FEL 2015
DAEJEON, KOREA

www.qrc.or.kr/fel2015

37th International Free Electron Laser Conference

23 - 28 August 2015
Daejeon Convention Center

Conference Chairs

Nikolay A. Vinokurov, *KAERI/BINP*
In Soo Ko, *PAL*

International Executive Committee

I. Ben-Zvi, *BNL & Stony Brook University*
M.-E. Couprie, *Synchrotron SOLEIL*
J. N. Galayda, *SLAC*
L. Giannessi, *ENEA & ELETTRA-Sincrotrone Trieste*
A. Gover, *Tel Aviv University*
H. Hama, *Tohoku University*
K.-J. Kim, *ANL & The University of Chicago*
V. N. Litvinenko, *Stony Brook University & BNL*
E. J. Minehara, *JAEA & WERC*
G. R. Neil, *Jefferson Lab.*
C. W. Roberson, *ONR (ret.)*
J. Rossbach, *DESY & Hamburg University*
T. I. Smith, *Stanford University*
H. Tanaka, *RIKEN Spring-8*
A. F. G van der Meer, *FELIX Facility, Radboud University*
N. A. Vinokurov, *BINP & KAERI*
R. P. Walker, *Diamond Light Source*
Z. T. Zhao, *SINAP*

Local Organizing Committee

Y. U. Jeong, *KAERI (Chair)*
D. E. Kim, *PAL*
K. Lee, *KAERI*
Y. Kim, *KAERI*
B. C. Lee, *KAERI*
S. H. Park, *KAERI*
K. Jang, *KAERI*

International Program Committee

H.-S. Kang, *PAL (Chair)*
S. Benson, *JLab*
S. Biedron, *CSU*
J. Byrd, *LBNL*
B. E. Carlsten, *LANL*
S. Di Mitri, *Elettra*
B. Diviacco, *Elettra*
P. Emma, *SLAC*
M. Ferrario, *INFN*
J. C. Frisch, *SLAC*
G. Geloni, *European XFEL*
J. Gruenert, *European XFEL*
J.-H. Han, *PAL*
T. Hara, *RIKEN*
Z. Huang, *SLAC*
R. Ischerbeck, *PSI*
Y. Kim, KAERI
M. Labat, *Soleil*
R. Lindberg, *ANL*
P. Musumeci, *UCLA*
H. Ohgaki, *Kyoto Univ.*
B. Patterson, *PSI*
D. Ratner, *SLAC*
S. Reiche, *PSI*
F. Sannibale, *LBNL*
E. Schneidmiller, *DESY*
S. Schreiber, *DESY*
O. Shevchenko, *BINP*
F. Stephan, *PITZ DESY-Zeuthen*
T. Tanaka, *RIKEN*
N. Thompson, *ASTEC*
S. Werin, *Maxlab*
D. Wang, *SINAP*
Y. K. Wu, *Duke Univ.*
A. A. Zholents, *ANL*

KAERI Korea Atomic Energy Research Institute
PAL POHANG ACCELERATOR LABORATORY
DAEJEON DAEJEON METROPOLITAN CITY

e-mail: kleegle@gmail.com


FEL 2015
DAEJEON, KOREA
37th International
Free Electron Laser Conference
23 - 28 August 2015
Daejeon Convention Center

Foreword

The 37th International Free Electron Laser Conference FEL 2015 was held from August 23rd to 28th, 2015 in Daejeon, Republic of Korea.

Daejeon is renowned for its world-class science complex. More than 800 high-tech companies, 70 of government or private research institutes and 6 of prominent universities are thriving in the City of Daejeon. In the southwestern of Daejeon city, there are many historical sites of Baekje-era (18BC ~ 660AD), which is known for an ancient Korean country to contribute international exchange with China and Japan. Recently, eight key relics of Baekje-era were designated as a UNESCO World Heritage Site.

In scientific aspect, two co-organizers of this Conference – Pohang Accelerator Laboratory (PAL) and Korea Atomic Energy Research Institute (KAERI) – have complementary FEL projects. PAL is developing the XFEL, which is expected to convey the commissioning next year, and KAERI is running several small-scale projects. Participants had an opportunity to visit these facilities through technical tour program.

We appreciate great interest of industrial companies to this conference to present their exhibitions and/or supports. Their financial contributions made it possible to offer a number of student fellowships making it possible for these young scientists to attend the conference.

In spite of more than 50 years of the FEL operation we still have many interesting talks and posters. This progress is, probably, based on continuous progress of accelerator and other related technologies. However, our conference was the last annual one. Next FEL conferences will be in 2017 (Santa Fe, USA) and 2019 (Hamburg, Germany).

We thank all participants who visited Daejeon and made their valuable contributions to the Proceedings of FEL 2015.

In Soo Ko

Nikolay Vinokurov

Young Uk Jeong

Heung-Sik Kang

Committees

Conference Chairs

Nikolay Vinokurov	KAERI/BINP
In Soo Ko	PAL/POSTECH

International Executive Committee

I. Ben Zvi	BNL & Stony Brook University
M.E. Couprie	Synchrotron SOLEIL
J.N. Galayda	SLAC
L. Giannessi	ENEA & ELETTRA-Sincrotrone Trieste
A. Gover	Tel Aviv University
H. Hama	Tohoku University
H.S. Kang	PAL/POSTECH
K.J. Kim	ANL & The University of Chicago
V.N. Litvinenko	Stony Brook University & BNL
E.J. Minehara	JAEA & WERC
G.R. Neil	Jefferson Lab.
S. Reiche	PSI
C.W. Roberson	ONR (ret.)
J. Rossbach	DESY & Hamburg University
T.I. Smith	Stanford University
H. Tanaka	RIKEN SPring-8
A.F.G van der Meer	FELIX Facility, Radboud University
N.A. Vinokurov	BINP & KAERI
R.P. Walker	Diamond Light Source
Z.T. Zhao	SINAP

International Program Committee of FEL2015

H.S. Kang (Chair)	PAL/POSTECH
S. Benson	JLab
S. Biedron	CSU
J. Byrd	LBNL
B. E. Carlsten	LANL
S. Di Mitri	Elettra
B. Diviacco	Elettra
P. Emma	SLAC
M. Ferrario	INFN
J. C. Frisch	SLAC
G. Geloni	European XFEL
J. Gruenert	European XFEL
J. H. Han	PAL
T. Hara	RIKEN
Z. Huang	SLAC
R. Ischerbeck	PSI
Y. Kim	KAERI
M. Labat	Soleil
R. Lindberg	ANL
P. Musumeci	UCLA
H. Ohgaki	Kyoto Univ.
B. Patterson	PSI
D. Ratner	SLAC
S. Reiche	PSI
F. Sannibale	LBNL
E. Schneidmiller	DESY
S. Schreiber	DESY
O. Shevchenko	BINP
F. Stephan	PITZ DESY-Zeuthen
T. Tanaka	RIKEN
N. Thompson	ASTEC
S. Werin	Maxlab
D. Wang	SINAP
Y. K. Wu	Duke Univ.
A. A. Zholents	ANL

Local Organizing Committee of FEL2015

Y. U. Jeong	KAERI	(Chair)
D. E. Kim	PAL	(Editor office)
K. Lee	KAERI	(Website and online registration)
Y. Kim	KAERI	(Exhibitions)
B. C. Lee	KAERI	
S. H. Park	KAERI	
K. -H. Jang	KAERI	

FEL2015 Prize Committee

L. Giannessi	ENEA & ELETTRA-Sincrotrone Trieste	(Chair)
T. Shintake	OIST	
W. M. Fawley	ELETTRA-Sincrotrone Trieste/SLAC	
Y. U. Jeong	KAERI	
J. N. Galayda	SLAC	

Contents

FIRST LASING OF THE THIRD STAGE OF NOVOSIBIRSK FEL*

O.A.Shevchenko#, V.S.Arbuzov, K.N.Chernov, I.V. Davidyuk, E.N.Dementyev, B.A.Dovzhenko, Ya.V.Getmanov, B.A.Knyazev, E.I.Kolobanov, A.A.Kondakov, V.R.Kozak, E.V.Kozyrev, V.V.Kubarev, G.N.Kulipanov, E.A.Kuper, I.V.Kuptsov, G.Ya.Kurkin, S.V.Motygin, V.N.Osipov, V.M.Petrov, L.E.Medvedev, V.K.Ovchar, A.M.Pilan, V.M.Popik, V.V.Repkov, T.V.Salikova, M.A.Scheglov, I.K.Sedlyarov, G.V.Serdobintsev, S.S.Serednyakov, A.N.Skrinsky, S.V.Tararyshkin, V.G.Tcheskidov, A.G. Tribendis, N.A.Vinokurov, P.D.Vobly
BINP, Novosibirsk, Russia

Abstract

Novosibirsk FEL facility is based on the first in the world multi-turn energy recovery linac (ERL). It comprises three FELs (stages). FELs on the first and the second tracks were commissioned in 2004 and 2009 respectively and operate for users now. The third stage FEL is installed on the fourth track of the ERL. It includes three undulator sections and 40-meters-long optical cavity. The design tuning range of this FEL is from 5 to 20 microns and the design average power at bunch repetition rate 3.74 MHz is about 1 kW. Recent results of the third stage FEL commissioning are reported.

OVERVIEW OF THE NOVOSIBIRSK FEL FACILITY

Accelerator Design and Basic Parameters

The Novosibirsk FEL facility is based on the multiturn energy recovery linac (ERL) which scheme is shown in Fig. 1. The advantage of this scheme is that high energy electrons can be obtained with shorter linac as the beam goes through the linac several times before it enters undulator.

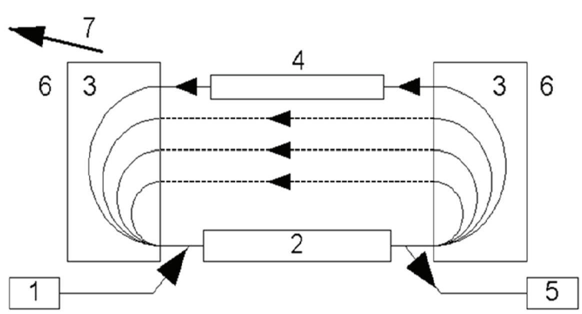

Figure 1: Simplest multiturn ERL scheme: 1 – injector, 2 – linac, 3 – bending magnets, 4 – undulator, 5 – dump.

Multiturn ERLs look very promising for making ERLs less expensive and more flexible, but they have some serious intrinsic problems. Particularly in the simplest scheme shown in Fig. 1 one has to use the same tracks for accelerating and decelerating beams which essentially complicates adjustment of the magnetic system.

*Work supported by by Russian Science Foundation (project 14-12-00480)
#O.A.Shevchenko@inp.nsk.su

At present the Novosibirsk ERL is the only one multiturn ERL in the world. It has rather complicated lattice as it can be seen from Fig. 2. The ERL can operate in three modes providing electron beam for three different FELs. The whole facility can be treated as three different ERLs (one-turn, two-turn and four-turn) which use the same injector and the same linac. The one-turn ERL is placed in vertical plane. It works for the THz FEL which undulators are installed at the floor. This part of the facility is called the first stage. It was commissioned in 2003 [1].

The other two ERL beamlines are placed in horizontal plane at the ceiling. At the common track there are two round magnets. By switching these magnets on and off one can direct the beam either to horizontal or to vertical beamlines. The 180-degree bending arcs also include small bending magnets with parallel edges and quadrupoles. To reduce sensitivity to the power supply ripples, all magnets on each side are connected in series. The quadrupole gradients are chosen so that all bends are achromatic. The vacuum chambers are made from aluminium. They have water-cooling channels inside.

The second horizontal track has bypass with the second FEL undulator. The bypass provides about 0.7 m lengthening of the second orbit. Therefore when the beam goes through the bypass it returns back to the linac in decelerating phase and after two decelerations it finaly comes to the dump. This part (the second stage) was commissioned in 2009. The final third stage will include full-scale four-turn ERL and FEL installed on the last track.

The basic beam and linac parameters common for all three ERLs are listed in Table 1.

Table 1: Basic ERL Parameters

Injection energy, MeV	2
Main linac energy gain, MeV	11
Charge per bunch, nC	1.5
Normalized emittance, mm·mrad	30
RF frequency, MHz	180.4
Maximum repetition rate, MHz	90.2

ISBN 978-3-95450-134-2

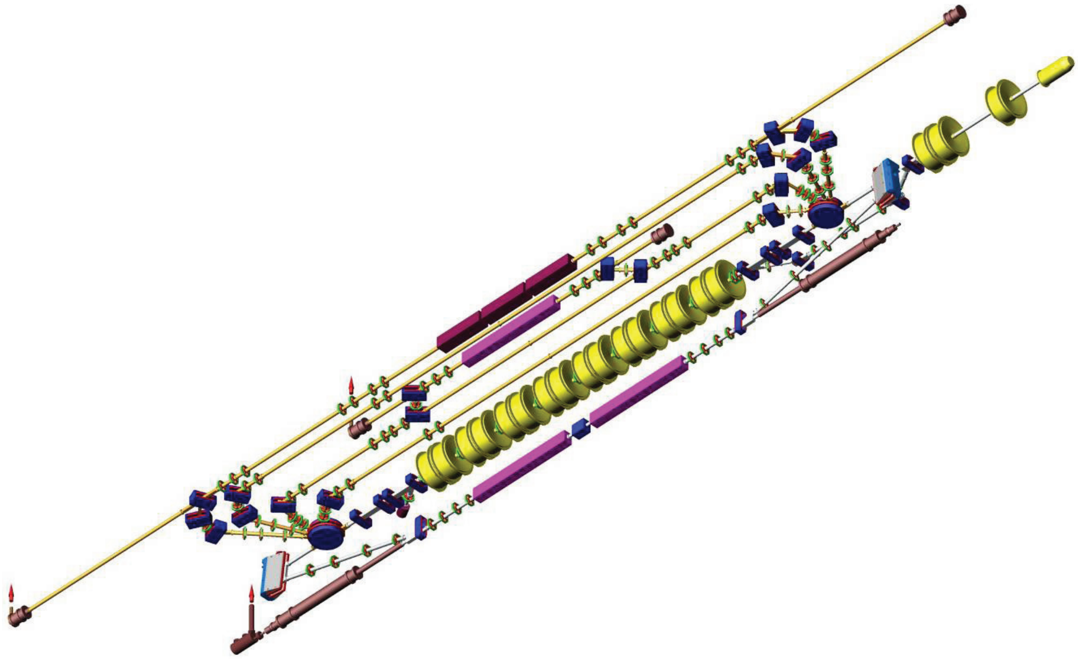

Figure 2: The Novosibirsk ERL with three FELs (bottom view).

Depending on the number of turns the maximum final electron energy can be 12, 22 or 42 MeV. The bunch length in one-turn ERL is about 100 ps. In two and four-turn ERLs the beam is compressed longitudinally up to 10-20 ps. The maximum average current achieved at one-turn ERL is 30 mA which is still the world record.

One essential difference of the Novosibirsk ERL compared to other facilities [2,3] is using of the low frequency non-superconducting RF cavities. On one hand it leads to increasing of the linac size but on the other hand it also allows to increase transversal and longitudinal acceptances which allows to tolerate longer electron bunches with large transversal emittance.

The location of different parts of the facility in the accelerator hall is shown in Fig. 3.

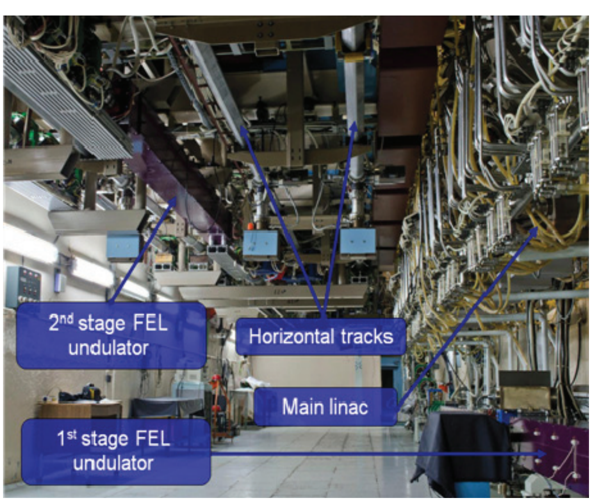

Figure 3: Accelerator hall (bottom view).

The First Stage FEL

The first stage FEL includes two electromagnetic undulators with period 12 cm, phase shifter and optical cavity. Undulator pole shape is chosen to provide equal electron beam focusing in vertical and horizontal directions. The matched beta-function is about 1 m. The phase shifter is installed between undulators and it is used to adjust the slippage. The optical cavity is composed of two copper mirrors covered by gold. The distance between mirrors is 26.6 m which corresponds to the repetition rate 5.64 MHz. Radiation is outcoupled through the hole made in the mirror center. The optical beamline is separated from the vacuum chamber by diamond window. The beamline pipe is filled with dry nitrogen.

The FEL generates coherent radiation tunable in the range 120-240 micron as a continuous train of 40-100 ps pulses at the repetition rate of 5.6 - 22.4 MHz. Maximum average output power is 500 W, the peak power is more than 1 MW [4]. The minimum measured linewidth is 0.3%, which is close to the Fourier-transform limit.

The Second Stage FEL

The second stage FEL includes one electromagnetic undulator with period 12 cm and optical cavity. The undulator is installed on the bypass where the electron energy is about 22 MeV. Therefore the FEL radiation wavelength range is 40 - 80 micron. The undulator design is identical to the first stage one but it has smaller aperture and higher maximum magnetic field amplitude. The optical cavity length is 20 m (12 RF wavelengths). Therefore the bunch repetition rate for initial operation is 7.5 MHz.

ISBN 978-3-95450-134-2

The first lasing of this FEL was achieved in 2009. The maximum gain was about 40% which allowed to get lasing at 1/8 of the fundamental frequency (at bunch repetition rate ~1 MHz).

The significant (percents) increase of beam losses took place during first lasing runs. Therefore sextupole corrections were installed into some of quadrupoles to make the 180-degree bends second-order achromatic. It increased the energy acceptance for used electron beam.

The optical beamline (Fig. 4) which delivers radiation from new FEL to existing user stations is assembled and commissioned. The output power is about 0.5 kW at the 9 mA ERL average current. In future we consider an option to use the new type of undulators with variable period [5] at this FEL. It will allow us to increase significantly the wavelength tuning range.

Figure 4: Optical beamlines for the first and the second stage FELs. Radiation of both FELs is delivered to the same user stations. Switching between FELs is done by retractable mirror.

THE THIRD STAGE FEL DESIGN

Energy of electrons in the third stage ERL is about 42 MeV as the beam is accelerated four times. Undulator of the FEL is installed on the fourth track as it is shown in Fig. 5 and Fig. 6. The whole undulator is composed of three 28 period sections. Each of them is a permanent magnet undulator with period 6 cm and variable gap. The wavelength range of this FEL will be 5-30 microns. The optical cavity of this FEL is about 40 meters long. It is composed of two copper mirrors (Fig. 7).

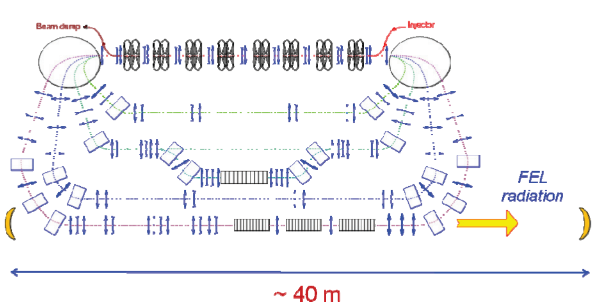

Figure 5: The third stage ERL with FEL undulators and optical cavity.

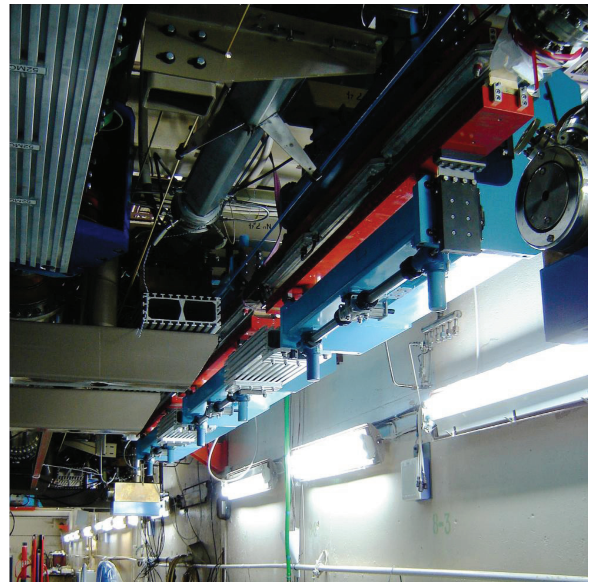

Figure 6: The third stage FEL undulator sections.

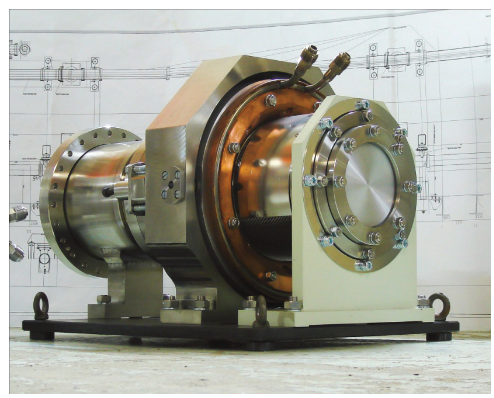

Figure 7: Copper mirrors.

The radiation is outcoupled trough the holes in the mirror center. But we also have an option to implement electron outcoupling scheme here (see Fig. 8) [6].

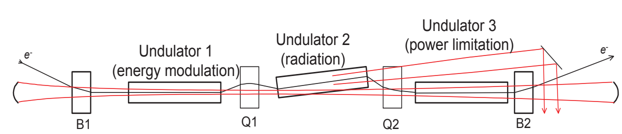

Figure 8: Electron outcoupling scheme.

COMMISSION CHALLENGES AND FIRST EXPERIMENTS

Commissioning of the third stage FEL could not be possible without solution of some physical and technical problems. The first one was obtaining of high recovery efficiency in multiturn ERL. Without it one could not get the high enough bunch repetition rate which is required for lasing. Adjustment of the ERL lattice allowed to decrease beam losses down to 10 %. As the result the average current 3.2 mA was obtained. The other problem was alignment of 40 meters long optical cavity. The

ISBN 978-3-95450-134-2

distance between mirrors had to be adjusted with accuracy better than 0.3 mm. One also had to align the beam trajectory in undulator with submillimetric accuracy. When all requirements were fulfilled getting lasing became a simple task. The first experiment with FEL radiation included measurement of radiation power and wavelength. The maximum power was 100 watts at wavelength about 9 microns (see Fig. 9). Future experiments at the third stage FEL will include study of selective photochemical reactions, infrared laser catalysis and separation of isotopes

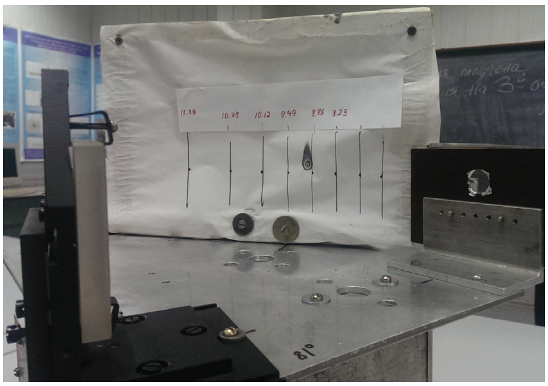

Figure 9: Radiation wavelength measurement experiment.

FUTURE PROSPECTS

Concerning the third stage FEL in the nearest future we plan to improve x-ray and neutron radiation shielding, install remote control units for undulator gap and optical cavity mirror angles, deliver FEL radiation to existing user stations, decrease beam losses and increase average current, increase DC gun voltage and improve beam quality in injector, optimize electron efficiency of FEL. The regular user shifts at the first stage FEL will be also continued.

REFERENCES

[1] A E. A. Antokhin et al. NIM A528 (2004) p.15.
[2] G.R. Neil et al. Phys. Rev. Lett. 84 (2000), p. 662.
[3] E.J. Minehara. NIM A483 (2002) p. 8.
[4] G.N. Kulipanov et al., IEEE Trans. Terahertz Science and Tech., v. 5, No 5, p. 798, (2015).
[5] N.A. Vinokurov et al., Proc. of FEL2010, p. 696.
[6] A.N. Matveenko et al., Proc. of FEL2007, p. 204.

ISBN 978-3-95450-134-2

THREE PLUS DECADES OF TAPERED UNDULATOR FEL PHYSICS*

William M. Fawley, Sincrotrone Trieste S.C.p.A., Trieste, Italy, and
SLAC National Accelerator Laboratory, Menlo Park, Califonia, 94025 USA†

Abstract

Beginning with the classic 1981 work of Kroll-Morton-Rosenbluth [1], multiple generations of FEL scientists have studied and used experimentally undulator tapering to improve and optimize the radiation output of both amplifier and oscillator FELs. Tapering has undergone a renaissance of interest, in part to make possible TW instantaneous power levels from x-ray FELs. In this talk, I will give a highly personalized (and undoubtedly strongly biased) historical survey of tapering studies beginning with the ELF 35-GHz experiments at Livermore in the mid-1980's and continuing up to quite recent studies at the LCLS at both soft and hard x-ray wavelengths.

SOME GENERAL COMMENTS

Not wanting to put together pages and pages of dusty, historical material covering my tapering experiences since the early 1980's, I will instead limit myself to a few suggestions to my younger, brighter, and far more energetic FEL colleagues concerning subject areas of our current millenium where it is *possible* (but not certain!) that additional work on tapering theory could be useful and productive.

Regarding optimizing "KMR-style" tapers, I think it is quite evident at this FEL 2015 conference that numerous groups (*e.g.,* UCLA/SLAC, Lund, DESY, Diamond/Daresbury) realize that allowing a variable ponderomotive phase $\psi_R(z)$ can lead to much greater power output over a fixed undulator length than would be keeping ψ_R rigidly fixed. (Moreover, as I tried to stress in my talk, KMR themselves knew this and T. Scharlemann and I from the mid-1980's had a ramping option for ψ_R in the FRED&GINGER self-design algorithm). However, it is not clear to me personally that there is a unique (or even semi-unique) strategy that can maximize the trapping fraction in the undulator region just downstream of the nominal saturation point z_{SAT} that will work over a broad range of FEL parameters such as Z_R/L_G, Twiss-β/L_G, $4\pi\varepsilon_N/\lambda_s$, σ_E/ρ , *etc.* (here all the standard abbreviations hold...). My guess is that when emittance and incoherent energy spread are non-trivial relative to the size of the FEL parameter ρ, one may need to be very careful in increasing ψ_R too rapidly in z. Effects such as these mean that if the bucket area does not increase sufficiently quickly with z due to an increasing radiation power, then there will likely be a lot of detrapping in the first couple gain lengths beyond the nominal saturation point from particles near the outer edges of bucket. There is also the issue for high electron beam energy FELs such as LCLS or XFEL that depend upon quadrupole-based strong focusing that the variation of wiggle-period-averaged $p_{\|}$ over a betatron period can be another source of detrapping lightly-bound electrons.

Regarding sidebands, during the olden days of the LLNL high gain amplifier work, I started a paper (never finished after my departure from the shortly-to-collapse LLNL FEL program) on SASE-stimulated sideband limits to stable tapering. This was stimulated by the desire to see if one could get a solid criterion for the necessary seed power (presumably higher due to the detrapping effects of sidebands than would be necessary from just final spectral bandwidth considerations). This subject is now (refreshingly???) current again with the interest in reaching TW power levels from x-ray FELs. My feeling is that there has been no truly definitive work on to what degree will tapering control sideband growth in situations where one wants reasonably stable trapping over as many as 10 gain lengths beyond z_{SAT}. I also suspect that whatever work was done in the 1990's concerning detrapping due to sidebands should likely be redone and extended by considering 2015-style high brightness e-beams in which the particles might be more deeply trapped initially in the saturation region. Moreover, with 3 (or is it 4) orders of additional computational power now available, it is useful for someone to look at the various characteristics of sideband growth (*e.g.*, radiation mode size and shape, sensitivity to different focusing schemes and different ratios of the betatron to the synchrotron wavelength). If in fact SASE-initiated sidebands are a true issue in terms of detrapping, perhaps there are clever schemes in terms of detuning *a' la* I-SASE that can reduce the effective sideband growth rate.

Regarding tapering SASE-mode amplifiers, I do not believe we in the community know at all what the best strategy is in terms of a variable $\psi_R(z)$ that will work over a broad range of parameters. The statistical irregularities of the depths of the ponderomotive wells from one SASE-spike to another suggests there may *not* be one taper that works best for all. Sam Krinsky and Robert Gluckstern) did some very nice work [2] in the early-2000's on the general statistical properties of SASE spikes in the exponential gain region leading up to z_{SAT}. Perhaps some clever soul can do similar analysis that could extend this analysis to a few gain lengths beyond z_{SAT}. Then ideally, this soul could *also* use the resultant properties to find an indication as to how best

* My FEL work over these last 3+ decades has been funded by numerous entities including the taxpayers of the European Union via the FERMI project of Elettra-Sincrotrone Trieste and the taxpayers of the USA via the Office of Science in the Dept. of Energy through grants to SLAC, Argonne, and Lawrence Berkeley National Labs, and also via DARPA and the Strategic Defense Initiative Organization (the "Star Wars" people) within the Dept. of Defense through grants to Lawrence Livermore National Laboratory. DISCLAIMER: the views and opinions expressed herein are those solely of the author, completely privately funded, and hopefully unpolluted by any publicly-supported political correctness or toadiness. Few neurons were harmed in the writing of this paper.

† william.fawley@elettra.eu

ISBN 978-3-95450-134-2

manipulate ψ_R in a way that maximizes both the trapping in the saturation region and then also leads to an optimized power extraction in the next five to ten gain lengths.

Since the effective group velocity of the SASE radiation spikes speeds up to c as one moves beyond z_{SAT}, this change of effective slippage rate might have some consequences in determining the statistically-optimized $\psi_R(z)$ that would not be seen in the time-steady situation. I note that the FEL01 work [3] that was done on SASE-tapering for LCLS-like parameters indicated that a reduced $\psi_R = 0.2$ (relative to the $\approx 0.35 - 0.45$ found for time-steady cases) could retain significant residual trapping out to $z = 200$ m. Thus, it does not seem that the particles fully debunch as a given electron slice passes though the valley of "darkness" between one SASE radiation spike to the next. But here too the great increase in computational power should allow a relatively easy investigation into what might be going on in the case of a very, very long hard x-ray FEL. Looking for various correlations between the relative spike power (including its nearby neighbors in the direction of the beam head) and the trapping/detrapping properties of the electron slices might be quite illuminating. It also might not be too surprising that the taper that optimizes SASE power for a given undulator length is not the exact same one that would maximize the far field brightness nor the one that minimizes shot-to-shot fluctuations in the situation where the electron beam length is comparable to a couple slippage lengths or less. For situations where the electron beam has strong longitudinal variation in properties such as emittance, incoherent energy spread and/or current, the situation is likely even more complex in finding an "optimized" taper for a SASE configuration.

In the end, it is almost certain that the "final" taper optimization will be done in the control room (much as is true for LCLS and FERMI today), perhaps with the benefit of some genetic algorithm. But we are very lucky to be entering a golden age regarding FEL amplifiers in which more than a half-dozen XUV to hard X-ray FELs will be operational by 2018 and the best is almost certainly yet to come for amplifier FELs.

REFERENCES

[1] N. M. Kroll, P. L. Morton, and M. N. Rosenbluth, *IEEE J. Quantum Elec.*, **QE-17**, 1436 (1981).

[2] S. Krinsky and R. L. Gluckstern, *Phys. Rev. ST Accel. Beams* **6**, 050701 (2003).

[3] W. M. Fawley, Z. Huang, K.-J. Kim and N. A. Vinokurov, *Nuc. Instr. Meth.* **A483**, 537Ð541 (2002).

ISBN 978-3-95450-134-2

X-RAY FEL R&D: BRIGHTER, BETTER, CHEAPER

Zhirong Huang
SLAC National Accelerator Laboratory, Menlo Park, CA, USA

Abstract

The X-ray free-electron lasers (FELs), with nine to ten orders of magnitude improvement in peak brightness over the third-generation light sources, have demonstrated remarkable scientific capabilities. Despite the early success, X-ray FELs can still undergo dramatic transformations with accelerator and FEL R&D. In this paper, I will show examples of recent R&D efforts to increase X-ray coherence and brightness, to obtain better control of X-ray temporal and spectral properties, and to develop concepts for compact coherent sources.

INTRODUCTION

X-ray FEL or XFEL is a breakthrough in light source development and enables atomic-scale imaging at femtosecond (fs) time resolution [1–3]. Despite the early success, it is widely recognized that XFELs continue to have significant potential for improvement. New methods have been rapidly developing to provide FEL seeding, extremely short x-ray pulses, variable double pulses, two-color FEL generation, and polarization control. Many of the proposals were implemented in the LCLS since 2011 through the so-called FEL R&D program that I have the privilege to contribute. Here I present a personal (incomplete) overview. I also like to discuss dreams/progress towards compact XFELs and conclude with some final remarks.

IMPROVING TEMPORAL COHERENCE (BRIGHTER)

Typical XFEL pulses are made of a few tens to hundreds of coherent spikes of fs duration, each with no fixed phase relation to the others due to the self-amplified spotaneous emission process. Longitudinal coherence can be imposed by a post-SASE monochromator, but typically with reduced intensity and increased intensity fluctuations. External seeding at radiation wavelengths down to a few nanometers was demonstrated at the FERMI FEL at Synchrotron Trieste with high-gain harmonics generation from an UV laser [4]. At shorter radiation wavelengths around 1 nm or below, external laser seeding becomes increasingly difficult, while self-seeding can be a viable alternative.

Following a proposal from DESY [5], a collaboration between SLAC, Argonne and the Technical Institute for Superhard and Novel Carbon Materials in Russia successfully implemented hard X-ray self-seeding at LCLS in 2012. One out of 33 undulator sections (U16) was removed in order to install a chicane and an in-line single diamond crystal. The thin crystal transmits most of the SASE pulse but also generates a trailing monochromatic seed pulse. The chicane can delay the electron bunch to temporally overlap with the seed and to amplify the seed in the second part of the undulator array (U17-U33). Self-seeding at the angstrom wavelength scale, with a factor of about 40 bandwidth reduction, was demonstrated [6]. Hard X-ray self-seeding is in operation since 2013 and provides seeded beams from 5 keV to 9.5 keV with two to four times more photons per pulse than SASE using a post-monochromator. In a recent warm dense matter dynamic compression experiment, the unique properties of the seeded X-rays provide plasmon spectra of this complex state that yield the temperature and density with unprecedented precision at micrometer-scale resolution [7].

After the success of hard X-ray self-seeding, a compact soft X-ray self-seeding system was designed and implemented upstream of the hard X-ray self-seeding section in 2013 [8]. This system covers the photon energy range from 0.5 keV to 1 keV with a fwhm bandwidth of $2{\times}10^{-4}$. The SXRSS system relies on a grating monochromator consisting of a variable line spacing toroidal grating followed by a plane mirror, slit and two mirrors. The four-dipole chicane is similar to the hard X-ray one and displaces, de-bunches and delays the electron beam. Although still being optimized, the soft X-ray self-seeding system has demonstrated a bandwidth of 3-5$\times10^{-4}$, wavelength stability of 1×10^{-4}, and an increase in peak brightness by a factor of up to 5 across the photon energy range [9].

One of the main challenges for seeded FELs is the electron energy stability. Since the radiation wavelengh is fixed by seeding, the relative electron energy jitter should be less than the fractional FEL bandwidth divided by 2. Intense efforts have been launched to reduce the LCLS energy jitter. These includes injector RF tune-up and compression scheme optimization [10]. Underlying hardware instability has also been carefully scrutinized and improved over recent years [11]. High-power RF terminating loads and higher-rated deuterium thyratrons are forthcoming. Since 2012, both hard and soft X-ray energy jitters have been reduced by a factor of 2, and the hard X-ray self-seeding pulse intensity has increased by about a factor of 3 [12].

The measured spectrum of the soft X-ray self-seeding at LCLS has a pedestal-like distribution around the seeded frequency [9], which limits the spectral purity and seeding applications without a post-undulator monochromator. In a separate contribution to these proceedings [13], we study the origins of the pedestals and focus on the contributions of microbunching instability prior to the FEL undulator. We show that both energy and density modulations can induce sidebands in a seeded FEL. Theory and simulations are used to analyze the sideband content relative to the seeding signal. The results place a tight constraint on the longitudinal phase space uniformity for a seeded FEL.

ISBN 978-3-95450-134-2

CONTROL X-RAY PULSE PROPERTIES (BETTER)

To accommodate user requests for shorter X-ray pulses, LCLS has developed two operating modes to deliver pulses with durations in the few-fs range: a low-charge operating mode [14] and a slotted-foil method [15]. In the low-charge mode (20 pC), the reduced bunch charge provides improved transverse emittance from the gun compared to nominal operation and also mitigates collective effects in the accelerator, allowing for extreme bunch compression. The compressed electron bunch length is measured to be < 5 fs fwhm, using the X-band transverse deflector installed after the LCLS undulator in 2013 [16]. In this low-charge mode, the FEL pulse consists of only 1 or 2 coherent spikes of radiation and has better temporal coherence. Another method for femtosecond pulse generation is to use an emittance-spoiling slotted foil, which has been used at LCLS since 2010. When the dispersed electron beam passes through a foil with single or double slots, most of the beam emittance is spoiled, leaving very short unspoiled time slices to produce femtosecond X-rays. To achieve a variable pulse duration and separation, an aluminum foil (3 μm thickness) with different slot arrays was implemented. Depending on the bunch charge and the final current, a single slot with variable slot width can control the X-ray duration from 50 fs down to ~ 4 fs, while V-shape double slots with different slot separation can provide two short X-ray pulses separated by about 10 fs to 80 fs for pump-probe experiments [17].

Two-color pulses are another example of custom-made X-rays from an FEL, where two pulses of different photon energy are generated with a variable time delay. One method relies on generating two X-ray colors by dividing the LCLS undulator beamline into two sections longitudinally with a distinct K associated with each section [18]. The same electron beam lases twice in two sections of the undulator so the FEL power of each color is between 5% and 15% of the full saturation power. The second method generates two colors simultaneously in one undulator using two electron bunches of different energies [19]. This method requires generation, acceleration and compression of double electron bunches within the RF wavelength of the accelerator system [20]. Each X-ray pulse is generated by one electron bunch and can reach the full saturation power, improving the two-color intensity by one order of magnitude in comparison with the first method. This "twin-bunch" approach can also be combined with hard X-ray self-seeding using appropriate crystal orientations to generated two-seeded hard X-ray colors [21]. The time delay between pulses can be adjusted from nearly overlapping to ~100 fs [19].

LCLS generates linearly polarized, intense, high brightness x-ray pulses from planar fixed-gap undulators. A new 3.2-m-long compact undulator (based on the Cornell University Delta design [22]) has been developed and installed in place of the last LCLS undulator segment (U33) in 2014 [23]. This undulator provides full control of the polarization degree and K value. Used on its own, it produces fully polarized radiation in the selected state (linear, circular or elliptical) but at low intensity. To increase the output power by orders of magnitude, the electron beam is micro-bunched by several (~ 10) of the upstream LCLS undulator segments operated in the linear FEL regime. As unavoidable by-product, this micro-bunching process produces moderate amounts of horizontally linear polarized radiation which mixes with the radiation produced by the Delta undulator. This unwanted radiation component has been greatly reduced by the reversed taper configuration [24]. Full elimination of the linear polarized component was achieved through spatial separation combined with transverse collimation. As a result, close to 100% circularly polarized soft X-rays with pulse intensity over 200 μJ have been delivered to study magnetic circular dichroism and ultrafast magnetization reversal [23].

COMPACT COHERENT SOURCES (CHEAPER)

Both synchrotron storage rings and XFEL are large X-ray light source facilities. At the moment, synchrotrons can provide 30-60 beamlines per machine, while XFELs only support 1-2 beamlines. Hence synchrotron facilities are much more cost effective to operate than XFELs even though they are both expensive to build. Therefore, it is very desirable to develop compact coherent X-ray sources that are at a small fraction of cost and size of big XFELs. Realization of compact XFELs that can be installed at many universities and research institutions will further revolutionize the ultrafast X-ray sciences. Many ideas exist to make compact coherent sources. Some rely on inverse Compton scattering (replacing cm-period undulator with μm wavelength laser and hence lower electron beam energy by a factor of 100. While others attempts to take advantage of the advanced accelerator methods to produce high-energy, high-brightness beams in a compact way (e.g., plasma accelerator boosts acceleration gradient by more than a factor of 100).

Laser plasma accelerators (LPAs) have made tremendous progress in generating high-energy (~ 1 GeV and above), high peak current (1-10 kA), and low-emittance (~ 0.1 μm) beams [25–28]. Such an accelerator was used to produce EUV spontaneous undulator radiation [29]. Due to the challenges in controlling the injection process, LPA beams have rather large energy spread, typically on a few percent level. Such energy spread hinders the short-wavelength FEL application. Nevertheless, active research and development efforts have been pursued to develop compact FELs based on these novel accelerators [30–32].

Transverse gradient undulator (TGU) has been proposed to reduce the sensitivity to electron energy variations for FEL oscillators [33] and to enhance the FEL interaction for high-gain FELs driven by large energy spread beams of laser plasma accelerators [31]. In Ref. [31], we have analyzed and simulated a compact soft x-ray FEL example using a laser plasma beam with 1 GeV central energy and 1% rms energy spread. For a peak current of 10 kA and a normalized emittance of 0.1 μm, the TGU-based FEL

ISBN 978-3-95450-134-2

reaches the multi-GW power in 5-m undulator length at the radiation wavelength of 3.9 nm (the so-called "water window" soft X-ray regime). We have also showed that the TGU improves the SASE power by about two orders of magnitude and the bandwidth by another order of magnitude over the normal undulator. A later study has also taken into account energy-time correlation of the beam that always exists in a laser plasma accelerator and have obtained similar results [34].

A TGU FEL demonstration experiment at 30 nm radiation wavelength is under development using the laser plasma accelerator [26] at Shanghai Institute of Optics and Fine Mechanics [35]. The electron beam energy is between 400 to 600 MeV, with the measured rms energy spread about 1% [36]. A 6-m TGU with the undulator period 2 cm and the transverse gradient of $\sim 50\ \mathrm{m}^{-1}$ is being manufactured at Shanghai Institute of Applied Physics for this experiment [37]. Controlling and transporting these beams with unusual characteristics (large angular divergence and energy spread) will be a major challenge in such an experiment.

CONCLUSIONS

In summary, I have showed examples that vigorous accelerator and FEL R&D can drastically improve FEL coherence and brightness. These improvements in turn demand much better control of electron beams, as well as advanced diagnostics and undulator development. I have briefly discussed possibilities and challenges for realizing compact XFELs. These efforts are worth pursuing and will be complementary to the development of large facilities.

ACKNOWLEDGEMENTS

I would like to thank Kwang-Je Kim, who introduced me to the beautiful and intricate FEL world, and thank Argonne LEUTL team that first demonstrated SASE saturation!

I wish to thank the entire LCLS team and talented SLAC accelerator research staff and engineers. They made all these possible and are so much fun to work with!

This work was supported by Department of Energy Contract No. DE-AC02-76SF00515.

REFERENCES

[1] W. Ackermann *et al.*, Nature Photon. **1**, 336 (2007).

[2] P. Emma *et al.*, Nature Photon. **4**, 641 (2010).

[3] T. Ishikawa *et al.*, Nature Photon. **6**, 540 (2012).

[4] E. Allaria *et al.* Nature Photon. **7**, 913 (2013).

[5] G. Geloni, V. Kocharyan, and E. Saldin, J. Mod. Opt. **58**, 1391 (2011).

[6] J. Amann *et al.* Nature Photon. **6**, 693 (2012).

[7] L. Fletcher *et al.* Nature Photon. **9**, 274 (2015).

[8] Y. Feng *et al.*, in proceedings of FEL2012, 205 (2012).

[9] D. Ratner *et al.*, Phys. Rev. Lett. **114**, 054801 (2015).

[10] L. Wang *et al.*, TUP070, these proceedings.

[11] F.-J. Decker *et al.*, in proceedings of FEL2013, 518 (2013).

[12] T. Maxwell, private communications.

[13] Z. Zhang *et al.*, WEP024, these proceedings.

[14] Y. Ding *et al.*, Phys. Rev. Lett. **102**, 254801 (2009).

[15] P. Emma *et al.*, Phys. Rev. Lett. **92**,074801 (2004).

[16] C. Behrens *et al.*. Nature Commun. **5**, 3762 (2013).

[17] Y. Ding *et al.*, submitted to App. Phys. Lett. (2015).

[18] A. Lutman *et al.*, Phys. Rev. Lett., **110**, 134801 (2013).

[19] A. Marinelli *et al.*, Nature Commun. **6**, 6369 (2015).

[20] Z. Zhang *et al.*, Phys. Rev. ST Accel. Beams **18**, 030702 (2015).

[21] A. Lutman *et al.*, Phys. Rev. Lett., **113**, 254801 (2014).

[22] A. Temnykh, Phys. Rev. ST Accel. Beams **11**, 120702 (2008).

[23] H.-D. Nuhn *et al.*, WED01, these proceedings.

[24] E. A. Schneidmiller and M. V. Yurkov, Phys. Rev. ST Accel. Beams 16, 110702 (2013).

[25] W. Leemans *et al.*, Nature Physics **2**, 696 (2006).

[26] J.S. Liu *et al.*, Phys. Rev. Lett. **107**, 035001 (2011).

[27] X. Wang *et al.* Nature Commun. **4**, 1988 (2013).

[28] W. Leemans *et al.*, Phys. Rev. Lett. **113**, 245002 (2014).

[29] M. Fuchs *et al.*, Nature Physics **5**, 826 (2009).

[30] A. Maier *et al.* Phys. Rev. X **2**, 031019 (2012).

[31] Z. Huang, Y. Ding, C. Schroeder, Phys. Rev. Lett. **109**, 204801 (2012).

[32] A . Loulergue *et al.* New J. Phys. **17** 023028, (2015).

[33] T. Smith *et al.*, J. Appl. Phys. **50**, 4580 (1979).

[34] Z. Huang *et al.*, in proceedings of AAC2014, SLAC-PUB-16100 (2014).

[35] T. Zhang *et al.*, in proceedings of FEL2013, 152 (2013).

[36] J.S. Liu, private communications.

[37] D. Wang, private communications.

ISBN 978-3-95450-134-2

TRANSFORMING THE FEL: COHERENCE, COMPLEX STRUCTURES, AND EXOTIC BEAMS

E. Hemsing*
SLAC National Accelerator Laboratory, Menlo Park, California 94025, USA

Abstract

Modern high brightness electron beams used in FELs are extremely versatile and highly malleable. This flexibility can be used to precisely tailor the properties of the FEL light for improved temporal coherence (as in external or self-seeding), but can also be exploited in new ways to generate exotic FEL modes of twisted light that carry orbital angular momentum (OAM) for new science. In this paper I briefly review the history of the work on OAM light production in FELs, and describe how lasers and undulator harmonics can be combined to produce both simple and complex e-beam distributions that emit intense, coherent, and highly tunable OAM light in future FELs.

INTRODUCTION: FEL TAILORING

Free-electron lasers (FELs) are composite systems of accelerators, electron beam (e-beam) optics, and undulators that produce widely tunable light with exceptional brightness at wavelengths down to hard x-rays for a broad range of studies. The versatility of FELs is derived from the fact that the e-beams that form the lasing medium can be precisely manipulated to tailor the properties of the radiated light. These 'beam shaping' manipulations, which range from coarse shaping of the e-beam current profile to precision shaping of the distribution at optical or shorter wavelengths, are used primarily to tailor the temporal shape of the FEL pulse. Because the typical SASE FEL pulse is composed of many temporal spikes, the aim of these schemes is to improve the longitudinal coherence and produce Fourier Transform-limited pulses. To this end, such techniques can also be combined with 'radiation shaping' techniques that exploit characteristic features of the undulator radiation to further broaden the landscape of designer FEL photon beams.

The past decade has shown tremendous progress in the development of such 'beam by design' concepts [1], in some cases turning proposed techniques into experimental realities over the course of just a few years. This is due in part to the confluence of rapidly advancing technologies that yield higher brightness e-beams, highly stable sub-ps lasers, and tunable undulator systems. The diagram in Figure 1 shows a sample of a number of different schemes designed to tailor the FEL output through either direct shaping of the electron beam (beam shaping) or through shaping using intrinsic features of the undulator radiation (radiation shaping). The slotted foil technique [2], for example, is a method of selecting only a short portion (or portions) of the electron beam to lase by spoiling the emittance of or removing the rest of the beam. Laser-based e-beam shaping techniques (shown

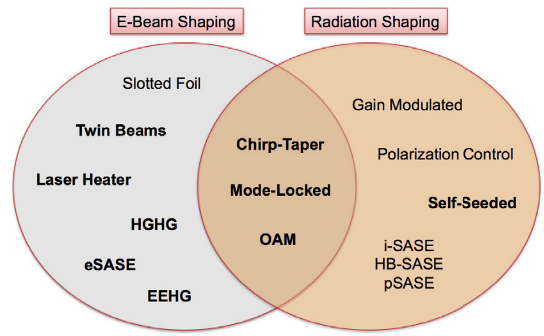

Figure 1: Diagram of example FEL pulse shaping schemes. In bold are those that are based on lasers.

in bold) such as HGHG and EEHG rely on external lasers to precisely rearrange the e-beam phase space to produce coherent density bunching at high harmonics. Such microbunched beams then radiate coherent pulses with bandwidths much narrower than the intrinsic FEL bandwidth. Radiation shaping with the i-SASE, HB-SASE, or pSASE techniques, on the other hand, seeks to take control over the natural slippage between the e-beam and the co-propagating radiation to communicate phase information over different portions of the beam to improve the temporal coherence. In another example, the polarization of the FEL pulse can be controlled using different combinations of linear or circularly polarized undulators, delays, and undulator tapering. Several schemes rely on specific combinations of both types of shaping. In the laser-based 'chirp-taper' technique designed to produce ultrashort pulses, for example, the resonant frequency of the undulators is tapered along the length to exactly match the energy chirp of a short portion of an e-beam that has been modulated by a few-cycle laser pulse.

The concentration on tailoring the temporal profile stems from the fact that the high-gain FEL is nearly diffraction limited and thus already has a high degree of transverse coherence, even for SASE. The lowest order transverse mode also has the highest gain, so the radiation at the fundamental frequency is gaussian-like and is peaked on axis. While it is fortunate that such ubiquitous modes are generated as a matter of course, there are numerous emerging applications and research opportunities where higher order transverse modes, specifically modes that carry orbital angular momentum (OAM), provide additional degrees of freedom that may be specifically exploited to probe the deep structure and behavior of matter.

* ehemsing@slac.stanford.edu

ISBN 978-3-95450-134-2

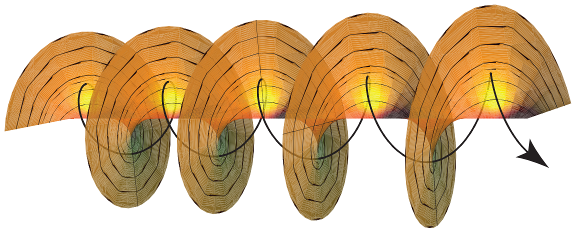

Figure 2: Helical phase and spiraling Poynting vector of OAM light.

A BRIEF HISTORY OF OAM LIGHT

The idea that light can carry spin angular momentum (SAM) dates back to the work of J.H. Poynting in 1909 [3]. He argued that circularly polarized light waves must carry angular momentum by virtue of the energy flux carried by the rotating electromagnetic fields, and that the associated torque could thus be measured in its transfer with matter. This was first confirmed by Beth in 1936 [4] in an experiment that measured the twist on a series of quarter wave plates suspended by a thin torsion fiber and normal to an incident circularly polarized beam. The conversion of the polarization state gave a measured angular momentum that was in agreement with expectations from quantum theory that predicted each photon carried $\pm\hbar$ of SAM.

Analysis of the total angular momentum of the electromagnetic fields reveals, however, that the spin does not necessarily account for all of the angular momentum carried by the light. It wasn't until 1992 that Allen et al [5] showed that Laguerre-Gaussian modes, which are eigenmodes of the paraxial wave equation, also carry discrete values of *orbital* angular momentum per photon[1]. Since then, there has been considerable work devoted to revealing the novel behaviors and uses of these exotic beams, because like the SAM, the OAM can also be transferred to matter. This leads to unique exploits in particle micro-manipulation [9–11], microscopy [12, 13], imaging [14], optical pump schemes [15], quantum entanglement [16, 17], and communications [18].

The most salient feature of OAM light is a characteristic helical phase front and associated spiraling Poynting vector that describes the flow of the linear momentum about the propagation axis. The depicted single twist helix shown in Figure 2 illustrates the phase of the lowest order non-zero OAM mode. Modes described by such phases have associated $l\hbar$ of OAM per photon, where l is an integer. This is in addition to the angular momentum defined by the polarization state where each photon has at most $\pm\hbar$ of SAM. The undefined phase along that axis also gives these modes a characteristic annular intensity profile, which has important implications for their generation in FELs.

[1] To the astute reader troubled by the assignment of OAM to the massless photon which should have only SAM by Lorentz invariance, I defer to the relevant discussions in [6], [7], and [8] regarding the subtleties of intrinsic and extrinsic angular momentum as they apply to the OAM modes.

OAM AMPLIFICATION IN FELS

Because of their exotic properties and multitude of applications at visible and longer wavelengths, it seems only natural to wonder how OAM light might be folded into the flexible FEL repertoire, particularly since these new insights overlapped with the development of the first x-ray FEL [19]. Among the promising x-ray OAM applications is an expanded x-ray magnetic circular dichroism technique [20] where it is proposed that angle-resolved energy loss spectrometry can distinguish spin-polarized atomic transitions subject to different photon OAM and polarization states [21, 22].

In reality, the first examinations into FEL OAM were more modestly motivated. They began at UCLA initially as an attempt to explain the strange hollow and swirling intensity profiles that were observed at the visible-infrared SASE amplifier (VISA) FEL at the ATF at Brookhaven [23, 24]. While in the end these profiles were likely not OAM in nature[2], it was soon realized that OAM light could indeed be generated in an FEL given the proper conditions.

This came as a result of a theoretical formalism that had been developed by myself, Avi Gover and James Rosenzweig to understand how OAM modes couple to the e-beam and are amplified [25, 26]. The basis of this formalism was the gain-guiding nature of the high-gain FEL process, in which the lasing e-beam tends to guide the radiation rather than let it diffract completely away [27]. This feature compels a mathematical description of the guided FEL radiation in terms of self-similar eigenmodes with fixed profiles rather than the diffracting modes of free space. In our formalism, the guiding properties of the lasing e-beam were modeled through a description of the e-beam as a 'virtual dielectric'. This approach is ultimately mathematically identical to previous analyses that described the radiation field through a mode expansion, but it had a particularly useful advantage. It turned out that, if the virtual dielectric is chosen to have a refractive index with a parabolic radial dependence (i.e., a so-called quadratic index medium), then the basis self-similar eigenmodes have precisely the same form as the OAM modes of free space paraxial propagation evaluated at the beam waist. In this way of describing the FEL, we had a useful connection between the guided FEL modes and the naturally occurring free-space modes such that the coupling characteristics of specific OAM modes in the FEL interaction could be calculated directly [25]. Subsequent extensions to the model were then developed that included energy spread [28] (where the equivalence between ours and other formalisms was also shown) and later on emittance and betatron motion [29]. From the full theoretical description, a fitting formula[3] for the gain length $L_{3D}/L_{1D} = 1 + \Lambda_{0,\pm 1}$ of the $l = \pm 1$ OAM modes was obtained in at the optimal

[2] The donut shapes were most likely the result of off-axis coupling to the radiation due to betatron motion and energy spread.

[3] in the spirit of the example set by Ming Xie for quickly calculating the FEL gain length [30]

ISBN 978-3-95450-134-2

detuning [29],

$$\begin{aligned}\Lambda_{0,\pm 1} =&1.1\eta_d^{0.57} + 3.0\eta_\gamma^2 + 0.60\eta_\epsilon^{1.56} + 950\eta_d^{1.5}\eta_\gamma^{3.7} \\ &+ 5.5\eta_d^{1.10}\eta_\epsilon^{0.5} + 11\eta_d^{0.7}\eta_\epsilon^{1.2} \\ &+ 1.14\eta_\gamma^{5.1}\eta_\epsilon^{1.6} + 20300\eta_d^{2.3}\eta_\gamma^{1.75}\eta_\epsilon^{2.1},\end{aligned} \tag{1}$$

where $\eta_d = L_{1D}/2k\sigma_x^2$ is the diffraction parameter, $\eta_\gamma = 2\sigma_\gamma k_u L_{1D}$ is the energy spread parameter for a gaussian distribution, and $\eta_\epsilon = 2k\epsilon_x k_\beta L_{1D}$ is the emittance parameter. An analogous fitting formula for the OAM gain length in a space charge dominated beam is given in Ref [29].

With the description of the FEL as an expansion of OAM modes it became relatively straightforward to calculate the requirements for an OAM mode to be amplified. One striking result was that, even in the presence of averaged betatron motion and energy spread for a round e-beam, the OAM modes in the FEL are orthogonal. Modes of a given l do not couple to each other unless the cylindrical symmetry is broken. This is related to the fact that the spatial structure of the bunching in the e-beam during amplification corresponds with the phase structure of the emitted light. As such, the bunching factor for OAM light should be written in a modified form to incorporate the helical phase,

$$b_{l_b}(k) = \frac{1}{N}\sum_{j=1}^{N} e^{iks_j - il_b\phi_j}. \tag{2}$$

When coupled to a radiation field of the form $e^{iks-il\phi}$, there is a direct relationship between the l_b mode in the e-beam and the l mode in the field at the fundamental lasing frequency,

$$l_b = l. \tag{3}$$

This means that, in an ideal system, an OAM mode can be amplified independent from other modes in the system and they will not cascade down to the fundamental $l = 0$ mode because they are tied to the helical e-beam distribution. Thus, an OAM mode with a sufficiently large head start in the amplification process will dominate up to saturation. But this also means that it has to be externally seeded in order to dominate over the SASE-driven fundamental mode that has the highest gain. This isn't necessarily a problem because there are numerous ways in which OAM modes can be produced to act as an EM seed. Mode conversions have been performed with conventional lasers by shaping the laser pulse front with dedicated optics [31–33]. But such methods are not optimal from the standpoint of harnessing the extreme wavelength tunability of the FEL down to x-ray wavelengths, where can also be difficult to obtain a sufficiently intense x-ray OAM seed.

FEL TAILORING FOR OAM

Without an external EM seed that carries OAM to jumpstart the FEL, one is left to rely on two possible options, vis-a-vis Figure 1. One is beam shaping, the other is radiation shaping. For beam shaping to work, the OAM seed comes from the electron beam itself. Because of the helical phase structure of the OAM modes, this option requires a precise helical manipulation of the e-beam structure at the level of the lasing wavelength as given by the bunching in Eq. 2. The e-beam must be helically bunched so that the EM emission in the undulator has the helical phase structure of the desired OAM mode, thereby initiating the FEL process [25]. But how does one make a spiral electron beam density distribution at the lasing wavelength?

A clue came from a 2008 paper by Sasaki and McNulty [34] where they showed that the phase structure of harmonic radiation from helically polarized undulators carries an azimuthal component that is characteristic of OAM light. It had in fact been known for some time that all harmonics $h > 1$ from helical undulators have an off-axis annular intensity profile (see e.g., [35]), which is characteristic of OAM modes. This profile structure was confirmed for coherent emission by Allaria et al [36]. That the associated phase was helical, however, had apparently gone previously unnoticed. Only recently was the predicted helical phase structure confirmed in experiments on second harmonic incoherent undulator radiation from a 3rd generation synchrotron light source [37].

The intimate connection between the helical phase and the harmonic radiation fields thus provided a beam-shaping mechanism to tailor the FEL for OAM amplification at the fundamental lasing frequency. A subsequent revisiting of the spatial coupling between the e-beam and the resonant undulator harmonics suggested that the correspondence between the helical bunching mode and the radiation l modes should be modified [38],

$$l_b = l \pm (h-1), \tag{4}$$

where the + or − sign indicates the right or left handedness of the helical undulator field. From the harmonic interaction it was shown that there is a way to couple azimuthal modes in the e-beam to different azimuthal modes in the fields. This feature essentially provided a solution to the problem of jumpstarting the FEL to emit an OAM mode without an OAM EM seed, namely, through harmonic coupling.

From these realizations came two different methods by which coherent OAM light can be produced in an FEL, illustrated in Figure 3. Though they appear similar in layout, the first method A) is essentially a beam shaping method whereas B) is a radiation shaping method. The interaction in each undulator is effectively governed by the coupling in Eq. 4, although the bunching is not revealed until the beam exits the chicane. In the beam shaping case A), the electron beam is energy modulated by the simple $l = 0$ laser (e.g, a Gaussian profile) at the second harmonic resonance of the helical undulator, assumed here to be right handed. In other words, the resonant frequency of the helical undulator is $\omega_{h,r} = \omega_L/2$ where ω_L is the laser frequency. This generates a spatially dependent energy modulation that, after passage through the simple chicane produces $l_b = 1$ helical bunching at the frequency ω_L. The bunched beam

ISBN 978-3-95450-134-2

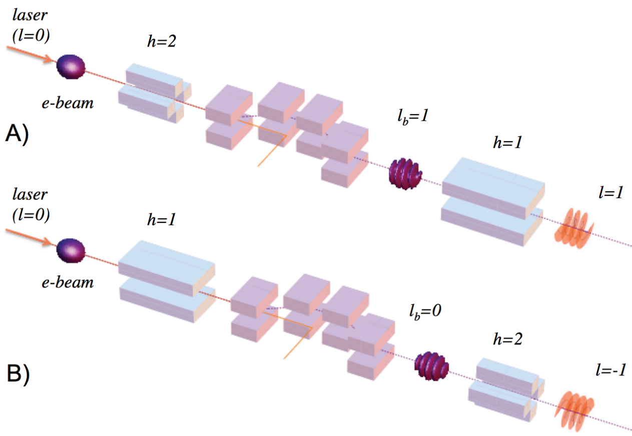

Figure 3: Two different OAM production methods in FELs. A) Beam shaping with helically microbunched e-beam. B) Radiation shaping with regularly microbunched e-beam radiating at 2nd harmonic.

then enters an FEL planar undulator tuned so that it's fundamental frequency is the same as that of the laser, $\omega_{p,r} = \omega_L$. Because the beam is also bunched at the fundamental frequency, the FEL lases and produces an $l = 1$ OAM mode at the frequency ω_L, which matches the $l_b = 1$ bunching (Eq. 3). The system effectively acts like a mode convertor and amplifier, where the initial $l = 0$ laser mode is converted to an $l = 1$ OAM mode at the same frequency.

In the radiation shaping method shown in B), the helical and planar undulators are simply swapped. No other tuning is changed, but the result is different. In this case, the $l = 0$ laser modulates the beam in a simple fashion, again with $\omega_{p,r} = \omega_L$. The resulting bunching at the chicane exit is of the ordinary sort and has no azimuthal dependence, so $l_b = 0$. In the helical undulator downstream, the beam, which is again bunched at ω_L, radiates at the second harmonic because $\omega_{h,r} = \omega_L/2$. By Eq. 4, this generates $l = -1$ OAM light at the frequency ω_L. Note that the OAM mode has reversed sign between case A) and case B), while the frequency of the light stays the same. This 'radiation shaping' scheme also acts like a mode convertor of the $l = 0$ laser, but in this case the OAM light is generated by exploiting the spatial features of the harmonic radiation rather than the beam distribution.

EXPERIMENTS

Several experiments designed to investigate the different OAM generation techniques followed. The first, performed at the Neptune Laboratory at UCLA in 2011 called HELiX [39], was a test of the helical microbunching concept proposed in [38] required by the beam shaping method of OAM generation. The setup of the experiment is shown in Figure 4. The 12-12.5 MeV electron beam was modulated by a 10.6 μm wavelength CO_2 laser in a short helical undulator, which was tuned to be resonant at 21.2 μm. The e-beam and the laser thus interacted at the second harmonic resonance, which generated a single twist helical energy modulation.

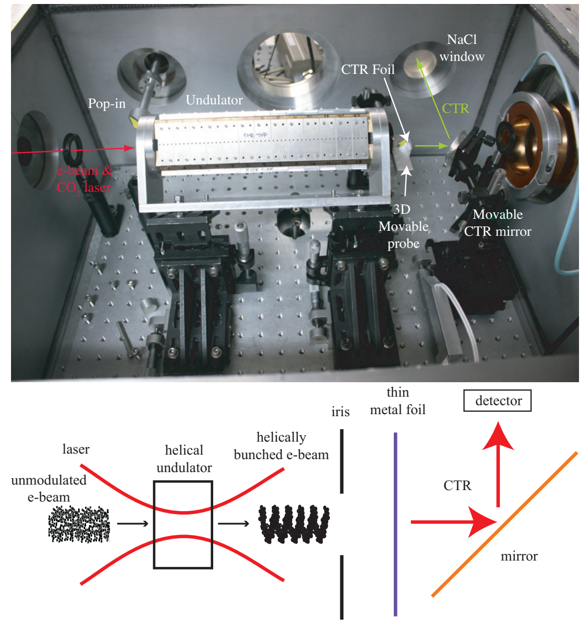

Figure 4: Picture (above) and cartoon (below) of the HELiX helical microbunching experiment at UCLA.

At these low e-beam energies, the longitudinal dispersion through the undulator was sufficient to turn the energy modulation into a helical density modulation, so no chicane was needed. The beam then hit a thin aluminum foil and emitted coherent transition radiation (CTR) with an imbedded helical phase. The integrated CTR signal intensity was measured and matched well with theoretical expectations for the CTR energy of a helically modulated beam [40], but direct experimental evidence for the helical phase was lacking.

A direct measurement of the helical phase in the radiation emitted by a helically microbunched beam was performed at the SLAC Next Linear Collider Test Accelerator (NLCTA) in 2013 [41]. The layout was identical to the beam shaping scheme in Fig. 3. Piggybacking on the infrastructure used for the echo enabled harmonic generation (EEHG) program [42–45], in this experiment, a helical undulator built by Andrey Knyazik at UCLA was used to modulate the 120MeV e-beam through the second harmonic interaction with an 800 nm laser [46]. Helical bunching was produced as the beam transited the chicane, and the coherent OAM light emitted in the following planar undulator was sent through a beam splitter and captured with two cameras set to image different focal planes. This enabled the phase to be determined by an iterative phase reconstruction algorithm from the measured intensities. Results showed that 85% of the radiation power was contained in the $l = 1$ azimuthal mode. Further direct evidence of the helical phase structure was obtained from images of the far field diffraction pattern of the light as it passed through a narrow slit, which showed clear evidence of a π phase difference across the beam and a shearing pattern that is the hallmark of traverse energy flow.

Following the beam shaping OAM experiment, the radiation shaping technique was then also tested at NLCTA by

ISBN 978-3-95450-134-2

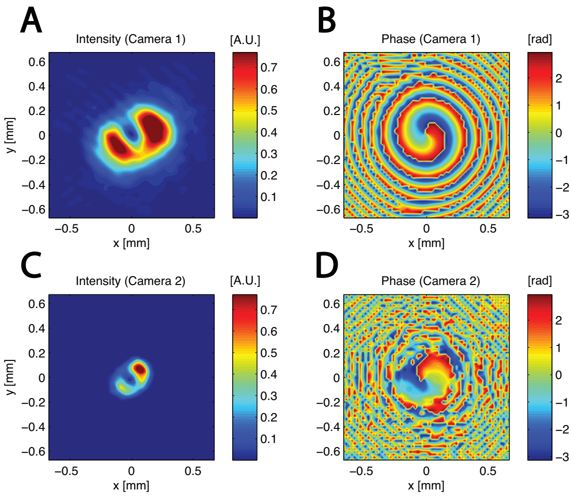

Figure 5: From [41]. Measured undulator radiation intensities (left) and reconstructed $l = 1$ OAM phases (right) from two cameras positioned to view the undulator radiation profiles at different planes. Intensity (A) and phase (B) at camera 1 are shown, and correspond to the intensity (C) and phase (D) at camera 2.

exchanging the positions of the helical and planar undulators [47]. Again, the phase reconstruction algorithm showed the presence of a helical phase in the coherent harmonic emission from the helical undulator, only this time with the opposite $l = -1$ handedness, as predicted by Eq. 4. Over 91% of the mode power was in this mode. The observed pattern of transverse interference between the coherent undulator radiation (CUR) and the CTR from the ejection screen also confirmed the helical phase via the presence of a forked pattern that is the signature of a phase singularity (See Figure 6).

Together, these two experiments confirmed the basic physics of in situ OAM light production in FELs using the e-beam as the mode conversion medium. In the beam shaping experiment, the beam radiates OAM light at the fundamental frequency of the undulator. This has the advantage that in principle the FEL can lase up to saturation to produce OAM light up to the GW level. A drawback of this technique is that the helical e-beam distribution is sensitive to asymmetries or transport effects that can wash out the carefully prepared structure and reduce the purity of the radiated OAM mode. In contrast, the radiation shaping technique, which relies primarily on the radiation emission profile of the helical undulator, is much less sensitive to these effects because the e-beam bunching does not have a helical structure. The result is higher mode purity, but because the harmonic emission is less intense than the fundamental, this scheme may produce less peak power. Even so, this technique is simpler, likely more robust in practice, and could be used in a simple FEL afterburner arrangement [48] where a helical undulator is placed downstream of an FEL to radiate coherent OAM light from the spent beam. This opens up new possibilities for pump-probe experiments with two pulses that carry different values of OAM, i.e, one $l = 0$ mode from the upstream FEL and one with $l \neq 0$ from the helical afterburner.

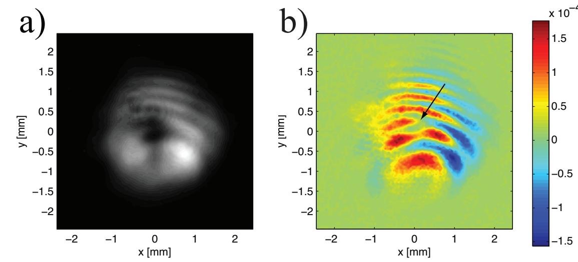

Figure 6: From Ref. [47]. Interference between CUR and off-axis CTR reveals the signature forked pattern (black arrow, right image) of a $l = -1$ vortex from the second-harmonic undulator emission. Image b) is the difference between image a) and an image taken with the e-beam is steered to remove the CTR interference (not shown).

FUTURE POSSIBILITES

Building on these concepts, new and more advanced schemes have been proposed. In a scheme dubbed Echo-v for vortex [49], the beam shaping method is integrated with an EEHG arrangement. In contrast to standard EEHG where two pairs of laser modulators and chicanes are used to generate high harmonic bunching [50, 51], in Echo-v, one or both of the modulators also imprints a helical energy modulation. Through the EEHG process the final helical bunching in the beam transforms just like the harmonics as $l_b = nl_1 + ml_2$ where n and m are the frequency harmonics of each laser and l_1 and l_2 are the helical modulations imprinted by the first and second lasers, respectively. With different combinations of l_1 and l_2, both the frequency and l_b can be up-converted simultaneously or independently to produce high harmonics at soft x-rays with either a large or small output l. Another scheme suggests the use of a simple transverse mask to seed the amplification of tunable OAM in a soft x-ray HGHG FEL [52]. The concept of OAM has also been applied directly to coherent electron beams where the quantum mechanical electron wave functions have a helical phase [53], as distinct from the classical helical bunching described here. This has become a rapidly advancing field of study in its own right.

CONCLUSION

It has become clear that FELs are extraordinarily powerful machines for discovery. They are highly flexible in that the character of the light they produce can in many ways be precisely tailored to suit an ever growing set of needs. The landscape of 'beam by design' techniques used previously to tailor the temporal profile of the light can now begin to include transverse tailoring schemes that open exciting new regimes of study in accelerator and photon science.

ISBN 978-3-95450-134-2

ACKNOWLEDGMENT

I would like to thank all of my friends and collaborators who have participated in the development of these ideas over the years. I would also like to thank the 2014 FEL Prize committee for the Young Scientist FEL Award.

REFERENCES

[1] E. Hemsing, G. Stupakov, D. Xiang, and A. Zholents, “Beam by design: Laser manipulation of electrons in modern accelerators,” *Rev. Mod. Phys.*, vol. 86, pp. 897–941, Jul 2014.

[2] P. Emma, K. Bane, M. Cornacchia, Z. Huang, H. Schlarb, G. Stupakov, and D. Walz, “Femtosecond and subfemtosecond x-ray pulses from a self-amplified spontaneous-emission–based free-electron laser,” *Phys. Rev. Lett.*, vol. 92, p. 074801, Feb 2004.

[3] J. H. Poynting, “The wave motion of a revolving shaft, and a suggestion as to the angular momentum in a beam of circularly polarised light,” *Proceedings of the Royal Society of London. Series A, Containing Papers of a Mathematical and Physical Character*, vol. 82, no. 557, pp. pp. 560–567, 1909.

[4] R. A. Beth, “Mechanical detection and measurement of the angular momentum of light,” *Phys. Rev.*, vol. 50, pp. 115–125, Jul 1936.

[5] L. Allen, M. W. Beijersbergen, R. J. C. Spreeuw, and J. P. Woerdman, “Orbital angular momentum of light and the transformation of laguerre-gaussian laser modes,” *Phys. Rev. A*, vol. 45, pp. 8185–8189, Jun 1992.

[6] S. J. van Enk and G. Nienhuis, “Spin and orbital angular momentum of photons,” *EPL (Europhysics Letters)*, vol. 25, no. 7, p. 497, 1994.

[7] A. T. O’Neil, I. MacVicar, L. Allen, and M. J. Padgett, “Intrinsic and extrinsic nature of the orbital angular momentum of a light beam,” *Phys. Rev. Lett.*, vol. 88, p. 053601, Jan 2002.

[8] M. V. Berry, “Paraxial beams of spinning light,” in *International Conference on Singular Optics* (M. S. Soskin, ed.), vol. 3487, pp. 6–11, SPIE, 1998.

[9] M. E. J. Friese, J. Enger, H. Rubinsztein-Dunlop, and N. R. Heckenberg, “Optical angular-momentum transfer to trapped absorbing particles,” *Phys. Rev. A*, vol. 54, pp. 1593–1596, Aug 1996.

[10] A. R. Carter, M. Babiker, M. Al-Amri, and D. L. Andrews, “Generation of microscale current loops, atom rings, and cubic clusters using twisted optical molasses,” *Phys. Rev. A*, vol. 73, p. 021401, Feb 2006.

[11] M. F. Andersen, C. Ryu, P. Clade, V. Natarajan, A. Vaziri, K. Helmerson, and W. D. Phillips, “Quantized rotation of atoms from photons with orbital angular momentum,” *Phys. Rev. Lett.*, vol. 97, no. 17, p. 170406, 2006.

[12] A. Jesacher, S. Fürhapter, S. Bernet, and M. Ritsch-Marte, “Shadow effects in spiral phase contrast microscopy,” *Phys. Rev. Lett.*, vol. 94, p. 233902, Jun 2005.

[13] P. Török and P. Munro, “The use of gauss-laguerre vector beams in sted microscopy,” *Opt. Express*, vol. 12, no. 15, pp. 3605–3617, 2004.

[14] B. Jack *et al.*, “Holographic ghost imaging and the violation of a bell inequality,” *Phys. Rev. Lett.*, vol. 103, p. 083602, Aug 2009.

[15] J. W. R. Tabosa and D. V. Petrov, “Optical pumping of orbital angular momentum of light in cold cesium atoms,” *Phys. Rev. Lett.*, vol. 83, pp. 4967–4970, Dec 1999.

[16] R. Fickler, R. Lapkiewicz, W. N. Plick, M. Krenn, C. Schaeff, S. Ramelow, and A. Zeilinger, “Quantum entanglement of high angular momenta,” *Science*, vol. 338, no. 6107, pp. 640–643, 2012.

[17] J. Leach, B. Jack, J. Romero, A. K. Jha, A. M. Yao, S. Franke-Arnold, D. G. Ireland, R. W. Boyd, S. M. Barnett, and M. J. Padgett, “Quantum correlations in optical angle–orbital angular momentum variables,” *Science*, vol. 329, no. 5992, pp. 662–665, 2010.

[18] J. Wang, J.-Y. Yang, I. M. Fazal, N. Ahmed, Y. Yan, H. Huang, Y. Ren, Y. Yue, S. Dolinar, M. Tur, and A. E. Willner, “Terabit free-space data transmission employing orbital angular momentum multiplexing,” *Nature Photonics*, vol. 6, pp. 488–496, 2012.

[19] P. Emma *et al.*, “First lasing and operation of an angstrom-wavelength free-electron laser,” *Nat Photon*, vol. 4, no. 9, pp. 641–647, 2010.

[20] B. T. Thole, P. Carra, F. Sette, and G. van der Laan, “X-ray circular dichroism as a probe of orbital magnetization,” *Phys. Rev. Lett.*, vol. 68, pp. 1943–1946, Mar 1992.

[21] M. van Veenendaal and I. McNulty, “Prediction of strong dichroism induced by x rays carrying orbital momentum,” *Phys. Rev. Lett.*, vol. 98, p. 157401, Apr 2007.

[22] J. Verbeeck, H. Tian, and P. Schattschneider, “Production and application of electron vortex beams,” *Nature*, vol. 467, no. 7313, pp. 301–304, 2010.

[23] A. Murokh, *Experimental Characterization of the Saturating, Near Infrared, Self-Amplified Spontaneous Emission Free Electron Laser: Analysis of Radiation Properties and Electron Beam Dynamics*. PhD thesis, University of California Los Angeles, 2002.

[24] G. Andonian, *Experimental and Analytical Study of a High Gain Self Amplified Spontaneous Emission Free Electron Laser Operating in a Large Spectral Bandwidth Regime*. PhD thesis, University of California Los Angeles, 2006.

[25] E. Hemsing, A. Gover, and J. Rosenzweig, “Virtual dielectric waveguide mode description of a high-gain free-electron laser. ii. modeling and numerical simulations,” *Physical Review A*, vol. 77, no. 6, p. 063831, 2008.

[26] E. Hemsing, A. Gover, and J. Rosenzweig, “Virtual dielectric waveguide mode description of a high-gain free-electron laser. i. theory,” *Physical Review A*, vol. 77, no. 6, p. 063830, 2008.

[27] G. T. Moore, “The high-gain regime of the free electron laser,” *Nuclear Instruments and Methods in Physics Research A*, vol. 239, pp. 19–28, Aug. 1985.

[28] E. Hemsing, A. Marinelli, S. Reiche, and J. Rosenzweig, “Longitudinal dispersion of orbital angular momentum modes in high-gain free-electron lasers,” *Phys. Rev. ST Accel. Beams*, vol. 11, p. 070704, Jul 2008.

ISBN 978-3-95450-134-2

[29] E. Hemsing, *Generation and Amplification of Coherent Radiation with Optical Orbital Angular Momentum in a Free-Electron Laser*. PhD thesis, University of California Los Angeles, 2011.

[30] M. Xie, "Design optimization for an x-ray free electron laser driven by slac linac," in *Proceedings of the 1995 Particle Accelerator Conference*, 1996.

[31] M. W. Beijersbergen, L. Allen, H. E. L. O. Van der Veen, and J. P. Woerdman, "Astigmatic laser mode converters and transfer of orbital angular momentum," *Optics Communications*, vol. 96, pp. 123–132, 1993.

[32] N. R. Heckenberg, R. McDuff, C. P. Smith, H. Rubinsztein-Dunlop, and M. J. Wegener, "Laser beams with phase singularities," *Optical and Quantum Electronics*, vol. 24, pp. S951–S962, 1992.

[33] M. W. Beijersbergen, R. P. C. Coerwinkel, M. Kristensen, and J. P. Woerdman, "Helical-wavefront laser beams produced with a spiral phaseplate," *Optics Communications*, vol. 112, no. 5-6, pp. 321 – 327, 1994.

[34] S. Sasaki and I. McNulty, "Proposal for generating brilliant x-ray beams carrying orbital angular momentum," *Phys. Rev. Lett.*, vol. 100, no. 12, p. 124801, 2008.

[35] W. Colson, "The nonlinear wave equation for higher harmonics in free-electron lasers," *IEEE J. Quant. Elect.*, vol. 17, no. 8, pp. 1417–1427, Aug 1981.

[36] E. Allaria, F. Curbis, M. Coreno, M. Danailov, B. Diviacco, C. Spezzani, M. Trovó, and G. DeNinno, "Experimental characterization of nonlinear harmonic generation in planar and helical undulators," *Phys. Rev. Lett.*, vol. 100, no. 17, p. 174801, 2008.

[37] J. Bahrdt, K. Holldack, P. Kuske, R. Müller, M. Scheer, and P. Schmid, "First observation of photons carrying orbital angular momentum in undulator radiation," *Phys. Rev. Lett.*, vol. 111, p. 034801, Jul 2013.

[38] E. Hemsing, P. Musumeci, S. Reiche, R. Tikhoplav, A. Marinelli, J. B. Rosenzweig, and A. Gover, "Helical electron-beam microbunching by harmonic coupling in a helical undulator," *Physical Review Letters*, vol. 102, no. 17, p. 174801, 2009.

[39] E. Hemsing, A. Knyazik, F. O'Shea, A. Marinelli, P. Musumeci, O. Williams, S. Tochitsky, and J. B. Rosenzweig, "Experimental observation of helical microbunching of a relativistic electron beam," *Applied Physics Letters*, vol. 100, no. 9, p. 091110, 2012.

[40] E. Hemsing and J. B. Rosenzweig, "Coherent transition radiation from a helically microbunched electron beam," *Journal of Applied Physics*, vol. 105, no. 9, p. 093101, 2009.

[41] E. Hemsing, A. Knyazik, M. Dunning, D. Xiang, A. Marinelli, C. Hast, and J. B. Rosenzweig, "Coherent optical vortices from relativistic electron beams," *Nature Phys.*, vol. 9, no. 9, pp. 549–553, 2013.

[42] D. Xiang, E. Colby, M. Dunning, S. Gilevich, C. Hast, K. Jobe, D. McCormick, J. Nelson, T. O. Raubenheimer, K. Soong, G. Stupakov, Z. Szalata, D. Walz, S. Weathersby, M. Woodley, and P.-L. Pernet, "Demonstration of the echo-enabled harmonic generation technique for short-wavelength seeded free electron lasers," *Phys. Rev. Lett.*, vol. 105, p. 114801, Sep 2010.

[43] D. Xiang, E. Colby, M. Dunning, S. Gilevich, C. Hast, K. Jobe, D. McCormick, J. Nelson, T. O. Raubenheimer, K. Soong, G. Stupakov, Z. Szalata, D. Walz, S. Weathersby, and M. Woodley, "Evidence of high harmonics from echo-enabled harmonic generation for seeding x-ray free electron lasers," *Phys. Rev. Lett.*, vol. 108, p. 024802, Jan 2012.

[44] E. Hemsing, D. Xiang, M. Dunning, S. Weathersby, C. Hast, and T. Raubenheimer, "Direct observation of fine-scale energy banding in echo-enabled harmonic generation," *Phys. Rev. ST Accel. Beams*, vol. 17, p. 010703, Jan 2014.

[45] E. Hemsing, M. Dunning, C. Hast, T. O. Raubenheimer, S. Weathersby, and D. Xiang, "Highly coherent vacuum ultraviolet radiation at the 15th harmonic with echo-enabled harmonic generation technique," *Phys. Rev. ST Accel. Beams*, vol. 17, p. 070702, Jul 2014.

[46] A. Knyazik, *Photons with a Twist: Coherent Optical Vortices From Relativistic Electron Beams*. PhD thesis, University of California Los Angeles, 2013.

[47] E. Hemsing, M. Dunning, C. Hast, T. Raubenheimer, and D. Xiang, "First characterization of coherent optical vortices from harmonic undulator radiation," *Phys. Rev. Lett.*, vol. 113, p. 134803, Sep 2014.

[48] E. L. Saldin, E. A. Schneidmiller, and M. V. Yurkov, "Optical afterburner for an x-ray free electron laser as a tool for pump-probe experiments," *Phys. Rev. ST Accel. Beams*, vol. 13, p. 030701, Mar 2010.

[49] E. Hemsing and A. Marinelli, "Echo-enabled x-ray vortex generation," *Phys. Rev. Lett.*, vol. 109, p. 224801, Nov 2012.

[50] G. Stupakov, "Using the beam-echo effect for generation of short-wavelength radiation," *Phys. Rev. Lett.*, vol. 102, p. 074801, 2009.

[51] D. Xiang and G. Stupakov, "Echo-enabled harmonic generation free electron laser," *Phys. Rev. ST Accel. Beams*, vol. 12, p. 030702, 2009.

[52] P. c. v. R. Ribič, D. Gauthier, and G. De Ninno, "Generation of coherent extreme-ultraviolet radiation carrying orbital angular momentum," *Phys. Rev. Lett.*, vol. 112, p. 203602, May 2014.

[53] K. Y. Bliokh, Y. P. Bliokh, S. Savel'ev, and F. Nori, "Semiclassical dynamics of electron wave packet states with phase vortices," *Phys. Rev. Lett.*, vol. 99, p. 190404, Nov 2007.

ISBN 978-3-95450-134-2

OPTIMIZATION OF A HIGH EFFICIENCY FREE ELECTRON LASER AMPLIFIER

E.A. Schneidmiller, M.V. Yurkov, DESY, Hamburg, Germany

Abstract

Technique of undulator tapering in the post-saturation regime is used at the existing X-ray FELs for increasing the radiation power. We present comprehensive analysis of the problem in the framework of one-dimensional and three-dimensional theory. We find that diffraction effects essentially influence on the choice of the tapering strategy. Our studies resulted in a general law of the undulator tapering for a seeded FEL amplifier as well as for SASE FEL.

INTRODUCTION

Effective energy exchange between the electron beam moving in an undulator and electromagnetic wave happens when resonance condition takes place. In this case electromagnetic wave advances electron beam by one radiation wavelength while electron beam passes one undulator period. When amplification process enters nonlinear stage, the energy losses by electrons become to be pronouncing which leads to the violation of the resonance condition and to the saturation of the amplification process. Application of the undulator tapering [1] allows to a further increase of the conversion efficiency. An idea is to adjust undulator parameters (field or period) according to the electron energy loss such that the resonance condition is preserved.

It is generally accepted that in the framework of the one-dimensional theory an optimum law of the undulator tapering should be quadratic [2–9]. Similar physical situation occurs in the FEL amplifier with a waveguide [2]. In this case radiation is confined within the waveguide. Parameters of FEL amplifiers operating in the infrared, visible, and x-ray wavelength ranges are such that these devices are described in the framework of three dimensional theory with an "open" electron beam, i.e. physical case of diffraction in a free space. In this case the diffraction of radiation is an essential physical effect influencing optimization of the tapering process. Discussions and studies on the optimum law of the undulator tapering in the three-dimensional case are in the progress for more than 20 years. Our previous studies were mainly driven by occasional calculations of perspective FEL systems for high power scientific (for instance, FEL based $\gamma\gamma$ - collider) and industrial applications (for instance, for isotope separation, and lithography [10–12]). Their parameter range corresponded to the limit of thin electron beam (small value of the diffraction parameter). In this case linear undulator tapering works well from almost the very beginning [6]. Comprehensive study devoted to the global optimization of tapered FEL amplifier with "open" electron beam has been presented in [4]. It has been shown that: i) tapering law should be linear for the case of thin electron beam, ii) optimum tapering at the initial stage should follow quadratic dependence, iii) tapering should start approximately two field gain length before saturation. New wave of interest to the undulator tapering came with the development of x-ray free electron lasers [13–20]. Undulator tapering has been successfully demonstrated at long wavelength FEL amplifiers [2, 21], and is routinely used at x-ray FEL facilities LCLS and SACLA [16, 17]. Practical calculations of specific systems yielded in several empirical laws using different polynomial dependencies (see [22, 23] and references therein).

Comprehensive analysis of the problem of the undulator tapering in the presence of diffraction effects has been performed in [24,25]. It has been shown that the key element for understanding the physics of the undulator tapering is given by the model of the modulated electron beam which provides relevant interdependence of the problem parameters. Finally, application of similarity techniques to the results of numerical simulations led to the universal law of the undulator tapering. In this paper we extend studies [24, 25] to the case of SASE FEL.

BASIC RELATIONS

We consider axisymmetric model of the electron beam. It is assumed that transverse distribution function of the electron beam is Gaussian, so rms transverse size of matched beam is $\sigma = \sqrt{\epsilon\beta}$, where ϵ is rms beam emittance and β is focusing beta-function. An important feature of the parameter space of short wavelength FELs is that the space charge field does not influence significantly the amplification process, and in the framework of the three-dimensional theory the operation of the FEL amplifier is described by the following parameters: the diffraction parameter B, the energy spread parameter $\hat{\Lambda}_{\mathrm{T}}^2$, the betatron motion parameter $\hat{k}_\beta$ and detuning parameter $\hat{C}$ [9, 26]:

$$B = 2\Gamma\sigma^2\omega/c\,, \qquad \hat{C} = C/\Gamma\,,$$
$$\hat{k}_\beta = 1/(\beta\Gamma)\,, \qquad \hat{\Lambda}_{\mathrm{T}}^2 = (\sigma_{\mathrm{E}}/\mathcal{E})^2/\rho^2\,, \qquad (1)$$

where $\Gamma = \left[I\omega^2\theta_{\mathrm{s}}^2 A_{\mathrm{JJ}}^2/(I_{\mathrm{A}}c^2\gamma_z^2\gamma)\right]^{1/2}$ is the gain parameter, $\rho = c\gamma_z^2\Gamma/\omega$ is the efficiency parameter, and $C = 2\pi/\lambda_{\mathrm{w}} - \omega/(2c\gamma_z^2)$ is the detuning of the electron with the nominal energy $\mathcal{E}_0$. Note that the efficiency parameter ρ entering equations of three dimensional theory relates to the one-dimensional parameter $\rho_{1\mathrm{D}}$ as $\rho_{1\mathrm{D}} = \rho/B^{1/3}$ [9, 27]. The following notations are used here: I is the beam current, $\omega = 2\pi c/\lambda$ is the frequency of the electromagnetic wave, $\theta_{\mathrm{s}} = K/\gamma$, K is the rms undulator parameter, $\gamma_z^{-2} = \gamma^{-2} + \theta_{\mathrm{s}}^2$, $k_{\mathrm{w}} = 2\pi/\lambda_{\mathrm{w}}$ is the undulator wavenumber, $I_{\mathrm{A}} = 17$ kA is the Alfven current, $A_{\mathrm{JJ}} = 1$ for helical undulator and $A_{\mathrm{JJ}} = J_0(K^2/2(1+K^2)) - J_1(K^2/2(1+K^2))$ for planar undulator. J_0 and J_1 are the Bessel functions of the first

ISBN 978-3-95450-134-2

kind. The energy spread is assumed to be Gaussian with rms deviation $\sigma_{\rm E}$.

In the following we consider the case of negligibly small values of the betatron motion parameter $\hat{k}_\beta$ and the energy spread parameter $\hat{\Lambda}^2_{\rm T}$ (i.e. the case of "cold" electron beam). Under these assumptions the operation of the FEL amplifier is described by the diffraction parameter B and the detuning parameter $\hat{C}$.

Equations, describing the motion of the particles in the ponderomotive potential well of the electromagnetic wave and the undulator, become simple when written down in the normalized form (see, e.g. [9]):

$$\frac{d\Psi}{d\hat{z}} = \hat{C} + \hat{P}, \qquad \frac{d\hat{P}}{d\hat{z}} = U\cos(\phi_U + \Psi)\,, \tag{2}$$

where $\hat{P} = (E - E_0)/(\rho E_0)$, $\hat{z} = \Gamma z$, and U and ϕ_U are the amplitude and the phase of the effective potential. Deviation of the electron energy is small in the exponential stage of amplification, $\hat{P} \ll 1$, and process of the beam bunching in phase Ψ lasts for a long distance, $\hat{z} \gg 1$. Situation changes drastically when amplification process enters nonlinear stage and deviation of the electron energy $\hat{P}$ approaches to the unity. The phase change on a scale of $\Delta\hat{z} \simeq 1$ becomes to be fast, particles start to slip fast in phase Ψ which leads to the reduction of the electron beam modulation, and the growth of the radiation power is saturated.

Undulator tapering [1], i.e. adjustment of the detuning according to the energy loss of electrons, $\hat{C}(\hat{z}) = -\hat{P}(\hat{z})$, allows to keep synchronism of trapped electrons with electromagnetic wave.

UNIVERSAL TAPERING LAW

During amplification process the electron beam is modulated periodically at the resonance wavelength. This modulation grows exponentially in the high gain linear regime, and reaches a value about the unity near the saturation point. Application of the undulator tapering allows to preserve beam bunching at a long distance. Electron beam current $I(z,t) = I_0[1 + a_{\rm in}\cos\omega(z/v_z - t)]$ is modulated with amplitude $a_{\rm in}$ in this case. Radiation power of the modulated beam is given by [28]:

$$\begin{aligned} W &= \frac{2\pi^2 I_0^2 a_{\rm in}^2 \sigma^2}{c\lambda\lambda_{\rm u}} \frac{K^2 A_{\rm JJ}^2}{1+K^2} f(\tilde{z})\tilde{z}\,, \\ f(\tilde{z}) &= \arctan(\tilde{z}/2) + \tilde{z}^{-1}\ln\left(\frac{4}{\tilde{z}^2+4}\right)\,. \end{aligned} \tag{3}$$

In the right-hand side of expression (3) we explicitly isolated z-dependence of the radiation power with function $f(\tilde{z})$ of argument $\tilde{z} = 1/N$ where $N = k\sigma^2/z$ is Fresnel number, and $k = 2\pi/\lambda$ is wavenumber. Plot of the function $f(\tilde{z})$ is shown in Fig. 1. Asymptotes of the function $f(\tilde{z})$ are:

$$\begin{aligned} f(\tilde{z}) &\to \pi/2 \quad &&\text{for} \quad \tilde{z} \gg 1 \quad (N \ll 1)\,, \\ f(\tilde{z}) &= \tilde{z}/4 \quad &&\text{for} \quad \tilde{z} \ll 1 \quad (N \gg 1) \end{aligned} \tag{4}$$

for thin and wide electron beam asymptote, respectively.

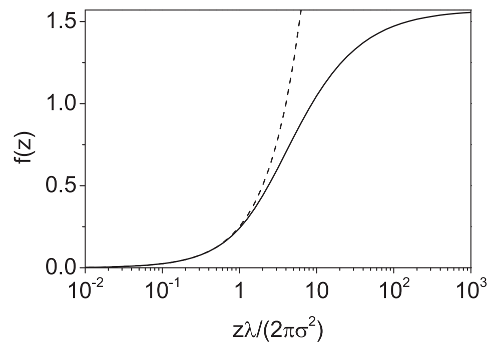

Figure 1: Function $f(z)$ entering equation (3). Dashed line shows the asymptote (4) for small values of z, $f(\tilde{z}) = \tilde{z}/4$.

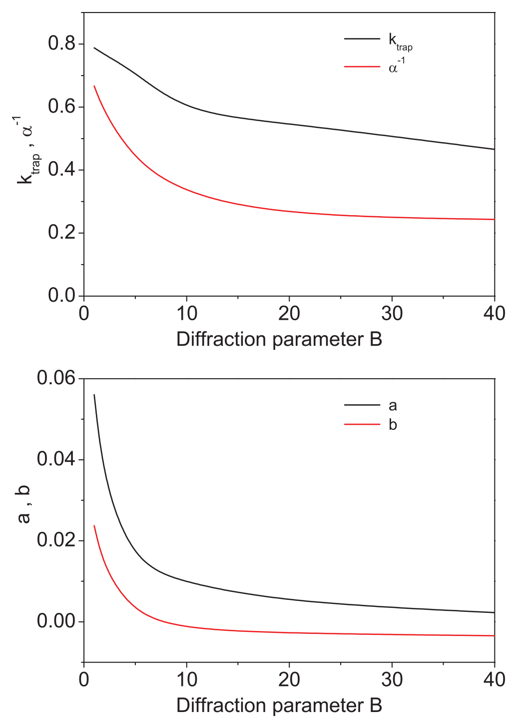

Figure 2: Upper plot: the trapping efficiency K_{trap} for the globally optimized undulator (black curve) and the fitting coefficient α^{-1}_{tap} of the global optimization entering Eq. (5) (red curve). Lower plot: coefficients a (black line) and b (red line) of the rational fit of the tapering law (6).

The detuning (undulator tapering) should follow the energy loss by particles given by (3) which suggests the following universal law [24, 25]:

$$\hat{C} = \alpha_{tap}(\hat{z} - \hat{z}_0)\left[\arctan\left(\frac{1}{2N}\right) + N\ln\left(\frac{4N^2}{4N^2+1}\right)\right]\,, \tag{5}$$

with Fresnel number N fitted by $N = \beta_{tap}/(\hat{z} - \hat{z}_0)$. Undulator tapering starts by two field gain length $2 \times L_g$ before the saturation point at $z_0 = z_{sat} - 2 \times L_g$. Parameter β_{tap} is rather well approximated with the linear dependency on diffraction parameter, $\beta_{tap} = 8.5 \times B$. Parameter α_{tap} is

ISBN 978-3-95450-134-2

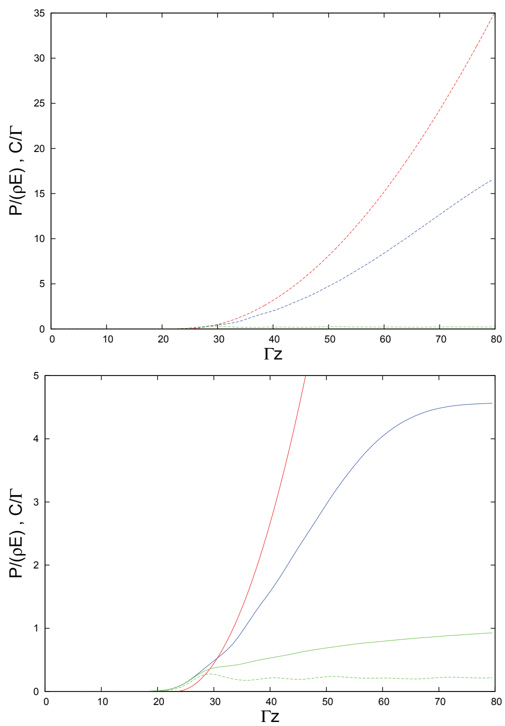

Figure 3: Evolution along the undulator of the reduced radiation power $\hat{\eta} = W/(\rho W_{\text{beam}})$ (blue curve) and of the detuning parameter $\hat{C} = C/\Gamma$ (red curve). Top and bottom plots correspond to the seeded and SASE case, respectively. Solid blue and green curve on the bottom curve correspond to tapered and untapered case, respectively. Dashed green line is radiation power of seeded untapered FEL. Diffraction parameter is $B = 10$.

plotted in Fig. 2. It is a slow varying function of the diffraction parameter B, and scales approximately to $B^{1/3}$.

Analysis of the expression (5) shows that it has quadratic dependence in z for small values of z (limit of the wide electron beam), and linear dependence in z for large values of z (limit of the thin electron beam). It is natural to try a fit with a rational function which satisfies both asymptotes. The simplest rational fit is:

$$\hat{C} = \frac{a(\hat{z} - \hat{z}_0)^2}{1 + b(\hat{z} - \hat{z}_0)} \ . \qquad (6)$$

The coefficients a and b are the functions of the diffraction parameter B, and are plotted in Fig. 2. Start of the undulator tapering is set to the value $z_0 = z_{sat} - 2L_g$. Analysis performed in [24, 25] have shown that the fit of the tapering law with the rational function also works well.

ANALYSIS OF THE TAPERING PROCESS

Seeded FEL

We proceed our paper with the analysis of the trapping process. Top plot in Fig. 3 shows evolution of the average radiation power of seeded FEL along the optimized tapered undulator. The trapping efficiency $K_{trap} = \hat{P}/\hat{C}$ falls down with the diffraction parameter B (see Fig. 2). This is natural

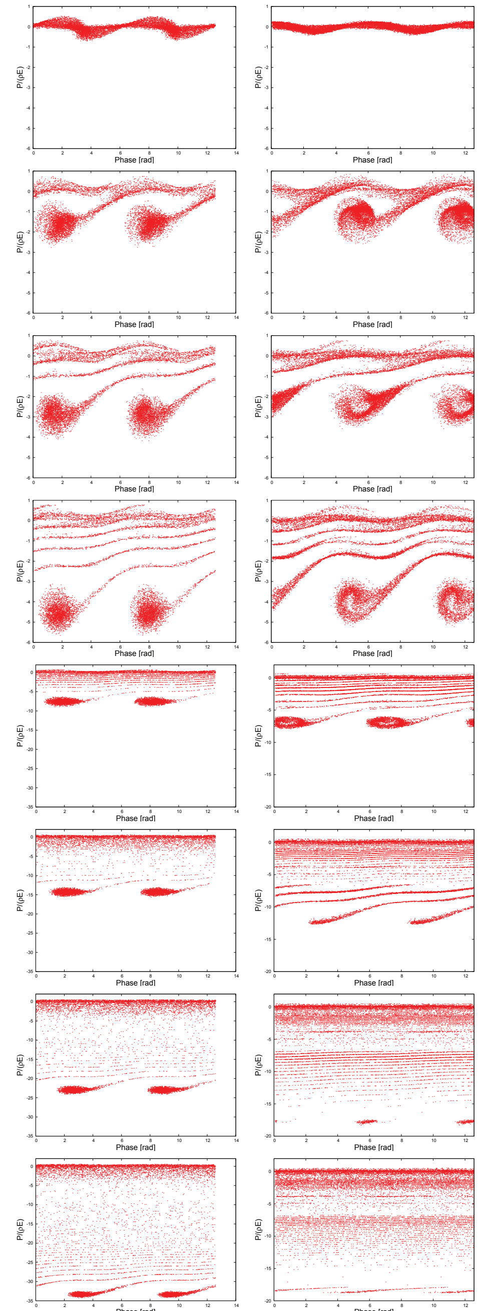

Figure 4: Phase space distribution of electrons at different stages of the trapping process. Diffraction parameter is $B = 10$. Plots from the top to the bottom correspond to $\hat{z} = 23.5$, 35.3, 39.2, 43.2, 49, 58.9, 68.7, and 78.5, respectively. Left column represents seeded FEL amplifier. Right column represents SASE FEL at the coordinate along the bunch $\hat{s} = \rho\omega t = 100$, see Figs. 5 and 6.

consequence of the diffraction effects discussed in earlier publications (see, e.g. Ref. [9], Chapter 4). Indeed, FEL radiation is not a plane wave. Transverse distribution of the radiation field (FEL radiation mode [9, 29]) depends on the value of the diffraction parameter B, and the field gradient (or, amplitude of ponderomotive well) across the electron

ISBN 978-3-95450-134-2

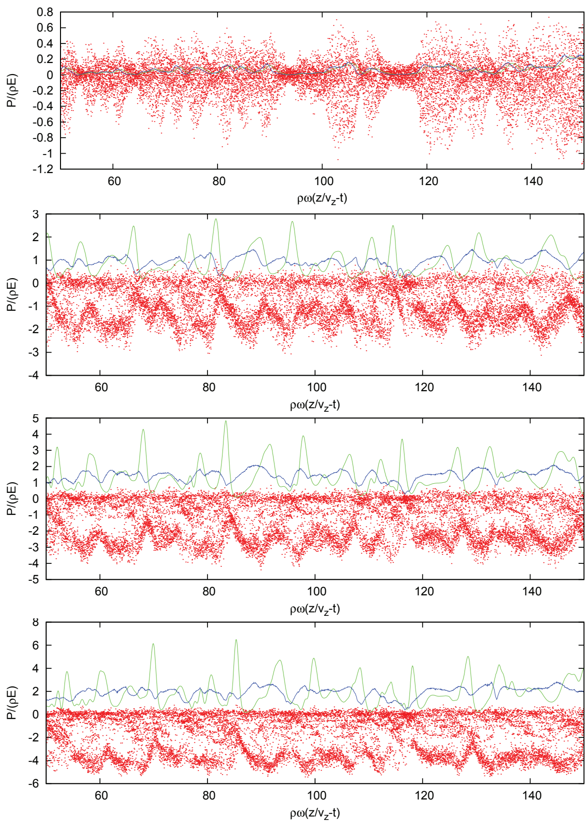

Figure 5: Phase space distribution of the particles along the bunch (red dots), average loss of the electron energy (blue line), and radiation power (green line) at different stages of the trapping process in SASE FEL. Here diffraction parameter is $B = 10$. Plots from the top to the bottom correspond to $\hat{z} = 23.5$, 35.3, 39.2, and 43.2, respectively.

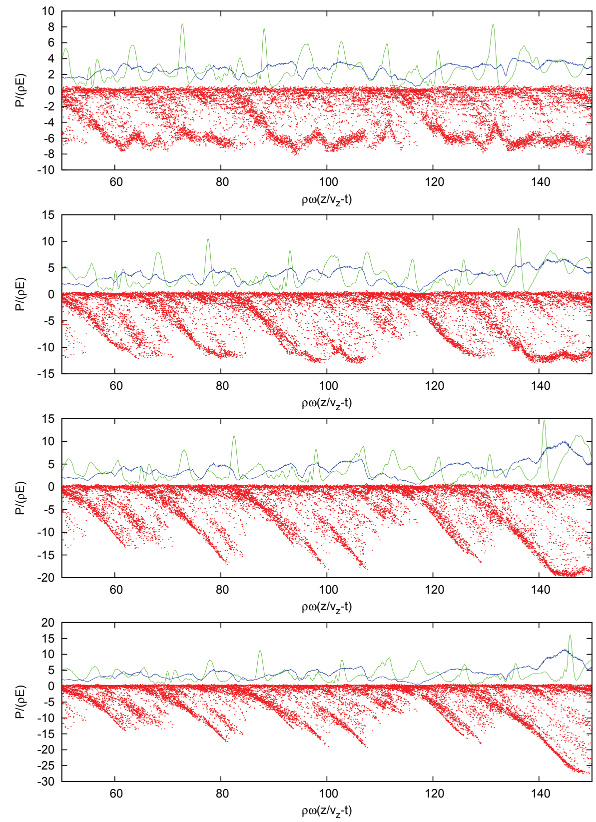

Figure 6: Phase space distribution of the particles along the bunch (red dots), average loss of the electron energy (blue line), and radiation power (green line) in the deep tapering regime. Diffraction parameter is $B = 10$. Plots from the top to the bottom correspond to $\hat{z} = 49$, 58.9, 68.7, and 78.5, respectively.

beam is more pronouncing for larger values of the diffraction parameter B. In the latter case we obtain situation when electrons located in the core of the electron beam are already fully bunched while electrons at the edge of the beam are not bunched yet (see phase space plot (a) in Fig. 4). As a result, the number of electrons with similar positions on the energy-phase plane falls down with the growth of the diffraction parameter, as well as the trapping efficiency in the regime of coherent deceleration. The trapping process is illustrated with the phase space plots presented on Figs. 4-6 for the value of the diffraction parameter $B = 10$. The particles in the core of the beam are trapped most effectively. Nearly all particles located at the edge of the electron beam leave the stability region very soon. The trapping process lasts for a several field gain lengths when the trapped particles become to be isolated in the trapped energy band for which the undulator tapering is optimized further. For the specific value of the diffraction parameter $B = 10$ the trapping proces is not finished even at three field gain lengths after saturation, and non-trapped particles continue to populate low energy tail of the energy distribution (see Fig. 7). There was an interesting experimental observation at LCLS that energy distribution of non-trapped particles is not uniform, but represent a kind of energy bands [30–32]. Graphs presented in Fig. 4 give a hint on the origin of energy bands which are formed by non-trapped particles. This is the consequence of nonlinear dynamics of electrons leaving the region of stability. Note that a similar effect can be seen in the early one-dimensional studies [7, 8].

Optimum Tapering of SASE FEL

The considerations on the strategy for the tapering optimization of a SASE FEL is rather straightforward. Radiation of SASE FEL consists of wavepackets (spikes). In the exponential regime of amplifications wavepackets interact strongly with the electron beam, and their group velocity visibly differs from the velocity of light. In this case the slippage of the radiation with respect to the electron beam is by several times less than kinematic slippage [9]. This feature is illustrated with the upper plot in Fig. 5 which shows onset of the nonlinear regime. We see that wavepackets are closely connected with the modulations of the electron beam current. When the amplification process enters nonlinear (tapering) stage, the group velocity of the wavepackets approaches to the velocity of light, and the relative slippage approaches to the kinematic one. When a wavepacket advances such that

ISBN 978-3-95450-134-2

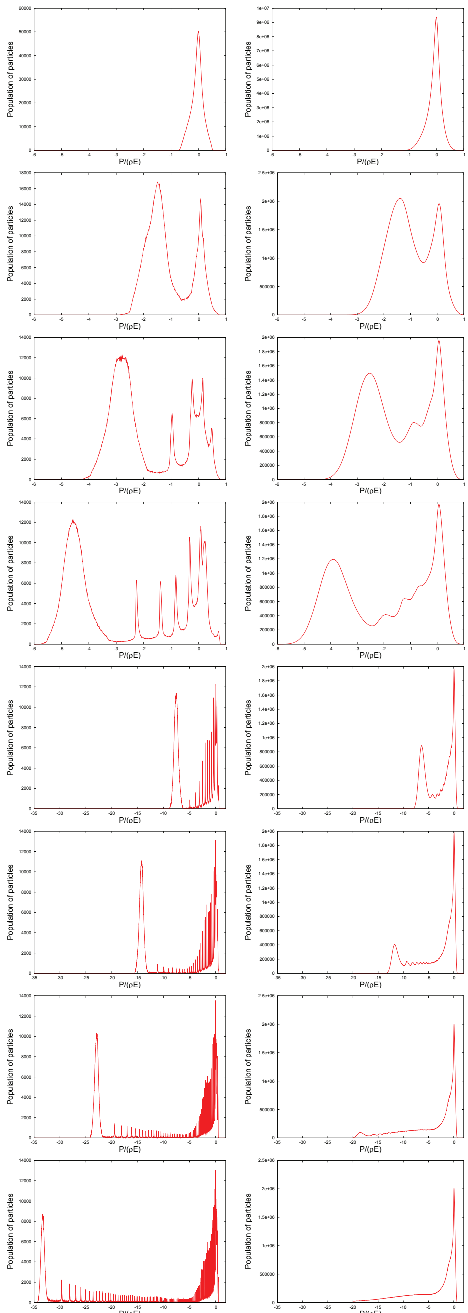

Figure 7: Population of the particles in energy at different stages of amplification. Diffraction parameter is $B = 10$. Plots from the top to the bottom correspond to $\hat{z} = 23.5$, 35.3, 39.2, 43.2, 49, 58.9, 68.7, and 78.5, respectively. Left and right columns represent seeded FEL amplifier and SASE FEL, respectively.

it reaches the next area of the beam disturbed by another wavepacket, we can easily predict that the trapping process will be destroyed, since the phases of the beam bunching and of the electromagnetic wave are uncorrelated in this case. Typical scale for the destruction of the tapering regime is coherence length, and the only physical mechanism we can use is to decrease the group velocity of wavepackets. This

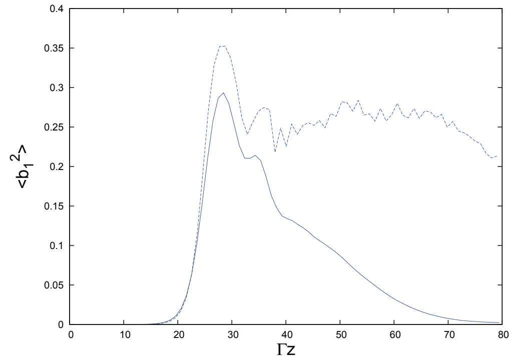

Figure 8: Evolution along the undulator of the squared value of the bunching factor for the FEL amplifier with optimized undulator tapering. Dashed and solid line represent seeded FEL amplifier and SASE FEL, respectively. Diffraction parameter is $B = 10$.

happens optimally when we trap maximum of the particles in the regime of coherent deceleration, and force these particles to interact as strong as possible with the electron beam. We see that this strategy is exactly the same as we used for optimization of seeded FEL. Global numerical optimization confirms these simple physical considerations. Conditions of the optimum tapering are the same as it has been described above for the seeded case. Start of the tapering is by two field gain lengths before the saturation. Parameter β_{tap} is the same, $8.5 \times B$. The only difference is the reduction of the parameter α_{tap} by 20% which is natural if one remember statistical nature of the wavepackets. As a result, optimum detuning is just 20% below the optimum seeded case.

We illustrate operation of SASE FEL with simulations with three-dimensional, time-dependent FEL simulation code FAST [33]. Bottom plot in Fig. 3 shows evolution of the average radiation power of SASE FEL along optimized tapered undulator. Details of the phase space distributions are traced with Figs. 4 - 6. Initially behavior of the process is pretty close to that of the seeded case. Initial values of the beam bunching is comparable with the seeded case (see Fig. 8). The rate of the energy growth is also comparable with the seeded case. The feature of the "energy bands" remains clearly visible in the case of SASE FEL as well (see Figs. 7 - 6). It is interesting observation that plots in Figs. 6 corresponding to the well trapped particles qualitatively correspond to experimental data from LCLS taken with transverse deflecting cavity [30–32].

The beam bunching gradually drop down when wavepackets travel along the bunch. As we expected, the amplification process is almost abruptly stopped when the relative slippage exceeded the coherence length. However, increase of the total radiation power with respect to the saturation power is about factor of 12.

ISBN 978-3-95450-134-2

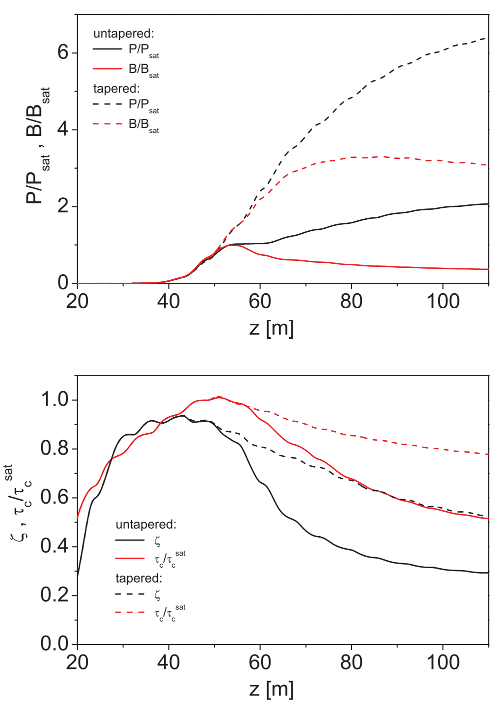

Figure 9: Fundamental harmonic: evolution of the radiation power and brilliance (top plot) and of coherence time and degree of transverse coherence (bottom plot) along the undulator for untapered (solid curves) and optimized tapered case (dashed curves).

PROPERTIES OF THE SASE RADIATION: TAPERED VERSUS UNTAPERED CASE

We perform comparative analysis of the radiation properties tapered and untapered case for the parameters of the SASE3 undulator of the European XFEL [34]. Undulator period is 6.8 cm, electron energy is 14 GeV, radiation wavelength is 1.55 nm. Undulator consists of 21 modules, each is 5 meters long with 1.1 m long intersections between modules. Parameters of the electron beam correspond to 0.25 nC case of the baseline parameters of the electron beam: emittance 0.6 mm-mrad, rms energy spread 2.5 MeV, peak beam current 5 kA [35]. Average focusing beta function is equal to 15 m. The value of the diffraction parameter is B = 1.1 which is close to the optimum conditions for reaching the maximum value of the degree of transverse coherence [36]. Two cases were simulated: untapered undulator, and the undulator optimized for maximum FEL efficiency as it has been described in previous sections [25].

Plots in Fig. 9 show evolution along the undulator of the radiation power, the degree of transverse coherence, the coherence time, and the brilliance for the fundamental harmonic. For the case of untapered undulator the coherence time and the degree of transverse coherence reach maximum values in the end of the linear regime. Maximum brilliance of the radiation is achieved in the very beginning of the nonlinear regime which is also referred as the saturation point [36]. In the case under study the saturation occurs at the undulator length of 53 m. Parameters of the radiation at the saturation point are: the radiation power is 108 GW, the coherence time is 1.2 fs, the degree of transverse coherence is 0.86, and the brilliance of the radiation is equal to 3.8×10^{22} photons/sec/mm^2/rad^2/0.1% bandwidth. The radiation characteristics plotted in Fig. 9 are normalized to the corresponding values at the saturation point.

General observations for the tapered regime are as follows. Radiation power grows faster than in the untapered tapered case. The coherence time and the degree of transverse coherence degrade, but a bit less intensive than in the untapered case. Brilliance of the radiation for the tapered case saturates at the undulator length of 80 m, and then drops down gradually. For this specific practical example the benefit of the tapered case against untapered case in terms of the radiation brilliance is factor of 3, and it is mainly defined by the corresponding increase of the radiation power. Coherence properties of the radiation in the point of the maximum brilliance of the tapered case are worse than those of the untapered SASE FEL in the saturation point: 0.86 to 0.68 for the degree of transverse coherence, and 1 to 0.86 in terms of the coherence time.

REFERENCES

[1] N.M. Kroll, P.L. Morton, and M.N. Rosenbluth, IEEE J. Quantum Electron. 17, 1436 (1981).

[2] T.J. Orzechowski, B.R. Anderson, J.C. Clark, e al., Phys. Rev. Lett. 57, 2172 (1986).

[3] R.A. Jong, E.T. Scharlemann, W.M. Fawley, Nucl. Instrum. Methods Phys. Res. A272, 99 (1988).

[4] W.M. Fawley, Nucl. Instrum. Methods Phys. Res. A375, 550 (1996).

[5] W.M. Fawley, Z. Huang, K.J. Kim, and N. Vinokurov, Nucl. Instrum. Methods Phys. Res. A483, 537 (2002).

[6] E.L. Saldin, E.A. Schneidmiller and M.V. Yurkov, Opt. Commun. 95, 141 (1993).

[7] E.T. Scharlemann, Laser Handbook, Volume 6, Free electron lasers, eds. W.B. Colson, C. Peilegrini and A. Renieri (North Holland, Amsterdam, 1991), p. 291.

[8] E.L. Saldin, E.A. Schneidmiller and M.V. Yurkov, Physics Reports 260, 187 (1995).

[9] E.L. Saldin, E.A. Schneidmiller, M.V. Yurkov, "The Physics of Free Electron Lasers" (Springer-Verlag, Berlin, 1999).

[10] E.L. Saldin, V.P. Sarantsev, E.A. Schneidmiller and M.V. Yurkov, Nucl. Instrum. and Methods A339. 583 (1994).

[11] C. Pagani, E.L. Saldin, E.A. Schneidmiller and M.V. Yurkov, Nucl. Instrum. and Methods A455, 733 (2000).

[12] E.A. Schneidmiller, V.F. Vogel, H. Weise and M.V. Yurkov, Journal of Micro/Nanolithogrphy, MEMS, and MOEMS 11(2), 021122 (2012).

[13] W. Ackermann, G. Asova, V. Ayvazyan et al., Nature Photonics 1, 336 (2007).

ISBN 978-3-95450-134-2

[14] M. Vogt, B. Faatz, J. Feldhaus et al., Proc. IPAC 2014 Conf., paper TUOCA02 (2014), http://accelconf.web.cern.ch/AccelConf/IPAC2014/papers/tupca02.pdf

[15] E. Allaria, R. Appio, L. Badano et al., Nature Photonics 6, 699 (2012).

[16] P. Emma, R. Akre, J. Arthur et al., Nature Photonics 4, 641 (2010).

[17] Tetsuya Ishikawa, Hideki Aoyagi, Takao Asaka et al., Nature Photonics 6, 540 (2012).

[18] Massimo Altarelli, Reinhard Brinkmann, Majed Chergui et al. (Eds), XFEL: The European X-Ray Free-Electron Laser. Technical Design Report, Preprint DESY 2006-097, DESY, Hamburg, 2006 (see also http://xfel.desy.de).

[19] R. Ganter (Ed.), Swiss FEL Conceptual Design Report, PSI Bericht Nr. 10-04, April 2012.

[20] H.S. Kang, K.W. Kim, I.S. Ko, Proc. IPAC 2014 Conf., paper THPRO019 (2014), http://accelconf.web.cern.ch/AccelConf/IPAC2014/papers/thpro019.pdf

[21] X.J. Wang, H.P. Freund, D. Harder et al., Phys. Rev. Lett. 103, 154801 (2009).

[22] Y. Jiao, J. Wu, Y. Cai et al., Phys. Rev. ST Accel. Beams 15, 050704 (2012).

[23] G. Geloni, V. Kocharyan, and E. Saldin, DESY Report 11-049, 2011.

[24] E.A. Schneidmiller and M.V. Yurkov, Proc. FEL2014 Conference, Basel, Switzerland, 2014, MOP065. http://accelconf.web.cern.ch/AccelConf/FEL2014/papers/mop065.pdf

[25] E.A. Schneidmiller and M.V. Yurkov, Phys. Rev. ST Accel. Beams 18, 030705 (2015).

[26] E.L. Saldin, E.A. Schneidmiller and M.V. Yurkov, Nucl. Instrum. and Methods A 475, 86 (2001).

[27] R. Bonifacio, C. Pellegrini and L.M. Narducci, Opt. Commun. 50 (1984) 373.

[28] E.L. Saldin, E.A. Schneidmiller and M.V. Yurkov, Nucl. Instrum. and Methods A539, 499 (2005).

[29] E.T. Scharlemann, A.M. Sessler, and J.S. Wurtele, Nucl. Instrum. and Methods A 239, 29 (1985).

[30] C. Behrens, Talk at the Workshop on Advanced X-Ray FEL Development, May 23, 2014, Hamburg.

[31] P. Krejcik, Talk at IPAC 2014, June 2014, Dresden, Germany. http://accelconf.web.cern.ch/AccelConf/IPAC2014/talks/weobb03/talk.pdf

[32] Y. Ding, F.-J. Decker, V.A. Dolgashev et al., Preprint SLAC-PUB-16105, SLAC National Accelerator Laboratory, 2014.

[33] E.L. Saldin, E.A. Schneidmiller, and M.V. Yurkov, Nucl. Instrum. and Methods A 429, 233 (1999).

[34] E.A. Schneidmiller and M.V. Yurkov, J. Mod. Optics (2015). DOI: 10.1080/09500340.2015.1035349

[35] E.A. Schneidmiller and M.V. Yurkov, Preprint DESY 11-152, Hamburg, 2011.

[36] E.L. Saldin, E.A. Schneidmiller, and M.V. Yurkov, Opt. Commun. 281(2008)1179.

ISBN 978-3-95450-134-2

ESTIMATE OF FREE ELECTRON LASER GAIN LENGTH IN THE PRESENCE OF ELECTRON BEAM COLLECTIVE EFFECTS*

S. Di Mitri#
Elettra Sincrotrone Trieste, 34149 Basovizza, Trieste, Italy
S. Spampinati
Department of Physics, University of Liverpool, Liverpool L69 7ZX, United Kingdom
Cockroft Institute, Sci-Tech Daresbury, Warrington WA4 4AD, United Kingdom

Abstract

A novel definition for the three-dimensional free electron laser gain length is proposed [1], which takes into account the increase of electron beam projected emittance as due, for example, to geometric transverse wakefield and coherent synchrotron radiation developing in linear accelerators. The analysis shows that the gain length is affected by an increase of the electron beam projected emittance, even though the slice (local) emittance is preserved, and found to be in agreement with Genesis code simulation results. It is then shown that the minimum gain length and the maximum of output power may notably differ from the ones derived when collective effects are neglected. The proposed model turns out to be handy for a parametric study of electron beam six-dimensional brightness and FEL performance as function, e.g., of bunch length compression factor, accelerator alignment tolerances and optics design.

WORK PLAN

Following our work in [1], which relies in turn on the formalism developed in [2,3,4]:

- We analytically evaluate the electron beam 6-D energy-normalized brightness, $B_{n,6D}$, in the presence of short-range geometric transverse wakefield (GTW) in accelerating structures and coherent synchrotron radiation (CSR) emitted in magnetic compressors. We extend our previous study [5] to include the analytical estimate of the final slice energy spread when microbunching instability (MBI) is suppressed with a laser heater [6]. This estimate makes use of the analytical model for the MBI given in [7,8].
- We show that the physical picture proposed in [4] for the beam motion in an undulator also applies to angular perturbations caused by GTW and CSR in the accelerator. Consequently, we establish an explicit connection between the FEL performance, so far only predicted on the basis of the electron bunch's slice parameters, and a more complete set of sources of $B_{n,6D}$ degradation that is including projected beam parameters.
- An analytical formula is given for estimating the self-amplified spontaneous emission (SASE) FEL [9,10] 3-D power gain length's [11] increase due to collective effects, the power saturation length and the peak power at saturation. We extend the discussion beyond SASE to the case of externally seeded FELs.

THEORETICAL MODEL

GTW and CSR offset individual "macro-slices" both in configuration and velocity spaces. The macro-slices are modelled to be as long as several cooperation lengths, since GTW and CSR-induced transverse kicks are typically correlated with z, the longitudinal coordinate internal to the bunch, on the length scale of few to hundreds microns. Neglecting for the moment any slice emittance growth from the injector to the undulator, the projected emittance growth is entirely due to mismatch of the bunch macro-slices in the transverse phase space. We take this growth into account through the mechanism described by Tanaka *et al.* [4]. In that work, the authors identify two distinct processes that increase $L_{g,1D}$. One is a lack of overlapping between the spontaneous undulator radiation, whose wavefront follows the electrons' local direction of motion, and the FEL radiation, whose wavefront is preserved when the electrons are transversally kicked by lattice errors. The other process is electrons' bunching smearing due to longitudinal dispersion of electrons transversally kicked by lattice errors.

We recognize that the electrons' angular divergence has two contributions: one is incoherent and due to the finite beam emittance as depicted in Xie's [11] and Saldin's [12] models; the other is coherent, being the tilt of the macro-slice centroids with respect to the reference trajectory. The coherent divergence adds to (and in some cases, surpasses) the incoherent one and may amplify the effect of bunching smearing. In order to take into account the coherent motion of electrons, we apply the physical picture depicted in [4] to individual macro-slices. Each macro-slice is transversally kicked by collective effects in the linac and thus moves along the undulator on a different trajectory than other macro-slices, as shown in Fig. 1.

We call $\sqrt{\langle\theta_{coll}^2\rangle}$ the rms angular divergence of the macro-slice centroids at the undulator. Being a quantity averaged over the bunch duration, $\sqrt{\langle\theta_{coll}^2\rangle}$ is an indicator of the mismatch of the macro-slices in the transverse phase space, projected onto the z-coordinate. We assume that the charge transverse distribution at the undulator is matched to some design Twiss parameters, and that a smooth optics is implemented along the

*Work supported by the FERMI project of Elettra Sincrotrone Trieste.
#simone.dimitri@elettra.eu

ISBN 978-3-95450-134-2

undulator line: β_u is the average betatron function and its variation is small along the undulator. Thus, the determinant of the so-called "sigma matrix" computed at the undulator provides the beam projected emittance as a function of $\sqrt{\langle\theta^2_{coll}\rangle}$ and β_u [1]:

$$\varepsilon_{n,f} \approx \varepsilon_{n,0}\sqrt{1+\frac{\gamma\beta_u\langle\theta^2_{coll}\rangle}{\varepsilon_{n,0}}}, \tag{1}$$

with $\varepsilon_{n,0}$, $\varepsilon_{n,f}$ being the rms initial (unperturbed) normalized and the final normalized emittance in the plane of interest, respectively, and γ the relativistic Lorentz factor at the undulator. Finally, we revise Tanaka's formula for the gain length [4] and make the following ansatz to estimate the 3-D gain length in the presence of collective effects [1]:

$$L_{g,coll} \approx \frac{L_{g,3D}}{1-\pi\langle\theta^2_{coll}\rangle/\theta^2_{th}}, \tag{2}$$

$L_{g,3D}$ is the 3-D power gain length in the sense of Xie [11]; $\theta_{th}=\sqrt{\lambda/L_{g,3D}}$ and λ the FEL wavelength. The electron beam slice transverse emittance and the slice energy spread at the undulator are taken into account in $L_{g,3D}$; the information on the degradation of the projected emittance is brought about by $\langle\theta^2_{coll}\rangle$. The range of application of Eq.2 is $\langle\theta^2_{coll}\rangle<\theta^2_{th}/\pi$; larger values of are assumed to inhibit the FEL process.

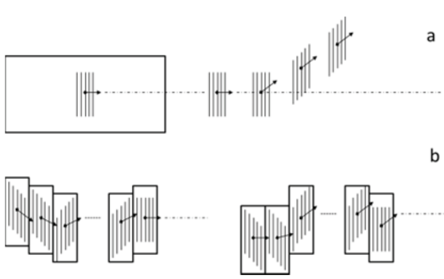

Figure 1: Effect of a transverse kick on electrons in an undulator. (a) All electrons in the bunch follow the same direction of motion as a whole. (b) Different macro-slices in the same bunch follow different directions of motion along the undulator by virtue of their initial different launching conditions. In the sketch, solid lines define the bunch (a) or a macro-slice (b); arrows indicate the electrons' direction of motion; vertical bars identify the FEL microbunch wavefront orientation. Copyright of American Physical Society [1].

DEPENDENCE ON THE BEAM OPTICS

Equation 2 aims to generalize Xie's formalism, so that $L_{g,coll}$ reduces to $L_{g,3D}$ either for null collective effects $\langle\theta^2_{coll}\rangle = 0$ or large β_u, for any *pre-set* emittance growth (see Eq.1). The dependence on β_u is explained as follows. We assume an electron beam whose normalized emittance grows along the linac according to $\Delta\varepsilon_n = \varepsilon_{n,f} - \varepsilon_{n,0}$. If such a growth only concerns the slice emittance, the gain length will be $L_{g,3D}$ according to [11]. If, instead, the emittance growth is only the projected one, and the slice emittance is preserved at the injector level, the gain length will be $L_{g,coll}$ in Eq.2. We point out that, in this modeling, the *projected* growth $\Delta\varepsilon_n$ is uniquely determined by the initial beam parameters and the linac setting and, as already said, it is due to the bunch slices' misalignment in the transverse phase space. Then, if β_u is large, as in a weak focusing undulator lattice, the macro-slices will tend to overlap in angular divergence, that is $\langle\theta^2_{coll}\rangle\to 0$, as shown in Fig. 2-d. In this case we expect $L_{g,coll}$ to approach $L_{g,3D}$. On the contrary, a small β_u as due, *e.g.,* by strong focusing, will force the macro-slice centroids to very different angular divergences. In this case $\langle\theta^2_{coll}\rangle\neq 0$ as shown in Fig. 2-c, and we expect $L_{g,coll}$ to diverge from $L_{g,3D}$.

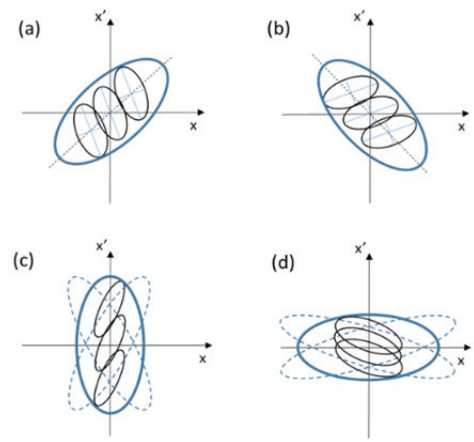

Figure 2: Mechanism of emittance growth in the transverse phase space, due to kicks by collective effects (cartoon). (a) Two macro-slices are displaced along the direction of the kick (dashed line) with respect to an unperturbed macro-slice (inner centered ellipse). The projected emittance has grown (outer ellipse). (b) Same as in (a), after $\pi/2$ betatron phase advance. The area of the outer ellipse remains constant after the kick. (c) The beam is matched at the entrance of the undulator to some design Twiss parameters. The optics is smooth in a way that Twiss parameters β and α vary little along the undulator (dashed outer ellipses). Since βu is small, the macro-slices are largely dispersed in angular divergence that is (solid line ellipse). (d) Same as in (c), but with βu large. The macro-slices largely overlap in angular divergence that is (solid line ellipse). Copyright of American Physical Society [1].

The parameters listed in Table.1 are considered for a quantitative comparison of $L_{g,coll}$ and the M.Xie-defined $L_{g,3D}$ as function of β_u, in Fig. 3. The FEL wavelength and the emittance growth were chosen in order to ensure $\langle\theta^2_{coll}\rangle<\theta^2_{th}/\pi$ over the entire range of β_u. $L_{g,3D}$ was

ISBN 978-3-95450-134-2

computed for beam slice normalized emittances of 0.5 μm (green dashed-dotted line) and 2.3 μm (red dashed line); in these cases the projected emittances coincide with the sliced values since all slices are well aligned in the phase space. $L_{g,coll}$, instead, was computed for a beam slice normalized emittance of 0.5 μm and 2.3 μm normalized projected emittance (blue solid line). The latter is determined by the misalignment of the bunch slices in the phase space. The analytical predictions are in agreement with the simulation results obtained with the Genesis code [13], over the entire range of β_u considered (symbols), thus demonstrating the validity of the proposed gain length model and its consistency with the existing 3-D theory.

Most of VUV and x-ray FELs, existing and planned, tend to have β_u small in order to maximize the transverse overlap of electrons and photons in the undulator. Figure 3 suggests that a beam focusing less tight than foreseen for an ideal beam might be more suitable in the presence of a highly diluted projected emittance.

Table 1. Parameters for the SASE FEL used to compare $L_{g,coll}$ (Eq.2) and $L_{g,3D}$ [11], as function of β_u

Parameter	Value	Unit
Energy	1.8	GeV
Peak Current	3.0	kA
Norm. Transv. Emittance at the Injector, rms	0.5	μm rad
Norm. Transv. Emittance at the Undulator, rms	2.3	μm rad
Undulator Parameter (Planar Undulator), K	√2	
Undulator Period	20	mm
FEL Parameter, 1-D (for β_u = 10m)	0.1	%

The physics depicted so far applies in principle both to SASE and to externally seeded FELs because, independently from the FEL start-up signal, they both rely on the amplification of undulator radiation through the formation of bunching at the resonance wavelength. In practice, however, in a SASE FEL the entire bunch participates to lasing, while for externally seeded FELs only the seeded potion of the electron bunch is relevant to lasing. In other words, the present analysis applies only to the lasing (seeded) portion of the electron bunch.

BRIGHTNESS AND FEL PERFORMANCE

The *electron* 6-D normalized electron beam brightness, $B_{n,6D}$, is defined as the total bunch charge over the product of the horizontal, vertical and longitudinal rms normalized *projected* emittance. The normalized longitudinal emittance is the product of bunch length and absolute energy spread. All three emittances are invariant under acceleration and linear bunch length compression, but are degraded by collective effects, i.e. CSR and GTW. These effects are modelled as angular kicks to the particles' coordinate. The final normalized emittance subjected to CSR in *n* consecutive compression stages and to GTW in *m* linac sections, is provided by the

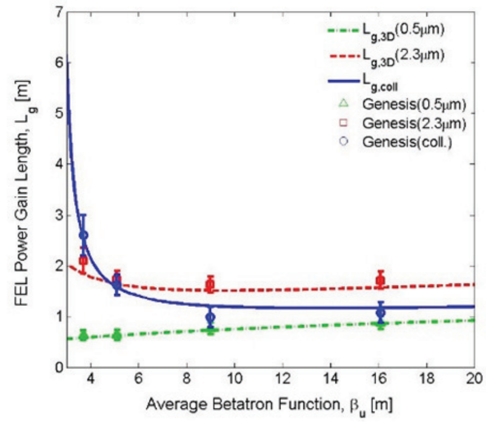

Figure 3: Gain length as function of the average betatron function in the undulator, analytical (lines) and from Genesis simulation (symbols), with parameters from Tab.1. The gain length from simulations fits the FEL power growth along the undulator. Error bars show the maximum variation of the fit value over several runs. For each run used to fit $L_{g,coll}$ (blue circles), several random distributions of the bunch's macro-slices in the transverse phase space were generated. In this case, each distribution (in each transverse plane) corresponds to a normalized projected emittance of 2.3 μm, while the slice emittance is 0.5 μm for all slices. The projected beam size is forced to fit the average betatron function selected for that run. Copyright of American Physical Society [1].

determinant of the "sigma matrix" computed at the linac end in the presence of those kicks. Since the emittance is also defined in Eq.1, we can compute $\left\langle \theta_{coll}^2 \right\rangle$ as a function of the perturbations once β_u and $\varepsilon_{n,f}$ are known.

We consider a single-pass linac driving SASE FEL in the ultra-violet wavelength range (see [1] for list of parameters). We investigated two options: one-stage compression at low energy and two-stage compression with fixed total compression factor C = C1 × C2. We then looked at $B_{n,6D}$ versus C1 to identify the compression scheme that maximizes the beam brightness for a given final peak current (1 kA), as shown in Fig. 4. That compression scheme was then used to compare in Fig. 5 the FEL 3-D output performance gain length in the presence of collective effects to those predicted by M.Xie. Finally, we selected the compression factor that minimizes $L_{g,coll}$ and, in Fig. 6, studied its sensitivity, as well as that of $B_{n,6D}$, to the linac-to-beam misalignment and the optics in the compressor.

CONCLUSIONS

We have extended the existing analytical models for the estimation of the electron beam brightness and of FEL properties – gain length, saturation length and power at saturation of a SASE FEL – by including the collective effects in the driving linac. Two major findings follow from the proposed model:

1) The degradation of the beam transverse projected emittance affects the FEL performance even though the

ISBN 978-3-95450-134-2

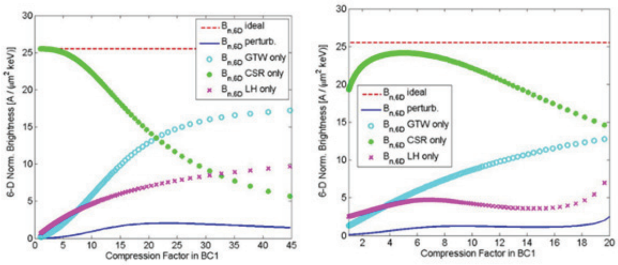

Figure 4: Analytical estimate of final $B_{n,6D}$ for the one-stage (left) and two-stage compression, as function of the compression factor in BC1. In the two-stage, the total compression factor is fixed to 20. Copyright of American Physical Society [1].

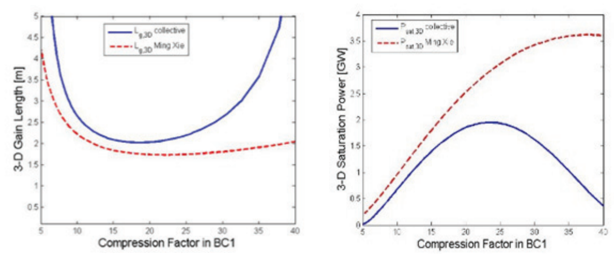

Figure 5: The 3-D gain length (left), and the 3-D SASE saturation power are evaluated in the M. Xie sense and in presence of collective effects. Copyright of American Physical Society [1].

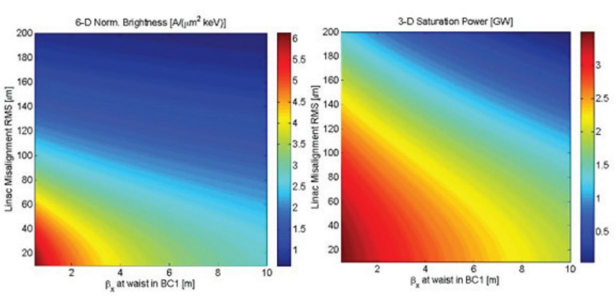

Figure 6: Contour plot of $B_{n,6D}$ (left) and $P_{sat,coll}$ as function of the rms linac-to-beam misalignment and of the minimum betatron function in BC1. A 500 pC bunch charge, compressed in one-stage by a factor 18. The final peak current is 0.9 kA. Copyright of American Physical Society [1].

slice emittance is preserved. Our analytical finding for the 3-D gain length in the presence of collective effects, *i.e.* Eq.2, is in agreement with Genesis simulation results within 5%–15% of the gain length, over the wide range of β_u considered (see Fig.3). The residual analysis *vs.* simulation discrepancy may originate from the lack of several approximations in the Genesis runs, which are instead part of our theory: the asymmetry of horizontal and vertical betatron function (at large β_u) whereas our model assumes perfect symmetry; the effect of multiple angular kicks on the bunch's macro-slices by offset quadrupole magnets, which are neglected in our model; the power gain computed from time-dependent simulations instead of the steady-state approximation (single longitudinal FEL mode), which is part of Tanaka's model.

2) The enlargement of the FEL power gain length due to a dilution of the projected emittance can be counteracted by a relatively large average betatron function in the undulator line. The optimum value of the average betatron function (*i.e.*, corresponding to the minimum gain length) turns out to be closer to the value dictated by the projected emittance with respect to that associated to the slice emittance.

Our model was then compared with that by Xie [11], with the following quantitative findings:

i) A deterioration of the FEL performance with respect to Xie's model is observed when collective effects are included. For the cases considered here, a discrepancy of ~15% between $L_{g,3D}$ and $L_{g,coll}$ is observed around the point of minimum gain length, and a much larger discrepancy at very small and very large values of C1.

ii) The collective effects halve the "good" range of C1 over which the gain length and the saturation length are little sensitive (*i.e.*, vary less than 10%) to the compression factor.

iii) The SASE power at saturation in the Xie's sense is reduced by the collective effects by a factor up to 3 in the C1 range considered.

The proposed analysis does not pretend to replace sophisticated FEL codes. Our analysis may be useful for an initial exploration of the design parameters of a high brightness linac-driven FEL and of the magnetic lattice in the undulator line. As a matter of fact, the analytical model described in this article allowed us to investigate and to optimize, as a practical case study, an accelerator layout by inspecting two compression schemes, and to scan the FEL properties vs. the compression strength, the linac-to-beam misalignment, and the betatron function in the magnetic compressor. Our study establishes the predominant influence of GTW on $B_{n,6D}$ for a high charge beam driven by an S-band linac, and that of CSR for a low charge beam in an X-band FEL driver (not shown). We observed a net dependence of the FEL saturation power on $B_{n,6D}$. We also found that the gain length and the saturation length can be made quite insensitive to the linac-to-beam misalignment (*i.e.*, GTW instability) and to the optics in the compressor (*i.e.*, CSR instability) with a proper choice of the compression scheme and strength.

ACKNOWLEDGEMENTS

The authors are in debt with M. Cornacchia for his encouragement, and with W. Fawley for stimulating discussions about the dependence of FEL performance on the beam optics. We acknowledge A. Zholents for his suggestion to extend our work to the 6-D brightness, and E. Allaria and for his advices on FEL physics. This work was funded by the FERMI project of Elettra Sincrotrone Trieste.

ISBN 978-3-95450-134-2

REFERENCES

[1] S. Di Mitri and S. Spampinati, Phys. Rev. Special Topics – Accel. Beams **17**, 110702 (2014).

[2] M. Xie, in Proc. of Part. Accel. Conf. 1995, TPG10, IEEE (1996).

[3] E. L. Saldin, E. A. Schneidmiller and M. V. Yurkov, in Proc. of the 26th Free Electron laser Conf., MOPOS15, Trieste, Italy (2004).

[4] T. Tanaka, H. Kitamura and T. Shintake, Nucl. Instrum. Methods Phys. Research A **528** (2004) 172–178.

[5] S. Di Mitri, Phys. Rev. Special Topics – Accel. Beams **16**, 050701 (2013).

[6] E. L. Saldin, E. A. Schneidmiller and M. V. Yurkov, Nucl. Instrum. Methods Phys. Res., Sect. A **528** (2004) 355.

[7] Z. Huang and K.-J- Kim, Phys. Rev. Special Topics – Accel. Beams **5**, 074401 (2002).

[8] Z. Huang, M. Borland, P. Emma, J. Wu, C. Limborg, G. Stupakov and J. Welch, Phys. Rev. Special Topics – Accel. Beams **7**, 074401 (2004).

[9] R. Bonifacio, C. Pellegrini and L. Narducci, Opt. Commun. **50** (1984) 373-378.

[10] A. M. Kondratenko and E.L. Saldin, Part. Accel. **10** (1980) 207–216.

[11] M. Xie, in Proc. of Part. Accel. Conf. 1995, TPG10, IEEE (1996).

[12] L. Saldin, E. A. Schneidmiller and M. V. Yurkov, in Proc. of the 26th Free Electron laser Conf., MOPOS15, Trieste, Italy (2004).

[13] S. Reiche et al., in Proc. of the 22nd Part. Accel. Conf., TUPMS038, Albuquerque, NM, USA (2007): http://pbpl.physics.ucla.edu/

ISBN 978-3-95450-134-2

OPERATING OF SXFEL IN A SINGLE STAGE HIGH GAIN HARMONIC GENERATION SCHEME

Guanglei Wang, Weiqing Zhang, Guorong Wu, Dongxu Dai, Xueming Yang#
State Key Laboratory of Molecular Reaction Dynamics, Dalian Institute of Chemical Physics, Chinese Academy of Sciences, Dalian 116023, P. R. China

Abstract

The beam energy spread at the entrance of undulator system is of paramount importance for efficient density modulation in high-gain seeded free-electron lasers (FELs). In this paper, the dependencies of high harmonic bunching efficiency in the high-gain harmonic generation (HGHG) schemes on the electron energy spread distribution are studied. Theoretical investigations and multi-dimensional numerical simulations are applied to the cases of uniform and saddle beam energy distributions and compared to a traditional Gaussian distribution. It shows that the uniform and saddle electron energy distributions significantly enhance the performance of HGHG-FELs. A numerical example demonstrates that, with the saddle distribution of sliced beam energy spread controlled by a laser heater, the 30th harmonic radiation can be directly generated by a single-stage seeding scheme for a soft x-ray FEL facility.

INTRODUCTION

In recent years, enormous progresses have been achieved in the seeded free-electron lasers (FELs), which hold great potential to deliver high brilliance radiation pulses with excellent longitudinal coherence in the extreme ultraviolet and even x-ray regions. The first seeding scheme, i.e., high-gain harmonic generation (HGHG) has been fully demonstrated at BNL [1-4] and is currently used to deliver coherent extreme ultraviolet FEL pulses to users at FERMI [5]. For a long time, it is thought that the frequency multiplication factor of a single-stage HGHG is usually limited within ~10 [1,6], due to the tradeoff between the energy modulation and the energy spread requirement for exponential amplification process of FEL. Therefore, a complicated multi-stage HGHG scheme [7-9] has been theoretically proposed and experimentally demonstrated for short wavelength production from a commercially available seed laser.

Up to now, the bunching performance assessment for seeded FELs is on the basis of assumption that the electron beam at the entrance of undulator has an energy spread of Gaussian distribution, which however is not true, e. g., in the specific case with a laser heater in the LINAC [10-11]. Laser heater is widely utilized in high-gain FEL facilities to suppress the gain of the micro-bunching instability via Landau damping by controllable increasing the beam energy spread. It is found that a non-Gaussian energy distribution can be induced by a laser heater and inherited in the main LINAC section, depending upon details of the transverse overlap between the laser beam and the electron beam in the laser heater system. A recent experiment at FERMI [5,12] demonstrates that the non-Gaussian beam energy spread induced by the laser heater may expand the harmonic number of a single-stage HGHG to several tens [13-14]. Meanwhile, one cannot exclude other unknown schemes lie beyond the horizon for controlling beam energy spread distribution in future.

Considering that the initial energy distribution of electron beam is one of the most critical elements in the bunching process of seeded FELs, in this paper, the possible beam energy distribution influences on density modulation efficiency in various seeded FEL schemes have been studied. In Section II, by using a set of nominal parameters of Shanghai soft x-ray free-electron laser facility (SXFEL) [15], the bunching efficiencies in HGHG schemes with different electron beam energy spread distribution are theoretically derived and numerically simulated, which shows that the uniform and saddle cases may significantly enhance the bunching performance of HGHG. It indicates that the beam energy distribution is of great importance for HGHG scheme, the frequency up-conversion number of a single-stage HGHG can be improved to 30 or even higher with a uniform or saddle electron energy distribution. A followed start-to-end example in Section III demonstrated that the saddle distribution of sliced beam energy spread controlled by a laser-heater can be maintained in the following accelerations of LINAC, and the saddle beam energy distribution is capable of driving a 30^{th} harmonic up-conversion in a single-stage HGHG operation of SXFEL, even though it has a larger sliced beam energy spread than a Gaussian case. Finally, we present our conclusions in Section IV.

ENERGY SPREAD DISTRIBUTION EFFECTS ON SEEDING SCHEME

In order to obtain a comprehensible idea of the energy spread distribution effects on different seeded configurations, by using the nominal parameters of SXFEL, uniform and saddle energy spread distributions are investigated for the density modulation process and compared to the previous Gaussian distribution case in this section, under the same RMS deviation, i.e., beam energy spread. SXFEL aims at generating coherent 8.8 nm FEL pulses from 264 nm seed laser through a two-stage HGHG. In the nominal design of SXFEL, an 840 MeV electron beam with sliced energy spread of 84 keV, i.e., a relative energy spread of 1×10^{-4},

#xmyang@dicp.ac.cn

ISBN 978-3-95450-134-2

normalized emittance of 1.0 μm-rad, bunch charge of 500 pC, and peak current of 500 A is expected at the exit of the LINAC for efficient FEL lasing. The sliced beam energy distributions used in the frame of analysis of this section are summarized in Fig. 1.

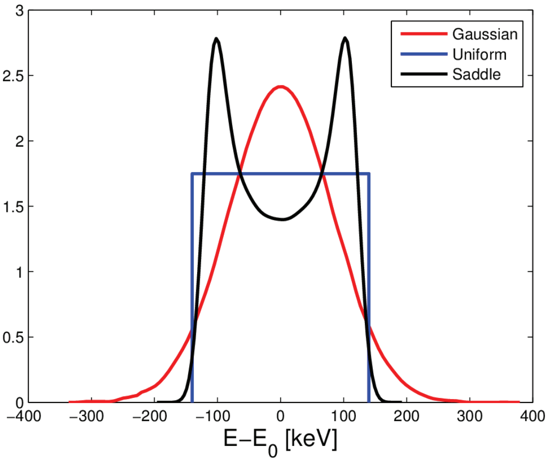

Figure 1: The different beam energy distributions with RMS energy spread of 84keV for the studies in this Section.

It is necessary to take some words to describe the saddle distribution before we step forward, while the Gaussian and uniform distributions are quite straight. As is well known, laser-heaters used for micro-bunching instability suppression in modern high-brightness LINACs have shown the possibility to control the RMS deviation and the distribution shape of sliced beam energy spread by choosing the laser spot size and the peak power [10,13]. In more detail, in the LINAC of SXFEL, electrons from the photo-injector are firstly accelerated up to 130 MeV, and then sent into the laser heater system where a 792 nm Ti-sapphire laser with the pulse length of 10 ps are used to increase the RMS energy spread from 2 keV to about 8.4 keV. After a total longitudinal compression factor of about 10, the sliced RMS energy spread should be about 84 keV at the undulator entrance (at 840 MeV) in the absence of impedance effects. If one supposes a fundamental Gaussian mode laser with spot much larger than the electron beam size co-propagates with a Gaussian electron beam in the laser heater undulator, the energy modulation amplitude is almost the same for all electrons, and the energy profile of heated beam is possibly a saddle distribution, as the black shown in Fig. 1.

Among the various seeding schemes, HGHG is the most compact and pioneering. The high harmonic bunching of HGHG can be described as [16]:

$$b = J_h(h\Delta\gamma_s D)\int dp f(p)e^{-ihD\sigma_E p}, \tag{1}$$

where h is the harmonic number, $D = k_s R_{56}/\gamma$, k_s is the wave number of the seed laser, R_{56} is the strength of the dispersive chicane, γ is the electron beam Lorentz factor, $\Delta\gamma_s$ is the seed laser-induced energy modulation amplitude and J_h is the h^{th} order Bessel function, $p = (E - E_0)/\sigma_E$ is the dimensionless energy deviation of a particle with an average energy E_0 and RMS energy spread σ_E, $f(p)$ is the initial longitudinal phase space distribution. For a Gaussian energy distribution, following Eq. (1), the bunching factor can be written as,

$$b_G = J_h(hD\Delta\gamma_s)\exp(-\frac{h^2D^2\sigma_E^2}{2}). \tag{2}$$

For a saddle distribution, which is caused by the energy modulation process in laser heater, using the notations in ref. [13], i.e., the net longitudinal bunch length compression between the laser heater and the main undulator C, the energy modulation induced in the laser heater system $\Delta\gamma_h$ and the energy spread at the exit of the photo-injector σ_H, the bunching factor can be written as [10, 13],

$$b_S = \left|J_h(hD\Delta\gamma_s)\exp(-\frac{h^2\sigma_H^2C^2D^2}{2})\times J_0(hCD\Delta\gamma_h)\right|. \tag{3}$$

The predictions made by Eq. (2) has been analyzed intensively in Ref. [11]. The bunching factor draw back fast for a Gaussian energy distribution and this feature limits the feasibility of HGHG at high harmonics. For the non-Gaussian case, FERMI's experiment results show an FEL output pulse energy oscillation with the increase of the laser heating [13], which is a meaningful demonstration of Eq. (3).

If we assume a more ideal case that the electron energy is uniformly distributed between [E_0-τ/2, E_0+τ/2], the RMS energy spread is then changed to $\sigma_E = 0.5\tau/\sqrt{3}$. According to Eq. (1) and the law of Fourier transform for a rectangular pulse [17], the bunching factor for the uniform energy distribution at h^{th} harmonic can be presented as

$$b_U = J_h(hD\Delta\gamma_s)\left|Sinc(hD\tau/2)\right|. \tag{4}$$

To verify the abovementioned theoretical predictions and compare different cases, we carry out the single frequency simulations using the universal FEL simulating code GENESIS [18]. In these simulations, we take the main parameters of SXFEL as an example to illustrate the effects of different energy distribution on FEL density modulation process. Considering that the effective energy spread induced by the seed laser in HGHG is limited by the FEL parameter ρ for the requirement of exponential amplification in the final 8.8nm radiator, the energy modulation amplitude $A = \Delta E/\sigma_E$ is chosen to be about 5, and the optimal dispersive strength is chosen to be $k_1R_{56}A \approx 1.2$ here.

Figure 2 shows the bunching factor distributions at various harmonic numbers for different cases. The bunching factor oscillations are clearly seen for the uniform and saddle energy spread distribution cases. The

ISBN 978-3-95450-134-2

amplitudes of the oscillations can be adjusted by setting the energy modulation amplitude and the strength of dispersive chicane. The simulation dots are all at the vicinity of the theoretical value, which is in good agreement with the derivation of Eqs. (2)-(4). This kind of bunching factor oscillation can be used to significantly extend the tuning range of the output wavelength of a single-stage HGHG down to very high harmonics, and makes the generation of soft X-ray FEL pulses in a single-stage HGHG possible.

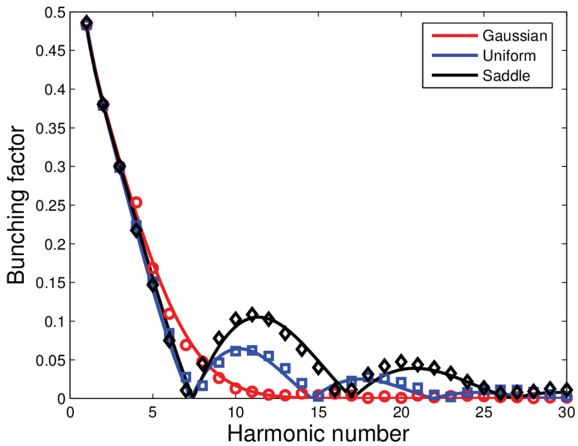

Figure 2: The evolution of bunching factor with the harmonic number, the red circle is Gaussian results, blue square and the black diamond is for uniform and saddle respectively, the corresponding color line is theoretical derivation of Eqs. (2)-(4).

OPERATING SXFEL WITH SINGLE-STAGE HGHG

It has been widely discussed that, seeded FELs with total frequency up-conversion factor of 30, e.g., SXFEL. In this section, we discuss the feasibility of operating SXFEL with a single-stage HGHG, by properly handling the distribution of the sliced beam energy spread with the laser heater.

It is widely known that, the Landau damping of the micro-bunching instability in the electron beam with a Gaussian energy spread is much more efficient than that with a saddle one. It means that, in order to achieve the same suppression of the micro-bunching instability, a larger laser energy in the laser heater, or equivalently a larger RMS deviation of the electron energy distribution could be needed for the non-Gaussian case. Therefore, to clearly understand and state the tradeoff of using a saddle-like energy distribution instead of the Gaussian one for seeded FELs, start-to-end tracking of the electron beam, including all the components of SXFEL has been carried out. The electron beam dynamics in the photo-injector was simulated with ASTRA [19] to take into account space-charge effects. ELEGANT [20] was then used for the simulation in the remainder of the LINAC. For simplicity, one bunch compressor setup of SXFEL is considered.

In the simulation, the total energy spread of about 20 keV is obtained in the absence of all the impedance effects, i.e., the energy sliced energy spread at the exit of photon injector of ~2 keV and the bunch compression factor of 10. In further micro-bunching studies, we first switch off the laser heater, and it is found that the typical sliced beam energy spread is 54 keV at the exit of LINAC. Then two laser-heater cases with the laser size of 0.3 mm and 1.2 mm are considered, respectively, while the electron beam size in the heater is 0.3 mm in both cases. The laser energy is independently optimized to obtain a better micro-bunching suppression, i.e., a lower sliced beam energy spread here for each case. The energy distribution at the exit of the LINAC is shown in Fig. 3. According to the simulation, the beam energy distribution shape controlled by the laser-heater can be maintained in the LINAC. The optimal energy spread is about 27 keV and 38 keV for Gaussian and saddle case, which are both better than the case without laser heater. In other words, it results more micro-bunching and larger energy spread in the saddle case than in the Gaussian one.

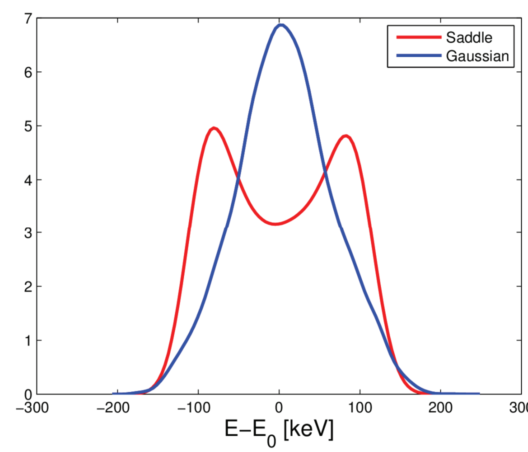

Figure 3: The saddle and Gaussian sliced beam energy distribution at the exit of the LINAC.

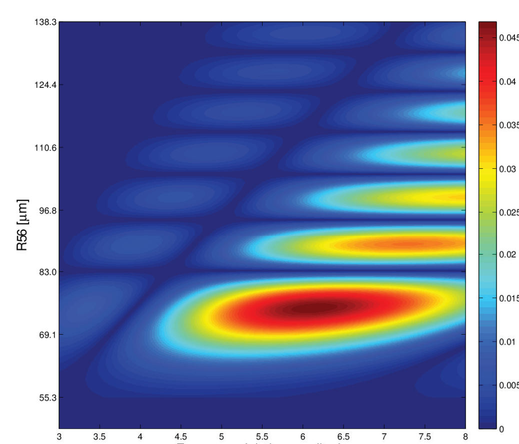

Figure 4: The 30th harmonic bunching factor in a single-stage HGHG v.s. the energy modulation amplitude and the strength of the dispersion. A saddle-like energy distribution from ELEGANT with a RMS energy spread of 38 keV is used.

ISBN 978-3-95450-134-2

According to the previous results, the bunching factor of HGHG can be significantly enhanced with a saddle energy distribution. Using the tracked saddle-like energy distribution, the optimized 30th harmonic bunching factor as a function of the HGHG scheme setup is shown in Fig. 4. One can find that the 30th harmonic bunching factor could be more than 4% for energy modulation amplitude A around 6, which is strong enough for driving intense coherent radiation at the beginning of the radiator. Moreover, in view of the tradeoff between the seed laser induced energy spread and the available bunching factor, a moderate modulation amplitude of A = 6.5 is chosen for FEL gain process in the radiator.

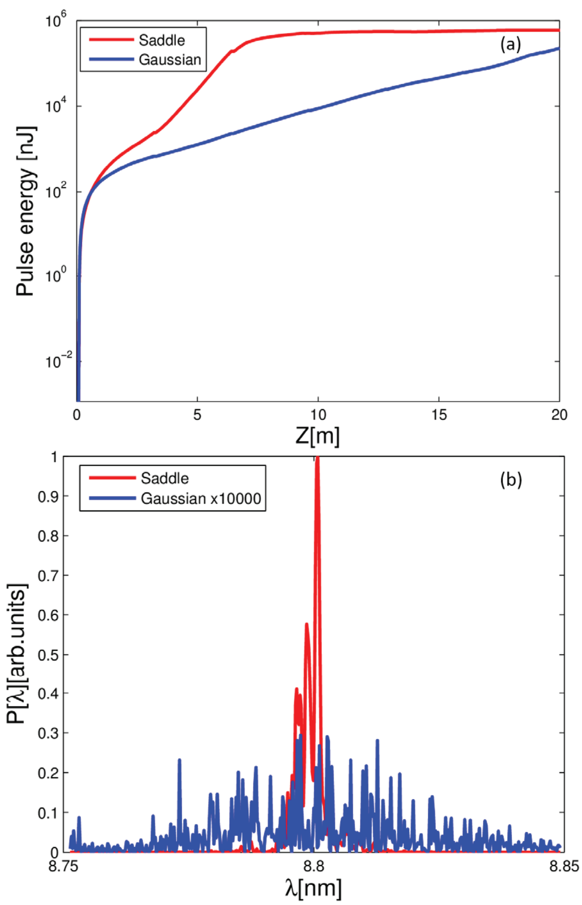

Figure 5: Comparison of final 8.8 nm radiation pulse energy (a) and spectra (b) of SXFEL with a single-stage HGHG. The spectra are exported at the undulator position of 10 m, where the saddle distribution is almost saturated, while the Gaussian one is still in exponential gain regime.

In the FEL simulation, the saddle energy distributions from ELEGANT are artificially imported to GENESIS [18] at the entrance of the modulator undulator. The FWHM pulse duration of the 264nm seed laser is supposed to be 500fs. In order to fairly compare the HGHG performance for both Gaussian and saddle distributions, the energy spread induced by the seed laser is assumed to be same in both cases. Figure 5 shows the comparison of output pulse energy along the radiator and the output spectra. The saddle energy spread beam drives a strong coherent radiation at the beginning of the radiator and the saturation length is about 10m, while the Gaussian one almost starts from shot noise and a much longer radiator is required. After passing through 10 m long radiator, the relative FWHM bandwidth of saddle case is about 0.05% and 5 times narrower than the Gaussian distribution. The noisy spike and FEL spectrum broaden in the saddle case is induced mainly by the nonlinear energy chirp in the electron beam [21-24]. It is worth stressing that with the recent technology [25-26], the FEL performance can be future improved by removing the beam energy curvature [27].

CONCLUSION

In this paper, the sliced energy distribution effects on the bunching process in seeded FELs are investigated by using theoretical analysis and numerical simulations. It is found that a bunching factor oscillation happens in HGHG for uniform and saddle distributions. Moreover, such a bunching factor oscillation in HGHG can be adjusted by setting the energy modulation amplitude and the strength of the dispersive chicane, thus to obtain a large bunching factor at high harmonics.

For the single-stage HGHG operation of a soft X-ray FEL, the start-to-end example in this paper demonstrates that the 30th or even higher harmonic is possible with a moderate energy spread control by using the laser-heater system in the LINAC, even though the saddle distribution has a larger sliced beam energy spread than a Gaussian case. Thus, by manipulating the energy spread distribution, a single-stage HGHG may be used to cover much larger harmonic range than the theoretical predictions under the assumption of Gaussian beam energy spread distribution. However, in order to avoid the temporal coherence degradation due to the nonlinear beam energy curvature, a much shorter seed laser is preferred for high harmonic operation of single-stage HGHG.

Finally, it is worth emphasizing that the control of the sliced beam energy spread, both RMS deviation and shape is quietly related to many issues, e.g., the required suppression of the micro-bunching instability, the detailed LINAC setup, and the FEL performances in pursuit. In general, larger laser heater energy, or equivalently a larger RMS for the electron energy distribution may be needed in non-Gaussian case. Then for a real FEL machine, except the robust design and self-consistent start-to-end beam tracking, it is likely that the machine flexibility, the accuracy of beam energy spread measurement, the commissioning experiences and efforts will determine the frequency up-conversion limit achievable for different seeded FELs.

ACKNOWLEDGEMENT

The authors are grateful to Bo Liu and Dao Xiang for helpful discussions. This work was supported by the National Natural Science Foundation of China (21127902, 11175240, 11205234 and 11322550).

REFERENCES

[1] L. H. Yu, Phys. Rev. A **44**, 5178 (1991).
[2] L. H. Yu et al., Science **289**, 932 (2000).
[3] L. H. Yu et al., Phys. Rev. Lett. **91**, 074801 (2003).
[4] T. Shaftan, and L. H. Yu, Phys. Rev. E **71**, 046501 (2005).
[5] E. Allaria et al., Nature Photonics **6**, 699 (2012).
[6] R. Bonifacio et al., Riv. Nuovo Cimento, **17**, 9 (1990).
[7] J. Wu and L. H. Yu, Nucl. Instrum. Methods Phys. Res., Sect. A **475**, 104 (2001).
[8] B. Liu et al., Phys. Rev. ST Accel. Beams **16**, 020704 (2013).
[9] E. Allaria et al., Nature Photonics **7**, 913 (2013).
[10] Z. Huang et al., Phys. Rev. ST Accel. Beams **7**, 074401 (2004).
[11] Z. Huang et al., Phys. Rev. ST Accel. Beams **13**, 020703 (2010).
[12] G. Dattoli et al., arXiv:1410.6614.
[13] E. Ferrari et al., Phys. Rev. Lett. **112**, 114802 (2014).
[14] S. Spampinati et al., Phys. Rev. ST Accel. Beams 17, 120705 (2014).
[15] J. Yan, M. Zhang, and H. Deng, Nucl. Instrum. Methods Phys. Res., Sect. A **615**, 249 (2010).
[16] K. J. Kim, Z. Huang, and R. Lindberg, Synchrotron Radiation and Free Electron Lasers, Principles of Coherent X-Ray Generation, (2014).
[17] Bochner S., Chandrasekharan K., Fourier Transforms, Princeton University Press, (1949).
[18] S. Reiche, Nucl. Instrum. Methods Phys. Res., Sect. A **429**, 243 (1999).
[19] K. Flottmann, ASTRA User Manual, http://www.desy.de/~mpyflo
[20] M. Borland, ANL Advanced Photon Source, Report No. LS-287, 2000.
[21] E. L. Saldin et al., Optics Communications **202**, 169 (2002).
[22] D. Ratner, A. Fry, G. Stupakov, and W. White, Phys. Rev. ST Accel. Beams **15**, 030702 (2012).
[23] C. Feng et al., Phys. Rev. ST Accel. Beams **16**, 070605 (2013).
[24] G. Wang et al., Nucl. Instrum. Methods Phys. Res., Sect. A **753**, 56 (2014).
[25] K. Bane and G. Stupakov, Nucl. Instrum. Methods Phys. Res., Sect. A **690**, 106 (2012).
[26] P. Emma et al., Phys. Rev. Lett. **112**, 034801 (2014).
[27] H. Deng et al., Phys. Rev. Lett. **113**, 254802 (2014).

ISBN 978-3-95450-134-2

INFLUENCE OF HORIZANTAL CONSTANT MAGNETIC FIELD ON HARMONIC UNDULATOR RADIATIONS AND GAIN

H. Jeevakhan, P. K. Purohit, Applied Science Department,NITTTR, Bhopal, India
G Mishra, SOP, DAVV, Indore, India

Abstract

Harmonic undulators has been analyzed in the presence of constant magnetic field along the direction perpendicular to the main undulator field. Effect of constant magnetic field magnitude on trajectory of electron beam, intensity of radiation and FEL gain at fundamental and third harmonics has been evaluated. Performance of harmonic undulator in the presence horizontal component of earth's magnetic field is the practical realization of the suggested scheme

INTRODUCTION

Current researches in science calls for an ultrafast, high brightness and X –ray light source . Fourth generation FEL systems are use to lase at X ray wavelength region [1, 2]. FEL is produced by interaction of relativistic electron beam, an electromagnetic wave travelling in the same direction and undulator. FEL differs from other conventional lasing systems in terms of operation mechanism and assembly as well [3, 4]. Novel design and error analysis of undulator are among the major and important part in FEL research. Concept of Harmonic undulator is given to use undulator assembly with slight modification and radiating lower wavelength with modest electron beam. Structure of undulator is optimized to enhance the output radiation and gain in FEL systems [5-9].

In this paper we have modeled an harmonic undulator with additional horizontal magnetic field. In real applications this component can be realized with earth's horizontal magnetic field component. In the related work, K Zhukovsky has given an analytical model and discus the effect of horizontal field constituent of undulator radiation and compare it with other factor such as energy spread in beam, emittance and focusing components [10]. N. O. Strelnikov et al presents experimental and modeling results concerning the effects of the interaction of Earth's magnetic field with different types of Insertion devices [11]. In the previous paper [9], we have presented semi analytical results for the effect of constant magnetic field along the direction parallel to undulator field. In this paper we have added a constant field perpendicular to undulator field. The effect of additional field in horizontal direction on harmonic undulator radiations and gain has been analyzed.

UNDULATOR FIELD

We have considered a constant magnetic field in the direction perpendicular to planar undulator magnetic field encompass with harmonic field

$$B = [B_0\kappa, a_0 B_0 sink_u z + a_1 B_0 sinhk_u z, 0] \tag{1}$$

where, $k_u = \frac{2\pi}{\lambda_u}$ undulator wave number, λ_u is undulator wave length, h is harmonic integer, B_0 is peak magnetic field, a_0 and a_1 controls the ratio of main undulator field to additional harmonic field κ is the magnitude of constant magnetic field. For practical purpose it is replica of horizontal component of earth magnetic field.

The velocity can be evaluated by using Lorentz force equation:

$$\frac{dv}{dt} = -\frac{e}{\gamma mc}(\vec{v} \times \vec{B}) \tag{2}$$

This gives

$$\beta_x = -\frac{K}{\gamma}\left[\cos(\Omega_u t) + \Delta\frac{\cos(h\Omega_u t)}{h}\right]$$

$$\beta_y = -\frac{K}{\gamma}[\kappa\Omega_u t] \tag{3}$$

$$\beta_z = \beta^* - \frac{K^2}{2\gamma^2}\left[\frac{1}{2}\cos(2\Omega_u t) + \frac{1}{2}\left(\frac{\Delta}{h}\right)^2\cos(2h\Omega_u t) + \left(\frac{\Delta}{h}\right)\cos(1+h)\Omega_u t + \left(\frac{\Delta}{h}\right)\cos(1-h)\Omega_u t + (\kappa\Omega_u t)^2\right] \tag{4}$$

where $K = \frac{a_0 e B_0}{\Omega_u m_0 c}$ is the undulator parameter and $\Delta = \frac{a_1}{a_0}$, and $\beta^* = 1 - \frac{1}{2\gamma^2}\left[1 + \frac{K^2+K_1^2}{2}\right]$ with $K_1 = \frac{\Delta K}{h}$.

The electron trajectory along z direction is given by

$$\frac{z}{c} = \beta^* t - \frac{K^2}{8\gamma^2\Omega_u}\sin(2\Omega_u t) - \frac{K_1^2}{8\gamma^2 h\Omega_u}\sin(2h\Omega_u t) - \frac{KK_1}{2\gamma^2(1-h)\Omega_u}\sin(1-h)\,\Omega_u t - \frac{KK_1}{2\gamma^2(1+h)\Omega_u}\sin(1+h)\,\Omega_u t - \frac{K^2\kappa^2{\Omega_u}^2 t^3}{6\gamma^2} \tag{5}$$

The spectral properties of radiation can be evaluated from Lienard-Wiechart integral [12],

$$\frac{d^2 I}{d\omega d\Omega} = \frac{e^2\omega^2}{4\pi^2 c}\left|\int_{-\infty}^{\infty}\{\hat{n} \times (\hat{n} \times \hat{\beta}\} exp\left[i\omega(t - \frac{z}{c})\right] dt\right| \tag{6}$$

where the integration is carried over undulator length, $T = \frac{2N\pi}{\Omega_u}$ and ω is the emission frequency. Introducing the variables

$$z_1 = -\frac{\omega K^2}{8\gamma^2\Omega_u}, \qquad z_2 = -\frac{\omega K_1^2}{8\gamma^2 h\Omega_u},$$

$$z_3 = -\frac{\omega KK_1}{2\gamma^2(1-h)\Omega_u} \text{ and } z_4 = -\frac{\omega KK_1\kappa}{2\gamma^2(1+h)\Omega_u}.$$

The brightness expression is reduced to

ISBN 978-3-95450-134-2

$$\frac{d^2I}{d\omega d\Omega} = \frac{e^2\omega^2}{4\pi^2 c}\left(\frac{K}{\gamma}\right)^2\left[\left|\hat{\imath}\int_0^T dt\left\{cos(\Omega_u t) + \frac{\Delta}{h}cos(h\Omega_u t)\right\}expi(\Phi t + \Psi t^3)J_m(0,z_1)J_n(0,z_2)J_p(z_3)J_q(z_4)\right|^2 + \left|\hat{\jmath}\int_0^T dt\{\kappa\Omega_u t\}\, expi(\Phi t + \Psi t^3)J_m(0,z_1)J_n(0,z_2)J_p(z_3)J_q(z_4)\right|^2\right] \quad (7)$$

$$\Phi = \frac{\omega}{\omega_1} - m\Omega_u - nh\Omega_u - p(1-h)\Omega_u - q(1+h)\Omega_u$$

$$\Psi = \frac{\omega K^2\kappa^2\Omega_u{}^2}{6\gamma^2}$$

and Eq. (7) can be further reduced to

$$\frac{d^2I}{d\omega d\Omega} = \frac{e^2\omega^2 T^2}{4\pi^2 c}\left\{|T_x|^2\, S(\Phi,\Psi) + |T_y|^2\frac{\partial S(\Phi,\Psi)}{\partial\Phi}\right\} \quad (8)$$

with

$$T_x = \frac{K}{2\gamma}\Big[\{J_{m+1}(0,z_1) + J_{m-1}(0,z_1)\}J_n(0,z_2)J_p(z_3)J_q(z_4) + \frac{\Delta}{h}\{J_{n+1}(0,z_2) + J_{n-1}(0,z_2)\}J_m(0,z_1)J_p(z_3)J_q(z_4)\Big]$$

$$T_y = \frac{2i\pi K\kappa N}{\gamma}$$

and $S(\Phi,\Psi) = \left|\int_0^1 \mathrm{e}^{(\Phi\tau+\Psi\tau^3)}\mathrm{d}\tau\right|^2$ and $\tau = {}^{t}/_{T}$ is unit interaction time.

FEL Gain

To calculate the small signal gain of the harmonic undulator with constant magnetic field, let us consider a radiation field as,

$$\vec{E} = E_0\cos(\psi)\hat{x} \quad (9)$$

where, $\psi = n_1 k_1 z - n_1\omega_1 t + \varphi$. n_1=1, 2, 3…. are the emission harmonics and φ is the phase of the electron with the radiation field. The change in energy of the electron is given by,

$$\frac{d\gamma}{dt} = -\frac{e}{m_0 c}\left[\vec{E}.\vec{\beta}\right] \quad (10)$$

Eq. (3) & Eq. (9) are used to solve Eq.(10) and we obtain,

$$\frac{d\gamma}{dt} = \frac{eE_0K}{2m_0c\gamma}\left[\begin{matrix}\{\cos(\psi+k_u z)+\cos(\psi-k_u z)\}\\ +(\Delta/h)\{\cos(\psi+k_h z)+\cos(\psi-k_h z)\}\end{matrix}\right] \quad (11)$$

The electron longitudinal motion from Eq. (5) is expressed by,

$$z = \bar{z} + \Delta z$$

where

$$\bar{z} = \beta^* ct - \frac{K^2\kappa^2\Omega_u{}^2 t^3}{6\gamma^2}$$

$$\Delta z = -\frac{K^2 c}{8\gamma^2\Omega_u}sin(2\Omega_u t) - \frac{K_1^2 c}{8\gamma^2 h\Omega_u}sin(2h\Omega_u t) - \frac{KK_1 c}{2\gamma^2(1-h)\Omega_u}sin(1-h)\,\Omega_u t - \frac{KK_1 c}{2\gamma^2(1+h)\Omega_u}sin(1+h)\,\Omega_u t \quad (12)$$

Using Eq.(12) ,the phase terms appearing in Eq.(11) are simplified to read as,

$$\psi \pm (k_u z) = n_1\xi + \varphi + n_1 k_1\Delta z - (n_1 \mp 1)k_u z - n_1 k_h z - n_1(1-h)k_u z - n_1(1+h)k_u z$$

$$\psi \pm (k_h z) = n_1\xi + \varphi + n_1 k_1\Delta z - (n_1 \mp 1)k_h z - n_1 k_u z - n_1(1-h)k_u z - n_1(1+h)k_u z \quad (13)$$

where,

$$\xi = (k_1 + k_u + k_h + (1+h)k_u + (1-h)k_u)\bar{z} - \omega_1 t.$$

Using, Eq. (13), Eq. (11) is simplified after averaging over the undulator to find ,

$$\frac{d\gamma}{d\tau} = \frac{eKE_0L_u}{2\gamma m_0 c^2}[b_0 + (\Delta/h)b_1]\cos(n_1\xi + \varphi) \quad (14)$$

$$b_0 = \{J_{m+1}(0,z_1) + J_{m-1}(0,z_1)\}J_n(0,z_2)J_p(z_3)J_q(z_4)$$

$$b_1 = \{J_{n+1}(0,z_2) + J_{m-1}(0,z_2)\}J_m(0,z_1)J_p(z_3)J_q(z_4)$$

Expressing,

$$n_1\frac{d^2\xi}{d\tau^2} = \frac{4\pi N}{\gamma}\left[n_1 + \frac{3\Psi\tau^2 L_u^2}{\Omega_u c^2}\right]\frac{d\gamma}{d\tau} - 6\Psi\tau\mathrm{T}^3 \quad (15)$$

ISBN 978-3-95450-134-2

we get,

$$n_1 \frac{d^2\xi}{d\tau^2} = \frac{4\pi NeKE_0 L_u}{2\gamma^2 m_0 c^2}\left[n_1 + \frac{3\Psi\tau^2 L_u^2}{\Omega_u c^2}\right]$$
$$\left(b_0 + (\Delta/h)b_1\right]\cos(n_1\xi+\varphi) - 6\Psi\tau\mathrm{T}^3\big) \tag{16}$$

Introducing the dimensionless optical field as,

$$a = \frac{4\pi NeKE_0 L_u}{2\gamma^2 m_0 c^2}\left[n_1 + \frac{3\Psi\tau^2 L_u^2}{\Omega_u c^2}\right][b_0 + (\Delta/h)b_1] \tag{17}$$

The pendulum equation is,

$$\frac{d^2\xi_s}{d\tau^2} = |a|\cos(\xi_s+\varphi) - 6\Psi\tau\mathrm{T}^3 \tag{18}$$

where, we have substituted $n_1\xi = \xi_s$.The wave equation for the vector potential $\vec{A}$ is written as

$$[\nabla^2 - \frac{1}{c^2}\frac{\partial^2}{\partial t^2}]\vec{A} = -\frac{4\pi}{c}\vec{J} \tag{19}$$

where, the vector potential is calculated from $E = -\frac{1}{c}\frac{\partial A}{\partial t}$

Solving Eq. (19) for the transverse current density $\vec{J} = -nec\vec{\beta}$ where β is taken from Eq. (3) we get the free electron laser gain, for

$\Psi << 1$

$$G = -\frac{j}{\nu_0^3}[2 - 2\cos(\nu_0) - \nu_0\sin(\nu_0)] \tag{20}$$

where,

$$j = \frac{2\pi^2 Ne^2 K^2 L_u}{\gamma^3 m_0 c^2} n_1 [b_0 + \Delta_1 b_1 + \Delta_2 b_2]^2 .$$

RESULT AND DISCUSSION

The undulator field analyzed in the paper can be realized as the effect of horizontal components of earth's magnetic field on the harmonic undulator radiation. For beam and undulator parameters, $\gamma = 100, K = 1, \lambda_u = 5cm, h = 3$, we have find the effect on intensity of fundamental frequency and third harmonic frequency with the variation of κ. Figure 1 (a, b) shows the trajectory along 'x' and 'y' direction, demonstrates the shifting of beam from mean position (x=0; y=0) with κ. The emittance effect due non alignment of electron beam predicts the degradation of intensity of beam and modification in the spectrum.

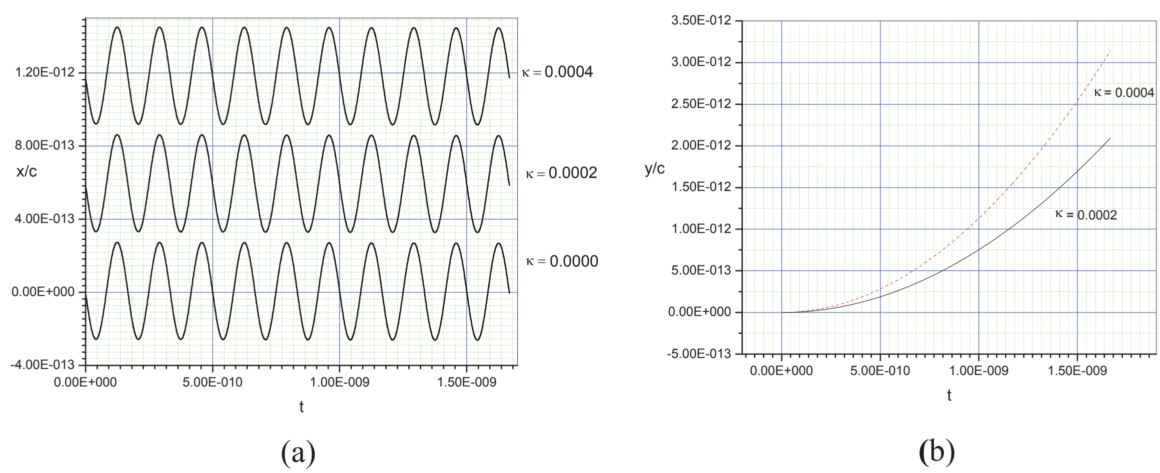

Figure 1: Trajectory along 'x' and 'y' directions.

Figure 2 illustrates the case of undulator radiation for the case of $m = 1,3,$ harmonic. For single peak beam energy distribution, the reduction of the intensity spectrum broadening is displayed. Figure 2 (a) and (b) reflects the intensity reduction for the fundamental and third harmonics respectively. The intensity reduction is proportional to the square of the harmonic number. So the reduction in intensity is substantial for harmonics $m = 3$. However with harmonic field amplitudes, the intensity at $m = 3$ the intensity loss is compensated.

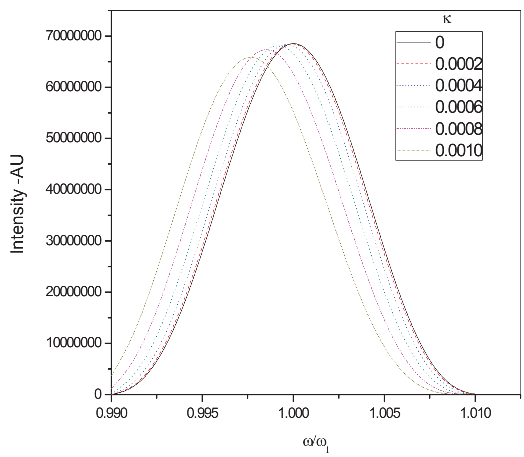

(a)

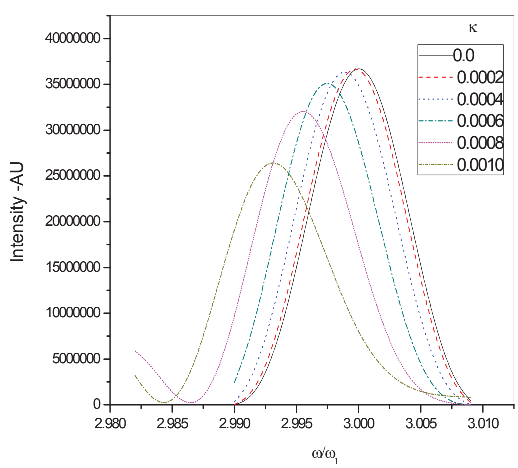

(b)

Figure 2 : Intensity at fundamental and third harmonic.

The shift in resonance and reduction in intensity at third harmonic is more as compare to first harmonics. In Fig. 2a it is shown that for κ =0.0010 the resonance shift is 0.0025 and the intensity reduction is nearly 5 % at fundamental and for similar value of additional field there is shift of 0.0067 and intensity reduction of 28% .However the overall normalized shift at first and third harmonics is 0.2%. The additional field in the directional along the 'y ' direction shows similar results but at a very low magnitude of additional constant field [9].

In conclusion we have reported the intensity distribution at fundamental and third harmonics of harmonic undulator radiations of harmonic undulator field associated with very low magnitude constant magnetic field.

The constant magnetic field present in undulator due to horizontal component cause shifting of resonance frequency at fundamental and third harmonics and loss of intensity at resonance frequency. The shift in the resonant frequency is very low almost 0.1 % matters in very low gain band width system otherwise, it has adjusted for optimum output in high gain band width amplifier systems but the intensity degradation is the issue of concern as it is higher at third harmonic as compare to fundamental .

We have compared this effect at fundamental and third harmonics. The additional harmonic field with addition of shims in the planar undulator structure is helpful to overcome the loss in the intensity further effect the overall gain.

REFERENCES

[1] K Nass et al., Journal of synchrotron radiation 22(2), 225-238 (2015)

[2] D Arnlund et al., Nature methods 11(9), 923-926 (2014)

[3] G.Dattoli et al., Lectures on FEL Theory and Related Topics,WorldScientific, Singapore, 1993.

[4] W. B. Colson, Free Electron Lasers, Lawrence Berkeley national Laboratory, University of California, http:// scholarship.org/uc/item/26c6t9rn.

[5] M. Gehlot et al., chin. phys. lett. Vol. 30, No. 8 084101 (2013)

[6] M. Asakawa et al., Nuclear Instruments and methods in Physics Research A 358, p. 399 (1995)

[7] N. Nakao et al.,Nuclear Instruments and methods in Physics Research A 407, p. 374 (1998)

[8] G. Dattoli,etal.,J.Appl.Phys.104,124507 (2008)

[9] H. Jeevakha, G. Mishra, Optic Communications, 335, 126-128 (2015)

[10] K Zhukovsky, Progress In Electromagnetics Research B, Vol. 59, 245-256 (2014)

[11] N.O. Strelnikov et al., Physical Review Special Topics - Accelerators and Beams 17, 062401 (2014)

[12] J.D. Jackson, “Classical Electrodynamics”, Wiley, New York, 1975.

ISBN 978-3-95450-134-2

THEORETICAL COMPUTATION OF THE POLARIZATION CHARACTERISTICS OF AN X-RAY FREE-ELECTRON LASER WITH PLANAR UNDULATOR

Gianluca Geloni, European XFEL GmbH, Hamburg, Germany
Vitali Kocharyan, Evgeni Saldin, Deutsches Elektronen-Synchrotron (DESY), Hamburg, Germany

Abstract

We show that radiation pulses from an X-ray Free-Electron Laser (XFEL) with a planar undulator, which are mainly polarized in the horizontal direction, exhibit a suppression of the vertical polarization component of the power at least by a factor $\lambda_w^2/(4\pi L_g)^2$, where λ_w is the length of the undulator period and L_g is the FEL field gain length. We illustrate this fact by examining the XFEL operation under the steady state assumption. In our calculations we considered only resonance terms: in fact, non resonance terms are suppressed by a factor $\lambda_w^3/(4\pi L_g)^3$ and can be neglected. While finding a situation for making quantitative comparison between analytical and experimental results may not be straightforward, the qualitative aspects of the suppression of the vertical polarization rate at XFELs should be easy to observe. We remark that our exact results can potentially be useful to developers of new generation FEL codes for cross-checking their results.

INTRODUCTION

In this paper we quantify the small component of the electric field in the vertical direction in radiation pulses produced by an XFEL with horizontal planar undulator. In particular, we show that for a typical XFEL setup the horizontally polarized component of radiation is greatly dominant, and that only less that one part in a million of the total intensity is polarized in the vertical plane.

The study of XFEL polarization characteristics is obviously deeply related to the problem of electromagnetic wave amplification in XFEL, which refers to a particular class of self-consistent problems. It can be separated into two parts: the solution of the dynamical problem, i.e. finding the motion of the electrons in the beam under the action of given electromagnetic fields, and the solution of the electrodynamic problem, i.e. finding the electromagnetic fields generated by a given contribution of charge and currents. The problem is closed by simultaneous solution of the field equations and of the equations of motion.

Let us consider the electrodynamic problem more in detail. The equation for the electric field $\vec{E}$ follows the inhomogeneous wave equation

$$c^2\nabla^2\vec{E} - \frac{\partial^2\vec{E}}{\partial t^2} = 4\pi c^2\vec{\nabla}\rho + 4\pi\frac{\partial\vec{j}}{\partial t} . \qquad (1)$$

Once the charge and current densities ρ and $\vec{j}$ are specified as a function of time and position, this equation allows one to calculate the electric field $\vec{E}$ at each point of space and time [1]. The current density source provides the main contribution to the radiation field in an FEL amplifier, and the contribution of the charge density source to the amplification process is negligibly small. This fact is commonly known and accepted in the FEL community.[1]

Due to linearity, without the gradient term the solution of Eq. (1) exhibits the property that the radiation field $\vec{E}$ points in the same direction of the current density $\vec{j}$. An important limitation of such approximation arises when we need to quantify the linear vertical field generated in the case of an XFEL with planar undulator. In the case $\vec{j}$ points in the horizontal direction (for a horizontal planar undulator), according to Eq. (1), which is exact, only the charge term is responsible for a vertically polarized component of the field: if it is neglected, one cannot quantify the linear vertical field anymore.

Similar to the process of harmonic generation, the process of generation of the vertically polarized field component can be considered as a purely electrodynamic one. In fact, the vertically polarized field component is driven by the charge source, but the bunching contribution due to the interaction of the electron beam with the radiation generated by such source can be neglected. This leads to important simplifications. In fact, in order to perform calculations of the radiation including the vertically polarization component one can proceed first by solving the self-consistent problem with the current source only. This can either be done in an approximated way using an analytical model for the FEL process or, more thoroughly, exploiting any existing FEL code. Subsequently, the solution to the self-consistent problem can be used to calculate the first harmonic contents of the electron beam density distribution. These contents enter as known sources in our electrodynamic process, that is Eq. (1). Solution of that equation accounting for these sources gives the desired polarization characteristics.

Approximations particularly advantageous for our theoretical analysis include the modeling of the electron beam density as uniform, and the introduction of a monochromatic seed signal. Realistic conditions satisfying these assumptions are the use of a sufficiently long electron bunch with a longitudinal stepped profile and the application of a scheme in the SASE mode of operation for narrowing down the radiation bandwidth. In the framework of this model it becomes possible to describe analytically all the polarization properties of the radiation from an XFEL.

[1] However, we have been unable to find a proof of this fact in literature, except book [2] and review [3], which are only the publications, to the authors' knowledge, dealing with this issue.

ISBN 978-3-95450-134-2

The simplicity of our model offers the opportunity for an almost completely analytical description in the case of an XFEL in the linear regime. A complete description of the operation of an XFEL can be performed only with time-dependent numerical simulation codes. Application of the numerical calculations allows one to describe the most general situation, including arbitrary electron beam quality and nonlinear effects. Finding an analytical solution is always fruitful for testing numerical simulation codes. Up to now, in conventional FEL codes the contribution of the the charge source is assumed to be negligible. However, the charge term alone is responsible for the vertically polarized radiation component, which is our subject of interest. Our analytical results for the high-gain linear regime are expected to serve as a primary standard for testing future FEL codes upgrades.

Here we will report only the main results of our calculations. Details can be found in [4].

RESONANCE APPROXIMATION

Paraxial Maxwell's equations in the space-frequency domain can be used to describe radiation from ultra-relativistic electrons (see e.g. [5]). We call the Fourier transform of the real electric field in the time domain $\vec{\bar{E}}_\perp(z,\vec{r}_\perp,\omega)$, where $\vec{r}_\perp = x\vec{e}_x + y\vec{e}_y$ identifies a point on a transverse plane at longitudinal position z, $\vec{e}_x$ and $\vec{e}_y$ being unit vectors in the transverse x and y directions. Here the frequency ω is related to the wavelength λ by $\omega = 2\pi c/\lambda$, c being the speed of light in vacuum. From the paraxial approximation follows that the electric field envelope $\vec{\tilde{E}}_\perp = \vec{\bar{E}}_\perp \exp[-i\omega z/c]$ does not vary much along z on the scale of the reduced wavelength $\lambda/(2\pi)$. As a result, it can be shown that the following field equation holds:

$$\left(\nabla_\perp^2 + \frac{2i\omega}{c}\frac{\partial}{\partial z}\right)\vec{\tilde{E}}_\perp(z,\vec{r}_\perp,\omega) = -4\pi \exp\left[i\int_0^z d\bar{z}\frac{\omega}{2c\gamma_z^2(\bar{z})}\right]\left[\frac{i\omega}{c^2}\vec{v}_{o\perp} - \vec{\nabla}_\perp\right] \times\tilde{\rho}(z,\vec{r}_\perp - \vec{r}_{o\perp}(z),\omega)\,, \qquad (2)$$

where $\vec{r}_{o\perp}(z)$, $s_o(z)$ and v_o are the transverse position, the curvilinear abscissa and the velocity of a reference electron with nominal Lorentz factor γ_o that is injected on axis with no deflection and is guided by the planar undulator field. Such electron follows a trajectory specified by $\vec{r}_{o\perp}(z) = r_{ox}\vec{e}_x + r_{oy}\vec{e}_y$ with $r_{ox}(z) = K/(\gamma_o k_w)\cos(k_w z)$ and $r_{oy}(z) = 0$. Here K is the undulator parameter defined in terms of the maximum magnetic field and $k_w = 2\pi/\lambda_w$, λ_w being the undulator period. The corresponding velocity is described by $\vec{v}_{o\perp}(z) = v_{ox}\vec{e}_x + v_{oy}\vec{e}_y$. Moreover, $\gamma_z(z) = 1/\sqrt{1 - v_{oz}(z)^2/c^2}$ and $v_{oz}(z) = \sqrt{v_o^2 - v_{o\perp}(z)^2}$. Finally, $\widetilde{\rho}$ is related to the Fourier transform of the macroscopic charge density, $\bar{\rho}$, by

$$\bar{\rho} = \widetilde{\rho}(z,\vec{r}_\perp - \vec{r}_{o\perp}(z),\omega)\exp\left[i\omega\frac{s_o(z)}{v_o}\right]\,, \qquad (3)$$

s_o being the curvilinear abscissa along the trajectory.

With the aid of the appropriate Green's function and using the far-zone approximation a solution of Eq. (2) can be found to be:

$$\vec{\tilde{E}}_\perp = -\frac{i\omega}{cz}\int d\vec{l}\int_{-\infty}^{\infty} dz'\tilde{\rho}(z',\vec{l},\omega)\exp\left[i\Phi_T(z',\vec{l},\omega)\right] \times\left[\left(\frac{K}{\gamma}\sin(k_w z') + \theta_x\right)\vec{e}_x + \theta_y\vec{e}_y\right]\,, \qquad (4)$$

where

$$\Phi_T = \omega\left\{\frac{z'}{2\gamma^2 c}\left[1 + \frac{K^2}{2} + \gamma^2\left(\theta_x^2 + \theta_y^2\right)\right] - \frac{K^2}{8\gamma^2 k_w c}\sin(2k_w z') - \frac{K\theta_x}{\gamma k_w c}\cos(k_w z')\right\} + \omega\left\{\frac{K\theta_x}{k_w\gamma c} - \frac{1}{c}(\theta_x l_x + \theta_y l_y) + (\theta_x^2 + \theta_y^2)\frac{z}{2c}\right\}. \qquad (5)$$

Here θ_x and θ_y indicate the observation angles x/z and y/z. Moreover, since in Eq. (4) we introduced explicitly the trajectory inside the undulator, we need to limit the integration in dz' to a proper range within the undulator. We assume that this is done by introducing a function of z' as a factor to $\widetilde{\rho}$, which becomes zero outside properly defined range, thus effectively limiting the integration range in z'.

In this article we are interested in considering fields and electromagnetic sources originating from an FEL process. Imposing resonance condition between electric field and reference particle, the self-consistent FEL process automatically restricts the amplification of radiation at frequencies around the first harmonic $\omega_{1o} = 2k_w c\bar{\gamma}_z^2$ and at emission angles $\theta_{\max}^2 \ll 1/\bar{\gamma}_z^2$, where $\bar{\gamma}_z^2 = \gamma^2/(1 + K^2/2)$. Our focus onto FEL emission also explains the definition in Eq. (3). In fact, introduction of $\widetilde{\rho}$ is useful when $\widetilde{\rho}$ is a slowly varying function of z on the wavelength scale. If the charge density distribution under study originates from an FEL process a stronger condition is satisfied, namely $\widetilde{\rho}$ is slowly varying on the scale of the undulator period λ_w and, as the FEL pulse itself, is peaked around the fundamental ω_{1o}. The words 'peaked' or 'around' the fundamental mean that the bandwidth is $\Delta\omega/\omega_{1o} \ll 1$. We quantify 'how near' the frequency ω is to ω_{1o} introducing the detuning parameter $C = (\Delta\omega/\omega_{1o})k_w$, with $\Delta\omega = \omega - \omega_{1o}$. The detuning parameter C should indeed be considered as a function of z, $C = C(z)$. All other dependencies on z, for example due to the fact that the energy of particles actually deviates from γ and actually decreases during the FEL process, is accounted for in $\tilde{\rho}$. We seek to calculate the first harmonic contribution at frequencies ω around ω_{1o}, $\vec{\tilde{E}}_{\perp 1}$, by making use of the well-known Anger-Jacobi expansion. Invoking the FEL process allows to take the limit for $C \ll k_w$ and $\theta_{\max}^2 \ll 1/\bar{\gamma}_z^2$. Keeping the dominant terms only we obtain

$$\vec{\tilde{E}}_{\perp 1} = \frac{\omega_{1o}}{cz}\exp\left[i\frac{\omega_{1o}}{2c}z(\theta_x^2 + \theta_y^2)\right]$$

ISBN 978-3-95450-134-2

$$\times\left[\frac{K}{2\gamma}\mathrm{A_{JJ}}\vec{e}_x+\frac{2K\gamma}{2+K^2}\mathrm{B_{JJ}}\theta_x\theta_y\vec{e}_y\right]$$
$$\times\int_{-\infty}^{\infty}dl_x\int_{-\infty}^{\infty}dl_y\int_{-\infty}^{\infty}dz'$$
$$\times\exp\left[-i\frac{\omega_{1o}}{c}\left(\theta_x l_x+\theta_y l_y\right)\right]$$
$$\times\exp\left[i\frac{\omega_{1o}}{2c}\left(\theta_x^2+\theta_y^2\right)z'\right]\tilde{\rho}(z',\vec{l},\omega)\exp[iCz'],(6)$$

where we have defined

$$\mathrm{A_{JJ}}=J_0\left(\frac{K^2}{2(2+K^2)}\right)-J_1\left(\frac{K^2}{2(2+K^2)}\right),\qquad(7)$$

$$\mathrm{B_{JJ}}=J_0\left(\frac{K^2}{2(2+K^2)}\right)+J_1\left(\frac{K^2}{2(2+K^2)}\right),\qquad(8)$$

and $J_p(\cdot)$ indicates the Bessel function of the first kind of order p. Note that usually computer codes present the product $\tilde{\rho}(z',\vec{l},\omega)\exp[iCz']$ combined in a single quantity tipically known as the complex amplitude of the electron beam modulation with respect to the phase $\psi=k_w z'+(\omega/c)z'-\omega t$. Regarding such product as a given function allows one not to bother about a particular presentation of the beam modulation. Eq. (6) is our most general result, and is valid independently of the model chosen for the current density and the modulation. It can be used together with FEL simulation codes for detailed calculations of the evolution of the vertically polarization contribution to the FEL radiation.

In the case of an FEL, due to the presence of a maximum angle $\theta_{\max}$ related with the self-consistent process, the angle-integrated correction to the power from the horizontally polarized radiation component only includes the leading resonant term, and Eq. (6) can always be used to calculate such correction at the first harmonic.

ANALYTICAL CASES

We now restrict our attention to the steady-state model of an FEL amplifier. Because of the steady state assumption we restrict our attention to one single frequency. This means that, in the time domain, the electric field envelope $\vec{\tilde{E}}_{\perp 1}$ must correspond to a real electric field at a certain frequency $\bar{\omega}=\omega_{1o}(1+Ck_w)$ given by $\vec{E}(z,\vec{r}_\perp,t)=\vec{\mathcal{E}}_{\perp 1}(z,\vec{r}_\perp)\exp[i\bar{\omega}(z/c-t)]+C.C.$, where the symbol $C.C.$ indicates complex conjugation.

The power fractions into the two modes of polarization are found to be

$$W_{(\sigma,\pi)}=\frac{c}{2\pi}\int_{-\infty}^{\infty}dx\int_{-\infty}^{\infty}dy|\mathcal{E}_{\perp 1(x,y)}(z,x,y)|^2,\qquad(9)$$

where

$$\vec{\tilde{E}}_{\perp 1}(z,\vec{r}_\perp,\omega)=2\pi\vec{\mathcal{E}}_{\perp 1}(z,\vec{r}_\perp)\delta(\omega-\bar{\omega}).\qquad(10)$$

In order to calculate $W_{(\sigma,\pi)}$ we make use of Eq. (9). The expression for $\mathcal{E}_{\perp 1(x,y)}$ can be found in terms of $\vec{\tilde{E}}_{\perp 1}$ with the help of Eq. (10). Finally, one needs to calculate $\vec{\tilde{E}}_{\perp 1}$, which can be done using Eq. (6).

Under the assumption of a one-dimensional steady state FEL amplifier we write the expression for the slowly-varying amplitude of the charge density as

$$\tilde{\rho}(z,\vec{r}_\perp,\omega)=\frac{j_o(\vec{r}_\perp)}{v_z}2\pi a(z)\delta(\omega-\omega_0),\qquad(11)$$

where we defined the current density

$$j_o(\vec{r}_\perp)=-\frac{I_o}{2\pi\sigma^2}\exp\left(-\frac{r_\perp^2}{2\sigma^2}\right),\qquad(12)$$

and where we dropped the term in $\delta(\omega+\bar{\omega})$ passing to complex notation, as done before with the field.

We will show that, typically, in the case of an XFEL with a horizontal planar undulator, only less that one part in a million of the total power at the first harmonic is polarized in the vertical direction. For some experiments even such small fraction of the π mode is of importance. The contribution of the second harmonic can be calculated using results in [6] and was studied in [4]. There it was found that the contribution from the even harmonics can be completely disregarded when the XFEL operates in linear regime. At saturation, the contribution from the second harmonic can be comparable with the first harmonic in the case when X-ray optics harmonic separation is absent.

High-gain Linear Regime

We first model the case of an FEL amplifier in the high-gain linear regime. We proceed approximating the detuning parameter C as constant along the undulator. Let us restrict, for simplicity, to the case of perfect resonance for $C=0$. This means that from now on $\bar{\omega}=\omega_{1o}$. The high-gain asymptote of the one-dimensional steady-state theory of FEL amplifiers yields

$$a(z)=a_f\exp[(\sqrt{3}+i)z/(2L_g)],\qquad(13)$$

where we set the exit of the undulator (in the linear regime) at $z=0$ and $a_f=$ constant is the modulation level at $z=0$. Here L_g is the field gain length. The number of undulator periods in the field gain length L_g is just $N_w=(4\pi\rho_{1\mathrm{D}})^{-1}$, where the FEL parameter $\rho_{1\mathrm{D}}$ is defined in [7]. Based on Eq. (6) we obtain

$$\begin{pmatrix}W_\sigma\\W_\pi\end{pmatrix}=W_o\begin{pmatrix}\mathrm{A_{JJ}}^2\rho_{1D}^{-1}G_\sigma(N)\\\mathrm{B_{JJ}}^2\rho_{1D}G_\pi(N)\end{pmatrix},\qquad(14)$$

where

$$G_\sigma(N)=\frac{1}{2\sqrt{3}}\exp[(1-i\sqrt{3})N]\{\pi$$
$$+\pi\exp\left[2i\sqrt{3}N\right]-i\exp\left[2i\sqrt{3}N\right]\mathrm{Ei}\left(N(-1-i\sqrt{3})\right)$$
$$+i\mathrm{Ei}\left(iN(i+\sqrt{3})\right)\}\qquad(15)$$

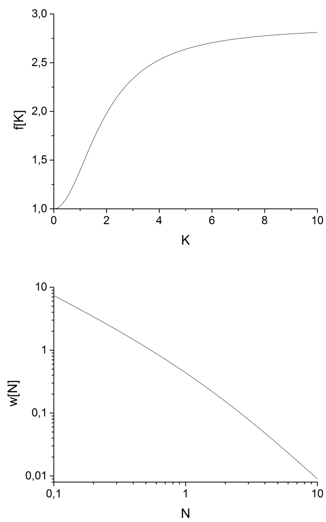

Figure 1: Illustration of the behavior of $f(K)$ (left) and $w(N)$ (right).

$$G_\pi(N) = \frac{1}{6}\left\{\frac{3}{N} - \left(-3i+\sqrt{3}\right)\exp[(1+i\sqrt{3})N] \times\left[\pi - i\mathrm{Ei}\left((-1-i\sqrt{3})N\right)\right] - \left(3i+\sqrt{3}\right) \times\exp[(1-i\sqrt{3})N]\left[\pi + i\mathrm{Ei}\left(i(i+\sqrt{3})N\right)\right]\right\} \quad (16)$$

and

$$W_o = W_b a_f^2 \left(\frac{I_o}{\gamma I_A}\right)\left(\frac{K^2}{2+K^2}\right) \quad (17)$$

where $W_b = m_e c^2 \gamma I_o/e$ is the total power of the electron beam and $N = \omega_{1o}\sigma^2/(cL_w)$ is the diffraction parameter (or Fresnel number) with $L_w = L_g$ in our case.

The ratio between the fractions radiated in the two modes of polarization is therefore conveniently expressed as a function of three separate factors:

$$\frac{W_\pi}{W_\sigma} = f(K)g(N_w)w(N) \quad (18)$$

with

$$f(K) = \frac{B_{JJ}^2}{A_{JJ}^2}, g(\rho_{1D}) = \rho_{1D}^2, w(N) = \frac{G_\pi(N)}{G_\sigma(N)}\ . \quad (19)$$

The first factor, $f(K)$, is only a function of the undulator K parameter and is plotted in Fig. 1. The second factor, $g(\rho_{1D})$ scales as the inverse number of undulator periods squared, and is a signature of the fact that the gradient term in the equation for the electric field scales as the inverse number of undulator periods. The third factor, $w(N)$, is only a function of the diffraction parameter that is, once the wavelength and the undulator length are fixed, a function of the electron beam size only. It is also plotted in Fig. 1. It is unity for values of the diffraction parameter around unity, but it quickly decreases for larger values of N. The power fraction radiated in the π mode increases drastically with the photon energy, partly due to a larger number of undulator period per field gain-length, but mainly because of a larger diffraction parameter.

As an example we consider a 250 pC electron beam at a photon energy of about 9 keV for the SASE2 line of the European XFEL, at the electron energy of 17.5 GeV. Here $K \simeq 3.6$, the peak current is about 5 kA, and the rms sizes of the electron beam in the horizontal and vertical directions are about $\sigma_x \simeq 15\ \mu$m and $\sigma_y \simeq 18\ \mu$m respectively. For our purposes of exemplification we consider a round beam with $\sigma = 16\mu$m. The peak current density can then be estimated as $I_0/(2\pi\sigma^2)$. Finally, the undulator period is $\lambda_w = 40$ mm. From these numbers we obtain the parameter $\rho_{1\mathrm{D}} \simeq 8 \cdot 10^{-4}$. Plugging these numbers in Eq. (18) and remembering the definition in Eq. (19)we obtain $f(K) \simeq 2.5$, $g(\rho_{1D}) \simeq 6.4 \cdot 10^{-7}$, $N \simeq 3$ and $w(N) \simeq 0.072$, so that the overall ratio $W_\pi/W_\sigma \simeq 1.13 \cdot 10^{-7}$.

Constant Density Modulation

In analogy with the previous paragraph, we now proceed to study the case of a constant density modulation along an undulator of fixed length L_w, imitating the behavior of an FEL at saturation. We can still set $C(z) = 0$. At variance with the previous model we now write

$$\tilde{\rho}(z,\vec{l}) = j_o\left(\vec{l}\right) 2\pi a_f H_{L_g}(z)\delta(\omega-\omega_{1o})\ . \quad (20)$$

Here a_f = const, $H_{L_w}(z) = 1$ for z in the range $(-L_w/2, L_w/2)$ and zero otherwise, with L_w the undulator length, and j_o is defined as in Eq. (12). One finds

$$\left(\begin{array}{c} W_\sigma \\ W_\pi \end{array}\right) = W_o \left(\begin{array}{c} \mathrm{A_{JJ}}^2(4\pi N_w)F_\sigma(N) \\ \mathrm{B_{JJ}}^2(4\pi N_w)^{-1}F_\pi(N) \end{array}\right), \quad (21)$$

where

$$F_\sigma(N) = \arctan\left(\frac{1}{2N}\right) + N\ln\left(\frac{4N^2}{4N^2+1}\right), \quad (22)$$

$$F_\pi(N) = \frac{1}{N(1+4N^2)}, \quad (23)$$

and where parameters N and W_o are defined above.

Similarly as before, the ratio between the two fractions radiated into the two modes of polarization is conveniently expressed as a function of three separate factors:

$$\frac{W_\pi}{W_\sigma} = f(K)g(N_w)h(N) \quad (24)$$

with

ISBN 978-3-95450-134-2

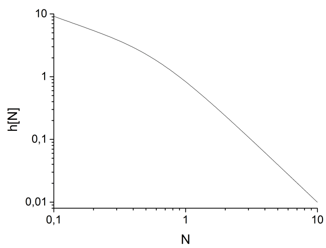

Figure 2: Illustration of the behavior of $h(N)$.

$$f(K) = \frac{B_{JJ}^2}{A_{JJ}^2}, g(N_w) = \frac{1}{(4\pi N_w)^2}, h(N) = \frac{F_\pi(N)}{F_\sigma(N)}. \quad (25)$$

The function f has been defined in the previous paragraph. Concerning the second factor g, we have an expression which is similar to that in Eq. (19). The only difference is that here we replaced ρ_{1D} with $(4\pi N_w)^{-1}$, with N_w the number of undulator periods in the undulator. The number of undulator periods in a field gain length is just $N_w = (4\pi\rho_{1D})^{-1}$, and therefore the second factor in Eq. (24) just amounts to ρ_{1D}^2 for an undulator length $L_w = L_g$, L_g being, as before, the field gain length. By setting the undulator length equal to the field gain length the two models can be directly compared by studying $w(N)$ as defined in Eq. (19) and $h(N)$ defined in Eq. (25). We plot $h(N)$ explicitly in Fig. 2. As one can see it differs from Fig. 1, due to the different model used.

Considering the same example made in the previous paragraph we find again $f(K) \simeq 2.5$, $g(\rho_{1D}) \simeq 6.4 \cdot 10^{-7}$, $N \simeq 3$. Plugging the value for N into Eq. (25) we obtain $h(N) \simeq 0.097$, so that the overall ratio $W_\pi / W_\sigma \simeq 1.5 \cdot 10^{-7}$.

The case of a constant density modulation treated in this paragraph not only pertains an FEL at saturation, but also the case of spontaneous emission in an undulator. A major difference compared to the FEL case is that the FEL process limits the detuning to values $C \ll k_w$ and the angle of interest up to $\theta_{\max}$. Such limitations are not automatically present in the case of spontaneous emission. However, if we limit the acceptance angle of the spontaneous emission to $\theta_{\max}$ and we assume the undulator length of order of the FEL gain length, we expect the same ratio of the fractions radiated in the two modes of polarization found in Eq. (24).

REFERENCES

[1] J. Jackson, "Classical Electrodynamics", 3rd ed., Wiley, New York, (1999).

[2] E. Saldin, E. Schneidmiller, M. Yurkov, "The Physics of Free-Electron Lasers, Springer", (1999).

[3] Z. Huang, K.-J. Kim, Physical Review Special Topics AB 10 (2007) 034801.

[4] G. Geloni, V. Kocharyan and E. Saldin, DESY 15-021, `http://arxiv.org/abs/1502.04627`, accepted for publication in Optics Communications, (2015).

[5] G. Geloni, E. Saldin, E. Schneidmiller, M. Yurkov, Optics Communications 276 167, (2007).

[6] G. Geloni, E. Saldin, E. Schneidmiller, M. Yurkov, Optics Communications 271 207, (2007).

[7] R. Bonifacio, C. Pellegrini, L. Narducci, Optics Communications 50 373, (1984).

EFFICIENT ELECTRON SOURCES OF COHERENT SPONTANEOUS RADIATION WITH COMBINED HELICAL AND UNIFORM MAGNETIC FIELDS

N. Balal[1#], V. L. Bratman[1, 2], E. Magori[1]
[1]Ariel University, Ariel, Israel
[2]Institute of Applied Physics, Russian Academy of Sciences, Nizhny Novgorod, Russia

Abstract

Two methods to mitigate repulsion of electrons in dense bunches from photo-injectors with a relatively low particle energy and to enhance the power of terahertz radiation have been studied. First method is based on using very short bunches and small undulator periods that allows a significant shortening radiation sections. According to simulations bunches with duration (50-100) fs and energy 6 MeV that presumably could be formed in the constructing Israeli THz FEL [1] would fairly effectively radiate at frequencies up to (10-20) THz. The second method is based on an idea recently proposed by A.V. Savilov for longitudinal electron bunching [2, 3]. This is possible when a bunch moves in a combined magnetic field of a solenoid and of a undulator and the electron cyclotron frequency is sufficiently large in comparison with their undulator frequency. In such situation, an increase/decrease of particle energy in the repulsed Coulomb field of space charge leads to a decrease/increase in particle longitudinal momentum. Correspondingly, Coulomb repulsion can lead to an effective attraction of the particles (this effect is analogous to the known cyclotron negative-mass instability). A large value of the uniform field that is necessary in this method can be used to easily obtain a undulator field by inserting a simple steel helix inside a pulsed solenoid. Simulations confirm that the particle attraction can provide a powerful and narrowband radiation of the bunch with electron energy (5-6) MeV and duration 0.3 ps at the frequencies up to 3 THz.

SHORT BUNCHES IN MICROUNDULATORS

The first opportunity may be realized if bunches with duration of about of 100 fs or even shorter are formed at the entrance of a radiation section. In this case, one can use a mm-period undulator (microundulator) and produce the radiation with the frequency up to 10 THz and higher. A small undulator period provides a relatively narrow-band radiation at comparably short radiation length where the longitudinal particles expansion is not too large even at very high bunch charges if the corresponding energy chirp is also used. For such situation, we propose a helical undulator in the form of a set of a helically spaced magnet block interspaced with a preliminarily non-magnetized steel helix; such a set with helically periodic elements being inserted into a solenoid redistributes its field adding the required helical component in it (Fig. 1). The magnet block should be permanently magnetized toward the solenoid field. This method was successfully developed for a plane prototype in [4]. A strong solenoid field prevents also the transverse particles expansion. According to simulations on the basis Microwave Studio code the optimized undulator systems of such a kind with the ratio of longitudinal helix thickness to the separations 1:2 can provide a strong transverse helical field with the amplitude up to (0.7-1.0) T at an acceptable gap-period ratio 1:3 (Table 1). Such fields provide, in particular, a sufficiently large undulator parameter K=0.3-0.4 at the small period of (4-5) mm. Simulations of Coherent Spontaneous Undulator Radiation of an electron bunch in a combined magnetic field of the solenoid and steel and preliminarily magnetized helical insertions was carried out on the basis of a self-consistent one-dimensional model of the bunch in the form of a charged plane layer using simple formulas for the field of an arbitrary moving charged plane [5]. Such one-dimensional simulations were used for estimations of interaction and radiation from thin disc-like electron bunches with the following parameters: charge (50-200) pC, radius 0.4 mm, duration (50-100) fs, energy 5.5 MeV and a large energy chirp (0.3-1.0) MeV moving in a waveguide mounted into the undulator with the length (5-10) cm. According to calculations one may expect to obtain in such situation narrowband picosecond pulses with the radiation frequency up to (10-20) THz and energy up to (0.1-0.4) μJ.

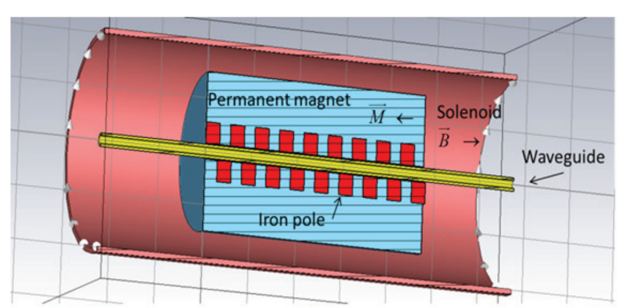

Figure 1: Microundulator for a source of Coherent Spontaneous Radiation of a dense electron bunch with the frequency up to (10-20) THz consisting of a solenoid and insertions in the form of a magnetized block and a non-magnetized steel helix.

#nezahb@ariel.ac.il

ISBN 978-3-95450-134-2

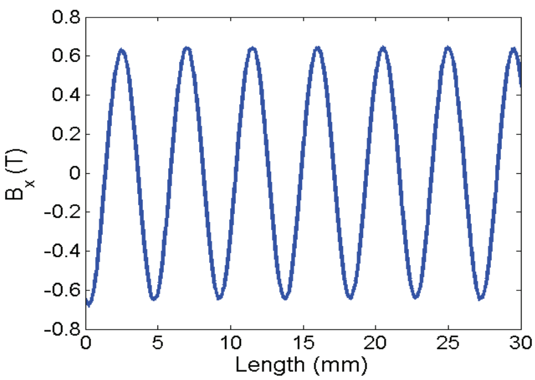

a)

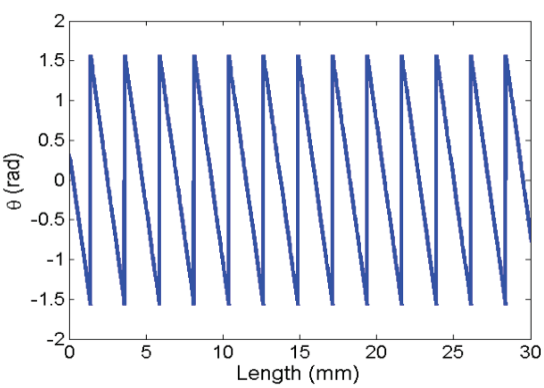

b)

Figure 2: Results of simulations for transverse magnetic field at the axis of symmetry of microundulator on the basis of Microwave Studio code: a) x-component and b) phase.

Table 1: Parameters of Microundulator

Field of solenoid, T	0.8
Period, mm	4.5
Gap, mm	1.5
Height of steel poles, mm	6
Height of magnet block, mm	15
Helical undulator field, T	0.7

NEGATIVE-MASS BUNCH STABILIZATION

The second considered method is intended to realization of a promising idea [2,3] for an effective longitudinal electron bunching in a combined helical and very strong (over-resonance) uniform magnetic fields. Such effect can occur when the cyclotron electron frequency is significantly larger than its undulator bounce-frequency. It is known that in this region of parameters the longitudinal velocity of a particle can decrease/increase with an increase/decrease in its energy [6,7]. Correspondingly, like in the classic cyclotron negative-mass instability of non-isochronously oscillating and interacting charged particles [8,9], the change of the particle energy in the repulsing Coulomb field of a bunch leads to the longitudinal electron attraction and bunching of particles. In this paper, we propose to use a very large value of the uniform magnetic field that is required for such Negative-Mass Stabilization for easy obtaining the transverse undulator field by inserting a one steel helix inside a pulsed solenoid with a strong field that leads to a proper redistribution of this field. For example, a steel helix with the period 2.5 cm mounted in the axial magnetic field 8 T (Fig. 3) can easily provide the undulator parameter K=0.5-1.0 (despite the fact that the axial field significantly exceeds the saturation value for steel and other magnetic materials). In such fields the cyclotron frequency of the particles with energy 5.5 MeV

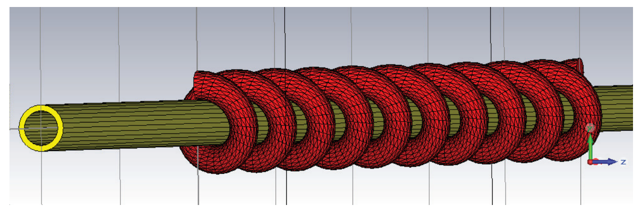

a)

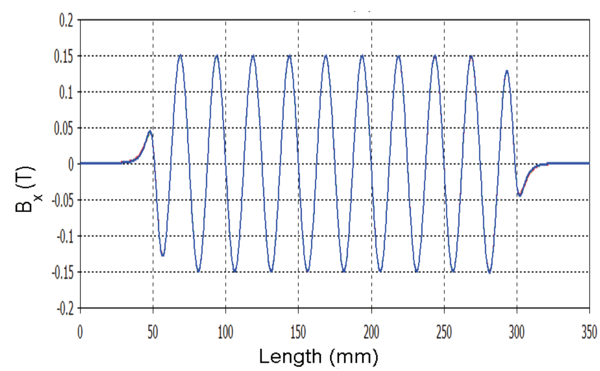

b)

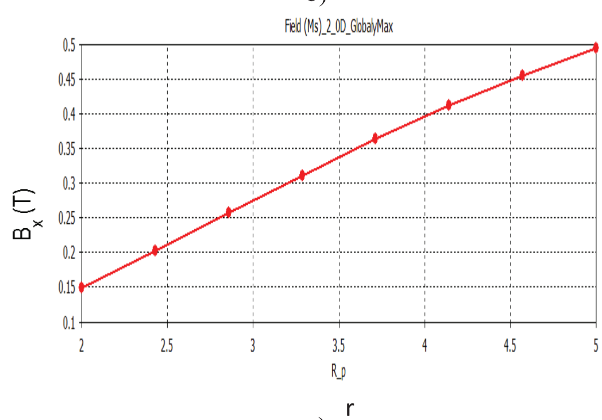

c)

Figure 3: Helical undulator for Negative-Mass Stabilization of the electron bunch: a) a steel helix wound on cylindrical waveguide with outside diameter 10 mm and inserted inside a solenoid with a strong field, b) axial distribution of transverse undulator field, c) dependence of amplitude of transverse field on helix radius r.

ISBN 978-3-95450-134-2

is 60% larger than their undulator frequency. Simulations for the bunch with the charge 300 pC on the basis of General Particle Tracer code (Fig. 4) demonstrate a good coincidence with results of calculations for an ideal model studied in [2]. Due to the Negative-Mass effect the longitudinal size of the nucleus of the electron beam is nearly constant at a large undulator length. Correspondingly, the effective particle attraction in such conditions can provide a powerful and narrowband radiation at the frequencies (1-3) THz.

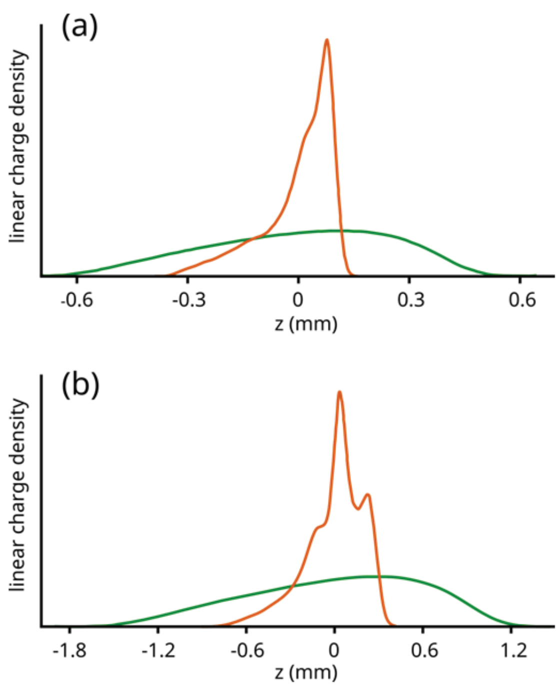

Figure 4: Density distribution for the electron bunch in the combined undulator and uniform magnetic fields in negative- and positive-mass regimes (solid and dashed curves correspond to the guiding field +8 T and -8 T, respectively) after the distance 45 cm (a) and 90 cm (b).

Table 2: Parameters of Electron Beam and Undulator for a THz Source with Negative-Mass Stabilization

Electron bunch		Undulator	
Energy, MeV	5.5	Period, mm	25
Charge, pC	300	Axial field, T	8
Duration, ps	330	Transverse field, T	0.15

CONCLUSION

Two methods have been proposed and theoretically studied for possible power and frequency enhancement in the constructing Israeli source of THz coherent spontaneous radiation of short ultrarelativistic electron bunches.

Use of very short electron bunches with duration of (50-100) ps and a large energy chirp together with a proposed helical modification of the microundulator based on redistribution of uniform magnetic field of a solenoid by a periodic set of preliminarily magnetized and non-magnetized materials (Fig. 1) could increase the maximum frequency of the source from (3-4) THz to (10-20) THz and significantly narrow its radiation spectrum.

The simple steel helical structure inserted into a strong field of solenoid (Fig. 3) can be also used for obtaining a helical undulator field and realization of Negative-Mass Stabilization regime that may lead to significantly higher efficiency and narrower bandwidth of radiation

REFERENCES

[1] A. Friedman, A. Gover , E. Dyunin, Y. Lurie, E. Magori, N. Balal, V. Bratman, "Configuration and status of the Israeli THz Free Electron Laser", 36th Int. Free-Electron Laser Conf. Basel (2014) 553.

[2] I. V. Bandurkin, A. V. Savilov, "THz Photo-Injector FEM Based on Spontaneous Coherent Emission from a Bunch of Negative-Mass Electrons", FEL 2015 Conference, TUP001.

[3] N. Balal, I. V. Bandurkin, V. L. Bratman, E. Magory, and A.V. Savilov,"Negative-Mass Mitigation of Coulomb Repulsion for Terahertz Undulator Radiation of Electron Bunches" (submitted to APL).

[4] A. A. Varfolomeev, A. S. Khlebnikov, S. N. Ivanchenkov, N. S. Osmanov and A. H. Hairetdinov, "Strong magnetic field microundulator with permanent magnets inserted into a solenoid", Nuclear Instruments and Methods in Physics Research A 331 (1993) 745.

[5] V. L. Bratman, S. V. Samsonov, "Radiation and radiative damping of a charged plane, oscillating with a relativistic velocity", Phys. Letters A206 (1995), pp. 377-382.

[6] N. S. Ginzburg and N. Yu. Peskov, "Nonlinear theory of relativistic ubitrons with electron beams formed in an adiabatically increasing undulator field and uniform magnetic field", Tech. Phys. **58**, 859 (1988).

[7] H. P. Freund and T. M. Antonsen, Principles of Free-Electron Lasers, (Chapman & Hall, London, 1996).

[8] C. Nielsen and A. Sessler, "Longitudinal Space Charge Effects in Particle Accelerators", Rev. Sci. Instrum. 30, 80-89 (1959).

[9] A. A. Kolomensky and A. N. Lebedev, "Stability of charged beams in storage systems", Atom. Energy 7, 549-554 (1959; in Russian).

ISBN 978-3-95450-134-2

LINAC DESIGN OF THE IR-FEL PROJECT IN CHINA*

Zhigang He, Wei Xu, Shancai Zhang†, Lin Wang, Qika Jia
NSRL USTC, HeFei, AnHui 230039, China

Abstract

We are building an infrared free-electron laser (IR-FEL) facility that will operate from 5 µm to 200 µm. This FEL source is drived by a linac, which is composed of a triode electron gun, a subharmonic prebuncher, a buncher, two accelerators, and a beam transport line. The linac is required to operate from 15 to 60 MeV at 1 nC charge, while delivering a transverse rms emittance of smaller than 30 mm-mrad in a 5 ps rms length, smaller than 240 keV rms energy spread bunch at the Far-infrared and Mid-infrared undulators. In this article, the preliminary Linac design studies are described.

INTRODUCTION

The basic layout of the FEL facility is shown in Fig. 1. The accelerating system consists of a 100 kV triode electron gun, a bunching system, and two accelerators. The energy range between 15 and 25 MeV will be covered with the first accelerator (A1) for the far-infrared radiation, and the range between 25 to 60 MeV with the second accelerator (A2) for the middle-infrared radiation. As to the requirement of the FEL physics [1], the electron beam characteristics are listed in Table 1.

Table 1: Electron Beam Characteristics

	Energy (E)	15-60 MeV
	Energy spread (δE)	< 240 keV
	Emittance (ε_n)	< 30 mm-mrad
micro pulse	Charge (Q)	1 nC
	Peak current (I_p)	> 95 A
	Pulse length (σ_t)	2-5 ps
	Repetition rate	$\frac{476}{n(=1,2,3,4,5)}$ MHz
macro pulse	Pulse width	5–10 µs
	Average current (I)	~300 mA
	Repetition rate	20 Hz

DESCRIPTION OF THE LINAC

As shown in Fig. 1, the Linac consists of a:

- 100 keV electron gun
- 476 MHz subharmonic standing wave pre-buncher
- 2856 MHz fundamental frequency traveling wave buncher
- two 2856 MHz fundamental frequency traveling wave accelerators
- set of solenoid focusing coil from the gun exit to the end of the first accelerator
- magnetic compressor (chicane)
- two beam transport systems

The triode gun can be driven by the grid for the pulsed mode. A 476 MHz signal during 10 µs is carried to the HV deck. A frequency divider is used to control the repetition rate of the micro pulses. The electron gun pulser could offer the pulsed signal of up to 200 V/1 ns every 2, 4, 8, 16, or 32 ns. We expect to obtain micro pulses of 1-2 A/1 ns at the gun output. The operating mode of the electron gun is similar to the gun of the CLIO FEL [2, 3], while RF gated electron guns are adopted by the FELIX FEL [4, 5] and FHI FEL [6].

The pre-buncher will be a 20 cm long stainless steel re-entrant standing wave cavity operating at 476 MHz. With a gap voltage of 40 kV, the bunch length could be compressed by about 20 times in 24 cm long drift space downstream from the pre-buncher exit at the entrance of the buncher.

For further bunch length compression, a traveling wave buncher operating at 2856 MHz is used, which consists of an input coupler, 11 cells , and an output coupler. The phase velocities β_ϕ of the fist four cells are 0.63, 0.8, 0.915, and 0.958 respectively, and that of the rest of the cells is 1. With a 9 MV/m gradient (about 5 MW input power), the bunch length can be compressed to 4.5 ps (rms) and the beam energy is about 3.1 MeV at the exit of the buncher.

The two 2 meters long traveling wave accelerators are also operating at 2856 MHz, which consists of input and output couplers and 57 cells. Because of the high average current, the beam loading effect should be considered in the accelerators. As to our design structures, the acceleration gradient of the cells are shown in Fig. 2. When the beam current is 300 mA, one accelerator can offer about 30 MeV beam energy increase with 20 MW input power.

To improve the gain of the short wavelength radiation, a higher peak current bunch may be required. The chicane could be as a backup apparatus to obtain a shorter bunch. Because the peak current is above 100 A at the exit of A1, the magnetic compressor is not used normally.

The main functions of the beam transport systems are beam matching and beam energy filtering. Energy slits will be used in the dispersion section to filter out the electrons with great energy spread.

BEAM DYNAMICS

The code PARMELA is used for beam dynamics simulation. The initial beam current and bunch length are 1.5 A and 1 ns respectively.

Figure 3 shows the simulated longitudinal distribution state and phase space of the electron bunch at the exit of the

* Supported by National Natural Science Foundation of China (No. 21327901).
† Corresponding author, email: shancai@ustc.edu.cn

ISBN 978-3-95450-134-2

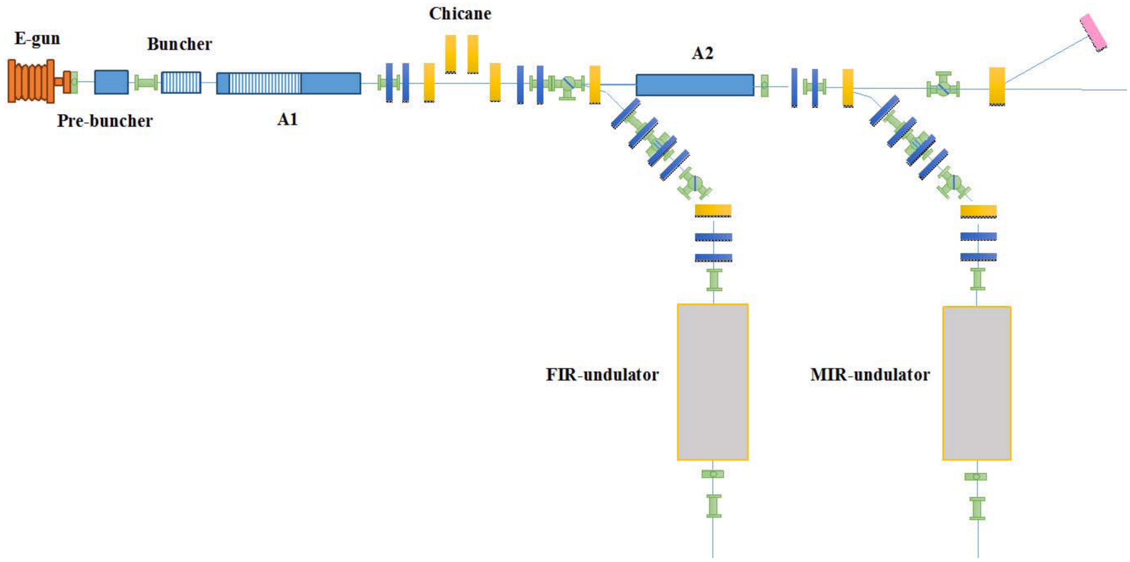

Figure 1: Basic layout of the FEL facility.

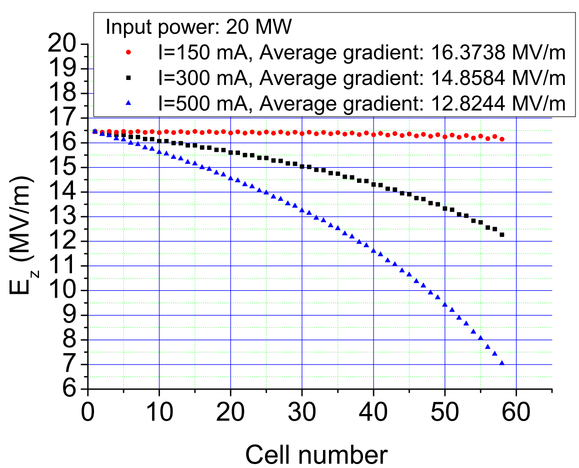

Figure 2: Acceleration gradient of the acceleration cells for different beam currents.

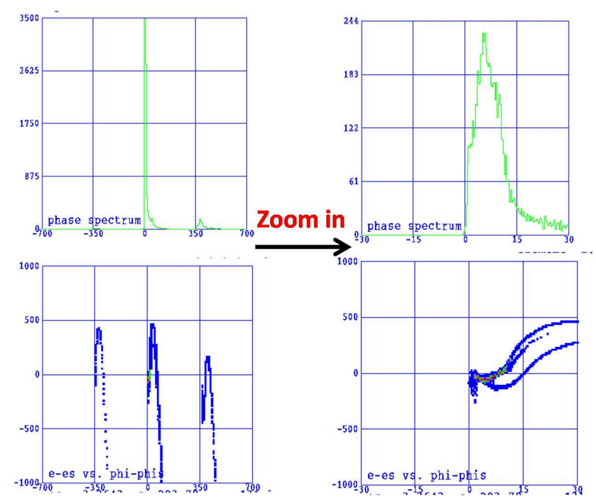

Figure 3: Longitudinal distribution state and phase space of the electron bunch at the exit of the buncher.

buncher. The electron bunch is compressed to about 30 ps width. In the core part, the bunch length is within 15 ps, and the energy spread is also small.

Figure 4 shows the current distribution state and phase space of the electron bunch at the exit of A1. The peak current is up to 120 A, the charge of electrons in the core part is about 1 nC, and the rms bunch length is 4.5 ps. When the beam energy is 20 MeV, the rms energy spread is about 80 keV. When the beam energy is 30 MeV, the spread could be increased to 120 keV, which is the maximum rms energy spread of the whole Linac, however the energy spread caused by errors is not included. The transverse emittances are about 10 mm-mrad in the horizontal and vertical directions, as shown in Fig. 5.

The lattice of the beam transport line is designed with the code MAD. As an example, the beta and dispersion functions for the MIR-undulator without the magnetic compressor are shown in Fig. 6. At the position of 0.9 m dispersion, the energy slit will be installed for energy filter.

STATUS AND SCHEDULES

The project is under technical design. The first 60 MeV electron beam is scheduled in September of 2017, the MIR laser would operate at the end of 2017, and the FIR laser would be available at the middle of 2018.

ISBN 978-3-95450-134-2

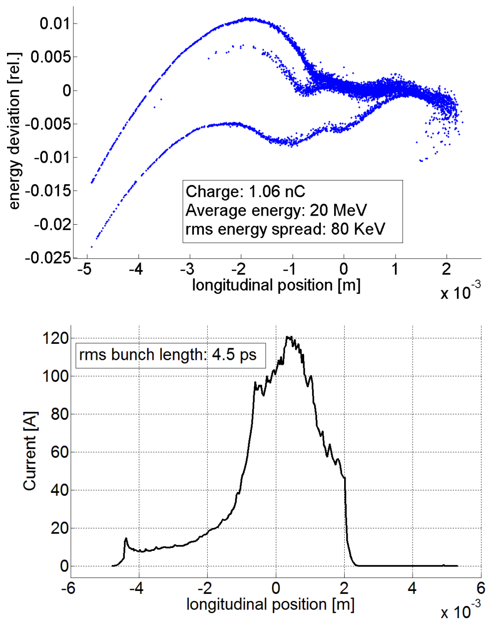

Figure 4: The current distribution state and phase space of the electron bunch at the exit of A1.

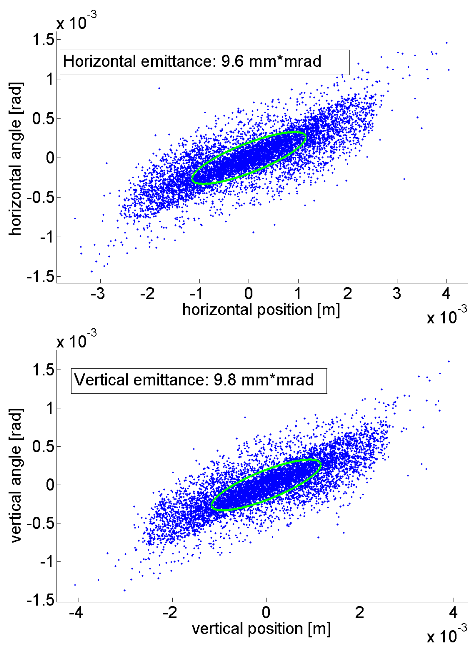

Figure 5: The transverse phase spaces of electron bunch at the exit of A1.

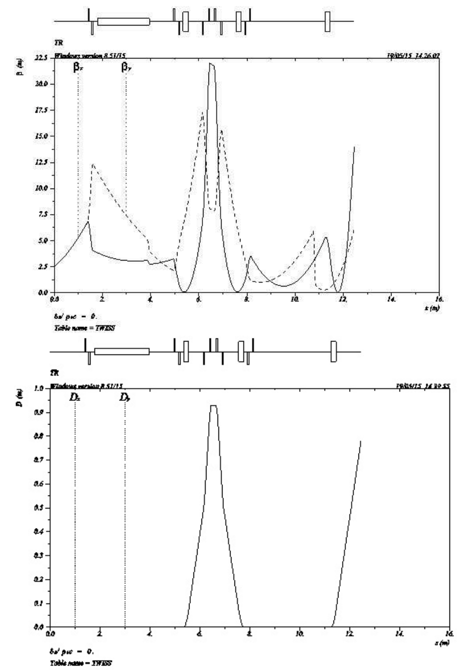

Figure 6: The beta function and dispersion function along the transport line.

REFERENCES

[1] Heting Li, presented at FEL'15, Daejeon, Korea, Aug 2015, paper TUP028, these proceedings.

[2] J. C. Bourdon, R. Belbéoch, P. Brunet, et al., proceeding of EPAC'1988, P. 314.

[3] R. Chaput, proceeding of EPAC'1988, P. 544.

[4] P. W. van Amersfoot, R. W. B. Best, C. A. J. van der Geer, et al., proceeding of EPAC'1988, P. 430.

[5] R. J. Bakker, C. A. J. van der Geer, A. F. G. van der Meer, et al., Nucl. Instrum. Methods Phys. Res., Sect. A **307**, 543(1991).

[6] H. Bluem, V. Christina, B. Dalesio, et al., proceeding of FEL'2010, MOPA09.

ISBN 978-3-95450-134-2

THE STATUS OF CLARA, A NEW FEL TEST FACILITY

J. A. Clarke[1], D. Angal-Kalinin[1], P. A. Atkinson, N. Bliss, A. D. Brynes[1], R. Buckley[1], S. Buckley[1], R. Cash, N. Collomb, L. Cowie[1], G. Cox, G.P. Diakun[1], S. Dobson, D.J. Dunning[1], B.D. Fell, A. Gallagher, P. Goudket[1], A.R. Goulden[1], S. A. Griffiths, C. Hill, C. Hodgkinson, D.M.P. Holland[1], P. C. Hornickel[1], F. Jackson[1], S.P. Jamison[1], J.K. Jones[1], T. J. Jones, K.B. Marinov[1], B. Martlew, P.A. McIntosh[1], J.W. McKenzie[1], K.J. Middleman[1], B.L. Militsyn[1], A.J. Moss[1], B.D. Muratori[1], M.D. Roper[1], L.K. Rudge[1], Y. Saveliev[1], B. J. A. Shepherd[1], E. Snedden[1], R.J. Smith[1], S.L. Smith[1], M. Surman[1], T. Thakker[1], N.R. Thompson[1], R. Valizadeh[1], A.E. Wheelhouse[1], J. Williams, P.H. Williams[1], STFC Daresbury Laboratory, Sci-Tech Daresbury, Warrington, UK
R. Bartolini[2], I. Martin, Diamond Light Source, Oxfordshire, UK
A. Kolano, University of Huddersfield, UK
G. Burt[1], P. Ratoff[1], University of Lancaster, UK
S. Spampinati[1], C. Welsch[1], Y. Wei[1], A. Wolski[1], University of Liverpool, UK
R.B. Appleby[1], K. Hanahoe[1], O. Mete[1], H.L. Owen[1], G. Xia[1], University of Manchester, UK
S. Boogert, A. Lyapin, E. Yamakawa, John Adams Institute at Royal Holloway, University of London, UK
L. Campbell, A.J.T. Colin, J.R. Henderson, B. Hidding, B.W.J. McNeil, University of Strathclyde, UK
J. Smith, Tech-X UK Ltd, Daresbury Innovation Centre, Daresbury, UK
V.V. Paramonov, A. K. Skasyrskaya, Institute for Nuclear Research, Moscow, Russian Federation
[1]Cockcroft Institute, Sci-Tech Daresbury, Warrington, UK
[2]John Adams Institute, University of Oxford, UK

Abstract

CLARA is a new FEL test facility being developed at STFC Daresbury Laboratory in the UK. The main motivation for CLARA is to test new FEL schemes that can later be implemented on existing and future short wavelength FELs. Particular focus will be on ultra-short pulse generation, pulse stability, and synchronisation with external sources. The project is now underway and the Front End section (photoinjector and first linac) installation will begin later this year. This paper will discuss the progress with the Front End assembly and also highlighting other topics which are currently receiving significant attention.

INTRODUCTION

CLARA will be a dedicated FEL test facility in the UK, capable of testing new FEL schemes that have the capability to enhance the performance of short wavelength FELs worldwide. The primary focus of CLARA will be on ultrashort pulse generation, stability, and synchronisation. Enhancements in these three areas will have a significant impact on the experimental capabilities of FELs in the future.

The wavelength range chosen for the CLARA FEL is 400 – 100 nm, appropriate for the demonstration of advanced FEL concepts on a relatively low energy accelerator. Key drivers for this choice are the availability of suitable seed sources for interacting with the electron beam and the availability of single shot diagnostic techniques for the characterisation of the output. The proposal is to study short pulse generation over the range 400 – 250 nm, where suitable nonlinear materials for single shot pulse profile characterisation are available. For schemes requiring only spectral characterisation (for example producing coherent higher harmonics of seed sources, or improving the spectral brightness of SASE) the operating wavelength range will be 266 – 100 nm. Generating these wavelengths will be readily achievable with the 250 MeV maximum energy of CLARA.

Since the Conceptual Design Report was published in 2013 [1] there has been significant progress in the overall design of the facility, with special attention paid to the Front End injection section (up to 50 MeV) and the FEL layout itself. The injection section is currently being procured and assembled offline and it will be installed in November 2015 with commissioning planned for April 2016. A schematic layout of the full facility is given in Fig. 1.

FRONT END SECTION

The CLARA Front End includes the RF photoinjector, a 2 m long S-band linac, a straight ahead line into a temporary combined Faraday cup/beam dump and a dog-leg to transport the beam into the already operational VELA facility [2]. Initially the existing 2.5 cell S-band RF gun currently used at VELA will be used for the CLARA Front End [3]. This is limited to 10 Hz repetition rate, at bunch charges of up to 250 pC. The gun is fed with a 10 MW klystron with a power available for the gun of 8.5 MW. Maximum beam momentum measured at this

ISBN 978-3-95450-134-2

power is 5.0 MeV/c [4]. To reach repetition rates of up to 400 Hz this will be replaced by a high repetition rate photoinjector which is currently being manufactured [5]. This new photoinjector is a 1.5 cell S-band gun with RF probe included for active monitoring and feedback. The cooling system has been optimised to cope with up to 10 kW of average power which means that at a maximum gradient of 120 MV/m it will be capable of 100 Hz, or alternatively 100 MV/m at 400 Hz. The gun also incorporates a vacuum load lock system for ready replacement of the cathode. CAD models of the gun cavity, which is currently being fabricated, are given in Figs. 2 and 3. The linac will also be capable of 400 Hz operation at a maximum gradient of 25 MV/m. A photo of the linac structure currently being fabricated and tested is given in Fig. 4. Detailed studies of the Front End performance with the existing 10 Hz gun and the new 400 Hz gun as a function of accelerating gradient, photoinjector laser pulse length, and also the impact of a velocity compression mode are all discussed in [6].

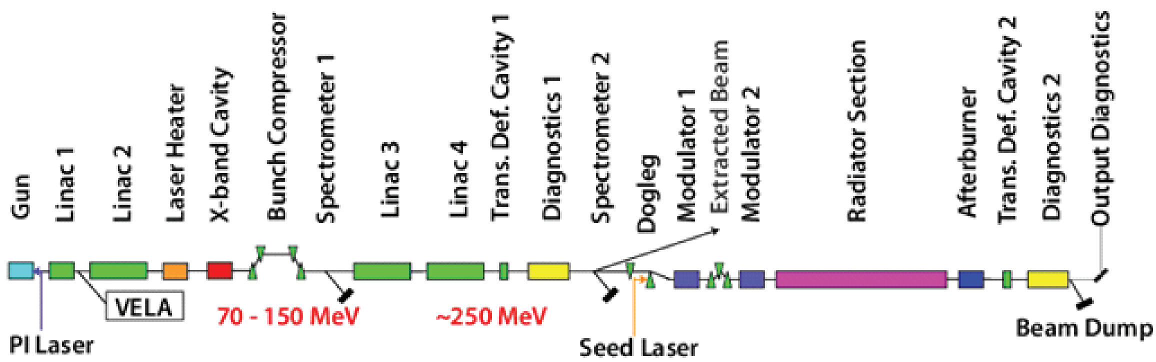

Figure 1: Schematic layout of CLARA.

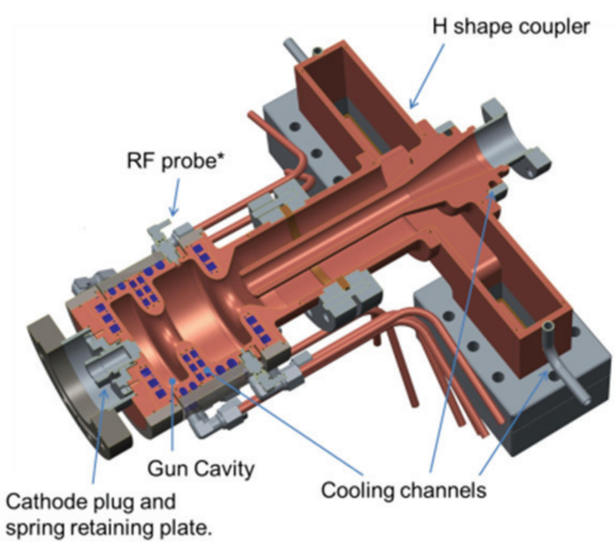

Figure 2: CAD model of the high repetition rate gun showing the key features.

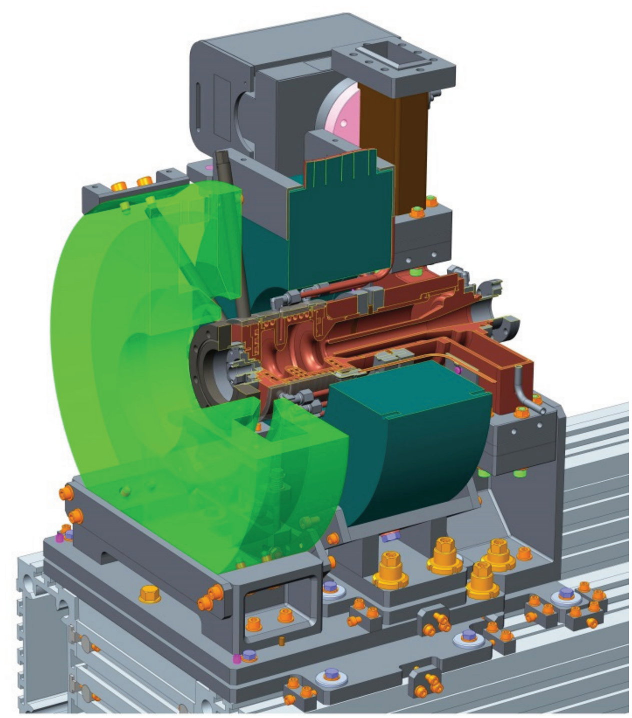

Figure 3: CAD model of the high repetition rate gun mounted on CLARA with the main solenoid in dark green and the bucking solenoid in light green. The load lock system attaches to the back of the gun within this bucking solenoid.

ISBN 978-3-95450-134-2

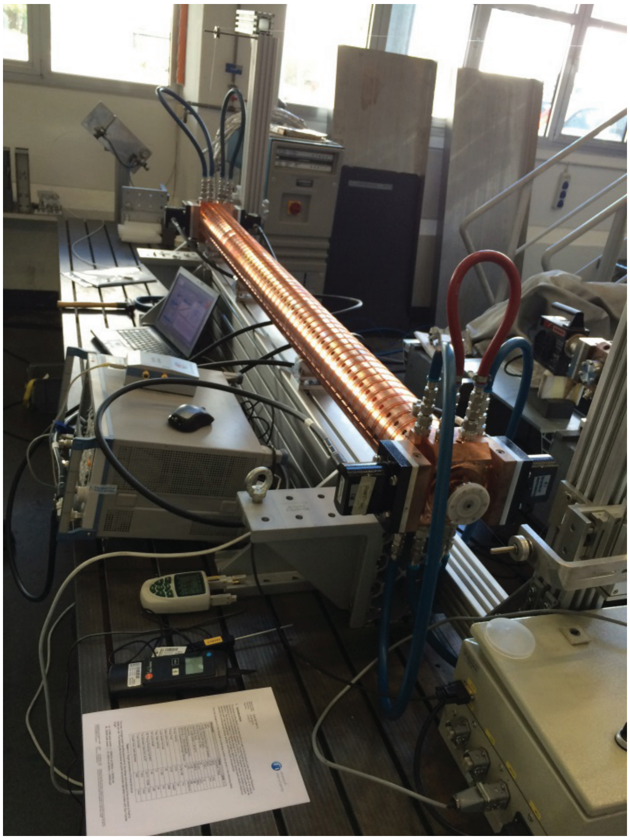

Figure 4: Photo of the 2 m long S-band linac undergoing low power RF testing following manufacture.

LASER HEATER STUDIES

The CLARA linac is potentially affected by longitudinal microbunching instability (MBI) [7-9], as are other accelerators that drive high gain free electron laser (FEL) facilities [10,11], which produces short wavelength (~1 – 5μm) energy and current modulations. These can both degrade the FEL spectrum and reduce the power by increasing the slice energy spread. This instability is presumed to start at the photoinjector exit growing from a pure density modulation caused by shot noise and/or unwanted modulations in the photoinjector laser temporal profile. As the electron beam travels along the linac to reach the bunch compressor, the density modulation leads to an energy modulation via longitudinal space charge. The resultant energy modulations are then transformed into higher density modulations by the bunch compressor. The increased current non-uniformity leads to further energy modulations along the rest of the linac. Coherent synchrotron radiation in the bunch compressor can further enhance these energy and density modulations [12,13]. The main solution to prevent MBI, used in several FEL facilities, is the laser heater [14,15].

A laser heater consists of a short, planar undulator located in a magnetic chicane where an external infra-red laser pulse is superimposed temporally and spatially over the electron beam. The electron-laser interaction within the undulator produces an energy modulation on a longitudinal scale length corresponding to the laser wavelength.

The second half of the laser heater chicane smears the energy modulation in time, leaving the beam with an almost pure incoherent energy spread. This controllable incoherent energy spread suppresses further MBI growth via energy Landau damping in the bunch compressor. A layout of a laser heater is shown in Fig. 5.

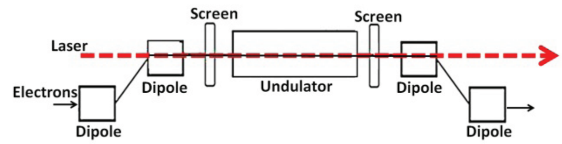

Figure 5: Laser heater layout.

Whilst our studies have shown that a laser heater will not be essential in order for CLARA to lase, the presence of the laser heater in a test facility like CLARA could be exploited to study further some less explored aspects of MBI such as the microbunching induced by the laser heater chicane and the microbunching competition between different sections of the accelerator [16].

The laser heater can also be used to modulate the electron beam energy spread to control the FEL temporal and spectral properties [17] or to deliberately increase the final energy spread to study energy spread sensitivities of the FEL schemes tested at CLARA. The laser heater chicane could be also used to implement the diagnostics presented in [18]. These are all possible experiments of relevance to future FEL facilities. Further details of the CLARA laser heater design and motivation are presented in [19].

REVISED FEL SECTION

The layout of the FEL section has been revised since the publication of the CDR. The previous layout included a single modulator undulator to provide an interaction between seed/modulating lasers and the electron beam. It was found in simulations however that for the 30 – 120 μm seed wavelength range the amplitude of the modulation obtained was smaller than that required for optimum performance in some modes. This was due to the modest seed power available and the fact that the slippage limited the interaction length to only a few undulator periods. The revised layout comprises two modulators with dispersive chicane in between, i.e. an optical klystron configuration. The small modulation induced in the first modulator can be bunched in the chicane giving strong coherent emission in the second modulator which then slips over the whole bunch driving the energy modulation more strongly. The amplitude of the energy modulation is expected to be enhanced by nearly an order of magnitude, compared to the original design comprising a single modulator.

The layout of the radiator section has also been revised. The length of the individual undulator modules has been reduced from 1.5 m to 0.75 m and the gaps between modules have also been halved in length from 1.1 m to

ISBN 978-3-95450-134-2

0.5 m. The number of modules is now 17 compared with 7 previously. There are several motivations for this change. First, two of the schemes to be investigated on CLARA, Mode-Locking [20] and HB-SASE [21], have been seen in simulations to perform more effectively for a lattice comprising a greater number of shorter undulators, in agreement with other research [22]. Second, reducing the FODO period reduces the FEL gain length which benefits all CLARA FEL schemes. Third, the natural focussing of the FEL undulators becomes less significant allowing easier matching into the FODO channel. In order to reduce the length of the intermodule gaps the diagnostic screens and vacuum components will now be incorporated within the length of the undulator modules, rather than in the gaps. Design of the vacuum solution and diagnostic screens is ongoing.

UNDULATOR TAPERING STUDIES

Undulator tapering is a well-known and widely used technique for improving the performance of free-electron lasers. It was originally proposed as a way to improve the energy extraction efficiency of an FEL, but has since found many other applications. For example, when tapering is combined with self-seeding, it provides a route to coherent, high-power, hard x-ray FELs. Alternatively, it can be used in combination with an external laser modulator to generate short, fully coherent radiation pulses by restricting high FEL-gain to the energy-chirped sections of the electron bunch. Similarly, energy-chirps arising from velocity bunching or longitudinal space charge can be compensated using an undulator taper. A reverse undulator taper can also be used to suppress FEL power, whilst still allowing a high degree of bunching to develop within the electron bunch. This can then be used for a variety of applications, such as generating circularly polarised light in a helical undulator after-burner.

In view of this diverse range of applications for undulator tapering, the topic is currently one of interest for study with CLARA. An investigation has been carried out into the suitability of the proposed FEL layout for improving both the final FEL pulse energy and spectral brightness via undulator tapering. The results have confirmed that the proposed layout is suitable for effective tapering experiments [23].

X-BAND DEVELOPMENTS

Initially CLARA will be based on S-band linac sections to achieve the required energy of 250 MeV. However, a study has shown that the replacement of the last 4 m linac section by an X-band linac designed for FEL applications does not have any adverse impact on the bunch quality and would have the useful advantage of increasing the maximum energy of CLARA to approximately 430 MeV, assuming a gradient of 65 MV/m [24]. This would enable CLARA to prove that X-band technology developed initially for the CLIC particle physics collider at CERN is applicable to FELs [25]. In the long term, as this technology matures and is further industrialised, X-band acceleration could form the basis of a future FEL user facility for the UK.

BUILDING UPGRADE

CLARA is being installed into an existing building on the Daresbury site. This building is approximately fifty years old and is 34 m by 110 m which is more than sufficient for CLARA (approximately 10 m by 95 m). However, the temperature variation within the building due to seasonal variation is very large due to poor environmental control and insufficient insulation. As a result the temperature control required within the shielded enclosure, which is specified to be within 0.1 °C, would be very difficult to achieve. Furthermore, the ancillary equipment outside of the shielded enclosure, such as the RF infrastructure, control racks, power convertors, cables, fibres, and lasers, also require the temperature to be well controlled in order to be able to achieve the extreme levels of synchronisation and stability required by CLARA. Therefore the building is being upgraded to stabilise the temperature within the complete building to within 1.0 °C. The walls and roof are being completely replaced by modern insulated panels, and all windows removed, in order to achieve this specification with the minimum of active control required. This building upgrade will be completed within approximately 18 months.

REFERENCES

[1] J.A. Clarke et al, "CLARA Conceptual Design Report", JINST 9 T05001, 2014.
[2] P.A. McIntosh et al, "VELA: A New Accelerator Technology Development Platform For Industry", Proceedings of IPAC2014, Dresden, Germany, p2471, WEPME083.
[3] J. Rodier et al, Proceedings of EPAC 2006, Edinburgh, UK, June 2006, p 1277.
[4] B.L. Militsyn, et al., "Beam Commissioning of VELA at Daresbury Laboratory", Proc. IPAC2014, Dresden, Germany, (2012) p2986.
[5] B.L. Militsyn, "Design of the High Repetition Rate Photocathode Gun for the CLARA Project", Proceedings of LINAC2014, Geneva, Switzerland, p1155, THPP126.
[6] J.W. McKenzie, A.D. Brynes & B.L. Militsyn, "Front End Simulations and Design for the CLARA FEL Test Facility", FEL2015, Deajeon, Korea, paper MOP057, these proceedings.
[7] E.L. Saldin, E.A. Schneidmiller, and M.V. Yurkov, Nucl. Instrum. Methods Phys. Res. A 490, 1(2002).
[8] T. Shaftan and Z. Huang, Phys. Rev. ST Accel. Beams 7, 080702 (2004).
[9] S. Seletskiy et al. Phys. Rev. ST Accel. Beams 14, 110701 (2011).
[10] Z. Huang et al., Phys. Rev. ST Accel. Beams 13, 020703 (2010).
[11] S. Spampinati et al., Phys. Rev. ST Accel. Beams 17, 120705 (2014).

ISBN 978-3-95450-134-2

[12] T. Limberg, P. Piot, and E. A. Schneidmiller, Nucl. Instrum. Methods Phys. Res., Sect. A 475, 353 (2001).

[13] S. Heifets, S. Stupakov, and S. Krinsky, Phys. Rev. ST Accel. Beams 5, 064401 (2002).

[14] E. L. Saldin, E. A. Schneidmiller, and M. V. Yurkov, Nucl. Instrum. Methods Phys. Res., Sect. A 528, 355 (2004).

[15] Z. Huang, M. Borland, P. Emma, J. Wu, C. Limborg, G. Stupakov, and J. Welch, Phys. Rev. ST Accel. Beams 7, 074401 (2004).

[16] D. Ratner at al Phys. Rev. ST Accel. Beams 18, 030704 (2015).

[17] E. Roussel et al. "Influence of a non-uniform longitudinal heating brightness electron beams for FEL", proceedings of IPAC 2015.

[18] R. Fiorito et al., Phys. Rev. ST Accel. Beams 17, 122803 (2014).

[19] S. Spampinati et al, "A laser heater for Clara", FEL2015, Daejeon, Korea, paper MOP044, these proceedings.

[20] N. R. Thompson and B. W. J. McNeil, "Mode-Locking in a Free-Electron Laser Amplifier", Phys. Rev. Lett. 100, 203901, 2008.

[21] B. W. J. McNeil et al, "Transform Limited X-Ray Pulse Generation from a High-Brightness Self-Amplified Spontaneous Emission Free-Electron Laser", Phys. Rev. Lett. 110, 134802, 2013.

[22] N. R. Thompson et al, "High-Brightness Operation of SASE FELs", Phys. Procedia 52, 52-61, 2014.

[23] I.P.S. Martin et al, "Studies of Undulator Tapering for the CLARA FEL", these proc.

[24] P. H. Williams et al, "Developments in the CLARA FEL Test Facility Accelerator Design and Simulations", FEL 2014, p589, TUP091.

[25] J. Pfingstner et al, "The X-Band FEL Collaboration", FEL2015, Daejeon, Korea, paper TUP013, these proceedings.

ISBN 978-3-95450-134-2

PRESENT STATUS OF SOURCE DEVELOPMENT STATION AT UVSOR-III*

Najmeh Sadat Mirian#, Jun-ichiro Yamazaki, Kenji Hayashi, Masahiro Katoh, UVSOR, Okazaki, Japan
Masahito Hosaka, Yoshifumi Takashima, Nagoya University, Nagoya, Japan
Naoto Yamamoto, Taro Konomi, KEK, Tsukuba, Japan
Heishun Zen, Kyoto University, Kyoto, Japan

Abstract

Construction and development of a source development station are in progress at UVSOR-III, a 750 MeV electron storage ring. It is equipped with an optical klystron type undulator system, a mode lock Ti:Sa Laser system, a dedicated beam-line for visible-VUV radiation and a parasitic beam-line for THz radiation. New light port to extract edge radiation was constructed recently. An optical cavity for a resonator free electron laser is currently being reconstructed. Some experiments such as coherent THz radiation, coherent harmonic radiation, laser Compton Scattering gamma-rays and optical vortices are in progress.

INTRODUCTION

UVSOR is a synchrotron light source, which was constructed in 1980's. Using a part of the ring, various light source technologies, such as resonator free electron laser [1] and its applications [2], coherent harmonic generation [3] and coherent synchrotron radiation via laser modulation [4], laser Compton scattering [5] have been developed. These research works had been carried out by parasitically using an undulator and a beam-line for photo-electron spectroscopy [6]. Under Quantum Beam Technology Program of MEXT in Japan, we started constructing a new experiment station dedicated for light source developments. FY2010, we created a new straight section by moving the injection line. FY2011, a new optical klystron was constructed and installed. FY2009-2010, the seed laser system was upgraded and moved to the new station. FY2011, two beam-lines dedicated for coherent light source development were constructed. In FY2012, another upgrade program for the storage ring was funded, in which all the bending magnets were replaced [7]. After this major upgrade, we started to call the machine UVSOR-III. Because we had to pay a lot of efforts for the machine conditioning, we have to slow-down the construction of the source development station for a few years. In FY2014, the mirror chambers of the optical cavity were installed. The experiments have started on coherent THz edge radiation, optical vortex beam, and laser Compton scattering gamma-rays. In this paper, we will report the most recent status of the source development station at UVSOR-III.

*Some parts of this work were supported by JSPS KAKENHI Grant Number 26286081, 26390111 and MEXT Quantum Beam Technology Program.
#nsmirian@ims.ac.jp

FACILITY STATUS

Accelerators

The recent view of UVSOR-III storage ring is shown in Fig. 1. The main parameters of the ring are listed in Table 1. The ring is normally operated at 750 MeV for synchrotron radiation users in multi-bunch mode. On the other hand, in many of the source development studies, the ring is operated at lower energy (600~500MeV) and in single bunch mode. The studies are carried out in dedicated beam times for machine studies. Usually every weekend and Monday can be used for machine studies. In addition, a few weeks a year are usually reserved for machine studies.

The electron beam is supplied by an injector which consists of a 15 MeV linear accelerator and a full energy booster synchrotron. Top-up operation is possible, even for the low energy single bunch operation.

Since the major upgrade in 2012, we have observed that the threshold current of the transverse single bunch instability was lowered. Currently we can accumulate around 50 mA in a single bunch, however, it is difficult to accumulate more. This problem is currently under investigation.

The source development station was constructed by utilizing one of 4m straight section in the ring. It is comprised of an optical klystron, an optical cavity, a seed laser system and beam-lines. The layout of the accelerator part is shown in Fig. 2.

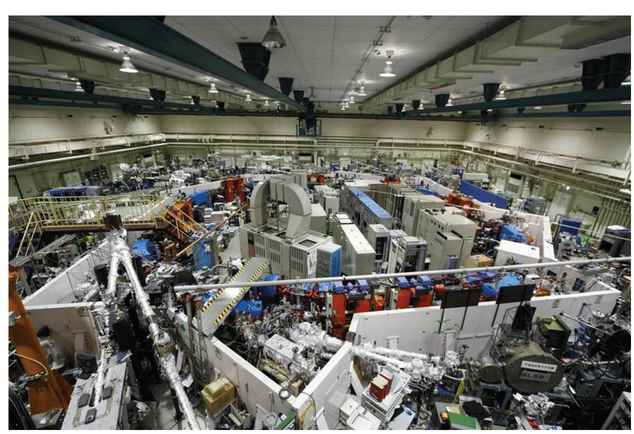

Figure 1: Recent View of UVSOR-III Storage Ring and Synchrotron Radiation beam-lines.

ISBN 978-3-95450-134-2

Table 1: Main Parameters of UVSOR-III

Electron Energy	750 MeV (max.)
Circumference	53.2 m
Beam Current	300 mA (multi-bunch) 50 mA (single bunch)
Emittance	17.5 nm-rad
Energy Spread	5.3×10^{-4}
Betatron Tunes (x,y)	(3.75, 3.20)
Harmonic Number	16
RF Frequency	90.1 MHz
RF Voltage	120 kV
Momentum Compaction	0.030
Natural Bunch Length	128 ps

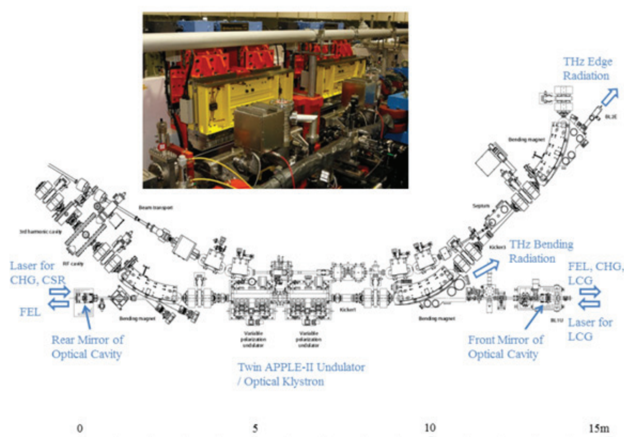

Figure 2: Layout of Source Development Station (Accelerator Part) with a picture of Optical Klystron. A part of the storage ring is shown. The electron beam is circulating counter clockwise (from left to right in this figure).

Optical Klystron

The optical klystron consists of two identical variable polarization undulators of APPLE-II configuration and a buncher magnet, which is a three pole electromagnetic wiggler, in between. The magnetic gaps and phases of the two undulators as well as the field strength of the buncher can be changed independently. The undulators were designed so that the fundamental wavelength of the undulators in the planer mode can be tuned to 800 nm for the electron energy of 600 MeV and to 400 nm for 750MeV. The former wavelength is that of the Ti:Sa laser described in the next section and the latter its second harmonics. So far, the laser seeding is carried out at the fundamental wavelength. In future, the second harmonics will be used to carry out the seeding experiments during normal users beam times. The main parameters of the optical klystron are listed in Table 2.

Table 2: Main Parameters of Optical Klystron

Magnetic Configuration	APPLE-II
Period Length	88 mm
Number of Periods	10 + 10
Max. R56 of Buncher	67µm (600MeV)
Max. Deflection Parameter	7.36 (horizontal) 4.93 (vertical) 4.06 (circular)

Laser

The original laser system for the seeding experiment at UVSOR consisted of a Ti:Sa oscillator and a regenerative amplifier (COHERENT: legend HE), which was synchronized with the RF acceleration of the storage ring [4]. FY 2010, a multipath amplifier (COHERENT: Hidra-50) and a single-path amplifier (COHERENT: Legend-cryo) were added toward a higher pulse energy. The main parameters of the laser system are listed in Table 3.

During the construction of the new experiment station, the laser system was moved to a new site which is close to the downstream end of the undulator beam-line. For the seeding experiment, we have constructed a laser transport line which quides the laser beam to the upstream end of the undulator and, then, into the storage ring [8]. In this new configuration, we have observed laser beam position instability which is likely caused by mechanical vibrations of the optical components. It is observed that this causes significant instabilities of the coherent radiation intensities. Therefore we are currently testing a beam stabilization system based on a commercial product.

Table 3: Main Parameters of Laser System

Legend-HE	Pulse Energy Pulse Width Repetition Rate	2.5 mJ 100fs-2ps 1 kHz
Legend-Cryo	Pulse Energy Pulse Width Repetition Rate	10 mJ 100fs-2ps 1kHz
Hydra-50	Pulse Energy Pulse Width Repetition Rate	50 mJ 100fs-2ps 10Hz

Beam Lines

In spring 2015, the front end of the beam line BL1U, which is dedicated for extracting the FEL or CHG radiation or LCS gamma-rays and injecting laser beams for LCS experiments, was improved as shown in Fig. 3. Just after the light port on the bending magnet chamber, there are a manual gate valve, a beam shutter and a pneumatic gate valve as in the other synchrotron radiation beam lines at UVSOR-III. Just downstream of these, there is a beam slit, which is to cut the unnecessary part of the radiation. This slit was prepared for future utilization of

ISBN 978-3-95450-134-2

the coherent radiation. After the slit, a dismountable 90 degree mirror was installed, which is to extract the light beams and transport those to an optical bench for diagnostics and to lead the laser beam for the LCS experiment to the storage ring. After the mirror, a mirror chamber of the optical resonator for the FEL was installed. The exit of the mirror chamber was sealed with a quartz window. Currently the mirror for the optical cavity is not mounted. Therefore, the undulator radiation can be extracted directly through the window without using mirrors. This may be useful to precisely investigate the phase properties of the undulator radiation.

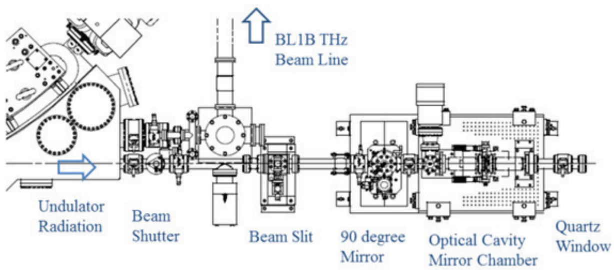

Figure 3: Beam Line Frontend at BL1U.

Another dedicated beam line BL2E was also constructed in FY2014. This beam line is located at the second bending magnet from the undulator, as shown in Fig. 2. This beam-line utilizes a small light port on the zero degree line of the bending magnet. A water cooled Cu mirror reflects the edge radiation from the bending magnet upwards. The radiation was extracted to the air through a quartz window. In adding to this beam line, there is another terahertz beam line BL1B, which is normally used by terahertz synchrotron radiation users, but can be used for the coherent terahertz experiment. In this beam line, a magic mirror is installed which collects infrared and terahertz synchrotron radiation from the bending magnet with a very wide aperture, 244x80 $mrad^2$. A Martin-Puplett type interferometer (JASCO FARIS-1) is also equipped.

SUMMARY AND PROSPECTS

A light source development station was constructed and is being developed at the UVSOR-III electron storage ring. Currently, coherent terahertz radiation experiment based on laser modulation technique, laser Compton scattering experiment and optical vortices beam study using the APPLE-II undulators in tandem are in progress. Resonator free electron laser experiment will be re-started in near future toward intra-cavity laser Compton scattering experiment. The combined use of multi-photon beams such as terahertz-pump and VUV-CHG probe experiments is under preparation.

ACKNOWLEDGMENT

The authors wish to thank all the collaborators in the source development studies, from Lille U., Synchrotron Soleil, Dortmund U., Hiroshima U., Osaka U., Yokohama N. U. and KEK.

REFERENCES

[1] e.g. S. Takano et al., Nucl. Instr. Meth. Phys. Res. A331 (1993) 20; M. Hosaka et al., Nucl. Instr. Meth. Phys. Res. A, 507 (2003), 289-293; C. Evain et al., Phys. Rev. Lett. 102, 134501 (2009).

[2] e.g. T. Gejo et al., Nucl. Instr. Meth. Phys. Res. A 528 (2004), 627-631; T. Nakagawa et al., Rev. Sci. Instr. 78, 023907 (2007); J. Takahashi et al., Internat. J. Molecular Sci., 10 (2009) 3044-3064; H. Nishino et al., Chemistry Euro. J. 2013, 19, 13929-13936.

[3] e.g. M. Labat et al., Phys. Rev. Lett. 101, 164803 (2008); T. Tanikawa et al., Appl. Phys. Express 3 (2010) 122702.

[4] e.g. M. Shimada et al., Jpn. J. Appl. Phys., 46, 12 (2007) 7939; M. Shimada et al., Phys. Rev. Lett. 103, 144802 (2009); S. Bielawski et al., Nat. Phys., 4 (2008) 390-393; I. Katayama et al., Appl. Phys. Lett. 100, 111112 (2012).

[5] e.g. Y. Taira et al., Nucl. Instr. Meth. A, 652, pp.696-700, (2011); Y. Taira et al., Rev. Sci. Instr. 84, 053305 (2013).

[6] S. Kimura et al., J. Electron Spectroscopy Relat. Phenomena 80 (1996) 437-440.

[7] M. Adachi et al., J. Physics: Conf. Ser. 425 (2013) 042013.

[8] S. Tanaka et al., Proc. FEL2012 (2012) 460.

ISBN 978-3-95450-134-2

THE FERMI SEEDED FEL FACILITY: OPERATIONAL EXPERIENCE AND FUTURE PERSPECTIVES

Luca Giannessi*, Enrico Allaria, Laura Badano, Filippo Bencivenga, Carlo Callegari, Flavio Capotondi, Davide Castronovo, Paolo Cinquegrana, Marcello Coreno, Riccardo Cucini, Ivan Cudin, Miltcho B. Danailov, Gerardo D'Auria, Raffaele De Monte, Giovanni De Ninno, Paolo Delgiusto, Alexander Demidovich, Simone Di Mitri, Bruno Diviacco, Alessandro Fabris, Riccardo Fabris, William M. Fawley, Mario Ferianis, Eugenio Ferrari, Paola Finetti, Paolo Furlan Radivo, Giulio Gaio, David Gauthier, Federico Gelmetti, Fatma Iazzourene, Maya Kiskinova, Stefano Krecic, Marco Lonza, Nicola Mahne, Michele Manfredda, Claudio Masciovecchio, Massimo Milloch, Fulvio Parmigiani, Giuseppe Penco, Lorenzo Pivetta, Oksana Plekan, Mauro Predonzani, Kevin Prince, Emiliano Principi, Emanuele Pedersoli, Lorenzo Raimondi, Primoz Rebernik Ribic, Fabio Rossi, Eléonore Roussel, Luca Rumiz, Claudio Scafuri, Claudio Serpico, Paolo Sigalotti, Michele Svandrlik, Cristian Svetina, Mauro Trovò, Alessandro Vascotto, Marco Veronese, Roberto Visintini, Dino Zangrando, Marco Zangrando
Elettra, Trieste, Italy

Abstract

FERMI is the seeded FEL user facility in Trieste, Italy, producing photons from the VUV to the soft X-rays with a high degree of coherence and spectral stability. Both FEL lines, FEL-1 and FEL-2, are available for users, down to the shortest wavelength of 4 nm. We report on the completion of the commissioning of the high energy FEL line, FEL-2, on the most recent progress obtained on FEL-1 and on the operational experience for users, in particular those requiring specific FEL configurations, such as two-colour experiments. We will also give a perspective on the improvements and upgrades which have been triggered based on our experience, aiming to maintain as well as to constantly improve the performance of the facility for our user community.

INTRODUCTION

The distinguishing features that make the FERMI FEL facility [1-3] attractive for the scientific community are the wavelength tunability, the spectral stability, the high degree of longitudinal and transverse coherence with pulses close to the Fourier limit. The capability of providing pulses with different polarizations in various controllable configurations [4,5] and the availablility of a synchronized user laser (IR &UV) with very low time jitter with respect to the FEL pulses [6], are other important and unique characteristics of FERMI.

FERMI FEL-1, the VUV to EUV line covering photon energies between 12 eV and 62 eV [2], has been operating for external users since December 2012. FEL-2, covering the EUV to soft X-rays photon energy range (62 eV to 310 eV) [3], reached in September 2014 the nominal energy per pulse of 10 µJ at the short-wavelength end of the spectral range (4 nm) [7] and is now also available for user experiments. In optimized conditions the spectral quality and operating characteristics of FEL-1 and FEL-2 are similar, with the latter more critical in terms of tuneup and stability requirements. An upgrade program has been started to guarantee for FEL-2 the same robustness, reliability and flexibility of FEL-1.

Three beamlines, each one with its own experimental station, are open for users: Diffraction and Projection Imaging (DiProI) [8], Elastic and Inelastic Scattering TIMEX (EIS-TIMEX) [9], Low Density Matter (LDM) [10]. Three more will be available for users in 2016.

FEL-2 COMMISSIONING RESULTS

In order to efficiently seed the electron beam at low wavelengths, FEL-2 is based on a double stage cascaded HGHG scheme. The external laser seeds the 1st stage that consists of a modulator and a radiator with two sections; the photon pulse generated in the 1st stage seeds the 2nd one, consisting of a second modulator and a radiator with six sections. The magnetic chicane after the 1st stage delays the electron beam with respect to the photon pulse, so that the latter overlaps with fresh electrons.

First lasing of FEL-2 was successfully demonstrated in October 2012 at 14.4 nm and 10.8 nm [3]. The performance of FEL-2 was extended to progressively shorter wavelengths and optimized during the following commissioning periods. In September 2014 specified operating conditions were attained at the lower end of the nominal wavelength interval of FEL-2, namely 4.0 nm [7]. These performances were confirmed in March 2015. These results were achieved after an accurate machine optimization, by setting the peak bunch current to 700 A and the beam energy at 1.5 GeV, by keeping the emittance around 1.5 mm mrad for a properly matched beam at the undulator entrance and by an accurate control of the beam transport along the undulators. The main parameters of FEL-2 are listed in Table 1.

*luca.giannessi@elettra.eu

ISBN 978-3-95450-134-2

The spectral quality of FEL-2 at 5.4 nm and at 4 nm is shown in Fig. 1. The FEL spectral line shapes show very high quality and the transverse profile is very close to the TEM_{00} Gaussian mode.

Table 1: FEL-2 Main Parameters

Parameter	Value
Beam Energy (GeV)	1.0 - 1.5
Peak Current (A)	700 - 800
Repetition Rate (Hz)	10 - 50
Wavelength range (nm)	20 - 4
Polarization	variable
Expected pulse length (fs)	< 100
Energy per pulse (μJ)	up to 100 (~10, 4 nm)
Typical rel. bandwidth,% rms	~0.03 (~0.07, 4 nm)
Shot to shot stability, % rms	~25%(~30%, 4 nm)

At 5.4 nm the harmonic conversion is 12x4, the 1st stage being seeded at 261 nm and the 2nd stage seeded at 21.7 nm and tuned at its 4th harmonic. At 4.0 nm the conversion factor is 13x5.

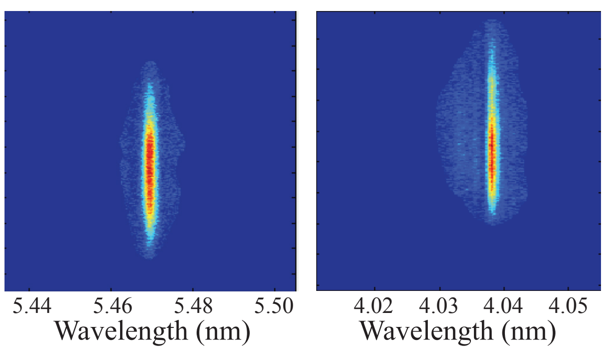

Figure 1: FEL-2 spectrum at 5.4 nm and at 4.0 nm.

In March 2015 in the same configuration at 4 nm an energy stability (rms) of about 30% (see Fig. 2) was achieved. At 4 nm the FEL tuning is more critical and the average line-width is larger than at 5.4 nm. In addition it is not straightforward to achieve simultaneously top energy figures and minimum shot to shot fluctuations together with good spectral linewidth performances. Based on the experience on FEL-2 at short wavelength, a series of upgrades has been initiated as described later.

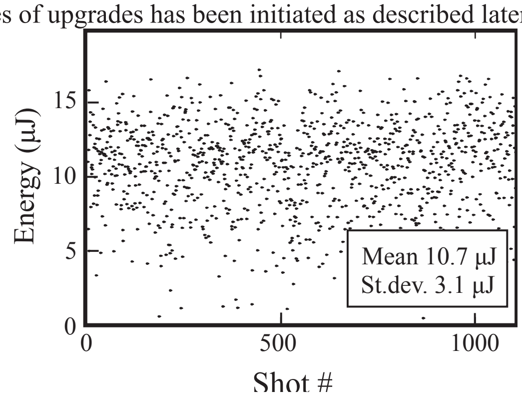

Figure 2: FEL-2 pulse energy.

FEL-1 RECENT EXPERIENCE AND SPECIAL USER MODES

The recent developments on FEL-1 were focused on the characterization and control of the source properties, in particular in terms of polarization [4,5] and pulse/coherence, showing the possibility to tailor the spectro-temporal content of the light pulses [11]. Concerning the latter, we also implemented a SPIDER [12-14] setup for the reconstruction, both in the temporal and spectral domains, of the envelope and phase of pulses generated by the FEL. The method is based on seeding the FEL with two identical replicas of a seed pulse to generate two FEL pulses, shifted in frequency relative one another, by an appropriate electron phase space energy-time quadratic curvature. SPIDER phase interferometry was then used to reconstruct the pulse properties (duration of about 71-73 fs, with deviation of 1.1-1.2 from the Fourier limit) [15]. Some of these studies were also carried out on the first stage of FEL-2, which has identical parameters to those of FEL-1 except for a reduced number of radiators.

Special user modes have been developed to offer to the scientific community extended operating conditions of the FEL with respect to the nominal design parameters, either in terms of wavelengths below the nominal spectral range [16], or in terms of pulse tailoring, with two FEL pulses produced by the same electron beam [17, 18, 19] for pump and probe experiments. Special optimization of the electron beam and of the FEL parameters allowed generation of coherent radiation from FEL-1 at 12 nm, well below its nominal spectral range, to perform user experiments with 10 μJ energy per pulse. After the pioneering two colour FEL-pump/FEL-probe experiment in 2012 [17], a new FEL configuration allowing two colour operations with a wide spectral separation between the two FEL pulses has been proposed and successfully used in experiments [20]. In this configuration, two seed laser pulses with slightly different wavelengths and a controllable delay interact with the same electron bunch. The final radiator is divided into two sections tuned at two different harmonics of the two seed lasers (Fig. 3a). Coherent emission is produced by each of the two bunched portions of the beam in only one of the two

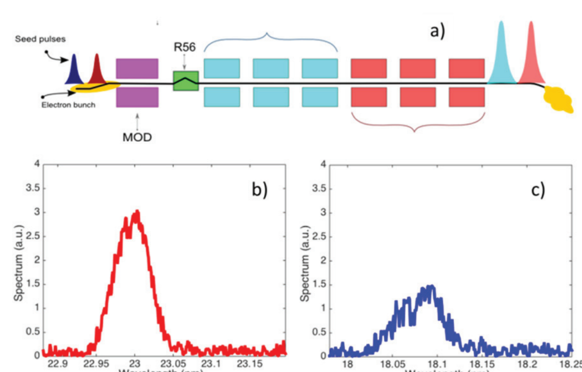

Figure 3: Layout used for two colour FEL operation (a) and measured spectra for the two FEL pulses (b, c).

ISBN 978-3-95450-134-2

radiator segments, generating two temporally and spectrally separated pulses (Fig. 3b and 3c).

Notwithstanding the high gain harmonic generation configuration of FERMI, it is also worth mentioning that lasing in SASE Optical Klystron mode was demonstrated [21]. This configuration is considered as an interesting back-up solution when the seed laser is, for any reason, unavailable.

OPERATION FOR USERS

FERMI operates for about 6500 hours a year; the rest of the time is dedicated to maintenance and upgrade activities [22]. In 2014 60% of the operation time was dedicated to users activities, one quarter of which was devoted to tuning and setting up the FEL and the beamlines. In the remaining 45% of total operation time the facility ran routinely for user experiments, with 86% average FEL uptime availability (with respect to the ideal 100% of the scheduled beamtime), thus improving from the 84.3% value in 2013. Besides internal beamtimes, 16 peer reviewed experiments were completed.

Based on the complexity of the specific experiment, its duration can vary between 3 and 6 days (with an average of about 5 days).

As we are approaching the conclusion of commi-ssioning, the time dedicated to user experiments is increasing. In 2015 it will reach 55% of the total operation time; the number of allocated experiments will increase from 16 to 19 in 2015.

In October 2014 the 4th call for proposals was published and it was opened both on FEL-1 and FEL-2. At the deadline in January 2015 68 proposals had been submitted, 30% on FEL-2. The expected number of allocated proposals is 21, i.e. an oversubscription factor 3.3 (3.1 for the 3rd call). A more efficient operating schedule, based on a weekly turnover between the experimental stations is considered. The preparation time for a standard experiment is between 1 and 2 days. The "special" user modes described in the previous section require careful optimization of all systems involved in the FEL process and close collaboration between scientists and machine experts, in order to define the best strategy to achieve the experimental goals. Therefore the preparation time can be as long as one week; thus only a limited number of experiments of this category can be allocated per year.

The total number of proposals submitted on FERMI to the four calls opened so far from 2012 to 2014 is 193, 76 on DiProI, 55 on EIS-TIMEX and 62 on LDM. About 35% of the proposers are from national institutions, 65% from international ones. The largest foreign community comes from Germany and accounts for 25% of the total.

UPGRADE PROGRAM

LINAC

The present maximum beam energy of the linac is 1.55 GeV (1.5 GeV with a compressed beam) [23]. Two additional accelerating structures by Research Instruments GmbH will be installed to increase the maximum beam energy to 1.65 GeV and to improve the beam quality at low energy [24]. The accelerating structures are 3-meter long, constant gradient, with symmetric input and output couplers and will replace the two single feed structures present in the 100 MeV injector part. The two existing sections will be reinstalled in the high energy part of the LINAC, where space and RF power are already available. Final installation is foreseen in the winter shutdown and commissioning with the increased beam energy will start in February 2016.

FEL-2

In order to reduce the required seed energy and ensure for FEL-2 similar performances in terms of continuous tunability and operability as FEL-1, a third undulator section will be added to the radiator of the 1st stage of FEL-2. This configuration was already foreseen in the original design and space to accommodate the additional undulator is available. The upgrade will allow extraction of higher energy per pulse from the 1st stage at equivalent seed power or alternatively to reduce the required seed power to reach an equivalent seed pulse energy for the 2nd stage. The latter will therefore open the possibility of using the OPA seed laser amplifier with a wider range of seed wavelengths. The stringent requirements on the electron beam quality will be relaxed as well.

The new section is a 2.5 m long Elliptically Polarized Undulator (EPU), 55.2 mm period length, 10 mm minimum gap, the same as the other two EPUs of the FEL-2 1st stage. It is under construction by Kyma srl. Delivery is scheduled in 2015, the installation in tunnel in January 2016 and the commissioning with beam in March.

SEED LASER

The addition of a second regenerative amplifier to the seed laser system, sharing the same femtosecond oscillator with the existing amplifier, will improve the quality of the laser pulse for seeding FEL-2, leading to an improvement of the FEL quality and flexibility. The new regenerative amplifier main features are: a shorter pulse duration in fixed wavelength (800 nm) mode, i.e. less than 50 fs FWHM, and a central wavelength tunability within ±2%. It will also improve the energy and pulse duration parameters of the seed laser pulse. This pulse is delivered with extremely low jitter, less than 7 fms rms [6], to the experimental stations, for pump-probe experiments, and the upgraded system will extend the available range of delays between the FEL pulse and the optical laser pulse.

THREE NEW BEAMLINES

EIS-TIMER

The EIS-TIMER beamline will offer an experimental method based on a Four-Wave-Mixing (FWM) process. In July 2014 a dedicated compact experimental set-up ("*mini-TIMER@DiProI*"), shown in Fig. 4a, was installed

ISBN 978-3-95450-134-2

on DiProI to demonstrate how the coherent FEL pulses delivered by FERMI can generate transient gratings (TGs) in the extreme ultraviolet range and how such TGs, when illuminated by an optical laser pulse, can stimulate an appreciable FWM response [25]. The latter has the form of a well-defined beam (Fig. 4b) that propagates downstream of the sample along the phase matched direction (k_{out} in Fig. 4c). This result is a fundamental milestone for more advanced EUV/soft X-ray FWM applications and a first validation of the EIS-TIMER beamline concept.

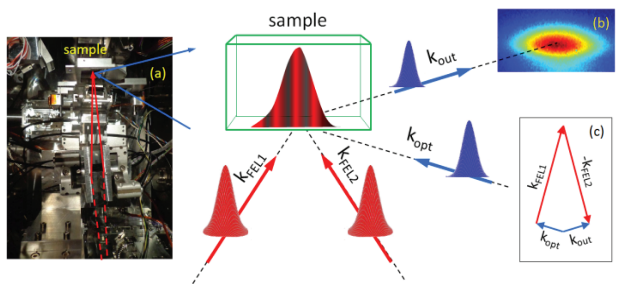

Figure 4: *miniTIMER* set-up (a) and results (b and c).

The first test experiment on EIS-TIMER beamline was performed in July 2015. The beamline will open to the users in 2016.

TeraFERMI

TeraFERMI will collect the THz radiation naturally emitted by the spent electron beam that exits the FEL undulators and will guide it into a dedicated THz laboratory in the FERMI experimental hall. Ultrashort (100's fs) pulses in the 0.1-15 THz range with 1-10 MV/cm electric fields and 0.3-3 Tesla magnetic field will then become available. The TeraFERMI source chamber was installed in January 2015. The optical layout and beamline design are completed and the installation started in July 2015. The first photons are expected for autumn 2015.

MagneDyn

MagneDyn is the beamline for time resolved magnetic dynamics studies and differently from other beamlines, it will receive photons only from the FEL-2 source, since the main scientific interest is in the soft X-ray energies, including the weaker radiation at the third harmonic of FEL-2 undulators.

MagneDyn construction is ongoing and it will see its first photons in the second semester of 2016.

CONCLUSION

The two FEL lines of FERMI, covering the spectral range from VUV to soft X-rays, are now both open for users. Thanks to the excellent FEL spectral stability and quality, high degree of coherence, flexibility of the source the number of users is steadily increasing.

The available experimental stations will be increased from three to six in 2016. A short-term upgrade plan is being implemented to further improve the robustness and the reliability of the facility.

REFERENCES

[1] C. J. Bocchetta et al., "FERMI@Elettra FEL Conceptual Design Report" (Sincrotrone Trieste, 2007).
[2] E. Allaria et al.,Nature Photonics **6**, 699-704 (2012).
[3] E. Allaria et al., Nature Photonics **7**, 913-918 (2013).
[4] E. Allaria et al., Phys. Rev. X **4**, 041040 (2014).
[5] E. Ferrari et al., Scientific Reports 5, 13531 (2015).
[6] M. B. Danailov et al., Optics Express **22**, 12869 (2014).
[7] E. Allaria et al., J. Synchrotron Rad. **22**, 485 (2015).
[8] F. Capotondi et al., Journal of Synchrotron Radiation, **22**, 544 (2015).
[9] C. Masciovecchio, et al. J. Synchrotron Rad. **22**, 553 (2015).
[10] C. Svetina et al., Journal of Synchrotron Radiation, **22**, 538 (2015).
[11] D. Gauthier et al. Spectro-temporal shaping of free-electron laser pulses, Phys. Rev. Lett., in press.
[12] C. Iaconis and I. A. Walmsley, Opt. Lett. **23**, 792 (1998).
[13] T. M. Shuman, et al., Opt. Express. **5**, 134–143 (1999).
[14] Y. Mairesse et al., Phys. Rev. Lett. **94**, 173903 (2005).
[15] G. De Ninno et al. Nature Communications **6**, 8075 (2015).
[16] L. Giannessi et al., "First lasing of FERMI FEL-2 (1°stage) and FERMI FEL-1 recent results" FEL Conference 2012, Nara, Japan, p. MOOB6 (2012).
[17] E. Allaria et al., Nature Commun. **4**, 2476 (2013).
[18] G. De Ninno et al., Phys. Rev. Lett. **110**, 064801 (2013).
[19] B. Mahieu et al., Optics Express **21**, 22728 (2013).
[20] M. Sacchi, Nat. Comm., submitted.
[21] G. Penco et al., Phys. Rev. Lett. **114**, 013901 (2015).
[22] M. Svandrlik, "Operation of FERMI FELs for Users", in Proceedings of the SPIE. Optics+Optoelectronics Conference, Prague 2015, 9512-29.
[23] S. Di Mitri et al., Nucl. Instrum. and Meth. **608**, 19 (2009).
[24] G. Penco et al., JINST **8**, P05015 (2013).
[25] F. Bencivenga et al., Nature **520**, 205 (2015).

ISBN 978-3-95450-134-2

STATUS OF THE SOFT X-RAY USER FACILITY FLASH

K. Honkavaara*, B. Faatz, J. Feldhaus, S. Schreiber, R. Treusch, M. Vogt
DESY, Hamburg, Germany†

Abstract

Since 10 years FLASH at DESY (Hamburg, Germany) has provided high brilliance FEL radiation at XUV and soft x-ray wavelengths for user experiments. Recently FLASH has been upgraded with a second undulator beamline, FLASH2, whose commissioning takes place parallel to user operation at FLASH1. This paper summarizes the performance of the FLASH facility during the last user period from January 2014 to April 2015.

INTRODUCTION

Since summer 2005, FLASH [1–4], the free-electron laser (FEL) user facility at DESY (Hamburg), has delivered high brilliance XUV and soft X-ray FEL radiation for photon experiments. In order to fulfill the continuously increasing demands on the beam time and on the photon beam properties, FLASH is now upgraded with a second undulator beamline (FLASH2), being the first FEL facility worldwide operating simultaneously two undulator lines. The first lasing of FLASH2 was achieved in August 2014 [5]. A brief history of FLASH from a superconducting accelerator technology test facility [6] to a soft x-ray FEL user facility can be found in [3] and references therein.

Figure 1 shows an aerial view of the north side of the DESY area in summer 2014. The FLASH facility with its two experimental halls is in the middle: the FLASH1 hall (recently named as "Albert Einstein") is on the right, the new FLASH2 hall ("Kai Siegbahn") on the left. Next to FLASH are the experimental hall of the PETRA III synchrotron light source (left) and the construction site of PETRA III extension (right).

Figure 1: Aerial view of the FLASH facility. The FLASH1 experimental hall is on the right, the new FLASH2 hall on the left.

This paper reports the status of the FLASH facility and its performance during the 5th user period in 2014/15. Part of this material has presented also in previous conferences, most recently in [4].

FLASH FACILITY

Up to 800 µs long trains of high quality electron bunches are generated by an RF-gun based photoinjector. An exchangeable Cs_2Te photocathode [7] is installed on the backplane of the normal conducting RF-gun. The photocathode laser system has two independent lasers, a third one is in the commissioning phase [8]. The bunch train repetition rate is 10 Hz, and different discrete bunch spacings between 1 µs (1 MHz) and 25 µs (40 kHz) are possible.

A linac consisting of seven superconducting TESLA type 1.3 GHz accelerating modules accelerates the electron beam up to 1.25 GeV. The linearization of the energy chirp in the longitudinal phase space is realized by a module with four 3.9 GHz (third harmonic of 1.3 GHz) superconducting cavities downstream the first accelerating module. The RF-gun and the accelerator modules are regulated by a sophisticated MTCA.4 based low level RF (LLRF) system [9, 10]. The electron beam peak current of the order of a few kAs is achieved by compressing the electron bunches by two magnetic chicane bunch compressors at beam energies of 150 MeV and 450 MeV, respectively.

The use of superconducting technology allows operation with long RF-pulses, i.e. with long electron bunch trains. The bunch train can be shared between the two undulator lines, allowing to serve simultaneously two photon experiments, one at FLASH1 and the other at FLASH2, both at 10 Hz pulse train repetition rate. The separation of the two bunch trains is realized by using a kicker-septum system downstream the last accelerating module.

The production of FEL radiation, both at FLASH1 and FLASH2, is based on the SASE (Self Amplified Spontaneous Emission) process. FLASH1 has six 4.5 m long fixed gap (12 mm) undulator modules, FLASH2 twelve 2.5 m long variable gap undulators. Later, FLASH2 can be upgraded with hardware allowing a seeded operation. A planar electromagnetic undulator, installed downstream of the FLASH1 SASE undulators, provides, on request, THz radiation for user experiments. A place for a THz undulator is available also at FLASH2.

A schematic layout of the FLASH facility is shown in Fig. 2. More details of the FLASH facility and its subsystems can be found, for example, in [3, 4], and references therein. Photon beamlines and photon diagnostics are described in [2, 11, 12].

* katja.honkavaara@desy.de
† for the FLASH team

ISBN 978-3-95450-134-2

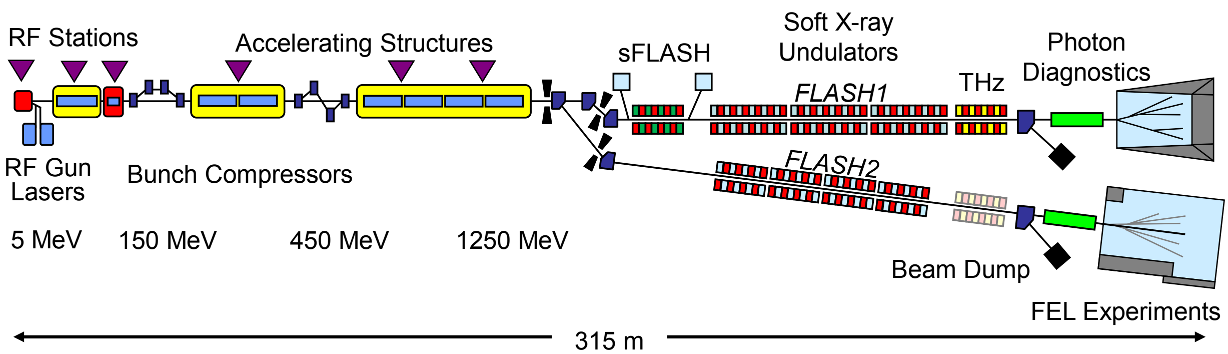

Figure 2: Layout of the FLASH facility (not to scale).

Simultaneous Operation

Each photon experiment has its own demands on the photon beam parameters concerning, for example, photon wavelength, pulse pattern, and pulse duration. In order to fully use the capacity of two undulator lines, the parameters of FLASH1 and FLASH2 need to be, as far as possible, independently tunable.

FLASH1 has fixed gap undulators, and therefore the electron beam energy of the FLASH linac is defined by the photon wavelength required at FLASH1. Thanks to the FLASH2 variable gap undulators providing wavelength tunability by up to a factor of 4, the FLASH2 wavelength can be adapted to the fixed electron beam energy. However, in order to take full advantage of the two undulator lines and to allow fast wavelength changes also at FLASH1, it is desirable to replace the FLASH1 undulators by variable gap ones in the future.

Unequal pulse pattern and pulse duration at FLASH1 and FLASH2 is realized by using two independent photocathode lasers in parallel. This allows production of two electron bunch trains with different parameters (number of bunches, bunch spacing, bunch charge) within the same RF-pulse. A gap of 30 to 50 µs (kicker pulse rise time) is needed between the bunch trains. The LLRF system permits, in certain limits, different accelerating amplitudes and phases for the FLASH1 and FLASH2 bunch trains. This feature, together with different bunch charges, allows lasing at FLASH1 and FLASH2 with different photon pulse durations.

An example of simultaneous operation with different parameters is shown in Fig. 3: FLASH1 has a train of 112 electron bunches with a bunch charge of 0.2 nC, and simultaneously FLASH2 is operated with one bunch of 0.4 nC. The electron beam (1.2 GeV) is not only transported through both beamlines, but both are also simultaneously lasing with wavelengths of 4.5 nm (FLASH1) and 5.5 nm (FLASH2).

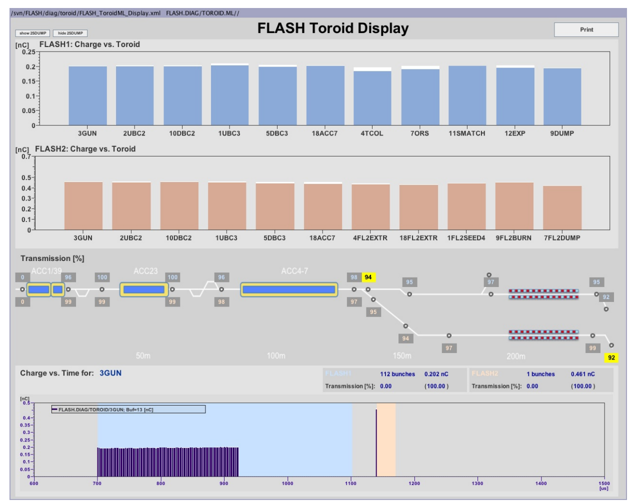

Figure 3: Example of simultaneous operation of FLASH1 and FLASH2. FLASH1 (blue): 112 electron bunches, bunch charge 0.2 nC. FLASH2 (salmon): single bunch with a charge of 0.4 nC.

FLASH1 OPERATION

During the 5th user period from January-27, 2014 to May-3, 2015 (462 days), 10180 hours of beam operation have been realized: 5628 hours (55%) were dedicated to photon user experiments, and 4552 hours (45%) for FEL and accelerator studies. The scheduled weekly maintenance took 199 hours, the yearly approval of the personnel interlock system 81 hours, and the Christmas shutdown 307 hours. Due to a vacuum leak in the RF-gun window, an additional 321 hours off time was accumulated in April 2014. As a consequence, one user experiment was postponed from April 2014 to April 2015.

After a 3 weeks shutdown in May 2015, to complete the radiation shielding between FLASH1 and FLASH2 tunnels with an additional 1000 tons of sand, the FLASH beam operation continued on May-26, 2015. The second half of 2015 will be dedicated to the 6th period of user experiments. From now on, FLASH will have two 6 months user periods per year.

User Operation

Table 1 shows the FLASH1 operating parameters in 2014-2015. These parameters are not all achieved simultaneously, but indicate the overall span of the performance.

ISBN 978-3-95450-134-2

Table 1: FLASH1 Parameters, 5th User Period 2014/15

Electron beam		
Energy	MeV	345 - 1250
Bunch charge	nC	0.08 - 1
Bunches / train		1 - 500
Bunch spacing	µs	1 - 25
Repetition rate	Hz	10
FEL radiation		
Wavelength (fundamental)	nm	4.2 - 52
Pulse energy	µJ	10 - 500
Pulse duration (fwhm)	fs	< 50 - 200
Peak power	GW	1 - 3
Photons per pulse		10^{11} - 10^{13}
Peak brilliance	*	10^{29} - 10^{31}
Average brilliance	*	10^{17} - 10^{21}

* photons / (s mrad^2 mm^2 0.1 % bw)

Similar to previous user periods, the 5th period was organized with an alternating pattern of user blocks (4 weeks) and study blocks (2-3 weeks). The time between the user blocks is also required to exchange experimental set-ups. In the near future, the exchange time for certain types of experiments will be significantly reduced, when two permanent end-stations will be in regular operation: the CAMP end-station for imaging and pump-probe experiments at BL1, and a Raman spectrometer at the PG1 beamline.

During the 5th user period the uptime of the FLASH facility was 96%. In total 4256 hours of FEL radiation was delivered to 32 experiments (25 external, 6 in-house, and one industry experiment). This corresponds to 75% of the total time reserved for user operation. 21% of the user time was used to tune the photon beam parameters to meet the versatile demands of the experiments.

FEL radiation at more than 50 different photon wavelengths between 4.3 nm and 52 nm was delivered to experiments. About 40% of experiments was carried out with a single photon pulse (10 Hz repetition rate), about 20% requested as many pulses as possible. Other desired a multi-pulse operation with a lower intra-train pulse repetition rate (100 kHz or 200 kHz). In addition many experiments require photon pulses shorter than 50 fs or with a small bandwidth (<1%). Arrival time stabilization to the 20 to 40 fs level is also often requested.

Some examples of realized parameter combinations are a single pulse operation at 4.3 nm, 400 pulses (1 µs pulse spacing) at 7.8 nm, 40 pulses (10 µs spacing) at 15 nm, and 60 pulses (5 µs spacing) at 52 nm. For all the cases, the pulse train repetition rate was 10 Hz.

Figure 4 shows the average photon pulse energy during 12 hours of FEL radiation delivery for a user experiment. The fundamental wavelength of the radiation is 9.9 nm. The experiment was carried out at the 3rd harmonics of it (3.3 nm) with 400 photon pulses per train. An example of the pulse energy along the pulse train is shown in Fig. 5.

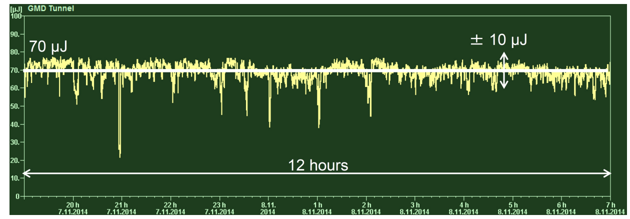

Figure 4: Average photon pulse energy during 12 hours of FEL radiation delivery. Photon wavelength 9.9 nm, 400 photon pulses per train, pulse train repetition rate 10 Hz, photon beamline aperture 3 mm.

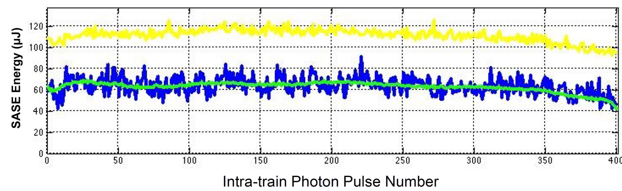

Figure 5: Pulse energy of 400 photon pulses in one train, pulse spacing 1 µs (1 MHz), photon wavelength 9.9 nm. Blue: Actual value, Green: Average, Yellow: Maximum.

Since FLASH1 has fixed gap undulators, the change of the photon wavelength requires the change of electron beam energy. As a consequence a substantial amount of tuning time is needed for wavelength changes (roughly one third). This time will be significantly reduced, when variable gap undulators are available also at FLASH1. Besides wavelength changes, tuning is also required to provide high photon pulse energies (>100 µJ per pulse), to adjust photon beam pointing, and to set up and keep operation with long pulse trains or with very short photon pulses. Additional tuning is also needed, when special FEL radiation properties (e.g. a narrow bandwidth) or parallel delivery of THz radiation are requested.

Two or three user experiments are simultaneously installed at different photon beamlines. Typically, three to five beam time blocks of 24 to 48 hours are reserved for each experiment. Only occasionally an experiment, due to its own constraints, is able to run continuously over several days. Since every experiment has its own parameter set, time (4-8 hours) is reserved for parameter change and tuning at the beginning of each beam time block. This scheduled tuning corresponds to about 20% of the total user time.

The total tuning time can be significantly reduced, when the same experiment runs continuously over a longer period. Two examples to demonstrate this are an experiment of 7 days in December 2014 (11.5 nm, single pulse), and an other one running 10 days in April 2015 (60 pulses, four different wavelengths between 44 nm and 52 nm). In the former case, the FEL radiation delivery was 96%, tuning 2%, and downtime 2% of the total time reserved for the experiment. In the latter one, the distribution was 87% delivery, 11% tuning (including wavelength changes), and 2% downtime.

ISBN 978-3-95450-134-2

FEL and Accelerator Studies

In addition to FEL user operation, FLASH beam time is allocated to FEL and accelerator studies. Study time is used to improve the FLASH performance as an FEL user facility, and to prepare it for the demands of the coming experiments, including also the photon beamlines. Time is reserved for general accelerator physics experiments and developments as well.

Examples of tasks carried out during the study periods are upgrades of the LLRF and the optical synchronization systems, preparation of reference settings for the user operation, and training of the operators. Time is also allocated, for example, to electron beam optics studies [13, 14], and to generate ultra short bunches [15, 16]. The latter uses a special short-pulse (~1 ps) photocathode laser system, and very low electron bunch charge (down to 20 pC) with the goal to produce single-spike, longitudinally fully coherent photon pulses with duration below 10 fs.

An other example of experiments carried out during study periods is the seeding experiment sFLASH, which is located upstream of the FLASH1 SASE undulators since 2010. During the first years sFLASH concentrated on HHG (High Harmonics Generation) seeding [17]. Later also other seeding schemes like HGHG (High Gain Harmonic Generation) have been investigated [18, 19]. In addition, sFLASH hardware has been used to study suppression of FEL radiation by seeded microbunching instabilities [20].

Many of the accelerator physics developments carried out at FLASH have been related to the European XFEL [21], concerning, for example, electron beam diagnostics [22], and operation of accelerating modules with XFEL operation parameters. A new project, FLASHForward, focusing on the plasma-based acceleration, has recently started its hardware installations at the third FLASH electron beamline, and already performed first tests of the production of "driver" and "witness" bunches.

COMMISSIONING FLASH2

Beam commissioning of FLASH2 started in spring 2014. The first lasing was achieved on August 20, 2014 at a wavelength of 40 nm [5]. During the following months, lasing with several wavelengths has been established. Figure 6 shows an example of an FEL beam spot on a YAG screen at a wavelength of 5 nm.

In January 2015, FLASH2 demonstrated fast tunability with the variable gap undulators: the wavelength was changed from 6 nm to 13.5 nm within 30 minutes with a wavelength step of 0.5 nm, i.e. 2 minutes per step.

From mid January 2015 to mid April 2015, FLASH2 had a 3 months shutdown to finalize the installation of photon beam diagnostics in the FLASH2 tunnel. After the re-establishment of the electron beam and SASE operation, the first FEL beam was transported to the experimental hall in June 2015. In the experimental hall, the installation of photon beamlines is on-going, and the first pilot experiments are foreseen later this year. The FLASH2 beam commissioning continues in 2015 parallel to FLASH1 user operation.

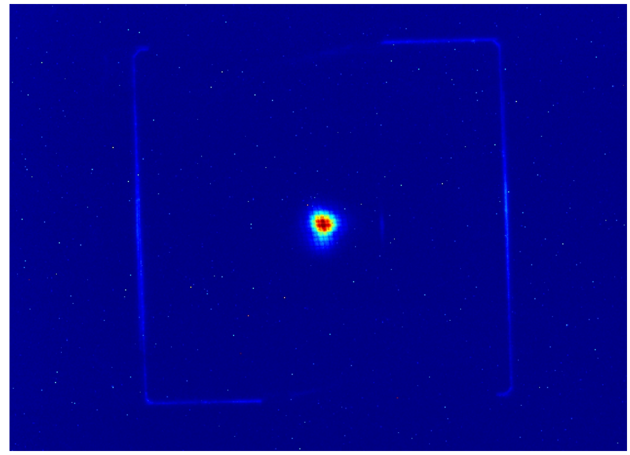

Figure 6: FLASH2 FEL radiation spot on a YAG screen. Photon wavelength 5 nm. The diffraction pattern is caused by a MCP mesh inserted upstream of the screen.

More details of the FLASH2 commissioning, and of the simultaneous FLASH1 and FLASH2 operation, can be found in [23].

SUMMARY AND OUTLOOK

FLASH1 has successfully completed its 5th user period. After a short shutdown in May 2015, the 6th user period started in June 2015 continuing to the end of 2015. Two user periods of 6 months each are scheduled for the year 2016.

The FLASH2 beam commissioning started in spring 2014 and takes place in parallel to the FLASH1 user operation. First lasing was achieved in August 2014. The first FLASH2 pilot photon experiments are expected late 2015, and regular user operation in 2016.

ACKNOWLEDGMENT

We like to thank all colleagues participating in the successful operation, meticulous maintenance, and continuous upgrading of the FLASH facility.

REFERENCES

[1] W. Ackermann *et al.*, "Operation of a free-electron laser from the extreme ultraviolet to the water window", Nature Photonics **1**, 336 (2007).

[2] K. Tiedtke *et al.*, "The soft x-ray free-electron laser FLASH at DESY: beamlines, diagnostics and end-stations", New J. Phys. **11**, 023029 (2009).

[3] K. Honkavaara *et al.*, "FLASH: the First Soft X-ray FEL Operating Two Undulator Beamlines Simultaneously", in *Proc. 36th Free-Electron Laser Conf.*, Basel, 2014, pp. 635-639.

[4] M. Vogt *et al.*, "Status of the Soft X-ray Free Electron Laser FLASH", in *Proc. 6th Int. Particle Accelerator Conf.*, Richmond, 2015, TUPWA033.

ISBN 978-3-95450-134-2

[5] S. Schreiber, B. Faatz, "First Lasing at FLASH2", in *Proc. 36th Free-Electron Laser Conf.*, Basel, 2014, pp. 7-8.

[6] D. A. Edwards, Ed., "TESLA Test Facility Linac, Design Report", DESY, Hamburg, Rep. TESLA-1995-01, March 1995.

[7] S. Schreiber, S. Lederer, "Lifetime of Cs2Te Cathodes Operated at the FLASH Facility", in *These Proceedings: Proc. 37th Int. Free-Electron Laser Conf.*, Daejeon, 2015, TUP042.

[8] S. Schreiber *et al.*, "Simultaneous Operation of Three Laser Systems at the FLASH Photoinjector", in *These Proceedings: Proc. 37th Int. Free-Electron Laser Conf.*, Daejeon, 2015, TUP041.

[9] M. Hoffmann *et al.*, "Operation of Normal Conducting RF Guns with MicroTCA.4", in *Proc. 6th Int. Particle Accelerator Conf.*, Richmond, 2015, MOPHA028.

[10] M. Omet *et al.*, "Operation Experiences with the MicroTCA.4-based Digital LLRF Control System at FLASH", in *Proc. 6th Int. Particle Accelerator Conf.*, Richmond, 2015, MOPHA029.

[11] K. Tiedtke *et al.*, "Challenges for Detection of Highly Intense FEL Radiation: Photon Beam Diagnostics at FLASH1 and FLASH2", in *Proc. 35th Free-Electron Laser Conf.*, New York, 2013, pp. 417-420.

[12] E. Ploenjes *et al.*, "FLASH2 Beamline and Photon Diagnostics Concepts", in *Proc. 35th Free-Electron Laser Conf.*, New York, 2013, pp. 614-617.

[13] J. Zemella *et al.*, "Measurements of the Optical Functions at FLASH", in *Proc. 5th Int. Particle Accelerator Conf.*, Dresden, 2014, pp. 1141-1143.

[14] J. Zemella *et al.*, "Progress in Optics Studies at FLASH", in *Proc. 6th Int. Particle Accelerator Conf.*, Richmond, 2015, TUPWA035.

[15] J. Roensch-Schulenburg *et al.*, "Operation of FLASH with Short SASE-FEL Radiation Pulses", in *Proc. 36th Int. Free-Electron Laser Conf.*, Basel, 2014, pp. 342-345.

[16] M. Yurkov *et al.*, "Low Charge Mode of Operation of Free Electron Laser FLASH", in *These Proceedings: Proc. 37th Int. Free-Electron Laser Conf.*, Daejeon, 2015, WEP021.

[17] S. Ackermann *et al.*, "Generation of Coherent 19- and 38-nm Radiation at a Free-Electron Laser Directly Seeded at 38 nm", Phys. Rev. Lett. **111**, 114801 (2013).

[18] J. Boedewadt *et al.*, "Recent Results from FEL Seeding at FLASH", in *Proc. 6th Int. Particle Accelerator Conf.*, Richmond, 2015, TUBC3.

[19] K. Hacker *et al.*, "HGHG Seeding at FLASH - First Lasing at 38 nm", in *These Proceedings: Proc. 37th Int. Free-Electron Laser Conf.*, Daejeon, 2015, WEP030.

[20] C. Lechner *et al.*, "FEL Lasing Suppression by a Seeded Microbunching Instability", in *These Proceedings: Proc. 37th Int. Free-Electron Laser Conf.*, Daejeon, 2015, TUA02.

[21] W. Decking, "Status of the European XFEL", in *These Proceedings: Proc. 37th Int. Free-Electron Laser Conf.*, Daejeon, 2015, WEA04.

[22] N. Baboi, D. Noelle, "Commissioning of the FLASH2 Electron Beam Diagnostics in respect to its use at the European XFEL", in *Proc. 3rd Int. Beam Instrumentation Conf.*, Monterey, 2014, pp. 712-721.

[23] M. Scholz *et al.*, "First Simultaneous Operation of Two Sase Beamlines in FLASH", in *These Proceedings: Proc. 37th Int. Free-Electron Laser Conf.*, Daejeon, 2015, TUA04.

ISBN 978-3-95450-134-2

STATUS OF THE FABRICATION OF PAL-XFEL MAGNET POWER SUPPLIES*

Seong Hun Jeong#, Ki-Hyeon Park, Hyung Suck Suh, Sang-Bong Lee, Bongi Oh, Young-Gyu Jung, Hong-Gi Lee, Dong Eon Kim, Heung-Sik Kang, In Soo Ko
PAL, Pohang, Republic of Korea

Abstract

The PAL-XFEL has been constructing including a 10 GeV linac, hard X-ray and soft X-ray beam lines. The PAL-XFEL required for about six hundreds of magnet power supply (MPS). The nine different prototypes of MPS are developing to confirm the performance, functions, size, heat load and so on. This paper describes the test results of the prototype MPS in major specifications. All MPSs have to be installed until the end of September in 2015. The installation progress of the MPS was also described.

INTRODUCTION

The PAL-XFEL accelerator needs many kinds of power supplies for different magnet types. Table 1 shows the specifications of the power supplies needed for the PAL-XFEL.

The MPS for corrector magnets are divided into 4 families based on the current rating and stability, 10 A 10 ppm, 10 A 50 ppm , 12 A 10 ppm and 12A 50 ppm.

The MPSs for the dipole and quadrupole were categorized into two types, unipolar and bipolar. And it was grouped to five types according to its current ratings.

Table 1: MPS Specifications

Magnet	MPS type	Qty	Stability (ppm)
Corrector	Digital	395	10 & 50
Quadrupole	Unipolar	122	100
	Bipolar	86	
Dipole	Unipolar	20	20
	Bipolar	2	
Solenoid	Bipolar	3	20

BASIC STRUCTURE

The configuration of the designed MPS was similar with others [1]. The input stage consisted of transformer, full rectifier and a damped low pass filter. The commercial switching mode power supply (SMPS) was often adopted for low power less than 400 W instead. Transformer connection was one of delta or wye windings or sometimes both of them where high stability was required. The low pass filter at the input stage should be needed. Figure 1 shows the general hardware configuration of the MPS.

The topology of the power convertor was either buck for unipolar or H- or half-bridge for bipolar. The output stage was composed of a low pass filter to reduce the switching noise. The output filter composed of two stage LC filters where the pole of the first stage was about ~KHz and second one was between higher than one-half and full of the switching frequency.

The DSP TMS320F28335 from TI Co was used to control the duty of the PWM and to interface surrounding peripherals. It has six enhanced PWM modules with 150 ps micro edge positioning (MEP) technology [2]. Thus effective PWM resolutions can be increased up to about 18-bit in case of switching frequency of 25 KHz. Without MEP, the normal PWM resolution is about 12-bit, which can't offer the sufficient resolution for the high stability.

The power supply performs the Ethernet communication by the single chip WEB server. The WEB server exchanges all power supply data via RS232 connection with the FPGA.

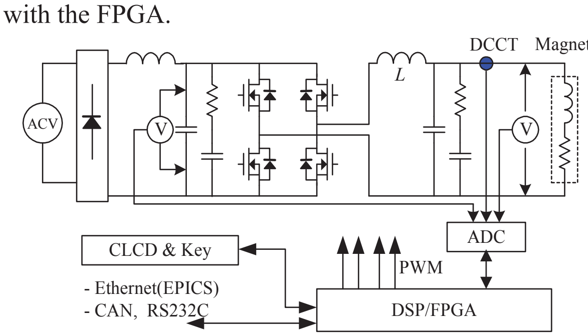

Figure 1: Block diagram of the buck type magnet power supply.

CONTROL SCHEME

The control loops for the developed MPS are given in Fig. 2. A cascaded current and voltage feedback loop was applied to the MPS compensator [3]. The inner voltage loop worked to reject the voltage fluctuation of the output stage. The voltage loop has a small time constant comparing to outer current loop. Thus it can be shown as constant by the outer loop.

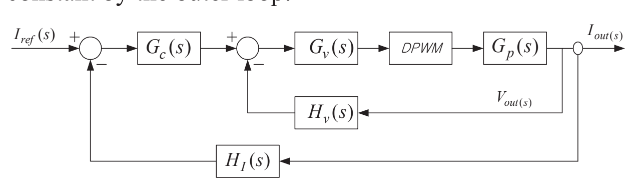

Figure 2: Block diagram of complete current loop system.

The current and voltage compensators were applied a proportional-integral (PI) type which was very common

*Work supported by Ministry of Science, ICT & Future Planning
#jsh@postech.ac.kr

ISBN 978-3-95450-134-2

in feedback systems. The coefficients of the current loop were 60 for proportional gain and 30000 for integral gain, respectively. Figure 3 showed the frequency and phase responses of the discrete PI compensator when the time period of the loop was 40 µs. The pole located at 0 and zero at the about 80 Hz.

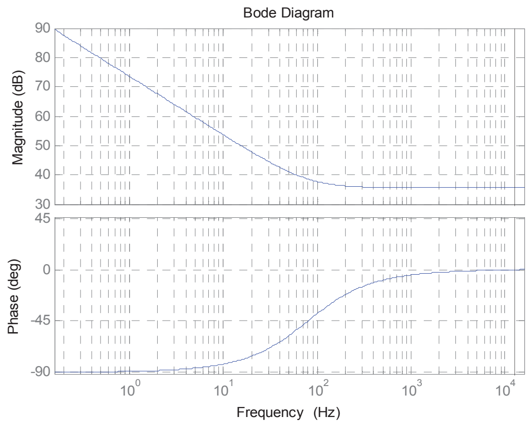

Figure 3: Bode plot of the discrete current PI compensator of the MPS.

PROTOTYPE POWER SUPPLY

All measurement system is consists of three part – HP3458A digital voltmeter from Agilent Co. with external DCCT MACC150 from HITEC, computer and load magnet. Two prototype power supplies are fabricated for verifying performance. The supplies underwent extensive testing at the factory. Testing included verifying the digital interlocks and running each unit for eight hours. The major specifications of MPS were examined about short term stability, step responses at the rising and falling times, zero cross response and long term stability.

Corrector MPS

The prototype MPSs for corrctor magnets were developed . The major specifications are given in Table 2. The total number of corrctor MPS is 432. The four MPSs were assembled into shelf of which height is 3 U. Figure 4 shows the 4 type corrector MPS for prototype.

Table 2: Corrector MPS Specifications

MPS Type	I [A]	V[V]	Qty[ea]	Stability[ppm]
C1	5	12	262	50
C2	10	15	74	50
C3	5	10	78	10
C4	12	15	18	10

Figure 4: Prototype corrector MPS.

The other hardware modules are standalone to each MPS. The MPS has a character LCD for display the basic information like set-current, interlock status, etc.

The cross effect tests, like step current set, bewteen MPSs in a same shlef were tested. We found that each MPSs were fully isolated in the cross coupling issues.

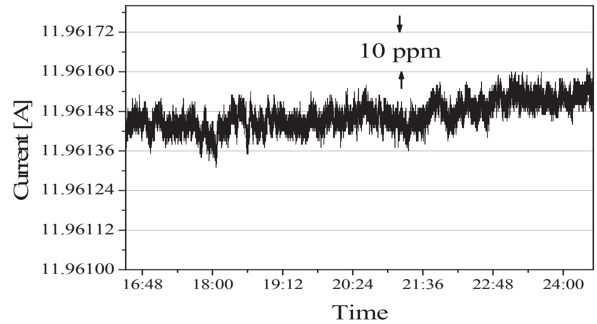

Figure 5: Long term stability of corrector power supply.

Figure 5 shows the long term current stability of corrector MPS. The current stability with the load was less than 20 ppm of ±12 A output current.

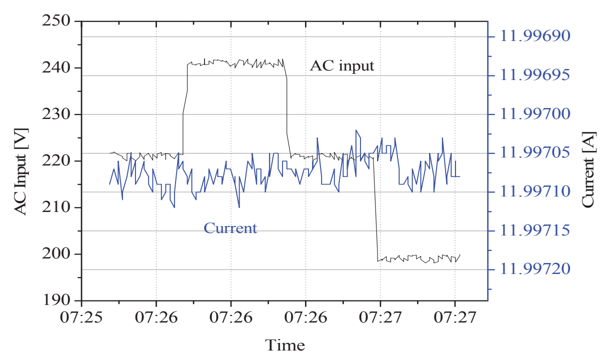

Figure 6: Resposses of the line regulation test.

Figure 6 shows the response of AC line regulation test. The AC line is change the ±10%, but current stability is not changed.

Dipole and Quadrupole MPS

The major specifications of MPSs for dipole and quadrupole magnets are given in Table 3. The total number of MPS for those magnets is 276.

Table 3: Dipole & Quadrupole MPS Specifications

MPS Type	I [A]	V[V]	Qty[ea]	Stability[ppm]
A-1	20	20	180	50 & 100
A-4	±20	20	38	50 & 100
B-1	190	110	31	10 & 50 &100
B-2	310	85	5	10 & 50
B-3	310	200	2	50

DAWON have manufactured the dipole and quadrupole power supply and prototype power supply has fabricated as shown in Fig. 7. This prototype A-1 MPS has a character LCD for display the basic imformation of MPS set-current, interlock status, etc.

ISBN 978-3-95450-134-2

Figure 7: Prototype A-1 power supply.

The long term current stability of A1-type, power supply was measured as shown in Fig. 8. The current stability was less than 50 ppm of 20 A output current for 2.5 °C ambient air temperature change.

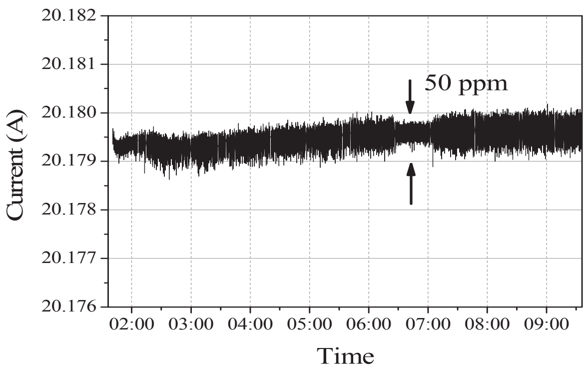

Figure 8: Long term stability of A-1 type power supply.

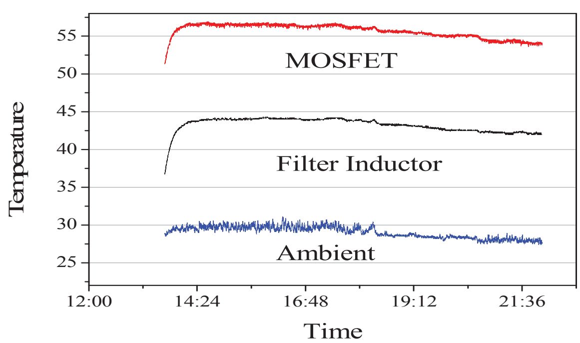

Figure 9: Temperature change of major component of A-1 type power supply.

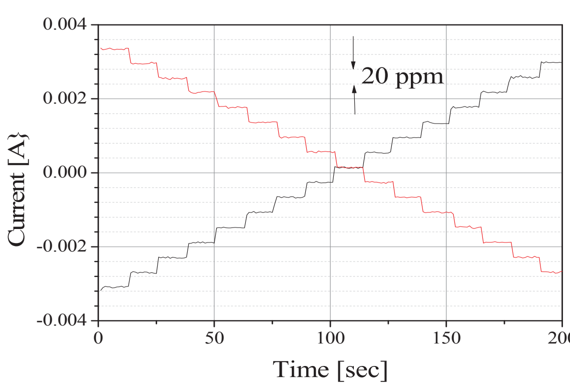

Figure 10: Zero cross response of the A-1 type MPS.

Figure 9 shows the major components operating temperature. It was measured to verify the stable operation for low MTBF (mean time between failures). The MOSFET surface temperature is about 56 °C and filter inductor is about 43 °C. It was normal operating range for reliable life time of MPS

Figure 10 shows the zero cross response of the A1-type MPS. When 20 ppm step of the input current was increased from -0.003 A to 0.003 A, the MPS showed good output responses. Figure 11 shows the reproducibility response of A-1 MPS. The output current is changed from 10% of maximum output current to maximum output current for 1 minute interval. It shows the good response.

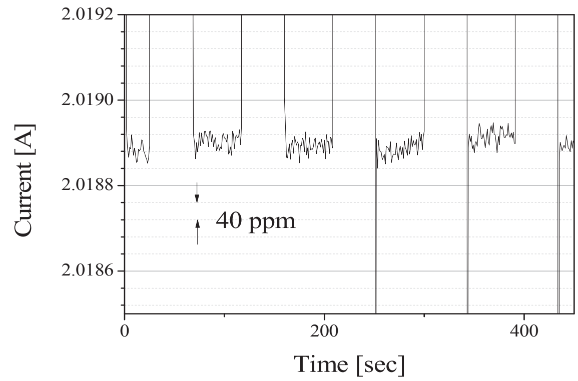

Figure 11: Reproducibility response of A-1 MPS.

CONCLUSION

This paper described the overall MPS requirements, control scheme, MPS assembling, test results, installation plan for PAL-XFEL. In factory stage, the acceptance test will focused on the power circuit. After the 8 hour-operation at 100% normal current, MOSFET and filter inductor temperature was checked. The temperature change is less than 20°C for A-1 type power supply. The experimental results with the assembled PS showed the high stability. The short term stability is about 10 ppm and long term stability for eight hours is about 50 &10 ppm each. These MPS included the small web server to make easy maintenance. The MPS will be installed from Aug., 2015 and the operation tests will begin in Dec., 2015.

REFERENCES

[1] K. H. Park, et al., “Implementation of high precision magnet power supply using the DSP”, in *Proc. Asian Pacific Accelerator Conf.* (*APAC2007*), Indore, January 2007, paper THPMA024, p.666.

[2] Texas Instruments Co., http://www.ti.com

[3] H. Jin, S.B. Dewan, “A Combined Feed-forward and feedback Control Scheme for Low-Ripple Fast-Response Switch-mode Magnet Power Supply”, IEEE Trans. on Magnetics, Vol.30, No.2, p.1801 (1994).

ISBN 978-3-95450-134-2

BEAM COMMISSIONING PLAN FOR THE SwissFEL HARD-X-RAY FACILITY

T. Schietinger on behalf of the SwissFEL team,
Paul Scherrer Institut, CH-5232 Villigen PSI, Switzerland

Abstract

The SwissFEL facility currently being assembled at the Paul Scherrer Institute is designed to provide FEL radiation in the photon wavelength range between 0.1 and 7 nm. The commissioning of the first phase, comprising the electron injector, the main electron linear accelerator and the first undulator line, named Aramis and dedicated to the production of hard X-rays, is planned for the years 2016 and 2017. We present an overview of the beam commissioning plan elaborated in accordance with the installation schedule to bring into operation the various subsystems and establish beam parameters compatible with first pilot user experiments in late 2017.

INTRODUCTION

SwissFEL is an X-ray Free-Electron-Laser facility under construction at the Paul Scherrer Institute (PSI) in Switzerland [1]. Its two undulator lines, named Aramis and Athos, are designed to deliver hard X-rays in the wavelength range between 0.1 and 0.7 nm and soft X-rays between 1 and 7 nm, respectively. Figure 1 shows a schematic overview of the facility, annotated with relevant machine and beam parameters. In a first phase, only the Aramis beamline will be realized, with Athos to be completed in a second phase, currently foreseen for the period 2018–20. After an extensive design and development phase, including beam development work [2] and component tests [3] at a dedicated injector test facility [4], the SwissFEL-Aramis facility is currently in the installation phase, with first beam commissioning scheduled for early 2016. The commissioning phase is foreseen to extend over two years, with installation activities continuing in parallel or in between. First pilot user experiments are expected for late 2017.

We give an overview of the various commissioning steps. While the sequence of commissioning tasks will remain the same apart from further refinements or small rearrangements due to possible changes, the dates are subject to change depending on the overall progress of component delivery and installation. The SwissFEL commissioning plan is part of a global project plan (dubbed Planning-Installation-Commissioning, or PIC, plan), which ensures the overall consistency of the project schedule taking into account all dependencies. It is updated on a regular basis reflecting progress achieved on building construction, component delivery and installation. The dates presented here have been derived from the latest PIC plan update (July 2015).

COMMISSIONING OVERVIEW

The SwissFEL commissioning, up to the end of the first project phase, can be split into three phases: the injector phase (first acceleration stage, up to a beam energy of 320 MeV), the linac phase (transmission through the full accelerator and undulator line, but no intentional generation of X-rays yet) and the FEL phase (final phase with X-rays from the undulators). The SwissFEL commissioning objectives have been formulated in terms of a set of milestones, specifying electron beam energy and bunch charge, repetition rate, and photon wavelength and pulse energy to be achieved for three specific dates, see Table 1.

The start of beam development activities is usually dictated by the installation and start-up schedule of the necessary infrastructure. In particular in the later stages of commissioning, progress towards reaching the final beam energy, and thus the final photon wavelength, will be driven entirely by the deployment schedule of the RF stations powering the main linac.

The special location of SwissFEL in a freely accessible forest outside the PSI site requires particular consideration to radiation issues. As a consequence, every commissioning step involving a significant change in beam parameters is followed by extensive radiation mappings of the building and the surrounding areas.

The commissioning work will be performed in eight-hour shifts, following the existing PSI shift schedule for simplicity. Due to the limited manpower available, only two shifts per work day will be staffed, with the third shift (during the night) being used for long-term stability tests and the like. On weekends it is foreseen to staff one shift per day on average. Shift crews will consist of a shift leader (typically a beam dynamics expert) a shift expert (from a PSI expert group, such as diagnostics, RF, controls etc., but also beam dynamics, depending on the specific commissioning task or issue), and, as far as available, a member of the PSI operation section. For all the critical hardware systems, on-call services will be maintained by the expert groups. The absence of scheduled, dedicated night shifts considerably simplifies both the organizational aspects of shift work and the associated formal approval procedure.

The numbers of shifts needed during each commissioning phase to reach the milestones have been estimated as 155 for injector commissioning, 135 for linac commissioning and 204 for FEL commissioning. In addition, some 28 weeks are needed for the commissioning of the photonics infrastructure in the optical and experimental hutches.

ISBN 978-3-95450-134-2

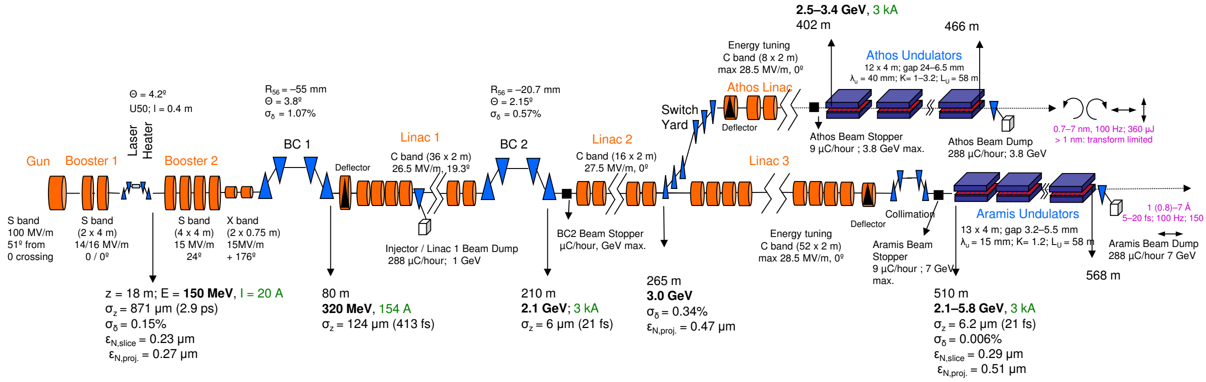

Figure 1: SwissFEL schematic overview showing the two beamlines Aramis (hard X-rays) and Athos (soft X-rays). The latter beamline will only be realized in a second phase and is shown here for information only.

Table 1: SwissFEL Aramis principal milestones with target dates according to current planning.

Parameter	**Milestone I** 30 June 2017	**Milestone II** 30 Sept. 2017	**Milestone III** 30 Dec. 2017
Electron beam energy [GeV]	3.0	3.8	5.8
Electron bunch charge [pC]	200	200	200
Repetition rate [Hz]	50	50	100
Photon wavelength [Å]	3.7	2.3	1.0
Photon pulse energy [μJ]	400	400	400

RF CONDITIONING

Every beam commissioning phase is preceded by a period of RF conditioning, during which the accelerating structures of newly installed RF stations are slowly brought up to their nominal accelerating gradients and somewhat further to ensure smooth operation with beam. The procedure is needed to remove remaining surface impurities as well as dust and humidity directly with RF power and may take from a few hours up to several weeks, depending on the state of the cavities. While this conditioning is done without beam, i.e., no electrons are injected during the conditioning RF pulses, it may proceed in parallel to beam operation, which would make use of already conditioned cavities only. In this case the timing of the electron bunches is set in a way that ensures their undisturbed passage through cavities under conditioning, i.e., between two RF pulses. Also, to prevent the acceleration of dark current electrons (from field emission at the cavity surface) produced in the cavities of one RF station by any of the following cavities, the RF conditioning pulses are all shifted, not only with respect to the electron bunch, but with respect to all other RF stations under conditioning as well.

INJECTOR COMMISSIONING

The commissioning of the SwissFEL injector proceeds in four main stages, summarized in Table 2. The first two stages after the RF conditioning are dedicated to the commissioning of the gun and booster sections of the injector, whereas the last two stages deal with the setup of the two chicanes (bunch compressor and laser heater). The stages typically include a few shifts for the beam-based commissioning of the diagnostics components involved in the new machine part. After every stage, the stability and reproducibility of the beam parameters will be verified before proceeding to the next stage. Provided that the first C-band RF station of linac 1, situated between the end of the booster and the injector spectrometer, is in operation at the time of completion of the injector commissioning, a further commissioning stage is foreseen to test and characterize this RF module with beam, taking advantage of the injector spectrometer for beam measurements.

The repetition rate for injector commissioning will generally be limited to 10 Hz to minimize beam losses. Exceptions are occasional gun tests at 100 Hz and overall booster tests at 50 or 100 Hz towards the end of injector commissioning, when orbit and optics are well understood. Some linac installation work is planned in parallel with injector operation in the linac 3 and undulator areas ($z > 245$ m). For the time of the injector commissioning, a temporary beam stopper, consisting of a 50 cm $\times$ 30 cm $\times$ 30 cm iron block, will prevent the direct propagation of the electron beam beyond the injector area.

The commissioning of the injector will mainly be performed at a nominal bunch charge of 200 pC. For first passes through machine sections, however, the bunch charge will be reduced to about 50 pC to minimize radiation losses. The charge will only be raised once a stable orbit and a reasonable optics have been established for a given section.

ISBN 978-3-95450-134-2

Table 2: Commissioning stages for the SwissFEL injector. Beam conditions refer to the nominal conditions during a given stage; E is the electron beam energy, Q the bunch charge and R the repetition rate.

Commissioning Stage	Approx. Dates	Beam Conditions	Main Tasks
RF Conditioning	Jan./Feb. 2016		Conditioning of gun and S-band booster cavities beyond nominal accelerating gradient. Conditioning of first C-band module as soon as available.
Gun Commissioning	Feb./March 2016	e^- to gun dump E = 7.1 MeV Q = 50–200 pC R = 10–100 Hz	Initial setup of the electron gun, commissioning of diagnostics in gun section, detailed characterization of the gun.
Booster Commissioning	April–June 2016	e^- to inj. dump E = 320 MeV Q = 50–200 pC R = 10 Hz	Transmission to injector beam dump, beam-based commissioning of diagnostics, RF commissioning of booster cavities, setup of beam orbit and optics, radiation mapping, beam emittance optimization.
BC1 Commissioning	June/July 2016	e^- to inj. dump E = 320 MeV Q = 50–200 pC R = 10 Hz	Setup of bunch compressor (orbit and optics), longitudinal phase space measurement (compression verification), commissioning of X-band cavity, emittance optimization of compressed beam.
Laser Heater Commissioning	July/Aug. 2016	e^- to inj. dump E = 320 MeV Q = 50–200 pC R = 10 Hz	Basic setup of the laser heater chicane (final setup will be done based on FEL signal).
C-band Module Test	Aug. 2016	e^- to inj. dump E = 590 MeV Q = 50–200 pC R = 10 Hz	Beam-based test and characterization of first C-band module.

LINAC COMMISSIONING

The goal of the linac commissioning phase, summarized in Table 3, is the safe transport of electrons through all linac sections as well as the transfer and undulator lines at a nominal beam energy of 2.1 GeV. The reduced beam energy reflects the fact that at this stage of the commissioning, only linac 1 will be equipped with operational power RF stations. (Linacs 2 and 3 will have cavities installed, but no RF power to drive them.) The final beam energy of 5.8 GeV, requiring all RF power stations, will only be achieved during the FEL phase of commissioning.

Once stable beam delivery from the injector has been established and the linac beamline has been fully assembled the commissioning of the linac stage can start. It is foreseen to perform a first pass of the machine up to the beam stopper installed in front of the Aramis undulator at the injector energy of 320 MeV. This approach will expose any obvious problems with the beamline at low beam power and allow for first diagnostics checks still in parallel to the conditioning of the linac-1 RF stations. In the subsequent commissioning stage, the beam energy will be raised gradually to the linac-1 energy of 2.1 GeV, followed by the setup of the second bunch compressor and the energy collimator chicane.

During these first commissioning stages, the beam will be deflected (by a movable permanent dipole magnet) to a beam stopper placed in front of the Aramis undulator line. Another beam stopper is available further upstream after the second bunch compressor (BC2 beam stopper). It will be used only rarely in conjunction with a profile monitor at the same location (whenever the beam profile needs to be checked before entering linac 2).

As soon as the beam parameters, as measured after the energy collimator, fulfill a set of predefined requirements, electrons will be transported through the undulator line onto the Aramis beam dump. During this first beam setup in the transfer and undulator lines the undulator gaps will remain in their open positions, such that no X-rays will be produced. For the first commissioning of the linac, transfer and undulator sections, the bunch charge will be kept at the intermediate value of 50 pC or even below, in particular when going through the undulators, to limit potential radiation losses. For the same reason the repetition rate will remain at 10 Hz for the early linac commissioning, to be raised to 50 Hz at the later stage in preparation for the first SASE attempts. The RF stations will run at 100 Hz throughout, irrespective of the bunch frequency. The nominal bunch frequency of 100 Hz can only be realized in the later stages of commissioning, since the handling of two zero-crossings with respect to the 50 Hz mains

ISBN 978-3-95450-134-2

supply will require some additional work by the low-level radiofrequency (adaptation of the feed-forward algorithm) and beam diagnostics groups.

FEL COMMISSIONING

In the last commissioning phase, the electron beam will finally be used to generate coherent X-ray radiation by having it pass through the undulators at closed gaps. After the alignment of the undulators and the verification of the nominal beam transport through the undulator section with closed gaps, the first goal will consist in the observation SASE radiation, thus establishing the distinctive signal of free-electron lasing.

The individual FEL commissioning stages, summarized in Table 4, essentially follow the installation progress of the linac RF modules. At every commissioning stage, a few weeks of beam operation are reserved for photonics commissioning. As the electron energy is increased, the accessible output photon wavelength decreases, down to the nominal 1 Å for the full linac energy of 5.8 GeV. At this stage, the very first pilot experiments are planned as a test of the facility under user operation conditions.

The bunch charge during FEL commissioning will vary between 50 and 200 pC depending on the specific commissioning task. The milestones defined for each FEL commissioning stage call for operation at 200 pC yielding photon pulse energies of 400 μJ. The repetition rate will remain at 50 Hz for the first FEL commissioning stages to avoid complications arising from the second mains zero-crossing, and will only be raised to 100 Hz during the very last commissioning stage.

TRANSITION TO USER OPERATION

Once the first commissioning goals have been reached, the facility will cycle through distinct periods of user operation (beginning with so-called friendly users), end station commissioning, and machine development. Corresponding operation modes (including some additional ones for machine tuning, shutdown etc.) have been defined. The exact details of the transition to regular user operation as well as the long-term organization of user operation at SwissFEL are the subject of current discussions and will be defined in the coming months.

CONCLUSION AND OUTLOOK

The SwissFEL Aramis hard-X-ray facility is approaching its commissioning phase, currently foreseen for the years 2016 and 2017. We have presented an overview of the main commissioning steps of the facility leading up to first pilot user experiments by the end of 2017. The commissioning plan is aimed at reaching a set of predefined milestones in accordance with the SwissFEL installation and system commissioning schedule, taking into account the available resources.

ACKNOWLEDGMENT

It is a pleasure to thank the various PSI expert groups for providing the input necessary for drawing up the SwissFEL commissioning plan. Special thanks go to Sven Reiche and his team for numerous invaluable discussions on commissioning issues.

REFERENCES

[1] R. Ganter (ed.), PSI Report 10-06 (2010).

[2] See, e.g., E. Prat, M. Aiba, S. Bettoni, B. Beutner, S. Reiche, and T. Schietinger, Phys. Rev. ST Accel. Beams **17**, 104401 (2014).

[3] See, e.g., R. Ischebeck *et al.*, in *Proc. 2nd Int. Beam Instrumentation Conference (IBIC'13),* Oxford, UK, Sep. 2013, p. 12.

[4] M. Pedrozzi (ed.), PSI Report 10-05 (2010).

ISBN 978-3-95450-134-2

Table 3: Commissioning stages for the SwissFEL linac. Beam conditions refer to the nominal conditions during a given stage; E is the electron beam energy, Q the bunch charge and R the repetition rate. The listed numbers of C-band modules do not include an additional module used to drive the transverse deflecting cavities.

Commissioning Stage	Approx. Dates	Beam Conditions	Main Tasks
RF Conditioning	Feb.–Aug. 2016		Conditioning of C-band modules up to z = 255 m beyond nominal accelerating gradient.
0.32-GeV Linac (no C-band modules)	Oct. 2016	e^- to Aramis stopper E = 320 MeV Q = 50 pC R = 10 Hz	Transmission through linac to Aramis beam stopper, beam-based commissioning of diagnostics, test of machine protection system, radiation mapping.
2.1-GeV Linac (9 C-band modules = linac 1)	Oct.–Dec. 2016	e^- to Aramis stopper E = 2.1 GeV Q = 50 pC R = 10 Hz	RF commissioning linac 1, beam-based commissioning of diagnostics, setup of beam orbit and optics, commissioning of transverse deflecting structures and bunch compressor 2, setup of energy collimator, global compression setup, radiation mapping.
Transfer- and Undulator Lines (9 C-band modules = linac 1)	Dec. 2016	e^- to Aramis dump E = 2.1 GeV Q = 50 pC R = 10–50 Hz	Transmission through undulator line, beam-based commissioning of diagnostics, orbit feedback, systematic beam-based alignment of quadrupoles and beam position monitors, final test of machine protection system, radiation mapping.

Table 4: Commissioning stages for the SwissFEL Free-Electron Laser. Beam conditions refer to the nominal conditions during a given stage; E is the electron beam energy, Q the bunch charge and R the repetition rate. The listed numbers of C-band modules do not include an additional module used to drive the transverse deflecting cavities.

Commissioning Stage	Approx. Dates	Beam Conditions	Main Tasks
RF Conditioning	Aug. 2016–July 2017		Conditioning of all remaining C-band modules beyond nominal accelerating gradient.
2.1–3.0-GeV FEL (λ = 3.7 Å) (9→13 C-band modules = linac 1&2)	Oct. 2016	e^- to Aramis dump E = 2.1–3.0 GeV Q = 50–200 pC R = 50 Hz	Undulator alignment, transport at closed gaps, first SASE, empirical SASE optimization, RF commissioning linac 2, linac energy management, FEL characterization and optimization, wavelength tuning, advanced diagnostics commissioning, routine operation studies. *Photonics:* optical hutch Aramis-2 and front-end.
3.8-GeV FEL (λ = 2.3 Å) (17 C-band mod. = linac 1&2, and part of linac 3)	July–Oct. 2017	e^- to Aramis dump E = 3.8 GeV Q = 50–200 pC R = 50 Hz	RF commissioning linac 3 (first 4 modules), FEL characterization and optimization, wavelength tuning, radiation mapping, routine operation studies. *Photonics:* optical and experimental hutch, end-station for Aramis-1.
5.8-GeV FEL (λ = 1.0 Å) (all 26 C-band mod. = linac 1–3)	Oct. 2017–Feb. 2018	e^- to Aramis dump E = 5.8 GeV Q = 200 pC R = 100 Hz	RF commissioning linac 3 (rest), FEL characterization and optimization, wavelength tuning, 100 Hz operation, radiation mapping, routine operation studies. *Photonics:* exp. hutch and end-station for Aramis-2.

ISBN 978-3-95450-134-2

COMPARISON OF ASTRA SIMULATIONS WITH BEAM PARAMETER MEASUREMENTS AT THE KAERI ULTRASHORT PULSE FACILITY

H. W. Kim[#,1,2], K. H. Jang[1,2], Y. U. Jeong[1,2], Y. Kim[1,2], K. Lee[1,2], S. H. Park[1,2],
N. Vinokurov[1,2,3], S. V. Miginsky[1,2,3],
I. Baek[1], M. Chae[1], B. Gudkov[1], B. Han[1], S. Park[1], S. Setiniyaz[1]
[1]KAERI, Daejon, Republic of Korea
[2]UST Acceleartor and Nuclear fusion physics engineering, Daejon, Republic of Korea
[3]Budker INP SB RAS, Novosibirsk, Russia

Abstract

An RF-photogun-based Linear accelerator for ultra-short electron beam generation is under construction at Korea Atomic Energy Research Institute (KAERI) [1]. This facility are mainly composed of an 1.5 cell S-band (2.856 GHz) RF gun, a travelling wave type linac 3m long and 90-degree achromatic bends.

We have performed computer simulation using ASTRA code to investigate the electron beam dynamics in the system with the input data of bead tested gun electric field distribution and the magnetic fields of the magnets [2]. We will present the simulated and experimental electron beam parameters.

INTRODUCTION

Ultrafast electron diffraction (UED) [3-7] are powerful tools for the study of the time-resolved molecular structure and material science. The UED can reveal inter-nuclear coordinates with high temporal and spatial resolution, therefore observing a change of structure on ultrafast time scale with milliangstrom accuracy.

Figure 1 shows the schematics of experimental setup for relativistic UED at KAERI. The UED beamline is designed to provide electron beams with low emittance and ultrashort pulses. The emitted electron beams are accelerated in high RF field to ~ 3 MeV. The electron beams can be deflected by a first bending magnet installed right after the RF gun. Each beamline has second bending magnet similar to the first one and three quadrupole magnets between the bending magnets. Two bending and three quadrupole magnets compose the 90-degree achromatic bend. The deflected electron beams will be used for UED experiments.

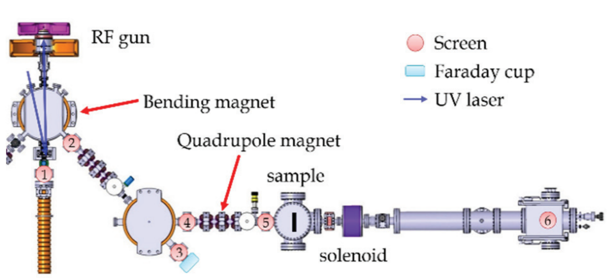

Figure 1: Schematic diagram of UED beamline at the KAERI and experimental setup.

We measured field distributions of all components and we simulated beam dynamics using measured field distributions.

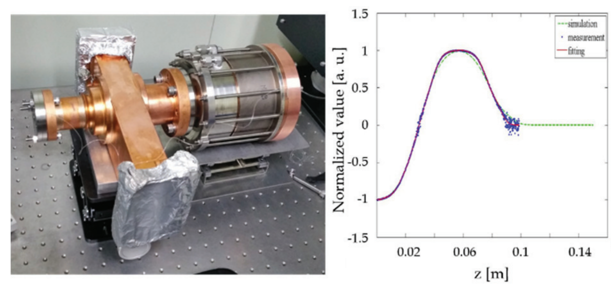

Figure 2: Photo of experimental setup for bead test and measured field distribution.

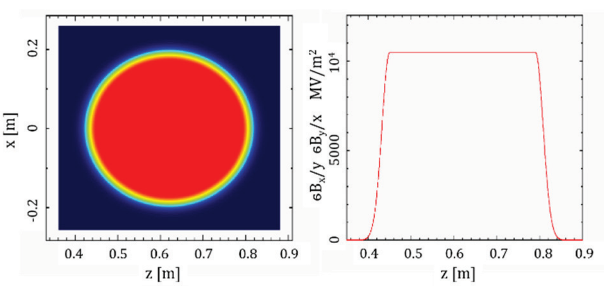

Figure 3: Magnetic field distribution of the 45-degree bending magnet.

Figure 2 shows experimental setup for bead test (left) and measurement data. The RF photogun has a coaxial coupler, which provide axisymmetric accelerating field.

Figure 3 shows magnetic field distribution of a 45-degree bending magnet. The shape of bending magnet is round which has horizontal focusing properties and simplifies alignment because of input and output directions cross in the centroid of the magnet. To achromaticity and isochronism UED beamline contains a second 45-degree bending magnet and three quadrupole lenses. The quadrupole lenses have square yoke (see Fig. 4). The manufacturing and assembly have been simplified.

We have performed computer simulation using ASTRA code to investigate the electron beam dynamics in the system with the measured field data.

#khw8412@kaeri.re.kr

ISBN 978-3-95450-134-2

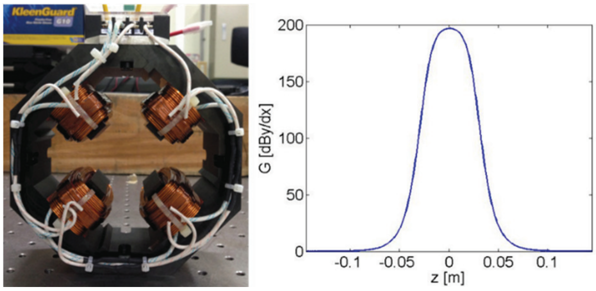

Figure 4: Photo and focusing field distribution of quadrupole lens.

COMPARISON OF SIMULATIONS WITH MEASUREMENTS

The electron beam is emitted from the copper cathode by a third harmonic of a Ti:Sapphire femtosecond laser (267 nm). The transverse and longitudinal profile of the laser both are Gaussian. A main solenoid with bucking coil is installed around the RF gun for suppress beam blow up due to space charge force.

The first electron beam has been generated on March and further optimization is in progress. Figure 5 shows a dark current image at the screen1 (see Fig. 1.).

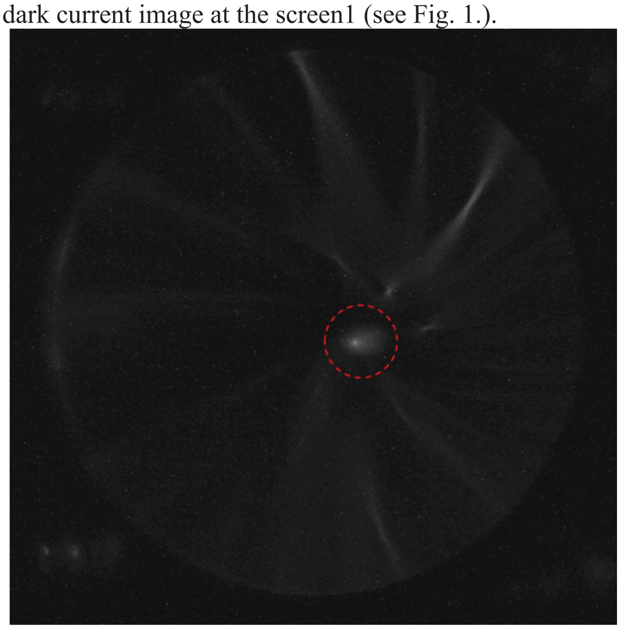
Figure 5: An electron beam image (red dot circle) with a dark current at the screen1.

The beam energy measured using the first 45-degree bending magnet. The momentum p is given by

$$p = 0.2998\mathrm{B}\rho,$$

where B is a magnetic field of bending magnet and ρ is a bending radius. The charge was measured at the screen3 (see Fig. 1.) by using a Faraday cup. We measured beam parameters varying a laser injection phase when a maximum energy gain is 0-degree. The measurement results as function of the laser injection phase are shown in Fig. 6. The blue dot line indicates a measured total energy and red line indicates a simulated total energy. The green line indicates the charge with 1 μJ laser and purple line indicates the charge with 0.4 μJ laser. The dark current is almost removed after the first bending magnet because of the energy of dark current is lower (2~2.5 MeV) than main beam. The ratio of dark current to main beam is 1.5% and the quantum efficiency of cathode is $1.2\text{x}10^{-5}$.

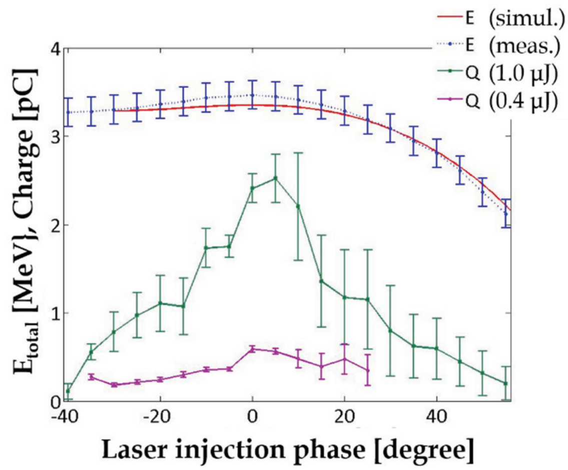

Figure 6: The measurement results of total energy and charge as function of a laser injection phase.

The energy spread estimated by using equation as follows,

$$\sigma_{S2} = \sqrt{\sigma_{S1} + \left(\eta \frac{\Delta E}{E}\right)^2},$$

where σ_{S1} is a rms beam size at the screen1, σ_{S1} is a rms beam size at the screen2 (just after the first 45-degree bending magnet) η is dispersion and $\Delta E/E$ is the energy spread. The estimated energy spread was 0.3%.

The emittance was measured at the screen5 (see Fig. 1.) by using the quadrupole scan technique [8]. The dispersion is compensated by three quadrupole lenses between two bending magnets. The dispersion compensation was checked to focus beam horizontally, as shown in Fig. 7.

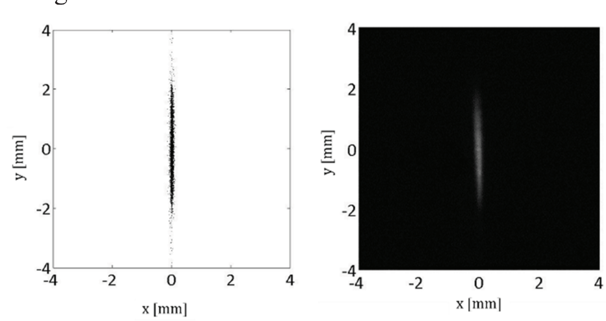

Figure 7: The simulated (left) and experimental (right) beam image at the screen5.

The experiment conditions were used initial value for simulation. It is summarized in Table 1.

ISBN 978-3-95450-134-2

Table 1: Experimental Condition and Initial Parameters for Simulation.

Experimental condition	
Laser pulse power	~ 0.5 μJ
Laser spot size	0.5 mm
Laser pulse length	130 fs
Quantum efficiency	10^{-5}
E_{z_peak}	61 MV/m
Solenoid current	0.205 T

The measured horizontal and vertical normalized emittance were 0.33 mm-mrad and 0.5 mm-mrad, respectively. The simulated horizontal and vertical normalized emittance were 0.31 mm-mrad and 0.28 mm-mrad, respectively. We assume that a difference of vertical emittance is un-uniformity of cathode surface, as shown in Fig. 8.

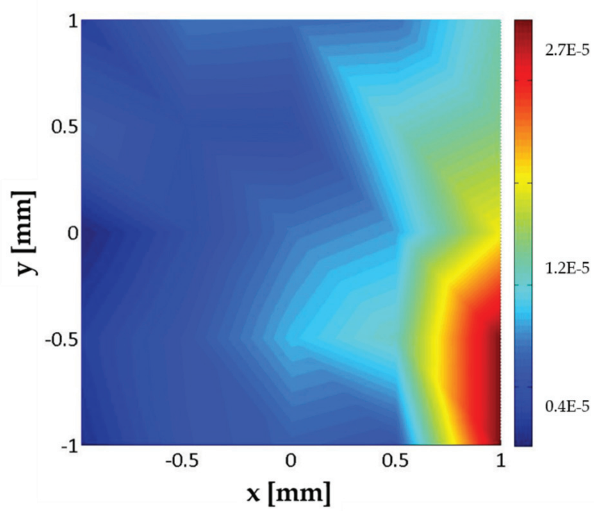

Figure 8: Quantum efficiency map of cathode at the UED beamline.

CONCLUSION

The first beam generation has succeeded in March this year. Baking and aging of the RF photogun and solenoid are in the march. We measured a beam energy, energy spread, charge and emittance. The experimental data and simulation data has showed a little different results. The differences between simulation and experiment might be misalignment of RF photogun, solenoid and the un-uniformity of cathode surface. We will align all components precisely and will try to get UED pattern.

REFERENCES

[1] N. Vinokurov, et al., in: Proceedings of the Free Electron Laser Conference 2013, New York, 2013, pp. 287.
[2] K. Floettmann, A Space Charge Tracking Algorithm ASTRA, http://www.desy.de/~mpyflo/
[3] X.J. Wang, et al., J. Korean Phys. Soc. 48 (2006) 390.
[4] J.B. Hastings, et al., Appl. Phys. Lett. 89 (2006) 184109.
[5] P. Musumeci, J.T. Moody, C.M. Scoby, Ultramicroscopy 108 (2008) 1450.
[6] R.K. Li, et al., Chin. Phys. C 33, Suppl. II. To appear.
[7] J. Yang, et al., Nucl. Instr. and Meth. A 637 (2011) S24.
[8] S. Setiniyaz et al., in: Proceedings of the Free Electron Laser Conference 2015, Daejeon, 2015, MOP063.

ISBN 978-3-95450-134-2

LCLS-II INJECTOR BEAMLINE DESIGN AND RF COUPLER CORRECTION*

F. Zhou#, D. H. Dowell, R.K. Li, T. O. Raubenheimer, J. F. Schmerge, SLAC, Stanford, CA 94309, USA
C. Mitchell, C. Papadopoulos, F. Sannibale, LBNL, Berkeley, CA 94720, USA
A. Vivoli, FNAL, Batavia, IL 60510, USA

Abstract

LCLS-II CW injector beamline consists of a 186 MHz normal conducting (NC) RF gun for beam generation and acceleration to 750 keV, two solenoids for the beam focusing, two BPMs, 1.3 GHz NC RF buncher for bunch compression down to 3-4 ps rms, 1.3 GHz superconducting standard 8-cavity cryomodule to boost beam energy to about 98 MeV. The beamline is being optimized to accommodate all essential components and maximize beam quality. The beamline layouts and beam dynamics are presented and compared. The 3D RF field perturbation due to cavity couplers where the beam energy is very low (<1 MeV) causes significant emittance growth especially for a large-size beam. A theory of rotated fields predicted and simulations verified using a weak skew quadrupole located even a significant distance from the perturbation can completely eliminate the emittance growth. A layout for future upgrade is developed. The results are presented and analysed.

INTRODUCTION

LCLS-II [1] currently under construction at SLAC National Accelerator Laboratory is a continuous wave (CW) x-ray free electron laser (FEL) user facility driven by a 4 GeV superconducting linac. To meet with the x-ray FEL requirements, the LCLS-II injector must simultaneously deliver high repetition rate up to 1 MHz and high brightness electron beam with normalized emittance of <0.4 µm at nominal 100 pC/bunch and peak current 12 A [2-3]. The major beam requirements for LCLS-II injector are summarized, as presented in Table 1.

Table 1: Major LCLS-II Injector Beam Requirements

Parameters	Nominal
RF gun energy (keV)	750
Electron energy (MeV)	98
Bunch repetition rate (MHz)	0.62 (0.93 max)
Nominal/max bunch charge (pC)	100/300
Peak current for 100/300 pC (A)	12/30
Nominal average current (mA)	0.062
Slice emittance for 100/300 pC (µm)	0.4/0.6
Bunch length for 100/300 pC (mm)	1/1.4
Slice energy spread 100/300 pC (keV)	1/5
Cathode QE lifetime	0.5%
Dark current (nA)	<400

*The work is supported by DOE under grant No. DE-AC02-76SF00515.
zhoufeng@slac.stanford.edu

The proposed full LCLS-II CW injector consists of a CW RF gun operating at 186 MHz (7^{th} sub-harmonic of 1.3 GHz for superconducting linac) for beam generation and acceleration, two solenoids for the beam focusing and emittance compensation, two BPMs for measurements of beam positions and bunch charge, 1.3 GHz 2-cell RF buncher for the bunch compression down to 3-4 ps rms from 10-15 ps rms, beam current diagnostic ICT, a standard 1.3 GHz superconducting 8-cavity cryomodule (CM) to boost beam energy from <1 MeV to 98 MeV, laser heater for suppression of micro-bunching instability, beam collimation systems and a dedicated diagnostic section. Figure 1 shows the schematic layout of the full LCLS-II injector. As the electron beam emittance and bunch length have been frozen at the CM end, the interest of this paper only focuses on the front part of the injector from the cathode to the CM end. This paper only discusses the beam dynamics issues. Technical details of the CW RF gun and cathode/laser performance are described elsewhere [4-5].

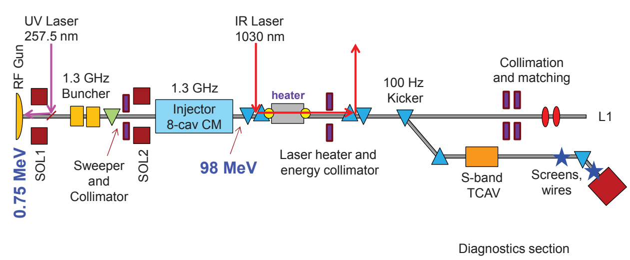

Figure 1: Schematic of the full LCLS-II injector. The front part of the injector discussed in this paper starts from the cathode to the CM end; downstream of the CM includes laser heater system, collimation systems and a dedicated beam diagnostics beamline.

INJECTOR BEAMLINE EVELOPMENTS

The injector front beamline (called injector for simplification) is being optimized since the conceptual design report (CDR) of the LCLS-II project launched in summer 2013. The LCLS-II injector beamline is required:

- To accommodate essential beam components and diagnostics, and adapt to the standard 8-cavity CM.
- To maximize electron beam performance in 6-d phase spaces.
- To make large half physical aperture for beam pipe, >4 times rms beam size to avoid the CW electron beam loss.

For the CDR, the distance from the 2^{nd} solenoid (SOL2) to the 1^{st} cavity (CAV1) of the 8-cavity CM was about 1

ISBN 978-3-95450-134-2

m. Although a good emittance of <0.6 µm for 300 pC was achieved from the simulations with the CDR layout, no space was available to accommodate a few essential components such as a 2nd BPM (BPM2) and gate valve. In 2014, a new layout was developed to add about 50 cm between SOL2 and CAV1 for the missing components with a customized reduced endcap for the CM. The emittance was found to increase ~10-15%, to 0.62 µm for 300 pC with the extra 0.5 m of drift-length. Later it was concluded that the CM would need to be modified for shortening the standard CM endcaps. Extra cost and potential construction delays prevented the modification of the CM for shortening the endcap. Thus it was decided the standard CM including endcaps is adopted for the LCLS-II injector source. For that purpose, another 21 cm was added in the distance between SOL2 and CAV1. Particle simulations using Astra code [6] show the emittance increases to 0.67 µm from 0.62 µm for 300 pC with this extra 21 cm. In addition, two pairs of solenoid/BPMs described in the CDR have small physical aperture, 1.4 cm of half aperture, ~2.6 times the rms beam size. According to the simulations, the beam starts to be lost at the 1st solenoid (SOL1) with only a 1 mm transverse offset of laser beam on the cathode. We determined to re-design the layout to reduce the emittance to < 0.6 µm with both added drifts and increase the solenoid/BPM aperture so the ratio of half aperture to rms beam size > 4.

New Baseline Layout Developments

To shorten the distance between the SOL2 and CAV1 and enlarge physical apertures of the solenoids and BPMs, we seek to redesign the solenoid and modify the BPM with large bores and shorter length [7] without compromising the electron beam performance. Table 2 presents the comparisons of the new solenoid/BPM with CDR design. With the new solenoid/BPM the physical apertures increase >50% and the lengths are shortened by 30%-50%. Combination of the new solenoid with the modified BPM saves about 15 cm in length in comparison to previous SOL/BPM. Figure 2 shows the comparison of the longitudinal solenoid field B_z vs. z for the new design and the CDR design. The new solenoid improves emittance, although its field quality factor is similar to the previous one. It is believed the new solenoid improves the emittance compensation process with space charge. Studies also show that moving SOL1 closer to the cathode can reduce the beam size thereby reducing chromaticity induced emittance. The new solenoid structure is compatible with a z-position shift in the cathode direction. After extensive simulations, with the new layout shown in Fig. 3 the emittance significantly improves. The optimized emittance is 0.25 µm and 0.43 µm for 100pC and 300 pC respectively, compared to 0.42 and 0.67 µm respectively for the CDR layout with added drifts ("CDR+71 cm"). The optimized emittance values are already close to the cathode thermal emittance contribution of 0.2 µm and 0.33 µm for 100 pC and 300 pC respectively. In addition, the ratio of the half physical aperture g to the rms beam size σ_x (i.e., g/σ_x) is >4.5 at all locations for 300 pC, compared to 2.6 for the "CDR + 71 cm" case. Table 3 presents the comparisons of the major beam performances for layouts. With the new layout, the slice emittance and longitudinal bunch distribution and higher order nonlinear energy spread at the end of CM are shown in Fig. 4. The slice emittance for 100 pC is <0.25 µm (100% particles) much smaller than 0.4 µm of required value, and the non-linear energy spread is about 6.3 keV rms comparable to previous layouts. The following changes are made compared with the "CDR + 71 cm" layout:

- moved the SOL1 5 cm closer to the cathode and
- moved SOL2 and 5 cm upstream
- reduced the distance between SOL2 and cavity1 about 15 cm
- increased physical apertures of SOL1, SOL2, BPM1, BPM2, and beam pipe for the laser injection area and ICT.

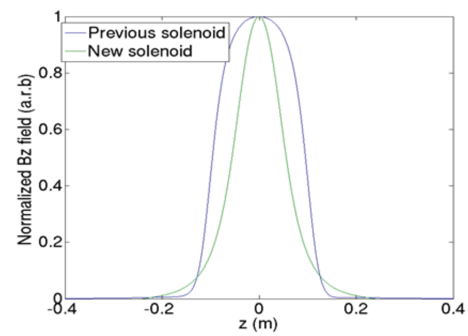

Figure 2: Magnetic field B_z along z for new and CDR solenoids.

Table 2: Comparisons of New and CDR Solenoid/BPM Dimensions for 300 pC

Parameters	CDR layout	New layout
SOL length	28.8 cm	17 cm
SOL: half aperture	1.44 cm	2.35 cm
BPM length	20 cm	15 cm
BPM: half aperture	1.44 cm	2.5 cm

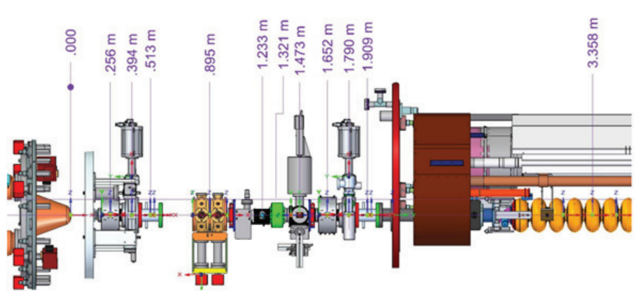

Figure 3: Schematic of new baseline layout from the cathode to CM. Major components are 186 MHz RF gun, two pairs of solenoid/BPM, 1.3 GHz NC RF buncher, ion pump, laser injection box, current diagnostic ICT, YAG screen, two valves, and standard 8-cavity CM.

ISBN 978-3-95450-134-2

Table 3: Electron Beam Performance Comparisons (g/σx is the ratio of the half aperture to rms beam size for 300 pC)

Parameters	"CDR + 71 cm"	New layout
g/σx at SOL1	2.6	4.6
g/σx at buncher	6.0	6.6
g/σx at SOL2	4.2	6
Proj. emittance (rms, 100%, μm)	0.67 (for 300 pC)	0.24/0.42 (100/300pC)
Higher order >3 δE (rms, keV)	14 (for 300 pC)	6.3/13.5 (100/300pC)
Peak Current (A)	30 (for 300 pC)	13/30 (100/300pC)

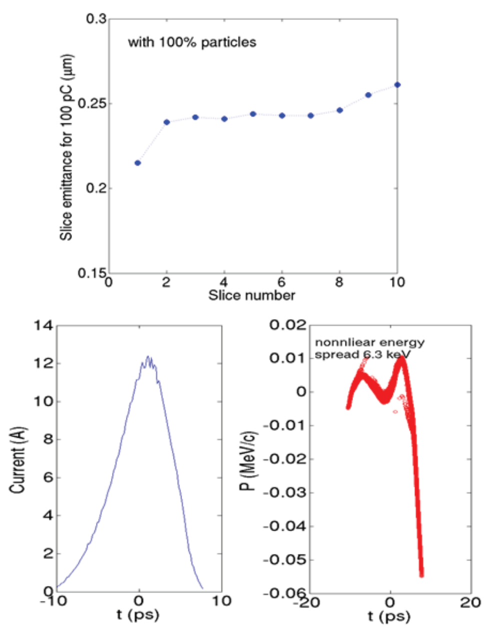

Figure 4: Slice emittance (top); longitudinal beam distribution (bottom left) and higher order energy spectrum (bottom right) at 98 MeV.

The significant emittance improvements with this new layout are mostly contributed by: 1) moving SOL1 closer to the cathode; 2) reduced distance between SOL2 and CAV1; and 3) new solenoid field map. The emittance can be further improved using a spatially truncated Gaussian distribution instead of a current spatially uniform distribution. Note that all beam dynamics simulations presented in this paper are performed using Astra code with 1 μm/mm of thermal emittance, transverse spatially uniform initial distribution and temporal flattop with 2 ps rise/fall time.

Novel Method for RF Coupler Correction

A standard 8-cavity CM is used to boost the electron beam energy to ~98 MeV from <1 MeV. The strong asymmetrical field from RF couplers located at the low energy of <1 MeV significantly increases the emittance for larger-size beams. Figure 5 shows the RF coupler induced emittance growth (green) in comparison to the perfect RF field (blue) for 300 pC. The results indicate ~40% emittance growth due to the RF couplers is expected from the simulations. The kicks of quadrupole terms induced by RF couplers can be expressed by:

$$\begin{pmatrix} x' \\ y' \end{pmatrix}_{coupler} = \begin{pmatrix} v_{xx}x + v_{xy}y \\ v_{yx}x + v_{yy}y \end{pmatrix}$$

where v_{xx} and v_{xy} are linear terms, and v_{xy} and v_{yx} are coupled terms. The emittance growth is mostly caused by the coupled terms. The kicks of linear and coupled term can be corrected with skew quadrupole [8], which is modeled as:

$$\begin{pmatrix} x' \\ y' \end{pmatrix}_{quad} = \begin{pmatrix} \dfrac{\cos 2\theta_q}{f_q}x - \dfrac{\sin 2\theta_q}{f_q}y \\ \dfrac{\sin 2\theta_q}{f_q}x + \dfrac{\cos 2\theta_q}{f_q}y \end{pmatrix}$$

where θ_q is the quadrupole rotation angle, f_q is the quadrupole focal length. With proper quadrupole parameters (rotation angle and strength), the RF coupler induced quadrupole terms can be completely cancelled. As shown in Fig. 5 (red) the RF coupler induced emittance growth is completely corrected with a very weak skew quadrupole (integrated strength 3 Gs and 10° of rotation angle). This method using quadrupole correction allows for adjustable corrections compared to traditional RF coupler correction with absorbers, or cavity coupler cell deformations and/or penetration to cancel quad terms.

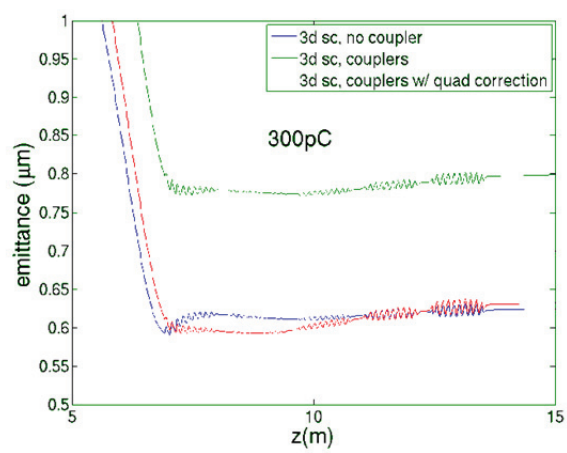

Figure 5: Emittance evolution with perfect RF field (blue), with RF couplers field (green) and correction using a weak skew quadrupole (red) for 300 pC.

Alternate Beamline Development

In the baseline layout we used single standard 8-cavity CM but the 2nd and 3rd cavities are powered off (i.e., ~4.2 m between the first two-powered cavities) for better emittance. It is believed that the drift distance between the CAV1 and next powered cavity improves the emittance compensation process. Further simulations showed that the emittance improves with longer separation between

ISBN 978-3-95450-134-2

the CAV1 and next powered cavity for 300 pC, as shown in Fig. 6. The optimum emittance is obtained with about 5.5-6 m of the distance between CAV1 and next powered cavity center. In an alternate configuration, we can replace the single standard 8-cavity CM in the baseline layout with two CMs. The first CM (CM1) has only one 9-cell cavity to gain about 10-MeV energy and the second CM is a standard 8-cavity (CM2). As shown in Fig. 7, excluding the space for CM endcaps, about 3.2 m of drift space is available for essential diagnostics including emittance station and energy spectrometer for ~10-MeV 6-d beam phase spaces measurements. The components from the cathode to the CM1 are identical to the new layout (not shown in Fig. 7). The alternate layout may not be adopted for the LCLS-II project due to cost. However, it can be used for future upgrade as it has significant advantages over the baseline layout:

- Emittance is independent of the cavity gradient on the cavities on the CM2. So all cavities of the CM2 can be powered on with at least one cavity as spare.
- The drift between the two injector CMs allows addition of essential diagnostics such as emittance station and energy spectrometer for measurement of 10-MeV beam and cavity alignments.
- Emittance is improved by 5-10% in comparison to the baseline layout.

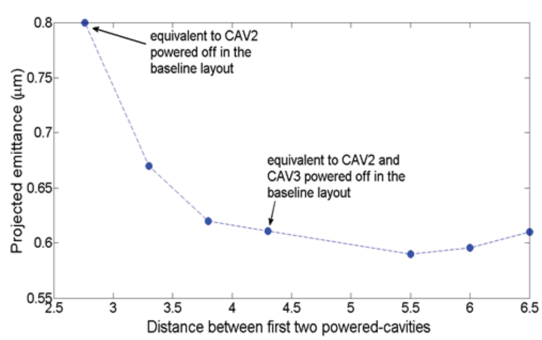

Figure 6: Emittance vs. distance between first two powered-cavities for 300 pC.

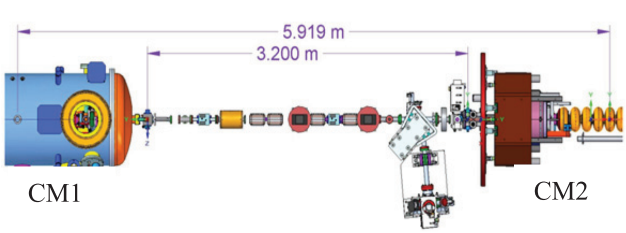

Figure 7: Schematic of the alternate layout (components from cathode to CM1 are identical to Fig. 3). Diagnostics installed in between CM1 and CM2 include the emittance station using slits, collimators, and energy spectrometer.

SUMMARY

LCLS-II injector layout was optimized with significant improvements of emittance and physical apertures. A simple model using a weak skew quadrupole is developed [9] and simulations show the RF couplers effect can be completely cancelled with the skew quadrupole. An alternate layout is also developed with improved emittance and addition of essential diagnostics such as emittance station and energy spectrometer at ~10 MeV.

REFERENCES

[1] T. Raubenhemier, “The LCLS-II, a new FEL facility”, FEL2014, Basel, Switzerland, 2014.
[2] C. Papadopoulos *et al.*, “RF injector beam dynamics optimization for the LCLS-II”, The 4th International Part. Accel. Conference, Dresden, Germany, pp. 1974-1976.
[3] J. Schmerge et al., “LCLS-II injector design”, FEL2014, Basel, Switzerland, 2014.
[4] F. Sannibale et al., “Advanced photoinjector experiment photogun commissioning results”, Phys. Rev. ST Accel. Beams 15, 103501 (2012)
[5] R. Huang et al., “Dark current studies on a normal-conducting high-brightness very-high-frequency electron gun operating in continuous wave mode”, Phy.s Rev. ST Accel. Beams 18, 013401 (2015).
[6] K. Floettmann, Astra manual, Desy, October 2011.
[7] M. Johnson, LBL, presentation at LCLS-II injector collaboration meeting July 2015.
[8] D. Dowell, “Analysis and cancellation of RF coupler-induced emittance growth due to astigmatism”, LCLS-II tech. note TN-15-05, 2015 and physics archive: http://arxiv.org/abs/1503.09142

ISBN 978-3-95450-134-2

STATUS, PLANS AND RECENT RESULTS FROM THE APEX PROJECT AT LBNL*

F. Sannibale, K.M. Baptiste, C.W. Cork, S. De Santis, M. Dickinson, L. Doolittle, J. Doyle, J. Feng, D. Filippetto, G. Harris, G. Huang, M. J. Johnson, M. Jones, T. D. Kramasz, S. Kwiatowski, D. Leitner, R. Lellinger, C.E. Mitchell, V. Moroz, E. Norum, H.A. Padmore, G.J. Portmann, H. Qian, J.W. Staples, D.L. Syversrud, M. Vinco, S. Virostek, R. Wells, M. Zolotorev, Lawrence Berkeley National Laboratory, Berkeley, CA 94720, USA
R. Huang, NSRL, University of Science and Technology of China, Hefei, Anhui, 230029, China

Abstract

The Advanced Photo-injector EXperiment (APEX) at the Lawrence Berkeley National Laboratory (LBNL) is dedicated to the demonstration of the capability of an electron injector based on the VHF-gun, the new concept RF gun developed at LBNL, of delivering the beam quality required by MHz-class repetition rate X-Ray free electron lasers. Project status, plans, and recent results are presented.

INTRODUCTION

APEX, the Advanced Photo-injector EXperiment at the Lawrence Berkeley National Laboratory (LBNL) is dedicated to the development and test of an injector based on the VHF-Gun [1-3], a new concept high repetition rate high-brightness electron gun. The successful development of such an injector will critically impact the performance of future 4th generation light sources when MHz-class repetition rates are required. In particular, the baseline of the SLAC LCLS-II project [4] includes an injector based on such a gun.

The VHF-Gun is a normal-conducting continuous wave (CW) RF gun where electrons are generated by laser-induced photo-emission on high quantum efficiency (QE) cathodes and accelerated up to the nominal energy of 750 keV. The gun cavity resonates at 186 MHz, the 7th sub-harmonic of 1.3 GHz or the 8th sub-harmonic of 1.5 GHz, the two dominant superconducting linac technologies. The low frequency makes the resonator size large enough to lower the power density on the cavity walls at a level that conventional cooling techniques can be used to run in CW mode, while maintaining the high accelerating fields required for the high brightness performance. A second advantage of the low frequency is the long wavelength that allows for large apertures on the cavity walls with negligible field distortion. Such apertures provide the vacuum conductance necessary to achieve the low pressures required to operate the sensitive QE cathodes with acceptable lifetime. A last advantage of such a scheme is that it is based on mature and reliable RF and mechanical technology, an important characteristic to achieve the reliability required to operate in a user facility.

The APEX project was initiated at the end of 2009 and was organized in 3 stages (Phase 0, I and II), with the first two (now completed) dedicated to the development and testing of the gun, cathode testing and electron beam characterization at the gun energy. In Phase II, presently in its very final installation phase, a buncher and a linac are added to the VHF-Gun to compress and accelerate the beam up to 20-30 MeV reducing space charge forces in order to perform a reliable characterization of the gun/injector brightness and compression performance.

The commissioning of the VHF-Gun and the demonstration of all its major design goals are reported elsewhere [5], here we concentrate on the status of the installation of Phase-II of APEX and on the more recent commissioning results.

* Work supported by the Director of the Office of Science of the US Department of Energy under Contract no. DEAC02-05CH11231

PHASE-II DESCRIPTION

Figure 1 shows the CAD layout of APEX Phase-II. The vacuum loadlock that allows replacing the reactive high quantum efficiency (QE) without breaking vacuum, and the VHF-Gun are visible in the left-bottom corner of the figure.

In Phase-II a 1.3 GHz CW buncher is inserted downstream the gun followed by a linac composed by three 1.3 GHz pulsed accelerating section. A suite of beam diagnostics systems capable of 6D beam phase-space characterization completes the accelerator layout.

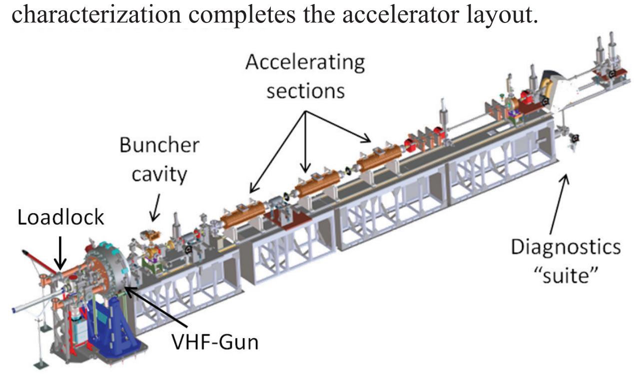

Figure 1: APEX Phase-II Layout.

The buncher, shown in Fig. 2, uses a two-cell design optimized for high shunt impedance and for being multipacting free over the whole range of power [6]. The main parameters for the buncher are shown in Table 1. The RF power is fed in each cell by two coaxial couplers terminated with a loop that couples the magnetic field in the cell. Two additional flanges in each of the cells are

ISBN 978-3-95450-134-2

used to connect a vacuum pump (combined NEG-Ion pumps- NEXTorr type from SAES) and an RF probe.

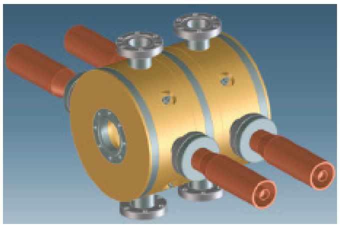

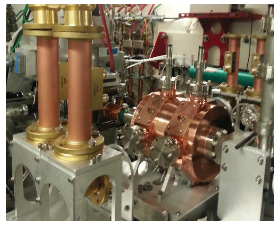

Figure 2. Left: APEX buncher CAD view. Right: a picture of the buncher installed in the Phase-II beamline.

The couplers ports and the additional two flanges were optimized to minimize dipolar and quadrupolar field components induced by the ports themselves and that could degrade beam emittance. The buncher resonance frequency is controlled by the cooling water temperature.

The fabrication of the buncher is completed, the two cells have been frequency tuned and their field balanced using the four dimples in each cell, and the unit is now installed in the beamline. A picture of the buncher is visible in the right part of Fig. 2, while in the left part a CAD view that includes also the four RF couplers is shown.

The buncher coupler, an LBNL design, is a coaxial structure with a bandpass response centered at 1.3 GHz and with few MHz bandwidth. The design incorporates a custom RF window to separate the vacuum in the buncher from the air side. The RF power from four CW 1.3 GHz 2.5 kW solid state amplifiers (from TOMCO) is fed to the four couplers by individual semi-rigid 1-5/8” heliax-type HCA158-50J cables.

Figure 3: APEX Buncher RF coupler.

Figure 3 shows a picture of one of the buncher couplers. In the right part of the figure, the copper loop that magnetically couples the field inside the buncher, is visible. The rotatable flange on the right, allows clocking the coupler to obtain the desired coupling factor.

Both the buncher and its couplers were completely designed and fabricated at LBNL with the only exception of the brazing operations that were performed by California Brazing (Newark, CA).

The Phase-II linac is composed by three 1m-long 1.3-GHz normal-conducting standing-wave accelerating sections. At the moment only two sections are installed, the third one, delivered with some delay, will be installed sometime later this year. The sections are a modified version of the 7-cell sections designed and used by the Argonne AWA group [7]. The central cell, where the RF power is fed, was modified to include two opposite located RF power couplers (only one in the original design) and two dummy couplers (perpendicularly to the real ones) to effectively minimize dipolar and quadrupolar field distortions that could affect the beam emittance.

Table 1: Buncher Main Parameters

Parameter	Value	Units
Frequency	1.3	GHz
Mode of operation	CW	
Mode separation	1.2	MHz
Ideal conductor Q_0	23500	
Nominal Voltage	240	kV
Nominal power	8	kW
Power per cell	4	kW
Power per coupler	2	kW
Resonant mode	π	
Shunt impedance	7.2	MΩ

Figure 4 shows the two accelerating sections installed in the Phase-II beamline. The two RF couplers and one of the dummies on top of the section are visible.

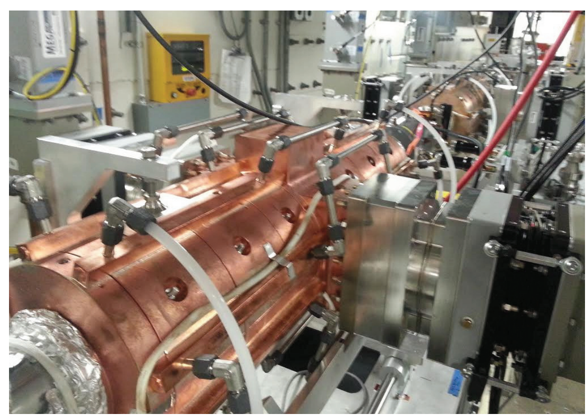

Figure 4: The modified AWA accelerating sections installed in the Phase-II beamline.

A single klystron (THALES TV 2022F) generates 25-MW peak power over a 10 µs pulses at 10 Hz for the 3 accelerating sections and for the 1.3 GHz transverse deflecting cavity used for beam diagnostics. The power from the klystron is delivered to the 4 devices by a complex network of SF_6 filled L-Band rectangular waveguides that includes a 4-port RF circulator and high power phase-shifters/attenuators for each of the branches.

While the VHF-Gun and the buncher run in CW mode, the linac operates in pulsed mode at 10 Hz repetition rate. The rationale behind this configuration is based on the fact that electron beam brightness (the main of the APEX Phase-II goals) is a single bunch property of the beam that is not affected by the repetition rate. This permitted using

ISBN 978-3-95450-134-2

a room temperature copper linac with a strong cost reduction and system simplification.

Downstream of the linac, a beam diagnostics suite with 6D beam phase-space characterization capability is located. It includes emittance monitors for space charge dominated or non-dominated beams, a spectrometer and a transverse deflecting cavity. More details on the diagnostics can be found elsewhere [8].

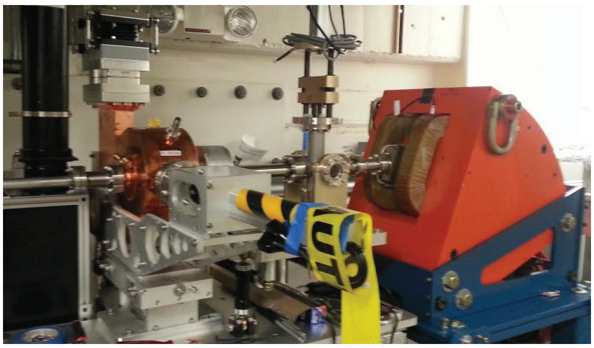

Figure 5: Part of the Phase-II diagnostics beamline. The 1.3-GHz single-cell transverse deflecting copper cavity is visible in the left of the picture followed downstream by the large orange spectrometer (vertical) bending magnet.

PHASE-II INSTALLATION STATUS

Phase-II beamline installation is close to completion and subsystem check-outs already started. High power RF conditioning of the linac sections and of the buncher will start as soon as the check-out is completed, and will be followed by beam commissioning.

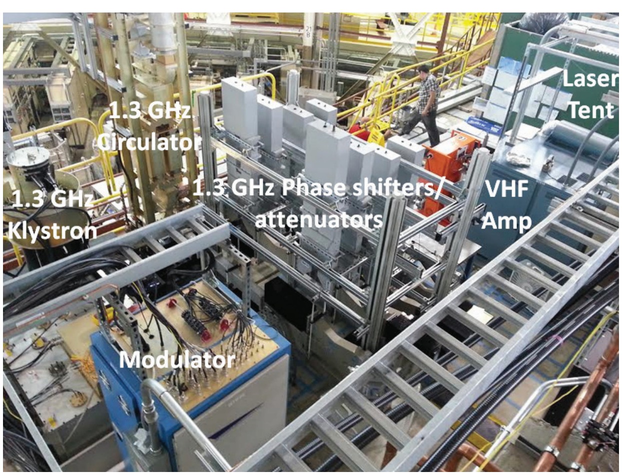

Figure 6: Several APEX subsystems on the BTF roof.

Figure 6 shows the Beam Test Facility (BTF) roof where all the RF power sources and the cathode driver laser are located.

Figure 7 shows the Phase-II beamline installed inside the BTF.

Figure 7: APEX Phase-II beamline installed in the BTF.

RECENT RESULTS

In April 2015 the beam tests were suspended to allow the installation of the Phase-II beamline. Before that, a number of beam measurements at the beam energy using the Phase-I beamline were performed.

Cs_2Te photocatode characterization campaign

Cesium-Telluride (Cs_2Te) photocathodes, produced by INFN/LASA in Milan, Italy, were extensively tested during a many days campaign.

The results demonstrated the capability of such a cathode to perform at the challenging unprecedented regime imposed by high repetition rate x-ray FELs such as the LCLS-II.

Multiple runs at 1 MHz repetition rate with constant charges per bunch of 20, 100 and 300 pC were performed to characterize the QE and the QE lifetime of such a cathode. Figure 8 shows an example of such runs.

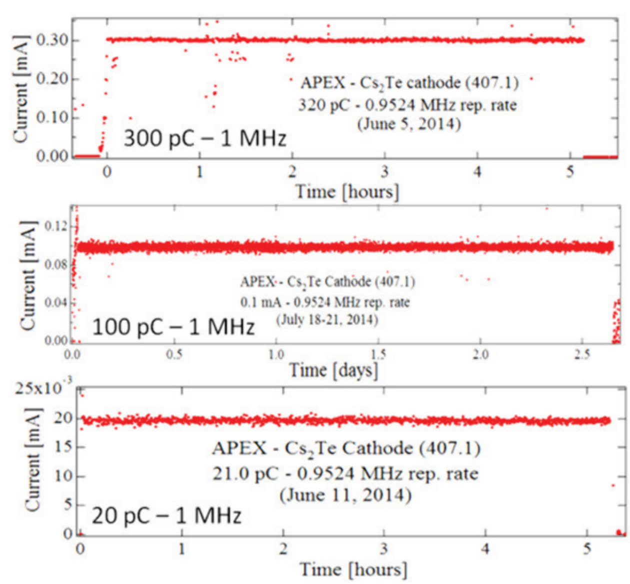

Figure 8: Example of constant current tests with Cs_2Te.

ISBN 978-3-95450-134-2

The measurements showed an extremely high QE with long lifetimes well beyond LCLS-II requirements. The reason for the slow QE lifetime was identified as a progressive oxidation of the photo-emitting material due to the residual oxygen that shows in the gun when the RF is ON (~10^{-11} Torr partial pressure). Figure 9 shows a summary of the QE lifetime measurements with the fit indicating the clear correlation between the integrated amount of oxygen and the QE value. More details on such measurements can be found elsewhere [9, 10].

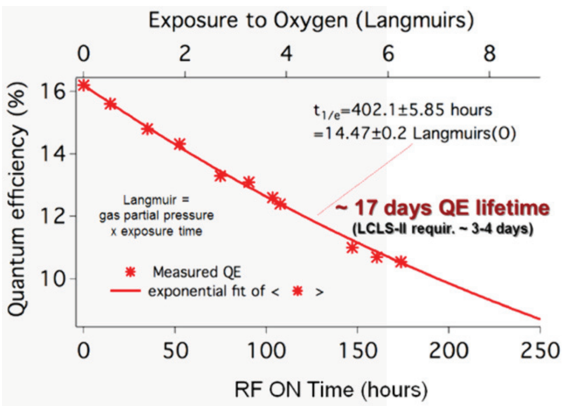

Figure 9: Cs_2Te QE vs. time and integrated Oxygen exposure.

Dark characterization and reduction

Dark current in high duty cycle accelerators can represent a serious issue. If not properly controlled, it can induce quench of superconducting RF structures and additional radiation dose that can degrade the performance of permanent magnet-based devices.

An extensive dark current characterization campaign was performed at APEX that allowed to quantify the current intensity as function of the beam energy (Fowler-Nordheim analysis) as well as to identify the location in the gun of the field emitters responsible for most of the dark current generation (around the copper area just outside of the cathode plug). These findings make it possible to define an effective multi-point strategy to reduce photoemission from the gun. Details of the measurements and the analysis can be found in [11].

On August 2014, a failure of one of the RF waveguides that bring the power to the VHF-Gun contaminated the gun and forced us to open the gun cavity for the necessary cleaning. Such a situation offered the possibility of actuating some of the points in our dark current reduction strategy. In particular, we carefully re-polished the area where the field emitters were located, and performed a dry-ice cleaning cycle of the whole cavity wall followed by an additional cleaning cycle of the cathode area.

When we restarted later in January 2015, the dark current intensity showed an impressive decrease by more than 3-orders of magnitude going from ~350 nA down to ~0.1 nA. Figure 10 shows the Fowler-Nordheim analysis before (top) and after (bottom) the cleaning/re-polishing operation.

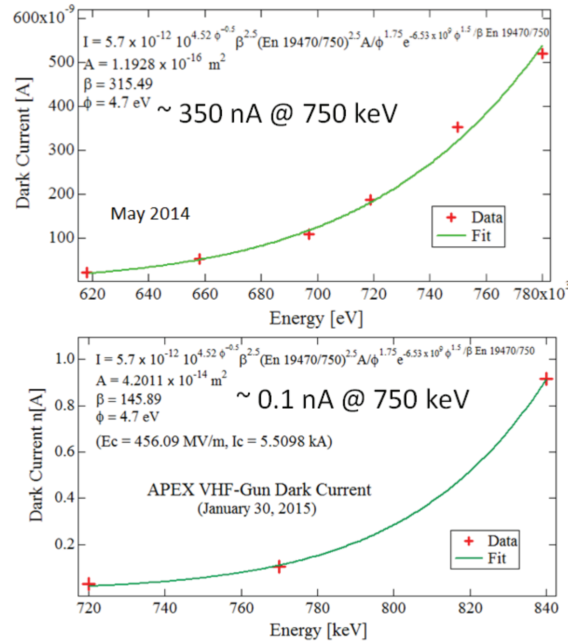

Figure 10: Dark-current Fowler-Nordheim analysis before (top) and after (bottom) the cleaning/re-polishing operation.

PLANS AND CONCLUSIONS

Plans for the near future include the beam commissioning of Phase-II beamline, and in particular the demonstration of the compression and emittance required by the different modes of operation of LCLS-II.

In addition, APEX will operate in support of HIRES, the high repetition rate ultrafast electron diffraction program at APEX funded by DOE-BES [12].

REFERENCES

[1] J. Staples, F. Sannibale, and S. Virostek, VHF Band Injector, CBP Technical Note No. 366, LBNL October 2006.
[2] K. Baptiste *et al*, NIM A **599**, 9 (2009).
[3] R. Wells *et al.*, Proceedings of IPAC2014, Dresden, Germany, p. 733 (2014).
[4] J. Galayda, Proceedings of IPAC2014, Dresden, Germany, p. 935 (2014).
[5] F. Sannibale *et al.*, PRST-AB **15**, 103501 (2012).
[6] H. Qian *et al.*, Proceedings of IPAC2014, Dresden, Germany, p. 3924 (2014).
[7] J. Power *et al.*, in Proceeding of IPAC10, Kyoto, Japan, p. 4310 (2010).
[8] D. Filippetto *et al.*, Proceedings of IPAC2012, New Orleans, Louisiana, USA, p. 963 (2012).
[9] H. Qian *et al.*, Presented at FEL'15, Daejeon, Korea, MOD03.
[10] D. Filippetto, H. Qian, and F. Sannibale, Appl. Phys. Lett. **107**, 042104 (2015).
[11] R. Huang *et al.*, PRST-AB **18**, 013401 (2015)
[12] D. Filippetto *et al.*, Proceedings of IPAC2014, Dresden, Germany, p. 726 (2014).

ISBN 978-3-95450-134-2

ELECTRON BEAM PROPERTIES FROM A COMPACT SEEDED TERAHERTZ FEL AMPLIFIER AT KYOTO UNIVERSITY

K. Damminsek#, S. Rimjaem, C. Thongbai
Plasma and Beam Physics (PBP) Research Facility, Department of Physics and Materials Science, Faculty of Science, Chiang Mai University, Chiang Mai 50200 Thailand
S. Suphakul, H. Ohgaki, H. Zen
Institute of Advanced Energy, Kyoto University, Gokasho, Uji, Kyoto 611-0011 Japan

Abstract

A compact seeded Terahertz FEL amplifier is started construction at the Institute of Advanced Energy, Kyoto University, Japan. The system consists of a 1.6 cell BNL type S-Band photocathode RF-gun, a magnetic bunch compressor in form of a chicane, triplet quadrupole magnets and a short planar undulator. Electron beams from the photocathode

RF-gun were measured and compared with the RARMELA simulation results. Numerical and experimental studies on the contribution of the space charge effect were carried out. By using the RF power of 9 MW, the RF phase of 40 degree, the laser pulse energy of 20 μJ and the solenoid magnet current of 135 A, the electron beam with a bunch charge of 50 pC, a beam energy of around 5 MeV and an RMS emittance of 6-8 mm-mrad was achieved.

INTRODUCTION

The Institute of Advanced Energy has developed the compact seeded THz-FEL (IR-FEL) amplifier [1]. The system was designed to be simple, compact and economical aimed to use in scientific researches. The system consists of a 1.6 cell BNL type S-Band photocathode RF-gun, a magnetic bunch compressor in form of a chicane, triplet quadrupole magnets and a short planar undulator. The photocathode RF gun succeeded to generate the first beam in May, 2015. The electron beam properties, i.e. a bunch charge, a beam energy and a transverse beam emittance from the photocathode RF gun were measured. These electron beam properties are compared with the simulation results using the program PARMELA [2] to check the system. Since the energy of the electron beam would be low, around 5 MeV, the space charge effect should affect the beam properties strongly and it might be difficult to obtain a short bunch beam to generate intense THz radiation. Therefore, the study on the beam properties from the RF gun is crucial both by experiment and by simulation.

The 1.6 cell BNL type S-Band photocathode RF-gun has been developed at KEK [3]. The gun has two cavities, the first cavity is a half-cell type and the second cavity is a full-cell type. The photocathode of the RF-gun is the copper one during this study. A high power microwave transported from a 10 MW klystron, travels through a waveguide, which is connected at the upper wall of the second cavity. The microwave is fed into the first cavity via the central iris between two cavities. The effective length of half-cell and full-cell are 3.4135 cm and 9.0405 cm, respectively. The microwave has a pulse duration of 2 μs with a maximum macro-pulse repetition rate of 10 Hz. The photocathode drive laser consists of a mode-locked Nd:YVO_4 laser (GE-100-VAN-89.25 MHz-CLX-Flexible AOM, Time-Bandwidth), two amplifiers, beam position stabilizers and SHG-FHG [4]. The laser wavelength is 266 nm with a pulse duration of 8 ps at FWHM. The repetition rate of the injected laser is one thirty second of the RF frequency (89.25 MHz), which is defined by mode-lock frequency and designed to synchronize the cavity frequency of the MIR-FEL system. This is because the laser system is also used for the photocathode mode operation of the existing S-band linac [4]. A solenoid magnetic field is used to compensate a very strong space-charge effect on the electron beam. The limitation of the power supply used for the solenoid magnet is 200 A with a solenoid field around 300 mT. Beside the experiments, numerical simulations using the program PARMELA were performed to study the electron motion in the RF gun as well as to investigate accelerated electron beam properties which are charge, energy, energy spread, emittance and pulse width.

METHODOLOGY

To investigate a transverse profile, dark current and bunch charge of the electron beam produced from the photocathode RF-gun of a compact seeded terahertz FEL amplifier, we used a fluorescence screen, a CCD camera, an electron exaction window and a Faraday cup as shown in Fig. 1(left). The typical Faraday cup signal of the electron charge measurement is shown in Fig. 1(right). Unfortunately, we did not have enough time to prepare in vacuum measurement. Thus, the charge measurement was performed in air. The photoelectron beams hit the exaction window inside a vacuum chamber. The window made of copper with a thickness of 0.2 mm. The energy loss of electron at the copper window is calculated to be 230 keV at the kinetic energy of the beam of 4.5 MeV [5]. An emitted electron beam from the copper window traveled in the air, then, it is observed by using the Faraday cup. The cup itself is made of graphite for absorbing the electron beam by using the in air measurement technique. The electron bunch charge is obtained by using an Eq. 1:

kantaphon.damminsek@gmail.com

ISBN 978-3-95450-134-2

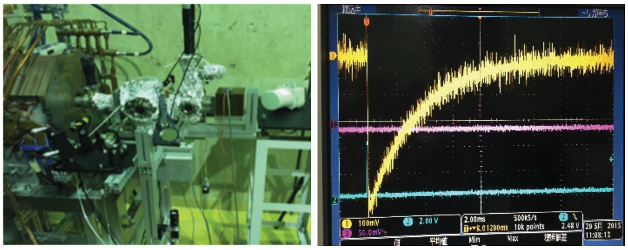

Figure 1: (left) Photogragh of the experimental set up for measurement of a dark current and electron bunch charges. (right) Typical Faraday cup signal of the electron charge measurement.

$$Q = \int I(t)dt = \frac{1}{R}\int U(t)dt\,, \qquad (1)$$

where $U(t)$ is the measured voltage observed by the oscilloscope and R is a resistance of the measurement system. The dark current is a background current, which comes from an effect of the RF wave even the drive laser is switched off. The dark current dependence on the microwave power is shown in Fig. 2.

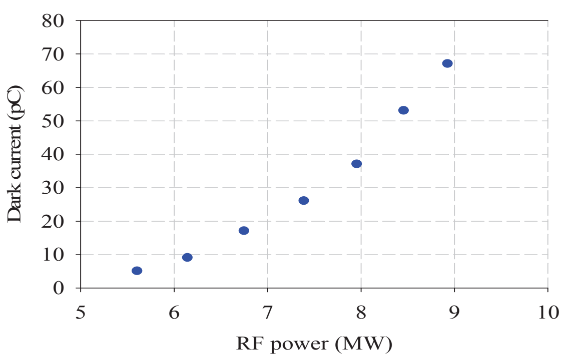

Figure 2: Relationship between the dark current and the RF power.

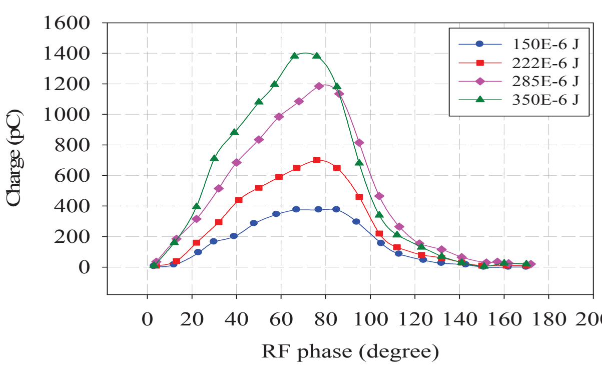

Figure 3: A relationship between the electron bunch charge and the RF phase.

We used an RF power of 9 MW and a solenoid current of 120 A to study the photoelectron bunch charge dependence on the RF phase. The relationships are shown in Fig. 3. Besides the bunch charge, the beam energy and beam emittance are other important properties of the electron beam. To study these properties, we used the measurement set-up as shown in Fig. 4.

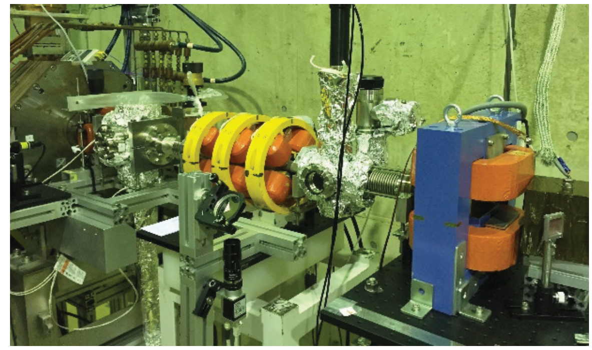

Figure 4: Photograph of the experimental set up for the measurements of beam energy and beam emittance.

The instrument system consists of a beam exaction window, which is a mylar window, a dipole magnet, three quadrupole magnets, a fluorescence screen and two CCD cameras. The energy measurement has been performed with the in air measurement as well. An emitted electron beam from the mylar window whose thickness is 0.3 µm traveled in the air. The mylar window is made of Aluminum coated one side with a polyimide [6]. The energy loss in the Aluminum window is calculated to be 110 keV at kinetic energy of the beam of 4.5 MeV [5]. On the other hand, the density of air inside the accelerator room is 1.20E-3 g/cm^3, the stopping power in the air is about 2.3 keV per 1 cm. When the beam travelling pass a dispersive region of the dipole magnet, which has the magnetic field perpendicular to a traveling path of the beam, the magnetic field acts on the electron beam related to the energy (E) of the beam [7] as

$$\frac{1}{\rho[m]} = \frac{0.2998 B_0[Tesla]}{\beta E_{total}[GeV]}\,, \qquad (2)$$

where B_0 is the peak magnetic field of the dipole magnet and ρ is the radius of curvature of the traveling path. Therefore, electrons with different energies bend in the dispersive region with different bending radii. A geometry length of the dipole magnet is 6.5 cm and an effective length is 11 cm. The beam energies are related to an RF power and phase.

A comparison between the measurement and simulation results of the beam energy dependence on the RF phase is shown in Fig. 5. The blue plots are the measurement results and other plots are the example of simulation results. The measurement results of the beam energies depending on the RF powers and the RF phases are shown in Fig. 6. An expected ratio of the accelerating gradient between the half-cell and the full-cell of the RF-gun is 1:1.

ISBN 978-3-95450-134-2

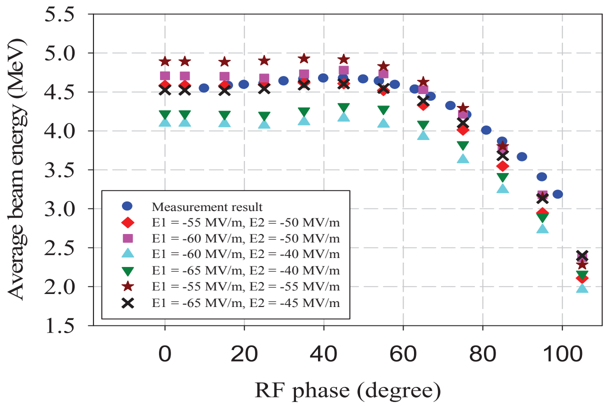

Figure 5: Measurement and simulation results of the beam energy dependence on the RF phases.

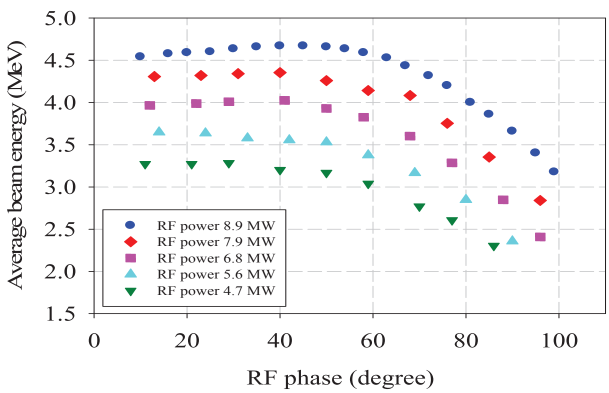

Figure 6: Measurement results of the beam energy dependence on the RF powers and the RF phases.

According to the measurement results in Fig. 6, at the RF phase lower than 40 degree, the beam energy slowly increases and it is almost constant around 40-50 degree for each RF power. The beam energy rapidly decreases at the phase larger than 50 degree. The beam energy for each phase are proportional to the RF power. The relationship of the beam energy and the RF phase for each RF power shows the same tendency.

Beam emittance is an important quantity for evaluation of the transverse electron beam quality. The emittance relates to area or volume of the phase space diagram, which is occupied by electrons. The emittance are defined as [8]

$$\varepsilon_x = \sqrt{\langle x^2\rangle\langle x'^2\rangle - \langle xx'\rangle^2}\,,\ \varepsilon_y = \sqrt{\langle y^2\rangle\langle y'^2\rangle - \langle yy'\rangle^2}\,, \quad (3)$$

where x, y are electron horizontal and vertical positions in Cartesian coordinate system. The angles x', y' are defined by the transverse momenta divided by the total momentum.

A measurement system is prepared in form of a quadrupole scan method with a thin lens approximation. The quadrupole magnets focus the electron beam in vertical or horizontal direction. A focal length of quadrupole magnet is given by this following equation

$$f[m] = 1/(k[m^{-2}]l[m])\,, \quad (4)$$

where k is the strength of the magnet and l is the effective length of the magnet, which is related to [7]

$$k = (0.2998G[T/m])/(p[GeV/c])\,, \quad (5)$$

where G is the gradient of the magnet and p is the momentum of the electron. An effective length of the quadrupole magnets in this experiment is 55 mm. We used an RF power of 9 MW with an RF phase of 40 degree and a solenoid current of 130 A to study the beam emittance dependence on the bunch charge and the drive laser pulse energy. The relationships of these parameters are shown in Fig. 7.

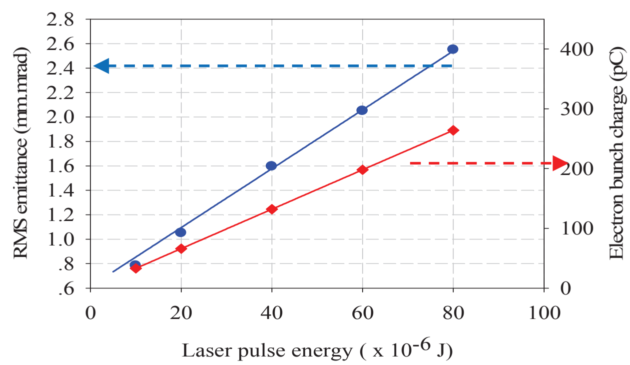

Figure 7: The beam emittance dependence on the bunch charge and the drive laser pulse energy.

As is shown in the Fig. 7, the bunch charges are proportional to the laser pulse energies. It is noted that the space charge effect, which is larger with a higher bunch charge, makes the beam getting a large divergence. Therefore, the beam emittance is getting larger according to the laser pulse energy.

The solenoid magnetic field changes a focusing condition of the beam. Therefore, it changes the RMS beam emittance. We used an RF power of 9 MW, an electron bunch charge of 50 pC and an RF phase of 40 degree for studying the beam emittance dependence on the solenoid field. The relationship is shown in Fig. 8. Blue and red plots refer to a property in x-axis and y-axis, respectively. The beam emittance is minimum at a solenoid current of 135 A. The results in both x-axis and y-axis show similar tendency with small difference in values.

A magnitude of the electric field inside the RF-gun changes with the time. Then, the beam energy depends on an accelerating gradient of the RF as a function of the RF phase. Therefore, the RMS emittance also related to the RF phase. We used the RF power of 9 MW, the solenoid current of 135 A and the bunch charge of 50 pC for this

ISBN 978-3-95450-134-2

investigation. The measurement and simulation results are shown in Fig. 9.

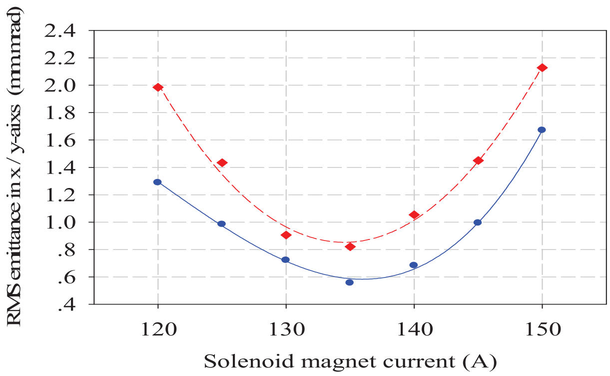

Figure 8: Relationship between the beam RMS emittance and the solenoid magnetic current.

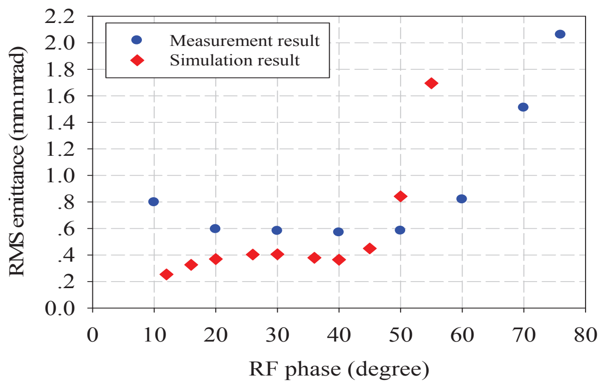

Figure 9: Relationship between the beam emittance and the RF phase.

It is clearly seen that the beam energies are high and almost constant at low RF phase region, where the space charge effect is low. Therefore, the beam emittance almost constant at this region. On the other hand, the beam energy rapidly decreases at high RF phase region, where the space charge effect is high. Therefore, the beam emittance rapidly increases.

CONCLUSTION AND OUTLOOK

The numerical and experimental studies on the electron beam properties have been carried out. Results of the investigation show that the electron beam with a bunch charge of 50 pC, a beam energy of around 5 MeV and an RMS emittance of 6-8 mm-mrad can be obtained by using the RF power of 9 MW, the RF phase of 40 degree, the laser pulse energy of 20 μJ and the solenoid magnet current of 135 A. Further investigation will be performed in order to improve the quality of the RF-gun, the measurement systems and the calculation methods for the better performance of the 1.6 cell BNL type photocathode RF-gun.

ACKNOWLEDGMENTS

The authors would like to acknowledge the support by the Joint Supervision Single Master Degree Program, the ASEAN University Network-Kyoto University (AUN-KU), Student Mobility Program toward Human Security Development, Japan Student Service Organization (JASSO) and the Development and Promotion of Science and Technology talents project (DPST).

REFERENCE

[1] S. Suphakul et al., "Development of Compact THz-FEL system at Kyoto University", TUP057, FEL2014, Basel, Switzerland (2014).
[2] L.M. Young and J.H. Billen, Los Alamos National Laboratory Technical Note LA-UR-96-1835, 2002.
[3] N. Terunuma et al., "Improvement of an S-band RF gun with a Cs_2Te photocathode for the KEK-ATF", Nucl. Instrum. Methods Phys. Res. A 613 1(2010).
[4] H. Zen et al., "Development of Photocathode Drive Laser System for RF Guns in KU-FEL", THP045, FEL2014, Basel, Switzerland (2014)
[5] Stopping-power and range tables for electrons: http://physics.nist.gov/cgi-bin/Star/e_ta ble. pl
[6] Sheldehl materials, "The red book": http://www. sheldahl.com/documents/RedBook.pdf
[7] J. Holmes, S. Henderson, Y. Zhang, "Magnetic Field and Magnet Design", USPAS, Vanderbilt (2009): http://uspas.fnal.gov/materials/09VU/Lectu re2.pdf.
[8] T. Rao and D. H. Dowell, An Engineering Guide to Photoinjectors, (New York, 2012).

ISBN 978-3-95450-134-2

PAL XFEL PULSE MODULATOR SYSTEM TEST RESULTS USING A HIGH PRECISION CCPS*

S.H. Kim[#,1], S.S. Park[1], S.J. Kwon[1], Y.J. Park[1], G.H. Kim[1], H.S. Lee[1], H.S. Kang[1], I.S. Ko[1], M.H. Cho[1], D.S. Kim[2], S.Y. Lee[2], M.H. Seo[2], H.S. Shin[3], K.Y. Jang[3]
[1]Pohang Accelerator Laboratory, Pohang City, Kyungbuk 790-784, Korea
[2]Dawonsy cop., Siheung City, Kyunki 429-850, Korea
[3]POSCO ICT, Seongnam City, Kyunki 463-400, Korea

Abstract

PAL XFEL is supposed to install 51 units of the pulse modulator power supplies for a 10-GeV linear accelerator using S-band (2856 MHz) cavities. The requirements of the modulator stability really become very tight. The stability on beam voltage is required to be less than 50 ppm. In order to obtain the high precision stability from the modulator system, we have newly produced a capacitor charging power supply (CCPS) and obtained the target stability with 10 ppm (STD) accuracy from measuring PFN (Pulse Forming Network). The CCPS generates a maximum output voltage of 50 kV at average current of 2.4 A with 4 units of the CCPS. The modulator peak output capacity is 400 kV, 500 A and 7.5 µs at a pulse repetition rate of 60 pps using CCPS, a modified type-E PFN, and a pulse transformer. In this paper, the test results of the modulator system will be described.

INTRODUCTION

In order to obtain the energy of 10 GeV from PAL XFEL, We are expecting to employ 51 units of pulse modulators with matching klystrons. Among the 51 units, s-band types are fifty units, and x-band type is one. The requirements of a beam voltage stability and RF phase stability are 0.005% (std) and 0.1 degree (std), respectively. The high precision CCPS has been employed to meet the requirement for the modulator stability. We are supposed to use three types of klystrons: an equal number of modulators with 48 of the s-band 80 MW klystrons, two of the s-band 25 MW klystrons, and one of the x-band klystron.

MODULATOR SYSTEM

51 units of the pulse modulator power supplies will be installed for a 10-GeV linear accelerator until the end of September this year. There are three types of klystrons: the s-band 80 MW, 25 MW klystrons, and the x-band 50 MW klystron.

Klystron Tube

The performance parameters of the s-band Toshiba E37320 klystrons and XL4 klystron are shown in the tables below. The XL4, x-band klystron, is used to power x-band structures of PAL XFEL for beam phase space linearization.

*Work supported by the Korean Ministry of Education
#ksangh@postech.ac.kr

Table 1: S-band Klystron Specifications

Description	Unit	Value
Frequency	MHz	2,856
Peak output RF power	MW	80
RF pulse	µs	4
Cathode voltage (V_k)	kV	400
Beam current (I_k)	A	500
µ-perveance		1.85~2.0
Repetition rate (Max)	Hz	60

Table 2: X-band Klystron Specifications

Description	Unit	Value
Frequency	GHz	11,424
Peak output RF power	MW	50
RF pulse	µs	2
Cathode voltage (V_k)	kV	450
Beam current (I_k)	A	360
µ-perveance		1.2
Repetition rate (Max)	Hz	120

Modulator

The specifications of the PAL XFEL modulator are output power of 200 MW, beam voltage of 400 kV, beam current of 500 A, pulse width of 7.5 µs and repetition rate of 60 Hz. Table 3 summarizes the specifications of the modulator.

Table 3: Modulator Specifications

Description	Unit	Value
Peak power	MW	200
Average charging power	kW	120
Repetition rate (normal)	Hz	60
Pulse peak output voltage	kV	400
Pulse peak output current	A	500
PFN voltage stability (rms)	ppm	< 10
Flat-top width	µs	4.0

Figure 1 shows the simplified circuit diagram of the PAL XFEL modulator. In order to charge to PFN capacitor, CCPS are used, which are newly produced by

ISBN 978-3-95450-134-2

Dawonsys and Posco ICT. The inverter power supply is a constant current source so that the PFN voltage is linearly increasing during active charging time. It takes about 14 msec to charge the PFN up to 45 kV, not including dwell time as using a maximum output voltage of 50 kV at an average current of 2.4 A with 4 units of the CCPS in a 200 MW PAL XFEL modulator. The CCPS total power rating is 120 kJ/s.

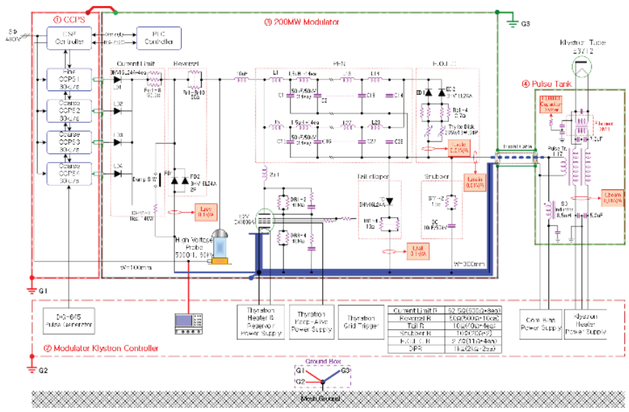

Figure 1: Circuit diagram of the PALXFEL modulator.

CAPACITOR CHARGING POWER SUPPLY

The modulator employees a high efficiency capacitor charging power supply that utilizes a high frequency, series resonant inverter topology. The power supply is specifically designed for constant current capacitor charging. With the help of the CCPS, the modulator system is naturally compact in spite of a 200 MW modulator power.

Configuration of CCPS

The block diagram of the inverter power supply is shown in Fig. 2. There are four basic modules: the input power module, the inverter section, the high-voltage tank, and the control system. Inverter part is a resonance method that consists of L and C to supply resonance current and full-bridge circuit using IGBT module. The resonance frequency is 40 kHz. High voltage rectifier circuits produce the rectified high voltage output. The control circuit utilizes a high regulation scheme that DSP 28335 is used to control primary power and inverter part of the CCPS, sensing output voltage and current in order to monitor various interlocks.

Control of CCPS

CCPS controls PFN voltage precisely by using a precision controller and a master controller. Figure 3 shows the configuration for precision control. The precision controller picks up the charged voltage in PFN by using a high voltage probe and transfers to a master controller in the CCPS after determining the gate pulse width of the IGBT to maintain setting value of the PFN charging voltage through a P-I control. The master controller controls the output by transmitting the gate

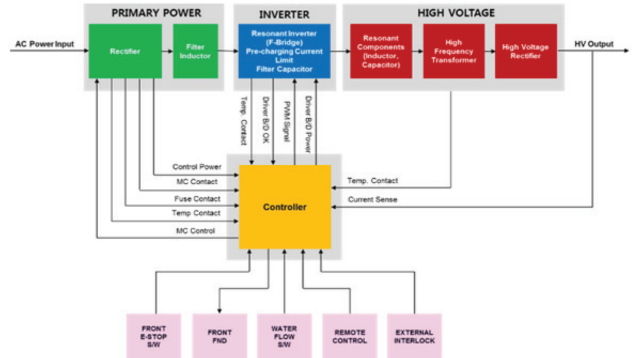

Figure 2: Block diagram of the inverter power supply.

signal of IGBT received from a precision controller and displays received interlock information of CCPS, then finally transfers the information to a machine controller. To meet a very tight stability two different types of CCPS mode are employed. One is a fine control mode which is a high precision type (< 10 ppm) and the other is a coarse CCPS (<1,000 ppm).

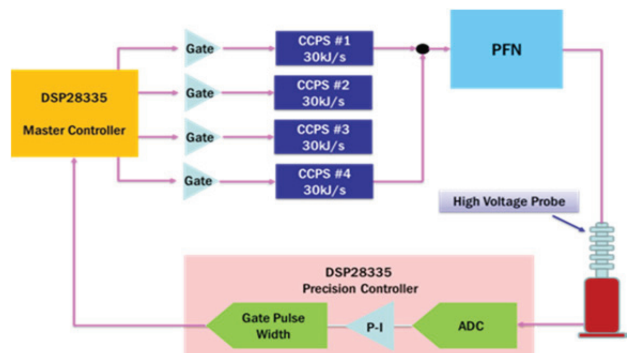

Figure 3: CCPS precision control configuration.

Stability Measurement

The experimental devices were set up to measure the modulator stability from PFN, beam voltage, and beam current as shown in Fig. 4. To obtain high precision of the voltage stability, we used a high voltage probe (VD60 Ross) which is very stable in temperature fluctuation. On the PFN, beam voltage, and beam current waveform, the zero offset is defined by a differential amplifier (DA1855A, Lecroy) setting a band width of 100 kHz. To

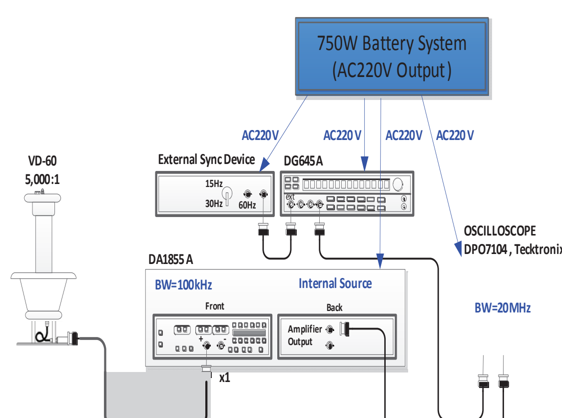

Figure 4: Test device for a stability measurement.

ISBN 978-3-95450-134-2

display the histogram, an oscilloscope (DPO7104, Tektronix) equipped with a high resolution mode in an acquisition mode is used [1].

PFN Charging Voltage Waveform

The capacitance of PFN in the 200 MW PAL XFEL modulator is 1.4 µs, and the test operation condition is 42 kV at 60 Hz. The load is Toshiba s-band klystron (E37320). Figure 5 shows the charging current waveform of PFN and bucket voltage during charging. The charging voltage will be changed when the PFN voltage reaches to the target value during charging. Figure 6 shows the expanded precision charging voltage waveform and control of voltage waveform in the regulation section of PFN. The size of the precision voltage in the regulation section is less than 2 V.

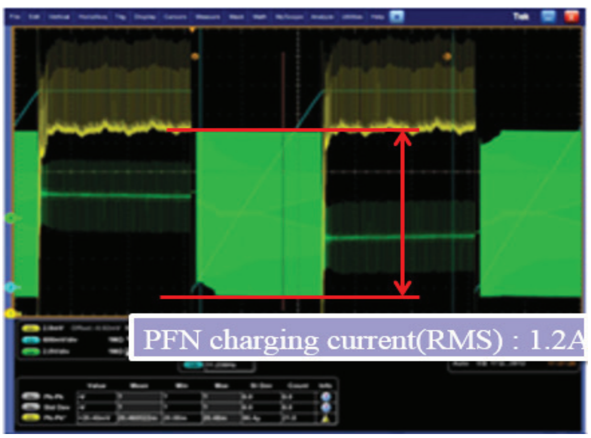

Figure 5: PFN charging current.

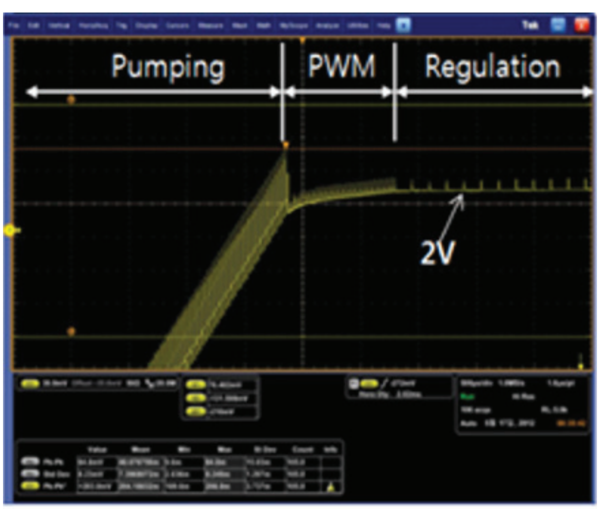

Figure 6: Current of PFN charging voltage.

Test Results

In order to reduce switching noise from a thyratron switch in a modulator system, separated AC power and optic cables were used to block the switching noise while measuring the stability of PFN voltage. The measuring position of PFN stability is 1 µs before switching of a thyratron. For each measurement it took about 3 minutes and performed 3 times after every 30 minutes waiting time. The stability of the PFN charging voltage was about 9 ppm shown in Fig. 7. In the same method as PFN measuring, the beam voltage stability was trying to do, and the measuring position of beam voltage stability was randomly selected from the flat-top, then set 5 ns for the time division. For each measurement it took about 3 minutes and performed 8 times for more accurate results after every 30 minutes waiting time. The stability of the beam voltage was about 29.6 ppm shown in Fig. 8. The slight deviation of the stability for each step was mainly due to temperature dependent time variation.

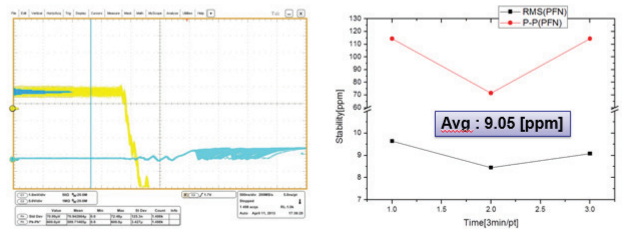

Figure 7: PFN voltage stability measurement.

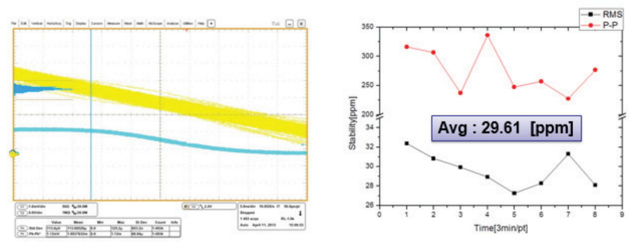

Figure 8: Beam voltage stability measurement.

HARMONICS OF CCPS INPUT POWER MEASUREMENT

We measured and analysed the harmonics that may be generated from CCPS input power, 480 V AC while the CCPS is running at 40 kV, 60 Hz. Plots for current waveforms measured from the 480 V AC are shown in Fig. 9.

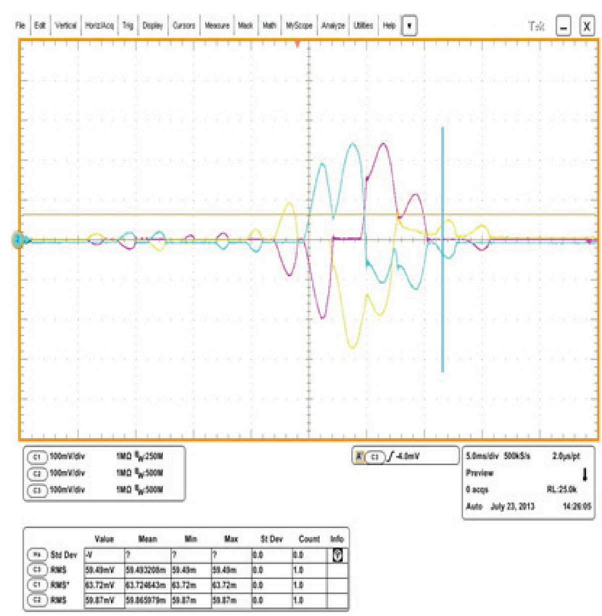

Figure 9: Current waveforms from AC 480 V.

ISBN 978-3-95450-134-2

The detailed harmonic trends measured from AC 480 V are summarized below while CCPS is working at 40 kV, 60 Hz. As shown in Fig. 10, those are 41.6 % of the 2nd harmonics, 14.7 % of 3rd, 30.7 % of 5th, and 10 % of 7th. As a result of analysing each phase and its harmonics, unexpected high harmonic distortions have occurred due to characteristic of making the CCPS operation that they are only working during the period of 13.4 ms at 60 Hz. An inductor of 1 mH was set up in the input source side of AC 480 V to solve that harmonic problem. After that there was a reduction effect of about 72 % at harmonic distortions. However, the voltage drops of AC 480 V get worse at the inductor test of 1 mH, so we need to consider an inductor of the appropriate values. In general, the inductor of installed capacity of 5 % is applied for harmonic current reduction of nonlinear load. Therefore, the inductor of about 5 % is expected to apply an inductor of around 600 μH when used shall be. The harmonics also bring the reduction by increasing capacitor values that used in the DC link in the CCPS.

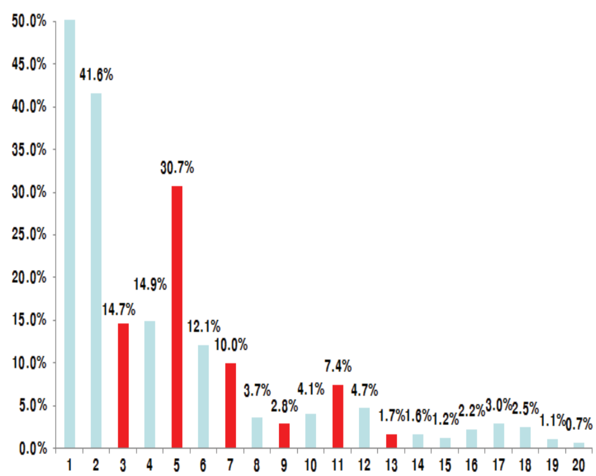

Figure 10: Harmonic current spectrum measured from AC 480 V.

CONCLUSION

The 200 MW pulse modulator for an 80 MW s-band klystron was designed and fabricated including a precise function of CCPS that is a maximum output voltage of 50 kV and an average power of 30 kW. The stability results of measuring at PFN and beam voltage were satisfying the requirement of < 10 ppm and < 50 ppm, respectively. Three-phase 480 V AC is used to supply CCPS input with the AC power. We have found lots of power factor measured more badly than the requirements set out while CCPS is working only for 13.3 ms at 60 Hz. In order to reduce unexpected high harmonic distortions we have to make a harmonic measurement of AC 480 V applied to CCPS input lines, then installed a inductor of 600 mH between CCPS input lines and AC 480 V. After that, we are satisfying the results due to reducing the high harmonic distortions and the voltage drop rate of AC 480 V.

REFERENCES

[1] J.S. Oh, S.S. Park, Y.J. Han, I.S. Ko, W. Namkung, “Design considerations for the stability improvement of klystron-modulator for PAL-XFEL”, Proceeding of 2005 Particle Accelerator Conference, Knoxville, Tennessee, 2005, pp. 1165-1167.

STUDY OF SMITH-PURCELL FREE ELECTRON LASER USING ELECTRON BUNCH PRODUCED BY MICRO-PULSE ELECTRON GUN

Jifei Zhao*, Deyu Yang, Ziqin Yang, Weiwei Tan, Yujia Yang, Xiangyang Lu†
Institute of Heavy Ion Physics, Peking University, Beijing100871, China

Abstract

A Micro-Pulse electron Gun (MPG) with the frequency of 2856 MHz has been designed, constructed and tested. Some primary experimental studies have been carried out and electron beam with the average current of 18 mA has been detected which holds promise to use as an electron source of Smith-Purcell Free Electron Laser (SP-FEL) to produced Coherent Radiation. It is well known that Smith-Purcell radiation is one of the achievable ways to produce FEL. After many years study in theory and experiment, lots of new mechanisms and appearances have been discovered. Coherent Smith-Purcell Radiation was discovered in 1990s as well. Obviously, MPG is one of ideal electron sources of CSPR for that S-band electron source can increase energy density and produce frequency-locked SP radiation at these frequencies. And this will be displayed in the simulation of this article.

INTRODUCTION

Since the multipacting effect was firstly discovered by Farnsworth in 1934[1], it has been deeply investigated in many areas, such as RF structure related accelerator [2-5], high power microwave generators [6, 7]. Some applications of the multipacting effect require suppressing the secondary-electron emission electron while the others, crossed-field devices for instance, need to enhance the emission [8]. Micro-Pulse electron Gun (MPG) which has been proposed by Mako for more than two decades [9] needs to select the materials judiciously. Due to its self-bunching property and choosing suitable secondary-electron-emission material, MPG is capable of providing high Pulse Repetitions Frequency (PRF) which means high current and short pulse electron beams [10]. The features of high PRF and short pulse make MPG one of the most appropriate electron sources to do some research of frequency locked Coherent Smith-Purcell Radiation (CSPR) which was discovered in 1990s.

This paper presents studies on the steady state multipacting in a MPG and the simulation of Smith-Purcell FEL using electron bunch produced by MPG. In the first section, the requirements for the steady multipacting are proposed by analyzing the self-bunching effects and conditions of secondary electron emission. In the second section, the primary experimental results are obtained through the experiments carried out on a 2.856 GHz MPG cavity. Finally, the further experimental arrangements are given. And Smith-Purcell FEL is investigated by using Particle In Cell (PIC) simulation method.

* Email: zjf@pku.edu.cn
† Corresponding author, email: xylu@pku.edu.cn

REQUIREMENTS FOR STEADY STATE MULTIPACTING

The MPG Model

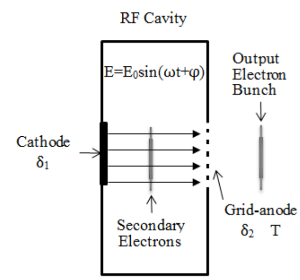

Figure 1: The schematic diagram of MPG model.

The MPG model is shown in Fig. 1. It consists three parts: an pill-box RF cavity working TM_{010} mode, a secondary emission surface with Secondary Emission Yield (SEY) δ_1, a grid-anode, SEY δ_2 and transmission coefficient T, which is opaque to the microwave field but let the electrons partially go out the RF cavity. When MPG working, the microwave electric field -anode changes as sine wave with time. And the secondary electrons move between cathode and grid under the action of electric field.

The Self-bunching Effects

The self-bunching effects have been reported in many articles [11, 12]. They can be explained by the following ways.

Firstly, we divide the cavity length into N parts and every part is dz. The electric field acting on every electron in nth can be expressed

$$E_n = E_0 \times \sin(\omega \sum_{i=1}^{n-1} t_i + \varphi) \tag{1}$$

where t_i is the travelling time of electron in ith part. And the acceleration can be written (non-relativistic electrons)

$$a_n = \frac{E_n e}{m} \tag{2}$$

Then the travelling time is

$$t_n = \frac{(v_{n-1}^2 + 2a_n dz)^{\frac{1}{2}} - v_{n-1}}{a_n} \tag{3}$$

where v_{n-1} is the velocity of electron in (n-1)th part.

ISBN 978-3-95450-134-2

The velocity of electron in nth and is

$$v_n = a_n t_n + v_{n-1} \tag{4}$$

The time of different initial phase electrons take to go across one cavity length in a specific MPG is obtained through carrying out recursive process above. Figure 2 shows travelling time versus the initial phase of different electrons for cavity length d=2mm, RF frequency f=2.856GHz (half a period is 171ps), N=10000, initial energy ε=2eV, in the case of E_0=0.7MV/m, E_0=0.8MV/m, E_0=0.9MV/m, E_0=1.0MV/m, E_0=1.1MV/m, E_0=1.2MV/m.

Taking example for E_0=1MV/m, one can clearly see there are two crossover points between the t=171ps (half a period) and the E_0=1MV/m curve. And the abscissa value of left one corresponds to the initial phase of synchrotron electron φ_c because it means that if an electron which was emitted from the emission surface with this phase it just can reach the grid in half a period. While the abscissa value of right one corresponds to the cutoff point of self-bunching effects.

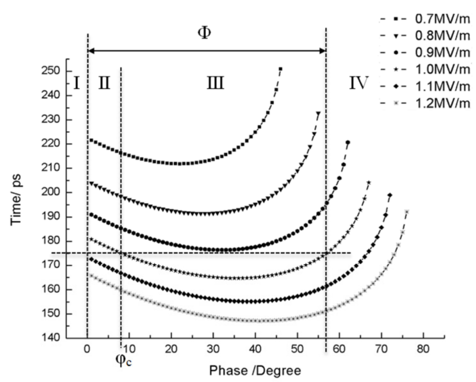

Figure.2: The travelling distance of electron vs its phase.

The integrated interval of self-bunching can be confirmed by comparing the time of different electrons take in a cavity length. In conclusion, the phase range of self-bunching is (0-Φ). Another piece of information Fig. 2 gives us is that there must exist two crossover points between the half a period time line and the electric field curve to make the MPG running stably-that is the electric field must be chosen properly for a parameters given MPG in order to produce self-bunching effects.

The Requirements of Secondary Electron Emission

Basically, the higher the electric field is, the more energy the electrons will be gained. According to the basic empirical SEY formula of common metal materials Eq. 8 [13], the SEY curve versus the energy of the incident electron can be got.

$$\frac{\delta}{\delta_{\max}} = (\nu e^{1-\nu})^k \tag{8}$$

where δ is the SEY of the material, $\delta_{\max}$ is the maximum value of δ, $\nu=(E_i-E_0)/(E_{\max}-E_0)$, in which $E_{\max}$ is the impact energy corresponding to $\delta_{\max}$, E_0 is the initial energy of secondary electrons and k=0.62 for ν<1; k=0.25 for ν>1.

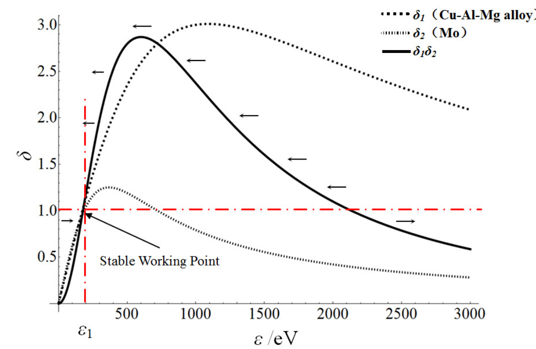

Figure 3: The effective SEY curve versus impact energy for Mo, Cu-Al-Mg ally and total of them.

The effective SEY curve versus impact energy for Mo, Cu-Al-Mg ally and total of them are shown in Fig. 3. Where the δ_{max} for Mo and Cu-Al-Mg ally are respectively 1.25 and 3 and corresponding ε_{max} are 375eV and 1000 eV. The stable working point is the crossover point in this figure because if there are power fluctuations, the working point can return to the stable working point. That is, there are power feedback mechanisms at this point.

Requirements for Steady State Multipacting

As was mentioned above, the impact energy must working at the stable working point and the electron bunch must produce self-bunching effects. In conclusion, to obtain steady state multipacting in the MPG, there must be a good match between the accelerating field required by self-bunching effects and impact energy. The accelerating field can be adjusted by frequency f and cavity length d to produced self-bunching effects. While the stable working point can be adjusted by changing δ of the cathode and the grid-anode as well as the transmission factor T.

PRIMARY EXPERIMENTS

Based on the requirements of steady state multipacting, two MPG cavities (PKUMP-I and PKUMP-II) with frequency of 2.856GHz have been designed and the RF parameters have been listed in Table 1. The PKUMP-I has been constructed and applied to do some primary experiments.

The schematic diagram of the experimental platform is shown is Fig. 4. The output electron beams are collected by a faraday cup which is connected to a 50 Ω resistance in parallel way. So the beam current can be detected by a oscilloscope.

ISBN 978-3-95450-134-2

Table 1: The Designed RF Parameters of the MPG Cavities

RF parameters	PKUMP-I	PKUMP-II
Resonant frequency f (GHz) :	2.856	2.856
Cavity length (mm)	1.8	1.75
Unloaded quality factor Q_0	100	~400
Shunt impedance r_{shunt} (MΩ)	0.036	~0.03
Unloaded coupling coefficient β_0	1.25	3~4

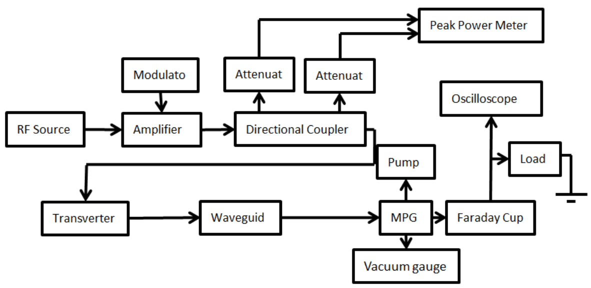

Figure 4: The schematic diagram of the experimental platform.

Three different materials have been tested as grid-anode by the platform using PKUMP-I. And the materials of different transmission are shown is Fig. 5. The test result is shown in Table 2. Form this table we can make some conclusion: (1) The higher the transmission is, the more electrons the MPG could produce. (2) Oxy free copper is a more appropriate choice for getting relatively large current. Although Grid-anodes of Stainless Steel and Molybdenum could not produce more electrons, they are useful for steady state multipacting. Taking the MO3 for example, the measured average current is 0.4 mA, just as what is shown in Fig. 6, but the stable working time is more than 70min.

Table 2: The Measured Current for Various Grid-anode

Materials	NO.	Transmission Coefficient	Measured Average Current (mA)
Stainless steel	SS1	6%	0.2
	SS2	18.3%	3.8
Oxy free copper	OFC1	6%	4
	OFC2	18%	9
	OFC3	25%	18
Molybdenum	MO1	11%	4
	MO2	14.125%	6
	MO3	30.65%	0.4

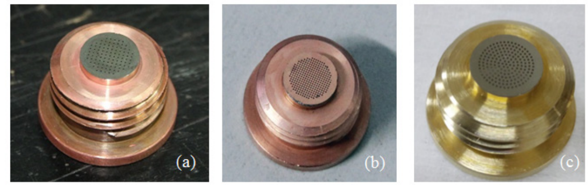

Figure 5: Three different grid-anodes (a) is stainless steel grid, (b) is Oxy Free Copper grid, (c) is Molybdenum grid.

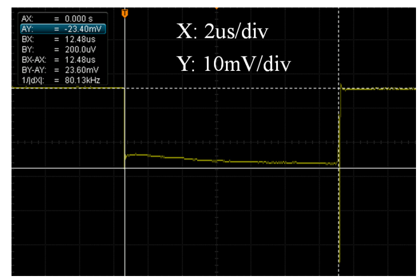

Figure 6: The output beam average current (≈0.4 mA) when the grid-anode is MO.

SIMULATION OF SMITH-PURCELL FEL

When a charged particle passes over a periodic grating, the Smith-Purcell Radiation (SPR) which was first observed in 1953[14] occurs. For electron bunch, the wavelength of the radiation is

$$\lambda = \frac{1}{n}\left(\frac{1}{\beta} - \cos\theta\right) \tag{9}$$

where n is the order of the radiation, l is the granting period, β is the ratio of the electron bunch velocity to the speed of light, and θ is the observation angle.

According to the feature of the electron bunch produced by MPG, the simulation of SP-FEL is carried out by PIC simulation method. The main setting parameters of the simulation are show in Table 3.

Table 3: The Main Parameters of the Simulation

Parameters	Value
Electron beam energy	100keV
Average current	18mA
Beam thickness	0.5mm
Frequency	2.856GHz
Beam length (longitudinal)	5ps
Grating period	1mm
Grating groove depth	1mm
Grating groove width	0.5mm
Number of periods	200
External magnetic field	2T

ISBN 978-3-95450-134-2

After the MPG, there is an accelerating gap between the MPG and the grating. And the voltage of the gap is -100 keV which can accelerate the electron beam to about 100 keV. The beam is supposed a parallel-beam and the emittance of it is 0 mm·mrad. The number of periods is assumed 200 with the grating period is 1mm so that there are three electron bunches passing over the grating at least. Figure 7 is the X-Y contour map of B_z obtained at 1.271 ns. Four electron bunches is passing over the surface of the grating. We can see the interference fringes apparently. And there are two cylindrical waves radiated from both ends of the grating appear. We conclude that those waves should be attributed to the so called evanescent wave radiation. The evanescent wave radiate at the ends of a grating where it undergoes partial reflection and partial diffraction. Figure 8 shows the Time signal of Bz and corresponding FFT from a detector placed at 35°. It can be clear seen from Fig. 8 that there are seven electrons arrived the terminal of the grating because there are seven nodes and the interval of the node is 350 ps corresponding to the period of the beam. The FFT from a detector strongly shows the frequency-locked SP radiation occurred and the frequency is 54.25 GHz corresponding to 19th harmonic of the rf frequency.

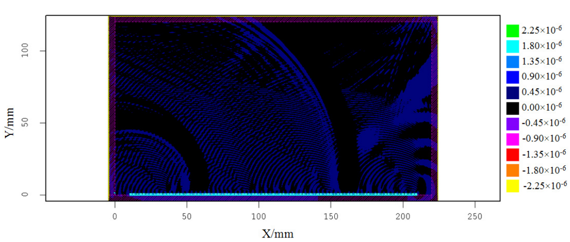

Figure 7: the x-y contour map of B_z obtained at 1.271ns.

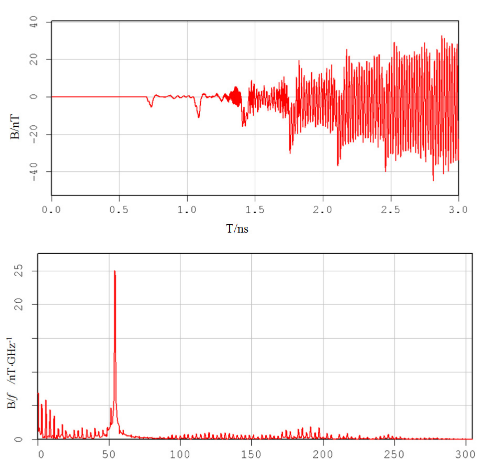

Figure 8: Time signal of B_z and corresponding FFT from a detector placed at 35.

CONCLUSION

In summary, the self-bunching effects and the requirements of secondary electron emission were investigated in theory. And the theoretical analysis shows that to obtain a steady state multipacting, a good match between the accelerating field and impact energy is required. According the theory, the experimental exploration was carried out with the PKUMP-I one of the two MPG designed by Peking university. Three different metal grid materials were used in the experiments. A maximum of 18mA with OFC3 was detected by a faraday cup and a more than 70 min of stable output with MO3 was got. To study the application of the electron bunch produced by MPG in SP FEL, the simulation was carried out by PIC method. The results show that the electron bunch could produce frequency-locked SP radiation.

REFERENCES

[1] P. T. Farnsworth, Journal of the Franklin Institute 218, 411 (1934).
[2] P. Ylä-Oijala, Part. Accel. 63, 105 (1999).
[3]C. M. Lyneis, H. A. Schwettman, and J. P. Turneaure, Appl. Phys. Lett. 31, 541 (1977).
[4] H. Padamsee, D. Proch, P. Kneisel, and J. Mioduszewski, IEEE Trans.Magn. 17, 947 (1981).
[5] R.L. Geng, H. Padamsee, S. Belomestnykh, P. Goudket, D.M. Dykes, and R.G. Carter, Nuclear Instruments and Methods in Physics Research Section A: Accelerators, Spectrometers, Detectors and Associated Equipment 508, 227 (2003).
[6] N.F. Kovalev, V.E. Nechaev, M.I. Petelin, and N. Zaitsev, IEEE Trans. Plasma Sci. 26, 246 (1998).
[7] A. Shih and C. Hor, IEEE Trans. Electron Devices 40, 824 (1993).
[8] A Shih, J Yater, C Hor, and R Abrams, Appl. Surf. Sci. 111, 251 (1997).
[9] F.M. Mako, and W. Peter, in Proceedings of the 1993 Particle Accelerator Conference, U.S. Washington, DC, 17 May-20 May 1993, IEEE (Piscataway, NJ, USA, 1993), pp. 2702-2704.
[10] K. Zhou, X.Y. Lu, S.W. Quan, J. F. Zhao, X. Luo., and Z. Q. Yang, Rev. Sci. Inst 85, 093304 (2014).
[11] L.K. Len, and F.M. Mako. in Proceedings of The 1999 Particle Accelerator Conference, New York, USA,
[12] X.F. Yang, Z. Xu, X. Jin, M. Li, X.S. Liu, G.H. Cai, H.P. Lu, and Z.F. Zhang, in Proceedings of the Third International Symposium on Pulsed Power And Plasma Applications, Mianyang, China, 22 Oct -26 Oct 2002, pp. 433-436
[13] J.R.M. Vaughan, IEEE Trans. Electron Devices 36(9), 1963-1967 (1989).
[14] S.J. Smith, and E. M. Purcell. Phys. Rev. 92, 1069 (1953).

ISBN 978-3-95450-134-2

NUMERICAL SIMULATIONS OF A SUB-THz COHERENT TRANSITION RADIATION SOURCE AT PITZ

P. Boonpornprasert*, M. Krasilnikov, F. Stephan, DESY, Zeuthen, Germany
B. Marchetti, DESY, Hamburg, Germany

Abstract

The Photo Injector Test facility at DESY, Zeuthen site (PITZ), develops high brightness electron sources for modern linac-based Free Electron Lasers (FELs). The PITZ accelerator can be considered as a proper machine for the development of an IR/THz source prototype for pump and probe experiments at the European XFEL. For this reason, the radiation generated by high-gain FEL and Coherent Transition Radiation (CTR) produced by the PITZ electron beam has been studied. In this paper, numerical simulations on the generation of CTR based on the PITZ accelerator are presented. The beam dynamics simulations of electron bunches compressed by velocity bunching are performed by using the ASTRA code. The characteristics of CTR are calculated numerically by using the generalized Ginzburg-Frank formula. The details and results of the simulations are described and discussed.

INTRODUCTION

The Photo Injector Test facility at DESY, Zeuthen site (PITZ), has been established to develop, study and optimize high brightness electron sources for modern linac-based short-wavelength Free-Electron Lasers (FELs) like FLASH and the European XFEL. The concept of generating IR/THz radiation by electron bunches from a "PITZ-like" linear accelerator for pump and probe experiments at the European XFEL was presented in Ref. [1]. In order to study and demonstrate the capabilities of IR/THz generation from such an accelerator, PITZ has continued the case study for such a prototype IR/THz source. The main goal of the development is to generate radiation that covers wavelengths from IR (μm) to THz (cm) with a variety of field patterns (from single-cycle to narrow-band), and with a high level of peak and average radiation power from the PITZ accelerator. In addition, developments and studies on radiation based electron bunch diagnostics and photon diagnostics can be done at the same time. The radiation generations using high-gain FELs and Coherent Transition Radiation (CTR) have been studied and preliminary results have been obtained.

The layout for the simulations of radiation generation as shown in Fig. 1 is similar to the current PITZ beamline with some additional radiators. The layout consists of a 1.6-cell L-band photocathode RF gun surrounded by main and bucking solenoids, a cut disk structure (CDS) booster, screen stations, quadrupole magnets and dipole magnets. The CTR station is placed at 16.30 m downstream from the cathode. An APPLE-II type undulator is placed at the end of beamline for the high-gain FEL radiation using Self-Amplification of Spontaneous Emission (SASE) process. Preliminary start-to-end simulations for the SASE FEL using the PITZ accelerator and covering radiation wavelength from 20 μm to 100 μm were studied and presented in Ref. [2].

In principle, the radiation wavelength of the CTR emitted from a relativistic electron bunch is longer than or comparable to the bunch length. Therefore, in order to cover radiation frequencies in the THz region, the electron bunch length must be in the sub-ps scale. The nominal FWHM bunch length of the electron beam at PITZ is about 2 ps to 20 ps, it is obvious then that the beam needs to be compressed in order to fulfill our request.

In this paper, we present methods and results of numerical simulations of the CTR source based on the PITZ accelerator. The paper is organized as follows: the details and results of the bunch compression simulations using the velocity bunching are described in the next section. Then, the characteristics of the CTR obtainable from the compressed bunches are calculated numerically and discussed. Finally, our conclusion and outlook are presented.

SIMULATIONS OF VELOCITY BUNCHING

We would like to maximize the electron bunch charge in order to increase the CTR intensity and to minimize the bunch length in order to broaden the spectral bandwidth. The photocathode laser system at PITZ is able to produce pulses having gaussian temporal pulse shape with minimum FWHM length of 2.43 ps. The electron bunch charge can be varied by adjusting the laser pulse energy. With this laser temporal length and large laser spot size on the cathode (rms size of 1 mm), it is possible to reach about 1 nC bunch charge.

When accelerating on-crest from the gun and the booster with their possible maximum peak electric fields, the beam can be accelerated up to about 22 MeV/c mean momentum. Since the peak electric field at the cathode has to be high enough for extracting the expected bunch charge from the cathode, the RF phase in the gun was fixed to its Maximum Mean Momentum Gain (MMMG) phase and we use only the booster for the velocity bunching. However, the minimum beam momentum is limited to about 15 MeV/c in order to prevent from too strong space-charge domination problems during the beam transport and a too big emission angle from the CTR which is directly proportional to $1/\gamma$ where γ is the Lorentz factor of the electron beam.

The ASTRA code [3] was used for tracking the electron beams from the cathode to the CTR station which is placed 16.30 m downstream from the cathode as shown in

* prach.boonpornprasert@desy.de

ISBN 978-3-95450-134-2

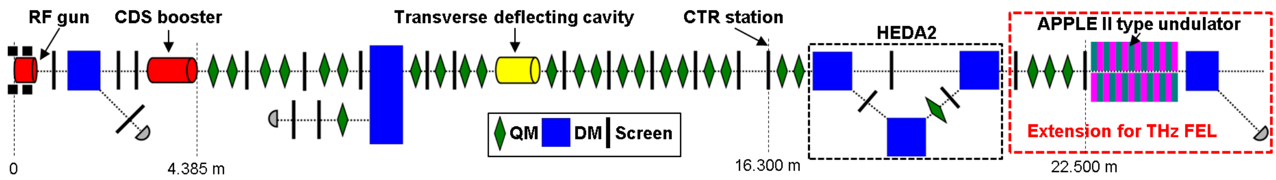

Figure 1: Schematic layout of the PITZ beamline including radiation stations, CTR and SASE FEL, for simulations studies. Here QM and DM represent quadrupole magnets and dipole magnets, respectively.

Fig. 1. A gaussian laser temporal shape with pulse duration of 2.43 ps FWHM and bunch charges of 20 pC, 100 pC, 200 pC, 500 pC and 1 nC were used as input for the simulations. The gun phase was set to its MMMG phase. The booster phase was set to −60° off-crest with respect to (w.r.t.) its MMMG phase in order to obtain the final electron beam momentum of about 15 MeV/c as required. Important input parameters for the ASTRA simulations are listed in Table 1.

Table 1: Input Parameters for ASTRA Simulations

Paramaters	Values
Rms laser spot size at the cathode, [mm]	1
Z_{start} to Z_{end}, [m]	0 to 16.30
Bunch charge [nC]	0.02 to 1
Peak electric field in the Gun, [MV/m]	60
Peak electric field in the booster, [MV/m]	18
Gun phase w.r.t. MMMG phase, [degree]	0
Booster phase w.r.t. MMMG phase, [degree]	−60

The evolution of the simulated rms bunch length from the cathode (0 m) to the CTR station (16.30 m) is shown in Fig. 2. The rms momentum spread and peak current as a function of the bunch charge at the CTR station are shown in Fig. 3 and the corresponding longitudinal phase spaces are shown in Fig. 4. The rms bunch length at the CTR station decreases by about 30 % w.r.t. its value at the booster exit for a 20 pC beam. On the other side, for a 1 nC beam there is only a reduction of about 14 %. The decreasing of the compression efficiency from the velocity bunching for higher bunch charge is due to the stronger longitudinal space-charge force. Furthermore, the rms momentum spread is lower for the higher bunch charge as can be seen from the plot in Fig. 3 and more obviously from the slopes of the longitudinal phase spaces in Fig. 4. This also reduces the compression efficiency.

CALCULATION OF THE CTR

For calculating the CTR produced by an electron bunch, a longitudinal form factor of the electron bunch is introduced as follows:

$$F_{long}(\omega) = \int_{-\infty}^{\infty} \rho_{long}(t) \exp(-i\omega t) dt \qquad (1)$$

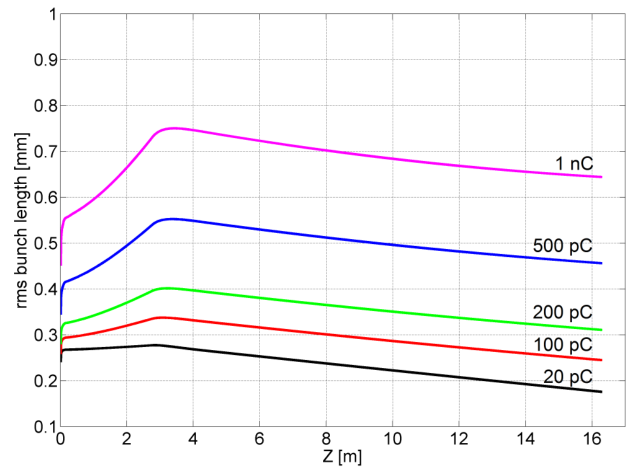

Figure 2: Simulated rms bunch lengths from the cathode (0 m) to the CTR station (16.30 m) for bunch charges of 20 pC to 1 nC.

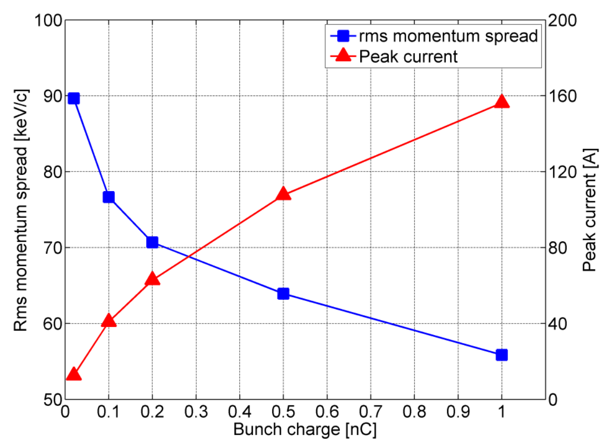

Figure 3: Simulated rms momentum spread and peak current of the compressed bunch as a function of bunch charge at the CTR station.

where $\rho_{long}(t)$ is the function that describes the longitudinal charge profile. The generalized Ginzburg-Frank formula [4] is used for calculating the radiation energy. This formula assumes that the radiator screen is a finite circular metallic screen with the radius a. Furthermore, the electron beam having a transverse radius size r_b and a Lorentz factor $\gamma = 1/\sqrt{1-\beta^2}$, where β is the electron speed normalized to the speed of light, impinges normally on the screen. Then the

ISBN 978-3-95450-134-2

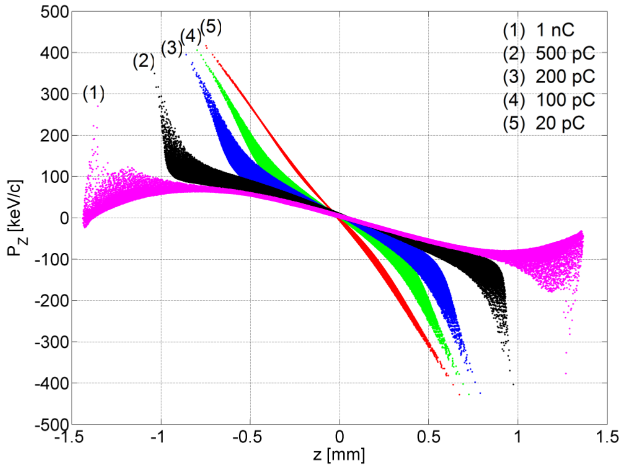

Figure 4: Simulated longitudinal phase spaces of the compressed bunch at the CTR station.

spectral and spatial radiation energy in the far-field regime for backward CTR are given by [4]

$$\begin{aligned}\frac{d^2U_{bunch}}{d\omega d\Omega} =& \frac{e^2}{4\pi^3\varepsilon_0 c}\frac{\beta^2\sin^2\theta}{(1-\beta^2\cos^2\theta)^2}\cdot N^2\left|F_{long}(\omega)\right|^2\\ &\times\left[\frac{2c}{\omega r_b\sin\theta}J_1\left(\frac{\omega r_b\sin\theta}{c}\right)-\right.\\ &\left.\frac{2c\beta\gamma}{\omega r_b}I_1\left(\frac{\omega r_b}{c\beta\gamma}\right)T(\gamma,\theta,\omega)\right]^2,\end{aligned} \tag{2}$$

where θ is the angle between an axis normal to the screen plane in backward direction and the emitted radiation direction, J_n is the Bessel function, K_n and I_n are the modified Bessel functions and the term $T(\gamma,\theta,\omega)$ is written as

$$\begin{aligned}T(\gamma,\theta,\omega) =& \frac{\omega a}{\beta\gamma c}J_0\left(\frac{\omega a\sin\theta}{c}\right)K_1\left(\frac{\omega a}{c\beta\gamma}\right)+\\ &\frac{\omega a}{\beta^2\gamma^2 c sin\theta}J_1\left(\frac{\omega a\sin\theta}{c}\right)K_0\left(\frac{\omega a}{c\beta\gamma}\right).\end{aligned} \tag{3}$$

The form factors of the simulated electron bunches in the previous section are calculated by Eq. 1 and shown in Fig. 5. The form factor of the bunch with 20 pC charge gives the widest spectrum that covers the frequency up to 0.5 THz but of course delivers only a very low CTR intensity when compared to the radiation from 1 nC bunch charge which will be shown later in this section.

For the calculations of the radiation characteristics, the screen radius is assumed to be 15 mm. Transverse focusing of the beam at the screen can be done by using quadrupole magnets between the booster exit and the CTR station. However, we will address this issue in further dedicated studies while for the moment we assume the transverse radius of the beams to be 0.5 mm for all the bunch charges.

Figure 6 shows contour plots of the radiation energy calculated by Eq. 2 versus radiation frequency and the angle θ for bunch charges of 20 pC and 1 nC. For the case of 20 pC (top plot), the plot shows that the radiation has the highest intensity in the frequency range from 0.1 to 0.25 THz within the measured angle of about 0.15 rad. While for the case of 1 nC (bottom plot), the highest intensity is in the frequency range of 0.05 to 0.1 THz within the measured angle of 0.3 rad.

The total pulse energy of CTR radiation is obtained by integrating Eq. 2 over the frequency band and the backward hemisphere. Figure 7 shows the calculated total pulse energy as a function of bunch charge by integrating the frequency up to 0.5 THz. The total pulse energy for the case of 1 nC reaches about 2 µJ while it reaches about only 4 nJ for the case of 20 pC.

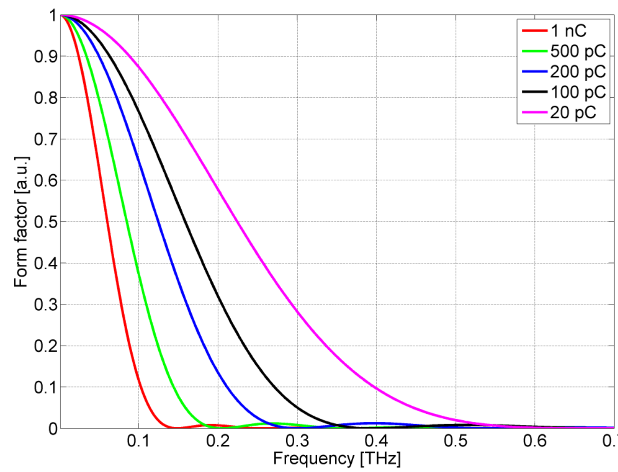

Figure 5: Form factors of the compressed bunch at the CTR station.

CONCLUSION AND OUTLOOK

We have obtained preliminary results for the calculation of CTR characteristics generated by the electron beam from the PITZ accelerator. In this case study the bunch is compressed by the velocity bunching using the booster cavity. These results will be used as a reference for preparing a CTR experiment at PITZ which is foreseen to take place in the beginning of 2016.

More realistic conditions are needed to be implemented in the CTR calculation, such as the radiation from an oblique target screen and calculation in the near-field regime. The calculation of the electric field of the CTR pulse has also been planed.

An other option for bunch compression is to use the HEDA2 section (Fig. 1). Studies on the feasibility of this option need to be done. The use of a modulated electron bunch by employing the flexibility of the PITZ photocathode laser is also an option to a produce CTR spectrum with narrow-band and higher harmonics frequencies as shown in example studies from Ref [5].

ISBN 978-3-95450-134-2

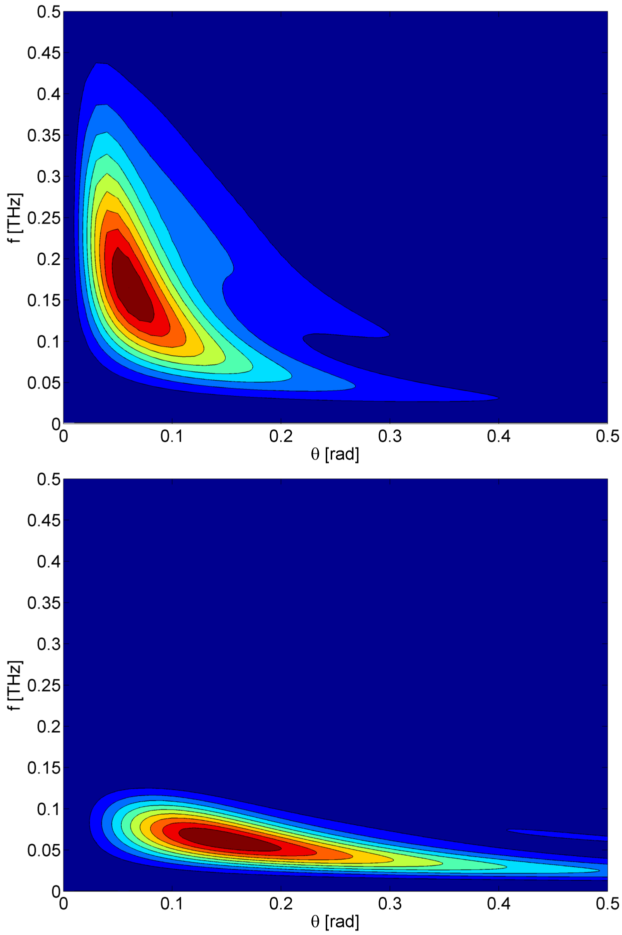

Figure 6: Contour plot of the normalized radiation energy as a function of the radiation frequency and the angle θ for bunch charges of 20 pC (top) and 1 nC (bottom).

ACKNOWLEDGMENT

The authors would like to thank C. Thongbai and S. Rimjaem from Chiang Mai University and colleagues at PITZ for useful comments and discussions.

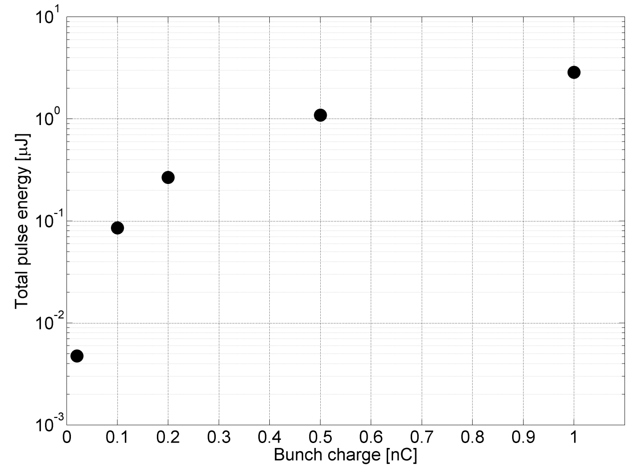

Figure 7: Calculated total radiation energy as a function of the bunch charge.

REFERENCES

[1] E. Schneidmiller et al., "Tunable IR/THz source for pump probe experiment at European XFEL", in *Proc. 34th Int. Free-Electron Laser Conf.*, Nara, Japan, 2012, WEPD55.

[2] P. Boonpornprasert et al., "Start-to-End simulations for IR/THz undulator radiation at PITZ", in *Proc. 36th Int. Free-Electron Laser Conf.*, Basel, Switzerland, 2014, MOP055.

[3] K. Flöttmann, ASTRA particle tracking code, `http://www.desy.de/~mpyflo`.

[4] S. Casalbuoni et al., "Far-infrared transition radiation and diffraction radiation, Part I", *TESLA Report 2005-15*, 2005.

[5] B. Marchetti et al., "Novel scnemes for the optimization of the SPARC narrow band THz source", *Review of Scientific Instruments 86*, 073301, 2015.

ISBN 978-3-95450-134-2

BEAM OPTICS MEASUREMENTS AT FERMI BY USING WIRE-SCANNER

G. Penco[# 1], A. Abrami[1], I. Cudin[1], S. Di Mitri[1], M. Ferianis[1], E. Ferrari[1], G. Gaio[1], L. Giannessi[1,2], S. Grulja[1], G.L. Orlandi[3], C. Ozkan Loch[3], R. Sauro[1], L. Sturari[1]
[1]Elettra-Sincrotrone Trieste S.C.p.A., Basovizza, Italy
[2]ENEA C.R. Frascati, Roma, Italy
[3]Paul Scherrer Institut, 5232 Villigen PSI, Switzerland

Abstract

Measuring and controlling the electron beam optics is an important ingredient to guarantee high performance of a free-electron laser. In the FERMI linac, the Courant-Snyder parameters and the transverse emittances are routinely measured by detecting the beam spot size as a function of a scanning quadrupole placed upstream (i.e. quadrupole scan method). The beam spot size is usually measured with an OTR screen that unfortunately suffers from coherent optical transition radiation (C-OTR) that introduces spurious light and corrupts the image. Moreover, the beam size at the end of the FERMI linac is focused to a few tens of microns and this makes it difficult to precisely measure it with the OTR system, which has an estimated resolution of 20 µm. For this reason, a wire-scanner system has been installed at the end of the linac just in the waist of the optics channel. The wire-scanner is a SwissFEL prototype (Paul Scherrer Institut, Villigen CH) installed in FERMI in order to study the hardware and beam loss monitor performances at the GeV energy scale. The beam optics measurements performed with the wire-scanner is here presented, and the obtained results are more in agreement with the theoretical expectations. A more reliable beam optics estimation at the end of the linac has allowed better matching it to the nominal lattice and transporting it up to the undulator chain, providing important benefits to the FEL performance.

INTRODUCTION

FERMI is a single-pass seeded free-electron laser (FEL) based upon the High Gain Harmonic Generation (HGHG) principle [1]. It is composed by two FEL lines that are now completely commissioned and in operation for providing intense photons (~100s uJ/pulse) for Users experiments: FEL-1 covers the range from 100nm to 10nm and FEL-2 from 20nm to 4nm [2,3].

The FERMI FEL high performance strongly relies on the capability of producing very high quality and bright electron beams.

The electron beam is generated in a RF photoinjector [4], and accelerated to 1.2-1.5 GeV by an S-band linac [5]. Two magnetic bunch compressors are placed respectively at 300MeV and at 650MeV and are utilized to shorten the electron bunch from few ps to hundreds of fs, increasing the peak current to 500-800A according to the desired operation parameters. One of the main goals in the beam transport and optimization from the injector to the undulators consists in preserving the transverse emittance and limiting the undesirable effects inducing emittance growth. At this purpose, the electron beam Courant-Snyder parameters, i.e. β and α functions, and the transverse emittance are routinely measured in strategic regions along the linac and the undulators lines, and an optimization procedure is implemented to match the optics to the lattice design. These diagnostic stations are placed after the injector (~100 MeV), after the first bunch compressor, at the end of the linac, and in front of the modulator. In this paper we focus on the 15-meter long optics diagnostic station located at the end of the linac, whose schematic layout is shown in Fig. 1.

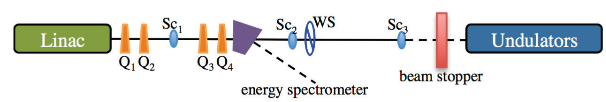

Figure 1: Diagnostic station layout at the end of the FERMI linac, including quadrupoles (Q), YAG-OTR multi-screens system (Sc) and the wire-scanner that has been installed 64 cm downstream the screen Sc_2.

THE WIRE-SCANNER PROTOTYPE AT FERMI

The nominal optics design at the end of the linac is reported in Fig. 2.

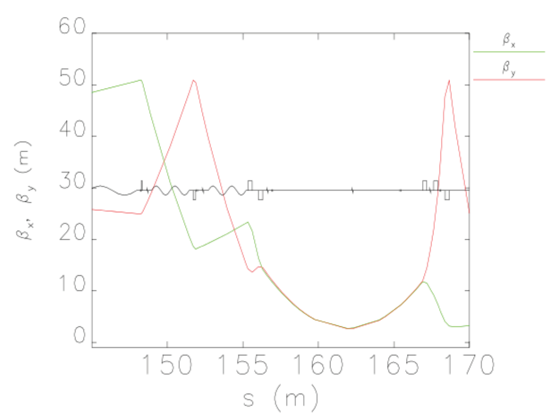

Figure 2: The horizontal and vertical β-function along the straight path at the end of the linac. The origin (s=0m) of the horizontal axis corresponds to the electron source, i.e. the photo-cathode plate.

The quadrupoles Q_3 and Q_4, see Fig. 1, are usually used only when the beam is sent into the spectrometer beam-line, to increase the measurement resolution of the longitudinal phase space [6], and are completely switched

ISBN 978-3-95450-134-2

off when the beam is routinely driven to the undulators. As a consequence the beam evolves from the second quadrupole (Q_2) to the third screen (Sc_3) as in a simple drift, with a very small waist ($\beta x=\beta y\sim 2m$) in correspondence to the second screen Sc_2.

The beam optics functions and transverse emittance are measured by using the quadrupole scan technique [7], consisting in changing the strength of the quadrupole Q_2 and measuring the correspondent beam spot size variation on a downstream screen. The screen Sc_2 has been conceived as the most suitable at this purpose since it is just in the beam waist (for the nominal lattice).

Each FERMI screen station has the option to use an OTR or a YAG target [8]. Despite of the higher spatial resolution of the OTR, strong spurious coherent-OTR signals emitted by the shortened electron bunch affect the beam spot size measurement [9]. The laser heater system [10] is used at high intensity to suppress, as much as possible any microbunching instabilities during the optics measurements. Unfortunately, it is hard to complete suppress any spurious signals that are still present, although not distinguishable. By the other hand, the YAG is limited by its low resolution (~40µm) and could be a reliable alternative only where the beam is not strongly focused. Moreover, the FERMI linac commissioning activities have required to set the screen system with a large field of view, for the slice parameters measurements [11], and this decreases the beam spot size measurement resolution also in the case of the OTR.

For all these reasons, a wire-scanner (WS) device has been installed as close as possible to the Sc_2 in order to evaluate the beam transverse profile and make a comparison with the OTR screen.

The WS is a SwissFEL prototype composed of an in-vacuum scanning hardware and scintillator-fibers for out-vacuum detection of the beam-losses [12]. The wire-fork can be inserted 45-deg with respect to vertical axis by means of a UHV linear-feed-through motorized by a stepper-motor. Two pairs of Tungsten wires are stretched on the fork frame to scan the beam profile along the horizontal and vertical directions. The two pairs of wires have a diameter of 5 and 13 µm, respectively, to ensure a geometrical resolution in the range 1.3-3.3 µm (rms).

When the wire intercepts the electron beam, a shower of high energy primary scattered electrons and secondary particles is forward emitted at a small angle in proportion to the fraction of the beam charge that is intercepted by the wire. Scanning the wire at constant speed and detecting the beam losses allow reconstructing the single projection of the beam profile. The wire losses have been measured with three Saint Gobain Scintillator fiber BCF-20 (1mm diameter): two were placed in the linac tunnel, before the beam stopper, respectively 2.48m and 5.52m downstream the WS device, while the third one was installed in the undulator hall (at 8.40m). A forth loss monitor, a Cerenkov fiber, has been placed in the linac tunnel, at about 4.5m from the WS. All four monitors signals are digitized by a vme multichannel adc board running at 250 Msamples/sec. Real-time software acquires, processes and stores shot-by-shot the waveforms coming out from board whereas a dedicated tango server manages the communication to higher level programs.

BEAM PROFILE MEASUREMENTS

The WS stepping motor system ensures a reliable constant wire scanning velocity. Wire mechanical vibrations are completely negligible for scanning speed lower than 1 mm/s as reported in [12].

Figure 3a shows a horizontal beam profile acquired by the four beam loss monitors when scanning the 5-µm vertical wire at 0.1mm/s. Since FERMI operates at 10Hz and the wires form an absolute angle of 45-deg with respect to the insertion axis of the wire-fork, the beam profile is sampled with a step of about 7µm.

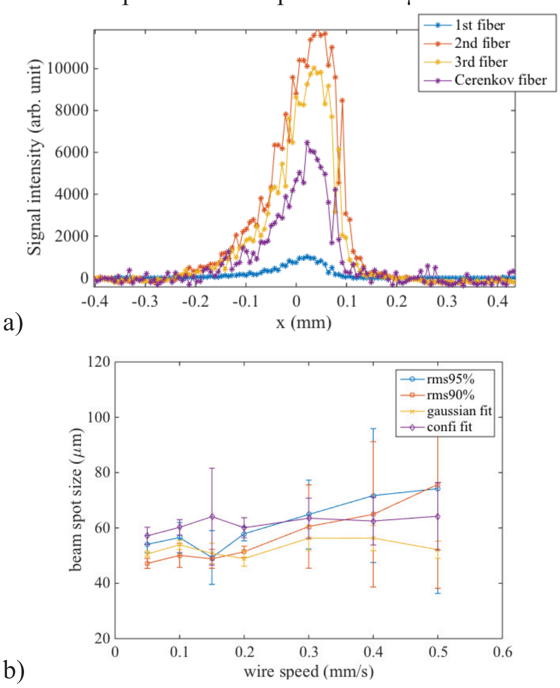

a)
b)

Figure 3: a) Horizontal beam profile acquired by the four monitors for the vertical 5-µm wire scanning at 0.1mm/s. b) Horizontal beam size (σ_x) versus the wire speed obtained by processing in four different ways the profile measured with the second fiber.

The second fiber is placed at the best distance from the WS to maximize the beam losses signal and it is taken as the reference for the measurement. By the way, when the beam stopper is closed, the backscattering shower saturates the fiber and only the first one could be used. The acquired profiles can be processed in different ways to estimate the beam spot size: by a Gaussian fit, or by an asymmetric Super-Gaussian function ("confi" fit [4]), or by calculating the raw rms over 90% or 95% of the whole bunch charge ("rms90%", "rms95%"). Figure 3b reports the horizontal beam size σ_x obtained with these 4 methods as a function of the 5-µm wire scanning speed (using the second fiber). The higher the speed the lower the resolution in sampling the beam profile, so one should expect the beam size tends to increase with the wire

ISBN 978-3-95450-134-2

speed. This is confirmed by processing the profile with the "rms90%" and "rms95%" methods. This is less evident for the Gaussian and "confi" fits, where the edges of the bunch profiles can lead respectively to underestimate and overestimate the beam size.

The noise in the beam profile obtained in a wire scan is mainly due to the beam trajectory jitter, usually about 10-µm (rms), that leads to an overestimation of the beam size. We have chosen to process the acquired data with the "rms95%" method, that results to be the best compromise between cutting the tails, more affected by trajectory jitter, without losing too much information about the actual beam profile. In order to "wash out" the effect of the trajectory jitter, we integrated several beam profiles acquired in the same machine condition for different wire speeds (see Fig. 4a). The four aforementioned fitting methods were applied to the integrated profiles and plotted in Fig. 4b. The values of σ_x are smaller than those in Fig. 3b and almost constant for wire speed <0.2mm/s. We therefore chose to set the wire speed at 0.2mm/s and integrate the beam profiles to have a reliable beam size measurement.

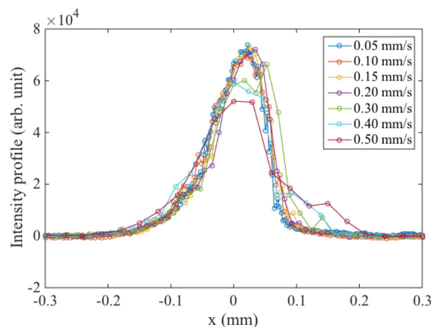

a)

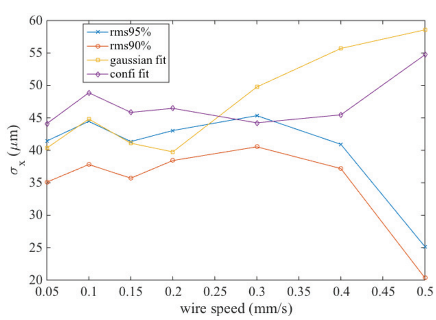

b)

Figure 4: a) Horizontal profile integrated over six profiles acquired with the second fiber at different wire speed; b) σ_x obtained with the four methods as a function of the wire speed. At wire speed = 0.5mm/s, the measurements are not reliable due to the poor resolution in sampling the beam profile.

BEAM EMITTANCE MEASUREMENTS

As mentioned above, the optics and transverse emittance measurements are performed by means of the quadrupole scan method. During these measurements, the linac beam stopper was closed to avoid too much radiation in undulator hall. In fact, changing the quad strength completely mismatches the beam downstream, with a consequent intolerable enhancement of the beam losses in the undulators. By the other hand, a beam profile measurement with the WS system at scanning speed of about 0.2mm/s and without varying the machine optics is almost transparent for the FEL: this permits to monitor the beam transverse size on-line and in a non-invasive way.

As said above, when the beam stopper is closed it is possible to use only the first fiber. Despite its signal is almost a factor 10 less intense than the second fiber one, it is anyway three orders of magnitude larger than the background noise, and it is perfectly suitable for the FERMI beam profile measurements.

We have compared the beam size measured by the WS and by the screen Sc_2 during a quadrupole scan, and consequently the Twiss functions and the emittance obtained (see Fig. 5).

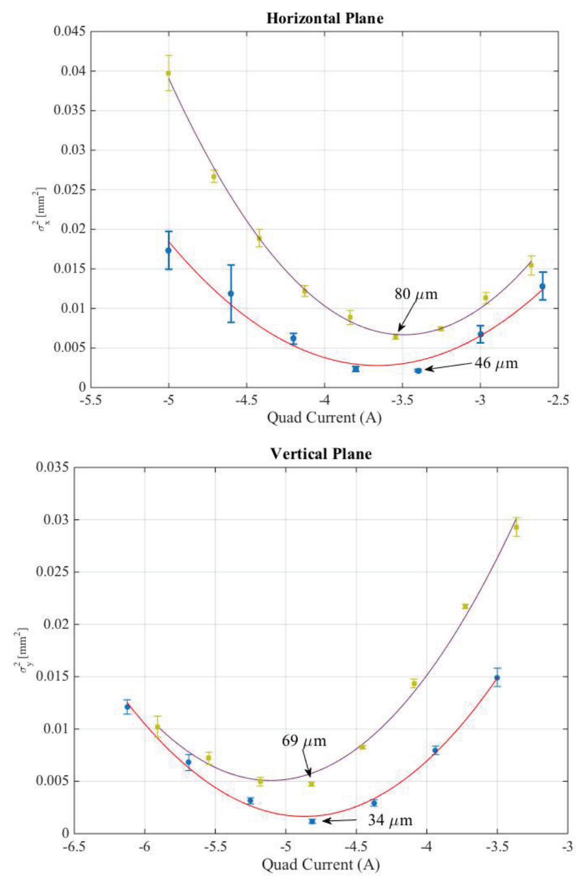

Figure 5: Horizontal (top) and Vertical (bottom) beam spot size versus the quadrupole Q_2 current measured by the WS device (blue circles data and red line) and by the Sc_2 (yellow squares data and purple line). The horizontal profile was measured with the 5-µm wire, while the vertical one with the 13-µm wire.

The beam spot on the OTR screen was filtered to clean-up the background noise and the beam sizes (σ_x and σ_y) were provided by calculating the RMS of the 90% of the total beam charge, with a two dimensional image cutting process. To be consistent, the beam profiles measured by the WS were processed with the "rms95%" method (one dimensional cutting).

ISBN 978-3-95450-134-2

The minimum beam sizes obtained with the two devices are reported in the plots of Fig. 5: the OTR measured a beam waist that is about two times larger than the WS. Since the emittance obtained by this kind of measurement is strongly correlated to the minimum beam spot size detected, the Sc_2 provides larger value of emittance than the WS, and different Twiss functions (see Table 1). During the FERMI commissioning, the screen Sc_3 has been usually utilized for this measurement because here the β-function assumes a larger value. Table 1 lists also the results of a quadrupole scan measurement performed using Sc_3: the emittances, β and α are closer to the values measured with WS than that obtained with the screen Sc_2.

Table 1: Twiss Functions and Emittance Measured at the Quadrupole Q2 by using the WS, the OTR Sc_2 and Sc_3, before the Matching Procedure

	WS	Sc_2	Sc_3
β_x [m]	18.79±1.98	15.49±0.70	16.75±0.88
α_x	9.47±1.07	7.79±0.40	8.44±0.49
ε_x [mm mrad]	2.42±0.25	5.92±0.27	3.31±0.17
β_y [m]	18.71±0.85	11.47±0.41	16.16±1.05
α_y	-6.78±0.30	-4.23±0.12	-5.58±0.34
ε_y [mm mrad]	1.81±0.08	4.28±0.15	2.95±0.19

The values of Table 1 are used to match the beam optics to the nominal lattice, by acting on the upstream quadrupoles. The matching procedure converges fast and reliable with the WS results, while it requires several iterations with the Sc_3 ones and it does not converge at all with the Sc_2 ones. Applying the quadrupoles setting foreseen by using the WS values as input, and measuring again the optics, we obtained the results reported in Table 2.

Table 2: Twiss Functions and Emittance Measured at the Quadrupole Q_2 by using the WS and the OTR Sc_2, after the Matching Procedure

	WS	Sc_2
β_x [m]	17.96±1.46	13.76±0.68
α_x	10.82±0.95	8.27±0.45
ε_x [mm mrad]	1.70±0.14	6.23±0.31
β_y [m]	14.48±0.35	10.42±0.40
α_y	-5.53±0.13	-4.06±0.15
ε_y [mm mrad]	1.62±0.04	4.35±0.17

As before the matching, the Sc2 is not able to provide reliable beam spot size, so that the measured optics and emittances are completely different from the WS results. The mismatch parameter $B=1/2(\beta_0\gamma_m-2\alpha_0\alpha_m+\beta_m\gamma_0)$, where the sub-fix "0" refers to the nominal lattice and "m" to the measurements, calculated by using the WS output is 1.042 in the horizontal plane and 1.008 in the vertical one.

CONCLUSION

A SwissFEL wire-scanner prototype has been installed and successfully tested in the diagnostic area placed at the end of the FERMI linac. The experimental results confirmed the feasibility at the GeV energy scale of the WS set-up for emittance measurements and beam profile monitoring during FEL operations. It has demonstrated the capability to measure beam size of few tens of μm (rms), constituting an important improvements with respect to the current OTR screens. Optics and emittance measurements performed with the WS device have provided reliable results, making converging the optics matching procedure faster and allowing a better optics transport up to the undulator chain, with relevant benefits to the FERMI FEL performance.

REFERENCES

[1] L. H. Yu, Phys. Rev. A **44**, 5178 (1991).
[2] E. Allaria et al., Nat. Photonics **6**, 699 (2012).
[3] E. Allaria et al., Nat. Photonics **7**, 913 (2013).
[4] G. Penco et al., JINST **8**, P05015 (2013).
[5] S. Di Mitri et al., Nucl. Instrum. Methods Phys. Res. Sect. A **608**, 19 (2009).
[6] P. Craievich et al., IEEE Transactions on Nuclear Science 62, issue 1, pages 1-11 (2015).
[7] G. Minty and F. Zimmermann, SLAC-R-621 (2003).
[8] L. Badano et al., Proceedings of the DIPAC'07 Conference, Venice, Italy, 2007, paper TUPC11.
[9] Z. Huang et al., Phys. Rev. ST Accel. Beams **13**, 020703 (2010).
[10] S. Spampinati et al., Phys Rev. ST Accel and Beams **17**, 120705 (2014).
[11] G. Penco et al., "Time-sliced emittance and energy spread measurements at FERMI", Proceedings of the 34th FEL Conference, Nara, Japan, 2012, paper WEPD20.
[12] G.L. Orlandi et al., "Design and Test of Wire-Scanners for SwissFEL", Proceedings of the 36th FEL Conference, Basel, Switzerland, 2014, paper THP091.

ISBN 978-3-95450-134-2

FEMTOSECOND SYNCHRONIZATION OF 80-MHz TI:SAPPHIRE PHOTOCATHODE LASER OSCILLATOR WITH S-BAND RF OSCILLATOR*

Heewon Yang#, Chan-Gi Jeon, Kwangyun Jung, Jungwon Kim, KAIST, Daejeon, South Korea
Byungheon Han, Young Uk Jeong, KAERI, Daejeon, South Korea
Hayun Chung, Korea University Sejong Campus, Sejong, South Korea

Abstract

We present the femtosecond synchronization between an 800-nm photocathode laser and an S-band RF oscillator using an optical-RF phase detection system at KAERI-WCI Accelerator. A 79.33-MHz commercial Ti:sapphire photocathode laser oscillator is locked to a 2.856-GHz RF master oscillator (RMO) using a fiber-loop-based optical-microwave phase detector (FLOM-PD), which results in 13 fs (rms) out-of-loop residual timing jitter integrated from 1 Hz to 10 MHz offset frequency. We also measured the long-term out-of-loop timing drift between the 800-nm optical pulse train and the RF signal, which results in 28 fs (rms) integrated over 1 hour.

INTRODUCTION

Investigation on atomic and molecular scale dynamics has recently become an active field of research. The time-resolved pump-probe experiment using ultrafast electron beams or X-rays can observe the atomic scale phenomena with femtosecond time resolution. In doing so, femto-second-precision synchronization between lasers and RF sources is crucial to achieve femtosecond-resolution measurements. As a result femtosecond-precision laser-RF synchronization has been actively studied in the last decade [1-5]. For large-scale FELs, RF-modulated cw lasers or low-jitter mode-locked lasers at telecommunication wavelength have been used as the optical master oscillator (OMO) and the timing signals generated from the OMO are distributed via stabilized fiber links. However, for smaller-scale FELs and UED, this approach may be a complex and high cost method. In this paper, as an alternative, we studied the possibility of using the commercial Ti:sapphire photocathode laser as the OMO as well. We show 13 fs (rms) synchronization between a Ti:sapphire photocathode laser and an RF oscillator. We also measured the long-term out-of-loop timing drift of 27.8 fs (rms) integrated over an hour. To achieve this <30 fs stability long-term synchronization, we used a fiber-loop optical-microwave phase detector (FLOM-PD) to measure and lock the phase difference between optical and RF signals [6].

SYNCHRONIZATION OF PHOTOCATHODE LASER TO RMO

A 79.33 MHz repetition rate Ti:sapphire laser (Coherent Vitara-T) and a 2.856-GHz RF oscillator (Keysight N5181B) are used in this work. Figure 1 shows the structure of the FLOM-PD. The FLOM-PD is based on the fiber Sagnac-loop interferometer, and it detects phase difference between optical pulse train and RF signal using phase error-dependent intensity imbalance between two detector outputs [6]. The FLOM-PD can reduce the excess phase noise and drift added in the optical-to-electronic conversion process compared to direct photodetection method.

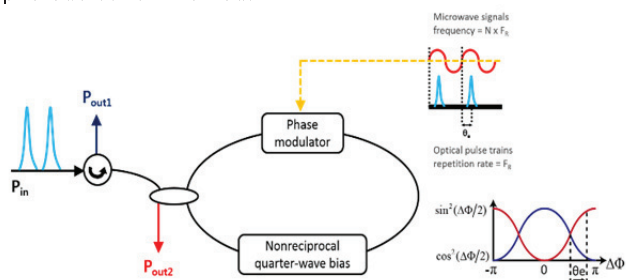

Figure 1: Schematic fiber-loop-based optical-microwave phase detector [6].

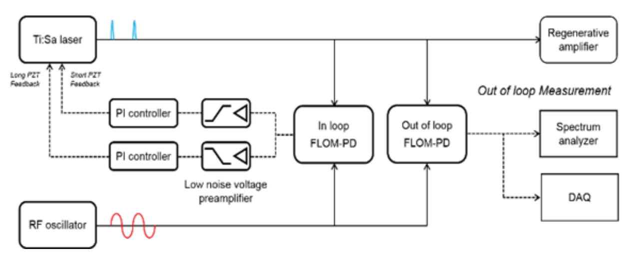

Figure 2: Schematic of the synchronization system.

Figure 2 shows the schematic of the synchronization between a photocathode laser and an RF oscillator. The synchronization setup is composed of three parts, a photocathode laser, an RF oscillator and a FLOM-PD. A Ti:sapphire laser generates 480 mW average output power with 79.33 MHz repetition rate. The laser is locked to a 2.856-GHz RF oscillator, which is used as an RF master oscillator (RMO). One FLOM-PD is used to lock the laser with the RMO and the other FLOM-PD is used to measure the residual phase noise and drift in an out-of-loop way. To operate a FLOM-PD, we used 12 mW average optical power and +19 dBm average RF power. The in-loop FLOM-PD measures phase difference between optical and RF signals and generates an error signal. Two piezoelectric transducers (PZT) inside the Ti:sapphire laser are controlled by using the error signal from FLOM-PD. The high and low offset frequency noise

*Work supported by the KAERI Project, South Korea.
#hwyang@kaist.ac.kr

ISBN 978-3-95450-134-2

is controlled by short and long PZTs, respectively. The synchronization feedback loop consists of a low-noise voltage preamplifier (Stanford Research Systems, SRS560) and a PI servo controller (Newport, LB1005). The out-of-loop FLOM-PD monitors the residual phase noise and drift between the locked optical and RF signals.

Figure 3 shows the collection of phase noise power spectral density. Curve (a) shows the phase noise of a free-running Ti:sapphire laser, measured by a signal source analyzer (SSA) and a balanced optical cross-correlator (BOC) in the low (<10 kHz) and high (>10 kHz) offset frequency, respectively. To measure the high offset frequency precisely, two-color balanced optical cross-correlator (TC-BOC) [7] is used with a 1550-nm solid-state laser (One-Five Laser, Origami-15) as an optical reference. Curve (b) shows the phase noise of an RF oscillator measured by the SSA. Curve (c) shows the residual phase noise when the OMO and RMO are locked, measured by an out-of-loop FLOM-PD. Note that the phase noise for >10 kHz offset frequency is limited by the FLOM-PD resolution. The RMO-OMO locking bandwidth is about 9 kHz. Outside this locking bandwidth, the optical pulse train carries the phase noise of free-running OMO. Curve (d) shows the residual timing jitter between a Ti:Sapphire laser and an RF oscillator projected in the optical domain (i.e., the timing jitter of optical pulse train follows the RMO phase noise inside the locking bandwidth and free-running laser jitter outside the locking bandwidth).

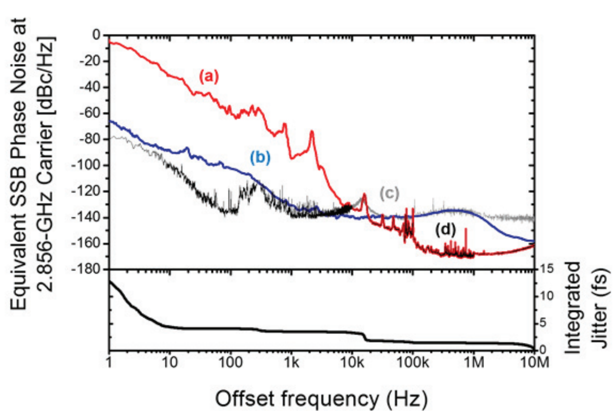

Figure 3: Phase noise measurement results. (a) Phase noise of a free-running Ti:sapphire laser, (b) Phase noise of an RF oscillator, (c) Residual phase noise measured by out-of-loop FLOM-PD, (d) Integrated timing jitter of locked optical pulse train.

For the optical pulse train, the rms timing jitter is 13 fs when integrated from 1 Hz to 10 MHz offset frequency. Note that the intrinsic rms timing jitter of the used Ti:sapphire laser is 2.6 fs [10 kHz – 10 MHz], which sets the fundamental limit in achievable synchronization. As can be seen from curve (d), majority of timing jitter is contributed in 1 – 10 Hz offset frequency. Preliminary analysis suggests that it is mostly originated from the amplitude-to-phase conversion in FLOM-PD. Figure 4 shows the long-term out-of-loop timing drift measurement. The measured long-term timing drift is 27.8 fs (rms) for an hour.

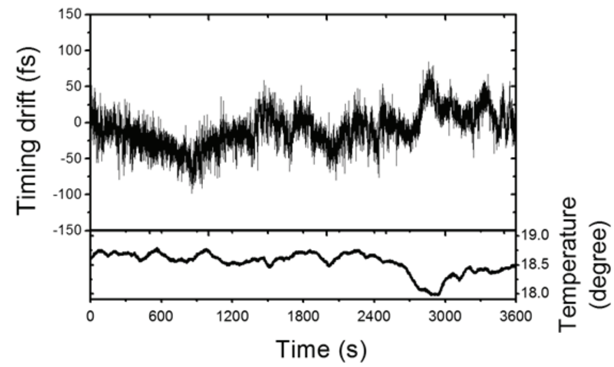

Figure 4: Long-term timing drift measurement for 1-hour.

SUMMARY

We show laser-RF synchronization between an 800 nm Ti:sapphire photocathode laser and a 2.856-GHz RF oscillator with 13 fs residual rms timing jitter. The measured long-term timing drift is 27.8 fs (rms) for an hour. These results suggest that a commercial Ti:sapphire photocathode laser can serve as an OMO, which is tightly locked to an RMO, for small-scale FELs and UEDs. With several technical improvements for reducing amplitude-to-phase conversion in FLOM-PD, few-femtosecond synchronization will be possible in the near future.

ACKNOWLEDGEMENT

This work was supported by the KAERI-WCI Project funded by the National Research Foundation of South Korea (under grant WCI-2011-001).

REFERENCES

[1] J. Kim et al, “Drift-free femtosecond timing synchronization of remote optical and microwave sources,” Nature Photon. **2**, 733 (2008).

[2] K. Gumerlock et al., "A Low-cost, high-reliability femtosecond laser timing system for LCLS," Proc. Free Electron Laser Conference 2014, p. 917 (2014).

[3] S. Schulz et al., "Femtosecond-precision synchronization of the pump-probe optical laser for user experiments at FLASH," Proc. SPIE 2013, p. 87780R-1 (2013).

[4] B. Liu et al., "Evolvement of the laser and synchronization system for the Shanghai DUV-FEL test facility," Proc. Free Electron Laser Conference 2014, p. 960 (2014).

[5] K. Jung et al, “Remote laser-microwave synchronization over kilometer-scale fiber link with few-femtosecond drift,” J. Lightw. Tech. **32**, 3742 (2014).

[6] K. Jung and J. Kim, “Subfemtosecond synchronization of microwave oscillators with modelocked Er-fiber lasers,” Opt. Lett. **37**, 2958 (2012).

[7] H. Li et al, “Remote two-color optical-to-optical synchronization between two passively mode-locked lasers,” Opt. Lett. **39**, 5325 (2014).

ISBN 978-3-95450-134-2

STABILIZATION OF MAGNETRON FREQUENCY FOR A MICROTRON-DRIVEN FEL*

B. A. Gudkov#, S. Bae, K. H. Jang, Y. U. Jeong, H. W. Kim, K. Lee, J. Mun, S. H. Park, G. I. Shim, KAERI, Daejeon, Korea
S. V. Miginsky, N. A. Vinokurov, KAERI, Daejeon, Korea, and Budker INP, Novosibirsk, Russia

Abstract

Under KAERI WCI program we develop a compact pulsed microtron-driven FEL. Electron bunches are accelerated in the microtron and transported by the beamline to the unlulator. The RF cavity in the microtron is fed by the magnetron. Any accelerator driver for a FEL should provide an electron beam having very stable parameters such as electron energy, beam current and especially repetition rate in a train. All mentioned parameters depend on magnetron current. It means that special attention should be paid for the shape of a current pulse, supplied to the magnetron from the modulator. We developed the modulator project with a computer control that will provide an arbitrary shape of the magnetron current. A simplified prototype was fabricated and tested. The methods of controlling of the pulse shape are considered. Simulation and experimental results are presented.

INTRODUCTION

If one wants to obtain the maximum monochromatic FEL emission, the repetition rate of microbunches should be equal within a train and in all the trains. If maximum power is necessary, while monochromaticity is not so important, frequency ramp within a train can be used, as described in [1]. In this case, initially the detuning is significant, optimal for amplification. It increases the rise time, thus lengthen the emission pulse. Then the detuning comes to zero, and a FEL transits to so called spiking mode, and the spectrum broadens. Thus, in different cases, one can need absolutely stable or increasing in a certain way through a train repetition rate.

A magnetron, unlike a klystron, is an oscillator, but not an amplifier, so one cannot obtain stable frequency using a high-stable low-power master oscillator. The magnetron frequency depends on many factors: the mechanical tuning, the magnetic field, the anode current, the load impedance, and the temperature.

The magnetron is coupled to RF cavity of the microtron via a waveguide and an isolator. Isolator usually is tuned to allow some portion of reflected power to come back to the magnetron. Quality factor of the RF cavity is approximately of order higher than of magnetron.

In case of narrow band resonant load, the frequency pulling effect may take place. The presence or absence of the effect depends on waveguide length, reflected power level and on cavity and magnetron detuning.

Thus, one should provide stable flat top current pulse through a magnetron or some specific current pulse shape for a frequency ramp within a train.

Ability to form an arbitrary shape of a current pulse is a universal solution.

*Work was supported by the World Class Institute (WCI) program of the National Research Foundation of Korea (NRF) funded by the Ministry of Education, Science and Technology of Korea (MEST) (NRF Grant Number: WCI 2011-001).
e-mail: b_a_gudkov@mail.ru

EQUIVALENT CIRQUIT

Volt-Ampere characteristic of a magnetron one can see in Fig. 1. Typical threshold voltage is 45-50kV depending on the magnetic field in a magnetron. There is no current for low voltage across the magnetron due to so-called magnetic isolation. Differential resistance dU/dI in the conducting area is 50-70 Ohm.

First approach for equivalent circuit of the magnetron may be series connected resistor, an ideal diode and Zener diode with a threshold voltage Vth. Another possibility is to use an ideal voltage source instead of Zener diode.

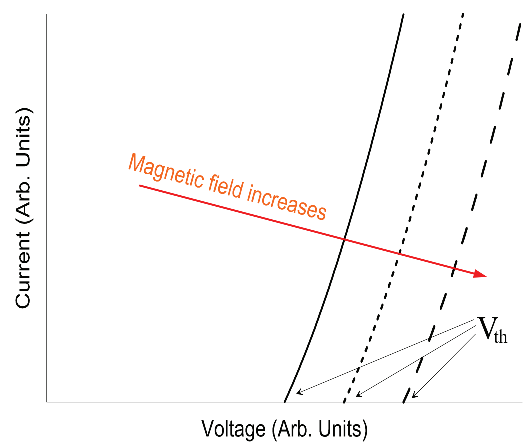

Figure 1: Volt –Ampere characteristic of a magnetron.

Simplified equivalent circuit of the modulator and the magnetron is shown in Fig. 2, where:

L_s is a leakage inductance of the HV transformer, referenced to the secondary side of the transformer,

C_s - the sum of the stray capacitances of the W2 and of a high voltage cable,

R_d - differential resistance of the magnetron,

D – ideal diode (magnetron conducts current only one direction)

V_{th} -Zener diode with threshold voltage V_{th}.

Capacitor C_1 is charged from power supply (not shown) before the pulse is triggered.

ISBN 978-3-95450-134-2

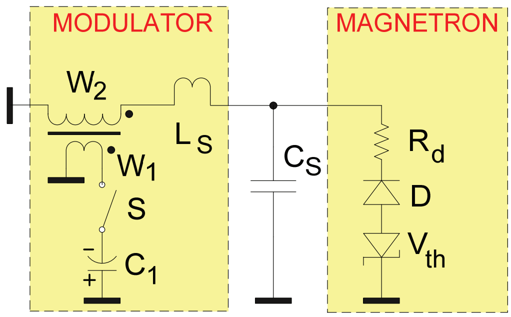

Figure 2: Modulator and magnetron equivalent circuit.

After closing the switch "S", the magnetron is still non-conducting; current comes to "C_s" through "L_s" and charges it cosine-like in time. When the voltage across "C_s" reaches threshold voltage of the magnetron V_{th}, the whole current through "L_s" is switched to magnetron, and the magnetron voltage V_m is stabilized at the level according to formula [1]

$$V_m = V_{th} + I_0 * R_d \,, \tag{1}$$

where I_0 is an amplitude current through "Ls" and may be estimated using formula [2]:

$$I_0 \cong V_1 \frac{W_2}{W_1} \sqrt{C_s / L_s} \,. \tag{2}$$

Further current behaviour depends on the initial secondary voltage, induced to W_2, which, in turn, depends on voltage, stored by C_1 and also on C_1 value, because the capacitor is partially discharged during the pulse. Typical current shape one can see in Fig. 7, trace "0".

Fine tuning of initial current I(0) is possible by means of the short (some tens of nanosecond) "preliminary pulse" which may be generated about 1 microsecond before the main pulse with duration about some tens of nanoseconds. In this case initial conditions for main pulse will be: zero current through L_s, but not zero voltage across C_s. As a result, initial magnetron current will be changed.

SIMPLE CORRECTOR

The main idea was to make the top of the current pulse as flat as possible.

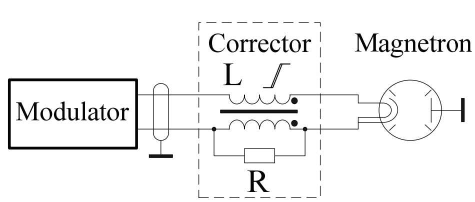

Figure 3. Simple corrector circuit.

We tested a simple corrector, which contains one switch as shown in Fig. 3. Inductor "L" with a saturable core acts like a switch and the corrector impedance is changed from R to almost zero approximately at the middle of the pulse. The magnetron operates with a dummy load. This corrector changes magnetron current as shown in Fig. 4. Black trace is the voltage across the magnetron, red solid trace is the magnetron current without corrector and red dashed trace – with corrector.

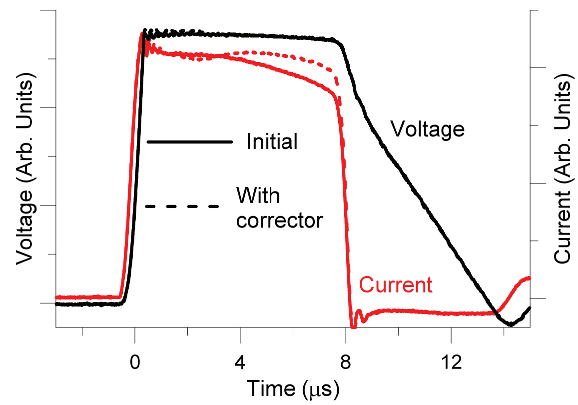

Figure 4. Current pulse shape modification.

As it is shown in Fig. 5, fluctuation of the instant frequency, generated by the magnetron, was reduced from 0.7 MHz p-p (red solid line) down to 0.2 MHz p-p (red dashed line).

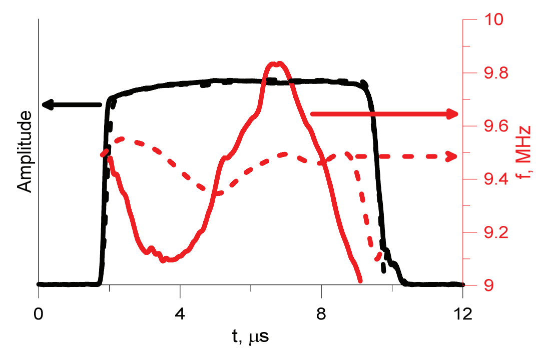

Figure 5. Instant frequency deviation modification.

It is clear that even such a simple corrector improved the situation drastically, so next evident step is to construct a corrector with a number of cells, in purpose to get a more fine control of a current pulse shape.

MULTI-CELL CORRECTOR

Corrector may be placed in series with the magnetron as it is shown in the Fig. 3, or in series with the secondary winding of the HV transformer at the low voltage terminal of W2, as shown in Fig. 6.

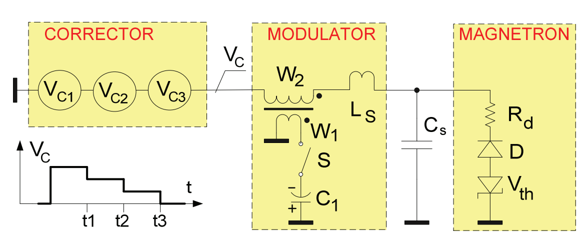

Figure 6. Modulator with a multi-cell corrector.

ISBN 978-3-95450-134-2

The minimal value of current deviation depends on the number of cells. Here three cells are shown. Each cell in the simplest case contains a resistor and a solid state switch (IGBT), connected in parallel. Also high efficiency voltage pulse sources may be used. Note that modulator instant output power is about 5MW (50kV, 100A), required corrector power is about 200kW (2kV peak voltage, 100A).

Current shapes for different circuits were simulated and are shown in Fig. 7:

- Trace “0” –modulator without corrector,
- Trace “1” –modulator with 1-cell corrector,
- Trace “3” –modulator with 3-cell corrector,

Current deviations are 4, 1, and 0.3A p-p, respectively.

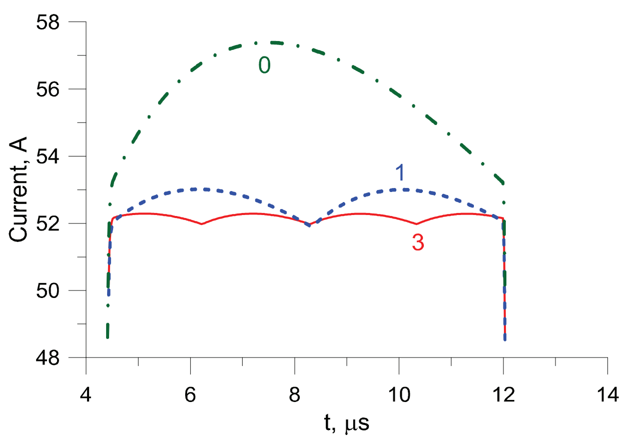

Figure 7. Current shape with different correctors.

For corrector composed from 2-state cells current deviation during the top of the pulse is decreased approximately as $1/(n+1)^2$, where n is the number of cells in a corrector.

PULSE SHAPE CONTROL

Now we can summarize methods of current shape control:

- magnetron voltage – by magnetic field tuning
- initial current value – by adjusting of Cs.
- average value of the first derivation dI/dt – by computer control of the primary voltage.
- shape details – by control of time diagram for the corrector, forming desirable shape of corrector voltage.
- initial current fine tuning – by control of the preliminary pulse duration

CONCLUSION

Methods of current shape control and the project of the modulator with corrector were developed. Simple corrector was tested. Multi-cell corrector now is fabricated.

REFERENCES

[1] R.J. Bakker, G.M.H. Knippels, A.F.G. van der Meer, et al. “Dynamic desynchronization of a free-electron laser”, Phys. Rev. E, 48 (1993), R3256-R3258.

[2] G. M. Kazakevitch, V. M. Pavlov, Y. U. Jeong, B. C. Lee, “Intrapulse frequency stability of a magnetron frequency-locked through a wave reflected from an accelerating cavity”, Nucl. Instr. and Meth. A647, 2011, pp. 10-16.

ISBN 978-3-95450-134-2

FIRST RESULTS OF COMMISSIONING OF THE PITZ TRANSVERSE DEFLECTING STRUCTURE

H. Huck*, G. Asova†, M. Bakr‡, P. Boonpornprasert, A. Donat, J. Good, M. Gross, C. Hernandez-Garcia§, I. Isaev, L. Jachmann, D. Kalantaryan, M. Khojoyan, W. Koehler, G. Kourkafas, M. Krasilnikov, D. Malyutin¶, D. Melkumyan, A. Oppelt, M. Otevrel, M. Pohl, Y. Renier, T. Rublack, J. Schultze, F. Stephan, G. Trowitzsch, G. Vashchenko, R. Wenndorff, Q. Zhao, DESY, Zeuthen, Germany
D. Churanov, L. Kravchuk, V. Paramonov, I. Rybakov, A. Zavadtsev, D. Zavadtsev, INR of the RAS, Moscow, Russia
M. Lalayan, A. Smirnov, N. Sobenin, MEPhI, Moscow, Russia
C. Gerth, M. Hoffmann, M. Hüning, DESY, Hamburg, Germany
O. Lishilin, G. Pathak, Hamburg University, Hamburg, Germany

Abstract

For successful operation of X-ray Free Electron Lasers, one crucial parameter is the ultrashort electron bunch length yielding a high peak current and a short saturation length. In order to effectively compress the bunches during the acceleration process, a detailed understanding of the full longitudinal phase space distribution already in the injector is required. Transverse deflecting RF structures (TDS) can shear the bunch transversely, mapping the longitudinal coordinate to a transverse axis on an observation screen downstream. In addition to the bunch length, the slice emittance along the bunch as well as the full longitudinal phase space can be obtained. At the Photo Injector Test Facility at DESY, Zeuthen site (PITZ), an S-band traveling wave TDS is under commissioning since 2015. This cavity is a prototype for the TDS in the injector part of the European XFEL and has been designed and manufactured by the Institute for Nuclear Research (INR RAS, Moscow, Russia). In this paper, first commissioning results of the system at PITZ are presented and discussed.

INTRODUCTION

Multi-GeV electron beams with high peak currents, required for the operation of X-ray Free Electron Lasers (XFELs), are generated as initially long bunches to reduce space charge effects, and are later compressed at moderate to high energies. Bunch compressors, typically realized as magnetic chicanes following off-crest acceleration, shape the longitudinal phase space for subsequent acceleration and, eventually, for the lasing process in the FEL undulators. To prevent degradation of the overall beam quality, bunch compression in the European XFEL is split into three stages at increasing beam energies. Three transverse deflecting structures are foreseen as diagnostic tools after the second and third bunch compressor and in the injector part of the European XFEL [1, 2]. A prototype of the latter, designed [3] and manufactured by the Institute for Nuclear Research of the Russian Academy of Sciences, is under commissioning at the Photo Injector Test Facility at DESY, Zeuthen site (PITZ).

TDS Working Principle

Quickly changing transverse RF fields deflect electrons depending on their arrival time with respect to the RF phase (Fig. 1). In the linear region around the zero-crossing phase, the longitudinal axis is projected linearly onto the vertical axis of a downstream screen, while the horizontal screen coordinate shows the horizontal beam size of the slices. By scanning the focusing strength of a quadrupole magnet, the slice emittance along the bunch can be obtained. Furthermore, live images of the full longitudinal phase space can be observed when combining the vertical TDS deflection with a horizontally dispersive dipole.

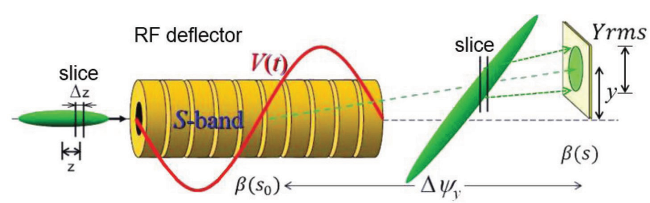

Figure 1: TDS principle: Depending on their longitudinal position, electrons are deflected by transverse RF fields and observed on a screen several meters downstream [4].

Assuming a pure drift space of length L between TDS and screen, a slice of momentum p at the relative longitudinal position z in the bunch hits the screen at vertical position [5]

$$y = S \cdot z = \frac{eV_0 k}{pc} \cdot L \cdot z, \tag{1}$$

where the S-parameter depends on the deflecting voltage V_0 and wave number k. In the general case, the longitudinal

* holger.huck@desy.de
† on leave from INRNE, Sofia, Bulgaria
‡ on leave from Assiut University, Assiut, Egypt
§ on leave from Jlab, Newport News, USA
¶ now at HZB, Berlin, Germany

ISBN 978-3-95450-134-2

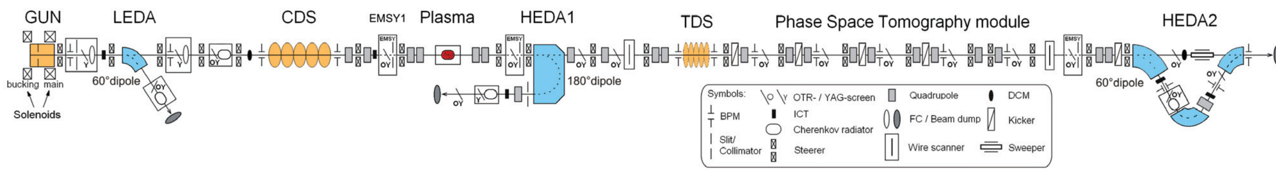

Figure 2: Current layout of the PITZ beamline (PITZ 3.0). Electron bunches which are streaked vertically by the TDS can be monitored on several YAG and OTR screens in the tomography module. Alternatively, their full longitudinal phasespace can be analyzed in the high energy dispersive arm HEDA2, 7.3 m downstream the TDS. During the measurements presented in this paper, the plasma cell was replaced by an empty beam tube.

resolution can be expressed as [4, 5]

$$\sigma_z \gtrsim \frac{2}{eV_0 k} \frac{m_0 c^2}{\sin(\Delta\psi)} \sqrt{\frac{\gamma\epsilon_n}{\beta_{\mathrm{TDS}}}} \tag{2}$$

with the normalized emittance ϵ_n, beta function β_{TDS} in the TDS, relativistic factor γ and betatron phase advance $\Delta\psi$ between TDS and screen.

Layout at PITZ

The PITZ TDS is installed in the high energy section of the beamline, between the first emittance measurement station EMSY1 and the phase space tomography module (Fig. 2). It is a traveling wave structure similar to the LOLA design [6]. The cell dimensions were selected to have the same cells for all three structures in the European XFEL TDS and are realized in its prototype for PITZ [7]. Table 1 summarizes the most important parameters.

Table 1: Design Parameters of the PITZ TDS

Deflecting voltage	1.7 MV
Input power	2.11 MW
RF Frequency	2997.2 MHz
Pulse length	3 µs
Structure Length	0.533 m
Number of cells	14+2
Phase advance per cell	$2\pi/3$
Quality factor at 20 °C	11780

COMMISSIONING STATUS

A ScandiNova [8] modulator was installed and commissioned at PITZ in early 2015. The on-site acceptance tests were very successful, showing a pulse flatness of 0.24 % within 3.3 µs and a pulse-to-pulse stability of approx. 66 ppm. Both of these values are well inside the ScandiNova specifications (0.3 %, 100 ppm). The modulator is capable of driving a 5-MW klystron, allowing for possible future upgrades of the PITZ RF system.

Following the conditioning of the currently installed 3-MW klystron and the final connection of the waveguide system and RF load to the TDS cavity, the first low-power RF pulses were sent to the structure in early July. Within one shift, the pulses could be synchronized to the electron bunches, and the deflected beam was observed on a YAG screen 1.3 m downstream the TDS.

The structure was conditioned up to intermediate power levels of about 0.5 MW within several days. Currently, the reflected power from the whole waveguide system precludes higher power levels, as reflection must stay below 75 dBm (32 kW) to prevent damage to the klystron. Possible sources of the unusually high reflection are under investigation using a diagnostic load.

The resonance temperature of the TDS was determined by observing the phase difference between signals from the two RF probes in the TDS cells adjacent to the RF input and output cells, while slowly changing the temperature of the cooling water. A value of 50.8 °C was found, which is almost within the designed temperature range of 30-50 °C for the frequency control. In agreement with cold tests [9], the reflected power from the structure does not change measurably within 10 K around resonance conditions.

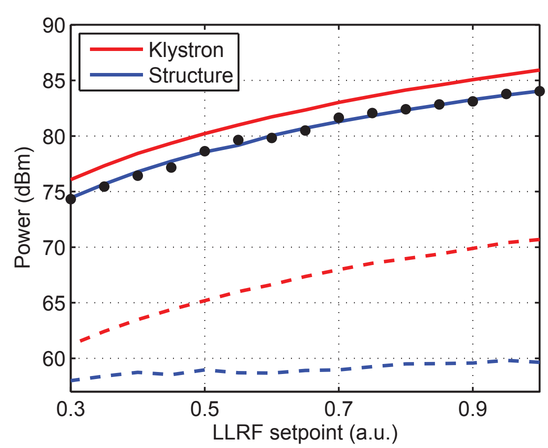

Figure 3: Forward (full lines) and reflected (dashed lines) power readings from the directional couplers at the klystron and deflecting structure. The black dots are estimations of the power in the structure based on the measured electron beam deflection.

Present RF power readings for intermediate power levels from the directional couplers at the klystron exit and at the structure entrance are shown in Fig. 3. The black dots are estimations of the power in the structure based on the actual deflection of the electron beam. For that, the S-parameter

ISBN 978-3-95450-134-2

was determined as described below with a pure drift space between TDS and screen, and then used to calculate the deflection voltage (Eq. 1), from which the power was estimated using simulation results and small corrections [9] accounting for increased attenuation at operating conditions. While these estimations fit very well to the coupler readings, the ratio between forward power at the klystron and structure is unexpectedly large, indicating either losses of more than 30 % in the whole waveguide system, or a wrong calibration of the klystron coupler, which was based on the nominal maximal klystron output.

FIRST MEASUREMENTS WITH ELECTRON BEAM

All measurements were done at machine conditions compliant to the emittance measurements [10] and stability tests for the commissioning phase of the European XFEL. The gun was operated with 640-µs RF pulses at 5 MW and maximum mean momentum gain phase. The booster was set to 3 MW, yielding a mean beam momentum of 21.5 MeV/c in the TDS. After roughly focusing the beam to the first emittance measurement station (see EMSY1 in Fig. 2) with just the main gun solenoid, the beam was further focused onto the observation screens with additional quadrupole magnets right before the TDS. Photocathode laser pulses with a Gaussian temporal profile of 11 to 12 ps length (FWHM) were used [11, 12]. These were generated by introducing a Lyot filter [13] into the regenerative amplifier, thus limiting the bandwidth of the usually 2 ps short laser pulses.

Calibration Procedure

Whenever the power in the structure, the energy or focusing of the beam or the observation screen changes, a new calibration is necessary in order to determine the new S-parameter (Eq. 1). For that, the screen position of the beam centroid was recorded under variation of the RF phase in the TDS. A linear fit of this phase scan yields the zero-crossing phase and the S-parameter.

Proper background subtraction and averaging can have a significant impact on the reliability and reproducibility of all TDS measurements, and can be a major challenge for an automated analysis. Different background subtraction methods are under investigation. The best results so far have been achieved with the operator manually defining a region of interest for the calibration code.

Temporal Profiles

A set of preliminary bunch length measurements for different bunch charges (Fig. 4) have been taken. Because the actual beam profiles show significant deviations from a Gaussian shape even at low charges of 100 pC, the real full-width-half-maximum value was determined in both measurement and simulation results, instead of using the statistical rms values. Examples of longitudinal profiles, measured at the first YAG screen after the TDS, are shown in Fig. 5, accompanied by ASTRA simulations assuming a perfect transverse laser profile. While the overall profile shape looks quite similar in experiment and simulation, measured bunch lengths are clearly shorter throughout all measurements. Furthermore, a slight dip near the bunch center is visible in all measurements. Simulations show similar features only at much higher bunch charges around 1 nC.

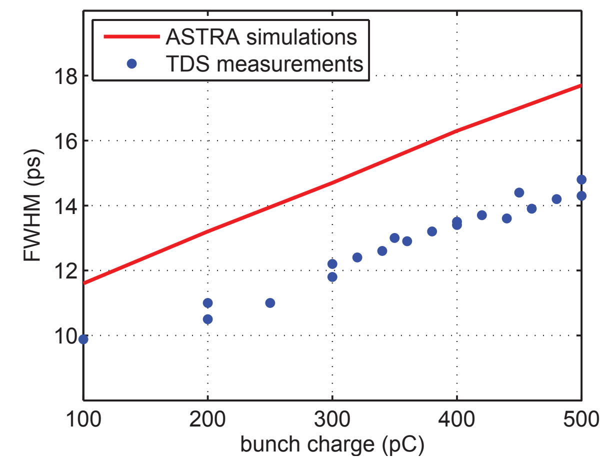

Figure 4: FWHM bunch lengths, measured and simulated, for bunch charges between 100 and 500 pC. The booster phase was tuned for maximum mean momentum gain.

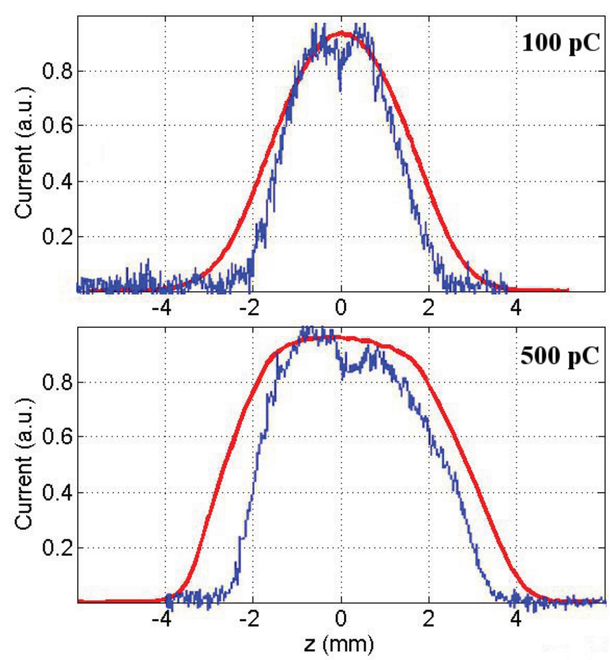

Figure 5: Longitudinal profiles of 100 pC (top) and 500 pC (bottom) bunches after the TDS. The smooth red curves are ASTRA simulations assuming a 11.5 ps (FWHM) long Gaussian photocathode laser pulse, the blue curves are TDS measurements.

ISBN 978-3-95450-134-2

For the lowest investigated charge (100 pC), most dicrepancies could be explained by more realistic simulations using the measured transverse laser distribution as input („core plus halo“ model, see [10] and references therein). Results of these simulations are shown in Fig. 6, where the bunch length is plotted versus the RF phase of the booster. The second set of data (green squares) was obtained one month after the first one (blue dots), which was used for the simulations. In that month, the quantum efficiency of the cathode degraded and the actual transverse laser profile presumably changed as well, resulting in different space charge forces during emission. Furthermore, the bunch length can be systematically underestimated in measurements by neglecting low-intensity parts of the beam or by subtracting too much noise or background.

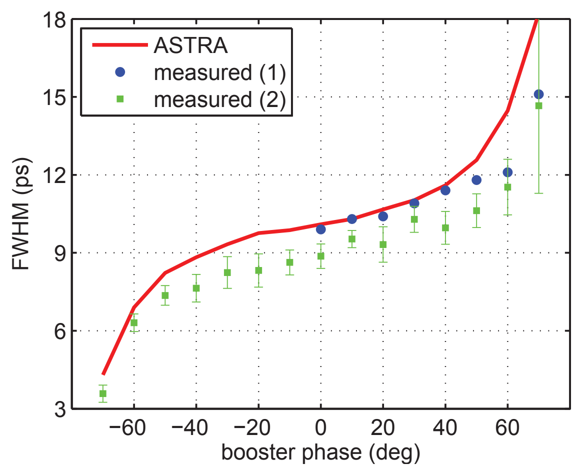

Figure 6: FWHM bunch length versus booster phase for a bunch charge of 100 pC, measured with the TDS (two data sets) and simulated (red line) using the measured transverse laser profile from the first data set (blue dots) as input.

Both the statistical shot-to-shot error of the bunch length measurements and the linearity error of the calibration curve were approx. 4 % for the measurements presented here. The resolution, given by the FWHM spot size of the unstreaked beam, varied between 0.5 and 1.0 ps. Once the nominal deflecting voltage is obtained and beam transport and focusing is optimized, a temporal resolution of ≈ 0.1 ps is expected for pure profile measurements, and 0.2 to 0.3 ps for slice emittance as well as for full longitudinal phase space measurements [4].

Full Longitudinal Phase Space

Sample images of the full longitudinal phase space in the HEDA2 section (Fig. 2) are presented in Fig. 7. These pictures were taken with a very low deflection voltage in the TDS and without optimized focusing between TDS and screen, therefore only exhibiting basic features with a low temporal and momentum resolution. For the center image, the electron bunch was accelerated on-crest in the booster, but on the rising slope of the RF for the left image. Consequently, the head of the bunch shows a higher momentum than the tail in the left image.

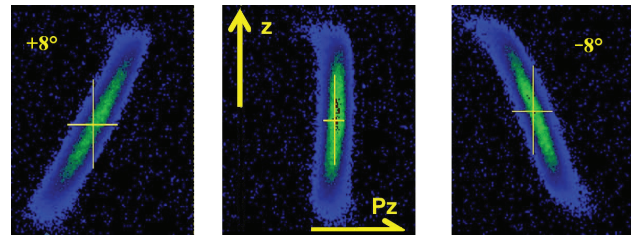

Figure 7: First low-resolution images of the full longitudinal phase space, viewed on a YAG screen after the first HEDA2 dipole magnet. The left and right pictures were taken at +8 and -8 degree booster phase with respect to the maximum mean momentum gain phase, respectively.

CONCLUSION

The PITZ TDS, a prototype for the injector TDS of the European XFEL, is under commissioning since July 2015. Currently, the deflecting voltage is limited to about 50 % of the nominal voltage by the reflected power measured at the klystron, which is under investigation. Power estimations based on the measured electron beam deflection are in good agreement with the reading from the directional coupler at the TDS. First preliminary bunch length measurements suggested a slight overestimation of the bunch length in simulations, which could be partly resolved by more detailed simulations. More detailed measurements and simulations using more realistic transverse laser profiles are foreseen for the upcoming weeks. In the near future, the TDS will also be employed for slice emittance measurements as well as for analyzing the self-modulation of electron bunches inside a plasma cell.

REFERENCES

[1] M. Altarelli et al. (Editors), “The European X-Ray Free-Electron Laser”, Technical Design Report, doi:10.3204/DESY_06-097, (2007).

[2] W. Decking and T. Limberg, “European XFEL Post-TDR Description”, XFEL.EU TN-2013-004-01 (2013).

[3] L. Kravchuk et al., “Layout of the PITZ transverse deflecting system for longitudinal phase space and slice emittance measurements”, LINAC2010, TUP011 (2010).

[4] D. Malyutin, “Time resolved transverse and longitudinal phase space measurements at the high brightness photo injector PITZ”, PhD thesis, University of Hamburg, Hamburg (2014).

[5] P. Emma et al., “A Transverse RF deflecting structure for bunch length and phase space diagnostics”, LCLS-TN-00-12 (2000).

[6] O.H. Altenmueller et al., “Investigations of Traveling-Wave Separators for the Stanford Two-Mile Linear Accelerator”, Rev. Sci. Instrum. 35, 438 (1964).

ISBN 978-3-95450-134-2

[7] A. Anisimov et al., “Input Couplers for the Dipole Mode Periodic Structures”, RuPac 2010, 328 (2010).

[8] ScandiNova website: `http://www.scandinovasystems.com/`

[9] V. Paramonov, A. Zavadtsev, “Summary for TDS design parameters and RF measurements after RF component construction”, INR note, May 2015.

[10] G. Vashchenko et al., “Emittance Measurements of the Electron Beam at PITZ for the Commissioning Phase of the European XFEL”, MOD04, *These Proceedings*, FEL’15, Deajeon, Korea (2015).

[11] I. Will et al., “Photoinjector drive laser of the FLASH FEL”, Opt. Express 19, 23770-23781 (2011).

[12] I. Will, G. Klemz, “Generation of flat-top picosecond pulses by coherent pulse stacking in a multicrystal birefringent filter”, Opt. Express 16, 14922-14937 (2008).

[13] B. Lyot, “Optical apparatus with wide field using interference of polarized light”, Acad. Sci. 197 (1933).

ISBN 978-3-95450-134-2

IMPLEMENTATION OF MTCA.4-BASED CONTROLS FOR THE PULSED OPTICAL SYNCHRONIZATION SYSTEMS AT DESY*

M. Felber#, L. Butkowski, M. K. Czwalinna, M. Fenner, C. Gerth, M. Heuer, M. Killenberg, T. Lamb, U. Mavrič, J. Mueller, P. Peier, K. Przygoda, S. Ruzin, H. Schlarb, C. Sydlo, M. Titberidze, F. Zummack, DESY, Hamburg, Germany
T. Kozak, P. Prędki, TUL-DMCS, Łódź, Poland
E. Janas, ISE-WUT, Warsaw, Poland

Abstract

With the current state of the synchronization system at FLASH (Free-electron Laser in Hamburg) the arrival time between electron bunches and optical laser pulses can be synchronized to a level of 30 fs rms, e.g. for pump-probe experiments. In the course of the development of an up-scaled system for the European XFEL and the migration of control hardware to the modern MTCA.4 (Micro Telecommunications Computing Architecture) platform, all involved components of the system will be replaced with new developments. The front-end devices are upgraded. FPGAs (Field Programmable Gate Arrays) are performing the data processing and feedback calculations. In order to facilitate the firmware development, a toolset (Rapid-X) was established which allows application engineers to develop, simulate, and generate their code without help from FPGA experts in a simple and efficient way. A software tool kit (MTCA4U) provides drivers and tools for direct register access e.g. via Matlab or Python and a control system adapter, which allows the server applications to be written control system independent.
In this paper, an overview on the synchronization setups and their upgrades as well as an introduction to the new hardware is given. The Rapid-X and MTCA4U tool kits are presented followed by a status report on the implementation of the new developments.

INTRODUCTION

Like most other accelerator sub-systems the various setups of which the optical synchronization systems at FLASH and the European XFEL are constructed can be divided in four layers:

1) The front-end device, usually an electro-optic and/or an opto-mechanic setup connecting another component of the accelerator with the signals from the synchronization system.

2) The electronic hardware which is the platform for readout and processing of signals generated by the front-end deviceand actuating on it. It also connects to a CPU providing a physical interface to the external world. For the computation usually FPGAs are used.

3) The firmware running on an FPGA which can be divided in two layers. The base is the hardware specific part which provides access to the peripherals like ADCs (Analog to Digital Converters), DACs (Digital to Analog Converters), and memory. The second part is application specific and can incorporate algorithms for the computation of physically meaningful numbers from the front-end signals and - in many cases - a feedback control loop.

4) The software layer which can also be separated in at least two parts. One is that it provides a framework for connecting to the firmware registers via specific drivers, e.g. to set and read parameters. The other is to process this data e.g. for displaying or performing supervision in an application code. The latter can also calculate algorithms and perform feedback control but opposed to the firmware the higher latency only allows for slower (low bandwidth) control loops. Usually the application software is integrated in the accelerator control system, in this case it is called server but it can also be an independent program or script.

Growing demands for the synchronization of FELs in number of setups and their performance triggers continuous upgrades on all four of the mentioned aspects which will be described in the following chapters.

FRONT-END DEVICES

The optical synchronization system has been operated at FLASH since 2009 [1]. It is based on the distribution of 200 fs long laser pulses at 1550 nm with a repetition rate of 216.7 MHz, 1/6 of the main 1.3 GHz RF. This reference signal can be used at remote locations in the accelerator for bunch arrival time monitors (BAMs) [2], RF reference stabilization (REFM-opt) [3] or laser synchronization (L2L) [4]. In a recent publication, a synchronization of 30 fs rms between the FEL and the Pump-Probe was experimentally shown [5]. In order to achieve this level of performance an active beam-based feedback (BBFB) stabilization [6] of the electron bunch arrival time with help of the fs-precise BAM measurements has to be applied as well as optical lock of the pump-probe laser to the reference with the scheme of two-color balanced optical cross-correlation. For attaining even better stability in future and to cope with the growing number of clients, all sub-systems of the optical synchronization are being improved. The European XFEL is being equipped with the improved designs from the start while FLASH is being upgraded and extended step by step.

*This work has partly been funded by the Helmholtz Validation Fund Project MTCA.4 for Industry (HVF-0016)
#matthias.felber@desy.de

ISBN 978-3-95450-134-2

Master Laser Oscillator (MLO)

As the source of each synchronization reference signal for the whole accelerator, the phase stability of the MLO is especially crucial. Up to now it is locked to the RF master oscillator using conventional methods [7] but in future a more sophisticated MZI (Mach Zehnder Interferometer) setup will be used which is very similar to the one in the optical-RF reference modules [3], described later. The performance is expected to be sub-5 fs rms short-term [1 kHz–10 MHz] and sub-5 fs peak-peak long-term.

Link Stabilization Units (LSUs)

The fiber link stabilization from the MLO to the client was and will be based on balanced optical cross-correlation (OXC) between a reference and a reflected pulse but the opto-mechanic design of the LSU has completely changed. The footprint decreased by more than a factor of two while providing more flexibility e.g. for the implementation of polarization-maintaining fiber. This way it is possible to supply additional end-stations at FLASH, e.g. the plasma acceleration experiment FLASHForward [8] or the new beamline FLASH2 [9] which would not have been possible with the old design. An in-house developed balanced detector for the OXC provides superior low-noise performance compared to available commercial products. In a realistic scenario of environmental accelerator conditions the a 3.6 km fiber link was stabilized to 3.3 fs rms over 24 hours [10].

Synchronization of External Lasers (L2L)

Besides an RF-based pre-locking [11] the ultimate performance of sub-5 fs rms between the synchronization reference and an external laser (usually Yb @ 1030 nm or TiSa @ 800 nm) a two-color OXC is used. In the past only individual bread-board assemblies were applied. Now we designed a versatile applicable engineered version which is more compact and robust [4].

Bunch Arrival Time Monitor (BAM)

With the current design it is possible to measure the arrival time with <10 fs rms accuracy [2]. The redesign [12] of the complete BAM front-end is prepared for low-charge operation by providing the possibility to exploit the bandwidth of the new 40 GHz pickups [13].

RF Reference Module (REFM-opt)

The REFM-opt [3] stabilizes the reference signal for the LLRF (Low-Level Radio Frequency) detection used for regulating the accelerating field. By synchronizing to the optical reference residual drifts are avoided and load is taken from the BBFB which increases performance and robustness. The stability was shown to be better than 5 fs.

HARDWARE UPGRADES TO MTCA.4

MTCA is a novel electronic framework for analog and digital signal processing. MTCA.4 [14] was released as an official standard by the PCI Industrial Manufacturers Group (PICMG [15]) in2011 and is supported by the xTCA for physics group, a network of physics research institutes and electronics manufacturers. Its main improvements over the preceding standards like VME (Versa Module Europa) are enhanced rear I/O connectivity and provisions for improved precision timing. MTCA.4 has many advantages including capabilities for remote monitoring, remote maintenance, hot-swap of components, and the option to duplicate critical components, making the standard highly modular and flexible.

MTCA.4 at DESY

In agreement between the involved groups, it was decided to use the MTCA.4 standard for the control electronics of the European XFEL and FLASH. This involves the LLRF field control [16], timing system, diagnostics like beam position monitors [17] and camera readouts, and the optical synchronization system [18].

Various boards were developed at DESY with collaboration partners in order to fulfil the different application tasks. In this paper we only provide a short summary of the boards developed and used for the synchronization system, because a detailed description of the modules is given already in [18]. The portfolio includes two AMCs (Advanced Mezzanine Cards) with Virtex FPGAs. One is built as a 10 Channel 125 MSPS digitizer card [19] and is used for laser synchronization while the other one has two FMC (FPGA Mezzanine Card) slots and is used for LSU control and BAM data processing. Another low-cost AMC is used as carrier board for stepper motor drivers, monitoring ADCs, or general purpose IO boards. In most cases the AMC is connected to an RTM (Rear Transition Module) which usually provides the interface to analog signals and e.g. analog processing for laser synchronization [20], ADCs and DACs for the LSU signals or a four channel piezo driver to drive the piezos that act as fast actuators in the control loop for lasers and fiber links.

FIRMWARE AND RAPID-X

The implementation of algorithms and procedures on a FPGA requires a hardware description language such as VHDL. Therefore application engineers are usually dependent on the availability of FPGA experts which implement their schemes. During debugging or when a change is required this can result in an ineffective and time-consuming iterative process between VHDL programming and testing. In order to overcome this challenge a toolset called Rapid-X [21] was developed. The idea is that the hardware specific part of the firmware is separated from the application algorithms. While the first is developed by the FPGA expert, the latter can be easily designed by a user who does not need deep knowledge of the underlying processes. Additionally, this approach makes it easy to reuse the algorithms developed for a certain application in projects that use other boards or to migrate a given project to a different board by simply substituting the hardware-specific VHDL code.

ISBN 978-3-95450-134-2

The platform for Rapid-X is the software Matlab/Simulink [22] which is used to describe complex systems and algorithms with block diagrams. The Xilinx System Generator tool already offers the possibility to design, simulate and test standard Simulink models with data processing in the FPGA. However, the model still needs to be connected to other parts of the HDL project, which includes elements such as clock distribution, external memories, signal sources and sinks (also from and to other boards), ADCs, DACs, etc. This becomes increasingly difficult, the more complex the hardware architecture and the entire system is. With the custom Simulink library Rapid-X the designer can directly integrate these peripherals in the design and compile it to a complete VHDL project without any more help from the expert.

Rapid-X was already extensively used e.g. to generate firmware for data acquisition or to develop, implement, and test advanced feedback control algorithms [23].

SOFTWARE TOOL KIT MTCA4U

At DESY a tool kit was developed in order to ease the development, debugging, and distribution of application software. It is the DESY MicroTCA.4 User Tool Kit (MTCA4U) which basically consists of three tools [24].

1) A PCI-express driver (Linux kernel module) which is universal for basic access to all devices developed at DESY. Modularity and expandability allow generating device-specific drivers with a minimum of code, inheriting the functionality of the base driver.

2) A C++ API (Application Programming Interface) which allows convenient access to all device registers by name, using mapping information which is automatically generated when building the firmware. A graphical user interface (Qt Hardware Monitor) allows direct read and write access to the device, including plotting functionality for recorded raw data. The API is also used to provide Matlab- and Python-bindings and command line tools which all use the same syntax.

3) The third tool is an adapter for easy integration of independent application code into a control system, e.g. DOOCS [25] at FLASH and the European XFEL. When the application is integrated to the control system with the adapter it becomes a server for a device or task. The idea is that the control system adapter makes it easy to reuse the developed code at facilities using other control systems e.g. EPICS or TANGO.

STATUS AND CONCLUSION

The implementation of MTCA.4-based controls and the redesign of all front-end devices for the synchronization systems at FASH and the European XFEL promise to improve the performance, increase flexibility and maintainability and reduce the space requirements. However, for a small team like ours this effort on all four presented aspects of the system is a big challenge. As a matter of fact, the migration is not as advanced as anticipated in the project plans.

The design for all of the front-end devices is finished, some are still in the prototyping phase and some are already in operation in the facilities.

Most of the MTCA hardware components which were developed in our group at DESY are available from industry partners due to licensing agreements thus making them available for the accelerator community and beyond. Only a few FMC modules still need to be revised.

The Rapid-X framework supports all AMC modules used by us and is continuously extended. After a rather long debugging phase it has proven to be an extremely valuable tool for our feedback algorithm development. Yet, the firmware for the three main applications laser synchronization, fiber link stabilization, and bunch arrival time monitors is not completed.

The MicroTCA.4 User Tool Kit is meanwhile in a mature state and its tools are widely used. However, none of the needed servers, meaning control system independent software connected to a DOOCS adapter have been programmed yet. For the development phase usually Matlab scripts making use of the MTCA4U tools to access data from the FPGAs are applied. For the laser synchronization which is the first setup needed in operation at several locations a Python script is being prepared to temporarily substitute for the missing server.

REFERENCES

[1] S. Schulz et al., IBIC 2013, WEPC32
[2] F. Loehl et al., Phys. Rev. Lett. 104, 144801 (2010)
[3] E. Janas et al., IPAC 2014, WEPRI115
[4] J. Mueller et al., IPAC 2015, MOPHA031
[5] S. Schulz et al., Nature Comm. 6, 5938 (2014)
[6] C. Schmidt et al., FEL 2011, THPA26
[7] M. Felber et al., FEL 2010, THOA3
[8] B. Foster et al., http://arxiv.org/abs/1508.03192
[9] M. Scholz et al., FEL 2015, ID1358
[10] C. Sydlo et al., FEL 2014, THP090
[11] M. Felber et al., IPAC 2014, TUPRI107
[12] H. Dinter et al., FEL 2015, TUP049
[13] M. K. Czwalinna et al., FEL 2014, THP069
[14] T.Walter et al., IPAC 2013, THPWA003
[15] http://www.picmg.org
[16] J. Branlard et al., IPAC 2012, MOOAC01
[17] F. Schmidt-Foehre et al., IPAC 2014, THPME117
[18] M. Felber et al., IBIC 2014, MOPD07
[19] http://www.struck.de
[20] E. Janas et al., FEL 2015, TUP045
[21] P. Predki et al., IEEE TNS (Vol:62, Issue 3)
[22] http://www.mathworks.com
[23] M. Heuer et al., IBIC 2014, MOCZB3
[24] M. Killenberg, IPAC 2014, THPRO104
[25] http://doocs.desy.de

ISBN 978-3-95450-134-2

TURBO-ICT PICO-COULOMB CALIBRATION TO PERCENT-LEVEL ACCURACY

F. Stulle*, J. Bergoz, Bergoz Instrumentation, Saint-Genis-Pouilly, France

Abstract

We report on the calibration methods implemented for the Turbo-ICT and the BCM-RF. They allow to achieve percent-level accuracy for charge and current measurements. Starting from the Turbo-ICT and BCM-RF working principle, we discuss the scientific fundaments of their calibration and the practical implementation in a test bench. Limits, both principle and practical, are reviewed. Achievable accuracy is estimated.

INTRODUCTION

The Turbo-ICT sensor and its corresponding BCM-RF electronics can accurately measure charges of ultra-short particle bunches as well as average currents of CW beams of such bunches [1,2].

When excited by a single bunch, the Turbo-ICT output signal is a short resonance at a fixed frequency f_{res} but charge-proportional amplitude. The BCM-RF works in sample-and-hold mode and measures the apex of this resonance. The maximum possible bunch repetition rate is approximately 2 MHz. For calibration the relation between Turbo-ICT input charge Q_{in} and BCM-RF output voltage U_{BCMRF} is determined.

When excited by a CW beam, the Turbo-ICT output signal is a sine wave of frequency f_{res} and current-proportional amplitude. The BCM-RF works in track-continuous mode and measures the apex of this sine wave. The Turbo-ICT resonance frequency f_{res} must match the bunch repetition rate f_{rep} or a harmonic. For calibration the relation between average input current $\langle I_{\mathrm{cw,in}}\rangle$ and BCM-RF output voltage U_{BCMRF} is determined.

In the following, we discuss the Turbo-ICT and BCM-RF working principle. The calibration methods for both modes of operation are described and the achievable accuracies are estimated.

TURBO-ICT / BCM-RF PRINCIPLE

To determine charge or current the BCM-RF measures on a logarithmic scale the apex of the Turbo-ICT output signal. Hence, the apex should depend only on input charge or current. Most notably, any current transformer's output pulse shape is usually dependent on input pulse shape, which could induce a variation of the apex even for constant charge or current. Only for "sufficiently short" input pulses this dependence is negligible.

It is required that an input pulse must be considerably shorter than the Turbo-ICT resonance wave length, which is fulfilled, e.g., in laser-plasma accelerators or X-ray free-electron lasers. Details are given in Appendix A.

*stulle@bergoz.com

Turbo-ICT Pulse Response

The spectral response $Q_{\mathrm{out}}(f)$ of a Turbo-ICT to an incoming current pulse $I_{\mathrm{in}}(t)$ is the product of the incoming pulse's spectrum $Q_{\mathrm{in}}(f)$ and the Turbo-ICT's transmission coefficient $S_{21}(f)$, e.g. as obtained from S-parameter measurements using a vector network analyser (VNA):

$$Q_{\mathrm{out}}(f) = Q_{\mathrm{in}}(f)\, S_{21}(f)\,.$$

Using the inverse Fourier transform the time-domain output current pulse $I_{\mathrm{out}}(t)$ can be determined:

$$I_{\mathrm{out}}(t) = \int_{-\infty}^{+\infty} Q_{\mathrm{in}}(f)\, S_{21}(f)\, e^{i\,2\pi\, f t}\, df\,.$$

For "sufficiently short" input pulses, $I_{\mathrm{out}}(t)$ can be approximated:

$$I_{\mathrm{out}}(t) \approx Q_{\mathrm{in}} \int_{-\infty}^{+\infty} S_{21}(f)\, e^{i\,2\pi\, f t}\, df = Q_{\mathrm{in}}\, M(t)\,. \quad (1)$$

That means, for "sufficiently short" input pulses the Turbo-ICT output pulse has always the same shape $M(t)$ scaled by the input pulse charge Q_{in}.

$M(t) = \int_{-\infty}^{+\infty} S_{21}(f)\, e^{i\,2\pi\, f t}\, df$ is the Turbo-ICT's response to a Dirac pulse, i.e. to an infinitely short current pulse, normalized by the pulse's charge; its units are Ampère per Coulomb. Figure 1 shows a typical $S_{21}(f)$ of a Turbo-ICT and the corresponding Dirac response.

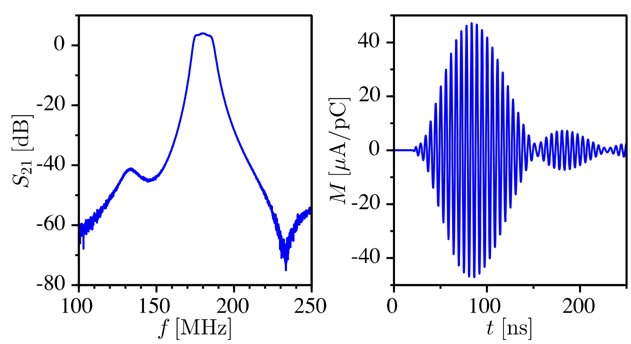

Figure 1: Typical Turbo-ICT response in frequency-domain (left) and in time-domain (right).

Turbo-ICT Dirac Response Correction

As mentioned above, the Turbo-ICT Dirac response can be reconstructed from the Turbo-ICT's S_{21}:

$$M(t) = \int_{-\infty}^{+\infty} S_{21}(f)\, e^{i\,2\pi\, f t}\, df\,.$$

While this equation is in theory correct, it is in practice not sufficient. Around the Turbo-ICT, the measurement setup is not perfectly matched to 50 Ω wave impedance. Reflections occur during the VNA measurements, lowering power and current passing the Turbo-ICT. Such effects will not be present in the accelerator. Consequently, the measured transmission coefficient $S_{21,\mathrm{VNA}}$ is not exactly representative of the real $S_{21,\mathrm{ACC}}$ in the accelerator.

ISBN 978-3-95450-134-2

The required correction can be obtained by exploiting the fact that the ratio of Turbo-ICT output voltage $U_{\text{out,VNA}}$ and input current I_{in} is constant. I_{in} is the current passing the Turbo-ICT, not the current I_0 sent by the source. If I_0 would enter the Turbo-ICT, as in the accelerator due to absence of reflections, the output voltage would be $U_{\text{out,ACC}}$. But the ratio must remain the same:

$$\frac{U_{\text{out,ACC}}}{I_0} = \frac{U_{\text{out,VNA}}}{I_{\text{in}}} = \frac{U_0\, S_{21,\text{VNA}}}{I_{\text{in}}}$$

$$\Leftrightarrow \frac{U_{\text{out,ACC}}}{U_0} = S_{21,\text{VNA}} \frac{I_0}{I_{\text{in}}} = S_{21,\text{ACC}}\,.$$

The input current I_{in} can be calculated either using the reflection coefficient $S_{11,\text{VNA}}$, i.e. the signal reflected at the Turbo-ICT input, or using the transmission coefficient $S_{31,\text{VNA}}$, i.e. the signal passing the Turbo-ICT:

$$I_{\text{in}} = I_0\left(1 - S_{11,\text{VNA}}\right) = I_0\, S_{31,\text{VNA}}$$

and we get:

$$S_{21,\text{ACC}} = \frac{S_{21,\text{VNA}}}{1 - S_{11,\text{VNA}}} = \frac{S_{21,\text{VNA}}}{S_{31,\text{VNA}}}.$$

In practice it is less error-prone to use $S_{31,\text{VNA}}$. Its phase has an impact only on the phase of $S_{21,\text{ACC}}$, but not on the absolute value. However, to obtain $S_{31,\text{VNA}}$ a 3-port S-parameter measurement is required.

The correct $M(t)$ that must be used for calculations is:

$$M_{\text{correct}}(t) = \int_{-\infty}^{+\infty} S_{21,\text{ACC}}(f)\, e^{i\,2\pi f t}\, df\,.$$

Charge Measurements

The results obtained can be directly exploited for single-bunch charge measurements. Rearranging Eqn. (1) gives:

$$Q_{\text{in}} \approx I_{\text{out}}(t)/M(t)\,.$$

Since Q_{in} is time independent it is, e.g., sufficient to divide the apex of $I_{\text{out}}(t)$ by the apex of $M(t)$ or to divide their respective peak-to-peak values:

$$Q_{\text{in}} \approx \frac{\max(|I_{\text{out}}(t)|)}{\max(|M(t)|)} \approx \frac{\max\left(I_{\text{out}}(t)\right) - \min\left(I_{\text{out}}(t)\right)}{\max\left(M(t)\right) - \min\left(M(t)\right)}\,. \qquad (2)$$

Current Measurements

The spectrum of a CW beam of equal bunches consists only of a DC component, a component at the bunch repetition frequency f_{rep} and its harmonics.

Since the Turbo-ICT includes a narrow band-pass filter around $f_{\text{res}} = f_{\text{rep}}$, or a harmonic of f_{rep}, only a single frequency is transmitted. That means, for a CW input beam the Turbo-ICT output signal is a sine wave. This can also be understood by considering that in time-domain the output signal must be the sum of the time-shifted resonances excited by consecutive bunches.

The output amplitude $I_{\text{rms,out}}$ can be related to the average input current $\langle I_{\text{cw,in}}\rangle$ (see Appendix B):

$$\langle I_{\text{cw,in}}\rangle \approx \frac{I_{\text{rms,out}}}{\sqrt{2}\, S_{21,\text{ACC}}\left(f_{\text{rep}}\right)}\,. \qquad (3)$$

SINGLE-BUNCH CHARGE CALIBRATION

For single-bunch charge calibration, the Turbo-ICT needs to be excited by a short current pulse, whose charge needs to be determined, to obtain a resonance which can be measured by the BCM-RF.

Equivalent Input Charge

It is important to understand that one has to determine the charge as seen by the Turbo-ICT, which will be excited only by the spectral power falling into its bandwidth.

As mentioned before, for pulse length independent measurements the input pulses need to be "sufficiently short". The pulses generated by our fast pulser, a CPS/1S by Kentech Instruments Ltd., have a FWHM length of 200ps, which could suffice in some cases. But in practice they are too long due to having a tail. Additionally, cable losses stretch the pulses further.

To circumvent this problem, an equivalent input charge is determined from the Turbo-ICT output resonance. The Turbo-ICT is excited using the fast pulser and a programmable step attenuator. The resonance peak-to-peak value is measured by an oscilloscope. The Turbo-ICT Dirac response is reconstructed from S-parameters. Eqn. (2) is applied to obtain the equivalent input charge, which is the charge of a Dirac pulse that would excite the same resonance as the fast pulser.

Charge Scan

To obtain the BCM-RF response, a charge scan is performed using the fast pulser and the programmable step attenuator. For each attenuator setting the BCM-RF output voltage U_{BCMRF} is recorded. Based on the attenuator settings and the previously determined equivalent input charge, output voltage and input charge are related.

Estimation of Calibration Accuracy

While the calibration principle is rather straight forward, there are a few issues that need to be considered to achieve good calibration accuracy. Some are also important for the measurements in the accelerator.

First, the accuracy of the equivalent input charge determination depends on the accuracy of the Turbo-ICT resonance as measured by the oscilloscope and the accuracy of the Turbo-ICT Dirac response reconstruction from VNA measurements. These two points are further discussed in the following sub-sections.

Second, the BCM-RF output voltage is a DC voltage which can be easily measured with sufficient precision. Hence, it has no impact on aggregate accuracy.

Third, the BCM-RF must properly measure the resonance apex. To achieve this, the sample-and-hold trigger has to be finely adjusted. Only if the trigger is set up correctly it does not impact accuracy.

Fourth, cable losses must be measured and signal amplitudes need to be corrected accordingly. For calibration, losses in the cable connecting Turbo-ICT and BCM-RF can be accurately measured using a VNA. In the accelera-

ISBN 978-3-95450-134-2

tor, on the other hand, it might be more difficult to measure these losses. When estimating the calibration accuracy a typical error of 1% is included due to cables.

Fifth, since Turbo-ICT and BCM-RF work at a narrow frequency band their adaptation to 50 Ω is very good. Standing waves on the cable connecting them are negligible. When using the same cable for calibration and in the accelerator, standing waves would in any case be correctly taken into account.

Sixth, during analysis of the charge scan the equivalent input charge needs to be scaled by the real attenuation of the programmable step attenuator, which is measured using a VNA. But also the determination of the equivalent input charge depends on this attenuator. Hence, any systematic scaling error of its real attenuation is compensated. Remaining errors can be neglected.

Accuracy of Resonance Measurements

The Turbo-ICT output resonance is characterized by measuring its peak-to-peak value with an oscilloscope. Noise is reduced by averaging. However, a scaling error might be present due to oscilloscope errors and incomplete knowledge of cable losses.

An improvement is to compare on the oscilloscope the Turbo-ICT resonance to a sine wave of same amplitude and frequency f_{res}. The sine wave is generated by a calibrated RF signal generator. Its peak-to-peak value is deduced from the RF signal generator power setting. By doing so, oscilloscope scaling errors are replaced by RF signal generator errors, which are usually smaller. Fewer cables need to be taken into account.

For Turbo-ICT calibration an Agilent N5181A RF signal generator is used. Its calibration report states an uncertainty of 0.2dB, i.e. about 2%. To remain conservative, a measurement error of 3% is assumed.

Accuracy of Dirac Response Reconstruction

The accuracy of the Dirac response reconstruction is given by the accuracy of the S-parameter measurements. These are performed using a factory calibrated Agilent E5071C 4-port vector network analyser. To correct for the influence of cables, an on-site calibration is performed using a factory calibrated Agilent 85033E calibration kit.

According to data sheets and calibration certificates the absolute accuracies of S_{21} and S_{31} measurements are of the order of 1% amplitude and 1° phase.

Since the ratio S_{21}/S_{31} is used, correlated errors will be eliminated. Uncorrelated errors will increase. It is assumed that the real error is a mixture of correlated and uncorrelated errors and that the error on the ratio will be similar to the error of a single measurement.

In addition, a coaxial structure is required geometrically adapting the cables to the Turbo-ICT aperture. The previously described S_{21} correction only corrects the error due to an impedance mismatch at this structure's input. If the wave impedance along the Turbo-ICT differs from this input impedance, an uncorrected error remains.

When testing the impact of adapting to different wave impedances, a variation of the S_{21} amplitude by 1-2% was observed. For calibration, the setup has been adapted to match a theoretical wave impedance of 50 Ω.

Taking into account these measurement setup uncertainties, an estimated error on the Dirac response amplitude of 2% seems to be justified.

Resulting Accuracy of Charge Calculation

Since above mentioned errors are systematic errors, the worst case would be if they all go in the same direction. In such a case, the errors of resonance measurement, Dirac response reconstruction and cable losses simply add:

$$\Delta_{\mathrm{charge,worst}} \approx 3\% + 2\% + 1\% \approx 6\%\,.$$

However, the errors are independent and the more realistic statistical error is

$$\Delta_{\mathrm{charge}} \approx \sqrt{(3\%)^2 + (2\%)^2 + (1\%)^2} \approx 4\%\,.$$

CW BEAM CURRENT CALIBRATION

Following from the relation between the CW beam's average input current $\langle I_{\mathrm{cw,in}}\rangle$ and the output sine wave's RMS amplitude $I_{\mathrm{rms,out}}$ (see Appendix B), calibration in track-continuous mode can be simplified by using a sine wave as input signal. Taking into account the required correction of the measured S-parameters, we get:

$$\langle I_{\mathrm{cw,in}}\rangle \approx \frac{I_{\mathrm{rms,out}}}{\sqrt{2}\,S_{21,\mathrm{ACC}}(f_{\mathrm{rep}})} = \frac{I_{\mathrm{rms,in}}}{\sqrt{2}}\,\frac{S_{21,\mathrm{VNA}}(f_{\mathrm{rep}})}{S_{21,\mathrm{ACC}}(f_{\mathrm{rep}})}\,.$$

Using a calibrated RF signal generator, the Turbo-ICT is excited by a sine wave of frequency f_{res} and known RMS amplitude. The BCM-RF measures the apex of the Turbo-ICT output sine wave. By applying above equation the average input current of a CW beam is deduced which would lead to the same BCM-RF output voltage.

Estimation of Calibration Accuracy

As for the single-bunch charge calibration, several effects need to be considered to obtain good accuracy.

The following assumptions seem justified. The BCM-RF output voltage is considered error free. A typical error of 1% is included due to cables. The Turbo-ICT Dirac response is known to 2%. And the RF signal generator amplitude accuracy is 2%.

Resulting Accuracy of Current Calculation

As for single-bunch charge calibration, the worst case would be if all errors add:

$$\Delta_{\mathrm{current,worst}} \approx 2\% + 2\% + 1\% \approx 5\%\,.$$

The more realistic statistical error is

$$\Delta_{\mathrm{current}} \approx \sqrt{(2\%)^2 + (2\%)^2 + (1\%)^2} \approx 3\%\,.$$

CONCLUSION

Turbo-ICT and BCM-RF can accurately measure single-bunch charges and CW beam average currents.

Their calibration is derived from a combination of time-domain and frequency-domain measurements. Standard techniques and mathematics are exploited. Based on the accuracy of the instruments used and considering measurement setup uncertainties, absolute calibration errors of

ISBN 978-3-95450-134-2

$\Delta_{\mathrm{charge}} \approx 4\%$ (single-bunch charge)
$\Delta_{\mathrm{current}} \approx 3\%$ (CW beam average current)
are estimated.
To achieve correct measurement results during calibration and in the accelerator, the particle bunch length has to fulfil $t_{\mathrm{FWHM,in}} \lesssim 0.05/f_{\mathrm{res}}$. The bunch should not have a tail.

ACKNOWLEDGMENT

The calibration methods were developed during a collaboration with PSI. Thanks to the allocation of SITF beam time to compare different charge diagnostics devices, calibration could be tested and improved. We would like to thank C. Ozkan, P. Pollet, V. Schlott and M Stadler for discussions and support.

APPENDIX A
SHORT-PULSE ASSUMPTION

The Fourier transform of a finite current pulse $I_{\mathrm{in}}(t)$ is:

$$Q_{\mathrm{in}}(f) = \int_{-\infty}^{+\infty} I_{\mathrm{in}}(t)\, e^{-i\,2\pi\, f t}\, dt$$
$$= \int_{0}^{t_{max}} I_{\mathrm{in}}(t)\, \big(\cos(2\pi\, f t) + i\, \sin(2\pi\, f t)\big)\, dt\,.$$

t_{max} is the total pulse length. If $f \ll 1/2\pi t_{\mathrm{max}}$ the sine approaches zero while the cosine approaches unity for any time t within the integration boundaries. That means, irrespective of the shape of $I_{\mathrm{in}}(t)$ its spectrum $Q_{\mathrm{in}}(f)$ must approach towards DC the value $\int_{-\infty}^{+\infty} I_{\mathrm{in}}(t)\, dt$, i.e. the pulse charge Q_{in}. The spectral amplitude $Q_{\mathrm{in}}(0)$ always exactly equals the pulse charge Q_{in}.

The smaller t_{max} the higher will be the frequencies for which $Q_{\mathrm{in}}(f)$ can be approximated by Q_{in}. In case of the Turbo-ICT, an input pulse can be considered "sufficiently short" only if $Q_{\mathrm{in}}(f) \approx Q_{\mathrm{in}}$ over the full Turbo-ICT bandwidth $S_{21}(f)$.

Assuming a Gaussian input pulse, the maximum length $\sigma_{\mathrm{in,max}}$ can be calculated for which $Q(f_{\mathrm{res}})$, i.e. the spectral amplitude at the Turbo-ICT resonance frequency, lies within a certain fraction ε of Q_{in}:

$$(1-\varepsilon)\, Q_{\mathrm{in}} < Q_{\mathrm{in}}\, e^{-2\pi^2\, \sigma_{\mathrm{in,max}}^2\, f_{\mathrm{res}}{}^2}$$
$$\Leftrightarrow \sigma_{\mathrm{in,max}} < \frac{1}{f_{\mathrm{res}}} \sqrt{\frac{\log(1-\varepsilon)}{-2\pi^2}}\,.$$

If the spectral amplitude $Q(f_{\mathrm{res}})$ should stay within 1% of Q_{in}, the input pulse length needs to fulfil

$$\sigma_{\mathrm{in,max}} < 0.0226/f_{\mathrm{res}}\,.$$

Pulse shapes other than Gaussians will lead to different, though comparable results. Considering only pulses that do not have any tail, we can generally assume that the FWHM of the input pulses should fulfil

$$t_{\mathrm{FWHM,in}} < 0.05/f_{\mathrm{res}}$$

for less than 1% error.

The same limit applies when measuring CW beams. In this case, f_{res} needs to be a harmonic of the pulse repetition rate f_{rep}. The higher the chosen harmonic the tighter is the limit imposed on the input pulse length.

Typically the Turbo-ICT resonance frequency is of the order of 200 MHz, while the spectra of sub-picosecond particle bunches, e.g. generated by laser-plasma accelerators or X-ray free-electron lasers, can reach beyond THz. Such particle bunches can be considered "sufficiently short".

APPENDIX B
TURBO-ICT RESPONSE TO CW BEAM

A CW beam of short and equal particle bunches can be mathematically approximated by a Dirac Comb:

$$I_{\mathrm{cw,in}}(t) \approx \sum_{n=-\infty}^{+\infty} Q_{\mathrm{b}}\, \delta(t - n\,T)\,.$$

Q_{b} is the single bunch charge. $T = 1/f_{\mathrm{rep}}$ is the bunch repetition period. The Dirac Comb can be expressed as a Fourier Series:

$$I_{\mathrm{cw,in}}(t) \approx Q_{\mathrm{b}}\, f_{\mathrm{rep}} \sum_{n=-\infty}^{+\infty} e^{i\,2\pi\, n\, f_{\mathrm{rep}}\, t}$$
$$\approx Q_{\mathrm{b}}\, f_{\mathrm{rep}} + 2Q_{\mathrm{b}}\, f_{\mathrm{rep}} \sum_{n=1}^{+\infty} \cos\big(2\pi\, n\, f_{\mathrm{rep}} t\big)\,.$$

$Q_{\mathrm{b}}\, f_{\mathrm{rep}}$ is the average beam current $\langle I_{\mathrm{cw,in}}\rangle$. It corresponds to a DC component in the beam spectrum, which is lost during measurements because current transformers cannot transmit DC components. All other components are scaled by the current transformer's $S_{21}(f)$:

$$I_{\mathrm{out}}(t) \approx 2\, Q_{\mathrm{b}}\, f_{\mathrm{rep}} \sum_{n=1}^{+\infty} \mathrm{S}_{21}\big(n\, f_{\mathrm{rep}}\big) \cos\big(2\pi\, n\, f_{\mathrm{rep}}\, t\big)\,.$$

By band-pass filtering at a single frequency $n\, f_{\mathrm{rep}}$ a cosine signal remains:

$$I_{\mathrm{out,filter}}(t) \approx 2\, Q_{\mathrm{b}}\, f_{\mathrm{rep}}\, \mathrm{S}_{21}\big(n\, f_{\mathrm{rep}}\big)\, \cos\big(2\pi\, n\, f_{\mathrm{rep}}\, t\big)\,.$$

The RMS amplitude of this signal is:

$$I_{\mathrm{out,RMS}} \approx \sqrt{2}\, Q_{\mathrm{b}}\, f_{\mathrm{rep}}\, \mathrm{S}_{21}\big(n\, f_{\mathrm{rep}}\big)$$
$$\Leftrightarrow \langle I_{\mathrm{cw,in}}\rangle = Q_{\mathrm{b}}\, f_{\mathrm{rep}} \approx \frac{I_{\mathrm{out,RMS}}}{\sqrt{2}\, \mathrm{S}_{21}\big(n\, f_{\mathrm{rep}}\big)}\,.$$

An input sine wave of amplitude

$$I_{\mathrm{in,RMS}} = \frac{I_{\mathrm{out,RMS}}}{\mathrm{S}_{21}\big(n\, f_{\mathrm{rep}}\big)}$$

would excite the same Turbo-ICT output signal as the Dirac Comb. This is a consequence of the fact that both input signals deliver the same spectral power at $n\, f_{\mathrm{rep}}$, despite having totally different shapes.

REFERENCES

[1] H.J. Choi, M.S. Chae, H.-S. Kang, and S.J. Park, "Introduction to the Test Results of Turbo-ICT in PAL-ITF", in *Proc. IBIC'14*, Monterey, CA, USA, Sep. 2014, paper WEPF09, pp. 553-557.
[2] K. Nakamura *et al.*, "Pico-coulomb charge measured at BELLA to percent-level precision using a Turbo-ICT", to be published in Plasma Phys. Control. Fusion, LPAW2015 Cluster Issue.

ISBN 978-3-95450-134-2

ALL-FIBER APPROACH TO LONG-TERM STABLE TIMING DISTRIBUTION SYSTEM

M. Xin*, K. Şafak, F. X. Kärtner, CFEL, DESY, Hamburg, Germany
P. T. Callahan, M. Y. Peng, F. X. Kärtner, MIT, Cambridge, Massachusetts, USA

Abstract

A complete fiber-optic, high-precision, long-term stable timing distribution system is demonstrated over a 3.5-km polarization-maintaining fiber link for synchronization of next generation X-ray free-electron lasers. The residual timing jitter at [1 Hz, 1 MHz] is below 0.7 fs, and the RMS drift (<1 Hz) is 3.3 fs over 200 hours of continuous operation. This all-fiber-optic implementation will greatly reduce the complexity of optical alignment in timing distribution and improve the overall mechanical and timing stability of the system.

INTRODUCTION

Next generation FELs, such as the European XFEL [1] in Hamburg and Linac Coherent Light Source II [2] in Stanford, are predicted to deliver X-ray pulses shorter than 10 fs. Unlocking the high temporal-resolution capabilities of these facilities will require extremely stable timing distribution systems [3, 4] delivering better than 10-fs precision between optical and radio frequency (RF) sources located over kilometer distances. Over the past decade, we have been advancing a pulsed-optical timing distribution system [5-7] that uses the ultralow-noise pulse train from a mode-locked (master) laser as its timing signal. The timing signal is transferred through timing-stabilized fiber links from a central location to multiple end stations, where efficient and robust synchronization is realized using balanced optical cross-correlators (BOC) [8] for optical sources and balanced optical-microwave phase detectors [7] for RF sub-systems. Real facilities such as FLASH and the European XFEL need fiber networks consisting of 20 or more timing links, which require tremendous attention to the alignment and stability of the free-space optics to minimize timing-drifts induced by beam pointing instabilities. This situation also necessitates preamplification of the master laser's output to overcome excessive free-space to fiber coupling losses to provide adequate power for all timing links. To eliminate free-space optics and its disadvantages from the timing distribution system, we have developed integrated, fiber-coupled balanced optical cross-correlators (FC-BOC) using periodically-poled $KTiOPO_4$ (PPKTP) waveguides [9, 10]. These waveguides exhibit second harmonic (SH) conversion efficiencies up to 1.02 % / [W·cm^2] (20 times higher than the bulk optical devices), which will decrease the power demand from the master laser and consequently support more timing links. Furthermore, the robustness and ease of implementation of these fiber-coupled devices will eliminate alignment-related problems observed in free-space optics. In this paper, we present an all-fiber implementation of the pulsed-optical timing distribution system using FC-BOCs.

EXPERIMENTAL SETUP

A diagram of the experimental setup is shown in Fig. 1(a). The master laser operates at 1554-nm center wavelength with +22.4-dBm average output power, 150 fs pulse width and 216.66-MHz repetition rate. Its repetition rate is locked to a RF synthesizer (RF-S) to reduce the timing drift below 10 Hz. The only free-space part built in this experiment is the initial power separation elements comprised of one polarization beam splitter (PBS) and 3 half-wave plates. Furthermore, polarization-maintaining (PM) fiber components are chosen over standard single-mode (SM) fiber for the construction of the setup, as previous results obtained with SM fiber has showed substantial polarization-mode-dispersion effects in the out-of-loop link stabilization measurements [3]. After the PBS, the output of the master laser is coupled into two separate fiber paths: the out-of-loop reference path and the link stabilization unit. The out-of-loop reference path is a 1-m long PM fiber serving as the reference arm for the out-of-loop FC-BOC. The link stabilization unit starts with a fiber-coupled polarization beam splitter (FC-PBS1) which divides the optical power further into two segments. The first segment (traveling to the right through FC-PBS1 in Fig. 1(a)) is directed into the timing link which consists of a fiber-coupled faraday rotator (FC-FR), a fiber-coupled motorized delay line (FC-MD) with 560-ps range, a PM fiber stretcher (PM-FS), and a 3.5-km PM dispersion-compensated fiber spool (PM-DCF). The second segment is sent into a 0.5-m fiber having a fiber-coupled faraday mirror (FC-FM) at the end. The FC-FM turns the polarization of the pulses by π/2 upon reflection and guides them into the in-loop FC-BOC to serve as the reference pulses for the timing stabilization of the 3.5-km link.

Both of the two FC-BOCs are PPKTP waveguide chips in fiber-coupled packages with internal temperature control [10]. A schematic of the module is shown in Fig. 1(b). The wavelength division multiplexer (WDM) consists of a fiber-coupled dichroic beam-splitter cube coupling the input pulses into the waveguide for cross-correlation and separates the SH return path from the fundamentals. The forward and backward SH signals are then fed to the ports of a fiber-coupled BPD (FC-BPD).

* ming.xin@desy.de

ISBN 978-3-95450-134-2

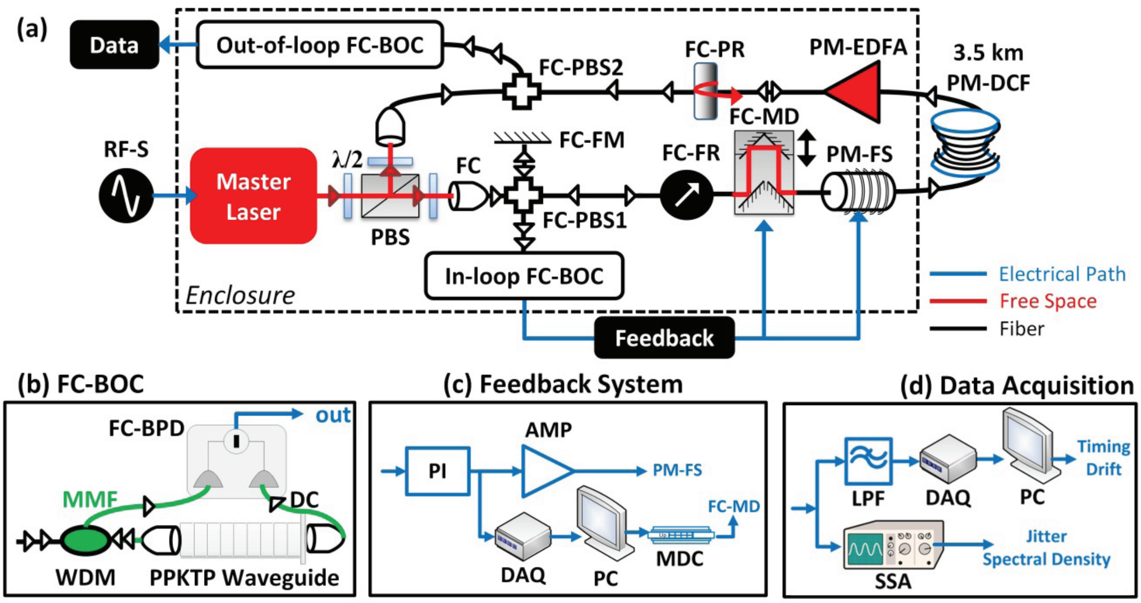

Figure 1: (a) Schematic of the link stabilization experiment. (b) Main elements the FC-BOCs. (c) Feedback system employed for the link delay compensation. (d) Data acquisition elements for the evaluation of the out-of-loop measurement results. Abbreviations: RF-S, RF synthesizer; FC, fiber coupler; FC-PBS, FC polarization beam splitter; FC-FM, FC faraday mirror; FC-FR, FC faraday rotator; FC-MD, FC motorized delay; PM-FS, PM fiber stretcher; PM-DCF, PM dispersion-compensated fiber; PM-EDFA, PM erbium doped fiber amplifier; FC-PR, fiber-coupled partial reflector; WDM, wavelength division multiplexer; MMF, multi-mode fiber; DC, dichroic coating; FC-BPD, fiber-coupled BPD; PI, proportional-integral controller; AMP, voltage amplifier; DAQ, data acquisition card with 1-Hz sampling rate; PC, personal computer; MDC, motorized delay controller; LPF, 2-Hz low-pass filter; SSA: Agilent 5052a signal source analyzer.

Power management of the fiber links is critical: high link output power is desirable for high signal-to-noise ratio, while low link operating power is needed to avoid fiber nonlinearity-induced timing errors. As a precaution, the fibers are operated with a maximum power of +13 dBm to avoid significant fiber nonlinearities. The input power to the timing link is set to +8 dBm such that after forward propagation, the link transmission loss results in +0-dBm link power. Custom-built bi-directional PM erbium doped fiber amplifier (PM-EDFA) is used in the last section of the timing link to boost the output power to +13 dBm. +3 dBm of power is reflected back by the fiber-coupled partial reflector (FC-PR with 10% back reflection) and reamplified by the PM-EDFA back to +13 dBm. The back-propagated pulses are then combined with new laser pulses from the reference arm of FC-PBS1 in the in-loop FC-BOC. The in-loop FC-BOC measures the propagation delay change in the timing link and generates an error voltage. The error signal is processed by a proportional-integral (PI) controller and then applied to the fiber stretcher with a PZT amplifier (AMP) to compensate the fast timing jitter (see Fig. 1(c)). The piezo resonance of the stretcher at 18 kHz permits a closed loop bandwidth higher than 10 kHz. The output of the PI controller is also recorded by a data acquisition card (DAQ) so that when it reaches its output voltage limit, the motorized-delay is activated through a computer program serving as the slow compensation to the fluctuating link delay. Finally, the output of the FC-PR and the out-of-loop reference fiber are combined in FC-PBS2 and coupled into the out-of-loop FC-BOC to evaluate the performance of the link stabilization experiment.

In order to minimize the drifts coming from the length fluctuations in the FC-BOC reference paths, all setup elements are placed in a temperature-stabilized enclosure, except the 3.5-km fiber link spool, which is put outside and exposed to environmental fluctuations.

RESULTS AND DISCUSSION

Figure 2 shows the measured voltage responses of the FC-BOCs against the time delay between the incoming orthogonal pulses. Due to excess coupling loss between the PM fiber and the waveguide for the reverse-generated SH, the SH power collected on the forward path is approximately 10 dB higher than that of the reverse path in FC-BOCs. Therefore, a 10-dB attenuator is inserted to symmetrize the cross-correlation curve. This issue has prevented us from reaching higher timing sensitivities for FC-BOCs when compared with bulk optics cross-correlators. Nevertheless, even with the current coupling losses we have achieved comparable results to the previous work [5, 6]. For each FC-BOC, five different measurements are performed and the mean values of the jitter-to-voltage conversion factors are 4.5 mV/fs (± 0.32 mV/fs) and 82.0 mV/fs (± 4.9 mV/fs) for the in-loop and out-of-loop FC-BOC respectively (BPD transimpedance gain: 2×10^{6} V/A, 3-dB bandwidth: 150 kHz, responsivity: 0.5 A/W).

ISBN 978-3-95450-134-2

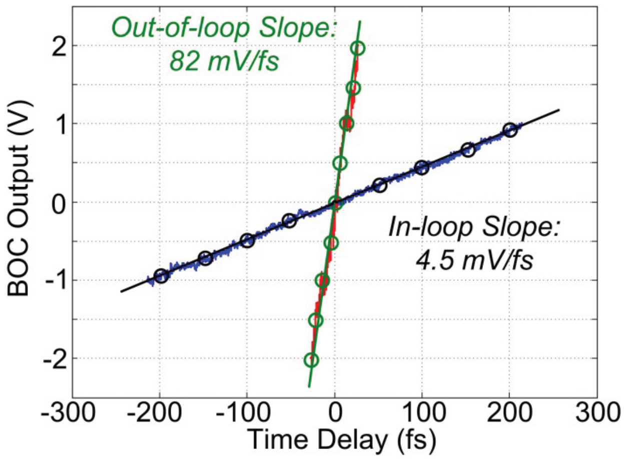

Figure 2: Measurement results of the FC-BOC output versus the delay between the pulses. Blue curve corresponds to the in-loop and red curve corresponds to the out-of-loop FC-BOC response.

The relative timing stability of the 3.5-km PM fiber link is continuously monitored for 200 hours without interruption. The black curve in Fig. 3(a) displays the residual timing drift measured by low-pass filtering the output of out-of-loop FC-BOC at 1 Hz (without any averaging). A remaining drift of only 3.3 fs (± 0.2 fs) RMS is measured for 200 hours of continuous link stabilization; and the motor delay has corrected for over 25-ps timing error. Relative temperature fluctuations of the 3.5-km fiber spool and the enclosure are plotted in Fig 3(b). The maximum deviation of the temperature is about 0.18 K and 0.06 K on the case of the fiber spool and inside the enclosure respectively. The correlation between the residual drift and the enclosure temperature confirms that the drift is mainly limited by the environmental fluctuations penetrating into the FC-BOCs. This is reasonable because the optical enclosure is large in volume, making it difficult to completely isolate the enclosed fibers from the laboratory environment. Even though we have spent considerable effort to splice as short fiber reference arms as possible, the system still contains in total ~2.5 m of uncompensated fiber (reference arms of the FC-BOCs and the fiber pigtail between FC-PR and FC-PBS2). A temperature fluctuation of ~0.1 K on 2.5-m uncompensated fiber would introduce ~7.5-fs error to the timing detection due to thermal expansion and contribute directly to the final drift. Hence, the observed residual drift in our experiment agrees well with the recorded relative temperature change.

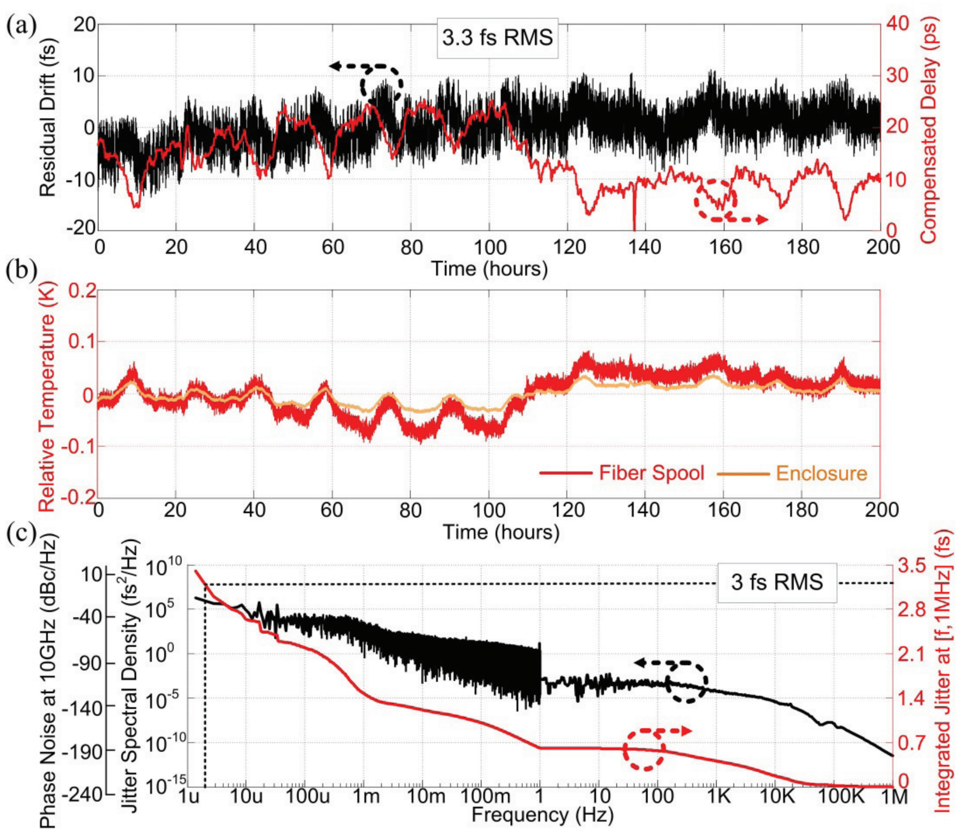

Figure 3: Out-of-loop measurement results. (a) Black curve: timing drift for 200 hours of continuous operation; red curve: corrected link propagation delay by the FC-MD. (b) Environmental conditions during the measurement, red curve: temperature measured on the 3.5-km fiber link spool; orange curve: temperature measured inside the enclosure. (c) Black curve: timing jitter spectral density and single-sideband phase noise (scaled at a 10 GHz carrier) from 1.4 μHz up to 1 MHz; red curve: its integrated jitter from frequency f up to 1 MHz.

ISBN 978-3-95450-134-2

The complete jitter spectral density of the link stabilization and its integrated jitter are shown in Fig. 3(c) (black and red curves respectively). The spectrum from 1 Hz up to 1 MHz is taken with a signal source analyzer (SSA) from the out-of-loop FC-BOC; whereas, the spectrum below 1 Hz is obtained by taking the Fourier transformation of the residual drift data shown in 3(a). The total jitter above 1 Hz is kept below 0.7 fs RMS, whereas the daily temperature fluctuations cause considerable jitter as can be seen from the frequency range below 1 mHz (red curve, Fig. 3(c)). Nevertheless, phase noise of only -20 dBc/Hz at an offset frequency of 2 μHz from a 10-GHz carrier is achieved and the total integrated jitter from 2 μHz up to 1 MHz is only 3 fs (± 0.18 fs) RMS which is more than sufficient for an efficient FEL synchronization.

CONCLUSION

In summary, we have successfully implemented a complete fiber-optic timing distribution system, which can be used for precise and long-term stable FEL synchronization.

We have demonstrated timing stabilization of a 3.5-km long fiber link using completely fiber-coupled elements. The out-of-loop measurement shows only 0.7-fs RMS link jitter integrated from 1 Hz to 1 MHz and 3.3-fs RMS residual drift below 1 Hz over 200 hours of continuous operation. Sub-fs precision over longer time intervals has been hampered by environmental fluctuations introducing timing detection errors via the uncompensated reference fiber arms. Local temperature stabilization of these reference arms would alleviate this effect and deliver better precision. Furthermore, the current efficiency of the FC-BOCs is limited by excess SH coupling loss, but still delivers a sensitivity comparable to the bulk-optic BOCs. The next generation device will include an integrated WDM to eliminate the coupling problem, thereby increasing the performance by an order of magnitude. Nevertheless, the current system based on FC-BOCs and PM fiber elements provides easy-to-implement, alignment-free, long-term stable, few-fs precision timing distribution under normal laboratory conditions. We believe that the demonstrated all-fiber timing distribution system can easily be deployed to an operating FEL, helping to both monitor and control electron bunch creation and fs X-ray pulse generation, to ultimately push the limits of spatially and temporally resolved imaging of molecular dynamics.

ACKNOWLEDGMENT

The authors acknowledge financial support by the Cluster of Excellence: The Hamburg Centre for Ultrafast Imaging-Structure, Dynamics and Control of Matter at the Atomic Scale of the Deutsche Forschungsgemeinschaft.

REFERENCES

[1] M. Altarelli, R. Brinkmann, M. Chergui, W. Decking, B. Dobson, S. Düsterer, G. Grübel, W. Graeff, H. Graafsma, and J. Hajdu, *XFEL: The European X-Ray Free-Electron Laser. Technical Design Report* (DESY, 2006).

[2] Stohr, J. Linac Coherent Light Source II (LCLS-II) Conceptual Design Report. No. SLAC-R-978. (SLAC, 2011).

[3] J. Kim, J. A. Cox, J. Chen, and F. X. Kärtner, "Drift-free femtosecond timing synchronization of remote optical and microwave sources," *Nature Photon.* **2**, 733-736 (2008).

[4] S. Schulz, I. Grguraš, C. Behrens, H. Bromberger, J. T. Costello, M. K. Czwalinna, M. Felber, M. C. Hoffmann, M. Ilchen, H. Y. Liu, T. Mazza, M. Meyer, S. Pfeiffer, P. Prędki, S. Schefer, C. Schmidt, U. Wegner, H. Schlarb, A. L. Cavalieri, "Femtosecond all-optical synchronization of an X-ray free-electron laser," *Nature Commun.* **6**, 6852 (2015).

[5] M. Y. Peng, P. T. Callahan, A. H. Nejadmalayeri, S. Valente, M. Xin, L. Grüner-Nielsen, E. M. Monberg, M. Yan, J. M. Fini, and F. X. Kärtner, "Long-term stable, sub-femtosecond timing distribution via a 1.2-km polarization-maintaining fiber link: approaching 10^{-21} link stability," *Opt. Express* **21**, 19982-19989 (2013).

[6] M. Xin, K. Şafak, M. Y. Peng, P. T. Callahan, F. X. Kärtner, "One-femtosecond, long-term stable remote laser synchronization over a 3.5-km fiber link," *Opt. Express* **22**, 14904-14912 (2014).

[7] M. Y. Peng, A. Kalaydzhyan, F. X. Kärtner, "Balanced optical-microwave phase detector for sub-femtosecond optical-RF synchronization," *Opt. Express* **22**, 27102-27111 (2014).

[8] A. J. Benedick, J. G. Fujimoto, and F. X. Kärtner, "Optical flywheels with attosecond jitter," *Nature Photon.* **6**, 97–100 (2012).

[9] A. H. Nejadmalayeri, F. N. C. Wong, T. D. Roberts, P. Battle, and F. X. Kärtner, "Guided wave optics in periodically poled KTP: quadratic nonlinearity and prospects for attosecond jitter characterization," *Opt. Lett.* **34**, 2522–2524 (2009).

[10] P. T. Callahan, K. Şafak, P. Battle, T. D. Roberts, F. X. Kärtner, "Fiber-coupled balanced optical cross-correlator using PPKTP waveguides," *Opt. Express* **22**, 9749-9758 (2014).

ISBN 978-3-95450-134-2

INFLUENCE OF ENVIRONMENT CHANGES ON LIBERA SYNC 3 LONG-TERM STABILITY

S. Zorzut, M. Cargnelutti, Instrumentation Technologies, Solkan, Slovenia
S.G. Hunziker, Paul Scherrer Institut, Villigen, Switzerland

Abstract

Libera Sync 3 is intended to be used as a reference clock transfer system in the latest fourth generation light sources where the required long-term stability is in the range of a few tens of femtoseconds of drift per day [1]. The system has an outstanding added jitter performance below 4 fs in the 10 Hz to 10 MHz frequency range. The system has been developed in collaboration with the Paul Scherrer Institute (PSI) and first units are already installed in the SwissFEL machine. In this article we present the influence of temperature and humidity changes on the long-term phase stability of the system.

INTRODUCTION

Libera Sync 3 solution is based on a continuous wave (CW) modulation of an optical carrier in which phase detection and stabilization are done in the radio frequency (RF) domain [2]. The system is composed of a transmitter and a receiver units (Figure 1) connected by two optical fiber links that are laid in the installation tunnel as it is depicted in Figure 2. Additional Ethernet connection is used for data exchange between the units and for remote monitoring and control of Libera Sync 3.

Figure 1: Libera Sync 3 transmitter and receiver units.

The two optical fiber links are used in order to overcome optical limitations, mainly due to the Rayleigh backscattering effect [3, 4]. One fiber is used to transfer a low-noise signal while the second is used to transfer a low-drift reference signal.

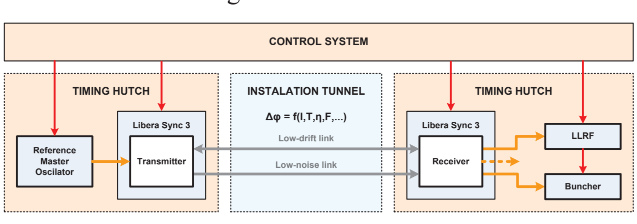

Figure 2: Installation of Libera Sync 3 system in the accelerator environment.

Libera Sync 3 compensates both the phase drifts in the electronics and in the low-drift optical link. All the components outside the phase compensation loops are sensitive to environmental changes, especially temperature and humidity changes. To reduce such influences different compensation techniques like thermal stabilization of critical components and usage of thermally compensated materials are applied, but nevertheless some residual sensitivity to environmental changes still exist.

PERFORMANCE MEASUREMENTS

Jitter and long term stability are two key performance parameters for Libera Sync 3.

Jitter Performance

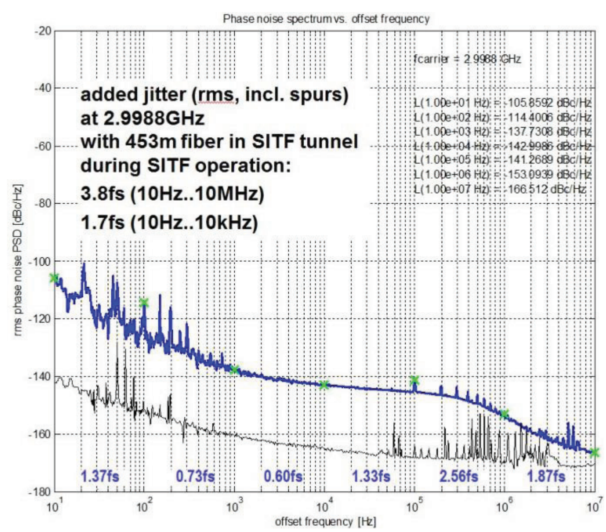

Figure 3: Libera Sync 3 added phase noise and jitter. The black curve shows the limit of the measuring setup.

Figure 3 shows Libera Sync 3 measured phase noise and jitter at 2998.8 MHz that was done at PSI. The added jitter in the frequency range from 10 Hz to10 MHz is 3.8 fs.

Long-term Phase Stability

The long-term phase stability of the Libera Sync 3 was measured using a standalone phase detector unit which compared the output RF signal from the Libera Sync 3 system with the reference signal. The drift of setup itself is estimated to be on the order of a few femtoseconds peak-to-peak per day. Figure 4 shows block diagram of the measurement setup.

ISBN 978-3-95450-134-2

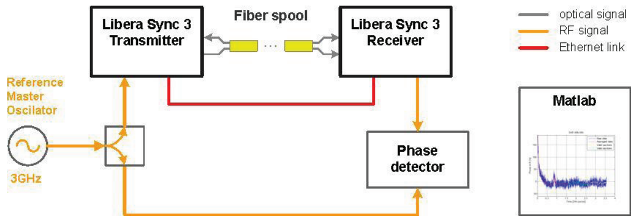

Figure 4: Phase drift measurement setup.

Figure 5 shows typical long-term phase drift of one of the Libera Sync 3 systems compared to the environmental conditions the system has been exposed to. After the installation, Libera Sync 3 and all RF cables normally require a couple of days to relax and stabilize. Typical long-term phase stability of Libera Sync 3 system is in the range of 10 to 30 femtoseconds peak to peak over one day of operation for environmental changes that are within specification (±1 °C and ±5 % RH).

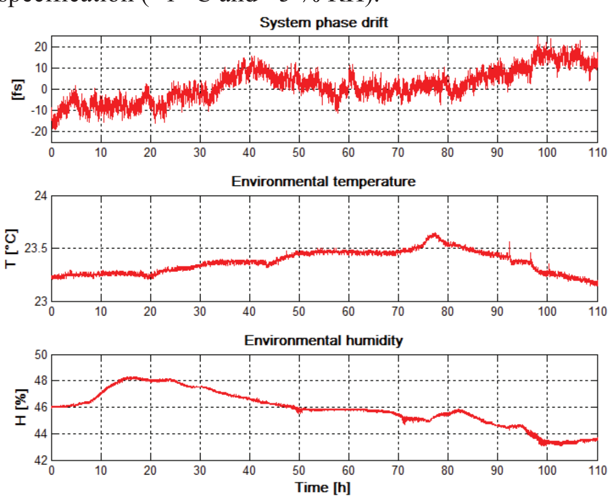

Figure 5: System phase drift and changes in environmental temperature and humidity.

The sensitivity of the Libera Sync 3 system to temperature and humidity changes was measured using environmental test chamber. RF generator, long-term stable phase detector and temperature stabilized RF splitter were placed outside the environmental test chamber as it is depicted in Figure 6. For all the RF connections temperature compensated RF cables with the temperature dependence in the range of some 10 fs/m/K were used. Length of all RF cables inside the chamber was approximately 1 m.

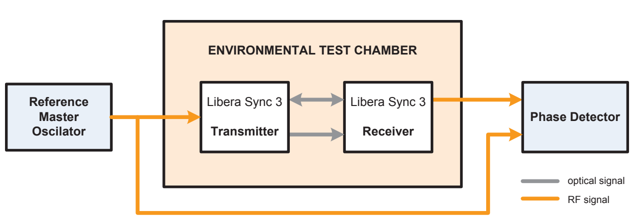

Figure 6: Temperature and humidity dependence measurement setup.

Figure 7 shows phase drift of first Libera sync 3 system in relation to trapezoidal changes in temperature and humidity. Temperature dependence is arround 25 fs/°C. System responded to humidity change with some delay. 20 % change in the environmental humidity caused 100 fs of phase drift.

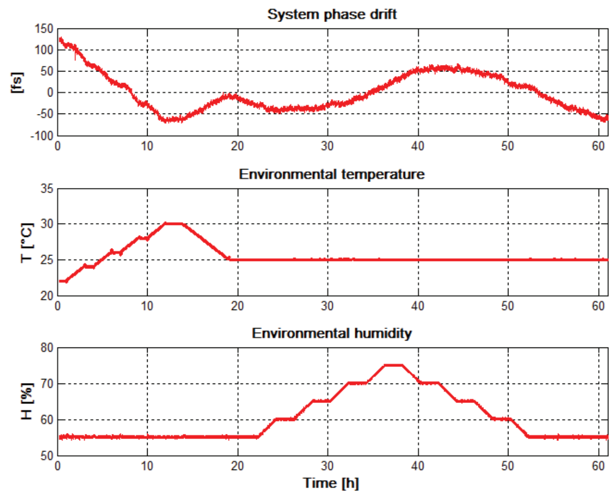

Figure 7: Libera Sync 3 long term phase drift and temperature and humidity changes.

Figure 8 shows the step response of second Libera Sync 3 system to humidity changes. Step change in environmental humidity caused some spikes in environmental temperature and some of them are noticed in the system phase drift too. The Libera Sync 3 system adapts to new conditions in 2 to 3 hours after humidity step change has been applied. Jump from 50 % to 60 % in environmental humidity caused 70 fs of systems phase drift while jump in humidity from 70 % to 80 % caused 110 fs of systems phase drift. Humidity dependence increases with theabsolute value of it.

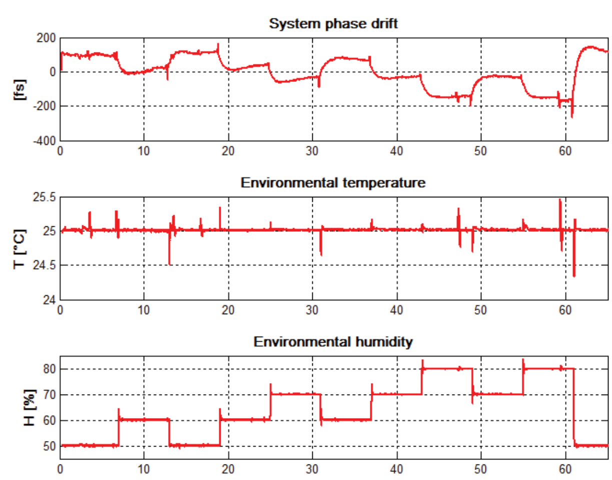

Figure 8: Libera Sync 3 phase drift response to step changes in environmental humidity.

ISBN 978-3-95450-134-2

Additional long-term performance measurements were done. In this case Libera Sync 3 system was removed from the environmental test chamber and only approximately 1 m of connecting RF cables remained inside the chamber. Figure 9 shows measured setup phase drift for the same humidity profile inside the chamber as it was used in previous case. Beside RF cables that are susceptible to environmental changes all other instruments that are outside test chamber are also exposed to some environmental changes that chamber is introducing to the room where it is located. A jump from 50 % to 60 % in humidity caused a 20-30 fs phase drift while a jump in humidity from 70 % to 80 % caused a 40-50 fs of setup phase drift. The correlation between humidity profile and phase drift measurement is not as obvious as in previous measurements.

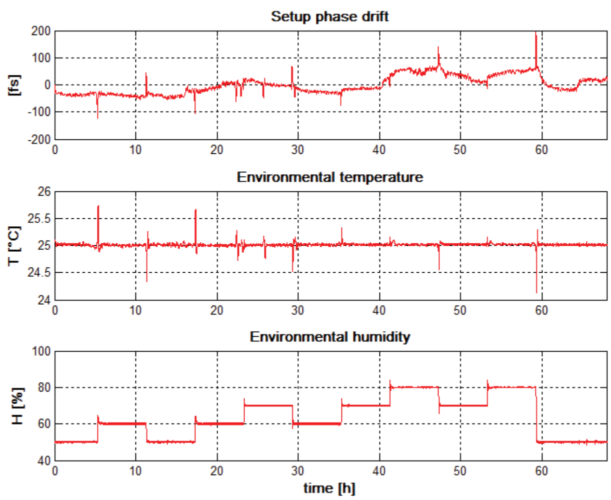

Figure 9: Setup phase drift.

CONCLUSION

In the presented paper one Libera Sync 3 system was exposed to trapezoidal changes in environmental temperature and humidity and one to the step changes in environmental humidity. The system adapts well on smooth changes in temperature and humidity while step changes introduce some transient response in sytems performance that settles down in 2 to 3 hours.

The presented measurements include the contribution of the RF cables inside the chamber that were exposed to the same environment changes as the system itself. Furthermore all the instruments and cables outside the chamber were also exposed to some environment disturbances that chamber caused to the room where it is installed. The estimation how much the testing setup contributed to the Libera Sync 3 long-term drift performance can be seen in the last measurement. The measurement error can be as high as 30 % of the measured value. This gives an insight about the complexity of the presented long-term measurements.

Libera Sync 3 system needs moderately stable environment to reach its nominal performance. The long term measurements of other Libera Sync 3 systems confirm these observations. On the other hand additional and improved measurements of systems dependence to environmental changes need to be performed in order to cancel out measurement uncertainty and get better statistics.

REFERENCES

[1] V. Schlott *et al.*, “Reference Distribution System for SwissFEL”, Libera Workshop, 2012.

[2] M. Vidmar, J. Tratnik, and P.L. Lemut, “Chasing Femtoseconds – How Accelerators Can Benefit from Economies of Scale in Other Industries”, in *Proc. IPAC’11*, San Sebastián, Spain, Sep. 2011, paper WEIB01, pp. 1973-1976.

[3] P. Orel, S. Zorzut *et al.*, “Next Generation CW Reference Clock Transfer System with Femtosecond Stability”, in *Proc. NAPAC’13*, Pasadena, CA, USA, Sep.-Oct. 2013, paper THPMA04, pp. 1358-1360.

[4] P. Orel *et al.*, “Test Results of the Libera Sync 3 CW Reference Clock Transfer System”, in *Proc. IPAC'14*, paper TUPRI079, pp. 1751-1753.

ISBN 978-3-95450-134-2

A LASER HEATER FOR CLARA

S. Spampinati, University of Liverpool and The Cockcroft Institute, Warrington, Cheshire, U.K.
B.D.Muratori, N.R. Thompson, P.H.Williams, ASTeC, Daresbury Laboratory, Warrington, Cheshire, U.K.

Abstract

CLARA is a new FEL test facility, being developed at STFC Daresbury Laboratory in UK, based on a high brightness electron linac. The electron beam of CLARA can potentially be affected by the longitudinal microbunching instability leading to a degradation of the beam quality. The inclusion of a laser heater in the linac design can allow control of the microbunching instability, the study of microbunching and deliberate increase of the final energy spread to study energy spread requirements of the FEL schemes tested at CLARA. We present the initial design and layout of the laser heater system for CLARA and its expected performance.

INTRODUCTION

CLARA (Compact Linear Accelerator for Research and Applications) is a proposed 250MeV, 100-400nm FEL test facility at Daresbury Laboratory [1]. The purpose of CLARA is to test, explore and ultimately validate new schemes for FEL light generation in areas such as ultra-short pulse generation, temporal coherence and pulse-tailoring. The accelerator itself will consist of 4 S-Band normal conducting linear accelerators with a medium-energy variable bunch compression scheme, feeding into a flexible arrangement of FEL modulators and radiators. For seeding purposes the accelerator includes a pre-FEL dogleg where modulated laser light can be introduced. The accelerator will be driven by a high rep-rate RF photo-cathode S-Band electron gun, operating in single bunch mode at up-to 100Hz, and with bunch charges up-to 250pC. Peak currents at the FEL are expected to be in the 500A range running the linac with the magnetic bunch compressor. An increased current in the 1-2 KA range can be obtained through the use of a velocity-bunching scheme in the first two linac structures [2]. The CLARA linac is potentially affected by the longitudinal microbunching instability (MBI) [3-5], as are other accelerators that drive high gain free electron laser (FEL) facilities [6,7], that produce short wavelength (~1-5µm) energy and current modulations. These can both degrade the FEL spectrum and reduce the power by increasing the slice energy spread. This instability is presumed to start at the photoinjector exit growing from a pure density modulation caused by shot noise and/or unwanted modulations in the photoinjector laser temporal profile. As the electron beam travels along the linac to reach the first bunch compressor (BC1), the density modulation leads to an energy modulation via longitudinal space charge. The resultant energy modulations are then transformed into higher density modulations by the bunch compressor. The increased current non-uniformity leads to further energy modulations along the rest of the linac. Coherent synchrotron radiation in the bunch compressor can further enhance these energy and density modulations [8,9]. The main solution to prevent MBI, used in several FEL facilities, is the laser heater (LH) [10,11].

A laser heater consists of a short, planar undulator located in a magnetic chicane where an external infrared laser pulse is superimposed temporally and spatially over the electron beam. The electron-laser interaction within the undulator produces an energy modulation on a longitudinal scale length corresponding to the laser wavelength.

The second half of the LH chicane smears the energy modulation in time, leaving the beam with an almost pure incoherent energy spread. This controllable incoherent energy spread suppresses further MBI growth via energy Landau damping in the bunch compressor. A layout of a laser heater is shown in Fig. 1.

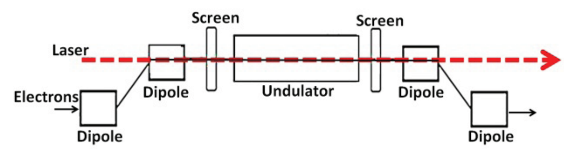

Figure 1: Laser heater layout.

The presence of the laser heater in a test facility like CLARA could be exploited to study further some less explored aspects of MBI such as the microbunching induced by the laser heater chicane and the MB competition between different sections of the accelerator [12].

The laser heater can also be used to modulate the electron beam energy spread to control the FEL temporal and spectral properties [13] or to deliberately increase of the final energy spread to study energy spread requirements of the FEL schemes tested at CLARA. The laser heater chicane could be also used to implement the diagnostics presented in [14]. These are all possible experiments of relevance to future FEL facilities. Consequently a space for a laser heater system has been left in the linac layout. Due to space constraints and to the necessity to avoid long strait sections at low energy the more convenient location for the laser heater is just before the bunch compressor at a beam energy of 125-210 MeV. In this case the beam present a significant energy chirp (~2%) and this is a difference respect to other facility [6,7]. The effect of the chirp on the laser heater will be analysed.

After the first acceleration stage a set of 4 quadrupoles allows matching of the optical functions into the laser heater chicane and 4 additional quadrupoles follow the

ISBN 978-3-95450-134-2

LH chicane to control the matching in the bunch compressor region. The values of the basic parameters of the electron beam in the laser heater region are reported in table 1.

Table 1: Electron Beam Parameters

Parameter	Value	Unit
Energy	125-210	MeV
Pulse duration	4-6	ps
Chirp	<2	%
Slice energy spread	3	keV
Emittance	0.6	mm·µrad
σ_x, σ_y	220	µm
$\sigma_x^{'}, \sigma_y^{'}$	11	µrad

SYSTEM DESCRIPTION

The laser pulse used for the laser heater could be a small portion of the photocathode infrared drive laser picked up just before the harmonic up-conversion to UV, similar to systems installed in other facilities [6,7]. The laser pulse has to be stretched to be 2-3 times longer than the electron beam. Pulse energy of 150-200 µJ should be available.

The chicane has to provide enough room for the insertion of the electron beam on the laser path and an effective smearing of the time energy correlation induced by the laser. The R_{56} and the dispersion of the chicane have to be kept small possible as the beam acquires a chirp.

A possible design of the chicane has bending angles of 4.5 degrees, a separation between the first and the second dipole as between the third and fourth dipole of 30 cm, a dipole length of 10 cm and a total chicane length of 2,0-2,7 m. The maximum dispersion (in the center of the chicane) and the R_{56} of this chicane are 4.5 mm and 31 mm, respectively. This design provides a horizontal trajectory bump of 3.1 cm, sufficient to overlap the laser and the electron beam, and a good smearing of the energy modulation at the laser wavelength. This smearing occurs because the path length, from the chicane center (where the energy modulation is induced) to the chicane end, depends on the electron's horizontal divergence trough the transport matrix element R_{52}. Therefore, the energy/position correlation, induced in the undulator, is smeared if the following relation is satisfied

$$\left|R_{52}\cdot\sigma_{x^{'}}\right| = \left|\eta_{\max}\cdot\sigma_{x^{'}}\right| > \frac{\gamma_r}{2\pi} \qquad (1)$$

with a dispersion value of 31 mm and an angular spread of 11 µrad, the rms temporal smearing is 340 nm, which is large compared to the reduced wavelength of 127 nm. Thus the 800 nm energy correlation is efficiently smeared.

The R_{56} of the laser heater chicane is around ten times smaller than the R_{56} of the bunch compressor chicane photoinjector accelerates approximately on crest), the laser heater chicane produces a small bunch compression (<10%) This effect is not critical for the subsequent compression. The laser heater undulator is a variable gap planar undulator composed of 7 periods of 5.5 cm each. This undulator is resonant with the 800 nm laser at beam energy of 150 MeV for a value of the strength parameter K equal to 1.2. Figure 2 shows the resonant K value as function of the beam energy. The minimum undulator gap required to have the resonance at 210 MeV is 24 mm (considering a remanent field of 1.25 T).

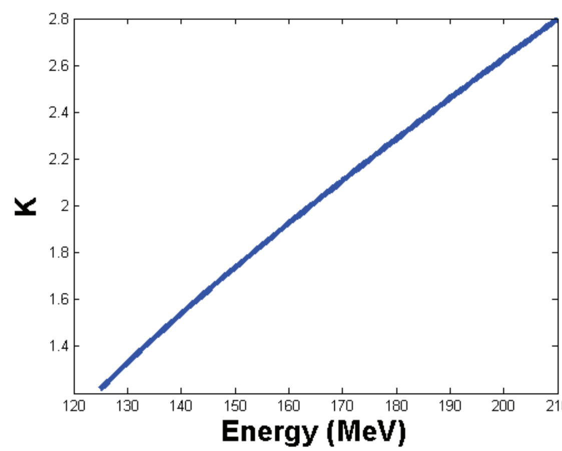

Figure 2: Resonant undulator factor K versus beam energy.

The basic parameters of laser, chicane and undulator are reported in table 2. It is possible to estimate the energy spread induced in the beam by the laser heater using the following formulas [4]

$$\sigma_\varepsilon = \int_0^{L_U}\sqrt{\frac{\sigma_r^2(x)}{2\cdot\left(\sigma_x^2+\sigma_r^2(x)\right)}}\sqrt{\frac{P_L}{P_0}}\cdot\frac{K}{\gamma_0}\frac{1}{\sigma_r(x)}m_0c^2[JJ]dx \qquad (2)$$

where σ_x and σ_r are the rms transverse dimension of the electron and the laser beam, respectively, L_U is the undulator length, γ_0 is the electron beam mean energy, P_L is the laser beam peak power, JJ is the undulator coupling factor [15] and P_0 = 8.9 GW. The integration is on the longitudinal undulator coordinate. Figure 3 reproduces the induced energy spread as function of the laser energy considering a laser pulse length (FWHM) of 15 ps.

ISBN 978-3-95450-134-2

Table 2: Laser Heater Parameters

Parameter	Value	Unit
Wavelength	800	nm
σ_x, σ_y	220	µm
Laser pulse duration	10-15	ps
Laser max energy	150-200	µJ
Bending angle	4.5	º
Dipole length	10	cm
Drift 1-2(3-4) dipoles	30	cm
Undulator period	5.5	cm
Number of period	7	

Figure 3 reproduces the induced energy spread as function of the laser energy considering a laser pulse length (FWHM) of 15 ps.

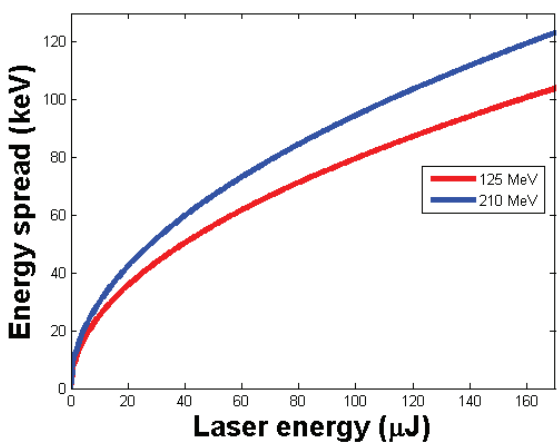

Figure 3: Slice energy spread versus Laser power.

Pulse energy of 0.3-0.5 µJ is required to have an energy spread of 5-10 keV and then suppress the microbunching. An Energy spread higher than this suppression threshold is amplified by bunch compression as the area of the longitudinal phase space is conserved. The maximum energy spread delivered at the end of the linac, is for a compression factor 5-8, 500-800 keV, equivalent to a relative energy spread of 0.2% -0.35% at 250 MeV.

This level of relative energy spread is comparable with the Pierce parameter [1,16] of CLARA and so is sufficient to affect the FEL process.

The level of heating provided by the system described is enough to study and suppress microbunching and to study the energy spread requirement of several FEL schemes tested at CLARA. Modulation of this large energy spread done with the technique described in [13] can modify the spectral and temporal properties of the FEL pulse.

Two CROMOX (Al2O3:Cr) screens, one on each side of the undulator, allow imaging both the laser beam and the electron beam in order to superimpose them transversely.

SIMULATIONS

Simulations including the beam energy modulation in the laser heater undulator and the transverse dynamic in the laser heater chicane have been performed with the code ELEGANT [17] to test the performance of system described above. A first set of simulations have been performed using the full beam distribution to study the effect of the energy chirp on the energy spread induced by the laser heater. 2M macro-particles have been used in these simulations. The phase space of the heated beam at the exit of the chicane is reproduced in fig. 4. The electron beam has a chirp of 2% and the laser pulse has a length (FWHM) of 15 ps and energy of 20 µJ.

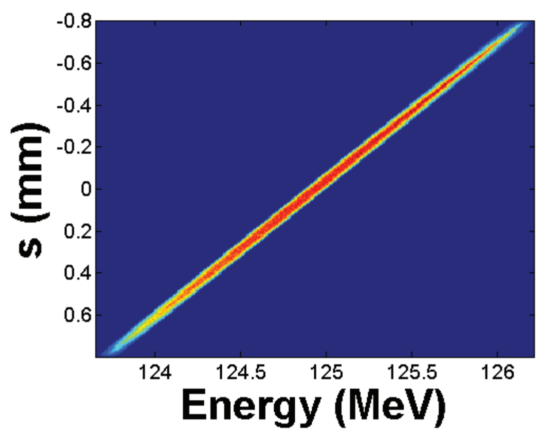

Figure 4: Electron beam phase space after the laser heater.

The slice energy spread along the beam is reproduced in fig 5. We see that the variation of the beam heating is about 20% on the total beam length and correspond to what is found experimentally in other working laser heaters where the beam has a more flat energy profile in the laser heater [7]. This seems to be a good level of uniformity.

Other simulations have been performed using only a small central part of the beam to study the smearing of the energy modulation in the second part of the chicane. Figure 6a and 6b reproduce the phase space after the laser heater undulator and after the chicane. In this case the pulse energy is 0.3 µJ. The energy spread induced in this case is 6 keV and should be close to the value that suppresses efficiently the microbunching instability. 2M macro-particles have been used in these simulations. We see that the energy correlation is removed be the beam dynamic in the second part of the chicane. We can see in fig 6c that the correlation is now transferred in the t-xp plane. This correlation can restore a microbunching on the laser wavelengths along the beam line in the point in which the transport element from the center of the chicane

ISBN 978-3-95450-134-2

goes to 0. This transient micobunching can induce a certain level of energy spread [6]. This effect is strongly depended by the optics from the laser heater to the bunch compressor [6,12]. In the bunch compressor any correlation is removed by the strong R_{56} of the chicane. The optics from the laser heater to the bunch compressor should avoid waist in the x plane between the laser heater and the bunch compressor.

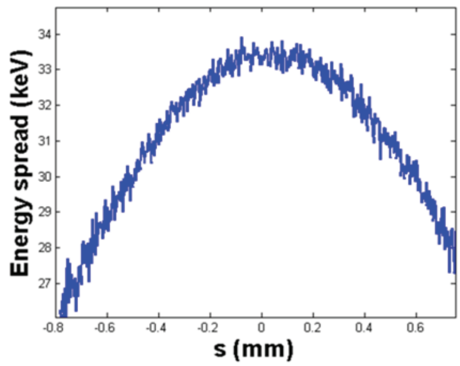

Figure 5: Energy spread after the laser heater.

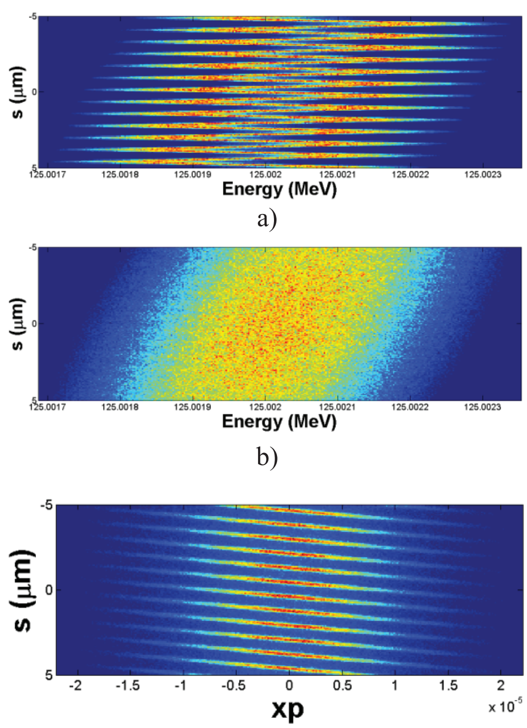

a)

b)

c)

Figure 6: a) Phase space in the center of the chicane after the undulator. b) Phase space after the chicane. c) *t-xp* correlation after the chicane.

CONCLUSION

We have presented a possible design of the CLARA laser heater and simulations of its operation. The level of heating provided by this design is enough to study and suppress microbunching and to study the energy spread requirement of the several FEL schemes tested at CLARA. The homogeneity of the heating along the beam is good despite the presence of the chirp used to compress the beam.

REFERENCES

[1] J. A. Clarke et al, JINST 9 T05001 (2014).
[2] M.Ferrario et al. Phys. Rev. Lett. 104, 054801 (2010).
[3] E.L. Saldin, E.A. Schneidmiller, and M.V. Yurkov, Nucl. Instrum. Methods Phys. Res. A 490, 1(2002).
[4] T. Shaftan and Z. Huang, Phys. Rev. ST Accel. Beams 7, 080702 (2004).
[5] S. Seletskiy et al. Phys. Rev. ST Accel. Beams 14, 110701 (2011).
[6] Z. Huang et al., Phys. Rev. ST Accel. Beams 13, 020703 (2010).
[7] S. Spampinati et al., Phys. Rev. ST Accel. Beams 17, 120705 (2014).
[8] T. Limberg, P. Piot, and E. A. Schneidmiller, Nucl. Instrum. Methods Phys. Res., Sect. A 475, 353 (2001).
[9] S. Heifets, S. Stupakov, and S. Krinsky, Phys. Rev. ST Accel. Beams 5, 064401 (2002).
[10] E. L. Saldin, E. A. Schneidmiller, and M. V. Yurkov, Nucl. Instrum. Methods Phys. Res., Sect. A 528, 355 (2004).
[11] Z. Huang, M. Borland, P. Emma, J. Wu, C. Limborg, G. Stupakov, and J. Welch, Phys. Rev. ST Accel. Beams 7, 074401 (2004).
[12] D. Ratner at al Phys. Rev. ST Accel. Beams 18, 030704 (2015).
[13] E. Roussel et al. "Influence of a non-uniform longitudinal heating brightness electron beams for FEL", proccedings of IPAC 2015.
[14] R. Fiorito et al., Phys. Rev. ST Accel. Beams 17, 122803 (2014).
[15] W. B. Colson, IEEE J. Quantum Electron. 17, 1417 (1981).
[16] R. Bonifacio, C. Pellegrini, and L. Narducci, Opt. Commun. 50, 373 (1984).
[17] M. Borland, ANL/APS Report No. LS-287 (2000).

ISBN 978-3-95450-134-2

THE BINP HLS TO MEASUREMENT VERTICAL CHANGES ON PAL-XFEL BUILDINGS AND GROUND*

Hyojin Choi†, Kwang Won Seo, Kyehwan Gil, Seung Hwan Kim, Heung-Sik Kang
Department of Accelerator, PAL-XFEL, Pohang, Korea

Introduction

General matters about the hydrostatic leveling system (HLS) to be installed in PAL-XFEL were explained in Reference [1]. This paper will introduce principles of measuring water pipes that are references of HLS and Ultrasonic-type HLS of the Budker Institute of Nuclear Physics (BINP).

WATER VOLUME CHANGING BY TIDAL EFFECTS

The strength of gravity of planets in the solar system follows Isaac Newton's law of gravity and the superposition principle. There are three elements changing the gravity of the earth: the earth's orbit, the moon's orbit and leaning of the earth's rotational axis. As shown by Figure 1, the orbit of the earth circling around the sun is oval. The sun's tide generating force changes according to positions of the earth's orbit.

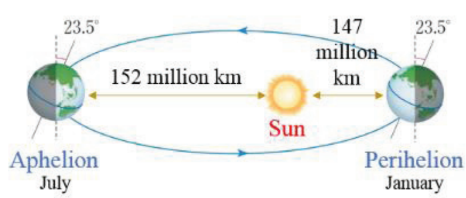

Figure 1: Earth's orbit.

As shown by Figure 2, the effects of tide generating force appear due to complex movements, such as the earth's rotation, the moon's orbit and the leaning of the moon's orbital plane. It is very difficult to gain theoretical access to them and they can be various depending on factors (such as composition of the continental ground, latitude, longitude and altitude) affecting regions whose tide generating force is to be measured, so it is difficult to analyze them. The effects of the tide generating force changing over time lead to changes in gravity and in consequence the earth's land and sea affected by gravity display tidal phenomena over time.

The tide generating force can be measured using an earth tide meter or a gravity meter. Figure 3 shows changes in the tide generating force measured in Korea using an earth tide meter. Changes in the tide generating force cause changes in the water volume and they appear as changes in the water height inside a water pipe in the process of measuring HLS. As explained in Reference [1], water produces volume changes because of various outside effects in addition to the tide generating force. In the case of water in a glass, the water height changes about 2μm/deg/cm because of temperature and the figure is about Max. 0.6μm/cm because of tides. There should be no temperature changes in order to observe the water height changing by tidal effects.

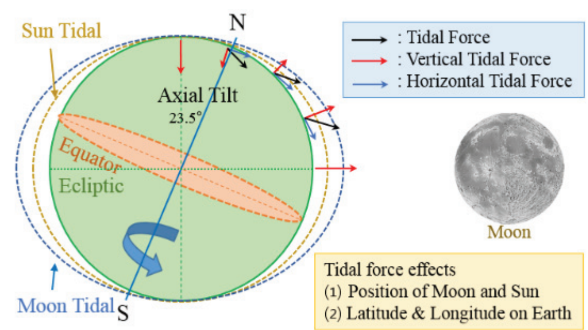

Figure 2: Distribution of the tidal force on the earth.

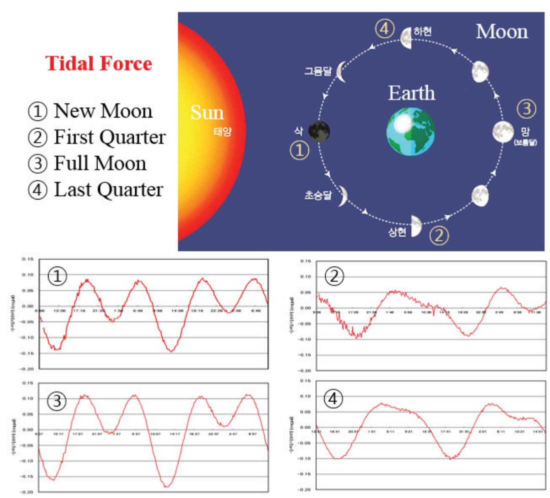

Figure 3: The tide generating force depending on positions of the sun and the moon.

Although the water volume inside a water pipe dynamically changes moment by moment due to temperature inside a tunnel and tides, the water height of the entire area of the water pipe will be maintained in the short term if the flow inside the water pipe is large enough. The space inside the water pipe is closed and hydrostatic levelling measurement is made under the condition where the amount of water is the same even if the water volume changes. As shown by Figure 4, water pipes are installed on the floor inside the tunnel. As long as an accelerator works, entries to the tunnel are prevented and there is no vibration caused by people.

*Work supported by Ministry of the Science, ICT and Future Planning
†choihyo@postech.ac.kr

ISBN 978-3-95450-134-2

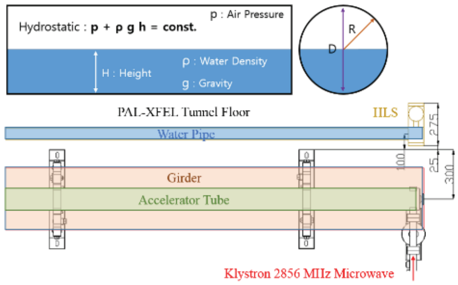

Figure 4: The position of water pipes inside the accelerator tunnel.

There should be sufficient water flow for all of the water inside the water pipes to maintain the same water surface. Figure 5 shows the diameter of a water pipe to secure proper flow in accordance with the length of the pipe. [2]

Distance (m)	Depth of water (m)	Period (sec)
1	0.0028	12
5	0.0053	44
10	0.0070	76
50	0.0133	277
100	0.0175	484
500	0.0334	1752
1000	0.0440	3050

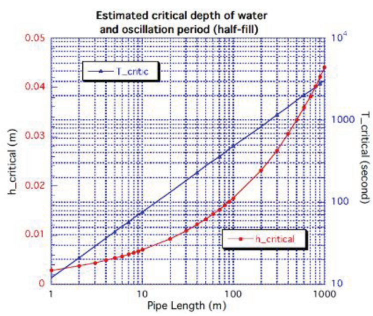

Figure 5: The critical (optimum) depth of water and the period of oscillation for different lengths of pipes in a half-filled system.

Figure 6 shows the length and diameter of water pipes to be installed in PAL-XFEL. The material of pipes is anti-corrosive stainless steel SUS304 whose surface was treated sanitarily. The right diameter of a pipe for the length of the pipe was calculated according to Figure 5 and then pipes whose diameter is close to the calculation result were selected among pipes commercially available.

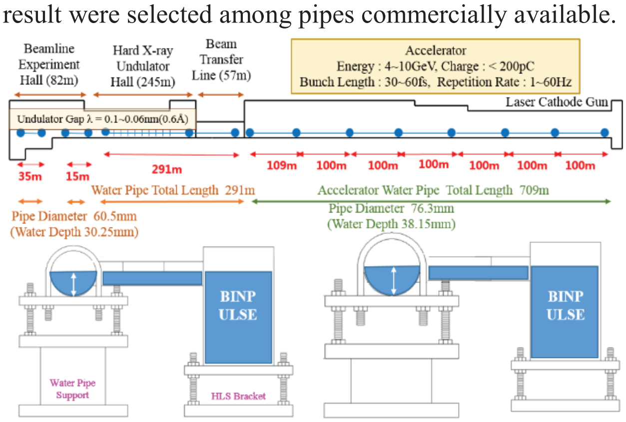

Figure 6: The length and diameter of a water pipe.

COMPOSITION OF BINP HLS AND PRINCIPLES OF MEASURING IT

A measurement concept of BINP HLS measuring the height of water using an ultrasonic transducer is shown in Figure 7. The transducer is H10KB3T (7MHz) used for ultrasonic flaw detectors made by GE Sensing & Inspection Technologies. The range that can be measured by the transducer is the far-field area. A reflector that adopts the role of an absolute ruler and the height of water surface can be measured correctly only when they are placed within the far-field area. [3] The height of the HLS bracket shown in Figure 6 should be adjusted properly so that the height of the water surface doesn't veer from the far field due to vertical changes in the building foundation. If there are serious vertical changes in the foundation, the water pipe support of Figure 6 should be adjusted too.

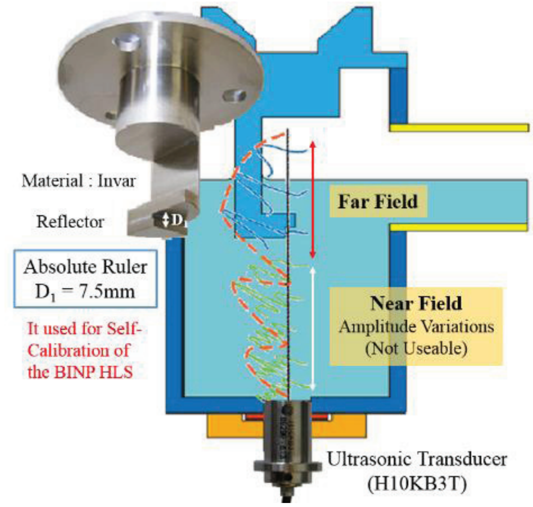

Figure 7: The HLS measurement concept using an ultrasonic transducer.

As shown by Figure 8, ultrasonic waves that take place in the transducer are reflected in the reflector and water surface and are conveyed to the transducer. Even when the performance of the transducer and water temperature change, the height of the water surface can be measured correctly because the time gap between Wave-t1 and Wave-t2 reflected by the absolute ruler (D1) is 7.5mm. Such a self-calibration function improves the accuracy and credibility in the measurement of BINP HLS.

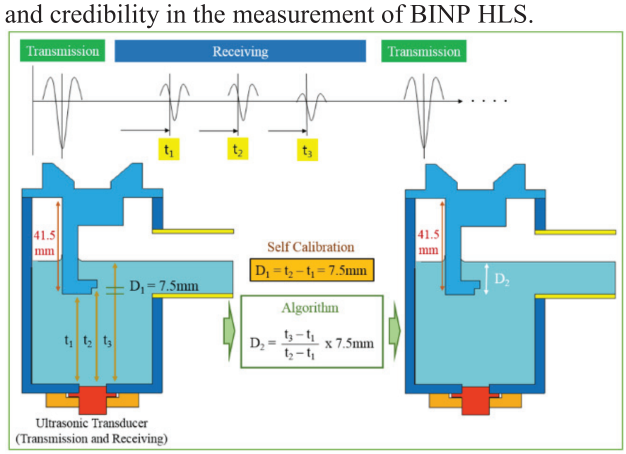

Figure 8: Measuring the height of water surface using ultrasonic waves.

Figure 9 shows a block diagram, an electronic circuit of BINP HLS. Reflected ultrasonic waves are recorded as time at the TDC (Time to digital converter) through a comparator. Timing jitters can occur at the system clock

ISBN 978-3-95450-134-2

8MHz of an electronic circuit or time delays can occur at a microcontroller, but these effects are equally applied to all return waves. As shown by Figure 8, timing jitter and time delay elements of the electronic circuit are removed with a formula [(t3-t1)/(t2-t1)] for calculating the length of D2. [4]

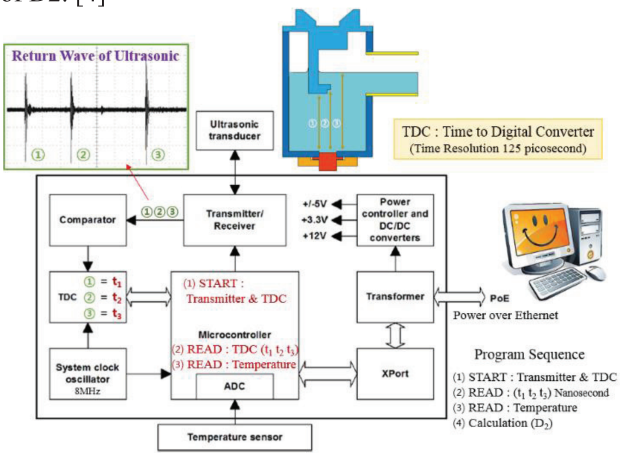

Figure 9: Block diagram of the ULSE Electronics.

The resolution for measuring the distance of HLS is determined by the sound velocity in water and TDC of an electronic circuit. The sound velocity is determined by the temperature of water and the time resolution of TDC is determined by a system clock 8MHz. Like Figure 10, the resolution for measuring the distance of BINP HLS is about 0.2μm.

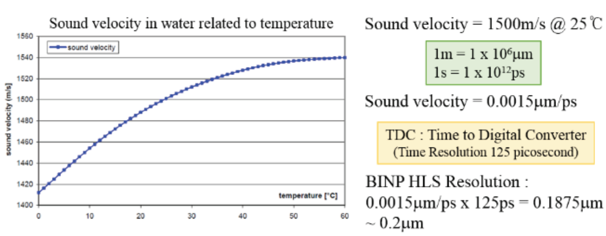

Figure 10: Resolution for measuring the distance of BINP HLS.

PAL-XFEL BUILDING FOUNDATION

The purpose of installing HLS is to continuously survey the vertical changes of a building and its foundation and record any changes. To analyse and understand the results of HLS measurement, people should know about the conditions of the building and its foundation. Conditions regarding the creation of the foundation of a PAL-XFEL building are shown in Figure 11. After deciding to construct a building at an altitude of 62 meters, earth at the altitude of 62 meters or higher was removed completely. In order not to construct the building on a weak foundation, the earth of the weathered zone, a weak foundation, was removed completely. After this, the space of the removed weak foundation was replaced with concrete to maintain an altitude of 62 meters. It did not pour the foundation piles for the foundation for enhanced bearing capacity due to construction of a PAL-XFEL building on the bedrock. Transformation of the building floor is connected with subsidence and upheaval of the foundation. Zones where the foundation is expected to change vertically can be found through continuously measuring vertical changes of the building floor using HLS. Measurement data of HLS is used for aligning accelerators.

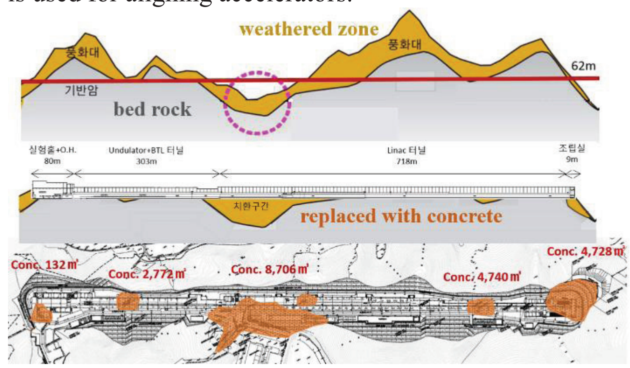

Figure 11: Conditions of creating the PAL-XFEL foundation.

BINP HLS TEST ON PAL-XFEL

Figure 12 shows the method of using BINP HLS and the result of testing ULSE 2 sets which was borrowed from BINP to learn about the operation. The tidal effect of the sun and moon could not be confirmed because of the changes in surrounding temperature (2.2 degrees). The tidal effect can be seen in HLS when the influence of surrounding temperature is less than the tidal effect.

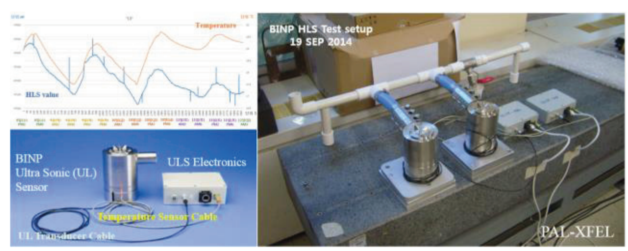

Figure 12: BINP ULSE Test on PAL-XFEL.

ACKNOWLEDGMENT

Thanks to Dr. A.G. Chupyra and Dr. M.N. Kondaurov of BINP for their technical support and cooperation on testing BINP HLS in PAL-XFEL.

REFERENCES

[1] H. Choi, et al., "Introduction to BINP HLS to Measure Vertical Changes on PAL-XFEL Buildings and Ground", Proc. of IPAC 2015, MOPTY028 (2015).
[2] C. Zhang, et al., "Primary Hydrokinetics Study and Experiment on the Hydrostatic Leveling System", Proc. of IWAA 2002, p. 2978, Spring-8, Japan, (2002).
[3] A.G. Chupyra, et al., "The Ultrasonic Level Sensors for Precise Alignment of Particle Accelerators and Storage Rings", Proc. of IWAA 2006, SLAC, USA (2006) paper FR004.
[4] A.G. Chupyra, et al., "BINP Capacitive and Ultrasonic Hydrostatic Level Sensors", Proc. of IWAA 2008, KEK, Tsukuba (2008), TU015, TU015.

ISBN 978-3-95450-134-2

THE DESIGN OF LOW NOISE MAGNET POWER SUPPLY*

K. H. Park#, S. H. Jeong, Y. G. Jung, D. E. Kim, H. S. Suh, H. G. Lee, S. B. Lee, B.G. Oh, W. S. Choi, I. S. Ko, PAL, POSTECH, Pohang, Korea

Abstract

The accelerator facility needs a high stable magnet power supply (MPS). The stability requirements of the some MPSs in accelerator facility were in the range of the ~10 ppm. There are many noise sources which affect the stability of the MPS. Thus the design of the MPS requests much attention on the noise reduction scheme from the design stage. The noise on the MPS divided into some sources such as the ripple voltage coming from rectifier on the DC link, switching noise from the high voltage switch, and so on. This paper dealt the ripple components analysis, oversampling converter and digital voltmeter for the high precision stability measurement.

INTRODUCTION

The stability of the magnet power supply (MPS) was related to the noise components generated by MPS itself. The sources to give the poor output stability of the MPS were divided into two types as ripple components and switching noise. The ripple components came from rectifier which inevitably generated by the harmonic components of the line frequency such as 60Hz, 120Hz and so on. And the other noises were developed at inter PCBs or cables between modules due to parasitic inductance and capacitance on fast rising and falling time of the pulse when switching state. The proper signal processing in digital and analogue to increase signal to noise ratio was needed to the high stability MPS.

This paper describes some design schemes that was implemented into the MPS were described such as ripple voltage analysis, and oversampling converter for high resolution. And this paper shows the working process of the dual slop integrator for analogue to digital converter (ADC). And the aperture time of the DVM3458A affects the measurement precision in the ~ppm range.

REDUCTION LINK VOLTAGE RIPPLE

The full wave rectifier of three-phase AC input of wye or delta-connection or both of them was composed for the DC link voltage of the MPS. The Fourier series expansion of the link voltage in the case of full wave rectifier of three phase AC line is given as the following equation

$$V_{link} = \frac{3\sqrt{3}}{\pi} V_m \left(1 - \sum_{k=1}^{\infty} \frac{2}{36k^2} \cos(6k\omega t)\right).$$

The spectrum of the V_{link} contains sixth multipole components of the line frequency. It is corresponded to 360 Hz in the case of the 60 Hz AC input. The switching frequency of 25 KHz of the MPS was much higher than the multipole components of 360 Hz, thus it was acted as sampling frequency while it satisfied the Nyquist sampling theorem as the following equation [1].

$$F_s \geq 2F_c,$$

where F_s is the sampling frequency and F_c is the highest frequency in the signal.

The FETs worked as analogue switch devices in the sampling process. The cut-off frequency of the output filter of the MPS was located around ~KHz, thus the rectified ripple components passed without any attenuation. Figure 1 showed the simulation results of the PSPICE for a three phase full rectifier. The ripple components of the link voltage were appeared at the output stage with 0.5 V_{pp}, which affected to the output stability about 10 mA_{pp} fluctuation with same frequency.

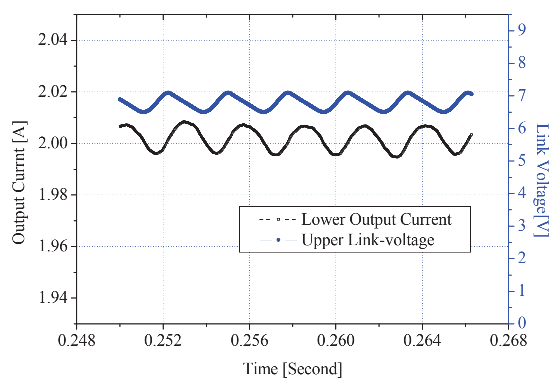

Figure 1: Ripple components on the output stage.

To reduce this effect of the ripple components, a proper low-pass filter should be configured into the input rectifier. The parallel damped filter was preferred to building the MPS as described in Ref. [2]. The cut-off frequency of the filter should be ranged ~10 Hz, that was dependent on the required stability.

OVERSAMOLING CONVERSION

Oversampling method represents that the ADC converts analogue signal into digital with a higher sampling rate than the required bandwidth of interest. This method combined with suitable digital signal processing like average and decimation is able to improve signal-to-noise ratio (SNR). With the improved SNR the effective bit resolution of ADC will be increased [3].

The MPS is designed by the switching mode thus it cannot be avoided switching noise generated during the switch transition. Furthermore, there are many other noise

*Work supported by Ministry of Science, ICT & Future Planning
#pkh@postech.ac.kr

ISBN 978-3-95450-134-2

sources in MPS introduced from DSP itself, induced noise voltage by the high current fluctuation, common mode noise from AC line, and etc.

All of these noises made the design of the high stable MPS difficult. Thus it was necessary to design hardware circuits in depth and to adapt suitable signal processing. The required current stability of the MPS was less than 10ppm. This means that the resolution of ADC for feedback control has to have higher than 17-bit.The switching frequency of the power converter of the MPS was 25 KHz. The ADC AD977 from the Analog Devices was adapted for the MPS which was specified 16-bit resolution, 200 KHz throughput, internal reference, etc. Two ADCs continuously sampled the output current with the same start of conversion clock of 200KHz.These sampled data were averaged and decimated in the field programmable gate array(FPGA) SPARTAN 3 comes from Xilinx Co. Whenever DSP requested the ADC data, FPGA sent them to DSP through SPI, which were calculated just before process. The DSP and FPGA were always synchronized by the time sharing access to the given clock period, thus there were no chance to loss the ADC data. Figure 2 showed the oversampling scheme applied into MPS.

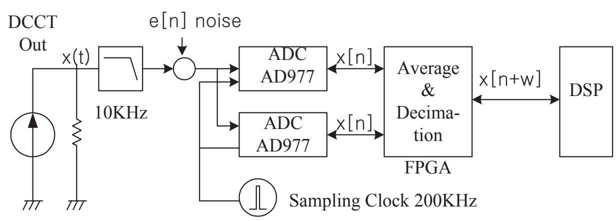

Figure 2: Oversampling and averaging to increase effective resolution.

In this case the oversampling factor k is 16. This will lead to improve SNR as following in Table 1.

Table 1: Oversampling Effectiveness

Factor k	SNR in dB	Extra bits
16	12	2.0

HIGH STABILITY MEASUREMENT

The required current stability of the MPS was less than 10 ppm. The digital volt meter (DVM) to measure the stability of the MPS has to have the high resolution up to about 8-digit.

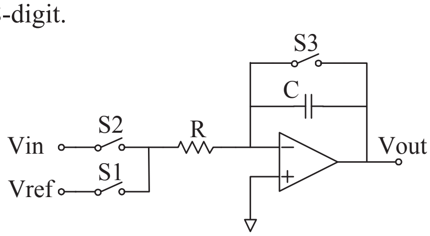

Figure 3: Dual-slop integrator circuits.

The DVM3458A from the Agilent was widely accepted for the stability measurement for the MPS. The DVM3458A uses basically the dual-slope AD converter to increase the resolution by the good noise rejection ratio [4]. Figure 3 showed a typical dual slope integrator which is the basic configuration of the dual-slope ADC. Its working process was described in Ref. [5]. Actual data conversion is accomplished in two phases: input signal integration and reference voltage de-integration. The first, the input voltage V_{in} is applied to the integrator with a fixed length of time t_u by closing the S2. Then output voltage was given as

$$V_{out}(t_u) = = -\frac{1}{RC} V_{in} t_u.$$

Next, V_{ref} with polarity opposite to that of V_{in} is connected by closing S1. Time counter was started at this time until the output of the integrator crosses through zero voltage. The typical waveform of the dual-slope was shown in Fig. 4.

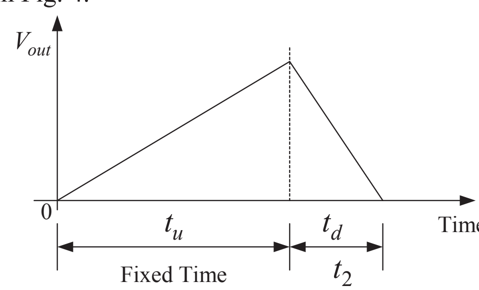

Figure 4: Dual-slope waveform.

This means that the counter contents are proportional to the unknown voltage V_{in}. The output voltage V_{out} at the t_2 was given as

$$V_{out}(t_2) = V_{out}(t_u) - \frac{1}{RC} V_{ref}(t_d) = 0.$$

Then the unknown input voltage V_{in} can be find by

$$V_{in} = -V_{ref}(t_d/t_u).$$

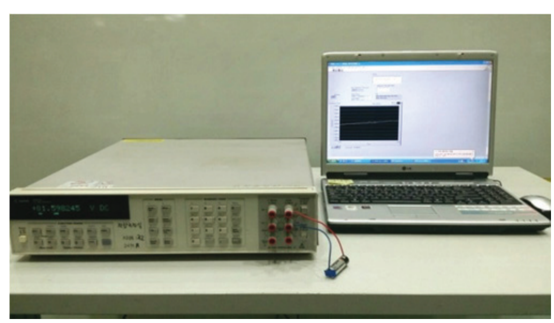

Figure 5: Test setup for the DVM with a battery input.

The DVM3458A has a function of choice for aperture time that is equal to the ADC integration time when direct current volt mode selected and it can be varied from 0.5 µs to 1 s. The default aperture time when power is on is 166.66 ms for 60 Hz AC line voltage. The DVM integrated the input signal thus input noise components averaged to be small during its aperture time. Figure 5

ISBN 978-3-95450-134-2

shows the DVM3458A to test the precision depending on the aperture time with battery input.

The DC battery voltage was measured with various aperture time of the DVM 3458A in the range from 1 μs to 100 ms. With the same conditions, the measured voltages to the battery have the different stability with the different aperture time as following table 2. To measure the a few ppm stability the aperture time should be larger than 10 ms. Figure 6 showed the stability measurement results at the aperture time of 100 ms.

Table 2: Stability Comparison with Various Aperture Time at the Battery Input

Aperture Time [ms]	0.001	0.01	0.1	1	10	100
Stability [ppm]	1000	250	40	20	2.5	1

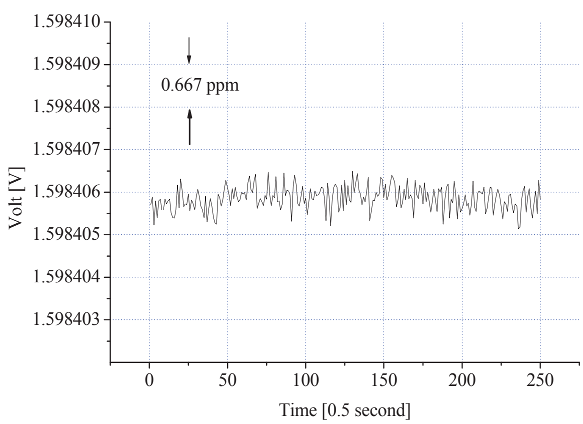

Figure 6: Stability test results at the aperture time of 100 ms.

EXPERIMENTAL RESULTS

The short term stability of the MPS was examined. Its stability was less than 3 ppm peak-to peak for 15 minutes shown in Figure 7.

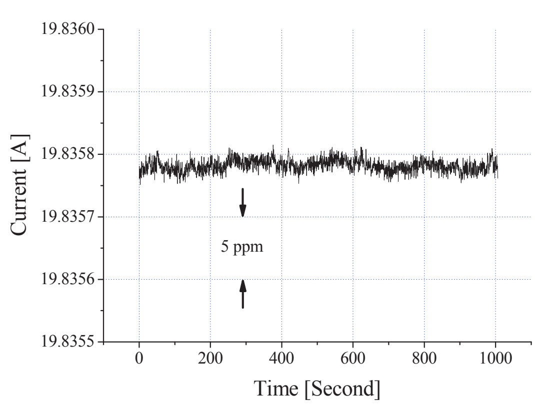

Figure 7: Short-term stability of the 20A bipolar power supply.

The stability variations as increase the output current were tested. The stabilities were become worse as output current increase as shown in Fig. 8.

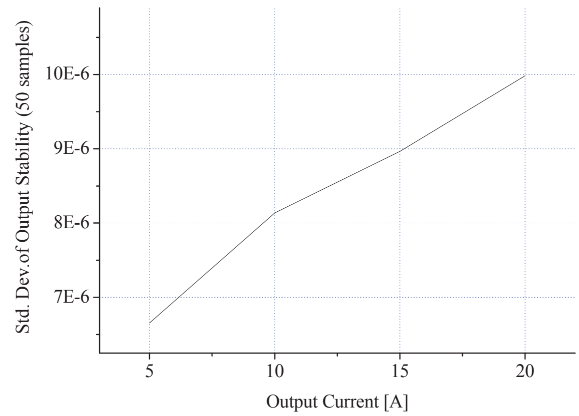

Figure 8: Stability variation on the output current.

CONCLUSION

This paper described the MPSs which had high stability for the output current. The ripple components of the rectified link voltage were affected the stability according to the sampling theory. Thus the ripple voltage should be attenuated by the filter which was cut-off frequency of 30 Hz. The DVM 3458A from the Agilent showed different measurement results depending on the aperture time selection with the battery input. This means that aperture time should be longer than 100 ms for 1 ppm stability guarantee.

The short term stability showed less than 3 ppm. The stability variation by the output current increase was tested. It showed that the output stability was become worse as increase output current.

REFERENCES

[1] P.P. Vaidyanathan, "Generalizations of the Sampling Theorem Seven Decades After Nyquist", IEEE Trans. on circuits and systems, Vol. 48, No. 9, p.1094 (2001)
[2] Rong Liang and Shashi B. Dewan, "A Low Ripple Power Supply for High Current Magnet Load", IEEE Trans. on Industry applications, Vol. 30, No. 4, p.1006 (1994)
[3] Oversampling Techniques using the TMS320C24x Family; http://www.ti.com
[4] Agilent Technologies 3458A Multimeter User's Guide; http://www.agilent.com
[5] AN1041: Understanding Integrating ADCs; http://www.maximintegrated.com

ISBN 978-3-95450-134-2

DESIGN, DEVELOPMENT AND TEST OF THE MAGNETS FOR PAL-XFEL*

Hyung Suck Suh, Bongi Oh, Dong Eon Kim, Heung-Sik Kang, Hong-Gi Lee, In Soo Ko, Ki-Hyeon Park, Moo Hyun Cho, Sang-Bong Lee, Seong Hun Jeong, Young-Gyu Jung
PAL, Pohang, Republic of Korea

Abstract

PAL-XFEL is now being constructed with the goal of 0.1 nm hard X-ray in Pohang, Korea. As the first phase we will construct 10 GeV linac, one hard X-ray and one soft X-ray beamlines which require 6 different families of 46 dipole magnets, 11 families of 209 quadrupole magnets, and 3 families of 48 corrector magnets. We have designed these magnets with considering the efficient production and the proper power supplies. This paper describes an outline of the design and test results of the magnets until now.

INTRODUCTION

The PAL(Pohang Accelerator Laboratory)-XFEL is a 0.1-nm hard X-ray FEL project starting from 2011. Three hard X-ray and two soft X-ray branches are planned. As the first phase of this project, one hard X-ray (HX1) and one soft X-ray (SX1) which consist of 51 dipole and 209 quadrupole magnets will be constructed [1].

We have designed all magnets on our own by using OPERA and ANSYS codes [2, 3]. Every magnet is designed to maintain the maximum temperature rise of coils below 20 K for 120% of the nominal currents. In the process of the design, it was helpful to parameterize the main variables of the magnets in a spread sheet for easy estimation by changing some parameter. Now we are manufacturing and testing the magnets. Two Hall probe measurement benches were used to measure the magnetic field for the dipole magnets and the quadrupole magnets respectively.

DIPOLE MAGNETS

The dipole magnets were classified into six kinds according to the pole gap, the effective magnetic length, and the maximum magnetic field. The results of the classification are listed in Table 1.

Most dipole magnets have the same pole gaps of 30 mm except D6 of 15 mm for the self-seeding. D1, D2, and D4 have H-type core shape, and D3, D6, and D7 have C-type. All dipole magnets of D1~D6 for the bunch compressor, the chicane, and the self-seeding have the trim coils with 1% of the main field.

The pole profiles of magnets are optimized by the small bumps at the tip of the pole for the field uniformity. The requirements for the field uniformity are different from each magnet.

Table 1: The Families of Dipole Magnets (D5 was replaced with D2.)

Family	Magnetic length [m]	Max. field [T]	Qty	Position
D1	0.20	0.80	6	BC1
D2	0.70	1.00	19	BC2,BC3, BAS1
D3	1.44	1.30	11	BAS2,3,4
D4	0.17	0.312	4	Laser Heater
D6	0.30	0.485	4	Self seeding
D7	0.75	1.164	2	Tune-up dump

We have tested all prototype dipole magnets. Most magnets satisfied the field requirements. But D1 and D7 didn't satisfy the field uniformity slightly. We have calculated the magnetic field by using B-H table of Chinese low carbon steel (DT4), and manufactured magnets by using the same materials. But a little difference between the calculated and measured field uniformities has arisen. So we used shims (10x10 mm^2 wide, 1mm thick, steel plates) to improve the field uniformity. The shims were placed on the chamfer sides of front and end sides of lower and upper poles. Figure 1 shows the field distribution of FEM model and the magnetic field measurement scene of D1.

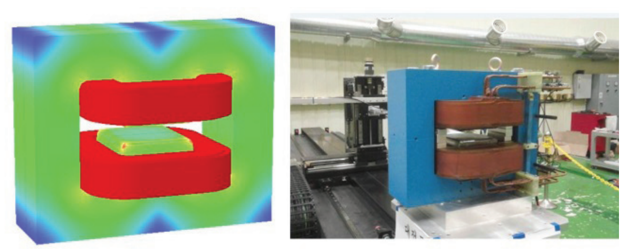

Figure 1: D1 dipole magnet (Left: magnetic field distribution of FEM model, Right: magnetic field measurement by Hall probe).

The field uniformities of D1 are shown in Figure 2, where the calculated one is drawn with a green dashed line, measured without shims with a blue dash-dot line, and measured with shims with a red line. The requirement of the 3-dimensional field uniformity is less than 1.0E-4 for |x| < 17 mm, and less than 5.0E-4 for |x| < 41 mm. And we confirmed that the field uniformities of field integral along straight line are very similar to that along the curved orbit.

ISBN 978-3-95450-134-2

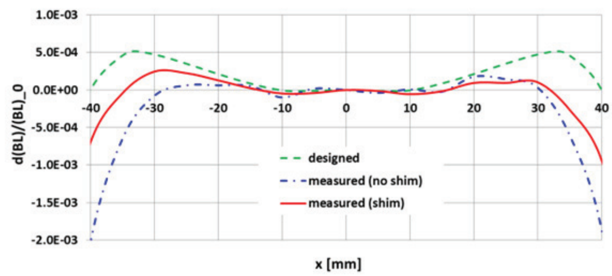

Figure 2: Magnetic field uniformity of D1 dipole magnet (green dashed line: designed, blue dash-dot line: measured without shim, red solid line: measured with shim), $\Delta(BL)/(BL)_0 < 5.0E-4$ for $|x| < 41$ mm.

The laminated cores are used for the magnets D2 and D3 which quantities are more than 10 magnets, and the solid cores are used for the rest of the dipole magnets which quantities are less than 10.

We measured D2 dipole magnet also. Figure 3 shows the magnetic field distribution of FEM model and the magnetic field measurement scene. Figure 4 shows the field uniformity of calculated and measured field integral. The requirement of the 3-dimensional field uniformity is less than 1.0E-4 for $|x| < 16$ mm, and less than 5.0E-4 for $|x| < 22$ mm.

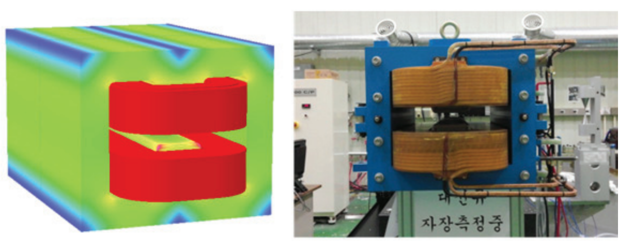

Figure 3: D2 dipole magnet (left: magnetic field distribution of FEM model, right: magnetic field measurement).

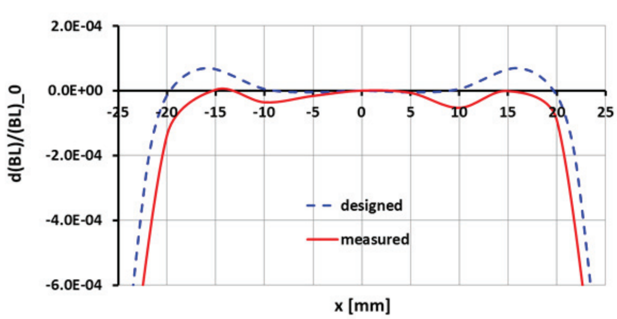

Figure 4: Field uniformity of D2 dipole magnet (blue dashed line: calculated, red line: measured), $\Delta(BL)/(BL)_0 < 5.0E-4$ for $|x| < 22$ mm.

QUADRUPOLE MAGNETS

The quadrupole magnets were classified into 11 kinds according to the aperture diameter, the effective length, and the maximum field gradient. The results of the classification are listed in Table 2.

Some quadrupole magnets (Q1, Q2, Q3, Q6, and Q9) have the horizontal and vertical steering fields for the bunch compressors and the inter-undulator.

Table 2: The Families of Quadrupole Magnets

Family	Aperture diameter [mm]	Magnetic length [m]	Max. gradient [T/m]	Qty
Q1	30	0.065	15	20
Q2	30	0.13	25	60
Q3	30	0.18	25	18
Q4	44	0.20	25	6
Q5	22	0.40	35	14
Q6	16	0.13	40	31
Q7	80	0.50	18	3
Q8	22	0.25	30	19
Q9	16	0.08	32	18
Q10	44	0.50	25	4
Q11	44	0.10	10	16

The multipole components were calculated by using an equation, the radial component: $B_r(r_0,\varphi) = \Sigma_n \{A_n \sin(n\varphi) + B_n \cos(n\varphi)\}$, where r_0 is the reference radius that is the good field radius. All magnets are optimized to have the relative multipole components less than 1.0E-4 in 3D calculations. Figure 5 shows the half pole contour. In this figure, the o-m line follows along an ideal hyperbola, the m-n is a straight line and a curve after n point. We could satisfy the multipole requirements by manipulating the position and the length of the straight section.

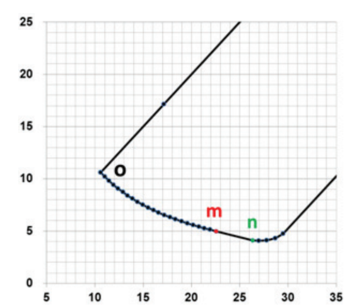

Figure 5: The half pole of quadrupole magnet.

The indirect cooling system (heat sink) for the quadrupole magnets (Q1, Q2, Q3, Q5, Q6, Q8, and Q9) was adopted. Figure 6 shows the cross section of the conductor and the temperature distribution of quadrupole magnet Q2. We used the effective thermal conductivity: $1/k_{eff} = \Sigma v_i/k_i$ for the turn insulation and the ground insulation, where v_i is the volume fraction.

We have tested nine families of quadrupole magnets with a hall probe, and confirmed the field qualities and the temperature rises satisfied the requirements (see Table 3) [4].

ISBN 978-3-95450-134-2

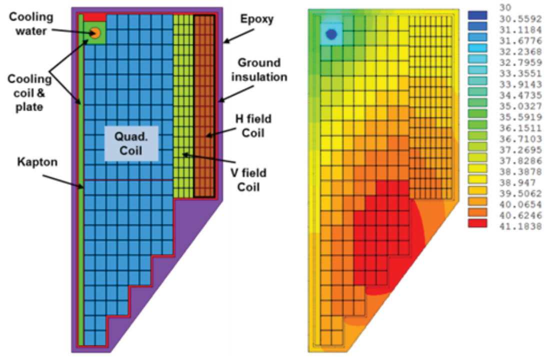

Figure 6: The conductor cross section and the temperature distribution of quadrupole magnet Q2 with a heat sink.

Table 3: Temperature Rise of Quadrupole Magnets

Magnets	Calculated temperature rise [K]	Measured temperature rise [K]
Q1	2	3
Q2	11	15
Q3	11	10
Q4	17	12
Q5	10	15
Q7	12	4
Q8	10	12
Q10	12	9
Q11	2	1

We measured the magnetic field of quadrupole magnets by only Hall probe. Figure 7 shows the field distribution of FEM model and the field measurement scene of Q8 quadrupole magnet. There is a little discrepancy of the field gradient integral of quadrupole magnets by about 2%. Figure 8 shows the field gradient profile of Q8, where the blue dash line is a calculated one and the red line is a measured one. We can see a stacking status of the laminated core by measuring field along the center line of a quadrupole magnet. The field integral would be zero in the ideal quadrupole magnet.

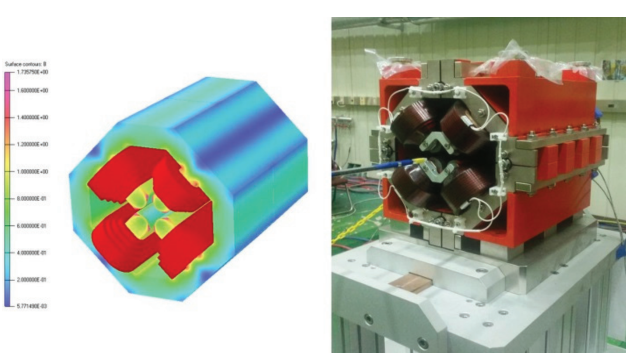

Figure 7: FEM model and field measurement scene of a quadrupole magnet Q8.

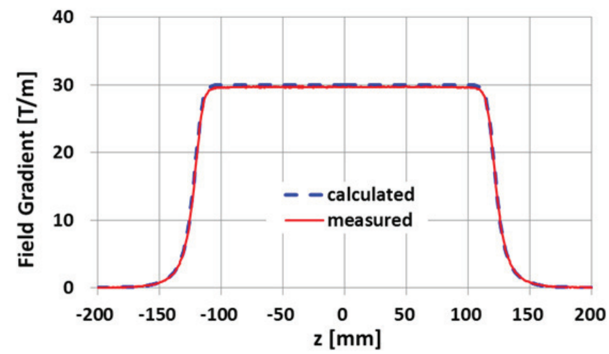

Figure 8: The field gradient profile of Q8 quadrupole magnet.

We have tested all quadrupole magnets of Q1, Q2, Q3, Q5, and Q8. Figures 9 and 10 show the relative field gradient deviations. All quadrupole magnets are excited by the individual power supplies.

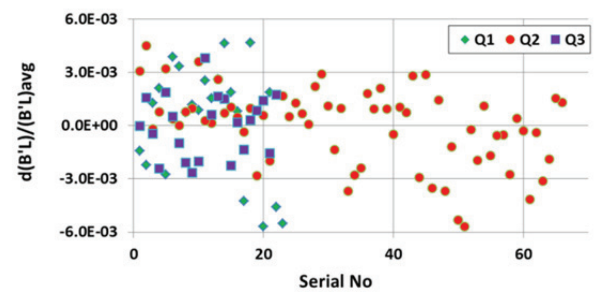

Figure 9: The relative field gradient deviations of Q1, Q2, and Q3 quadrupole magnets.

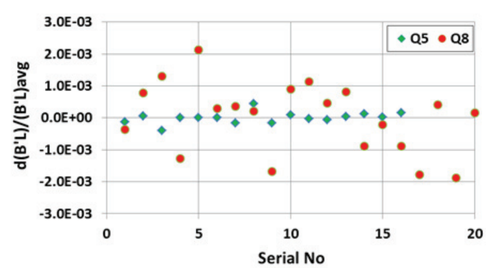

Figure 10: The relative field gradient deviations of Q5, and Q8 quadrupole magnets.

CORRECTOR MAGNETS

The dipole magnets and the quadrupole magnets for the chicanes and the beam analysing have the trim coils or the horizontal/vertical steering coils respectively. Beside these, we prepared the independent corrector magnets of three families of 50 magnets.

Figure 11 shows the corrector magnets, where the right drawing is for the corrector magnets for the undulator, that have an air core in order to maintain no remanent field. Table 4 shows the main parameter of corrector magnets.

ISBN 978-3-95450-134-2

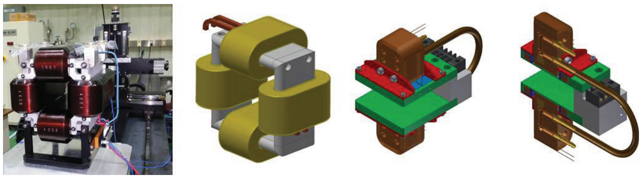

Figure 11: Corrector magnets (left: C1 and C2, right: corrector for undulator).

Table 4: The Main Parameters of Corrector Magnets

Corrector type	C1	C2	C3
Core	iron	iron	iron
Cooling type	air	heat sink	air
Field integral [Gcm]	5000	5000	500
Whole magnet length [mm]	295	144	54
Current density [A/mm^2]	1.1	2.6	0.7
Temperature rise [K]	7	12	9
Quantity(+spare)	36	6	8

CONCLUSION

When we classified the magnets and determined the coil and core sizes, we should consider the connection condition of magnets in series or stand alone, the electrical properties of magnets, and the number of cooling circuit. If the number of cooling circuits is increased in order to reduce the temperature rise, then the magnets become more complicate with the risk of leakage.

We have designed all magnets, and are testing magnets now. Also we confirmed the flow rates of the cooling water that were almost same with estimated ones, and the temperature rises of coils that were below 15 K. Magnetic capabilities of all the magnets have satisfied the requirements till now.

REFERENCES

[1] Heung-Sik Kang, “Current Status of PAL-XFEL Project”, IPAC’13, Shanghai, China (2013).
[2] Vector Fields Software, http://www.cobham.com
[3] ANSYS, http://www.ansys.com
[4] Jack T. Tanabe, “Iron Dominated Electromagnets”, 2005, pp. 113-126

ISBN 978-3-95450-134-2

DEVELOPMENT OF COHERENT TERAHERTZ WAVE SOURCES USING LEBRA AND KU-FEL S-BAND LINACS*

N. Sei, H. Ogawa, Research Institute for Measurement and Analytical Instrumentation, National Institute of Advanced Industrial Science and Technology (AIST),
1-1-1 Umezono, Tsukuba, Ibaraki 305-8568, Japan
K. Hayakawa, T. Tanaka, Y. Hayakawa, K. Nakao, T. Sakai, K. Nogami, M. Inagaki, Laboratory for Electron Beam Research and Application (LEBRA), Nihon University,
7-24-1 Narashinodai, Funabashi, 274-8501, Japan
H. Ohgaki, H. Zen, Institute for Advanced Energy, Kyoto University, Gokasho, Uji,
Kyoto 611-0011, Japan

Abstract

In an infrared free-electron laser (FEL) facility using an S-band linac, a short-bunched electron beam is required to obtain a high FEL gain. Generally, the bunch length of the electron beam is compressed to 1 ps or less before interaction with the photons accumulated in the FEL resonator. This suggests that the electron beam dedicated to the FEL lasing is suitable for generation of high-peak-power coherent radiation in terahertz (THz) wave region. With the compressed electron beams the coherent THz-wave sources have been developed at Laboratory for Electron Beam Research and Application in Nihon University and mid-infrared FEL facility in Kyoto University. The observed energy has been higher than 100 μJ per macropulse in both infrared facilities.

INTORODUCTION

To increase a gain of a free-electron laser (FEL), high electron charge and short pulse width are required for the electron beam used in an infrared FEL facility. Although it is necessary to consider slippage of the electron beam in an insersion device, the root-mean-square (RMS) bunch length of the electron beam is often compressed to 1 ps or less before the insersion device.

Then, the electron beam in the infrared FEL facility is suitable for generating intense coherent radiation in a terahertz (TH) wave region, which lies between the microwaves and the infrared region. A lot of materials have unique absorptive and dispersive properties in the THz wave region [1]. Because the coherent radiation is broad band, it is useful for THz spectroscopy [2]. By combining the probe light of the coherent radiation with the pump light of the infrared FEL, it is expected to clarify dynamics of the molecular vibrations. Because the maximum electric field of the coherent radiation becomes more than 100 kV/cm, it can cause nonlinear optical effects in the THz region [3]. Multiphoton absorption will be also observed by using high-repetition coherent radiation.

Therefore, National Institute of Advanced Industrial Science and Technology (AIST) has developed intense THz-wave sources at infrared FEL facilities in cooperation with Nippon University and Kyoto University. We have already observed coherent synchrotron radiation (CSR) in both infrared FEL facilities. In this article, we will report the status and the new plan of the developments of the coherent radiation THz-wave sources.

THZ-WAVE SOURCES AT LEBRA

At the Laboratory for Electron Beam Research and Application (LEBRA) at Nihon University, an S-band linac is used to generate unique light sources. The electron-beam energy can be adjusted from 30 to 125 MeV, and the charge in a micropulse is approximately 30 pC in full-bunch mode, where the electron beam is bunched in 350-ps intervals. The LEBRA has two monochromatic light sources, which are the infrared FEL in a wavelength region of 1–6 μm and the parametric X-ray radiation (PXR) in an energy region of 5–34 keV [4, 5]. The electron beam is transported from the S-band linac to the FEL straight section or the PXR straight section with the separate 90° arc sections, which can

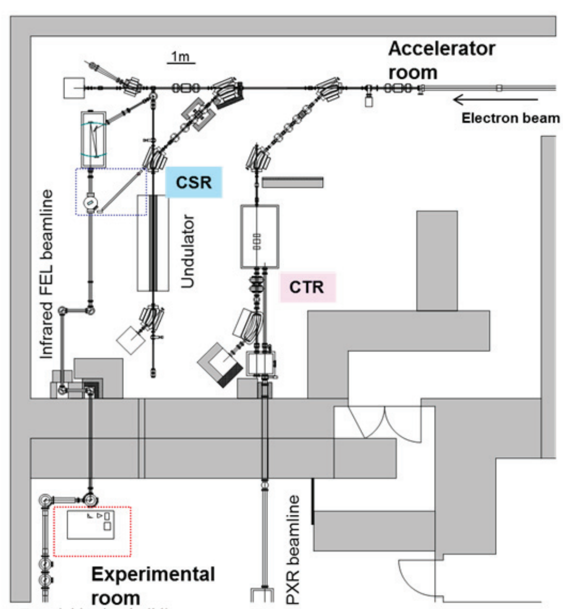

Figure 1: Layout of the experimental setup of coherent radiations at the LEBRA.

*Work supported by sei.n@aist.go.jp

ISBN 978-3-95450-134-2

compress the RMS bunch length to 1 ps or less. The macropulse duration determined by the flat-top pulse width of the 20 MW klystron output power is approximately 20 μs. However, the width of the flat-top pulse is adjusted to be 5 μs or less to avoid heating damage of a silicon crystal for PXR generation. Layout of the experimental setup at the LEBRA is shown in Fig. 1.

Although the bunch length is minimized at the FEL straight section, there is no view port to extract the CSR at the downstream bending magnet. In the PXR straight section, the electron beam is not operated in the long macropulse mode. Then, we developed the CSR beam at the upstream bending magnet in the FEL straight section at first. Because the RMS bunch length was calculated to be approximately 2 ps at the upstream bending magnet, we expected that the intense CSR was emitted in a frequency range of 0.1–0.3 THz. We observed intense THz wave beam extracted from a fused-quartz vacuum window with using a D-band diode detector (Millitech Inc., DXP-06), and we confirmed that it was the CSR beam by measuring dependency of the intensity on the electron charge of the micropulse and the two-dimension distributions of the horizontally and vertically polarized radiations [6]. The energy of the CSR beam extracted from the vacuum window was approximately 0.4 μJ per macropulse.

Because ionizing radiation generated due to the relativistic electron beam of the linac in the accelerator room, we transport the CSR beam to an experimental room by using the infrared FEL beamline. To match the profile of the CSR beam to that of the infrared FEL beam, we used a thin $LiTaO_3$ crystal substrate in the infrared FEL beamline. It has an average reflectance of 67% in the frequency range of 0.1–0.3 THz and an average transmission of 75% in the wavelength range of 0.5–5 μm. The energy of the transported CSR was 50 nJ per macropulse, and it was available at frequency range of 0.1–0.3 THz [7]. The qualities of the THz-wave beam were sufficient to be used in evaluation of the bunch length, imaging experiments, and spectroscopy [8]. Figure 2 shows a transmission imaging of a banded agate with a thickness of 6 mm by using the CSR beam. It is noted that a druse and bands in the banded agate cause interference of the CSR. The CSR beam can be applied with the infrared FEL beam, and a preliminary experiment of two color spectroscopy have been already conducted with the CSR and infrared FEL beams at the LEBRA.

To obtain more powerful THz waves, we have undertook developments of new coherent radiation sources. In the PXR straight section, there is a device of transition radiation to observe the profile of the electron beam. Because it is located behind the silicon crystal, it does not avoid to generate the PXR beam. Moreover, the RMS bunch length can be compressed to 1 ps or less. As shown in Fig. 3, intensity of coherent transition radiation (CTR) is more than 100 times as high as that of the CSR. The CTR energy is expected to be more than 1 mJ per macropulse. Because the CTR can be handled as a point

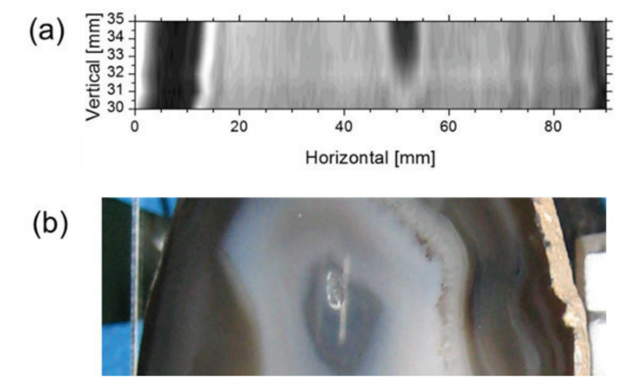

Figure 2: (a) Transmission imaging of a banded agate with using the CSR beam and D-band diode detector and (b) photograph of the banded agate.

light source, it is easy to transport the CTR beam to the experimental room. Then, an alumina fluorescent screen was replaced with a 50–μm titanium film, and characteristics of the CTR were investigated. We have already observed intense THz waves which has a maximum at a frequency of 0.3 THz. The energy of the intense THz waves was much higher than 0.1 mJ per macropulse. The THz waves can be simultaneously used with the PXR beam, so that we plan to transport the intense THz waves with using the PXR beamline. The identity of the intense THz waves will be reported in the near future.

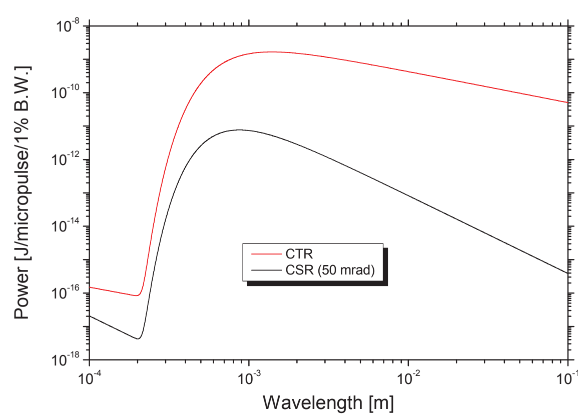

Figure 3: Calculated spectra of the CTR (red line) and CSR (black line) with the RMS bunch length of 0.5 ps at LEBRA. The radiation angle which CSR can be integrated is assumed to be 50 mrad.

THZ-WAVE SOURCES AT KU-FEL

At a mid-infrared FEL facility named as KU-FEL, which is located in Institute of Advanced Energy, Kyoto University, an S-band linac is also used to generate high peak-power light sources [9]. The KU-FEL consists of a 4.5-cell thermionic RF gun, a dog-leg section for an energy filtering, a 3-m accelerator tube, a 180° arc section for a bunch compression, an undulator, and an optical cavity. Recently, a photocathode gun has been developed

ISBN 978-3-95450-134-2

as an exchangeable electron source. A schematic layout of the KU-FEL is shown in Fig. 4. A pulse width of the klystron is approximately 8 µs. However, when the pulse width becomes longer than 3us, the electron-beam qualities are influenced during the macropulse duration by back-bombardment effect. Although the electron energy is maintained fixedly by changing the high voltage of the klystron modulator, the electron charge of the micropulse changes from 20 to 40 pC. The FELs oscillate in a wavelength region of 5–22 µm, and the maximum energy of the FEL is 33 mJ per macropulse [10].

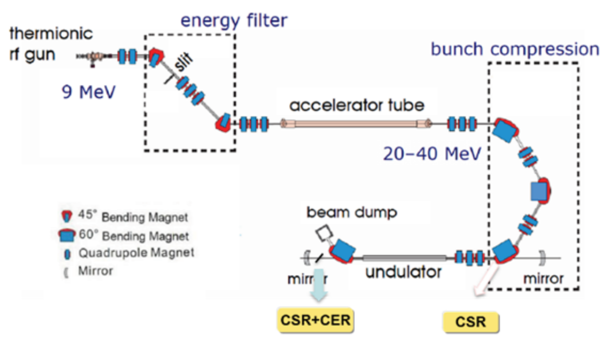

Figure 4: Layout of the experimental setup of coherent radiations at the KU-FEL.

The RMS bunch length of the electron beam in the KU-FEL can be compressed to 1 ps or less in the undulator section. However, a vacuum window to extract radiation is far from the downstream bending magnet, and an inner diameter of a vacuum pipe between the vacuum window and the bending magnet is narrow. The radiation angle which synchrotron radiation emitted from the downstream bending magnet can be extracted from the vacuum window is only 30 mrad. Then, we started to develop CSR at upstream bending magnet, which has a vacuum window at a bending angle of 30°. The radiation angle which synchrotron radiation emitted from the upstream bending magnet can be extracted from the vacuum window is 100 mrad. A fused silica with a diameter of 38 mm and a thickness of 3.5 mm is inserted in the vacuum window.

The RMS bunch length was calculated to be 1–2 ps at the radiation point in the upstream bending magnet. Therefore, the maximum of the CSR spectrum was expected to be in a wavelength region of 0.1–0.2 THz, so that we used a G-band diode detector (Millitech Inc., DXP-05) to investigate evolution of THz waves extracted from the vacuum window. As shown in Fig. 5, we observed intense THz waves, of which macropulse structure was different from that of core monitor signal. The intensity of the THz waves was almost proportional to the second power of the charge up to 6 pC when the macropulse width was 2.8 µs. We measured two-dimensional distributions of the coherent THz waves, and it was found that it almost accorded with the two-dimensional distributions of synchrotron radiation at a frequency of 0.14 THz. Then, the intense THz waves were confirmed to be the CSR. Figure 5 suggests that the bunch length of the micropulse changed during the macropulse duration. We measured energy of the CSR extracted from the vacuum window by a pyrodetector (Gentec-EO Inc., QE8SP-I-MT-BNC) which was set on a two-dimensional moving stage, and it was approximately 55 µJ per macropulse. The CSR spectrum was measured by a simple Michelson interferometer, and it was clarified that the maximum was in a frequency region of 0.1–0.2 THz. The detailed characteristics of the CSR beam will be report in another paper [11].

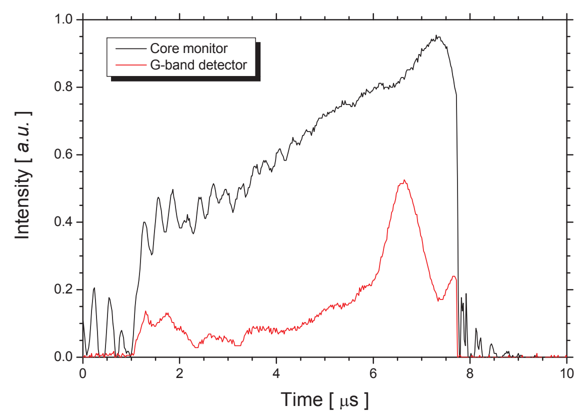

Figure 5: Evolutions of core monitor signal (black line) and CSR intensity measured be G-band diode detector (red line) during the macropulse duration.

Although the radiation angle in the downstream bending magnet is small, the CSR power at the entrance of the downstream bending magnet is higher than that at the observation point in the upstream bending magnet. We also expected to observe coherent edge radiation (CER) at the vacuum window near the downstream bending magnet [12]. Then, we measured profiles of a THz-wave beam with a Teflon lens and a pyroelectricity camera (Ophir Optronics Solutions Ltd., Pyrocam IV), which was located 0.7 m from the entrance of the downstream bending magnet. As shown in Fig. 6, the measured profile had nonuniform hollow structure. This experimental result suggests that the CSR and CER were emitted from

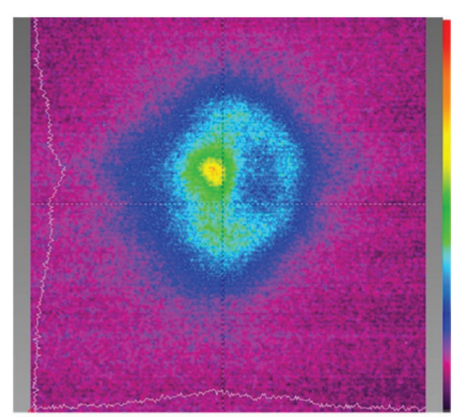

Figure 6: Measured profile of the intense THz waves emitted from the entrance of the downstream bending magnet in the undulator section.

ISBN 978-3-95450-134-2

the entrance of the downstream bending magnet. The THz-wave energy extracted from the vacuum window was measured by the pyrodetector, and it was 100 μJ or more. As the infrared FEL system with the storage ring NIJI-IV at the AIST has developed quasi-monochromatic X-ray beams via FEL-Compton backscattering [13, 14], FEL facilities have potential to develop complex light sources. We plan to clarify the characteristics of the intense THz waves.

CONCLUSION

We have developed intense THz-wave sources by using short-pulse electron beams in the infrared FEL facilities. At the LEBRA, the CSR emitted from the upstream bending magnet in the FEL straight section was transported to the experimental room by using the FEL beamline. It was applied to the imaging experiments and spectroscopy with the infrared FELs. The new CTR, of which energy is 1 mJ per macropulse or more, is under development in the PXR straight section. At the KU-FEL, the CSR with energy of 55 μJ per macropulse has been developed in the upstream bending magnet of the undulator section. The more powerful THz-wave source is under development in the downstream bending magnet. We will advance pioneering studies in which the intense THz waves are used with the infrared FEL or the PXR.

ACKNOWLEDGMENT

This work has been supported in part under the Visiting Researcher's Program of the Research Reactor Institute, Kyoto University, and ZE Research Program ZE26B-1 and ZE27B-6, Kyoto University.

REFERENCES

[1] P. H. Siegel, "Terahertz technology", IEEE Trans. Microw. Theory Tech., **50** (2002) 910.

[2] N. Sei *et al.*, "Design of Terahertz-Wave Spectrophotometry by Compton Backscattering Using Relativistic Electron Bunches and their Coherent Synchrotron Radiations", Appl. Phys. Express, **1** (2008) 087003.

[3] M. Jewariya *et al.*, "Ladder climbing on the anharmonic intermolecular potential in an amino acid microcrystal via an intense monocycle terahertz pulse", Phys. Rev. Lett., **105** (2010) 203003.

[4] Y. Hahakawa *et al.*, "First lasing of LEBRA FEL at Nihon University at a wavelength of 1.5 μm", Nucl. Instrum. Methods Phys. Res. A, **483** (2002) 29.

[5] Y. Hahakawa *et al.*, "X-ray imaging using a tunable coherent X-ray source based on parametric X-ray radiation", J. Inst., **8** (2013) C08001.

[6] N. Sei *et al.*, "Observation of intense terahertz-wave coherent synchrotron radiation at LEBRA", J. Phys. D: Appl. Phys., **46** (2013) 045104.

[7] N. Sei *et al.*, "Complex light source composed from subterahertz-wave coherent synchrotron radiation and an infrared free-electron laser at the Laboratory for Electron Beam Research and Application", J. Opt. Soc. Am. B, **31** (2014) 2150.

[8] N. Sei *et al.*, "Measurement of a bunch length of a relativistic electron beam using a narrow-band diode detector in a terahertz region", J. Jpn. Soc. Infrared Science & Technology (in Japanese), **25** (2015) 97.

[9] H. Ohgaki *et al.*, "Lasing at 12 μm Mid-Infrared Free-Electron Laser in Kyoto University", Jpn. J. Appl. Phys., **47** (2008) 8091.

[10] H. Zen *et al.*, "Present status of Kyoto University free electron laser", FEL2013, New York, USA, 711.

[11] N. Sei *et al.*, *in preparation*.

[12] G. Geloni *et al.*, "Theory of edge radiation. Part I: Foundations and basic applications", Nucl. Instrum. Methods Phys. Res. A, **605** (2009) 409.

[13] N. Sei *et al.*, "Lasing of middle-infrared free-election lasers using the storage ring NIJI-IV", Opt. Lett., **36** (2011) 3645.

[14] N. Sei *et al.*, "Operation of higher harmonic oscillations in free-electron lasers", Opt. Express., **20** (2012) 308.

ISBN 978-3-95450-134-2

LINEAR VLASOV SOLVER FOR MICROBUNCHING GAIN ESTIMATION WITH INCLUSION OF CSR, LSC AND LINAC GEOMETRIC IMPEDANCES

C. -Y. Tsai#, Department of Physics, Virginia Tech, Blacksburg, VA 24061, USA
D. Douglas, R. Li, and C. Tennant, Jefferson Lab, Newport News, VA 23606, USA

Abstract

As is known, microbunching instability (MBI) has been one of the most challenging issues in designs of magnetic chicanes for short-wavelength free-electron lasers or linear colliders, as well as those of transport lines for recirculating or energy recovery linac machines. To more accurately quantify MBI in a single-pass system and for more complete analyses, we further extend and continue to increase the capabilities of our previously developed linear Vlasov solver [1] to incorporate more relevant impedance models into the code, including transient and steady-state free-space and/or shielding coherent synchrotron radiation (CSR) impedances, the longitudinal space charge (LSC) impedances, and the linac geometric impedances with extension of the existing formulation to include beam acceleration [2]. Then, we directly solve the linearized Vlasov equation numerically for microbunching gain amplification factor. In this study we apply this code to a beamline lattice of transport arc [3] following an upstream linac section. The resultant gain functions and spectra are presented here, and some results are compared with particle tracking simulation by ELEGANT [4]. We also discuss some underlying physics with inclusion of these collective effects and the limitation of the existing formulation. It is anticipated that this more thorough analysis can further improve the understanding of MBI mechanisms and shed light on how to suppress or compensate MBI effects in lattice designs.

INTRODUCTION

The beam quality preservation is of a general concern in delivering a high-brightness beam through a transport line or recirculation arc in the design of modern accelerators. Microbunching instability (MBI) has been one of the most challenging issues associated with such beamline designs. Any source of beam performance limitations in such recirculation or transport arcs must be carefully examined in order to preserve the beam quality, such as the coherent synchrotron radiation (CSR), longitudinal space-charge (LSC) and/or other high-frequency impedances that can drive microbunching instabilities.

To accurately quantify the direct consequence of microbunching effect, i.e. the gain amplification factor, we further extend our previously developed semi-analytical simulation code [1] to include more relevant impedance models, including CSR, LSC and linac geometric impedances. The LSC effect stems from (upstream) ripple on top of an electron beam and can accumulate an amount of energy modulation when the beam traverses a long section of a beamline. Such energy modulation can then convert to density modulation via momentum compaction R_{56} downstream the beamline [5, 6]. In addition, along the beamline, CSR due to electron radiation emission inside bending dipoles can have a significant effect on further amplifying such density to energy modulation [5, 6]. The accumulation and conversion between density and energy modulations can possibly cause serious microbunching gain amplification (or, MBI).

In this paper, we first introduce the methods of microbunching gain calculation: a kinetic model based on linearized Vlasov equation [7, 8], and particle tracking by ELEGANT as a benchmarking against our code. Then we briefly summarize the impedance models used in our simulations. After that, we illustrate simulation results: the gain functions and spectra for our example lattice, including a transport arc following a section of upstream linac. Finally, we discuss the underlying physics and summarize our observation from the simulation results.

METHODS

To quantify the MBI in a transport or recirculation beamline, we estimate the microbunching amplification factor G (or, bunching factor g_k) by two distinct methods. The first one, based on a kinetic model, is to solve a (linearized) Vlasov equation [7,8]. This method is of our primary focus in this paper. The second one, served as a benchmarking of the first method, is based on particle tracking method (here we use ELEGANT [4]). For the former, after mathematical simplification of the linearized Vlasov equation, we actually solve a general form of Volterra integral equation for the bunching factor. In our code, to facilitate us in simulating ERL-based lattices which sometimes contain vertical spreaders and/or recombiners, we extend the existing formulation to include both transverse horizontal and vertical bends. Also, we consider the presence of linac sections in a general beamline; the formulation of Volterra integral equation would be slightly modified [2] to accommodate RF acceleration or deceleration. In sum, the governing equation for bunching factor g_k is summarized below,

$$g_k(s) = g_k^{(0)}(s) + \int_0^s K(s,s')g_k(s')ds' \quad (1)$$

where the kernel function can be particularly expressed as

$$K(s,s') = \frac{ik_0 C(s)}{\gamma_0}\frac{I_0 C(s')}{I_A}\hat{R}_{56}(s'\to s)Z\left(kC(s'),s'\right)\times[\text{Landau damping}] \quad (2)$$

for the [Landau damping] term

jcytsai@vt.edu

ISBN 978-3-95450-134-2

$$\exp\left\{\frac{-k^2}{2}\left[\begin{array}{l}\varepsilon_{x0}\left(\beta_{x0}\hat{R}_{51}^2(s,s')+\dfrac{\hat{R}_{52}^2(s,s')}{\beta_{x0}}\right)\\+\varepsilon_{y0}\left(\beta_{y0}\hat{R}_{53}^2(s,s')+\dfrac{\hat{R}_{54}^2(s,s')}{\beta_{y0}}\right)+\sigma_\delta^2\hat{R}_{56}^2(s,s')\end{array}\right]\right\} \quad (3)$$

with

$$\hat{R}_{56}(s'\to s)=\hat{R}_{55}(s')\hat{R}_{56}(s)-\hat{R}_{55}(s)\hat{R}_{56}(s')+\hat{R}_{51}(s')\hat{R}_{52}(s)-\hat{R}_{51}(s)\hat{R}_{52}(s') +\hat{R}_{53}(s')\hat{R}_{54}(s)-\hat{R}_{53}(s)\hat{R}_{54}(s') \quad (4)$$

$$\hat{R}_{5i}(s,s')=C(s)\hat{R}_{5i}(s)-C(s')\hat{R}_{5i}(s') \quad (5)$$

and the bunch compression factor

$$C(s)=\frac{1}{\hat{R}_{55}(s)-h_0\hat{R}_{56}(s)} \quad (6)$$

Here the kernel function K(s,s') describes relevant collective effects, g_k(s) the resultant bunching factor as a function of the longitudinal position given a wavenumber k, and $g_k^{(0)}$(s) is the bunching factor in the absence of collective effect (i.e. from pure optics effect). We note that the above formulation can be applicable to the case with focusing in combined-function dipoles.

In the above formulation, we have made the coasting beam approximation, i.e. the modulation wavelength is assumed much shorter than the bunch duration. The transport functions $\hat{R}_{5i}(s)$ (i = 1, 2, 3, 4, 6) can be obtained directly from ELEGANT by tracking a (sufficient) number of macroparticles and deriving the 6 by 6 transport matrix at separate locations by proper transformation of the dynamic variables [2]:

$$\begin{bmatrix}\hat{x}\\ \hat{y}\end{bmatrix}=\begin{bmatrix}x\\ y\end{bmatrix}\sqrt{\frac{E_r(s)}{E_0}};\ \begin{bmatrix}\hat{p}_x\\ \hat{p}_y\end{bmatrix}\simeq\begin{bmatrix}p_x\\ p_y\end{bmatrix}\sqrt{\frac{E_r(s)}{E_0}};\ \hat{z}=z;\ \hat{\delta}=(\delta+1)-\frac{E_r(s)}{E_0} \quad (7)$$

Here E_0 is the initial beam energy and $E_r(s)$ is the reference energy at a specific location s. $\delta\equiv(E-E_0)/E_0$. Note here that the transformation assumes the energy gain due to acceleration (or deceleration) varies slowly, i.e. $1/E_r\, dE_r/ds = 1$.

To quantify MBI in a single-pass system, we define the microbunching gain as functions of the global longitudinal coordinate s as well as the initial modulation wavelength λ (or, $k = 2\pi/\lambda$):

$$G(s,k=2\pi/\lambda)\equiv\left|\frac{g_k(s)}{g_k^{(0)}(0)}\right| \quad (8)$$

Hereafter, we simply call G(s) the gain function, which is a function of s for a given modulation wavenumber, and denote $G_f(\lambda)$ as the gain spectrum, which is a function of modulation wavelength at a specific location (e.g. denoted with a subscript "f" at the exit of a beamline). It is worth mentioning the general physical meaning of Eqs. (1-3): a density perturbation at s' induces an energy modulation through a collective impedance [$Z(k(s'))$] and is subsequently converted into a further density modulation at s via non-vanishing momentum compaction $R_{56}(s'\to s)$.

IMPEDANCE MODELS

For an electron beam traversing an individual dipole, CSR can have both steady-state and transient effects. In addition, when a beam goes through a long transport line, LSC can have a significant effect on accumulating energy modulations. Moreover, when a beam is accelerated the RF cavity is characteristic of the (high-frequency) geometric impedance which can also accumulate an amount of energy modulation. Here we quote the relevant impedance expressions without further derivation:

CSR in Free Space

For a relativistic electron beam ($\beta = 1, \gamma < \infty$) traversing a bending dipole, the free-space steady-state CSR impedance per unit length can be expressed as [9]:

$$\mathrm{Re}\left[Z_{CSR}^{s.s.NUR}(k(s);s)\right]=\frac{-2\pi k(s)^{1/3}}{|\rho(s)|^{2/3}}\mathrm{Ai}'\left(\frac{(k(s)|\rho(s)|)^{2/3}}{\gamma^2}\right)+\frac{k(s)\pi}{\gamma^2}\left(\int_0^{(k(s)|\rho(s)|)^{2/3}/\gamma^2}\mathrm{Ai}(\varsigma)d\varsigma-\frac{1}{3}\right)$$

$$\mathrm{Im}[Z_{CSR}^{s.s.NUR}(k(s);s)]\simeq\frac{2\pi k(s)^{1/3}}{|\rho(s)|^{2/3}}\left\{\frac{1}{3}\mathrm{Bi}'(x)+\int_0^x\left[\begin{array}{l}\mathrm{Ai}'(x)\mathrm{Bi}(t)\\-\mathrm{Ai}(t)\mathrm{Bi}'(x)\end{array}\right]dt\right\} \quad (9)$$

where $x=\left(k(s)|\rho(s)|\right)^{2/3}/\gamma^2$, $k = 2\pi/\lambda$ is the modulation wavenumber, $\rho(s)$ is the bending radius, and Ai and Bi are Airy functions. Under ultrarelativistic approximation ($\gamma\to\infty$), Eq. (9) is reduced to the well-known expression [10,11]

$$Z_{CSR}^{s.s.UR}\left(k(s);s\right)=\frac{-ik(s)^{1/3}A}{|\rho(s)|^{2/3}},\ A=-2\pi\left[\mathrm{Bi}'(0)/3+i\mathrm{Ai}'(0)\right] \quad (10)$$

Prior to reaching steady state, the beam entering a bend from a straight section would experience the so-called entrance transient state, where the impedance per unit length can be obtained by Laplace transformation of the corresponding wakefield [12-14]:

$$Z_{CSR}^{ent}\left(k(s);s\right)=\frac{-4}{s^*}e^{-4i\mu(s)}+\frac{4}{3s^*}\left(i\mu(s)\right)^{1/3}\Gamma\left(\frac{-1}{3},i\mu(s)\right) \quad (11)$$

where $\mu(s) = k(s)z_L(s)$, s^* is the longitudinal coordinate measured from dipole entrance, $z_L=\left(s^*\right)^3/24\rho^2$, and Γ is the upper incomplete Gamma function.

There are also exit CSR transient effects as a beam exits from a dipole. For the case with fields generated from an upstream electron (at retarded time) propagating across the dipole to downstream straight section, i.e. Case C of Ref. [14], the corresponding impedance per unit length can be similarly obtained by Laplace transformation:

$$Z_{CSR}^{exit}\left(k(s);s\right)=\frac{-4}{L_b+2s^*}e^{\frac{-ik(s)L_b^2}{6|\rho(s)|^2}\left(L_b+3s^*\right)} \quad (12)$$

where s^* is the longitudinal coordinate measured from dipole exit and L_b is the dipole length.

For the impedance expression of the case where fields generated from an electron (at retarded time) within a dipole propagating downstream the straight section, we use the following expression for the exit transient impedance [15]:

$$Z_{CSR}^{drif}(k(s);s) \approx \begin{cases} \frac{2}{s^*}, \text{ if } \rho^{2/3}\lambda^{1/3} \le s^* \le \lambda\gamma^2/2\pi \\ \frac{2k(s)}{\gamma^2}, \text{ if } s^* \ge \lambda\gamma^2/2\pi \\ 0, \text{ if } s^* < \rho^{2/3}\lambda^{1/3} \end{cases} \tag{13}$$

where s^* is again the longitudinal coordinate measured from dipole exit. This expression assumes the exit impedance comes primarily from coherent edge radiation in the near-field region (i.e. $z < \lambda\gamma^2$), and in our simulation we only include transient effects right after a nearby upstream bend.

Here we note that these CSR models are valid only when the wall shielding effect is negligible. The wall shielding effect becomes important when the distance from the beam orbit to the walls h satisfies $h \le \left(\rho\lambda^2\right)^{1/3}$. In this situation, one should consider to use the shielded CSR impedance in evaluating the CSR-induced microbunching gain. Currently we adopt the steady-state impedance based on parallel-plate model [16, 17] as

$$Z_{CSR}^{p.p.}(k) = \frac{8\pi^2}{h}\left(\frac{2}{k(s)\rho(s)}\right)^{\frac{1}{3}} \sum_{p=0}^{\infty} F_0(\beta_p),\ \beta_p = (2p+1)\frac{\pi}{h}\left(\frac{\rho(s)}{2k^2(s)}\right)^{\frac{1}{3}} \tag{14}$$

where

$$F_0(\beta) = \mathrm{Ai}'(\beta^2)\left[\mathrm{Ai}'(\beta^2) - i\mathrm{Bi}'(\beta^2)\right] + \beta^2\mathrm{Ai}'(\beta^2)\left[\mathrm{Ai}(\beta^2) - i\mathrm{Bi}(\beta^2)\right].$$

For a more realistic beam pipe geometry, such as rectangular cross section, we consider to load impedance data externally calculated by another dedicated program. We are also working in progress on a numerical approach to obtain the impedance model which takes into account the straight-bend-straight section with rectangular beam pipe [18]. The results shall be valid for non-ultrarelativistic and finite wall resistivity, including both CSR and LSC.

LSC in Free Space

Below we present two slightly different LSC impedance expressions [19] implemented in our code. The first one is on-axis model, which assumes a transversely uniform density with circular cross section of radius r_b,

$$Z_{LSC}^{on-axis}(k(s);s) = \frac{4i}{\gamma r_b(s)}\frac{1-\xi K_1(\xi)}{\xi} \tag{15}$$

where $\xi = \frac{k(s)r_b(s)}{\gamma}$ and $r_b(s) \approx \frac{1.747}{2}\left(\sigma_x(s) + \sigma_y(s)\right)$ [20]. The second one is the average model, which integrates the radial dependence [19, 21],

$$Z_{LSC}^{ave}(k(s);s) = \frac{4i}{\gamma r_b(s)}\frac{1-2I_1(\xi)K_1(\xi)}{\xi} \tag{16}$$

where ξ is defined above the same way. In the following we use the first model, in accordance with ELEGANT.

Linac Geometric Effect

If a beam experiences acceleration, deceleration or chirping along a section of a linac with RF cavities, the periodic structure in general features a geometric impedance. We consider this collective effect by adopting the following expression [22-24],

$$Z_{linac}^{UR}(k) = \frac{4i}{ka^2}\frac{1}{1+(1+i)\frac{\alpha L}{a}\sqrt{\frac{\pi}{kg}}} \tag{17}$$

where $\alpha \approx 1 - 0.4648\sqrt{g/L} - 0.07\,g/L$, a is the average iris radius, g is the gap distance between irises, and L is the cell/period length.

SIMULATION RESULTS

In this section we take a high-energy transport arc [3] following an upstream linac section as an example for our analysis. Table 1 summarizes some beam parameters used in our simulations. In this beamline lattice, the electron beam is accelerated from 50 MeV to 1.11 GeV through a section of linac including 200 cavities with assumed voltage gradient ~10 MV/m, frequency 1497 MHz and on-crest acceleration phase. We note that, at the exit of the linac, beam phase-space distribution is not particularly optimized to match that of the downstream transport arc. However, the purpose here is to demonstrate the microbunching gain evolution along a general beamline with inclusion of beam acceleration. Thus, this imperfect match should not be a concern. The transport arc is a second-order achromat and being globally isochronous with a large dispersion modulation across the entire arc. Figure 1 shows the dispersion R_{16}(s) and momentum compaction functions R_{56}(s) along the linac-arc beamline. It can be seen in Fig. 1 that the transport function R_{56}(s) has taken non-ultrarelativistic effect into consideration.

Table 1: Initial Beam Parameters for the Example Lattice

Name	Value	Unit
Beam energy (at linac entrance)	50	MeV
Beam energy (at linac exit)	1.11	GeV
Peak bunch current	88	A
Normalized emittance	0.3	μm
Initial beta function	18	m
Initial alpha function	-3.6	
Energy spread (uncorrelated)	~3×10^{-4}	

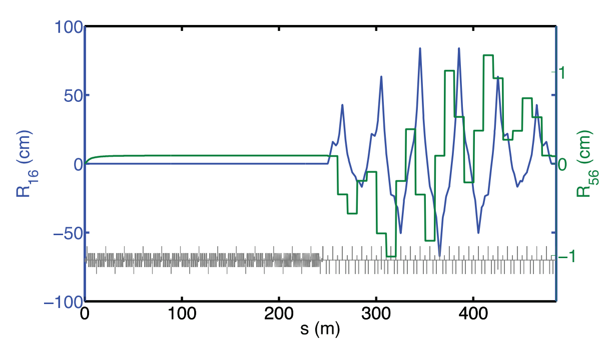

Figure 1: Dispersion (blue) and momentum compaction (green) functions of the example linac-arc lattice.

Figures 2 and 3 show the evolution of gain functions G(s) along the beamline. ELEGANT tracking simulation

ISBN 978-3-95450-134-2

was performed for a Gaussian beam of 70M macroparticles with flattop z-distribution. LSC effect is only considered within drift elements and RF cavities. In other elements such as dipoles, focusing or defocusing quads this effect is neglected. In Fig. 3, the CSR effects include both transient and steady states inside individual dipoles, as well as exit transient effect in the downstream drift sections. We found in Fig. 2 the gain is slightly decreased in the linac section, because of LSC-induced plasma oscillation along with beam acceleration (see also R_{56} in Fig. 1). Our Vlasov solutions match well with ELEGANT tracking results throughout the lattice except some "special" locations (see, e.g. at s = 410-440 m, in Figs. 2 and 3). After carefully examining numerical parameters to ensure the convergence of ELEGANT tracking results, we found the gain deviation (between our Vlasov solutions and ELEGANT) does not stem from numerical issues but is due to physical non-uniformity of the bunch profile as a result of RF curvature. Here we assume this RF curvature from the linac is not compensated by a harmonic cavity, as is done in several linac-based FELs.

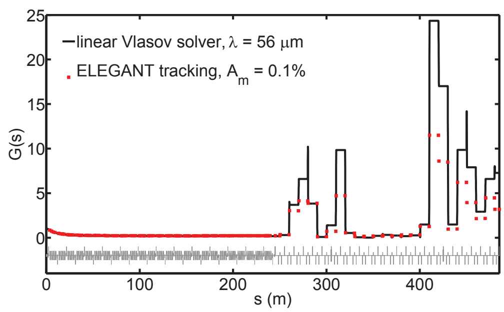

Figure 2: LSC-induced microbunching gain function G(s) for the linac-arc lattice.

Here we would show that this bulk non-uniformity can cause the microbunching gain to be a bit reduced, compared with that of our Vlasov solution which does exclude this effect from gain estimation. Due to the presence of an RF cavity, the accelerated beam is characteristic of an RF curvature (see top figure of Fig. 4). In our case with on-crest acceleration, we can simply assume the particle energy deviation related to its longitudinal coordinate to be

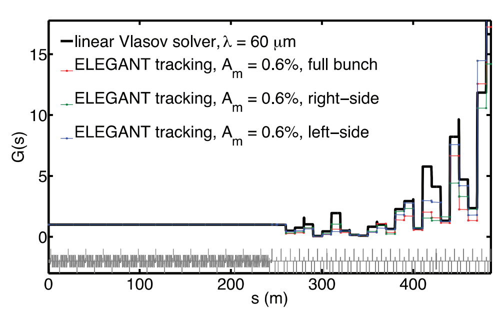

Figure 3: CSR-induced microbunching gain function G(s) for the linac-arc lattice. Here the CSR effects include both entrance and exit transients as well as steady-state effect.

$$\delta_i = hz_i + qz_i^2 \tag{18}$$

where the linear chirp h vanishes but quadratic chirp q does exist (< 0 in our case). With this (z-δ) correlation, we can define an effective (and local) chirp to be

$$h^{eff}(z_i) \equiv -\frac{\partial \delta_i}{\partial z_i} = -2qz_i \Rightarrow \begin{cases} <0, \text{ for bunch tail } (z_i<0) \\ >0, \text{ for bunch head } (z_i>0) \end{cases} \tag{19}$$

The local bunch compression factor can be described as

$$C(s,z_i) = \frac{1}{R_{55}(s) - h^{eff}(z_i)R_{56}(s)} \Rightarrow \begin{cases} >1, \text{ for bunch head } \& \ R_{56}(s)>0 \\ <1, \text{ for bunch tail } \& \ R_{56}(s)>0 \end{cases} \tag{20}$$

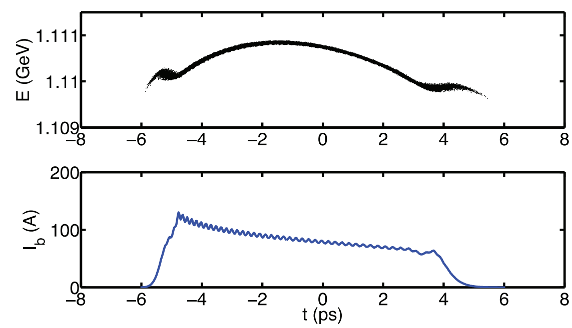

Figure 4: (Top) longitudinal phase space distribution at s = 410 m. (Bottom) bunch current density. Note here the bunch head is to the left.

By the above simple analysis we can explain the presence of bunch non-uniformity in Fig. 4. Note that in Fig. 4 the bunch head is to the left since we use t as the variable instead of z. Now we would like to illustrate how such bulk non-uniformity affects the bunch spectrum (or, the bunching factor) and thus the microbunching gain.

Without resorting to rigorous mathematical derivation, we only illustrate numerically the difference of bunch spectra between uniform density-modulated and non-uniform density-modulated bunch profiles. Figure 5 highlights the following three different functions:

$$f_1(t) = A_0 + A_1\sin(\omega t), \quad f_2(t) = A_0 t + A_1 \sin\left[(\omega - A_2 t)t\right] \tag{21}$$
$$f_3(t) = A_0 t + A_1 \sin\left[(\omega + A_2 t)t\right]$$

where f_1 describes the coasting-beam model, while f_2 and f_3 approximately represent the non-uniformity of the bunch profile (in bottom figure of Fig. 4, corresponding to the right-side and left-side of the bunch profile, respectively).

From Fig. 5 it can be obviously seen that with non-uniform bunch profile (f_2 and f_3) the corresponding bunch spectral amplitudes are smaller than the uniform one. This indeed causes the microbunching gain to be reduced at certain locations with local bunch compression.

ISBN 978-3-95450-134-2

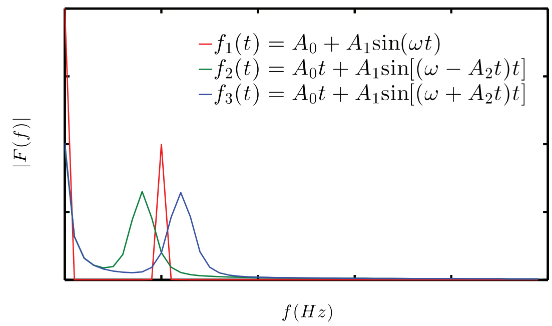

Figure 5: Bunch spectra (as Fourier transformation) of three different functions in Eq. (21). Assume A_0=A_1=1, A_2=4π, and the nominal frequency f = 10 Hz.

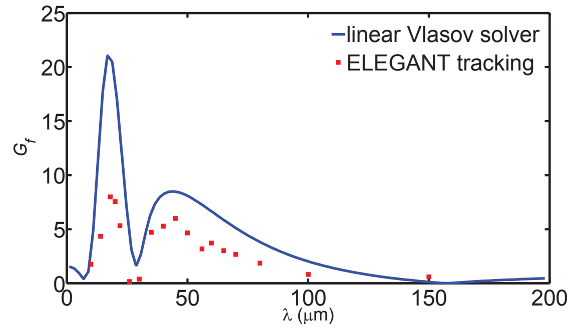

Figure 6: Microbunching gain spectra with LSC effects. Note here that in ELEGANT simulation we vary the initial modulation amplitudes around 0.1-0.6%.

Figures 6-8 show the microbunching gain spectra including different collective effects. In Fig. 6, we can see the dependence of modulation wavelength on LSC-induced microbunching gain. In Fig. 7, both our Vlasov solver and ELEGANT include all relevant CSR effects, i.e. entrance, exit transient, and steady-state CSR effects. We believe the difference comes from: (i) non-uniformity of the bulk bunch; (ii) the different models of exit transient CSR used in our simulation [see Eq. (13)] and in ELEGANT [4, 14]. We also notice the gain reduction of non-ultrarelativistic (NUR, black curve) CSR compared with ultrarelativistic (UR, blue curve) approximation. The fluctuations shown in Fig. 7 are likely due to the CSR drift model we applied [Eq. (13)], which requires further investigation. Thus far in ELEGANT, it is not trivial to include all relevant collective effects such as CSR, LSC and linac geometric wakes into thorough consideration for MBI estimation. However, with our linear Vlasov solver, it is straightforward to add these relevant impedance models into consideration. In Fig. 8 we add these collective effects altogether for microbunching gain estimation. We observe that the overall microbunching gain is in fact an accumulation effect of density-energy conversion throughout the beamline. In the long section of the upstream linac, LSC and linac geometric wake have accumulated an amount of energy modulation, and later such energy modulation converts to density modulation through the downstream nonvanishing R_{56} [e.g. at s = 280 m in Fig. 2]. Then, the modulation can be further amplified via CSR effect (in this case, mainly steady-state CSR) downstream the bends. Note that with the large gain shown in Fig. 8 the microbunching may reach nonlinear regime where linearized Vlasov solution is no longer valid for a practical point of view. For the validity of linear analysis, we assume the initial perturbation is sufficiently small (although in fact it may not be so small) that the magnitude of the bunching factor along the beamline does not exceed a certain value (e.g. less than 10%).

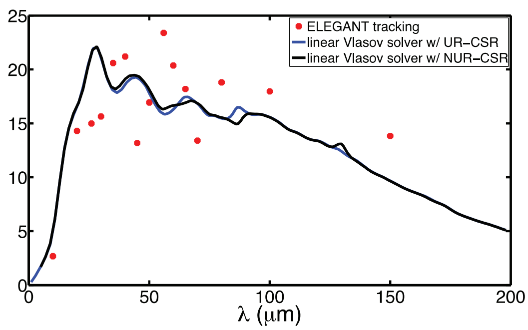

Figure 7: Microbunching gain spectra with all relevant CSR effects. ELEGANT results include both entrance and exit transient as well as steady-state impedances. The initial modulation amplitudes are varied around 0.1-0.6% to ensure numerical convergence.

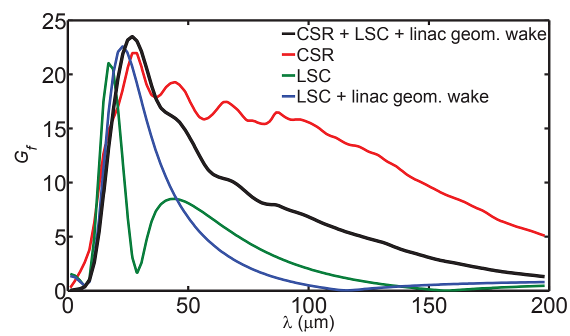

Figure 8: Microbunching gain spectra with various combinations of collective effects. To simulate the gain with linac geometric impedance, here we assume the linac parameters are: a = 3.07 cm; L = 10.0 cm; g = 8.0 cm; α = 0.528. For comparison, the illustrated gain values with all effects included (black curve) are ten times smaller than the calculated values.

ISBN 978-3-95450-134-2

SUMMARY AND CONCLUSION

We have presented the theoretical formulation to include the case with beam acceleration based on the scaled dynamical variables [2]. Then, we summarized various collective impedance models relevant to the microbunching instability for our subsequent analysis. After that, we demonstrated a linac-arc beamline as our microbunching gain estimation. Our simulation results match well with ELEGANT tracking except at some locations with local bunch compression. We identify that such local bunch compression is due to non-uniformity of the bunch profile which stems from RF curvature in the upstream acceleration section, and can result in microbunching gain reduction. With inclusion of all relevant collective effects (CSR, LSC and linac geometric effects) in the simulation, the results show that microbunching gain can be significantly enhanced due to energy-density conversion along the beamline.

ACKNOWLEDGMENT

We thank Steve Benson for bringing many motivating issues for our studies and proofreading this draft. This work is supported by Jefferson Science Associates, LLC under U.S. DOE Contract No. DE- AC05-06OR23177.

REFERENCES

[1] C.-Y. Tsai *et al.*, FEL'14 (THP022), IPAC'15 (MOPMA028) and ERL2015 (TUICLH2034).

[2] M. Venturini, Microbunching instability in a single-pass systems using a direct two-dimensional Vlasov solver, Phys. Rev. ST Accel. Beams 10, 104401 (2007).

[3] D. Douglas *et al.*, Control of coherent synchrotron radiation and microbunching effects during transport of high brightness electron beams, arXiv: 1403.2318v1 [physics.acc-ph] and D. Douglas *et al.*, Control of synchrotron radiation effects during recirculation, IPAC'15 (TUPMA038).

[4] M. Borland, elegant: A Flexible SDDS-Compliant Code for Accelerator Simulation, APS Light Source Note LS-287 (2000) and Modeling of microbunching instability, Phys. Rev. ST Accel. Beams 11, 030701 (2008).

[5] E. L. Saldin *et al.*, Klystron Instability of a Relativistic Electron Beam in a Bunch Compressor, Nucl. Instrum. Meth. A 490 (2002) 1.

[6] Z. Huang *et al.*, Suppression of microbunching instability in the linac coherent light source, Phys. Rev. ST Accel. Beams 7, 074401 (2004).

[7] S. Heifets *et al.*, Coherent synchrotron radiation instability in a bunch compressor, Phys. Rev. ST Accel. Beams 5, 064401 (2002).

[8] Z. Huang and K.-J. Kim, Formulas for coherent synchrotron radiation microbunching in a bunch compressor chicane, Phys. Rev. ST Accel. Beams 5, 074401 (2002).

[9] R. Li and C.-Y. Tsai, CSR impedance for non-ultrarelativistic beams, IPAC'15 (MOPMN004).

[10] J. Murphy *et al.*, Longitudinal wakefield for an electron moving on a circular orbit, Part. Accel. 1997, Vol. 57, pp. 9-64.

[11] Ya. S. Derbenev *et al.*, Microbunch radiative tail-head interaction, TESLA-FEL-Report 1995-05

[12] D. Zhou, An alternative 1D model for CSR with chamber shielding, IPAC'12 (MOOBB03).

[13] C. Mitchell *et al.*, Effects of transient CSR wakefields on microbunching in a bunch compressor, IPAC'13 (TUPWA057).

[14] E. L. Saldin *et al.*, On the coherent radiation of an electron bunch moving in an arc of a circle, NIMA 398, 373 (1997).

[15] R. Bosch *et al.*, Longitudinal wake of a bunch of suddenly accelerated electrons within the radiation formation zone, Phys. Rev. ST Accel. Beams 10, 050701 (2007).

[16] R. Warnock, Shielded coherent synchrotron radiation and its effects on very short bunches, SLAC-PUB-5375, 1990.

[17] T. Agoh and K. Yoloya, Calculation of coherent synchrotron radiation using mesh, Phys. Rev. ST Accel. Beams 7, 054403 (2004).

[18] R. Li, Radial eigenmodes for a toroidal waveguide with rectangular cross section, IPAC12 (WEPPR095).

[19] M. Venturini, Models for longitudinal space charge impedance for microbunching instability, Phys. Rev. ST Accel. Beams 11, 034401 (2008).

[20] J. Wu *et al.*, Analytical Analysis of longitudinal space charge effects for a bunched beam with radial dependence, Phys. Rev. ST Accel. Beams 11, 040701 (2008).

[21] M. Venturini *et al.*, Dynamics of longitudinal phase-space modulation in an RF compressor for electron beams, Phys. Rev. ST Accel. Beams 13, 080703 (2010).

[22] R. L. Gluckstern, Longitudinal impedance of a periodic structure at high frequency, Phys. Rev. D 39, 2780 (1989).

[23] K. Yokoya and K. Bane, The longitudinal high-frequency impedance of a periodic accelerating structure, PAC 1999.

[24] Z. Huang *et al.*, Effect of linac wakefield on CSR microbunching in the Linac Coherent Light Source, PAC 2003.

ISBN 978-3-95450-134-2

INTRABEAM SCATTERING IN HIGH BRIGHTNESS ELECTRON LINACS*

S. Di Mitri#, Elettra Sincrotrone Trieste, 34149 Basovizza, Trieste, Italy

Abstract

Intra-beam scattering (IBS) of a high brightness electron beam in a linac has been studied analytically, and the expectations found to be in reasonable agreement with particle tracking results from the Elegant code. It comes out that, under standard conditions for a linac driving a free electron laser, IBS plays no significant role in the development of microbunching instability. A partial damping of the instability is envisaged, however, when IBS is enhanced either with dedicated magnetic insertions, or in the presence of an electron beam charge density at least 4 times larger than that produced by present photo-injectors.

INTRODUCTION

The question to which extent intra-beam scattering (IBS) affects the properties of high brightness electron bunches in linacs was posed in [1,2], with attention to the interplay of IBS and microbunching instability (MBI). Following our study in [3], here we aims to provide a quantitative answer and an outlook, by comparing the analysis and particle tracking runs of the ELEGANT code [4], whereas IBS was simulated following prescriptions given in [2,5].

In particular, we wonder whether IBS could play a role when the beam transverse dimension is squeezed with strong focusing ("low-beta") FODO cells, so to increase the IBS longitudinal growth rate. At first glance, the idea of using IBS to increase the energy spread of an electron bunch traveling in a dedicated FODO channel seems to be attractive for the following reasons: i) IBS heats the beam by avoiding cost, complexities and maintenance of a laser heater (LH) system [6]; ii) the heating level is tunable with the quadrupoles' focusing strength; iii) it provides longitudinally uncorrelated energy spread, thus avoiding any side effect associated to the energy modulation induced in a LH at the infrared laser wavelength (*e.g.*, the so-called trickle heating) [7]. We will see however that, to be as effective as a LH, the enhancement of IBS requires a long and densely packed FODO channel. An alternative compact lattice in which the beam recirculates through low-beta FODO channels is investigated. This solution, however, turns out to be not practical because of the coherent synchrotron radiation (CSR) instability that develops through the arcs.

THEORETICAL BACKGROUND

Ultra-relativistic electron bunches in modern accelerators generally have much smaller velocity spread in the longitudinal direction of motion than in the transverse planes owing to the relativistic contraction by the Lorentz factor γ: $\sigma_\delta/\gamma << \sigma_{x'},\sigma_{y'}$, where σ_δ is the beam rms fractional energy spread and $\sigma_{x',y'}$ the rms angular divergence. If the bunch's charge density is high enough and the bunch travels a long path, multiple Coulomb scattering tends to redistribute the beam momenta from the transverse degree of freedom to the longitudinal one. This process is called IBS and its longitudinal growth rate may be comparable to the beam damping time in low emittance electron storage rings. The instantaneous growth rate of the energy spread of a bunched beam circulating in a ring was given in [8,9]. Since there are no synchrotron oscillations in a linac, the formula for a coasting beam should be used here (which results in a growth rate a factor 2 larger than that of a bunched beam) [8]:

$$\frac{1}{\sigma_\delta}\frac{d\sigma_\delta}{dt} \approx \frac{r_e^2 cN}{8\gamma^2\varepsilon_{n,x}\sigma_x\sigma_z\sigma_\delta^2}\ln\left(\frac{\Delta\gamma_{\max}}{\Delta\gamma_{\min}}\right) \tag{1}$$

Here r_e is the electron classical radius, $\beta c \approx c$ the electron velocity, N the number of electrons in the bunch, $\varepsilon_{n,x} = \varepsilon_{n,y}$ the rms normalized transverse emittance of a round beam, and σ_z the rms bunch length. The argument of the Coulomb logarithm is the ratio of the maximum and the minimum energy exchange due to a single scattering event, and $\Delta\gamma_{\max} \propto \gamma^2\sigma_{x'}$, $\Delta\gamma_{\min} \propto r_e/(\sigma_x\sigma_{x'}) \approx \gamma\, r_e/\varepsilon_{n,x}$ [1].

Following an argument made in [10], we consider that the IBS energy distribution has a nearly Gaussian core with a long tail. Since we are mostly interested in the energy spread of the Gaussian core, we set the maximum energy transfer to $\Delta\gamma_{\max} = \gamma\cdot 10^{-5}$ as also done in [1], and find that the logarithm is of the order of 10 for a normalized emittance of ~1 μm. Then, Eq. 1 can be integrated and it yields to the final fractional rms energy spread in the presence of IBS cumulated over the distance Δs [3]:

$$\sigma_\delta \approx \sqrt{\sigma_{\delta,0}^2 + \frac{2r_e^2 N}{\gamma^2\varepsilon_{n,x}\sigma_x\sigma_z}\Delta s} \equiv \sqrt{\sigma_{\delta,0}^2 + \sigma_{\delta,IBS}^2}, \tag{2}$$

with $\sigma_{\delta,0}$ the initial rms fractional incoherent energy spread. Equation 2 is an approximate expression for smooth betatron oscillations, neither energy dispersion nor particle acceleration.

If we apply Eq. 2 to the low energy part of a linac, we find that an electron beam from a state-of-the-art photo-injector, *e.g.* with beam charge Q = 0.5 nC, σ_z = 750 μm, ε_n = 0.6 μm rad, σ_x = 150 μm and γ = 300, collects an absolute rms energy spread $\sigma_{E,IBS} \approx$ 3 keV over Δs ~ 30 m. This is comparable to the typical value of $\sigma_{E,0} \approx$ 2 keV out of the photo-injector [11], and still far from the amount of

*Work supported by the FERMI project of Elettra Sincrotrone Trieste.
#simone.dimitri@elettra.eu

ISBN 978-3-95450-134-2

heating required to suppress MBI in an FEL-driver [12,13]. Then, if we assume that the bunch length is magnetically compressed by a factor of, say, C ~30, $\sigma_{E,IBS}$ may grow up to ~100 keV over hundreds of meters, but its contribution to Landau damping of MBI remains small for two reasons. First, in the linac region immediately following the compressor, $\sigma_{E,IBS}$ is negligible compared to the incoherent energy spread of the compressed beam, which is increased to $C\sigma_{E,0} \approx 60$ keV by virtue of the preservation of the longitudinal emittance. Second, $\sigma_{E,IBS}$ grows with *s* at a lower rate than the relative energy modulation amplitude of MBI (respectively, square root *vs.* linear dependence) [5,14]. In conclusion, the impact of $\sigma_{E,IBS}$ on the development of the MBI is expected to be small. In particular, it is negligible with respect to the effect of a LH *unless* important modifications to the magnetic lattice and/or to the beam parameters are introduced. We finally remark that, with the aforementioned beam parameters, the transverse emittances and the bunch length are substantially unchanged by IBS.

FODO CHANNEL

Equation 2 says that, for injected beam parameters like those in Table 1, $\sigma_{E,IBS} \approx 6$ keV if the rms transverse beam size $\sigma_{x,y}$ shrinks down to 25 μm (average value) along a beam line 30 m long. With such a system designed for the *maximum* beam heating, *i.e.* minimum betatron function β, a reduction of the total $\sigma_{E,IBS}$ can be obtained by re-arranging the quadrupole strengths so to allow β to expand to higher values. On the opposite, the lower limit of β is set by the optical aberrations excited by strong focusing and by the technical design of the quadrupole magnets. In order to make our system more flexible, compact and easy to build, we set β = 0.3 m. This solution ensures a standard technical design of the quadrupole magnets and negligible emittance growth due to optical aberrations.

Table 1: Electron Beam Parameters out of a State-of-the-art Photo-injector and FODO Lattice Parameters

Charge	500	pC
Bunch duration, rms	2.5	ps
Norm. slice emittance, rms	0.6	μm
Incoherent energy spread, rms	2.0	keV
Mean energy	150	MeV
FODO length	30	m
Average betatron function in FODO	0.3	m
IBS-induced energy spread, rms (Eq. 3)	6.0	keV

$\sigma_{E,IBS}$ cumulated in the FODO channel is evaluated with Eq. 2 and shown in Fig. 1, in the (β,Q) and the (β,L) space, with L the FODO channel total length. We assume that the three-dimensional charge density out of the photo-injector remains constant as the injected bunch charge is varied. In other words we assume the following scaling: $\varepsilon_n[\mu m] \approx Q[nC]^{1/3}$ and $\sigma_z[mm] \approx 1.2 \cdot Q[nC]^{1/3}$ so that $Q/(\sigma_z \varepsilon_n^2) = const.$. In general, $\sigma_{E,IBS}$ turns out to be quite insensitive to Q if compared to its dependence on *s*, γ and β, because in our scaling the effect of a higher charge is compensated by a longer bunch duration and a larger transverse emittance.

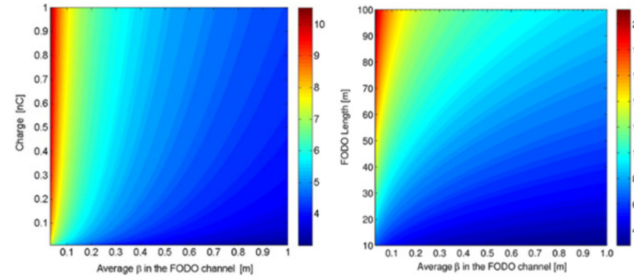

Figure 1: IBS-induced rms energy spread in keV, in the (β,Q) space for L = 30 m (left), and in the (β,L) space for Q = 500 pC. Both plots are for a beam energy of 150 MeV. The beam transverse emittances and the bunch duration are scaled with Q as explained in the text. Notice that the colour scale is different in the two plots. Copyright of American Physical Society (APS) [3].

We benchmarked the analytical estimation of $\sigma_{\delta,IBS}$ for the beam parameters in Tab.1, with particle tracking runs of the ELEGANT code. ELEGANT implements Bjorken and Mtingwa's formulas [15] for calculating the emittance growth rate in all directions of motion. To take into account non-Gaussian distributed beams, ELEGANT allows beam slice analysis: within each slice, particles are assumed to be Gaussian-distributed in the transverse phase space and in energy, and uniformly distributed in *z*. The incoherent energy spread induced by IBS along the FODO channel is shown in Fig. 2. Its final rms value, averaged over the bunch slices, is 4.5 keV for the sliced beam (not shown) and 6.0 keV for the unsliced one. Such a discrepancy is due to the non-uniform heating of the sliced beam because of the lower charge density at the bunch edges. The simulations confirm that the bunch length remains substantially unchanged in the presence of IBS (not shown).

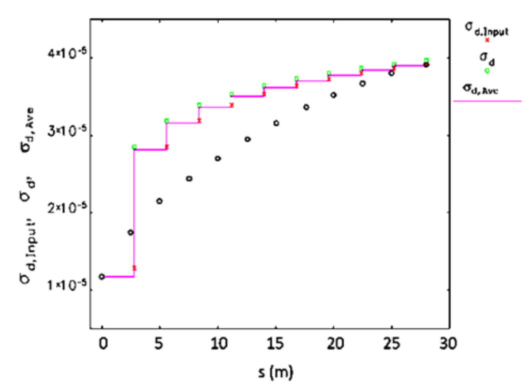

Figure 2: Electron beam slice rms fractional energy spread along the FODO channel in the presence of IBS, for the unsliced beam (see parameters in Table 1). In the legend, "$\sigma_{d,Input}$" is the energy spread at the entrance of each "IBS module" depicted in ELEGANT; "σ_d" is the energy spread at the exit of each IBS module and "$\sigma_{d,Ave}$" is the rms fractional energy spread, averaged over all bunch slices. The rms fractional energy spread estimated with Eq. 2 is also shown (circles). Copyright of APS [3].

ISBN 978-3-95450-134-2

By scaling the simulation result with Eq. 2, we estimate a FODO channel as long as ~100 m to achieve $\sigma_{E,IBS}$ ~10 keV. At this point, the scheme would start having a large impact on the machine design and cost. Alternatively, while keeping the 30 m long FODO channel, a beam charge density ~4 times higher than in Tab.1 should be provided, which seems to be out of the horizon of present facilities. We can therefore conclude that a relatively *compact single-pass* low-beta FODO channel could only about double the incoherent energy spread of typical high brightness electron beams produced by nowadays photo-injectors. This is not sufficient for best performance of x-ray FELs, although it might be suitable, *e.g.*, for longer wavelength FELs driven by shorter linacs, lower peak current and/or requiring weaker magnetic compression than in FERMI and LCLS, *i.e.*, having a lower MBI gain.

RECIRCULATION

As an alternative to the single-pass FODO channel, we investigated a recirculating IBS beam line (RIBS) to cumulate a larger $\sigma_{E,IBS}$ and to minimize the impact on the total linac length. The bunch is injected into, and extracted from, the RIBS by fast kicker magnets. After M-turns into the RIBS, the beam has passed through a low-beta FODO channel 2M+1 times. A sketch of the RIBS at 150 MeV with realistic sizes is shown in Fig. 3. The two arcs are basically a copy of the design by Douglas *et al.* [16]. In our design, the arcs are achromatic and quasi-isochronous ($R_{56} = 2\times10^{-4}$ m, $T_{566} = 4\times10^{-3}$) and connected to the FODO channels by matching sections made of additional quadrupole magnets. An ultra-relativistic bunch takes approximately 360 ns to make one turn in the RIBS. Kickers with rise and fall time pulse duration of a few tens of nanosecond are therefore adequate for our purposes.

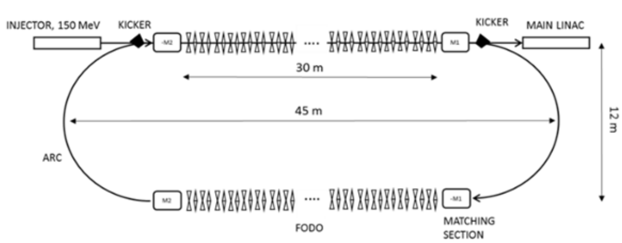

Figure 3: Schematic layout of the recirculating IBS beam line (not to scale). Copyright of American Physical Society [3].

A 150 MeV, 250 pC beam at the entrance of RIBS was generated by including the relativistic velocity spread, the geometric longitudinal wakefield and the RF curvature in an upstream 12 m long S-band injector. Other beam parameters are: ε_n = 0.4 µm rad, σ_z = 375 µm and $\sigma_{E,0}$ = 2 keV. The total rms energy spread is 0.1%. This beam is expected to generate $\sigma_{E,IBS} \approx$ 10 keV in half a turn (see Eq. 2). In principle, the number of turns in RIBS should be a compromise between the amount of desired $\sigma_{\delta,IBS}$, which is proportional to the square root of the length of the traversed FODO channel, and the tolerable degradation of the beam six-dimensional emittance due to chromatic aberrations and CSR instability. After one turn, the incoherent energy spread has grown to 10 keV rms, but largely at the expense of the deeply modulated longitudinal phase space, as shown in Fig. 4. We conclude that the longitudinal CSR instability prevents beam recirculation. In addition, the CSR-induced energy loss modulates the beam correlated energy spread through the arc. This amplifies the variation of the bunch length at the dipole magnets (since R_{56} oscillates in the range ±30 mm, see [10]) and partially invalidates the optics scheme for emittance preservation in the presence of CSR, which requires the same bunch length at the dipoles [17,18].

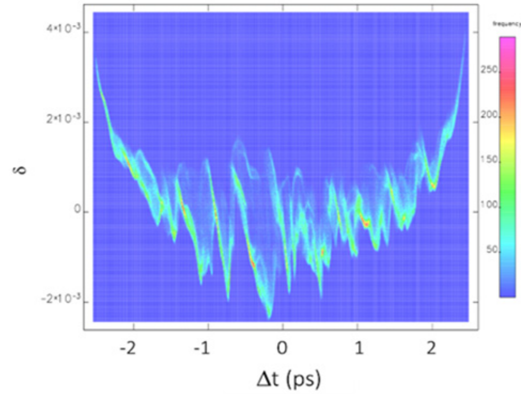

Figure 4: Electron beam longitudinal phase space after one turn in RIBS. Copyright of American Physical Society [3].

CONCLUSIONS

The impact of IBS on the six-dimensional emittance of high brightness electron beams like those driving x-ray FELs, has been studied. The analytical estimation based on the Piwinski's formalism is in rough agreement with the particle tracking results obtained with the ELEGANT code. They confirm that IBS is relevant neither to the FEL energy-normalized bandwidth in the ultra-violet – x-ray wavelength range, nor to the gain of the MBI in the main linac. A low-beta FODO channel has been investigated to increase the longitudinal growth rate of IBS at the linac injection. This solution is far from being as efficient as a LH system: the channel requires tens of quadrupole magnets over tens of meters to generate an incoherent energy spread in the range 5–10 keV rms, for beam charges in the range 100–500 pC. As an alternative, a recirculating beam line was explored to cumulate IBS-induced energy spread in a relatively compact lattice. Unfortunately, the CSR instability in the arcs, driven by the high charge density and the low beam rigidity, deeply modulates the beam longitudinal phase space after only one turn. In conclusion, a relatively compact single-pass low-beta FODO channel at the linac injection could almost double the incoherent energy spread of high brightness beams with charge in the range 100–500pC. A beam heating above the 10 keV rms level is envisaged at the end of the FODO channel for charge densities at least ~4 times higher than generated by state-of-the-art photo-injectors.

ISBN 978-3-95450-134-2

ACKNOWLEDGEMENTS

This work was funded by the FERMI project of Elettra Sincrotrone Trieste.

REFERENCES

[1] Z. Huang, Technical Note LCLS-TN-02-8 (2002).
[2] A. Xiao and M. Borland, in Proc. of the 23rd Part. Accel. Conf., TH5PFP038, Vancouver, BC, Canada (2009).
[3] S. Di Mitri, Phys. Rev. Special Topics – Accel. Beams **17**, 074401 (2014).
[4] M. Borland, APS LS-287 (2000).
[5] A. Xiao, in Proc. of the 24th Linear Accel. Conf., MOP093, Victoria, BC, Canada (2008).
[6] E. L. Saldin, E. A. Schneidmiller and M.V. Yurkov, Nucl. Instrum. Methods Phys. Res., Sect. A **528**, 355 (2004).
[7] Z. Huang *et al.*, Phys. Rev. Special Topics – Accel. Beams **13**, 020703 (2010).
[8] A. Piwinski, "Intrabeam Scattering" in CERN Accelerator School (1991) 226.
[9] A. Piwinski, in Proc. of the 1983 SSC Workshop, Ann Arbor, MI (1983) 59.
[10] T. Raubenheimer, Part. Accel. **45** (1994) 111.
[11] M. Hüning and H. Schlarb, Proc. of the 2003 Part. Accel. Conf., WUPAB017, Portland, OR, USA. IEEE Catalog Number *03CH37423C,* ISBN 0-7803-7739-7 (2003).
[12] Z. Huang e*t al.*, Phys. Rev. Special Topics – Accel. Beams **7**, 074401 (2004).
[13] S. Spampinati *et al.*, Phys. Rev. Special Topics – Accel. Beams 1**7**, 120705 (2004).
[14] E. L. Saldin, E. A. Schneidmiller and M. V. Yurkov, Nucl. Instrum. Phys. Res. A **490** (2002) 1.
[15] J. D. Bjorken and S. K. Mtingwa, Part. Accel. **13** (1983) 118.
[16] D. R. Douglas et al., JLAB-ACP-14-1751 (2014), arXiv:1403.2318.
[17] D. Douglas, JLAB-TN-98-012 (1998).
[18] S. Di Mitri, M. Cornacchia, S. Spampinati, Phys. Rev. Letters **110**, 014801 (2013).

WAKE FIELD POTENTIALS OF "DECHIRPERS"*

A. Novokhatski#, SLAC National Accelerator Laboratory, Menlo Park, CA 94025, USA

Abstract

A corrugated structure, which is used in "dechirper" devices, is usually a pipe or two plates with small corrugations (bumps) on the walls. There is a good single-mode description of the wake potentials excited by a relativistic bunch if the wave length of the mode is much longer than the distance between the bumps in the pipe. However, ultra-short bunches, which are now used in FELs, excite much higher frequency fields and the corresponding wake potentials will be very different from the single-mode description. We have made analyzes of these wake potentials based on a numerical solution of Maxwell's equations. It was confirmed that the behavior of the wake fields of ultra-short bunches in corrugated structures is not much different from the fields excited usually in accelerating structures where the wake potentials are described by the exponential function. We also carried out calculations for a similar device, that was installed and measured at the Pohang Accelerator Laboratory, Korea. We find very good agreement with the experimental results.

INTRODUCTION

The precise knowledge of the wake fields generated in different elements of free electron lasers (FEL) including accelerator, beam transport and undulators has become very important with increasing power and efficiency of X-ray production. Usually it is a "negative" effect. For example in Ref.[1] it is demonstrated how the wake fields generated in collimators may decrease the FEL performance. However the effect from wake fields can also be "positive" if this field is used to improve the energy spectrum. These wake fields can be generated in the accelerator (linac) or in special devices – "dechirpers". To our knowledge this word was introduced in ref. [2] for the first time.

There are several publications which have some sort of formula for the wake fields in corrugated structures. The references to these publications can be found in Ref. [3-4]. These formulas are derived from the assumption of a single dominating mode and the Green's function for the wake potentials is described as a damped cosine function. Although they referred to our 1997 publication [5], where we found a similarity to the wake fields in corrugated structures with the fields in a tube with a thin dielectric layer, the authors do not fully analyze the applicability of the single mode approach to describe wake fields of very short bunches. A corrugated wall structure is planned for use in the device that makes an additional energy loss along the very short bunches of the LCLS [4]. It now becomes very important to check how well a single mode approach can describe the fields, that are excited in corrugated structures and perhaps another description must be used. For the FEL application the dechirper has a small sized corrugation structure, of order of millimeters. Electron bunches in the FEL have a length of micron. If we scale the bunch length together with the structure size up ten times or more we will get geometry environments that are very similar to the linear accelerating structures. As we know, the wake fields in the accelerating structures are not described by a single mode. There is another description, which contains all modes. Such as the Green's function for the TESLA accelerating structure [6] or the SLAC accelerating structure [7]. We may assume that the wake potentials of a corrugated structure excited by short bunches are also described by this or a similar function. To check this assumption we calculated wake potentials of the corrugated structure using a computer code NOVO [8], which was specially designed to calculate wake fields of very short bunches. This code has been benchmarked based on a good agreement with the wake fields measured in the LCLS-LTU [9]. Recently the code was extended for the wake field calculations in rectangular beam chambers [10].

A DECHIRPER

As mentioned above, a dechirper takes energy from the beam through the interaction of the bunch electro-magnetic field with a metal corrugated structure. The practical design of the dechirper consists of two identical movable parallel plates (jaws) with corrugated walls in a form of the periodic set of planar diagrams. A schematic drawing of the dechirper is shown in Fig. 1. The dechirper, which is planned to be installed at LCLS, has the following parameters of the corrugated structure. The period is 0.5 mm, the thickness of a diaphragm is a half of a period and the transverse sizes of a diaphragm are: h=0.5 mm, Lx=12 mm. Definitions of the sizes are given in Fig. 1. The total length L of the corrugated structure is 2 m. The gap between two jaws is adjustable. The nominal gap is 1.4 mm.

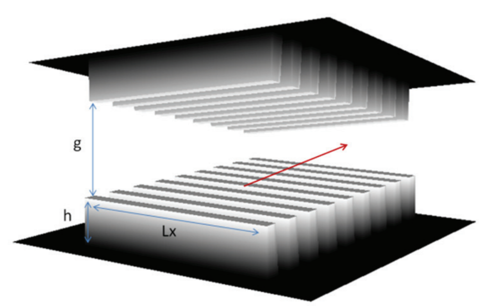

Figure 1: A schematic drawing of a dechirper. The red line shows a bunch trajectory.

*Work supported by DoE Contract No. DOE-AC02-76SF00515
#novo@slac.stanford.edu

ISBN 978-3-95450-134-2

We start with calculations to make a comparison with the single mode approach. We calculated wake potential of a relatively long bunch of 25 micron and for a relatively long range of distance after a bunch for a nominal gap. This wake potential is show in Fig. 2.

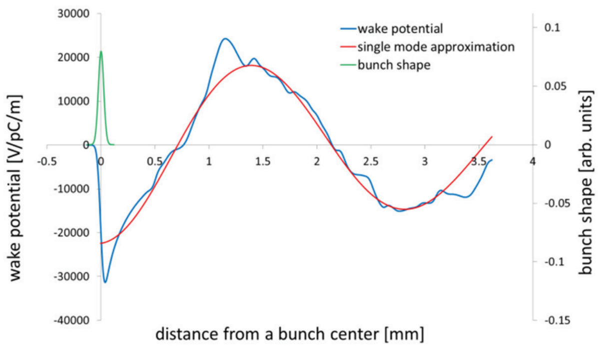

Figure 2: Wake potential (a blue line) of a 25 micron bunch passing through a 2 m rectangular corrugated structure with a full gap of 1.4 mm. The red line shows a single mode approximation. The green line shows the bunch charge distribution.

The shape of the wake potential seems to be easily fitted by a damped cosine function. This approximation is shown by a red line in Fig. 2. The frequency of this mode is 105.5 GHz or the wave length of this mode is 28.4 mm which is in agreement with calculations in Ref. [4]. However, as we can see from the plot, this fit does not give a good approximation at small distances: in the bunch region. For a shorter bunch such kind of approximation can bring much more mistake. Calculated wake potentials of 10 and of 5 micron bunches are shown in Fig. 3 by magenta and green lines. We can see a great difference in the shape of the wake potentials, which have a dependence upon the distance in this region of a bunch while the single mode approach gives an almost constant value (red line). In the Fig. 3 we also include a wake potential of a 25 micron bunch to show that all three wake potentials have a common part, which can be very well approximated by an exponential function (a pink line).

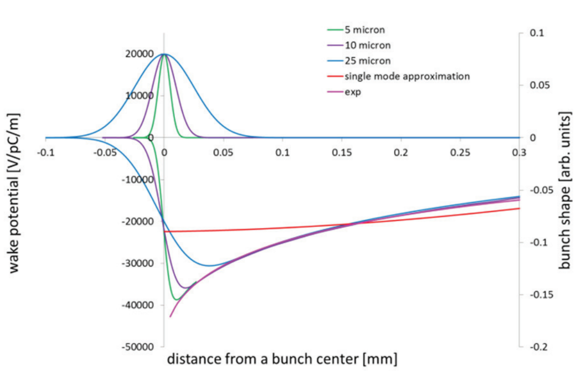

Figure 3: Wake potential of a 5 micron bunch (green line), 10 micron (magenta line) and 25 micron (blue line). The red line shows a single mode approximation and the pink line show the exponential function.

Based on this approximation we suggest using the following approximation of the Green's function for corrugated structures

$$w_{\|}(s) = A(g)\exp\sqrt{\frac{s}{s_0(g)}} \qquad (1)$$

The fitting parameters $A(g)$ and $s_0(g)$ are functions of the gap size g (full gap). We can use this approximation as a Green's function to calculate wake potentials of bunches with any complicated charge distribution $q(s)$

$$W(s) = \int_{-\infty}^{s} q(s')w_{\|}(s-s')ds' \qquad (2)$$

We show an example of a complicated bunch shape (two horn distribution) in Fig. 4. The bunch distribution is shown by the blue line. The "head" of the bunch is on the left.

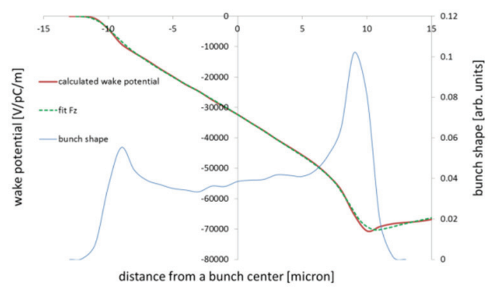

Figure 4: Comparison of the wake potential calculated using a computer code (red line) and calculated using a Green's function (green line) for a two horn bunch passing a dechirper with a 1 mm gap.

The comparison of the wake potentials calculated using a computer code (red line) and using a convolution with a Green's function (green line) is also shown in Fig. 4. We can conclude based on this good agreement, that we can use the above mentioned Green's function (1) to calculate wake fields in the dechirper. In these calculations the gap was 1 mm. It is interesting to note that the wake potential of a two horn bunch has two slopes. According to Fig. 4 we can compensate a possible energy chirp of the main part of a bunch, but the energy chirp of the second horn will be not compensated.

We made wake field calculations for different gaps in order to find approximate values for $A(g)$ and $s_0(g)$. We have found that a more or less good approximation (±5%) for A and s_0 over the range of gaps from 1 to 2 mm to be the following:

$$A(g) \approx A_0 L \frac{Z_0 c}{g^2} \qquad s_0(g) \approx g\sqrt{\frac{g}{L}} \qquad (3)$$

with parameters: $A_0 \approx 0.85 \quad L \approx 55\ mm.$

ISBN 978-3-95450-134-2

TRANSVERSE WAKE FIELD

The main purpose of the dechirper is to introduce energy loss along the bunch. While interacting with a longitudinal force, which is responsible for the energy loss or gain, the particles of the bunch may also interact with a transverse force. We calculate the integral of the transverse forces (transverse kick) when a bunch is in the center of the dechirper in the vertical as well as is in the horizontal direction. A two dimensional plot of the vertical and horizontal kicks is shown in Fig. 5. The orientation of the dechirper jaws is as shown in Fig. 1.

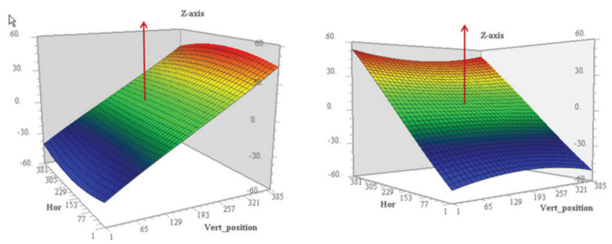

Figure 5: Integrated vertical and horizontal force distribution when a bunch trajectory lies in the center, between the jaws and in the middle of the diaphragms of the dechirper. Red arrows show the bunch trajectory.

It can be seen that the dechirper acts as a quadrupole lenses: defocusing in the direction of the jaws and focusing in the perpendicular direction. In general, we may represent the Green's function of the transverse kick using a Tailor expansion. In the vertical direction we have:

$$w_y(s,y) = w_y^0(s,y_1) + \\ + \sum_{n=1} \frac{\partial^n}{\partial y^n} w(s,y)|_{y=y1} (y-y_1)^n \tag{4}$$

When the leading particles have no offset $y_1 = 0$ and $w_y^0(s,0) = 0$ due to symmetry, then the first important term is the first derivative

$$w_y(s,y) = w_y^1(s)y = \frac{\partial}{\partial y} w_y(s,y)|_{y=0}\ y \tag{5}$$

A vertical gradient of the wake fields acting on the bunch particles will be a convolution of this function and the bunch charge distribution. We calculate this gradient for a 10 micron bunch moving through a dechirper with a gap of 1.4 mm. Fig. 6 shows this calculation. We have found that the transverse Green's function, which defines the vertical gradient, can be approximated by the following formula:

$$\mathrm{w}_{\mathrm{y}}^1(s) \approx \frac{1}{\Delta(g)} \frac{s}{s_0(g)} w_{\|}(s) \tag{6}$$

The parameter $\Delta(g)$ is approximately 2.2 mm for gaps of 1-2 mm. One can check how well this formula describes a vertical gradient. In Fig. 6 a green dashed line shows the vertical gradient calculated using Green's function (6). We get very good agreement in the bunch region.

It was interesting to find that the Green's function for the gradient of horizontal kick has the same form like (6) but with a negative sign.

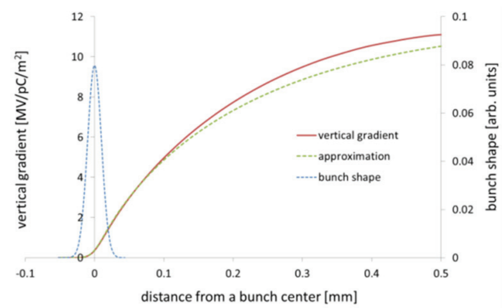

Figure 6: Vertical gradient of the transverse wake fields of a 10 micron bunch (red line), approximation of the vertical gradient (green dashed line) and bunch charge distribution (dotted blue line).

PAL-ITF EXPERIMENT

The single mode approach was also been used for calculating the wake fields in order to make a comparison with the experimental measurement of the corrugated dechirper in Pohang Accelerator Laboratory [2]. They found a 20% difference. They concluded the bunch charge must have been 150 pC instead of measured 200 pC. We decided to check this statement even the bunch length in the experiment was relatively large - 0.67 mm. The geometry of the corrugated structure can be found in Ref. [2]. It has the same period of 0.5 mm as the SLAC dechirper, but with a little bit thicker diaphragms. The main difference is a larger transverse size (Lx=50 mm), which allows using it with larger gaps.

We calculated wake potentials for an experimentally measured bunch distribution. Fig. 7 shows this distribution and corresponding wake potential for a gap of 6 mm. It is interesting to note that again the wake potential has two slopes for a two horn bunch, so there will not be full compensation of the chirp in the dechirper. Comparing the computed wake potential, we find good agreement with the shape of the measured wake potential, which is presented in the right middle plot of Fig. 5 in Ref. [2].

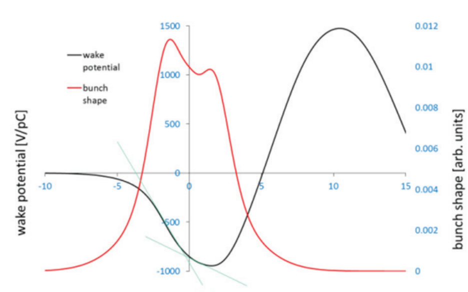

Figure 7: The shape of the experimentally measured two horn bunch (red line) and the corresponding wake potential (black line). Light green lines show two slopes.

ISBN 978-3-95450-134-2

We also calculated the loss factor as a function of the gap size. The results for the relative energy loss of a 70 MeV bunch with a charge of 150 pC (green line with red triangles) and 200 pC (black line with blue stars) are shown in Fig. 8.

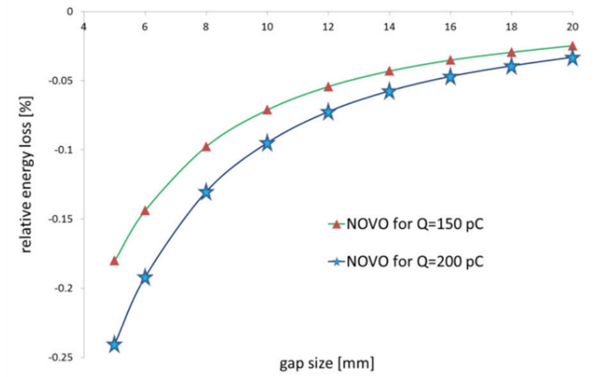

Figure 8: Relative energy loss of a bunch with a charge of 150 pC (green line with red triangles) and 200 pC (black line with blue stars).

Comparison with a plot in Fig. 6 of Ref. [2] shows that our calculations for a 200 pC bunch are in better agreement with the experimental measurement than for a bunch of 150 pC. We also have good agreement for the focusing effect in the horizontal direction (Fig. 9) and the vertical transverse kick (Fig. 10) for a bunch charge of 200 pC. In these calculations we assume that the total distance to the screen (where the transverse position is measured) is 5.25 m, which is the sum of the distance from the end of the dechirper to the screen (4.75 m) plus half of the dechirper length (0.5 m). One can compare our result with the right plot of Fig. 9 in Ref. [8] and find very good agreement. The calculated vertical position of the bunch due to an offset position of the bunch in the dechirper (red line in Fig. 10) is also in very good agreement with the measurement data (Fig. 8 in Ref. [2]).

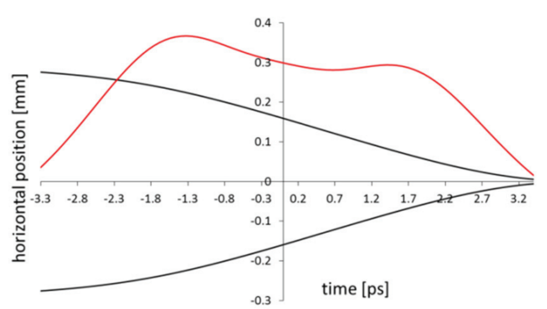

Figure 9: Horizontal position of the bunch boundary particles (black lines) downstream of the dechirper for a bunch charge of 200 pC. The red line shows the bunch charge distribution.

A blue line in Fig. 10 shows the energy loss of the bunch. It can be seen that the losses increase with the offset of the beam.

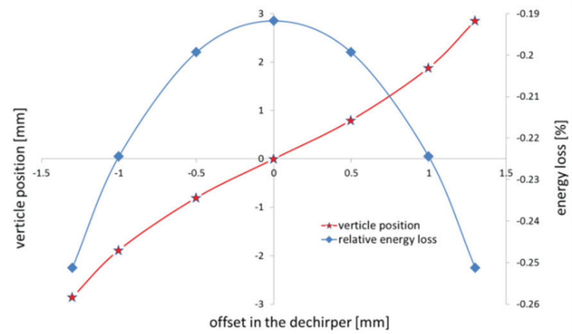

Figure 10: Vertical position of the bunch downstream of the dechirper (red line with red stars) and energy loss (blue line with diamonds) as a function of the vertical offset in the dechirper for a gap of 6 mm. The bunch charge is 200 pC.

To understand the reason for the difference between the wake potential calculated by our code and the single mode approach used for wake field calculations in Ref. [2], we carried out calculations of shorter bunches for this dechirper to derive the Green's function. We found that the difference came from the difference of Green's function at small distances. This difference is important even for a bunch length of 0.67 mm.

ACKNOWLEDGMENT

The author would like to thank Mike Sullivan for help and valuable comments, Axel Brachmann, Rick Iverson, Yunhai Cai, Paul J. Emma, Zhirong Huang and Franz-Josef Decker for support and interest in this work, and physicists of the Beam Physics Department for useful discussions.

REFERENCES

[1] A. Novokhatski et al., Phys. Rev. ST Accel. Beams 17, 124401 (2014).
[2] P. Emma et al., Phys. Rev. Let. 112, 034801 (2014).
[3] K. L. F. Bane and G. V. Stupakov, Phys. Rev. ST Accel. Beams 6, 024401 (2003).
[4] Z. Zhang et al., Phys. Rev. ST Accel. Beams 18, 010702 (2015).
[5] A. Novokhatski and A. Mosnier, in Proceedings of the 1997 Particle Accelerator pp. 1661–1663.
[6] A. Novokhatski and A. Mosnier, DAPNIA/SEA-96-08, 1996.
[7] A. Novokhatski Nuclear Instruments and Methods in Physics Research A684 (2012), 46–51.
[8] A. Novokhatski, SLAC-PUB-11556, 2005.
[9] A. Novokhatski, in Proceedings of the 31st (FEL09), Liverpool, UK.
[10] A. Novokhatski, Phys. Rev. ST Accel. Beams 14, 060707 (2011).

THE EFFECT OF WAKE FIELDS ON THE FEL PERFORMANCE*

A. Novokhatski#, F.-J. Decker, Yu. Nosochkov, M. Sullivan
SLAC National Accelerator Laboratory, Menlo Park, California, 94025, U.S.A.

Abstract

When a beam travels near collimator jaws, it gets an energy loss and a transverse kick due to the back reaction of the beam field diffracted on the collimator's jaws. The effect becomes very important for an intense short bunch when a tight collimation of the background beam halo is required. In the Linac Coherent Light Source (LCLS) at SLAC a collimation system is used to protect the undulators from radiation due to particles in the beam halo. The collimators in the LCLS must remove the halo particles before they affect and eventually degrade the very precise fields of the permanent magnet undulators [1]. The wake field effect from the collimators not only brings an additional energy jitter and change of the trajectory of the beam, but also rotates the beam on the phase plane that consequently leads to a degradation of the performance of the Free Electron Laser (FEL) at LCLS. In this paper, we describe a model of the wake field radiation in the SLAC linac collimators. We also present results of experimental measurements, which clearly confirm our model.

INTRODUCTION

The effect of collimators with small apertures on the transverse beam dynamics was observed during the operation of the Stanford Linear Collider (SLC) [2]. The problem of wake fields excited by collimators becomes more important for linac operation and x-ray production at LCLS. The backward reaction of the wake field from the collimators on the beam brings an additional energy jitter and a change of the trajectory of the beam. It leads also to a degradation of the FEL performance at the LCLS. This is because of the special character of the wake fields: the response reaction depends on the longitudinal position of the particles in the bunch. The "head" of the bunch is not deflected at all, but the "tail" gets the maximum deflection force. This kind of kick leads to the bunch being geometrically tilted. Because the "tail" of the bunch may oscillate in the lattice, the orientation of the bunch in space will oscillate too. Effectively the transverse projected emittance is increased and the FEL performance is degraded.

SLAC LINAC COLLIMATOR

Nine adjustable beam collimators are used in the LCLS operation, mainly accomplished in two main sections: at end of the SLAC linac and in the region from the linac to the undulators (LTU). Each collimator is composed of horizontal and vertical pairs of rectangular collimator jaws. The geometry of a collimator assembly is very complicated because each jaw is independently and remotely adjustable and can completely shadow the beam path. A collimator is essentially a kind of assembly of RF cavities coupled to the beam. Bellows with a chamber form two quarter-wave coaxial cavities. There are several trapped RF modes inside the collimator volume. In a multi-bunch operation, some energy is deposited in this region. One jaw can be in a position that is too close to the beam path while the other jaw is moved out. The jaws have a titanium alloy body with a slightly curved face (10-m radius) and a titanium-nitride jaw surface for improved conductivity and survivability against beam hits [3]. Currently the gap between jaws is kept approximately ±1.6 mm in all collimators. However, the spontaneous beam halo requires smaller gaps.

A TRANVERSE KICK FROM A COLLIMATOR JAW

Based on the analytical estimates [4] we assume that the kick from a collimator jaw is inversely proportional to the distance to this jaw. We estimate a kick for a particle with longitudinal position s in a bunch as

$$g(s) = \frac{Z_0}{4\pi} I_b \frac{s}{\delta}, \tag{1}$$

where δ is a transverse distance from the bunch to the collimator jaw, I_b is the bunch current, and Z_0 is impedance of free space. The average bunch kick will be

$$g_{av} = \frac{1}{8\pi\varepsilon_0} \frac{Q}{\delta}. \tag{2}$$

Opposite to the energy loss, which is proportional to the bunch current, the average kick is determined by a bunch charge Q and the proximity of the beam to the edge of the collimator jaw. The nonlinear behaviour of the kick leads immediately to emittance growth if a bunch travels very close to a collimator jaw edge. However, even a linear kick may increase the effective or projected emittance because a bunch "head" and a bunch "tail" will get different kicks. A "head" will receive nothing, but a "tail" will get a maximum kick.

A DIPOLE KICK FROM A COLLIMATOR WITH TWO JAWS

If we know a kick from one jaw, we can calculate a kick from a collimator with two jaws. Each jaw attracts the beam and the total kick must be the sum of the two kicks

*Work was supported by DOE-AC02-76SF00515.
#novo@slac.stanford.edu

ISBN 978-3-95450-134-2

$$g_{av} = \frac{Q}{8\pi\varepsilon_0}\left(\frac{1}{\delta_1} - \frac{1}{\delta_2}\right), \tag{3}$$

where δ_1 and δ_2 denote displacements from the two jaws.

If a bunch has a small offset Δx relative to a symmetry plane between the two jaws, then we get a dipole kick

$$g_{av} \approx \frac{Z_0 c Q}{4\pi}\frac{\Delta x}{a^2} \quad \Delta x << a\,. \tag{4}$$

Here we assume that the distance between the two jaws is *2a*. The average kick is proportional to the displacement of a bunch from a symmetry plane and inversely proportional to the square of the distance between the jaws, contrary to the theoretical model in reference [2]. The latter model predicts a kick inversely proportional to the bunch length and the distance between jaws. This model did not get agreement with experimental results.

MEASUREMENTS AND DATA ANALYSIS

The SLAC collimators are installed mainly at the end of the linac and in the LTU beam line. The beam line regions containing the collimators are detailed in [1]. We use upstream and downstream beam position monitors (BPMs) to determine the incoming and outgoing trajectories of the beam. The measurement of the beam positions at the locations of these BPMs allow us to measure the kick angle created by the transverse wake fields. The BPMs also provide information about the bunch charge. Controlling the bunch charge, we may determine position of a jaw when it touches the beam. The initial beam trajectory corresponds to a normal LCLS operation when the beam is centered in the collimators by using feedback kicks. We record BPMs dataset for each position of a collimator jaw (20 machine pulses). For each measurement only one jaw is moved in the direction to the collimator center, while the other jaw is taken far away from the beam. Each time the jaw position is changed in a step of 0.05 mm or less. Measurements of the beam kick due to the collimator wake fields were made with the beam energy of 11.5 GeV and the bunch charge of 150 pC.

For every position of a jaw we averaged all dataset (20 machine pulses) removing any failed pulse or BPM malfunction. We also calculated a ratio of a bunch charge before and after the measuring collimator using the BPM data. This ratio is shown in Fig. 1 for the vertical collimator with a vertical jaw moving down. The red circles correspond to the measured values. As the collimator jaw touches the beam, the ratio is decreased. When a bunch charge loss reaches 50%, the collimator jaw edge is in the center of the bunch. We have to note that the measured position of the beam may not be exactly in the center of the collimator. Assuming that the transverse distribution of the bunch charge has a Gaussian shape, we approximate the measured data by the Error function and determine the displacement of a bunch relative to a collimator jaw and the bunch size. The black solid line in Fig. 1 shows this approximation. We found that the displacement is 106 micron for this collimator and the vertical bunch size is equal to 65 micron. Measurement with a horizontal collimator showed that the horizontal beam size is the same as the vertical of 65 micron.

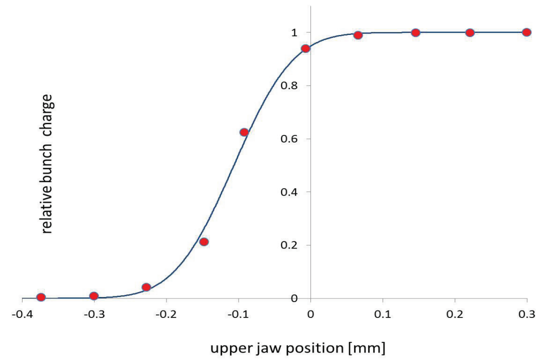

Figure 1: Ratio of a bunch charge after and before a collimator as a function of the collimator jaw position, where the upper jaw is moving down. Red circles: measurement, black solid line: analytical approximation.

For the transverse kick analysis we chose only those positions of a jaw where the bunch charge due to a collimator is not changed much. The first goal was to determine the direction of a kick induced by the wake fields. To resolve it, we measured a beam trajectory along the linac, LTU and undulator regions, where a jaw position was close to the beam, and compared it to a reference trajectory where a jaw was moved far away from the beam. Figure 2 shows the difference of the horizontal projections of these trajectories downstream of the measured horizontal collimator corresponding to the left jaw moving towards the beam. One can see that the beam receives a negative kick.

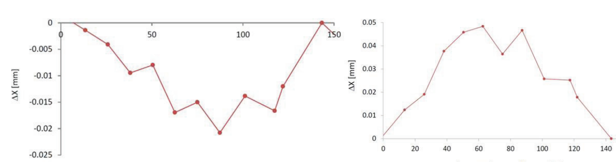

Figure 2: Difference of the horizontal projections of the measured and reference beam trajectories downstream of a horizontal collimator when the left or right jaw moved towards the beam.

When the right jaw of the same collimator was moved towards the beam, it resulted in a positive kick, as can be seen in Fig. 3 showing the difference of the horizontal projections of the measured and reference trajectories. Here the orbit effect due to the right jaw is larger since it was moved closer to the beam as compared to the left jaw. In both cases the beam gets a kick in the direction of

ISBN 978-3-95450-134-2

the closest jaw. In some sense, one can say that a jaw "attracts" the beam. The same effect was observed with the vertical collimators. This is a good experimental check of our theory.

The collimator kick leads to beam oscillations downstream of the collimator. Figure 3 shows the beam trajectory in the case where the bottom jaw of a vertical collimator is moved closer to the beam. The solid line is the vertical projection of the beam trajectory and the dotted line shows the horizontal projection.

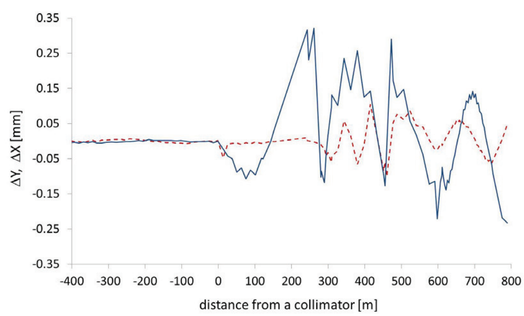

Figure 3: The vertical (solid line) and horizontal (dotted line) projections of the beam trajectory, where the bottom jaw of a vertical collimator is moved close to the beam.

In Fig. 3 we can see vertical oscillations in the undulator region (the last 100 meters), caused by the wake field effect from the vertical collimator. It is interesting to note that this is also accompanied by a horizontal oscillation indicating some unexplained coupling in this region.

To check the dependence of the average kick upon the collimator jaw position we analyse the BPM data at the place where the bunch gets the maximum displacement. As one can see in Fig. 2, this region is approximately 60-80 m downstream of the collimator. The measurement results for different collimators are presented below. Figure 4 shows a beam position and a relative bunch charge after a collimator as a function of a bottom jaw position. One can see that the beam starts to get a kick before it touches the collimator jaw. These measurement results were compared with the formula (2), which predicts a kick to be inversely proportional to the distance between the beam and the collimator jaw. Based on this prediction, we calculated the averaged beam displacement using the linac lattice parameters.

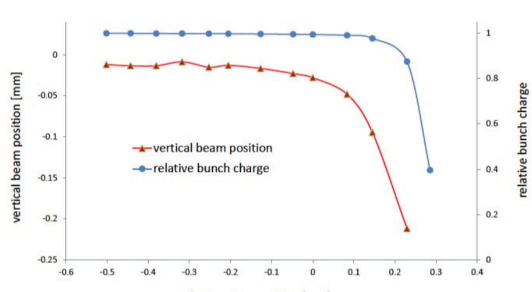

Figure 4: A vertical beam position (the line with triangles) and a relative bunch charge (line with circles) versus position of the collimator bottom jaw.

To make an accurate comparison, we approximate the measured data by our analytical prediction, optimising the possible mistakes in measuring of a jaw edge position and a position of a BPM. The results are shown in Fig. 5 for four jaws of a horizontal and a vertical collimator. In the measurement, each jaw was moved towards the beam keeping the other jaws far away from the beam. In these plots the horizontal axis is an inverse position of a jaw which makes the displacement a straight line. One can see a good agreement with our prediction for all the jaws. However, we found that the calculated approximate position of a collimator jaw is about 100 microns closer to the beam as compared to a jaw position measured at the point where a loss of 50% of the bunch charge occurs. This discrepancy can be explained by the fact that the beam, as we discussed before, has a non-zero transverse size. The latter can be included in the formula (2). The error of the BPM position was found to be inside a 5-10 micron range.

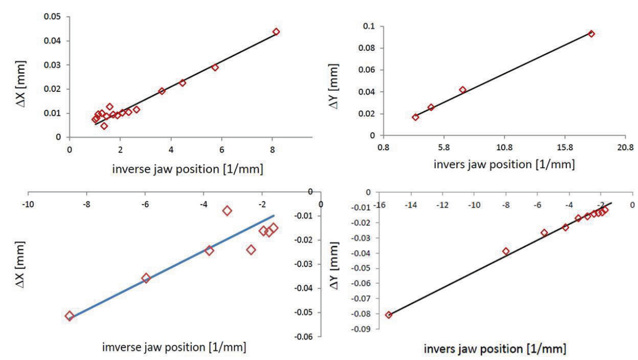

Figure 5: Comparison of the measured beam displacement after a collimator (red diamonds) with the theoretical prediction (black solid line) for four jaws of the horizontal and vertical collimators.

The special character of the wake fields is that the response reaction depends on the longitudinal particle position in the bunch. The "head" of the bunch is not deflected at all, but the "tail" receives the maximum deflection force. Since the transverse kick leads to the oscillations in the focusing system, the particles at different positions in the bunch will oscillate with different betatron phases. This makes the bunch geometrically tilted. This tilt angle will also perform oscillation in the lattice. In practice, the feedback system makes the head of the bunch oscillate too as it acts against the averaged kick. For this reason the feedback system cannot completely compensate the kick from a collimator.

In the beam phase space, the bunch tilt is rotating along the focusing system. Consequently, the transverse emittance may be increased. We can make an estimate of this additional emittance using a formula for the emittance and values of the β–functions, and assuming that the transverse beam size is twice the value of the beam displacement. We found that at some locations in the linac or LTU the effective (or projected) emittance can be comparable with the real beam emittance and reaching more than 1 mm-mrad. To verify this estimate,

ISBN 978-3-95450-134-2

we did an emittance measurement using the LCLS diagnostic in the LTU region [5]. The measurement was done downstream of the collimator using 4 wire scanners with a 45° phase advance between them. The results are shown in Fig. 6 for three different positions of the collimator jaw. The left plots show the measured beam sizes in the vertical plane, and the right plots the respective normalized phase space ellipses. The dashed lines indicate the projection angle for each measurement. The projected emittance increases when a collimator jaw approaches the beam. One can also see the tilt of the bunch, which is rotating on the phase plane relative to its center.

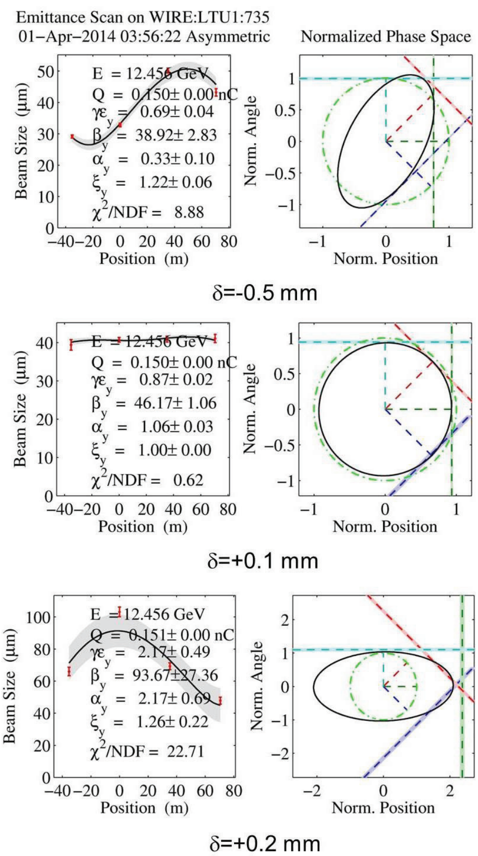

Figure 6: Emittance measurements for different positions of the collimator jaw: -0.5, +0.1, +0.2 mm.

The tilt of the bunch performs oscillations in the focusing system of the FEL. This indicates that different particles of a bunch oscillate with different betatron phases, which may disturb the coherent radiation in the FEL undulators. In this way the efficiency of the FEL performance may be reduced. We found confirmation of this prediction in the measurements. Usually the pulse energy of the X-ray beam describes the efficiency of the FEL. At LCLS this parameter is measured in a different way. Specifically, a gas detector is used to measure the FEL efficiency when a collimator jaw is moved towards the beam. The result of the measurement is shown at Fig. 7, where the relative bunch charge and the projected emittance are also shown. One can see a strong correlation between the growth of the projected emittance and the reduction of pulse energy. When a beam is close to a collimator jaw, a small change of the jaw position leads to a dramatic change in the X-ray production. We found that in this case the pulse energy exponentially depends upon the particle loss. The pulse energy decreases by 50% when only 3% of the beam particles are absorbed by a collimator jaw.

We also see the rotation of the bunch on the energy-coordinate phase plane using a new X-band transverse deflector at LCLS [6]. This deflector gives a linear kick along the bunch in the horizontal direction; hence, particles along the bunch obtain different horizontal positions.

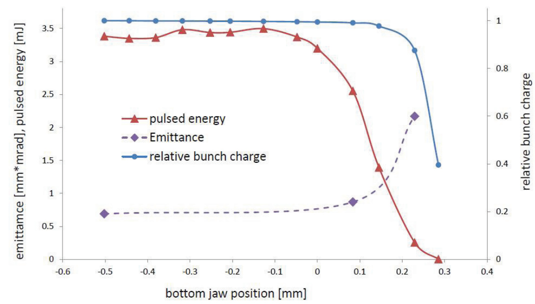

Figure 7: The FEL pulse energy (triangles), the beam emittance (diamonds) and the relative bunch charge (circles) versus the collimator jaw position.

As the bunch travels to the screen after the vertical bending magnet, particles with different energies obtain different vertical positions. In the measurement we change the position of a jaw in a vertical collimator and then take images from the screen. A typical image of a bunch, which produces an X-ray pulse energy of 3 mJ, is shown on the left plot of Fig. 8. As the collimator jaw comes closer to the beam (center and right plots in Fig. 8) the particles get transverse kicks opposite to the kick from the deflector. The energy spread also decreases as the X-ray production in the undulators is reduced. However, the horizontal size of the beam is also increasing. The latter could be explained by the existence of the vertical-horizontal coupling in the LTU as we mentioned before.

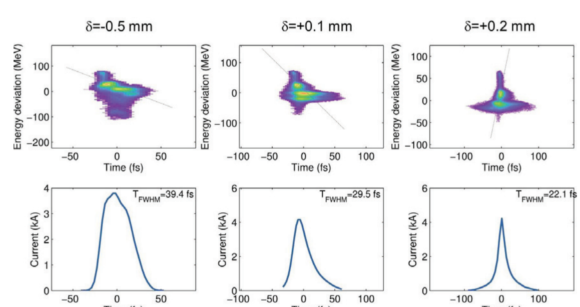

Figure 8: Bunch images on the phase plane for different positions of the collimator jaw.

REFERENCES

[1] P. Emma et al, in Proceedings of the European Particle Accelerator Conference (EPAC 2006),

Edinburgh, Scotland, MOPCH048.
[2] F.-J. Decker, et al., in Proceedings of the XVIII International Linac Conference (LINAC96), Geneva, Switzerland, August 1996.
[3] D. Walz et al., PAC89, Chicago, SLAC-PUB-4965.
[4] A. Novokhatski, "On the estimation of the wake potential for an ultra-relativistic charge in an accelerating structure", Institute of Nuclear Physics, Novosibirsk, Preprint INP 88-39, 1988.
[5] H. Loos et al., in Proceedings of the 14th Workshop, BIW10, Santa Fe, USA, May 2-6, 2010.
[6] Y. Ding et al., PR STAB, 14, 120701 (2011).

ISBN 978-3-95450-134-2

REVERSIBLE ELECTRON BEAM HEATER WITHOUT TRANSVERSE DEFLECTING CAVITIES

G. Stupakov and P. Emma
SLAC National Accelerator Laboratory, Menlo Park, CA, USA

Abstract

In Ref. [1] a technique to suppress the instability with the help of a reversible electron beam heater was proposed. It employs transverse deflecting cavities synchronized in a way that one of the cavities, located before a bunch compressor, generates a slice energy spread, while the other one removes it after the beam passes through the bunch compressor. In this paper we demonstrate that a reversible heater equivalent to that of [1] can be designed using much simpler elements: bend magnets and quadrupoles in combination with the energy chirp of the beam.

INTRODUCTION

The performance of modern free electron lasers is often limited by the microbunching instability in the electron beam that develops during its acceleration and transportation to the undulator. A search of new methods for effective suppression of the instability is crucial for future FELs, especially the ones that use external seeding. One of the promising approaches to this problem is the idea of a reversible electron beam heater proposed in Ref. [1]. It employs transverse deflecting cavities (TDS) synchronized in a way that one of the cavities, located before a bunch compressor, introduces a slice energy spread, and the other one removes it after the bunch compressor. Being an attractive concept, it however imposes extremely tight tolerances on the synchronization of the cavities. It also adds a considerable cost of the RF structures and an additional RF power system to the accelerator.

An ideal reversible heater has to perform two actions. First, it should increase the slice energy spread in the beam before the bunch compressor to the level that suppresses generation of microbunching instability due to coherent synchrotron radiation in the compressor, and to remove it afterwards restoring the beam to the original energy spread (amplified by the compression factor). Second, it is also desirable that the heater destroys energy and density modulations in the beam which are accumulated before the compressor—these are usually associated with the longitudinal space charge impedance and earlier compressing stages. Of course, the heater should not noticeably increase the transverse emittance of the beam.

In this paper we show how a reversible heater can be implemented using DC magnets without TDS. We simplify our analysis by assuming thin elements and neglecting the optics associated with drifts between them.

REVERSIBLE HEATER USING TDS

Here we give a brief description of the reversible heater based on transverse deflecting cavities and analyze, following [1], its effect on the energy spread of the beam and the beam emittance. While our analysis can be easily extended for a broader range of distribution functions, to evaluate the effect of the heater, for specificity, we consider an initial 4D Gaussian distribution function of the beam

$$f_0(x, x', z, \eta) = A \exp\left[-\frac{1}{2}\left(\frac{x^2}{\sigma_{x0}^2} + \frac{x'^2}{\sigma_{x'0}^2} + \frac{z^2}{\sigma_{z0}^2} + \frac{\eta^2}{\sigma_{\eta 0}^2}\right)\right], \tag{1}$$

where x and x' are the transverse coordinate and angle, z is the longitudinal coordinate in the beam, $\eta = \Delta E/E$ is the relative energy deviation, and σ_{x0}, $\sigma_{x'0}$, σ_{z0} and $\sigma_{\eta 0}$ are the standard deviations for the corresponding variables. In the distribution function (1) we ignore the transverse coordinates y and y'. The normalization constant A is such that $\int f_0 dx dx' dz d\eta = 1$.

When the beam with the initial distribution function (1) passes through a system under consideration the distribution function is transformed, $f_0(x, x', z, \eta) \to f_1(x, x', z, \eta)$, where f_1 is the distribution function at the exit. To find f_1, we use the formalism of linear optics with 4×4 beam transport matrices that act on vector (x, x', z, η). To take into account the acceleration before the BC that generates an energy chirp h (that is a linear correlation between the energy η and the longitudinal coordinate z) we will use the matrix $R_c(h)$,

$$R_c(h) = \begin{pmatrix} 1 & 0 & 0 & 0 \\ 0 & 1 & 0 & 0 \\ 0 & 0 & 1 & 0 \\ 0 & 0 & h & 1 \end{pmatrix}. \tag{2}$$

For a bunch compressor (BC) we will use the matrix

$$R_{BC} = \begin{pmatrix} 1 & 0 & 0 & 0 \\ 0 & 1 & 0 & 0 \\ 0 & 0 & 1 & r \\ 0 & 0 & 0 & 1 \end{pmatrix}, \tag{3}$$

with r being the $\{5, 6\}$ element of the 6-dimensional transport matrix of the compressor.

In linear optics, the R-matrix for a short transverse deflecting cavity is given by

$$R_{TDS}(K) = \begin{pmatrix} 1 & 0 & 0 & 0 \\ 0 & 1 & K & 0 \\ 0 & 0 & 1 & 0 \\ K & 0 & 0 & 1 \end{pmatrix}, \tag{4}$$

ISBN 978-3-95450-134-2

where the parameter K (K has dimension of inverse length) defines the strength of the transverse deflection, $K = e\omega_{\rm rf} V_{\rm cav}/\gamma mc^3$ with $\omega_{\rm rf}$ the cavity resonant frequency and $V_{\rm cav}$ the cavity voltage. The $\{4,1\}$ element of this matrix introduces an energy spread in the beam that is proportional to the beam transverse size. As a result, after passing through the cavity the beam energy spread increases from $\sigma_{\eta 0}$ to σ_η where

$$\sigma_\eta^2 = \sigma_{\eta 0}^2 + K^2\sigma_{x0}^2. \tag{5}$$

This is a reversible "heating" of the beam that can be used to suppress the microbunching instability and can be removed by a second TDS with opposite polarity. In addition to the slice heating, there is also another unavoidable side effect of the TDS: it tilts the beam in the x'-z plane and increases the beam projected transverse emittance. Calculations show that the beam emittance ϵ_x after the cavity is given by

$$\epsilon_x = \epsilon_{x0}\sqrt{1 + K^2\sigma_{z0}^2/\sigma_{x'0}^2}, \tag{6}$$

where $\epsilon_{x0} = \sigma_{x0}\sigma_{x'0}$ is the initial emittance before the cavity (we remind that there is no initial correlations in the beam between x and x').

In the reversible heater [1], the needed slice energy spread is generated by a first TDS placed before the bunch compressor, and then removed from the beam by a second TDS after the BC. The full transport matrix $R_{\rm rh}$ of such reversible heater, from the entrance to the RF section that generates the energy chirp to the exit from the second TDS, is obtained as a product of several matrices [1]

$$R_{\rm rh} = R_{\rm TDS}(-CK)\cdot R_{\rm BC}\cdot R_{\rm TDS}(K)\cdot R_{\rm c}(h) \tag{7}$$

where $C = (1+hr)^{-1}$ is the compression factor. Matrix $R_{\rm c}(h)$ on the right hand side accounts for the beam energy chirp h needed for compression, and matrix $R_{\rm TDS}(-CK)$ removes the energy spread introduced by $R_{\rm TDS}(K)$. Multiplying the matrices we find[1]

$$R_{\rm rh} = \begin{pmatrix} 1 & 0 & 0 & 0 \\ -CK^2r & 1 & 0 & -CKr \\ Kr & 0 & \frac{1}{C} & r \\ CKhr & 0 & h & 1 \end{pmatrix}. \tag{8}$$

Note that the second TDS also compensates the emittance growth (6) introduced by the first TDS. While this compensation is not complete, the residual emittance growth after the reversible heater for the parameters of Ref. [1] is small, $\Delta\epsilon_x/\epsilon_{x0} \approx 1.3\%$.

Finally, as is shown through computer simulations in [1], the TDS reversible heater satisfies the second condition outlined in the introduction: it smears out initial energy and density modulations accumulated in the beam before the compression. In Appendix we demonstrate the smearing in an analytical model of a cold beam.

[1] Matrix $R_{\rm rh}$ differs from the corresponding matrix in [1]. We believe that this is due to an error in the original publication—the matrix in [1] is not symplectic.

BEAM HEATING WITHOUT TDS

A reversible energy spread generated by TDS is not a unique property of deflecting cavities—it can also be obtained in passive systems that do not require RF power (assuming that the beam has already an energy chirp). To illustrate this statement we begin from a simple observation: a combination of a beam energy chirp and a bend magnet introduces a slice energy spread in a cold beam.

Let us assume that the beam with the distribution function (1) passes through an accelerating system that generates an energy chirp h and then through a *thin* bend magnet with a bending angle θ. For simplicity, we consider the case of a cold beam, $\sigma_{\eta 0} = 0$. The transport matrix for the bend, $R_{\rm b}$, is

$$R_{\rm b}(\theta) = \begin{pmatrix} 1 & 0 & 0 & 0 \\ 0 & 1 & 0 & \theta \\ -\theta & 0 & 1 & 0 \\ 0 & 0 & 0 & 1 \end{pmatrix}. \tag{9}$$

The combined effect of the chirp and the bend are given by the product $R_{\rm b}(\theta)\cdot R_{\rm c}(h)$. It transforms the initial variables to the final (indicated by the subscript 1): $x_1 = x$, $\eta_1 = \eta + hz$, $x_1' = x' + \theta(\eta + hz)$, $z_1 = z - \theta x$. Expressing from these equations x, x', z, η through x_1, x_1', z_1, η_1 and substituting them into (1) gives the distribution function after the bend $f_1(x_1, x_1', z_1, \eta_1)$ (hereafter, we drop the indices in the arguments of f_1). To find the beam distribution over η and z we integrate f_1 over x, x'. A straightforward calculation gives

$$\int dx\,dx'\,f_1(x,x',z,\eta) = A_1\exp\left(-\frac{\eta^2}{2\sigma_\eta^2} + a\eta z - bz^2\right). \tag{10}$$

with the slice energy spread after the bend as

$$\sigma_\eta = \frac{|h\theta|\sigma_{z0}\sigma_{x0}}{\sqrt{\theta^2\sigma_{x0}^2 + \sigma_{z0}^2}} \approx |h\theta|\sigma_{x0}, \tag{11}$$

and parameters a and b that are of no interest for what follows. In the last equation we assumed $|\theta|\sigma_{x0} \ll \sigma_{z0}$. We can see from (10) that each slice in the beam with a given value of coordinate z has now a Gaussian distribution in energy with the rms spread proportional to the product of the bending angle and the energy chirp.

The mechanism behind this heating is illustrated in Fig. 1. An initial cold beam distribution of a chirped beam in the longitudinal z-η phase space is a narrow line shown in the left part of the figure. After passage through the bend, particles with different horizontal coordinates, x, in each slice of the beam are shifted along z by $-\theta x$, as shown by the horizontal arrow, due to the $\{31\}$ element of matrix $R_{\rm b}$, see Eq. (9). This widens the original thin-line distribution of the beam into an ellipse, and introduces slice energy spread σ_η shown in the right plot.

A unavoidable side effect of the slice heating in this process is increasing of the beam transverse emittance through

ISBN 978-3-95450-134-2

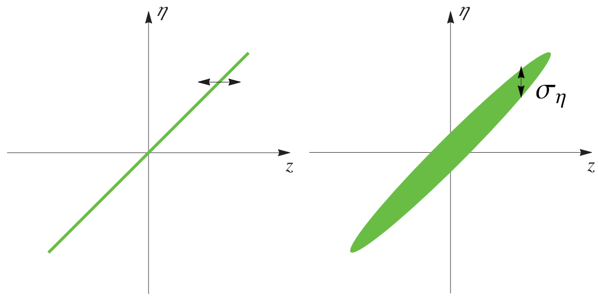

Figure 1: Illustration of beam heating.

tilting the phase space x-z. A direct calculation of the beam emittance ϵ with the distribution function f_1 gives the following expression for ϵ:

$$\epsilon = \sqrt{\epsilon_0{}^2 + h^2\theta^2\sigma_{z0}^2\sigma_{x0}^2}, \tag{12}$$

where $\epsilon_0 = \sigma_{x0}\sigma_{x'0}$ is the initial emittance. Note a similarity with the TDS case, Eq. (6).

To illustrate the magnitude of the heating and the emittance increase, we consider the following numerical example: the beam energy $E = 100$ MeV, $\sigma_{z0} = 1$ mm, $h = 0.01/\text{mm}$ corresponding to 1% of the total energy, $\sigma_{x0} = 0.2$ mm, $\theta = 50$ mrad. Using Eq. (11) we find

$$\sigma_\eta E \approx |h\theta|\sigma_{x0}E \approx 10 \text{ keV}. \tag{13}$$

In addition, assuming the initial horizontal projected normalized emittance $\epsilon_{x0} = 1$ μm we find from (12) that the final beam emittance, after the chirp-bend system, will be increased to about 20 μm, that is twenty times.

It is important to emphasize that the heating and the emittance increase due to the mechanism discussed above are reversible. Adding two bending magnets of opposite polarity before and after the bunch compressor would lead to an effective increase of the slice energy spread (11) ("beam heating") prior to the compressor, and removing the energy spread after the passage through the system ("beam de-heating"). This should result in the suppression of the beam microbunching due to the coherent synchrotron radiation of the beam inside the BC [2–5]. Note that in this arrangement, due to the bends, the beam line becomes tilted at an angle with respect to the direction of the beam line before (and after) the auxiliary bending magnets. Note also that while this arrangement is similar to the setup proposed in Ref. [6], it is however not the same: in particular, the beam energy chirp in Ref. [6] is generated between the bends, and in our case it is outside of the bends.

A simple reversible heater using the two bend magnets is not completely satisfactory: it does not suppress the incoming energy and density modulations in the beam. Indeed, if we calculate the R-matrix of the sequence "bend–bunch compressor–bend of opposite polarity" we find that this matrix is equal to the original R_{BC} matrix,

$$R_\text{b}(-\theta) \cdot R_\text{BC} \cdot R_\text{b}(\theta) = R_\text{BC}. \tag{14}$$

This means that while suppressing microbunching due to CSR in the BC, the system converts an energy modulation, accumulated by the beam in the linac before the compression, into a density modulation through the r matrix element exactly the same way as without the auxiliary bends. In the next section we will show how this can be improved with the help of additional accelerating cavities that modify the beam chirp after the first bending magnet.

REVERSIBLE HEATER WITHOUT TDS

We first show that the TDS matrix itself can be implemented as a combination of energy chirps, bends and focusing. In this analysis we use the following thin-quad matrix with the focal length F:

$$R_\text{q}(F) = \begin{pmatrix} 1 & 0 & 0 & 0 \\ -1/F & 1 & 0 & 0 \\ 0 & 0 & 1 & 0 \\ 0 & 0 & 0 & 1 \end{pmatrix}. \tag{15}$$

With the matrices defined earlier, it is a matter of simple matrix multiplication to show the product of the matrices

$$R_\text{q}(f) \cdot R_\text{b}(-\theta) \cdot R_\text{chirp}(-h) \cdot R_\text{b}(\theta) \cdot R_\text{chirp}(h), \tag{16}$$

is identical to the matrix $R_\text{TDS}(K)$ given by Eq. (4) if parameters F and h and θ are chosen such that

$$F = -\frac{1}{K\theta}, \qquad h = \frac{K}{\theta}. \tag{17}$$

For a given K, the bending angle θ in these relations can be considered as a free parameter.

Eq. (16) proves that the TDS matrix can be implemented as a sequence "energy chirp–bend–opposite energy chirp–opposite bend–quad". With this result, it is not surprising that full matrix (8) of the reversible heater can be implemented as a sequence of the following elements: "energy chirp–thin bend–energy de-chirp–bend of opposite sign–thin quad" (as above, we keep ignoring the transverse optics effects due to the finite length of each element). Indeed, as can be verified by direct matrix multiplication, the following combination $R_\text{rh}^{(1)} = R_\text{b}(\theta_1) \cdot R_\text{BC} \cdot R_\text{chirp}\left(-h(1+\theta/\theta_1)\right) \cdot R_\text{b}(\theta) \cdot R_\text{chirp}(h)$ gives the matrix

$$R_\text{rh}^{(1)} = \begin{pmatrix} 1 & 0 & 0 & 0 \\ h\theta(\theta+\theta_1) & 1 & 0 & \theta+\theta_1 \\ -C^{-1}(\theta+\theta_1) & 0 & \frac{1}{C} & r \\ \frac{h\theta(\theta+\theta_1)}{\theta_1} & 0 & -\frac{h\theta}{\theta_1} & 1 \end{pmatrix}, \tag{18}$$

where the compression factor now is $C^{-1} = 1 - rh\theta/\theta_1$. It is easy to check that selecting the angles θ and θ_1 such that

$$\theta = -\frac{C^2Kr}{C-1}, \qquad \theta_1 = \frac{CKr}{C-1}, \tag{19}$$

reduces $R_\text{rh}^{(1)}$ to matrix (8). Note that because angles θ and θ_1 have different absolute values, the result of the system (18) is the rotation of the beam line by the angle $\theta_1 - |\theta|$, which

ISBN 978-3-95450-134-2

imposes a certain constrain on the geometry of the beam line.

To illustrate that the system with the matrix (18) offers a practical approach, we calculate the bending angles θ and θ_1 that make the reversible heater without TDS equivalent to the one with TDS from Ref. [1] with the parameter K of the first TDS equal to $K = 9.6 \times 10^{-4}$ cm. Following [1] we take the beam energy $E = 360$ MeV, the compression factor $C = 13$, $r = -138$ mm. Using Eqs. (18) we find the bending angles of the dipole magnets in our system

$$\theta_1 = 10.8°, \qquad \theta = -0.83°. \tag{20}$$

The heating inside the bunch compressor will be

$$\sigma_\eta E \approx |h\theta_1|\sigma_{x0} E \approx 10 \text{ keV}. \tag{21}$$

The projected emittance growth inside the BC will be $\epsilon_x/\epsilon_{x0} \approx 32$; it will be almost completely removed at the exit from the heater.

BUILDING BLOCKS FOR REVERSIBLE HEATER

Using a bend magnet as an elementary building block of a reversible heater has an evident disadvantage that, if not compensated by a subsequent bend of opposite polarity, it might require the downstream beam line to be angled relative to the direction at the entrance to the heater. As pointed out above, matrix (18), results in rotation of the downstream beam line by an angle $\theta_1 - |\theta|$. In this regard, it might be advantageous to replace bends as elementary building blocks with a sequence of magnetic elements that neither rotate not displace the beam line. One of such examples is provided by the following combination:

$$\begin{aligned} &R_\mathrm{b}\left(\frac{1}{4}\theta\right) \cdot R_\mathrm{d}(l) \cdot R_\mathrm{q}(F) \cdot R_\mathrm{d}(l) \cdot R_\mathrm{b}\left(-\frac{1}{2}\theta\right) \\ &\cdot R_\mathrm{d}(l) \cdot R_\mathrm{q}(F) \cdot R_\mathrm{d}(l) \cdot R_\mathrm{b}\left(\frac{1}{4}\theta\right) \cdot R_\mathrm{q}\left(\frac{F}{2}\right), \end{aligned} \tag{22}$$

where $R_\mathrm{d}(l)$ is the R-matrix of a drift of length l. Choosing an arbitrary F and $l = 2F$ and multiplying the matrices gives matrix (9). Since the total bending angle in (24) is zero, replacing bends in our previous analysis by this sequence eliminates beamline tilts and offsets for the price of additional complexity of the beam line.

ACKNOWLEDGMENT

This work is supported by the U.S. Department of Energy under contract No. DE-AC02-76SF00515.

APPENDIX: EFFECT OF THE REVERSIBLE HEATER ON INITIAL MODULATION

To analyze the effect of the reversible heater on an initial beam modulation, we make two simplifying assumptions. First, we assume a cold beam, $\sigma_\eta = 0$. Second we consider a long bunch, formally corresponding to the limit $\sigma_z \to \infty$. The latter is justified if the period of the modulation λ_0 is much smaller than $2\pi\sigma_z$.

We consider two cases: an initial energy modulation and an initial density modulation of the beam. In the first case the initial beam distribution function is

$$\begin{aligned} f_0(x, x', z, \eta) = \frac{n_0}{2\pi\sigma_x\sigma_{x'}} \exp\left(-\frac{x^2}{2\sigma_{x0}^2} - \frac{x'^2}{2\sigma_{x'0}^2}\right) \\ \times \delta(\eta - \Delta\eta \sin k_0 z), \end{aligned} \tag{23}$$

and in the second case we have

$$\begin{aligned} \Delta f_0(x, x', z, \eta) = \frac{\Delta n_0 \cos(k_0 z)}{2\pi\sigma_x\sigma_{x'}} \exp\left(-\frac{x^2}{2\sigma_{x0}^2} - \frac{x'^2}{2\sigma_{x'0}^2}\right) \\ \times \delta(\eta). \end{aligned} \tag{24}$$

In these equations, $k_0 = 2\pi/\lambda_0$ is the wavenumber of the modulation, $\Delta\eta$ is the amplitude of the energy modulation, Δn_0 is the amplitude of the density modulation, and n_0 is the beam density (number of particle per unit length). Note that in the second case we consider only the part Δf of the distribution function responsible for the density perturbation.

To evaluate the effect of the heater on modulations we will compute the Fourier component of the density perturbation $\Delta\hat{n}(k)$ before and after the the heater. For the first case, we do not have an initial density perturbation and hence $\Delta\hat{n}_0(k) = 0$. For the second case we initially have

$$\begin{aligned} \Delta\hat{n}_0(k) &= \int_{-\infty}^{\infty} dz\, dx\, dx'\, d\eta\, e^{-ikz} \Delta f_0(x, x', z, \eta) \\ &= \Delta n_0 \int_{-\infty}^{\infty} dz\, e^{-ikz} \cos(k_0 z) \\ &= \frac{1}{2}\Delta n_0(\delta(k - k_0) + \delta(k + k_0)). \end{aligned} \tag{25}$$

To calculate $\hat{n}(k)$ after the system we need to transform the distribution function from the initial (Eq. (23) or (24)) and then to calculate the Fourier integrals again. The transformation from the initial to final coordinates according to the R-matrix (8)

$$\begin{aligned} &x_1 = x, \qquad z_1 = Krx + \frac{1}{C}z + r\eta, \\ &\eta_1 = CKhrx + hz + \eta, \end{aligned} \tag{26}$$

where the subscript 1 indicates the variables after the heater and the variables without the subscript are before the heater and $C = (1 + hr)^{-1}$. Instead of expressing the initial coordinates in terms of the final ones and substituting then into the distribution function, one can, equivalently, integrate the initial distribution function replacing the final coordinate in e^{-ikz_1} by $e^{-ik(Krx+z/C+r\eta)}$. Hence, one needs to compute

$$\Delta\hat{n}(k) = \int_{-\infty}^{\infty} dz\, dx\, dx'\, d\eta\, e^{-ik(Krx+z/C+r\eta)} f_0(x, x', z, \eta).$$

ISBN 978-3-95450-134-2

In the case of the energy modulation, Eq. (23), we have

$$\Delta\hat{n}(k) = \frac{n_0}{2\pi\sigma_{x0}\sigma_{x'0}} \int_{-\infty}^{\infty} dz\, dx\, dx'\, d\eta\, e^{-ik(Krx+z/C+r\eta)} \times \exp\left(-\frac{x^2}{2\sigma_{x0}^2} - \frac{x'^2}{2\sigma_{x'0}^2}\right)\delta(\eta - \Delta\eta \sin k_0 z). \quad (27)$$

For comparison, consider first the effect of the bunch compressor, that is when there are no TDS cavities, $K = 0$. Integrating over dx and dx' and using the identity

$$e^{-ia\sin\zeta} = \sum_{m=-\infty}^{\infty} e^{im\zeta} J_m(-a) \quad (28)$$

we find

$$\Delta\hat{n}(k) = n_0 \sum_{m=-\infty}^{\infty} J_m(-kr\Delta\eta) \int_{-\infty}^{\infty} dz e^{-iz(k/C-mk_0)} = 2\pi C n_0 \sum_{m=-\infty}^{\infty} J_m(-mCk_0 r\Delta\eta)\delta(k - mCk_0). \quad (29)$$

This is the standard effect of conversion of the energy modulation into the density one through r (augmented by the compression factor C). We see that $\Delta\hat{n}(k)$ consists of infinitely many harmonics of the initial wavenumber k_0 with the harmonic number given by the integer m.

Returning to the original equation (27) with nonzero K we find that $\Delta\hat{n}(k)$ given by (29) is now multiplied by an additional suppression factor

$$\frac{1}{\sqrt{2\pi}\sigma_x} \int_{-\infty}^{\infty} dx\, e^{imCk_0Krx} \exp\left(-\frac{x^2}{2\sigma_x^2}\right) = e^{-(mCk_0rK\sigma_{x0})^2/2}. \quad (30)$$

We see that if the exponent in this equation is large enough the final density modulation converted from the initial energy modulation is exponentially suppressed by the heater.

For the initial density modulation, Eq. (24), we have

$$\Delta\hat{n}(k) = \frac{\Delta n_0}{2\pi\sigma_{x0}\sigma_{x'0}} \int_{-\infty}^{\infty} dz\, dx\, dx'\, d\eta\, e^{-ik(Krx+z/C+r\eta)} \times \cos(k_0 z) \exp\left(-\frac{x^2}{2\sigma_{x0}^2} - \frac{x'^2}{2\sigma_{x'0}^2}\right)\delta(\eta) = \frac{1}{2} C\Delta n_0 e^{-(Ck_0rK\sigma_{x0})^2/2}(\delta(k - Ck_0) + \delta(k + Ck_0)). \quad (31)$$

We see that it is compressed by a factor of C and suppressed by the same factor (30) with $m = 1$.

REFERENCES

[1] C. Behrens, Z. Huang, and D. Xiang, *Reversible electron beam heating for suppression of microbunching instabilities at free-electron lasers*, Phys. Rev. ST Accel. Beams, 15 (2012), p. 022802.

[2] M. Borland, *Simple method for particle tracking with coherent synchrotron radiation*, Phys. Rev. ST Accel. Beams, 4 (2001), p. 070701.

[3] S. Heifets, G. Stupakov, and S. Krinsky, *Coherent synchrotron radiation instability in a bunch compressor*, Phys. Rev. ST Accel. Beams, 5 (2002), p. 064401.

[4] Z. Huang and K.-J. Kim, *Formulas for coherent synchrotron radiation microbunching in a bunch compressor chicane*, Phys. Rev. ST Accel. Beams, 5 (2002), p. 074401.

[5] E. L. Saldin, E. A. Schneidmiller, and M. V. Yurkov, *Klystron instability of a relativistic electron beam in a bunch compressor*, Nucl. Instrum. Meth., A490 (2002), pp. 1–8.

[6] J. Qiang, C. E. Mitchell, and M. Venturini, *Suppression of microbunching instability using bending magnets in free-electron-laser linacs*, Phys. Rev. Lett., 111 (2013), p. 054801.

ISBN 978-3-95450-134-2

FRONT END SIMULATIONS AND DESIGN FOR THE CLARA FEL TEST FACILITY

J.W. McKenzie, A.D. Brynes, B.L. Militsyn, STFC Daresbury Laboratory, Warrington, WA4 4AD, UK

Abstract

We present the design and simulations of the Front End for CLARA (Compact Linear Accelerator for Research and Applications), the proposed UK FEL test facility at Daresbury Laboratory. This is based around an S-band RF photocathode gun. Initially this will be the 2.5 cell gun, currently used on VELA facility at Daresbury, which is limited to 10 Hz repetition rate. Later, this will be upgraded to a 1.5 cell gun, currently under development, which will allow repetition rates of up to 400 Hz to be reached. The beam will be accelerated up to 50 MeV with a booster linac which will be operated in both bunching and boosting modes for different operating regimes of CLARA. Simulations are presented for a currently achieved performance of the RF system and drive laser with optimisation of the laser pulse lengths for various operational modes of CLARA.

INTRODUCTION

CLARA (Compact Linear Accelerator for Research and Applications) is a proposed 250 MeV FEL test facility at Daresbury Laboratory [1]. It will comprise a photoinjector, a four section S-band linac and FEL test area. The first 2 m long linac section serves as a booster or a buncher. CLARA is designed to test out various novel FEL schemes which require different beam pulses varying from ultra short very high current bunches for single-spike SASE to relatively long for seeded FEL. To cover all the range of the bunch lengths, longitudinal compression is going to be provided through both magnetic compression and velocity bunching. For many of these schemes, the required beam parameters can be met by either compression scheme. However, seeded FEL operation can only be met with the magnetic compression as a constant current profile is desired along the bunch, while single-spike SASE can only be met with velocity bunching to a very short bunch with high peak current. A comparison of the compression schemes can be found in [2].

A staged approach is taken to construction and commissioning, with stage one comprising of a photoinjector and booster linac to be installed in 2016. This links in to the existing VELA facility at Daresbury [3] and shares its RF and laser infrastructure.

The electron source for CLARA will initially be the 2.5 cell S-band RF gun currently used at VELA. This is limited to 10 Hz repetition rate, at bunch charges of up to 250 pC. The gun is fed from a 10 MW klystron with 8.5 MW of power available at the gun. The maximum beam momentum measured around 5.0 MeV/c. To reach repetition rates of up to 400 Hz, a 1.5 cell High Repetition Rate S-band Gun (HRRG) has been designed and is currently under construction [4].

The VELA photoinjector laser will also be used to drive CLARA, with a beam split in the transport line. The laser pulse has a length of 76 fs rms that allows short low charge electron bunches to be produced. In this paper we analyse the beam parameters which can be obtained with the currently achieved performance of the RF system and laser and investigate the use of a longer pulse laser for the different modes of CLARA.

OPERATION OF THE BASELINE INJECTOR WITH REDUCED GUN FIELD

The original design of the 2.5-cell gun assumed operation at a peak field of 100 MV/m. However, the measured beam momentum in VELA is lower than was expected based on simulations and measured quality factors [5]. To match the measured beam momentum of 5 MeV/c, simulations show the peak electric field to be 70 MV/m.

In this work, beam dynamics simulations were carried out with the ASTRA code. The photoinjector laser spot size was simulated as a 1 mm diameter flat-top with a 76 fs rms Gaussian temporal profile. An intrinsic emittance of the beam from the copper photocathodes assumed to be of 0.9 mm·mrad per mm rms as per LCLS measurements [6].

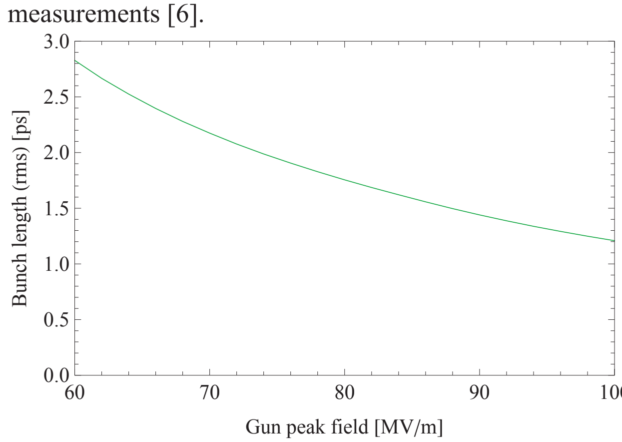

Figure 1: Simulated dependence of the length of a 250 pC bunch at the exit of the 2.5 cell gun.

Due to the short laser pulse length, the gun operates in the “blow-out” regime, where the space-charge expands emitted bunch. Thus, the electron bunch length in this case is determined by the bunch charge and the rate of acceleration. Fig. 1 shows how the rms length of a 250 pC bunch after the gun depends on the peak field (for the same operational phase). It can be seen then that reducing the gun peak field from 100 MV/m to 70 MV/m, causes

ISBN 978-3-95450-134-2

an increase of almost a factor of two in the electron bunch length.

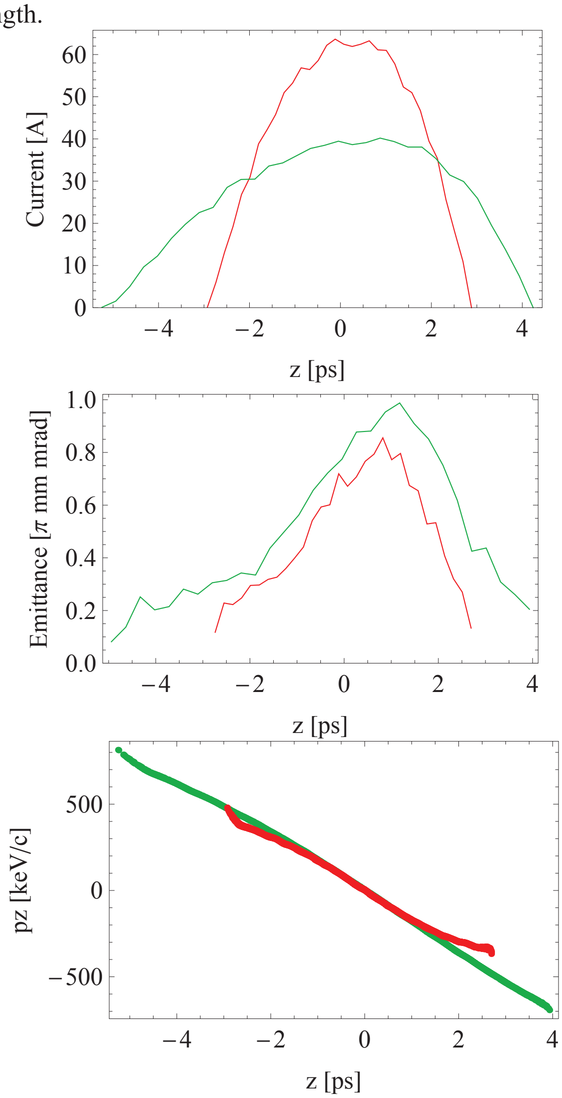

Figure 2: Distribution of the current (top), slice emittance (middle) and the momentum deviation (bottom) in 250 pC electron bunch for 100 MV/m (red) and 70 MV/m (green).

Figure 2 shows the results of comparison of the original, published in the CDR [1], CLARA bunch simulation at the FEL entrance at 100 MV/m and 250 pC, and that at reduced gun peak field of 70 MV/m. A few further modifications are included in the simulation. The main one being that the distance from photocathode to the entrance of the linac has been reduced slightly due to engineering considerations. The reduction in gun peak field also causes a rise in transverse emittance. The solenoids, surrounding first linac section, have been switched off to allow for a flat transverse beam profile at the exit of the second linac section and the linac phase set to give the same chirp in longitudinal phase space for compression downstream in the magnetic chicane.

Simulations with linac wakefields have shown no effect on the transverse beam dynamics and only have a small effect on the longitudinal beam dynamics (increasing the energy spread) as the bunch length is relatively long.

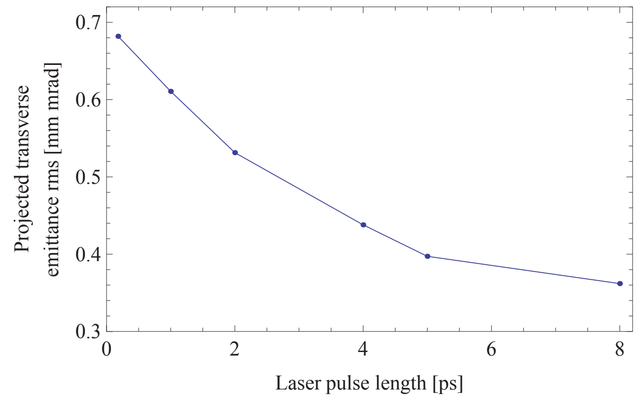

Figure 3: Dependence of the projected rms emittance of 250 pC bunch on drive laser pulse length.

OPTIMISATION OF THE LASER PULSE LENGTH

Since the electron bunch length increases to such a large extent in the “blow-out” regime, longer laser pulse lengths were investigated where the length of the electron bunch thus depends on the length of the drive laser pulse directly. To see any effect, the drive laser pulse length should be longer than the “natural” electron bunch length which is formed due to the space-charge induced blow-up. To investigate this, the drive laser pulse length was scanned in simulation.

For the simulations, a flat-top laser pulse was varied in 1 ps steps, with 0.2 ps rise and fall times. For each case, the gun phase and solenoid were optimised to produce minimum projected transverse emittance after the first linac section. The linac solenoids were then adjusted to further reduce the transverse emittance without overfocussing which had been seen to result in halo development in previous simulations. The scan was repeated for the 2.5-cell gun at a peak field of 70 MV/m, and for the 1.5 cell HRRG at a peak field of 100 MV/m and 120 MV/m.

2.5 Cell Gun at a Field of 70 MV/m

Figure 3 shows the biggest effect from increasing the laser pulse length is the reduction in transverse emittance. As is seen in the slice emittance profiles, shown in Fig. 4, this arises due to the reduction in the sharp peak in slice emittance that presents with the short laser pulse. Increasing the laser pulse length and flattening of its temporal profile, decreases this hump in slice emittance until there is a flat profile. It can be seen from these profiles, and also the current profiles that the overall bunch length does not change until the laser pulse length is longer than the natural space-charge blow-out bunch length. At this point, the bump in slice emittance is flattened out. Therefore there is an optimum laser pulse length for reducing slice emittance whilst keeping the electron bunch length as short as possible, in this case around 5 ps.

ISBN 978-3-95450-134-2

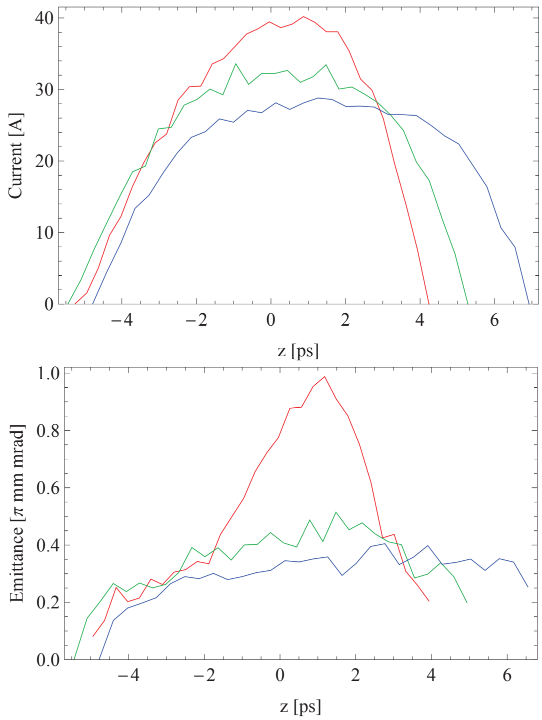

Figure 4: Current (top) and emittance (bottom) profiles for laser pulse lengths of 5ps (green), 8 ps (blue), compared to the previous 76 fs rms laser pulse (red).

1.5 Cell HRRG at 100 MV/m and 120 MV/m

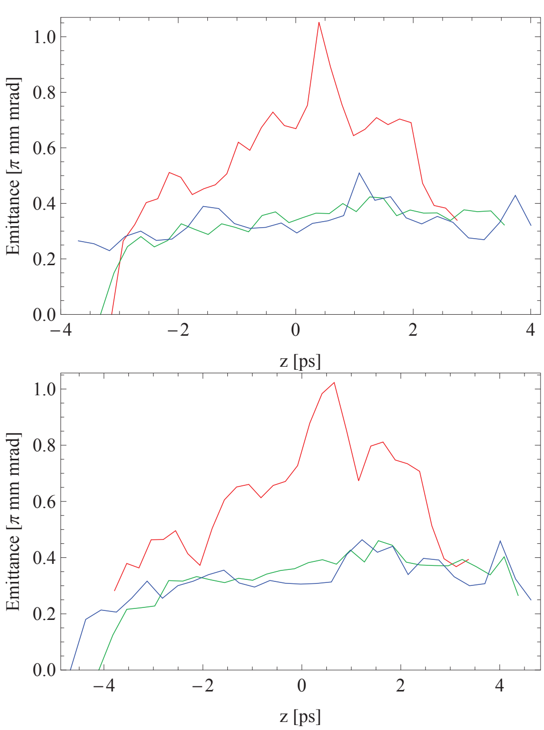

Figure 5: Current profiles at 120MV/m (top) and 100 MV/m (bottom) for laser pulse lengths of 3ps (green), 5 ps (blue), compared to the previous 76 fs rms laser pulse (red).

The above scans were repeated for the 1.5 cell HRRG at the design peak field of 120 MV/m, and a reduced field of 100 MV/m, as contingency for not achieving the design field. The behaviour is the same as for the 2.5 cell gun at 70 MV/m, but with a different optimum for the laser pulse length of 3 ps, as shown in Fig. 5.

Rise/Fall Times

A further investigation was made to look at the effect of the rise and fall times for the laser pulse. The 4 ps laser pulse was used, and simulations carried out at a higher number of macroparticles (100,000) to see the effect, with varying the rise and fall times in 0.1 ps steps. There was no effect on the current profile, however longer rise and fall times give rise to spikes in the slice emittance at the start and end of the bunch, as shown in Fig. 6. To reduce these spikes, the rise and fall times should be kept 0.2 ps or shorter. However, it is under question whether these slice emittance spikes where the current is low have any consequence to overall machine performance of the FEL.

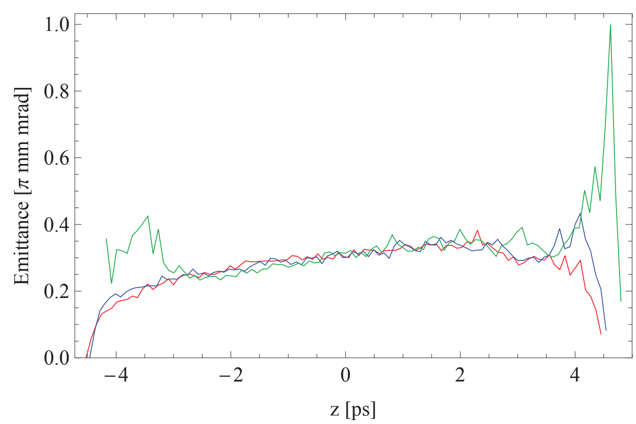

Figure 6: Slice emittance rise/fall times of 0.2 (red), 0.3 (blue), and 1 ps (green) for a 4 ps long laser.

VELOCITY BUNCHING MODE

The alternative to the magnetic bunch compression mode of CLARA is velocity bunching in the low energy section of the machine. Gentle compression with velocity bunching can provide similar bunch lengths as magnetic compression, however, it can also be used to produce very short bunches with high peak current, which are necessary for single-spike SASE FEL operation.

The optimal parameters of a 100 pC CLARA bunches using velocity bunching scheme were achieved with a 50 fs Gaussian laser pulse of diameter 1.8 mm on the photocathode. These laser parameters were found as result of a larger optimisation to provide the shortest bunches via velocity bunching in CLARA operated with the 2.5 cell gun [7]. The optimal velocity bunching compression was already obtained at the lower gun field of 70 MV/m, as at lower beam momentum for the same energy chirp velocity difference of the particles within the bunch is greater.

ISBN 978-3-95450-134-2

The effect of changing the laser specifications in the velocity bunching mode to the currently available drive laser parameters – a diameter of 1 mm and a length of 76 fs rms Gaussian, is shown in Fig. 7. The beam has similar rms length, but a less sharp current profile, with a drop of peak current by almost a factor of two. There is also a large increase in slice emittance. Further simulations have shown that the slice emittance can be reduced, but at the expense of further decreasing the peak current.

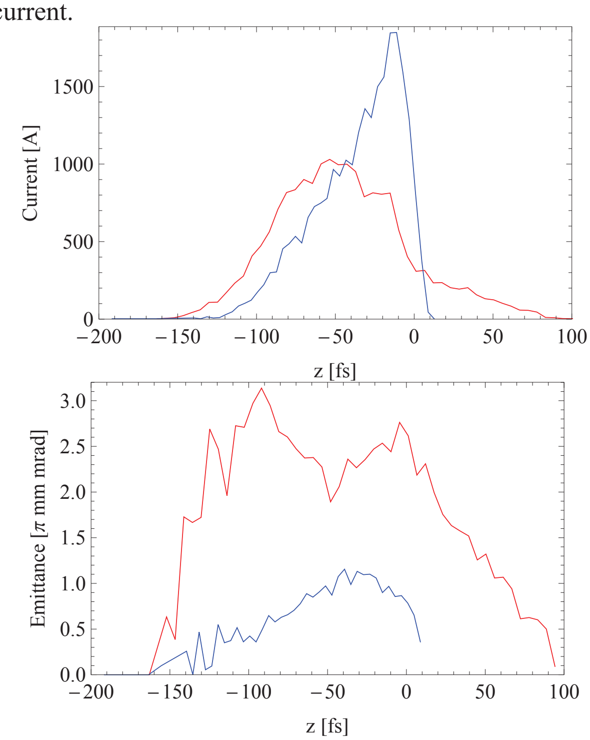

Figure 7: Optimised laser pulse (blue) and VELA laser pulse (red)

As with the magnetic compression case, longer laser pulses were also investigated (whilst keeping the laser spot diameter at 1 mm). For each case, the beamline settings were optimised at the exit of the second linac section. As can be seen in Fig. 8, increasing the laser pulse length causes a reduction in the peak current, but in all cases slice emittance can be kept reasonably low, unlike in the case of the existing laser pulse.

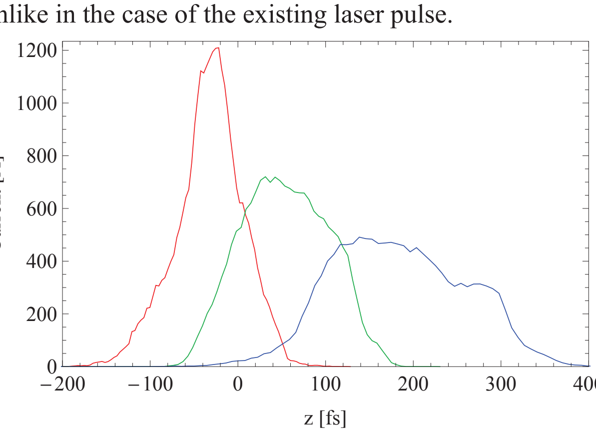

Figure 8: Current profiles for laser pulse lengths of 1 ps (red), 2 ps (green), 4 ps (blue).

It is seen then, that to produce the very high peak currents that make velocity bunching scheme ideal for single-spike SASE FEL operation, that a different photoinjector laser tuning has to be used compared to the magnetic compression mode.

A further consideration has to be made for wakefields as the bunch length is so short. Wakefields were then included for the booster and linac sections in the ASTRA simulations. For the case of the original optimised laser pulse, the simulated wakefields significantly decrease high peak current spike, although the overall bunch length remains similar, as shown in Fig. 9. Further investigation is required to analyse these wakefield effects.

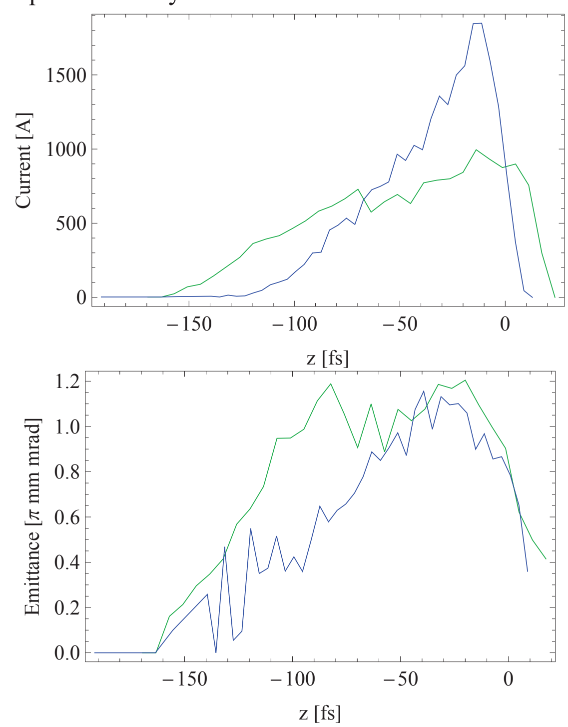

Figure 9: Current (top) and emittance (bottom) profiles with (green) and without (blue) linac wakefields.

CONCLUSION

Detailed analysis of the possibility of CLARA front end to deliver beams required for operation of the FEL in SASE, single spike SASE and seeded modes can be achieved with the current operational performance of the laser and RF system. However, the optimised beam parameters are met for a different photoinjector laser tuning for each case that may require an upgrade of the drive laser. Preliminary estimation of the impact of wakefields in booster and linac on the beam parameters at FEL shows that these leads to significantly decrease of the peak current for the single-spike case.

REFERENCES

[1] J.A. Clarke et al,. "CLARA Conceptual Design report", JINST **9** T05001, 2014

ISBN 978-3-95450-134-2

[2] P.H. Williams, et al., "Comparison of Compression Schemes for CLARA", Proc. IPAC2012, New Orleans, USA, (2012)1756-1758
[3] P.A. McIntosh et al, "A New Electron Beam Test Facility (EBTF) at Daresbury Laboratory for Industrial Accelerator System Development," IPAC'12, New Orleans, USA, (2012) 4074-4076
[4] B.L. Militsyn et al., "Design of the High Repetition Rate Photocathode Gun for the CLARA Project", Proc. LINAC'14, Geneva, Switzerland, (2014)1155-1158
[5] B.L. Militsyn, et al., "Beam Commissioning of VELA at Daresbury Laboratory", Proc. IPAC2014, Dresden, Germany, (2012)2986-2988
[6] Y. Ding et al., PRL **102**, 254801(2009)
[7] J.W. McKenzie & B.L. Militsyn, "A Velocity Bunching Scheme for Creating Sub-picosecond Electron Bunches from an RF Photocathode Gun", Proc. IPAC2011, San Sebastian, Spain, (2011)3194-3196

ISBN 978-3-95450-134-2

RFTweak 5 – AN EFFICIENT LONGITUDINAL BEAM DYNAMICS CODE

Bolko Beutner*, Martin Dohlus, Hannes Dinter
Deutsches Elektronen-Synchrotron (DESY), Hamburg, Germany

Abstract

The shaping of the longitudinal phase space in bunch compression systems is essential for efficient FEL operation. RF systems and self-field interactions contribute to the overall phase space structure. The design of the various facilities relies on extensive beam dynamics simulations to define the longitudinal dynamics. However, in everyday control room applications such techniques are often not fast enough for efficient operation, e.g. for SASE tuning. Therefore efficient longitudinal beam dynamics codes are required while still maintaining reasonable accuracy. Our approach is to pre-calculate most of the required data for self-field interactions and store them on disc to reduce required online calculation time to a minimum. In this paper we present the fast longitudinal tracking code RFTweak 5, which includes wakes, space charge, and CSR interactions. With this code the full European XFEL with a 1M particles bunch is calculated on the order of minutes on a standard laptop. Neglecting CSR effects this time reduces to seconds.

INTRODUCTION

RFTweak 5 is a fast tracking code for longitudinal phase space dynamics. A strong use case is the online setup of bunch compression in the control room during e.g. SASE tuning. The concept of the code is similar to LiTrack [1], which is written in MATLAB as well. RFTweak 5 includes effects of longitudinal wakes, space charge interactions as well as coherent synchrotron radiation (CSR) emission. While the underlying code is applicable to different electron linacs, the graphical user interface (GUI) of the code is build specifically for FLASH and the European XFEL. An example is shown in Fig. 1.

OVERVIEW OF THE TRACKING PROCEDURE

Beam-lines defined in RFTweak 5 consisting primarily of two different element types. Elements which keep the individual longitudinal particle position offset fixed while the energy is altered (Type 1) and the opposite in which the energy is constant and the position is modified (Type 2). Examples are RF structures or bunch compression chicanes respectively. We assume a sufficiently high beam energy to justify the assumption of fixed longitudinal position offsets in straight sections (Type 1 elements like drifts, quadrupoles, or RF structures). Furthermore, the assumption is made that elements with longitudinal dispersion (Type 2 like chicanes or energy collimator) consist purely of magnetic fields.

* bolko.beutner@desy.de

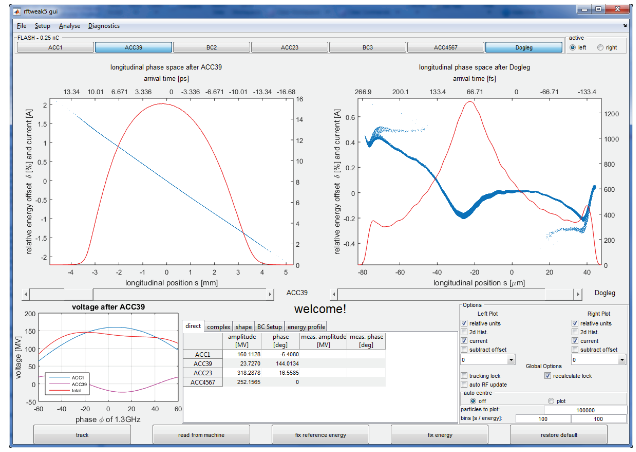

Figure 1: Layout of the main GUI for FLASH. Two phase space distributions are displayed at selected positions along the machine. Various options are available, like the display as point cloud or density histograms or the subtraction of polynomial offsets of various order. RF parameters of the linac can be entered by the user or read from the control system. Resulting voltage profiles after the lineariser cavities are directly displayed.

Self field interactions are neglected but CSR effects can be included as described later.

Both types of elements are described by the polynomial expansion

$$s^i_{n+1} = s^i_n + R_{56}\delta_{E_{i,n}} + T_{566}{\delta_{E_{i,n}}}^2 + \cdots \quad (1)$$

$$\delta_{E_{i,n+1}} = \delta_{E_{i,n}} + A + Bs^i_n + C{s^i_n}^2 + \cdots, \quad (2)$$

with the normalised energy offset $\delta_{E_{i,n}}$ of particle i at element n, some coefficients A, B, C representing longitudinal fields, and the longitudinal dispersion parameters $R_{56}, T_{566}, \ldots$.

In the first case the coefficients are obtained from a Taylor expansion of the longitudinal dispersion [2], in the latter the Taylor series expansion represents the longitudinal electric fields, e.g. the RF voltage.

Elements of Type 2 can include additional effects of longitudinal wakes. These wakes are either determined by geometry (e.g. cavities, changes in beam pipe diameter) or space charge. For FLASH and the European XFEL the geometric wakes are stored in a database [3]. In this database the integrated wakes per section are summarised as greens functions (wakes of an infinitesimal short bunch). Space charge wakes, which are dependent on the energy profile and the transverse beam dimensions, are summarised per section as well. These wake functions are calculated given

ISBN 978-3-95450-134-2

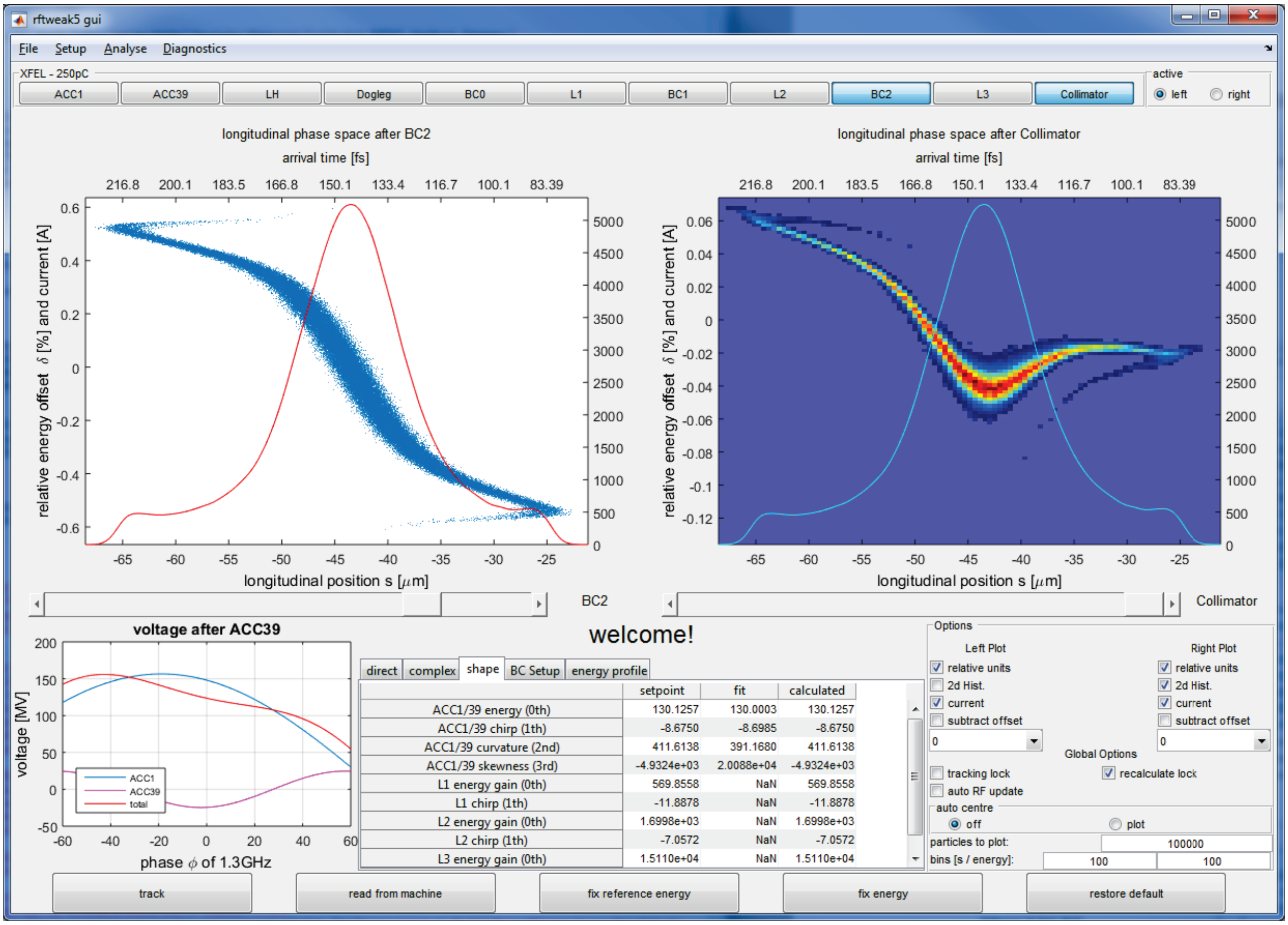

Figure 2: Layout of the main GUI for European XFEL. In this example RF parameters are controlled via abstract knobs corresponding to the desired shape of the longitudinal phase space for compression.

certain assumptions on the transverse dimensions from the design optics and a given energy profile. These wakes kernels are calculated before the actual tracking run, based on assumptions on the transverse beam size and a predefined energy profile. Wake fields, and the corresponding energy changes, are represented by a convolution of the sum of the wake-greens-functions with the actual longitudinal current profile.

Initial particle distributions are taken from ASTRA. From these 6D particle dumps only the longitudinal position and momentum information are directly used. Derived quantities like emittance or beam spot size are calculated and stored for later usage. The booster, ACC1 in the example of FLASH, is included in these ASTRA runs. To accommodate a variable setup of the booster in the code we apply the RF tracking first backwards to the entrance and then forward again.

To obtain CSR wakes in the relevant sections transverse phase space information are required. They are estimated from the initial particle distribution moments and linear transport from the start to the sections containing CSR effects. The tracking consists of a sequence of transport- and wake-steps. That transport is represented by 4D coefficients up to second order while the CSR wake kernels are taken from pre-calculated tables stored on disc.

Since these tables contain integrated wakes as well large transport steps, not necessarily smaller than the magnet dimensions, are possible. This allows for large tracking steps and thus efficient CSR calculations. The pre-calculation of these tables, however, can be very demanding. Especially since the tables need to be determined for each possible bending angle of the chicanes.

PROGRAM OVERVIEW

The principles outlined in the last section are combined into a MATLAB graphical user interface for use at the DESY FLASH and the European XFEL facilities. This graphical user interface was designed using the MATLAB datagui library developed at DESY [4].

The main functionality of the code is the ability to manipulate RF parameters of the machine and directly observe the resulting longitudinal profiles and phase space distributions, allowing for intuitive setup of bunch compression scenarios.

Bunch compression and the required shaping of the longitudinal phase space is not determined by individual RF stations voltage V and phase φ alone, but by an interplay of multiple stations. Therefore it is convenient to accept not only the voltage and phase of the individual stations

ISBN 978-3-95450-134-2

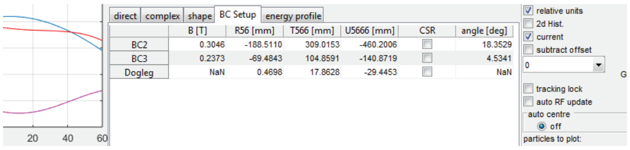

Figure 3: An example of the setup of dispersive sections. While the chicanes can be adjusted by the field, or bending angle, the dogleg or collimator sections are represented by the matrix elements. CSR calculations can be activated for each chicane individually.

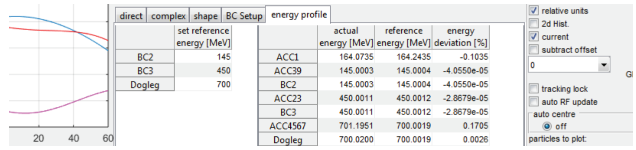

Figure 4: An overview of the energy profile in the currently selected model. On the left hand side the energies at the chicanes are defined as a basis for the wake table calculations. on the right hand side the actual profile is compared with these set values and the deviation is monitored.

as input parameters, as shown in Fig. 1. An obvious disadvantage of direct voltage and phase setup is the fact that each of these knobs changes the beam energy. However the compression is mostly tuned with a fixed beam energy at the chicanes while the chirp needs to be modified. Our approach here is to allow the user to set the RF not in Polar but in Cartesian coordinates, namely the real and imaginary part of $V \cdot \exp(i\varphi)$. The energy gain of a bunch is determined only by the real part while the imaginary part determines the chirp. This is equivalent to set a voltage V_0, the net energy gain, and to make the actual voltage a function of the phase as $V = V_0/\cos(\varphi)$.

In general compression tuning is more involved than correcting the voltage for off-crest acceleration to maintain energy. The total, voltage especially of the booster and lineariser higher harmonic cavity, upstream each chicane is important. In [5] a model is developed which allows to calculate the required RF parameters resulting in desired phase space shapes, namely the polynomial expansion of the longitudinal position correlation upstream and after each chicane. In Fig. 2 the input mask of these parameters is shown. The user can set-up the linearisation of the phase space basically independent of the desired chirp. A later modification of the chirp maintains the shape of the current profile but changes the bunch length, which is very useful for FEL tuning or setup of seeding schemes.

Apart from the RF parameters the bunch compressor chicanes can be set-up or read from the control system (see Fig. 3). CSR interactions are activated for each chicane individually. Since the charge density is highest after the last chicane it is often accurate enough to only calculate the CSR effects optimising calculation time.

As mentioned above part of our approach for fast calculations self-field effects are treated by pre-calculated files stored to disc. As an example the CSR kernel tables for European XFEL are about 4 GB of data since data needs to be calculated for each bending angle and each chicane (in our case tables are calculated in 0.05 deg steps covering the corresponding bending angle range of the chicanes). Kernel files for the space charge and wake calculations (about 150 MB for European XFEL) are energy dependent, so they have, in contrast to CSR tables, be recalculated if the energy profile changes to obtain correct results. This calculations take about 2 minutes on a standard laptop, so they can in principle be recalculated "on-the-fly".

Since the RF parameters are meant to be modified we can not assume that the energy profile is constant. The tool is constantly calculating the deviation of the actual model profile with the set-values for the tables (see Fig. 4). We estimate that energy deviations up to about 5% are tolerable before the tables need to be recalculated. The GUI offers different methods to deal with larger energy deviations. Either the voltages are modified automatically in an iterative process that the beam energy matches the target values ("fix energy" button) or the target energy profile is set to the actual values, recalculating the tables ("fix reference energy" button).

SIMULATED DIAGNOSTICS

To further help the user in the control room setting up the machine actual diagnostic components are simulated.

An important tool is the use of a transverse deflecting structure (TDS) in combination with a spectrometer dipole to image the longitudinal phase space (see Fig. 5). The image is obtained from the 2D longitudinal phase space distribution using 6D transport between the deflector and the screen including the whole beam-line section. The missing transverse components are randomised based on the design Twiss parameters at the deflector assuming some user defined slice emittance. The effect of the transverse deflecting structure is included as a transport matrix [6]. As seen in Fig. 5 it is valuable to see how the resolution limitations of such measurements "smear out" the current profile to help understand high frequency excitations on the beam even if sharp edges are not visible in the TDS images.

Another important diagnostic are the bunch compression monitors (BCM). These diagnostics measure integrated intensity from coherent radiation to give a single number corresponding to the bunch length. Such devices are valuable for setup and feedback systems. In the GUI (Fig. 6) this number is calculated from the longitudinal profile following the methods outlined in [7].

The virtual diagnostics offered in the GUI are the spectra obtained from the synchrotron radiation cameras as seen in Fig. 7.

All the diagnostics are representing the actual diagnostics as much as possible. The image presented for the TDS measurements for example represent the same pixel size and chip dimensions, as well as the real RF power to streak conversion. Even the colourmap used in the control system

ISBN 978-3-95450-134-2

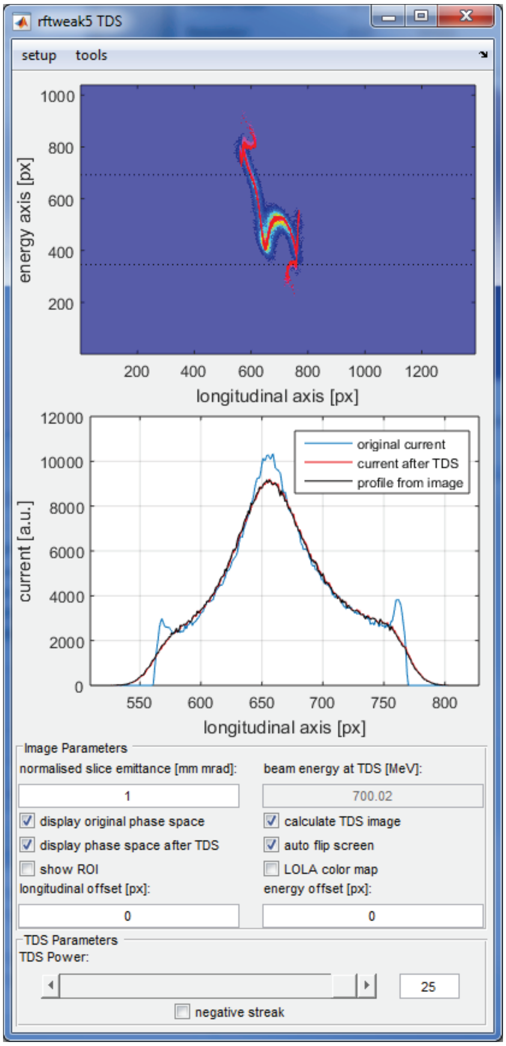

Figure 5: A simulated view of the LOLA transverse deflecting structure image for FLASH. The longitudinal phase space (red) is compared with the estimated image on the corresponding screen.

display can optionally be used. The BCM data are calculated using measured detector response data.

SUMMARY AND OUTLOOK

In this paper we presented a fast and efficient tracking tool for the longitudinal beam dynamics of electron linacs. Detailed GUI versions of the code were developed for FLASH and the European XFEL, but the code can in principle be applied to other machines as well. This tool is tested and in use at FLASH and intended as standard bunch compression setup aid at the European XFEL.

Pre-calculated wake kernel tables as well as a careful optimisation of tracking step size management allows efficient calculations on a time scale usable for control room applications. As an example the full European XFEL with 1 million macro-particles including geometric wakes, and longitudinal space charge is calculated in 5 seconds on a

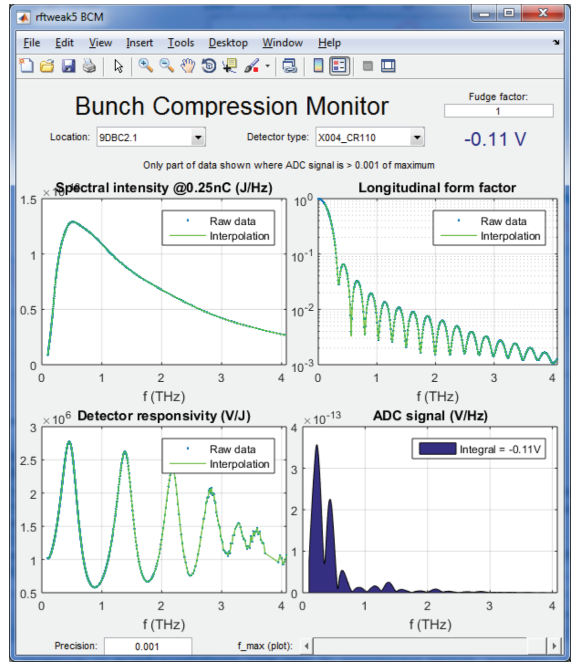

Figure 6: The expert GUI for the simulated bunch compression monitor (BCM) data. For the user the relevant number are the –0.11 V in the upper right corner, which corresponds to the actual ADC reading of FLASH in this example.

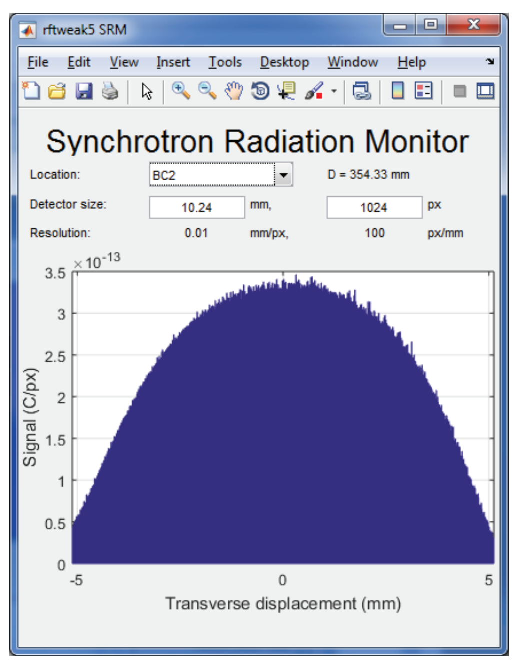

Figure 7: Beam energy spectra measured with the synchrotron radiation cameras in the chicanes are plotted for the chicanes as a tuning aid.

ISBN 978-3-95450-134-2

standard laptop. Switching CSR interactions on increases the calculation time to the order of a minute.

In the future this project will be combined with our new project "XTrack", which is a full 6D fast tracking algorithm. We imagine that we set-up the compression in RFTweak 5 and transfer the data to the new code to obtain a full 6D phase space representation on the order of about 10 minutes at the undulators to judge FEL performance.

REFERENCES

[1] K. Bane, P. Emma, "*LiTrack*: A Fast Longitudinal Phase Space Tracking Code with Graphical User Interface", SLAC-PUB-11035 (2005).

[2] K.L.Brown,"A First- and Second-Order Matrix Theory for the Design of Beam Transport Systems and Charged Particle Spectrometers", SLAC-R-75, (1982).

[3] O. Zagorodnova, T. Limberg, "Impedance Budget Database for the European XFEL", Proceedings of PAC09, Vancouver, BC, Canada (2009).

[4] S. Meykopff, "Advanced Matlab GUI Development with the DataGUI Library", Proceedings of ICALEPCS 2015, Melbourne, Australia (2015).

[5] I. Zagorodnov and M. Dohlus, "Semianalytical modeling of multistage bunch compression with collective effects", Phys. Rev. ST Accel. Beams 14, 014403 (2011).

[6] M. Cornacchia and P. Emma, "Transverse to longitudinal emittance exchange", Phys. Rev. ST Accel. Beams 5, 084001 (2002).

[7] S. Wesch, "Echtzeitbestimmung longitudinaler Elektronenstrahlparameter mittels absoluter Intensitäts- und Spektralmessung einzelner kohärenter THz Strahlungspulse", PhD Thesis, University of Hamburg (2012).

ISBN 978-3-95450-134-2

TECHNOLOGY MATURATION FOR THE MaRIE 1.0 X-FEL*

J.W. Lewellen#, K. Bishofberger, B.E. Carlsten, L. Duffy, F.L. Krawczyk, Q.R. Marksteiner, D.C. Nguyen, S.J. Russell, R. L. Sheffield, N. Yampolsky, LANL, Los Alamos, NM 87545, USA

Abstract

Los Alamos National Laboratory is proposing a high-energy XFEL, named MaRIE, to meet its mission needs. MaRIE will be required to generate coherent 42+ keV photons, and, due to space constraints at the LANSCE accelerator complex at Los Alamos, MaRIE's design electron beam energy is 12 GeV. This combination places significant restrictions upon the MaRIE electron beam parameters, in particular the transverse emittance and energy spread at the undulator entrance. We are developing approaches to meet these requirements, but these often require solutions extending beyond the current state-of-the-art in X-FEL design.

To reduce overall project risk, therefore, we have identified a number of key experimental and modeling / simulation efforts intended to address both the areas of greatest uncertainty in the preliminary MaRIE design, and the areas of largest known risk. This paper describes the general requirements for the MaRIE X-FEL, our current areas of greatest concern with the preliminary design concept, and our corresponding Technology Maturation Plan (TMP).

INTRODUCTION

The Matter-Radiation Interactions in Extremes (MaRIE) facility is intended to provide unprecedented time- and space-resolved measurements on multiple scales, but with particular emphasis on mesoscale phenomena in dense materials such as metals at up to GHz measurement rates [1]. The MaRIE concept leverages the existing LANSCE 1-MW, 0.8-GeV proton accelerator [2] for multi-probe measurement capabilities.

MaRIE 1.0 is the initial implementation of the MaRIE facility, and includes at its core a 42-keV X-ray free-electron laser (X-FEL) driven by a 12-GeV superconducting linac. The X-FEL must be co-located with the existing LANSCE facility to fully realize the multi-probe promise of MaRIE; however, this imposes several constraints on the overall design of the MaRIE X-FEL linac, in particular the length available for the accelerator, over and above the stringent beam quality required by the 42-keV photon energy goal.

Electron beam radiography (eRad) is a highly desirable option for MaRIE. While most of our initial modelling and simulation work has focused upon the requirements for the X-FEL, the option to support eRad operations should not be precluded by the MaRIE linac design. Emittance and bunch length are not critical parameters for eRad bunches, but eRad requires bunch charges of 2 nC, and the MaRIE linac must be capable of providing both eRad and XFEL bunches within the same macropulse.

While our initial design simulations indicate the MaRIE linac design is feasible, we have identified several areas of particular concern where the performance of the MaRIE driver linac must be extended beyond the current state-of-the-art. A technical maturation plan (TMP) has been developed to explore the relevant physics and ameliorate risk early in the MaRIE project.

*Work supported by the US DOE / NNSA under contract DE-AC52-06NA25396.
jwlewellen@lanl.gov

REQUIRED PERFORMANCE

MaRIE requires an extraordinarily bright electron beam in order to drive the SASE process to saturation within the X-FEL. (While the eRad beam should not be challenging to generate, copropagating it with an X-FEL drive beam raises additional questions and concerns. However, the MaRIE TMP is currently focused primarily on the challenges surrounding the X-FEL design.) Table 1 summarizes the parameters and performance requirements for the MaRIE linac.

Table 1: MaRIE Drive Linac Performance Requirements

Parameter	Units	Value
Beam energy	GeV	12
Linac frequency	GHz	1.3
Cavity gradient	MV/m	31.5
Max. macropulse duration	μs	100
Bunches / macropulse		10 – 100
X-FEL bunch charge	nC	0.1 nominal 0.2 max
eRad bunch charge	nC	2
Intrabunch energy spread		$\leq 1 \cdot 10^{-4}$
Slice energy spread		$\leq 1.5 \cdot 10^{-4}$
RMS slice emittance	μm	≤ 0.2
RMS bunch length	fs	12

IDENTIFIED KEY RISK AREAS

The MaRIE beam requirements at the undulator drive requirements for the remainder of the linac. While based on existing technology to the extent feasible, MaRIE's performance requirements demand beyond-state-of-the-art performance in several areas.

ISBN 978-3-95450-134-2

The MaRIE Technology Maturation Plan (TMP) [3] identifies the following areas of risk: photoinjector emittance; long-range wakes; coherent synchrotron radiation (CSR)-induced emittance growth; correlated energy spread reduction; longitudinal space charge and microbunching; emittance preservation; and distributed seeding.

The TMP calls for the risks to be addressed by a series of experiments where possible, as well as enhanced modelling and simulation (M&S). The subsections below describe the particular concerns identified for each risk area, and briefly discuss the remediation strategies. Generally, all experimental approaches will also include modelling and simulation.

Photoinjector Emittance and Energy Spread

MaRIE requires an 0.2 μm RMS normalized slice emittance at the undulator at 100-pC bunch charge. While recent results from PITZ indicate this level of performance is achievable directly from the injector [4], we must allow for degradation of the emittance as the beam is accelerated and compressed. Therefore the MaRIE photoinjector has a target emittance goal of 0.1 mm RMS at a bunch charge of 100 pC, inclusive of thermal emittance. Assuming a copper cathode with thermal emittance of ~0.6μm/mm [5], this implies a sub-mm emission spot. In turn, to keep emission current density low enough to avoid space-charge-induced beam quality degradation, a relatively long bunch must be generated, on the order of 10 – 20 ps with flattop emission. Finally, as discussed below the beam at the photoinjector must have a slice energy spread of less than 3.6 – 7.2 keV, depending on the bunch length, or on the order of 0.1%. The present MaRIE photoinjector design concept is, essentially, a PITZ-type photoinjector with a reconfigured solenoid, to provide better focusing earlier, as illustrated in Figure 1.

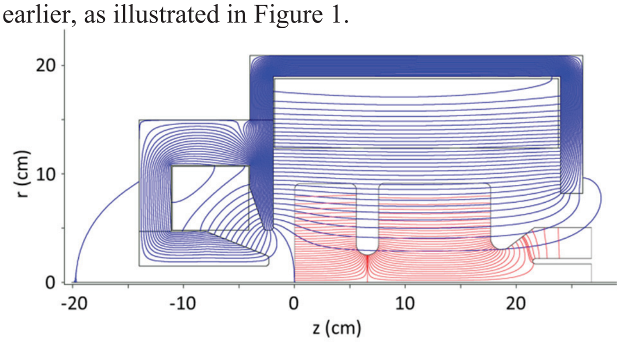

Figure 1: MaRIE photoinjector, showing RF cavity based on the PITZ design (red field contours) with a new solenoid design (blue contours).

To reduce technical risk associated with the photoinjector design, we are proposing construction of a full-scale MaRIE RF photoinjector and solenoid to validate the baseline performance assumptions. We are also proposing additional cathode R&D focused on thermal emittance reduction; this would help relax requirements on the emission spot size, with concurrent reduction in bunch length from the photoinjector and relaxation of the linac bunch compression requirements.

Long-Range Linac Wakefields

The requirement for a 100-μs beam pulse duration drives the selection of superconducting technology for the linac; in particular, TESLA-type cavities and cryomodules are used in the conceptual design. The overall space constraints drive a target accelerating gradient of 31.5 MV/m (based on cavity, not overall real-estate, gradient). We view this as aggressive but possible; the baseline MaRIE concept also includes length contingency in case this gradient is not achievable.

The flexible bunch pattern incorporates a minimum spacing of 1 RF period between X-FEL driver bunches, and also should accommodate 2-nC eRad bunches being accelerated in tandem with the X-FEL drive beam, but with greater intra-bunch spacing. The interaction of a variable-spacing, variable-charge bunch train with cavity short- and long-range wakefields must be well-understood, including effects of and tolerances on cavity alignment. While short-range wakes are now well-understood [6,7], long-range wakes require additional exploration.

A series of drive / witness beam experiments can be conducted on existing TESLA-type modules [8] to thoroughly map out the long-range wakefields in a typical module, complemented by modelling and simulation via the Lucretia code [9]. This experiment will also help determine requirements for cavity and module alignment tolerances for MaRIE.

CSR Emittance Growth and Chirp Control

At 12 GeV, a relative energy spread of 0.015% equals 1.8 MeV. A starting bunch length of 10 – 20 ps (quasi square pulse) requires an overall bunch compression ratio of 250 – 500:1 to obtain the required 12 fs RMS bunch duration at the undulator.

The MaRIE design incorporates multiple compression stages, nominally at 250 MeV and 1 GeV with compression ratios of 25:1 and 10 – 20:1, respectively. These energies were chosen based on the potential for mitigation of net energy spread increase [10], and also to reduce net energy spread increase at the end of the linac, as the linac energy can be changed to tune the FEL wavelength.

Each compression stage is nominally a 2-chicane compressor, designed to help mitigate the time-dependent kick in the x'-t plane induced by CSR effects within each chicane [11,12]. Initial optimization studies indicate a single dual-chicane compressor can provide up to ~50:1 compression without significant slice, and greatly reduced projected, emittance degradation; for instance, Figure 2 shows the difference in t-x' phase space between a conventional 4-dipole chicane and a dual-chicane compressor for a 57:1 compression ratio. However, such an arrangement has not as yet been experimentally tested.

The dual-chicane compressor provides considerable flexibility in how each compressor is tuned; other approaches such as the Z-bend or zig-zag [13] and the 5-dipole compressor [14] are also of interest and will be

ISBN 978-3-95450-134-2

further explored in modelling and simulation as part of the overall MaRIE design optimization effort.

As part of the general CSR mitigation strategy, the compressors are set to somewhat undercompress relative to the chirp; however, this leaves a residual chirp on the beam. At a final compressed duration of 12 fs, using an RF-based dechirper is infeasible. Since the accelerator structures do not provide a sufficiently strong short-range wake to dechirp the beam, a dedicated dechirping system such as the one in [15] is planned for installation in the switchyard between the end of the linac and the undulator entrance.

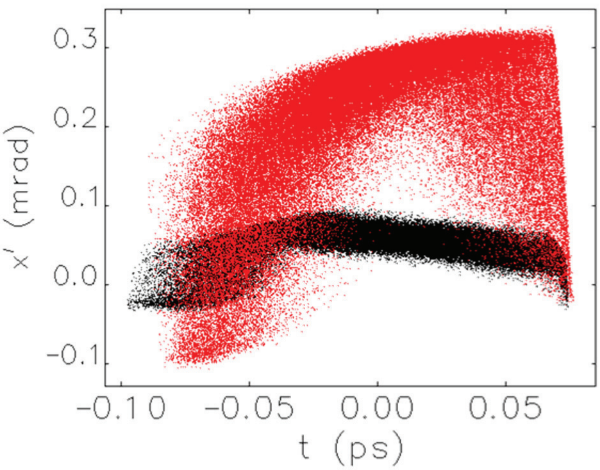

Figure 2: **elegant** [20] simulation of t-x' phase space for a 57:1 compression ratio with a single (red) and dual (black) chicane compressor.

We propose constructing a full dual-chicane compressor at a suitable test facility to map out the performance space of the dual-chicane design. The chicane will also provide a compressed beam for experiments with corrugated and smooth-wall dechirpers.

Longitudinal Space Charge and Microbunching

The high compression ratios at relatively low beam energies, combined with the low energy spread of the beam, tend to drive longitudinal space charge (LSC)-induced microbunching and associated energy spread growth. Indeed, in the baseline design for the MaRIE linac, the beam is space-charge dominated [16] along a large fraction of its length (see Figure 3). In particular, a significant fraction of the energy spread growth occurs between 1 and 2 GeV. At present, the growth in uncorrelated energy spread is the main point of concern for the MaRIE linac reference design, as it exceeds the tolerances presented above. The longitudinal phase space at the end of the MaRIE linac is shown in Figure 4 below.

The now-traditional method for dealing with LSC in X-FEL driver linacs is inclusion of a laser heater at the front end of the linac [17]. Typical laser heater designs, such as that at LCLS-I, impart too large an energy spread on the beam and thus cannot be used in MaRIE. Operating existing laser heaters at low energy tends to lead to a "trickle heating" effect [18], resulting in a greater, rather than lower, final energy spread. While it is possible a "low-energy" laser heater can be designed specifically for MaRIE, and will be part of our design effort, it is prudent to consider other means of ameliorating LSC in MaRIE. These include maintaining a larger beam radius in sections of the linac currently in the space-charge-dominated regime, and introducing controlled residual dispersion along portions of the linac [19].

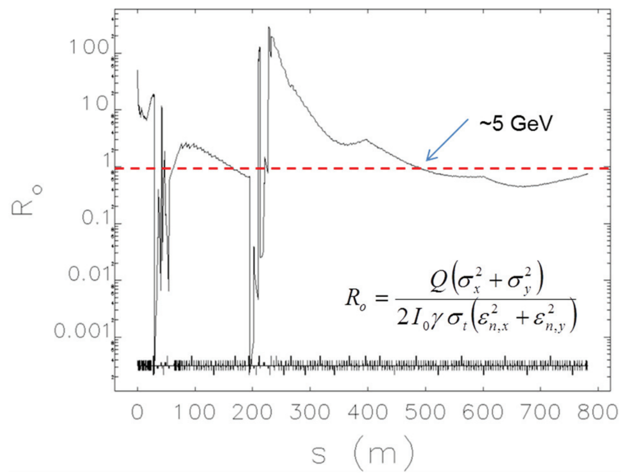

Figure 3: Space charge impact parameter along the MaRIE linac. R_o > (<) 1 implies space-charge (emittance) dominated beam dynamics.

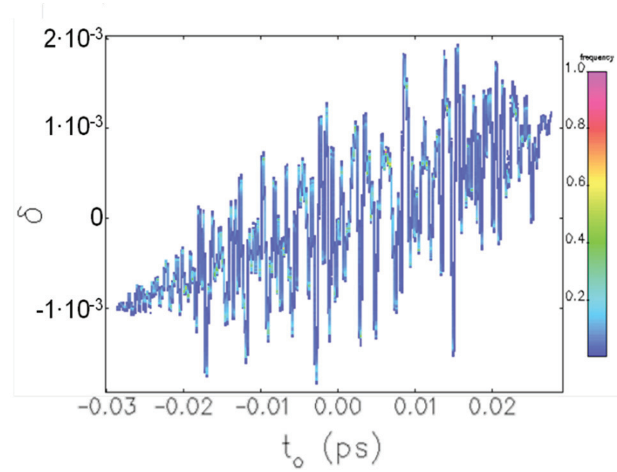

Figure 4: Longitudinal phase space at the end of the MaRIE linac.

Most of these techniques can be tested at existing facilities to a greater or lesser extent; with the exception of a low-energy laser heater, which may require a new undulator or drive laser, hardware costs should be minimal.

Modelling and simulation will also play a critical role in mitigating this area of concern; for instance, further optimization of the bunch compressor placement along the linac is warranted. Also, at the present time **elegant** [20] is our primary modelling tool for the MaRIE linac. **elegant**'s space charge model is longitudinal only; our modelling and simulation strategy includes extending the use of the OPAL code [21] beyond the injector, as it can be

ISBN 978-3-95450-134-2

used to include true 3-D space charge effects along the entire linac.

Emittance Preservation and Distributed Seeding

Generation and preservation of the low-emittance beam is discussed above for specific areas of concern; here, we refer to a general effort to improve the fidelity of the start-to-end modelling of the MaRIE linac, including detailed design of the beam switchyard area between the linac and undulator lines, and beam transport along the undulator.

The distributed seeding (DS) technique [22] is intended to improve the stability of the X-FEL output while reducing its bandwidth. DS makes use of chicanes within the undulator line to serve as time delays; the effects from these chicanes, such as CSR-induced energy spread and emittance growth, must be incorporated into the general modelling of electron beam transport along the undulator.

Both of these areas of concern will be addressed by modelling and simulation. Ideally the DS concept would be experimentally explored, but doing so would require significant modification to an existing SASE-FEL.

CONCLUSIONS

The current reference design for the MaRIE linac appears to meet most of the criteria presented above, with the residual slice energy spread being a notable exception. While aggressive, most of the assumptions in the design are based on proven SASE-FEL linac technology. The MaRIE TMP is intended to buy down risk early in the project by placing additional emphasis on areas identified as being of particular concern. This will be done, wherever feasible, by a combination of experimental and modelling / simulation. We believe the work to be done is interesting from both the standpoint of fundamental accelerator physics as well as technology maturation and improvement, and welcome discussions regarding collaboration in these and related areas.

ACKNOWLEDGEMENTS

The authors wish to thank Cris Barnes, MaRIE capture manager, for useful discussions and suggestions.

This research was funded by the Matter-Radiation Interactions in Extremes program at Los Alamos National Laboratory. Los Alamos National Laboratory, an affirmative action / equal opportunity employer, is operated by Los Alamos National Security, LLC, for the National Nuclear Security Administration of the U. S. Department of Energy under contract DE-AC52-06NA25396.

REFERENCES

[1] Please see http://marie.lanl.gov for more details of the MaRIE project and measurement capabilities.

[2] N.S.P. King et al., "An 800-MeV proton radiography facility for dynamic experiments," Nucl. Instrum. Meth. **A**, Vol. 424, issue 1, pp. 94-91 (3 Nov 1999).

[3] LANL internal document; please contact R. Sheffield (sheff@lanl.gov) for more information or copies.

[4] M. Krasilnikov et al., "Experimentally minimimzed beam emittance from an L-band photoinjector," Phys. Rev. ST-AB **15**, 100701 (2012).

[5] D.H. Dowell and J.F. Schmerge, "Quantum efficiency and thermal emittance of metal cathodes," Phys Rev. ST-AB **12**, 074201 (2009).

[6] A. Mosnier, "Longitudinal and Transverse Wakes for the TESLA Cavity," TESLA Report 93-11, DESY Print, May 1993.

[7] A. Novokhatski and A. Mosnier, "Short bunch wake potentials for a chain of TESLA cavities," Nucl. Instrum. Meth. A 763 (2014), 202-209.

[8] R. Brinkmann et al. eds., *TESLA Technical Design Report Part II – The Accelerator*. (Hamburg; DESY, 2001).

[9] The LUCRETIA Project: http://www.slac.stanford.edu/accel/ilc/codes/Lucretia

[10] R.D. Ryne et al., "Using a Leinard-Weichert Solver to Study Coherent Synchrotron Radiation Effects," Proc. 2013 FEL Conf., New York, NY (August 2013).

[11] J.W. Lewellen, "Progress on the MaRIE 1.0 Linac Baseline Design," LA-UR-13-25445 (2013).

[12] J.W. Lewellen et al., "Status of the MaRIE X-FEL Accelerator Design," Proc. 2015 Int'l Part. Accel. Conf., Richmond, VA, USA (May 2015).

[13] V.N. Litvinenko et al., "Merger designs for ERLs," Nucl. Instrum. Meth. **A** 557 (2006), 165-175.

[14] D.Z. Khan and T.O. Raubenheimer, "LCLS-II Bunch Compressor Study: 5-Bend Chicane," Proc. 2014 FEL Conf., Basel, Switzerland (August 2014).

[15] P. Emma et al., "Experimental Demonstration of Energy-Chirp Control in Relativistic Electron Bunches using a Corrugated Pipe," Phys. Rev. Lett. **112**, 034801 – Published 23 January 2014.

[16] S.G. Anderson et al., "Space-charge effects in high brightness electron beam emittance measurements," Phys. Rev. ST-AB, Vol. 5, 014201 (2002).

[17] Z. Huang et al., "Suppression of microbunching instability in the linac coherent light source," Phys. Rev. ST-AB, Vol. 7, 074401 (2004).

[18] Z. Huang et al., "Measurement of the linac coherent light source laser heater and its impact on the x-ray free-electron laser performance," Phys. Rev. ST-AB **13**., 020703 (2010).

[19] Ji Qiang et al., "Suppression of Microbunching Instability Using Bending Magnets in Free-Electron Lasers," Phys. Rev. Lett 111.5 (2013): 054801.

[20] M. Borland, Argonne National Laboratory Report LS-287, 2000.

[21] A. Adelmann et al., "The Object Oriented Parallel Accelerator Library (OPAL), Design, Implementation and Application," Proc. 2009 Int'l Comp. Accel. Phys. Conf., San Franscisco, CA, USA (2009).

[22] D.V. Nguyen, "Distributed Seeding for Narrow-band X-ray Free-Electron Lasers," presented at FEL'15, Daejeon, Korea, May 2015, paper TUB02, these Proceedings.

ISBN 978-3-95450-134-2

TRANSVERSE EMITTANCE MEASUREMENT OF KAERI LINAC WITH THICK LENS QUADRUPOLE SCAN

Sadiq Setiniyaz*, In-Hyung Baek, MoonSik Chae, Boris Gudkov, Byung-Heon Han, Kyu Ha Jang, Young Uk Jeong, Hyun Woo Kim, Jinhee Nam, Sunjeong Park, KAERI, Daejeon, Republic of Korea
Sergey Miginsky and Nikolay Vinokurov
Budker INP RAS, Novosibirsk, Russia and KAERI, Daejeon, Republic of Korea

Abstract

The UED (Ultrafast Electron Diffraction) beamline of KAERI (Korea Atomic Energy Research Institute) WCI (World Class Institute) Center has been completed and successfully commissioned. Transverse emittance of the electron beam was measured at the entrance of the UED chamber with the quadrupole scan technique. In this technique, larger drift distance between the quad and screen is preferred because it gives better thin lens approximation. A space charge dominated beam however, will undergo emittance growth in the long drift caused by the space charge force. We suggest mitigating this growth by introducing quadrupole scan with short drift and without thin lens approximation. We shall discuss the measurement process and results.

INTRODUCTION

The RF photogun of KAERI WCI Center is designed to generate sub-picosecond electron bunches with energy around 3.2 MeV. The beam can be delivered to UED experiments or can be further accelerated up to 20-30 MeV by the main accelerating cavity for X-ray/THz pump and probe experiments as shown in the Fig. 1. The UED section of beamline is designed to supply electron bunches with 0.1 ps length, 1 pC charge, and nominal energy of 3 MeV a ninety degree using an achromatic bend by velocity bunching [1].The UED section has been successfully commissioned recently and electron beam parameters were measured.

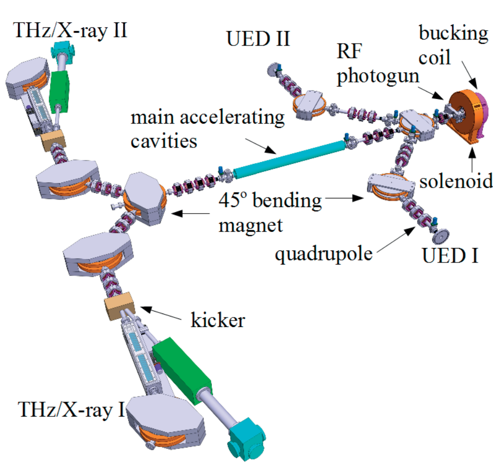

Figure 1: KAERI WCI center electron beamline layout.

* sadik82@gmail.com

Transverse emittance and Twiss parameters are important parameters of an accelerator to quantify the beam quality and match optics. Most common methods to measure emittance are quadrupole scan [2–6], the slit and collector [7, 8], the pepper-pot [9]. In the quadrupole scan, the beamsize is measured as a function of the quadrupole magnetic field strength [2]. Imaging screens like OTR (Optical Transition Radiation), YAG (Yttrium aluminium garnet), or phosphor screens are used to observe beam profile along with a synchronized camera. Generally, thin lens approximation is applied and rms beamsizes obtained from the beam profile are used to extract the emittance and Twiss parameters by fitting a parabolic function.

The thin lens approximation is effective when $\sqrt{k_1}L << 1$, where k_1 is quad strength and L is its effective length. The quad here is viewed as a thin focusing/de-focusing lens. In quadrupole scanning method, for a better thin lens approximation k_1 is kept small while the drift distance between the quad and screen is set as large as possible (usually few meters). But a space charge dominated beam pass through a long drift will experience emittance growth due to the space charge force [10]. This growth can be mitigated by shortening drift length and extracting emittance without using thin lens approximation. In our case, drift length is 23 cm.

THICK LENS QUADRUPOLE SCAN

In quadrupole scan, a quadrupole magnet and a screen are used to measure the emittance ans Twiss parameters of the beam. The screen is separated from the quad by a drift distance. Transfer matrix of the scanning region **M** is given by the matrix product of the transfer matrices of drift **S** and quad **Q**

$$\mathbf{M} = \mathbf{SQ} = \begin{pmatrix} m_{11} & m_{12} \\ m_{21} & m_{22} \end{pmatrix}. \tag{1}$$

Here **S** and **Q** are given by

$$\mathbf{Q} = \begin{pmatrix} cos\sqrt{k_1}L & \frac{1}{\sqrt{k_1}}sin\sqrt{k_1}L \\ -\sqrt{k_1}sin\sqrt{k_1}L & cos\sqrt{k_1}L \end{pmatrix}, \tag{2}$$

$$\mathbf{S} = \begin{pmatrix} 1 & l \\ 0 & 1 \end{pmatrix}, \tag{3}$$

where l is the drift length. The beam matrix at the screen ($\sigma_\mathbf{s}$) is related to the beam matrix of the quadrupole ($\sigma_\mathbf{q}$) using the similarity transformation [11]

$$\sigma_\mathbf{s} = \mathbf{M}\sigma_\mathbf{q}\mathbf{M}^\mathrm{T}. \tag{4}$$

ISBN 978-3-95450-134-2

where the $\sigma_\mathbf{s}$ and $\sigma_\mathbf{q}$ are defined as

$$\sigma_{\mathbf{s},x} = \begin{pmatrix} \sigma^2_{\mathrm{s},x} & \sigma_{\mathrm{s},xx'} \\ \sigma_{\mathrm{s},xx'} & \sigma^2_{\mathrm{s},x'} \end{pmatrix}, \ \sigma_{\mathbf{q},x} = \begin{pmatrix} \sigma^2_{\mathrm{q},x} & \sigma_{\mathrm{q},xx'} \\ \sigma_{\mathrm{q},xx'} & \sigma^2_{\mathrm{q},x'} \end{pmatrix}. \tag{5}$$

The matrix element $\sigma_{\mathrm{s},x}/\sigma_{\mathrm{q},x}$ is the horizontal rms beam size at the screen/quad. $\sigma_{\mathrm{s},x}$ can be expressed as the function of the matrix elements m_{11} and m_{12} as

$$\sigma^2_{\mathrm{s},x} = \sigma_{\mathrm{q},x}\beta_{\mathrm{q},x}\left(m_{11} + m_{12}\frac{-\alpha_{\mathrm{q},x}}{\beta_{\mathrm{q},x}}\right)^2 + m^2_{12}\frac{\sigma_{q,x}}{\beta_{q,x}}. \tag{6}$$

The transfer matrix elements m_{11} and m_{12} are given as

$$\begin{aligned} m_{11} &= cos\sqrt{k_1}L - l\sqrt{k_1}sin\sqrt{k_1}L, \\ m_{12} &= \tfrac{1}{\sqrt{k_1}}sin\sqrt{k_1}L + lcos\sqrt{k_1}L. \end{aligned} \tag{7}$$

When thin lens approximation is valid, Eq. (6) becomes a parabolic function. The emittance and Twiss parameters are extracted by measuring $\sigma_{\mathrm{s},x}$ and fitting the parabolic function. Since we used short drift distance to mitigate emittance growth, the thin lens condition $k_1 L \ll 1$ is no longer satisfied. So, we obtained emittance and Twiss parameters by directly fitting Eq. (6) and by treating the quad as a thick lens.

EMITTANCE MEASUREMENT

Experiment Setup

The experimental setup of the emittance measurement with quad scan is shown in the Fig. 2. Electron beam from the RF photogun is delivered to the UED chamber using two 45$^{\mathrm{o}}$ dipole magnets and 6 quads. Five retractable imaging screens s1-s5 as shown are used observe the beam. The current quad 6 (q6) shown in the Fig. 2 is varied to perform scanning. A P-22 type phosphor screen s5 with 12.7 mm diameter is located at 23.0 cm downstream of the q6. A synchronized camera (Basler scout scA 600-28fm) placed under the screen are used to observe beam profile.

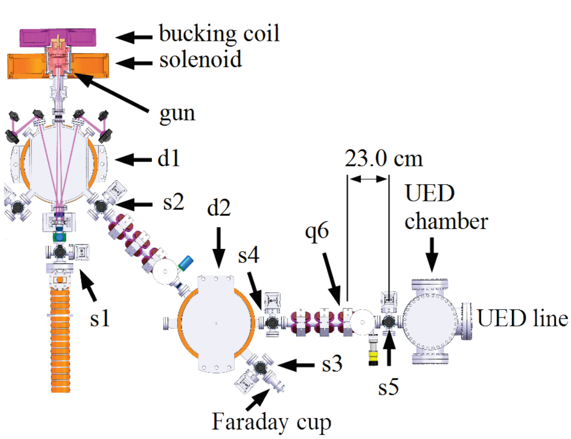

Figure 2: Quadruple scan experimental setup.

The beam energy and energy spread are measured using dipole d1 and screen s2. The magnetic field of the d1 is mapped to determine the energy of the beam when it bent by 45$^{\mathrm{o}}$. A Faraday cup is placed at the end of the 45$^{\mathrm{o}}$ line to measure electron bunch charge. The effective length of the quad was measured to be 8.335 cm by mapping the quad magnetic field.

Experiment Procedure

As shown in the Fig. 2, the electrons in the gun is focused by a solenoid. The beam is first observed at screen s1 where it is tuned to round shape. Then it is bent 45$^{\mathrm{o}}$ by d1 and observed on s2. By observing beam position on s2, the beam energy is maximized by adjusting laser delay. Then d1 is turned off and beam is observed on s1 and tuned to round shape again. Then beam is bent again by d1 and observed on s2. The coil current of the d1 is recorded to estimate energy and energy spread of the beam.

Then this beam is then delivered s3 using d1 and q1-q3. The beam is centered and tuned to round shape at s3. Then the screen s3 is retracted from the beamline and beam is delivered to FC. The electrical signals from FC created by electron bunches are amplified by a preamplifier and observed using a oscilloscope. The upstream magnets tuned to obtain maximize the oscilloscope which is used to calculate electron bunch charge.

Then d2 is turned on beam is delivered s4 first and s5 later. The horizontal beamsize at s5 usually is larger than vertical because of the beam dispersion. The dispersion is suppressed by adjusting q1-q3 while turning off q4 and q5. When dispersion is suppressed, q6 can focus the beam into a horizontally narrow shape on s5. Then q4 and q5 tuned to form a round beam on s5 while q6 is off. The scan is performed by changing q6 coil current and recording beam image.

DATA ANALYSIS AND RESULTS

Beam images from camera were calibrated using the screen target frame which has 12.7 mm diameter. The scaling factor can be obtained by dividing the diameter of the frame with the number of pixels in the diameter. The result is a horizontal scaling factor of 0.0158 ± 0.0006 mm/pixel. Beam images processed using a MATLAB based script. Beam profile observed on phosphor is shown in the Fig. 3. The yellow lines are beam projections and fitted with Gaussian distribution as shown by red curve.

The emittance measurement was performed by changing the quadrupole current, which changes quad strength k_1, and measuring the corresponding beam image on the view screen. The measured two-dimensional beam image was projected along the image's abscissa and ordinate axes. The rms value is extracted by fitting Gaussian distribution to the beam projection. Measurements of σ_s for several quadrupole currents/k_1 is then fit using the function in Eq. (6) to determine the emittance and the Twiss parameters. The Fig. 4 shows the square of the rms (σ^2_s) vs k_1 for x (horizontal)

ISBN 978-3-95450-134-2

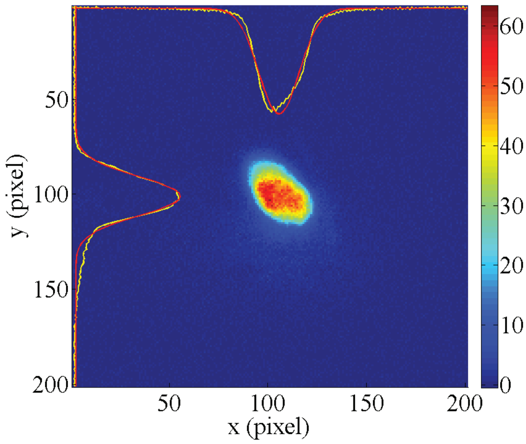

Figure 3: Electron beam profile observed on phosphor screen when q6 is off. The yellow/red line is projection/Gaussian fits.

and y (vertical) beam projections along with the fits using Eq. 6. The emittances and Twiss parameters from these fits are summarized in Table. 1.

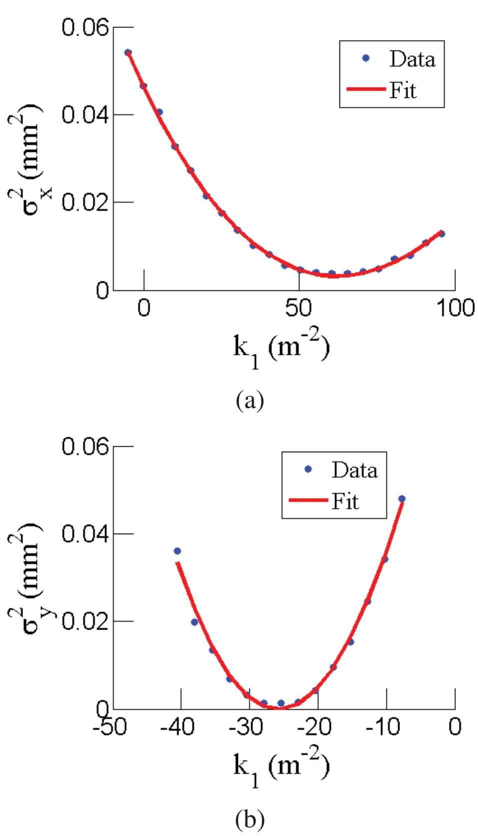

Figure 4: Squares of rms beamsize *vs* k_1 and fit using thick lens equation; (a) beam horizontal projection, (b) beam vertical projection.

The vertical emittance is significantly larger than horizontal one. One possible reason is vertical beam size reached its waist during the scanning and couldn't be focused further. However, the curve in Eq. (6) follows smaller vertically minimum beamsize as can be seen in the Fig. 4 (b). We plan to perform a test by beginning the quad scan with a with larger vertical size instead of round shape.

Table 1: Emittance Measurement Results

Parameter	**Unit**	**Value**
normalized emittance $\epsilon_{n,x}$	µm	0.23 ± 0.03
normalized emittance $\epsilon_{n,y}$	µm	0.42 ± 0.07
β_x-function	m	0.63 ± 0.10
β_y-function	m	5.5 ± 1.6
α_x-function	rad	0.9 ± 1.1
α_y-function	rad	0.23 ± 0.03
bunch charge	pC	1.12 ± 0.03
total energy E	MeV	3.26
relative energy spread $\Delta E/E$	%	0.32

CONCLUSIONS

We have used quadrupole scanning method with thick lens equation to measure the beam emittance of the WCI cetner UED Linac at the KAERI. The horizontal/vertical emittance was measured to be 0.23 ± 0.03/0.42 ± 0.07 µm for 1.12 ± 0.03 pC bunch charge. The vertical emittance is significantly larger than horizontal one. We plan to conduct further investigation on this matter. We also plan to measure emittance *vs* charge in the near future and compare emittances obtained with and without thin lens approximations as charge grow.

ACKNOWLEDGMENT

This work was supported by the World Class Institute (WCI) Program of the National Research Foundation of Korea (NRF) funded by the Ministry of Science, ICT and Future Planning (NRF Grant No. WCI 2011-001).

REFERENCES

[1] N. Vinokurov *et al.*, in *Proc. FEL2013*, New York, USA (2013).

[2] S. Setiniyaz *et al.*, in *Proc. IPAC2012*, New Orleans, USA (2012).

[3] B. E. Carlsten *et al.*, "Nucl. Instrum. Methods. A", 1993.

[4] E. Chiadroni *et al.*, in *Proc. DIPAC2009*, Basel, Switzerland (2009).

[5] R. Spesyvtsev *et al.*, in*Proc. FEL2008*, Gyeongju, South Korea (2008).

[6] C. Thomas, *et al.*, JINST 6, P07004 (2011).

[7] A. V. Steenbergen, *Nucl. Instrum. Methods* 51, 245 (1967).

[8] M. Walter *et al.*, in *Proc. PAC2003*, Portland, USA (2003).

[9] K. Kubo, ATF internal report ATF-98-35 (1998).

[10] C. Sawyer and N. Norris, in *Proc. LINAC84*, Seeheim, Germany (1984).

[11] S.Y. Lee, *Accelerator Physics*, (Singapore: World Scientific, 2004), 61.

ISBN 978-3-95450-134-2

ELECTRON BUNCH LENGTH MEASUREMENT USING RF DEFLECTING CAVITY

Sunjeong Park#, Kyunpook National University, Daegu and KAERI, Daejon, Republic of Korea
Hyun Woo Kim, Sangyoon Bae, Jungho Mun, Kyuha Jang, Young Uk Jeong, Nikolay Vinokurov, KAERI, Daejon, Republic of Korea
Eun-San Kim, Kyunpook National University, Daegu, Republic of Korea

Abstract

Recently, the RF photogun based-ultrafast electron diffraction (UED) system has been developed in KAERI. In the system, the emitted electron bunches are experimentally confirmed to be accelerated up to 3 MeV at 5 MW of RF power. And the time duration of the each bunch is initially designed to be less than 50 fs at the sample position. To analyses the performance of the system and to measure exactly the length of the electron bunches, we developed a rectangular type of S-band deflecting cavity working on TM_{120} mode. The principle of electron deflecting in the cavity, design & mechanical fabrication process and test results will be present in the conference.

INTRODUCTION

To understand the ultrafast dynamics of atoms or molecules, we use the X-FEL or ultrafast electron diffraction (UED) system. Those systems can provide the pulses with high temporal and spatial resolution. UED system using electron bunches with a few MeV has compact size compared with X-FEL, while it still can make the femtosecond time resolution or over sub nanometers of atomic spatial dimension [1].

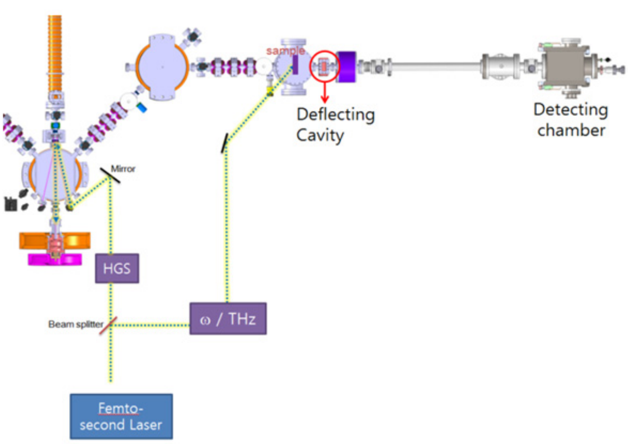

Figure 1: Schematic of the Korea Atomic Energy Research Institute (KAERI) UED system.

*Work supported by the WCI Program of NRF of Korea (NRF Grant Number: WCI 2011-001) and the RFBR Grant 11-02-91320-SIG_a.
#Sunjeong@kaeri.re.kr

Figure 1 shows schematics of the KAERI UED system. The RF photocathode gun is equipped at the system for the electron generation. The electron beam emitted from photocathode by fs laser is accelerated to 3 MeV by input RF power to reduce the space charge effect. After the gun, the electron beam is focused by several magnets, and the electron bunch length would be less than 50 fs. To measure the longitudinal distribution of the electron bunch, we are going to use an RF deflecting cavity working on TM_{120} mode. A strong transverse magnetic field deflects the beam passing through the cavity. After that the transverse beam size at the screen located downstream at the cavity is related to the bunch length at the deflector position.

The temporal resolution of deflecting cavity can be calculated by using following equation:

$$\Delta t = \Delta x \frac{U/e}{L\pi f V_t} .$$

To get the temporal resolution less than 20 fs, the RF input power at the cavity is estimated to be 2 MW. To improve the resolution of measurement, the 10 um slit would be used at upstream of the deflecting cavity.

RF DESIGN

We design the RF deflecting cavity similar to a rectangular cavity which drives 2.856 GHz working on TM_{120} mode [2]. The distribution of electromagnetic field in the cavity is shown in Figure 2.

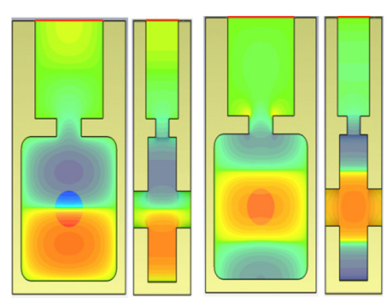

Figure 2: Electric field (left) and magnetic field (right) distribution of TM_{120} mode in the deflecting cavity.

Figure 3 shows the simulation results of the RF deflecting cavity. The resonance frequency of the results is higher than expected value because of error at the simulation.

ISBN 978-3-95450-134-2

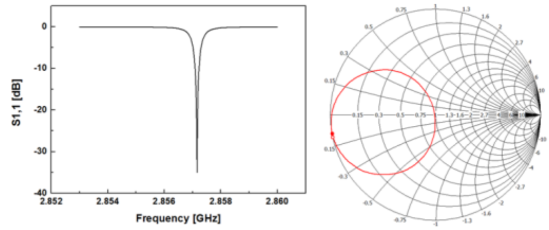

Figure 3: S11 parameter (left) and Smith chart (right) of the simulation of the deflecting cavity.

The measured results of fabricated deflecting cavity are shown in Figure 4 below.

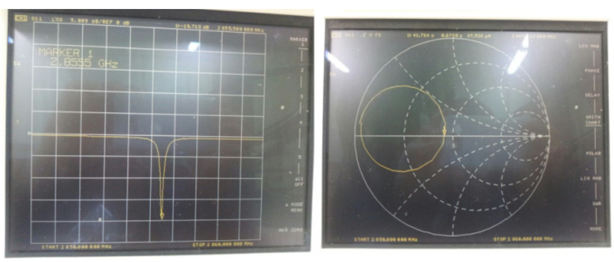

Figure 4: Cold test results of S11 parameter (left) and smith chart (right) of the deflecting cavity.

The resonance frequency and Q-value of cavity is 2.8555 GHz and 12326 respectively. Table 1 below shows the simulation and measured results of the cavity.

Table 1: DeflectingCavity Parameters

Parameter	Simulation	Real
Resonance frequency	2.8572 GHz	2.8555 GHz
Loaded Q-factor Q_L	6968	7103
Coupling constant β	0.96	0.73
Unloaded Q-factor Q_0	13332	12326

BEAM DYNAMICS

The electron beam deflected vertically after a drift space, and the vertical beam size would be related to the bunch length. The force in the deflecting cavity is given by

$$F_y(z) = q\left[\widetilde{E_y}(z) + c\widetilde{B_x}(z)\right],$$

where

$$\widetilde{E_y}(z) = E_y(z)e^{-j(\omega t+\varphi)},$$
$$\widetilde{B_x}(z) = B_x(z)e^{-j(\omega t+\varphi-\pi/2)}.$$

The maximum deflecting voltage, V_{def}, is defined when the RF phase in the cavity is 90 degree:

$$V_{\mathrm{def}} = -\int_{-L/2}^{L/2}\left[E_y(z)\sin(kz) + cB_x(z)\cos(kz)\right]dz,$$

and the change in the angular divergence of the electron beam is given by

$$y_f' = \frac{1}{E_0}\int F_y dl = \frac{q}{E_0}\int E_y dl = \frac{-qV_y}{E_0}$$
$$= \frac{-qV_{def}\sin(\varphi - ks)}{E_0}.$$

Using those equations, the vertical electron beam size can be calculated [3, 4].

$$\sigma_y^2 = \sigma_{y,0}^2 + \left(\frac{kqV_{def}}{E_0}\sigma_z D\right)^2.$$

Beam simulation has been progressed for the deflecting cavity. We used particle tracking code of ASTRA to consider the space charge effect. The energy of electron beam is 3 MeV and the horizontal and vertical rms beam sizes are 1.2 mm and 1.4 mm respectively. The electron bunch length at the deflecting cavity is about 50 fs. The electron beam would be transferred to the screen located after 2 meters downstream from the deflecting cavity. Figure 5 shows the simulation results. We measured the electron beam sizes after the drift space without RF field and with RF field in the deflecting cavity to obtain the electron bunch length.

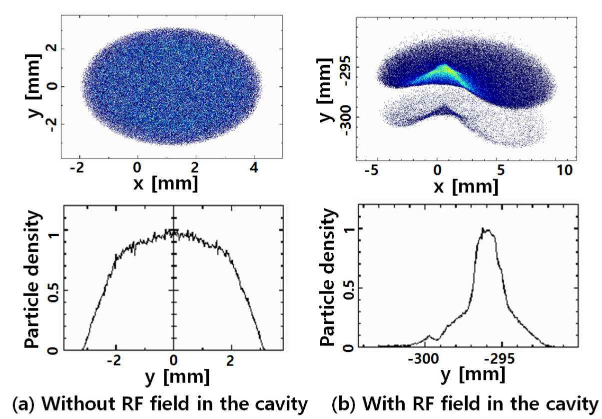

Figure 5: ASTRA simulation results. (a) is the beam distribution after the deflecting cavity without RF field in the cavity, (b) is the beam distribution after the deflecting cavity with RF field in the cavity.

The calculated bunch length is about 58 fs. We applied the 10-µm slit at the simulation to compensation of vertical beam effect for the electron bunch length measurement.

SUMMARY

The KAERI UED will use ultrafast electron bunches with a bunch duration less than 50 fs at the sample position. To measure the longitudinal distribution of the electron bunch, we will use an RF deflecting cavity working at TM_{120}-like mode. We studied beam dynamics in the deflecting cavity using code ASTRA. The beam optimization should be needed. According to the results of simulation and cold test, the deflecting cavity would be used for bunch-length measurement at KAERI UED system.

ISBN 978-3-95450-134-2

REFERENCES

[1] A.M. Michalik *et al.*, “Theory of ultrafast electron diffraction: The role of the electron bunch properties”, *J. Appl. Phys.* 104, 54905 (2001).
[2] S. Matsuba *et al.*, “Deflecting cavity for bunch length diagnostics at compact ERL injector”, Proceeding of IPAC’10, Kyoto, Japan (2010).
[3] R. Akre *et al.*, “Bunch length measurements using a transverse RF deflecting structure in the SLAC linac”, Proceeding of EPAC’02, Paris, France (2002).
[4] P. Emma *et al.*, “A transverse RF deflecting structure for bunch length and phase space diagnostics”, LCLS-TN-00-12 (2000).

ISBN 978-3-95450-134-2

TRANSVERSE-EMITTANCE PRESERVING TRANSFER LINE AND ARC COMPRESSOR FOR HIGH BRIGHTNESS ELECTRON SOURCES*

S. Di Mitri#, M. Cornacchia, Elettra Sincrotrone Trieste, 34149 Basovizza, Trieste, Italy
S. Spampinati, Department of Physics, University of Liverpool, Liverpool L69 7ZX, United Kingdom, and Cockroft Institute, Sci-Tech Daresbury, Warrington WA4 4AD, United Kingdom

Abstract

Minimizing transverse emittance is essential in single- or few-passes accelerators designed to deliver high brightness electron beams. Emission of coherent synchrotron radiation (CSR) is an important factor of emittance degradation. We have demonstrated, with analytical and experimental results, that this perturbation may be cancelled by imposing certain conditions on the electron optics when the bunch length is constant along the line. This scheme of CSR suppression is then enlarged, analytically and numerically, to cover the case of varying bunch length in a periodic arc compressor. The proposed solution holds the promise of cost-saving of compact transfer lines with large bending angles, and new schemes for beam longitudinal gymnastics both in recirculating and in single-pass accelerators driving free electron lasers.

INTRODUCTION

The advent of sub-ps electron beams with very high brightness in free electron lasers (FELs) [1] and in linear colliders has raised the awareness of the accelerator community to the effect of the coherent synchrotron radiation (CSR) on beam transverse emittance [2–5]. The CSR field affects the electron transverse motion both with radial forces and by changing the particle energy in the dispersive line. In the latter case, the particle starts a betatron oscillation around a new reference trajectory, thus increasing its Courant-Snyder (C-S) invariant [6]. The synchrotron radiation emission is coherent for wavelengths comparable to the electron bunch length and it induces a variation of the particle energy that is correlated with the longitudinal coordinate along the bunch. The removal of that correlation may therefore suppress the CSR-driven emittance growth [7,8].

In the following, we show that linear optics formalism can be used to describe the effect of consecutive *identical* CSR energy kicks on the beam transverse emittance; CSR emission is assumed to happen in the 1-D (longitudinal) and steady-state approximation [9]. The analytical prediction for the final emittance as function of the optics setting in a substantially isochronous transfer line was validated experimentally in the FERMI FEL [10,11] high energy Spreader line [12]. We then show that the same formalism can be extended to the case of a non-isochronous beam line, made of several large-angle dipole magnets, with limited impact on the beam emittance [13].

*Work supported by the FERMI project and the ODAC project of Elettra Sincrotrone Trieste.
#simone.dimitri@elettra.eu

ISOCHRONOUS LINE

The FERMI achromatic system, denoted henceforth as Spreader, is made of two identical double bend achromats (DBA), as sketched in Fig.1. Each DBA includes two FODO cells and their nominal setting ensures $\Delta\mu = \pi$ between the dipoles, and symmetric Twiss functions β and α, with values β_1 (α_1) and β_4 (α_4) in the dipoles of the first and the second achromat, respectively. The two DBAs are separated by 7 quadrupoles with a phase advance of π between them. In the following, the C-S formalism is applied to the particle motion in the Spreader with the aforementioned notation. Only the motion in the bending plane is considered.

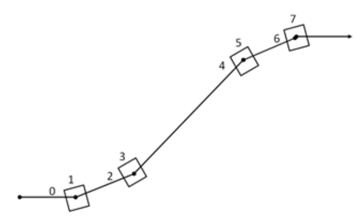

Figure 1: Sketch of the FERMI Spreader (not to scale). The design optics gives a betatron phase advance of π in the bending plane between two consecutive dipoles. There are quadrupoles between the dipoles (not shown here). Copyright of American Physical Society [12].

The initial particle coordinates relative to the reference trajectory are $x_0 = 0, x_0' = 0$ and the initial particle C-S invariant is $2J_0 = 0$. The variable subscript refers to the point along the lattice, as indicated in Fig.1. After the CSR kick in the first dipole, the particle transverse coordinates become:

$$\begin{cases} x_1 = \eta\delta \equiv \sqrt{2J_1\beta_1}\cos\Delta\mu\big|_{\Delta\mu=0} = \sqrt{2J_1\beta_1} \\ x_1' = \eta'\delta \equiv -\sqrt{\dfrac{2J_1}{\beta_1}}(\alpha_1\cos\Delta\mu + \sin\Delta\mu)\big|_{\Delta\mu=0} = -\alpha_1\sqrt{\dfrac{2J_1}{\beta_1}} \end{cases} \quad (1)$$

Here δ is the single particle relative energy deviation induced by CSR. After the CSR kick, the particle C-S invariant has grown to $2J_1 = \gamma_1 x_1^2 + 2\alpha_1 x_1 x_1' + \beta_1 x_1'^2 = H_1\delta^2$, where $H_1 = \gamma_1\eta^2 + 2\alpha_1\eta\eta' + \beta_1\eta'^2$ and $\gamma_1 = \left(\dfrac{1+\alpha_1^2}{\beta_1}\right)$. At the second dipole, after π phase advance and in the presence of the second CSR kick, we have:

ISBN 978-3-95450-134-2

$$\begin{cases} x_3 = x_2 + \eta\delta = -\sqrt{2J_1\beta_2} + \sqrt{2J_1\beta_1} = 0 \\ x_3' = x_2' - \eta'\delta = \alpha_2\sqrt{\frac{2J_1}{\beta_2}} + \alpha_1\sqrt{\frac{2J_1}{\beta_1}} = \sqrt{\frac{2J_1}{\beta_1}}(\alpha_1 + \alpha_2) \end{cases} \quad (2)$$

Equation 2 was obtained by substituting the dispersive terms as in Eq.1 and by using the symmetry of β at the dipoles (no specific choice for α is made at this stage). The same steps followed so far can easily be repeated till the end of the line. A new invariant will be defined after each CSR kick by the algebraic addition of the dispersive terms to the particle coordinates. With the additional equality $2J_i = \gamma_i x_i^2 + 2\alpha_i x_i x_i' + \beta_i x_i'^2$ for $i = 3,5,7$, each invariant J_i will be expressed as a function of J_1 and the C-S parameters. Doing this, after the last CSR kick we obtain:

$$2J_7 = 2J_1 4\alpha_1^2 \left(1 - \sqrt{\frac{\beta_5}{\beta_1}}\right)^2 \equiv 2J_1 X_{17}, \quad (3)$$

with the prescription $2J_1 = H_1\delta^2, \sigma^2_{\delta,CSR} = \langle \delta^2_{CSR} \rangle$, we estimate a residual emittance growth at the Spreader's end:

$$\Delta\gamma\varepsilon = \gamma\varepsilon\left[\sqrt{1 + \frac{H_1\sigma^2_{\delta,CSR}}{\varepsilon} X_{17}} - 1\right] < 0.1\mu m, \quad (4)$$

where ε is the unperturbed geometric emittance and γ is the relativistic Lorentz factor for the beam mean energy. The experimental demonstration of cancellation of CSR kicks, i.e. $X_{17} = 0$ in Eq.4, is shown in Fig.2.

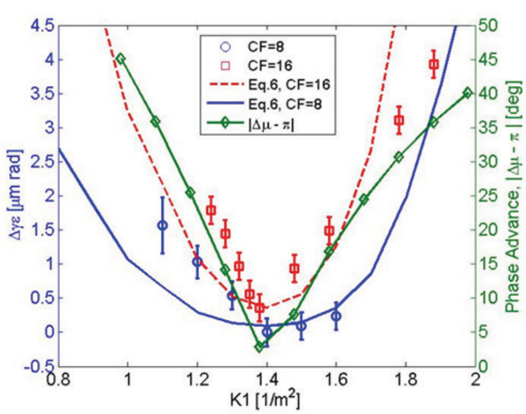

Figure 2: Horizontal normalized emittance growth at the end of the Spreader (markers with error bars) as a function of the strength of a quadrupole placed between the two DBAs. The squares (circles) are for a bunch length compression factor CF=16 (8) carried out in the upstream linac. The horizontal betatron phase advance between the DBAs (diamonds) was computed with ELEGANT on the basis of the experimental machine settings; the absolute value of its distance from π is shown. The dashed (solid) line is the evaluation of Eq.4 for CF=16 (8). Copyright of American Physical Society [12].

The emittance growth was measured at the end of the Spreader as the phase advance between the two achromats and the C-S parameters in the second achromat were changed by varying a quadrupole's strength in the intermediate dispersion-free region, thus breaking the optics balance. The perturbed optics was computed for each quadrupole's strength with the ELEGANT code [14], and thereby used to evaluate Eq.4. The experimental growth rate was higher for the shorter beam, in agreement with the expected CSR dynamics and well described by the analytical model. Minimum emittance growth was achieved for a π phase advance between the two achromats and design C-S parameters at the second achromat, again in agreement with the theoretical expectation.

It is worth mentioning that the expression for the CSR kick in Eq.1 was recently re-modelled in [15] with a more accurate expression that takes into account a non-zero length of the dipole magnets. That modeling was shown to provide a more accurate control of the final beam emittance, and an exact solution for the optical cancellation of the CSR-induced invariant in a single symmetric DBA.

NON-ISOCHRONOUS LINE

Bunch length magnetic compression is routinely used in high brightness electron linacs driving FELs and particle colliders in order to shorten the bunch that is to increase the peak current of the injected beam from few tens to kilo-Amperes. To date, magnetic compression is performed in dedicated non-isochronous insertions made of few degrees bending magnets inserted on the accelerator straight path; the compression factor is limited by the degradation of the beam transverse emittance owing to emission and absorption of CSR. For this reason, if a high peak current is needed, for instance, at the end of recirculating accelerators like energy-recovery linacs (ERLs) driving FEL, the photo-injected beam is recirculated in isochronous beam lines and magnetically time-compressed only after the very last stage of acceleration [16], e.g. with a magnetic chicane [17,18]. Although this approach tends to preserve beam brightness during recirculation [19], it may put an upper limit to either the compression factor or the beam charge or both, thus to the final peak current, because of CSR-induced emittance growth in a single-stage compression [20].

In the following, we reformulate the concept introduced above of CSR-driven optics balance [12] for the more general case of varying bunch length [13], and show that it works for bending angles larger than previously thought advisable and practical. The proposed solution applies adiabatic compression throughout the arc. Optical aberrations and longitudinal nonlinearities are controlled with sextupole magnets. We show that it is feasible to redistribute a compression factor of up to 45 for a 500 pC beam, by means of a periodic 180 deg arc at 2.4 GeV, while keeping CSR transverse kicks under control. The total growth of the normalized emittance does not exceed

ISBN 978-3-95450-134-2

the 0.1 μm level for peak currents of up to 2 kA. In comparison with existing literature [21–24], our solution allows larger compression factors at higher charges, and simplifies ERL lattice designs since, in principle, a dedicated chicane is no longer needed for compression as the arc acts both as final stage of recirculation *and* compressor. Although it finds an immediate application to ERLs, the proposed CSR-immune arc compressor promises to be applicable to more general accelerator design, thus offering the possibility of new and more effective layout geometries of single-pass accelerators and of new schemes for beam longitudinal gymnastic.

The 180 deg arc compressor is made of 6 modified Chasman-Green achromats (one cell shown in Fig.3; linear optics functions in Fig.4) separated by drift sections that allow optics matching from one DBA to the next one. The arc is 125 m long (40 m long radius) and functional up to 2.4 GeV. The bending angle per sector dipole magnet is $\theta = 0.2618$ rad and the dipole arc length $l_b = 1.4489$ m. R_{56} of one dipole is 17.2 mm, while that of the entire arc is 207.1 mm. If, for example, a total compression factor C = 45 were required at the end of the arc, an energy chirp $h = \left(\frac{1}{C} - 1\right)\frac{1}{R_{56}} \approx 4.7 m^{-1}$ would be needed at its entrance, which corresponds roughly to a fractional rms energy spread of $\sigma_{\delta,0} \approx h\sigma_{z,0} = \frac{1}{E}\frac{dE}{dz}\sigma_{z,0} \approx 0.3\%$ for a 3 ps rms long bunch.

According to the analysis depicted above, the normalized emittance growth in the bending plane and in the presence of CSR for a *single* DBA cell can be estimated by:

$$\Delta\varepsilon_{nf} = \varepsilon_{nf} - \varepsilon_{n0} \cong \varepsilon_{n0}\left(\sqrt{1 + \frac{\gamma J_3}{\varepsilon_{n0}}} - 1\right), \quad (5)$$

where the single particle C-S invariant $2J_3$ is:

$$2J_3 = \beta_2 x_3'^2 + 2\alpha_2 x_3 x_3' + \left(\frac{1+\alpha_2^2}{\beta_2}\right)x_3^2 \quad (6)$$

$$\cong \left(\frac{k_1\rho^{1/3}\theta^2}{2}\right)^2 \left\{\left[\sqrt{\beta_2}\left(C^{4/3}+1\right) - \frac{\alpha_2}{\sqrt{\beta_2}}\left(\frac{l_b}{6}\right)\left(C^{4/3}-1\right)\right]^2 + \left[\frac{1}{\sqrt{\beta_2}}\left(\frac{l_b}{6}\right)\left(C^{4/3}-1\right)\right]^2\right\}$$

It is worth noticing that $(k_1\rho^{1/3}\theta)$ in Eq.6 is the rms value of the fractional energy spread induced by CSR in the first dipole magnet of a DBA cell, and that its evolution along the cell (thus the arc), as well as that of the bunch length, is taken into account by the cell compression factor C. The invariant has a minimum for $\beta_2 \cong \beta_{2,\min} = \frac{l_b}{6}\left(\frac{C^{4/3}-1}{C^{4/3}+1}\right)$; β_2 is the betatron function inside the dipole magnet, where the beam size is forced to a waist, and l_b is the dipole's length. In the lattice under consideration we expect to have minimal CSR effect on the emittance for $\beta_{2,\min} \sim 0.2$ m.

In summary, in order to minimize the CSR-induced emittance growth in a periodic 180 deg arc compressor, we prescribe the use of several symmetric DBA cells with linear compression factor not far from unity in most of the cells. We also impose a beam waist in the dipoles of all the DBAs and find that, unlike in a magnetic chicane (see [25] and references therein), there is an optimum value for β_2 inside the dipoles that minimizes the chromatic emittance growth due to CSR.

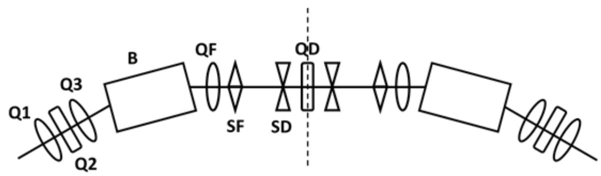

Figure 3: Sketch (not to scale) of the arc compressor DBA cell. Dipole magnets (B), focusing (QF, Q1 and Q3) and defocusing (QD, Q2) quadrupole magnets, focusing (SF) and defocusing sextupole magnets (SD) are labelled. The geometry and the magnets' arrangement is symmetric with respect to the middle axis (dashed line). Copyright of Europhysics Letters [13].

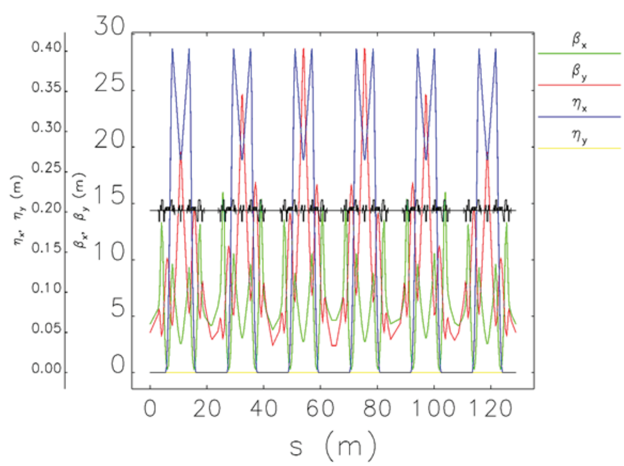

Figure 4: Linear optics functions along the 180 deg arc compressor. Optics functions are quasi-symmetric in each DBA cell of the arc compressor, and totally symmetric with respect to the middle axis of the arc. The minimum β_x is in the dipole magnets, and it ranges from 0.14 m to 0.26 m over the six cells.

Table 1 summarizes the arc input and output beam parameters used in ELEGANT particle tracking runs. Two sets of initial beam parameters are considered, one for high charge–long bunch, the other for low charge–short bunch. Five million particles in a bunch were tracked. Quiet start of the electron beam input distribution and filtering were adopted to ensure suppression of numerical sampling noise at uncompressed wavelengths shorter than 35 μm. The rms normalized projected emittance of the

ISBN 978-3-95450-134-2

500 pC beam grows from 0.80 μm to 1.05 μm at the arc's end, with contributions from incoherent synchrotron radiation (ISR), chromatic aberrations and CSR, as shown in Fig.5. Chromatic aberrations are responsible for the emittance modulation along the line, as well as for the (small) horizontal slice emittance growth, shown in Fig.6-top plot. Non-uniformity of the horizontal C-S slice invariant (i.e., the invariant of the slice centroid) along the bunch, shown in Fig. 6-bottom plot, reflects the slices misalignment in the transverse phase space due to CSR kicks. Residual CSR-induced microbunching shows up in the longitudinal phase space at final wavelengths longer than 10 μm. Final slice energy spread is around 2 MeV and substantially dominated by the initial uncorrelated energy spread times the total compression factor.

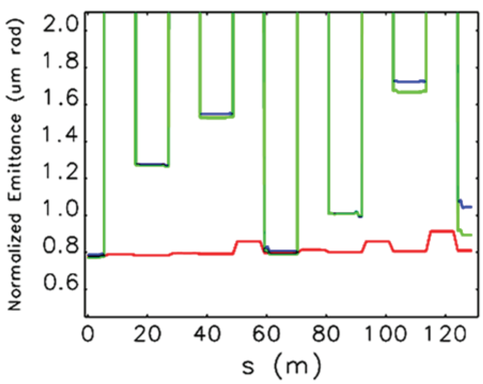

Figure 5: Projected normalized emittance (rms value) in the bending plane along the arc, for the 500 pC beam (see Table 1). The emittance evolution is shown, respectively, in the presence of ISR-only for the fully compressed beam (red), with the addition of compression and optical aberrations (green) and with the further addition of CSR (blue). Copyright of Europhysics Letters [13].

Table 1. Electron Beam Parameters at the Entrance and at the Exit of the Arc Compressor (Simulation Results). Rms values are computed over 100% of the beam charge. Input values are only indicative and do not necessarily reflect optimized beams from the injector

Input beam			
Energy	2.4	2.4	GeV
Charge	100	500	pC
Bunch length, rms	300	900	μm
Peak current	30	45	A
Proj. norm. emittance, rms	0.20,0.20	0.80,0.80	μm rad
Uncorr. energy spread, rms	30	40	keV
Corr. energy spread, rms	0.14	0.42	%
Output beam			
Compression factor	45	45	
Peak current	1400	2000	A
Proj. norm. emittance, rms	0.34, 0.23	1.05, 0.82	μm rad
Slice energy spread, rms	≤1.6	≤2.0	MeV
CSR energy spread, rms	0.003	0.003	%

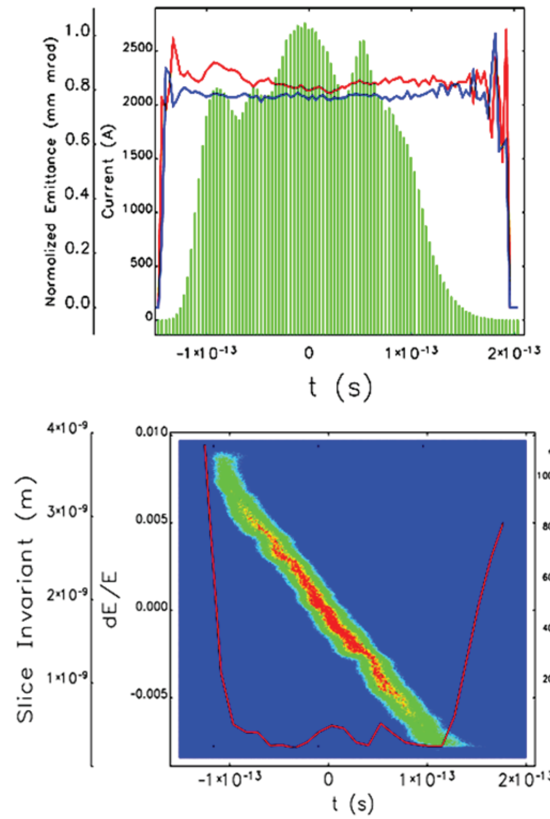

Figure 6: Top: current profile (histogram), superimposed to the slice rms normalized emittance. Bottom: longitudinal phase space, superimposed to the slice Courant-Snyder invariant (solid line): the horizontal one varies along the bunch because of CSR kicks. Bunch head is at negative time coordinates. Copyright of Europhysics Letters [13].

FINAL REMARKS

The capability of controlling CSR effects in an arc compressor (not necessarily constrained to a 180 deg total bending angle) – and thus to increase the beam peak current while preserving its 6-D normalized brightness using an approach that goes beyond those offered by the existing literature – quite generally opens the door to new geometries in accelerator design and new schemes of beam longitudinal gymnastic. For example, after single- or multi-pass acceleration in an FEL linac-driver, the beam can be arc-compressed at high energy and counter-propagated into an undulator, which could then lie parallel to the accelerator. At least two advantages are seen: one is that cost savings are achieved in civil construction, the other is that the operation of the system is simplified, as much as the beam does not undergo any manipulation other than acceleration until it reaches the arc compressor. On the basis of our findings, the arc could be investigated as either compressor (together with a proper setting of the upstream RF phases to match the arc's positive R_{56}) or a CSR-immune transfer line, if the beam has no energy chirp at its entrance. Our arc compressor design is also recommended for an ERL, or recirculated linac-driven FEL such as that described in [26]. In this case, the

ISBN 978-3-95450-134-2

electron beam may be accelerated and recirculated in isochronous beam lines until it reaches the target energy and energy chirp, and eventually compressed. From the entrance to the exit of the arc compressor, the energy spread, normally dominated by the energy chirp, remains substantially unchanged. In order for the FEL amplification process to be efficient, σ_δ must be matched to the normalized FEL energy bandwidth, ρ [27]. For lasing in x-rays, $\rho \geq 10^{-4}$ and this may require a removal of the energy chirp downstream of the arc, i.e. with a dedicated RF section. With the 500 pC beam parameters of Table 1, we estimate [28] lasing at 1.3 nm with $\rho = 1.1\times10^{-3}$, a 2.1 m-long 3-D gain length, and FEL power saturating at 2.6 GW in a 36 m long undulator.

ACKNOWLEDGEMENTS

The authors are grateful to D.R. Douglas for encouragements and fruitful discussions on arcs design, and to Y. Jiao for discussions on emittance control in DBAs. The authors are also in debt to the FERMI Team for their support in running the machine and for the development of the diagnostic tools that permitted the analysis of the experimental observations at FERMI. This work has been funded by the FERMI project and the ODAC project of Elettra Sincrotrone Trieste.

REFERENCES

[1] S. Di Mitri, M. Cornacchia, Physics Reports **539** (2014) 1-48.
[2] R. Talman, Phys. Rev. Lett. **56**, 1429 (1986).
[3] T. Nakazato et al., Phys. Rev. Lett. **63**, 2433 (1989).
[4] Ya.S. Derbenev, J.Rossbach, E.L. Saldin, and V.D. Shiltsev, TESLA-FEL 95-05 (1995).
[5] B. E. Carlsten and T. O. Raubenheimer, Phys. Rev. E **51**, 1453 (1995).
[6] E.D. Courant and H.S. Snyder, Annals of Phys. **3**, 1 (1958).
[7] D. Douglas, JLAB-TN-98-012 (1998).
[8] P. Emma and R. Brinkmann, SLAC-PUB-7554 (1997).
[9] E.L. Saldin, E.A. Schneidmiller, and M.V. Yurkov, Nucl. Instrum. Methods Phys. Res., Sect. A **398**, 373 (1997).
[10] E. Allaria *et al., Nat. Photon.* **6** (2012) 699–704.
[11] E. Allaria *et al., Nat. Photon.* **7** (2013) 913–918.
[12] S. Di Mitri, M. Cornacchia and S. Spampinati, Phys. Rev. Letters **110**, 014801 (2013).
[13] S. Di Mitri, M. Cornacchia, Europhys. Letters **109**, 62002 (2015).
[14] M. Borland, APS Tech Note LS-207 (2000).
[15] Y. Jiao, X. Cui, X. Huang and G. Xu, Phys. Rev. Special Topics – Accel. Beams **17**, 060701 (2014).
[16] S.V. Benson et al., Journal of Modern Optics, **58**:16, 1438-1451 (2011).
[17] P. Piot, D. R. Douglas, and G. A. Krafft, Phys. Rev. Special Topics – Accel. Beams, **6**, 030702 (2003).
[18] G.H. Hoffstaetter and Y. H. Lau, Phys. Rev. Special Topics – Accel. Beams, **11**, 070701 (2008).
[19] D.R. Douglas et al., Thomas Jefferson National Accelerator Facility Report No. JLAB-ACP-14-1751 (2014), arXiv:1403.2318.
[20] Y. Jing, Y. Hao and V. N. Litvinenko, Phys. Rev. Special Topics – Accel. Beams, **16**, 060704 (2013).
[21] J.H. Wu, J.B. Murphy, V. Yakimenko, I. Ben-Zvi, W. Graves, E. Johnson, S. Krinsky and T. Shaftan, in Proc. of the 2001 Part. Accel. Conf., RPAH012, edited by P.W. Lucas and S. Webber, Chicago, IL, U.S.A. (2001).
[22] R. Hajima, Nucl. Instrum. Meth. Phys. Research, Sect. A **528**, 335 (2004).
[23] M. Shimada, K. Yokoya, T. Suwada and A. Enomoto, Nucl. Instrum. Meth. Phys. Research, Sect. A **575**, 315 (2007).
[24] M. Borland and V. Sajaev, in Proc. of the 24th Linear Accel. Conf., TUP023, edited by B. Laxdal and P.W. Schmor, Victoria, BC, Canada (2008).
[25] S. Di Mitri and M. Cornacchia, Nucl. Instrum. Meth. Phys. Research, Sect. A **735**, 60 (2014).
[26] R.C. York, Phys. Rev. Special Topics – Accel. Beams **17**, 010705 (2014).
[27] R. Bonifacio, C. Pellegrini and L. Narducci, Opt. Commun. **50**, 373-378 (1984).
[28] M. Xie, in Proc. of 1995 Part. Accel. Conf., Dallas, TX, USA, IEEE, 183–185 (1995).

ISBN 978-3-95450-134-2

FIRST SIMULATION RESULTS ON FREE ELECTRON LASER RADIATION IN DISPLACED PHASE-COMBINED UNDULATORS*

N.S. Mirian,†
UVSOR Facility, Institute for Molecular Science (IMS), Okazaki, Japan and
School of Particle and Accelerator Physics, IPM, Tehran, Iran
E. Salehi, Department of Physics, Amirkabir University of Technology, Tehran, Iran

Abstract

This report deals with self amplified spontaneous emission free electron laser (FEL) amplifier where the FEL emission is obtained from displaced phase combined undulators. Magnetic field of this adjustment methods in three dimensions is presented. The electron dynamics is investigated. The simulation method and results are explained. The radiation properties of the fundamental resonance and third harmonic through the phase combined undulators are compared with the normal undulator with the same undulator deflection parameter.

INTRODUCTION

In free electron laser (FEL), a relativistic and high current electron beam passes through a periodic, transverse magnetic undulator field and produces electromagnetic wave. Undulator, as a major component in the FEL, converts the energy of the electron beam to that of the radiation field [1,2].

We know that when the gap between the top and bottom magnetic arrays is relatively narrow, the magnetic arrays of undulators subject to a significant attractive force. Therefor, the undulators usually require rigid mechanical components and frames to control the magnetic gap precisely. Further, a large number of components are required to administrate the mechanical load along the undulator axis and forbear the deformation of the magnetic arrays. If we remove the attractive force between the two arrays of the undulator, the heavy and large base frame is not necessary, and the undulator will be designed to be much more compact and lightweight.

Recently, Kinjo et. al in Ref. [3] have employed phase-combined undulators (PCUs) in two new methods to make fine adjustment of the magnetic force in the insertion device. In the PCUs the phase between the lower and upper Halbach arrays is shifted such that the undulator has no magnetic force without using any cancellation system. By developing the principle of PCU, Kinjo et al. [3] divided the undulator into a number of sections such that half of them are phase-shifted in one direction and the others are shifted in opposed direction, without breaking the periodic condition in the undulator field. In their first method, they suggested an additional phase shift by a relative longitudinal displacement of δ to each section of the PCU; this method is referred to as the displacement method. In the second method, they used the easy axis rotation, which is hereinafter referred to as the rotation method.

In this report, we investigate the evolution of the electron beam and radiation in the FEL by employing the displaced PCU.

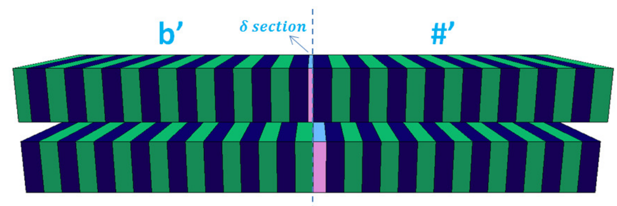

Figure 1: Conceptual diagram of the PCU.

GENERAL DISCUSSION

According to Ref. [3], by displacing upper or lower magnet array by $-\lambda_u/4$, the vertical force between the two arrays can be eliminated; while the shear longitudinal force that appears in the two arrays may be positive or negative depending on whether the upper or lower magnetic array is displaced. For significant reduction of the attractive force between the two arrays and longitudinal force, the PCU is composed of two kinds of sections as shown in Fig. 1. The blue blocks show the vertical polarization and the green blocks show the horizontal polarization. In one kind of section called♭, the upper magnets array are displaced by $-\lambda_u/4$, while in the next kind of section called #, the lower magnets array are displaced by $-\lambda_u/4$. Composition of these two sections can eliminate the shear longitudinal force. In the displacement adjusting method the relative longitudinal displacement of δ is added to each section, as shown in Fig. 1. In this figure, D shows the number of sections and the symbol #′(♭′) denotes the lower (upper) array of magnets that is displaced by $-\lambda_u/4-\delta$. Then, the magnetic field in three dimensions takes form

$$\mathbf{B}_{\#',b'} = \begin{bmatrix} \pm\frac{B_0}{2}\sinh(\frac{k_u}{\sqrt{2}}x)[\cos(k_u z)e^{\pm\frac{k_u y}{\sqrt{2}}} - \cos(k_u z - k_u(\frac{\lambda_u}{4}+\delta))e^{\mp\frac{k_u y}{\sqrt{2}}}] \\ \frac{B_0}{2}\cosh(\frac{k_u}{\sqrt{2}}x)[\cos(k_u z)e^{\pm\frac{k_u y}{\sqrt{2}}} + \cos(k_u z - k_u(\frac{\lambda_u}{4}+\delta))e^{\mp\frac{k_u y}{\sqrt{2}}}] \\ \pm\frac{B_0\sqrt{2}}{2}\cosh(\frac{k_u}{\sqrt{2}}x)[-\sin(k_u z)e^{\pm\frac{k_u y}{\sqrt{2}}} + \sin(k_u z - k_u(\frac{\lambda_u}{4}+\delta))e^{\mp\frac{k_u y}{\sqrt{2}}}] \end{bmatrix}. \quad (1)$$

The magnetic filed of the displaced PCU on axis is

$$\mathbf{B}(z) = B_0 cos(k_u(z-\Delta))\left[cos(k_u\Delta)\hat{j} + (-1^d)sin(k_u\Delta)\hat{k}\right], \quad (2)$$

* Work supported by Institute for Research in Fundamental Sciences (IPM)
† nsmirian@ims.ac.jp

where $\Delta = \lambda/8 + \delta/2$ is the half longitudinal displacement, and d is an even number for $\flat'$ section and an odd number for # section.

Following the Colson's analysis [4], we can find the the zero order dimensionless velocities of electrons. For the transverse velocities we obtain:

$$\beta_y(z) = (\beta_0 - (-1)^d \beta_z(z)) tan(\Delta), \quad (3)$$

$$\beta_x = \beta_0 \Bigg(2(-1)^d tan^2(\Delta) \left(\frac{\beta_z}{\beta_0}\right) - \left(\frac{\beta_z}{\beta_0}\right)^2 (tan^2(\Delta) + 1) - (tan^2(\Delta) - 1) \Bigg)^{1/2}, \quad (4)$$

and for longitudinal velocity we find

$$(-1)^d sin^2(\Delta)(sin^{-1}(\frac{\beta_z}{\beta_0} - (-1)^d tan^2(\Delta)) - \frac{\pi}{4}) - \sqrt{cos^2(\Delta) - \left(\frac{\beta_z}{\beta_0} - (-1)^d sin^2(\Delta)\right)^2} = \frac{-eB_0}{k_u \gamma mc^2} sin(k_u z - \Delta). \quad (5)$$

Further, simplification of the above Equations is impossible. In case of $\Delta = 0$ in Eq. (5), the simple longitudinal velocity equation in normal planar undulator, $\beta_z/\beta_0 = 1 - (eB_0/2\gamma mc^2 k_u)^2 sin^2(k_u z)$ can be obtained. Since the resonance condition, and radiation spectrum are obtained from the longitudinal velocity, one expects the resonance and spectrum equation in the PCUs to be different from those in the normal undulator.

In the FEL analysis, by using the electron velocity and the radiation electromagnetic fields, variation of electron energy and radiation field equations can be obtained. Further, the gain lengths of radiation wave can be found by means of the standard linear analysis of the variation of electron energy and radiation field equations. However, working with the velocity equations in the PCUs is not straight forward, we need simpler longitudinal velocity to calculate the resonance equation, FEL gain length, FEL parameters and pendulum equation. In other words, the FEL analysis is not easy in the PCUs. So, in order to extract the radiation wave evolution and information, we prefer to go straight to the simulation [5].

The electromagnetic field in simulation is assumed to be in the form of Gauss-Hermit modes that can be explained in terms of a complete basis set consistent with the planar undulator. The vector potential can be expressed as

$$\mathbf{A}(x,t) = \hat{e}_x \sum_{l,n,h} e_{l,n,h}(x,y)[A^{(1)}_{l,n,h} \cos\varphi_h + A^{(2)}_{l,n,h} \sin\varphi_h] \quad (6)$$

where summations over l and n denote the transverse modes, h is the harmonic number, $A^{(1,2)}_{l,n,h}$ are the slowly varying complex radiation field amplitudes, and

$$e_{l,n,h}(x,y) = \exp(-r^2/w_h^2) H_l(\sqrt{2}x/w_h) H_n(\sqrt{2}y/w_h)$$

represents the transverse structure of each mode, where H_r is the Hermit polynomial and w_h is the waist of the h^{th} harmonic. In this equation, $\varphi_h = h(k_0 z - \omega_0 t) + \alpha_h r^2/w_h^2$ is the vacuum phase while $k_0 (= \omega_0/c)$ is the vacuum wavenumber and α_h is the curvature of the phase front. It is assumed that $A^{(1,2)}_{l,n,h}$, α_h, and w_h are slowly varying function of z.

Substituting Eq. (6) into Maxwell's equations and using slowly varying envelope approximation, leads to a parabolic diffusion equation for the harmonic amplitudes, that can be averaged over one wave period to obtain an equation for the vector potential.

The momentum equation of motion for electrons can be obtained by inserting the electric and magnetic fields of radiation as well as the undulator magnetic field in the relativistic Lorentz force equation.

SIMULATION RESULTS

The set of coupled nonlinear differential equations for the undulator magnetic field and radiation electromagnetic field, as well as the electron momentum equations can be solved numerically by the Cyrus 3D code [6]. The simulation was done in time independent approximation. The wiggler parameters in all cases of PCUs are $\lambda_u = 3.3$ cm, $B_0 = 4.8$ kG. Also we choose an entrance taper region of $N_i = 10$ undulator period in length such that the tapered magnetic field amplitude is $B_0 \sin^2(k_0 z/4N_i)$. The electron current I has been fixed at 150 A, with the initial radius $r_b = 0.015$ cm, while the electron energy is chosen as 200 MeV. The thermal and the diffraction effects of the electron beam are ignored.

The initial conditions of the radiation fields is assumed such that the fundamental wavelength is seeded with a 5 W of optical power which is totally in the lowest mode of the fundamental resonance. The initial radiation waist is assumed to be 0.05 cm and the initial alpha parameter is zero.

For the displacement PCU simulation, we choose the longitudinal displacement $\delta = 0.008\lambda_u$ to have an adjustment such that the vertical force becomes 0.5% of the maximum force between the two arrays. By considering Eq. (3) in Ref. [3] , the deflection parameter for the PCU with this displacement becomes 1.019. With this condition the resonance wavelength is found approximately to be 156.75 nm. Note that the resonance wave length is found from several simulations.

In Fig. 2, the comparison of the fundamental and the third harmonic radiation power growth for different number of sections in the displaced PCU with D=400, D=100, D=10, and D=2 with the normal undulator (NU) with the same undulator deflection (K=1.019), are presented as a function of the distance through the undulator. To keep the K value in the normal undulator the magnetic field is chosen as

ISBN 978-3-95450-134-2

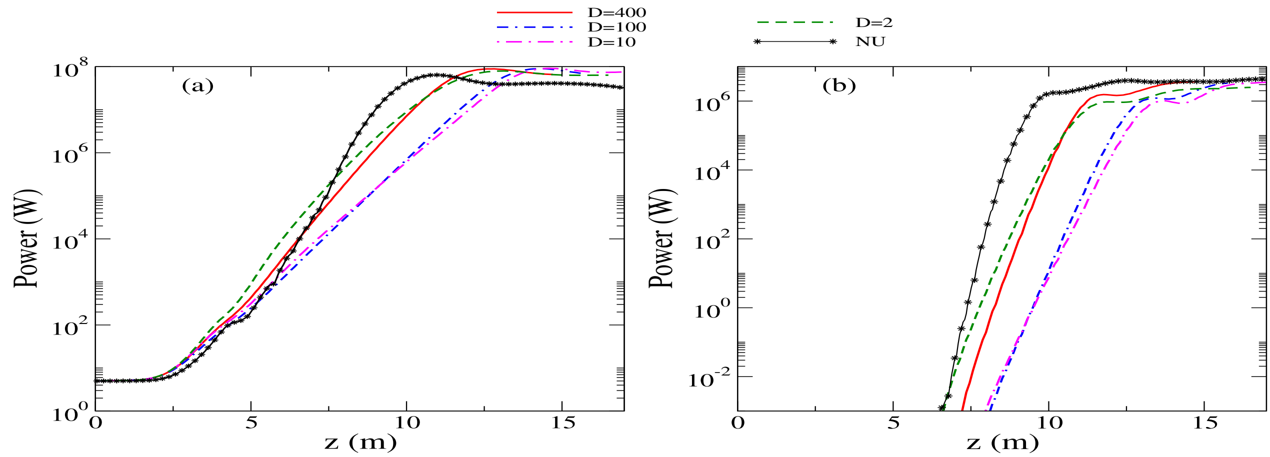

Figure 2: Power growth of (a) the fundamental resonance and (b) the third harmonic in the displaced PCUs with D sections and normal undulator (NU).

Table 1: The optical characteristics of the saturation point of the fundamental resonance and the third harmonic in different displaced PCUs with D sections and in the normal undulator (NU).

	NU	PCU, D=400	PCU, D=100	PCU, D=10	PCU, D=2
α_1	0.44	0.38	0.36	0.28	0.46
α_3	0.99	0.59	0.9	0.5	1.43
w_1	0.26 mm	0.28 mm	0.28 mm	0.25 mm	0.4 mm
w_3	0.14 mm	0.16 mm	0.19 mm	0.16 mm	0.27 mm

B=3.31 KG. In the PCU with D=400 sections, the length of each section is equal to the period of the undulator λ_u. Obviously the number of sections in the PCU can change the gain length of the radiation power growth. As can be seen from Fig. 2 (a), the radiation in the normal undulator saturates near z = 11m with the power of P_s = 68 MW, while in the phase combined undulator with 400 sections, the saturation point is near z = 12.8 m and the power is P_s = 86 MW. Likewise when the number of sections is D = 100, D = 10, and D = 2 the saturation point, respectively, are located at z = 14.5, 14.8, and 13.5 m; while the saturation powers are, respectively, P_s = 64, 64, and 57 MW. The average gain length of radiation in the normal undulator is L_g = 55 cm and in the PCU with different sections of D = 400, 100, 10, and 2 is, respectively, L_g = 66, 77, 79, and 71 cm.

In Fig. 2 (b) where the third harmonic power growth curves are compared, we can observe that the third harmonic power reaches saturation at (z_s =10 m, P_s = 1.7 MW) in normal undulator and in 400, 100, 10, 2-section PCU reaches saturation, respectively, at (z_s = 11.5 m, P_s = 1.3 MW), (z_s = 13.5 m, P_s = 0.81 MW), (z_s = 13.8 m, P_s = 0.62 MW), and (z_s = 12 m, P_s = 0.44 MW). From these figures it can be seen that the gain length and the saturation point of the normal undulator are shorter than that of the PCUs, and the saturation power in normal undulator and 400-section PCU is higher than that in the PCUs. In the following, we consider the properties of radiation of the fundamental and third harmonic at saturation points for these undulators.

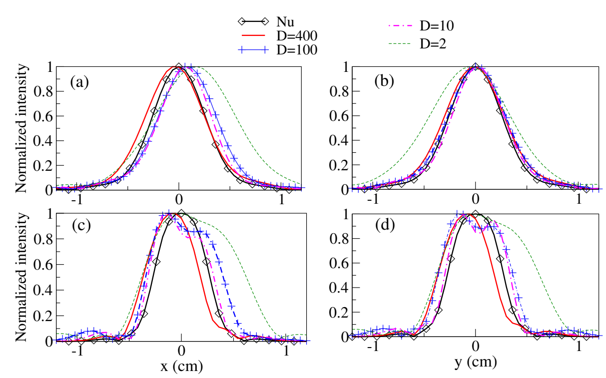

Figure 3: Normalized intensity in the x and y direction for (a) the fundamental resonance (b) the 3rd harmonic radiation in different displaced D-section PCUs and normal undulator (NU).

Table 1 reports the phase front curvature and the waist of the fundamental resonance ($\alpha_1$and w_1), and the third harmonic (α_3 and w_3) at the saturation point of each undulator. The phase front curvature of radiation at the saturation point in 2-section PCU and normal undulator is higher than that in other PCUs. Also the radiation waist in the PCU with two sections is wider than that in other PCUs and the normal undulator.

Figures 3(a) and (c) illustrate the fundamental resonance and third harmonic normalized intensity distribution, respec-

ISBN 978-3-95450-134-2

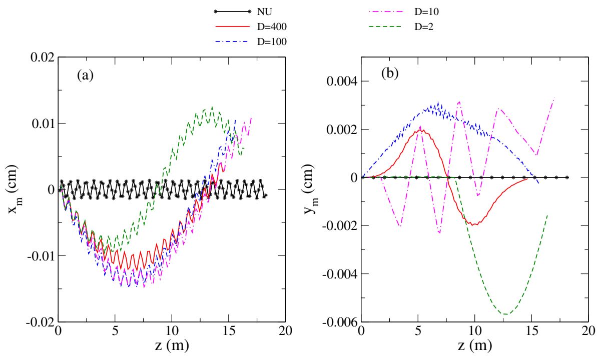

Figure 4: The center of mass motion of the bunch through the undulator in (a) x and (b) y directions for different cases.

tively, in the x direction; and Figures 3(b) and (d) show those in y direction for different D values. It is clear that the standard deviation of the normalized intensity radiation in the case of normal undulator is less than other cases. And the standard deviation of radiation in two-section PCU is wider than other cases. Further, Fig. 3(d) shows the y-distribution of the third harmonic radiation in the cases of PCU with 100 and 10 sections have two peaks near $y = -0.13$ cm and $y = 0.9$ cm.

Actually, at the beginning and end of each PCU section (♭ and # section), magnetic field changes, which modifies the transverse dynamics of electrons. Mathematically, the transverse coordinate y of the electrons are continuous but its first and second derivatives , that correspond to the momentum and acceleration, respectively, are not continuous. This means that we have critical points in electron dynamics at the beginning of each section of PCU. Figure 4 presents the center of mass motion of the bunch through the undulator in the x and y directions for different cases. In normal undulator, the center of mass motion of the bunch in the x and y directions oscillates very rapidly around the origin. There is a large kick in the y-trajectory of electron in the middle of the undulator, which is due to the switch from section ♭ to section #. In section ♭ the velocity of the electron in the y direction is $\beta_y(z) = (\beta_0 - \beta_z(z))1.05$, but in section # the electron velocity in the y direction is $\beta_y(z) = (\beta_0 + \beta_z(z))1.05$.

SUMMARY

This report focuses on studying simulation of FEL amplifier with a displaced phase-combined undulator, in which a magnetic attractive force is eliminated. By obtaining the electron velocity components on the axis of the displaced PCU, we have shown that analysis of the FEL and finding important FEL parameters by employing the linear analysis in the PCUs is not straight forward. Also, calculation of resonance condition with longitudinal velocity of the electrons in PCUs is not straight forward. Then the simulation of radiation and electron motion has been performed. The radiation properties of the fundamental resonance and the third harmonic through the displaced PCUs and normal undulator with the same undulator deflection parameter are compared. Some differences in saturation length and saturation power were found.

REFERENCES

[1] W. Ackermann, G. Asova, V. Ayvazyan, A. Azima, and N. Baboi, Nat. Photon. 1, 336 (2007).

[2] B. McNeil, Nat. Photonics 3, 375 (2009).

[3] R. Kinjo, T. Tanaka, Phys. Rev. ST Accel. Beams 17, 122401 (2014).

[4] W.B. Colson, IEEE Journal of Quantum Electronics QE-17, 1417 (1981).

[5] N.S. Mirian, E. Salehi, et al., submitted to publication (2015).

[6] M. H. Rouhani, N. S. Mirian, S. Salehi, reference available at, `http://particles.ipm.ir/Cyrus1D.jsp`

ISBN 978-3-95450-134-2

HARMONIC GENERATION IN TWO ORTHOGONAL UNDULATORS*

Najmeh Sadat Mirian†
UVSOR Facility, Institute for Molecular Science (IMS), Okazaki, Japan and
School of Particle and Accelerator Physics, IPM, Tehran, Iran

Abstract

In this report, the harmonic generation in two orthogonal undulators is under discussion. There is a possibility of generation of the even and odd harmonics as well as no-integer harmonics in two orthogonal undulators. By considering the first order of electron velocity, the total energy radiated per unit solid angle per unit frequency interval for a single electron traveling along the undulators is derived. Also a numerical simulation of one-dimensional non-averaged equations is conducted to present the self amplified spontaneous emission of harmonic generation in two orthogonal undulators.

INTRODUCTION

Modern high intensity sources are based on the electron radiation through undulator in synchrotrons and free electron lasers (FEL). Free electron lasers that are mostly based on self amplified spontaneous emission, hold great prospects as high power, coherent, and tunable radiation in the high frequency region of the electromagnetic spectrum [1,2]. The angular distribution of the radiation in undulators is obtained by computing the amount of energy lost by the particle in a retarded time during the emission of the signal. In practice, the spectrum of the radiation depends on the detailed motion of the electron and on the direction from which the electron is observed.

In a planar undulator with an ideal sinusoidal periodic magnetic field, the electrons radiate at odd harmonics due to their non-uniform axial motion. In ideal helical undulator, because of the constant longitudinal velocity, the spectrum is centered about the resonance frequency and there is no significant harmonic growth.

The two orthogonal undulators in FEL has been proposed as away toward the product of two tunable color radiation pulses with different polarizations, while the total length of device dose not change with the respect to the usual single-color FEL [3,4]. The form of this undulator is composed of two linear undulators orthogonally polarized with different periods. The possibility of generation of two radiation waves with different frequencies and different polarizations was investigated. We showed that by changing dependently the strength of the two magnetic fields, we can control the final power and the saturation length.

This report focuses on studying the harmonic generation in the two-orthogonal undulators in two different methods.

* Work supported by Institute for Research in Fundamental Sciences (IPM)
† nsmirian@ims.ac.jp

FIELD EQUATIONS

The undulator magnetic field, in the paraxial approximation, is described by the following expression

$$\mathbf{B}_w = B_{w2}\cos(k_{02}z)\hat{e}_x + B_{w1}\cos(k_{01}z)\hat{e}_y, \quad (1)$$

where B_{wi} is the untapered undulator field amplitude, $k_{01,02} = 2\pi/\lambda_{01,02}$ are undulator wave numbers and $K_{1,2} = \left|eB_{w1,2}\lambda_{01,2}/mc^2\right|$ are the deflecting parameters. We assume $n\lambda_{01} = m\lambda_{02}$, which permits us to treat the cases of a harmonic relation between λ_{01} and λ_{02} and of rational m/n. The proper resonance relation in this magnetic file has been obtained as [3,4]

$$\lambda_{1,2} = \frac{\lambda_{01,02}}{\gamma}(1 + \frac{K_1^2}{2} + \frac{K_2^2}{2}), \quad (2)$$

where λ_1 and λ_2 are, respectively, fundamental resonance wavelength in the x and y direction. The one-dimensional vector potential can be assumed to be

$$\mathbf{A} = i\sum_h \left[A_{1h}e^{i(k_1z-\omega_1t)}\hat{e}_x + A_{2h}e^{i(k_2z-\omega_2t)}\hat{e}_y\right], \quad (3)$$

where h is the harmonic number. The vector potential amplitudes $A_{1,2h} = A^{(1)}_{1,2h} + i\,A^{(2)}_{1,2h}$, are assumed to vary slowly in z and t. By using Maxwell-Poisson equation in Gaussian gauge, and the slowly varying envelope approximation (SVEA), the two polarization amplitudes take the following independent differential form:

$$\begin{aligned}\frac{\partial}{\partial z}A_{1,2h} + \frac{1}{c}\frac{\partial}{\partial t}A_{1,2h} &= \tfrac{2\pi en}{k_{1,2}}\textstyle\sum_h \beta_{x,yj}\delta(z-z_j)e^{-i\alpha_{1,2hj}},\\ \alpha_{1,2h} &= h(k_{1,2}z - \omega_{1,2}t) = h\alpha_{1,2}, \quad (4)\end{aligned}$$

where $\omega_{1,2} = k_{1,2}c$ is radiation frequency for fundamental resonance. Similar to the way used in Ref [4] after averaging of Maxwell's equation over time scale ℓ/c (where $\ell = n\lambda_1 = m\lambda_2$), we have

$$\left(\frac{\partial}{\partial z} - \frac{\partial}{\partial t}\right)\begin{pmatrix} a^{(1)}_{1h} \\ a^{(2)}_{1h}\end{pmatrix} = \frac{\omega_p^2}{2h\omega_1 c}\beta_{z,0}\begin{pmatrix} \left\langle \frac{u_x}{|u_z|}\cos(\alpha_{1h})\right\rangle \\ -\left\langle \frac{u_x}{|u_z|}\sin(\alpha_{1h})\right\rangle\end{pmatrix}, \quad (5)$$

$$\left(\frac{\partial}{\partial z} - \frac{\partial}{\partial t}\right)\begin{pmatrix} a^{(1)}_{2h} \\ a^{(2)}_{2h}\end{pmatrix} = \frac{\omega_p^2}{2h\omega_1 c}\beta_{z,0}\begin{pmatrix} \left\langle \frac{u_y}{|u_z|}\cos(\alpha_{2h})\right\rangle \\ -\left\langle \frac{u_y}{|u_z|}\sin(\alpha_{2h})\right\rangle\end{pmatrix}, \quad (6)$$

$a^{(1,2)}_h = e\frac{A^{(1,2)}_h}{mc^2}$ is the normalized amplitude, $\omega_p^2 = 4\pi e^2 n/mc^2$ is the square of plasma frequency, and $\mathbf{u} = \mathbf{P}/mc = \gamma\beta$ is a dimensionless variable. The averaging operator is defined as

ISBN 978-3-95450-134-2

$$\langle(\cdots)\rangle = \int_0^{2\pi} \frac{\sigma(\psi_0)}{2\pi} d\psi_0(\cdots), \tag{7}$$

where $\sigma(\psi_0)$ is the phase distribution at the entry time t_0 , and ψ_0 is the initial phase $\psi_0 = \omega t_0$.

MOMENTUM EQUATION

By using Lorentz force equation, the momentum equations for the ith electron of the beam can be derived as

$$\begin{aligned}
\frac{dp_{ix,y}}{dt} &= e\beta_{iz} B_{w1,2}\cos(k_{01,2}z) \\
&\quad - \sum_h ehk_{1,2}(1-\beta_{iz})[A_{1,2h}e^{ih\alpha_{i1,2}} + cc], \\
\frac{dp_{iz}}{dt} &= e\beta_{iy}B_{w2}\cos(k_{02}z) - \sum_h ehk_2\beta_{iy}[A_{2h}e^{ih\alpha_{i2}} + cc] \\
&\quad - eh\beta_{ix}B_{w1}\cos(k_{01}z) - \sum_h ek_1\beta_{ix}[A_{1h}e^{ih\alpha_{i1}} + cc],
\end{aligned} \tag{8}$$

where $\beta_{x,y,zj} = v_{x,y,zj}/c$ are the normalized velocity components. In first order longitudinal velocity takes following form [4]

$$\beta_z = \frac{1}{4}\left[\left(\frac{K_1}{\gamma}\right)^2\cos(2k_{01}z) + \left(\frac{K_2}{\gamma}\right)^2\cos(2k_{02}z)\right] + \beta_0, \tag{9}$$

where $\beta_0^2 = 1 - 1/\gamma^2$. The trajectories of the electrons in first order takes form:

$$\begin{aligned}
\mathbf{r}_j &= \beta_0 ct\hat{e}_z - \frac{\lambda_{01}}{2\pi}\frac{K_1}{\gamma_0}\sin(\omega_{01}t)\hat{e}_x - \frac{\lambda_{02}}{2\pi}\frac{K_2}{\gamma_0}\sin(\omega_{02}t)\hat{e}_y \\
&+ \frac{\lambda_{01}}{16\pi}\left(\frac{K_1}{\gamma_0}\right)^2\sin(2\omega_{01}t)\hat{e}_z + \frac{\lambda_{02}}{16\pi}\left(\frac{K_2}{\gamma_0}\right)^2\sin(2\omega_{02}t)\hat{e}_z.
\end{aligned} \tag{10}$$

HARMONIC GENERATION

The total energy radiated per unit solid angle per unit frequency interval for a single electron in an undulator with length $L_w = N_{wi}\lambda_{0i}$ is obtained by

$$\frac{d^2I}{d\omega d\Omega} = \frac{e^2}{4\pi^2 c}\left|\int_{-L_w/2c}^{L_w/2c} dt\,\mathbf{n}\times[\mathbf{n}\times\boldsymbol{\beta}(t)]e^{i\omega[t-\mathbf{n}.\mathbf{r}(t)/c]}\right|^2, \tag{11}$$

here, $\mathbf{n}$ is a unit vector from the electron to the observer. Only the emission in the forward direction ($\mathbf{n} = \hat{e_z}$) is considered, then

$$\begin{aligned}
\hat{e_z}.\mathbf{r} \approx \beta_0 ct + \frac{\lambda_{01}}{16\pi}\left(\frac{K_1}{\gamma_0}\right)^2\sin(2\omega_{01}t) + \frac{\lambda_{02}}{16\pi}\left(\frac{K_2}{\gamma_0}\right)^2 \\
\times\sin(2\omega_{02}t),
\end{aligned} \tag{12}$$

$$\hat{e_z}\times[\hat{e_z}\times\boldsymbol{\beta}(t)] = -\frac{1}{\gamma}[K_1\sin(\omega_{01}t) + K_2\sin(\omega_{02}t)],$$

where $\omega_{01,2} = k_{01,2}c$. By using following expansion

$$e^{-i\xi\sin\theta} = 2\pi\sum_{l=-\infty}^{l=\infty} J_l(\xi)e^{-il\theta}, \tag{13}$$

where $J_l(\varsigma)$ is a Bessel function of the first kind, one can write

$$\begin{aligned}
&\hat{e_z}\times[\hat{e_z}\times\boldsymbol{\beta}(t)]e^{i\omega(t-\hat{e}_z.\mathbf{r}/c)} = \frac{2\pi}{2i\gamma^2}\sum_d\sum_{d'}[J_d(\chi_1)J_{d'}(\chi_2) \\
&[K_1[e^{it(\omega(1-\beta_0)-\omega_0(2(d+d\varsigma)-1))} - e^{it(\omega(1-\beta_0)-\omega_0(2(d+d'\varsigma)+1))}]\hat{e}_x \\
&+K_2[e^{it(\omega(1-\beta_0)-\omega_0(2(d+d\varsigma)-\varsigma))} - e^{it(\omega(1-\beta_0)-\omega_0(2(d+d'\varsigma)+\varsigma))}]\hat{e}_y],
\end{aligned} \tag{14}$$

here, $\chi_{1,2} = K_{1,2}\omega/8\pi c\gamma^2 k_{w1,2}$, and $\varsigma = \omega_2/\omega_1 = m/n$. Therefore, by integration of Eq. (14) in Eq.(11), we have

$$\begin{aligned}
\frac{d^2I}{d\omega d\Omega} = \frac{e^2}{\gamma^2\omega_{01}^2 c}\Bigg\{&\left[K_1\sum_d\sum_{d'} J_d(\chi_1)J_{d'}(\chi_2)\left(\frac{\sin\left(\frac{(\omega-\omega_r(1-2(d-d'\varsigma)))N\pi}{\omega_r}\right)}{\left(\frac{(\omega-\omega_r(1-2d-d'\varsigma))N\pi}{\omega_r}\right)} - \frac{\sin\left(\frac{(\omega-\omega_r(1+2(d+d'\varsigma))N\pi}{\omega_r}\right)}{\left(\frac{(\omega-\omega_r(1+2(d+d'\varsigma))N\pi}{\omega_r}\right)}\right)\right]^2 + \\
&\left[K_2\sum_d\sum_{d'} J_d(\chi_1)J_{d'}(\chi_2)\left(\frac{\sin\left(\frac{(\omega-\omega_r(\varsigma-2(d+d'\varsigma))N\pi}{\omega_r}\right)}{\left(\frac{(\omega-\omega_r(\varsigma-2(d-+d\varsigma))N\pi}{\omega_r}\right)} - \frac{\sin\left(\frac{(\omega-\omega_r(\varsigma+2(d-+d\varsigma))N\pi}{\omega_r}\right)}{\left(\frac{(\omega-\omega_r(\varsigma+2(d+d'\varsigma))N\pi}{\omega_r}\right)}\right)\right]^2,
\end{aligned} \tag{15}$$

Equation (15) shows depending on value of ς, we can have even and odd harmonics. If ς is the odd number, instead, odd harmonics domain. As well, if ς is even, certainly we have growth of even harmonics. Further, this equation shows in some cases we can observe the no-integer harmonics.

Figure 1 displays this equation for different values of ς at z=4 m. As can be seen in case (c) where the ς is non-integer number, we can observe the integer and non-integer harmonics.

Polarization angle of radiation is another important issue in two orthogonal undulators. However, we know it depends on the magnetic field intensity of each undulator. Figure 2 presents the radiation polarization angle in various frequencies.

ISBN 978-3-95450-134-2

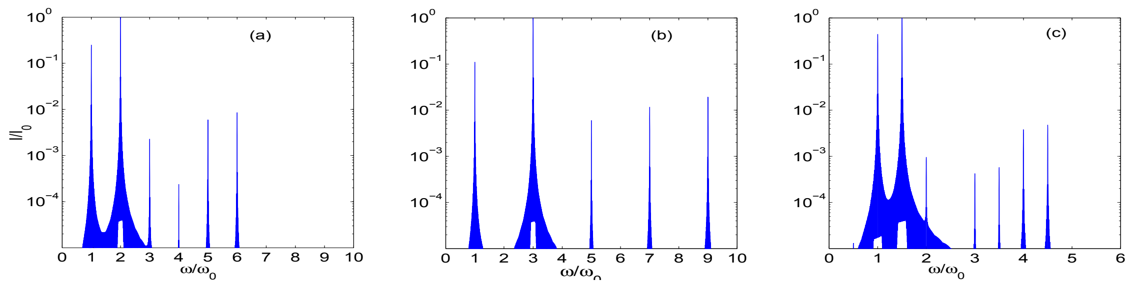

Figure 1: Spectrum of the radiation of one electron at z=4 m (a) m/n=2, (b)m/n=3 and (c) m/n=3/2, $K_1 = K_2 = 2.1$, $\lambda_{01} = 2.8\,cm$.

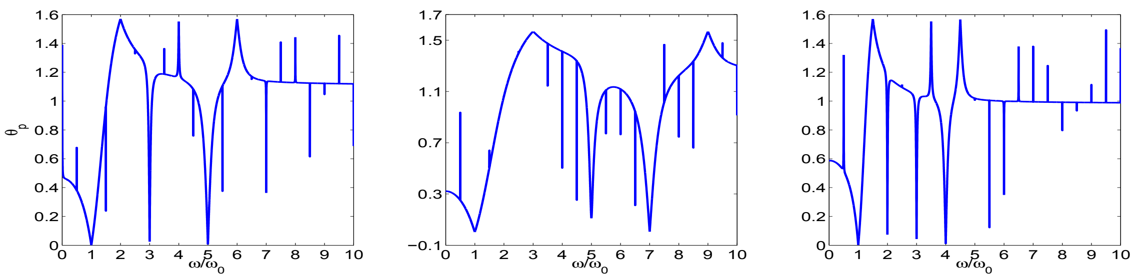

Figure 2: Radiation polarization angle of one electron radiation, while (a) m/n=2, (b)m/n=3 and (c) m/n=3/2, $K_1 = K_2 = 2.1$, $\lambda_{01} = 2.8\,cm$.

TIME DEPENDENT SIMULATION AND SHOT NOISE ALGORITHM

The set of the vector potential fields, phases and the non averaged dynamic equations includes $4N_e + 2N_h$ self-constant first order differential equations, where N_e indicates the macroparticle numbers in one beamlet, and N_h is the number of harmonics. In this case the length of the beamlet is $\ell = n\lambda_1 = m\lambda_2$. For simulation, we extended the Cyrus 1D code [6]. Cyrus 1D follows the approach of MEDUSA 1D [5]. This code shows very significant agreement with T1 code [7] corresponding to averaged FEL code and logistic map formula proposed with G. Dattoli [8].

To include shot noise in the simulation, the macroparticles are assumed to load over $[0, 2\pi]$ and perturbation due to shot noise is imposed to the phases, such that

$$\alpha'_j = \alpha_j + \delta\alpha \sin(\alpha_j - \phi)$$

where ϕ is chosen randomly over the interval $[0, 2\pi]$ and $\delta\alpha \ll 1$ describe the Poisson statistics. The phase of macroparticle, in x-polarization and y-polarization of electromagnetic radiation, are defined as

$$\alpha_{1j} = n\alpha', \qquad \alpha_{2j} = m\alpha'_j. \tag{16}$$

For time dependent (i.e slippage) simulation we use approach explained in Ref [9], however in this case the electron bunch with L_b length is divided to L_b/ℓ slices and the time dependent operation in Rung-Kutta loop is imposed on every spatial interval $\ell_w = n\lambda_{01} = m\lambda_{02}$.

In simulation the electron current is assumed to be 100 A and $\gamma = 300$. Fig.3 presents the evolution of pulse energy of (a) x-polarization (λ_1) and (b) y-polarization (λ_2) for different harmonics through undulator interaction, while the $m/n = 2/1$. It shows the growth of the even harmonics as well as the odd harmonics. For x-polarization, the intensity of the fifth harmonic at saturation point is higher than intensity of the third harmonic. For y-polarization, the intensity of the second harmonic is higher than the odd harmonics.

Figure 4 shows, when m/n=3/1, both m and n are the odd number, the odd harmonics of the x-polarization and y-polarization have higher intensity respect to the even harmonics. In fact, the growth of the odd harmonics are faster. Further, this plot shows that the pulse energy at the saturation point, z=4 m, for the third harmonic of the x-polarization, which has the wavelength equal to the fundamental resonance of the y-polarization, is higher than the fundamental resonance of x-polarization.

Figure 5 demonstrates the evolution of harmonic pulse energy, when m/n=3/2. Plat (a) indicates that the energy of the second harmonic pulse is equal to the third harmonic pulse energy at z=6 m.

Figures 6 and 7 show the pulse shape near saturation point $z = 4.5\,m$, for different harmonics of x-polarization and y-polarization when, respectively, $m/n = 2$ and $m/n = 3$.

ISBN 978-3-95450-134-2

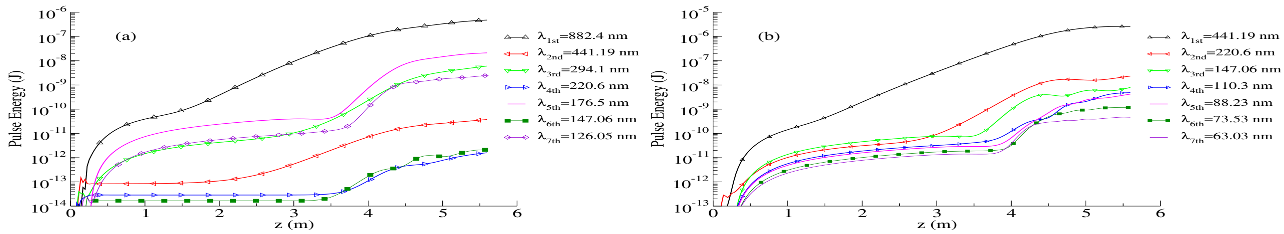

Figure 3: Evolution of pulse energy through undulator interaction for different harmonics (a) x- polarization , (b) y-polarization, m/n=2/1.

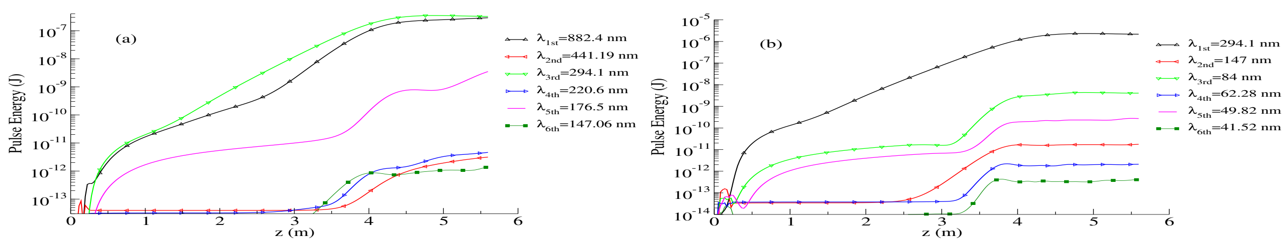

Figure 4: Evolution of pulse energy through undulator interaction for different harmonics (a) x- polarization , (b) y-polarization,m/n=3/1.

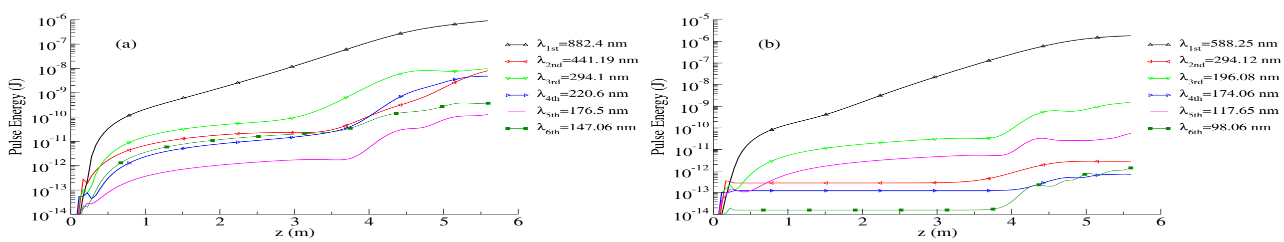

Figure 5: Evolution of pulse energy through undulator interaction for different harmonics(a) x- polarization , (b) y-polarization, m/n=3/2.

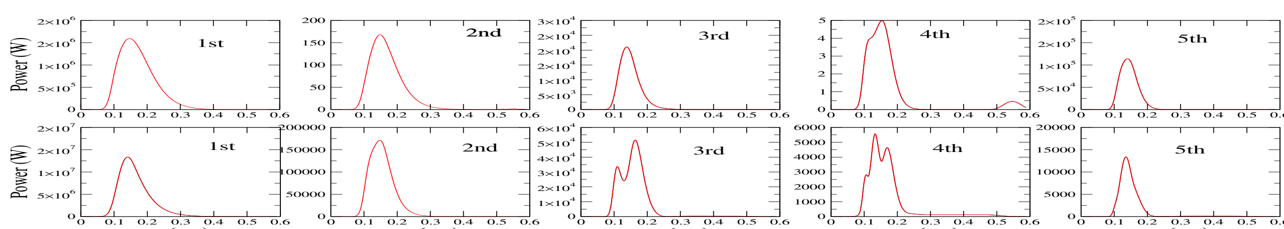

Figure 6: Power pulse shape in z=4.5, up : x-polarization, down: y-polarization; m/n=2.

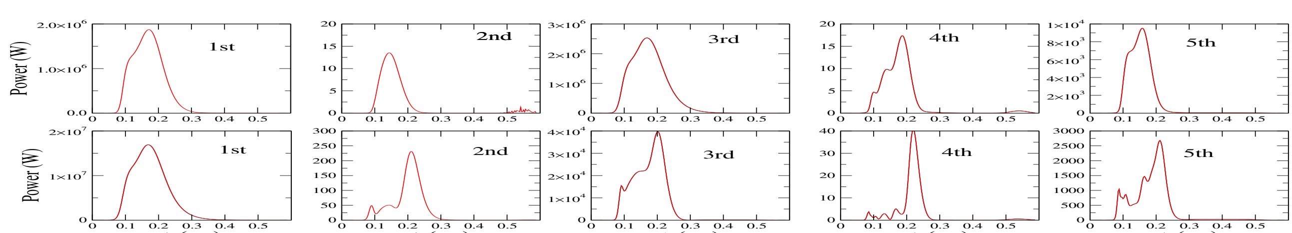

Figure 7: Power pulse shape in z=4.5, up : x-polarization, down: y-polarization; m/n=3.

ISBN 978-3-95450-134-2

CONCLUSION

This report focuses on studying the harmonic generation in the two-orthogonal undulators in two different methods. By considering the total energy radiated per unit solid angle per unit frequency interval for a single electron traveling the undulators and also by numerical simulation of one-dimensional non-averaged equations, we have demonstrated the possibility of generation of the even and odd harmonics as well as no-integer harmonic in two orthogonal undulators.

REFERENCES

[1] W. Ackermann, G. Asova, V. Ayvazyan, A. Azima, and N. Baboi, Nat. Photon. 1, 336 (2007).

[2] B. McNeil, Nat. Photonics 3, 375 (2009).

[3] G. Dattoli, N.S. Mirian, E. DiPalma, and V. Petrillo, Phys. Rev. ST Accel. Beams, 17, 5, 050702, (2014).

[4] N.S. Mirian, G. Dattoli, E. DiPalma, and V. Petrillo, Nuclear Instruments and Methods in Physics Research Section A, 767,227, (2014).

[5] H.P. Freund, L. Giannessi, and W.H. Miner, Jr., Applied Phys 104, 123114 (2008).

[6] N.S. Mirian, reference available at `http://particles.ipm.ir/Cyrus1D.jsp`.

[7] N.S. Mirian, E. Salehi, reference available at `http://particles.ipm.ir/Cyrus1D.jsp`.

[8] G. Dattoli, P.L. Ottaviani, and S. Pagnutti, Report No. ENEA RT/2007/40/FIM.

[9] N. Mirian, B. Maraghech, Phys. Plasmas 21, (2014).

CARRIER-ENVELOPE-PHASE STABLE LINEARLY AND CIRCULARLY POLARIZED ATTOSECOND PULSE SOURCES

Z. Tibai#, Zs. Nagy-Csiha, G. Almási, J. Hebling, Institute of Physics, University of Pécs, Hungary
Gy. Tóth, J.A. Fülöp, MTA-PTE High Field Terahertz Research Group, 7624 Pécs, Hungary

Abstract

We recently proposed a robust method for producing few-cycle attosecond pulse generation in the extreme ultraviolet spectral range. It is based on radiation of relativistic ultrathin electron layers, which are produced with inverse free electron laser process. In the present article the energy of this attosecond source is investigated numerically for the linearly and circularly polarized cases.

INTRODUCTION

In recent years a few phenomenon depending on carrier-envelope-phase (CEP) was recognized [1]. Waveform-controlled few-cycle laser pulses enabled the generation of isolated attosecond pulses and their application to the study of electron dynamics in atoms, molecules, and solids [2].

EUV pump—EUV probe experiments can be carried out at free-electron lasers (FELs) [3,4]; however, the temporal resolution is limited to the fs regime. Various schemes, such as the longitudinal space charge amplifier [5], or two-color enhanced self-amplified spontaneous emission (SASE) [6] were proposed for attosecond pulse generation at FELs. A very recent scheme suggests possible generation of sub-attosecond pulses in the hard X-ray region [7]. But the stochastic pulse shape is disadvantageous; furthermore there are no reliable techniques available for CEP control of attosecond pulses. Recently we proposed a robust method for producing waveform- and CEP-controlled attosecond pulses in the EUV spectral range [8]. Here we investigate numerically the feasibility and stability of this technique.

SIMPLE SETUP

Our proposed setup is shown in Fig. 1. A relativistic electron beam e.g. from a LINAC is sent through a modulator undulator (MU) where a TW-power laser beam is superimposed on it in order to generate nanobunches by the inverse free-electron laser (IFEL) action. The nanobunched electron beam then passes through a radiator undulator (RU) consisting of a single or a few periods. The radiator undulator is placed behind the modulator undulator at a position where the nanobunch length is shortest. Of course, efficient coherent radiation generation is possible only if the nanobunch length is shorter than the half period of the radiation.

#tibai@fizika.ttk.pte.hu

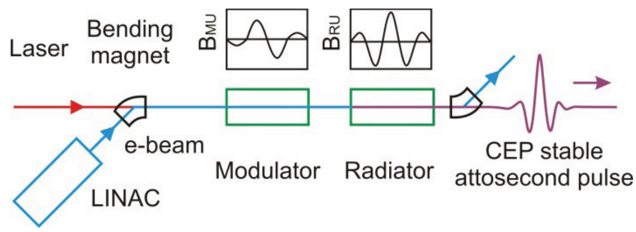

Figure 1: Layout of the setup.

SIMULATION METHOD

The General Particle Tracer (GPT) [9] numerical code was used for simulation of nanobunching in the modulator undulator. In the simulations the parameters of the electron bunch before the nanobunching were chosen according to published parameters of the electron bunches created by the accelerator of FLASH at DESY, Germany (Table 1) [10,11]. Electron bunches with 60 μm transversal size were assumed.

Table 1: Parameters used in the Simulations

Parameter	Value
E-beam energy (γ)	2000
E-beam charge	250 pC
E-beam energy spread (1σ)	0.05 %
E-beam Normalized emittance	1.4 mm mrad

Inside the modulator undulator the interaction between the electrons, the magnetic field of the undulator, and the electromagnetic field of the modulator laser with 516 nm wavelength and 10 TW power (P_L) introduces a periodic energy modulation of the electrons. This energy modulation leads to the formation of nanobunches in the drift space behind the MU. The charge of a single nanobunch is 1.0 pC and according to the simulations, its length can be as short as 6 nm (at 4.9 m behind the center of the modulator undulator).

The temporal shape of the ultrashort pulses emitted by these extremely short electron nanobunches in the RU, were calculated at a plane 8 m behind the middle of the RU.

The wavelength of the EUV radiation (λ_r) is determined by the well-known resonance condition:

$$\lambda_r = \frac{\lambda_{RU}\left(1+K_{RU}^2/2\right)}{2\gamma^2}, \qquad (1)$$

ISBN 978-3-95450-134-2

where λ_{RU} is the period of the RU, $K_{RU} = eB_0\lambda_{RU}/2\pi mc$ is the undulator parameter, B_0 is the peak magnetic field of the RU, e and m are the electron charge and mass, respectively, γ is the relativistic factor, and c is the speed of light.

The EUV radiation waveform is determined by the magnetic field distribution of the RU along the electron beam propagation direction (z). The magnetic field distribution of the RU is given by Eq. 2 for linearly polarized case:

$$B_{RU} = B_0 \cdot \exp\left(-z^2/2\sigma^2\right)\cos\left(2\pi/\lambda_{RU}\right), \quad (2)$$
$$\text{if} \quad -L/2 < z < L/2, \quad \text{otherwise} \quad 0,$$

where σ is the standard deviation of the Gauss envelope and L is the length of the RU. These parameters were set to $\sigma = 1.5/\sqrt{4\ln(2)}\lambda_{RU}$ (the FWHM of the envelope of the magnetic field is $1.5\lambda_{RU}$) and $L = 2.5\lambda_{RU}$ [8,12]. Similarly, magnetic field distribution of the RU in the circularly polarized case was described in [13].

EUV PULSE GENERATION AND RESULTS

The simulated waveform of the generated EUV pulses closely resembles the magnetic field of the RU (Eq. 2) [14]. The shapes of the pulses for different modulator laser pulse powers – for constant spot sizes, while the peak electric field was varied – are shown in Fig 2. The period length (42.7 cm) of the RU was chosen so that the radiation wavelength was 60 nm for K = 0.5 undulator parameter according to Eq. (1). The peak electric field of the generated attosecond pulse is 2.5 MV/cm for 2 TW and 3.2 MV/cm for 10 TW modulator laser power, respectively. The reason of the lower EUV intensity for lower modulator laser power is that lower laser power results lower energy-modulation in electronbunch and the drift space will be longer. Therefore, the transversal sizes of the nanobunches are bigger for lower laser power and the solid angle of radiated field decreases [8]. As it expected, the temporal shapes of radiated electric fields are CEP stable and the shape is practically independent of the power of the modulator laser pulse.

The EUV pulse energy as a function of the radiation wavelength in the range of 20-200 nm – calculated at different modulator laser powers for γ = 2000 and K = 0.5 – is shown in Fig. 3. The radiation wavelength, given by the resonance condition Eq. (1), can be set by the choice of the RU period λ_{RU}. The pulse energy first increases with increasing the wavelength. This range is followed by saturation at the 10 TW case and a subsequent energy decrease (blue line in Fig. 3) for the longest wavelength. The reason of the latter is that longer undulator periods are needed to generate longer wavelengths. Due to the associated longer path inside the RU the average nanobunch length increases and creates two separated nanobunch from each other, thereby reducing coherence in the radiation process. For lower powers the average length of the nanobunch does not increase as fast as for 10 TW, therefore there the energy increases with increasing the wavelength on the whole investigated EUV wavelength range.

According to the calculations, single-cycle EUV pulses with 50, 86, 111, and 134 nJ energy can be generated at λ_r = 60 nm for 2, 4, 6 and 10 TW modulator laser powers, respectively.

In another series of calculations the wavelength of the modulator laser power was varied (516, 800 and 1032 nm). The EUV pulse energy as a function of the radiation wavelength in the range of 20-220 nm (similarly to Fig. 3) for γ = 2000, P_L = 10 TW and K = 0.5 is shown in Fig. 4.

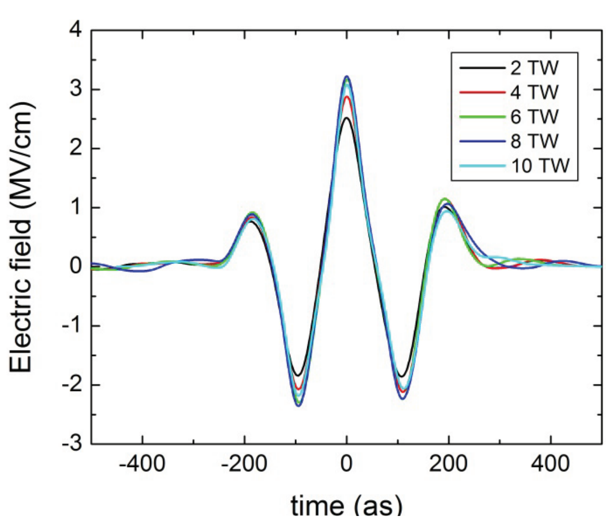

Figure 2: The temporal shape of the electric field of the EUV pulse for different modulator laser powers.

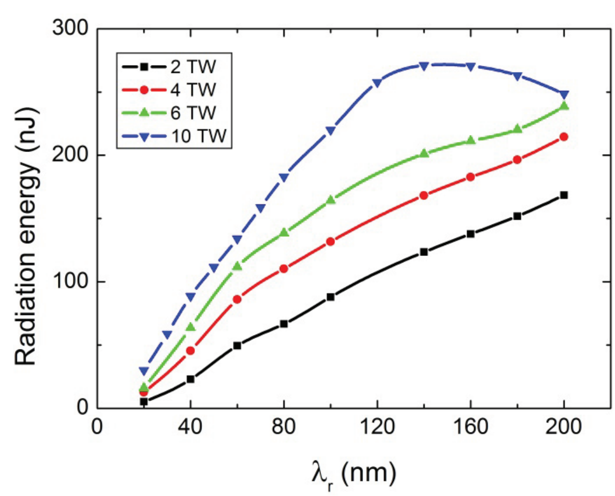

Figure 3: Dependence of the EUV pulse energy on the wavelength of the generated pulses.

ISBN 978-3-95450-134-2

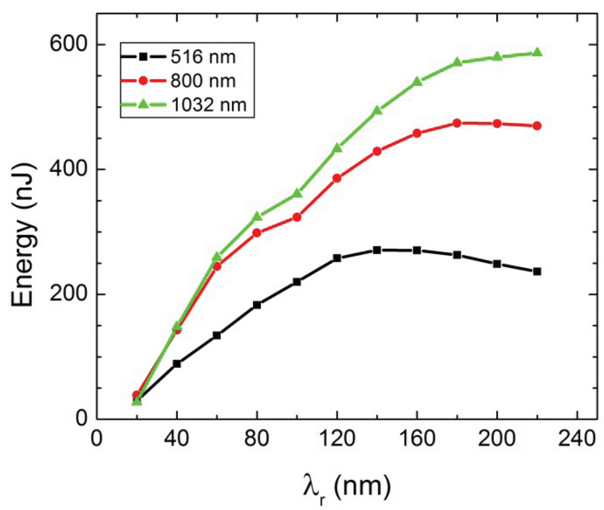

Figure 4: Dependence of the EUV pulse energy on the radiation wavelength for γ = 2000 and P_L = 10 TW and three different modulation laser wavelengths.

The largest EUV pulse energy is obtained with the longest modulator laser wavelength. Certainly, the energy of the EUV pulse depends on the charge of the nanobunch. Using longer modulator laser it is possible to concentrate larger charge in a nanobunch . We note, however, that using the longer laser wavelength (1032 nm; green line in Fig 4.) for modulation is disadvantageous below 20 nm, because for this case the length of the nanobunch is almost two times longer than for the shorter wavelength case (516 nm). Therefore this effect reduces the coherence in the radiation process, and the energy for 1032 nm is lower than for 516 nm at 20 nm. Above 60 nm, the energies for the 1032 nm laser are about two times higher, than for the 516 nm wavelength case.

According to the calculations, single-cycle 240-as pulses with 134, 244 and 260 nJ energy can be generated at λ_r = 60 nm for 516, 800 and 1032 nm modulator lasers, respectively. In the VUV range generation of sub-fs pulses with around half a microjoule energy is possible.

The above discussed robust method for production of CEP-stable, pulse-shape-controlled, linearly polarized attosecond pulses [5, 12, 14], can be easily modified (by using helical undulator) in order to generate circularly polarized attosecond pulses [13]. The electric field of the calculated pulse with this setup is shown in Fig 5. The blue and the green curves are the x and y electric field components, respectively. Using λ_{RU} = 42.6 cm undulator period and K = 0.5 undulator parameter for the RU (B_0 = 80.1 mT, γ = 2000) simulations predict $E_{max} \approx$ 4 MV/cm maximum value of the electric field, of the generated 240-as-long EUV pulses.

The main results of the linearly and circularly polarized EUV pulses are summarized in Table 2. The CEP stability of both the linearly and circularly polarised attosecond pulses is better than 50 mrad.

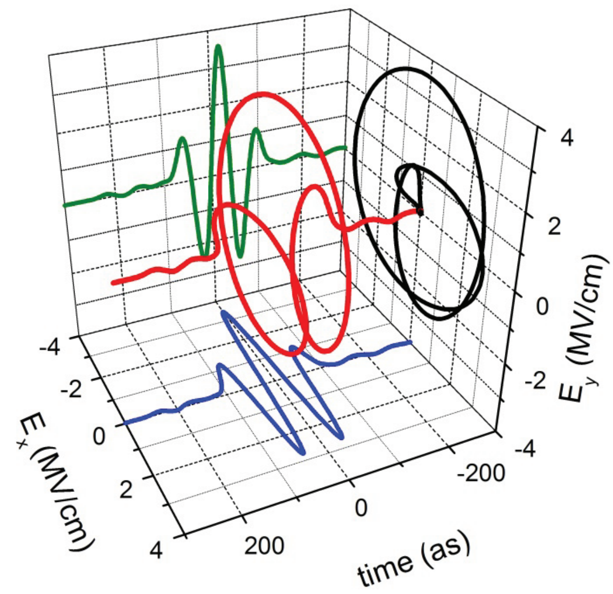

Figure 5: The electric field of the generated few cycle, circularly polarized attosecond pulse (red) and the x (blue) and y (green) components of the field. (γ = 2000, K = 0.5, λ_r = 60 nm).

Table 2: Summarized Results

Wavelength	Pulse duration	Polarization (C/L)	Energy
20 nm	80 as	Linear	30 nJ
60 nm	240 as	Linear	260 nJ
100 nm	400 as	Linear	360 nJ
20 nm	90 as	Circularly	30 nJ
60 nm	270 as	Circularly	170 nJ
100 nm	450 as	Circularly	300 nJ

CONCLUSION

In summary, practical aspects of the method proposed in our previous work [8,13] for CEP stable linearly and circularly polarized attosecond EUV pulse generation were investigated in detail by means of numerical simulations. The energy of the generated attosecond EUV pulse with various parameters was studied.

Our calculations predict for example single-cycle linearly polarized CEP-stable pulses with 260 nJ energy at 60 nm wavelength and 240 as duration, and circularly polarized pulses with 170 nJ energy at 60 nm wavelength and 270 as duration.

The predicted tens- or hundreds-of-nJ energy of the attosecond pulses enables to use them as pump pulse in pump-probe measurements. Pulses with the predicted exceptional parameters can enable time- and CEP-resolved measurements with sub-100-as resolution.

ISBN 978-3-95450-134-2

ACKNOWLEDGMENT

Financial support from Hungarian Scientific Research Fund (OTKA) grant No. 113083 and 101846 is acknowledged. JAF acknowledges support from János Bolyai Research Scholarship (Hungarian Academy of Sciences). The present scientific contribution is dedicated to the 650th anniversary of the foundation of University of Pécs, Hungary.

REFERENCES

[1] P. Dombi, J. Mod. Opt., **53**, 163-172 (2006) and references therein.
[2] F. Krausz and M. Ivanov, Rev. Mod. Phys. **81**, 163 (2009).
[3] Y. Jiang et al., Phys. Rev. Lett. **105**, 263002 (2010).
[4] M. Magrakvelidze et al., Phys. Rev. A **86**, 013415 (2012).
[5] A. Marinelli *et al*., Phys. Rev. Lett. **110**, 064804 (2013).
[6] A. Zholents and G. Penn, Phys. Rev. ST Accel. Beams **8**, 050704 (2005)
[7] D. J. Dunning *et al*., Phys. Rev. Lett. **110**, 104801 (2013).
[8] Z. Tibai *et al*., Phys. Rev. Lett. **113**, 104801 (2014).
[9] online at http://www.pulsar.nl/gpt
[10] K. Honkavaara *et al*., “Status of the FLASH II Project”, in Proceedings of the 34th International Free-Electron Laser Conference, (FEL2012, Nara, Japan, 2012), Report No. WEPD07.
[11] S. Ackermann *et al*., “Optimization of HHG Seeding between 10 nm to 40 nm”, in Proceedings of the 34th International Free-Electron Laser Conference, (FEL-2012, Nara, Japan, 2012), Report No. TUPD11.
[12] Z. Tibai *et al*., Phys. Rev. ST Accel. Beams, submitted.
[13] Gy. Tóth *et al*., Opt. Lett., accepted.
[14] Gy. Tóth *et al*., “Investigation of novel shape-controlled linearly and circularly polarized atto-second pulse sources”, in Proceedings of the International Workshop on PIPAMON Conference, Debrecen, Hungary, March 2015, submitted.

ISBN 978-3-95450-134-2

EFFICIENCY ENHANCEMENT OF A HARMONIC LASING FREE ELECTRON LASER

E. Salehi, Department of Physics, Amirkabir University of Technology, Tehran, Iran
N.S. Mirian*, UVSOR Facility, Institute for Molecular Science, Okazaki, Japan and
School of Particle and Accelerator Physics, Institute for Research in Fundamental Sciences (IPM), Tehran, Iran
B. Maraghechi, Department of Physics, Amirkabir University of Technology, Tehran, Iran

Abstract

The harmonic lasing free-electron laser amplifier, in which two wigglers is employed in order for the fundamental resonance of the second wiggler to coincide with the third harmonic of the first wiggler to generate ultraviolet radiation, is studied. A set of coupled nonlinear first-order differential equations describing the nonlinear evolution of the system, for a long electron bunch, is solved numerically by CYRUS code. Thermal effects in the form of longitudinal velocity spread are also investigated. The second wiggler field decreases linearly and nonlinearly at the point where the radiation of the third harmonic saturates to enhance the efficiency. The optimum starting point and the slope of the tapering of the amplitude of the wiggler are found by a successive run of the code. It is found that tapering can increase the saturated power of the third harmonic considerably.

INTRODUCTION

High-gain free-electron laser(FEL) amplifiers hold great prospects as high power, coherent, and tunable radiation in the x-ray regions of the electromagnetic spectrum. Utilizing nonlinear harmonic generation when bunching the harmonics is driven by the fundamental frequency in the vicinity of saturation is a possible way for obtaining x-ray wavelengths [1–7].

Recently, McNeil et al. [8] proposed a harmonic lasing FEL amplifier in a one-dimensional limit that can be extended to higher harmonics by suppressing the interaction at the fundamental resonance while allowing the harmonics to evolve to saturation. To suppress the interaction at the fundamental resonance without affecting the third harmonic lasing, they proposed two different settings for the undulator are considered by changing the wiggler magnetic field while keepingthe wiggler period, λ_w , and the initial average electron beam energy, γ, constant.

The intrinsic efficiency of the FEL is low. By increasing the energy of the electron beam, the efficiency reduces further. Therefore, for the x-ray FEL, efficiency is very low.For this reason, much attention has been givenin the literature to schemes for the FEL efficiency enhancement [9–13].

The purpose of the present study is to use the concept of the linear and nonlinear tapering of the wiggler field to increase the efficiency of the harmonic lasing FEL. To this end, by decreasing the wiggler amplitude linearly or nonlinearly at the saturation point, the resonance condition of the FEL is restored, which will result in higher intensity UV radiation. The slippage of the radiation with respect to the long electron bunch is ignored. Equations describing harmonic lasing FEL are derived. This set of equations is solved numerically using CYRUS 1D code in one-dimension [14]. CYRUS, which was developed by N. S. Mirian et al to study nonlinear harmonic generation. This code like MEDUSA employs nonaveraged equations [15,16]. The third harmonic lasing is considered so that the operating wavelength is in the ultraviolet (UV) domain.

* nsmrian@ims.ac.jp

BASIC EQUATIONS

The numerical simulation of the harmonic lasing is conducted using the CYRUS 1D code that is written in standard FORTRAN 90. This code like MEDUSA [15, 16] employs nonaveraged equations. The formulation treats the planar wiggler model and the radiation field is represented as a superposition of Gaussian modes [17]. The vector potential of the radiation field, in plane-polarized form, is

$$\delta\mathbf{A}(\mathbf{z},t) = \sum_{l,n,h}[\delta A_h^{(1)} sin(\varphi_h) + \delta A_h^{(2)} cos(\varphi_h)]\hat{\mathbf{e}}_x \quad (1)$$

where $\delta A_h^{(i)}$ with $i = 1, 2$ are the amplitudes that are assumed to vary slowly in z and t and $h = 1, 3, ...$ denotes the harmonic number, $\alpha_h = h(k_0 z - \omega t)$ is the phase of the hth harmonic of the angular frequency ω. Averaging Maxwell's equations over the time scale $2\pi/\omega$, the field equations take the form

$$\left(\frac{\partial}{\partial z}\right)\begin{pmatrix}\delta a_h^{(1)}\\ \delta a_h^{(2)}\end{pmatrix} = \frac{\omega_b^2}{2h\omega c}\begin{pmatrix}\langle\frac{u_x}{|u_z|}cos\alpha_h\rangle\\ \langle-\frac{u_x}{|u_z|}sin\alpha_h\rangle\end{pmatrix} \quad (2)$$

where $\delta a_h^{(i)} = e\delta A_h^{(i)}/m_e c^2$ are the normalized amplitudes, $\omega_b^2 = 4\pi e^2 n_b/m_e c^2$ is the square of the beam plasma frequency. The averaging operator is defined as

$$\langle(\cdots)\rangle = \int_0^{2\pi}\frac{\sigma(\psi_0)}{2\pi}d\psi_0\int_0^{\infty}dpG_0(p_z)(\cdots) \quad (3)$$

.

Here, $\sigma(\psi_0)$ is the phase distribution at entry time. Also, $G_0(p_z)$ is the initial momentum space distribution which is

ISBN 978-3-95450-134-2

chosen to have a spread in the longitudinal momentum, in the form of a Gaussian distribution function, without any spread in the transverse momentum. We chose the thermal distribution function as

$$G_0(p_z) = \sqrt{\frac{2}{\pi}}\frac{1}{\triangle p_z} exp\left(-\frac{2(p_z - p_0)^2}{\triangle p_z^2}\right) \quad (4)$$

where p_0 and $\triangle p_z$ are the initial bulk momentum and momentum spread, respectively. Electron trajectories are integrated using the Lorentz force equations in the magnetostatic and electromagnetic fields. It is important to emphasize that no average is performed over the Lorentz force equation.

$$\frac{d\boldsymbol{P}}{dt} = -e\delta\mathbf{E} - \frac{e}{c}\mathbf{v}\times(\delta\mathbf{B} + \mathbf{B}_w) \quad (5)$$

Here $\mathbf{B}_w$ is the planar wiggler magnetic field in one dimension that is written as

$$\mathbf{B}_w(z) = B_w(z)sin(k_w z)\hat{e_y}.$$

The details of the formulation is explained in Ref. [18].

In this paper, we consider a harmonic lasing FEL in which the wiggler consists of two halves with two different magnetic field strengths but the same wavelength λ_w. We reduce the wavelength of the fundamental harmonic of the first part by reducing the rms wiggler $a_n = \overline{\Omega}_n/\sqrt{2}$ (for planar wiggler). Suppose that in the first part the rms wiggler parameter is a_1 and the fundamental resonant wavelength is λ_1 with the harmonic resonant wavelength $\lambda_h = \lambda_1/h$, $h = 3, 5, 7, \ldots$. In the second part the rms wiggler parameter is a_n so that the new resonant fundamental wavelength is the nth harmonic of the first mode setting, $\lambda_1' = \lambda_n$.We assume that the beam energy and the undulator period are fixed. Therefore the retuned wiggler parameter a_n is obtained from the FEL resonance relation:

$$\frac{1 + a_1^2}{1 + a_n^2} = n. \quad (6)$$

Obviously, there are no real solutions fora_n if $a_c = \sqrt{n-1}$.

NUMERICAL SIMULATION

The complete set of coupled nonlinear differential equations is solved numerically using the fourth-order Rounge-Kutta method. For the particle averaging, the Gaussian quadrature technique in each of the degrees of freedom (ψ_0, p_{z0}) is used. In this work, an attempt was made to match the third harmonic resonance of the first part of the wiggler to the fundamental resonance of the second part in order to obtain UV radiation. The common parameters of the wigglers, radiation, and the electron beam which are used in this study are as follows: the electron beam has the relativistic factor of 300 with peak current of 200A and the initial radius of 0.15 mm. The wavelength of both parts of the wiggler is 2.8 cm. The peak value of the on-axis amplitude of the first part of the wiggler is 8.33 KG over the length

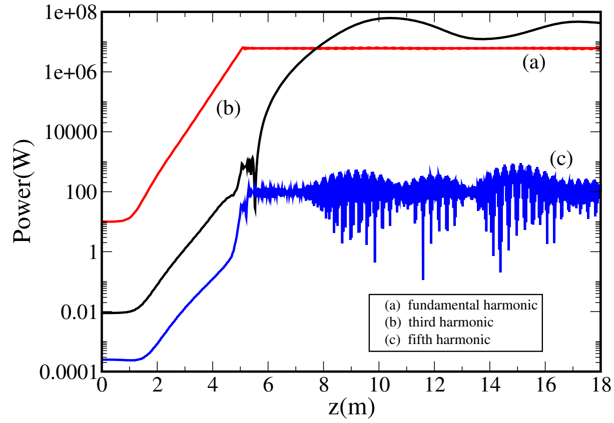

Figure 1: Power of the fundamental resonance (a), the third harmonic (b), and the fifth harmonic (c) versusz(m).

of 5 m, and the entry tapered region is $N_w = 10$ wiggler period in length. Using relation (6), we obtain $a_3 = 0.349$, and optimize the step taper and overall length for the maximum output. Using these beam and wiggler parameters, the fundamental resonance is at the wavelength of 523.9 nm, and the initial power is 10 W. The third harmonic resonance wavelength is 174.63 nm and starts from zero initial power. Figure 1 demonstrates the harmonic lasing scheme as described above. The resonant, cold beam limit is assumed. It is seen that the fundamental scaled intensity (a) is disrupted at $z = 5\,m$. Also, the intensity of the third harmonic (b), which is the fundamental of the second part of the wiggler when the undulator parameter is re-tuned at $\overline{\Omega}_3 = 0.49$, and the intensity of the fifth harmonic (c) are shown in Fig. 1. It is seen that the third harmonic grows to $3.8 \times 10^7 W$ and the fifth harmonic is also disrupted.

Figure 2 shows the longitudinal phase space of the electrons at different coordinates z along the wiggler for $\triangle\gamma/\gamma = 0.002$. Plots (a), (b), and (c) are for the first part of the wiggler and plots (d), (e), and (f) are related to the second part. The uneven distribution of initial phase, in plot (a), is the artifact of the Gauss quadrature weightings. Observe that as electrons move along the wiggler their energy gets redistributed in pondermotive phase $\psi = \alpha_3 + k_w z$ along a straight line with a sinusoidal modulation. This straight line is an indication of the energy spread. It is evident that the spread of energy becomes progressively larger as the beam approaches the saturation point. At $z = 6\,m$, the sinusoidal modulation is an indication that the untrapped electrons move along and pass over the pondermotive potential. The trapped particle at saturation is shown by the non-sinusoidal phase-space plot at $z = 17\,m$. We can conclude, therefore, that the plot of γ versus ψ truly represents the conventional phase space of $d\psi/dz$ versus ψ. Also, the variations of energy of the electrons is shown in Fig. 3 as a function of the distance through the wiggler. It is seen that the energy of the electrons after saturation point changes oscillationary.

The radiation intensity, $|A|$, indicates the efficiency of the FEL system. The lower (higher) intensity yields a lower

ISBN 978-3-95450-134-2

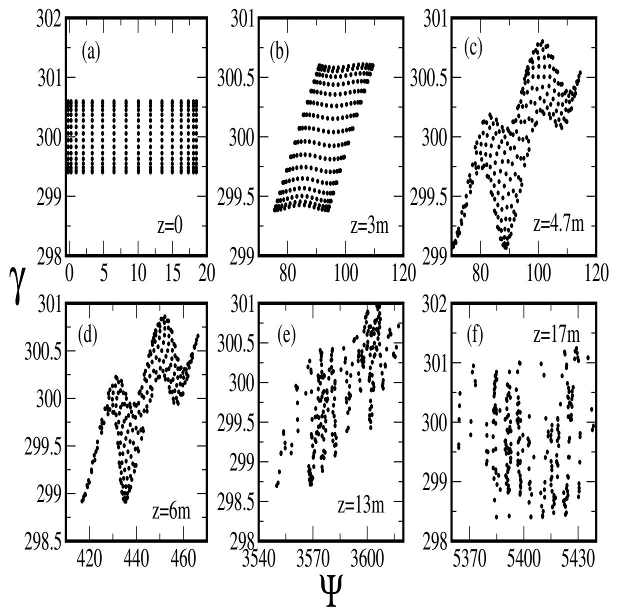

Figure 2: Distribution of energy γ versus the distribution of pondermotive phase of the electron beam at different values of the coordinate z along the undulator.

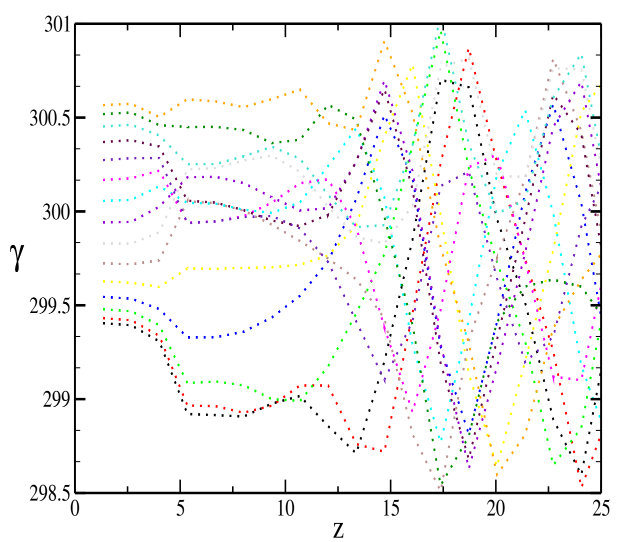

Figure 3: The variations of energy of the electrons as a function of the distance through the wiggler

(higher) efficiency. In the absence of tapering, oscillation of the radiation power beyond the saturation point persists. In one period, electrons give their energy to the radiation to increase the radiation amplitude and reduce the energy of electrons. This will cause the electrons to lose their resonance with the electromagnetic radiation and go to the phase in which they will extract energy from the radiation. Following this situation, the amplitude of radiation decreases up to the point at which electrons gain energy and their resonance with the radiation is established. This will cause the electrons to lose their energy to radiation. This cycle will repeat itself It has been shown that by decreasing the amplitude of

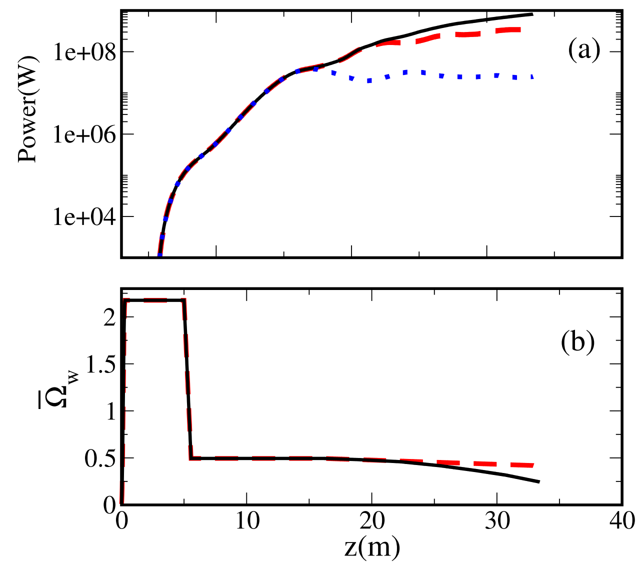

Figure 4: Comparison of the growth in the third harmonic power for a linearly tapered (dashed line), nonlinearly tapered (solid line), and untapered (dotted line) wiggler (a). Plot (b) shows Ω_w versus z for the linear tapering (dashed line) and nonlinear tapering (solid line) of the wiggler.

the wiggler a portion of the transverse energy of the electron beam will be transferred to the longitudinal motion and therefore accelerate the electron beam. This reduction can be linearly or linearly, that nonlinear decreasing can obtain more suitable restoration of the resonance condition.

It is assumed that the FEL has a constant wiggler field B_w (beyond the injection region) up to the point z_T (the saturation point), and after that the wiggler amplitude decreases linearly by the slope m. The linearly tapered wiggler may be written as

$$\overline{\Omega}_{wh}(\overline{z}) = \begin{cases} \overline{\Omega}_{wh}, & \overline{z} < \overline{z}_T \\ \overline{\Omega}_{wh} - m(\overline{z} - \overline{z}_T), & \overline{z} \geq \overline{z}_T \end{cases} \tag{7}$$

And the nonlinearly tapered wiggler can be as

$$\overline{\Omega}_{wh}(\overline{z}) = \begin{cases} \overline{\Omega}_{wh}, & \overline{z} < \overline{z}_{T1} \\ \overline{\Omega}_{wh} - m_i(\overline{z} - \overline{z}_{Ti}), & \overline{z}_{Ti} < \overline{z} < \overline{z}_{Ti+1} \end{cases} \tag{8}$$

$\overline{z}_{Ti+1}$ with $i = 1, 2, 3, \ldots$ are slopes of the lines between $\overline{z}_{Ti}$ and m_i. The second part of the wiggler in at apered harmonic lasing has been optimized over the entire length of 16.1 m. In Fig. 4(a), a comparison is made between the linearly tapered (dashed line), nonlinearly tapered (solid line), and untapered (dotted line) wigglers for the power of the third harmonic lasing. The wiggler amplitude is decreased at $z_T = 16.1\,m$ with the slope $m = 0.2\times10^{-4}$ for the linearly tapered wiggler. For nonlinear tapering, the amplitude of the wiggler is decreased at $z_{T1} = 16.1\,m$, $z_{T2} = 19\,m$, $z_{T3} = 22.6\,m$, $z_{T4} = 25.5\,m$, $z_{T5} = 28.3\,m$, $z_{T6} = 30.7\,m$ with slopes of $m_1 = 0.2\times10^{-4}$, $m_2 = 0.3\times10^{-4}$, $m_3 = 0.6\times10^{-4}$,

ISBN 978-3-95450-134-2

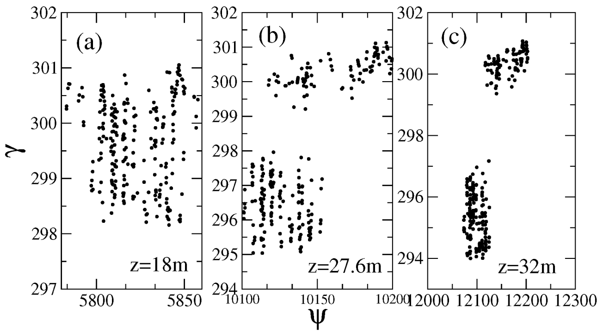

Figure 5: Distribution of energy γ versus the distribution of pondermotive phase of the electron beam at different values of the coordinate z along the linearly tapered wiggler.

$m_4 = 0.8 \times 10^{-4}$, $m_5 = 0.9 \times 10^{-4}$, $m_6 = 1.2 \times 10^{-4}$, respectively. The parameters m and z_T are chosen to obtain the maximum intensity of the third harmonic lasing, which are found by a successive run of the code. We can see significant increases in the third harmonic power from 3.8×10^7 to 8.1×10^8W for the linear tapering, and from to W for thenonlinear tapering. It can be seen that the nonlinear tapering of the wiggler amplitude with different slopes has higher efficiency. The profile for the variation of the wiggler parameter $\overline{\Omega}_w$ with $z(m)$ for the nonlinear tapering (solid line) and linear tapering (dashed line) of the wiggler is shown in Fig. 4(b).

The longitudinal phase space of the electrons at different coordinates z along the linearly tapered wiggler is represented in Fig. 5. It can be seen that in the tapered region and beyond the energy of the electron beam is reduced. Because of the restoration of the resonance condition, electrons give their energy to the radiation and the radiation amplitude increases.

SAMMARY

In this paper, a one-dimensional simulation is conducted to analyze harmonic lasing FEL. In order to generate UV radiation, the fundamental resonance disrupted by reducing the undulator magnetic field and the third harmonic grows up to the saturation point. The thermal effect of the electron beam is taken into account. By relating the energy distribution function to the distribution function of the pondermotive phase,chaotic patterns at the saturation point are revealed. It is found that by suitably tapering the amplitude of the second wiggler field, saturation of the radiation for a shorter wavelength can be postponed leading to further amplification. In the case of the tapered wiggler, it is found that the efficiency can be enhanced more effectively by the nonlinear reduction of the second wiggler field at saturation point compared to that of the linear tapering.

REFERENCES

[1] W. Ackermann, G. Asova, V. Ayvazyan, A. Azima, N. Baboi, Nature Photon. 1, 336 (2007).

[2] R. Bonifacio, L. De Salvo, and P. Pierini, Nucl. Instrum.Methods Phys. Res., Sect. A 293, 627 (1990).

[3] H.P. Freund, S. Biedron, and S. Milton, Nucl. Instrum. Methods Phys. Res., Sect. A 445, 53 (2000).

[4] Z. Huang and K. Kim, Phys. Rev. E 62, 7295 (2000).

[5] E.L. Saldin, E. A. Schneidmiller, and M.V. Yurkov, Phys. Rev. ST Accel. Beams 9, 030702 (2006).

[6] D. Ratner, A. Brachmann, F.J. Decker, Y. Ding, D. Dowell, P. Emma, A. Fisher, J. Frisch, S. Gilevich, Z. Huang, P. Hering, et al., Phys. Rev. ST Accel. Beams 14, 060701 (2011).

[7] L.H. Yu, Phys. Rev. A 44, 5178 (1991).

[8] B.W.J. McNeil, G.R.M. Robb, M.W. Poole, and N.R. Thompson, Phys. Rev. Lett. 96, 084801 (2006).

[9] H.P. Freund and S.H. Gold, Phys,. Rev. Lett. 52, 926 (1984).

[10] P. Sprangle, C.M. Tang, and W.M. Manheimer, Phys. Rev. Lett.43, 1932 (1979).

[11] P. Sprangle, C.M. Tang, and W.M. Manheimer, Phys. Rev. A 21, 302 (1980).

[12] H.P. Freund and J. Pasour, Phys. Rev. Lett.91, 094801 (2003).

[13] X.J. Wang, T. Watanabe, Y. Shen, R.K. Li, J.B. Murphy, T. Tsang, and H.P, Freund, Appl. Phys. Lett.91, 181115 (2007).

[14] N.S. Mirian, M.H. Rouhani, `http://particles.ipm.ir/Cyrus1D.jsp`

[15] H.P. Freund, S.G. Biedron, and S.V. Milton, IEEE J. Quantum Electron.36, 275 (2000).

[16] H.P. Freund, L. Giannessi, and W.H. Miner, Jr, J. Appl. Phys. 104, 123114 (2008).

[17] H.P. Freund, S.G. Biedron, and S.V. Milton, IEEE J. Quantum Electron.27, 243 (2003).

[18] E. Salehi, B. Maraghechi, and N.S. Mirian, Phys. Plasmas 22, 033110 (2015).

ISBN 978-3-95450-134-2

THREE-DIMENSIONAL SIMULATION OF A HARMONIC LASING FREE-ELECTRON LASER AMPLIFIER

E. Salehi, B. Maraghechi
Department of Physics, Amirkabir University of Technology, Tehran, Iran,
N.S. Mirian*
UVSOR Facility, Institute for Molecular Science, Okazaki, Japan and
School of Particle and Accelerator Physics, IPM, Tehran, Iran

Abstract

Three-dimensional simulation of harmonic lasing Free-electron laser is represented in the steady-state regime. Here, the third harmonic of the first wiggler is adjusted at the fundamental resonance of the second wiggler by reducing the magnetic field strength of the second wiggler. The hyperbolic wave equations can be transformed into parabolic diffusion equations by using the slowly varying envelope approximation. A set of coupled nonlinear first-order differential equations describing the nonlinear evolution of the system is solved numerically by CYRUS3D code. This set of equations describes self-consistently the longitudinal spatial dependence of the radiation waists, curvatures, and amplitudes together with the evaluation of the electron beam. Thermal effects in the form of longitudinal velocity spread are also investigated.

INTRODUCTION

High-gain free electron laser (FEL) amplifiers hold great prospects of reaching coherent high power radiation in the x-ray region of the electromagnetic spectrum. In recent years, a great effort of researchers has been devoted to studying the process of higher harmonic generation in achieving lasing at shorter wavelengths [1–5].

Radiation of the electron beam in the planar wiggler contains odd harmonics but the output power at the hth harmonics is rather small and is of the order of 10^{-h} times the power of the fundamental [1, 3–5]. Recently, McNeil et al. [6] proposed a harmonic lasing method for FEL amplifiers that can amplify the higher harmonics by suppressing the interaction at the fundamental resonance. They showed that this configuration can significantly extend the operation band of user facilities.

Reference [6] has outlined two methods for suppressing the interaction at the fundamental resonance while allowing the third harmonic to evolve to saturation. The first method is based upon shifting the phase of the fundamental between the wiggler segments, which can be controlled by various techniques [7]. For the hth harmonic, this phase shift should be $2\pi n/h$, where $n = 1, 2, 3, \ldots$ is an integer number and $h = 3, 5, 7, \ldots$ is the harmonic number. The second method is detuning of the fundamental by considering two different segments for the wiggler. Two segments of the wiggler have different magnetic field intensity while the wiggler period, λ_w, and the initial average electron beam energy, γ, are kept constant.

The thermal effect of the electron beam is particularly important for higher harmonics, because they are more sensitive to the energy spread than the fundamental one [8, 9]. The energy spread is considered as a Gaussian energy distribution in MEDUSA code for nonlinear harmonic generation [10]. Also, in reference [7], the energy spread effects are included that the gain length for the detuning of the fundamental is compared with the third harmonic in conventional FEL.

The aim of this paper is to present a three-dimensional simulation of the emission at the fundamental and third harmonic in the non-wiggler-averaged-orbit approximation of the harmonic lasing FEL with source-dependent expansion [11–14]. Therefore, the source function is incorporated self-consistently into the functional dependence of the radiation waist, the radiation wavefront curvature, and the radiation amplitude instead of using the usual modal expansion consisting of vacuum Laguerre-Gaussian or Hermite-Gaussian functions. It is important to emphasize that no wiggler average is imposed on the orbit equations. Therefore, It is possible to treat the injection of the beam into the wiggler, with the ease of inclusion of external focusing or dispersive magnetic components in the beam line and the facility for using an actual magnetic field in the numerical solution. The third harmonic lasing is considered so that the operating wavelength is in the EUV domain. The slippage of the radiation with respect to the long electron bunch is ignored.

The code which is written for this purpose is named CYRUS 3D, which was developed by PhD students in Amirkabir University and Institute for Research in Fundamental Sciences (IPM). This code follows MEDUSA 3D [10] formulation.

DESCRIPTION OF THE SIMULATION CODE

The simulation code for three-dimensional non-wiggler averaged-orbit formulation is CYRUS 3D code, that was written in standard Fortran 95. This code is time independent with harmonics and thermal effects taken into account. It models planar wiggler and the electromagnetic field is represented as a superposition of Gauss-Hermit modes in the slowly varying amplitude approximation. Electron trajectories are integrated using the three-dimensional(3D) Lorentz

* nsmirian@ims.ac.jp

ISBN 978-3-95450-134-2

force equations in the magnetostatic and electromagnetic fields.

This code like MEDUSA 3D employs nonaverage equations. The details of the formulation is explained in Ref. [10]. We simulate harmonic lasing FEL in which the wiggler consists of two segments. In the harmonic lasing FEL the wiggler segments have two different magnetic field strengths but the same wavelength λ_w.

The thermal effect of the electron beam on the harmonic gain is particularly important. Higher harmonics are more sensitive to the energy spread than the fundamental one [4, 6, 8]. It was concluded in Ref. [6] that harmonic lasing with phase shifting is more sensitive to the emittance and the energy spread than the harmonic lasing with detuning of the fundamental. In Refs. [15], a spread in the traverse momentum with constant total energy is considered. They showed that a longitudinal spread is more effective than a transverse spread in reducing the growth rate.

To consider effects of the energy spread, we assume longitudinal spread without any spread in the transverse momentum. So, the initial conditions is chosen to model the axial injection of the electron beam with the energy in the form of a Gaussian distribution function that is peaked around the initial energy of the beam. We choose the thermal distribution function as

$$G_0(p_z) = \sqrt{\frac{2}{\pi}}\frac{1}{\Delta p_z} exp\left(-\frac{2\,(p_z - p_{z0})}{\Delta p_{z^2}}\right), \qquad (1)$$

where p_0 and Δp_{z0} are the initial bulk momentum and momentum spread, respectively.

$$\langle(\cdots)\rangle = \int\frac{d\psi_0}{2\pi}\sigma_{\parallel}(\psi_0)\iint dx_0 dy_0 \sigma_{\perp}(x_0, y_0)\int dp G_0(p_z)(\cdots) \qquad (2)$$

To consider harmonic lasing FEL using the retuned fundamental resonant wavelength, the wiggler is composed of two segments and the wavelength of the fundamental resonance of the second segment is decreased by reducing the magnetic field strength of the second segment of the wiggler. In this case, for the first segment, the rms wiggler parameter is a_1 and the fundamental resonant wavelength is λ_1 giving the harmonic resonant wavelengths as $\lambda_h = \lambda_1/h$, $h = 3, 5, 7, \ldots$. In the second segment, the rms wiggler parameter is reset to a_n so that the new resonant fundamental wavelength is the nth harmonic of the first segment, $\lambda_1' = \lambda_n$. For the assumed fixed beam energy and wiggler period, the retuned wiggler parameter a_n is obtain from the FEL resonance relation

$$\frac{1 + a_1^2}{1 + a_n^2} = n. \qquad (3)$$

Obviously, a_1 must be larger than $a_c = \sqrt{n-1}$. Because there are no real solutions for a_n for $a_1 < a_c$. So, the wiggler can not be reduced to a fundamental wavelength $\lambda_1' = \lambda_n$ for $a_1 < a_c$. We consider tuning the harmonic interaction by decreasing the wiggler magnetic field; it is clear this is impractical for an operating X-ray FEL.

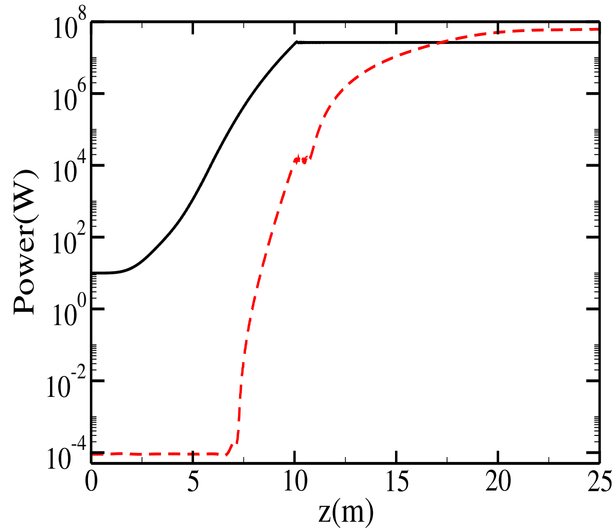

Figure 1: Evolution for the power for the fudamental resonance (solid line) and the third harmonic (dashed line).

NUMERICAL ANALYSIS

Self-consistent first-order nonlinear differential equations are solved numerically using the forth-order Runge-Kutta algorithm subject to the appropriate initial conditions and in the time independent approximation where the pulse length is much longer than the slippage length over the course of the wiggler. The particle averages are carried out using a Gaussian quadrature technique in each of the degrees of freedom $(x_0, y_0, \psi_0, \varphi_0, p_{z0}, \gamma_0)$. The number of Gauss-Hermite modes that are needed in the code depends on each particular example. The self-guiding effects of the electron beam in an FEL during exponential gain become dominant over the diffraction, and the balance depends on the Rayleigh length, the growth rate, and the evolution of the beam envelope. Therefore, it is necessary to choose a suitable basis set in order to determine the optical mode content. The number of modes that are determined by an empirical procedure in which successive simulation runs are made with an increasing number of modes until convergence of the saturation power and saturation length are achieved.

The parameters for the electron beam, the wiggler, and the radiation in the simulation are as follows. The electron beam has the relativistic factor of 964, a peak current of 300 A, an initial radius of 0.01495 cm, and an energy spread of 0.01%. The wiggler period is 3.3 cm and exhibits a peak of on-axis amplitude equal to 10.06 kG. An entry taper region is $N_w = 10$ wiggler period in length which is necessary in order to inject the electrons into the steady-state trajectories. Using these beams and wiggler parameters, the fundamental resonance is at a wavelength of 102.9 nm in the 1D resonance formula. Because of betatron motion in three dimensions, fundamental resonance is found at the wavelength of 103.6 nm, which is seeded with a 10 W of optical

ISBN 978-3-95450-134-2

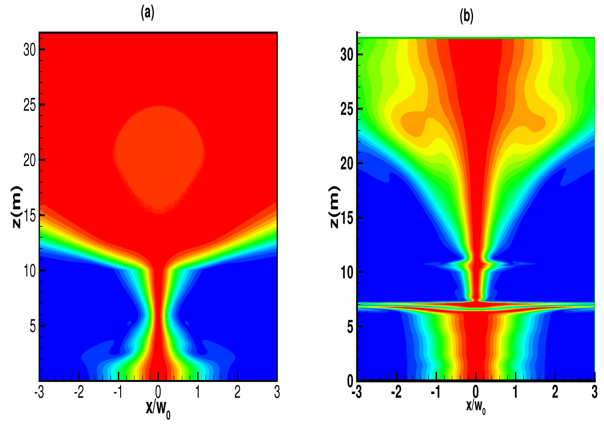

Figure 2: Transverse intensity profile of the fundamental resonance wavelength (a) and the third harmonic wavelength (b) in the x direction for $y = 0$

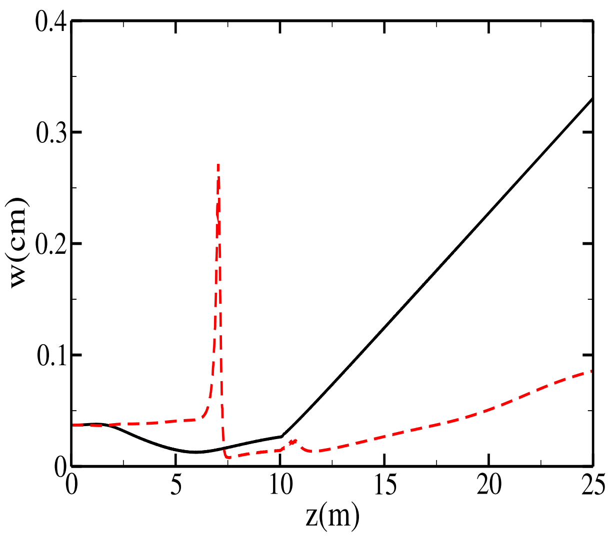

Figure 3: Evolution of the radiation spot size for the fundamental resonance (solid line) and third harmonic (dashed line).

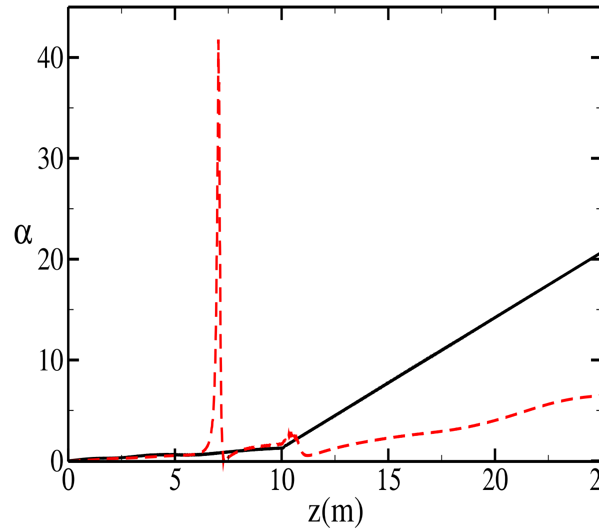

Figure 4: Evolution of $\alpha_1$and $\alpha_3$with longitudinal coordinate.

power. The third harmonic wavelength is at 34.5 nm and starts from zero initial power. The initial radiation waists are 0.037 cm and the initial alpha parameters are chosen to be zero. The initial state of electron beams is chosen to model the injection of an axisymmetric electron beams with the flattop density profiles, i.e., $\sigma_\perp = 1$. For unbunched electron beam, the particles are uniformly distributed in phase.

The fundamental resonance is suppressed by reducing the wiggler magnetic field strength at $L_1 = 10$ m with $a_3 = 0.97$ while the third harmonic grows to saturation. In Fig. 1, the power of the fundamental resonance (solid line) and the third harmonic (dashed line) are plotted as a function of the distance through the wiggler. The intensity of the shorter wavelength is larger than the intensity of the fundamental wavelength. Therefore, reducing the wiggler magnetic field, the fundamental resonance will be suppressed and the third harmonic of the first segment of the wiggler is a seed for the fundamental harmonic of the second segment of the wiggler leading to higher power. The fundamental resonance in Fig. 1 is suppressed at $z = 10$ m with the power of 2.7×10^7 W. The third harmonic approaches to saturation point at $z = 19.5$ m with the power of 4.8×10^7 W.

Evolution of the radiation amplitude in the transverse plane is shown in Figs. 2(a) and 2(b) as a function of z for the fundamental mode and the third harmonic, respectively. Although, these figures do not show the amplification of the radiation because of normalization of transverse profile to peak intensity of 1, they show that the amplitude profile of the radiation in the transverse plane becomes narrower as the radiation propagates toward the point of saturation and this mode narrowing is greater for the third harmonic. As it is seen in Fig. 2(b), the transverse intensity profile for the third harmonic initially widens until z=6.6 m, the point where the small gain ends. Because the radiation undergoes diffraction in the small gain region and experiences rapid focusing so-called gain guiding, at the onset of exponential growth it leads to narrowing transverse intensity profile. Thus, the transverse profile of the radiation appears to be guided with an exponentially growing amplitude. The position of the saturation point can be inferred from the point where mode narrowing stops and the intensity profile widens. Because the gain guiding is no longer effective after the saturation point the radiation waist begins to grow.

In Fig. 3, the radiation waist of the fundamental resonance and third harmonic are plotted. The radiation waist for the third harmonic is observed to expand, from its initial size, during the small signal region because of vacuum diffraction. This can also be seen in Fig. 2(b). At the exponential growth region, optical guiding becomes strong and focusing is rapid. Finally, the radiation waist expends rapidly as the saturation point is reached. The radiation waist for the fundamental

ISBN 978-3-95450-134-2

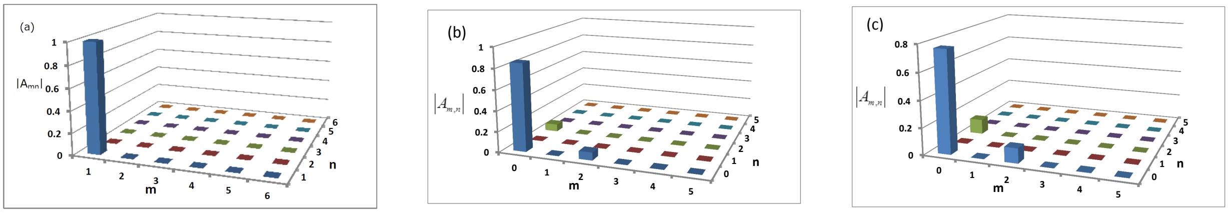

Figure 5: Composition histogram of modes at the beginning wiggler (a), the suppresion point (b), and the saturation point (c).

resonance behaves similar to the third harmonic, and grows faster at the suppressing point.

The curvature of the phase front, α, is shown in Fig. 4. Both fundamental and the third harmonic, which are plane waves at the entrance to the wiggler at $z = 0$, deviate from plane waves as radiation travels along the wiggler. The curvature of the phase front of the third harmonic increases abruptly as saturation occurs but for the fundamental resonance, it increases rapidly at the suppression point.

The composition process will introduce higher-order modes in an attempt to account. Figure 5 shows the mode content histogram at the beginning, suppression and saturation point of the third harmonic. Figure 5 represents that a purely (0,0) mode at the beginning of the wiggler. It can be seen that the lowest order mode $TEM_{0,0}$ is dominant at the saturation point.

CONCLUSION

In this paper, we analyzed harmonic lasing to enhance harmonic generation in the frame work of the realistic 3D model of the FEL process by using a nonaveraged simulations, which is named CYRUS 3D. In the absence of slippage, the variation of radiation waists, curvatures, and amplitudes for fundamental resonance and the third harmonic are studied. The radiation power of the third harmonic is larger than that of the fundamental resonance in contrast to the nonlinear harmonic generation. Also, the composition of significant modes of the third harmonic is presented which shows that the lowest order mode is dominant.

REFERENCES

[1] W. Ackermann,G. Asova, V. Ayvazyan, A. Azima, N. Baboi, Nature Photon. **1**, 336 (2007).

[2] R. Bonifacio, L. De Salvo, and P. Pierini, Nucl. Instrum. Methods Phys. Res., Sect. A **293**, 627 (1990).

[3] H. P. Freund, S. Biedron, and S. Milton, Nucl. Instrum. Methods Phys. Res., Sect. A **445**, 53 (2000).

[4] Z. Huang and K. Kim, Phys. Rev. E **62**, 7295 (2000).

[5] E. L. Saldin, E. A. Schneidmiller, and M. V. Yurkov, Phys. Rev. ST Accel. Beams **9**, 030702 (2006).

[6] B. W. J. McNeil, G. R. M. Robb, M. W. Poole, and N. R. Thompson, Phys. Rev. Lett. **96**, 084801 (2006).

[7] E. A. Schneidmiller and M. V. Yurkov, Phys. Rev. ST Accel. Beams **15**, 080702 (2012).

[8] E. L. Saldin, E. A. Schneidmiller, and M. V. Yurkov, Opt. Commun. **281**, 1179 (2008).

[9] L. H. Yu and J. Wu, Nucl. Instrum. Methods Phys. Res A **483**, 493 (2002).

[10] H. P. Freund, S. G. Biedron, S. V. Milton, IEEE J. Quantum Electron. **36**, 275 (2000).

[11] L. H. Yu and J. Wu, Nucl. Instrum. Methods Phys. Res A **483**, 493 (2002). P. Sprangle, A. Ting, and C. M. Tang, Phys. Rev. Lett. **59**, 202 (1987).

[12] B. Hafizi, P. Sprangle, and A. Ting, Phys. Rev. A **36**, 1739 (1987).

[13] P. Sprangle, A. Ting, and C. M. Tang, Phys. Rev. A **36**, 2773 (1987).

[14] B. Hafizi, P. Sprangle, and J. R. Penano, Nucl. Instrum. Methods Phys. Res.Sect. A **581**, 601 (2007).

[15] A. Chakhmachi and B. Maraghechi, Phys. Plasmas **16**, 043110 (2009).

FREE-ELECTRON LASER DRIVEN BY A 500 MeV LASER PLASMA ACCELERATOR BEAM

W.Qin, S.Huang, L.Zeng, X.Yan, K.Liu, J.Chen, IHIP, Peking University, Beijing 100871, China
Y. Ding, Z. Huang, SLAC, Menlo Park, CA 94025, USA

Abstract

A laser plasma accelerator is under construction at Peking University and several hundred MeV electron beams are expected. In this paper we discuss applying a 500 MeV beam with 1% relative energy spread to FEL. Bunch decompression method is considered to deal with the large energy spread of the beam. Emittance growth induced by large divergence and energy spread during beam transport has been treated with the chromatic matching manipulation. Simulation shows that 100 MW level, 6.3 fs , 0.008 bandwidth output can be obtained for 30 nm FEL. TGU method with assumed matched beam is also discussed as a comparison.

INTRODUCTION

Laser Plasma Accelerator (LPA) is considered as a promising candidate to drive compact short-wavelength Free-Electron Laser (FEL) owing to its capability to generate high energy electron beams in centimeter scale, which is of great interest for university scale labs. Undulator radiation utilizing laser plasma accelerated beam has been reached in the VUV and soft-X region [1, 2]. However, the percent level relative energy spread and chromatic induced emittance degradation during beam transport hinder the application of LPA beam to short-wavelength FEL. Controlled injection to improve beam quality and stability is being pursued by the LPA community. Even though, with presently demonstrated LPA beam, FEL may be realized when undulator adjustment and beam manipulation are performed to meet the requirement of high-gain FEL. To overcome the energy spread issue, two methods have been proposed, i.e., a proper dispersed beam coupled to a Transverse Gradient Undulator (TGU) [3] and a decompressed beam coupled to a longitudinally tapered undulator [4, 5]. However, chromatic effect induced emittance growth during beam transport can seriously affect either of the two energy spread compensation scheme. Recently, a so-called chromatic matching manipulation which synchronizes the energy slice waist slippage and the FEL slippage is proposed to address the chromatic effect for the decompression scheme [6]. For the TGU scheme, a matching beamline with sextupoles to correct the chromaticity is necessary [7].

In this paper, we discuss the application of an expected 500 MeV LPA beam at Peking University to a 30 nm FEL. Bunch decompression method with chromatic matching manipulation is considered, while TGU scheme with the LPA beam assumed to be matched at the undulator entrance is also discussed as a comparison.

LASER PLASMA ACCELERATOR AT PKU

Peking University is developing a multi-functional laser plasma acceleration experimental platform (see Fig.1) utilizing a high contrast 5 Hz, 200 TW, 800 nm laser system. After two stage CPA compression, the laser pulse with 5J energy is compressed to 25 fs. For laser proton acceleration, the laser is transported to the plasma mirror chamber to further increase its contrast ratio, then interact with a solid target to produce 15 MeV proton beam. For laser electron acceleration, the laser pulse is directly delivered to the gas target chamber to interact with a supersonic gas jet. The 200 TW laser system is ready to deliver the pulse, while the first experiment is still under preparation. A gas jet of adjustable length and several diagnostic devices including a 2 GeV electron spectrometer are also ready. Expected electron beam parameters for the first experiment are several hundred MeV energy with several MeV energy spread, tens of pC bunch charge, 0.1 mm·mrad normalized emittance.

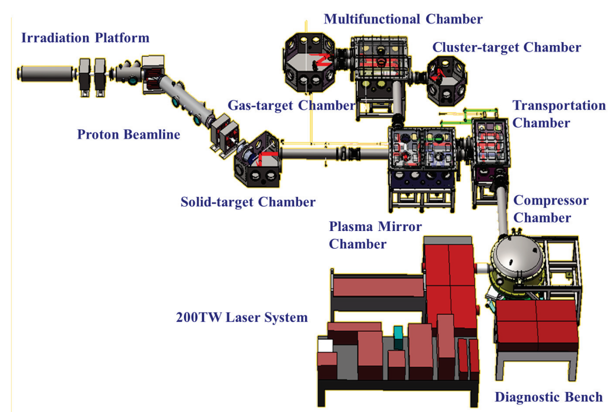

Figure 1: Laser plasma accelerator at Peking University.

BEAM MANIPULATION

Based on the capability of laser plasma accelerator at PKU, we discuss using a 500 MeV, 10 fs (FWHM), 40 pC LPA beam with 1% rms relative energy spread and 0.1 mm·mrad rms normalized emittance to drive 30 nm FEL. The parameters are summarized in Table 1. The beam is assumed to be 6D Gaussian in phase space and no correlation in both transverse and longitudinal phase space. Due to the μm scale beta function in plasma accelerator, the initial rms beam divergence is at mrad level, which is orders larger than that of electron beam from conventional accelerator. Large beam divergence leads to fast beam expansion at the very beginning of the transport beamline. Along with large energy spread, beam divergence drastically increase the chromatic

ISBN 978-3-95450-134-2

emittance. With second order optics notation, geometric emittance after a transport beamline is given by [6]

$$\varepsilon_{total} \approx \sqrt{\varepsilon_0^2 + \left(\frac{t_{126}}{r_{11}}\sigma_\delta \sigma_{x_0'}^2\right)^2}, \tag{1}$$

where ε_0 is the initial geometric emittance, σ_δ is the relative energy spread and $\sigma_{x_0'}$ is the initial beam divergence. For the LPA case, chromatic term dominates over the initial emittance, resulting several mm·mrad emittance growth after the transport beamline. Noting that the chromatic effect increase the beam emittance by rotating different energy slice to different phase space orientation, thus introducing an energy related slice waist slippage along the undulator, it is possible to sort these energy slices and synchronize them with the FEL pulse. As a result, the FEL pulse can always 'see' a low emittance slice focused at its waist.

Table 1: LPA and FEL Parameters

LPA parameters	Symbol	Value	Unit
pulse energy	E_l	5	J
pulse duration	τ_l	25	fs
laser wavelength	λ_l	800	nm
rep. rate	f_l	5	Hz
Beam parameters			
beam energy	E_b	500	MeV
bunch charge	Q	40	pC
rms norm. emittance	$\gamma\varepsilon_{x,y}$	0.1	mm·mrad
rms beam divergence	$\sigma_{x',y'}$	1	mrad
bunch duration(FWHM)	τ_b	10	fs
rms energy spread	σ_γ/γ	1%	
FEL parameters			
radiation wavelength	λ_r	30	nm
undulator period	λ_u	15	mm
undulator length	L_u	6	m
undulator strength	K	2.38	

A schematic of the chromatic matching beamline coupling the LPA beam to a 6 m long 15 mm period undulator is shown in Fig.2. It is composed of a triplet to refocus the beam, a chicane to introduce the energy sorting and another four quadrupoles to tune the synchronization. The chicane also reduces the beam slice energy spread since it decompresses the bunch, which is of benefit. The quadrupole strength for the refocusing triplet is up to 200 T/m, while for the tune quadrupoles is below 80 T/m.

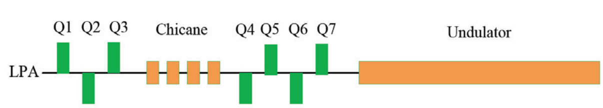

Figure 2: schematic of the chromatic matching beamline.

Figure 3 shows the ELEGANT [8] tracked transverse beam phase space at the undulator entrance (a,d), center (b,e) and exit (c,f), up to second order. Here transport matrix element $r_{12} = r_{34} = 0$, $r_{11} = r_{33} = 30$, $t_{226} = t_{446} = 0$, $t_{126} = t_{346}$. Chicane strength is scanned from 100 µm to 1 mm to obtain maxmium FEL power. Slice to slice focusing along the undulator can be seen clearly in the x plane while is distorted by the undulator natural focusing in the y plane. Only part of all energy slices are successively focused to waist, corresponding to high current region of the decompressed beam (see Fig. 4). The beam is decompressed by a factor 6 through the chicane and an energy chirp of 0.01/7.19 µm is introduced, with peak current decreased from 3.5 kA to 650 kA. It should be noted that the total normalized beam emittance is increased from 0.1 mm·mrad to 5.7 mm·mrad due to the chromatic effect, mainly in the first triplet.

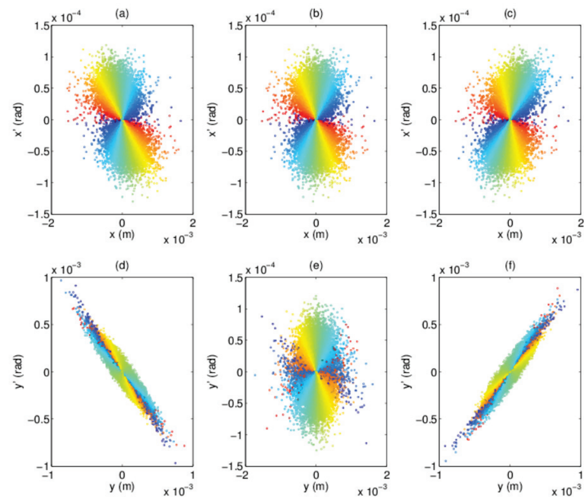

Figure 3: Transverse phase space at undulator entrance (a,d), center (b,e) and exit (c,f) for x (up) and y (down) plane.

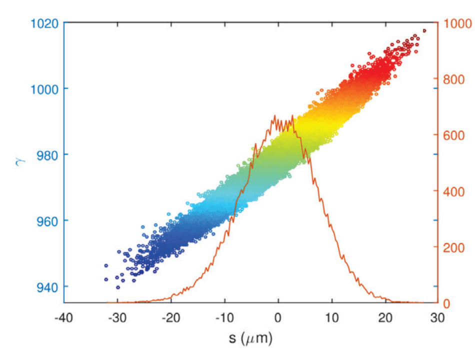

Figure 4: Longitudinal phase space and beam current distribution at undulator center.

FEL SIMULATION

FEL simulation is conducted with GENESIS [9] using ELEGANT tracked beam distribution. To compensate the energy chirp created by the decompression, a linear undula-

ISBN 978-3-95450-134-2

tor taper is applied according to

$$\frac{\Delta a_w/a_{w0}}{\Delta z} = -\frac{\lambda_r}{\lambda_u}\left(\frac{1+a_w^2}{a_w^2}\right)\frac{\Delta\gamma/\gamma_0}{\Delta s}, \quad (2)$$

where a_{w0} is undulator strength at center, γ_0 is beam central energy. To apply the taper to the whole 6 m undulator, the relative taper strength $\Delta a_w/a_{w0}$ is about -2.2% for the chirp.

As is shown in Fig.5, significant FEL power gain is obtained with chromatic matching manipulation. Without the manipulation, there would be no amplification since the emittance is increased to about 6 mm·mrad due to the chromatic effect. Without undulator taper, FEL tends to saturate at 5 m with 10 MW power. With undulator taper, the amplification lasts longer and FEL power reaches 100 MW level.

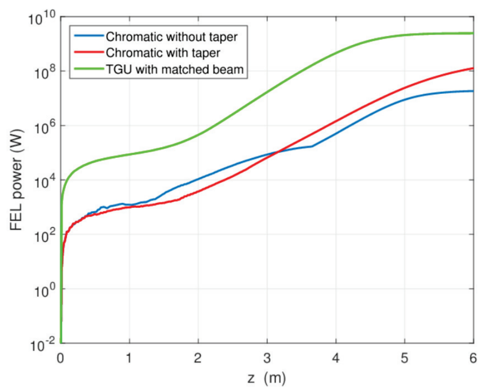

Figure 5: FEL power for untapered chromatic matching (blue), tapered chromatic matching (red) and TGU with assumed matched beam (green).

As a comparison, we simulated a TGU case with transverse gradient parameter $\alpha = 54\mathrm{m}^{-1}$ and beam dispersion $\eta = 2.5\,\mathrm{cm}$ for the same LPA beam, assuming it is matched to the undulator entrance, i.e., $\sigma_x = \sqrt{\beta_x\varepsilon_x} \approx \sqrt{L_u\gamma\varepsilon_x/2\gamma} \approx \sqrt{3m \times 0.1\,\mu\mathrm{m}/978.5} = 17.5\,\mu\mathrm{m}$. TGU case is able to reach higher FEL power up to GW level owing to its much higher peak current than the decompressed beam. All electrons matched to its resonant condition contribute to the FEL power for the TGU case, while only those slices focused to wasit contribute to the FEL gain for the chromatic matching case, which further increases the power difference for the two cases.

Fig.6 shows the time profile for untapered chromatic matching (blue) and tapered chromatic matching (red) and TGU (green) simulation. A 6.3 fs (FWHM) single spike FEL pulse is obtained, owing to lasing of only the part of slices which are focused to waist along the undulator. This is even shorter than the initial bunch length before decompression. The TGU case can also obtain single spike FEL pulse with 13.3 fs (FWHM) duration since the slippage length is comparable to the bunch length when no decompression is applied. The corresponding sprectrum is shown in Fig.7, where single spike spectrum is also obtained. Undulator taper can narrow the bandwidth to 0.008(FWHM) since it compensates the energy chirp, which is comparable to the TGU method.

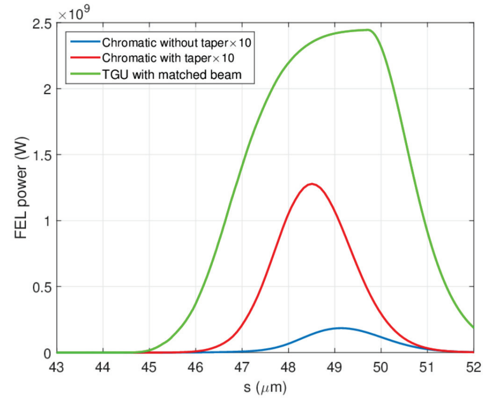

Figure 6: Time profile for untapered chromatic matching (blue) and tapered chromatic matching (red) and TGU case (green).

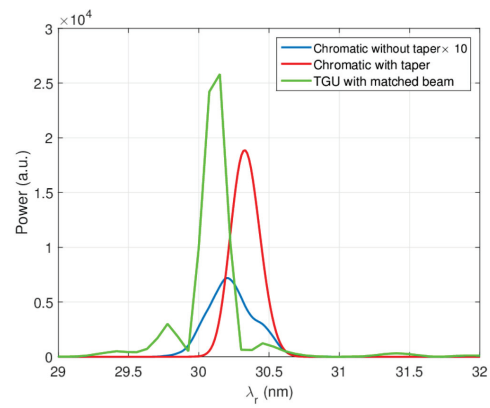

Figure 7: Spectrum for untapered chromatic matching (blue) and tapered chromatic matching (red) and TGU case (green).

It is worth noting that matching the 0.1 mm·mrad LPA beam to TGU entrance requires complicated beamline to correct the chromatic effect. Since initial beam size before dispersion acts as an equivalent energy spread and reduces the FEL performance, the TGU case requires to minimize the beamsize before dispersion, making it quite sensitive to initial emittance, while chromatic matching case is insensitive because the chromatic emittance is the dominant term.

CONCLUSION

We present here a preliminary study of applying an expected 500 MeV LPA beam at Peking University to FEL. It is shown that with chromatic matching manipulation, the 30 nm FEL can reach 100 MW power at 6 m undulator exit, with single spike FEL pulse of 6.3 fs and 0.008 bandwidth. The TGU method may reach higher FEL power but requires more complicated transport beamline to correct the chromatic effect and the FEL pulse length is longer than the chromatic matching method.

ISBN 978-3-95450-134-2

REFERENCES

[1] Anania et al., Appl. Phys. Lett. 104, 264102 (2014).

[2] M. Fuchs et al., Nature Physics 5, 826 - 829 (2009).

[3] Z. Huang et al., Phys. Rev. Lett. 109, 204801 (2012).

[4] A.R. Maier et al., Phys. Rev. X 2 031019 (2012).

[5] T. Seggebrock et al., Phys. Rev. ST Accel. Beams 16, 070703 (2013).

[6] A. Loulergue et al., New J. Phys. 17 023028 (2015).

[7] C. Widmann et al., IPAC'14, Dresden, Germany, THOBA03.

[8] M. Borland, Advanced Photon Source Report No. LS-287, (2000).

[9] S. Reiche, Nucl. Instr. Meth. A 429 (1999) 243.

ISBN 978-3-95450-134-2

SUB-RADIANCE AND ENHANCED-RADIANCE OF UNDULATOR RADIATION FROM A CORRELATED ELECTRON BEAM*

R. Ianconescu, University of Tel-Aviv, Tel-Aviv and Shenkar College, Ramat Gan, Israel
E. Hemsing, A. Marinelli, SLAC, Menlo Park, California, USA
A. Nause, UCLA, Los Angeles, USA
A. Gover, University of Tel-Aviv, Tel-Aviv, Israel

Abstract

The radiant intensity of Synchrotron Undulator Radiation (UR) depends on the current noise spectrum of the electron beam injected into the wiggler. The current noise spectrum and intensity can be controlled (suppressed or enhanced relative to the shot-noise level) by the effect of collective longitudinal space charge interaction in drift and dispersion sections [1]. This new control lever is of significant interest for possible control of SASE in FEL, since UR is the incoherent seed of SASE. Thus, control of spontaneous UR is a way to enhance the coherence of seeded FEL [2, 3], or alternatively, obtain enhanced radiation from a cascade noise-amplified electron beam [4]. The dependence of UR emission on the current noise is primarily a result of the longitudinal correlation of the e-beam distribution due to the longitudinal space charge effect. However, at short wavelengths, 3-D effects of transverse correlation and effects of emittance disrupt the proportionality relation between the UR intensity and e-beam current noise. We present analysis and simulation of UR sub-radiance/enhanced-radiance under various ranges of beam parameters, and compare to recent experimental observations [1].

INTRODUCTION

This study is an extension of previous work on current noise correlation effects due to longitudinal space charge (LSC) interactions effects in a drifting electron beam, such as microbunching instability [5] and e-beam noise suppression effects [6–14] which are of particular interest at the short wavelength limit [15] where it may be relevant for coherence enhancement of XUV FELs. The understanding and control of UR from a correlated electron beam is of major interest because UR is an important source of radiation for applications, and it is the start radiation field of SASE FEL. UR can be also an efficient diagnostic mean for evaluating e-beam current noise in a wide range of the spectrum, especially because it emits radiation on axis (contrary to OTR diagnostics). 3D correlation effects on UR that have been observed experimentally [1] have received little attention so far. The model presented in this paper is intended for study of such 3D effects.

SPONTANEOUS RADIATION EMISSION FROM FREE ELECTRONS

The radiation mode expansion analysis of superradiant emission from particulate current in [16] can be extended to analysis of radiation into plane waves from any free electron radiation source in the far field zone. This results in a dipole antenna expression for the spectral radiant intensity

$$\frac{d^2\breve{W}}{d\omega d\Omega} = \frac{\eta_0 k^2}{16\pi^3}|\breve{d}|^2 \sin^2\psi, \tag{1}$$

where

$$\underline{\breve{d}}(\omega, \underline{k}) \equiv \sum_j \Delta\underline{\breve{d}}_j, \tag{2}$$

$$\Delta\underline{\breve{d}}_j \equiv -e\int_{-\infty}^{\infty} dt\underline{v}_j(t)e^{i\omega t - i\underline{k}\cdot\underline{r}_j(t)}, \tag{3}$$

and

$$\underline{k} = k(\hat{e}_x \sin\Theta_x + \hat{e}_y \sin\Theta_y + \hat{e}_z \cos\Theta) \tag{4}$$

SPONTANEOUS EMISSION FROM A CORRELATED ELECTRON BEAM

Here we extend the radiation mode expansion formulation of [16] for superradiance and stimulated superradiance from an electron beam to the case of emission from a correlated or uncorrelated electron beam into plane waves in the far field. This includes the cases of a randomized (Poisson distribution) electron beam producing conventional incoherent spontaneous emission, a prebunched beam producing superradiant emission, a random beam of super-Poissonian distribution producing enhanced radiance spontaneous emission or a beam of sub-Poissonian distribution that produces sub-radiance (suppressed spontaneous emission). So far, the formulation is valid for general radiation schemes of free electrons. In the next section we specify to the case of undulator radiation.

For spontaneous emission, the system is stationary in the sense that it is not sensitive to the absolute time of the interaction. Defining t_{0j} the time electron j enters the interaction region, $\Delta\underline{\breve{d}}_j$ in Eq. (3) is written as

$$\Delta\underline{\breve{d}}_j = -e\int_{t_{0j}}^{t_j(L)} dt\underline{v}_j^{(0)}(t - t_{0j})e^{i\omega t - i\underline{k}\cdot\underline{r}_j^{(0)}(t-t_{0j})}, \tag{5}$$

and we set the integration limits from the entering time t_{0j} to the exit time $t_j(L)$, L being the interaction length. By changing variable $t' = t - t_{0j}$, we obtain

$$\Delta\underline{\breve{d}}_j = \Delta\underline{\breve{d}}_j^{(0)}e^{i\omega t_{0j}} \tag{6}$$

where

$$\Delta\underline{\breve{d}}_j^{(0)} = -e\int_0^{\Delta t_j(L)} dt'\underline{v}_j^{(0)}(t')e^{i\omega t' - i\underline{k}\cdot\underline{r}_j^{(0)}(t')}. \tag{7}$$

* This research was supported in part by a grant from the United States-Israel Binational Science Foundation(BSF), Jerusalem, ISRAEL

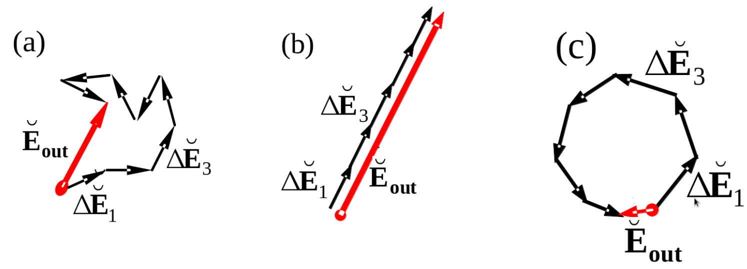

Figure 1: Different cases of e-beam correlations, showing how the fields add for each. Panel (a) shows an uncorrelated beam and fields add according to "random walk". Panel (b) shows full superradiance, in which case all the fields add with the same phase and panel (c) shows full subradiance in which case the electrons are anti-correlated and the radiation sums to something close to 0.

The upper limit $\Delta t_j(L) \equiv t_j(L) - t_{0j}$ depends on the trajectory of the electron, but is independent of the entering time t_{0j}. Setting Eqs. (2) and (6) into (1), we obtain

$$\frac{d^2\breve{W}}{d\omega d\Omega} = \frac{\eta_0 k^2}{16\pi^3}\sin^2\psi \left|\sum_j \Delta\breve{d}_j^{(0)} e^{i\omega t_{0j}}\right|^2 . \tag{8}$$

This result can be averaged over the transverse statistics of electron trajectories, and over the longitudinal distribution statistics of the arrival times t_{0j}: $\langle\rangle$ means averaging over an ensemble of different realizations (different electron beam pulses). Putting the averaging inside the sums we obtain

$$\left\langle\frac{d^2\breve{W}}{d\omega d\Omega}\right\rangle = \frac{\eta_0 k^2}{16\pi^3}\sin^2\psi \left[\sum_j \left\langle\left|\Delta\breve{d}_j^{(0)}\right|^2\right\rangle + \sum_{j\neq k}\left\langle\Delta\breve{d}_j^{(0)}\Delta\breve{d}_k^{(0)*}e^{i\omega(t_{0j}-t_{0k})}\right\rangle\right]. \tag{9}$$

Considering that $\breve{d}^{(0j)}$ is independent of t_{0j} (see Eq. (6)) the averaging over the ensemble of realizations can be split into averaging over t_{0j} and averaging over the other trajectory parameters $(\underline{r}_{\perp 0j}, \underline{\beta}_{0j})$.

$$\left\langle\frac{d^2\breve{W}}{d\omega d\Omega}\right\rangle = \frac{\eta_0 k^2}{16\pi^3}\sin^2\psi \left[\left\langle\sum_j \left|\Delta\breve{d}_j^{(0)}\right|^2\right\rangle + \sum_{j\neq k}\left\langle\Delta\breve{d}_j^{(0)}\Delta\breve{d}_k^{(0)*}\right\rangle\left\langle e^{i\omega(t_{0j}-t_{0k})}\right\rangle\right]. \tag{10}$$

Often the transverse correlation effect between the electrons is neglected (in particular in the case of a narrow electron beam [17, 18]) and then (and only then) $\left\langle\Delta\breve{d}_j^{(0)}\Delta\breve{d}_k^{(0)*}\right\rangle = \left\langle\Delta\breve{d}_j^{(0)}\right\rangle\left\langle\Delta\breve{d}_k^{(0)*}\right\rangle = \left\langle\left|\Delta\breve{d}_j^{(0)}\right|^2\right\rangle$, and one obtains the 1D case result:

$$\left\langle\frac{d^2\breve{W}}{d\omega d\Omega}\right\rangle = \frac{\eta_0 k^2}{16\pi^3}\sin^2\psi \left\langle\left|\Delta\breve{d}^{(0)}\right|^2\right\rangle \left[N + \sum_{j\neq k}\left\langle e^{i\omega(t_{0j}-t_{0k})}\right\rangle\right]. \tag{11}$$

where $\langle|\Delta\breve{d}^{(0)}|^2\rangle$ is an average over the trajectories $(\underline{r}_{\perp 0j}, \underline{\beta}_{0j})$. In case of a random beam (shot-noise), the arrival times of each pair of electrons are independent, and one may again decompose $\left\langle e^{i\omega(t_{0j}-t_{0k})}\right\rangle = \left\langle e^{i\omega t_{0j}}\right\rangle\left\langle e^{-i\omega t_{0k}}\right\rangle$ and each individual term is 0, resulting in

$$\left.\left\langle\frac{d^2\breve{W}}{d\omega d\Omega}\right\rangle\right|_{shot} = \frac{\eta_0 k^2}{16\pi^3}\sin^2\psi \left\langle\left|\Delta\breve{d}^{(0)}\right|^2\right\rangle N, \tag{12}$$

which is the expression for the spectral radiant energy intensity of conventional spontaneous radiation emission produced by the "shot-noise" of an uncorrelated electron beam. This case happens if:

$$\left\langle e^{i\omega(t_{0j}-t_{0k})}\right\rangle = 0, \tag{13}$$

As is evident from Eq. (11) there is enhanced radiant emission if the beam is correlated such that:

$$\left\langle e^{i\omega(t_{0j}-t_{0k})}\right\rangle > 0, \tag{14}$$

and there is subradiance if the beam electrons are anti-correlated:

$$\left\langle e^{i\omega(t_{0j}-t_{0k})}\right\rangle < 0. \tag{15}$$

Full superradiance occurs when all arrival times are identical, so that $t_{0j} = t_{0k}$ (maximum bunching). In such a case $\left\langle e^{i\omega(t_{0j}-t_{0k})}\right\rangle = 1$, and Eq. (11) results in

$$\left\langle\frac{d^2\breve{W}}{d\omega d\Omega}\right\rangle = \frac{\eta_0 k^2}{16\pi^3}\sin^2\psi \left\langle\left|\Delta\underline{\breve{d}}^{(0)}\right|^2\right\rangle N^2 = N\left.\left\langle\frac{d^2\breve{W}}{d\omega d\Omega}\right\rangle\right|_{shot}, \tag{16}$$

Superradiance occurs also if the e-beam is periodically bunched (see [16]). See also [19] in which it is shown an extreme case of subradiance in case the granularity of the current is 0, meaning 0 shot noise.

These different cases of correlated beam radiance are displayed schematically in Figure 1 as a complex field summation of the radiation wavepackets field from the individual electrons.

Note that if one wants to keep 3D effects in the analysis, it is necessary to stay with the exact expression in Eq. (8), as we do in our simulations.

ISBN 978-3-95450-134-2

EXPLICIT EXPRESSION FOR RADIATION FROM A LINEAR UNDULATOR

We consider here a beam in a linear undulator having a known transverse velocity in the $\hat{e}_x$ direction due to the undulator: $v_w = c\beta_w = ca_w/\gamma$, $a_w = eB_w/(mck_w)$ being the "wiggler parameter", $k_w = 2\pi/\lambda_w$ is the undulator wavenumber and B_w is the amplitude of the magnetic field. In addition, there are transverse initial velocities in the $\hat{e}_x$ and $\hat{e}_y$ directions for each electron injected into the undulator at $z = 0$: $\underline{v}_{\perp 0j}$ and initial positions in the $\hat{e}_x$ and $\hat{e}_y$ directions at the undulator entry, which we call $\underline{r}_{\perp 0j}$.

Neglecting now betatron oscillation inside the undulator, the velocity of electron j inside the undulator entering at t_{0j} is

$$\underline{v}_j(t) = \underline{v}_{\perp 0j} + Re[\tilde{\underline{v}}_w e^{-ik_w z_j(t)}] + \hat{e}_z v_{0zj}. \quad (17)$$

We neglect for now the longitudinal quiver ($a_w \ll 1$), so that we assume $v_{zj} = v_{0zj}$ is a constant in z. Hence we use the electron longitudinal velocity averaged over the undulator period:

$$z_j(t) = v_{zj}t, \quad (18)$$

and the transverse position is

$$\underline{r}_{\perp j}(t) = \underline{r}_{\perp j} + \underline{v}_{\perp 0j}t + Re[\tilde{\underline{r}}_w e^{-ik_w z_j(t)}] \quad (19)$$

From the real part in Eq. (17), $\tilde{v}_w e^{-ik_w z_j(t)}$ contributes the forward radiation, while its complex conjugate contributes the backward radiation at Doppler down shifted low frequency. Hence we neglect the complex conjugate. We shall also neglect the transverse quiver in Eq. (19) (which can produce harmonic emission off-axis). Setting Eqs. (18) and (17) into Eq. (7), and changing the integration variable $z = v_{zj}t$ one obtains

$$\Delta\check{d}_j^{(0)} = -e\frac{\tilde{\beta}_w}{2\beta_{zj}} e^{-i\underline{k}_\perp \cdot \underline{r}_{\perp 0j}} \int_0^L dz e^{i\theta_j z}, \quad (20)$$

which results in

$$\Delta\check{d}_j^{(0)} = -e\frac{\tilde{\beta}_w}{2\beta_{zj}} e^{-i\underline{k}_\perp \cdot \underline{r}_{\perp 0j}} e^{i\theta_j L/2} L \,\mathrm{sinc}(\theta_j L/2), \quad (21)$$

where

$$\theta_j(\omega) = \omega/v_{zj} - k_z - k_w - \underline{k}_\perp \cdot \beta_{\perp j}/\beta_{zj} \quad (22)$$

is the detuning parameter. So the expression for the radiant spectral energy intensity is obtained from Eq. (8)

$$\frac{d^2\check{W}}{d\omega d\Omega} = \frac{e^2\eta_0 k^2}{16\pi^3} \sin^2\psi \frac{|\tilde{a}_w|^2 L^2}{4\gamma^2\beta_z^2} \left| \sum_j \mathrm{sinc}(\theta_j L/2) e^{i\theta_j L/2} e^{i\omega t_{0j} - i\underline{k}_\perp \cdot \underline{r}_{\perp 0j}} \right|^2, \quad (23)$$

where the z velocity of the j electron inside the undulator averaged over the longitudinal quiver is given by

$$\beta_{zj}^2 = \beta_j^2 - \beta_w^2/2 - \beta_{0x}^2 - \beta_{0y}^2, \quad (24)$$

and the wiggler velocity square β_w^2 is divided by 2 for the case of linear wiggle. β_j is the total velocity of electron j (or the velocity before entering the wiggler).

RADIANT ENERGY INTENSITY

For small angular spread and small energy spread (cold beam) all θ_j are approximately equal, so one may write the spectral energy radiant intensity as

$$\frac{d^2\check{W}}{d\omega d\Omega} \simeq \frac{e^2\eta_0 k^2}{16\pi^3} \sin^2\psi \frac{|\tilde{a}_w|^2 L^2}{4\gamma^2\beta_z^2} \mathrm{sinc}^2(\theta L/2) \left| \sum_j e^{i\omega t_{0j} - i\underline{k}_\perp \cdot \underline{r}_{\perp 0j}} \right|^2, \quad (25)$$

and neglecting the velocity spread, θ is approximately

$$\theta \simeq \omega/v_z - k_z - k_w = \omega/v_z - \omega\cos\Theta/c - k_w. \quad (26)$$

The condition $\theta = 0$ defines the center frequency at observation angle Θ:

$$\omega_0 = \frac{ck_w}{1/\beta_z - \cos\Theta}, \quad (27)$$

so θ can be written

$$\theta = k_w \frac{\omega - \omega_0}{\omega_0}. \quad (28)$$

Considering the width of the sinc^2 function, one can define the spectral width $\Delta\omega$ at any observation angle Θ as

$$\frac{\Delta\omega}{\omega_0} = \frac{\lambda_w}{L} = 1/N_w, \quad (29)$$

By direct integration one can show that the total frequency integrated radiant energy intensity is

$$\frac{dW}{d\Omega} = \int_{-\infty}^{\infty} \frac{d^2\check{W}}{d\omega d\Omega} d\omega = \left.\frac{d^2\check{W}}{d\omega d\Omega}\right|_{\omega_0} \Delta\omega. \quad (30)$$

For small angular and energy spread the line broadening (29) is the same as in a cold beam limit (“homogeneous broadening”). Using the above in Eq. (23), one gets

$$\frac{dW}{d\Omega} = \frac{e^2\eta_0 k_0^2}{16\pi^3} \sin^2\psi \frac{|\tilde{a}_w|^2 L^2}{4\gamma^2\beta_z^2} \frac{\omega_0}{N_w} \left| \sum_j \mathrm{sinc}(\theta_{j0} L/2) e^{i\theta_{j0} L/2} e^{i\omega_0 t_{0j} - i\underline{k}_{\perp 0} \cdot \underline{r}_{\perp 0j}} \right|^2, \quad (31)$$

where $\omega_0 = \omega_0(\Theta)$ is defined by (27) and θ_{j0}, $\underline{k}_{\perp 0}$ are defined by (22), (4) with $\omega = \omega_0(\Theta)$, $k = \omega_0(\Theta)/c$.

ISBN 978-3-95450-134-2

EXPERIMENTAL OBSERVATIONS AND SIMULATION RESULTS

We have recently demonstrated for the first time control over spontaneous emission of undulator radiation by establishing in the e-beam, prior to injection into the undulator, longitudinal (temporal) correlation between the electrons. This was done in a set-up composed of a drift section (in which longitudinal space charge interaction correlates the velocities of the electrons) and a dispersive section (chicane) that correlates the longitudinal positions (or the injection times t_{0j}) of the electrons [1]. Figure 2 shows the UR radiant intensity on-axis as a function of the chicane compaction parameter R_{56}. The curve is normalized to the UR radiant intensity of an almost uncorrelated beam ($R_{56} = 0$). The experiment shows attainment of up to ×2.6 suppression factor of the UR (sub-radiance) and up to ×2.6 enhancement factor (enhanced-radiance) at higher R_{56}. The experiment was carried out in NLCTA with a 120 MeV, 25 pC beam and a periodic wiggler that generated $\lambda = 800$ nm UR on axis. In the experiment [1] also the UR radiant intensity dependence on off-axis angle Θ was measured for various levels of R_{56}. Figure 2 shows the suppression ratio of the UR dependence on Θ for various values of R_{56} relative to the case of $R_{56} = 0$. The data shows that there is significant UR suppression also at off-axis angles, however the suppression factor deteriorates (gets closer to 1) at larger off-axis angles, especially when the on-axis suppression factor is minimal ($R_{56} \simeq 2$ mm).

Another interesting experimental result is described by the red data points in Fig. 2(b) and 3. They show the deterioration of both the suppression and the enhancement effects (the gain factor relative to an uncorrelated beam gets closer to 1) when a thin foil is placed on the way of the beam before it is injected into the wiggler. It is expected that the angular scattering in the foil diminishes the longitudinal and transverse correlation that was established in the beam prior to injection.

In a 1D model it is expected that the undulator radiation is proportional to the spectral density of the e-beam current (which is the current shot-noise when the beam is uncorrelated). However a 3D model would reveal deviations from such proportionality. In particular it is evident from Eqs. (22) and (31) that the UR emission off-axis would be affected not only by the longitudinal correlation in the beam (t_{0j}) but also by the transverse correlations ($\underline{r}_{\perp 0j}$, $\underline{\beta}_{\perp 0j}$) that develop in the beam drift section. We presume that these 3D effects should explain the experimental results displayed in Figs. 2 and 3. This is the motivation for the analysis and simulations of the correlated beam UR that are presented in this paper.

In order to simulate the UR from a correlated electron beam including 3D effects of transverse e-beam correlation and off-axis radiation emission we use a 3D particle simulation code (GPT) that simulates the electron dynamics in the drift section, including 3D Coulomb interaction between the particles in a finite cross section e-beam [17]. The effect of the dispersive section is taken into consideration using a Matlab program based on the transformation equation $z'_j \to z_j + R_{56}(\gamma_j - \gamma)/\gamma$. The 6D coordinates of all particles are then used in the Matlab program (based on equations (22) and (23)) as the initial condition parameters ($\underline{\beta}_{0j}$, $\underline{r}_{\perp 0j}$, t_{0j}) needed for the computation of the spectral radiant intensity as function of frequency ω and emission angle Θ. The GPT 3D simulation establishes the longitudinal beam correlation effect and the suppression (or enhancement) of the electron beam shot noise [17]. But it also establishes transverse correlation [18] between the electrons $\underline{r}_{\perp 0j}$ which come into expression in the full 3D model of UR (Eqs. (22) and (23)), especially when we consider off-axis emission and e-beam angular spread. We show in Fig. 4 some initial results of simulation of correlated beam UR. Because of limited computer resources, simulations were not carried out with the same experimental parameters of [1], but for a lower energy beam (100 MeV) that generates on axis with

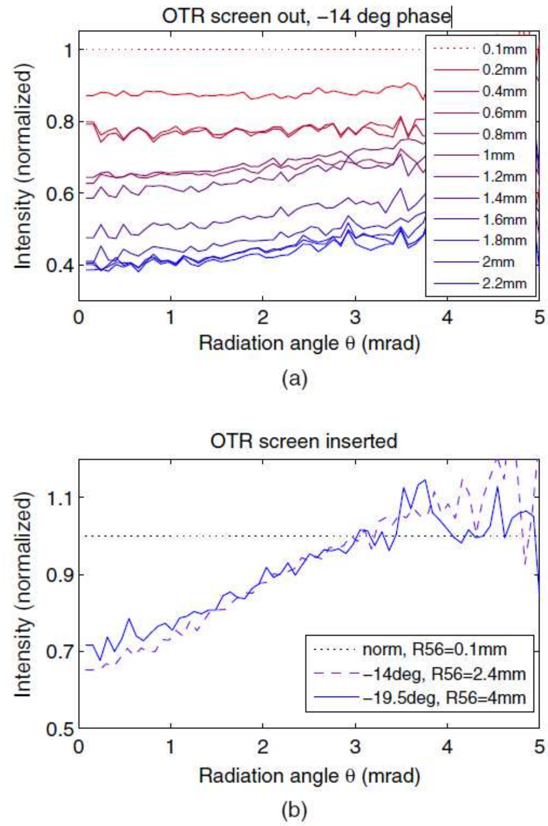

Figure 2: from [1]: Radiation intensity as a function of angle from direction of motion normalized by the measurement with $R_{56} = 0.1$ mm. (a) Case of -14 deg gun phase for different values of R_{56}. Suppression is slightly stronger on axis, but is relatively uniform across the FWHM beam (2 mrad). (b) Inserting an OTR screen increases emittance, which amplifies angular effects. At optimal suppression for both -14 deg and -19 deg gun phases, the degree of suppression is angle dependent, with suppression predominantly on axis. Data for the -14 deg case corresponds to the red square, $R_{56} = 2.4$ mm in Fig. 3.

ISBN 978-3-95450-134-2

the same wiggler parameters a longer wavelength ($\lambda = 2\,\mu$m) instead of 0.8 µm used in [1].

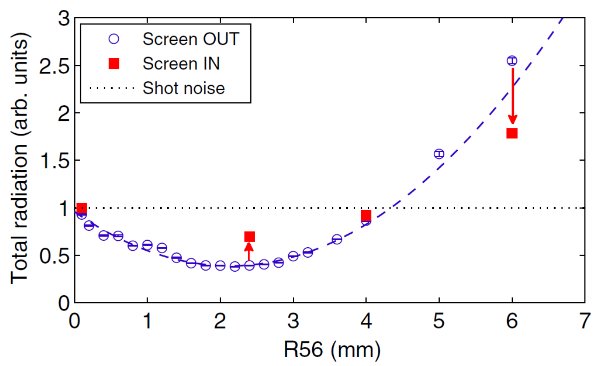

Figure 3: from [1]: Intensity on the camera as a function of chicane R_{56} at -14 deg phase with OTR screen OUT (blue circles) and screen IN (red squares). The dotted black line shows the inferred shot noise level. Insertion of a thin foil on the way of the beam before injection into the wiggler scatters the beam, spoils the correlation, and shifts intensity towards the shot noise level (but does not fully suppress coherent effects).

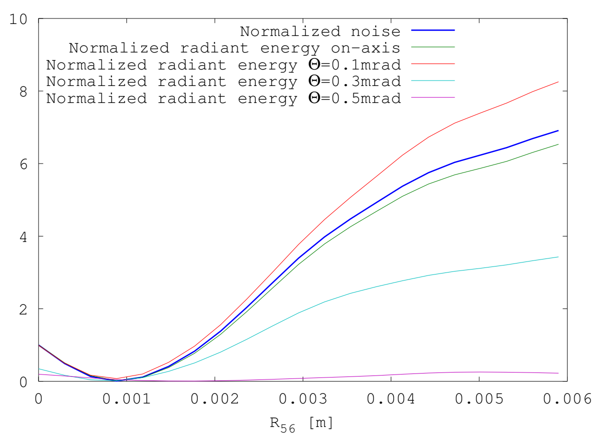

Figure 4: Noise and radiant energy intensity as function of R_{56}. Both the noise and the radiant energy intensity are computed at the center frequency for the same realization, namely the same random initial condition of an injected beam (single pulse). The noise is normalized to its value for $R_{56} = 0$ and the radiant energy intensity is normalized relative to it's value for $R_{56} = 0$, on axis, i.e. $\Theta = 0$. The diagram demonstrates deviation of the correlated beam UR from the current noise for large values of R_{56} and Θ.

In Fig. 5 we show correlated current noise and radiant intensity on axis, as function of frequency, and in Fig. 5b the ratio between them. The ratio of the spectra (Fig. 5b) replicates the ideal sinc^2 dependence. In Fig. 4 noise and radiant energy intensity at different observation angles as function of R_{56}. The figure shows good proportionality

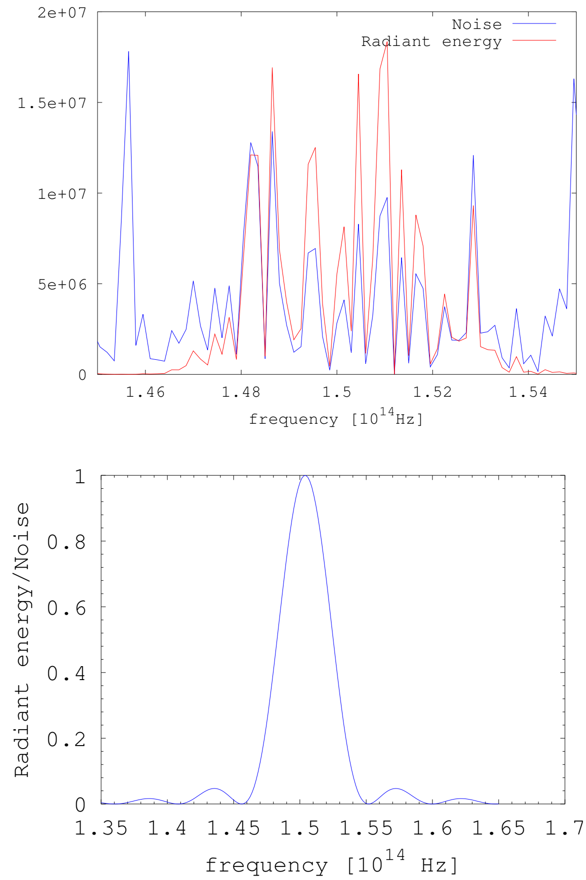

Figure 5: (a) Current noise spectrum of a random cold beam with Poissonian distribution (shot-noise) and the corresponding UR spectrum on-axis for the same electron distribution (same realization). The UR spectrum spikes are correlated to the current noise spikes. (b) The ratio of the UR to current noise for the same beam realization shown in (a) replicates $\mathrm{sinc}^2(\theta_0 L/2)$ dependence.

between the noise and the radiant energy intensity on axis, but reveals significant deviation off-axis due to 3D effect.

CONCLUSIONS

In this paper we presented formulation and numerical analysis of controlled suppression/enhancement of spontaneous emission of Undulator Radiation from a correlated electron beam. The electron correlation in the beam is established and controlled by propagating the beam through a drift section followed by a dispersive section (Chicane). The beam drift is simulated by a 3D code (GPT) that takes into account space charge interactions (Coulomb interaction between particles). The collective undulator radiation radiant intensity and spectral radiant intensity are calculated in the far diffraction zone by coherent summation of the wave packet fields emitted by the individual electrons and modeled by analytic expressions taking into account all 3D effects, including longitudinal and transverse correlation, e-beam spread and off-axis radiation emission. The 3D simulations

ISBN 978-3-95450-134-2

are motivated by observation of 3D effects in emission of correlated beam UR (both suppression and enhancement) that were measured in a recent experiment that we presented earlier [1]. At present, we applied the simulations to an arbitrary example of an undulator of 10 periods $\lambda_w = 15.4$ cm operating with a 100 MeV cold e-beam of radius $r_b = 1$ mm, emitting UR of central wavelength $\lambda = 2\,\mu$m on axis. The drift section simulation was done for the same beam parameters for a drift length $L_d = 10$ m that corresponds to plasma oscillation phase of $\phi_p = \pi/6$. The simulations demonstrate the presence of 3D effects of transverse correlation, that are usually not taken into consideration. However, they do not really simulate the experiment of [1] that was conducted with different parameters.

REFERENCES

[1] D. Ratner et al., PRST - ACCELERATORS AND BEAMS 18, 050703 (2015)

[2] E. Allaria et al., Nat. Photonics 7, 913 (2013)

[3] M. Labat et al., "High-Gain Harmonic-Generation Free-Electron Laser Seeded by Harmonics Generated in Gas", Phys. Rev. Lett., 107, 224801 (2011).

[4] A. Marinelli et al., Phys. Rev. Lett. 110, 264802 (2013)

[5] Z. Huang, J. Wu and T. Shaftan, "Microbunching Instability due to Bunch Compression", SLAC-PUB-1159, (December, 2005)

[6] H. Haus and N. Robinson, "The minimum noise figure of microwave beam amplifiers", Proc. IRE 43, 981 (1955).

[7] A. Gover and E. Dyunin, "Collective-Interaction Control and Reduction of Optical Frequency Shot Noise in Charged-Particle Beams", PRL 102, 154801, (2009).

[8] A. Marinelli and J. Rosenzweig, "Microscopic kinetic analysis of space-charge induced optical microbunching in a relativistic electron beam", Phys. Rev. ST Accel. Beams, 13, 110703 (2010).

[9] K.-J. Kim, in Proceedings of the 2011 FEL Conference (2011).

[10] D. Ratner, Z. Huang and G. Stupakov, "Analysis of shot noise suppression for electron beams", Phys. Rev. ST-AB 14, 060710 (2011).

[11] A. Gover, T. Duchovni, E. Dyunin, and A. Nause, "Collective microdynamics and noise suppression in dispersive electron beam transport", Physics of Plasmas, 18 (2011).

[12] A. Gover and E. Dyunin, Journal of Quantum Electronics 132166 (2010).

[13] A. Gover, A. Nause, E. Dyunin, and M. Fedurin, "Beating the shot-noise limit", Nature Physics, 8, 877 (2012).

[14] D. Ratner and G. Stupakov, "Observation of shot noise suppression at optical wavelengths in a relativistic electron beam", Phys. Rev. Lett., 109, 034801 (2012).

[15] A. Nause, E. Dyunin, and A. Gover, "Short wavelength limits of current shot-noise suppression", Phys. Plasmas 21, 083114 (2014) ; Erratum: Phys. Plasmas 21, 129904 (2014)

[16] A. Gover, "Superradiant and stimulated-superradiant emission in prebunched electron-beam radiators. I. Formulation", Phys. Rev. Special Topics - Accelerators and Beams 8, 030701 (2005)

[17] A. Nause, E. Dyunin and A. Gover, "Optical frequency shot-noise suppression in electron beams: Three-dimensional analysis", Jour. Appl. Phys. 107, 103101 (2010).

[18] M. Venturini, Phys. Rev. ST Accel. Beams 11, 034401

[19] R. Ianconescu, "Radiation from charges in the continuum limit" , AIP Advances, 3 (6), (2013).

ISBN 978-3-95450-134-2

ON THE IMPORTANCE OF ELECTRON BEAM BRIGHTNESS IN HIGH GAIN FREE ELECTRON LASERS*

S. Di Mitri#, Elettra Sincrotrone Trieste, 34149 Basovizza, Trieste, Italy

Abstract

Linear accelerators delivering high brightness electron beams are essential for driving short wavelength, high gain free-electron lasers (FELs). The FEL radiation output efficiency is often parametrized through the power gain length that relates FEL performance to the electron beam quality at the undulator. Experimental data and simulation results of existing and planned FEL facilities, collected in [1], are used to explicit the relationship between the FEL output wavelength and the electron beam six-dimensional brightness. Following [2], practical formulas are provided that show the dependence of the exponential gain length on the beam brightness.

6-D ELECTRON BEAM BRIGHTNESS

In the context of an electron bunch, the 4-dimensional (4-D) brightness, B_{4D}, can be defined as the peak current divided by its 4-D transverse phase space volume that is the product of the transverse emittances [3]. Owing to the fact that linac-driven free electron lasers (FELs) are sensitive to the beam relative energy spread and local charge density, it is convenient to parameterize the linac performance in terms of the 6-D brightness, B_{6D}, which is the total bunch *charge* divided by its 6-D phase space volume. The 6-D volume includes, in addition to the four transverse positions and slopes, the normalized longitudinal emittance, which scales as the product of bunch length and absolute energy spread. In the following, we assume the particle beam in the ultra-relativistic approximation, so that the longitudinal charge distribution is assumed to be constant during acceleration.

In general, we may define the brightness either locally, *i.e.*, for each bunch *slice* (in this case, the brightness depends on the z-coordinate inside the bunch), or for the whole bunch, thus involving the bunch total charge and *projected* emittances. The transverse rms normalized emittances are invariant under acceleration and linear transport, presuming collective effects, such as space charge, may be neglected. The same is true for the longitudinal rms normalized emittance if the energy spread is intended as uncorrelated, *i.e.*, without any energy chirp.

The presence of nonlinear motion and collective effects along the beam delivery system may dilute the normalized emittances from their values at the injection point. Following [2], we introduce an effective degradation factor $\zeta \geq 1$ in each plane of the particle motion so that $\varepsilon_{nx,f} = \varsigma_x \gamma_0 \varepsilon_{x,0}$, $\varepsilon_{ny,f} = \varsigma_y \gamma_0 \varepsilon_{y,0}$, and $\varepsilon_{nz,f} = \sigma_{z,f}\sigma_{E,f} = \varsigma_z \sigma_{z,0}\sigma_{E,0}$, with obvious notation. We are now able to relate the 6-D normalized brightness at the undulator, $B_{n,f}$, to that at the linac injection, $B_{n,0}$:

$$B_{n,f} \equiv \frac{Q}{\varepsilon_{nx,f}\varepsilon_{ny,f}\varepsilon_{nz,f}} = \frac{Q}{\zeta_x \zeta_y \zeta_z \gamma_0^2 \varepsilon_{x,0}\varepsilon_{y,0}\varepsilon_{z,0}} = \frac{B_{n,0}}{\zeta_x \zeta_y \zeta_z} \qquad (1)$$

In the ideal case of vanishing nonlinear and collective effects, $\varsigma_x, \varsigma_y, \varsigma_z \to 0$ in Eq. 1 and thereby the 6-D normalized brightness is preserved at the injector level under acceleration and linear bunch length compression.

IMPORTANCE OF PROJECTED BEAM PARAMETERS

In contrast to linear colliders, where particle collisions effectively integrate over the entire bunch length, the FEL process takes place over short fractions of the electron bunch length. In fact, slice emittance and slice energy spread may vary significantly along the bunch and thus give local regions where lasing may or may not occur [4]. One could therefore argue that only *slice* electron beam quality is of interest, each slice being at maximum as long as the slippage length of the photon beam over the electrons, cumulated along the undulator length. In the following, we make the case that other considerations related to the electron beam control and optimization of the FEL performance justify an optimization of B_{6D} defined in terms of the projected beam emittances. We will limit the discussion to the transverse emittances; correlations in the longitudinal plane are discussed in [1,2].

The need to control beam size and angular divergence along the undulator calls for measurements and manipulation of the electron beam optical (Twiss or envelope) parameters, which have to be matched to the design ones [5–8]. As a practical matter, optics matching is routinely performed by measuring the *projected* electron bunch transverse size [9]. From an operational point of view, it is therefore important to ensure that the projected transverse emittances and Twiss parameters be as close as possible to the slice ones, because this guarantees that most of the bunch slices are matched to the design optics and that they overlap in the transverse phase space. During beam transport and acceleration, at least two collective effects threaten locally to offset bunch slices in the transverse (and longitudinal) phase space, namely coherent synchrotron radiation (CSR) and geometric transverse wakefield (GTW). Specific optics designs can be adopted to minimize those collective effects (for a review of these topics, see for example [1]).

The projected emittance can be considered a good marker also for externally-seeded FEL performance. In

*Work supported by the FERMI project of Elettra Sincrotrone Trieste.
#simone.dimitri@elettra.eu

ISBN 978-3-95450-134-2

such FELs, output FEL properties reflect the high longitudinal coherence of the seeding laser, which can be tens to hundreds of femtoseconds long. In order to maximize the FEL efficiency and the peak current, the final electron bunch duration is commonly specified to be as long as the seed laser duration plus some room (typically, from tens to hundreds of femtoseconds) for accommodating the shot-to-shot arrival time jitter of the electron bunch with respect to the seed laser. The electron bunch duration has to be even longer when the so-called "fresh bunch" scheme is implemented for lasing at high harmonic jumps [10–12]. Consequently, high performance from a seeded FEL requires uniformity of the slice beam parameters over most of the bunch duration in order to ensure the same strength of lasing from different slices. That is, seeded FELs also require a large value of electron beam brightness, defined in terms of projected transverse and longitudinal emittance.

Another point in favor of carefully considering projected beam parameters is illustrated in [13], where it is shown that the output power gain length of a self-amplified spontaneous emission (SASE) FEL [14,15] depends on the mismatch of bunch slices in the transverse phase space, thus on the projected emittance, even if the slice emittance is unperturbed. A similar result is expected to be valid for externally seeded FELs as well. The projected emittance growth due to mismatch of bunch slices in the transverse phase space is taken into account through the mechanism described by Tanaka *et al.* [16]. In that work, the authors identify two distinct processes that increase the FEL gain length. The first effect is referred to as the (lack of) electron-photon transverse spatial overlap along the undulator. The second one describes the accumulation of longitudinal phase error between electrons and radiation by virtue of the slowing down of individual electrons due to their local angular divergence. We recognize that the electrons' angular divergence has two contributions (similar considerations can be found in [17,18]): one is incoherent and due to the non-zero beam emittance as depicted in Xie's [19] and Saldin's [20] models; the other is coherent, originating from the possible tilt of the slices' centroid with respect to the reference trajectory. The coherent divergence adds to (and in some cases, surpasses) the incoherent one and may amplify the effect of bunching smearing. One source of coherent divergence occurs when each slice is transversely kicked by collective effects in the linac and moves along the undulator on a trajectory different from that of other slices. In this case, Tanaka's formula for the gain length is revised via the following *ansatz*, to estimate the 3-D gain length in the presence of collective effects [13]:

$$L_{G,coll} \approx \frac{L_{G,3D}}{1-\pi\left\langle \theta_{coll}^2 \right\rangle / \theta_{th}^2} \tag{2}$$

$L_{G,3D}$ is the 3-D power gain length as calculated by Xie [19] and $\theta_{th} = \sqrt{\lambda / L_{G,3D}}$. The electron beam slice transverse emittance and the slice energy spread at the undulator are taken into account in $L_{G,3D}$; the information on the projected emittance growth $\Delta\varepsilon$, which is uniquely determined by the initial beam parameters and its dynamics in the linac, is brought about by $\theta_{coll} \propto \Delta\varepsilon / \beta_u$ [13], with β_u the average betatron function along the undulator.

FEL REQUIREMENTS FOR THE ELECTRON BEAM

It is well-known that in the so-called 1-D, cold limit, where electron beam energy spread, transverse emittance and radiation diffraction effects are all neglected, the radiation peak power at the resonant wavelength grows exponentially along the undulator with a gain length $L_G = \lambda_u/(4\pi\sqrt{3}\rho)$. Here λ_u is the undulator period length, and ρ is the "FEL parameter" [4]:

$$\rho = \left(\frac{\Omega_p \lambda_u a_w [JJ]}{8\pi c\gamma}\right)^{2/3} = \frac{1}{2\gamma}\left(\frac{I}{I_A}\right)^{1/3}\left(\frac{\lambda_u a_w [JJ]}{2\pi\sigma_x}\right)^{2/3}, \tag{3}$$

with Ω_p being the plasma frequency, I the electron bunch peak current, I_A = 17045 A the Alfven current, γ the relativistic Lorentz factor for the beam mean energy, σ_x the standard deviation of the (assumed round) electron beam transverse size; $a_w = K$ for helically- and $a_w = K/\sqrt{2}$ for planar-polarized undulator, where $K = 0.934 B_0[T]\lambda_u[cm]$ in practical units, is the so-called undulator parameter, B_0 the undulator peak magnetic field, and c the speed of light in vacuum. $[JJ]$ is the undulator-radiation coupling factor [21], equal to 1 for a helical undulator, and to $J_0(\xi) - J_1(\xi)$ for a planar undulator, where J_0 and J_1 are Bessel's functions of the first kind with argument $\xi = K^2/(4+2K^2)$. The FEL fundamental wavelength of emission satisfies:

$$\lambda = \frac{\lambda_u}{2\gamma^2}\left(1 + a_w^2\right) \tag{4}$$

Typically $\rho \approx 10^{-3}$ in the UV wavelength regime but may drop to $\sim 10^{-4}$ in the X-ray regime for kA-current beams. If the undulator length is equal or longer than $\sim 18 L_G$, the conversion of electrons' kinetic energy to photon energy considerably enlarges the electron beam energy spread. Once the spread in the longitudinal momentum of the electrons becomes sufficiently large to cause significant de-bunching over one power gain length, the FEL gain process strongly diminishes. Consequently, the FEL gain grows exponentially as far as the following numerical condition applies to the beam fractional energy spread [22]:

$$\sigma_\delta \le 0.5\rho, \tag{5}$$

ISBN 978-3-95450-134-2

with an eventual reduction in the FEL gain; the associated FEL power saturates at a level $P_{sat} \approx 1.6\rho EI/e$. An electron beam at multi-GeV energies and kA-scale peak currents is able to produce GW-scale radiation peak powers. For SASE devices, the value of ρ also defines the approximate number of undulator periods $N_{sat} \sim 1/\rho$ and the length $L_{sat} \approx \lambda_u/\rho$ necessary to reach saturation.

The spread in longitudinal momentum in Eq. 5 has two major sources: (1) the incoherent energy spread that is "uncorrelated" with the particle longitudinal position inside the bunch, and (2) the non-zero transverse emittance. In other words, Eq. 5 refers both to the spread of longitudinal momentum and to the energy spread associated with the square of the beam transverse angular divergence [23]. Beam divergence scales as $(\varepsilon/\beta_u)^{1/2}$, with β_u the average betatron function along the undulator and ε the geometrical electron beam transverse emittance (the two parameters are measured in the same plane; the divergences in the two planes add in quadrature). At the same time, in order to minimize emittance effects and to ensure optimal transverse overlap of the co-propagating radiation and electron beam, the electron beam trajectory, transverse size and angular divergence must be controlled with steering and quadrupole magnets that are interleaved between the undulator segments. The most efficient electron-photon beam interaction occurs when the transverse beam phase space area and distribution matches that of the radiation, whereas the transverse electron beam size scales as $(\varepsilon\beta_u)^{1/2}$. Considerations on both the maximum allowable effective energy spread and the transverse overlap lead to an rms value of ε that must be smaller than, or of the same order as, that of the diffraction-limited photon beam [24]:

$$\varepsilon_{x,y} \le \frac{\lambda}{4\pi} \tag{6}$$

Equation 6 implies an "optimum" average betatron function along the undulator of the order of the FEL power gain length. More details on this relationship are discussed in the following Section. In general, Eq. 6 allows to maximize the FEL gain and it also optimizes the FEL transverse coherence.

OPTIMUM BETATRON FUNCTION

It should be noticed that the term "optimum" used above refers to the condition for minimum SASE FEL power gain length. Some deviations are usually found when the SASE FEL output power at saturation is maximized. The existence of an "optimum" average betatron function in the undulator, in the assumption of periodic smooth focusing, can be inferred already by considering the effective size and divergence of a photon beam propagating over one FEL gain length, in the presence of a non-zero emittance electron beam. Those are, respectively, $\sigma^2_{\gamma,eff} = \varepsilon\beta_u + \lambda L_G/(4\pi)^2$ and $\sigma'^2_{\gamma,eff} = \varepsilon/\beta_u + \lambda/L_G$, whereas the expressions apply to each transverse plane separately, or we may intend the (square of) electron beam size and divergence as the sum in quadrature of the size and divergence in the two planes. The photon beam *brilliance* is maximized when the effective photon beam emittance $\sigma_{\gamma,eff}\sigma'_{\gamma,eff}$ is minimized, which implies simultaneously $\varepsilon \le \lambda/(4\pi)$, $\beta_u \le L_G/(4\pi)$ and $\beta_u \ge L_G/(4\pi)$. That would be true when Eq. 6 holds and at the same time $\beta_u \approx L_G/(4\pi)$.

The found expression, however, suggests an optimum value of β_u which is commonly at the sub-meter level, and therefore not practical. As a matter of fact, it is not correct since that was derived by considerations solely related to the transverse overlap of the electron beam and the FEL radiation. When the electrons' longitudinal motion w.r.t. the FEL radiation is also considered, one finds that the betatron motion affects the synchronism between electron and emitted photons, so that the transverse emittance causes Landau damping of the electrons bunching. Considerations on the bunching smearing leads to the lower limit $\beta_u \ge (0.25-0.50)L_G$ for the optimum betatron function [25,26]. When the constraint on the total energy spread is considered, Eq. 6, together with the target of maximum FEL gain, Eq. 3, an equation for the optimum β_u is found [27]. In this case, when the cold beam limit (no energy spread) and the emittance diffraction limit are considered at the same time, we find an optimum value $\beta_u \approx 2L_G$ (actually, a betatron phase advance of 0.5 rad over one gain length) [27]. This analytical evaluation was somehow supported from simulation results [28], which provided the optimum condition $\beta_u \approx 3L_G$ for non-zero energy spread. One should notice that those results are consistent with a photon beam weakly affected by radiation diffraction. Indeed, if we assume a photon beam size at waist that matches the electron beam size, then the ratio of the Rayleigh length over the FEL gain length must be $4\pi\varepsilon\beta_u/\lambda L_G \ge 1$. At the diffraction limit, we have again $\beta_u \ge L_G$. In conclusion, in most practical cases the approximate equation $\beta_u \approx L_G$ is taken as a reference.

SCALING LAWS

Since a smaller transverse emittance is usually associated with shorter FEL wavelengths, and since we can observe a proportionality between transverse emittance and $B_{n,f}$, we wonder if we could establish any relationship between $B_{n,f}$, and λ. This is done below, neglecting for the moment any emittance dilution, by substituting Eq. 4 into Eq. 1, and assuming the electron beam transverse emittance (equal in the two planes) at the diffraction limit (see Eq. 6):

$$B_{n,f} = \frac{Q}{\varepsilon_{nx,f}\varepsilon_{ny,f}\varepsilon_{nz,f}} = \frac{I}{c\sigma_E\gamma_0^2\varepsilon_0^2} \approx \frac{32\pi^2}{c}\frac{I}{\sigma_E}\frac{1}{\lambda_u\left(1+a_w^2\right)}\frac{1}{\lambda} \tag{7}$$

It is worth noticing that the ratio I/σ_E is invariant under acceleration and compression (whereas the peak current

ISBN 978-3-95450-134-2

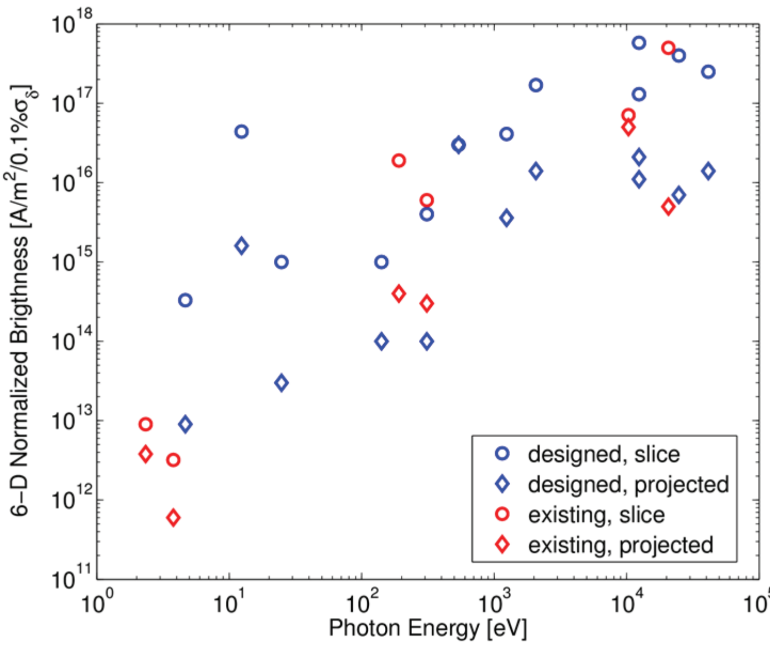

Figure 1: Six-dimensional normalized electron beam brightness *vs.* maximum photon energy at fundamental FEL emission, for facilities in the ultra-violet (UV) to X-rays, designed (blue) or running (red). Data taken from [1] and updated to 2013. From lower to higher energies, now-running facilities are: SPARC (Italy), SDUV-FEL (China), FLASH-I (Germany), FERMI (Italy), LCLS (USA), SACLA (Japan). The brightness refers to the projected (circle) or slice value in the bunch (diamond). Copyright of Photonics MDPI [2].

and the energy spread must be evaluated at the same location along the accelerator), when collective effects are ignored. We find that, for any given undulator, a shorter λ requires a higher $B_{n,f}$. This is confirmed in Fig. 1, where $B_{n,f}$ of designed and existing single-pass linac-driven FEL facilities, is shown as a function of the maximum photon energy (*i.e.*, minimum fundamental wavelength) from UV to X-rays (inferred or measured data are taken from [1] and updated to 2013). Moreover, Fig. 1 shows $B_{n,f}$ evaluated for projected and slice emittances (where the slice length is approximately one tenth of the total bunch duration, and located in the bunch core). A gap of one or two orders of magnitude occurs typically between the two brightness values. The closer the projected and the slice brightness, the more efficient the FEL process is, since most of the electrons are distributed in identical manner in 5-D (x,x',y,y',γ) phase space along the bunch. Usually, a smaller gap between the projected and the slice brightness is gained at the expense of the flexibility of the FEL facility in wavelength, intensity, polarization, *etc.*

Since ρ(λ) determines the efficiency of the electron-to-photon energy transfer in the undulator at a given wavelength, a large ρ is typically desired because that implies a shorter gain length, or a higher FEL power at saturation. Some restrictions to the upper value of ρ may be considered in a SASE FEL that targets a relatively narrow spectral bandwidth because in this kind of FEL the output bandwidth is also proportional to ρ. We can explicit the dependence of ρ on $B_{n,f}$ by substituting Eq. 7 into Eq .3, similarly to what was done in [29] for the longitudinal brightness. We impose 4πε = λ, re-define the energy spread like the rms value of γ, and consider a specific, typical value K = 1 in a helical undulator. Finally we get:

$$\rho \approx 0.016\frac{E[GeV]^{4/3}\lambda[nm]}{\beta_u[m]^{1/3}}\sigma_\delta^{1/3}B_{n,f}\left[\frac{A}{\mu m}\right]^{1/3}, \qquad (8)$$

from which we see that the strongest dependence of ρ is on the electron beam energy. The latter can be increased with a longer linac or higher accelerating gradient RF structures, but it is also quite expensive. It is worth noting that since the FEL resonance condition in Eq. 4 imposes λ ~ $1/E^2$, ρ is not expected to vary much when λ is made short, and in fact we typically have ρ ≈ 10^{-3}–10^{-4} in the entire XUV range (*i.e.*, λ ≈ 0.1–100 nm).

Equation 8 can be further manipulated and ρ written as a function of the electron beam transverse and longitudinal parameters at the undulator, whereas still we retain 4πε = λ and K = 1:

$$\rho \approx 3.1\times10^{-4}\left(\frac{I[A]\varepsilon_{n,x}[\mu m]}{\beta_u[m]}\right)^{1/3} \qquad (9)$$

Equation 9 tells us that, in order to have ρ large at any given λ and for any fixed optics in the undulator, it is always convenient to increase the peak current, while there might be no practical convenience in reducing the *normalized* emittance below the diffraction limit, because this could reduce ρ with much improvement neither in the FEL output power, nor in the FEL transverse coherence. A closer look to Eq.9 tells us that, when Eq.6 is forced to equality, if $\varepsilon_{n,x} = \gamma\varepsilon_x$ is lowered because γ is lowered

ISBN 978-3-95450-134-2

(while ε_x is kept fixed), then λ is fixed that implies λ_u is lowered (see Eq. 4); $\rho \sim \gamma^{1/3}$ is also lowered. If $\varepsilon_{n,x} = \gamma\varepsilon_x$ is lowered because ε_x is lowered (while γ is kept fixed), then λ is lowered that implies λ_u is lowered; $\rho \sim \lambda_u^{1/3}$ is lowered as well.

Alternatively, if the equality in Eq. 6 is broken and the geometric emittance is left "free" to span lower values than λ, Eq. 9 is not valid anymore and, for same peak current and undulator optics, a higher FEL gain is expected by virtue of both a reduced beam size (see Eq. 3), and of an overall smaller effective energy spread (see Eq. 5). A notable improvement of SASE FEL output power by virtue of a transverse emittance well below the diffraction limit was in fact observed is simulation runs and recently reported in [30].

We conclude this Section by noticing that by replacing that "optimum" value $\beta_u \approx L_G$ in Eq. 9, we find that ρ scales like $\sim\sqrt{I}$, instead of the cubic power of I as in Eq. 3. In fact, Eq. 3 assumes a scaling with I which is independent from the transverse beam size. The condition $\beta_u \approx L_G$, instead, implies that the transverse charge density changes as the current changes and, in particular, the beam size squeezes as the current increases, so leading to a more favourable dependence of ρ on I. Moreover, by virtue of Eq. 2, a larger β_u than usually considered on the basis of the previous discussion could be considered, when the projected emittance *growth* becomes comparable to the unperturbed value of the slice emittance.

CONCLUSIONS

The importance of projected electron beam parameters for FEL performance were highlighted, in regard of operational aspects of an FEL facility and of a new definition for the SASE FEL 3-D gain length. Scaling laws for the FEL parameter in the 1-D approximation with the electron beam 6-D brightness were discussed, as well as the relationship between the brightness and the FEL wavelength. Considerations on the beam optics in the undulator were refreshed, which suggest an optimum range for the average betatron function also in consideration of the importance of the projected emittance for the FEL performance.

ACKNOWLEDGEMENTS

The author is in debt to W. Fawley, whose generous sharing of knowledge and experience has made this work possible. E. Allaria and M. Venturini are acknowledged for insights into scaling laws of the FEL parameter, and L. Giannessi for a careful reading of this article and suggestions. This work was funded by the FERMI project of Elettra Sincrotrone Trieste.

REFERENCES

[1] S. Di Mitri, M. Cornacchia, Physics Reports **539** (2014) 1–48.
[2] S. Di Mitri, Photonics, **2** (2015) 317–341.
[3] C. Leujeune and J. Aubert, "*Emittance and Brightness: Definitions and Measurements*", Adv. In Electronics and Electr. Phys., Suppl. 13A, Academic Press, Inc., 159-259 (1980).
[4] R. Bonifacio, B.W. McNeil, P. Pierini, Phys. Rev. A **40** (1989) 4467–4475.
[5] H.P. Freund, P.G. O'Shea, Phys. Rev. Lett. **80**, 520 (1998).
[6] S. Reiche, Nucl. Instr. Meth. Phys. Res. A **445** (2004) 90–94.
[7] G. Geloni, V. Kocharyan, E.L. Saldin, DESY 11–081 (2011); http://arxiv.org/abs/1105.3878v1
[8] M.W. Guetg *et al.*, Phys. Rev. Special Topics – Accel. Beams **18**, 030701 (2015).
[9] M.G. Minty, F. Zimmermann, Report No. SLAC-R-621, Palo Alto, CA, USA (2003).
[10] I. Ben-Zvi, K.M. Yang, and L.-H. Yu, Nucl. Instrum. Methods Phys. Res. A **318** (1992) 726–729.
[11] L.-H. Yu, I. Ben-Zvi, Nucl. Instrum. Methods Phys. Res. A **393** (1997) 96–99.
[12] E. Allaria et al., Nature Photonics **7** (2013) 913–918.
[13] S. Di Mitri and S. Spampinati, Phys. Rev. Special Topics – Accel. Beams **17**, 110702 (2014). See also S. Di Mitri and S. Spampinati, this conference.
[14] A.M. Kondratenko and E.L. Saldin, Partic. Accel. **10** (1980) 207–216.
[15] R. Bonifacio, C. Pellegrini, L.M. Narducci, Opt. Commun. **50** (1984) 373–378.
[16] T. Tanaka, H. Kitamura and T. Shintake, Nucl. Instrum. Methods Phys. Research A **528** (2004) 172–178.
[17] G. Dattoli, A. Renieri, A. Torre, and R. Caloi. Il Nuovo Cimento D, **11**(3) (1989) 393–404.
[18] G. Dattoli, L. Giannessi, P. L. Ottaviani, and C. Ronsivalle, Journal of Applied Physics, **95**(6) (2004) 3206–3210.
[19] M. Xie, in Proc. of Part. Accel. Conf. 1995, TPG10, IEEE (1996).
[20] E. L. Saldin, E. A. Schneidmiller and M. V. Yurkov, in Proc. of the 26th Free Electron laser Conf., MOPOS15, Trieste, Italy (2004).
[21] W.B. Colson, IEEE J. Quant. Electron. **17** (1981) 1417.
[22] J. Murphy, C. Pellegrini, R. Bonifacio, Opt. Commun. **53** (1985) 197.
[23] A. Luccio, C. Pellegrini, in *Free Electron Lasers*, ed. S. Martellucci and A.N. Chester, Plenum, NY (1983) 28. Also: J. Murphy and C. Pellegrini, in Proc. of the International Conference on Quantum Electronics, San Diego, CA, USA, November 1984.
[24] K.-J- Kim, Nucl. Instrum. Meth. Phys. Res. A, **246** (1986) 71–76.
[25] S. Reiche, Nucl. Instrum. Meth. Phys. Res. A, **445** (2000) 90–94.
[26] G. Geloni, V. Kocharyan, and E. Saldin, DESY Note 11-081, ISSN 0418-9833 (2011).
[27] Y.H. Chin, Nucl. Instrum. Meth. Phys. Res. A, **331** (1993) 424–428.
[28] H.P. Freund and P. O'Shea, Phys. Rev. Letters **80**, 3 (1998).

ISBN 978-3-95450-134-2

[29] C. Pellegrini, Nucl. Instrum. Meth. Phys. Res. A, **272** (1988) 364–367.
[30] M.W. Guetg, B. Beutner, E. Prat, and S. Reiche, Phys. Rev. Special Topics – Accel. Beams **18**, 030701 (2015).

ISBN 978-3-95450-134-2

GENERATING A SINGLE-SPIKE SASE PULSE IN THE SOFT X-RAY REGIME BY VELOCITY BUNCHING*

Jaeyu Lee, Bonghun Oh, Moohyun Yoon#, POSTECH, Pohang, Korea

Abstract

A bright ultrashort X-ray pulse emerges as a valuable tool for many fields of research nowadays. The single-spike operation of X-ray FEL is one way of making a bright ultrashort X-ray pulse. It requires extreme bunching and a magnetic chicane is a conventional compressor. In a low charge range, a magnetic chicane can be replaced by the velocity bunching technique. In this paper, we present the result of particle tracking simulation generating a single-spike soft X-ray SASE pulse without a magnetic chicane.

INTRODUCTION

XFEL based on SASE principle generates a fully coherent radiation in the transverse plane because the transverse emittance of the electron beam is usually tailored to smaller than the diffraction-limited emittance. In the longitudinal plane however, the coherence is rather poor because radiation starts from the shot noise. Therefore, efforts have been made to improve the SASE FEL's longitudinal coherence. One of the methods which is rather straightforward to implement is to create a single-spike radiation pulse on the order of a few hundred attosecond, two orders of magnitude shorter than the pulse length from a typical SASE FEL so that great enhancement of the longitudinal coherence is achieved.

In this regard, there are two different schemes to obtain an attosecond XFEL. The first scheme is to manipulate an initially long electron bunch and achieve lasing only part of the bunch in the longitudinal axis which is short enough for single-spike radiation. The other scheme is to enhance the bunching process to make an ultrashort electron bunch. As mentioned above, the radiation of SASE FEL has temporal fluctuation; it is a stream of many coherent pulses which separate each other. Single coherent pulse or single spike has space of $2\pi L_{c,1D}$ in between, which is given by

$$2\pi L_{c,1D} = \frac{\lambda_r}{2\sqrt{3}\rho}, \tag{1}$$

where $L_{c,1D}$ is called the cooperation length and λ_r is the radiation wavelength, and ρ is the pierce parameter. Making ultrashort electron bunch for single-spike operation has advantages in the clearness of single spike but making ultrashort bunch is technically difficult. Low charge is preferred to shorten the electron bunch but it also increases difficulties in the beam diagnosis.

The velocity bunching (VB) [1] is a technique to achieve bunching of electrons in the longitudinal direction which is effective when the electron speed is not close to the speed of light. Therefore, the VB process can take place between the rf gun and main accelerating cavities. VB can be an alternative of the magnetic chicane usually employed in the SASE FEL and is effective especially when the bunch charge is low. Therefore, it will be a very interesting question if one can achieve a desirable bunch length to generate a single spike radiation pulse in SASE FEL with a very small charge of a several pico-Coulombs. One may also anticipate that even VB can eliminate the need for magnetic chicane or at least minimize the use of chicane. The aim of this report is to propose the use of VB combined with a low charge of picocoulomb order for a single spike generation of SASE soft X-ray FEL.

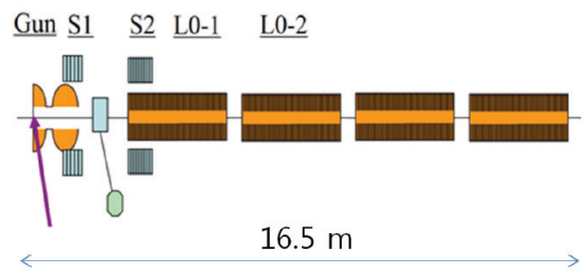

Figure 1: Layout of the injector lattice for the Soft X-ray FEL design.

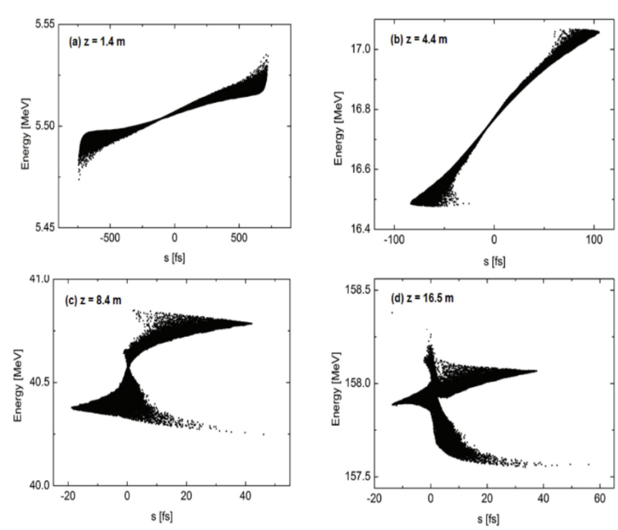

Figure 2: Longitudinal phase space distribution in the injector.

INJECTOR AND LINAC

We designed the injector linac similar to the LCLS injector [2] which is consists of a photo-cathode gun, two solenoids, and two 3-m long S-band accelerating sections L01 and L02. 200,000 particle tracking in the injector linac was performed with ASTRA [3]. Optimization for parameters was carried out through the Multi-Objective

*Work supported by POSTECH Basic Science Research Institute Grant and Ministry of Science, ICT and future Planning (MISP) of Korean government.
#moohyun@postech.ac.kr

ISBN 978-3-95450-134-2

Genetic Algorithm (MOGA) [4]. The optimized parameters for the injector linac are listed in Table 1. The ranges of the laser parameters and initial beam parameters for optimization are determined from simple scaling of LCLS 20-pC operation parameters [5]. When charge is decrease from 20 pC to 5 pC, beam and laser length parameters are scaled as $\propto Q^{1/3}$ [6].

At the injector design, we need to maximize the VB to make the soft XFEL without a magnetic chicane. We added another two rf cavities to the hard Xray FEL injector design to maximize the VB and increase electron energy at the matching section between injector rf cavities and the linac rf cavities. We expected that it helps suppressing the current reduction caused by the LSC effect. The total length of the injector system is now 16.5 m (Fig. 1). Among the four cavities, the first and second cavities are used to VB and the last are used to acceleration and energy spread compensation.

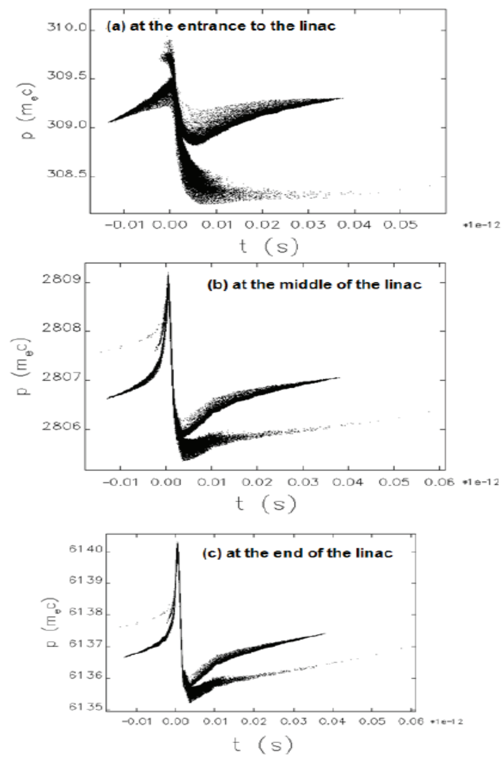

Figure 3: Longitudinal phase space distribution in the linac.

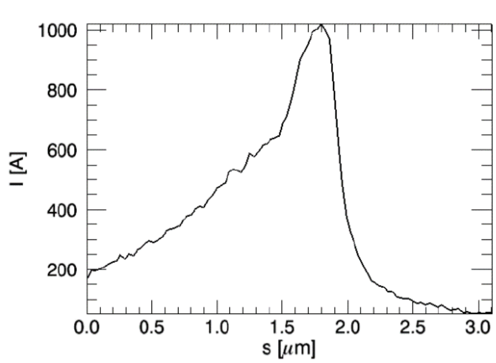

Figure 4: Longitudinal phase space distribution in the linac.

The change of the longitudinal phase space distribution at the injector is plotted in Fig. 2. The coordinate z is the position starts from the cathode and the z = 1:4 m at the start of the first rf cavity. Length of the one rf cavity is 3.0 m. From Fig. 2(a) to Fig. 2(c), electron bunch length is decreased by VB process. Figure 2(d) is at the injector end and it evolves to Fig 3(a) which is at the entrance to the linac rf cavities. Fig 3 shows that the shape of the longitudinal phase space distribution is preserved at the linac. The code Elegant [7] was used for the linac simulation. The current distribution at the end of the linac is presented in Fig. 4. Peak current is 1 kA and rms bunch length of current peak is 0.2 μm which is equivalent to 0.67 fs.

Table 1: FEL Parameters for the Single-Spike Mode 1 nm XFEL

Parameter	Unit	Value
Electron energy	GeV	3.136
Rms bunch length (of current peak)	fs	0.67
Peak current	kA	1
Undulator period	cm	3
Magnet full gap	mm	11.04
Undulator parameter K		1.7395
Average betatron function	m	30
Rms energy spread $\sigma_{\Delta\gamma}$		1.0
FEL (pierce) parameter ρ		0.00088
Cooperation length	fs	1.25/2π
Radiation wavelength	nm	1.00086
Peak saturation power (untapered)	GW	2
Saturation length	m	35

SINGLE SPIKE 1 NM FEL

FEL parameters for the single-spike mode 1 nm FEL is presented in Table 1. Electron energy has been lowered to 3.136 GeV from the hard X-ray XFEL design which is 5 GeV because the longer FEL wavelength loosen the parameter requirements. With the fixed current and undulator parameter, the Pierce parameter ρ is proportional to $(\gamma\lambda^2)^{1/3}$. Rms bunch length of the current peak is shorter than 2πLc but there is long low current tail where from s = 0 μm to s = 1.5 μm in Fig. 4. We need to suppress the lasing of that part of the electron bunch. Other FEL parameters are chosen considering the physical limit and optimization of FEL performance. For an untapered case, we expect a peak saturation power is 2 GW and a saturation length is 35 m. GENESIS 1.3 code [8] was used to perform FEL simulation.

ISBN 978-3-95450-134-2

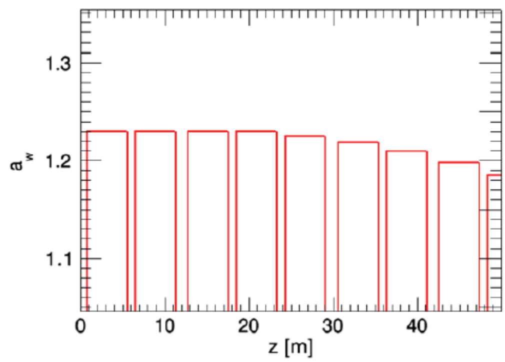

Figure 5: Stepwise tapering of the undulator parameter for the soft XFEL simulation.

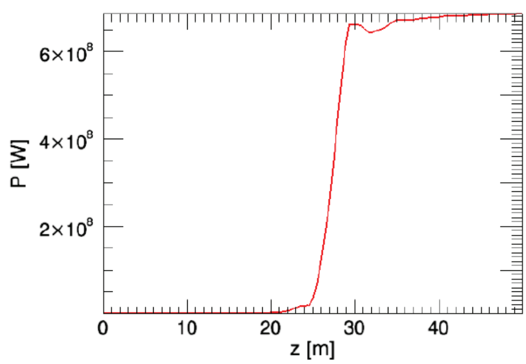

Figure 6: Average radiation power along the undulator position z.

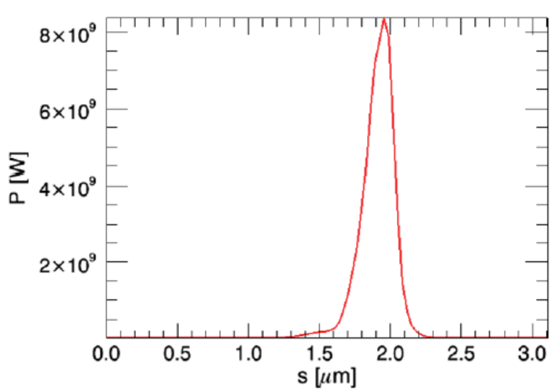

Figure 7: Temporal power profile at z = 30 m.

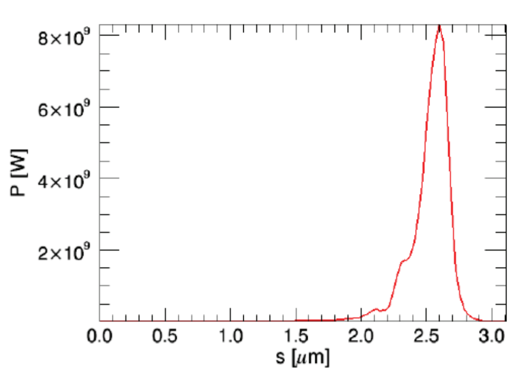

Figure 8: Temporal power profile at z = 50 m.

In order to suppress the lasing of the low current part of the electron bunch and increase the radiation power, we introduce the undulator tapering (Fig. 5). The current peak is lased prior to the low current part, strong undulator tapering after the saturation of the current peak will prevent the lasing of the low current part. The average radiation power along the undulator position z is presented in Fig. 6. The saturation length is 29 m and there is no power increase after 30 m because of the strong tapering. That cease of the power increase is express the suppression of the lasing of the low current part.

Figure 7 and 8 shows the temporal radiation power profile at z = 30 m and 50 m respectively. It shows the effect of the undulator tapering. There is small side peak after the main single-spike radiation but it is negligible. Peak saturation power is 8 GW and rms duration of the single-spike radiation is 0.1 μm or equivalently 0.33 fs. Figure 9 shows the spectral power density at z = 30 m. It has the relative bandwidth of 1.0×10^{-3}.

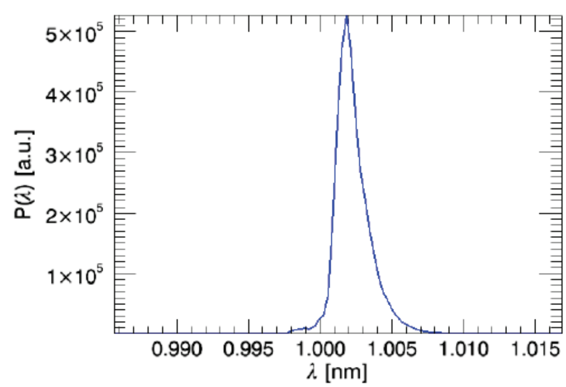

Figure 9: Spectral power density after the saturation.

CONCLUSION

We simulated XFEL design which generates single-spike radiation for the 1 nm FEL with 5 pC, 3.1 GeV electron beam. Velocity bunching technique was used to replace magnetic chicane and we obtained the single-spike radiation with 8 GW at z = 30 with 5 pC and 3.1 GeV electron beam with the help of strong undulator tapering. Because of the simplicity and compactness of the design, we expect it will be an economical soft X-ray light source. Error study is needed especially for the injector rf system and we will conduct in near future.

ACKNOWLEDGMENT

Work supported by POSTECH Basic Science Research Institute Grant and Ministry of Science, ICT and future Planning (MISP) of Korean government.

REFERENCES

[1] E.L. Saldin, E.A. Schneidmiller and M.V. Yurkov, Opt. Commun. 148, 383-403 (1998).
[2] P. Emma et al., Nature photon. 4, 641 - 647 (2010).
[3] Floettmann, ASTRA User Manual, see http://www.desy.de /mpyflo/Astra_dokumentation/

ISBN 978-3-95450-134-2

[4] Ivan V. Bazarov and Charles K. Sinclair, Phys. Rev. ST Accel. Beams 8, 034202 (2005).
[5] https://portal.slac.stanford.edu/sites/lclscore public/ Accelerator_Physics_Published_Documents=LCLS-parameters.pdf
[6] J. Rosenzweig et al., Nucl. Instrum. Methods A 593, 39 (2008).
[7] M. Borland, elegant: A flexible SDDS-Compilant Code for Accelerator Simulation, APS LS-287 (2000).
[8] S. Reiche, Nucl. Instr. Meth. A 429, 243 (1999).

ISBN 978-3-95450-134-2

NEW SOFT X-RAY UNDULATOR LINE USING 10 GEV ELECTRON BEAM IN PAL-XFEL

C. H. Shim, I. S. Ko, Pohang University of Science and Technology, Pohang 790-784, Korea
Y. W. Parc#, Pohang Accelerator Laboratory, Pohang 790-784, Korea

Abstract

PAL-XFEL is designed to have five undulator lines and only two undulator lines, the HXR undulator line with 10 GeV electron beam and the SXR undulator line with 3.15 GeV electron beam, will be installed during phase I. A photon beam energy from 0.28 to 1.24 keV will be provided at the SXR undulator line and different range from 2 to 20 keV will be supplied at the HXR undulator line. According to existing schedule, however, photon beam energy from 1.24 to 2 keV won't be provided in PAL-XFEL. In this research, new soft X-ray undulator line for PAL-XFEL using 10 GeV electron beam in main linac is proposed to cover the vacant photon energy. Four candidates are evaluated by estimating and comparing FEL performances using Ming Xie's formula.

INTRODUCTION

Pohang Accelerator Laboratory X-ray Free Electron Laser (PAL-XFEL) is designed to have three undulator lines at the end of 10 GeV main linac and two undulator lines at the end of 3.15 GeV branch linac as shown in Fig.1 [1,2]. But only two among five undulator lines will be installed during phase I. One is the hard X-ray (HXR) undulator line with 10 GeV electron beam and the other is the soft X-ray (SXR) undulator line with 3.15 GeV electron beam. Main parameters of PAL-XFEL are listed in Table.1.

A photon beam with energy from 2 to 20 keV will be supplied at the HXR undulator line. Another photon beam with different energy from 0.28 to 1.24 keV will be provided at the SXR undulator line. According to existing schedule, photon beam with energy from 1.24 to 2 keV won't be usable in PAL-XFEL. In this vacant region, however, it is estimated that there are some demands for outstanding experiments [3] and therefore that region has to be covered in the near future. There are two main ways to cover the vacant region: One is extending photon energy supply of existing undulator lines. The other is designing new undulator line using one of three available undulator lines.

In this research, new SXR undulator line for PAL-XFEL using 10 GeV electron beam in main linac is proposed.

Table 1: Main Parameters of Current PAL-XFEL

	Hard X-Ray	**Soft X-Ray**
Location	Main Linac	Branch Linac
Energy	4 – 10 GeV	2.5 – 3.15 GeV
FEL Photon Energy	Und. Gap Change (Max. Energy Fix)	
	12.4 – 20.0 keV (0.1 – 0.06 nm)	0.41 – 1.24 keV (3 – 1 nm)
	Energy Change (Min. Und. Gap Fix)	
	2.0 – 12.4 keV (0.6 – 0.1 nm)	0.28 – 0.41 keV (4.5 – 3 nm)
Und. Period	26 mm	35 mm
Peak Current	3 kA	2 kA
Normalized Slice Emittance	0.4 mm-mrad	0.6 mm-mrad
Slice Energy Spread	1.5 MeV	1.5 MeV
Bunch Length	18 um (60 fs)	27 um (90 fs)

Evaluation is conducted by comparing estimated FEL performances of existing undulator lines and newly designed undulator lines in the vacant region. All estimation of FEL performances are based on Ming Xie's formula [4]. Time-dependent simulation is also performed with selected solution by GENESIS 1.3 using real beam parameter [5].

EXISTING UNDULATOR LINE

There are two undulator lines, the HXR and SXR undulator lines, according to existing schedule in PAL-XFEL, so two specific candidates are also available. Each parameters of two lines are listed in Table 1.

Soft X-Ray (SXR) Undulator Line

In the SXR undulator line, electron beam energy is fixed at maximum values, 3.15 GeV, as shown by blue dashed

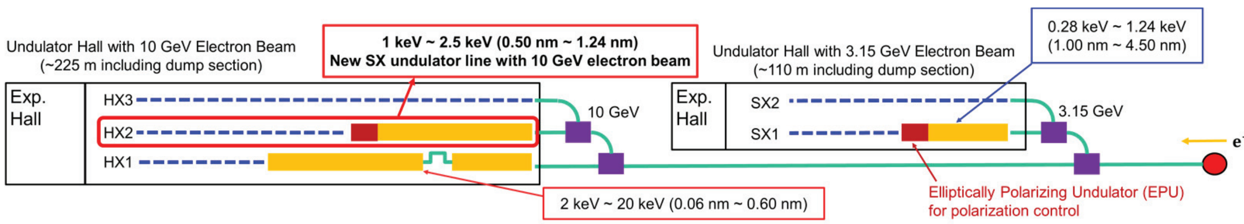

Figure 1: Schematic diagram about undulator lines of PAL-XFEL.

#young1@postech.ac.kr

ISBN 978-3-95450-134-2

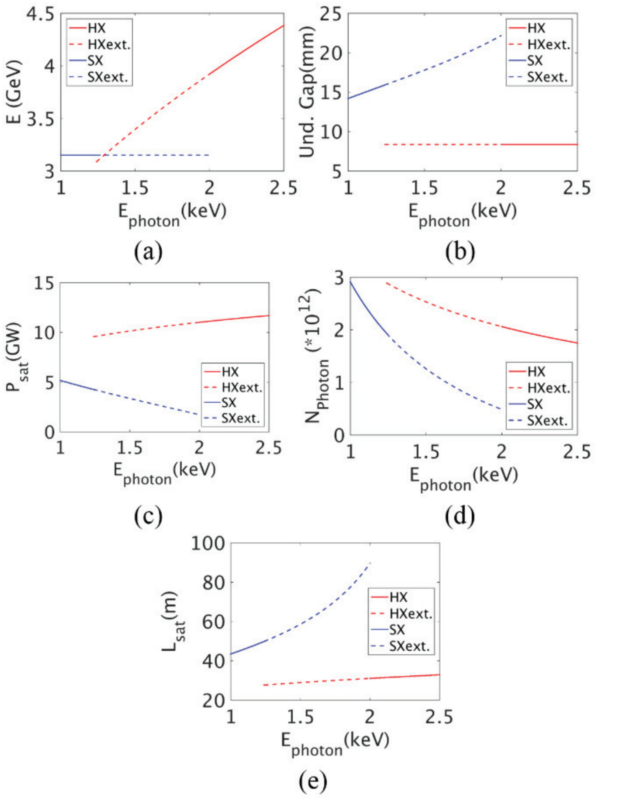

Figure 2: Blue (red) line indicates the existing SXR (HXR) undulator line. Solid (dashed) line means provided (vacant) photon energy region (a) Electron beam energy (b) Undulator gap (c) Saturation power (d) Number of photons (e) Saturation length.

line in Fig. 2 (a). Resonance photon energy is adjustable by changing undulator gap and photon energy supply can be extended. The wider undulator gap is opened, the higher photon energy is obtained as plotted by blue dashed line in Fig. 2 (b). Saturation power and number of photons are decreasing as photon energy becomes higher as drawn in Fig. 2 (c) and (d) by blue dashed line. 1×10^{12} is minimum number of photons standard of SXR in PAL-XFEL project and it can't be reached over 1.63 keV as shown in Fig. 2 (d) by blue dashed line. Furthermore, saturation length is increasing rapidly as photon energy becomes higher as shown in Fig. 2 (e). Therefore, it is hard to cover the vacant region at the existing SXR undulator line in PAL-XFEL.

Hard X-Ray (HXR) Undulator Line

In the HXR undulator line, undulator gap is fixed at minimum values, 8.37 mm, as shown in Fig. 2 (b) by red dashed line. Resonance photon energy is adjustable by changing electron beam energy and photon energy supply can be extended. The lower energy electron beam has, the lower photon energy is gained as plotted by red dashed line in Fig. 2 (a). FEL performances such as saturation power, number of photons and saturation length are not bad in vacant region as shown by red dashed line in Fig. 2 (c), (d) and (e). However, required electron beam energy

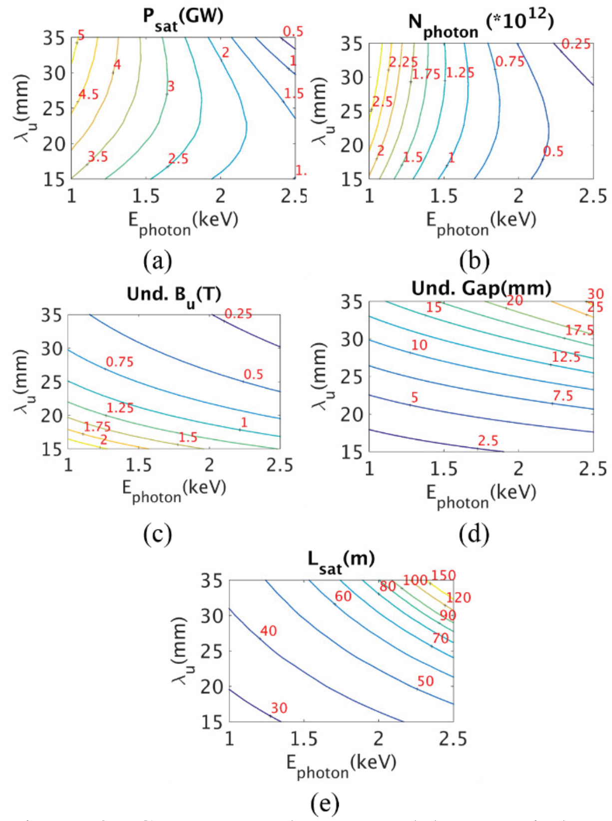

Figure 3: Contour graphs vs. undulator period and resonance photon energy in 3.15 GeV branch linac (a) Saturation power (b) Number of photons (c) Undulator peak magnetic field (d) Undulator gap (e) Saturation length.

is too low (< 4 GeV) and it can't be realized because of technical limit in accelerator section. Thus, it is also hard to cover the vacant region at the existing HXR undulator line in PAL-XFEL.

NEW SOFT X-RAY UNDULATOR LINE

There are two available locations for new SXR undulator line. One is the end of branch linac with 3.15 GeV electron beam energy and the other is the end of main linac with 10 GeV electron beam energy. Thus, two candidates will be evaluated. Electron beam parameters at each linacs are listed in Table 1.

3.15 GeV Branch Linac

In the new SXR undulator line at the end of branch linac, electron beam energy is fixed at 3.15 GeV over the vacant region. Ordinary saturation power is expected as shown in Fig. 3 (a). Number of photons, however, can't satisfy minimum standard, 1×10^{12}, above 1.5 ~ 1.6 keV photon energy as plotted in Fig. 3 (b). If the undulator period is shorter than 25 mm, requisite peak magnetic field is above 1 T as shown in Fig. 3 (c). It is hard to realize such high field by undulator, so undulator period has to be longer than 25 mm to cover the vacant region. Undulator gap respond to needed peak magnetic field is shown in Fig. 3 (d). Minimum gap is restricted by diameter of beam tube

ISBN 978-3-95450-134-2

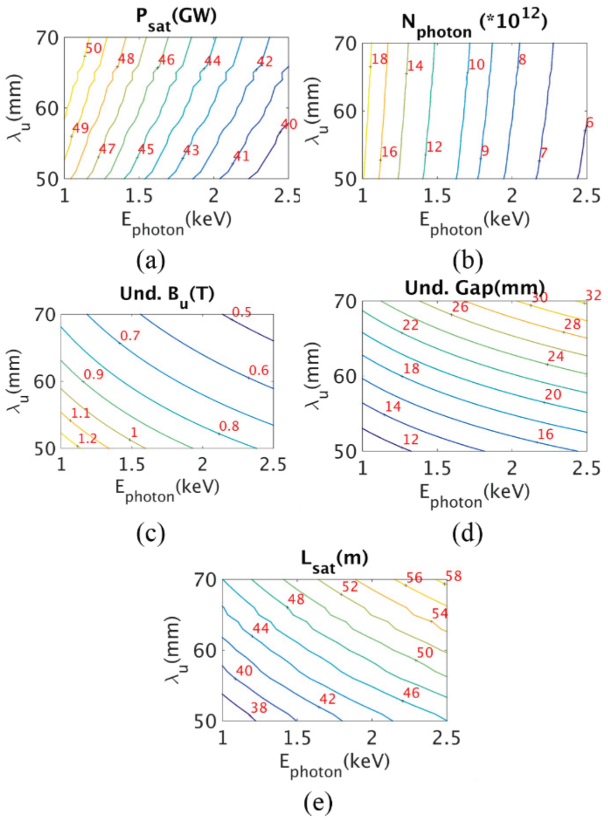

Figure 4: Contour graphs vs. undulator period and resonance photon energy in 10 GeV main linac (a) Saturation power (b) Number of photons (c) Undulator peak magnetic field (d) Undulator gap (e) Saturation length.

and mechanical margin. So undulator period has to be longer than 28 mm when same minimum gap of existing undulator line, 8.37 mm, is applied. Furthermore, saturation length is rapidly increasing as photon energy becomes higher when undulator period is longer than 30 mm as shown in Fig. 3 (e). Therefore, new SXR undulator line with any undulator period in 3.15 GeV branch linac is inappropriate to cover the vacant region.

10 GeV Main Linac

In the new SXR undulator line at the end of main linac, electron beam energy is fixed at 10 GeV over the vacant region. Sufficiently high power and number of photons at any photon energy are expected as shown in Fig. 4 (a) and (b). If the undulator period is longer than 60 mm, requisite values of peak magnetic field and undulator gap are enough reasonable as plotted in Fig. 4 (c) and (d). Furthermore, proper saturation length is estimated at any undulator period and photon energy as shown in Fig. 4 (e). So, the new SXR undulator line with 60 mm undulator period in 10 GeV main linac is the best candidate to cover the vacant photon energy region, 1.24 ~ 2 keV.

SIMULATION RESULTS

Time-dependent simulation is conducted about selected candidate. Real beam parameters for 10 GeV main linac with wakefield effect is used in simulation [6].

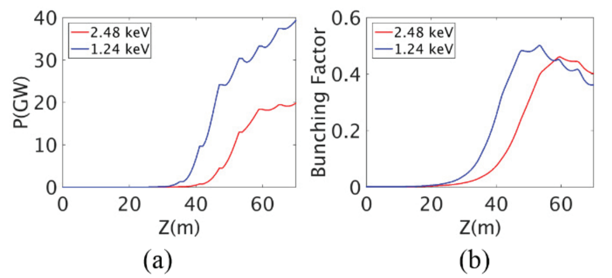

Figure 5: SASE simulation results with non-tapering. Blue (red) line indicates 1.24 (2.48) keV photon energy. (a) Radiation power (b) Bunching factor.

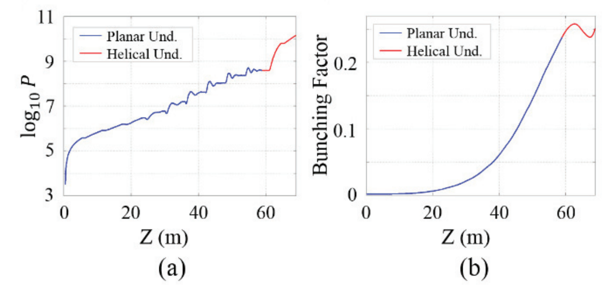

Figure 6: Polarization control with EPU simulation results. Blue (red) line indicates planar (helical) undulator output. (a) Logarithmic radiation power (b) Bunching factor.

SASE Simulation

Only 5 m-long planar undulator lattice is used in SASE simulation with non-tapering [6]. Simulations about two different photon energies are carried out. Radiation powers are sufficiently high as shown in Fig. 5 (a). Radiation power at 60 m is 33.28 (18.38) GW when photon energy is 1.24 (2.38) keV as indicated by blue (red) line in Fig. 5 (a). Both saturation points where the bunching factor has the maximum value are occurred within 60 m as plotted in Fig. 5 (b). With proper tapering scheme after saturation, radiation power will grow much higher than this.

Polarization Control with EPU

In the soft X-ray regime, polarization control is essential and it can be realized using additional elliptically polarizing undulator (EPU) with reverse tapering method [7]. Ten 5 m-long planar undulators are used and reverse tapering method is applied to them. Two additional 3.5 m-long EPUs are used for polarization control [6]. Simulation is conducted about 1.24 keV photon beam. Logarithmic power graph is shown in Fig. 6 (a). Linearly polarized radiation power at the end of planar undulators is 0.38 GW. Circularly polarized radiation power at the end of EPUs is 14.06 GW which is 5 times higher than previous results at the existing SXR undulator line by virtue of high electron beam energy [8]. According to definition of degree of polarization [7], it is 98.65% in this case. By optimizing reverse tapering method, higher circularly polarized radiation power and degree of polari-

ISBN 978-3-95450-134-2

zation will be obtained. Bunching factor of this case is shown in Fig. 6 (b).

CONCLUSION

To cover the vacant photon energy region from 1.24 to 2 keV in PAL-XFEL, four candidates are evaluated by estimating and comparing FEL performances using Ming Xie's formula. New soft X-ray undulator line with 60 mm undulator period at the end of 10 GeV main linac is the best solution to cover it. Moreover, FEL performances of overlapped photon energy region such as 1.24 keV is quite improved by virtue of high electron beam energy.

REFERENCES

[1] I. S. Ko, J.-H. Han, in *Proceedings of LINAC2014* (Geneva, Switzerland, 2014), p.26.
[2] H. S. Kang, K.-W. Kim, I. S. Ko, in *Proceedings of IPAC2015* (Richmond, USA, 2015), p.2439.
[3] B. I. Cho et al., Phys. Rev. Lett. 109, 245003 (2012).
[4] M. Xie, Proceedings of the 1995 Particle Accelerator Conference, IEEE, Piscataway, NJ, 1996, p. 183.
[5] S. Reiche, Nucl. Inst. And Meth. A **429**, 243 (1999).
[6] C. H. Shim, I. S. Ko, J.-H. Han and Y. W. Parc, in *Proceedings of IPAC2015* (Richmond, USA, 2015), p. 1678.
[7] E. A. Schneidmiller and M. V. Yurkov, Phys. Rev. ST AB **16**, 110702 (2013).
[8] C. H. Shim, I. S. Ko, Y. W. Parc and J.-H. Han, J. Korean Phys. Soc., accepted.

FEL OPERATION MODES OF THE MAX IV SHORT PULSE FACILITY

Alan Mak*, Francesca Curbis, Sverker Werin, MAX IV Laboratory, Lund University, Sweden

Abstract

The Short Pulse Facility (SPF) of the MAX IV Laboratory in Lund, Sweden features the production of ultrashort, incoherent x-ray pulses. It is driven by a 3-GeV linac and comprises two 5-metre undulator modules. While the SPF is designed for spontaneous radiation, we explore alternative operation modes in which the SPF functions as a simple free-electron laser (FEL). In this article, we characterize two of them in time-dependent numerical simulations. We perform a sensitivity study on the electron beam parameters and examine the technique of single-step tapering.

INTRODUCTION

The MAX IV facility in Lund, Sweden includes a Short Pulse Facility (SPF) [1] in addition to two storage rings. Commissioning is in progress as of 2015.

The SPF is situated at the end of the 3-GeV injector (see Fig. 1). It consists of two variable-gap, planar undulator modules, with a length of 5 metres each. The injector provides short electron bunches, which enable the SPF to produce incoherent x-ray pulses as short as 100 fs. From the same injector, electrons are also extracted at 1.5 GeV and 3 GeV for the top-up of the two storage rings (see Fig. 1).

In addition, the MAX IV facility was designed to enable future expansion. Two x-ray FELs (shown in grey in Fig. 1) can potentially be constructed as branch lines parallel to the SPF. They are set out in the long-term strategic plan of the laboratory [2]. In one of the branch lines, an extra linac section is envisaged, so as to provide the FEL with an electron energy of 5 – 6 GeV.

While the SPF is designed for spontaneous radiation, we explore alternative operation modes which enable the observation of coherent gain as a result of self-amplified spontaneous emission (SASE). In these operation modes, the SPF functions as a simple FEL, whereby the necessary techniques for a full-fledged FEL can be developed and tested.

To lay the foundation for future experimental work, we investigate two of such operation modes with the simulation code GENESIS [3]. In the first case, we study the sensitivity of the radiation power to the electron beam parameters. In the second case, we study the technique of single-step tapering [4, 5].

THEORETICAL BACKGROUND

Saturation Length and Power

Many properties of a high-gain FEL are characterized by the dimensionless Pierce parameter, which is defined as [6]

$$\rho = \frac{1}{2\gamma}\left(\frac{I}{I_A}\right)^{1/3}\left(\frac{\lambda_w K f_B}{2\sqrt{2}\pi\sigma_x}\right)^{2/3}. \tag{1}$$

* alan.mak@maxlab.lu.se

Here γ is the electron beam energy normalized to the electron rest energy $m_e c^2$. I is the peak current. $I_A = m_e c^3/e = 17.045$ kA is the Alfvén current. σ_x is the rms radius of the electron beam. λ_w is the undulator period. K is the undulator parameter. $f_B = J_0(\xi) - J_1(\xi)$ is the Bessel factor for planar undulators, with $\xi = K^2/[2(K^2+2)]$.

Using the Pierce parameter, the saturation length can be estimated by the relation

$$L_{\text{sat}} \approx \frac{\lambda_w}{\rho}, \tag{2}$$

and the saturation power by the relation

$$P_{\text{sat}} \approx \rho P_{\text{beam}}, \tag{3}$$

where $P_{\text{beam}} = \gamma m_e c^2 I/e$ is the electron beam power [6]. According to these relations, L_{sat} decreases with ρ, while P_{sat} increases with ρ.

In the SPF, the total undulator length L_w is only 10 m. In order to observe exponential power growth, it is preferable to choose an operation mode with $L_{\text{sat}} < L_w$, so that the exponential growth regime will, in principle, occur completely within the undulator line.

Single-Step Tapering

The purpose of single-step tapering is to enhance the power, and hence the energy extraction efficiency, of an FEL. It involves the use of two undulator segments with different undulator parameters. While the parameter of the first segment is K, the parameter of the second segment is decreased to $K - \Delta K$. A recent work by Li and Jia [5] provides a theoretical estimate of the optimal ΔK, given by

$$\frac{\Delta K}{K} = 2\sqrt{2}\rho\left(1 + \frac{2}{K^2}\right). \tag{4}$$

According to this relation, the optimal ΔK depends on the Pierce parameter ρ.

OPERATION MODES

We study two selected operation modes of the SPF using the simulation code GENESIS [3] in the time-dependent mode. The main parameters are shown in Table 1.

In Table 1, the saturation length L_{sat} and saturation power P_{sat} are estimated by Eqs. (2) and (3). For case A, the parameters are chosen so that the estimated L_{sat} is slightly shorter than the total undulator length L_w. For case B, the parameters are chosen so that the estimated L_{sat} is within the first of the two undulator modules.

In the simulations, there is a break section of 1 m between the two 5-metre-long undulator modules. As in the real facility, no focusing elements are inserted to the break section. The electron beam size in the SPF can be adjusted only by changing the twiss parameters at the entrance.

ISBN 978-3-95450-134-2

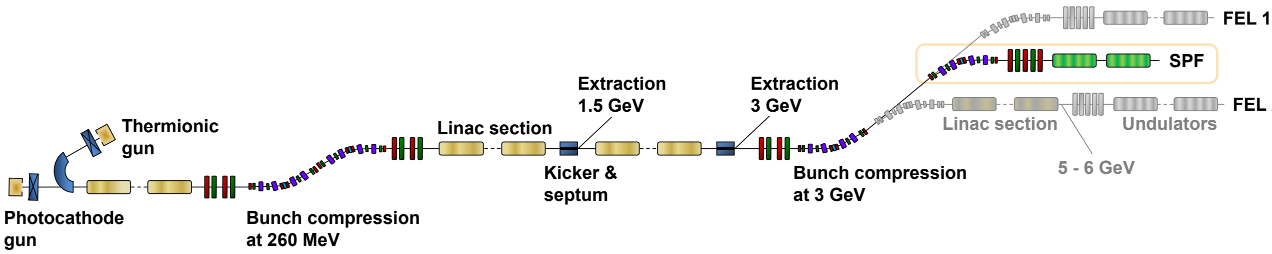

Figure 1: Schematic diagram of the SPF (in highlighted box) and its injector. Two potential FELs foreseen in the long-term strategic plan of the laboratory are shown in grey.

Table 1: Main Parameters of the Two Operation Modes Selected for the Simulation Studies

Parameter	Case A	Case B
Electron beam energy (GeV)	1.8	0.5
RMS bunch length (µm)	8	8
Peak current (kA)	2.5	2.5
Normalized emittance (µm rad)	0.4	0.4
Relative energy spread	1×10^{-4}	1×10^{-4}
Average β function (m)	13	11
Undulator period (mm)	15	15
Undulator parameter K	2.1	1.8
Radiation wavelength (nm)	2	20
Pierce parameter ρ	0.0017	0.0039
Estimated L_{sat} (m)	9	4
Estimated P_{sat} (GW)	7.7	4.8

RESULTS AND DISCUSSIONS

General Results for Case A

The results of the GENESIS time-dependent simulation for case A are summarized in Fig. 2.

Figure 2(a) shows the radiation power as a function of the distance z along the undulator line. Within the first undulator module ($z \leq 5$ m), the radiation does not exhibit any appreciable growth. Exponential growth occurs within the second undulator module ($z = 6 - 11$ m). At the exit of the undulator line ($z = 11$ m), the final power is 2.64 GW. While the estimated saturation length is $L_{\mathrm{sat}} = 9$ m, power saturation is not seen within the total undulator length of $L_w = 10$ m.

Figure 2(b) shows the evolution of the beam sizes along the undulator line. The blue and red solid curves correspond to the rms radius of the electron beam in the horizontal and vertical planes, respectively. The green dotted curve corresponds to the rms radius of the optical beam. At $z = 3 - 5$ m, the effect of optical guiding manifests itself in the decrease in optical beam size. In the break section ($z = 5 - 6$ m), the increase in optical beam size is due to vacuum diffraction. In the second undulator module ($z = 6 - 11$ m), the exponential power growth [see Fig. 2(a)] causes strong gain guiding, and hence a rapid decrease in optical beam size. At around $z = 10$ m, the decrease slows down, and the optical beam size approaches a turning point. This reflects the weakening of gain guiding, which is an indication that the radiation power is close to saturation.

Figure 2(c) shows the on-axis field amplitude as a function of z. The field grows monotonically within the undulator modules. In the break section ($z = 5 - 6$ m), there is a small decrease in field amplitude, due to the increase in the optical beam size [see Fig. 2(b)]. At around $z = 10$ m, the growth in field amplitude begins to slow down, as the power is approaching saturation.

Figure 2(d) shows the bunching factor as a function of z. Here the bunching factor is defined as the absolute value of $\langle e^{-i\psi} \rangle$, where the brackets denote the average over all particles, and ψ is the particle phase in the ponderomotive potential. The bunching factor grows with the field amplitude [see Fig. 2(c)], and the growth also begins to slow down at around $z = 10$ m. As the power is approaching saturation, the microbunching is close to fully developed, and the bunching factor reaches 0.35 at $z = 11$ m.

Sensitivity Study on Case A

The emittance, energy spread and peak current listed in Table 1 are stringent requirements on the quality of the electron beam. To quantify the effect of loosening these requirements, we perform a sensitivity study on case A using GENESIS time-dependent simulations. In particular, we probe the reduction in final radiation power (at $z = 11$ m) upon varying the emittance, the energy spread and the peak current, one at a time. The study is summarized in Table 2. The results show that the radiation power is very sensitive to the emittance and the peak current, and is fairly sensitive to the energy spread.

Single-Step Tapering in Case B

Since the SPF is made up of two variable-gap undulator modules, single-step tapering can be implemented by setting the parameters of the first and the second modules to K and $K - \Delta K$, respectively. In case B, the estimated saturation length $L_{\mathrm{sat}} = 4$ m is within the first module. By applying a single-step taper, we aim to observe post-saturation power growth in the second module.

The first module is fixed at $K = 1.8$. In GENESIS time-dependent simulations, we vary ΔK and probe the final radiation power at the exit of the second module ($z = 11$ m). The results are summarized in Fig. 3.

ISBN 978-3-95450-134-2

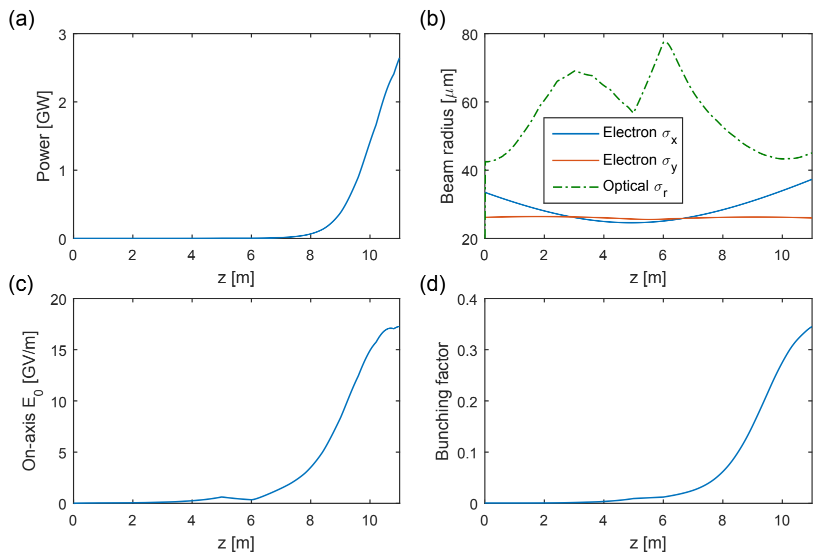

Figure 2: Simulation results for case A. The following quantities are plotted as functions of the distance z along the undulator line: (a) the radiation power; (b) the rms radii of the electron beam (solid curves) and the optical beam (dotted curve); (c) the field amplitude on axis; (d) the bunching factor.

Table 2: Results of the Sensitivity Study on Case A

Normalized emittance (μm rad)	Final power (GW)	Percentage power decrease
0.4	2.64	-
0.6	0.70	73.6%
0.8	0.13	95.0%
Relative energy spread	**Final power (GW)**	**Percentage power decrease**
1×10^{-4}	2.64	-
3×10^{-4}	1.82	31.3%
5×10^{-4}	1.06	59.9%
Peak current (kA)	**Final power (GW)**	**Percentage power decrease**
2.5	2.64	-
1.8	0.74	72.1%
1.2	0.09	96.7%

Without any tapering ($\Delta K/K = 0$), the final power is 2.58 GW. With single-step tapering, the final power is maximized at $\Delta K/K = 1.4\%$. The maximized final power is 3.51 GW, which is 36% higher than the final power in the no-taper scenario. In comparison, the theoretical estimate of the optimal $\Delta K/K$, given by Eq. (4), is 1.8%.

In Fig. 4, we compare the evolution of various quantities in the simulations of the optimized taper ($\Delta K/K = 1.4\%$) and no taper ($\Delta K/K = 0$).

As seen in Figure 4(a), the radiation power grows exponentially between $z = 3$ m and 5 m. Saturation is reached at the end of the first undulator module ($z = 5$ m), which is a little further than the estimated 4 m. The saturation power is 2.58 GW, which is lower than the estimated 4.8 GW. Without

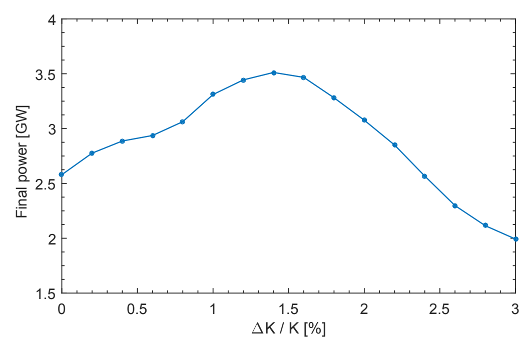

Figure 3: Simulation results for single-step tapering in case B. The final radiation power at the exit of the undulator line is plotted as a function of the step size $\Delta K/K$.

tapering, the power remains at the same level subsequently. With the optimized single-step taper, the power continues to grow after the 1-metre break section, and reaches final saturation at around $z = 7$ m in the second module.

In Figure 4(b), the decrease in optical beam size between $z = 3$ m and 5 m matches the regime of the exponential power growth, due to gain guiding. After the exponential regime, the optical beam size increases again, due to the absence of gain guiding.

In Figure 4(c), the on-axis field amplitude reaches its maximum at $z = 5$ m. Beyond the power saturation, the curve for optimized taper shows an additional bump at $z = 6-8$ m over the curve for no taper.

In Figure 4(d), the bunching factor also reaches its maximum at $z = 5$ m. Beyond the power saturation, the optimized taper yields a smaller bunching factor than in the case of no taper. This can be attributed to the detrapping of particles during the deceleration of the ponderomotive bucket in phase space.

ISBN 978-3-95450-134-2

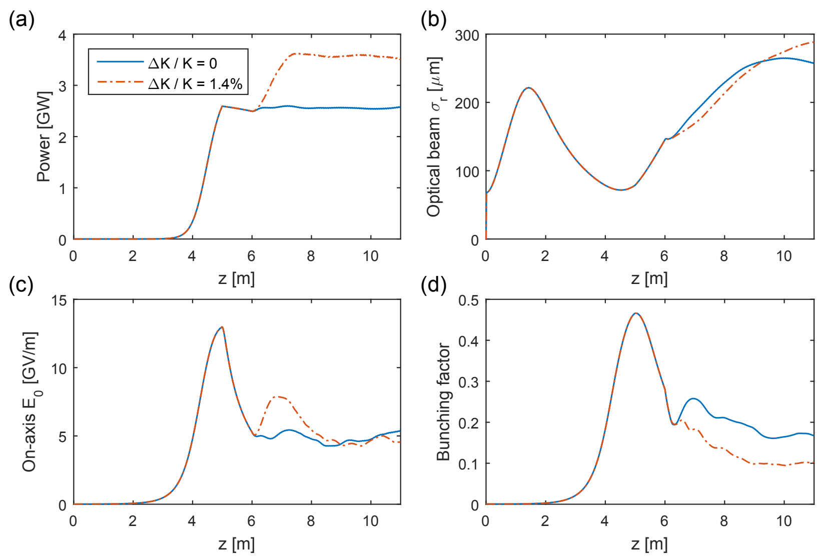

Figure 4: Simulation results for optimized taper ($\Delta K/K = 1.4\%$) and no taper ($\Delta K/K = 0$) in case B. The following quantities are plotted as functions of z: (a) the radiation power; (b) the rms radius of the optical beam; (c) the field amplitude on axis; (d) the bunching factor.

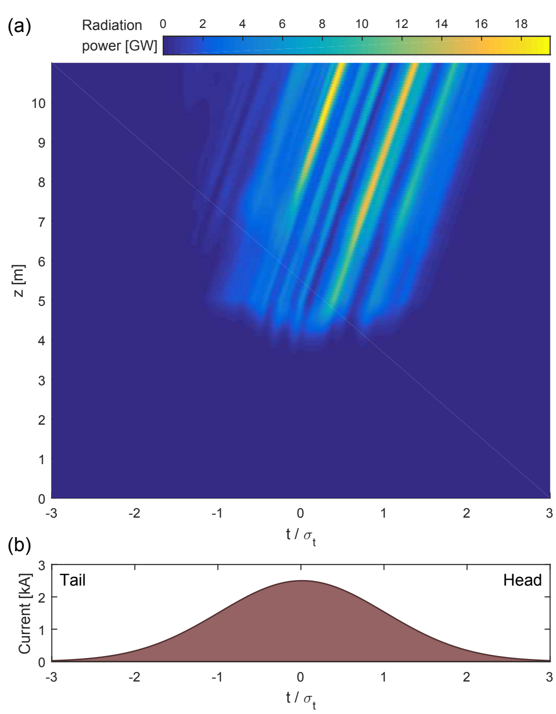

Figure 5: Simulation results for the optimized taper ($\Delta K/K = 1.4\%$) in case B. (a) Radiation power of different slices within the electron bunch. (b) The longitudinal profile of the electron bunch.

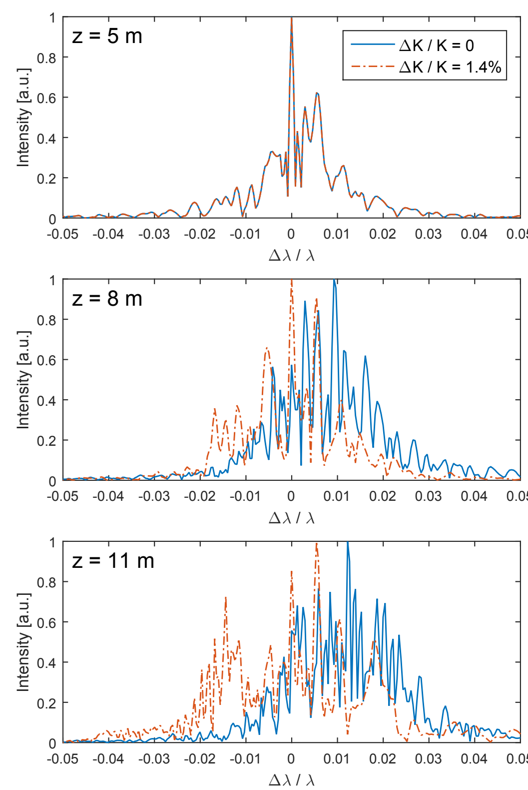

Figure 6: Spectral intensity spectra for optimized taper ($\Delta K/K = 1.4\%$) and no taper ($\Delta K/K = 0$) at $z = 5$ m, 8 m and 11 m.

Radiation Properties of Case B

As the simulations are performed in the time-dependent mode, we can also compare the radiation power at different slices within the electron bunch. This comparison is made in Fig. 5(a) for the case of optimized taper ($\Delta K/K = 1.4\%$). The colour scale shows the radiaion power. The vertical axis shows the distance z along the undulator line. The horizontal axis shows the longitudinal position t within the electron bunch, normalized to the rms bunch length σ_t. Meanwhile, the longitudinal profile of the electron bunch is shown in Fig. 5(b).

ISBN 978-3-95450-134-2

From Fig. 5(a), we see that the radiation is the most intense in the second undulator module ($z = 6-11$ m). Furthermore, it is the central part of the electron bunch ($-\sigma_t \leq t \leq 2\sigma_t$) that contributes significantly to the average radiation power shown in Figure 4(a). Towards the head and the tail of the bunch, the contribution is much smaller.

In Fig. 6, we compare the spectral intensity distributions for the scenarios of optimized taper ($\Delta K/K = 1.4\%$) and no taper ($\Delta K/K = 0$). At $z = 5$ m, the radiation power has just reached saturation, there is very little difference in the two spectral intensity distributions.

Beyond the saturation point, the single-step taper sustains the radiation at the central wavelength, and the central spike is still seen in the spectral intensity distribution at $z = 8$ m and 11 m (see Fig. 6). But in the no-taper scenario, the original resonant condition is no longer maintained after the saturation point. As a result, the radiation power shifts towards longer wavelength in the spectral intensity distributions for $z = 8$ m and 11 m (see Fig. 6).

Another observation in the spectral intensity distribution is the growth of sidebands (see Fig. 6). For the optimized taper, at $z = 11$ m, sidebands are seen around $\Delta\lambda/\lambda = 0.018$ and -0.014. The sideband at $\Delta\lambda/\lambda = 0.005$ even surpasses the central spike in intensity. The growth of the sidebands can be attributed to synchrotron oscillations [7].

CONCLUSION AND OUTLOOK

In this article, we have discussed two operation modes of the SPF, referred to as case A and case B. With the use of time-dependent simulations in GENESIS, we have demonstrated that these operation modes lead to exponential power growth within the length of the undulator line. In these operation modes, the SPF functions as a simple FEL.

In case A, we have performed a sensitivity study, quantifying the effect on the radiation power after loosening the requirements on the quality of the electron beam.

In case B, we have applied the technique of single-step tapering, and compared the optimal step size $\Delta K/K$ obtained in our simulations to that given by theoretical estimation in Li and Jia [5]. With the simulation results, we have examined the radiation properties, which include the evolution of the spectral intensity distribution along the undulator line.

Beyond this article, we envision to test the two FEL operation modes experimentally at the SPF. The experience of operating the SPF as a simple FEL shall provide insight into the laboratory's future development of a full-fledged FEL.

REFERENCES

[1] S. Werin et al., "Short Pulse Facility for MAX-lab", Nucl. Instrum. Methods Phys. Res., Sect. A **601**, 98 (2009).

[2] F. Curbis et al., "Towards an X-Ray FEL at the MAX IV Laboratory", in Proceedings of the 36th International Free-Electron Laser Conference, Basel, Switzerland, 549 (2014).

[3] S. Reiche, "GENESIS 1.3: a Fully 3D Time-Dependent FEL Simulation Code", Nucl. Instrum. Methods Phys. Res., Sect. A **429**, 243 (1999).

[4] D. A. Jaroszynski et al., "Free-Electron Laser Efficiency Enhancement, Gain Enhancement, and Spectral Control Using a Step-Tapered Undulator", Phys. Rev. Lett. **74**, 2224 (1995).

[5] H. Li, Q. Jia., "Optimization of Single-Step Tapering Amplitude and Energy Detuning for High-Gain FELs", Chinese Physics C **39**, 018101 (2015).

[6] Z. Huang, K.-J. Kim, "Review of X-Ray Free-Electron Laser Theory", Phys. Rev. ST Accel. Beams **10**, 034801 (2007).

[7] R. W. Warren, J. C. Goldstein, "The Generation and Suppression of Synchrotron Sidebands", Nucl. Instrum. Methods Phys. Res., Sect. A **272**, 155 (1988).

ISBN 978-3-95450-134-2

SEEDED FEL STUDY FOR CASCADED HGHG OPTION FOR FLASH2

G. Feng#, I. Zagorodnov, M. Dohlus, T. Limberg, W. Decking, J. Boedewadt, DESY, Hamburg, Germany
K. Hacker, Technische Universität Dortmund, Germany
T. Plath, University of Hamburg, Germany

Abstract

The free electron laser (FEL) facility at DESY in Hamburg (FLASH) is the world's first FEL user facility which can produce extreme ultraviolet (XUV) and soft X-ray photons. In order to increase beam time delivered to users, a major upgrade named FLASH II is in progress. As a possibility, a seeding undulator section can be installed between the extraction arc section and the SASE undulator of FLASH2. In this paper, a possible seeding scheme for the cascaded HGHG option for FLASH2 is presented. The SASE undulator of FLASH2 can be used as the second radiator of the cascaded HGHG section. Parameters optimization for the accelerating modules and for the bunch compressors has been done to meet the requirement for the electron bunches. In the beam dynamics simulation, collective effects were taken into account. Particle distribution generated from the beam dynamics simulation was used for the seeded FEL study. Space charge and CSR impacts on the microbunches were included during the cascaded HGHG simulation. The simulation results show that FEL radiation with the wavelength of a few nms and with high monochromaticity can be seeded at FLASH2.

INTRODUCTION

FLASH has been an FEL user facility since 2005 which can produce FEL radiation in the wavelength range from 4.1nm to 45nm [1]. In order to increase the beam time, a major upgrade, FLASH II, is in progress. Behind the main linac, three fast vertical kickers and a DC Septum distribute the electron beam either to the dogleg section of FLASH1 or to the extraction arc of FLASH2 [2]. As the extension of FLASH, the beamline of FLASH2 has been constructed in a separate tunnel. SASE FEL radiation in the wavelength range from 4 nm to 80nm can be produced from the SASE undulator of FLASH2 [3]. Gap of the SASE undulator is variable for relaxing the dependency of the radiation wavelength on the electron beam energy and for independent operation of FLASH1 and FLASH2. As a possibility, a seeding undulator section can be installed between the extraction arc and the SASE undulator of FLASH2. Maybe it can allow for different seeding schemes, like HHG, HGHG and several combinations of them [4]. In this paper, seeded FEL study for the cascaded HGHG option for FLASH2 is presented. The SASE undulator of FLASH2 has been used as the second radiator of the cascaded HGHG in the simulation.

A single stage HGHG section which can also be used as the first stage of the cascaded HGHG consists of a dispersive chicane and two undulator sections: a modulator and a radiator. In the modulator, a seeding laser modulates the electron energy distribution. In the dispersive chicane, the energy modulation is transformed into a density modulation: microbunching. Because the microbunching will have a significant harmonic content, the radiator can be tuned to a higher harmonic of the seed laser. When the bunched electron beam enters the it can emit coherent, intense FEL radiation.

The seed laser which will be used for FLASH2 is a Ti:Sapphire laser at a repetition rate of 100 kHz. After frequency up conversion, the laser wavelength ranges from 200 nm to 270 nm [5]. In the seeded FEL study, the electron beam with energy of 1 GeV has been used and the seeding laser has wavelength of 266 nm. In order to avoid particle loss in terms of FEL bandwidth and to reduce the beam instability due to microbunching, the amplitude of energy modulation in the modulator is limited to less than 1 MeV. Figure 1 gives the estimation of bunching factor as a function of harmonics of the seed laser for different initial uncorrelated energy spread. One can see at the 7th harmonic, the bunching factor can reach 0.2 in the case of 100 keV uncorrelated energy spread. For FLASH, it is possible to obtain electron bunches with a smaller uncorrelated energy spread, when the peak current is low enough. Therefore, in the following study, the peak current of the electron bunch is limited lower than 1.5 kA and the first radiator is tuned to the 7th harmonic of the seed laser.

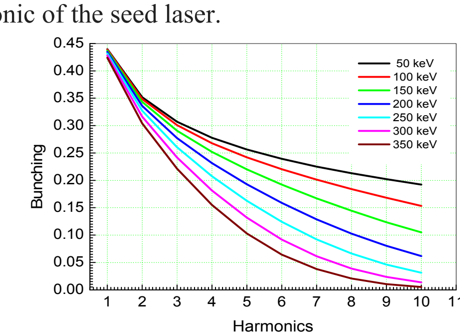

Figure 1: Bunching factor for HGHG with different initial slice energy spreads.

BEAM DYNAMICS SIMULATION

The seed laser has the wavelength of 266nm, the pulse duration is 100 fs and the pulse energy is 6 μJ [5]. The total length of the pulse is about 90 um. In order to get long enough electron bunch for HGHG option, especially for cascaded HGHG, beam dynamics with 1 nC bunch charge case has been studied.

Description of the RF cavities and the magnets is from the FLASH 2 lattice definition which has been written in Elegant format [6].There are some restrictions in the beam dynamics simulation. Same as the normal operation case, the beam energies which were used in the

guangyao.feng@desy.de

ISBN 978-3-95450-134-2

simulation before BC2 and BC3 are 145.5 MeV, 450 MeV respectively. The technical restriction of maximum energy gain for each accelerating module has also been taken into account [7].

Transformation of the longitudinal coordinate in the i^{th} bunch compressor can be described with the following formula [8], where R_{56i}, T_{566i} and U_{5666i} are the momentum compaction factors in the i^{th} compressor. δ_i is the relative energy deviation.

$$s_i = s_{i-1} - \left(R_{56i}\delta_i + T_{566i}\delta_i^2 + U_{5666i}\delta_i^3\right) \quad i = 1, \dots, N$$

For the fixed values of RF parameters and momentum compaction factors, the global compression function can be defined by the following formulas, where $C_N(s)$ describes the increase of the peak current in the slice with initial position s and $Z_N(s)$ is the inverse global compression function.

$$C_N = \frac{1}{Z_N}, Z_N = \frac{\partial s_N}{\partial s}$$

For a two-stage bunch compression scheme, like FLASH, if the collective effects are not included, one can get the relation among the RF parameters, the beam energies and the inverse global compression functions.

$$E_1 = E_1(V_1, \varphi_1, V_{39}\ \varphi_{39}),$$
$$E_2 = E_2(V_1, \varphi_1, V_{39}, \varphi_{39}, V_2, \varphi_2),$$
$$Z_1 = \frac{\partial s_1}{\partial s}(0), Z_2 = \frac{\partial s_2}{\partial s}(0), Z_2' = \frac{\partial^2 s_2}{\partial s^2}(0), Z_2'' = \frac{\partial^3 s_2}{\partial s^3}(0)$$

In the above formulas, V_{39} and φ_{39} are the voltage amplitude and phase shift of ACC39. V_i and φ_i (i=1, 2) are the RF parameters of ACC1 and ACC2-3. In general case, beam bunches are accelerated on crest in ACC4-7. The partial compression functions $C_i = 1/Z_i$ (i=1, 2) describe the amount of the compression achieved after the i^{th} compressor. In principle, for a linear compression in the middle of the bunch, Z_N' and Z_N'' can be set to zero. But they should be adjusted slightly if the collective effects are taken into account.

Typically BC2 is operated with a bending angle of 18° [1]. So the curvature radius of the reference trajectory (r_1) in BC2 has been set to 1.618 m. In order to reduce space charge effects between the BC2 and BC3, a not strong compression (C_1=2.7) in BC2 has been selected in the simulation. Table 1 shows the parameter settings for the bunch compressors. During the parameters selection, the technical restriction of curvature radius [8] has been taken into account. Considering collective effects, a fast tracking code written with matlab was used for the RF parameters optimization. RF settings for the accelerating modules are shown in Table 2. In principle, beam bunches with small energy chirp are needed to get FEL radiation with high monochromaticity. For this purpose, the phase of ACC4-7 was adjusted to obtain beam bunches with small energy chirp.

Table 1: Parameter Settings for the Bunch Compressors

Charge Q, nC	Curvature radius in BC2, r_1 [m]	$R_{56,BC2}$ [mm]	Compr. In BC2	Curvature radius in BC3, r_2 [m]	$R_{56,BC3}$ [mm]	Total compr. C
1.0	1.618	180.7	2.7	5.4	95.7	~20

Table 2: RF Parameter Settings for the Accelerating Modules

V_{acc1} [MV]	φ_{acc1} [deg]	V_{acc39} [MV]	φ_{acc39} [deg]	$V_{acc2,3}$ [MV]	$\Phi_{acc2,3}$ [deg]	$V_{acc4,5,6,7}$ [MV]	$\Phi_{acc4,5,6,7}$ [deg]
160.3	-3.2	21.9	153.4	322.3	19.0	623.0	-28.0

Beam dynamics simulation from the RF gun to the entrance of the first modulator has been completed. For the arc sections, CSRTrack code [9] was used and CSR impact has been taken into account. Beam tracking in the straight sections with space charge effects was simulated by using ASTRA code [10]. The longitudinal cavity wake field effects [11] were included at the exit of each accelerating section with matlab scripts. A million particles were used in the simulation. Figure 2 shows description of the bunch properties before the first modulator. In the middle of the bunch, the maximum uncorrelated energy spread is about 150 keV.

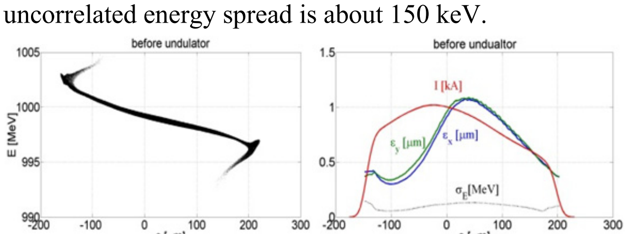

Figure 2: Bunch properties before the modulator for 1.0 nC case. Longitudinal phase space (left), Current profile, slice emittances and slice energy spread (right).

CASCADED HGHG SIMULATION

The technical restriction of K parameter for SASE undulator of FLASH2 can be described as $0.78 \leq K_{rms} \leq 1.91$. According to the formulas for K parameter $K = \frac{\sqrt{2}}{2} 0.934 B_0[\mathrm{T}]\lambda_u[\mathrm{cm}]$ and for resonant radiation wavelength $\lambda = \frac{\lambda_u}{2\gamma^2}(1 + K^2)$ [12], the reasonable K with different period length for each undulator section has been obtained. The first radiator and the second modulator will have same period length because radiation in them has the same wavelength. Table 3 gives the parameter selections for the undulator sections. It is impossible to tune the second radiator to the 7^{th} harmonic because the K parameter will be out of the limit.

The formula $\hat{I} = \frac{cqkE_{mod}}{\sqrt{\pi}\sigma_E}$ can be used to estimate the peak current of the microbunches after an ideal compression, where E_{mod} is the amplitude of the energy modulation and σ_E is the uncorrelated energy spread. The formula $P_L = 8.7 \times 10^9 \times \left(\frac{E_0 E_{mod}}{511000^2} \cdot \frac{\sigma_{Laser}}{L_u K_{ut}}\right)^2$ gives the relation among the laser power, the beam energy, the energy modulation, the size of the laser, the total length and K parameter of the first modulator. Considering the above points, a possible description of the first stage HGHG section is given: The period length of the modulator is 8.3 cm and the total number of periods is 27. There are four dipole magnets in the dispersive chicane. The length of the magnet is 0.1 m, with the same length as FLASH correctors. The distance between the first two dipole magnets is 0.5 m. The radiator has the period length of 4.3 cm and the number of periods is 49. The particle distribution will be up converted to the 7th harmonic of the seed laser in the radiator.

Table 3: Parameter Selections for the Undulator Sections

Undulator sections	λ [nm]	K (rms)	λu [cm]
Modulator 1	266	4.852	8.3
Radiator 1	38	2.402	4.3
Modulator 2	38	2.402	4.3
Radiator 2 (SASE undulator)	12.67 7.6	1.446 0.924	3.14

According to the design optics of FLASH2 SASE option [6], beam optics matching has been done before the SASE undulator. The average beta function in the undulator sections is about 10 meters.

Particle distribution generated from the beam dynamics simulation was used for the radiation study. Simulations in the modulator and in the radiator have been done with Genesis 1.3 [13]. In order to take into account space charge and CSR impacts, ASTRA and CSRTrack codes were used for the beam dynamics simulation on the beamline between the modulator and the radiator. To obtain the input particle files for ASTRA, CSRTrack and Genesis, particle distribution conversion among these codes has been done with matlab scripts. Figure 3 gives the longitudinal phase space at the exit of the first modulator. One can see the amplitude of energy modulation is about 0.8 MeV. An adjustment has been done to shift the laser with respect to the electron bunch to reserve a new part of the bunch for the second stage HGHG.

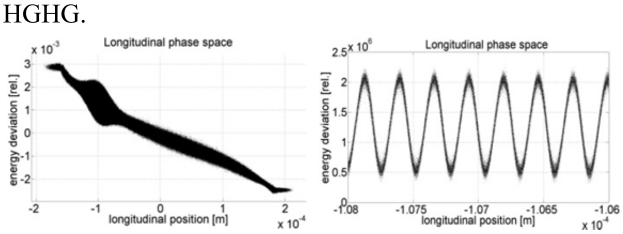

Figure 3: Longitudinal phase space after the modulator.

Before CSRtrack simulation in the first dispersive chicane, some estimation for CSR impact on the microbunches has been done. For an ideal compression, r56 of the chicane should be 53 µm and the curvature radius is 14.5 m. One can get the microbunch length of 8 nm after ideal compression with formula $\sigma = \frac{r_{56}\sigma_E}{E}$. The steady state CSR field [14] has also been estimated. Figure 4 shows the longitudinal field of a microbunch in circular motion. In the center of the bunch, the maximum field is about 18 MV/m. The density modulation and CSR impact on the microbunches in the chicane are shown in Figure 5. One can see the total CSR effect is less than 500 keV.

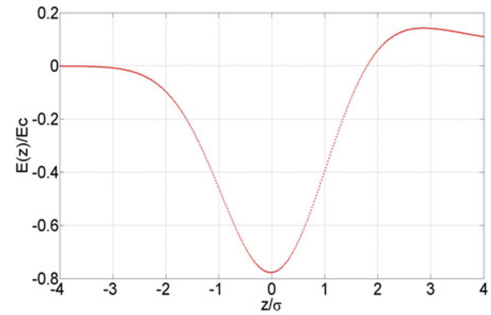

Figure 4: Normalized longitudinal field of an ultra-relativistic thin Gaussian bunch in circular motion.

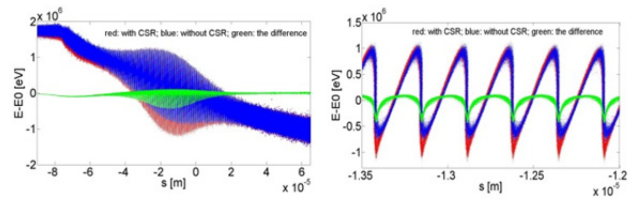

Figure 5: Density modulation and CSR impact on microbunches in the dispersive chicane.

Bunching factor at the entrance of the first radiator and the bunching distribution along the radiator are shown in figure 6. At the exit of the first radiator, radiation with peak power about 0.3 GW has high monochromaticity.

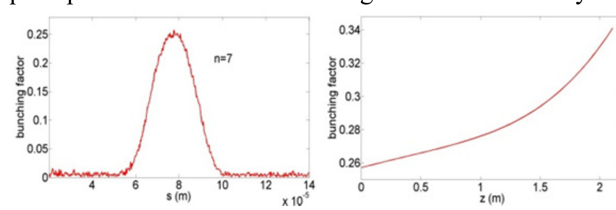

Figure 6: Bunching factor before the radiator (left) and bunching distribution along the radiator (right).

Figure 7 shows the schematic layout of the cascaded HGHG section. A fresh bunch chicane is placed between the first sage and the second. The FEL radiation generated from the first radiator passes the chicane and slips ahead, while the electron bunches are bent on a bump like trajectory and fall behind. Therefore the FEL radiation coincides with a different part of the bunch in the second modulator. This new part has not been seeded before and can be used for the second stage HGHG study. Considering uncorrelated energy spread distribution (Figure 8) after the first radiator, difference between the electron bunch trajectory and the photon pulse trajectory is chosen with a value of 107 µm. Figure 9 shows the longitudinal phase space after the second modulator.

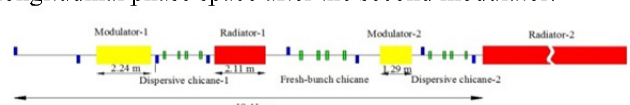

Figure 7: Schematic layout of a cascaded HGHG section.

ISBN 978-3-95450-134-2

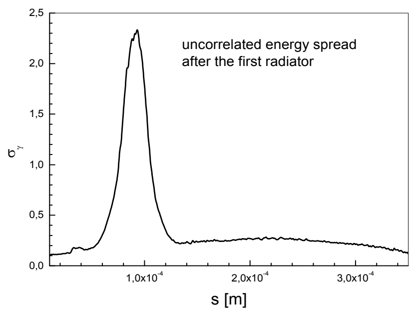

Figure 8: uncorrelated energy spread distribution after the first radiator.

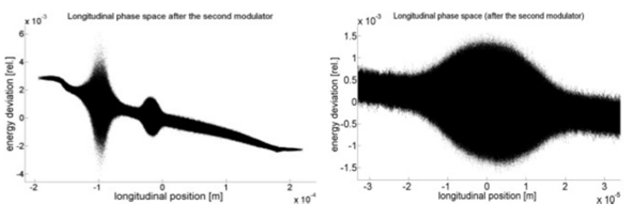

Figure 9: longitudinal phase space after the second modulator.

Before the simulation in the second dispersive chicane, CSR impact on the microbunches has been estimated with the same method like the previous work. r56 of the second dispersive chicane for ideal compression is 5.13 μm and the curvature radius is 47 m. The rms microbunch length after compression is about 1nm. Longitudinal CSR field of a microbunch in circular motion has been estimated. In the center of the bunch, the maximum field is about 4 MV/m. It is not very strength because of the large curvature radius in the chicane. Simulation results show the total CSR effect is less than 100 keV.

In order to obtain high power radiation beyond nominal saturation level, undulator can be tapered to keep the resonant condition as the electron bunches lose energy. It's possible to use tapered undulator for the second radiator because the gap of the SASE undulator of FLASH2 is variable. After adjusting the K parameter of each undulator section, FEL radiation with peak power about 3.5 GW and with high monochromaticity has been obtained when the radiator is tuned to the 3rd harmonic. Bunching factor before the radiator is shown in Figure 10. Figure 11 gives the radiation power at the exit of the radiator and the spectrum. At the exit of the radiator, the radiation energy is about 243 μJ. When the radiator is tuned to the 5th harmonic, one can get the FEL radiation with peak power of 1.0 GW and the resonant wavelength is 7.6 nm.

CONCLUSION

A possible seeding scheme for the cascaded HGHG option for FLASH2 is presented. A start-to-end simulation from the RF gun to the seeding undulator section has been done for this option. Parameters optimization for the accelerating modules and for the bunch compressors was achieved to meet the requirement for the electron bunches. Space charge, CSR and longitudinal cavity wake field effects were taken into account in the simulation. The simulation results show that it is possible to obtain HGHG FEL radiation with the wavelength of a few nms and with high monochromaticity.

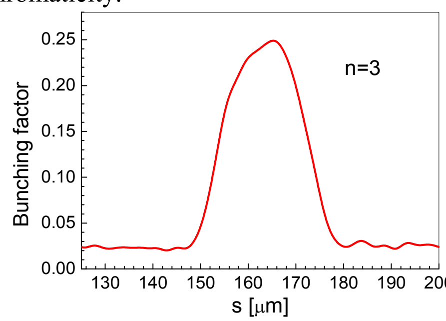

Figure 10: Bunching factor before the second radiator.

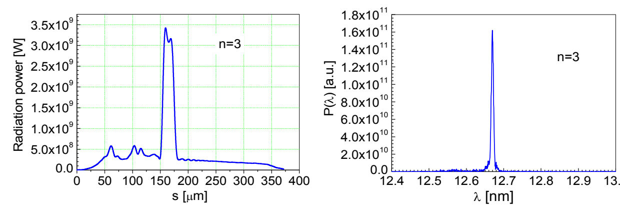

Figure 11: Radiation power at the exit of the radiator (left) and the spectrum (right).

ACKNOWLEDGMENT

We are grateful to Bart Faatz, Sven Reiche, Matthias Scholz, Yauhen Kot and Sascha Meykopff for their support and help for this work.

REFERENCES

[1] M. Vogt, B. Faatz, et al., "Status of the free electron laser FLASH at DESY", Proceedings of IPAC'11, San Sebastian, Spain, 2011, paper THPC081.

[2] M. Scholz, W. Decking, et al., "Extraction arc for FLASH II", Proceedings of FEL'12, Nara, Japan, August 2012, paper TUPD33.

[3] B. Faatz, et al., "FLASH II: A seeded future at FLASH", Proceedings of IPAC'10, Kyoto, Japan, 2010, paper TUPE005.

[4] K. Hacker, "A Concept for Seeding 4-40 nm FEL Radiation at FLASH2", TESLA-FEL, 2013-01.

[5] T. Tanikawa, "Seeding Preparation at the FLASH2 Beamline", presented at FEL'14, Basel, Switzerland 2014, MOP081, unpublished.

[6] M. Scholz, FLASH-lattice files, http://www.desy.de/fel-beam/ flash2_elegant_2012_09_19.zip.

[7] http://www.desy.de/fel-beam/s2e/flash/Information/RF.txt

[8] I. Zagorodnov, M. Dohlus, "A semi-Analytical Modelling of Multistage Bunch Compression with Collective Effects", Physical Review STAB 14 (2011).

[9] M. Dohlus,T. Limberg, "CSRtrack: faster calculation of 3D CSR effects", Proceedings of FEL'04, Trieste, Italy, August 2004, paper MOCOS05.

[10] K. Floettmann, "ASTRA", DESY, Hamburg, http:// www.desy.de/~mpyflo/, (2011).

[11] T. Weiland, I. Zagorodnov, "TESLA cryomodule wake", TESLA Report 2003-19, DESY (2003).

ISBN 978-3-95450-134-2

[12] E. L. Saldin, E. A. Schneidmiller, M.V. Yurkov, The Physics of Free Electron Lasers, Springer Science & Business Media, 2000.
[13] S. Reiche, "GENESIS 1.3", NIM A 429 (1999) 243.
[14] M. Dohlus, T. Limberg, Bunch Compression for Linac-based FELS, Beam Dynamics Newsletter, No. 38, December, 2005.

ISBN 978-3-95450-134-2

SCHEME TO INCREASE THE OUTPUT AVERAGE SPECTRAL FLUX OF THE EUROPEAN XFEL AT 14.4 keV

Gianluca Geloni, European XFEL GmbH, Hamburg, Germany
Vitali Kocharyan, Evgeni Saldin, Deutsches Elektronen-Synchrotron (DESY), Hamburg, Germany

Abstract

Inelastic X-ray scattering and nuclear resonance scattering are limited by the photon flux available at SR sources, up to 1e10 ph/s/meV at 14.4 keV. A thousand-fold increase may be obtained by exploiting high repetition rate self-seeded pulses at the European XFEL. We report on a feasibility study for an optimized configuration of the SASE2 beamline combining self-seeding and undulator tapering at 14.4 keV. One should perform monochromatization at 7.2 keV by self-seeding, and amplify the seed in the first part of the output undulator. Before saturation, the electron beam is considerably bunched at the 2nd harmonic. A second part of the output undulator tuned to 14.4 keV can thus be used to obtain saturation at this energy. One can further prolong the exchange of energy between the photon and the electron beam by tapering the last part of the output undulator. Start-to-end simulations demonstrate that self-seeding, combined with undulator tapering, allows one to achieve more than a hundred-fold increase in average spectral flux compared with the nominal SASE regime at saturation, resulting in a spectral flux of order 1e13 ph/s/meV. A more detailed description of this study can be found in [1].

INTRODUCTION AND METHOD

Inelastic X-ray scattering from electrons [2]- [8] (IXS) and Nuclear Resonant Scattering [9]- [13] (NRS) are important techniques for probing condensed matter by successfully exploiting the high brightness of synchrotron radiation sources. Inelastic scattering relies on the transfer of momentum and energy from the photon field to the sample. Such transfer is detected as a change of momentum and energy of the scattered photons, and allows for the study of a number of excitations with different characteristic lengths and time scales, related to the momentum and energy transfer. In particular, the highest temporal resolution is achieved for very small energy transfer, and calls for a very high average spectral density of the incident X-ray radiation.

In [14] it was studied how sub-meV inelastic X-ray scattering experiments could benefit from high-repetition rate, seeded XFELs. In that case, the method exploited Hard X-ray Self-Seeding (HXRSS) and tapering at the European XFEL around the photon energy of 9 keV in combination with a new concept for monochromatization and spectral analysis [15–17], which is expected to lead to Ultra-High Resolution IXS (UHRIX) momentum-resolved experiments with 0.1-meV spectral and 0.02-nm^{-1} momentum transfer resolution. In that work we showed that the European XFEL equipped with HXRSS can lead to a photon flux of order

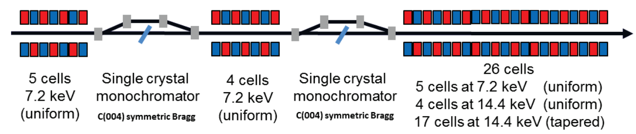

Figure 1: Layout of the SASE2 undulator at the European XFEL configured for HXRSS and tapered operation, as discussed in this work.

10^{14} ph/s/meV at the sample, about four orders of magnitude larger than what is presently achievable at synchrotrons.

A continuation of that kind of studies includes the investigation of the average spectral density achievable at high-repetition self-seeded FEL at higher X-ray energies. The most natural application of these kind of X-ray sources is for NRS experiments. Similarly as for IXS applications, also NRS analyzers are limited, in resolution, by the flux available at synchrotrons. For instance, at 14.4 keV, the maximum spectral flux available at third generation synchrotron radiation sources is of order 10^{10} photons per second per meV bandwidth.

Here we propose a way to increase such spectral flux up to about three orders of magnitude at the SASE2 beamline of the European XFEL. This will enable NRS experiments with very high, sub-meV resolution, and can be achieved by exploiting a combination of three different factors and techniques: first, the high-repetition rate of the European XFEL [18]; second, the HXRSS setup [19]- [37] that will be installed at SASE2 [38]; third, Coherent Harmonic Generation (CHG) [39]- [57]; and finally, fourth, post-saturation tapering [58]- [70].

X-Ray Free Electron Lasers (XFELs) are capable of producing X-ray pulses with unprecedented power spectral density. However, the average spectral flux strongly depends on the maximal repetition rate that can be achieved by the linac driver of each XFEL setup. In particular, the European XFEL [18] will be driven by a superconducting accelerator, which enables up to 27000 pulses per second, more than two orders of magnitude higher than what can be achieved with a normal-conducting linac. A straightforward analysis (see section) for the case of the SASE2 beamline of the European XFEL at 14.4 keV shows that one can obtain up to about 10^{11}ph/s/meV for the SASE case at saturation. This number is already one order of magnitude better than what can be achieved at synchrotrons that can provide about 10^{10} ph/s/meV around 14.4 keV. However, the average spectral flux can be further increased of other two orders of magnitude by combining together HXRSS, CHG, and post-saturation tapering techniques.

ISBN 978-3-95450-134-2

HXRSS enables active spectral filtering by FEL amplification of a monochromatized SASE signal produced in the first part of an XFEL setup. Recently, a monochromatization scheme based on a single diamond crystal [32] was successfully realized at the LCLS [36] and at SACLA [37].

The simplest realization of a HXRSS setup based on a single crystal monochromator is composed by three parts. In the first part, a SASE pulse is produced in the linear regime, as in conventional XFELs. In the second part the electron beam is sent through a bypass composed of a short (few-m long) magnetic chicane, which washes out the electron beam microbunching, enables a tunable delay with respect to the photon beam, and allows for the introduction of a monochromator on the radiation path. The monochromator itself is composed by a single, thin diamond crystal (in our case 100 μm thin) in transmission geometry. The crystal works as a filter, imposing a narrow dip in the XFEL SASE spectrum around the Bragg energy. In the time domain, such dip corresponds to a 'wake' of monochromatic radiation following the main XFEL pulse, which is transmitted unperturbed. When the relative delay between electrons and X-ray pulse is properly chosen, this wake can be used to seed the electron bunch and gets amplified up to saturation in the third part of the setup, composed by an output undulator. This procedure typically allows for a reduction in bandwidth down to almost the Fourier limit, and thus corresponds to a manyfold increase in the spectral density of the original X-ray pulse.

When dealing with high-repetition rate XFELs, special care must be taken to avoid excessive heat-load of the diamond crystal. One way to increase the ratio between the seeded signal and the SASE noise is to perform the monochromatization process twice. At the position of the second crystal the signal is already almost Fourier-limited and monochromatization allows an increase of the seed signal, compared to the SASE background, of a factor roughly equal to the ratio between the SASE bandwidth and the seeded bandwidth, typically an order of magnitude. This increase in the signal-to-noise ratio can be used to diminish the length of the XFEL preceding the HXRSS setups, thus reducing the heat-load on the crystals [27]. This scheme, see Fig. 1 will be realized at the SASE2 line of the European XFEL [38].

The HXRSS setup can be tuned in energy by changing the pitch angle of the diamond crystal. The exploitation of several (symmetric and asymmetric) reflections allow in principle to cover all the XFEL spectrum starting from about 3 keV. However, while increasing the energy (here we consider the remarkable energy point at 14.4 keV) one faces the problem that the HXRSS efficiency decreases, due to a combination of several reasons. Suppose that one works with a given crystal and with fixed reflection, for example C(004), increasing the photon energy. This leads to a smaller and smaller Bragg angle. However, due to the presence of a spatio-temporal coupling phenomenon [34, 35], the field transmitted by the crystal behaves as $E[t, x - ct\cot(\theta_B)]$. Therefore, when θ_B decreases, the superposition between electron beam and photon beam becomes worse and worse, leading to a decrease in efficiency. One may try to solve the issue by using other reflections, for C(444), where the Bragg's angle is very near to $\pi/2$ radians around the target energy of 14.4 keV. However, as the Miller indexes increase the Darwin width narrows. As a result, the maximum of the impulse response of the filter decreases and therefore the seeded pulse become smaller, thus decreasing the overall efficiency. Furthermore, as the energy increases, the equivalent SASE shot-noise increases, as does the gain length. These factors concur to a decrease in the final spectral density of self-seeded pulses at high energies, which we observed in simulations.Here we propose a scheme to overcome this problem, without changes to the HXRSS hardware.

The undulator system of the European XFEL is long enough to allow one to use CHG techniques to overcome this problem without changing the HXRSS hardware, e.g. without the need for a crystal optimized for high-energy applications. Near saturation, the bunching at harmonics of the fundamental begins to increase, the bunching being driven by the interaction of the first harmonic and the magnetic field of the undulator with the electron beam. This mechanism is well-known goes under the name of Coherent Harmonic Generation (CHG) and was extensively studied both theoretically and experimentally [39]- [57]. To see how we can take advantage of CHG, let us consider the Fe^{57} nuclear resonance at 14.4 keV as target energy. With reference to Fig. 1 one seeds at 7.2 keV, using the C(004) symmetric reflection, where HXRSS is quite efficient. Following the two HXRSS setups one lets the X-ray beam at 7.2 keV to be amplified in the first part of the third undulator. In order to exploit the CHG mechanism we now tune the fundamental of the second part of the radiator at the second harmonic, which is the target energy 14.4 keV. Simulation shows that the second harmonic content in the electron beam bunching is large enough to reach saturation in a few segments. The rest can be used to increase the output power of about an order of magnitude. This tenfold increase, together with a likewise narrowing of the spectral bandwidth yields an advantage of two orders of magnitude in the spectral density of the output radiation compared to SASE.

In particular, our simulations shows that one can indeed reach about $4 \cdot 10^{13}$ ph/s/meV in the case of seeded-tapered pulses at the SASE2 line of the European XFEL at 14.4 keV. These simulations studies are reported in a detailed way in the next section , while in section we come to conclusions.

FEL STUDIES

The source discussed in the previous section, Fig. 1 was studied using the code Genesis [71]. We ran a statistical analysis consisting of 100 runs. Start-to-end simulations [72] were used as input information for GENESIS, and define the electron beam quality. The main parameters summarizing the mode of operation of the European XFEL discussed here can be found in Table 1.

ISBN 978-3-95450-134-2

Table 1: Main Parameters for the Mode of Operation of SASE2 (considered here)

	Units	
Undulator period	mm	40
Periods per cell	-	125
Total number of cells	-	35
Intersection length	m	1.1
Energy	GeV	17.5
Charge	pC	100

The first five undulator segments produce SASE radiation at 7.2 keV, one half of the target energy. When considering application of HXRSS methods to the European XFEL, one always needs to account the high-repetition rate of the setup, which poses strict limits on the energy per pulse incident onto the crystal. In our case, this amounts to an average of about 0.75 μJ per pulse, which is below the limiting heat load level even for the full-repetition rate of the European XFEL case. Following the first crystal, the X-ray seed pulse proceeds through the second undulator in Fig. 1, where it is amplified by the interaction with the electron beam.

Due to the competition with the SASE process there is a relatively large spectral background at the entrance of the second crystal. Moreover, the power level in the second pulse is lower than that on the first, and the average energy per pulse incident on the second crystal is about 0.44 μJ. However, at the seed frequency the spectral density is much higher (about one order of magnitude) than that at the first crystal. As a result, also the seed level after the second crystal, Fig. 2 (left) is about an order of magnitude larger than that after the first crystal. This is the advantage of the two-chicane scheme, which betters the signal-to-noise ratio (signal being the seeded FEL, noise being the SASE FEL pulse) of a factor roughly equal to the ratio between the SASE FEL bandwidth and the seeded FEL bandwidth, roughly equal to an order of magnitude.

After the second crystal, the seed signal is amplified into the first four segments of the final in Fig. 1. At this point, the electron beam is significantly bunched at the second harmonic of the fundamental, around 14.4 keV, and the microbunching is well correlated along the longitudinal direction, because it is driven by the fundamental. Hence the idea, first considered but not fully exploited in [73] to tune the final part of the radiator at 14.4 keV in order to exploit such bunching.

The last 17 cells are tapered segment by segment as illustrated in Fig. 3. The optimal tapering was found on an empirical basis, in order to optimize the final spectral density of the output signal.

In Fig. 4 we plot the energy and variance of energy fluctuations of the seeded FEL pulse as the latter develops along the undulator. Note the high maximum variance in Fig. 4 (right), which can be ascribed to the statistical properties of the second harmonic. From Fig. 4 (left) it can be seen that we are able to produce pulses up to a few mJ energy.

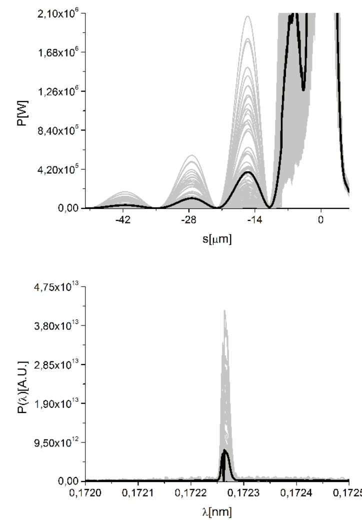

Figure 2: Power distribution and spectrum after the second HXRSS monochromator. Grey lines refer to single shot realizations, the black line refers to the average over a hundred realizations.

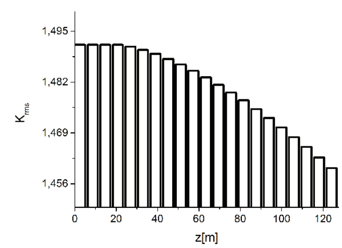

Figure 3: Taper configuration for the output undulator (21 segments).

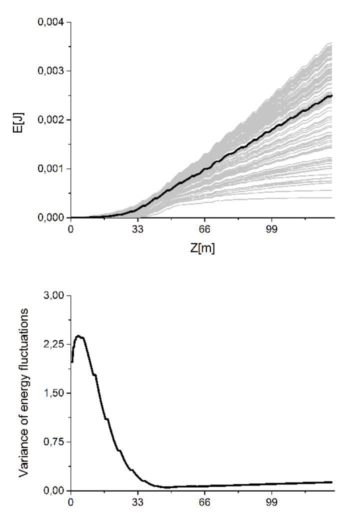

Figure 4: Energy and variance of energy fluctuations of the seeded FEL pulse as a function of the distance inside the output undulator. Grey lines refer to single shot realizations, the black line refers to the average over a hundred realizations.

ISBN 978-3-95450-134-2

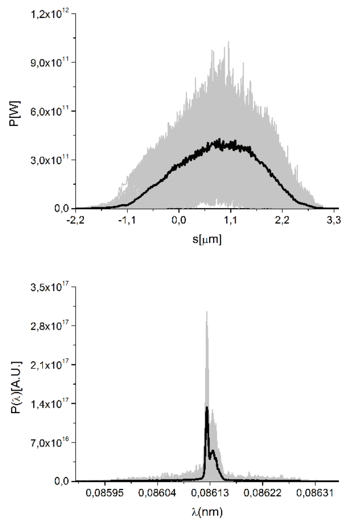

Figure 5: Power distribution and spectrum at the exit of the setup. Grey lines refer to single shot realizations, the black line refers to the average over a hundred realizations.

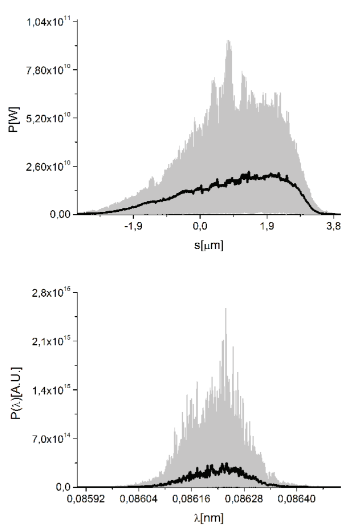

Figure 6: Power and spectrum in the conventional SASE mode of operation at saturation, to be compared with Fig. 5. Grey lines refer to single shot realizations, the black line refers to the average over a hundred realizations.

In Fig. 5 one can see the final output of our setup in terms of power and spectrum.

A comparison with the output power and spectrum for the conventional SASE mode at saturation can be made by inspecting Fig. 6. The average peak power for the SASE pulse at saturation, Fig. 6, is about $2 \cdot 10^{10}$ W with an average energy per pulse of about 0.25 mJ. In the seeded case, Fig. 5, it reaches about $4 \cdot 10^{11}$ W with an average energy per pulse of about 3 mJ.

This corresponds to an increase in flux from about 10^{11} photons per pulse to about $1.3 \cdot 10^{12}$ photons per pulse. Such increase, of about one order of magnitude, is due to tapering.

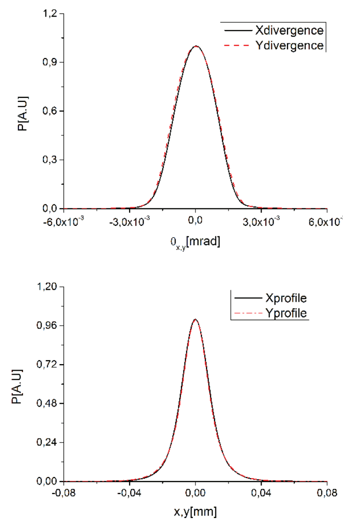

Figure 7: Divergence and profile of the seeded FEL pulse at the exit of the output undulator.

Moreover, the final SASE spectrum relative bandwidth is $\Delta\lambda/\lambda \sim 1.4 \cdot 10^{-3}$ corresponding to about 20 eV while, due to the enhancement of longitudinal coherence, the seeded spectrum has a FWHM relative bandwidth $\Delta\lambda/\lambda \sim 7 \cdot 10^{-5}$, corresponding to about 1 eV. This translates to an increase in spectral density of about a factor 20.

Summing up, we obtain a bit more than one order of magnitude increase in peak power due to tapering, and more than an order of magnitude decrease in spectral width due to seeding. Combining the two effects, we obtain more than two orders of magnitude increase in spectral flux density from the SASE to the seeded-tapered case. Accounting for the high repetition rate of the European XFEL (27000 pulses per second), this correspond to about 10^{11} ph/s/meV for SASE case at saturation, compared to about $4 \cdot 10^{13}$ ph/s/meV in the case of the seeded-tapered case. Finally it should be noted that the background radiation flux at 7.2 keV, mainly due to the first five segments of the radiator, see Fig. 1, is limited to about two orders of magnitude less than the main output signal.

To close this section, in Fig. 7, we show size and divergence at the exit of the undulator, which are important in dealing with the beam transport through the X-ray beamline up to the experiment. The beam shape is about round with a FWHM size of about 20 μm, and a FWHM divergence of about 2 μrad. A more detailed description of this study can be found in [1].

CONCLUSIONS

In this paper we investigated the potential of the European XFEL for experiments requiring high-average spectral flux and high photon energies like Nuclear Resonance Scattering (NRS) applications at 14.4 keV. In particular, we showed how a combination of Hard X-ray Self-Seeding (HXRSS), Coherent Harmonic Generation (CHG) and post-saturation

ISBN 978-3-95450-134-2

tapering techniques, coupled with the high-repetition rate of the European XFEL can be advantageously used. HXRSS and tapering provide a combined increase in spectral flux of about two orders of magnitude, one to be ascribed to the bandwidth narrowing resulting from self-seeding, one due to tapering. CHG allows to overcome the decrease of HXRSS efficiency at high photon energy by exploiting the high-harmonic bunching in a HXRSS setup tuned at a sub-harmonic of the target energy, the second in our case, without the introduction of any hardware change in the HXRSS setup. According to our start-to-end simulations this method should allow for a maximum flux of order 10^{13} photons per second in a meV bandwidth around 14.4 keV, with a background at 7.2 keV less than two orders of magnitude smaller. We underline that 10^{13} photons per second in a meV bandwidth at 14.4 keV is more than two orders of magnitude larger than what would be achievable at the European XFEL in the nominal SASE mode at saturation, and three orders of magnitude larger than what is presently available at synchrotron radiation sources. We are thus confident that this method may constitute the key for NRS experiments with ultra-high resolution of the order of 0.1 meV.

REFERENCES

[1] G. Geloni, V. Kocharyan and E. Saldin, "Scheme to increase the output average spectral flux of the European XFEL at 14.4 KeV", DESY 15-141 (2015).

[2] E. Burkel, B. Dorner, and J. Peisl. "Observation of inelastic x-ray scattering from phonons". Europhys. Lett., 3:957–61, (1987).

[3] E. Burkel. "Inelastic Scattering of X rays with Very High Energy Resolution", volume 125 of *Springer Tracts in Modern Physics*. Springer, Berlin, (1991).

[4] F. Sette, M. H. Krisch, C. Masciovecchio, G. Ruocco, and G. Monaco. "Dynamics of glasses and glass-forming liquids studied by inelastic x-ray scattering". Science, 280:1550–1555, (1998).

[5] E. Burkel. "Phonon spectroscopy by inelastic x-ray scattering". Rep. Prog. Phys., 63:171–232, (2000).

[6] Michael Krisch and Francesco Sette. "Light Scattering in Solids IX", volume 108 of Topics in Applied Physics, chapter Inelastic X-Ray Scattering from Phonons, pages 317–370. Springer, Berlin, (2007).

[7] Giulio Monaco. "The high-frequency atomic dynamics of disordered systems studied by high-resolution inelastic x-ray scattering". In Settimio Mobilio, Federico Boscherini, and Carlo Meneghini, editors, Synchrotron Radiation, pages 461–482. Springer Berlin Heidelberg, (2015).

[8] Alfred Q.R. Baron. "Introduction to high-resolution inelastic x-ray scattering", arXiv:1504.01098, (2015).

[9] S.L. Ruby and J. de Physique 35, C6-209-C6-211, (1974).

[10] E. Gerdau et al., Phys.Rev. Lett. 54, 835, (1985).

[11] J.B. Hastings et al., Phys. Rev. Lett. 66, 770, (1991).

[12] R. Roehlsberger, "Nuclear Condensed Matter Physics with Synchrotron Radiation:Basic Principles, Methodology and Applications", Springer Tracts in ModernPhysics, vol. 208, Springer, Berlin, (2005).

[13] E. Gerdau, H. de Waard (Eds.), Hyperfine Interact. 123/124, (1999).

[14] O. Chubar et al., "Novel opportunities for sub-meV inelastic X-ray scattering experiments at the European XFEL", MOP086, this conference, (2015).

[15] Yuri Shvyd'ko, Stanislav Stoupin, Kiran Mundboth, and Jungho Kim. "Hard-x-ray spectrographs with resolution beyond 100 μeV". *Phys. Rev. A*, 87:043835, (Apr 2013).

[16] S. Stoupin, Yu. V. Shvyd'ko, D. Shu, V. D. Blank, S. A. Terentyev, S. N. Polyakov, M. S. Kuznetsov, I. Lemesh, K. Mundboth, S. P. Collins, J. P. Sutter, and M. Tolkiehn. "Hybrid diamond-silicon angular-dispersive x-ray monochromator with 0.25-mev energy bandwidth and high spectral efficiency". *Opt. Express*, 21(25):30932–30946, (Dec 2013).

[17] Yu. Shvyd'ko. "Theory of angular dispersive imaging hard x-ray spectrographs". *arXiv:1501.05052*, (2015).

[18] M. Altarelli, et al. (Eds.) XFEL, "The European X-ray Free-Electron Laser", Technical Design Report, DESY 2006-097, Hamburg (2006).

[19] J. Feldhaus et al., Optics. Comm. 140, 341, (1997).

[20] E. Saldin, E. Schneidmiller, Yu. Shvyd'ko and M. Yurkov, NIM A 475 357, (2001).

[21] E. Saldin, E. Schneidmiller and M. Yurkov, NIM A 445 178, (2000).

[22] R. Treusch, W. Brefeld, J. Feldhaus and U Hahn, Ann. report 2001 "The seeding project for the FEL in TTF phase II", (2001).

[23] A. Marinelli et al., "Comparison of HGHG and Self Seeded Scheme for the Production of Narrow Bandwidth FEL Radiation", Proceedings of FEL 2008, MOPPH009, Gyeongju, (2008).

[24] G. Geloni, V. Kocharyan and E. Saldin, "Scheme for generation of highly monochromatic X-rays from a baseline XFEL undulator", DESY 10-033, (2010).

[25] Y. Ding, Z. Huang and R. Ruth, Phys.Rev.ST Accel.Beams, vol. 13, p. 060703, (2010).

[26] G. Geloni, V. Kocharyan and E. Saldin, "A simple method for controlling the line width of SASE X-ray FELs", DESY 10-053 (2010).

[27] G. Geloni, V. Kocharyan and E. Saldin, "A Cascade self-seeding scheme with wake monochromator for narrow-bandwidth X-ray FELs", DESY 10-080, (2010).

[28] Geloni, G., Kocharyan, V., and Saldin, E., "Cost-effective way to enhance the capabilities of the LCLS baseline", DESY 10-133, (2010).

[29] J. Wu et al., "Staged self-seeding scheme for narrow bandwidth , ultra-short X-ray harmonic generation free electron laser at LCLS", proceedings of 2010 FEL conference, Malmo, Sweden, (2010).

[30] Geloni, G., Kocharyan V., and Saldin, E., "Generation of doublet spectral lines at self-seeded X-ray FELs", DESY 10-199 (2010), and Optics Communications, 284, 13, 3348, (2011).

[31] Geloni, G., Kocharyan, V., and Saldin, E., "Production of transform-limited X-ray pulses through self-seeding at the European X-ray FEL", DESY 11-165, (2011).

ISBN 978-3-95450-134-2

[32] Geloni, G., Kocharyan V., and Saldin, E., "A novel Self-seeding scheme for hard X-ray FELs", Journal of Modern Optics, vol. 58, issue 16, pp. 1391-1403, DOI:10.1080/09500340.2011.586473, (2011).

[33] J. Wu et al., "Simulation of the Hard X-ray Self-seeding FEL at LCLS", MOPB09, FEL 2011 Conference proceedings, Shanghai, China, (2011).

[34] Y. Shvyd'ko and R. Lindberg, Phys. Rev. ST Accel. Beams 15, 100702, (2012).

[35] G. Geloni et al., "Wake monochromator in asymmetric and symmetric Bragg and Laue geometry for self-seeding the European XFEL", DESY 13-013, (2013).

[36] J. Amann et al., Nature Photonics, DOI: 10.1038/NPHOTON.2012.180, (2012).

[37] T. Inagaki et al., "Hard X-Ray Self-Seeding setup and results at SACLA", Proceedings of the 2014 FEL Conference, Basel, Switzerland, TUC01, (2014).

[38] XFELSEED, "Design and construction of Hard X-ray Self-Seeding Setups for the European XFEL", Project approved in the framework of the coordinated German-Russian call for proposals "Ioffe-Roentgen Institute", (2014).

[39] M. Schmitt and C. Elliot, Phys. Rev. A 34, (1986).

[40] R. Bonifacio, L. De Salvo, and P. Pierini, Nucl. Instrum. and Methods A 293, 627, (1990).

[41] W.M. Fawley et al., "Large harmonic bunching in a high-gain free-electron laser", Proc. IEEE Part. Acc. Conf., 219, (1995).

[42] H. Freund, S. Biedron and S. Milton, Nucl. Instrum. and Methods A 445, (2000).

[43] Z. Huang and K.-Je Kim, Phys. Rev. E, 62, 7295, (2000).

[44] H. Freund, S. Biedron and S. Milton, IEEE J. Quant. Electr. 36, 275, (2000).

[45] Z. Huang and K. Kim, Nucl. Instrum. and Methods A 475, 112, (2001).

[46] S. Biedron et al., Nucl. Instrum. and Methods A 483, 94, (2002).

[47] S. Biedron et al., Phys. Rev. ST 5 030701, (2002).

[48] A. Tremaine et al., Phys. Rev. Lett. 88 204801, (2002).

[49] W. Brefeld et al., Nucl. Instrum. and Methods A 507, 431, (2003).

[50] H.P. Freund, P.G. O'Shea and S.G. Biedron, Nucl. Instrum. Methods Phys. Res. A 528, 44, (2004).

[51] E.L. Saldin, E.A. Schneidmiller and M.V. Yurkov, Phys. Rev. ST 9 030702, (2006).

[52] G. Geloni, E. Saldin, E. Schneidmiller and M. Yurkov, Opt. Comm., 271, 1, 207, (2007).

[53] G. Geloni, E. Saldin, E. Schneidmiller, and M.Yurkov, Nucl. Instrum. Methods Phys. Res., Sect. A 581, 856, (2007).

[54] E. Allaria et al., Phys. Rev. Lett. 100, 174801, (2008).

[55] R.Treusch and J. Feldhaus, NewJ. Phys. 12, 035015, (2010).

[56] E. Allaria et al., Opt. Express 19, 10619, (2011).

[57] C. Spezzani et al., PRL 107, 084801, (2011).

[58] A. Lin and J.M. Dawson, Phys. Rev. Lett. 42 2172, (1986).

[59] P. Sprangle, C.M. Tang and W.M. Manheimer, Phys. Rev. Lett. 43 1932, (1979).

[60] N.M. Kroll, P. Morton and M.N. Rosenbluth, IEEE J. Quantum Electron., QE-17, 1436, (1981).

[61] T.J. Orzechovski et al., Phys. Rev. Lett. 57, 2172, (1986).

[62] W. Fawley et al., NIM A 483 p 537, (2002).

[63] M. Cornacchia et al., J. Synchrotron rad. 11, 227-238, (2004).

[64] X. Wang et al., Phys. Rev. Letters 103, 154801, (2009).

[65] G. Geloni, V. Kocharyan and E. Saldin, "Scheme for generation of fully coherent, TW power level hard x-ray pulses from baseline undulators at the European XFEL", DESY 10-108, fulltext available at `http://arxiv.org/`, (2010).

[66] J. Wu et al., "Staged self-seeding scheme for narrow bandwidth, ultra-short X-ray harmonic generation free electron laser at LCLS", Proceedings of the 2010 FEL conference, Malmo, Sweden, TUPB08, (2010).

[67] G. Geloni, V. Kocharyan, and E. Saldin, "Production of transform-limited X-ray pulses through self-seeding at the European X-ray FEL", DESY 11-165, fulltext available at `http://arxiv.org/`, (2011).

[68] W.M. Fawley et al., "Toward TW-level LCLS radiation pulses", Proceedings of the FEL 2011 Conference, Shanghai, China, TUOA4, (2011).

[69] J. Wu et al., "Simulation of the Hard X-ray Self-seeding FEL at LCLS", Proceedings of the 2011 FEL Conference, Shanghai, China, MOPB09, (2011).

[70] Y. Jiao et al. Phys. Rev. ST Accel. Beams 15, 050704, (2012).

[71] S. Reiche et al., Nucl. Instr. and Meth. A 429, 243, (1999).

[72] I. Zagorodnov, "Beam Dynamics Simulations for XFEL", `http://www.desy.de/fel-beam/s2e/` (2012).

[73] G. Geloni, V. Kocharyan, and E. Saldin, "Extension of self-seeding to hard X-rays > 10 keV as a way to increase user access at the European XFEL", DESY 11-224, (2011).

ISBN 978-3-95450-134-2

NOVEL OPPORTUNITIES FOR SUB-meV INELASTIC X-RAY SCATTERING AT HIGH-REPETITION RATE SELF-SEEDED X-RAY FREE-ELECTRON LASERS

Oleg Chubar, Brookhaven National Laboratory, New York, USA
Gianluca Geloni, Anders Madsen, European XFEL GmbH, Hamburg, Germany
Vitali Kocharyan, Evgeni Saldin, Svitozar Serkez, DESY, Hamburg, Germany
Yuri Shvyd'ko, Advanced Photon Source, Argonne National Laboratory, Argonne, IL 60439, USA
John Sutter, Diamond Light Source Ltd, Didcot, Oxfordshire, OX11 0DE, UK

Abstract

Inelastic x-ray scattering (IXS) is an important tool for studies of equilibrium dynamics in condensed matter. A new spectrometer recently proposed for ultra-high-resolution IXS (UHRIX) has achieved 0.6 meV and 0.25 nm^{-1} spectral and momentum transfer resolutions, respectively [1]. However, further improvements down to 0.1 meV and 0.02 nm^{-1} are required to close the gap in energy-momentum space between high and low frequency probes. We show that this goal can be achieved by further improvements in x-ray optics and by increasing the spectral flux of the incident x-ray pulses. UHRIX performs best at energies from 5 to 10 keV, where a combination of self-seeding and undulator tapering at the SASE2 beamline of the European XFEL promises up to a hundred-fold increase in average spectral flux compared to nominal SASE pulses at saturation, or three orders of magnitude more than possible with storage-ring based radiation sources. Wave-optics propagation shows that about 7×10^{12} ph/s in a 90-μeV bandwidth can be achieved on the sample. This will provide unique new possibilities for IXS. Extended information about our work can be found in [2].

INTRODUCTION

Momentum resolved inelastic x-ray scattering (IXS) is a technique introduced [3, 4] and widely used [5–9] at synchrotron radiation facilities for studies of atomic-scale dynamics in condensed matter. A photon with energy E_{i} and momentum $\boldsymbol{K}_{\text{i}}$ changes its energy and momentum to E_{f} and $\boldsymbol{K}_{\text{f}}$ in a inelastic scattering process in the sample and leaves behind a collective excitation with energy $\varepsilon = E_{\text{i}} - E_{\text{f}}$ and momentum $\boldsymbol{Q} = \boldsymbol{K}_{\text{i}} - \boldsymbol{K}_{\text{f}}$, respectively. IXS provides access to dynamics on a length scale $\lambda = 2\pi/Q$ and a time scale $t = 2\pi\hbar/\varepsilon$ simultaneously. Presently, together with IXS there are a few inelastic scattering techniques allowing probes of a limited region in the time-length scale: in fact, a gap remains in experimental capabilities between the low-frequency (visible and ultraviolet light) and the high-frequency (x-rays and neutrons) inelastic scattering techniques. Because of this, dynamics in the range from about 1-100 picosecond (ps) on atomic- and meso-scales is still inaccessible. However, this region is of vital importance for disordered systems and, therefore, to the study of many outstanding problems in condensed matter dynamics, such as the nature of the liquid to glass transition.

IXS could in principle penetrate this unexplored dynamic range of excitations[1], but this would require solving two long-standing challenges. First, IXS spectrometers in their traditional implementation have not improved the best numbers in energy ($\simeq$ 1.5 meV) and momentum transfer ($\simeq$ 1.5 nm^{-1}) resolutions for the past 20 years [10, 11]. Second, the IXS signal is very weak. Hence, more efficient IXS spectrometers with better resolution and more powerful x-ray sources are required to advance the field. Recently, a new type of dispersive spectrometer was tested for the first time. This ultra-high-resolution IXS (UHRIX) spectrometer [1] achieved a spectral resolution of 0.6 meV at a momentum transfer down to 0.25 nm^{-1}. Additionally, the spectral contrast improved by an order of magnitude compared to the traditional IXS spectrometers [3, 10–14]. To sharpen the desired resolution to 0.1 meV and 0.02-nm^{-1} and to ensure higher countrates, we propose to further develop the angular dispersive x-ray optical scheme [15, 16] and to replace scanning IXS spectrometers with broadband imaging spectrographs [17][2].

Complementarily, high-repetition rate seeded x-ray free-electron lasers (XFELs) hold the promise to overcome the problem of weak IXS signals. Low-gain x-ray free-electron laser oscillators (XFELOs) may in time produce a spectral flux of up to 10^{14} – 10^{15} photons/s/meV [19, 20], but currently they are still under development [21]. High-gain XFELs under operation are limited, in average flux, by their low repetition rate [22, 23]. In contrast, at the European XFEL [24], owing to superconducting accelerator technology, Self-Amplified Spontaneous Emission (SASE) will allow for the production of average output fluxes of about 10^{12} photons/s/meV at 9 keV (the optimum working energy of the UHRIX setup), which is already more than one order of magnitude greater than at synchrotron radiation facilities [9]. The spectral flux can be further substantially increased by self-seeding [25, 26], which will be first be available, at the European XFEL, at the SASE2 beamline [27]. Another order of magnitude increase in flux can be gained by tapering the magnetic field of the seeded undulator [28–35].

[1] INS cannot enter this region because of the kinematic limitation. The low-frequency probes cannot enter this region because their photon wavelengths are too long.

[2] A Fourier-transform IXS technique has been demonstrated recently [18], which could be considered as a powerful complementary approach for studies of *non-equilibrium* excitation with ultra-high spectral resolution.

ISBN 978-3-95450-134-2

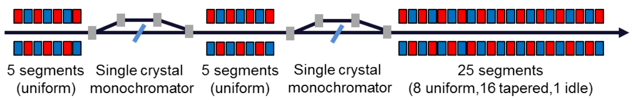

Figure 1: Layout of the baseline SASE2 undulator (35 segments).

In this work we propose to enable UHRIX in combination with an optimized configuration of the SASE2 x-ray source exploiting self-seeding and undulator tapering techniques in order to reach more than 10^{14} photons/s/meV, the same figure estimated in Ref. [36]. This may become a real game-changer for ultra-high-resolution x-ray spectroscopy, for IXS in particular, and for the studies of dynamics in disordered systems.

HIGH AVERAGE FLUX X-RAY SOURCE FOR ULTRA-HIGH-RESOLUTION IXS

The implementation of hard x-ray self-seeding (HXRSS) at European XFEL [27] will be based on a two cascade scheme in order to deal with the heat-load on the crystals at the high-repetition rate of the facility (up to 27000 X-ray pulses per second distributed in ten macropulses with up to 2700 pulses each). HXRSS will first be enabled at the SASE2 undulator line, which includes 35 segments, each consisting of 5 m long undulators, for a total of 175 m of magnetic length with an undulator period of 40 mm. We could then operate the SASE2 baseline in HXRSS mode followed by post-saturation tapering according to the scheme in Fig. 1, which optimizes the average output spectral flux around the optimum working point of the UHRIX setup, 9 keV. For seeding purposes we considered the (004) symmetric Bragg reflection from a 100 μm thick crystal. We performed numerical simulations of the high average-flux source in Fig. 1 using the code GENESIS [37]. Simulations are based on a statistical analysis consisting of 100 runs. Start-to-end simulations [38] yield the input information about the 250 pC, 17.5 GeV electron beam used for our study, which is fed into GENESIS.

The first five undulator segments work in the SASE mode, and yield the output power and spectrum in Fig. 2(a) and (b), respectively. The filtering process performed by the first crystal is illustrated in Fig. 2(c) and (d). The x-ray pulse then proceeds through the second undulator in Fig. 1, where it seeds the electron beam. Power and spectrum at the exit of the second undulator are shown in Fig. 2(e) and (f), respectively. This figure shows seed amplification in competition with the SASE process, given the relatively low seed power level from the first part of the setup. This is particularly evident in the time domain, where the reader can see the seeded pulse following about 20 μm after the SASE pulse. Note that the power levels in the two pulses are about the same. Moreover each of the pulses (seeded and SASE) carries about the same energy as the initial SASE pulse incident on the first crystal, for a total incident average energy per pulse of about

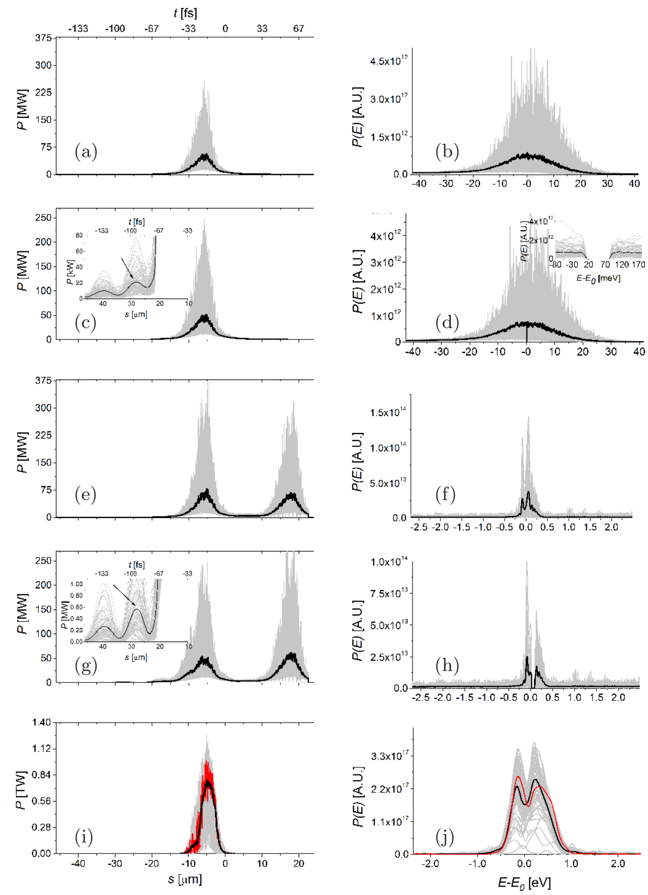

Figure 2: Power distribution and spectrum of the x-ray pulse along the undulator: (a) and (b) at the exit of the first undulator (5 segments); (c) and (d) after the first HXRSS monochromator; (e) and (f) at the exit of the second undulator (5 segments); (g) and (h) after the second HXRSS monochromator; (i) and (j) at the exit of the setup. Grey lines refer to single shot realizations, the black line refers to the average over a hundred realizations. The insets in (c) and (h) are an enlarged part of the main plot, showing the seed appearing after the filtering process. The black arrows indicate the position of the seed relative to the electron slice with maximum current. The red lines in graphs (i) and (j) refer to the particular FEL shot that is used for wavefront propagation simulations (see Section 'UHRIX OPTICS').

2.7 μJ, still within the heat-load limits. In the frequency domain, one notices a greatly increased peak power spectral density for the seeded signal [compare Fig. 2(d) and (f)] while the SASE pulse contributes a wide-bandwidth, noisy background. The fact that the power spectral density for the seed signal is larger than that for SASE by about an order of magnitude (roughly corresponding to the ratio of the SASE bandwidth to the seeded bandwidth) is what actually allows the x-ray beam to impinge on the second HXRSS crystal at relatively low power, but with a large signal (seeded) to noise (SASE) ratio, thus reducing heat loading effects by about one

ISBN 978-3-95450-134-2

order of magnitude compared to a single-chicane scheme. The filtering process performed by the second crystal is illustrated in Fig. 2(g) and (h), respectively. After this, the seed signal is amplified to saturation and beyond, exploiting a combination of HXRSS with post-saturation tapering.

Tapering is implemented by changing the K parameter of the undulator segment by segment. The tapering law used in this work [2] has been implemented on an empirical basis, in order to optimize the spectral density of the output signal. On the average, we expect to be able to produce pulses of about 11 mJ energy. The beam shape is nearly round with a FWHM size of about 50 μm, and a FWHM divergence of about 1.8 μrad. The final output of our setup is presented in Fig. 2(i) and (j), respectively, in terms of power and spectrum.

This result should be compared with the output power and spectrum for SASE at saturation, which corresponds to the *conventional* mode of operation foreseen for the European XFEL. Considering as before an average over 100 shots, the peak power for the SASE saturation case is about 4×10^{10} W, while for the seeded case in Fig. 2(i), it has increased to 7.5×10^{11} W. This corresponds to an increase in flux from about 7×10^{11} photons per pulse to about 7×10^{12} photons per pulse. This increase of about one order of magnitude is due to tapering. Moreover, the final SASE spectrum has a FWHM of about 11.6 eV, corresponding to a relative bandwidth of about 1.2×10^{-3} while, due to the enhancement of longitudinal coherence, the seeded spectrum has a FWHM of about 0.94 eV, corresponding to a relative bandwidth of about 1×10^{-4}.

Summing up, we obtain more than one order of magnitude increase in peak power due to tapering, and a bit less than an order of magnitude decrease in spectral width due to seeding. Combining the two effects, we obtain an increase of slightly over two orders of magnitude in spectral flux density from the SASE to the seeded-tapered case. This corresponds to about 2.1×10^{14} ph/s/meV for the seeded-tapered case, compared to about 1.5×10^{12} ph/s/meV in the case of SASE at saturation.

UHRIX OPTICS

Ultra-high-resolution IXS (UHRIX) studies with the 0.1-meV spectral and the 0.02-nm^{-1} momentum transfer resolution require a significant amount of x-ray photons with an energy $E_0 = 9.13185$ keV and a momentum $K = E_0/\hbar c = 46.27598$ nm^{-1} to be delivered onto the sample within a $\Delta E \lesssim 0.1$ meV spectral bandwidth, with a transverse momentum spread $\Delta K \lesssim 0.02$ nm^{-1}, and concentrated on the sample on a spot of $\Delta s \lesssim 5$ μm (FWHM) in diameter. The aforementioned fixed photon energy E_0 is required by the use of the (008) Bragg backreflection from a Si crystal, one of the central components of the ultra-high-resolution optics, presented in detail in [2].

We consider a scenario in which the UHRIX instrument is installed at a SASE2-undulator beamline of the European XFEL. In particular, we consider an option of integrating

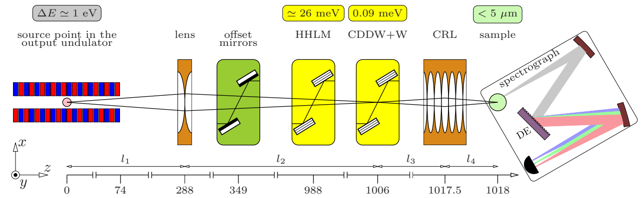

Figure 3: Main optical components of the proposed UHRIX instrument at the SASE2-undulator beamline of the European XFEL shown schematically together with the output undulator. Optical components are presented as pictographs at certain distances from the source position measured at the beam waist in the SASE2 undulator, which is at 74 m from undulator's downstream end. See text for descriptions.

UHRIX into the 'Materials Imaging and Dynamics' (MID) instrument [39], presently under construction at the European XFEL. A schematic view of optical components essential to deliver photons with the required properties on the sample for UHRIX studies is shown in Fig. 3. Optics are shown as pictographs at certain distances from the source. The source position is around 74 m inside the undulator. This number was determined by back-propagation in free space of the XFEL radiation from the undulator end.

The main optical components are as follows. A biconcave parabolic refractive lens [40], creates a secondary source on the 6-bounce angular dispersive ultra-high-resolution CDDW+W monochromator. This is essential in order to achieve a tight focal spot size on the sample because it eliminates the blurring that the strong angular dispersion of the CDDW+W monochromator would otherwise cause [17]. The CDDW+W monochromator then selects a 0.1 meV spectral bandwidth from the incident x-ray beam. CDDW+W is a modification of a CDW-type angular dispersive monochromator [16,41,42], which uses a three-step process of collimation (C), angular dispersion (D), and wavelength selection (W) [43]. Finally, a parabolic compound refractive lens CRL [40,44] focuses the monochromatic x-rays on the sample.

The x-ray spectrograph captures photons scattered from the source in a sufficiently large solid angle and images them in a spectral window a few meV wide with an 0.1-meV spectral resolution in the dispersion plane. The dispersing element (DE), a hard x-ray analog of optical diffraction gratings, is a key component of the spectrograph. The spectrograph is also capable of simultaneously imaging scattered intensity perpendicular to the dispersion plane in a range of 0.2-nm^{-1} with 0.01-nm^{-1} resolution.

Supplementary optical components include a pair of offset mirrors, which separate XFEL radiation from unwanted high-energy bremsstrahlung, and the two-bounce, two-crystal non-dispersive high-heat-load monochromator (HHLM). The HHLM narrows the 1-eV bandwidth of the incident x-rays to about 26 meV and thus reduces the heat-load onto the ultra-high-resolution CDDW+W monochromator by a fac-

ISBN 978-3-95450-134-2

tor of 36. The choice of optical elements of the UHRIX instrument and their design parameters were determined by dynamical theory calculations for monochromatization, and by geometrical optics for focusing.

Verification of the design parameters, determination of the efficiency of the system and calculation of the radiation characteristics were performed by wavefront propagation simulations from the XFEL source to the sample. GENESIS [37] calculates the original wavefront of the SASE radiation at the exit of the output undulator. SRW [45], calculates the wavefront after propagation from the undulator through each drift space and optical component in the beamline by using Fourier optics. Simulations of the diffracting crystals with SRW have just recently been made possible by the addition of a new module [46], which has already been applied to the design of the planned IXS beamline 10-ID at NSLS-II [47].

Results of the wavefront propagation simulations related to the sample area are presented graphically in Fig. 4. The spectral, time, spatial, and angular radiation pulse distributions and their parameters at the sample location (image plane at $z = 1018$ m in Fig. 3), are provided in captions to Fig. 4. The calculated radiation parameters at the sample location are in good agreement with design values obtained by the ray-transfer matrix approach and dynamical theory calculations. Thus, the wavefront propagation simulations confirm the soundness of the optical design of the UHRIX instrument worked out initially by the ray-transfer matrix approach and dynamical theory calculations. They also confirm the feasibility of the target specification.

The wavefront propagation simulations show that the spectral flux from the XFEL undulator can be transported to the sample through the UHRIX x-ray optics with a 30% efficiency and reach a remarkably high value of $\simeq 7 \times 10^{13}$ ph/s/meV. This number exceeds by more than three orders of magnitude the spectral flux numbers reported for the state of the art IXS instruments at synchrotron radiation facilities [9]. The specially designed crystal and focusing optics ensure that $\simeq 6.3 \times 10^{12}$ ph/s/meV photons on the sample can be concentrated in a spectral band of 0.09 meV, on the spot with a $3.3(\mathrm{V}) \times 6.5(\mathrm{H})\ \mu\mathrm{m}^2$ size, and with a momentum transfer spread of $\lesssim 0.015\ \mathrm{nm}^{-1}$.

DISCUSSION AND CONCLUSIONS

This article explores novel opportunities for ultra-high-resolution IXS (UHRIX) at high repetition rate XFELs unlocked by the recent demonstration of a conceptually new spectrometer [1] with unprecedented specifications (0.6 meV spectral resolution and 0.25 nm^{-1} momentum transfer), operating around 9 keV. Its exploitation, together with the broadband ultra-high-resolution imaging spectrograph proposed in [17] will make it possible to fill the energy-momentum gap between high and low frequency inelastic probes and to provide exciting new opportunities for studies of dynamics in condensed matter. In particular, UHRIX experiments can be enabled at the European XFEL, where an increase of more than three orders of magnitude in average spectral flux is expected compared to what is available today at synchrotrons. The gain is due to two main factors: firstly, the high repetition rate of the European XFEL, owing to the superconducting linac accelerator driver, which allows up to 27000 X-ray pulses per second, and secondly, the presence of long undulators, allowing the combined implementation of hard X-ray self-seeding (HXRSS) and post-saturation tapering techniques. In particular, a double-chicane HXRSS scheme increases the signal-to-noise ratio and eases the heat-load on the HXRSS crystals to a tolerable level. This scheme is expected to yield up to TW-level X-ray pulses. Simulations of pulse propagation up to the sample position through the UHRIX optics show that an unprecedented average spectral flux of 7×10^{13} ph/s/meV is feasible. The power delivered to the sample can be as high as 350 W/mm^2 and radiation damage can become a limitation but liquid jets and scanning setups for solid samples can be employed to circumvent eventual problems, see Ref. [39] and references therein.

ACKNOWLEDGMENTS

We are grateful to Massimo Altarelli for many useful discussions and support, and to Thomas Tschentscher, Serguei Molodtsov, Harald Sinn, Stephen Collins, Giulio Monaco, Alexei Sokolov, Kwang-Je Kim, Kawal Sawhney, Alexey Suvorov and Igor Zagorodnov for useful discussions and interest in this work. Work at the APS was supported by the U.S. Department of Energy, Office of Science, Office of Basic Energy Sciences, under Contract No. DE-AC02-06CH11357. The development of SRW code is supported in part by the US DOE Office of Science, Office of Basic Energy Sciences under SBIR awards DE-SC0006284 and DE-SC0011237.

REFERENCES

[1] Y. Shvyd'ko, S. Stoupin, D. Shu, S. P. Collins, K. Mundboth, J. Sutter, and M. Tolkiehn, Nature Communications **5:4219** (2014).

[2] O. Chubar et al., 'Novel opportunities for sub-meV inelastic X-ray scattering at high-repetition rate self-seeded X-ray free-electron lasers', http://arxiv.org/abs/1508.02632, DESY 15-140, (2015).

[3] E. Burkel, B. Dorner, and J. Peisl, Europhys. Lett. **3**, 957 (1987).

[4] E. Burkel, *Inelastic Scattering of X rays with Very High Energy Resolution*, vol. 125 of *Springer Tracts in Modern Physics* (Springer, Berlin, 1991).

[5] F. Sette, M. H. Krisch, C. Masciovecchio, G. Ruocco, and G. Monaco, Science **280**, 1550 (1998).

[6] E. Burkel, Rep. Prog. Phys. **63**, 171 (2000).

[7] M. Krisch and F. Sette, *Light Scattering in Solids IX* (Springer, Berlin, 2007), vol. 108 of *Topics in Applied Physics*, chap. Inelastic X-Ray Scattering from Phonons, pp. 317–370.

[8] G. Monaco, *Synchrotron Radiation* (Springer Berlin Heidelberg, 2015), chap. The High-Frequency Atomic Dynamics of Disordered Systems Studied by High-Resolution Inelastic X-Ray Scattering, pp. 461–482.

ISBN 978-3-95450-134-2

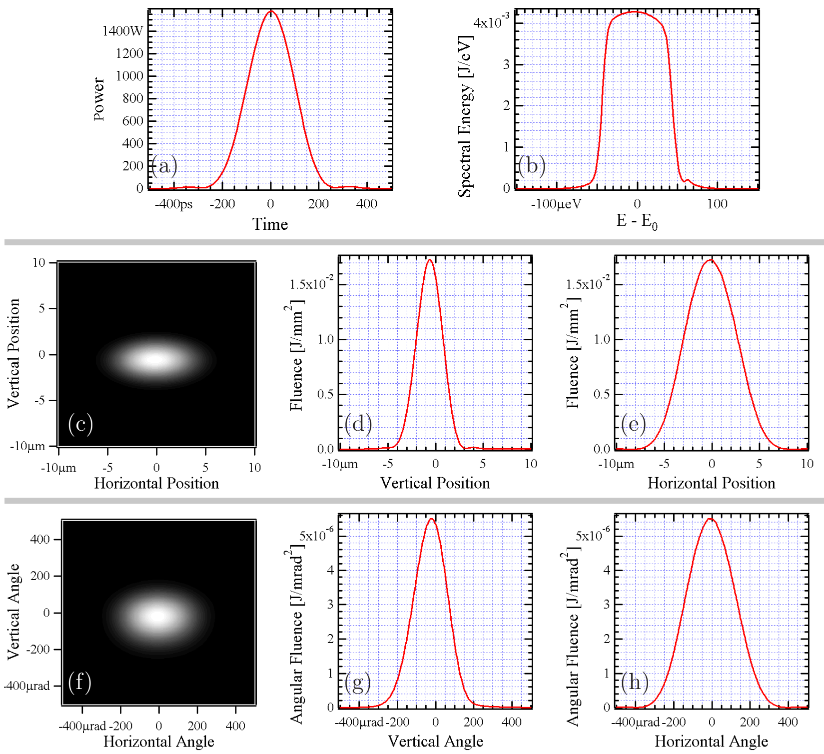

Figure 4: Time, spectral, spatial and angular distributions of the radiation pulse on the sample (z = 1018 m in Fig. 3). (a) Pulse power, pulse duration is $\simeq$ 225 ps (FWHM) (b) Spectrum, spectral bandwidth is $\simeq$ 0.090 meV (FWHM). (c) Spatial distribution, 2D plot; (d) vertical x-cut through the center of the fluence distribution; and (e) horizontal y-cut. Beam footprint size on the sample is 3.3 μm (V)×6.5 μm (H) (FWHM). (f) Angular distribution, 2D plot; (h) vertical cut through the center of the fluence distribution; and (g) horizontal cut. Beam divergence on the sample is 220 μrad (V)×310 μrad (H) (FWHM), corresponding to a 0.01 nm^{-1} $\times$ 0.015 nm^{-1} transverse momentum spread.

[9] A. Q. R. Baron, arXiv:1504.01098 (2015).

[10] C. Masciovecchio, U. Bergmann, M. Krisch, G. Ruocco, F. Sette, and R. Verbeni, Nucl. Instrum. Methods Phys. Res. B **117**, 339 (1996).

[11] A. H. Said, H. Sinn, and R. Divan, Journal of Synchrotron Radiation **18**, 492 (2011).

[12] F. Sette, G. Ruocco, M. Krisch, U. Bergmann, C. Masciovecchio, Mazzacurati, G. Signorelli, and R. Verbeni, Phys. Rev. Lett. **75**, 850 (1995).

[13] A. Q. R. Baron, Y. Tanaka, D. Miwa, D. Ishikawa, T. Mochizuki, K. Takeshita, S. Goto, T. Matsushita, H. Kimura, F. Yamamoto, et al., Nucl. Instrum. Methods Phys. Res. A **467-468**, 627 (2001).

[14] H. Sinn, E. Alp, A. Alatas, J. Barraza, G. Bortel, E. Burkel, D. Shu, W. Sturhahn, J. Sutter, T. Toellner, et al., Nucl. Instrum. Methods Phys. Res. A **467-468**, 1545 (2001).

[15] Y. Shvyd'ko, S. Stoupin, K. Mundboth, and J. Kim, Phys. Rev. A **87**, 043835 (2013).

[16] S. Stoupin, Y. V. Shvyd'ko, D. Shu, V. D. Blank, S. A. Terentyev, S. N. Polyakov, M. S. Kuznetsov, I. Lemesh, K. Mundboth, S. P. Collins, et al., Opt. Express **21**, 30932 (2013).

[17] Y. Shvyd'ko, Phys. Rev. A **91**, 053817 (2015).

[18] M. Trigo, M. Fuchs, J. Chen, M. P. Jiang, M. Cammarata, S. Fahy, D. M. Fritz, K. Gaffney, S. Ghimire, A. Higginbotham, et al., Nature Physics **9**, 790–794 (2013).

[19] K.-J. Kim, Y. Shvyd'ko, and S. Reiche, Phys. Rev. Lett. **100**, 244802 (2008).

[20] R. R. Lindberg, K.-J. Kim, Y. Shvyd'ko, and W. M. Fawley, Phys. Rev. ST Accel. Beams **14**, 010701 (2011).

[21] T. J. Maxwell, J. Arthur, Y. Ding, W. M. Fawley, J. Frisch, J. Hastings, Z. Huang, J. Krzywinski, G. Marcus, K.-J. Kim, et al., in *Proceedings of the 2015 International Particle Accelerator Conference* (SLAC Publication: SLAC-PUB-16286, 2015).

[22] P. Emma, R. Akre, J. Arthur, R. Bionta, C. Bostedt, J. Bozek, A. Brachmann, P. Bucksbaum, R. Coffee, F.-J. Decker, et al., Nature Photonics **4**, 641 (2010).

[23] T. Ishikawa, H. Aoyagi, T. Asaka, Y. Asano, N. Azumi, T. Bizen, H. Ego, K. Fukami, T. Fukui, Y. Furukawa, et al., Nature Photonics **6**, 540–544 (2012).

[24] M. Altarelli, R. Brinkmann, M. Chergui, W. Decking, B. Dobson, S. Dusterer, G. Grübel, W. Graeff, H. Graafsma, J. Hajdu, et al., *XFEL: The European X-Ray Free-Electron Laser : Technical design report* (DESY, Hamburg, 2006).

[25] G. Geloni, V. Kocharyan, and E. Saldin, Journal of Modern Optics **58**, 1391 (2011a).

ISBN 978-3-95450-134-2

[26] J. Amann, W. Berg, V. Blank, F.-J. Decker, Y. Ding, P. Emma, Y. Feng, J. Frisch, D. Fritz, J. Hastings, et al., Nature Photonics **6** (2012).

[27] *XFELSEED, 'Design and construction of Hard X-ray Self-Seeding Setups for the European XFEL'*, Project approved in the framework of the coordinated German-Russian call for proposals 'Ioffe-Röntgen Institute' (2014).

[28] P. Sprangle, C.-M. Tang, and W. M. Manheimer, Phys. Rev. Lett. **43**, 1932 (1979).

[29] N. Kroll, P. Morton, and M. Rosenbluth, IEEE J. Quantum Electronics **QE-17**, 1436 (1981).

[30] T. J. Orzechowski, B. R. Anderson, J. C. Clark, W. M. Fawley, A. C. Paul, D. Prosnitz, E. T. Scharlemann, S. M. Yarema, D. B. Hopkins, A. M. Sessler, et al., Phys. Rev. Lett. **57**, 2172 (1986).

[31] W. M. Fawley, Z. Huang, K.-J. Kim, and N. A. Vinokurov, Nucl. Instrum. Methods Phys. Res. A **483**, 537 (2002).

[32] X. J. Wang, H. P. Freund, D. Harder, W. H. Miner, J. B. Murphy, H. Qian, Y. Shen, and X. Yang, Phys. Rev. Lett. **103**, 154801 (2009).

[33] G. Geloni, V. Kocharyan, and E. Saldin, arXiv:1007.2743 (2010), DESY 10-108.

[34] W. Fawley, J. Frisch, Z. Huang, Y. Jiao, H.-D. Nuhn, C. Pellegrini, S. Reiche, and J. Wu, Tech. Rep., SLAC National Accelerator Laboratory, Menlo Park, CA 94025, USA (2011), SLAC-PUB-14616.

[35] Y. Jiao, J. Wu, Y. Cai, A. W. Chao, W. M. Fawley, J. Frisch, Z. Huang, H.-D. Nuhn, C. Pellegrini, and S. Reiche, Phys. Rev. ST Accel. Beams **15**, 050704 (2012).

[36] X. Yang and Y. Shvyd'ko, Phys. Rev. ST Accel. Beams **16**, 120701 (2013).

[37] S. Reiche, Nucl. Instrum. Methods Phys. Res. A **429**, 243 (1999).

[38] I. Zagorodnov (2012), http://www.desy.de/fel-beam/s2e/.

[39] A. Madsen, J. Hallmann, T. Roth, and G. Ansaldi, Technical Design Report, XFEL.EU TR-2013-005, European X-Ray Free-Electron Laser Facility GmbH, Hamburg, Germany (2013).

[40] B. Lengeler, C. Schroer, J. Tümmler, B. Benner, M. Richwin, A. Snigirev, I. Snigireva, and M. Drakopoulos, J. Synchrotron Radiation **6**, 1153 (1999).

[41] Y. V. Shvyd'ko, M. Lerche, U. Kuetgens, H. D. Rüter, A. Alatas, and J. Zhao, Phys. Rev. Lett. **97**, 235502 (2006).

[42] Y. Shvyd'ko, S. Stoupin, D. Shu, and R. Khachatryan, Phys. Rev. A **84**, 053823 (2011).

[43] Y. Shvyd'ko, *X-Ray Optics – High-Energy-Resolution Applications*, vol. 98 of *Optical Sciences* (Springer, Berlin Heidelberg New York, 2004).

[44] A. Snigirev, V. Kohn, I. Snigireva, and B. Lengeler, Nature **384**, 49 (1996).

[45] O. Chubar and P. Elleaume, EPAC-98 Proceedings pp. 1177–1179 (1998).

[46] J. P. Sutter, O. Chubar, and A. Suvorov, Proc. SPIE **9209**, 92090L (2014).

[47] A. Suvorov, Y. Q. Cai, J. P. Sutter, and O. Chubar, Proc. SPIE **9209**, 92090H (2014).

ISBN 978-3-95450-134-2

MULTISTAGE CSR MICROBUNCHING GAIN DEVELOPMENT IN TRANSPORT OR RECIRCULATION ARCS

C. -Y. Tsai#, Department of Physics, Virginia Tech, Blacksburg, VA 24061, USA
D. Douglas, R. Li, and C. Tennant, Jefferson Lab, Newport News, VA 23606, USA

Abstract

Coherent synchrotron radiation (CSR) induced microbunching instability has been one of the most challenging issues in the design of modern accelerators. A linear Vlasov solver has been developed [1] and applied to investigate the physical processes of microbunching gain amplification for several example lattices [2]. In this paper, by further extending the concept of stage gain as proposed by Huang and Kim [3], we develop a method to characterize the microbunching development in terms of stage orders that allow the quantitative comparison of optics impacts on microbunching gain for different lattices. We find that the microbunching instability in our demonstrated arcs has a distinguishing feature of multistage amplification (e.g, up to 6th stage amplification for our example transport arcs, in contrast to two-stage amplification for a typical 4-dipole bunch compressor chicane). We also try to connect lattice optics pattern with the obtained stage gain functions by a physical interpretation. This Vlasov analysis is validated by ELEGANT [4] tracking results with excellent agreement.

OVERVIEW OF CSR MICROBUNCHING INSTABILITY THEORY IN A SINGLE-PASS SYSTEM

Theoretical formulation of the CSR-induced microbunching instability in a single-pass system (e.g. a bunch compressor chicane) has been developed based on the linearized Vlasov equation [3, 5]. The formulation assumes initial modulation wavelength is small compared with the whole bunch duration (i.e. coasting-beam approximation) and treat the CSR effect as a small perturbation. By the method of characteristics, the equation that governs the evolution of the complex bunching factor can be written as [5]

$$b_k(s) = b_k^{(0)}(s) + \int_0^s K(s,s') b_k(s') ds' \tag{1}$$

where the bunching factor $b_k(s)$ is defined as the Fourier transform of the perturbed phase space distribution and the kernel function is particularly expressed as

$$K(s,s') = \frac{ik}{\gamma}\frac{I(s)}{I_A} C(s') R_{56}(s'\to s) Z\left(kC(s'),s'\right) \times [\text{Landau damping}] \tag{2}$$

for [Landau damping] term

$$[\text{Landau damping}] = \exp\left\{\frac{-k^2}{2}\left[\varepsilon_{x0}\left(\beta_{x0}R_{51}^2(s,s') + \frac{R_{52}^2(s,s')}{\beta_{x0}}\right) + \sigma_\delta^2 R_{56}^2(s,s')\right]\right\} \tag{3}$$

with

$$R_{56}(s'\to s) = R_{56}(s) - R_{56}(s') + R_{51}(s')R_{52}(s) - R_{51}(s)R_{52}(s') \tag{4}$$

and $R_{5i}(s,s') = C(s)R_{5i}(s) - C(s')R_{5i}(s')$.

Here the kernel function K(s,s') describes relevant collective effects, g_k(s) the resultant bunching factor as a function of the longitudinal position given a wavenumber k, and $g_k^{(0)}$(s) is the bunching factor in the absence of collective effect. $I(s)$ is the beam current at s and I_A is the Alfven current.

In this paper, we are interested in the bunching factor evolution subject to the CSR effect. For an ultrarelativistic electron beam traversing through a bending magnet, the CSR effect, described in terms of the impedance, can be expressed as [6, 7]

$$Z_{CSR}^{ss}\left(k(s);s\right) = \frac{-ik(s)^{1/3}A}{\left|\rho(s)\right|^{2/3}},\ A \approx -0.94 + 1.63i \tag{5}$$

where $k = 2\pi/\lambda$ is the modulation wave number, ρ is the bending radius.

Here we presumed the CSR interaction be in the steady state and only in the longitudinal direction with negligible shielding effect. So far we have obtained the governing equation for the bunching factor and given the 1-D steady-state ultrarelativistic CSR impedance. In the following two sections, we would introduce two methods to solve Eq. (1), i.e. the direct solution and iterative solution, and define the microbunching gain functions associated with the two kinds of solutions, respectively, for our subsequent analysis.

DIRECT SOLUTION

Here by "direct solution" we mean self-consistent solution of Eq. (1), as summarized below. First, we re-write Eq. (1) by expressing the bunching factors in vector forms and the kernel function in a matrix form, and we have after taking the inverse on both sides,

$$\mathbf{b}_k = \left(\mathbf{I} - \mathbf{K}\right)^{-1}\mathbf{b}_k^{(0)} \tag{6}$$

provided the inverse matrix of (**I-K**) exists.

To quantify the microbunching instability in a single-pass system, we define the microbunching gain as functions of the global longitudinal coordinate s as well as the initial modulation wavelength λ (or, $k = 2\pi/\lambda$)

$$G(s,k=2\pi/\lambda) \equiv \left|\frac{b_k(s)}{b_k^{(0)}(0)}\right| \tag{7}$$

Hereafter, we simply call G(s) the gain function as a function of s given a specific modulation wavenumber, and denote $G_f(\lambda)$ gain spectrum as a function of λ at a specific location (e.g. denoted with a subscript "*f*" at the exit of a beamline). Before ending this section, it deserves to mention the physical meaning of Eq. (1 or 6) and Eq. (7) with CSR effect [3]: a density perturbation at s' induced an energy modulation through CSR impedance

jcytsai@vt.edu

ISBN 978-3-95450-134-2

and is subsequently converted into a further density modulation at s via momentum compaction function R_{56}.

ITERATIVE SOLUTION

Another approach to solve Eq. (1) is resorted to iterative method, thus called iterative solution. Here we presume the zeroth order solution to be

$$\mathbf{b}_k^{(0)} = \mathbf{b}_k^{(0)} \tag{8}$$

and define the first order solution as

$$\mathbf{b}_k^{(1)} = \left(\mathbf{I}+\mathbf{K}\right)\mathbf{b}_k^{(0)} \tag{9}$$

Then, the second order solution can be defined accordingly

$$\mathbf{b}_k^{(2)} = \left(\mathbf{I}+\mathbf{K}+\mathbf{K}^2\right)\mathbf{b}_k^{(0)} \tag{10}$$

In general, we have the n-th order solution to be expressed as

$$\mathbf{b}_k^{(n)} = \left(\sum_{m=0}^{n}\mathbf{K}^m\right)\mathbf{b}_k^{(0)} \tag{11}$$

It can be shown that Eq. (6) and Eq. (11) are equivalent when $n \to \infty$, provided the sum converges. For a storage ring rather than a single-pass system, the convergence may not be held, which is however beyond the scope of this paper. We define the stage gain function with respect to Eq. (11) as follows

$$\tilde{G}^{(n)}(s,k=2\pi/\lambda) = \frac{\mathbf{b}_k^{(n)}(s)}{\mathbf{b}_k^{(0)}(0)}, \quad \text{and} \quad G^{(n)}(s,k) = \left|\tilde{G}^{(n)}(s,k)\right| \tag{12}$$

We have mentioned the physical meaning of Eqs. (1) or (6) subject to CSR effect in the previous section. Here we give another interpretation by Eq. (11): the overall CSR gain at a specific position, say, at the exit of a lattice, can be contributed by many “staged gains.” Let us take a 3-dipole bunch compressor chicane lattice as an example (see Fig. 1). The 0th-satge gain comes from pure optics effect [i.e. in the absence of collective effect, Eq. (8)]. The 1st-stage gain is contributed from initial density modulations (located at the beamline entrance, the first and/or second dipole entrance), converted to energy modulation via CSR interaction within the first and/or second dipole, then freely propagated by optics through R_{56}, to the last dipole via *one* interaction [second term on R.H.S. of Eq. (9)]. The 2nd-stage gain evolves from an initial density modulation (located at the beamline entrance or the first dipole), converted to energy modulation (via CSR within the first dipole) and then further density modulation (via R_{56}) till the second dipole, and such density modulation (which had experienced one-time CSR-R_{56} conversion earlier) eventually turns into farther energy modulation via CSR within the second dipole and downstream R_{56} till the last dipole, contributing to (part of) the resultant overall CSR gain [third term on R.H.S. of Eq. (10)]. To express in an alternative but more general way: the 1st-stage amplification refers to CSR interaction taking place inside only in *one* dipole (either 1st or 2nd dipole) where CSR impedance induces energy modulation as a result of density modulation. The microbunching structure in the beam evolves under optical propagation for the rest of the beamline. The 2nd-stage amplification refers to CSR interaction taking place inside *two* dipoles, with the beam phase space evolving under optical propagation for the rest of the beamline.

Figure 1 gives a conceptual diagram for the process to evolve. In this paper we consider multi-dipole system in a transport or recirculation arc lattice (e.g. 24 dipoles in our demonstrated arcs) in terms of multi-stage amplification scheme. In the following section of the stage gain analysis, we would quantify such multi-stage behavior of CSR microbunching gain in a general linear lattice.

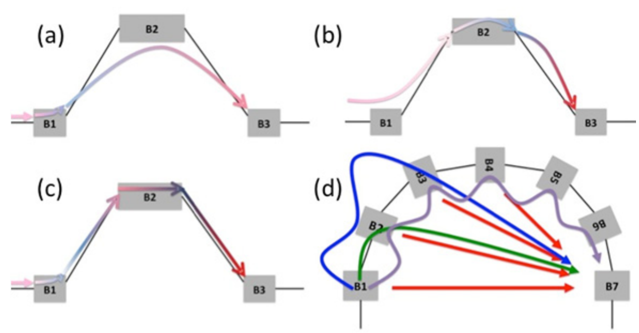

Figure 1: Conceptual illustration of multistage CSR microbunching gain evolution. For a typical 3- or 4-dipole bunch compressor chicane (a-c), (up to) 2-stage amplification can describe the microbunching gain evolution. Here for (a-c) the red color indicates the density modulation and the blue color represents energy modulation. Deeper colors indicate further amplified (or, more induced) modulations than for shallower colors.

STAGE GAIN ANALYSIS

In this section, we intend to quantify the CSR gains by separating the contributions of beam parameters from the lattice properties and to extract individual stage gains from the overall CSR gain. To achieve this, we expand Eq. (12) in a series of polynomials of the beam current I_b up to a certain order M,

$$\tilde{G}_f^{(M)} = \tilde{G}^{(M)}(s=s_f) = \tilde{G}_0 + \tilde{G}_1 I_b + \ldots + \tilde{G}_M I_b^M = \sum_{m=0}^{M}\tilde{G}_m I_b^m \tag{13}$$

By inspecting the kernel function, Eq. (2), the above expression can be further formulated to be

$$\tilde{G}_f^{(M)} = \sum_{m=0}^{M} A^m d_m^{(\lambda)}\left(\frac{I_b}{\gamma I_A}\right)^m \tag{14}$$

where A is given in Eq. (5), γ is the relativistic factor and $d_m^{(\lambda)}$ is the dimensionless coefficient (given a certain modulation wavelength) which now reflects the properties from lattice optics at m^{th} stage (m = 0, 1, 2,…), as well as Landau damping through finite beam emittances and energy spread [Eq. (3)]. For our interest in the following discussion, λ is chosen to correspond to the maximal CSR gain, denoted as λ_{opt}. Here we point out that Eq. (38) of Ref. [3] can be a special case of Eq. (14) for M = 2 in a typical bunch compressor chicane.

Obtaining the coefficients $d_m^{(\lambda)}$ of Eq. (14) can be straightforward. Here we remark the close connection between Eq. (2) and Eqs. (11) and (12) for determination of $d_m^{(\lambda)}$. For now, we can define the *individual* stage gain, which shall be convenient for our further discussion,

$$\mathcal{G}_f^{(m)} = \left| A^m d_m^{(\lambda)} \left(\frac{I_b}{\gamma I_A} \right)^m \right| \tag{15}$$

In the following section, we would take two comparative example arc lattices to demonstrate the stage gain analysis and its connection to both direct and/or iterative solutions.

EXAMPLES

In this section we take two 1.3 GeV high-energy transport arcs as our comparative examples (hereafter dubbed Example 1 and Example 2 lattice). The detailed description of the two example lattices can be found in Ref. [8]. Table 1 summarizes some initial beam parameters used in our simulations. Here, Example 1 lattice is a 180° arc with large momentum compaction (R_{56}), as well as a second-order achromat and being globally isochronous with a large dispersion modulation across the entire arc. In contrast to the first example, Example 2 is again a 180° arc with however small momentum compaction. This arc is also a second-order achromat but designed to be a locally isochronous lattice within superperiods. Local isochronisity ensures that the bunch length is kept the same at phase homologous CSR emission sites. The lattice design strategy was originally aimed for CSR-induced beam emittance suppression, while our simulation results show that it appears to work for microbunching gain suppression as well. Figure 2 shows the Twiss functions and transport functions $R_{56}(s)$ (or, the momentum compaction functions) across the arcs. Note that $R_{56}(s)$ for Example 2 (Fig. 2d) is much smaller in amplitude than that for Example 1 (Fig. 2c) due to local isochronicity.

Table 1: Initial Beam and Twiss Parameters for the Two Example Arc Lattices

Name	Example 1 (large R_{56})	Example 2 (small R_{56})	Unit
Beam energy	1.3	1.3	GeV
Bunch current	65.5	65.5	A
Normalized emittance	0.3	0.3	µm
Initial beta function	35.81	65.0	m
Initial alpha function	0	0	
Energy spread (uncorrelated)	1.23×10^{-5}	1.23×10^{-5}	

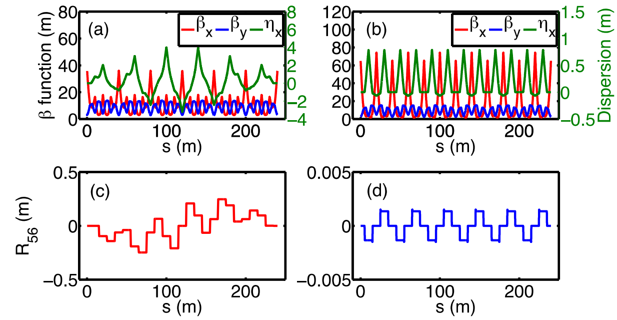

Figure 2: Lattice and transport functions for 1.3 GeV high-energy transport arc: (a)(c) with large momentum compaction function R_{56} (Example 1); (b)(d) with small momentum compaction function R_{56} (Example 2).

CSR microbunching gains for the two transport arcs are shown in Figs. 3 and 4. Figure 3 shows the gain spectra $G_f(\lambda)$ at the exits of the lattices as a function of modulation wavelength, from which one can obviously see a significant difference between them: Example 1 is vulnerable to CSR effect while the microbunching gain in Example 2 remains around unity. Figure 4 demonstrates the evolution of CSR microbunching gains as a function of s for several different wavelengths. One can see, in Fig. 3, that the shorter wavelengths enhance the Landau damping through Eq. (3), while longer wavelengths feature negligible CSR effect.

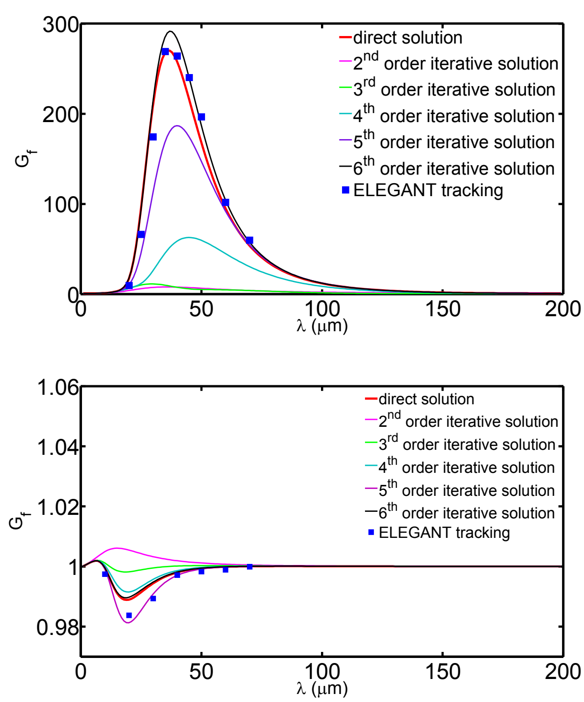

Figure 3: CSR gain spectra $G_f(\lambda)$ as a function of initial modulation wavelength for Example 1 (top) and 2 (bottom) lattice. The iteration solutions are obtained by Eq. (12).

ISBN 978-3-95450-134-2

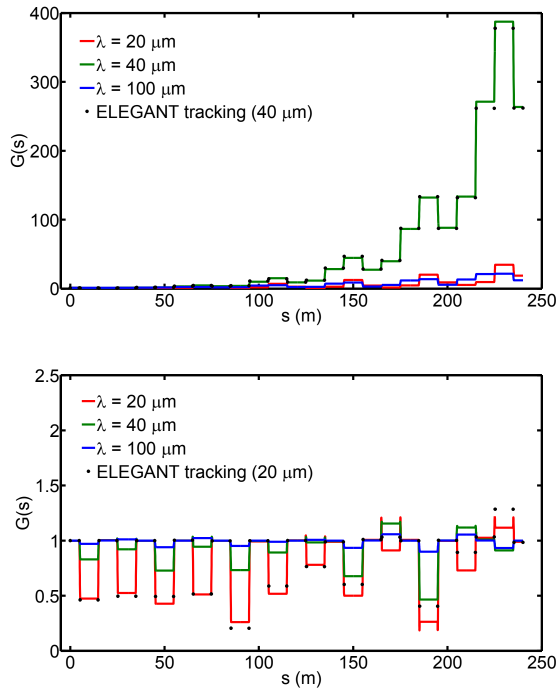

Figure 4: CSR gain functions $G(s)$ for Example 1 and 2 lattice.

From the simulation results (Figs. 3 and 4), we conclude that different lattice optics can give dramatically different CSR microbunching gains, although the geometric layout of the two lattices is identical. Also, we observe an interesting phenomenon: the two transport arcs are characteristic of (up to) 6th stage gain, which is distinguished from the (up to) 2nd-stage gain in a bunch compressor chicane [3]. Now, we would like to look into the gain amplification (or, gain evolution) in further depth by raising the following two questions: (i) how does CSR gain evolve along the beamline, i.e. based on the stage gain concept, can we quantify the CSR gain for each individual stages? (ii) Is there any advantage to employing the stage gain concept?

We still take Example 1 and 2 arcs as examples to extract the coefficients $d_m^{(\lambda)}$ [see Eq. (14)] so that we can quantify and compare optics impacts on the microbunching gains due to the CSR interaction. Here we choose the (optimum) wavelengths 36.82 µm and 19 µm for Example 1 and 2, respectively. Figure 5 illustrates and compares the stage gain coefficients for the two arcs. Here we can see the coefficients for Example 1 are at least three orders of magnitude larger than those for Example 2, showing the essential difference in $d_m^{(\lambda)}$ between the two arcs. The dramatic difference of CSR microbunching gain for the two Example arcs can be attributed to the difference in $d_m^{(\lambda)}$. Figure 6 shows the bar charts representing the individual staged gains at lattice exits $\mathcal{G}_f^{(m)}$ [see Eq. (15)] as functions of beam current and stage index for both transport arcs. Here we have two observations in Fig. 6: first, given a specific stage order (say, q), as the beam current increases, $\mathcal{G}_f^{(q)}$ also increases; second, for the same beam current, as the stage order increases, it does not necessarily imply $\mathcal{G}_f^{(q)}$ increase accordingly. This is because the stage gain coefficient's behavior depends on the properties of a lattice itself.

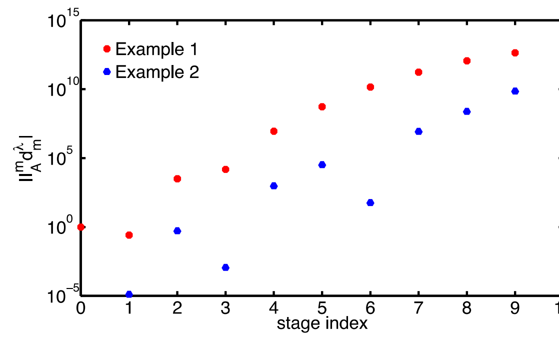

Figure 5: Comparison of $I_A^m d_m^{(\lambda)}$ for the two 1.3 GeV high-energy transport arcs; Example 1: red square and Example 2: blue triangle. Note the log scale in the vertical axis.

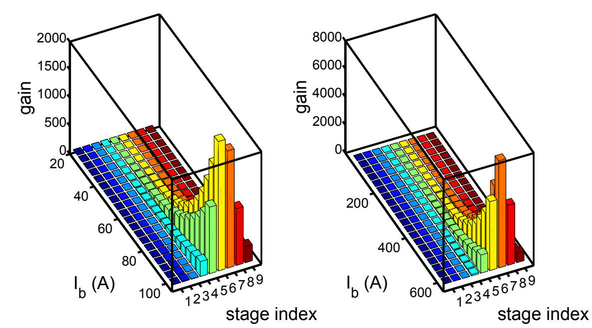

Figure 6: Bar chart representation of the individual staged gains [Eq. (18)] at the exits of the Example 1 and 2 lattices for several different beam currents. (Left) Example 1 (λ = 36.82 µm); (right) Example 2 (λ = 19 µm).

Regarding the advantage of the stage gain concept, since $d_m^{(\lambda)}$ is independent of beam current and beam energy, it can be used to quickly estimate the beam current dependence of the maximal CSR gain, provided an optimum wavelength is given. Figure 7 compares the current dependence of final overall gain from Eq. (14) for the two lattices at a selected wavelength that is in the vicinity of optimal wavelengths for maximal gains. It can be seen, in Example 2 case (Fig. 7b), the nominal beam current (65.5 A) is well described by including up to 6th order stage coefficient (red curve), while at further high currents (e.g. I_b > 160 A), it needs to include higher stage orders into account (e.g. M = 9, green curve). This observation is consistent with the 6th order iterative solutions presented in Fig. 3.

ISBN 978-3-95450-134-2

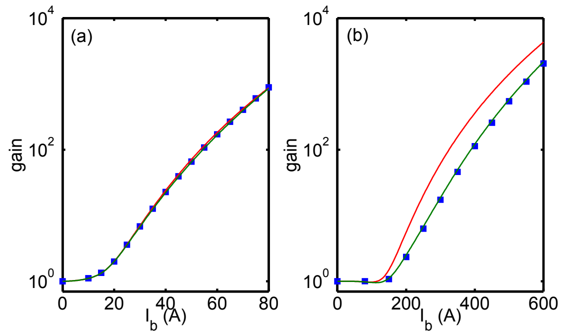

Figure 7: Current dependence of maximal CSR gain for the two high-energy transport arc lattices: (a) Example 1; (b) Example 2. Solid red curve from Eq. (14) with $M = 6$, solid green curve from Eq. (14) with $M = 9$ and blue square dots from Eq. (7).

So far we have quantified the individual stage gains by extracting the coefficients $d_m^{(\lambda)}$ from the kernel function. The advantage of the extracted $d_m^{(\lambda)}$ has been used to make quick estimation of maximal CSR gains for a range of beam currents in a beamline. To answer our first question with our developed stage gain concept, it would be better to present $R_{56}(s'\to s)$ [defined in Eq. (4)] together in the analysis. Figure 8 shows the "quilt" pattern for the two example arcs. The upper left area in the figures vanishes due to causality. It is obvious that in Example 1 (left figure) those block areas with large amplitude, particularly the bottom right deep red blocks, can potentially accumulate the CSR gain. To be specific, for Example 1, energy modulation at s' = 15 m can cause density modulation at s = 60 m, where CSR can induce further energy modulation at the same location. Then such modulation propagates by $R_{56}(s'\to s)$ from s' = 60 m to s = 100 m, and so on. It is this situation that causes multi-stage CSR amplification. Here we note that more complete analysis needs to take Landau damping effect into account. In contrast, the situation for Example 2 (right figure) is more alleviated because of much smaller amplitudes in $R_{56}(s'\to s)$. The microbunching amplification up to 6 stage in Example 1 and up to 9 stage in Example 2 are also manifested in Fig. 8.

Up to now, we have the above physical but qualitative interpretation of the multi-stage gain development along a beamline. We would like to more quantitatively connect the physical picture with our developed stage gain concepts. For simplicity, we exclude Landau damping effect and only consider the CSR microbunching amplification.

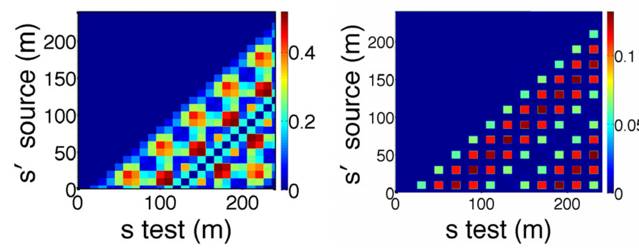

Figure 8: $R_{56}(s'\to s)$ quilt patterns for the two Example lattices: Example 1 (left) and Example 2 (right).

Figure 9 plots the staged gain functions $G^{(n)}(s)$ [defined in Eq. (12 or 14)] for Example 1 lattice without Landau damping effect [i.e. $\varepsilon_{nx} = \sigma_\delta = 0$], where we find the stage gain function is characteristic of periodic-like oscillation for lower-staged amplification (i.e. closely followed block patterns in left figure of Fig. 8) while features a stepwise increasing function for higher-staged amplification. It is this situation that reflects multi-stage CSR amplification. Similarly, for Example 2 lattice, there also exist many (even more) modular blocks (right figure of Fig. 8); however, in contrast to Example 1, the microbunching growth is less of a concern for Example 2 at a comparable bunch current (65.5 A) because of the smaller amplitudes of $R_{56}(s'\to s)$. The fact of even more modular blocks for Example 2 lattice would reflect its higher multi-stage gain behavior at higher currents, as can be seen in Fig. 7 (b). Note here that a higher stage does not correlated with higher amplitude of gain. Also it's important to remark that the staged-gain description in Eq. (11) has limited applications. For example, it is convergent only for a single-pass beamline when CSR interaction takes place in finite number of dipoles. For the same reason, a multistage gain amplification concept as Eq. (11) may not be valid for longitudinal space charge (LSC) effect.

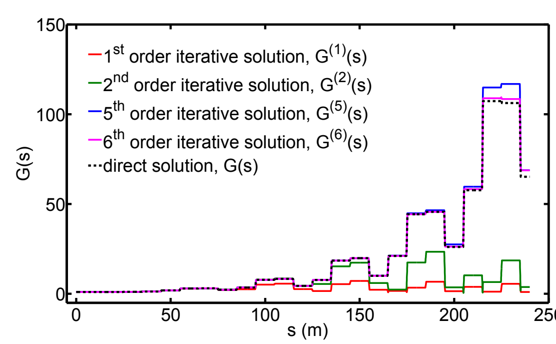

Figure 9: Gain functions $G^{(n)}(s)$ (solid curves) and $G(s)$ (dashed curves) for Example 1 lattice with λ = 80 μm in the absence of Landau damping [Eq. (4)].

CONCLUSION

In this paper, we have first outlined the theoretical formulation based on (linearized) Vlasov equation by treating the CSR effect as a perturbation and making the

ISBN 978-3-95450-134-2

coasting beam approximation. The solution to the governing equation [Eq. (1)] can be obtain self-consistently (i.e. direct solution) or found through numerical iteration (i.e. iterative solution). With introduction of stage gain concept, the individual iterative solutions can be connected through the lattice optics pattern [i.e. $R_{56}(s' \to s)$] in a physical and quantitative way. Moreover, the stage gain coefficient [defined in Eq. (14)], due to its independence of beam current and beam energy, can be applied to make quick estimation for the maximal CSR gain, provided a lattice is given (Fig. 7).

ACKNOWLEDGMENT

We thank Steve Benson for the interest of this work and proofreading this draft. This work is supported by Jefferson Science Associates, LLC under U.S. DOE Contract No. DE- AC05-06OR23177.

REFERENCES

[1] C. -Y. Tsai *et al.*, Linear Vlasov Solver For Microbunching Gain Estimation with Inclusion of CSR, LSC, And Linac Geometric Impedances (MOP052, these proceedings)

[2] See, for example, C. -Y. Tsai *et al.*, ERL2015 (TUICLH2034), IPAC'15 (MOPMA028), and FEL'14 (THP022)

[3] Z. Huang and K. -J. Kim, Formulas for coherent synchrotron radiation microbunching in a bunch compressor chicane, Phys. Rev. ST Accel. Beams 5, 074401 (2002)

[4] M. Borland, elegant: A Flexible SDDS-Compliant Code for Accelerator Simulation, APS Light Source Note LS-287 (2000) and Modeling of microbunching instability, Phys. Rev. ST Accel. Beams 11, 030701 (2008)

[5] S. Heifets *et al.*, Coherent synchrotron radiation instability in a bunch compressor, Phys. Rev. ST Accel. Beams 5, 064401 (2002)

[6] J. Murphy *et al.*, Longitudinal wakefield for an electron moving on a circular orbit, Part. Accel. 1997, Vol. 57, pp. 9-64

[7] Ya. S. Derbenev *et al.*, Microbunch radiative tailhead interaction, TESLA-FEL-Report 1995-05

[8] D. R. Douglas *et al.*, Control of coherent synchrotron radiation and microbunching effects during transport of high brightness electron beams, arXiv: 1403.2318v1 [physics.acc-ph] or D. R. Douglas *et al.*, Control of synchrotron radiation effects during recirculation, IPAC'15 (TUPMA038)

ISBN 978-3-95450-134-2

REVIEW OF EXPERIMENTAL RESULTS FROM HIGH BRIGHTNESS DC GUNS: HIGHLIGHTS IN FEL APPLICATIONS

Nobuyuki Nishimori, JAEA, Tokai, Naka, Ibaraki 319-1195, Japan

Abstract

Future energy recovery linac light sources and high repetition rate X-ray FELs require high-brightness and high-current electron guns. A DC photoemission gun is one of the most promising candidates for such guns, because a record high current of 75 mA and generation of high brightness beam satisfying LCLS-II injector specifications were recently demonstrated at the Cornell photoinjector with a 400 kV photoemission gun. Further increases of gun high voltage and cathode gradient are desirable to reduce space charge induced emittance growth especially for higher bunch charge applications. Employment of a segmented insulator is a key to reach higher voltage. This technique led to generation of a 500 keV beam from the JAEA gun with 160 mm acceleration gap, conditioning voltage more than 500 kV at the Cornell gun with gap < 50 mm, and demonstration of 500 kV holding for 10 hours at the KEK gun with 70 mm gap. In this paper, recent experimental results of high brightness DC guns are presented.

INTRODUCTION

High repetition rate FELs such as LCLS-II and high power FEL for EUV lithography require a high-brightness and high-current electron gun [1,2]. A normal conducting RF gun operating at 186 MHz has been developed for the next generation FELs and recent experimental results are described in the FEL2014 [3]. In this paper we focus on experimental results from high brightness DC guns as another candidates for the high repetition rate FELs. Those DC gun-based photoinjectors are designed and constructed being inspired by the great success of Jefferson laboratory energy recovery linac (ERL) FEL [4].

The recent highlight in FEL applications is the first demonstration of cathode thermal emittance dominated high bunch charge beams satisfying LCLS-II injector specifications at the Cornell photoinjector [5]. The cathode thermal emittance is given by [6]

$$\varepsilon_{n,th} = \sigma_x \sqrt{\frac{MTE}{mc^2}},$$

where MTE is cathode mean transverse energy, σ_x is the initial rms size of the beam and mc^2 is the electron rest energy. The charge q can be generated from cathode as long as the external cathode gradient E is greater than the image charge field given by $q/\varepsilon_0 \pi (2\sigma_x)^2$ [7]. The thermal emittance for charge q and cathode gradient E is thus given by [6]

$$\varepsilon_{n,th} \geq \frac{1}{2}\sqrt{\frac{q}{\pi\varepsilon_0 E}}\sqrt{\frac{MTE}{mc^2}}.$$

Substitution of cathode gradient E = 4.3 MV/m, and MTE = 140 meV of NaKSb cathode used for the Cornell experiment yields minimum thermal emittance of $\varepsilon_{n,th}$ = 0.11 µm for 20 pC, 0.24 µm for 100 pC, and 0.41 µm for 300 pC. Although those emittance values are within the LCLS-II specifications summarized in Table 1, it had been considered to be difficult to preserve the thermal emittance through a DC gun-based photoinjector. Recently the Cornell photoinjector demonstrated that the emittance at the injector exit increases only by 50% or less from the cathode thermal emittance, satisfying the LCLS-II specifications [5]. The sophisticated injector design, excellent injector components including the 400 kV photoemission gun and advanced beam transport techniques relying on space charge simulation codes led to preservation of the high brightness performance from the cathode through the injector accelerator with bunch compression required for LCLS-II specifications.

Generation of a record high average current of 75 mA demonstrated at the Cornell photoinjector is also a highlight in FEL applications [8,9]. The average current is three orders of magnitudes greater than LCLS-II specification and high enough for high power EUV FEL. Generation of both cathode emittance dominated high bunch charge and high current beams was achieved with the same NaKSb cathode.

Table 1: LCLS-II Injector Specifications [5]

Bunch charge	95% ε_n (µm)	Peak current (A)
20 pC	0.25	5
100 pC	0.40	10
300 pC	0.60	30

Further increase of the gun high voltage is desirable to reduce space charge induced emittance growth especially for FELs driven by high bunch charge. Employment of a segmented insulator is a key to reach higher voltage [10]. This technique led to the first demonstration of 500 keV beam from a photoemission DC gun with 160 mm acceleration gap at Japan Atomic Energy Agency (JAEA) [11]. The cathode gradient is 5.8 MV/m without Pierce-type focusing electrode. The gun has been used for commissioning of the compact ERL (cERL) at KEK for more than two years [12]. The gun operational voltage at the cERL is however limited to 390 kV, because the insulator is operated with eight segments due to the failures of two segments out of the full ten. Recently a new two segmented insulator was installed on the top of

nishimori.nobuyuki@jaea.go.jp

ISBN 978-3-95450-134-2

the existing insulator. The insulator with 2+8 segments was successfully conditioned up to 550 kV without the central stalk. Beam generation from the gun with the additional insulator will be performed at the cERL in the near future.

Higher cathode gradient along with high voltage has been pursued at KEK and Cornell. The 70 mm gap photogun at KEK demonstrated holding at 500 kV for 50 hours [13]. The cathode gradient is 6.9 MV/m without Pierce-type focusing electrode. The HV conditioning up to 550 kV was achieved with small number of HV trip events about 50. The trip number is much fewer than the JAEA and other DC guns. Although there are a few differences such as the insulator material used at KEK and the HV chamber design, it is still unclear what mainly contributes to the much better HV performance of the KEK gun, compared with the JAEA gun. The beam generation test will be performed soon.

A photogun with a segmented insulator has been also developed at Cornell University [14]. The unique feature is a movable anode, allowing the cathode-anode gap to be adjusted. The measured breakdown voltage as a function of the gap length was found to agree well with the empirical equation given by $V(\mathrm{kV}) = 123 \times g^{0.34}(\mathrm{mm})$ [15]. They pointed out that the KEK result at 500 kV with 70 mm gap is consistent with the equation and that the normalized emittance for bunch charges higher than 150 pC approaches thermal emittance as the voltage approaches 500 kV [16].

In this paper, we describe recent experimental results of high brightness DC guns. In Sec. 2, the results from the Cornell photoinjector are described. As already mentioned, various developments of the photoinjector components and advanced beam transport techniques based on space charge simulation codes contribute to the unprecedentedly high brightness and high current beam generation. In Sec. 3, the results from the JAEA 500 kV gun are described. In Sec. 4, high gradient 500 kV gun at KEK and Cornell are described.

CORNELL PHOTOINJECTOR

Generation of high brightness electron beam satisfying LCLS-II specifications has been demonstrated at the Cornell photoinjector. Their success relies on various developments in the whole injector system.

The Multi Objective Genetic Algorithm (MOGA) optimization developed for design of the Cornell ERL injector [17,18] has been used to find optimum parameter sets for the high brightness beam satisfying LCLS-II injector specifications. Three dimensional space charge simulation codes such as GPT [19] along with realistic models of gun acceleration field, injector cavity fields, and magnetic fields have been used in the MOGA optimizations. The 3D space charge code is shown to agree well with phase space measurements of space charge dominated beams at the Cornell photoinjector [5,20-22]. The MOGA optimization is now widely used for injector designs at other facilities [23,24].

Before the measurements of space charge dominated bunches, the GPT model for the Cornell photoinjecotor was verified with sophisticated measurements at near-zero bunch [22], as briefly described in the following. The transverse beam position change was measured with downstream BPMs by changing the initial position of the beam on cathode or kicking the beam with a corrector magnet. This was repeated for each element in the injector. The measured responses were found to agree well with the GPT model for all the elements including the 3D rf field maps used to model the cavities and fields due to the input power couplers. The alignment of the beam through the whole injector is also found to be very important to generate the low emittance beam. An element by element alignment procedure was developed for the gun, the buncher cavity, and the SRF cavities with corrector coils within accuracy of 50 μm. The solenoids were physically moved to align their magnet centers with beam trajectory within accuracies of 50 μm and 0.2 mrad. As the final check, the injector was set up with parameters for 20 pC/bunch and the emittance at the injector exit was measured with a two slit Emittance Measurement System (EMS). The emittance was verified to agree well with thermal emittance at the cathode measured with a solenoid scan technique. The beam sizes at several locations along the injector are also verified to agree well with the GPT model.

After all the injector components were verified to have responses predicted by the GPT model for near-zero bunch, an optimum parameter set for each bunch charge was loaded to the injector. The measured emittance and longitudinal current profile at the EMS location are shown to agree well with the GPT model and to satisfy the LCLS-II specifications [5]. Small discrepancy between the simulation and the measurement seen in a graph of optimized emittance vs. rms bunch length is attributed to the difference between ideal and measured transverse laser distributions. This suggests that further improvement of emittance is anticipated with an improved laser shaping technique [25].

Recently a beam asymmetry after the first emittance compensation solenoid was discovered and attributed to the stray quadrupole fields in the solenoid. The asymmetry was mitigated with a correcting quadrupole coil. This greatly contributed to demonstration of the cathode emittance dominated beams [26].

The gun at the Cornell photoinjector is operated at 400 kV with a non-segmented insulator and the cathode-anode gap length of 50 mm [27]. The cathode gradient is 4.3 MV/m with Pierce-type focusing electrode. They developed various types of photocathodes [6,28,29] and used a NaKSb with a 140 meV cathode mean transverse energy to demonstrate both high brightness and high current performance. The gun has a high voltage power supply capable of delivering 100 mA beam.

HGH VOLTAGE GUN AT JAEA

As demonstrated at the Cornell photoinjecotor, it is feasible to generate cathode emittance dominated beam

ISBN 978-3-95450-134-2

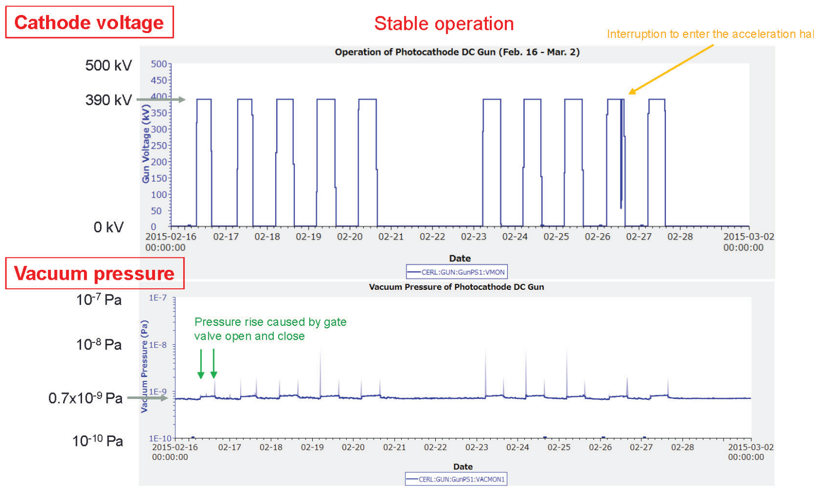

Figure 1: Typical gun cathode voltage and vacuum pressure during two weeks of the cERL operation.

when the whole injector system is carefully set up and the beam response is well reproduced by space charge simulation codes. Development of higher voltage and higher gradient gun will help further improve the performance of the DC gun-based photoinjector. In this section, development of a high voltage photoemission gun at JAEA is described.

The details of the gun system are described in Refs. [10,11,30]. A segmented insulator with guard rings employed to protect the ceramics from field emission is a key to reach high voltage without giving fatal damage to the insulator. The high voltage conditioning up to 550 kV with the stalk was achieved in 2009 [10], and 500 keV beam with current up to 1.8 mA from a photoemission DC gun was demonstrated in 2012 [11]. The cathode-anode gap length was changed from the original design of 100 mm to 160 mm to demonstrate 500 keV beam [30]. This is because field emitters that could not be pacified were created repeatedly at 100 mm gap, preventing the stable gun operation at 500 kV.

The gun was installed at the cERL at KEK and stably delivered beam for more than two years since April 2013. The gun operational voltage has been limited to 390 kV. This is because failures of two out of ten segments of the insulator were found at KEK after the gun shipment from JAEA. Short bars have been connected between the electrodes of the failed segments. The gun insulator has been operated with eight segments during the commissioning instead of full ten segments.

Figure 1 shows a typical operational status of the gun voltage and vacuum pressure during two weeks. The gun is operated from 12:00 to 23:00 on a week day. The stability of the gun voltage is excellent and no HV breakdown event was observed in the past two years. This is very good for such a future industrial application as EUV lithography [2]. The gun vacuum pressure during the operation is 8×10^{-10} Pa. The average beam current at the cERL is increased 10 times every year starting from 1 μA, as they monitor the radiation level outside the accelerator hall. The maximum average current generated so far is 100 μA and will be increased up to 1 mA by the end of FY 2015 [12]. The ERL beam has been used for laser Compton scattering (LCS) X-ray generation [31]. The cathode material is GaAs. The quantum efficiency at 530 nm laser measured during the LCS experiment from January to July in 2015 is plotted in Fig. 2. The 1/e life time is 6000 hours long enough for the LCS commissioning, although the charge extracted is only 6 C. The cathode lifetime study at the cERL will be continued with elevated beam current. This would provide an estimation of the cathode life time of a DC gun-based photoinjector for high repetition rate FELs.

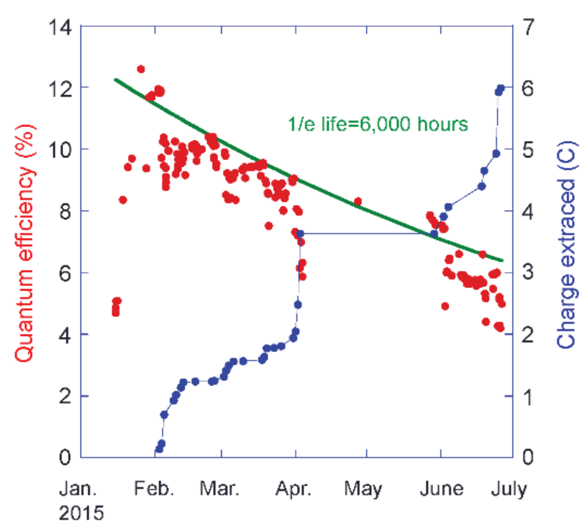

Figure 2: Quantum efficiency of GaAs photocathode and charge extracted during the cERL commissioning from January to July in 2015.

Recently a newly manufactured two segmented insulator was installed on the top of the existing insulator to recover 500 kV operation, as shown in Fig. 3. The insulator with 2+8 segments was successfully conditioned

ISBN 978-3-95450-134-2

up to 550 kV without the central stalk (see Fig. 4). Beam generation from the gun with the additional insulator will be performed in the near future.

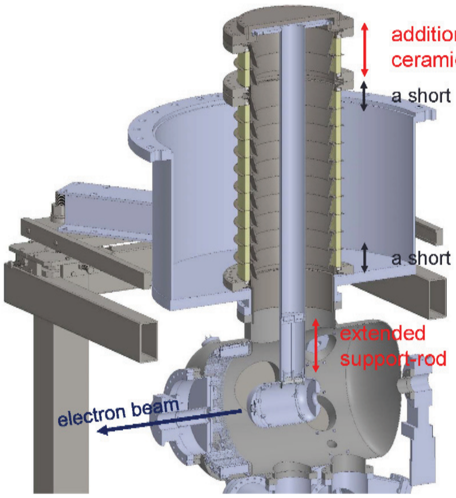

Figure 3: Gun configuration with additional two segmented ceramics at the cERL.

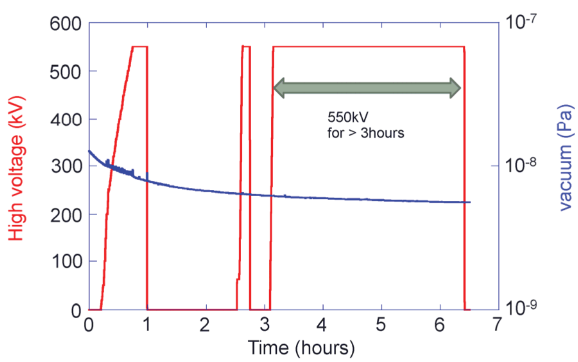

Figure 4: HV test without central stalk with additional ceramics at the cERL. Red is high voltage and blue is gun vacuum.

A simulation study of the cERL photoinjector for FEL applications is presented in Ref. [24]. Although there are many differences between the cERL and Cornell pohtoinjectors, the simulation suggests that LCLS-II specifications could be satisfied at the cERL photoinjector if higher acceleration gradient becomes available at the injector cavity. At the moment, we try to reproduce the cERL beam generated with presently available injector parameters by space charge simulation codes [32]. This will eventually lead to generation of cathode emittance dominated beam at the cERL.

HIGH VOLTAGE GUNS WITH NARROW GAPS AT KEK AND CORNELL

The photoemission gun developed at KEK is similar to that at JAEA. The most significant difference is the short cathode-anode gap of 70 mm [13]. The cathode gradient is 6.9 MV/m at 500 kV and the maximum gradient of the cathode electrode surface is 11.0 MV/m. Although the short-gap is believed to yield difficulty in HV application [30], the gun was successfully conditioned up to 550 kV with the HV trip number less than 50, which is much fewer than the JAEA gun. Holding test at 500 kV for 50 hours without any breakdown event nor any vacuum activity was also demonstrated. The gun vacuum is 4×10^{-10} Pa good enough to avoid photocathode damage due to ion back-bombardment created by residual gas in the cathode-anode gap. The structure of the segmented insulator with guard ring is almost the same as that of the JAEA gun. The insulator material is high voltage resistant Al_2O_3 based ceramic called TA010 fabricated by Kyocera. It is different from 99.8 % Al_2O_3 used at JAEA [33]. The material used for both KEK and JAEA guns is titanium. The design of the chamber is different from each other. It is under investigation what mainly contributes to much better HV performance at the KEK gun, compared with the JAEA gun. The downstream beam line including radiation shield is under construction at KEK. The beam generation test will be performed soon.

A segmented gun has also been developed at Cornell University [14]. Although the design of the insulator is similar to the JAEA/KEK gun, the insulator diameter and the number of the segments are greater than those of the JAEA/KEK gun. This would be better for operation at such high voltage as 750 kV. The gun was successfully conditioned up to > 500 kV with 50 mm gap using combination of UHV and noble gas conditioning. The helium gas processing was found to be effective in suppressing field emitters observed at voltages above 400 kV. This is different from JAEA experience that the gas conditioning is not effective once the field emitter appeared [34]. The most unique feature is a movable anode, allowing the cathode-anode gap to be adjusted from 20 to 50 mm. The measured breakdown voltage as a function of the gap length is found to agree well with the empirical equation given by $V(kV) = 123 \times g^{0.34}(mm)$ in a textbook [15]. Those measured data are 400 kV for 30 mm gap and 450 kV for 50 mm gap. The optimum set of gun voltage, transverse focusing fields by Pierce-type electrode, and field strength at the photocathode are studied numerically [14,35]. The simulation suggests that a 30 mm gap at 400 kV has smaller emittance than a 50 mm gap at 450 kV for charges up to 100 pC, when the segmented gun is placed in the Cornell photoinjector [14]. They pointed out that the result of 70 mm gap KEK gun is consistent with the empirical breakdown voltage equation and that the normalized emittance for bunch charges higher than 150 pC approaches thermal emittance as the voltage approaches 500 kV [16].

SUMMARY

Recent experimental results from high brightness DC guns are presented. The DC gun-based Cornell photoinjector successfully demonstrated both cathode emittance dominated and high current beam satisfying the LCLS-II specifications with a 400 kV non-segmented insulator gun with 50 mm gap and Pierce-type focusing electrode. The success relies on various developments in the whole injector system and further improvement is anticipated with improved laser shaping. Efforts to increase the gun high voltage and cathode gradient are in progress with employment of segmented insulators. A 500-keV electron beam was demonstrated at JAEA and gun operational experience at the cERL is accumulated. Gun operation at 500 kV with 70 mm gap was demonstrated at KEK indicating further improvement of the DC gun-based photoinjector is feasible. The experimental and numerical studies at the Cornell segmented insulator gun with variable cathode-anode gap suggest that there is an optimum set of gun voltage, electrode shape and cathode field strength depending on the application.

ACKNOWLEDGMENTS

We acknowledge Adam Bartnik, Colwyn Gulliford, Jared Maxson, Bruce Dunham, and Ivan Bazarov at Cornell University for useful discussion on the Cornell photoinjector developments. We thank Masahiro Yamamoto, Tsukasa Miyajima, Yosuke Honda at KEK, Masao Kuriki at Hiroshima University, Ryoji Nagai and Ryoichi Hajima at JAEA for helpful discussion on KEK/JAEA gun developments. This work is partially supported by JSPS Grants-in-Aid for Scientific Research in Japan (15H03594).

REFERENCES

[1] P. Emma et al., "Linear accelerator design for the LCLS-II FEL facility", in *Proc. of FEL2014*, Basel, Switzerland (2014), THP025.
[2] N. Nakamura et al., "Design work of the ERL-FEL as the high intense EUV light source", in *Proc. of ERL2015*, Stony Brook, NY (2015), MOPCTH010.
[3] D. Filippetto, "APEX: A photo-injector for high average power light sources and beyond", in *Proc. of FEL2014*, Basel, Switzerland (2014), TUA01; J.F. Schmerge et al., "The LCLS-II injector design", *ibid.*, THP042.
[4] G.R. Neil et al., Phys. Rev. Lett. 84, 662 (2000).
[5] C. Gulliford et al., Appl. Phys. Lett. 106, 094101 (2015).
[6] I.V. Bazarov et al., Phys. Rev. Lett. 102, 104801 (2009).
[7] D. Nguyen et al., "RF Linac for High-Gain FEL Photoinjectors", US Particle Accelerator School (2014), LA-UR 14-23995.
[8] L. Cultrera et al., Appl. Phys. Lett. 103, 103504 (2013).
[9] B. Dunham et al., Appl. Phys. Lett. 102, 034105 (2013).
[10] R. Nagai et al., Rev. Sci. Instrum. 81, 033304 (2010).
[11] N. Nishimori et al., Appl. Phys. Lett. 102, 234103 (2013).
[12] S. Sakanaka et al., "Recent progress and operational status of the compact ERL at KEK", in *Proc. of IPAC2015*, Richmond, VA (2015), TUBC1.
[13] M. Yamamoto et al., "Development of a 500 kV DC gun with narrow gap", in *Proc. of ERL2015*, Stony Brook, NY (2015), TUIBLH1021.
[14] J. Maxson et al., Rev. Sci. Instrum. 85, 093306 (2014).
[15] P. Slade, *The Vacuum Interrupter: Theory, Design, and Application* (Taylor & Francis, 2007).
[16] J. Maxson, "High accuracy adaptive laser and electron beam shaping and a bit about DC gun emittance vs. gun gap", in *Proc. of ERL2015*, Stony Brook, NY (2015).
[17] I.V. Bazarov and C.K. Sinclair, Phys. Rev. STAB 8, 034202 (2005).
[18] I.V. Bazarov et al., Phys. Rev. STAB 14, 072001 (2011).
[19] http://www.pulsar.nl/gpt/
[20] I.V. Bazarov et al., Phys. Rev. STAB 11, 100703 (2008).
[21] I.V. Bazarov et al., Appl. Phys. Lett. 98, 224101 (2011).
[22] C. Gullidord et al., Phys. Rev. STAB 16, 073401 (2013).
[23] C.F. Papadopoulos et al., "Longitudinal and transverse optimization for a high repetition rate injector", in *Proc. of FEL2014*, Basel, Switzerland (2014), THP057.
[24] T. Miyajima et al., "Beam simulations of high brightness photocahotde DC gun and injector for high repetition FEL light source", in *Proc. of FEL2014*, Basel, Switzerland (2014), THC04.
[25] J. Maxson et al., Phys. Rev. STAB 18, 023401 (2015).
[26] Adam Bartnik, "Cornell injector performance", in *Proc. of ERL2015*, Stony Brook, NY (2015).
[27] B.M. Dunham et al., "Performance of a very high voltage photoemission gun for a high brightness, high average current ERL injector", in *Proc. of PAC07*, Albuquerque, New Mexico (2007), TUPMS021.
[28] I.V. Bazarov et al., J. Appl. Phys. 103, 054901 (2008).
[29] L. Cultera et al., Appl. Phys. Lett. 99, 152110 (2011).
[30] N. Nishimori et al., Phys. Rev. STAB 17, 053401 (2014).
[31] R. Nagai et al., "Demonstration of high-flux photon generation from an ERL-based laser Compton photon source", in *Proc. of IPAC2015*, Richmond, VA (2015), TUPJE002.
[32] T. Miyajima et al., "Status of higher bunch charge operation in compact ERL", in *Proc. of IPAC2015*, Richmond, VA (2015), TUPWA067.
[33] B.M. Dunham et al., "ERL2011 summaries of working group 1: Progress with DC photoemission electron sources", in *Proc. of ERL2011*, Tsukuba, Japan (2011), WG1000.
[34] N. Nishimori et al., "Status of photoemission DC gun development at JAEA", in *Proc. of FLS2012*, Newport News, VA (2012), WEWBERL04.
[35] J.M. Maxson et al., "Optimization of DC photogun electrode geometry", in *Proc. of PAC2011*, New York, NY (2011), WEP245.

ISBN 978-3-95450-134-2

OVERVIEW OF ALTERNATIVE BUNCHING AND CURRENT-SHAPING TECHNIQUES FOR LOW-ENERGY ELECTRON BEAMS*

Philippe Piot[1,2]
[1] Department of Physics and Northern Illinois Center for Accelerator & Detector Development, Northern Illinois University, DeKalb, IL 60115, USA
[2] Accelerator Physics Center, Fermi National Accelerator Laboratory, Batavia, IL 60510, USA

Abstract

Techniques to bunch or shape an electron beam at low energies ($\mathcal{E}$ < 15 MeV) have important implications toward the realization of table-top radiation sources or to the design of compact multi-user free-electron lasers. This paper provides an overview of alternative methods recently developed including techniques such as wakefield-based bunching, space-charge-driven microbunching via wave-breaking, ab-initio shaping of the electron-emission process, and phase space exchangers. Practical applications of some of these methods to foreseen free-electron-laser configurations are also briefly discussed.

INTRODUCTION

Schemes to enhance the peak current of electron bunches have a vast range of applications. In radiation processes radiating at a given wavelength λ, electrons within a duration $\tau \leq \lambda/c$ radiate in phase thereby enhancing the radiation flux [1]. Likewise low-energy *short* electron bunches can be injected in short-wavelength accelerators, e.g., based on laser-plasma wakefield [2]. In addition to compression, the capability to tailor the current profile of these electron bunches can also serve further applications, e.g., to produced narrow-band radiation (using a train of short electron bunches) [1], enhance the transformer ratio for beam-driven accelerator (ramped current profiles [3]) or mitigate phase-space dilutions arising from collective effects, e.g., coherent synchrotron radiation [4].

Techniques to alter the current distribution can be casted into four categories: (i) ab-initio tailoring of the emission process, (ii) introduction of energy-position correlation within the bunch with subsequent bunching in longitudinally-dispersive beamline, (iii) the direct shaping of the beam by ab-initio shaping of the bunch at its formation stage, and (iv) phase-space manipulations between two degrees of freedoms to map a transversely tailored distribution onto the current profile.

Throughout this paper we employ the longitudinal phase space (LPS) coordinates (ζ, δ) associated to an electron within the bunch. Here ζ is the axial position with respect to the bunch centre and δ is the fractional momentum spread.

* This work was supported by the US-DOE contract DE-SC0011831 with Northern Illinois University. Fermilab is operated by Fermi Research Alliance, LLC under Contract No. DE-AC02-07CH11359 with the US DOE.

AB INITIO METHODS

Photoemission from Shaped Laser Pulses

Photoemission electron source are widespread in operating and foreseen FEL facilities. The electron bunches produced in this type of sources have, at best, durations comparable to the illuminating laser pulse. However the duration is influenced by space charge and RF effects (in the case of RF guns). Figure 1 illustrates the typically achieved compression for a low (0 nC) and high (1 nC) bunch charge. Some bunch compression can be achieved by phasing the laser closer to zero crossing phase ($\varphi = 0°$ in our convention) to the detriment of the transverse emittance. On another hand employing shorter laser bunch results in operating the source in the "blow-out" regime which leads to a large space-charge-induced bunch lengthening [5–7]. The latter regime of operation leads to linearized longitudinal phase space (LPS) which can be subsequently manipulated to yield very short bunches [5].

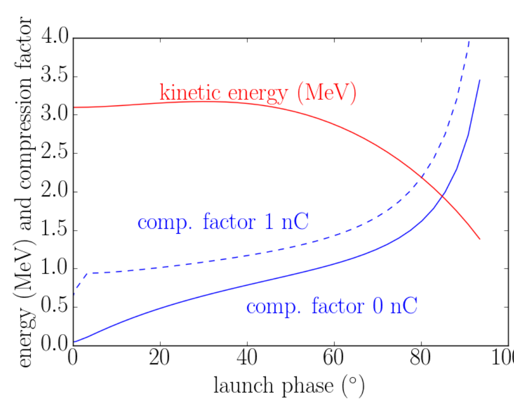

Figure 1: Compression factor (defined as the ratio of the final electron-bunch duration to laser-pulse duration) computed for an L-band RF gun with a 3-ps laser pulse with (dash line) and without (solid trace) accounting for space charge effects.

An interesting area of research is the possibility of tailoring the temporal profile of the emission process. This is particularly attractive in photoemission sources where the emitted electron-bunch distribution initially mirrors the temporal profile of the laser pulse impinging on the cathode. Consequently, laser shaping plays a central role and methods to temporally tailor the laser have been extensively investigated in combination with photo-emission electron sources.

These pulse-shaping techniques include frequency-domain techniques based on spatial-light modulators [8], and DAZZLER systems [9], or simpler time-domain methods using delay lines [10], birefringent crystals [11] or lens with échelon profiles [12]. However these pulse-shaping techniques provide limited ability to form short bunches directly out of an electron source (as pointed out above).

A shape of wide interest is a train of laser pulses to form train of electron bunches. This type of bunches can support the production of coherently enhanced narrowband radiation, or are capable of resonantly exciting a given mode in multi-mode beam-driven accelerating structures. At very low charges, shaping was shown to lead to the formation of electron bunch train [12]. However as the charge increase the density modulation quickly dissipates (it become an energy modulation). Reference [13] pointed out that the information on the initial density modulations is actually imprinted on the LPS and can be eventually recovered after, e.g., after acceleration, using a beamline with the proper longitudinal dispersion R_{56}.

An emerging demand for shaped electron bunches also comes from the mitigation of collective effects. Laser shaping was suggested in Ref. [14] to form electron bunches current profile able pre-compensate for energy spread induced by geometric wakefield in, e.g., accelerating cavities. This capability was recently demonstrated at the FERMI@ELETTRA facility [15] where the “flattening" of the LPS was directly measured.

Finally, an important application of shaped electron beams regards the improvement of the transformer ratio $\mathcal{R}$ in collinear beam-driven acceleration methods [3]. In this class of acceleration methods, a drive bunch excites wakefields which can accelerate a delayed "witness bunch". Maximizing $\mathcal{R}$ – the ratio between minimum decelerating field within the drive bunch with the maximum accelerating field experienced by the witness bunch – can enable longer interaction lengths thereby giving rise to higher energy gain for a given energy depletion of the drive bunch. Symmetric drive-bunch distributions are limited to $\mathcal{R} \leq 2$. A recent proposal for a compact short-wavelength mutli-user FEL facility based on multiple beam-driven linacs call for transformer ratio $\mathcal{R} \sim 5$ [16]. Most of the transformer-ratio-enhancing shapes that have been proposed so far exhibit discontinuities and are therefore challenging to experimentally realized [17]. Recent numerical investigations pointed out to a class of smooth current profiles adequate to support beam-driven acceleration with enhanced transformer ratios [18]. Figure 2 depicts a simulated laser shape (from a DAZZLER system) and resulting electron-bunch distribution (green-shaded curve) downstream of a linac with wakefield (blue trace) produced in a DLW; see details in [18] .

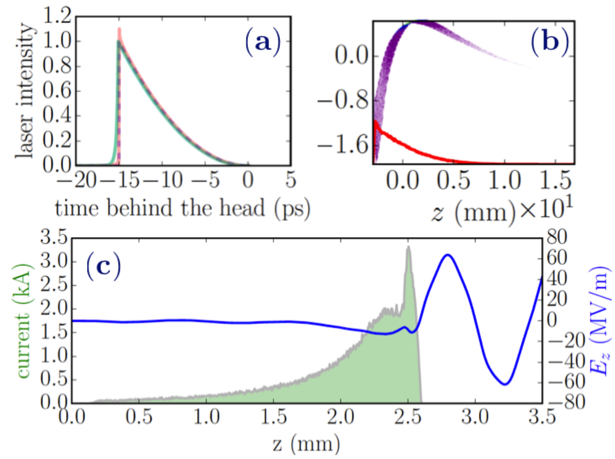

Figure 2: Example of ab-initio temporal shaping of a laser pulse (a) with resulting longitudinal phase space (density plot) and current distribution (red trace) (b) along with final (c) current distribution (green-shaded curve) and excited wakefield in a dielectric accelerator (blue trace). Figure adapted from Ref. [18].

Optically-assisted Field Emission

The capability of forming spatially and temporally localized electron packets via optically-enhanced field-emission from sharp tips has been demonstrated by several groups [19–21]. In brief field emission is a macroscopic manifestation of quantum tunneling, i.e. the "bending" of the potential barrier under the influence of an applied external field. Field emission typically occurs in the presence of high electric field O(GV/m). This field can be locally achieved due to sharp tips or cathode-surface roughness with macroscopic fields on the order of $E \sim 10$ MV/m only. Given the locally-enhanced field $E_e \equiv \beta_e E$, where β_e is the enhancement factor, the field-emitted current density is described by the Fowler-Nordheim (FN) law [22]

$$\boldsymbol{j} = aE_e^2 \exp\left(-\frac{b}{E_e}\right)\hat{\boldsymbol{n}}, \tag{1}$$

where $\hat{\boldsymbol{n}}$ is the normal to the local surface and a and b are positive constants that depend on the material. When the applied field is time dependent i.e. $E(t) = E_0 \cos \omega t$, the field emission is pulsed $\boldsymbol{j}(t)$ and bunches are formed. In a regime where a high-intensity laser pulse impinges the cathode, the bunch duration is given by the laser period ($\tau \sim 2$ fs for a 800-nm laser pulse).

Figure 3 presents particle-in-cell simulations results of an optically-assisted field emission process from a nanohole using the program WARP [23]. The resulting LPS recorded on a plane 300-nm downstream of the cathode displays modulation with periodicity on the order of 800 nm consistent with the laser wavelength. The noise on this simulation is dominated by the statistics: a single nanohole produces only 200 electrons. Combining several nanoholes in an array [24] would reduce the shot noise and increase the bunching factor at the triggering-laser wavelength. Preserving this imprinted information on the LPS during the downstream acceleration, e.g., in an RF gun, would be crucial to ensure the density modulation can eventually be recovered and further compressed.

ISBN 978-3-95450-134-2

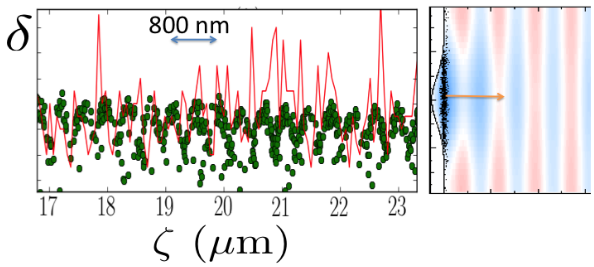

Figure 3: Particle-in-cell simulation of optically-enhanced field emission. Zoomed view (left) of the LPS recorded 300-nm from the cathode surface (the circles represent macroparticle and the red trace is a population histogram) and (right) overview of simulated nanohole geometry. Figure courtesy from A. Lueangarawong (NIU).

This optically-enhanced field-emission technique could in principle be extended by considering a two-dimensional arrays of nanoholes thereby allowing for the generation of electron “crystals" tailored for coherent emission in, e.g., inverse Compton scattering setups.

ENERGY-MODULATIONS TECHNIQUES

Bunching low energy-electron (non-relativistic) beams is often accomplished via the introduction of velocity modulations. This technique was further adapted for higher energy electron beam, e.g., typically produced in photoinjectors using energy-modulation methods to bunch the beam prior to its injection in a downstream linac [25], or to produce ultra-short bunch for, e.g., ultra-fast-electron-diffraction application [5].

Introducing an energy modulation of the form $\delta_0 = \sum_{i=1}^{n} A_i \cos(k_i \zeta_0 + \phi_i)$ (where A_i, k_i and ϕ_i are respectively the energy-normalized amplitude, wavevector and phase associated to the electromagnetic waves used to introduce the modulation). Given the energy modulation and a downstream beamline with longitudinal dispersion R_{56}, the final electron position within the bunch is $\zeta = \zeta_0 + R_{56}\delta_0$ (linear approximation). Typically the R_{56} is introduced by dispersive beam lines, e.g. chicanes. Here we note that for non ultra-relativistic beam, a drift of length D has a longitudinal dispersion given by $R_{56} = -\frac{D}{\beta^2\gamma^2}$.

Modulations via Radiation Fields

It has long been recognized that the short-range radiation field or wakefield could be capitalized on to introduce correlation in the LPS. Wakefields have been recently employed to introduce energy modulation or remove remanent time-energy chirps downstream of bunch compressors [26, 27]. The ability of some compact structures, e.g., dielectric-lined waveguides (DLWs), to support high-frequency modes (e.g. in the THz regime) has also enable the impression of energy modulation for possible bunch-train generation [28]. It was recently recognized that the introduced energy modulation is large enough to directly enable bunching in a subsequent drift when combine with low-energy beams [29]. The interaction of a bunch with its wakefield lead to an energy change described by the convolution integral

$$\Delta\mathcal{E}(\zeta) = LQ\int_{-\infty}^{\zeta} G(\zeta-\zeta')\Lambda(\zeta')d\zeta', \qquad (2)$$

where Q is the bunch charge, L the length of the structure, $\Lambda(\zeta)$ is the charge distribution (satisfying $\int \Lambda(\zeta)d\zeta = 1$), and the Green's function taken to be $G(\zeta) = 2\kappa\cos(k\zeta)$ for a single-mode structure with wavevector k and loss factor κ. In order to illustrate the scheme we consider a parabolic charge-density profile $\Lambda(\zeta) = [3Q/(2a^3)](a^2 - \zeta^2)$ for $|\zeta| \le a$ where a is the half-width of the distribution; see Fig. 4(a). Figure 4(b) illustrates for two case of mode wavelength. When the rms bunch length fulfills $\sigma_\zeta \simeq \lambda/2$; the wakefield introduces a single-cycle energy modulation while in the case $\sigma_\zeta \simeq 4\lambda$ the wakefield impresses a few-period energy modulation. The former case yields to an energy depression between the head and tail of the bunch which has the proper sign to be compressed via ballistic bunching in a subsequent drift. Although the introduced chirp is nonlinear, it can eventually lead to the production of a high-peak current for a fraction of the bunch population while the remaining population is debunched. Despite this drawback, this scheme is appealing given its simplicity and absence of need for a precisely synchronized external field as required in, e.g., ballistic bunching based on a buncher cavity [5]. Additionally, for the case of an energy modulation [red trace in Fig. 4(b)], the modulation converts into a density modulation in the drift following the wakefield structure and leads to the generation of a train of bunches as illustrated in Fig. 5. The numerical simulations were carried out for a configuration consisting of an RF gun, a dielectric-lined waveguide (DLW), and two solenoids [29]. Overall the formation of bunch trains with

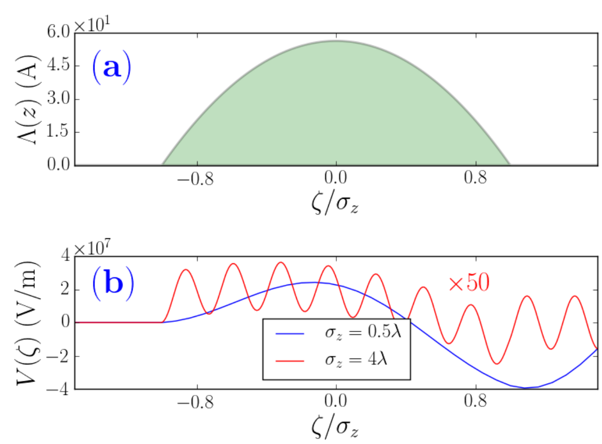

Figure 4: Parabolic charge distributions (a) and corresponding wake potential (b) for two cases of ratio between the rms bunch length σ_ζ and DLW fundamental-mode wavelength λ. The head of the bunch corresponds to $\zeta \le 0$. The wake potential associated to the $\sigma_\zeta = 4\lambda$ case is scaled by a factor 50 for clarity.

ISBN 978-3-95450-134-2

this technique leads to higher peak current and bunching factors than the wave-breaking method discussed in the next section.

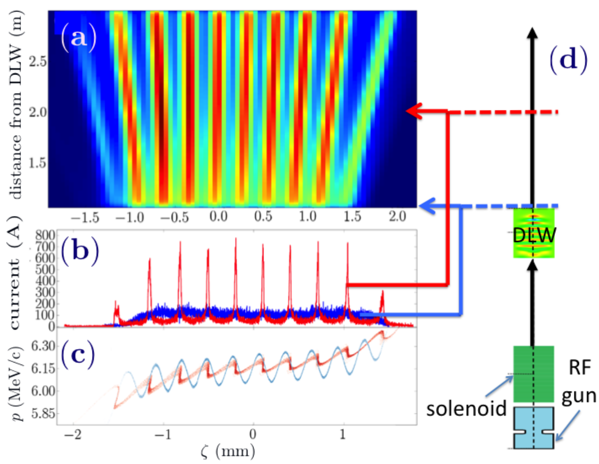

Figure 5: Example of bunch train formation using wakefields. Evolution of the bunch density distribution behind the DLW structure (a) with corresponding initial (blue) and final (red) current (b) and longitudinal phase space (a). The schematic (d) shows the simulated setup. Figure adapted from Ref. [29].

It was also suggested to cascade several DLWs to form ultrashort temporal structures on the bunch in a manner similar to the EEHG technique [30]. The scheme, dubbed wakefield-assisted high-harmonic generation (WAHHG), was simulated using a 5-MeV beam produced in a S-band photoinjector. At these low energies, the chicanes required to introduce the required longitudinal motion can be replaced by drift spaces [31]. Figure 6 demonstrates the concept of WAHHG, the beam evolution is identical to the EEHG method albeit for the reduced number of modulation (given that the bunch length is only one order of magnitude larger than the wavelength of the mode supported by the DLW mode (typically $\lambda \sim 100\ \mu$m). Scaling the technique to shorted wavelength is possible but would require DLWs with smaller apertures with associated impact on the electron beam transmission. The technique was also implemented at higher beam energy using a series of modulator-chicane modules as done for the EEHG approach [32].

Finally, it should be pointed out that other wakefield mechanisms, e.g., the use of a corrugated pipes [3] or plasmas could provide alternatives to DLWs while leading to similar results.

Modulations via Velocity Fields

An interesting and rather counter-intuitive technique for producing comb-like electron distributions consist in exploiting the space-charge forces occurring in beam with initial density modulations Ref. [33]. The idea recognizes that in a modulated cold plasma, plasma oscillations occur (with period T_p) and the density modulation cycles to energy modulation and vice versa every $T_p/4$. When the initial modulation becomes large (corresponding to an initial bunching factor $b \simeq 1/4$, a phenomenon akin to wave breaking occurs and leads to an enhancement of the bunching factor after $T_p/2$. The technique was experimentally demonstrated at UCLA [33]. Additionally the method was shown to be controllable and capable of forming bunch trains after acceleration in a linac [34].

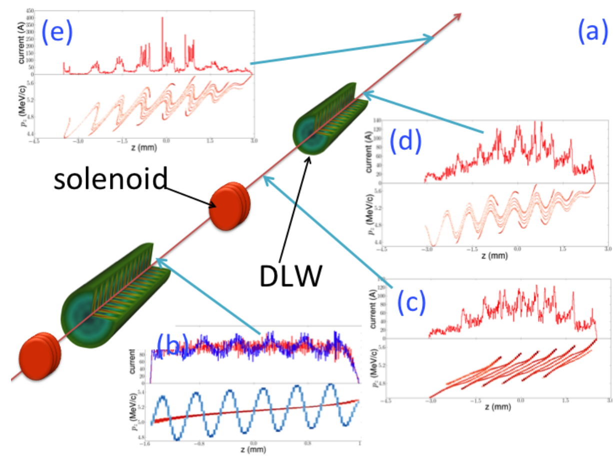

Figure 6: Concept for wakefield assisted high harmonic generation (WAHHG). A modulation is introduced (b) in the first dielectric-lined waveguide (DLW), the subsequent drift over bunch the beam (c) and a final DLW structure superimposes another energy modulation resulting in energy bands (d). After a subsequent drift the energy bands eventually lead to multiple spikes (e). Figure adapted from Ref. [31].

Modulations via External Fields

Energy modulations can also be introduced via external field as commonly done in conventional setups based on RF components. Here we note that recent progress in the efficient generation of THz pulses have open new possibilities. The THz regime is of interest as the wavelengths $\lambda \in [0.1, 1]$ mm are comparable to the electron bunch lengths typically generated by RF guns. THz radiation generation via optical rectification of an IR laser pulse using a cooled lithium niobate wedged crystal has achieved efficiency on the order of 10% thereby opening the path to mJ THz pulses [35, 36].

A possible configuration for a THz buncher involves an IFEL process [37]. The energy-depleted IR laser pulses used to produce the required UV pulses for photoemission can be directed to an optical-rectification stage to generate $\sim \mu$J THz pulses. The produced THz pulse is then co-propagated in an undulator to interact with the electron bunch via an IFEL interaction (coupling through transverse field/velocity). In order to control the phase velocity of the THz pulse, a waveguide is introduced in the undulator. This bunching scheme has the advantage of being immured to jitter as both the bunch and THz pulse are derived from the same laser system. Simulations performed for the PEGASUS photoinjector indicate that the method is well matched to the bunching of ~ 5 MeV electron bunches typically formed in the blow-out

ISBN 978-3-95450-134-2

regime and could lead to bunch durations on the order of ~ 10 fs [37].

In the latter THz buncher, the co-propagated THz pulse is a TEM_{00} mode and the energy exchange occurs through the transverse field. Converting this mode into a radially polarized mode TEM^*_{01} (which as an axial electric field) could essentially enable the THz pulse to introduce an energy modulation via coupling through its axial field, e.g., as done in a conventional linac. The challenge resides in the need for mJ pulse compared to the IFEL buncher. In addition, for non ultra-relativistic beams relative phase slippage between the beam and THz pulse becomes important so that the interaction naturally leads to compression via velocity bunching as discussed in [38].

MANIPULATIONS BETWEEN TWO DEGREES OF FREEDOM

Phase-space manipulations within two, or three, degrees of freedom have emerged the past decade [39] and can offer flexible alternative to shape the longitudinal distribution of electron bunches [17]. At low energies these methods can be combined with an interceptive mask, or can directly exploit correlation introduced during the electron-emission process.

In brief the technique rely on exchanging phase-space coordinate between one of the transverse degree of freedoms [here taken to be the transverse phase space (x, x')] with the longitudinal one (ζ, δ). The main challenge is to devise accelerator beamlines, in the $\widetilde{\boldsymbol{X}} \equiv (x, x', \zeta, \delta)$ coordinate system, capable of providing a 2×2 anti-block diagonal transverse matrix [14]. Over the years various beamline – or phase-space exchanger beamlines – have been proposed. Most of the exchangers incorporate a deflecting cavity located between either two doglegs [40] or within a chicane [41]. Other schemes include the possible use of transverse-gradient undulators [42].

These techniques were tested at low energies (~ 15 MeV) at the Fermilab's AOPI photoinjector [43]. A multi-slit mask was used to generate a transversely segmented electron bunch which was subsequently transformed into a train of bunch [44, 45]; see Fig. 7. The experiment especially showed the flexibility of the method: varying the input Courant-Snyder parameters upstream of the exchanger beamline could provide control over the bunch train parameters (e.g. separation).

The method was later combined with a transverse shaping of the laser spot on the photocathode and the experiment demonstrated the possibility to map the transverse distribution generated at the cathode surface in the temporal domain; see Fig. 8 [46].

This latter idea was further expanded to combine structured cathodes with nanoscale periodicities to produce trains of bunches at the attosecond scale [47, 48].

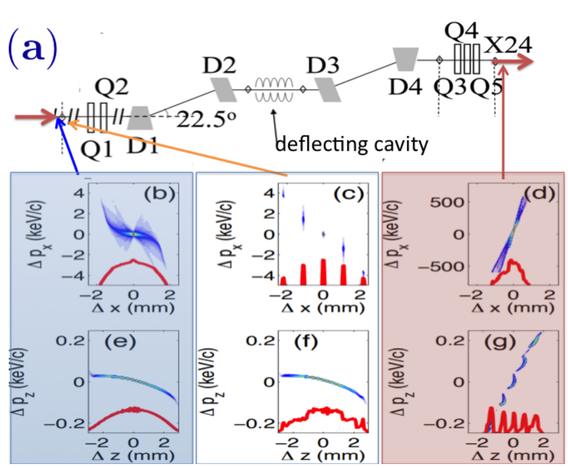

Figure 7: Example of phase space exchanger beam line (a) with corresponding initial (b,e), collimated (c,f) and final (d,g) transverse (b-d) and longitudinal (e-g) phase spaces.

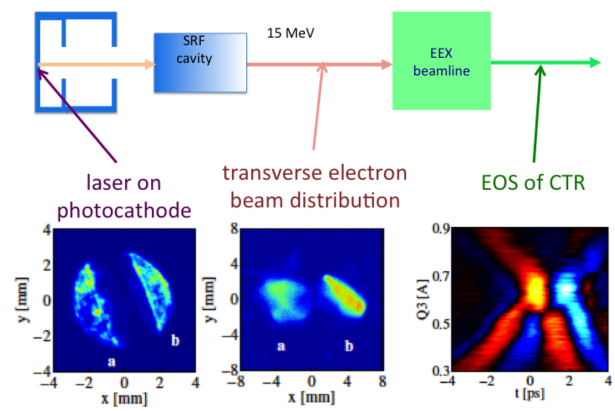

Figure 8: Formation of a twi bunch using a transversely segmented photocathode laser pulse via a phase space exchange (top). A twin pulse (to transversely seperated laser pulse (lower left image) produces a transversely segmented electron beam (lower middle image) converted into two bunches with variable delay (lower right image). Adapted from Ref. [46].

SUMMARY

This paper provides a non-exhaustive review of concepts recently devised to longitudinally compress or shape the current distribution of non-ultra-relativistic electron bunches.

This paper represents the work of many people and has in particular greatly benefited from collaborations with W. S. Graves (MIT), F. Lemery (CFEL/U. Hamburg), A. Halavanau (NIU), A. Lueangaramwong (NIU), T. Maxwell (SLAC), D. Mihalcea (NIU), and Y.-E Sun (ANL). I am grateful to the FEL15 scientific program committee for the invitation to present this review.

REFERENCES

[1] A. Gover, Phys. Rev. ST Accel. Beams **8**, 030701 (2005).

[2] T. Tajima and J. M. Dawson Phys. Rev. Lett. **43**, 267 (1979).

[3] K. L. F. Bane, P. Chen, P. B. Wilson, SLAC-PUB-3662 (1985).

[4] C. Mitchell, J. Qiang, and P. Emma, Phys. Rev. ST Accel. Beams **16**, 060703 (2013).

ISBN 978-3-95450-134-2

[5] T. van Oudheusden, P. L. E. M. Pasmans, S. B. van der Geer, M. J. de Loos, M. J. van der Wiel, and O. J. Luiten Phys. Rev. Lett. **105**, 264801 (2010).

[6] P. Musumeci, J. T. Moody, R. J. England, J. B. Rosenzweig, and T. Tran, Phys. Rev. Lett. **100**, 244801 (2008).

[7] P. Piot, Y.-E Sun, T. J. Maxwell, J. Ruan, E. Secchi, J. C. T. Thangaraj, Phys. Rev. ST Accel. Beams **16**, 010102 (2013).

[8] A. M. Weiner, Rev. Sci. Instrum., **71**, 1929 (2000).

[9] P. Tournois, Opt. Commun. **140**, 245 (1997).

[10] C. W. Siders, J. L. W. Siders, A. J. Taylor, S. Park, and A. M. Weiner, Appl. Opt. **37**, 5302 (1998).

[11] S. Zhou, D. Ouzounov, H. Li, I. Bazarov, B. Dunham, C. Sinclair, and F. W. Wise, Appl. Opt. **46**, 8488 (2007).

[12] Y. Li, K.-J. Kim, Appl. Phys. Lett., **71**, 1929 (2000).

[13] M. Boscolo, M. Ferrario, I. Boscolo, F. Castelli, S. Cialdi Nucl. Instrum. Meth. A **577** 409 (2007).

[14] M. Cornacchia, S. Di Mitri, G. Penco, and A A. Zholents, Phys. Rev. ST Accel. Beams **9**, 120701 (2006).

[15] G. Penco, M. Danailov, A. Demidovich, E. Allaria, G. De Ninno, S. Di Mitri, W.?M. Fawley, E. Ferrari, L. Giannessi, and M. Trovó, Phys. Rev. Lett. **112**, 044801 (2014).

[16] A. Zholents, W. Gai, R. Limberg, J. G. Power, Y.-E Sun, C. Jing, A. Kanareykin, C. Li, C. X. Tang, D. Yu Shchegolkov, E. I. Simakov, in Proc. of the 2014 Free-Electron Laser conference (FEL14), 993 (2014).

[17] P. Piot, Y.-E Sun, J. G. Power, and M. Rihaoui, Phys. Rev. ST Accel. Beams **14**, 022801 (2011).

[18] F. Lemery and P. Piot, Phys. Rev. ST Accel. Beams **18**, 081301 (2015).

[19] P. Hommelhoff, C. Kealhofer, M. A. Kasevich, Phys. Rev. Lett. **97**, 247402 (2006).

[20] R. Bormann, M. Gulde, A. Weismann, S.V. Yalunin, and C. Ropers, Phys. Rev. Lett. **105**, 147601 (2010).

[21] M. Krüger, M. Schenk, P. Hommelhoff, Nature **475**, 78 (2011).

[22] R.H. Fowler and L. Nordheim, Proc. Royal Soc. of London. Series A, **119**, 173-181 (1928).

[23] J. L. Vay, D. P. Grote, R. H. Cohen, A. Friedman, Comput. Sci. Disc. **5** 014019 (2012).

[24] R. K. Li, H. To, G. Andonian, J. Feng, A. Polyakov, C. M. Scoby, K. Thompson, W. Wan, H. A. Padmore, P. Musumeci, Phys. Rev. Lett. **110**, 074801 (2013).

[25] G. A. Krafft, in Proc. of the Microbunches Workshop, AIP Conference Proceedings **367**, 46 (1996).

[26] S. Antipov, C. Jing, M. Fedurin, W. Gai, A. Kanareykin, K. Kusche, P. Schoessow, V. Yakimenko, and A. Zholents, Phys. Rev. Lett. **108**, 144801 (2012).

[27] P. Emma, M. Venturini, K. L. F. Bane, G. Stupakov, H.-S. Kang, M. S. Chae, J. Hong, C.-K. Min, H. Yang, T. Ha, W. W. Lee, C. D. Park, S. J. Park, and I. S. Ko, Phys. Rev. Lett. **112**, 034801 (2014).

[28] S. Antipov, M. Babzien, C. Jing, M. Fedurin, W. Gai, A. Kanareykin, K. Kusche, V. Yakimenko, A. Zholents, Phys. Rev. Lett. **111**, 134802 (2013).

[29] F. Lemery, P. Piot, Phys. Rev. ST Accel. Beams **17**, 112804 (2014).

[30] G. Stupakov, Phys. Rev. Lett. **102**, 074801 (2009).

[31] F. Lemery, P. Piot, to appear in Proc. of the 16th Advanced Accelerator Concept (AAC14) workshop, San Jose CA (in press, 2015).

[32] P. Piot, F. Lemery, manuscript in preparation (2015).

[33] P. Musumeci, R. K. Li, A. Marinelli, Phys. Rev. Lett. **106**, 184801 (2011).

[34] P. Musumeci, R. K. Li, K. G. Roberts, Phys. Rev. ST Accel. Beams **16**, 100701 (2013).

[35] J. Hebling, K.-L, Yeh, M. C, Hoffmann, B. Bartal, K. A. Nelson, J. Opt. Soc. Am.B **25**, 6 (2008).

[36] J. Fülöp, L. Pálfalvi, M. C. Hoffmann, János Hebling, Opt. Express **19**, 15090 (2011).

[37] J. T. Moody, R. K. Li, P. Musumeci, C. M. Scoby, H. To, AIP Conf. Proc. **1507**, 722 (2012).

[38] L. J. Wong, A. Fallahi, F. X. Kärtner, Opt. Express **21**, 9793 (2013).

[39] M. Cornachia, P. Emma, Phys. Rev. ST Accel. Beams **6**, 030702 (2003).

[40] P. Emma, Z. Huang, K.-J. Kim, P. Piot, Phys. Rev. ST Accel. Beams **9**, 100702 (2006).

[41] D. Xiang and A. Chao, Phys. Rev. ST Accel. Beams **14**, 114001 (2011).

[42] L.D. Duffy, K.A. Bishofberger, B.E. Carlsten, A. Dragt, Q.R. Marksteiner, S.J. Russell, R.D. Ryne, N.A. Yampolsky, Nucl. Instrum. Meth. Sec. A **654**, 52 (2011).

[43] J. Ruan, A. S. Johnson, A. H. Lumpkin, R. Thurman-Keup, H. Edwards, R. P. Fliller, T. W. Koeth, Y.-E Sun, Phys. Rev. Lett. **106**, 244801 (2011).

[44] Y.-E Sun, P. Piot, A. Johnson, A. H. Lumpkin, T. J. Maxwell, J. Ruan, and R. Thurman-Keup, Phys. Rev. Lett. **105**, 234801 (2010).

[45] P. Piot, Y.-E Sun, T. J. Maxwell, J. Ruan, A. H. Lumpkin, M. M. Rihaoui, R. Thurman-Keup, Appl. Phys. Lett. **98**, 261501 (2011).

[46] T. Maxwell, J. Ruan, P. Piot, A. Lumpkin, R. Thurman-Keup, A. Johnson, Y.-E Sun, in Proc. of IPAC2012, New Orleans LA, 2789 (2012).

[47] W. S. Graves, F. X. Kärtner, D. E. Moncton, P. Piot, Phys. Rev. Lett. **108**, 263904 (2012)

[48] E. A. Nanni and W. S. Graves, preprint arXiv:1503.03493 [physics.acc-ph] to appear in Phys. Rev. ST Accel. Beams (2015)

ISBN 978-3-95450-134-2

ALKALI CATHODE TESTING FOR LCLS-II AT APEX*

H. Qian, D. Filippetto, J. Feng, J. Nasiatka, H. Padmore, F. Sannibale†,
LBNL, Berkeley, CA 94720, USA
R. Li, J. Schmerge, F. Zhou, SLAC, Menlo Park, CA 94025, USA

Abstract

Electron sources of high brightness and high bunch charge (~ 300 pC) with MHz repetition rate are one of the key technologies for next generation X-FEL facilities such as the LCLS-II at SLAC and the Euro XFEL at DESY. The Advanced Photoinjector EXperiment (APEX) at the Lawrence Berkeley National Laboratory (LBNL) is developing such an electron source based on high quantum efficiency (QE) alkali photocathodes and the VHF-Gun, a new scheme normal conducting RF gun developed at LBNL. The VHF-Gun already demonstrated stable CW operation with high gradient (20 MV/m), high gun voltage (~ 750 kV) and low vacuum pressure (~ 3×10^{-10} torr) laying the foundation for the generation of high brightness electron beams. In this paper, we report the test and characterization of two different alkali cathodes in high average current (several hundreds of pC per bunch with MHz repetition rate) operation at APEX. Measurements include cathode life time, QE map evolution and thermal emittance characterization, to investigate the compatibility of such cathodes with APEX gun for the challenging requirements of LCLS-II.

INTRODUCTION

Next revolutionary FEL light source facilities, such as the LCLS-II at SLAC [1], requires MHz beam repetition rate with similar peak brightness as the state of the art ~ 100 Hz FEL drivers [2]. From the perspective of electron source, such a requirement translates to an electron gun of both high electric field and high duty cycle, and a photocathode of high quantum efficiency(~ 1%), low thermal emittance (< 1 mm.mrad/mm) and long life time (> 1 week) [3].

R&D on innovative electron gun technologies addressing the need of simultaneous high peak field and high duty cycle, from DC sources to Superconducting Radiofrequency Guns has made a lot of progress [3]. Though normal conducting high frequency (~ GHz) RF guns have provided beams of tremendous high peak brightness with 100 Hz repetition rate, they are criticized for not being able to reach higher duty cycle due to thermal load. Our group at Lawrence Berkeley National Laboratory has focused the effort on the new type of normal conducting RF gun resonating in the VHF frequency range (APEX, [4]), which has achieved reliable operation in continuous wave mode (CW) with accelerating fields (in excess of 20 MV/m) required to produce low emittance-high charge electron beams with high peak current needed to drive the next generation of Free Electron Lasers [5]. The basic gun parameters for cathode testing are shown in Table 1.

Table 1: Nominal APEX VHF Gun Parameters

Parameter	Value	Unit
$E_{cathode}$ in CW mode	20	MV/m
f_{rf}	185.71	MHz
E_k	758	keV
Base Pres. rf off	4×10^{-11}	Torr
Base Pres. rf on	3×10^{-10}	Torr

High brightness, high-yield photocathode materials are essential for high repetition rate electron sources. Unfortunately, such materials are usually very reactive semiconductors and their performances tend to degrade very fast with time and extracted charge, which can be a serious limitation to the operation of a future facility like LCLS-II and has been subject of intense studies in recent years [6]. The degradation of high QE semiconductor photocathodes are mainly due to three reasons, first is reaction with residual gases in vacuum, second is back bombardment of ionized residual gases or field emitted electrons, third is laser heating. Two categories of alkali photocathodes are tested at APEX gun to characterize its feasibility to host high QE semiconductor cathodes. First is UV sensitive Cs_2Te cathode, and second is the green sensitive antimonide cathodes (Cs_3Sb and K_2CsSb). The Cs_2Te cathode testing inside APEX gun has finished [7], and testing of antimonide cathodes just started, both are presented in this paper.

APEX BEAMLINE AND LASER SYSTEM

Cathode testing is done using the APEX phase I beamline, as shown in Fig. 1. It starts with the core part, the VHF gun and cathode loadlock system, and a set of beam diagnostics follows, such as ICT, YAG screen, Farady cup, emittance slits, deflecting cavity and energy spectrometer magnet, which are used to characterize both cathode and beam transverse and longitudinal phase space.

The Cs_2Te cathode is tested with a home made Yb-doped fiber laser system [8]. The 37.14 MHz oscillator seed a chain of Yb-doped fiber amplifiers. The repetition rate is reduced down to 1 MHz during amplification. The total IR beam is about 1 W, and after two second harmonic generations, both green and UV laser are available for the cathode testing. Recently, a similar commercial laser with 2 W IR power is installed, and will be used for antimonide cathode testing and APEX phase II commissioning.

* Work supported by the Director of the Office of Science of the US Department of Energy under Contract no. DEAC02-05CH11231
† fsannibale@lbl.gov

ISBN 978-3-95450-134-2

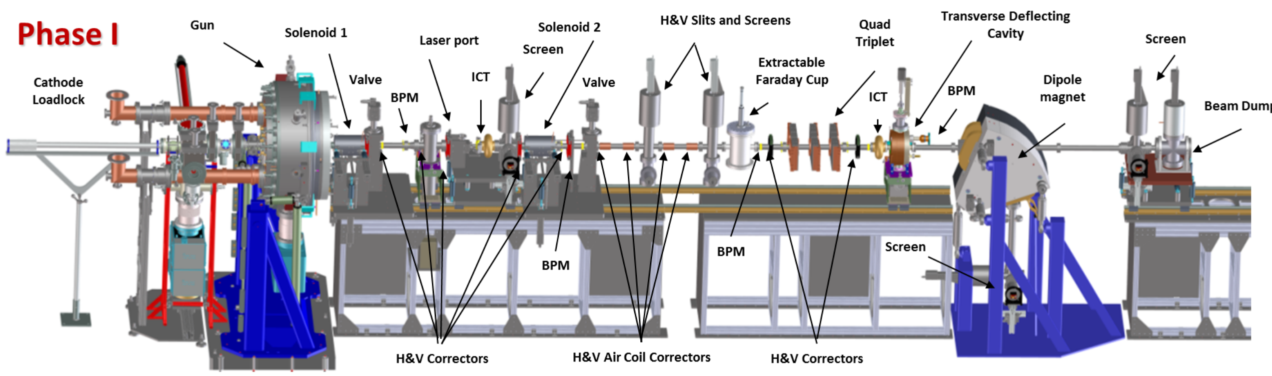

Figure 1: Cathode tested at APEX phase I beamline.

CESIUM TELLURIDE

The photoemission threshold of Cs_2Te is in UV, and with QE above 1%, it's a good candidate to produce high bunch charge (~ 300 pC) beam at 1 MHz required by LCLS-II. Besides, it has been tested in pulsed normal conducting RF guns [9,10], and has shown both good QE and good life time with vacuum above 10^{-9} torr, but whether Cs_2Te cathode can survive the CW normal conducting gun is still an open question.

APEX Cs_2Te cathodes are purchased from INFN-LASA [11], which are round thin film of Cs_2Te deposited at the top of the polycrystalline molybdenum plug [12] on a region of 5 mm diameter. The cathodes were shipped to Berkeley in a vacuum suitcase, and stored for more than a year before installation in the experimental apparatus. During the entire period the total pressure in the chamber was kept below 10^{-9} Torr via Non Evaporable Getter pumps (NEGs). A map of the quantum efficiency of the fresh cathode is reported on the left side of Fig. 2, together with a picture of the deposited area on top of the plug.

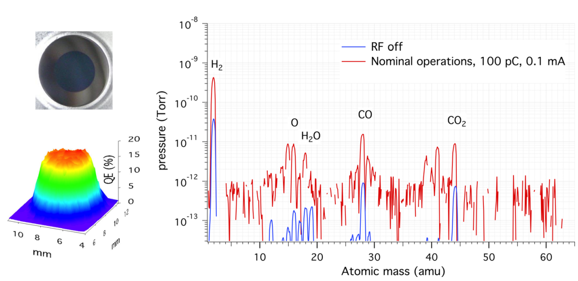

Figure 2: Left: image and QE map of the Cs_2Te cathode before operations (Courtesy of D. Sertore, INFN/LASA). Right: residual gas analysis in the APEX gun without RF power (blue) and during 0.1mA operations (red) (from [7]).

Gun Vacuum

As already mentioned, low gas pressure in the gun is of paramount importance for cathode lifetime: the total pressure determines the rate of ion production, causing cathode bombardment, while the presence of specific elements and compounds leads to chemical contamination. In the case of Cs_2Te, it has been demonstrated its receptivity to O and CO_2, while it has shown to be fairly insensitive to CO, N_2, and CH_4 [13]. The right plot of Fig. 2 reports residual gas analysis traces in the VHF gun in absence of electric field and during operations, with nominal CW power and 0.1 mA average current. In both cases, the total pressure is dominated by the partial pressure of hydrogen, with the other chemical species down by about two decades. The gas pressure is fairly insensitive to the value of extracted average current, while directly dependent on the average RF power feeding the cavity.

QE Degradation

In order to characterize and understand the dependencies of the cathode performance on the specific operating conditions, we performed continuous measurements of the same cathode plug for a period of a week, changing the average current extracted. The measurements were done on the same cathode plug, characterized by QE values and QE maps.

According to the previous findings [13], the main cause of contamination is caused by reaction of cesium with oxygen and carbon dioxide, with the poisoning effect of oxygen being about 100 times faster. Therefore, to a good approximation, only oxygen pressure can be considered in assessing the degradation by contamination. Residual gas analysis of the APEX gun volume (Fig. 2) shows an increase of the oxygen line by about 2 orders of magnitude when the RF power is feeding the cavity. Oxygen is desorbed by the cavity walls during operations, due to RF heating and X-rays absorption by the cavity surface. Most of the contamination will therefore happen during operations. Figure 3 reports QE evolution during operations. The horizontal axis reports the hours of operation of the electron gun, with RF power feeding the cavity, both with and without electron beam extraction. The top-axis shows the total exposure to oxygen, expressed in Langmuirs (10^{-6}torr·s). A fit of the measurements reveals a $1/e$ lifetime of about 14.5 Langmuirs which, in our case, corresponds to about 402 h of operations, consistent with the previous measurements at low fields and low currents [13], and fulfils the baseline requirement of LCLS-II.

ISBN 978-3-95450-134-2

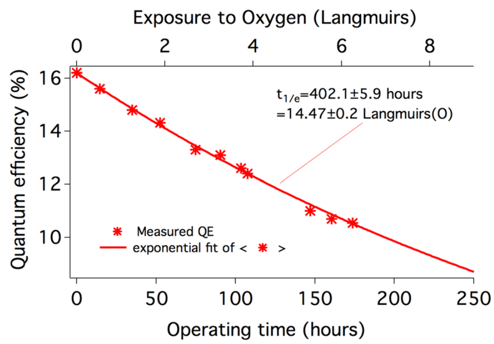

Figure 3: Exponential fit of QE as function of operational time and exposure to oxygen (from [7]).

Besides, cathode sputtering by ion and electrons bombardment is a major concern when running at high average currents. Such effect is generally very large in DC guns, as the static accelerating field captures all the positively charged ions and accelerate them back to the cathode creating dips in QE at the center of the cathode [14]. In our case the accelerating field is oscillating at a frequency of about 186 MHz, and only a small fraction of ions are captured by the field and find their way back to the cathode [15]. The damage rate of ion back-bombardment is proportional to the total pressure in the gun and to the average beam current. We measured cathode lifetime against different average beam currents, and no correlation between QE lifetime and average current was detected within the experimental accuracy upon variation of average current by more than one order of magnitude (from 0.02 mA to 0.3 mA), implying negligible contribution to the degradation by the back-bombardment at such currents and vacuum levels. In particular there was no evidence of locally enhanced degradation due to either bombardment or laser heating, enabling beam operations at the rf center of the cathode. The right plot of Fig.4 gives an example of QE map, taken at the end of the measurement campaign, which shows quasi-uniform QE degradation of the cathode.

RF assisted QE Rejuvenation

It has already been shown [13] that QE degradation can be partially recovered. Such rejuvenation requires heating and illumination with UV light for breaking the strong ionic bonds formed between oxygen and cesium. Consistently with such previous findings we observed a slight increase of QE at the beginning of each run.

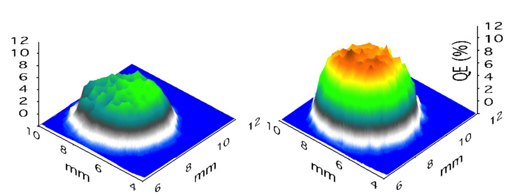

Figure 4: QE degradation after the 3-week shutdown and QE rejuvenation after few hours of gun operation at full power (from [7]).

Quantum efficiency degrades also during machine shutdowns. Without rf power in the cavity oxygen levels are too low for explaining the measured rate of degradation with cathode oxidation. One possible alternative is the formation of weak bonds (Van der Walls-like) between the cathode surface elements and the residual gas molecules in the cavity (expecially water). Such bonds are very weak, with characteristic distances in the range of 0.3-0.6 nm and energies in the 0.2-20 meV range, and an externally applied field of 20MV/m is sufficient to break them apart. QE rejuvenations at the beginning of each restart of APEX gun running were routinely observed, and one example is shown in Fig. 4. The QE at the cathode center before the 3-week shutdown was 11%, while it dropped down to about 5.5% at the restart (left map of Fig. 4). After few hours of operation following the shutdown, it recovered 11% QE as well as the flat QE distribution before the shutdown (right plot of Fig. 4).

Thermal Emittance

Thermal emittance was characterized, by measuring the electron beam size at the first viewscreen as function of the solenoidal lens strength. The emittance of 500 fC beam was measured for different laser spot sizes at the cathode, and a linear regression of the results lead to a value of respectively 0.72 ± 0.07 and 0.79 ± 0.05 $\mu m/mm$ RMS for horizontal and vertical emittances, in line with previous results on the same type of cathode [16].

Cathode Surface Analysis

We have demonstrated negligible correlation of cathode lifetime with average current, and indicated the surface oxidation during operations as the main mechanism of QE degradation. In fact, we experienced another deterioration mechanism: field-emitted electron sputtering.

Some fied emission electrons can be directed toward the cathode plug causing erosion and ejection of atoms from the active film. Others hit the anode walls producing secondary electrons that are then accelerated back at the opposite phase of the field, hitting the cathode [12]. Figure 5-A shows the evolution of iso-QE lines (12%) of a fresh cathode at constant time intervals (5.5 hours) during operations. After a quick degradation of the right side of the cathode the QE stabilizes. The inset of Fig.5-A shows the imaging on a downstream screen of field-emitted distribution at the cathode, after compensation for the solenoid rotation. The field emitters are distributed along the edges of the circular gap between cathode plug and cavity wall, and are concentrated on the right side of the cathode.

Post-mortem analysis of the cathode confirms the cause of asymmetric degradation. Figure 5-B shows interferometric measurements done on the plug. The white inner circle delimits the active region of the plug (deposition area). The macroscopic features of the area include a peak and a valley corresponding to the high and low QE areas of the cathode. The difference in height is on the order of the initial Cs_2Te coating, suggesting reduction of deposited material.

ISBN 978-3-95450-134-2

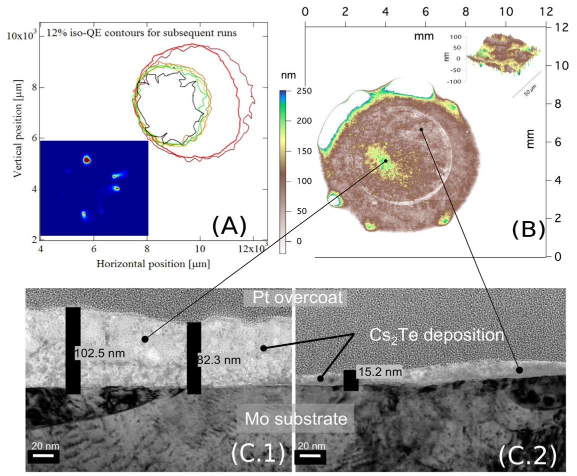

Figure 5: (A) Iso-QE lines during operations. The inset shows the asymmetric distribution of field-emitted particles, imaged at the beamline viewscreen. (B) Post-mortem interferometry on the cathode surface showing asymmetric erosion. The difference between peaks and valleys is at the level of film deposition thickness. (C.1-C.2) Post-mortem TEM measurements of the Cs_2Te layer in the peak and valley as shown in figure (from [7]).

Such hypothesis is confirmed by TEM measurements in Fig. 5-C.1(C.2). Two $5\mu m$-wide samples, chosen from the peak and the valley as shown in the figure, were prepared by Focused Ion Beam lift-out technique and exposed to 200 kV electron beam for imaging. Platinum were deposited on the region of interest to protect from ion implantation and damage of the surface of interest. The large thickness difference of active deposition measured between the two areas explains the difference in quantum efficiency [17]. Such cathodes are grown by deposition of 10 nm of Tellurium and consequent deposition of Cesium by evaporation. About 70 nm of Cesium have been experimentally found to be the optimum for QE, with an atomic ratio between Cs and Te of about 2.5 [13]. We have performed Energy dispersive X-ray spectroscopy on the film to measure the element composition. Nine different point spectra at different locations around the film were measured with 10 and 20 kV beam energies, and an overall mapping using 8 kV beam was performed. Traces of molybdenum (substrate) have been found on all the measurements, as well as small amounts of oxygen and carbon. The atomic percent of Te and Cs varies along the cathode and, while in the high-QE region (lower-right side of the film) the atomic percent ratio Cs/Te is close to 1.5, it rapidly decreases well below 1 moving toward the low-QE region (upper-left side). Such decrease of Cesium on the surface explains the difference in QE between different areas [13], while the asymmetric distribution of field emitted electrons matching the cathode QE map suggests the cause of the degradation speed between different areas of the film to be electron sputtering.

GUN IMPROVEMENTS BENEFIT CATHODE OPERATION

After the Cs_2Te cathode testing, the APEX gun went through a full refurbishment. The mating surface between cathode and anode halves of the cavity showed signs of degradations. In particular the rf spring was damaged in some points due to poor RF contacts. The mating surface was polished and machined again, and the RF spring was substituted with a new one of thicker gold coating, which improved the unloaded Q and thus reduced the RF heat load by 15%. The highest temperature of the anode cavity wall dropped from lim 100°C to ~ 70°C, and the vacuum pressure at nominal gun voltage went from 8×10^{-10} torr to 3×10^{-10} torr. Besides, the cathode/anode region were processed with dry ice cleaning and mirror-like hand polishing, which reduced the transported dark current downstream the APEX beamline from 350 nA to < 0.1 nA at nominal gun voltage, more than 3 orders of magnitude reduction. With the above improvements of the gun, life time of the Cs_2Te cathode is expected to be even longer than the one reported in Fig. 3.

ALKALI ANTIMONIDE CATHODES

Alkali antimonide cathodes are sensitive to green laser, which could simplify the photoinjector driving laser system in terms of power, transverse profile quality, feedback control and diagnostics. Besides, alkali antimonide cathodes have smaller thermal emittance compared with Cs_2Te cathodes [18], which can help in further improving LCLS-II beam emittance. APEX is collaborating with ALS photocathode lab on alkali anotimonide cathode preparation, and antimonide cathode testing results inside APEX gun will help optimize cathode preparation recipe, such as deposition sequence, thickness, roughness et al. Initial testing results have shown QE above 1% for CsK_2Sb inside the APEX gun, and further alkali antimonide cathode testing is still to be done.

CONCLUSION

We have tested two categories of alkali cathodes for continuous operations in high average current electron injectors for the next generation of Free Electron Lasers. The UV sensitive Cs_2Te cathode has been characterized for the first time in a normal conducting CW system providing simultaneous high accelerating fields and mA-scale current. The results demonstrate that such cathodes are robust enough to withstand continuos operations in the APEX-like operating conditions. The green sensitive alkali antimonide cathodes testing is still in progress. The successful blending between the normal conducting APEX VHF gun and semiconductor cathodes opens the doors to a new generation of scientific instruments, as high repetition rate Free Electron Lasers, where peak brightness meets high flux.

ISBN 978-3-95450-134-2

ACKNOWLEDGMENT

The authors would like to thank M. Zolotorev for useful discussions, Russell Wells for the coordination of all mechanical activities that allowed to perform the presented measurements, and D. Sertore for providing the cathodes. The authors acknowledge support from DOE grants No. DE-AC02-05CH11231.

REFERENCES

[1] T. Raubenheimer et al., WEB01, Proc. FEL2014, `http://www.JACoW.org`

[2] R. Akre et al., Phys. Rev. ST Accel. Beams 11, 030703 (2008).

[3] F. Sannibale et al., Journal of Modern Optics 58, 1419 (2011).

[4] F. Sannibale et al., Phys. Rev. ST Accel. Beams 15, 103501 (2012).

[5] J.F. Schmerge et al., THP042, Proc. FEL2014, `http://www.JACoW.org`

[6] D. Dowell et al., Nucl. Instrum. Methods A 622, 685 (2010).

[7] D. Filippetto et al., Applied Physics Letters 107, 042104 (2015).

[8] J. Feng et al., THP222, Proc. PAC'11, `http://www.JACoW.org`

[9] S. Schreiber et al., FRAAU05, Proc. FEL2008, `http://www.JACoW.org`

[10] N. Terunuma et al., Nucl. Instrum. Methods A 613, 1 (2010).

[11] `http://wwwlasa.mi.infn.it/ttfcathodes/`

[12] R. Huang et al., Phys. Rev. ST Accel. Beams 18, 013401 (2015).

[13] A. Di Bona et al., J. Appl. Phys. 80, 3024 (1996).

[14] B. Dunham et al., Appl. Phys. Lett. 102, 034105 (2013).

[15] J. Qiang, Nucl. Instrum. Methods A 614, 1 (2010).

[16] D. Sertore et al., MOPKF045, Proc. EPAC'04, `http://www.JACoW.org`

[17] P. Michelato, Nucl. Instrum. Methods A 393, 464 (1997).

[18] S. Karkare et al., TUOAB1, Proc. PAC'13, `http://www.JACoW.org`

ISBN 978-3-95450-134-2

EMITTANCE MEASUREMENTS OF THE ELECTRON BEAM AT PITZ FOR THE COMMISSIONING PHASE OF THE EUROPEAN XFEL

G. Vashchenko*, G. Asova†, M. Bakr‡, P. Boonpornprasert, J. D. Good, M. Gross, C. Hernandez-Garcia§, H. Huck, I. Isaev, D. Kalantaryan, G. Kourkafas, M. Krasilnikov, D. Malyutin, D. Melkumyan, A. Oppelt, M. Otevrel, Y. Renier, T. Rublack, F. Stephan, Q. Zhao¶, Deutsches Elektronen-Synchrotron, Zeuthen site, Zeuthen, Germany
O. Lishilin, G. Pathak, Hamburg University, Hamburg, Germany

Abstract

For the operation of free electron lasers (FELs) like the European XFEL and FLASH located at DESY, Hamburg Site, high quality electron beams are required already from the source. The Photo Injector Test facility at DESY, Zeuthen Site (PITZ), was established to develop, characterize and optimize electron sources for such FELs. Last year the work at PITZ focused on the optimization of a photo injector operated very close to the startup parameters of the European XFEL. This implies photocathode laser pulses with a Gaussian temporal profile of about 11 – 12 ps FWHM to drive the photo gun operated at a gradient of about 53 MV/m. Significant effort was spent on the electron beam characterization and optimization for various bunch charges. Emittance measurements were performed as a function of major accelerator parameters such as main solenoid current, laser spot size on the cathode and the gun launching phase. The requirement on the beam emittance for a bunch charge of 500 pC for the European XFEL commissioning phase has been demonstrated. Results of these studies accompanied with the corresponding simulations are presented in this paper.

INTRODUCTION

Free electron lasers like the European XFEL and FLASH require high quality electron beams already from the photo injector [1, 2]. The commissioning phase of the European XFEL injector section is planned to start end of 2015. For the commissioning phase there are reduced requirements on the operation conditions and electron beam quality as compared to the nominal ones in order to simplify the commissioning phase and operate the machine at most stable, reliable and robust conditions. Namely, it is planned to use a gun gradient reduced from 60 MV/m to 53 MV/m which corresponds to a reduced electron beam momentum after the gun from about 6.7 MeV/c to 6.1 MeV/c. The photocathode laser system used for the commissioning phase will produce transversally uniform pulses which correspond to the nominal operation, while the temporal profile will be Gaussian with a full width at half maximum (FWHM) of about 13 ps as compared to the nominal flat-top profile with an FWHM of 20 ps and rise/fall times of 2 ps. Various electron beam charges (0.1 – 1 nC) with corresponding electron beam quality are planned to be used for the nominal operation of the European XFEL [3]. For SASE (Self Amplified Spontaneous Emission) commissioning it is currently planned to use a bunch charge of 500 pC, which is in the middle of the nominal charge range. For this charge the requirement on the normalized transverse slice emittance during the commissioning phase is 1 mm mrad at the undulator section.

The possibility to run the European XFEL photo injector with the aforementioned parameters was validated at the Photo Injector Test facility at DESY, Zeuthen site (PITZ), which serves as an injector test-bed for FLASH and the European XFEL. A schematic layout of PITZ is presented in Fig. 1. Conditioning and characterization of the normal conducting L-band RF gun cavities is performed at PITZ for their further usage at the European XFEL and FLASH. The photoelectrons are produced with a Cs_2Te semiconductor photocathode. UV laser pulses which are transversely uniform and temporally Gaussian, with an estimated FWHM of about 11 – 12 ps, are currently used. The produced photoelectrons are accelerated in the gun cavity and are focused with the main solenoid installed at the exit of the gun. The bucking solenoid installed upstream the cavity is used to compensate the field of the main solenoid at the cathode plane in order to avoid initial angular momentum in the electron beam which spoils the electron beam quality. During the last run period the RF gun was operated at a maximum on-axis peak field of about 53 MV/m and 640 μs RF pulse length as required for the commissioning phase of the European XFEL. Several diagnostic devices are installed downstream the gun for the electron beam characterization (see Fig. 1). Further beam acceleration is done using a normal conducting L-band Cut Disk Structure (CDS) booster cavity which can increase the momentum of the electron beam up to about 22 MeV/c. The first Emittance Measurement SYstem (EMSY1) is installed directly at the exit of the CDS booster at about 5.3 m downstream the cathode. The transverse projected normalized emittance of the electron beam is measured using the conventional slit scan method based on a direct measurement of the electron beam size and angular spread [4]. More details about the PITZ setup can be found elsewhere [4–6].

* Grygorii.Vashchenko@desy.de
† on leave from INRNE-BAS, 1784 Sofia, Bulgaria
‡ on leave from Assiut University, 71515 Assiut, Arab Republic of Egypt
§ on leave from JLab, Newport News, VA 23606, USA
¶ on leave from IMP/CAS, 730000 Lanzhou, China

ISBN 978-3-95450-134-2

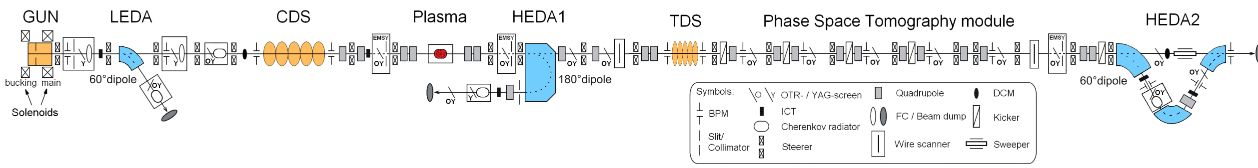

Figure 1: Schematic layout of the Photo Injector Test facility at DESY, Zeuthen site (PITZ).

BEAM DYNAMICS SIMULATIONS WITH REALISTIC TRANSVERSE LASER PROFILE

A Space charge TRacking Algorithm (ASTRA) code was used to perform beam dynamics simulations [7]. Electron beams of 1 nC, 500 pC, 250 pC and 100 pC were used in simulations as well as during the measurements. The gun on-axis peak field at the cathode was fixed to 53.25 MV/m based on the matching of the electron beam momentum of about 6.1 MeV/c measured experimentally and found during the simulations for the gun launching phase which provides the Maximum Mean Momentum Gain (MMMG). The CDS booster on-axis peak field was tuned in the same manner and resulted in 17.1 MV/m in order to achieve the electron beam momentum of about 21.0 MeV/c at MMMG phase as during the experimental measurements. The CDS booster launching phase was fixed to MMMG phase for simulations and measurements as it has a minor impact on the quality of the electron beam in a wide range [8]. Laser pulses with a Gaussian temporal profile and an FWHM of about 12 ps were used during the simulations as well as for measurements. The main solenoid current, gun launching phase and laser spot size on the cathode were used as input parameters for the multi-parameter optimization.

The transverse laser profile used in the simulation was generated using two different approaches. In the first, conventional approach the uniform transverse profiles of different sizes were used like in previous simulations [4–6] where the laser spot size was a parameter of optimization and was assumed to fit to the experiment. In a second more sophisticated approach, in order to better match the real laser transverse distribution at the cathode measured with the help of a CCD camera installed at an equivalent position, the transverse laser profile was generated as follows. At first, the measured laser transverse distribution is analyzed and converted to a radial profile by integrating over the azimuthal angle in 2π as shown in Fig 2a. The obtained radial profile can be split in two parts: the core part with a uniform distribution and the halo part with a Gaussian transition as shown in Fig. 2a. By fitting the experimental data with the corresponding model the radius of the uniform part Rc and the rms size of the Gaussian transition sigH are found. Using these values the corresponding cathode distribution, which will be used for simulations as shown in Fig. 2b, is generated. A small discrepancy between the values of Rc and sigH in Fig. 2a and 2b is caused by limited statistics during the generation of the initial cathode distribution for ASTRA: only $2 \cdot 10^5$ particles were generated in this case. More details on the generation of such distributions and their influence on beam dynamics can be found in [9]. When using a uniform

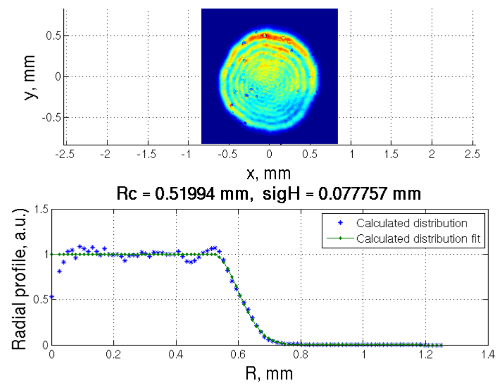

(a) Example of an analysis of a real laser transverse profile and generation of its radial profile. The generated radial profile is fitted with a multi curve: an uniform distribution with radius Rc and a Gaussian transition with an rms of sigH.

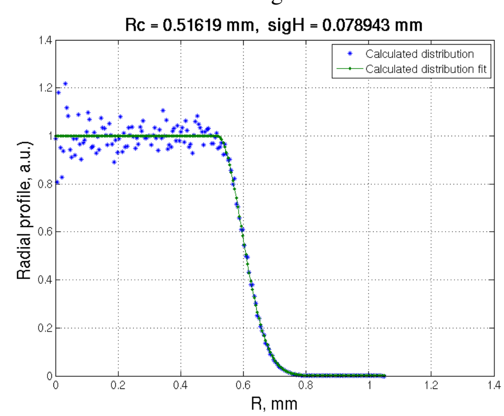

(b) Example of an ASTRA distribution (radial profile) generated with parameters found in the upper figure. Radial profile is fitted with the model described above and the fit parameters found are in a good agreement.

Figure 2: Example of generating an ASTRA input laser distribution with a realistic laser profile.

laser transverse distribution the beam dynamics simulations are quasi-continuous, while by using a more realistic distribution, as in the second approach, the beam dynamics simulations are performed only for the ceratin experimental conditions. Simulation results with both approaches for var-

ISBN 978-3-95450-134-2

ious electron beam charges are presented in the following section together with experimental data.

EMITTANCE SIMULATIONS AND MEASUREMENT RESULTS

Emittance dependencies on the main solenoid current, gun launching phase and rms laser spot size on the cathode were measured for various electron beam charges. At first, for a fixed electron beam charge the emittance dependence on the laser spot size on the cathode was measured at the MMMG gun launching phase as a phase which expects to deliver the minimum emittance [4]. For each laser spot size a solenoid scan was done in order to minimize the emittance and for the main solenoid current delivering the best emittance several statistical measurements were performed. The results of such measurements for 500 pC electron beams are presented in Fig. 3 together with simulation results. As

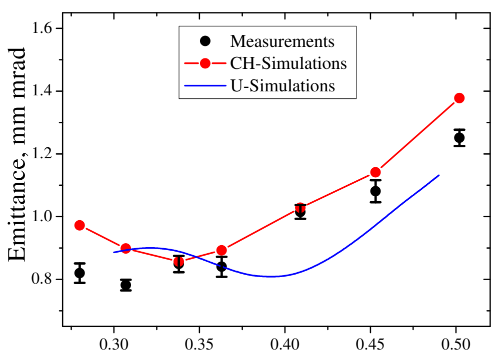

Figure 3: Emittance dependence on the rms laser spot size on the cathode for an electron beam with 500 pC bunch charge. Statistical error bars are shown in experimental measurements. "CH-" states for simulations with realistic transverse laser profile while "U-" for the simulations with uniform laser transverse profile, see text.

it can be seen from Fig. 3 for rms laser spot sizes of less than 0.37 mm the emittance dependence is weak and taking into account the systematic errors during the measurements, which are estimated to be about 10 % (see [4]), the laser spot size delivering the best emittance value cannot be conclusively determined. Taking into account that the slice emittance would be smaller than the projected one and that the emittance increase from the injector to the undulator section is small, it can be concluded that the requirement for the commissioning phase of the European XFEL on the emittance of less than 1 mm mrad for an electron bunch charge of 500 pC is fulfilled within good margins.

The red dotted curve in Fig. 3 represents the simulations with a realistic transverse profile which includes core and halo parts as described in the previous section, while the blue curve shows the simulations with an uniform profile. It can be seen that inclusion of the realistic transverse laser profiles in the simulation delivers better agreement to measurements not only by the obtained emittance values but also by better agreement for the machine parameters delivering the minimum emittance value. Additionally, as can be seen in Fig. 3, in the simulations with the uniform transverse laser distribution it is not possible to extract the desired charge for rms laser spot sizes on the cathode of less than 0.3 mm due to space-charge limitations at the cathode, while for the measurements it is limited at about 0.28 mm.

For the rms laser spot of about 0.31 mm, which delivered the smallest measured emittance during the laser spot size scan, the dependance of emittance on gun launching phase was measured as presented in Fig. 4. As well as in

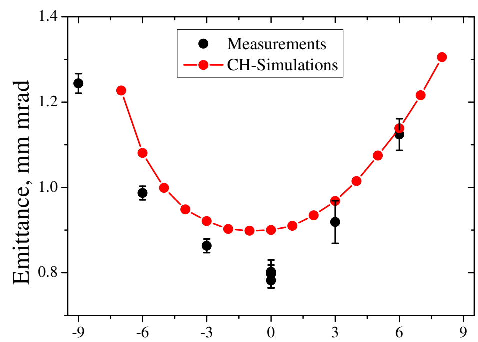

Figure 4: Emittance dependence on the gun launching phase for an electron beam with 500 pC bunch charge and rms laser spot size of 0.31 mm. Statistical error bars are shown in experimental measurements.

the previously described measurements for each gun phase the main solenoid current was scanned in order to find the minimum emittance for each gun launching phase and for the solenoid current delivering the minimum emittance value several statistical measurements were performed. Again a comparable trend between the measurements and simulations is observed. Additionally, one has to point out the emittance measurements at MMMG phase which are represented by three tightly positioned points in Fig. 4. These measurements were done at the same machine conditions. Between these measurements the machine conditions were changed to perform different studies. As in total four days passed between the first and the last measurement it can be concluded that the machine stability and reproducibility is very good at least within this short period.

A summary plot of the emittance for different electron beam charges is shown in Fig. 5 for parameters corresponding to the commissioning phase as well as for nominal conditions of the European XFEL [4, 6]. As it can be seen from Fig. 5 and was expected in advance the obtained emittance values for the machine operating at the parameters close to those for the commissioning phase of the European XFEL are systematically higher than for the nominal conditions but will allow a stable and robust first commissioning of the European XFEL.

ISBN 978-3-95450-134-2

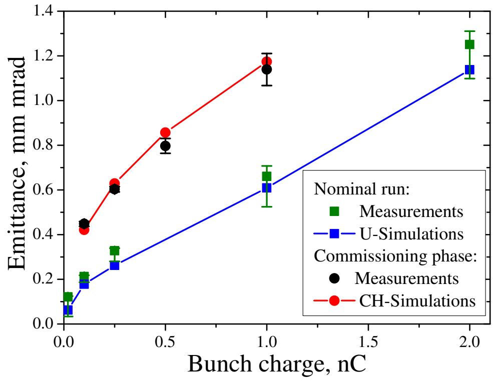

Figure 5: Emittance dependence on electron bunch charge for different stages of the European XFEL.

SUMMARY AND OUTLOOK

Operation of the PITZ photo injector at parameters very close to the ones planned for the commissioning phase of the European XFEL has revealed that the requirement on electron beam quality in terms of emittance is well fulfilled and that the RF gun is operated reliably. Beam dynamics simulations with improved modeling of the transverse laser distribution were performed and yield a better agreement between the simulated and measured data as a function of machine parameters. On the way to further improve the electron beam quality beyond the nominal European XFEL parameter set, the commissioning of a new type of photocathode laser system, capable of producing 3D-ellipsoidal laser pulses, has started at PITZ [10, 11]. In addition to the already existing very flexible photocathode laser system [12] this should allow to ultimately optimize the electron beam parameters.

REFERENCES

[1] W. Ackermann et al., Nature Photon. 1, 336 (2007).

[2] M. Altarelli et al., DESY Hamburg Report No. DESY 2006-097, 2007.

[3] W. Decking et al., “European XFEL construction status”, FEL2014, Basel, Switzerland, August 2014, WEB03, p. 623.

[4] G. Vashchenko, *Transverse phase space studies with the new CDS booster cavity at PITZ.* PhD thesis. DESY-THESIS-2013-043, 2013.

[5] F. Stephan et al., Phys. Rev. ST Accel. Beams 13, 020704 (2010).

[6] M. Krasilnikov et al., Phys. Rev. ST Accel. Beams 15, 100701 (2012).

[7] K. Floetmann, A Space charge TRacking Algorithm, `http://www.desy.de/~mpyflo`.

[8] G. Vashchenko et al., “Emittance optimization for different bunch charges with upgraded setup at PITZ”, IPAC2011, San Sebastian, Spain, September 2011, THPC115, p. 3155.

[9] C. Hernandez-Garcia et al., “Studies on charge production from Cs_2Te photocathodes in the PITZ L-band normal conducting radio frequency photo injector”, in preparation, to be submitted to Phys. Rev. ST Accel. Beams.

[10] M. Khojoyan et al., “Optimization of the PITZ photo injector towards the best achievable beam quality”, FEL2014, Basel, Switzerland, August 2014, THP006, p. 685.

[11] J. Good., “New ellipsoidal laser at the upgraded PITZ facility”, *These Proceedings*, TUP034, FEL2015, Daejeon, Korea (2015).

[12] I. Will and G. Klemz, Optics Express 16, 14922 (2008).

ISBN 978-3-95450-134-2

SUPPRESSION OF FEL LASING BY A SEEDED MICROBUNCHING INSTABILITY*

C. Lechner†, A. Azima, M. Drescher, L. L. Lazzarino, Th. Maltezopoulos, V. Miltchev,
T. Plath, J. Rönsch-Schulenburg, J. Rossbach, University of Hamburg, Hamburg, Germany
K. E. Hacker, S. Khan, R. Molo, DELTA, TU Dortmund University, Dortmund, Germany
S. Ackermann, J. Bödewadt, G. Brenner, M. Dohlus, N. Ekanayake, T. Golz, T. Laarmann,
T. Limberg, E. Schneidmiller, N. Stojanovic, M. Yurkov, DESY, Hamburg, Germany

Abstract

Collective effects and instabilities due to longitudinal space charge and coherent synchrotron radiation can degrade the quality of the ultra-relativistic, high-brightness electron bunches driving free-electron lasers (FELs). In this contribution, we demonstrate suppression of FEL lasing induced by a laser-triggered microbunching instability at the free-electron laser FLASH. The interaction between the electron bunches and the 800-nm laser pulses takes place in an undulator upstream of the FEL undulators. A significant decrease of XUV photon pulse energies has been observed in coincidence with the laser-electron overlap in the modulator. We discuss the underlying mechanisms based on longitudinal space charge amplification (LSCA) [1] and present measurements.

INTRODUCTION

The microbunching instability (MBI) due to longitudinal space-charge (LSC) forces in linear accelerators can compromise the quality of high-brightness electron bunches. This affects electron beam diagnostics as well as the FEL performance. For instance, emission of coherent optical transition radiation (COTR) was observed at several facilities [2–5] and it has to be mitigated for accurate measurements of the transverse beam profile. The longitudinal space-charge amplifier (LSCA) proposed in Ref. [1] is a concept to exploit these instabilities for the production of short-wavelength radiation. As illustrated in Fig. 1, an LSCA comprises multiple amplification stages, each one consisting of an electron beamline followed by a dedicated dispersive element. In the beamline, the electrons in the higher-density regions expand longitudinally introducing an energy change. The longitudinal dispersion R_{56} of the chicanes converts these energy changes into a density modulation. Starting from shot noise, a strong density modulation can be achieved in two to four stages.

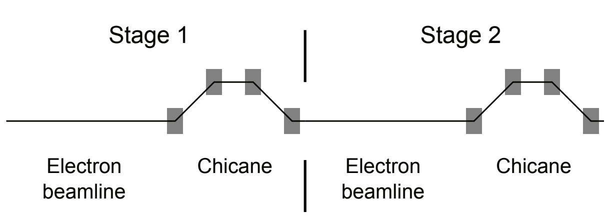

Figure 1: Schematic layout of a two-stage longitudinal space-charge amplifier (LSCA) configuration [1].

LSC amplification was studied experimentally at the Next Linear Collider Test Accelerator (NLCTA) at SLAC, where the impact of compression changes on spontaneous undulator radiation was measured [6]. At the Source Development Laboratory (SDL) at the National Synchrotron Light Source (NSLS) at Brookhaven National Laboratory (BNL), a modulated current profile was generated at the photoinjector with a modulated laser pulse. Microbunching gain was observed at wavelengths suitable for THz generation [7]. In Ref. [8], detailed investigations of the MBI using direct measurements of electron bunches with an RF deflector are presented.

In this contribution, we give an overview of LSCA studies performed at the FEL user facility FLASH [9] in which the amplification process was initiated by modulating the electron bunch by means of an external laser pulse. The amplified energy modulation is applied to suppress the lasing process. First results of these experiments have already been presented in Refs. [10, 11].

EXPERIMENTAL SETUP

The measurements presented in this contribution were performed at the FEL user facility FLASH at DESY, Hamburg [9]. The schematic layout of the facility is shown in Fig. 2. The superconducting linear accelerator (linac) driving the FEL delivers high-brightness electron bunches with energies up to 1.25 GeV. At a repetition rate of 10 Hz, bunch trains consisting of up to 800 bunches at a 1-MHz repetition rate can be produced. The facility has been upgraded by a second undulator beamline FLASH2, which is currently under commissioning [12].

For these measurements, the hardware of the sFLASH seeding experiment has been used. It is installed in the FLASH1 electron beamline between the collimation section (dogleg) and the undulator system, compare Fig. 3. The electron bunches arriving from the collimation section of FLASH1 are modulated in an electromagnetic undulator (5 periods of $\lambda_u = 20\,\mathrm{cm}$, $K_{\max} = 10.8$) by the 800-nm laser pulses arriving from the seeding laser system. After the modulator, chicane C_1 with variable R_{56} is installed. For studies of LSC effects, we use a combination of a transverse-

* Work supported by Federal Ministry of Education and Research of Germany under contract No. 05K10PE1, 05K10PE3, 05K13GU4, 05K13PE3, and the German Research Foundation program graduate school 1355.

† christoph.lechner@desy.de

ISBN 978-3-95450-134-2

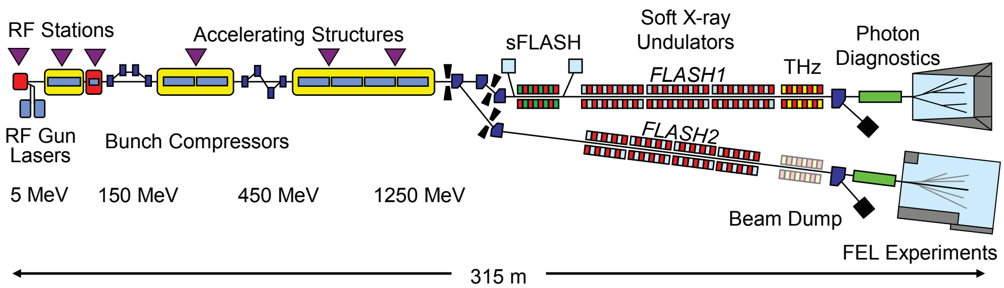

Figure 2: Schematic layout of FLASH user facility. The electron bunch is laser-manipulated in a combination of modulator and chicane installed in the *sFLASH* experiment.

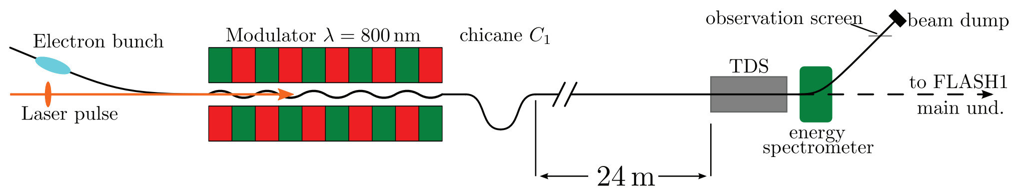

Figure 3: Hardware used for the measurements. The electron bunch arrives from the collimation section (dogleg) of the FLASH1 beamline and the 800-nm pulse from the laser system. In the modulator, the electron-light interaction imprints an energy modulation onto the bunch that is converted into a current modulation in the subsequent chicane C_1. After propagating along a 24-meter-long electron beamline, the electron bunches are characterized by the combination of a transverse-deflecting structure (*TDS*) and a dipole spectrometer.

deflecting structure (TDS) [4] and a dipole spectrometer installed about 13 m upstream of the FLASH1 SASE undulators. First, an arrival-time dependent vertical kick is applied in the TDS, an RF-structure operated at 2856 MHz. After introducing this longitudinal-to-vertical correlation, the longitudinal phase-space distribution can be measured on the observation screen in the dispersive section downstream of the energy spectrometer.

For the measurements with FEL operation, the TDS and the energy spectrometer have to be disabled to allow for transport of the density modulated electron bunches to the FLASH1 main undulator. The energy of the XUV photon pulses is measured with the "gas-monitor detector" (GMD) [13], a gas-filled volume in the XUV photon beamline leading to the FLASH1 experimental hall. In the GMD, the XUV photons ionize gas atoms and the ion and electron currents indicate the FEL pulse energy. Additionally, spectra of XUV photon pulses were measured with a high-resolution spectrometer.

OVERVIEW OF MEASUREMENTS

The experiment was designed to meet two objectives: (i) investigation of the LSC-driven amplification mechanism and (ii) study of the impact of the LSC-amplified initial energy modulation on the FEL process in the FLASH1 SASE undulator.

Characterization of Amplification Process

To study the LSC-driven evolution of the electron bunches, we used electron bunches with an energy of 700 MeV, a peak current of 0.3 kA, and an rms bunch duration of 0.3 ps. After generating an energy modulation by interaction with 800-nm, approx. 60-fs (full-width half maximum, FWHM) laser pulses in the modulator, a current modulation is generated in a chicane installed at the exit of the modulator. The manipulated electron bunches are then transported along a 24-m-long electron beamline. There, LSC forces drive the longitudinal expansion of high-current regions of the electron bunch. This process entails the accumulation of an energy modulation amplitude at the expense of the current modulation. At the end of this beamline, the longitudinal phase-space distributions of the seeded electron bunches have been characterized using the TDS in combination with a dipole energy spectrometer. From these measured longitudinal phase-space distributions, the slice energy spread has been extracted. This analysis has been carried out for a set of energies of the modulating laser pulses as well as for different longitudinal dispersions R_{56} of the chicane used to generate the current modulation. The initial parameters have been deduced by applying a fitting procedure based on an LSC model simulated with the code `QField` [14].

Suppression of FEL Lasing

In the second part of the experiment, the electron bunches were re-compressed to enable the SASE FEL process in the FLASH1 SASE undulator at $\lambda = 13.1$ nm. Here, the initial current modulation was generated using 0.2-ps-long (FWHM) laser pulses while the relative temporal jitter between the laser pulses and the electron bunches was 58 fs rms [15]. With this ratio of the temporal jitter to the laser

ISBN 978-3-95450-134-2

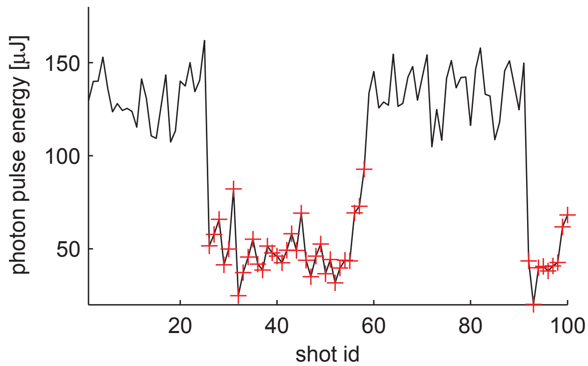

Figure 4: Suppression of FEL lasing for moderate initial laser modulation. The photon pulse energies emitted by the electron bunches have been measured with the GMD detector. Samples obtained with the modulating laser switched on are marked with *red crosses*.

pulse duration, the initial modulation is supposed to be well-reproducible [16]. As the manipulated electron bunches propagate to the FLASH1 SASE undulator, the energy modulation amplitude grows. This degradation of the electron bunch parameters results in a reduction of the XUV photon pulse energy, as shown in Fig. 4. Using the GMD to diagnose photon pulse energies, we studied this suppression of FEL lasing for different laser pulse energies and electron beamline configurations. In particular, a significantly stronger suppression effect has been observed in a configuration with two chicanes. Moreover, measurements have been performed with a high-resolution spectrometer installed at the PG beamline in the FLASH1 user hall [17, 18] for various settings of laser-generated initial energy modulation amplitude and longitudinal dispersion R_{56} of the chicane.

SUMMARY AND OUTLOOK

We reported on measurements of a laser-seeded longitudinal space-charge oscillation. The laser-induced current modulation initiates a growth of the energy modulation amplitude, which has been used to study suppression of FEL lasing. These measurements have been performed for different laser and electron beamline configurations. A more detailed data analysis will be presented in [19].

Potential applications of these seeded LSC effects include the reduction of slice energy spread in HGHG-seeded FELs [20–22] and the selective suppression of FEL lasing [19].

ACKNOWLEDGEMENTS

We thank DESY and the FLASH team for the opportunity to perform our experiment. Supported by Federal Ministry of Education and Research of Germany under contract No. 05K10PE1, 05K10PE3, 05K13GU4, 05K13PE3, and the German Research Foundation program graduate school 1355.

REFERENCES

[1] E.A. Schneidmiller and M.V. Yurkov, *Using the longitudinal space charge instability for generation of vacuum ultraviolet and x-ray radiation*, Phys. Rev. ST Accel. Beams 13, 110701 (2010).

[2] H. Loos, et al., *Observation of coherent optical transition radiation in the LCLS linac*, Proc. 30th Intl. Free-Electron Laser Conf., Gyeongju, Korea, 2008, 485–489.

[3] S. Wesch, et al., *Observation of coherent optical transition radiation and evidence for microbunching in magnetic chicanes*, Proc. 31st Intl. Free-Electron Laser Conf., Liverpool, UK, 2009, 619–622.

[4] C. Behrens, et al., *Electron beam profile imaging in the presence of coherent optical radiation effects*, Phys. Rev. ST Accel. Beams 15, 062801 (2012).

[5] S. Matsubara, et al., *Improvement of screen monitor with suppression of coherent-OTR effect for SACLA*, Proc. of 1st Intl. Beam Instrumentation Conf., Tsukuba, Japan, 2012, 34–37.

[6] A. Marinelli, et al., *Generation of Coherent Broadband Photon Pulses with a Cascaded Longitudinal Space-Charge Amplifier*, Phys. Rev. Lett. 110, 264802 (2013).

[7] S. Seletskiy, et al., *Seeding, Controlling, and Benefiting from the Microbunching Instability*, Phys. Rev. Lett. 111, 034803 (2013).

[8] D. Ratner, et al., *Time-resolved imaging of the microbunching instability and energy spread at the Linac Coherent Light Source*, Phys. Rev. ST Accel. Beams 18, 030704 (2015).

[9] K. Honkavaara, et al., *Status of the Soft X-Ray FEL User Facility FLASH*, These Proceedings: Proc. 37th Intl. Free-Electron Laser Conf., Daejeon, 2015, MOP014.

[10] C. Lechner, et al., *Demonstration of SASE Suppression Through a Seeded Microbunching Instability*, Proc. 36th Intl. Free-Electron Laser Conf., Basel, 2014, 177–180.

[11] J. Bödewadt and C. Lechner, *Results and perspectives on the FEL seeding activities at FLASH*, Proc. 35th Intl. Free-Electron Laser Conf., New York, NY, USA, 2013, 491–495.

[12] M. Scholz, B. Faatz, and Siegfried Schreiber, *First Simultaneous Operation of Two SASE Beamlines in FLASH*, These Proceedings: Proc. 37th Intl. Free-Electron Laser Conf., Daejeon, 2015, TUA04.

[13] K. Tiedtke, et al., *Gas detectors for x-ray lasers*, J. Appl. Phys. 103, 094511 (2008).

[14] M. Dohlus, Ch. Henning, *Periodic Poisson Solver for Particle Tracking*, submitted (2015); preprint available as (i) DESY-15-071 or (ii) `http://arxiv.org/`, code 1505.01330.

[15] C. Lechner, et al., *Measurements on the Timing Stability at the FLASH1 Seeding Experiment*, Proc. 36th Intl. Free-Electron Laser Conf., Basel, 2014, 913 – 916.

[16] C. Lechner, *Temporal Control of Laser-Electron Interaction at High-Gain Free-Electron Lasers*, PhD thesis, University of Hamburg (2015).

[17] N. Gerasimova, S. Dziarzhytski, and J. Feldhaus, *The monochromator beamline at FLASH: performance, capabilities and upgrade plans*, J. Mod. Opt. 58, 1480 (2011).

ISBN 978-3-95450-134-2

[18] M. Martins, et al., *Monochromator beamline for FLASH*, Rev. Sci. Instrum. 77, 115108 (2006).

[19] C. Lechner, et al., *in preparation*

[20] K. Hacker, *A Concept for Seeding 4-40 nm FEL Radiation at FLASH2*, TESLA-FEL 2013-01 (2013).

[21] E. Hemsing, et al., *Correlated Energy-Spread Removal with Space Charge for High-Harmonic Generation*, Phys. Rev. Lett. 113, 134802 (2014).

[22] K. Hacker, et al., *Measurements and Simulations of Seeded Electron Microbunches with Collective Effects*, These Proceedings: Proc. 37th Intl. Free-Electron Laser Conf., Daejeon, 2015, WEP031.

ISBN 978-3-95450-134-2

MULTI-BEAMLINE OPERATION TEST AT SACLA

Toru Hara*, Takahiro Inagaki, Kazuaki Togawa, Ryota Kinjo, Hideki Takebe#, Chikara Kondo, Yuji Otake, Hitoshi Tanaka
RIKEN SPring-8 Center, Sayo-cho, Hyogo 679-5198, Japan
Kenji Fukami
JASRI, Sayo-cho, Hyogo 679-5149, Japan

Abstract

After the installation of the second undulator beamline (BL2), multi-beamline operation has been started at SACLA since January 2015. 30 Hz electron bunches are alternately deflected to two beamlines using a kicker magnet and a DC twin-septum magnet. Since all undulator beamlines are placed downstream of the linear accelerator at SACLA, the beam energies are changed from bunch to bunch to obtain broad tunability of the laser wavelengths between the beamlines. In the multi-beamline operation, stable lasing is successfully achieved at the two beamlines with pulse energies around 100-150 μJ. The peak current is currently limited to about 1 kA due to the CSR effects at a doglegged beam transport to BL2. The status and operational issues related to the multi-beamline operation of SACLA are reported.

INTRODUCTION

In order to meet the growing demand for XFEL user operation, a new undulator beamline (BL2) was installed in September 2014 at SACLA. Following this installation, a DC switching magnet was replaced by a kicker magnet and a DC twin-septum magnet in January 2015 to start pulse by pulse multi-beamline operation [1].

The undulator hall of SACLA can accommodate five undulator beamlines and they are all placed in parallel to each other [2]. In conventional facility designs, the beamlines of low photon energies branch off from the middle of a linear accelerator, where the electron beam energy is still low (Fig. 1 (a)) [3, 4]. At SACLA, however, all beamlines are placed downstream of the accelerator to make the facility compact (Fig. 1 (b)). Instead, the electron beam energy is controlled from bunch to bunch to obtain a wide spectral range between beamlines [5].

Figure 2 is a schematic of the SACLA facility. BL3 is the first undulator beamline installed in the midst of the five beamlines, so the electron beam travels straight from the end of the accelerator. The second beamline, BL2, is placed next to BL3. The undulators of BL2 and BL3 have the same parameters with a magnet period of 18 mm. In the beam transport to BL2, the electron beam is deflected twice by 3° in a dogleg.

*toru@spring8.or.jp
#Present address: Okinawa Institute of Science and Technology (OIST)

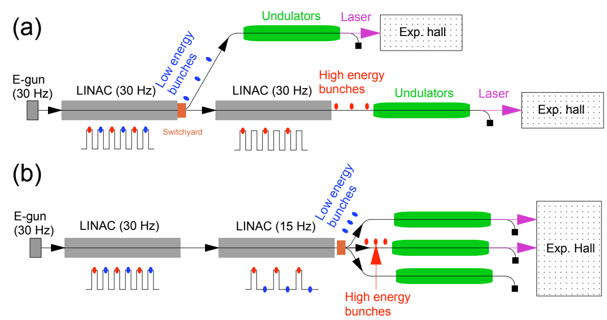

Figure 1: Multi-beamline schemes of XFEL facilities, (a) conventional layout and (b) SACLA.

In addition to the XFEL beamlines, there is a beam transport line to the SPring-8 storage ring, which is called XSBT (XFEL to Synchrotron Beam Transport). Since SACLA is planned to be used as a low-emittance injector in the upgrade project of SPring-8, XSBT will be used for the electron beam injection to the upgraded low-emittance ring in future [6].

BEAMLINE SWITCHYARD

A beamline switchyard is composed of a kicker magnet and a DC twin-septum magnet installed at the end of the linear accelerator. The switchyard deflects the electron beam in three directions (+3°, 0° and -3°), and each direction corresponds to BL2, BL3 and XSBT respectively. To ensure the electron beam orbit stability, the deflection angle of the kicker is kept small as ±0.53°. Then the DC twin-septum, locating 5.2 m downstream of the kicker (Fig. 3), deflects the beam by ±2.47°. The stability requirement for the kicker is 1×10^{-5} (peak-to-peak) equivalent to an angular orbit error of 0.1 μrad.

The kicker has a length of 0.4 m and its yoke is made with laminated silicon steel plates of 0.35 mm thickness. A ceramic vacuum duct is used at the kicker magnetic gap to eliminate the effects of eddy currents.

The DC twin-septum is composed of two identical septum magnets symmetrically-placed from side to side. Each septum magnet deflects the electron beam in opposite direction and the electron bunches for BL3 pass through between the two septums [1].

A pulsed power supply of the kicker magnet is a non-resonant type. It generates a bipolar trapezoidal waveform of current at up to 60 Hz, which is the maximum repetition of the electron beam at SACLA. The polarity, amplitude and repetition of the pulses can be arbitrarily changed according to the direction of deflection, beam energy and repetition of the electron bunches.

ISBN 978-3-95450-134-2

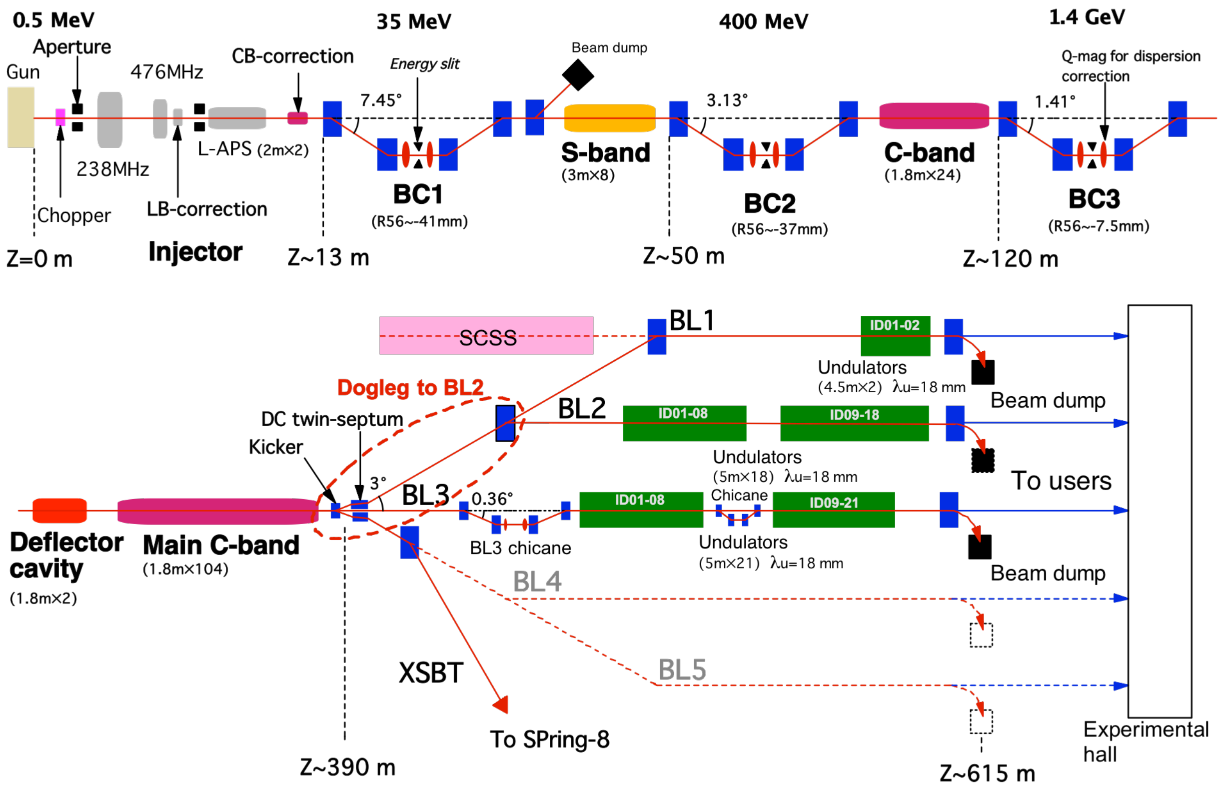

Figure 2: Schematic of SACLA facility.

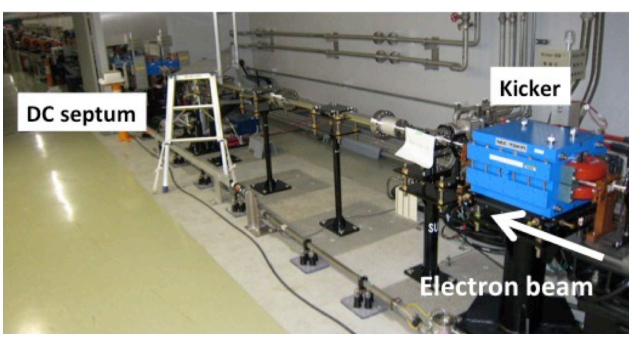

Figure 3: Photograph of a beamline switchyard.

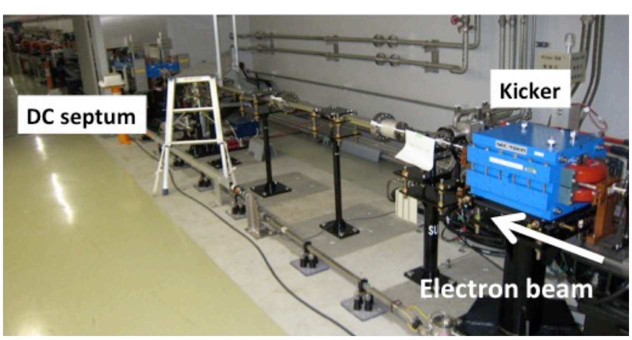

Figure 4: An example of a beamline switching pattern. Colored dots show the arrival timing of the electron bunches to the kicker.

Figure 4 is an example of a beamline switching pattern. The duration of a single trapezoidal waveform is 16.6 ms (60 Hz) and four waveforms compose the switching pattern. In this example, the electron bunches of 60 Hz are deflected to BL2 at 15 pps, BL3 at 15 pps and XSBT at 30 pps. The arrival timing of the electron bunches is set at the end of the flat top of each trapezoidal waveform, where the output current is well regulated and stabilized.

Before installation, the stability and reproducibility of the pulsed magnetic fields are checked using a gated NMR detector, which scans the resonant frequency only when a 0.6 ms gate is opened. Thus the peak magnetic fields can be accurately measured [1]. Except for a slow drift, which can be corrected using a beam orbit feedback system, the pulse-to-pulse stability of 1×10^{-5} (peak-to-peak) is confirmed.

CSR EFFECTS AT BL2 DOGLEG

Figure 5 shows the beam optics and the magnet configuration of the beam transport to BL2. The dogleg is made not only achromatic, but also isochronous by using two small inversed bending magnets to prevent the change of the longitudinal electron bunch shape and length.

In order to pursue higher laser pulse intensity, the peak current has been increased by strong compression of the electron bunches at SACLA. Currently the peak current reaches around 10 kA, which is more than three times higher than the original design value [7]. Short electron bunches and photon pulses are desirable for XFEL users, but they impose a severe condition for beam transport due to the CSR effects [8-11]. Since the deflection angle of 3°

ISBN 978-3-95450-134-2

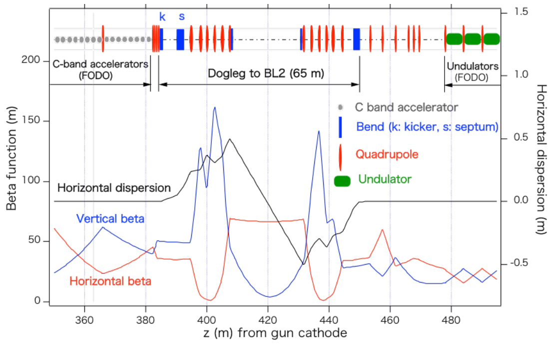

Figure 5: Beam optics and magnet configuration of the BL2 transport line.

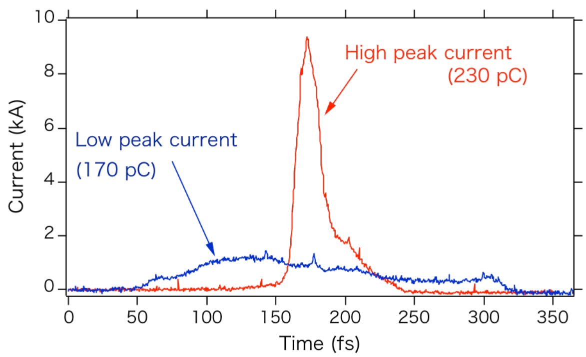

Figure 6: Longitudinal electron bunch profiles measured by a C-band RF deflector.

is unevenly distributed to the kicker and the septum magnet at the switchyard, a DBA lattice can not be applied to cancel the CSR effects [12, 13].

Figure 6 is the longitudinal bunch profiles measured by a C-band RF deflector cavity [14]. When the 10 kA bunches (Fig. 6, "High peak current") of 7.8 GeV are transported to BL2, large fluctuation of the horizontal beam orbit is observed after the dogleg. Although the lasing was successfully obtained at BL2, the laser intensity largely fluctuates from pulse to pulse and the pulse energy stayed around 30 μJ, which is one order smaller than the value routinely obtained at BL3.

As reducing the peak current, the fluctuations of the horizontal beam orbit and the laser pulse intensity decrease. At around 1 kA of the peak current, whose longitudinal electron bunch profile is shown as Fig. 6 "Low peak current", the maximum pulse energy of 100-150 μJ is obtained.

Table 1 compares the electron beam orbit fluctuations of the two beamlines under different peak currents. The beam orbit fluctuations are measured using two BPMs in front of the undulators of each beamline. Although the orbit fluctuations of BL2 are always larger than those of BL3, they reduce to sufficiently small level at 1 kA compared to the transverse emittance size of 33 pm-rad assuming 0.5 μm-rad normalized emittance and a 7.8 GeV beam energy.

Table 1: Fluctuations of the Electron Beam Orbit in Front of the Undulators. Both position and angle are measured using two BPMs and the area of distribution (rms) is shown. The conditions of high and low currents correspond to the electron bunches shown in Fig. 6.

	Horizontal plane (pm-rad)	**Vertical plane (pm-rad)**
BL2, high current	16.3	0.74
BL2, low current	2.7	0.64
BL3, high current	1.4	0.27
BL3, low current	0.83	0.24

MULTI-BEAMLINE OPERATION

The multi-beamline operation is tested using the 7.8 GeV electron bunches with a 1.2 kA peak current (Fig. 6, "Low peak current"). The repetition of the electron bunch is 30 Hz and the kicker magnet alternately deflects the bunches to BL2 and BL3. The undulator K-values are set to K=2.85 and K=2.1 at BL2 and BL3 respectively. Figure 7 shows the laser pulse intensities measured at the two beamlines. The photon energies are 6.38 keV at BL2 and 10.07 keV at BL3. The pulse intensity fluctuations are about 10 % (STD) at both beamlines and stable XFEL operation is achieved.

Fixing the electron beam energy the same for the two beamlines limits the wavelength tunability, which is an important feature of XFELs as a light source. In order to enlarge the spectral range, multi-energy operation of the accelerator is applied [5].

There are 52 C-band klystrons (104 accelerator structures) downstream of the final bunch compressor BC3 at SACLA, and the electron bunches are accelerated at a crest RF phase. In normal single-energy operation, all the klystrons run at the same repetition as the electron bunches. For the multi-energy operation, some of the klystrons are operated at sub-harmonics of the bunch repetition to change the beam energy of individual bunches.

In the demonstration, the repetition of 12 klystrons is changed to 15 Hz, which is half of the electron bunch repetition of 30 Hz. As a result, half of the electron bunches are not accelerated by the accelerator structures powered by these klystrons. Therefore the beam energies of the electron bunches can be alternately changed between 6.3 GeV and 7.8 GeV at the end of the accelerator. Then the kicker magnet deflects the lower energy bunches to BL2.

Figure 8 is the averaged spectra measured by a monochromator. The photon energy of BL2 is now lowered from 6.38 keV to 4.09 keV, while that of BL3 is

ISBN 978-3-95450-134-2

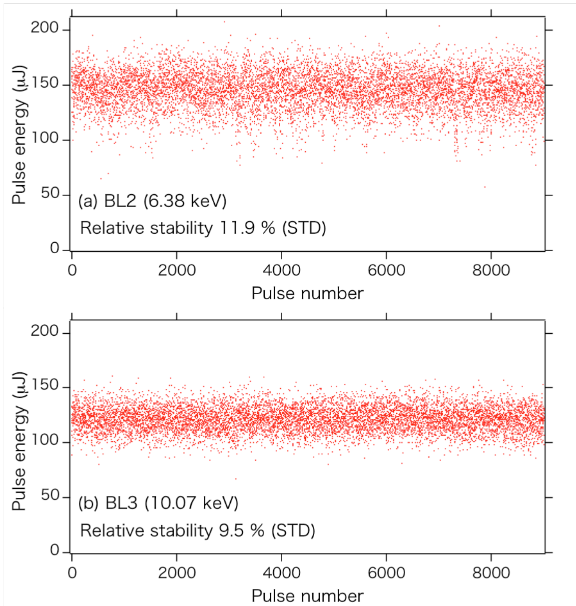

Figure 7: Stability of the photon pulse intensity, (a) BL2 and (b) BL3. Red dots are single-shot results. The electron beam energy is 7.8 GeV. The undulator K-values are 2.85 and 2.1 for BL2 and BL3 respectively.

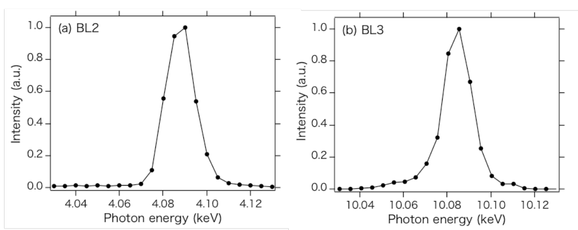

Figure 8: Averaged laser spectra measured at (a) BL2 and (b) BL3.

maintained the same as 10.09 keV. Figure 9 is the laser pulse intensities of the two beamline. Compared to Fig. 7, no degradation of the laser stability is observed. By optimizing the beam energies for each beamline, the wavelength tunable range of the multi-beamline operation can be largely extended.

SUMMARY

The multi-beamline operation using two undulator beamlines installed at the end of the accelerator has been successfully demonstrated at SACLA. 30 Hz electron bunches are alternately deflected to the two beamlines and simultaneous lasing has been obtained. By changing the beam energies of individual electron bunches, a broad spectral range can be achieved in the multi-beamline operation.

The CSR effects observed at the BL2 dogleg currently limit the peak current and the laser pulse energy stays around 100-150 μJ. To increase the laser intensity, rearrangement of the beam optics at the dogleg is under consideration to mitigate the CSR effects.

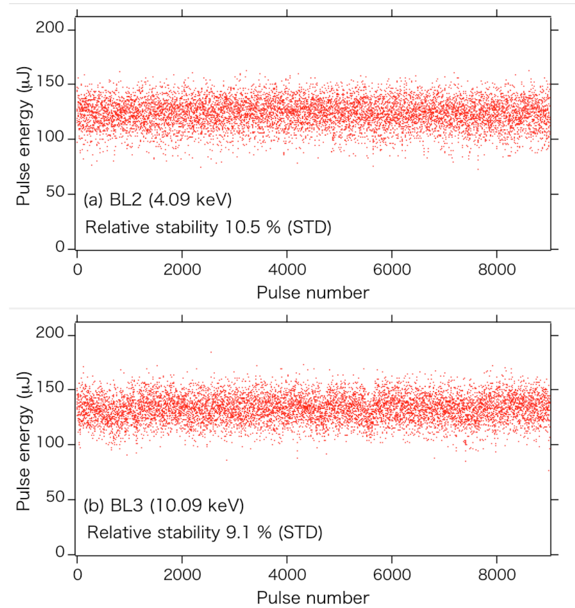

Figure 9: Stability of the photon pulse energy, (a) BL2 and (b) BL3. Red dots are single-shot resultsThe electron beam energy is 6.3 GeV for BL2 and 7.8 GeV for BL3. The undulator K-values are 2.85 and 2.1 for BL2 and BL3 respectively.

REFERENCES

[1] T. Hara et al., in Proceedings of FEL2014, Basel, August 2014, 71 (2014).
[2] T. Ishikawa et al., Nat. Photon. 6, 540 (2010).
[3] J. H. Han, H.S. Kang and I. S. Ko, in Proceedings of IPAC2012, New Orleans, May 2012, 1735 (2012).
[4] S. Reiche, in Proceedings of FEL2011, Shanghai, August 2011, 223 (2011).
[5] T. Hara et al., Phys. Rev. ST Accel. Beams 12, 080706 (2013).
[6] H. Tanaka, et al., to be published in Synchrotron Radiation News.
[7] T. Hara, K. Togawa and H. Tanaka, in Proceedings of FEL2010, Malmö, August 2010, 111 (2010).
[8] R. Talman, Phys. Rev. Lett. 56, 1429 (1986).
[9] B. E. Carlsten and T. O. Raubenheimer, Phys. Rev. E 51, 1453 (1995).
[10] M. Dohlus and T. Limberg, Nucl. Instr. and Meth. A 393, 494 (1997).
[11] E. L. Saldin, E. A. Schneidmiller and M. V. Yurkov, Nucl. Instr. and Meth. A 398, 373 (1997).
[12] D. Douglas, Thomas Jefferson National Accelerator Facility JLAB-TN-98-012 (1998).
[13] S. Di Mitri, M. Cornacchia and S. Spampinati, Phys. Rev. Lett. 110, 014801 (2013).
[14] E. Ego et al., Nucl. Instrum. Methods {¥bf A795}, 381 (2015).

ISBN 978-3-95450-134-2

FIRST SIMULTANEOUS OPERATION OF TWO SASE BEAMLINES IN FLASH

M. Scholz*, B. Faatz, S. Schreiber, J. Zemella, DESY, Hamburg, Germany

Abstract

FLASH2, the second undulator beamline of the FLASH FEL user facility at DESY (Hamburg, Germany) is under commissioning. Its first lasing was achieved in August 2014. FLASH is the first soft X-ray FEL operating two undulator beamlines simultaneously. Both undulator beamlines are driven by a common superconducting linear accelerator with a beam energy of up to 1.25 GeV. Fast kickers and a septum are installed to distribute one part of the electron bunch train to FLASH1 and the other part to FLASH2 with full repetition rate. The commissioning of FLASH2 takes place primarily in parallel to FLASH1 user operation. Various beam optics measurements have been carried out in order to ensure the required electron beam quality for efficient SASE generation. This paper reports the status of the FLASH2 commissioning.

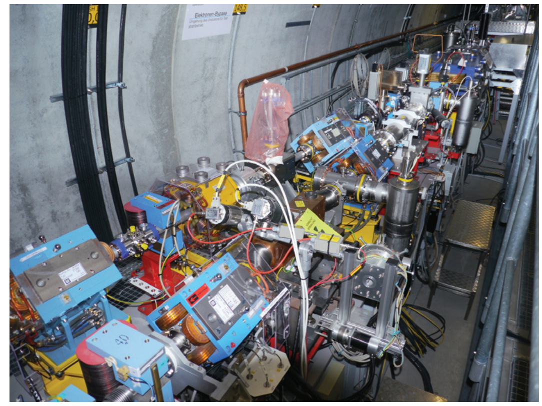

Figure 1: The first elements of the extraction arc leading the electrons to the new beamline FLASH2 are depicted on the left hand side. The beamline on the right hand side is FLASH1.

INTRODUCTION

FLASH [1–3], the free-electron laser (FEL) at DESY, Hamburg, Germany, delivers high brilliance XUV and soft X-ray FEL radiation for photon experiments. The superconducting accelerator technology used in the FLASH linac allows RF pulse lengths up to 800 µs. That makes it possible to accelerate electron bunch bursts with several hundred bunches. The bursts come with a repetition rate of 10 Hz and the maximum repetition rate of the single bunches within the bursts is 1 MHz. The bursts can be divided into parts, which can then be assigned to different undulator beamlines.

During a shutdown in 2013, FLASH was upgraded with a second undulator beamline [4, 5]. Fast kickers and a DC Lambertson-Septum are installed downstream the FLASH linac allowing to distribute the electron beam either to FLASH1 or to the extraction arc leading to FLASH2. Figure 1 shows the first extraction components. The schematic layout of the FLASH facility is shown in Fig. 2.

Due to fixed gap undulators, the photon wavelength delivered by FLASH1 determines the electron beam energy. FLASH2 is equipped with a variable gap undulator thus the photon energy can also be changed, within limits, by varying the undulator gap size. First lasing in the new undulator beamline was achieved on August 20, 2014 [6] and several different machine setups have been tested since then. The commissioning of FLASH2 takes place mostly in parallel to FLASH1 user operation. In this paper, we describe the parallel operation of the two undulator beamlines as well as the commissioning status of FLASH2.

* matthias.scholz@desy.de

RF CONTROL FOR SIMULTANEOUS OPERATION

The RF-pulse is shared between the electron bunch trains for FLASH1 and FLASH2. For a 800 µs long FR-pulse, the total maximum number of bunches, with a bunch repetition rate of 1 MHz, is 800. The bunch pattern (number of bunches and intratrain repetition rate) and bunch charge can be different for FLASH1 and FLASH2. This is realized by using two independent injector lasers in parallel.

Between the two bunch trains there is a gap of about 50 µs, which is required to rise the current of the FLASH2 extraction kickers and to establish a current flattop that ensures the same kick for all bunches in the burst. The kicked bunches are deflected by a septum magnet to the FLASH2 beamline. Other bunches travel straight through the septum to FLASH1.

The gap between the bunch trains can also be used to change the RF pulse amplitudes and phases (both within limits) in the accelerating modules in order to adjust the beam energy and the compression for both beamlines separately. Figure 3 shows the RF steps of two coupled modules (ACC4 and ACC5) during parallel operation of FLASH1 and FLASH2. The picture shown is taken after a FLASH2 dispersion measurement during which the beam energy in FLASH2 was changed by ± 3 MeV. This was achieved by changing the FLASH2 RF amplitude in the modules accordingly. FLASH1 delivered FEL beam for a user experiment during this measurement thus its RF settings must stay unchanged. In addition to the different amplitudes, the phases of the modules were set to 1.5 degree off-crest for FLASH1 while the FLASH2 bunches were accelerated on-crest.

ISBN 978-3-95450-134-2

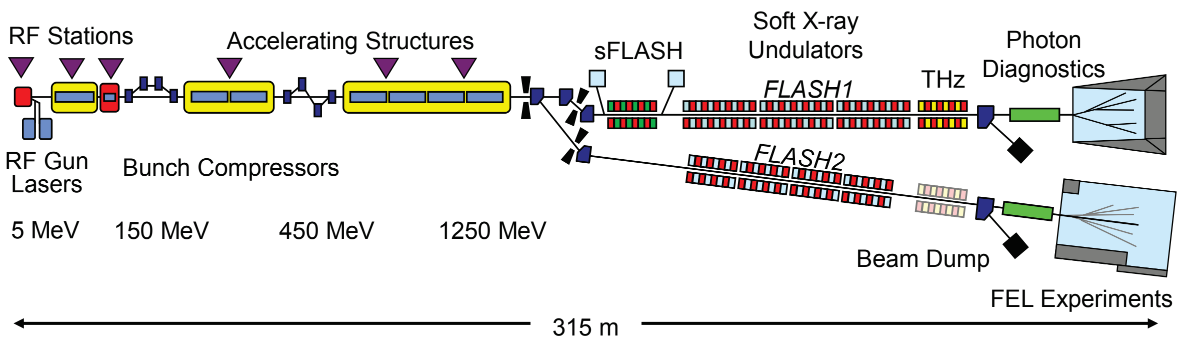

Figure 2: Schematic layout of the FLASH facility including the superconducting linac, the bunch compressors and the undulator beamlines FLASH1 and FLASH2. The location of a seeding experiment sFLASH is indicated.

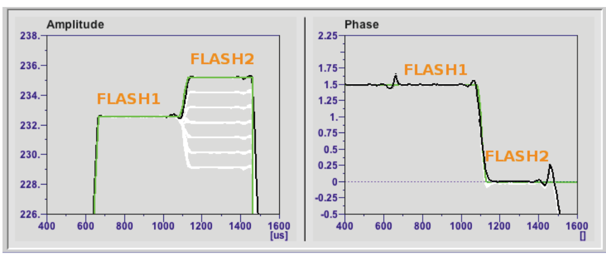

Figure 3: RF amplitude (left) and phase (right) of accelerating modules. The RF pulse length (800 µs) is split in two parts, one for each beamline. Both, the amplitude and the phase have different settings for FLASH1 and FLASH2. The units of the horiztontal axes are micro seconds. The untit for the RF amplitude is energy gain in MeV and the unit for the RF phase its degree.

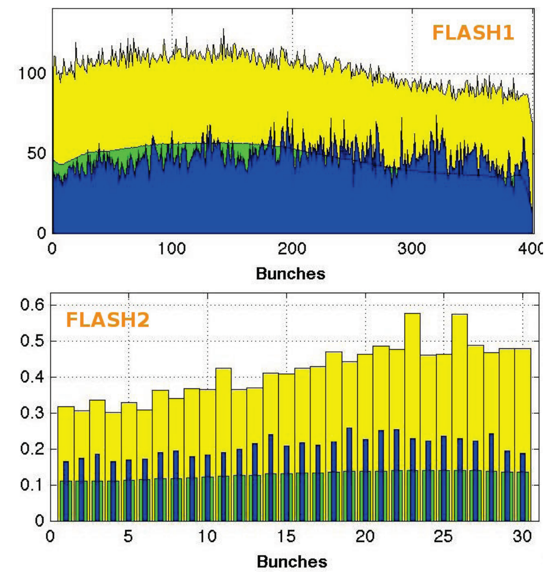

Figure 4: SASE pulse energy per bunch (in a.u.) for 400 bunches in FLASH1 (upper plot) and for 30 bunches in FLASH2 (also in a.u.). Blue: Actual value, Green: Average, Yellow: Maximum.

A slow bunch compression feedback uses the RF steps to keep the compression of the bunches constant over time for both beamline separately.

PARALLEL OPERATION OF TWO UNDULATOR BEAMLINES

The first electron beam in the FLASH2 extraction arc could be realized on March 4, 2014 and the first electrons in the FLASH2 dump could be achieved on May 23, 2014. Most of the FLASH2 commissioning has taken place in parallel to FLASH1 user operation. Dedicated beam time for FLASH2 has been restricted to a few days per month. During the first tests with electron beam, the gap of the FLASH2 undulators was open in order to avoid radiation damage of the permanent magnets.

First SASE operation in FLASH2 was achieved August 20, 2014 [6] during FLASH1 operation with 250 bunches per burst delivering photons at a wavelength of 13.5 nm. The FLASH2 undulator was closed to 9.5 mm which led, with a beam energy of 680 MeV, to a photon wavelength of 40 nm. This was the first time that two soft X-ray FEL beamlines driven by the same linac were operated in parallel.

So far, the maximum number of bunches per burst during a parallel SASE operation of both beamlines has been 400 bunches in FLASH1 and 30 bunches in FLASH2, both with a bunch repetition rate of 1 MHz. Figure 4 shows the SASE pulse energy, measured by the MCP (Microchannel plate [7]) detectors, along the bunch trains in FLASH1 and FLASH2.

The plots presented in Figures 5 and 6 give an overview of parallel SASE operations of FLASH1 and FLASH2. The first plot covers the period from August, 2014 to August, 2015 and the second plot covers the period from June 2015 to August 2015.

In Fig. 5 photon wavelengths generated by FLASH1 and FLASH2 during parallel SASE operation are depicted as a function of the electron beam energy. Due to the fixed gap undulator, the wavelength of FLASH1 is coupled to the electron beam energy. However, FLASH2 can produce different wavelength at a fixed electron beam energy (within limits) by adjusting the undulator gap size. Already in the beginning of September 2014, several wavelengths below 40 nm

ISBN 978-3-95450-134-2

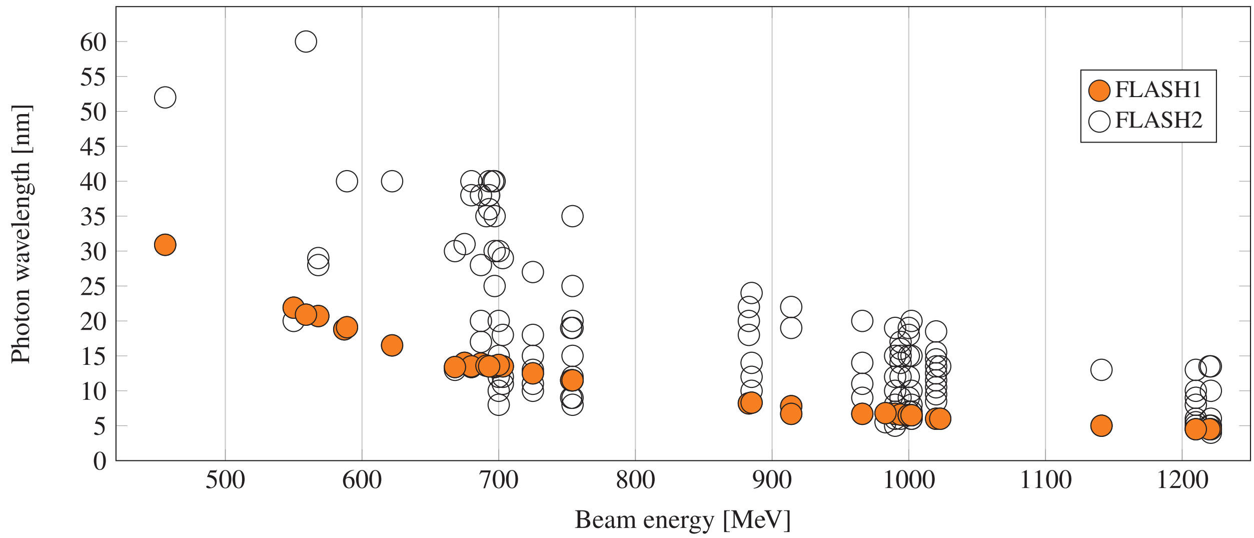

Figure 5: Photon wavelengths achieved in the FLASH1 and FLASH2 beamlines during parallel SASE operation in the period from August 2014 to August 2015. The photon wavelength in FLASH1 is determined — due to the fixed gap undulator — by the electron beam energy. FLASH2 is equipped with a variable gap undulator and the wavelength can be varied at fixed electron beam energy by changing the gap size.

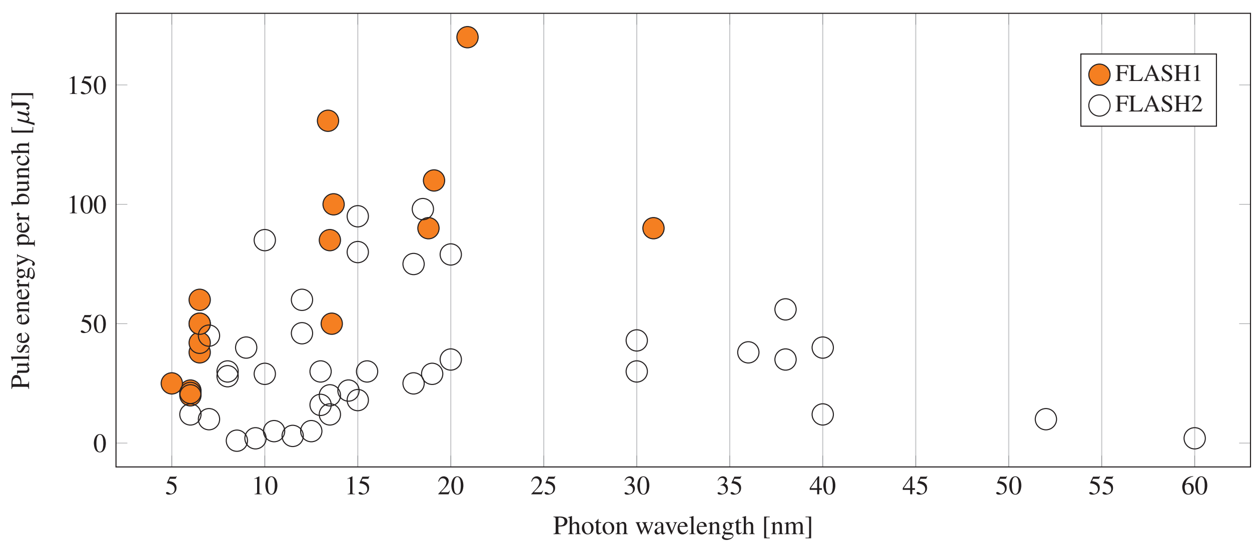

Figure 6: SASE pulse energies per bunch for photon wavelengths delivered by FLASH1 and FLASH2 achieved during parallel SASE operation in the period from June 2015 to August 2015.

were achieved as well. The shortest wavelength produced by FLASH2 so far, 4 nm, was obtained during an intense study week in January 2015. Due to installations of photon beam diagnostics in the FLASH2 tunnel, no parallel SASE operation was possible from mid January 2015 to June 2015. After that, further successful runs were carried out in summer 2015. The maximum photon wavelength at FLASH2, 60 nm, was achieved in June 2015.

The GMD detector, to measure the absolutely calibrated photon pulse energy, has been available at FLASH2 since June 2015. Therefore the data shown in Fig. 6 covers only the period from June to August 2015. The presented plot shows the pulse energy in both beamlines during parallel SASE operation for different photon wavelengths. Although FLASH2 has not yet reached the maximum photon energies of FLASH1, the achieved pulse energy of about 100 μJ at different wavelengths between 10 nm and 20 nm is promising.

For the long wavelengths, the pulse energies reached so far was rather small. The main reason for this is that for any given energy, emphasis has been on optimizing the FEL for shorter wavelengths, which is considered to be the more demanding challenge.

FLASH2 SASE commissioning continues during the next months.

ISBN 978-3-95450-134-2

SUMMARY AND OUTLOOK

We have had a very successful year with great advances in the commissioning of the new undulator beamline at FLASH2. The simultaneous SASE operation of FLASH1 and FLASH2 emphasizes the unique status of FLASH among the free-electron lasers.

The maximum SASE pulse energy of FLASH2 is still below the energy of the SASE pulses at FLASH1 but we are optimistic that FLASH2 can achieve similar level in the future. The minimum wavelength in FLASH2 reached so far with saturated photon beam is 5 nm. Simulations show that for nominal parameters, 4 nm can be reached at 1.25 MeV, and we are confident that we can reach also shorter wavelengths in the near future. Many tools and diagnostic devices have been developed or adapted from FLASH1 to the new beamline, and further tools are under commissioning. First photon experiments are expected 2016.

ACKNOWLEDGMENT

We like to thank all colleagues who have been involved in the FLASH II project and participated in the commissioning of the new FLASH2 undulator beamline.

REFERENCES

[1] W. Ackermann et al., *"Operation of a free-electron laser from the extreme ultraviolet to the water window"*, Nature Photonics 1, 336 (2007).

[2] K. Tiedtke et al., *"The soft x-ray free-electron laser FLASH at DESY: beamlines, diagnostics and end-stations"*, New J. Phys. 11, 023029 (2009).

[3] K. Honkavaara et al., *"Status of the soft x-ray user facility FLASH"*, presented at FEL'15, Daejeon, Korea, Aug 2015, MOP014, these proceedings.

[4] M. Scholz, *"Design of the Extraction Arc for the 2^{nd} Beam Line of the Free-Elelctron Laser FLASH"*, DESY-Thesis-2014-002.

[5] M. Scholz et al., *"Extraction Arc for FLASH II"*, THP073, Proceedings of FEL2012, Nara, Japan.

[6] S. Schreiber, B. Faatz, *"First Lasing at FLASH2"*, MOA03 Proceedings of FEL2014, Basel, Switzerland.

[7] E. Syresin et al., *"Radiation detectors based on microchannel plates for free-electron lasers"*, DOI:10.1134/S1547477114060144.

DISTRIBUTED SEEDING FOR NARROW-LINEWIDTH HARD X-RAY FREE-ELECTRON LASERS*

D.C. Nguyen#, P.M. Anisimov, C.E. Buechler, J.W. Lewellen, Q.R. Marksteiner
LANL, Mail Stop H851, Los Alamos, New Mexico, USA

Abstract

We describe a new FEL line-narrowing technique called distributed seeding (DS), using Si(111) Bragg crystal monochromators to enhance the spectral brightness of the MaRIE hard X-ray free-electron laser. DS differs from self-seeding in three important aspects. First, DS relies on spectral filtering of the radiation at multiple locations along the undulator, with a monochromator located every few power gain lengths. Second, DS performs filtering early in the exponential gain region before SASE spikes start to appear in the radiation longitudinal profile. Third, DS provides the option to select a wavelength longer than the peak of the SASE gain curve, which leads to improved spectral contrast of the seeded FEL over the SASE background. Time-dependent Genesis simulations show the power-vs-z growth curves for DS exhibit behaviors of a seeded FEL amplifier, such as exponential growth region immediately after the filters of the seeding approaches considered, the two-stage DS spectra produce the highest contrast of seeded FEL over the SASE background and that the three-stage DS provides the narrowest linewidth with a relative spectral FWHM of 8 X 10^{-5}.

INTRODUCTION

X-ray free-electron lasers (XFELs) routinely operate in the SASE mode, whereby the radiation power grows exponentially with distance in a long undulator as a single electron bunch amplifies its own undulator radiation all the way to saturation. The radiation slips ahead of the electrons by the slippage distance $N_u\lambda_0$, where N_u is the number of undulator periods and λ_0 is the resonance wavelength, forming randomly distributed wave-packets within a single radiation pulse. In the exponential gain regime, these wave-packets develop into high-intensity longitudinal spikes, each of which is coherent within a coherence length given by

$$l_c = \frac{\lambda_0}{6\sqrt{\pi}\rho}\sqrt{\frac{z}{L_G}},$$

where λ_0 is the resonance wavelength, z is the distance traversed by the electrons in the undulator, L_G is the 1D power gain length, and ρ is the Pierce parameter. At saturation ($z \sim 20\ L_G$), the coherence length is

$$l_c^{sat} \approx \frac{\lambda_0}{2\sqrt{\pi}\rho}.$$

For an XFEL with sub-Angstrom output wavelength, ρ is on the order of 5 x 10^{-4}, and thus the coherence length at saturation is on the order of 20 nm. The mean separation between these spikes is $\Delta z_{spike} \leq 2\pi l_c$, or about 100 nm, much shorter than the overall radiation pulse length (~tens of μm). The frequency spectrum of a SASE XFEL consists of hundreds of narrow spectral lines, each being the Fourier transform of the radiation overall temporal duration, within an envelope that is the Fourier transform of the individual temporal spikes. The overall SASE spectrum has a relative bandwidth FWHM of

$$\frac{\Delta\lambda}{\lambda_0} = \frac{4\ln 2}{\sqrt{\pi}}\rho,$$

or about 0.1% for the typical ρ of an XFEL. The large bandwidth and poor temporal coherence of the SASE XFEL preclude its use in applications that require a high degree of longitudinal coherence such as three-dimensional coherent X-ray diffractive imaging.

SASE self-seeding has been studied and successfully employed to reduce the XFEL bandwidth to a fraction of an electron volt [1-5]. This technique relies on monochromatizing the SASE radiation from the first part of the undulator and then re-injecting the monochromatic seed into the second part of the undulator for amplification. Hard X-ray self-seeding can be performed either with a Bragg crystal monochromator as suggested by Saldin *et al.* [1], or a diamond wake crystal as suggested by Geloni *et al.* [2]. Self-seeding at both hard and soft X-ray energies has been demonstrated at the Linac Coherent Light Source [3, 4], where the seeded FEL spectra typically exhibit a narrow spectral line on top of a broadband SASE background. Geloni *et al.* also proposed using cascade self-seeding [5] to improve the contrast of self-seeded FEL over SASE.

We present a new concept of distributed seeding (DS) using multiple silicon Bragg crystal monochromators. DS differs from SASE self-seeding in three important aspects. First, DS relies on spectral filtering of the radiation at more than one location along the undulator. For this study, we consider both the two-filter and three-filter DS with a spectral filter located every five power gain lengths. Second, DS performs filtering early in the exponential gain region before SASE spikes start to appear in the radiation longitudinal profile to ensure the

*Work supported by the US DOE / NNSA under contract DE-AC52-06NA25396.
#dcnguyen@lanl.gov

ISBN 978-3-95450-134-2

Figure 1: Schematic of the MaRIE XFEL undulator with 14 FODO periods and three locations for the spectral filters.

radiation is dominated by a coherent seed and not SASE noise. Third, DS provides the option to select a wavelength longer than the peak of the SASE gain curve, which leads to improved spectral contrast of the seeded FEL over the SASE background.

MaRIE X-RAY FEL

The MaRIE XFEL is a proposed hard X-ray FEL driven by 12-GeV electron beams to generate coherent 42-keV photons. At a resonance wavelength of 0.2936 Å, four Si(111) Bragg crystals, each deflecting the X-ray beam by 5.4°, can be used in a four-bounce crystal monochromator (4BCM). The 4BCM increases the X-ray beam path by 1.2 ps (0.36 mm), which can be matched by delaying the electron beams in a small-angle bypass chicane that will be described later in this paper. The bypass chicane R_{56} is sufficiently large to erase the FEL-induced microbunching so that each electron bunch behaves like a fresh bunch upon entering the next undulator segment.

Using time-dependent numerical FEL simulations with Genesis 1.3 [6], we model the DS FEL with either two or three monochromators along the undulator. Two cases of the two-filter configuration are studied, one with the first filter at the end of the first two FODO periods, and the other at the end of the four FODO periods. The three-filter configuration involves filtering at every two FODO periods starting at the end of the first two FODOs. We present the number of photons versus distance along the undulator for these three cases.

The electron beams traversing the bypass chicane are expected to experience loss of beam brightness caused by coherent synchrotron radiation (CSR) and to a lesser extent, by incoherent synchrotron radiation (ISR). Beam dynamic simulations using Elegant [7] to compute the effects of CSR and ISR on the beam energy, energy spread and emittance in each bypass chicane. These simulations show the dominant effect is CSR-induced reduction in the peak current and slice energy in the latter part of the electron bunch. CSR also causes a small increase in the slice emittance but this has no noticeable effects on the FEL performance.

Figure 1 shows the MaRIE XFEL undulator with fourteen FODO periods and three locations for the spectral filters. The two-filter configurations under study are AB, with the monochromators at locations A and B, and BC with the filers at locations B and C. The three-stage configuration ABC has monochromators at all three locations.

Figure 2a illustrates the small-angle, four-dipole chicane to temporally delay the electron beam to synchronize it with the X-ray beam, including the monochromator (in between the middle dipoles). The dipole length is 35 cm and the center-to-center distance between the first and second (also the third and fourth) dipoles is 3.3 m. The four-bounce crystal monochromator is illustrated in Fig. 2b. The first and last Si(111) crystals are flat; however, the second and third crystals are curved to produce a 0.7 μm rms radius at the slit in the middle of the 4BCM. The function of the slit is to select a narrow spectrum at the long wavelength and reject the SASE signal.

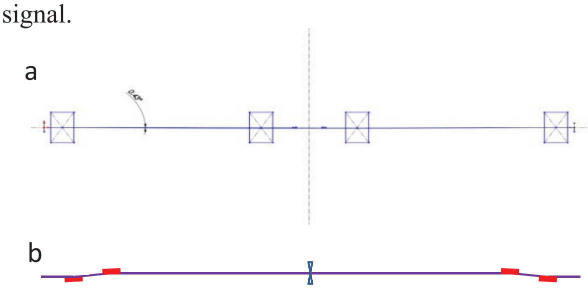

Figure 2: a) The four-dipole bypass chicane with the 4BCM in between the two middle dipoles; b) expanded view of the 4BCM showing the four Si(111) crystals in red and the slit in blue. The total length of the bypass chicane (2a) is 8.63 m whereas the length of the 4BCM (2b) is 0.4 m.

By filtering the undulator radiation early in the exponential growth curve, we can increase the throughput of the 4BCM at the longer wave as the undulator radiation at this point is dominated by longer wavelength radiation. Figure 3 plots the averaged single-shot undulator radiation spectrum at the end of four gain lengths (blue), the averaged SASE power (red), and the spectral response of the four-crystal monochromator with its wavelength centered at 0.2940 Å (green). Since the DS signal is at a longer wavelength but SASE is shifted toward shorter wavelength, the contrast of DS over SASE is enhanced.

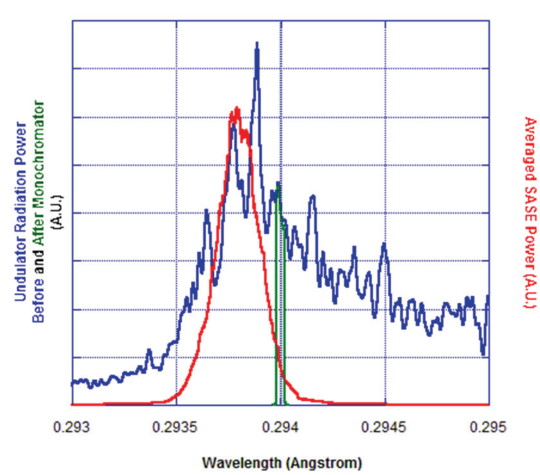

Figure 3: The undulator radiation spectrum before (blue) and after (green) the 4BCM, and the average SASE signal in the exponential gain regime (red).

ISBN 978-3-95450-134-2

We anticipate that bending the electron beams in the bypass chicane will result in beam quality degradations, mainly caused by coherent synchrotron radiation (CSR) and to a lesser extent, by incoherent synchrotron radiation (ISR). Beam dynamic simulations using Elegant [7] to compute the effects of CSR and ISR on the beam energy, energy spread and emittance in each bypass chicane, show the dominant effect is CSR-induced reduction in the peak current and slice energy (gamma) in the latter part of the electron bunch (Fig. 4), which can be compensated for by a small taper in the undulator *K* parameter. CSR also causes a negligible increase in the slice emittance with no noticeable effects on the FEL performance.

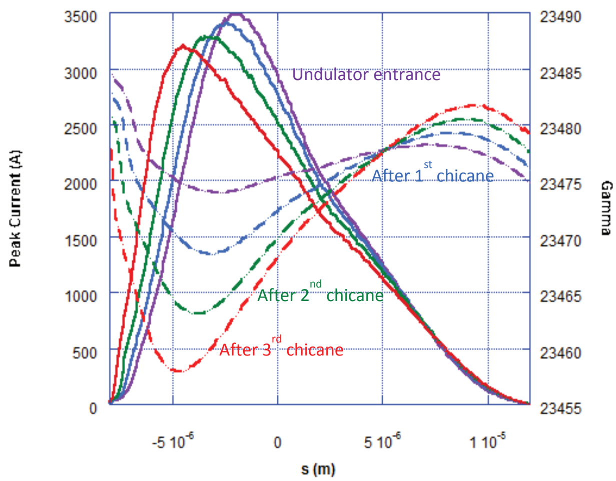

Figure 4: The CSR-induced reduction in peak current (solid lines) and slice beam gamma (dashed lines) as functions of the electron bunch position at three different undulator locations: purple = undulator entrance, blue = after the first chicane, green = after the second chicane, and red = after the third chicane.

SIMULATIONS

We use the full 4D (time-dependent) Genesis to predict the DS performance using the MaRIE XFEL parameters [8]. Numerically, the on-axis power and phase of the Genesis output at the ends of the second, fourth and sixth FODO cells was used with the assumption that the radiation beam has full coherence across the transverse profile. Fourier transform was applied to the complex electric field to produce the radiation spectrum, which is then multiplied by the spectral response of the four silicon crystals to produce the filtered spectrum. The latter is Fourier-transformed back into the time domain and then serves as the monochromatic seed for the subsequent undulator segments. Figure 5 plots the log of the numbers of photons versus undulator length for the two-filter DS cases (AB and BC) and the three-filter DS case ABC.

CONCLUSIONS

We have shown via time-dependent 3D Genesis simulations that the DS technique, using multiple Bragg crystal monochromators, can provide a high degree of temporal coherence for the MaRIE XFEL. The DS confi-

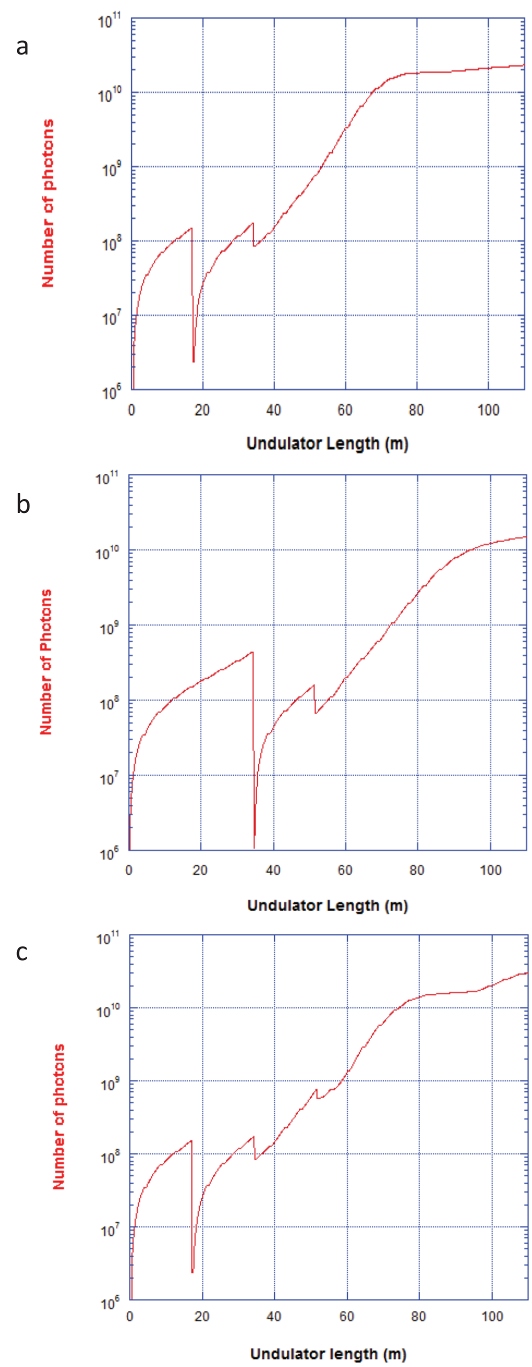

Figure 5: a) Plots of the number of photons versus undulator length for the DS configurations a) two-filter AB; b) two-filter BC; and c) three-filter ABC.

guration with only two monochromators already achieves a 10X enhancement in X-ray brightness compared with the traditional SASE technique and produces a narrow-line seeded FEL spectrum with good contrast between the monochromatic output and the SASE background. The DS configuration with three monochromators provides additional spectral narrowing but with a slight increase in the SASE background. Both the two-stage and three-stage DS FEL output has a filled-in longitudinal profile with a coherence length on the order of 200 nm. It also exhibits a

ISBN 978-3-95450-134-2

power-versus-z plot characteristic of a true seeded amplifier FEL. For the MaRIE XFEL, the two-stage DS technique appears to be the more practical than the three-stage DS as a spectral line narrowing technique.

We have performed Elegant simulations to model beam degradation due to CSR and ISR in the chicanes that are used to delay the electron bunch to match with the X-ray delays in the monochromators. Although the CSR-induced beam degradations are small, they are cumulative with the number of chicanes. The dominant effect is a steady reduction in the peak current and the slice electron beam energy in the region of the electron bunch where most of the FEL interaction occurs, i.e., at the electron beam energy minimum near the end of the bunch. This cumulative change in beam energy requires that the undulator K_{rms} parameter be reduced (step-tapered) to maintain the FEL resonance.

One of the key features of the DS method is the ability to tune the central wavelength away from the SASE resonance wavelength. A combination of the judicious choice of the central wavelength and the undulator K_{rms} parameters can put the DS central wavelength in between the SASE backgrounds of different undulator stages, thereby enabling subsequent spectral filtering to improve the contrast between the seeded spectral line and the SASE background.

ACKNOWLEDGMENTS

The authors benefited from helpful discussions with Bruce Carlsten, Richard Sheffield and Nikolai Yampolsky at LANL, and Craig Ogata and Yuri Shvyd'ko at Argonne National Laboratory. This research was funded by the Los Alamos National Laboratory Matter-Radiation Interactions in Extremes (MaRIE) program, led by Cris Barnes and John Tapia.

REFERENCES

[1] E.L. Saldin, E.A. Schneidmiller, Yu.V. Shvyd'ko, and M.V. Yurkov, *Nucl. Instr. Meth. Phys. Res.* **A 475** 357-362 (2001).

[2] G. Geloni, V. Kocharyan, and E. Saldin, *J. Mod. Opt*., 58:1391–1403 (2011).

[3] J. Amann *et al*., *Nature Photonics* **6**, 693-698 (2012).

[4] D. Cocco *et al*., in *Proc. SPIE 8849, "X-ray lasers and coherent X-ray sources,"* 88490A-1, (2013).

[5] G. Geloni *et al.*, DESY **10-080** (2010).

[6] S. Reiche, *Nucl. Instr. Meth. Phys. Res.* **A 429** 243-248 (1999).

[7] M. Borland, *Phys. Rev. ST Accel. Beams* **4**, 070701 (2001).

[8] J.W. Lewellen *et al.*, these proceedings, paper MOP062.

ISBN 978-3-95450-134-2

TUNABLE HIGH-POWER TERAHERTZ FREE ELECTRON LASER AMPLIFIER*

G. Zhao#, S. Huang, W. Qin, L. Zeng, K. Liu
Institute of Heavy Ion Physics, School of Physics, Peking University, Beijing 100871, China
C. H. Chen, Y. C. Chiu, Y. C. Huang
Institute of Photonics Technologies, Department of Electrical Engineering,
National Tsinghua University, Hsinchu 30013, Taiwan

Abstract

In this paper we present an ongoing project under the collaboration between Peking University (PKU) in Beijing and National Tsinghua University (NTHU) in Taiwan to develop tunable wavelength THz with high peak and average power from a THz free-electron laser (FEL) amplifier driven by a superconducting accelerator system at PKU and a tunable THz seed which is provided by a THz parametric amplifier (TPA). Simulation results show that narrow-band, wavelength-tunable THz radiation with 0.05-0.8 MW peak power and Watt-level average power can be expected.

INTRODUCTION

THz have attracted much interest in many undisclosed phenomena. Especially in non-invasive diagnosis, security scanning, physics study and manufacturing. THz radiation sources are developing very fast. Free-electron laser (FEL) is an important technology to generate high-power THz radiation [1]. SASE THz FEL is difficult to realize because it requires high electron bunch charge, so most of the THz FEL devices are operating in the FEL oscillator [2,3]. We would like to develop another method—seeded amplifier. We try to use THz seed and superconducting accelerator to generate THz radiation with high peak power and average power simultaneously. THz FEL amplifier was first proposed by C.Sung et al in 2006. They used a TW CO_2 laser through different frequency generation (DFG) in GaAs crystal to generate THz seed [4,5]. We will choose a more compact design to generate THz seed by optical technology—THz parametric amplifier (TPA), which can produce wavelength tunable from 1 to 6 THz and narrow-band spectrum THz. In this paper, we present FEL simulation of THz FEL amplifier and preliminary study on TPA THz seed.

SYSTEMLAYOUT

Our THz FEL amplifier system comprises two major components, the FEL amplifier and the THz seed. Figure 1 shows the configuration of the THz parametric amplifier. A pulse laser at 1064 nm and a wavelength tunable external-cavity diode laser (ECDL) pump a lithium niobate (LN) or KTiOPO4 (KTP) crystal, then generate a tunable narrow-band THz seed. Figure 2 shows the superconducting accelerator system at PKU, including the DC-SRF photoinjector which has been put into operation since 2014 and can provide 3MeV electron beam with bunch charge up to 60 pC, a SRF linac with two 1.3GHz Tesla-type cavities and a planer undulator. This superconducting system is expected to deliver high repetition rate electron beam with the energy of 8-25 MeV. It is under installation and will be operated in this autumn.

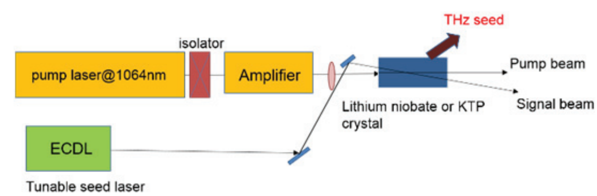

Figure 1: Configuration of the TPA THz seed system.

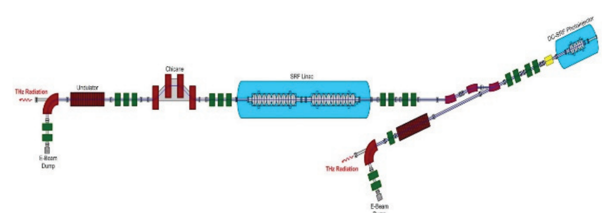

Figure 2: Superconducting accelerator system at PKU.

THz PRARMETRIC AMPLIFIER

In recent years, tunable THz-wave sources with high temporal and spatial coherence using the resonant frequency of ferroelectric crystal lattices at room temperature are popular. TPA can generate tunable coherent radiation [6]. This optical technology is based on tunable light scattering from the long wavelength side of the A1-symmetry mode in LN which has a high gain coefficient from 0.5 THz to 3 THz [7]. Molecular of crystal absorb photons of pump laser and transit to a virtual energy level. Near-infrared (NIR) photons and THz photons from the vibrational mode of molecular will be generated through Stimulated Raman Scattering (SRS) process. The frequency of THz photon equals to the difference between the frequency of pump laser and seed laser. The output NIR, which has the same frequency with the seed laser, usually used to derive the THz information. The output THz is distributed in a certain angle which

* Institute of Heavy Ion Physics, School of Physics, Peking University, Beijing 100871, China
# zhaogang@pku.edu.cn

ISBN 978-3-95450-134-2

satisfies the phase-matching condition. The TPA has been proved to be a useful coherent, narrow-band THz source which can continuously tunable in 0.5 to 3 THz at room temperature [8]. The tuning is accomplished by controlling the wavelength of signal beam. In the past several years, THz frequency has been extended to 3-6 THz by using KTP which has higher response frequency and higher damage threshold [9].

We have successfully built a TPA test system at NTHU with a 500ps mode-locked laser which can produce more than 2mJ pump laser after a side-pumped Nd:YAG amplifier. The system is shown in Fig. 3. With this system, the pumping intensity can reach a few GW/cm^2, the ECDL can operate in CW mode with 600mW output power which is tunable from 1066nm to 1082nm. Finally, we can get THz radiation with 10W peak power from LN crystal. The THz power measured by a Golay cell is shown in Fig. 4.

Figure 3: TPA test system at NTHU.

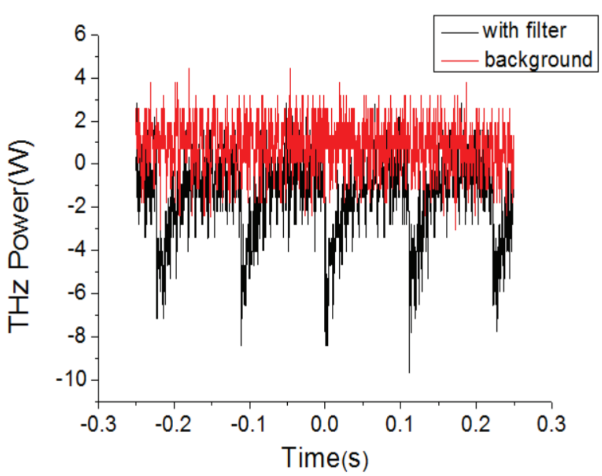

Figure 4: The measurement of THz power.

FEL SIMULATION

We use Genesis code for FEL simulation. The basic parameters of electron beam before undulator used for simulation are shown in Table1. We suppose that beam distribution is uniform in transverse and Gaussian in longitudinal.

We investigate the relationship between THz peak power and bunchlength. As shown in Fig. 5, the maximum peak power is obtained with the bunch length of 2.5 ps. Because THz wavelength is long, the slippage effect would be serious when the electron bunch is too short. On the other hand, if the beam length become longer, the peak power of THz also decreases due to the lower peak current of electron beam.

Table 1: Electron Beam Parameters for FEL Simulation

Parameter	Value	Unit
Electron beam energy	10~25	MeV
Bunch length	2.5	ps
Energy spread	0.5%	
Emittance	2	mm-mmrad
Beam size	200	μm

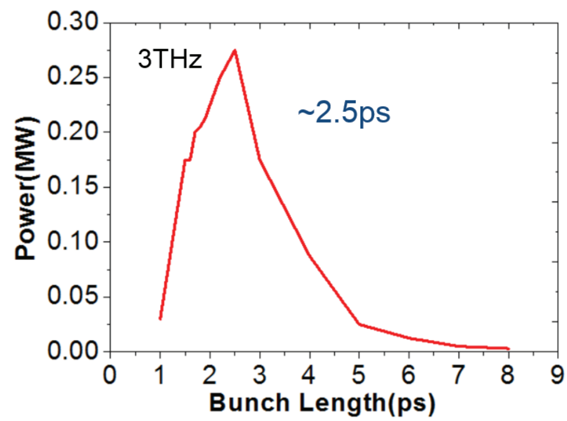

Figure 5: The relationship between THz peak power and bunch length.

We compare the gain curves along z coordinate with different power of THz seed. When the seed power is 0, it is a process of SASE. When the seed power is 1W, only 1THz FEL reaches saturation at 4m. When the seed power is increased to 10W, 2 and 3THz reach satiation at 4m. It is obvious that higher seed power is better, but it is difficult to obtain the peak power higher than 10W with TPA. We also find that THz radiation with higher frequency has higher peak power. For 4 to 6 THz, longer undulator whose length is about 4.6m is needed for saturation. Here we choose the undulator period length of 4cm, which is the same as our existed undulator. Due to the limited space, the period number is chosen to be 100.

In Fig. 6, we plot the power profiles and spectra with different frequency. The peak power is from 0.2 MW to 0.8MW when the THz frequency is from 2THz to 6THz. If we suppose the repetition rate is 1MHz, then the average power is from 0.6W to 2.4W. The product of fwhm spectral width (Δf) and pulse duration (Δt) is 0.59, close to Fourier transform limit for Gaussian distribution. That means the THz radiation has good temporal coherence.

ISBN 978-3-95450-134-2

The THz power could be further increased by using tapered undulator. The peak power increased to from 0.25MW to 2MW at 3THz when the taper is 12% starting from 1.5m.

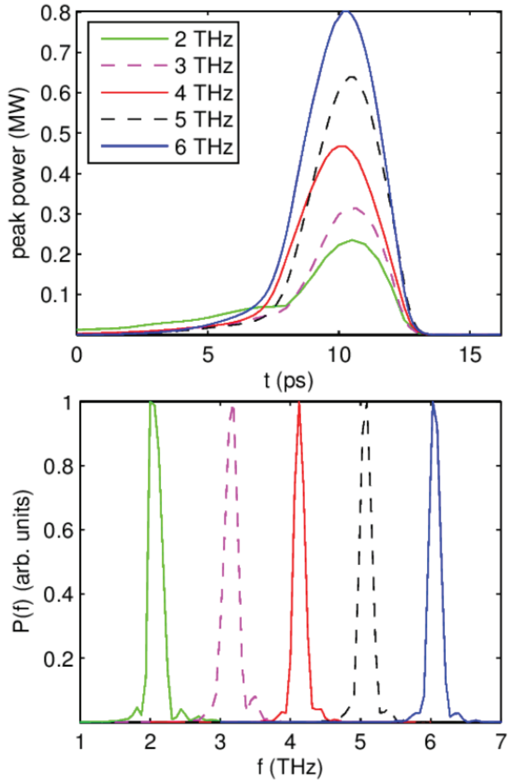

Figure 6: Power profiles and spectra with different frequency.

SUMMARY

In this paper, we present a plan of THz FEL amplifier based on TPA seed and 8~25 MeV superconducting accelerator was proposed by PKU and NTHU. On the test system of THz seed, we have obtained narrow-band, frequency tunable THz radiation with 10W peak power.

Simulation results show that THz radiation with tunable frequency from 1 to 6 THz, peak power higher than 0.8 MW and average power of several watt can be generated.

REFERENCES

[1] J. S. Sokolowski *et al.*, "First lasing of the Israeli tandem electrostatic accelerator free electron laser", PAC'97, p. 906, (1997).

[2] G. M. H. Knippels *et al.*, Phys. Rev. Lett. **83**, 1578 (1999).

[3] G. N. Kulipanov *et al.*, Terahertz Science and Technology **1**, 107 (2008).

[4] C. Sung *et al.*, Phys. Rev. ST Accel. Beams **9**, 120703 (2006).

[5] S.Ya. Tochitsky *et al.*, J. Appl. Phys. **98**, 026101 (2005).

[6] K. Kawase, J. Shikata, H. Ito, "Terahertz wave parametric source" (Topical Review), J. of Phys. D: Appl. Phys., **35**(3), R1-R14 (2002).

[7] K. Kawase, J. Shikata, K. Imai, H. Ito, "A transform-limited, narrow-linewidth, THz-wave parametric generator", *Appl*. *Phys*. *Lett*., **78**, 2819 (2001).

[8] T. D. Wang, Y. Y. Lin, S. Y. Chen, A. C. Chiang, S. T. Lin, and Y. C. Huang, Opt. Express 16, 12571 (2008).

[9] Weitao Wang *et al.* Opt. Lett. **39**(13), 3706-3709 (2014).

ISBN 978-3-95450-134-2

THE MICROBUNCHING INSTABILITY AND LCLS-II LATTICE DESIGN

M. Venturini*
Lawrence Berkeley National Lab, Berkeley, CA 94720 USA

Abstract

The microbunching instability is a pervasive occurrence when high-brightness electron beams are accelerated and transported through dispersive sections, like bunch-compression chicanes or distributions beamlines. If left uncontrolled, the instability can degrade the beam brightness and compromise the FEL performance. This paper contains a discussion of how consideration of the microbunching instability is informing the LCLS-II design and determining the specifications for the laser heater and transport lines. We review some of the expected and not so-expected phenomena that we have encountered while carrying out high-resolution macroparticle simulations of the instability and the analytical models developed to interpret the numerical results.

INTRODUCTION

LCLS-II is a 4^{th}-generation high-rep rate FEL light source soon to enter the construction phase at SLAC [1,2]. The 4 GeV super-conducting Linac will occupy the first third of the existing SLAC Linac tunnel; a long (~ 2 km) transport line will bypass the remaining sections of the normal-conducting machine and deliver the beam to the existing undulator hall, with a fast kicker distributing the beam between the hard (HXR) and soft (SXR) x-ray FEL undulators. The baseline design (100 pC bunches with $I_f \simeq 800$ A or higher peak current at the FELs and $I_{gun} \simeq 3$ A at the gun) calls for two-stage magnetic-compression at 250 and 1600 MeV beam energy in addition to significant velocity-bunching or 'ballistic' compression in the injector before the beam becomes ultra-relativistic. Use of a third magnetic chicane placed immediately before the spreader at full 4 GeV beam energy is under consideration but will not be discussed here. For a summary of relevant machine parameters, see Table 1.

As in all 4^{th}-generation light sources the microbunching instability is expected to be significant. The instability can be seeded by shot noise or other noise sources at the injector photo-cathode and develops through a combination of collective effects (primarily space-charge) and transport/compression along dispersive sections. The main adverse effect is the generation of uncorrelated or micro-correlated energy-spread growth. The instability can result into loss of radiated power and/or degradation of the radiation spectral properties, with tolerance to the instability depending on the mode of FEL operation (SASE, self-seeding, external seeding).

There are two aspects relevant to the instability that are specific to LCLS-II: the presence of long transport lines between the Linac and the undulators and reliance on velocity bunching for compression. Both have potentially aggravating effects. While in low rep-rate LCLS-class injectors, which are usually operated without velocity bunching, plasma oscillations at low energy tend to have a generally smoothing effect on perturbations to the charge density [3], the effect can be reduced or reversed in the presence of velocity bunching compression [4,5]. This is most relevant for the instability seeded by non-uniformity in the photo-gun laser profile. Here we will not address this issue, focusing instead on consideration of microbunching seeded by shot noise, for which it is appropriate to model the development of the instability starting from the exit of the injector. In our study we use a combination of analytical and numerical methods to characterize the main drivers of the instability and related phenomena, and identify strategies for machine-design optimization. Topics of interest discussed here include the anomalous heating induced by the laser heater, the development of the instability through the magnetic compressors, and its further amplification through the transport lines downstream of the Linac. Our macroparticle simulations, carried out with the code IMPACT [6], are based on idealized models of the beam distribution (*e.g.* temporal flat-top, 6D water-bag) having the nominal characteristics (emittance, peak current) of the baseline beam at the exit of the injector and always employ the same number of macroparticles as the number of electrons to minimize spurious effects. Results from start-to-end simulations starting from the photo-cathode and including modelling of the radiation output are reported elsewhere [7,8].

Table 1: LCLS-II Baseline Settings

Charge/bunch	100 pC
Peak current at exit of injector, I_{inj}	14 A
Peak current at FEL, I_f	800 A
Transverse normalized rms emittance, ε_n	0.3 μm
Beam energy at exit of injector, E_{inj}	100 MeV
Beam energy at BC1, E_{bc1}	250 MeV
Beam energy at BC2, E_{bc2}	1.6 GeV
Beam energy at FEL, E_f	4 GeV
BC1 R_{56}, R_{56}^{bc1}	-55 mm
BC2 R_{56}, R_{56}^{bc2}	-38 mm
BC1 compression factor, C_{bc1}	~ 6
BC2 compression factor, C_{bc2}	~ 10

* mventurini@lbl.gov

ISBN 978-3-95450-134-2

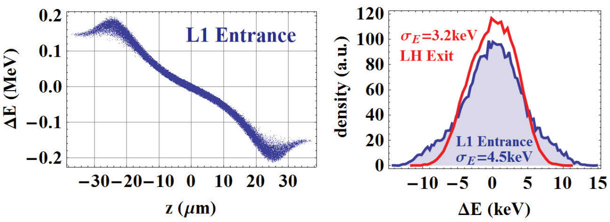

Figure 1: Longitudinal phase-space (left) of bunchlet at entrance of the first section of the Linac (L1) and energy density in the core (right, blue curve). For comparison, the red curve on the right figure is the energy density at exit of the LH chicane: the difference between the two is the result of trickle heating; $\sigma_{E0} = 2$ keV.

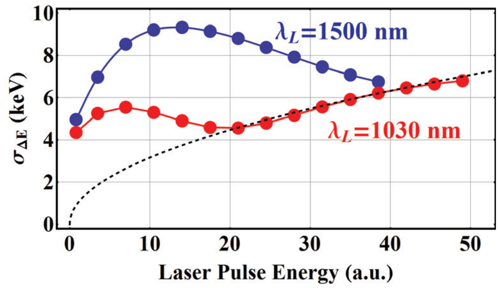

Figure 2: Energy spread at the entrance of L1 (two choices of laser wavelengths) showing evidence of the 'trickle' heating effect; $\sigma_{E0} = 0.1$ keV. The dashed line is the nominal heating in the absence of collective effects.

ANOMALOUS HEATING

'Trickle' Heating

The Laser Heater (LH) is the established method to control the microbunching instability, exploiting the microbunching sensitivity to energy-spread induced mixing. In LCLS-II the LH is located at the exit of the injector at about 100 MeV beam energy; it consists of a 0.54 m undulator placed in the middle of a weak 4-dipole chicane and a $\lambda_L = 1030$ nm laser system. Concerns about the 'trickle' heating effect, discovered during LCLS commissioning [9], motivated the close analysis reported here. Trickle heating is an echo-like phenomenon, in which the E/z micro-correlations generated by the laser/electrons interaction in a finite-dispersion region induce x/y correlations on the same micro-scale downstream of the LH (while the E/z micro-correlations are eventually washed out by the finite transverse emittance). The x/y correlations appear at relatively well localized points along the lattice separated by π phase advance in the horizontal betatron motion. The associated longitudinal space-charge forces modify the electron energy resulting into anomalous heating, which is undesirable, as it may compromise accurate control of the heater operation. To speed up the numerical calculations without sacrificing accuracy, we simulate a flat-top bunchlet meant to model a short section of the bunch core (but long enough to span many laser wavelengths).

We track the bunchlet with initial gaussian energy density and σ_{E0} slice rms energy spread, starting from the exit of the injector, a few meters upstream of the LH chicane; σ_{E0} from high brightness injectors is not known very well but is expect to be on the order of 1-2 keV, including IBS effects: in our simulations we exercised a range of values, down to 0.1 keV. The action of the laser on the beam is modeled as a point-like interaction inducing a sinusoidal energy modulation and occurring in the middle of the physical undulator. The electron dynamics through the undulator itself is modeled as that of a drift (IMPACT has the capability to track the electrons through the undulator and laser pulse fields, but it is time consuming and unnecessary for our purposes here). The bunch is followed through the LH chicane and a 50-m long collimation section to the entrance of the first Linac section (L1).

An example of bunchlet longitudinal phase space is shown in Fig. 1, left picture. The prominent energy chirp, entirely due to longitudinal space charge (LSC) in the short bunchlet, is removed in the analysis (linear as well nonlinear terms) before determining the energy spread distribution shown in the right picture. For comparison, the density observed at the exit of the LH chicane (red curve) is also shown: the difference between the two is (mostly) a consequence of the trickle heating effect. The results of a systematic study, shown in Fig. 2, also include data points obtained with $\lambda_L = 1500$ nm (blue dots), longer than the design $\lambda_L = 1030$ nm (red dots), to illustrate the dependence of trickle heating on the laser wavelength. The black-dashed curve is the nominal rms energy spread $\sigma_{\Delta E} \propto \sqrt{E_L}$ induced by the LH as a function of the laser pulse energy E_L (normalized units). Anomalous heating is apparent for small E_L but remains below the $6-7$ keV LH baseline design specification. The data points follow a behavior qualitatively consistent with the analytical model discussed in [9]. Notice that in the limit of vanishing laser pulse energy, the observed energy spread does not converge to the energy spread of the incoming beam ($\sigma_{E0} \simeq 0.1$ keV, in these simulations), as explained below. The above results are for an earlier and now outdated design of a 4 m long LH chicane with $|R_{56}| = 14$ mm.

Shot-noise Induced Heating

Another potential source of anomalous heating is the microbunching seeded by shot noise that develops through the LH chicane as a result of energy modulations accrued upstream of the LH. The linear gain of the instability is relatively modest but it may be sufficient for longitudinal space charge in the long section between LH chicane and first magnetic compressor BC1 to cause a few keV amplitude energy-modulation. Strictly speaking, this is a correlated energy spread (with E/z correlations on the μm scale). However, as the beam experiences the relatively large $|R_{56}|$ in BC1 the microcorrelation is flattened causing the energy spread to become effectively uncorrelated. Evidence of enhanced heating is shown on the left picture of Fig. 3 in the (top) data points for the energy spread observed at the entrance of BC1: for low laser-pulse energy, the energy spread is significantly larger than that observed at the entrance of

ISBN 978-3-95450-134-2

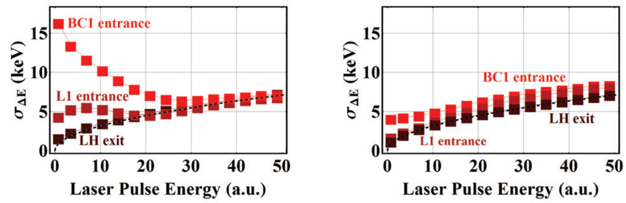

Figure 3: Slice energy spread as observed at the exit of the LH chicane, entrance of L1, and entrance of bunch compressor for a 4 m (left) and improved 8 m long (right; baseline design) LH chicane, showing evidence of shot-noise induced heating; $\sigma_{E0} = 0.1$ keV.

L1 (the latter is for the most part dominated by the trickle heating effect). The data points at the exit of the LH chicane track the nominal heating closely, as expected. The reported energy spread is calculated over a distance within the beam that encompasses several wavelengths of the dominant energy modulation. Once again, this unintended heating is undesirable as it may compromise the ability to tune the LH and set a lower bound to the minimum beam energy spread. The effect is also difficult to predict accurately because of a strong dependence on the not very well-known slice energy spread at the exit of the injector. In addition, there may be contributions to the microbunching instability from the gun and injector, not captured here, also not easy to predict accurately. It is therefore wise to adopt a lattice-design strategy aiming at reducing microbunching amplification through the LH chicane.

The instability is sensitive to the choice of R_{56} in the chicane, a variable over which the lattice designer has some degree of control. All the other relevant parameters kept fixed, there tends to be a value of $|R_{56}|$ that maximizes microbunching. Given the relatively small value of the slice energy spread involved, linear theory shows that here decreasing, rather than increasing, $|R_{56}|$ is the more effective way to reduce the instability. This can be seen from the basic scaling predicted by the simplified linear-theory model of the instability gain for the longitudinal mode with wavenumber k

$$G \simeq 4\pi \frac{I}{\gamma I_A} k|R_{56}| e^{-(\sigma_\delta k R_{56})^2/2} \int ds \frac{|Z(k)|}{Z_0}, \qquad (1)$$

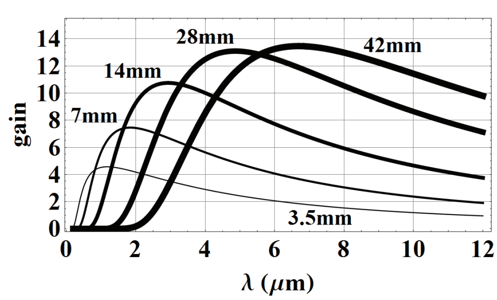

Figure 4: Linear gain curve of the microbunching instability through the LH chicane for several choices of $|R_{56}|$ as indicated. (Constant $\sigma_E = 2.5$ keV through the chicane.)

where I is the bunch peak current, $I_A \simeq 17$ kA the Alfven current, Z the longitudinal space charge impedance per unit length, $Z_0 = 120\pi$ the vacuum impedance and the integral is over the drift space preceding the LH chicane. Several gain curves of the microbunching instability through the LH chicane for various choices of R_{56} are reported in Fig. 4. The model is not very accurate (*e.g.* the beam slice relative energy spread $\sigma_\delta = \sigma_E/E_{inj}$ is assumed to have an effective value constant through the chicane, whereas the generation of the laser-induced heating is localized in the middle of the chicane) but it gives a good sense of the scaling involved. We redesigned the chicane to decrease $|R_{56}|$ to 3.5 mm. In order to keep the trajectory horizontal offset unchanged at 7.5 cm this was achieved by lengthening the chicane to 8 m while reducing the bend angle in the dipoles. Overall, anomalous heating in the presence of the modified chicane is much reduced (right picture in Fig. 3). Both pictures in Fig. 3 were obtained with a conservative choice for the beam natural slice energy spread out of the injector ($\sigma_{E0} = 0.1$ keV).

INSTABILITY THROUGH THE BC'S

It is well known that multi-stage magnetic compression will tend to magnify the development of microbunching [10–12], with the overall instability gain depending on the overlap in frequency domain of the gain curves through each compressor. As the gain through a compressor is sensitive to the details of the beam-slice energy distribution, it is important in the analysis to include the exact form of the energy distribution induced by the laser heater. To illustrate this point let us consider in some detail the development of the instability through BC1 and BC2. Consider the regime in which shot noise is the dominant noise source in the beam exiting the laser heater. As the beam travels toward the first bunch compressor, space-charge induced energy modulations develop and cause bunching as the beam undergoes compression in BC1.

A finite slice energy-spread $\sigma_{\delta,bc1} = \sigma_{E,lh}/E_{bc1}$ introduces a frequency cutoff in the current-profile spectrum of the beam emerging from BC1, suppressing noise amplification at wavelengths shorter than $\lambda_{bc1} \simeq 2\pi|R_{56}^{bc1}|\sigma_{\delta,bc1} \simeq 8.5$ μm (wavelength observed after compression), roughly corresponding to the peak gain, having assumed $\sigma_{E,lh} = 6$ keV heating by the laser heater. (For the other parameters, see Table 1.)

Further LSC-induced energy modulations are then accrued by the beam on its way toward BC2. The spectrum of these modulations exhibiting an expected peak at $\lambda_{bc1}/C_{bc2} \sim 0.85\mu$m is shown in the top-picture of Fig. 5 for a macroparticle beam tracked starting from the exit of the injector with initial water-bag (WB) distribution (*i.e.* a uniformly populated ellipsoid in the 6D phase space). Note that in the figure the spectrum is reported as a function of the wavelength *after* compression through BC2, with $C_{bc2} \simeq 10$. In the simulation we assumed $\sigma_{E0} = 1$ keV for the slice energy spread before passage through the laser heater.

ISBN 978-3-95450-134-2

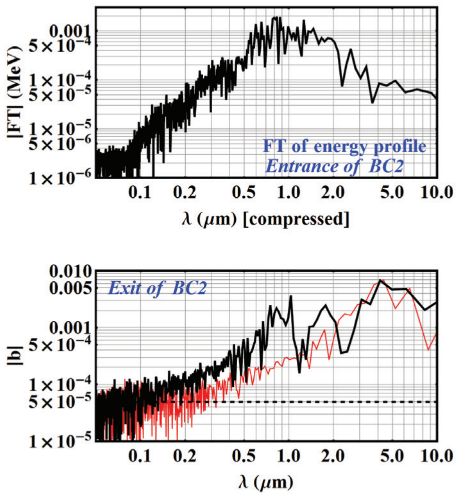

Figure 5: Spectrum of the energy profile of a simulated beam observed at the entrance of BC2 (top) and bunching observed at the exit of BC2 (bottom, black line). In the top picture the spectrum is expressed in terms of mode wavelengths observed after BC2 compression. In the bottom picture the dashed line indicates the shot-noise level; the red line is the bunching exhibited by an equivalent beam with the same $\sigma_E \simeq 36$ keV rms slice energy spread (as observed right before BC2) but with a gaussian slice energy density.

Now, as the slice energy spread after BC1 is $\sigma_{E,bc1} = C_{bc1}\sigma_{E,lh} \simeq 36$ keV we expect bunching to peak at

$$\lambda_{bc2} \simeq 2\pi|R_{56}^{bc2}|\sigma_{\delta,bc2} \simeq 5\ \mu\text{m} \tag{2}$$

(again, as observed after compression through BC2). Because the spectral components at $\lambda_{bc1}/C_{bc2} \sim 0.85\ \mu$m are significantly shorter than λ_{bc2}, the expectation based on a model like (1) is that they should be mostly washed out. In fact, inspection of the spectrum of the beam profile downstream of BC2 shows a strong component in the neighborhood of $\sim 1\ \mu$m, comparable in magnitude to bunching at $\simeq 5\ \mu$m, see black curve in the bottom picture of 5. To understand this feature, which leads to interesting consequences further downstream (see next section), we have to account for the effect of the laser heater on the beam energy distribution with more care. (To avoid possible confusion, we should point out that the wavelengths of interest here only coincidentally happen to be in the range of that of the LH laser, $\lambda_L \simeq 1\mu$ m).

Consider a beam model with a sinusoidal energy modulation $\hat{\delta}\sin(k_1 z)$, $k_1 = 2\pi/\lambda_1$ and (uncorrelated) energy density $V(\delta)$. For starters, assume that the beam has no long-scale energy chirp so that no compression occurs. As the beam propagates through a chicane with momentum compaction R_{56} and energy E_{bc}, the beam develops bunching according to

$$\rho(z) = 1 + 2\sum_{n=1}^{\infty}\tilde{\rho}(k_n)\cos k_n z, \tag{3}$$

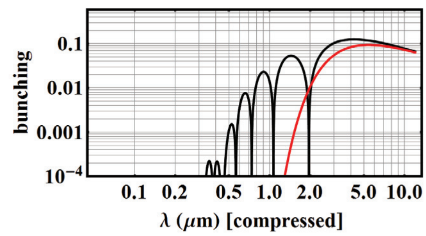

Figure 6: Bunching at the exit of BC2 (black curve) as predicted by Eq. (5) for a model beam with slice energy density as induced by the laser heater and assuming, for simplicity, a uniform spectrum of the energy profile on the beam entering BC2. For comparison, the red curve is the expected bunching from an equivalent beam with identical rms slice energy spread but gaussian distribution, showing a much sharper cut-off at shorter wavelengths. Black and red curve here are meant to capture the essential features of the corresponding curves in the bottom picture of Fig. 5, obtained from macroparticle simulations.

where the FT of the beam density at the exit of the chicane $\tilde{\rho}(k_n) = \lambda_1^{-1}\int_{-\lambda_1/2}^{\lambda_1/2}\rho(z)e^{-ik_n z}dz$ is given by

$$\tilde{\rho}(k_n) = J_n(\hat{\delta}k_1|R_{56}|)\int d\delta e^{ik_1|R_{56}|\delta}V(\delta). \tag{4}$$

J_n is the Bessel function and $k_n = nk_1$. This is the generalization of a formula better known when $V(\delta)$ is gaussian [13].

If the laser pulse and the electron beam in the LH are transversally matched one can derive a manageable expression for $V(\delta)$ [14] and evaluate the integral in (4) in terms of a first-order Bessel function

$$\tilde{\rho}(k_n) = J_n(\hat{\delta}k_1|R_{56}|)\left[\frac{2J_1(x)}{x}\right]e^{-(k_n R_{56}\sigma_{\delta 0})^2/2}, \tag{5}$$

where $x = \sqrt{2}k_n|R_{56}|\sigma_E/E_{bc}$ and σ_E is the rms energy spread at the entrance of the chicane. With the heater turned off, the beam is assumed to have a gaussian uncorrelated energy distribution with $\sigma_{\delta 0} = \sigma_{E0}/E_{bc}$ rms relative energy spread. In the presence of compression the formulas above are still valid provided that k_n is interpreted as the wavenumber of the beam perturbation as seen *after* compression.

This model applied to the beam dynamics through BC2 is a useful tool for interpreting the simulation results. Plot of Eq. (5) in Fig. 6 for $n = 1$, the only significant component for our parameters, shows that the energy spread induced by the laser heater is associated with a relatively shallow cutoff at shorter wavelengths. Whereas the peak of the gain is not far from the value predicted by Eq. (2), longitudinal modes at shorter wavelength down to 0.5 μm are not strongly suppressed. As a result, modes in the neighborhood of 1 μm after compression in BC1 can pass through BC2 and remain quite visible in the current profile.

Having noted the microbunching amplification in the μm range, we should add that for a LH setting of 6 keV or so, the

ISBN 978-3-95450-134-2

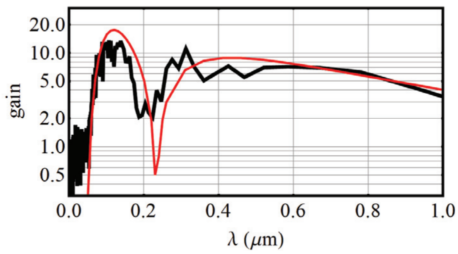

Figure 7: Gain of the instability accrued by the beam traveling from the exit of BC2 through the DL1 dogleg (see text for a description of the machine layout). Linear theory (red curve) agrees fairly well with simulations (black curve). The latter was obtained from a 4-shot average of the bunch profile spectrum.

instability by the exit of BC2 remains modest, amounting to a current ripple of a few percent, see the black curve in Fig. 12. (This curve represents the current profile over a short segment of the same bunch in the example just discussed but observed at the end of the extension line past the Linac). This level of bunching and the concurrent energy spread/modulation would have limited consequences on the FEL performance. However, further amplification of the instability is to be expected as the beam is transported from the Linac to the FELs [15].

TRANSPORT THROUGH THE BYPASS LINE

R_{56} in the Doglegs and its Compensation

The last section of the Linac is followed by an extension line (to accommodate possible future energy upgrades) and a ∼ 80 m long, tilted, two-bend dogleg achromat (DL1) designed to gently lift the beam from the floor to the ceiling of the tunnel into the bypass line. Transport past the Linac can add significantly to the instability. A rough, order-of-magnitude estimate of the instability peak gain accrued by the beam from BC2 through DL1, can be done using

$$G \sim \frac{I}{I_A}\frac{mc^2}{\sigma_E}\frac{L_s}{\gamma^* r_b}\xi \qquad (6)$$

where L_s is the BC2-to-DL1 distance, r_b is an average effective transverse size of the beam and γ^* and effective relativistic factor. This formula is based on the approximation $|Z|/Z_0 \simeq 0.3/\pi\gamma^* r_b$ for the LSC impedance valid when the factor $\xi = 2\pi r_b/\lambda\gamma^*$ is not too far from unity. With a slice energy spread on the order of $\sigma_E = 0.5$ MeV, $I = 850$ A, $L_s = 550$ m, taking for γ^* the geometric mean between the values at BC2 and DL1, and $r_b \simeq 100$ μm, we expect a peak gain at about $\lambda \simeq 2\pi(\sigma_E/E_f)|R_{56}| \simeq 0.2$ μm, yielding $\xi \sim 0.7$ and hence $G \sim 40$. This is a fairly large number, considering that further amplification is to be expected through the additional transport sections downstream of DL1. It turns out that the above formula overestimates the effect somewhat; however, a more accurate calculation still yields

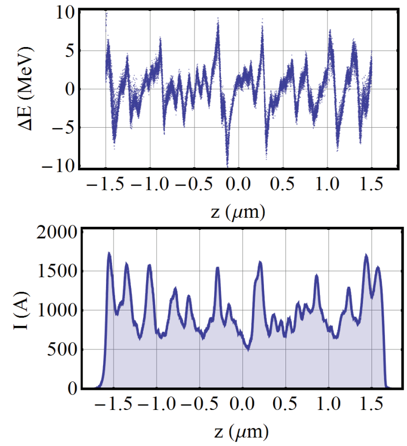

Figure 8: Images of the longitudinal phase space (top) and current profile (bottom) at the entrance of the HXR FEL beamline in the absence of compensating chicanes in the transport line downstream of DL1 show very large instability. (Short flat-top bunchlet with $I = 850$ A current tracked from the exit of BC2).

a significant peak gain $G_{\rm peak} \sim 15$. This is shown in Fig. 7, where a comparison between the results from linear theory based on an impedance model for space-charge effects (red curve) and macroparticle simulations (black) also provides a reassuring cross-validation of the methods used in our study; in both cases only the longitudinal component of the self-fields is included in the physics model (more on this in the next section). Here, the numerical simulation is for a flat-top beam, with gaussian energy density, propagated from the exit of BC2 and initially carrying no other bunching than that deriving from shot-noise. The black curve is the average of four runs using different seeds in the random number generator employed to populate the macroparticle distribution. The dip observed at about $\lambda \simeq 2$ μm is the result of phase differences due to the wavelength-dependent plasma oscillations along the Linac (at these wavelengths the plasma-oscillation period is not very long compared to the distance traveled by the beam; in other words, the kinetic $\propto 1/\gamma^2$ component of R_{56} cannot be neglected, particularly in the vicinity of BC2).

If we now extend the numerical simulation beyond DL1 to the entrance of the FEL we observe a dramatic amplification of the instability, Fig. 8, with maximum seen to occur at the sub-μm wavelength, about consistent with our estimate of the peak gain through DL1. Striking as it is, we should keep in mind that this simulation does not capture the full extend of the instability, as it excludes the beam dynamics upstream of BC2 and bunching that may have occurred therein.

The magnitude of the effect is of serious concern. Fortunately, there exists a simple but effective remedy consisting of introducing R_{56}-compensation in the dispersive sections downstream of the Linac as a way to prevent conversion of modulations in the energy profile into longitudinal slippage (barring the small slippage that may occur as a result of plasma oscillations, which is generally benign).

ISBN 978-3-95450-134-2

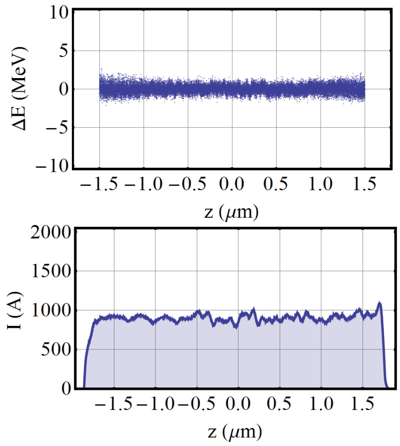

Figure 9: As in Fig. 8 but in the presence of R_{56}-compensating chicanes adjacent to the dipoles of the bypass-line doglegs, showing a much reduced instability.

Let us consider in some detail the beam transport to the HXR FEL undulator. The main R_{56} contributors to this transport are DL1 (R_{56} = 200 μm) and a combination of two double-bend achromats downstream of the spreader (R_{56} = 65 + 65 μm) also arranged in a dogleg configuration. With each dipole in DL1 and downstream dogleg contributing positively to R_{56} a local R_{56}-compensation can be simply achieved by placing standard 4-bend chicanes (contributing negative R_{56}) next to the dogleg dipoles. Because of the small momentum compaction involved, the required compensating chicanes (CCs) are weak and short (~ 1 m). Numerical simulations show a remarkable improvement, Fig. 9, with a similarly beneficial outcome observed in the transport to the SXR FEL.

Exact compensation of the momentum compaction, however, does not completely solve our problems. This becomes apparent when the effect of microbunching accumulated by the beam upstream of, and through BC2, is properly included in the picture, as discussed below.

Effect of Transverse Space-charge Fields

A somewhat surprising finding of our study was the discovery of a new mechanism for the amplification of microbunching occurring in the presence of imperfect damping of the microbunching instability through BC2 and driven by the transverse rather than the longitudinal component of the self-fields. We first observed this effect while investigating the beam dynamics through DL1, including acceleration and transport from the exit of the injector.

Despite the presence of the compensating chicanes we observe a small but significant enhancement of bunching, caused by the transverse space-charge (TSC) forces within the dogleg. The mechanism is somewhat reminiscent of the trickle heating effect [9]: in both cases an energy modulation couples with dispersion to cause the appearance of a 2D longitudinal/horizontal pattern in the beam density on the scale of the energy modulation wavelength at certain locations along the dogleg.

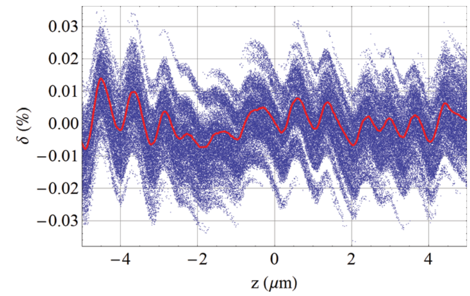

Figure 10: Longitudinal phase space of the beam core at the entrance of DL1. The red curve is the slice centroid energy. The apparent ~ 1 μm energy modulation is the result of LSC during acceleration and transport following the second bunch compressor, placed about 700 m upstream of DL1.

Referring to the WB-beam example discussed earlier, a 6 keV setting of the laser heater leaves a few % microbunching on the beam at $\lambda \simeq 1$ μm at the exit of BC2, which by the entrance of the dogleg DL1 results into a noticeable energy modulation, see Fig. 10. Further downstream in the dogleg this modulation gives rise to the pattern seen in Fig. 11. The transverse component of the space charge associated with this 2D x/z pattern causes a μm modulated $\Delta x'$ kick on the particles horizonal angular coordinate. Because the matrix entry R_{52} from location of the kick to exit of the dogleg is generally finite, a longitudinal shift is induced, $\Delta z = R_{52}\Delta x'$, enhancing the existing bunching, as observed at the exit of the dogleg, Fig. 12. The unequivocal 3D nature of the effect is confirmed by simulations where only the longitudinal component of the self-fields is applied in tracking the beam particles. In this case the observed amplification of the observed ~ 1 μm microbunching disappears.

Under certain simplifying assumptions one can work out an analytical model for the TSC-induced bunching in the form [16]

$$b_k \simeq \delta_p \frac{2Ik}{\varepsilon_{xn}\gamma^2 I_A} \int_{s_0}^{s_f} ds \frac{\eta_x^2}{\sqrt{\beta_x \beta_y}} e^{-\frac{\varepsilon_{xn}\eta_x^2 k^2}{\gamma\beta_x}},$$

where δ_p is the relative energy-modulation amplitude at the entrance of the dogleg with wavenumber k, $\beta_{x,y}$ and η_x

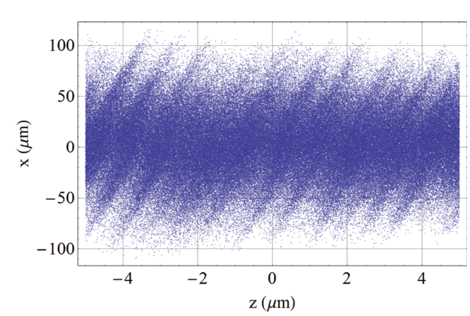

Figure 11: Section x/z of the beam phase space observed just before the first quad of DL1 showing the longitudinal/transverse microbunching induced by the energy modulation of Fig. 10.

ISBN 978-3-95450-134-2

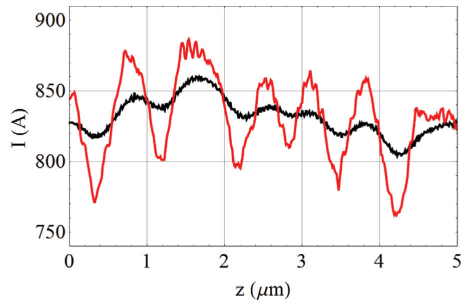

Figure 12: The beam current profile as seen at the entrance of DL1 (black curve) shows ∼ 1% longitudinal bunching amplitude at about $\lambda \simeq 1$ μm wavelength. By the exit of the dogleg (red curve) bunching has grown to about 4%, implying a net ∼ 3% contribution from TSC in the dogleg. The quoted numbers are about the middle of the observed value ranges.

are the betatron and the dispersion functions, and ε_{xn} is the normalized rms emittance (same as the vertical emittance). The integral is over the dogleg length and the expression is valid for the case where R_{56} has been locally compensated. The formula agrees reasonably well with the results of the numerical simulations and shows that high-brightness beams are most vulnerable to this effect.

The net result of the TSC-induced microbunching from DL1 and the downstream transport sections, including the various other sources of the instability starting from the injector is shown in the right pictures of Fig. 13, for σ_E = 6 keV LH setting. The observed microbunching is significant. Similar bunching but with somewhat larger magnitude is also observed at the exit of the transport line toward the SXR FEL.

Nonlinear Momentum Compaction

At the entrance of DL1 the bunch carries a significant energy chirp left over from compression and transport through the last section of the Linac and the extension line. Unlike the current LCLS copper machine, the longitudinal wakefields associated with the L-band SC structures are too weak to remove the post-compression chirp. Chirp removal is complete only after transport through the bypass line thanks to the action of the vacuum-chamber resistive-wall wakefields.

It turns out that the $T_{566} \simeq 0.1$ m nonlinear momentum compaction contributed by DL1 in conjunction with substantial energy chirp has the potential to generate further amplification of microbunching. To see this let $\delta_c(z) \simeq hz$ be the energy chirp of the beam at the entrance of DL1, with dominant linear component h. As it travels through the dogleg a particle experiences longitudinal slippage $z' = z + R_{56}\delta + T_{566}\delta^2$.

Consider two particles with approximately the same longitudinal coordinate z_0 but different energy, $\delta_1 = \delta_c(z_0) + \Delta_1$ and $\delta_2 = \delta_c(z_0) + \Delta_2$. Through first order in Δ_1 and Δ_2 the relative slippage between the two reads $\Delta z = R_{56}\Delta\delta + [2T_{566}\delta_c(z_0)]\Delta\delta$, with $\Delta\delta = \Delta_2 - \Delta_1$. In the presence of the

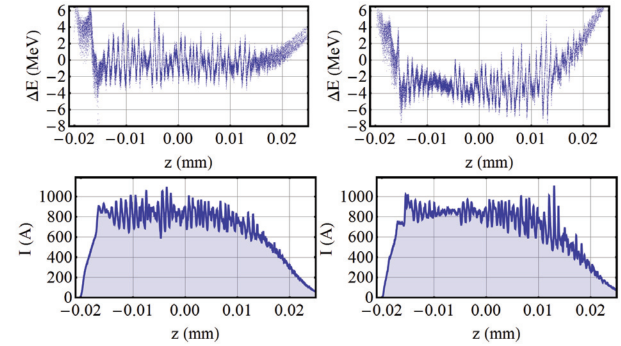

Figure 13: Bunch longitudinal phase space (top) and current profile (bottom) at the entrance of the HXR FEL. The comparison is between a complete physics-model simulation (right) and one (left) where the linear energy chirp is removed as the beam enters DL1 as a way to highlight the T_{566} effect. (WB beam with σ_E = 6 keV LH setting. Compensating chicanes are inserted. Bunch head is to the left.)

CCs set to exactly cancel the contribution from the doglegs, we have $R_{56} = 0$ and the effect of T_{566} can be thought of as being equivalent to a z−dependent effective $R_{56}^{\text{eff}} = 2T_{566}hz_0$. With $T_{566} \simeq 0.1$ m, $h \simeq 50$ m^{-1}, we have $R_{56}^{\text{eff}} \simeq 100$ μm for $z_0 = 10$ μm away from the beam center, *i.e.* a value comparable in magnitude to the actual linear momentum compaction of the DL1 dogleg in the absence of the compensating chicanes. The simplest way to gauge the T_{566}-effect is by a macroparticle simulation in which 'by hand' we remove the beam linear energy chirp right at the entrance of DL1 and compare the result (left pictures in Fig. 13) with that of the baseline simulation (same figure, right pictures, where the T_{566} effect is included). The T_{566} effect is particularly visible toward the tail of the bunch; in other parts of the beam the behavior is more complicated as it appears to interfere with other sources of the instability. Incidentally, we should note that, for better comparison, in the simulation the resistive wall wakefields were turned off in order to preserve the longitudinal phase-space flatness of the beam delivered to the FEL.

CONCLUSIONS

To summarize our main findings, we have determined that *i)* transport through the bypass and distribution lines downstream of the Linac can significantly amplify the microbunching instability and *ii)* the instability is fueled by two distinct sources: longitudinal and transverse space charge. We showed that introducing local R_{56} compensation in the transport lines downstream of the Linac has a beneficial effect but still leaves a sizeable level of instability when the laser heater is operated at its design specification.

Is there a way, short of heating the beam more, to reduce the instability further? We recognize that setting the compensating chicanes to cancel R_{56} minimizes the LSC-induced microbunching. However, in view of *ii)* it is conceivable that LSC- and TSC-induced bunching could, to some de-

ISBN 978-3-95450-134-2

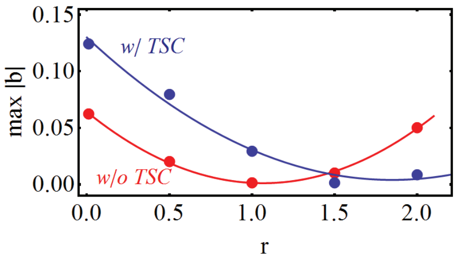

Figure 14: Amplitude of the instability observed on the beam at the entrance of the HXR FEL as a function of the strength of the compensating chicanes with (blue data) and without (red data) inclusion of transverse space-charge effects in the simulation. See the text for the meaning of r. Water-bag beam with 6 keV LH setting. The simulations do not include the T_{566}-effect.

gree, offset each other, suggesting that a different tuning of the compensating chicanes may yield an improved lattice. Indeed, simulations starting from the injector show minimum bunching when the CCs overcompensate rather than exactly cancel the R_{56} contribution from the adjacent dogleg dipoles.

Fig. 14 reports a measure of the instability at the FEL as a function of the parameter r defined as $r = |R_{56}^{\mathrm{CC}}|/|R_{56}^{\mathrm{B-DL}}|$, where $R_{56}^{\mathrm{B-DL}}$ and R_{56}^{CC} are the contributions to the momentum compaction from the dipole(s) in the dogleg and the associated CC; $r = 1$ corresponds to exact compensation as in the simulations of Fig.'s 9 and 13. The measure of the instability in Fig. 14 is the maximum bunching $|b(k)|$ for $\lambda = 2\pi/k \leq 3$ μm obtained from the FT of the current profile in the bunch core. While $r = 1$ represents the optimum in simulations where we exclude account of the transverse component of space-charge fields on the beam dynamics (red dots), with the full 3D model of space charge the minimum instability shifts to about $r \simeq 1.5$ (blue dots). To facilitate the interpretation of the results, in these simulations we removed the linear energy chirp from the beam at the entrance of DL1 as a way to eliminate the T_{566} effect. Including the latter, however, does not alter the results significantly.

To further validate these conclusions, we studied the dependence of the beam energy spread at the FEL (an alternate measure of the microbunching instability more directly related to the FEL performance) as a function of the LH setting for $r = 1$ and $r = 1.5$, see Fig. 15. The dashed line represents the expected energy spread in the absence of collective effects $\sigma_E = C\sigma_{E,lh}$, where C is the overall magnetic compression. In the data analysis, σ_E is calculated as the projected rms energy spread within the ~ 20 μm long beam core after we remove the long-scale nonlinear energy chirp from the beam distribution as determined by a low-order polynomial interpolation (therefore, properly speaking, σ_E is not a *slice* energy spread). The simulations include the T_{566} effect and indicate a minimum achievable energy spread, as defined above, of 0.65 MeV corresponding to laser heater settings of about 9 keV.

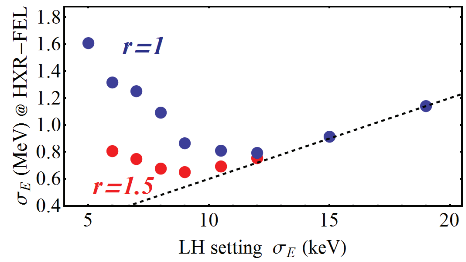

Figure 15: Energy spread observed on the beam at the entrance of the HXR FEL as a function of the LH setting for two lattice designs: with exact compensation ($r = 1$, blue data) and over-compensation ($r = 1.5$, red data) of R_{56} in the bypass doglegs. The simulations include the T_{566}-effect.

Additional machine optimization to reduce the instability further may be possible in principle targeting, for example, the reduction of the ~ 1 μm bunching observed at the exit of BC2. This could be pursued, *e.g.*, by retuning the bunch compressor chicanes R_{56} to minimize the overlap of the instability gain curves through each compressor. In practice, other constraints limit the freedom to set the BC parameters and the payoff from further lattice optimization is likely to be modest. On the other hand, we believe that the current baseline lattice with the compensating chicanes properly tuned should already deliver beams meeting the desired FEL performance in both the SASE and self-seeding modes of operation.

ACKNOWLEDGMENTS

Work supported by DOE, in part under Contract No. DE-AC02-05CH11231 and through the LCLS-II Project. J. Qiang's assistance with the IMPACT simulations is gratefully acknowledged as well as support from the LCLS-II design team and in particular P. Emma, Z. Huang, Y. Nosochkov, T. Raubenheimer, and M. Woodley.

REFERENCES

[1] J. Galayda, IPAC 2014, Dresden, Proc., p. 935 (2014).

[2] T. Raubenheimer, 'LCLS-II: Status of the CW X-ray FEL Upgrade to the SLAC LCLS facility', Proc. 37th Int. Free-Electron Laser Conf., Daejeon (2015).

[3] C. Limborg-Deprey, P. Emma, Z. Huang, and J. Wu, EPAC 2004, Lucerne, Proc. p. 1506 (2004).

[4] M. Venturini, *et al.*, PRST-AB, **13**, 080703 (2010).

[5] J. Qiang, J. Corlett, C.E. Mitchell, C.F. Papadopoulos, G. Penn, M. Placidi, M. Reinsch, R.D. Ryne, F. Sannibale, C. Sun, M. Venturini, P. Emma, and S. Reiche, PRST-AB, **17**, 030701 (2014).

[6] J. Qiang, *et al.*, PRST-AB **12**, 100702 (2009).

[7] J. Qiang, *et al.* 'Start-to-end simulation of the LCLS-II beam delivery system with real number of electrons', Proc. 37th Int. Free-Electron Laser Conf., Daejeon (2015).

[8] G. Marcus, *et al.*, 'High-fidelity start-to-end numerical particle simulations and performance studies for LCLS-II', Proc. 37th Int. Free-Electron Laser Conf., Daejeon (2015).

ISBN 978-3-95450-134-2

[9] Z. Huang, *et al.*, PRST-AB **11**, 020703 (2010).

[10] M. Venturini, PRST-AB **7**, 104401 (2007).

[11] E.A. Schneidmiller and M.V. Yurkov, PRST-AB **13**, 110701 (2010).

[12] A. Marinelli, *et al.* , PRL **110**, 26480-2 (2013).

[13] L. H. Yu, Phys. Rev. A **44**, 5178 (1991).

[14] Z. Huang, M. Borland, P. Emma, J. Wu, C. Limborg, G. Stupakov, and J. Welch, PRST-AB **7**, 074401 (2004).

[15] M. Venturini and A. Zholents, NIM-A **539**, 53 (2008).

[16] M. Venturini and J. Qiang, PRST-AB **18**, 054401 (2015).

ISBN 978-3-95450-134-2

THZ PHOTO-INJECTOR FEM BASED ON SPONTANEOUS COHERENT EMISSION FROM A BUNCH OF NEGATIVE-MASS ELECTRONS*

I.V. Bandurkin, A.V. Savilov #, Institute of Applied Physics, Nizhny Novgorod, Russia

Abstract

It is proposed to utilize the effect of negative mass for stabilization of the effective axial size of very dense and short electron bunches produced by photo-injector guns by using combined undulator and strong uniform magnetic fields. It has been shown that in the "abnormal" regime, in which an increase in the electron energy leads to a decrease in the axial velocity of the electron, due to the negative-mass effect the Coulomb repulsion of electrons leads to their attraction and formation of a fairly stable and compact bunch “nucleus”. The use of the negative-mass regime may provide realization of a source of the terahertz radiation, which is based on a long-pulse coherent spontaneous undulator emission from a short dense moderately-relativistic (5.5 MeV) photo-injector electron bunch with a high (up to 20%) efficiency and a narrow frequency spectrum.

INTRODUCTION

Laser-driven photo-injectors allow formation of fairly compact and accessible sources of dense electron bunches with a moderate energy of 3-6 MeV, sub-picosecond and picosecond pulse durations, and charges of up to 1 nC and greater. These bunches can be further accelerated up to the GeV energy level for the use in short-wavelength FELs or directly exploited for radiation in the THz frequency range. In the latter case, they can be used, in particular, for realization of comparatively simple and compact sources operating in the regime of spontaneous coherent undulator radiation of electrons [1-4]. This type of radiation is realized, when the effective axial length of bunches in the radiation section is shorter than the operating wavelengths. In this situation, the wave packets emitted by each of the electrons add up basically in phase; this provides high level of radiation power.

Evidently, the length of the operating region is strictly limited by the Coulomb particle repulsion leading to an increase in bunch sizes and, first of all, in the axial size of the bunch. In this letter, we propose a method of weakening the axial repulsion significantly and, simultaneously, of confining particles in the transverse direction by means of using the radiation of electrons in combined undulator and strong uniform guiding magnetic fields. The corresponding effect is similar to the Negative Mass Instability which is well-known in cyclic accelerators [5,6] and Cyclotron Resonance Masers [7-9]. In the combined field, the negative-mass effect can occur when the electron cyclotron frequency corresponding to the guiding magnetic field exceeds the bounce frequency of electron oscillations in the periodic undulator field. In such “abnormal” regime, an increase in the energy of the particle leads to a decrease in its axial velocity [10-13] and axial Coulomb repulsion of the electrons leads to their effective mutual attraction which slows down bunch degradation. The use of this regime can result in a substantial increase in the effective length of the coherent spontaneous emission, and, therefore, an increase in the power and narrowing of the spectrum of the output radiation pulse.

In this letter, we study a possibility to realize a powerful and very efficient source of long-pulse coherent radiation of the terahertz frequency range on the basis of the Israeli THz Source [3] as an example of the proposed approach. This THz source is based on the using coherent spontaneous undulator emission from a short dense photo-injector electron bunch with moderate energy (5.5 MeV). The stabilization of the axial size of the bunch (which is required to provide the coherent character of the radiation) is due to the negative-mass regime of the motion of the bunch through a long operating undulator. An undulator with a strong uniform magnetic field providing the negative-mass effect is proposed and designed for this experiment [14].

NEGATIVE-MASS EFFECT

For demonstration of the negative-mass effect, let us first recall the known properties of the electron motion in a helical undulator with period $\boldsymbol{d_u}$ and a homogeneous axial magnetic field $\boldsymbol{B_0}$ (Fig. 1a) within the approximation of negligible transverse inhomogeneity of the undulator field as well as the perturbations caused by the Coulomb and radiated fields [10-12]. The normalized oscillatory (transverse) electron momentum obeys the equation:

$$p_\perp = K \,/\, \Delta\,,$$

where K is the undulator parameter in the absence of the guiding field, $B_0 = 0$, and $\Delta = 1 - \Omega_c/\Omega_u$ is the mismatch between the relativistic electron cyclotron frequency $\Omega_c = eB_0/mc\gamma$ and the undulator (bounce) frequency $\Omega_u = h_u V_z$. The dependence of the transverse electron velocity on the cyclotron frequency has a resonance character (Fig. 1b); $V_\perp(\Omega_c)$ is an increasing function at low axial magnetic fields ($\Omega_c < \Omega_u$) and a decreasing function at high magnetic fields ($\Omega_c > \Omega_u$).

The Coulomb interaction leads to an increase in the energies of the particles placed in the bunch front and to decrease in the energies of the electrons being in the tail. The type (positive/negative mass) of the Coulomb interaction is determined by the dependence of the axial

*Work partially supported by the Russian Scientific Foundation (Project 14-19-01723).
#savilov@appl.sci-nnov.ru

ISBN 978-3-95450-134-2

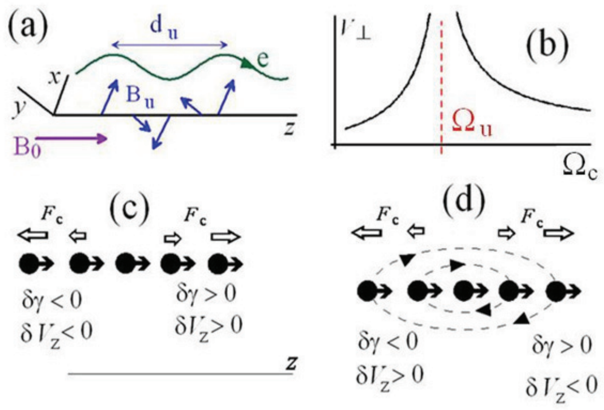

Figure 1: (a) Electron motion in the combined helical undulator and uniform axial fields. (b) Characteristic dependence of the transverse electron velocity on the cyclotron frequency. (c) Coulomb repulsion in the "positive-mass" regime. (d) Coulomb attraction and oscillations of electrons in the "negative-mass" regime.

velocity on the energy (relativistic mass-factor, γ):

$$\mu = \frac{dV_z}{d\gamma} = \frac{c}{\gamma^3}\left(1 + \frac{K^2}{\Delta^3}\right).$$

In the normal, "positive-mass" regime, μ>0. In this case, the Coulomb interaction results in repulsion of the particles (Fig. 1c) and, therefore, in degradation of the bunch. However, it is possible to provide the "negative-mass" regime, when the axial electron velocity decreases with an increase in the energy, μ<0 . Actually, if the cyclotron frequency exceeds the undulator frequency, and the mismatch Δ is small enough,

$$\Delta < 0 \text{ and } |\Delta|^3 < K^2,$$

then an increase in the energy of a particle shifts this particle closer to the cyclotron-undulator resonance $\Omega_c = \Omega_u$. This results in an increase in the particle transverse momentum. Moreover, in the vicinity of the resonance, the transverse momentum may increase so fast, that it can lead to a decrease in the axial velocity, so that the negative-mass condition is fulfilled. In the "negative-mass" regime the Coulomb interaction leads to oscillations of particles around the "nucleus" of the bunch (Fig. 1d). This effect can be utilized in a straightforward way for stabilization of the dense electron bunch moving through a relatively long undulator.

NUMERICAL SIMULATIONS

The proposed regime has been studied on the basis of the original 3D numerical code using the exact relativistic formulas for Liénard–Wiechert potentials. We have studied the motion of the electron bunch with the parameters close to those discussed for the Israeli THz Source [3]: an initial charge of 0.3 nC, a length of 0.1 mm, diameter 1 mm, and the Lorentz-factor γ =12 in the helical undulator with a period of 2.5 cm and the undulator parameter K=0.45. In this case, the resonance magnitude of the guiding magnetic field is close to 5 T. When the axial magnetic field is high enough ($B_0 = 7 - 9\,T$), the dependencies of the transverse momentum and axial velocity of a particle on its Lorentz-factor (Fig. 2) indicate the possibility of the negative-mass regime. To ensure accurate pumping of the electron undulator oscillations, a smooth entrance into the undulator with gradually increasing amplitude of the transverse field was provided at the first 5 periods. The typical number of large particles in simulations was of the order of 10^3.

From the simulation results it can be clearly seen that the speed of bunch degradation decreases substantially, when the guiding field exceeds the resonant value (Fig. 3). Moreover, despite the rms length of the bunch increases in all regimes, in the negative-mass regime (μ < 0) the main part of the bunch stays concentrated within a fairly small nucleus comparable with the initial volume.

Existence of a nucleus in the bunch allows efficient coherent spontaneous undulator radiation as soon as the length of this nucleus is less than the radiation wavelength. Figure 4 illustrates intensity and spectra of the forward radiation of the bunch in the far-field zone. In the positive-mass regimes ($B_0 < 5\,T$) the coherent spontaneous emission is provided during the bunch motion through several undulator periods; then, it is stopped due to the Coulomb repulsion. In contrast, in regimes of the negative-mass stabilization ($B_0 > 5\,T$), the coherent spontaneous emission is provided at the undulator length of about 1 m (40 undulator periods).

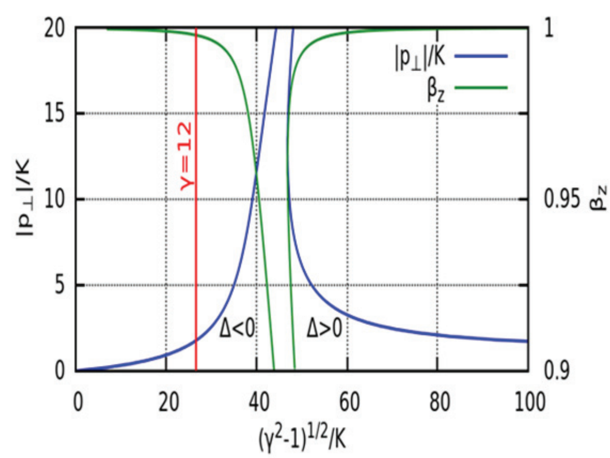

Figure 2: Dependency of the transverse momentum and axial electron velocity on the Lorentz-factor, γ. Vertical line marks the point corresponding to $\gamma = 12$.

ISBN 978-3-95450-134-2

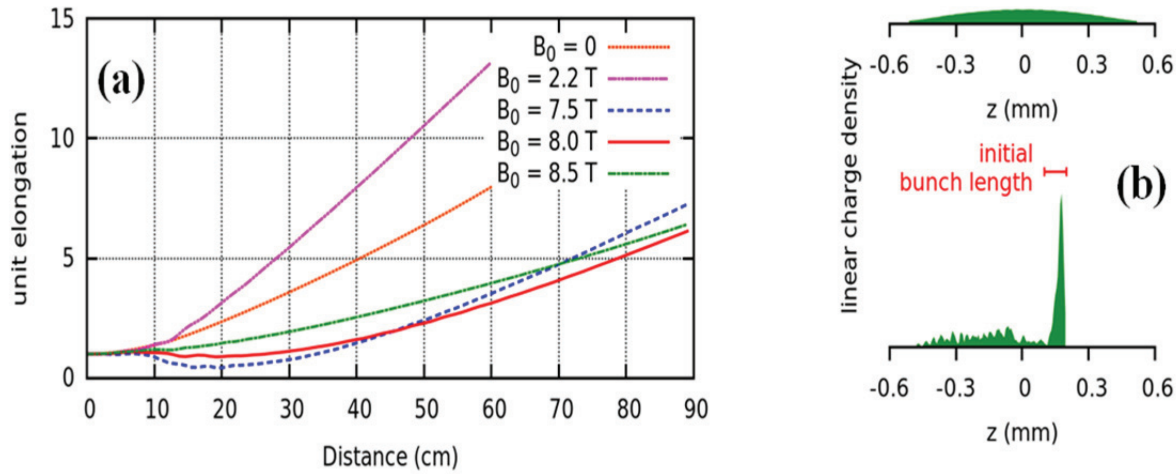

Figure 3: (a): Dependency of the rms unit elongation of the bunch l/l_0 on the trip distance in various regimes. (b): Comparison of the initial bunch with one after a 60 cm trip at $B_0 = 0$, and with the bunch after a 90 cm trip in the regime of negative-mass stabilization.

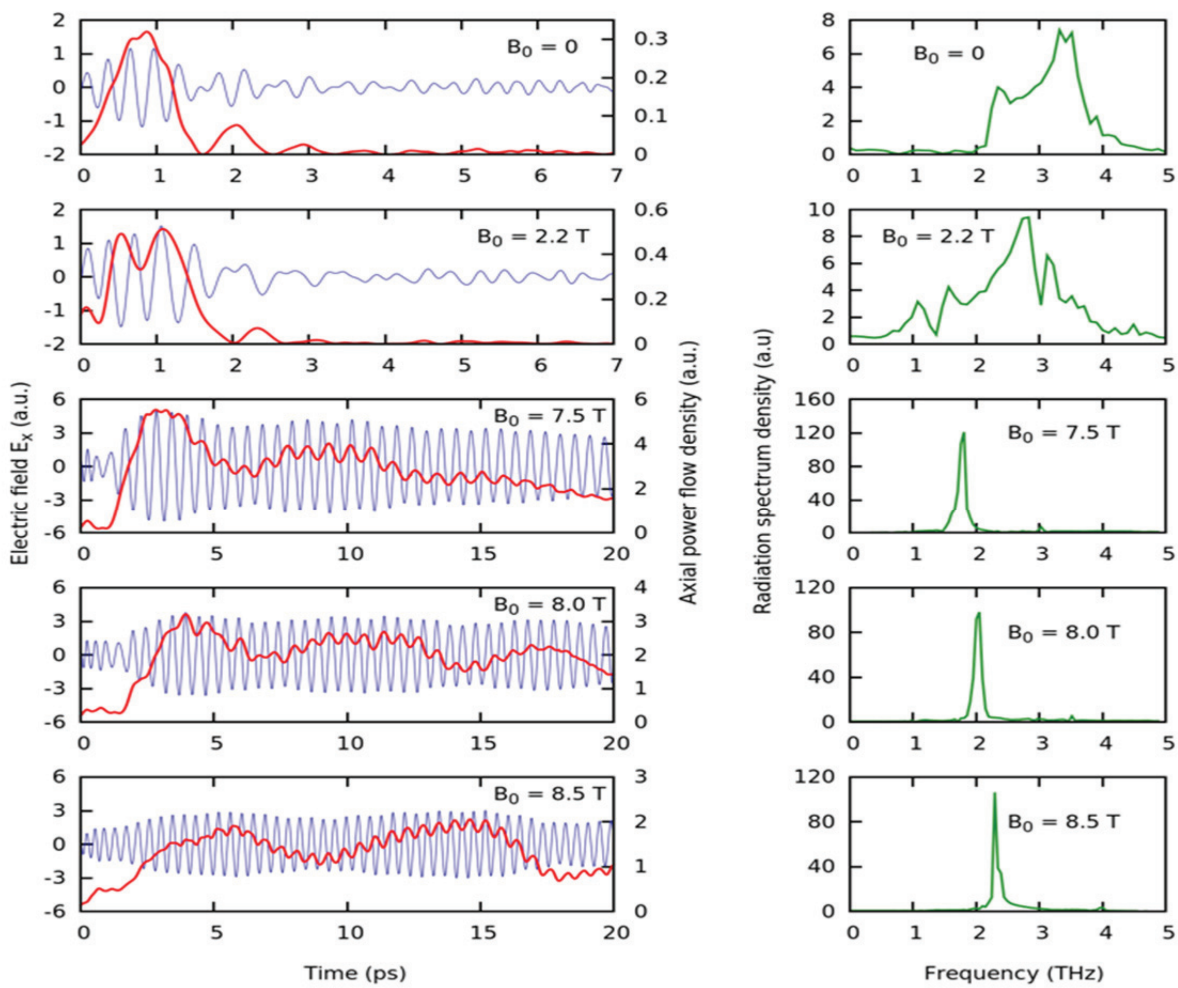

Figure 4: Forward radiation of the bunch in the far-field zone: x-component of electric field (thin blue curves) and axial power flow density (thick red curves) on the left, as well as the field spectrum density on the right.

ISBN 978-3-95450-134-2

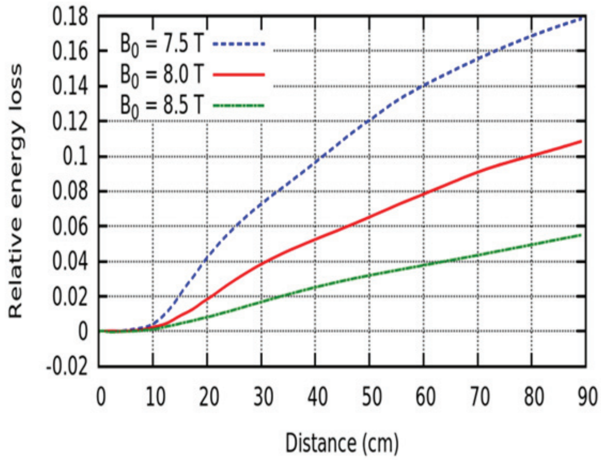

Figure 5: Energy losses of the electron bunch versus the axial position of the bunch in the negative-mass regimes.

The negative-mass effect leads to a significant enhancement in both the power and the duration of the radiated pulse, whereas the radiation frequency is lower than in the regime with the zero guiding field. The latter is due to a smaller Doppler upshift caused by the greater transverse and smaller axial electron velocities. According to simulations, the total bunch energy loss after of approximately 1 meter trip in the negative-mass regime can amount to 18% (Fig. 5). This corresponds to an average power of the order of 10 MW in the 20 ps forward-radiated THz pulse.

A large value of the uniform magnetic field that is required for realization of the negative-mass regime can be used to easily obtaining the required helical undulator field. It can be done, for example, by means of insertion of periodic conducting or magnetic structures into the solenoid creating the guiding magnetic field. In these cases, the undulator field is obtained due to excitation of eddy currents inside the conductors and due to magnetization of magnetics and redistribution of a uniform magnetic field, respectively. In particular, simple copper or iron helices can be placed inside a pulsed solenoid for obtaining a helical undulator field. For example, an iron helix with a period of 2.5 cm and an inner diameter of 10 mm wound of a wire with a radius of 3 mm and mounted into the solenoid with a uniform field of 8 T, provides the undulator parameter K=0.45 [14].

CONCLUSION

The simulations presented in this work confirm that realization of effective negative-mass stabilization of a short electron bunch is possible. They predict stability of the electron bunch during a 1 meter trip along the undulator (in contrast to ~10 cm in the positive-mass regime realized at low axial magnetic fields).

Using such a regime can provide significant power enhancement, a very high electron efficiency (up to 20%), and a significant spectrum narrowing for a radiation source, which operates at the frequencies ranging from 1 to 3 THz and is based on the spontaneous coherent undulator radiation from a short (0.1 mm) dense (0.3 nC) electron bunch with moderate energy (5.5 MeV).

Evidently, the proposed method could be also useful to provide the bunch stabilization in free-electron lasers, which are based on the stimulated undulator radiation.

REFERENCES

[1] A. Doria, R. Bartolini, J. Feinstein, G.P. Gallerano, and R.H. Pantell, IEEE J. Quantum Electron. 29, 1428–1436 (1993).

[2] A. Gover, F.V. Hartemann, G. P. Le Sage, N.C. Luhmann, Jr., R.S. Zhang, and C. Pellegrini, Phys. Rev. Lett., 1192–1195 (1994).

[3] A. Friedman, A. Gover , E. Dyunin, Y. Lurie, E. Magori, N. Balal, V. Bratman, “Configuration and status of the Israeli THz Free Electron Laser”, FEL’2014, Basel, August 2014, p. 553 (2014); http://www.JACoW.org

[4] K. Lee, J. Mun, S. Hee Park, R.-H. Jang, Y. Uk Jeong, N.A.Vinokurov, Nuclear Instr. Meth. Phys. Res. A 776, 27 (2015).

[5] C. Nielsen and A. Sessler, Rev. Sci. Instrum. 30, 80 (1959).

[6] A.A. Kolomensky and A.N. Lebedev, Atom. Energy 7, 549 (1959).

[7] V.L. Bratman, Tech. Phys. 46, 2030 (1976).

[8] V.L. Bratman and A. V. Savilov, Phys. Plasmas 2, 557 (1995).

[9] A. V. Savilov, Phys. Plasmas 6, 2276 (1997).

[10] N.S. Ginzburg and N.Yu. Peskov, Tech. Phys. 58, 859 (1988).

[11] H. P. Freund and T. M. Antonsen, *Principles of Free-Electron Lasers*, (London: Chapman & Hall, 1996).

[12] N.S. Ginzburg and N.Yu. Peskov, Phys. Rev. ST Accel. Beams 16, 090701 (2013).

[13] I.V. Bandurkin, S.V. Kuzikov, and A.V. Savilov, Appl. Phys. Lett. 105, 073503 (2014).

[14] N. Balal, V.L. Bratman, E. Magory, “Efficient Electron Sources of Coherent Spontaneous Radiation with Combined Helical and Uniform Magnetic Fields”, these proceedings, FEL’2015, Daejeon, Korea (2015).

ISBN 978-3-95450-134-2

FURTHER STUDIES OF UNDULATOR TAPERING IN X-RAY FELs

Alan Mak*, Francesca Curbis, Sverker Werin, MAX IV Laboratory, Lund University, Sweden

Abstract

We further the studies of the model-based optimization of tapered free-electron lasers presented in a recent publication [Phys. Rev. ST Accel. Beams **18**, 040702 (2015)]. Departing from the ideal case, wherein the taper profile is a smooth and continuous function, we consider the more realistic case, with individual undulator segments separated by break sections. Using the simulation code GENESIS, we apply our taper optimization method to a case, which closely resembles the FLASH2 facility in Hamburg, Germany. By comparing steady-state and time-dependent simulations, we examine how time-dependent properties alter the optimal taper scenario. From the simulation results, we also deduce that the "traditional" empirical method, whereby the intermediate radiation power is maximized after closing every undulator gap, does not necessarily produce the highest final power at the exit of the undulator line.

INTRODUCTION

Present-day imaging experiments at x-ray free-electron laser (FEL) facilities call for an increased number of photons within a shorter pulse duration [1, 2]. To meet the stringent demand on the radiation power, the technique of undulator tapering has been revisited in recent years, and much theoretical effort has been dedicated to the optimization of this technique [3–6].

In a recent publication [6], we propose a modification to the Kroll-Morton-Rosenbluth (KMR) model [7], which serves as a method of optimizing the taper profile. The method features a variable phase of the resonant particle, and opens up possibilities for further enhancement of radiation power beyond the constant-phase model.

In the ideal case, the taper profile $K(z)$ is a smooth and continuous function. However, most existing taperable x-ray FELs, such as FLASH2 [8] and SACLA [9], consist of individual undulator segments separated by break sections. With these limitations, a reduction of radiation power from the ideal case is inevitable.

The break sections are needed for beam focusing, trajectory correction and diagnostics. However, vacuum diffraction of the optical beam in the break sections leads to a decrease in the on-axis field strength, which also causes particle detrapping [3].

Also, as each undulator segment is uniform within itself, the segment length sets a limit on the rate at which K can decrease, and hence a limit on the bucket deceleration rate. Furthermore, if the segment length is larger than the synchrotron period, the electron beam can absorb energy momentarily from the optical beam [6].

* alan.mak@maxlab.lu.se

In this article, we study a case with 2.5-m undulator segments separated by break sections. Using the simulation code GENESIS [10], we adapt our taper optimization method to these limitations, and obtain the highest possible power. We then compare the simulation results obtained in the steady-state mode and the time-dependent mode, quantifying the effects of time-dependent properties.

The case chosen for our simulation studies is intended to match the design parameters of the FLASH2 facility, which achieved its first lasing [11] in August 2014.

CASE DEFINITION

For the simulation studies in this article, we choose a case with main parameters as shown in Table 1. These parameter values are within the designed range for the FLASH2 facility [8].

Table 1: Main Parameters for the Simulated Case

Parameter	**Symbol**	**Value**
Electron beam energy	E	1.25 GeV
Peak current	I	2.5 kA
Bunch charge	Q	630 pC
Bunch length	σ_t	30 µm
Energy spread	σ_E	0.5 MeV
Normalized emittance	$\varepsilon_{x,y}$	1.4 µm rad
Average beta function	$\langle\beta_{x,y}\rangle$	6 m
Radiation wavelength	λ	6 nm
Undulator period	λ_w	31.4 mm
Undulator segment length	L_{seg}	2.5 m

The undulator segments considered in this case are planar. The lattice for the transverse focusing of the electron beam is in a FODO configuration. The period of the FODO cell is 6.6 m, in which two quadrupole magnets are 3.3 m apart from one another.

The FLASH2 facility has 12 undulator segments [8]. But in our simulation studies, we first consider a total of 30 segments, for the purpose of understanding the FEL dynamics over a long distance. After that, we consider the more realistic 12-segment case, by discarding all the subsequent segments in the simulations.

TAPER OPTIMIZATION METHOD

Our taper optimization method is detailed in a recent publication [6]. The method is based on the KMR model [7] and a modification thereto. It considers a resonant particle with phase-space coordinates (ψ_R, γ_R). With a constant phase $\psi_R(z) = \psi_R(0)$, it is known as the ordinary KMR

ISBN 978-3-95450-134-2

method. With an increasing phase

$$\psi_R(z) = \frac{\pi}{2}\left(\frac{z}{L_d}\right)^n,$$

it is known as the modified KMR method, where L_d and n are positive real numbers at our choice.

L_d is known as the detrapping length. At $z = L_d$, the phase ψ_R reaches $\pi/2$. The area of ponderomotive bucket then becomes zero, and total detrapping occurs. Adjusting L_d allows us to control the rate at which ψ_R increases.

The degree n does not have to be an integer. But in Ref. [6], we have shown with another case that the output power is maximized by choosing $n = 1$. In this article, we restrict ourselves to $n = 1$.

The method involves iterative simulations, with step size Δz along the undulator line. In the ideal case, Δz should be as small as possible, such as $\Delta z = \lambda_w$. But in the case at hand, the individual undulator segments require us to make the adaptation $\Delta z = L_{\mathrm{seg}}$. Furthermore, we adapt the method to the presence of break sections. In each step Δz, the decrease in on-axis field amplitude due to vacuum diffraction in the preceding break section is taken into account.

The iterative simulations are performed in the steady-state mode of GENESIS. Upon choosing a constant resonant phase ψ_R for the ordinary KMR method or a detrapping length L_d for the modified KMR method, the iterative simulations will result in a taper profile $K(z)$. Upon obtaining the taper profile, we input it to GENESIS again and run it in the time-dependent mode.

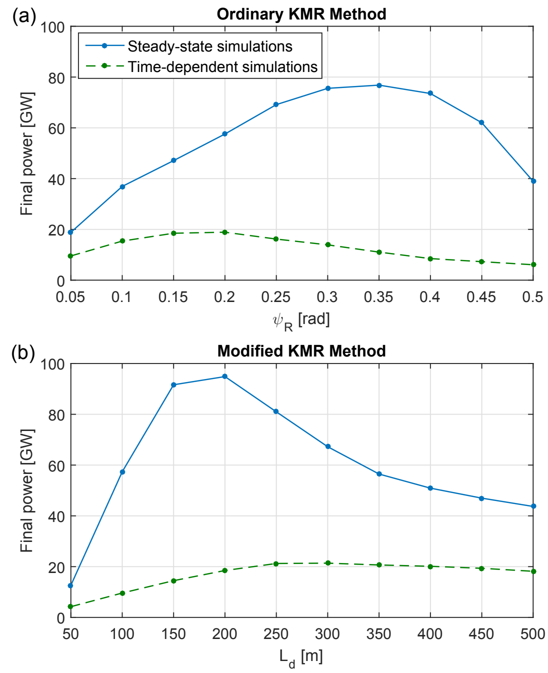

Figure 1: The final radiation power at the exit of the 30th undulator segment (a) as a function of the resonant phase ψ_R in the ordinary KMR method and (b) as a function of the detrapping length L_d in the modified KMR method. The blue solid curves are the results of steady-state simulations, and the green dashed curves are the results of time-dependent simulations.

RESULTS AND DISCUSSIONS

General Results with 30 Undulator Segments

To examine the FEL dynamics over a long distance, we simulate a total of 30 undulator segments with GENESIS.

For the ordinary KMR method, we vary the resonant phase ψ_R from 0.05 rad to 0.5 rad at intervals of 0.05 rad. For the modified KMR method, we vary the detrapping length L_d from 50 m to 500 m at intervals of 50 m.

In all these runs, we probe the final radiation power at the exit of the 30th undulator segment. The results are summarized in Fig. 1. The blue solid curves are the results of steady-state simulations, and the green dashed curves are the results of time-dependent simulations.

Ordinary KMR versus Modified KMR In the steady-state mode (see blue solid curves in Fig. 1), the final power is maximized at $\psi_R = 0.35$ rad for the ordinary KMR method, and at $L_d = 200$ m for the modified KMR method. The maximized final powers are 76.8 GW and 94.9 GW, respectively. The maximized final power for the modified KMR method is 123% that for the ordinary KMR method.

In the time-dependent mode (see green dashed curves in Fig. 1), the final power is maximized at $\psi_R = 0.2$ rad for the ordinary KMR method, and at $L_d = 300$ m for the modified KMR method. The maximized final powers are 18.9 GW and 21.4 GW, respectively. The maximized final power for the modified KMR method is 113% that for the ordinary KMR method.

In both the steady-state and the time-dependent modes, the modified KMR method produces a higher final power than the ordinary KMR method. This shows that an increasing ψ_R is more favourable than a constant ψ_R for maximizing the final power, even when time-dependent properties are taken into account. The benefit of using an increasing ψ_R over a constant ψ_R has been justified in Ref. [6] in terms of the initial capturing of particles and the rate of bucket deceleration.

Steady-state versus Time-dependent For the ordinary KMR method [see Fig. 1(a)], the maximized final power in the time-dependent mode constitutes a 75% drop from that in the steady-state mode. For the modified KMR method [see Fig. 1(b)], the maximized final power in the time-dependent mode constitutes a 77% drop from that in the steady-state mode. These show that time-dependent properties are a significant cause of power reduction.

The power reduction can be understood as follows. In GENESIS, a steady-state simulation is equivalent to considering only the central slice in a time-dependent simulation. Thus, a taper profile $K(z)$ obtained in the steady-state mode is only optimal for the centremost part of the longitudinal bunch profile, when running in the time-dependent mode. Towards the head and the tail of a Gaussian bunch profile,

ISBN 978-3-95450-134-2

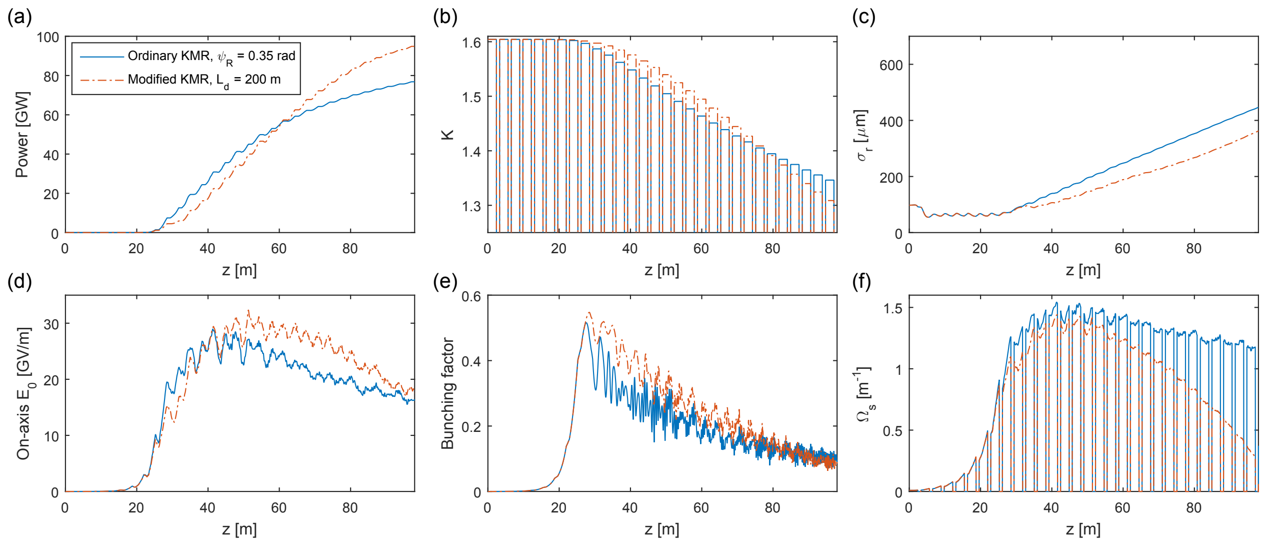

Figure 2: Results of steady-state simulations, showing the optimal scenarios of the ordinary KMR method (blue) and the modified KMR method (red) with the use of 30 undulator segments. The following quantities are plotted as functions of the distance z along the undulator line: (a) the radiation power; (b) the undulator parameter K; (c) the rms radius of the optical beam; (d) the field amplitude on axis; (e) the bunching factor; (f) the synchrotron frequency.

the slice current is significantly lower. These parts of the bunch behave in a non-optimal fashion under a taper profile $K(z)$ optimized for the central slice, thus reducing the average power produced by the bunch.

Another observation is that the optimal scenarios are not the same in the steady-state mode and in the time-dependent mode. When going from steady-state to time-dependent in the ordinary KMR method, the optimal ψ_R decreases. Similarly, when going from steady-state to time-dependent in the modified KMR method, the optimal L_d increases, which corresponds to an overall decrease in the range of ψ_R.

As discussed in Ref. [6], the area of the ponderomotive bucket decreases with ψ_R, while the bucket deceleration rate increases with ψ_R. This implies that in the presence of time-dependent effects, it is preferable to maintain a relatively large bucket at the expense of slowing down the bucket deceleration. This trade-off can be justified by the fact that time-dependent effects constitute an additional source of particle detrapping [3].

Optimal scenarios with 30 Segments

Without any tapering, power saturation occurs at around $z = 30$ m in the 10th undulator segment. This is known as the initial saturation point. The saturation power is 2.5 GW in the steady-state mode and 1.7 GW in the time-dependent mode.

The optimal taper scenarios in the steady-state mode are examined in Fig. 2. The blue solid curves correspond to the ordinary KMR method with $\psi_R = 0.35$ rad, while the red dashed curves correspond to the modified KMR method with $L_d = 200$ m.

Figure 2(a) shows the evolution of the radiation power along the undulator line. At the exit of the undulator line, the modified KMR method yields a higher power than the ordinary KMR method does, in agreement with Fig. 1. But upstream at $z = 30 - 60$ m, the situation is actually the opposite, i.e. the modified KMR method gives a *lower* power. This shows that it is possible to obtain a higher power downstream by sacrificing the power upstream. In other words, the "traditional" empirical method, whereby the radiation power is maximized after closing every undulator gap, does not necessarily yield the highest power at the end of the undulator line.

Figure 2(b) shows the taper profiles obtained from the iterative simulations. The individual undulator segments and the break sections are clearly seen. For both the ordinary KMR method and the modified KMR method, the K value hardly changes within the first seven segments. The decrease in K begins slightly before the initial saturation point. Immediately after the initial saturation point, the particle trapping development region begins [3]. In this region, the K value for the modified KMR method decreases more slowly than that for the ordinary KMR method. Downstream in the undulator line, the K value for the modified KMR method decreases more rapidly than that for the ordinary KMR method. Note that the rate of K decrease reflects the rate of bucket deceleration. For the modified KMR method, the bucket deceleration is kept slow in the particle trapping development region, thus allowing more particles to be captured in the bucket for the subsequent energy extraction.

Figure 2(c) shows the optical beam size as a function of z. Before the initial saturation point ($z = 30$ m), gain guiding keeps the optical beam size small. Beyond the initial saturation point, gain guiding is weakened, and refractive guiding becomes dominant. The strength of refractive guiding varies with the phase ψ_R as $\cos\psi_R$ [6]. For the modified KMR method, ψ_R increases with z, making the refractive guiding stronger. This partly explains why the optical beam size is

ISBN 978-3-95450-134-2

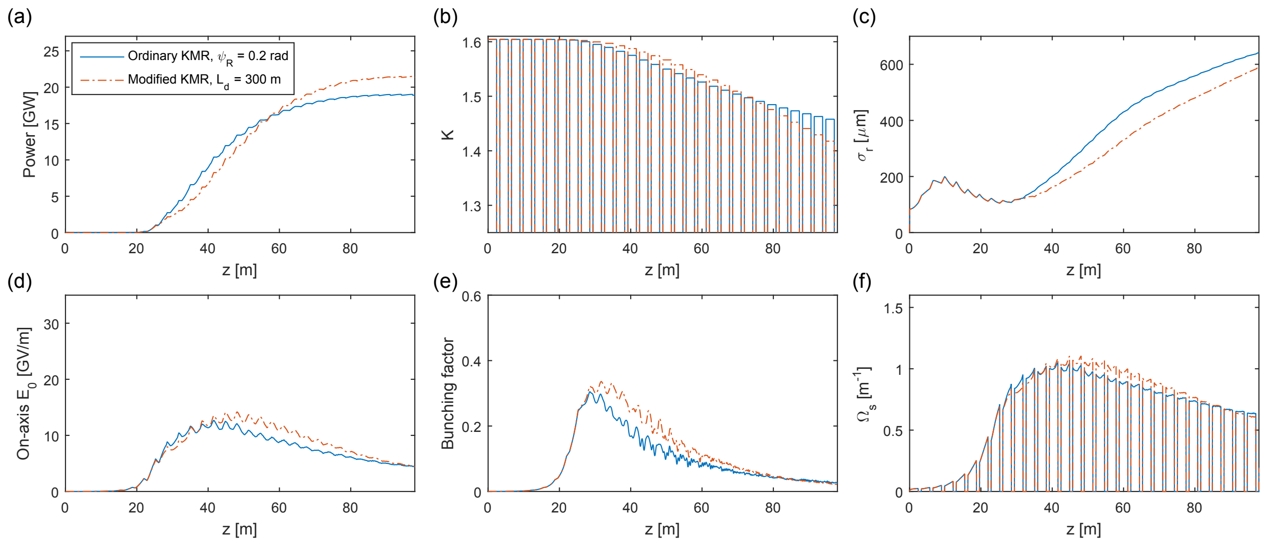

Figure 3: Results of time-dependent simulations, showing the optimal scenarios of the ordinary KMR method (blue) and the modified KMR method (red) with the use of 30 undulator segments. The following quantities are plotted as functions of z: (a) the radiation power; (b) the undulator parameter K; (c) the rms radius of the optical beam; (d) the field amplitude on axis; (e) the bunching factor; (f) the synchrotron frequency. These quantities are averaged over the electron bunch, and weighted by the slice current.

smaller for the modified KMR method than for the ordinary KMR method beyond the initial saturation point.

The effect of keeping the optical beam size small is also seen in Fig. 2(d), which shows the evolution of the on-axis field amplitude. With a smaller optical beam size beyond the initial saturation point, the modified KMR method gives a stronger field on axis.

Figure 2(e) shows the bunching factor as a function of z. Here the bunching factor is defined as the absolute value of $\langle e^{-i\psi} \rangle$, where the brackets denote the average over all particles, and ψ is the particle phase in the ponderomotive potential. In the particle trapping development region immediately beyond $z = 30$ m, the bunching factor for the modified KMR method is higher than that for the ordinary KMR method. This can be attributed to the larger on-axis field amplitude and the slower decrease in K value.

Figure 2(f) shows the synchrotron frequency as a function of z. The synchrotron frequency is given by [6, 12]

$$\Omega_s(z) = \sqrt{\frac{2\pi e}{m_e c^2 \lambda_w} \frac{K(z) f_B(z) E_0(z)}{\gamma_R^2(z)} \cos[\psi_R(z)]}.$$

For both the ordinary KMR method and the modified KMR method, the synchrotron frequency increases from zero at the entrance to the undulator line and reaches its maximum value slightly after the initial saturation point. Afterwards, the ordinary KMR method exhibits a relatively uniform synchrotron frequency, while the modified KMR method shows a rapid decrease in synchrotron frequency. The behaviour of the synchrotron frequency is a combined effect of the variations in K, E_0 and ψ_R along the undulator line.

Figure 3 shows the corresponding results in the time-dependent mode. The radiation power, K parameter, optical beam size, on-axis field amplitude and the bunching factor exhibit mostly the same patterns as in Fig. 2. However, the radiation power is lower overall [see Fig. 3(a)]. The diffraction of the optical beam is stronger [see Fig. 3(c)], and the on-axis field weaker [see Fig. 3(d)]. The bunching factor is also smaller overall [see Fig. 3(e)].

In the two optimal taper profiles Fig. 3(b), K decreases more slowly than in their steady-state counterparts [see Fig. 2(b)]. This also shows that in the presence of time-dependent effects, a slower deceleration of the ponderomotive bucket is preferable.

Comparing Fig. 3(f) to Fig. 2(f), we see that time-dependent effects give rise to a different behaviour of the synchrotron frequency. At $z = 40 - 80$ m, the synchrotron frequency is higher for the modified KMR method than for the ordinary KMR method in the time-dependent mode, but the situation is the opposite in the steady-state mode. Also, while the synchrotron frequency for the modified KMR method decreases very rapidly in the steady-state mode, it remains relatively uniform in the time-dependent mode.

Figure 4 shows the the spectral power distributions at the exit of the 30th undulator segment. The blue and red curves correspond to, respectively, the ordinary KMR method with $\psi_R = 0.2$ rad and the modified KMR method with $L_d = 300$ m, which are the the optimal scenarios in the time-dependent mode. The two distributions are largely similar.

Considering Only 12 Segments

The case studied in this article is intended to resemble the FLASH2 facility as closely as possible. The actual FLASH2 facility has 12 undulator segments [8]. Therefore, we now consider the more realistic 12-segment case by discarding all the subsequent segments in our simulation results.

ISBN 978-3-95450-134-2

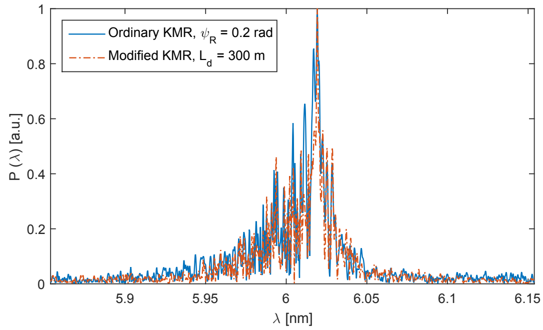

Figure 4: The spectral power distributions for the ordinary KMR method with $\psi_R = 0.2$ rad (blue) and for the modified KMR method with $L_d = 300$ m (red).

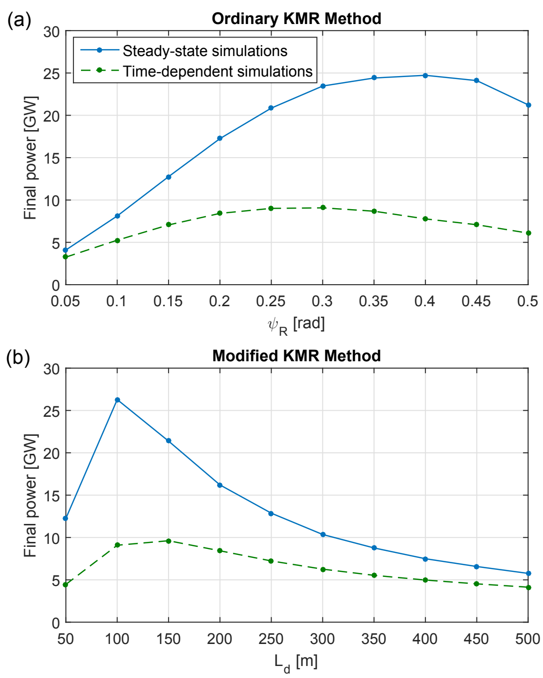

Figure 5: The final radiation power at the exit of the 12th undulator segment (a) as a function of the resonant phase ψ_R in the ordinary KMR method and (b) as a function of the detrapping length L_d in the modified KMR method. The blue solid curves are the results of steady-state simulations, and the green dashed curves are the results of time-dependent simulations.

The final power at the exit of the 12th segment is shown in Fig. 5 for different ψ_R and L_d values. With only 12 segments, the optimal ψ_R and L_d values are, of course, different from those in the 30-segment case. The reason is explained in Ref. [6].

In the steady-state mode (see blue solid curves in Fig. 5), the optimal ψ_R is 0.4 rad, which gives a final power of 24.7 GW; the optimal L_d is 100 m, which gives a final power of 26.3 GW.

In the time-dependent mode (see green dashed curves in Fig. 5), the optimal ψ_R is 0.3 rad, which gives a final power of 9.1 GW; the optimal L_d is 150 m, which gives a final power of 9.6 GW.

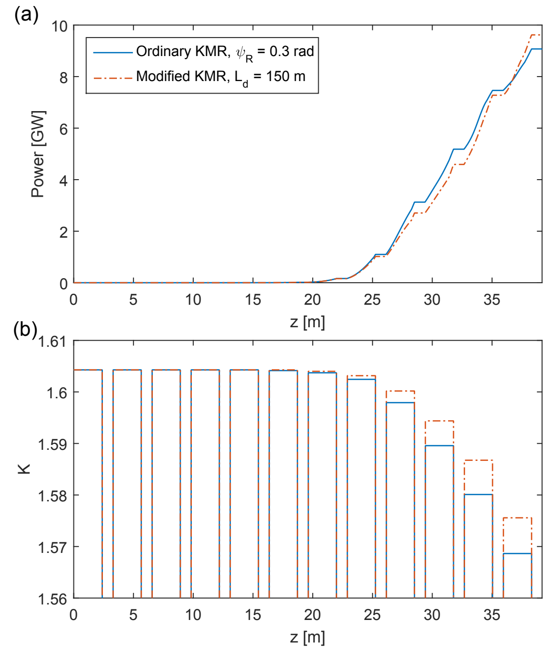

Figure 6: Results of time-dependent simulations, showing the optimal scenarios of the ordinary KMR method (blue) and the modified KMR method (red) with the use of only 12 undulator segments. (a) The bunch-averaged radiation power and (b) the undulator parameter K are plotted as functions of z.

With only 12 undulator segments, there is not a huge difference in final power between the ordinary KMR method and the modified KMR method. But compared to the case of no taper, the optimized tapers increase the final power by almost a factor of 11 in the steady-state mode, and a factor of 6 in the time-dependent mode.

The optimal scenarios in the time-dependent mode are shown in Fig. 6. It is apparent from Fig. 6(b) that the K value hardly changes in the first seven undulator segments. The post-saturation power growth is mainly due to the tapering of the last five segments.

As seen from Fig. 6(a), the modified KMR method yields a slightly higher final power at the exit of the 12th segment, compared to the ordinary KMR method. Nonetheless, upstream at $z = 25-35$ m, the power produced by the modified KMR method is actually *lower*. Once again, this shows that a higher power can be obtained at the exit of the undulator line by sacrificing the intermediate power upstream. This also implies that the "traditional" empirical method, whereby the intermediate power is maximized after closing every undulator gap, does not necessarily yield the highest final power.

SUMMARY AND OUTLOOK

In this article, we have furthered the study of a previously presented [6] taper optimization method, by adapting the

ISBN 978-3-95450-134-2

method to individual undulator segments separated by break sections. Using the simulation code GENESIS [10], we have applied the method to an x-ray FEL case, which closely resembles the FLASH2 facility [8] in Hamburg, Germany. By comparing the simulation results in the steady-state mode and the time-dependent mode, we have quantified the effects of time-dependent properties on the FEL dynamics. It would be an interesting experiment to test the 12-segment time-dependent simulation results on the FLASH2 facility.

REFERENCES

[1] R. Neutze et al., "Potential for Biomolecular Imaging with Femtosecond X-Ray Pulses", Nature **406**, 752 (2000).

[2] H. N. Chapman et al., "Femtosecond Diffractive Imaging with a Soft-X-Ray Free-Electron Laser", Nature Physics **2**, 839 (2006).

[3] Y. Jiao et al., "Modeling and Multidimensional Optimization of a Tapered Free Electron Laser", Phys. Rev. ST Accel. Beams **15**, 050704 (2012).

[4] C. Emma et al., "Terawatt X-Ray Free-Electron-Laser Optimization by Transverse Electron Distribution Shaping", Phys. Rev. ST Accel. Beams **17**, 110701 (2014).

[5] E. Schneidmiller, M. Yurkov, "Optimization of a High Efficiency Eree Electron Laser Amplifier", Phys. Rev. ST Accel. Beams **18**, 030705 (2015).

[6] A. Mak, F. Curbis, S. Werin, "Model-Based Optimization of Tapered Free-Electron Lasers", Phys. Rev. ST Accel. Beams **18**, 040702 (2015).

[7] N. M. Kroll, P. L. Morton, M. N. Rosenbluth, "Free-Electron Lasers with Variable Parameter Wigglers", IEEE J. Quantum Electronics **17**, 1436 (1981).

[8] K. Honkavaara et al., "Status of the FLASH II Project", in Proceedings of the 34th International Free-Electron Laser Conference, Nara, Japan, 381 (2012).

[9] T. Ishikawa et al., "A Compact X-Ray Free-Electron Laser Emitting in the Sub-Ångström Region", Nature Photonics **6**, 540 (2012).

[10] S. Reiche, "GENESIS 1.3: a Fully 3D Time-Dependent FEL Simulation Code", Nucl. Instrum. Meth. A **429**, 243 (1999).

[11] S. Schreiber, B. Faatz, "First Lasing at FLASH2", in Proceedings of the 36th International Free-Electron Laser Conference, Basel, Switzerland, 7 (2014).

[12] D. Prosnitz, A. Szoke, V. K. Neil, "High-Gain, Free-Electron Laser Amplifiers: Design Considerations and Simulation", Phys. Rev. A **24**, 1436 (1981).

ISBN 978-3-95450-134-2

THRESHOLD OF A MIRROR-LESS PHOTONIC FREE-ELECTRON LASER OSCILLATOR PUMPED BY ONE OR MORE ELECTRON BEAMS

A. Strooisma, P.J.M. van der Slot*, K.J. Boller
Mesa+ Institute for Nanotechnology, University of Twente, Enschede, The Netherlands

Abstract

Transmitting electrons through a photonic crystal can result in stimulated emission and the generation of coherent Cerenkov radiation. Here we consider a photonic-crystal slab consisting of a two-dimensional, periodic array of bars inside a rectangular waveguide. By appropriately tapering the bars at both ends of the slab, we numerically show that an electromagnetic wave can be transmitted through the photonic-crystal slab with close to zero reflection. Furthermore, the photonic-crystal slab allows transmission of electrons in the form of one or more beams. We design the tapered photonic-crystal slab to have a backward wave interaction at low electron-beam energy of around 15 kV, that results in distributed feedback of the radiation on the electrons without any external mirrors being present. Here we discuss the dynamics of the laser oscillator near threshold and numerically show that the threshold current can be distributed over multiple electron beams, resulting in a lower current per beam.

INTRODUCTION

Electron beams have been used to generate incoherent and coherent radiation over a large spectral range. Among the huge range of sources are microwave devices [1, 2], gyrotrons [1, 3], synchrotrons [4] and free-electron lasers (FELs) [5–8]. These sources can be divided in two classes, the so-called fast-wave (e.g., gyrotrons, synchrotrons and FELs) and slow-wave or Cerenkov devices (e.g., traveling wave tubes, Smith-Purcell and Cerenkov free-electron lasers). Here we focus on the slow-wave devices that use an interaction structure to slow down the phase velocity of the wave to make the electron move synchronous with the wave. This phase matching results in bunching of the electrons on the scale of the radiation wavelength and is responsible for the generation of coherent radiation [1, 2, 9]. The slow-wave devices are very efficient and powerful sources of radiation at microwave frequencies, however, when scaled to higher frequencies the output power drops. The reason for this is that the characteristic size of the interaction structure reduces when the operating frequency increases. The maximum current that can be transported through the interaction structure is also reduced and, hence, the output power. However, in a photonic free-electron laser (pFEL) a photonic crystal is used as interaction structure to slow down the wave. Electrons streaming through a photonic crystal can move synchronous with a co-propagating wave and emit coherent Cerenkov radiations [9, 10]. A photonic crystal typically has many parallel channels through which

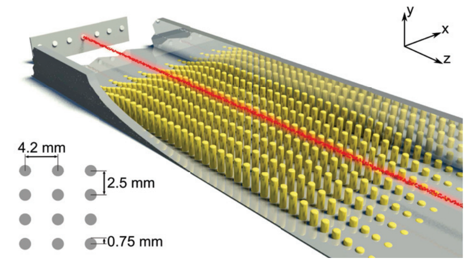

Figure 1: Schematic view of the photonic free-electron laser with a single electron beam. The red dots represent the electrons. The inset shows the orientation of the coordinate system.

the electrons can propagate. For example, the photonic crystal shown in Fig. 1 allows up to seven beams to propagate in parallel through the photonic structure. Therefore, when the photonic crystal shrinks in size to support higher operating frequencies, one can increase the transverse extend of the crystal to create more parallel channels for the electrons and keep the total current streaming through the crystal constant. As the current per individual electron beam will decrease, it is of interest to investigate the behavior of a photonic free-electron laser near threshold when pumped by one or multiple electron beams.

The remainder of this paper is organized as follows. We first present the photonic crystal considered in this paper and then we use a particle-in-cell code (CST particle studio 2014) to investigate the performance near threshold of the backward-wave pFEL oscillator when pumped by a single electron beam in the center of the photonic crystal. This is followed by investigating the performance when the same oscillator is pumped by several electron beams and the paper concludes with a discussion and outlook.

TAPERED PHOTONIC CRYSTAL

The photonic free-electron laser considered here is shown schematically in Fig. 1. The photonic crystal consists of 8 rows of 40 posts placed in a rectangular waveguide, where the height of the nth post in a row is given by:

$$h_n = \begin{cases} h_0 \cos^2\left(\frac{\pi}{2}\left(\frac{n}{11} - 1\right)\right) & \text{if } 1 \leq n \leq 10 \\ h_0 & \text{if } 10 < n \leq 30 \\ h_0 \cos^2\left(\frac{\pi}{2}\frac{n-30}{11}\right) & \text{if } 30 < n \leq 40 \end{cases}, \quad (1)$$

where $h_0 = 4$ mm is the full post height. The other dimensions of the photonic crystal are a post radius of 0.75 mm, a distance between post centers of 2.5 mm along the z axis and 4.2 mm along the x axis. The waveguide has a cross-section of 33.6 by 8.0 mm. The taper at both ends of the crystal is

* p.j.m.vanderslot@utwente.nl

ISBN 978-3-95450-134-2

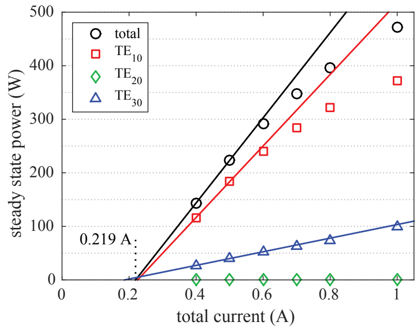

Figure 2: The output power of the pFEL as a function of electron beam current. The electron energy is 14 keV for all data points, and the pFEL is pumped by a single beam in the center of the photonic crystal.

used to suppress reflections at the transition between empty waveguide and waveguide loaded with the photonic crystal [10]. As a consequence, the pFEL has no external mirrors, as the waveguide is assumed to terminate in matched ports and therefore does not reflect any radiation. Still, due to the periodicity of the dispersion of the Bloch modes [11], the pFEL can be operated in the so-called backward-wave regime where the group velocity is directed opposite to the phase velocity. Because of this, light generated at the downstream side of the photonic crystal travels to the upstream side, where it bunches the electron beam. Consequently, the backward wave provides feedback for the electron bunching and thereby creates an oscillator configuration. For more details on the photonic-crystal slab and its dispersion, the reader is referred to Ref. [10].

SINGLE BEAM THRESHOLD CURRENT

First we consider the structure of Fig. 1 when pumped with a single electron beam in the center having a beam voltage $V_b = 14$ kV. Note that after the tapered section the empty waveguides continues for another 13.75 mm before it ends in a matched waveguide port where the radiation is analyzed in terms of waveguide modes. As the waveguide modes and photonic crystal Bloch eigenmodes couple one-to-one [10], the waveguide modes are representative for the Bloch eigenmodes inside the crystal. Figure 2 shows the output power of the backward-wave pFEL oscillator as a function of the electron beam current for the three lowest order modes, TE_{10} (squares), TE_{20} (diamonds), and TE_{30} (triangles), and the total power P_{tot} (circles). Because the electron beam and therefore the gain is purely in the center of the waveguide, only modes with a strong on-axis longitudinal field are expected to couple strongly to the electron beam. Indeed, Fig. 2 shows that 99.5 % of the total power is in modes one and three and that the even modes, with zero on-axis longitudinal field, contain negligible power. The power in higher order odd modes is also negligible.

Figure 2 shows that the output power behaves like any other laser oscillator. The pumping power, which is set by the accelerated electrons, has to overcome a minimum threshold that is defined by the roundtrip loss of the oscillator. Although 100 % of the wave is coupled out of the photonic crystal slab the backward-wave interaction still provides feedback between the wave and the electrons. In this case, the bunching induced by the wave, that grows in the direction towards the electron gun, must be sufficient to dominate the noise in the electron beam. Due to a threshold in the pumping current, the slope efficiency, η_{sl}, defined by [12, 13]

$$\eta_{sl} = \frac{dP_{out}}{dP_{in}} = \frac{1}{V_b}\frac{dP_{out}}{dI_b}. \qquad (2)$$

is considered instead of the intrinsic efficiency η_{int} given by [14, 15]

$$P_{out} = \eta_{int} P_{in} = \eta_{int} I_b V_b, \qquad (3)$$

where for a free-electron laser (including the pFEL) the input power P_{in} is the product of the total electron beam current, I_b, and the total accelerating voltage, V_b. As is known from many other laser oscillators [12, 13] the slope efficiency is more or less constant when pumped up to a few times the threshold pump power. From Figure 2 it is clear that the slope efficiency is not constant for the total power and the power in the fundamental mode, whereas the slope efficiency is approximately constant for the third order mode. Therefore, the lowest available current data are taken to determine the threshold beam current via linear extrapolation, giving a threshold current of 0.22 ± 0.03 A. This means that the highest beam current investigated is far above threshold (by nearly a factor of 5), and that for the total power the slope efficiency is nearly constant ($\eta_{sl} = 5.7$ %) up to a beam current that is about 3 times the threshold current. Analysis of the $P_{out}(I_b)$ relation, as shown in Fig. 2, shows that the slope efficiency does not follow a simple power relation, and, consequently, differs from the 4/3-power relationship found for η_{int} off an FEL [14, 15]. Furthermore, these results show that the feedback provided by the photonic crystal in combination with the gain provided by the electron beam is sufficient to obtain lasing as long as the electron beam current is above a threshold.

MULTI-BEAM THRESHOLD CURRENT

When pumping with multiple electron beams, it is of special interest to investigate if lasing is still obtained when the current per beam is dropped below the current threshold for single-beam pumping. This is a necessary condition to scale the pFEL to higher operating frequencies. To investigate this, we used the same structure, beam voltage and total current as in the previous section, while the number of electrons beams is increased from 1 to 5 in steps of 2 (i.e. by filling adjacent free channels). Figure 3 shows the total output power versus the current per electron beam for pumping with one electron beam (circles), three electron beams (triangles) and five electron beams (stars). The current thresholds have been obtained in the same way as described above. The threshold current per beam is found to be 0.219, 0.088 and 0.071 A

ISBN 978-3-95450-134-2

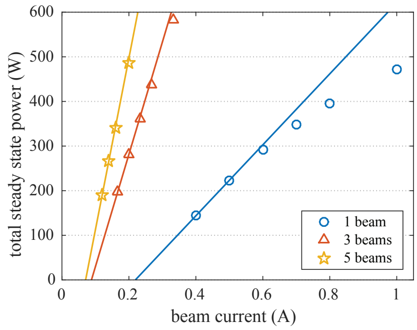

Figure 3: The output power of the pFEL for one (circle), three (triangle) and five (star) electron beams with varying current per beam. The electron energy is 14 keV for all data points.

when pumping with one, three and five beams, respectively. We observe that the total threshold current increases with the number of pump beams. This is caused by the lower field strength at the location of the additional beams [10], which results in a lower gain [16]. The most important conclusion that can be drawn from this data is that it is possible to distribute the current over multiple beams, such that the current in each beam is lower than the single-beam threshold and the laser oscillator still turns on if the total current is above a threshold.

Using Eq. 2 where I_b is now the total current, we find for the slope efficiency 5.7 %, 6.0 % and 5.4 % when pumping with one, two and three beams, respectively. In more detail, we observe that up to a total beam current of 0.7 A, the single-beam pFEL produces the highest output power. For higher total current, the three-beam pFEL produces the highest output power, more than 100 W more than the single-beam pFEL for a total current of 1 A. The five-beam pFEL only just surpasses the single-beam pFEL in output power at a total current of 1 A and remains below the output level of the three-beam pFEL for all total beam currents investigated. On the other hand, the mode purity increases when the number of pump beams increases [10].

OUTPUT FREQUENCY

The pFEL oscillator of Fig. 1 has no external resonator and the oscillator can therefore be continuously tuned due to the absence of longitudinal modes. An estimate of the operating frequency can be obtained from the intersection of the dispersion of an appropriate Bloch eigenmode [10] with the dispersion of the slow space-charge wave given by [1]

$$\omega = k_z v_e - p\gamma^{-3/2}\omega_p, \qquad (4)$$

where $\omega_p = \sqrt{\frac{e^2 n_e}{m_e \epsilon_0}}$ is the non-relativistic plasma frequency, v_e is the electron velocity, γ is the Lorentz factor, e, n_e and m_e are the electron charge, density and mass, respectively, ϵ_0 is the permittivity of free space and p is the so-called plasma reduction factor. Note, there also exists a fast space-charge wave, but only the slow space-charge wave can give

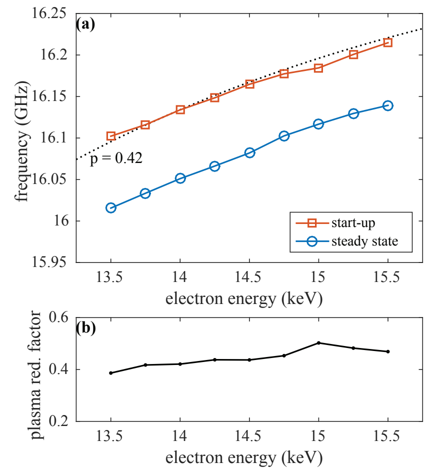

Figure 4: Spontaneous emission (squares) and steady-state (circles) frequency as a function of total electron energy as obtained from the PIC simulations (a). The dotted and dashed lines show the frequency expected from velocity-matching using $p = 0.42$. The plasma reduction factor as calculated from the spontaneous emission frequency (b).

up energy [1] and facilitate the pFEL interaction. The fast space-charge wave will be ignored in the remainder of this paper.

A more accurate prediction of the output frequency is obtained from the PIC simulations. To obtain the output frequency, we apply a Fourier transform to the electric field when the laser is in steady state. Figure 4a shows the steady-state output frequency (blue circles) as a function of the beam voltage for the pFEL oscillator of Fig. 1 pumped by a single, 1-A electron beam. Note, the same photonic crystal without tapered end sections would have reflections at the end facets, and the resulting resonator would have a free spectral range of about 0.15 GHz.

Calculating the operating frequency from the velocity matching requires knowledge about the plasma frequency reduction factor p. This parameter can not readily be calculated independently for this geometry. However, using the operating frequency obtained from the PIC simulations, it should be possible to calculate the plasma reduction factor as function of the electron beam energy. As in steady state the electrons will have on average a reduced longitudinal velocity with an increased spread and a non-uniform longitudinal distribution, the frequency during start-up of the laser, where the electron velocity distribution is still uniform with small spread, will be used. To obtain this frequency, the Fourier transform is applied to the electric field for the first 4.2 ns and zero-padding is used to increase the resolution of the Fourier transform. This is essentially the frequency of spontaneous emission of the pFEL oscillator. This spontaneous emission frequency is plotted as well in Fig. 4a (red squares). We observe that the steady-state frequency is slightly lower (< 100 MHz) than the spontaneous emission frequency that is emitted when the gain is below or just above threshold.

ISBN 978-3-95450-134-2

This difference is under investigation and could be caused by an interaction induced change in the wave phase.

Using the average longitudinal electron velocity from the PIC simulations, which takes into account the buildup of potential energy in the metallic structure [17], and the frequency of the spontaneous emission, Eq. 4 is used to calculate the plasma frequency reduction factor p. This factor is plotted in Fig. 4b as a function of the initial total electron energy. From Fig. 4b it follows that p increases slightly with increasing electron energy, which agrees with the dependency found for other geometries [18]. For comparison, the operating frequency predicted from velocity matching using the average value $p = 0.42$ is also shown in Fig. 4a as dotted line.

CONCLUSION

A backward-wave photonic free-electron laser oscillator is numerically investigated using a particle-in-cell code. We have determined the threshold current for laser operation when pumped by a single and by multiple electron beams. We find that the threshold current per beam reduces with the number of beams, but the total threshold current increases. The latter is due to the reduced field strength of the Bloch eigenmodes of the crystal near the sidewalls of the waveguide. This reduces the overall gain and consequently raises the total threshold current. Still, when the number of electron beams is increased, the current per beam can be reduced while approximately maintaining the output power. Using multiple beams has the added advantage that a higher mode purity can be be obtained. We have observed that the frequency of spontaneous emission is slightly higher than the steady-state frequency of the oscillator. Due to absence of any external resonator, the output frequency can be continuously tuned by varying the accelerating voltage for the electrons.

The multi-beam performance of the pFEL oscillator suggests an interesting scaling route to increase the operating frequency to well into the THz domain, compared to the microwave frequencies investigated here. This requires the crystal to be scaled down in size by two orders of magnitude. Instead of increasing the current density in a single beam, the same total current can now be obtained by propagating many electron beams in parallel through the pFEL. Such a massively parallel set of electron beams may be produced by so-called field-emitter arrays [19]. Switching individuals beams on and off, or providing a chirp in the accelerating voltage, either in time or as a function of transverse position, may provide the source with interesting capabilities to manipulate the light produced.

ACKNOWLEDGMENT

This research is supported by the Dutch Technology Foundation STW, which is part of the Netherlands Organisation for Scientific Research (NWO), and which is partly funded by the Ministry of Economic Affairs.

REFERENCES

[1] A.S. Gilmour Jr., *Klystrons, traveling wave tubes, magnetrons, crossed-field amplifiers, and gyrotrons*, (Norwood: Artech House, 2011).

[2] E. Jerby et al., “Cylclotron maser oscillator experiments in a periodically loaded waveguide”, IEEE J. Quant. Electr. **31**, 970 (1995).

[3] M.V. Kartikeyan, E. Borie, M. Thumm, *Gyrotrons, high-power microwave and millimeter wave technology* (Berlin: Springer, 2004).

[4] D.H. Bilderback et al., “Review of third and next generation synchrotron light sources”, J. Phys. B: At. Mol. Opt. Phys. **38**, S773 (2005).

[5] L.R. Elias, et al., “Observation of Stimulated Emission of Radiation by Relativistic Electrons in a Spatially Periodic Transverse Magnetic Field”, Phys. Rev. Lett. **36**, 717 (1976).

[6] P. Emma et al., “First lasing and operation of an Ångstrom-wavelength free-electron laser” Nat. Phot. **4**, 641 (2010).

[7] J. Feldhaus, “FLASH—the first soft x-ray free electron laser (FEL) user facility”, J. Phys. B: At. Mol. Opt. Phys. **43**, 194002 (2010).

[8] E. Allaria et al., “Highly coherent and stable pulses from the FERMI seeded free-electron laser in the extreme ultraviolet”, Nat. Phot. **6**, 699 (2012).

[9] P.J.M. van der Slot et al., “Photonic Free-Electron Lasers”, IEEE Photon. J. **4**, 570 (2012).

[10] A. Strooisma et al., “A mirror-less, multi-beam photonic free-electron laser oscillator pumped far beyond threshold”, TUP005, *These Proceedings*, FEL’15, Daejeon, Korea (2015).

[11] J.D. Joannopoulos, R.D. Meade and J.N. Winn, *Photonic Crystals: Molding the Flow of Light*, (Princetong: Princeton University Press, 1995).

[12] O. Svelto and D.C. Hanna, *Principles of Lasers*, (Berlin: Springer, 1998).

[13] A.E. Siegman, *Lasers*, (Herdon: University Science Books, 1986).

[14] E.L. Saldin, E.A. Schneidmiller and M.V. Yurkov *The physics of free-electron lasers*, (Berlin: Springer, 2000).

[15] H.P. Freund and T.M. Antonsen Jr., *Principles of Free-electron Lasers, 2nd edition*, (London: Chapman & Hall, 1996).

[16] G.S. Nusinovich et al., “Wave coupling in sheet- and multi-beam travelling wave tubes”, Phys. Plasmas **16**, 063103 (2009).

[17] S. Humphries Jr., *Charged particle beams*, (Minealo: Dover Publications, 2013).

[18] G.M. Branch and T.G. Mihran, “Plasma-frequency reduction factors in electron beams”, IRE Trans. Electron Devices textbf2, 3 (1955).

[19] C.A. Spindt, “A thin-film field-emission cathode”, J. Appl. Phys. **39**, 3504 (1968).

ISBN 978-3-95450-134-2

THREE-DIMENSIONAL, TIME-DEPENDENT SIMULATION OF FREE-ELECTRON LASERS

H.P. Freund
Department of Electrical and Computer Engineering, Colorado State University, Fort Collins, USA
P.J.M. van der Slot#
Mesa+ Institute for Nanotechnology, University of Twente, Enschede, the Netherlands,
Department of Electrical and Computer Engineering, Colorado State University, Fort Collins, USA

Abstract

Simulation codes modeling the interaction of electrons with an optical field inside an undulator are an essential tool for understanding and designing free-electron lasers (FELs). A new code under development, named MINERVA, uses a modal expansion for the optical field. A Gaussian expansion is used for free-space propagation, and an expansion in waveguide modes for fully guided propagation, or a combination of the two for partial guiding at THz frequencies. MINERVA uses the full Newton-Lorentz force equation to track the particles through the optical and magnetic fields. We describe the main features of MINERVA, and show comparisons between simulations and experiments conducted using the LCLS.

INTRODUCTION

Simulation codes modeling the interaction of electrons with an optical field inside an undulator are an essential tool for understanding and designing free-electron lasers (FELs). As there exists a large variety of FELs ranging from long-wavelength oscillators using partial wave guiding to single-pass soft and hard x-ray FELs that are either seeded or starting from noise (*i.e.*, Self-Amplified Spontaneous Emission or SASE), a simulation code should be capable of modeling this huge variety of FEL configurations. A new code under development, named MINERVA, is capable of modeling such a large variety of FELs. The code uses a modal expansion for the optical field including a Gaussian expansion for free-space propagation, or an expansion in waveguide modes for fully-guided propagation, or a combination of the two for partial guiding, which is typically used at THz frequencies. MINERVA uses the full Newton-Lorentz force equations to track the particles through the optical and magnetic fields. Here we describe the main features of MINERVA and compare simulations with experiments conducted using the LCLS at SLAC.

A variety of different free-electron laser (FEL) simulation codes have been developed over the past several decades such as GINGER [1], MEDUSA [2], TDA3D [3], and GENESIS [4], among others. These codes typically undergo continuous development over their usable lifetimes. As a result, the codes become increasingly complex as new capabilities are added or older capabilities are deleted, and this tends to compromise their performance. It also renders it increasingly more difficult to make further modifications that might be needed. Because of this, we decided to develop a new code using a "clean-slate" approach having the properties and characteristics that we desired.

#p.j.m.vanderslot@utwente.nl

SIMULATION PROPERTIES

The formulation used in MINERVA describes the particles and fields in three spatial dimensions and includes time dependence as well. Electron trajectories are integrated using the complete Newton-Lorentz force equations. No wiggler-averaged-orbit approximation is made. The magnetostatic fields can be specified by analytical functions for a variety of analytic undulator models (such a planar or helical representations), quadrupoles, and dipoles. These magnetic field elements can be placed in arbitrary sequences to specify a variety of different transport lines. As such, MINERVA can set up field configurations for single or multiple wiggler segments with quadrupoles either placed between the undulators or superimposed upon the undulators to create a FODO lattice. Dipole chicanes can also be placed between the undulators to model various optical klystron and/or high-gain harmonic generation (HGHG) configurations. A variety of undulator models is available, including: (1) either flat- or parabolic-pole-face planar undulators, (2) helical undulators, and (3) a representation of an APPLE-II undulator that can treat arbitrary elliptic polarizations. The fields can also be imported from a field map.

The electromagnetic field is described by a modal expansion. For free-space propagation, MINERVA uses Gaussian optical modes, while waveguide modes are used when the wavelength is comparable to the dimensions of the drift tube. As a result, MINERVA can treat both long and short wavelength FELs. A combination of the Gaussian and waveguide modes is also possible when there is partial guiding at, for example THz frequencies.

The electromagnetic field representations are also used in integrating the electron trajectories, so that harmonic motions and interactions are included in a self-consistent way. Further, the same integration engine is used within the undulator(s) as in the gaps, quadrupoles, and dipoles, so that the phase of the optical field relative to the electrons is determined self-consistently when propagating the particles and fields in the gaps between the undulators.

ISBN 978-3-95450-134-2

Particle loading is done in a deterministic way using Gaussian quadrature that preserves a quiet start for both the fundamental and all harmonics. Shot noise is included using the usual Poisson statistics algorithm [5] so that MINERVA is capable of simulating SASE FELs; however, provision is made for enhanced shot-noise due to various levels of micro-bunching.

MINERVA has also been linked to the Optics Propagation Code (OPC) [6, 7] for the simulation of FEL oscillators or propagating an optical field beyond the end of the undulator line to a point of interest. We focus in this paper on the simulation of the LCLS SASE FEL so we will not discuss the coupling between MINERVA and OPC further, but this will appear in future papers.

MINERVA is written in Fortran 95 using dynamic memory allocation and supports parallelization using the Message Passing Interface. The memory allocated for a given simulation run is determined by the needs for a specific configuration. Since the field is described by a discrete set of wave modes characterized by distinct amplitudes, the description of the field requires relatively little memory. The principal demand on memory is, therefore, determined by the number of particles in the simulation but the amount of memory required is relatively modest for most cases studied to date.

Table 1: Parameters of the LCLS FEL Experiment

Electron Beam	
Energy	13.64 GeV
Bunch Charge	250 pC
Bunch Duration	83 fsec
Peak Current	3000 A (flat-top)
x-Emittance	0.4 mm-mrad
y-Emittance	0.4 mm-mrad
rms Energy Spread	0.01%
rms Size (x)	215 microns
α_x	1.1
β_x	30.85 m
rms Size (y)	195 microns
α_y	-0.82
β_y	25.38 m
Undulators	33 segments
Period	3.0 cm
Length	113 Periods
Amplitude (1st segment)	12.4947 kG
K_{rms} (1st segment)	2.4748
Taper Slope	-0.0016 kG
Gap Length	0.48 m
Quadrupoles	
Length	7.4 cm
Field Gradient	4.054 kG/cm

THE LCLS SASE FEL

The LCLS [8] is a SASE FEL user facility that became operational in 2009 and operates at a 1.5 Å wavelength. The fundamental operating parameters are listed in Table 3. It employs a 13.64 GeV/250 pC electron beam with a flat-top temporal pulse shape of 83 fsec duration. The normalized emittance (x and y) is 0.4 mm-mrad and the rms energy spread is 0.01%. The undulator line consisted of 33 segments with a period of 3.0 cm and a length of 113 periods including one period each in entry and exit tapers. A mild down-taper in field amplitude of -0.0016 kG/segment starting with the first segment (which has an amplitude of 12.4947 kG and K_{rms} = 2.4748) and continuing from segment to segment of was used to compensate for energy loss due to Incoherent Synchrotron Radiation (ISR). This is referred to as a "gain taper". The electron beam was matched into a FODO lattice consisting of 32 quadrupoles each having a field gradient of 4.054 kG/cm and a length of 7.4 cm. Each quadrupole was placed a distance of 3.96 cm downstream from the end of the preceding undulator segment. The Twiss parameters for this FODO lattice are also shown in Table 1.

The LCLS produces pulses of about 1.89 mJ at the end of the undulator line, and saturation is found after about 60 m. A comparison between the measured pulse energies (green circles) and the simulation (blue) is shown in Fig. 1. The data is courtesy of H.-D. Nuhn and P. Emma at SLAC, and the simulation results represent an average over an ensemble of runs performed with different noise seeds. As shown in the figure, the simulations are in good agreement with the measurements and with each other in the start-up and exponential growth regions. The simulation exhibits saturation where the exponential gain regime ends after 60 m at a pulse energy of 1.5 mJ. However, the pulse energy grows more slowly to about 1.92 mJ after 110 m, which is in good agreement with the measurements.

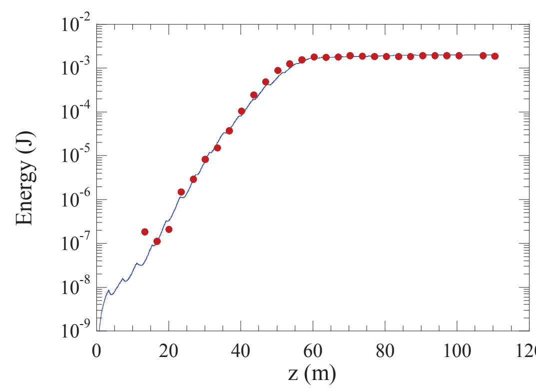

Figure 1: Comparison between experimental data (red circles) from the LCLS (data courtesy of P. Emma and H.-D. Nuhn) and simulation (blue).

Experiments have also been performed at the LCLS [9] to investigate enhancing the efficiency using a tapered undulator. This taper is referred to as the "saturation taper". Saturation in an FEL occurs when the bulk of the electrons become trapped in the ponderomotive wave formed by the beating of the undulator and radiation fields. At that point the electrons have lost energy and dropped out of resonance with the wave. The tapered undulator has the effect of accelerating the electrons in

ISBN 978-3-95450-134-2

the axial direction and maintaining the resonance over an extended length [10]. Comparisons between tapered undulator amplifiers and simulation have demonstrated good agreement and high efficiencies [11]. Comparison between the use of tapered undulators in a seeded amplifier and an equivalent SASE FEL shows that while the efficiency enhancement is lower in the SASE FEL, substantial efficiency enhancements are possible [12].

The LCLS configured with a stronger taper for the last segments has demonstrated such enhancements in the efficiency [9]. This experiment employed an undulator in which the aforementioned mild linear down-taper is enhanced by the addition of a more rapid down-taper starting at the 14th undulator segment. The experimental taper profile is shown in Fig. 2 (data courtesy of D. Ratner).

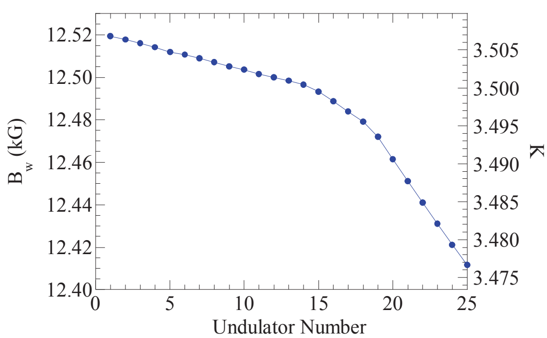

Figure 2: The experimentally applied saturation taper profile (courtesy of D. Ratner).

In comparison with the undulator and electron beam properties employed in the first lasing experiments, the tapered undulator experiment employed undulators tuned to somewhat different field strengths and an electron beam parameters that may have varied from the initial experiments. The pulse energies in the experiment were obtained by measuring the energy loss in the electron beam. Simulations were conducted over a parameter range including emittances of 0.40 mm-mrad – 0.45 mm-mrad and energy spreads of 0.010% – 0.015% that are thought to characterize the electron beam.

A comparison between the measured pulse energies and simulations over the parameter range that most closely agree with the experiment is shown in Fig. 3, where the experimental results are shown in red. Observe that the maximum pulse energy shown represents a substantial enhancement over that reported in the first lasing experiment. The simulation results represent averages over many noise seeds. As is evident from the figure, the simulations for the three choices are all very similar and are in good agreement with the measurements, indicating that the efficiency enhancement could be achieved for a variety of electron beam parameters.

SUMMARY AND CONCLUSION

As shown in the paper, the current state of development of MINERVA yields good agreement for the experiments studied using the LCLS at SLAC. Consequently, we feel that MINERVA can accurately, and with confidence, predict the performance of short wavelength FELs.

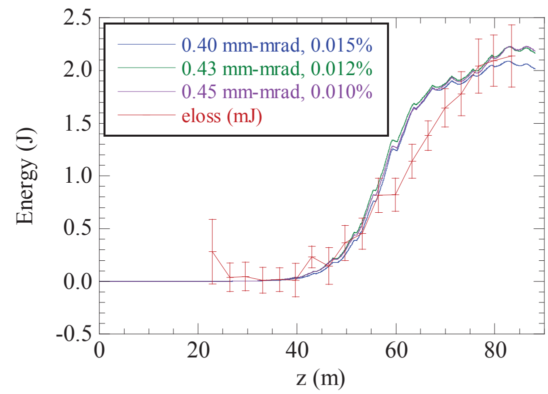

Figure 3: Comparison between the experimental data (red) and simulations for a variety of emittances and energy spreads (data courtesy of D. Ratner).

MINERVA is currently in beta-test and development will continue. At present, the inclusion of waveguide modes is under development that will permit the simulation of long wavelength THz FELs. In addition, several techniques necessary to import particles from beam generation and tracking codes and to export particles to these beam generation and tracking codes for start-to-end simulations are being developed including both statistical algorithms and the direct importation of particles on a one-to-one basis. These developments will be reported in future publications.

ACKNOWLEDGEMENTS

The authors would like to acknowledge many helpful discussions with P. Emma, H.-D. Nuhn, and D. Ratner.

REFERENCES

[1] W.M. Fawley, “An Informal Manual for GINGER and its’ post-processor XPLOTGIN”, LBID-2141, CBP Tech Note-104, UC-414, 1995.
[2] H.P. Freund, S.G. Biedron, and S.V. Milton, IEEE J. Quantum Electron **36**, 275 (2000).
[3] T.M. Tran and J.S. Wurtele, Comput. Phys. Commun. **54**, 263 (1989).
[4] S. Reiche, Nucl. Instr. Meth. A **429**, 243 (1999).
[5] H.P. Freund, L. Giannessi, and W.H. Miner, Jr., J. Appl. Phys. **104**, 123114 (2008).
[6] J. Karssenberg *et al.*, J. Appl. Phys. **100**, 093106 (2006).
[7] http://lpno.tnw.utwente.nl/opc.html
[8] P. Emma *et al.*, Nat. Photon. **176**, 1038 (2010).
[9] D. Ratner *et al.*, SLAC-PUB-14194 (2010).
[10] P. Sprangle, C.M. Tang, and W.M. Manheimer, Phys. Rev. Lett. **43**, 1932 (1979).
[11] X.J. Wang, H.P. Freund, W.H. Miner, Jr., J.B. Murphy, H. Qian, Y. Shen, and X. Yang,, Phys. Rev. Lett. **103**, 154801 (2009).
[12] H.P. Freund and W.H. Miner, Jr., J. Appl. Phys. **105**, 113106 (2009).

ISBN 978-3-95450-134-2

A MIRROR-LESS, MULTI-BEAM PHOTONIC FREE-ELECTRON LASER OSCILLATOR PUMPED FAR BEYOND THRESHOLD

A. Strooisma, P.J.M. van der Slot*, K.J. Boller
Mesa+ Institute for Nanotechnology, University of Twente, Enschede, The Netherlands

Abstract

In a photonic free-electron laser one or multiple electron beams are streaming through a photonic crystal to generate coherent Cerenkov radiation. Here we consider a photonic-crystal slab consisting of a two-dimensional, periodic array of bars inside a rectangular waveguide, with both ends tapered to provide complete transmission of an electromagnetic wave. By appropriately designing the photonic-crystal slab, a backward wave interaction at low electron beam energy of around 15 kV can be obtained. The backward wave interaction provides distributed feedback without any external mirrors being present. We numerically study the dynamics of the laser oscillator when pumped far beyond threshold with one or multiple electron beams. We show that using multiple beams with the same total current provide better suppression of higher-order modes and can produce more output power, compared to the laser pumped by a single beam of the same total current.

INTRODUCTION

The coherent emission of traditional laser oscillators is typically limited to a discrete set of emission frequencies, which is determined by the transition between bound-electron states having discrete energy levels, by the the discrete set of longitudinal modes of the resonator or by a combination of both [1]. Free-electron lasers (FELs) partly overcome this by generating coherent radiation using unbound, also called free, electrons, which have a continuous energy distribution and can therefore emit at any desired frequency [2, 3]. However, whenever an oscillator configuration is used, the emission of an FEL will again be in the longitudinal modes of the resonator. Note that the free electrons need higher kinetic energy to emit shorter wavelengths, e.g., energies of a few MeV are required to generate THz radiation, while several to tens of GeV are required to emit soft- and hard x-ray radiation.

It is therefore desirable to have a coherent radiation source based on free electrons that would be compact, continuously tunable and preferably require much lower energy electrons (compared to undulator-based FELs) to generate a specific frequency. At the same time this source should provide a feedback mechanism that does not require an external resonator. The photonic free-electron laser (pFEL) [4] is a such a light source that fulfills these requirements and has other advantages as well.

In a pFEL gain is provided by electrons streaming through a photonic crystal embedded in a waveguide as shown in Fig. 1. The photonic crystal slab considered here consists of a periodic array of metal posts placed inside a metallic waveguide that provides the vacuum required to transport the electrons. Note that this photonic crystal possesses many natural channels for the electrons to propagate through (e.g., up to seven in Fig. 1). This allows the total current to be divided over many electron beams, lowering the current density in each individual beam. This results in higher quality electron beams and easier beam transport [5] than would be possible with a single electron beam. On the other hand, when keeping the current density in the individual beams constant, increasing the number of electron beams provides a simple way of scaling the output power of the source.

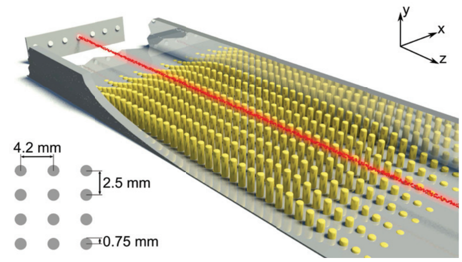

Figure 1: Schematic view of the photonic free-electron laser with a single electron beam. The red dots represent the electrons. The inset shows the orientation of the coordinate system.

When an electron beam streams through the photonic crystal, spontaneous Cherenkov radiation is emitted [6], albeit with different properties [7] compared to the emission in bulk materials. The spontaneous emission will contain Bloch eigenmodes of the photonic crystal slab that are velocity matched with the electrons for a low-order spatial harmonic. If the Bloch eigenmode has a longitudinal electric field component, then the mutual interaction between radiation field and electrons results in bunching of the electrons and hence the build-up of a coherent radiation field at the velocity-matched frequency.

The remaining part of this paper is organized as follows. We first investigate the properties of the tapered photonic crystal slab considered in this paper which includes the dispersion of the lowest order Bloch eigenmode. Then we investigate the performance of the mirrorless pFEL oscillator when pumped by a single electron beam in the center of the photonic crystal slab. This is followed by investigating the performance when the same oscillator is pumped by several electron beams and the paper concludes with a discussion and outlook.

* p.j.m.vanderslot@utwente.nl

ISBN 978-3-95450-134-2

TAPERED PHOTONIC CRYSTAL

Because of the periodicity of the dispersion (i.e., spatial harmonics) of the Bloch modes [8], the pFEL can be operated in the so-called backward-wave regime where the group velocity is directed opposite to the phase velocity. Because of this, light generated at the downstream side of the photonic crystal travels to the upstream side, where it bunches the electron beam. Consequently, the backward wave provides feedback on the bunching and thereby creates an oscillator configuration without requiring any external mirrors. This means that the longitudinal modes induced by external mirrors are also absent and the pFEL can be continuously tuned in frequency.

To avoid that the end facets of the photonic crystal slab reflect the electromagnetic waves (and thus act as mirrors), the height of the posts that form the photonic crystal is tapered down at each of the end facets, creating a crystal as is schematically shown in Fig. 1. This photonic crystal consists of 8 rows of 40 posts, where the height of the nth post in a row is given by:

$$h_n = \begin{cases} h_0 \cos^2\left(\frac{\pi}{2}\left(\frac{n}{11} - 1\right)\right) & \text{if } 1 \leq n \leq 10 \\ h_0 & \text{if } 10 < n \leq 30 \\ h_0 \cos^2\left(\frac{\pi}{2}\frac{n-30}{11}\right) & \text{if } 30 < n \leq 40 \end{cases}, \quad (1)$$

where $h_0 = 4$ mm is the full post height. The other dimensions of the photonic crystal are a post radius of 0.75 mm, a distance between post centers of 2.5 mm along the z axis and 4.2 mm along the x axis. The waveguide has a cross-section of 33.6 by 8.0 mm.

The transmission of a wave through the crystal has been numerically calculated using a frequency-domain solver (CST Studio Suite 2014). The structure shown in Fig. 1, when made out of copper, reflects only 0.4 % of the incident power at 16 GHz, the typical operation frequency of this laser. This shows that the tapers have a very low reflection. 70.4 % of the power is transmitted, so the losses in a single pass through the copper photonic crystal are 29.2 %. These calculations also show that the transmitted and reflected waves only contain the incident mode and no other modes, indicating that the photonic crystal modes and waveguide modes couple one-to-one.

The dispersion curve of the lowest order Bloch mode with non-zero longitudinal electric field for the photonic crystal of Fig. 1 is shown in Fig. 2 where the frequency (ν) is plotted versus longitudinal wavenumber, k_z, for the first (shifted) Brillouin zone. Figure 2 also shows the electron beam dispersion for the slow space-charge wave that is given by [9]

$$\nu = \frac{k_z v_{el}}{2\pi} - p\gamma^{-3/2}\nu_p, \quad (2)$$

$$\nu_p = \frac{1}{2\pi}\sqrt{\frac{e^2 n_{el}}{m_{el}\epsilon_0}}. \quad (3)$$

Here, v_{el} is the electron velocity, γ is the Lorentz factor, ν_p is the the non-relativistic plasma frequency, e, n_{el} and m_{el} are the electron charge, density and mass, respectively, ϵ_0 is the permittivity of free space and p is the so-called plasma reduction factor, which varies between 0 and 1. Figure 2 clearly shows that the laser operates in the backward-wave regime with a phase velocity in the direction of the electron velocity and a group velocity pointed in the opposite direction, i.e. towards the direction of the electron gun.

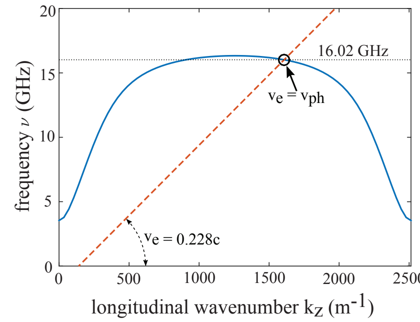

Figure 2: The calculated dispersion curve of the first Bloch mode with a non-zero longitudinal field component for the photonic crystal shown in Fig. 1 (the blue solid line) and the dispersion of the slow space-charge wave (red dashed line) for an electron beam with a $I_b = 1$ A, $E_b = 14$ keV and $p = 1$. The intersection of the two lines gives an indication of the frequency for velocity matching.

Note that in determining the operating frequency, the electron velocity inside the photonic crystal slab needs to be calculated from the kinetic energy, which is not necessarily the same as the total energy of the electron (eV_b, where e is the absolute value of electron charge and V_b is the accelerating potential of the electron gun) as the electrons will also attain potential energy when they are injected into the metallic waveguide structure that contains the metallic photonic crystal slab. Due to the periodic structure of the photonic crystal, this can not be calculated analytically. However, the average reduction in kinetic energy can be obtained from simulations that we use for studying the laser dynamics in the next section.

SINGLE BEAM PUMPING

To study the performance of the mirrorless pFEL oscillator, i.e., with a tapered photonic crystal slab as shown in Fig. 1, we perform so-called particle-in-cell (PIC) simulations [10] (CST Studio Suite 2014) to study the dynamics of the oscillator. Unless otherwise specified, the waveguide and photonic crystal are assumed to be lossless and an electron beam with zero energy spread is used (a so-called cold electron beam). The radius r_b of the electron beam is 1 mm. A guiding magnetic field of 0.5 T provides an immersed flow for the electrons and balances the radial space-charge force of the electron beam [5].

A typical output signal obtained by these simulations is shown in Fig. 3a for $I_b = 1$ A and $E_b = 14$ keV. This beam current is almost 5 times the threshold current for this device

ISBN 978-3-95450-134-2

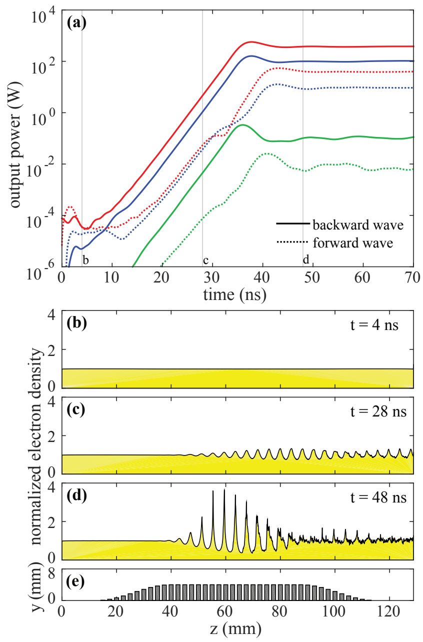

Figure 3: The power as a function of time (a) in the backward (solid lines) and forward (dotted lines) direction for the first three waveguide modes (red: TE_{10}, green: TE_{20}, blue: TE_{30}). Here, I_b = 1 A and E_b = 14 keV. The times for subfigures (b-d) are indicated by vertical dotted lines. The electron line density at various times: spontaneous emission (b), exponential growth (c) and steady state (d). A side view of the photonic crystal (e).

[11]. The output power for the three lowest order waveguide modes is shown. Note that after the tapered section the empty waveguides continues for another 13.75 mm before it ends in a matched waveguide port where the radiation is analyzed in terms of waveguide modes. Because the electron beam and therefore the gain is purely in the center of the waveguide, only modes with a strong on-axis longitudinal field are expected to couple strongly to the electron beam. Indeed, Fig. 3a shows that 99.5 % of the total power is in modes one and three and that the even modes, with zero on-axis longitudinal field, contain negligible power. The power in higher order odd modes is also negligible. Even though the pFEL only amplifies light in the backward direction, Fig. 3a shows that there is still a small amount of power leaving the crystal in the forward direction. This is caused by incomplete destructive interference of the wave in the forward (upstream) direction, due to non-homogeneous gain in the crystal. A frequency of ν = 16.047 GHz with a full width at half maximum of 0.58 MHz[1] was found. By varying the beam voltage from 13.5 kV to 15.5 kV, the frequency changed continuously from 16.02 GHz to 16.14 GHz.

[1] For the calculation of the bandwidth, the metallic parts had the properties of copper in order to obtain a realistic estimate for the bandwidth. In this case the total power was 334 W (cf. Fig. 3).

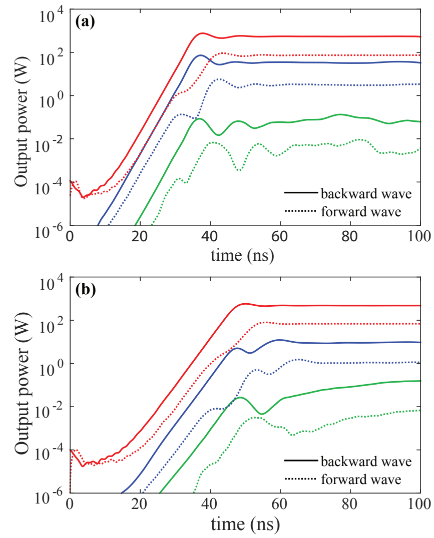

Figure 4: The output power as a function of time for the pFEL pumped with 3 (a) and 5 (b) beams. Just as in Fig. 3, shown are the backward (solid) and forward waves (dotted) for the first three waveguide modes (red: TE_{10}, green: TE_{20}, blue: TE_{30}). The total current in the beams is 1 A and E_b = 14 kV.

The dynamics can be divided into three phases that are determined by the electron bunching. Figures 3b-d show the electron line-charge density along the electron beam for the three phases. A side-view of the photonic crystal is shown in Fig. 3e to give context to the horizontal axis of sub-figures b-d. Initially, the electron beam is homogeneous and the output is dominated by spontaneous emission (Fig. 3b). Spontaneous emission into the lasing mode will start bunching the electrons and, subsequently, start the feedback mechanism that results in exponential growth (Fig. 3c). After some time the gain will saturate: the electrons slow down because their kinetic energy is transferred to the radiation field, which causes electrons and the wave to go out of phase. Finally, this effect becomes so strong that the growth will stop completely and the system reaches its steady state (Fig. 3d), i.e. the total single pass gain equals the total round-trip loss. Here, the total loss is determined by the 100 % out-coupling of the electromagnetic field from the photonic crystal.

MULTIPLE BEAM PUMPING

As mentioned before, multiple electron beams could stream through the photonic crystal. In combination with the scale invariance of Maxwell's equations [8], this can be used to maintain a certain drive current, and therefore output power, for the laser when the pFEL is scaled to operated at higher frequencies [4]. It is therefore of interest to investigate the pFEL pumped by multiple electron beams moving in parallel through the photonic crystal.

Figure 4a and b show the output power over time when pumping with the three and five most central beams, respec-

ISBN 978-3-95450-134-2

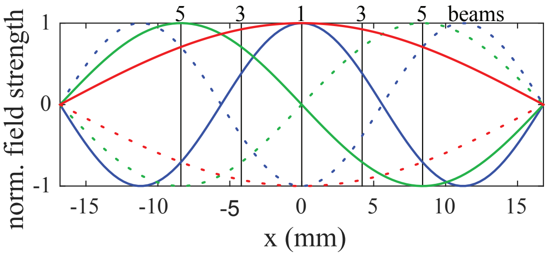

Figure 5: The empty waveguide mode profiles for the TE_{10} (red), TE_{20} (green) and TE_{30} (blue) modes. The vertical black lines show the position of the electron beams for pumping with 1, 3 or 5 beams.

tively. The same configuration is used as for the single beam simulations presented in Fig. 3 (i.e. PEC as metal and a cold electron beam) and the sum of the current in the beams is equal to 1 A. When pumped with multiple beams the pFEL behaves very similar to when pumped with a single beam. However, the multibeam pFEL does take longer to start up, which is due to the lower current per beam. Fig. 4 shows that the fraction of the power in the fundamental mode increases with the number of beams: 81 ± 3 % for one beam, 93 ± 2 % for three beams and 99 ± 1 % when five beams are used. The reason for this is that the gain depends on the field strength at the location of the electrons. The field strength of the first three waveguide modes is shown as a function of the position on the x-axis in Fig. 5. The envelope of the corresponding Bloch eigenmodes of the photonic crystal slab have a similar shape. This figure indicates that the field weighted overlap with the electron beams is highest for the fundamental mode and increases with the number of electron beams. Hence, the gain of the fundamental mode is expected to increase relative to that of the other modes, when the number of electron beams increases. For the configuration investigated, pumping with three beams gives the highest output power while five beams delivers an output with highest mode purity at the expense of a lower output power. This means that the number of pump beams can be used to optimize the tapered pFEL oscillator for maximum output power, maximum mode purity, or possibly both.

DISCUSSION AND OUTLOOK

A photonic free-electron laser oscillator without an external resonator is proposed and investigated numerically using a particle-in-cell code. In this study the metal parts are assumed to be perfect conducting and a cold electron beam is used. A backward-wave interaction provides the feedback that results in oscillator-like behavior of the pFEL. By tapering the ends of the photonic crystals, reflections at the end of the crystal can be reduced to well below the 1 % level. Keeping the total current constant at almost 5 times the threshold current, it is found that the output power and mode purity could be controlled by using multiple electron beams. It is also shown that the oscillator can be continuously tuned. Finally, using copper as metal to provide a more realistic simulation, it was shown that the dynamic oscillator behavior was very similar to the ideal case, albeit with a somewhat lower output power. Using a beam voltage of 14 kV, an output frequency of 16.0470±0.0006 GHz is found with a total power equal to 334 W.

The multi-beam performance of the pFEL oscillator suggests an interesting scaling route to increase the operating frequency to well into the THz domain, compared to the microwave frequencies investigated here. This requires the crystal to be scaled down in size by two orders of magnitude. Instead of increasing the current density in a single beam, the same total current can now be obtained by propagating many electron beams in parallel through the pFEL. Such a massively parallel set of electron beams may be produced by so-called field-emitter arrays [12]. Switching individuals beams on and off, or providing a chirp in the accelerating voltage, either in time or as a function of transverse position, may provide the source with interesting capabilities to manipulate the light produced.

ACKNOWLEDGMENT

This research is supported by the Dutch Technology Foundation STW, which is part of the Netherlands Organisation for Scientific Research (NWO), and which is partly funded by the Ministry of Economic Affairs.

REFERENCES

[1] A.E. Siegman, *Lasers*, (Herdon: University Science Books, 1986).

[2] H.P. Freund and T.M. Antonsen Jr., *Principles of Free-electron Lasers, 2nd edition*, (London: Chapman & Hall, 1996).

[3] L.R. Elias, et al., "Observation of Stimulated Emission of Radiation by Relativistic Electrons in a Spatially Periodic Transverse Magnetic Field", Phys. Rev. Lett. **36**, 717 (1976).

[4] P.J.M. van der Slot et al., "Photonic Free-Electron Lasers", IEEE Photon. J. **4**, 570 (2012).

[5] S. Humphries Jr., *Charged particle beams*, (Minealo: Dover Publications, 2013).

[6] J.V. Jelley", *Cherenkov radiation and its applications*, (London: Pergamon press, 1958).

[7] C. Luo et al., "Cerenkov Radiation in Photonic Crystals", Science **299**, 368 (2003).

[8] J.D. Joannopoulos, R.D. Meade and J.N. Winn, *Photonic Crystals: Molding the Flow of Light*, (Princetong: Princeton University Press, 1995).

[9] A.S. Gilmour *Principles of Traveling Wave Tubes*, (Norwood: Artech House, 1994).

[10] J.M. Dawson, "Particle Simulation of Plasmas", Rev. Mod. Phys. **55**, 403 (1983).

[11] A. Strooisma et al., "Threshold of a mirror-less photonic free-electron laser oscillator pumped by one or more electron beams", TUP003, *These Proceedings*, FEL'15, Daejeon, Korea (2015).

[12] C.A. Spindt, "A thin-film field-emission cathode", J. Appl. Phys. **39**, 3504 (1968).

ISBN 978-3-95450-134-2

QUANTUM NATURE OF ELECTRONS IN CLASSICAL X-RAY FELS*

Petr M. Anisimov#, LANL, Los Alamos, NM 87545, USA

Abstract

An x-ray free electron laser (FEL) is considered by many to be a completely classical device. Yet, some have investigated operating regimes where the underlying physics transitions from a classical to a quantum description. Focusing on the collective behaviour of electrons, they have introduced symmetrized bunching operators and have found an additional energy spread due to recoil, mediated through a quantum FEL parameter.

This work focuses on the quantum nature of a single electron, which is best described, not by a point particle, but by a wave packet. Owing to free space dispersion, one can define the smallest-sized wave packet at an FEL entrance that remains as such throughout an FEL. By utilizing this packet size, we have developed a 1D FEL theory that includes how quantum effects affect bunching.

The smallest-sized wave packet is related to the quantum FEL parameter and offers new insights into the classical-to-quantum transition. It can be generalized to include 3D effects and offers a convenient way to classify FELs. Our theory indicates that gain reduction due to quantum averaging is much stronger than previously believed and will significantly affect harmonic lasing in x-ray FELs (XFELs).

INTRODUCTION

Interest in XFELs has grown in response to the expanding scientific demand in coherent x-ray light sources. XFELs, such as the LCLS at SLAC (USA) [1] and SACLA at Spring-8 (Japan) [2], deliver ultra-bright X-ray pulses having femtosecond duration. Their peak brilliance is about eight orders of magnitude higher than that from most other X-ray sources. The combination of high pulse energy and femtosecond pulse duration of coherent XFEL pulses has created new fields of research in ultrafast chemistry, structural biology and coherent diffractive imaging [3].

The FEL was invented by John Madey [4] who used a quantum mechanical description to arrive at a classical result for the low-gain lasing regime. Thus, the FEL is considered by many to be a completely classical device [5-7]. However, there has been a significant effort to formulate a quantum mechanical description for FELs [8-12] even though XFELs built to date are well described by the classical theory (as their bandwidth is much larger than the recoil frequency) [13].

The quantum regime for FEL operation discussed in Ref. [13] was further investigated in Refs. [14-19]. It was shown that the classical-to-quantum transition is controlled by a "quantum FEL parameter", defined as the ratio between the FEL bandwidth and the photon recoil energy [20]. The quantum regime of operation requires the quantum FEL parameter to be small, a regime that cannot be reached by existing XFELs [1, 2].

Future XFELs are now being designed in response to demand for ever shorter radiation wavelengths and narrower bandwidths. However, cost limitations for future facilities drives their design to utilize accelerators with as low a beam energy as possible. These opposing design criteria exacerbate quantum mechanical effects requiring careful consideration of their impact on lasing performance.

Here we focus on the quantum nature of a single electron and determine how it affects classical XFEL performance. Starting with the classical 1D theory and an analysis of the free space dispersion of an electron wave packet, we construct a hybrid 1D FEL theory that accounts for quantum uncertainty of the electron position inside an XFEL. This theory facilitates a unified description of XFELs and indicates that the planned MaRIE XFEL at Los Alamos National Lab [21] will be affected.

CLASSICAL 1D THEORY

XFELs are lasers that use relativistic electrons moving freely through a periodic magnetic structure in order to generate radiation. The magnetic structure, an undulator, is characterized by wiggle period λ_u and strength parameter $K = eB_0/k_u mc$, where B_0 is a peak magnetic field and $k_u = 2\pi/\lambda_u$. In a planar undulator, electrons with energy γ_0 in mc^2 units generate x-ray radiation at a wavelength $\lambda = \frac{\lambda_u}{2\gamma_0^2}\left(1+K^2/2\right)$.

The fundamentals of FEL instability are captured by the 1D theory with universal scaling in terms of the FEL parameter $\rho = \frac{1}{2\gamma_0}\sqrt[3]{\frac{I}{I_A}\frac{\lambda_u^2 K^2 JJ_1}{8\pi A}}$ for an electron beam with the peak current I and the transverse area A. Here I_A =17 kA is the Alfven current and $JJ_n = J_{\lfloor n/2\rfloor}(nY) + J_{\lfloor n/2\rfloor+1}(nY)$ with $Y = -K^2/(4+2K^2)$ is the energy exchange parameter. The independent variable is the distance along the undulator, $z = \bar{v}_z t / L_{g0}$, measured in the units of the 1D gain length $L_{g0} = \lambda_u / 4\pi\rho$; and the α^{th} electron is described by its ponderomotive phase with respect to the radiation, $\theta_\alpha = (k+k_u)\bar{v}_z t - kct$, and the relative energy detuning, $\eta_\alpha = (\gamma - \gamma_0)/\rho\gamma_0$. The complete set of coupled first-order differential equations has the following form:

*Work supported by the U.S. Department of Energy through the LANL/LDRD Program. LA-UR–15– 26403
#petr@lanl.gov
ISBN 978-3-95450-134-2

$$\frac{d\theta_\alpha}{dz} = \eta_\alpha \tag{1}$$

$$\frac{d\eta_\alpha}{dz} = -2\,\mathrm{Re}\left(Ee^{i\theta_\alpha}\right) \tag{2}$$

$$\frac{dE}{dz} = \frac{1}{N}\sum_{\alpha=1}^{N} e^{-i\theta_\alpha} \tag{3}$$

where the radiation field, E, is normalized to the field at saturation $E_{sat} = \frac{\mu_0 cKJJ_1}{2\gamma_0}\frac{I}{A}L_{g0}$.

Equations (1) and (2) are the pendulum equations and describe the motion of an electron in the ponderomotive potential created by the x-ray radiation. There are two classes of electrons – trapped (in the well) and untrapped. Trapped electrons bunch together and emit coherent radiation according to Eq. (3), which in turn deepens the ponderomotive well. This captures a fraction of the untrapped electrons and provides additional energy for further increasing x-ray radiation and trapping efficiency. Once all electrons are trapped at about $z_{\mathrm{sat}} = 10$, the saturation is reached.

We analyse the growth of FEL instability using the Vlasov equation for an ensemble of electrons with the distribution, $F_0(\eta) = 1/(2\Delta)$ for $|\eta - \delta| \le \Delta$ [5] and show that the x-ray radiation field obeys the equation:

$$\frac{dE^3}{dz^3} + 2i\Delta\frac{dE^2}{dz^2} - \left(\delta^2 - \Delta^2\right)\frac{dE}{dz} - iE = 0$$

Looking for a solution of the form $E = E_0 e^{-i\delta z + i\lambda z}$, one obtains the cubic characteristic equation:

$$(\lambda - \delta)\left(\lambda^2 - \Delta^2\right) + 1 = 0 \tag{4}$$

where the growth rate for the FEL instability is given by the negative imaginary part of a complex root (see Figure 1).

QUANTUM ELECTRON

Classical FEL theory depends on the localization of an electron in its ponderomotive well. According to quantum mechanics, an electron is not a point particle and therefore must be treated as a wave packet:

$$\psi(s,z) = e^{ik_0(s-z)}\frac{e^{-(s-z)^2/4\Delta s(z)^2}}{\sqrt{\sqrt{2\pi}\,\Delta s(z)}}$$

having energy $\gamma_0 = \sqrt{1 + \hbar^2 k_0^2 / m_0^2 c^2}$ in mc^2 units. Consequently, electrons can only be localized in the ponderomotive well to no better than $2\Delta s/\lambda$ and the ponderomotive phase of the α^{th} electron is distributed as:

$$W_\alpha(\theta, z) = \frac{e^{-(\theta-\theta_\alpha)^2/2\sigma(z)^2}}{\sqrt{2\pi}\,\sigma(z)}$$

with $\sigma(z) = 2\pi\Delta s(z)/\lambda$.

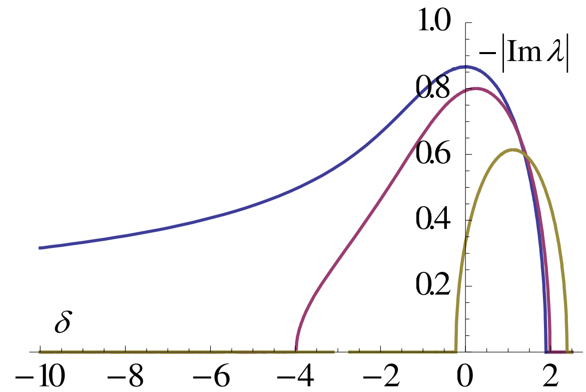

Figure 1: Growth rate for different energy spreads: $\Delta = 0$ (blue), $\Delta = 1/2$ (red), $\Delta = 1/0.8$ (yellow).

Owing to free space dispersion, the size of the wave packet cannot be infinitely small. Starting with a width Δs_0, it grows according to

$$\Delta s^2(z) = \Delta s_0^2 + \frac{d_z^2 L_{g0}^2}{\bar{v}_z^2 \Delta s_0^2} z^2$$

where $\bar{v}_z = c\beta\left(1 - K^2/4\gamma_0^2\right)$ is the average electron longitudinal velocity in an undulator and $d_z = \frac{\lambda_c c}{4\pi\gamma_0^3}\left(1 + \frac{K^2}{2}\right)$ is the free space dispersion modified by the presence of the undulator field. Thus, the initial size of the wave packet, Δs_0, that minimizes the spreading of the wave packet inside an undulator of the dimensionless length, L, is $\Delta s_0^2 = d_z L_{g0} L / \bar{v}_z$.

The quantum mechanical nature of electron limits the smallest-sized wave packet at the end of an undulator to $\Delta s_f^2 \approx \frac{\lambda_c L_{g0} L}{2\pi\gamma_0^3}\left(1 + \frac{K^2}{2}\right)$, which is 7% of the radiation wavelength for MaRIE parameters [21]! Therefore, modification of the 1D theory is needed to include wave packet spreading in order to properly describe MaRIE XFEL performance.

HYBRID 1D THEORY

The 1D FEL theory can be amended by including wave packet spreading and quantum averaging. The modified set of coupled first-order differential equations takes the following form:

$$\frac{d\theta_\alpha}{dz} = \eta_\alpha$$

$$\frac{d\eta_\alpha}{dz} = -2\sum_n \frac{JJ_n}{JJ_1}\mathrm{Re}\left(E_n \left\langle e^{in\theta}\right\rangle_\alpha\right)$$

$$\frac{dE_n}{dz} = \frac{JJ_n}{JJ_1}\frac{1}{N}\sum_{\alpha=1}^{N}\left\langle e^{-in\theta}\right\rangle_\alpha$$

$$\frac{d\sigma^2}{dz} = \frac{1}{2\bar{\rho}^2\sigma_0^2}z$$

ISBN 978-3-95450-134-2

where the quantum averaging is $\left\langle e^{in\theta}\right\rangle_\alpha = e^{-n^2\sigma^2/2}e^{in\theta_\alpha}$, the quantum FEL parameter is $\bar{\rho} = \rho(mc\gamma/\hbar k)$, and n is the harmonic lasing number [22-25].

The solution of the last equation is $\sigma(z)^2 = \sigma_0^2 + z^2/4\bar{\rho}^2\sigma_0^2$ and for $z_f = z_{sat}$ the minimal final uncertainty for the ponderomotive phase is $\sigma_f = \sqrt{z_{sat}/\bar{\rho}}$. This smallest-sized electron wave packet depends on the quantum FEL parameter and provides new insights into the classical-to-quantum transition.

In the classical regime, $\bar{\rho} >> 1$ (i.e. $\sigma_f << \pi$) an electron can be treated as a point particle since this smallest-sized wave packet fits easily inside a ponderomotive well. In the intermediate regime, where $\bar{\rho} = 1$ (i.e. $\sigma_f \approx \pi$), an electron extends slightly into neighbouring wells (see Figure 2). Lastly, in the quantum regime where $\bar{\rho} << 1$ (i.e. $\sigma_f >> \pi$), an electron occupies more than a single ponderomotive well. In the particular case where $\bar{\rho} = 0.4$ (see Ref. [16]), the FEL spectrum makes a transition from continuous to discreet, as an electron has a significant probability of being located in multiple nearest-neighbour wells (see Figure 2).

DISCUSSION

Previous theoretical works focused on collective bunching behaviour and used a symmetrized momentum bunching operator for quantization [19]. It has been found that the growth rate equation is similar to that from the dispersion relation for the classical FEL with initial energy spread $\Delta = 1/2\bar{\rho}$ (see Eq. 4). This extra term represents the intrinsic quantum momentum spread due to recoil that, in dimensional units, is given by $\hbar k/2$.

Hybrid 1D FEL theory provides new insight into FEL operation in the quantum regime by relating the smallest-sized wave packet to the size of the ponderomotive well. The wave packet description of an electron also carries an intrinsic quantum momentum spread that, in dimensionless units, has an initial energy spread

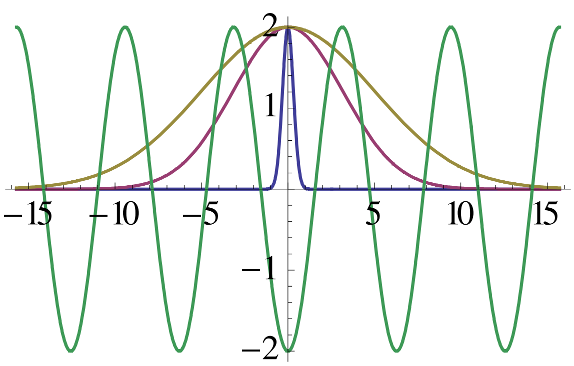

Figure 2: Electron probability distribution at the end of an undulator, $W_\alpha(\theta, \sigma_f)$, in the ponderomotive potential (green) for different values of the quantum FEL parameter: $\bar{\rho} = 100$ (blue), $\bar{\rho} = 1$ (red), and $\bar{\rho} = 0.4$ (yellow).

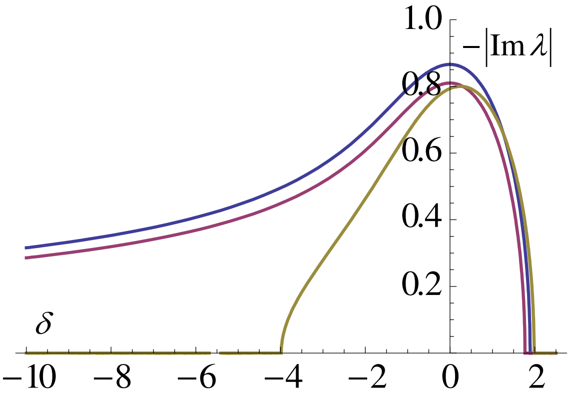

Figure 3: Growth parameter for a mono-energetic beam without quantum averaging (blue) and with quantum averaging for $\bar{\rho} = 50$ (red). The yellow line is for the growth parameter based on Ref. [16] for $\bar{\rho} = 1$.

$\Delta_0 = 1/\sqrt{2z_{sat}\bar{\rho}}$. Here, contrary to expectations, the energy spread tends to zero for a point particle, $\bar{\rho} >> 1$.

One can perform a growth rate analysis for 1D hybrid theory by assuming a constant-sized wave packet since the minimum uncertainty wave packet spreads little inside an undulator:

$$\frac{dE_n^3}{dz^3} + 2i\delta\frac{dE_n^2}{dz^2} - \left(\delta^2 - \Delta^2\right)\frac{dE_n}{dz} - q_n^2 iE_n = 0$$

where $q_n = \frac{JJ_n}{JJ_1}e^{-n^2\sigma^2/2}$. Here, we assume single harmonic lasing, where only the n^{th} harmonic is generated and all other harmonics are suppressed [22-25].

The quantum nature of an electron, captured by the 1D hybrid theory, does not introduce energy spread. However, the FEL growth rate is still reduced due to quantum averaging. Figure 3 shows the FEL growth parameter as a function of detuning including reductions of the growth parameter based on quantum averaging and on the theory from Ref. [16]. For example, the on-resonance growth rate for a mono-energetic electron beam is reduced due to quantum averaging by $e^{-n^2\sigma^2/3}$, which is much stronger than one would expect based on the previous analysis.

1D theory does not take into account 3D effects that increase the gain length over L_{g0} and require a longer undulator in order to reach saturation. The quantum FEL parameter does not take into account such effects. The smallest-sized wave packet, on the other hand, becomes larger in size in order to accommodate the longer undulator length and thus behaves more quantum than would be otherwise expected. For a given smallest-sized wave packet with an FEL parameter ρ, there is a family of XFELs which generate x-ray radiation at a given energy that are equally affected by the quantum nature of electrons. Therefore, one can classify the quantum nature of XFELs based on the smallest-sized wave packet.

ISBN 978-3-95450-134-2

Figure 4 shows the x-ray FEL families for different wave packet sizes.

The final point of our discussion concerns harmonic lasing [22-25]. The reduction in performance caused by quantum averaging is stronger here due to the quadratic dependence on the harmonic number. Table 1 shows the expected gain reduction for the 3rd harmonic lasing with suppressed fundamental for current/planned facilities. While the growth rate for the fundamental is reduced by a few percent in a case of MaRIE facility, quantum averaging will reduce the on-resonance growth rate by 60%.

CONCLUSIONS

The quantum nature of an electron expresses itself through its wave nature. The wave packet description of an electron is closer to a classical point particle description than it is to a plane wave description but free space dispersion effects remain. We have amended 1D FEL theory in order to include quantum averaging over the nonlocal electron wave packet. A long wave packet does not spread as much as a short wave packet, but it might still be longer at the end of the undulator. Thus, we have focused on the smallest wave packet that minimizes wave packet spreading at the end of an undulator.

We have showed that classification of quantum FELs can be done based on either the quantum FEL parameter or the minimum uncertainty of wave packet spreading. However, when 3D effects are included, the later approach seems to be preferred over former. Furthermore, our approach provides new insights into the classical to the quantum regime transition.

Based on the information in Table 1, one can estimate σ_f including 3D effects for different FEL facilities. Using the 1D expression for the minimal final uncertainty of the ponderomotive phase, one can define an effective quantum FEL parameter. In the case of the MaRIE facility, $\bar{\rho}_{eff} = 50$, putting it in the classical domain based on the previous classification. However, its on-resonance growth parameter is reduced by as much as one would expect from the previous treatment with $\bar{\rho} = 1$.

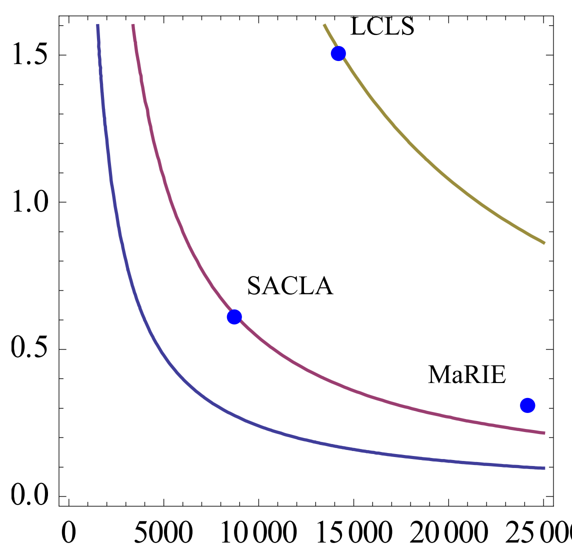

Figure 4: X-ray FEL families for $\sigma_f = 0.45$ (blue), $\sigma_f = 0.30$ (red), and $\sigma_f = 0.15$ (yellow) for $\rho = 5\times10^{-4}$. The vertical axis is in Angstrom and the horizontal axis is the energy of electrons in mc^2 units.

Table 1: Gain Reduction Comparison for Various Facilities

XFEL	**Energy**	λ_r	$2\Delta s_f/\lambda_r$	Γ_{qu}/Γ_{3rd}
LCLS	14 GeV	1.5A	5%	0.93
European	17.5 GeV	0.5A	8%	0.82
PAL	10 GeV	0.6A	10%	0.75
SACLA	8.5 GeV	0.6A	12%	0.64
MaRIE	12 GeV	0.3A	14%	0.58

REFERENCES

[1] P. Emma, et al., Nat. Photonics 4 (2010) 641.
[2] T. Ishikawa et al., Nat Photonics 6 (2012) 540.
[3] M. Yabashi, H. Tanaka, and T. Ishikawa, J. Synch. Rad. 22 (2015) 477.
[4] J.M.J Madey, J. Appl. Phys. 42 (1971) 1906.
[5] P. Schmuser, et al., “Free-Electron Lasers in the Ultraviolet and X-ray Regime,” (Springer Tracts in Modern Physics 2014).
[6] E.L. Saldin, E.A. Schneidmiller, and M.V. Yurkov, “The Physics of Free Electron Lasers,” (Springer, Berlin Heidelberg 2000).
[7] H.P. Freund and T.M. Antonsen, “Principles of Free-Electron Lasers,” (Chapman & Hall, London, 1996).
[8] W. Becker and M.S. Zubairy, Phys. Rev. A 25 (1982) 2200.
[9] W. Becker and J.K. McIver, Phys. Rev. A 27 (1983) 1030.
[10] R. Bonifacio and F. Casagrande, Optics Comm. 50 (1984) 251
[11] R. Bonifacio, C. Pellegrini and L. Narducci, Opt. Commun. 50 (1984) 373.
[12] G. Preparata, Phys. Rev. A 38 (1988) 233.
[13] I.V. Smetanin, Laser Physics 7 (1997) 318.
[14] R. Bonifacio, et al., Europhys. Lett. 69 (2005) 55.
[15] R. Bonifacio, N. Piovella and G.R.M. Robb, Nucl. Instrum. and Meth. in Phys. Res. A 543 (2005) 645.
[16] R. Bonifacio, et al., Phys. Rev. ST Accel. Beams 9 (2006) 090701.
[17] R. Bonifacio, et al., Opt. Commun. 274 (2007) 347.
[18] N. Piovella, et al., Phys. Rev. Lett 100 (2008) 044801.
[19] C.B. Schroeder, C. Pellegrini and P. Chen, Phys. Rev. E 64 (2001) 056502.
[20] R. Bonifacion and F. Casagrande, Nucl. Inst. and Meth. A 237 (1985) 168.
[21] B.E. Carlsten et al., in Proceedings of the Particle Accelerator Conference 2011, Paper TUODS1.
[22] B.W.J. McNeil, et al., Phys. Rev. Lett. 96 (2006) 084801.
[22] E.A. Schneidmiller and M.V. Yurkov, Phys. Rev. ST Accel. Beams 15 (2012) 080702.
[24] H.P. Freund, Phys. Rev. ST Accel. Beams 17 (2014) 010702.
[25] G. Penn, Phys. Rev. ST Accel. Beams 18 (2015) 060703.

ISBN 978-3-95450-134-2

HIGH FIDELITY START-TO-END NUMERICAL PARTICLE SIMULATIONS AND PERFORMANCE STUDIES FOR LCLS-II

G. Marcus, Y. Ding, P. Emma, Z. Huang, T. O. Raubenheimer, L. Wang
SLAC, Menlo Park, CA 94025, USA
J. Qiang, M. Venturini, LBNL, Berkeley, CA 94720, USA

Abstract

High fidelity numerical particle simulations that leverage a number of accelerator and FEL codes have been used to analyze the LCLS-II FEL performance. Together, the physics models that are included in these codes have been crucial in identifying, understanding, and mitigating a number of potential hazards that can adversely affect the FEL performance, some of which are discussed in papers submitted to this conference [1, 2]. Here, we present a broad overview of the LCLS-II FEL performance, based on these start-to-end simulations, for both the soft X-ray and hard X-ray undulators including both SASE and self-seeded operational modes.

INTRODUCTION

The LCLS-II is an advanced x-ray FEL light source that consists of two independently tunable undulators capable of producing radiation covering a large spectral range that can be fed by both a CW superconducting RF (SCRF) linac or by the existing copper linac [3]. Each undulator beamline will be dedicated to the production of either hard (HXR) or soft (SXR) x-ray photons and will incorporate self-seeding [4, 5] infrastructure to produce narrow-bandwidth and longitudinally coherent FEL pulses. Addtional details regarding the baseline design can be found elsewhere [3, 6, 7].

It has been found that the relatively low electron beam energy of 4 GeV (compared to the nominal operation of LCLS) along with an extended transport distance from the end of the linac to the entrance of the undulators leaves the electron beam susceptible to a space-charge driven microbunching instability (MBI) [8–10]. This MBI manifests as large slice current and energy modulations that can potentially degrade the FEL performance. In addition, the space-charge MBI is the leading candidate responsible for the production of a self-seeded spectral 'pedestal' which is seen in both experiment [11] and in simulation [12] and is the topic of current theoretical study [2, 13].

This paper reports the results of high fidelity numerical particle simulations using the suite of codes IMPACT [14–16] and GENESIS [17]. These simulations include the effects of three-dimenstonal space charge, coherent and incoherent synchrotron radiation, RF cavity wakefields and resistive wall wakefields in the generation, acceleration and transport of the electron beam from the cathode to the undulator for three charge distributions: 20 pC, 100 pC, and 300 pC. To model the initial shot noise of the electron beam, which may act as the seed for the space-charge driven MBI, the real number of electrons were tracked from the cathode. The various charge distributions were then used to define the electron beams in GENESIS, where resistive wall wakefield effects are also included in the FEL simulations. SASE has been studied across the tuning ranges for each of the individual charge distributions for both the HXR and SXR undulators and include fully time-dependent taper optimizations. Preliminary results for self-seeding with the 100 pC electron beam will also be discussed.

ELECTRON BEAM PROPERTIES

A detailed start-to-end simulation study of the accelerator beam delivery system is reported elsewhere [1, 18]. Below, we present the electron beam longitudinal phase space (LPS) and critical slice parameters for each of the charge distributions discussed above at the entrance to the SXR undulator. The LPS of the electron beams at the entrance to the HXR undulator show less effects of MBI for reasons discussed in [18]. This sets the stage for detailed FEL simulations in the following section.

20 pC

Figure 1 shows the LPS along with various slice properties of the 20 pC electron beam that has been tracked to the SXR undulator. The core of the distribution is roughly 8 μm long,

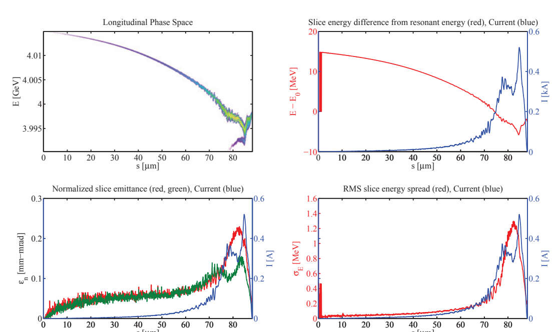

Figure 1: Slice properties of the 20 pC electron beam that has been tracked to the SXR undulator. Top left: longitudinal phase space; top right: slice energy deviation from the resonant energy (red) and current (blue); bottom left: normalized slice emittance (x-red, y-green) and current (blue); bottom right: rms slice energy spread (red) and current (blue).

is slightly chirped with the head of the beam having a lower energy, and has a $I \sim 300$ A current. The normalized slice emittance is less than $\epsilon_n \sim 0.2$ μm in both transverse planes, so while the current is rather low, the beam is sufficiently bright such that it can produce greater than 20 μJ of energy

ISBN 978-3-95450-134-2

per pulse at the high end of the tuning range in the HXR undulator (5 keV), which is important for operations. The rms slice energy spread in the core of the beam reads as greater than $\sigma_E \sim 1.2$ MeV, but is really closer to $\sigma_E \sim 0.45$ MeV if one neglects the filamentation seen in the LPS from the calculation.

100 pC

Figure 2 shows the LPS along with various slice properties of the 100 pC electron beam that has been tracked to the SXR undulator. It is obvious that the space-charge driven

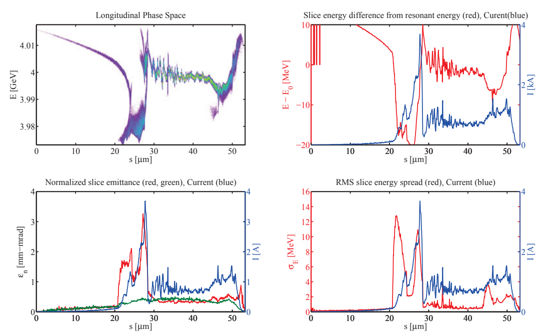

Figure 2: Slice properties of the 100 pC electron beam that has been tracked to the SXR undulator. Top left: longitudinal phase space; top right: slice energy deviation from the resonant energy (red) and current (blue); bottom left: normalized slice emittance (x-red, y-green) and current (blue); bottom right: rms slice energy spread (red) and current (blue).

MBI has severely impacted the LPS of the beam where large current and energy variations can be seen along the longitudinal profile. Nevertheless, the current in the core, which is roughly 20 μm long, is about $I \sim 750$ A. Peak to peak energy variations along the longitudinal profile can be as large as 8 MeV just after the large current spike in the tail of the beam. The normalized slice emittance is less than $\epsilon_n \sim 0.43$ μm in both transverse planes while the rms slice energy spread is roughly $\sigma_E \sim 0.55$ MeV.

300pC

Figure 3 shows the LPS along with various slice properties of the 300 pC electron beam that has been tracked to the SXR undulator. The core of this distribution, which is less impacted by the space-charge induced MBI than the 100 pC electron beam, is roughly 50 μm long and has a current of $I \sim 900$ A. The normalized slice emittance is less than $\epsilon_n \sim 0.70$ μm in both transverse planes while the rms slice energy spread is roughly $\sigma_E \sim 0.40$ MeV. While the larger transverse emittance for this charge distribution will negatively impact the performance at the high end of the tuning range of the HXR undulator, the relatively flat LPS in the core may be useful for self-seeded or externally seeded applications [12].

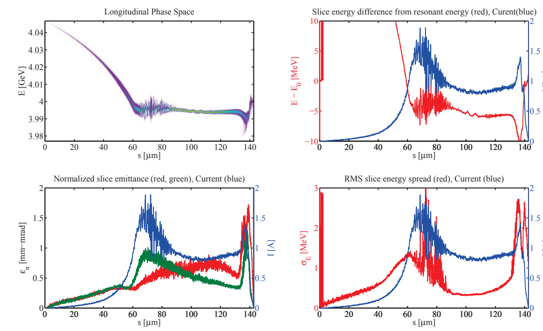

Figure 3: Slice properties of the 300 pC electron beam that has been tracked to the SXR undulator. Top left: longitudinal phase space; top right: slice energy deviation from the resonant energy (red) and current (blue); bottom left: normalized slice emittance (x-red, y-green) and current (blue); bottom right: rms slice energy spread (red) and current (blue).

SASE PERFORMANCE STUDY

Undulator Parameters

Details of the undulator layout can be found elsewhere [6,7]. Figure 4 shows the main parameters of the HXR and SXR undulators. The undulator vacuum chamber will be

Parameter	Value SXR (HXR)	Unit
Type	Hybrid PM, planar	-
Full gap height	Variable	-
Period	39 (26)	mm
Segment length	3.4	m
Break length	1.0	m
# segments	21 (32)	-
Total length	96 (140)	m

Figure 4: LCLS-II undulator parameters.

made of aluminum and will have a rectangular cross section with a 5 mm gap height, which is used to define the resistive wall wakefield for the FEL simulations.

Tapering Optimization and Performance

The tapering scheme employed here follows the strategy laid out in [19] and is based on a three parameter optimization (z_0, ξ, d) of the final FEL pulse energy. Here the taper is given by

$$a_w(z) = a_w(z_0) \times \left[1 - c\,(z - z_0)^d\right], \qquad (1)$$

where z_0 is the taper starting location, which is typically a few power gain lengths before saturation; $c = \frac{\xi}{(L_w - z_0)^d}$, where $\xi = 1 - \frac{a_w(L_w)}{a_w(z_0)}$ is the taper ratio (the % change of the rms undulator parameter a_w over the tapered part of the

ISBN 978-3-95450-134-2

undulator) and L_w is the length of the tapered part of the undulator; and d is the taper profile order. Full time-dependent (not single slice or single frequency) taper optimizations are needed in order to capture the dynamics of SASE in the post-saturation regime accurately. The optimal taper that is nominally given by single-slice optimization scans over the three parameters listed above is more appropriate for seeded FELs. This is because particles in distinct coherence regions (SASE spikes) tend to have uncorrelated ponderomotive phases [20]. We have found that the optimal taper given by a single-slice parameter scan often produces less than half the energy that could be achieved by a full time-dependent parameter scan, which is a significant result. Figure 5 shows the result of a typical parameter scan for the 100 pC electron beam resonant at $E_\gamma = 1.5$ keV in the HXR undulator for one particular taper starting location, z_0. The taper profile order, d, is typically around 2 and the optimal taper ratio, ξ, depends on the undulator length and various electron beam and radiation properties. A summary of the LCLS-II SASE performance with post-saturation tapering can be found in Figure 6 for the charge distributions and tuning ranges that span the relevant parameter spaces. The FEL seems to be insensitive to the MBI induced energy and current modulations at all but highest photon energies in the HXR undulator, where the beam is more sensitive to slice energy spread.

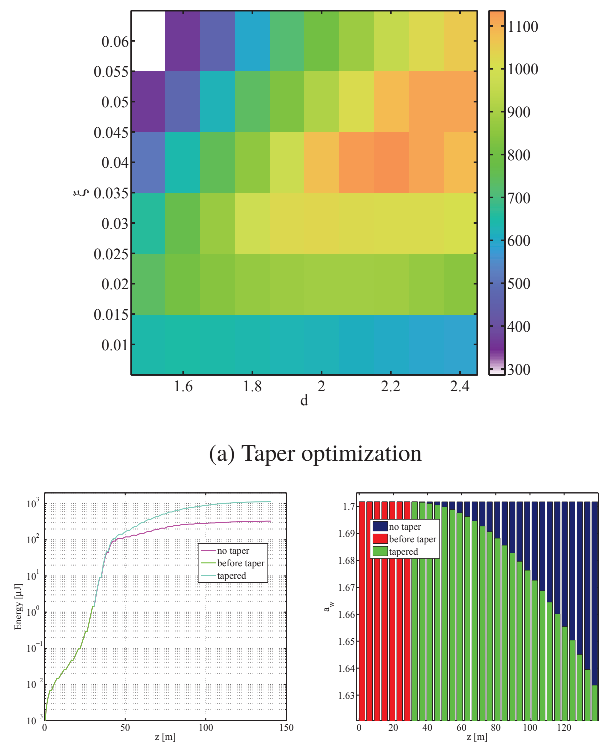

(a) Taper optimization

(b) Gain curve (c) Undulator taper

Figure 5: (a) taper optimization showing the energy at the end of the undulator as a function of d and ξ; (b) gain curve for the optimal taper and for the un-tapered case; (c) the taper profiles for the optimal taper and the un-tapered case.

SELF-SEEDED PERFORMANCE STUDY

Simulation Strategy

The SXR beamline will incorporate a self-seeding system (SXRSS) to produce longitudinally coherent soft x-ray free electron laser pulses. It will consist of two undulators that are separated by a monochromator and a magnetic chicane. The first undulator will consist of 7-8 independent segments while the second undulator consists of 13-14 independent segments. The monochromator design will be based on the existing LCLS SXRSS monochromator [21] with additional flexibility built in. It will have a compact footprint that is designed to allow both the chicane and monochromator to occupy the equivalent space of a single undulator segment along the strong focusing quadrupole FODO cell strongback.

The resolving power is nominally specified to be $R = 15,000$, but upgrade paths to $R \sim 30,000$ are being explored.

The specification of the individual components of both the monochromator and chicane are not yet established. As such, a phenomenological approach is used to model the bandwidth reduction of the seed. The nominal monochromator design relative bandwidth $(1/R)$ and overall efficiency ($\sim 5\%$) are used to specify the amplitude of a Gaussian frequency filter function. The phase of the filter function is defined through Kramers-Kronig relations such that causality

	SXR			HXR		
	250eV	750eV	1.25keV	1.5keV	3.25keV	5keV
20pC	267 (42)	239 (43)	168 (41)	206 (27)	147 (22)	25 (7)
100pC	1205 (260)	795 (135)	527 (76)	1136 (111)	469 (46)	10 (6)
300pC	5482 (1013)	3844 (519)	1897 (422)	2364 (300)	642 (147)	- (0.4)

Figure 6: LCLS-II start-to-end SASE performance study with optimized post-saturation tapering. The left column indicates the electron beam charge while the top two rows indicate either the SXR or HXR undulator and the photon energy in each undulator that was studied. The parentheses indicate the energy at saturation, which is not necessarily the energy at the end of the undulator without a post-saturation taper.

ISBN 978-3-95450-134-2

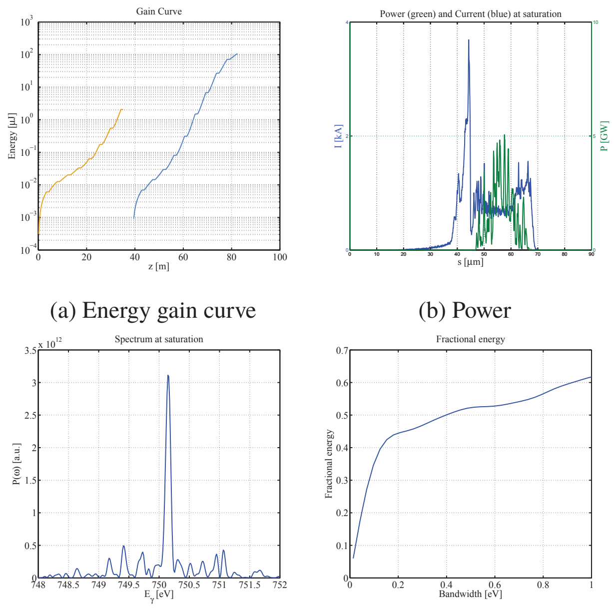

(a) Energy gain curve (b) Power

(c) Spectrum (d) Fractional energy

Figure 7: (a) Energy gain curve for the SASE undulator (orange) which generates the seed to be monochromatized and amplified downstream (blue); (b) Power (green) and current (blue) at saturation; (c) On-axis spectrum at saturation; (d) Fractional energy within a given bandwidth at saturation.

is not violated when the filter is applied to the fully three-dimensional FEL pulse exiting the seventh or eigth undulator section. The fields exiting the monochromator are then used to specify the seed into the next undulator. Diffraction through the actual monochromator setup is not modeled. This is, however, a small effect at these photon energies. In addition, a new and simple optical propagation theory has been developed to track the full three-dimensional field through the optical lattice and will be explored when the monochromator design has matured [22].

The magnetic chicane serves the dual role of compensating for the delay introduced by the monochromator and destroying any residual electron beam microbunching from the first undulator. This is modeled in a very simple way by using the dumped particle distribution and re-initializing the shotnoise.

Performance

The nominal performance for the SXRSS system using the 100 pC electron beam distribution tuned to produce $E_\gamma = 750$ eV photons is illustrated in Figure 7. The first undulator terminates the field growth well before saturation after 8 undulator sections (orange, Figure 7a). Here, the FEL energy is roughly 2 μJ while the longitudinal profile in both the spectral and temporal domain display the typical SASE spiking. The field is then frequency filtered while the electron beam shotnoise is re-initialized according to the description above. The field is amplified to saturation in a downstream undulator (blue, Figure 7a). The temporal duration at this point is roughly $\Delta T_{FWHM} \sim 36$ fs (Green, Figure 7b), which is consistent with the resolving power of $R = 15,000$ at this photon energy. Some spiking due to the fluctuating electron beam slice properties is evident. The spectrum at this point (Figure 7c) has a dominant spike with a spectral width $\Delta E_\gamma \sim 100$ meV, which is roughly twice as large as the initial bandwidth, which is defined by the monochromator bandwidth. This is a result of the longer wavelength energy and density modulations present along the LPS of the electron beam. Additionally, the higher frequency modulations produces the additional frequency content shown in the figure. These effects conspire to lower the fractional energy which is stored within the primary bandwidth of the FEL pulse, which in turn lowers the overall peak spectral brightness.

SUMMARY AND CONCLUSION

The relatively low energy of the LCLS-II electron beam and the long transport from the linac to the undulators leaves the beam susceptible to a strong space-charge driven microbunching instability, which in turn generates longitudinal variations of the electron beam slice properties. These variations may negatively impact the FEL performance. As such, high fidelity numerical particle simulations have been performed in an attempt to capture the relevant physics and to evaluate the performance of the FEL under these circumstances. Three separate charge distributions were evaluated in both the SXR and HXR undulators across the their full tuning ranges. In addition, time-dependent taper optimizations were performed in order to more accurately characterize an optimal performance. It was found that the MBI induced energy and current variations had only a small impact on the SASE FEL performance while the seeded performance showed the production of a broadband spectral 'pedestal.' Schemes to mitigate the pedestal are currently under investigation.

ACKNOWLEDGMENT

This work was supported by U.S. Department of Energy Contract No. DE-AC02-76SF00515.

ISBN 978-3-95450-134-2

REFERENCES

[1] M. Venturini *et al.*, "The microbunching instability and LCLS-II lattice design: lessons learned", in *These Proceedings: Proc. 37th Int. Free-Electron Laser Conf., Daejeon*, 2015, TUC01.

[2] Z. Zhang *et al.*, "Microbunching-induced sidebands in a seeded free-electron laser", in *These Proceedings: Proc. 37th Int. Free-Electron Laser Conf., Daejeon*, 2015, WEP084.

[3] T. Raubenheimer, "LCLS-II: Status of the CW X-ray FEL Upgrade to the LCLS Facility", in *These Proceedings: Proc. 37th Int. Free-Electron Laser Conf., Daejeon*, 2015, WEP014.

[4] J. Feldhaus *et al.*, *Opt. Comm.* **140**, 341 (1997).

[5] G. Geloni *et al.*, *Journ. Mod. Opt.* **58**, 16 (2011).

[6] T. O. Raubenheimer,"Technical Challenges of the LCLS-II", *in Proceedings: Proc. 6th Int. Part. Acc. Conf., Richmond*, 2015, WEYC1.

[7] G. Marcus, "FEL Simulation and Performance Studies for LCLS-II', *in Proceedings: Proc. 36th Int. Free-Electron Laser Conf., Basel*, 2014, TUP032.

[8] M. Borland *et al.*, *Nucl. Instrum. Methods Phys. Res. Sect. A*, **483**, 268 (2002).

[9] E. L. Saldin *et al.*, *Nucl. Instrum. Methods Phys. Res. Sect. A*, **490**, 1 (2002).

[10] Z. Huang *et al.*, *Phys. Rev. ST Accel. Beams*, **7**, 074401 (2004).

[11] D. Ratner *et al.*, *Phys. Rev. Lett.*, **114**, 054801 (2015).

[12] G. Penn *et al.*, "Effect of Microbunching on Seeding Schemes for LCLS-II", in *These Proceedings: Proc. 37th Int. Free-Electron Laser Conf., Daejeon*, 2015, WEP025.

[13] R. Lindberg, unpublished.

[14] J. Qiang *et al.*, *Phys. Rev. ST Accel. Beams*, **9**, 044204 (2006).

[15] J. Qiang *et al.*, *J. of Comp. Phys.*, **163**, 434 (2000).

[16] J. Qiang *et al.*, *Phys. Rev. ST Accel. Beams*, **12**, 100702 (2009).

[17] S. Reiche, *Nucl. Instr. Meth. Phys. Res. Sec. A* **429**, 243 (1999).

[18] J. Qiang *et al.*, "Start-to-End Simulation of the LCLS-II Beam Delivery System with Real Number of Electrons", in *These Proceedings: Proc. 37th Int. Free-Electron Laser Conf., Daejeon*, 2015, WEP070.

[19] Y. Jiao *et al.*, *Phys. Rev. ST Accel. Beams*, **15**, 050704 (2012).

[20] W. M. Fawley, *Nucl. Instr. Meth. Phys. Res. Sec. A* **483**, 537 (2002).

[21] Y. Feng *et al.*, "System Design for Self-Seeded the LCLS at Soft X-ray Energies", in *Proc. 34th Int. Free-Electron Laser Conf.*, Nara, 2012, TUoBI01.

[22] G. Marcus, *to be published.*

ISBN 978-3-95450-134-2

HIGH-GAIN FEL IN THE SPACE-CHARGE DOMINATED RAMAN LIMIT

I. Gadjev, C. Emma, A. Nause, J. Rosenzweig, UCLA, Los Angeles, USA

Abstract

While FEL technology has reached the EUV and X-ray regime at existing machines such as LCLS and SACLA, the scale of these projects is often impractical for research and industrial applications. Sub-millimeter period undulators can reduce the size of a high-gain EUV FEL, but will impose stringent conditions on the electron beam. In particular, a high-gain EUV FEL based on undulators with a sub-millimeter period [1] will require electron beam currents upwards of 1 kA at energies below 100 MeV. Coupled with the small gap of such undulators and their low undulator strengths, K < 0.1, these beam parameters bring longitudinal space-charge effects to the foreground of the FEL process. When the wavelength of plasma oscillations in the electron beam becomes comparable to the gain-length, the 1D theoretical FEL model transitions from the Compton to the Raman limit [2]. In this work, we investigate the behavior of the FEL's gain-length and efficiency in these two limits. The starting point for the analysis was the one-dimensional FEL theory including space-charge forces. The derived results were compared to numerical results of Genesis 1.3 simulations. This theoretical model predicts that in the Raman limit, the gain-length scales as the beam current to the -1/4th power while the efficiency grows as the square root of the beam current.

INTRODUCTION

The attractiveness of sub-millimeter undulators is the ability to produce EUV and X-ray FELs in a compact space. A 100 MeV electron beam is easily obtainable in 10 meters with current acceleration technology and produces EUV light in an undulator of 800 μm period. A high-gain FEL requires beam currents in the kA scale in order to achieve saturation. The small aperture of such micro-undulators drives the transverse size of the beam to the 10 μm scale while their small undulator strength, $K_{und} \approx 0.01$, reduces the coupling of the beam and radiation. All these factors contribute to bring longitudinal space-charge effects to the foreground of compact FELs based on micro-undulators.

The typical FEL operation regime is the Compton regime, in which space charge is negligible. Marcus et al. [3] have shown that longitudinal space-charge increases the gain-length and provided a Ming Xie type of fit to the gain. However, if the longitudinal space-charge is strong enough, it can no longer be treated as only a correction to the Compton regime. Gover and Sprangle [2] treat the limit in which space-charge is dominant as a separate FEL regime. The transition into the Raman regime can be quantified as the set of undulator and beam parameters such that: $2k_pL_G > \pi$.

We will show that in the Raman limit, the gain-length and efficiency of the FEL change their scaling with the beam current from the typical scaling in the Compton regime. The gain-length tapers off to a $I_0^{-1/4}$ scaling at very high beam currents, while the efficiency is boosted to a $I_0^{1/2}$ scaling. The Raman limit presents a new mode of operation of the FEL. We investigate the behavior of gain and efficiency in the Raman limit. The analysis is carried out solely through the one-dimensional FEL theory in order to isolate the effects of longitudinal space-charge. To study FEL efficiency we begin by providing insight into the conditions for saturation. The 1D FEL theory yields analytic solutions for the gain, whose validity extends to the Compton and Raman limits. The efficiency is deduced by finding the saturation power that results for a given gain and saturation distance. The analytic expressions are then compared to simulations. A simple numerical approach was treated by a linear finite-difference numerical integration of the one-dimensional FEL equations with and without the space-charge terms. As a third consistency check, genesis 1.3 simulations were implemented. Since genesis 1.3 includes three-dimensional effects, the beam parameters for the simulated beams were chosen so as to minimize the effect of 3D space-charge, diffraction, and emittance.

1-D FEL THEORY

Longitudinal space charge is quantified by the relativistic plasma wave-number, and its effects on the FEL performance can be studied in the 1-D limit. The relativistic plasma wave-number is defined as:

$$k_p = \sqrt{\frac{2I_0}{I_A\gamma^3\sigma_x^2}}$$

The Alfein current is, $I_A = 4\pi\varepsilon_0 m_e c^3/e$. The beam current, energy, and transverse size are I_0, γ, σ_x, respectively. The transition into the Raman regime can be quantified as the set of undulator and beam parameters such that:

$$2k_pL_G > \pi$$

The gain-length is defined through the solutions of the third-order ODE for the electric field. Assuming the field has the form, $\tilde{E}(z)\sim\exp(\alpha z)$, then the root with a positive real part defines the gain-length as:

$$\alpha^3 + i4k_u\alpha^2 + \left(k_p^2 - 4k_u^2\eta^2\right)\alpha - i8k_u^3\rho^3 = 0$$
$$\rightarrow L_G = \frac{1}{2\Re[\alpha_+]}$$

ISBN 978-3-95450-134-2

The undulator wavenumber is, k_u, the Pierce parameter is ρ, and the detuning from resonance is η. For completeness we quote the Pierce parameter:

$$\rho = \left[\frac{K[JJ]}{4\sqrt{2}}\frac{\gamma_z}{\gamma}\frac{k_p}{k_u}\right]^{2/3}$$

The following definitions are in order: k_u is the undulator wave-number, the peak magnetic field is B_u, so that the undulator parameter is $K = eB_u/mck_u$, and $[JJ]$ is a constant on the order of unity that describes the coupling between the elctron motion and radiation.

Now we take the two limits in the cubic equation for the 1D FEL gain. In the Compton limit, the case with no space-charge, $k_p = 0$, we obtain the usual definition of the gain-length:

$$L_G^C = \frac{1}{2\sqrt{3}k_u\rho} \propto I_0^{-1/3}$$

When k_p can no longer be neglected in the cubic equation, the maximum gain is shifted to a detuning of, $\eta_{max} = k_p/2k_u$, and the gain-length's dependence on beam current shifts to:

$$L_G^R \propto I_0^{-1/4}$$

Efficiency of an FEL is defined as the power extracted from the electron beam. If the system's energy is to be conserved, the extracted beam energy has to be fed into the energy of the electromagnetic field. Therefore, we can write the following definition for FEL efficiency:

$$Q_{FEL} = \frac{\Delta U_{beam}}{U_{beam}} = \frac{\Delta P_{rad}}{P_{rad}} = \frac{e(P_{sat} - P_0)}{\gamma_0 mc^2 I_0}$$

Following the arguments presented in [2], we can derive the efficiency's dependence on the beam current for the two regimes:

$$Q_{eff}^C \propto I_0^{1/3}$$
$$Q_{eff}^R \propto I_0^{1/2}$$

To investigate these scaling rules through numerical methods, we take the saturation power to be the average power of the FEL after the exponential gain has subsided. This approach is useful in analysing simulations, but not analytically meaningful like the quasi non-linear methods implemented by Zhirong et al [4], [5] to study saturation. The topic of saturation power is a delicate one and is inherently a non-linear effect that is not the topic of this work.

NUMERICAL METHODS

A 1D solver was implemented to study the behavior of the FEL gain-length and saturation power as longitudinal space-charge effects become dominant. The coupled FEL equations [6] can be numerically integrated by a linear integration method as shown below.

$$\theta_j^n = \theta_j^{n-1} + 2k_u\eta_j^{n-1}\Delta z$$
$$\eta_j^n = \eta_j^{n-1} - \frac{e}{\gamma_0 mc^2} Re\left[\left(\frac{K[JJ]}{2\gamma_0}\tilde{E}^{n-1} - \frac{i\mu_0 c^2}{\omega_r}\tilde{j}_1^{n-1}\right)e^{i\theta_j^{n-1}}\right]\Delta z$$
$$\tilde{E}^n = \tilde{E}^{n-1} - \frac{\mu_0 cK[JJ]}{4\gamma_0}\tilde{j}_1^{n-1}\Delta z$$
$$\tilde{j}_1^n = j_0\frac{2}{N}\sum_{j=1}^{N} exp(-i\theta_j^{n-1})$$
$$j_0 = -\frac{ec}{\pi\sigma_x^2\lambda_r}N$$

Space charge in these equations is strictly a longitudinal term and is proportional to the first harmonic of the electron bunching. Since the Raman limit arises in the one-dimensional FEL theory, it should manifest itself in the results obtained by "pushing" a particle distribution through the above equations. However, because the equations are general, they should also reproduce the Compton limit. Genesis 1.3 [7] is a 3D FEL code that is the standard in the community and we can use it to bench-mark the 1D code and as a second point of comparison. In order to replicate the 1D condition in genesis, we must use pancake beams in which longitudinal space-charge is dominant. Care was also taken in preparing simulations that minimize the effects of diffraction and emittance.

GAIN AND DETUNING

Figure 1 shows the gain curves as functions of the detuning of the beam from resonance. The blue plot is made for a set of parameters that put the FEL in the Compton regime, but with enough space-charge for there to be detuning. The red plot is obtained for a set of parameters that drive the FEL into the Raman regime. There is good agreement between the analytic solutions, 1D model, and genesis1.3. The maximum gain (shortest gain-length) for a specific set of beam parameters is obtained for an energy detuning that depends on the space charge parameter, $\eta_{max} = k_p/2k_u$.The close agreement between the analytic solutions, the 1D model, and the genesis1.3 output for these two vastly different beam currents is encouraging and justifies our use of the 1D model.

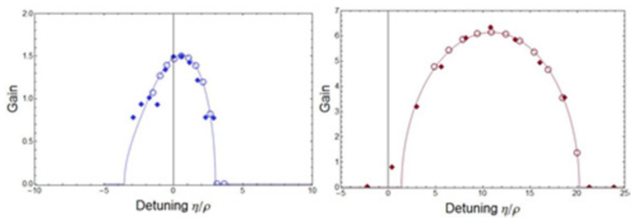

Figure 1: FEL gain as a function of the energy detuning of the electron beam. The solid line is the solution the cubic equation for the electric field, the circles correspond to 1D simulations, and the solid diamonds are genesis1.3 simulations. The left (blue) plot is an FEL in the Compton limit and the right (red) is the Raman limit.

LONGITUDINAL PHASE-SPACE

Figure 2 shows snapshots of the longitudinal phase-space of the electrons close to saturation of the high-gain FEL in the Compton (blue) and Raman (red) limits. We see that as the FEL approaches the point of saturation, the electrons lose energy and reach the bottom of their synchrotron oscillation inside the pondermotive bucket. In the Compton case, the particles continue to spin around the center of the bucket as a whole. However, in the Raman case, there is a point of charge pile-up that causes particles to significantly accelerate and alter their trajectories inside the bucket [8]. This prevents the synchrotron oscillations to continue undisturbed through saturation and smears out the energy distribution. The inclusion of longitudinal space-charge disturbs the synchrotron oscillations. In the simulations without space-charge the energy has a better defined oscillation that corresponds to the synchrotron frequency. Once space-charge effects are included, the average energy after saturation does not execute a well-defined oscillation.

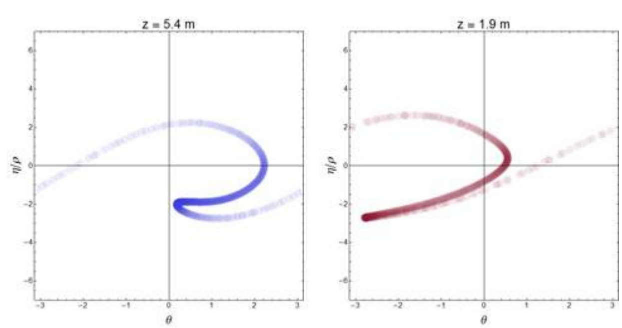

Figure 2: The longitudinal phase-space at the onset of saturation for the Compton (left and blue) and Raman (right and red) limits.

GAIN-LENGTH AND EFFICIENCY

The final two plots show the scaling of the gain-length and efficiency through the Compton and Raman regions of operation. To obtain these plots, we transition the FEL by varying the beam current while holding the rest of the set of undulator and beam parameters constant. Increasing the beam current indefinitely is not practical, but serves as the most straightforward way to study the Compton-Raman transition and the FEL's performance there. The current directly increases the space charge's influence and, as seen above, changes the required detuning for maximum gain. The plot has Ln-Ln axes so that the slope of the lines corresponds to the power of the current dependence, $L_G \propto I_0^{\alpha} \rightarrow ln(L_G) \propto \alpha \cdot ln(I_0)$. The two sets of beam parameters for which we bench-marked our code with genesis are included (diamonds), and they show complete agreement with our 1D code (solid circles) and the asymptotic analytic behavior (solid lines).

Figure 3 confirms the scaling law for the FEL gain-length for a wide range of beam current values (1kA to 1.6MA). For low beam currents, the gain-length shortens as $I_0^{-1/3}$ for an increase in current. Although there is detuning and space charge is not negligible in this region, this is still the Compton limit. As the beam current is increased, the plasma wave-length approaches a gain-length and begins to strongly influence micro-bunching. This increases the gain-length and an increase in current no longer translates in as much of a shortening of the gain-length as in the Compton limit. In fact, in the Raman regime, the gain-length is proportional to, $I_0^{-1/4}$.

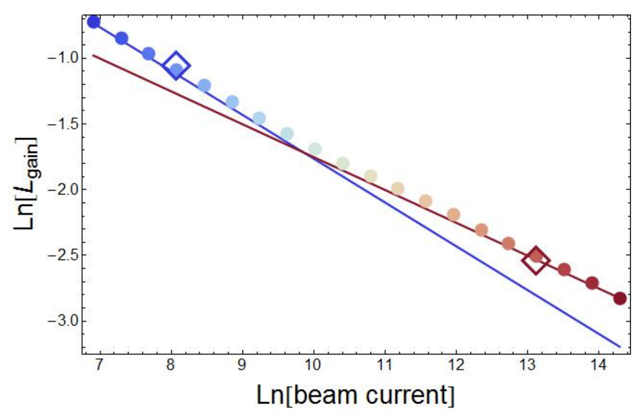

Figure 3: Gain-length scaling with beam current. Blue is the Compton limit and red Raman.

Although the gain-length increases for as more current is added, the efficiency of the FEL process begins to increase. Gover and Sprangle [2] derive the efficiency in the Raman limit to be proportional to the plasma wave-number, which in turn depends on the square root of the beam current, $Q_{eff}^{R} \propto k_p \propto I_0^{1/2}$. The efficiency boost stems from the large detuning needed for the space charge dominated FELs. Because the electrons are higher off resonance initially, once saturation occurs and the particle distribution has reached the bottom of its synchrotron oscillation in the pondermotive bucket, there has been more energy lost to the radiation as compared to a slightly detuned beam. Figure 4 confirms the efficiency increases from, $Q_{eff}^{C} \propto I_0^{1/3}$, to $Q_{eff}^{R} \propto I_0^{1/2}$, as the FEL transitions from the Compton to the Raman regime.

ISBN 978-3-95450-134-2

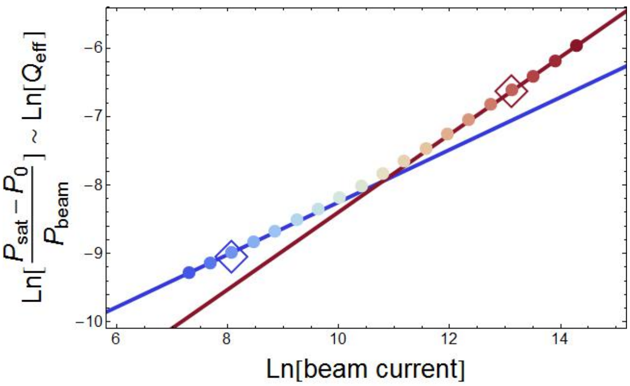

Figure 4: Efficiency scaling with beam current. Blue is the Compton limit and red Raman.

DISCUSSION

Space charge effects in high-gain FELs are usually a corrective term that increases the ideal gain-length and postpones saturation. We have studied the extreme case of a Raman FEL, where longitudinal space charge is dominant. Once in the Raman limit, there is a trade-off between the gain-length and efficiency of the FEL. We have confirmed through simulations that while the gain-length tapers off to a $I_0^{-1/4}$ scaling at very high beam currents, the efficiency of the FEL is boosted to a $I_0^{1/2}$ scaling. The onset of saturation has been shown to be affected by the space dynamics as shown in the longitudinal phase-space plots.

The push towards sub-millimeter period undulators for the construction of compact XFELs requires electron beams that have high current and small transverse size at energies of hundreds of MeV. These micro-undulators have small undulator parameters, $K_{und} \approx 0.01$, which further decreases the coupling of the beam and radiation. It is not unreasonable to expect that Raman effects will surface in such scenarios.

REFERENCES

[1] J. Harrison, A. Joshi, J. Lake, R. Candler, and P. Musumeci, "Surface-micromachined magnetic undulator with period length between 10 μm and 1 mm for advanced light sources," *Phys. Rev. Spec. Top. - Accel. Beams*, vol. 15, no. 7, p. 070703, Jul. 2012.

[2] A. Gover and P. Sprangle, "A Unified Theory of Magnetic Electrostatic Bremsstrahlun Scattering , and Cerenkov-," *IEEE J. Quantum Electron.*, vol. QE-17, no. July, pp. 1196–1215, 1981.

[3] G. Marcus, E. Hemsing, and J. Rosenzweig, "Gain length fitting formula for free-electron lasers with strong space-charge effects," *Phys. Rev. Spec. Top. - Accel. Beams*, vol. 14, no. 8, p. 080702, Aug. 2011.

[4] Z. Huang and K.-J. Kim, "Review of x-ray free-electron laser theory," *Phys. Rev. Spec. Top. - Accel. Beams*, vol. 10, no. 3, p. 034801, Mar. 2007.

[5] N. . Vinokurov, Z. Huang, O. . Shevchenko, and K.-J. Kim, "Quasilinear theory of high-gain FEL saturation," *Nucl. Instruments Methods Phys. Res. Sect. A Accel. Spectrometers, Detect. Assoc. Equip.*, vol. 475, no. 1–3, pp. 74–78, Dec. 2001.

[6] P. Schmüser, *Springer Tracts in Modern Physics 258 Free-Electron Lasers in the Ultraviolet and X-Ray Regime.*

[7] S. Reiche, "Numerical Studies for a Single Pass High Gain Free-Electron Laser Dissertation," 1999.

[8] E. Peter, a. Endler, F. B. Rizzato, and a. Serbeto, "Mixing and space-charge effects in free-electron lasers," *Phys. Plasmas*, vol. 20, no. 12, p. 123104, 2013.

ISBN 978-3-95450-134-2

COHERENT THOMSON SCATTERING RADIATION GENERATED BY USING PEHG

S. Chen, K. Ohmi, D. Zhou, KEK, 1-1 Oho, Tsukuba 305-0801, Japan

Abstract

Electron beam is density modulated by the phase-merging effect to obtain ultra-short longitudinal structures in the phase space. Coherent radiations are then generated by the coherent Thomson scattering between the phase-merged beam and a long wavelength laser pulse.

INTRODUCTION

It is able to generate intense short wavelength radiation by the Thomson scattering between relativistic electron beam and an incident high-field laser beam. In the case of back-scattering, the radiation wavelength is expressed by [1]

$$\lambda_r = \frac{\lambda_L}{4\gamma^2}\left(1 + \frac{a_L^2}{2} + \gamma^2\theta^2\right) \tag{1}$$

where the dimensionless vector potential a_L of the incident laser can be expressed as

$$a_L = \frac{eE_L}{m_e c\omega_L} = 0.85 \times 10^{-9}\lambda_L[\mu m]I_0^{1/2}[W/cm^2] \tag{2}$$

Equation 1 has the similar form with the radiation wavelength of undulator radiation except for a Doppler-shift factor of $4\gamma^2$ rather than $2\gamma^2$. Usually the wavelength of incident laser is much shorter than undulator period length. Therefore, to obtain radiation with same wavelength, it requires much lower electron beam energy than that of the undulator radiation. However, the radiation of Thomson scattering is usually incoherent.

If the electron bunch has longitudinal structure shorter than the radiation wavelength, coherent Thomson scattering radiation can be generated. Several methods to obtain such a longitudinal structure have been discussed previously [2–4]. In this paper, we propose to use the phase-merging effect method realized by transverse gradient undulator (TGU), which is referred as PEHG in FEL [5–7], to modulate the electron bunch and generate short longitudinal phase space structures. Then a long wavelength laser in THz region [8] is used as laser undulator to generate coherent Thomson scattering radiation with such a beam.

LASER-BEAM INTERACTION IN UNDULATOR

The Hamiltonian of laser-beam interaction in a planar undulator is expressed as follows

$$H = (1+\delta) - \sqrt{(1+\delta)^2 - (\boldsymbol{p} - \frac{\boldsymbol{a}}{\gamma})^2 - \frac{1}{\gamma^2}}, \tag{3}$$

where $a_x = \hat{a}_u \cos k_u s + \hat{a}_L \cos k_L z$.

The equations of electron motion are expressed by

$$\begin{aligned}
x' &= \left(p_x - \frac{a_x}{\gamma}\right)\frac{1}{p_s},\\
p_x' &= \frac{1}{\gamma p_s}\left(p_x - \frac{a_x}{\gamma}\right)\frac{da_x}{dx}\\
z' &= -\frac{\left(p_x - \frac{a_x}{\gamma}\right)^2 + p_y^2 + \frac{1}{\gamma^2}}{p_s(p_s + 1 + \delta)},\\
\delta' &= \frac{1}{\gamma p_s}\left(p_x - \frac{a_x}{\gamma}\right)\frac{da_x}{dz}\\
p_s &= \sqrt{(1+\delta)^2 - (\boldsymbol{p} - \frac{\boldsymbol{a}}{\gamma})^2 - \frac{1}{\gamma^2}}
\end{aligned} \tag{4}$$

Equation 4 can be solved numerically by, for example, Runge-Kutta integration. The radiation emitted by an electron can be calculated by the Heaviside-Feynman expression

$$\boldsymbol{E}_i(\boldsymbol{x}_0, t) = \frac{e}{4\pi\varepsilon_0}\left[\frac{\boldsymbol{R}_i}{R_i^3} + \frac{R_i}{c}\frac{d}{dt}\frac{\boldsymbol{R}_i}{R_i^3} + \frac{1}{c^2}\frac{d^2}{dt^2}\frac{\boldsymbol{R}_i}{R_i}\right] \tag{5}$$

Here "i" denotes the i-th electron and $\boldsymbol{R}_i$ is the vector between observation point $\boldsymbol{x}_o$ and the election position $\boldsymbol{x}_i$. Then the total radiation field can be calculated using the superposition principle. A numerical simulation code using this method has been developed by K. Ohmi [2] and will be used in this work.

DENSITY MODULATION BY PEHG

Basic Principle of PEHG

In traditional HGHG [9, 10], the harmonic components contained in the density modulated bunch are measured by the bunching factor

$$b_n =< e^{-in\theta_j} >= e^{-\frac{1}{2}n^2\sigma_\gamma^2(\frac{d\theta}{d\gamma})^2} J_n(n\Delta\gamma\frac{d\theta}{d\gamma}). \tag{6}$$

As is seen in Eq. 6, the bunching factor reduces exponentially with the harmonic number increases due to the none-zero energy spread σ_γ. The performance of density modulation of traditional HGHG is restricted so that it is hard to obtain sufficiently short longitudinal structures in the phase space.

PEHG [5, 7] was proposed to improve the harmonic number of traditional HGHG by replacing the modulator undulator with a TGU with transverse field gradient α. Meanwhile, a dog-leg section with a dispersion strength η is put

ISBN 978-3-95450-134-2

in the front stream of the TGU to provide the transverse-longitudinal coupling. The principle equation inside the TGU is shown in Eq. 7,

$$\frac{\gamma' - \gamma_0'}{\gamma - \gamma_0} = 1 - \frac{2\pi N_u \Delta\gamma}{\gamma_0}\left(\frac{\alpha\eta {K_0}^2}{K_0^2 + 2} - 1\right). \tag{7}$$

By choosing the values of transverse gradient α of TGU and the dispersion strength η of the dog-leg properly, one can make the right hand side of Eq. 7 becomes zero. The electrons with the same energy merge to the same phase during the energy modulation process. After passing through the dispersion section with proper value of R_{56}, ultra-short longitudinal structures are obtained inside the electron bunch.

Density Modulation

We assume an 100 MeV electron beam of an Energy Recovery Linac (ERL). Firstly, only 1-D simulations are carried out, i.e., assumeing the transverse emittance is neglectable. The simulation parameters are shown in Table 1.

Table 1: Simulation Parameters

TGU modulator		
Period length	λ_u	2 cm
Period number	N_u	15
Central Undulator strength	K_0	2.0316
Electron beam		
Central beam energy	E_0	100 MeV
Beam energy spread	σ_E	30 keV
Seeding laser		
Wavelength	λ_s	800 nm
Vector potential	a_s	3.7761×10^{-5}
Max. energy modulation	$\Delta\gamma$	180 keV

From Eq. 7, the optimized value of $\alpha\eta$ is

$$(\alpha\eta)_{opt} = \left(\frac{\gamma_0}{2\pi N_u \Delta\gamma} + 1\right)\frac{K_0^2 + 2}{K_0^2}. \tag{8}$$

With the parameters in Table 1, Eq. 8 gives the theoretical optimized value of $\alpha\eta \approx 10.24$. In actually, the optimized value of $\alpha\eta$ is slightly different with the theoretical value. Meanwhile, the R_{56} value of the dispersion section should also be optimized to achieve a better rotation inside the longitudinal phase space. In this simulation, the values of $\alpha\eta$ and R_{56} are optimized for the 40th harmonic of the seeding laser. The 3-D plot of the bunching factor optimization result is shown Fig. 1.

From Fig. 1, the optimized value is $\alpha\eta \approx 9.2$ and $R_{56} \approx 6.425 \times 10^{-5}$ m^{-1}. With such parameters, the longitudinal phase space after the density modulation of PEHG is shown in Fig. 2(a).

The longitudinal phase space modulated by a traditional HGHG with the similar parameters is also shown as a comparison (with a slight slippage to distinguish the two longitudinal phase space). It shows an obvious phase-merging

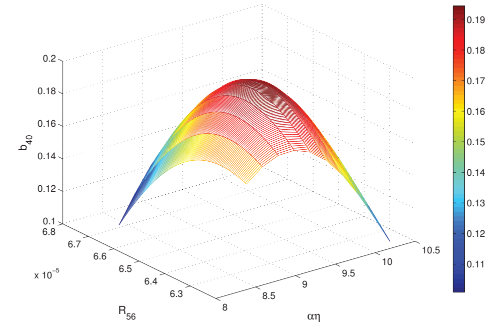

Figure 1: Optimization of the 40th harmonic of the seeding laser

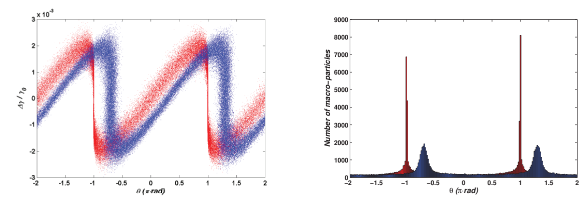

(a) (b)

Figure 2: Longitudinal phase space after dispersion section. PEHG in red and HGHG in blue for comparison. 2(a): Longitudinal phase space; 2(b): Particle distribution.

phenomenon around the phase $\theta = \pm\pi$ in the PEHG modulated phase space. Although there is also a broadening effect on other phase, the particle distribution shown in Fig. 2(b) indicates that most particles are concentrated near the phase $\theta = \pm\pi$. The length of this ultra-short longitudinal structure is less than 20 nm.

COHERENT THOMSON SCATTERING

The modulated bunch are used to collide with an incident laser pulse to generate coherent Thomson scattering radiation. For simplicity, only the head-on collision case (back-scattering) is considered. The incident laser has a wavelength $\lambda_L = 2$ mm, dimensionless vector potential $a_L \approx 1.0314$ and pulse length $\sigma_L = 2\lambda_L$. The electric field of the scattered radiation observed on the direction of electron motion (i.e., $\theta = 0$) is shown in Fig. 3. A single pulse length is about 600 atto-seconds. The radiation spectrum is shown in Fig. 4. The amplitude of radiation with phase-merged beam is significantly enhanced compared with the amplitude with out phase-merging, almost three order of magnitude. Since the dimensionless vector potential of incident laser is larger than 1, some higher harmonic components appears due to the non-linear effect of Thomson scattering. However, because of the coherence of the fundamental mode and incoherence of higher harmonics, the fundamental mode has much higher amplitude than the higher harmonics.

ISBN 978-3-95450-134-2

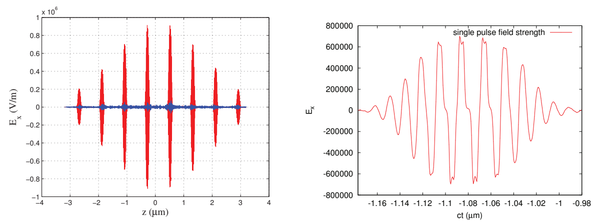

Figure 3: Electrical field strength distribution of the scattering radiation.

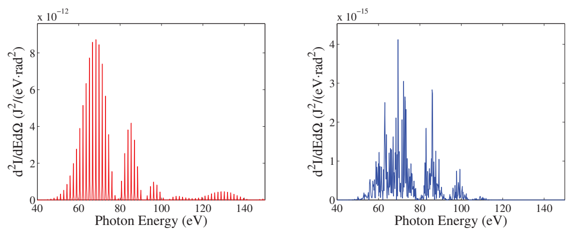

Figure 4: Spectrum of the scattered radiation.

INFLUENCE OF THE INITIAL TRANSVERSE EMITTANCE

In the simulation above, we assume the electron beam has a extremely small transverse emittance, i.e., in 1-D scene. We can get a set of ultra-short electron slices to generate coherent Thomson scattering radiation. However, in 3-D case, the effect of the initial transverse emittance which acts as a equivalent energy spread should be considered. The correlation between electron energy and it's transverse position after the dog-leg is smeared by the initial transverse distribution. In order to counteract this effect, the dispersion strength of dog-leg should be enlarged to provide a stronger transverse-longitudinal coupling and improve the resolution in TGU.

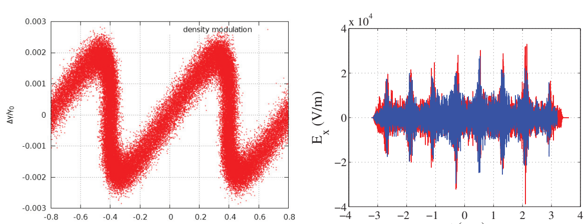

(a) $\eta = 0.2$ m, $\alpha = 46$ m^{-1}

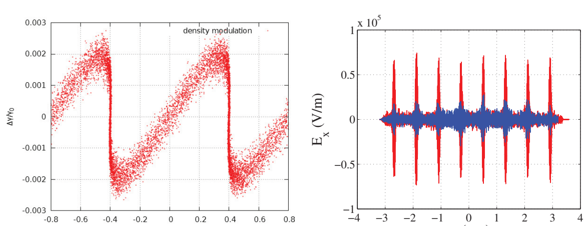

(b) $\eta = 2.0$ m, $\alpha = 4.6$ m^{-1}

Figure 5: 3-D simulation with the transverse emittance $\varepsilon_x = 1$mm·mrad

In Fig. 5, the results of 3-D simulation with initial transverse emittance $\varepsilon_x = 1$ mm·mrad are shown. By increasing the dispersion strength η, coherent radiation can still be obtained after Thomson scattering. We should also notice that because the longitudinal charge density also reduces because of a longer bunch length after the stronger dispersion, the amplitude of electric field is one order of magnitude lower than the 1-D result. Even though, it is still much stronger than the radiation without PEHG modulation.

SUMMARY

We have studied the coherent Thomson scattering radiation emitted by the head-on collision of the density modulated electron bunch and a long-wavelength laser pulse. Electron bunch is density modulated using the phase-merging effect in a TGU to generate ultra-short longitudinal structures (shorter than 20 nm) in the phase space and then scattering with an incident laser with 2 mm wavelength. The scattered radiation is significantly improved compared with the case using beam without phase-merging. Transverse emittance could be a possible limitation to this method. However, by increasing the dispersion strength of dog-leg, coherent radiation can still be obtained.

ACKNOWLEDGEMENT

The authors thank Prof. K. Liu and Dr. S. Huang of Peking University for their support. Thanks to Dr. Y. Ding of SLAC and Dr. H. Deng of SINAP for their helpful suggestion and discussion.

REFERENCES

[1] Chao, Alexander Wu, et al. *Handbook of accelerator physics and engineering, 2nd ed.*. Published by World Scientific Publishing Co. Pte. Ltd., 2013.

[2] Ohmi, K., et al., in Proceedings of IPAC2013, Shanghai, China, pp:1592-1594

[3] Kashiwagi, S., Kato, et al., Physics and Chemistry, 78(12), 1112–1115(2009).

[4] Wu, H.-C., Meyer-ter-Vehn, J., Fernández, J., & Hegelich, B. M., PRL, 104(23), 234801(2010).

[5] Deng, H., & Feng, C., PRL, 111(8), 084801(2013).

[6] Wang, G., Feng, C., Deng, H., Zhang, T., & Wang, D. . NIM A, 753(2014), 56–60

[7] Feng, C., Deng, H., Wang, D., & Zhao, Z. (2014). New Journal of Physics, 16(4), 043021

[8] Shimada, M., & Hajima, R., PRST-AB 13(2010), 100701

[9] Yu, L.H., PR A, 44(8), 5178–5193(1991).

[10] Yu, L.H., Wu, J., NIM A, 483(2002) 493-498.

ISBN 978-3-95450-134-2

RECENT PROGRESS IN UPGRADE OF THE HIGH INTENSITY THz-FEL AT OSAKA UNIVERSITY

G. Isoyama#, M. Fujimoto, S. Funakoshi, K. Furukawa, A. Irizawa, R. Kato, K. Kawase, A. Tokuchi, R. Tsutsumi, M. Yaguchi, ISIR, Osaka University, Ibaraki, Osaka 567-0047, Japan

Abstract

The THz-FEL based on the 40 MeV, L-band electron linac is working in the wavelength region from 25 to 150 μm or in the frequency region from 2 to 12 THz. For basic study on FEL physics and its applications, the linac and the FEL are upgraded to have higher stability and intensity in operation of the FEL. The high voltage power supply of the inverter type is remodelled and the solid state switch is developed in place of the thyratron for the klystron modulator, so that fractional variations of the klystron voltage are reduced from 2×10^{-4} to 8×10^{-6} (rms). As a result, fractional variations of the FEL macropulse energy are reduced to 2.4 % (rms). A new grid pulser for the thermionic electron gun of the linac is developed, which generates a series of pulses with the duration of 5 ns at intervals of 36.8 ns. Using the grid pulser, charge in an electron bunch is increased four times higher though the bunch intervals quadruple, so that the micropulse energy increases more than ten times higher than that in the conventional operation mode. The maximum micropulse energy in the new operation mode exceeds 0.1 mJ/micropulse at wavelengths around 70 μm (4.3 THz). Application experiments have begun using the high intensity and stable FEL beam.

INTRODUCTION

We have been conducting a free-electron laser based on the L-band electron linac at the Research Laboratory for Quantum Beam Science of the Institute of Scientific and Industrial Research (ISIR), Osaka University. The first lasing was achieved in 1994 at wavelengths from 32 to 40 μm. We then began remodelling the FEL to expand the wavelength region towards the longer wavelength side and obtained lasing at 150 μm or 2 THz in 1998 [1], which was the longest wavelength at that time obtained with FELs based on RF linacs. However, the intensity of the FEL was not high enough to reach the power saturation level and its stability was low because the linac was constructed in 1970s and not for FEL. We had an opportunity to upgrade the linac for higher stability and reproducibility in operation in 2003. In doing so, we have added a new operation mode for FEL, in which the RF pulse duration is increased from 4 μs for the standard operation mode to 8 μs, and the number of amplifications is increased not twice but three times higher because the first 2 μs part of the electron pulse is lost in the FEL beam line owing to an energy variation there generated by the filling time of the RF power and the onset of the beam loading in the acceleration tube of the linac. As a result, the FEL is operated in the high intensity reaching power saturation and operational stability is significantly improved [2].

We have been upgrading the THz-FEL further. In this paper, we will report results of the recent progress of the FEL in stability and power.

STABILIZATION

The stability of the FEL output power is crucial for basic study on FEL and its applications. It depends strongly on stability of the linac and hence all the possible measures at that time were taken in the previous remodelling of the linac. Nevertheless, the macropulse energy of FEL fluctuated by some tens of a percent. Crucial parameters for the linac stability are the RF power and its phase provided to the 1.3 GHz RF structures, including the pre-buncher, the buncher, and the 3 m long acceleration tube. These parameters strongly depend on the voltage generated with the klystron modulator and applied to the klystron. The stability of the klystron voltage V_k is primarily determined by a high voltage power supply of the klystron modulator. The large energy

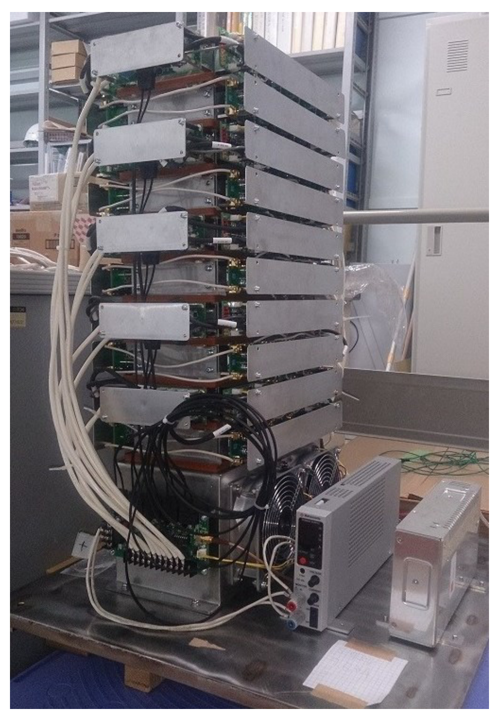

Figure 1: Solid state switch 2nd model for the klystron modulator. The maximum holding volate is 25 kV and the peak current is 6 kA for 8 μs pulses at a repetition frequency of 60 Hz.

#isoyama@sanken.osaka-university. ac.jp

ISBN 978-3-95450-134-2

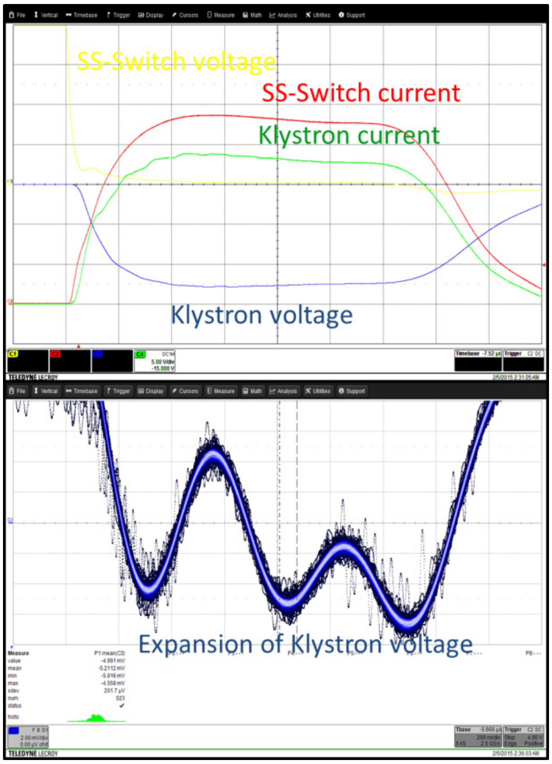

Figure 2: Voltage and current waveforms of the solid state switch and those of the klystron (upper panel) and expansion of the klystron voltage (lower panel). The klystron voltage in the lower panel is 523 pulses overlaid on the screen and its fractional variation is 8×10^{-6} (rms) or 8 ppm.

fluctuation of the FEL pulses indicates that the high voltage power supply we used is not stable enough, which is an inverter type power supply charging the PFN with fractional stability of $\sim10^{-3}$ or less. The two step charging process is employed to charge the PFN with the power supply; the coarse charging to 90 % in steps of 0.5 % and the fine charging to a target voltage by reducing the width of charging pulses. In order to make the stability higher, a new charging procedure has been developed. Instead of the pulse-width modulation circuit, a sub charging line with higher impedance is added to reduce charge per pulse, and the charging line is switched from the main line to the sub one when the PFN voltage reaches 99 % of the target value and the fine charging continues in steps of an order of 10^{-5} in the remaining part to the target value. The stability of the charged PFN voltage is measured to be 8×10^{-6} (rms), which is measured using a differential amplifier (Lecroy DA1855A). The measured value is significantly smaller than that obtained with the previous system.

The PFN is discharged using a thyratron and high voltage pulses are generated for the klystron. The fractional stability of the klystron voltage should be equal to that of the PFN voltage, but the measured stability of the klystron voltage is 2×10^{-4}, which is much larger than the stability of the PFN voltage, 8×10^{-6}. The source of the instability is considered to be the thyratron, which is a gas filled discharge tube. We have developed a solid state switch that can replace the thyratron [3]. The switch is made of sixty static induction thyristors; ten of them connected in series with six such connected in parallel. The maximum specifications of the solid state switch are a holding voltage of 25 kV and a pulse duration of 8 μs at a repetition frequency of 10 Hz, which are sufficient for operation of the linac. Figure 1 shows a photograph of the second model of the solid state, which is improved compared to the first model in that an operation mode can be chosen by changing wirings in the switch between 25 kV/6 kA and 50 kV/3 kA to be used for common klystron modulators and that the repetition rate is increased from 10 Hz to 60 Hz by reinforcement of the air cooling system. As shown in Fig. 2, the stability of the klystron voltage is measured for the second model using the differential amplifier to be $dV_k/V_k = 7.8\times10^{-6}$, which is nearly equal to that of the high voltage power supply for PFN charging, so that the stability of the solid state switch is much higher than that of the high voltage power supply. As a result of introduction of the solid state switch, the fluctuation of the FEL macropluse energy is reduced from 5.4 % for the thyratron to 2.4 % for the solid state switch.

HIGH POWER OPERATION

In the conventional mode of linac operation for FEL, which is named the 108 MHz mode, the grid pulser for

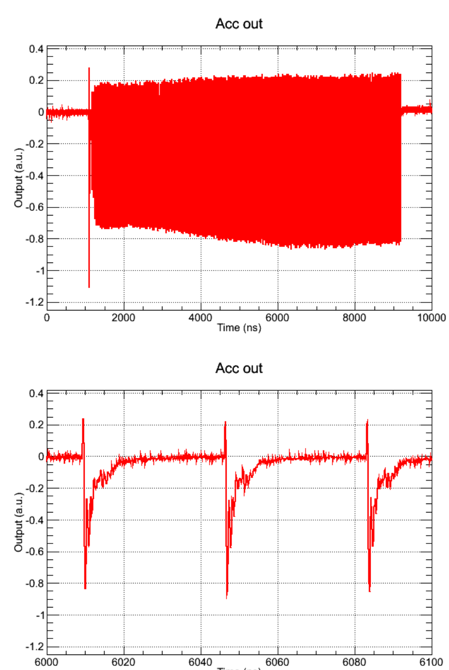

Figure 3: Electron beam current measured with a core monitor at the exit of the linac operated using the 27 MHz grid pulser. The upper panel shows the whole electron pulse of an 8 μs duration and the lower panel is its expansion showing electron bunch singals at 36.8 ns intervals.

ISBN 978-3-95450-134-2

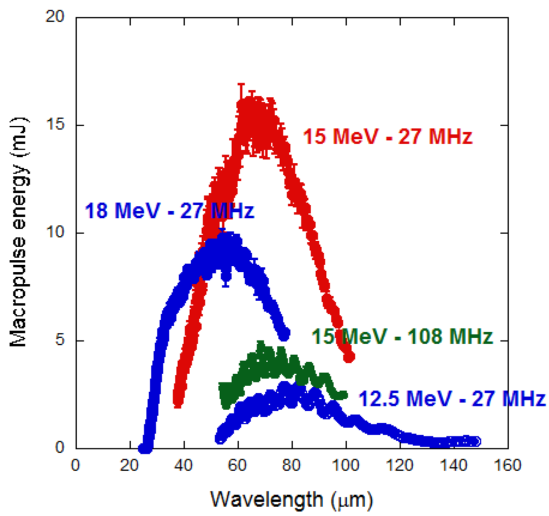

Figure 4: Macropulse energy measured with an energy meter in various operation modes at the zero detning by varying the wiggler gap.

the thermionic cathode generates 8 μs long square pulses and the electron gun generates rectangular pulses with the same duration and a peak current of 0.6 A. The second 108 MHz and the 216 MHz cavities of the three-stage sub-harmonic buncher (SHB) system are excited, so that a series of bunches, each of which has 1 nC charge, separated by 8.2 ns and continuing for 6 μs are generated at the FEL. The roundtrip time of FEL pulses in the optical cavity is 36.8 ns, so that four FEL pulses lase independently in the cavity. The electron current injected to the linac is limited by the beam loading in the acceleration tube and the current of 0.6 A in the 108 MHz mode is the maximum. In order to increase the bunch charge while maintaining the average beam current, we have developed a new grid pulser for the electron gun to generate a series of electron pulses with 5 ns duration and a peak current of 2.4 A continuing at intervals of 36.8 ns for 8 μs so that a single FEL pulse can develop in the optical cavity. The electron beam from the gun has a frequency component of 108 MHz, so that all the SHB cavities are excited to generate an electron beam with uniform energy over 6 μs for FEL. Figure 3 shows the electron beam measured at the exit of the linac using a core monitor and its expansion in time. The new

Table 1: Main Parametrs of the THz-FEL

Wavelength/Frequency range	25~150 μm/2~12 THz
Repetition frequency	10 Hz
Macropulse length	3 ~ 4 μs
Micropulse length	< 20 ps
(High power mode / Conventional mode)	
Macropulse energy	10~27 / 3~10 mJ at 70~80 μm
Micropulse intervals	36.8 / 9.2 ns
Micropulse energy	100~260 / 10~30 μJ

operation mode of the linac named the high power mode or the 27 MHz mode is successfully commissioned and electron bunches with charge of 4 nC/bunch continuing at intervals of 36.8 ns for 8 μs are generated and transported to the FEL [4].

The FEL is successfully operated in the 27 MHz mode at an electron energy of 15 MeV. As can be seen in Fig. 4, the macropulse energy of the FEL is measured to be higher than 10 mJ at wavelengths around 70 μm, which is more than three times higher than that obtained in the 108 MHz mode. The number of micropulses in the 27 MHz mode is approximately 100, which is a quarter of that in the 108 MHz mode, so that the micropulse energy exceeds 0.1 mJ, which is ten times higher than the value obtained in the 108 MHz mode.

CHARACTERIZATION

The main parameters of the THz-FEL are listed in Table 1. The characteristics of the FEL have been measured, including detuning curves, wavelength spectra, macropulse structures consisting of many micropulses measured with fast THz detectors, time structures of micropulses using a Michelson interferometer, and so on. Two examples among them are shown below.

Figure 5 shows wavelength spectra of the FEL operated in the 108 MHz mode at the electron energy of 15 MeV and an optical cavity detuning for the maximum FEL gain by varing the wiggler gap in steps of 1 mm. The wavelength can be varied from 50 to 105 μm or from 2.9 to 6 THz for the fixed electron energy of 15 MeV. Another example is an interferogram shown in Fig. 6, which is measured for the micropulses in the 27 MHz mode operated at 15 MeV, the wiggler gap 30 mm, the wavelength 105 μm, and the zero-detuning position, where the macropulse energy is highest. The fine

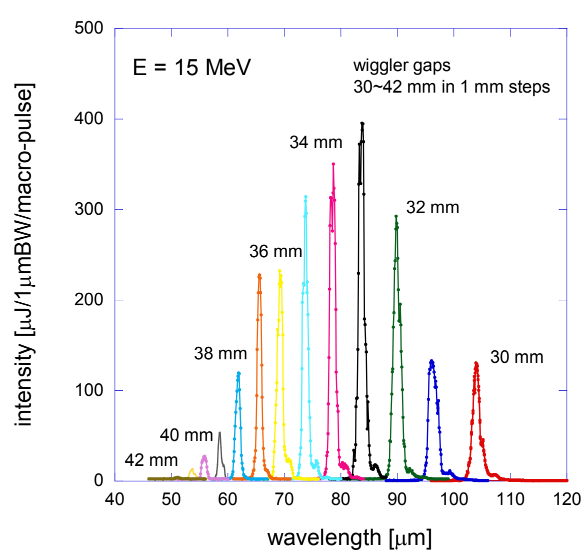

Figure 5: Wavelength spectra measured with a monochrometer in the conventional operation mode (108 MHz mode) of the FEL at the electron energy of 15 MeV by varying the wiggler gap.

ISBN 978-3-95450-134-2

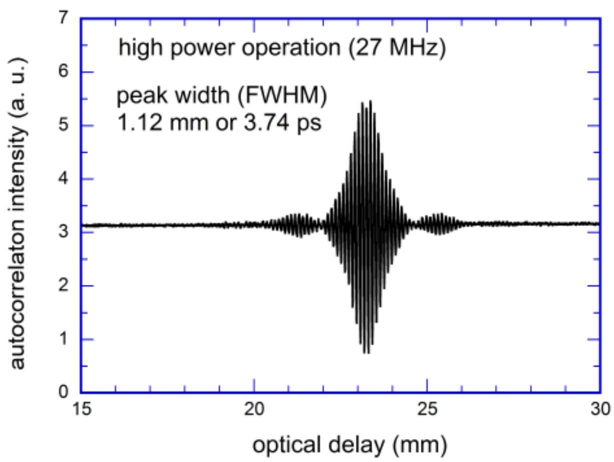

Figure 6: Autocorrelation pattern of FEL micropulses measured with a Michelson interferometer and an energy meter in the high power mode (27 MHz mode) at the electron energy of 15 MeV, the wiggler gap of 30 mm, and the zero detuning. The wavelength is 105 µm.

structure is due to interference of the monochromatic light, so that intervals of the interferences are a half of the wavelength 105 µm. The width of the interference peak is 1.12 mm or 3.74 ps. If it is assumed that the peak width is equal to twice the micropulse duration, though there are some discussions on interpretation of the interference pattern, the micropulse duration is estimated to be 0.6 mm or 2 ps.

APPLICATIONS

We began application experiments with spectroscopic and imaging studies using the THz-FEL. A Czerny-Tuner monochromator is used for spectroscopic studies. The wiggler gap for the FEL and the wavelength of the monochromator are synchronously scanned to measure a high resolution spectrum. Figure 7 shows an transmission spectrum of water vapor in the air measured with the FEL operated in the conventional mode and compared with a

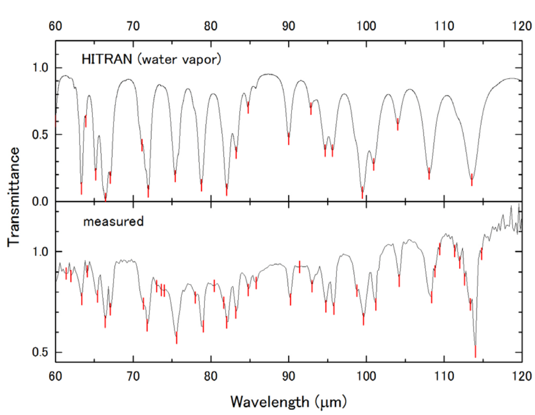

Figure 7: Transmission spectrum of water vapor in the air measured with the FEL in the conventional mode (lower panel) and calculated one of HITRAN (upper panel).

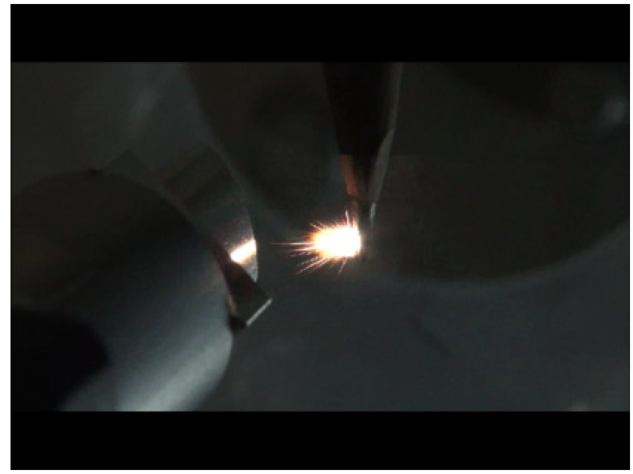

Figure 8: Spark generated by the FEL beam in the high power mode or the 27 MHz mode focused on the lead of a pencil using an off-axis paraboloidal mirror with a focal length of 12.5 mm.

calculation of HITRAN. The measure fine structures are in good agreement with the calculated ones. Another example is a wavelength resolved imaging by the raster method. The FEL is also used for measurement of characteristics of THz cameras conducted in collaboration with NEC Corporation [5].

In the high intensity operation of the FEL, the FEL beam can make aerial discharge and a plume on a pencil lead, as shown in Fig. 8, when it is focused with an off-axis paraboloidal mirror with a focal length of 12.5 mm. The peak power of the micropulse at a wavelength around 70 µm or 4.3 THz is calculated to be P = 50 MW for the micropulse energy 0.1 mJ and the duration of 2 ps. The FEL beam coming out through the window of the evacuated beam line to the experimental station is nearly circular and its size is measured to be σ_r = 1.7 mm (rms). When it is focused using the mirror with f = 12.5 mm, the focused beam radius is estimated to be 47 µm (rms) using the relation for diffraction-limited light, $\sigma_r \times \sigma_r' \sim \lambda/4\pi$, and the cross sectional area of the FEL beam at the focal point is calculated to be $S = \pi\sigma_r^2 = 7.0\times10^{-5}$ cm^2. Then the power density there is calculated as I = P/S = 0.7 TW/cm^2, from which the electric field and the magnetic field are calculated as

$$\mathrm{E\,[V/cm]} = 27.5 \times \sqrt{I\,[\mathrm{W/cm^2}]} = 27\,[\mathrm{MV/cm}] \quad (1)$$

$$\mathrm{B\,[T]} = \mathrm{E\,[V/m]}/c = 9\,[\mathrm{T}] \quad (2)$$

Using this high intensity THz radiation, studies on various non-linear effects are being conducted in collaboration with some groups working on THz science and technology [6].

SUMMARY

The recent progress in development of the THz-FEL at ISIR, Osaka University was reported. Pulse-to-pulse fluctuations of FEL macropulse energy are reduced by upgrading the high voltage power supply and the

ISBN 978-3-95450-134-2

introduction of the solid state switch for the klystron modulator. Application experiments have begun using the stable and intense THz beam.

ACKNOWLEDGMENT

A part of this work was supported by JSPS KAKENHI Grant Numbers 24310069 and 24651102.

REFERENCES

[1] R. Kato et al., Nucl. Instrum. Methods Phys. Res., Sect. A 429 (1999) 146.
[2] G. Isoyama et al., Infrared Phys. Technol. 51 (2008) 371.
[3] A. Tokuchi et al., Nucl. Instrum. Methods Phys. Res., Sect. A 769 (2015) 72.
[4] S. Suemine et al., Nucl. Instrum. Methods Phys. Res., Sect. A 773 (2015) 97.
[5] N. Oda et al., Proc. of SPIE Vol. 9102 910202, (5-6 May 2014, Baltimore, Maryland, USA).
[6] M. Nagai et al., Proc. of IRMME-THz 2014, (14-19 September 2014, Zcson, Arizona, USA), IEEE 10.1109/IRMMW-THz.2014.6956352.

ISBN 978-3-95450-134-2

PERFORMANCE AND TOLERANCE STUDIES OF THE X-RAY PRODUCTION FOR THE X-BAND FEL COLLABORATION

J. Pfingstner*, E. Adli, University of Oslo, Oslo, Norway

Abstract

The X-band FEL collaboration is currently designing an X-ray free-electron laser based on X-band acceleration technology. This paper reports on the recent progress on the design of the undulator part of this machine including simulations of the X-ray production process. The basic parameters have been chosen and a beam transport system has been designed, considering strong and weak focusing of quadrupole and undulator magnets. Simulations of the X-ray production process have been carried out with realistic input beam distributions from particle tracking studies of the linac design team. The expectable X-ray properties for SASE and seeded FEL operation have been investigated and also undulator taper options have been studied.

INTRODUCTION

The X-band collaboration is a group of 12 institutes and universities with the common interest of using X-band acceleration technology for FEL applications. The higher acceleration gradients achievable with X-band structures allow making linacs shorter and more power efficient as S-band and C-band linac used nowadays. The recent advances in the X-band technology [1] have encouraged the X-band collaboration to design a soft and a hard XFEL based on the X-band technology [2]. An important part of this effort is the design of the undulator section and the simulation of the X-rays production process, which is the subject of this paper. Topics that will be covered are the basic parameter choice, the beam transport lattice, and the simulations of the most important X-ray parameters for different modes of operation.

UNDULATORS AND ELECTRON BEAM

The parameter of the electron beam and the undulator section are chosen by taking into account the experience of existing facilities, e.g. SwissFEL [3] and LCLS [4]. The undulator section consists of 13 permanent magnet undulators [5] of each 3.96 m in length. The undulator magnets have a period length λ_u of 15 mm and a maximal undulator parameter K of 1.3, which allows reaching an X-rays wavelength of 1 Å with a beam energy of 6 GeV. The modules are separated by gaps of 0.72 m to provide space for quadrupole magnets, beam position monitors, beam loss monitors and phase shifters. The quadrupole magnets are used to control the beam size (FODO lattice) as will be discussed below.

With the described undulator parameters, a beam energy of about 6 GeV is necessary to reach the specified X-ray wavelength of 1 Å. The beam current has to be >3 kA to enable the production of X-ray with on a GW level, and to achieve a reasonably short saturation length. Preferably the beam current should be uniform along the bunch, which implies a bunch charge of 200 pC assuming a bunch length of about 15 μm. To keep the electrons and the X-rays in a resonance condition, there are limits on the transverse emittance ϵ and the energy spread σ_E of the electron beam [6], which are for the chosen parameters <0.3 μm and <2x10^{-4}, respectively.

An electron beam B0 with the stated properties has been created artificially and will act in the performed simulations as a reference. Complementary, two beams, B1 and B5, have been provided by the linac team, which have been created with particle tracking using PLACET [7]. In contract to B0, the bunch charge of B1 and B5 is 250 pC. The two beams correspond to different bunch compressor setups. As can be seen in Fig. 1, neither B1 nor B5 reach the specified beam current yet, since the optimisation of the linac and the bunch compressors is an on-going effort.

BEAM TRANSPORT SYSTEM

The electron beam size is controlled in the undulator section due to the focusing of the quadrupole magnets, which are located in the gap between the undulator magnets. The magnet strengths are adjusted to form a FODO lattice. The size of the β-function is a trade off between high current density (small β-function), and small longitudinal velocity change of the electrons due to their betatron motion (large β-function). An expression for the optimal average β-function β_{opt} has been derived in [8] and is for our parameters 15 m.

If only the strong focusing of the quadrupole magnets is considered, the lattice design can be performed with simple

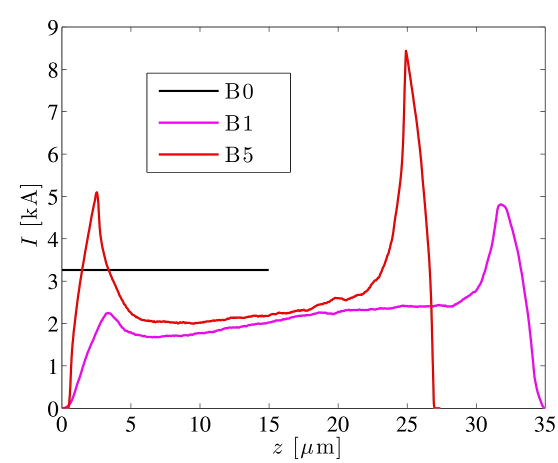

Figure 1: Current profile along the different considered bunches. B0 is an artificially created reference bunch.

* juergen.pfingstner@cern.ch

ISBN 978-3-95450-134-2

analytic expressions. However, also the weak focusing of the magnets in vertical direction (due to the pole fringe fields) has to be taken into account. For this reason, a generalised FODO lattice is used, where different magnet strengths K_1 and K_2 for the focusing and defocusing quadrupole magnets can be chosen. This additional degree of freedom allows compensating the distortion of the β-function due to the weak focusing, and a periodic solution can be found.

To find such magnet strengths K_1 and K_2 the following optimisation problem was implemented in OCTAVE [9]

$$\min_{K_1,K_2} J(K_1, K_2), \tag{1}$$

where the target function J represents the quadratic error of horizontal and vertical β-functions for the magnet strengths K_1 and K_2 from β_{opt}

$$J(K_1, K_2) = \sum_{i\in\{x,y\}} \left(\frac{\sqrt{\beta_{i,1}} + \sqrt{\beta_{i,2}}}{2} - \sqrt{\beta_{opt}} \right)^2 .$$

The β-functions at the centres of the focusing and defocusing magnets $\beta_{x,1}$, $\beta_{x,2}$, $\beta_{y,1}$ and $\beta_{y,2}$ are calculated from the according beam transport matrices M as [10]

$$\beta_{x,1} = \frac{M_{x,1}(1,2)}{\sin(\mu_{x,1})} \quad \text{with}$$
$$\mu_{x,1} = \operatorname{acos}\left(\frac{\operatorname{trace}\,(M_{x,1})}{2} \right).$$

In this case $M_{x,1}$ is the horizontal beam transport matrix for one FODO period starting from the centre of the quadrupole magnet with strength K_1. The matrices M are computed by the multiplication of the transport matrices of the individual elements. While an undulator magnet is modelled as a simple drift space in the horizontal direction, the vertical transport matrix is given by

$$M_{y,U} = \left(M_{y,P/2}\right)^{2N_p},$$

where N_p is the number of undulator periods of length λ_u, and $M_{y,P/2}$ is the transport matrix of one undulator pole given by

$$M_{y,P/2} = \begin{bmatrix} 1 & 0 \\ -\frac{1}{f_f} & 1 \end{bmatrix} \begin{bmatrix} 1 & \lambda_u/2 \\ 0 & 1 \end{bmatrix} \begin{bmatrix} 1 & 0 \\ -\frac{1}{f_f} & 1 \end{bmatrix}. \tag{2}$$

Eq. 2 represents fringe field kicks at the entrance and the exit of a magnet pole and a drift space in between the poles. The kick strength $1/f_f$ of the vertical fringe fields is given by [10]

$$\frac{1}{f_f} = \frac{\pi^2 K^2}{2\gamma^2 \lambda_u},$$

where γ is the relativistic factor of the electron beam. The OCTAVE optimisation routine `fminsearch` was used successfully to find a solution to the optimisation problem Eq. 1. In tracking simulations with GENESIS [11], it has been verified that the corresponding β-functions are regular and of the desired size β_{opt} in both transverse dimensions.

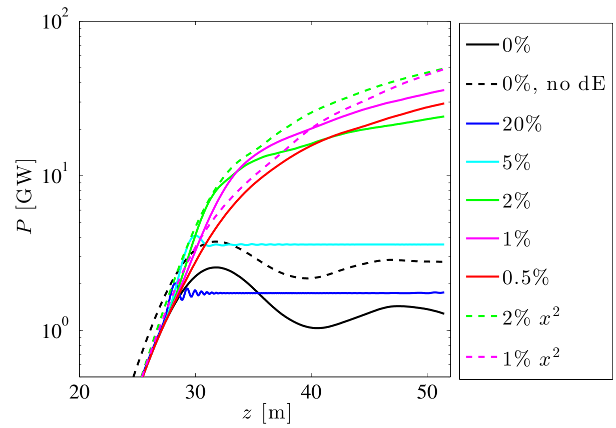

Figure 2: X-ray power along the undulator section for different undulator taper types. The percentage mentioned in the label corresponds to the decrease of the undulator parameter K at the end of the undulator section.

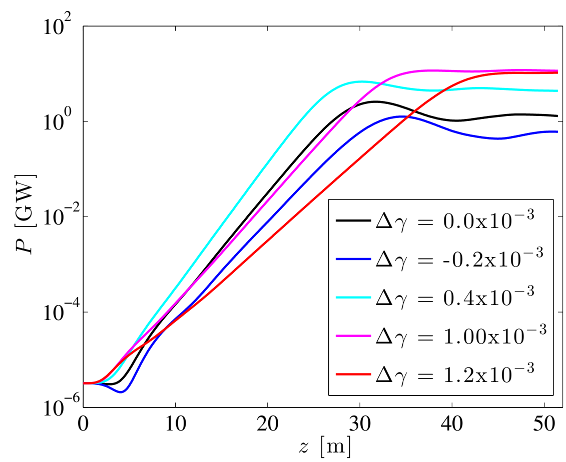

Figure 3: X-ray power along the undulator section for seeded operation with different beam energy detuning $\Delta\gamma$.

SIMULATION STUDIES

The studies of the X-ray production process are mainly carried out with the help of simulation with the FEL code GENESIS [11]. The plausibility of the results is checked with analytical estimates known from FEL theory, e.g. [6]. In the following, the performed simulations will be grouped according to the used simulation mode. Single micro-bunch simulations can be performed very rapidly and are a good approximation for the operation with a strong seed laser. Even though single micro-bunch simulations can be used to study many effects, computationally much more expensive multiple micro-bunch simulations are necessary to be able to take into account all properties of the used electron beam. This is in particular necessary to study the SASE process.

Before the study of the X-ray production process started, suitable simulation parameters were determined. In systematic studies it was found that a particle number per slice of 2^{13} was sufficient. Also it was found that space charge

ISBN 978-3-95450-134-2

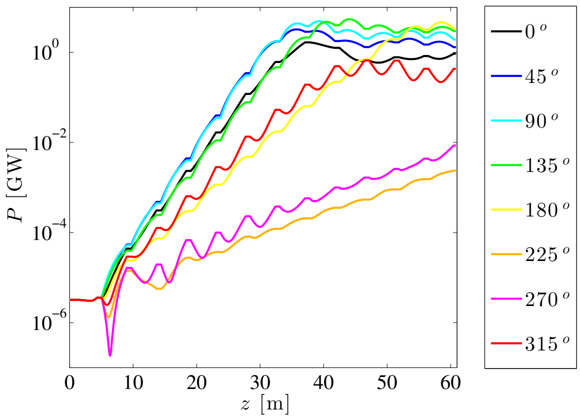

Figure 4: X-ray power along the undulator section for different phase mismatches between electron and X-ray beam introduced in the gaps between the undulator magnets.

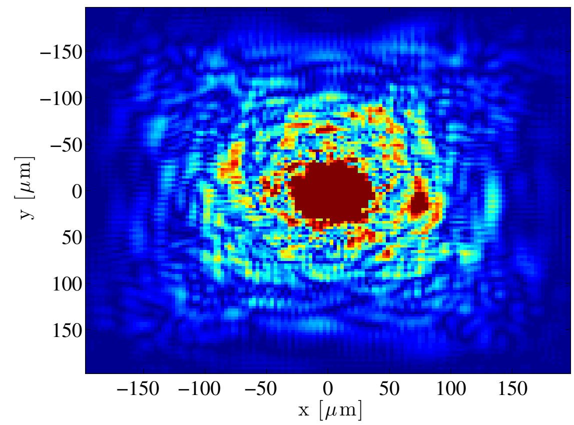

Figure 5: Transverse X-ray intensity at the end of the undulator section created with beam B0 in seeded operation.

effects have a negligible effect on the X-ray production, due to the high energy of the electron beam. Hence, the time-consuming space charge calculation was turned of in the GENESIS simulations. Also the effect of incoherent synchrotron radiation was investigated. While the corresponding beam energy spread increase can be neglected, the average association beam energy loss has a rather strong impact on the simulation results and has to be taken into account, as can be seen from the solid and dashed black lines in Fig. 2.

Single Micro-Bunch Simulations

The produced X-ray power for a seeded operation is around 1–2 GW with an saturation length of 32 m, as can be seen in Fig. 2 (solid black line). Since in this particular simulation the gaps have not been considered, the saturation length including gaps is about 37 m, which has been confirmed with simulations including the gaps.

To increase the X-ray power further, undulator strength tapering can be applied [12]. The effect of linear and quadratic tapers has been evaluated and the results are shown in Fig. 2. The tapering starts to decrease the undulator parameter K at 27 m up to a maximal percentage at the end of the undulator section. With a quadratic taper of 1–2%, the X-ray power can be increased to 52 GW. From these results it is also clear that tapering is not only compensating the beam energy loss by restoring the undulator resonance condition. This would only result in an X-ray production corresponding to the dashed black line, where the energy loss has been turned of artificially in the simulation. Instead, tapering is keeping the electrons at a relative phase with respect to the X-rays such that they continuously lose energy in the saturation regime, instead of performing synchrotron oscillations. A similar effect can be achieved in seeded operation, if the beam energy is chosen slightly higher than given by the resonance condition. With an energy detuning of 1 per mil, the X-ray power can be increase to 10 GW, as can be seen in Fig. 3.

In Fig. 4, the effect of a phase mismatch of the electron beam and the X-rays due to a wrong length of the undulator gaps has been investigated. The black curve shows the X-ray power when the resonance condition is perfectly maintained. Interestingly, for a large range of phase shifts the output power is increased, since the electrons are moved to a relative phase with respect to the X-rays where they lose more energy as for the nominal condition. This suggests that phase shifters could be used as an alternative to tapering to increase the X-ray power. The simulation results also indicate that the necessary phase shifter resolution should be in the order of 10-20°, which is consistent with phase shifter designs from existing facilities.

In Fig. 5, the intensity distribution of the X-rays (no tapering) at the end of the undulator section is shown. The plot is saturated in the centre where the highest X-ray power is located. This high intensity area is at the same location as the electron beam and both have about the same size. The corresponding X-rays have been created shortly before the end of the undulator (near field radiation). The radiation further away from the electron beam is of lower intensity. It has been produced further upstream in the undulator section and has diffracted to larger distances from the centre (far field radiation).

Multiple Micro-Bunch Simulations

Simulations with multiple micro-bunches are computational expensive. For the beams B0, B1 and B5, a total number of 6393, 14625 and 11433 micro-bunches have been simulated, respectively. This corresponds to a simulation of each 24th micro-bunch of the real beam, which is sufficient according to the suggested parameter choice of GENESIS. The simulations have been performed on a 32-core computer with the MPI parallelised version of GENESIS. One simulation takes about 2 1/2 hours with this setup.

The average power of the X-ray pulse along the undulator section for different beam distributions is depicted in Fig. 6. For the seeded operation, a seeding laser power of 10 kW

ISBN 978-3-95450-134-2

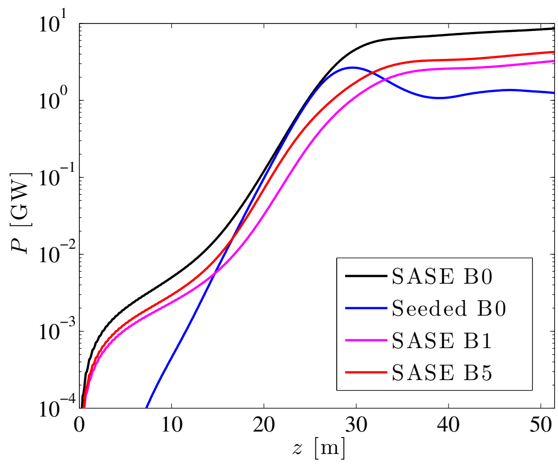

Figure 6: Average power of the X-ray pulse plotted along the undulator section. Different electron beams are considered in SASE and seeded mode.

was used, and the shot noise of the electron beam was artificially turned off. The simulations show, that the beam B0 produces 9 GW of X-ray power in the SASE mode, which is significantly more than the corresponding 1–2 GW produced in seeded operation.

Also the performance of the beam distributions created from tracking simulations with an realistic lattice setup has been evaluated. Both beams, B1 and B5, cannot reach the same X-ray power level as the benchmark beam B0. As a reason for the worse performance, the lower peak current of these beams has been identified (see Fig. 1). The currently produced beams will have to be shortened in the future to reach the necessary 3 kA. Even though B5 is shorter than B1, the produced X-ray power is hardly increased compared to B1. This is due to the fact that the current is only larger at spikes at the head and the tail of the bunch, where also the energy spread is increased, which inhibits the X-ray production process. This outcome is a valuable input for the linac and bunch compressor team as a guideline for their design.

CONCLUSIONS

The design of the undulator section and the simulations of the X-ray production process for the hard X-ray FEL of the X-band collaboration have been described. For the chosen parameters, the expectable X-ray power level is 1–2 GW and 9 GW for SASE and seeded operation, respectively. The saturation length of the FEL process is about 37 m including the gaps between undulator magnets and the expectable spectral bandwidth is 1 per mil at the end of the undulator section. Also advanced methods to increase the X-ray output power have been studied, such as tapering, detuning and a phase shifting with phase shifter magnets. For a quadratic taper of 1–2‰ the X-ray power can be increase to 52 GW.

In collaboration with the linac and bunch compressor team, different realistic electron beam distributions have been studied with respect to the X-ray power produced by them. This effort has resulted in design guidelines that will help to improve the overall performance of the proposed XFEL facility. In the future, it is planned to perform tolerance studies and investigate the influence of resistive wall wakefields on the X-ray production. Also, the undulator magnet parameter will be re-evaluated with the intention to minimise the cost of the overall XFEL facility.

REFERENCES

[1] A. Degiovanni et al., *High-gradient test results from a CLIC prototype accelerating structure: TD26CC*, In Proc. of IPAC14, WEPME015 (2014).

[2] J. Pfingstner et al., *The X-band FEL collaboration*, In Proc. of FEL15, TUP013 (2015).

[3] SwissFEL CDR, *SwissFEL Conceptual Design Report*, PSI Bericht Nr. 10-04 (2012).

[4] LCLS CDR, *Linac Coherent Light Source (LCLS) Conceptual Design Report*, SLAC-R-593 (2002).

[5] J. A. Clarke, *The Science and Technology of Undulators and Wigglers*, Oxford University Press 2004, ISBN 978-0-19-850855-7.

[6] P. Schmüser et al., *Free-Electron Lasers in the Ultraviolet and X-Ray Regime*, Springer International Publishing Switzerland 2014, ISBN 978-3-319-04080-6.

[7] D. Schulte et al., *The PLACET Tracking Code*, `http://clicsw.web.cern.ch/clicsw/`.

[8] E. L. Saldin et al., *Design Formulas for VUV and X-Ray FELs*, In Proc. of FEL04, MOPOS15 (2004).

[9] J. W. Eaton. Octave. `www.gnu.org/software/octave`.

[10] H. Wiedemann, *Particle Accelerator Physics*, Springer-Verlag Berlin Heidelberg 2007, ISBN: 978-3-540-49043-2.

[11] S. Reiche, *GENESIS 1.3*, `http://genesis.web.psi.ch/`.

[12] D. Ratner et al., *FEL gain length and taper measurements at LCLS*, In Proc. of FEL09, THOA03 (2009).

ISBN 978-3-95450-134-2

PLANS FOR AN EEHG-BASED SHORT-PULSE FACILITY AT THE DELTA STORAGE RING*

S. Hilbrich†, F.H. Bahnsen, M. Bolsinger, M. Jebramcik, S. Khan, C. Mai, A. Meyer auf der Heide, R. Molo, H. Rast, G. Shayeganrad, P. Ungelenk,
Center for Synchrotron Radiation (DELTA), TU Dortmund University, 44227 Dortmund, Germany

Abstract

The 1.5-GeV synchrotron light source DELTA, operated by the TU Dortmund University, includes a short-pulse facility based on the coherent harmonic generation (CHG) technique, which allows for the generation of radiation pulses with wavelengths down to 53 nm and durations of 50 fs. In order to reach even shorter wavelengths, the present setup will be modified to employ the echo-enabled harmonic generation (EEHG) and femtoslicing techniques.

INTRODUCTION

At DELTA, a 1.5-GeV synchrotron light source operated by the TU Dortmund University (see Fig. 1), ultrashort coherent synchrotron radiation pulses are provided by a short-pulse facility [1] based on coherent harmonic generation (CHG) [2]. The goal is to generate radiation at wavelengths down to 53 nm with a pulse duration of 50 fs. In order to access even shorter wavelengths, the present facility will be modified [3] to employ the echo-enabled harmonic generation (EEHG) technique [4] and the femtoslicing scheme [5] as additional radiation sources.

Coherent Harmonic Generation

As part of the CHG technique [2], the electron energy is modulated sinusoidally by a co-propagating laser pulse in an undulator (modulator). The laser pulse is typically 1000 times shorter than the electron bunch in the storage ring. Downstream of the modulator, the electrons pass a magnetic chicane resulting in a microbunching which gives rise to coherent radiation at the laser wavelength or harmonics thereof in a second undulator (radiator). The bunching factor characterizes the correlation between the longitudinal positions of the electrons with respect to the laser wavelength λ and is defined as [6]

$$b_n = \frac{1}{N}\left|\sum_{k=1}^{N} e^{-2\pi i z_k n/\lambda}\right|, \qquad (1)$$

where n is the harmonic number, N is the number of electrons and z is the longitudinal position of an electron. The power of the CHG radiation scales as $P_n(\lambda) \sim N^2 b_n^2(\lambda)$ with $b_n(\lambda) \sim e^{-n^2}$ [7, 8]. This short-pulse technique can only be employed if the intensity of the short coherent pulse is higher than that of the long incoherent background ($\sim N$). This is the case for harmonics up to $n \approx 5$.

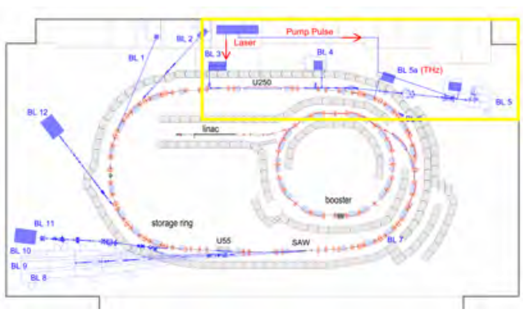

Figure 1: Sketch of the synchrotron light source DELTA. The yellow frame marks the CHG facility in the northern part of the storage ring. Synchrotron radiation is provided by dipole magnets, the undulators U55, U250 and the superconducting asymmetric wiggler (SAW).

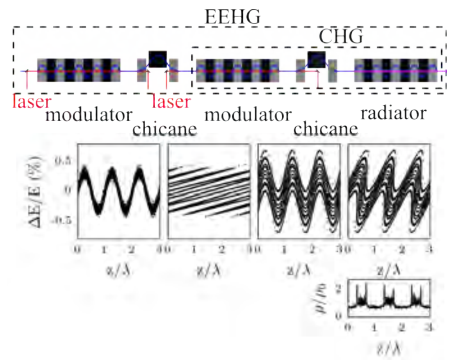

Figure 2: Top: Schematic view of the EEHG and CHG setup. Center: The electron distribution in longitudinal phase space (relative energy deviation $\Delta E/E$ versus longitudinal coordinate z in units of the laser wavelength λ) before and after the first and second chicane. Bottom: Electron density distribution after the second chicane in the case of EEHG.

Echo-Enabled Harmonic Generation

The EEHG scheme [4], which was originally proposed for FEL seeding, requires one more modulator and chicane compared to the CHG setup. In the first modulator, the electron energy is modulated sinusoidally with the periodicity of the laser wavelength. In the first chicane, the electron distribution is strongly sheared in the longitudinal phase space (see Fig. 2). In the second modulator, the electron energy is modulated again with a second laser pulse and in the following chicane, a density modulation with high harmonic content is generated. For EEHG, the bunching factor scales as $b_n(\lambda) \sim n^{-1/3}$, if the energy modulation amplitude and chicane strength are optimized for each harmonic [9].

* Work supported by DFG, BMBF, FZ Jülich and by the Federal State NRW.
† svenja.hilbrich@tu-dortmund.de

ISBN 978-3-95450-134-2

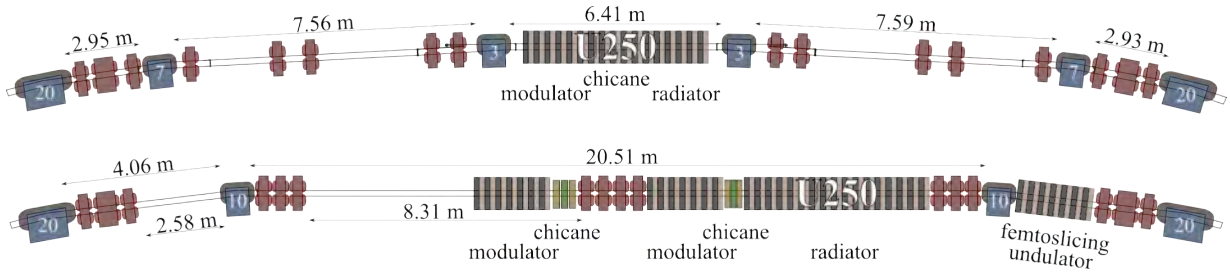

Figure 3: Top: Present magnetic setup in the northern part of DELTA. Bottom: Planned magnetic setup for the implementation of EEHG and femtoslicing in which the 3- and 7-degree dipole magnets are replaced by two 10-degree dipole magnets (adapted from [10]).

Femtoslicing

In contrast to the CHG and EEHG schemes, the femtoslicing technique [5] is based on a spatial separation of energy-modulated electrons downstream of the modulator by a dispersive element, e. g., a dipole magnet. In a following radiator, the off-energy electrons radiate incoherently at the radiator wavelength. In contrast to CHG and EEHG, the radiator can be tuned to arbitrary wavelengths and polarization. However, the intensity of incoherent radiation from a small fraction of the electrons in the bunch is very low. In the future DELTA short-pulse facility, EEHG and femtoslicing radiation initiated by the same laser pulse will be used simultaneously.

Modification of the Present Short-Pulse Facility

The present short-pulse facility at DELTA [1] is located in the northern part of the storage ring. A 17-period electromagnetic undulator (U250) serves as modulator, chicane and radiator. In order to implement the EEHG technique, two additional 7-period electromagnetic undulators were procured and are already in house. They will be employed as modulators, whereas the undulator U250 will be used as radiator only.

For a successful implementation of EEHG, both modulators, the chicanes, and the radiator should be placed in one long straight section because dipole magnets would smear out the microbunches. Furthermore, the distance between the second modulator and the radiator has to be minimized because the angular spread of the electrons results in different path lengths along a drift space. In order to create the required straight section, the storage ring has to be modified without changing its circumference significantly [10]. The resulting new magnetic layout of the short-pulse facility is shown in Fig. 3 and Table 1 summarizes the properties of the present and future storage ring lattice.

LATTICE OF THE FUTURE SHORT-PULSE FACILITY

The model of the new short-pulse facility proposed in [10] and [11] is based on a storage ring lattice showing discrepancies to the actual layout of the storage ring, e. g., the circumference differs by 3.8 cm between the model and the length calculated from the RF frequency of the accelerating cavity. In 2014, the positions of the storage ring magnets were surveyed and based on this data, an improved model with a circumference constistent with the RF frequency was obtained [12]. In this model, asymmetries in the optics due to a misalignment of the magnets were detected which will be reduced by realigning the whole storage ring.

Table 1: Lattice Properties of the Present and Future DELTA Storage Ring

Parameter	Present	EEHG
circumference	115.164 m	115.176 m
bunch length (FWHM)	100 ps	100 ps
horizontal emittance	17.5 nm rad	16.5 nm rad
horizontal tune	9.23	9.13
vertical tune	3.33	3.95

In addition, the model of the future short-pulse facility was adapted to fit the survey results [12]. Figure 4 shows the optical functions of the future short-pulse facility, where the beta functions and dispersion are reduced compared to the present lattice.

SIMULATION OF MICROBUNCHING

In order to study the obtainable bunching factor, a modified version of the code *elegant* [13] including a laser beam quality factor M^2 larger than unity [14] was used. As an example, the bunching factor for the 40th harmonic of the laser wavelength 800 nm was optimized. In the simulation, a laser pulse energy of 4 mJ, a pulse length of 60 fs and a beam quality factor M^2 of 1.1 were assumed, resulting in optimum R_{56} values of the magnetic chicanes of 1.25 mm and 24 µm. The waist radius w_0 (two standard deviations of intensity) for optimum energy modulation is 0.5 mm in both modulators [10], while the restriction that the energy modulation may not exceed the energy acceptance of the storage ring, leads to laser waist radii of 2.68 mm and 1.71 mm. These parameters yield a maximum energy modulation of 0.33% and 0.49%. The resulting bunching factor optimized for the 40th harmonic of the 800 nm laser radiation is shown in Fig. 5. The achievable value is sufficient to exceed the background of incoherent radiation [11].

ISBN 978-3-95450-134-2

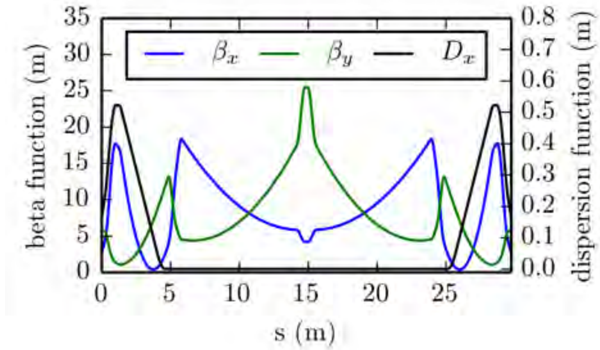

Figure 4: Calculated optical functions of the future short-pulse facility [12].

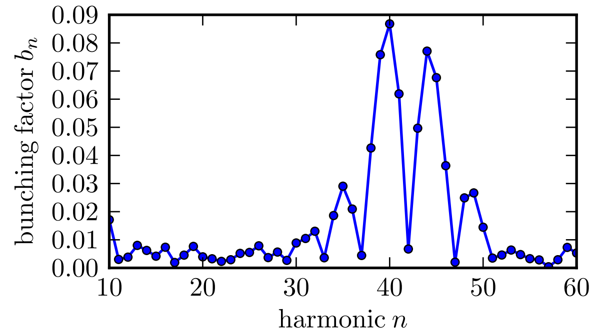

Figure 5: Calculated bunching factor versus harmonic n of the 800 nm laser radiation. The bunching factor was optimized for the 40th harmonic [11].

FEMTOSLICING RADIATION

For the following calculations of the femtoslicing radiation, a radiator with a period length of 56 mm and 30 periods was considered. Using the modified version of the code *elegant*, the energy-modulated electron distribution at the femtoslicing undulator was simulated by tracking the electrons from the first modulator to the femtoslicing undulator. Figure 6 shows the angular distributions of the electrons with and without laser-induced energy modulation. As an example, a laser pulse energy of 8 mJ, a waist radius w_0 of 1.28 mm, a pulse length of 60 fs (FWHM) and a beam quality factor of $M^2 = 1.1$ were assumed. The resulting maximum energy modulation amplitude is 0.90 % corresponding to the energy acceptance of the RF cavity [11].

The angular distribution of the femtoslicing radiation generated by a single electron at a photon energy of 237 eV and at the third harmonic at 711 eV was simulated using the code *Spectra* [15] (see Fig. 6) [11].

A convolution of both angular distributions was used to calculate the angular distribution of the radiation generated in the femtoslicing undulator at a photon energy of 711 eV (Fig. 6). The short-pulse component exceeds the background radiation for observation angles above 1.5 mrad [11].

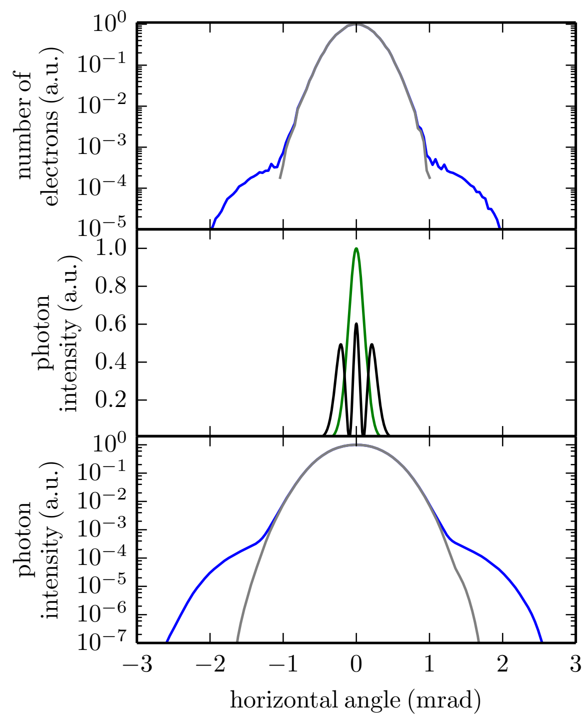

Figure 6: Top: Angular distribution of the electrons at the beginning of the femtoslicing undulator with (blue) and without (grey) energy modulation. Center: Angular distribution of the radiation generated by a single electron in the femtoslicing undulator at a photon energy 237 eV (green) and at the third harmonic (black). Bottom: Angular distribution of the femtoslicing radiation at a photon energy of 711 eV with (blue) and without (grey) the energy modulation [11].

MODIFICATION OF THE VACUUM SYSTEM

The new magnetic layout requires a modification of the present vacuum system including chambers and pumps. In order to reduce the cost, as many of the existing chamber parts as possible will be reused in the new setup. Since the 10-degree dipole magnets have a different bending radius than the 3- and 7-degree magnets (see Fig. 3), new dipole chambers have to be manufactured. In addition, tapers and a new design of the vacuum chambers are needed, due to a reduced gap height of the new modulators.

Since both chicanes in the EEHG section displace the electron beam only by a few millimeters [10], no mirrors can be placed at the chicane bumps without decreasing the electron beam lifetime. As a consequence, the laser radiation for the second modulator has to be coupled in at the first 10-degree dipole magnet chamber. In view of the additional impedance, the tube diameter should be as small as possible. In contrast to this, the laser radiation requires an aperture larger than 4.6 times the beam size $w(z) = w_0\sqrt{1 + (z/z_R)^2}$, where z is the longitudinal coordinate and z_R is the Rayleigh length, to avoid diffraction effects which may impair the laser beam quality [16].

ISBN 978-3-95450-134-2

In order to generate two laser pulses from one pulse provided by the existing laser system, a beamsplitter for 800-nm or a second harmonic generation (SHG) unit producing 400-nm radiation could be used. Using a laser waist radius of 500 µm for an optimum energy modulation in both modulators, the 4.6w radiation envelope along the vacuum chamber was calculated for different beam quality factors M^2. This calculation was performed for 800-nm as well as 400-nm radiation for both laser beams. As shown in Fig. 7, the 800-nm beam is incompatible with a waist size of 500 µm and a diameter of the incoupling tube of 31 mm, which is the diameter of already existing beamline tubes. Therefore, a setup for the laser-electron interaction using 800-nm in the first modulator and 400-nm radiation in the second modulator will be adopted.

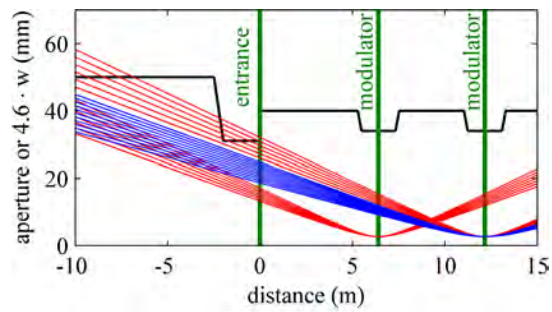

Figure 7: Laser radiation diameter (4.6w) of the 800-nm (red) and 400-nm (blue) radiation versus distance to the exit of the laser beam pipe. The aperture (black) is determined by the beamline and by the storage ring chamber dimensions. The beam quality factor M^2 varies between 1.0 and 1.3 for 800-nm and between 1.3 and 2.0 for 400-nm laser radiation in steps of 0.05 while keeping the laser waist radius constant at $w_0 = 500\,\mu$m.

Simulation of a 1-d Pressure Profile

In order to determine pump positions and types in the modified part of the storage ring, a one-dimensional pressure profile was calculated. As a first step, the distribution of the photon flux along the vacuum chamber wall from the bending magnets was determined (see Fig. 8). The radiation caused by the insertion devices was neglected in this model. The thermal and synchrotron-radiation-induced desorption rates were adjusted such that a lifetime of around 10 hours at 130 mA and 18 hours at 15 mA for the present setup of DELTA was achieved by numerical calculation [17] including residual gas scattering as well as the Touschek effect. The pressure simulation was carried out for a pure nitrogen (N_2) gas load. For a more refined simulation, the measured gas composition [18] will be included in the model.

The new vacuum system is supposed to keep the average pressure at the present level in order to maintain a similar beam lifetime. Pressure profiles for the present and one possible EEHG pump configuration are shown in Fig. 8.

CONCLUSION

Based on the spatial survey of the storage ring, an improved model for the future short-pulse facility was developed, and the simulation of the EEHG microbunching and of the femtoslicing radiation show that both techniques can be applied at DELTA.

Resulting from the calculations of the radiation envelope in the vacuum chamber, a setup for a laser-electron interaction using two different wavelengths for the two laser pulses will be investigated. Indicated by the calculated pressure profile, the relative change of the pressure due to modifications of pump positions and types is predictable. Including measured gas compositions, a more precise simulation will be possible.

ACKNOWLEDGMENT

It is a pleasure to thank our colleagues at DELTA and the faculty of Physics of the TU Dortmund University for their support. This work was supported by BMBF (05K13PE3), by the DFG (INST 212/236-1 FUGG), by the Helmholtz ARD Initiative, by the FZ Jülich and by the Federal State NRW.

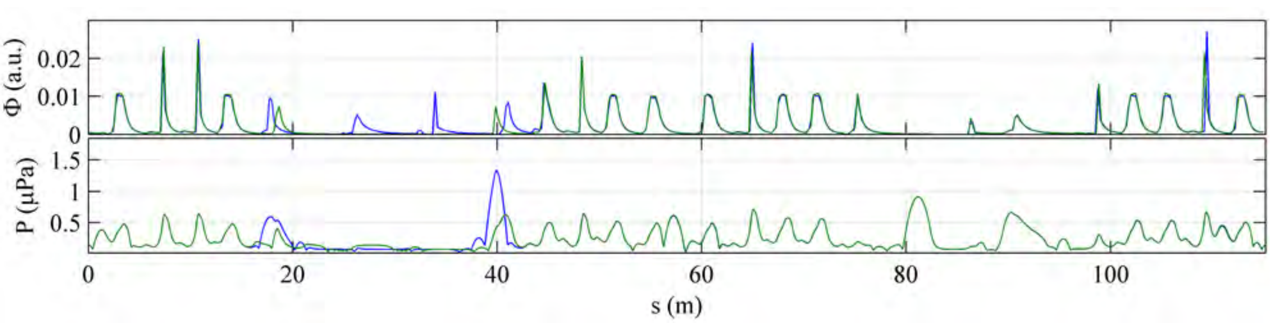

Figure 8: Simulated dipole radiation photon flux Φ on the outer wall of the vacuum chamber (top) at a beam current of 130 mA and pressure P (bottom) versus the longitudinal postion s in the storage ring for the present setup (blue) and for the storage ring modified in the region between s = 14 m and 43 m (green).

ISBN 978-3-95450-134-2

REFERENCES

[1] S. Khan et al., "Generation of Ultrashort and Coherent Synchrotron Radiation Pulses at DELTA", *Sync. Rad. News* 26, pp. 25-29, 2013.

[2] R. Prazeres et al., "Coherent harmonic generation in the vacuum ultraviolet spectral range on the storage ring ACO", *Nucl. Instr. and Meth. A* 272, pp. 68-72, 1988.

[3] R. Molo et al., "EEHG and Femtoslicing at DELTA", in *Proc. 35th Int. Free-Electron Laser Conf.*, New York, 2013, pp. 594-597.

[4] G. Stupakov, "Using the Beam-Echo Effect for Generation of Short-Wavelength Radiation", *Phys. Rev. Lett.* 102, pp. 074801 ff., 2009.

[5] A.A. Zholents, M.S. Zolotorev, "Femtosecond X-Ray Pulses of Synchrotron Radiation", *Phys. Rev. Lett.* 76, pp. 912-915, 1996.

[6] P. Schmüser et al., *Ultraviolet and Soft X-Ray Free-Electron Lasers*, Springer, 2008.

[7] L.H. Yu, "Generation of intense uv radiation by subharmonically seeded single-pass free-electron lasers", *Phys. Rev. A* 44, pp. 5178-5193, 1991.

[8] J. Wu, L. Yu, "X-ray Production by Cascading Stages of a High-Gain Harmonic Generation Free-Electron Laser I: Basic Theory", *SLAC-PUB-10494*, 2004.

[9] D. Xiang, G. Stupakov, "Echo-enabled harmonic generation free electron laser", *PRSTAB* 12, pp. 030702, 2009.

[10] S. Hilbrich et al., "Upgrade Plans for the Short-Pulse Facility at DELTA", *Proc. 36th Int. Free-Electron Laser Conf.*, Basel, 2014, pp. 255-259.

[11] R. Molo, PhD Thesis, TU Dortmund University, Germany, in preperation.

[12] S. Hilbrich, "Studies of the DELTA Lattice in View of a Future Short-Pulse Facility Based on Echo-Enabled Harmonic Generation", Master thesis, TU Dortmund University, Germany, 2015.

[13] M. Borland, Advanced Photon Source LS-287, 2000.

[14] R. Molo, "Investigation of Short-Pulse Radiation Sources at DELTA Based on Coherent Harmonic Generation and Echo-Enabled Harmonic Generation", Diploma Thesis, TU Dortmund University, Germany, 2011.

[15] T. Tanaka, H. Kitamura, "SPECTRA: A Synchrotron Radiation Calculation Code", *J. Synchrotron Rad.* 8. pp. 1221, 2001.

[16] A.E. Siegmann, *Lasers*, Univ. Science Books, 1986.

[17] M.A. Jebramcik et al., "Study of the Beam Lifetime at the Synchrotron Light Source DELTA", *Proc. of 5th Int. Particle Accelerator Conf.*, Dresden, 2014, pp. 222-224.

[18] A. Strasser, "Simulation des longitudinalen Druckverlaufs im Vakuumsystem von DELTA und Untersuchung der Strahllebensdauer", Master thesis, TU Dortmund University, Germany, 2014.

ISBN 978-3-95450-134-2

THE X-BAND FEL COLLABORATION

J. Pfingstner*, E. Adli, University of Oslo, Oslo, Norway
A. Aksoy, Ö. Yavaş, Ankara University, Ankara, Turkey
M. J. Boland, T. K. Charles, R. Dowd, G. S. LeBlanc, Y.-R. E. Tan, K. P. Wootton, D. Zhu, Synchrotron Light Source Australia, Clayton, Australia
N. Catalan-Lasheras, A. Grudiev, A. Latina, D. Schulte, S. Stapnes, I. Syratchev, W. Wünsch, CERN, Geneva, Switzerland
G. D'Auria, S. Di Mitri, C. Serpico, Elettra-Sincrotrone, Trieste, Italy
C. J. Bocchetta, A. I. Wawrzyniak, Solaris, Jagiellonian University, Krakow, Poland
G. Burt, Lancaster University, Lancaster, UK
A. Charitonidis, E. N. Gazis, National Technical University of Athens, Greece
Z. Nergiz, Nigde University, Nigde, Turkey
W. Fang, Q. Gu, Shanghai Institute of Applied Physics, Shanghai, China
D. Angal-Kalinin, J. Clarke, STFC, Daresbury Laboratory, Cockcroft Institute, Daresbury, UK
T. Ekelöf, M. Jacewicz, R. Ruber, V. Ziemann, Uppsala University, Uppsala, Sweden
X. J. A. Janssen, VDL ETG T&R B.V., Eindhoven, Netherlands

Abstract

The X-band FEL collaboration is currently designing an X-ray free-electron laser based on X-band acceleration technology. Due to the higher accelerating gradients achievable with X-band technology, a X-band normal conducting linac can be shorter and therefore potentially cost efficient than what is achievable with lower frequency structures. This cost reduction of future FEL facilities addresses the growing demand of the user community for coherent X-rays. The X-band FEL collaboration consists of 12 institutes and universities that jointly work on the preparation of design reports for the specific FEL projects. In this paper, we report on the on-going activities, the basic parameter choice, and the integrated simulation results. We also outline the interest of the X-band FEL collaboration to use the electron linac CALIFES at CERN to test FEL concepts and technologies relevant for the X-band FEL collaboration.

INTRODUCTION

A major factor in the cost of the construction of a linac driven FEL facility is the accelerator technology adopted. For normal conducting facilities, a substantial part of the costs is determined by the linac operating frequency, which strongly influences space requirements and power consumption. Most of the operational facilities use S-band linacs, operating at 3 GHz, or newly designed C-band linacs, operating at 6 GHz. The use of higher frequencies can allow an increase of the operating gradient and the efficiency, with an overall reduction of the machine length and the cost. These advantages could be further enhanced if the operating frequency can be extended to the X-band region (i.e. 12 GHz), where the operating gradients can be almost doubled compared to those of C-band structures. During the last decades, research and development of X-band accelerator technologies has seen a tremendous progress within the context of the next generation of electron-positron Linear Colliders, where very high gradients are necessary to achieve the multi-TeV beam energies within reasonable lenght. The possibility to operate X-band accelerating structures at gradients higher than 100 MV/m, has been recently demonstrated in the context of the CERN CLIC (Compact Linear Collider) Collaboration, with a very low RF Breakdown Rate (BDR/m < 3 x 10^{-7}) [1]. This has suggested that the X-band technology may represent a useful solution to get very compact and cost effective multi-GeV linacs, opening the way for new less expensive FEL facilities. This option seems to be even more attractive if we consider that most of the future X-ray FELs will be designed to operate with very short and low-charge electron bunches, minimising unwanted wake field effects. Starting from the FEL output specifications provided by users (i.e. wavelength range, energy per pulse, pulse duration, pulse structure, etc.), the objective of the X-band FEL collaboration is to analyse three possible scenarios: a soft X-ray FEL, a hard X-ray FEL and the extension of an existing facility. Other efforts involve identifying, designing and testing, a common X-band RF unit for the three sources, on a dedicated test stand. This effort will demonstrate the maturity of the technology, validating the hardware and the use of X-band in this area of strategic scientific interest.

COLLABORATION AND SPECIFIC INTERESTS

The X-band FEL collaboration consists of 12 institutes and universities (see affiliation of authors), which share the common interest of using X-band technology for FELs. Some of the envisioned projects within this collaboration are summarised in the following.

* juergen.pfingstner@cern.ch

ISBN 978-3-95450-134-2

Light Source Australia

The Australian Synchrotron (ASLS) is a third generation storage ring based light source in Melbourne. Presently, upgrade plans are being made to improve the X-ray beams available to the large user community. In the proposed upgrade concept, called AXXS (Australian X-band X-ray Source) [2], it is foreseen to exchange the existing DBA lattice of the storage ring with an MBA lattice. Since the current injector complex is not capable of producing beams with small enough emittances to allow an efficient injection into the MBA lattice, a new, low-emittance injector linac is being designed. It is based on X-band technology and accelerates the beams to the necessary energy of 3 GeV. Since the X-band linac can operate at a high repetition rate, it can be used simultanuously as an injector for a soft X-ray FEL. Also hard X-rays can be produced if the beam energy is increase by a second X-band linac from 3 GeV to 6 GeV. Due to the high acceleration gradients of the X-band technology, the restricted site length of 550 m is sufficient to accommodate such an hard XFEL.

Daresbury Laboratory

The CLARA FEL Test Facility project is under development at STFC Daresbury Laboratory, with the first accelerating section being installed later this year [3]. CLARA will be capable of testing new FEL schemes that have the capability to enhance the performance of short wavelength FELs worldwide. The primary focus of CLARA will be on ultrashort pulse generation, stability, and synchronisation. Enhancements in these three areas will have a significant impact on the experimental capabilities of FELs in the future. In addition to these stated aims CLARA will also be an ideal test bed for the demonstration of new accelerator technologies related to FELs. Initially CLARA is designed to be based on S-band linac sections to achieve the required energy of 250 MeV. However, a study has shown that the replacement of the last 4 m linac section by an X-band linac designed for FEL applications does not have any adverse impact on the bunch quality and would have the advantage of increasing the maximum beam energy to approximately 430 MeV, assuming a gradient of 65 MV/m [4].

FERMI@Elettra

FERMI [5, 6] is a fourth generation light source at the Elettra – Sincrotrone Trieste (Italy) Laboratory that functions as a user facility producing photons in the ultraviolet and soft X-ray wavelength regions (100–4 nm), with an S-band linac (3 GHz) presently operated up to 1.5 GeV. Its capabilities and photon range could be improved and extended to hard X-rays (λ<0.5 nm) by increasing the linac energy up to 3.0–3.5 GeV. Using infrastructures and spaces already available, this upgrade can be reached adding a new X-band (12 GHz) linac segment working with a gradient of 65–70 MV/m, downstream the second bunch compressor of the present machine, as sketched in Fig. 1. This solution will also give the possibility to operate two independent sources

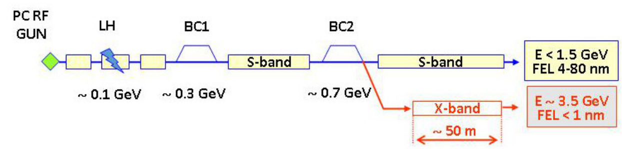

Figure 1: Schematic view of the Electra facility with the planned upgrade in red.

at different wavelengths, which could be simultaneously used for experiments [7].

Shanghai Photon Science Center

Since 2009 the ring-based third generation light source SSRF (Shanghai Synchrotron Radiation Facility) supplies a large number of users with synchrotron radiation in the X-ray regime. To even further extend the capabilities of the Shanghai Photon Science Center, the Shanghai Soft X-ray FEL (SXFEL) was officially approved in 2011. In the first phase, the electron beam will be accelerated to an energy of 0.84 GeV with a combination of S-band and C-band acceleration structures. In the second phase, the beam energy will be increased to 1.3 GeV by replacing the C-band with X-band structures. For that reason, SINAP launched a significant R&D activity on the X-band technology [8], which includes a dedicated workshop. SINAP is also working on a proposal for a compact hard X-ray FEL (HXFEL), which will employ, apart from the S-band injector, exclusively X-band structures with an acceleration gradient of 65 MV/m to reach a beam energy of 6.4 GeV. In the studied upgrade scenario, the beam energy is increased to 8 GeV by raising the gradient to 80 MV/m.

Turkish Accelerator Center

The currently proposed program of the Turkish Accelerator Center (TAC) [9] has three relevant light source projects – Construction of TARLA (Turkish Accelerator and Radiation Laboratory in Ankara), and preparation of conceptual design reports of the Synchrotron Radiation Facility and the X-Ray Free Electron Laser facility. TARLA is a free electron laser operating in the infrared regime using superconducting RF acceleration, whereas the X-ray FEL will produce wavelengths of 0.1–10 nm or 5–10 nm. These facilities will cover a wide range of scientific interests in physics, chemistry, biology, life sciences, medicine, nanotechnology and engineering.

The TAC team has been working on a conceptual design report of these projects since 2010 with support of the Ministry of Development of Turkey. The team has been studying different accelerating structure such as the TESLA structure which is also related to the technology being employed in TARLA. Considering the cost of an XFEL facility, TAC wants to take advantage of the novel X-band cavities operating at room temperature which would reduce the overall price. The TAC team considers two different types of single pass FELs: (i) high repetition rate soft X-rays, (ii) low repeti-

ISBN 978-3-95450-134-2

Table 1: Design Parameter Summary of the Hard X-ray FEL

Parameter	Symbol	Value
Energy after injector	E_{inj}	0.3 GeV
Bunch length after injector	$\sigma_{z,inj}$	44 μm
Injector frequency	f_{inj}	3 or 12 GHz
Injector gradient	G_{inj}	20 or 65 MV/m
Energy after linac	E	6.0 GeV
Bunch length after linac	σ_z	<8 μm
Normalised emittance	$\epsilon_{x,y}$	0.3 μm
Bunch charge	n	250 pC
Linac frequency	f	12 GHz
Linac gradient	G	65 MV/m
Repetition rate	f_{rep}	100 Hz
Structure length	L_{str}	0.75 m
Undulator period	λ_U	15 mm
Undulator parameter (max)	K_0	1.4
X-ray wave length (min)	λ_γ	1 Å
X-ray power (SASE at 1 Å)	P_γ	9 GW

tion rate hard X-rays. To design both facilities they consider an S-band based injector, which would operate at low repetition rate, and an X-band based injector, which would allow the entire accelerator to operate at high repetition rate.

PROGRESS IN DETAILED DESIGN

In the following, the status of the design of the X-band based XFEL for hard X-rays will be summarised. The soft X-ray version and the options for the extension of existing facilities are not covered in this document.

Machine Layout and Fundamental Parameters

The layout of the X-band XFEL consists of the same principle elements as employed by all operating FEL facilities and is depicted in Fig. 2. An S-band gun creates a low-emittance (<0.3 μm) electron beam with a bunch charge of 250 pC. This bunch in accelerated with an S-band injector to an energy of 0.3 GeV and is then compressed in the bunch compressor BC1 to a length of about 44 μm. An X-band linearizer upstream of BC1 is used to correct distortions of the longitudinal phase space before the compression. Alternatively, designs employing an X-band gun and/or an all X-band injector are also being studied. After BC1 the electron bunch is accelerated with X-band accelerating structures to an energy of 2.24 GeV before it is compressed in BC2 to a bunch length below 8 μm. Then the bunch is further accelerated to its final energy of 6 GeV and fed into in-vacuum permanent magnet undulators, where X-rays with a nominal wavelength of 1 Å are produced (tuning is not discussed here). The X-ray beams are guided via photon beamlines into the experimental area, where they are focusing and used in a variety of different instruments. The most important parameters are summarised in Table 1.

Injector

Two different types of injectors have been considered: (i) a 2.6 cell photo cathode RF gun operating at 3 GHz with 100 MV/m peak accelerating field similar to the SwissFEL [10], and (ii) a 5.6 cell photo cathode RF gun operating at 12 GHz with a maximum 200 MV peak accelerating field, which is similar to the one being developed at SLAC [11]. To extract charge from the cathode, we assumed a 9 ps full width half maximum (FWHM) laser pulse length for the S-Band gun, and a 3 ps FWHM laser pulse length for the X-band gun. For both types of RF guns the cathode is assumed to deliver 250 pC bunch charge. After the extraction, the beam is accelerated to 100 MeV by using either S-band traveling wave accelerating structures that are operating with a gradient of 20 MV/m at 3 GHz, or X-band traveling wave accelerating structures that are identical to the main linac structures operating with 65 MV/m gradient at 12 GHz. We have used the Poisson/Superfish code [12] to make a preliminary design for both, the gun and the generated field maps. The Astra code [13] has been used for the simulations performed to optimise the injector section. The beam sizes and emittances along the S-band and X-band based injectors are given in Fig. 3. As it can be seen, the projected normalised emittance ϵ_x is about 0.25 mm.mrad and 0.5 mm.mrad for the S-band and X-band based design.

Linac

The linac design process has proceeded through three main steps: RF parameters definition, longitudinal phase-space setup, and beam transport optimization. In the first step, the parameters of the acceleration structure and the RF unit were optimised in collaboration with the RF experts. The parameters (see RF section for details) were chosen to minimise the linac cost, while keeping the impact of transverse the wakefields at an acceptable level. Defining the parameters of the accelerating structure allowed to design and optimize the longitudinal phase space evolution along the machine. As it is expected that an X-band machine exhibits high sensitivity to RF stability [14], a semi-numerical optimization has been used, where analytical expressions of the sensitivities have been derived and used as figures of merit for a numerical minimization. This generated a layout that is "robust by design". The transverse beam transport has been provided with a lattice where the optimal balance between transverse focusing and transverse wakefield effects is achieved. Also a design entirely based on X-band components, i.e. using an X-band gun and injector (described in the injector section) is under study. Tests of beam-based alignment, using Dispersion-Free Steering and Wakefield-Free Steering have been performed with the PLACET tracking code [15]. The average emittance of 100 simulated machines (per line) with 100 μm RMS misalignment of the elements is depicted in Fig. 4, where each machine has been corrected using beam-based alignment (BBA), assuming a 5 μm BPM resolution. The tests confirm that the emittance growth can be kept below 0.03 μm in both axes, as shown in Fig. 4.

ISBN 978-3-95450-134-2

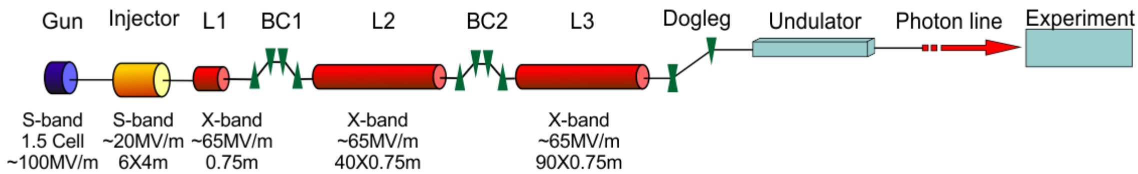

Figure 2: Schematic view the X-band XFEL for the S-band injector option.

RF Design

Based on an optimisation considering wakefield effects (described in the linac section), an optimal structure has been found with the following parameters: 72 cells, 0.75 m long, a/λ of 0.12, and a gradient of 65 MV/m. Ten of these structures will be installed on one RF module and will be fed by one RF station. This RF station consists of commercially available klystrons, modulators and pulse compressors (see Fig. 5). In the baseline option, two klystrons VKX-8311A from CPI will be driven by individual modulators K2-3 from Scandinova and will produce a 1.5 μs long RF pulse. Two of these pulses will be added by a hybrid combiner to a 1.5 μs pulse of 100 MW, which is then compressed to a 150 ns pulse via a pulse compressor. After this compression the 418 MW RF pulse is distributed via an RF network to the ten structures, which results in an acceleration gradient of 65 MV/m. With this option a repetition rate of 100 Hz can be reached. An alternative option, which is currently studied, is to power each structure with an individual 6 MW tubes E37113 from Toshiba and the modulator K2-1 from Scandinova. The RF pulses of length of 5 μs also would have to be compressed with a pulse compressor. This option would allow to operate with an increased repetition rate of up to 400 Hz with approximately the same installation cost, but with lower energy efficiency.

Bunch Compressors

The baseline X-band FEL collaboration design includes a 2-stage bunch compression scheme. Harmonic lineariza-

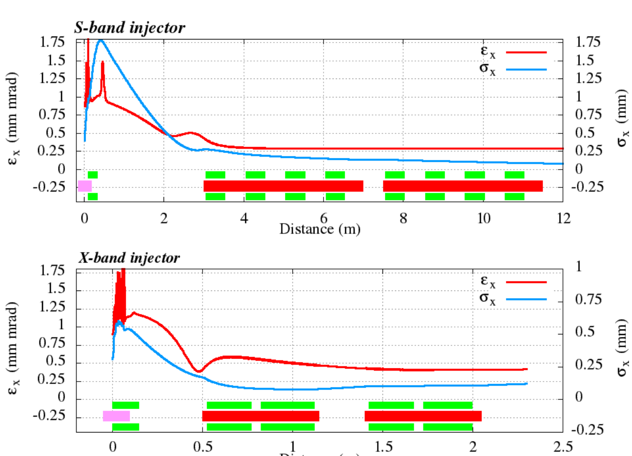

Figure 3: Emittance and beam size evolution along the S-band (top) and X-band (bottom) based injector.

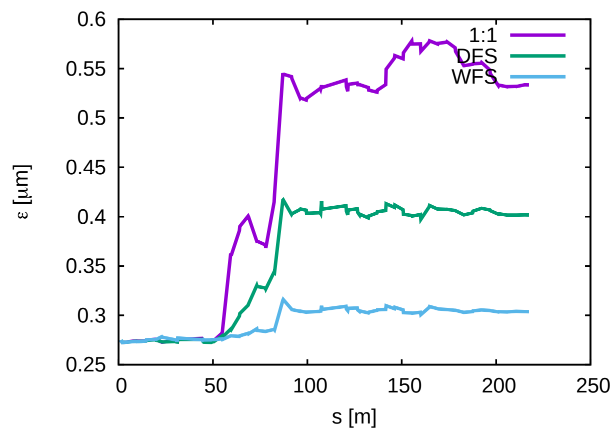

Figure 4: Horizontal normalised emittance along the FEL linac after beam-based alignment.

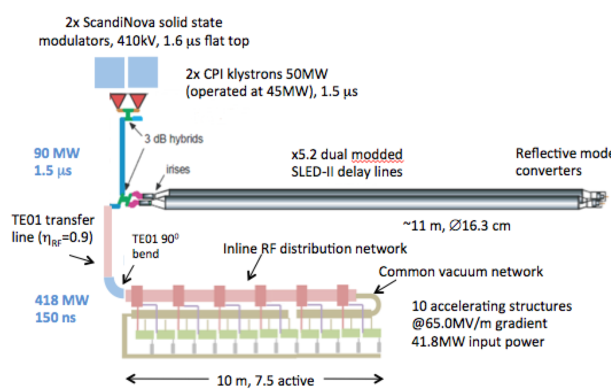

Figure 5: Schematic view of proposed RF unit (module).

tion is utilized through an S-band injector followed by a 12 GHz linearizing structure positioned just before the first chicane. This scheme allows of an overall compression ratio of 100 to be achieved, corresponding to a final bunch length of 26.7 fs. Figure 6 shows the Elegant [16] simulation results of the longitudinal phase space at the beginning and end of the first bunch compressor (BC1) and second bunch compressor (BC2). Alternative compression schemes are also being considered, including Optical linearization and Phase Modulation Linearization [17] employed with a dogleg compressor, for an all X-band machine.

Undulator Section

The baseline design for the undulator sections consists of 13 permanent magnet undulators of 3.96 m in length, with a

ISBN 978-3-95450-134-2

magnetic period length λ_u of 15 mm [18]. The modules are separated by gaps of 0.72 m to provide space for quadrupole magnets, beam position monitors, beam loss monitors and phase shifters. The maximal undulator parameter K of 1.3 results in an X-rays wavelength of 1 Åfor a 6 GeV electron beam. The beam size is controlled in the undulator section with quadrupole magnets that form a FODO lattice. Since there is also weak focusing from the undulator magnets present, the quadrupole magnet strengths have been adapted in order to restore a regular β-function of the specified magnitude. This results in slightly different strengths for the focusing and the defocusing quadrupoles. The evaluation of the expectable FEL performance relies mainly on numerical simulations with the codes GENESIS [19] and GINGER [20]. Using electron beams with the target parameters given in Table 1, the predicted X-ray output power is about 1 GW and 9 GW for seeded and SASE operation, respectively. The saturation length is about 37 m including the gaps. The output power can be increased with different tapering options, as shown in Fig. 7. Besides tapering, also the effect of energy detuning has been investigated. The undulator team works in close collaboration with the linac and bunch compressor group to optimise the quality of the produced electron bunches with respect to the produced output power via integrated simulations. An on-going effort is the determination of the mechanical and electrical tolerances of the undulator magnets and phase shifters.

UNDULATOR TECHNOLOGY DEVELOPMENTS

Undulator technology continues to make advances and FELs are able to take advantage of these improvements. The use of in-vacuum undulators has already been adopted by SACLA and SwissFEL, rather than out of vacuum technology. This enables shorter periods to be used, compared with standard out of vacuum undulators, and so lower electron beam energies, for the same output wavelength, are required.

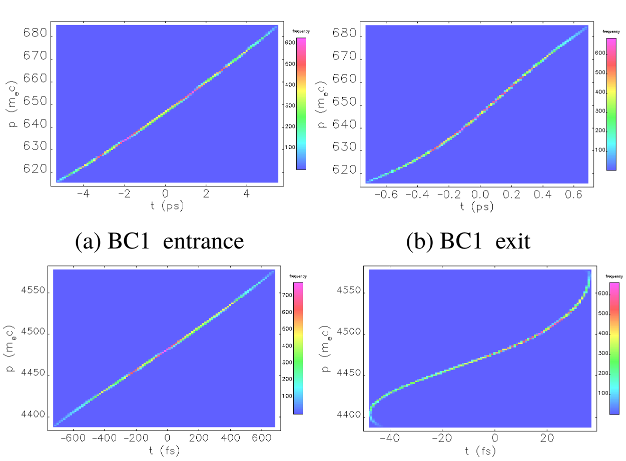

(a) BC1 entrance (b) BC1 exit

(c) BC2 entrance (d) BC2 exit

Figure 6: Longitudinal phase space evolution, through the two bunch compressors.

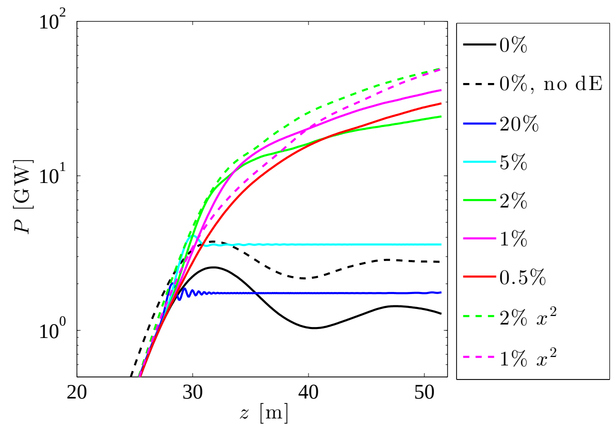

Figure 7: X-ray output power for different tapering options (here for seeded operation). For more details see [18].

The additional cost to the project of employing in-vacuum undulators instead of out of vacuum undulators is more than compensated for by the savings generated (in both capital and operating costs) by this lower electron energy requirement. This general approach of investing more in the undulator technology in order to make cost savings elsewhere in the facility appears to hold true for the other two technologies which we are considering: cryogenic permanent magnet undulators and superconducting undulators.

Cryogenic permanent magnet undulators (CPMUs) have been implemented in several 3rd generation storage rings [21–24] but not yet in a FEL. The advantages of operating at low temperature with NdFeB (~140 K) or PrFeB (77 K) are the much increased coercivity and 20% higher remanence. This allows for further reduced magnet period compared with in-vacuum undulators. An issue with both CPMU and in-vacuum undulators is that the output wavelength is varied by changing the magnet gap, and this then alters the resistive wall wakefield experienced by the electron bunch. It is possible that this could affect the electron bunch properties sufficiently that the beam will need to be retuned to optimise lasing. The alternative to gap tuning is beam energy tuning which obviously requires beam retuning as well. This issue may be an operational advantage for not just out of vacuum undulators but also superconducting undulators, which typically have a fixed aperture vessel for the electron beam and vary their magnetic field by changing the current in the coils. Superconducting undulators (SCUs) are not as mature as CPMUs but several groups are actively pursuing different designs and two storage rings have implemented them so far [25,26]. SCUs have the potential to generate the strongest fields of all the undulator technologies and so even shorter periods can be implemented whilst still maintaining reasonable tuning ranges. Typically SCUs employ NbTi wire but even stronger fields will be achieved if Nb_3Sn can be implemented. The advantages of SCUs for FELs is so significant that a dedicated R&D collaboration has been established for the LCLS-II project [27]. We plan to consider each of the

ISBN 978-3-95450-134-2

above undulator technologies from a facility cost perspective to establish the optimum facility parameters for each technology. Clearly the smallest possible undulator period results in the lowest electron energy requirements but this is not necessarily the optimum choice as the K parameter may well be too small and hence the gain length too long and also the wavelength tuning range from the adjustment of K (and not beam energy) may be unacceptable for the user.

PROPOSED TEST FACILITY AT CTF3

CALIFES is a 200 MeV electron linac [28], which is part of the CLIC Test Facility 3 (CTF3) at CERN. The linac is capable of producing an electron beam with a wide range of parameters. Of particular note are the low emittance (2 mm mrad), short bunch length (down to 300 μm), and range of bunch charge capabilities (up to 1.5 nC), available in single- or multi-bunch trains (up to > 100 bunches at 1.5 GHz). After the planned CTF3 shutdown at the end of 2016, the community has proposed to convert CALIFES into an advanced test facility for X-band FEL applications, as well as other users. The CALIFES linac is located close to the existing high power X-band RF test-stands [29] which can be used to power X-band structures.

Tests with beam are needed to demonstrate that sufficiently high peak current and good beam quality can be obtained with X-band. In CALIFES a number of X-band components can be tested, including phase-space linearizers, transverse deflecting cavities (for bunch length diagnostics and RF spreaders) and wakefield monitors. CALIFES would also provide an opportunity to test novel bunch compression schemes including purely magnetic compression systems. CALIFES would be the only facility in Europe where a significant amount of time could be dedicated to X-band tests, until the completion of CLARA at Daresbury.

CONCLUSIONS

The X-band FEL collaboration is a group of 12 institutes and universities that works jointly towards the design of an X-ray FEL based in X-band acceleration technology. The advantage of the X-band technology is that the linac can be much shorter, due to the higher achievable gradients. This reduces the overall cost of the facility, which could in the future increase the availability of coherent X-rays for the user community. Due to the combined efforts, the design studies are progressing rapidly, as reported in this paper. The collaboration also follows closely the developments in the undulator sector, since technological advances in this area have the potential to further reduce the cost of a proposed facility. There are also plans to use the existing electron linac CALIFES at CERN to test FEL technologies that are of relevance for the collaboration. As a long-term goal, the efforts of the X-band FEL collaboration will hopefully grant more users the access to the highly demanded, high-brightness, coherent X-ray beams.

REFERENCES

[1] A. Degiovanni et al., *High-gradient test results from a CLIC prototype accelerating structure: TD26CC*, In Proc. of IPAC14, WEPME015 (2014).

[2] M. J. Boland et al., *Plans for an Australian XFEL using a CLIC X-band linac*, In Proc. of IPAC14, THPME081 (2014).

[3] J. A. Clarke et al., *The Status of CLARA, A New FEL Test Facility*, In Proc. of FEL15., (2015).

[4] P. H. Williams et al., *Developments in the CLARA FEL Test Facility Accelerator Design and Simulations*, In Proc. of FEL14, TUP091 (2014).

[5] E. Allaria et al., *Highly coherent and stable pulses from the FERMI seeded free-electron laser in the extreme ultraviolet*, Nat. Photon. 6, 699-704 (2012).

[6] E. Allaria et al., *Two-stage seeded soft-X-ray free-electron laser*, Nat. Photon. 7, 913-918 (2013).

[7] G. D'Auria, *X-band technology for FEL sources*, In Proc. of LINAC14, MOPP023 (2015).

[8] W. C. Fang, *R&D of X-band accelerating structures for compact XFEL at SINAP*, In Proc. of LINAC14, TUPP127 (2014).

[9] `http://tac.en.ankara.edu.tr/`.

[10] E. Prat et al., *Emittance measurements and minimization at the SwissFEL Injector Test Facility*, Phys. Rev. ST Accel. Beams 17, 104401 (2014).

[11] R. A. Marsh et al., *Modeling and design of an X-band rf photoinjector*, Phys. Rev. ST Accel. Beams 15, 102001 (2012).

[12] James H. Billen, *Poisson/Superfish User's Manual*, LA-UR-96-1834 (2006).

[13] K. Floettmann, *ASTRA User Manual*, (2011).

[14] A. Aksoy, *Beam Dynamics for 6 GeV X-FEL Design using X-band Structure*, In Proc of CLIC Workshop 2015, (2015).

[15] D. Schulte et al., *The PLACET Tracking Code*, `http://clicsw.web.cern.ch/clicsw/`.

[16] M. Borland, *Elegant: A Flexible SDDS-Compliant Code for Accelerator Simulation*, Advanced Photon Source LS-287, (2000).

[17] T. K. Charles et al., *Comparison of Bunch Compression Schemes for the AXXS FEL*, In Proc. of IPAC15, TUPWA005, (2015).

[18] J. Pfingstner et al., *Performance and tolerance studies of the X-ray production for the X-band FEL collaboration*, In Proc. of FEL15, TUP011 (2015).

[19] S. Reiche, *GENESIS 1.3*, `http://genesis.web.psi.ch/`.

[20] W. Fawley, *A user Manual for GINGER and Its Post-Processor XPLOTGIN*, LBNL-49625-Rev. I ed., Lawrence Berkley National Laboratory (2004).

[21] J. Chavanne, *Recent Progress in Insertion Devices at the ESRF*, In Proc. of IPAC11, THPC153 (2011).

[22] T. Tanaka et al., *In-situ Magnetic Correction for Cryogenic Undulators*, In Proc. of IPAC10, WEPD026 (2010).

[23] J. Schouten et al., *Electron Beam Heating and Operation of the Cryogenic Undulator and Superconducting Wigglers at Diamond*, In Proc. of IPAC11, THPC179 (2011).

ISBN 978-3-95450-134-2

[24] C. Benabderrahmane et al., *Development of PrFeB Cryogenic Undulator (CPMU) at SOLEIL*, In Proc. of IPAC11, THPC149 (2011).

[25] S. Casalbuoni et al., *Recent Developments on Superconducting Undulators at ANKA*, In Proc. of IPAC15, WEBD3 (2015).

[26] Y. Ivanyushenkov et al., *Development and operating experience of a short-period superconducting undulator at the Advanced Photon Source*, Phys. Rev. ST Accel. Beams 18, 040703 (2015).

[27] P. Emma et al., *A Plan for the Development of Superconducting Undulator Prototypes for LCLS-II and Future FELs*, In Proc of FEL14, THA03 (2014).

[28] A. Mosnier et al., *The Probe Beam Linac in CTF3*, In Proc. of EPAC06, MOPLS059 (2006).

[29] N. Catalan-Lasheras et al., *Experience Operating an X-band High-Power Test Stand at CERN*, In Proc. of IPAC14, WEPME016 (2014).

ISBN 978-3-95450-134-2

BEAM COMMISSIONING AND INITIAL MEASUREMENTS ON THE MAX IV 3 GeV LINAC

S. Thorin, J. Andersson, F. Curbis, , M. Eriksson, L. Isaksson, O. Karlberg,
D. Kumbaro, F. Lindau, E. Mansten, D. Olsson, S. Werin, MAX IV Laboratory, Lund, Sweden

Abstract

The linear accelerator at MAX IV was constructed for injection and top-up to the two storage rings and as a high brightness driver for the Short Pulse Facility. It is also prepared to be used as an injector for a possible future Free Electron Laser.

Installations were completed and beam commissioning started in the early fall of 2014.

In this paper we present the progress during the first phase of commissioning along with results from initial measurements of optics, emittance, beam energy and charge.

BACKGROUND

The MAX IV facility [1] is the successor of the MAX-lab accelerators at Lund University and includes two storage rings, a full energy linac and a Short Pulse Facility (SPF). The rings will be operated at 1.5 and 3 GeV. The SPF will be a single pass spontaneous linac lightsource, producing sub-ps spontaneous X-ray pulses. The injector will be flexible enough to drive both injection and top-up for the storage rings, and produce high brightness pulses for the SPF. The long term strategic plan for the facility include an X-ray FEL, and the linac was developed to be fully prepared to handle the high demands for an FEL driver.

The first phase of linac commissioning was completed in the beginning of May 2015, and after a few months shutdown for final installations and system tests of the 3 GeV MAX IV storage ring, the linac was recommissioned and started the process of injections for storage ring commissioning.

MAX IV LINAC GENERAL DESIGN

For injection and top up to the storage rings a thermionic gun with a pulse train chopper system is used [2]. In high brightness mode we use a 1.6 cell photo cathode gun capable of producing an emittance of 0.4 mm mrad at a charge of 100 pC [3]. The gun will be operated together with a kHz Ti:sapphire laser at 263 nm. The same laser will be used for timing and synchronisation of the whole accelerator and the SPF.

The acceleration is done in 39 warm S-band linac sections together with 18 RF units, each consisting of a 35 MW klystron and a solid state modulator. The klystrons are operated at the lower power of 25 MW which reduces the operational cost and gives a total redundancy in energy of 0.6 GeV.

The beam is kicked out for injection into the storage rings at 1.5 and 3 GeV. Bunch compression is done in double achromats [4] at 260 MeV and at full energy, 3 GeV, after extraction to the storage ring. A schematic view of the layout can be seen in Figure 1.

STATUS OF BEAM COMMISSIONING

Commissioning of the MAX IV linac started in August 2014 using the thermionic RF gun. While high power conditioning was still ongoing in the main linac, the injection system including thermionic gun, chopper and first linac structure was started up and characterised. In November 2014 the hight brightness photo cathode gun produced electrons at MAX IV for the first time. During December we reached both transfer lines to the storage rings (Figure 3) and entered the second bunch compressor where we could measure the electron energy. Full energy, 3 GeV, was reached in February 2015. Beam from the high brightness gun was delivered through the SPF section to the main beam dump in the following month. A first hint of light at MAX IV was detected from an old MAX-lab undulator that is now temporarily installed the SPF [5] (Figure 2).

In the beginning of august 2015, after a few months machine shut-down, the linac was recommissioned with the purpose to start injecting in to the 3 GeV storage ring. The beam reached the first screen in the storage ring on the August 11 (Figure 4).

CHARGE MEASUREMENTS

Beam charge is measured with Current Transformers at several points through the machine and with Faraday Cups at each beam dump (Figure 5). The charge specification for storage ring injection with the thermionic gun is 1 nC within a 100 ns bunch train for each linac shot. This was achieved at the beam dump in the centre of the 3 GeV transferline, but for radiation safety reasons not more than 750 pC is accelerated during normal operation and ring commissioning.

The nominal charge specification for the SPF is 100 pC, which has been achieved and delivered though the undulator section. A charge range from 20 to 200 pC has been accelerated though the whole linac and into the second bunch compressor.

EMITTANCE SCANS

Emittance and twiss parameters are measured before and after both bunch compressors using quad scans. The quad scan station before BC1 is the first point to measure emittance from the electron guns.

Thermionic Gun

For the thermionic gun the measured horizontal normalized emittance is around 30 mm mrad, which is higher than

ISBN 978-3-95450-134-2

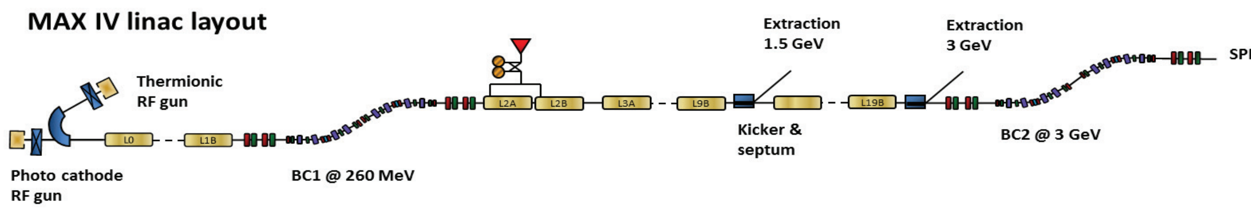

Figure 1: Layout of the MAX IV linac.

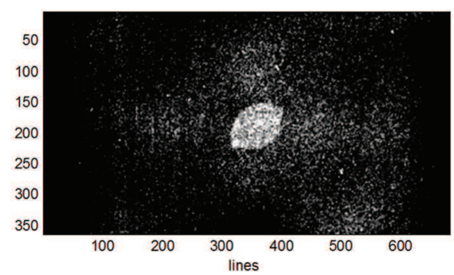

Figure 2: First "‘blip"’ of light detected from an undulator in the Short Pulse Facility.

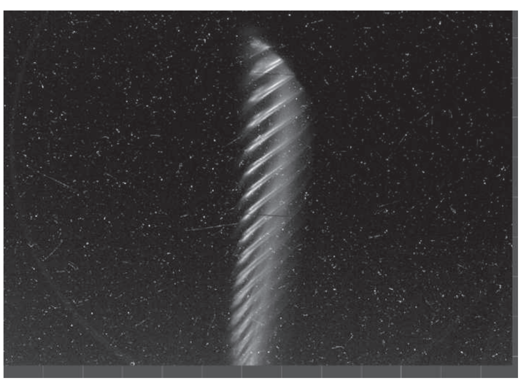

Figure 3: In the dispersive maximum in the 3 GeV transfer-line it is possible to resolve individual S-band pulses in the 500 MHz structure created by the gun and chopper.

the design value. The vertical emittance is at the same point below 7 mm mrad, which corresponds to simulations. A typical quadscan plot can be seen in Figure 6.

Photo Cathode Gun

For the photo cathode gun a normalised emittance down to 1.5 mm mrad has been measured before BC1 at 100 pC. This is a factor 3 higher than the design value of 0.5 mm mrad. It has later been discovered that the length of the laser pulse is below 2 ps which in combination with slightly too low RF power to the gun can be a reasonable explanation to the large emittance. Activities to stretch the laser pulse and increase the RF power to the gun are in progress.

More information about commissioning of the MAX IV electron guns can be found in [6].

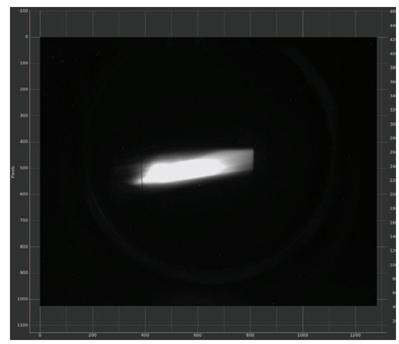

Figure 4: Image of the electron beam at the first screen in the 3 GeV storage ring.

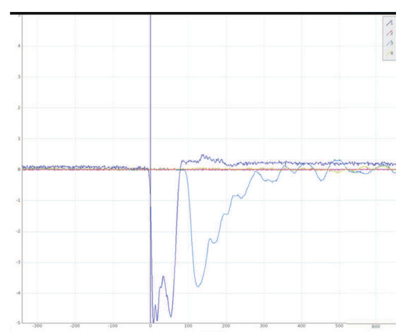

Figure 5: Trace on oscilloscope from the current transformer (dark blue) and Faraday cup (light blue) at the extraction to the 3 GeV storage ring.

At the quad scan station before the second compressor emittances as low as 0.8 mm mrad at 50 pC has been measured after using scrapers inside BC2 to get rid of some unwanted transverse beam halo.

BUNCH COMPRESSION

The two magnetic double achromats used as bunch compressors in the MAX IV linac have a positive R56 unlike the commonly used magnetic chicane which has a negative R56. The energy chirp needed for compression is done by accelerating the electrons on the falling slope of the RF voltage. Both types of bunch compressors naturally have a positive T566 and in the case of a BC with positive R56 this has a linearising effect on the longitudinal phase space. We can thus choose the optical parameters in the achromat to achieve linearisation without needing a harmonic cavity for this purpose.

ISBN 978-3-95450-134-2

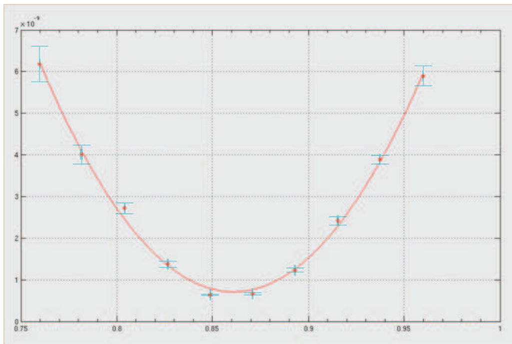

Figure 6: Typical plot from a quad scan emittance measurement just before BC2.

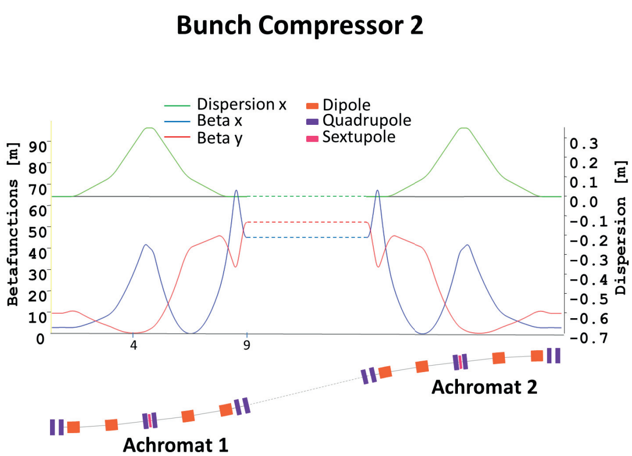

Figure 7: Layout and optics of the second bunch compressor. BC1 is very similar.

A sextupole is used in the centre of each achromat to minimize the second order dispersion at the end of the linac. This sextupole is rather weak and could be compared with the chromaticity compensating sextupoles in a storage ring. These sextupoles are also used to tweak the linearisation through the bunch compressor. R56 of the achromats is fixed and the compression is varied using the RF phase in the linac.

A schematic view of the layout and optics of bunch compressor 2 can be seen in Figure 7.

Relative Bunch Length Measurements

A relative bunch length measurement using horn antennas [7] was carried out with the beam from the photo gun after only compressing in BC1. The antennas were placed outside a ceramic gap after the compressor and a phase scan indicated full compression at around 26∘ which agrees with simulations.

Sextupole Influence on Bunch Length

Although it was not yet possible to determine the absolute bunch lengths of the compressed photo cathode beam, a measurement of the sextupole influence on bunch length and longitudinal profile was performed. The beam was accelerated at zero crossing in the last 8 linac structures, and viewed on a screen at maximum dispersion in BC2 [8]. This induces a correlated energy spread in the beam, and the dispersive region in BC2 will streak the beam horizontally, making the profile along the x-axis on the screen proportional to the longitudinal profile of the beam. The phase of the linacs before BC1 was set for maximum compression, and the sextupoles in BC1 varied from 0 to maximum current. A clear influence of the sextupoles on the profile can be seen. Figures 9 shows a projection of the horizontal plane on screen images (Figure 8) with sextupoles off and on. Both the RMS and FWHM beam size decreases with increasing sextupole strength, and has a minimum at k2 = 50 m^{-3}, see Figure 10. This corresponds very well with simulations. We did not have enough control of the optics of the beam at the screen to make assumptions about the absolute bunch length.

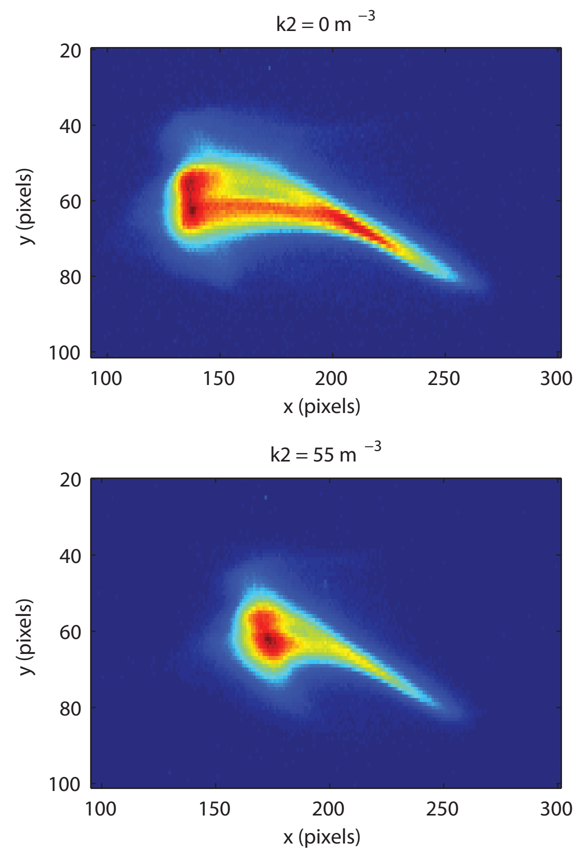

Figure 8: The electron beam from the photogun in the maximum dispersion section of BC2 for two different settings of the BC1 sextupoles. The bunch was at maximum compression in BC1 and the 8 last linac structures phased to zero crossing.

SUMMARY AND OUTLOOK

Phase one of the MAX IV linac commissioning was completed early May 2015. The linac had then delivered elec-

ISBN 978-3-95450-134-2

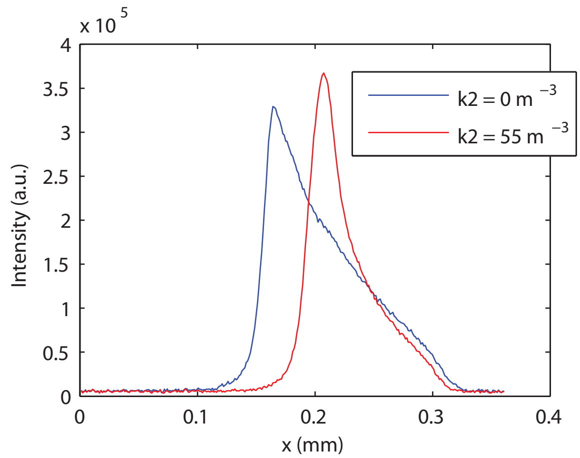

Figure 9: The longitudinal profile of the beam depends on strength of the bunch compressor sextupoles.

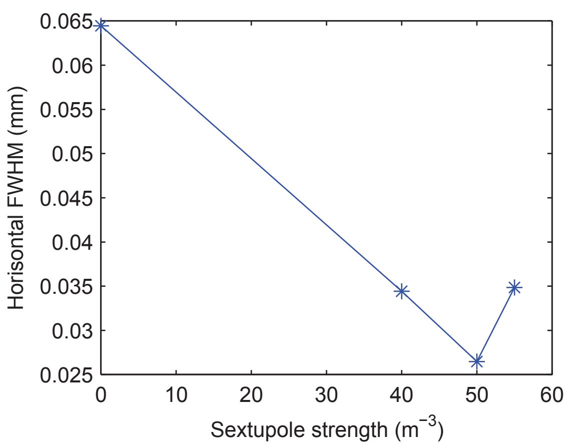

Figure 10: Bunch length dependence of the bunch compressor sextupoles which help to linearise longitudinal phase space and increase peak current.

trons from a thermionic RF gun into transfer lines to both MAX IV storage rings, and electron from a photocathode gun to a Short Pulse facility. In the beginning of August 2015 the linac delivered the first electrons into the 3 GeV storage ring and will now operate for storage ring injection.

The plan for coming steps for MAX IV linac commissioning include improving beam quality from both electron guns, achieving an absolute measurement of bunch length for the compressed high brightness beam and top up injection to the storage rings.

REFERENCES

[1] *Detailed Design Report-MAX IV facility* (2010) Lund, Sweden.

[2] D. Olsson et al, Nuclear Instruments and Methods in Physics Research A, 759, p. 29–35 (2014)

[3] E. Elafifi et al, “An Electron Gun Test Stand to Prepare for the MAX IV Project”, TUPPD065, IPAC2012.

[4] S. Thorin et al., “Bunch Compression by Linearising Achromats for the MAX IV Injector” WEPB34, FEL2010

[5] S. Werin, et al., “Short pulse facility for MAX-lab,” Nucl. Instr. and Meth. in Phys. Res. A 601, pp. 98- 107, (2009).

[6] J. Andersson et al., “Initial Commissioning Results of the MAX IV Injector” presented at FEL’15, Daejeon, Korea, Aug 2015, paper TUP036, these proceedings

[7] R. Appio et al., “Absolute Bunch Length Measurements at Fermi@ELETTRA FEL” TUAL3, IBIC2013

[8] F. Curbis et al., “Prospects for Longitudinal Phase-space Measurements at the MAX IV Linac” THPME170, IPAC14

ISBN 978-3-95450-134-2

STATUS OF THE ALICE IR-FEL: FROM ERL DEMONSTRATOR TO USER FACILITY

N.R. Thompson[1], J.A. Clarke[1], T. Craig[2], D.J. Dunning[1], O.V. Kolosov[3], A. Moss[1], Y.M. Saveliev[1], M.R.F. Siggel-King[1,2], M. Surman[1], P.D. Tovee[3], P. Weightman[2]
[1]Accelerator Science and Technology Centre (ASTeC), STFC Daresbury Laboratory, UK
[2]Department of Physics, The University of Liverpool, L69 3BX, UK
[3]Department of Physics, Lancaster University, LA1 4YB, UK

Abstract

The ALICE (Accelerators and Lasers In Combined Experiments) accelerator at STFC Daresbury Laboratory in the UK was conceived in 2003. It was constructed as a short-term Energy Recovery Linac (ERL) demonstrator to develop the underpinning technology and expertise required for a proposed 600MeV ERL-based FEL facility. In this paper we present an update on the performance and status of ALICE which now operates as a funded IR-FEL user facility. We discuss the technological challenges of evolving a short-term demonstrator into a stable, reliable user facility and present a summary of the current scientific programme.

BRIEF HISTORY OF ALICE

In 2000 a proposal was developed at Daresbury Laboratory for 4GLS, a combined XUV/VUV/IR FEL facility driven by a 600MeV ERL [1]. This was to be a complementary photon source to the hard and soft X-ray sources of the ESRF and Diamond Light Source respectively. In 2003 funding was obtained to build a lower energy prototype, ERLP, to enable development of the underpinning technologies and expertise: assembling and operating TESLA cavities and cryomodules; operation of an ERL and associated RF, synchronisation and optics; photoinjector technologies; FEL techniques and operation; longitudinal beam dynamics and simulation; and diagnostic techniques and instrumentation. ERLP was sited in reused experimental areas, leading to some layout restrictions. The project benefitted greatly from collaboration with Jefferson Laboratory. In particular, the 350kV DC photocathode gun was based on the JLab design and a number of quadrupole magnets and chicane assemblies were provided on loan. The FEL wiggler had previously been used on the JLab IR-Demo FEL [2] and was re-engineered for variable gap operation. The FEL mirror cavities were loaned by LURE where they had previously been used on the CLIO FEL. The intention was to run ERLP for two years as an accelerator test facility before decommissioning.

Procurement and construction began through 2004/5. First beam from the gun was in August 2006 followed by a period of commissioning using a dedicated gun diagnostic beamline. 2007 was a challenging year: the gun suffered from strong field emission, rapidly deteriorating QE, mechanical failure inside the cathode ball, conditioning resistor failure and vacuum leaks. Nevertheless, by the end of 2007 100pC was achieved at 350keV with QE>3%. Unfortunately, the linac suffered field emission which limited the gradient to 27 MeV rather than the design value of 35 MeV.

In 2008 the 4GLS project was cancelled and ERLP was renamed ALICE. By October, after repairs to the booster linac cryomodule at ACCEL and the installation of a smaller ceramic in the gun (generously loaned by Stanford University) the milestone of energy recovery was achieved.

As suggested by the new name, the purpose of the facility shifted in 2009 towards laser-related experiments and user exploitation. Coherently enhanced broadband THz was extracted from the final dipole of the bunch compression chicane, Compton back-scattering off a TW laser in a head-on geometry was successfully demonstrated [3] and electro-optic sampling was implemented as an electron bunch length diagnostic.

By 2010 the FEL undulator was installed and lasing was achieved in October that year. Details of the commissioning process up to first lasing, including a summary of the beam optics design, can be found elsewhere [4].

Larger scale user programmes commenced in 2011 after commissioning of the THz and FEL beamlines. The THz beam was transported to a tissue culture laboratory for biological experiments to determine safe limits of exposure of human cells to THz and the effect of THz on the differentiation of stem cells [5]. A Scanning Near-Field Optical Microscope (SNOM) was installed and integrated with the IR beamline—further details are given later in this paper.

In 2012, while the user programmes progressed, time was also spent studying the transverse and longitudinal beam dynamics [6] and the effect of chicane R_{51} and R_{52} on the THz emission.

ALICE is now funded via a three-year EPSRC grant [7] to provide three months of user IR-FEL/THz beamtime per year. A number of technology upgrades and operational improvements have been implemented to transition ALICE from a test facility to a stable, reliable user facility. These are described in subsequent sections. The layout of ALICE is shown in Figure 1.

RECENT UPGRADES

Digital Low-Level RF (DLLRF) Work had been started at Daresbury in 2009 to develop DLLRF systems to replace the existing analog systems. The motivations were: to have the ability to modify loop parameters during operations; to allow complicated control algorithms such as adaptive feed forward to overcome beam loading; to en-

ISBN 978-3-95450-134-2

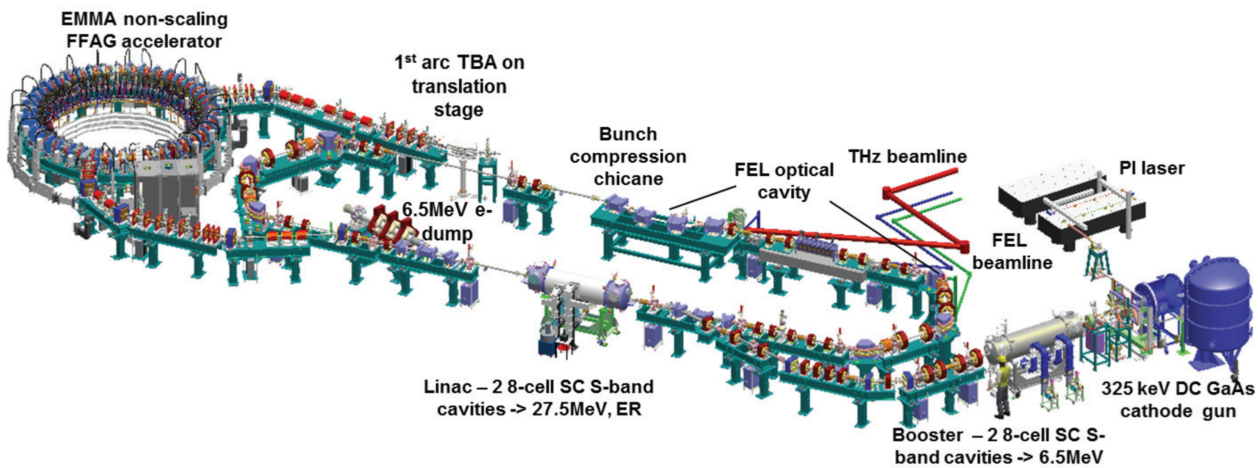

Figure 1: ALICE layout.

able controlled cavity filling to limit the RF power reflection in the waveguide and Lorentz force induced detuning control; and to introduce more extensive diagnostics. DLLRF has now been in operation for the ALICE buncher cavity for three years where *rms* phase and amplitude stability of 0.024° and 0.05% has been measured. Similarly, a 1.3GHz DLLRF system was successfully tested on the superconducting booster cavity demonstrating *rms* phase and amplitude stability of 0.028° and 0.04%.

The DLLRF system for the main linac was installed in 2014 and successfully commissioned at the start of 2015, immediately before user operations commenced. The improved reliabilty, stability and control of the new system soon became apparent and allowed introduction of a new system to stabilise drift in the photoinjector laser which markedly improved the stability of the FEL, as described in the next section.

Photoinjector Laser Synchronisation In 2012 correlations had been observed between the FEL output power and the relative phase between the photo-injector laser and the RF. This year, to provide a more stable FEL beam for the user programme, more investigations were carried out. A LLRF4 digital card (designed by Larry Doolittle (LBNL) and produced by Dimtel) was clocked from the ALICE master oscillator at 1.3 GHz. Two 81 MHz signals connected to the ADC inputs of the LLRF4 were processed to provide I and Q measurements of the RF laser drive signal and a signal from the laser output cavity, both CW signals at 81 MHz. It was then observed that the FEL power variation was correlated with drift and step changes in I and Q of the laser cavity signal which indicated the signal had changed phase with respect to the 81 MHz drive signal. The correlation between laser phase and FEL power is shown clearly in Figure 2.

To compensate, a phase shifter was introduced in the laser drive signal and a PID control in EPICS was used to monitor and control the position of the phase shifter. This greatly improved the performance of ALICE—the short term stability

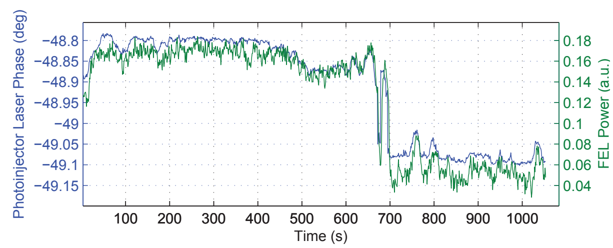

Figure 2: Observed correlation between photoinjector laser phase and FEL output power, prior to introduction of feedback.

of the FEL average power (measured on a macropulse basis) was improved from typically 5-10% to 1-2% and longer term drift was much reduced, greatly improving the utility of the beam for SNOM imaging which requires good stability over a one-hour timescale.

Diagnostic and Operational Improvements A current monitor and BPM were installed in the main beam dump which proved useful for optimising the energy recovery efficiency. By minor 'missteering' in the dispersive dump beamline the change in beam energy at the onset of lasing could be resolved. This provided a useful online diagnostic for FEL optimisation and monitoring. The BPM system around the rest of the accelerator was upgraded to allow all BPMs to be monitored simultaneously (rather than in 4 switchable banks as previously) and an orbit correction algorithm was implemented and commissioned. This will be invaluable in maintaining the trajectory within the FEL undulator while the gap is rapidly scanned over its full range.

The ALICE hall has poor temperature stability - variations of several degrees over the course of 24 hours are typical. This can lead to local phase changes due to cable temperature variation, drifts in the FEL cavity length (see next section) and changes in the position of the PI laser spot on the cathode. To reduce the temperature variation for the last user run,

ISBN 978-3-95450-134-2

the magnets were left on overnight when the machine was operating on a 16 hour cycle. This was found to markedly reduce setup time the following morning, primarily due to better RF phase reproducibility. It then typically took one hour to achieve stable lasing from powering up. Later, operations commenced on a 24 hour/5 day cycle. In this regime lasing was maintained stably and continuously with the only interruptions due to cathode recaesiations which took about half an hour and were required every 2-3 days.

IR-FEL Feedback One of the main uses of the ALICE FEL light is SNOM imaging which requires stable wavelength, bandwidth, and power over scans lasting approximately one hour. Past FEL operation experience indicated cavity length variation over 16-hour runs with the rate of change initially linear at up to 5 μm/hr then slowing and reversing later in the day. This was consistent with a sinusoidal variation on a 24-hour timescale. Laser tracker measurements were used to confirm the 24-hour cavity length variation and correlate it to temperature. Tracker points mounted on the exterior of the FEL cavity showed cavity length variations of ± 10 μm strongly correlated to ± 0.5°C air temperature variation. The width of the FEL detuning curve is ~ 20 μm, and variation of more than $1-2$ μm is sufficient to cause an unacceptable variation in FEL power and wavelength. Therefore, to meet the stability requirements action was required to maintain the cavity length to this level.

Several options that have been successfully used at other FELs were discounted, such as temperature stabilisation of the hall (due to cost) and interferometric measurement and correction of the cavity length (due to space restrictions in the cavity). An initial solution was a feedback system based on the measured spectrum of the FEL light. Different options were trialled, including feedback on cavity length based on the measured wavelength, and the use of response matrices to feed back on undulator gap based on measurements of measured wavelength, linewidth and FEL power. While these approaches were suitable under certain conditions they were unusable during extended sequences of rapid wavelength scans which were often required by users. Consequently, a second feedback technique was implemented in which temperature sensors were mounted on the girders around the FEL. The system was commissioned by recording temperature against cavity length for the peak of the detuning curve over an extended period of several days. A linear response was found, and a simple open loop control system implemented to vary the cavity length over the course of a scan to maintain constant wavelength. For SNOM scans this was used in tandem with a more rapid feedback on the undulator gap to compensate for any other parameter variation that directly or indirectly affected the FEL wavelength. Using these two systems together it was possible to achieve *rms* wavelength stability of $\sigma_\lambda/\lambda_0 \leq 0.1\%$ (approximately 10% of the relative bandwidth) over periods of several hours.

IR-FEL Beamline and End-station The beamline and end-station have been recently upgraded. The beamline was originally designed for 4μm radiation but because ALICE operates at a lower energy than the original design energy of 35 MeV the output is at longer wavelengths. The beamline toroidal mirror has therefore been replaced with a larger mirror to avoid over-filling at these longer wavelengths. Computer controlled in-vacuum movement was added to enable better control and alignment. This upgrade contributed to a five-fold increase in FEL-IR power at the end of the beamline. A second exit port, and retractable mirror, were added to the end of the beamline to enable rapid switching between experiments.

SCIENTIFIC PROGRAMME

The scientific programme on ALICE is aimed at developing more accurate and sensitive diagnostic techniques to improve oesophageal, prostate and cervical cancer survival rates. The capabilities of the IR-FEL and broad-band THz sources make the ALICE accelerator ideally suited to the programme [7].

IR radiation is routinely used for the identification of molecules and materials. It can be used to create a chemical image of a sample, however, the spatial resolution with usual imaging techniques is limited by diffraction to half of the wavelength of the radiation. At this resolution one may resolve cells but not sub-cellular features. The ability to achieve nanoscale spatial resolution in biomedical research can help provide new medicines and treatments. Two complementary techniques, IR Scanning Near-field Optical Microscopy (IR-SNOM) and Atomic Force Microscopy in the IR (AFM-IR), have been developed and used to obtain spectrally selective IR images at complementary sub-micron spatial resolutions.

Infrared Studies

The accelerator and FEL are now optimised to cover the range of wavelengths 5.7-8.3 μm, which includes many of the characteristic absorption lines found in cells, tissue and cancerous materials. For both IR-SNOM and AFM-IR techniques, a fixed wavelength of the 10 Hz pulsed IR-FEL light is focussed onto the sample. A tip is positioned at the intersection of the light and sample at a fraction of a micron above the surface of the sample. The sample is then scanned relative to the tip whilst the sample-to-tip distance is kept constant. The tip is used to measure both the topography and the sensitivity of the sample to the absorption of IR light.

IR-SNOM IR-SNOM is being developed and used to obtain images with spatial resolutions down to 0.1 μm (Figure 3). At this level sub-cellular structures can be imaged and identified. A specially prepared tapered fibre tip is used to collect the light. The spatial resolution is determined by the diameter of the tip. The amount of light collected by the tip depends on the type of molecule or tissue directly under the tip. Reflection IR-SNOM is a well-developed tech-

ISBN 978-3-95450-134-2

nique where the IR radiation is focussed onto the sample at a grazing angle and the non-diffracting evanescent wave is collected by the fibre [8]. In this work, IR-SNOM has been extended to include transmission SNOM, where the IR radiation is focussed onto the underside of the sample and the fibre collects radiation transmitted through the sample. Both SNOM techniques have benefitted from a new SNOM instrument, which is mounted onto an inverted microscope.

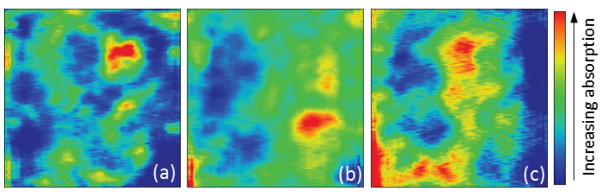

Figure 3: Images of oesophageal tissue recorded with IR-SNOM showing the relative amount of light collected by the fibre tip in reflection mode. (a) 8.05 μm, (b) 7.3 μm, (c) 6.5 μm. Image size is 250×250 μm..

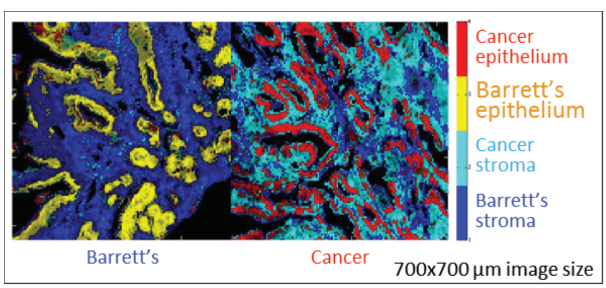

Figure 4: Results of image analysis development on FTIR hyper-spectral images of oesophageal tissue.

Images from biopsies of benign and cancerous tissue have been obtained using both SNOM techniques. The wavelengths were chosen to differentiate different types of tissue. Computerised algorithms, that have the potential to contribute to rapid analysis of biopsies, are being developed. These are initially based on analysis of IR hyperspectral images (HSI) [9]. The potential of IR imaging for cancer identification is illustrated in Figure 4, where cancerous and benign tissues are readily differentiated.

AFM-IR A recently developed atomic force microscopy technique, AFM-IR, which enables images with spatial resolutions of tens of nm to be obtained [10], was deployed. When the frequency of the radiation is tuned to a molecular absorption, the molecule becomes vibrationally excited. This excitation is converted to heat, which in turn causes the sample material to expand to release thermal stress. The reliable detection of this tiny expansion by the sharp (few nm in size) AFM tip has been demonstrated. The deflection of the tip is proportional to the amount of IR absorption. Therefore, by tuning the wavelength chemical analysis can be achieved. Successful AFM-IR imaging was demonstrated on breast cancer cell cultures and Aβ amyloid fibres [10]. Figure 5(b) shows fixed wavelength line scans across one line of a topographic image. Each profile is an average of 128 intensity normalised line scans. Using this set-up, the difference between peptide fibres folded in β-sheets (which are indicators of the Alzheimer disease) and normally folded α-helix protein was observed.

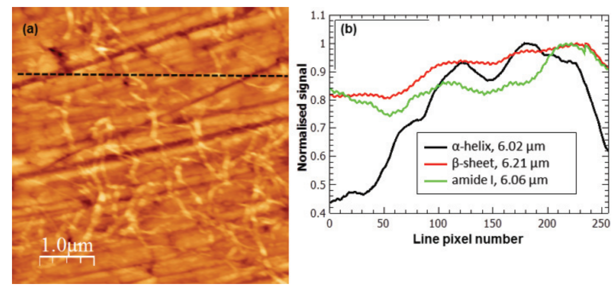

Figure 5: (a) Topographic image of Aβ amyloid fibres on CaF_2 with a dotted line showing the line from where the profiles were taken and (b) normalised line profiles for fixed wavelength line scans: α-helix (6.02μm), β-sheet (6.21μm) and amide I (6.06μm).

THz Studies

The high-intensity broadband THz radiation from ALICE is ideally suited to two projects aimed at advancing the development of cheap portable THz instruments for the diagnosis of cancer. The first project is extending compressive THz spectroscopic imaging to three dimensions [11, 12]. The second project is developing an ultra-sensitive Imaging Fourier Transform Spectrometer, which is an alternative to the traditional THz-TDS (Time-Domain Spectroscopy) imaging technique [13].

ACKNOWLEDGEMENTS

MS-K, TC, JI and PW are grateful to Peter Gardner, Mike Pilling and Paul Bassan for their help and use of their infrared hyperspectral imaging system. The contributions of A. Cricenti, M. Luce, D. Martin, towards the acquisition of SNOM data, are acknowledged. We acknowledge support from the Engineering and Physical Sciences Research Council (EP/K023349/1). The SCAnCan collaboration is grateful to the ASTeC accelerator staff and technical support at Daresbury and Liverpool. OVK and PDT acknowledge support from D. Allsop, C. Tinker-Mill, F. Martin, EU FUNPROB grant 269169 and EPSRC EP/K023373/1.

REFERENCES

[1] '4GLS Conceptual Design Report', CCLRC (2006) `http://www.4gls.ac.uk/cdr/4GLS_CDR.online.pdf`

[2] S. Benson *et al.*, 'First lasing of the Jefferson Lab IR Demo FEL', Nucl. Instrum. Methods Sect. A, 429(1-3) (1999) 27-32

[3] D. Laundy *et al.*, 'Results from the Daresbury Compton backscattering X-ray source ', Nucl. Instrum. Methods Sect. A, 689 (2012) 108-114

ISBN 978-3-95450-134-2

[4] N. R. Thompson *et al*., 'First lasing of the ALICE infra-red Free-Electron Laser ', Nucl. Instrum. Methods Sect. A, 680 (2012) 117-123

[5] R. Williams *et al*,'The influence of high intensity terahertz radiation on mammalian cell adhesion, proliferation and differentiation', Phys. Med. Biol 58 (2) (2013)

[6] F. Jackson *et al*, 'Electron Beam Dynamics in the ALICE IR-FEL Facility', Proceedings of FEL2012, (2012) 464-467, WEPD42, `www.jacow.org`

[7] Engineering and Physical Sciences Research Council funded SCAnCan collaboration grant (EP/K023349/1) `http://gow.epsrc.ac.uk/NGBOViewGrant.aspx?GrantRef=EP/K023349/1`

[8] A. D. Smith *et al*., 'Near-field optical microscopy with an infra-red free electron laser applied to cancer diagnosis', Appl. Phys. Lett. 102 (2013) 053701 and references therein.

[9] E. Gazi, *et al*., J. Pathology 201 99 (2003) and M.J. Baker *et al*., B. J. Cancer 99 1859 (2008).

[10] P. D. Tovee, *et al*. 'Time dynamics of photothermal vs opto-acoustic response in mid-IR nanoscale biospectroscopy', in preparation.

[11] Project lead by Y.-C. Shen, Department of Electrical Engineering and Electronics, The University of Liverpool, Liverpool, UK

[12] Y.C. Shen *et al*., 'Terahertz pulsed spectroscopic imaging using optimized binary masks', Appl. Phys. Lett., 95 231112 (2009).

[13] Project lead by C. Tucker and P. Ade, School of Physics and Astronomy, University of Cardiff, UK in combination with their commercial partners QMC Instruments, Cardiff, UK.

ISBN 978-3-95450-134-2

HPC SIMULATION SUITE FOR FUTURE FELS

R.J. Allan[1], L.T. Campbell[2,3], A.J.T. Colin[4], D. Dunning[3], B.W.J. M^{c}Neil[2], B. Muratori[3], J.D.A. Smith[5], N.R. Thompson[3], P. Traczykowski[2], P. Williams[3]
[1]The Hartree Centre, STFC Daresbury Laboratory, Warrington, UK
[2]SUPA, Department of Physics, University of Strathclyde, Glasgow, UK
[3]ASTeC, STFC Daresbury Laboratory and Cockcroft Institute, Warrington, UK
[4]SUPA, Department of Physics and Astronomy, University of Glasgow, Glasgow, UK
[5]Tech-X UK Ltd, Sci-Tech Daresbury, Warrington, UK

Abstract

A new HPC simulation suite, intended to aid in both the investigation of novel FEL physics and the design of new FEL facilities, is described. The integrated start-to-end suite, currently under development, incorporates both plasma (VSim) and linac (ELEGANT, ASTRA, VSim) accelerator codes, and will include the 3D unaveraged FEL code Puffin to explore novel FEL methods.

INTRODUCTION

Free Electron Lasers are now operating successfully in SASE mode at X-ray wavelengths [1, 2] with others planned or under development [3]. Like the first conventional lasers developed in the early 1960s, X-ray FELs are in their infancy and have the potential for further significant development, particularly with respect to their temporal coherence, pulse durations, potential to deliver synchronised, multi-colour output, and the possibility of being driven by new electron beam sources. Research is now focussing on these future possibilities. Experimental facilities such as [4] and [5] are designed with the dedicated purpose of testing out new techniques for such improved output. At the same time, plasma accelerators have emerged as a promising potential driver of future FELs, with the potential to reduce the size and cost of the facilities.

FEL simulation codes are fundamental tools in the investigation of FEL theory, novel methods and the design of facilities. The most commonly used codes perform approximations including the Slowly Varying Envelope Approximation (SVEA) on the radiation field [6], averaging the electron motion over an undulator period, and discretisation of the electron beam and radiation field into 'slices' (of minimum width equal to the radiation wavelength) over which periodic boundary conditions are applied [7].

As a consequence of these approximations, the averaged SVEA codes are unable to model processes occurring at a sub-resonant wavelength scale (equivalently radiation outside a narrow bandwidth centred on the resonant frequency) [8], or significant changes in the electron beam phase space such as current redistribution during the FEL interaction [9, 10]. While these effects are not important for the basic operation of the FEL, some advanced methods currently proposed to improve the temporal output in the next generation of FELs rely on just such processes [11, 12]. SVEA codes are also unable to model the Coherent Spontaneous Emission (CSE) arising from current gradients in the electron pulse; this can act as a strong seed for the FEL interaction [13]. For these reasons it is necessary to use unaveraged, non-SVEA codes to model FELs driven by Laser Plasma Accelerators (LPAs), which typically produce short, broadband electron beams.

The FEL simulation code PUFFIN (Parallel Unaveraged Fel INtegrator) was developed [14] to be free of the averaging and SVEA approximations which limit other commonly used codes. The primary aim of PUFFIN was to provide a flexible research resource that can be adapted to test new ideas and methods for future FEL development. It was therefore not focused on FEL facility design and leaves it lacking in some features desirable to those designing real experiments. It also lacks simulation paths to and from other accelerator codes, and a good visual on-site interface for outputs.

In the following, we describe a start-to-end (s2e) simulation suite currently under development. It is anticipated that it will aid in the design of the UK CLARA FEL test facility [5] and in interpreting the results of experiments to be performed there. As part of the project, Puffin will undergo development, both to optimize algorithms for new HPC architectures and to implement useful physical features required for proper facility simulation. The suite will include a common visual interface throughout the simulator which will use ASTRA [15], elegant [16, 17] and VSim [18] for the accelerator simulators in conjunction with Puffin for

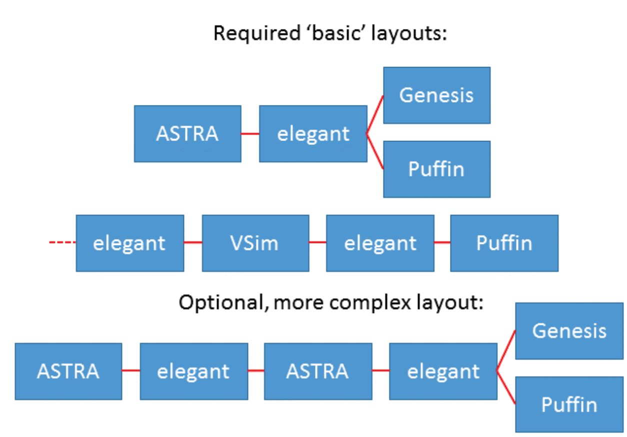

Figure 1: Various simulation layouts afforded by the suite.

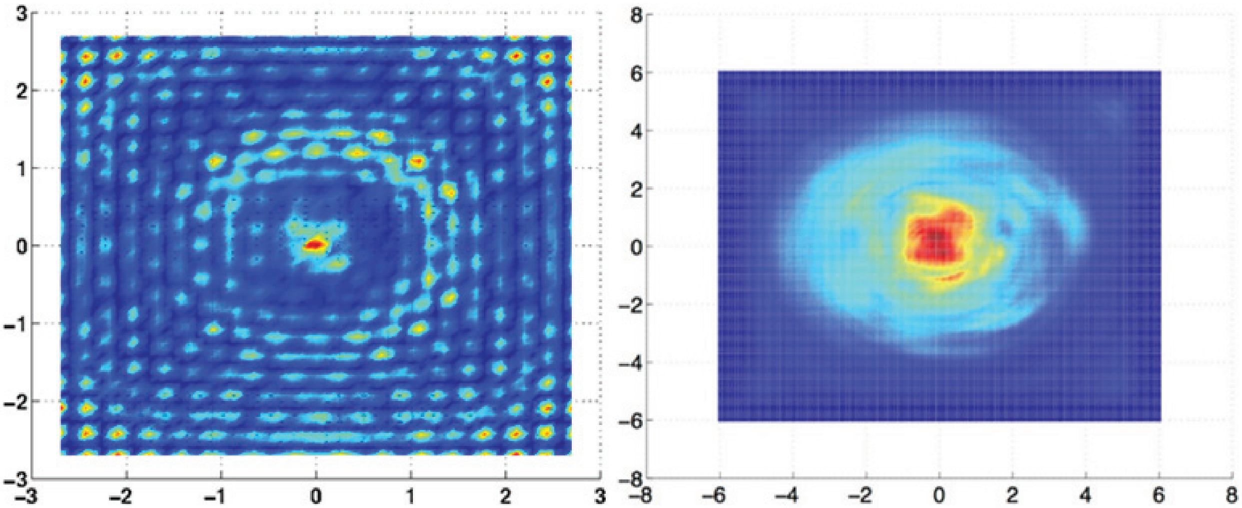

Figure 2: Diffraction before (left) and after (right) the implementation of the absorbing boundary conditions, for identical parameters.

the FEL. Genesis [19] will probably also be included for situations where the extra computational resolution of Puffin is not required. This will result in a s2e suite able to model both plasma accelerator and linac driven FELs that may implement novel accelerator and FEL methods.

SOFTWARE AND LICENCING

The existing codes which will be used in the main simulation chain (elegant, ASTRA, VSim, Puffin) will require simulation 'handshakes' to be written which will pass the electron beam between codes. Further extensions to this model are probable, e.g. it would be useful to include Genesis for benchmarking results with Puffin. These software packages should provide a good platform to perform s2e simulations of the most crucial parts of a facilty. The 2 most basic setups, see Figure 1, allows s2e simulation of a simple RF-linac or plasma accelerator driven FEL. However, more complex scenarios will also be developed and supported.

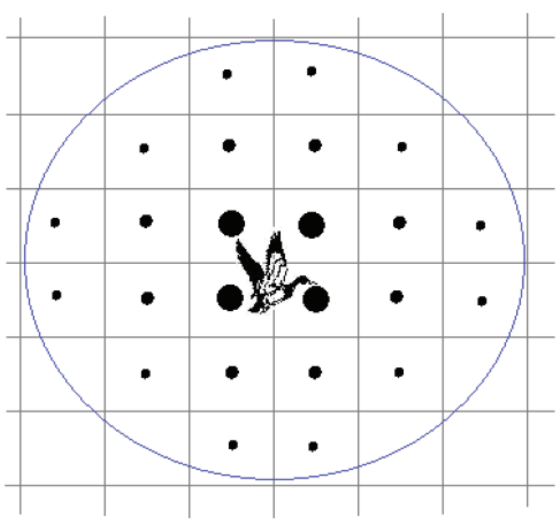

Figure 3: The 'shotgun' model of particle spreading. The heavier macroparticle from the coarse accelerator distribution is the shotgun cartridge and the finer shot (of varying size) are the microparticle. The pellets from the shotgun cartridge spread out over the blast radius according to a spreading factor.

The deployment of the s2e suite onto HPC facilities will be simplified through use of the bilder [21] package management system and the scimake [20] extensions to cmake for finding scientific simulation software packages. Puffin, with the new software and documentation will be released under a BSD or other non-restrictive licence, while extensions to bilder and scimake will be available under their existing open source licenses. As the entire s2e suite supports both closed and open software, hooks will be provided for detection of the presence of other codes (VSim, ASTRA) that have been licensed on the system and addition of the appropriate 'handshakes' for passing data between them. As the configuration software is open source, other software tools may be added in future.

In Puffin, the required resolution of simulation particles is at the sub-resonant wavelength scale. However, in accelerator codes such as elegant, the electrons are usually not required to be so finely sampled. A general code written in C for converting a coarse distribution of few macro-particles into a finer distribution consisting of a greater number of micro-particles is therefore being developed which converts the coursely sampled electron beam from the output of the accelerator codes for input into Puffin. The code takes the coarse macroparticle distribution and breaks it up to distribute them in phase space to a finer distribution consisting of many more microparticles, with the correct Poissonian shot-noise statistics of [22]. An analogy is made in Figure 3 as the spread of pellets (microparticles) from a shotgun car-

ISBN 978-3-95450-134-2

tridge (macroparticle)[1]. A number of spreading profiles of the microparticles are available, the simplest of which are gaussian and top-hat. User-defined spreading profiles may also be used.

IMPROVEMENTS TO PUFFIN

Improvements to Puffin over that as described in [14] include the implementation of transverse boundary conditions to absorb radiation diffracting out the numerical grid. The algorithm involves the use of a transverse 'mask', similar to that described in [23], to absorb a broadbandwidth of frequencies. Previously, periodic boundary conditions, present as a consequence of solving the field diffraction in Fourier space, caused artificial transverse interference when in highly diffractive regimes. See Figure 2 for an example of this, and the subsequent clean-up observed with the absorbing boundaries.

The current 3D undulator field models were described previously in [24], and in the future may utilize field maps to try to correctly simulate *e.g* APPLE II type undulators. The addition of quadrupoles and phase shifters is also a priority for this project to allow e.g. FODO focussing. Current work involving 'ramping' up the undulator field at the start and end of each module indicates that auto phase-matching between undulator modules of the radiation field to a bunched electron beam is a non-trivial task if one has a broadband and/or multi-peaked-spectra beam, and such issues require further work.

The undulator field tapering can be performed by utilizing the model initially developed to produce 2-colour output, (see [10] for an example of the use of tapering in Puffin).

Puffin currently utilizes MPI for parallelism, but there is a requirement to also implement OpenMP to properly utilize resources on the largest HPC machines. A rudimentary hybrid MPI/OpenMP version of Puffin has now been developed, and exhibits a modest scaling with the number of OpenMP threads (depending on the number of macroparticles).

After performance benchmarking and optimization, development to test Puffin on new architectures will also be performed; further development will involve porting to the Intel Xeon Phi architecture, and the appropriateness of using GPU's with Puffin has yet to be evaluated. While Puffin currently implements parallelism with the electron beam, it may be necessary to also develop a parallel field algorithm as larger field grid sizes begin to be used for e.g. high harmonic simulations.

Puffin has not yet been benchmarked against experiment. However, it has been benchmarked against analytic expressions for the broadband spontaneous output, and also the M. Xie fitting formulae [25], and gives excellent agreement in both cases. As part of this project, there will be direct benchmarking against Genesis results and experiments in a variety of cases. This will help to identify the regimes where unaveraged codes are necessary.

[1] No ducks were harmed in the writing of this article.

VISUALISATION

Throughout the the full s2e chain, a suggested or idealized workflow is that the output data will be processed by SDDS [26], then converted to HDF5 [27] formatting with VizSchema compliance for visualization using VisIt [28] (see Figure 4). The SDDS package has extensive, well-tested post-processing scripting routines for extracting relevant, commonly used measurements for accelerator physicists, and the use of VisIt will provide a convenient common interface for all stages of the design process for users.

However, it is expected that pragmatic considerations may alter this visualization chain in some specific cases. For example, VSim already uses VisIt for plotting, meaning it is convenient to utilize those routines which are already in place.

CONCLUSIONS

The HPC suite currently under development and described here will enable the exploration of new FEL methods and allow designs to test them to be developed at facilities such as CLARA and the NLCTA. The suite will also assist in research towards plasma accelerator driven FELs. It is hoped that the portability afforded by the build system will lower the technical barrier of installing and linking these codes together at HPC facilities. The build system produced will also be useful for building Puffin more easily for running on smaller local machines, e.g. in 1D mode on personal laptops.

ACKNOWLEDGEMENTS

We gratefully acknowledge the support of Science and Technology Facilities Council Agreement Number 4163192 Release #3; ARCHIE-WeSt High Performance Computer, EPSRC Grant EP/K000586/1; EPSRC Grant EP/M011607/1 and John von Neumann Institute for Computing (NIC) on JUROPA at Jülich Supercomputing Centre (JSC), under project HHH20. We acknowledge use of Hartree Centre resources in this work. The STFC Hartree Centre is a research collaboratory in association with IBM providing High Performance Computing platforms funded by the UK's investment in e-Infrastructure. The Centre aims to develop and demonstrate next generation software, optimised to take advantage of the move towards exa-scale computing.

REFERENCES

[1] P. Emma *et al.* Nat. Photonics **4** (2010) 641

[2] T. Ishikawa *et al.* 2012 Nat. Photonics **6** (2012) 540

[3] B.W.J. McNeil and N.R. Thompson, Nature Photon. **4** (2010) 814

[4] M. Dunning *et al.*, Proceedings of 2011 Particle Accelerator Conference, New York, NY, USA, MOP014, 130

[5] J.A. Clarke *et al.*, JINST **9** (2014) T05001

[6] F.T. Arecchi and R. Bonifacio, IEEE J. Quantum Electron. **QE-1** (1965) 169

ISBN 978-3-95450-134-2

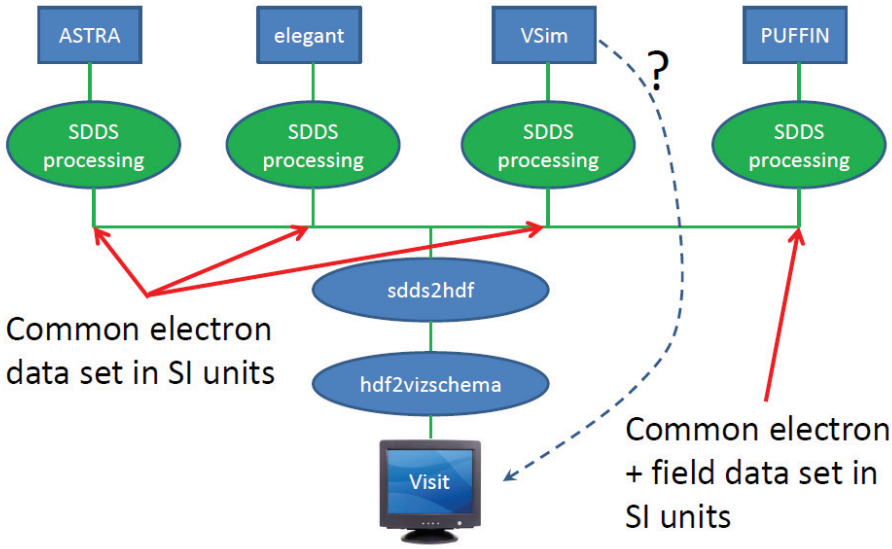

Figure 4: Schematic of the proposed, idealised visualization chain for the simulation suite. SDDS is used for post-processing and VisIt is used for viewing the results after conversion to HDF5 format. Note that VisIt can already directly visualize VSim data, so it may be be more convenient to utilize this functionality within this project.

[7] S. Reiche, Proceedings of FEL2010, Malmö, Sweden (JACoW, 2010), MOOCI1, 165

[8] L.T. Campbell, B.W.J. McNeil and S. Reiche, New J. Phys.**16** (2014) 103019

[9] L.T. Campbell and B.W.J. McNeil, Proceedings of FEL2012, Nara, Japan, THPD41, 626

[10] L.T. Campbell and A.R. Maier, *ibid*

[11] E. Hemsing, G. Stupakov and D. Xiang, Rev. Mod. Phys. **86** (2014) 897

[12] J.R. Henderson, L.T. Campbell and B.W.J. McNeil, New J. Phys. **17** (2015) 083017

[13] B.W.J. McNeil, M. Poole and G. Robb, Phys Rev ST AB **6** (2003) 070701

[14] L.T. Campbell and B.W.J. McNeil, Phys. Plasmas **19** (2012) 093119

[15] Klaus Floettmann, 'ASTRA A Space Charge Tracking Algorithm', `http://www.desy.de/~mpyflo/`, 2015

[16] M. Borland 'elegant: A Flexible SDDS-Compliant Code for Accelerator Simulation', Advanced Photon Source LS-287, September 2000

[17] Y. Wang and M. Borland, Proceedings of the 12th Advanced Accelerator Concepts Workshop, AIP Conf. Proc. 877, 241 (2006).

[18] C. Nieter and J. Cary, Journal of Computational Physics **196** (2004) 448

[19] S. Reiche, Nucl. Instrum. Methods Phys. Res. A **429** (1999) 243

[20] `http://sourceforge.net/p/scimake/wiki/Home/`

[21] `http://sourceforge.net/projects/bilder/`

[22] B.W.J. McNeil, M.W. Poole, and G. R.M. Robb, PRST-AB, **6** (2003) 070701

[23] A.A. Gonoskov and I.A. Gonoskov, Suppression of reflection from the grid boundary in solving the time-dependent Schroedinger equation by split-step technique with fast Fourier transform, arXiv:physics/0607120, (2006)

[24] J. R. Henderson, L.T. Campbell, A.R. Maier and B.W.J. McNeil, Proceedings of FEL2014, Basel, Switzerland, TUP022, 416

[25] M. Xie, Nucl. Inst. Meth. Phys. Res. A 445 (2000) 59

[26] M. Borland, Proc. 1995 PAC, Dallas, Texas (1996) 2184

[27] `https://www.hdfgroup.org/HDF5/doc/index.html`

[28] `https://wci.llnl.gov/simulation/computer-codes/visit/`

ISBN 978-3-95450-134-2

TIME LOCKING OPTIONS FOR THE SOFT X-RAY BEAMLINE OF SwissFEL

E. Prat and S. Reiche
Paul Scherrer Institut, Villigen, Switzerland

Abstract

SwissFEL is an FEL facility presently under construction at the Paul Scherrer Institute that will serve two beamlines: Aramis, a hard X-ray beamline which is under construction and will provide FEL radiation in 2017 with a wavelength between 0.1 and 0.7 nm; and Athos, a soft X-ray beamline which is in its design phase and is expected to offer FEL light in 2021 for radiation wavelengths between 0.7 and 7 nm. A passive synchronization of the FEL signal to a laser source is fundamental for key experiments at Athos, such as time-resolved resonant inelastic X-ray scattering (RIXS) experiments. In this paper we explore different options to achieve this time synchronization by means of energy modulating the electron beam with an external laser.

INTRODUCTION

The SwissFEL facility, presently under construction at the Paul Scherrer Institute, will provide SASE and self-seeded FEL radiation at hard (1–7 Å) and soft (7–70 Å) X-ray FEL beamlines [1]. SwissFEL will operate with electron beam charges varying between 10 and 200 pC and beam energies from 2.1 to 5.8 GeV. The hard X-ray beamline, Aramis, is expected to have the first user experiments in 2017, while the soft X-ray beamline Athos will lase by 2021.

Pivotal experiments for Athos, such as time-resolved resonant inelastic X-ray scattering (RIXS) experiments [2], require a very precise knowledge of the arrival time of the FEL pulse. More generally, pump-probe experiments need an accurate synchronization between the pump and the probe (FEL pulse). This can be achieved with a passive synchronization between the FEL pulse and a conventional laser. One possibility would be to use a laser-based seeding scheme, either direct seeding with a strong HHG source [3] or by employing more complicated layouts like the High-Gain Harmonic Generation (HGHG) [4] and the Echo-Enabled Harmonic Generation [5] schemes. However, laser-based seeding has at present limitations at a radiation wavelength of around 5 nm [6], and going beyond seems very difficult due to shot noise degradation issues [7] from the spontaneous undulator radiation. An alternative approach to passively lock the FEL pulse with an external laser is by energy modulating the electrons that will produce FEL radiation via interaction with a laser pulse in a wiggler magnet. Unlike the methods mentioned above, which induces a coherent signal at the resonant wavelength, the following methods slice the bunch by allowing the bunch to drive the SASE FEL amplification only where it had an overlap with the laser signal.

One possibility to do that is with the ESASE (Enhanced-SASE) mechanism [8], in which a dispersive section (normally a magnetic chicane) is used to convert the energy modulation of the electrons into a density modulation prior to the FEL generation in the undulator beamline. The higher current will drive the FEL amplification faster than the unmodulated beam.

Another option [9] is that the electrons are injected after the modulator directly into the radiator without the need of any dispersive section. The modulation generates an effective energy chirp in the beam that can be exactly compensated with a linear tapering of the undulator field [10]. By tapering one can force that only a very short slice of the bunch produces FEL radiation, while the rest of the electrons will not lase since the tapering will bring them out of the resonance condition. This scheme requires a more powerful laser system than in the ESASE configuration.

The ideal configuration is with an one-period modulator and a few-cycle laser pulse – in such a case a perfectly synchronized FEL pulse is generated. If the modulator has more periods, several short FEL pulses will be generated, which will not be perfectly locked since the modulation and therefore the FEL signal are lengthened. The advantage of this latter option is that the required laser power will be reduced.

In this contribution we will explore the ESASE and the "energy chirp" schemes to achieve the time synchronization of the FEL pulse. Figure 1 shows a schematic layout for these two options.

SIMULATION SETUP

The numerical simulations are done for a radiation wavelength of 1 nm, considering the layout for the soft X-ray beam line Athos with 4 m long undulator modules and 75 cm intra-undulator break sections, which hold the focusing quadrupole and the measurements of the beam positions. The FEL process in the radiator section is simulated with

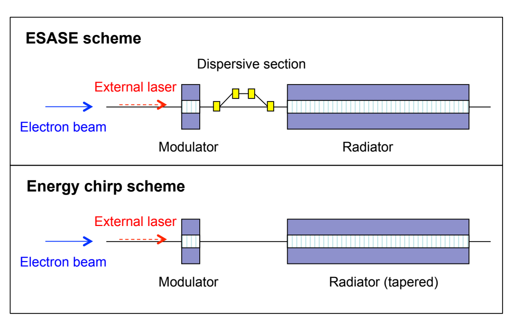

Figure 1: Conceptual layout for slicing the electron beam by an external signal. Either a current modulation or a strong energy chirp (upper and lower plot, respectively) is used to select the part of the bunch which lases.

ISBN 978-3-95450-134-2

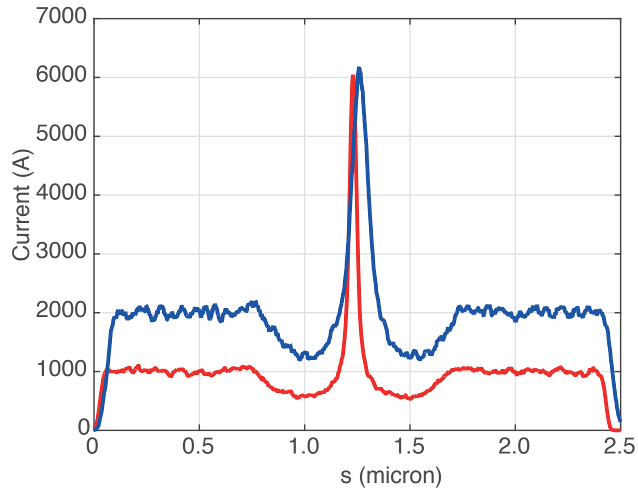

Figure 2: Current and FEL profiles (left and right plot, respectively) for an input beam with 1 and 2 kA beam current (red and blue line, respectively).

Table 1: Parameters of Soft X-ray Beamline at SwissFEL, Used for Simulations

Parameter	Value
Current (flat top)	1–2 kA
Charge	200 pC
Mean energy	3 GeV
RMS energy spread	350 keV
Normalized emittance	300 nm
Average β-function	10 m

the code Genesis 1.3 [11]. Table 1 shows the properties of the electron beam distribution that we used as input for the simulations. The considered normalized emittance value is consistent with our measurements at the SwissFEL Injector Test Facility [12]. We assume that the laser has a wavelength of 800 nm, and that the dispersive section in the ESASE scheme imposes an R_{56} of 0.6 mm.

PERFORMANCE OF ESASE SCHEME

Unlike an HGHG source, where the induced current modulation has a significant harmonic content at the final wavelength, the current spike length in the ESASE scheme is longer than the FEL wavelength. The synchronization occurs because the enhanced current provides locally a faster amplification than the rest of the electron bunch. A strong contrast between current spike and initial current yields a better signal-to-noise of the time-locked FEL pulse.

This argument is only valid if the amplification within the current spike does not suffer from slippage effects with reduced gain in this so called "weak super radiance" regime [13]. To avoid this problem the rms current spike length σ_s has to fulfill the condition [14]:

$$\sigma_s \geq 2L_c \quad , \tag{1}$$

where L_c is the cooperation length. For the SwissFEL case of 1 nm the cooperation length is 50 nm and thus the FWHM of the spike has to be longer than 200 nm. The left plot of Fig. 2 shows two current profiles, where the current has been enhanced in the spike by factors of 3 and 6, respectively. The lower the input current of the electron bunch, the shorter the current spike. For the two cases studied the FWHM lengths are 120 nm and 50 nm, both not fulfilling the criteria for the minimal spike length. As expected the performance suffers and hardly any signal is seen in the profile among the noise (right plot of Fig. 2). Higher compression factors by the ESASE scheme do not help because the spike length drops inversely proportional to the current while the cooperation scales only as $I^{-1/3}$.

The only possible optimization is to increase the spike length by increasing the laser wavelength. At least 2 micron is needed for 1 nm FEL wavelength but at the lowest photon energy the cooperation is about 7 times longer pushing the wavelength of the laser modulation field into the IR range of about 15 microns. While ESASE would work well for hard X-ray FELs it is not considered a viable option for the soft X-ray beam line of SwissFEL.

PERFORMANCE OF LOCAL ENERGY CHIRP AND STRONG TAPERING

An alternative approach is to induce a strong energy modulation. If this beam is injected into an untapered undulator then the slippage will shift the radiation into parts of the bunch where the beam energy does not match the resonance condition any longer. This can be compensated by applying a taper to the undulator field. For the modeling we assume a peak-to-peak energy modulation of 20 MeV as shown in Fig. 3 by a sinusoidal single-cycle laser signal. The strongest chirp (around 4 micron in the plot) will be compensated by the taper. In all other parts of the bunch the electrons are shifted out of resonance due to the taper, where the two

ISBN 978-3-95450-134-2

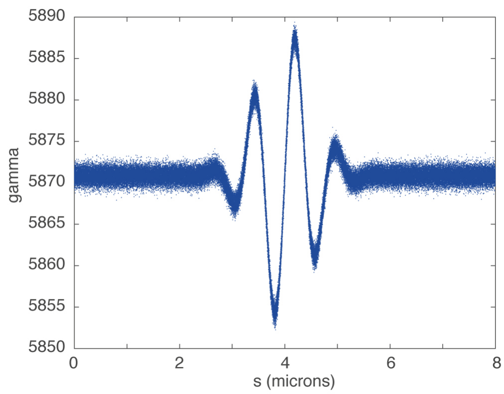

Figure 3: Energy modulation used for the simulation for the injection into a strongly tapered undulator.

smaller positive chirps at 3 and 5 microns have the tendency to stay in resonance the longest. For the best performances we were required to apply stronger taper than needed for the central part. While it degrades the peak power a little bit the two adjacent positive chirps are suppressed even stronger and the contrast ratio between signal and noise is improved. The radiation profile at the end of the taper is shown in Fig. 4 .

It is also possible to change both the sign of the energy chirp and taper gradient with the same efficiency in the slicing performance. If only one sign is flipped then the slicing process selects not one but two areas where the FEL performance is kept in resonance, resulting in two spikes with 3 fs separation and a relative wavelength difference of about 0.3%.

Because the taper gradient is strong a stepwise taper with the 4 m long undulator modules for the soft X-ray beam line of SwissFEL, significantly reduces the performance. Within the 4 m the slippage is sufficiently large to be off resonance either in the beginning or the end of the module and the amplification is reduced. In the same moment the parts which are supposed to be suppressed can stay longer in resonances. Overall the signal-to-noise ratio breaks down

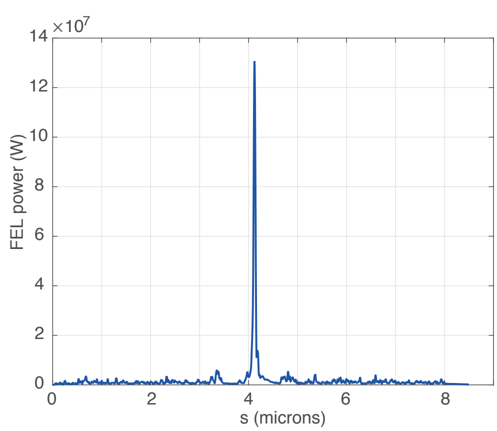

Figure 4: Radiation profile towards the end of the undulator for the strongly tapered undulator field.

and no clear sliced signal is visible. Therefore we consider a smooth linear taper to be mandatory.

A limitation of the valid slippage region is given because the strong energy modulation can only be applied roughly over half the laser wavelength. In our case it is 400 nm. Compared to the two ESASE cases it is 3.5 or 8 times longer, respectively, and allows for a significant build-up of the FEL power. In the case studied we reached 130 MW peak power till the spike reached the upper end of the positive energy chirp (around 4.2 microns in Fig. 3). A reduction in the taper gradient brings up the peak power to saturation at about 5 GW but also reduces the signal-to-noise ratio because two adjacent spikes, 800 nm before and after the main spike, become noticeable in amplitude. However further amplification is possible by either inverting the taper gradient to allow the radiation spike to slip into the region of negative chirp while staying in resonance or by shifting the radiation field into regions of the electron bunch with a small delay of one to two microns, where the beam quality has not been exhausted by the FEL process.

Overall this method seems to be feasible for the soft X-ray FEL beam line at SwissFEL. In particular the design for the undulator modules allows for a linear taper. The APPLE III type modules can generate a transverse gradient, which then translates into a linear taper when the module is rotated around the yaw axis.

ENERGY MODULATION

An external laser provides the input field for the energy modulation based on the interaction with the electron beam in the magnetic field of the modulator undulator. We assume a Ti:Sapph laser system with a wavelength of 800 nm because it generates short but highly intense laser pulses. Because of a wavelength 800 time longer than the FEL wavelength, the modulator parameters are rather extreme with a possible configuration for an undulator with a period of 25 cm and a K-value of 25. Multiple periods are possible but it lengthens the region of the energy modulation due to the slippage within the modulator. In particular single-cycle energy modulations are not possible unless the number of periods is reduced to one. The laser field has to scale inversely with the number of undulator periods. As a consequence reducing the modulator length from 10 to 1 period requires a peak power 100 times larger.

The reduction in the modulator length can actually be extended below a single undulator period. In fact half a period should be sufficient, which corresponds to a single dipole. In the case of the soft X-ray beamline at SwissFEL the transfer line to the undulator has several dipoles. The last one has a bending angle of 2.5 degrees. Replacing the modulator undulator with the last dipole has the additional benefit that the laser can be injected on a straight path with sufficient clearance for the laser optics, unlike a modulator, where the electron beam has an additional bypass chicane so that the laser can be coupled in on a straight line. Also the exit of the last dipole in the transfer line has the smallest

ISBN 978-3-95450-134-2

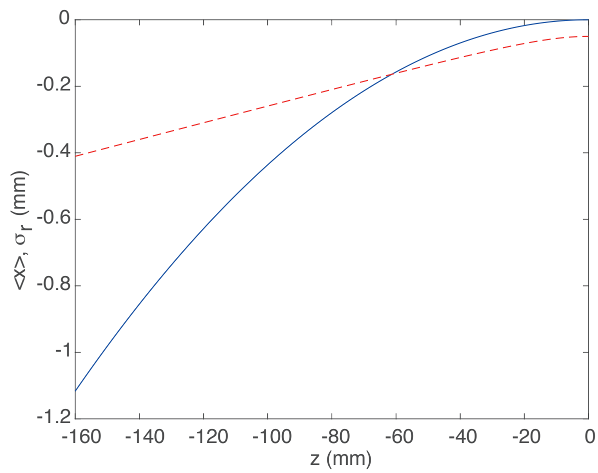

Figure 5: Electron orbit (blue line) and radiation field envelope (red dashed line) within a dipole for energy modulation.

dispersion and therefore the energy modulation is coupled only weakly to a change in the orbit in the order of one micron or less.

In the following we are considering the modulation by means of a dipole. From the simulations presented above a peak-to-peak energy modulation of 0.63% is needed. The laser is aligned that its waist is placed at the exit of the dipole with a direction colinear to the design orbit after the dipole. The bend radius is stronger than the divergence of the laser field so that the electron will fly into the field within the last few centimeters of the dipole. The relation of the orbit to the converging laser field is shown in Fig. 5 for a waist size of 100 µm and a laser wavelength of 800 nm.

The change of the electron energy is given by

$$\begin{aligned} \dot{\gamma} &= \frac{e}{mc^2}\vec{v}\cdot\vec{E} \\ &\approx \frac{eE_0}{mc^2}v_0 \sin\left(\frac{v_0}{R}t\right)\frac{w_0}{w(z)}e^{-\frac{x^2}{w(z)^2}}\cos(\phi(z)), \end{aligned} \quad (2)$$

where v_0 is the total electron velocity, R the bending radius of the dipole, E_0 the maximum field amplitude of the laser field, w_0 the mode size at the waist, $w(z) = w_0\sqrt{1 + z^2/z_r^2}$, z_r the Rayleigh length of the converging laser field, and $\phi(z)$ the interaction phase

$$\phi(z) = kz - \omega t + \phi_0 + \tan^{-1}(z/z_r) \quad , \quad (3)$$

with k and ω the wave number and frequency of the laser field, respectively, and ϕ_0 the injection phase of the laser. The time is chosen so that at $t = 0$ the electron has reached the exit of the dipole with $x, z = 0$. Contributions of any field components in the z-direction have been ignored.

The change in energy is shown in Fig. 6 for $\phi_0 = 0$. Initially the energy is oscillating because the electron moves under an angle, where the interaction phase is varying rapidly up to the point where the electron propagates parallel to the field towards the exit of the dipole. However here the transverse velocity component is also vanishing and the interaction is zero. The major energy change occurs in the last 200 ps for the case presented. Integrating Eq. 2 for various phases gives the net energy change of the electron as shown in Fig. 7.

To match an energy modulation of 0.64%, used for the simulation presented above, an absolute variation of about ±10 MeV is needed. Changes in the waist sizes can be balanced with the power of the laser pulse. In Table 2 various configuration are listed, which are providing the same energy modulation. Larger spot sizes require more radiation power however the optimization towards the smallest values are

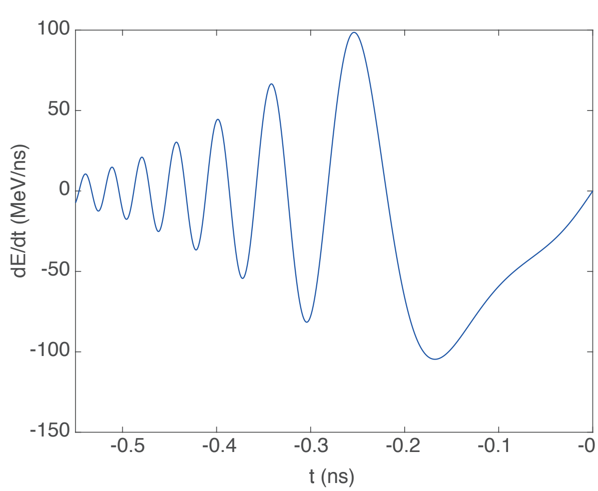

Figure 6: Instantaneous energy change of the electron, interacting with a laser field within a dipole.

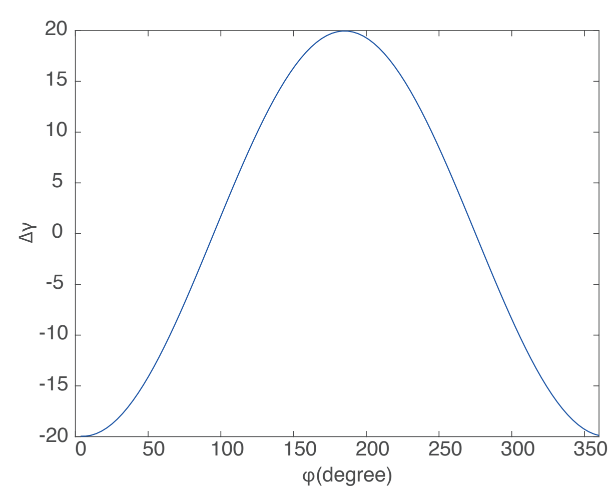

Figure 7: Performance of the energy modulation with a dipole magnet. The amplitude of the laser has been scaled to obtain a peak-to-peak modulation of 20 MeV.

ISBN 978-3-95450-134-2

Table 2: Various Laser Parameters to Obtain the Needed Energy Modulation foR Slicing

Waist Size	Power
60 µm	420 GW
120 µm	740 GW
180 µm	1600 GW

limited by the need for a homogeneous energy modulation for all transverse positions of the electrons within the beam distribution. Therefore the waist has to be significantly larger than the electron beam size. Typical values for SwissFEL are about 45 microns, thus for practical reasons the limit in the laser spot size is given by 100 microns.

We would like to emphasize that the use of a dipole as the modulator is driven by the idea to generate a single attosecond FEL pulse, which is time-locked to the laser pulse. Therefore the overall energy of the laser pulse is about 2.5 mJ, assuming a pulse duration of 3 fs, which seems reasonable for a Ti:Sapph laser system.

TIMING SYNCHRONIZATION

The preferred method of compensating an energy chirp with a strong linear taper yields an FEL spike, which is located close to the end of the positive chirp around the maximum in the energy modulation. Because the start-up is still based on the shot noise of the spontaneous radiation the position is not precise but if the undulator length is matched so that the radiation spike moves with its group velocity over the maximum length of the chirp, then those spikes which are generated at the beginning of the chirp close to the minimum in the energy modulation have the largest amplification. The simulations for different shot-noise seeds yield always the maximum spike within 40 degrees of the energy modulation wavelength, locking the FEL within 300 attosecond to the phase of the external laser signal. This resolution is only preserved if the laser source utilizes a carrier envelope phase stabilization. Otherwise the phase of the laser signal is undefined and the jitter of the FEL pulse is at least 3 fs. For the single spike operation the CEP stabilization is mandatory to provide a matching chirp to the taper of the undulator field.

CONCLUSION

To stabilize the arrival time of the FEL pulse the signal can be locked with an external laser signal. Unlike seeding, which has its challenges to provide a sufficient signal to drive the FEL below 5 nm, slicing is rather robust because it only restricts the region within the electron bunch, where SASE amplification can occur. With a carrier envelope phase stable laser signal the synchronization can be brought down to below 1 fs.

For the wavelength considered for the soft X-ray beam line at SwissFEL, the ESASE scheme has the disadvantage that the FEL process in the induced current spikes suffers significantly from slippage and no good signal can be generated. More favorable is to compensate a strong energy chirp with a linear tapering of the undulator field. A sub-femtosecond spike is generated, which is significantly larger than the background signal and phase locked to the laser signal applying the energy modulation.

To aim for a single spike multi-period modulator have to be avoided. Instead the interaction between electron beam and the laser field can be generated by a single dipole magnet. The expected power is in the order of one Terawatt with a pulse duration of about 3 fs, which in reach of existing Ti:Saphh laser systems.

ACKNOWLEDGMENT

We thank T. Schmidt and M. Calvi for explaining to us the feasibility of a linear taper with the UE40 undulytor modules for Athos and B. Patterson to initiate the discussion of passive locking of the FEL signal with an external laser.

REFERENCES

[1] R. Ganter (ed.), PSI Report No. 10-04, 2012.

[2] B. D. Patterson and Mirjam van Daalen (eds.), PSI Report No. 14-01, 2014.

[3] M. Ferray et al., Journal of Physics B: Atomic Molecular and Optical Physics 21, L31 (1988).

[4] L.H. Yu, Phys. Rev. A, 44, 5178 (1991).

[5] G. Stupakov, Phys. Rev. Lett. 102, 074801 (2009).

[6] E. Allaria et al., Nat. Photonics 7, 913 (2013).

[7] E. L. Saldin, E. A. Schneidmiller, and M. V. Yurkov, Opt. Commun. 202, 169 (2002).

[8] A. A. Zholents, Phys. Rev. ST Accel. Beams 8, 040701 (2005).

[9] E. L. Saldin, E. A. Schneidmiller, and M. V. Yurkov, Phys. Rev. ST Accel. Beams 9, 050702 (2006).

[10] N. M. Kroll, P. L. Morton, and M. Rosenbluth, IEEE J. Quantum Electron., 17, 1436 (1981).

[11] S. Reiche, Nucl. Instr. Meth. A 429, 243 (1999).

[12] E. Prat, M. Aiba, S. Bettoni, B. Beutner, S. Reiche, and T. Schietinger, Phys. Rev. ST Accel. Beams 17, 104401 (2014).

[13] R. Bonifacio, B. W. J. McNeil, and P. Pierini, Phys. Rev. A 40, 4467 (1989).

[14] S. Reiche, P. Musumeci, C. Pellegrini and J.B. Rosenzweig, Nucl. Instr. Meth. A 593, 45 (2008).

ISBN 978-3-95450-134-2

RECENT STUDY IN iSASE

K. Fang, C. Pellegrini, J. Wu, SLAC National Accelerator Laboratory, Menlo Park, CA 94025, USA
S. Hsu, University of California, San Diego, CA, 92093, USA
C. Emma, C. Pellegrini, University of California, Los Angeles, CA 90095, USA

Abstract

The Improved Self-Amplified Spontaneous Radiation (iSASE) scheme has the potential to reduce SASE FEL bandwidth. This is achieved by repeatedly delaying the electrons with respect to the radiation pulse using phase shifters in the undulator break sections. It has been shown that the strength, locations and sequences of phase shifters are important to the iSASE performance. The particle swarm optimization algorithm is used to explore the phase shifters configuration space globally.

INTRODUCTION

Improved Self Amplified Spontaneous Emission (iSASE) [1, 2] is capable of improving spectrum by increasing cooperation length. Electrons are delayed with respect to the optical field by phase shifters in the FEL lattice. And connection is built up between electrons that are separated by several coherent spikes width away. With proper interference between new grown field and optical field, bandwidth can be reduced.

There has been effort to investigate the mechanism of study the proper phase delay configuration. There is study proposes to arrange phase shifter strength in a geometric or reverse geometric sequence. In this kind of configuration, the largest phase delay creates a small period frequency comb modulation in the power spectrum. When the second largest phase delay, which is half of the largest delay, has a good phase match, it eliminates some of the side band peaks and amplifies the central peak. Using this scheme, the central peak can be effectively selected. There are also other schemes uses prime number phase delay [3] and random phase delay [4] to improve the FEL bandwidth.

Some optimization method, such as simulated annealing method [5], has been used to optimize iSASE. The method is able to explore the solution space locally around a reverse geometric sequence configuration, but not yet conclusive. This study focuses on the global optimization of iSASE phase delay configuration.

iSASE

FEL bandwidth is improved by repeatedly delaying the electron bunch with respect to the optical field. After each phase delay, the interference effect between the shifted light field and the new grown field from energy and density modulated electron beam appears as a modulation to the FEL power spectrum [6],

$$P(\nu; z) = P_0(\nu; z)T(\nu, \phi, a), \quad (1)$$

$$T(\nu, \phi, a) \propto 1 + |a|^2 + 2|a|\cos(\nu\phi + \varphi). \quad (2)$$

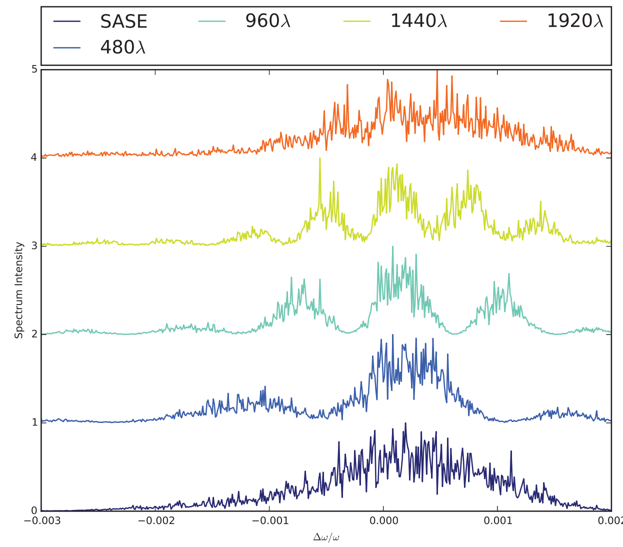

Figure 1: Modulation can be seen in the FEL power spectrum after the first phase shifter. The modulation period decreases with larger phase delay. Yet there is a limit (960λ) where the modulation pattern no longer exists. This is because the dispersive effect in the phase shifter strong enough to wash out the density modulation in the electron bunch. Only the optical field carries the pure SASE spectrum through the phase shifter.

Here ϕ is the integer phase delay. The modulation period is inversely proportional to ϕ. φ, the fractional phase delay, controls the center of the modulation function. a is the relative amplitude between the shifted optical field and the new grown field. The dispersive effect in the phase shifter can cause damping to electron bunching and even distort the electron bunch density modulation. The interference effect is degraded by the dispersive effect. Therefore it sets a upper limit to the tolerable phase delay value (Fig. 1). A narrow filtering function can be generated using multiple modulation functions with different modulation periods.

PARTICLE SWARM OPTIMIZATION

Particle swarm optimization algorithm mimics the behavior of bird flocking. The candidate solutions, which are called particles, have position and velocity. At the beginning, particles are randomly distributed in the solution space with random velocity. As particles sweep through the solution space, particles find solutions with different cost values. During the process, particles are also attracted by the good solutions, with lower cost values, that have been experienced by the particles. And these good solutions may

ISBN 978-3-95450-134-2

be replaced by the even lower cost solutions found by the particles. Eventually particles cluster around the global optimal solutions. Therefore the particle swarm optimization algorithm is known for its ability to search for global minimum. The evolution equation for the algorithm can be written as,

$$x^i(n+1) = x^i(n) + v^i(n) \tag{3}$$

$$v^i(n+1) = \alpha v^i(n) + U(0,\beta)(p^i(n) - x^i(n)) + U(0,\beta)(g^i(n) - x^i(n)). \tag{4}$$

Here $x^i(n), v^i(n)$ are the i^{th} particle position and velocity respectively after the n^{th} iteration. α is the particle inertia. $U(0,\beta)$ is a random number that sampled uniformly between $(0,\beta)$. $p^i(n)$ is the best solution the i^{th} particle has experienced after n iterations. $g^i(n)$ is the best solution among the neighbors of the i^{th} particle. There are two general definition of neighbors. One assumes that the all particles fully connected. In this topology, particles are attracted by the best solution that ever experienced by the whole group. The second setting assumes that particles can only communicate with their adjacent neighbors. The first setting usually converges faster than the latter topology. Yet, the latter one is less likely to be attracted by local minimums than the first one. In our study, we consider the particles are only connected to their adjacent neighbors.

OPTIMIZATION RESULT

Particle swarm optimization algorithm is applied to optimize iSASE configuration. The algorithm searches for the optimal bandwidth in the phase delay variable space. In this study, we consider inserting five phase shifters to a LCLS-II type machine. In such machine, the gain length is about the length of a undulator section. The phase shifters are placed between the gap sections with the first one locating after the fourth undulator section. Drift space is taken out so that the center of modulations function align with SASE center frequency.

Phase delay upper bound in the optimization is set at 1800λ so that the electron beam can maintain its bunching after a dispersive chicane (Fig. 1). 100 particles are uniformly distributed in the parameter space (Fig. 2). The algorithm converges after 200 iterations (Fig. 3). Particles are clustering around the global minimum. There are particles scattering around the cluster. This is coming from the last two terms on the right hand side of Eq. 4. Particles tend to oscillate around the global minimum.

The global best solution (Fig. 4) yields a 9×10^{-5} bandwidth (Fig. 5), which is 4 times smaller than the SASE bandwidth. Figure 6 demonstrates that the solution is a minimum point. The FEL bandwidth tends to increase, as the Euclidian distance to the global best solution increases. By investigating the particles that has Euclidian distance larger than 10, we find that they are solutions that basically switch the values of the first two phase shifters. It is one of the local minimums the algorithm finds before converging to the global minimum. This confirms with the fact that as the

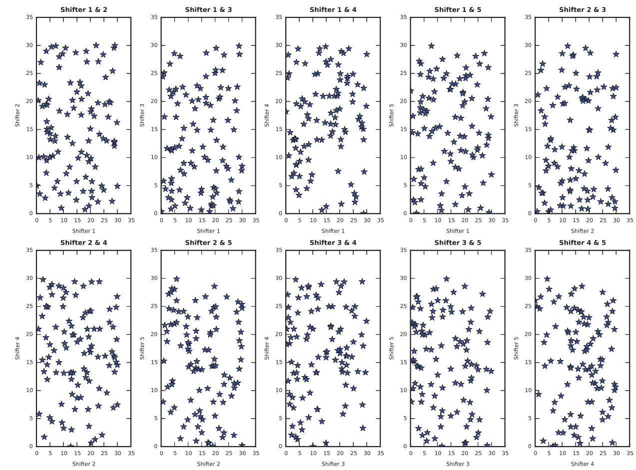

Figure 2: Particles are distributed uniformly in the solution space initially.

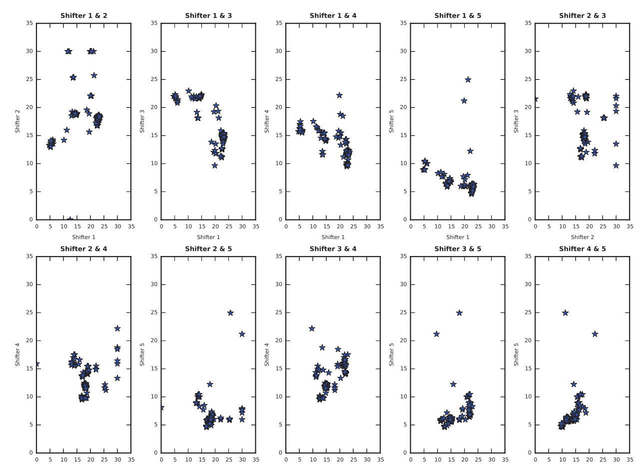

Figure 3: At the end of the optimization, particles cluster around the global best solution.

energy modulation amplitude increases in the linear regime, the tolerable phase delay decreases. Thus the golbal best solution has large phase delay at beginning and small phase delay at the end.

We also notice that the first phase delay value almost reaches the limit of the phase delay values where interference can be well maintained. The first phase shifter defines the finest modulation period. The configuration can be divided into two parts. The 1st, 4th and 5th phase delays are 1380λ,720λ and 360λ respectively. This three phase delays form a reverse geometric sequence. This kind of configuration can effectively eliminate the side bands as it is shown in the middle plot of Fig. 7. However, since the largest one has already reach the limit, the reverse geometric sequence cannot continue. With a isochronous chicane, it can be shown that a 20 times bandwidth reduction can be achieved by extending the existing reverse geometric sequence with five phase shifters (Fig. 5). On the other hand, the algorithm is able to find a compromising solution. The 2nd and 3^{rd}

ISBN 978-3-95450-134-2

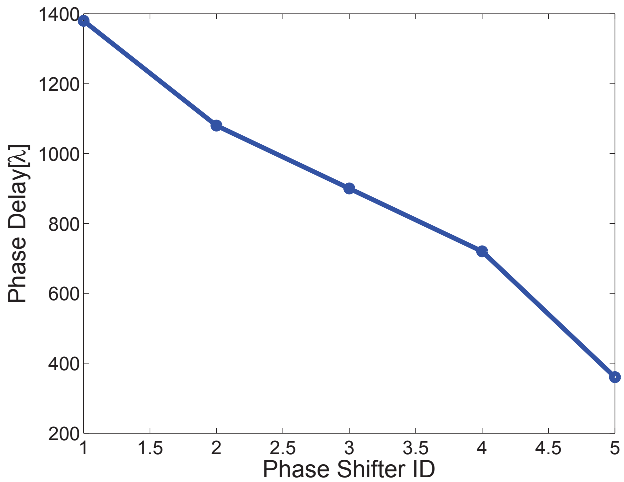

Figure 4: The optimal phase shifter values from the particle swarm optimization.

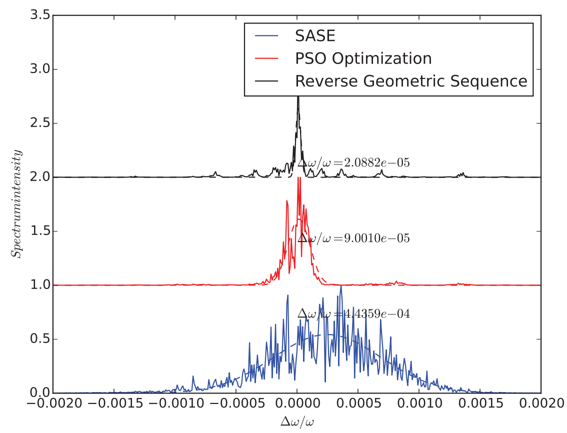

Figure 5: The FEL bandwidth is reduced by a factor of four from 4.4×10^{-4} to 9.0×10^{-5} with dispersive effect. It can be further reduced to 2×10^{-5} with isochronous chicanes.

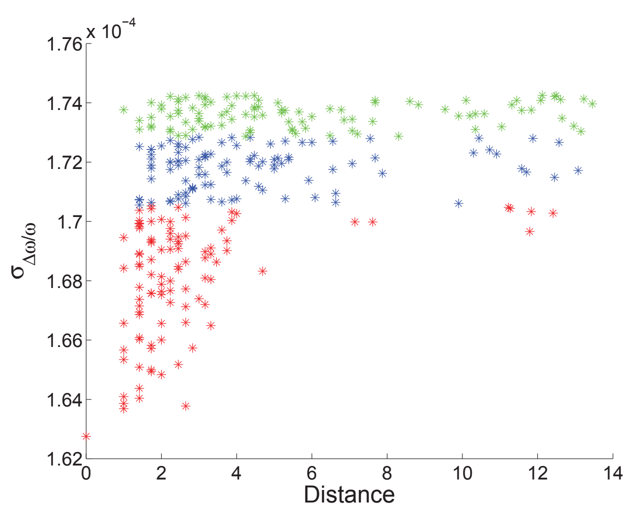

Figure 6: The Euclidian distance to the global best solution for the first 300 best solutions is plotted against their bandwidth.

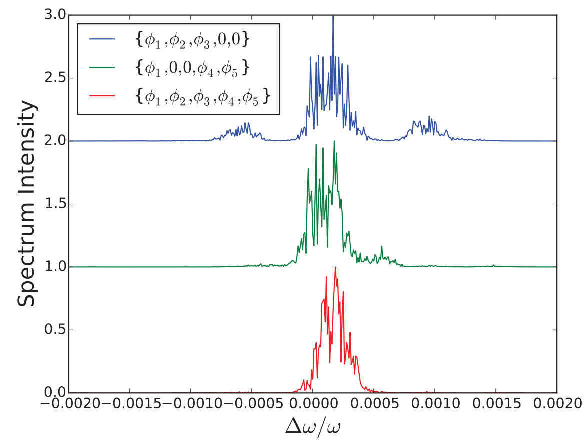

Figure 7: The upper figure plots the final power spectrum with first three phase shifters. The middle figure plots the spectrum with reverse geometric sequence. The last one is the global best solution found by the optimization.

phase shifters are used to further narrow the central peak. With the first three phase shifters, the FEL power spectrum has a narrower distribution and with small sidebands (the upper plot in Fig. 7). Therefore the combination of these two mechanisms finally shape the FEL power spectrum and yield a narrow bandwidth.

CONCLUSION

Particle swarm optimization is applied to iSASE to search the optimal phase shifter configuration. The algorithm is able to avoid multiple local minimums and find the global minimum. The FEL bandwidth is reduced by a factor of 4 from 4.4×10^{-4} to 9×10^{-5}. And the global best solution also confirms that the reverse geometric sequence configuration is able to remove sidebands effectively. The limitation is caused by the dispersive effect of the phase shifter. By introducing nonlinear chicane, the reduction factor can at least be further enhanced to 20.

ACKNOWLEDGEMENT

This work was supported by the US Department of Energy (DOE) under the US DOE Office of Science Early Career Research Program grant FWP-2013-SLAC-100164

REFERENCES

[1] J. Wu et al, "Generation of longitudinally coherent ultra high power X-Ray FEL pulses by phase and amplitude mixing", in *Proceedings of the 32th International Free Electron Laser Conference, Nara, Japan, 2012* (JACoW,2012), p. 237.

[2] J. Wu et al, "X-Ray spectra and peak powr control with iSASE" in *Proceedings of the 4th International Particle Accelerator Conference, Shanghai, China, 2013* (JACoW,2013), p. 2068.

[3] B.W.J. McNeil, N.R. Thompson, and D.J. Dunning, "Transform-Limited X-Ray Pulse Generation from a High-

ISBN 978-3-95450-134-2

Brightness Self-Amplified Spontaneous-Emission Free-Electron Laser”, Phys. Rev. Lett., **110**, 134802 (2013).

[4] N.R. Thompson, D.J. Dunning, and B.W.J. McNeil, “Improved temporal coherence in SASE FELS”, in *Proceedings of the 1st International Particle Accelerator Conference, Kyoto, Japan, 2010* (IEEE,Newyork,2010), p. 2257.

[5] L. Gupta, K. Fang, and J. Wu, “Optimization of an improved SASE (iSASE) FEL”, in *Proceedings of the 6th International Particle Accelerator Conference, Richmond, USA, 2015* (JACoW,2015), p. 1881.

[6] K. Fang, et al. “iSASE Study”,in *Proceedings of the 36th International Free Electron Laser Conference, Basel, Switzerland, 2014* (JACoW,2014), p. 442.

FUNDAMENTAL LIMITATIONS OF THE SASE FEL PHOTON BEAM POINTING STABILITY

E.A. Schneidmiller, M.V. Yurkov, DESY, Hamburg, Germany

Abstract

The radiation from Self Amplified Spontaneous Emission Free Electron Laser (SASE FEL) [1, 2] has always limited value of the degree of transverse coherence. Two effects define the spatial coherence of the radiation: the mode competition effect, and the effect of poor longitudinal coherence. For the diffraction limited case we deal mainly with the effect of the poor longitudinal coherence leading to significant degradation of the spatial coherence in the post-saturation regime. When transverse size of the electron beam significantly exceeds diffraction limit, the mode competition effect does not provide the selection of the ground mode, and spatial coherence degrades due to contribution of the higher azimuthal modes. Another consequence of this effect are fluctuations of the spot size and pointing stability of the photon beam. These fluctuations are fundamental and originate from the shot noise in the electron beam. The effect of pointing instability becomes more pronouncing for shorter wavelengths. Our study is devoted to the analysis of this effect and description of possible means for improving the degree of transverse coherence and the pointing stability.

INTRODUCTION

Previous studies have shown that coherence properties of the radiation from SASE FEL strongly evolve during the amplification process [3–7]. At the initial stage of amplification the spatial coherence is poor, and the radiation consists of a large number of transverse modes [7–15]. Longitudinal coherence is poor as well [16–18]. In the exponential stage of amplification the transverse modes with higher gain dominate over modes with lower gain when the undulator length progresses. This feature is also known as the mode competition process. Longitudinal coherence also improves in the high gain linear regime [18–20]. The mode selection process stops at the onset of the nonlinear regime, and the maximum values of the degree of the transverse coherence and of the coherence time are reached at this point. The undulator length required to reach saturation is in the range from about nine (hard x-ray SASE FELs) to eleven (visible range SASE FELs) field gain lengths [3]. The situation with the transverse coherence is favorable when the relative separation of the field gain between fundamental and higher modes exceeds 25-30%. In this case the maximum degree of transverse coherence can exceed the value of 90% [3, 7]. Further development of the amplification process in the nonlinear stage leads to visible degradation of the coherence properties.

Relative separation of the gain of the FEL radiation modes depends on the value of the diffraction parameter. Increase of the value of the diffraction parameter results in a smaller relative separation of the gain of the modes. In this case we deal with the mode degeneration effect [9, 12]. Since the number of gain lengths to saturation is limited, the contribution of the higher spatial modes to the total power grows with the value of the diffraction parameter, and the transverse coherence degrades. Large values of the diffraction parameter are typical for SASE FELs operating in the hard x-ray wavelength range [21–25].

In this paper we perform analysis of the radiation modes, and find their ranking in terms of the field gain. The main competitor of the ground TEM_{00} is the first azimuthal TEM_{10} mode. When contribution of TEM_{10} mode to the total power exceeds a few per cent level, a fundamental effect of bad pointing stability becomes to be pronouncing. The power of the effect grows with the electron beam size in the undulator. We present detailed analysis of this effect for Free Electron Laser FLASH [26, 27] which currently takes place due to the weak focusing in the undulator resulting in large values of the diffraction parameter and conditions of the "cold" electron beam [28]. Our analysis shows that operation with a stronger focusing of the electron beam and a lower peak current would allow one to improve both, the degree of transverse coherence and the pointing stability of the photon beam at FLASH.

The figure of merit for operation of optimized SASE FEL is the ratio of the geometrical emittance to the radiation wavelength, $\hat{\epsilon} = 2\pi\epsilon/\lambda$ [3–5]. Parameter space of optimized SASE FELs is typical for the hard x-ray regime. We show that SASE FELs operating at short wavelengths and low electron beam energy with the value of $\hat{\epsilon} > 1$ suffer from the mode degeneration effect resulting in significant degradation of the spatial coherence and pointing stability of the photon beam. The effect of the photon beam pointing jitter is a fundamental one, and can not be eliminated by eliminating of the jitters of machine parameters.

ANALYSIS OF THE RADIATION MODES

We consider an axisymmetric model of the electron beam. It is assumed that the transverse distribution function of the electron beam is Gaussian, so the rms transverse size of matched beam is $\sigma = \sqrt{\epsilon\beta}$, where ϵ is the rms beam emittance and β is the beta-function. In the framework of the three-dimensional theory, the operation of a short-wavelength FEL amplifier is described by the following parameters: the diffraction parameter B, the energy spread parameter $\hat{\Lambda}_T^2$, the betatron motion parameter $\hat{k}_\beta$ and detuning parameter $\hat{C}$ [11, 12]:

$$\begin{aligned} B &= 2\Gamma\sigma^2\omega/c\,, \qquad \hat{C} = C/\Gamma\,, \\ \hat{k}_\beta &= 1/(\beta\Gamma)\,, \qquad \hat{\Lambda}_T^2 = (\sigma_E/E)^2/\rho^2\,, \end{aligned} \tag{1}$$

ISBN 978-3-95450-134-2

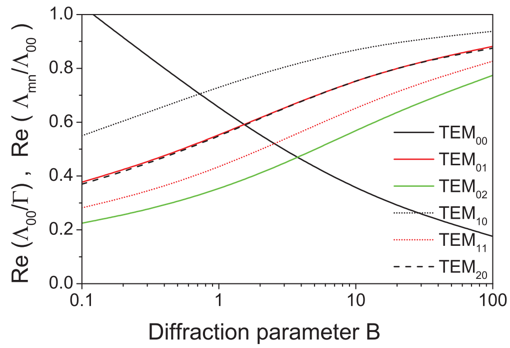

Figure 1: Ratio of the maximum gain of the higher modes to the maximum gain of the fundamental mode $\mathrm{Re}(\Lambda_{mn})/\mathrm{Re}(\Lambda_{00})$ versus diffraction parameter B. The energy spread parameter is $\hat{\Lambda}_{\mathrm{T}}^2 \to 0$, and the betatron motion parameter is $\hat{k}_\beta \to 0$. Color codes refer to the radial index of the mode: 0 - black, 1 - red, 2 - green. Line type codes refer to the azimuthal index of the mode: 0 - solid line, 1 - dotted line, 2 - dashed line. Black solid line shows the gain of the fundamental mode $\mathrm{Re}(\Lambda_{00})/\Gamma$.

where $E = \gamma mc^2$ is the energy of electron, γ is relativistic factor, $\Gamma = \left[I\omega^2\theta_{\mathrm{s}}^2 A_{\mathrm{JJ}}^2/(I_{\mathrm{A}} c^2\gamma_{\mathrm{z}}^2\gamma)\right]^{1/2}$ is the gain parameter, $\rho = c\gamma_{\mathrm{z}}^2\Gamma/\omega$ is the efficiency parameter, and $C = 2\pi/\lambda_{\mathrm{w}} - \omega/(2c\gamma_{\mathrm{z}}^2)$ is the detuning of the electron with the nominal energy $\mathcal{E}_0$. Note that the efficiency parameter ρ entering equations of three dimensional theory relates to the one-dimensional parameter ρ_{1D} as $\rho_{\mathrm{1D}} = \rho/B^{1/3}$ [12, 29]. The following notations are used here: I is the beam current, $\omega = 2\pi c/\lambda$ is the frequency of the electromagnetic wave, λ_{w} is undulator period, $\theta_{\mathrm{s}} = K/\gamma$, K is the rms undulator parameter, $\gamma_z^{-2} = \gamma^{-2} + \theta_{\mathrm{s}}^2$, $I_{\mathrm{A}} = mc^3/e = 17$ kA is the Alfven current, $A_{\mathrm{JJ}} = 1$ for helical undulator and $A_{\mathrm{JJ}} = J_0(K^2/2(1+K^2)) - J_1(K^2/2(1+K^2))$ for a planar undulator. J_0 and J_1 are the Bessel functions of the first kind. The energy spread is assumed to be Gaussian with the rms deviation σ_{E}.

The amplification process in SASE FEL starts from the shot noise in the electron beam. At the initial stage of amplification, the coherence properties are poor, and the radiation consists of a large number of transverse and longitudinal modes [7–15]:

$$\tilde{E} = \sum_{m,n} \int \mathrm{d}\omega A_{mn}(\omega, z)\Phi_{mn}(r,\omega) \times \exp[\Lambda_{mn}(\omega)z + im\phi + i\omega(z/c - t)] \,. \quad (2)$$

Each mode is characterized by the eigenvalue $\Lambda_{mn}(\omega)$ and the field distribution eigenfunction $\Phi_{mn}(r,\omega)$. The real part of the eigenvalue $\mathrm{Re}(\Lambda_{mn}(\omega))$ is referred to as the field gain. The field gain length is $L_g = 1/\mathrm{Re}(\Lambda_{mn}(\omega))$. Eigenvalues and eigenfunctions are the solutions of the eigenvalue equation [10, 11]. Each eigenvalue has a maximum at a certain frequency (or, at a certain detuning), so that the detunig for each mode is chosen automatically in the case of a SASE FEL (in contrast with seeded FELs where the detuning can be set to any value). Thus, we use the three dimensionless parameters: B, $\hat{k}_\beta$, and $\hat{\Lambda}_{\mathrm{T}}^2$.

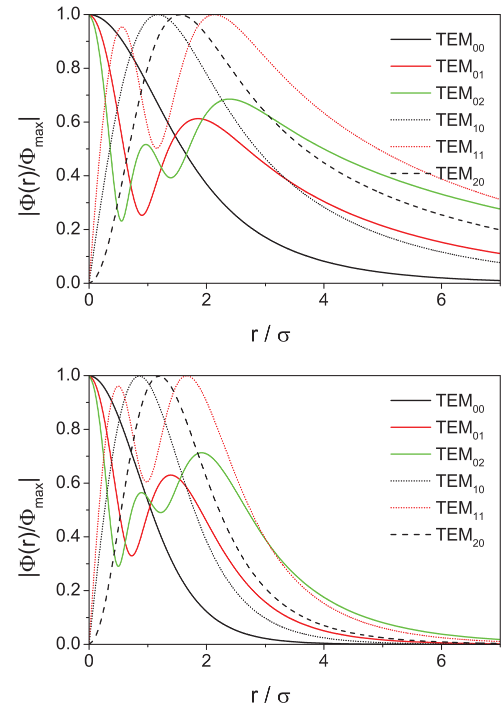

Figure 2: Amplitude of the eigenfunctions of the FEL radiation modes, $|\Phi_{mn}(r)|/|\Phi_{\max}|$. Top and bottom plots correspond to the diffraction parameter $B = 1$ and $B = 10$, respectively. The detuning corresponds to the maximum of the gain. The energy spread parameter is $\hat{\Lambda}_{\mathrm{T}}^2 \to 0$, and the betatron motion parameter is $\hat{k}_\beta \to 0$. Color codes refer to the radial index of the mode: 0 - black, 1 - red, 2 - green. Line type codes refer to the azimuthal index of the mode: 0 - solid line, 1 - dotted line, 2 - dashed line.

Let us look closer at the properties of the radiation modes. The gains for several modes are depicted in Fig. 1 as functions of the diffraction parameter. The values for the gain correspond to the maximum of the scan over the detuning parameter $\hat{C}$. The curve for the TEM$_{00}$ mode shows the values of the normalized gain $\mathrm{Re}(\Lambda_{00}/\Gamma)$. Curves for the higher spatial modes present the ratio of the gain of the mode to the gain of the fundamental mode, $\mathrm{Re}(\Lambda_{mn}/\Lambda_{00})$. Sorting the modes by the gain results in the following ranking: TEM$_{00}$, TEM$_{10}$, TEM$_{01}$, TEM$_{20}$, TEM$_{11}$, TEM$_{02}$. The gain of the fundamental TEM$_{00}$ mode is always greater than the gain of higher order spatial modes. The difference in the gain between the fundamental TEM$_{00}$ mode and higher spatial modes is pronounced for small values of the diffraction parameter $B \lesssim 1$. The gain of higher spatial modes approaches asymptotically the gain of the fundamental mode for large values of the diffraction parameter. In other words, the effect of the mode degeneration takes place. Its origin can be understood with the qualitative analysis of the eigenfunctions (distribution of the radiation field in the near zone). Figure 2

ISBN 978-3-95450-134-2

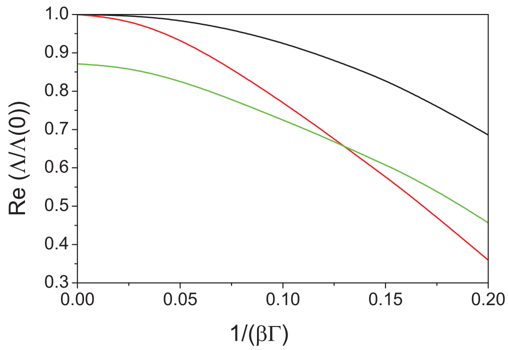

Figure 3: Dependence of the gain of TEM_{00} mode (black curve) and TEM_{10} mode (red curve) on the betatron motion parameter $\hat{k}_\beta = 1/(\beta\Gamma)$. The values are normalized to those at $\hat{k}_\beta \to 0$. Green curve shows the ratio of the gain of TEM_{10} mode to the gain of TEM_{00} mode. The diffraction parameter is $B = 10$. The energy spread parameter is $\hat{\Lambda}_T^2 \to 0$.

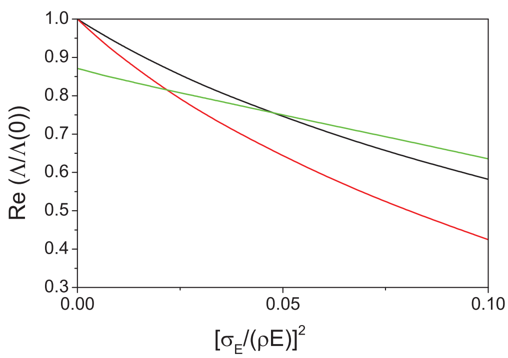

Figure 4: Dependence of the gain of TEM_{00} mode (black curve) and TEM_{10} mode (red curve) on the energy spread parameter $\hat{\Lambda}_T^2$. The values are normalized to those at $\hat{\Lambda}_T^2 \to 0$. Green curve shows the ratio of the gain of TEM_{10} mode to the gain of TEM_{00} mode. The diffraction parameter is $B = 10$. The betatron oscillation parameter is $\hat{k}_\beta \to 0$.

shows eigenfunctions of the FEL radiation modes for two values of the diffraction parameter, $B = 1$ and $B = 10$. We observe that for small values of the diffraction parameter the field of the higher spatial modes spans far away from the core of the electron beam while the fundamental TEM_{00} mode is more confined. This feature provides a higher coupling factor of the radiation with the electron beam and higher gain. For large values of the diffraction parameter all radiation modes shrink to the beam axis which results in an equalizing of coupling factors and of the gain. Asymptotically, the eigenvalues of all modes tends to the one dimensional asymptote as [5]:

$$\Lambda_{mn}/\Gamma \simeq \frac{\sqrt{3}+\mathrm{i}}{2B^{1/3}} - \frac{(1+\mathrm{i}\sqrt{3})(1+n+2m)}{3\sqrt{2}B^{2/3}} \qquad (3)$$

For a SASE FEL, the undulator length to saturation is in the range from about nine (hard x-ray range) to eleven (visible range) field gain lengths [3,4,6]. The mode selection process stops at the onset of the nonlinear regime, about two field gain lengths before saturation. Let us make a simple estimate for the value of the diffraction parameter $B = 10$ and a cold electron beam, $\hat{\Lambda}_T^2 \to 0$, and $\hat{k}_\beta \to 0$. We get from Fig. 1 that the ratio of the gain $\mathrm{Re}(\Lambda_{10}/\Lambda_{00})$ is equal to 0.87. With an assumption of similar values of coupling factors, we find that the ratio of the field amplitudes at the onset of the nonlinear regime is about of factor of 3 only. An estimate for the contribution of the higher spatial modes to the total power is about 10 %. Another numerical example for $B = 1$ gives the ratio $\mathrm{Re}(\Lambda_{10}/\Lambda_{00}) = 0.73$, and the ratio of field amplitudes exceeds a factor of 10. Thus, an excellent transverse coherence of the radiation is not expected for SASE FEL with diffraction parameter $B \gtrsim 10$ and a small velocity spread in the electron beam.

Longitudinal velocity spread due to the energy spread and emittance serves as a tool for the selective suppression of the gain of the higher spatial modes [9,12]. Figures 3 and 4 show the dependence of the gain of TEM_{00} and TEM_{10} modes on the betatron motion parameter and the energy spread parameter. We see that with the fixed value of the diffraction parameter, the mode degeneration effect can be relaxed at the price of gain reduction. The situation with transverse coherence is favorable when relative separation of the gain between the fundamental and higher spatial modes is more than 25-30 %. In this case the degree of transverse coherence can reach values above 90% in the end of the high gain linear regime [5,7]. Further development of the amplification process in the nonlinear stage leads to a significant degradation of the spatial and of the temporal coherence [3,4,6].

FLASH

In the present experimental situation, many parameters of the electron beam at FLASH depend on practical tuning of the machine [27]. Analysis of measurements and numerical simulations shows that depending on the tuning of the machine, the emittance may change from about 1 to about 1.5 mm-mrad. Tuning at small charges may allow one to reach smaller values of the emittance down to 0.5 mm-mrad. Peak current may change in the range from 1 kA to 2 kA depending on the tuning of the beam formation system. An estimate for the local energy spread is σ_E [MeV] $\simeq 0.1 \times I$ [kA]. The average beta function in the undulator is about 10 meters.

Let us choose the reference working point with the radiation wavelength 8 nm, rms normalized emittance 1 mm-mrad and beam current 1.5 kA. Parameters of the problem for this reference point are: the diffraction parameter is $B = 17.2$, the energy spread parameter $\hat{\Lambda}_T^2 = 1.7 \times 10^{-3}$, betatron motion parameter $\hat{k}_\beta = 5.3 \times 10^{-2}$.
Then the reduced parameters at other working points can be easily recalculated using the scaling:

$$B \propto \frac{\epsilon_n \beta I^{1/2}}{\lambda^{1/4}}, \qquad \hat{k}_\beta \propto \frac{1}{\beta I^{1/2}\lambda^{1/4}} \qquad \hat{\Lambda}_T^2 \propto I\lambda^{1/2}.$$

Analyzing these simple dependencies in terms of their effect on mode separation, we can state that

ISBN 978-3-95450-134-2

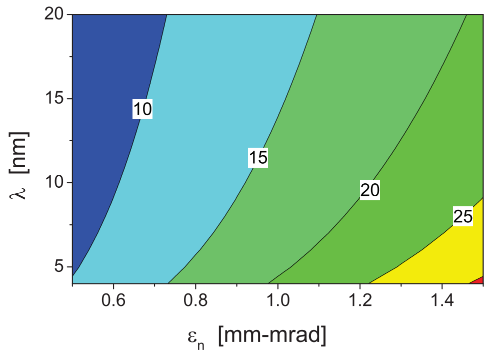

Figure 5: FLASH: contour plot for the value of the diffraction parameter B versus normalized emittance and radiation wavelength. Beam current is 1.5 kA, beta function is 10 m.

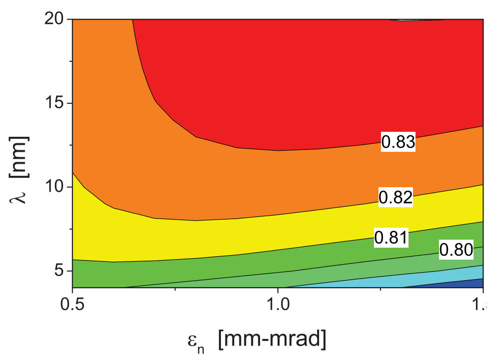

Figure 6: FLASH: contour plot of the ratio of the maximum field gain of TEM_{10} to the field gain of the ground TEM_{00} mode versus radiation wavelength and emittance. Beam current is 1.5 kA, beta function is 10 m.

- Dependencies on the wavelength are relatively weak (except for $(\hat{\Lambda}_T^2)_{eff}$), i.e. one should not expect a significantly better transverse coherence at longer wavelengths. Moreover, mode separation can even be somewhat improved at shorter wavelengths due to a significant increase in $(\hat{\Lambda}_T^2)_{eff}$.
- Reduction of the peak current (by going to a weaker bunch compression) would lead to an improvement of mode separation (even though the energy spread parameter would smaller). Obviously, the peak power at the saturation would be reduced.
- Dependence on the normalized emittance is expected to be weak because of the two competing effects. Mode separation due to a change of the diffraction parameter can be to a large extent compensated by a change of the longitudinal velocity spread. As we will see below, this happens indeed in the considered parameter range.
- Reduction of the beta-function would be the most favorable change because it would reduce the diffraction parameter, and increase the velocity spread at the same time. Unfortunately, there are technical arguments not supporting such a change in the FLASH undulator [30].

A contour plot for the value of the diffraction parameter B for the value of beta function of 10 m and the value of beam current 1.5 kA is presented in Fig. 5. We see that the value of the diffraction parameter is $B \gtrsim 10$ in the whole parameter space of FLASH. Figure 6 shows the ratio of the field gain $\mathrm{Re}(\Lambda_{10}(\omega))$ to the value of the field gain $\mathrm{Re}(\Lambda_{00}(\omega))$ of the fundamental mode. We see that this ratio is above 0.8 in the whole range of parameters, and we can expect significant contribution of the first azimuthal mode to the total radiation power. We can also notice relatively weak dependencies on the emittance and on the wavelength.

Spatial Coherence

In our studies of coherent properties of FELs [3] we have found that for an optimized SASE FEL the degree of transverse coherence can be as high as 0.96. One can see from Fig. 7 that in the considered cases the degree of transverse coherence is visibly lower. We should distinguish two effects limiting the degree of transverse coherence at FLASH. The first one is called mode degeneration and was intensively discussed in this paper. This physical phenomena takes place at large values of the diffraction parameter [12]. Right plot in Fig. 8 shows the contribution of higher azimuthal modes to the total power for a specific example of emittance of 1 mm-mrad and a peak current of 1.5 kA (the results have been obtained with time-dependent, three-dimensional FEL simulation code FAST [31]). The averaged contribution of the first azimuthal modes falls down in the high gain linear regime, but to the value of 12% only, and then starts to grow in the nonlinear regime, and reaches the value of 16% at the undulator end.

The second effect is connected with a finite longitudinal coherence, it was discovered in [7] and discussed in [3, 4]. The essence of the effect is a superposition of mutually incoherent fields produced by different longitudinally uncor-

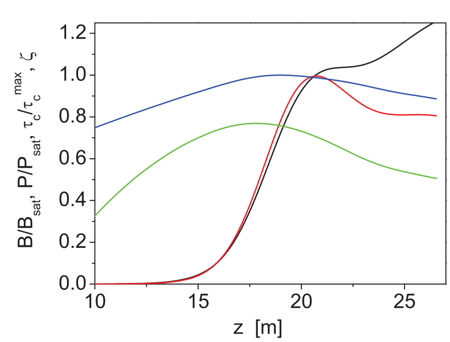

Figure 7: FLASH: evolution of the radiation power (black curve), coherence time (blue curve), degree of transverse coherence (green curve), and brilliance (red curve) along the undulator. Brilliance and radiation power are normalized to saturation values. Coherence time is normalized to maximum value of 5.5 fs. Radiation wavelength is 8 nm. Beta function is 10 m. Beam current is 1.5 kA. rms normalized emittance is 1 mm-mrad.

ISBN 978-3-95450-134-2

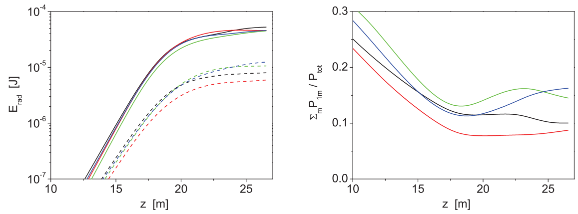

Figure 8: Left plot: evolution of the energy in the radiation pulse versus undulator length. Color codes (black to blue) correspond to different shots. Line style correspond to the total energy in the azimuthally symmetric $\sum TEM_{0m}$ modes (solid lines), and in of the first azimuthal $\sum TEM_{1m}$ (dashed lines). Right plot: partial contribution of the first azimuthal modes to the total radiation power, $\sum P_{1m}/P_{tot}$. FLASH operates at the radiation wavelength of 8 nm. Beta function is 10 m. Beam current is 1.5 kA. rms normalized emittance is 1 mm-mrad.

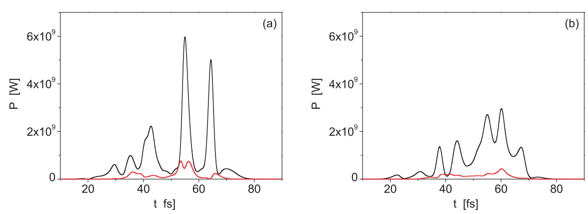

Figure 9: Temporal structure of two radiation pulses. Black lines show the power of the azimuthally symmetric modes, and the curve in the red color show the power of the first azimuthal modes. Radiation wavelength is 8 nm. Beta function is 10 m. Beam current is 1.5 kA. rms normalized emittance is 1 mm-mrad. Undulator length is 27 m.

related parts of the electron bunch. In the exponential gain regime this effect is relatively weak, but it prevents a SASE FEL from reaching full transverse coherence, even in the case when only one transverse eigenmode survives [7]. In the deep nonlinear regime beyond FEL saturation, this effect can be strong and can lead to a significant degradation of the degree of transverse coherence [3, 4]. In particular, as one can see from Fig. 7, this effect limits the degree of transverse coherence to the value about 50% when FLASH operates in the deep nonlinear regime.

Pointing Stability and Mode Degeneration

Mode degeneration has significant impact on the pointing stability of SASE FEL. Let us illustrate this effect with a specific example for FLASH operating with an average energy in the radiation pulse of 60 μJ. The left plot in Fig. 8 shows the evolution along the undulator of the radiation energy in azimuthally symmetric modes and of the energy in the modes with azimuthal index $n = \pm 1$. The right plot in this figure shows the relative contribution to the total radiation energy of the modes with azimuthal index $n = \pm 1$. Four consecutive shots are shown here. Temporal profiles of the radiation pulses are presented in Fig. 9. Intensity distributions in the far zone for these two shots are shown in two rows in Fig. 10. The four profiles on the left-hand side of each row show intensity distributions in the single slices for the time 40 fs, 50 fs, 60 fs, and 70 fs. The right column presents intensity profiles averaged over full shots. We see that the transverse intensity patterns in slices have a rather complicated shape due to the interference of the fields of statistically independent modes with different azimuthal indices. The shape of the intensity distributions changes on a scale of the coherence length. Averaging of slice distributions over a radiation pulse results in a more smooth distribution. However, it is clearly seen that the spot shape of a short radiation pulse changes from pulse to pulse. The center of gravity of the radiation pulse visibly jumps from shot to shot. The position of the pulse also jumps from shot to shot which is frequently referred to as poor pointing stability. Note that the effect illustrated here is a fundamental one, which takes place due to the mode degeneration when the contribution of the higher azimuthal modes to the total power is pronounced (10% to 15% in our case). Only in the case of a long radiation pulse, or after averaging over many pulses, the intensity distribution approaches asymptotically to an azimuthally symmetric shape.

OPTIMIZED SASE FEL

Target value of interest for XFEL optimization is the field gain length of the fundamental mode. For this practically important case the solution of the eigenvalue equation for the field gain length of the fundamental mode and optimum beta function are rather accurately approximated by [3, 4, 32, 33]:

$$
\begin{aligned}
L_{\mathrm{g}} &= 1.67 \left(\frac{I_A}{I}\right)^{1/2} \frac{(\epsilon_n \lambda_{\mathrm{w}})^{5/6}}{\lambda^{2/3}} \frac{(1+K^2)^{1/3}}{K A_{JJ}} (1+\delta) , \\
\beta_{\mathrm{opt}} &\simeq 11.2 \left(\frac{I_A}{I}\right)^{1/2} \frac{\epsilon_n^{3/2} \lambda_{\mathrm{w}}^{1/2}}{\lambda K A_{JJ}} (1+8\delta)^{-1/3} , \\
\delta &= 131 \, \frac{I_A}{I} \frac{\epsilon_n^{5/4}}{\lambda^{1/8} \lambda_{\mathrm{w}}^{9/8}} \frac{\sigma_\gamma^2}{(K A_{JJ})^2 (1+K^2)^{1/8}} , \qquad (4)
\end{aligned}
$$

where $\sigma_\gamma = \sigma_{\mathrm{E}}/mc^2$. In the case of negligibly small energy spread, the diffraction parameter B and parameter of betatron oscillations, $\hat{k}_\beta$ are functions of the only parameter $\hat{\epsilon}$ for optimized x-ray FEL. As a result, saturation characteristics of the SASE FEL written down in the dimensionless form are functions of two parameters, $\hat{\epsilon} = 2\pi\epsilon/\lambda$ and parameter $N_{\mathrm{c}} = I L_{\mathrm{g}} \lambda/(e \lambda_{\mathrm{w}} c)$ defining the initial conditions for the start-up from the shot noise [3–5]. Dependence of characteristics on the value of N_{c} is very slow, in fact logarithmic. The values of the diffraction parameter and of the betatron motion parameter are given by (see Fig. 11):

$$
B \simeq 13 \times \hat{\epsilon}^{5/2} , \qquad \hat{k}_\beta \simeq 0.154/\hat{\epsilon}^{3/2} .
$$

The maximum value of the degree of transverse (which occurs in the end of the linear regime) degrades gradually with the growth of the emittance parameter (see Fig: 12). The origin of this is the mode degeneration effect. The value of the diffraction parameter grows with the value of the emittance parameter, and starting from $\hat{\epsilon} > 1$ the gain of the TEM_{10}

ISBN 978-3-95450-134-2

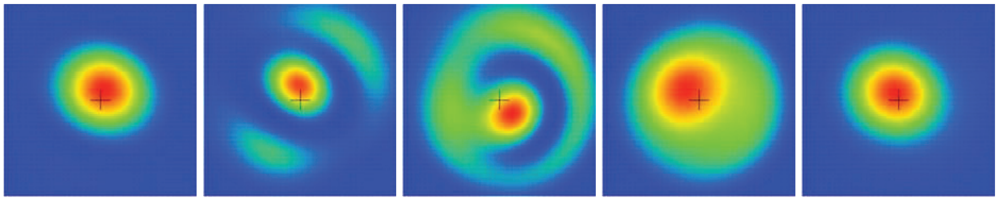

(a)

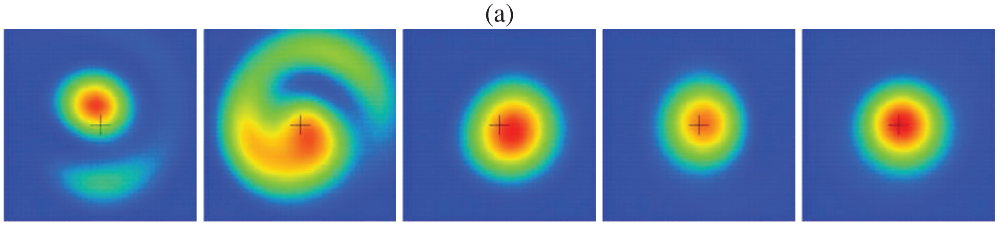

(b)

Figure 10: Profiles of the radiation intensity in the far zone. Rows correspond to specific shots with temporal structure presented in Fig. 9. Profiles on the right-hand side show average intensity over full pulse. Profiles 1 to 4 from the left-hand size show intensity distribution of selected slices corresponding to the time 40 fs, 50 fs, 60 fs, and 70 fs, respectively. Cross denotes geometrical center of the radiation intensity averaged over many shots. FLASH operates at the radiation wavelength of 8 nm. Beta function is 10 m. Beam current is 1.5 kA. rms normalized emittance is 1 mm-mrad. Undulator length is 27 m.

Table 1: Parameter Space of X-ray FELs

	LCLS	SACLA	EXFEL	SWISS FEL	PAL XFEL
Energy [GeV]	13.6	8.0	17.5	5.8	10
Wavelength [A]	1.5	0.6	0.5	0.7	0.6
ϵ_n [mm-rad]	0.4	0.4	0.4	0.4	0.4
$\hat{\epsilon}$	1	2.7	1.5	3.4	2.1

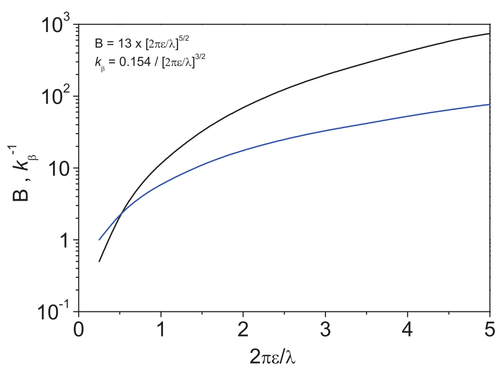

Figure 11: Optimized SASE FEL: diffraction parameter and betatron oscillation parameter versus the emittance parameter $\hat{\epsilon} = 2\pi\epsilon/\lambda$.

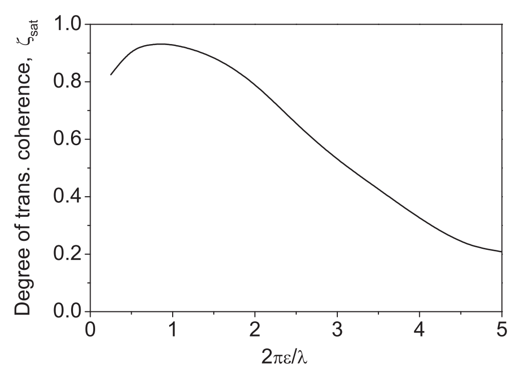

Figure 12: Optimized SASE FEL: maximum degree of transverse coherence versus the emittance parameter $\hat{\epsilon} = 2\pi\epsilon/\lambda$.

mode approaches closer to the gain of the ground TEM_{00} mode (see Fig. 13). Contribution of the TEM_{10} mode to the total power progresses with the growth of the emittance parameter (see Fig. 14). Starting from $\hat{\epsilon} > 2$ the azimuthal modes TEM_{2n} apear in the mode contents, and so on.

Table 1 presents comparative table of the main parameters of the x-ray FELs compiled for the shortest design wavelength [21–25]. To make comparison more simple, we assume the normalized emittance to be the same for all cases, $\epsilon_n = 0.4$ mm-mrad. General tendency is that parameter range of hard x-ray FELs driven with low energy electron beam corresponds to large values of the emittance parameter. As a result, output radiation will have poor spatial coherence and poor pointing stability of the photon beam. In the previous section we illustrated this problem for Free Electron Laser FLASH. Mode content of FLASH corresponds to that expected for optimized x-ray FEL operating with the value of the emittance parameter $\hat{\epsilon}$ around 2. Situation will become much worse for larger values of $\hat{\epsilon}$. Note that spatial jitter is of a fundamental nature (shot noise in the electron beam), and takes place even for an 'ideal' machine.

The reasonable question arises about possible ways to suppress the mode degeneration effect. The spread of longi-

ISBN 978-3-95450-134-2

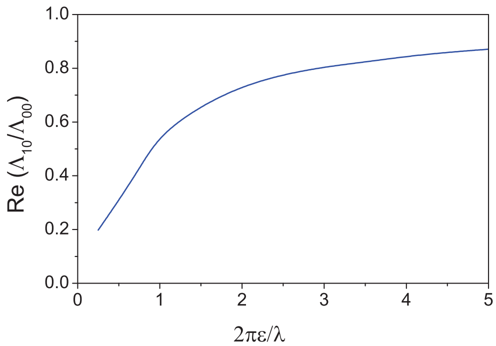

Figure 13: Optimized SASE FEL: Ratio of the gain $\mathrm{Re}(\Lambda_{10})/\mathrm{Re}(\Lambda_{00})$ versus the emittance parameter $\hat{\epsilon} = 2\pi\epsilon/\lambda$.

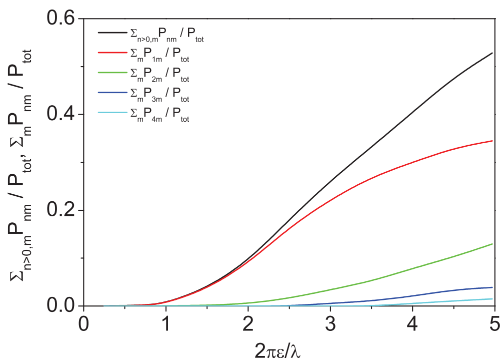

Figure 14: Optimized SASE FEL: partial contributions of the modes with azimuthal index $m = 0 \ldots 4$ to the total power versus the emittance parameter $\hat{\epsilon} = 2\pi\epsilon/\lambda$. SASE FEL operates in the saturation.

tudinal velocities (due to energy spread and emittance) helps to suppress high order modes thus improving transverse coherence properties. The energy spread can be increased with the laser heater [34]. Features of this effect are demonstrated with Fig. 4. However, the price for this improvement is a significant reduction of the gain of the fundamental mode and of the FEL power. A tight focusing of the electron beam in the undulator can be important for reaching higher coherence due to a reduction of the diffraction parameter and an increase of the velocity spread. This trick works for the case of FLASH, currently operating with large beta function with respect to optimum (maximum) FEL gain. Reduction of the beat function will reduce saturation length and improve spatial coherence. However, it is not the case of x-ray FEL optimized for maximum of the FEL gain. Reduction of the focusing beta function will result in the increase of the saturation length. In the end, with fixed energy of the electron beam, an available undulator length will define the level of spatial coherence and spatial jitter of the photon beam.

ACKNOWLEDGEMENT

We thank Reinhard Brinkmann for many useful discussions.

REFERENCES

[1] Y.S. Derbenev, A.M. Kondratenko, E.L. Saldin, Nucl. Instrum. Methods 193, 415 (1982).

[2] J.B. Murphy, C. Pellegrini, Nucl. Instrum. Methods A 237, 159 (1985.)

[3] E.L. Saldin, E.A. Schneidmiller, and M.V. Yurkov, Opt. Commun. 281(2008)1179.

[4] E.L. Saldin, E.A. Schneidmiller, and M.V. Yurkov, New J. Phys. 12 (2010) 035010, doi: 10.1088/1367-2630/12/3/035010.

[5] E.L. Saldin, E.A. Schneidmiller, and M.V. Yurkov, Opt. Commun. 281(2008)4727.

[6] E.A. Schneidmiller, and M.V. Yurkov, Proc. FEL 2012 Conference, http://accelconf.web.cern.ch/AccelConf/FEL2012/papers/mopd08.pdf.

[7] E.L. Saldin, E.A. Schneidmiller, and M.V. Yurkov, Opt. Commun. **186**(2000)185.

[8] G. Moore, Opt. Commun. 52, 46 (1984).

[9] E.L. Saldin, E.A. Schneidmiller and M.V. Yurkov, Optics Commun 97(1993)272.

[10] M. Xie, Nucl. Instrum. and Methods A 445, 59 (2000).

[11] E.L. Saldin, E.A. Schneidmiller and M.V. Yurkov, Nucl. Instrum. and Methods A 475, 86 (2001).

[12] E.L. Saldin, E.A. Schneidmiller, M.V. Yurkov, "The Physics of Free Electron Lasers" (Springer-Verlag, Berlin, 1999).

[13] K.J. Kim, Phys. Rev. Lett. 57(1986)1871.

[14] J.M. Wang and L.H. Yu, Nucl. Instrum. and Methods A250(1986)484.

[15] S. Krinsky and L.H. Yu, Phys. Rev. A 35(1987)3406.

[16] R. Bonifacio et al., Nucl. Instrum. and Methods **A341**(1994)181.

[17] R. Bonifacio et al., Phys. Rev. Lett. **73**(1994)70.

[18] E.L. Saldin, E.A. Schneidmiller and M.V. Yurkov, Opt. Commun. 148(1998)383.

[19] K.J. Kim, Phys. Rev. Lett. **57**(1986)1871.

[20] E.L. Saldin, E.A. Schneidmiller and M.V. Yurkov, Phys. Rev. ST-AB 9(2006)030702

[21] P. Emma et al. Nature Photonics 4, 641 (2010).

[22] T. Ishikawa et al., Nature Photonics 6, 540 (2012).

[23] R. Ganter (Ed.), Swiss FEL Conceptual Design Report, PSI Bericht Nr. 10-04, April 2012.

[24] H.S. Kang, K.W. Kim, I.S. Ko, Proc. IPAC 2014 Conf., paper THPRO019 (2014), http://accelconf.web.cern.ch/AccelConf/IPAC2014/papers/thpro019.pdf

[25] M. Altarelli et al. (Eds.), XFEL: The European X-Ray Free-Electron Laser. Technical Design Report, Preprint DESY 2006-097, DESY, Hamburg, 2006 (see also http://xfel.desy.de).

[26] W. Ackermann et al., Nature Photonics **1**(2007)336

ISBN 978-3-95450-134-2

[27] K. Honkavaara, B. Faatz, J. Feldhaus, S. Schreiber, R. Treusch, M. Vogt, Proc. FEL2014 Conference, Basel, Switzerland, 2014, web05. http://accelconf.web.cern.ch/AccelConf/FEL2014/papers/web05.pdf

[28] E.A. Schneidmiller and M.V. Yurkov, J. Mod. Optics (2015). DOI: 10.1080/09500340.2015.1066456.

[29] R. Bonifacio, C. Pellegrini and L.M. Narducci, Opt. Commun. 50 (1984) 373.

[30] B. Faatz and E. Prat, Alternative Focusing for FLASH, TESLA FEL Report 2009-10, DESY, Hamburg, 2009.

[31] E.L. Saldin, E.A. Schneidmiller, and M.V. Yurkov, Nucl. Instrum. and Methods **A 429**(1999)233.

[32] E.L. Saldin, E. A. Schneidmiller, and M.V. Yurkov, Opt. Commun. 235(2004)415.

[33] E. A. Schneidmiller, and M.V. Yurkov, Phys. Rev. ST AB, 15, 080702 (2012).

[34] E.L. Saldin, E.A. Schneidmiller, and M.V. Yurkov, Nucl. Instrum. and Methods A 528, 355 (2004).

MEASUREMENT OF SPATIAL DISPLACEMENT OF X-RAYS IN CRYSTALS FOR SELF-SEEDING APPLICATIONS

A. Rodriguez-Fernandez*, B. F. Pedrini, S. Reiche, Paul Scherrer Institut, 5232 Villigen PSI, Switzerland
K. D. Finkelstein, CHESS, Cornell University, Ithaca, New York, USA

Abstract

SASE Free-electron laser (FEL) radiation arises from shot noise in the electron bunch, which is amplified along the undulator section and results in X-ray pulses consisting of many longitudinal modes [1]. The output bandwidth of FELs can be decreased by seeding the FEL process with longitudinally coherent radiation. In the hard x-ray region, there are no suitable external seeding sources. Self-seeding represents a viable alternative. The X-ray beam is separated from the electrons using a magnetic chicane, and then monochromatized. The monochromatized X-rays serve as a narrowband seed, after recombination with the electron bunch, along the downstream undulators. This scheme generates longitudinally coherent FEL pulses.

Geloni et al. [2] have proposed monochromatization based on Forward Bragg Diffraction (FBD), which introduces a delay of the narrowband X-rays pulse of the order of femtoseconds that can be matched to the delay of the electron bunch due to the chicane. The FBD process produces a small transverse displacement of the X-ray beam, which may result in the loss of efficiency of the seeding process [3]. Preliminary results from an experiment performed at Cornell High Energy Synchrotron Source (CHESS) seem to confirm the predicted transverse displacement, which is therefore to be taken into account in the design of self-seeding infrastructure for optimizing the FEL performance.

INTRODURCTION

X-ray free-electron lasers (FELs) relying on the self-amplified spontaneous emission (SASE) exhibit peak brightnesses many orders of magnitude larger than that from insertion devices at third-generation synchrotron sources [4,5]. The SASE radiation spectrum consists of many longitudinal modes, as a result of shot noise initiation of the amplification process in the electron beam [1,6]. For high-gain FELs, the normalized frequency bandwidth is $\Delta\omega/\omega \sim \rho$, where ρ is the FEL Pierce parameter [7]. At the future Swiss Free Electron Laser facility $\rho = 4\cdot10^{-4}$.

The bandwidth can be reduced by seeding the FEL with longitudinally coherent radiation coming from an external source. In the hard X-ray regime, where no external sources are available, a self-seeding scheme has been proposed by Geloni et al. [2]. This method exploits the time-domain features of the radiation transmitted in forward direction by a thin crystal in Bragg or Laue diffraction geometry, called the "wake monochromator". Unfortunately, the Forward Bragg Diffraction (FBD) process produces a small transverse displacement of the narrow-bandwidth, time-delayed X-ray seeding pulse, which results, if not compensated, in the loss of efficiency of the seeding process [3,8]. Until now the transverse displacement has not been studied experimentally. For a proper design of the seeding infrastructure, a quantitative understanding is mandatory, especially at the shorter wavelengths of 1 Å and below that will be offered at the Swiss Free Electron Laser (SwissFEL) facility.

With this contribution, we intend to present first results from an experimental study of the transverse displacement due to FBD. Our first experiment was performed at beamline C1 of the CHESS facility. These first results help to guide new experiments at FEL facilities. The present investigations will serve to validate or ameliorate our simulation tool. This will then be applied to calculate the propagation of the X-ray signal through the designed self-seeding unit of SwissFEL with the simulation software for FELs, GENESIS [9].

THEORY OF TIME DEPEDENT X-RAY DINAMICAL DIFFRACTION

Shvyd'ko et al. [3] present a series of analytic expressions resulting from a spatiotemporal system of wave equations which represent the shape and power of the monochromatic wave generated by an incident broad spectrum beam. In a previous work Lindberg et al. [8] presented how, from the coupled wave system of Bragg diffraction one can obtain solutions for both reflected and transmitted wave fields. They showed the relation between the resulting temporal profile and crystal properties, which include the x-ray extinction length Λ, the incident angle θ for specific reflection, and in the case of the forward diffracted contribution, thickness d of the crystal. If the system of waves is solved for an incoming pulse beam it is possible to observe 'echos'. The transverse displacement Δx_0 is given by

$$\Delta x_0 = c\,\tau\cos(\theta)\,, \qquad (1)$$

where c is the speed of light and τ denotes the time difference between the undiffracted beam and the 'echo' leaving the rear surface.

Spatiotemporal Dynamical Diffraction

Lindberg and co-workers in Ref [8] derive an expression for the reflected and forward diffracted

*angel.rodriguez@psi.ch

ISBN 978-3-95450-134-2

wavefields at the surface of the crystal as a function of A_0 the initial incident wave. For the study of a wake monochromator crystal they obtain the following approximation to the outgoing wave

$$A_{0|P} = R_0 A_{0|Q} - \int_A^Q d\zeta' R_0(\zeta,\xi;\zeta',\zeta') \frac{ik_0\chi_h}{2\sin(\theta)} A_h - \int_A^Q d\zeta' A_0(\zeta',\zeta') \frac{\partial}{\partial\zeta'} R_0(\zeta,\xi;\zeta',\zeta')\Big|_{\xi'=\zeta'}, \quad (2)$$

Here, h denotes reciprocal lattice vectors inside the crystal that satisfy the diffraction condition. The amplitude R_0 denotes the forward diffracted signal at the rear and front surfaces, respectively. R_0 denotes the well-known Riemann function from the dynamical theory [3,8,10]. k_0 is the modulus of the x-ray wavevector inside/outside the crystal and χ_h is h-Fourier component of crystal polarizability [10].

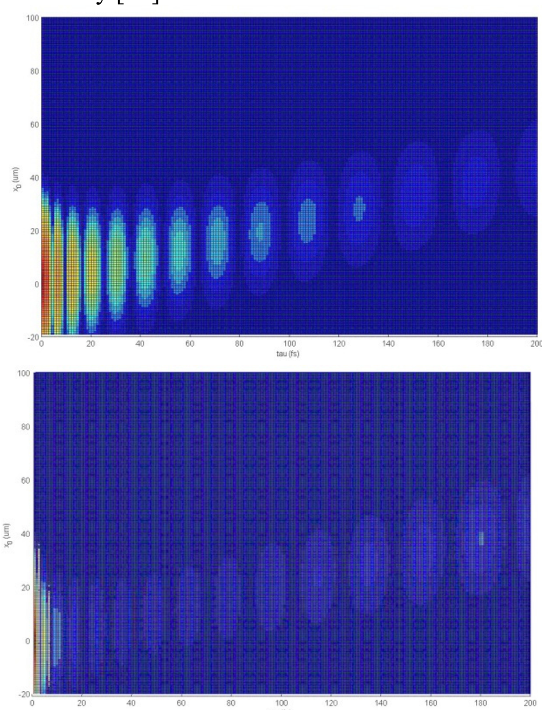

Figure 1: Forward diffracted field magnitude $|E_h|$ from the (400) Bragg reflection at 10 keV for a 600 μm thick Diamond crystal in the case of a 10 μm size incident x-ray beam. (Above) Calculated following Lindberg and Shvyd'ko approximation for (3) and (below) calculated taking into account all the terms in (2).

In equation (2), the authors of [8] consider only the third term, which is relevant for time delays $0 < c\tau < 2d/\sin(\theta)$. With several assumptions, the obtained amplitude of the forward diffracted wavefield becomes

$$E_{0|P|3} = \frac{d\pi^2}{\Lambda^2\sin(\theta)} e^{ik_0\chi_h(d+c\tau/\sin(\theta))/2\sin(\theta)} e^{-\frac{[x_0-c\tau\cot(\theta)]^2}{4\sigma_x^2}} \times \frac{J_1\left[\pi\sqrt{c\tau\left(2d/\sin(\theta)+c\tau/\sin^2(\theta)\right)}/\Lambda\right]}{\pi\sqrt{c\tau\left(2d/\sin(\theta)+c\tau/\sin^2(\theta)\right)}/\Lambda}, \quad (3)$$

where σ_x is the width of the incoming pulse in the transverse direction. For a 100 μm thick diamond crystal at $\theta = 44.04$ º, the range of validity for the approximation is $0 < c\tau < 300$ fs, and the first echoes are predicted to emerge at 10-20 fs delay relative to the undiffracted pulse.

In our first experiments taking place at synchrotron sources, the total pulse lengths was of the order of tens of picoseconds, and the signal from the forward diffracted beam results from integration over all positive time delays $\tau = 0$. Therefore, we must also take into account the first two terms neglected in equation (2). Using analog approximations as those used in Ref [8] for the third term, we calculated the corresponding two wave amplitudes of the forward diffracted beam and obtained

$$E_{0|P|1} = \frac{1}{4\pi\sin(\theta)} e^{ik_0\chi_h(d+c\tau/\sin(\theta))/2\sin(\theta)} e^{-\frac{[x_0-c\tau\cot(\theta)]^2}{4\sigma_x^2}} \times \left\{ J_0\left[2\pi\sqrt{\frac{c\tau}{2\sin(\theta)}\left(d+\frac{c\tau}{2\sin(\theta)}\right)}\Big/\Lambda\right] + \frac{c\tau}{d\,2\sin(\theta)+c\tau} J_2\left[2\pi\sqrt{\frac{c\tau}{2\sin(\theta)}\left(d+\frac{c\tau}{2\sin(\theta)}\right)}\Big/\Lambda\right]\right\}, \quad (4)$$

and

$$E_{0|P|2} = \frac{k_0^2\chi_h\chi_{\bar{h}}}{\sin^2(\theta)} e^{ik_0\chi_h(d+c\tau/\sin(\theta))/2\sin(\theta)} e^{-\frac{[x_0-c\tau\cot(\theta)]^2}{4\sigma_x^2}} \times \left\{ J_0\left[2\pi\sqrt{\frac{c\tau}{2\sin(\theta)}\left(d+\frac{c\tau}{2\sin(\theta)}\right)}\Big/\Lambda\right] + \frac{c\tau}{d\,2\sin(\theta)+c\tau} J_2\left[2\pi\sqrt{\frac{c\tau}{2\sin(\theta)}\left(d+\frac{c\tau}{2\sin(\theta)}\right)}\Big/\Lambda\right]\right\} \times \frac{J_1[\pi(c\tau)/\Lambda]}{\pi(c\tau)/\Lambda}. \quad (5)$$

Figure 1 shows the amplitude transmitted in forward direction as a function of transverse displacement and time delay, for a 600 μm thick diamond crystal in symmetric (4,0,0) Bragg geometry, and assuming a 10 keV, 10 μm wide x-ray beam. Figure 1a and 1b are obtained neglecting and considering (4,5), respectively. The dependence of the echo transverse displacement on the echo delay expressed in (1) is clearly visible in both panels. However, the figure also illustrates that the second term in (2) causes echoes at later times and correspondingly enhanced transverse displacement.

EXPERIMENTAL SET-UP

The simulations presented in Fig. 1 correspond to conditions of experiments performed at beamline C1 at CHESS to study diamonds of different thicknesses (200 and 600 μm) using the (400) Bragg reflection. We plan to validate the obtained results and to extend the within a

ISBN 978-3-95450-134-2

second experiment which will take place at Material Science beamline at Swiss Light Source (SLS).

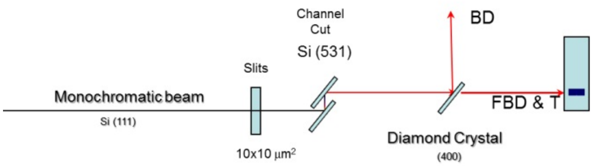

Figure 2: Experimental set-up for the experiment performed at C line at CHESS.

The beam characteristics required for the experiments (small energy bandwidth, beam size of about 10 μm and small angular divergence) are crucial. For this reason, after a Si (111) monochromator the beam is refined with a channel cut set of Si (531) crystals that reduce the angular width of incoming beam to 1.075'', which is slightly smaller than the expected Darwin acceptance for Diamond (400) Bragg reflection at 10 keV of 1.485''.

The layout of at the CHESS C-line is shown in Fig. 2. The beam size was set to 12±2 μm by slits located upstream the channel cut set of crystals. A NaI detector was situated in the Bragg diffraction direction, 44.04º, which mission was record the width and intensity of the Bragg diffracted signal. The detector in the forward direction uses a GGG scintillator crystal to convert x-ray to visible photons, which are recorded with an Andor camera with conventional resolution 6.5 μm/pixel after 10x magnification by means of an objective lens, leading to a resolution of 0.65μm/pixel. The sample under study was a diamond single crystal of 600 μm thickness. The crystal was set up to the maximum Bragg diffraction signal of the NaI detector at 10 keV, one fixed the channel cut set was rotated allowing just a determined energy to go throw it with high resolution. Recording the signal transmitted thru the crystal in the Andor camera.

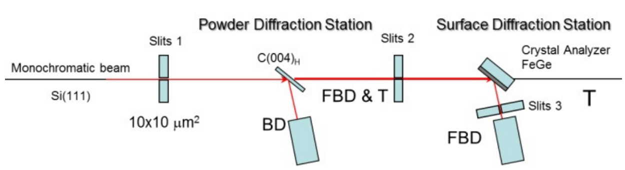

Figure 3: Experimental set-up at Material Science Beamline, SLS.

We have studied different diamond single crystals of thicknesses in the range 200 and 600 μmat the (400) reflection in symmetric Bragg geometry, and at 10 keV photon energy.

The foreseen setup for the future experiment at the SLS-MS beamline is shown Fig. 3. Beam divergence and size will be tuned with slits 0 and slits 1 in such a way to have parallel beam of 10 × 10 μm^2 size at the Powder Diffraction (PD) station. The crystals will be mounted at the center of the powder diffractometer on a high-precision goniometer, and will be oriented appropriately by monitoring the Bragg Diffracted beam with the Mythen detector D1 placed on the PD diffractometer arm.

The transmitted beam, which includes the echoes generated from the FBD process, will proceed through the high-precision slits 2 located in the Surface Diffraction (SD) hutch. These will select transversally the portion of the beam impinging on the spectrometer, placed on the arm of the SD diffractometer. The spectrometer will consist of an analyzer crystal diffracting the beam through slits 3 onto a Pilatus detector D2. The X-ray spectra are acquired by rotating the analyzer crystal. This will be made of InSb, from which we do not expect any fluorescence signal, and which, in combination with a proper setting of slits 3, will fulfill the resolution requirements of better than the Darwin width of the diamond reflection under consideration.

We will first record reference spectra without crystal in the beam, at different transverse positions of slits 2. Then, the crystal will be mounted and oriented to be in perfect Bragg reflection geometry, determined by requiring the intensity of the Bragg diffracted beam on D1 to be maximal. At this point, a number of spectra will be recorded, again at different positions of slits 2. The procedure will be repeated at slightly different energies of the incoming beam, set with the Si(111) monochromator.

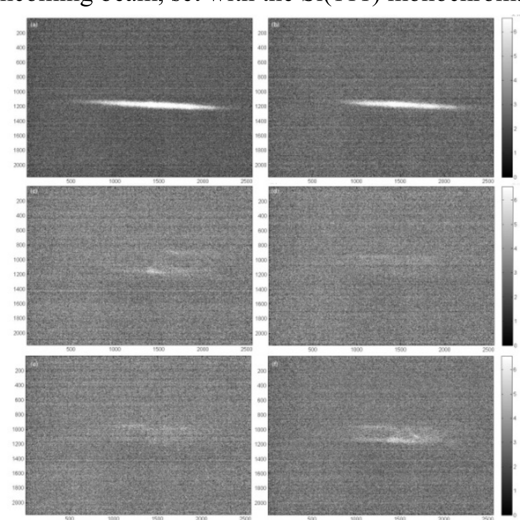

Figure 4: Forward Bragg Diffracted signal at six different energies for the 600 μm thick Diamond Crystal at the (400) reflection. (a) -2.50 eV, (b) -1.00 eV, (c) -0.87 eV, (d) 0 eV, (e) +0.03 eV and (f) +0.06 eV from 10 keV.

For this experiment we will be able to study five single crystal of diamond with different thicknesses 50, 100, 200, 500 and 600 μm. We also expect to be able to study the (400) reflection in the Bragg symmetry together with the Laue symmetry reflections (400), (220) and some asymmetric reflections as the (311).

ISBN 978-3-95450-134-2

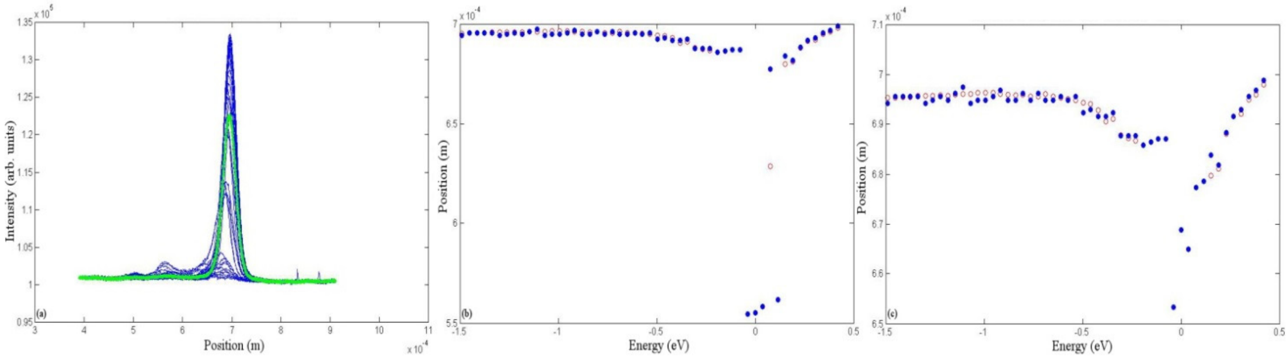

Figure 5: (a) Vertical cut of the forward diffracted signal recorder by the detector (Fig. 4) at different Energies near 10 keV. The reflection study was the symmetric (400) from a 600 µm thick diamond, (b) Position of the Maximum peak for the different energies scan performed and (c) Position of the first maxima follow over the different energy scans.(Energy units are refer from the centre of the Bragg condition at 10 keV.

FIRST RESULTS

In the experiment performed at C-line at CHESS, a 600 µm thick diamond single crystal was studied for the (400) reflection at 10 keV, θ = 44.04º. As presented in Fig. 4, while rocking the channel cut set, keeping the diamond fixed to the maximum Bragg condition, we are able to perform energy scans that allow us to take pictures of the forward diffracted spatial distribution in x_0 with high resolution.

It was observed how the intensity of the transmitted beam decreases considerably near the energy (10 keV) where the Bragg reflected beam intensity was maxima. This result tells us nearly all photons in the incident beam satisfied Bragg's law for the diamond 400 reflection. Since very few photons were "outside" the match to Bragg's law, the forward diffracted beam had a very small "contamination" from undiffracted radiation.

The vertical profile of the FWD signal, as presented in Fig. 5a, showed a decreasing of the transmitted intensity as a reduction of the area below the curve while approaching the Bragg condition as it is expected, due to the Bragg dispersion. What is interesting for our study is the displacement of the maxima, Fig. 5b, if the initial maxima (outside the Bragg condition) is follow, it is observed a displacement of 40 µm, this displacement can be related to the calculation presented by Lindberg and Sdvyd'ko [3,8]. Although, we also observed a second main peak that is related to the second term in (2), this maximum is 120 µm displace from the initial maxima position and in terms of intensity, near the Bragg condition, is even bigger than the initial maxima. Time speaking this maximum will appear at times much larger than 200 fs, so it should not be considered for self-seeding.

CONCLUSIONS

The initial step in the study of the transverse displacement occurring in the FBD process has been performed in view of its future application for self-seeding at FELs. For a 600 µm thick diamond single crystal, a transverse displacement of the order of 40 µm is observed as we expected from the calculations by Shvyd'ko and Lindberg [8].The future experiment that will be performed at SLS, where different thickness diamonds will be study at different Bragg reflections (220), (400) and (311) for both Laue and Bragg geometries, will help to increase our knowledge about this process.

ACKNOWLEDGMENT

We will like to acknowledge Cornell High Energy Synchrotron Source for the beamtime given for perform the study. CHESS is supported by the NSF & NIH/NIGMS via NSF award DMR-1332208 Also to Bruce Patterson, who helped us in the discussion for the developing of the experimental technique.

REFERENCES

[1] J. S. Wark and R. W. Lee, J. Apply. Crystallogr. 32, 692 (1999)
[2] G.Geloni, V. Kocharyan and E. Saldin DESY report 10-053 (2010).
[3] Y. Shvyd'ko and R. Lindberg Phys. Rev. ST Accel. Beams 15, 100702 (2012)
[4] A. M. Kondratenko and E. L. Saldin, Part. Accel. 10, 207 (1980)
[5] J. Als-Nielsen and D. McMorrow Elements of Modern X-ray Physics, John Wiley & Sons, Inc, New York, 2011 (second edition).
[6] F. N. Chukhovskii and E. Foster, Acta Crystallogr. Sect. A 51, 668 (1995)
[7] R. Bonifacio, C. Pellegrini, and L. M. Narducci, Opt. Commun. 50, 373 (1984)
[8] R. R. Lindberg and Y. V. Shvyd'ko, Phys. Rev. ST Accel. Beams 15, 050706 (2012)
[9] S. Reiche, Nuclear Instruments and Methods in Physics Research A 429, 243 (1999)
[10] B. W. Batterman and H. Cole, Rev. of Modern Phys. 26, 681 (1964)

ISBN 978-3-95450-134-2

A MODIFIED SELF-SEEDED X-RAY FEL SCHEME TOWARDS SHORTER WAVELENGTHS

L. Zeng#, S. Huang, W. Qin, K. Liu, J. Chen
Institute of Heavy Ion Physics, School of Physics, Peking University, Beijing 100871, China
Y. Ding, G. Marcus, Z. Huang
SLAC National Accelerator Laboratory, Menlo Park, CA 94025, USA

Abstract

We present a modified self-seeded free-electron laser (FEL) scheme of harmonic generation to extend soft x-ray FEL towards shorter wavelength. Different from classical HGHG scheme whose seed laser is a conventional laser with a longer wavelength, this scheme uses a regular self-seeding monochromator to generate a seed laser, followed by a HGHG configuration to produce shorter-wavelength radiations. We perform start-to-end simulations to demonstrate the second and third harmonic FELs from a soft x-ray self-seeding case at the fundamental wavelength of 1.52 nm. The FEL performance will be discussed.

*INTRODUCTION

There are two main schemes for single pass short wavelength FELs: SASE [1,2] and HGHG [3,4]. Until recently, most of the modern high-gain FELs in short wavelength (e.g., x-ray) region have been operated in SASE mode (Emma et al., 2010 [5]; Ishikawa et al., 2012 [6]), which is characterized by excellent transverse coherence. However, SASE has poor temporal coherence and large shot-to-shot fluctuations in both the time and frequency domain because it starts from shot noise.

HGHG scheme can generate fully coherent and high gain harmonic radiation of seed laser. However, single stage harmonic number n is limited since the energy spread is increased n times during the energy modulation which makes the induced energy spread exceed the ρ of radiator. So far, the highest harmonic obtained with single HGHG is the 13th harmonic at 20nm using a 1.2 GeV beam at FERMI FEL [7]. In order to reach higher harmonics, so as to obtain ultrashort wavelength and fully coherent FEL, several schemes have been suggested in recent years. Among them, the cascaded HGHG scheme with the help of "fresh bunch" technique was first proposed in 2001 [8]. Recently, 4.3 nm radiation (60th harmonic of a 260 nm UV laser) has been achieved with a two stage HGHG configuration at FERMI [9]. Another harmonic bunching technique, EEHG [10], has been proof-of-principle demonstrated at SLAC [11] and the third harmonic has been observed at SDUV-FEL, then further amplified to saturation (Zhao et al., 2012 [12]). Currently, coherent radiation at 160 nm (15th harmonic of a 2400 nm seed laser) has been produced at SLAC [13].

#zengling@pku.edu.cn

So far, the cascaded HGHG and EEHG have difficulty in generating hard X-ray FEL. For classic HGHG scheme, it cannot reach hard x-ray region due to lack of external seeds with short enough wavelengths [14]. Besides, the optical properties of HGHG FEL are determined by the quality of seed laser, so a high quality seed laser is required. On the other hand, self-seeding [15] starts from SASE, and a monochromator is used before saturation to generate a purified seed. This seed is then well aligned and interact with the electron beam, which is delayed by a bypass chicane, until saturation to produce near Fourier-transform-limited X-ray pulses. This self-seeding scheme works for both soft and hard x-ray FELs and has been demonstrated recently [14]. For x-ray FEL with the photon energy below 2 keV, a grating-based monochromator can be used [14]; while for x-ray FEL with the photon energy above 4.5 keV, diamond-based monochromator is more popular [16]. The self-seeded FEL in the energy region between 2 to 4.5 keV is more difficult due to lack of monochromator materials. In this paper, we study a new scheme combining the self-seeding and HGHG scheme to produce fully coherent x-rays which could fill the above energy gap not easily achieved by regular seeding schemes.

HGHG BASED ON SELF-SEEDING

The proposed scheme, HGHG based on self-seeding, is shown in Fig. 1, which consists of two stages: SASE stage and HGHG stage. In this preliminary work, we are trying to generate 0.76 nm and 0.51 nm x-ray FELs which are the second and third harmonic of the 1.52 nm radiation from SASE undulator, respectively.

The first stage follows the regular self-seeding setup, including a SASE undulator, a monochromator, and a bypass chicane. A 4.3 GeV electron beam is sent to the 19.8-m-long undulator (U_S) which is resonant at 1.52 nm and operates in the linear amplification region, so the output radiation has the usual SASE properties. The monochromator filters out a narrow bandwidth signal from the SASE radiation, which is used as the seed laser for the downstream HGHG.

The second stage FEL uses the seed laser and electron beam from the former stage to generate harmonic radiation. Here we should notice that, different from external seed laser whose peak power is at hundred megawatt level (e.g., 100 MW in FERMI FEL-1 [7]) in classic HGHG scheme, our seed power is limited to be lower than several hundred kilowatts in order to avoid damage to the monochromator optics [14]. As a result, we

ISBN 978-3-95450-134-2

need to use a longer undulator for electron energy modulation. This long modulator has two functions here: the first one is to amplify the few hundred kilowatt seed to few hundred megawatt, which is mainly achieved with the front part of the modulator; the second one is to modulate the electron bunch, as in a normal HGHG modulator.

.

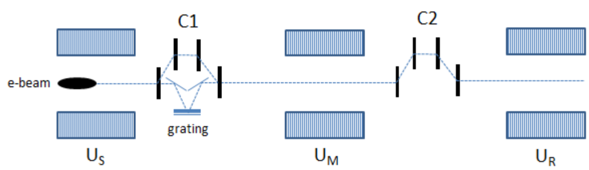

Figure 1: Schematic of HGHG based on self-seeding. U_S is a SASE undulator resonated at 1.52nm. U_M is a modulator resonated at 1.52 nm while U_R is a radiator resonated at 0.76 nm or 0.507 nm. C1 and C2 are chicanes with different values of R_{56}.

FEL SIMULATION

Table 1: Parameters used for HGHG based on Self-seeding Simulation

Parameter	Value	Unit
Electron beam		
Energy	4.3	GeV
Peak current	3	kA
Energy spread	1	MeV
Emittance	0.5	mm-mrad
Mono / Chicane		
Resolving power	5000	
Power efficiency	0.02	
R_{56} of C2	0.28	µm
Undulators		
U_S (U_M and U_R) period	0.03	m
U_S length	19.8	m
U_S strength, A_u	2.4749	
U_M length	9.9	m
U_M strength, A_u	2.4749	
U_R length	39.1	m
U_R strength, A_u	1.6	

We use LCLS parameters as a representative example for start-to-end simulations. The simulations were performed with GENESIS [17]. Table 1 shows the parameters of the scheme which have been optimized for the maximum FEL power at the exit of monochromator. Time-dependent simulation result of the first stage is shown in Fig. 2. It is clear that after the monochromator, the seed power of radiation is about 200 kW.

For modulator, the optimal $\Delta\gamma_m$ is about $n\sigma_\eta$ [18], where n is the harmonic number, σ_η is the relative energy spread and $\Delta\gamma_m$ is the maximum energy modulation amplitude. Three LCLS-type undulator sections are used for modulator which have a total length of 9.9 m. The dispersion of the chicane is chosen to approximately satisfy $R_{56}\Delta\gamma_m/\gamma \approx \lambda/4$[10], where λ is the wavelength of the seed laser. The value of R_{56} here is 0.28 µm.

Figure 3 illustrates the evolution of the peak power of the second harmonic and the third harmonic along radiator. The second harmonic reaches saturation at 39 m and the saturation power is 29 GW, while the third harmonic reaches saturation at 36 m and the saturation power is 0.6 GW. At the position of saturation the 2nd and 3rd harmonic spectrum is shown in Fig. 4. We can see a second harmonic at 0.76 nm whose relative bandwidth is about $2\text{x}10^{-3}$ and a third harmonic at 0.76 nm whose relative bandwidth is about $1.5\text{x}10^{-3}$.

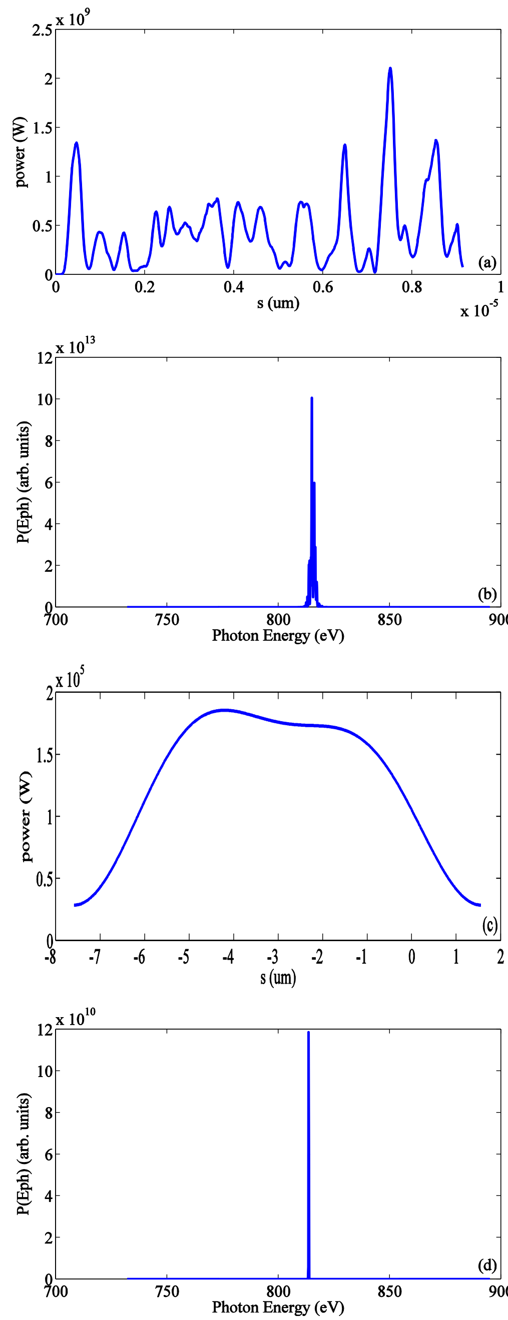

ISBN 978-3-95450-134-2

Figure 2: The FEL power at monochromatic SASE stage in time and frequency domain.(a) temporal profile at the exit of U_S; (b) spectrum at the exit of U_S; (c) temporal profile at the exit of monochromator; (d) spectrum at the exit of monochromator.

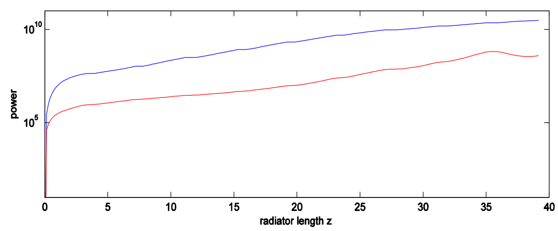

Figure 3: The 2nd (blue line) and 3rd (red line) harmonic power evolution along the radiator undulators (Different A_u values.)

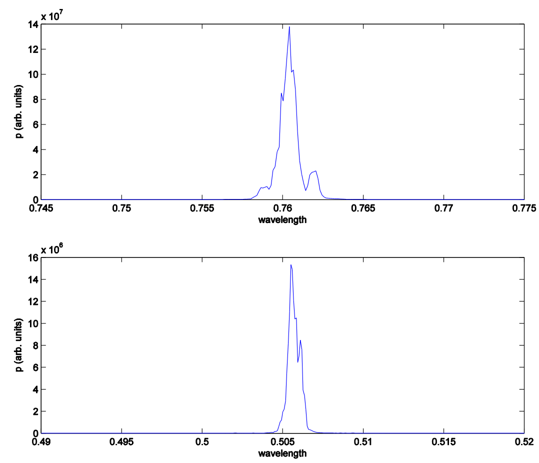

Figure 4: 2nd (a) and 3rd (b) harmonic FEL spectrum at the radiator exit.

CONCLUSION

In this paper, we proposed a new scheme to produce fully coherent shorter-wavelength radiations. It is a modified HGHG setup based on a seed from regular self-seeding scheme. The simulation shows promising results that with wavelength of 0.76 nm (2nd harmonic) and 0.51 nm (3rd harmonic), fully coherent radiation of 30 GW and 0.6 GW are obtained. Further study including optimization and higher harmonic generation is ongoing.

REFERENCES

[1] SLAC Report No. SLAC-R-593, 2002.

[2] DESY Report No. DESY-2006-097, 2006.

[3] I. Ben-Zvi et al., Nucl. Instrum. Methods Phys. Res., Sect. A 304, 181 (1991).

[4] L. Yu. Phys. Rev. A 44. 5178 (1991).

[5] Emma P, Akre R, Arthur J, et al. First lasing and operation of an ångstrom-wavelength free-electron laser, Nature Photonics, 2010, 4(9): 641-647.

[6] Ishikawa T, Aoyagi H, Asaka T, et al. A compact X-ray free-electron laser emitting in the sub-angstrom region, Nature Photonics, 2012, 6(8): 540-544.

[7] Allaria, E., et al., 2012, Nature Photonics 6, 699.

[8] Wu J H, Yu L H. Nucl. Instrum. Methods A, 2001, 475: 10

[9] Allaria, E., et al., 2013, Nature Photonics 7, 913.

[10] Xiang D, Stupakov G. Echo-enabled harmonic generation free electron laser, Physical Review Special Topics-Accelerators and Beams, 2009, 12(3): 030702.

[11] Dunning M, et al. A proof-of-principle echo-enabled harmonic generation FEL experiment at SLAC, Conf. Proc. 2010, C100523 (IPAC-2010-TUPE069).

[12] Zhao Z.T, Wang D, Chen J H, et al. First lasing of an echo-enabled harmonic generation free-electron laser, Nature Photonics, 2012, 6(6): 360-363.

[13] Hemsing, E., M. Dunning, C. Hast, T. Raubenheimer, S. Weathersby, and D. Xiang, 2014, "Highly coherent vacuum ultraviolet radiation at the 15th harmonic with echo-enabled harmonic generation technique", Phys.Rev.ST Accel.Beams 17 (2014) 070702; doi: 10.1103/ PhysRevSTAB. 17. 070702

[14] Ratner D, Abela R, Amann J, et al. Experimental Demonstration of a Soft X-Ray Self-Seeded Free-Electron Laser. Physical review letters, 2015,114(5): 054801.

[15] Feldhaus J, Saldin E L, Schneider J R, et al. Possible application of X-ray optical elements for reducing the spectral bandwidth of an X-ray SASE FEL, Optics Communications, 1997, 140(4): 341-352.

[16] J. Amann et al. "Demonstration of self-seeding in a hard-X-ray free-electron laser", Nature Photonics 6, 693–698 (2012) doi:10.1038/nphoton.2012.180

[17] S. Reiche, Nucl. Instr. Meth. Phys. Res. Sec. A 429, 243 (1999).

[18] Kwang-Je Kim and Zhirong Huang. Introduction to the physics of free electron lasers.

ISBN 978-3-95450-134-2

STUDIES OF UNDULATOR TAPERING FOR THE CLARA FEL

I.P.S. Martin, Diamond Light Source, Oxfordshire, UK
R. Bartolini, Diamond Light Source, Oxfordshire, UK
and John Adams Institute, University of Oxford, UK
D. Dunning, N. Thompson, ASTeC, STFC Daresbury Laboratory, UK

Abstract

Undulator tapering is a well-known method for enhancing the performance of free-electron lasers [1]. It works by keeping the resonant wavelength constant, despite variation in the electron beam energy. Both the energy-extraction efficiency and the spectral brightness of the FEL can be improved using this technique. In this paper we present recent studies of undulator tapering for the CLARA FEL in both SASE and seeded modes. The methods used to optimise the taper profile are described, and the properties of the final FEL pulses are compared.

INTRODUCTION

Undulator tapering is a well-known and widely used technique for improving the performance of free-electron lasers [1]. It works by keeping the resonant wavelength matched to the bunching in the electron beam, despite the changing energy of the electrons as they travel along the length of the undulator. It was originally proposed as a way to improve the energy extraction efficiency of an FEL [2–5], but has since found many other applications. For example, when tapering is combined with self-seeding, it provides a route to coherent, high-power, hard x-ray FELs [5,6]. Alternatively, it can be used in combination with an external laser modulator to generate short, fully coherent radiation pulses by restricting high FEL-gain to the energy-chirped sections of the electron bunch [7–9]. Similarly, energy-chirps arising from velocity bunching or longitudinal space charge can be compensated using an undulator taper [10, 11]. A reverse undulator taper can also be used to *suppress* FEL power, whilst still allowing a high degree of bunching to develop within the electron bunch. This can then be used for a variety of applications, such as generating circularly polarised light in a helical undulator after-burner [12].

In view of this diverse range of applications for undulator tapering, the topic is currently one of interest for study at the CLARA FEL currently under construction [13, 14]. CLARA aims to provide a test facility at which a wide range of current and future FEL schemes can be tested experimentally, and so the suitability of the proposed layout for effective tapering needs to be established at an early stage.

In this paper we present preliminary studies of undulator tapering using the CLARA FEL. We study two cases, namely seeded and SASE operation at 266 nm, and for each case investigate the performance of undulator tapering at improving the final FEL pulse quality.

TAPER OPTIMISATION METHODS

The basic principle of undulator tapering is simple, that is, the resonant wavelength should be kept constant by matching the undulator strength parameter a_u to the changing electron energy. In practice however, establishing the optimum taper profile is not straight-forward. Here, we compare two contrasting techniques.

The first method relates to the 1D Kroll-Morton-Rosenbluth (KMR) formalism [1,3]. In this, a Hamiltonian method is used to define a fixed synchronous phase Ψ_r that relates the rate of energy-extraction to the particle energy, the field amplitude and a_u. The Ψ_r parameter also defines the ponderomotive bucket area, and so the selection of Ψ_r becomes a trade-off between capturing the greatest number of particles (small Ψ_r) and maximising the rate at which energy is extracted from the electron beam (large Ψ_r). A modification of this method was recently proposed in [15], in which Ψ_r is allowed to vary along the radiator. The problem then changes from finding the optimal fixed-value of Ψ_r to one of optimising $d\Psi_r/dz$. In this study, we investigate a linear increase of the form:

$$\Psi_r(z) = \frac{\pi}{2L_d} z \tag{1}$$

where L_d is the so-called *detrapping length* (bucket area shrinks to zero at $z = L_d$, see [15] for details). With this parameter defined, the problem reduces to one of iteratively solving the equation:

$$a_u(z + \Delta z) = a_u(z) - \frac{\sqrt{2}e}{m_e c^2}\frac{\lambda_r}{\lambda_u} f_B(z)E_0(z)\sin\Psi_r(z)\Delta z \tag{2}$$

where f_B is the Bessel factor for a planar undulator and the radiation field amplitude E_0 is found at each step from time independent GENESIS calculations [16]. Solving Eqn. 2 gives a continuous taper profile; this has been converted to a stepped taper for later analysis using full, time dependent simulations.

The second method investigated is direct optimisation of the taper profiles using time-dependent GENESIS simulations. Whilst 3D, time-dependent simulations are slow, they automatically include various limiting effects such as radiation refraction and diffraction, radial dependence of the radiation field and the growth of sidebands that are missing from the 1D, steady-state method outlined above [17].

In principle, arbitrary taper profiles can be optimised in this way. However, to simplify the problem we investigate

ISBN 978-3-95450-134-2

a stepped taper of the form:

$$a_u(z) = \begin{cases} a_u(0), & \text{if } z \le z_0 \\ a_u(0) - b(z - z_0)^2, & \text{otherwise} \end{cases}$$

where b and z_0 are parameters to be optimised. In this study, each of the parameters are scanned in a grid in order to identify the best values.

CLARA FEL PARAMETERS

The latest proposal for the CLARA FEL is that the radiator section should be composed of many short undulator modules interleaved in a FODO focussing channel, with space reserved for mini-chicanes, diagnostics, etc. after each undulator. This layout would bring it closer to short-wavelength FEL facilities in terms of matching the undulator length to the FEL gain length, and has been selected in order to make it suitable for demonstration of the HB-SASE [18] and Mode-Locking [19] FEL schemes. The downside is that the undulator packing-faction remains relatively low at 0.62, potentially allowing significant radiation diffraction to take place between the undulator modules. The main parameters of the FEL are given in Table 1, and a plot of the electron beam size through the first two FODO periods are shown in Fig. 1.

Table 1: Summary of CLARA Parameters

Parameter	Unit	Value
Electron energy	MeV	232
Normalised emittance	mm.mrad	0.5
Energy Spread	keV	100
Bunch charge	pC	250
RMS bunch length	fs	250
Radiator period	mm	27.5
RMS undulator parameter, a_u		1.7285
Number of periods		28
Number of undulator modules		17
FODO period	m	2.475

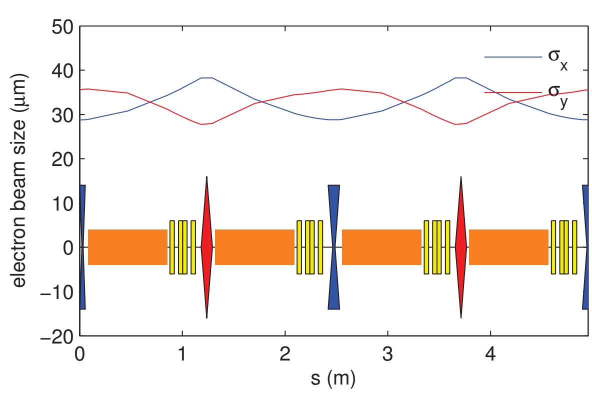

Figure 1: Electron beam size through two FODO periods of the radiator section in CLARA.

TAPERING FOR SEEDED OPERATION

Due to the limited space available for the CLARA radiators, demonstration of a full self-seeding plus tapered undulator set-up has not been considered here. Instead, these studies aim to simulate the scheme by providing an external laser seed. In the baseline design it is foreseen that an 800 nm seed-laser will be provided [13]. This could be used in combination with a chicane to provide initial bunching at 800 nm, with the radiators set to be resonant at 266 nm. For simplicity however, these studies have assumed direct seeding of the electron bunch at 266 nm. Such a seed laser could be considered as potential future upgrade of the facility.

In order to match the characteristics of self-seeding as closely as possible, it has been assumed that the seed power is ~$10^{-4} \times P_{sat}$. The length of the seed pulse has been set equal to the electron bunch at 250 fs rms, giving a pulse energy of 50 nJ at the entrance to the radiator.

Figure 2 shows the results of scanning the taper parameters z_0 and b. Two options are considered, either maximising the pulse energy or the spectral brightness (defined here as the integrated spectrum in the region 264.67 nm to 267.33 nm). Without tapering, the FEL reaches an initial saturation at 4.56 m into the radiator (4 undulator modules). The results indicates that for both options the taper should begin before this, and in order to maximise pulse energy the profile should be gradual ($b = 0.0002$ starting after 1 module). In contrast, maximising the spectral brightness favours a stronger reduction in a_u ($b = 0.0019$) starting after 3 modules.

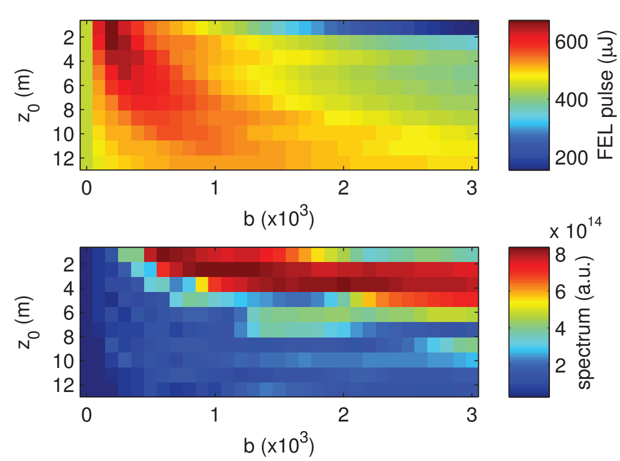

Figure 2: FEL pulse energy (top) and integrated spectrum (bottom) as a function of quadratic taper parameters.

When using the modified KMR technique to optimise the taper profile, a similar trade-off is observed. Selecting a relatively large value of $L_d = 17.8$ m leads to a gradual increase in Ψ_r, resulting in a larger bucket area that maximises the number of captured particles. The rate of energy extraction is slow, but the final pulse energy is maximised. Alternatively, selecting a smaller value of $L_d = 8.9$ m leads to more rapid energy extraction, but sacrifices the number of parti-

ISBN 978-3-95450-134-2

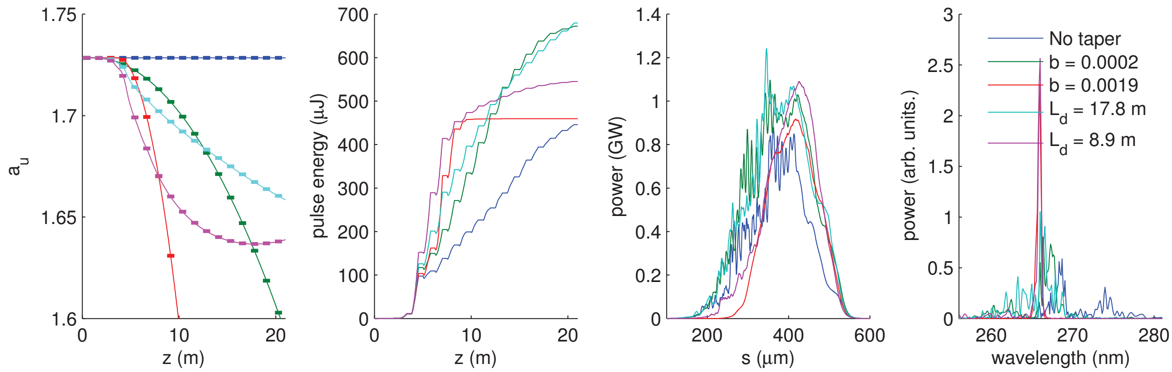

Figure 3: Comparison of optimum pulse properties found using quadratic (red and green lines) and modified KMR (cyan and magenta lines) taper profiles (seeded operation). A pulse calculated for an un-tapered FEL is also given for reference (blue lines). Far left: undulator taper profiles. Middle left: pulse energies as a function of z. Middle right: pulse profiles at $z = 21.01$ m. Far right: pulse spectra at $z = 21.01$ m.

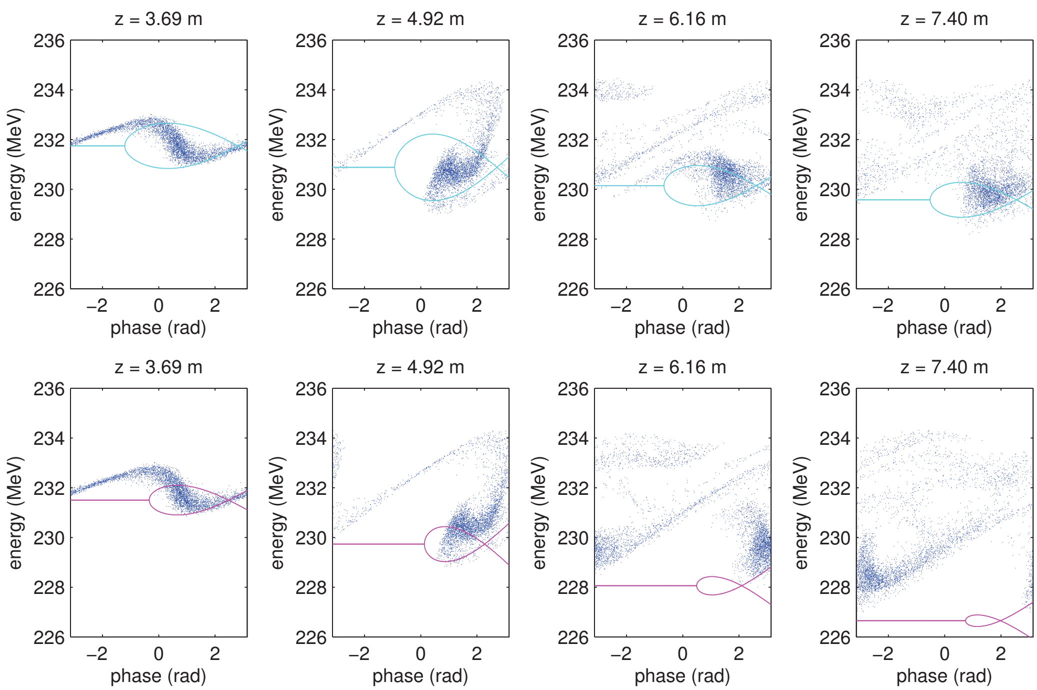

Figure 4: Electron bunch phase space at various points along the radiator for two taper profiles, each calculated using the modified KMR method. Top: $L_d = 17.8$ m. Bottom: $L_d = 8.9$ m.

cles captured in the bucket. The final pulse energy in this case is lower, but the spectral brightness is maximised.

A comparison of the FEL pulse properties is given in Fig. 3. As can be seen, the modified KMR method marginally outperforms the simple quadratic taper profile when optimising for either pulse energy or spectral brightness, despite the inherent simplifications of the 1D analysis. The taper profiles arrived at using this technique quickly deviate from quadratic, approaching a linear variation of a_u with z for $L_d = 17.8$m, and levelling off completely for $L_d = 8.9$ m.

The increase in pulse energy is modest, going from 440 μJ in the untapered case to 680 μJ for the modified KMR case with $L_d = 17.8$ m. The pulse durations are also reasonably similar, ranging from 480 fs for the modified KMR case with $L_d = 8.9$ m to 635 fs for the untapered case (FWHM). The feature that benefits the most from tapering is the line-width, which reduces by up to a factor of 10 over the non-tapered case, with a similar increase in the spectral brightness. The final FEL pulse for the modified KMR case with $L_d = 8.9$ m has a time-bandwidth product of 0.86, close to that of a transform-limited Gaussian pulse.

When optimising for pulse energy, the increase comes mainly from side-band growth rather than an increase at the target wavelength. A faster taper is clearly beneficial

ISBN 978-3-95450-134-2

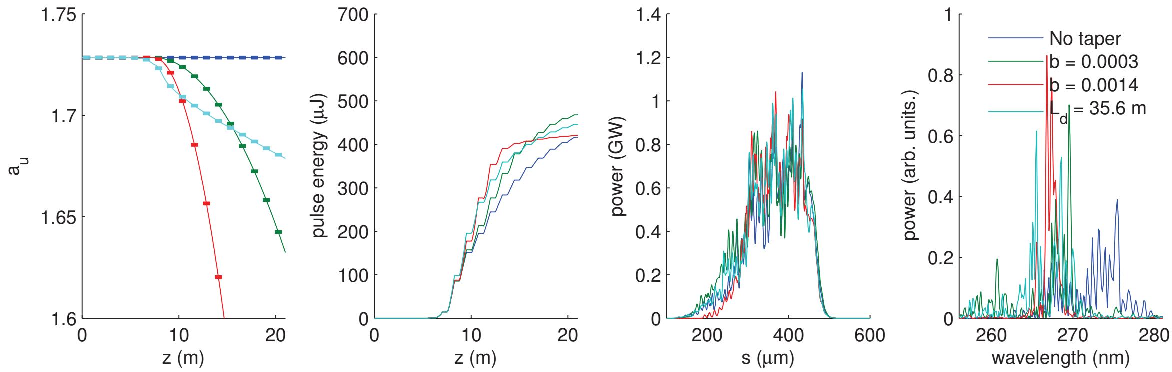

Figure 5: Comparison of optimum pulse properties found using quadratic (red and green lines) and modified KMR (cyan lines) taper profiles (SASE operation). A pulse calculated for an un-tapered FEL is also given for reference (blue lines). Far left: undulator taper profiles. Middle left: pulse energies as a function of z. Middle right: pulse profiles at $z = 21.01$ m. Far right: pulse spectra at $z = 21.01$ m.

at preventing this, as the detrapped particles are moved further from resonance, limiting their ability to form sidebands. This can be seen by examining the electron phase space (see Fig. 4). Here, the two modified KMR cases of maximum pulse energy (L_d = 17.8 m, top) and maximum spectral brightness (L_d = 8.9 m, bottom) are compared. For maximum pulse energy, the ponderomotive bucket is large, with a high fraction of particles either inside or close to the separatrix. For maximum spectral brightness, the more aggressive taper profile means that the bucket area is smaller and the number of captured particles is reduced. However, for those particles that are captured, more energy is extracted at the target wavelength, with the remaining particles left further from from resonance (thereby preventing side-band growth). In the case of a quadratic taper profile with b = 0.0019, the FEL pulse decouples completely from the electron bunch after 9.6 m.

TAPERING FOR SASE OPERATION

The impact of undulator tapering for CLARA in SASE mode has also been investigated. It is anticipated that the tapering will be less effective in this mode due to the stochastic nature of the radiation growth. In SASE mode, each radiation spike is uncorrelated in phase with respect to its neighbours, leading to a mismatch between radiation phase and electron bunching as the FEL pulse moves forward. This in turn limits the ability to maintain particle trapping simply by adjusting a_u.

For the case of no tapering, the FEL reaches an initial saturation point at 9.5 m into the radiator, although as with the seeded case the pulse energy continues to increase after this point due to sideband growth. After applying the modified KMR technique to identify the optimum taper profile, it was found that when setting L_d to 35.6 m that both the pulse energy and spectral brightness could be simultaneously maximised. When applying a quadratic taper profile starting after 6 undulator modules (z = 7.9 m), it was found that it is possible to improve on either the pulse energy or the spectral brightness over and above what could be achieved with the modified KMR technique, although not simultaneously.

The results of this analysis are shown in Fig. 5. As with the seeded FEL simulations, the pulse duration is left largely unchanged by the tapering, ranging from 450 fs FWHM for the b = 0.0014 case (maximum spectral brightness) to 580 fs for the b = 0.0003 case (maximum pulse energy). The increase in pulse energy found from tapering is ~10-15 %. The main improvement is once again observed in the integrated spectrum around the target wavelength, which in this case can be improved by more than a factor 5.

CONCLUSIONS

An investigation has been carried out into the suitability of the proposed CLARA FEL structure for improving both the final FEL pulse energy and spectral brightness via undulator tapering. Two contrasting taper optimisation techniques have been investigated, and the analytic modified KMR method was found to produce comparable, and in some cases superior, results to those given by direct 3D, time-dependent optimisation of a quadratic taper profile (despite the inherent simplifications). However, it remains a possibility that direct optimisation of an arbitrary taper profile would still be beneficial; this option is feasible given modern cluster computing resources and numerical optimisation techniques (see [20] for example).

As expected, undulator tapering has been found to be more effective for seeded operation than for SASE. Both spectral brightness and pulse energy can be significantly increased by using a tapered undulator, although indications are that the increase in pulse energy comes largely from sideband growth.

Finally, the authors would like to express their thanks to the members of the CLARA FEL and accelerator working groups for valuable discussions and for providing the input parameters used during these studies.

ISBN 978-3-95450-134-2

REFERENCES

[1] N.M. Kroll, P.L. Morton, M.N. Rosenbluth, "Free-Electron Lasers with Variable Parameter Wigglers", J. Quantum Electronics **17**, 8 (1981).

[2] T.J. Orzechowski, et al., "High-Efficiency Extraction of Microwave Radiation from a Tapered-Wiggler Free-Electron Laser", Phys. Rev. Lett. **57**, 17 (1986).

[3] W.M. Fawley, Z. Huang, K.-J. Kim, N.A. Vinokurov, "Tapered Undulators for SASE FELs", Nucl. Inst. Methods A **483**, 537 (2002).

[4] X.J. Wang, et al., "Efficiency and Spectrum Enhancement in a Tapered Free-Electron Laser Amplifier", Phys. Rev. Lett. **103**, 154801 (2009).

[5] G. Geloni, V. Kocharyan, E. Saldin, "Scheme for Generation of Full-Coherent, TW Power Level Hard X-ray Pusles from Baseline Undulators at the European X-ray FEL", DESY 10-108, (2010).

[6] W.M. Fawley, et al., "Toward TW-Level, Hard X-ray Pulses at LCLS", in Proc. FEL2011, Shanghai, TUOA4 (2011).

[7] E.L. Saldin, E.A. Schneidmiller, M.V. Yurkov, "Self-Amplified Spontaneous Emission FEL with Energy-Chirped Electron Beam and its Application for Generation of attosecond x-ray Pulses", Phys. Rev. ST Accel. Beams **9**, 050702 (2006).

[8] W.M. Fawley, "Production of Ultrashort FEL XUV Pulses via a Reverse Undulator Taper", Nucl. Inst. Methods A **593**, 111 (2008).

[9] I.P.S. Martin, R. Bartolini, "Comparison of Short Pulse Generation Schemes for a Soft X-ray Free Electron Laser", Phys. Rev. ST Accel. Beams **14**, 030702 (2011).

[10] L. Giannessi, et al., "Self-Amplified Spontaneous Emission Free-Electron Laser with an Energy-Chirped Electron Beam and Undulator Tapering", Phys. Rev. Lett. **106**, 144801 (2011).

[11] S. Huang, Y. Ding, Z. Huang, J. Qiang, "Generation of Stable Subfemtosecond Hard X-ray Pulses with Optimised Nonlinear Bunch Compression", Phys. Rev. ST Accel. Beams **17**, 120703 (2014).

[12] E.A. Schneidmiller, M.V. Yurkov, "Obtaining High Degree of Circular Polarisation at X-ray Free-Electron Lasers via a Reverse Undulator Taper", Phys. Rev. ST Accel. Beams **16**, 110702 (2013).

[13] J.A. Clarke, et al., "CLARA Conceptual Design Report", JINST **9**, T05001 (2014).

[14] J.A. Clarke, et al., "The Status of CLARA, a New FEL Test Facility", in Proc. FEL2015, Daejeon, MOP011 (2015).

[15] A. Mak, F. Curbis, S. Werin, "Model-Based Optimisation of Tapered Free-Electron Lasers", Phys. Rev. ST Accel. Beams **18**, 040702 (2015).

[16] S. Reiche, "GENESIS 1.3: A Fully 3D Time-Dependent FEL Simulation Code", NIM-A **429**, p. 243-248, (1999).

[17] Y. Jiao, et al., "Modeling and Multidimensional Optimisation of a Tapered Free Electron Laser", Phys. Rev. ST Accel. Beams **15**, 050704 (2012).

[18] B.W.J. McNeil, N.R. Thompson, D.J. Dunning, "Transform-Limited X-ray Pulse Generation from a High-Brightness Self-Amplified Spontaneous Emission Free-Electron Laser", Phys. Rev. Lett. **110**, 134802 (2013).

[19] N.R. Thompson, B.W.J. McNeil, "Mode Locking in a Free-Electron Laser Amplifier", Phys. Rev. Lett. **100**, 203901 (2008).

[20] K. Deb, "A Fast and Elitist Multiobjective Genetic Algorithm: NSGA-II", IEEE Trans. Evolutionary Computing. **6**, 2, p. 182 (2002).

ISBN 978-3-95450-134-2

MEASUREMENT UNCERTAINTIES IN GAS-BASED MONITORS FOR HIGH REPETITION RATE X-RAY FEL OPERATIONS*

Y. Feng#, J. Krzywinski, M. Campell, D. W. Schafer, E. Ortiz, M. Rowen, T. O. Raubenheimer, SLAC, Menlo Park, CA 94025, USA

Abstract

Thermodynamic simulations using a finite difference method were carried out to investigate the measurement uncertainties in gas-based X-ray FEL diagnostic monitors under high repetition rate operations such as planned for the future LCLS-II soft and hard X-ray FEL's. For monitors using relatively high gas pressures for obtaining sufficient signals, the absorbed thermal power becomes non-negligible as repetition rate increases while keeping pulse energy constant. The fluctuations in the absorbed power were shown to induce significant measurements uncertainties, especially in the single-pulse mode. The magnitude of this thermal effect depends nonlinearly on the absorbed power and can be minimized by using a more efficient detection scheme in which the gas pressure can be set sufficiently low.

INTRODUCTION

The Linac Coherent Light Source (LCLS) currently operating at SLAC National Accelerator Laboratory will soon start to construct, under the LCLS-II project, a new 4 GeV continuous-wave (CW) superconducting radio frequency (SCRF) linear accelerator, in addition to the existing normal conducting RF Cu linac (CuRF). There will be two new variable-gap undulators to be placed in the existing LCLS undulator tunnel: a new soft X-ray undulator and a hard X-ray undulator that would replace the existing LCLS fixed-gap undulator. Both new undulators, when fed by the SCRF linac, could run at a very high repetition rate up to ~ 1 MHz, nearly 4 orders of magnitude higher than the LCLLS 120 Hz operation. Both undulators will operate in the Self Amplified Spontaneous Emission [1] (SASE) mode with the option to be self-seeded over certain energy ranges. Due to the intrinsic stochastic nature of the SASE lasing process and other extrinsic random mechanisms in the linac, many important parameters of the FEL beam fluctuate randomly from pulse to pulse [2]. For example, the pulse intensity can vary by as much as a 10% in the SASE mode to nearly 100% in the seeded mode [3]. Many diagnostic devices are needed to help the accelerator operators to optimize the lasing performance, and to enable the users to normalize the experimental data [4-8].

The various diagnostic devices are typically located in the Front-End Enclosure (FEE) just downstream of the undulator but upstream of any experimental endstations. They are often required to be highly transmissive and minimally intrusive as to introduce only negligible wavefront distortion or transverse coherence degradation. Because of the close proximity of FEE to the effective source location, which is somewhere between the FEL saturation point and the end of undulators (EOU), the power density of the beam at the device locations is quite high, and the diagnostic devices must be based on using a gas medium or a thin solid film to avoid damages while assuring the transmission requirement. For soft X-ray FEL beams in particular, gas-based concepts are the only viable solutions because of the high absorption cross-section at these energies even for the very low Z materials. For pulse energy measurement, LCLS-II is planning to install two Gas Detector Monitors [9] (GMD's), one of the original design for very soft X-rays and another the latest version specifically optimized for covering higher X-ray energies, on the soft X-ray transport line in the FEE for the SCRF high repetition rate FEL beam. Both GMD's should be capable of providing pulse-to-pulse measurements at greater than 1 MHz repetition rate, but would require very low operating pressures on the order of only 10^{-5} hPa because of the highly efficient direct detection of the ions/electrons from photoionization by the impinging FEL beam.

On the LCLS-II hard X-ray transport line in the FEE, the existing LCLS N_2 gas energy detectors [10] (GED's) shown in Figure 1 will be re-purposed with upgrades for providing pulse-to-pulse measurements of both the high repetition rate FEL when driven by the SCRF linac as well as the 120 Hz high pulse energy FEL when driven by the CuRF linac. The GED concept is based on the detection of the near ultraviolet (UV) optical radiation from the N_2 molecules excited by the secondary electrons, which are produced by the primary photoelectron via collisions with the N_2 molecules. This indirect radiation process in a GED, in contrast to what happens in a GMD, is far less efficient, and thus requires the use of a much higher operation pressure of order 0.01 to 1 hPa, an increase of 3 to 5 orders of magnitude.

Gas-based systems such as the gas attenuator used for LCLS and also being planned for LCLS-II, however, have been shown to exhibit density depression or the so-called "filamentation" effect [11], when the energy absorbed in the gas medium is sufficiently high so that it can no longer be considered as being merely a small perturbation. The effective attenuation not only depends on the pressure, but also on many other physical attributes of the attenuator system itself, including gas type and it thermal properties, the length and radius of the gas tube, the transverse profile of the FEL beam [12]. If the input pulse energy fluctuates as in any SASE based FEL pulses, the attenuation received by any given pulse also varies substantially but in a delayed and hysteric manner and is

*Work supported by DOE under Contract #. DE-AC02-76SF00515.
#yfeng@slac.stanford.edu

ISBN 978-3-95450-134-2

essentially not predictable [13]. This non-deterministic behaviour presents a rather serious operational challenge to the users and could cause irreparable damages to equipment that the attenuator is designed to protect. One of the mitigation strategies is to measure the attenuated intensity by a separate diagnostic device and use it as a feedback to make the proper adjustment to the operating pressure to obtain the requirement attenuation.

Since the downstream intensity diagnostic device is also gas based, a similar filamentation or density depression effect is expected to be present, which would in turn impact the measurement as well. As stated earlier, for gas-based energy monitors the absorbed energy is typically designed to be very small, although in the case of GED it is not entirely negligible because of the higher operating pressure to compensate for the lower light production efficiency. In this report, we will investigate the uncertainties in the pulse intensity measurement using a GED under the LCLS-II high repetition rate operations, especially when the input pulse energy thus the running average of the input power fluctuates randomly. It was found that these random variations would lead to significant measurements uncertainties on a pulse-by-pulse basis. The magnitude of this thermal effect depends nonlinearly on the averaged absorbed power and can be minimized by using a more efficient detection scheme such as that of the GMD's, for which the gas pressure can be set sufficiently low.

GAS MONITORS SIMULATIONS

The ultrafast interaction between the FEL pulses and the gas atoms/molecules in a gas monitor is very complex and is the subject of many pioneering research activities ranging from nonlinear atomic and molecular science to FEL driven atomic X-ray lasers [14, 15], which often involving focusing the already small FEL beam down to an even tinier spot. However, in either a gas attenuator or an energy monitor and for the purpose of this investigation, the FEL beam is unfocused and the light-matter interaction remains linear, and can be modelled simply as an energy deposition mechanism via photoabsorption that takes place instantaneously upon arrival of each pulse, creating a local temperature and a simultaneous pressure gradient in the gas medium along the beam path while the global density remains unchanged. The pressure gradient in turn drives hydrodynamic motions of the atoms/molecules to establish a global pressure equilibrium, resulting in a density gradient coexisting with the temperature gradient. What ensues is a slow process at a few nanoseconds and longer time scales dominated by thermal diffusion, dissipating eventually all of the deposited energy. The time-dependent behaviour of this thermodynamic process after each pulse is used to predict what temperature and density profile the next trailing pulse would effectively "see", from which the responses such as the intensity of the near UV production in a GED can be determined and the extent to which the fluctuations in input pulse energy can impact the measurement accuracy can be evaluated.

Time-dependent Behaviour with Random Input Pulse Energies

The simulation techniques used to study the steady state and time dependent solutions of a gas attenuator [12,13] were used. Potential modifications for taking into account the specific GED geometry shown in Figure 1 and operating conditions turned out to be not necessary. Because of the relatively rare gas pressure, the temperature gradient along the beam direction remains small in comparison to that in the radial direction. As such the computational procedures developed earlier [13] can be readily applied here, whereby the time-dependent temperature and density profiles were obtained by solving a one-dimensional partial differential heat equation for a thin slab starting at the entrance of the gas pipe and repeating it sequentially towards the exit.

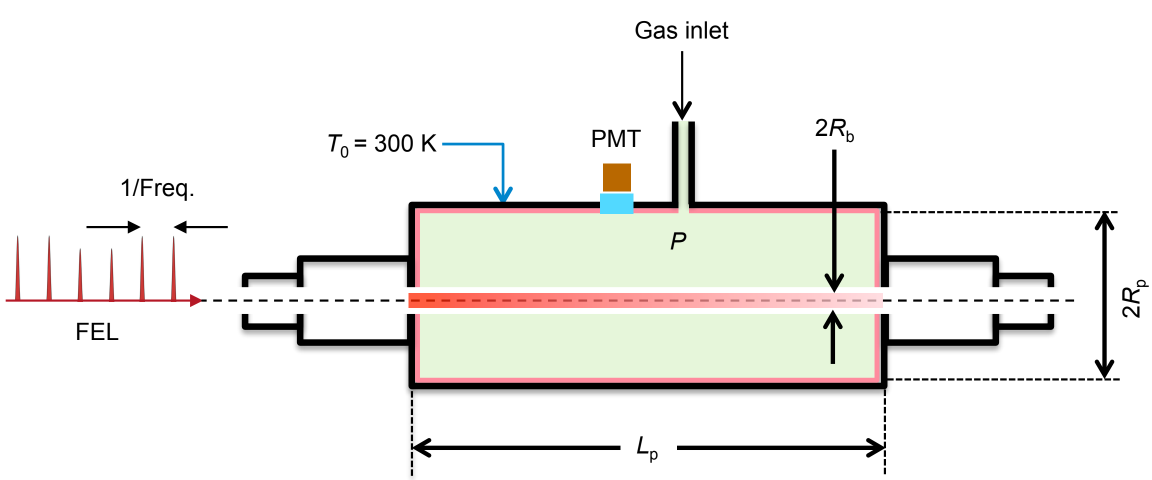

Figure 1: Schematic of the LCLS-II hard X-ray gas detector, consisting of a cylindrical pipe filled with N_2 gas bookended by two differential pumping sections. The pipe has a length L_p and diameter of $2R_p$, and the FEL beam $2R_b$. The wall of the pipe is cooled to 300 K, and the gas inlet maintains the pressure P ranging from tens of mTorr to a few Torr. The PMT is used to collect near UV radiation created by the passage of the FEL.

ISBN 978-3-95450-134-2

The simulation was done for a 1 keV X-ray FEL beam running at 100 kHz with an average per-pulse energy of 2 mJ distributed randomly from 0 to 4 mJ and an average power of 200 W. The energy of any given pulse was generated by using a standard pseudorandom scalar algorithm. The GED is 300 mm in length and 50 mm in diameter, with the outer wall cooled to 300 K, and the pressure P regulated to an equilibrium of 0.985 Torr to effectively attenuate the beam by 5%, about 2x higher than 0.345 Torr, which was calculated in the low-power limit when the filamentation effect due to the absorbed power is neglected. The gas pressure in the two differential pumping sections is assumed to be negligible as well. The isobaric specific heat of the N_2 gas was assumed to be constant at $7R/2$ due to it being in a fully excited rotational state but in the vibrational ground state, where R = 8.31 J/K·mol is the gas constant. In Figure 2, the time evolution of the temperature at the central entrance of the gas pipe is shown, exhibiting instantaneous rise immediately after the arrival of each pulse, and then a relaxation process towards the steady state value T_{eq} ~ 810 K, which depends on the average absorbed power Q in the gas volume. Because of the fluctuations in the input pulse energy, the asymptotic temperatures "seen" by the trailing pulses also vary randomly by as much as 150 K.

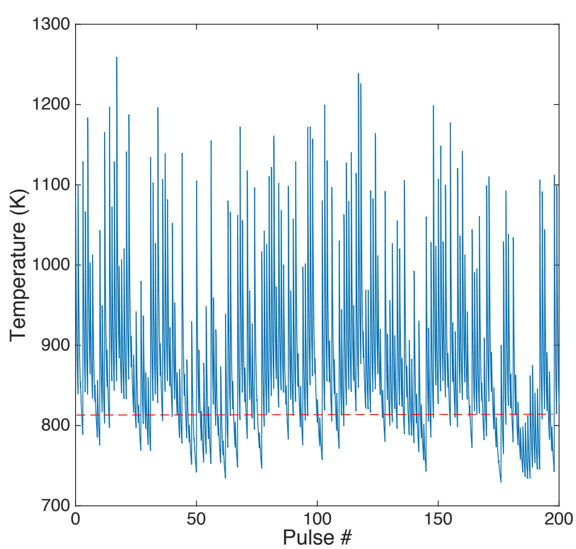

Figure 2: The time evolution of the temperature at the center of the entrance of the gas pipe as 200 random pulses of average energy of 2 mJ pass through. The targeted attenuation $A(0)$ was set for 0.05, resulting an average absorbed power of 10 W.

There are corresponding variations in the density distribution after each pulse, given by the assumed local equilibrium condition $n(r, z, t)T(r, z, t) = P/k_B$, where r, and z are the spatial coordinates, and P the equilibrium pressure [13] The actual achieved attenuation $A(Q)$ for any given pulse can be calculated from the density profile $n(r, z, t)$ and the photoabsorption cross-section of the N_2 gas and is plotted in Figure 3.

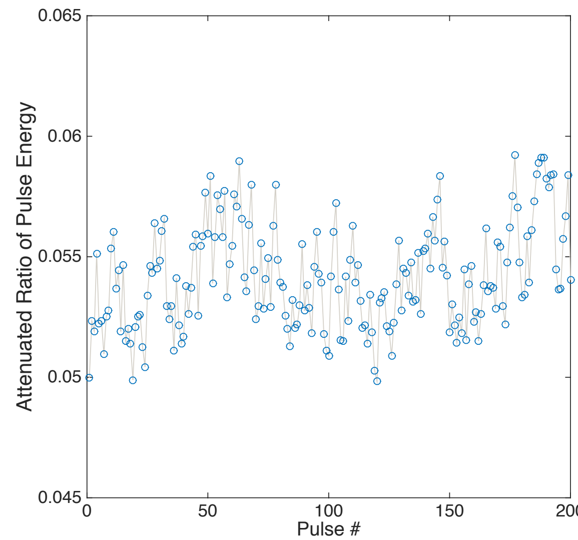

Figure 3: The actual received attenuation by each of the 200 pulses with randomly varying energy from 0 to 4 mJ. The targeted attenuation $A(0)$ was set for 0.05.

The achieved attenuation $A(Q)$ for any given pulse is no longer constant as expected in the low-power limit when the filamentation effect is negligible, and changes by as much as 20% peak-to-peak or 4.4% in standard deviation from the average value of 0.055, in addition, there is an overall shift of 0.005 in the average from the targeted value $A(0)$ of 0.05 to 0.055, reflecting the fact that the gas pressure was set a bit higher than required when using the result from the CW steady state simulation [13].

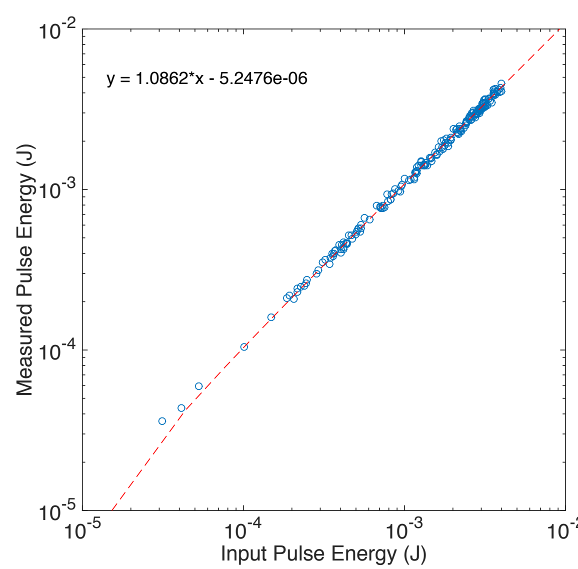

Figure 4: The measured pulse energy vs. the input pulse energy for the case that the effective attenuation is set for 5% or 10 W. The red dotted line is a linear fit.

Measured Pulse Energies

The photo multiplier tube (PMT) in Figure 1 is used to collect the near UV radiation generated indirectly by the

ISBN 978-3-95450-134-2

primary electrons via the photoabsorption process, which was assumed to be the dominant attenuation mechanism. The normalized pulse intensity measured by the PMT is proportional to the attenuated pulse energy, i.e., $I_m = I_0 \cdot A(Q) \cdot \eta / A(0)$, where I_0 is randomized input pulse energy, η is the quantum efficiency of the detector and is set to 1 for simplicity and for properly evaluating the measurement uncertainties, and $A(0)$ is the targeted attenuation in the low-power limit.

In Figure 4, the normalized measured pulse energy is plotted directly against the randomized input pulse energy, and a linear fit is also shown by the red dotted line. It can be seen that I_m correlates in general with the input energy I_0, but also exhibits substantive deviations that depend critically on the total power absorbed in the gas volume as evidenced by a similar simulation for $A(0) = 0.125\%$ shown in Figure 5, where the deviations are greatly reduced, exemplifying the performance expected for an intensity monitor if the filamentation effect is absent.

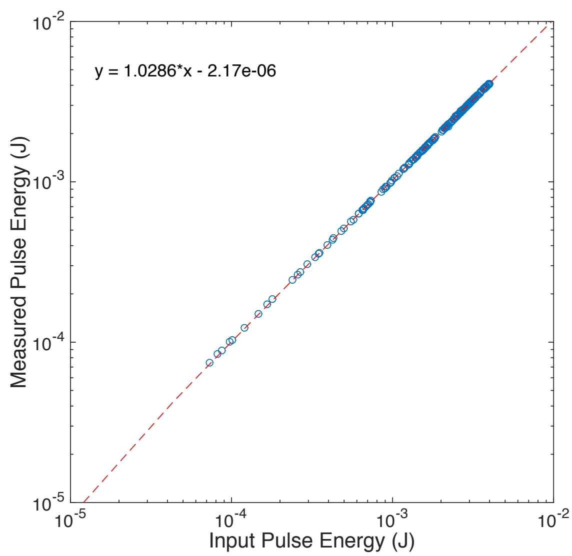

Figure 5: The measured pulse energy vs. the input pulse energy for the case that the effective attenuation is set for 0.125% or 0.25 W. The red dotted line is a linear fit.

Energy Measurement Uncertainties

To quantitatively assess the measurement uncertainties, the ratio of the measured over the input pulse energy is plotted against the input pulse energy in Figure 6 and Figure 7 for the 5% and 0.125% attenuation cases, respectively. The scatter in the data sets are markedly different, reaching as much as 20% peak-to-peak or σ = 4.3% in standard deviation for 5% or 10 W attenuation, but only 2.2% peak-to-peak, and 0.48% in σ for the 0.125% or 0.25 W attenuation. The ratios are both greater than unity because of the pressure settings were slightly higher than required in both cases, reflecting some small differences in steady state and time-dependent simulations in determining the equilibrium pressure [13]. This result is rather important since in order to reach the 1% relative accuracy requirement for pulse energy measurement, the absorbed power must be reduced to less than 0.5 W, and the attenuation to less than 0.25%. This finding will be used to help guide the LCLS N_2 gas detector upgrade to first emphasizing maximizing the near UV detection efficiency including more sensitive PMT's and lower electronics noise, thus reducing the required operating pressure. Additional gain can be made by reducing the pipe diameter to improve cooling of the gas molecules.

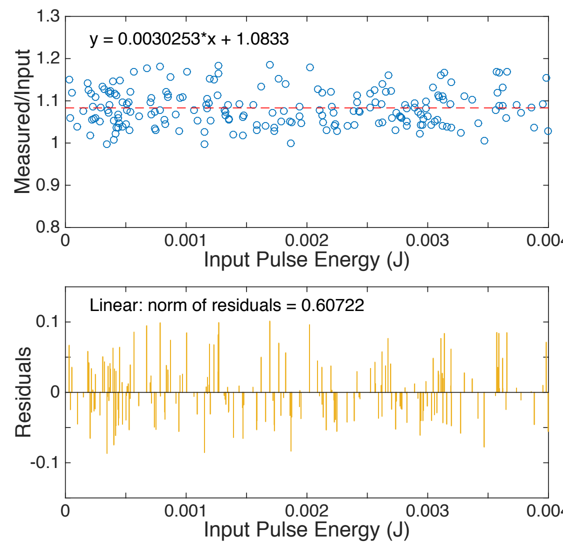

Figure 6: The ratio of the measured over the input pulse energy for the case that the effective attenuation is set for 5% or 10 W. The red dotted line is a linear fit, with the residuals shown in the bottom plot.

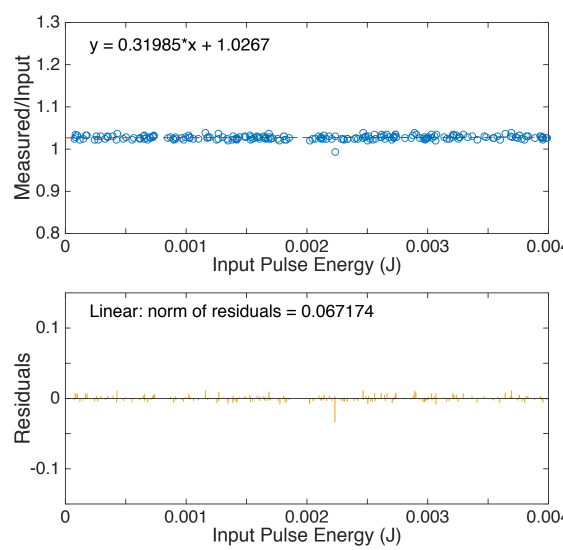

Figure 7: The ratio of the measured over the input pulse energy for the case that the effective attenuation is set for 0.125% or 0.25 W. The red dotted line is a linear fit, with the residuals shown in the bottom plot.

ISBN 978-3-95450-134-2

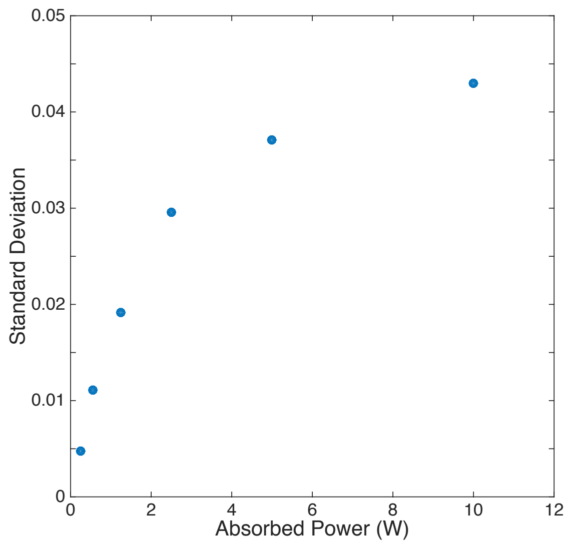

Figure 8: The dependence of the standard deviation σ for the pulse energy measurement on the power absorbed in the gas volume. The red dotted line is a polynomial fit. To achieve a relative accuracy of 1%, the power must be kept below 0.5 W given the specific design of the current LCLS N_2 gas detector.

CONCLUSION

We have carried out thermodynamic simulations to study the impact of filamentation effect on the measurement uncertainties in gas-based pulse energy monitors, when the absorbed power in the gas volume is not negligible. This is particularly applicable to the case of the LCLS-II N_2 gas detector under high repetition rate operations, in which the pressure or the density in the gas volume must be set sufficiently high to produce required signal strength for reliable measurements. It was found that the absorbed energy in the gas interaction volume exhibit random variations in response to the fluctuations in the input pulse energy as is the case for most SASE based FEL sources. Consequently, there could be substantial uncertainties in the pulse energy measurement, approaching 20% peak to peak or 4.3% in standard deviation, when the average absorbed power is set at 10 W. This undesirable effect can be minimized by devising more efficient monitoring technique whereby smaller gas pressure/density could be used, such as the GMD's planned for the soft X-ray transport line of the LCLS-II. For the GMD's, a potential issue could be the gas diffusion time being sufficiently short, since the ions and electrons generated from the photoabsorption process are designed to be swept from the interaction volume after each pulse, thus depleting the effective gas density. In principle, similar studies looking into the gas diffusion process in the GMD's should be performed. For other gas-based monitors designed for measurements other than energy such as capturing soft X-ray FEL single-shot spectra from analysing the kinetic energy of primary photoelectrons, the filamentation effect is expected to be not as important, because typically a gas jet is used, and the gas molecules in the interaction region are being replaced for every pulse.

ACKNOWLEDGMENT

Use of the Linac Coherent Light Source (LCLS), SLAC National Accelerator Laboratory, is supported by the U.S. Department of Energy, Office of Science, Office of Basic Energy Sciences under Contract No. DE-AC02-76SF00515.

REFERENCES

[1] A. M. Kondratenko, and E. L. and Saldin, Sov. Phys. Dokl. 24, 986 (1979); R. Bonifacio, C. Pellegrini, and L. M. Narducci, Opt. Commun. 50, 373 (1984).
[2] For example, E. L. Saldin, E. A. Schneidmiller, and M. V. Yurkov, Optics Communications 148, 383 (1998).
[3] P. Emma, private communication.
[4] Y. Feng, J. Feldkamp, D. M. Fritz, M. Cammarata, A. Robert, C. Caronna, H. T. Lemke, D. Zhu, S. Lee, S. Boutet, G. Williams, K. Tono, M. Yabashi, and J. Hastings, Proc. SPIE 8140, 81400Q (2011).
[5] For example, Bionta et al, Opt. Express 19, 21855 (2011).
[6] D. Zhu, M. Cammarata, J. M. Feldkamp, D. M. Fritz, J. B. Hastings, S. Lee, H. T. Lemke, A. Robert, J. L. Turner, and Y. Feng, Appl. Phys. Lett. 101, 034103 (2012).
[7] C. Behrens, et al, Nat. Comm. 5, 3762 (2014).
[8] E. Allaria, et al., Phys. Rev. X 4, 041040 (2014).
[9] K. Tiedtke et al. J. Appl. Phys. 103, 094511 (2008).
[10] S. P. Hau-Riege, R. M. Bionta, D. D. Ryutov, R. A. London, E. Ables, K. I. Kishiyama, S. Shen, M. A. McKernan, D. H. McMahon, M. Messerschmidt et al., Phys. Rev. Lett. 105, 043003 (2010).
[11] Y.-H. Cheng, J. K. Wahlstrand, N. Jhajj, and H.M. Milchberg, Optics Express 21, 4740 (2013).
[12] Y. Feng, J. Krzywinski, D. W. Schafer, E. Ortiz, M. Rowen, and T. O. Raubenheimer, submitted to J. Synch. Rad. (2015).
[13] Y. Feng, J. Krzywinski, D. W. Schafer, E. Ortiz, M. Rowen, and T. O. Raubenheimer, submitted to Proc. SPIE (2015).
[14] L. Young, E. P. Kanter, B. Krässig, Y. Li, A.M. March, S. T. Pratt, R. Santra, S. H. Southworth, N. Rohringer, L. F. DiMauro, et al., Nature 446, 56 (2010).
[15] N. Rohringer, D. Ryan, R. A. London, M. Purvis, F. Albert, J. Dunn, J. D. Bozek, C. Bostedt, A. Graf, R. Hill et al., Nature 481, 488 (2012).

ISBN 978-3-95450-134-2

FACILITY UPGRADES FOR THE HIGH HARMONIC ECHO PROGRAM AT SLAC'S NLCTA

B. Garcia*, M.P. Dunning, C. Hast, E. Hemsing, T.O. Raubenheimer
SLAC, Menlo Park, California, USA
D. Xiang, Shanghai Jiao Tong University, Shanghai

Abstract

The Echo program currently underway at SLAC's Next Linear Collider Test Accelerator (NLCTA) aims to use Echo-Enabled Harmonic Generation (EEHG) to produce considerable bunching in the electron beam at high harmonics of a 2400 nm seed laser. The production of such high harmonics in the EUV wavelength range necessitates an efficient radiator and associated light diagnostics to accurately characterize and tune the echo effect. We have installed and commissioned the Visible to Infrared SASE Amplifier (VISA) undulator, a strong focusing two meter long planar undulator of Halbach array design with 1.8 cm period length. To characterize the output radiation, we have designed, built, and calibrated a grazing incidence EUV spectrometer which operates between 12–120 nm with resolution sufficient to resolve individual harmonics. An absolute wavelength calibration is achieved by using both EEHG and High Gain Harmonic Generation (HGHG) signals from the undulator.

INTRODUCTION

The NLCTA at SLAC is a low-energy X-band test accelerator which delivers a beam at up to 165 MeV with normalized projected emittance of <2 mm-mrad, and bunch charge of up to 200 pC. The current layout of the main NLCTA beamline is shown in Figure 1 (for a discussion of the previous state of the facility and upgrades, see [1]), and we briefly review it here. The beam is generated from a UV photocathode illuminated by a 266 nm, 1 ps long laser pulse and accelerated through a 1.6 cell BNL/SLAC/UCLA S-band gun. After, it is boosted to 60 MeV by an X-band accelerating structure (X1), and continues to the Echo portion of the beamline where it is accelerated again to 120 MeV (X2). An orbital bump is generated by small chicane (C0) to allow insertion of the first seed laser, which modulates the beam in the first undulator (U1), followed by the first dispersive chicane (C1), second modulator (U2), and final dispersive chicane (C2). An additional boost is provided by the third X-band structure (X3) to bring the beam energy to ~160 MeV, where the beam then enters the two meter VISA undulator (U3) to radiate. Finally, photons can be diverted into either the Extreme Ultraviolet (EUV) or Vacuum Ultraviolet (VUV) spectrometer and associated diagnostics, and electron beam energy is finally measured with a dipole energy spectrometer.

The NLCTA is currently involved in investigating advanced beam phase space manipulation techniques, particularly Echo-Enabled Harmonic Generation (EEHG) [2]. This technique involves using a two-modulator, two-chicane setup in order to generate density modulations in the electron beam at a high harmonic of the initial seed laser. The first laser modulator imprints an energy modulation on the beam, which is then macroscopically sheared by a strong first chicane. This creates a fine energy banding structure in the electron beam, effectively decreasing the slice energy spread of the individual beamlets. The beam is then modulated in a second undulator, and this modulation converted into density modulation by standing the energy modulation upright (similar to the manipulation in the more common High-Gain Harmonic Generation scheme [3]). Thus, a density modulation recoheres at a wavenumber given by $k = nk_1 + mk_2$, where n, m are integers, and k_1, k_2 are the wavenumbers of the first and second laser (which may be identical). This allows, for example, the single stage seeding of a x-ray free-electron laser via conventional lasers with harmonic numbers of perhaps up to 100 [4]. It is worth noting that such single stage seeding is difficult with alternate schemes, as the required energy modulation to reach high harmonics quickly exceeds the FEL bandwidth ρ, while in EEHG the required modulation remains comparatively small even for high harmonics.

At SLAC, this technique has been demonstrated in a series of proof of principle experiments, first to generate the 3rd and 4th harmonic of a 1600 nm seed [5]. This was then extended to the 15th harmonic of a 2400 nm seed, reaching down into the VUV at 160 nm [6]. One ultimate goal for the harmonic extension of the EEHG technique is to demonstrate the ~75th harmonic of a seed laser. At this harmonic, one can seed a x-ray FEL with a 266 nm laser and reach solidly into the x-ray regime, obtaining fully coherent light. Therefore, there has been a push to reach to these high harmonics at NLCTA, which has required the installation of a new radiating undulator along with an associated EUV photon spectrometer to characterize the harmonic generation.

THE VISA UNDULATOR

The previous radiation of the 15th harmonic of a 2400 nm seed laser was obtained using a 120 MeV beam and an X-band microwave undulator with tuneable K value and effective undulator period of 1.39 cm [7]. In order to more effectively radiate low wavelengths, we both increased the beam energy and installed a new, longer undulator.

To boost the beam energy, we added one additional X-band accelerating structure (X3) of 1 meter length following C2. This structure in the current configuration provides an additional 45 MeV of beam energy, bringing the total

* bryantg@stanford.edu

ISBN 978-3-95450-134-2

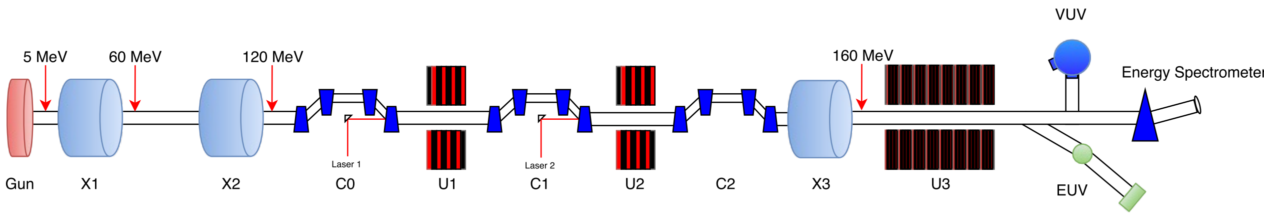

Figure 1: Layout of the NLCTA Echo beamline

energy entering the radiating section to 165 MeV. Furthermore, this acceleration occurs following the EEHG phase space modulation. Experimentally, we see that the EEHG bunching survives this final acceleration section. This observation hints at the possibility of performing complicated phase space manipulations at low beam energy, thus allowing lower powered lasers, and only later boosting to a final beam energy.

The installation of X3 and facility limitations in RF power necessitated a permanent magnet undulator. For this purpose, a two meter long planar undulator, known as the Visible to Infrared SASE Amplifier (VISA) was installed [8]. The VISA was originally designed as a test undulator for LCLS to reach saturation within a short distance by means of a high FEL paramater ρ and short period length. As such, the VISA is a permanent magnet array of Halbach array design and has a period length of 1.8 cm, undulator parameter $K = 1.26$, and is equipped with a strong focusing array to minimize the beta function during radiation. The focusing is achieved by a FODO array with 24.7 cm period, resulting in an average matched beta function of about 50–100 cm for an 160 MeV beam.

The VISA undulator is equipped with four Optical Transition Radiation (OTR) screens which allow viewing of the beam and radiation at positions along the undulator. To aid in steering, the VISA has also been equipped with four "window frame" corrector magnets, which each provide up to a 2×10^{-3} rad kick independently in each the x and y direction. The individual VISA magnets were first aligned using the pulsed-wire setup, providing an accuracy near 50 µm for the magnetic axis [9]. Once on the beamline, the VISA was then aligned by means of a small guide laser injected into the beam pipe by means of a pop-in screen. The currently installed VISA in place on the NLCTA beamline is shown in Figure 2.

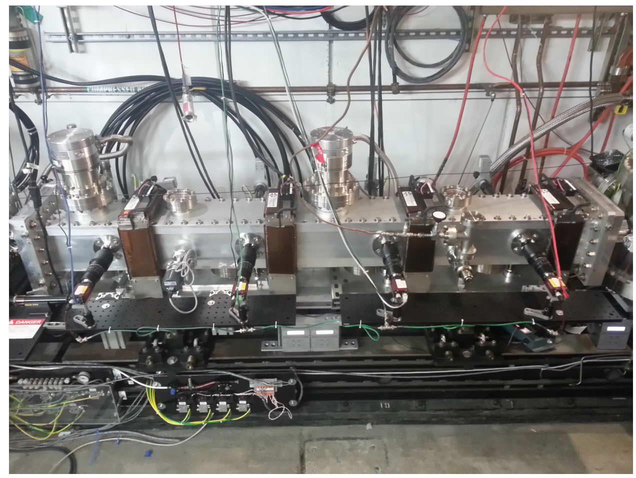

Figure 2: The VISA undulator in place on the NLCTA beamline. Visible are the four corrector magnets and pop-in observation screens.

THE EUV SPECTROMETER

In order to investigate the high harmonic radiation of the 2400 nm seed laser, we required additional diagnostics beyond those used in previous echo studies. In particular, the previous spectrometer was the commercially available McPherson model 234/302 scanning monochromator, equipped with a 2400 G/mm or 1200 G/mm corrected concave grating. Originally, this spectrometer was equipped with an Andor CCD camera and the efficiency of the setup was observed to drop precipitously below ~150 nm. Therefore, we constructed a custom grazing incidence EUV spectrometer to measure the light in the wavelength range 12–120 nm. The full assembly of the custom EUV spectrometer is shown in Figure 3. The light is first ejected from the beam path by means of a gold mirror at 15° angle of incidence

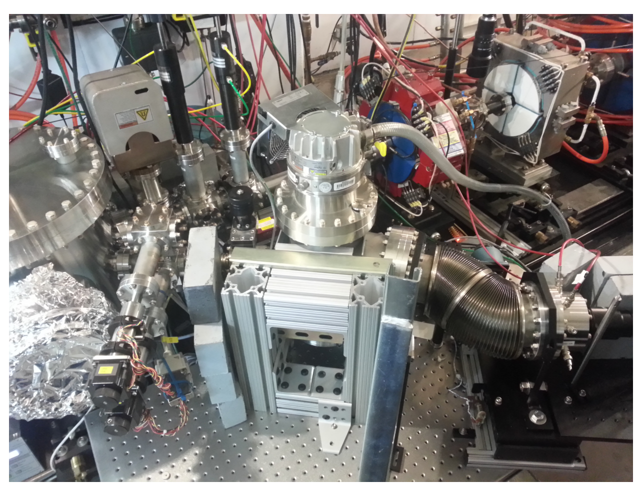

Figure 3: The custom EUV spectrometer. Light is ejected from the main beamline in the large chamber at the left, and passes through the double cube slit assembly. The chamber containing the grating is in the center, and the exit bellows is shown near the maximal shear position.

ISBN 978-3-95450-134-2

into the spectrometer arm of the assembly with a reflectivity of 60-80% over wavelengths of interest. During the design, several commercial slit solutions were considered but ultimately rejected due to limited available space, the need for high vacuum, and the desire to have a wide aperture range. We constructed a custom slit assembly using two small vacuum cubes with attached stepper motors to allow two parallel blades to close or open as a slit. A computer drawing of the slit assembly is shown in Figure 4. This setup also provides independent motion of each blade, allowing for translation of the combined slit while maintaining the aperture. Furthermore, the vertical design of the slit creates a minimal beamline footprint, allowing a relatively compact spectrometer assembly. The light then strikes a Hitachi 001-0639 (001-0640) aberration-corrected concave grating at an angle of 4.7°, corresponding to either the high or low energy configuration. These gratings have 600 (1200) G/mm, and a 3.7° blaze angle, focus to a flat field 469 mm from their center. These gratings allow reasonable focusing and efficiency in the range 22-124 (11-62) nm. This grating is mounted in a fixed configuration in a custom high-vacuum chamber.

Upon leaving the grating chamber, the light enters a large, 6" diameter bellows which is approximately 14" long. The diameter of the bellows was chosen to allow the dispersed light (including the zeroth order dispersion) to travel all the way to the focal plane without reflection. In order to capture the entire frequency spectrum from the grating, the end of the bellows is required to translate (parallel to the focal plane) approximately 120 mm. This large shear in the bellows structure necessitates a highly corrugated bellows, and the buckling of the individual bellows welds ultimately limits the spectrometer's upper wavelength range. The translation of the free bellows end is accomplished via a linear motion stage with a readback which is ultimately converted into a visible wavelength range.

The bellows end is then attached to a 40 mm MicroChannel Plate (MCP) detector (Model BOS-40, Beam Imaging Solutions). The MCP has a dual chevron configuration, CsI coating, 5 µm pore size, and gives a gain of approximately 10^4 when operated with a 2 kV high voltage power supply. The CsI coating provides relatively high detection efficiency from 10-150 nm, covering the whole range of interest for the Echo program. Behind the MCP is a P-43 phosphor screen, powered by a 5 kV power supply, which is then directly imaged with a camera.

Finally, the McPherson VUV spectrometer was moved to a separate portion of the beamline and equipped with a similar MCP detector (BOS-18, Beam Imaging Solutions). The gain of the MCP has allowed use of the McPherson spectrometer as a diagnostic tool down to ~50 nm.

CALIBRATION

Due to the flat field focusing of the EUV grating, the dispersion along the MCP is not constant, and varies depending on linear position (or equivalently, central wavelength). From the grating equation and the flat focus criterion, it is easy to see that

$$x = r_{\text{focal}} \left(\frac{\sqrt{1 - (n\lambda - \sin\alpha)^2}}{n\lambda - \sin\alpha} \right)$$

Where x is the linear distance along the focal plane to the diffracted wavelength λ, n is the groove density, r_{focal} is the distance to the focal plane, and α is the angle of incidence.

In practice, the linear location of the zeroth order diffraction is first found and marked on the MCP screen as the reference zero pixel position. Then, displacements to desired wavelengths are calculated and the linear stage moved accordingly. The linear stage can be controlled to within a fraction of a mm, leading to a pointing accuracy in wavelength of $\lesssim$0.3 nm. Based on the central pointing wavelength and the known pixel position relative to the zeroth order, a wavelength scale can be established seamlessly over the entire range of spectral visibility.

In order to begin tuning of echo harmonics, attention is typically focused on the most easily attainable first. Therefore, typically the upgraded VUV spectrometer is first used to establish signals in the range 160-60 nm. From this configuration, using the low energy grating in the EUV spectrometer, the signal can be seamlessly tuned down into lower wavelength ranges.

Various misalignments and uncertainties can conspire to give theoretical uncertainties for wavelength pointing in the range of 1 nm. Therefore, it is desirable to have wavelength calibration guides to verify against. For this purpose, we use the radiated harmonics themselves to verify and calibrate the wavelength scale. As the laser wavelengths are highly stable and known, the corresponding echo harmonic positions are known to great accuracy. Although the beam energy may contain some significant jitter and chirp, the insensitivity of echo to this noise results in an incredibly reliable wavelength marker when echo signals are present [10]. Incidentally, this instability, present in the HGHG signal but not the EEHG, is often used to distinguish between the two when tuning for the echo effect. At high harmonic number, however, nearby harmonics may be nearly indistinguishable, leading to an ambiguity on the order of ~1 nm. First, where this ambiguity exists, one can investigate all relevant possibilities

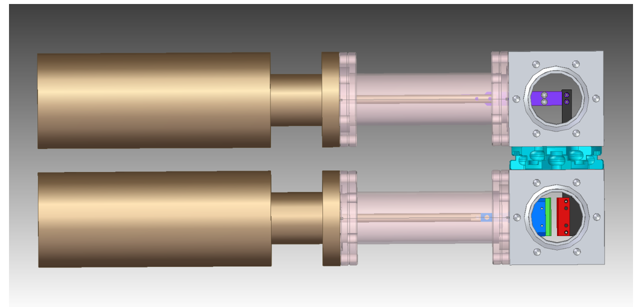

Figure 4: The custom slit assembly, showing the two blades on independent stepper motors.

ISBN 978-3-95450-134-2

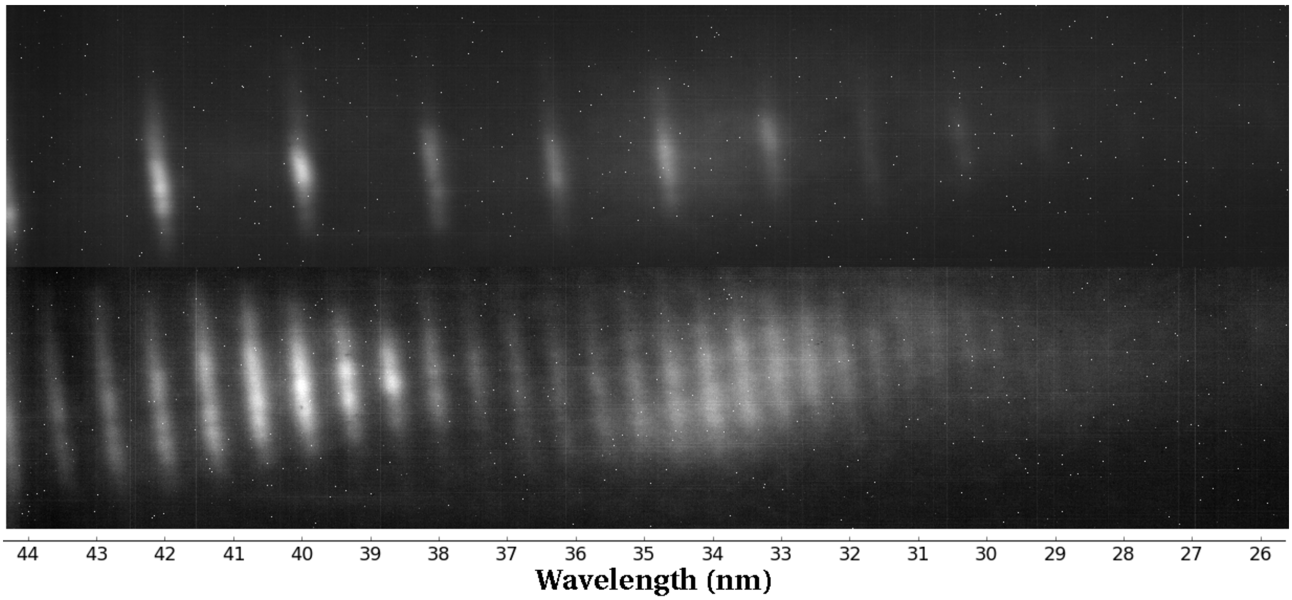

Figure 5: Calibration of the EUV spectrometer using images from the 800 nm (top) and 2400 nm (bottom) seed lasers. It is clear to identify the corresponding harmonic, providing a fine tune of the wavelength calibration as well as a check on the other methods described in this paper.

of harmonics and select the correct one via a χ^2 type analysis. To illustrate, select a particular harmonic and suppose it is the nth, knowing then that the nearby harmonics are the $n-1$, $n+1$, $n+2$ etc. The wavelength is known unambiguously enough to know the pixel dispersion $d(px)/d\lambda$, so that a set of calculated pixel positions for the various harmonics can be compared against their observed pixel positions. With this set of data, one can see which choice for n yields the lowest residual, and in practice there is always a clear choice.

To further strengthen the wavelength calibration of the device, the 800 nm laser was used to generate echo signals in the same region as the 2400 nm. Unfortunately, due to present constraints in the laser system, we are unable to quickly switch between the two, although with a stable beam the turnover time is low enough to cause only inconvenience. The 800 nm provides harmonics far enough apart to eliminate any ambiguity, and one can readily observe the overlap the nth harmonic from the 800 nm laser and the $3n$th from the 2400 nm laser as a final post in the wavelength calibration scale. This technique is demonstrated in Figure 5 where one can clearly identify 800 nm harmonics with their 2400 nm counterpart.

CONCLUSION

In order to investigate high harmonics of a 2400 nm seed laser, it was necessary to upgrade the beam energy, radiating undulator, and photon diagnostics at SLAC's NLCTA. To this end, the beam energy has been boosted by roughly 40 MeV by an additional accelerating structure (X3), a highly efficient strong focusing two meter VISA undulator was installed, and a custom EUV spectrometer for photon diagnostics in the range 12–120 nm was designed, installed, and calibrated.

These upgrades should enable the generation and radiation of laser harmonics up roughly through the 75th. Below this point, the VISA undulator will be radiating on its 6th harmonic, and it may prove difficult to detect any photons from this low efficiency radiation. To increase harmonic number, one can either increase the beam energy by adding an additional accelerating structure or increase the laser wavelength further into the infrared. RF limitations currently cap the energy gain of the structure X3 to about 45 MeV, but the addition of a SLED line could roughly double this energy, providing a beam of about 210 MeV. This upgrade would move the fundamental undulator harmonic to below 100 nm, and in principle allow the radiation of laser harmonics up past 100. We see no other limitations in terms of the NLCTA facility, so this upgrade would provide an environment to test the fundamental limits, and ultimate breakdown, of the EEHG process.

REFERENCES

[1] M. Dunning, C. Adolphsen, T. S. Chu, E. Colby, S. Gilevich, C. Hast, K. Jobe, C. Limborg-Deprey, D. McCormick, B. McKee *et al.*, "Status and upgrade of nlcta for studies of advanced beam acceleration, dynamics and manipulations," in *Proceedings of the 2011 Particle Accelerator Conference*, New York, NY, USA, 2011. [Online]. Available: http://jacow.org

[2] G. Stupakov, "Using the beam-echo effect for generation of short-wavelength radiation," *Phys. Rev. Lett.*, vol. 102, p. 074801, Feb 2009. [Online]. Available: http://link.aps.org/doi/10.1103/PhysRevLett.102.074801

[3] L. H. Yu, "Generation of intense uv radiation by subharmonically seeded single-pass free-electron lasers," *Phys. Rev. A*, vol. 44, pp. 5178–5193, Oct 1991. [Online]. Available: http://link.aps.org/doi/10.1103/PhysRevA.44.5178

ISBN 978-3-95450-134-2

[4] D. Xiang and G. Stupakov, "Echo-enabled harmonic generation free electron laser," *Phys. Rev. ST Accel. Beams*, vol. 12, p. 030702, Mar 2009. [Online]. Available: http://link.aps.org/doi/10.1103/PhysRevSTAB.12.030702

[5] D. Xiang, E. Colby, M. Dunning, S. Gilevich, C. Hast, K. Jobe, D. McCormick, J. Nelson, T. O. Raubenheimer, K. Soong, G. Stupakov, Z. Szalata, D. Walz, S. Weathersby, M. Woodley, and P.-L. Pernet, "Demonstration of the echo-enabled harmonic generation technique for short-wavelength seeded free electron lasers," *Phys. Rev. Lett.*, vol. 105, p. 114801, Sep 2010. [Online]. Available: http://link.aps.org/doi/10.1103/PhysRevLett.105.114801

[6] E. Hemsing, M. Dunning, C. Hast, T. O. Raubenheimer, S. Weathersby, and D. Xiang, "Highly coherent vacuum ultraviolet radiation at the 15th harmonic with echo-enabled harmonic generation technique," *Phys. Rev. ST Accel. Beams*, vol. 17, p. 070702, Jul 2014. [Online]. Available: http://link.aps.org/doi/10.1103/PhysRevSTAB.17.070702

[7] S. Tantawi, M. Shumail, J. Neilson, G. Bowden, C. Chang, E. Hemsing, and M. Dunning, "Experimental demonstration of a tunable microwave undulator," *Phys. Rev. Lett.*, vol. 112, p. 164802, Apr 2014. [Online]. Available: http://link.aps.org/doi/10.1103/PhysRevLett.112.164802

[8] R. Carr, M. Cornacchia, P. Emma, H.-D. Nuhn, B. Poling, R. Ruland, E. Johnson, G. Rakowsky, J. Skaritka, S. Lidia, P. Duffy, M. Libkind, P. Frigola, A. Murokh, C. Pellegrini, J. Rosenzweig, and A. Tremaine, "Visible-infrared self-amplified spontaneous emission amplifier free electron laser undulator," *Phys. Rev. ST Accel. Beams*, vol. 4, p. 122402, Dec 2001. [Online]. Available: http://link.aps.org/doi/10.1103/PhysRevSTAB.4.122402

[9] R. Ruland, D. Arnett, G. Bowden, R. Carr, B. Dix, B. Fuss, C. LeCocq, Z. Wolf, J. Aspenleiter, G. Rakowski *et al.*, "Visa undulator fiducialization and alignment," in *Proceedings of the 6th International Workshop on Accelerator Alignment, ESRF*, 1999.

[10] Z. Huang, D. Ratner, G. Stupakov, and D. Xiang, "Effects of energy chirp on echo-enabled harmonic generation free-electron lasers," in *Proceedings of the 2009 FEL Conference*, Liverpool, UK, 2009.

ISBN 978-3-95450-134-2

DESIGN OF THE MID-INFRARED FEL OSCILLATOR IN CHINA

Li Heting, Jia Qika, Zhang Shancai#, Wang Lin
NSRL, University of Sicence and Technology of China, Hefei, 230029, China

Abstract

In 2014, Xiamen University and other three research organizations received the approval to realize an infrared free electron laser (IR-FEL) for fundamental of energy chemistry. The IR-FEL covers the spectral range of 2.5-200 μm and will be built in NSRL. Two FEL oscillators driven by one Linac will be used to generate mid- infrared and far-infrared lasers. In this article we describe the design studies for the mid-infrared FEL oscillator.

INTRODUCTION

Under the financial support of Natural Science Foundation of China, the project of infrared laser for fundamental of energy chemistry is building up an infrared light source in Hefei. The National Synchrotron Radiation Laboratory (NSRL) of USTC is responsible for the design, construction and commissioning of IRFEL apparatus. It will be a dedicated experimental facility aiming at energy chemistry research, whose core device is a free electron laser (FEL) generating 2.5-200 μm laser for photo excitation, photo dissociation and photo detection experimental stations. Similar as the IR-FEL at the Fritz-Haber-Institute in Berlin [1,2], two oscillators driven by one Linac will be used to generate mid- infrared (2.5-50 μm) and far-infrared (40-200 μm) lasers.

The MIR-FEL is planned to laser earlier and in this paper, we will focus on the design of the MIR-FEL oscillator. To meet the user requirements, the undulator, optical cavity and electron beam for the MIR-FEL are designed and described. Then simulations using Optical-Propagate Code (OPC) [3] have been done and the results will be shown. We finally summarize in the last section.

DESIGN GOAL

As mentioned above, there will be three experimental stations in the first stage. The users of these stations have brought out their requirements on the IR-FEL performance, as given in Table.1. In addition, some users have extra requirements, for example, the photo excitation and dissociation stations require that the peak and average power of IR-FEL should be as high as possible. in the next section.

It is worth pointing out that the broad wavelength range and high radiation intensity brings us much difficulties in the design of electron Linac and optical cavities. For example, the short-wavelength FEL requires short electron bunch to achieve high peak current while the long-wavelength FEL requires long electron bunch to suppress the slippage effect, and the short-wavelength FEL requires a short Rayleigh length of the optical cavity to get a considerable big spot size and an appropriate outcoupling on the mirror while the case of the short-wavelength FEL is opposite. Therefore, the design is to find a balance for the object wavelength range.

Table 1: Design Goal of the IR-FEL

Parameters	Specification
Covering spectrum	2.5 ~ 200 μm
MIR FEL oscillators	2.5 ~ 50 μm
FIR FEL oscillators	40 ~ 200 μm
Macro-pulse length(FW)	5~ 10 μs
Repetition of macro-pulse	20 Hz
Macro-pulse energy	~100 mJ
Micro-pulse length (RMS)	5 ~ 10 ps
Micro-pulse energy	1 ~ 50 μJ
Bandwidth	0.3 ~ 3 %
Continuous tunability	200 ~ 300 %

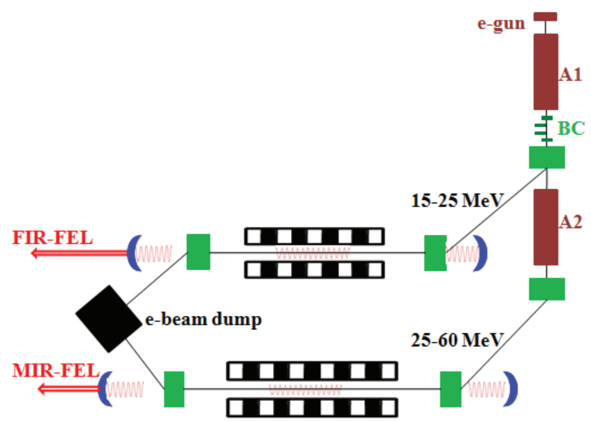

Figure 1: Schematic of the projected IR-FEL.

MIR-FEL DESIGN

Layout

As shown in Fig. 1, the IR-FEL is composed of two FEL oscillators driven by one electron Linac. Two accelerating tubes are used to accelerate the electron beam. Between the first and the second accelerating tube, a four-dipole magnetic chicane is designed as an optional operation condition. Its purpose is to reduce the micro-pulse length and increase the peak current of the electron bunch for the short-wavelength FEL, and for the long-wavelength FEL, it also can increase the micro-pulse length to suppress the slippage effect.

It is very important that we choose the thermionic electron gun as the electron source [4]. Using special gate control system, the electron bunch chain will be extracted from the gun, with micro-pulse length of 1 ns, optional

#shancai @ustc.edu.cn

ISBN 978-3-95450-134-2

repetition frequency of 476/238/119/59.9 MHz, and the charge of larger than 1 nC.

The electron beam energy for FIR oscillator is lower (15-25 MeV), and one accelerating tube is capable of reaching this energy level. Therefore, we extract the beam into the FIR oscillator after the first accelerating tube, for leaving enough space between the two oscillators. Between the electron Linac and FEL oscillators, the achromatic transfer lines are designed, where energy collimators will be used to eliminate the electrons with large energy spread, and the quadrupole doublets will be used to adjust transverse matching between the electron beam and the laser beam inside the oscillators.

Undulator

In a planar undulator, the FEL radiation wavelength is determined by the resonance condition. On the other hand, there is an empirical formula describing the relations between the peak magnetic field and the ratio of g/λ_u, where g is the undulator gap.

Briefly speaking, we need to determine the undulator period appropriately, so that we can achieve the FEL in the objective wavelength range with appropriate electron energies, and furthermore, combining with the design of undulator length we can get enough high FEL gains at all the wavelengths. In addition, we have to consider the continuous tunability of the FEL wavelength.

Table 2: Undulator Parameters for MIR-FEL

Parameter	Specification
Period length	46 mm
Period number	50
Min. gap	16 mm
Strength parameters	0.5~3.2
Peak magnetic field	0.1~0.72 T

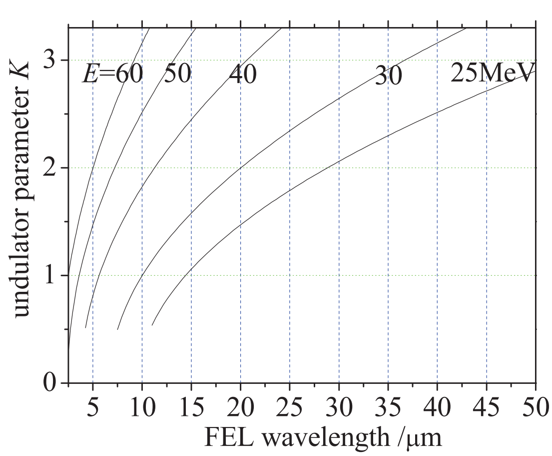

Figure 2: The wavelength tunability with different electron beam energy for MIR-FEL.

In this project, a planar hybrid undulator with NdFeB permanent magnets is used and the remanence of NdFeB is selected to be 1.2 T. The designed undulator parameters for MIR-FEL are given in Table 2. Under this condition, the radiation wavelength tunability with different electron beam energy is shown in Fig. 2, from which one can find that the continuous tunability can easily reach 300%. Note that the the maximum electron beam energy is designed to be 60 MeV, mainly for enhancing the performance of radiation around 2.5 μm, as shown in Fig. 3.

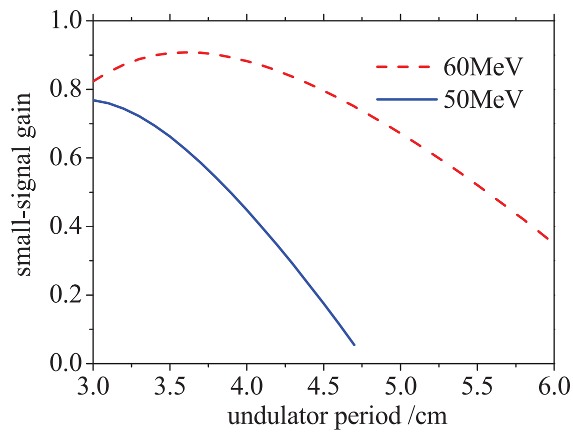

Figure 3: The variation of small signal gain of 2.5 μm FEL with the undulator period.

Optical Cavity

There are several key parameters for the optical cavity, such as cavity length, reflectivity of mirrors, curvature radius of mirrors and outcoupling hole size, and so on. The cavity length is determined by following factors, such as installation space of other components, the time structure of the electron beam, the saturation time of the radiation field, the requirements of optical beam sizes on mirrors, etc. The curvature radius of the mirrors determines the Rayleigh length, stability factor, optical beam size on the mirrors, and the matching of the electron beam and the optical beam. The size of the outcoupling hole contributes to the single-pass loss and then affects the saturation process. When the FEL wavelength varies in a broad range, these relations become more complicated.

In this project, two same mirrors are used to form a symmetrical optical cavity. The 2.3 m long undulator will be symmetrically placed in the optical cavity such that we have 1.37 m of space available for beam transport and diagnostic on the two sides. We once considered asymmetrical placement but unfortunately our architectural condition enforce the FEL being extracted from the downstream mirror so that the undulator can't be moved closer to the upstream mirror since there is no space in that side. The parameters of the optical cavity are shown in Table 3. The Rayleigh length is designed to be one third of the undulator length (0.77 m), which is mainly for the consideration of 2.5 μm FEL case. Figure 4 shows the intra-cavity modes, from which one can note that 2.5 μm FEL has a small spot size on the mirror, and at this moment the outcoupling of 1 mm hole is about 8%. from Fig. 4 we also can find that only for the wavelength longer than 30 μm there is a little diffraction loss.

ISBN 978-3-95450-134-2

Table 3: Parameters of MIR Optical Cavity

Parameter	Specification
Cavity length	5.04 m
Curvature radius of mirrors	2.756 m
Rayleigh length	0.77 m
Reflectivity	99%
Diameters of coupling hole	1.0, 1.5, 2.5, 3.5 mm

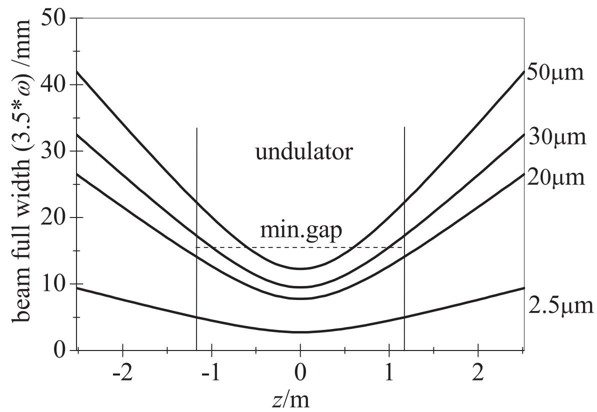

Figure 4: The modes in the MIR optical cavity.

Electron Beam

When the electron gun type is determined, the possible quality of the electron beam is roughly fixed. After optimization, the requirements of the electron beam for MIR-FEL are given in Table 4.

Table 4: Parameters of Electron Beam for MIR-FEL

Parameter	Specification
Energy	25-60 MeV
Energy spread	<240 keV
Emittance	<30 mm•mrad
Charge	1 nC
Pulse length (RMS)	2-5 ps

MIR-FEL PERFORMANCE

Based on the designed parameters in the previous Part, the small signal gain of MIR-FEL is calculated and given in Fig. 5. We can see that the gain is very high in the wavelength range of 4-30 μm. For short wavelength, small *K* leads to the small gain while for short wavelength, large relative energy spread and slippage effect are the reasons. In Fig. 6, we give the macro-pulse energy of MIR-FEL simulated by OPC code. Note that the cavity length detuning is fixed to be two times the radiation wavelength. One can find that the macro-pulse energy can reach the 100 mJ level for most of the object wavelengths. We still can enhance the macro-pulse energy by increase the micro-pulse repetition rate.

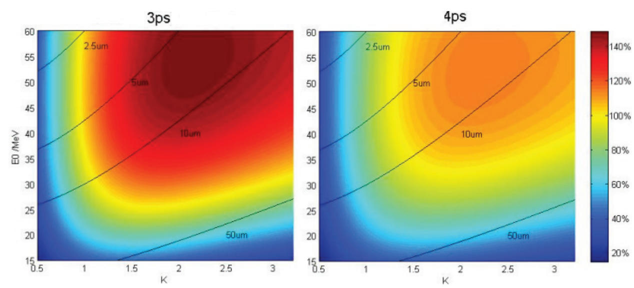

Figure 5: The small signal of MIR-FEL.

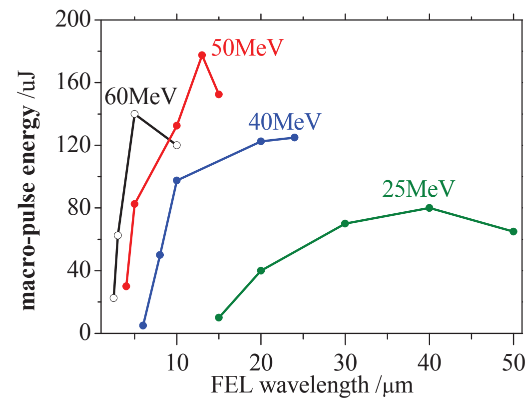

Figure 6: The macro-pulse energy of MIR-FEL based on the micro-pulse repetition rate of 119 MHz.

SUMMARY

In summary, we have introduced the IR-FEL project to be built in NSRL and designed the MIR-FEL oscillator. Brief design results are given in this paper and tell us that it should be possible to achieve the design goal. In fact, the design is more detailed and considers much more specific aspects, such as the discussion of each system's error effects, the feasibility of every designed parameter, and so on. Much more design work is underway, such as the FIR oscillator design, the S2E simulations and so on. However, all the design work will keep on till the machine lasers well.

ACKNOWLEDGEMENT

It is a pleasure to thank the FHI, CLIO and FELIX people for generously sharing their valuable experience in IR-FEL oscillator. This work is support by National Natural Science Foundation of China (21327901).

REFERENCES

[1] W. Schöllkopf et al., "First Lasing of the IR FEL at the Fritz-Haber-Institut, Berlin", FEL'12, paper MOOB01, pp1-4.
[2] W. Schöllkopf et al., "The IR and THz FEL at the Fritz-Haber-Institut", FEL'13, paper WEPSO62, pp657-660.
[3] J. Karssenberg et al., J. Appl. Phys. 100, 093106 (2006).
[4] He Zhigang, et al., FEL'15, paper MOP010, these proceedings.

ISBN 978-3-95450-134-2

SINGLE PICOSECOND THz PULSE EXTRACTION FROM THE FEL MACROPULSE USING A LASER ACTIVATING SEMICONDUCTOR REFLECTIVE SWITCH

K. Kawase[#], R. Kato, A. Irizawa, M. Fujimoto, K. Furukawa, K. Kubo, G. Isoyama,
Osaka University, Osaka, Japan

Abstract

The THz-FEL at the Institute of Scientific and Industrial Research (ISIR), Osaka University can generate high-intensity THz pulses or FEL macropulses, which comprise approximately 100 micropulses at 37 ns intervals in the 27 MHz mode or 400 micropulses at 9.2 ns intervals in the 108 MHz mode. The maximum macropulse energy in the 27 MHz mode reaches 26 mJ at a frequency of 4.5 THz and the micropulse energy is estimated to be 0.2 mJ. To open new areas of studies with high intensity THz radiation for user experiments, we are developing a single pulse extraction system from the pulse train using a laser activating semiconductor reflective switch. We have succeeded in extracting a single THz pulse, duration of which is estimated to be less than 20 ps, from the FEL macropulse using a gallium arsenide wafer for the switch.

INTRODUCTION

THz radiation sources recently have been demanded from various scientific and industrial fields [1]. Although there is some THz source, the FEL-based THz radiation source has a great advantage comparing with the other types of source. The remarkable aspects of the THz-FEL are its peak intensity and narrowness of the bandwidth.

The THz-FEL at the ISIR is an oscillator type FEL driven by an rf-linac. Thus, the generated FEL forms a pulse train (macropulse). The macropulse consists of a number of THz micropulses. The micropulse duration is typically similar to the electron bunch duration, thus that duration is about 20 ps in ours. In our case, we have two types of the linac operation for the FEL experiment. The first type of the operation is the dc-beam extraction from the electron-gun and pulsing by the rf-cavity with the frequency of 108 MHz. In this case, the FEL macropulse consists of approximately 400 micropulses with the separation of 9.2 ns. The second type is the pulsed-beam extraction from the gun using the grid-pulser electric circuits with the repetition frequency of 27 MHz. In this case, the FEL macropulse consists of approximately 100 pulses with the separation of 37 ns. In the latter case, we achieved the macropulse energy of 26 mJ at the radiation frequency of 4.5 THz. The maximum micropulse energy is estimated to be over 200 μJ [2, 3].

There are requirements to extract a single micropulse for the investigations of the nonlinear response of materials in order to avoid thermal effects due to the irradiation of the pulse train. To meet these requirements, we are developing the single pulse extraction using a laser activating semiconductor reflective switch, which is also referred as a plasma mirror [4 - 9].

Generally non-doped semiconductors are insulators and thus they have a high transmittance for the radiation in the THz range. Because the THz-FEL radiation is linearly polarized, we can quench the reflecting radiation from the surface of a semiconductor wafer by setting the incident angle to Brewster's angle. Using an intense infrared laser pulse with the photon energy above the band gap energy and irradiating it on the semiconductor wafer, electron-hole plasma is generated on the surface and it becomes a high reflector for the THz radiation. After the diffusion and recombination of the excited electrons, it returns the insulator with a high transmittance. Therefore, we can apply this mechanism into the reflective switching technique to extract a single THz-pulse. The schematic diagram of this mechanism is shown in Fig. 1.

In this paper, we report the overview and present status of the single THz pulse extraction in our FEL facility.

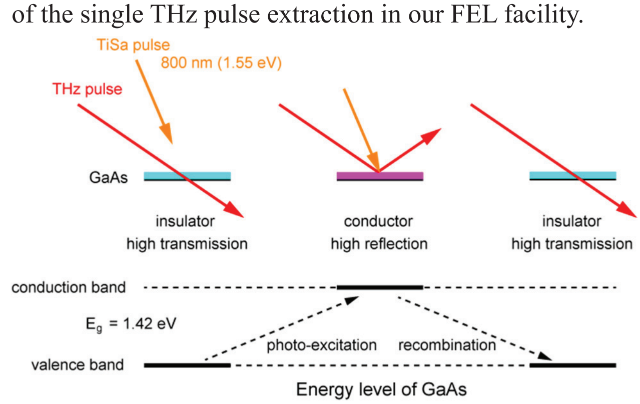

Figure 1: Schematic diagram of the laser activating semiconductor reflective switching for the THz pulse.

EXPERIMENTAL SETUP

The experiment is done using the L-band linac and THz-FEL system at the ISIR, Osaka University [3]. A schematic diagram of the L-band linac and FEL system is shown in Fig. 2. The generated THz-FEL pulses are transported through the vacuum duct to the outside of the radiation shielding area. To activate the semiconductor reflective switch, we use a mode-locked Ti:Sapphire laser system (Spit Fire, Spectra-Physics). The pulse repetition rate of the laser system is 960 Hz and the pulse energy is about 1 mJ. The pulse duration is typically 100 fs and the wavelength is centered at 800 nm. The pulse timing is synchronized to the rf of the linac system. The laser system is placed just beside the user area for the THz-FEL as shown in Fig. 2.

#kawase@sanken.osaka-u.ac.jp

ISBN 978-3-95450-134-2

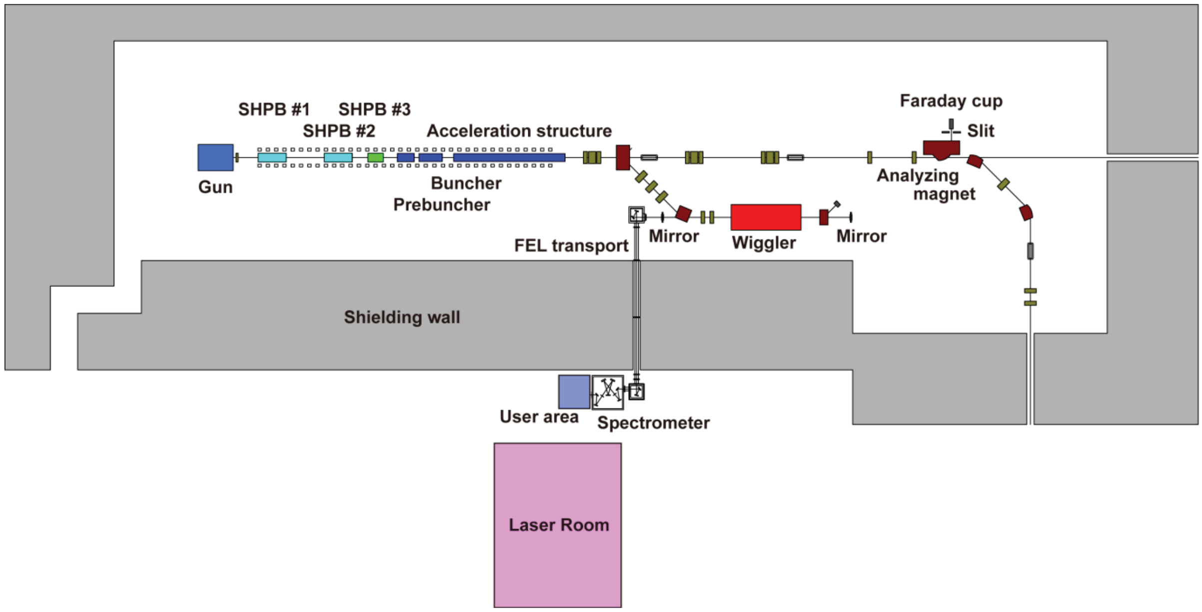

Figure 2: Schematic diagram of the L-band electron linac and THz-FEL. The linac and FEL system are installed inside the restricted room surrounded by the shielding wall. The generated THz-FEL beam is transported to the user area at the outside of the restricted room. The laser room is just beside the user area.

The experimental setup at the user area is shown in Fig. 3. The FEL transverse size at the output of the transport is about 20 mm in diameter. The Brewster's angle of the GaAs at the THz range is about 75 degrees. Thus, the beam size of the THz-FEL beam is needed as small as possible with the small divergence. Using a pair of off-axis parabola mirrors (focal lengths of 3 inches and 0.5 inches), the THz beam is down-collimated with the diameter of about 3 mm. The transmitted and reflected THz-FEL pulse is detected by a calibrated energy sensor (Coherent Inc. J-10), pyroelectric sensor (Molectron, P-5), or diode sensor (Quasi Optical Detector, Virginia Diode Inc.). The Ti:Sapphire laser pulse is transported with an optical delay. To control the irradiance, a half waveplate and polarized beam splitter cube is installed in front of the semiconductor wafer.

As the samples for the switching material, we use a non-doped GaAs wafer and two non-doped Si wafers with the resistivities of 1,000 Ω cm and 10,000 Ω cm. Each wafer has a thickness of 500 μm and a diameter of 2 inches.

RESULTS

As the results of using a GaAs wafer for the switching material and adjusting the laser irradiation timing, we succeed the single THz pulse extraction. The waveforms of the reflected THz radiation detected by the pyroelectric sensor are shown in Fig. 4. On the other hand, in case of using a Si wafer, there are a few reflected pulses after the switching timing. Comparing with the GaAs, Si has a long life-time of the electron-hole plasma [6]. The results shown in Fig. 4 are consistent with that.

To estimate the macropulse contrast which is the ratio between the net switched pulse energy and the total residual reflected energy, we measure the reflected macropulse energy with and without switching. At the radiation frequency of 4.5 THz, the net switched pulse energy is 4.4 ± 0.5 μJ and the macropulse contrast is 2.0.

The reflectance of the switch is estimated from the transmission waveform shown in Fig. 5. Ignoring the absorption of the THz radiation by the GaAs wafer, the reflectance is estimated to be 0.6 ± 0.1.

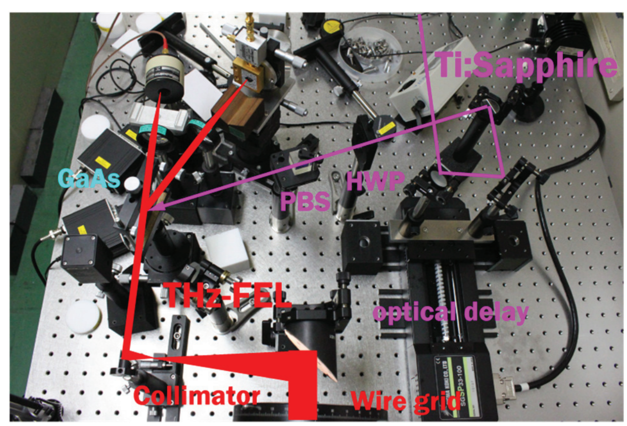

Figure 3: Experimental setup at the user area. The THz-FEL is collimated by using a pair of off-axis parabola mirrors and incident on the semiconductor wafer (GaAs) at the Brewster's angle. Ti:Sapphire laser pulse is transported through the optical delay (two right-angle mirrors mounted on the linear stage), half-waveplate (HWP) and polarized beam splitter cube (PBS).

ISBN 978-3-95450-134-2

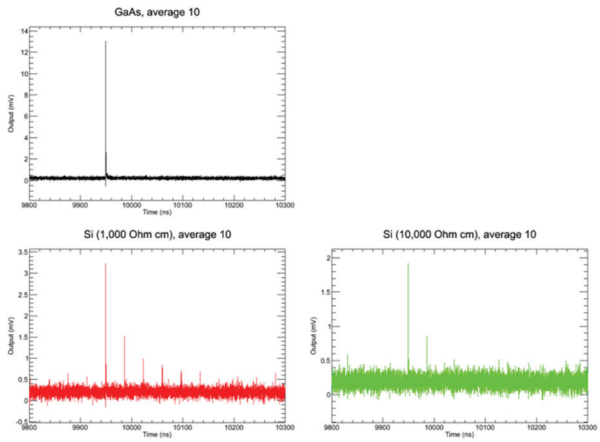

Figure 4: Waveforms of the reflected THz-pulse(s) by the pyroelectric sensor. In case of GaAs, only one pulse is observed in the linear scale. On the other hand, in Si cases, a few pulses are observed.

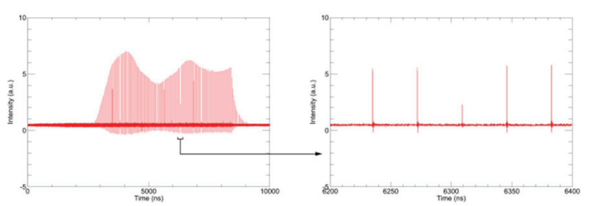

Figure 5: Waveform of the transmitted THz-pulses. Left side is a whole macropulse and right side is enlarged around the switching timing.

CONCLUSION

By using the Ti:Sapphire laser and the GaAs wafer as the reflective switching material, we succeed the single THz-pulse extraction from the FEL macropulse. As the present results, the extracted pulse energy is 4.4 μJ at the radiation frequency of 4.5 THz and the macropulse contrast is 2. Optimization of the single pulse extraction is continuing.

High intense single THz pulse beam is useful for various applications to investigate the materials science and other fields. We will make intense single THz pulse source based on the FEL and the laser activating reflective switching technique in near future.

ACKNOWLEDGMENT

A part of this work was supported by JSPS KAKENHI Grant Numbers 24310069, 24651102 and 15K13407.

REFERENCES

[1] R. Chulkov, et al., Phy. Rev. ST Accel. Beams 17, 050703 (2014).
[2] S. Suemine, et al., Nul. Instrum. and Meth. in Phys. Res. A 773, 97 (2015).
[3] K. Kawase et al., “High Power Operation of the THz FEL at ISIR, Osaka University”, Proceedings of FEL2014, Basel, Switzerland, August 2014, p. 531 (2014); http://www.JACoW.org
[4] A.J. Alcock and P.B. Corkum, Can. J. Phys. 57, 1280 (1979).
[5] J.P. Kaminski, et al., Appl. Phys. Lett. 57, 2770 (1990).
[6] F.A. Hegmann and M.S. Sherwin, “Generation of Picosecond Far-infrared Pulses Using Lase-activated Semiconductor Reflection Switches”, Proceedings of SPIE, vol. 2842, International Conference on Millimeter Waves and Applications III (1996).
[7] E.H. Haselhoff, et al., Nucl. Instrum. and Meth. in Phys. Res. A 358, ABS 28 (1995).
[8] X. Wang et al., Appl. Phys. Lett. 103, 191105 (2013).
[9] J. Schmidt et al., Rev. Sci. Instrum. 86, 063103 (2015).

ISBN 978-3-95450-134-2

TIME DEPENDENT STUDY FOR AN X-RAY FEL OSCILLATOR AT LCLS-II

J. Zemella[1,2], W. M. Fawley[1], R. R. Lindberg[3], and T. J. Maxwell[1]

[1]DESY, Hamburg, Germany
[2]SLAC, Menlo Park CA, USA
[3]ANL, Argonne IL, USA

Abstract

The LCLS-II with its high repetition rate and high quality beam will be capable of driving an X-ray free electron laser oscillator at higher harmonics in the hard X-ray regime (0.1 nm). The oscillator consists of a low loss X-ray crystal cavity using diamond Bragg crystals with meV bandwidth. The expected average spectral flux has been estimated to be at least two orders of magnitude greater than present synchrotron-based sources with highly stable, coherent pulses of duration 1 ps or less for applications in Mössbauer spectroscopy and inelastic x-ray scattering. A more detailed study of the start up of a fifth-harmonic X-ray FEL oscillator at LCLS-II will be presented with full, time-dependent simulations.

INTRODUCTION

The planned LCLS-II cryogenic linac based on TESLA technology [1, 2] at SLAC will be operated in 'cw-mode' with a repetition rate of 0.929 MHz. This enables one to develop new concepts for generating hard X-rays including low-gain FEL schemes such as X-ray free electron laser oscillators (XFELO) based on a high reflectivity crystal cavity with narrow bandwidth in the order of 10 meV [3]. The advantages of an XFELO are the full coherence and spectral purity of the X-ray pulse compared to state of the art sources like SASE (self amplified spontaneous emission) FELs (LCLS-I [4], SACLA [5]) based on a stochastic process leading to fluctuating pulse properties. Self seeding technique is able to improve longitudinal coherence in hard X-ray [6] but not reaching full, stable longitudinal coherence and typically include a broad SASE background that may complicate, e.g., precision inelastic X-ray scattering (IXS) experiments.

The design beam energy of the LCLS-II cryogenic linac is 4 GeV. To generate Ångstrom wavelengths one can instead amplify a higher harmonic of the FEL pulse [7]. We consider in this paper the fifth harmonic at 14.4 keV using the Bragg reflection of Diamond (hkl)=(733) where (hkl) are the Miller indices.

We present progress on the feasibility study started last year where initial performance estimates were presented in [8]. This paper is focused on verifying the startup process of the XFELO and saturation pulse properties using the time-dependent simulation code Ginger [9] in oscillator mode, extended to simulate higher harmonics.

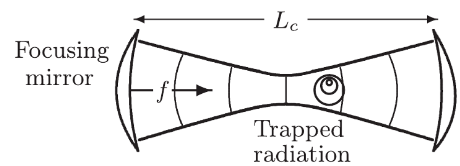

Figure 1: Used cavity design used in Ginger simulations.

LAYOUT

The cavity model used in simulations is depicted in Fig. 1. Two focusing elements define the waist ω_0 inside the undulator which can be expressed by the Rayleigh length Z_R and the wavelength λ

$$Z_R = \frac{\pi\omega_0^2}{\lambda}, \tag{1}$$

$$f = \frac{L_c}{4} + \frac{Z_R^2}{L_c}, \tag{2}$$

with cavity length L_c and focal strength f of the mirrors. Spectral filtering from the Bragg reflectors is done by applying the wavelength-dependent complex reflectivity of the two Bragg crystals, one thick (high-reflectivity) and one thin (extraction mirror) crystal. The path length change induced by Bragg reflection leading to cavity length detuning is compensated here by multiplying the complex reflectivity with the proper group delay phase factor as described in [10]. The assumed crystal reflectivity of both Bragg C*(733) crystals is shown in Fig. 2. For the present study the modified cavity design shown in Fig. 1 is a modification of the tunable, four crystal, zig-zag cavity scheme previously discussed. However, for gain studies only matched mode size, Rayleigh length, and electron beam beta function in the undulator must be matched which can be achieved by the cavity described. Of course this may change with a more precise description of the 3D angular divergence which is not addressed here.

SIMULATIONS

For simulating an XFELO for LCLS-II a 167 fs long Gaussian current profile with 120 A peak current and 200 keV Gaussian energy spread is assumed. Further parameters are gathered in Table 1.

Some optimization steps were performed for optimizing FEL gain. The first step is to find the right energy detuning, shown in the scan of Fig. 3 to maximize gain in steady state.

ISBN 978-3-95450-134-2

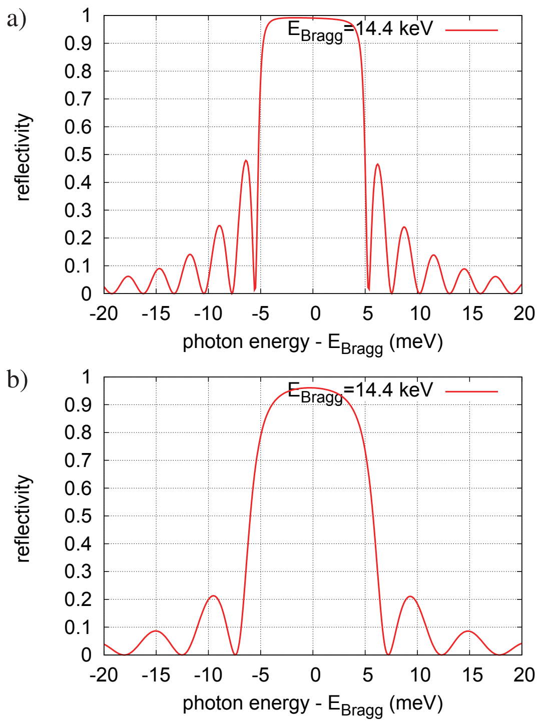

Figure 2: a) Reflectivity of a diamond crystal using Bragg reflex (733) with 200 micron thickness. b) Reflectivity of a diamond crystal using Bragg reflex (733) with 107 micron thickness. Transmission of crystal is about 4 %.

Table 1: Electron Beam and Cavity Parameters

Parameter	Value	Units
e^--beam energy	4.0	GeV
Peak current	120.0	A
Bunch charge	50.0	pC
Bunch length (rms)	166.7	fs
Energy spread	200.0	keV
Norm. emittance	0.3	µm
Photon energy at 5^{th} harmonic	14.4	keV
Undulator period	26.0	mm
Number of undulator periods	1250	
Undulator parameter K	1.433	
loss per round-trip	15.0	%
Rayleigh length	12.0	m
Distance rad. waist-undulator center	-1.0	m

The proper phase shift to compensate the exact cavity path length is done by several simulation runs. To obtain the maximum gain versus beta function at undulator center and the corresponding Rayleigh length of the light in the undulator a scan of both quantities was also performed. The last step is a scan of the undulator center/electron beam waist and the radiation waist position. A 1 m upstream shift of the undulator center with respect to the cavity center optimizes the gain, though this dependence is quite weak.

After these optimizations, we find the following. The

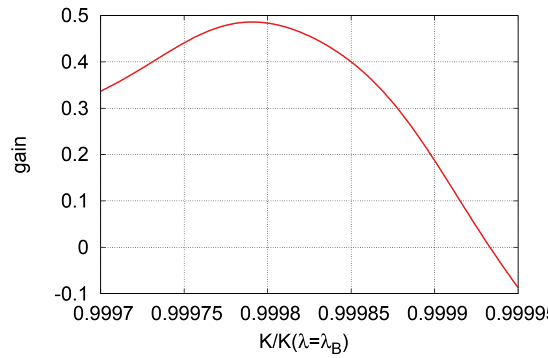

Figure 3: Single pass gain in dependence of the undulator parameter. $K(\lambda = \lambda_B)$ is the undulator parameter for the center wavelength of Bragg reflection.

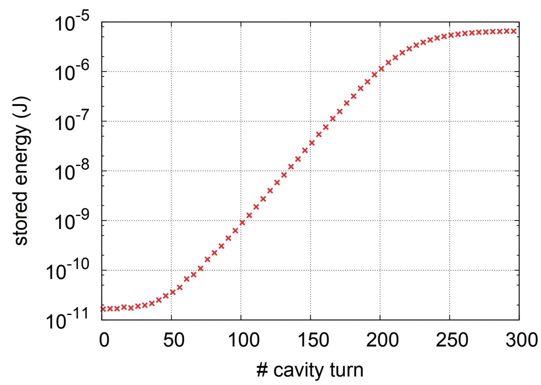

Figure 4: Evolution of the pulse energy for number of cavity round-trips.

photon pulse energy dependence on cavity round-trip number is shown in Fig. 4. The intra-cavity saturation power is $E_{Sat} = 6.6\,\mu$J after 275 cavity passes. Per-pass gain becomes exponential after just 50 passes. The net gain per pass is 7.6 % (including the 15 % loss per turn). This is noticeably less than the single-pass gain indicated by previous steady state estimates. The decrease of the gain is explained by the short bunch duration and much narrower actual crystal bandwidth which in this case are not a near-optimal Fourier limit pair. This leads to a reduced overlap between electrons and photons and therefore to a smaller gain. We find (not shown) that when increasing bunch length to 400 fs (rms) gain is a factor 2.5 higher and peak power is increased to 40 MW for a combined factor of 5 greater flux than in the present comparison. However in this case, the charge is necessarily increased to 120 pC to maintain sufficient peak current.

The pulse profile and spectrum are shown in Fig. 5. The temporal pulse profile is with 205 fs (rms) longer than the electron bunch length of 167 fs (rms). There are trailing pulses which are a result of the wavelength-dependent crystal reflectivity. The spectral width of 5 meV is slightly narrower than the reflectivity bandwidth of the crystals.

The photon pulse parameters are listed in Table 2.

ISBN 978-3-95450-134-2

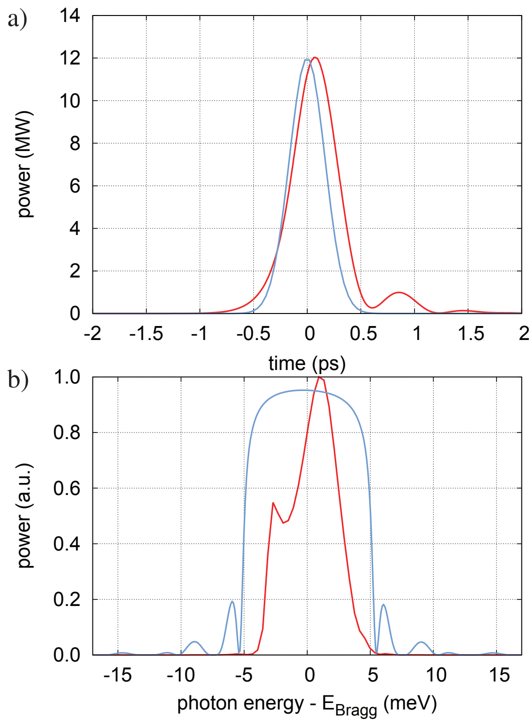

Figure 5: a) Temporal pulse profile at saturation in red. The current profile is also drawn in blue without y scaling. b) Spectral pulse profile at saturation in red. The combined crystal reflectivity of the thick and the thin crystal is also drawn in blue.

Table 2: Intra Cavity Photon Pulse Parameters

Parameter	Value	Units
Net gain per cavity pass	7.6	%
Applied loss per cavity pass	15.0	%
FEL gain per cavity pass	22.6	%
Pulse length at saturation (rms)	205.0	fs
Pulse bandwidth at saturation	5.0	meV
Pass number to saturation	250	
Intra-cavity pulse energy at saturation	6.6	μJ
Out-couple ratio	4.0	%
Output photons per pulse	$1.1 \cdot 10^{8}$	
Output spectral flux (~2 MHz rep. rate)	$4.2 \cdot 10^{13}$	ph/s/meV

CONCLUSION

An XFELO driven by the LCLS-II superconducting linac at 5^{th} harmonic photon energies of 14.4 keV using 50 pC bunches leads to a high brightness source which is able to improve achievable spectral flux by orders of magnitude for applications such as IXS and X-ray photon correlation spectroscopy, hungry for high coherence X-rays in a very narrow bandwidth. The time-dependent simulation with ideal Gaussian bunch shape leads to promising results in reasonable agreement to initial estimates while suggesting design modification to reach desired performance goals in the 10^{14} ph./s/meV range. Due to beam power limitations bunch lengthening is not suitable solution but would help to improve electron bunch - photon pulse overlap. A different Bragg reflex with a larger bandwidth shall increase the overlap the same manner helping to improve the performance of an XFELO at LCLS-II. With this benchmarking complete, further optimization and numerical studies will now be further extended to include the more realistic start to end-simulated electron bunches to investigate gain degradation from sub-optimal longitudinal phase space distributions.

REFERENCES

[1] SLAC National Accelerator Laboratory, Linac Coherent Light Source II Conceptual Design Report, No. SLAC-R-978 (2011).

[2] B. Aune et al., "Superconducting TESLA cavities", Phys. Rev. ST Accel. Beams **3**, 092001 (2000).

[3] K.-J. Kim, Y. Shvyd'ko, and S. Reiche, "A Proposal for an X-Ray Free-Electron Laser Oscillator with an Energy-Recovery Linac", Phys. Rev. Lett. **100**, 244802 (2008).

[4] P. Emma et al., First lasing and operation of an ångstrom-wavelength free-electron laser", Nature Photonics **4**, 641 (2010).

[5] T. Ishikawa et al., "A compact X-ray free-electron laser emitting in the sub-ångstrom region", Nature Photonics **6**, 540 (2012).

[6] J. Amann et al., "Demonstration of self-seeding in a hard-X-ray free-electron laser", Nature Photonics **6**, 693 (2012).

[7] J. Dai, H. Deng, and Z. Dai, "Proposal for an X-Ray Free Electron Laser Oscillator with Intermediate Energy Electron Beam", Phys. Rev. ST Accel. Beams **108**, 034802 (2012).

[8] T. J. Maxwell et al., "Feasibility study for an X-ray FEL oscillator at the LCLS-II", TUPMA028, 6-th IPAC 2015, Richmond VA, USA.

[9] W. M. Fawley, "A User Manual for GINGER-H and its Post-Processor XPLOTGINH", Version 2.0k, June 2012.

[10] R.R. Lindberg et al., "Performance of the x-ray free-electron laser oscillator with crystal cavity", Phys. Rev. ST Accl. Beams **14**, 010701 (2011).

ISBN 978-3-95450-134-2

NUMERICAL STUDIES OF THE INFLUENCE OF THE ELECTRON BUNCH ARRIVAL TIME JITTER ON THE GAIN PROCESS OF AN XFEL-OSCILLATOR FOR THE EUROPEAN XFEL

C. Maag, J. Zemella, DESY, Hamburg, Germany
J. Rossbach, University of Hamburg, Germany

Abstract

The superconducting linac of the European XFEL Laboratory in Hamburg will produce electron bunch trains with a time structure that allow in principle the operation of an XFELO (X-ray FEL-Oscillator). The electron bunches of the European XFEL have an expected length between 2 and 180 fs (FWHM) with an expected arrival time jitter of about 30 fs (RMS). A jitter of the electron bunch arrival time leads to a detuning between the electron and photon pulse. Since an XFEL-Oscillator relies on a spatial overlap of electron and photon pulse, the influence of a lack of longitudinal overlap is studied. The simulations are performed for different bunch lengths and levels of arrival time jitter. The results of a simulation are presented where angular, transversal and arrival time jitter are taken into account simultaneously, assuming parameters expected for the European XFEL Linac.

INTRODUCTION

The recently proposed concept of an XFELO described in [1, 2] potentially offers performance complementary to a SASE (self-amplified spontaneous emission) based FEL. The proposed XFELO uses a crystal cavity to provide narrow band feedback of the SASE radiation and has the potential to produce hard x-rays with energies between 5 and 20 keV. While the extracted peak power of such an XFELO (about 50 MW) is predicted to be lower by about 3 orders of magnitude compared to SASE-FELs, the bandwidth will be in the order of $\Delta\nu/\nu \approx 10^{-5}$ - 10^{-7} which is 2 - 4 orders of magnitude more narrow than the bandwidth of a SASE-FEL ($\Delta\nu/\nu \approx 10^{-3}$). The pulses of an XFELO will have a significantly larger longitudinal coherence up to full longitudinal coherence along the photon pulse [3]. Building an XFELO requires components which have to perform on the edge of today's technical feasibility, including the production and acceleration of high-brightness electron beams, the optimization of radiation generation in the undulator and the electron and x-ray beam guidance so as to overlap the electron bunch with the x-ray pulse to obtain optimal FEL gain. In this paper the influence of a lack of overlap is studied, whereby the focus rests on the arrival time jitter between electron bunch and x-ray pulse. The currently lowest arrival time jitter of 30 fs was achieved with a synchronization system reported in [4] using 60 fs (RMS) long electron bunches. At the European XFEL a synchronization system similar to that is planned to be implemented [5] and it is assumed that the arrival time jitter will decrease for bunches shorter than 60 fs. At the European XFEL electron bunches with a length between 180 fs and 2 fs are planned to be generated. Due to the fact that the arrival time jitter of the electron bunches at the European XFEL will be of the order of the bunch length some impact on the XFELO operation can be expected. To quantify the impact of the arrival time jitter on the XFELO operation simulations using the code GENESIS 1.3 [6] have been performed. The simulations have been performed for bunch lengths of 178 fs and 18.8 fs (FWHM) with three levels of arrival time jitter each. Since not only the arrival time is subjected to jitter exemplarily a simulation has been performed that incorporates bunch position and angular jitter as well. The jitter levels used in this exemplary simulation are the levels expected for European XFEL Linac.

Table 1: Input Parameters of the Simulations

Parameter	unit	Setup 1	Setup 2
Electron energy	GeV	14.5	14.5
Bunch charge	nC	1	0.1
Bunch length (FWHM)	fs	178	18.8
Peak current	kA	4.9	5
Normalized emittance	μm	1	0.3
Slice energy spread	MeV	1.5	2.04
Beta function at waist	m	7.5	7.5
Radiation wavelength	Å	1.027	1.027
Undulator length	m	15	15
Undulator period	m	0.03	0.03
Cavity length	m	66.62	66.62
Outcoupled radiation	%	4	4
Cavity losses	%	4	4

SIMULATIONS

The simulations where performed with the single pass FEL code GENESIS 1.3 together with an oscillator extension code [7] which calculates the propagation of the output radiation field in the cavity of one GENESIS run and use it as the seed radiation for a subsequent GENESIS run. The calculation of the field propagation inside the cavity comprises the free space propagation, the spectral filtering due to the Bragg reflection, the transformation due to the focusing elements and the outcoupling of a fraction of the radiation at one of the crystal mirrors. The spectral bandpass filter that is applied to the radiation to simulate the Bragg reflection (4 4 4) at a Diamond crystal has a width of $\Delta\lambda/\lambda \approx 1.66 \cdot 10^{-6}$ (FWHM) which corresponds to a Fourier-limited pulse duration of about 180 fs (FWHM).

ISBN 978-3-95450-134-2

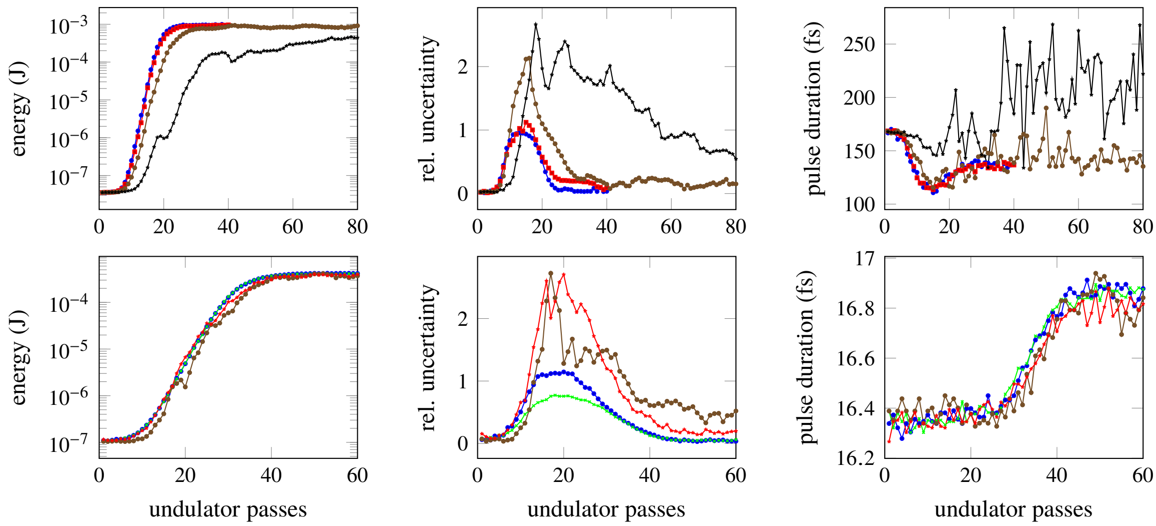

Figure 1: Effect of the arrival time jitter on the XFELO process for jitter levels of 0 fs (blue), 6.3 fs (green), 30 fs (red), 60 fs (brown), and 120 fs (black). In the top row the results of the simulation with 178 fs long electron bunches are shown. In the bottom row the results of the simulation with 18.8 fs long electron bunches are shown. The plots on the left show the mean pulse energy versus the number of undulator passes for the different jitter levels. The centered plots show the relative deviation of the mean pulse energy and the plots on the right show the mean pulse duration of the x-ray pulses.

For the generation of the arrival time jitter a script was written that shifts the radiation pulse by the deviation in the arrival time relative to a reference point within the simulated time window. The value of the deviation in the arrival time is generated by a random number generator that generates Gaussian distributed random numbers. Since GENESIS has input variables for angular and positional deviations of the electron beam the implementation of this kind of jitter could be done in a different way. Hence a script was written generating uniformly distributed random numbers and writing these numbers into the GENESIS input file. Both scripts have to be executed for each cavity round trip to generate the respective jitter. The input parameter of the simulations are shown in Table 1. One run of a jitter simulation presented here starts with a first electron bunch that generates an x-ray pulse via the SASE process and continues until the XFELO has reached saturation. Since jitter is a statistical process the simulations presented here consist of 25 runs, allowing to calculate the mean and variance of the results.

RESULTS

The arrival time jitter simulations have been performed for two different setups shown in Table 1. The essential difference in these two setups is the electron bunch length of 178 fs and 18.8 fs respectively. The results of the simulations are shown in Figure 1. The top row shows the results of setup 1. The first plot of the top row shows the mean pulse energy versus the number of undulator passes and the center plot in the top row shows the corresponding deviation of the mean for the jitter levels (RMS) of 0 fs (blue), 30 fs (red), 60 fs (brown) and 120 fs (black). For the jitter levels of 30 fs and 60 fs the impact on the gain process is quite low whereas at 120 fs the impact is significant. This result is in good agreement with the expectation that a jitter significantly shorter than the bunch length should only have a low effect on the gain process. In the plot of the energy deviation from the mean pulse energy it is noticeable that the deviation of the mean has a maximum roughly at the point where the gain is maximum. The reason for that is that at high gain levels a relatively small disturbance gets amplified and thus broadens the relative uncertainty. At saturation, lower pulse energies get amplified more than higher pulse energies and this leads to a narrowing of the relative uncertainty. The right picture in the top row shows the pulse duration versus the number of undulator passes. The pulse duration has a minimum about the point of the maximum gain. The reason for that could be that the amplitude of the electrical field in the center of the x-ray pulse is higher than at the head or the tail. If an electron bunch meets the circulating x-ray pulse it should therefore take longer for the microbunching to form at positions where the amplitude of the electrical field is lower compared to positions where the amplitude is higher. This should lead to a higher gain in the center of of the x-ray pulse until saturation is reached. Intensifying the center of the pulse more than the tails should thus shorten the over-all pulse duration. Furthermore the plot shows that the pulse duration increases with increasing jitter and that the fluctuation of the pulse duration increases with increasing jitter as well. The reason for the increase in the pulse duration is that due to the jitter the circulating pulse in the cavity and the electron bunch do not overlap completely, which leads to an asymmetrical growth of the x-ray pulse and thus the pulse duration increases.The plots in the bottom row show

ISBN 978-3-95450-134-2

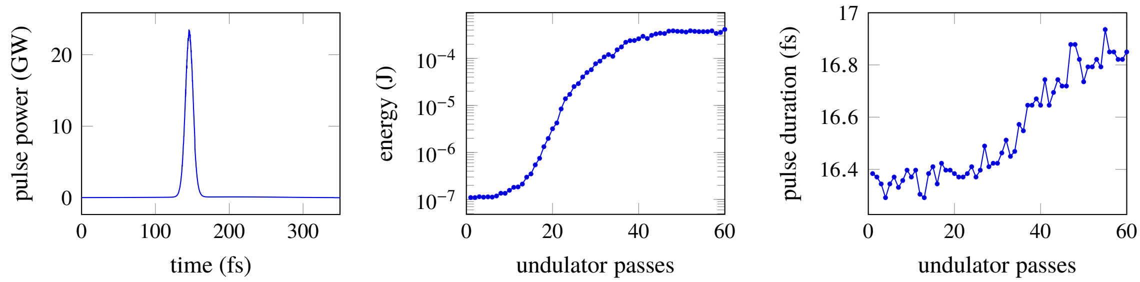

Figure 2: Performance of an XFELO considering the arrival time jitter (30 fs), angular jitter (100 nrad) and positional jitter (1 µm) expected for the European XFEL Linac. The left plot shows an exemplary pulse at saturation. The center plot shows the mean pule energy as a function of the number of undulator passes and the right plot shows the mean pulse duration as a function of the number of undulator passes.

the results of setup 2 (see Table 1). It should be noticed that in the bottom row the assumed jitter levels, if compared to the bunch length, are much bigger than in the top row. However, as the first and second plot (bottom row) show, the gain process at the same jitter levels is almost as stable as in the simulations using 178 fs electron bunches. The reason for that is the constant length of the circulating x-ray pulse. As mentioned above the Fourier-limited pulse length is due to the Bragg-reflection about 180 fs (FWHM). If a shorter pulse is generated only that fraction of the pulse within the bandwidth of the Bragg-reflection will be reflected. That leads to a circulating pulse much longer than the pulse generated in the undulator. Taking the circulating x-ray pulse of about 180 fs into account it becomes clear that the jitter sensitivity of an XFELO run with 18.8 fs electron bunches is almost the same as for an XFELO run with 178 fs electron bunches. Apart from this interesting fact the first two plots in the bottom row show the same characteristic like the first two plots in the top row. The right plot in the bottom row shows the mean pulse duration versus the number of undulator passes. All curves show a slight increase in pule duration and depending on the jitter level the pulse duration fluctuates more or less.The results of the simultaneous simulation of arrival time jitter, angular jitter and positional jitter are shown in Figure 2. For the simulation the setup 2 (see Table 1) has been used. The jitter levels are with 30 fs for the arrival time jitter, 100 nrad for the angular jitter and 1 µm for the positional jitter chosen like expected for the European XFEL Linac. The first plot shows an exemplary x-ray pulse at saturation. The pulse has an almost Gaussian shape with only some spikes on top which indicates a high level of longitudinal coherence. Even though it cannot be recognized very well it should be noticed that the 17 fs (FWHM) pulse has the weak circulating pulse of 180 fs (FWHM) as a background. The plot in the center shows the mean pulse energy versus the number of undulator passes. The curve has some small spikes and saturates at a mean pulse energy of about 300 µJ. The plot on the left shows the mean pulse duration as a function of the undulator passes. It can be seen that the mean pulse duration increases during the gain process and after saturation it stabilizes at about 16.8 fs. Overall this simulation shows a very similar characteristic to the simulation of setup 2 only taking arrival time jitter into account (see Figure 1).

CONCLUSION

In this paper the influence of electron beam jitter on the XFELO gain process was studied. An interesting result of the simulations is that for bunch lengths below the Fourier-limited pulse length of the mirrors the sensitivity to arrival time jitter does not significantly increase when the bunch length decreases. Therefore it turned out that the levels of arrival time jitter which can be achieved with today's technology are low enough to allow stable XFELO operation for all electron bunch lengths. At arrival time jitter levels significantly below the duration of the circulating pulse the jitter has only a weak impact on the mean gain, the mean saturation energy, and the mean pulse duration. However the fluctuation of these quantities increase noticeable. The simultaneous simulation of arrival time jitter, angular jitter and positional jitter have shown that it should be possible to run an XFELO under jitter conditions expected for the European XFEL Linac. Even though the fluctuations of the pulse energy and pulse duration are noticeably increased by the jitter the operation can be considered stable.

REFERENCES

[1] K. J. Kim et al., Phys. Rev. Lett. **100** (2008), 244802.

[2] R. R. Lindberg et al., Phys. Rev. ST A&B **14** (2011), 010701.

[3] J. Zemella et al.,WEPD29, Proc. FEL'2012.

[4] S. Schulz et al., Nature Communications **6** (2015), 5938.

[5] R. Abela et al., "The Technical Design Report of the European XFEL", European XFEL Laboratory (2007).

[6] S. Reiche, "User's Manual for GENESIS", `http://genesis.web.psi.ch/download/documentation/genesis_manual.pdf`

[7] J. Zemella, "Untersuchungen zu einem Freie-Elektronen-Laser-Oszillator im Röntgen-Wellenlängenbereich für den European XFEL", Dissertation (2013).

ISBN 978-3-95450-134-2

NEW ELLIPSOIDAL LASER AT THE UPGRADED PITZ FACILITY

J. Good[#], G. Asova [†], M. Bakr [‡], P. Boonpornprasert, M. Gross, C. Hernandez-Garcia[§], H. Huck, I. Isaev, D. Kalantaryan, M. Khojoyan[θ], G. Kourkafas, M. Kraslinikov, D. Malyutin[$], D. Melkumyan, A. Oppelt, M. Otevrel, Y. Renier, T. Rublack, F. Stephan, G. Vashchenko, Q. Zhao[¶], Deutsches Elektronen-Synchrotron, Zeuthen, Germany
I. Hartl, S. Schreiber, Deutsches Elektronen-Synchrotron, Hamburg, Germany
A. Andrianov, E. Gacheva, E. Khazanov, S. Mironov, A. Poteomkin, V. Zelenogorsky, Institute of Applied Physics, IAP, Nizhny Novgorod, Russia
E. Syresin, JINR, Dubna, Moscow Region, Russia
O. Lishilin, G. Pathak, Hamburg University, Hamburg, Germany

Abstract

High brightness photoinjectors for superconducting linac-based FELs are developed, optimized and characterized at the Photo Injector Test facility at DESY in Zeuthen (PITZ). Last year the facility was significantly upgraded with a new prototype photocathode laser system capable of producing homogeneous ellipsoidal pulses. Previous simulations have shown that the corresponding pulses allow the production of high brightness electron bunches with minimized emittance. Furthermore, a new normal conducting RF gun cavity was installed with a modified two-window waveguide RF feed layout for stability and reliability tests, as required for the European XFEL. Other relevant additions to the facility include beamline modifications for improved electron beam transport through the PITZ accelerator, refinement of both the cooling and RF systems for improved parameter stability, and preparations for the installation of a plasma cell. This paper describes the facility upgrades and reports on the operational experience with the new components.

ELLIPSOIDAL LASER SYSTEM

Previously reported [1] low emittance beams were obtained using a flat-top temporal laser profile with 60 MV/m in the RF gun, and more recently new measurements have been taken with a Gaussian temporal laser profile and 53 MV/m [2]. Also recently it was found that the transverse halo of the laser must be taken into account [3]. In earlier simulations it was found that uniform ellipsoidal charge distributions with sharp charge transition boundaries would produce even higher beam quality. Furthermore, it was shown that such electron bunches are also less sensitive to machine parameter jitter [4] and therefore increase the reliability and stability - crucial parameters for single-pass FELs such as FLASH and the European XFEL.

Naturally, a homogenous ellipsoidal photocathode laser pulse can be used to produce such charge distributions. Consequently, such a laser system has been developed for PITZ by the Institute of Applied Physics in Nizhny Novgorod, under the framework of a joint German-Russian research activity [5].

The system produces quasi-ellipsoidal laser pulses in the infrared through spectral amplitude-phase masking.

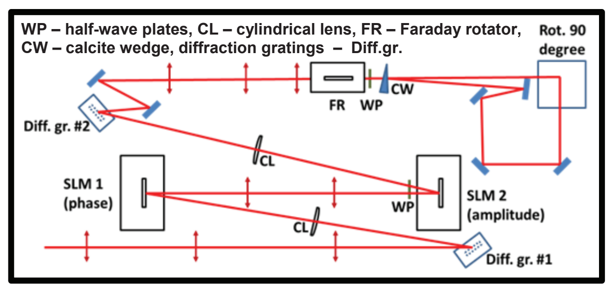

Figure 1: Schematic overview of the 3D shaper.

The shaper consists of two diffraction gratings, two Spatial Light Modulators, and various optical elements (Fig. 1). A chirped infrared laser pulse is transformed into the spectral domain with a diffraction grating and imaged onto Spatial Light Modulators (SLMs) whereupon masks such as in Fig. 2 are applied. The beam is then recombined via another grating, rotated 90º about its propagation axis, and passed back through the shaper again. This shapes the perpendicular transverse axis and produces a quasi-ellipsoidal distribution. Finally, the beam is converted from infrared to the ultraviolet via non-linear 4^{th} harmonic frequency conversion.

Simulations have been done to produce the mask in Fig. 2a) which is expected to roughly produce the quasi-ellipsoidal distribution in Fig. 2b).

Simulations have shown that these improved laser pulses have the potential to further reduce the emittance of the generated electron bunches at PITZ [4].

james.david.good@desy.de
† on leave from BAS INRNE, 1784 Sofia, Bulgaria
‡ on leave from Assiut University, 71515 Assiut, Egypt
§ on leave from JLab, Newport News, VA 23606, USA
¶ on leave from IMP/CAS, 730000 Lanzhou, China
$ now at Helmholtz-Zentrum Berlin, Berlin, Germany
θ now at Synchrotron SOLEIL, Paris, France

ISBN 978-3-95450-134-2

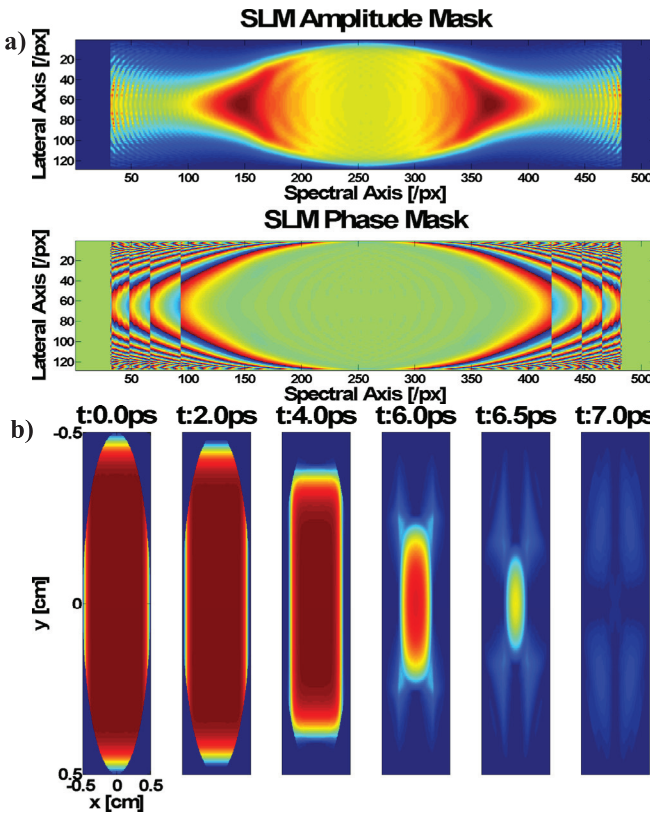

Figure 2: a) The corresponding normalized amplitude and phase masks. b) Temporal slices of a simulated quasi-ellipsoidal laser pulse. t=0 ps corresponds to the temporal center of the laser pulse.

The laser pulses are characterized by a cross-correlator coupled camera in the infrared (Fig. 3) prior to frequency conversion to the ultraviolet. Owing to the non-linarites inherent to the conversion process a UV:IR scanning cross-correlator is planned in order to fully characterize the shaped UV pulses. The first photoelectrons were produced with this system in spring and captured with a Faraday cup. The beamline and system are currently undergoing testing, commissioning, and further improvements.

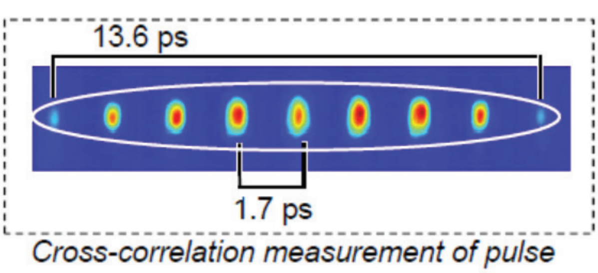

Figure 3: Cross-correlation measurement of a shaped pulse produced in the lab. Shown are ~250 fs time slices of the transverse distributions of the shaped laser pulse taken at 1.7 ps intervals throughout the entire pulse duration of 13.6 ps.

NEW GUN AND RF FEED SYSTEM

During the summer/autumn of 2014 the RF feed system and the gun at PITZ were replaced (Fig. 4). Gun 4.4 was exchanged with a Gun 4.2, while the RF feed changed from a single Thales RF window layout [6] to a double RF window-pair layout [7]. This was owing to high-load induced damage of the Thales window. Naturally, sharing of the load across two windows has reduced both the potential damage to the components and the likelihood of interruptive instances, thereby improving stability and reliability of the system.

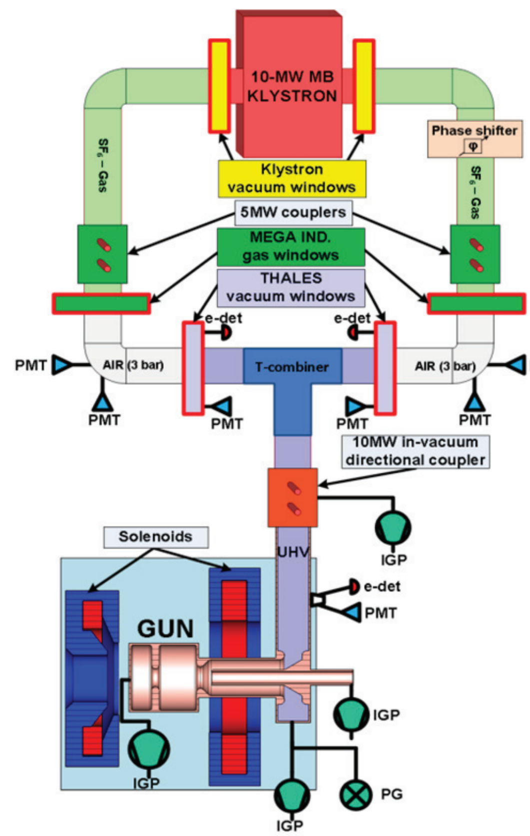

Figure 4: New gun interlock and RF distribution scheme.

However, the nominal operation target of FLASH and XFEL has not been reached owing to limitations of the gun itself. This can be attributed to the gun's troubled history [7]. Reduction of the operating power to 5 MW has shown a remarkable improvement in gun stability.

RF GUN STABILITY

One of the main tasks of PITZ is demonstration of stable operation of the RF gun at the European XFEL injector specifications. The specifications are an RMS amplitude jitter of less than 0.01% as well as an RF phase RMS jitter smaller than 0.01 deg. These challenging stability requirements have to be achieved within the RF pulse and from pulse-to-pulse.

ISBN 978-3-95450-134-2

Nominal RF pulses of 650 us flattop length at ~6.4 MW peak power in the gun cavity and 10 Hz repetition rate have to be stably supported for the European XFEL RF gun.

For the initial start-up conditions a reduced peak power of 4.5-5 MW is foreseen. A new low-level RF (LLRF) system has been implemented at PITZ since November 2014. It is based on μTCA [8] technology and imparts an increased measurement sampling rate within the RF pulse as well as extended feedback (FB) tools permitting improved regulation of the amplitude and phase of the RF gun.

Another tool to stabilize the normal conducting RF gun is the water cooling system (WCS). High temperature stability of the gun cavity is realized by heat transport control. The WCS implemented at PITZ currently has two functional modes: operation (WCS=oper) and stabilization (WCS=stab). The former actively regulates the gun's water circuit through valve-controlled mixing of cold water into the loop. Whereas, the latter employs a heat exchanger to regulate the closed warm water loop thereby reducing flow perturbations. Results of the stability measurements based on the statistical analysis of 800 subsequent RF pulses are shown in Fig. 5, where RMS phase and amplitude jitters within the RF pulse are plotted for various WCS and FB modes. These measurements have been performed for the peak RF power in the gun of 4.5 MW and 640 μs RF pulse duration.

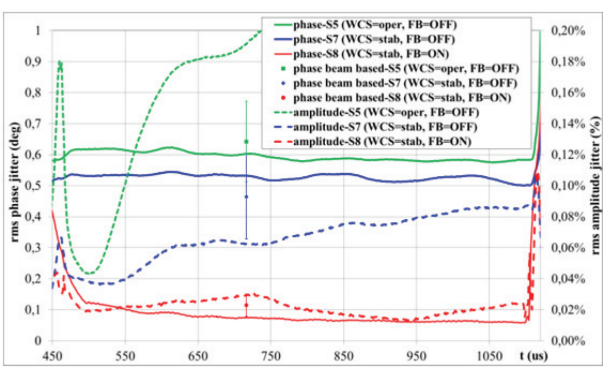

Figure 5: RF gun stability measurements. The RMS phase and amplitude jitter is plotted at left and right axis correspondingly for two regimes of the WCS and deactivated/activated LLRF feedback (measurements S5, S7 and S8). Results of the correspondent beam-based measurements are shown with markers. The horizontal position of these points corresponds to the time of the first electron bunch within the RF pulse.

As can be seen from these measurements, without feedback switching the WCS from operation mode to the stabilization mode improves the amplitude stability by a factor of 3 and the phase jitter is reduced by ~10%. Whereas, application of the LLRF feedback results in further reduction of the amplitude jitter by a factor of ~3 and significant reduction of the phase jitter (~75%). However, further improvements to the RF gun stability have to be implemented (factor 5 for the phase and factor 2 for the amplitude) in order to achieve the European XFEL injector specifications.

The RF stability measurements were cross-checked with electron beam measurements based on the fluctuations of the electron bunch charge as a function of the RF gun launch phase. The analytic approach used to fit the measured mean charge <Q> and charge fluctuations δQ assumed three independent and normally distributed sources of charge fluctuation: phase jitter, laser pulse energy fluctuations, and electronic noise of the charge measurement device (Faraday cup). It is also presumed that the temporal profile of the photocathode laser pulse is Gaussian as it was in the measurements. In order to minimize the influence of the space charge effect the space charge density at the cathode was reduced by decreasing the photocathode laser fluence. An example of the measured <Q> and δQ together with fitted curves are shown in Fig. 6. The phase RMS jitter obtained from these fits is plotted in Fig. 5.

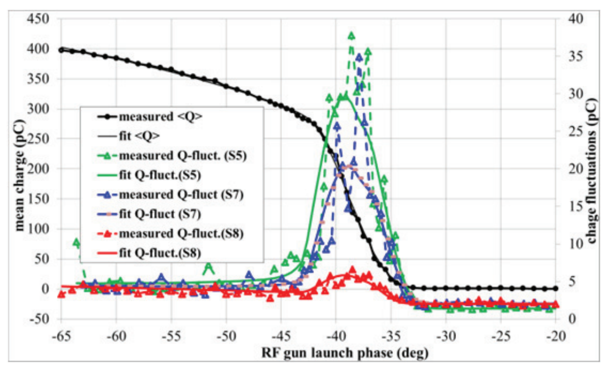

Figure 6: Beam based measurements of the RF gun stability. Measured mean charge and its analytical fit are plotted at the left axis. Charge fluctuations together with fits for three cases of WCS and FB (measurements S5, S7 and S8) are plotted at right axis.

PHOTOEMISSION STUDIES

One of the many areas of interest is the charge production behaviour of the Cs_2Te cathodes used in both FLASH and PITZ. While significant amounts of charge can be extracted from the cathodes it has been observed that the quantum efficiency (QE) of the cathode constantly decreases as a function of time (~1 year) before partially recovering (Fig. 7) [9].

ISBN 978-3-95450-134-2

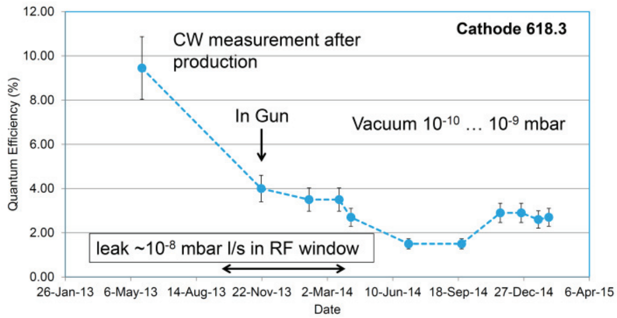

Figure 7: Quantum Efficiency of FLASH's Cs_2Te Cathode 618.3 during 2013/2014.

To investigate this behaviour one of the measurement programs embarked upon has been to map the QE over the surface of the cathode as a function of time.

It was seen that the QE consistently degrades across the entire surface of the cathode, within a period of one month, despite charge extraction occurring primarily at the centre. The evolution of existing defects and the formation of new ones can also be observed (Fig. 8). On longer time scales, on another cathode at PITZ, effects similar to those measured at FLASH have been observed.

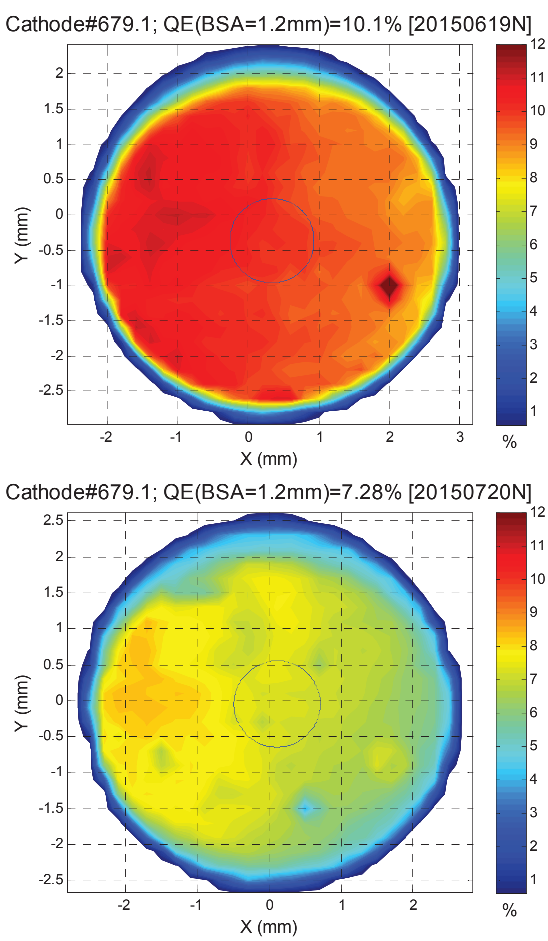

Figure 8: Evolution of cathode surface QE over one month.

Similarly, another unexplained aspect of charge extraction from the cathode was the increase of photoemission with laser pulse energy contrary to previous simulations (Fig. 9). According to simulation a uniform (flat-top) transverse laser profile, the extracted charge should saturate beyond certain laser pulse energy, corresponding to specific beam parameters and gun operating settings.

However, in reality the photocathode laser does not have a perfect flat-top transverse profile. Therefore a detailed investigative measurement program was begun to fully characterize the transverse profile of the laser and to produce a comparative set of photoemission data [3].

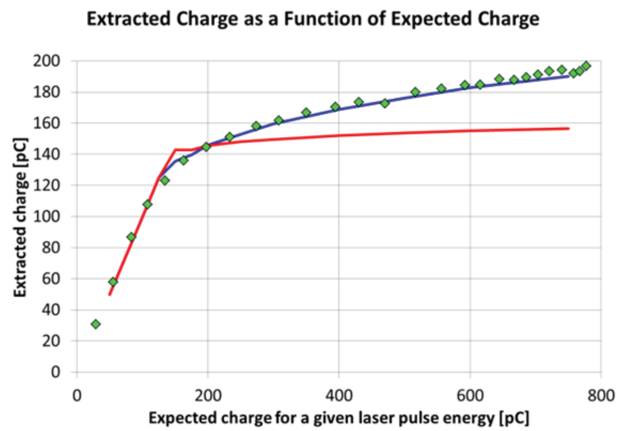

Figure 9: Extracted charge and expected charge given by simulation of a homogenous, transversely flat-top laser pulse (red) and the same distribution with a photonic halo (blue), and measurement of charge actually extracted (green).

The resulting simulations have shown that the previously observed discrepancy can be easily explained by rising Gaussian edges of the transverse laser profile generating a "halo" of charge around the core beam. Furthermore, this effect is constantly more pronounced across all gun gradients for more narrow transverse profiles where the ratio of core:halo area is decreased.

FURTHER FACILITY DEVICES

Additionally, commissioning of a transverse deflecting cavity (TDS) started in July 2015. The preliminary results are promising [10] as beam measurements are in good agreement with RF readings However, full operation of the device was limited by high reflection in the waveguide line.

A plasma cell was constructed in 2013 for doing proof of concept measurements for the AWAKE experiment at CERN [11]. The device consists of a heatpipe oven for the vaporization of lithium, Kapton foil windows to separate the volume from the beamline vacuum, and a 193nm ionizing laser to produce the plasma. The chamber has recently undergone successful mechanical, vacuum, and thermal stress tests and was placed into the beamline for the first time in July.

ISBN 978-3-95450-134-2

SUMMARY AND OUTLOOK

Preparatory simulations were done for the new ellipsoidal photocathode laser system. This has yielded trial phase-amplitude masks which have been tested and characterized with a scanning IR cross-correlator coupled camera. Photoelectrons have been generated with the system and development is ongoing.

The RF system has shown itself to be very reliable under a two RF window-pair solution and has been operated at full XFEL RF specifications without issue. The RF system will be fully assessed with the newly manufactured gun 4.6 which is planned to be installed until the end of 2015.

The phase and amplitude regulation of the RF gun has been improved by switching the LLRF to a µTCA-based system and by further improvement of the gun's water cooling system.

Photoemission studies have been performed and it was also determined by simulation, and confirmed by experimental data, that the irregularities of the transverse laser profile on the cathode have to be fully included in simulation.

Finally, the Transverse Deflecting Structure is in the commissioning phase and is expected to deliver extended diagnostic capability and insightful experimental data. Also experiments with a plasma cell have started to do proof-of-principle experiments in the field of particle beam driven plasma wakefield acceleration.

REFERENCES

[1] M. Krasilnikov et al., Experimentally minimized beam emittance from an L-band photoinjector, PRST AB 15, 100701 (2012).

[2] G. Vashchenko et al., Emittance Measurements of the Electron Beam at PITZ for the Commissioning Phase of the European X-FEL, these proceedings (MOD04), FEL'15, Daejeon, Korea.

[3] C. Hernandez-Garcia et al., "Studies on charge production from Cs2Te photocathodes in the PITZ L-band normal conducting radio frequency photo injector," in preparation, to be submitted to Phys. Rev. ST Accel. Beams.

[4] M.Khojoyan et al., Optimization of the PITZ photo injector towards the best achievable beam quality,Proc. FEL2014, Basel, Switzerland (2014).

[5] T.Rublack, First Results Attained with the Quasi 3-D Ellipsoidal Photo Cathode Laser Pulse System at the High Brightness Photo Injector PITZ, IPAC'15, Richmond, VA, USA (2015).

[6] M.Otevrel et al., Report on Gun conditioning activities at PITZ in 2013, Proc. IPAC'14, Dresden,Germany (2014).

[7] A. Oppelt et al., Facility Upgrade at PITZ and First Operation Results, IPAC'15, Richmond, VA, USA (2015).

[8] M.Hoffmann et al., Operation of Normal Conducting RF Guns with MTCA.4, IPAC'15, Richmond, VA, USA (2015).

[9] S. Schreiber and S. Lederer, Lifetime of Cs2Te Cathodes Operated at the FLASH Facility, these proceedings (TUP042), FEL'15, Daejeon, Korea.

[10] H. Huck et al., First Results of Commissioning of the PITZ Transverse Deflecting Structure, these proceedings (MOP039), FEL'15, Daejeon, Korea.

[11] M. Gross, et al., Preparations for a plasma wakefield acceleration (PWA) experiment at PITZ, Nuclear Instruments and Methods in Physics Research A 740 (2014), pp. 74-80.

ISBN 978-3-95450-134-2

OPERATION OF A SLIT EMITTANCE METER IN THE MAX IV GUN TEST STAND

J. Andersson*, F. Curbis, M. Isinger, F. Lindau, S. Werin
MAX IV Laboratory, Lund University, Lund, Sweden

Abstract

The MAX IV facility in Lund, Sweden is currently under commissioning. There are two guns in the current MAX IV injector, one thermionic gun for storage ring injection and one photocathode gun for the Short Pulse Facility. There is a possibility of extending the facility to include a Free Electron Laser. To investigate how the beam from the injector can be improved and how to match it to the future requirements for a FEL, the emittance meter from SPARC has been recommissioned at the MAX IV gun test stand. In this paper we report on the progress of this work and results from the first measurements.

INTRODUCTION

The MAX IV facility [1] is under construction in Lund, Sweden and includes two storage rings for production of synchrotron radiation and a short pulse facility (SPF) [2]. Both storage rings and the SPF are injected from a full energy LINAC and the injector for the LINAC has two different guns, a thermionic gun and a photocathode gun. The thermionic gun is used for ring injection but due to the requirements of short bunches and the long tail of low energy electrons, the thermionic gun is unsuitable for injection to the SPF. A 1.6 cell photocathode gun will be used instead, based on the BNL/SLAC type for FERMI@Elettra [3], operating at a frequency of 2.9985 GHz.

The performance of the photocathode gun needs to be improved, especially with regards to the emittance. Better experimental understanding of the different components of the injector is needed to find parameters to deliver an electron beams that meets the requirements. One of the diagnostic possibilities is to measure the emittance and beam envelope evolution along the injector. Earlier experiments using a pepperpot [4] has been carried out, but that setup was limited to one longitudinal position. The SPARC [5] emittance meter was placed in the vicinity to the MAX IV gun test stand after earlier experiments, and it was investigated to see if the slit- and mechanical parameters of the emittance meter was compatible with the expected beam performance from the MAX IV test gun.

MEASUREMENT PARAMETERS

The beam properties from the gun were simulated using ASTRA [6]. The result from simulations is a beam with kinetic energy of 3-5 MeV, charge of 50 - 500 pC and an emittance in the range of 0.3 to 5 mm mrad depending on operating parameters. In the first stage it is planned that the measurements are made using a single slit measurement device. Using the formulas from the appendix in [7] it is possible to estimate the dimensions of the mask and drift length to be able to resolve a beam with these properties.

The dimensions of the slit are a thickness of at least 0.5 mm tungsten to scatter the unwanted parts of the beam and a slit width of 50 μm to create emittance dominated beamlets. A slit separation of 200 μm was decided upon and to properly be able to resolve the divergence of the beam a drift space of 0.2 - 0.4 meters was used. The first tests were done using the same slit separation for all positions along the beam.

MEASUREMENT SYSTEM

The parameters for the emittance measurement device for the MAX IV gun test stand [8] are compatible with the SPARC emittance meter parameters. It was decided to recomission the SPARC emittance meter and install it into the MAX IV gun test stand to use it to investigate the beam performance. Motors, motor control and cameras was changed, but no mechanical changes were made to the system and it is in principle as described in reference [5]. The different motor axis were configured and calibrated, and after calibration the position accuracy was checked to make sure that the different axis positions could be repeated.

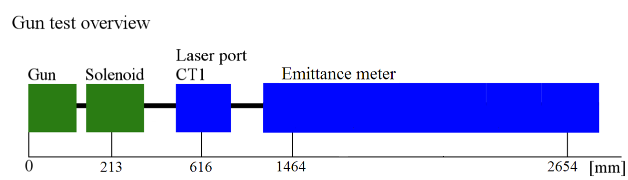

Figure 1: Schematic over the MAX IV test gun stand with emittance meter installed, the minima and maxima positions of the slit is marked.

A schematic of the test stand after the installation of the emittance meter can be seen in Figure 1 and Figure 2 shows a picture of the actual complete system. With the emittance meter installed at its current position in the beamline it is possible to measure with slit positions from 1.46 m up to 2.65 m.

The gun used in the test stand is of the same design as the gun currently used in the injector for the SPF at MAX IV. Measurements using the bead pull technique has verified that the field in this gun matches the field in the installed gun well. For the test setup a solenoid magnet produced by Scanditronix is used which is able to produce a maximum

* joel.andersson@maxlab.lu.se

ISBN 978-3-95450-134-2

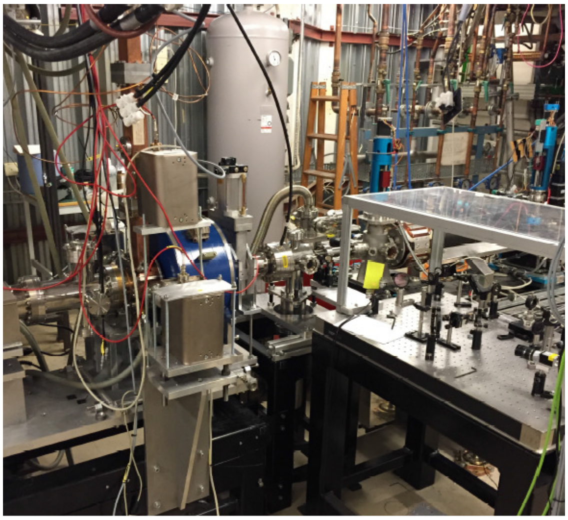

Figure 2: Picture of the gun test stand with the emittance meter visible behind the laser table.

field of 0.3 T along the main axis. The current out from the gun is measured with a in flange fast current transformer from Bergoz connected to an oscilloscope.

The laser system is a Ti:sapphire system, an oscillator locked to the 3 GHz RF feed laser pulses into a regenerative amplifier. The output from the amplifier is then fed into a multipass amplifier, and the output from this stage is frequency tripled using a BBO crystal. After the frequency tripling there is a delay stage to make it possible to adjust the timing, i.e. the injection phase. The transport system from the laser room to the test setup is in air but inside tubes. The beam is transported to a laser table next to the gun where it is focused on an iris that can cut the beam transversely. Finally the iris is imaged to the cathode, and the laser beam enters the gun system close to on axis through a port in the laser chamber.

A YAG screen is used to image the electron beam after the drift space, and the images was captured using a CCD camera from Basler. Calibration was done using existing measurement marks on the YAG screen of the emittance meter. The resolution of the camera with lens is 12.97 μm per pixel.

DATA COLLECTION

At an early stage it was realized that the test system had a lot of shot to shot fluctuations. To mitigate this problem it was investigated if it was possible to sort out bad data at an early stage in the measurement. The fast current transformer was connected to a Red Pitaya [9] board used as an oscilloscope, which in turn was connected to the control system. This created the possibility to filter captured images based on both charge output and intensity after the slit, so even though the measurement is multishot it is possible to discard measurement shots that deviates significantly.

In practice this was done by collecting 20 measurements, taking the average of these measurements with regards to charge and intensity and then acquiring 10 images that matches this average. The idea is that similar beam properties would have similar charge out from the gun and similar intensity after the slit.

DATA ANALYSIS

To get consistent results from the emittance measurement a good signal to noise ratio is needed, and it is important to handle the acquired data in a robust way. A set of MATLAB scripts were created to do background subtraction and filtering of the data.

The background subtraction was done in three steps. First a background image from the camera was subtracted from the real image to get rid of most of the background. After that a 2d median algorithm was applied to remove smaller spots and similar artifacts. Finally the image is summed in the horizontal (vertical) direction. For the summed image it was seen in many cases that the background subtraction did not manage to remove all of the background. For the images were the background was not removed, it was possible to do subtraction of a linear average and remove most of the remaining background data without affecting the signal shape.

At this point the RMS width and position of the data is calculated. For each summed image a gaussian fit is made to find the center position. The ROI of the data is then narrowed to better include only relevant data and the gaussian fit is done again. After that the data is analysed and the RMS width, position and intensity (area) of each peak is calculated.

In the next step the results are analysed to try to filter out datapoints that are too far from the nominal. It is assumed that captured images coming from shots with similar beam properties should also give similar analyzed values. After this filtering, the arithmetic mean of the acceptable data points for each slit is used as the data for that slit.

Finally the emittance and spot sizes are calculated using the formulas and method from Zhang [10].

RESULTS

The gun was put into operation in the MAX IV gun test stand during late 2014. The cathode used was a machined copper cathode similar to the cathode used with the commissioned gun. For the commissioned gun the quantum efficiency is measured to be $2.2 \cdot 10^{-5}$, and similar performance was expected from the new installation due to the similarity in manufacture and material. After initial conditioning of the gun the power could be brought up to around 90 MV/m maximum field amplitude along the main axis, and beam investigations started. The quantum efficiency was measured to $1 \cdot 10^{-6}$ and the cathode was baked to try to improve the quantum efficiency without any measurable success.

Due to the low quantum efficiency the charge in the measurements were typically between 50 and 100 pC. It was still possible to do a number of measurements and to test the

ISBN 978-3-95450-134-2

experimental setup under real operations. A complete set of methodical measurements of the emittance evolution along the beamline for different parameters was not possible in the available operations timeframe during the spring of 2015.

The measurements were all done for horizontal beam properties, but the system is also able to characterize the vertical emittance.

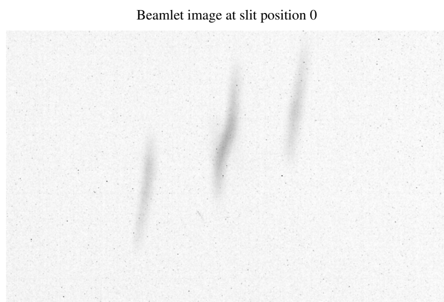

Figure 3: Beamlet image for slit position 0.

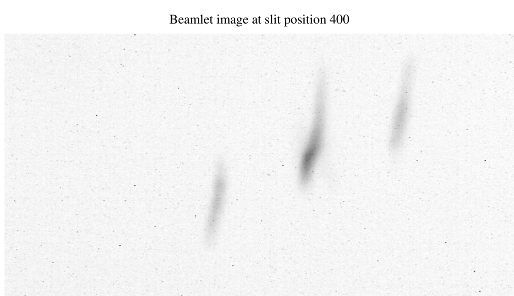

Figure 4: Beamlet image for slit position 400.

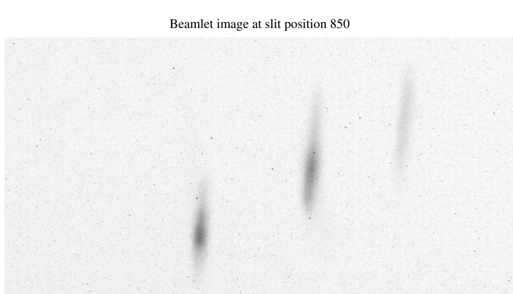

Figure 5: Beamlet image for slit position 850.

In Figures 3, 4, 5 a set of beamlet images from an emittance measurement can be seen. This set is for a measurement for 45 pC charge and 84 MV/m at positions 1.46 (0), 1.84 (400) and 2.25 (850) from the cathode. Not all beamlets are shown, every 5th beamlet is shown, and the distance is about 1 mm between each beamlet.

Figure 6 shows the measured emittance and the RMS spot size evolution at a field of 78 MV/m with 60 pC of charge

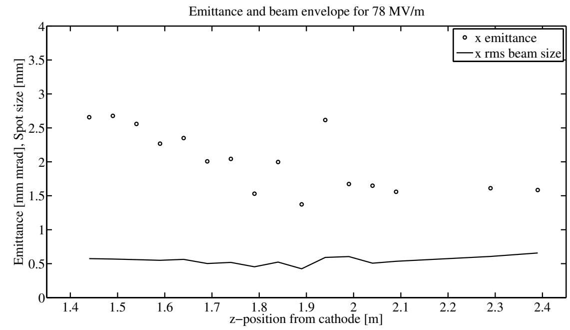

Figure 6: Emittance and beam envelope for 78 MV/m beam.

and a solenoid setting of 0.152 T. The injection phase of the laser was 30° where phase is measured from the zero crossing and checked for every measurement with a phase scan. The laser spot size was about 1 mm in diameter on the cathode.

Figure 7 shows the measured emittance and the RMS spot size evolution at a field of 84 MV/m with 45 pC of charge and a solenoid setting of 0.156 T. The injection phase is 30°m and the laser spot size about 1 mm in diameter on the cathode.

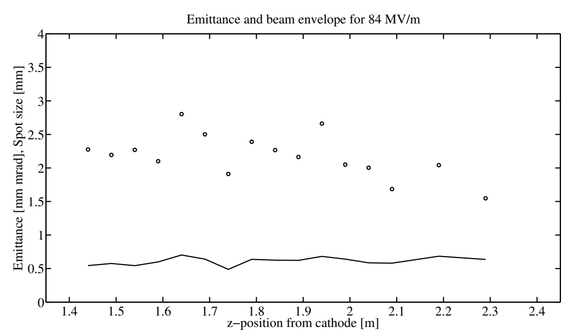

Figure 7: Emittance and beam envelope for 84 MV/m beam.

Compared to simulations, the measured emittance was larger than expected, and the emittance evolution does not match the one seen in simulations. The original simulations show an emittance around 1.5 mm mrad for the parameters of the test setup. Further investigations indicated that a larger spot size on the cathode, in the order of 2 mm, shows a larger emittance with an emittance evolution that is similar to the measured one. Further work will be put into verifying the beam size on the cathode and match the measured data to simulations.

A typical measurement took 4 hours for a total longitudinal movement of 900 mm with measurements points every 50 mm. This time needs to be reduced, the long measurement time is an issue both from the operating point of view and from the data stability point of view. It was also discovered during the measurements that there was a phase drift of about two degrees every hour. To limit the effect on the measurements the phase was rechecked periodically during every measurement, about every 20 minutes.

ISBN 978-3-95450-134-2

FUTURE WORK

The position where the emittance meter today is installed limits the measurement range to be from 1.46 to 2.65 m. The current design of the MAX IV injector has the first LINAC structure at 1.5 m from the cathode plane and the emittance evolution needs to be measured from a position closer to the cathode in the test setup. To do this a mechanical redesign for some parts of the test stand is needed and it is being investigated in what way this could be done.

During the next operating period more measurements will be made with focus on the impact of different parameters of the injector. There will also be further investigations into the cathode performance to figure out why the quantum efficiency is so low and how this can be improved. Experience will be collected from other labs to be able to do this investigation more efficient.

CONCLUSIONS

The SPARC emittance meter has been re-comissioned at the MAX IV gun test stand. A package of scripts and tools has been developed and tested to be able to do automatic measurement, and analyze data from the emittance meter. Within the the operating period we were able to show stable results from the emittance meter, but it was not possible to completely match the results to simulations.

In the next operating period more detailed studies will be done. The data analysis will also be improved further and errors in the system will be looked into in more detail to be able to create a realistic error model for the measurements results.

REFERENCES

[1] M. Eriksson et al., “The MAX-IV Design: Pushing the Envelope”, in Proc. of Particle Accelerator Conference, Albuquerque, 2007, pp. 1277 - 1279.

[2] S. Werin et al., “Short pulse facility for MAX-lab”, Nucl. Instr. and Meth. A, Volume 601, 2009, pp. 98 - 107.

[3] M. Trovo et al., “Status of the FERMI@ELETTRA Photoinjector”, in Proc. of European Particle Accelerator Conference, Genoa, 2008, pp. 247 - 249.

[4] J.Andersson et al., “Beam Performance of the Photocathode Gun for the MAX IV Linac” , in Proc. 36th Int. Free-Electron Laser Conf., Basel, 2014, pp. 799 - 802.

[5] M. Ferrario et al., “Design Study of a Movable Emittance Meter Device for the SPARC Photoinjector”, in Proc. of European Particle Accelerator Conference, Lucerne, 2004, pp. 2622 - 2624.

[6] K. Flöttman, ASTRA, `http://www.desy.de/~mpyflo/`.

[7] S.G. Andersson et al., “Space-charge effects in high brightness electron beam emittance measurements”, Phys. Rev ST Accel. Beams 5, 014201, 2002.

[8] E. Elafifi et al., “An Electron Gun Test Stand to Prepare for the Max IV Project”, in Proc. of Int. Particle Accelerator Conference, New Orleans, 2012, pp. 1551 - 1553.

[9] Red Pitaya, `http://redpitaya.com/`.

[10] M. Zhang, “Emittance formula for slits and pepper-pot measurements”, Fermilab, Fermilab-tm-1988, Oct. 1996.

ISBN 978-3-95450-134-2

INITIAL COMMISSIONING RESULTS OF THE MAX IV INJECTOR

J. Andersson*, F. Curbis, M. Eriksson, D. Kumbaro, F. Lindau, E. Mansten, D. Olsson, S. Thorin, S. Werin MAX IV Laboratory, Lund University, Lund, Sweden

Abstract

The MAX IV facility in Lund, Sweden is currently under commissioning. In the MAX IV injector there are two guns, one thermionic gun for storage ring injection and one photocathode gun for the Short Pulse Facility. The commissioning of the injector and the LINAC has been ongoing for the last year and ring commissioning is due to start shortly. In this paper we will present the results from beam performance experiments for the injector at the current stage of commissioning.

INTRODUCTION

The MAX IV facility [1] is under commissioning in Lund, Sweden. The facility has two storage rings for production of synchrotron radiation, one with 1.5 GeV and one with 3 GeV electrons. There is also a short pulse facility (SPF) [2] for the production of short pulses. The storage rings and the SPF are injected from a full energy LINAC. The injector for the LINAC has two electron guns, one thermionic gun [3] and one photocathode gun where the thermionic gun is used for ring injection. Due to the requirements of short bunches the thermionic gun is unsuitable for injection to the SPF and instead a 1.6 cell photocathode gun is used.

The commissioning of the injector and the LINAC started during the fall of 2014 and beam was commissioned until the recent shutdown period in May of 2015. During the commissioning all subsystems in the injector have been tested and brought online.

THE MAX IV INJECTOR

The injector system can be seen pictured in Figure 1. There are two parts of the injector, one leg where the thermionic gun is installed that injects into the main beam line through a 120 degree bend in an energy filter, and one straight leg for the photocathode gun.

Thermionic Gun Leg

The thermionic gun produces a beam from a BaO cathode using thermal heating. The beam is focused on an aperture using a solenoid, and between the solenoid and the aperture a chopper system [4] is shaping the beam into a suitable temporal structure for ring injection. For the initial ring commissioning scheme this will be three 3 GHz bunches within 10 ns (100 MHz) repetition time. The pulse length for each LINAC shot is 100 ns, where the pulse length is controlled using a stripline that is excited with a high-voltage pulse. The beam is refocused using a second solenoid, and then the beam proceeds into the first quad of the energy filter. The energy filter consist of four quadrupole magnets

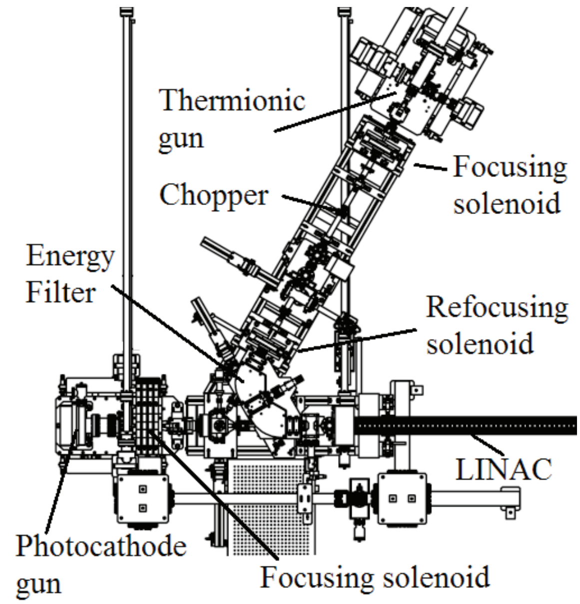

Figure 1: Blueprint of MAX IV pre-injector.

for focusing in the horizontal and vertical planes, two are located before the bending magnets and two located after. Between the two bending magnets there is a quadrupole magnet used to control the dispersion. There is also a scraper in the center of the energy filter, making it possible to adjust how much of the low energy tail of the beam that is accepted into the LINAC. The energy filter has a mechanical energy acceptance of about 200 keV and the beam is after the energy filter sent into the first structure of the LINAC. There exists multiple current transformers along the thermionic leg to measure the charge after the gun, before the energy filter and after the energyfilter.

Photocathode Gun Leg

The photocathode gun is operating at 2.9985 GHz and is based on the BNL/SLAC type for FERMI@Elettra [5]. The gun is powered by a 4 µs RF pulse via a SLED system. A laser with a wavelength of 263 nm is used to extract electrons from a copper cathode. The laser system is a KM Labs Dragon with cryogenic cooled Ti:Sapphire crystals. The laser has a oscillator at 76.9 MHz and its pulses are amplified, first in a regenerative amplifier and secondly in a multipass amplifier. Two kHz pump lasers are used to pump the amplifiers in the laser system. The pulse from the multipass amplifier is frequency tripled to a wavelength of 263 nm. The laser pulse is transported in an evacuated transport system from the laser room into the LINAC tunnel and is then focused on an iris where the beam size can be adjusted. The iris is imaged onto the cathode and the laser

* joel.andersson@maxlab.lu.se

ISBN 978-3-95450-134-2

beam is coupled into the gun in the laser chamber close to on-axis. The solenoid is manufactured by Radiabeam and is installed close to the gun. For diagnostics there is a in flange fast current transformer from Bergoz directly following the solenoid, and in the laser chamber there is a YAG screen for imaging of the cathode. After the laser chamber the beam is sent into the first structure of the LINAC.

There are three LINAC structures following the injector and following the last structure there is a matching section where it is possible to do emittance measurements using the quad scan technique. The beam is then sent into the first bunch compressor and further on to the main line of the LINAC. The bunch compressor contains dipole magnets that are also used for energy measurements.

SIMULATIONS

Simulations have been done for both legs of the injector system. The simulations were made using Parmela [6] using a model of the electric field in the gun based on a 2D symmetric model in Supefish [7]. For validation the first meter of the thermionic leg has also been simulated in Astra [8] using a full 3D model of the thermionic gun produced in COMSOL Multiphysics [9]. No large discrepancies have been found between the two simulations. The thermionic injector should be able to produce a beam with at least 20 pC of acceptable charge per 3 GHz bucket, 2.3 MeV kinetic energy and an emittance below 10 mm mrad after the first LINAC structure. The simulations in Parmela show an emit-tance of 5.6 mm mrad after the first LINAC structure at 100 MeV. The beta functions along the injector can be seen in Figure 2, there is both a horizontal and vertical focus in the center of the energy filter at approximately 2.5 m from the cathode.

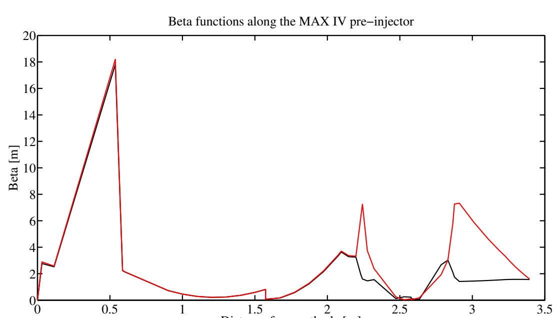

Figure 2: Simulated optics of the thermionic injector.

The photocathode beam simulations were made in ASTRA using a 3D gun field model from COMSOL, a transverse gaussian laser profile with a beam size of 1 mm and a longitudinal top hat profile with a length of 6 ps. The charge was set to be 100 pC . Using these parameters it is expected that the injector produces an electron beam with an emittance of 0.4 mm mrad at an energy of 100 MeV after the first LINAC structure. The energy spread is about 0.5 percent, and the simulated emittance and spot size evolution along the injector can be seen in Figure 3.

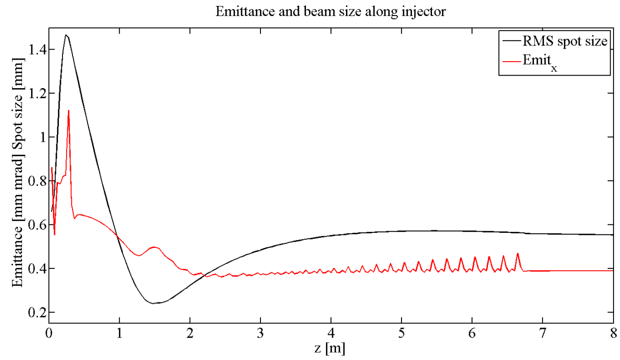

Figure 3: Emittance and beam envelope of the photocathode injector.

BEAM PERFORMANCE

Thermionic Gun

The thermionic gun has been conditioned during two different periods. The gun was first conditioned and basic measurements done in the MAX IV gun test stand [10]. The gun was then moved and installed at the MAX IV site where it was further conditioned. During the commissioning the gun performed well and very few RF breakdowns were experienced. The expected charge was delivered, and during commissioning it was possible to control the beam properties through the thermionic leg using solenoids and quadrupole magnets. A typical transverse beam going into the first LINAC can be seen in Figure 4, in this case for a 500 MHz bunch train structure, from a YAG crystal screen.

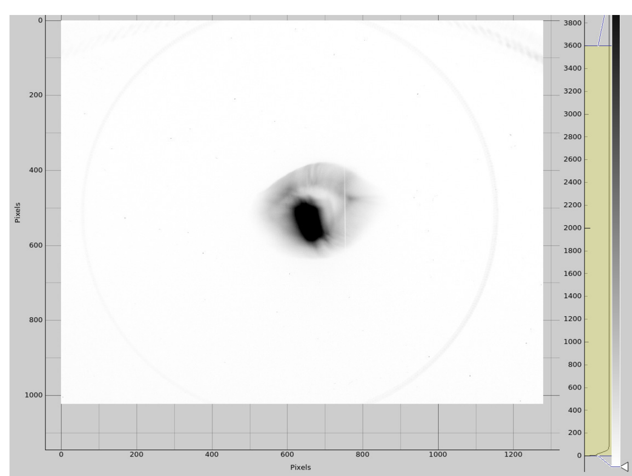

Figure 4: Thermionic beam on a YAG screen before first LINAC structure.

The aperture after the first solenoid in combination with the focusing properties of the solenoid acts as an additional energy filter. By combining the aperture with the energy filter it is possible to dump most of the low energy electrons. In Figure 5 a typical CT measurement can be seen, where

ISBN 978-3-95450-134-2

the scales are different for the different signals. The pink curve is the signal out from the gun corresponding to a total charge of about 300 nC. The chopper in combination with the aperture cuts the beam, the blue signal corresponds to the signal after the chopper and aperture, and has total charge of 3.5 nC. The yellow curve shows the signal after the energy filter, i.e. what is sent into the first LINAC structure, and the total beam charge per shot is about 1 nC.

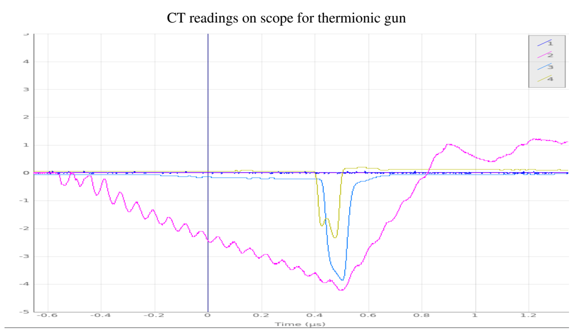

Figure 5: Beam current at the exit of the gun (pink), before (blue) and after (yellow) the energy filter, the scales for the vertical signal is different between the different channels.

The chopper was commissioned to produce the required bunch structure. Figure 6 shows the induced signal of a LINAC shot at a BPM strip. Here, the chopper operates at 100 MHz and it is configured for injection into ten 100 MHz storage ring buckets, and as can be seen the temporal pattern is ten buckets with 10 ns spacing. The emittance of the thermionic gun was not fully characterized at the time of this proceeding.

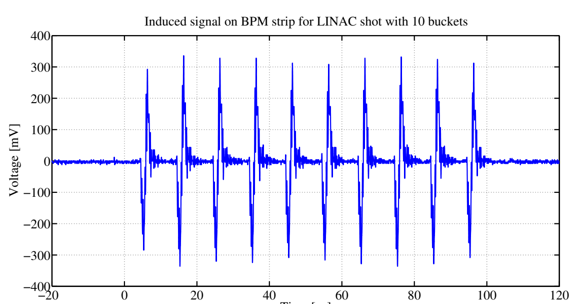

Figure 6: The induced signal of a LINAC shot at a BPM strip.

Photocathode Gun

The photocathode gun was also conditioned and initially commissioned in the MAX IV gun test stand. Figure 7 shows the measured charge out from the photocathode gun, as can be seen the delay is set so that the laser hits the cathode at the end of the RF pulse to maximize the field in the gun. The phase of the gun is set using a phase scan, and then set the delay stage of the laser system to a phase 30° from the zero-crossing. A typical phase scan result can be seen in Figure 8.

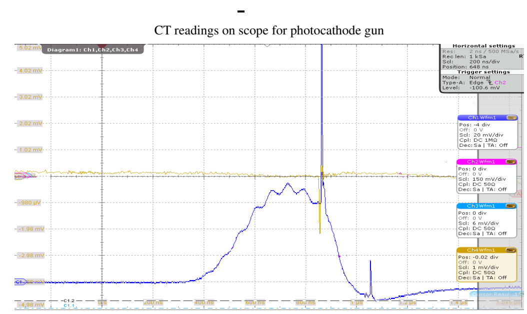

Figure 7: Typical charge output for the photogun.

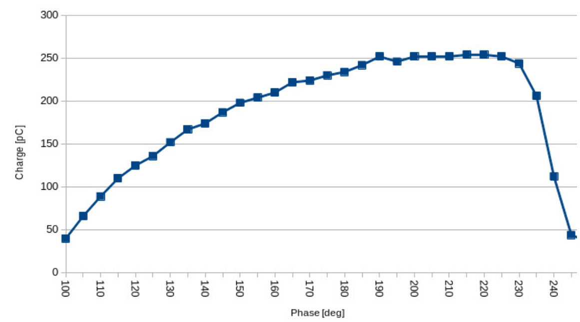

Figure 8: Typical phase scan for the photogun.

The quantum efficiency of the copper cathode was measured to be $2.2 \cdot 10^{-5}$ in the test stand and this was also the measured QE after the gun was moved and installed at the MAX IV site. At the moment there is no emittance diagnostics available close to the photocathode gun, the emittance is measured after the first three LINAC structures using the quad scan diagnostics available there. A plot of a quad scan result can be seen in Figure 9.

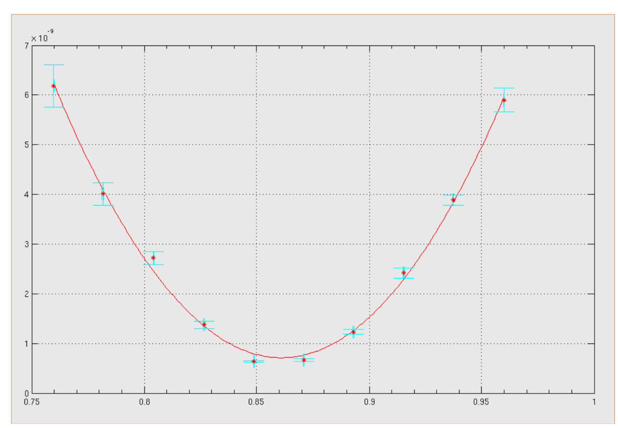

Figure 9: Typical quad scan curve at matching section one for the photocathode beam.

Initially the measured emittance out from the gun was higher than expected, measurements initially showed an

ISBN 978-3-95450-134-2

emittance of around 6 mm mrad at 170 pC. After investigation it was believed that the laser pulse was shorter than earlier thought and by increasing the length of the laser pulse it was possible to get the emittance down to 1.5 - 2 mm mrad at 100 pC. Further investigations will be made to determine what causes the decrease of the emittance.

FURTHER INJECTOR COMMISSIONING STEPS

The optics of the thermionic injector are being evaluated to see if there is some improvement to be made, both from higher energy out from the gun and from another operating scheme. These are being evaluated based on the experience gained during the commissioning and how the machine is performing with the beam that is being forwarded.

For the SPF the emittance requirement is below 1 mm mrad. Work will continue to improve the emittance out from the gun, using the improved diagnostics and also using the experience gained from the MAX IV gun test stand where a gun of the same design as the commissioned photocathode gun is currently being operated. One step is a cathode program to increase the understanding of the performance of the cathodes and to carry out long time investigations of the cathode performance.

SUMMARY

The MAX IV injector for the MAX IV project contains one thermionic leg and one photocathode leg, and it has been commissioned during fall 2014 / spring 2015. Results of beam measurements after the initial commissioning shows that the injector is able to produce a photocathode beam of 100 pc at 1.6 mm mrad and a thermionic beam with the correct bunch structure for ring injection at 20 pC per S-band bunch.

Work will continue to optimize the beam parameters using the installed system and test systems available.

REFERENCES

[1] M. Eriksson et al., “The MAX-IV Design: Pushing the Envelope”, in Proc. of Particle Accelerator Conference, Albuquerque, 2007, pp. 1277 - 1279.

[2] S. Werin et al., “Short pulse facility for MAX-lab”, Nucl. Instr. and Meth. A, Volume 601, 2009, pp. 98 - 107.

[3] B. Andersson et al., “The design of a 3 GHz thermionic RF-gun and energy filter”, Nucl. Instr. and Meth. A, Volume 491, 2002, pp. 307 - 313.

[4] D. Olsson et al., “A chopper system for the max iv thermionic pre-injector”, Nucl. Instr. and Meth. A, Volume 759, 2014, pp. 29 - 35.

[5] M. Trovo et al., “Status of the FERMI@ELETTRA Photoinjector”, Proc. of EPAC’08, Genoa, Italy, 2008, pp. 247 - 249.

[6] J.H. Billen, PARMELA, LA-UR-98-4478 (2001).

[7] K.Halbach et al., "SUPERFISH - A Computer Program for Evaluation of RF Cavities with Cylindrical Symmetry", Particle Accelerators 7 (1976) 213-222.

[8] K. Flöttman, ASTRA, `http://www.desy.de/~mpyflo/`.

[9] COMSOL Multiphysics, `http://www.comsol.com/`.

[10] E. Elafifi et al., “An Electron Gun Test Stand to Prepare for the Max IV Project”, in Proc. of International Particle Accelerator Conference, New Orleans, 2012, pp. 1551 - 1553.

ISBN 978-3-95450-134-2

CONSTRUCTION OF THE EU-XFEL LASER HEATER*

M. Hamberg*, V. Ziemann, Uppsala University, Uppsala, Sweden

Abstract

Installation of the laser heater for the EU-XFEL is completed and first commissioning runs are imminent. We discuss the installation of the key elements and provide an outlook of the commissioning phase.

INTRODUCTION

The low momentum spread of the cold electron bunches emitted from the photo-cathode of the EU-XFEL makes the accelerator sensitive to micro bunching instabilities. A laser heater is implemented to overcome this. In this proven concept a laser beam is overlapping the electron bunches as they are travelling through an undulator in a chicane. The net result after leaving the chicane is a decreased phase-space density i.e. warmer electron bunches [1-2].

The EU-XFEL laser heater is a Swedish in-kind contribution. Setup and tests were described earlier [3-4]. This paper focus on the installation of the key elements such as laser laboratory setup, laser transport vacuum system, laser routing and stabilisation system, optical stations and ultra-high vacuum (UHV) chambers before ending with an outlook.

IR LASER SOURCE SETUP

Directly after the IR laser source located on level 5 in the injection building all optical parts such as: Mirror mounts, beam-expansion telescope, retro-reflector stage (for time delay adjustment), safety shutter, active mirror mount and flip mirror for realignment are now installed. The system is also prepared for easily implementing motorized filter wheel and $\lambda/2$ rotation stage if the commissioning shows that this is a favorable position.

Furthermore a PLC system box is constructed, programmed, tested and ready to work in this location. The last mirror in this location is actively adjusted with the routing and stabilization system described below.

LASER TRANSPORT VACUUM SYSTEM

Leaving the optical table on level 5 the laser directly enters a 40 m long DN63 vacuum pipe system used to preserve the laser beam from atmospheric disturbances. The system was assembled during November to May. The strategy of the system is to use ion pumps to reduce disturbances from vibrations.

Initially the system was closed and turbo stations left to work one week before the ion pumps were switched on and the turbo stations removed. After two weeks monitoring at the three ion pumps in the system the pressure was below 10^{-6} mbar and the trend a steady decrease.

In early June, test of the motorised routing system inside of the vacuum was undertaken. We investigated the behaviour of the pressure when the stepper motors work inside of the vacuum. It was clear that the pressure up to that time had decreased to about 2×10^{-7} mbar. When the motors started and therefore also start outgassing in the process, the pressure rised to below 4×10^{-6} mbar (well in the safe region). After turning off the motors, the pressure quickly dropped down to 6×10^{-7} mbar. A view of part of the system is shown in Figure 1 whereas the pressure rise is illustrated in Figure 2.

In the last passage of the IR laser transport vacuum system at level 7 the laser enters goes from the wall out over the optical station 0 and towards the remaining laser heater setup (see overview in Figure 3).

Figure 1: Vacuum chamber located close to the electron gun in the injector hall (red mount). The laser is redirected from the vertical shaft downstream the tunnel wall.

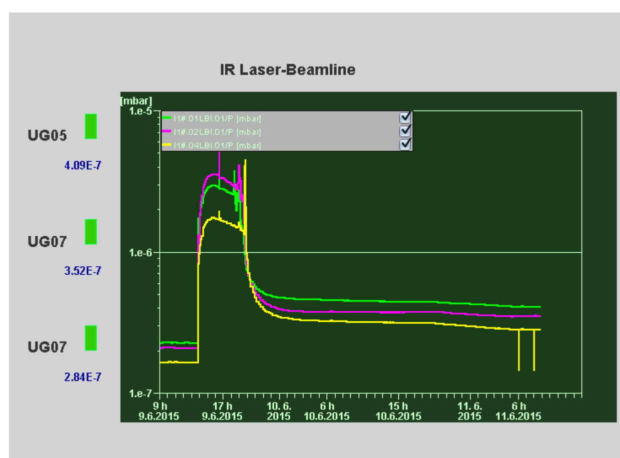

Figure 2: Pressure rise in laser transport vacuum system due to motors outgassing.

Figure 3: Overview over the laser heater on LVL7 (injector). The large optical table (OS0) is to the right side, undulator in the middle and the small table (OS1) on the left side. On top of OS0 the horizontal beam contains part of the laser vacuum system which continues along the wall to the right.

LASER ROUTING AND STABILISATION SYSTEM

This system consists of two parts build together. 1) The routing system which reads out the signal from a photo-diode behind each mirror while scanning an upstream mirror. 2) The stabilization system which quickly adjust the beam position and angle (4D stabilization) utilizing piezo actuators, microstepper motors and readout from PSD detectors. An example of signal from scanning the laser on top of the mirror is shown in Figure 4. The signal shows a clear peak when the laser is impinging on the centre of the mirror. Ring structures appear outside the centre position due to reflections in the pipe when scanning far outside. The routing system was first tested in March with good results running the full distance in air. The system was re-tested in June with better collimated beam and with the major parts of the mirrors inside vacuum. The full routing process passing each mirror from laser lab down to optical station 0 and passing 7 active mirrors lasted six hours when thoroughly tested.

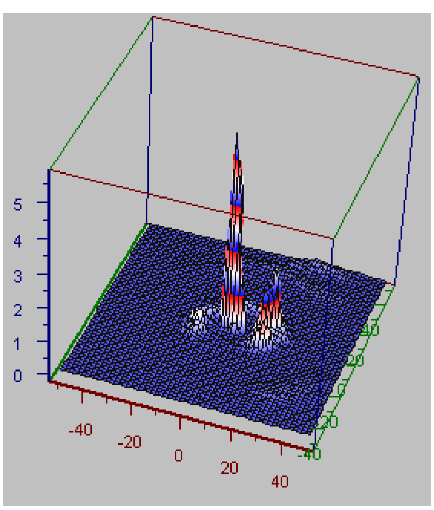

Figure 4: The 3D image shows that the signal is strongest when the laser is hitting the center of the mirror. The bottom plane is the scan area whereas the height represents signal intensity, units are arbitrary.

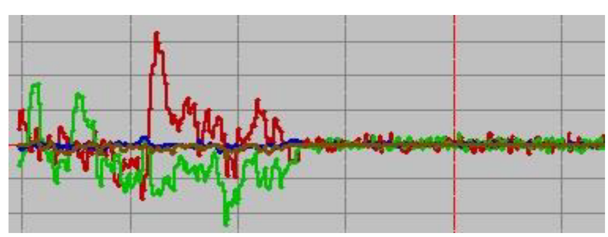

Figure 5: Signal from PSD located at the same distance as the undulator center (arbitrary units). Horizontal-axis is time (~10 s), vertical-axis is position (red is x-position, green y-position). The stabilisation system is turned on after half the time and the position is stabilised significantly.

ISBN 978-3-95450-134-2

Figure 6: The OS0 when looking downstreams. The telescope lenses are clearly visible in the center of the optical table. More optical components toward the end of the table are at the time covered with plastic bags for dust protection.

The 4D stabilization system was subsequently tested and found to be working well. After a calibration made by TEM-Messtechnik they concluded that the typical jitter at the undulator position ~50 m downstream from laser source was in the order of 4 µm (below 30 µm is wanted for good laser heater functionality). See Figure 5.

OPTICAL STATION 0

The optical station 0 (OS0 see Figure 6) is the 3.6x0.9 m optical table in the in the injector building used for reading out laser properties and focusing it into the centre of the undulator. All essential hardware is there and the system is working.

OPTICAL STATION 1

The optical station 0 consists of a 0.75x0.75 m optical table downstream the undulator in the injector building. The OS1 has periscope, PSD and camera.

UHV VACUUM CHAMBERS

The Ultra High Vacuum (UHV) chambers are located in the electron beamline behind the optical tables in the injector building. This include inlet/outlet chambers for coupling in the laser into the vacuum; crosses for OTR screen positioning readout; L-pipes going from below the OTR crosses down to pumps; undulator pipe with implemented bellows. All vacuum chambers are mounted and leak tight.

UNDULATOR

The undulator is tested, in position and awaits alignment and subsequent commissioning in location.

OUTLOOK: REMAINING PARTS AND TASKS

The installation of the laser heater is finished. Commissioning will follow. The system needs further adjustment and fine tuning during the coming year. This includes:

- Handling the laser power dynamic range of 5 orders of magnitude without disturbing the laser positioning or destroying detectors
- Precise alignment throughout the laser pathway including the movable focusing telescope located at OS0
- Lead shielding of the optical stations
- Full implementation of the PLC system including control and update of the interfacing system
- Photo-diode implementation at OS1 and readout for timing
- Pipes will be implemented around the laser beam on the laser table on LVL5. This will further reduce disturbances caused acoustic wave fluctuations in air faster than the laser repetition rate of 10 Hz which are impossible to stop with the stabilization system.

ACKNOWLEDGMENT

We thank the Swedish research council under Project number DNR-828-2008-1093 for financial support.

REFERENCES

[1] Z. Huang et al., Phys. Rev. ST Accel. Beams 13 (2013) 020703
[2] S. Spampanati et al., Phys. Rev. ST Accel. Beams 17 (2014) 120705.
[3] M. Hamberg and V. Ziemann, TUPSO25, Proceedings of FEL2013, New York, NY, USA.
[4] M. Hamberg and V. Ziemann, THPRO024, Proceedings of IPAC2014, Dresden, Germany.

ISBN 978-3-95450-134-2

SIMULATION AND DESIGN OF LOW EMITTANCE RF ELECTRON GUN

C. Saisa-ard*, S. Rimjaem, Plasma and Beam Physics (PBP) Research Facility,
Department of Physics and Materials Science, Faculty of Science,
Chiang Mai University, Chiang Mai 50200, Thailand

Abstract

Generation of high-brightness electron beam is one of the most critical issues in development of advanced electron accelerators and light sources. At the Plasma and Beam Physics (PBP) Research Facility, Chiang Mai University, a low emittance RF electron gun is under the development. This RF-gun is planned to be used as an electron source for a future IR/THz FEL facility. An extra resonant cavity is added to the modified design of the existing PBP-CMU RF-gun in order to reduce the transverse sliced emittance. This cell is coupled to the main full-cell via a side-coupling cavity. The electromagnetic field distributions inside the cavities are simulated by using the CST Microwave Studio 2012@. Then, beam dynamic simulations utilizing the program PARMELA are performed. Both RF and beam dynamic simulation results are reported and discussed in this contribution.

INTRODUCTION

The high brightness electron beam is essential in development of the next generation electron accelerators and light sources. The brightness of electron beams depends on the beam peak current and 6-dimensional emittance. This characteristic requires the high quality beams emitting from the electron injector. An electron gun of the linac-based THz radiation source at the Plasma and Beam Physics (PBP) Research Facility, Chiang Mai University, is driven by a 7 MW-klystron at the resonant frequency of 2856 MHz. It consists of 1.6 cell S-band standing-wave structure and a tungsten dispenser thermionic cathode with Os/Ru coating. The present RF-gun design was optimized to produce electron beams with longitudinal distribution suitable for using an alpha magnet as a magnetic bunch compressor. Together with a downstream linac section and related beam transport components, electron beams with the bunch length in order of fermtosecond can be obtained [1]. In order to improve the transverse properties of electron beams, new modified design of the RF-gun is conducted [2]. The previous study results suggest that by adding TM_{010} pillbox cavity next to the main full-cell is able to reduce the sliced emittance and line up the sliced phase spaces [3].

In this work, an extra resonant cavity is added to the PBP-CMU RF electron gun to modify the dynamics of electrons. This extra cell is connected to the end of the full-cell and the RF power is coupled from the full cell to the extra cell via the side coupling cavity. The electromagnetic fields inside the resonant cavities are simulated by using the program CST Microwave Studio (MWS) 2012@ [4]. The dynamics of electrons under the influence of the electromagnetic fields are studied by using a particle tracking program PARMELA [5]. RF parameters of the cavities and beam dynamics study results of electron beams are the main points, which are presented and discussed here.

* chaipattana_s@cmu.ac.th

SIMULATION OF ELECTROMAGNETIC FIELDS

The PBP-CMU RF gun consists of two main cavities, which operates in $\pi/2$ mode for acceleration at the resonant frequency of 2856 MHz. The existing RF-gun has asymmetric shape due to side-coupling cavity opening holes and an RF waveguide input port, which lead to asymmetric beam distribution. By rotating the direction of the side-coupling cavity to vertical direction, the asymmetric feature of electron beams reduced [2]. In this research, an extra cell is added downstream the full cell and it is coupled via a side coupling cavity in vertical direction as shown in Fig. 1 and Fig. 2. The mode of acceleration is kept to be at $\pi/2$ mode and at this mode the resonant frequency of the whole gun is around 2857.3 MHz. The RF parameters for each cell are listed in Table 1.

The electromagnetic field distributions in each mode is solved by using the *Eigenmode Solver* feature in CST MWS. Only boundary conditions at the end of the RF input port and at the end of the extra cell are Dirichelet, otherwise the Neumann boundary conditions is used. The hexahedral mesh is chosen and the total number of mesh cells is 265,650. The amplitude of axial electric field ratio between each cell, which implies to energy gain, can be adjusted by moving tuning rod inside the side coupling cavity. The axial electric field distribution along the beam propagating direction is shown in Fig. 3. The peak field ratio between the cells shown, in Table 2, are adjusted for optimizing electron bunch compression using the alpha magnet, which will be discussed later in other report.

Table 1: RF Parameters of Each Cell at $\pi/2$-mode

RF parameters	half cell	full cell	extra cell
Resonant frequency (MHz)	2866.3	2876.0	2870.0
Shunt impedance (MΩ)	3.45	7.99	5.75
Power (W)	290.8	358.2	318.6
Stored energy (mJ)	0.225	0.378	0.257
R-upon-Q	248	419.34	392.5
Accelerating Voltage (MV)	2.11	2.65	2.63

ISBN 978-3-95450-134-2

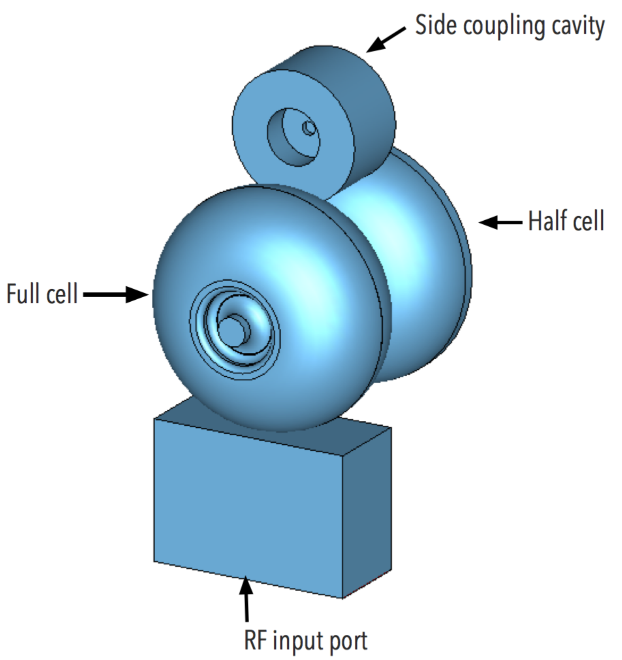

Figure 1: 3D CST MWS model of the thermionic RF-gun at the Plasma and Beam Physics Research Facility, Chiang Mai University.

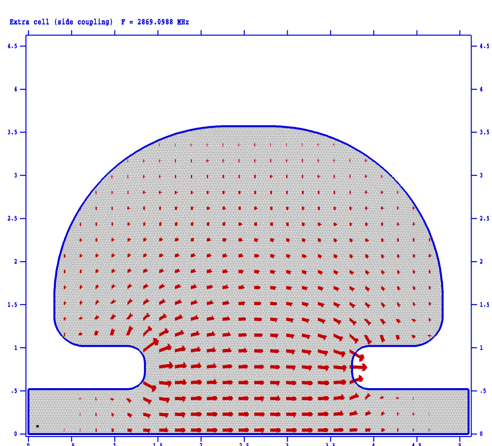

Figure 2: 2D internal geometry and SUPERFISH electric field vectors of the extra-cell (only half of the cell cross-section is shown here).

The axial electric field profile along z-axis can be investigated by varying the tuning rod position inside the side coupling cavity located between the full-cell and the extra-cell. By tuning the length of the tuning rod to be 1.15 mm, the peak field average field ratio between the cells are obtained as listed in Table 2.

BEAM DYNAMICS SIMULATIONS

The electromagnetic field distributions inside the new design RF-gun obtained from the program CST MWS and SUPERFISH [6] are used in the particle-in-cell program PARMELA. In simulations, 100,000 particles are assumed

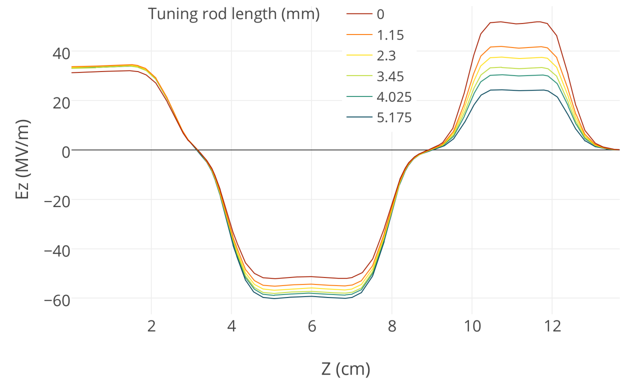

Figure 3: Axial peak electric field along z-direction inside the RF-gun

Table 2: The Peak and Average Field Ratios between Cells

Field ratio	full-cell / half-cell	full cell / extra cell
Peak field ratio	1.52	1.84
Average field ratio	1.59	1.31

to be uniformly emitted from a 3-mm radius thermionic cathode with a total beam current of 2.9 A. An initial energy of the reference particle is set to be 0.10971 eV, corresponding to the cathode temperature of 1,273 K. Energy spreads in both transverse and temporal directions are included in simulations.

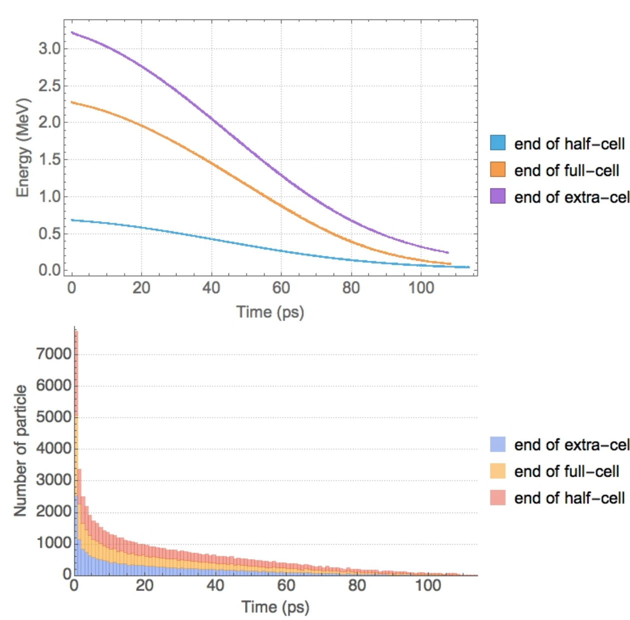

Figure 4: Longitudinal phase spaces and histograms at the ends of the half-cell, full-cell and extra-cell.

Longitudinal phase spaces and their temporal histograms at the ends of half-cell, full-cell and extra cell are shown in Fig. 4. Obviously, the electrons gain kinetic energy while they are moving inside the extra cell. However, it still has the

ISBN 978-3-95450-134-2

linear relation between energy and time at both directions, which is required for the bunch compression by using the alpha magnet.

Simulation results in the transverse direction at the end of the half-cell, full-cell and extra-cell are shown in Figs. 5–7. The vertical phase spaces at the ends of these three cells show asymmetric beam distributions due to non-symmetric magnetic fields in vertical direction (y-axis). This is caused by open holes at the side coupling cavity and the RF input port. The asymmetric beam distribution results in larger transverse beam emittance value and also leads to the off-center of the transverse beam profile.

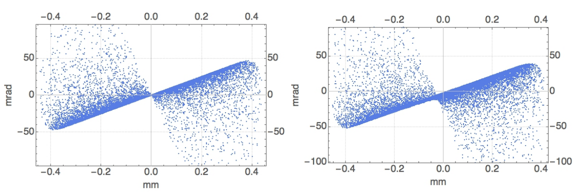

(a) x-axis (b) y-axis

Figure 5: Transverse phase spaces at the end of the half-cell

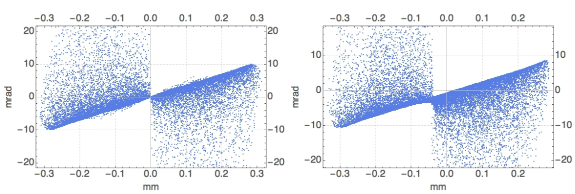

(a) x-axis (b) y-axis

Figure 6: Transverse phase spaces at the end of the full-cell

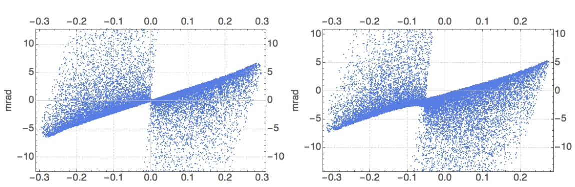

(a) x-axis (b) y-axis

Figure 7: Transverse phase spaces at the end of the extra-cell

The geometrical emittance can be calculated from $\epsilon = \sqrt{< t_i^2 >< (t_i')^2 > - < t_i t_i' >^2}$, where t_i and t_i' are the transverse positions (x or y) and their corresponding transverse momenta, respectively. The normal emittance is then be $\epsilon_n = \beta\gamma\epsilon$. The emittance values at the ends of full-cell and extra-cell are shown in the Table 3.

The sliced phase spaces are studied for the time periods of 0–10 ps and 10–20 ps along the bunch. The results at the ends of full-cell and extra-cell exits are compared in Fig. 8. The two sliced phase spaces at the end of the extra cell are more lined up than ones. The transverse projected emittance value for 90 % of high energetic beam for each time slice along the bunch are plotted in Fig. 9. It is clearly seen that at the tail of electron bunch with the time longer than 45 ps, the transverse projected emittance values at the end of the extra-cell are lower than the beam at the end of the full-cell. The number of electron within 45 ps is approximately 89.5% of the whole bunch.

Table 3: Transverse Emittance Values at The Ends of Full-Cell and Extra-cell

Exit of		**100% beam** x	**100% beam** y	**90% beam** x	**90% beam** y
ϵ (mm mrad)	full-cell	19.3	20.7	5.45	6.85
	extra-cell	9.6	10.4	3.57	4.75
ϵ_n (mm mrad)	full-cell	63.3	68.0	19.4	24.4
	extra-cell	46.5	50.4	18.6	24.8

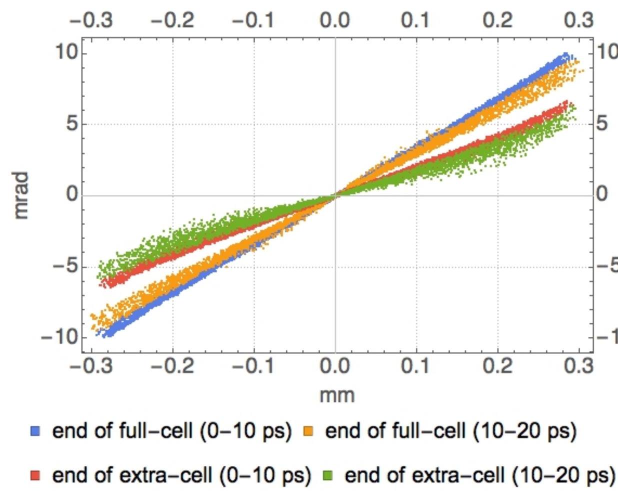

(a) x

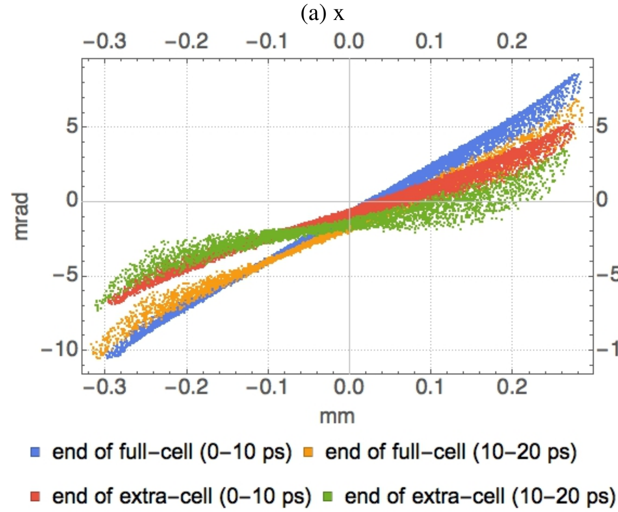

(b) y

Figure 8: The sliced phase spaces for the time periods of 0–10 ps and 10–20 ps along the bunch at the ends of full-cell and extra-cell.

CONCLUSION

Development of a new RF-gun at the PBP-CMU linac facility is on going. The design of the main accelerating

ISBN 978-3-95450-134-2

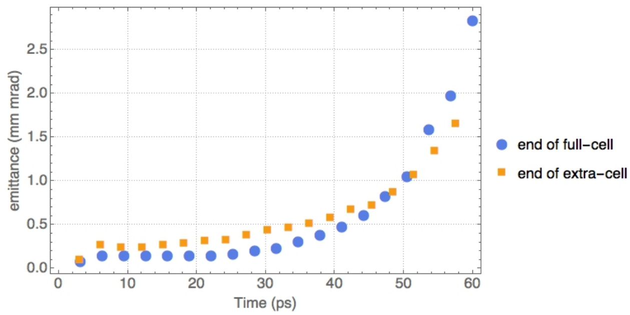

Figure 9: The sliced transverse emittance values, $\epsilon_{xy} = \sqrt{\epsilon_x \epsilon_y}$ along electron bunch at the ends of the full-cell and the extra-cell.

cavities is based on the first PBP-CMU RF-gun with RF-coupling in vertical direction for both RF input port and side-coupling cavity. The extra-cell is added to the full-cell to reduce the transverse emittance in both x and y directions. Although the force due to the electric field inside the extra-cell accelerates the beam, the linear relation between energy-time, which is necessary for bunch compression, still remains. The transverse projected emittance values at the end of the extra-cell are lower than at the end of the full-cell in both x and y directions. The sliced phase spaces within 0-10 ps and 10-20 ps for the x-direction at the extra-cell exit are more lined up than that y-direction.This is due to asymmetric vertical magnetic field distribution which is effected by the opening holes of the side coupling cavity. Furthermore, the sliced emittance values of the particles at the tail of the bunch (> 45 ps) at the end of the extra-cell are lower than that at the end of the full-cell. The trend of the growth of sliced emittance along the whole bunch at the end of extra-cell is also lower.

ACKNOWLEDGMENT

The authors would like to acknowledge the support from the CMU Junior Research Fellowship Program and the Department of Physics and Materials Science, Faculty of Science, Chiang Mai University.

REFERENCES

[1] C.Thongbai et al., Nucl. Instrum. Meth. A **587**, p. 130 (2008).

[2] S. Rimjaem et al., Nucl. Instrum. Meth. A **736**, p. 10 (2014).

[3] K. Kusoljariyakul et al., Nucl. Instrum. Meth. A **645**, p. 191 (2011).

[4] Microwave Studio, Computer Simulation Technology, Darmstadt, Germany. `http://www.cst.com`

[5] L.M. Young et al., PARMELA, Los Alamos National Laboratory Technical Note LA-UR-96-1835 (2002).

[6] K. Halbach et al., Part.Accel. **7**, p. 213 (1976).

SIMULTANEOUS OPERATION OF THREE LASER SYSTEMS AT THE FLASH PHOTOINJECTOR

S. Schreiber*, J. Roensch-Schulenburg, B. Steffen, C. Gruen, K. Klose, DESY, Hamburg, Germany

Abstract

The free-electron laser facility FLASH at DESY (Hamburg, Germany) operates two undulator beamlines simultaneously. Both undulator beamlines are driven by a common linear superconducting accelerator with a beam energy of up to 1.25 GeV. The superconducting technology allows the acceleration of trains of several hundred microsecond spaced bunches with a repetition rate of 10 Hz. A fast kickers-septum system is installed to distribute one part of the electron bunch train to FLASH1 and the other part to FLASH2 keeping the full 10 Hz repetition rate for both beamlines. In order to deliver different beam properties to each beamline, the FLASH photoinjector uses two independent laser systems to generate different bunch pattern and bunch charges. One laser serves the FLASH1 beamline, the other the FLASH2 beamline. A third laser with adjus ö laser pulse duration is used to generate ultra-short bunches for single spike lasing.

INTRODUCTION

FLASH [1–3], the free-electron laser (FEL) user facility at DESY (Hamburg) simultaneously operates two undulator beamlines [4–6]. It delivers high brilliance XUV and soft X-ray SASE radiation to photon experiments. FLASH is a user facility since 2005.

FLASH is a linear accelerator with a photoinjector followed by a superconducting linear accelerator. The maximum electron beam energy is 1.25 GeV, allowing SASE lasing down to 4 nm. The FLASH1 undulator beamline is in operation since 2004, the new FLASH2 beamline since 2014.

More details on the FLASH facility and its present status as well as on simultaneous operation of two beamlines can be found in these proceedings [3, 6].

A unique feature of FLASH is its superconducting accelerating technology. It allows to accelerate several thousand electron bunches per second. The bunches come in bursts with a repetition rate of 10 Hz. The maximal burst duration is 0.8 ms, the smallest distance between single bunches is 1 µs allowing a maximum number of 800 bunches per burst or 8000 bunches per second. FLASH has two undulator beamlines: FLASH1 and FLASH2. The burst of electron bunches is shared between them, keeping the 10 Hz repetition rate of the accelerator for each beamline.

An important and unique feature of FLASH is, that beam parameters and bunch pattern can vary for the two undulator beamlines: experiments with different wavelengths, pulse durations, and pulse pattern are possible at the same time.

The flexibility is realized with three main features. Firstly, variable gap undulators allow to adjust the wavelength for FLASH2 experiments, while the beam energy is determined by the wavelength required for FLASH1 lasing with its fixed gab undulators. Secondly, different photoinjector laser systems operated in parallel allow different charges, different pulse pattern, and to create a variable gap between the sub-bursts for FLASH1 and FLASH2. Thirdly, the low-level RF control of the accelerating structures are able to adjust phases and amplitudes – to a certain extend – independently for both beamlines, thus making different compression schemes possible. For details on FLASH2 photon beam parameters, the reader is referred to [4].

FLASH has three photoinjector lasers. Two lasers provide bursts of laser pulses with high single pulse energy but fixed single pulse duration. A third system has the feature of short and variable pulse duration optimized for high compression for ultra-short single spike SASE photon pulses.

The most promising method to achieve such short pulses is to compress the electron bunch to the femtosecond level. In the most extreme case the lasing part of the bunch is as short as one longitudinal optical mode. These so-called single-spike SASE pulses [7, 8] are bandwidth limited, longitudinally coherent.

In order to mitigate space charge forces, a low bunch charge of 20 pC is applied. It is generated at the gun by a short laser pulse of less than 1 ps (rms), thus substantially reducing the bunch compression factor required for bunch durations of a few femtoseconds only.

THE ELECTRON SOURCE

The electron source of FLASH is a photoinjector based on a normal conducting L-band 1.5 cell RF-gun. The gun is operated with an RF power of 5 MW at 1.3 GHz, corresponding to a maximal accelerating field at the cathode of 52 MV/m. The RF pulse duration is up to 850 µs, sufficient for generation of the required bunch trains of 800 µs duration. The repetition rate is 10 Hz. The beam momentum at the gun exit is 5.6 MeV/c.

As discussed in the introduction, the RF pulse length of the gun is adapted to the high duty cycle of the superconducting accelerator.

FLASH can accelerate many thousands of electron bunches per second. In order to keep the average power of the laser system reasonably small, a photocathode with a high quantum efficiency is used.

Cesium telluride has been proven to be a reliable and stable cathode material with a quantum efficiency above 5 % for a wavelength around 260 nm. The lifetime is more than 400 days of continuous operation [9]. The bunch charge

* siegfried.schreiber@desy.de

ISBN 978-3-95450-134-2

required for FLASH SASE operation is between 20 pC and a bit more than 1 nC. Assuming a very conservative quantum efficiency of the cathode of 0.5 %, a laser pulse energy of not more then 1 µJ on the cathode is sufficient to produce a 1 nC electron bunch. For 8000 bunches per second this corresponds to a reasonable intra train power of 1 W (0.8 ms burst) and an average power of 8 mW at 262 nm.

A challenge for the laser system is its burst mode structure with 0.8 ms long flat bursts of laser pulses. In addition, the picosecond long pulses must be synchronized to the RF of the accelerator to the 100 fs level.

THE LASER SYSTEMS

Laser 1 and Laser 2

The two laser systems [10] described in this section have been installed in 2010 [11] and 2012, and are a substantial upgrade compared to the previous lasers in operation at FLASH and the former TESLA Test facility (TTF) [12, 13]. The lasers have been developed in the Max Born Institute, partially tested at DESY, Zeuthen at PITZ and finally installed at FLASH.

Both lasers are used to drive the FLASH1 and FLASH2 beamlines for user runs. Both lasers can run for either beamline and also on the same beamline simultaneously, and also serve as a backup system for the other.

The layout of both lasers are very similar. Both systems consist of a pulsed laser oscillator with subsequent amplification stages. Figure 1 shows a schematic overview. A recent description of the laser systems can be found in [14], where the upgrade plans now realized have been described. The laser material chosen is Nd:YLF, lasing at a wavelength of 1047 nm. The material has together with a high gain, a long upper-state lifetime of 480 µs, and exhibits only a weak thermal lensing. This makes it suitable to produce pulse trains with milliseconds duration. After amplification, the wavelength is converted in two steps using an LBO and BBO crystal to the UV wavelength of 262 nm. Figure 2 shows an example of a scope trace of laser pulse trains.

The laser is equipped with two Pockels cell based pulse pickers before and after the pre-amplification stages. The one before the preamplifier is operated at a constant 1 MHz, the second just before the last high power amplifiers are used by the operator to control the number and distance of pulses per train – according to the requirements determined by the experiment of the facility. The protection system of the accelerator acts on the laser to realize an emergency switch-off of the electron beam.

In addition to the Pockels-cell based pickers in the IR, a new UV pulse picker is being tested based on an acousto-optic modulator [15].

For details on the pulse train oscillator [13] and amplification stages, the reader is referred to [10, 14]. Table 1 summarizes the pulse parameters for the lasers.

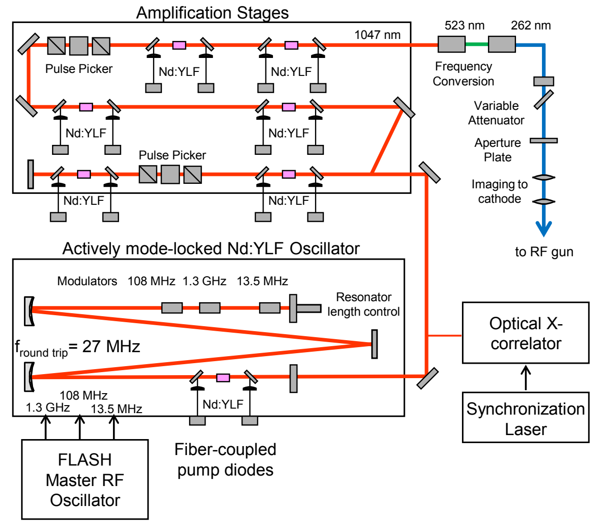

Figure 1: Schematic overview of laser 2 [14]. The oscillator and amplifiers are pulsed with 10 Hz, pulses are a few milliseconds long. The laser 1 amplification stages are very similar. Laser 1 has a shorter oscillator operating at 108 MHz using a 54 MHz AOM and a 1.3 GHz EOM.

Laser 3

Laser 3 has been installed and commissioned in 2013 [16]. The laser system consists of an oscillator [17] and a Yb:YAG amplifier [18]. The oscillator provides 400 fs pulses at 1030 nm with a repetition rate of 54 MHz. An acousto-optic modulator (AOM) picks with 1 MHz before final amplification to nominal 10 W average output power. The single pulse energy is about 10 µJ at 1030 nm. A second AOM picker before wavelength conversion is used by the operator to adjust the number and distance of pulses sent to the RF gun.

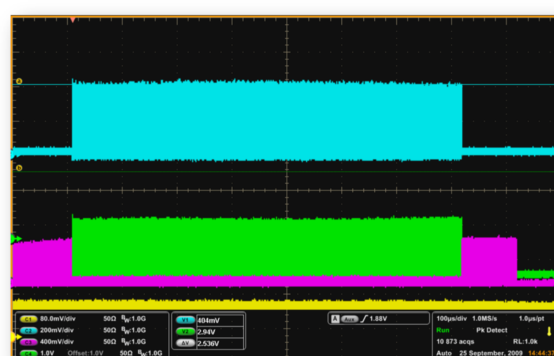

Figure 2: Example of a train of laser pulses [14]. The oscilloscope traces show the pulse train of the 27 MHz oscillator (yellow trace), after preamplification (3 MHz, wavelength 1047 nm, magenta), after conversion to 523 nm (3 MHz, 523 nm, green), and after conversion to the UV (3 MHz, 262 nm, blue). The time scale is 100 µs per division. Neither the 27 MHz nor the 3 MHz pulse structure is not resolved. Usually the laser is operated in the 1 MHz mode.

ISBN 978-3-95450-134-2

Frequency conversion is obtained with an LBO to the green, and with a BBO crystal to the UV (257.5 nm). The efficiency is 10 %; additional losses are due to the pulse stretcher and the transverse beam shaping. Overall, the pulse energy is sufficient for for electron bunch charges up to 200 pC.

Pulse Duration

The lasers do not apply longitudinal beam shaping, thus the longitudinal shape is close to a Gaussian. The duration of the UV-pulse is measured with a streak camera [19]. The measured pulse duration is $\sigma = 4.5 \pm 0.1$ ps for laser 1 and 6.5 ± 0.1 ps for laser 2 (sigma of a Gaussian fit). The pulse duration difference is due to their different laser oscillator.

The special feature of laser 3 is its adjustable pulse duration. The initial 800 fs long UV pulses are stretched by two transmissive gratings with 4000 lines per cm. A pulse duration between $\sigma = 0.8$ and 1.6 ps is adjustable.

Energy Control and Recombination Technique

The pulse energy is adjusted by two remote controlled attenuators. One attenuator is used by a feedback system to compensate for slow drifts in pulse energy, the other by the operators of FLASH to adjust the electron bunch charge emitted at the cathode.

The attenuators consist of a remote controlled half-wave plate together with Brewster angle polarizer plate.

These type of polarizer plates are also used to combine the three lasers into one common beamline. With a similar technique, pulse stacking [20] and double pulses by the split and delay technique are produced for certain experiments [21]. The Brewster angle polarizer plate is a thin coated fused silica plate oriented at the Brewster angle of 56°, transmitting 94 % of the p-polarization and reflecting 99.7 % of the s-polarization component.

The incoming UV laser pulse is linear polarized. The half-wave plate turns the polarization angle to the desired value while the polarizer transmits the p-polarized state only. For split and delay units, the relative intensities of the transmitted and the reflected beam are also adjusted with a remote controlled half-wave plate.

Combination of two laser pulses into one beamline – either from two laser systems or after the split and delay-unit –, are done in a similar way simply reversing the beam direction. The advantage of Brewster plate polarizers compared to polarizing independent beam splitters is that the recombination avoids the usual 50 % beam loss.

Beamline

Lasers 1 and 2 consequently use relay imaging together with spatial filtering. All amplification stages are imaged to the next amplifier head, and then to the frequency conversion crystals, followed by the last spatial filter in the UV.

The laser beam is then expanded and collimated to overfill a beam shaping aperture (BSA). A set of remotely controlled hard edge apertures of various sizes can be put into the laser beam. Usually an aperture size of 1.2 mm in diameter is used. Finally, the pulse shaping aperture is imaged onto the cathode of the RF-gun. The beam shaping aperture produces a quasi flat truncated Gaussian pulse on the cathode with negligible pointing jitter.

The laser beamline from the BSA to the cathode has a horizontal geometry with a length of about 5 m and traverses the radiation shielding of the accelerator. The beamline is sealed in tubes which are not evacuated. A quartz window separates the laser hutch with the tunnel to avoid air flows in the tubes. Finally, a fused silica vacuum window is followed by an all metal in vacuum mirror with an optically polished surface and and an enhanced UV-reflectivity. The cathode is hit under a small angle of 3°. Using linear translation stages the laser beam can be moved and aligned on the cathode with a precision of better than 10 µm. The laser beam can be deflected to a so-called virtual cathode, a Ce:YAG scintillator screen placed at the exact distance as the photo cathode.

Table 1: Main Parameters for the Photoinjector Laser Systems. Some parameters are adjustable and are set according to the requirements of the specific experiment.

Item	**Laser 1**	**Laser 2**	**Laser 3**
Laser material	Nd:YLF		Yb:YAG
Wavelength	1047 nm		1030 nm
4th harmonic	261.7 nm		257.5 nm
Train repetition rate	10 Hz		
Max. train duration	800 µs		
Intra-train rate	1 MHz (*)		
Pulses per train	1 – 800		
Pulse energy UV	50 µJ		1 µJ
Average power (IR)	2 W		10 W
Arrival time jitter	60 fs (rms)		—
Longitudinal shape	Gaussian		
Pulse duration (σ)	4.5±0.1 ps	6.5±0.1 ps	0.8–1.6 ps
Transverse profile	flat, truncated Gaussian		
Spot size on cathode	1.2 mm diam. ($^+$)		0.8 mm ($^+$)
Charge stability	0.5% rms		1% rms

* also: 500, 250, 200, 100, 50, or 40 kHz; 3 MHz optional
$^+$ truncated Gaussian; 15 different diameters are available

Combining the Lasers into One Beamline for Simultaneous Operation

Figure 3 shows how the laser beams of all three lasers are combined to one beamline. The Brewster plate polarizers are used for this purpose. Laser 1 is s-polarized and reflected by combiner 1 into the beamline of laser 2, which is p-polarized. Laser 3 is injected in a similar way using combiner 2.

Since laser 1 and laser 2 exhibit s- and p-polarization resp., a half wave plate turns the polarization state of both lasers such that both lasers are transmitted by combiner 2. The energy loss for lasers 1 and 2 is acceptable. This would not be the case for laser 3.

Combiner 2 is mounted on a translation stage and can be completely removed from the beamline if required. A

ISBN 978-3-95450-134-2

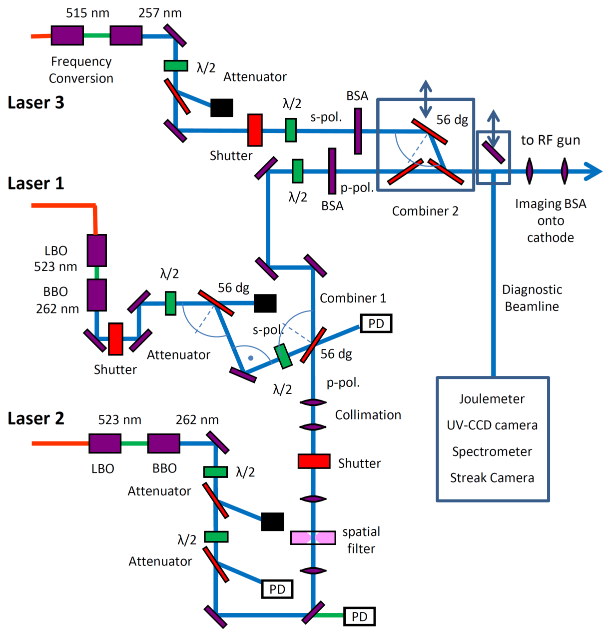

Figure 3: Beamline to combine all three laser systems. See explanations in the text.

second plate compensates the lateral shift of the polarizer plate. Laser 1 and laser 2 have the same beam shaping aperture (BSA), laser 3 has its own. The position of the BSA plates are such, that the aperture is imaged onto the photo cathode.

A diagnostic beamline features various instruments, a joulemeter, a UV enhanced CCD-camera, a spectrometer, and a streak camera.

SIMULTANEOUS OPERATION FLASH1 AND FLASH2

To allow different photon pulse pattern simultaneously for both FLASH undulator beamlines, two laser systems are used to serve FLASH1 and FLASH2. This is usually laser 1 and laser 2.

For operational reasons and the realization of different bunch pattern and charge, using two laser systems is a straightforward solution. An alternative would be to use a flexible pulse picker in the UV as described in [15] controlling the number of pulses, the amplitudes, and the distance independently for both beamlines. Such a pulse picker is in preparation.

As discussed above, FLASH operates with 0.8 ms long RF-pulse. The first part of the RF-pulse is used for FLASH1, the second part for FLASH2 (or vice versa). Between the sub-trains, a gap of 50 µs allows for the transition time of the kicker-septum system and the low level RF system to adjust (see Fig. 4).

For certain experiments, the short pulse laser 3 can be diploid to either of the two beamlines or in parallel with laser 1 or laser 2. This is done for example for experiments to generate ultra-short single-spike SASE pulses [22].

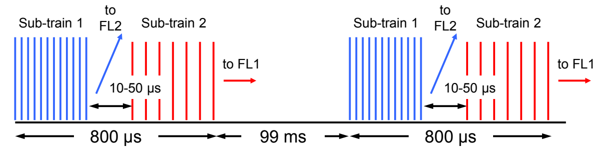

Figure 4: Bunch train sharing between FLASH1 (FL1) and FLASH2 (FL2): one RF pulse (10 Hz repetition rate) is shared by two sub-bunch trains. One train goes to FLASH1, the other is kicked to FLASH2. The sub-trains may have different bunch pattern or charge.

In the near future, FLASH will be equipped with a 3rd beamline, operated simultaneously in a similar way.

CONCLUSION

The three photoinjector laser systems are operated at the same time simultaneously to produce flexible electron bunch pattern for the FLASH beamlines, FLASH1 and FLASH2, and in the future also FLASH3.

ACKNOWLEDGMENT

We like to thank our colleagues from DESY and MBI, Berlin for their valuable and constant support.

REFERENCES

[1] W. Ackermann *et al.*, “Operation of a free-electron laser from the extreme ultraviolet to the water window”, Nature Photonics **1**, 336 (2007).

[2] K. Tiedtke *et al.*, “The soft x-ray free-electron laser FLASH at DESY: beamlines, diagnostics and end-stations”, New J. Phys. **11**, 023029 (2009).

[3] K. Honkavaara *et al.*, “Status of the Soft X-ray User Facility FLASH”, in *These Proceedings: Proc. 37th Int. Free-Electron Laser Conf.*, Daejeon, Korea, 2015, MOP014.

[4] B. Faatz *et al.*, “FLASH II: Perspectives and challenges”, Nucl. Instr. Meth. A **635**, S2 (2011).

[5] K. Honkavaara *et al.*, “FLASH: First Soft X-ray FEL Operating Two Undulator Beamlines Simultaneously”, in *Proc. 36th Int. Free-Electron Laser Conf.*, Basel, Switzerland, 2014, WEB05.

[6] M. Scholz *et al.*, “First Simultaneous Operation of Two SASE Beamlines in FLASH”, in *These Proceedings: Proc. 37th Int. Free-Electron Laser Conf.*, Daejeon, Korea, 2015, TUA04.

[7] R. Bonifacio, L. De Salvo, P. Pierini, N. Piovella, and C. Pellegrini, “Spectrum, temporal structure, and fluctuations in a high-gain free-electron laser starting from noise”, Phys. Rev. Lett. **73**, 70 (1994).

[8] J.B. Rosenzweig *et al.*, “Generation of ultra-short, high brightness electron beams for single-spike SASE FEL operation”, Nucl. Instr. Meth. A **593**, 39 (2008).

[9] S. Schreiber *et al.*, “Lifetime of Cs2Te Cathodes Operated at the FLASH Facility”, in *These Proceedings: Proc. 37th Int. Free-Electron Laser Conf.*, Daejeon, Korea, 2015, TUP042.

[10] I. Will, H.I. Templin, S. Schreiber, and W. Sandner, "Photoinjector drive laser of the FLASH FEL", Optics Express **19**, 23770 (2011).

[11] S. Schreiber *et al.*, "Operation of the FLASH Photoinjector Laser System", in *Proc. 33th Int. Free-Electron Laser Conf.*, Shanghai, China, 2011, p. 507.

[12] S. Schreiber, D. Sertore, I. Will, A. Liero, and W. Sandner, "Running experience with the laser system for the RF-gun based injector at the TESLA Test Facility linac", Nucl. Instr. Meth. A **445**, 427 (2000).

[13] I. Will, G. Koss, and I. Templin, "The upgraded photocathode laser of the TESLA Test Facility", Nucl. Instr. Meth. A **541**, 467 (2005).

[14] S. Schreiber *et al.*, "Upgrades of the Photoinjector Laser System at FLASH", in *Proc. 34th Int. Free-Electron Laser Conf.*, Nara, Japan, 2012, p. 385 (WEPD08).

[15] M. Gross *et al.*, "Laser Pulse Train Management with an Acousto-optic Modulator", in *Proc. 34th Int. Free-Electron Laser Conf.*, Nara, Japan, 2012, p. 189 (MOPD61).

[16] T. Plath *et al.*, "Commissioning and Diagnostics Development for the New Short-Pulse Injector Laser at FLASH", in *Proc. 2nd International Beam Instrumentation Conf.*, Oxford, United Kingdom, 2013, p. 353 (TUPC03).

[17] Origami 10XP by Onefive GmbH, Zurich, Switzerland, `http://www.onefive.com`

[18] Amplifer by AMPHOS, Aachen, Germany, `http://www.amphos.de`

[19] Femtosecond streak camera C6138 (FESCA-200), Hamamatsu Photonics K.K., Hamamatsu, Japan.

[20] S. Schreiber, "Pulse Stacker for the Photoinjector Laser System", in *Proc. TESLA Collaboration Meeting*, Zeuthen, Germany, Jan 21-23, 2004, WG3, `http://www-zeuthen.desy.de/tesla2004/agenda_wg3.html`

[21] O. Grimm, K. Klose, and S. Schreiber, "Double-pulse Generation with the FLASH Injector Laser for Pump/Probe Experiments", in *Proc. 10th European Particle Accelerator Conf.*, Edinburgh, Scotland, 2006, p. 3143 (THPCH150).

[22] J. Roensch-Schulenburg *et al.*, "Operation of FLASH with short SASE-FEL Radiation Pulses", in *Proc. 36th Int. Free-Electron Laser Conf.*, Basel, Switzerland, 2014, p. 342 (TUB04).

ISBN 978-3-95450-134-2

LIFETIME OF Cs_2Te CATHODES OPERATED AT THE FLASH FACILITY

S. Schreiber#, S. Lederer, DESY, Hamburg, Germany

Abstract

The injector of the free-electron laser facility FLASH at DESY (Hamburg, Germany) uses Cs_2Te photocathodes. We report on the lifetime, quantum efficiency (QE), and darkcurrent of photocathodes operated at FLASH during the last year. Cathode 618.3 has been operated for a record of 439 days with a stable QE in the order of 3 %. The fresh cathode 73.3 shows an enhancement of emitted electrons for a few microseconds of a 1 MHz pulse train.

INTRODUCTION

FLASH [1–3], the free-electron laser (FEL) user facility at DESY (Hamburg) delivers high brilliance XUV and soft X-ray SASE radiation to photon experiments. FLASH is a user facility since 2005.

The maximum electron beam energy is 1.25 GeV, allowing SASE lasing down to 4 nm. The FLASH1 undulator beamline is in operation since 2004, a new FLASH2 beamline since 2014. More details on the FLASH facility and its present status as well as on simultaneous operation of two beamlines can be found in these proceedings [3, 4].

A unique feature of FLASH is its superconducting accelerating technology. It allows to accelerate several thousand electron bunches per second. The bunches come in bursts with a repetition rate of 10 Hz. The maximal burst duration is 0.8 ms, the smallest distance between single bunches is 1 µs allowing a maximum number of 800 bunches per burst or 8000 bunches per second.

THE ELECTRON SOURCE

The electron source of FLASH is a photoinjector based on a normal conducting L-band 1.5 cell RF-gun. The gun is operated with an RF power of 5 MW at 1.3 GHz, corresponding to a maximal accelerating field at the cathode of 52 MV/m. The RF pulse duration is up to 850 µs, sufficient for generation of the required bunch trains of 800 µs duration. The repetition rate is 10 Hz. The beam momentum at the gun exit is 5.6 MeV/c.

As discussed in the introduction, FLASH can accelerate many thousands of electron bunches per second. In order to keep the average power of the laser system reasonably small, a photocathode with a high quantum efficiency is used.

Cesium telluride (Cs_2Te) has been proven to be a reliable and stable cathode material with a good quantum efficiency (QE) for a wavelength around 260 nm [5, 6]. The bunch charge required for FLASH SASE operation is between 20 pC and a bit more than 1 nC. For a QE of 5 %, a single laser pulse of 100 nJ at 262 nm produces a charge of 1 nC (linear regime). For a burst of 800 pulses with 1 MHz and 10 bursts per second, this corresponds to a burst power of 100 mW and an overall average power of 0.8 mW. With a laser pulse duration of 6.5 ps (rms), the peak power is 80 kW. These are all reasonable low numbers to avoid damage or ablations of the cathode thin film or of laser beamline components. For details on the FLASH injector laser systems, the reader is referred to [7] and references therein.

siegfried.schreiber@desy.de

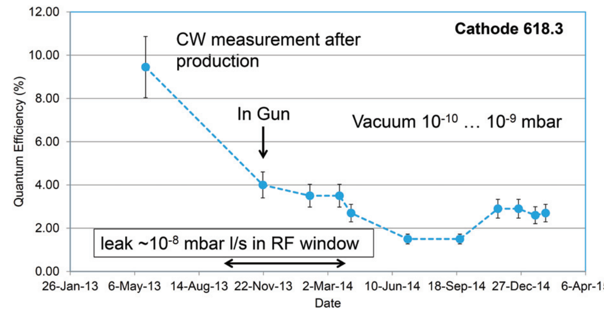

Figure 1: Quantum efficiency of cathode 618.3 during operation at FLASH.

QUANTUM EFFICIENCY

For practical reasons, we define the quantum efficiency (QE) as the ratio of the numbers of photons impinging the photocathode and the number of electrons emitted – while the RF-gun is operated at its nominal working point. The extracted charge is measured with a calibrated toroid at the RF-gun exit, the laser energy with a calibrated joulemeter [8] in front of the vacuum window. The transmission of the quartz window and the reflectivity of the in-vacuum mirror is taken into account. Finally the QE is obtained by a linear fit of the charge as a function of laser energy – before space charge effects saturate the emission. For an example of such a fit, the reader is referred for instance to [9, 10].

The nominal working point of the RF-gun is at an accelerating field of 52 MV/m (on-crest) and a launch phase of 38° from the zero-crossing point. This phase has been chosen years ago and has been kept as a reference since then. The launch phase for maximum energy gain and minimum energy spread is 45° and is used for SASE operation.

Longterm Operation of a Cs_2Te Cathode

Figure 1 shows the quantum efficiency of cathode 618.3 during operation at FLASH for a period of 439 days. The cathode has been produced with the usual recipe. A thin film of Cs_2Te with a diameter of 5 mm is deposited on a polished molybdenum plug. Figure 2 shows a photo of the cathode. For details on the production of cathodes see [10, 11].

The QE is always measured at the center of the cathode with RF-gun operation parameters as discussed above. Figure 1 also shows the QE measured just after production with a Hg-lamp at the preparation chamber. During operation in

ISBN 978-3-95450-134-2

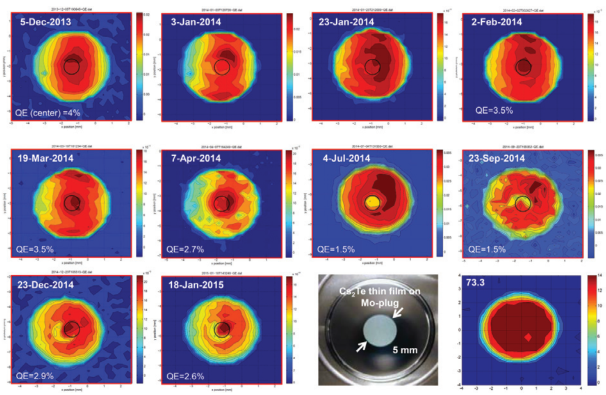

Figure 2: QE-map evolution of cathode 618.3 from December 2013 to January 2015. Each map shows the measured charge as a function of the horizontal and vertical position of the laser beam spot on the cathode surface. The charge is color coded and is given in nC. The maximum charge is adjusted to 20 to 30 pC. The cathode diameter is 5 mm. The black circle indicated the approximate size and position of the laser beam during beam operation. The QE measured in the center of the cathode is indicated at the lower left corner of each map and is also shown in Fig. 1. In the lower right corner we show as an example the inital QE-map of cathode 73.3 right after production and a photo of the cathode plug with the thin film cathode visible by the light blue color.

October 2013, the RF-window of the RF-gun developed a small leak to air of 10^{-8} mbar l/s. The leak had only been discovered later and was repaired in April 2014 by exchanging the RF-window.

This explains the low but stable quantum efficiency around a good 3 %. During conditioning time of the new window from April to June 2014 the QE dropped to 2 % and recovered later due to the improved vacuum pressure when a stable operation with the new window has been achieved. Previous studies have shown, that the QE strongly depends on vacuum conditions [12]. The total amount of charge extracted by this cathode is 3.2 C.

QE-Map Evolution

A QE-map is obtained by scanning a laser beam with constant energy over the cathode. The size of the laser beam is 100 µm in diameter obtained with a hard edge aperture imaged onto the cathode. The scanning step size is 85 µm. We use absolutely calibrated linear translation stages moving beamline mirrors in horizontal and vertical direction. For each scan point, the average charge of a train of 30 bunches is measured with a toroid right after the gun, averaged over 5 trains. The charge is adjusted to 20 to 30 pC, small enough to avoid space charge related saturation effects.

Figure 2 shows a series of QE-maps measured during the 439 days of operation of cathode 618.3 in the RF-gun. The slight left-right QE reduction visible at most maps is due to the narrow aperture of 5 mm of the in-vacuum mirror in horizontal direction. The overall picture is, that initially the QE degrades faster at the cathode center where the laser hits. The surrounding QE reduces slowly but steadily, where the center part recovers. Due to the vacuum conditions, we expected a slow reduction of the overall QE. The recovering of the QE at the center might be explained by laser cleaning effects.

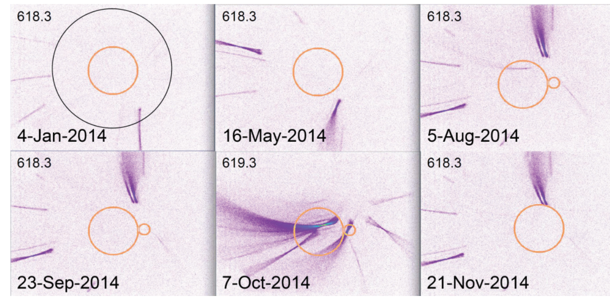

Figure 3: Darkcurrent of the RF-gun with cathode 618.3 and 619.3 measured with a Ce:YAG powder screen during operation in 2014. The red circle indicates the position of the Cs_2Te film, the black circle the rim of the cathode. The streaks are due to the solenoid field. Pictures were taken under normal operating conditions of the gun (see text).

DARKCURRENT

Darkcurrent is usually emitted by particles on the cathode or defects of the copper structure close or at the RF-contact spring [13, 14]. The RF-gun has been cleaned with dry-ice reducing the darkcurrent emitted at the gun backplane by an order of magnitude. Most of the residual darkcurrent is due to particles on the cathode plug surface.

The cathode is produced in the preparation chamber, either at LASA (cathode 73.3) or DESY (cathode 618.3), put into a transport box keeping ultra-high vacuum conditions. The transport box is shipped to FLASH where it is connected to the cathode load-lock system, pulled out of the carrier and inserted into the gun. During operation, whenever for example titan sublimation pumps are activated, the cathode has to be pulled back from the gun. Due to these frequent handling of the cathode plug, particles may appear and also disappear.

Figure 3 shows several images of darkcurrent taken from January 2014 to November 2014 with cathode 618.3 and one image with cathode 619.3. The images are taken with a Ce:YAG powder screen 1.6 m from the cathode downstream the RF-gun. The RF-gun was operated with standard parameters: with a field of 52 MV/m on the cathode (on-crest), an RF-pulse length of 500 µs, and a solenoid focusing field of 180 mT. Since the emitted darkcurrent has a large energy spread, streaks develop due to the focusing solenoid field. The camera settings and RF-pulse length have been equal for all images of cathode 618.3, so that the relative strength of the darkcurrent emitter can be compared. The image for cathode 619.3 has been taken with a by a factor of 10 reduced pulse length of 60 µs. The absolute darkcurrent measured with a Faraday cup (same size as the screen) is 5 µA. During

ISBN 978-3-95450-134-2

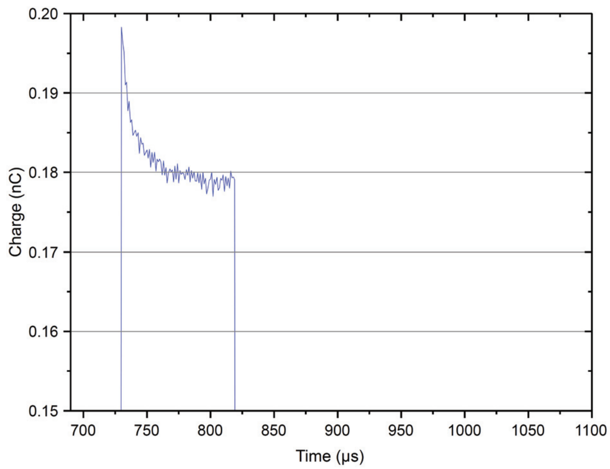

Figure 4: Measured charge along the electron bunch train for a flat laser pulse train as shown in Fig. 5. The bunch to bunch distance is 1 us.

standard operation the amount of darkcurrent entering the linac is reduced with a resonant kicker operating at 1 MHz together with a circular collimator.

The images show, that new emitters have been appearing in May 2014 and Aug 2014. The emitter from May disappeared shortly, the emitter from August stayed at a constant level.

Cathode 619.3 from the same production batch shows, that cathodes might actually be contaminated by emitters (Fig. 3). Cathode 619.3 emitted a darkcurrent of 20 µA and has therefore not been used for beam operation.

EMISSION ISSUE

Cathode 618.3 has been replaced by cathode 73.3 in February 2015. The motivation for the change was to test a fresh cathode. Certainly cathode 618.3 could have been operated for much longer than 439 days.

As already observed earlier, fresh cathodes do not emit uniformly along a bunch train. Figure 4 shows a non-flat emission of a 1 MHz pulse train – even though the laser pulse energy was flat along the train (Fig. 5). More charge is emitted for the first bunch and then drops within a few microseconds by 10 % and stays flat until the end of the bunch train. Assuming an exponential decay $Q(t) = Q_0 \exp(-t/\tau)$, the decay rate is $\tau = 10\,\mu s$. As said, the distance of the bunches within the train is 1 µs.

In this section, we show, that the enhanced emission is due to the emission process of the cathode and is not related to an artifact of the laser nor the accelerating field amplitude or phase of the RF-gun.

To exclude an effect of the RF-field, we shifted the laser pulse train along the RF-pulse by more than 100 µs. No change of the spike could be observed.

To exclude an artifact of the laser pulse train, we used two independent laser systems, laser 1 and laser 2. Both lasers have been adjusted to have a flat pulse train measured

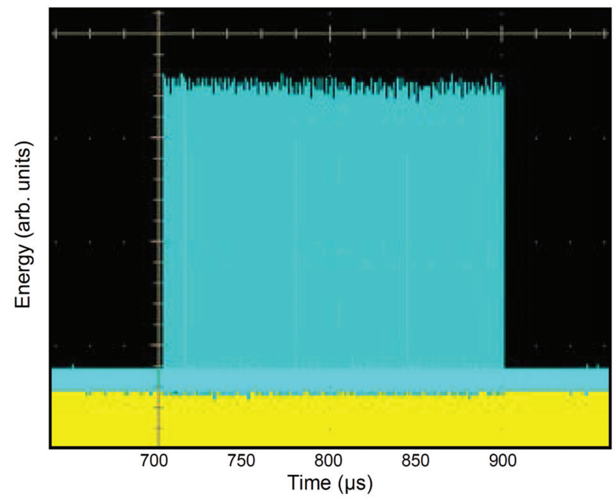

Figure 5: Oscilloscope trace of the laser pulse train used in this experiment. The spacing of the individual pulses is 1 µs (1 MHz), the train length is variable, in this example 200 µs. The wavelength is 262 nm. The laser pulse energy is measured with a UV sensitive photodiode.

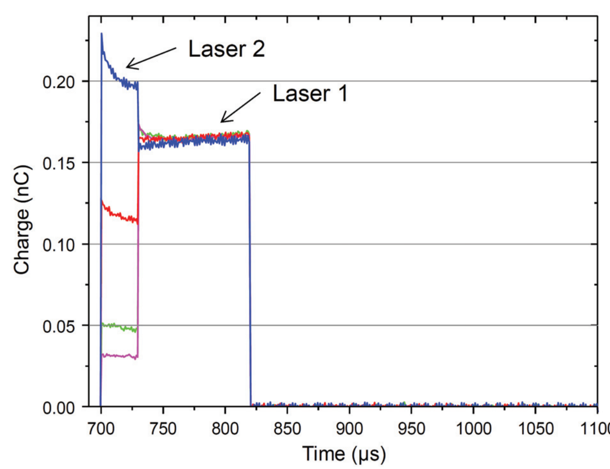

Figure 6: Measured charge along the pulse train generated by two independent laser systems, laser 1 and laser 2. The bunch distance is 1 µs. Initially, the electron bunches created by laser 2 show the emission spike, while the bunches generated by laser 1 not. The charge for laser 1 is intentionally reduced to show this effect. Gradually reducing the laser 2 pulse energy reduces the emission spike for laser 2 and enhances the spike for laser 1 (note : the color changes from blue, red, green to magenta). With laser 2 switched off (not in this plot), the emission spike by laser 1 is exactly the same as for laser 2 (Fig. 4).

ISBN 978-3-95450-134-2

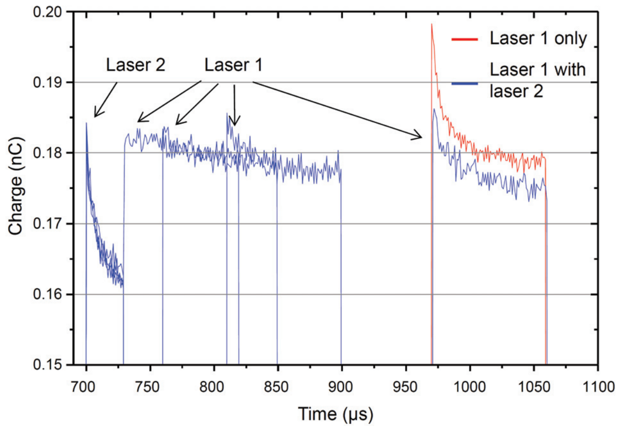

Figure 7: Measured charge along the pulse train generated by two independent laser systems, laser 1 and laser 2 (blue). The bunch distance within the train is 1 µs. The electron bunches created by laser 2 show the emission spike, while the bunches generated by laser 1 – when attached to the laser 2 train – not. Gradually shifting laser 1 in time away from laser 2 enhances the spike for laser 1. After a shift of 250 µs the spike generated by laser 1 is almost as pronounced as if laser 2 was switched off (red).

by a UV-sensitive fast photodiode using an oscilloscope as shown in Fig. 5. For both lasers alone, the emission spike appears as in Fig. 4.

To exclude a measurement artifact with the photodiode, we used both lasers at the same time. Laser 2 starts at 700 µs (an arbitrary chosen starting time but within the flat top of the RF-gun pulse) with a flat-top length of 30 µs and with a 1 µs bunch to bunch distance (1 MHz) – long enough to develop the decaying emission spike. Laser 1 runs also at 1 MHz with a longer pulse train of 100 µs.

The trick is, that laser 1 starts just where the laser 2 train ends, at 730 µs. With laser 2 switched on, the electron emission for laser 1 is flat! However, switching laser 2 off, the emission spike now appears for laser 1.

Figure 6 shows this effect: when the energy of laser 2 is gradually decreased, the laser 2 pulse train flattens and at the same time, the emission spike appears for laser 1. This excludes an effect of the lasers and shows, that the enhanced emission is due to a yet unknown property of the emission process of the cathode.

Keeping laser 2 on, and delaying laser 1 further in respect to laser 2, an emission spike for laser 1 appears step by step and is almost fully exploited after a delay of 250 µs (Fig. 7).

Further observations are, that laser 2 can only switch the emission spike for laser 1 off as in Fig. 6, if the charge of laser 2 is actuality extracted. Moving the start of the RF-field exactly between laser 2 and laser 1, the emission spike now appears for laser 1 (laser 2 does not emit electrons).

Another observation is, that reducing the accelerating field of the RF-gun from 52 MV/m below 20 MV/m, the enhanced emission is gone.

A last important finding is that the decay time of the enhanced emission at the beginning of the bunch train increases slowly with time, in other words, the trains become flatter. After 4 months of continuous operation, the decay time of the enhanced emission increased from the initial $\tau = 10\,\mu\mathrm{s}$ to 130 µs.

ACKNOWLEDGMENT

Besides our colleagues from LASA, Milan, and DESY Hamburg and Zeuthen we like to especially acknowledge C. Grün, DESY for his help in timing the laser systems and L. Monaco, LASA for producing cathode 73.3.

REFERENCES

[1] W. Ackermann *et al.*, "Operation of a free-electron laser from the extreme ultraviolet to the water window", Nature Photonics **1**, 336 (2007).

[2] K. Tiedtke *et al.*, "The soft x-ray free-electron laser FLASH at DESY: beamlines, diagnostics and end-stations", New J. Phys. **11**, 023029 (2009).

[3] K. Honkavaara *et al.*, "Status of the Soft X-ray User Facility FLASH", in *These Proceedings: Proc. 37th Int. Free Electron Laser Conf.*, Daejeon, Korea, 2015, MOP014.

[4] M. Scholz *et al.*, "First Simultaneous Operation of Two SASE Beamlines in FLASH", in *These Proceedings: Proc. 37th Int. Free Electron Laser Conf.*, Daejeon, Korea, 2015, TUA04.

[5] D. Sertore *et al.*, "First operation of cesium telluride photocathodes in the TTF injector RF gun", Nucl. Instr. Meth. A **445**, 422 (2000).

[6] S. Schreiber *et al.*, "On the Photocathodes used at the TTF Photoinjector", in *Proc. 2003 Particle Acc. Conf.* , Portland, Oregon, USA, 2003, p. 2071.

[7] S. Schreiber *et al.*, "Simultaneous Operation of Three Laser Systems at the FLASH Photoinjector", in *These Proceedings: Proc. 37th Int. Free Electron Laser Conf.*, Daejeon, Korea, 2015, TUP041.

[8] Molectron, J-5, `http://lasers.coherent.com`

[9] S. Schreiber *et al.*, "Cathode Issues at the FLASH Photoinjector", in *Proc. 30th Int. Free-Electron Laser Conf.*, Gyeongju, Korea, 2008, p. 552 (FRAAU05).

[10] S. Lederer *et al.*, "Photocathode Studies at FLASH", in *Proc. 11th European Particle Acc. Conf.*, Genoa, Italy, 2008, p. 232 (MOPC072).

[11] D. Sertore *et al.*, "Review of the Production Process of TTF and PITZ Photocathodes", in *Proc. 2005 Particle Acc. Conf.*, Knoxville, Tennessee, USA, 2005, p. 671.

[12] P. Michelato *et al.*, "Cs_2Te Photocathodes Robustness Studies", in *Proc. 11th European Particle Acc. Conf.*, Genoa, Italy, 2008, p. 241 (MOPC075).

[13] J.H. Han *et al.*, "Dark Current and Multipacting in the Photocathode RF Guns at PITZ", in *Proc. 2005 Particle Acc. Conf.*, Knoxville, Tennessee, USA, 2005, p. 895.

[14] L. Monaco *et al.*, "Dark Current Investigation of FLASH and PITZ RF Guns", in *Proc. 10th European Particle Acc. Conf.*, Edinburgh, Scotland, 2006, p. 2493 (WEPLS051).

ISBN 978-3-95450-134-2

PAL-XFEL CAVITY BPM PROTOTYPE BEAM TEST AT ITF

Sojeong Lee, Young Jung Park, Changbum Kim, Seung Hwan Kim, D.C. Shin
Heung-Sik Kang, Jang Hui Han, In Soo Ko
PAL, Pohang, Kyungbuk, Korea

Abstract

To achieve sub-micrometer resolution, The Pohang Accelerator Laboratory X-ray Free electron Laser (PAL-XFEL) undulator section will use X-band Cavity beam position monitor (BPM) systems. Prototype cavity BPM pick-up was designed and fabricated to test performance of cavity BPM system. Fabricated prototype cavity BPM pick-up was installed at the beam line of Injector Test Facility (ITF) at PAL for beam test. Under 200 pC beam charge condition, the signal properties of cavity BPM pick-up were measured. Also, the dynamic range of cavity BPM was measured by using the corrector magnet. In this paper, the design and beam test results of prototype cavity BPM pick-up will be introduced.

INTRODUCTION

The Pohang Accelerator Laboratory X-ray Free Electron Laser (PAL-XFEL) facility will use 10 GeV linac and undulator beamlines to provide X-ray FEL radiation to users. By using the self-amplified spontaneous emission (SASE) schematic, PAL-XFEL will provide X-rays in ranges of 0.1 to 0.06 nm for hard X-ray line and 3.0 nm to 1.0 nm for soft X-ray line [1]. To generate X-ray FEL radiation, the PAL-XFEL undulator section requires high resolution beam position monitoring systems with <1 µm resolution. At first phase, the PAL-XFEL will be operated at a repetition rate of 60 Hz with 0.2 nC electron beam charge [2]. To achieve this high resolution requirement under single electron beam with low charge condition, the PAL-XFEL undulator section will use the cavity Beam Position Monitors (cavity BPMs) for beam trajectory monitoring. Total 49 units of cavity BPM system will be installed in between each undulators with other diagnostics tools. Before fabrication of the PAL-XFEL cavity BPM pick-ups, the prototypes of cavity BPM were fabricated to test the performance of cavity BPM pick-ups.

PAL-XFEL CAVITY BPM PICK-UP DESIGN

The operation frequency of PAL-XFEL cavity BPM system was set as X-band frequency. Due to the limitation of installation space, the compact cavity BPM pick-up was required. To achieve high resolution and compact pick-up size, the X-band operation frequency, 11.424 GHz, was chosen for PAL-XFEL cavity BPM system. Also, for easy installation and maintenance, the PAL-XFEL cavity BPM pick-ups adopt the SMA feed through as output signal port. Under these two conditions, the PAL-XFEL cavity BPM pick-up was designed.

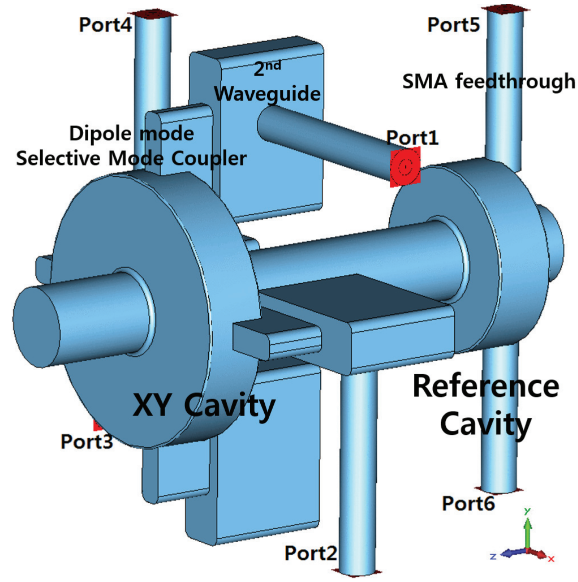

Figure 1: Modeling of PAL-XFEL cavity BPM pick-up vacuum part.

The PAL-XFEL cavity BPM pick-up consists of two cavities, reference cavity and XY cavity. The reference cavity uses TM_{010} mode, monopole mode, of pill box cavity. The amplitude of TM_{010} mode is proportional to the electron beam charge. By using this property of monopole mode, the reference cavity can measure the bunch charge, and this reference cavity signal is used to normalize the amplitude of XY cavity signal. On the other hand, the XY cavity uses TM_{110} mode, dipole mode, of pill box cavity. The amplitude TM_{110} mode is proportional to the bunch charge and offset of electron beam. Thus, the XY cavity can measure beam position by using excited dipole mode of XY cavity and reference cavity signal.

Figure 1 shows the inner structure modeling result of PAL-XFEL cavity BPM pick-up. Reference cavity is designed as simple structure, for easy fabrication. In case of XY cavity, the dipole mode selective coupler for suppressing the monopole mode signal of XY cavity. This dipole mode selective coupler structure was proposed and adopted for LCLS cavity BPM pick-ups [3,4]. Each SMA feed through is installed on the second waveguide of XY cavity. This second waveguide was adopted to minimize the brazing effect on the pill box part of XY cavity.

Table 1 shows the RF parameters of PAL-XFEL cavity BPM pick-up. The RF parameters of each cavity were calculated by using CST Microwave Studio module [5]. Both cavities were designed as high Q value and over coupled structure. Also, R/Q value of each cavity, one of factor de-

ISBN 978-3-95450-134-2

Table 1: Simulation Results of PAL-XFEL Cavity BPM Pick-up Properties

	Reference Cavity	XY Cavity
Frequency [GHz]	11.424	11.424
Q_L	2290	2544
Q_{ext}	3470	3882
β	1.94	1.90
R/Q	114.13 Ω	3.77 Ω/mm^2

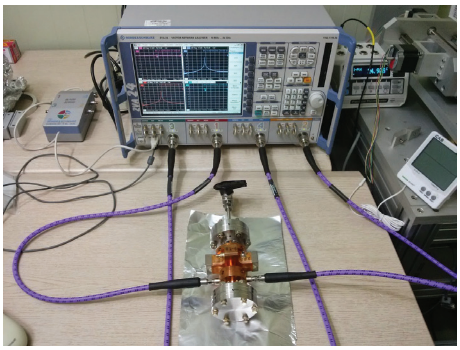

Figure 2: Fabricated prototype cavity BPM pick-up.

ciding the output signal amplitude, is enough to meet the high resolution of cavity BPM system.

CAVITY BPM PICK-UP FABRICATION AND MEASUREMENT RESULTS

The prototypes of cavity BPM pick-up were fabricated to test RF parameters of pick-up. Also, usual commercial SMA feed through does not support X-band region. Due to this reason, the SMA feed through was designed and fabricated for X-band cavity BPM pick-up. The prototype of PAL-XFEL cavity BPM pick-up was fabricated by using these SMA feed through

Table 2 and Table 3 show the measured result of one of prototype cavity BPM pick-up. To measure the RF parameters of each port, the vector network analyzer was used. In case of reference cavity, the simulation and measured value of Q-factors have difference. At first fabrication test, the Q_L factor of reference cavity was decreased after brazing process, lower than 2000. Due to close distance between pill box cavity and brazing point of feed through comparing with XY cavity, the reference cavity structure was highly sensitive to the brazing process error. To decrease the brazing process effect on the quality factor, the brazing points and dimension of reference cavity were modified and Table 2 shows the

Table 2: RF Parameters of Prototype Cavity BPM #02 – 06 Reference Cavity Measurement Result

	f[GHz]	β	Q_L	Q_{ext}
Port1	11.424	2.241	2876.61	4160.52
Port2	11.424	2.534	2887.96	4027.74

Table 3: RF Parameters of Prototype Cavity BPM #02 – 06 XY Cavity Measurement Result

	f[GHz]	β	Q_L	Q_{ext}
Port1	11.4242	2.394	2534.01	3592.54
Port2	11.4242	2.020	2532.51	3786.17
Port3	11.4242	1.934	2525.06	3830.41
Port4	11.4242	2.291	2526.84	3629.78

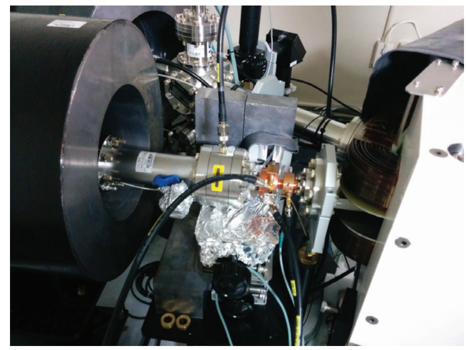

Figure 3: Installed prototype cavity BPM pick-up at ITF dump section.

modified version result. On the other hand, the XY cavity measurement result is quite similar to simulation result.

BEAM TEST AT ITF

After measuring RF parameters, the prototype cavity BPM pick-up was installed in the beam line of Injector Test Facility (ITF) at PAL. ITF can provide 200 pC electron beam [6] to the prototype cavity BPM pick-up, and by using this electron beam, the output signal properties of pick-up can be measured. The cavity BPM pick-up was installed at the dump section of ITF due to small diameter beam pipe of cavity BPM pick-up, as 9 mm. Three coaxial cables, RF signal amplifier and oscilloscope were used for monitoring response of XY cavity and reference cavity.

Figure 4 shows the y-direction port signal of XY cavity BPM under the 200 pC electron beam condition. However, due to sampling rate of oscilloscope, the 11.424 GHz output port signal was down-converted as 200 MHz. The measured

Figure 4: Raw signal of cavity BPM pick-up y-direction port. This output signal was down converted as 200 MHz and measured by using oscilloscope.

ISBN 978-3-95450-134-2

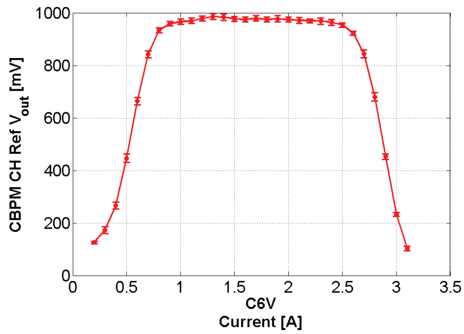

Figure 5: Reference cavity output voltage response to corrector C6V.

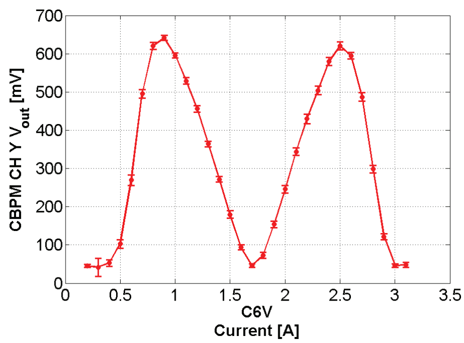

Figure 6: XY cavity y-direction output voltage response to corrector C6V.

decaying time of y-direction port signal was 30 ns. Comparing with the calculated decaying time of XY cavity, 35 ns calculated based on the measurement result by using network analyzer, the down-converted signal also gives similar values.

After measuring the raw signal of each port, dynamic range of cavity BPM pick-up was measured by using corrector magnet of ITF. However, there are no corrector magnets near the ITF dump section to scan precisely. Also, there was installation space limitation, the cavity BPM could not installed with its own support system. Due to these reasons, the linearity scan of pick-up could not be done within the interest region, ±1 mm. Instead, the dynamic range of cavity BPM pick-up was measured over than ±4 mm.

For the dynamic range measurement, the frequency mixer, oscilloscope and RF power detector were used. Due to the trigger problem of frequency mixer, the measurement by using oscilloscope was unstable. For stable pick-up signal measurement, RF power detector was used during the data acquisition. On the other hand, the beam offset at the cavity BPM was changed by using Cor6 corrector magnet. Also, two stripline BPMs are used to monitor the beam position. Considering distance between two stripline BPMs and cavity BPM pick-up, estimated beam offset change of the cavity BPM is 4.594 mm for Cor6 MPS 1 A current change. As shown Fig. 5 and Fig. 6, the cavity BPM pick-up response to Cor6 current change is similar to the monopole and dipole mode electric field distribution. For the reference cavity, the response of cavity BPM pick-up is almost constant and its amplitude does not depend on the beam offset change. On the other hand, the XY cavity, near the center, the y-direction port shows a good linearity to the beam offset change. However, the minimum output signal of the XY cavity is not zero for both ports. This non-zero value can be caused from the angle of the beam trajectory. On the other hand, the response of the cavity BPM pick-up is taken to 2.5 A current change of Cor6 MPS. This can be calculated as ∼ 11 mm at the cavity BPM position. This value is bigger than the beam pipe of the cavity BPM. Thus, decreasing y-direction port signal at both end side of scan could be caused from the beam charge loss. Also, maximum reference cavity port signal is maintained for 1.7 A current change of Cor6 MPS current. This current change can be converted to ∼ 7.8 mm beam offset changing. By considering the error of calculation and the beam size at the dump section, the dynamic range of this cavity BPM pick-up will be ∼ ±4 mm. However, by using this beam test, the output voltage change ratio within ±10 µm region cannot be measured with high precision.

RESULTS

The prototype PAL-XFEL cavity BPM pick-up was designed and fabricated to test the performance of X-band cavity BPM pick-up. After fabrication, the resonance frequency and Q-factors of cavity BPM pick-up were measured. In case of XY cavity, the measurement results shows good agreement with simulation results. Also, the prototype cavity BPM pick-up was installed in the beam line of ITF to measure the raw signal properties and dynamic range of cavity BPM pick-up. The measured decaying time of XY cavity signal was 30 ns and the dynamic range was ∼ ±4 mm. These value show good agreement with simulation results and Q-factor measurement results.

REFERENCES

[1] I. S. Ko and J.-H. Han, "Current status of PAL-XFEL project." in *Proceedings of 27th Linear Accelerator Conf.*, Geneva (2014).

[2] J.-H. Han et al., "Status of the PAL-XFEL project." in *Proceedings of 3rd Int. Particle Accelerator Conf.*, New Orleans (2012), p.1735.

[3] Li, Zenghai et al., "Cavity BPM with Dipole-Mode-Selective Coupler", in *Proceedings of the 2003 Particle Accelerator Conf.*, Portland, OR (2003).

[4] Waldschmidt, G. et al., "Electromagnetic design of the RF cavity beam position monitor for the LCLS." in *Proceedings of the 2007 Particle Accelerator Conf.*, Albuquerque, New Mexico (2007).

[5] CST MICROWAVE STUDIO, v. 2015, Computer Simulation Technology AG, www.cst.com

[6] Han, J. H., et al., "Beam operation of the PAL-XFEL Injector Test Facility.", in *Proceedings of 36th Int. Free Electron Laser Conf.* Basel (2014), p.615.

ISBN 978-3-95450-134-2

SPARK EL - SINGLE PASS BPM

M. Znidarcic, Instrumentation Technologies, Solkan, Slovenia

Abstract

Monitoring and subsequent optimization of the electron linacs and beam transfers requires specific instrumentation for beam position data acquisition and processing. Spark EL is the newly developed prototype intended for position monitoring in single or multi bunch operation linacs and transfer lines. The motivation, processing principles and first results are presented.

INTRODUCTION

In this paper we introduce a compact platform that aims to host a wide range of applications. First instrument built on this platform is Libera Spark EL (see Fig. 1 and Fig. 2). The instrument is designed for processing of electron beam in linear accelerators and beam transfers.

Figure 1: Housing prototype.

Figure 2: Libera Spark EL back panel.

A NEW PLATFORM

Looking at the beam instrumentation used to monitor and stabilize an accelerator, every device suits a specific role, but it is possible to identify some key components that are always present:

- RF front-end and analogue signal processing chains
- Internal communication buses
- Power supply unit
- Cooling system

In this new development, we take advantage of the latest advances in SoC technology to introduce a compact platform (see Fig. 3) that combines a high level of hardware integration with our knowledge regarding reconfigurable analogue signal processing.

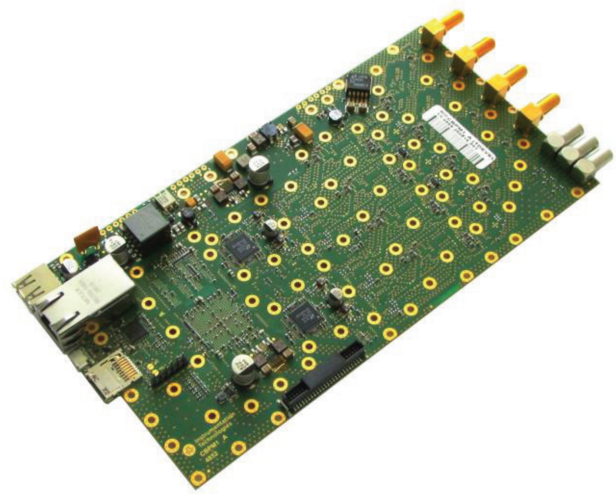

Figure 3: Libera Spark EL.

HW and SW Integration

Hardware and software are designed taking in account the balance between generality and optimization. It will be always possible to add specific features to customize it, opening at the same time the way for developing different applications, as shown in Fig. 4.

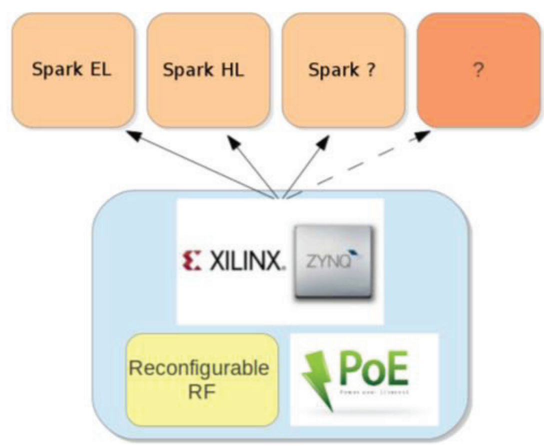

Figure 4: Platform concept based on SoC.

The core part is the SoC Xilinix Zynq 7020 [1] which combines the high-speed processing of the FPGA together with the flexibility of a CPU, all within the same chip. The inner communication between the two entities and the chance to share the same memory removes at the same time two of the biggest bottle-necks that still characterize separate-chip solutions:

- No communication protocols needed
- No data copy between FPGA and CPU.

The specifics of the analogue front-end cover the user requirements. Integrations with specific band-pass filters, phase-locked-loop (PLL) and variable attenuators are

ISBN 978-3-95450-134-2

possible if the application requires them. Figure 4 shows an example of the HW architecture of a BPM application.

Low Power Instrument

SoC requires less power than a multiple-board solution. Furthermore proper selection of the RF components (amplifiers, analog-to-digital converters, etc.) reduces the amount of heat that the cooling system has to treat. This enables the way towards passive cooling with the integration of the heat sink in the crate. Consequently fans are no longer needed, and from the system point of view, the main advantages are:

- No moving parts means no maintenance required
- Fans-induced noise is no longer present on the signals
- Less space and less power required from the system.

With the low power requirement, precisely less than 15 Watt, the system can be powered over Ethernet according to the PoE standard IEEE802.3af. In the case of accelerator applications, if the unit is powered over Ethernet, it is possible to put it closer to the machine (e.g. 5m), reducing at the same time the cost of cables and noise on the signal.

Easy SW Maintenance

The unit software can be basically divided in the design that configures the FPGA, application and other interfaces supported by the operating system on the CPU side. The operating system running on Xilinx Zynq SoC is Linux OS. The software packages are not installed in the device memory, but both FPGA and Linux code are loaded from the same image when the unit is turned on. In more details two different boot procedures will be supported:

- Memory card boot: if a memory card is inserted in the device socket, then the Linux OS will boot from the image contained in the memory
- File Transfer Protocol (TFTP) boot: if no memory is inserted, the boot procedure will start from the FLASH memory, and the software image will be downloaded from a configured TFTP server

In both cases a software update can easily be realized replacing the software image in each unit, with no need to deal with packages and configuration files in the operating system. In particular for a complete set of units configured to use TFTP, only one image should be modified.

CONTROL SYSTEM INTEGRATION

On the top layer, Libera Spark provides the MCI with a development package and Command Line utilities for open interaction in different control systems. On top of the MCI, various adaptors to different control systems can be implemented (EPICS, Tango, etc.). The EPICS interface is part of the standard software package.

DATA PROCESSING

The Spark EL data processing is initiated by the external event signal. The short signal from the detector is first shaped by the analog front-end filtering, designed in relation to the accelerator parameters and than sampled with 14 bit ADC converters. The maximal sampling frequency can be set to 125 MHz.

Through the configuration of various software parameters, Libera Spark offers processing of various beam types (flavors). After the hardware triggers signal which announces the arrival of the bunch, the search of bunch signal is started. The bunch signal is detected in comparison with the threshold parameter, then a useful part of the signal is defined with the pre-trigger and post-trigger parameters. The sum of the pre-trigger and post-trigger defines the processing window. The signal energy is calculated from the signal as defined by the processing window. After calculating the four signal amplitudes – Va, Vb, Vc and Vd – the beam position is calculated using formulas for X and Y. Four options can be used for position calculation:

- Diagonal pickup orientation – Linear formula
- Diagonal pickup orientation – Polynomial formula (3rd order)
- Orthogonal pickup orientation – Linear formula
- Orthogonal pickup orientation – Polynomial formula (3rd order):

$$X = X_{OFFSET} + \sum_{ij=0}^{3} K_{Xij} \left(\frac{(V'_A - V'_C)}{(V'_A + V'_C)} \right)^i * \left(\frac{(V'_B - V'_D)}{(V'_B + V'_D)} \right)^j$$

$$Y = Y_{OFFSET} + \sum_{ij=0}^{3} K_{Yij} \left(\frac{(V'_A - V'_C)}{(V'_A + V'_C)} \right)^i * \left(\frac{(V'_B - V'_D)}{(V'_B + V'_D)} \right)^j$$

In the case of longer beam structures, similar data processing is used, based on the appropriate signal windowing [2]. The data calculation is initiated by the external trigger event and is automatically stopped after the bunch structure is over (see Fig. 5). The decimated batch of data is available for transmission to the control system. In the case of continuous wave operation, the unit continuously processes and outputs the stream of decimated beam position data.

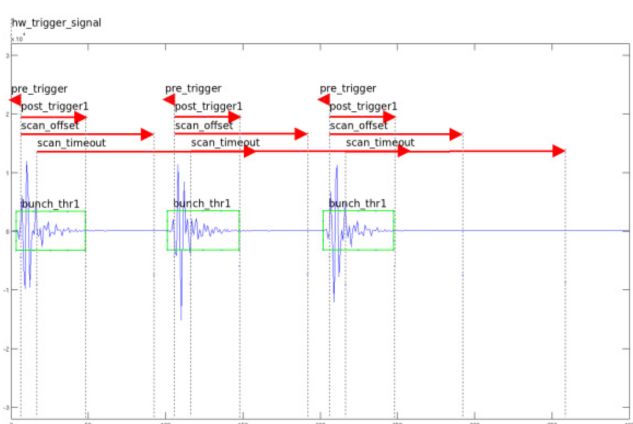

Figure 5: Macro-pulse mode.

ISBN 978-3-95450-134-2

POSITION MEASURING PERFORMANCE

Measurement performance mostly depends on the Spark front-end configuration [2]. Its parameters are set in accordance with main accelerator parameters. The driver for the RF front end configuration is type of sensor (stripline or capacitive) and beam flavor (single bunch, macro-pulse, etc.).

Spark EL

The standard type of Libera Spark EL implements 500 MHz SAW filters with 10 MHz bandwidth. Relatively narrow filter serves to lengthen the short, few picoseconds long signal, to a longer structure (nanoseconds). At operational beam charges, the position measurement resolution is close to 3 µm (kx = ky = 10 mm) for a single-bunch beam structure (see Fig. 6). Input signal is presented on Fig. 7.

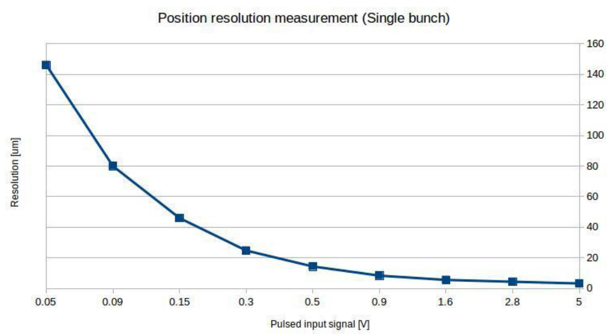

Figure 6: Single bunch measurement performance versus input signal level (0 dBFS = 5 V peak).

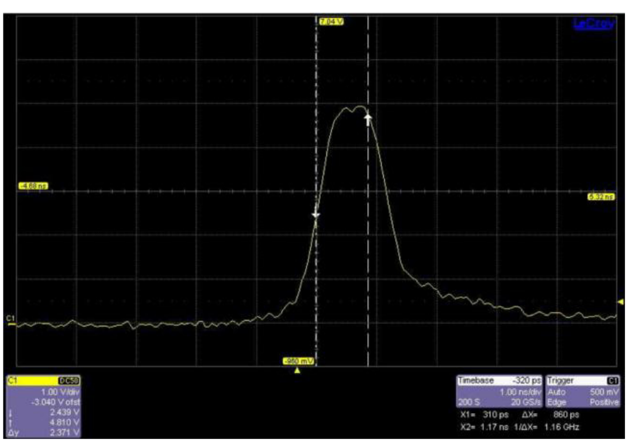

Figure 7: Input signal.

Default operational full-scale of the instrument is 5V, but can be configured in accordance to the accelerator beam dynamic range.

CONCLUSION

The development of new BPM for linear machines based on the SoC technology has been presented in this article. The introduced platform combines knowledge about reconfigurable RF front-ends with the advantages of a compact and passively cooled instrument that can be powered over Ethernet and booted from a server using SW image.

As a first development, the linear BPM instrument is promising application that shows very good performances, simple and straightforward architecture and an excellent price-to-performance ratio.

REFERENCES

[1] M. Cargnelutti, “Beam position electronics based on system on chip platform”, PAC 2013, Pasadena, CA USA, September 13, THPAC04
[2] Instrumentation Technologies, “Libera Single Pass E User Manual v1.00”, Solkan (September 2011)

ISBN 978-3-95450-134-2

MTCA.4 PHASE DETECTOR FOR FEMTOSECOND-PRECISION LASER SYNCHRONIZATION

E. Janas[1,2,*], K. Czuba[2], M. Felber[1], M. Heuer[1], U. Mavrič[1], H. Schlarb[1]
[1] DESY, Hamburg, Germany
[2] ISE, Warsaw University of Technology, Poland

Abstract

For time-resolved experiments at FELs such as the European XFEL an accurate synchronization of the machine is essential. The required femtosecond- level synchronization we plan to achieve with an optical synchronization system, in which an inherent part is the master laser oscillator (MLO) locked to the electrical reference. At DESY we develop a custom rear transition module in MTCA.4 standard, which will allow for different techniques of phase detection between the optical and the electrical signal, as well as locking to an optical reference using a cross-correlator. In this paper we present the current status of the development, including two basic solutions for the detection to an RF. One of the methods incorporates an external drift free detector based on the so-called MZI setup. The other one employs the currently used down-converter scheme with subsequent improvements. The module can serve for locking a variety of lasers with different repetition rates.

INTRODUCTION TO OPTICAL SYNCHRONIZATION SYSTEM AT THE EUROPEAN XFEL

The optical synchronization system planned for the European XFEL has a range of uses. It is employed in these locations of the facility, where the most demanding synchronization precision is necessary. First of all, it serves as a reference for a number of lasers in the machine, including pump-probe laser for time resolved experiments. The lasers can be directly locked to the optical synchronization system using laser-to-laser locking stations (L2L) described in [1]. Another applications are precise bunch arrival-time monitors or a support for the 1.3 GHz coaxial cable based timing distribution, suffering from the drifts arising with a distance from the signal source in the cables because of their thermal expansion. The electrical synchronization system, mainly supplying the LLRF stations along the FEL, comprises of so-called interferometer links which task is to extend the possible synchronization distances [2]. Nevertheless, to achieve the required stabilities of the timing signal at different locations along over 3km long accelerator, the system has to be resynchronized to the optical reference. At DESY, we have developed a module called REFM-OPT, which promises to achieve sub-10fs synchronization precision between electrical and optical signal over longer time periods [3]. The REFM-OPT utilizes the laser-to-RF phase detector (L2RF)

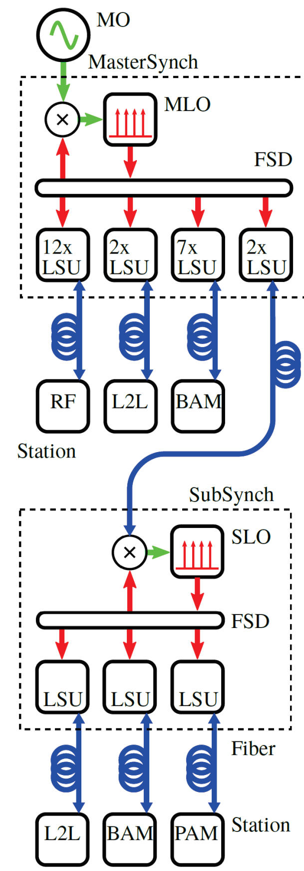

Figure 1: Optical synchronization scheme of the European XFEL. Description of system components: Master Oscillator (MO), Master Laser Oscillator (MLO), Slave Laser Oscillator (SLO), Free-Space Distribution (FSD), Link Stabilization Unit (LSU), Laser-to-Laser synchronization (L2L), Laser-to-RF synchronization (RF), Bunch Arrival-time Monitor (BAM) - beam diagnostics directly using the laser pulse train, Photon Arrival-time Monitor (PAM). Figure source: courtesy of Cezary Sydlo

of an extraordinary performance presented in [4], where we obtained 3.6 fs peak-to-peak phase drift over 24 h.

An overview of the optical synchronization system is shown in Figure 1. It incorporates the current solution used at DESY's mother facility FLASH (about ten times smaller than the European XFEL), with subsequent improvements and extensions. The signal source is a master laser oscillator (MLO), which is a commercial mode-locked laser with pulse duration of 200 fs at a repetition rate of 216.67 MHz. The MLO in turn is locked to the master oscillator (MO), the

* Ewa.Janas@desy.de

ISBN 978-3-95450-134-2

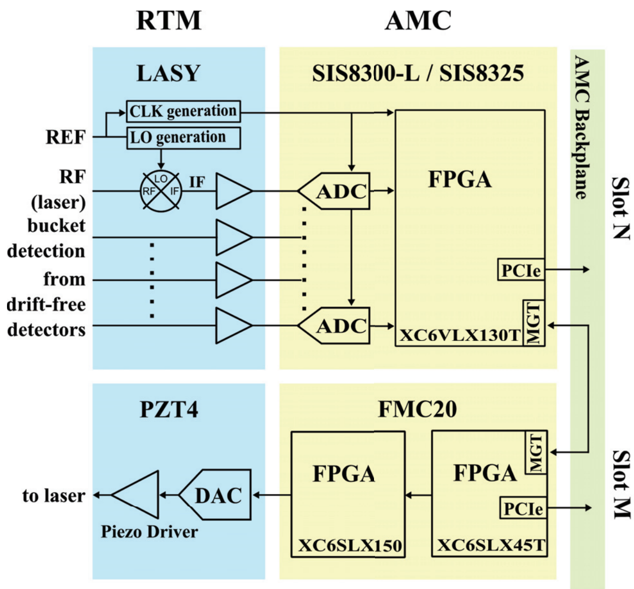

Figure 2: MTCA.4 components for laser locking application. Description of the terms: RTM-Rear Transition Module, a board connected to a specific AMC from the rear side of a MTCA.4 crate, AMC-Advanced Mezzanine Card, LASY-LAser SYnchronization board, SIS8300-L/SIS8325-digitizer board, where the controller is implemented, PZT4-4 channel piezo driver to control the piezo of the laser, FMC20-dual FPGA mezzanine card, here used for backplane and RTM interconnections.

ultra-stable signal source of a six times higher frequency (1.3 GHz) for the electrical reference distribution system. The signal distribution is done through the free-space distribution (FSD) and link stabilization units (LSUs) and it has been presented in more detail in [1], whereas the MLO locking scheme together with supplementary locking schemes implemented on the same hardware for another lasers is a subject of this paper.

LASER LOCKING SCHEME BASED ON MTCA.4 STANDARD

Laser synchronization in the European XFEL will utilize the MTCA.4 standard [5]. In the current development state, the system is built out of MTCA.4 cards, from which the phase detector item DRTM-DWC10 was designed to fulfill LLRF system needs and adapted for laser locking purpose with external RF components [6]. In the near future, the setup will be enriched by a dedicated rear transition module DRTM-LASY, first mentioned in [7]. It will exchange the currently used external RF components and DRTM-DWC10 board, and provide a set of new functions. The laser locking MTCA.4 setup supplemented with this module is presented in Figure 2.

In order to lock the laser to the reference (which can be either optical link end or RF signal), the phase difference between these two signals is first detected on LASY board (in one of the methods described below) or by a connected to it drift-free detector. The resulting error signal is processed to its Advanced Mezzanine Card (AMC). There it is digitized and the phase difference is stabilized by a controller, which acts on the laser's frequency/phase via piezo driver board called DRTM-PZT4 [8]. Alternatively, an external actuator can be used, but it has naturally a disadvantage of more external components. Taking into account the flexibility of the setup, the photo detectors to convert the laser signal to RF are not placed on LASY. However, there is foreseen a regulated power supply to drive an external photo diode. Additional feature enabling extension of board usage are two DAC outputs, which are planned to be added at the front panel. Having discussed what the complete synchronization setup looks like, the following sections move on to review various phase detection methods supported by LASY RTM.

DOWN-CONVERTER LOCKING SCHEME

The laser lock using a down-converter scheme is the most straightforward and bases on two-steps locking procedure described in [6]. All the RF components placed before out of a MTCA.4 system are now integrated on the LASY PCB (Figure 3). In order to achieve a flexibility over possible LO frequencies, independent of available reference, the board provides an LO generation functionality. Similarly, there is a clock generation section foreseen, thus an optimal clock frequency at ADC for non-IQ detection may be derived. For the sake of better performance in case of noise and phase drift, two compensation methods are implemented.

Reference Tracking

One of the methods to suppress the phase detection error due to the noise and drifts in the detector hardware is reference tracking. The method requires incorporation of another down-converter channel, where the reference can be injected instead of the measured laser signal. Assuming the reference is drift-free, any detected phase differences (measured against LO derived from the same signal) could be treated as coming from the setup itself. Expressed another way, by tracking the reference, one can detect the false part of the phase difference measured between the reference and the laser signal, coming from the LO generation block, RF components or PCB traces. Consequently, the phase difference detected on the reference tracking channel can be subtracted from the one from the laser channel.

The method requires, that both down-converter channels are possibly identical. Any inaccuracy in this matter, such as component's tolerance, yields to limitation of phase correction within this scheme. From the other hand the problem can be addressed, at least to a certain degree under another constrains, by using a two-tone calibration method described in the next section.

Two-tone Calibration

To date, several studies investigating various configuration with different applications have been carried out on this phase drift calibration method [9,10], here one more method

ISBN 978-3-95450-134-2

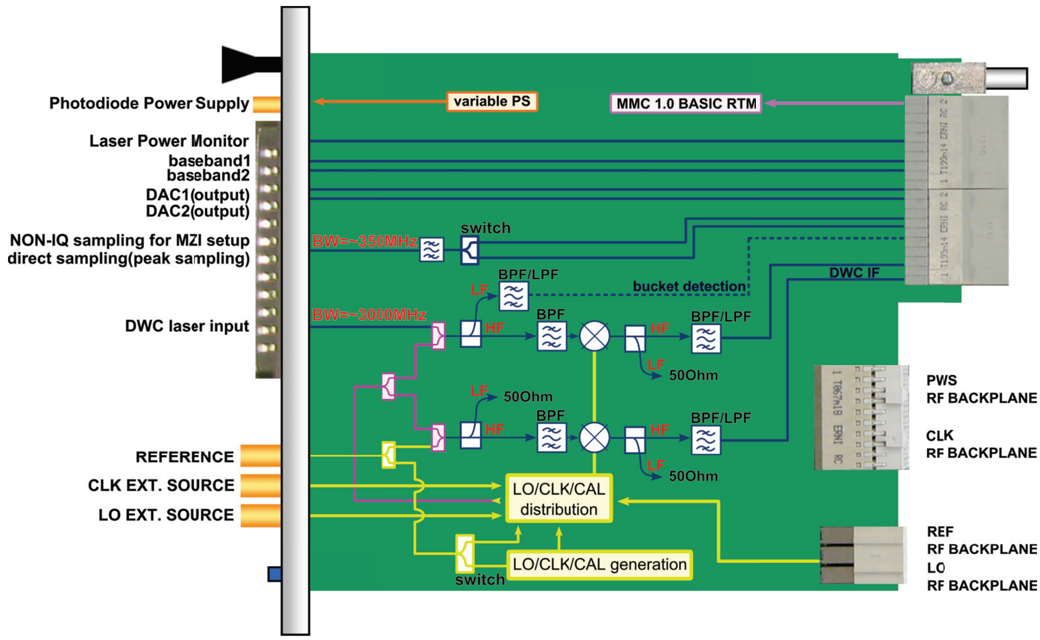

Figure 3: Block diagram of a DRTM-LASY module.

variation is applied, which corresponds to the specific application. Its advantage in respect of reference tracking consists in that the calibration signal is injected into the same hardware as the measured signal. Because of this, the frequency of a calibration signal has to be of different frequency than the measured laser harmonic to be thereby distinct from it. On the other hand, studies have shown that the chosen frequency should be also possibly close to it. Choosing an optimal calibration signal has conclusively been discussed in [10].

The method requires, that the calibration signal injection area (marked in magenta in Figure 3) is drift free, because any drift occuring here is not calibrated. The challenge lies in the fact, that the section must be also very wideband when used for this application - the same components conduct also a bucket detection signal, which is a base laser harmonic, thus of much lower frequency that the one likely used in the down-converter chain. The are several ideas how to overcome this problem, which will be addressed in the near future.

LASER LOCK USING DRIFT-FREE DETECTOR

The DRTM-LASY supports several locking methods exploiting so-called drift-free detectors. In both detectors, the phase is compared in the optical domain, converted to an electrical signal and then processed further to the digitizer.

Optical Cross-correlator

Thus far, the most precise method to lock the laser is a lock to the optical reference using a cross-correlation method. Its principle and the necessary external components can be explored in various sources [1, 11, 12], the most recent report

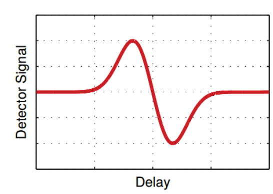

Figure 4: Example signal derived from the balanced optical cross-correlator. Figure source: [13].

can be found in [13]. The optical cross-correlator measures the relative timing between two optical pulses. These two pulses are mixed with each other on a nonlinear crystal, so that the intensity of the sum signal shows their overlap. To learn which pulse was first, there is a second setup with a known delay introduced additionally between the pulses. Then both overlapped ('sum') signals are detected on a balanced photo detector and processed via two baseband tracks on LASY to be subtracted from each other in the digital control system, giving the characteristic signal shown in Figure 4. The signals cannot be subtracted before the processing in the control system because of a certain ambiguity of the difference signal. Subtraction results in zero in both cases when the pulses do not overlap at all or if they are perfectly overlapping with each other (zero crossing on the plot). If we process both sums, then we can distinguish the situation of perfect synchronization by looking at the individual sum signals.

Laser-to-RF Detector

Locking the MLO to the reference coming from a MO will be performed using a L2RF phase detector, originally developed for a REFM-OPT module as was mentioned in the introduction to this paper. The L2RF detector principles

ISBN 978-3-95450-134-2

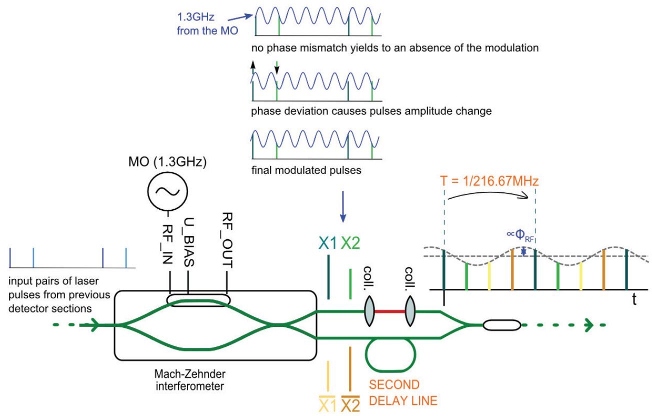

Figure 5: A scheme briefly showing phase detection in an L2RF setup. An output signal containing information about phase mismatch is in case of an MLO of frequency equal 216.67 MHz, which is also a laser pulse repetition rate. Its amplitude is proportional to the phase error.

were described in [14]. This phase detector compares the optical pulses with a RF signal in an EOM, where the optical pulses are modulated in amplitude depending on the phase shift between the signals. The phase mismatch is proportional to the modulation depth as shown in Figure 5. The amplitude of an output signal of 216.67 MHz (1/6 of 1.3 GHz) can be detected either by direct sampling or by readout electronics presented in [15]. Depending on repetition rate of the laser pulses the frequency of the L2RF output signal will change accordingly [16].

In case of using readout electronics, one can process an information signal via LASY baseband inputs like the ones from an optical cross-correlator. In the other case, there will be used a direct sampling input. An optimal configuration in which a L2RF detector should be used for MLO synchronization will be a subject of investigation in the near future.

CONCLUSION

This paper has introduced a new MTCA.4 card for laser synchronization DRTM-LASY and presented its features which are to be implemented. The board has been presented in the context of MLO synchronization to the accelerator electrical reference, although it is supposed to be used also for other lasers at FLASH, the European XFEL or other facilities. DRTM-LASY supports different synchronization schemes, including laser-to-laser method, laser-to-RF synchronization using drift-free detector or a down-converter scheme.

REFERENCES

[1] C. Sydlo et al. Femtosecond timing distribution for the European XFEL. *Proc. FEL2014, THP090*.

[2] K. Czuba et al. Overview of the RF synchronization system for the European XFEL. *Proc. IPAC2013, WEPME035*.

[3] E. Janas et al. Design and integration of the optical reference module at 1.3 GHz for FLASH and the European XFEL. *Proc. IPAC2014, WEPRI115*.

[4] T. Lamb et al. Femtosecond stable Laser-To-RF phase detection for optical synchronization systems. *Proc. IBIC2013, TUPC33*.

[5] http://mtca.desy.de.

[6] M. Felber et al. Compact MTCA.4 based laser synchronization. *Proc. IPAC2014, TUPRI107*.

[7] M. Felber et al. New MTCA.4-based hardware developments for the control of the optical synchronization systems at DESY. *Proc. IBIC2014, MOPD07*.

[8] K. Przygoda et al. MTCA.4 module for cavity and laser piezo operation. *Proc. IPAC2014, THPRO105*.

[9] G. Huang et al. Signal processing for high precision phase measurements. *Proc. BIW10, TUPSM082*.

[10] S. Jablonski et al. 2pi low drift phase detector for high precision measurements. *Real Time Conference (RT), 2014 19th IEEE-NPSS*.

[11] F. Zummack et al. Status of the fiber link stabilization units at FLASH. *Proc. IBIC2013, MOPC33*.

[12] S. Schulz et al. Femtosecond-precision synchronization of the pump-probe optical laser for user experiments at flash. *Proc. of SPIE Vol. 8778 87780R-2*.

[13] J. Müller et al. All-optical synchronization of pulsed laser systems at FLASH and XFEL. *Proc. IPAC2015, MOPHA032*.

[14] T. Lamb et al. Femtosecond stable Laser-To-RF phase detection using optical modulators. *Proc. FEL2011, THPA32*, 2011.

[15] E.Janas. Precise optical-electrical synchronization system for accelerators FLASH and XFEL. Master's thesis, WUT, Warsaw, Poland, 2012.

[16] M. Titberidze et al. Novel femtosecond level synchronization of titanium sapphire laser and relativistic electron beams. *Proc.IBIC2014 MOPD12*.

ISBN 978-3-95450-134-2

PROTOTYPE OF THE IMPROVED ELECTRO-OPTICAL UNIT FOR THE BUNCH ARRIVAL TIME MONITORS AT FLASH AND EUROPEAN XFEL

H. Dinter*, M.K. Czwalinna, C. Gerth, K. Przygoda, R. Rybaniec, H. Schlarb, C. Sydlo
DESY, Hamburg, Germany

Abstract

At today's free-electron lasers, high-resolution electron bunch arrival time measurements have become increasingly more important in fast feedback systems providing accurate timing stability for time-resolved pump-probe experiments and seeding schemes. At FLASH and the upcoming European XFEL a reliable and precise arrival time detection down to the femtosecond level has to cover a broad range of bunch charges, which may even change from 1 nC down to 20 pC within a bunch train. This is fulfilled by arrival time monitors which employ an electro-optical detection scheme by means of synchronised ultra-short laser pulses. At both facilities, the new bunch arrival time monitor has to cope with the special operation mode where the MHz repetition rate bunch train is separated into several segments for different SASE beam lines. Each of the segments will exhibit individual timing jitter characteristics since they are generated from different injector lasers and can be accelerated with individual energy gain settings. In this paper, we describe the recent improvements of the electro-optical unit developed for the bunch arrival time monitors to be installed in both facilities.

INTRODUCTION

The signal creation, detection and analysis in the electron bunch arrival time monitor is split into several subsystems, each fulfilling a particular task at their respective position in the signal processing chain. These include:

- The **RF unit** comprising four broadband pickups mounted in the beam tube in order to capture the electric field induced by the passing electron bunches [1]. The signals of opposite pickups are combined for a reduced position dependence of the measurement, resulting in two independent RF channels for the arrival time detection: Left + Right and Top + Bottom [2].
- The **electro-optical (EO) unit** converting the RF signal into an amplitude modulation of time-stabilised, ultra-short laser pulses provided by the optical synchronisation system [3,4] in order to achieve a high temporal sensitivity.
- **Electronics** for signal readout and control of the individual subsystems [5]. This part also performs communication with high-level control systems.

The general layout of the signal processing chain is illustrated in Fig. 1.

ELECTRO-OPTICAL UNIT

In this paper, we focus on the recent developments for the electro-optical part of the detection system. A schematic of the optical signal chain is shown in Fig. 2. Synchronised laser pulses enter the optical circulator at the top left and exit it on the right. A subsequent fast bidirectional fibre-optical switch acts as a selector which optical delay line is to be used for the current electron bunch subtrain.

After passing the delay stage and travelling back through the optical switch, the laser pulses are directed to the downward facing port of the circulator. An optical amplifier increases the signal level before it is split into three branches: one clock channel used as a trigger input for the sampling electronics and two channels leading to electro-optical modulators (EOM) corresponding to the two RF signal channels.

One of the signal paths leading to the EOMs provides the possibility of introducing an additional time delay through a separate optical delay stage. This can be used for adjusting the relative timing between the two channels, which might be necessary due to different RF cable lengths.

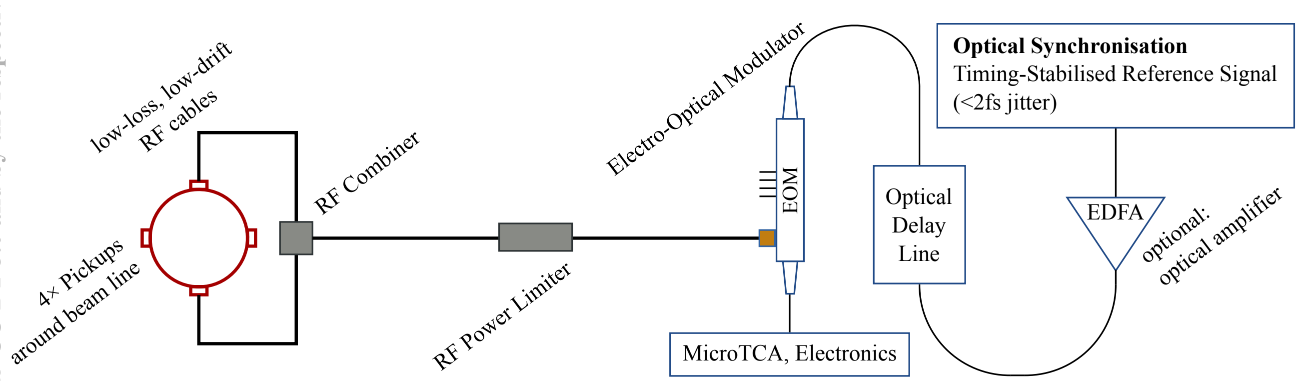

Figure 1: Basic layout of the cabling scheme (only one detection channel is shown).

* hannes.dinter@desy.de

ISBN 978-3-95450-134-2

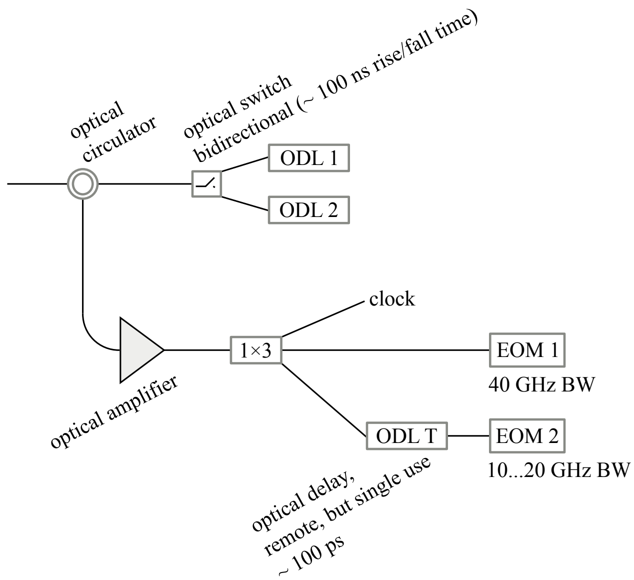

Figure 2: Optical signal processing chain.

In the EOMs, the laser pulses undergo an amplitude modulation depending on the arrival time of the electric signals coming from the RF pickups in the beam tube [6]. Changes in the timing of the electron bunches and thus of the electric signals result in a different modulation of the laser intensity, which is then detected by the readout electronics. By making use of the ultra-short, time-stabilised pulses from the optical synchronisation system, this detection scheme provides a high resolution combined with a timing accuracy in the range of a few femtoseconds [3].

OPTICAL DELAY STAGE

In order to achieve a high timing resolution, the EOMs are operated at a working point where the modulation of the laser pulses depends linearly with a steep slope on the arrival time of the electric signal. If the timing of the electron bunches and thus of the pickup signals changes by a large amount, the EOM is not longer driven in its linear regime, leading to measurement errors. In order for the system to stay within the working range, it is in such cases necessary to adjust the relative timing between the reference pulses and the electron bunches.

Figure 3 shows a photograph of the newly developed optical delay stage designed for this task. The adjustable timing delay is introduced by a retroreflector mounted on a commercially available motorised stage.[1] The laser pulses entering the setup through the optical fibre at the bottom right are coupled out by a collimator, directed to the retroreflector by two mirrors and coupled back into fibre by a second collimator. On its way, the free-space beam passes two wave plates which can be used for adjusting the polarisation.

By driving the motor stage, the optical path between the collimators and thus the transit time of the laser pulses is changed. The stage has a travelling distance of $\Delta z = 70$ mm, leading to a dynamic range of $2\Delta z = 140$ mm, or 467 ps, as the light passes this path twice on its way to the retroreflector and reverse. The optical power variation at the output is less than 10%, measured over the whole travelling distance.

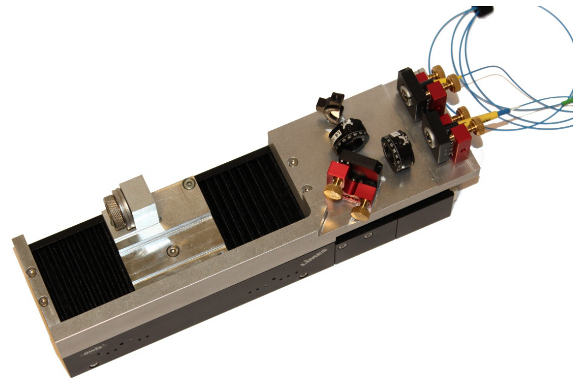

Figure 3: Optical delay stage.

Optionally, the second collimator can be replaced by a plane mirror, doubling the optical path length and the dynamic range of the system at the cost of reducing the positioning accuracy. In this case, the maximum delay is 934 ps. It is still to be investigated which of the two options provides better performance in terms of operating range vs. positioning precision and reproducibility.

BIDIRECTIONAL OPTICAL SWITCH

A key feature of FLASH and the European XFEL is the operation mode of a common linear accelerator driving multiple SASE beam lines [7]. The separate experimental end stations pose individual requirements on photon wavelength, spectral profile and pulse duration, raising the necessity of accelerating different parts of the electron bunch train with differing energies as well as unequal charges (see Fig. 4). This results in individual and varying timing characteristics among the separate bunch subtrains.

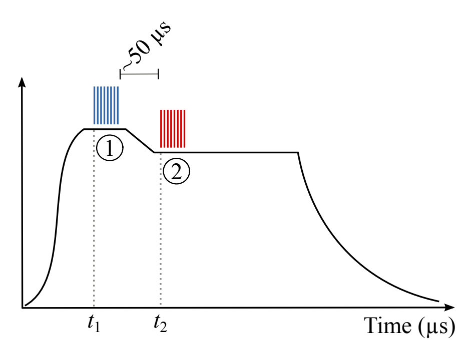

Figure 4: Electron bunch subtrains for different SASE beam lines.

The linear range of the modulated output signal of the EOMs is typically 2 ps to 4 ps. This is a consequence of the high sensitivity of the detection scheme. The timing between the electron bunches and the optical reference pulses needs

[1] OWIS LIMES 60-70 HSM

ISBN 978-3-95450-134-2

to be adjusted for each subtrain individually as soon as it leaves the linear region.

The transition time between the different parts of the bunch train lies in the range of a few tens of microseconds, which exceeds the feasible driving speed of the optical delay stage. Instead, the different timings are realised by using a separate optical delay stage per subtrain.

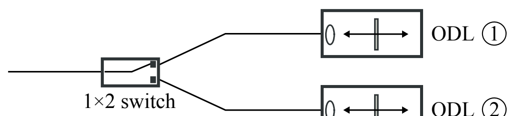

Figure 5: Individual optical delay stages for different electron bunch subtrains.

The toggling of the laser pulses' path between the different delay stages is carried out by a fast optical switch, as indicated in Fig. 5. The light passes the switch in both directions, therefore the use of a bidirectional device is necessary. An extension of this scheme to three or more optical delay lines is possible by using multiple switches in series or a switch with more than two outputs.

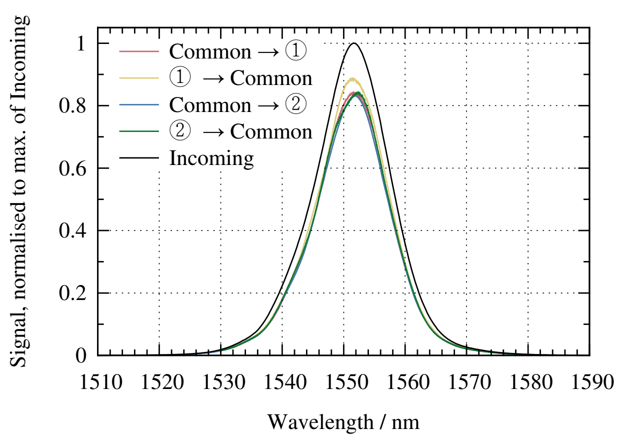

Figure 6: Optical spectrum of laser pulses after travelling in different directions through different ports of a bidirectional optical switch, compared to the spectrum of the incoming light.

Tests of the performance of a commercially available fast, bidirectional, polarisation maintaining fibre-optical switch[2] have been conducted in order to evaluate the switching speed and the device's influence on the optical spectrum of the laser pulses. The rise and fall times of laser light travelling in different directions through different ports of the switch have been measured to be around 100 fs at a repetition rate of 100 kHz. This duration is well below the available switching time of ~ 50 µs needed for the transition of the RF field in the accelerating cavities. At the exit of the switch the laser pulse amplitude is reduced by approximately 15% compared to the incoming light. The spectral shape is preserved, as shown in Fig. 6.

[2] AGILTRON NanoSpeed™ 1 × 2 bidirectional fibre-optic switch with 100 kHz driver

ELECTRONICS

For the control and monitoring of all subsystems several supporting electronic components are included in the setup:

- **TMCB** (Temperature Monitoring and Controls Board), developed at DESY for general purpose use in stand-alone devices. It is a versatile FPGA (Spartan6) board with 14 diverse ADC channels, 10 DAC channels, 4 temperature read-outs and 20 configurable GPIOs. It provides interface via Ethernet (RJ45) or optical communication (SFP+).

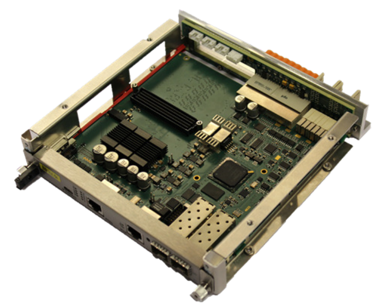

Figure 7: TMCB.

- **LDD** (Laser Diode Driver), developed at DESY. It is a high-precsion, low noise laser diode current driver and TEC controller. It has a compact mezzanine form factor with CAN and Ethernet interfaces and is suited for stand-alone operation.

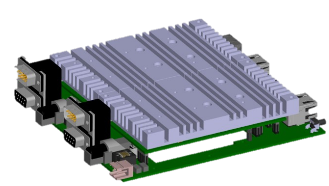

Figure 8: LDD.

- **FRED** (Fuse and Relay Board). This board was developed at DESY and is used in many 19" devices in electron diagnostics and beam control. It allows for remote monitoring and control of up to 8 DC voltage channels with individual fuses and current-limitations.

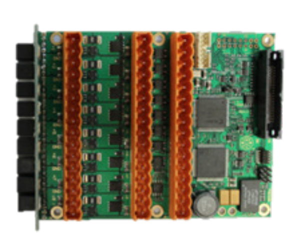

Figure 9: FRED3M.

- As temperature controller, a commercially available TEC controller[3] is used. It is remotely supervised using digital pins on the TMCB over the RS232 protocol.

[3] Meerstetter TEC-1091

ISBN 978-3-95450-134-2

THERMAL CONCEPT

In order to maintain the high timing stability of all involved components, the environmental conditions inside the unit have to be kept as stable as possible. Temperature variations lead to timing drifts in optical fibres (typically 30 – 50 fs / (K · m)) and working point shifting, e.g. of the EOMs. For a reduced susceptibility to external changes, all timing-critical components are mounted inside a thermally insulated and actively temperature stabilised compartment.

The electro-optical unit is housed in a 19" box, accommodating all optics, fibre-optics, DC and RF electronic devices. Only the DC power supplies are assembled as an external device.

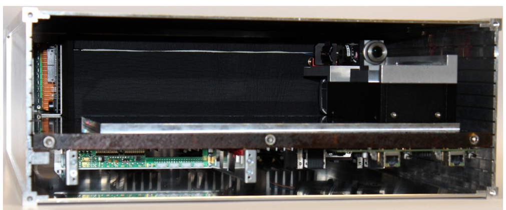

Figure 10: Front view of the 19" box housing the electro-optical unit. The middle plate separates the two temperature compartments.

The chassis is separated into two compartments, see Fig. 10. In the lower compartment (see Fig. 11), all components which introduce larger heat load, like TMCB, LDD, TEC controller and radiators of peltier elements, are mounted. The upper compartment (see Fig. 12) is thermally insulated from the lower part. In the front, a passively temperature stabilised area for the optical delay stages is located. In the rear, an actively temperature stabilised box with the sensitive fibre-optics and RF components is mounted.

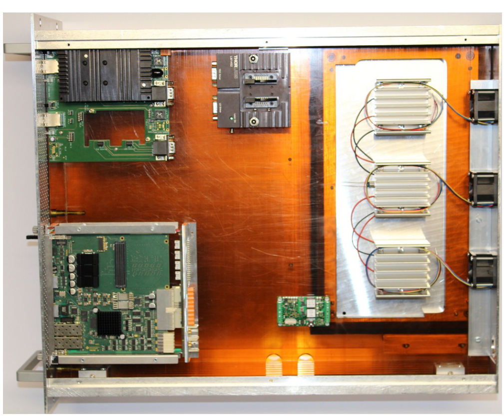

Figure 11: Lower compartment.

The temperature regulation by means of thermoelectric heating/cooling acts on a metallic base plate on which all parts are fixed. The thermally stabilised air volume is enclosed by a plastic box which is encased in heat insulation. A PID temperature controller is used for stabilising the base plate to $|\Delta T| < 0.01$ K.

Figure 12: Upper compartment.

Venting is achieved from front to rear with fans. This fits to the air conditioning concept of the 19" racks, which should deliver a stability of ±0.1 K by design.

SIGNAL READOUT

For sampling the modulated laser pulses exiting the EOMs a setup based on MicroTCA [8] electronics components is used. The digitalisation is done using an FMC board specially designed for the BAM readout (DFMC-DSBAM). It incorporates 4 ADCs for two channel interleaved sampling at up to 250 MSPS with 16 bit resolution, and has photo diodes and clock generation on board [9].

Figure 13: MicroTCA chassis equipped with x2timer, DAMC-FMC25 and DFMC-DSBAM modules.

Currently ongoing activities include circuit board design and evaluation, firmware development and high-level software programming. In Fig. 13, a photograph of a MicroTCA system used as a laboratory setup is shown. It is equipped with general-purpose timing and compute cards as well as the DFMC-DSBAM used for testing and development activities.

Figures 14a and 14b show test results from this setup. A series of laser pulses coming from a reference oscillator was scanned by changing the delay between the clock and sampling channels of the DFMC-DSBAM. The temporal

ISBN 978-3-95450-134-2

profile of the laser pulses is reproduced within the analogue bandwidth of 1 GHz.

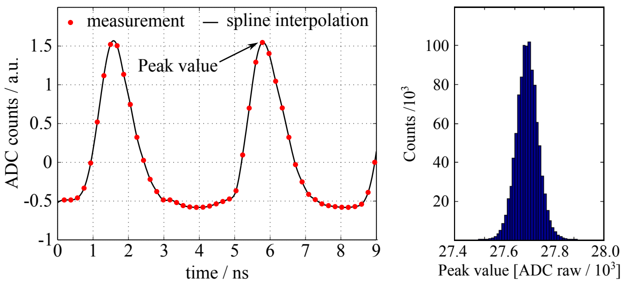

(a) Laser pulse train sampled by scanning the ADC clock delay.

(b) Distribution of detected peak values (1000 pulses).

Figure 14: Readout of optical pulses using the direct sampling electronics of DFMC-DSBAM.

A peak detection accuracy with better than 0.3% (STD) (from Fig. 14b) gives an upper limit of the cumulative amplitude jitter including laser pulse input, clock jitter and ADC resolution. Developments are ongoing to improve the amplitude detection accuracy in hardware and firmware.

CONCLUSION

A prototype of the improved electro-optical unit for the bunch arrival time monitors at FLASH and the European XFEL has been developed and is currently under construction. All included as well as supporting external components have been assembled and have been or are presently being tested. First measurements using the new signal processing and acquisition electronics show promising results and are in agreement with the expectations.

Current activities include the finalisation of the unit's internal cabling, mounting of the optics and ongoing firmware and high-level software developments. Further tests and performance evaluations will be conducted as soon as the setup reaches its final state. After completion of these steps the device will be installed in the injector section of the European XFEL for testing and commissioning with electron beam.

In the long term, at FLASH, eight bunch arrival time monitors will be installed or upgraded to the improved design, while up to ten setups are planned for the European XFEL, yielding in total 18 diagnostics stations needing to be equipped with electro-optical units of this kind. Once the prototype has proven its functionality in operation with beam, further devices are planned to be series manufactured and commissioned at the respective locations. An installation and testing routine is currently being developed on the basis of the experience gained with the prototype unit.

ACKNOWLEDGEMENT

The authors would like to thank Falco Zummack for his extensive support in setting up, maintaining and enhancing optical installations needed for the characterisation and testing of different subsystems. The contribution of Martin Schäfer and the mechanical workshop at DESY, Hamburg site, for carrying out the mechanical work, as well as Nicole Leuschner and the workshop at DESY, Zeuthen site, for the mechanical design and manufacturing of the optical delay stage, is highly appreciated.

REFERENCES

[1] A. Angelovski et al., "High bandwidth pickup design for bunch arrival-time monitors for free-electron laser", Phys. Rev. ST Accel. Beams 15, 112803 (2012).

[2] A. Angelovski et al., "Evaluation of the cone-shaped pickup performance for low charge sub-10 fs arrival-time measurements at free electron laser facilities", Phys. Rev. ST Accel. Beams 18, 012801 (2015).

[3] F. Löhl et al., "Electron Bunch Timing with Femtosecond Precision in a Superconducting Free-Electron Laser", Phys. Rev. Lett. 104, 144801 (2010).

[4] S. Schulz et al., "Femtosecond all-optical synchronization of an X-ray free-electron laser", Nature Communications 6, 5938 (2014).

[5] M.K. Czwalinna et al., "New Design of the 40 GHz Bunch Arrival Time Monitor Using MTCA.4 Electronics at FLASH and for the European XFEL", IBIC'13, Oxford, WEPC31, pp. 749–752 (2013), `http://accelconf.web.cern.ch/AccelConf/IBIC2013/papers/wepc31.pdf`

[6] A. Kuhl et al., "Comparative Analysis of Different Electro-Optical Intensity Modulator Candidates for the New 40 GHz Bunch Arrival Time Monitor System for FLASH and European XFEL", IBIC'13, Oxford, WEPC41, pp. 782–785 (2013), `http://accelconf.web.cern.ch/AccelConf/IBIC2013/papers/wepc41.pdf`

[7] K. Honkavaara et al., "FLASH: First Soft X-ray FEL Operating Two Undulator Beamlines Simultaneously", FEL'14, Basel, WEB05, pp. 635–639 (2014), `http://accelconf.web.cern.ch/AccelConf/FEL2014/papers/web05.pdf`

[8] MicroTCA website: `http://mtca.desy.de/`

[9] J. Szewinski et al., "MTCA Upgrade of the Readout Electronics for the Bunch Arrival Time Monitor at FLASH", ICALEPS'13, San Francisco, THPPC140, pp. 1380–1383 (2013), `http://accelconf.web.cern.ch/AccelConf/ICALEPCS2013/papers/thppc140.pdf`

EXTENSION OF EXISTING PULSE ANALYSIS METHODS TO HIGH-REPETITION RATE OPERATION: STUDIES OF THE "TIME-STRETCH STRATEGY"

E. Roussel, C. Evain, M. Le Parquier, C. Szwaj, S. Bielawski,
PhLAM/CERLA, Villeneuve d'Ascq, France
L. Manceron, J.-B. Brubach, M.-A. Tordeux, J.-P. Ricaud, L. Cassinari, M. Labat,
M.-E Couprie, P. Roy, Synchrotron SOLEIL, Gif-Sur-Yvette, France

Abstract

We examine how the "photonic time-stretch strategy" can be used to upgrade existing FEL Electro-Optic Sampling (EOS) setups to high repetition rates. Tests made at SOLEIL showed a capability of 88 MHz acquisition rate of single-shot EOS signals. The time-resolution limits is found to be identical to the limits of classical spectral encoding. Technically, time-stretch EOS systems can be build from existing spectral encoding systems, by adding an output optical device.

BRIEF REVIEW OF THE SPECTRAL ENCODING AND TIME-STRETCH METHODS

Spectrally Encoded Electro-optic Sampling (Time to Wavelength Conversion)

A powerful technique to analyze electron bunch shapes (or short THz pulses produced, e.g., by CSR) consists to convert the temporal information into the spectral domain of a laser pulse [1–6] (spectral encoding). The principle is displayed in Fig. 1. The spectral information is analyzed by a single-shot optical spectrum analyzer, which is composed of a grating and a CCD or CMOS camera. Although very efficient and widely used for electron bunch diagnostics, this strategy present a limitation in term of acquisition rate, because of the speed limitation of currently available cameras (typically hundreds of kilo frame/s). Hence it will be challenging to use further this technique in high-repetition rate FELs (as well as LINACs, storage rings, etc.).

Time Stretch Strategy (Time-to-time Conversion)

The photonic time-stretch technique has been developed in a different context than accelerator physics [7]. The idea consists in converting the ultrafast signal under investigation into a "slowed-down" replica. This is two-step process (Fig. 2). First the pulse is encoded into the spectral domain (as for the classical spectral encoding method). The second step consists in using dispersion in a long fiber, so that the optical spectrum is converted back into the time domain. Using a sufficient length of fiber, the output replica can be easily stretched up to the nanosecond domain, and thus can be recorded using a photodetector and an oscilloscope. This technique can typically reach tens to hundreds of MHz acquisition rates.

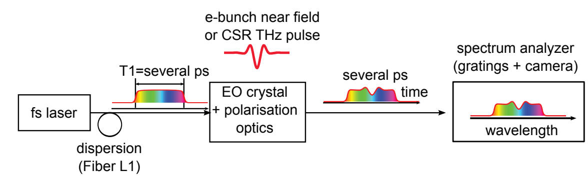

Figure 1: Classical electro-optic detection with spectral encoding. The pulse information is encoded into the spectral domain and recorded using a single-shot spectral analyzer. The main acquisition rate limitations stems from the camera used in the spectrum analyzer.

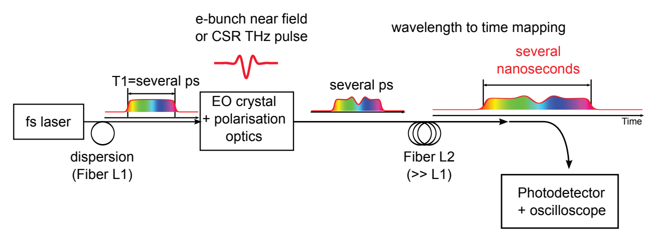

Figure 2: Principle of electro-optic sampling with time-stretch: a "slowed-down" replica of the bunch shape (or THz pulse) is produced. The output signal is recorded using a single pixel detector and an oscilloscope.

EXPERIMENTAL TESTS OF THE TIME-STRETCH EOS STRATEGY AT SOLEIL

We have explored the possibility to use this method to record electric fields produced by electron bunches at SOLEIL. Instead of probing the near-field electric field of an electron bunch, we attempted to detect the CSR THz pulses emitted by the electron bunch. As for the SLS EOS system [3], we used a GaP crystal and a 1040 nm mode-locked Yb fiber laser. The complete time-stretch setup is detailed in Ref. [8].

A typical series of single pulse is represented in Fig. 3. The stretch factor between the THz pulses and the oscilloscope pulses is $M = 190$ (i.e., 1 ps correspond to 190 ps at the oscilloscope input). The acquisition rate was fixed by the laser repetition rate (88 MHz). This speed enabled to study the CSR pulses emitted at the AILES beamline in

ISBN 978-3-95450-134-2

single bunch (0.85 MHz repetition rate), and 8 bunch (6.8 MHz).

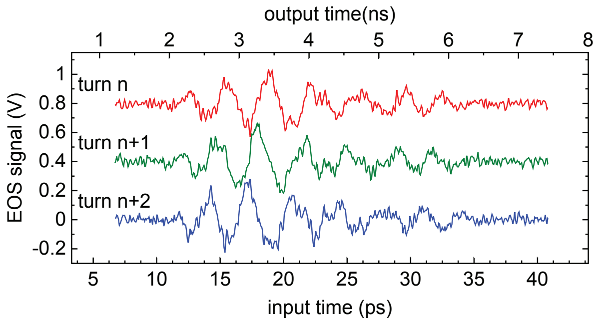

Figure 3: Typical EOS recording of successive THz CSR pulses emitted at SOLEIL every 1.2 μs. See [Roussel *et al.*, Scientific Reports 5, 10330 (2015)], for the detailed experimental setup. The stretch factor is $M = 190$. Note that the acquisition rate (88 Mega pulses/s) was well above the requirement of this recording.

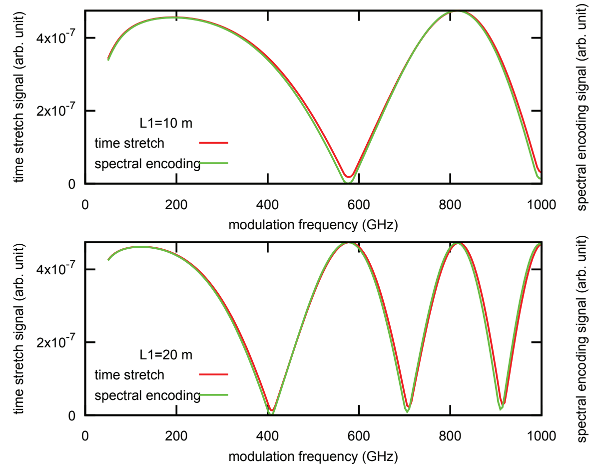

Figure 4: Comparison of the frequency responses (amplitude versus frequency) calculated in the case of spectral encoding (green curve) and time-stretch (red curves). (a) $L_1 = 10$ m and (b) $L_1 = 20$ m. $L_2 = 2000$ m. For other parameters, see Ref. [8].

TIME-STRETCH VERSUS SPECTRAL ENCODING METHODS: PERFORMANCES

Acquisition Speed

In the time-stretch technique, the use of a "single pixel" detector and an oscilloscope enables to reach much higher acquisition speeds. For the data shown in Fig. 2, the detector has a 20 GHz bandwidth, and the oscilloscope bandwidth is 30 GHz. It can thus be considered as equivalent to a spectrometer equipped with a camera with ≈20 GHz pixel clock.

Temporal Resolution/Bandwidth: Numerical Results

In addition to the crystal performances, it is well-known that spectral encoding method presents a limitation in temporal resolution that is due to the conversion process (from time to wavelength). Hence we have also examined the temporal resolution of the time-stretch strategy and compared it to the spectral encoding case.

Let us remember that the temporal resolution in the classic spectral encoding case is:

$$T_{res} \approx \sqrt{T_0 T_S}, \tag{1}$$

with T_S the duration of the stretched pulse at the crystal input, and T_0 the compressed pulse duration of the laser.

In order to compare the two methods, we have computed the output signal to a sine modulation of the crystal birefringence. We assume that the dispersion in the fibers is linear, and neglect nonlinear effects, and we compute the ouput modulation amplitude versus the modulation frequency f_m. As a main result (Fig. 4), the bandwidth (and thus the temporal resolution) were found to be the same for both the time-stretch and the spectral encoding methods.

CONCLUSION

The time-stretch strategy can be an alternative to the classical spectral encoding method, when high repetition rate electron bunches are used. From the experimental point of view, a time-stretch system can be obtained using an existing spectral encoding EOS system, by a relatively straighforward upgrade. Moreover no loss of performance is expected concerning the temporal resolution.

This strategy can also be potentially applied to any diagnostics for which an information can be encoded onto a laser pulse, as, e.g., transient reflectivity [9].

APPENDIX: DETAILS OF THE EXPERIMENTAL SETUP

In the case of CSR detection at SOLEIL, we used a setup optimized for sensitivity to the electric field. Hence, instead of using directly the setup presented in Fig. 2, we build a variant allowing to perform a balanced detection (at the analog level) between the two outputs of the EOS polarizing cube beam-splitter. This setup is shown in Fig. 5.

ACKNOWLEDGMENT

The work was supported by the ANR (Blanc 2010-042301) and the LABEX CEMPI project (ANR-11-LABX-0007). The CERLA is supported by the French Ministère chargé de la Recherche, the Région Nord-Pas de Calais and the FEDER. The project used HPC resources from GENCI TGCC/IDRIS (2013-x2013057057, 2014x2014057057).

ISBN 978-3-95450-134-2

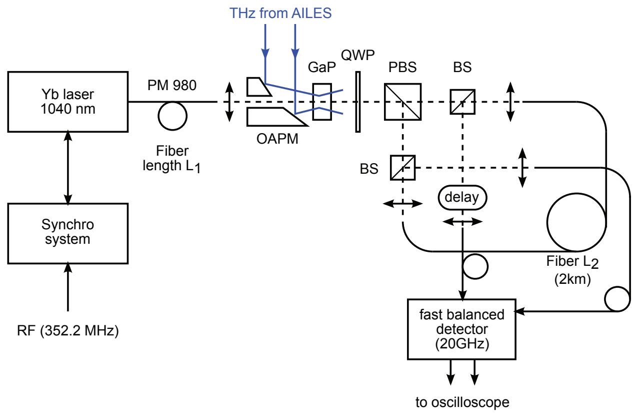

Figure 5: Detail of the experimental setup (from Ref. [8]). (P): polarizer, (OAPM): off-axis parabolic mirror, (PBS): polarizing beam splitter, (BS): non-polarizing beam-splitter. Expect the fiber with length L_1, all fibers are HI1060. L_1 = 10 m, and L_1 = 2 km.

REFERENCES

[1] Z. Jiang and X.-C. Zhang, Electro-optic measurement of THz field pulses with a chirped optical beam, Appl. Phys. Letters, **72**, 1945, 1998.

[2] I. Wilke *et al.*, Single-Shot Electron-Beam Bunch Length Measurements, Phys. Rev. Lett., **88**, 124801 (2002).

[3] F. Müller *et al.*, Electro-optical measurement of sub-ps structures in low charge electron bunches, Phys. Rev. ST Accel. Beams **15**, 070701 (2012).

[4] B. Steffen *et al.*, Electro-optic time profile monitors for femtosecond electron bunches at the soft x-ray free-electron laser FLASH, Phys. Rev STAB **12**, 032802 (2009).

[5] S. Casalbuoni *et al.*, Numerical studies on the electro-optic detection of femtosecond electron bunches, Phys. Rev. STAB **11**, 072802 (2008).

[6] N. Hiller *et al.*, "Electro-optical Bunch Length Measurements at the ANKA Storage Ring", IPAC'13, Shanghai, China, MOPME014 (2013).

[7] F. Coppinger *et al.*, Photonic time stretch and its application to analog-to-digital conversion, IEEE Tran. Microw. Theory and Techn. **47**, 1309 (1999).

[8] E. Roussel *et al.*, Observing microscopic structures of a relativistic object using a time-stretch strategy, Scientific Reports **5**, 10330 (2015).

[9] O. Krupin *et al.*, Temporal cross-correlation of X-ray free electron and optical lasers using soft X-ray pulse induced transient reflectivity. Optics Express **20**, 11396 (2012).

ISBN 978-3-95450-134-2

REAL-WORLD CONSIDERATIONS FOR CROSSED-POLARIZED UNDULATOR RADIATION CONVERSION*

W.M. Fawley†, E. Allaria, and E. Ferrari, Sincrotrone Trieste S.C.p.A., Trieste, Italy

Abstract

Cross-polarized (X-POL) configurations are a means to produce circularly-polarized radiation output from purely planar-polarized undulators. Recent polarization results from both the FERMI FEL-1 [1] at XUV wavelengths and Shanghai DUV-FEL [2] at visible wavelengths have confirmed that such configurations do work for single pass FELs. However, analysis of both FERMI and SINAP results indicate that the quantitative degree of planar to circular conversion can be significantly affected by several experimental details. Full conversion requires not only equal intensity of the two cross-polarized beams but also perfect overlap in space and time of their far-field amplitude and phase patterns. From simple theoretical analysis we examine a number of possible factors that can degrade the net linear to circular conversion efficiency. In addition to the previous suggestions by Ferrari *et al.* of problems with unbalanced powers and transverse phase variation arising from different effective emission z locations for the two cross-polarized radiation pulses, we also consider separate degradation effects of imperfect downstream overlap of the two linearly-polarized beams arising from different emission tilt angles and mode sizes. We also discuss optimizing the conversion efficiency by aperturing the radiation pulses downstream of the undulators.

INTRODUCTION

In addition to such attractive properties such as wavelength tunability, ultrashort and ultrabright output radiation, and multiple pulse production, free-electron lasers (FELs) with the proper undulator configurations can also produce variable polarization pulses. Because in many facilities linearly-polarized undulators have been favored due to their lower cost and often lower error content in comparison with variable-polarization designs such as the APPLE [3] and DELTA designs [4], the cross-polarized (X-POL) configuration has been suggested [5] as a relatively straight-forward means to produce output radiation with a high degree of circular polarization from purely linearly-polarized undulators. The X-POL arrangement has been studied for FEL amplifiers both theoretically [6, 7] and experimentally in the optical wavelength regime with circular-polarization degree 80% or greater [2].

Recently, experiments in October 2013 [1, 8] and more recently in February 2015 at the seeded FERMI FEL-1 facility [9] have shown the X-POL idea works reasonably well at wavelengths down to 26 nm. However, the 2013 results showed a global, maximum circular degree of polarization $P_{CIR} \leq 0.5$, suggesting that a careful tuning of the overall FEL system can be crucial for proper X-POL optimization. Indeed, the more recent X-POL results of February 2015 that included a careful optimization of the FEL using an online polarization diagnostic have shown significant improvement with a maximum $P_{CIR} \geq 0.8$. For the 2013 results, Ferrari *et al.* [8] suggested that an angular variation in far-field transverse eikonal phase between the horizontal- and vertically-polarized radiation due to different longitudinal source points in the undulator underlaid much of poor X-POL conversion. However, there are other possible degradation effects such as power imbalance of the two polarized fields and also imperfect spatial overlap arising from different emission tilt angles and mode sizes.

In the remainder of this paper we discuss these degradation issues and also the experimental procedures by which we believed we strongly improved the X-POL conversion efficiency as shown by the 2015 results.

THEORETICAL ANALYSIS

Inasmuch we are interested in the degree of circular polarization at a measurement point produced by spatial and temporal overlap of linearly-polarized sources the radiation properties are best described by the linear polarization basis for the Stokes parameters (see, *e.g.*, Eq. 7.27 of Jackson [10]):

$$\begin{aligned} S_0 &\equiv a_H^2 + a_V^2 \qquad & S_2 &\equiv 2a_H\, a_V\, \cos\phi_{HV} \\ S_1 &\equiv a_H^2 - a_V^2 \qquad & S_3 &\equiv 2a_H\, a_V\, \sin\phi_{HV} \end{aligned} \tag{1}$$

where a_H and a_V are the *local* field amplitudes of the two polarized beams, and $\phi_{HV} \equiv \varphi_H - \varphi_V$ is the difference of their eikonal phases. S_1 is the local, linearly-polarized signal lying in the horizontal/vertical plane while S_2 gives the strength of the signal component that is linearly-polarized in the skew planes at 45°/135°. Finally, S_3 measures the strength of the component with perfect circular polarization. The local value of the linear degree of polarization (the quantity that is actually measured in the FERMI studies discussed in the next section) $P_{LIN} = \sqrt{S_1^2 + S_2^2}/S_0$. The area integral of S_0 is proportional to the total power P_{TOT} of the two polarized beams while that of S_1 directly scales as $P_H - P_V$. The area integrals of S_2 and S_3 depend upon the details of their spatial overlap and relative phase at the measurement point. For the remainder of this discussion, we presume that the two sources are time-steady, monochromatic, exactly orthogonal, and define the horizontal and vertical planes.

Because the polarization measurements (see §III) are made in a "global" sense (here global refers to the total area

* This work was funded by the FERMI project of Elettra- Sincrotrone Trieste, supported in part by the Italian Ministry of University and Research under grants FIRB-RBAP045JF2 and FIRB-RBAP06AWK3

† william.fawley@elettra.eu

ISBN 978-3-95450-134-2

measured by the polarization detector), it becomes necessary to consider how local values of the Stokes parameters contribute to the global value. Clearly if the global value $\langle\langle S_1\rangle\rangle$ is non-zero, there must be residual linear polarization for all values of the relative phases ϕ_{HV} of the two beams and thus $P_{CIR} < 1$. However, it is also true that even if globally $\langle\langle S_1\rangle\rangle = 0$ but at local positions $S_1 \neq 0$, then both at those positions locally and more importantly *globally* $P_{CIR} < 1$. Such a situation can occur if for example the overall powers in the two linearly-polarized beams are exactly equal but either their mode shapes or sizes are different or, alternatively, if there is a transverse tilt between the two beams.

Similar phenomena are true for the S_2 and S_3 components where local values of $|S_2|$ might be large but the global value of $|\langle\langle S_2\rangle\rangle|$ can be zero. Unlike the S_1 parameter which by definition is insensitive to the relative phase ϕ_{HV}, both the local and, more importantly, global values of S_2 and S_3 depend upon this phase. For the FERMI X-POL experiments, the orthogonally-polarized sources originate in two different sets of undulators and ϕ_{HV} is varied by changing phase shifter strengths in the break sections. If we now make the *ansatz* that the temporal pulse shapes, radiated emission strength and transverse mode patterns of the two polarized beams are completely insensitive to variation of ϕ_{HV}, then if $\langle\langle S_2\rangle\rangle$ is non-zero for some given ϕ_{HV}, it must be *exactly* zero at some angle ϕ^0_{HV} in the interval $[\phi_{HV}, \phi_{HV} + \pi]$. At the two specfic angles ϕ^0_{HV} and $\phi^0_{HV} + \pi$, we have must have the global minimum value of $P_{LIN} = |\langle\langle S_1\rangle\rangle| \,/\, \langle\langle S_0\rangle\rangle$ given our *ansatz* that neither locally nor globally S_0 or S_1 depend upon ϕ_{HV}.

Defining $x \equiv \min P_{LIN} = |P_H - P_V|/P_{TOT}$, one sees that $P_H = 0.5\,(1 + x)\,P_{TOT}$ and $P_V = 0.5\,(1 - x)\,P_{TOT}$, presuming $P_H \geq P_V$. If the two beams exactly overlap at the detector with the same profile, then the maximum possible circular polarization is $\sqrt{1 - x^2}$. For example, if $\min P_{LIN} = 0.5$, then 75% of the total power is in one of the two linear polarizations while only 25% is in the other; $\max P_{CIR} = 0.866$ presuming both perfect spatial overlap and constant eikonal phase difference between the two beams.

Measure of the linear polarization angle $\psi = 0.5\tan^{-1} S_2/S_1$ while globally varying the phase shift between the two orthogonal sources also gives an indication of the downstream spatial and phase overlap properties. For perfect overlap and power balance, $\psi = \pm 45°$ and swings instantly at $\phi^0_{HV}, \phi^0_{HV} + \pi$ from one value to the other. For unbalanced powers but identical intensity and eikonal phase profiles,

$$\max|\psi| = 0.5\,\tan^{-1}\frac{0.5\sqrt{1 - x^2}}{x} \tag{2}$$

with the maxima in $|\psi|$ and $|d\psi/d\,\phi_{HV}|$ occurring in ϕ_{HV} at the locations of the maxima and minima of P_{LIN}, respectively. For $x = 0.5$, $\max\psi = 18.4°$ while for $x = 0.25$ the corresponding value is 31.3°. As we discuss in the next section, the behavior of both P_{LIN} and ψ as one scans in ϕ_{HV} can give an indication of the uniformity of the spatial overlap and relative eikonal phase variation of the two polarized beams.

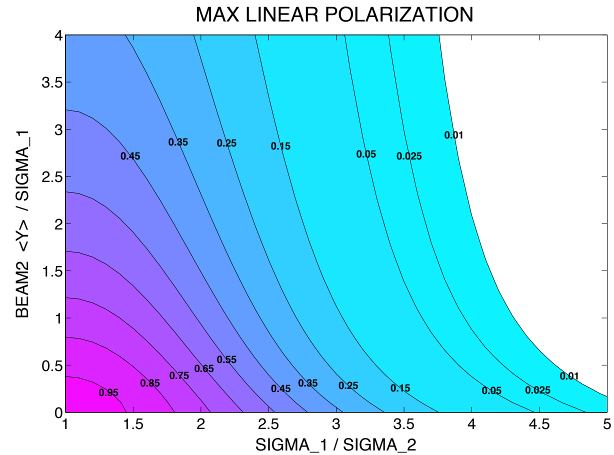

Figure 1: Contours mapping the maximum possible degree of linear polarization for two cross-polarized, gaussian profile beams with varying ratio of RMS radius σ_1/σ_2 and transverse offset of beam #2 from beam #1 in units of σ_1. There is perfect power balance and constant eikonal phase difference between the two beams.

In the case of perfect power balance (*i.e.*, $P_{LIN} = 0$ and $x = 0$), the maximum degree of linear polarization as one sweeps in over a full wavelength in phase shift between the two cross-polarized sources gives an indication of the uniformity of both the spatial overlap in intensity and eikonal phase difference of the two beams at the detector. In Figure 1 we plot the maximum degree of linear polarization for two equal power, cross-polarized sources in which the ratio σ_1/σ_2 of their downstream radii varies from 1 to 5 and for which the smaller beam's transverse offset $|\bar{y}|$ varies from 0 to 4 times the larger beam's electric field radius. Here we have presumed Gaussian profiles and a constant eikonal phase difference. One sees that for $\sigma_1/\sigma_2 \leq 1.5$ and $|\bar{y}|/\sigma_2 \leq 0.5$, one can still achieve greater than 85% linear polarization. Experimentally, such large values are quite obvious on downstream diagnostic screens and we believe in general that problems with maximum achievable polarization being significantly less than 0.9 are most likely due to a varying eikonal phase difference and/or different mode contents between the two beams.

FERMI EXPERIMENTAL RESULTS

The FERMI X-POL data of interest were taken with an electron time-of-flight (e-TOF) polarimeter developed at DESY and installed at FERMI under a collaborative effort (see [11–13] for more detail). On a shot-by-shot basis, this instrument measures at 16 individual stations equispaced in azimuthal angle θ the photoelectron signals produced by FEL radiation photoionization of He gas. The degree of *linear* polarization P_{LIN} and its angle ψ is then determined

ISBN 978-3-95450-134-2

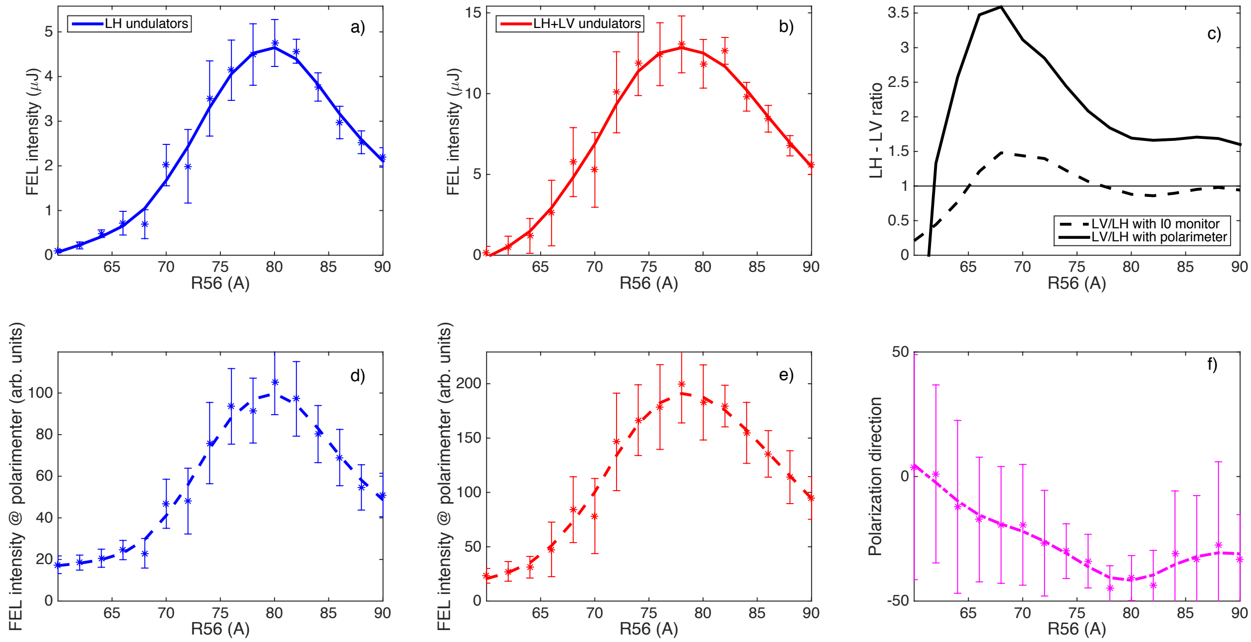

Figure 2: Variation of the output radiation power and its downstream degree of linear polarization via changing the FERMI FEL-1 post-modulator chicane current strength. This data was taken in February 2015. The panels labels a) and d) on the left display I0 and polarimeter power measurements, respectively, when only the upstream LH-polarized undulators were closed to FEL resonance. The center panels b) and e) refer to the measurements with all the LH- and LV-polarized undulators being closed. To the the right, panel c) shows the extacted power balance between the two polarizations (dashed line: I0 monitor data; solid line: polarimeter data) while panel f) indicates the measured polarization angle ψ. All error bars are the nominal RMS estimates.

from the signal data by using the theoretical relation

$$P(\theta) = 1 + \frac{1}{2}\{1 + 3\,P_{LIN}\ \cos[2(\theta - \psi)]\} \quad . \qquad (3)$$

In the process of optimizing an FEL for a cross-polarized configuration, it is critical to control the electron beam size and trajectory in the undulators. Moreover, the FEL needs to be controlled in a way that the emissions generated in the two groups of undulators have the same downstream properties. Since in the FERMI FEL-1 the field grows exponentially with z, balancing the power generated by each set of cross-polarized undulators can be difficult for the standard X-POL configuration where first a long undulator is used for one polarization, thus allowing the bunching and field to build up, followed by a second, much shorter undulator that produces the orthogonally-polarized radiation beam. Typically, there is little increase of bunching in the second undulator region and the second radiation beam is dominated by coherent spontaneous emission of a prebunched e-beam. In the case of an externally-seeded FEL such as FERMI, we found that power balance between the two beams is best achieved by manipulating the seeding and post-modulator chicane strength parameters. Importantly, we found in a recent set of experiments done in February 2015 that the best way to optimize matching between the two polarized radiation beams is to measure separately the FEL power of the two orthogonal sources at the downstream point where polarization control is actually wanted, or, alternatively, to examine the degree of the linear polarization of the combined fields.

Figure 2 reports an example of using an output intensity scan as a function of FERMI FEL-1's dispersive section strength as a means to balance the relative power between the two polarized sources. As one can see in Fig. 2a,b, according to measurements of the FEL power with the I0 gas-ionization monitor alone (whose position is quite close to the FEL source), it apparently is not possible in the present condition to get balanced emission between linear horizontal and linear vertical fields. Here we assumed that the measured output power from the two polarized beams will add linearly in the diagnostic; thus power balance would require twice the power in panel b) at a given dispersion strength relative to that in panel a). Considering only I0 measurements would then lead one to choose to a very different undulator configuration with respect to the one used here (*i.e.*, 4 undulators polarized LH and 2 LV). However if one use the FEL energy measurements from the polarimeter (*i.e.*, Fig. 2d,e), one sees a changing power balance ratio between the two polarizations as we change the chicane current and that an optimal, extracted ratio of 1.0 occurs at ≈ 78 A. Moreover, one can also measure directly the polarization properties while doing the optimization scan. Since in the case of a LH + LV cross-polarization, P_{LIN} depends on their relative phase ϕ_{HV} that is not known *a priori*, a better parameter for the optimization scans is the polarization angle ψ. As shown by Eq. 2 for power balance, this angle ideally does

ISBN 978-3-95450-134-2

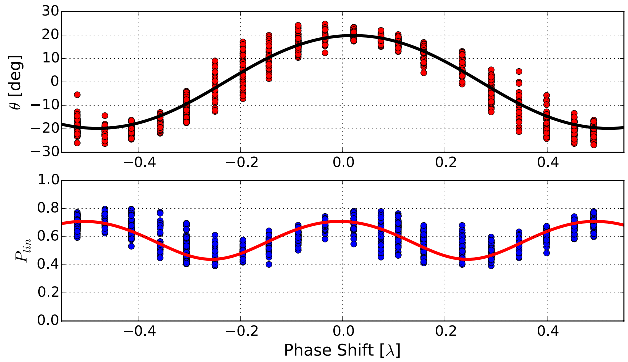

Figure 3: An example of the variation of linear polarization with phase shifter setting. In this case there is poor power balance and/or spatial overlap. The 32−nm data was taken in October 2013 on FERMI's FEL-1 with the DESY TOF polarimeter with the dots representing individual shots; typical statistical errors are of the order of 5%. The solid lines represent the predicted polarization dependence of two Gaussian profile sources with equal 100 μm waists separated by 3.7 m and whose field amplitudes differ by a factor of two.

not depend upon the relative phase and, for optimal power balance and overlap, should exhibit sudden changes from −45 to +45 degrees as one passes through the regime producing maximum circular polarization. Results reported in Fig. 2f show a clear trend for ψ with a local minimum at 43° for a dispersion section current ≈ 78 A. As would expected from perfect overlap theoretically, this corresponds to the dispersion section current value that also balances the power contributions from the LH- and LV-polarized undulator sections as seen in Figs. 2b,e.

These new results show the importance of an efficient, accurate, online diagnostic to determine the relative power between two cross-polarized sources. Indeed, if we had set the FEL based on the I0 detector power measurements, we would have obtained a condition where one of the two fields would be significantly stronger than the other. In retrospect, we believe such a situation occurred in our October 2013 X-POL measurements [8] which led to a reduced capability in polarization control as shown in Fig. 3. Indeed, it is important to note that the FEL power balance optimization done in the 2013 measurements used only the I0 monitor and we found that apparent balance required adopting a [4-LH + 1-LV] configuration rather than the far more successful [4-LH + 2-LV] configuration used more recently. For this situation, the power imbalance and the intensity and eikonal phase differnce effects of longitudinally-separated source points degrade both the degree of linear polarization and the maximum ψ achieved.

In February 2015 there were also a series of measurements in which the degree and angle of linear polarization was measured as a function of downstream, transverse position before which the combined beams were apertured upstream through an opening much smaller than their total size. Here we found that both the maximum and minimum polarization degree could be quite close to the perfect values of 1.0 and 0.0, again suggesting the smaller global values were due to relative intensity and eikonal phase variations. These results will be more fully reported elsewhere.

The authors are pleased to thank the FERMI operations crew and in particular the PADReS group for enabling the polarization observations of October 2013 and February 2015. We also gratefully acknowledge the FERMI collaboration with the DESY TOF polarimeter group and discussions with various team members.

REFERENCES

[1] E. Ferrari *et al.*, "Experimental Characterization of FEL Polarization Control with Cross Polarized Undulators", in *Proc. FEL'14*, Basel, Switzerland, Aug. 2014, paper THA02, pp. 644-648.

[2] H. Deng et al., *Phys. Rev. ST Accel. Beams* **17**, 020704 (2014).

[3] S. Sasaki, *Nucl. Instrum. Meth.* **A347**, 83-86 (1994).

[4] A.B. Temnykh, *Phys. Rev. ST Accel. Beams* **11**, 120702 (2008).

[5] K.-J. Kim, *Nucl. Instrum. Meth.* **A445**, 329 (2000).

[6] Y. Ding and Z. Huang, *Phys. Rev. ST Accel. Beams* **11**, 030702 (2008).

[7] Y. Li, B. Faatz, and J. Pflueger, *Nucl. Instrum. Meth.* **A613**, 163 (2010).

[8] E. Ferrari *et al.*, *Sci. Reports*, in press (2015).

[9] E. Allaria *et al.*, *Nat. Photonics* **6**, 699 (2012).

[10] J.D. Jackson, *Classical Electrodynamics*, 3rd Edition, Wiley, New York, p. 301 (1999).

[11] J. Viefhaus *et al.*, in *Coincidence Studies of Electron and Photon Impact Ionization*, ed. C.T. Whelan and H.R.J. Walters, *Physics of Atoms and Molecules*, Springer, pp. 145-153 (1997).

[12] J. Viefhaus, "An Online Diagnostic Unit for FEL Photon Parameter Determination and Optimization", presented at Proc. FEL'15, Daejeon, Korea, Aug. 2015, paper WED02, these proceedings.

[13] E. Allaria *et al.*, *Phys. Rev. X* **4**, 041040 (2014).

ISBN 978-3-95450-134-2

TECHNICAL OVERVIEW OF BUNCH COMPRESSOR SYSTEM FOR PAL XFEL

H.G. Lee, D.H. Na, S.B. Lee, B.G. Oh, Y.J. Suh, H.S. Suh, Y.G. Jung, D.E. Kim, K.H. Park, H.S. Kang, K.W. Kim
Pohang Accelerator Laboratory, POSTECH, KOREA

Abstract

Pohang Accelerator Laboratory(PAL) is developing a SASE X-ray Free Electron Laser based on 10 GeV linear accelerator. Bunch compressor (BC) systems are developed to be used for the linear accelerator tunnel. It consists of three(BC1, BC2, BC3_H) hard X-ray line and one(BC3_S) soft X-ray line. BC systems are composed of four dipole magnets, three quadrupole magnet, BPM and collimator. The support system is based on an asymmetric four-dipole magnet chicane in which asymmetry and variable R_{56}. can be optimized. This flexibility is achieved by allowing the middle two dipole magnets to move transversely. In this paper, we describe the design of the stages used for precise movement of the bunch compressor magnets and associated diagnostics components.

INTRODUCTION

A bunch compressor support system has been fabricated and tested for the PAL XFEL. The machine of the PAL XFEL consists of four main sections: the linear accelerator, the hard x-ray undulator hall, the soft x-ray undulator hall and the experimental area. The accelerator, schematically shown in Figure 1, comprises the gun, the laser heater, four accelerating sections groups (L1–L4), four bunch compressors (BC1, BC2, BC3_H and BC3_S) and the spreader. The physics design of the magnetic bunch compressor is based on an asymmetric four-dipole chicane configuration [1]. The BC purpose is to reduce the electron bunch length, thus increasing the peak current, taking advantage of the beam correlated energy spread. Due to the accelerating process, there is an inherent longitudinal energy spread in the electron bunch. Passing through four bending magnets chicane, the path length is energy dependent and the electron bunch is compressed. At each bend, the electron bunch head delays with respect to the tail. Mounting high homogeneity magnetic field dipoles and having diagnostic devices centre on the beam at each chicane position are the main advantages of the movable chicane.

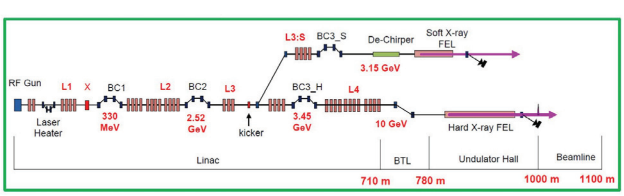

Figure 1: The schematic layout of the 3-BC lattice.

BUNCH COMPRESSOR OVERVIEW

The BC support system, shown in Figure 2 and Table 1, consist of four dipole magnets (DM), two tweak quadrupole magnets and a skew quadrupole magnet, two corrector magnets, BPM, collimator, screen and CSR monitor. The position of such diagnostic devices remains fixed with respect to the central dipoles.

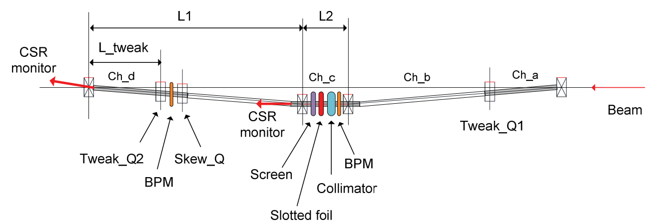

Figure 2: Layout of the BC support system.

Table 1: Major Parameters of the BC Support System

	BC1	BC2	BC3_H	BC3_S
Dipole angle , deg	4.9	3.0	1.7	1.7
Dipole length , m	0.2	0.7	0.7	0.7
L1 , m	4.4845	7.1905	7.597	6.397
L2 , m	1.2	1.8	1.8	1.8
L_tweak , m	1.146	1.3483	2.349	1.349
Aperture diameter of Tweak Quad , mm	44 (Q11)	44 (Q11)	44 (Q11)	44 (Q11)

The support systems of BC are composed of two fixed support and a moving support. The two central dipoles are mounted on a moving support that can have up to 627.0 mm motion orthogonal to the beam axis. A servo motor provides movement to the central stage and a linear encoder controls its exact position. The position accuracy of dipoles is within 50 µm.

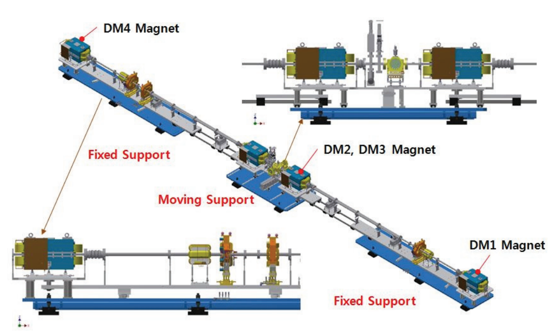

Figure 3: 3D modelling of BC support system.

The chicane is symmetric (DM1–DM2 distance is equal to DM3–DM4 distance). Tweak Q1 (Q2) is placed between DM1 (DM3) and DM2 (DM4). The quadrupole

ISBN 978-3-95450-134-2

magnets rotate and remain at a fixed distance from the pivot points DM1 and DM4. Figure 3 shows the BC layout and its overall 3D modeling.

MECHANICAL DESIGN OF SUPPORT

The BC support structure consists of three structural steel tables with 30 mm thick aluminum top plates. The moving table top plate house two sets of linear motion guide rails, each with a roller bearing cart, on which an aluminum sliding main plate is mounted. The main plate supports the two central dipoles and an adjustable aluminum plate. This plate carries the DM2, DM3 dipole magnet, and the BPM mounted on support independently adjustable. The dipole movements are controlled by means of a transverse support table for dipoles DM2 and DM3. The table travel on a pair of linear rails each with two linear guide blocks.

Figure 4 shows the component of the moving support system which is composed of basic support, moving table, sliding table, positioner and servo motor [2][3]. The mechanical parameters of the BC2 support systems are summarized in Table 2. The 406XR Positioner is capable of carrying relatively high loads up to a distance of 500 mm. Its quick and accurate positioning capability can be attributed to a high strength extruded housing, square rail ball bearing system, and precision ground ballscrew drive. It is equipped with 5mm lead ballscrew, linear encoder, electromagnetic break and limits switch.

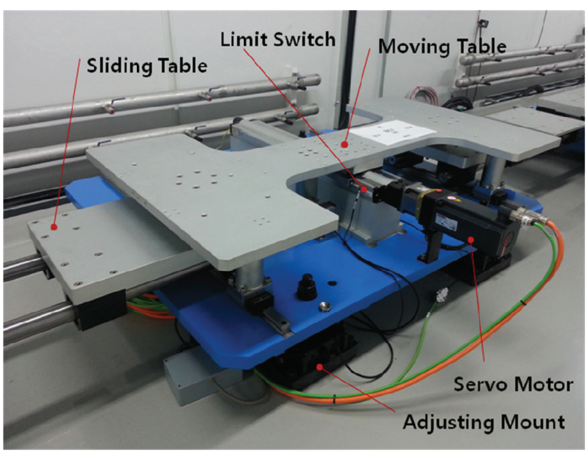

Figure 4: Component of moving support.

Table 2: Parameters of the BC2 Moving Support

Description	Moving Support
Dimension of Support[LxWxH][m^3]	5.0 x 1.3 x 0.53
Static torque of Servo Motor[N.m]	8.2
Working range of Positioner[mm]	500
Gear ratio	10:1
Resolution of Linear Encoder[μm]	0.5
Limit Switch & Hard Stopper	

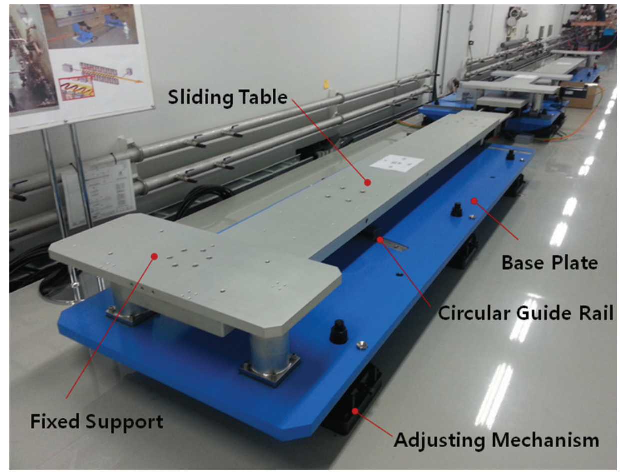

Figure 5: Component of fixed support.

Figure 5 shows the component of the fixed support system. DM1 and DM4 are mounted on the two fixed supports. Two rotating platforms supporting tweak quadrupole and skew quadrupole magnet are guided by two circular rails and a cam follower by adjustable ball transfer units. The cam follower is a compact bearing with a high-rigidity shaft and a built-in needle bearing. Most suitable as a guide roller for cam mechanisms and linear motion guided.

Each platform is driven by a rigidly connected ball spline unit on the fixed table and connected to the movable platform by a sliding constraint. There are four pivot assemblies which are mounted on rotating platforms for the equipment. The ball bearing is assembled inside a bearing housing pressed firmly by a cover plate and a collar nut. The pivot is fastened to the magnet support table and the rotating platform is attached to the bearing housing. The beam pivots are accurately located under each dipole center, and therefore all devices are rigidly connected to the beams stay aligned with the dipoles geometrical center. The basic structural steel beam design is aimed at minimizing deformations, guarantee of system position accuracy and reproducibility, keeping under control the total mass and the overall dimensions.

CONTROL SYSTEM

The motor is controlled with a PC running *Twincat* PLC, a software by *Beckhoff* that will be used in PAL-XFEL. The software has been coded in Structured Text, following the IEC 61131-3 standard. It is driven by a single servo motor. Also has a one Incremental linear encoder, the two contact sensor. It is simple moving because of one axis drive. The length of the actuator has three types. 500 mm 2sets, 600 mm 1set, 700 mm 1set. Controller is used the Beckhoff PLC C6920 can be installed the EPICS IOC.

MAGNET DESCRIPTION

Dipole magnet for the bunch compressor is applied two types, D1 and D2. D1 is used for BC1 and D2 is used for BC2, BC3_H, BC3_S. The distance of the offset of each

ISBN 978-3-95450-134-2

magnet is different in BC system. Table 3 is shows the offset distance of each dipole magnet in BC from the center line of the Beam. The quadrupole magnets are classified into 11 kinds according to the aperture diameter, the effective length and the maximum gradient. Quadrupole Q11 and Q11 skew type are installed the bunch compressor.

Table 3: The Offset Distance of Dipole Magnets

	Magnet Type	DM1	DM2	DM3	DM4
BC1	D1(mm)	5.13	2.83	2.83	5.13
BC2	D2(mm)	11.00	6.03	6.03	11.00
BC3_H	D2(mm)	6.23	3.42	3.42	6.23
BC3_S	D2(mm)	6.23	3.41	3.41	6.23

VACUUM CHAMBER DESIGN

On the basic design of LCLS Bunch compressor vacuum chamber, we implemented some modification, fabricated and tested [4][5][6]. Bellows at each side of the bending magnet are installed to respond the bending angle for vacuum chamber. The four dipole magnet chambers, also drift vacuum chamber, are made from extruded 6063-T5 aluminum alloy, chosen for its high mechanical accuracy, better electrical conductivity, high strength and superior weldability and is suitable for use as a vacuum chamber material. Aluminum alloys allow easy extrusion of complicated cross sections using porthole dies, and the Al-Mg-Si alloy provides superior performance in extrusion. So relative permeability (μ_r) is under 1.03.

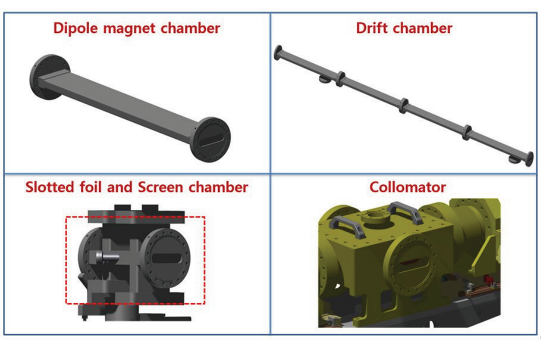

Figure 6: 3D modelling of unified beam chamber.

Figure 6 shows the dipole magnet chamber, slotted foil and screen chamber, collimator and the drift vacuum chamber. All chambers are approximately 800 mm long with internal 100 mm × 25 mm rectangular cross section. In order to reduce the deformation of the chamber, edge of cross section has rounded with 10R. Because it becomes the wall thickness is no more than 2 mm. An internal surface roughness of 150 nm was achieved with chemical treatment. The flange of the aluminum chamber is generally made of bi-metal method, especially friction welding which welded to the aluminum and stainless steel. Another method is that TiC coating on aluminum flange for high hardness. PAL-XFEL bunch compressor is adopted both methods. No detectable leak (< 1×10^{-10} mbar ℓ/s) is permitted for each components. We designed under 1×10^{-7} mbar after 48hr pumping. For maintained vacuum performance, We installed four sputter ion pumps (SIP) for 60 ℓ/s with RF pumping slits. Figure 7 shows the design of the RF shielded chamber. The diagnostic section, between DM2 and DM3, consists of BPM, Slotted foil and Screen monitor. Two sputter ion pumps near diagnostic instrument to reduce pressure rise induced by collimator, slotted foil and screen monitor. One cold cathode gauge is placed to measure pressure at collimator. To reduce wakefield effect and energy loss, we designed unified beam chamber dimension and RF shielded chamber such as dipole magnet chamber.

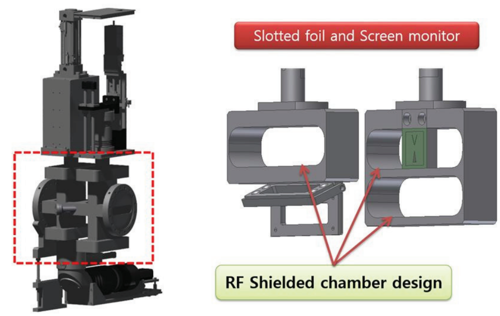

Figure 7: Design of the RF shielded chamber.

SUMMARY

In this report, the status of the PAL-XFEL bunch compressor system is briefly described. Three bunch compressor lattices for PAL XFEL are designed so as to minimize emittance growth due to CSR and mitigate microbunching instability. The support system has been successfully fabricated, load tested and installed.

REFERENCE

[1] H.S.Kang, J.H.Han, T.H. Kang, I. S. Ko, "Start to end simulation of three bunch compressor lattice for PAL-XFEL ", IPAC2012, New Orleans, USA.
[2] E. Rotela, S. Sharma, A. Barcikowski, and J. Biggs "Mechanical Design of a Flexible Bunch Compressor for APA Linac" APS, ANL.
[3] D. Lacivita, G. Lanfranco, G. Pangon, D. Zangrando, C. Belliero, M. Cenetti and F. Gangini, "FERMI@ELETTRA bunch compressor chicane mechanical design" Diamond Light Source Proceedings, Vol 1, e19, page 1 of 4 MEDSI-6 2010.
[4] D. La Civita et al., "FERMI@ELETTRA bunch compressor chicane mechanical design", Diamond Light Source Proceedings, Vol 1, e19, (2010).
[5] Gian Luca Orlandi et al., "Bunch-Compressor Transverse Profile Monitors of the SwissFEL Injector Test Facility", IBIC2012, Tsukuba, Japan.
[6] "LCLS CDR", SLAC-R-593, April 2002.

ISBN 978-3-95450-134-2

DESIGN CHALLENGE AND STRATEGY FOR THE LCLS-II HIGH REPETITION RATE X-RAY FEL PHOTON STOPPERS*

J. Krzywinski, J. T. Delor, P. A. Montanez, E. Ortiz, M. Rowen, T. O. Raubenheimer, Y. Feng#, SLAC, Menlo Park, CA 94025, USA

Abstract

The unique combination of the extremely high single-pulse peak fluence and the enormous average power density of the high repetition rate X-ray FEL's such as the future LCLS-II presents tremendous technical challenges to design, implementation, and operation of the photon stoppers. We have carried out finite-element-analysis studies of potential working designs including water-cooled normal-incidence CVD diamond and water-cooled grazing-incidence B_4C constructions to verify the validity of these concepts, in terms of remaining below the safe limits of melting or mechanical failure from fatigue. The CVD diamond design is new, novel, and compact, but bears the risk of not having been experimentally tested; whereas the B_4C approach is less practical due to a very small incidence angle required for sufficiently reducing the power density to not to melt. It was also shown that analytical methods for calculating the temperature distribution are reasonably accurate and can provide, for simple design geometries, immediate design guidance without often time-consuming numerical simulations.

INTRODUCTION

The X-ray beam properties of the LCLS-II high repetition rate Free-Electron Laser (FEL) present both conceptual and implementation challenges to developing insertable devices that will stop such a beam securely and reliably. Existing stopper designs currently deployed on LCLS-I operating at a repetition rate of only 120 Hz will not work for LCLS-II which produces similar single pulse energies but with a maximum repetition rate up to 1 MHz; an nearly four orders of magnitude increase. The unique combination of the extremely high peak fluence and the enormous average power density for even an unfocused beam, unprecedented at existing third generation synchrotron sources or the current fourth generation low repetition rate X-ray FEL's, requires new solutions.

In this report we explore some of the possible solutions that can push the limits of the allowable average and peak power beyond what were considered up until now. As a starting point we set the requirement that the stopper should be able to stop/absorb a beam with an average power of up to 200 W and maximum credible single-pulse energy from 2 to 10 mJ [1]. The specific beam parameters considered were: 100 kHz, 2 mJ and 20 - 50 fs long pulses over the X-ray energy range of 0.2 to 5 keV, producing an average power of 200 W. The authors have not identified a solution for stopping a beam at a kW level average power at the writing of this paper.

The combination of an enormous average incident power density (W/cm^2) and an extremely high peak fluence (J/cm^2 per pulse) suggests that the ideal material for stopping such X-ray beams should have both high thermal conductivity and low-*Z* number; a low-*Z* material is needed to avoid instantaneous damage. While there are several materials that can be considered, the most compelling candidate is the chemical-vapor-deposition (CVD) diamond that possesses exceptional high thermal conductivity. However we also recognize that there is a potential risk that diamond has not been tested with respect to the instantaneous damage limit (usually specified in the unit of eV/atom), especially under high repetition conditions when other factors such as the cyclical thermal fatigue, phase transitions, and chemical stability are to be considered. A further challenge is the operation at or near the carbon *K*-edge where the X-ray absorption length decreases dramatically, thus creating very high instantaneous radiation dosage. This instantaneous damage problem can be possibly mitigated by coating the CVD diamond by a thin layer of also low-*Z* material B_4C, which is better damage-resistant but has a poor thermal conductivity. The results of this study are described in section 2.

We have also investigated the possibility of using B_4C-based stoppers at a grazing incidence to alleviate potential issues because of its low thermal conductivity. It has been proven that the LCLS B_4C-based stoppers can effectively handle the FEL peak fluence, but the relatively poor thermal conductivity of B_4C (~ 30 W/m·K at room temperature) raises a serious question of whether such a material can be used as stoppers for high power density beams. We have thus explored solutions using grazing incidence conditions where the power is spread over a sufficiently large area. Grazing incidence copper-based stoppers have been successfully used at synchrotron sources to stop many kilowatts X-ray beams, and grazing incidence B_4C-based stoppers are also being planned for at the European XFEL facility. We sought to answer the question of how the maximum allowable average power density depends on the angle of incidence. The results of this study are given in section 3. The conclusions of these studies together with some comparisons are presented in section 4.

CVD DIAMOND BASED STOPPERS

CVD diamond has an excellent thermal conductivity, almost two orders of magnitude higher than that of B_4C at room temperatures and above. Therefore, one could expect it to work at normal incidence. Two cases were

*Work supported by DOE under Contract #. DE-AC02-76SF00515.
#yfeng@slac.stanford.edu

ISBN 978-3-95450-134-2

considered, one corresponding to the maximum photon energy of 1.3 keV for the Soft X-ray (SXR) and the other 5 keV for hard X-ray (HXR) transport lines, respectively. The X-ray FEL beam sizes at the worst-case scenarios at the stopper locations in the Front-End-Enclosure (FEE) (without the use of focusing lenses or mirrors) and the X-ray attenuation lengths at these two energies are given in Table **1**. The thermal conductivity of CVD diamond assumed in the simulations is shown in Figure 1, in comparison to that of copper.

Table 1: X ray FEL FWHM Beam Sizes and Attenuation Lengths for CVD Diamond

Photon Energy (eV)	FWHM Beam Size (μm)	Attenuation Length (μm)
1300	1160	2.7
5000	322	150

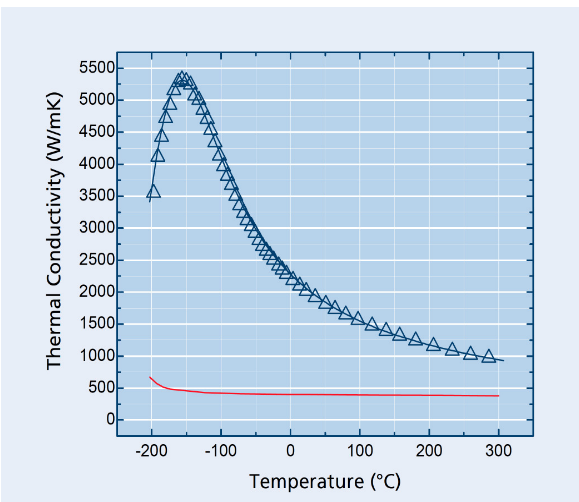

Figure 1: The thermal conductivity of CVD diamond (blue line) and copper (red line) for comparison [data taken from Diamond Materials GmbH].

The simulations were performed using the finite element analysis (FEA) method. The average power was applied as if it were a continuous-wave (CW) source, and the pulse structure of the FEL beam was not considered for simplicity. The instantaneous temperature in the material is expected to oscillate around that obtained using the CW FEA analysis, and depends on the exact temporal structure of the pulses. In addition, the FEA calculations were crosschecked with the help of several finite difference algorithms to assure that there are no significant numerical errors due to the fact that the absorption length was much smaller than the dimensions of the stopper. The finite difference algorithms assumed constant thermal conductivity and crosschecks were performed at low power levels resulting in small temperature variations. We started our simulations with an edge-cooled model (fixed temperature). The geometry is depicted in Figure 2.

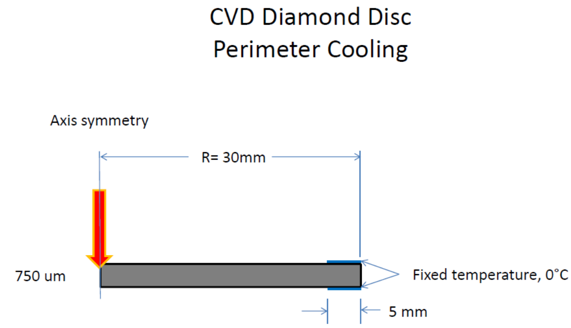

Figure 2: The schematic of a perimeter cooled CVD diamond used in simulations. The FEL beam is incident normal to the top surface and at the center of a 750 μm thick diamond disk of 30 mm in radius with the edge being held to a fixed temperature of 0°C.

The simulated maximum temperature as a function of the average incidence power for the 1.3 keV case and the 5 keV case is illustrated in Figure 3. For the SXR 1.3 keV simulation, the energy absorbed in the material was assumed to be applied to the surface due to the very short absorption length of < 3 μm, whereas in the 5 keV HXR case, a volumetric heating model was used. As expected the maximum temperature in the diamond for the two cases stays in a safe region well below the graphitization temperature for diamond (1300 °C) at power levels up to 200 W.

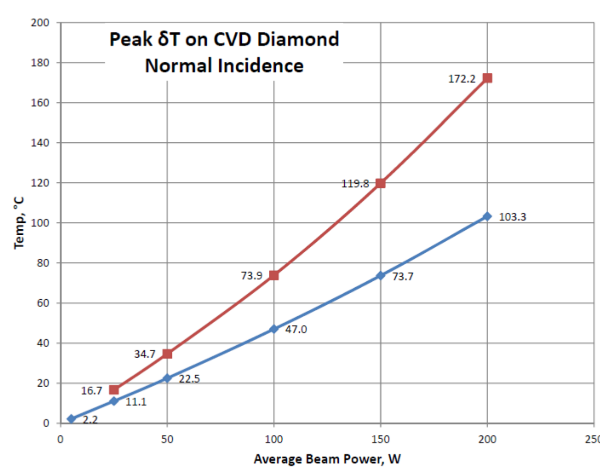

Figure 3: The steady state maximum temperature in the diamond for the 1.3 keV SXR (blue line) and 5 keV HXR (red line) cases as a function of the (CW) incident power for the geometry shown in Figure 2.

We have also simulated the thermal stress arising from the temperature gradient in the diamond. The boundary conditions are shown in Figure 4. Here we used the most conservative conditions where cooled edges were bound. The stress distributions for the 5 keV and 200 W cases are given in Figure 5 and Figure 6. The maximum stress is more than one order of magnitude smaller than the tensile strength of 500 MPa, at which the material is likely to be mechanically damaged. Therefore we have concluded that

ISBN 978-3-95450-134-2

perimeter cooled CVD discs should be able to withstand the maximum average input power of 200 W. In addition, the stress analysis of the CVD diamond disc with the bounded edges leads to the conclusion that one can use indium foil as the thermal contact material between the diamond and a cooper cooling block.

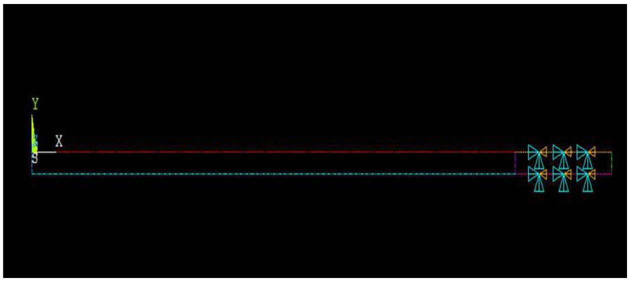

Figure 4: The Boundary conditions with clamped edges, where the 5 mm edge is restricted from movement in X and Y directions.

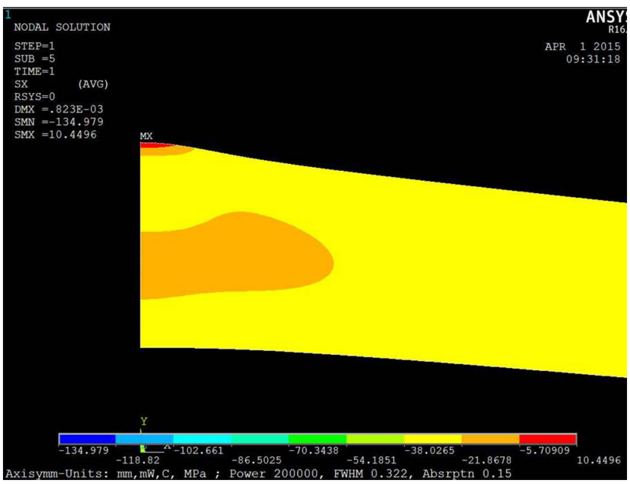

Figure 5: Radial stresses. Extreme values: 10.45 MPa (tensile), -38 MPa (compressive).

The instantaneous damage problem has been studied extensively both theoretically and experimentally at LCLS and other FEL facilities [e.g. 2, 3]. The instantaneous damage happens on a time scale ranging from a few femtoseconds to tens of picoseconds. The energy of femtosecond photon pulses is first absorbed in the atom's electron system, which then thermalizes with the lattice on the time scale of 1 to 50 ps [4]. When the absorbed dose is higher than the heat of fusion (or a specific heat related to other phase transitions), melting and subsequent damages occur. The typical heat of fusion scale is on the order of 1 eV/atom. Both thermal and non-thermal damage mechanisms have been reported in the literature [3, 6]. In the case of CVD diamond both the theory and the experiment support the non-thermal induced damage mechanism with a threshold around 0.5 eV/atom [6, 7].

Fatigue related damages should also be considered in addition to the instantaneous damage [7]. The theory predicts that the fatigue related damage could occur if the instantaneous absorbed dose is larger than a certain fraction of the heat of fusion. However, the current theory [7] is directly applicable to ductile materials such as Beryllium or Aluminium. It is not clear how the same theory can be extended to other materials in which the yield strength is anisotropic. For example, in the case of B_4C no multi-shot damage was observed when the B_4C sample was exposed to 650,000 X-ray pulses depositing 0.16 eV/atom at the surface of the sample (the heat of fusion for B_4C is close to 0.5 eV/atom). The dose of 0.16 eV/atom is more than twice as high as the dose derived if one applies the lowest value of the yield strength, the tensile yield strength, to estimate the fatigue related damage for B_4C [8]. The reason that the experimentally determined fatigue threshold is at least twice higher than derived from the theory presented in [7] can be attributed to the fact that the thermal stress here has mainly a compressive component and that the compressive yield strength in B_4C is much higher than the tensile one. One can expect that a similar situation may occur in the case of CVD diamond.

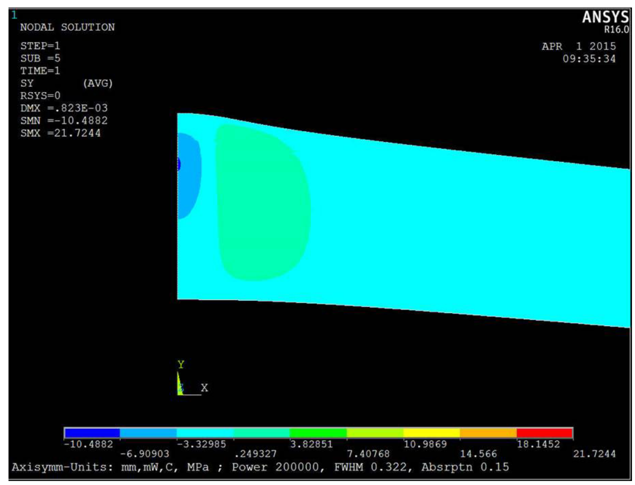

Figure 6: Axial stresses. Extreme values: 7.4 MPa (tensile), -10.5 MPa (compressive).

The instantaneous damage problem is most severe at the lowest photon energies as the absorption coefficient increases with the third power of the wavelength. For CVD diamond the maximum absorption occurs at the photon energy close to 290 eV, which corresponds to the carbon K absorption edge. Taking into account expected LCLS-II beam parameters and the location of the stopper; one derives the peak dose of 0.1 eV/atom at this photon energy. We have calculated the maximum increase of the temperature ΔT at the surface by taking into account the nonlinear dependence of the specific heat. The expected peak dose of 0.1 eV/atom corresponds to a ΔT of about 700 ^{o}K. The peak dose of 0.1 eV/atom has the same order of magnitude as the safe limit for the multi-shot damage. Therefore, in order to mitigate the multi-shot damage risk, we propose to coat the CVD surface with thin layer (1-2 μm) of B_4C. The effect of the coating on the peak dose absorbed in CVD diamond is shown in Figure 7. We are also planning to perform multi-shot damage tests to mitigate the thermal fatigue risk even further.

ISBN 978-3-95450-134-2

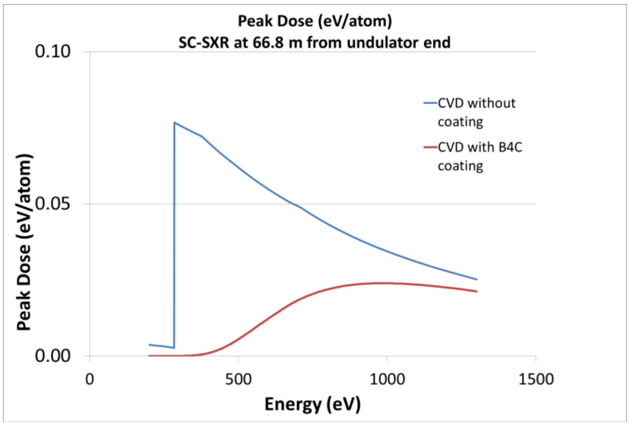

Figure 7: The peak dose of coated (red line) and uncoated CVD diamond (blue line).

The B_4C coated CVD diamond discs with the perimeter cooling will be placed in front of other stopper's elements fabricated from SiC and tungsten and designed to stop higher photon energies (see Figure 8). The role of the diamond discs is twofold: 1) to dissipate the heat and to reduce the thermal load on the SiC parts from 200 W to less than 2 W between 200 eV and 5 keV, and 2) to protect the SiC block from instantaneous damage in the same photon range. For photon energies higher than 5 keV up to 25 keV, the stopper will be working at the 120 Hz pulse frequency with the average power on the order of 1 W. The SiC block will protect the tungsten (for bremsstrahlung attenuation purpose) and other metals from instantaneous damage at photon energies higher than 5 keV. The dimensions of the SiC and tungsten blocks will be optimized later.

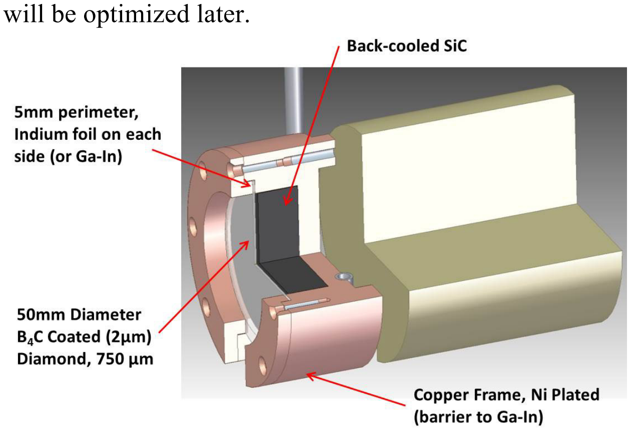

Figure 8: A 3D rendering of the CVD stopper (active burn-through monitor not shown).

B_4C BASED STOPPERS

In this section we consider only the average power for a B_4C based stopper. The instantaneous damage issues for B_4C are well understood and have been investigated experimentally at LCLS. Grazing incidence, copper based stoppers have been successfully used at third generation X-ray sources to stop kilowatt synchrotron radiation beams. Grazing incidence B_4C based stoppers are planned to be used at European XFEL [9].

The idea of managing the temperature by spreading the average power over larger areas works well when the absorption length is much smaller than the beam size. In the opposite case a pencil like beam generates most of the heat inside the volume of a stopper and changing the angle of incidence is not very effective with respect to the diminishing of surface temperature.

In order to address this problem we have investigated a model of the stopper which consists of a 6 mm thick B_4C material brazed to a molybdenum block (compatible CTE for brazing) and is cooled at the back side such that its temperature is kept at zero °C. The geometry and boundary conditions (for the normal incidence case) are presented in Figure 9.

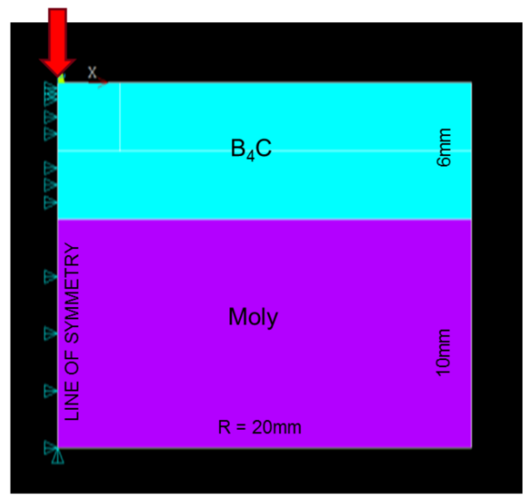

Figure 9: The geometry and boundary conditions of the B4C stopper model at normal incidence.

We have considered two cases, which correspond to the maximum photon energy of 1.3 keV, and 5 keV for the SXR and HXR beam lines, respectively. The beam sizes and attenuation lengths are given in Table **2**. The thermal conductivity of B_4C assumed in simulations is shown in Fig. 10.

Table 2: X-ray FWHM Beam Sizes and Attenuation Lengths for B_4C

Photon Energy (eV)	FWHM Beam Size (μm)	Attenuation Length (μm)
1300	1160	6
5000	322	351

The low absorption coefficient of B_4C (which is necessary to mitigate the instantaneous damage problem) results in a large absorption length. For example, at the photon energy of 5 keV, the absorption length is in the same order as the beam size. Therefore one should study in more detail how the spreading of the average power works in the case of B_4C based stoppers at this photon energy. For the normal incidence condition the steady state surface temperature of the stopper reaches the

ISBN 978-3-95450-134-2

melting temperature for the incidence power on the order of 50 W. The distribution of the stopper's temperature is shown in Figure 11.

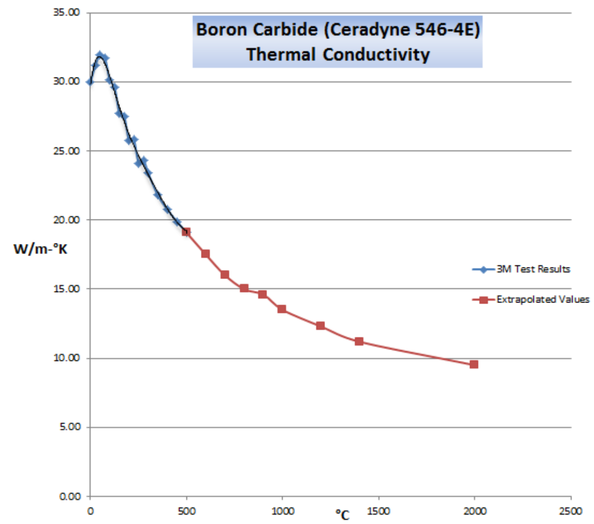

Figure 10: Dependence of the B_4C thermal conductivity on temperature.

The stress distribution is presented in Figure 12. The thermal stress has mainly the compressive component. The tensile stress is much lower and it is approximately one order of magnitude smaller than the tensile strength, which is in order of 500 Mpa. The main conclusion form this result is that the temperature damage will precede the stress related damage.

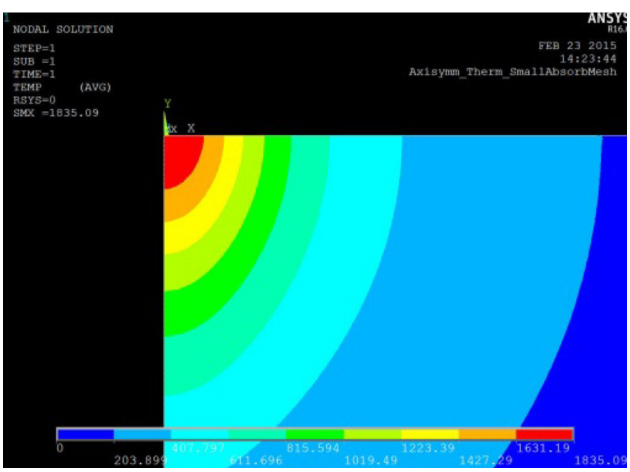

Figure 11: Temperature distributon in B_4C under normal incidence.

The dependence of the incidence angle on the temperature of the stopper's surface is discussed next. The summary of simulations is presented in Figure 13. In this figure we plot the dependence between the incidence average power and the incidence angle, which results in the same temperature at the surface. We plot three dependencies which correspond to the increase of temperature at the surface by 1000 °K, 1500 °K and up to near the melting temperature of 2445 °C.

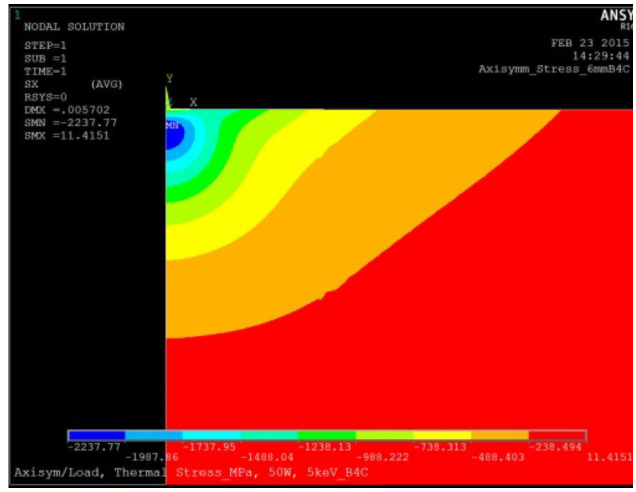

Figure 12: Radial Stress distributon in B_4C under noraml incidence.

One can clearly see from the figure that spreading the area of the illumination at the surface by the factor up to 10 times is not very effective. It increases the tolerable incidence power only up to 1.5 times. In order to gain an increase in the power by more than 3 times it is necessary to decrease the incidence angle below 3 degrees.

It can also be seen in this figure that in order to stay 400 °K below the melting temperature at the incidence power of 200 W the angle of incidence should be smaller than 2.2 degrees. Such a shallow angle will largely increase the longitudinal dimension of a stopper, which in turn will occupy more of the limited, valuable space of the diagnostics area. This would also increase the volume and the cost of B_4C material.

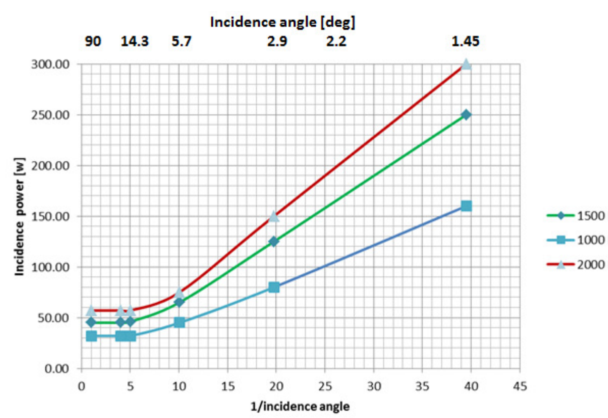

Figure 13: Dependence between the angle of incidence and the incident power for constant surface temperature.

For the 1.3 keV SXR case we have concluded that to stay below 2000 °C at the incidence power of 200 W, the angle of incidence should be smaller than 9 degrees. For the same power the angle of incidence should be smaller than 5 degree in order to keep the surface temperature below 1000 °C.

ISBN 978-3-95450-134-2

DISCUSSIONS AND CONCLUSIONS

In this section we will discuss feasibility of building the LCLS-II stoppers according to the two approaches discussed above. We will estimate the physical dimensions, and consider engineering efforts and costs. Then we will debate on other aspects such as risk, and going beyond the initial requirements, keeping in mind possible further developments of LCLS-II which can result in increasing the photon energy range and the instantaneous power and the average power. The considerations presented in the previous sections suggest that two concepts could be realized in practice.

CVD Diamond-based Stoppers

The normal incidence geometry allows designing very compact stoppers. Two redundant stoppers should use only around 300 mm space of the FEE transport beamline. Miniaturization of FEE elements has a great value because it gives room for more diagnostics, which can be needed as the development of the LCLS-II machine progresses.

Temperature and stress analysis suggests that CVD Diamond-based stoppers should endure twice or more of the design target average power of 200 W at 5 keV photon energy. B_4C coated CVD diamond should also survive higher pulse energies than specified in the physics requirement document. This prediction is based on the measured radiation hardness B_4C and the fact that both materials have similar compressive and tensile yield strength. However, the issue of resistance of CVD diamond to high instantaneous doses has not been explored yet experimentally and needs to be tested.

Here the main concern is that CVD diamond has a phase transition to graphite at the temperature around 1300 °C. Therefore the surface temperature should always be kept below this value and the stresses re-evaluated with each increase. The limits of the performance of the CVD diamond-based stopper with respect to the average power and the maximum pulse energy should be evaluated experimentally.

The FEA simulations should be revisited when the actual values for conductance are known at the cooling boundaries. This will result in an increase of the steady state peak temperatures differences from the “fixed temperature” scenario assumed above. Initial studies indicate this might be on the order of a 50% increase in peak temperature increase for CVD diamond, but still only a fraction of the graphitization temperature.

The significant advantage of CVD diamond-based stopper is that it has basically the same design for both SXR and HXR beam lines and this significantly reduces engineering efforts and promotes commonality between beamline devices; and also an operational benefit for having essentially the same device as LCLS.

B_4C-*based Stoppers*

The cost analysis of the B_4C-based stopper suggests that material cost should be similar to the CVD diamond-based stopper. The length of two redundant stoppers is estimated to be around 800 mm (9 degrees grazing incidence) and 1500 mm (2.2 degrees grazing incidence) for the SXR and HXR cases, respectively. Because SXR and HXR stoppers are different, an additional engineering cost is required here. This additional cost offsets the cost of tests required to determine radiation hardness of B_4C coated CVD diamond.

The performance of B_4C stoppers barely meets the design target of 200 W of average power at the discussed grazing angle. While there is still possible to increase the tolerable average power for the SXR stoppers, by decreasing the angle of incidence, there is no much room for improvements for the HXR stopper. 400 W of acceptable average power will require changing the grazing incidence angle to 1.07 degrees and increasing the length of the stopper to 3 m, which is impractical.

In summary we have shown that CVD diamond-based concept of the LCLS-II stopper is better and more practical with respect to B_4C based stopper. The CVD diamond- based concept has two main advantages:

- CVD Diamond handles higher average power and power density than B_4C stopper.
- CVD Diamond occupies significantly less beamline space in FEE than the B_4C stopper.

The radiation hardness of CVD diamond is less understood than the B_4C hardness, but the risk of radiation damage will be mitigated by coating CVD diamond with 1 - 2 μm thick B_4C layer. The limits of the performance of the CVD diamond based stoppers with respect to the average power and the maximum pulse energy should be evaluated experimentally as a follow-up to this initial analysis.

ACKNOWLEDGMENT

Use of the Linac Coherent Light Source (LCLS), SLAC National Accelerator Laboratory, is supported by the U.S. Department of Energy, Office of Science, Office of Basic Energy Sciences under Contract No. DE-AC02-76SF00515. We would like to thank L. Zhang of LCLS for helpful discussions.

REFERENCES

[1] X-ray Transport and Experimental Systems Physics Requirements document: LCLSII-3.5-PR-0051-R1.
[2] S. P. Hau-Riege et. al., Optics Express 18, 23933 (2010).
[3] S. P. Hau-Riege et. al., Appl. Phys. Lett. 95, 11104 (2009).
[4] B. Ziaja, et. al., High Energy Density Phys. 9, 462 (2013).
[5] J. Gaudin, et. al., Phys. Rev. B 88, 060101 (2013).
[6] N. Medvedev, et. al., Phys. Rev. B 88, 224304 (2013).
[7] D.D. Ryutov, Rev. Sci. Instr. 74, 3722 (2003).
[8] S. P. Hau-Riege, LCLS-TN-06-5 (2006).
[9] H. Sinn, private communication.

ISBN 978-3-95450-134-2

THE HIGHLY ADJUSTABLE MAGNET UNDULATOR

M. Hamberg, Uppsala University, Uppsala, Sweden

Abstract

The highly adjustable magnet undulator is a concept aiming for flexibility and extensive tunability of undulator settings in the linear as well as the helical regime. I report about suggested layout, magnetic simulations.

INTRODUCTION

Insertion devices such as undulators play and important role in accelerator physics in synchrotron storage rings as well as free electron lasers. Typical use is for creating photon radiation used for various investigations in medicine, biology, crystallography, chemistry, physics and other scientific areas. It can also be used for charged particle beam manipulation together with or without external radiation sources in order to manipulate the particle beam in various ways such in HGHG, EEHG and ORS setups.

The undulators used today are typically limited by their flexibility. This includes having a fixed undulator period, limited tapering options, inability to be quasiperiodically tuned and more. To overcome these limitations I present an idea of a highly adjustable magnet (HAM) undulator.

UNDULATOR CONCEPT

In the HAM-undulator, magnets are mounted in stacked rotating discs. Each disc comprises a magnet-couple, or magnetic structure pair, where their separations towards each other and the beamline can be adjusted independently. A center cross section view of three discs (in a real undulator many more discs will be implemented), and a front view are depicted in Fig. 1. The electron beam will travel through the center hole of the setup in which a vacuum pipe is implemented.

The system is modular and based on that each disc is identically constructed and then stacked in front of each other and secured in undulator end-plates on each side of the disc stack providing rigid reference surfaces. The full disc setup structure comprising the undulator end-plates and the disc stack can be secured on to a girder.

Since the magnet couples are built into a rotating disc the rotation around the beam axis can be adjusted arbitrary compared to the other discs. Furthermore, depending on the rotation angle between each disc, the helical angle can be changed. Additionally tapering of the magnetic field can be achieved in longitudinal and transversal direction. Tapering effects can also be achieved for helical cases.

The permanent magnet structures are connected to the rotation disc via adjustment means, so that the position of one magnet can be adjusted relative the other permanent magnet structure in the magnet pair. The adjustment means could be arranged to both adjust position of the magnet and to tilt the magnet relative a thought normal to the electron beam. This allow for transverse tapering of the undulator. Longitudinal tapering is achieved by for each disc decrease (or increase) the permanent magnet structure pair separation slightly throughout the undulator.

Each magnet structures in the structure pair could be made up as a simple transverse triple combination of directed permanent magnets to amplify the magnetic flux at the beam position. To alleviate the effect from magnet forces a thin layer of magnet material in longitudinal direction may be added on each magnet structure.

The undulator setup can be controlled by a standard PLC system. Due to the inherent construction no shimming is necessary.

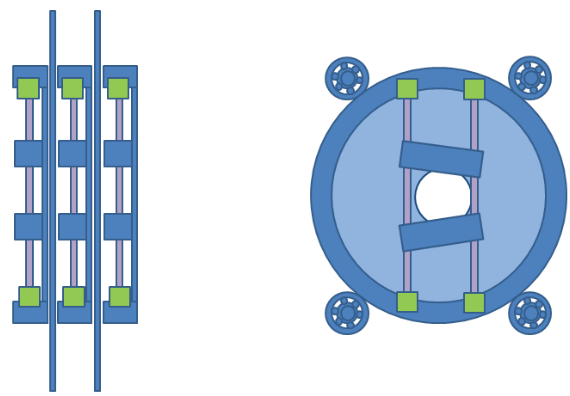

Figure 1: Left: Centre cross section view of three discs (in a real undulator many more discs will be implemented). Right: Front view of one disc with the magnet structure pair on each side of the centre hole.

EXAMPLE OF USAGE AND BENIFITS

Due to the flexibility of the construction one undulator can be used for many purposes.

- Linearly polarized light can be produced when the magnet couples are aligned with interchanging magnetic field of each disc (up down up etc.).
- Linearly polarized light of longer wavelengths can be produced by pairing rotating discs, as schematically illustrated in Fig. 2 (figure seen from side view with electron beam in centre).
- Circularly polarized light can be produced when the discs are rotated such that an additional rotation angle of up to 90 degrees is implemented for each passed dic, as schematically illustrated in Fig. 3, where figure is depicted from front with electron beam in center. In the figure the rotation angle is called alpha and four magnet structure pairs are implemented.
- Combinations of disc rotations can be implem-ented aiming for producing light with e.g. two

ISBN 978-3-95450-134-2

wavelengths simultaneously or simply for particular phase space manipulation.

- Quasiperiodic settings are possible.
- Longitudinal and transverse tapering is possible for linear as well as helical case.
- Modular design will ease process building and rebuilding the undulator.

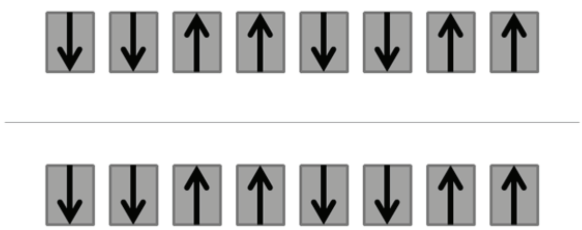

Figure 2: Example of configuration for linearly polarize light with paired configuration which doubles the undulator period. Figure is depicted from the side of the undulator.

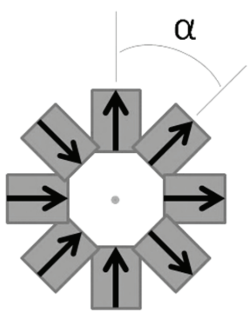

Figure 3: Example of configuration for circularly polarized light configuration as seen where each subsequent disc is rotated with an additional angle α. Figure is depicted as electron beam goes into the paper.

SIMULATIONS

The HAM undulator setup was simulated with COMSOL doing FEM analysis. Benchmark studies were also made for an APPLE II type undulator for comparison. In the simulation magnets were modeled as permanent magnets lying in pairs and all the magnets were placed in a box of air. For the linear case all the magnets will be aligned as in Fig. 4 where the magnet pairs are indicated with wire frames.

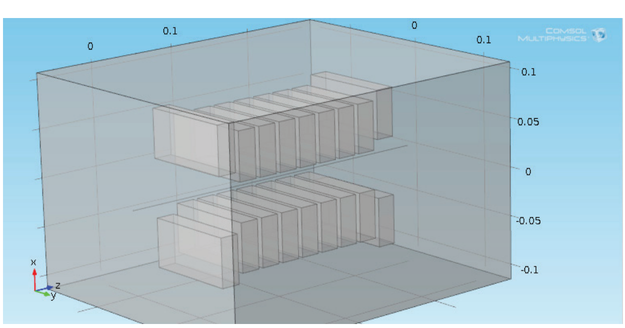

Figure 4: Simulation configuration of linear case illustrating magnet pairs linearly matched within a box of air.

Examples of how the magnets can be aligned for the helical case are found in Fig. 5.

The flux intensity the vector field along the undulator centre axis is indicated with arrows. It is clear that the magnetic field is rotating around the centre beam axis and interchanging as wanted. The worst case scenario with alpha increase 90-degrees scenario is illustrated.

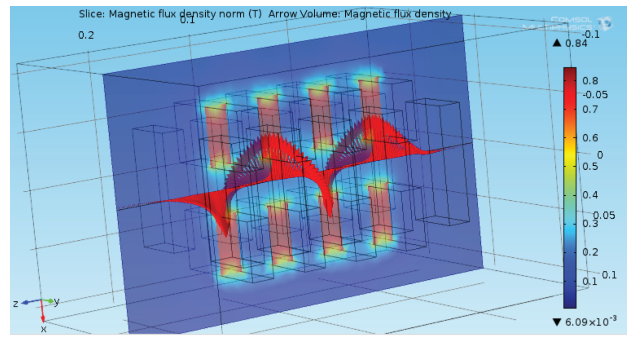

Figure 5: Simulation configuration of maximum circular case illustrating magnet pairs rotated 90-degrees between each disc. The red arrows indicate the flux intensity vector along the electron beam pathway and it is clearly rotating along the trajectory.

CONCLUSION

The concept and its first simulations show valuable behaviour with unsurpassed flexibility. Especially the ability to change the undulator period within wide ranges and to divide the undulator into sub intervals may be of particular interest. The physical behaviour needs further simulations. Engineering challenges exist but can most likely be overcome by existing technology which could be proven by construction of a test prototype. Patent is pending.

ACKNOWLEDGMENT

I thank KYMA and Bruno Diviacco for benchmarking studies and valuable discussions. I also thank Uppsala University Innovation centre and Claes Djurberg and ALMI Business partner Sweden for valuable support.

ISBN 978-3-95450-134-2

BEAM DYNAMICS SIMULATION FOR THE UPGRADED PITZ PHOTO INJECTOR APPLYING VARIOUS PHOTOCATHODE LASER PULSES

Mahmoud Bakr #, G. Vashchenko, M. Khojoyan*, M. Krasilnikov, F. Stephan
DESY Zeuthen 17538, Germany

Abstract

Production of electron bunches with extremely small transverse emittance is the focus of the PITZ (Photo Injector Test facility at DESY in Zeuthen) scientific program. PITZ is one of the leading laboratories on generation and optimization of high brightness electron bunches with different charges for free electron laser (FEL) machines such as FLASH and the European XFEL. In 2011 using a photocathode laser with a flattop temporal profile, PITZ has revealed record low transverse properties emittance values at different bunch charges. However, further improvement of beam quality with smaller emittance is foreseen using a cathode laser system, capable of producing 3D ellipsoidal bunches. Numerical simulations were performed to study and compare the beam dynamics of electron beams produced with 3D ellipsoidal and flattop laser profiles. Different bunch charges from 20 pC up to 4 nC are considered in the simulation, in order to find an optimum PITZ machine setup which yields the lowest transverse emittance. In the present paper, the simulation setup, conditions, and results of the comparison are presented and discussed.

INTRODUCTION

The handiness of a high brightness electron source is one of the key issues for successful operation of linac-based free electron lasers like, FLASH [1] and the European XFEL [2]. The self-amplified spontaneous emission (SASE) of the FELs process requires an extremely high space charge density of the radiating electron bunches implying high peak current, low energy spread and small transverse emittance of the electron beam. Such high quality beams are mandatory for efficient SASE generation in a single pass through long undulators with narrow gaps [3]. However, the above-mentioned properties are hard to be improved in a linac and thus the emittance has to be minimized already in the photocathode injector.

The Photo Injector Test facility at DESY, Zeuthen site (PITZ), aims to produce electron bunches with extremely small transverse emittance. A flattop temporal profile of the cylindrical pulses has been used at PITZ to reduce the transverse emittance of space charge dominated beams compared to the Gaussian pulse shape previously used [4]. The lower beam emittances reported from PITZ were obtained with a flattop temporal laser profile from Cs_2Te cathodes. The photocathode laser pulse shaping is considered as a powerful tool to optimize the photo injector performance. Thus, a further improvement is foreseen from the cathode laser pulse shaping. The overall brightness of a photo injector can be further improved by using an ideal electron bunch profile, which, according to simulations, is 3D ellipsoidal (hereinafter ellipsoidal) in space and time [5]. Because of the fact that the space charge force fields inside the bunch are linear, the ellipsoidal beam distribution is an ideal beam distribution for high brightness charged beam applications with the best transverse and longitudinal bunch compression. Such electron bunches not only have lower emittance, but are also less sensitive to jitter of machine parameters, thus allowing more stable and reliable operation, which is a key requirement for SASE-FELs facilities like FLASH and the European XFEL.

Simulations have been performed at PITZ to study the feasibility of using an ellipsoidal laser shape instead of flattop and Gaussian laser profiles [6]. The results have revealed a better injector performance when using the ellipsoidal laser profile. Further improvement was expected when shifting the second accelerating cavity (CDS booster) and the first emittance measurement screen (EMSY1) by ~40 cm upstream. Moreover, simulations for the imperfections of the ellipsoidal laser shape for 1 nC showed that the transverse emittance value is still smaller than the optimized emittance value for the flattop laser shape [7]. Recently, a new photocathode laser system capable of producing ellipsoidal pulses has been installed at PITZ [8]. It is foreseen to operate the new system in parallel to the nominal one that generates cylindrical pulses with various temporal profiles. First electrons were already generated by the new laser system; however, emittance measurements are not yet performed.

A schematic layout of the current PITZ setup is shown in Fig. 1. The PITZ photocathode RF gun delivers electron bunches up to several nC with a maximum mean momentum of up to 7 MeV/c generated from a Cs_2Te cathode. The gun is surrounded by two solenoids: main and bucking. The main solenoid is used for the transverse beam focusing, while the bucking solenoid is meant to compensate the remaining longitudinal magnetic field at the cathode. The final maximum momentum after the booster is up to 25 MeV/c. The transverse emittance of the electron beam is measured by the emittance measurement system, (EMSY1 located at 5.27 m downstream the cathode), using a single slit scan technique [9]. Additionally, there are many diagnostics devices available for the full characterization of electron beams. A detailed description of the PITZ setup can be found elsewhere [10].

The aim of this contribution is to check the feasibility of using the ellipsoidal laser beams in comparison to the flattop shaped pulses by means of the lowest transverse

On leave from: Physics Department, Assiut University, Assiut 71516, Egypt, mahmoud.bakr@desy.de.
*Now working in LOLA lab France

ISBN 978-3-95450-134-2

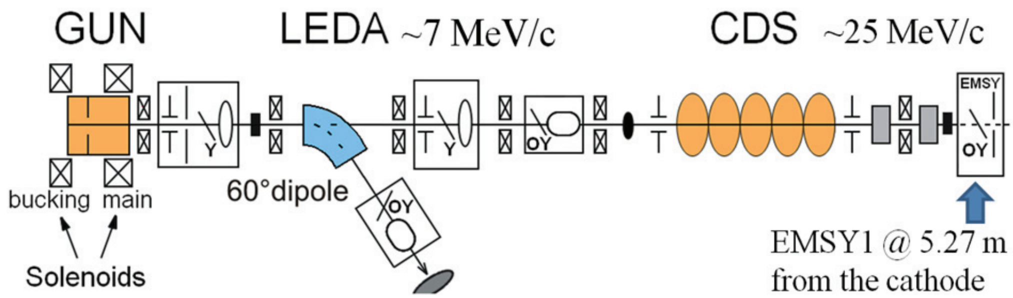

Figure 1: Schematic layout of the current PITZ beamline used in ASTRA simulations up to EMSY1.

emittance at EMSY1. This will be done by studying and comparing the beam dynamics of ellipsoidal and flattop beams with different bunch charges, from 20 pC up to 4 nC, for the actual PITZ setup.

SIMULATION SETUP AND CONDITIONS

Two different laser shapes, flattop temporal profile and an ellipsoidal distribution on the cathode, have been compared by tracking the generated electron beam using A Space charge Tracking Algorithm (ASTRA) [11]. For each of the profiles, the transverse emittance at the position of EMSY1 was optimized. Different bunch charges from 20 pC up to 4 nC are considered in the simulation, each was assumed to have 200000 macro particles with initial average kinetic energy of 0.55 eV [12]. In the simulation, the gun and booster peak electric fields were fixed at the phase of maximum mean momentum gain to 58.8 and 17.6 MV/m, which correspond to respectively beam momenta of 6.7 and 22 MeV/c downstream of gun and booster. This corresponds to the actual run conditions at PITZ [13]. The beam length of the ellipsoidal laser was chosen so that the produced electron beam has the same rms length at EMSY1 as the electron beam produced by the flattop laser with 2/21.5/2 ps rise, FWHM length and fall times respectively. A perfect ellipsoidal laser shape was considered in this simulation. For all bunch charges, the rms laser spot was simultaneously tuned with the main solenoid current and the gun phase to achieve the best transverse emittance of the electron beam at the position of EMSY1. The CDS booster phase was always tuned to deliver the maximum mean momentum of the electron beam. The space charge settings in ASTRA were optimized in order to minimize the impact of numerical errors on the emittance values.

RESULTS AND DISCUSSION

Results for 2 nC Bunch Charge

In the first part of this section, the results of 2 nC bunch charge with the two laser profiles are determined and presented as an example of the simulations in Figs. 2-4. The electron beam transverse projected emittances and rms beam sizes along the PITZ beamline up to EMSY1 are depicted in Fig. 2. The electron beam current and transverse slice emittance distributions within the bunch

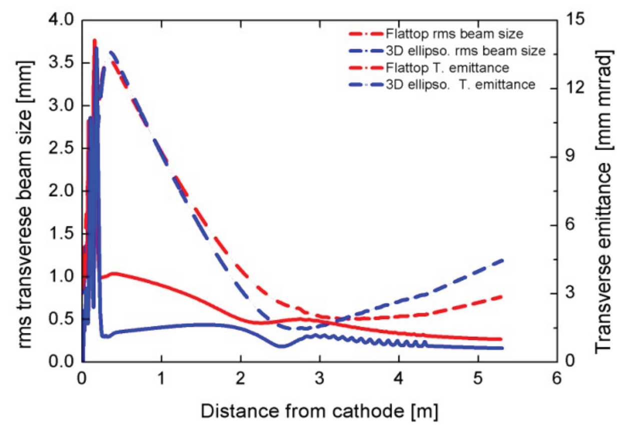

Figure 2: Transverse projected emittance and rms beam size for 2 nC bunch charge along the beamline up to EMSY1.

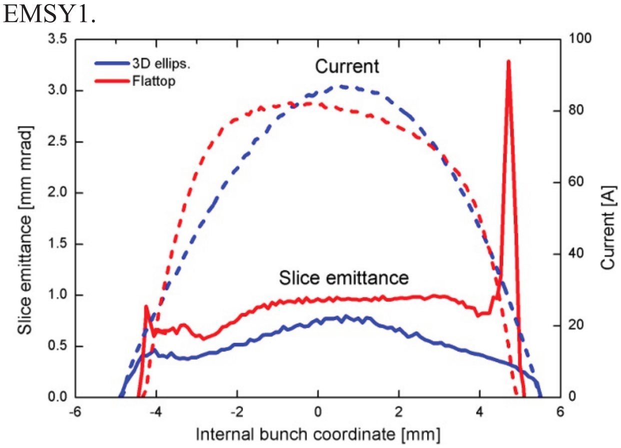

Figure 3: Beam current and slice transverse emittance distribution within the bunch for 2 nC bunch charge at EMSY1.

are plotted in Fig. 3. In addition, the electron beam longitudinal phase spaces for the two laser profiles are compared in Fig. 4.

It can be seen from Fig. 2, the optimized (best emittance at EMSY1) beam size for the ellipsoidal beam is higher than that for the flattop one; however, the transverse projected emittance is smaller. This tendency is related to the space charge effect in the booster. The peak current for 2 nC bunch charge generated from the ellipsoidal beam is estimated to be 88 A compared to 82 A generated from flattop beams as shown from Fig. 3.

ISBN 978-3-95450-134-2

Moreover, one can observe the existence of a high peak in the slice transverse emittance distributions for the flattop beam, while, the curve is almost flat for the ellipsoidal beam. This spike originates from the halo in the head of the bunch and it starts to be even from the emission when the head of the bunch is only emitted, it corresponds to a very short bunch length and therefore to the strong nonlinear transverse space charge force resulting in the blowup of the slice emittance of the bunch head.

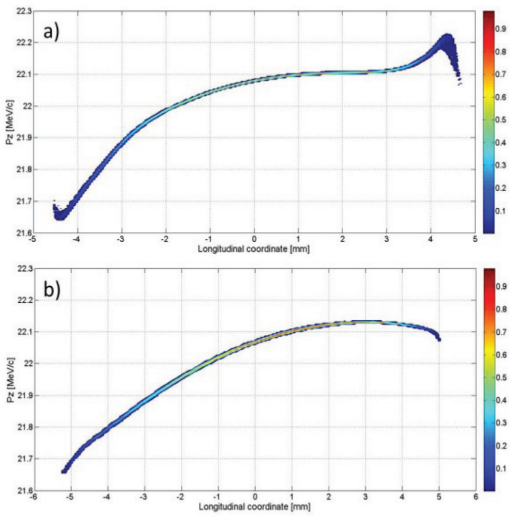

Figure 4: Electron beam longitudinal phase space for 2 nC bunch charge generated from (a) flattop and (b) ellipsoidal cathode laser pulses.

From Fig. 4 one can observe clearly the advantages of using an ellipsoidal laser profile compared to a flattop one, in terms of less nonlinearity in the longitudinal phase space and one obtains 91 mm-keV longitudinal emittance for the ellipsoidal beam compared to 114 mm-keV for the flattop one. Moreover, the ellipsoidal beam has a more regular shape without halo as compared to the flattop one. The simulated transverse emittance from the simulation at EMSY1 is 0.617 mm-mrad for the ellipsoidal beam compared to 1.008 mm-mrad for flattop one. This means ~40% improvement of the transverse emittance and 36% improvement in the average slice emittance are expected when using an ellipsoidal laser profile with respect to a flattop. Thus, the results have yielded a beam brightness for the ellipsoidal beam ~280% higher than that for the flattop beam.

Results for 20 pC to 4 nC Bunch Charges

The normalized transverse emittance and the brightness of the electron beam as a function of bunch charge from 20 pC up to 4 nC generated from the ellipsoidal and flattop laser profiles are shown in Figs. 5 and 6, respectively. The emittance gain and the brightness gain from using the ellipsoidal beams with respect to the flattop ones are also depicted in the right axis of Figs. 5 and 6 respectively. As seen from Fig. 5 there is ~30-42% improvement in transverse emittance for the case of ellipsoidal as compared to flattop profile for bunch charges higher than 100 pC. However, for bunch charge less than 100 pC the emittance gain is dramatically decreased and reaches only ~5% for 20 pC bunch charge. This behavior can be explained by the fact that at low bunch charge the contribution of the space charge in the emittance growth is very small compared to the higher bunch charge. Another reason for this degradation is that the beam emittance was optimized for the fixed laser pulse duration. Therefore the cathode laser pulse shape for the low charge case correspond to more thin linear charge column whereas the high charge case is close to the 3D cylinder with comparable transverse and longitudinal dimensions.

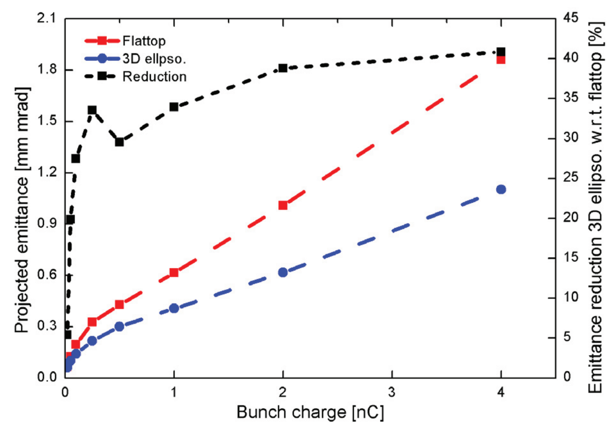

Figure 5: Electron beam transverse emittance as a function of bunch charge for flattop and ellipsoidal laser profiles at EMSY1 in the left axis, and in the right axis the emittance gain from ellipsoidal beams with respect to flattop ones.

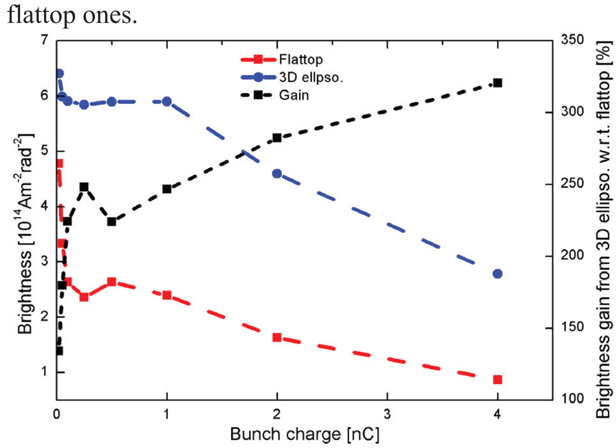

Figure 6: Brightness of the electron beam as a function of bunch charge for flattop and ellipsoidal laser profiles in the left axis, and in the right axis the brightness gain from ellipsoidal beams with respect to flattop ones.

It is well known that to increase the brightness ($b=2I/\varepsilon^2$ A mm^{-2} mrad^{-2}, where I (A) is the peak current, and ε (mm-mrad) is the transverse emittance) of an electron source it is necessary to increase its peak current while keeping a very small transverse emittance. This leads to the usage of high electric fields at the cathode to reduce

ISBN 978-3-95450-134-2

the influence of space charge forces. The peak currents for different bunch charges generated from ellipsoidal distributions are ~6-18% higher than that generated from flattop ones, however, the transverse emittances are 30-42% smaller. Moreover, the average slice emittance from the flattop pulse can be reduced by ~25-40% by using ellipsoidal laser pulses. Thus impressive increase in the beam brightness is expected. The beam brightness of the ellipsoidal beam was estimated to be ~225-320% higher than that for a flattop beam for bunch charges more than 100 pC.

As mentioned in the previous paragraph significant improvements on the electron beam brightness can be obtained by applying ellipsoidal pulses of the cathode laser. These advantages of ellipsoid laser pulses motivate experimental studies on such a cathode laser system in order to provide further improvement on emittance/ brightness from the electron sources for a extend the scientific reach of modern FEL facilities. In the near future, comparative measurements of the beam emittance with both ellipsoidal and flattop cathode laser profiles at PITZ are planned in order to verify the simulations. However, more investigations are required for the low bunch charges.

CONCLUSION

Beam dynamics simulations using ASTRA were performed for the current PITZ setup to compare the electron beam quality for the range of bunch charges from 20 pC to 4 nC generated from two different temporal shapes of the photocathode laser pulses (flattop and ellipsoidal). Emittance vs. bunch charge optimization was performed by tuning the rms laser spot size together with the main solenoid current and the gun phase to achieve the best transverse emittance of the electron beam, at the same rms bunch length for each bunch charge, at EMSY1. The simulation results yielded great improvement ~30-42%, and ~225-320% in the electron beam transverse emittance and brightness, respectively, when the flattop temporal shape is replaced by the ellipsoidal profile. Almost no beam halo and less nonlinearities of the electron beam shape in longitudinal phase space were observed for the electron beams created from the ellipsoidal laser profile. Overall, ~5-10% increase in the peak current is expected from ellipsoidal laser pulses compared to flattop pulses. The above-mentioned improvements should give sufficient headspace in the experimental realization of the ellipsoidal laser system to be able to demonstrate significant improvement with respect to the nominal flattop case.

REFERENCES

[1] M. Ackermann *et al.*, Nature Photon. 1, pp. 336-342, (2007).
[2] M. Altarelli *et al.*, DESY, Report No. 2006-097, (2006).
[3] P. Schmuser, M. Dohlus, and J. Rossbach, Ultraviolet and Soft X-Ray Free-Electron Lasers: Introduction to Physical Principles, Experimental Results, Technological Challenges (Springer-Verlag, Berlin, 2008).
[4] M. Krasilnikov *et al.*, Experimentally minimized beam emittance from an L-band photoinjector, PRST AB 15, 100701 (2012).
[5] O. D. Kellogg, Foundations of Potential Theory (The Murray Printing Company, Cambridge, MA, 1929).
[6] M. Khojoyan *et al.*, "Beam dynamics optimization for the high brightness PITZ photo injector using 3D ellipsoidal cathode laser pulses", in Proc. 35th Int. Free-Electron Laser Conf., New York, 2013, pp. 298-302.
[7] M. Khojoyan *et al.*, "Studies on the Application of the 3D Ellipsoidal Cathode Laser Pulses at PITZ", in Proc. 5th Int. Particle Accelerator Conf., Dresden, 2014, pp. 2958-2961.
[8] T. Rublack *et al.*, First Results Attained with the Quasi 3-D Ellipsoidal Photo Cathode Laser Pulse System at the High Brightness Photo Injector PITZ, IPAC 15 proceeding, Richmond, VA, USA (2015).
[9] L. Staykov, "Characterization of the transverse phasespace at the photo-injector test facility in DESY, Zeuthen site". PhD thesis, Hamburg University, 2012.
[10] F. Stephan *et al.*, "Detailed characterization of electron sources yielding first demonstration of European X-ray Free-Electron Laser beam quality", Physical Review Special Topics – Accelerators and Beams, vol. 13, p. 020704 (2010).
[11] K. Flöttmann, A Space charge TRacking Algorithm, ASTRA, http://www.desy.de/~mpyflo
[12] K. Flöttmann, "Note on the Thermal Emittance of Electrons Emitted by Cesium Telluride Photo Cathodes", TESLA-FEL, DESY, 1997.
[13] G. Vashchinko *et al.*, "Emittance measurements of the electron beam at PITZ for the commissioning of the European XFEL", presented at FEL'15, Daejeon, Korea, August 2015, these proceedings.

ISBN 978-3-95450-134-2

BENCHMARK OF ELEGANT AND IMPACT *

L. Wang#, P. Emma and T. Raubenheimer SLAC, Stanford, CA 94309, USA
J. Qiang, LBNL, Berkeley, CA 94720, USA

Abstract

The beam dynamics codes ELEGANT and IMAPCT have many users. We use these two codes for the design of LCLSII. Both codes use a 1D model for the coherent synchrotron radiation (CSR) in bend magnets. In addition, IMPACT has a 3D space-charge model, while ELEGANT uses a 1D model. To compare the two codes, especially the space-charge effects, we systematically benchmark the two codes with different physics aspects: wakefields, CSR and space-charge forces.

INTRODUCTION

The new LCLS-II high-repetition rate FEL project at SLAC [1] will use a new superconducting linac composed of TESLA-like RF cavities in continuous wave (CW) operation, in order to accelerate a 1-MHz electron beam to 4 GeV. Fig. 1 shows the optics of the hard x-ray beam of LCLS-II linac. The new superconducting linac is driven by a new high-rate injector [2], will replace the existing SLAC copper linac in sectors 1-7 (101.6 m/sector), while the remaining Cu RF structures in sectors 7-10 will be removed and replaced with a simple beam pipe and focusing lattice (the “linac extension”). The existing 2-km PEP-II bypass line (large β section in Fig. 1) will be modified to transport electrons from the linac extension in sector 10 through more than 2.5 km and into either of two undulators in the existing LCLS undulator hall. The overall design of the linac can be found in [3].

We use both ELEGANT and IMPACT codes for the LCLS-II design. The main difference in term of physics included is the space charge: ELEGANT uses 1D longitudinal space charge (LSC) model while IMPACT has 3D model. The long pass beamline at LCLS-II makes the space charge effect stronger compared to LCLS and the beam energy of LCLSII is low. Therefore strong micro-bunching instability is expected. Recently, it is found that the transverse space charge is also important and can add addition energy modulation to the beam [4]. Therefore it is important to check the impact of 3D space charge model compared to the 1D LSC model.

In this benchmark we use LCLS-II Hard X-ray linac as shown in Fig 1. The initial beam energy is 100 MeV and has an ideal Gaussian distribution in longitudinal direction with *rms* beam size of 1.0 *mm* and energy spread of 1 keV. The uncorrelated energy spread is increased downstream by using a 6 keV laser heater. The bunch charge is 100 pC. The particles are tracked through LCLS-II linac to the beginning of the undulator. We did step-by-step comparisons: first step for pure optics, all collective effects are turned off. Then the wakefields, CSR and space charge are added one-by-one.

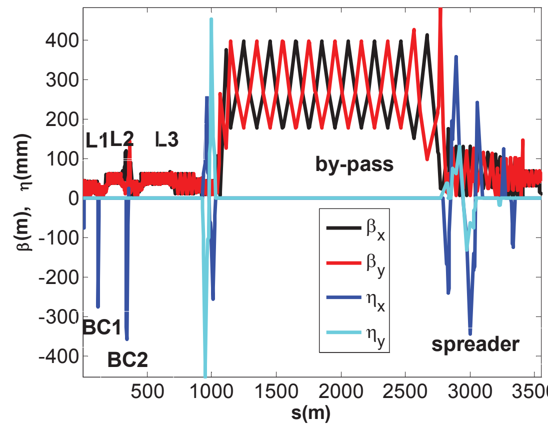

Figure 1: Optics (HXR) of the LCLS-II linac.

PURE OPTICS

To compare different collective effects, it is important to study a case when all collective effects are turned off. This means the wake fields (geometric wake of rf linac and resistive wall wake of the beam pipe), CSR and space charge are not included. The main parameters of the linac set-up are: the rf phase at L1, linearizer and L2 are -12.7^{o} -150^{o} and -15.5^{o}, respectively.

Figure 2 shows the phase space and the current profile before the undulator. There is an excellent agreement between both codes as expected. The peak current is about 1 kA with single spike. If the simulation starts with real injector beam, the final beam usually is flat at core of the beam with double horns at head and tail of the bunch. The beam energies are 250 MeV and 1.647 GeV at BC1 and BC2, respectively. Note that the BC2 beam energy in nominal design is 1.6 GeV. We use slight different beam energy here.

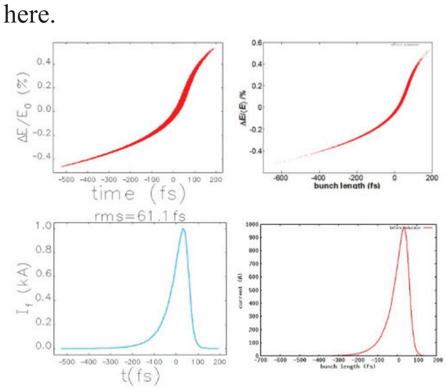

Figure 2: Longitudinal phase space (top) and current profile (bottom) at the beginning of undulator without collective effects from ELEGANT (left) and IMPACT (right).

*Work supported by Department of Energy Contract No. DE-AC02-76SF00515
#wanglf@SLAC.stanford.edu

ISBN 978-3-95450-134-2

EFFECT OF WAKE FIELDS

In this case the geometric wake of RF structure and the resistive wall wake of the beam pipe are included. These wakefields de-chirp the bunch and therefore reduce the beam energy chirp and peak current as shown in Fig. 3. The final peak current reduces from 1kA to 0.8kA. There is same current profile and similar phase space. IMPACT shows slightly stronger effect of wakefield.

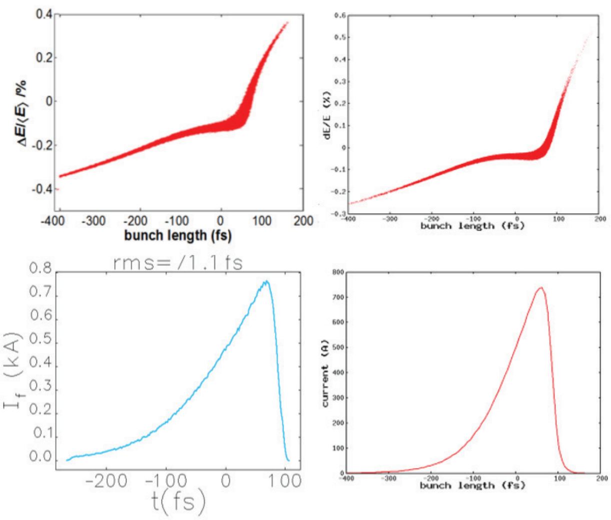

Figure 3: Longitudinal phase space at the end of BC2 with geometric wake and resistive wall wake effects: ELEGANT (left) and IMPACT (right).

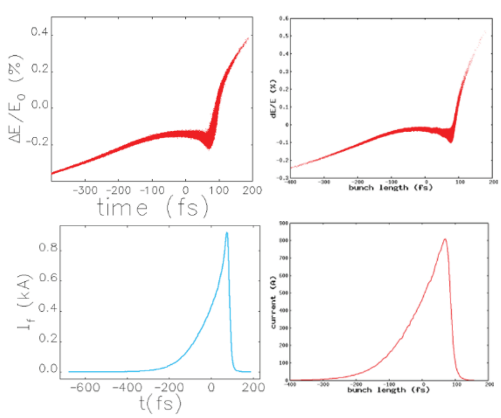

Figure 4: Longitudinal phase space with geometric wake, resistive wall wake and CSR: ELEGANT (left) and IMPACT (right).

WITH WAKEFIELD AND CSR

1D CSR is used in both codes. Similar as wake field effect, the CSR can de-chirper the beam in the longitudinal phase space. Figure 4 shows the comparisons. The phase space is hard to compare due to the different centroid in energy.

One noticeable difference is the peak current: ELEGNAT gives a larger peak current (0.9 kA vs 0.8 kA). Apparently it is caused by CSR. Detail study shows that the CSR in the 2nd bunch compressor (BC2) increases the peak current in ELEGNAT. This is typical CSR effect in LCLSII. The CSR in the 3rd bend of BC2 de-chirp the bunch and change the peak current due to the non-zero dispersion there. Although the last bend has stronger CSR and therefore larger energy kicker, it has negligible effect on the current profile due to the very small dispersion there.

Another benchmark is done with ideal Gaussian beam right before the BC2. There is good agreement for the beams at the end of BC2. So we are unable to identify the causes of the difference in previous case. The CSR may interplay with other things. It seems that the CSR in ELEGNAT play important role for sharp current profile.

WITH WAKE AND SPACE CHARGE

Wakefields and space charge are included in this comparison. IMPACT uses 3D space charge model while ELEGNAT uses 1D LSC. Figure 5 shows the comparison with the same numerical parameters for both codes: 50 million particles and 1024 slices in the space charge computation. The overall current profile is similar although it is spikier for Impact. The scale in the phase plot is quite different. IMPACT shows stronger overall de-chirper effect (smaller energy chirp near peak current center). Detail comparison shows similar energy modulation near the peak current: 0.15% for ELEGNAT and 0.14% for IMPACT. The modulation wavelength is also similar: 3 μm for ELEGANT and 2.3 μm for IMPACT. Actually the wavelength of modulation in ELEGNAT ranges from 2–3 μm if we look at the bunching result.

We are able to run IMPACT with real number particles to reduce the numerical noise. Figure 6 shows the IMPACT results with 624 million particles and 2048 slices. There are fine spikes in the current profile compared to the 50 million particles case. And the energy modulation has the same wavelength with smaller modulation (0.10% compared to 0.14%).

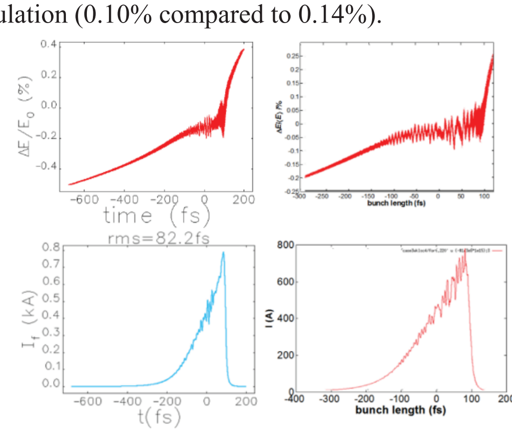

Figure 5: Both ELEGANT (left) and IMPACT (right) use 50 million particles and 1024 slices. Wake fields and space charge are included.

ISBN 978-3-95450-134-2

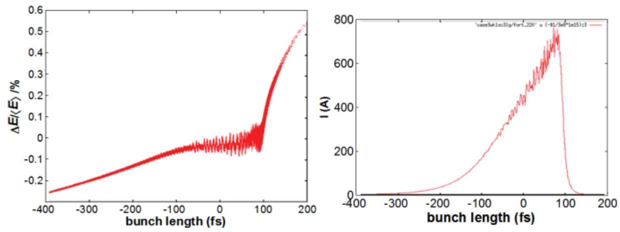

Figure 6: IMPACT with 624 million particles and 2048 slices.

WITH WAKE, CSR AND SPACE CHARGE

Wakefields, CSR and space charge are included in this comparison. Again, we run both codes using the same numerical parameters: 50 million particles and 1024 slices. The results are shown in Fig. 7. For both codes, the energy modulation wavelength and amplitude are very close to the previous case (with wake and space charge). The peak current increases compared to the previous case when the CSR is added in both codes. ELEGNAT gives a larger peak current. The IMPACT result with real number of particles is shown in Fig. 8. The results are quite close to that of 50 million particles case. For instance, the energy modulation reduces from 0.16% to 0.15%. The modulation wavelength doesn't change with the number of particles.

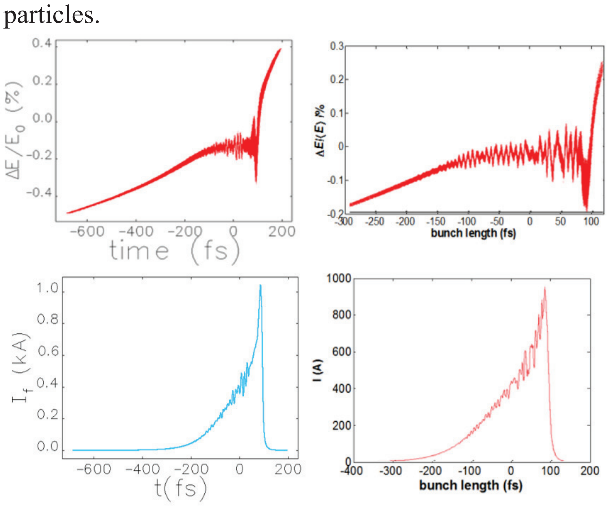

Figure 7: Wakefield, CSR and space charge are included. Both ELEGANT (left) and IMPACT (right) use 50 million particles and 1024 slices.

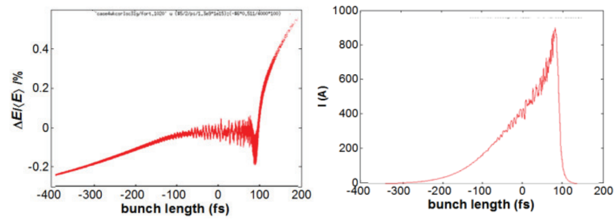

Figure 8: IMPACT with 624 million particles and 2048 slices. Wakefield, CSR and space charge are included

SUMMARY

We have done step-by-step benchmark for ELEGNAT and IMPACT. The overall agreements are good between ELEGANT and IMPACT codes for different effects: pure optics, wake and space charge. One noticeable effect is CSR on the peak current.

The most important to us is the space charge effects. Although the difference in the space charge model (3D in IMPACT compared to 1D in ELEGNAT), the results (such as the amplitude and wavelength of the energy modulation) are quite similar. The IMPACT with real number of particles shows similar result as 50 million particles with smoother current profile and smaller energy modulation.

ACKNOWLEDGEMENTS

This work is supported by Department of Energy Contract No. DE-AC02-76SF00515.

REFERENCES

[1] T. O. Raubenheimer, "Technical challenges of the LCLS-II CW X-ray FEL," in proceedings of IPAC2015, Richmod, VA, USA.

[2] J. Schmerge *et al.*, "The LCLS-II Injector Design", in Proc. of 36th Int. Free-Electron Laser Conf., Basel, 2014, THP042.

[3] P. Emma, *et al.*, "Linear Accelerator Design for the LCLS-II FEL Facility ", in Proc. of 36th Int. Free-Electron Laser Conf., Basel, 2014, THP025.

[4] M. Venturini and J. Qiang, Phys. Rev. ST Accel. Beams 18, 054401 (2015).

ISBN 978-3-95450-134-2

EFFECT OF HOT IONS AT LCLS-II*

L. Wang#, T. O. Raubenheimer, SLAC, Stanford, CA 94309, USA

Abstract

The ions in a linac with high repetition rate, such as ERL, draw more attention recently. LCLS-II has a long linac with 1 MHz repetition rate. The ions, in general, are not deeply trapped due to the long bunch spacing. The effect of ion thermal energy becomes important in this regime. The beam dynamics with ions are studied both theoretically and numerically. There is a linear growth in amplitude, instead of exponential growth as traditional fast ion instability. This linear growth set a maximum bunch-train length to limit the beam amplitude to fractional beam sigma. We also extend our works to different regimes where the motions of ions from stable to partially stable.

INTRODUCTION

The new LCLS-II high-repetition rate FEL project at SLAC [1] will use a new superconducting linac composed of TESLA-like RF cavities in continuous wave (CW) operation, in order to accelerate a 1-MHz electron beam to 4 GeV. Figure 1 shows the optics (top) of the hard x-ray beam and the beam size (100 pC) of LCLS-II linac (bottom). The new superconducting linac is driven by a new high-rate injector [2], will replace the existing SLAC copper linac in sectors 1-7 (101.6 m/sector), while the remaining Cu RF structures in sectors 7-10 will be removed and replaced with a simple beam pipe and focusing lattice (the "linac extension"). The existing 2 km PEP-II bypass line (large β section in Fig. 1) will be modified to transport electrons from the linac extension in sector 10 through more than 2.5 km and into either of two undulators in the existing LCLS undulator hall. The overall design of the linac can be found in [3].

There is a low temperature (~2K) for the superconducting linac (L1, L2, L3 in Fig. 1), while the rest linac has room temperature (~300K) with a thermal energy about 0.04eV. In most storage ring light source, the beam potential is much large than 1eV, for instance 100eV for SPEAR3 beam. Therefore, the thermal energy of the ion can be safely neglected. In LCLS-II, the beam is small and the bunch spacing is long where the thermal energy is comparable and even larger than the beam potential. In this case, the thermal energy should be included. The effective ion size with the thermal energy effect can be estimated as

$$\sigma_i^2 \approx \frac{\sigma_e^2}{2} + \frac{\upsilon_0^2}{2\omega^2} = \alpha^2 \sigma_e^2, \qquad (1)$$

where σ_e is the electron beam size, υ_0 is the ion speed at the thermal energy. When the thermal energy is negligible, the ion size is about $1/\sqrt{2}$ times of the electron beam size.

This paper is organized as the following: section II presents the detail simulations and section III introduces our theoretical model to explain the feature of the simulations.

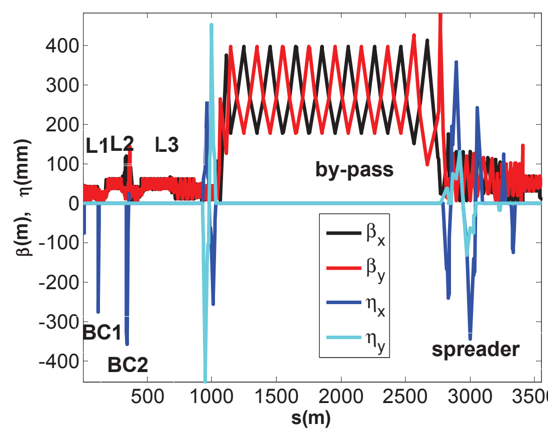

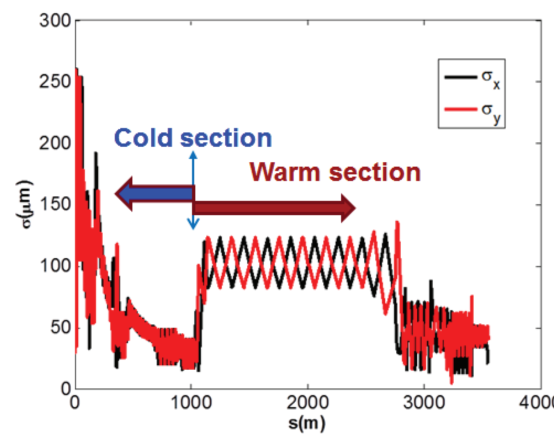

Figure 1: Optics (HXR) (top) and beam size (100 pC, bottom) of the LCLS-II linac.

SIMULATION

Simulations have a number of advantages: the non-linearity of the ion-cloud force is automatically included; the effects of beam optics and bunch-train with arbitrary beam filling pattern can be easily handled; a realistic vacuum model with multi-gas species is straightforward in simulation. A Particle in Cell (PIC) code based on a wake-strong model is used here [4].

The temperature is set to 10 K and 300K in the superconducting linac and warm section, respectively. In simulation we use multiple gases vacuum model [H2 (90%), H2O (1%), CO2 (1%), CO (7%) and CH4 (1%)]. We will use this vacuum component through this paper. The total vacuum pressure of 1 *nTorr* and 10 *nTorr* are assumed for the cold and warm section, respectively. The real vacuum should be better.

*Work supported by Department of Energy Contract No. DE-AC02-76SF00515
#wanglf@SLAC.stanford.edu

The simulation is done from injector exit (100MeV beam) to the beginning of the undulator. Figure 2 shows the ion distribution along the linac for 100 pC bunch charge. The ions are accumulated mainly at L1, L2 and bypass beam line due to the large beam size there. The motions of ions in other locations are basically unstable due to the over-focusing of the electron beam to the ion particles. Figure 3 shows the *rms* ion size along the linac. It is about twice of the electron beam size at the long-bypass beamline (warm section). The ion beam size estimated from Eq. (1) (using *CO* ion) is about 3 times of the electron beam size, which is close to the simulation where multiple gas species are used. The transverse distribution of ions at the long by-pass beamline is close to a Gaussian distribution (there is a long tail for far away particles which are excluded) as shown in Fig. 4. This is totally different from the case when the thermal energy is negligible where the ion size is smaller than the electron beam size and there is a sharp peak density at the core part of ion beam [4]. The thermal energy and long bunch spacing makes the dynamics of the beam-ion in LCLS-II totally different from the typical storage ring light sources.

Figure 5 shows the growth of the amplitude of electron bunches along the bunch train at the end of LCLS-II linac. The growth is linear along the bunch train [or time] instead of exponential one in the case of Fast Beam Ion Instability [5]. The linear growth is the result of the linear growth of the ions density along the bunch train. Therefore the amplitude roughly linearly depends on the ion density. Since the electron beam is round, there is a similar growth in both horizontal and vertical planes. The detail oscillation of electron beam and ion beam [Fig. 5 bottom] doesn't show the same oscillation pattern between the two beams, which indicates the lack of coherent motion. One possible reason is that the length of the bunch train is not long enough to allow the instability [coupled motion] start. However simulation with longer bunch train and high vacuum pressure always give linear growth.

Figure 6 shows the case of 300 pC bunch. It basically shows the similar feature as 100 pC, linear growth in time and incoherent motion. The growth is slightly faster than 100 pC case. In short summary, the growth of electron bunch amplitude linearly depends on the ion density. In other words, the amplitude grows linearly with along the bunch train length.

Large beam oscillation amplitude can degrade the performance of LCLS-II FEL. Therefore the ion effect sets a maximum length of the bunch train. For example, tolerable amplitude growth of 1% (10%) beam size limits the bunch train length to 0.5 seconds (15 seconds) and 0.38 seconds (12.5 seconds) for 100 pC and 300 pC bunch charge, respectively. For lower bunch rate than 1 MHz, the tolerable bunch train length should be longer.

A bunch train gap can be used to clear the ions. In general a train gap of a few ion oscillation periods can effectively clear the ions. A simulation shows that a train gap with 10 missing bunches is good enough to clear more than 95% ions.

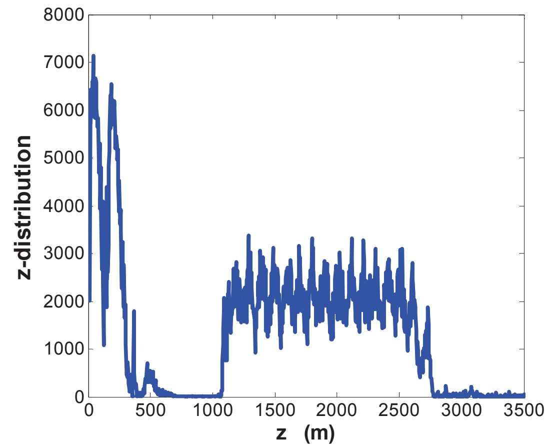

Figure 2: The distribution of ions along the linac, 100 pC bunch.

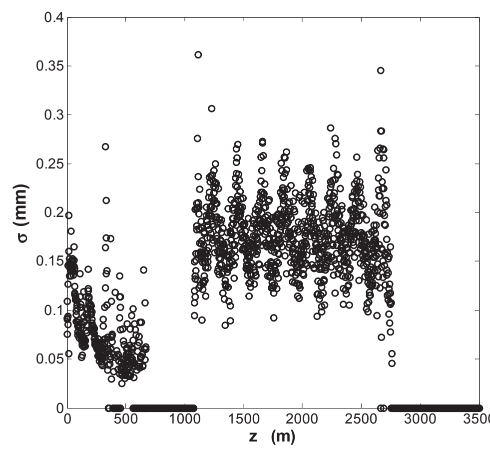

Figure 3: The transverse *rms* size of ions along the linac.

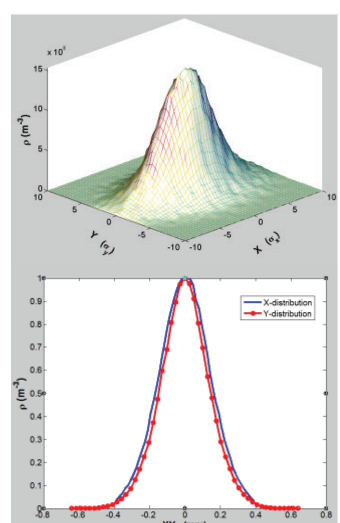

Figure 4: Transverse ion distribution (2D, top) (1D, bottom) at the long bypass beam line for 100 pC bunch charge.

ISBN 978-3-95450-134-2

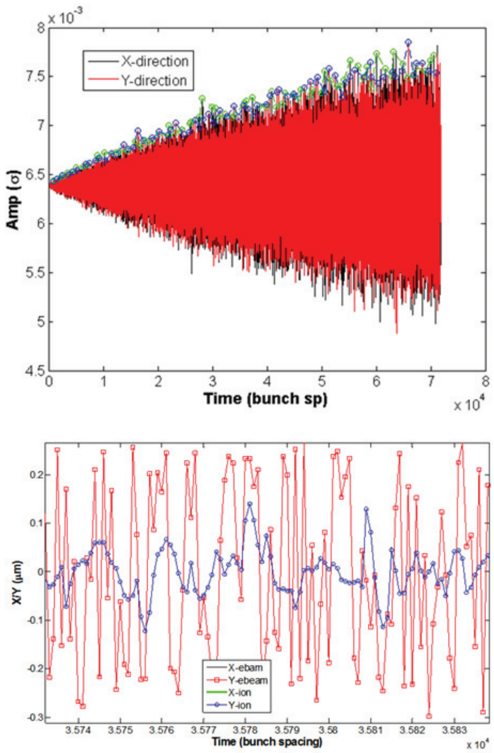

Figure 5: Electron bunch amplitude at the end of linac for a long bunch train (top) and oscillation of electron beam (red line) and ion beam (blue line) (bottom). Bunch charge is 100 pC.

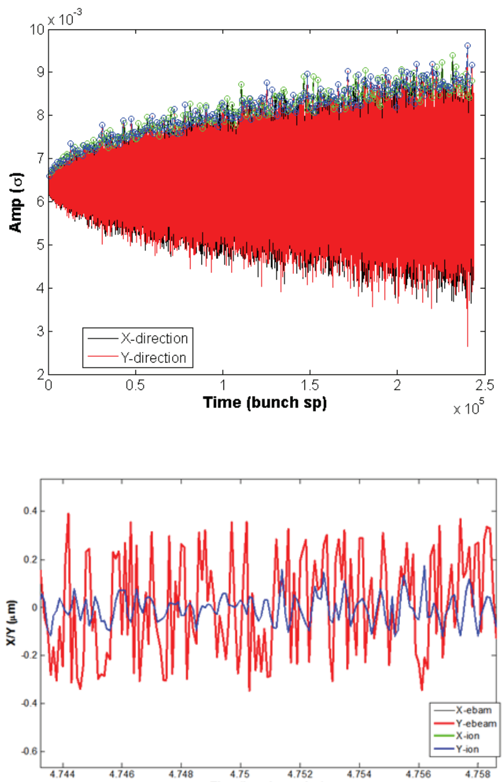

Figure 6: Electron bunch amplitude at the end of linac for a long bunch train (top) and oscillation of electron beam and ion beam (bottom). Bunch charge is 300 pC.

ION FREQUENCY SPREAD OF COLD AND HOT IONS

To understand the simulation, the motion of ions and their frequency spread under different conditions are investigated in this section for both cold and hot ion beams, coasting and bunched electron beam.

Cold ions with Coasting Electron Beam

For a round beam, the potential and field can be written as

$$U(r) = \frac{\lambda_e e}{4\pi\varepsilon_0}\left[\gamma - Ei\left(-\frac{r^2}{2\sigma^2}\right) + \ln\left(\frac{r^2}{2\sigma^2}\right)\right] \quad (2)$$

$$E_r(r) = \frac{e\lambda_e}{4\pi\varepsilon_0}\frac{1}{r}\left[1 - e^{-\frac{r^2}{2\sigma^2}}\right] \quad (3)$$

where γ=0.57721 is the Euler gamma constant and Ei is the exponential integral function. λ_e is the bunch line density and σ is the transverse root mean square (*rms*) beam size of the electron bunch. The period of ion oscillation depends on the position of the ion was born r_0 as

$$T(r_0) = 4\int_0^{r_0}\frac{1}{v(r)}d = 2\sqrt{2m}\int_0^{r_0}\frac{1}{\sqrt{U(r_0)-U(r)}}dr \quad (4)$$

The energy conservation law is used and the thermal effect is neglected here. Figure 7 shows the calculated ion frequency from the above equation and the results from particle tracking. There is an excellent agreement.

The frequency distribution in general case is given by

$$\rho(\omega_x) = \int_0^{\infty}\int_0^{\infty} f(\omega_x, x_0, y_0)\, g(x_0, y_0)\, dx_0 dy_0 \quad (5)$$

Here ω_x refers to the horizontal frequency and $f(\omega, x_0, y_0)$ is the frequency distribution function of ions with amplitude of $r_0 = \sqrt{x_0^2 + y_0^2}$. $g(x_0, y_0)$ is the distribution function of ion oscillation amplitude, which varies with time when beam instability happens. When the thermal energy is negligible (strong beam) compared to the beam potential and the electron beam amplitude is smaller compared to its beam size, the distribution of ion oscillation amplitude is a Gaussian distribution with the same *rms* as the electron beam.

Figure 8(a) shows the distribution of ion frequency with a round electron beam when $g(r_0)$ is a Gaussian distribution with *rms* size equal to the electron beam size σ. This is the case of the beginning of the instability where the amplitude is smaller than the beam size.

After instability occurs, the ions oscillate at larger amplitude. The ion frequency spread also increases accordingly. Figure 8(b) and 8(c) show the cases of ion amplitude has a amplitude of $\sqrt{2}\sigma$ and 2σ, respectively. The larger amplitude induces a larger frequency spread and therefore a stronger damping to the instability. The self-damping mechanism is one important character of

ISBN 978-3-95450-134-2

beam ion instability, which limits the amplitude of electron beam on orders of beam size at saturation level in most storage ring light sources.

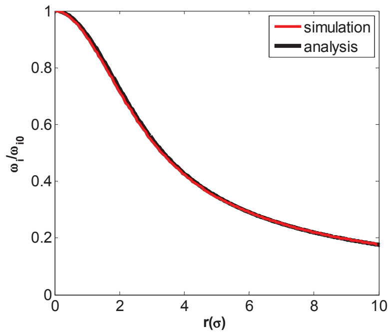

Figure 7: Comparison of the ion frequency with a round electron beam. The analysis is given by Eq. (4).

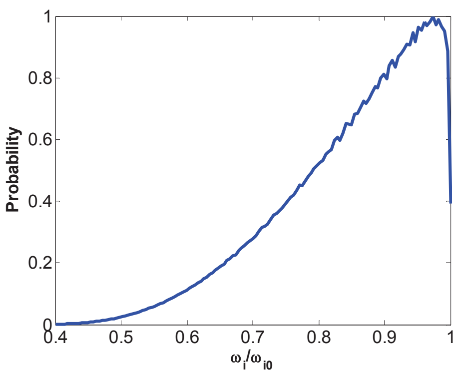

(a)

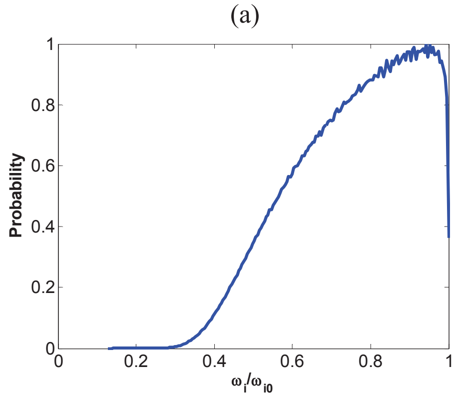

(b)

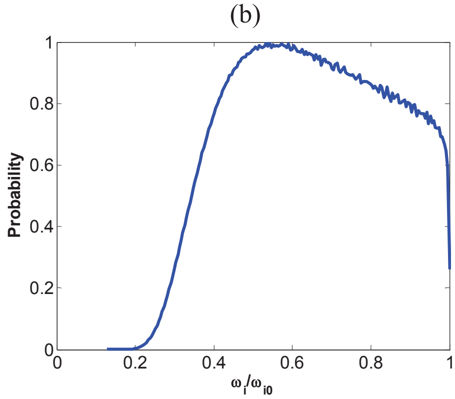

(c)

Figure 8: Horizontal ion frequency distribution of a round beam. r_0 has Gaussian distribution with $rms = \sigma$ (a); $\sqrt{2}\sigma$ (b); 2σ(c).

Cold Ions with Bunched Electron Beam

In real accelerators, most electron beams are short bunched beam. When the bunch spacing is much shorter compared to the period of the ion oscillation, as for most storage ring light sources, the electron bunch can be treated as a continuous beam. In this section we investigate the bunch spacing effect on the stable motion of the ions. A particle tracking program is used to estimate the frequency of the ions with different amplitudes.

Figure 9 shows the frequency dependence on the ion amplitude for different bunch spacing Δt=T_0/20, T_0/9, T_0/6.4, T_0/4.5 and T_0/3.7. Here T_0 is the period of the ions near beam centre. The ion frequency with short bunch spacing, such as $\Delta t < T_0/10$, is close to the case with coasting electron beam. When the bunch spacing is long, for example $\Delta t > T_0/9$, the motion of ions with large amplitude becomes unstable (with noisy distribution or zero frequency in the plots). The area of stable motion becomes smaller when the bunch spacing increases. Note that there are some stable/unstable zones for the last three cases. It is a feature of bunched beam. The motion of ion is unstable at smaller amplitude while it can become stable at large amplitude. Here the motion of ions with long bunch spacing is far from sinusoidal oscillations with single frequency. For example, the motion with a period of 5 bunch spacing is unstable; however it becomes stable if the period is 4 bunch spacing. That explains why the ion motion becomes stable at larger amplitude. It is the effect of bunched beam where the ion receives only a few discrete kickers from the electron bunches over one ion oscillation period. If the bunch spacing is longer than T_0/5, the motion of the ions is unstable except the core part ($r{\sim}\sigma$).

Hot Ions with Bunched Electron Beam

In the above studies, the effect of ion temperature is neglected. When the thermal energy of an ion is smaller compared to the beam potential energy ($kT \ll m\omega^2 \sigma^2$), the temperature effect is negligible. This is true for most electron beam in rings where the bunch spacing is short. For instance, the SPEAR3 beam has a bunch spacing of 2 *ns* and $T_0/\Delta t = 36$. The horizontal frequency at 300K is shown in Fig. 10, which is similar to the result at zero temperature except some noisy feature at large amplitude. It is clear that the effect of temperature is negligible for such strong electron beam.

When bunch spacing is long, the ion drift during one bunch spacing due to the thermal energy can be comparable to the transverse beam size. In LCLS-II, the maximum bunch repetition rate is 1*MHz*. The bunch charge varies from 10 pC to 300 pC. For a 100 pC bunch, the CO^+ frequency at the long by-pass beamline is shown in Fig. 11 for zero temperature and 300k, respectively. With zero temperature the bunch spacing effect ($T_0/\Delta t \sim 6$ here) is similar as one shown in Fig. 9. The long bunch spacing makes the ion motion at large amplitude unstable. The effect of temperature at 300K causes the frequency

ISBN 978-3-95450-134-2

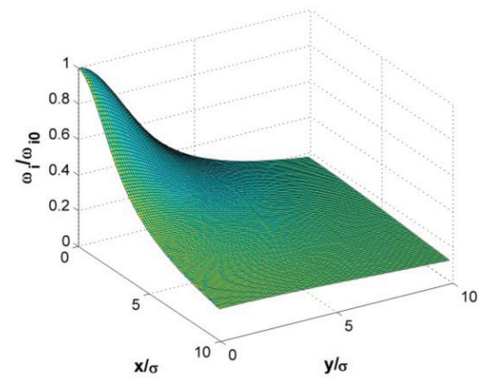

(a) $T_0/\Delta t$ =20

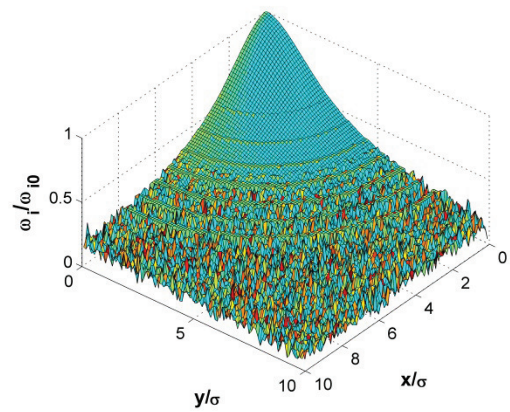

(b) $T_0/\Delta t$ =9

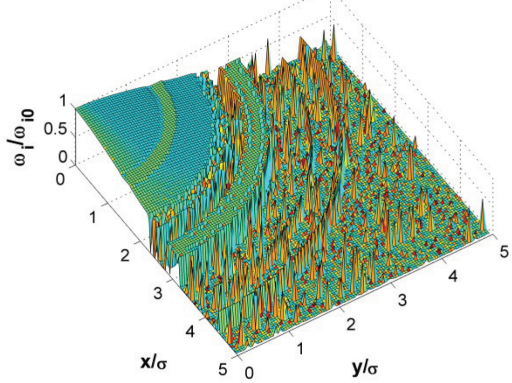

(c) $T_0/\Delta t$ =6.4

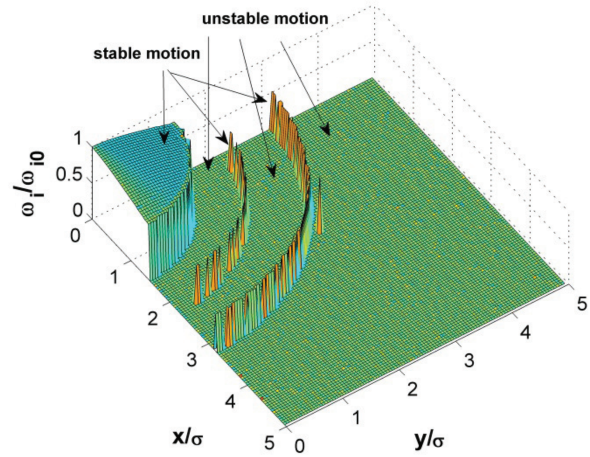

(d) $T_0/\Delta t$ =4.5

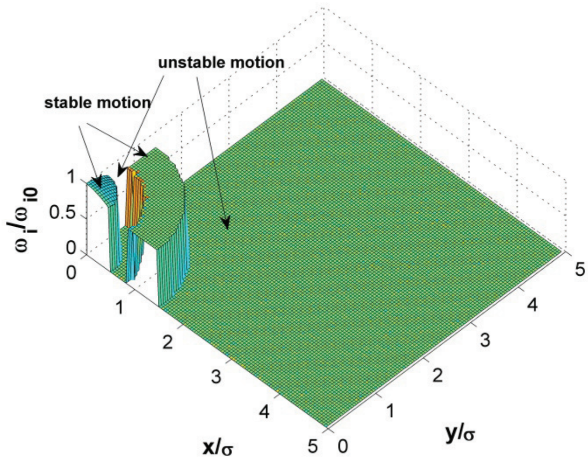

(e) $T_0/\Delta t$ =3.7

Figure 9: Horizontal Ion frequency distribution of a round beam with various bunch spacing.

distribution more randomly distributed (Fig. 11, bottom). This means that there is weak coherent central motion due to the long bunch spacing. The effect of temperature further supresses the coherent motion of ions.

BENCHMARK WITH IDEAL LINAC

To better check the effect of temperature and bunch spacing, we set-up one simple numerical test here: a 9 *km* long linac with regular FODO optics and single gas species vacuum. There is small variation in ion frequency for FODO cell optics. Therefore we can check the pure effect of bunch spacing and temperature with such ideal linac. The temperature is set to 300K in all cases while the bunch spacing is varied. Figure 12 shows three cases with different bunch spacing of $T_0/\Delta t$ =30, 9 and 5. There is an exponential growth for both electron and ion beams with a short bunch spacing of $T_0/30$, which is expected by the theory of fast beam ion instability [5]. The electron beam acts to the ions like a coasting beam due to the short

ISBN 978-3-95450-134-2

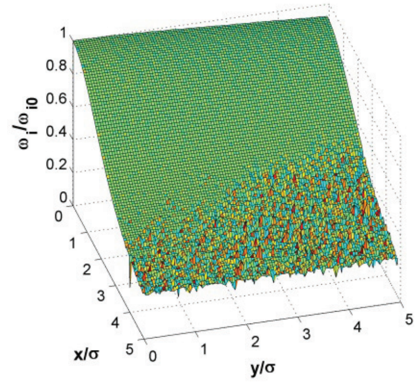

Figure 10: Horizontal ion frequency of a Bi-Gaussian electron beam with $\sigma_x/\sigma_y = 20$ and bunch spacing of 2 *ns* and Temperature of 300K. $T_0/\Delta t = 36$.

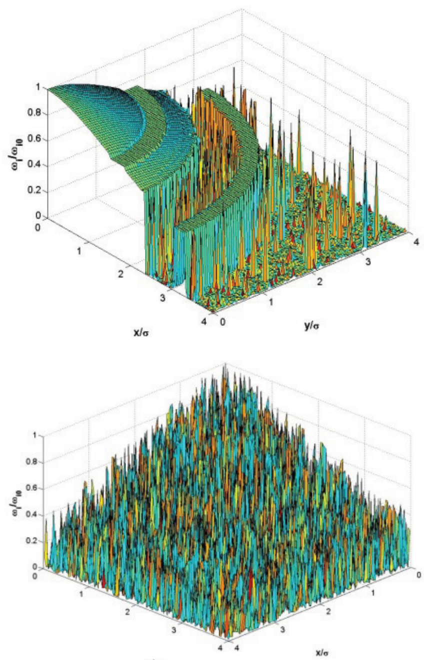

Figure 11: Frequency spread of *CO* ion at LCLS-II long bypass beamline with $T_0/\Delta t\sim 6$ (100 pC) and bunch repetition rate of 1 *MHz* at zero temperature (top) and 300K (bottom), respectively.

bunch spacing. When the bunch spacing increases to $T_0/9$, both beams show non-exponential growth with strong beating. The growth becomes linear when the bunch spacing is even longer as $T_0/5$, which is close to the LCLS-II case. Note that ion cloud oscillates at smaller amplitude compared to the electron beam in short bunch spacing case (Fig. 12 top) where the ions are deeply trapped. However the amplitude of ion cloud becomes larger than the electron beam when the bunch spacing is $T_0/5$ long (not shown here) where the ions are not deeply trapped.

The simulation with ideal linac confirms the linear growth in LCLS-II and agrees with the effect frequency spread of hot ions and long bunch spacing.

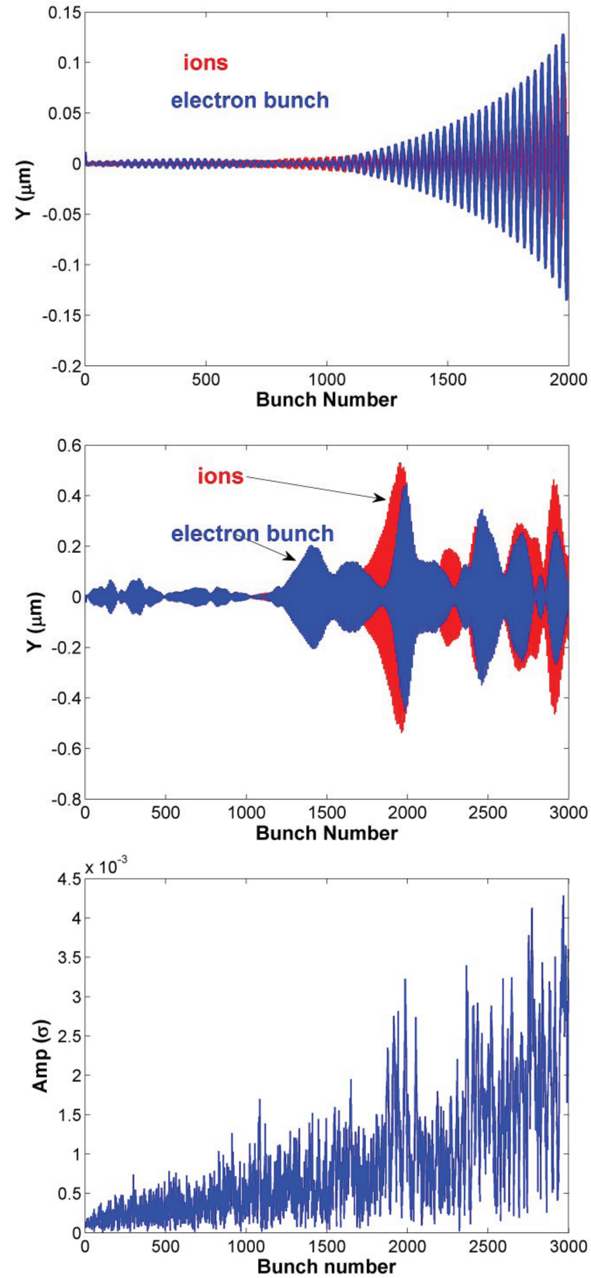

Figure 12: Beam and ion oscillation for various bunch spacing $1/30T_0$ (top), $1/9T_0$ (middle) and $1/5\ T_0$ (bottom) in 9 *km* long FODO cell linac with temperature of 300K. The vertical electron beam size is $15\mu m$.

SUMMARY AND DISCUSSION

A large number of ions can be accumulated due to the attractive force even with long bunch spacing in LCLS-II. However there is a lack of coherent motion between ion and electron beams because of the effects of long bunch spacing and hot ions. As a result, there is a linear growth in amplitude along the bunch train in our case and this growth sets one maximum length of bunch train for the operation. The ions can be effectively cleared by a bunch train gap with length on the order of ion oscillation period.

ISBN 978-3-95450-134-2

The frequency spread with hot ions can clearly explain the underlying physics in our case: the long bunch spacing and hot ions together induce large spread and noise in the ion frequency, which causes incoherent ion motion and linear growth of the electron beam.

ACKNOWLEDGEMENTS

We thank our colleagues Gennady Stupakov and William Fawley for fruitful discussions. This work is supported by Department of Energy Contract No. DE-AC02-76SF00515.

REFERENCES

[1] T. Raubenheimer, "The LCLS-II, a New FEL Facility at SLAC", in Proc. of 36th Int. Free-Electron Laser Conf., Basel, 2014, WEB001.

[2] J. Schmerge *et al.*, "The LCLS-II Injector Design", in Proc. of 36th Int. Free-Electron Laser Conf., Basel, 2014, THP042.

[3] P. Emma, *et al.*, "Linear Accelerator Design for the LCLS-II FEL Facility", in Proc. of 36th Int. Free-Electron Laser Conf., Basel, 2014, THP025.

[4] L. Wang, Y. Cai, T. O. Raubenheimer and H. Fukuma, Phys. Rev. ST Accel. Beams 14, 084401 (2011).

[5] T. O. Raubenheimer and F. Zimmermann, Phys. Rev. E 52, 5487 (1995).

ELECTRON BEAM PHASE SPACE TOMOGRAPHIE AT THE EUROPEAN XFEL INJECTOR

M. Scholz*, B. Beutner, DESY, Hamburg, Germany

Abstract

Transverse emittances as well as the energy spread and the peak current of the electron bunches are important parameters for high-gain free electron lasers such as the European XFEL. Investigations of the 6D phase space characterization would give important indications to optimize the beam quality for SASE operation. The injector of the European XFEL includes, inter alia, a laser heater, a transverse deflecting cavity (TDS), a spectrometer, a diagnostic section with four screens as well as several quadrupole magnets. In this paper, we will discuss the possibilities to characterize the 6D phase space of the electron beam in the injector of the European XFEL.

INTRODUCTION

Crucial electron beam parameters like the minimum slice and projected emittances as well as the minimum energy spread are defined by the injector system. SASE FELs like the European XFEL [1] depend strongly on the emittance and the energy spread, thus it is significant to investigate and optimize these parameters. A reconstruction of the two transverse phase spaces, preferably time resolved, and of the longitudinal phase space will be of use to accomplish this task.

A separate beam dump at the end of the European XFEL injector and a concrete shielding wall between the injector and the subsequent machine components allow to start the injector commissioning while the linac is still under construction.

In this paper we study the possibilities to use the XFEL injector components for measurements that are required to reconstruct the transverse and longitudinal phase spaces of the electron beam.

EUROPEAN XFEL INJECTOR

A schematic layout of the European XFEL injector is presented in the upper part of Fig. 1. Two superconducting accelerating modules are installed in the linac, a 1.3 GHz module and a third harmonic module to linearize the longitudinal phase space of the particle distributions. The beam energy downstream these modules is 130 MeV.

A subsequent diagnostic section including a transverse deflecting cavity as well as four screens [2] and a spectrometer allow to study the electron beam quality. The TDS installed in the XFEL injector is a 16 cell traveling wave S-band RF waveguide structure operating with a frequency of 2.997 GHz [3]. The streak is applied in the vertical plane. A following periodic FODO section is designed such that the betatron phase advances between the TDS and the screens are optimized for emittance and bunch length measurements. Figure 1 shows the default beta functions in the XFEL injector from the electron gun to the injector dump.

Four fast kickers can deflect single bunches out of a long bunch train such that one bunch can be observed on each screen. That makes it possible to measure electron beam optics and emittances online during SASE operation. The screens can also be moved into the electron beam so that the measurements can take place without kickers.

The default beam optics in the injector was not designed to measure the slice emittances with quadrupole scans as required for the reconstruction of the transverse phase spaces. Several special beam optics that fulfill the requirements and that can be realized with the available beam optics elements had to be developed.

TOMOGRAPHY

The tomography technique [4] allows to reconstruct an inner structure using cross sections of the volume taken from different viewing angles. The reconstruction of an electron beam's transverse phase space can be obtained with several projections of the particle distribution while the beam rotates in the respective phase space [5]. The latter can be achieved with a scan of the betatron phase ϕ_x respectively ϕ_y using quadrupole magnets between an optics reference point and a screen where the measurements take place. The optics reference point is the position where the Twiss functions and the emittance will be reconstructed. The range of the phase scan $\Delta\phi_{i,\,\mathrm{ref}\to\mathrm{screen}}$ has to be about 180 deg [6]. The number of required projections depends on the reconstruction algorithm. More projections will lead to a better reconstruction result. We decided to apply the maximum entropy (MENT) algorithm [7] that requires a comparatively small number of measurement steps. However, a fixed electron beam optics and a measurement with the four screens in the diagnostic section is not sufficient. The four steps that can be achieved with these screens are not enough for the tomographic reconstruction. For this reason, a phase scan with quadrupoles, in steps of 10 degree phase advance, will be used. The beam will be observed on the last screen upstream the spectrometer magnet.

All beam optics calculations were carried out using the optimization and tracking code elegant [8].

Horizontal Phase Space

The injector TDS enables horizontal slice emittance measurements. This makes it possible to reconstruct the horizontal phase space of single bunch slices. The use of the TDS entails additional constrains on beam optics. The vertical

* matthias.scholz@desy.de

ISBN 978-3-95450-134-2

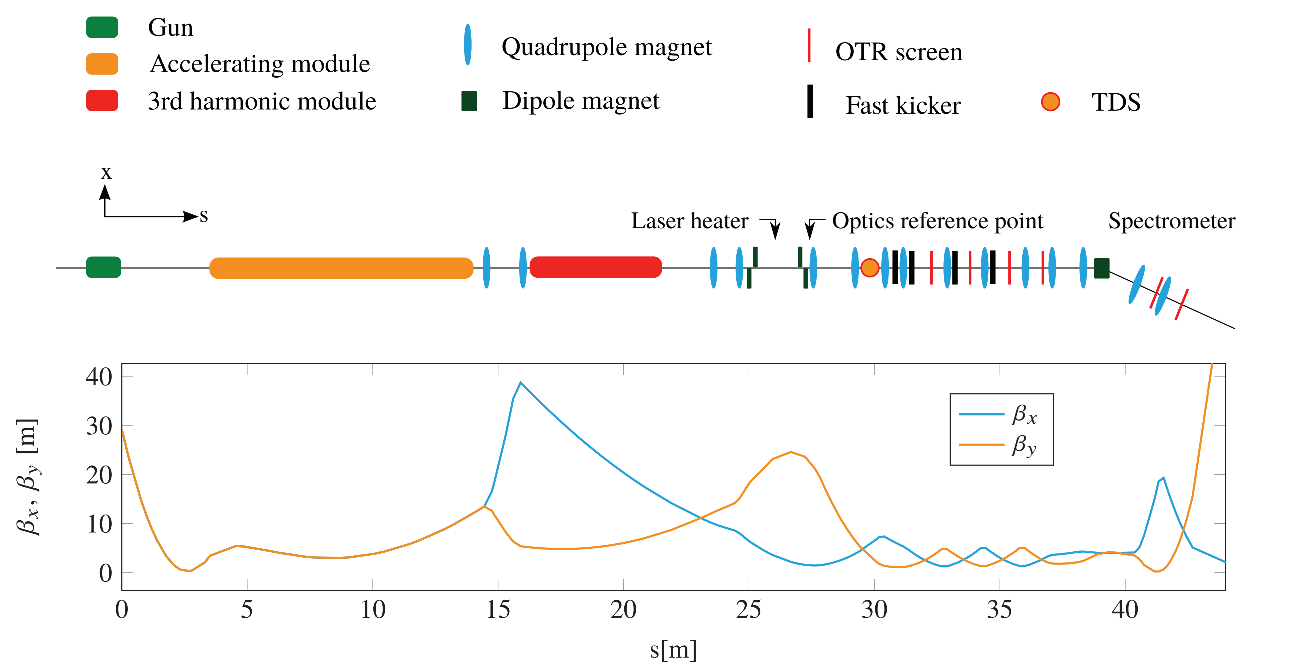

Figure 1: The default beta functions in the XFEL injector starting at the photo cathode and ending in the injector dump. Above the plot one can find a schematic layout of the XFEL injector.

offset of a particle at the screen, y_{screen}, deflected by the TDS, at the observation screen can be described as follows [3]:

$$y_{\text{screen}} = y_0 \pm \sqrt{\beta_y(s_{\text{screen}})\beta_y(s_{\text{TDS}})} \sin\left(\phi_{\text{y, TDS} \rightarrow \text{screen}}\right) K\, z,$$

with the initial offset y_0, the vertical beta function β_y at the position of the TDS as well as at the position of the screen. $\phi_{\text{y, TDS} \rightarrow \text{screen}}$ describes the vertical betatron phase advance between the TDS and the screen. K can be calculated as follows: $K = (eV_0 k)/(pc)$ with e, the elementary charge, k, the wave number of the structure, p, the momentum of the electrons and c, the velocity of light. The longitudinal position of the particle in the bunch is described with z.

A large vertical beta function at the position of the TDS as well as $\Delta\phi_{\text{y, TDS}\rightarrow\text{screen}} = 90$ deg is suggested to optimize the streak effect. The formula presented above indicates also a large vertical beta function at the position of the screen. However, that would also lead to a larger unstreaked beam thus it will not increase the streak's resolution. It has to be considered that the requirements on the beta functions and on the phase advances are not independent.

Demands on the beam optics in the horizontal plane are: The betatron phase has to be scanned over 180 degree as discussed before. The horizontal beta function in the TDS should be small in order to minimize additional energy spread induced by off axis field components. At the position of the screen, β_x has to be large enough that the beam size is larger than the screen's resolution.

A set of 18 different beam optics setups for the horizontal slice emittance measurements were developed fulfilling the specifications as discussed before. The electron beam optics reference point was chosen between the laser heater and the TDS. For this reason, the beam optics stays unchanged in the linac as well as in the laser heater during the scans. In total 7 quadrupoles were used and the setups are presented in Figures 2, 3 and 4. All three plots are presented as functions of the horizontal phase advance between the optics reference point and the observation screen. The first one, Fig. 2, shows the horizontal and the vertical beta functions at the position of the TDS. As required, the horizontal beta function is small and β_y is around 10 m or larger.

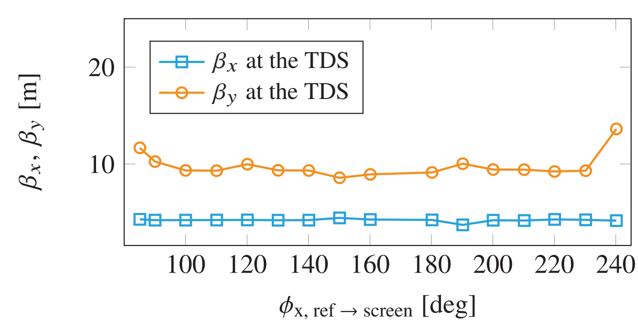

Figure 2: Beta functions at the position of the transverse deflecting cavity.

Figure 3 presents the beta functions at the observation screen. The horizontal function is, for all steps, around 30 m and the vertical beta function is for most of the steps below 0.5 m.

All quadrupole magnet's strengths for each measurement step are depicted in Fig. 4. The magnets are all within their maximum gradients and the unipolar quadrupoles in the FODO section were considered.

ISBN 978-3-95450-134-2

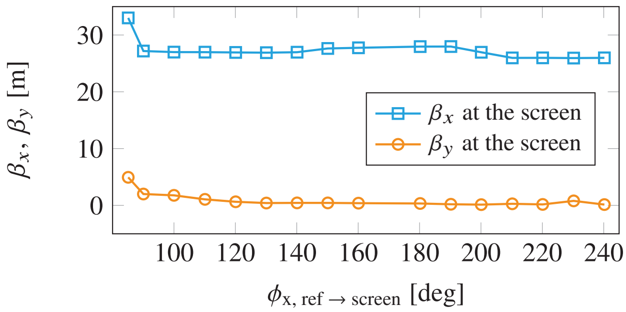

Figure 3: Horizontal and vertical beta functions at the screen for all steps of the horiztonal phase scan.

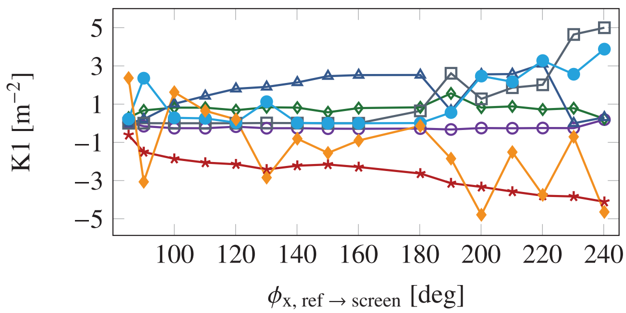

Figure 4: Normalized gradients of the quadrupoles used for the horizontal betatron phase scan.

The maximum effective voltage of the TDS installed in the injector is $V_{0,\text{max}} = 1.84$ MeV [3]. With the above mentioned TDS frequency and a longitudinal position of a particle in the bunch of $z = 3$ mm (The bunches are not compressed in the injector), with an average vertical beta function at the transverse deflecting cavity of $\beta_\text{y}(s_\text{TDS}) = 10$ m and with an average vertical beta function at the screen of $\beta_\text{y}(s_\text{screen}) = 0.3$ m, the maximum offset of a particle with no initial vertical offset ($y_0 = 0$ m) is about $y_\text{screen} \approx 4.5$ mm, which is much larger than the expected size of the unstreaked beam:

$$\sigma_y = \sqrt{\beta_\text{y}(s_\text{screen}) * \epsilon} \approx 25\mu\text{m},$$

calculated with an emittance of $\epsilon = 0.5\ \mu m$ ($\epsilon_\text{phys} = 2$ nm). The resolution of the screen is 10 μm [2]. Thus, the beam optics setups as presented are suitable to get a sufficiently streaked beam at the screen for horizontal slice emittance measurements, even when the maximum effective voltage of the TDS is not applied.

Vertical Phase Space

Since there is no TDS in the injector streaking in the horizontal plane it was necessary to find another way to do the vertical slice emittance measurements. When a linear chirp is applied on the electron bunches it is possible to streak them with the spectrometer magnet in a suitable way. The linearity of the energy chirp can be verified with a measurement of the longitudinal phase space, as it will be described below.

As for the horizontal slice emittance measurement, 18 quadrupole setups were developed that scan the vertical betatron phase over 180 degree while the dispersion at the observation screen downstream the spectrometer bending magnet is constant within small limits. The horizontal and vertical beta functions at the screen have to be such that the beam sizes are above the resolution limit of the screens [2].

The normalized gradients of the quadrupoles during the scan of the vertical betatron phase advance are depicted in Fig. 5. In total, 11 quadrupoles between the optics reference point and the screen were used. All quadrupoles stay within their maximum gradients and the unipolar magnets are considered.

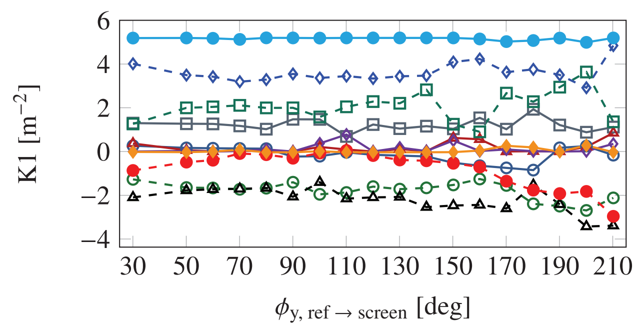

Figure 5: Normalized gradients of the quadrupoles used for the vertical betatron phase scan.

The dispersion at the screen during the scan of the vertical betatron phase advance is depicted in Fig. 6. Its around 0.6 m for all steps.

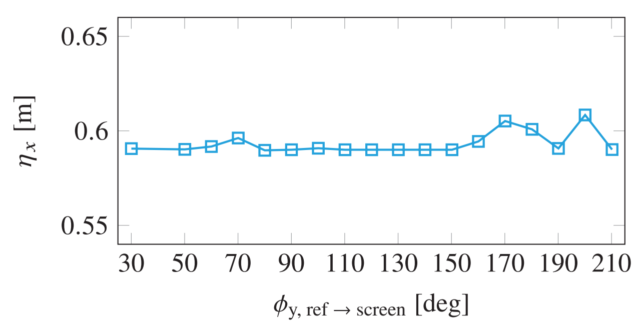

Figure 6: Dispersion at the screen downstream the spectrometer during the vertical betatron phase scan.

Figure 7 shows the horizontal and vertical beta functions at the observation screen. For most of the steps both parameters could be kept around 6 m.

A particle offset at the screen due to the dispersion can be calculated as follows:

$$x_\eta = \eta_\text{x}\delta,$$

with the horizontal dispersion η_x and the relative energy deviation of the particle $\delta = \Delta\text{p}/\text{p}_0$. Assuming an energy chirp of 0.5 % and a dispersion $\eta_\text{x} = 0.6$ m, this leads to a horizontal offset of $x_\eta \approx 3$ mm. The expected (unstreaked)

ISBN 978-3-95450-134-2

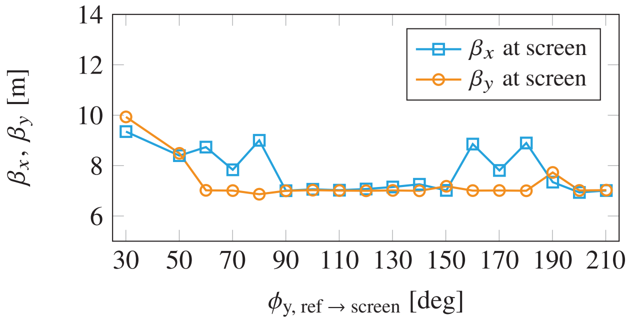

Figure 7: Beta functions at the screen downstream the spectrometer during the vertical betatron phase scan.

beam sizes at the screen are, under the assumption that the $\beta_x = \beta_y = 6$ m:

$$\sigma_x = \sigma_y = \sqrt{\beta_y(s_{\text{screen}}) * \epsilon} \approx 20\mu\text{m}.$$

With that, the horiztontal streak is much larger than the unstreaked horizontal beam size and the vertical beam size is larger than the resolution of the screen.

Longitudinal Phase Space

The vertically streaking TDS and the horizontally deflecting spectrometer bending magnet allow, with small restrictions, to observe the longitudinal phase space on the screen in the dispersive section [5]. The additional energy spread added to the particle distributions by the longitudinal electromagnetic fields in the TDS has to be taken into account while evaluating the taken pictures. An optimized optics solution was developed providing a vertical betatron phase advance of $\phi_{\text{y, TDS} \to \text{screen}} = 90$ degree and suitable beta functions at the screen. The beta functions between the electron gun and the observation screen are depicted in Fig. 8.

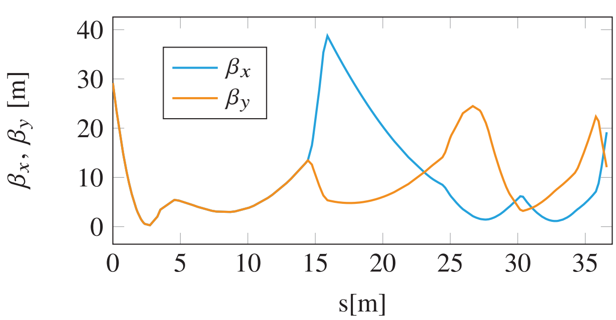

Figure 8: Beta functions in both planes as designed for the longitudinal phase space measurement on the screen downstream the spectrometer.

CONCLUSIONS

It was shown that the existing magnets, the transverse deflecting cavity and the screens installed in the European XFEL injector can be used for a horizontal and vertical slice emittance measurement. This makes it possible to reconstruct the transverse phase spaces of the bunch slices. In addition with the longitudinal phase space, which can be observed in the dispersive section of the injector, this gives an overview of significant beam parameters and allows optimizing the electron beam for SASE operation.

ACKNOWLEDGMENT

We like to thank all colleagues who have been involved in the construction, building and commissioning of the European XFEL injector.

REFERENCES

[1] M. Altarelli et al., *"The European X-Ray Free-Electron Laser, Technical design report"*, DESY 2006-097 July 2007.

[2] Ch. Wiebers et al., *"Scintillating screen monitors for the transverse electron beam profile diagnostics at the European XFEL"*, WEPF03, Proceedings of IBIC2013, Oxford, UK.

[3] M. Yan, *"Online diagnostics of time-resolved electron beam properties with femtosecond resolution for x-ray FELs"*, PhD thesis, University of Hamburg, to be published 2015.

[4] J. Radon, *"Über die Bestimmung von Funktionen durch ihre Integralwerte längs gwisser Manigfaltigkeiten"*, Akademie der Wissenschaften Leipzig, 69, Page 262-277, 1917.

[5] M. Röhrs et al., *"Time-resolved electron beam phase space tomography at a x-ray free-electron laser"*, Phys. Ref. ST 12, 050704, 2009.

[6] E. Prat et al., *"Emittance measurements and minimization at the SwissFEL injector test facility"*, Phys. Ref. ST 17, 104401, 2014.

[7] J. J. Scheins, *"Tomographic reconstruction of transverse and longitudinal phase space distributions using the maximum entropy algorithm"*, TESLA Report 2004-08.

[8] M. Borland, *"elegant: A Flexible SDDS-Compliant Code for Accelerator Simulation"*, Advanced Photon Source LS-287, September 2000.

ISBN 978-3-95450-134-2

THz BASED PHASE-SPACE MANIPULATION IN A GUIDED IFEL*

E. Curry†, S. Fabbri, P. Musumeci, UCLA, Los Angeles, CA 90049, USA
A. Gover, Tel-Aviv University, Tel-Aviv 69978, Israel

Abstract

We propose a guided IFEL interaction driven by a broadband THz source to compress a relativistic electron bunch and synchronize it with an external laser pulse. A high field single-cycle THz pulse is group velocity-matched to the electron bunch inside a waveguide, allowing for a sustained interaction in a magnetic undulator. The THz pulse is generated via optical rectification from the external laser source, with a measured peak field of up to 4.6 MV/ m. We present measurements of the THz waveform before and after a parallel plate waveguide with varying aperture size and estimate the group velocity. We also present results from a preliminary 1-D multi-frequency simulation code we are developing to model the guided broadband IFEL interaction. Given a 6 MeV, 100 fs electron bunch with an initial 10^{-3} energy spread, as can be readily produced at the UCLA PEGASUS laboratory, the simulations predict a phase space rotation of the bunch distribution that will reduce the initial timing jitter and compress the electron bunch by nearly an order of magnitude.

INTRODUCTION

As the development of THz sources pushes towards higher power, the pursuit of THz applications in accelerator physics has become an active field of research. In addition to the unique advantages of THz radiation for imaging and spectroscopy [1], the THz frequency range offers a middle ground in beam manipulation between the high-acceleration-gradient of laser wavelengths and the broad phase-acceptance window of RF. The transverse kick imparted to an electron bunch in an X-band RF deflector, like the one used for temporal diagnostics at LCLS [2], could be accomplished by a THz field that is over fifty times smaller. The higher frequency of THz relative to RF may also allow for improvement of the breakdown limitations in an accelerating structure [3]. Where laser coupling in a typical FEL results in microbunching of the electron beam, an FEL interaction with THz radiation could capture and compress the entire bunch within a single ponderomotive bucket.

At the UCLA PEGASUS laboratory, we intend to demonstrate the compression of a 1 pC electron bunch using ponderomotive coupling with a THz pulse. A single Ti:Sapph laser source will be used to generate THz through optical rectification while simultaneously driving a 1.6 cell S-band photogun. The ponderomotive force produced by the THz and undulator fields gives the electron bunch an energy chirp, resulting in longitudinal compression after a drift section.

* Work supported by DOE grant DE-FG02-92ER40693 and NSF grant PHY-1415583.
† ejcurry@physics.ucla.edu

The THz pulse is synchronized with the external laser pulse. When the phase of the ponderomotive bucket is centered on the average arrival time of the electron bunches, the induced energy chirp works to accelerate late bunches and decelerate early bunches towards the optimal timing, compensating for the inherent time-of-arrival jitter that accrues over the course of the initial electron bunch acceleration.

ZERO-SLIPPAGE IFEL

The resonance condition of a standard inverse free electron laser (IFEL) assumes slippage between the electron bunch and the laser waveform to maintain a phase synchronism condition as they propagate in free-space. For the single-cycle THz pulse produced by optical rectification, an interaction can be sustained by satisfying a "zero-slippage" condition, or grazing dispersion curve condition, in which the THz group velocity is matched to the average longitudinal speed of the electron bunch [4][5], in addition to satisfying the phase synchronism condition. This velocity-matching occurs when the dispersion curves for the waveguide and electron beam, shown in Fig. 1, have the same slopes. The control of THz pulse group velocity can be accomplished by a waveguide. This technique has the added benefit of preserving the on-axis field intensity over the length of the guide rather than operating in the diffraction limited regime.

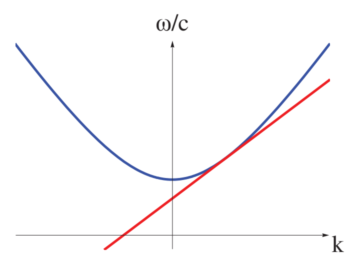

Figure 1: The dispersion curves for a waveguide (blue) and electron beam (red). The "zero-slippage" condition occurs when their slopes, corresponding to radiation group velocity and average longitudinal bunch velocity, are equal.

The THz frequency range is an ideal candidate for this guided IFEL technique. Although higher frequencies can offer a larger acceleration gradient, the size of the guiding structures becomes prohibitively difficult for co-propagation of electrons and laser. The length scales necessary for a THz guiding structure are large enough to permit alignment of the electron beam and accommodate the oscillating trajectory of the electrons in an IFEL without clipping. For reasonably low charge, wakefield effects in the guiding structure are negligible.

ISBN 978-3-95450-134-2

The IFEL-type phase-space manipulation we have proposed relies on ponderomotive coupling with the transverse field in the guide. Given excitation of the appropriate mode, a guiding structure can also provide a longitudinal field for direct coupling to the electron beam. This method of acceleration has been successfully demonstrated in ref. [6] for low energy electrons. However, for relativistic electrons, like those generated at PEGASUS laboratory, ponderomotive coupling is more efficient [7].

THz SOURCE CHARACTERIZATION

We use optical rectification in stoichiometric lithium niobate (sLN) to generate picosecond scale THz pulses. To enhance the conversion efficiency from IR to THz, the pulse front of the IR laser is tilted using a diffraction grating and imaged onto the sLN with a focusing lens [8][9]. With .1% conversion efficiency, we have 1.2 μJ pulses with a peak field of 3 MV/m after the diverging THz pulse is collimated and focused by a pair off-axis parabolic mirrors (OAP). By increasing the laser spotsize along with laser power, we can stay below the sLN damage threshold. Using 2.3 mJ of IR power, we produce a peak field of 4.6 MV/m, shown in Fig. 2b. We are developing a cooling chamber to further improve the conversion efficiency at the sLN crystal. With this modification, we can expect the peak field to increase by at least a factor of two [10].

Measurements of the temporal field profile are conducted with electro-optic sampling (EOS) in .5 mm thick zinc telluride. Within this nonlinear optical crystal, a THz induced rotation of the fast and slow axes changes the relative intensity between the horizontal and vertical polarization components of an IR probe pulse. A balanced detection scheme utilizes a quarter waveplate and Wollaston prism to separate these components onto two photodiodes. The original THz field is then calculated in terms of the intensity difference [11].

The IR probe pulse is brought into collinear propagation with the THz using a pellicle that is transparent to THz. For measurements of the THz profile after the waveguide, the IR probe travels within the guide, before interacting with the THz in the ZnTe crystal placed at the exit. The relatively high-frequency probe pulse is undistorted in the guide.

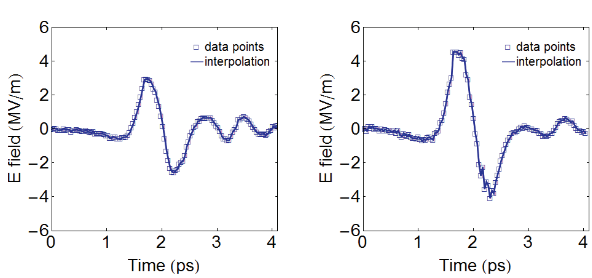

(a) (b)

Figure 2: THz profile with (a) undoubled spot size and (b) doubled spot size.

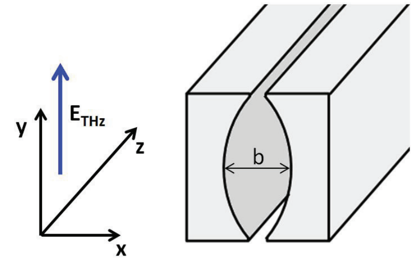

Figure 3: Diagram showing cross section of PPWG, with plate spacing b, and the orientation of THz polarization to excite the TE_{01} mode.

GUIDED THz PROPAGATION

We have adopted the curved parallel plate waveguide (PPWG) to control the propagation of the THz pulse. This choice was inspired by the investigation of guiding structures for a THz FEL oscillator in ref. [12] and [13]. The PPWG structure, shown in Fig. 3, offers the unique advantage of variable plate spacing which allows for tuning of the guide's dispersive properties and the corresponding group velocity of the THz pulse. Using an OAP, we focus the THz pulse into the entrance of the PPWG. This direct coupling of the THz pulse, with a gaussian transverse profile, excites the TE_{01} mode in the PPWG [14].

In Fig. 4, we show the THz longitudinal pulse profile after a 20 cm PPWG for three different plate spacings. The pulse profile before the waveguide is shown in Fig. 2a. The plates were machined from aluminum with a 3 mm radius of curvature. Because the plate alignment was set by eye, we list the plate spacings as nominally "3.5 mm," "2.5 mm," and "1.5 mm" in accordance with caliper measurements taken at both ends. Shown on the right in Fig. 4 are predicted pulse profiles based on the entering profile and the dispersion relation of the TE_{01} mode for the particular plate spacing. In the "1.5 mm" plate spacing measurement, the PPWG reached the limit at which the plate edges touched, resulting in some changes to the plates' alignment.

The group velocity of the THz pulse within the PPWG can be estimated by comparing the IR probe delay between the peak field in the initial and final THz pulse profile. After the "1.5 mm" plate spacing, the delay between the entering and exiting peak field was 4.03 ps, giving $\beta_g = .9940$. After the "2.5 mm" plate spacing, the delay was 2.47 ps, giving $\beta_g = .9963$. The delay for the THz pulse propagating in the "3.5 mm" plate spacing shown in Fig. 4 could not be determined because of backlash in the translation stage between measurements. However, a THz pulse generated by an IR pulse with doubled spotsize experienced a delay of 1.62 ps after the same "3.5 mm" spacing, giving $\beta_g = .9976$. The theoretical group velocities of .84 THz, the peak frequency of the pulse, for the three plate spacings are .9903 at 1.5 mm spacing, .9962 at 2.5 mm spacing, and .9979 at 3.5 mm spacing. The discrepancies between the measured and expected delays are most likely the result of plate misalignment, as well as plate contact for the case of the "1.5 mm" spacing.

ISBN 978-3-95450-134-2

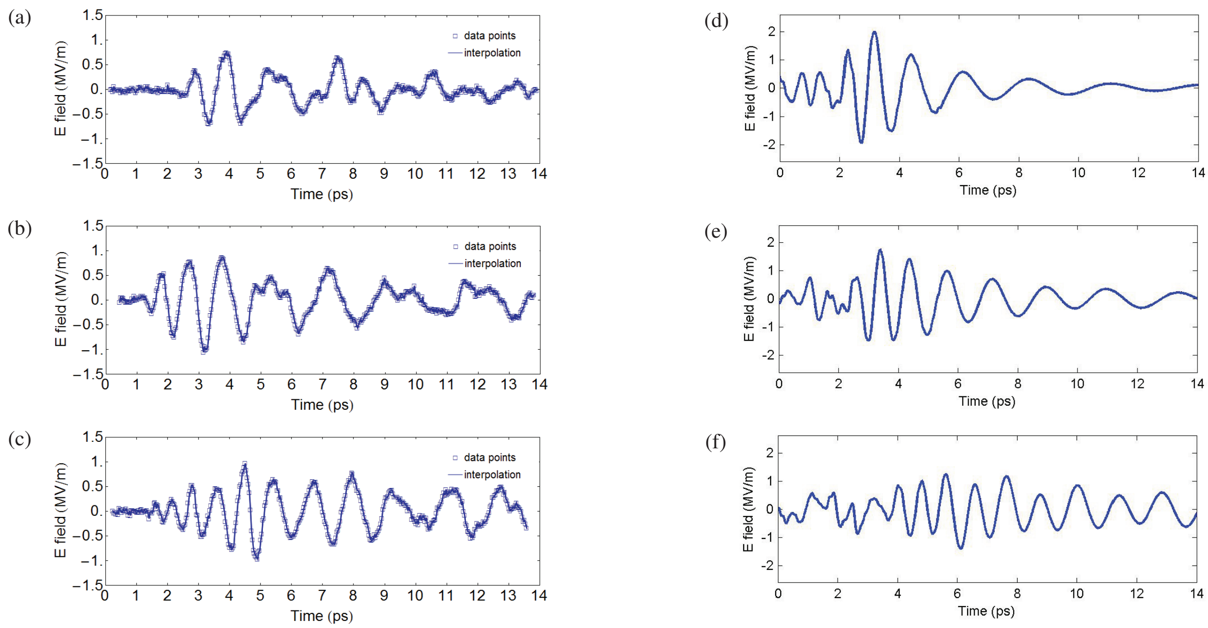

Figure 4: On the left, EOS measurements of the THz profile after a 20 cm PPWG with a plate spacing of (a) "3.5 mm," (b) "2.5 mm," and (c) "1.5 mm." On the right, predicted THz profile after the PPWG with plate spacing (d) "3.5 mm," (e) "2.5 mm," and (f) "1.5 mm," based on the THz profile measured at the entrance of the PPWG and shown in Fig. 2a.

SIMULATION STUDIES

Ponderomotive coupling with a single cycle THz pulse cannot be well-described by the single frequency approximation used by most FEL simulation codes because of the broad spectral content of the THz pulse. We are currently developing a multi-frequency simulation code, similar to MUFFIN [15], which will track the evolution of the THz pulse spectrum. The calculation does not rely on the slowly varying envelop approximation or period averaging and includes the waveguide-induced dispersion of the THz pulse.

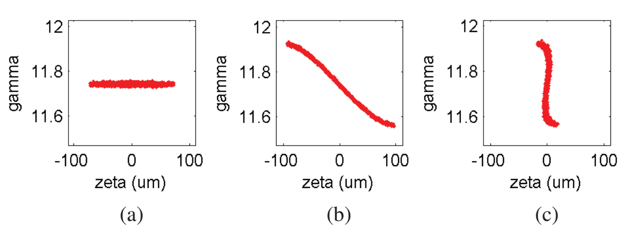

Figure 5: Simulation results showing the longitudinal phase space distribution (a) before the undulator, (b) at the exit of the undulator, and (c) after a .7 m drift period.

Preliminary simulation results are shown in Fig. 5, with the corresponding simulation parameters in Table 1. These waveguide parameters were chosen for the simulation because at the peak frequency they correspond to a theoretical group velocity of $\beta_g = .994$ which we have already experimentally achieved using the "1.5 mm" plate spacing. The selected electron bunch parameters are well within the range that can be routinely generated at PEGASUS laboratory [16] [17]. The sample 100 fs electron bunch, shown in Fig. 5, is compressed to 12.5 fs, almost an order of magnitude, after a .7 m drift. Given a timing jitter as great as 100 fs, the ponderomotive interaction cuts the timing jitter down to 40 fs while still compressing the bunch by a factor of 3.

Table 1: Simulation Parameters

Bunch energy	6 MeV
Energy spread	10^{-3}
Bunch length	100 fs rms
Undulator period	3 cm
Undulator parameter, K	1.32
# of undulator periods	8
PPWG spacing, b	2.06 mm
Plate curvature radius	2 mm
Peak THz field	10 MV/ m
Peak frequency	.84 THz
FWHM of spectrum	2.35 THz
# of frequency points	51
Frozen field approximation	On

CONCLUSION

To efficiently harness the power of a single cycle THz pulse for beam manipulation, the problem of extending the interaction time must be solved. Towards achieving a sustained interaction, we have demonstrated tunable control of the group velocity of a THz pulse inside a PPWG. Using velocity matching between the THz pulse and an electron bunch, we will sustain a "zero-slippage" IFEL interaction

ISBN 978-3-95450-134-2

to both compress the electron bunch and reduce its time-of-arrival jitter. Based on the 1-D multifrequency simulation code that we are currently developing, we should achieve up to an order of magnitude of bunch compression. Looking forward, the "zero-slippage" interaction that we will demonstrate in the PPWG can be extended to a transverse deflection mechanism, like the one proposed in ref. [18], without the need for an additional RF deflecting cavity to resolve the THz streaking.

ACKNOWLEDGMENT

We are grateful for the support of the U.S. Department of Energy through grant DE-FG02-92ER40693 and the National Science Foundation through grant PHY-1415583.

REFERENCES

[1] P.U. Jepsen, D.G. Cooke, and M. Koch. In: *Laser and Photonics Reviews* 5.1 (2011), pp. 124–166. ISSN: 1863-8899.
[2] C Behrens et al. In: *Nature communications* 5 (2014).
[3] A. Hassanein et al. In: *Physical Review Special Topics-Accelerators and Beams* 9 (6 2006), p. 062001.
[4] A Doria, GP Gallerano, and A Renieri. In: *Optics communications* 80.5 (1991), pp. 417–424.
[5] A. Gover et al. In: *Physical review letters* 72 (8 1994), pp. 1192–1195.
[6] E.A. Nanni et al. In: *preprint arXiv:1411.4709* (2014).
[7] A. Gover et al. *Encyclopedia of Modern Optics*. 2005. http://www.eng.tau.ac.il/research/FEL/Encyclopedia%20of%20Modern%20Optics1.pdf
[8] A.G. Stepanov, J. Hebling, and J. Kuhl. In: *Applied physics letters* 83.15 (2003), pp. 3000–3002.
[9] J Hebling et al. In: *Applied Physics B* 78.5 (2004), pp. 593–599.
[10] B. Bartal et al. English. In: *Applied Physics B* 86.3 (2007), pp. 419–423. ISSN: 0946-2171.
[11] M. Brunken et al. DESY, 2003.
[12] I.M. Yakover, Y. Pinhasi, and A. Gover. In: *Nuclear Instruments and Methods in Physics Research Section A: Accelerators, Spectrometers, Detectors and Associated Equipment* 375.1 (1996), pp. 260–263.
[13] I.M. Yakover, Y. Pinhasi, and A. Gover. In: *Nuclear Instruments and Methods in Physics Research Section A: Accelerators, Spectrometers, Detectors and Associated Equipment* 358.1 (1995), pp. 323–326.
[14] Rajind Mendis and Daniel M Mittleman. In: *Journal of the Optical Society of America B* 26.9 (2009), A6–A13.
[15] N. Piovella. In: *Physics of Plasmas (1994-present)* 6.8 (1999), pp. 3358–3368.
[16] P Musumeci et al. In: *Physical review letters* 100.24 (2008), p. 244801.
[17] J. T. Moody et al. In: *Physical Review Special Topics-Accelerators and Beams* 12 (7 2009), p. 070704.
[18] G. Andonian et al. In: *Physical Review Special Topics-Accelerators and Beams* 14.7 (2011), p. 072802.

ENERGY JITTER MINIMIZATION AT LCLS*

Lanfa Wang#, Timothy Maxwell, Franz-Josef Decker, Andrew Benwell, Axel Brachmann, Anatoly Krasnykh, Zhirong Huang, James Turner, William Colocho, Tang Tao
SLAC, Stanford, CA 94309, USA

Abstract

The energy jitter of the electron beam affects FELs in self-seeded modes if the jitter is large compared to the FEL parameter, effectively reducing the average brightness when shots are seeded off-energy. We work in multiple ways to reduce jitter, including hardware improvement and optimizing linac set-up. Experiments demonstrated better than 20% and 40% relative energy jitter reduction for 13.6 and 4 GeV linac operation, respectively. This paper discusses the global optimization of linac set-up using Multi-Objective Genetic Algorithm (MOGA). The solutions always suggest that we can largely reduce the energy jitter from a weak compression at BC1 and a stronger compression at BC2. Meanwhile low beam energy at BC2 also reduces the energy jitter, which is confirmed by the experiment.

INTRODUCTION

The impact of energy jitter on self-seeded FELs is understood by considering the flux transmitted through an X-ray monochromator. Assuming SASE with Gaussian bandwidth σ_{SASE} incident on a monochromator, the ratio F of off-energy transmitted X-ray flux to on-energy flux due to *rms* electron relative energy jitter σ_e is given by

$$F(\sigma_e)=\frac{\sigma_{SASE}}{\sqrt{\sigma_{SASE}^2+4\sigma_e^2}}. \quad (1)$$

For self-seeding, this implies the average available seed power degrades unless $\sigma_e << \sigma_{\mathrm{SASE}} / 2$. Should sufficient undulator length be available to reach post-saturation, slightly weaker seed intensities can in principle be stabilized to near-nominal in post-mono amplification. In this way, self-seeding can be slightly more robust against energy jitter vs. direct SASE filtering alone.

Figure 1 illustrates this energy dependence during the 2014 development of soft X-ray self-seeding (SXRSS) at the LCLS [1] at 540 eV. The fraction of X-ray power within twice the self-seeded bandwidth plotted as a function of δe shows the 0.12% rms energy jitter yields a 50% reduction of the average narrow-band X-ray intensity (0.1 vs. 0.2 mJ). Therefore, improving linac energy stability has the potential double the average spectral brightness achievable by SXRSS.

Over the years the beam stability and jitter have been investigated [2-7] to study and identify jitter sources and improve stability of the LCLS. Over recent years, a group of experts worked together to improve the energy jitter, including improving klystron station stability and other hardware, automated data logging, developing online linear models, etc. Experiments demonstrated better than 25% and 40% relative energy jitter reduction for 13.6 and 4 GeV linac operation, respectively, over the past year.

Here we present our global optimization of the linac to reduce the machine energy jitter. The simulation model and the optimized solutions for hard x-ray and soft x-ray beams are discussed in the following sections. Hardware upgrades will be briefly discussed towards the end.

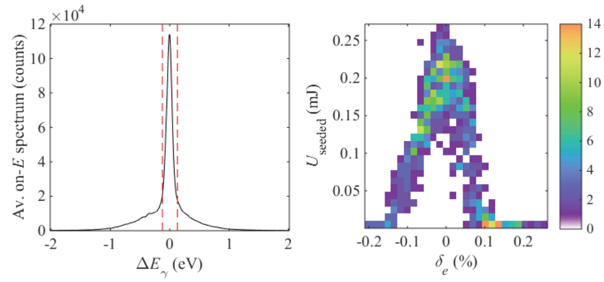

Figure 1: Average on-energy SXRSS spectra and range of fractional integration range (left). 2D histogram of partial pulse intensities U_{seeded} as a function of δ_e (right).

JITTER SOURCE AND SIMULATION MODEL

The primary source of the jitter is from the linac rf. The variation of pulse-to-pulse energy and timing jitter accumulates along the linac, each station adding in quadrature, and therefore has a large impact on beam jitter. Timing jitter at an rf station induces energy jitter as

$$\delta E(\varphi_0) = -e\omega_{rf}\hat{V}sin(\varphi_0)\delta t. \quad (2)$$

Additionally, amplitude fluctuations of rf klystrons along the linac generate an additional term to beam energy jitter as

$$\delta E(\varphi_0) = -e\hat{V}sin(\varphi_0)\delta\varphi + ecos(\varphi_0)\delta\hat{V}. \quad (3)$$

The first and secondary term on the left of the equation comes from the phase jitter and voltage jitter, respectively. For off-crest acceleration prior to bunch compression, the dominant contribution of the beam energy jitter is the beam timing/phase jitter at the rf stations as shown in Eq. 2. This timing jitter works similar as the rf phase jitter. Its effective rf phase jitter is

$$\delta\varphi_{rf,eff} = \omega_{rf}\delta t \quad (4)$$

*Work supported by Department of Energy Contract No. DE-AC02-76SF00515
#wanglf@SLAC.stanford.edu

ISBN 978-3-95450-134-2

However, the timing jitter seen at each rf station is not purely localized, being accumulated from upstream acceleration. For given rf phase and voltage jitter, we can optimize the linac configuration to reduce the energy jitter by minimizing the timing jitter effect in Eq. 2.

The magnet in bunch compressors (BCs) has very good stability and its jitter has negligible impact on the beam energy jitter. However BC acts as a dispersive element, converting energy jitter to correlated timing jitter. The effective *E-t* correlation provided by a BC is

$$\left(\frac{\delta E/E}{\delta t}\right)_{BC} = c/R_{56}, \qquad (5)$$

where c is the speed of light in vacuum and R_{56} is the momentum compaction factor of the BC. Since R_{56} at BC is negative, it contributes to a negative chirp.

Finally the collective effects such as wakefields and coherent synchrotron radiation (CSR) also add to the energy jitter through the jitters of bunch charge and current profile. These effects are not simply formulized.

As discussed above, the rf and BC elements can be treated as linear system for small variation. We can approximate the machine as a simple linear system to estimate jitter in the absence of nonlinear effects and collective effects. To fully and accurately optimize the machine, Multi-Objective Genetic Algorithm (MOGA) is applied to optimize the machine parameters in order to minimize the jitters (timing jitter, energy jitter and current jitter), energy spread and collective effects and provide zero energy chirp and certain peak current at the end of linac. For instance the overall jitters is defined as

$$jitter^2 = \sum_i \left[\frac{(\delta I/I)_i^2}{(\delta I/I)_0^2} w_I + \frac{(\delta E/E)_i^2}{(\delta E/E)_0^2} w_E + \frac{(\delta t/t)_i^2}{(\delta t/t)_0^2} w_T\right], \quad (6)$$

where $w_{I,E,T}$ are the weight factors for current, energy and timing jitter. The sum on the left is over all runs (seeds). The particles are tracked using LiTrack code in this paper, which includes the wakefields. But CSR and space charge are not modelled.

HARD X-RAY

Table 1 lists two optimized solutions for hard x-ray beam with a small energy jitter and 3 kA peak current. The configuration close to old operational configuration is also listed for comparison (The machine configuration change rapidly to improve the performance). The two optimized solutions are for 5.0 GeV and 6.3 GeV beam energy at BC2, respectively. There are about 100% improvements in energy jitter for both two fully optimized solutions.

The final beam before the undulator for solution 1 is shown in Fig. 2. The phase space is also optimized to get zero energy chirp. The current profile is similar as the nominal one. It has flat top at the core part of beam with horns at both head and tail of the bunch. Fig. 3 shows the detail of the jitters for the case with zero L3 phase. The energy jitters are widely distributed with large contributions from the phase of L1S, L2 and L1X. The total rms energy jitter is 0.01%.

The timing and energy jitter in general is correlated. This correlation comes primarily from the uncorrelated jitter growth from rf phase and voltage jitters being stretched by compression R_{56}. Fig. 4(left) shows the energy and timing jitter for solution 1 when L3 phase is set to zero. Apparently there is a correlation between the energy jitter and rf phase jitter. The relation between the beam energy jitter and beam timing jitter observed at each rf station is $\delta\varphi = \omega_{rf}\delta t$. If we define the correlation between the energy and timing jitter as $h = (\delta E/E)/\delta t$, then the *E-t* correlation provided by rf linac is

$$\left(\frac{\delta E/E}{\delta t}\right)_{rf} = -e\omega_{rf}\hat{V}sin(\varphi_0)/E \qquad (7)$$

here E is the beam energy at that element. Therefore we can apply an appropriate rf phase at L3 to conceal the residual correlation and provide the same energy gain. This correlation can be minimized to zero by setting a non-zero *L3* phase so that the final energy jitter is a minimal:

$$\varphi_{L3} = atan\left[\frac{E}{\omega_{rf}\hat{V}_{L30}} h_0\right]. \qquad (8)$$

Where $\hat{V}_{L30}$ is the *L3* voltage with zero rf phase and h_0 is the E-t correlation when L3 phase is set to zero. In the derivative of Eq. 8 we assume the whole L3 has the same rf phase. In operation, the rf phase along the L3 varies. But the idea is the same: the E-t chirper provided the L3 totally conceal the original chirper h_0 from upstream. For different operation modes, this *E-t* correlation and the beam energy gain at L3 varies. Therefore the optimal L3 phase also changes.

Co-author Decker first proposed the above idea at the LCLS to reduce the energy jitter which we refer to as "Decker phasing." The underlying physics of Decker phasing is to remove correlated energy jitter via L3 chirp. Fig.4(right) shows the E-t jitter with an optimal L3 phase of -13.8^{o}, where the final E-t correlation becomes zero. The final energy jitter is about 21% smaller compared to the case with zero L3 phase. The detail dependence of energy jitter on the L3 phase is shown in Fig. 5.

The major changes of the optimized solution includes L2 phase and R_{56}. A smaller L2 phase and $|R_{56}|$ at BC1 is prefered. With the same jitter sources, the energy jitter with the nominal configuration is about 0.022%. Therefore the optimized solution reduces the energy jitter to only 36% of that with nominal configuration. The improvement is significant.

Figure 6-7 shows the impact of L3 phase for the nominal configuration. There is a minimum energy jitter at L3 phase of –20 degree. Fig. 8 shows the observed dependence of energy jitter on the L3 phase. There is large improvement (25%) at the optimal L3 phase of

ISBN 978-3-95450-134-2

Table 1: Example of LCLS Operational and Optimized Solutions for Hard X-Ray

Variables	Solution1	Solution2	~old operational
BC2 energy(GeV)	5.0	6.3	5.0
I_{pk} (kA)	3.0	3.0	3.0
Charge(pC)	150	150	150
V_{0A}(MV)	57.5	57.5	57.7
V_{0B}(MV)	71.5	71.5	71.5
ϕ_{0A} (degree)	0	0	−5
ϕ_{0B} (degree)	−5	−5	−5
ϕ_{L1} (degree)	−29.85	−27.8	−26.1
V_{L1S}(MV)	125	122	118
ϕ_{Lx} (degree)	−159.4	−157	−160
V_{Lx}(MV)	25	25	22
ϕ_{L2} (degree)	−19.5	−19.5	−38.7
V_{L2}(GV)	5.0758	6.455	6.15
ϕ_{L3} (degree)	−13.8	−10.8	−20
V_{L3}(GV)	8.9	10.7	8.778
R_{56}@BC1(mm)	−35.4	−36	−45.5
R_{56}@BC2(mm)	−47.3	−47.1	−20.6
(Δt) (fs)	26	26	22
(ΔE/E) (%)	0.0078	0.0082	0.022

range from −14 to −20 degree. The simulation agrees reasonably well with the experiment.

There is a possibility to increase the LCLS final beam energy by increasing the rf acceleration at L2 and therefore the beam energy at BC2. We assume that the beam energy at BC2 is 6.3 GeV so we can have the maximum final beam energy up to 17.0 GeV [8]. The 2nd solution at Table 1 shows the main parameters of such solution. This solution (except rf voltage at L2 and L3) is close to solution 1 and the jitters are also similar to that solution. The energy jitter is about 0.010% and 0.0082% with zero and −10.8 degree L3 phase, respectively. Fig. 9 shows the solution in detail.

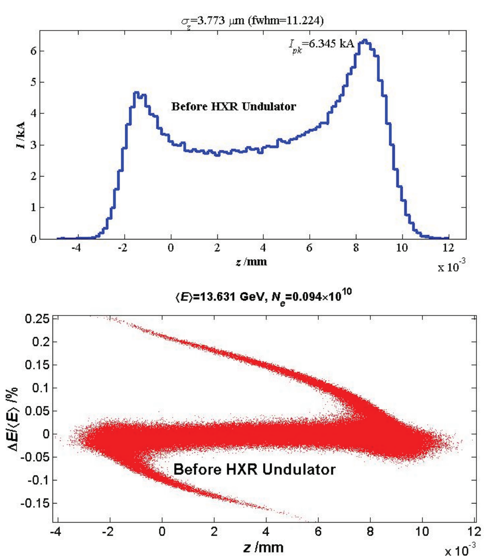

Figure 2: The final beam before the undulator listed for solution 1 in Table1. The beam energy at BC1 and BC2 is 220MeV and 5GeV, respectively. The final beam energy is 13.6GeV. Bunch lead is to the left.

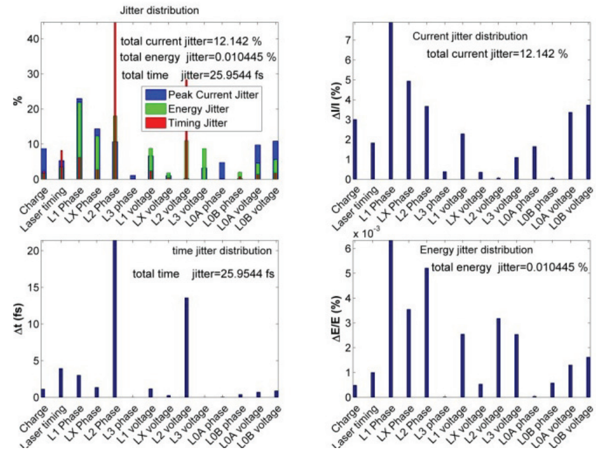

Figure 3: The distributions of jitters in energy, timing and current for the solution 1. But the L3 phase is zero in this study.

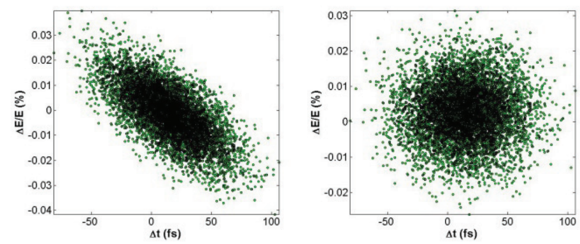

Figure 4: The energy and timing jitter at the end of linac for solution 1 with different L3 phases: 0 (left, energy jitter 0.01%) and −13.8° (right, energy jitter 0.0078%).

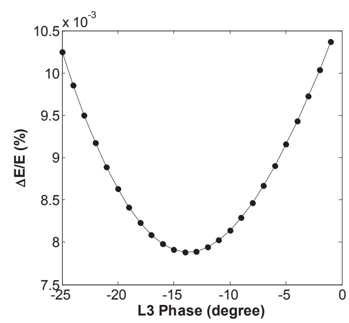

Figure 5: Simulated effect of L3 phase on the energy jitter for the optimized solution 1. The optimized L3 phase is −13.8 degree.

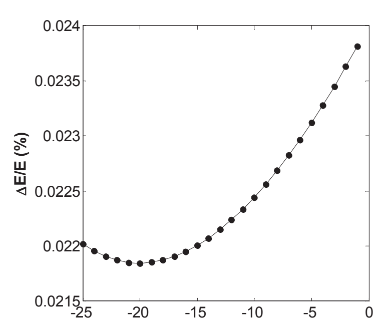

Figure 6: Simulated effect of L3 phase on the energy jitter for the old operational configuration. The optimized L3 phase is −20 degree.

ISBN 978-3-95450-134-2

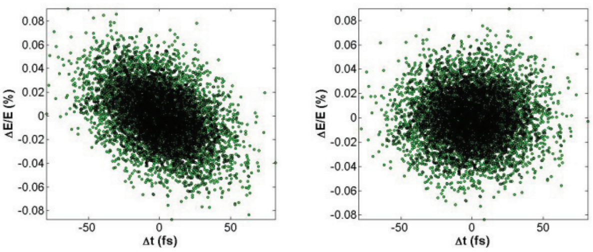

Figure. 7: Simulated effect of L3 phase on the energy jitter for the old operational configuration listed in Table 1. The L3 phase is zero (left) and −20 degree (right), respectively.

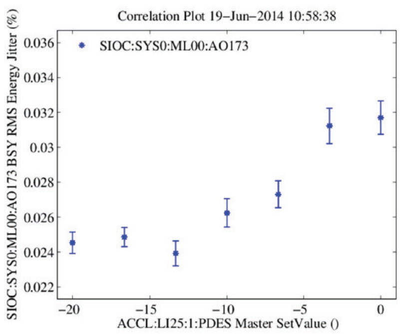

Figure 8: Observed energy jitter for different L3 phase for hard x-ray beam on June 19 of 2014.

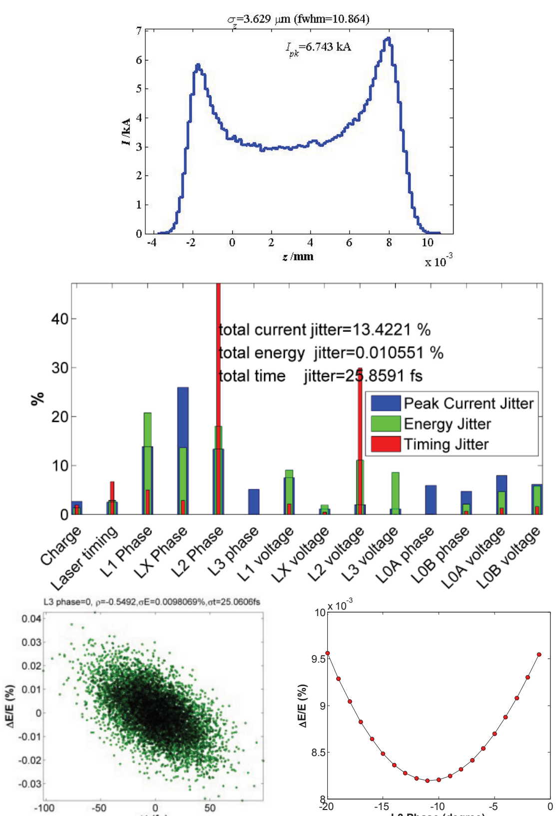

Figure 9: Current profile (top), jitters (middle) and impact of L3 phase on energy jitter (bottom) for solution 2 with beam energy of 6.3 GeV at BC2. The final beam energy is 17.0 GeV.

SOFT X-RAY

In LCLS the beam energy at the 2nd bunch compressor (BC2) is historically fixed at 5.0 GeV for both hard X-ray and soft X-ray beams. For example for a soft x-ray beam energy of 3.0 GeV, the beam is decelerated by linac 3 (L3) from 5.0 GeV to 3.0 GeV. In this way, for practical reasons, we fix the machine set-up before BC2 and use only L3 to adjust the final beam energy.

Simulation has shown that lower beam energy at BC2 can reduce the energy jitter for low energy running. We simply reduce the beam energy at BC2 from 5.0 GeV to 3.5 GeV while the finally beam energy at the end of linac is kept the same 3.5 GeV. In the first case the L3 decelerates the beam from 5.0 GeV to 3.5 GeV (left column of Fig. 10), while it does nothing in the 2nd case (right column of Fig. 10). In both cases the R_{56} at BC2 is set to −24.7 mm and the L2 phase is adjusted to get 1.5 kA current at the core of the beam shown in Fig. 10. The energy jitter reduces from 0.076% to 0.044% when the beam energy at BC2 is reduced from 5.0 GeV to 3.5 GeV.

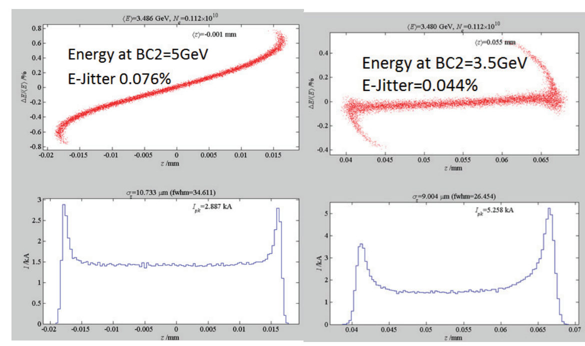

Figure 10: Simulated beam and energy jitter with different beam energy at BC2: 5.0 GeV(left) and 3.5 GeV (right). The final beam energy is 3.5GeV in both cases.

The strong dependence of the energy jitter on the beam energy at BC2 is confirmed by the experiment as shown in Fig. 11. The beam energy at BC2 is gradually reduced from 5.0 GeV to 3.5 GeV. The final beam energy is kept at 4.0 GeV by adjusted the rf at L3. Meanwhile the rf phase at L2 is adjusted (by the feedback) to keep a peak current of 1.5 kA. The *rms* energy jitter is reduced from 0.11% to 0.08%, about 27% improvement (top of the figure). Then the R_{56} at BC2 is adjusted from −24.7 mm to −27.2 mm, there is no apparent jitter impact. In the previous steps, the rf phase of L3 is kept at 0 phase (on crest). Finally the rf phase of L3 is changed to −15°. There is no clear impact on the jitter, which can be explained by the insufficient E-t correlation provide by L3 (Eq. 7). We will discuss more on that aspect shortly.

Both simulation and experiments show improvement of energy jitter with low beam energy at BC2. From quasi-linear theory including individual klystron station jitter contributions adding in quadrature in an *E-t* correlated fashion, it is clear a large jitter reduction stems from the dramatically reduced number of L2 and L3 rf stations (22 vs. 32) needed to achieve the final beam energy of 4 GeV

ISBN 978-3-95450-134-2

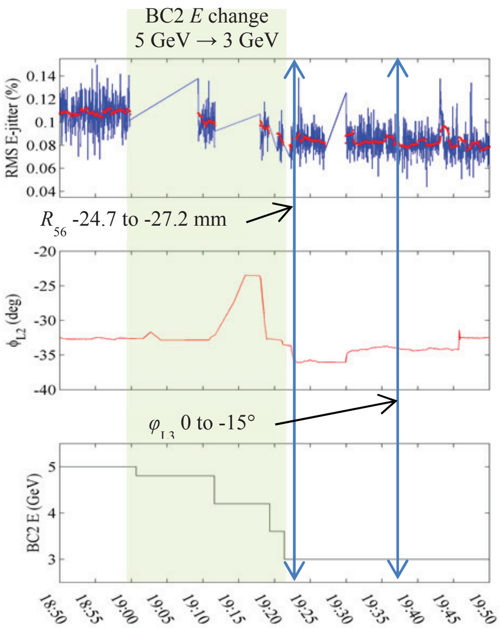

Figure 11: Observed energy jitter in LCLS when we scan the beam energy at BC2. The R56 at BC2 (1st line) and the rf phase of L3 (2nd line) are also adjusted to verify impact on the jitter. The figure shows the final energy jitter (top), the rf phase of L2 (middle) and the beam energy at BC2 (bottom), respectively.

by not over-accelerating in L2 leading to a 30-40% jitter reduction now used in low-E operation by fixing BC2 energy at 3 GeV if L3 energy is < 6 GeV. This approach yields jitter numbers consistent in scale with experimental results, but models only jitter evolution for a given configuration not including individual bunch longitudinal dynamics, collective effects such as wakefields, or optimization of final chirp. In the MOGA approach, we optimize the LCLS linac for different beam energies at BC2 with each linac treated as one rf station, and including wake effects. Table 2 shows two optimized solutions (1st and 2nd column) and the one close to the old operational mode (3rd column).

There are additional improvements in the energy jitter for the two further optimized solutions compared to the old operational configuration. These large improvements are the integrated effects of the optimized machine and are even better than the one with reduced BC2 energy alone (0.044%, Fig. 10). The beam energy at BC2 is 3.0 GeV and 5.0 GeV for the solution 1 and 2 respectively with similar energy jitters for the two sets of optimized solutions. We find the energy jitter can be even further reduced by full optimization under the condition of avoiding over-acceleration of the beam.

The beam and energy jitter of the three configurations are shown in Fig. 12-14. There are the same beam current of 1.5 kA at the core part of beam for all cases. There clear difference in the phase space, especially the energy chirp. Current “horns” for the old operational mode are small, indicating our machine is well tuned for that purpose.

The configurations in Table 2 do not apply Decker phasing. There are clear correlations between the energy and timing jitter in all cases. In principle the energy jitter can be further reduced using Decker phasing similar to the hard x-ray case. The required L3 rf phase is much larger (far away from crest) due to a low energy gain (or loss) at L3 for soft x-ray beam. As shown in Eq. 7-8, a large phase is required for Decker phasing if the rf voltage is low. It is also confirmed by the simulations shown in Fig. 12-14. A much large L3 phase (more than 60 degree) is required. This may explain the observation at LCLS where weak Decker phasing doesn’t help much for soft x-ray beam when rf phase of L3 is varied only with 20 degree from the crest. Apparently this phase is not sufficient.

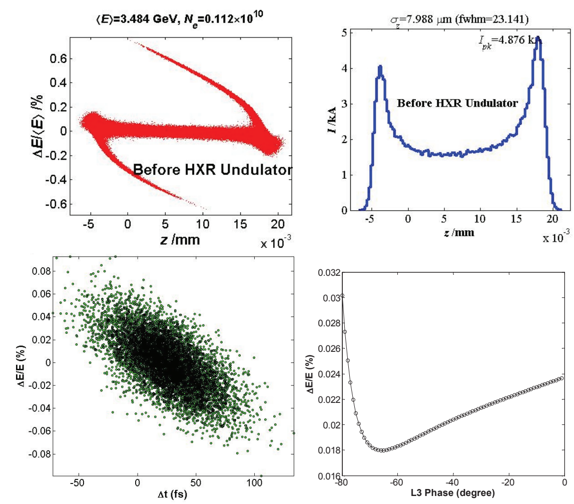

Figure 12: Beam and energy jitter of solution 1 as shown in Table 2: longitudinal phase space (top left); current profile (top right); energy and timing jitters when the L3 phase is zero (bottom left); impact of L3 phase on the energy jitter (bottom right).

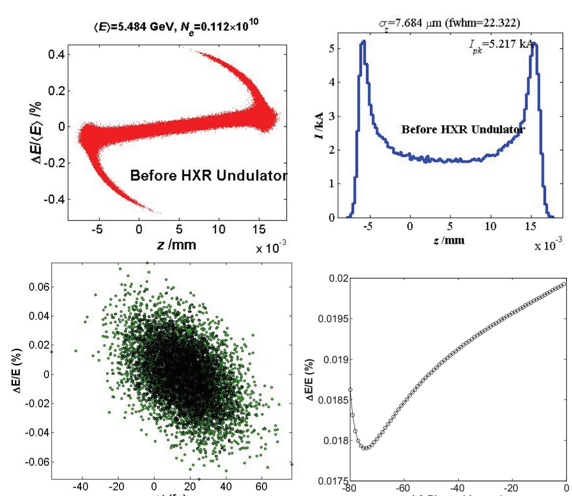

Figure 13: Beam and energy jitter of solution 2 as shown in Table 2: longitudinal phase space (top left); current profile (top right); energy and timing jitters when the L3 phase is zero (bottom left); impact of L3 phase on the energy jitter (bottom right).

ISBN 978-3-95450-134-2

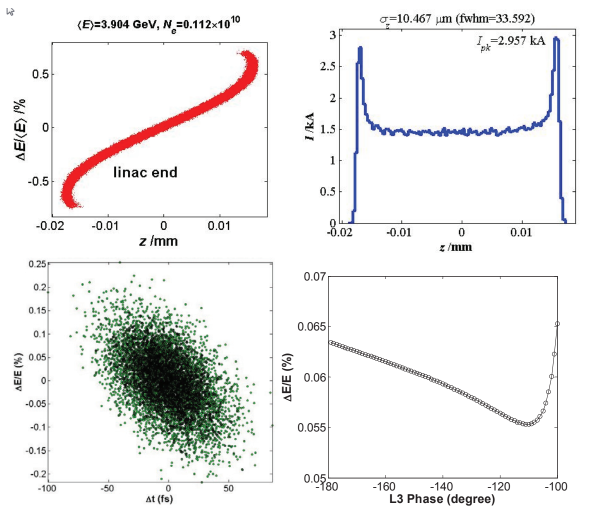

Figure 14: Beam and energy jitter with operational confiuration as shown in Table 2: longitudinal phase space (top left); current profile (top right); energy and timing jitters when the L3 phase is –180° (bottom left); impact of L3 phase on the energy jitter (bottom right).

Table 2: Examples of Two Fully Optimized Solutions for Soft X-Ray and Operational Configuration

Variables	Solution1	Solution2	*~operational*
E at BC2(GeV)	*3.0*	*5.0*	5.0
Final E (GeV)	*3.5*	*5.5*	3.9
I_{pk} (kA)	1.5	1.5	*1.5*
Charge(pC)	180	180	*180*
V_{0A}(MV)	57.5	57.5	*57.5*
V_{0B}(MV)	71.9	71.9	*71.9*
ϕ_{0A} (degree)	0	0	*–0*
ϕ_{0B} (degree)	–5	–5	*–5*
ϕ_{L1} (degree)	–26.7	–27.35	*–27.2*
V_{L1S}(MV)	119	120	*115*
ϕ_{Lx} (degree)	–159	–159.8	*–160*
V_{Lx}(MV)	23	23	*18.2*
ϕ_{L2} (degree)	–21.47	–19.5	*–34.2*
V_{L2}(GV)	2.987	5.058	*5.79*
ϕ_{L3} (degree)	–0	–0	*–180*
V_{L3}(GV)	0.5	0.5	*1.086*
R_{56}@BC1(mm)	–35.1	–36.7	*–45.5*
R_{56}@BC2(mm)	–47.6	–47.1	*–24.7*
(Δt) (fs)	27	15	*23*
(ΔE/E) (%)	0.024	0.020	*0.0635*

HARDWARE IMPROVEMENTS

Beyond optimization of the linac configuration, underlying hardware instability has also been carefully scrutinized and improved over recent years [4-7, 9-11]. Some of these have included regular maintenance of critical injector stations from the rf gun through the first bunch compressor. These "seed" significant downstream energy jitter growth as the first compressor converts incoming energy jitter into a phase jitter, increasing susceptibility to energy jitter growth due to phase instability in linac 2.

One item under development is improved high-power RF loads. With gradual SLAC klystron improvements over the years, the peak power klystron output has been raised to > 20 MW. The existing 2 MW SLAC RF loads no longer provide stable termination, as shown in Fig. 15 (top). Unstable reflected power is found to interfere in the later portion of the RF pulse. This issue is exacerbated in SLED mode operation shown with randomly fluctuating reflected power interfering with beam-time RF.

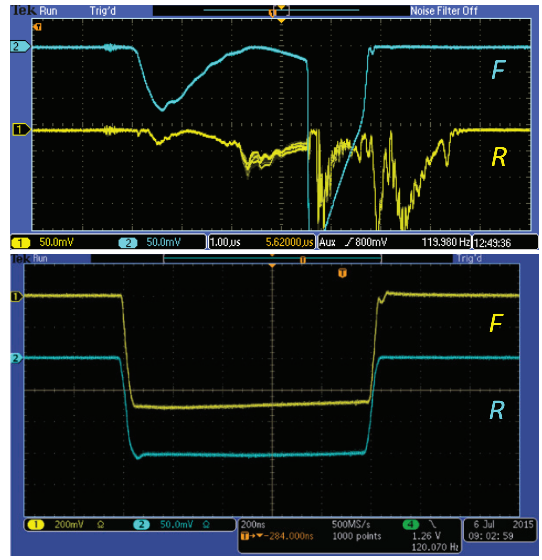

Figure 15: Scope traces of Forward and Reflected RF power for a SLEDed SLAC rf station with 2 MW SLAC RF old (top) and unSLEDed station with new, 20 MW SLAC RF load (bottom).

In answer to this, SLAC has developed a 20 MW-class, all-metal RF load. High-power RF conditioning of the first two loads has been successfully completed, with results from the first complete load shown in Fig. 15 (bottom) [10,11]. This shows stable RF termination at over 18 MW peak forward power for 1 μs pulses at 120 Hz stably terminated at 3 kW average. Upgrade of critical, SLEDed injector stations is currently being planned with long term roll out to remaining LCLS sectors under evaluation.

Additionally we are investigating the upgrade from hydrogen thyratrons to new, deuterium thyratrons with a higher beam voltage rating. The hydrogen thyratrons currently in use are run at > 90% of their maximum rating of 47 kV for the majority of stations. These results in frequent thyratron ranging and replacement resulting in degraded station performance and increased cost. In contrast, the thyratron driving the LCLS gun is operated at lower voltage (78% derated) and has run with excellent stability without thyratron replacement for over 20 years.

The deuterium thyratron replacement is plug compatible and rated for 80 kV @ 1 kHz while also auto-ranging. One has been in operation on a non-critical LCLS station for over 6 months showing a 48% improvement to pulse forming network stability, 30% reduction of beam voltage jitter, and with output phase and amplitude jitter reduced to present measurement limits while requiring no thyratron maintenance since

ISBN 978-3-95450-134-2

installation. This also is under consideration for rollout to critical injector stations with potential deployment to the remainder of the LCLS linac over future years.

SUMMARY AND DISCUSSION

The global computer optimizations have been done to minimize the energy jitter in LCLS. The benefit of low beam energy at BC2 is confirmed by experiment. The measured energy jitter for soft x-ray is improved about 27% by reducing the beam energy at BC2 from 5.0 GeV to 3.0 GeV.

We also confirm that "Decker phasing" can be used at L3 to conceal the residual E-t correlation for hard x-ray case. The optimal phase of –20 degree is close to the experiment. The experiment shows a larger reduction of 25% in energy jitter. Decker phasing is explained by a simple formula for a given residual correlation between energy and timing jitters. Studies show that a much large L3 phase is required for soft x-ray beam "Decker phasing". We will test that in the machine.

The global optimizations for the whole linac show significant energy jitter reduction (from 2.2×10^{-4} to 8×10^{-5} for hard x-ray beam and from 6.4×10^{-4} to 2.4×10^{-4} for soft x-ray beam). We will explore these solutions to further improve the jitter. Besides Decker phasing and lower beam energy at BC2 for soft X-ray operation, other ideas to reduce the energy jitter proposed include:

- *Reduce the compression (R56) at the first BC (BC1) and increase the compression (R56) at the 2nd BC (BC2).*
- *Reduce the rf phase of L2*

The maximum |R56| at BC2 is limited by the power supply of the magnets. We can operationally set the R56 of BC2 close to its maximum and optimize other parameters.

The simulations agree reasonable well with the observations with guidance for improving stability. Recent improvements in hardware should also reduce jitter while reducing maintenance. Since the sources of jitters vary time to time, it is more accurate and also straight forward to do online optimization to incorporate known, present sources of instability while maximizing the requested FEL performance simultaneously. A better simulation model, such as including CSR, will be updated. The online and off-line start-to-end optimization is our plan for next step along with ongoing hardware improvements.

ACKNOWLEDGEMENTS

This work is supported by Department of Energy Contract No. DE-AC02-76SF00515.

REFERENCES

[1] D. Ratner, et al., Phys. Rev. Lett. 114, 054801 (2015).
[2] P. Emma, J. Wu, "Trajectory Stability Modelling and Tolerances in the LCLS", EPAC06 Edinburgh, p.151.
[3] R. Akre et al., "Beam Stability Studies in the LCLS Linac", FEL08, Korea, Aug 2008.
[4] F.-J. Decker, et al., "Identifying Jitter Sources in the LCLS Linac", Linac08, Victoria, BC, Canada, p. 506.
[5] F.-J. Decker, et al., "Improving Beam Stability in the LCLS Linac", PAC09, Vancouver, BC, Canada, 2009, p. 2349.
[6] F.-J. Decker, et al., "Identifying Longitudinal Jitter Sources in the LCLS Linac", IPAC'10, Kyoto, Japan, 2010, p. 2296.
[7] F.-J. Decker, et. al., Increased Stability Requirements for Seeded Beams at LCLS, WEPSO10, in the proceedings of the 35th International Free-Electron Laser (FEL 2013).
[8] F.-J. Decker, et. al., Photon Energies beyond the Selenium K-Edge at LCLS, WEP022, these proceedings.
[9] F.-J. Decker, A. Krasnykh, B. Morris, and M.Nguyen, "A stability of LCLS Linac Modulators", SLAC-PUB-15083.
[10] A. Krasnykh, et. al., S-Band loads for SLAC Linac, MOPB087, in Proceedings of LINAC2012, Tel-Aviv, Israel.
[11] A. Krasnykh, et. al., online at http://slac.stanford.edu/pubs/slacwps/wp06/slac-wp-099.pdf

ISBN 978-3-95450-134-2

FAST PARTICLE TRACKING CODE*

L. Wang#, SLAC, Stanford, CA 94309, USA

Abstract

This paper presents a fast particle tracking (FPT) code for linac beam dynamics. It includes wake fields, coherent synchrotron radiation (CSR) and longitudinal space charge. We systematically benchmark the FPT with ELEGANT with different physics aspects: pure optics, wakefields, CSR and space-charge forces.

MODEL

The FPT code is originally developed to study the collective effects, including wakefields and CSR. There are two models for CSR: 1D CSR in free space [1] and 2D CSR with resistive wall beam pipe. In the 2D case, the CSR is calculated by another Finite Element Method (FEM) code based on the paraxial equation [2] and input it to FPT. Currently, the transverse collective effect is off. We are able to simply turn on/off different collective effects. These features make the code much fast compared other detail codes, meanwhile it includes the main physics we are interested.

The longitudinal spacing charge (LSC) has been recently added. It includes analytical methods for both round Gaussian and uniform beam model and numerical LSC module. The LSC impedances of a round Gaussian and uniform beam are

$$\frac{Z_{||}^{gau,free}(k)}{L} = i\frac{1}{4\pi\varepsilon_0}\frac{k}{\gamma^2\beta c}e^{-\frac{k^2\sigma_r^2}{2\gamma^2}}Ei\left(-\frac{k^2\sigma_r^2}{2\gamma^2}\right), \quad (1)$$

$$\frac{Z_{||}^{rd,free}(k)}{L} = i\frac{1}{k\pi a^2\varepsilon_0\beta c}\left[1-\frac{ka}{\gamma}K_1\left(\frac{ka}{\gamma}\right)\right]. \quad (2)$$

where E_i is the exponential integral function and K_1 is the modified Bessel function of the second kind. Note that the LSC impedance of the Gaussian beam can be approximated as the one of uniform beam with $\sigma = a/\sqrt{2}$ and $\sigma = a/\sqrt{3}$ at short and long wavelength regime, respecttively. But there is no simple approximation at the frequencies near $\frac{ka}{\gamma}\sim 1$ as shown in Fig. 1. The LSC impedance for arbitrary transverse beam shape with arbitrary beam pipe can be calculated numerically with FEM method [3].

In the following sections we benchmark FPT with ELEGANT with different physics aspects: pure optics, wakefields, CSR and space-charge forces. The collective effects are added step-by-step. In the benchmark we use LCLS-II linac. The initial beam has ideal Gaussian distribution in longitudinal direction with *rms* beam size of 1.0 mm and energy spread of 1.0 keV. The initial beam energy is 100 MeV. The particles are tracked through the linac and we compare the beam after the second bunch compressor (BC2).

WITHOUT COLLECTIVE EFFECTS

To compare different collective effects, it is important to study a case when all collective effects are turned off. This means the wake field, CSR and space charge are not included. The main parameters of the linac set-up are: the rf phase at L1, linearizer and L2 are –12.7, –150 and –15.5 degree, respectively. Figure 2 shows the phase space and current profile after BC2. There is an excellent agreement. The beam energies are 250 MeV and 1.60 GeV at BC1 and BC2, respectively. If we increase the energy at BC2 to 1.647 GeV (we use this energy for the rest of comparisons), the peak current reduced to 1.0 kA due to the reduction of relative energy chirper as shown in Fig. 3. There are excellent agreements for both beam energies when the collective effects are turned off.

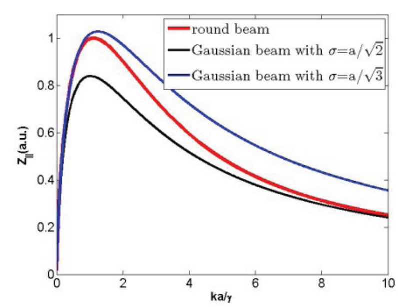

Figure 1: Comparison of the longitudinal space charge impedance of a round uniform and Gaussian beam.

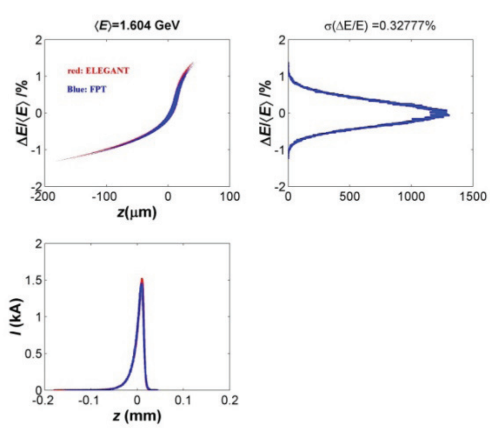

Figure 2: Longitudinal phase space at the end of BC2 without collective effects, beam energy at BC2 is 1.6 GeV. ELEGANT (red); FPT (blue).

*Work supported by Department of Energy Contract No. DE-AC02-76SF00515
#wanglf@SLAC.stanford.edu

ISBN 978-3-95450-134-2

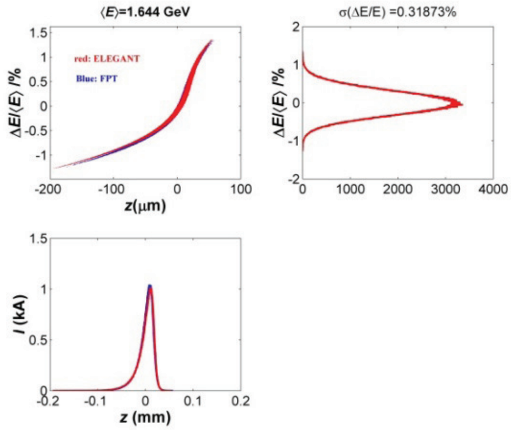

Figure 3: Longitudinal phase space without collective effects. Beam energy at BC2 is 1.644 GeV. ELEGANT (red); FPT (blue).

WAKEFIELDS ONLY

In this case the geometric wake of rf structure and the resistive wall wake are included. We will use a new superconducting linac composed of TESLA-like RF cavities (1.3 GHz) in continuous wave (CW) operation, in order to accelerate a 1 MHz electron beam to 4 GeV. Those wakefields de-chirp the bunch and therefore reduce the final peak current from 1.0 kA (Fig. 3) to 0.8 kA (Fig. 4). There is a 2 km long bypass beamline after the rf linac, the strong resistive wall wake of the beam pipe continue de-chirp the beam and make the phase space flat without changing the peak current. This is typical scheme for LCLS-II to control the energy chirp. Again, Fig. 4 shows excellent agreemens.

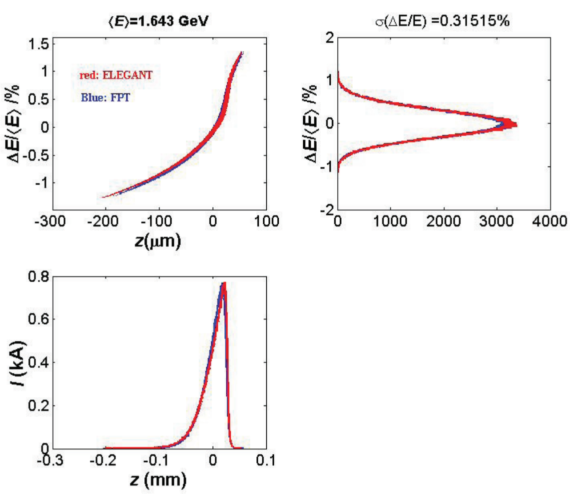

Figure 4: Longitudinal phase space with geometric wake and resistive wall wake effects. ELEGANT (red); FPT (blue).

WAKEFIELDS + CSR

1D free space CSR is used in both codes for this comparison. Similar as wake field effect, the CSR can de-chirp the beam in the longitudinal phase space and therefore can change the beam current profile. This is typical CSR effect in LCLS-II. The CSR in the third bend of BC2 de-chirp the bunch and change the peak current due to the non-zero dispersion there. Although the last bend has stronger CSR and therefore larger energy kicker, it has negligible effect on the current profile due to the very small dispersion there.

Figure 5 shows the phase space at the end of the last bend magnets at BC2. Again the agreement is very good. In our case the CSR in the drift regime after the last bending magnet is not smaller and even larger than the CSR inside the magnet.

2D CSR will be compared with the 1D model late to check the shielding effect. The shielding effect is small for very short bunch. Figure 6 shows the CSR in the last dipole magnet for a wave number k=1e6 [1/m]. The shielding starts to be effective with smaller aperture <8 mm. The actual aperture in LCLS-II design is larger (~40 mm). With such large aperture, the shielding effects on the CSR seen by the beam are small.

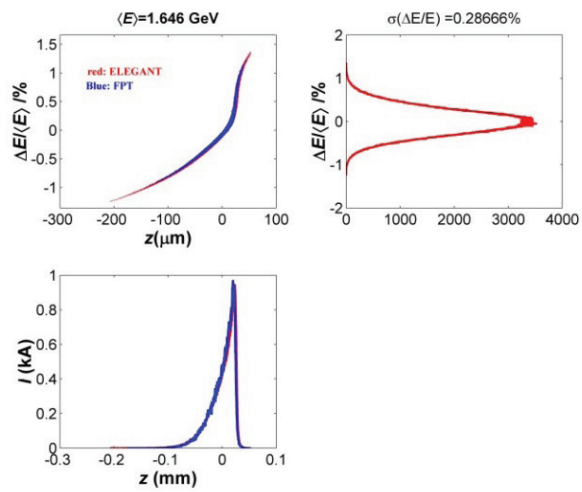

Figure 5: Longitudinal phase space with geometric wake, resistive wall wake and CSR. ELEGANT (red); FPT (blue).

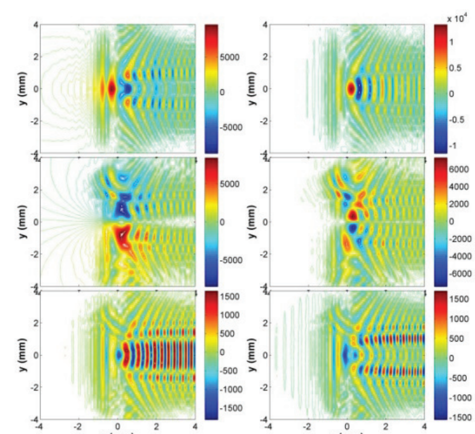

Figure 6: CSR field at the end of last bending magnet for wave number k=1.0e6 [1/m]. The horizontal field (top), vertical field (middle), and longitudinal field (bottom) are shown. Positive x represents outside direction.

ISBN 978-3-95450-134-2

WAKEFIELDS+CSR+LSC

The longitudinal space charge (LSC) effect is finally included. Both codes use 1D space charge model for this comparison. The LSC kicker in FPT is benchmarked with analysis. However the micro-bunching instability has large sensitivity to the numerical issue, such as noise (number of particles used in the simulation, grid size, etc.). ELEGANT uses 50 million macro-particles in the simulation, while FPT uses only 8 million.

Since the shot noise is proportional to the square root of the number of particles, we manually add one window on the LSC impedance by a factor of $\sqrt{N_{sim}/N_{real}}$. Where N_{real} and N_{sim} represents the real number particles and the number of particles used in the simulation, respectively. Note that we only apply this trick before the first bunch compressor (BC1). The results are shown in Fig. 7. The overall de-chirp due to LSC is very similar for both codes because the LSC impedance at Linac 2 (L2) (after BC1) is much larger than that before BC1. So the trick effectively reduces the noise at L2. FPT has smoother current profile simply due to the noise reduction trick at L1. At this moment it is not sure whether this is a proper way to treat the initial noise with less number particles because it is complicated by the grid size used in the simulation.

The bunching factor (Fig. 8) shows a modulation wave-length around 2~3μm. The START-to-END simulations from IMPACT-T/Z and ELEGANT always shows similar spectrum even at the end of linac [4]. This indicates the micro-bunching at that wavelength range is amplified along the downstream of the linac. In theory the simulated wavelength of micro-bunching (resolution) has strong dependence on the slice number, instead of the number of particles.

The micro-bunching instability is complicated by the initial noise and numerical parameters. We shall do further detail studies, such as reducing the initial noise with less number of macro-particles and more damping with 2D LSC. The energy spread due to 2D LSC provides additional damping to the instability. Figure 9 shows the LSC field of a uniform beam. The LSC field over the beam is not uniform. The field has a much larger spread for a Gaussian beam compared to a uniform beam. The spread over a Gaussian beam increases at short wave-length and the 2D effect becomes stronger.

Similar as CSR, LSC may add chirp to the beam and change the overall current profile. The peak current increases when LSC is added (comparing Fig. 5 with Fig. 7). If we are interested in this de-chirp effect, instead of the micro-bunching instability, we can simplify the LSC model to do fast computation: add high frequency pass filter to include the overall de-chirp effect from the LSC as shown in Fig. 10. In this case the requirement for the number of particles is largely reduced.

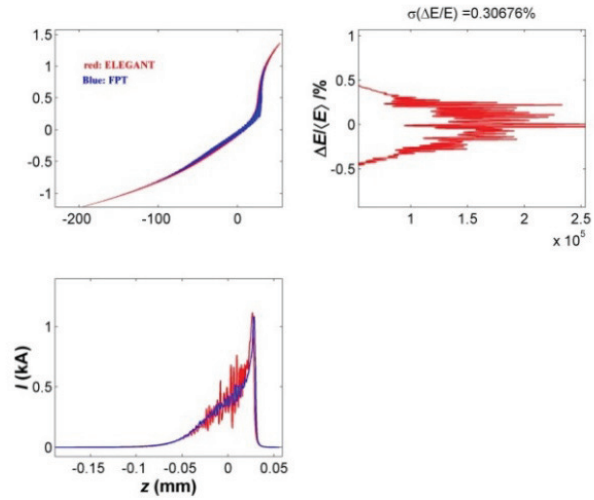

Figure 7: Longitudinal phase space at the end of BC2 with geometric wake, resistive wall wake, CSR and LSC. FPT applies noise reduction trick at L1 and uses 8 million particles, while ELEGANT uses 50 million particles.

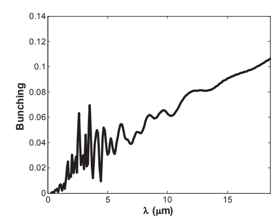

Figure 8: Bunching factor of beam.

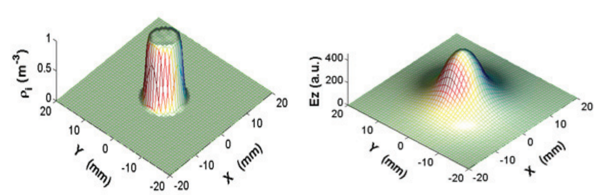

Figure 9: A uniform beam (left) and the LSC electric field (right) in a free space at $\frac{ka}{\gamma} = 1$.

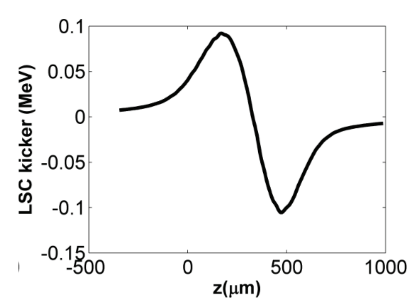

Figure 10: Example the LSC kicker along a Gaussian bunch, bunch head to the left.

ISBN 978-3-95450-134-2

SUMMARY

FPT model with different physics aspects is discussed and it is benchmarked with ELEGANT. There are excellent agreements between FPT and ELEGANT codes for different effects: pure RF linac, wake fields and CSR. There is also good agreement for LSC wake. We will continue to study the micro-bunch instability with better noise reduction schemes and reduced number macro-particles in the simulation. 2D effect of CSR and LSC will be studied.

ACKNOWLEDGEMENTS

This work is supported by Department of Energy Contract No. DE-AC02-76SF00515.

REFERENCES

[1] E.L Saldin. et al. Nucl.Instrum.Meth. A398 (1997) 373-394 DESY-TESLA-FEL-96-14, JINR-E9-97-51.
[2] T. Agoh and K. Yokoya. "Calculation of coherent synchrotron radiation using mesh", Phys. Rev. ST Accel. Beams, 7(5):054403, May (2004).
[3] L. Wang and Y. Li, "Analysis of the longitudinal space charge impedance of a round uniform beam inside parallel plates and rectangular chambers", Phys. Rev. ST Accel. Beams, 18, 024201 (2015).
[4] L. Wang, P. Emma, J. Qiang and T.O. Raubenheimer, presented at FEL'15, Daejeon, Korea, TUP066.

ISBN 978-3-95450-134-2

CATHODE ION BOMBARDMENT IN LCLS AND LCLS-II RF GUN*

L. Wang#, A. Brachmann, F. Decker, Z. Li, T.O. Raubenheimer,
J. Schmerge, F. Zhou, SLAC, Stanford, CA 94309, USA

Abstract

This paper studies the ions bombardment on the cathode in the LCLS and LCLS-II gun. LCLS operates at a low repetition rate of 120 Hz while LCLS-II will operate at 1 MHz rate. Therefore, it is important to estimate the ion bombardment.

A PIC code is used to track arbitrary particles (ions and electron here) in arbitrary 2D/3D electromagnetic field and solenoid field to estimate the possibility of ion bombardment. The LCLS gun has 1.6 cells while the LCLS-II gun is a quarter wave resonator (LBNL APEX gun) so the frequencies of the two guns are quite different. These characteristics make the ion dynamics quite different. In this paper we estimate the bombardment for various ion species.

LCLS GUN

The surface analysis of the first LCLS cathode provides evidence for complex hydrocarbon contamination [1]. The trajectory simulation of ions in LCLS gun shows strong possibility of ion back bombardment [2-3]. Here we do the trajectory simulation with one purpose-written code which can accurately model the ion generation (position and timing) and RF pulse. Both RF field and emittance compensation solenoid field are included. Electrons emitted from the cathode enter the rf cavity and move towards the solenoid region while ions are generated along the electrons' path. The electrons move quickly out of the cavity but the ions move much slower. Ions are tracked until they hit the cathode, hit the cavity surface or exit the cavity.

The on-axis electric field and the solenoid field for the LCLS gun are shown in Fig. 1. The cathode is located at the z=0. The electric field has a peak value at the cathode surface and the center of the full cell with the minimum field located at z=3.34 cm at the iris. Fig. 2 shows the electric fields of the rf gun. When an electron emitted from the cathode surface enters the second cavity, the rf electric field changes direction and the electron continues to accelerate through the second cell. The focusing solenoid is located 20 cm downstream of the cathode with zero field at the cathode. In all simulations, 2D field maps are used for both gun rf and solenoid fields.

The LCLS gun is pulsed at 120 Hz with an rf pulse that has a flat top order of 1 μs duration and decay time approximately 0.5 μs [4]. Electrons are generated at the peak rf pulse and therefore ions are also generated at the peak rf pulse. Since ions move slowly, they see the remaining rf pulse and their dynamics are strongly affected by the decaying pulse. Most ions run away from the cavity regime or hit the cathode before the next rf pulse.

Table 1 lists the main parameters for the LCLS gun and solenoid. For comparison, the parameters for the LCLS-II gun are also listed. The LCLS gun operates pulsed at 2856 MHz, while the LCLS-II gun is continuous-wave (CW) at a much lower frequency of 187 MHz. The LCLS gun has two cells while the LCLS-II gun is comprised of a single cell. Multiple cells make the ion dynamics much more complicated.

In this study we consider only the ions generated by beam gas ionization. Ions are uniformly generated along the electron beam path (z-direction) in the simulation. In reality, the beam ionization cross-section varies with beam energy with a large cross-section for low beam energy ranging from 100eV to 1 MeV. Ions born at different locations will see different initial rf field as shown in Fig. 3.

Table 1: Main Simulation Parameters

Description	LCLS	LCLS-II
rf frequency (MHz)	2856	187
Peak field (MV/m)	140	22
rf phase (degree)	–60	–8
rf Pulse length (μs)	~3	CW
Repetition rate (kHz)	0.12	1000
Solenoid field (T)	0.24	0.04
Beam energy(MeV)	5.9	0.8

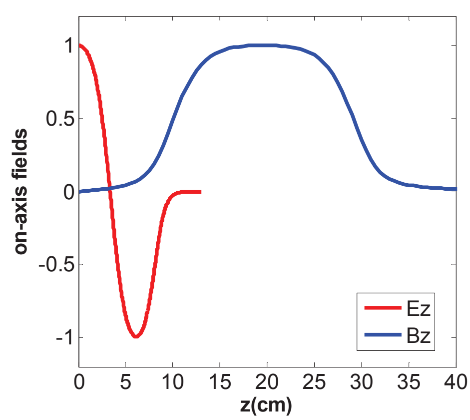

Figure 1: The normalized on-axis gun rf electric field and solenoid field.

*Work supported by Department of Energy Contract No. DE-AC02-76SF00515
#wanglf@SLAC.stanford.edu

ISBN 978-3-95450-134-2

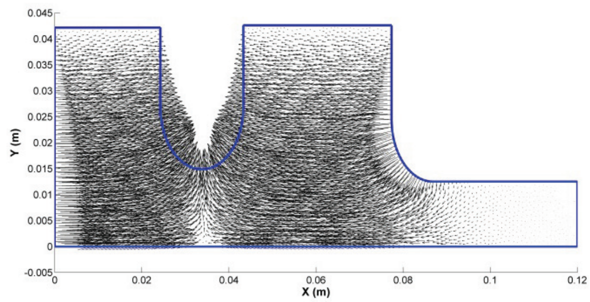

Figure 2: Geometry and electric field of the LCLS rf gun. The blue line shows the boundary (2D approximation).

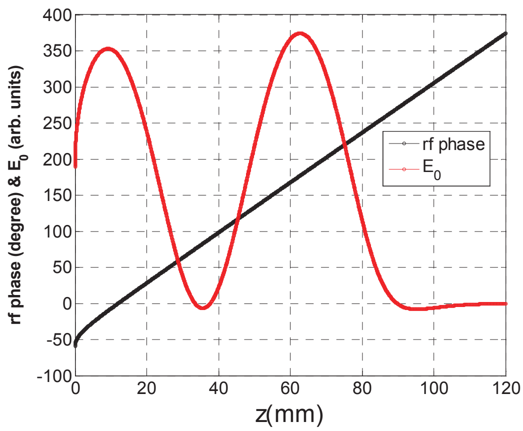

Figure 3: The initial rf phase (black line) and electric field (red line) seen by ions born at different location in the cavity.

H_2^+ ion

The hydrogen ion has small mass and moves fast. In most cases for the LCLS gun, hydrogen ions either hit the cathode or exit the gun during the rf pulse. Figure 4 shows the dependence of the ions striking the cathode and exiting the gun on their starting location. There are several narrow regions between 2 and 6 cm where ions strike the cathode (red line). The dynamics in this region is complicated by the decay of the rf pulse, rf phase and the variation of field amplitude shown in Fig. 1. The ions born near the cathode always hit the cathode because the rf phase is negative when the ions are generated and the ions are accelerated towards the cathode.

About 39% of the total ions reach the cathode surface; while 58% exit the gun longitudinally. The remaining ions move significantly off axis and eventually hit the cavity surface. No secondary particles are generated in the simulation. If the energy dependence of the cross-section is included, 44% ions hit the cathode and 53% exit the gun.

It is very useful to look at detail of individual ions born at different longitudinal location along the cavity. Figure 5 shows the final energy at the cathode or at the gun exit for ions born at different location. Each dot represents one ion particle used in the simulation. The red and black dots are for ions reaching the cathode and exiting the gun respectively. The ions born near the cathode (z<1cm) hit the cathode with energy up to 3500eV with random energy distribution even they are born at the same longitudinal cavity position. The ions are born at different radial positions and hit the cathode at slightly different times with very different energies. The ions are initially born with the same radial distribution as the electron beam, which is assumed to be Gaussian with a *rms* beam size of order of mm. Besides the ions near the cathode, a large number of ions born at the first part of the 2nd cell impact on the cathode as shown in Fig. 5. The multiple regions where ions impacting on the cathode as shown in Figs. 4-5 is one important feature of multiple cell guns. There are similar results in another study [5].

On the other hand, the ions exiting the gun (black dots), have very similar energy regardless of initial radius.

Note that the peak energy of ion hitting the cathode has strong dependence on the rf frequency, ion mass and rf field. It can be approximated as

$$T_{max} \approx \frac{2q^2 E_{z=0}^2}{A m_p \omega_{rf}^2} \ . \qquad (1)$$

Where $E_{z=0}$ is the amplitude of the rf field at the cathode, ω_{rf} is the angular frequency of the rf gun, A is the ion mass number and m_p is the proton mass.

Figure 6 shows radius distribution of ions impacting on the cathode. Most ions hit the cathode with $r < 10$ *mm*.

Figure 7 shows the energy distribution for the ions hitting the cathode. The high energy ions (> 2*keV*) are from the ions born near the cathode as shown by Fig. 5.

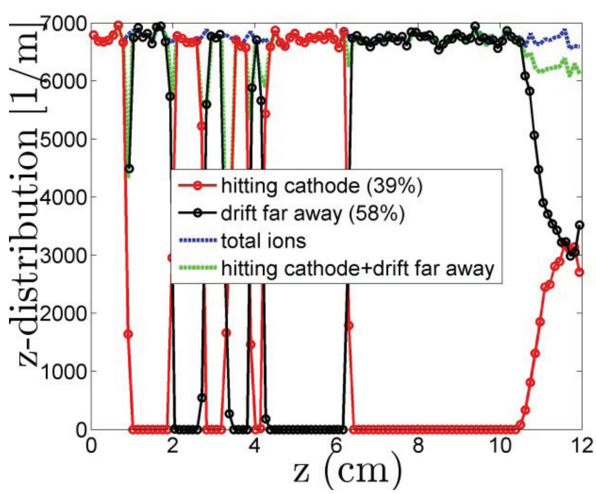

Figure 4: The dependence of the H2 ions striking the cathode and exiting the gun based on their initial position along the cavity. The red and black lines represent ions reaching the cathode and exiting the gun, respectively.

ISBN 978-3-95450-134-2

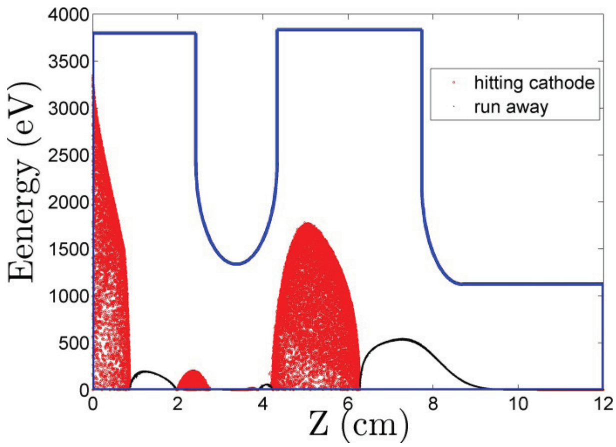

Figure 5: The final H_2+ ion energy for ions born at different position along the cavity. The red and black dots represent ions reaching the cathode and exiting the gun, respectively. The blue line shows the geometry of the gun cavity.

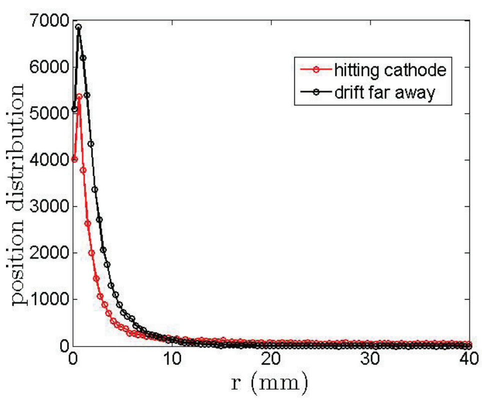

Figure 6: Radius distribution of the H2 ions hitting the cathode (red line).

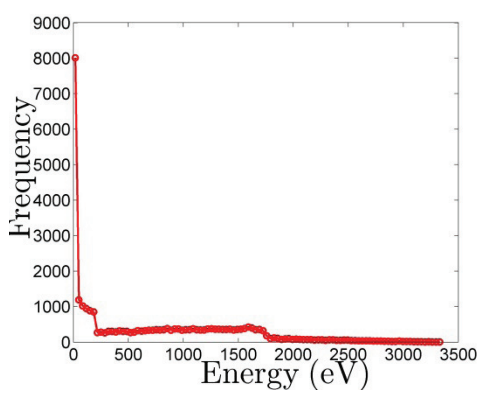

Figure 7: Energy distribution of the H2 ions hitting the cathode.

CO^+ ion

The CO ion moves slowly compared to the H2 ion. Therefore it takes longer time to reach the cathode. Except the ions born near the cathode surface, other ions reaching the cathode see much lower rf field due to the decay of the rf pulse. Figure 8 shows the ion distribution along its initial position in the cavity for both ions impacting on the cathode and exiting the gun. The distribution of ions hitting the cathode is simple compared to the H2 ion case. The CO ions born in two regions hit the cathode surface: near the cathode and 1st part of the 2nd cell with z ranging from 3.8 cm to 6 cm. About 36% of CO ions hit the cathode.

The final energy of individual ion particles is shown in Fig. 9. Four regions are clearly shown from the plot. The energy of the CO ion is smaller compared to that of H2 ion due to its large mass as described by Eq(1). Figure 10 shows the final energy distribution for ions hitting the cathode. The distribution can be explained by results shown in Fig. 9.

Figure 11 shows the radial distribution of ions impacting on the cathode. Similar to H2 ions, most CO ions hit the cathode with r <10 mm.

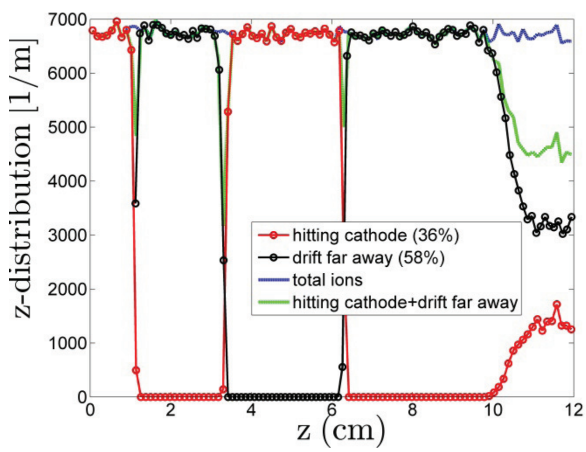

Figure 8: The dependence of the CO ions reaching the cathode and exiting the gun based on their initial position along the cavity.

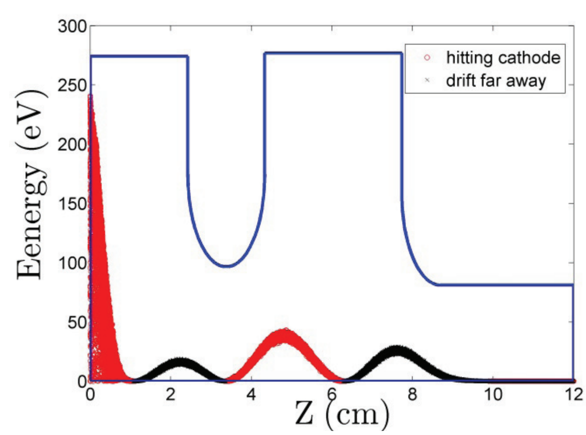

Figure 9: The final CO+ energy for ions born at different position along the cavity. The red and black dots represent ions reaching the cathode and exiting the gun respectively.

ISBN 978-3-95450-134-2

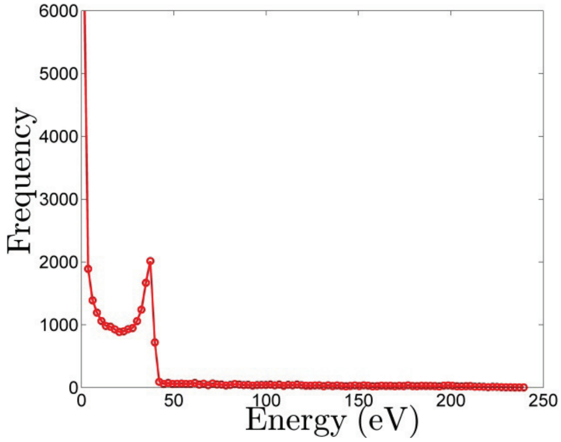

Figure 10: Energy distribution of the CO ions hitting the cathode.

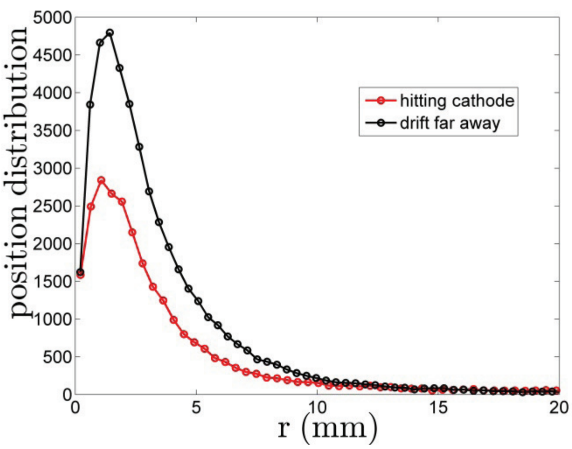

Figure 11: Impact radius distribution of the CO ions hitting the cathode (red line).

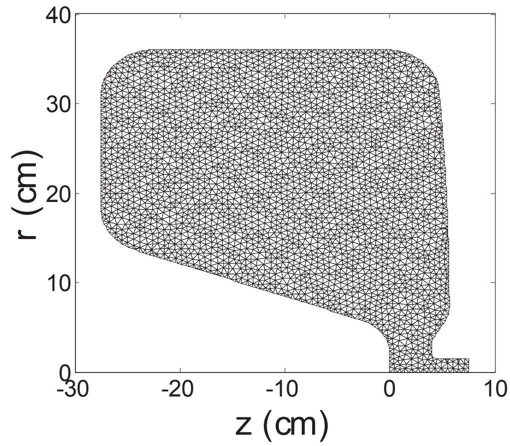

Figure 12: LCLS-II gun. The cathode is located at z=0 cm. Electron beam moves from left to the right.

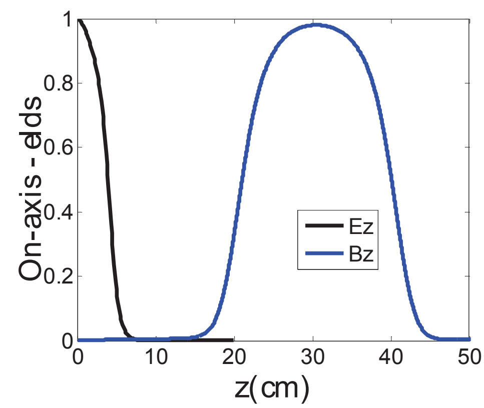

Figure 13: The normalized on-axis LCLS-II gun rf electric field (black line) and solenoid field (blue line).

LCLS-II GUN

The LCLS-II gun operates at 187 MHz. Figure 12 shows the geometry of the LCLS-II gun with the cathode centre located at (z, r)=(0,0). The low frequency makes the ion dynamics different from the LCLS gun. There is a peak electric field at the cathode and the electric field decays monotonically along the beam direction as shown in Fig. 13 where both the on-axis rf electric field and the focusing solenoid field are shown. The solenoid field inside the cavity is very weak and its effect on the ions is negligible.

H_2^+ ion

Figure 14 shows the simulation results for H2 ions: only 7% of the H2 ions reach the cathode. Those ions are generated near the cathode with z<0.5 *cm*. A large number of H2 ions (91%) exit the gun. Most H2 ions born at *z* between 5 *mm* and 7 *mm* move off axis and eventually hit the cavity surface. When the energy dependent cross-section is included, the percentage of ions hitting the cathode increases to 37% due to the large cross-section at low energy. The number of ions lost on the cavity surface also increase to 22%.

Figure 15 shows the typical trajectories of H2 ions: One ion hits the cathode and the second exits the gun. The oscillation due to rf fields are clearly shown for both cases.

Figure 16 shows the final energy when H2 ions hit the cathode (black dots) or run away from the cathode (red dots). Again there is a strong correlation between the final energy and their initial position. For the ions born at the same z-position, the energy of ions impacting on the cathode has large spread because the ion's energy at the cathode largely depends on the rf phase at that moment.

ISBN 978-3-95450-134-2

On the other hand, the energy of ions exiting the gun has much smaller energy spread.

The distributions of impact energy and radial position at the cathode surface are shown in Figs. 17 and 18 respectively. The peak energy is about 9 *keV*, which is larger than that of the LCLS gun although the LCLS-II gun has lower peak field. The lower rf frequency makes the impacting energy larger as shown in Eq.(1). Most H2 ions hit the cathode within 5.0 *mm* radius. It is interesting that the peak in the distribution is located at 1.5 *mm*, instead of the center of the cathode (r=0 *mm*).

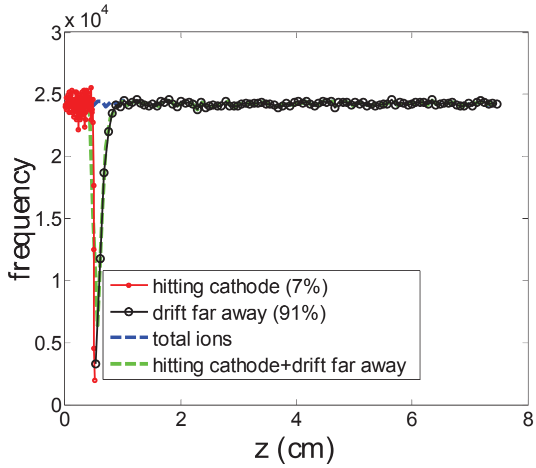

Figure 14: The dependence of the H2 ions reaching the cathode and exiting the gun on their initial position along the cavity.

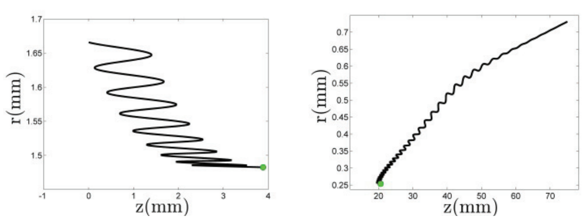

Figure 15: Trajectories of H2 ions born at different cavity positions. One ion hits the cathode (left) and one ion exits the gun (right).

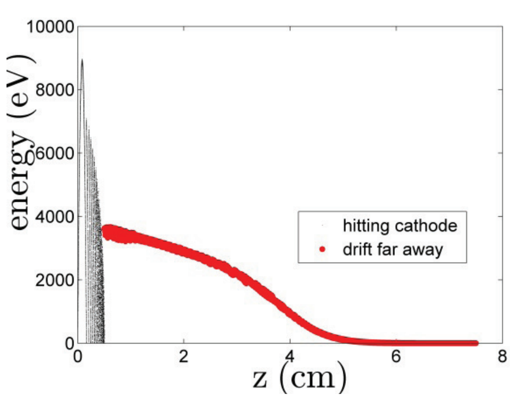

Figure 16: The final H_2+ ion energy for ions born at different position along the cavity. The black and red dots represent ions finally reaching the cathode and exiting the gun respectively.

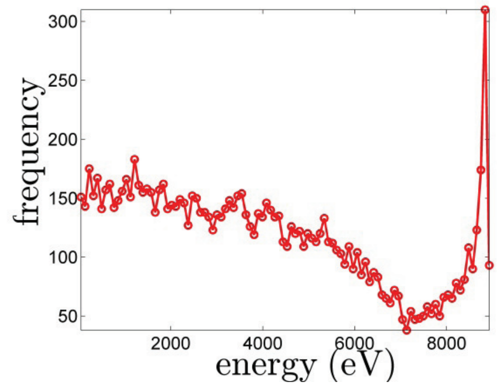

Figure 17: Energy distribution of the H2 ions hitting the cathode.

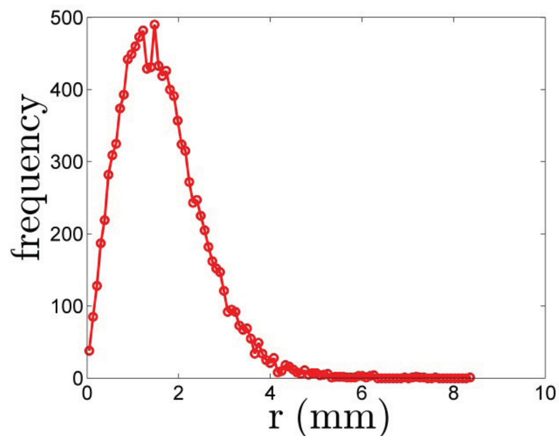

Figure 18: Impact radius distribution of the H2 ions hitting the cathode.

CO^+ ion

Because CO ion has large mass, the energy of CO ion is relatively low compared to the H2 ion. Other than the energy, the dynamics of CO ion is very similar to the H2 ion for the LCLS-II gun. Figures 19 to 21 shows the main results from simulation.

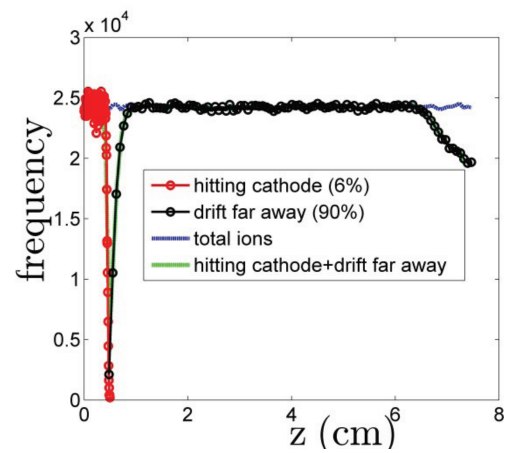

Figure 19: The dependence of the CO ions reaching the cathode and exiting the gun on their initial position along the cavity.

ISBN 978-3-95450-134-2

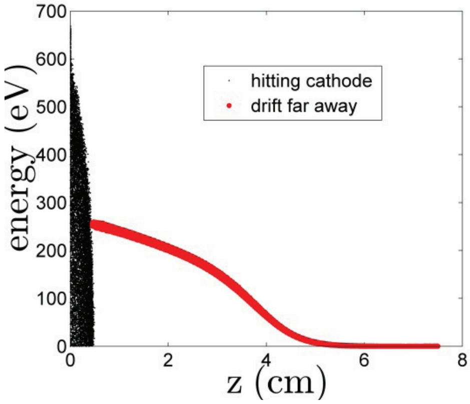

Figure 20: The final CO ion energy for ions born at different positions along the cavity. The black and red dots represent ions reaching the cathode and exiting the gun respectively.

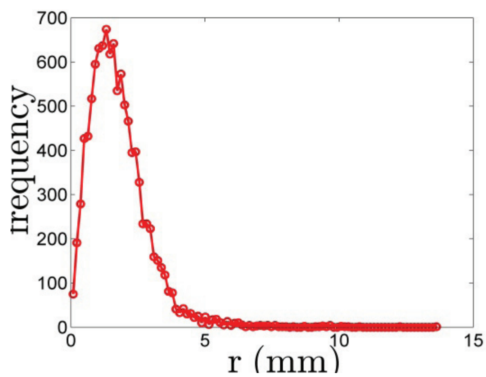

Figure 21: Impact radius distribution of the CO ions hitting the cathode.

SUMMARY AND DISCUSSION

A PIC code has been developed to simulate the dynamics of electron and ion particles in the rf gun. Arbitrary electric and magnetic fields can be modelled. Beside rf fields, the focusing solenoid is also included in the simulation although it has a small effect on the ions hitting the cathode surface.

The studies show very strong effects of the rf frequency, field variation along the cavity in beam direction and the rf phase. The ion dynamics for LCLS gun is complicated by its multiple-cell structure and pulsed rf.

We demonstrate that there are large potential ion back bombardment in the LCLS and LCLS-II rf guns. About 44% and 37% H_2 ions can hit the cathode surface for the LCLS and LCLS-II guns respectively. There is a similar number for CO ions. The chance of ions impacting on the cathode has strong dependence on the rf phase. A large negative rf phase, such as the LCLS gun, increases the probability of hitting the cathode. For example if the LCLS gun phase is -24^{o}, then only 15% H2 ions can impact on the cathode.

The impacting energy on the cathode is larger for low rf frequency guns, such as LCLS-II. The spot size of ions impacting on the cathode is on the order of 10 *mm* and 5 *mm* for the LCLS gun and LCLS-II gun respectively.

ACKNOWLEDGEMENTS

We thank Christos Papadopoulos for providing LCLS-II injector fields. This work is supported by Department of Energy Contract No. DE-AC02-76SF00515.

REFERENCES

[1] A. Brachmann et al., Surface Characterization of the LCLS RF Gun Cathode. This Conference, TUPE065.
[2] J. W. Lewellen, Phys. Rev. ST Accel. Beams 5:020101 (2002).
[3] A. Brachmann and D. Dowell, Proceedings of the 2010 International Particle Accelerator Conference (23-28 May 2010, Kyoto, Japan), p2281,TUPE064
[4] J.F. Schmerge, D.H. Dowell and S.M. Gierman, SLAC technical Note, LCLS-TN-07-1(2007), also J.F. Schmerge, LCLS-TN-02-7 (2002).
[5] John W. Lewellen, Phys. Rev. ST Accel. Beams 5, 20101 (2002).

ISBN 978-3-95450-134-2

RESULTS FROM THE NOCIBUR EXPERIMENT AT BROOKHAVEN NATIONAL LABORATORY'S ACCELERATOR TEST FACILITY*

N. Sudar, P. Musumeci, J. Duris, I. Gadjev, Department of Physics and Astronomy, UCLA, Los Angeles, CA 90045, USA

M. Polyanskiy, I. Pogorelsky, C. Swinson, M. Fedurin, K. Kusche, M. Babzien, BNL ATF, Upton, NY 11973, USA

Abstract

Conversion efficiencies of electrical to optical power in a Free Electron Laser are typically limited by their Pierce parameter, ρ ~0.1%. Introducing strong undulator tapering can increase this efficiency greatly, with simulations showing possible conversion efficiencies of ~40%. Recent experiments performed with the Rubicon Inverse Free Electron Laser have demonstrated acceleration gradients of ~ 100 MeV/m and high particle trapping efficiency by coupling a pre-bunched electron beam to a high power CO2 laser pulse in a strongly tapered helical undulator [1,2]. By reversing the undulator period tapering and re-optimizing the field strength along the Rubicon undulator, we obtain an Inverse Free Electron Laser decelerator, which we have aptly renamed Nocibur. This tapering profile is chosen so that the change in beam energy defined by the ponderomotive decelerating gradient matches the change in resonant energy defined by the undulator parameters, allowing the conversion of a large fraction of the electron beam power into coherent narrow-band radiation [3]. We discuss this mechanism as well as results from a recent experiment performed with the Nocibur undulator at Brookhaven National Laboratory's Accelerator Test Facility.

INTRODUCTION

The UCLA Particle Beam Physics Laboratory, in collaboration with Brookhaven National Laboratory's Accelerator Test Facility (ATF), has recently utilized the Inverse Free Electron Laser (IFEL) mechanism to use optical energy from a high power CO2 laser to accelerate a 52 MeV electron beam to 92 MeV in ~0.5 m [1]. These experiments utilized the strongly tapered helical Rubicon undulator to demonstrate highly efficient conversion between optical and electrical energy. This process in reverse, electro-optical conversion, represents a potentially attractive source for high peak power and high average power radiation source.

The Nocibur experiment at ATF utilizes a strongly tapered helical undulator to couple a pre-bunched electron beam to a high power CO2 laser, using the Inverse Free Electron Laser mechanism to now decelerate the electrons (Fig. 1). By designing the undulator tapering such that the FEL resonance condition is maintained as the beam decelerates, energy lost by the beam is converted into coherent radiation by way of stimulated emission [3]. By decelerating large fractions of the beam to ~50% the initial beam energy, electro-optical conversion efficiencies of up to ~40% are attainable.

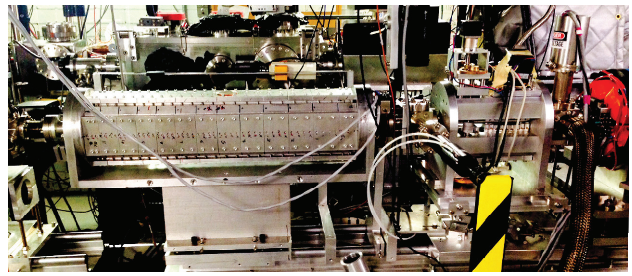

Figure 1: Nocibur undulator and pre-buncher installed in ATF beamline.

DESIGN OF UNDULATOR TAPERING

The undualtor tapering is designed to match the ponderomotive gradient set by the undulator and laser parameters to the FEL resonance condition, chosen such that the resonant phase remains constant throughout the deceleration (Fig. 2). In the case of this experiment we choose the resonant phase to be Ψr = -π/4.

Description	Definition
Undulator wavelength	$k_w = 2\pi/\lambda_w$
Laser wavelength	$k = 2\pi/\lambda$
Normalized laser vector potential	$K_l = \frac{e E_0}{m_0 c^2 k}$
Normalized undulator vector potential	$K = \frac{e B}{m_0 c k_w}$
Decelerating Gradient	$\frac{d\gamma}{dz} = \frac{e}{mc^2} E \cdot \beta \rightarrow \frac{d\gamma^2}{dz} = 2 k K_l K \mathrm{Sin}(\psi_r)$
Resonance Condition ($\frac{d\psi}{dz} = 0$)	$\gamma^2 = \frac{\lambda_w}{2\lambda}(1+K^2)$
Undulator Tapering Differential Equation	$\frac{dK}{dz} = \frac{2 k K K_l \mathrm{Sin}[\psi_r] - \frac{d\lambda_w}{dz}\frac{1+K^2}{2\lambda}}{\lambda_w K/\lambda}$

Figure 2: Derivation of differential equation determining K tapering.

The Nocibur undulator was previously used in the Rubicon IFEL acceleration experiments. To create the necessary decelerating gradient the Rubicon undulator period tapering was reversed and the field strength was re-tuned to match the K tapering solution to the differential equation (Fig. 3). The undulator was modeled in Radia, tuned and measured with a hall probe and the second integral was zeroed using pulse wire measurements (Fig. 3).

*Work supported by U.S. Dept. of Energy grant DE-FG02-92ER40693.

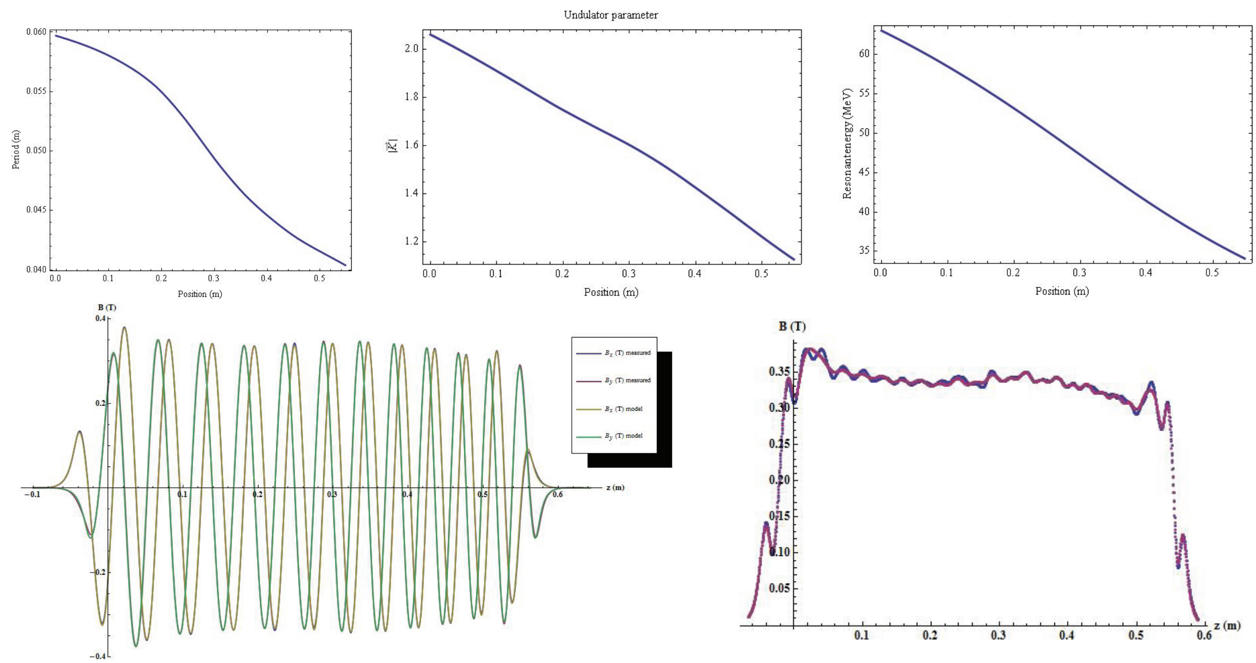

Figure 3: (Top) Design parameters for period tapering, K tapering and resonant energy along undulator. (Bottom) Actual field measurements compared with Radia model field maps.

EXPERIMENTAL PROCEDURE

The deceleration mechanism requires a strong seed to support the desired gradient. For this we copropagate the electron beam with a laser pulse from ATF's high power CO2 laser, parameters described in Table 1.

Table 1: Experimental Laser and E-Beam Parameters

Parameters	Values
E-Beam Energy	65 MeV → 35 MeV
E-Beam Current	100 A
Laser Focal Intensity	4 TW/cm²
Laser Wavelength	10.3 µm
Rayleigh Range	0.3 m
Laser Waist	1 mm
Peak Power	200 GW

Rough overlap between the laser and e-beam was achieved using a Germanium switch inserted into the beamline. Fine timing to place the E-beam at peak laser intensity was then done by varying a delay stage in the laser transport path and observing the increase or decrease in the amount of charge decelerated.

To maximize the amount of charge captured we control the injection into the ponderomotive bucket defined by the undulator and laser parameters using a pre-buncher.

The pre-buncher consists of a planar modulator section and a variable gap chicane. The modulator section creates a sinusoidal modulation at the resonant wavelength. The chicane dispersion serves to increase the bunching and also introduce a small delay such that the bunched beam enters the bucket at the decelerating resonant phase chosen in the design.

As seen in Fig. 2, the decelerating gradient depends on the laser vector potential. Taking diffraction into account, the tapering equations were solved considering the laser focal point to be at the center of the undulator. To focus the laser, a NaCl lens was placed outside of vacuum, upstream of a NaCl window that served to couple the CO2 laser into vacuum. By moving this lens and observing the laser spot on a pyrocamera located at an equivalent distance to the undulator center, we were able to set the waist position as desired.

RESULTS

Seeding the undulator with ~ 1 J of laser we were able to observe consistent full deceleration from 65 MeV to 35 MeV. Varying the pre-buncher chicane gap we were able to increase the fraction of electrons fully decelerated from ~5-10% with no pre-buncher installed, to ~30%, corresponding to ~100 pC (Fig. 4). We expect this to contribute ~3 mJ of laser energy to the seed and ~ 1 GW of power, demonstrating an electro-optical conversion efficiency of ~15 %.

RADIATION MEASUREMENTS

Using the FEL simulation code, Genesis 1.3, we were able to simulate the radiation growth, showing a direct correlation between the energy extracted from the electron beam and the growth of the radiation field [4]. Figure 5 shows results from a Genesis simulation showing 80% of a 1 kA beam decelerated by 30 MeV, producing 25 GW of radiation on top of a 100 GW seed

ISBN 978-3-95450-134-2

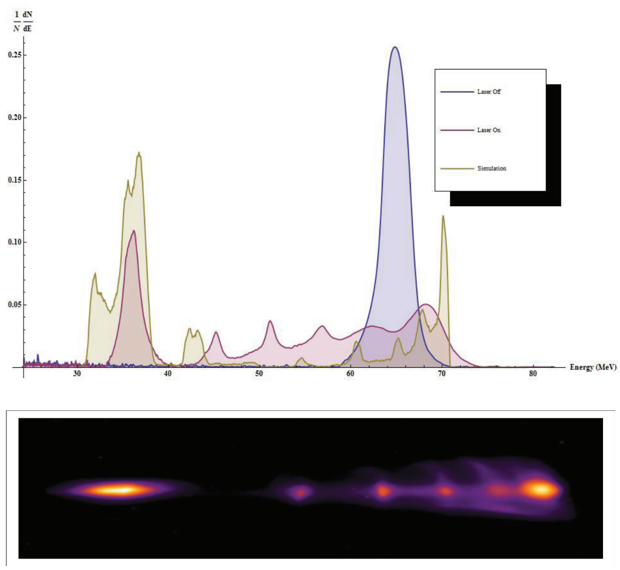

Figure 4: (Above) Deceleration data from Nocibur experiment showing 30% trapping compared with simulation and no laser shot. (Below) Spectrometer image of E-Beam energy spectrum corresponding to the spectra plotted above.

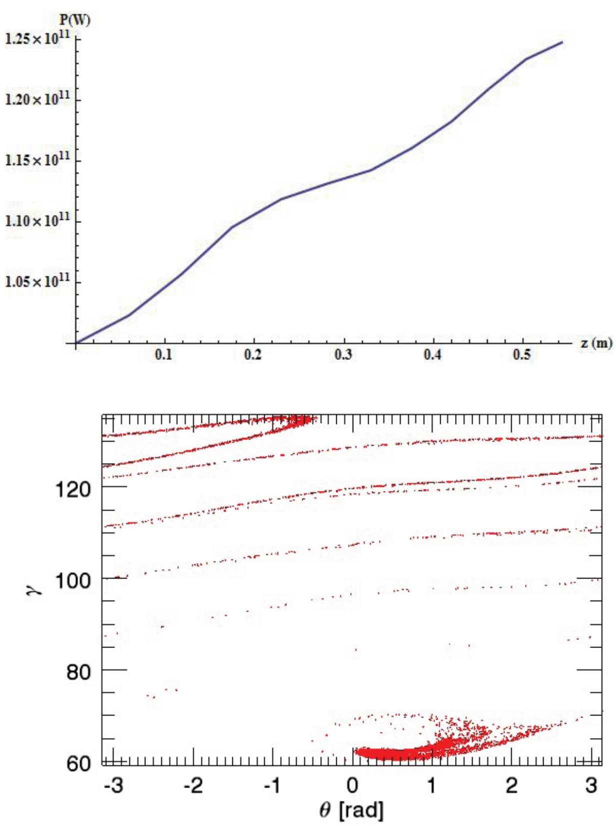

Figure 5: Genesis simulation results showing 25 GW radiation growth and deceleration using 1 kA peak current electron beam.

through the process of stimulated emission [5]. Experimental limitations forced us to run at 100 A, decreasing the radiation power generated to ~1 GW. Observing this radiation growth above the 100 GW seed is nontrivial. Increasing the peak current would not only increase the generated radiation power, but also increase the spectral bandwidth of the generated radiation allowing us to potentially use spectral filtering to observe the produced radiation. Efforts to increase the peak current at ATF are under way for future experimental runs.

CONCLUSIONS

High electro-optical conversion efficiencies (~40%) have been demonstrated at long wavelengths (35 GHz) where a waveguide could be utilized to maintain high laser intensities [6]. The Nocibur experiment serves as an important proof of principle experiment for short wavelength, highly efficient lasing utilizing strong tapering. The demonstration of a potential 15% conversion efficiency is a large step forward, and can be improved by increasing the peak current of the electron beam, and better optimization of the pre-buncher.

Future plans for measuring the produced radiation are being considered, potentially taking advantage of the spectral broadening when lasing with a short bunch or increased diffraction of the produced radiation.Extending this technology such that the signal becomes comparable to the seed or larger can be realized in an oscillator configuration or a longer tapered section FEL after burner. This high gain regime is an attractive solution for high average power, high peak power radiation sources, and these results from the recent Nocibur experiment affirm the practicality of pursuing these schemes.

REFERENCES

[1] J.Duris, P. Musumeci, R. Li. Phys. Rev. ST Accel. Beams, 15:061301, 2012.

[2] J. Duris et al., Nat. Commun. 5:4928 doi: 10.1038/ncomms5928, 2014.

[3] J. Duris, A. Murokh, P. Musumeci 2015 *New J. Phys.* **17** 063036.

[4] Y. Jiao, J. Wu, Y. Cai, A. W. Chao, W. M. Fawley, J. Frisch, Z. Huang, H.-D. Nuhn, C. Pellegrini, and S.Reiche Phys. Rev. STAB 15, 050704, 2012.

[5] A. Gover, Phys. Rev. ST Accel. Beams, 8, 030701, 2005.

[6] T. J. Orzechowski, B. R. Anderson, J. C. Clark, W. M. Fawley, A. C. Paul, D. Prosnitz, E. T. Scharlemann, S. Yarema. D. B. Hopkins, A. M Sessler and J. S. Wurtele. Phys. Rev. Letters 57, 2172 1986.

ISBN 978-3-95450-134-2

LASER WAKEFIELD ACCELERATION USING A LASER PRODUCED ALUMINIUM PLASMA*

Jaehoon Kim#, Younghoon Hwangbo, Seok-Gy Jeon, KERI, Ansan, Korea
Woo Je Ryu, Kyung Nam Kim, Seong Hee Park, Nikolay Vinokurov, KAERI, Daejeon, Korea

Abstract

In laser wakefield accelerator, usually a gas target is used to generate plasma medium. With this gas target, the pressure of the system cannot be keep as low as possible for electron beam application such as seeding the storage ring. To reduce this vacuum problem in LWFA, a plasma generated from solid Al target was used as plasma medium. A fundamental beam from the Q-switched ns pump laser in the Ti:sapphire power amplifier was used to generate a plasma from solid Al target. The plasma density was controlled by changing the distance between the main laser pulse for electron acceleration and the solid target. The plasma density was measured by the interferometer. The measured density indicates that the average charge of the ion in pre-plasma was 4.4. The main pulse ionized the Al plasma up to Al XII which means that the ionization injection could be used as an injection scheme. A 28 TW fs laser was used to accelerate the electron. A quasi-monochromatic electron was generated. The peak energy was 70 MeV and energy spread was 15 %. The divergence of the beam was 12 mrad in horizontal direction and 6 mrad in vertical direction.

INTRODUCTION

An interaction between ultrahigh intensity fs laser and plasma can be used as an electron accelerator which is called as a laser wakefield accelerator (LWFA) [1]. Due to the development of the chirped pulse amplification (CPA) technology, a compact table top ultrahigh intensity fs laser is available [2,3]. The feasibility of LWFA to accelerate the electron is already demonstrated. The main difference between the LWFA and conventional electron accelerator is the acceleration media. In LWFA, a plasma is used as acceleration medium, and such medium can support much higher acceleration field. A compact high energy electron accelerator is possible due to this strong acceleration field in LWFA. Besides the small system size, LWFA can generate a very short femtosecond time scale electron bunches because the acceleration region is very narrow [4]. The measured electron bunch length was less than 50 fs which was measured by using the coherent radiation transition[5,6]. A femtosecond x-ray can be generated using these femtosecond electron bunches which is very useful for the measurement of the dynamics of materials in femtosecond time scale [7-9].

In LWFA, typically a gas target is used to generate a plasma medium for the acceleration. But in vacuum sensitive applications such as an injector for a storage ring, the gas nozzle is not feasible because the gas injected into the vacuum chamber increases the pressure of the whole system. A plasma generated from a solid target can be used such an application because the number of particle injected into the vacuum chamber is much less than gas target. With solid target, the method to control the plasma density is needed because the plasma generated from a solid target by a laser expands very fast [10].

In this work, the feasibility of the laser produced plasma from solid target as an acceleration medium for a laser wakefield acceleration was studied. A density of the plasma was controlled by the distance between the main laser and the target and it was measured by using a Nomarski interferometer. The experimental results show that a laser produced plasma can be a good candidate of the acceleration medium for LWFA in vacuum sensitive applications.

#jkim@keri.re.kr

EXPERIMENT

To remove vacuum problem in LWFA with gas target, a plasma generated from a solid target was used as an acceleration medium for the LWFA. The experimental setup is shown in Fig. 1. The residual fundamental laser beam after the second harmonic generation from the pump laser of the main amplifier in the Ti:sapphire laser was used to generate a pre-plasma. By this method, the other laser is not needed to generate the pre-plasma. The laser was focused in line at a pure Al target by using a cylindrical lens and a biprism. The biprism was used to generate a uniform line intensity. If the intensity of the pre-pulse is too high, the plasma density at the interaction is too low because of the fast plasma expansion [10]. The size of the solid target is 2 mm wide and 25 mm long. After each laser shot, the target was moved 1 mm in x direction to supply a fresh surface. The laser line width at the target was controlled by the distance between the target and the cylindrical lens. In this experiments, the line width was 0.7 mm.

A ultrahigh intensity Ti:sapphire laser was used to accelerate electrons. The pulse duration of the laser was 25 fs and the peak power was 28 TW. The laser was focused at the pre-plasma by an off-axis parabolic mirror. The focal length of the OAP was 326 mm. The measured laser spot size was 5.4 μm. The time delay between the pre- and main pulse was fixed due to the optical pass length and was 140 ns.

The density of the pre- and main plasma was measured by using a Nomarski interferometer. A parts of the main pulse is used as a probe pulse after converted to the second harmonic pulse. A fast Fourier transform was used

ISBN 978-3-95450-134-2

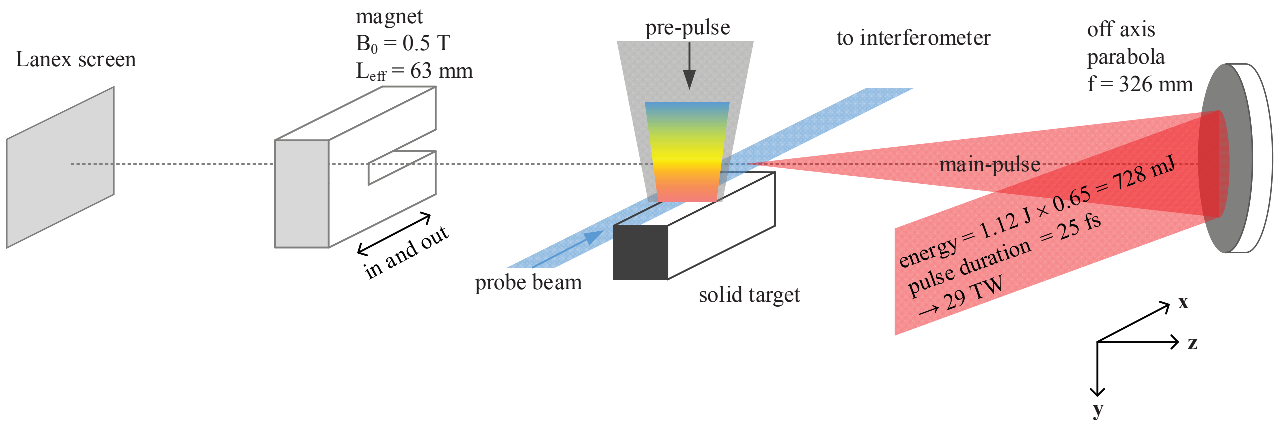

Figure 1: Experimental setup. A ns pre-pulse is from the fundamental laser of the pump laser for the amplifier of Ti:sapphire laser system. A pure Al target is on the 3-axis stage to control the position of the target relative to the laser beam. Some parts of the fs laser beam is used as a probe beam for the interferometer shown as blue line. Bending magnet is used to measure the electron beam energy. The peak power of the main pulse is 29 TW.

to recover the phase change due to the plasma [11]. The density was measured by using an Abel inversion [12].

After the target, an integrated current transformer was used to measure the bunch charge and after that a Lanex film was placed to measure the shape of the electron beam. A dipole mount was used to measure the energy of the beam by bending the electron. The magnetic field strength at the center of the pole was 0.5 T. The CCD camera was used to record the image of the Lanex.

RESULTS

Profiles of the pre- and main plasma were measured by interferometer. The density profiles are shown in Fig. 2. Uniform pre-plasma was generated due to the focusing optics for the ns laser as shown in Fig. 2-a). Due to the target width, the length of the pre-plasma is 2 mm. The density profile at 0.5 mm from the target surface is shown as a blue dashed line in Fig. 2-c). When the main pulse focused at the pre-pulse, the density profile was changed as in Fig. 2-b). The distance between the target and the main pulse was 0.5 mm. The profile of the main plasma density at 0.5 m from the target is shown in Fig. 2-c) with red solid line. The density of the main plasma increased because the main pulse ionized the ion in the pre-plasma. The density at the center of the plasma were 4×10^{18} cm^{-3} for pre-plasma and 1.6×10^{19} cm^{-3} for main plasma. Comparing the density profile of the pre- and main plasmas, the average charge of the ion in pre-plasma was 4.4 which means that the initial ionization of the plasma Al V.

The main pulse ionized the Al plasma up to Al XII by the optical field ionization. The density was very sensitive to the distance between the main laser and the target because the density exponentially decreased along the normal direction to the target.

Figure 3 show the electron beam profile and the energy distribution. The generation of the beam was very sensitive to the distance between the target and the main pulse. The electron beam was generate only when this distance was 0.5 mm due to the fast expansion of the plasma generated from the solid target. If the distance is longer than 0.5 mm, the density is too low. If that is shorter than 0.5 mm, the density is too high. The electron beam shape is elongated in horizontal direction.

As shown in Fig. 3-a), the beam divergence is 12 mrad in horizontal direction and 6 mrad in vertical direction. Blue dots in Fig. 3-a) show the center of the beam for each measurement. From this measurement, the pointing stability of the beam is 2 mrad in horizontal and 3.3 mrad in vertical direction.

Figure 3-b) shows the measured electron energy distribution. Quasi mono-energetic electron beams are generated by this solid target scheme. The average peak energy over 5 shots is 46 ± 3 MeV. The bunch charge is 13 ± 2 pC. The best electron beam generated from this scheme is the beam with peak energy 70 MeV and 15 % energy spread. With this result, the solid target can be used to accelerate electrons in LWFA.

ISBN 978-3-95450-134-2

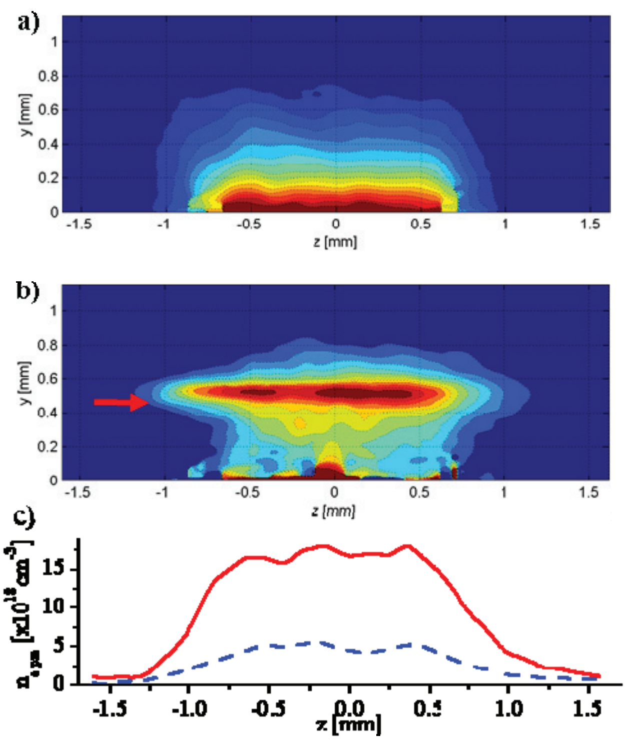

Figure 2: Plasma density profile. Density profile of the pre-plasma is shown in a) and the main plasma shown in b). A red arrow at b) indicates the positon of the main pulse. The cross sectional view of the density profile in shown in c).

CONCLUSION

To reduce the effect of the gas to the vacuum chamber for the vacuum sensitive application in LWFA, a plasma generated from solid Al target was used as plasma medium. A ns YAG laser was used to generate pre-plasma from the Al target. Due to the rapid expansion of the plasma, the plasma density was controlled by changing the distance between the main laser pulse for electron acceleration and the solid target. The electron beam was generate when the distance between the main and the target was 0.5 mm. The generation of the beam was sensitive to this distance because the plasma density. The plasma density was measured by the interferometer. A 29 TW fs laser was used to accelerate the electron. A quasi-monochromatic electron was generated. The peak energy was 70 MeV and energy spread was 15 %. The divergence of the beam was 12 mrad in horizontal direction and 6 mrad in vertical direction. The electron beam generated with this scheme will be used as the injector for the storage ring to generate strong THz radiation.

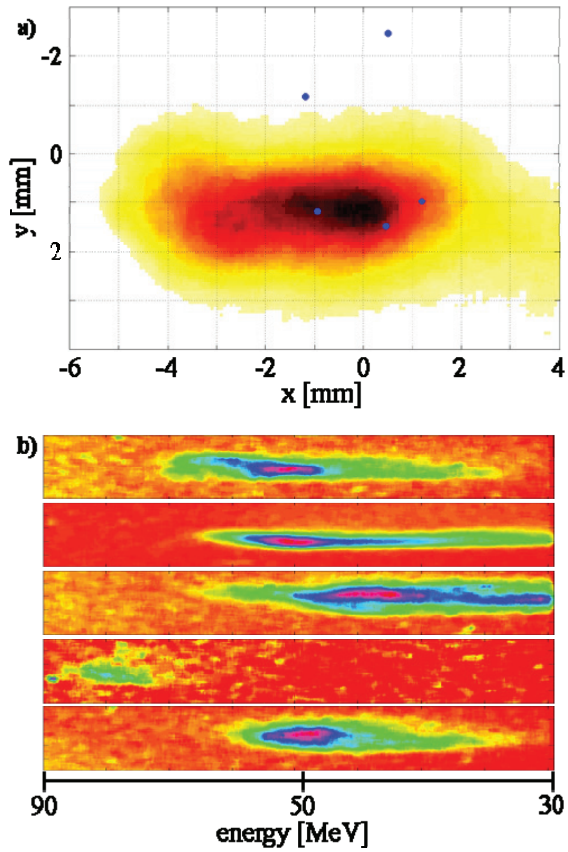

Figure 3: Accelerated beam image and the energy distribution. The beam shape and the center of the beams are shown in a). The measured electron energy in 5 series experiments are shown in b).

REFERENCES

[1] T. Tajima, and J. M. Dawson, Phys. Rev. Lett. 43, 267 (1979).
[2] D. Strickland and G. Mourou, Opt. Commun. 56, 219 (1985).
[3] P. Maine, D. Strickland, P. Bado, M. Pessot, and G. Morou, IEEE J. Quantum Electron. 24, 398 (1988).
[4] E. Esarey, P. Sprangle, J. K. Krall, and A. Ting, IEEE Trans. Plas. Sci. 24, 252 (1996).
[5] W. P. Leemans, J. van Tilborg, J. Faure, c. G. R. Geddes, C. Toth, C. B. Schroeder, E. Esarey, and G. Fubiani, Phys. Plasma 11, 2899 (2004).
[6] J. van Tilborg, C. B. Schroeder, C. V. Filip, C. Toth, C. G. R. Geddes, G. Fubiani, R. Huber, R. A. Kaindl, E. Esarey, and W. P. Leemans, Phys. Rev. Lett. 96, 014801 (2006).
[7] C. Rose-Petrucks, R. Jimenez, T. Guo, A. Cavalleri, C. W. Siders, F. Raksi, J. A. Squier, B. C. Walker, K. R. Wilson, and C. P. J. Barty, Nature 398, 310 (1999).
[8] C. Rischel, A. Rousse, I. Uschmann, P.-A. Albouy, J.-P. Geindre, P. Audebert, J.-C. Gauthier, E. Forster, J.-L. Martin, and A. Antonetti, Nature 390, 490 (1997).
[9] J. Kim, H. Jang, S. Yoo, M. Hur, I. Hwang, J. Lim, V. Kulagin, H. Suk, I. W. Choi, N. Hafz, H. T. Kim, K.-H. Hong, T. J. Yu, J. H. Sung, T. M. Jeong, Y.-C. Noh, D.-K. Ko and J. Lee, J. Korean Phys.Soc. 51,397 (2007).

ISBN 978-3-95450-134-2

[10] D. Giuliettie and L. A., Gizzi, La Rivista del Nuovo Cimento **21**, 1 (1998).
[11] K. A. Nugent, Appl. Opt. 18, 3101 (1985).
[12] M. Kalal and K. A. Nugent, Appl. Opts. 27, 1956 (1988).

ISBN 978-3-95450-134-2

TERAHERTZ SOURCE UTILIZING RESONANT COHERENT DIFFRACTION RADIATION AT KEK ERL TEST ACCELERATOR*

Y. Honda†, A. Aryshev, M. Shevelev, M. Shimada, KEK, Tsukuba, Ibaraki, Japan

Abstract

A test accelerator of energy recovery linac scheme, cERL, has been under commissioning at KEK. One of the feature of ERL is that it can realize a high repetition rate and continuous operation of a short bunched beam. It is a suitable place to test a light source based on resonant coherent radiation, such as an resonant coherent diffraction radiation (CDR) system. An optical cavity is formed on the beam orbit to build-up CDR. If the fundamental frequency of the cavity coincides with the beam repetition rate, the stored radiation can stimulate the radiation in the following bunches. We show a simple estimation of the radiation power based on a model of coupling between beam and cavity eigen modes. An ideal case example for cERL beam parameter is shown.

INTRODUCTION

One of the feature of ERL type of accelerator is that it can produce a short bunched beam at high repetition rate. It enables us to use it as a THz radiation source based on coherent radiation. CDR (Coherent Diffraction Radiation) is a coherent radiation produced by beam passing near a conductive target. Since it does not destroy a beam, the radiator can be installed in a loop of high averaged current ERL machine. As an advanced layout of CDR, it can be arranged to be a resonator scheme [1]. By coherently adding the radiation in a multi-bunched beam, it can extract radiation power much effectively. A test accelerator, cERL, which has been constructed recently in KEK, should be an ideal place to test the resonant CDR scheme.

Figure 1 shows the schematic of the resonant CDR system. An optical resonator of fundamental frequency that matches with beam repetition is placed on the beam axis. The cavity mirrors has a hole in the center so that beam can pass through. Electromagnetic wave excited in the resonator by a beam can be understood as CDR or higher-order modes of the resonator. Since the transverse profile of the mode is a donuts shape, it can be stored in a resonator formed by mirrors with hole.

Since electromagnetic wave in the resonator positively stimulates the radiation of the following bunches, the radiation power grows in square relation to bunch number. In order to extract the radiation, one of the cavity mirrors is designed to have transmission. Then it can be reflected to a transverse port using a parabolic mirror.

Here, we show the calculation of interaction of beam and resonator, and estimate radiation power assuming cERL beam parameter in an ideal case [2].

* Work supported by KAKENHI

† yosuke@post.kek.jp

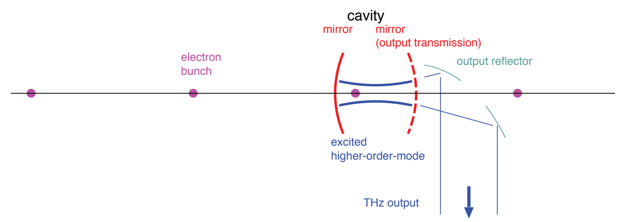

Figure 1: Schematic of resonant CDR.

HIGHER-ORDER GAUSS BEAM

The excited modes are odd order transverse modes of the resonator. Here we calculate the lowest one, TM_{10} mode.

Transverse field of TM_{10} mode is written as follows.

$$\begin{aligned} E^x_{10} &= \frac{A}{w(z)}\frac{x}{w(z)}\exp(-\frac{x^2+y^2}{w^2(z)}) \\ &\cdot\exp[i(\omega t - kz + \phi(z))] \end{aligned} \tag{1}$$

$$w(z) = w_0\sqrt{1+\frac{z^2}{z_0^2}} \tag{2}$$

$$z_0 = \frac{\pi w_0^2}{\lambda} \tag{3}$$

$$\phi(z) = 2\tan^{-1}(\frac{z}{z_0}) \tag{4}$$

ν is the optical frequency of radiation, c is the speed of light, $k = 2\pi/\lambda$, $\omega = 2\pi\nu$, $\omega/k = c$. A is a scale factor for normalization. $w(z)$ is the size at location z, w_0 is the size at the waist. $\phi(z)$ is known as Gouy phase which depends on the order of transverse mode, the factor 2 means the first order mode. z_0 is Rayleigh length.

Electromagnetic wave is a transverse wave in the case of an uniform plane wave. But, in cases of waves with spatial structure such as higher-order transverse modes, there exists a longitudinal field. The following relation can be shown from Helmholtz equation.

$$ikE^z = \frac{\partial E^x}{\partial x} \tag{5}$$

From Eq. 1, longitudinal field of TM_{10} mode is obtained as follows.

$$\begin{aligned} E^z_{10} &= -\frac{i}{k}\frac{A}{w^2(z)}(1-\frac{2x^2}{w^2(z)})\exp(-\frac{x^2+y^2}{w^2(z)}) \\ &\cdot\exp[i(\omega t - kz + \phi(z))] \end{aligned} \tag{6}$$

When beam of speed c passes on the center axis, it feels the longitudinal field of

$$E^z_{10}(x=y=0) = -\frac{A}{kw^2(z)}\exp[i2\phi(z)] \quad . \tag{7}$$

ISBN 978-3-95450-134-2

It accumulates the field while experiencing phase shift due to Gouy phase.

INTERACTION WITH THE RESONATOR

Here, we compare two types of two-mirror resonator shown in Fig. 2. (A) is formed with two concave mirrors of same radius of curvature. (B) is a half-cavity, formed with one flat mirror and one concave mirror. One of the mirror has power transmission ratio of T, it is the extraction port.

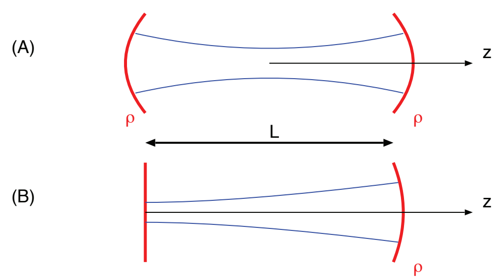

Figure 2: Configuration of resonator.

Electromagnetic energy of TM_{10} mode U can be written as

$$U = 2 \times \frac{\epsilon_0}{2} \int |E_{10}^x|^2 dV \quad , \tag{8}$$

here, we ignore contribution of longitudinal field. Using Eq. 1, it is calculated to be

$$U = \frac{\epsilon_0 \pi A^2 L}{8} \quad . \tag{9}$$

We calculate excitation of one longitudinal mode by a charged particle. (R/Q) of the mode is defined as follows.

$$(R/Q) = \frac{|\int E^z dz|^2}{\omega U} \tag{10}$$

Using Eq. 7, excited energy by charge q is

$$\begin{aligned} U_1 &= \frac{\omega}{4}(R/Q)q^2 & (11)\\ &= \frac{1}{2\epsilon_0 \pi L}\left|\int \frac{1}{1+p^2}\exp[i2\tan^{-1}p]dp\right|^2 & ,(12) \end{aligned}$$

here $p = z/z_0$.

Integration of p depends on design of the resonator. For example, in the case of Fig. 2(A), z should be integrated in $-\alpha z_0 \sim \alpha z_0$, and in the case of Fig. 2(B), z should be integrated in $0 \sim \alpha z_0$.

The integration part of Eq. 12 is calculated as a function of α, which is the half-cavity length in the unit of z_0. Figure 3 and Fig. 4 show the case (A) and (B), respectively. In the case (A), longer cavity than optimum can cancel the field due to the phase shift. The optimal case is $\alpha = 1$, it means $L = 2z_0$. As for in the case (B), phase shift is half of case (A), it can not be cancelled by phase shift. In both cases, the maximum of the integral part is 1. So, in the ideal case,

$$U_1 \sim \frac{q^2}{2\epsilon_0 \pi L} \quad . \tag{13}$$

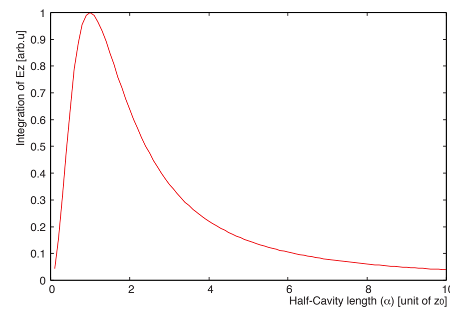

Figure 3: Integration in case (A).

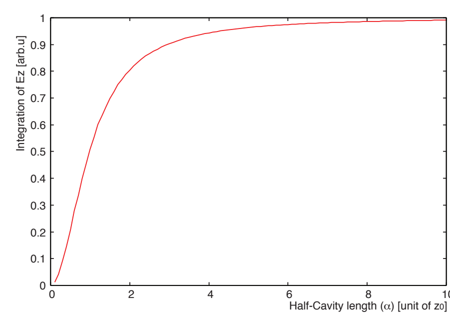

Figure 4: Integration in case (B).

EXTRACTED POWER

Power in the resonator P_{in} can be written as

$$P_{in}\frac{2L}{c} = U_1 \quad , \tag{14}$$

The power extracted from the resonator becomes

$$P_{out} = P_{in}T = U_1 \frac{c}{2L} T \tag{15}$$

here T is the mirror transmittance.

We consider the case of multi-bunch excitation. Here, we assume an ideal case that the resonator loss is negligible to the excitation mirror transmittance. And bunch repetition perfectly matches with resonator fundamental frequency, so that the radiation adds up coherently.

Field in the resonator decays due to the power extraction at the mirror. The amplitude becomes factor $\sqrt{1-T}$ in one round-trip. Field extracted in multi-bunch excitation V_∞ can be written using the single bunch excitation V_1 as follows.

$$\begin{aligned} V_\infty &= V_1 + V_1\sqrt{1-T} + V_1(\sqrt{1-T})^2 + \cdots \\ &= \frac{V_1}{1-\sqrt{1-T}} \sim \frac{2V_1}{T} \end{aligned} \tag{16}$$

Power is the square of amplitude.

$$P_\infty = V_\infty^2 = \frac{4}{T^2}V_1^2 = \frac{4}{T^2}P_{out} \sim \frac{cq^2}{\epsilon_0 \pi L^2 T} \tag{17}$$

So far, we discussed about single longitudinal mode. There should be many longitudinal mode spaced in every FSR (free-spectral-range) of the resonator. These are excited by the beam at the same time. It forms a mode-locked pulse in the resonator. Since Eq. 17 does not depend on frequency or w_0, all the longitudinal modes can be excited, except for diffraction loss or frequency dependence of mirrors.

For example, we assume the center frequency to be 1.6 THz and FSR to be 160 MHz, there are 100 longitudinal modes in 1 % bandwidth. The total power is sum of all the modes.

CALCULATION IN THE CASE OF CERL

We assume bunch compression mode of operation. So, we assume form-factor to be 1 around a few THz region. The parameter is as follows. Bunch charge is q = 10 pC/bunch, bunch repetition rate is FSR=162 MHz, number of longitudinal mode in 1% band width is $N_{mode} = 10^2$, the resonator length L = 0.925 m (162 MHz), transmission of extraction mirror $T = 10^{-3}$.

Photon flux F is calculated to be

$$F = \frac{cq^2}{\epsilon_0 \pi L^2 T}\frac{N_{mode}}{h\nu} \sim 2\times 10^{23} \quad \text{photons/s/1\%BW} \tag{18}$$

In averaged power, it is $P_\infty = F \times h\nu \sim$ 30W. By counting another transverse mode of perpendicular direction, TM_{01}, there should be another factor 2.

Finally, we compare with a single-path radiation without resonator. We use the formula of transition ratiation (TR), called Ginzburg-Frank equation in the follwing.

$$\frac{dW_{TR}}{d\omega d\Omega} = \frac{e^2}{4\pi^3 \epsilon_0 c}\frac{\beta^2 \sin^2\theta}{(1-\beta^2\cos^2\theta)^2} \tag{19}$$

θ is radiation angle.

Integrating all solid angle and coherently add number of particle (N^2), and also integrating in 1% bandwidth around 1.6 THz, the radiation flux is calculated to be $\sim 3 \times 10^{19}$ photons/s/1%BW at same beam parameter. Comparing with Eq. 18, it shows that there is four orders of magnitude enhancement because of the stimulation by resonator configuration.

SUMMARY

Here, we discussed CDR in a resonator configuration. It can be understood as excitation of a higher-order transverse mode of the resonator through its longitudinal electric field. So, it can be calculated from beam to cavity mode interaction. Calculating coherent addition of excitation in a multi-bunch beam, in an ideal case of loss is dominated by power extraction, the photon flux in cERL beam parameter results in $\sim 10^{23}$ photons/s/1%BW at THz region. This can be a very strong radiation source in this frequency.

This work is partially supported by Photon and Quantum Basic Research Coordinated Development Program from the Ministry of Education, Culture, Sports, Science and Technology, Japan, and JSPS KAKENHI 25600146.

REFERENCES

[1] A. Aryshev *et al.* "Observation of the stimulated coherent diffraction radiation in an open resonator at LUCX facility", Nucl. Instr. Meth. A 763, pp 424-432 (2014)

[2] Y. Honda "THz source utilizing an resonant CDR system at cERL", Proceedings of 11th Japanese Particle Society Meeting (2015)

ISBN 978-3-95450-134-2

LEBRA FREE-ELECTRON LASER ELICITS ELECTRICAL SPIKES FROM THE RETINA AND OPTIC NERVE OF THE SLUG LIMAX VALENTIANUS

F. Shishikura#, K. Hayakawa, Y. Hayakawa, M. Inagaki, K. Nakao, K. Nogami, T. Sakai, T. Tanaka
Laboratory for Electron Beam Research and Application, Nihon University, Chiba, Japan
Y. Komatsuzaki
Departments of Physics, College of Science and Technology, Nihon University Chiba, Japan

Abstract

Since 2001, the Laboratory for Electron Beam Research and Application (LEBRA) has been providing tunable free-electron lasers (FELs) encompassing the near-infrared (IR) region and part of the mid-IR region (0.9–6.5 µm), and generating visible wavelengths up to 400 nm by means of nonlinear optical crystals. We used LEBRA-FEL to irradiate the retina of slugs (*Limax valentianus*), and determined which FEL wavelengths generate electrical spikes from a retina-optic nerve preparation. In the dark-adapted state, blue FEL light (peak wavelength: 470 nm) efficiently elicited electrical spikes from the retina. The results are consistent with a previous study where a xenon arc lamp with interference filters was used to produce monochromatic visible light. The retina produced detectable electrical spikes when repeatedly irradiated with pulsed FEL below 5 Hz. We extended the wavelengths to the near-IR regions (0.8–2.5 µm); however, we detected no electrical response.

INTRODUCTION

Free electron lasers (FELs), such as the one developed by the Laboratory for Electron Beam Research and Application (LEBRA), produce high-energy, tunable pulsed radiation (wavelength range: 0.4–6.5 µm), which is ideal as a radiation source for investigating photochemical reactions in living organisms. Previously, we verified that visible FELs can control the germination of lettuce seeds, a well-known photochemical reaction in plants that is promoted by red light (660 nm) and inhibited by far-red light (740 nm) [1].

In this work, we investigated the efficiency of FEL for photic stimulation in an electrophysiological study. The eye (or retina) and optic nerve of the slug *Limax valentianus* is particularly useful for this purpose because the retina and optic nerve can be readily dissected free from the amputated eyestalk of the adult animal. The dissected retina-optic nerve preparation can be used for more than 12 h in a plastic chamber filled with snail Ringer solution [2]. Furthermore, the retina is big enough to be illuminated easily by the LEBRA-FEL micro-irradiation system, which contains a quartz fiber, and the optic nerve is large enough for signals to be recorded using a conventional capillary suction electrode. In the dark-adapted state, FEL irradiation experiments show that the peak wavelength of the spectral sensitivity curve is 470 nm.

#shishikura@lebra.nihon-u.ac.jp

MATERIALS AND METHODS

Animals

L. valentianus slugs, which are terrestrial and nocturnal, were collected locally and maintained for at least seven generations. These animals were kept under dark, wet conditions in plastic boxes placed in an incubator (SLC25A, Mitsubishi-Engineering Co., Japan) at 19.0 °C.

Dissection

Adult specimens (2.1–2.4 g) were used. Each animal was anesthetized with an injection of 500 µL of snail Ringer's solution [2] containing 50 mM $MgCl_2$. The snail Ringer's solution was a modification of Ramsey's Ringer solution [3]. The retina (about 0.25 mm diameter) and optic nerve (about 40 µm diameter) were isolated by micro-dissection in snail Ringer's solution. The optic nerve was removed free from surrounding tissue, and cut apart from the base of the retina. The retina-optic nerve preparations of both eyes were fixed with small tungsten wire pins (3 mm long, 0.1 mm diameter) on a sloping transparent sheet of silicon in fresh Ringer's solution in a small plastic chamber. The preparations in Ringer's solution were used in experiments for 1 day.

FEL Stimulation

In an earlier experiment [2], a xenon arc lamp (500 W) with a series of interference filters was used for producing monochromatic light. Here, we used the LEBRA-FEL as a radiation source, the beam specifications of which are detailed elsewhere [4,5]. LEBRA-FEL can generate sharp peak emissions of high-energy, high-coherency, tunable pulsed radiation from 0.4–6.5 µm, and narrow spectral bandwidths. LEBRA can generate 4 or 5 wavelengths for the irradiation experiments over a day.

The setup of the LEBRA-FEL micro-irradiation systems has been described in our previous study [1]. A quartz fiber (0.6 mm diameter; Edmund Optics, Tokyo, Japan) was installed on a holder (H-7; Narishige Group, Tokyo, Japan) of a micro-manipulator (MMO-220A, Narishige Group), and delivered visible light wavelengths and near-infrared (IR) wavelengths up to 3 µm. A dissection microscope and recording apparatus were placed in a Faraday cage, as shown in Fig. 1.

We used a light-emitting diode (LED) at a constant wavelength of 460 nm (20 $\mu W\ s^{-1}$ at 4.7 V) as a test light that was placed in the FEL delivery path and removed when the FEL was switched on. The intensities of the

ISBN 978-3-95450-134-2

light sources, FEL and LED, were measured at the tip of the quartz fiber by power meters (FieldMax-II and OP-2VIS, respectively, Coherent, Inc., Portland, OR) at the beginning and end of experiments. The FEL radiation energies could be reduced by a series of combined neutral density (ND) glass filters (Kenko Tokina Co. Ltd., Tokyo, Japan). In contrast to the LED power, the optical power of the FELs varied between experiments, and the average power was 8.70 μJ/pulse for visible wavelengths (420–710 nm) and 35.10 μJ/pulse for near-IR wavelengths (0.8–2.5 μm).

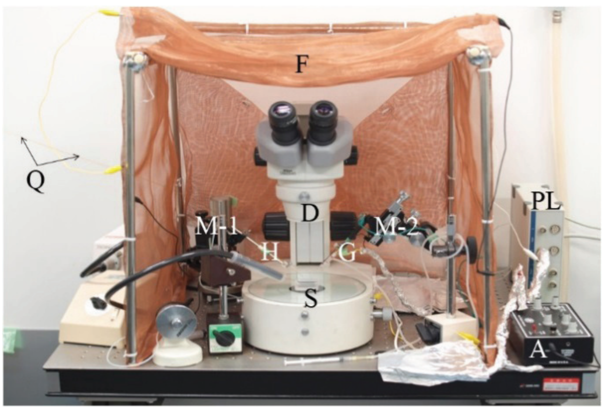

Figure 1: FEL micro-irradiation system. A, amplifier; D, dissection microscope; F, Faraday cage; G, glass capillary suction electrode and reference electrode; H, holder and quartz fiber; M-1, manipulator 1 for irradiation; M-2, manipulator 2 for recording electrodes; PL, data acquisition device (PowerLab 2/26); Q, quartz fiber; S, sample.

Recording and Analysis

Prior to irradiation experiments the retina-optic nerve preparations were fixed on a sloping silicon plate in a small plastic chamber (30 × 60 mm, 8 mm deep). The whole optic nerve bundle was suctioned by the tip of a glass capillary suction electrode at one of the three suction sites (Fig. 2). We used a silver chloride reference electrode consisting of an Ag/AgCl wire (0.25 mm diameter) coiled around the glass capillary suction electrode and immersed in snail Ringer's solution. Using manipulators, a FEL wavelength delivered through the quartz fiber could precisely irradiate the surface of the lens by bringing the tip of the fiber into contact. The retina-optic nerve preparations were irradiated for 1 s at 2 to 5 min intervals in most experiments, as this interval allowed the signal to return to the background discharge as a control.

Electrical signals were fed into a high-input impedance amplifier (DAM80 Differential Amplifier, World Precision Instruments, Inc., Sarasota, FL), which was connected to a data acquisition device (PowerLab 2/26, ADInstruments, Inc., Dunedin, New Zealand; settings: low filter, 1 Hz; high filter, 10 kHz; and gain, 1000). The oscilloscope trace was recorded continuously on a personal computer. Recordings and all irradiation experiments were performed at room temperature (22 °C) in a darkened room. Data analyses were performed with LabChart 7 software (ADInstuments, Inc.).

RESULTS AND DISCUSSION

Recording Site on the Optic Nerve

The recording sites on the optic nerve are shown in Fig. 2 (top left), and are designated *a*, *b*, and *c* according to their proximity to the retina. The results from site *a* gave large, steady electrical spikes when stimulated by the LED test light and the FEL. The suction electrode was fixed firmly to site *a* without losing electrical signals, and was used for the study. Suzuki et al. [2] used a site similar to site *a*, allowing us to compare our results with their previous results.

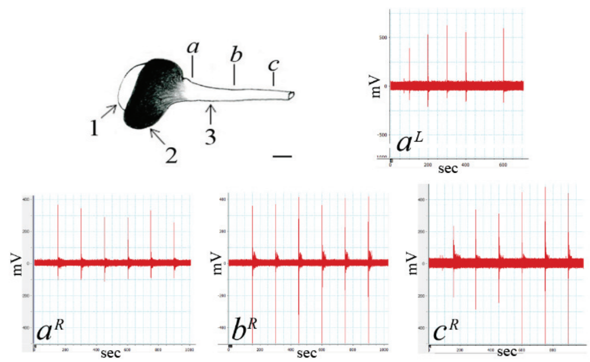

Figure 2: Effect of recording site on the optic nerve. Top left: schematic of the slug's right eye. Labels *a*, *b*, and *c* indicate recording sites. During recording, the eye was held at one of the sites with a glass capillary suction electrode. Signals were recorded at a^R, b^R, c^R, and a^L were obtained from the right eye (^{R}) and the left eye (^{L}), respectively, of the same individual. The stimulus lasted 1 s and was repeated 5 or 6 times at 100 or 200 s intervals. 1: Lens; 2: retina; 3: optic nerve. The scale bar indicates 50 μm.

Comparison of Spike Responses to Continuous Wavelength (LED) and Pulsed Wavelength (LEBRA-FEL)

The patterns of electrical spikes for continuous and pulsed wavelength light are compared in Fig. 3A and B. The patterns are similar, except for two prominent spikes detected in Fig. 3A in response to 2 Hz pulsed light. The first electrical spike was always large compared with the subsequent spikes. Figure 3B also shows a typical example; the two spikes generated by different light intensities demonstrated that the intensity of the electrical spikes was a function of the light source intensity. A 1–2 min interval between irradiation was sufficient for the signal to return to the static background discharge, even for full intensity signals (right side, Fig. 3B). However, when the irradiation continued, the intensity of the electrical spikes hardly decreased over 70 min (data not shown). The electrical responses from the retina-optic nerve of the slugs appeared to arise from complex reactions, as suggested by other studies [6,7].

ISBN 978-3-95450-134-2

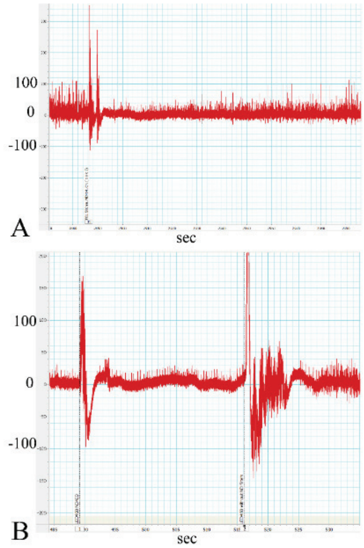

Figure 3: Comparison of electrical spikes between continuous (LED) and pulsed (LEBRA-FEL) irradiation. A: Data obtained from 560 nm LEBRA-FEL irradiation (1/16 intensity = 0.27 µJ/pulse), B; data obtained from LED 460 nm irradiation (left; 1/400 intensity = 0.05 µW s^{-1}, right; full intensity). Stimulus was 1 s in duration.

Spectral Sensitivity Curve

Figure 4 shows that the spectral sensitivity reached a maximum wavelength at about 470 nm, which is close to those of other gastropods, for example, 475 nm in *Helix pomatia* [8] and 480 nm in *L. flavus* [2]. At wavelengths

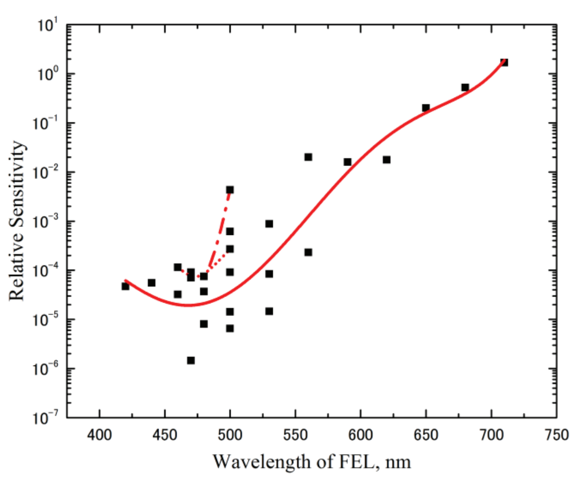

Figure 4: Spectral sensitivity curve of the dark-adapted *L. valentianus* retina-optic nerve as a function of the wavelength. Sensitivity is determined as the smallest amount of FEL energy at each wavelength required to generate electrical spikes slightly larger than background discharge. To examine the minimum radiation energy of each wavelength, a combination of ND glass filters was used. The dotted and dashed lines indicate results obtained from single preparations of the right and left eyes, respectively. The data was fitted with the straight line by OriginPro (OriginLab, Co., Northampton, MA).

from the near-IR region to 2.5 µm, any electrical spikes would have been too small to detect and would have been masked by the background discharge (Table 1). In contrast, for shorter wavelengths, the electrical spikes were visible up to 420 nm, which is the limit of LEBRA-FEL. Therefore, the slug's eyes responded well to blue light rather than to near-IR, suggesting the presence of only a single visual pigment having peak absorption at around 470 nm. Suzuki et al. [2] reported a shift in the maximum wavelength to 460 nm in response to the light-adapted state of the retina of *L. flavus*. However, we have not yet investigated the light-adapted state for our preparation. Kataoka [9] suggested that *L. flavus* slug eyes are sensitive to IR light, whereas our current data (Table 1) indicate that the eyes of *L. valentianus* are not sensitive to near-IR wavelengths (0.8–2.5 µm). We are currently performing further analysis of our data.

Table 1: Slug Retina-Optic Nerve Responses to Near-IR Radiation Stimuli from LEBRA-FEL

Wavelength, µm	Energy, µJ/pulse	Electrical Spike [1]
0.80	5.86	ND [2]
0.90	13.37	ND
1.00	33.25	ND
1.10	12.12	ND
1.25	42.90	ND
1.50	33.54	ND
1.70	90.90	ND
1.90	121.60	ND
2.00	52.60	ND
2.50	33.80	ND

[1]: Results of 10–15 reciprocals.
[2]: Not detected.

Responses to Repetitive Stimulation

Figure 3A indicates that the retina-optic nerve system can elicit two electrical spikes during irradiation for 1 s by LEBRA-FEL (2 Hz). To measure the response of one eye to the frequency of light pulses, we used LEBRA-FEL and LED light sources. Figure 5 shows that the right and left eyes both responded to increasing rates of repetitive stimulation up to 5 Hz with difficulty (Fig. 5C). This rate was defined as the flicker fusion threshold of the slug's eye. To generate higher frequency stimulation, we used an arbitrary/function generator (AFG3052C, Tektronix, Inc., Portland, OR) connected to the 460 nm LED (20 µW s^{-1} at 4.7 V). The flicker fusion threshold was below 4 Hz (data not shown). The different frequencies for the light sources may arise from the different intensity of the peak emission. The flicker fusion threshold of *L. valentianus* was much lower than animals, insects (*Locusta migratoria*, *Glossina morsitans* and *Drosophila hydei*), and birds (*Sturnus vulgaris* and *Columba livia*) that stalk prey, which typically have flicker fusion thresholds of over 100 Hz [10,11]. *L.*

ISBN 978-3-95450-134-2

valentianus can react to frequencies of up to 5 Hz at the higher peak emission energy for the LEBRA-FEL.

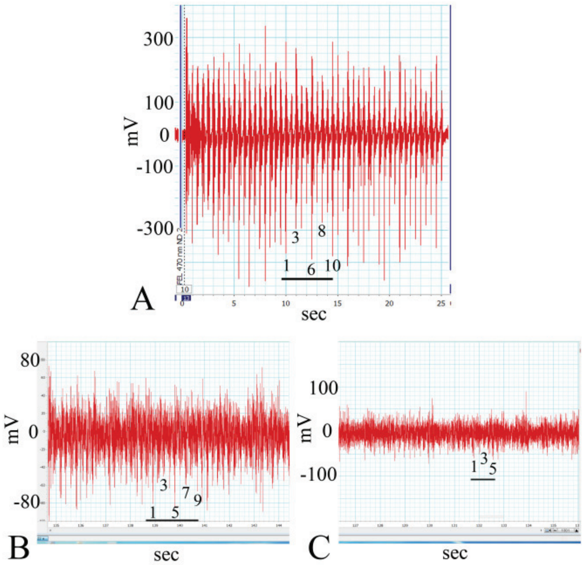

Figure 5: Flicker fusion rate (Hz) of *L. valentianus* eye preparation. The stimulus was 470 nm FEL (10 µJ/pulse) at A, 2.0 Hz; B, 4.55 Hz; and C, 5.0 Hz. Bars indicate irradiation times: A, 5 s; B, 2 s; and C, 1 s. The numbers on each graph indicate the frequency of LEBRA-FEL pulses.

ACKNOWLEDGMENT

We thank Mr. T. Kuwabara (a graduate of Departments of Physics, College of Science and Technology, Nihon University) for assistance.

REFERENCES

[1] F. Shishikura et al., "Potential photochemical applications of the free electron laser irradiation technique in living organisms", in *Proc.36th Int. FEL Conf.*, Basel, Switzerland, 2014, pp. 505-508.
[2] H. Suzuki et al., J. Comp. Physiol. 133, 125-130 (1979).
[3] A. J. Ramsey, J. Exp. Biol. 17, 96-115 (1940).
[4] K. Hayakawa et al., "The LEBRA 125 MeV electron linac for FEL and PXR generation", in *Proc. 27th Int. LINAC Conf.*, Lubeck, Germany, 2004, pp. 90-92.
[5] T. Tanaka et al., "Tunability and power characteristics of the LEBRA infrared FEL", in *Proc.26th Int. FEL Conf.*, Trieste, Italy, 2004, pp.247-250.
[6] K. T. Brown, Vis. Res. 8, 633-677 (1968).
[7] M. L. Wiederhold et al., J. Gen. Physiol. 61, 24-55 (1973).
[8] E. Berg and G. Schneider, Vis. Res., 12: 2151-2152 (1972).
[9] S. Kataoka, Vis. Res., 15, 681-686 (1975).
[10] K. L. Woo et al., Naturwissenschaften 96:415-419 (2009).
[11] R. C. Miall, Physiol. Entomol., 3, 99-106 (1978).

ISBN 978-3-95450-134-2

COTR RESISTANT PROFILE MONITOR*

H. Loos†, SLAC National Accelerator Laboratory, Menlo Park, CA 94025, U.S.A.

Abstract

Electron beam accelerators used as drivers for short wavelength FELs need ultra-high brightness beams with small emittances and highly compressed bunch lengths.The acceleration and beam transport process of such beams leads to micro-bunching instabilities which cause the emergence of coherent optical transition radiation (COTR). The effect of COTR on profile monitors based on OTR or fluorescent screens can be quite detrimental to their intended use to measure beam sizes and profiles. This presentation will review past observations of the beam diagnostics issues due to COTR and discuss various mitigation schemes for profile monitors as well as present experience with such implementations.

INTRODUCTION

Free electron laser facilities for the generation of soft and hard x-rays [1–5] utilize high brightness linear accelerators which have to produce electron beams of exceptional quality to achieve lasing in a feasible length of undulator. The beams of multi-GeV energy need to have sub-micrometer transverse emittance, 10^{-4} energy spread and 10s of fs or even shorter bunch durations for a total charge of the order of few 100 pC. Such parameters necessitate the measurement of transverse beam sizes and profiles from the injector area all the way to the unduators to establish beam emittance measurements throughout the accelerator so that machine tuning and optimization to maintain the high brightness beam into the undulators becomes possible. Furthermore, the 2-dimensional transverse beam distribution is needed to diagnose transverse coupling and to measure the time-resolved beam size or energy spread in conjunction with a transverse deflecting structure [6]. The most convenient method to obtain images of the transverse beam distribution is to use a profile monitor, i.e. a screen of some material intercepting the electron beam and emitting visible light imaged onto a CCD camera. The small, typically only several 10s of µm beam sizes make the use of scintillating crystals or thin foils generating optical transition radiation (OTR) [7] advantageous. The latter method was envisioned as the main transverse beam diagnostic for many XFEL accelerators because of the instantaneous response of OTR, and the absence of charge density dependent saturation effects or image resolution diluting depth effects as for thick scintillating crystals [8].

The ultra-high brightness of the XFEL accelerators—needed to enable coherent radiation at x-ray wavelengths—however poses a challenging problem for transverse beam diagnostics as became apparent for the first time during the commissioning of the LCLS injector [9]. It became obvious then that imaging beam distributions using OTR screens can lead to completely unreliable results due to coherent effects from the longitudinal structure in the bunch distribution, i.e. the emission of coherent optical transition radiation (COTR).

The following sections first provide a brief summary of the COTR issue, then a review of various mitigation schemes to provide images of the beam distribution that are not affected by COTR artifacts, and concluding with results from tests of the PSI design profile monitor at SwissFEL and LCLS.

COTR OBSERVATIONS

Coherent optical transition radiation is the process by which the light emission of a charged particle intercepting the boundary between two different media is not just the sum of the intensity of the light from individual particles as desired for OTR based beam diagnostics, but where longitudinal structure in the bunch at visible wavelengths leads to a coherent superposition of the emitted light fields, and hence an increase of the light intensity which can be a factor up to the number of particles if the bunch length itself is shorter than visible wavelengths.

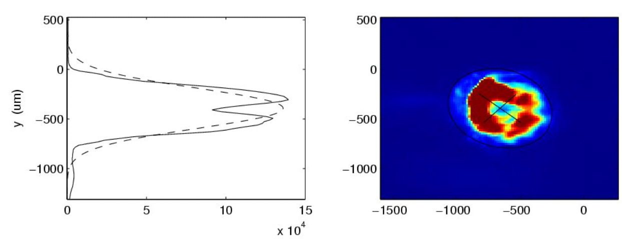

Figure 1: An image of the COTR radiation in the LCLS injector after BC1 observed with extreme bunch compression. From [9].

The initial observation of COTR [10] occurred in a deliberate way from an electron beam temporally modulated by the SASE process at visible wavelengths, which lead to the coherent enhancement of the incoherent OTR intensity by several orders of magnitude within the narrow SASE bandwidth. The first observation of broadband visible COTR at LCLS [9, 11] as shown in Fig. 1 was unexpected, but soon explained as a result of micro-bunching induced by the longitudinal space charge instability [12]. Subsequently the COTR effect has also been documented at most other high-brightness accelerators, both equipped with photo or thermionic cathode guns [13–16], with the latter requiring several bunch compression stages. Summaries of these observations can be found in [14, 17].

There are several implications of the COTR effect on the beam profile measurement. The light intensity can be greatly increased from a small factor for uncompressed

* Work supported by US DOE contract DE-AC02-76SF00515.
† loos@slac.stanford.edu

ISBN 978-3-95450-134-2

beams of ps duration to up to 5 orders of magnitude for highly compressed bunches with current spikes of few fs duration, even leading to CCD damage. Figure 2 shows the intensity enhancement for different bunch compression settings at FLASH [14]. For longer bunches, spurious changes to the measured OTR beam size can be observed which are not related to the actual beam size, but rather stem from non-uniform coherent enhancement across the transverse beam profile. Lastly, the entire transverse shape of the light distribution can change so that the COTR distribution from a Gaussian electron beam profile becomes a doughnut-shaped ring structure for bunches exhibiting sufficient transverse correlation of the longitudinal micro-bunching or current spikes (see Fig. 1).

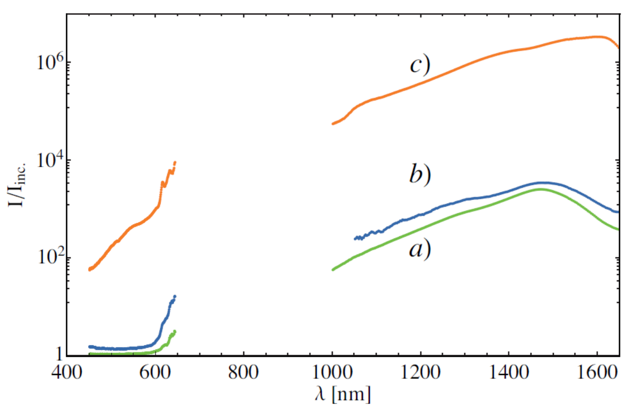

Figure 2: Visible and near IR relative spectral intensities of COTR w.r.t. incoherent OTR for three different bunch compression setups at FLASH. From [14].

COTR MITIGATION

A great number of methods has been proposed or tested over the last years to circumvent the detrimental coherent effects occurring when a high-brightness electron beam intercepts a screen, and to provide an image of the electron beam that is strictly proportional to its transverse charge density distribution. The schemes address this by changing one or more parameters in the OTR imaging process. The electron beam itself can be tailored to suppress its coherence, or the OTR emission can get spatially or spectrally filtered, or a different physical process to generate a beam distribution image can be chosen to avoid the sensitivity to the longitudinal particle distribution. The challenge for all the schemes is to overcome the potentially many orders of magnitude dominance of the COTR over the desired radiation process, considering that just an equal or even lesser fraction of COTR can already significantly alter measured beam profiles.

Beam Manipulation

As the LSC instability is driven by a small slice energy spread, one expects the inclusion of a laser heater in the injector of an accelerator to mitigate or sufficiently suppress the COTR emission by increasing the energy spread of the beam. Such suppression has indeed been observed [18] with the COTR intensity after the second LCLS bunch compressor being lowered by two orders of magnitude, however still a factor 6 above the incoherent level (see Fig. 3) with OTR beam sizes not representative of the true electron beam distribution.

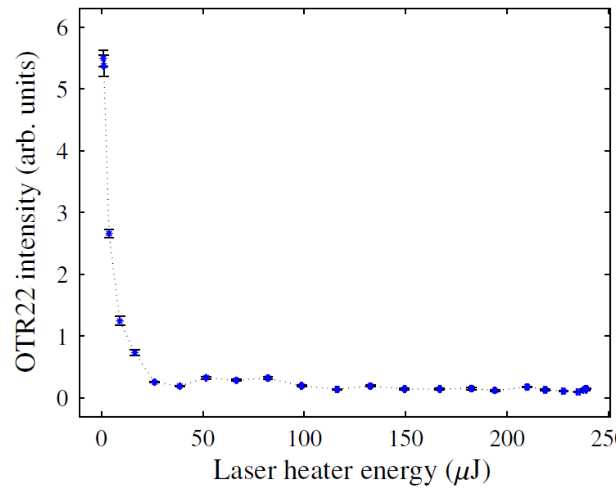

Figure 3: Reduction of COTR intensity at LCLS after the second bunch compressor with increasing laser heater power. From [18].

In the LCLS injector the required chicane for the laser heater manifests itself already the LSC instability due to the 8 mm R_{56}. As shown in Fig. 4 the OTR light intensity downstream of the laser heater doubles with just the chicane turned on, but is still about 25% above the incoherent OTR when the beam is heated by the laser [19]. Also an artificially 30% lower projected beam emittance is measured with just the chicane turned on [20], the effect on the measured emittance of smaller COTR effect with the heater on has not yet been determined.

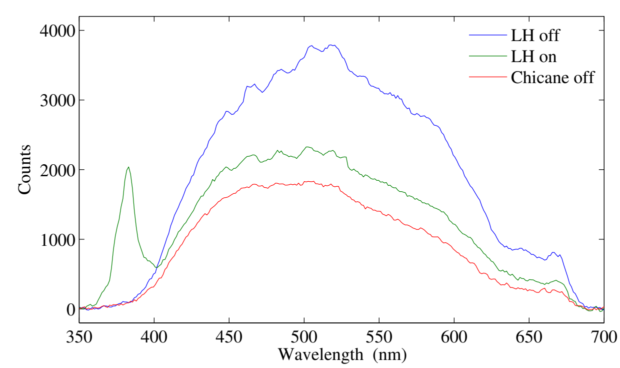

Figure 4: OTR spectrum after LCLS injector laser heater of 135 MeV beam and 150 pC charge. Incoherent spectrum with heater chicane turned off.

A different approach to change the beam phase space to suppress COTR emission was proposed in [21] for typical

ISBN 978-3-95450-134-2

injector beam energies. In this scheme a thick foil acts both as a spoiler to substantially increase the beam divergence and as the beam exits the foil to generate backwards OTR which is viewed via a downstream mirror. The increased beam divergence broadens the far-field COTR distribution which is equivalent to state that it limits the COTR source size and hence the ability of different parts of the beam to radiate coherently. While no direct implementation of this scheme has been reported, the suppression of COTR on downstream OTR screens by spoiling the beam emittance with inserted upstream OTR foils was observed at LCLS. The scheme has however limitations for high GeV beams where the required spoiler thickness to sufficiently increase the beam divergence becomes impractical.

Selective OTR Filtering

The different characteristics of OTR and COTR in terms of angular and spectral distribution can be utilized to preferably detect the OTR component and to suppress the COTR part. These techniques are also important for the use of scintillators as such crystals also represent a media boundary which emits OTR and consequently COTR.

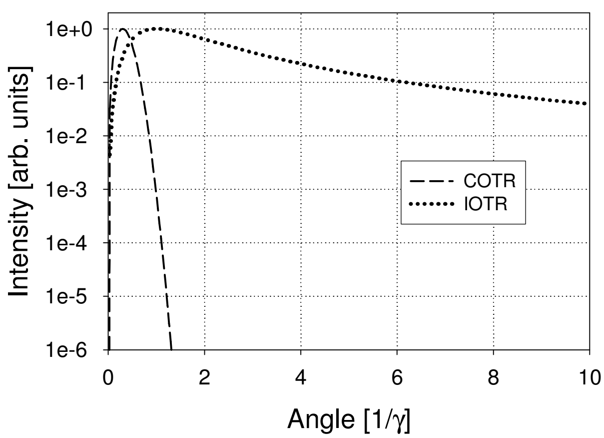

Figure 5: Comparison of the far-field angular emission distribution of COTR and incoherent OTR for an electron beam with 250 MeV LCLS beam parameters. From [22].

COTR is emitted from a larger source dimension than the OTR point spread function, and this size can be as large as the beam size for fully transverse coherent micro-bunching. This leads to a much narrower angular distribution of the COTR which can be exploited by spatially blocking the narrow COTR far-field cone in the Fourier plane of an imaging setup, while allowing the larger spatial frequencies of the incoherent OTR to pass.

The principle as proposed in [22] is shown in Fig. 5 where in case of the LCLS injector at 250 MeV the COTR emitted by the entire transverse extent of the beam is already completely suppressed within the $1/\gamma$ cone of the incoherent OTR. COTR emitted from smaller fractions of the transverse beam profile would however have much larger divergence and therefore be suppressed to a much lesser extent. Although no direct experimental verification of this scheme for OTR screens has been reported, it is now used in many scintillator screen applications to suppress COTR as described in the following section.

The strong wavelength dependence of the COTR as shown in Fig. 2 which has increasing intensity towards longer wavelength from the LSC instability gain [12] suggests spectral filtering of the OTR at shorter wavelengths where the relative COTR contribution can be smaller [13]. The COTR observed at the APS injector from a compressed beam at 325 MeV could be suppressed using a narrow bandpass filter at 400 nm, and the fluorescence from an LSO:Ce scintillator crystal did not exhibit any coherent effects.

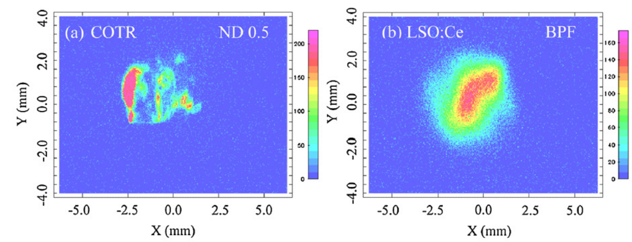

Figure 6: Spectral COTR mitigation using a 400 nm bandpass filter at the APS injector. From [13].

While this scheme can be successful for certain beam conditions with no micro-bunching gain at the blue end of the spectrum, it cannot be applied generally for highly compressed bunches with strong COTR intensity in the entire visible spectrum and possible beyond into the UV from few fs long current spikes. Much shorter wavelengths for OTR are necessary to utilize a spectral range with negligible bunching form-factor contributions.

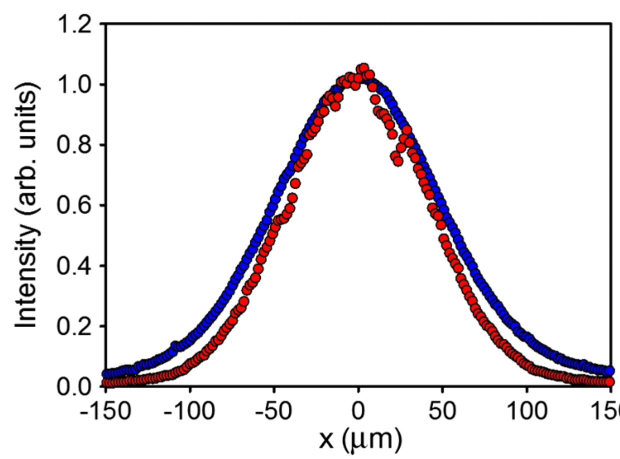

Figure 7: OTR beam profiles measured in the visible (blue) and in the EUV (red) for 855 MeV beam at MAMI. From [23].

Such OTR imaging has been proposed and demonstrated in the EUV [23]. As the OTR yield from a foil is essentially determined by the reflectivity at the respective wavelength, this is not a critical issue in the visible when using a metal foil, but becomes important at much shorter wavelengths. In this experiment at MAMI, a molybdenum target was used at a

ISBN 978-3-95450-134-2

grazing incidence angle for high reflectivity, and a multilayer spherical mirror was used to image the OTR onto a CCD camera. The reported somewhat smaller beam sizes in the EUV compared to the visible range are are shown in Fig. 7 and not yet fully understood. Although demonstrated as a viable beam size diagnostics, the complexity of the necessary in-vacuum setup makes this diagnostics not attractive for widespread use in an accelerator with multiple beam imaging stations.

OTR Avoidance Schemes

The most successful COTR mitigation scheme has been to avoid using OTR all together and instead use physical processes which do not probe the electron beam's Coulomb field at visible wavelengths. This is usually done via the detection of bremsstrahlung induced beam energy loss via scintillators or beam loss signal detection in wire scanners. The latter has been the main diagnostics where the observation of COTR made already installed OTR screens unreliable, e.g. at LCLS, but they only provide beam profiles and not images. Another mechanism which has been proposed is to use parametric x-rays (PXR) to generate a photon distribution proportional to the beam charge distribution which is then detected with a scintillator [24]. Since hard x-rays would be generated, the diagnostics should be impervious to coherence effects.

The renaissance of the scintillator raises again issues of resolution for small beam sizes and saturation for high charge densities as they were originally investigated [8]. Both were conveniently absent from OTR diagnostics which is only limited in resolution by the point spread function of typically sub-10 µm, and in charge density by material damage.

The scintillator resolution is mainly limited due to the crystal thickness and viewing geometry because the entire path of the beam through the crystal acts as a line source. The choice of thinner crystals with free-standing ones available as thin as 20 µm can shorten the length of the line source considerably and also limit beam losses from the beam interception with the crystal. The conventional geometry of a crystal oriented perpendicular to the beam with a downstream mirror or foil to direct the fluorescence away from the beam to a camera needs to be avoided to prevent additional COTR generation from the mirror. Extensive studies of the optimum viewing geometry without a mirror intercepting the beam as well were done in [25, 26] showing beam sizes measured from even a 300 µm thick LYSO crystal close to the OTR measurement for a 15 µm beam size as shown in Fig. 8. Even smaller vertical beam sizes of 7 µm from a 50 µm thick YAG crystal have been recently reported using a gated CCD [27].

Even when using a scintillating crystal, OTR and hence COTR are still generated at the entrance and exit boundaries of the crystal. The much larger efficiency of scintillators compared to OTR already provides a few orders of magnitude suppression. Furthermore, the same filtering as for OTR can be used here to suppress COTR much more effectively. Spatial filtering benefits from the nearly isotropic light emission from the scintillator and the COTR can be suppressed with a mask blocking the central COTR cone [28] or by tilting the YAG crystal to direct both the COTR from the crystal surface and a preceding viewing mirror away from the lens of the camera [6, 29]. In both cases no COTR could be observed from the respective screens. The same spatial separation is also implemented in the later discussed PSI profile monitor [30].

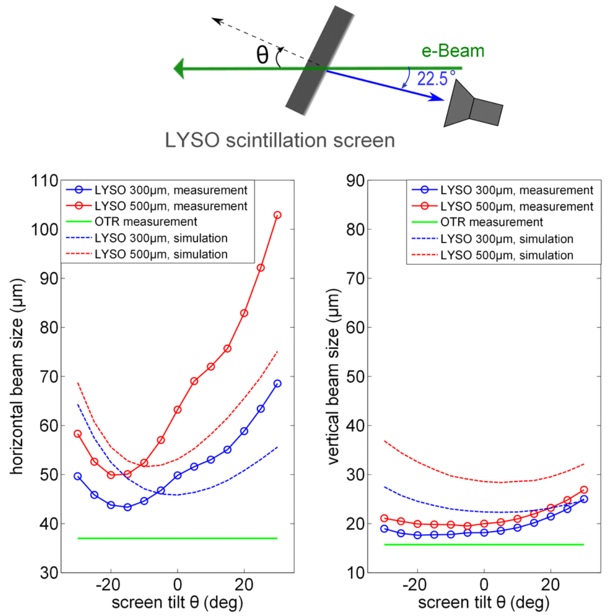

Figure 8: Measured beam sizes for LYSO crystals for various screen tilt angles compared to simulation and OTR measurement at MAMI. From [25].

Another effective method is to exploit the different time scales of the OTR and scintillation process. Whereas the OTR emission is prompt and happens within the duration of the bunch, the fluorescence in crystals typically used occurs with a lifetime of the order of 100 ns. By using a fast gated CCD camera, the trigger can be delayed w.r.t. the beam by 10s of ns so that the instantaneous COTR is blocked and only the fluorescent light emission is captured by the camera [31]. The complete disappearance of COTR effects from the LuAG screen can be seen in Fig. 9 when the camera trigger is delayed by 100 ns to the beam time.

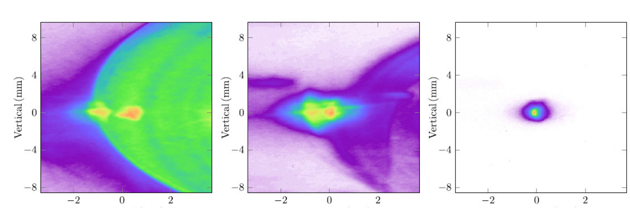

(a) OTR screen, no time delay. (b) LuAG screen, no time delay. (c) LuAG screen, time delay.

Figure 9: Beam images from OTR and LuAG screens for different trigger delays of a gated CCD showing COTR suppression in the delayed case at FLASH. From [31].

ISBN 978-3-95450-134-2

Whereas the temporal separation of scintillation and COTR light requires the use of expensive intensified CCD cameras, a combination of optimized tilt geometry of the scintillator and using a tilted image plane was developed for the profile monitor at PSI which uses standard cameras and is described in greater detail in the following section.

PSI PROFILE MONITOR

A COTR suppressing profile monitor was developed at PSI and has since been tested both in the SwissFEL test injector and at LCLS [30]. The design takes advantage of a tilted crystal geometry to separate the COTR from the desired fluorescence while maintaining the best screen resolution. The principle is shown in Fig. 10 demonstrating that a certain observation angle exists where the line that the beam prescribes while passing through the crystal will appear as a point to the observer. From the law of refraction this angle is given by $\beta = -\arcsin(n \sin\alpha)$ for a crystal tilt angle α. At the same time this observation angle will differ from the angle of specular reflection 2α which the COTR will be emitted, thus effectively directing the COTR away from the camera for a large enough tilt angle.

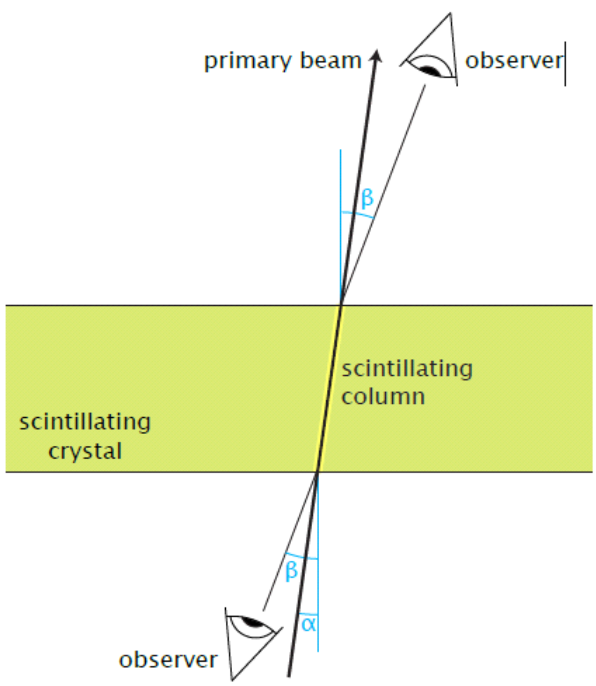

Figure 10: Diagram of the tilted crystal geometry showing the angles between the crystal normal, the beam axis, and the observation axis. From [30].

The implementation of the principle is shown in Fig. 11 with a 8.1° crystal tilt and an in-vacuum off-axis mirror to direct the fluorescence towards a CCD camera mounted at 90° to the beam axis. The COTR in this setup completely misses the in-vacuum mirror. The tilt of the crystal plane w.r.t. the camera viewing axis can be compensated by mounting the CCD with a similar tilt angle to the camera lens, but adjusted by the image magnification (Scheimpflug principle). This way the entire crystal can be in focus.

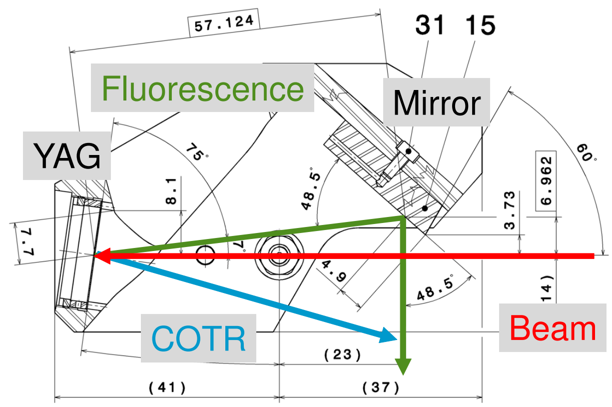

Figure 11: Schematic of the SwissFEL YAG screen. Adapted from [30].

At LCLS this profile monitor was installed in a diagnostics section upstream of the undulators where previously the largest COTR enhancement of about 10^5 was observed leading to camera destruction from the light intensity. The initially used 100 µm thick YAG crystal was soon replaced by a 100 µm version to limit the beam losses and enable 10 Hz beam operation, while stopping the beam at a tune-up dump upstream of the undulators. A number of beam tests were performed there at different beam energies and bunch charges, while varying the beam size, bunch compression, and having the injector laser heater on and off.

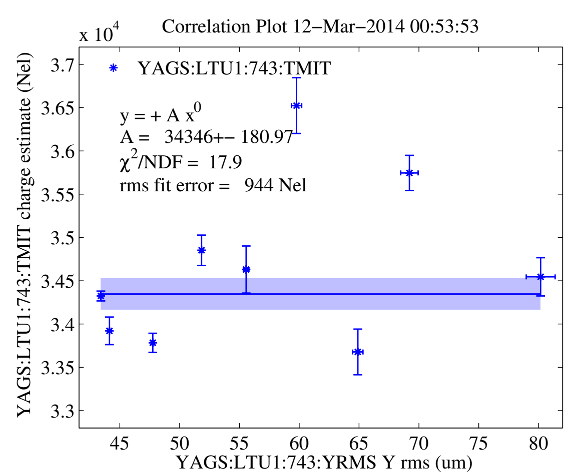

Figure 12: Test of saturation effect of the PSI profile monitor at LCLS for 13 GeV energy and 20 pC bunch charge. From [19].

Figure 12 shows a measurement of the integrated image intensity for various beam sizes at 20 pC and 13 GeV. The intensity varies by less than 10% in a non-systematic way without a visible drop at smaller charges, indicating that no saturation of the YAG fluorescence appears at this beam energy and charge density.

ISBN 978-3-95450-134-2

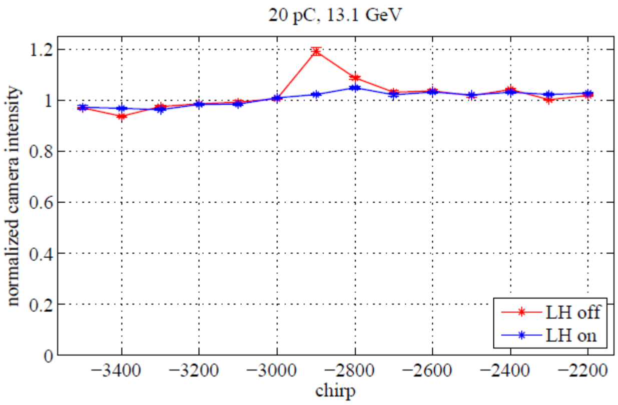

Figure 13: Integrated intensity from the PSI profile monitor at LCLS for different RF settings (chirp in MeV) at 20 pC charge. From [30].

Changing the accelerating RF phases and bunch compression, the suppression of COTR can be studied which is most prevalent at peak compression. Although no recent quantitative measurements of COTR at this location were available, it's presence could still be confirmed by the damage occurring to a CCD exposed to COTR from an OTR screen also mounted on the actuator as part of the PSI profile monitor. The results are shown in Figs. 13 and 14 at 13 GeV beam energy for 20 and 150 pC, respectively.

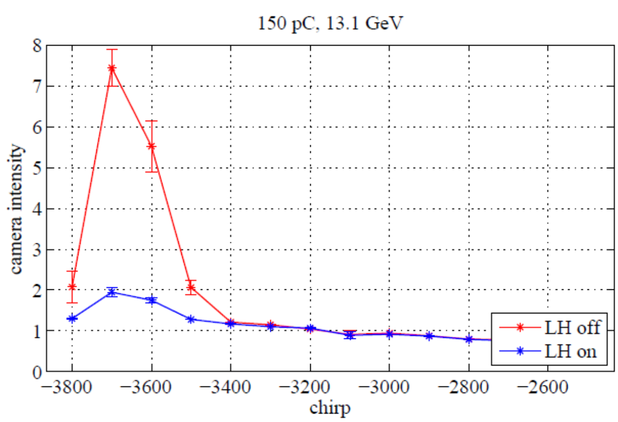

Figure 14: Same as previous figure for 150 pC. From [30].

Both measurements with the injector laser heater on and off are shown. For the low charge case, only a small increase in light intensity at the peak compression setting can be observed without the laser heater, which disappears completely when it is turned on. For the higher charge case, significant intensity enhancement by a factor of seven is still observed for the highest compression settings (corresponding to above 5 kA peak current) while for the normally used LCLS bunch compression settings of less than 4 kA only a minor change can be seen. When the laser heater is turned on, the enhancement at peak compression is reduced to less than a factor two, which can still be detrimental to beam size measurements. However, while previously the laser heater was only able to partially suppress COTR on the LCLS OTR screens, now a complete suppression for most beam setups on the YAG screen can be achieved.

Presently, an upgrade is underway using a different in-vacuum mirror to avoid coherent diffraction radiation being emitted from the edge of the mirror which points directly towards the camera.

The remaining enhancement can be understood as fluorescence being incited in the crystal via bunch form-factor components in the UV or shorter wavelengths which generate coherent radiation traveling through the crystal at these wavelengths. Strong indication for this effect could also be observed in the beam overlap diagnostics used in the LCLS soft x-ray self-seeding setup [32] where the electron beam passes by a 20 µm thick YAG crystal within a few mm. In the setup, an annular mirror prevents a direct path of coherent diffraction radiation from the crystal towards the camera, yet strong coherent light effects can be seen [19] which are also attributed to the same effect.

SUMMARY

The coherence effects seen in high brightness accelerators for x-ray FELs have made the use of standard OTR screen unfeasible for most situations after the bunches have been compressed or LSC instability gain has created micro-bunching. Mitigation schemes for OTR screens themselves were not successful in fully suppressing COTR with the option remaining to move to much shorted detection wavelengths. However, scintillator screens have reemerged as a viable alternative with demonstrated resolution at the 10 µm level. Temporal and spatial separation have been demonstrated to sufficiently suppress COTR in most cases. Scintillator screens using spatial COTR separation schemes are now planned for several XFEL projects under construction.

REFERENCES

[1] P. Emma, R. Akre, J. Arthur, R. Bionta, C. Bostedt, *et al.* Nature Photon. 4 (2010), 641.

[2] T. Ishikawa, *et al.* Nature Photon. 6 (2012), 540.

[3] *The european x-ray free-electron laser technical design report*. Technical Report DESY 2006-097, DESY (2007).

[4] H. S. Kang, K.-W. Kim, I. S. Ko. Proceedings of the 2015 International Particle Accelerator Conference, Richmond, VA. p. WEYC2 (2015).

[5] *SwissFEL conceptual design report*. Technical Report 10-04, Paul Scherrer Institut (2012).

[6] C. Behrens, F.-J. Decker, Y. Ding, V. Dolgashev, J. Frisch, *et al.* Nature Commun. 5 (2014), 3762.

[7] B. Yang, J. L. Bailey, D. R. Walters, S. J. Stein. Proceedings of the 2005 Particle Accelerator Conference, Knoxville, TN. pp. 4209–4211 (2005).

[8] A. Murokh, J. Rosenzweig, I. Ben-Zvi, X. Wang, V. Yakimenko. Proceedings of the 2001 Particle Accelerator Conference, Chicago, IL. pp. 1333–1335 (2001).

[9] R. Akre, D. Dowell, P. Emma, J. Frisch, S. Gilevich, *et al.* Phys. Rev. ST Accel. Beams 11 (2008), 030703.

ISBN 978-3-95450-134-2

[10] A. H. Lumpkin, R. Dejus, J. Lewellen, W. Berg, S. Biedron, *et al.* Phys. Rev. Lett. 88 (2002), 234801.

[11] H. Loos, *et al.* Proceedings of the 2008 FEL Conference, Gyeongju, Korea. pp. 166–172 (2008).

[12] D. Ratner, A. Chao, Z. Huang. Proceedings of the 2008 FEL Conference, Gyeongju, Korea. pp. 338–341 (2008).

[13] A. Lumpkin, N. Sereno, W. J. Berg, M. Borland, Y. Li, *et al.* Phys. Rev. ST Accel. Beams 12 (2009), 080702.

[14] S. Wesch, B. Schmidt. Proceedings of the 2011 DIPAC Conference, Hamburg, Germany. pp. 539–543 (2011).

[15] S. Weathersby, M. Dunning, C. Hast, K. Jobe, D. McCormick, *et al.* Proceedings of the 2011 PAC Conference, New York, NY. pp. 2426–2428 (2011).

[16] K. Togawa, *et al.* Proc. of the Fifth Microbunching Instability Workshop, Pohang, Korea (2013).

[17] A. H. Lumpkin. Proceedings of the 2013 FEL Conference, New York, NY. pp. 169–172 (2013).

[18] Z. Huang, A. Brachmann, F.-J. Decker, Y. Ding, D. Dowell, *et al.* Phys. Rev. ST Accel. Beams 13 (2010), 020703.

[19] H. Loos. Proceedings of the 2014 IBIC Conference, Monterey, CA. pp. 475–485 (2014).

[20] F. Zhou, K. Bane, Y. Ding, Z. Huang, H. Loos, *et al.* Phys. Rev. ST Accel. Beams 18 (2015), 050702.

[21] A. Murokh, E. Hemsing, J. Rosenzweig. Proceedings of the 2009 Particle Accelerator Conference, Vancouver, BC. pp. 3991–3993 (2009).

[22] R. B. Fiorito. Proceedings of the 2009 Particle Accelerator Conference, Vancouver, BC. pp. 741–745 (2009).

[23] L. G. Sukhikh, G. Kube, S. Bajt, W. Lauth, Yu, *et al.* Phys. Rev. ST Accel. Beams 17 (2014), 112805.

[24] A. Gogolev, A. Potylitsyn, G. Kube. Journal of Physics: Conference Series 357 (2012), 012018.

[25] M. Yan, C. Behrens, C. Gerth, G. Kube, B. Schmidt, *et al.* Proceedings of the 2011 DIPAC Conference, Hamburg, Germany. pp. 440–442 (2011).

[26] G. Kube, C. Behrens, C. Gerth, B. Schmidt, M. Yan, *et al.* Proceedings of the 2012 IPAC Conference, New Orleans, LA. pp. 2119–2121 (2012).

[27] T. Naito, T. Mitsuhashi. Proceedings of the 2014 IBIC Conference, Monterey, CA. pp. 426–429 (2014).

[28] H. Tanaka. Proceedings of the 2011 IPAC Conference, San Sebastian, Spain. pp. 21–25 (2011).

[29] H. Loos, *et al.* Proceedings of the 2010 Beam Instrumentation Workshop, Santa Fe, NM. pp. 34–43 (2010).

[30] R. Ischebeck, E. Prat, V. Schlott, V. Thominet, M. Yan, *et al.* Proceedings of the 2014 IBIC Conference, Monterey, CA. pp. 259–262 (2014).

[31] C. Behrens, C. Gerth, G. Kube, B. Schmidt, S. Wesch, *et al.* Phys. Rev. ST Accel. Beams 15 (2012), 062801.

[32] D. Ratner, R. Abela, J. Amann, C. Behrens, D. Bohler, *et al.* Phys. Rev. Lett. 5 (2015), 054801.

ISBN 978-3-95450-134-2

DIFFRACTION RADIATION MONITOR

Y. Taira#, AIST, Tsukuba, Japan

Abstract

Diffraction radiation is one of non-destructive electron beam diagnostic techniques. A circular aperture, rectangular slit, and edge are used as a diffraction radiation targets. A transverse size, divergence, bunch charge, position, and bunch length can be measured by analysing a spatial distribution of DR. In the case of that the electron beam energy is low and the bunch length of the electron beam is in the range of few ps to sub-ps, coherently enhanced diffraction radiation with the wavelength of sub-mm to mm range is used. A spatial distribution of coherently enhanced diffraction radiation generated from an edge and slit was measured with a terahertz camera.

INTRODUCTION

Diffraction radiation (DR) is generated when a charged particle moves in the vicinity of a boundary between two media with different dielectric constants. The charged particle does not directly interact with the material. An electric field with an effective electric field radius of $\gamma\lambda/2\pi$ (γ is the Lorentz factor of the charged particle, λ is the observed wavelength of DR) interact with the material. In the condition that the distance between the charged particle and the boundary, d, is larger than the effective electric field radius, no radiation generats. The boundary gets close to the charged particle, DR is generated.

DR is mainly used for the non-destructive electron beam diagnostics. Visible wavelength of DR is usually used for the beam diagnostic of a high energy electron beam. Beam size measurement as small as 14 µm was achieved at KEK-ATF by a rectangular slit [1]. Simultaneous measurement of the beam size, divergence, and position of the electron beam was proposed and experimentally investigated at the FLASH, DESY [2].

On the other hand, long wavelength of DR is used for low energy electron beam diagnostics. If the Lorentz factor and wavelength of DR are 100 and 500 nm, the effective electric field radius is calculated to be 8.0 µm. This value is much smaller than the typical beam size. Thus, long wavelength of DR such as a far-infrared or terahertz radiation have to be measured. When $\gamma = 80$ and $\lambda = 0.2$ mm, the effective electric field radius is calculated to be 2.5 mm. This value is much larger than the typical beam size and a fabrication of the mechanical slit is also easy.

Long wavelength radiation of DR is generated via coherent radiation. Coherent radiation is generated when the electron bunch length is much smaller than the wavelength of DR generated from the electron. Frequency spectrum of coherent radiation is strongly depended on the electron bunch length. Thus the beam diagnostic using the coherent diffraction radiation (CDR) is applied to the bunch length measurement at the low energy electron beam facilities [3-6].

In the previous research [7], feasibility study of beam position measurement using CDR generated from the slit was reported. It was found that an asymmetry distribution of CDR was sensitive to the beam position with respect to the slit center.

In this proceedings, spatial distribution and relative intensity of CDR generated from an edge and slit is reported to make clear the basic properties of CDR.

#yoshitaka-taira@aist.go.jp

EXPERIMENT SETUP

Spatial distribution measurement of CDR was conducted at an S-band compact electron linac at AIST. The electron beam was generated from a photocathode RF gun and accelerated up to 40 MeV by two accelerating tubes. Number of bunch in the macro pulse was 23 and repetition rate of the macro pulse was 25 Hz. The electron beam was then compressed in the longitudinal direction at an achromatic arc section. The compressed electron beam passed through a slit target for generating CDR. The electron beam size was controlled by three quadrupole magnets installed in the upper stream of the slit target. The bunch charge was 0.1 ~ 0.3 nC/bunch.

Schematic illustration of the spatial distribution measurement of CDR is shown in Fig. 1. The slit target was tilted at 45 degree. Thus the backward CDR was emitted toward the perpendicular direction against the electron beam trajectory. Backward CDR was collimated by a 100 mm focal length lens and leaves the vacuum duct through a z-cut crystal quartz window with the thickness of 9 mm. The radiation was then reflected by two silver mirrors, and passes through a wire grid linear polarizer (Specac, GS57203), a lens with the focal length of 50 mm, infrared blocking filter (NEC, IRV-TF030),

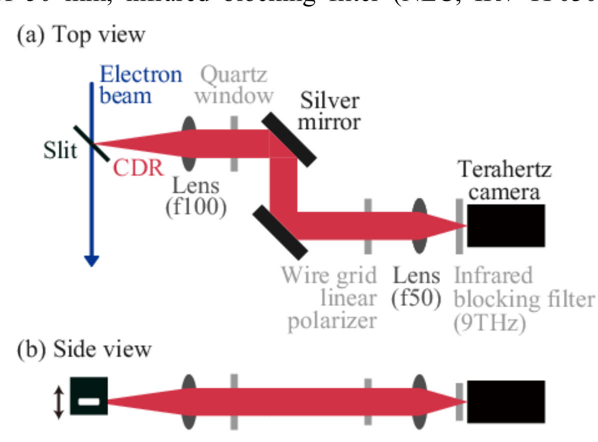

Figure 1: Schematic illustration of the spatial distribution measurement of CDR using a terahertz camera.

ISBN 978-3-95450-134-2

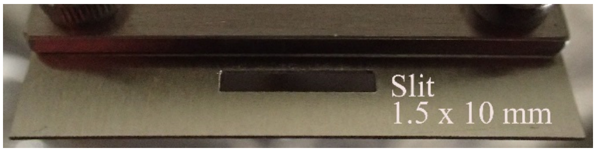

Figure 2: Picture of the rectangular slit target with the dimension of 1.5 mm x 10 mm and edge for generating the CDR.

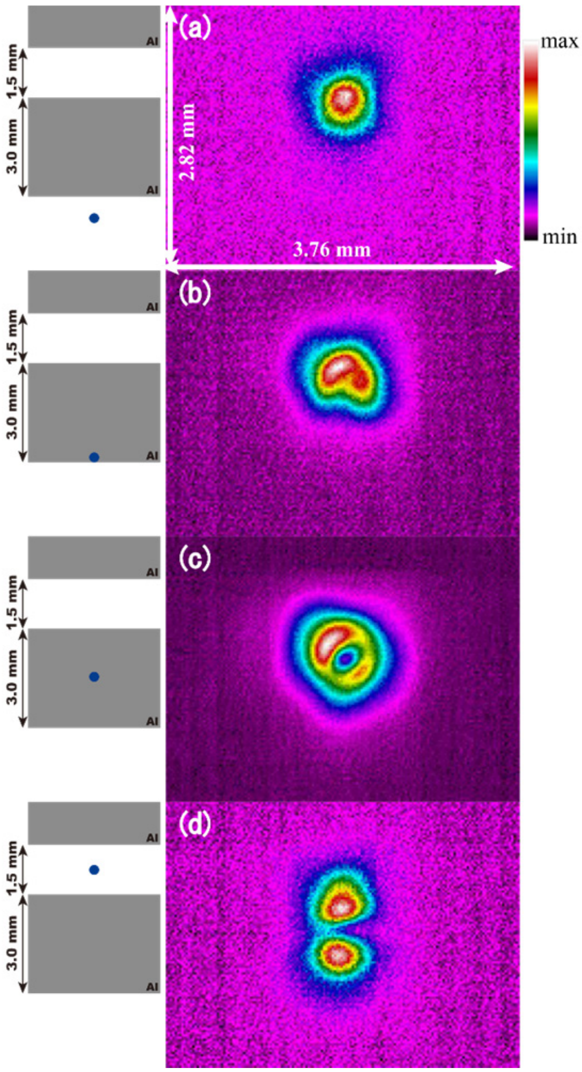

Figure 3: Spatial distribution of the CDR and CTR measured with the terahertz camera. (a) CDR: The electron beam passed in vacuum where 0.7 mm away from the edge. (b) CDR+CTR: The electron beam passed through the aluminium where 0.2 mm inside from the edge. (c) CTR: The electron beam passed through the central of the semi-plane. (d) CDR: The electron beam passed through the central of the rectangular slit.

and finally detected by a terahertz camera (NEC, IRV-T0832). In the experimental condition, the terahertz camera mainly detected the frequency of 1.5 THz. Thus the effective electric field radius is calculated to be 2.5 mm.

An image of the rectangular slit and edge target is shown in Fig. 2. The slit was made a hole with the dimension of 1.5 mm x 10 mm in 0.5 mm thick aluminium. There are semi-plane to generate coherent transition radiation (CTR) with the width of 3 mm under the rectangular slit. We also used the edge of semi-plane to generate the CDR. The slit target was fixed to the holder mounted on a linear manipulator. Thus the slit can be moved in the vertical direction against the beam trajectory. In order to observe the CDR, the beam trajectory and the beam size of the electron beam have to be adjusted. First, the spatial distribution of CTR emitted from the semi-plane was checked. The beam parameters were adjusted to obtain the ring profile of CTR. Then, we measured the spatial distribution of CDR.

RESULTS AND DISCUSSION

Figure 3 shows the spatial distribution of CDR and CTR measured with the terahertz camera.

The spatial distribution of CDR emitted from the edge of the semi-plane is shown in Fig. 3 (a). The electron beam moved in a position where 0.7 mm away from the edge of the semi-plane. The spatial distribution with a single peak was observed.

If the electron passed a position where a lower side of semi-plane, the distribution is changed like a new moon as shown in Fig. 3(b). This is because a low frequency component of CDR is suppressed. The semi-plane is cut at the distance shorter than the wavelength of low frequency CDR. Terahertz camera has a low sensitivity for long wavelength terahertz radiation. Thus the intensity of lower side is decreased.

When the electron passed through the central position in semi-plane, the distribution is almost similar to the CTR (Fig. 3 (c)).

If the electron passed through the center of the slit, main intensity is aligned along the vertical direction (Fig. 3 (d)). This result is similar to the distribution which is measured with the slit width of 1.0 mm [7].

Normalized total counts in area detecting the CDR is shown in Fig. 4. Total counts of background is subtracted. The measurement was carried out at three times. The plus symbol in Fig. 4 shows that the edge of the semi-plane got close to the electron. The target was moved at 80 μm step. The cross symbol in Fig. 4 is the CDR generated from the edge and slit was measured. The target was moved at 200 μm step. The square symbol in Fig. 4 is the vertically polarized CDR generated from the slit by moving the target at 120 μm step. No CDR was observed when the distance between the electron and the edge of the semi-plane was larger than the effective electric field radius. The total counts was increased as the edge of the semi-plane got close. Total counts was maximized at around the center of the semi-plane and was decreased as the edge of slit got close. Once the total counts was minimized at the slit center. It was slightly increased as the upper side edge of the slit got close, however, it was immediately decreased. Originally, the total intensity

ISBN 978-3-95450-134-2

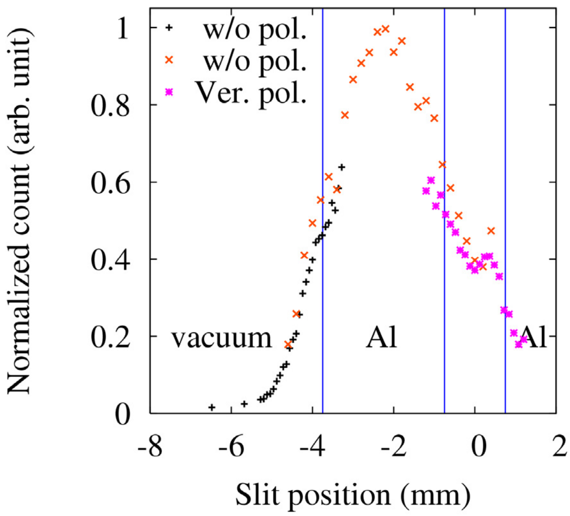

Figure 4: Normalized total counts in area the CDR is detected. The plus and cross symbols are the normalized counts when the polarizer was not used. The square symbol is the normalized counts of the vertically polarized component.

inside the slit describes a parabolic curve as observed in Ref [3]. A decline of the total counts around the upper edge of the slit is due to a structural asymmetry around the slit. There are a material of a holder on the slit.

CONCLUSION

Spatial distribution and relative intensity of CDR generated from the edge and slit target was measured with the terahertz camera. No radiation was observed when the distance is longer than the effective electric field radius of CDR. The spatial distribution of CDR is dramatically changed by the target position. In the near future, spatial distribution of horizontally polarized and vertically polarized CDR generated from the edge and slit will be measured with the polarizer and be compared with a calculation.

REFERENCES

[1] P. Karataev et al., Phys. Rev. Lett. 93, 244802 (2004).

[2] A. Cianchi et al., Phys. Rev. ST Accel. Beams 14, 102803 (2011).

[3] M. Castellano et al., Phys. Rev. E 63, 056501 (2001).

[4] A. H. Lumpkin et al., Nucl. Instr. Meth. Phys. Res. A 475, 470 (2001).

[5] X. Dao et al., Chin. Phys. Lett. 25, 2440 (2008).

[6] M. Veronese et al., Phys. Rev. Lett. 110, 074802 (2013).

[7] Y. Taira et al., TUPD12, Proceedings of IBIC2014, 442, (2014).

ISBN 978-3-95450-134-2

FIRST RESULTS OF THE SRF GUN TEST FOR CeC PoP EXPERIMENT*

I. Pinayev#, Z. Altinbas, S. Belomestnykh, K. Brown, J.C. Brutus, A. Curcio, A. Di Lieto, C. Folz, D. Gassner, M. Harvey, J. Jamilkowski, Y. Jing, D. Kayran, R. Kellerman, R. Lambiase, V.N. Litvinenko, G. Mahler, M. Mapes, W. Meng, T. Miller, M. Minty, G. Narayan, P. Orfin, T. Rao, J. Reich, B. Sheehy, J. Skaritka, L. Smart, K. Smith, L. Snydstrup, V. Soria, R. Than, C. Theisen, J. Tuozollo, E. Wang, G, Wang, B. Xiao, T . Xin, W. Xu, A. Zaltsman, BNL, Upton, NY 11973, USA

Abstract

We have started the first tests of the equipment for the coherent electron cooling proof-of-principle experiment. After tests of the 500 MHz normal conducting cavities we proceeded with the low power beam tests of a CW SRF gun. The results of the tests with record beam parameters are presented.

INTRODUCTION

The coherent electron cooling experiment (CeC PoP) [1, 2] is expected to demonstrate cooling of a single hadron bunch in RHIC. A superconducting RF gun operating at 112 MHz frequencies generates the electron beam. 500-MHz normal conducting cavities provide energy chirp for ballistic compression of the beam. 704-MHz superconducting cavity will accelerate beam to the final energy. The electron beam merges with the hadron beam and after cooling process is steered to a dump. The FEL-like structure enhances the electron-hadron interaction. The electron beam parameters are shown in the Table 1.

Table 1: Parameters of the Electron Beam

Parameter	Value
Energy	22 MeV
Bunch charge	1-5 nC
Normalized emittance	< 5 mm mrad
Energy spread	< 10^{-3}

GUN DESIGN

The CeC PoP gun has quarter-wave structure and operates at 113 MHz. Its design is shown in Fig. 1. The gun cavity is placed inside cryostat with thermal and magnetic shields. The cathode stalk is inserted into cone and is kept at room temperature. Such design allows having at room temperature a CsK_2Sb cathode, which is inserted inside of the stalk. The stalk itself serves as a cavity field pick-up.

The hollow fundamental power coupler (FPC) is inserted from the flat side of the cavity and let the generated beam go outside. The RF power is provided by a 2-kW solid-state amplifier. The FPC is surrounded by a gun solenoid, which is the first focusing element.

The cavity is coarsely tuned with two manual tuners while the fine frequency change is performed with help of the FPC, which is placed on a translation stage.

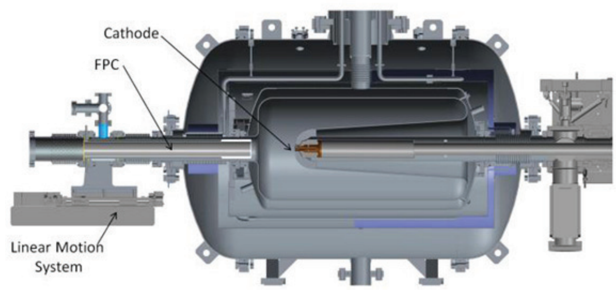

Figure 1: Layout of the superconducting gun.

The fundamental power coupler is followed by a laser cross which serve for launching of the drive laser beam onto the cathode and allows to serve the cathode as well.

TEST SET-UP

The tests performed were done with partially installed equipment and the components are shown in Fig. 2. The main systems components are:

- cathode manipulation system with “garage”, which serves for storage and insertion of the photocathodes.
- the gun itself.
- six solenoids for beam focusing.
- two copper 500 MHz cavities for energy chirp.
- beam diagnostics.
- drive laser.

A brief description of each system is below.

Drive Laser

The drive laser is Picolo AOT-1 built by Innolas. It generates up to 6 μJ pulse at 532 nm wavelength. The pulse duration is 0.7 ps and maximal repetition rate is 5 kHz. The initial r.m.s. spot size on the cathode is 1.5 mm. This laser is used for the test only an will be replaced with a new one capable to generate 78 kHz pulses with 1 kW peak power and tunable pulse length.

Diagnostics

The beam diagnostics include integrated current transformer (ICT) with sensitivity of 0.8 nV s/nC. During test the ICT output was connected to the LeCroy digital oscilloscope. The ICT is installed immediately after the laser cross allowing observing beam leaving the gun.

*Work supported by Department of Energy
#pinayev@nnl.gov

ISBN 978-3-95450-134-2

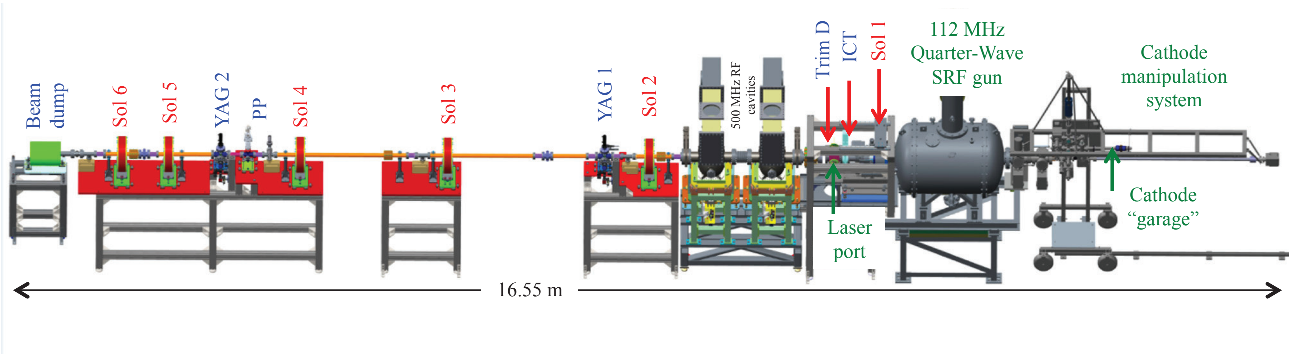

Figure 2: Rendering of the test set-up for the gun test. The overall length is about 16 meters. The gun on the right has cathode launch mechanism attached.

The transverse beam profile can viewed with two profile monitors equipped with 1.3 MP GigE cameras. In front of the second profile monitor there is a set of slits for the emittance measurement of the beam.

Beam position can be monitored with two BPMs with Libera Single Pass E+ receivers.

The beamline was terminated with low power (uncooled) beam dump, which also can serve as Faraday cup.

TEST PREPARATION

There was substantial amount of preparation job performed before he successful beam observation. The main hurdle was multipacting in the cavity and cathode stalk. One of the problematic spots was fundamental power couple, which is inside the first solenoid and has a bellow in the same location. The multipacting was suppressed by lengthy conditioning. We also observed multipacting after insertion of the photocathode. The multipacting zone was on the cathode side also coated with photoemissive material, which has tremendous secondary emission coefficient. We withdraw a cathode a performed laser cleaning of the side. Such operation required rejuvenation of the cathode by heating to 80ºC [3].

In order to suppress the cold emitters we employed helium processing of the cavity surface by letting small amount of helium into the cavity exciting it with available power.

We also observed substantial pressure spikes during the cathode transfer. We added a few NEG cartridges to improve vacuum in the system.

It needs to be mentioned that we have access to the system only for one day each two weeks during RHIC maintenance. Such circumstances substantially delayed project progress.

BEAM OBSERVATION

The tests were performed at the end of RHIC in parallel with condition of one of the RF cavities. We have much easier access to the tunnel.

We were able to observe beam charge after phase scan. The charge value was 0.5 nC. We found that beam current is limited by the space charge forces and increased the laser sport size by 50%. After this operation we were able to observe 3-nC beam charge (see Fig. 3).

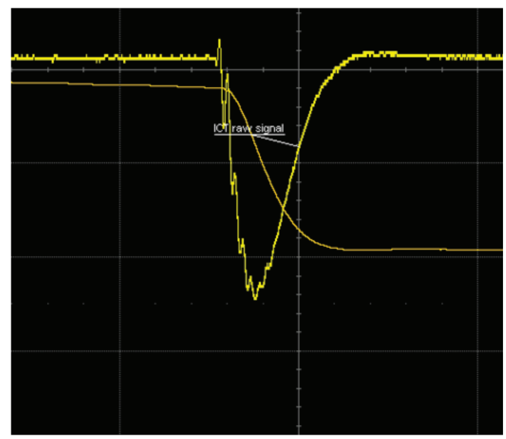

Figure 3: Trace of the ICT signal on the LeCroy oscilloscope. The pulse area indicated by built-in application is 3.6 nV s.

We increased the pulse rate to the maximum and generated 15 μA photocurrent. We tried to observe beam on the first profile monitor but were able to see only faint image on the edge of the fluorescent screen.

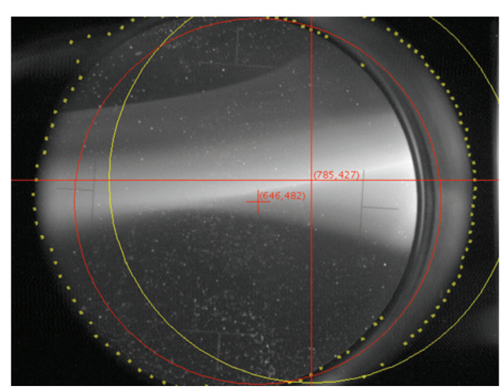

Figure 4: Image generated by dark current on the first beam profile monitor.

We found that one ion pump next to the laser cross has substantial, 200 Gs, stray magnetic field. The yoke of the

ISBN 978-3-95450-134-2

pump was removed to avoid the beam steering. Unfortunately, by this time the quantum efficiency of the cathode was essentially zero. Nevertheless we were able to observe dark current on the first and later on the second profile monitors.

ENERGY MEASUREMENT

We performed calibration of the field pick-up by measuring beam displacement on the first profile monitor with varying of calibrated trim placed after the first solenoid. No other focusing elements were utilized. The dependence of beam position on the trim current is shown in Fig. 5.

Using this measurement as the calibration point, we determined that we generated photo-emitted electron beam with kinetic energies between 1.6 and 1.7 MeV according to our logged RF pick-up data. We used an expected ratio of 1.02 between the energy of photoelectrons emitted at 78.5º of RF phase, compared with energy of dark current beam peaking at the crest (e.g. at 90º). We also used this calibration to determine that in pulsed mode of SRF gun operation the kinetic energy of the beam exceeded 2 MeV.

CONCLUSION

We had proven experimentally that SRF gun can operate with high efficiency CsK_2Sb photocathode and generate CW electron beam with record-high charge per bunch, which is accelerating in record high field.

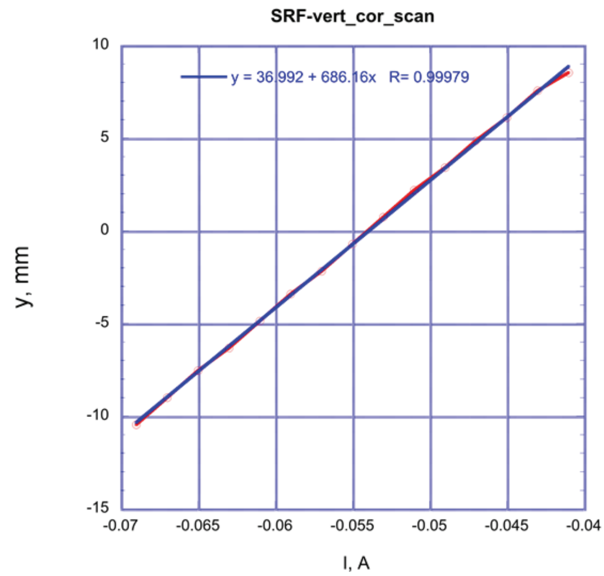

Figure 5: Dependence of beam position on the first profile monitor on the vertical trim current. The corresponding RF voltage is 1.6 MV.

REFERENCES

[1] V.N. Litvinenko *et al.*, "Proof-of-principle Experiment for FEL-based Coherent Electron Cooling", THOBN3, PAC'11.

[2] I. Pinayev *et al.*, "Present Status Of Coherent Electron Cooling Proof Of Principle Experiment", WEPPO14, COOL 2013.

[3] E. Wang *et al.*, In Proc. of ERL2015.

ISBN 978-3-95450-134-2

SwissFEL STATUS REPORT

R. Ganter on behalf of the SwissFEL team, PSI, Villigen, Switzerland

Abstract

SwissFEL is a 5.8-GeV linac which sends electron bunches at 100 Hz into a 60-m long in-vacuum undulator line to produce hard X-rays between 0.1 nm and 0.7 nm (Aramis line). The SwissFEL machine design is based on a low emittance beam with tight tolerances on RF phase stability. The first lasing of SwissFEL is planned for early 2017 and two end-stations should then be brought into operation in the same year. The delivery of the SwissFEL building to PSI is planned for fall this year, but some rooms are already completed and currently in use for component assembly. The production of the C-band RF accelerating structures has now reached the nominal rate of 5 structures/month. Two different RF solid-state modulator prototypes have demonstrated voltage pulse stability lower than 20 ppm but reliability tests are still ongoing. The undulator assembly and measurement sequences have started and 13 undulators are planned to be ready in the tunnel by October 2016. Large series of components like magnets, vacuum systems and mechanical supports are already in house and undergoing assembly. Photonics components for beamlines and for two end stations are ordered and planned to be ready for 2017. The next important milestone is the commissioning of the injector, the first 120 meters, in Spring 2016.

INTRODUCTION

The overall layout of SwissFEL is shown in Fig. 1. In order to tune the FEL wavelength of Aramis between 1 and 7 Angström, the electron beam energy can be varied between 2.1 and 5.8 GeV. This is achieved with Linac 3 which either accelerates or decelerates the beam. This enables the energy at the extraction point towards Athos (end of Linac 2) to stay always constant and equal to 3 GeV. Genesis simulations, assuming a slice emittance of 0.2 µm, lead to a pulse energy as high as 1.4 mJ at 1 Å in the case of long pulses with 200-pC charge (Fig. 2). At the end of the undulator line, electrons are deviated vertically down towards a 240-ton shielded beam dump [1]. The SwissFEL injector will produce two bunches separated by 28 ns at a repetition rate of 100 Hz. The second bunch is deflected after Linac 2 in the transfer line (Fig. 1) towards the soft X-ray Athos line.

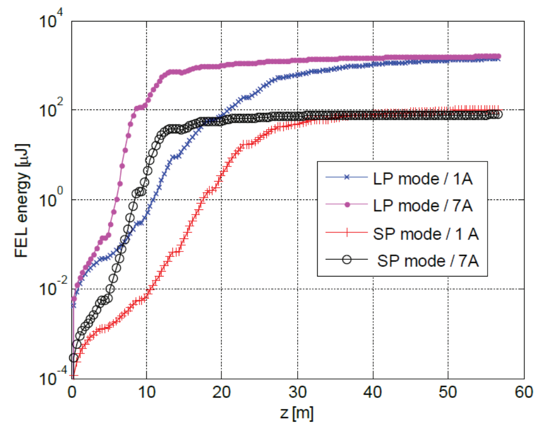

Figure 2: Genesis simulation of FEL pulse energy growth for two bunch charges, 200-pC long pulses (LP) and 10-pC short pulses (SP), and for two wavelengths: 1 and 7 Angström (graph from [2]).

STATUS OF BUILDING AND INFRASTRUCTURE

SwissFEL is a two-storey building from cathode source (z = 0 m) to the end of last linac (z ~ 460 m). All the RF power plants as well as the rest of the infrastructure are situated on the top floor. As a consequence, all the cabling and cooling lines come down from the ceiling as can be seen in the pictures of Fig. 3.

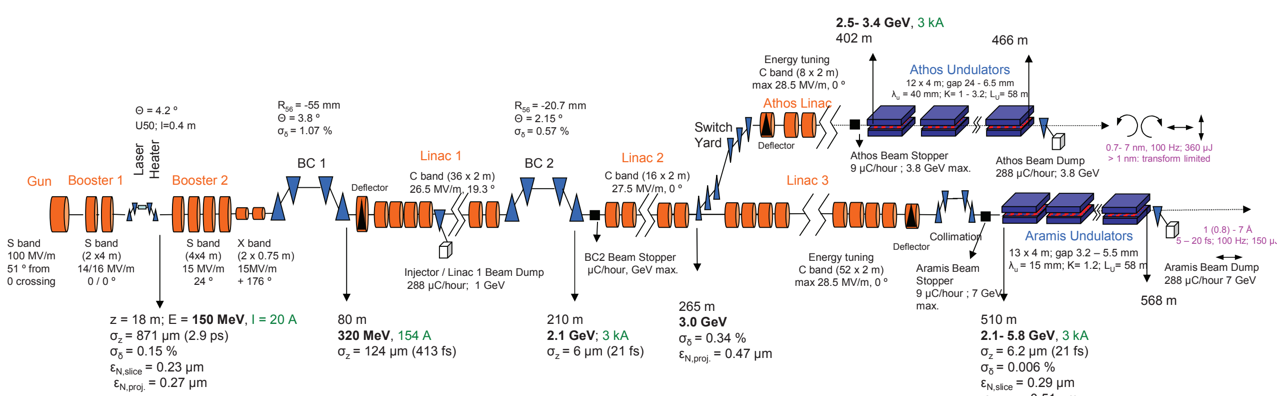

Figure 1: SwissFEL layout with the hard X-ray FEL line Aramis and the future Athos line to be built after 2018 (some parameters are merely indicative and only valid for a specific mode of operation).

ISBN 978-3-95450-134-2

The raw construction of the building is completed as illustrated in Fig. 3. Electrical and water infrastructure is currently being installed until Fall 2015. The Aramis undulator line is located in a single floor building and most of the electronic infrastructure is situated in the gallery beside the tunnel.

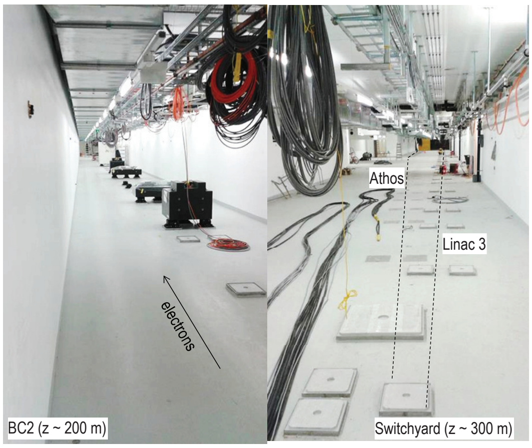

Figure 3: Pictures of the SwissFEL beam tunnel at z = 200 m (distance from cathode), near BC2, and at z = 300m, near switchyard.

The hard X-ray optical components are located in the optical hutch downstream of the front end wall of the Aramis undulator line (Fig. 3). The FEL pulses are then distributed over three end stations: A, B and C. The completion of the building is planned for Fall 2015, but some areas are already used by PSI for the assembly of components such as the injector part of the tunnel or the undulator preparation laboratory.

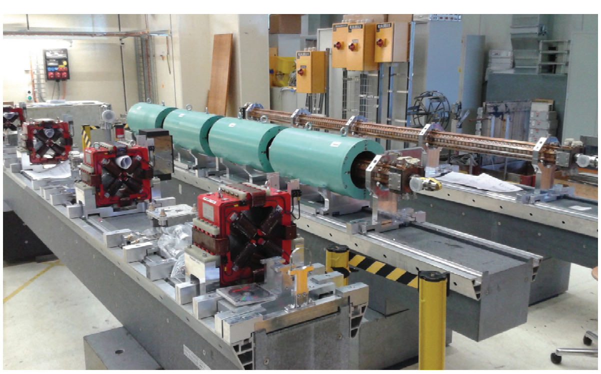

Figure 4: Injector girders assembled with new S band structures in the SITF building.

STATUS COMPONENTS

The SwissFEL injector test facility (SITF) was shut down in October 2014 after four years of operation. Many components will be re-used for the SwissFEL injector and the pre-assembly of girders has started in the SITF building (Fig. 4). The S-band RF structures are new, with a constant gradient RF design and dual-feed racetrack couplers. The C-band structure production has now reached a nominal rate of five structures per month (Fig. 5). In July 2015, 46 units out of 104 were already brazed and ready for conditioning at SwissFEL. One of the structures was conditioned up to 52 MV/m and showed a negligible breakdown rate at the nominal gradient of 28 MV/m. The BOC cavities are produced and brazed in house and 16 BOCs out of 27 are now ready for installation.

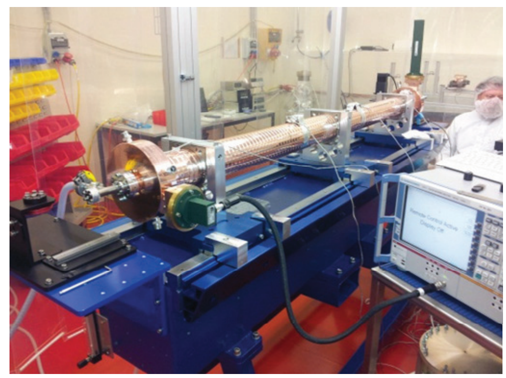

Figure 5: Picture of a newly produced C-band structure under RF frequency check after brazing.

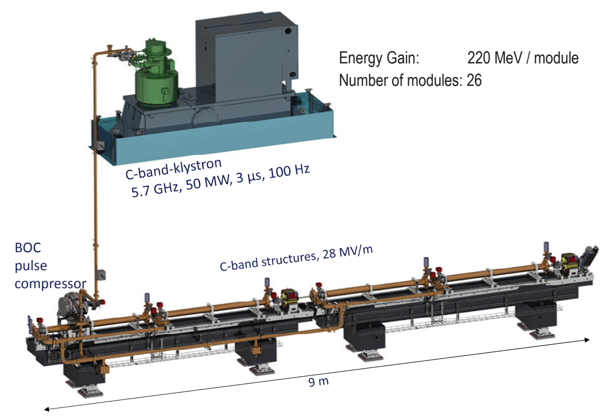

Figure 6: 3D Drawing of an RF module with the klystron–modulator assembly powering four C–band structures of 2-m length each.

There are twenty six C-band RF modules distributed over three linacs in order to accelerate the electron beam from 0.35 GeV to 5.8 GeV. Each module (Fig. 6) consists of four structures of 2-m length [3]. The RF power is generated by a solid state modulator coupled to a C-band klystron producing 3-microsecond-long pulses at 100 Hz with 50 MW of power. These pulses are then compressed to 300 MW thanks to an RF pulse compressor; the so-called barrel open cavity (BOC) [4]. This peak power allows a gradient of 28 MV/m (with 10% margin) leading to an energy gain of 220 MeV per module.

ISBN 978-3-95450-134-2

The solid-state RF modulator is a key component for SwissFEL since the accelerator design for a low emittance beam requires a very good stability level of the RF phase which means a modulator voltage pulse-to-pulse stability around 20 ppm rms [3]. Such stability levels have been demonstrated at PSI with two commercial modulator prototypes. Further reliability tests are however still required before launching a series production.

The Aramis line consists of 13 undulator modules each of 4-m length. These in-vacuum undulators have a variable rms *K* value ranging between 1 and 1.8. In order to adjust the gap, both magnet arrays are attached to wedges which change the gap by sub-micron steps when moved longitudinally (Fig. 7). The robust mechanical frame gives the stability and reproducibility of the magnetic field map. The magnet array is a hybrid lattice with a period of 15 mm with NdFeB(Dy) magnets and Permendur poles [5]. The whole undulator sits on eccentric cam-shaft movers giving five degrees of freedom (x, y, pitch, yaw and roll) for the alignment of the 4-m-long undulator with respect to the electron beam axis.

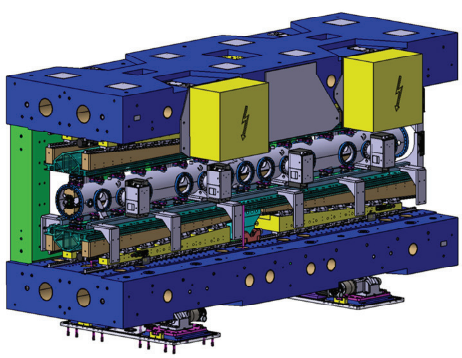

Figure 7: Cut-away view of the Aramis in-vacuum undulator revealing the wedges (in yellow) which open or close the gap.

Nine undulator frames together with 4 magnet arrays out of a total of 13 units have been delivered. The magnet array assembly in the undulator frame (Fig. 8) is done at PSI within the SwissFEL building. The magnet arrays are attached to the undulator frame thanks to adjustable columns (Fig. 9). These columns are then used to correct for the phase error of the magnet lattice. The local magnetic field amplitude errors are corrected by adjusting the height of each individual pole/magnet set via an automatic screw driver. An rms phase error below 2 degrees, along with a trajectory straightness within 2 µm, has been achieved with this method on a prototype [6]. The first undulator of the series is currently under magnetic optimisation and will be installed in the SwissFEL tunnel in October 2015. The rest of the series will then follow at a rate of one per month.

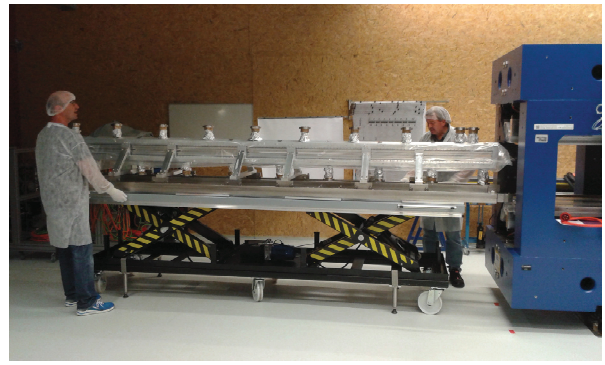

Figure 8: Insertion of the magnet arrays within the undulator frame for the first round of magnetic optimisation (without the vacuum chamber).

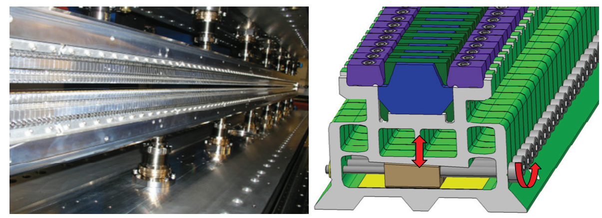

Figure 9: Magnet arrays attached to the undulator frame with adjustable columns prior to the vacuum tank installation (left). Individual magnet/pole sets are sitting on flexible supports (right).

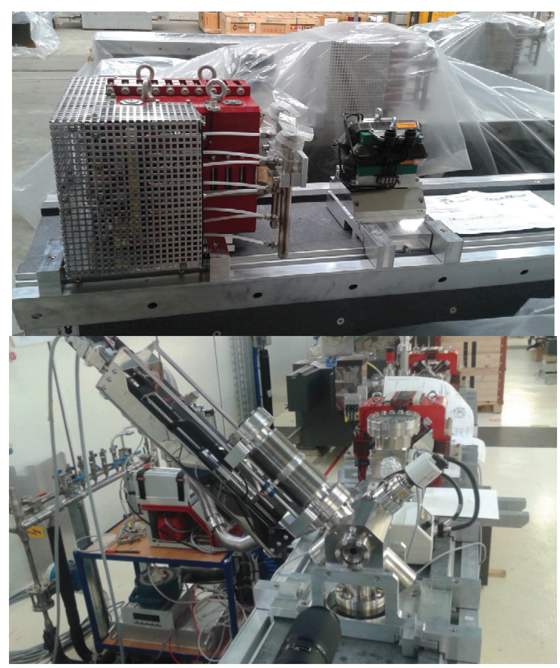

Figure 10: Quadrupole and steering magnets positioned on a girder before vacuum pipe installation (top). Prototype of the PSI wire scanner mounted on the girder for the site acceptance test of the linear feed-through (bottom).

ISBN 978-3-95450-134-2

Many components are already produced and tested such as, for example, the power supplies and magnets. About 450 magnets (steerers, dipoles, quadrupoles, etc.) have been produced and measured at PSI. These are currently being installed on girders (Fig. 10). Several electron diagnostic component prototypes have been successfully tested (OTR screens, BPMs, etc.) and series production is currently under way. SwissFEL will be equipped with Wire-scanners (WSCs) for emittance measurements and transverse profile monitoring during FEL operations (Fig. 10). WSC in-vacuum hardware and beam-loss-monitors (scintillator fiber) have been tested at the 250-MeV SITF and at the GeV energy scale in FERMI [7,8]. The gun laser system (Table 1) which will illuminate the photocathode and drive the laser heater is in production and should be delivered by the end of 2015.

Table 1: Summary of Gun Laser Specifications

Wavelength	1040 nm
Pulse energy at 260 nm before shaping	800 µJ
Energy stability	0.5% rms
Minimum pulse duration (Gaussian)	500 fs FWHM

In addition, the first photonics components have arrived at PSI. The X-ray pulse energy and position monitor has been provided by DESY and was recently delivered to PSI (Fig. 11).

Figure 11: X ray pulse energy and position monitor in the SwissFEL building.

The designs of the two end stations (ESA & ESB) which will be operated in the first phase of SwissFEL are completed. End station A is dedicated to ultrafast photochemistry and photobiology, and End Station B will focus more on pump-probe crystallography. Key components (diffractometer, heavy load goniometer, pump lasers, etc.) are now in the procurement phase. Some special components like the 2D detector “Jungfrau” are developed directly in house at PSI. The two end stations should be ready for Fall 2017 in time for the first pilot experiments.

Figure 12: 3D drawings of the End Station A (top) and End station B (bottom).

CONCLUSION

Despite a few months of delay in the delivery of the building infrastructure the preparation of key components like the RF modules and the undulators are progressing according to the schedule. The procurement of the RF modulator is the critical path item of the project but recently pulse to pulse voltage stability tolerances could be demonstrated with two different prototypes. The injector test facility has been shut down in order to prepare the new version of the injector. The next important milestone will be the commissioning start of this injector in March 2016.

REFERENCES

[1] R. Ganter *et al.*, in *FEL'12*, Nara, Japan, Aug. 2012.
[2] E. Prat and S. Reiche, in *FEL'14*, Basel, Switzerland, Aug. 2014.
[3] F. Loehl, in FEL'15, Daejeon, Korea, Aug. 2015.
[4] R. Zennaro *et al.*, in *IPAC'13*, Shanghai, China, May 2013.
[5] T. Schmidt *et al.*, in *FEL'12*, Nara, Japan, Aug. 2012.
[6] M. Calvi *et al.*, in *FEL'14*, Basel, Switzerland, Aug. 2014.
[7] G. Orlandi *et al.*, in *FEL'14*, Basel, Switzerland, Aug. 2014.
[8] G. Penco *et al.*, in FEL'15, Daejeon, Korea, Aug. 2015.

A TWO-COLOR STORAGE RING FEL*

J. Yan†, Y.K. Wu, H. Hao, S. Mikhailov, V. Popov
DFELL/TUNL and Department of Physics, Duke University, Durham, NC, USA
J.Y. Li, NSRL, University of Science and Technology of China, Anhui, China
N.A. Vinokurov, Budker Institute of Nuclear Physics, Novosibirsk, Russia
S. Huang, Institute of Heavy Ion Physics, Peking University, Beijing, China
J. Wu, SLAC National Accelerator Laboratory, Menlo Park, CA, USA

Abstract

Using different undulator configurations on the Duke storage ring, we have successfully achieved lasing with a novel two-color storage ring FEL. Using a pair of dual-band FEL mirrors, simultaneous lasing was realized in IR (around 720 nm) and in UV (around 360 nm). With this two-color FEL, we have demonstrated independent wavelength tuning of either IR or UV lasing. With careful tuning, we have also realized harmonic lasing with the UV lasing tuned to the second harmonic of the IR lasing. The tuning of harmonic two-color lasing has also been demonstrated with the locked wavelengths. Furthermore, we have demonstrated good control of the FEL power sharing between the two colors. The two-color FEL has created new opportunities to drive a two-color Compton γ-ray beam at the High Intensity γ-ray Source at Duke.

INTRODUCTION

Multi-color lasers have found many important applications in scientific research. One example is wavelength-division multiplexing, which utilizes multiple optical signals at different wavelengths multiplexed into a shared fiber for enhancing the efficiency of communication systems. Multi-color lasers with good colinearity are particularly important in research, since the laser beams of different colors can be co-propogated over a long distance, collimated and focused simultaneously. For example, two optical pulses with different wavelengths but controllable time delay can be used in pump-probe spectroscopy to measure the fast dynamics of the system under investigation. Some other applications of multi-color lasers include photomixing processes for terahertz radiation generation and differential absorption lidar. The typical approach to realize simultaneous multi-color lasing is using a dispersive or diffractive wavelength filter such as a prism or grating, either intracavity or in an external feedback cavity. Such a technology has been implemented in conventional lasers with different gain media such as dye [1,2], solid-state [3,4], semiconductor [5,6] and fiber [7]. However, the wavelength tunability of these lasers is typically limited by the bandwidth of the gain medium.

Since the theoretical prediction and the first experimental demonstration by Madey in the 1970s [8,9], free-electron lasers (FELs) have seen great development over the past few decades, and have become increasingly attractive light sources in a number of research areas. A common low-gain FEL configuration uses an optical cavity to trap and amplify electron beam radiation in a device termed an oscillator FEL [10]. An oscillator FEL can be driven either by an electron storage ring or a linac. Oscillator FELs mainly operate in the spectral region from IR to vacuum UV. The natural advantages of an FEL such as its broadband gain medium (an electron beam) and the single optical cavity configuration make the oscillator FEL an excellent device for the multi-color lasing with good wavelength tunability and colinearity. Since early 1990s, multi-color, especially two-color FEL operations have been developed and realized with several linac based FELs. The first two-color linac FEL operation was demonstrated on CLIO [11], an oscillator FEL operating in the mid-infrared regime, where two FEL wavelengths were produced by the same electron beam and two undulators with different undulator strengths inside a single optical cavity. Two other linac based oscillator FELs reported successful two-color operations later [12,13]. Another FEL configuration, the high-gain single-pass FEL, is mainly driven by linacs and does not use an optical cavity. In these FELs, the amplification of the FEL beam is realized in a single pass via the interaction between the electron beam and its radiation in a long undulator array [14,15] or with an external laser [16,17]. Single-pass FELs are now high-performance coherent light sources in the extreme UV and x-ray regimes. Recently two-color operations have also been experimentally demonstrated with several single-pass FELs [18–22] in the short-wavelength spectral regions.

Unlike in a linac, an electron beam in a storage ring is recycled so that it participates in the FEL interaction repeatedly over a large number of passes. Therefore, the physics challenges for the two-color operation of a storage-ring FEL include the control and management of two competing lasing processes and maintanance of simultaneous lasing at two wavelengths in multiple passes. The first experimental demonstration of two-color FEL operation at the Duke FEL facility, in which simultaneous generation of two FEL wavelengths (IR and UV) with a harmonic relationship was realized, was reported in Ref [23]. In this article, we report an experimental study of two-color lasing using a different undulator configuration. The experimental results show good performance of this two-color operation in terms of wavelength tunability, power tunability and power stability. In addition, this two-color FEL can serve as a photon

* Work supported in part by the US DOE grant no. DE-FG02-97ER41033.
† junyan@fel.duke.edu, 1-919-660-2667.

ISBN 978-3-95450-134-2

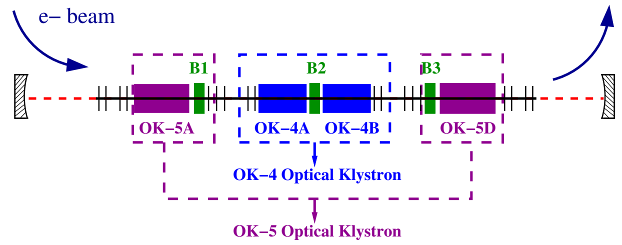

Figure 1: A four-undulator configuration for two-color FEL operation. All the four undulators are powered up, with two OK-4 undulators and two OK-5 undulators forming two sets of interleaved optical klystrons.

source for the two-energy γ-ray production via Compton backscattering at the High Intensity γ-ray Source [24].

EXPERIMENTAL SETUP

The operation of the Duke FEL system can use a variety of undulator configurations with four available electromagnetic undulator magnets, two planar OK-4 undulators and two helical OK-5 undulators (see Figure 1). This provides the possibility of operating a multi-color FEL using the same electron beam and a shared optical cavity. We have achieved two-color lasing with both three-undulator and four-undulator configurations. In the three-undualtor configuration, three undulators are powered up, including the upstream OK-5 undulator (OK-5A) and two OK-4 undulators (OK-4A and OK-4B) as an optical klystron in the middle section. The downstream OK-5 undulator (OK-5D) is disconnected. In the four-undulator configuration, OK-5D undulator is also energized so that two OK-5 undulators also form an optical klystron as shown in Figure 1. In this two-color FEL, OK-5 undulators are tuned to lase at λ_1 in IR while OK-4 undulators to lase at λ_2 in UV.

By changing either the electron beam energy or undulator field strength, the FEL lasing wavelength can be tuned around the center wavelength of the undulator radiation, λ_{cen},

$$\lambda_{\mathrm{cen}} = \frac{\lambda_u}{2\gamma^2}\left(1 + p\frac{K^2}{2}\right), \qquad (1)$$

where λ_u is the undulator period, $\gamma = E/(mc^2)$ is the Lorentz parameter for an electron with energy E and rest mass m, $K = eB_0\lambda_u/(2\pi mc^2)$ is the undulator strength of an undulator with peak magnetic field strength B_0, and the polarization parameter $p = 1$ (or 2) for a planar (or helical) undulator. The wavelength tuning is done by changing the magnetic field strength in the OK-4 and OK-5 undulators. Further, three buncher magnets, $B1$, $B2$ and $B3$ (see Figure 1) are used to provide fine tuning of the two-color FEL lasing, both the wavelength and power level.

The two-color FEL lasing is typically tuned to the IR wavelength around 720 nm (λ_1) and the UV wavelength around 360 nm (λ_2), and allows for harmonic lasing with $\lambda_1 \simeq 2\lambda_2$. To enable lasing at two wavelengths with such a large spectral separation, a pair of dual-band FEL mirrors

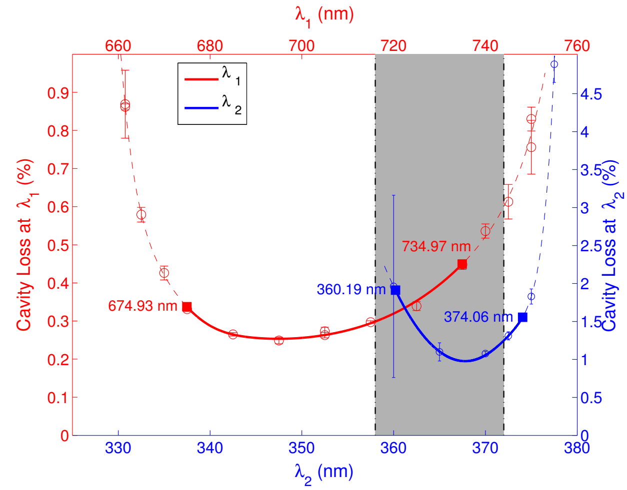

Figure 2: Measured round-trip FEL cavity losses in two high-reflectivity bands as a function of the wavelength. The mirrors have degraded after being exposed to the electron beam radiation for a substantial amount of time compared to the case with fresh mirrors reported in Ref [23]. The solid parts of the curves represent the wavelength tuning range of one color while fixing the lasing wavelength of the other color. The shaded region enclosed by the black dash-dot lines represents the tuning range for harmonic wavelength tuning ($\lambda_1 \simeq 716 \sim 744$ nm; $\lambda_2 \simeq 358 \sim 372$ nm).

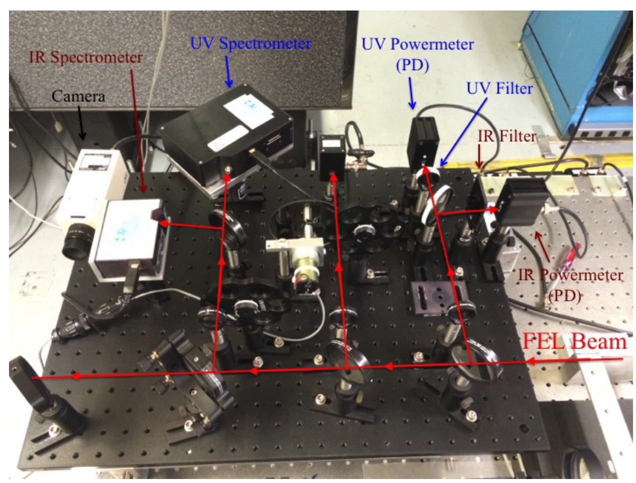

Figure 3: Optical system for two-color FEL diagnostics. The power measurement for each color is done using a photodiode after filtering out the signal of the other color. The wavelength measurements are done by two spectrometers covering IR and UV wavelength ranges, respectively.

have been developed with two highly reflective wavelength bands centered around 720 nm and 360 nm, respectively. Figure 2 shows the measured round-trip losses in the IR and UV bands after the FEL mirrors have degraded by substantial exposure to the electron beam radiation. As shown in Figure 2, the minimum cavity loss in UV is roughly four times as high as that in IR.

ISBN 978-3-95450-134-2

Since the same electron beam is used as the shared gain medium, it is critical to keep the net lasing gains at two wavelengths close to each other. The OK-5 FEL has a relatively low gain since the helical undulators are located about 10 m away from the center of the optical cavity. The lower gain of OK-5 undulators is compensated by operating the OK-5 FEL in IR where the optical cavity has a lower loss (see Figure 2). Located in the middle of the optical cavity, the OK-4 FEL has a higher gain and is chosen to be operated in UV where the cavity loss is also higher. To provide good gain matching, the gain of the OK-4 FEL needs to be further reduced. In these experiments, several tuning knobs, e.g. RF frequency detune df_{RF} which controls FEL detune, bunchers $B1$, $B2$ and $B3$, are found to be useful for adjusting the relative gains at the two wavelengths. For example, we devised a special setup of the OK-4 optical klystron to significantly reduce its gain by forcing it to lase with a lower gain via the tuning of buncher $B2$.

The FEL measurements reported in this article were conducted with the four-undulator configuration, the cavity loss shown in Figure 2 and a single-bunch, 500 MeV electron beam in the Duke storage ring. Figure 3 is a picture of a typical FEL optical diagnostic system to characterize the two-color FEL beams. The FEL spectra at two wavelengths are measured using two spectrometers from Ocean Optics, a USB4000 spectrometer with a wavelength range of 477 – 1146 nm, and a HR4000 spectrometer with a wavelength range of 220 – 447 nm. The extracted FEL power in each color is measured using a photodiode after filtering out the signal of the other color. The intracavity power in each color can be estimated by properly calibrating the two photodiodes with the FEL active power.

EXPERIMENTAL RESULTS

Wavelength Tuning

For many important research applications using a two-color laser, it is critical to have the ability to tune one of the lasing wavelengths while fixing the other. In Ref [23], we have demonstrated the tuning of λ_1 (IR) with a large tuning range while fixing λ_2 (UV) using the three-undulator configuration. Figure 4 shows a tuning using the four-undulator configuration in which λ_1 was fixed at 720.06±0.07 nm, while λ_2 was tuned from 374.06 nm to 360.19 nm, demonstrating a wavelength tuning range of $\Delta\lambda_2 \approx 14$ nm. Such wavelength tuning was achieved by varying the magnetic field strength of OK-4 undulators as the primary tuning knob as well as the setting of buncher B2 as an auxiliary knob for fine wavelength adjustments. Since B2 was a shared buncher by OK-4 and OK-5 optical klystrons, the OK-5 undulators, as well as B1 and B3 were also tuned to compensate for the small wavelength shift of λ_1, so that λ_1 stayed fixed at 720 nm. Figure 5 shows two of measured spectra normalized to their respective peak intensity, one in the second harmonic relationship and the other with λ_2 tuned away from $\lambda_1/2$ by 8 nm. It should be noticed that the signal-to-noise ratio of UV spectra in Figure 5(a) is much lower than other measured spectra, indicating that this spectral region is close to the lower wavelength limit for the UV lasing due to large cavity loss (See Figure 2).

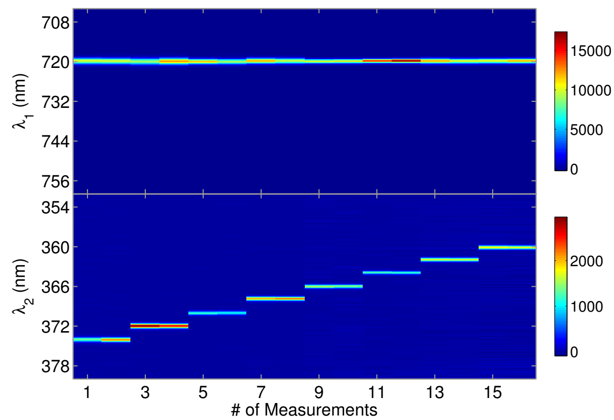

Figure 4: Single wavelength tuning. λ_2 is tuned while the fundamental λ_1 is fixed. The beam current is maintained between 12.2 mA and 12.7 mA.

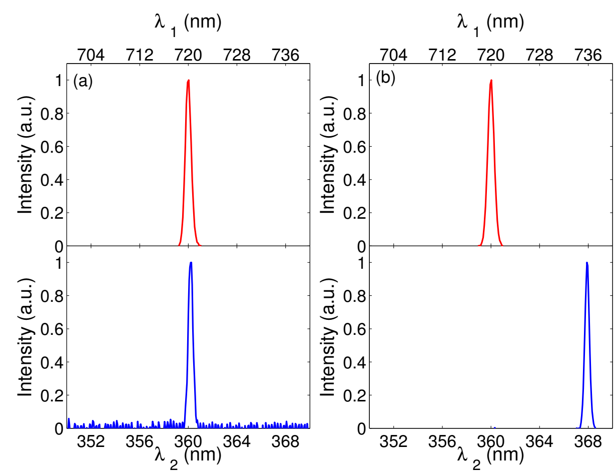

Figure 5: Measured spectra (normalized) in the wavelength tuning measurement shown in Figure 4: (a) $\lambda_1 = 719.99$ nm; $\lambda_2 = 360.19$ nm. The rms spectral widths of λ_1 and λ_2 are $\sigma_1 = 0.49$ nm and $\sigma_2 = 0.20$ nm, respectively; (b) $\lambda_1 = 720.00$ nm; $\lambda_2 = 367.91$ nm. $\sigma_1 = 0.53$ nm and $\sigma_2 = 0.19$ nm.

To demonstrate the wavelength tuning of harmonic two-color lasing, the magnetic field strengths of OK-4 and OK-5 undulators as well as bunchers were varied simultaneously to keep two wavelengths in the second harmonic relationship. In this case, λ_1 was tuned from 716.15 nm to 744.08 nm ($\Delta\lambda_1 \simeq 28$ nm) while λ_2 was accordingly varied from 358.25 nm to 371.99 nm ($\Delta\lambda_2 \simeq 14$ nm). The wavelength tuning range of harmonic lasing was limited by the amount of overlap of the low-loss regions of the high-reflectivity wavelength bands in IR and UV of the specially developed dual-band FEL mirrors.

ISBN 978-3-95450-134-2

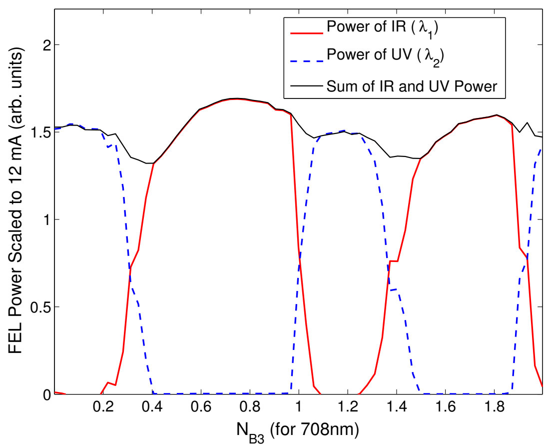

Figure 6: Two-color FEL power control using N_{B3}. A roughly 100% power modulation for IR (solid red) and UV (dashed blue) was achieved with the total power (solid black) maintained stable with a 6.8% power variation. The beam current was maintained between 12.2 and 12.5 mA with top-off injection. $N_{B1} = 0$; $N_{B2} = 0.68$ for 367 nm. The average λ_1 and λ_2 is 709.17 nm and 367.01 nm, respectively.

Power Control

The two lasing processes at two different wavelengths share the same gain medium, the electron beam. The experimental results in the previous section showing two-color lasing with wavelength tunability have clearly demonstrated the capability of providing effective gain balance for two lasing processes, as well as a mastery of the FEL power control. Additional measurements were made to demonstrate a precise control of the partitioning of the FEL power for two different wavelengths by adjusting N_B, the relative optical phase slippage between the laser and electron beams produced by a buncher. Power control via N_{B1} tuning has been demonstrated for the three-undulator configuration in Ref [23]. Since OK-5 is an optical klystron in the four-undulator configuration, it is found that buncher B1 or B3 can be used as a knob to control the FEL power partition in two colors without significantly impacting the lasing wavelength of OK-4 (λ_2). For example, the two-color power tuning using B3 is shown in Figure 6, where the measured extracted FEL powers are first linearly scaled to 12 mA and then cross-calibrated with P_{FEL}, the direct FEL power emitted by the electron beam in the FEL interaction. P_{FEL} can be written as [25–27]

$$P_{\text{FEL}} \approx \alpha\, P_{\text{syn}}\, \frac{\sigma_{\text{FEL}}^2 - \sigma_0^2}{\sigma_{\text{FEL}}}, \qquad (2)$$

where P_{syn} is the total synchrotron radiation power emitted by the electron bunch in the entire storage ring; α is a numerical factor depending on the undulator configuration and FEL operation conditions; σ_{FEL} and σ_0 are the relative electron beam energy spread with FEL turned on and off, respectively. The electron beam energy spread is determined from the electron bunch length which is measured using an image dissector tube. Further, in steady state operation P_{FEL} balances against the total cavity loss and thus is proportional to the total intracavity power. Therefore, the cross calibration of the extracted power at two wavelengths allows us to study the levels of intracavity power modulation. As shown in Figure 6, a roughly 100% power modulation for IR and UV was achieved while the total FEL power is maintained quite stable within 6.8% (rms). The periodic power modulation in this measurement can be attributed to the gain modulation mechanism of an optical klystron, where, by tuning N_{B3}, the IR beams emitted in OK-5A and OK-5D produce constructive and destructive inteference alternately for electrons of a certain energy. As shown in the previous sections, the bunchers are used not only to balance the gain for two colors but as an auxiliary knob for fine wavelength adjustments. Therefore, accompanying the power modulation, the wavelength of IR lasing is periodically shifted around the mean value (709.17 nm) by about 6.43 nm (0.9%), while the wavelength of UV lasing is maintained constant at 367.01 ± 0.02 nm.

Overall, we realized complete control of the FEL power for each of the lasing wavelength, producing stable two-color lasing with either equal power, or a pre-determined power ratio of two wavelengths. During this process, the total FEL power remained roughly constant.

Two-color FEL Operation with Three-undulator Configuration

Our two-color FEL was first successfully operated using a three-undulator configuration with OK-5A and two OK-4 undulators (see Figure 1). Using this configuration, we demonstrated precision wavelength control and tuning, as well as full control of FEL power in two colors. Details on the storage ring setup and experimental results can be found in Ref [23]. With the same set of FEL mirrors which were fresher with less radiation induced degradation, the wavelength range of UV single wavelength tuning was larger with $\Delta\lambda_2 \simeq 24$ nm. The wavelength tuning ranges with harmonic lasing were also larger with $\Delta\lambda_1 \simeq 36$ nm and $\Delta\lambda_2 \simeq 18$ nm. In addition, the FEL power partition between the two colors could be well controlled by tuning the buncher B1. The two-color power stability was also examined with the three-undulator configuration and found to be related to many factors such as the stability of FEL optical axes due to the movement of FEL mirrors and the variation of the FEL cavity detune due to the temperature change. We also studied the temporal structure of the two-color beams under various operation conditions.

SUMMARY

In this paper, we report the successful operation of a two-color FEL using a four-undulator configuration. We have demonstrated wavelength tunability in a wide range by changing one of the two lasing wavelengths or simultaneously changing both wavelengths while maintaining the second harmonic relationship in wavelength. Furthermore,

ISBN 978-3-95450-134-2

we have demonstrated full control of the FEL power in two colors while maintaining the total FEL power at a steady level. The Duke storage ring is primarily operated as a photon driver for the High Intensity γ-ray Source. The preliminary work on two-color γ-beam production using the two-color FEL is well under way. This two-color γ−ray beam will provide new possibilities for experimental nuclear physics research.

ACKNOWLEDGMENT

We would like to thank V.N. Litvinenko and P. Wallace for useful discussions, S. Günster for producing the dual-band mirrors, and the engineering and technical staff at DFELL/TUNL for their support. This work was supported by DOE Grant DE-FG02-97ER41033.

REFERENCES

[1] H. S. Pilloff, Appl. Phys. Lett. **21**, 339 (1972).

[2] H. Lotem and R. T. Lynch Jr., Appl. Phys. Lett. **27**, 344 (1975).

[3] R. Scheps and J. F. Myers, IEEE Photon. Technol. Lett., **4**, 1 (1992).

[4] F. Siebe et al., IEEE J. Quantum Electron. **35**, 1731 (1999).

[5] T. Hidaka and Y. Hatano, Electron. Lett. **27**, 1075 (1991).

[6] C.-L. Wang and C.-L. Pan, Appl. Phys. Lett. **64**, 3089 (1994).

[7] S. Reilly et al., Electron. Lett. **38**, 1033 (2002).

[8] J. M. J. Madey, J. Appl. Phys. **42**, 1906 (1971).

[9] L. R. Elias et al., Phys. Rev. Lett. **36**, 717 (1976).

[10] Y. K. Wu et al., Phys. Rev. Lett. **96**, 224801 (2006).

[11] D. A. Jaroszynski et al., Phys. Rev. Lett. **72**, 2387 (1994).

[12] T. I. Smith et al., Nucl. Instr. and Meth. in Phys. Res. A **407**, 151 (1998).

[13] A. Zako et al., Nucl. Instr. and Meth. in Phys. Res. A **429**, 136 (1999).

[14] R. Bonifacio, C. Pellegrini, and L. M. Narducci, Opt. Commun. **50**, 373 (1984).

[15] P. Emma et al., Nat. Photon. **4**, 641 (2010).

[16] L. H. Yu et al., Science **289**, 932 (2000).

[17] L. H. Yu et al., Phys. Rev. Lett. **91**, 074801 (2003).

[18] A. A. Lutman et al., Phys. Rev. Lett. **110**, 134801 (2013).

[19] A. Marinelli et al., Phys. Rev. Lett. **111**, 134801 (2013).

[20] S. Ackermann et al., Phys. Rev. Lett. **111**, 114801 (2013).

[21] E. Allaria et al., Nat. Commun. **4**, 2476 (2013).

[22] T. Hara et al., Nat. Commun. **4**, 2919 (2013).

[23] Y.K. Wu et al., “A Widely Tunable Two-Color Free-Electron Laser on a Storage Ring”, submitted for publication.

[24] H. R. Weller et al., Prog. Part. Nucl. Phys. **62**, 257 (2009).

[25] N.A. Vinokurov and A.N. Skrinsky, Tech. Rep. (Budker Institute of Nuclear Physics, Novosibirsk, 1977) preprint INP 77-67.

[26] A. Renieri, Il Nuovo Cimento B **53**, 160 (1979).

[27] B. Jia et al., Phys. Rev. ST Accel. Beams **13**, 080702 (2010).

ISBN 978-3-95450-134-2

WAVEGUIDE THz FEL OSCILLATORS*

Sergey Miginsky#, Nikolay Vinokurov, KAERI, Daejon, Korea; Budker INP, Novosibirsk, Russia
Sangyoon Bae, Boris Gudkov, Kyu Ha Jang, Young Uk Jeong, Hyun Woo Kim, Kitae Lee, Jungho Mun, Seong Hee Park, Gyu Il Shim, KAERI, Daejon, Korea

Abstract

In today's world there is a significant demand for FEL-based THz radiation sources. They have a wide tuning range, a narrow band of radiation, and comparably high peak and average emission power. There are a significant number of these machines in the world, operating or in the development.

The main difference between a long-wave FEL, of THz or a millimeter band, and a conventional one is a too big transverse size of the fundamental mode of an open optical resonator. It claims a large gap in an undulator that dramatically decreases its strength. Both factors sorely decrease the amplification and the efficiency, and often make lasing impossible.

The main way to solve this problem is to use a waveguide optical resonator. It decreases and controls the transverse size of the fundamental mode. However, the waveguide causes a number of problems: power absorption in its walls; higher modes generation by inhomogeneities, as it is not ideal; electron beam injection into a FEL is more sophisticated; also outcoupling is more complicated; finally, the resonator detuning control claims some special solutions. The waveguide dispersion relation differs from one in the free space. It shifts up the wavelength of the FEL, changes the optimal detuning, and creates a parasitic mode near the critical wavelength of the waveguide. These problems and possible solutions to them are considered.

INTRODUCTION

Outstanding parameters of THz FELs, like a wide tuning range, a narrow band of radiation, and comparably high peak and average emission power cause a significant number of these machines in the world. Several examples one can find in [1–7]. These machines differ significantly from each other and are intended for different purposes. One can easily found that FELs provide incomparably higher power than oscillators of other types in THz region [8].

However, there are several significant problems in development of THz FELs. Most one is that the fundamental mode of an open optical resonator has too big size in this case. It causes a decrease of the gain directly by weakening interaction between a wave and electrons and indirectly by an increase in an undulator gap that causes a sharp decline in strength of the latter. Thereby, extremely high peak current is necessary to obtain lasing. An effective method to improve the situation is the use of a waveguide optical resonator instead of open one. In this case the size of its mode can be significantly reduced together with an undulator gap. Wherein, a number of other problems arise. Energy absorption in the waveguide walls reduces the loop gain. Higher modes generation on waveguide inhomogeneities produces a similar effect. Beam injection into this resonator can be a complicated problem. Light outcoupling can be also not so easy. The wave group velocity in a waveguide depends on the wavelength, so the resonator should be retuned for each wavelength to keep the detuning. It is another sophisticated problem. Conducting of a beam through a narrow waveguide is not easy problem too. All these problems should be solved for a waveguide FEL.

WAVEGUIDE RESONATORS

Several types of waveguides shown in Fig. 1 can be used in FELs. Electric field in all the cases is horizontal. Each of them has some advantages and drawbacks.

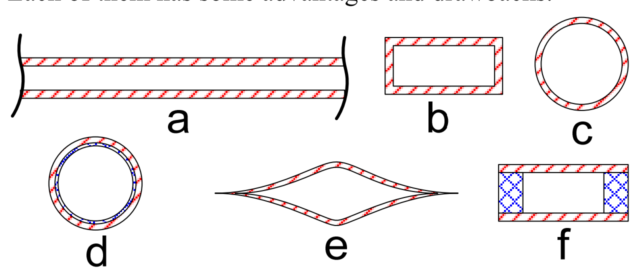

Figure 1: Types of waveguides: a – parallel-plate, b – rectangular, c – circular, d – with dielectric coating, e – special shape, f – rectangular with dielectric walls.

A parallel-plate waveguide concentrates wave power along the vertical coordinate only, while along the horizontal one it is similar to empty space. Thus, in the vertical plane the electric field distribution is cosine-like with zeroes at the walls, and in the horizontal one it is the well-known Gaussian free-space mode. It can be placed in a planar undulator only. One can conclude that the most effect of this waveguide is the decrease of the undulator gap. Power loss in this waveguide typically is not so big and can be easily evaluated using the following formula

$$\alpha \cong \frac{\pi}{2l} \frac{1}{1+\frac{i\zeta}{kl}}, \tag{1}$$

*Work was supported by the World Class Institute (WCI) program of the National Research Foundation of Korea (NRF) funded by the Ministry of Education, Science and Technology of Korea (MEST) (NRF Grant Number: WCI 2011-001).
#Miginsky@gmail.com

ISBN 978-3-95450-134-2

where l is the waveguide half-height, k is the wavenumber, and $\zeta = Z_s / Z_0$, the ratio of the surface impedance to the one of free space [9].

A rectangular waveguide provides much smaller fundamental mode size, thus much bigger primary gain. In the other hand, wave losses in it are very high, so the system should be optimized well and, even in this case can be unable to work. A special shape (like Fig. 1e) can be applied to reduce losses.

Also dielectric walls of a rectangular waveguide (like Fig. 1f) give similar and even stronger effect. Nevertheless, this waveguide has many drawbacks. It is very hard to manufacture such a structure, as it should be extremely uniform and vacuum-tight simultaneously. The dielectric is to be refractory and slightly conductive, so its choice is not obvious. The latter property is necessary to discharge of the current absorbed from the beam halo.

A circular waveguide is useful together with a helical undulator. In this case the gain is twice bigger than with a planar one, other things being equal. The properties of this waveguide are similar to ones of a rectangular one.

The inner surface of a circular waveguide can be coated by a dielectric to dramatically reduce power absorption. In this case the fundamental mode being used for lasing is not H_{11} as in a pure-metal waveguide, but hybrid HE_{11} one [10]. Also change in the wave structure intensifies the beam-to-light interaction. The results for an aluminium pipe of the inner diameter of 4.8 mm are placed in Fig. 2. Optimal thickness coating of low-density polyethylene (LDPE, 45 μm) or corundum (20 μm) was used. λ is the wavelength, E is the electric field of the wave, P is its power, k" is the imaginary part of the wavenumber, and Z_0 is the impedance of free space. The data were obtained from numerical simulations. The plot shows that an optimally coated circular waveguide is up to 70 times more effective than pure-metal one. The kind of polymer almost does not matter, so technological reasons and radiation hardness are most important in its selection.

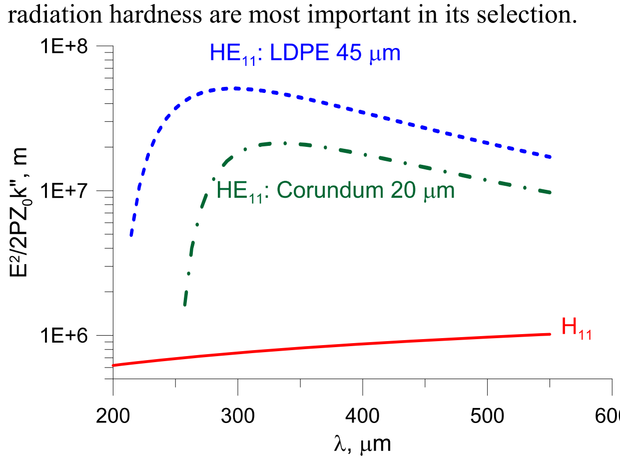

Figure 2: Efficiency of a circular waveguide: all-metal – solid, LDPE coated – dotted, corundum coated – dash-dot.

Losses in a waveguide optical resonator are shown in Fig. 3. If the mirrors are placed close to the waveguide, reflections losses and beyond the mirror ones are absent. In this case the mirrors should be cylindrical for a parallel-plate waveguide and flat in other case. If there is significant distance between a flange and a mirror, the latter should be elliptical for a parallel-plate waveguide and spherical in other cases.

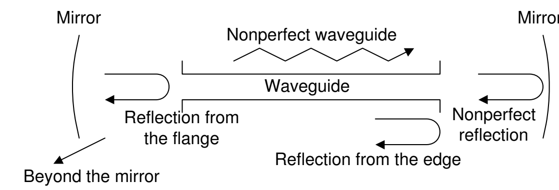

Figure 3: Possible losses in waveguide resonators.

Reflection from a flange is caused by diffraction and depends on the parameter $\kappa = kl^2 / R$, where R is the distance to the mirror. Limits for κ for various losses and field distributions are placed in Table 1.

Table 1: Maximum Allowable κ

Losses \ Distribution	Cos-like	Rectangular
1%	0.64	0.34
10%	2.1	1.06

Most frequent nonuniformity of a waveguide is its variable curvature. Higher order modes are generated in the places where the curvature is changed. These modes damp more rapidly than the fundamental one. Some part of power is also reflected. These losses can be estimated using the following formulae [9]:

$$\cong \frac{0.2376(kl)^6}{(kR_y)^2} \tag{2}$$

and

$$\cong \frac{4d^2}{3R_x^2} . \tag{3}$$

The meanings of variables in the formulae above are explained in Fig. 4.

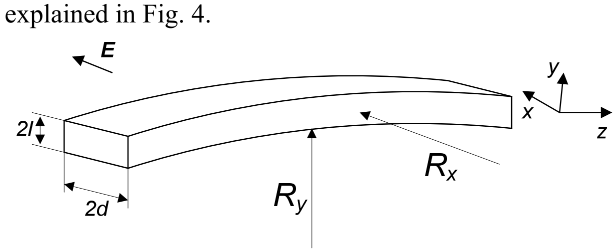

Figure 4: Curvature of a waveguide.

ISBN 978-3-95450-134-2

BEAM INJECTION AND EXTRACTION

Possible injection and extraction schemes depend on the type of the optical resonator. If there are significant distances from the waveguide flanges to the mirrors, the conventional scheme can be used, like in Fig. 5. The advantages of this scheme are that an electron moves in the empty space and the length of the resonator is controlled easily. The main drawback is losses on places with limited aperture, namely mirrors and flanges.

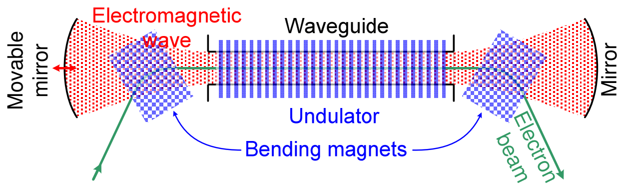

Figure 5: A conventional injection and extraction scheme.

If the mirrors of the optical resonator are adjacent to the waveguide, and the latter is parallel-plate, an injection and extraction scheme could be as in Fig. 6. In this case there is no power loss at the right (as in Fig. 6) waveguide flange. The movable mirror has some small distance to the waveguide flange, so power loss here is unavoidable due to diffraction. Another advantage of this scheme is that it is shorter than the previous one. A drawback is that the waveguide is longer, so power loss in it is bigger.

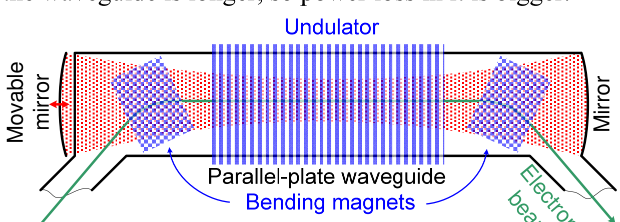

Figure 6: An injection and extraction scheme for a parallel-plate waveguide and adjacent mirrors.

If the average beam power is not so high, a scheme like in Fig. 7 can be used. It does not contain bending magnets. An electron beam is injected into a circular waveguide through a thin mesh. Outcoupling is through the same mesh. A blind movable mirror at the opposite end of the waveguide is simultaneously a beam dump. The main advantage of the scheme is that the waveguide is short and there is no flange power loss simultaneously. Also the resonator length is the shortest. There are some drawbacks too. A gap between the plunger and the waveguide absorbs some small part of electromagnetic power. The mesh mirror also absorbs and scatters some part of incoming electron beam.

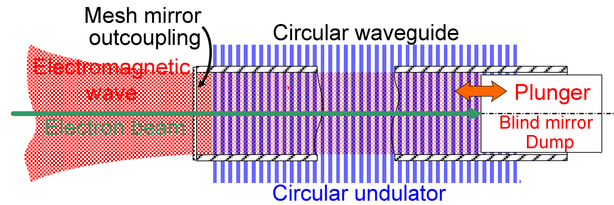

Figure 7: An injection and extraction scheme for a helical geometry and adjacent mirrors.

A ring optical resonator can be used together with the conventional scheme, as in Fig. 8. Its advantage is that all the power losses caused by the waveguide are twice smaller than in the simplest case. The drawbacks are that its alignment is terribly sophisticated and power losses on mirrors are twice bigger.

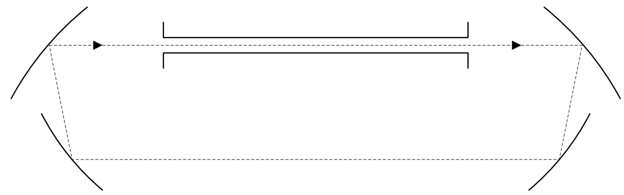

Figure 8: A ring optical resonator.

OUTCOUPLING

The simplest outcoupling is a hole in the centre of a mirror, as in Fig. 9. It is used most frequently in FELs. The main drawback is 50% loss of extracted power, as the hole is a radiator emitting waves both sides equally. Radiation toward the resonator has the pattern almost orthogonal to its fundamental mode if the hole is small enough.

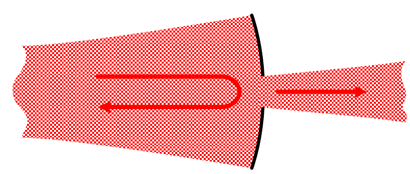

Figure 9: Centre hole outcoupling.

There is a well-known method to solve this problem: the use of huge number of very small radiators instead of large one. This is mesh outcoupling shown in Fig. 10. If the distance between the mesh holes is much smaller than the wavelength, their emission interferes constructively in both directions, and the total pattern is almost equal to this of the incident wave. The transparency of the mesh strongly depends on its period and geometrical transparency. An electron beam of moderate power can be injected through the mesh with moderate loss. The scheme has some drawbacks. The mesh hardly can be shaped well like a solid mirror, so can be flat only. Even in this case it can be easily deform due to non-uniform heating. The mesh transparency significantly depends on the wavelength.

ISBN 978-3-95450-134-2

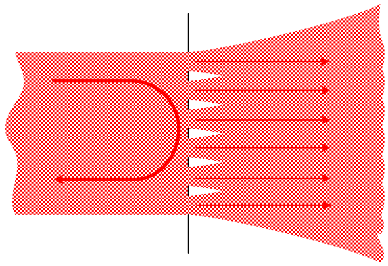

Figure 10: Mesh outcoupling.

One more possibility is an inclined dielectric plate in the way of electromagnetic wave. It reflects a part of wave power out of the resonator. In this case there are two reflecting surfaces. If the plate is thin enough, there is interference between two reflected pulses, that results strong dependency of the outcoupling coefficient on the wavelength. The plate can be made so that the optical paths for the two pulses differ approximately by their length. In this case there is almost no interference, but the pulse length is doubled.

RESONATOR RETUNING

Significant retuning of the optical resonator is necessary when wavelength tuning, as the group velocity in a waveguide depends on the wavelength, and the detuning (the difference between the bunch repetition rate and the appropriate harmonic of the resonator) should be preserved. For example, if one needs to control the wavelength within 200 to 400 μm in a FEL with a parallel-plate waveguide of the height of 5 mm and the length of 3 m, he needs to change the length of the resonator within approximately 1.8 mm. It is comparable to the bunch length of an S-band accelerator and can not be ignored. All the resonators described above have this property.

CONCLUSION

- The design of a THz FEL typically differs from this of a conventional FEL.
- The use of a waveguide seems to be a good idea.
- Several various designs of waveguide resonators are possible. Each one has its own advantages and posers and is intended for appropriate applications.

REFERENCES

[1] CLIO FEL website: http://clio.lcp.upsud.fr/clio_eng/clio_eng.htm

[2] UCSB FIR-FEL website: http://sbfel3.ucsb.edu/ctst/Top.html/

[3] Y. U. Jeong, et al., " A Compact THz Free Electron Laser at KAERI", Infrared Millimeter Waves and 14th International Conference on Teraherz Electronics, 18-22 Sept. 2006, p. 551.

[4] ELBE U100-FEL website: http://www.hzdr.de/db/Cms?pNid=471

[5] ENEA Far Infrared Compact FEL website: http://www.frascati.enea.it/fis/lac/fel/fel2.htm

[6] G N Kulipanov et al., The international electronic journal of THz, 107 (2008).

[7] A Super-radiant THz FEL website: http://www.eng.tau.ac.il/research/FEL/

[8] Microtech Instruments THz generators website: http://www.mtinstruments.com/thzsources/

[9] S. Miginsky, et al. "Analysis of far-infrared waveguide open resonators", AFEL'97, Hirakata, Osaka, Japan, Jan. 1997.

[10] S. Miginsky et al., Bulletin of the Russian Academy of Sciences. Physics 79, 31 (2015).

ISBN 978-3-95450-134-2

SATURATION DYNAMICS, FINE SPECTRUM, AND CHIRP CONTROL IN A CW FEL OSCILLATOR

H. S. Marks#, A. Gover, H. Kleinman, Tel Aviv University, Israel
D. Borodin, A. Damti, M. Einat, A. Friedman, M. Kanter, Y. Lasser, Y. Lurie, Y. Vashdi, A. Yahalom, Ariel Universi, Israel

Abstract

Here we report in brief the results of an experimental study of the saturation dynamics and the optimal conditions for maximal radiation power extraction in a Free Electron Laser (FEL) oscillator. The Israeli Electrostatic Accelerator Free Electron Laser (EA-FEL) is capable of providing lasing pulses at frequencies between 95-110 GHz (depending on the electron beam energy). A critical parameter affecting the performance of the laser is the reflectivity and transmission of the out-coupling element of the resonator.

By attaching a variable reflectivity out-coupling element (based on a series of wire-grid polarisers) to the resonator of our EA-FEL we demonstrate the ability to optimise performance depending upon the desired output. For maximum lasing time the out-coupling from the resonator must be minimized, although sufficient for some radiation to leave. For maximum peak-power the reflectivity must be set differently depending upon the energy of the electron-beam (in MeV), which relates to the frequency emitted, and to the magnitude of the electron-beam current (in A). Mode competition ceases and a single longitudinal resonator mode is established more quickly the higher the reflectivity (important for short pulses).

The variable out-coupling allows us to operate optimally over a large range of frequencies and beam currents which would be impossible with an element with fixed reflectivity.

INTRODUCTION

Most FELs are based on RF-Linac acceleration technology that provides a periodic train of picosecond range e-beam pulses. FEL oscillators constructed based on such accelerators operate in principle as analogues of conventional mode-locked lasers [1]. In such oscillators, the laser radiation pulses are a superposition of numerous longitudinal modes of the resonator. By contrast, FEL oscillators based on electrostatic acceleration, which are the focus of the current article, can operate in a quasi-CW mode, namely their pulse duration is much longer than the time for several photon round-trips in the resonator. Such FEL oscillators operate analogously to conventional CW lasers of homogenously broadened gain medium.

Consequently, they can operate at a single longitudinal radiation mode, and the physics of their steady state saturation and output coupling power optimization can be analysed in terms of conventional laser theory. Though there are many FEL oscillators operating in the world [2], there are few operating electrostatic accelerator FELs in which the laser oscillator physics and specifically the problem of power out-coupling optimization can be studied experimentally. The Israeli Electrostatic Accelerator FEL (EA-FEL) is one of them. Another is the UCSB FEL [3]. Both can operate in a quasi-CW mode. The Dutch FOM-FEL operated along similar principles and at higher power but has since been dismantled [4]. An EA-FEL has also been built in Korea [5]. The Israeli Tandem EA-FEL has at its heart a fixed linearly polarised Halbach Wiggler [6].

POWER OUT-COUPLING OPTIMISATION

The subject of optimal power outcoupling for attaining maximum lasing power output is treated by most standard texts on lasers [7-10]. This same subject of optimal power outcoupling in EA-FEL has not been studied extensively so far. The Israeli FEL group experimented with optimisation of power outcoupling of an FEM operating at microwave frequencies [11]. The matter was also treated by us theoretically in relation to our Tandem EA-FEL, which is the subject of this paper [12].

Table 1: General System Parameters of the EA-FEL

Beam Current	0.5-3 A
B_w(Wiggler Field Amplitude)	0.193 T
λ_w	44.4 mm
A_e (Effective area of mode)	$40.1 \times 10^{-6}\ m^2$
L_w – Wiggler Length	989 mm
Beam Kinetic Energy	1.4 MeV

Within the limitations of our measurement range, single mode operation is generally observed. The time for single mode operation depends upon the roundtrip reflectivity. We arrive at this conclusion from looking at the lasing spectra, which we obtain from heterodyne mixing of the attenuated laser signal. We use an oscilloscope with a sampling rate of 5 GHz (Agilent – DSO-X3104A), with an analog bandwidth of 1 GHz. In producing the output the mixer doesn't discriminate between lasing frequencies above or below the local oscillator; so the 1 GHz bandwidth of the oscilloscope shows scanning over a range of over 2 GHz (±1 GHz from the local oscillator). So any demonstration of single mode operation is limited to 2 GHz. Though, the gain bandwidth of lasing is also limited, lasing further from the

#harrym@post.tau.ac.il

ISBN 978-3-95450-134-2

maximal gain point is less likely to survive the mode competition.

In Fig. 1 and 2 the spectra produced by the mixer are shown. The first time windows of the spectra in these figures are presented from the moment build-up begins, not from the time the electron beam starts! That is, depending upon the reflectivity there is a period of between 0.5 to 2.5 µs before there is any measurable lasing occurring.

In Fig. 1, it appears single mode operation is established after the second time window, between 1.5-2.5 µs. For the case shown in Fig. 1 the reflectivity of the out-coupling element was set to 0.89. By contrast, in Fig. 2, where the reflectivity of the out-coupling element was set to just 0.81, the mode competition is still evident in the third time window. Single mode operation is attained only after another 0.7 µs, where the two small satellite modes in the third frame disappear (not shown). For both Figs 1 and 2 the beam energy was ~1.36 MeV, the beam current 1.3 A, the lasing at frequencies close to 96.4 GHz and the internal losses of the resonator ~0.65 (at this frequency). During these pulses the accelerating voltage was falling at ~0.7kV/µs.

We expect that the gain curve will shift nearly linearly with the accelerator terminal voltage. This was found to be for the parameters of the EA-FEL [13] $\Delta f_{max}/\Delta V = 166\ MHz/kV$, due to a given drop in voltage ΔV over time t. When the voltage drop was $\Delta V/\Delta t \sim -0.5kV/\mu s$, this meant a change in the central frequency of the gain curve of $\Delta f_{max}/\Delta t = 83.05$ MHz/µs. So for a FWHM net-gain bandwidth of 5 GHz the gain curve needs to shift by roughly 2.5 GHz for lasing to cease, this should take ~2.5/0.08305 = 30.1 µs (assuming the dominant mode is built up at a frequency close to the maximum gain frequency). Although due to frequency pulling, despite the large shift in the gain curve, the lasing frequency will only change by ~5 MHz.

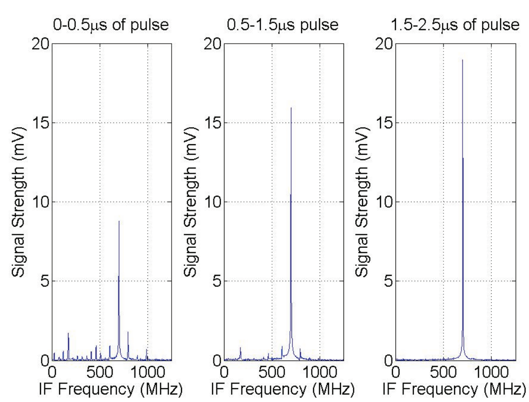

Figure 1: With the out-coupling element set to a reflectivity of 0.89 we observe the development of the lasing over three time windows. The lasing is 701 MHz above the LO which was set to 95.7 GHz. It appears that by the period of the final time window single mode lasing is established.

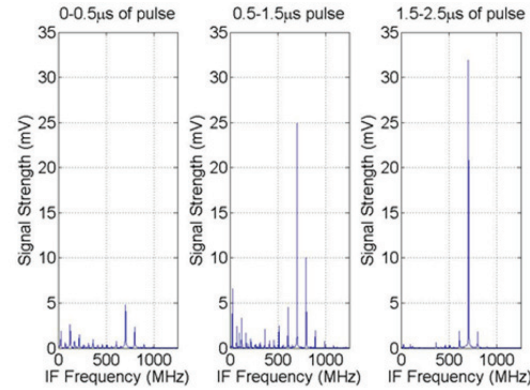

Figure 2: With the out-coupling element set to a reflectivity of 0.81 we observe the development of the lasing over three time windows. The lasing is 702 MHz above the LO which was set to 95.7 GHz. It appears that by the period of the final time window single mode lasing is not yet established.

LASER OUTPUT POWER OPTIMISATION

Earlier we considered how changing the out-coupling of the resonator changes the parameters of the lasing. Now we present measurements, which are compared to simulations, of the results of lasing power output as a function of out-coupling. We present this for a beam energy of ~1.36 MeV which corresponds to a frequency of 96.4 GHz, whilst the beam current was 1.3A (see Fig. 3). The variability from pulse to pulse is not due to uncertainty in the measurement but instability in the accelerating potential. Remarkably, this beam energy fluctuation having little effect on the small signal gain, often did not cause change from pulse to pulse in the lasing frequency, but dispersed the saturation power output. The simulated curves were produced in FEL3D [14].

Noting that the lasing ceases below a reflectivity of ~0.784 whilst the internal losses in the resonator at 96.4 GHz are ~0.65 we calculate the gain to be G=3.64.

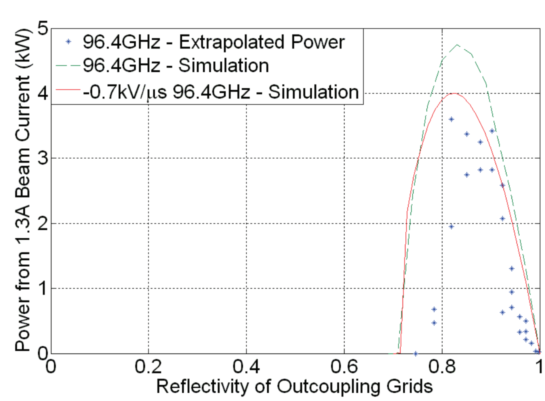

Figure 3: Power as a function of resonator exit reflectivity at 96.4 GHz, extrapolated from measurements in the user room to the output of the resonator.

ISBN 978-3-95450-134-2

CONCLUSION

The optimisation of power output from a free electron laser oscillator based on an electrostatic accelerator has been demonstrated and the effect of voltage fluctuations on the saturation power observed. This optimal coupling point was achieved experimentally by remote-control tuning of the transmission of a variable reflection mm-wave mirror at the end of the resonator. FEL3D simulations of output power maximisation and oscillation build-up and saturation were consistent with the experimental conclusions. We demonstrated FEL oscillation build-up and establishment of narrow bandwidth single mode operation within a few microseconds. A more expanded version of this text is to be published shortly in IEEE MTT.

REFERENCES

[1] A. Gover, E. Dyunin, “Coherence of e-Beam radiation sources and FELs – A Theoretical Overview”, *Proceedings of FEL 2006*, BESSY, Berlin, Germany, 2006.

[2] Neil, George R. "FEL oscillators." In *Particle Accelerator Conference, 2003. PAC 2003. Proceedings of the*, vol. 1, pp. 181-185. IEEE, 2003.

[3] L. R. Elias, J. Hu, G. Ramian, "The UCSB electrostatic accelerator free electron laser: First operation." *Nuclear Instruments and Methods in Physics Research Section A: Accelerators, Spectrometers, Detectors and Associated Equipment*, vol 237, no. 1, pp. 203-206, 1985.

[4] A. G. A.Verhoeven, W. A. Bongers, V. L. Bratman, M. Caplan, G. G. Denisov, C. A. J. Van Der Geer, P. Manintveld et al. "First microwave generation in the FOM free-electron maser." *Plasma physics and controlled fusion,* vol. 40, no. 8A, pp. 139-156, 1998.

[5] Cho, Sung Oh, Byung Cheol Lee, Young Uk Jeong, Sun Kook Kim, Jongmin Lee, and Kie Hyung Chung. "Transient behavior of the terminal voltage in a recirculating electrostatic accelerator for a long-pulse free-electron laser." *Review of scientific instruments*, vol. 67,no. 10, pp. 3491-3493, Oct. 1996.

[6] H. S. Marks, M. Volshonok, E. Dyunin, A. Gover, Y. Lasser, R. Shershevski, and A. Yahalom. "Wiggler improvement based on single axis magnetic measurement, synthesized 3-D field simulation of trajectories and sorting of lateral focusing magnets." *Nuclear Instruments and Methods in Physics Research Section A: Accelerators, Spectrometers, Detectors and Associated Equipment* 660, no. 1, 15-21, 2011.

[7] P. W. Milonni, J. H. Eberly, “Lasers”, John Wiley & Sons, 1988.

[8] K. Shimoda, “Introduction to Laser Physics”, *Springer Series in Optical Sciences*, vol. 44, Apr. 1986.

[9] A. Yariv, "Introduction to optical electronics", 2nd Edition, Holt McDougal, 1976.

[10] A. E. Siegman, “Lasers”, University Science Books, 1986

[11] A. Abramovich, H. Kleinman, A. Eichenbaum, Y. M. Yakover, and A. Gover, Y. Pinhasi, “Efficiency Enhancement of Free Electron Maser Oscillator by Mode Selection with a Prebunched Electron Beam”, *Applied Physics Letters*, vol. 76, no. 1, Jan. 2000.

[12] A. Abramovich, Y. Pinhasi, A. Yahalom, D. Bar-Lev, S. Efimov, A. Gover, “Optimization of Power Output and Study of Electron Beam Energy Spread in a Free Electron Laser Oscillator”, *Nuclear Instruments and Methods in Physics Research A*, vol. 475, no. 1-3, pp. 579-582, Dec. 2001.

[13] Y. Socol, A. Gover, A. Eliran, and M. Volshonok, Y. Pinhasi, B. Kapilevich, A. Yahalom, Y. Lurie, M. Kanter, M. Einat, and B. Litvak, “Coherence limits and chirp control in long pulse free electron laser oscillator”, *Phys. Rev. Special Topics – Accelerators and Beams,* Vol. 8, no. 8, pp. 1-5, Aug. 2005.

[14] Y. Pinhasi, M. Cohen, A. Gover, “Three-dimensional codes for simulating electron beam transport and free-electron laser operation including space-charge effects”. *International journal of electronics*, vol. 78, no. 3, pp. 581-590, 1995.

ISBN 978-3-95450-134-2

RF GUN DARK CURRENT SUPPRESSION WITH A TRANSVERSE DEFLECTING CAVITY AT LCLS*

James R. Lewandowski, R. Clive Field, Alan Fisher, Heinz-Dieter Nuhn, James Welch SLAC National Accelerator Laboratory, Menlo Park, California 94025, U.S.A

Abstract

A significant source of radiation signals in the LCLS Undulator has been identified as being generated by dark current emitted from the LCLS RF Photocathode Gun. Radiation damage to permanent magnets over time can lead to degraded performance and significant cost for replacement. A method of using an existing transverse deflector cavity with a modified RF pulse has been tested and shows promise for eliminating the radiation dose from RF gun dark current that is generated in time before and after the production beam pulse.

DARK CURRENT IN ACCELERATOR STRUCTURES

Dark current in high gradient accelerator structures results from electrons being emitted from the surfaces of the accelerator cavity walls. With the proper phase of the electric field these particles can be captured and accelerated along with the main production beam. Even though these stray particles are accelerated within the acceptance envelope of main beam they may have slightly different energy and orbit. In FEL machines such as LCLS this dark current can be transported through the entire linac and then lost in the Undulator magnets depositing their energy into magnet material causing degradation of the magnetic field over time [1]. An existing S-Band Transverse RF deflector which is used for beam diagnostic bunch length measurements is located in the LCLS injector and is the tool used for our dark current suppression tests.

TRANSVERSE DEFLECTOR CAVITIES

RF deflector structures as in Figure 1, were developed in the early days of SLAC for use in high energy physics experiments as fast kickers to send beam to multiple experiments, separate particles with different momentum [2] or they can be used to streak the beam for measuring bunch length as in LCLS or any other beam measurement experiment. In our application as a dark current suppression device we take advantage of the fast fill time characteristics of the traveling wave deflector structure. The fill time of the S-Band deflector used in the LCLS injector is around 55ns.

This fast fill time allows us to create an rf pulse with two lobes which has a zero field between the lobes. We can time the arrival of the beam such that it sits between the lobes and is minimally perturbed while

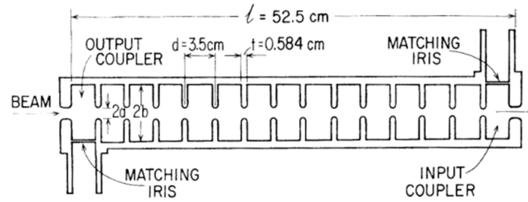

Figure 1: S-Band LOLA deflector sketch[2].

any dark current will see the maximum deflection with proper phasing of the cavity. The perturbed dark current can then be intercepted by existing collimators and purged out of the system. This scheme has been tested during several machine development days and is ready to be tested with user operation.

DARK CURRENT RADIATION SIGNAL

The LCLS undulator is instrumented with lead shielded optically stimulated luminescent dosimeters, or OSL dosimeters, electronic RADFETs, and Lucite detectors with photomultiplier tubes [1]. The initial dark current signals were observed on the PMT signals when the rf gun cathode laser was shuttered. With no production electron beam being produced there were still radiation signals present in the undulator which encompassed the rf pulse length of the gun. When power to the rf gun was taken away the signal disappeared. Even with collimation some particles which are on energy and orbit were getting through the entire linac system and depositing their energy in the undulator. A typical configuration for 9.5keV x-ray energy can yield a dose measured in the RADFET monitors of 4R/day as shown in Figure 2.

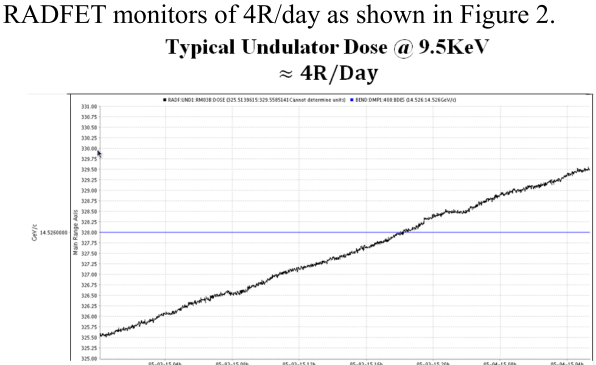

Figure 2: 24 hour RADFET 24 hour dose for 9.5KeV X-rays.

A reduction of the dose accumulated from the stray dark current electrons would be beneficial to the lifetime of the undulator magnets. The method of using the transverse deflector cavity has shown to be an effective solution in this endeavour.

*Work supported by U.S. Department of Energy, Office of Basic Energy Sciences, under Contract DE-AC02-76SF00515
#jiml@slac.stanford.edu

ISBN 978-3-95450-134-2

DEFLECTOR DARK CURRENT SWEEPER

RF Waveform

Initial tests of using the deflector structure as a dark current sweeper involved creating an rf waveform which would give unwanted dark current particles a kick while leaving the production beam unperturbed. The initial test was performed using a double pulse waveform with a 150ns and 50ns gap. The I&Q 150ns gap input waveform for the low level rf is shown in Figure 3a. Downmixed output waveforms from the deflector structure are seen in Figure 4.

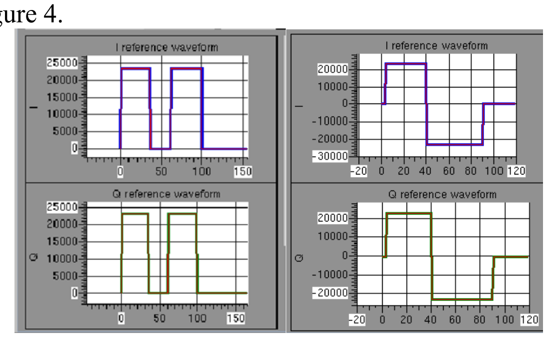

Figure 3: LCLS Control system display of I&Q waveform for dark current sweeper. 3a: RHS:150ns gap. 3b: LHS- “NoGap”.

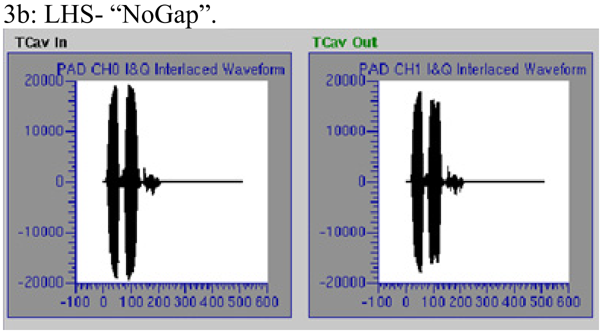

Figure 4: LCLS Control system display of Deflector RF Output with Sweeper 150ns Gap.

A waveform with a 50ns gap was also tested. Both the 150ns and 50ns gap provided the required “zero amplitude” zone which the beam could traverse the structure with little perturbation.

A final waveform with no gap, only a phase flip which results in an opposite kick for dark current which comes after the beam will be the standard running configuration when we are able to run during experiments, Figure 3. The FPGA firmware in the RF Phase and Amplitude Control Chassis (PAC) was modified to allow 30ps timing step resolution. This was achieved through shifting the FPGA clock phase. This waveform was successfully tested with beam and subsequent running will use the “no gap” waveform. The beam data in the next section was taken using the 50ns gap rf setup.

DETECTION OF DARK CURRENT IN UNDULATOR

As was stated earlier in this document and presented in [1] detection of dark current radiation signals in the LCLS undulator using Lucite Cherenkov light counters, which detect lost beam particles, were used to both characterize dark current signals and confirm the effectiveness of the deflector kicker system.

DAQ Hardware

Scintillator signals were acquired into SLAC designed DAQ hardware which is integrated into the control system. A Matlab program was written which integrates signal which displays the PMT signal as you would view on an oscilloscope. The large spike in the middle is time 0, where the FEL production beam is located. Two green boxes indicate times before and after the arrival of the main beam pulse. The image is made to have a persistence quality that allows old data spikes to fade after about 20 seconds. The image in Figure 5 clearly shows the radiation signature of dark current particles both before and after the main beam time. During our experiment we monitor this signal for some period of time and then turn on the Sweeper and observe the effect.

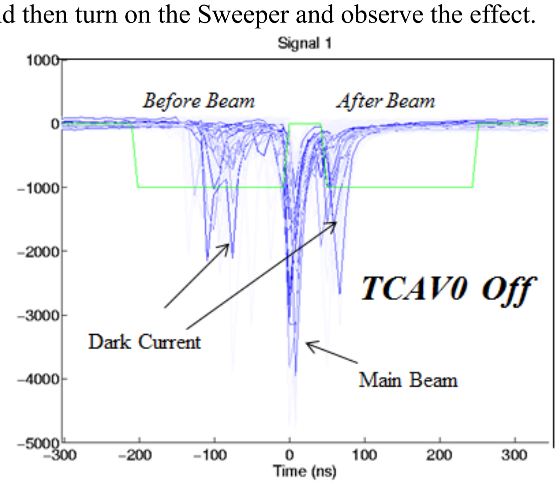

Figure 5: Dark Current Radiation observed in undulator PMT with TCAV suppression off, 9.5KeV FEL.

When the TCAV deflector operating with our double pulse waveform is enabled the radiation signature from the dark current is no longer present. A faded persistence image can be seen in Figure 6.

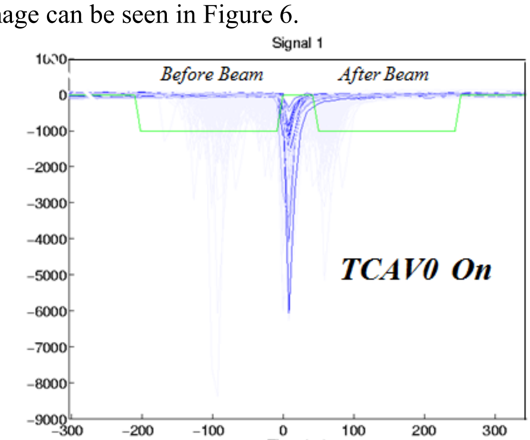

Figure 6: Dark Current Radiation is no longer observed in undulator when the TCAV is enabled with the double pulse.

ISBN 978-3-95450-134-2

Integrated Dark Current Signals

The next test was to look at the integration of the radiation signals in time as shown in Figure 7. Scans were made looking at our 3 different detectors, 2 early in the undulator and the 3rd toward the end. The integrated signals show a clear response from having the TCAV dark current suppression system working. A more negative signal indicates more radiation detected.

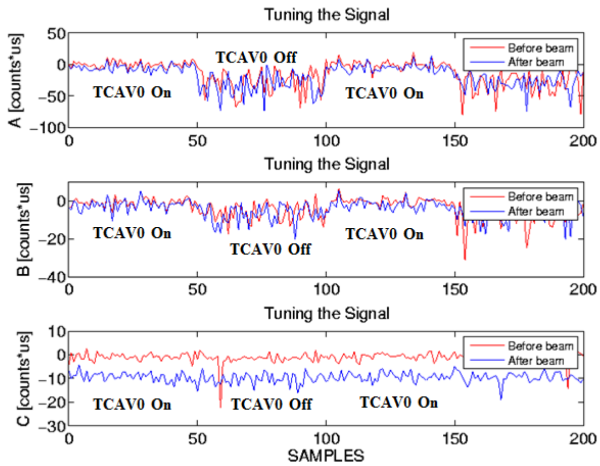

Figure 7: Undulator PMT radiation "Persistence" Scope Integration strip chart with/without TCAV0 Double Pulse Dark Current Suppression.

Integrated RADFET Signal during Operation

During one operational test we were able to leave the TCAV deflector operating for over an hour of time. This allowed a bit of dose to accumulate in the RADFET detectors. A comparison with similar running conditions a few hours before during user delivery, Figure 8, shows a 300mR/hr dose rate in a detector which is early in the undulator. For the 1.5hr integration with the dark current sweeper enabled, the detector shows an unmeasurable dose, see Figure 9. The dose rate change was not observed on other RADFET's downstream. This may indicate that the majority of dark current is lost early in the undulator.

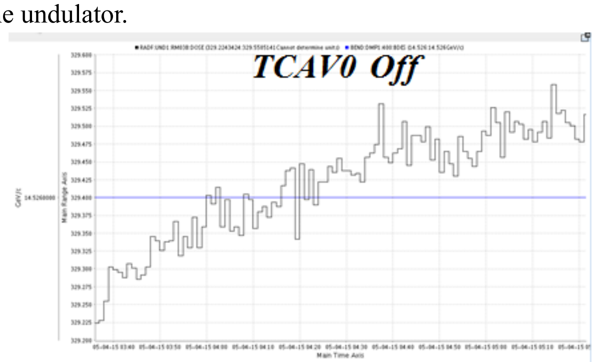

Figure 8: Typical 300mR/hr Radiation dose during 9.5KeV operation.

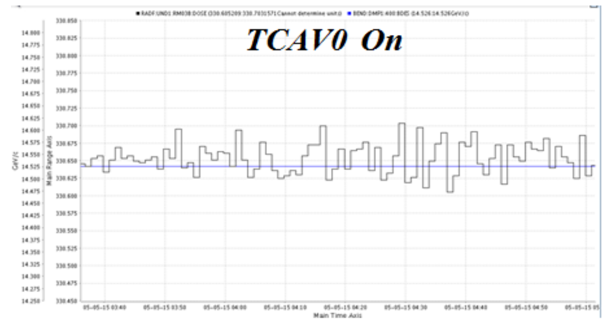

Figure 9: 0mR/hr with TCAV suppression enabled.

DEFLECTOR EFFECTS ON BEAM QUALITY

Potential concerns about passing the core beam through an active deflector cavity while operating the FEL must be addressed. Issues to be concerned about are steering effects on the beam immediately after the structure and perturbations to beam quality due to residual fields when the beam passes through the deflector structure.

Our beam tests have shown that there is no noticeable effect on the beam quality or orbit due to passing through the deflector structure with the sweeper enabled.

Figure 10 shows the beam spot immediately after passing through the deflector as viewed on an Optical Transition Radiation (OTR) foil. The orbit deflection was minimized with a 30ps RF timing trigger developed specifically for the application. A comparison of sweeper on/off shows not orbit shift.

As no detrimental effects are evident in the local vicinity of the deflector cavity we then focused our attention on downstream effects by using the XTCAV deflector in the LCLS dump line. The XTCAV is able to achieve femtosecond time and energy resolution measurements on the electron beam after it passes through the undulator magnets. Images of the beam were taken with the Dark Current sweeper disabled in Figure 11, and enabled as seen in Figure 12. There was no discernable effect to the beam quality or the FEL intensity from the sweeper operation.

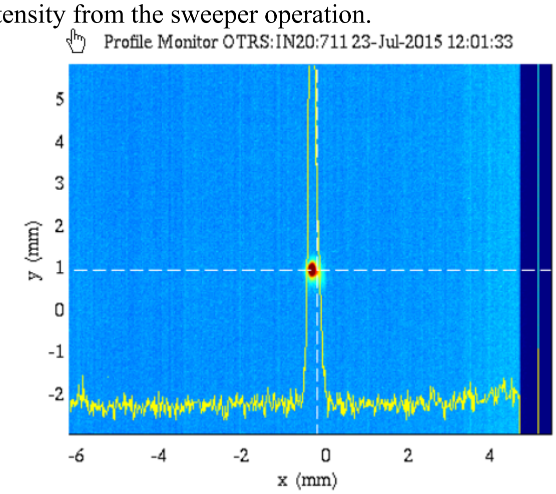

Figure 10: OTR beam image with deflector cavity enabled. Orbit corrected with fine timing of RF drive.

ISBN 978-3-95450-134-2

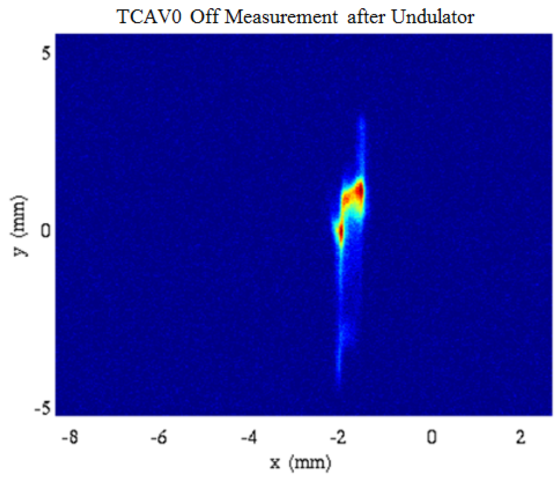

Figure 11: Beam Profile measurement after undulator with Dark Current Sweeper disabled.

During one test there was an increase in FEL energy jitter on the order of 4-5%. We are confident that with regular maintenance to this system it will perform within the operating specifications of other klystron powered systems.

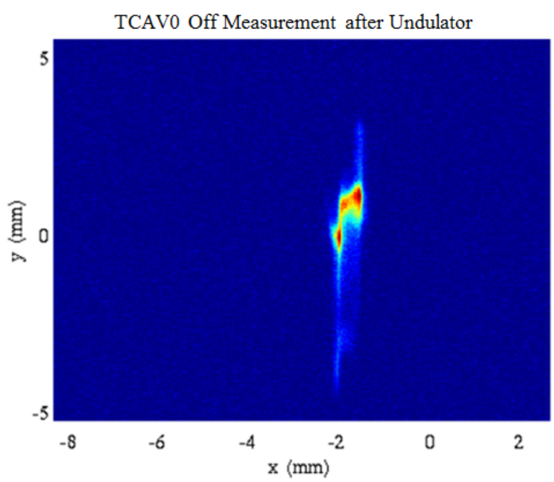

Figure 12: Beam Profile measurement after undulator with Dark Current Sweeper enabled.

APPLICATIONS FOR HIGH REP RATE FELS SUCH AS LCLS-II

Dark current that is mostly on energy and orbit can find its way through kilometre long accelerator systems, even with good collimation schemes. When pulse repetition rates of 1MHz, such as is proposed for LCLS-II, become reality the radiation doses deposited into undulator magnets from random capture of particles will accumulate very quickly. A dark current sweeper based on an rf deflector may be a good solution. Fast fill times (t_{fill}) can allow deflecting fields time to clear gaps between production beam pulses. Recent X-Band deflectors have even faster fill times and higher transverse gradients in shorter packages [3] than the S-Band structure used in our tests. For example a system based on the SLAC 27cell X-Band structure (t_{fill}=27ns) could yield a .152MV kick with 10KW input running at CW with a commercially produced klystron[4] [5].

CONCLUSIONS

A system for sweeping RF-Gun generated dark current away while leaving the production beam unperturbed has been successfully tested at the LCLS FEL operating at its usual 120Hz repletion rate. A reduction in the radiation generated by dark current has been observed when the transverse deflector in the LCLS injector operates using a special "double pulse" configuration. This added functionality can help prolong the lifetime of magnets lifetime by reducing the integrated dose absorbed in the magnetic material over time and also can improve experimental conditions by eliminating out of time particles which can contribute to experiment noise. The concept has implications for future higher repetition rate machines such as LCLS-II where the dose rates from this dark current will be much higher. It is hoped that in the upcoming run at LCLS this system can be activated for all runtime activities except those that use the deflector cavity for beam diagnostic functions.

REFERENCES

[1] H.-D. Nuhn, C. Field, et al, "Undulator Radiation Damage Experience at LCLS." FEL 2014, SLAC-Pub-16120
[2] O. H. Altenmueller, R. R. Larsen and G. A. Loew, "Investigations of Traveling-Wave Separators for the Stanford Two-Mile Linear Accelerator." Review of Scientific Instruments 35:438 (1964).
[3] V. A. Dolgashev, et al, "Design and Application of Multi Megawatt X-Band Deflectors for Femtosecond Electron Beam Diagnostics." PhysRevSTAB 17, 102801 (2013)
[4] CPI Model VA-864, 10KW CW klystron. http://www.cpii.com/product.cfm/1/20/48
[5] Private communication with V. A. Dolgashev.

ISBN 978-3-95450-134-2

SIMULATING SINGLE CRYSTAL COPPER PHOTOCATHODE EMITTANCE*

T. Vecchione#, SLAC National Accelerator Laboratory, Menlo Park, CA 94025, U.S.A.

Abstract

The performance of free-electron lasers depends on the quality of the electron beam used. In some cases this performance can be improved by optimizing the choice of photocathode with respect to emittance. With this in mind, electronic structure calculations have been included in photoemission simulations and used to predict the emittance from single crystal copper photocathodes. The results from different low-index surfaces are reported. Within the model assumptions the Cu(100) surface was identified as having minimal emittance, particularly when illuminated by 266 nm light and extracted in a 60 MV/m gradient. These findings may guide future experimental work, leading to improved machine performance.

INTRODUCTION

In photocathode-based free-electron lasers (FEL) much of the overall emittance comes from the photocathode itself. Surprisingly, the choice of which photocathode to use is often a result of historical precedent rather than systematic study. In these cases it is important to optimize the choice of photocathode with respect to emittance. Reductions in emittance can increase both the brightness and the energy of the x-rays produced and can save money by allowing undulators to be installed that are shorter in length.

Xie published a model that is useful for illustrating the dependence of FEL performance on emittance [1]. In this model the undulator saturation power, P_{sat}, is given as a function of the beam power, P_{beam}

$$P_{sat}\left[\varepsilon_x\right]=1.6\rho\left[\varepsilon_x\right]\left(\frac{L_{1d}\left[\varepsilon_x\right]}{L_g\left[\varepsilon_x\right]}\right)^2 P_{beam} \tag{1}$$

and the saturation length, L_{sat}, is given as a function of the input noise power, P_n.

$$L_{sat}\left[\varepsilon_x\right]=L_g\left[\varepsilon_x\right]Ln\left[\frac{P_{sat}\left[\varepsilon_x\right]}{\alpha P_n}\right] \tag{2}$$

Both the saturation power and the saturation length depend on the FEL parameter, ρ, which in turn depends implicitly on emittance, ε_x, through the beam size, σ_x. The FEL parameter for a planar undulator is given by

$$\rho\left[\varepsilon_x\right]=\left(\frac{\left(\frac{I}{I_A}\right)\left(\frac{\lambda_u}{2\pi\sigma_x\left[\varepsilon_x\right]}\right)^2\left(\frac{1}{2\gamma}\right)^3\times}{\left(\frac{K}{\sqrt{2}}\left(J_0\left[\frac{K^2}{4+2K^2}\right]-J_1\left[\frac{K^2}{4+2K^2}\right]\right)\right)^2}\right)^{1/3} \tag{3}$$

*Work supported by US DOE contract DE-AC02-76SF00515.

#tvecchio@slac.stanford.edu

For the sake of brevity, all other important definitions can be found in either [1] or in a comprehensive review of FEL theory by Huang and Kim [2].

Figure 1 uses Eq. (1), (2) and (3) to plot the projected percent increase in radiated power and the percent decrease in saturation length as functions of a percent decrease in emittance for the LCLS-I.

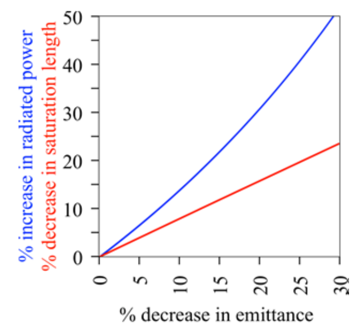

Figure 1: A significant improvement in FEL performance is predicted from lower emittance. For the LCLS-I at 8 keV and an initial emittance of 1 μm a 20% decrease in emittance gives either a 31% increase in radiated power or a 16% decrease in saturation length.

It is reasonable to assume that a change in emittance at the photocathode will lead to a similar change in emittance at the undulator.

The biggest challenge in evaluating photocathodes for use in FELs is in accurately predicting their emittance. Analytical expressions for metal photocathdoes have been derived by Dowell and Schmerge [3], Eq. (4), and by Vecchione [4], Eq. (5). Equation (5) maintains the full Fermi-Dirac distribution in the final result. One consequence of this is that the emittance at non-zero temperatures is non-zero even when the photon energy, ħω, equals the effective work function, ϕ_{eff}. In the zero temperature limit Eq. (5) reduces to Eq. (4).

$$\varepsilon_n=\sigma_x\sqrt{\frac{\hbar\omega-\phi_{eff}}{3mc^2}} \tag{4}$$

$$\varepsilon_n=\sigma_x\sqrt{\frac{kT}{mc^2}}\sqrt{\frac{Li_3\left[-Exp\left[\frac{e}{kT}\left(\hbar\omega-\phi_{eff}\right)\right]\right]}{Li_2\left[-Exp\left[\frac{e}{kT}\left(\hbar\omega-\phi_{eff}\right)\right]\right]}}$$
$$Li_n\left[z\right]=\frac{\left(-1\right)^{n-1}}{\left(n-2\right)!}\int_0^1\frac{1}{t}Log\left[t\right]^{n-2}Log\left[1-zt\right]dt \tag{5}$$

ISBN 978-3-95450-134-2

To derive Eq. (4) or (5) two physical models are used. The first is the Sommerfeld free electron model describing electronic states and their occupational probabilities. In this model electrons are bound by a uniform potential, they have a constant density of states and the occupational probability of these states is governed by Fermi-Dirac statistics. The second model used is the Spicer 3-step model identifying a sequence of steps involved in photoemission. In the first step electrons absorb photons gaining energy $\Delta E=\hbar\omega$ normal to surface. In the second step these electrons diffuse to surface. In the third step these electrons escape if they can, loosing energy $\Delta E=\phi_{eff}$ normal to surface.

In the Sommerfeld model all metallic surfaces are treated identically. Unfortunately this is not always reliable for predicting emittance. The reason for this is that the electronic structure of the material has not been accounted for. Figure 2 illustrates the importance of crystallographic grains in photocathodes. It is generally agreed that the electronic structure should be included to improve the accuracy of emission models.

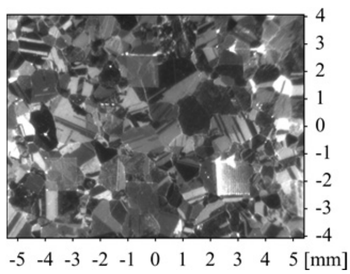

Figure 2: Optical image of a copper photocathode showing a large number of single crystal grains and illustrating the importance of crystallographic orientation.

METHODS

Electronic structure calculations have been incorporated into a photoemission model. The electronic structure calculations were performed using Density-Functional Theory (DFT), a widely accepted technique for calculating the ground state electronic structure of a material. The basis of DFT is an assumption that the exact N-body Schrödinger equation for a system of electrons

$$\begin{pmatrix} -\frac{1}{2}\nabla^2 \\ +\frac{1}{2}\sum_{i\neq j}\frac{1}{|r_i-r_j|} \\ -\sum_{i,I}\frac{Z_I}{|r_i-R_I|} \\ +\frac{1}{2}\sum_{I\neq J}\frac{Z_I Z_J}{|R_I-R_J|} \end{pmatrix}\Psi(r_1,r_2,\rightleftharpoons)=E\Psi(r_1,r_2,\rightleftharpoons) \qquad (6)$$

can be described by an equivalent set of N, 1-body Kohn-Sham equations.

$$\begin{pmatrix} -\frac{1}{2}\nabla_i^2 \\ +\frac{1}{2}\int\frac{n(r')}{|r-r'|}dr' \\ -\sum_I\int\frac{Z_I n(r')}{|r'-R_I|}dr' \\ +\frac{1}{2}\sum_{I\neq J}\frac{Z_I Z_J}{|R_I-R_J|} \\ +\varepsilon_{xc}\left[n(r)\right] \end{pmatrix}\psi_i(r)=\varepsilon_i\psi_i(r) \qquad (7)$$

An "exchange-correlation" term is added ad-hoc to the Kohn-Sham equations and defined to be anything such that this equivalency is true. The approach was laid down in the 1960s [5, 6] and has been improved on since then.

ABINIT was used in these simulations. ABINIT is a freely distributed software package for DFT calculations. It emphasizes valence band phenomena by replacing the core electron charge density with norm-conserving pseudopotentials. This simplifies the problem, allowing for a decreased plane-wave basis set to be used in solving the Kohn-Sham equations. In these simulations Troullier-Martins type pseudopotentials were used.

ABINIT relies on periodic boundary conditions. As a result, surface electronic structure can be calculated using a slab supercell. Bulk calculations were done with a fixed lattice constant (3.615 Å) but the ionic positions in the slab calculations were allowed to relax. The final slab thicknesses were 42.1 Å for Cu(100), 30.4 Å for Cu(110) and 30.2 Å for Cu(111).

Additional simulation details are as follows. A local density approximation Teter-Pade parameterization was used for the exchange-correlation functional. The occupational probability of states was calculated using 0.01 Hartree "cold smearing". The energy cutoff was 30 Hartree for the slab calculations and 50 Hartree for the bulk calculations. In general the DFT convergence criterion was that of a difference in total energy of $1\text{x}10^{-6}$ Hartree twice in a row.

Once a set of eigenvectors and eigenvalues were calculated then they were expanded using symmetry operations to fill the Brillouin Zone. The number of eigenvectors used varied from a minimum of 16^2=256 for slab calculations to 50^3=125000 for bulk calculations. The discrete set of eigenvectors and eigenvalues were made continuous by linearly interpolating between them.

The physical model governing the emission aspects of the simulations was based on the Spicer model used to derive Eq. (4) and (5) with step 2 omitted. K-space was searched randomly until at least 10^3 states (or more) with sufficient energy and momentum for emission were found. These states were emitted and RMS values were calculated based on the resulting distribution.

ISBN 978-3-95450-134-2

RESULTS

The first results reported are simple demonstrations that the electronic structure of copper was calculated correctly. Figure 3 shows the Fermi surface from copper made by mapping the Fermi energy in K-space. The resulting shape is common to face-centered cubic metals.

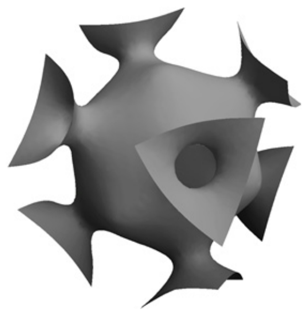

Figure 3: Fermi surface from copper. The shape of this surface is common and serves as a demonstration that the electronic structure was calculated correctly.

Figure 4 gives the simulated bulk density of states from copper. This result was also in line with expectations.

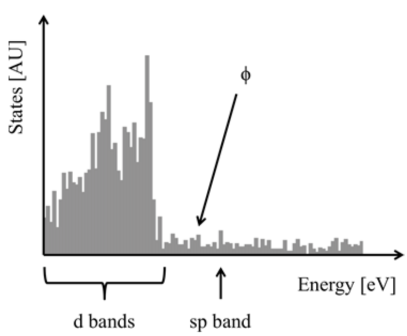

Figure 4: Bulk density of states for copper. The sp band in copper is separated from the d bands and is the reason that copper behaves like a free-electron metal.

Table 1: Surface Work Function Calculations using Supercell Slabs. The results of the current simulations are given in the first line of the table. The values are reasonably consistent with other published work.

Cu(111)	Cu(100)	Cu(110)		Source
5.02	4.88	4.65	calc	Vecchione, T.
5.02	4.64	4.52	calc	Schroder, A. *unpublished at present
5.31	5.02	4.81	calc	Fall, C.
5.19	4.95	4.9	calc	Rodach, T., Bohnen, K. P., & Ho, K. M.
5.2	4.94	4.68	calc	Li, W., & Li, D. Y.
4.94	4.59	4.48	exp	Gartland, P. O., Berge, S., & Slagsvold, B. J.
4.98	4.83	4.45	exp	Haas, G. A., & Thomas, R. E.
4.63	4.45	4.4	exp	Peralta, L., Margot, E., Berthier, Y., & Oudar, J.
5.54	5.15	4.92	exp	Delchar, T. A.

The supercell slab calculations produced values for work functions that were reasonably consistent with other published work. These results are summarized in Table 1.

The emission components of the simulations were verified by comparing the results with available angle-resolved photoemission spectroscopy (ARPES) data from copper. This comparison is shown in Figure 5.

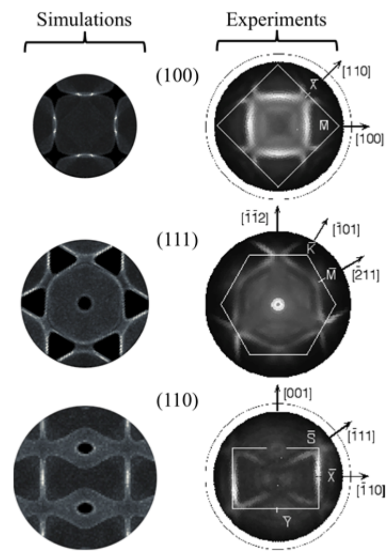

Figure 5: Verifying the emission model. The experimental data is reproduced from [7]. The excitation energy was $\hbar\omega$=21.2 eV (He) and in the simulations a bandwidth of ΔE = 0.1 eV was applied to the final result.

Having demonstrated that the simulations give reasonable results, the following are the results from copper, shown in Figures 6, 7 and 8.

Cu(100) and Cu(110) are well described by the Sommerfeld free electron model. Cu(110) has a much lower work function the Cu(100) but based on parameterized fits to the Dowell-Schmerge formula (Eq. (4) it also a much lower effective mass.

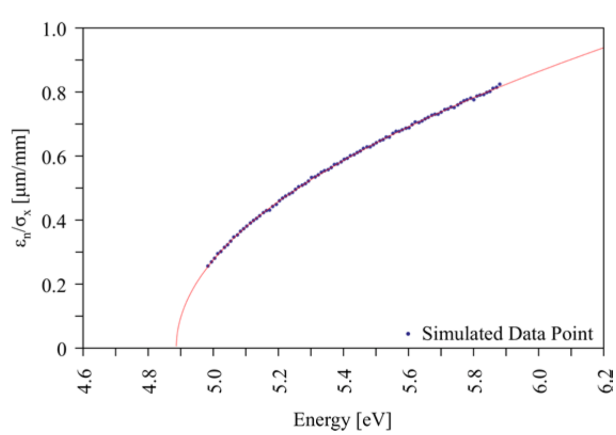

Figure 6: Emittance as a function of excitation energy for Cu(100). The slab calculation gives a work function of ϕ = 4.88 eV. Fitting the simulated data gives the same work function with an effective mass of m = 0.98 m_e.

ISBN 978-3-95450-134-2

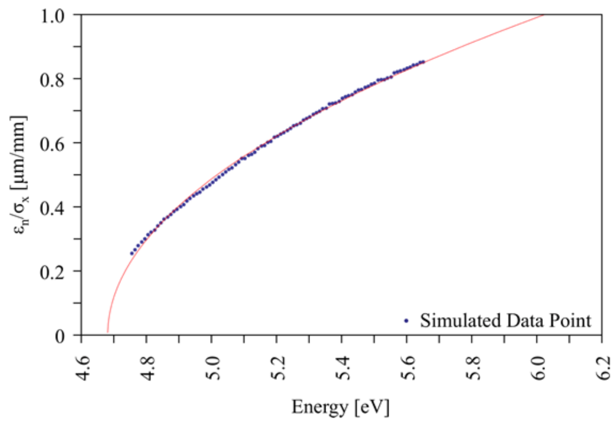

Figure 7: Emittance as a function of excitation energy for Cu(110). The slab calculation gives a work function of $\phi = 4.65$ eV. Fitting the simulated emittance data gives a slightly different parameterization of $m = 0.88\ m_e$ and $\phi = 4.68$ eV.

Cu(111) has a discontinuity in emission due a neck in the Fermi surface in this direction. Bulk Cu(111) would make a poor photocathode. However the gap in emission provides an interesting opportunity for a surface state to create a possibly lower emittance photocathode. This needs further study.

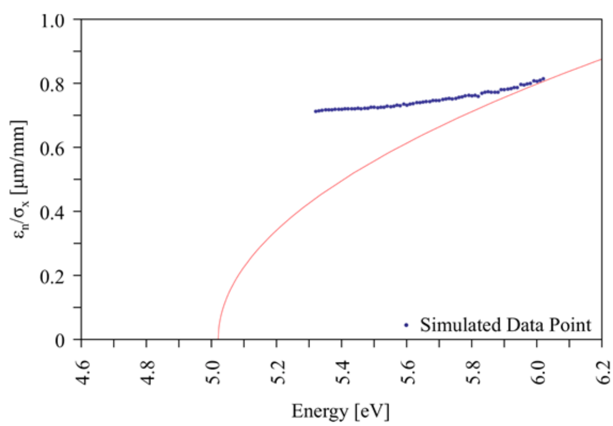

Figure 8: Emittance as a function of excitation energy for Cu(111). The slab calculation gives a work function of $\phi = 5.02$ eV. The region where there is no emission comes from the neck in Fermi surface.

The effect of an applied electric field on the surface of a photocathode is to effectively lower the work function an amount given by Equation 8.

$$\Delta\phi = \sqrt{\frac{eF}{4\pi\varepsilon_0}} \tag{8}$$

This so called "Schottky effect" at 60 MV/m produces a 0.294 eV reduction in the work function. Figure 9 is a plot of emittance from Cu(100) and Cu(110) using Equation 4, the parameterized model fits from above and in the presence of a 60 MV/m extraction field.

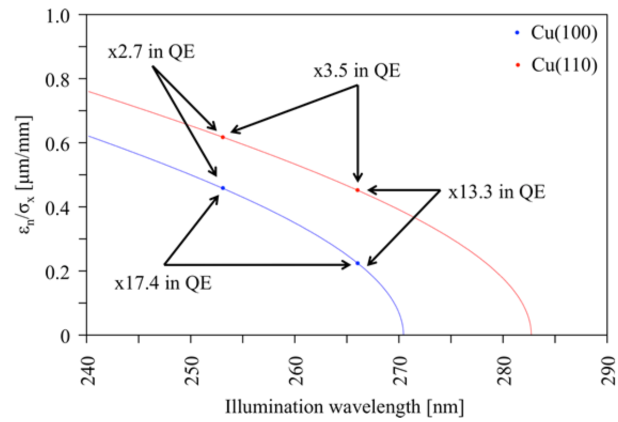

Figure 9: A comparison of emittance from Cu(100) and Cu(110) in the presence of a 60 MV/m extraction field. Factor differences in quantum efficiency are also listed to aid the comparison.

One finds that:
ε_n for Cu(100) at 253 nm = σ_x (0.46 μm/mm)
ε_n for Cu(110) at 253 nm = σ_x (0.62 μm/mm)
ε_n for Cu(100) at 266 nm = σ_x (0.22 μm/mm)
ε_n for Cu(110) at 266 nm = σ_x (0.45 μm/mm)

If quantum efficiency (QE) isn't a concern due to both an excess in overhead laser budget for a specific amount of charge and from being far from the damage threshold of the surface then minimal emittance would come from the Cu(100) surface illumined by 266 nm light. The projected value is actually a little below to the thermal limit of 0.23 μm/mm. This comes from having ignored Fermi statistics (temperature) in the model. The real value will be slightly higher than this but not so much so as to change the overall result. Under realistic operating conditions this is probably the best value that can be achieved.

CONCLUSIONS

In summary, the benefits to FELs from reducing photocathode emittance can be significant. Recognizing that experimental work is expensive, cost-effective numerical simulations have been performed. Within the model assumptions the Cu(100) surface was identified as having minimal emittance, particularly when illuminated by 266 nm light and extracted in a 60 MV/m gradient. These findings will guide future experimental work, leading to improved machine performance.

FUTURE PLANS

Several important physical phenomena have been left out of these simulations. In the near future it will be important to repeat these simulations including the effects of finite temperature occupational probabilities, the work function shift in the presence of surface oxide layers and having considered contributions from surface states.

ISBN 978-3-95450-134-2

In general the (111) surfaces of the face-centered cubic and the (100) surfaces of the body-centered cubic metals have exposed surface states. Figure 10 gives an example of one such case. This is important because surface states have well defined dispersion relations. The energy of a transition from an initial surface state (ħω) limits the transverse momentum allowed in the final state. If the final state is in vacuum, the result is anisotropic emission that is confined in both energy and momentum. It has been hypothesized that surface states could be a source for low emittance electron beams so the overall contribution of surface states needs to be considered.

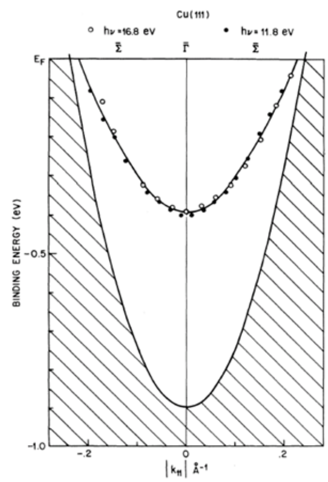

Figure 10: Image reproduced from [8] showing a clear dispersion relationship of the exposed Cu(111) surface state. The region where there is no emission from the bulk states comes from the neck in the Fermi surface.

The set of face-centered cubic and body-centered cubic metals shown in Figure 11 are expected to exhibit phenomenogically similar emission characteristics to those found in copper. In the future emittance simulations from these metals will be systematically parameterized to identify surfaces with large effective masses that could possibly produce low emittance beams. A group led by W. A. Schroeder has recently published results [9,10] showing good success with similar structure based comparative efforts.

bcc

fcc

Li	Be									
Na	Mg									
K	Ca	Sc	Ti	V	Cr	Mn	Fe	Co	Ni	Cu
Rb	Sr	Y	Zr	Nb	Mo	Tc	Ru	Rh	Pd	Ag
Cs	Ba		Hf	Ta	W	Re	Os	Ir	Pt	Au

Figure 11: The set of face-centered cubic and body-centered cubic metals for which the effective masses of low index surfaces will be calculated.

Simulations are a preliminary step to identifying photocathodes for use. Before this can happen the results of the simulations must be experimentally verified. For this a strategy such as the one illustrated in Figure 12 could be used to test single crystal photocathodes for the LCLS-I.

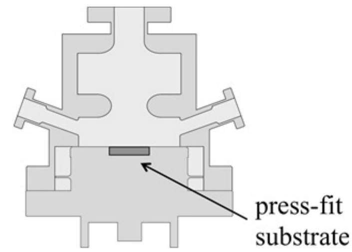

Figure 12: Experimental setup for testing single crystal photocathodes in a high gradient RF gun. This press-fit substrate strategy is similar to one that has been used at the UCLA/PEGASUS facility.

Finally the algorithm for calculating emittance from metallic photocathodes can be adapted to calculate emittance from semiconductor photocathodes. This will make the work relevant for future FELs such as the LCLS-II. The goal will be to search through appropriate semiconductors to find ones with large effective masses at their band gaps that could possibly produce low emittance beams.

ACKNOWLEDGMENT

The author would like to thank W. Andreas Schroeder at the University of Illinois at Chicago for all of his helpful suggestions.

REFERENCES

[1] M. Xie, "*Design optimization for an X-ray free electron laser driven by SLAC linac*", Proceedings of the 1995 Particle Accelerator Conference, May 1-5, 1995, Dallas, USA, 183-185.

[2] Z. Huang and K. J. Kim, *Phys. Rev. ST Accel. Beams* **10** 3, 034801 (2007).

[3] D. Dowell and J. Schmerge, *Phys. Rev. ST Accel. Beams* **12** 11, 074201 (2009).

[4] T. Vecchione et al, "*Quantum Efficiency and Transverse Momentum from Metals*", Proceedings of FEL'13, August 25-30, 2013, New York, USA, TUPSO83.

[5] P. Hohenberg and W. Kohn, *Phys. Rev.* **136**, B864 (1964).

[6] W. Kohn and L.J. Sham, *Phys. Rev.* **140**, A1133 (1965).

[7] P. Aebi et al., *Surf. Sci.* **307**, 917-921 (1994).

[8] S. D. Kevan, *Phys. Rev. Lett.* **50** 7, 526 (1983).

[9] T. Li, B. L. Rickman and W. A. Schroeder, *J. Appl. Phys.* **117** 13, 134901 (2015).

[10] T. Li, B. L. Rickman and W. A. Schroeder, *Phys. Rev. ST Accel. Beams* **18** 7, 073401 (2015).

ISBN 978-3-95450-134-2

RECENT UNDERSTANDING AND IMPROVEMENTS OF THE LCLS INJECTOR*

F. Zhou+, D. Bohler, Y. Ding, S. Gilevich, Z. Huang, H. Loos, and D. Ratner
SLAC, Stanford, CA 94309, USA

Abstract

Ultraviolet drive laser and copper photocathode are the key systems for reliably delivering <0.4 μm of emittance and high brightness free electron laser (FEL) at the linac coherent light source (LCLS). Characterizing, optimizing and controlling laser distributions in both spatial and temporal directions are important for ultra-low emittance generation. Spatial truncated Gaussian laser profile has been demonstrated to produce better emittance than a spatial uniform beam. Sensitivity of the spatial laser distribution for the emittance is measured and analysed. Stacking two 2-ps Gaussian laser beams significantly improves emittance and eventually FEL performance at the LCLS in comparison to a single 2-ps Gaussian laser pulse. In addition, recent observations at the LCLS show that the micro-bunching effect depends strongly on the cathode spot locations. The dependence of the micro-bunching and FEL performance on the cathode spot location is mapped and discussed.

INTRODUCTION

The cost and performance of the x-ray free electron laser (FEL) [1-2] depends critically on the emittance of the electron beam from the injector source. Producing and maintaining the desired ultra-small emittance (<0.4 μm for 180-250 pC) is one of the major challenges for operations of Linac Coherent Light Source (LCLS). Major injector source emittance includes cathode thermal emittance, space charge, and RF-contributed emittance [3-4]. According to the LCLS operational experience, the photocathode drive laser distributions sensitively affect injector emittance thereby hard x-ray FEL performance. The LCLS drive laser system is a frequency tripled, chirped-pulse amplification system based on Ti:sapphire. The system consists of mode-locked oscillator, followed by a pulse stretcher oscillator, a regenerative amplifier, two multi-pass amplifiers, pulse compressor, and finally a frequency tripler to convert the IR laser to 253 nm. The 253 nm laser beam is finally delivered to the copper photocathode through a long in-vacuum transport from the laser room on the ground to the 10-m deep SLAC linac tunnel.

The performance of the complex LCLS laser systems is sensitive to the external environment such as humidity, temperature and dusts and aging equipment. For 24/7 operating laser systems, minor environment change may cause optical misalignments, even optics damage, resulting in changes of spatial and temporal laser distributions on the cathode. Measuring, optimizing and controlling the desired spatial and temporal laser profiles on the cathode are of particular importance for maintaining the desired ultra-low emittance and maximizing x-ray FEL performance. As the drive laser systems, the LCLS copper photocathode is also of importance for the emittance and the micro-bunch instability (μBI). Recently we observed at the LCLS that the μBI is different at different cathode spots, causing different hard x-ray FEL performance (e.g., pulse intensity and bandwidth). Impacts of drive laser distributions and photocathode on the emittance, μBI and FEL performance are measured and analysed. This paper is organized as follows. Section II will introduce the measures of the spatial laser distribution and laser impacts on emittance. Emittance dependence on the temporal laser distribution is presented in Section III. In section IV, the dependence of the μBI and x-ray FEL performances on the laser location across the photocathode is mapped and discussed. The results are finally summarized.

MEASURING, OPTIMIZING AND CONTROLLING SPATIAL LASER DISTRIBUTION FOR ULTRA-LOW EMITTANCE

Many previous studies showed the drive laser must be uniform in transverse dimensions on the photocathode to produce the best emittance beam. However, recently simulations and experimental observations at the LCLS [5] show that the truncated-Gaussian spatial laser beam produces a better emittance beam than uniform laser does. Figure 1 (top) shows the different spatial lineout-intensity distributions including uniform-like (a), truncated-Gaussian (b), and Gaussian-like (c). The projected and time-sliced emittances of three distributions are simulated, as shown in Fig. 1 (bottom), using ImpactT code [6] for 150 pC. The emittance with the truncated-Gaussian distribution improves ~30% in comparison to the uniform-like laser or Gaussian-like beam.

Maintaining and controlling the spatial truncated-Gaussian laser beam on the photocathode, however, is not trivial for 24/7 operational laser systems. For example, it is difficult to maintain both shoulders a1 and a2 shown in Fig. 1(b) of the truncated-Gaussian distribution to be balanced through the complex laser systems and 10's meters-long laser transport. Extensive simulations show that the unbalanced shoulders increase the emittance. Therefore, having quantitative measures is crucial for characterizing, optimizing and controlling the spatial laser beam shapes and degree of asymmetry of both shoulders for ultra-small emittance beam. The following sub-

* The work is supported by DOE under grant No. DE-AC02-76SF00515.
+ zhoufeng@slac.stanford.edu

ISBN 978-3-95450-134-2

sections describe two major measures (parameters for spatial laser lineout distribution and laser Zernike polynomials [7]) of the spatial laser shapes and emittance dependence on shapes. When the laser on the photocathode has regular smooth spatial distribution, either of two measures is good for quantitative characterization of laser beam. However, in reality, the laser distribution sometimes is irregular from the laser systems due to misalignment and mirror damages. In such a case, using parameters for lineout laser distribution may not fully represent a true laser beam, as only emittance number cannot represent an irregular electron beam. The parameters for laser Zernike polynomials are found as a better measure of the laser spatial distributions for the case, although it is more complicated. With these two vital measures, the desired parameters for spatial laser distribution can be maintained within the criteria for high-brightness electron beam generation.

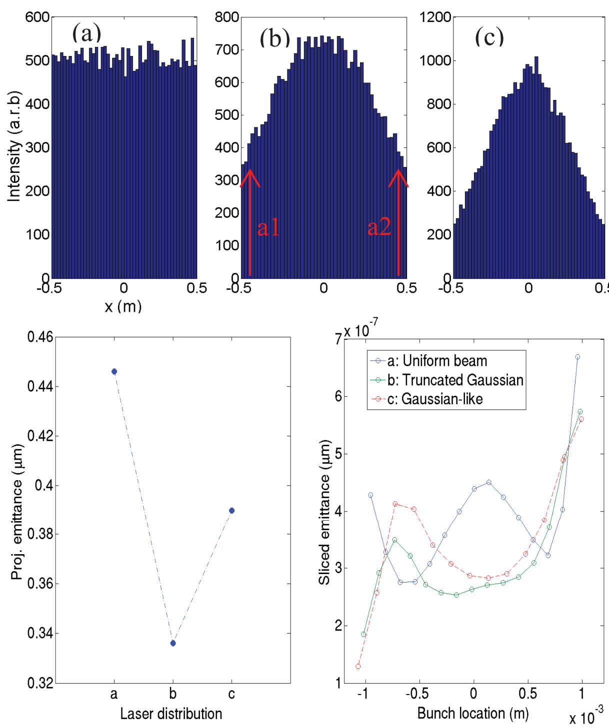

Figure 1: Spatial laser lineout distributions (top), (a), (b) and (c) represent uniform-like, certain truncated-Gaussian and Gaussian-like spatial distributions; corresponding projected (bottom, left) and slice emittances (bottom, right) for 150 pC.

Parameterized With Lineout Laser Distribution

When the laser spatial distribution is reasonably smooth, as shown in Fig. 2, the method of using lineout-distribution is the best way to quantify laser profile. The lineout intensity ratio g/h shown in Fig.2 is used to determine the laser shape. The laser is in uniform-like with g/h<0.1, while it is close to Gaussian distribution with g/h>3. Figure 3 shows both simulated (left) and measured (right) emittance for different laser lineout intensity ratio of g/h for 150 pC. Both measurements and simulations show that the range of g/h for maintaining ultra-low emittance is in between 0.5 and 1.5. For a regular smooth-like spatial Gaussian laser beam, the lineout intensity ratio g/h can be adjusted within the desired range using an optical telescope.

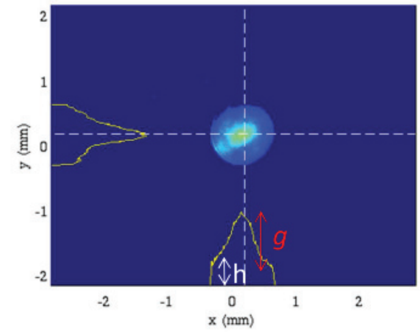

Figure 2: Example of regular smooth beam distribution parameterized by g/h of the lineout intensity ratio.

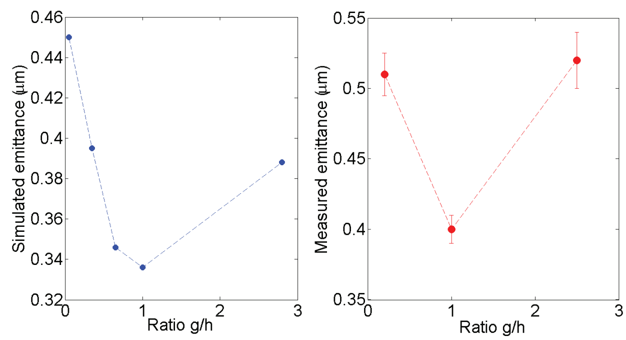

Figure 3: Simulated (left) and measured (right) emittance for different g/h of lineout intensity ratio for 150 pC.

Parameterized With Laser Zernike Polynomials

Zernike functions are usually used in the optical systems to characterize the measured structures of deformations and aberrations because these form a complete, orthogonal basis over the unit circle. The Zernike functions are a product of the Zernike radial polynomials and sine- and cosine-functions. As these functions are orthogonal on the unit circle, any function defined on the unit circle can be expressed as a sum of Zernike polynomials. The coefficients associated with the dominated Zernike polynomials can be used to represent optical data. For simplification, instead of using large amount of Zernike polynomials, two parameters [8], symmetry and asymmetry powers, are used to represent summed different types of polynomials for an optical spatial laser beam on the cathode. The symmetry power summing all symmetrical polynomials is to determine the spatial laser shapes, e.g., uniform or truncated Gaussian or Gaussian. In this study, the laser is close to uniform-like distribution with the symmetry power <0.01, while it is near Gaussian-like with the symmetry power >0.07. The asymmetry power summing asymmetrical polynomials is to determine the degree of laser beam symmetry with respect to the centroid spot location. The

ISBN 978-3-95450-134-2

laser beam is near symmetry with the asymmetry power <0.01, otherwise the beam is in not symmetric. For a fixed asymmetry power <0.01, emittance dependence on the symmetry power for different spatial laser shapes shown in Fig. 4 (top, a, b and c) is measured, as shown in Fig. 4 (bottom), for 150 pC. The data shows that the small emittance can be achieved with the symmetry power in 0.025-0.04 (truncated Gaussian distributions). Figure 5 shows the measured emittance dependence on the laser beam asymmetry power for a fixed symmetry power of 0.025. It shows the beam emittance can be maintained at ultra-low value with the asymmetry power <0.015.

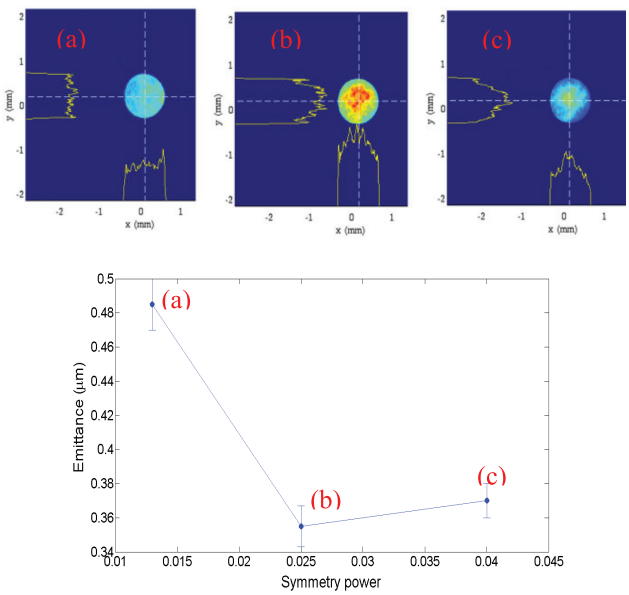

Figure 4: Laser shapes and related symmetry power vs. measured emittance for a fixed asymmetry power <0.01.

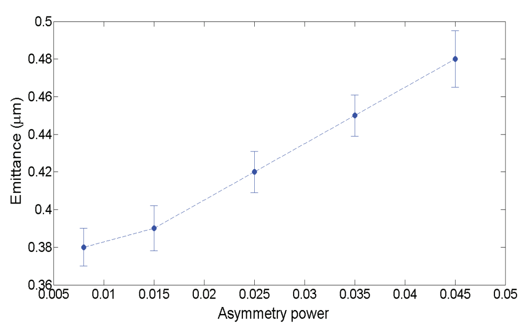

Figure 5: Measured emittance dependence on the asymmetry power for a fixed symmetry power of 0.025.

OPTIMIZATIONS OF TEMPORAL LASER DISTRIBUTION FOR ULTRA-LOW EMTTANCE

RF and space charge emittance strongly depends on the photocathode drive laser pulse length [9], expressed by:

$$\varepsilon_{rf} \sim E.\sigma_r^{\,2} \cdot \sigma_z^{\,2} \qquad (1)$$

$$\varepsilon_{sc} \sim \frac{Q}{E \cdot \sigma_z} \mu_x \qquad (2)$$

where E is the peak accelerating gradient on cathode, μ_x is the transverse space charge factors related to the aspect ratio of the rms beam size σ_r to rms bunch length σ_z, and Q is the bunch charge. Eqs. 1 and 2 indicate that the laser pulse length has to be traded off for space charge and RF emittance for optimum emittance. Systematic simulations of the emittance dependence on the single Gaussian laser are performed for 180 pC, as shown in Fig. 6. The projected (left) and sliced emittance (right) is close to optimum for single ~3.5 ps FWHM Gaussian laser.

Current LCLS drive laser pulse has 1.9±0.2 ps FWHM, and the laser systems are not flexible to lengthen laser pulse length >3 ps FWHM without compromising the laser temporal profile. Recently, two ~1.9-ps different polarization Gaussian lasers are stacked together to lengthen the laser pulse. The advantages using pulse stacking over single Gaussian laser: 1) easier to adjust overall laser pulse length for various needs; 2) relatively sharper edges of the final laser pulse for emittance compensation process. As shown in Fig. 6, a better projected emittance is simulated with a stacked 4 ps pulse (~2 ps separation for stacking two 2-ps pulses) than single 3.5 ps Gaussian laser, although the slice emittance with 4 ps stacked laser is similar to 3.5 ps single Gaussian. The 4 ps stacked pulse has better emittance compensation than single 3.5ps Gaussian.

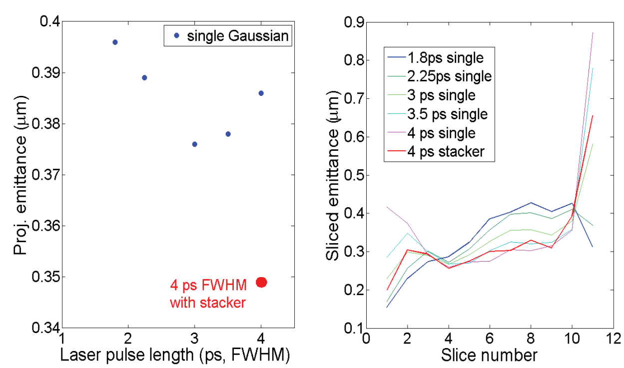

Figure 6: Simulated projected (left) and slice (right) emittance dependence on the single Gaussian laser and a stacked pulse 4 ps FWHM for 180 pC.

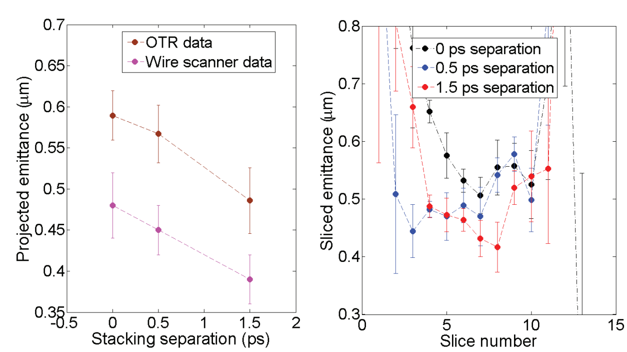

Figure 7: Measured projected (left) and slice (right) emittance (250 pC) with different separation for stacking two ~1.9 ps FWHM pulses.

ISBN 978-3-95450-134-2

Figure 7 shows the comparison of the measured projected (left) and slice (right) emittance for single Gaussian and stacked laser beam. At the LCLS, projected emittance can be measured with one OTR screen and wire scanner. The data shows the projected emittance measured with the OTR screen is ~20% higher than wire scanner. The higher emittance with the OTR method is probably caused by the microbunching effect at the OTR screen. Further understanding for the emittance difference using OTR and wire scanner is needed. The slice emittance can be measured only with the OTR screen and a transverse RF cavity. Although the measured projected and slice emittance using the OTR screen may be overestimated in comparison to wire scanner, the measured trend clearly shows emittance with stacked pulse is significantly improved compared with a single Gaussian laser for 250 pC. During the emittance measurements the spatial laser profile on the cathode is not setup for optimum emittance but it is kept unchanged for fair comparisons. The stacked laser pulse eventually improves the x-ray FEL pulse intensity by 30-50% compared with singe Gaussian ~2 ps FWHM laser pulse.

MAPPING MICRO-BUNCHING OF THE PHOTOCATHODE

Micro-bunching as well as emittance plays critical roles on the x-ray FEL performance. Laser heater [10] in principle can suppress the μBI, but cannot completely eliminate its effect thereby resulting in deterioration of FEL qualities such as pulse intensity and/or bandwidth. Photocathode is one of the major sources inducing the μBI. Recently the micro-bunching effects observed at the LCLS cathode are found very different for different spots on the same cathode. We measured the coherent optical transition radiation (COTR) effect (i.e., integrated counts) at one OTR screen located immediately after the 1st stage of magnetic bunch compressor (BC1). 1-mm-size of laser spot is used to scan across the cathode with 0.1 mm of step size. The COTR signal on the cathode is mapped, as shown in Fig. 8.

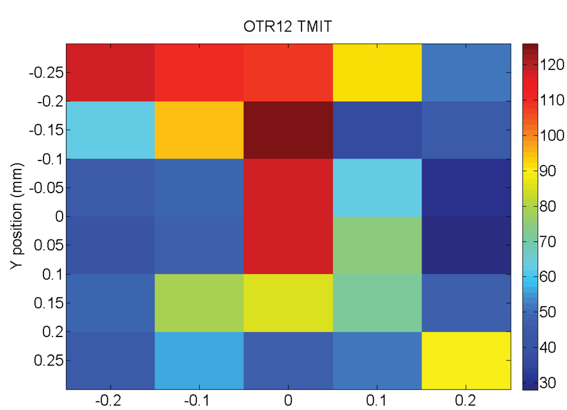

Figure 8: Measured COTR signal in arbitrary units for different laser locations on the same cathode.

The micro-bunching effect on different spots on the same cathode can vary by a factor of 3-4. The effect is expected to be significantly magnified through next magnetic bunch compressor and long-distance beam transport. A question is naturally asked: how is the different spot location correlated to different μBI?

Subsequent measured electron emission profiles are found different for different spots on the cathode, and also the measured QE uniformity varies with the spot location. The resulting different uneven electron emission profile is probably caused by the recent laser cleaning [11-12] for the increase of QE for the copper photocathode. The different transverse electron emission profiles on the photocathode may induce different transverse space charge forces on the beam. A recently developed analytical model [13] may qualitatively explain how to transform the transverse into the longitudinal effects. In the model, for a finite angular spread x_0' with an initial uniform longitudinal coordinate but have a relative energy modulation of δ, when the beam enters dispersive area, transverse and longitudinal coordinates x and z are correlated, expressed by:

$$x = R_{12}x_0' + R_{16}\delta\cos\left[k(z - R_{52}x_0')\right] \qquad (3)$$

where R_{12}, R_{52}, and R_{16} are transfer matrix, k is the oscillation wave number for energy modulation. With this correlation, transverse space charge induced by microstructure (such as uneven surface on the cathode) may couple to longitudinal plane to generate permanent longitudinal microbunching via leaked-out dispersions.

The measurements indicate that the FEL pulse intensity and/or bandwidth are correlated to different laser spot locations, as given in Table 1. As discussed above, different spot location is correlated to different micro-bunching on the cathode. The microbunching caused extra energy spread resulting in lower FEL pulse intensity or larger bandwidth. The data presented in Table 1 may indicate lower FEL pulse intensity or wider bandwidth is probably correlated to worse microbunching effects. Further thorough understanding for the observations is needed.

Table 1: Measured FEL performance and micro-bunching effect for different locations on the cathode. (Note N/A means the data is not measured).

Laser position x/y in mm	FEL pulse intensity	FEL bandwidth, FWHM	COTR signal (a.r.b.)
+0.2/-0.3	2.1 mJ	N/A	50
+0.2/+0.2	0.8-1 mJ	N/A	90
+0.2/-0.25	N/A	27 eV	50
-0.1/-0.25	N/A	40 eV	110

ISBN 978-3-95450-134-2

SUMMARY

Controlling spatial laser distribution on the cathode is of importance for ultra-low emittance beam. Quantitative measures of laser spatial distribution using parameters for lineout intensity and Zernike polynomials are developed. According to simulation and measurement results, optimum emittance are achieved and maintained with truncated–Gaussian spatial laser distribution, g/h in between 0.5-1.5 using lineout distribution measure or symmetry power in between 0.025-0.04 using Zernike polynomials measure. Simulations and measurements also concluded ultra-small emittance is achieved with 3.5-4 ps either single Gaussian or stacked laser pulse for 180-250 pC. Following these quantified criteria for spatial and temporal laser profiles, ultra-low emittance beam can be maintained.

The micro-bunching effects are found different for different cathode spots. The observations indicate that the FEL pulse intensity or bandwidth could be correlated to the micro-bunching effect for different spots. It is believed that different electron emission profiles at different cathode spot location causes different transverse space charge, which is eventually transformed into longitudinal space charge via the leaked dispersion along the beam transport. The longitudinal microbunching effect affects the energy spread thereby x-ray FEL performance.

REFERENCES

[1] P. Emma et al., "First lasing and operation of an Angstrom-wavelength free electron laser", Nature Photon. 4 641 (2010).
[2] T. Ishikawa et al., "A compact x-ray free electron laser emitting in the sub-angstrom region", Nature Photonics 6, 540-544 (2012).
[3] K-J. Kim, Nucl. Instrum. Methods Phys. Res. Sect. A 275, 201 (1989).
[4] F. Zhou et al., "Experimental characterization of emittance growth induced by the nonuniform transverse laser distribution in a photoinjector", Phys. Rev. ST-AB 5, 094203 (2002).
[5] F. Zhou et al., "Impact of the spatial laser distribution on photocathode gun operation", Phys. Rev. ST-AB 15, 090701 (2012).
[6] J. Qiang, ImpactT code manual, LBNL-62326, 2007.
[7] Zernike function see link below: https://en.wikipedia.org/wiki/Zernike_polynomials
[8] D. Bohler, private communication.
[9] K.-J. Kim, "RF and space charge effects in laser-driven RF electron guns", Nucl. Instrum. Methods, A275, 201 (1989).
[10] Z. Huang *et al.*, "Measurements of the linac coherent light source laser heater and its impact on the x-ray free-electron laser performance", Phys. Rev. ST Accel. Beams 13, 020703 (2010).
[11] F. Zhou et al., "High-brightness electron beam evolution following laser-based cleaning of a photocathode", phys. Rev. ST-AB 15, 090703 (2012).
[12] F. Zhou et al., "Establishing reliable good initial quantum efficiency and in-situ laser cleaning for the copper cathodes in the RF gun", Nucl. Instru. Methods in Phys. Res. Section A 783 (2015).
[13] M. Venturini and J. Qiang, "Transverse space charge induced microbunching instability in high-brightness electron bunches", Phys. Rev. ST-AB 18, 054401 (2015).

ISBN 978-3-95450-134-2

ENERGY SPREAD CONSTRAINTS ON FIELD SUPPRESSION IN A REVERSE TAPERED UNDULATOR*

J. MacArthur, A. Marinelli, A. Lutman, H.-D. Nuhn, Z. Huang
SLAC National Accelerator Laboratory, Menlo Park, CA, USA

Abstract

A 3.2 m variable polarization Delta undulator [1] has been installed at the end of the LCLS undulator line. The Delta undulator acts an an afterburner in this configuration, using bunching from upstream planar undulators to produce radiation with arbitrary polarization. To optimize the degree of polarization from this device, a reverse taper has been proposed [2] to suppress background radiation produced in upstream undulators while still microbunching the beam. Here we extend previous work on free electron lasers with a slowly varying undulator parameter [3] to show there is a strong energy spread dependence to the maximum allowable detune from resonance. At LCLS, this energy spread limitation keeps the reverse taper slope in the slowly varying regime and limits the achievable degree of circular polarization.

INTRODUCTION

Circularly polarized x-rays can be used to probe ultrafast demagnetization processes [4], image nanoscale spin order [5], and probe the chirality of biomolecules [6]. However, no x-ray Free Electron Lasers (FELs) offer direct production of circular x-rays. A helical undulator called the Delta undualtor is being commissioned at the Linac Coherent Light Source (LCLS) to address this shortcoming [7].

The Delta undulator is not long enough operate alone and reach appreciable power levels. The electron beam must therefore be prepared in advance of the Delta undulator to maximize the power produced in the circular polarization mode. A reverse tapered planar undulator line preceding the Delta undulator was proposed [2] to maximize the microbunching in a beam entering the Delta undulator while suppressing the background linear field. In this paper we present a constraint on the effectiveness of the reverse taper technique in FELs with a relatively large energy spread.

In the following sections, the 1D FEL equations are explored in the slowly varying detune regime. For an undulator of period λ_u, Pierce parameter ρ, and z-dependent resonant energy $\gamma_r(z)$, the detune from the initial energy γ_0 is

$$\delta = \frac{\gamma_0 - \gamma_r(z)}{\gamma_0}. \tag{1}$$

The detune is slowly varying when it's change over a gain length $L_G \approx \lambda_u/4\pi\rho$ is significantly less than the gain bandwidth, which is typically several ρ [3]. Thus the slowly varying technique is valid when

$$\frac{\lambda_u}{4\pi\rho}\left|\frac{d\delta}{dz}\right| < \rho. \tag{2}$$

At LCLS, successful 720 eV reverse taper configurations operate with a maximum reverse taper detune of $\delta = -0.005$ applied over six undulator modules, or 20 m. These conditions mandate a Pierce parameter satisfying

$$\rho > \sqrt{\frac{\lambda_u}{4\pi}\left|\frac{d\delta}{dz}\right|} = 7.7 \times 10^{-4}. \tag{3}$$

Typical 720 eV reverse taper runs operate at a peak current of 5 kA with a 30 um transverse beam size, resulting in a Pierce parameter of 2.2×10^{-3}. It is therefore instructive to apply the slowly varying solution of the FEL equations to soft x-ray experiments at LCLS.

In the following section we review important aspects of FELs with slowly varying parameters. In subsequent sections we apply this formalism to a reverse tapered undulator to calculate an energy spread limit on the effectiveness of a reverse tapered undulator line. Finally, 3D simulations are compared with results from the 1D theoretical framework.

WKB REVIEW

The Vlasov and Maxwell equations can be expressed in matrix form [3],

$$\frac{d}{d\bar{z}}\begin{pmatrix} a_\nu \\ f_\nu \end{pmatrix} = iM\begin{pmatrix} a_\nu \\ f_\nu \end{pmatrix}, \tag{4}$$

$$M = \begin{pmatrix} -\bar{\nu} & -i\int_{-\infty}^{\infty} d\bar{\eta} \\ -i\frac{dV}{d\bar{\eta}} & -\left(\bar{\eta} - \bar{\delta}\right) \end{pmatrix}. \tag{5}$$

The dimensionless FEL variables used here are

$$\bar{z} = 2\rho k_u z \tag{6}$$

$$\bar{\eta} = \frac{\gamma(z) - \gamma_c(z)}{\gamma_0\rho} \tag{7}$$

$$\bar{\delta} = \frac{\gamma_c(z) - \gamma_r(z)}{\gamma_0\rho} \tag{8}$$

$$\bar{\nu} = \frac{\Delta\nu}{2\rho} \tag{9}$$

$$a_\nu = -\frac{eK[\mathrm{JJ}]}{4\gamma_0^2 mc^2 k_u\rho}e^{-i\Delta\nu k_u z}E_\nu \tag{10}$$

$$f_\nu = \frac{2k_u\rho^2}{k_0}F_\nu, \tag{11}$$

where ρ and k_u are the Pierce parameter and undulator wavenumber. The Lorentz factor γ_0 defines the mean beam

* Work supported by U.S. DOE Office of Basic Energy Sciences under Contract No. DE-AC02-76SF00515.

ISBN 978-3-95450-134-2

energy at the start of the undulator line, while $\gamma_c(z)$ and $\gamma_r(z)$ represent the mean beam energy in the absence of FEL interaction and the beam energy resonant with the rms undulator parameter value $a_u(z)$,

$$\gamma_r(z) = \sqrt{\frac{k_0}{2k_u}\left(1 + a_u(z)^2\right)} \tag{12}$$

The radiation wavenumber resonant at the start of the undulator line is k_0. In an undulator line in a reverse taper configuration, a_u increases with z.

The frequency detune is $\Delta\nu = (k-k_0)/k_0 = \nu-1$, where k is the radiation wavenumber. The Fourier component of the electric field is E_ν. The electron energy distribution is represented by a smooth distribution $V(\eta)$ and a microbunched perturbation $\delta F(\theta, \eta, z)$. The Fourier component of the of the distribution function is

$$F_\nu = \frac{1}{2\pi}\int \delta F(\theta, \eta, z) e^{-i\nu\theta} d\theta, \tag{13}$$

which can be integrated to give the bunching parameter

$$b_\nu = \int F_\nu d\eta. \tag{14}$$

Eq. (4) has been solved in the case of a slowly varying $\bar{\delta}(z)$ to be of the form

$$\begin{pmatrix} a_\nu \\ f_\nu \end{pmatrix} = \Psi_0 \exp\left(-i\int_0^{\bar{z}} \left(\mu_0(\tau) + \mu_1(\tau)\right) d\tau\right), \tag{15}$$

where μ_0 is the zeroth order growth rate and μ_1 is a small first order correction. The eigenvector Ψ_0 is

$$\Psi_0(z) \propto \begin{pmatrix} 1 \\ \frac{i}{\mu_0-(\bar{\eta}-\bar{\delta})}\frac{dV}{d\bar{\eta}} \end{pmatrix}. \tag{16}$$

With the change of variables

$$\hat{\mu} = \mu_0 - \bar{\delta} \tag{17}$$

$$\hat{\nu} = \bar{\nu} - \bar{\delta}, \tag{18}$$

the zeroth order growth rate satisfies

$$\hat{\mu} - \hat{\nu} = \int_{-\infty}^{\infty} \frac{d\bar{\eta}}{\bar{\eta} - \hat{\mu}}\frac{dV}{d\bar{\eta}} \tag{19}$$

The imaginary part of $\hat{\mu}$ and leads to exponential field growth. In subsequent sections we ignore the imaginary part of μ_1 as it is small and negative in a reverse tapered undualtor [3].

UPPER BOUND ON THE DETUNE

Given an energy distribution $V(\bar{\eta})$, the growth rate $\mathrm{Im}(\hat{\mu})$ can be calculated numerically. The growth rate is typically largest at a small negative $\hat{\nu}$. In a reverse taper, however, $\bar{\delta}$ may take on large negative values, leading to a large positive $\hat{\nu}$. If $\hat{\nu}$ is too large, the imaginary part of $\hat{\mu}$ reaches zero, killing the FEL interaction. In this section we explore the energy spread dependent limit on the combined detune $\hat{\nu}$.

For a Gaussian beam with an energy standard deviation of ζ, $V(\bar{\eta})$ takes the form

$$V(\bar{\eta}) = \frac{1}{\sqrt{2\pi}\zeta} e^{-\bar{\eta}^2/2\zeta^2}. \tag{20}$$

Using this energy distribution, Eq. (19) can be expressed in terms of the error function $\mathrm{erf}(x)$,

$$\hat{\mu} - \hat{\nu} = -\frac{1}{\zeta^2} - i\sqrt{\frac{\pi}{2}}\frac{\hat{\mu}}{\zeta^3} e^{-\hat{\mu}^2/2\zeta^2}\left(1 + \mathrm{erf}\left(\frac{i\hat{\mu}}{\sqrt{2}\zeta}\right)\right), \tag{21}$$

where

$$\mathrm{erf}(x) = \frac{2}{\sqrt{\pi}}\int_0^x e^{-t^2} dt. \tag{22}$$

FEL growth stops when $\mathrm{Im}(\hat{\mu}) = 0$. The detune $\hat{\nu}$ and energy spread ζ are purely real, so FEL growth stops when

$$0 = \mathrm{Re}\left[\hat{\mu}\, e^{-\hat{\mu}^2/2\zeta^2}\left(1 + \mathrm{erf}\left(\frac{i\hat{\mu}}{\sqrt{2}\zeta}\right)\right)\right] \tag{23}$$

However, the error function is purely imaginary for purely imaginary argument, so Eq. (23) implies $\mathrm{Re}(\hat{\mu}) = \mathrm{Im}(\hat{\mu}) = 0$. Referring back to Eq. (21), this implies the upper limit on $\hat{\nu}$ at a given energy spread ζ is simply

$$\hat{\nu} \le \frac{1}{\zeta^2}. \tag{24}$$

A contour plot of $\mathrm{Im}(\hat{\mu})$ is shown as a function of the scaled energy spread and detune in Fig. 1. The $\mathrm{Im}(\hat{\mu}) = 0$ contour is parameterized by $\hat{\nu} = 1/\zeta^2$, as denoted by the dotted line.

Table 1: Distribution Dependent $\hat{\nu}$ Boundary

$V(\bar{\eta})$	Width (rms)	Boundary
Eq. (20)	ζ	$\hat{\nu} = 1/\zeta^2$
Eq. (A5)	ζ	$\hat{\nu} = 1/2\zeta^2$

X-ray FEL's often use a laser heater to combat the microbunching instability [8]. The laser heater imparts a non-Gaussian energy spread on an initially Gaussian beam, modifying $V(\bar{\eta})$. If the pre-laser heater energy spread is ingorably small, the $\hat{\nu}$ boundary still takes a simple form. Coincidentally, as observed by one of us[1], the growth rate itself resulting from a matched laser heater is algebraic. These results are discussed in the appendix. Table 1 presents a summary, where the energy spread dependent upper limit on the detune is reported for FEL's operation with different energy distributions.

[1] A. Marinelli

ISBN 978-3-95450-134-2

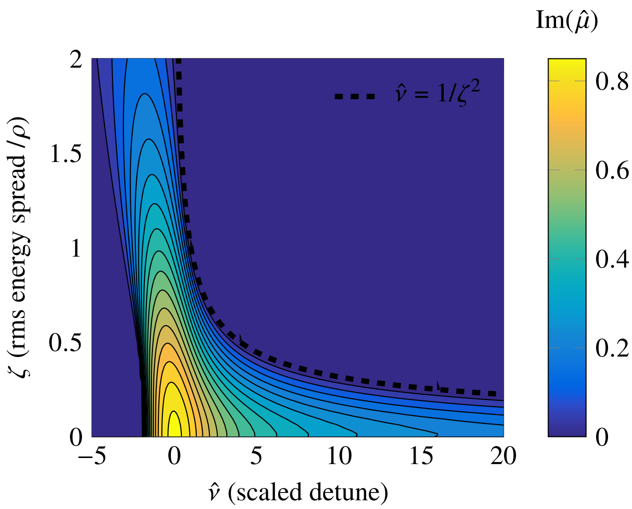

Figure 1: A numerical calculation of the growth rate Im($\hat{\mu}$) as a function of the scaled detune $\hat{\nu}$ and the scaled rms energy spread ζ. FEL's with a finite energy spread operate most efficiently with a small negative $\hat{\nu}$ (yellow, green). However, a reverse tapered FEL may operate near the Im($\hat{\mu}$) = 0 boundary. This boundary is parametrized by Eq. (24). In this calculation the energy distribution is assumed to be Gaussian with a standard deviation of ζ.

IMPLICATIONS FOR REVERSE TAPER EXPERIMENTS

The purpose of a reverse tapered undulator line is to suppress the field growth relative to the bunching. At a given frequency ν, this means

$$\left|\frac{b_\nu}{a_\nu}\right| \gg 1 \tag{25}$$

is desirable. In this section, we relate this condition to the scaled detune $\hat{\nu}$.

Using the definition of b_ν given in Eq. (14) and the evolution of f_ν and a_ν shown in Eqs. (15,16), the ratio of the bunching factor to the field is

$$\left|\frac{b_\nu}{a_\nu}\right| = \left|\frac{\int d\bar{\eta}\exp\left(-i\int_0^{\bar{z}}(\mu_0+\mu_1)\,d\tau\right)\frac{1}{\bar{\eta}-\hat{\mu}}\frac{dV}{d\bar{\eta}}}{\exp\left(-i\int_0^{\bar{z}}(\mu_0+\mu_1)\,d\tau\right)}\right| \tag{26}$$

$$= \left|\int \frac{d\bar{\eta}}{\bar{\eta}-\hat{\mu}}\frac{dV}{d\bar{\eta}}\right|, \tag{27}$$

which can be simplified with the dispersion relation in Eq. (19),

$$\left|\frac{b_\nu}{a_\nu}\right| = |\hat{\mu}-\hat{\nu}|. \tag{28}$$

Evidently, the ratio of the bunching to the field at a given location along the undulator line depends only on the present detune and growth parameter. As long as the slowly varying approximation is satisfied, $|b_\nu/a_\nu|$ is independent of the taper history.

Often the magnitude of $\hat{\mu}$ is close to zero, so $|\hat{\nu}| \gg |\hat{\mu}|$ for a large detune. In fact $\hat{\mu}$ is exactly zero on the boundary discussed in the previous section. Therefore a large scaled detune $\hat{\nu}$ means

$$\left|\frac{b_\nu}{a_\nu}\right| \approx \hat{\nu}. \tag{29}$$

As seen in previous section, the energy spread places an upper limit on $\hat{\nu}$. This upper limit transfers to the present situation,

$$\left|\frac{b_\nu}{a_\nu}\right| \le \frac{1}{\zeta^2} = \frac{\rho^2\gamma_0^2}{\sigma_\gamma^2}, \tag{30}$$

where σ_γ is the rms beam energy spread in units of m_ec^2. A beam with a relatively large energy spread cannot suppress the field strength relative to the bunching strength.

3D SIMULATION

In a SASE FEL with a reverse tapered undulator, the bunching and field evolve over a range of frequencies. The framework presented above is relevant for a particular frequency ν, but it can help explain the bunching evolution in a 3D reverse taper simulation with a large energy spread.

In Fig. 2, the bunching spectrum evolution during two time-dependent Genesis simulations is shown. Both simulations were done in a reverse tapered undulator, where the resonant energy decreases (black line) because of a stepwise-increasing undulator K value. The common simulation parameters are shown in Table 2.

Table 2: Genesis Simulation Parameters

Qauntity	Value	Units
energy ($\gamma_0 m_e c^2$)	3.969	GeV
energy spread ($\sigma_\gamma m_e c^2$)	3.5, 7.0	MeV
transverse emittance	0.6	µm
photon energy (nominal)	700	eV
undulator period	3.0	cm
starting K value	3.50	
ending K value	3.52	
undulator gap K value	0.0	
undulator modules	6	
peak current	5.5	kA
phase space	ideal Gaussian beam	
Pierce Parameter (ρ)	2.2×10^{-3}	

The difference between the two simulations is in energy spread. The top simulation in Fig. 2 uses a 3.5 MeV rms energy spread, while the bottom simulation uses a 7.0 MeV energy spread. In both simulations bunching grows at a range of energies between what is resonant at the start and end of the undulator line (693 eV - 700 eV).

In the 3.5 MeV energy spread simulation, bunching grows at a wide range of frequencies, peaking in intensity at a frequency in the middle of the reverse taper range. This

ISBN 978-3-95450-134-2

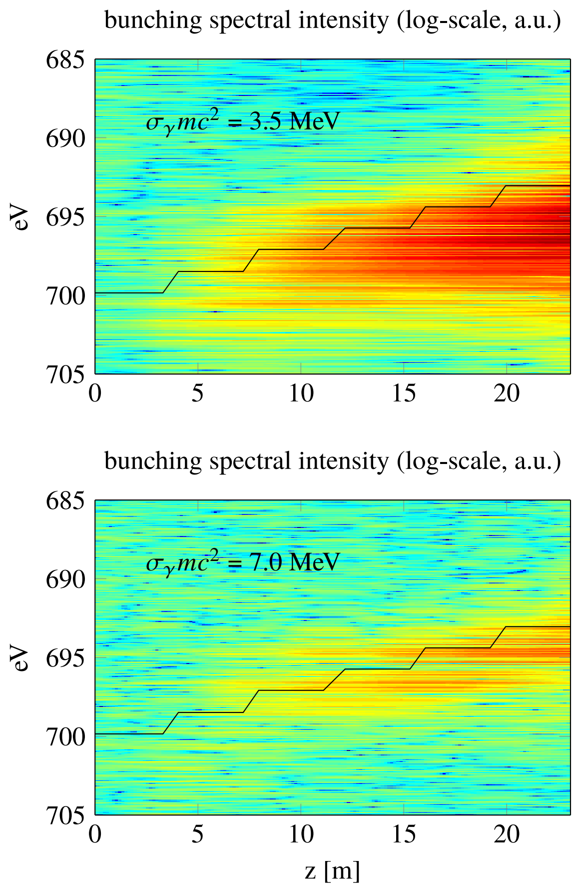

Figure 2: The bunching spectral intensity evolves as a function of distance along the undulator line in two time dependent Genesis simulations: $\sigma_\gamma mc^2 = 3.5\,\mathrm{MeV}$ (top), and 7.0 MeV (bottom). The spectral intensity is plotted in arbitrary units but on the same scale in the top and bottom simulations. The black line traces the energy resonant to the reverse tapered undulator at a particular location.

is consistent with the theoretical expectation for a slowly varying reverse taper [3]. In the 7.0 MeV case, however, bunching growth is less successful. Bunching initiated at a particular frequency early on in the undulator line cannot be amplified in undulator segments with a larger detune. This is a result of the limitation in Eq. (24), which can be rewritten in a more illuminating form

$$E_{h\nu,\max}(z) = 2E_{h\nu_0}\left(\rho^3 \frac{\gamma_0^2}{\sigma_\gamma^2} + \frac{\Delta\gamma(z)}{\gamma_0}\right) + E_{h\nu_0}, \qquad (31)$$

where $E_{h\nu_0} = 700\,\mathrm{eV}$, $\Delta\gamma(z)/\gamma_0$ reaches a minimum of -0.0049 at the end of the undulator line, and other parameters are given in Table 2. $E_{h\nu,\max}(z)$ is the maximum photon energy that will experience exponential growth due to the FEL instability. Plugging in the two different energy spread values, this means

$$E_{h\nu,\max}(\mathrm{end}) = \begin{cases} 714\,\mathrm{eV}, & \sigma_\gamma m_e c^2 = 3.5\,\mathrm{MeV} \quad (32) \\ 698\,\mathrm{eV}, & \sigma_\gamma m_e c^2 = 7.0\,\mathrm{MeV} \quad (33) \end{cases}$$

at the end of the undulator line. In the high energy spread case, no FEL growth will take place above 698 eV. This matches the drop in bunching spectral intensity in the bottom panel if Fig. 2 above 698 eV in the final undulator segment. No such constraint on FEL growth is placed on the 3.5 MeV energy spread simulation, all relevant frequencies are amplified.

CONCLUSION

The electron beam energy spread places a strong constraint on the FEL field growth at large detunes from resonance. This in turn limits the maximum achievable bunching to field strength ratio. A high bunching to field strength ratio is critical for successful operation of a helical undulator like the Delta undulator following a reverse tapered planar undulator line. The energy spread of LCLS in the soft x-ray regime is large enough for this effect to limit the power contrast seen in the Delta undulator, restricting the maximum achievable degree of polarization.

APPENDIX: LASER HEATER DISTRIBUTION

A laser heater is used at LCLS to combat the microbunching instability by increasing the slice energy spread of the beam. The electron energy distribution exiting a laser heater depends on the initial distribution and the laser and electron beam transverse matching. In this section the initial energy distribution is assumed to be negligible relative to the energy modulation from the laser heater.

For a beam with zero initial energy spread, a transverse beam size of σ_x, and a laser energy modulation of $\Delta\bar{\eta}_L(r)\sin(k_L z)$ at the laser wavenumber k_L, the post-laser heater distribution function is

$$V(r,z,\bar{\eta}) = \delta\left(\bar{\eta} - \Delta\bar{\eta}_L(r)\sin k_L z\right)\frac{1}{2\pi\sigma_x^2}e^{-r^2/2\sigma_x^2}, \quad \text{(A1)}$$

where δ is the Dirac's delta function and the radial dependence of the energy modulation is

$$\Delta\bar{\eta}_L(r) = 2\zeta\, e^{-r^2/4\sigma_r^2} \qquad \text{(A2)}$$

for an interaction with a maximum energy modulation of 2ζ. As in previous sections, the scale factor 2ζ will dictate the width of the energy distribution. The factor of 2 is used to set the resultant energy distribution to an rms width of ζ. The distribution in Eq. (A1) can be integrated over the transverse and longitudinal coordinates to find the energy distribution function,

$$V(\bar{\eta}) = \int 2\pi r dr \int V(r,z,\bar{\eta})dz \qquad \text{(A3)}$$

$$= \frac{1}{2\pi\zeta}\int_0^{2B\log(2\zeta/\bar{\eta})} \frac{e^{-x}}{\sqrt{e^{-B^2 x} - \bar{\eta}^2/4\zeta^2}}dx \qquad \text{(A4)}$$

where $B = \sigma_r/\sigma_x$ and the assumption $B \geq 1$ has been applied. This integral can be rewritten in terms of Hypergeometric functions, but it is more instructive to examine two

ISBN 978-3-95450-134-2

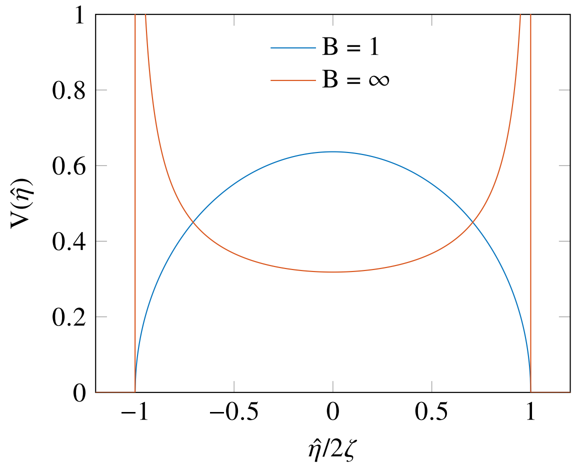

Figure 3: The energy distribution from a matched beam ($B = 1$) and an unmatched beam ($B = \infty$) exiting the laser heater. By assuming the energy spread entering the laser heater is negligibly small, exact expressions for these distributions are given by Eqs. (A5, A6).

special cases,

$$V(\bar{\eta}) = \begin{cases} \frac{1}{\pi\zeta}\left(1 - \bar{\eta}^2/4\zeta^2\right)^{1/2}, & B = 1 \quad \text{(A5)} \\ \frac{1}{2\pi\zeta}\left(1 - \bar{\eta}^2/4\zeta^2\right)^{-1/2}, & B \to \infty. \quad \text{(A6)} \end{cases}$$

These distributions are shown in Fig. 3. The matched beam ($B = 1$) case, where laser heaters typically operate, exhibits a centrally peaked and relatively narrow distribution. We therefore proceed to solve for the growth rate using this distribution.

Inserting Eq. (A5) into Eq. (19), it is clear that the growth rate is the solution to an algebraic equation

$$2\zeta^2 (\hat{\mu} - \hat{\nu}) = \left(1 - 4\frac{\zeta^2}{\hat{\mu}^2}\right)^{-1/2} - 1. \tag{A7}$$

The roots of this polynomial are easily calculated with symbolic processing software. As before, we seek the upper limit on $\hat{\nu}$ for a given energy spread ζ. The upper limit is the solution to the equation $\mathrm{Im}(\hat{\mu}) = 0$. As before, this implies $\hat{\mu} = 0$, and the boundary is

$$\hat{\nu} \leq \frac{1}{2\zeta^2}. \tag{A8}$$

This boundary is plotted above the solution to Eq. (A7) in Fig. 4. The rms energy spread of Eq. (A5) and the Gaussian distribution in Eq. (20) are ζ. The detune limit is a factor of two more stringent in the laser heater case for the same rms spread.

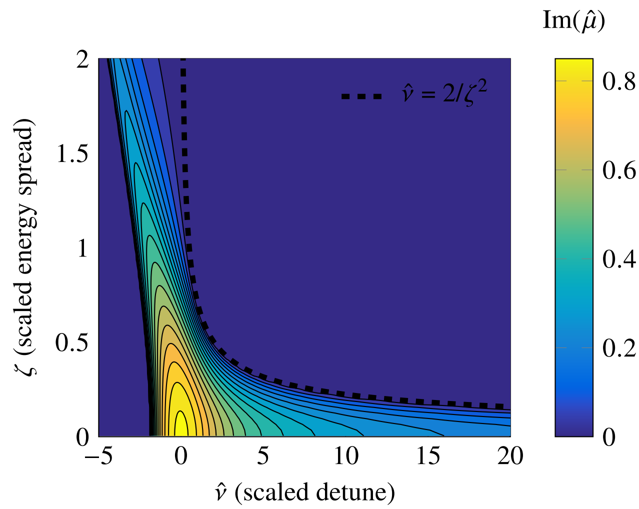

Figure 4: A numerical calculation of the growth rate $\mathrm{Im}(\hat{\mu})$ as a function of the scaled detune $\hat{\nu}$ and the scaled rms energy spread ζ. In contrast to Fig. 1, here the growth rate is calculated assuming a laser heater energy distribution given by Eq. (A5). The upper limit on the scaled detune is given by Eq. (A8).

REFERENCES

[1] A. B. Temnykh. "Delta undulator for Cornell energy recovery linac." In: *Phys. Rev. ST Accel. Beams* 11 (12 Dec. 2008), p. 120702.

[2] E. A. Schneidmiller and M. V. Yurkov. "Obtaining high degree of circular polarization at x-ray free electron lasers via a reverse undulator taper." In: *Phys. Rev. ST Accel. Beams* 16 (11 Nov. 2013), p. 110702.

[3] Z. Huang and G. Stupakov. "Free electron lasers with slowly varying beam and undulator parameters." In: *Phys. Rev. ST Accel. Beams* 8 (4 Apr. 2005), p. 040702.

[4] B. Pfau et al. "Ultrafast optical demagnetization manipulates nanoscale spin structure in domain walls." In: *Nature communications* 3 (2012), p. 1100.

[5] T. Wang et al. "Femtosecond Single-Shot Imaging of Nanoscale Ferromagnetic Order in Co/Pd Multilayers Using Resonant X-Ray Holography." In: *Phys. Rev. Lett.* 108 (26 June 2012), p. 267403.

[6] U. Hergenhahn et al. "Photoelectron circular dichroism in core level ionization of randomly oriented pure enantiomers of the chiral molecule camphor." In: *The Journal of Chemical Physics* 120.10 (2004), pp. 4553–4556.

[7] H-D Nuhn et al. "R&D; Towards a Delta-Type Undulator for the LCLS." In: *Presented at FEL 2013*. SLAC-PUB-15743. 2013.

[8] Z. Huang et al. "Suppression of microbunching instability in the linac coherent light source." In: *Phys. Rev. ST Accel. Beams* 7 (7 July 2004), p. 074401.

ISBN 978-3-95450-134-2

LASER HEATER TRANSVERSE SHAPING TO IMPROVE MICROBUNCHING SUPRRESSION FOR X-RAY FELS

S. Li*, A. Fry, S. Gilevich, Z. Huang, A. Marinelli, D. Ratner, J. Robinson
SLAC, Menlo Park, CA 94025, USA

Abstract

In X-ray free electron lasers (FELs), a small amount of initial density or energy modulation in the electron beam can be amplified through the acceleration and bunch compression process. The undesired microbunching on the electron bunch will increase slice energy spread and degrade the FEL performance. The Linac Coherent Light Source (LCLS) laser heater (LH) system was installed to increase the uncorrelated energy spread in the electron beam in order to suppress the microbunching instability. The distribution of the induced energy spread depends strongly on the transverse profile of the heater laser and has a large effect on microbunching suppression. In this paper, we present theoretical calculations for the LH induced energy spread and discuss strategies to shape the laser profile in order to obtain better suppression of microbunching. We present analysis and potential methods to achieve Gaussian and Gaussian-like energy spread on the electron beam.

INTRODUCTION

At the Linear Coherent Light Source (LCLS), the laser heater (LH) system was installed in the injector area to suppress the microbunching instability by increasing the uncorrelated energy spread [1, 2]. The interaction between the heater laser and the electron beam takes place in a short undulator and gives rise to an energy modulation on the electron beam. The distribution of the laser-heater-induced energy spread affects the suppression of the microbunching instability. The energy modulation amplitude each electron experiences varies depending on the location of the electron relative to the laser transverse profile. Therefore one can control the energy spread distribution by transversely shaping the heater laser profile, and hence improve the suppression of microbunching instability.

In this paper we present theoretical calculations to relate the laser transverse profile with laser-heater-induced energy spread distribution. We discuss two methods of generating Gaussian-like energy spread using a fundamental Gaussian mode and a Laguerre-Gaussian (LG) mode, and compare their microbunching suppression effect and power efficiency. Lastly, we investigate the possibility of implementing a Gaussian speckle distribution, an approach independent of the transverse electron distribution.

* siqili@slac.stanford.edu

LASER HEATER SUPPRESSION THEORY

The energy modulation induced by laser-electron interaction is obtained in [1],

$$\begin{aligned}\delta_L(r) &= \sqrt{\frac{P_L}{P_0}}\frac{KL_u}{\gamma_0\sigma_r}\left[J_0[\frac{K^2}{4+2K^2}] - J_1[\frac{K^2}{4+2K^2}]\right] f(r)\\ &\equiv Af(r),\end{aligned} \tag{1}$$

where P_L is the peak laser power, $P_0 = I_A mc^2/e \approx 8.7\text{GW}$, K is the undulator strength parameter, γ_0 is the relativistic factor of electron beam energy, L_u is undulator period, σ_r is the rms spot size of the laser, $J_{0,1}$ are the Bessel functions, r is the radial position of the electron, and $f(r)$ describes any arbitrary transverse profile of the laser beam. On the right hand side of the equation, we group the constants in front of the laser profile $f(r)$ into one constant A.

If we assume a Gaussian electron distribution and integrate the energy-modulated electron beam in transverse and longitudinal coordinates, we get the expression for the modified energy distribution,

$$\begin{aligned}V(\delta) &= \frac{1}{\pi\sigma_x^2\sqrt{2\pi}\sigma_{\delta 0}}\int r dr d\xi \frac{e^{-\frac{r^2}{2\sigma_x^2}-\frac{\xi^2}{2\sigma_{\delta 0}^2}}}{\sqrt{\delta_L(r)^2-(\delta-\xi)^2}}\\ &\approx \int\frac{1}{\pi\sigma_x^2} r\, dr\, e^{-\frac{r^2}{2\sigma_x^2}}\frac{1}{\sqrt{\delta_L(r)^2-\delta^2}},\end{aligned} \tag{2}$$

where σ_x is the rms size of the electron beam, and $\sigma_{\delta 0}$ is the initial energy spread in the electron beam. $\sigma_{\delta 0}$ is typically 1 to 3 keV, and is relatively small compared to the induced energy spread which will be shown below to be around a few tens of keV. Thus we ignore its contribution in the last line of Eq. (2) and throughout the rest of this paper.

The microbunching gain is defined as the ratio of the final bunching factor to the initial bunching factor $\left|\frac{b_f}{b_0}\right|$, which can be approximated as [1]

$$G \approx \frac{I_0}{\gamma I_A}\left|k_f R_{56}\int_0^L ds\frac{4\pi Z(k_0;s)}{Z_0}\right| S_L(k_f R_{56}A, \frac{\sigma_r}{\sigma_x}), \tag{3}$$

where I_0 is the peak current, I_A is the Alfven current, $k_f = Ck_0$ is the compressed modulation wave number through compression C, $Z(k;s)$ is the longitudinal space charge impedance defined below (Eq. (4)), and S_L is the gain suppression factor defined as the Fourier transform of $V(\delta)$. The impedance function is

$$Z(k,s) = \frac{iZ_0}{\pi k r_b^2}\left[1-\frac{kr_b}{\gamma}K_1\left(\frac{kr_b}{\gamma}\right)\right], \tag{4}$$

ISBN 978-3-95450-134-2

where r_b is the radius of the transverse cross section for a uniform distribution. In the following, we take $r_b \approx 2\sigma_x$. The suppression factor is

$$S_L(kR_{56}A, B) = \int R\,dR\,e^{-\frac{R^2}{2}} J_0[kR_{56}Af(r)]\,, \qquad (5)$$

with

$$R \equiv \frac{r}{\sigma_x},\; B \equiv \frac{\sigma_r}{\sigma_x}\,. \qquad (6)$$

To get a desired Gaussian energy distribution $V(\delta)$, we need a Gaussian suppression factor S_L because they are related to each other by Fourier transform. Note that for a Gaussian transverse electron distribution, a linear R dependence of the laser profile will generate a perfect Gaussian suppression factor, hence a Gaussian energy distribution:

$$S_L(A') = \int_0^\infty R\,dR\,e^{-\frac{R^2}{2}} J_0(A'R) = e^{-A'^2/2}, \qquad (7)$$

where $A' \equiv kR_{56}A$ and k and R_{56} are kept fixed.

At the end of compression, the gain becomes

$$G \approx \frac{I_0}{\gamma I_A}\left|k_f R_{56} L \frac{4\pi Z(k_f)}{Z_0}\right| S_L(k_f R_{56}A, \frac{\sigma_r}{\sigma_x})\,. \qquad (8)$$

Again, we use the approximation that $\sigma_{\delta 0}$ is negligible compared to the induced energy spread in the above equation. The variance of current profile is proportional to $\int_0^\infty dk_0 |G(k_0)b_0(k_0)|^2$ [1]. In the approximation of $b_0(k_0)$ being the white noise and independent of wave length, we can use the following integral as a measure of how well the laser heater suppresses the microbunching gain

$$I = \int_0^\infty G^2(k_0)dk_0\,. \qquad (9)$$

The smaller I, the better the laser heater suppresses the microbunching gain. In the following analysis, we will use the I integral to compare the different methods of generating a desired energy spread distribution.

Note that in Eq. (5) the suppression factor is defined in terms of the energy modulation amplitude A, whereas the FEL performance is evaluated in terms of the rms energy spread. We would like to compare microbunching suppression of different laser profiles with the same induced rms energy spread. By definition, the square of rms energy spread is $\sigma_\delta^2 = \int \delta^2 V(\delta)\,d\delta$, where $V(\delta)$ also depends on δ_L. We get

$$\sigma_\delta = A\sqrt{\int_0^\infty \frac{r\,dr}{2\sigma_x^2} e^{-\frac{r^2}{2\sigma_x^2}} f^2(r)}. \qquad (10)$$

Therefore we can convert between energy modulation amplitude and rms induced energy spread using the factor in Eq. (10) for any radially symmetric laser profile $f(r)$.

TWO EXAMPLES: FUNDAMENTAL GAUSSIAN MODE AND LAGUERRE-GAUSSIAN MODE

There are several methods to generate a perfectly Gaussian or Gaussian-like energy spread by manipulating the laser heater transverse profile. Here in this section, we go through two examples. In the analysis in this section, the beam goes through one linac (L1) and one bunch compressor (BC1) with the following parameters:

Table 1: Simulation Parameters

Parameter	Value
R_{56}	45 mm
r_b	300 μ m
Peak current I_0	30 A
γ	489
L1 length L	12 m
σ_δ	15 keV
BC1 compression C_1	7

Fundamental Gaussian Laser Mode

We can now plug in specific laser profiles to the theories in the above section. Let's start with a fundamental Gaussian mode laser,

$$\delta_L(r) = Ae^{-\frac{r^2}{4\sigma_r^2}} = Ae^{-\frac{R^2}{4B_G{}^2}}\,, \qquad (11)$$

with $B_G = \frac{\sigma_r}{\sigma_x}$ as in Eq. (6). The subscript G denotes Gaussian mode. Plugging Eq. (11) into Eq. (10), we get $A = \sqrt{2(1+\frac{1}{B_G^2})}\sigma_\delta$, consistent with [2].

We can calculate the suppression factor and gain, which will give us the I integral as a function of B_G. Physically, this tells us the suppression effect as a function of the laser size relative to the electron beam size. Figure 1 shows that the best suppression occurs at $B_G = 0.9$. As we move away from $B_G = 0.9$ in either direction, the I integral starts to increase, suggesting we should operate in the range of $0.8 < B_G < 1.2$. We refer to the case when $B_G = 1$ as "matched Gaussian" or MG.

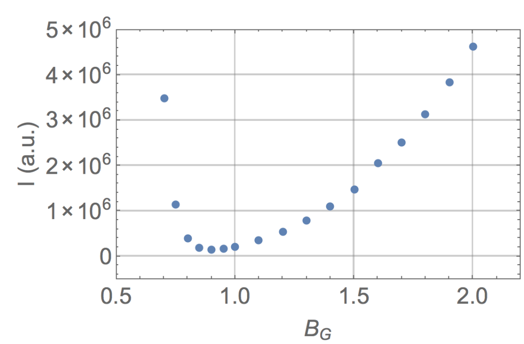

Figure 1: Gaussian laser profile suppression integral I as a function of B_G.

Laguerre-Guassian Laser Mode

We have shown that a linear R dependence of the laser profile produces a perfectly Gaussian energy spread (Eq. (7)).

ISBN 978-3-95450-134-2

One way to approach the linear R dependence is to use the first order Laguerre-Gaussian (LG_0^1) mode,

$$\delta_L(r) = ARe^{-\frac{R^2}{2B_{LG}^2}}, \tag{12}$$

again with $B_{LG} = \frac{\sigma_r}{\sigma_x}$ as in Eq. (6). Note by the above definition of LG_0^1 mode, the σ_r in the equation is the same as the rms laser beam size. When B_{LG} is large, the electron sees a linearly increasing energy modulation as it moves from the center to the edge on the transverse plane. Following the same procedure as in the previous section, we can find the normalization factor $A = (1 + \frac{2}{B_{LG}^2})\sigma_\delta$. Similarly, from suppression factor and gain, we can get I integral as a function of B_{LG} (Fig. 2). The horizontal line refers to the suppression due to matched Gaussian laser profile. When $B_{LG} = 3$, the LG mode is better than a matched Gaussian by a factor of 3. As B_{LG} reaches 3.5, the I integral starts to flatten, making it meaningless to further increase B_{LG}. At the current LCLS laser heater, the Gaussian laser profile has approximately $B_G = 1.5$. In this case, the LG mode with $B_{LG} = 3$ improves over the Gaussian profile by a factor of 23 in terms of the I integral.

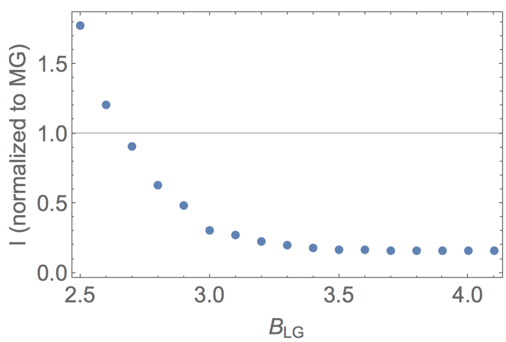

Figure 2: LG laser profile suppression integral I as a function of B_{LG}. The horizontal line corresponds to the integral I for matched Gaussian laser profile.

To produce an LG mode at LCLS, we can use a liquid crystal spatial light modulator (SLM) to convert the existing Gaussian mode to the helical LG mode by phase modulation. The LG_0^1 mode requires a helical phase pattern linearly dependent on azimuthal angle ϕ and independent of radial position r. We can control the output beam size by adding a blazed phase pattern to the helical phase pattern with a defined aperture. Matsumoto et. al. in [3] present the detailed procedure of phase compensation and demonstrate efficient conversion of Gaussian beam to higher-order LG modes.

Comparison

To compare the Gaussian mode and LG mode, we can use the suppression factor and the final energy spread as a metric to measure which one suppresses microbunching better.

Figure 3 shows the suppression factor S_L as a function of modulation wavenumber k for different laser profiles. $B_{LG} = 10$ resembles the linear R dependence profile that produces a Gaussian suppression factor. $B_{LG} = 3$ shows oscillatory behaviors deviating away from a smooth Gaussian. With smaller B_{LG} the oscillation becomes more obvious. The matched Gaussian case shows a stronger oscillation than $B_{LG} = 3$. The current LCLS operation ($B_G = 1.5$) shows the strongest oscillation among the curves.

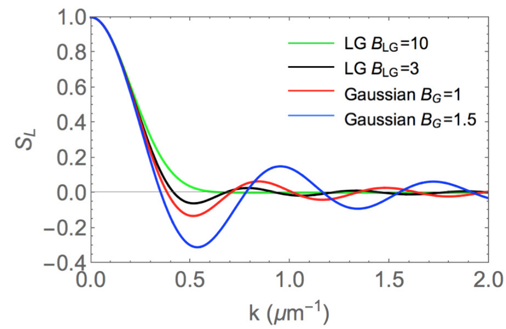

Figure 3: Suppression factor S_L as a function of modulation wavenumber k.

A more quantitative way of comparison is the FEL final energy spread. The simulation takes in analytical expression for the suppression factor, so we compare the Gaussian profiles with several B_G values with a linear R dependence laser profile. In this simulation, we take initial energy spread to be 1 keV, final beam energy 4.3 GeV. As shown by Fig. 4, the linear R dependence profile reduces final SES by 25% compared to matched Gaussian mode. Compared to Gaussian profile with $B_G = 1.5$, the linear R dependence profile improves the final SES by 66%. The result indicates that if we could produce a sufficiently Gaussian-like energy spread, the final energy spread will be improved significantly.

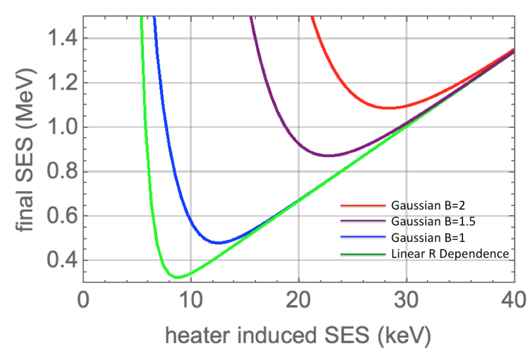

Figure 4: Final slice energy spread (SES) as a function of heater induced SES.

Another important consideration is power efficiency. We would like to compare the ratio of averaged induced energy modulation to power for both LG mode and Gaussian mode. In Eq. (13) we ignore the normalization factors because they cancel as we consider the ratio.

$$\left(\frac{\langle\delta^2\rangle}{P}\right)_{MG} \Big/ \left(\frac{\langle\delta^2\rangle}{P}\right)_{LG} = \frac{(2 + B_{LG}^2)^2}{4(1 + B_G^2)}, \tag{13}$$

ISBN 978-3-95450-134-2

Table 2 illustrates the efficiency ratio to achieve same energy spread for various values of B_G and B_{LG}. This is a theoretical calculation. Additional power loss comes from converting a Gaussian mode to LG mode, and the spatial modulator efficiency.

Table 2: Efficiency ratio for different B_G and B_{LG}

B_G	B_{LG}	$P_{LG}/P_{Gaussian}$
1	3	15
1	4	41
1.5	3	9
1.5	4	25
2	3	6
2	4	16

SPECKLE PATTERN

One drawback of the above schemes is that they require careful measurement of the beam size (matched Gaussian) or beam distribution (LG mode). An alternative approach is to create a speckle pattern so that different electrons see different modulation amplitudes. By modulating with a single frequency laser of wavenumber k and transversely varying amplitude $A(x, y) sin(kz)$, an electron receives an energy modulation, δ, with a probability distribution $P(\delta)$ determined by the laser profile, $A(x, y)$. The expected modulation is given by

$$P(\delta) = \int_{\delta}^{\infty} Q(\eta)R(\eta, \delta)d\eta, \tag{14}$$

where $Q(\eta)$ is the probability that an electron interacts with a transverse laser field of amplitude $A(x, y) = \eta$, and $R(\eta, \delta)$ is the probability that a field $\eta \sin(kz)$ produces a modulation of amplitude δ (due to the sinusoidal variation in time). The interpretation of $R(\eta, \delta)$ is the probability density function of a sine wave, $R(\eta, \delta) = 2/(\pi\eta\sqrt{1 - \delta^2/\eta^2})$ (where we have normalized so that $\int_0^{\eta} R d\delta = 1$). Note that $R(\eta, \delta) = 0$ for $\eta < \delta$, so the lower limit of the integral is δ.

Choosing an appropriate intensity distribution $Q(\eta)$ will give a Gaussian energy spread independent of the electron distribution. With

$$Q(\eta) = \frac{\eta}{\sigma_r^2} e^{-\eta^2/2\sigma_r^2}, \tag{15}$$

we find a Gaussian energy distribution

$$P(\delta) = \frac{2}{\pi\sigma_r^2} \int_{\delta}^{\infty} d\eta \frac{\eta e^{-\eta^2/2\sigma_r^2}}{\sqrt{\eta^2 - \delta^2}} = \sqrt{\frac{2}{\pi\sigma_r^2}} e^{-\delta^2/2\sigma_r^2}. \tag{16}$$

As for the LG mode, a spatial modulator can also produce an approximate intensity distribution given by $Q(\eta)$. To minimize the effect of transverse smearing of both electrons and laser, we group the pixels by intensity. Each block of pixels have intensities given by $Q(\eta)$, and we repeat the block throughout the transverse plane, requiring the block feature small compared to the electron rms beam size (Fig. 5). We then find a Gaussian-like energy distribution regardless of the electron beam's transverse distribution, as shown in Fig. 6.

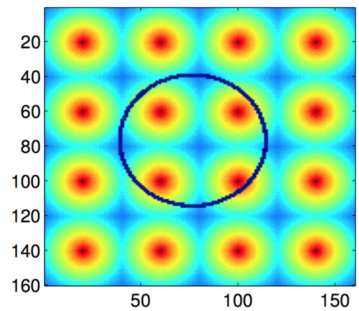

Figure 5: An example of speckle pattern with the blue ring representing the FWHM of a Gaussian electron beam with a random offset.

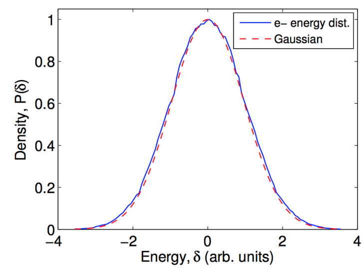

Figure 6: Electron energy distribution produced by the speckle pattern shown in Fig. 5.

The speckle approach assumes that the pattern is maintained throughout the undulator length in the LCLS LH system, i.e. the undulator length L_u must be shorter than the confocal parameter $b = 2\pi w_0^2/\lambda$, with smallest feature size w_0 and wavelength λ. For the current LCLS LH design, the confocal parameter, $b \sim 2$ cm, is much to small for the beam to maintain imaging, and implementing this approach would require new hardware. However, if designing a laser heater system from scratch, it should be possible to accommodate a sufficiently long confocal parameter; for example, using the LCLS cathode laser ($\lambda = 260$ nm), $\sigma_r = 300\ \mu$m, and $w_0 = 100\ \mu$m, gives a reasonable confocal parameter of $b = 0.25$ m.

CONCLUSION

In this paper, we have presented the theoretical background of the effect of transverse laser profile on the electron beam energy spread in the LCLS LH system. In particular, we have shown that a linear R dependence in the laser profile generates a perfectly Gaussian energy spread. As examples, we considered the fundamental Gaussian mode and the Laguerre-Gaussian mode laser, to generate a Gaussian-

ISBN 978-3-95450-134-2

like energy spread. For the fundamental Gaussian mode, our analysis is consistent with the result in [1] that a matched Gaussian laser is optimal in terms of suppressing the microbunching instability. With LG mode we are able to achieve even better suppression of microbunching when the rms laser beam size is larger than the rms electron beam size. The challenge lies in implementing LG mode with reasonable efficiency. We also investigated the possibility of generating a Gaussian energy spread with a speckle pattern by enforcing an intensity distribution (Eq. (15)) on a spatial modulator. This method has an advantage of being resistant to transverse motion and overlap, but proves difficult with the current LCLS laser heater setup.

REFERENCES

[1] Huang, Zhirong, et al. "Suppression of microbunching instability in the linac coherent light source." *Physical Review Special Topics-Accelerators and Beams* 7.7 (2004): 074401.

[2] Huang, Zhirong, et al. "Measurements of the linac coherent light source laser heater and its impact on the x-ray free-electron laser performance." *Physical Review Special Topics-Accelerators and Beams* 13.2 (2010): 020703.

[3] Matsumoto, Naoya, et al. "Generation of high-quality higher-order Laguerre-Gaussian beams using liquid-crystal-on-silicon spatial light modulators." *JOSA A* 25.7 (2008): 1642-1651.

ISBN 978-3-95450-134-2

FOUR-DIMENSIONAL MODELS OF FREE ELECTRON LASER AMPLIFIERS AND OSCILLATORS

J. Blau*, K. Cohn, W. B. Colson
Physics Department, Naval Postgraduate School, Monterey, CA 93943, USA

Abstract

New four-dimensional models of free electron lasers (FELs) are described, for both amplifier and oscillator configurations. Model validation and benchmarking results are shown, including comparisons to theoretical formulas and experiments.

INTRODUCTION

Over the past 25 years at the Naval Postgraduate School, we have developed a suite of computer programs to model free electron lasers [1, 2]. We have separate programs for different types of FELs (i.e., single-pass amplifiers or multi-pass oscillators) under various conditions (i.e., short or long pulses), with graphics optimized to understand the results for each type of FEL.

Our programs can be classified according to the number of dimensions in the model. The one-dimensional (1D) and two-dimensional (2D) programs run very rapidly on laptop and desktop computers. The 1D programs are helpful in visually understanding basic principles such as electron bunching, optical gain and saturation, and in many cases give good descriptions of FEL performance. The 2D programs are useful when longitudinal effects such as pulse slippage and desynchronism are dominant. The three-dimensional (3D) and four-dimensional (4D) programs typically run on multi-core or cluster computers, and are useful when transverse effects such as optical mode distortion are significant. Each of the programs produces extensive graphical output to enhance physical understanding and reveal trends.

This paper describes the new 4D models that we have developed over the past several years, taking advantage of advances in computer technology that enable these programs to run efficiently on readily available hardware such as Linux clusters. We also present results showing how we have validated and benchmarked the new models.

DESCRIPTION OF THE MODELS

Dimensionless Parameters

All of our models use dimensionless parameters that simplify the equations, provide intuitive insight, and generalize the results [3]. Longitudinal coordinates are normalized to the undulator length L, and transverse coordinates are normalized to a characteristic optical mode radius $\sqrt{L\lambda/\pi}$, where λ is the optical wavelength. The dimensionless time is defined by $\tau = ct/L$ where c is the speed of light.

Phase space coordinates follow the microscopic bunching of the electrons on the scale of an optical wavelength. The electron phase is defined as $\zeta = (k + k_0)z - \omega t$ where $k = 2\pi/\lambda$ is the optical wavenumber, $k_0 = 2\pi/\lambda_0$ is the undulator wavenumber, λ_0 is the undulator period, $\omega = kc$ is the optical frequency, and z is the electron's position along the undulator axis at time t. The dimensionless phase velocity then becomes $\nu = d\zeta/d\tau = L[(k + k_0)\beta_z - k]$ where $\beta_z = v_z/c$.

The dimensionless undulator parameter is given by $K = eB\lambda_0/2\pi mc^2$, where B is the rms field strength, e is the electron charge and m is the electron mass (in cgs units). For most FELs, $K \sim 1$.

The dimensionless optical field amplitude is defined as $|a| = 4\pi NeKLE/\gamma^2 mc^2$, where N is the number of undulator periods, E is the electric field amplitude, and γ is the Lorentz factor. When $|a| \ll \pi$ the optical fields are weak and there is very little electron bunching. When $|a| \sim \pi$, there can be significant electron bunching, producing growth of the optical fields. When $|a| \gg \pi$, strong optical fields can cause many of the electrons to become trapped in closed phase space orbits, leading to the onset of saturation.

The optical fields are driven by the dimensionless current density, $j = 8N(e\pi KL)^2\rho/\gamma^3 mc^2$, where ρ is the particle density. When $j \lesssim 1$, the weak-field gain is low, but when $j \gg 1$, the FEL can have high gain. A typical FEL oscillator has $j \sim 100$ and moderate weak-field gain. An FEL amplifier, with a much longer undulator, can have $j \sim 10^5$ and very high gain over a single pass.

Model Assumptions and Methods

The first 4D model that we developed in the early 1990s assumed the electron beam is well inside the optical mode [4]. In that case, all of the electrons in each longitudinal slice of the pulse interact with the same optical field, so the microscopic bunching is uniform across each slice. This assumption significantly reduces the computational and memory requirements for the simulation; for instance, instead of large 3D arrays for the electron phase ζ and phase velocity ν, only 1D arrays are required.

Our new 4D models are more general, including the full evolution in (x, y, z, t) of the electrons and optical pulses. The programs are parallelized, with each process following an optical wavefront $a(x, y)$ and sample electrons for a single longitudinal slice of the optical pulse $a(z)$ along the undulator axis. In each slice, the optical wavefront is represented by the field amplitude and phase over a rectangular grid, and approximately 30,000 sample electrons are assigned transverse phase space coordinates $(x, \theta_x, y, \theta_y)$ in addition to their longitudinal phase space coordinates (ζ, ν). To reduce shot noise effects, a quiet start algorithm [5] is used to assign the initial phase space coordinates, taking

* blau@nps.edu

ISBN 978-3-95450-134-2

into account the emittance and energy spread of the electron beam. The effective charge corresponding to each sample electron is weighted by the current density profile of the electron pulse.

The number of transverse modes included in our models is limited only by the number of transverse grid points; typically a 300 × 300 grid is adequate, but in some cases a 1000 × 1000 grid is needed. The number of longitudinal slices determines the number of longitudinal modes; typically we use 100 slices, but in some cases several hundred slices are needed. The optical wavelength is allowed to evolve self-consistently.

On each time step, the electrons advance in phase space according to the relativistic Lorentz force equation, using a fourth-order Runge-Kutta method. Their transverse coordinates are updated according to the undulator betatron focusing. The undulator can have a step or linear taper starting at an arbitrary position; the Lorentz force equation is adjusted accordingly. The optical field evolves according to the parabolic wave equation, using a Fourier transform method. Electrons are continually passed from one optical slice to the next to account for pulse slippage. An important feature of our models is that they do not assume axial symmetry, so they can include arbitrary shifts and tilts of the electron beam and cavity mirrors with respect to the undulator axis to study the effects of misalignments on FEL performance [6].

A single-pass amplifier model was developed first. The initial optical field can be specified in terms of the seed laser parameters, or it can develop from spontaneous emission to simulate a SASE FEL. The initial electron beam can be described by statistical quantities such as the spread in positions and velocities along each dimension, or a particle tracking code such as PARMELA [7] or GPT [8] can be used to produce the initial electron distribution. Graphical output from the simulation includes the evolution of the optical power and gain along the undulator, the electron phase space, slices through the optical field in each dimension, the optical power spectrum, and a modal decomposition of the final optical field.

Next we developed multi-pass oscillator simulations. A transformation matrix is used to represent each mirror, with the radius of curvature determined by the cavity length and the dimensionless Rayleigh range. One of the mirrors can be partially transparent, or it can use hole out-coupling. Including mirrors within the program allows it run efficiently compared to other approaches that require exchanging the wavefronts with an external optics code on each pass. An expanding coordinate grid outside of the undulator [9] allows for the significant diffraction that occurs in a typical FEL oscillator, with a significant reduction in computation time and memory requirements.

The first oscillator model that we developed uses periodic boundary conditions, with the assumption that the pulse length is much greater than the slippage distance ($N\lambda$). The results of this model depend mainly on three key parameters: the dimensionless current density j, the cavity quality factor, and the Rayleigh length. This model is useful for studying effects such as coherence evolution, the trapped-particle instability, the development of sidebands, and limit-cycle behavior.

We have recently developed another oscillator model that incorporates short pulses (comparable to the slippage distance). In this model, the longitudinal window is wide enough to contain the full extent of the electron and optical pulses as they evolve through the undulator, so it does not require periodic boundary conditions. Desynchronism is implemented by a steadily increasing shift of the optical pulse with respect to the electron pulse on each pass.

Graphical Output

To aid in analyzing the large amounts of data, our 4D simulations produce extensive graphical output. Figure 1 shows an example of simulation output for the Jefferson Laboratory infrared FEL oscillator [10]. The green shaded window at the top of the figure lists the dimensionless parameters used in the simulation. Near the middle on the left side of the figure is a plot labeled a(x, 0, 0) which shows the amplitude of the optical field (blue) versus x at $y = z = 0$ at the beginning of the first pass; the narrower electron beam is superimposed in red. Directly above that is an intensity plot showing the evolution of this optical field profile over $n = 300$ passes through the undulator; here light blue corresponds to the largest optical field amplitude, and dark blue corresponds to zero field. The white lines indicate the $1/e$ value of the field amplitude, and the red dots indicate the $1/e$ value of the electron beam current at each pass. In the upper left is the final optical field profile; notice that the peak value, shown in the upper right corner of each plot, has increased from 6.7 to 26.6. Next to those plots is a similar series of plots, now showing the evolution of an optical field slice versus y at $x = z = 0$. These are virtually identical to the previous plots because the input parameters for this example had azimuthal symmetry (although our 4D model does not require that).

The next column of plots, labeled a(0, 0, z), show the evolution of the electron and optical pulses versus z, at $x = y = 0$. The initial electron pulse (red) starts out slightly ahead of the optical pulse (blue), but ends up trailing the optical pulse by the slippage distance $N\lambda$ at the end of each pass. The z coordinate in these plots is normalized to the slippage distance. The evolution of the optical pulse over many passes depends on the interaction between the electron and optical pulses, and the desynchronism (or "detuning") of the optical cavity [1].

In the upper right is a series of plots labeled $P(0,0,\nu)$, showing the evolution of the optical power spectrum. This is obtained by taking the Fourier transform of the optical power $P(0,0,z) = |a(0,0,z)|^2$ at $x = y = 0$, as representative of the pulse spectrum. Notice that the power spectrum is initially peaked near resonance, $\nu = 0$, but shifts to a larger value $\nu \approx 8$ after $n \approx 200$ passes. This corresponds to a shift in the lasing wavelength of $\Delta\lambda/\lambda = \Delta\nu/2\pi N \approx 4\%$ as the FEL evolves from weak fields to saturation in strong

ISBN 978-3-95450-134-2

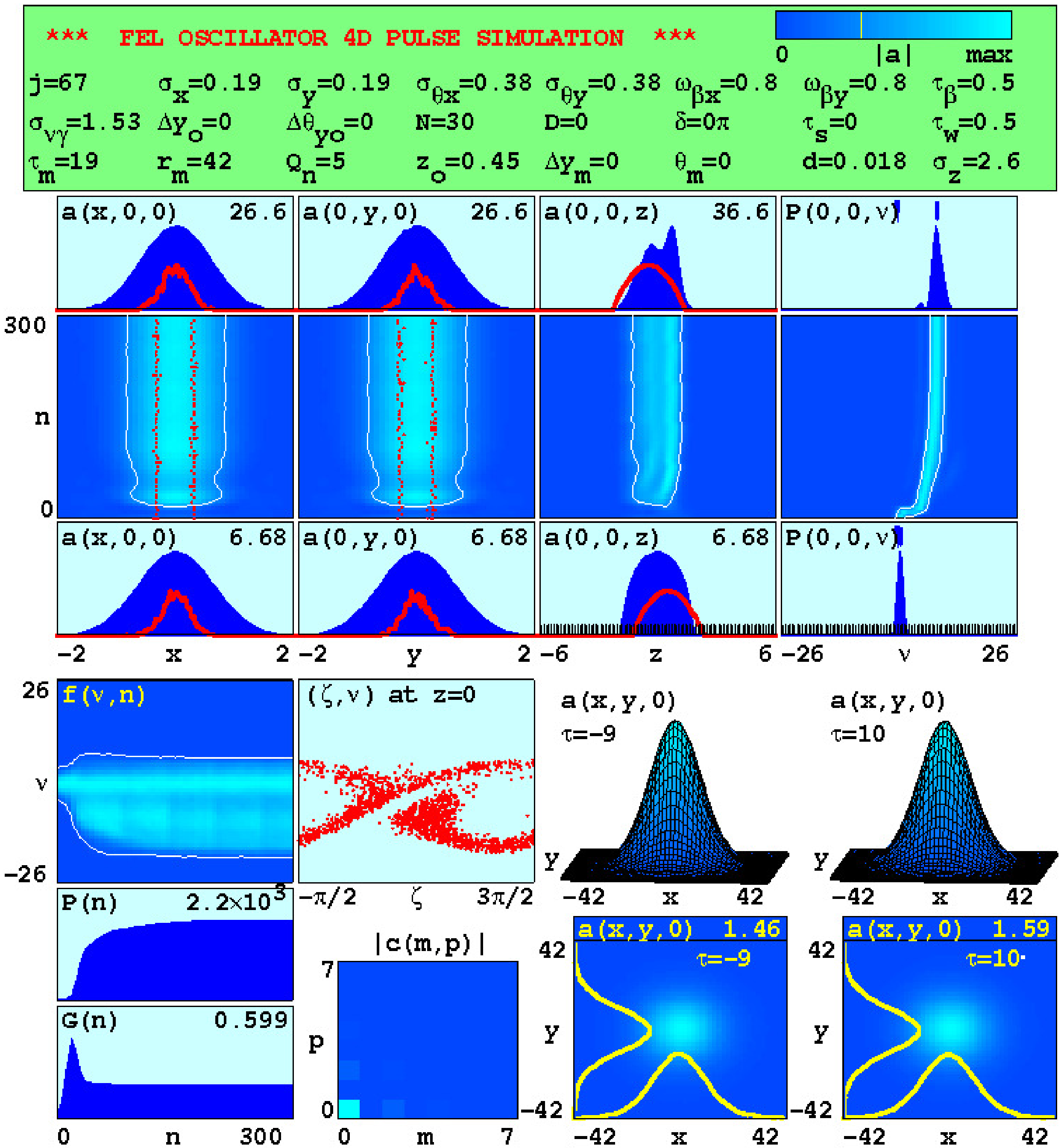

Figure 1: Output from a 4D simulation of the Jefferson Lab infrared FEL oscillator. The various plots are described in the text.

ISBN 978-3-95450-134-2

fields, a well-known effect predicted by FEL theory [1] and observed in many experiments.

In the lower half of the figure, the plot on the left labeled $f(\nu,n)$ shows the evolution of the electron phase velocity distribution. Notice that the electrons initially have a rather narrow phase velocity distribution due only to emittance and energy spread, but as they interact with the growing optical field in the undulator over many passes they develop a broader distribution in phase velocities. Next to that plot shows the final distribution of the electrons in phase space (ζ,ν) at $z = 0$, indicating good bunching of the electron beam. In the bottom left of the figure are two plots showing the evolution of the optical power $P(n)$ and gain $G(n)$. Notice that the optical power saturates at a fixed value after $n \approx 200$ passes.

On the bottom of the figure near the center is a plot labeled $|c(m,p)|$, which depicts the modal composition of the optical wavefront, using a color scale to represent the values of the coefficients of the Hermite-Gaussian cavity modes. In this case, a light blue square at $p = m = 0$ indicates the wavefront is primarily in the fundamental (0,0) mode. This is confirmed by the four plots in the lower right of the figure, which show a nearly Gaussian optical wavefront $|a(x,y,0|$ at the left ($\tau = -9$) and right ($\tau = 10$) mirrors, in both 2D and 3D representations.

VALIDATION AND BENCHMARKING OF THE MODELS

First we will compare results from our simulations to well-known theoretical formulas. These formulas typically assume idealized cases, but they are useful to give rough approximations of FEL performance, and with careful choices of parameters they can be used to validate our models. We will also provide benchmarks by comparing simulation predictions to results from FEL experiments.

Weak-field Gain

In weak optical fields ($|a| \ll \pi$) and low current density ($j \lesssim 1$), the single-pass gain can be expressed as [1]

$$G = j\left(\frac{2 - 2\cos\nu_0 - \nu_0\sin\nu_0}{\nu_0^3}\right). \tag{1}$$

This formula assumes all of the electrons are injected with the same initial electron phase velocity ν_0 (i.e., no emittance or energy spread). It also assumes perfect overlap between the electron and optical beams, and it ignores effects such as diffraction, pulse slippage, and optical mode distortion. However, we can compare it to the results from our 4D amplifier model if we choose appropriate initial conditions. The electron and optical beams are given identical top-hat profiles with a large radius to minimize diffraction. Long, flat pulses are used to remove slippage effects. The resulting weak-field gain spectrum for $j = 1$ is shown in Fig. 2. The blue theory line corresponds to Eq. 1, and the red dots correspond to results from the 4D amplifier model. The results show excellent agreement between the theory and the model for this idealized case. The slight differences are expected since Eq. 1 does not allow the optical fields to evolve self-consistently.

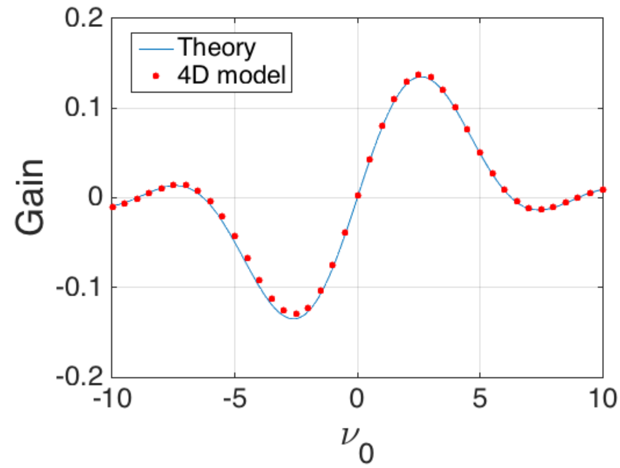

Figure 2: Weak field gain spectrum: single-pass gain vs. initial phase velocity ν_0 for a low-gain FEL ($j = 1$).

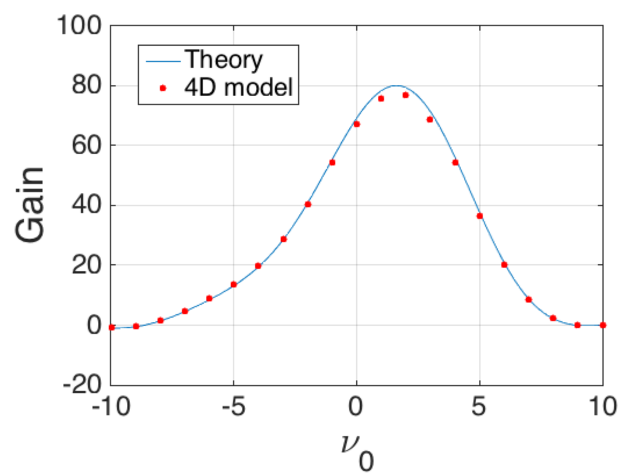

Figure 3: Weak field gain spectrum: single-pass gain vs. initial phase velocity ν_0 for a high-gain FEL ($j = 100$).

For a high-gain FEL ($j \gg 1$), Eq. 1 is no longer valid. Instead, the FEL integral equation described below can be used to estimate the gain. Now the gain spectrum is broader and more symmetric with a peak near resonance, $\nu_0 \approx 0$, as shown in Fig. 3. Here we have used $j = 100$; the blue theory line was obtained using the FEL integral equation, and the red dots are from our 4D amplifier model, with the same idealized conditions as before. Again, there is good agreement between the model and the theory.

For a high-gain FEL at resonance, $\nu_0 = 0$, the weak-field gain can be approximated as [1]

$$G \approx \frac{1}{9}e^{(j/2)^{1/3}\sqrt{3}} \tag{2}$$

Figure 4 shows results for gain versus current density j for our 4D model (red dots) compared to Eq. 2 (blue line).

ISBN 978-3-95450-134-2

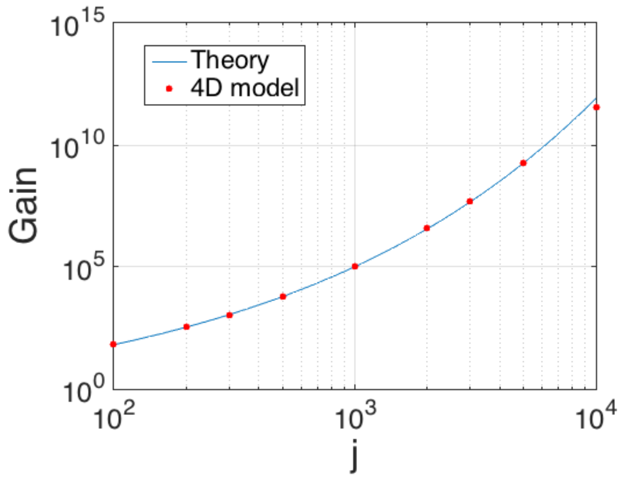

Figure 4: Weak-field gain vs. dimensionless current density j for high-gain FELs ($j \gg 1$) at resonance ($\nu = 0$).

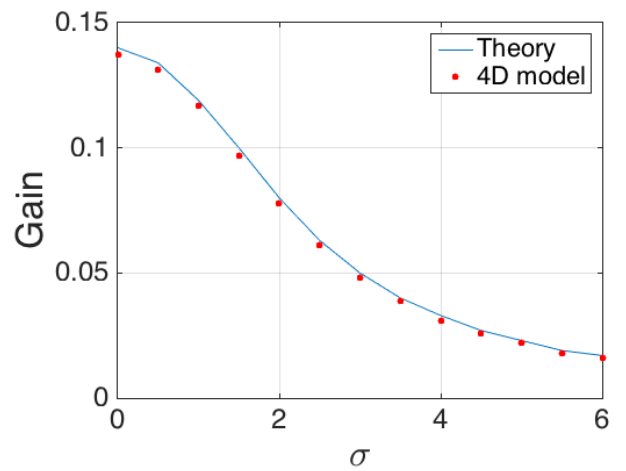

Figure 5: Weak-field gain vs. the rms spread σ in phase velocities due to an energy spread for a low-gain FEL ($j = 1$).

There is excellent agreement between the model and the theory over about 10 orders of magnitude change in gain (note the logarithmic scale on each axis).

The previous results all assume an idealized electron beam, with no energy spread or emittance. The effects of a realistic beam can be incorporated into the theory using the FEL integral equation [11,12], which describes the evolution of the dimensionless, complex optical field,

$$\frac{da}{d\tau} = \frac{ij}{2}\int_0^\tau \tau' F(\tau') e^{-i\nu_0\tau'} a(\tau - \tau') d\tau' \tag{3}$$

where $F(\tau') = \int f(q)e^{-iq\tau'}dq$ is the characteristic function of the distribution $f(q)$ of electron phase velocities $\nu_i = \nu_0 + q$ about ν_0 and $\int f(q)dq = 1$.

For example, if an electron beam has a Gaussian spread of energies, it will have a corresponding distribution in phase velocities $f(q) = \exp(-q^2/2\sigma^2)/\sqrt{2\pi}\sigma$ where $\sigma = 4\pi N\Delta\gamma/\gamma$ is the standard deviation. For a low-gain FEL, it is clear from Fig. 2 that when the spread in phase velocities is on the order of π, there will be significant gain degradation. Figure 5 shows the effect of increasing electron energy spread on FEL gain. The blue line corresponds to Eq. 3 and the red dots are results from our 4D model. Again, we see excellent agreement between the model and the theory.

Strong-field Gain

In strong optical fields, $|a| \gg \pi$, an analytic formula for gain is not available, but features of saturation can be explored and compared to a 1D model. Figure 6 shows results for 4D simulations of single-pass gain versus initial phase velocity ν_0 and optical field amplitude a_0. As the FEL evolves from weak fields $a_0 \approx 0$ up to moderately strong fields $a_0 = 20$, the peak gain decreases from $G \approx 13\%$ to $G \approx 3\%$, the gain spectrum $G(\nu_0)$ becomes broader and the peak shifts away from resonance, from $\nu_0 \approx 3$ to $\nu_0 \approx 5$. Simulations with our 1D model produce a nearly identical plot [1].

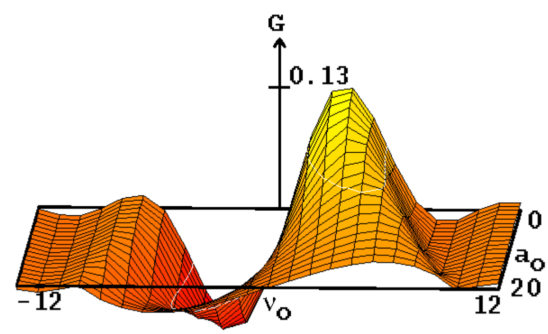

Figure 6: Results for 4D simulations of single-pass gain G vs. initial phase velocity ν_0 and optical field amplitude a_0 for a low-gain FEL ($j = 1$).

Extraction

The FEL extraction η is defined as the ratio of the output optical power to the input electron beam power. Our simulations predict extraction by first determining the average change in phase velocity $\langle\Delta\nu\rangle$ of the sample electrons, then the corresponding extraction is calculated using $\eta = \langle\Delta\nu\rangle/4\pi N$.

A low-gain FEL will saturate when the optical field amplitude reaches $|a| \approx 4\pi^2$. In that case, the trapped electrons will undergo an average phase velocity shift of $\langle\Delta\nu\rangle \approx 2\pi$, which gives an approximate theoretical extraction of $\eta_{th} \approx 1/2N$. Indeed, that is what our simulations invariable obtain for low-gain FELs, so long as the gain is above threshold. For example, the Jefferson Lab FEL oscillator has $N = 30$ periods, so the above formula predicts an extraction of $\eta_{th} \approx 1.67\%$. The actual experiment obtained extractions between 1.5% and 1.7% [10]. In our 4D simulation of this FEL shown in Fig. 1, the power evolution plot $P(n)$ near the lower left indicates saturation after $n = 200$ passes. The final phase velocity distribution $f(\nu, n)$

ISBN 978-3-95450-134-2

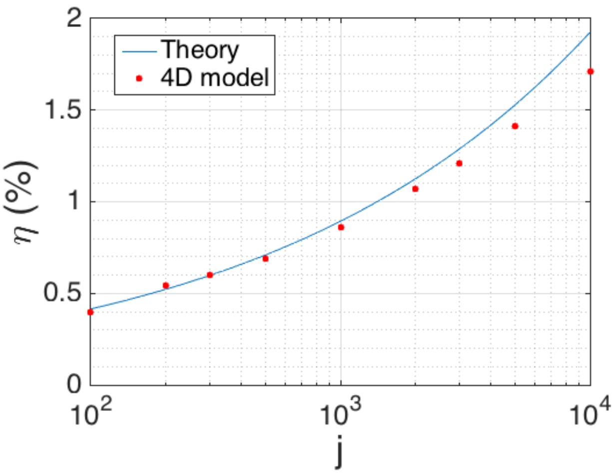

Figure 7: Extraction η vs. dimensionless current density j for high-gain FELs ($j \gg 1$) at resonance ($\nu = 0$).

shown above it yields an extraction of $\eta = 1.63\%$, in good agreement with the theory formula and the experimental results.

A high-gain FEL will saturate at a larger optical field amplitude $|a| \approx 2(j/2)^{2/3}$ [1], causing the trapped electrons to undergo an average phase velocity shift of $\langle \Delta\nu \rangle \approx 2\sqrt{2}(j/2)^{1/3}$. Assuming half of the electrons are trapped, the resulting theoretical extraction is

$$\eta_j \approx \frac{2\sqrt{2}(j/2)^{1/3}}{8\pi N}. \quad (4)$$

Figure 7 shows results for extraction versus current density for our 4D model (red dots) compared to Eq. 4 (blue line). There is good agreement between the model and the theory over a couple orders of magnitude change of the current density j. The slight differences at large j may be due to the assumption in Eq. 4 that half of the electrons are trapped.

Tapered Undulator

As an FEL approaches saturation, the electrons lose energy and are no longer in resonance with the optical field, thus reducing energy exchange. To further enhance extraction, the undulator can be tapered to restore resonance [13]. Typically this is done by a linear change in the undulator gap, resulting in a linear slope of the on-axis undulator field, $\Delta B/B$. This produces an effective acceleration of the electron phase velocity [1],

$$\delta = -4\pi N \left(\frac{K^2}{1+K^2}\right)\left(\frac{\Delta B}{B}\right)\left(\frac{1}{1-\tau_s}\right), \quad (5)$$

where τ_s is the dimensionless location of the taper start along the undulator axis (recall $\tau = 1$ corresponds to the end of the undulator). If half of the electrons remain trapped, the resulting extraction can be estimated as $\eta_\delta \approx \delta(1-\tau_s)/8\pi N$.

For example, the Brookhaven National Laboratory (BNL) seeded FEL amplifier had $N = 256$ periods and an undulator parameter of $K = 0.78$, with a 4% field taper along the the last 2.5m of the 10m long undulator [14]. The corresponding phase acceleration is thus $\delta \approx 63\pi$ starting at $\tau_s = 0.75$, and the estimated extraction is $\eta_\delta \approx 0.74\%$. The actual experiment obtained an extraction of $\eta \approx 0.8\%$.

Figure 8 shows the output from a 4D simulation of the BNL FEL amplifier. The various plots shown in this figure are similar to those in Fig. 1, except the evolution plots are now for a single pass through the undulator from $\tau = 0$ to $\tau = 1$. Since this is a high-gain FEL ($j = 7782$), the optical beam is "guided" along the axis near the electron beam, as seen in the evolution of the transverse profiles $a(x,0,0)$ and $a(0,y,0)$ near the upper left of the figure. Beneath those plots, the evolution of the electron phase velocity, $f(\nu,\tau)$ shows the phase acceleration due to taper beginning at $\tau_s = 0.75$. The final phase space picture next to that indicates about half of the electrons remain trapped. The power and gain evolution plots in the lower left reveal a plateau at saturation $\tau \approx 0.75$, and then the power and gain continue to increase as the taper takes effect. Next to those plots, the modal composition plot $|c(m,n)|$ indicate the presence of numerous higher-order modes, as expected in a high-gain FEL. In this case, since there is no optical cavity, the basis set for the modal decomposition assumes the seed laser is in the fundamental (0,0) Hermite-Gaussian mode. Higher-order mode content is also observed in the strongly-peaked optical wavefront $a(x,y,0)$ shown in the lower right at $\tau = 1$. The simulation obtained an extraction of $\eta = 0.84\%$, in good agreement with the theory formula and the experimental result.

CONCLUSION

Our new 4D models of FEL amplifiers and oscillators have been validated and benchmarked by comparison to theoretical formulas and experimental results. We have demonstrated excellent agreement between our simulations and the theory formulas for various regimes of FEL operation, and we have also shown good agreement with experimental results. We are now using the new 4D models to study the interaction between transverse and longitudinal effects, such as how diffraction affects desynchronism in short-pulse FELs.

ACKNOWLEDGMENT

The authors are grateful for support from the High Energy Laser Joint Technology Office.

ISBN 978-3-95450-134-2

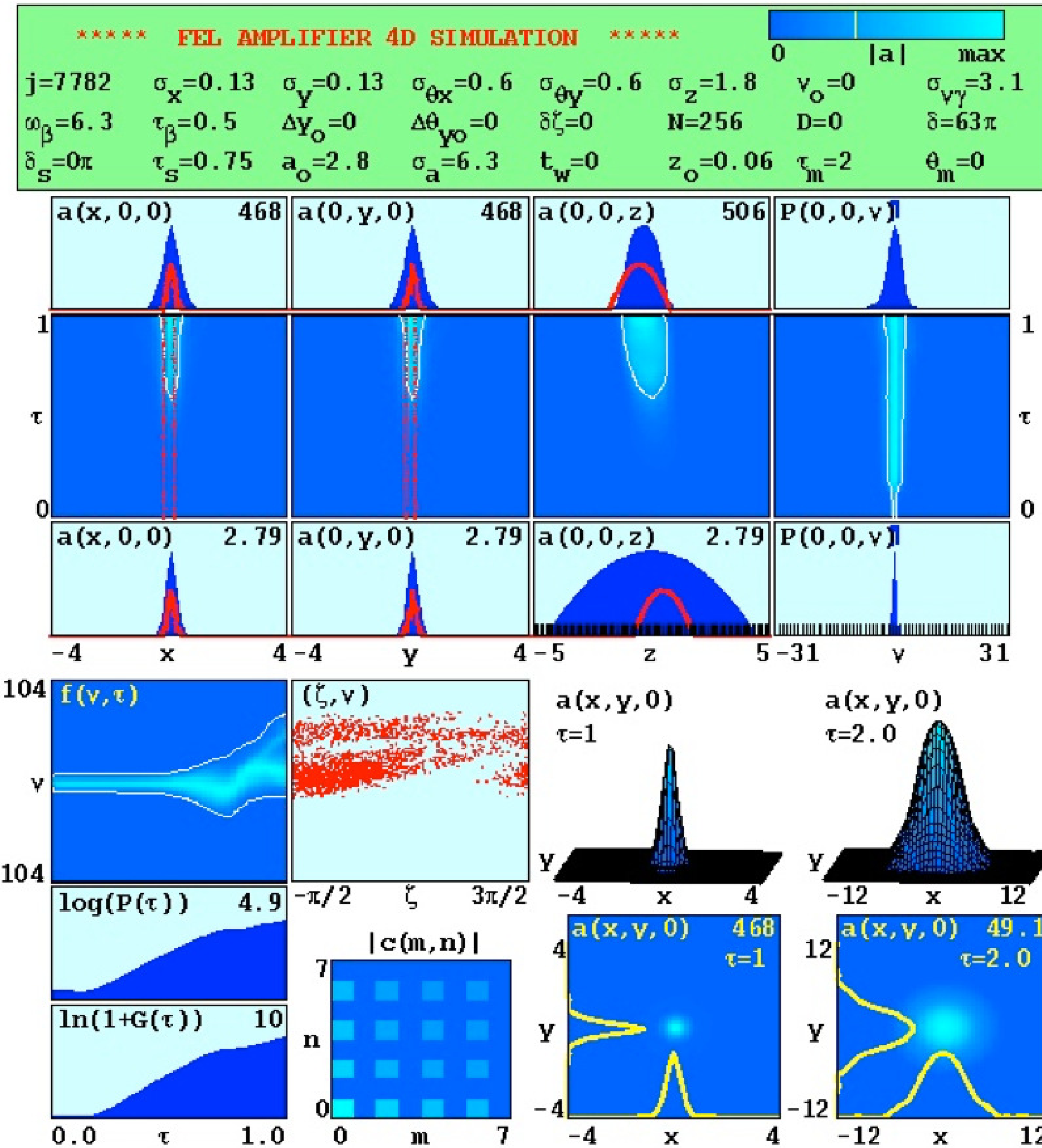

Figure 8: Output from a 4D simulation of the Brookhaven National Laboratory seeded FEL amplifier.

ISBN 978-3-95450-134-2

REFERENCES

[1] W. B. Colson, in *Laser Handbook*, (Amsterdam: North-Holland, 1990), Chap. 5.

[2] J. Blau, Ph.D. Thesis, Naval Postgraduate School, Monterey, CA (2002).

[3] W. B. Colson and J. Blau, "Parameterizing Physics Effects in Free Electron Lasers", Nucl. Instr. Meth. Phys. Res. A 272, 386 (1988).

[4] J. Blau and W. B. Colson, "Four Dimensional Simulations of the CEBAF Infrared Free Electron Laser", Nucl. Instr. Meth. Phys. Res. A 318, 717 (1992).

[5] W. M. Fawley, "Algorithm for Loading Shot Noise Microbunching in Multidimensional, Free-Electron Laser Simulation Codes", Phys. Rev. ST Accel. Beams 5, 070701 (2002).

[6] P. P. Crooker et. al., "Vibrations Effects in Short Rayleigh Length FELs", FEL'05, Stanford, CA, USA, August 2005.

[7] L. M. Young and J. H. Billen, "The Particle Tracking Code PARMELA", PAC'03, Portland, OR, USA, May 2003.

[8] M. J. de Loos and S. B. van der Greer, "General Particle Tracer: A New 3D Code for Accelerator and Beam Line Design", EPAC'96, Barcelona, Spain, June 1996.

[9] R. L. Armstead, W. B. Colson and J. Blau, "Short Rayleigh Length Free Electron Laser Simulations in Expanding Coordinates", FEL'04, Trieste, Italy, August 2004.

[10] S. Benson et. al., "High Power Operation of the JLAB IR FEL Driver Accelerator", PAC'07, Albuquerque, NM, USA, June 2007.

[11] W. B. Colson, J. C. Gallardo and P. M. Bosco, "Free-Electron Laser Gain Degradation and Electron Beam Quality", Phys. Rev. A 34, 4837 (1986).

[12] W. B. Colson and J. Blau, "Free Electron Laser Theory in Weak Optical Fields", Nucl. Instr. Meth. Phys. Res. A 272, 386 (1987).

[13] N. M. Kroll, P. L. Morton and M. N. Rosenbluth, "Free-electron Lasers with Variable Parameter Wigglers", IEEE J. Quant. Elect. QE-17, 1436 (1981).

[14] X. J. Wang et. al., "Efficiency and Spectrum Enhancement in a Tapered Free-electron Laser Amplifier", Phys. Rev. Lett. 103, 154801 (2009).

ISBN 978-3-95450-134-2

DEVELOPMENT OF PHONON DYNAMICS MEASUREMENT SYSTEM BY MIR-FEL AND PICO-SECOND LASER

T. Murata#, H. Zen, T. Katsurayama, T. Nogi, S. Suphakul, K. Torgasin, T. Kii, K. Masuda, H. Ohgaki, Institute of Advanced Energy, Kyoto University, Kyoto 611-0011, Japan
K. Yoshida, Kumamoto institute for Photo-Electro Organics, Kumamoto 862-0901, Japan and Department of Applied Chemistry and Biochemistry, Kumamoto University, Kumamoto 860-8555, Japan
K. Hachiya, Graduate School of Energy Science, Kyoto University, Kyoto 606-8501, Japan

Abstract

Coherent control of a lattice vibration in bulk solid (mode-selective phonon excitation: MSPE) is one of the attractive methods in the solid state physics because it becomes a powerful tool for the study of ultrafast lattice dynamics (e.g. electron-phonon interaction and phonon-phonon interaction). Not only for that, MSPE can control electronic, magnetic, and structural phases of materials. In 2013, we have directly demonstrated MSPE of a bulk material with MIR-FEL (KU-FEL) by anti-Stokes Raman scattering spectroscopy. For the next step, we are starting a phonon dynamics measurement to investigate the difference of physical property between thermally excited phonon (phonon of equilibrium state) and optically excited phonon (phonon of non-equilibrium state) by time-resolved method in combination with a pico-second laser and MIR-FEL. By using pico-second laser, we can also expect to perform the anti-Stokes hyper-Raman scattering spectroscopy to extend MSPE method to the phonon mode which has Raman inactive (or some of the infrared inactive modes). As the first step, we have commissioned the time-resolved phonon measurement system and started the measurement on 6H-SiC. Consequently, we succeeded in a development of a phonon dynamics measurement system and the temporal resolution of the developed system was around 10 ps.

INTRODUCTION

The electron-phonon interaction influences physical properties of solid-state materials. Thus, the clarification of the interaction is required for understanding basic physical properties of solid-state materials and developing high-performance devices [1,2]. To clarify the interaction, it is important to understand the relation between the electronic state and the excitation of a particular lattice vibration (phonon).

Mode-selective phonon excitation (MSPE) is one of the useful methods for clarification of the relation between electronic state and the excitation of a particular phonon mode. Especially, a mid-infrared pulse laser is strong tool for MSPE. By irradiating a mid-infrared pulse laser tuned absorption wavelength of a specific phonon, the direct excitation of a specific phonon mode is available [3,4]. We have developed a technique which can directly observe excitation condition of particular phonon mode by using anti-Stokes Raman scattering spectroscopy (Fig. 1) [3]. By using the technique, the MSPE by MIR-FEL has been directly demonstrated with the sample material of 6H-SiC (Fig. 2) [3]. Then, we have started development of phonon dynamics measurement system by MIR-FEL and pico-second laser to investigate the differences of phonon property between selective excitation and thermal (non-selective) excitation.

murata.tomoya.46s@st.kyoto-u.ac.jp

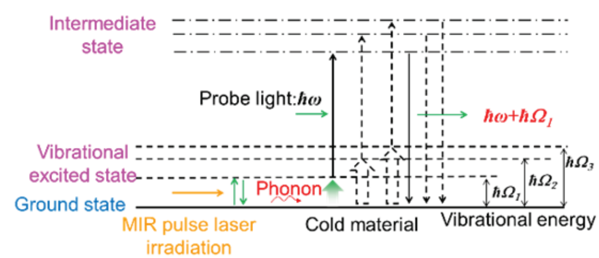

Figure 1: Schematic of the principle of anti-Stokes Raman scattering by MIR laser irradiation with cold material [3].

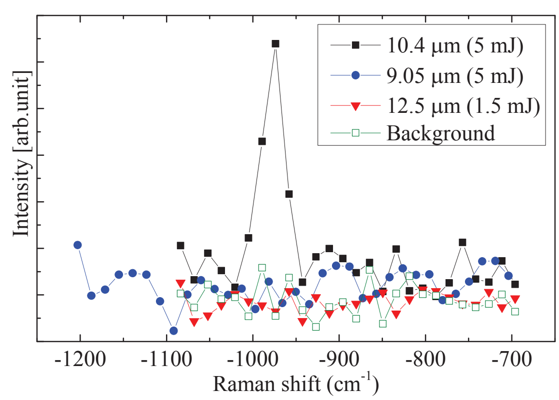

Figure 2: Anti-Stokes Raman scattering spectra with MIR-FEL and nano-second laser at 14 K [3].

PHONON DYNAMICS MEASUREMENT SYSTEM

Figure 3 shows the schematic diagram of developed phonon dynamics measurement system. In this system, the second harmonic of pico-second Nd-YVO_4 laser (probe light) [5] and MIR-FEL (pump light) are simultaneously irradiated. The wavelength and pulse

ISBN 978-3-95450-134-2

width of the pico-second laser were 1064 nm, 7.5 ps, respectively. To pick up the near-infrared light, mirror was installed in front of half-wave plate before SHG crystal [see Fig. 2 of Ref. 5], and transported around 15 m to the user room. A beam expander was installed to parallelize the laser beam. The transported laser light was injected to BBO crystal for second harmonic generation. A bandpass filter was used to cut light from the fundamental wavelength (1064 nm). A quartz lens focused the laser on the sample surface. The pico-second laser is synchronized to the RF signal which was used for electron beam acceleration for MIR-FEL by using a piezo stage in the pico-second laser oscillator. The timing delay of MIR-FEL pulse against the pico-second laser can be adjusted by using a mechanical phase shifter installed in the RF signal line of driver linac of the MIR-FEL and an optical delay was also used. The emitted light from the sample was collimated by a quartz lens and focused on the entrance slit of the monochromator (Triax 190, Horiba Scientific). Notch filters (NF533-17, thorlabs: central wavelength of 532-nm and blocking bandwidth of 17-nm) were installed to supress the background photons caused by Rayleigh scattering on the sample. The spectrum of the emitted anti-Stokes Raman scattering light was measured by using a monochromator and a photomultiplier with a gating system (R3896 and C1392, Hamamatsu Photonics) under the photon counting condition. The gating timing of photomultiplier was synchronized to the oscillation timing of MIR-FEL. The output current signal from the photomultiplier tube was measured by a digital oscillo-scope.

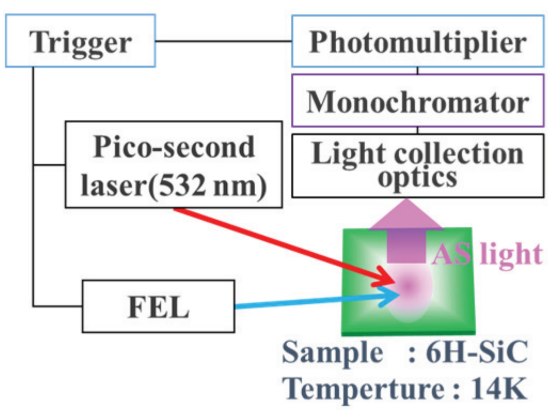

Figure 3: Schematic of the measurement system for anti-Stokes Raman scattering.

Table 1: Phonon Modes of 6H-SiC [6]

Wavenumber (Wavelength)	Infrared active	Raman active
965 cm^{-1} (10.4 μm)	○	○
797 cm^{-1} (12.5 μm)	○	×
787 cm^{-1} (12.7 μm)	×	○
767 cm^{-1} (13.0 μm)	×	○

TEST MEASUREMENT

Test experiments have been performed to evaluate the performance of the developed system and investigate the phonon dynamic of 6H-SiC which is the same sample with reference [3] and was a commercially available SiC (6H-semi-insulator type SiC, Xlamen Powerway Advanced Material Co., LTD:SiC) with dimension of 15 mm × 15 mm × 0.33 mm and the crystal orientation of (0001). First, the sample was cooled to 14 K using a closed-cycle Helium refrigerator, and thermal phonon excitation was suppressed. The known phonon modes of this sample around 10 μm are listed in Table 1 [6]. The FEL wavelength was tuned to 10.4 μm and the delay between the pico-second laser and MIR-FEL was varied to find the condition of simultaneous irradiation of two lasers. Next, the anti-Stokes scattering light intensity depending on the delay was measured to know the temporal resolution of the developed system. Moreover, under the simultaneous irradiation condition, the wavelength of MIR-FEL was varied to check the dependence on MIR-FEL wavelength.

RESULTS AND DISCUSSION

Timing Scan

To investigate the temporal resolution of the developed system, the MIR-FEL wavelength was tuned to 10.4 μm. Figure 4 shows the dependence of anti-Stokes Raman scattering intensity on the delay of the MIR-FEL. Horizontal axis indicates the delay time of the probe light (pico-second laser) against the pump light (MIR-FEL). At the optimum timing, we observed a strong anti-Stokes Raman scattering light at the Raman shift of -975 cm^{-1} as obviously shown in Fig. 4. As is shown in Fig. 4 the width of the delay time was around 20 ps in FWHM and the temporal resolution was evaluated around 10 ps. It would be worth to note that there is very weak tail in the positive delay side in Fig. 4. The origin of this tail is possibly decayed lattice vibration.

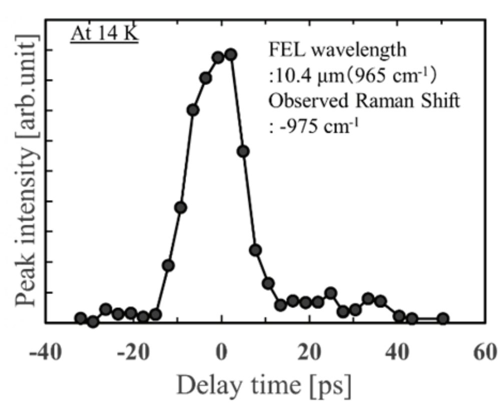

Figure 4: Dependence of anti-Stokes light intensity on delay time pico-second laser against MIR-FEL.

Since the predicted lifetime of the observed phonon excitation mode in 6H-SiC is about 2 ps at 20 K [use

ISBN 978-3-95450-134-2

Eq. 5 of Ref. 7], the developed measurement system could not extracted any detail information of the lifetime by this test experiment. The developed system, however, can be available to measure the samples of longer lifetime, i.e. hydrogenated amorphous silicon, whose phonon lifetime are several tens pico-second [8].

FEL Wavelength Dependence

Figure 5 shows the measured anti-Stokes Raman scattering spectra at 14 K. When the wavelength of MIR-FEL was tuned to 10.4 μm, a peak emerged at 975 cm^{-1}. Comparing to the previous system which used a nano-second laser, S/N ratio was improved from 4:1 to 22:1. But when the wavelength of MIR-FEL was tuned to 8.95 μm and 9.60μm, the peak was observed in wavelength that does not correspond to absorption energy of lattice vibration of 6H-SiC. On the other hand, the sample has infrared active and Raman inactive phonon mode at 12.5μm, but anti-Stokes light peak was not observed in the case of 12.5-μm FEL irradiation. Consequently, either excitation of a special vibrational mode or sum frequency generation was suspected as a cause. Figure 6 shows dependence of wavenumber of the peak in anti-Stokes Raman scattering spectra on FEL wavenumber. The peak wavenumber of the observed anti-Stokes Raman scattering light was almost linear to the wavenumber of

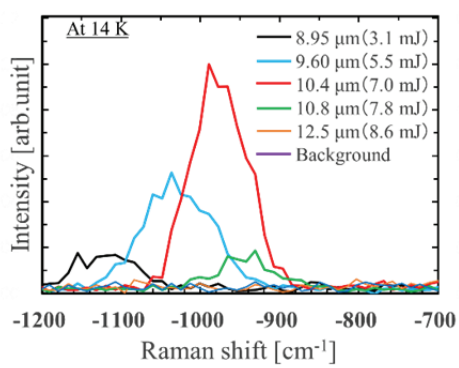

Figure 5: Anti-Stokes Raman scattering spectra with MIR -FEL and pico-second laser at 14K.

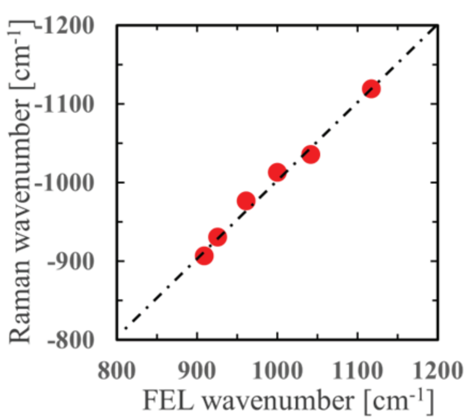

Figure 6: Dependence of the peak wavenumber in anti-Stokes light on FEL wavenumber.

MIR-FEL used as the pump laser. Further studies in experimental and theoretical studies are required to reveal the phonon excitation mechanism by a mid-infrared pulse laser.

CONCLUSION

We developed a phonon dynamics measurement system by MIR-FEL and pico-second laser to study the differences of phonon property between a selective excitation and a thermal (non-selective) excitation. The system was checked by using 6H-SiC which has been studied previous nano-second laser system. The test measurement showed that by using pico-second laser, S/N ratio was enhanced by 5 times in comparison to the nano-second laser.

The temporal resolution of the developed system was evaluated to be around 10 ps. Therefore the developed measurement would be available to the samples whose phonon lifetime are longer, i.e. hydrogenated amorphous silicon which has several tens pico-second of lifetime.

In addition, we have observed unexpected peaks in wavelength (8.95, 9.60 μm) during this study which do not correspond to any known phonon mode in 6H-SiC. The sample has infrared active and Raman inactive phonon mode at 12.5μm. But anti-Stokes light peak was not observed in the case of 12.5-μm FEL irradiation. Further study is required to reveal the phonon excitation mechanism by a mid-infrared pulse laser.

REFERENCES

[1] K. Kato, et al., J. Appl. Phys. 111, 113520 (2012).
[2] T. Sonobe, et al., AIP Conf. Proc., 1214, 23 (2010).
[3] K. Yoshida, et al., Appl. Phys. Lett. 103, 182103 (2013).
[4] M. Rini, et al., Nature 449, 72 (2007).
[5] H. Zen, et al., Proceedings of FEL2014, 828 (2014).
[6] S. Nakashima, et al., phys. stat. sol. (a) 162, 39 (1997).
[7] S. Anand, et al, Physica B 226, 331 (1996).
[8] M. van der Voort, et al., Physica B 263-264, 283 (1999) .

ISBN 978-3-95450-134-2

LCLS-II: STATUS OF THE CW X-RAY FEL UPGRADE TO THE SLAC LCLS FACILITY*

T.O. Raubenheimer# on behalf of the LCLS-II Collaboration,
SLAC, Menlo Park, CA 94025, USA

Abstract

The LCLS-II will be a CW X-ray FEL upgrade to the existing LCLS X-ray FEL at the SLAC National Accelerator Laboratory (SLAC). This paper will describe the overall layout and performance goals of the upgrade project.

INTRODUCTION

The LCLS-II is an X-ray Free-Electron Laser (FEL) which will upgrade the LCLS FEL at SLAC. The LCLS-II is designed to deliver photons between 200 eV and 5 keV at repetition rates as high as 1 MHz (929 kHz) using a superconducting RF linac (SCRF) linac while still providing pulses at short wavelengths and high X-ray pulse energy over the photon range of 1 to 25 keV using the existing 120 Hz copper RF (CuRF) LCLS linac. The project consists of a new 4 GeV SCRF linac, extensive beam transport systems, and two new variable gap undulators.

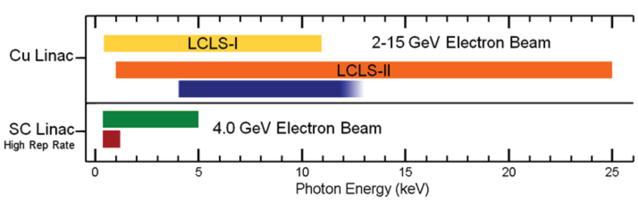

Figure 1: Schematic illustrating the performance of the LCLS and the LCLS-II upgrade where [orange] represents SASE at 120 Hz, [blue] represents Self-Seeding at 120 Hz, [green] represents SASE at high rate, and [red] represents Self-Seeding at high rate.

The LCLS-II will extend the high peak brightness capability and flexibility of LCLS while also having the ability to provide MHz rate beams from a CW SCRF linac; the parameters are shown in Table 1. The operating regimes are illustrated in Figure 1 and listed below:

1. Soft X-ray photons from SASE and self-seeding between 0.2 and 1.3 keV at MHz rates, with an average X-ray power in excess of 20 Watts;

2. Hard X-ray photons from SASE between 1.0 and 5.0 keV at MHz rates with an average X-ray power in excess of 20 Watts and with the possibility of a future upgrade to self-seeding operation at energies between 1 and 4 keV;

3. Hard X-ray photons with SASE between 1 and 25 keV and self-seeding between 4 keV and 13 keV at 120 Hz, with mJ-class pulses and performance comparable to or exceeding that of LCLS.

The upgrade is expected to significantly extend the XFEL science capability at SLAC; elements of the science program that will be enabled by the LCLS-II is documented in Ref. [1].

The LCLS-II project is being constructed by a collaboration of US laboratories consisting of Argonne National Lab. (ANL), Cornell University (CU), Fermilab (FNAL), Jefferson Lab. (JLab), Lawrence Berkeley National Lab. (LBNL), and SLAC. In addition, the project has substantial assistance from the EuXFEL project as well as the other international laboratories focused on SCRF development and XFEL's.

The SCRF linac will be installed in the first third (1 km) of the SLAC linac tunnel and a bypass line will bring the high rate beam around the middle third of the existing linac and the existing LCLS CuRF linac as illustrated in Figure 2. Beams from both the CuRF and the SCRF linac will be transported to the existing LCLS Undulator Hall where, to cover the full photon-energy range, the existing LCLS fixed gap undulator will be removed and the facility will install two variable-strength (gap-tunable) undulators, one dedicated to the production of Soft X-rays (SXR Undulator) from 0.2 to 1.3 keV and one dedicated to production of Hard X-rays (HXR Undulator) from 1.0 to 25.0 keV. The facility will also allow the possibility of generating near transform-limited pulses using self-seeding as well as downstream monochromators.

As illustrated in Figure 2, the facility is constructed to either deliver high-rate beam from the SCRF linac to both the SXR and HXR undulators, or to deliver the high-rate beam to the SXR undulator and deliver beam from the existing copper CuRF linac at 120 Hz to the HXR undulator.

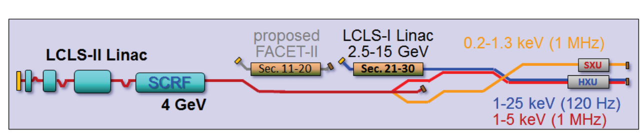

Figure 2: Schematic layout of the LCLS-II project.

* Work supported by DOE Contract: DE-AC02-76-SF00515
# torr@stanford.edu

ISBN 978-3-95450-134-2

Table 1: LCLS-II Electron and X-ray Parameters

SCRF Parameters	nominal	range	CuRF Parameters	nominal	range	units
Electron Energy	**4.0**	2.0 - 4.14	Electron Energy	**15**	2.5 – 15.0	GeV
Bunch Charge	**100**	10 - 300	Bunch Charge	**150**	10 - 250	pC
Bunch Repetition Rate in Linac	**0.62**	0 - 0.93	Bunch Repetition Rate in Linac	**120e-6**	0 – 120e-6	MHz
Beam Power in Linac	**0.25**	0.0 – 1.2	Beam Power in Linac	**270e-6**	0.0 – 500e-6	MW
Rms slice emittance at undulator	**0.40**	0.2 - 0.7	Rms slice emittance at undulator	**0.40**	0.2 - 0.7	µm
Final peak current	**800**	300 - 1200	Final peak current	**3000**	1000 - 5000	A
Final slice E-spread	**500**	125 - 1500	Final slice E-spread	**1500**	500 - 3000	keV
RF frequency	**1.3**	-	RF frequency	**2.8**	-	GHz
Avg. RF gradient	**16**	-	Avg. RF gradient	**~20**	-	MV/m
Avg. Cavity Q0	**2.7e10**	1.5 - 5e10	Avg. Cavity Q0	**1.3e4**	-	-
Photon energy range of SXR	-	**0.2 - 1.3**	Photon energy range of SXR	-	**N/A**	keV
Photon energy range of HXR	-	**1 - 5**	Photon energy range of HXR	-	**1 - 25**	keV
Typical photon pulse energy	**0.2**	0.01 - 5	Typical photon pulse energy	**2**	1 - 5	mJ

Bunches from the SCRF linac will be directed to either the HXR or SXR with a high rate magnetic kicker that will allow independent control of the beam rate being delivered to either undulator. The SCRF linac will be intrinsically more stable than the LCLS linac and the energy stability of the electron beams is specified to be <0.01% rms which is over10x more stable than that from the CuRF linac. The timing stability in the initial implementation of LCLS-II is specified to be better than 20 fs rms and is expected to be less than 10 fs rms. It is expected that the stability of the SCRF beams will be improved after the initial operation with the implementation of additional feedback systems that are possible due to the high repetition rates of the linac.

The LCLS-II will be flexible in its operating modes consistent with the maximum x-ray beam power, the maximum electron beam power to the BSY and undulator dumps, the maximum repetition rate and the range of bunch charges. As noted above, the HXR can be fed from either the SCRF linac or the CuRF linac, while the SXR can be fed only from the SCRF linac. The BSY Beam Spreader can direct the SCRF linac beam arbitrarily toward either undulator or to the BSY dump. The design does not presently include the capability of delivering different bunch charges or peak currents to the two undulators simultaneously, however that capability may be developed in the future.

The beams from the CuRF linac at 120 Hz will retain all of the flexible operating modes that are being developed at LCLS [2-6]. These include pulse-length control, two-color pulses and two pulses with delay at the 100 fs scale [4, 5]. New techniques are being developed as well which may allow pulse-by-pulse pulse length control and limited shaping of the x-ray pulses. Many of these techniques will be implemented on the SCRF linac as well however these capabilities are beyond the baseline project and will take time after initial operation to develop the full capability.

CONFIGURATION AND CHALLENGES

The LCLS-II will consist of a new CW injector and SCRF linac, extensive transport line, and two new variable gap undulators. The layout of the new systems is similar to the design of the LCLS. The primary differences are also related to the technical challenges the project faces:

1. The CW SCRF linac.
2. High brightness CW injector.
3. Variable gap undulators.
4. High power beams.
5. Beam dynamics of high brightness low energy beams.

These issues will be described further below.

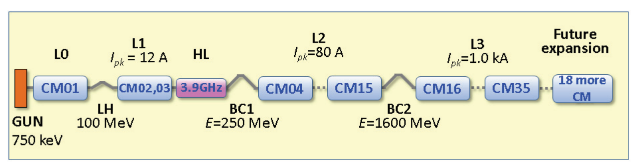

Figure 3: Schematic of LCLS-II SCRF linac.

SCRF Linac

The LCLS-II SCRF linac will be constructed from 35 1.3 GHz cryomodules (CM), each containing eight 9-cell cavities. Like the LCLS linac, the linac will contain a Laser Heater at roughly 100 MeV to suppress the microbunching stability and two bunch compressors, BC1 at 250 MeV and BC2 at 1.6 GeV as illustrated in Figure 3. In addition, two 3.9 GHz CM with eight 9-cell cavities will be installed upstream of BC1 to linearize the longitudinal phase space.

Parameters are listed in Table 2.

ISBN 978-3-95450-134-2

Table 2: SCRF 1.3 GHz Linac Parameters

Gradient	16 MV/m
Average Q_0	2.7×10^{10}
Num. Cavities	280 (35 CM)
Total voltage at 16 MV/m	4.65 GV
Max. Beam Energy	4.5 GeV
Max. bunch rep. rate	929 kHz
Max. bunch charge	300 pC

The SCRF cavities are based on the TESLA design pioneered at DESY and the CM's are similar to those developed for the ILC and EuXFEL program but modified for CW operation.

In a CW SCRF linac, the heat load is dominated by the rf losses in the cavities which scales as $Grad^2/Q$. The state-of-art at 1.3 GHz is the EuXFEL cavities which achieve Q's of roughly 1.5×10^{10} and gradient's in excess of 25 MV/m. The dynamic heat load due to these cavities is fine at the low duty-cycle of the EuXFEL but would be prohibitive in the CW LCLS-II. To minimize the rf losses, the LCLS-II project is supporting R&D aimed at developing Q's in excess of 2.7×10^{10} at a gradient of 16 MV/m.

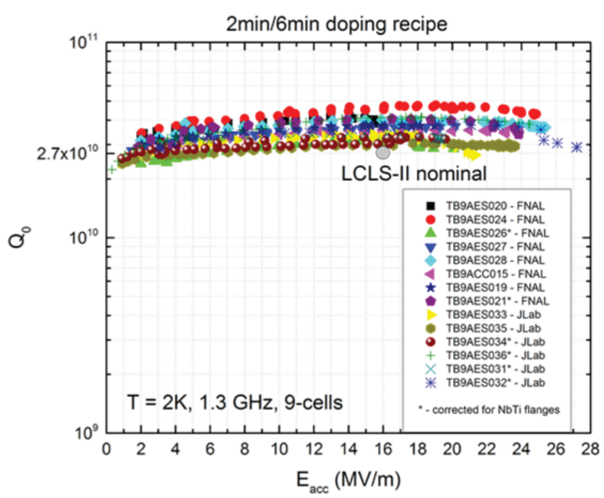

Figure 4: Q versus gradient for N-doped 9-cell cavities tested at FNAL and JLab.

This enormous challenge is being met using the Nitrogen-doping technique that has been developed at FNAL. This technique has improved the Q's of the 1.3 GHz 9-cell cavities by more than a factor of two as illustrated in Figure 4. While the cavity processing has proceeded very well, there are still challenges in translating these benefits to a full CM and the LCLS-II will likely design for additional cryogenic overhead to ensure success in meeting the design goal of a 4 GeV electron beam. An excellent summary of the present high-Q SCRF cavity status can be found in Ref. [7].

The cavity processing procedure is being developed at FNAL, JLab, and CU. FNAL and JLab will each build one prototype 8-cavity CM by the end of 2015 and these will be verified during the first half of 2016. The construction of the rest of the CM's for the LCLS-II will be shared between FNAL and JLab.

The SCRF linac will be cooled with two 4 kW cryoplants. The cryoplants will be similar to that built for the JLab 12 GeV upgrade [8] and will provide cooling for 4 kW at 2°K. The plant is being designed by JLab while FNAL is designing the cryo-distribution systems. The plants will be located roughly halfway along the linac (adjacent to BC2) and will feed cryogenics both upstream toward the injector and downstream. The layout for one of the plants is illustrated in Figure 5.

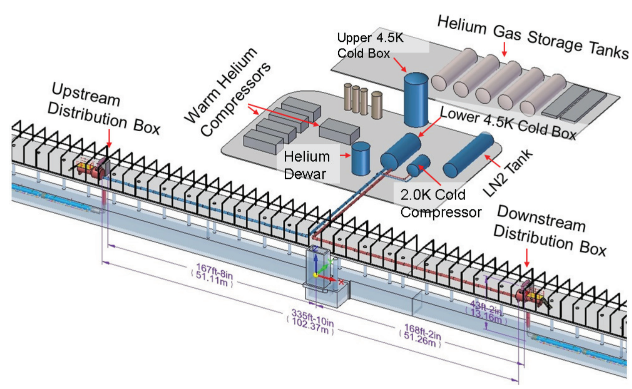

Figure 5: Schematic of a single cryoplant for the LCLS-II SCRF linac.

The SCRF linac is being designed to accelerate 300 µA up to greater than 4 GeV for 1.2 MW of beam power, which is sufficient to ultimately generate more than 100 Watts of X-rays in up to 10 individual undulator beamlines. The initial LCLS-II configuration will be limited to a maximum power of 250 kW, supplying beam to only the first two undulators. It only includes sufficient RF power to accelerate 100 uA up to 4 GeV at 16 MV/m with 10-Hz detuning or, as illustrated in Figure 6, 30 uA up to 4.5 GeV at 18 MV/m with 10 Hz detuning. The specification of 10 Hz detuning is expected to be conservative in which case high current beams could be accelerated.

ISBN 978-3-95450-134-2

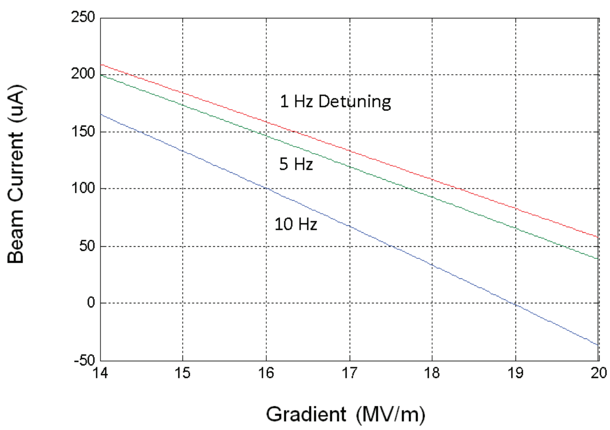

Figure 6: Beam current versus cavity gradient for the initial RF system for various detuning values from Ref. [9].

The two configurations considered for the RF power configuration were a single high-power source powering multiple (48) cavities or a single-source, single cavity configuration. While the single-source, multiple-cavity configuration was expected to be a significant cost savings, the project will be based on the single-source, single cavity configuration because it is expected to have much better control of the cavity fields. The RF power will be supplied by 3.8 kW solid-state amplifiers and the LLRF system for the LCLS-II is described in Ref. [10].

High-Brightness CW Injector

The performance of an FEL depends critically on the incoming electron beam brightness. For CW operation, a normal conducting high gradient rf gun is not possible and, while lots of potential exists, superconducting rf guns have not yet demonstrated the desired brightness.

Instead, the LCLS-II will use a low voltage rf gun very similar to the 186 MHz rf gun being developed as part of the APEX project at LBNL [11]. The normal-conducting photo-cathode gun, shown in Figure 7, will provide a beam of 750 keV which is then bunched with a 1.3-GHz normal conducting buncher cavity before being injected into a standard 1.3 GHz CM where it is captured and accelerated to 100 MeV. It is expected that the relatively high voltage of the rf gun will provide a higher beam brightness than a DC gun operating at 400 to 500 kV.

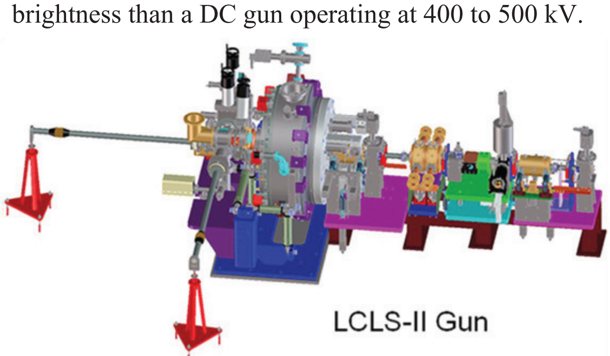

Figure 7: Schematic of the LCLS-II injector, based on the LBNL APEX rf gun.

The APEX project has demonstrated the operation of the rf gun at 800 kV and is in the-process of installing the 1.3 GHz buncher cavity and downstream accelerator structures to accelerate the beam to 30 MeV and verify the beam brightness [12]. Brightness measurements are expected in the fall of 2015.

In parallel, the Cornell DC gun which was developed for an Energy Recovery Linac [13], has been operated at 400 kV and the beam brightness has been measured for bunch charges across the LCLS-II operating range of 10 - 300 pC using a new NaKSb cathode [14]. The gun was optimized to meet the LCLS-II emittance and peak current requirements and the studies provided an excellent benchmark of the ASTRA and GPT gun simulation codes, providing confidence in the LCLS-II injector design. These codes are being use to optimize the detailed implementation at LCLS-II to increase the beam aperture and improve the emittance performance [15, 16].

The baseline cathode will be Cs_2Te illuminated in the UV. The laser system has been sized for a 0.5% QE and the emittance performance is based on a 1 mm-mrad per mm thermal emittance. Measurements at the APEX rf gun of the thermal emittance and QE exceed the design specifications.

In addition, alkali-antimonide cathodes are being developed around the world and, if proven robust, will be adopted by the LCLS-II project to improve the beam emittance and simplify the gun laser system. As noted, measurements on the Cornell dc gun were made using a NaKSb cathode with a thermal emittance ~30% smaller than the typical Cs_2Te cathodes of 0.8 mm-mrad/mm.

Variable-Gap Undulators

As noted, the SXR undulator can be fed from the SCRF linac, while the HXR undulator can be fed from either the SCRF or the CuRF linacs, although not from both simultaneously. The undulators will be installed side-by-side in the existing LCLS Undulator Hall. A schematic of the undulator layout appears in Figure 8.

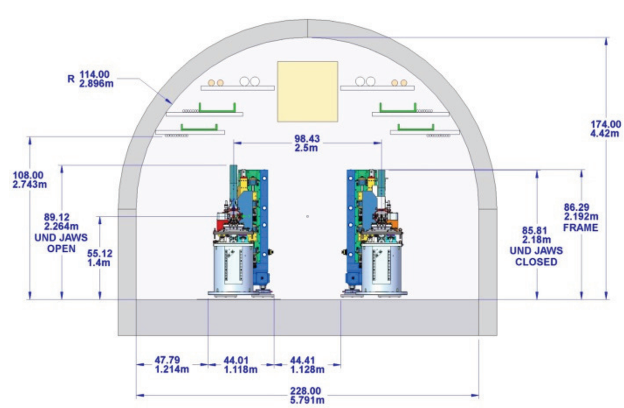

Figure 8: Schematic of HXR and SXR undulators in the LCLS Undulator Hall.

ISBN 978-3-95450-134-2

Both undulators are variable-gap hybrid permanent-magnet undulators; the existing fixed gap LCLS undulators will be removed. The HXR undulator has a period of 26 mm, close to that of the existing LCLS undulator, while the SXR undulator has a period of 39 mm. The maximum length of the existing LCLS Undulator Hall is roughly 150 meters. As illustrated in Figure 9, this will allow for the installation of up to 35 segments for the HXR, with each segment being 3.4 meters long followed by an interspace of 1.0 meters for a quadrupole, phase shifter, RF BPM, and x and y steering coils. To support self-seeding, two of these undulator slots will be reserved for self-seeding monochromators. The baseline will include 32 HXR segments plus two self-seeding slots, one of which contains the existing LCLS HXR self-seeding monochromator [17]; the other is reserved for a future upgrade.

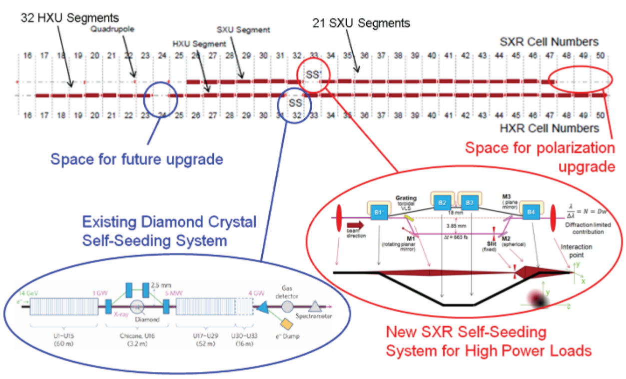

Figure 9: LCLS-II undulator layout.

The SXR undulator can be shorter, and there will be 21 SXR undulator segments plus one empty slot for the self-seeding monochromator which will be based on the LCLS SXRSS monochromator but modified for higher average power with a resolving power over 10,000. Development of the SXRSS monochromator is ongoing. The last three SXR undulator slots are reserved for the future installation of polarization control undulators such as DELTA undulators [18, 19], and the space upstream of the SXR undulator may be used for future seeding installations or additional undulators for two-color X-ray generation or other upgrades.

Table 3: Parameters for the HXR and SXR Undulators

	HXR	SXR
Period	26 mm	39 mm
Mag. Material	$N_d2Fe_{14}B$	$N_d2Fe_{14}B$
Max. K	2.44	5.48
Min. gap	7.2 mm	7.2 mm
Seg. Length	3.4 m	3.4 m
Num. Segments	32	21
Interspace Length	1 m	1 m
Total Length	96 m	140 m

The baseline LCLS-II undulators are being developed at LBNL [20]. The undulator parameters are listed in Table 3. A 3.4-meter prototype has been constructed and is shown in Figure 10.

The LCLS-II project is also exploring the option of a horizontal-gap, vertically polarizing undulator (VPU) which would significantly reduce losses in the horizontally deflecting optics downstream of the HXR undulator at photon energies about a few keV. A prototype VPU is being developed at Argonne National Laboratory with testing expected in the Fall of 2015 [20].

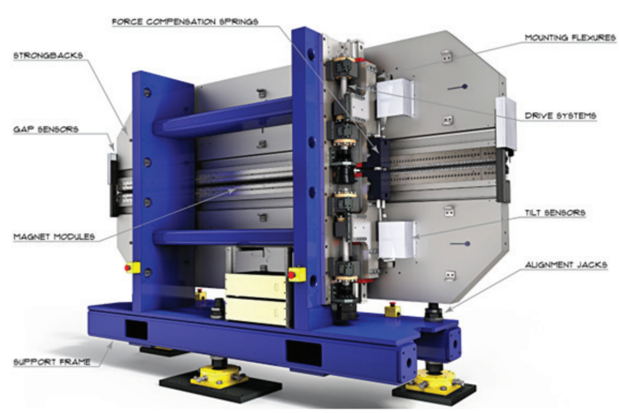

Figure 10: Prototype LCLS-II variable gap undulator.

High Beam Power

The LCLS-II SCRF linac is being designed to deliver 1.2 MW at 4 GeV of electron beam power although the initial rf system will only support a maximum of 400 kW at 4 GeV. Each of the two undulator systems (SXR and HXR) is design to operate with up to 120 kW of electron beam power which can generate as much as 1 kW of X-rays. The X-ray transport systems are designed for a maximum of 200 W across the operating spectrum however many components are challenged by the intense x-ray beam. The collimators and stoppers need additional attention [21] and, in gas-based attenuators or diagnostics, the x-ray beam can create a hollow channel [22] reducing their effectiveness and possibly amplifying intensity jitter effects.

Furthermore, to ensure a 10-year operating lifetime, beam loss in the hybrid permanent magnet undulator systems must be limited to an average of 12 mW, i.e. $1\text{x}10^{-7}$ of the maximum beam power. Control of the electron and X-ray beam power requires careful design of passive and active systems.

SLAC has operating experience with high power beams and the beam dumps and operating systems are being designed with this experience. The beam dumps are water-cooled dumps based on previous designs and the collimation system to limit the beam losses in the undulators is a four-stage design in which each stage will collimate in (x, x', y, y' and ΔE). Additional collimation of parasitical (off-time) buckets may also be implemented.

Because of transients induced when changing the beam current profile and timing in the SCRF linac, the time required to change the rate is limited by the damping time of the feedback systems. When operating with a high-repetition-rate beam in the linac, we expect that this time will be a fraction of a second. The time needed to switch between the SCRF linac and the CuRF linac will be dominated by the time required to change out the DC magnets and re-establish the electron beam. This should take less than one hour. To simplify operations, the beam power in the undulators is controlled using a magnetic kicker located at the end of the SCRF linac. This will allow the full power linac beam to be tuned up onto a high power dump before beam is taken to and through the undulators. Using the kicker, the rate to each of the undulators can be rapidly controlled from single-shot to maximum rate.

The very high average power of the accelerated CW electron beam can damage components within a few 100 μs. For this reason, several accelerator operating modes are envisioned for initial low-power commissioning, recovery from RF trips, recovery from beam-loss trips, and startup from shut-down periods. The Machine Protection System (MPS) is being designed with a 100 μs trip rate which is facilitated using the segmented design; if a fault arises near the undulator systems, beam can first be put onto the high power linac beam dump and then stopped at the electron source.

Beam Dynamics

The LCLS-II beam from the CuRF linac is very similar to that of the operating LCLS and thus is well quantified however understanding the beam from the SCRF linac has a new set of challenges. As noted, the design of the linac is similar to that of the LCLS with a laser heater and two-stage bunch compressor.

To ensure the performance of the LCLS-II analytic studies and detailed Start-to-End (S2E) simulations of the LCLS-II are being performed using the IMPACT [23] and Elegant [24] tracking codes and the Genesis FEL simulation code [25]. The low energy of the beam from the SCRF linac and the long transport makes the space charge and micro-bunching effects much more significant than in LCLS. A number of new effects driven by space charge have been observed including micro-bunching effects driven by transverse space charge in dispersive regions and the impact of longitudinal nonlinearities [26, 27].

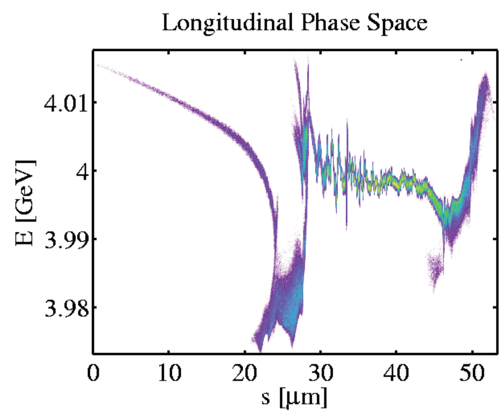

Figure 11: Longitudinal phase space illustrating micro-bunching instability.

These new effects have led to design modifications to moderate their impact. With these changes, it is believed that the high-rate HXR and SXR FEL's will exceed the specification of 20 W across the parameter range as illustrated in Figure 12 and described in Ref. [28].

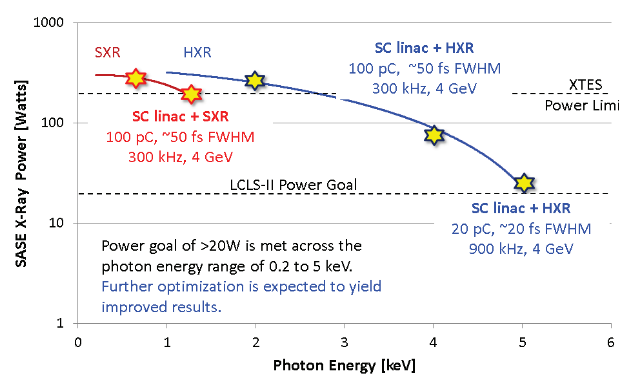

Figure 12: SASE X-ray average power from LCLS-II high-rate beam.

In parallel, experimental studies are being performed on the LCLS to verify the simulation codes in a parameter regime similar to that expected for the LCLS-II operation [29, 30]. When complete, this confirmation is expected to provide significant confidence in the LCLS-II accelerator design.

ISBN 978-3-95450-134-2

CONCLUSION

The LCLS-II project is developing an upgrade to the LCLS X-ray FEL at SLAC that is based on a 4 GeV SCRF linac and two variable-gap undulators. The project is being constructed by a collaboration of six institutions from across the US. The design of the accelerator and required hardware is well advanced and proceeding toward first X-rays at the end of 2019.

REFERENCES

[1] Science Driven Instrumentation for LCLS-II, https://portal.slac.stanford.edu/sites/lcls_public/Instrument_Document_Repository/LCLS-II_Instrumentation_Whitepaper_DOE.pdf (2015).
[2] Z. Huang, MOB02, FEL'15, these proceedings.
[3] Y. Ding, TUA01, FEL'15, these proceedings.
[4] A. Marinelli, *et al.*, WEP080, FEL'15, these proceedings.
[5] Z. Zhang, *et al.*, WEP059, FEL'15, these proceedings.
[6] J. MacArthur, *et al.*, WEP004, FEL'15, these proceedings.
[7] A. Grassellino, MOYGB2 IPAC'15, Richmond, VA (2015) and references within.
[8] A. Freyberger, MOXGB2 IPAC'15, Richmond, VA (2015) and references within.
[9] C. Nantista and C. Adolphsen, LCLSII-TN-15-29 (2015).
[10] C. Hovater, MOPWI021 IPAC'15, Richmond, VA (2015).
[11] F. Sannibale *et al.*, PRST-AB 15, 103501 (2012).
[12] F. Sannibale, *et al.*, MOP024, FEL'15, these proceedings.
[13] C. Gulliford *et al.*, PRST-AB 16, 073401 (2013).
[14] C. Guilliford, *et al.*, http://arxiv.org/abs/1501.04081 (2015).
[15] F. Zhou, *et al.*, MOP021, FEL'15, these proceedings.
[16] C. Mitchell, *et al.*, TUP073, FEL'15, these proceedings.
[17] J. Amann, *et al.*, Nature Photonics 6, 693 (2012).
[18] A. Temnykh, Phys. Rev. ST Accel. Beams'11, 120702 (2008).
[19] H.D. Nuhn, *et al.*, WED01, FEL'15, these proceedings.
[20] E. Gluskin, TUXC1 IPAC'15, Richmond, VA (2015) and references within.
[21] Y. Feng, *et al.*, TUP056, FEL'15, these proceedings.
[22] Y. Feng, *et al.*, TUP026, FEL'15, these proceedings.
[23] J. Qiang, *et al.*, PRST-AB 12, 100702 (2009).
[24] M. Borland, APS LS-287 (2000).
[25] S. Reiche, Nucl. Instr. & Meth. A429, 243 (1999).
[26] Y. Ding, *et al.*, TUPMA003, IPAC'15, Richmond, VA (2015) and references within.
[27] M. Venturini, *et al*, TUC01, FEL'15, these proceedings.
[28] G. Marcus, *et al.*, TUP007, FEL'15, these proceedings.
[29] D. Ratner *et al.*, PRSTAB 18, 030704 (2015).
[30] D. Ratner *et al.*, MOP058, FEL'15, these proceedings.

ISBN 978-3-95450-134-2

FREE ELECTRON LASERS IN 2015

K. Cohn#, J. Blau, W. B. Colson, J. Ng, M. Price
Physics Department, Naval Postgraduate School, Monterey, CA 93943, USA

Abstract

Thirty-nine years after the first operation of the free electron laser (FEL) at Stanford University, there continue to be many important experiments, proposed experiments, and user facilities around the world. Properties of FELs operating in the terahertz (THz) infrared (IR), visible, ultraviolet (UV), and X-ray wavelength regimes are tabulated and discussed.

LIST OF FELS IN 2015

The following tables list existing (Table 1) and proposed (Tables 2, 3) relativistic free electron lasers (FELs) in 2015. The 1st column lists a location or institution, and the FEL's name in parentheses. References are listed in Tables 4 and 5; another useful reference is: http://sbfel3.ucsb.edu/www/vl_fel.html.

The 2nd column of each table lists the operating wavelength λ, or wavelength range. The longer wavelength FELs are listed at the top and the shorter wavelength FELs at the bottom of each table. The seven orders of magnitude of operating wavelengths indicate the flexible design characteristics of the FEL mechanism.

In the 3rd column, t_b is the electron bunch duration (FWHM) at the beginning of the undulator, and ranges from almost continuous-wave to short sub-picosecond time scales. The expected optical pulse length in an FEL oscillator can be several times shorter or longer than the electron bunch depending on the optical cavity Q, the FEL desynchronism and gain. The optical pulse can be many times shorter in a high-gain FEL amplifier, or one based on self-amplified spontaneous emission (SASE). Also, if the FEL is in an electron storage-ring, the optical pulse is typically much shorter than the electron bunch. Most FEL oscillators produce an optical spectrum that is Fourier transform limited by the optical pulse length.

The electron beam kinetic energy E and peak current I are listed in the 4th and 5th columns, respectively. The next three columns list the number of undulator periods N, the undulator wavelength λ_0, and the rms undulator parameter $K = eB\lambda_0/2\pi mc^2$ (cgs units), where e is the electron charge magnitude, B is the rms undulator field strength, m is the electron mass, and c is the speed of light. For an FEL klystron undulator, there are multiple undulator sections as listed in the N-column; for example 2x7. Some undulators used for harmonic generation have multiple sections with varying N, λ_0, and K values as shown. Some FELs operate at a range of wavelengths by varying the undulator gap as indicated in the table by a range of values for K. The FEL resonance condition, $\lambda = \lambda_0(1+K^2)/2\gamma^2$, relates the fundamental wavelength λ to K, λ_0, and the electron beam energy $E = (\gamma-1)mc^2$, where γ is the relativistic Lorentz factor. Some FELs achieve shorter wavelengths by using coherent harmonic generation (CHG), high-gain harmonic generation (HGHG), or echo-enabled harmonic generation (EEHG).

The last column lists the accelerator types and FEL types, using the abbreviations listed after Table 3.

The FEL optical power is determined by the fraction of the electron beam energy extracted and the pulse repetition frequency. For a conventional FEL oscillator in steady state, the extraction can be estimated as 1/(2N); for a high-gain FEL amplifier, the extraction at saturation can be substantially greater. In a storage-ring FEL, the extraction at saturation is substantially less than this estimate and depends on ring properties.

In an FEL oscillator, the optical mode that best couples to the electron beam in an undulator of length $L = N\lambda_0$ has a Rayleigh length $z_0 \approx L/12^{1/2}$ and has a fundamental mode waist radius $w_0 \approx (z_0\lambda/\pi)^{1/2}$. An FEL typically has more than 90% of its power in the fundamental mode.

At the 2015 FEL Conference, there were three new lasings reported: the mid-IR FEL oscillator at Kyoto University was operated with a photocathode, the 3rd stage of the Novosibirsk THz FEL operated at 9 µm, and the XUV FEL at DESY (FLASH) demonstrated cascaded SASE operation. Progress continues on many other existing and proposed FELs around the world; several large X-ray FEL facilities are scheduled to come online over the next couple of years.

ACKNOWLEDGMENTS

The authors are grateful for support from the HEL-JTO.

#krcohn@nps.edu

ISBN 978-3-95450-134-2

Table 1: Existing Free Electron Lasers (2015)

LOCATION (NAME)	λ(μm)	t_b(ps)	E(MeV)	I(A)	N	λ_0(cm)	K(rms)	Type
Ariel (EA-FEL)	3000	5×10^7	1.4	0.5-3	26	4.44	0.8	EA,O
Frascati (FEL-CATS)	430-760	15-20	2.5	5	16	2.5	0.5-1.4	RF
UCSB (mm FEL)	340	25000	6	2	42	7.1	0.7	EA,O
Dresden (TELBE)	100-3000	0.15	15-34	15	8	30	≤5.7	RF,SU
Nijmegen (FLARE)	100-1400	3	10-15	50	40	11	0.5-3.3	RF,O
KAERI (THz FEL)	100-1200	20	4.5-6.7	0.5	80	2.5	1.0-1.6	MA,O
Novosibirsk (FEL1)	90-240	100	12	10	2x32	12	0-0.9	ERL,O
Osaka (ISIR, SASE)	70-220	20-30	11	1000	32	6	1.5	RF,S
Himeji (LEENA)	65-75	10	5.4	10	50	1.6	0.5	RF,O
UCSB (FIR FEL)	60	25000	6	2	150	2	0.1	EA,O
Osaka (ILE/ILT)	47	3	8	50	50	2	0.5	RF,O
Novosibirsk (FEL2)	37-85	20	22	50	32	12	0-1.1	ERL,O
Osaka (ISIR)	25-150	20-30	13-20	50	32	6	≤1.5	RF,O
Tokai (JAEA-FEL)	22	2.5-5	17	200	52	3.3	0.7	RF,O
Bruyeres (ELSA)	20	30	18	100	30	3.2	0.8	RF,O
Dresden (ELBE U100)	18-250	1-4	15-34	30	40	10	0.5-2.7	RF,O
Osaka (iFEL4)	18-40	10	33	40	30	8	1.3-1.7	RF,O
Novosibirsk (FEL3)	9	10	42	100	3x28	6	0.3-1.8	ERL,O
Kyoto (KU-FEL)	5-21.5	<1	20-36	17-40	52	3.3	0.7-1.56	RF,O
Darmstadt (FEL)	6-8	2	25-50	2.7	80	3.2	1.0	RF,O
Osaka (iFEL1)	5.5	10	33.2	42	58	3.4	1.0	RF,O
Beijing (BFEL)	5-25	4	30	15-20	50	3	0.5-0.8	RF,O
Daresbury (ALICE)	5-11	~1	27.5	80	40	2.7	0.35-0.9	ERL,O
Dresden (ELBE U27)	4-21	1-4	15-34	30	68	2.73	0.3-0.7	RF,O
Berlin (FHI MIR FEL)	4-50	1-5	15-50	200	50	4	0.5-1.5	RF,O
Tokyo (MIR-FEL)	4-16	2	32-40	30	43	3.2	0.7-1.8	RF,O
Nijmegen (FELIX)	3-250	1	50	50	38	6.5	1.8	RF,O
Orsay (CLIO)	3-150	10	12-50	100	38	5	≤1.4	RF,O
Nijmegen (FELICE)	3-40	1	60	50	48	6.0	1.8	RF,O
Hawaii (MkV)	2-10	2-5	30-45	30-60	47	2.3	0.1-1.3	RF,O
Osaka (iFEL2)	1.88	10	68	42	78	3.8	1.0	RF,O
Nihon (LEBRA)	1.5-6.5	1	58-100	10-20	50	4.8	0.7-1.4	RF,O
UCLA-BNL (VISA)	0.8	0.5	64-72	250	220	1.8	1.2	RF,S
JLab (IR upgrade)	0.7-10	0.35	120	300	30	5.5	3.0	ERL,O
Osaka (iFEL3)	0.3-0.7	5	155	60	67	4	1.4	RF,O
JLab (UV demo)	0.25-0.7	0.35	135	200	60	3.3	1.3	ERL,O
Duke (OK-5)	0.25-0.79	5-20	270-800	10-50	2x30	12	3.18	SR,O,K
Okazaki (UVSOR-II)	0.2-0.8	6	600-750	28.3	2x9	11	2.6-4.5	SR,O,K
SINAP (SDUV-FEL)	0.2-0.35	2-8	100-180	20-100	360	2.5	0.98	RF,A,H,E
DELTA (U250)	0.2	100	1500	40	2x7	25	7.3-10	SR,K,H
Duke (OK-4)	0.19-0.4	50	1200	35	2x33	10	4.75	SR,O,K
ELETTRA (SR-FEL)	0.09-0.26	70	1000	150	2x19	10	4.2	SR,A,K,H
PSI (SwissFEL Test)	0.07-0.8	0.5-3	100-220	20-160	265	1.5	0.5-1.3	RF,S
Frascati (SPARC)	0.066-0.8	0.15-8	80-177	40-380	450	2.8	0.5-1.55	RF,A,S,H
DESY (sFLASH)	0.038	0.5	700	1000	180 120	3.14 3.3	1.9 2.1	RF,S,H
ELETTRA (FERMI-1)	0.02-0.1	0.7-1.2	900-1500	300-700	252	5.5	1-3	RF,A,H
ELETTRA (FERMI-2)	0.004-0.0144	0.7-1.6	900-1500	300-700	396	3.5	0.85-1.6	RF,A,H
DESY (FLASH2)	0.004-0.08	0.05-0.5	500-1250	2500	768	3.14	0.5-2	RF,S
DESY (FLASH1)	0.004-0.05	0.05-0.5	350-1250	2500	981	2.73	0.87	RF,S
SLAC (LCLS)	0.12 nm	0.07	15400	3500	3696	3	2.5	RF,S
SPring-8 (SACLA)	0.06-0.25 nm	0.02-0.03	8300	3000-4000	6300	1.8	1.52	RF,S

ISBN 978-3-95450-134-2

Table 2: Proposed Free Electron Lasers (2015)

PROPOSED FELs	$\lambda(\mu m)$	t_b(ps)	E(MeV)	I(A)	N	λ_0(cm)	K(rms)	Type
KAERI (Table-top THz)	400-600	20	6.5	1	28	2.3-2.6	2.1-2.4	MA,O
Tokyo (FIR-FEL)	300-1000	5	10	30	25	7	1.5-3.4	RF,O
Colorado State University	200-800	5-15	6	100	50	2.5	1.0	RF,O
India (CUTE-FEL)	50-100	1000	10-15	20	50	5	0.57	RF,O
Berlin (FHI FIR FEL)	40-500	1-5	20-50	200	40	11	1-3	RF,O
Ariel (THz FEL)	75-300	0.3	3-6	1000	20	2.5	0.47	RF,A
Beijing (PKU-FEL)	4.7-8.3	1	30	60	50	3	0.5-1.4	ERL,O
Turkey (TARLA U25) (TARLA U90)	3-20 18-250	0.4-6 0.4-6	15-40 15-40	12-155 12-155	60 40	2.5 9	0.25-0.7 0.7-2.3	RF,O
Tallahassee (Big Light)	2-1500	1-10	50	50	45	5.5	4.0	ERL,O
Daresbury (CLARA)	0.1-0.4	0.5	250	400	500	2.9	0.7-1.5	RF,A
Dalian (DCLS)	0.05-0.15	1	300	300	360	3.0	0.3-1.6	RF,A,H

Table 3: Proposed Short Wavelength Free Electron Lasers (2015)

PROPOSED FELs	λ(nm)	t_b(ps)	E(GeV)	I(kA)	N	λ_0(cm)	K(rms)	Type
JLab (JLAMP)	10-100	0.1	0.6	1	330	3.3	1.0	ERL,O,A
SINAP (SXFEL)	8.8	0.26	0.84	0.6	720	2.5	0.95	RF,H,E
Glasgow (ALPHA-X)	2-300	0.001-0.005	0.10-1.0	1	200	1.5	0.5	PW,A
Groningen (ZFEL)	0.8	0.1	1-2.1	1.5	2600	1.5	0.85	RF,S,H
PSI (SwissFEL Athos) (SwissFEL Aramis)	0.7-7 0.1-0.7	0.002-0.015 0.002-0.015	2.5-3.4 2.1-5.8	1.5-2.7 1.5-2.7	1200 3192	4 1.5	0.7-3.5 0.5-1.3	RF,S,SS RF,S,SS
SLAC (LCLS-II SXR) (LCLS-II HXR)	1.0-6.2 0.05-1.2	0.01-0.1 0.01-0.1	2.0-4.0 2.5-15.0	0.5-1.5 0.5-4	1827 4160	3.9 2.6	1.4-3.9 0.36-1.7	RF,S,SS RF,S,SS
Pohang (PAL SXFEL) (PAL HXFEL)	1-4.5 0.06-1	0.06-0.18 0.045-0.09	2.6-3.2 4-10	1-3 2-4	1300 4100	3.43 2.44	1.6-3.4 1.3-2.1	RF,S
DESY (European XFEL)	0.4-5 0.05-0.4	0.002-0.18	8-17.5	5	1544 4375	6.8 4	4-9 1.65-3.9	RF,S
LANL (MaRIE)	0.03	0.03	12	3.4	5600	1.86	0.86	RF,S,H,E

Accelerator type:
MA - Microtron Accelerator
ERL - Energy Recovery Linear Accelerator
EA - Electrostatic Accelerator
RF - Radio-Frequency Linear Accelerator
SR - Electron Storage Ring
PW- Laser Plasma Wakefield Accelerator

FEL type:
A - FEL Amplifier
K - FEL Klystron
O - FEL Oscillator
S - Self-Amplified Spontaneous Emission (SASE)
H - Harmonic Generation (CHG, HGHG)
E - Echo-Enabled Harmonic Generation (EEHG)
SS - Self-Seeded Amplifier
SU - Super-radiant FEL

ISBN 978-3-95450-134-2

Table 4: References and Websites for Existing FELs

LOCATION (NAME)	Internet Site or Reference
Ariel (EA-FEL)	http://www.ariel.ac.il/research/fel
Beijing (BFEL)	http://www.ihep.ac.cn/english/BFEL/index.htm
Berlin (FHI MIR)	http://fel.fhi-berlin.mpg.de
Bruyeres (ELSA)	P. Guimbal et al., Nucl. Inst. and Meth. **A341**, 43 (1994).
Daresbury (ALICE)	http://www.stfc.ac.uk/ASTeC/Alice/projects/36060.aspx
Darmstadt (FEL)	M. Brunken et al., Nucl. Inst. and Meth. **A429**, 21 (1999).
DELTA (U250)	H. Huck et al., Proceedings of FEL 2011, Shanghai, China. http://accelconf.web.cern.ch/AccelConf/FEL2011/papers/mooa5.pdf
DESY (FLASH, sFLASH)	http://flash.desy.de
Dresden (ELBE)	http://www.hzdr.de/FELBE
Duke (OK-4, OK-5)	http:// https://www.phy.duke.edu/duke-free-electron-laser-laboratory
ELETTRA (SR-FEL)	http://www.elettra.trieste.it/elettra-beamlines/fel.html
ELETTRA (FERMI)	http://www.elettra.trieste.it/FERMI
Frascati (FEL-CATS)	http://www.frascati.enea.it/fis/lac/fel/fel2.htm
Frascati (SPARC)	http://www.roma1.infn.it/exp/xfel
Hawaii (MkV)	M. Hadmack, Ph.D. Dissertation, University of Hawaii, December 2012.
Himeji (LEENA)	T. Inoue et al., Nucl. Inst. and Meth. **A528**, 402 (2004).
JLab (IR upgrade)	G. R. Neil et al., Nucl. Inst. and Meth. **A557**, 9 (2006).
JLab (UV demo)	S. V. Benson et al., Proceedings of FEL 2011, Shanghai, China. http://accelconf.web.cern.ch/AccelConf/FEL2011/papers/weoci1.pdf
KAERI (THz FEL)	Y. U. Jeong et al., Nucl. Inst. and Meth. **A575**, 58 (2007).
Kyoto (KU-FEL)	H. Zen et al., Proceedings of FEL 2013, New York, NY, USA http:// https://accelconf.web.cern.ch/accelconf/FEL2013/papers/wepso84.pdf
Nihon (LEBRA)	K. Hayakawa et al., Proceedings of FEL 2007, Novosibirsk, Russia. http://accelconf.web.cern.ch/AccelConf/f07/papers/MOPPH046.pdf
Nijmegen (FELICE, FELIX)	http://www.ru.nl/felix
Nijmegen (FLARE)	http://www.ru.nl/flare
Novosibirsk (FEL1)	N. G. Gavrilov et al., Nucl. Inst. and Meth. **A575**, 54 (2007).
Novosibirsk (FEL2)	N. A. Vinokurov et al., Proceedings of FEL 2009, Liverpool, UK. http://accelconf.web.cern.ch/AccelConf/FEL2009/papers/tuod01.pdf
Novosibirsk (FEL3)	G. Kulipanov et. al., IEEE Trans. Terahertz Sci. Technol. **5**, no. 5, 798 (2015).
Okazaki (UVSOR- II)	H. Zen et al., Proceedings of FEL 2009, Liverpool, UK. http://accelconf.web.cern.ch/AccelConf/FEL2009/papers/wepc36.pdf
Orsay (CLIO)	http://clio.lcp.u-psud.fr
Osaka (iFEL4)	T. Takii et al., Nucl. Inst. and Meth. **A407**, 21 (1998).
Osaka (iFEL1,2,3)	H. Horiike et al., Proceedings of FEL 2004, Trieste, Italy. http://accelconf.web.cern.ch/AccelConf/f04/papers/THPOS17/THPOS17.pdf
Osaka (ILE/ILT)	N. Ohigashi et al., Nucl. Inst. and Meth. **A375**, 469 (1996).
Osaka (ISIR)	R. Kato et al., Proceedings of IPAC 2010, Kyoto, Japan. http://accelconf.web.cern.ch/accelconf/IPAC10/papers/tupe030.pdf
PSI (SwissFEL Test)	S. Reiche, Proceedings of FEL2014, Basel, Switzerland.
SINAP (SDUV-FEL)	Z. T. Zhao and D. Wang, Proceedings of FEL 2010, Malmo, Sweden. http://accelconf.web.cern.ch/AccelConf/FEL2010/papers/moobi1.pdf
SLAC (LCLS)	http://lcls.slac.stanford.edu
Tokai (JAEA-FEL)	R. Hajima et al., Nucl. Inst. and Meth. **A507**, 115 (2003).
Tokyo (MIR-FEL)	http://www.rs.noda.tus.ac.jp/fel-tus/English/E-Top.html
UCLA-BNL (VISA)	A. Tremaine et al., Nucl. Inst. and Meth. **A483**, 24 (2002).
UCSB (mm, FIR FEL)	http://sbfel3.ucsb.edu

ISBN 978-3-95450-134-2

Table 5: References and Websites for Proposed FELs

LOCATION (NAME)	Internet Site or Reference
Ariel (THz FEL)	A. Friedman et. al., Proceedings of FEL 2014, Basel, Switzerland, http://accelconf.web.cern.ch/AccelConf/FEL2014/papers/tup081.pdf
Beijing (PKU-FEL)	Z. Liu et al., Proceedings of FEL 2006, Berlin, Germany. http://accelconf.web.cern.ch/AccelConf/f06/papers/TUAAU05.pdf
Berlin (FHI FIR)	http://fel.fhi-berlin.mpg.de
Colorado State University	S. Milton et. al., Proceedings of IPAC 2014, Dresden, Germany. http://accelconf.web.cern.ch/AccelConf/IPAC2014/papers/thpri074.pdf
Dalian (DCLS)	T. Zhang et. al., Proceedings of IPAC2013, Shanghai, China http://accelconf.web.cern.ch/accelconf/IPAC2013/papers/weodb102.pdf
Daresbury (CLARA)	J. A. Clarke et. al., Proceedings of IPAC 2012, New Orleans, LA, USA. http://accelconf.web.cern.ch/AccelConf/IPAC2012/papers/tuppp066.pdf
DESY (Europe XFEL)	http://www.xfel.eu
Glasgow (ALPHA-X)	http://phys.strath.ac.uk/alpha-x/
Groningen (ZFEL)	J. P. M. Beijers et al., Proceedings of FEL 2010, Malmo, Sweden. http://accelconf.web.cern.ch/AccelConf/FEL2010/papers/mopc22.pdf
India (CUTE-FEL)	S. Krishnagopal and V. Kumar, Proceedings of FEL 2007, Novosibirsk, Russia. http://accelconf.web.cern.ch/accelconf/f07/papers/MOPPH074.pdf
JLab (JLAMP)	S. V. Benson et al., Proceedings of FEL 2009, Liverpool, UK. http://accelconf.web.cern.ch/accelconf/FEL2009/papers/mopc70.pdf
KAERI (Table-top THz)	Y. U. Jeong et al., J. Korean Phys. Soc., Vol. **59**, No. 5, 3251 (2011).
LANL (MaRIE)	http://marie.lanl.gov
NPS-Niowave (THz)	http://www.niowaveinc.com
Pohang (PAL XFEL)	J.-H. Han et. al., Proceedings of IPAC 2012, New Orleans, LA, USA. http://accelconf.web.cern.ch/accelconf/IPAC2012/papers/tuppp061.pdf
PSI (SwissFEL Athos,Aramis)	http://www.psi.ch/swissfel
SINAP (SX-FEL)	Z. T. Zhao and D. Wang, Proceedings of FEL 2010, Malmo, Sweden. http://accelconf.web.cern.ch/AccelConf/FEL2010/papers/moobi1.pdf
Tallahassee (Big Light)	http://www.magnet.fsu.edu/usershub/scientificdivisions/emr/facilities/fel.html
Tokyo (FIR-FEL)	http://www.rs.noda.tus.ac.jp/fel-tus/English/E-Top.html
Turkey (TARLA U25,U90)	http://www.tarla.org.tr

ISBN 978-3-95450-134-2

PHOTON ENERGIES BEYOND THE SELENIUM K-EDGE AT LCLS*

F.-J. Decker, W. Colocho, Y. Ding, R.H. Iverson, H. Loos, J.C. Sheppard, H.V. Smith,
J. L. Turner, SLAC, Menlo Park, CA 94025, USA

Abstract

The Linac Coherent Light Source (LCLS) was designed for photon energies of 830 eV to 8.3 keV [1]. This range was widened and up to 11.2 keV photons have been already delivered to users. The selenium K-edge at 12.6578 keV is very interesting since selenium can replace sulphur in biological structures and then that structure can be precisely measured. To reach 12.7 keV, the electron energy would need to be raised by about 6% which initially did not seem possible. The trick was to change the final compression scheme from a highly correlated energy spread and moderate R56 in the compression chicane to moderate energy spread and large R56. The same bunch length can be achieved and RF energy is freed up, so the overall beam energy can be raised. Photons up to an energy of 12.82 keV (1.3% above the K-edge) with a pulse intensity of 0.93 mJ were achieved. The photon energy spread with this setup is wider at around 40-50 eV FWHM, since less correlated energy spread is left after the compression.

INTRODUCTION

To achieve FEL lasing above the selenium K-edge, it was necessary to increase to electron beam energy to 16.9 GeV which is above the energy reach of the standard LCLS linac configuration. A crucial component of the energy increase was accomplished through raising the beam energy in the second bunch compressor (BC2) by accelerating closer to the crest of the RF in second Linac section (L2). The reduced energy spread from nearer to crest operation required an increase in the R56 of the BC2 chicane to achieve to nominal bunch compression required for FEL performance.

This paper starts with a brief historical perspective. A discussion of the BC2 chicane issues follows along with a note on the changes to L2 and expectations from LiTrack simulations. The paper concludes with a discussion of the FEL performance at the selenium K-edge energy.

HISTORY

In May of 2013 an experiment started with the third harmonic to reach 11.2 keV. The low flux caused a try to use the fundamental at higher than "normal" photon energy. This yielded 50 times more photons. A final test followed quickly by pushing the limits; 11.92 keV was reached. The corresponding wavelength was still 4% longer than an Ångstrom (or 12.4 keV) and even further away from an interesting energy at 12.6578 keV, the selenium K-edge. The corresponding electron energy difference of 6% (five RF stations) seemed too much to overcome easily. Adding a modulator and RF klystron and splitting the four accelerating sections of an existing station into 2+2 would give only 41% more energy, so about 12 additional modulator plus klystrons would be required. In the search for ways to raise the energy and since we had already performed a beam test, we missed the now obvious way to do it (using the available energy better).

This changed in July of 2014 when one of our Variable Voltage Substations (VVS) burnt up. We lost the energy contribution of 16 klystrons and were limited to about 7.0 keV, right where the then current experiment wanted to run. One of us felt the pressure that someone might ask him the next morning: "Why didn't you think of …?", and came up with the brilliant idea, that we can trade the correlated energy spread (chirp) in L2 versus the R56 in the BC2 (Bunch Compressor 2) chicane. He also recognised the major limit since the bend magnets have to be raised for the R56 and then again for the higher energy, giving a quadratic behaviour and the power goes then with the fourth order of the required change.

BC2 BEND MAGNETS

The bend magnets for the BC2 bunch compressor have to carry the main burden for the highest energy running. The maximum field strength was raised to 10 kG-m or 250 A current (from 200 A), which is 50% more in the maximum power and about three times than typical running conditions.

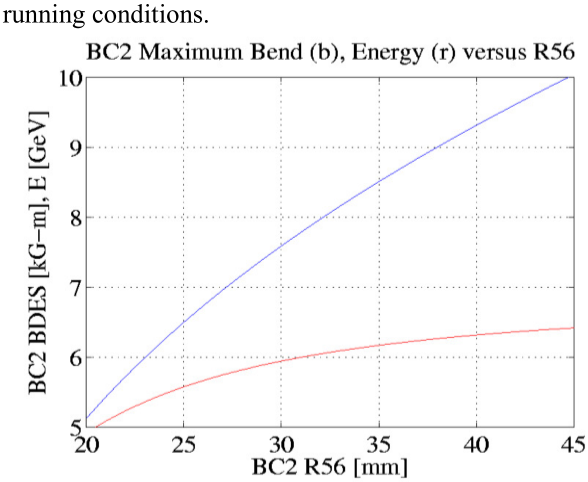

Figure 1: BC2 maximum bend strength and L2 energy versus R56 of the BC2 chicane.

*Work supported by U.S. Department of Energy, Contract DE-AC02-76SF00515.

The Figure 1 shows dependence of the desired bend strength (BDES) versus the R56 value, while the L2 energy is raised to the maximum possible, but still maintaining the same compression. Finally the chicane R56 was raised from 28 to 45 mm, the energy from 5 GeV (with lots of energy overhead) to 6.25 GeV and the bend field from 6.2 to 9.8 kG-m (235 A).

Temperature

The temperatures of the magnet and its cooling water were measured during 250 A operation test. The input water had 35°C and output 55°C, with the highest point on the coil at 62°C. During that initial test an underrated wall breaker tripped, which had to be finally upgraded for continuous running. Going to even higher currents like 300 A (other available power supply) would push the temperature increase to 30°C, the magnet into saturation, and the R56 to its maximum of 50 mm.

Polynomials

The four bend magnets of the chicane have trim windings which are adjusted correspondingly to compensate the measured differences in the IvsB-polynomial. Since the magnets were only measured up to 200 A, (or 8.5 kG-m) the extrapolation to 10 or even 12 kG-m (see Fig. 2) is wrong and has to be extrapolated more carefully. The estimated orbit variation of about 2 mm can be handled with upstream and downstream correctors and was not corrected with the trims (Fig. 3).

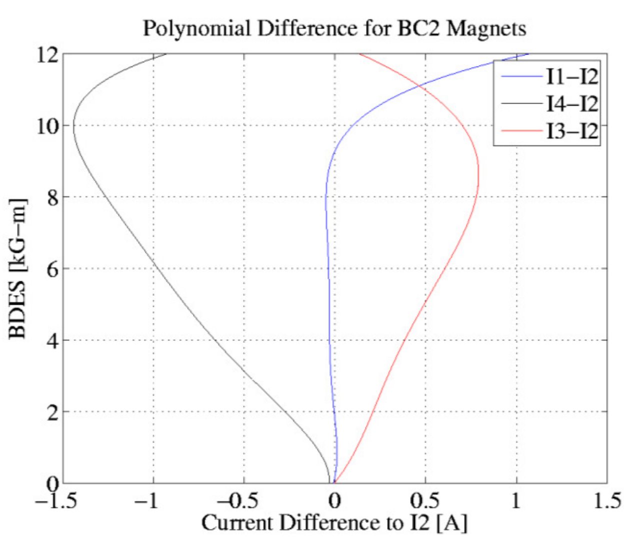

Figure 2: The difference of the bend fields with the respect to the second magnet is plotted versus the required current difference to achieve the same field strength.

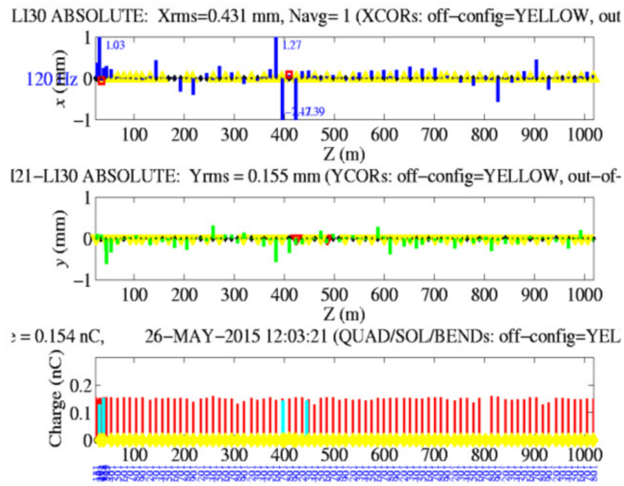

Figure 3: The orbit around BC2 (z = 400 m) had variations of +1.3 mm and -2.4 mm in x, about ten times worse than the rest of the linac.

L2 PHASE

Since R56 of the chicane was raised from 28 to 45 mm, the L2 phase had to be adjusted correspondingly from 35° to 22°, closer to the RF crest to get the same bunch length after compression. This change gains about 0.7 GeV in energy (Fig. 4) corresponding to about three RF stations worth of energy.

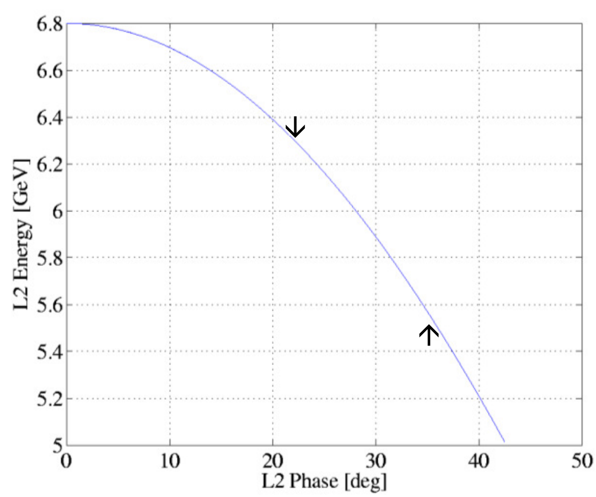

Figure 4: Energy gain due to reduced L2 phase.

ISBN 978-3-95450-134-2

LITRACK SIMULATIONS

LiTrack simulations were done at 16.9 GeV (Fig. 5) and compared with the typical design setup at 13.6 GeV (Fig. 6). Since the wakefields relative to the higher energy are less, the energy spread is remarkably good. The distribution has some more tails. The horns in the longitudinal distribution split into two peaks near the front and end of the bunch.

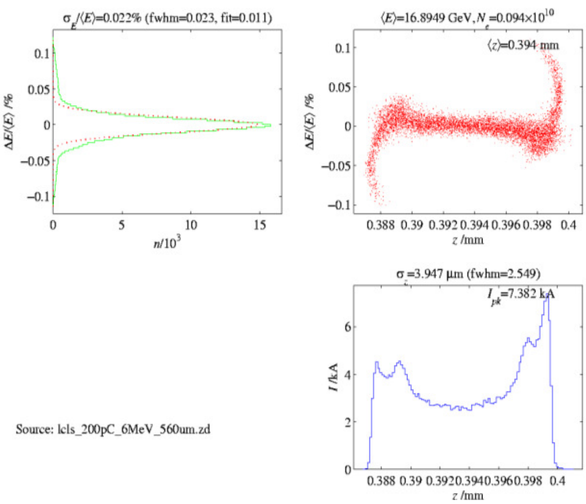

Figure 5: 16.9 GeV, R56 = -45 mm.

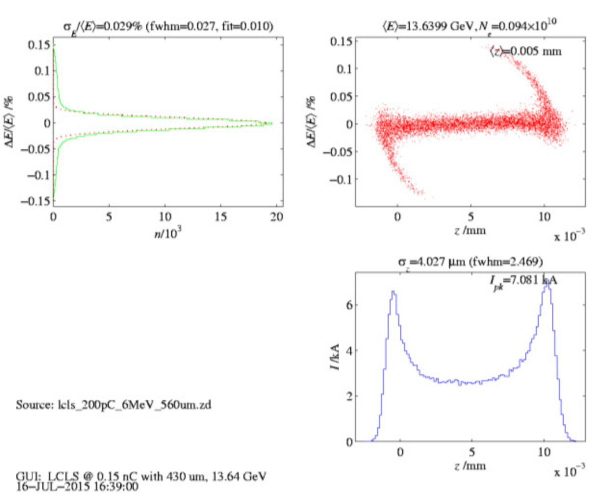

Figure 6: 13.6 GeV, R56 = -28 mm.

FEL PERFORMANCE

The initial FEL performance was very bad by a factor of 10-20 and tuning efforts were hampered by a low FEL gas detector signal. The R56 was even temporally reduced to increase tuning efficiency. Finally from a low jittery intensity the beam was tuned up and most of the jitter was non-linearly correlated with the peak current in BC2 (IMAX) (red in Fig. 7). Launch set points and vertical dispersion correction into the undulator reduced the peak current dependency and stable beam up to 1.2 mJ was achieved (blue in Fig. 7). The high energy of 12.82 keV with the initial performance of 0.93 mJ put us off the chart (Fig. 8).

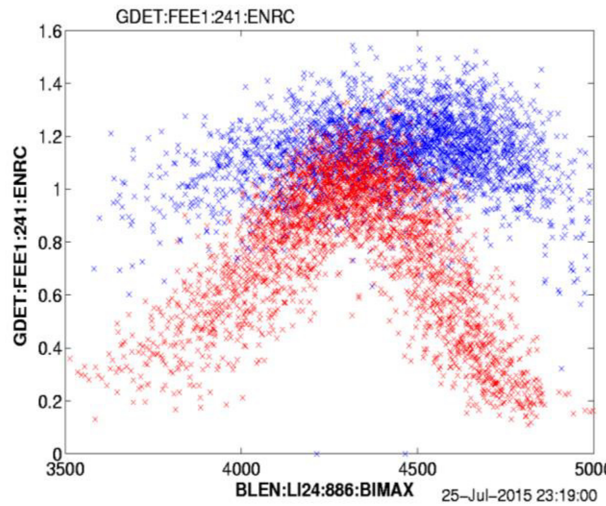

Figure 7: FEL performance via Gas Detector (GDET) [mJ] versus the BC2 peak current [A]. The initial red distribution shows a strong the dependence to peak current, while the tuned up data in blue shows the final performance.

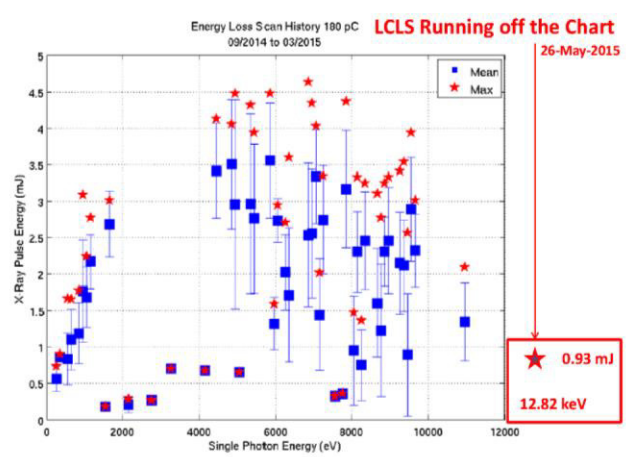

Figure 8: Pulse energy [mJ] versus Photon Energy [eV] shows the 12.8 keV nearly 30% above the typical hard x-ray running conditions.

Energy Spread

The relative energy spread of 0.023% FWHM (30 eV at 12.8 keV) is close to the typical energy spread of 20 eV at 9 keV (0.022%), see Fig. 9. Two effects play a role. It gets smaller due to the higher energy, but also gets bigger since the lower correlation of the energy spread is less reduced by wakefields.

ISBN 978-3-95450-134-2

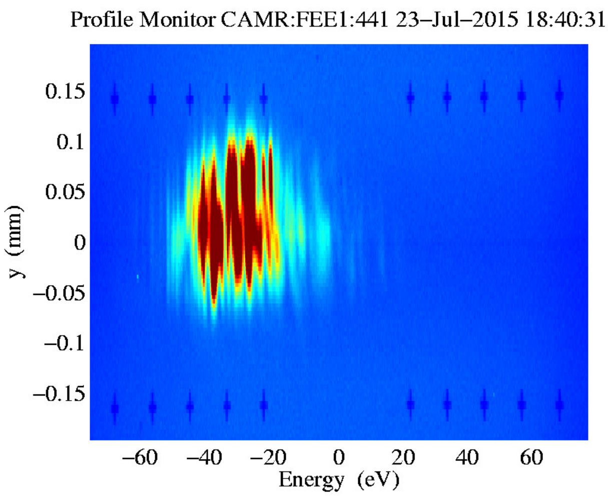

Figure 9: SASE energy distribution at 12.8 keV.

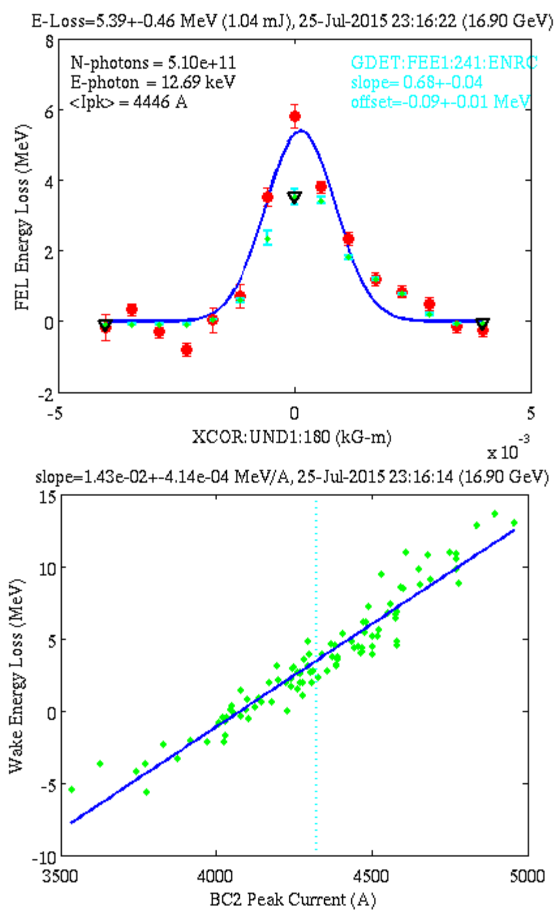

Figure 10: Energy loss scan at 12.8 keV (top) and the calibration measurement with peak current (bottom).

Performance Measurement

Typically the FEL performance is measured by an energy loss measurement, where the FEL process gets suppressed by introducing a trajectory oscillation in the undulator [2]. From the measured energy loss in MeV the FEL intensity in mJ is calculated (Fig. 10). The plot is more jittery than typical, which might have two reasons. The energy is higher, therefore the relative energy change is smaller and the typical correction due to peak current fluctuations is not smaller. And second it seems to be not just a linear dependence to peak current, but a slightly quadratic term too (Fig. 10 bottom).

CONCLUSION

The run at a photon energy of 12.8 keV was a big success.

ACKNOWLEDGMENT

Without the dedicated work of Power Electronic Maintenance and the RF group the 12.8 keV run would not have been possible. With their preparation, they achieved the high reliability which was necessary for the success. Also the Radiation Physics group was involved solving the problem at running at or just beyond the typically allowed electron energy limit of 17 GeV.

REFERENCES

[1] P. Emma et al., “First Lasing and Operation on an Ångstrom-Wavelength Free-Electron Laser”, Nature Photonics 4, 641–647; 2010.

[2] H. Loos, “LCLS accelerator operation and measurement of electron beam parameters relevant for the X-ray beam”, Proc. SPIE 8778, Advances in X-ray Free-Electron Lasers II: Instrumentation, 87780J (May 3, 2013); doi:10.1117/12.2021569.

TWO BUNCHES WITH NS-SEPARATION WITH LCLS*

F.-J. Decker, S. Gilevich, Z. Huang, H. Loos, A. Marinelli, C.A. Stan, J.L. Turner, Z. van Hoover, S. Vetter, SLAC, Menlo Park, CA 94025, USA

Abstract

The Linac Coherent Light Source (LCLS) delivers typically one electron bunch. Two-bunch operation is also possible, and is used to generate XFEL (x-ray free electron laser) pulse pairs for pump / probe experiments. Pulse pairs from two electron bunches with up to 100 fs separation have been already produced using a split and delay in the laser which produces them on the gun cathode [1]. Here we present a method to produce two bunches with longer separations by the combining two laser systems. This method allows any time separation within the limits imposed by RF and safety systems. We achieved separations up to 35 ns (limited by a beam safety system), different beam energies, and also vertical separations of several beam diameters. The vertical separation enabled a successful user experiment, and although it led to large fluctuations in the X-ray pulse energy it also provided an efficient pulse intensity scan.

INTRODUCTION

An early two-bunch test in 2010 [2] with 8.4 ns bunch separation revealed the possibilities and constrains of multi-bunch operation. This two-bunch mode was initially envisioned to increase the hit rate in LCLS experiments as jets carrying samples could move sufficiently between bunches to expose a new part of the jet. Unfortunately, XFEL pulses also induce pressure waves and explosions, which damage the jets over distances longer than the jet translation between bunches, even for delays of a few hundred ns [3]. Two-bunch operation with ns delays is nevertheless ideal for the investigation of these shock waves and explosions. The setup used in 2010 was upgraded and adjusted, as described in the next sections, for a user experiment [4] on XFEL explosions.

LASERS

Two mostly identical laser systems are used for the gun cathode at LCLS, and in standard operation a mirror selects one of the beams (Fig. 1). We added a 50/50 splitter (combiner) that can be interchanged with the mirror to either select one of the beams or combine them. The timing of each laser and the intensity of the combined beam could be controlled remotely. For the experiments reported here, we did not have remote and separate intensity control for the two lasers to adjust continuously the charge of the electron bunches, but we could set the ratio of the final FEL intensities to either 1:10 or 2.5:5 by moving the timing of the heater laser to coincide with the arrival of either the second or the first laser pulse. Only one bunch could be heated, since the timing delay stage is after the combination. This setup was sufficient for the experiments, and several improvements remain possible for the laser system concerning two-bunch operation, such as individual intensity control, laser heater for both bunches, and pointing control. Figure 2 shows the control layout used to run either one of the lasers for single bunches, or to combine them for two bunches.

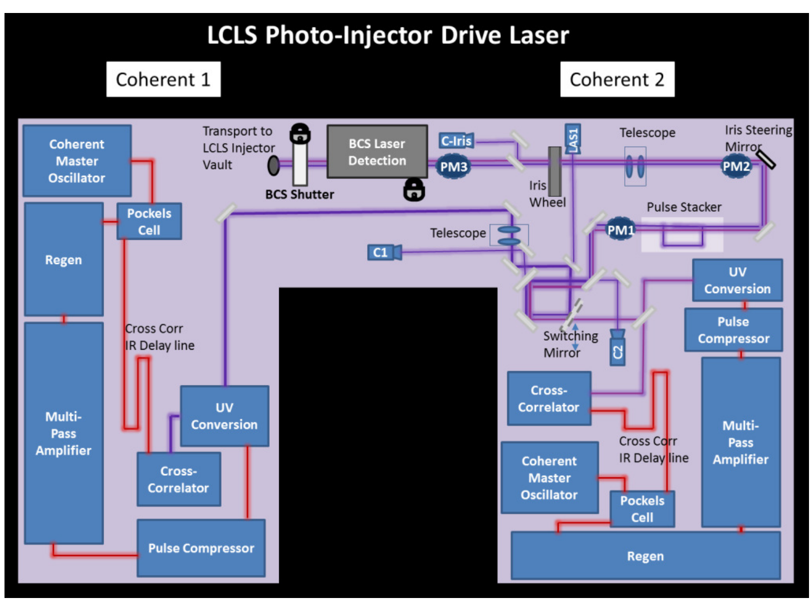

Figure 1: The laser system setup consists of two Coherent lasers, which can be selected with the switching mirror.

*Work supported by U.S. Department of Energy, Contract DE-AC02-76SF00515.

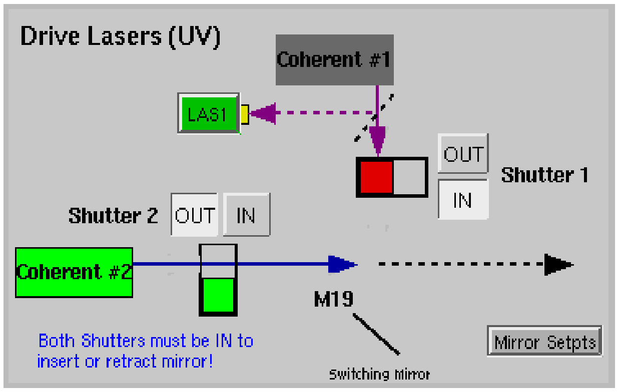

Figure 2: Controls layout to allow the different lasers or both with beam shutters.

TIMING AND BEAM CONTAINMENT

Typically the lasers are timed that they are contained inside a 40 ns BCS gate (Beam Containment System). Two timing scans were performed to detect the edges of the gate, one positive and the other negative. Figure 3 shows a timing scan with the Vitara 1 oscillator in positive direction with steps of 360°. The energy change in BC1 is measured as different positions in x and 1 mm corresponds to about 1° or 1 ps timing change. Two things are visible, there is a three step periodicity of about 0.3° variations and after about 11,000° a timing step happens of nearly 1° when the trigger time changes. Since the two lasers can be adjusted separately in time (phase), it was used up to 2° to reduce the beam difference early in the accelerator. The beam stayed on for 38.2 ns (+20, -18 ns), which is close to the "40 ns" BCS gate (Fig. 4). The BCS gate of the lasers was the main constraint in the spring of 2015, but should be lifted for the fall running, so that only real accelerator RF will limit the bunch separation in time.

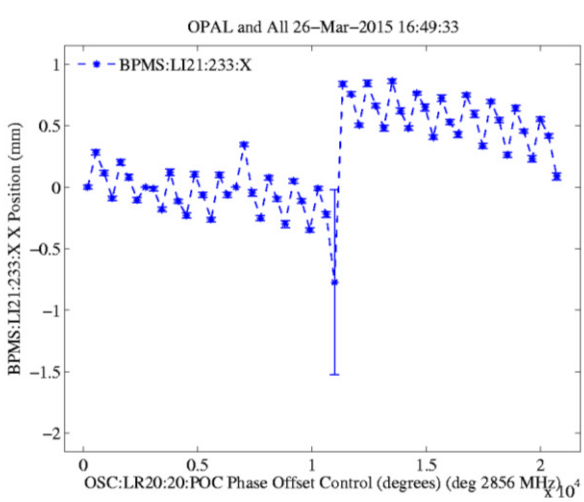

Figure 3: Timing scan of Vitara1 oscillator in RF degrees.

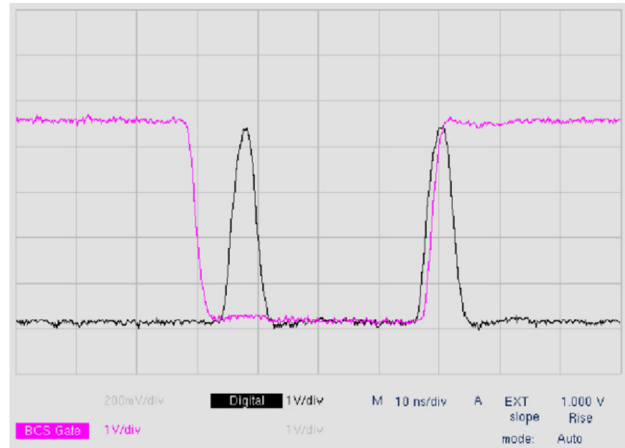

Figure 4: BCS gate (pink) and the two laser pulses close to the edges.

RF ISSUES

The RF pulses in the linac are long enough to allow up to about 400 ns separation of the two bunches, but since only one bunch was envisioned for LCLS, special setups are shorter. This includes the Gun and L1X RF pulses (Fig. 5 and 6).

Gun RF

Since the gun has a 1.6 cell structure it resembles a standing wave setup, where the plateau is achieved exponentially. To reduce the RF pulse energy that plateau is never reached since the pulse length is short. To achieve a flat pulse top the drive can be reduced suddenly to the necessary level for steady state condition.

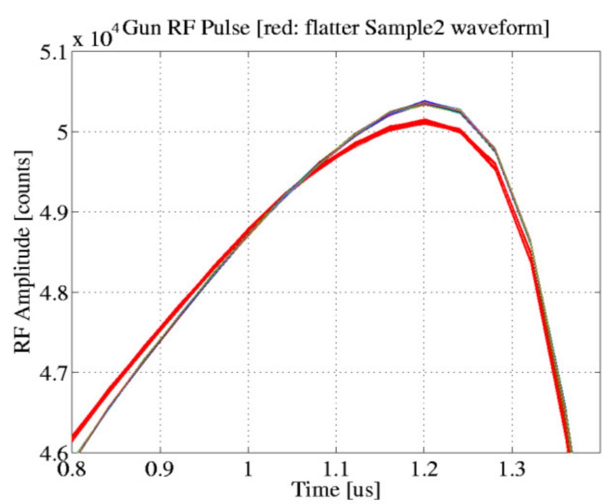

Figure 5: Gun RF pulse shows the filling time of the standing wave setup. By lowering suddenly the drive the equilibrium can be reached faster and a flattop achieved. Here it got flatter (red), but not yet flat.

ISBN 978-3-95450-134-2

L1X RF

Figure 6 shows the timing scan of the x-band linearizer klystron L1X. The RF pulse has to be lengthened to achieve more separation than 100 ns.

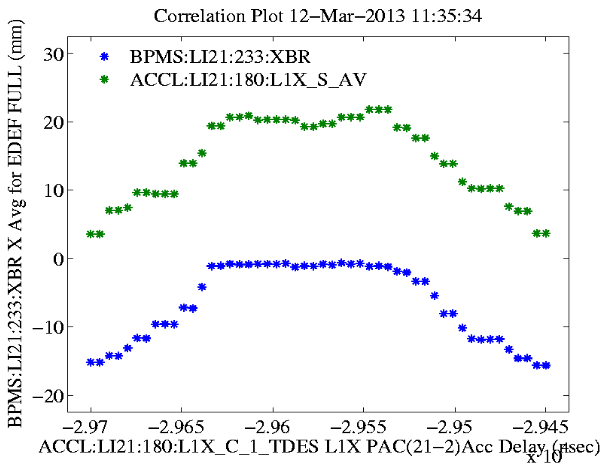

Figure 6: Timing scan for the L1X station, showing a 100 ns flat distribution.

BPM RESPONSE

The beam position monitor system (BPM) measures the position in x and y and also the beam intensity or beam charge. Since it down-samples to a certain frequency its intensity signal response is sensitive to the bunch separation of the two bunches. The signals of the two bunches get added like vectors and the response can be calculated using the sampling frequency of 140, 200, or 40 MHz of the different processors (Fig. 7 and 8).

By using the raw waveform of the BPMs and taking the expected bunch separation into account a bunch difference signal can be achieved (Fig. 9).

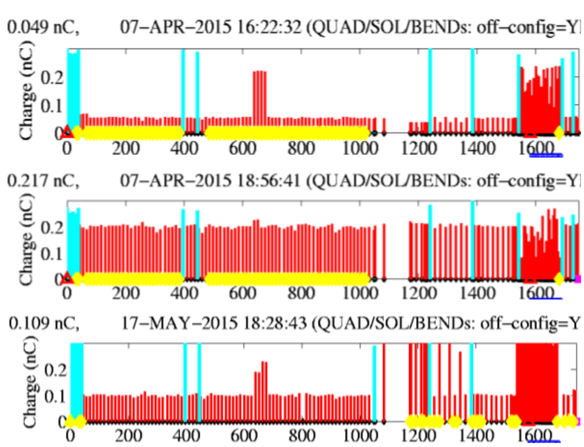

Figure 7: BPM response for roughly 18, 35 and 25 ns bunch separation along the accelerator distance z in meters. In cyan are toroid readings which are seeing 2*0.15 nC = 0.3 nC, while the first BPM "measures" 50 pC, 220 pC, 110 pC for the three time separations.

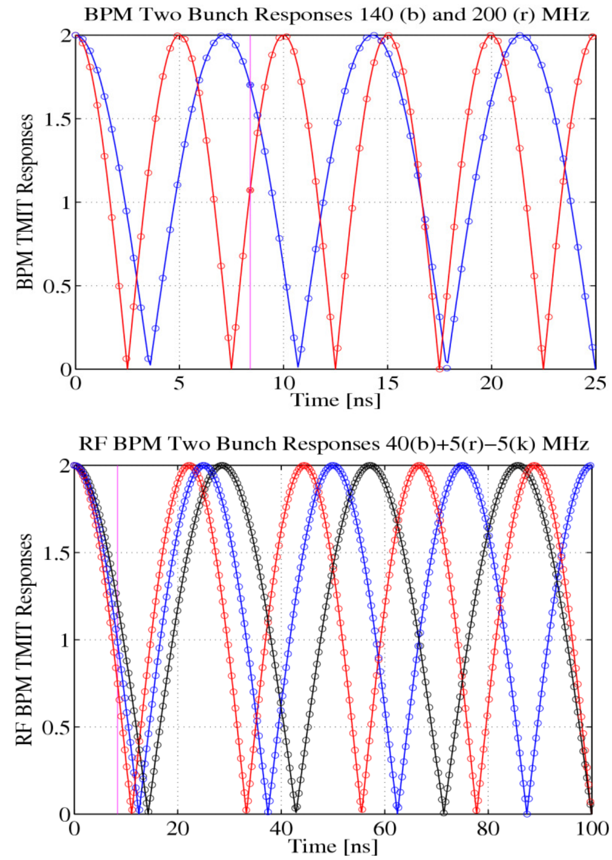

Figure 8: BPM intensity (TMIT) response for two strip line style BPM electronics (top) and RF cavity BPMs of the undulator (bottom). At certain delays no response is possible, but a little off and a signal with good positions is achieved.

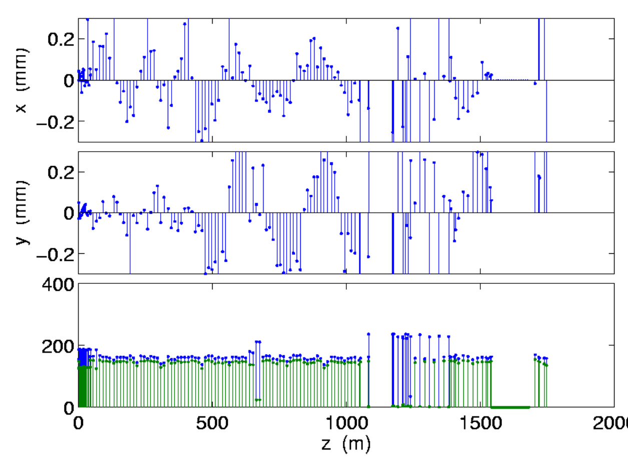

Figure 9: Difference orbit of two bunches with 25.2 ns (72 RF buckets) time separation. The intended kick in y with TCAV3 (at z = 500 m) is visible, but also an un-intended x difference is visible which starts early in the linac.

ISBN 978-3-95450-134-2

ENERGY CONTROL

The beam energy of the two bunches can be controlled by adjusting the time of the RF pulse since the SLED pulse is not flat. This can be done in the region where the beam gets its correlated energy spread before BC2 (Fig. 10) and also afterwards to achieve different energies at the end for the photon experiment (Fig. 11).

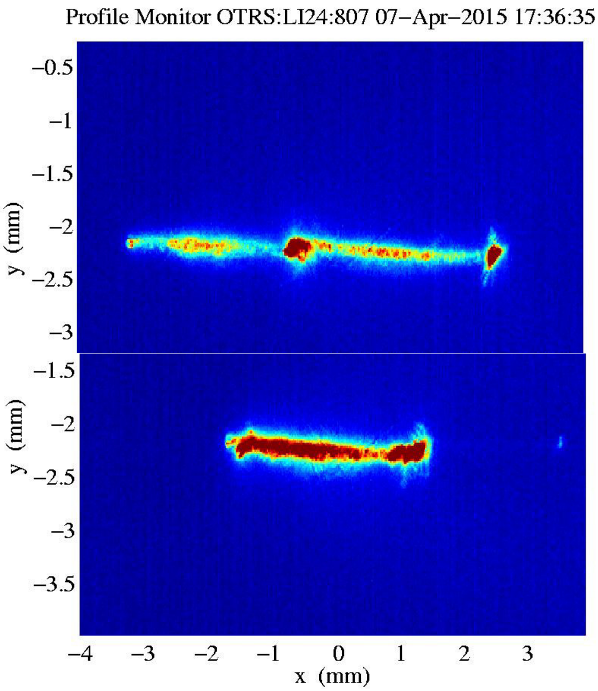

Figure 10: Energy distribution inside the BC2 chicane. Top: the two bunches have about 3 mm difference orbit, while at the bottom they overlap after adjusting the timing of the RF envelope.

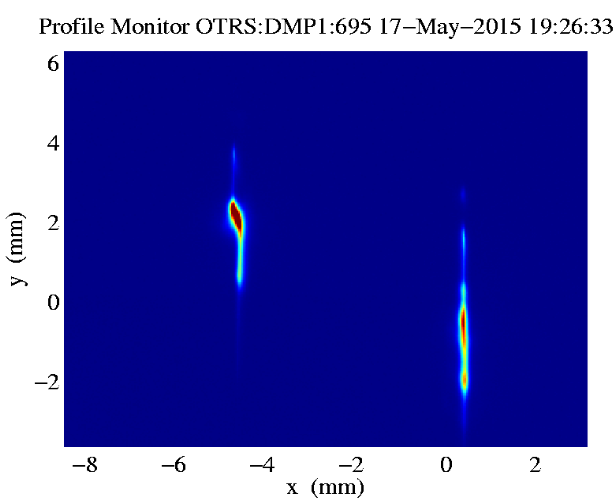

Figure 11: Beam distribution in energy (vertical) and time (horizontal) at the end on the dump screen. Left is the first bunch with higher energy than the second bunch to the right, which is also shorter. The big phase separation is not really understood yet.

Finally the photon beam energy can be measured with a spectrometer and the energy adjusted carefully so the first beam is above and the second beam is below the Cu K-edge of 8.98 keV (Fig. 12).

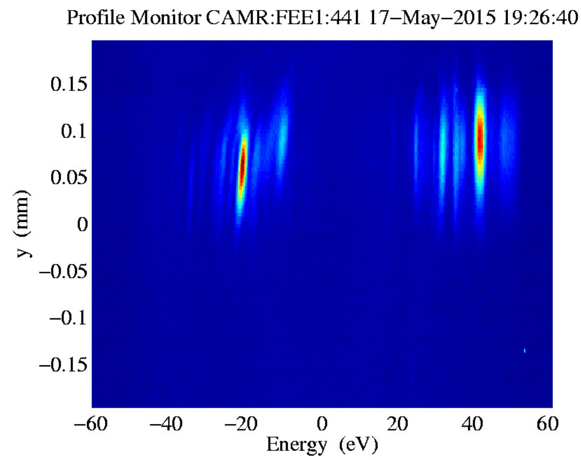

Figure 12: FEE (Front End Enclosure) spectrometer shows the two SASE photon pulses with about 60 eV energy separation (and 25 ns time separation).

TRANSVERSE CONTROL

The experiment asked also for a transverse separation in y of a few sigmas for the two bunches so the second bunch would hit the expanding sample. This was envisioned to be introduced with TCAV3 in Sector 25 (see Fig. 9), but a nasty instability of 3.6 Hz made the jitter three times worse, so it could not be used. But since there was also an x separation (Fig. 9) which had to be dealt with we decided to use the same approach for x and y. Since the two bunches have different energies an introduced dispersion will separate (or combine) them. Three corrector bumps after DL2 (Dog Leg 2) created enough dispersion so the two bunches were combined in x and separated in y (Fig. 13).

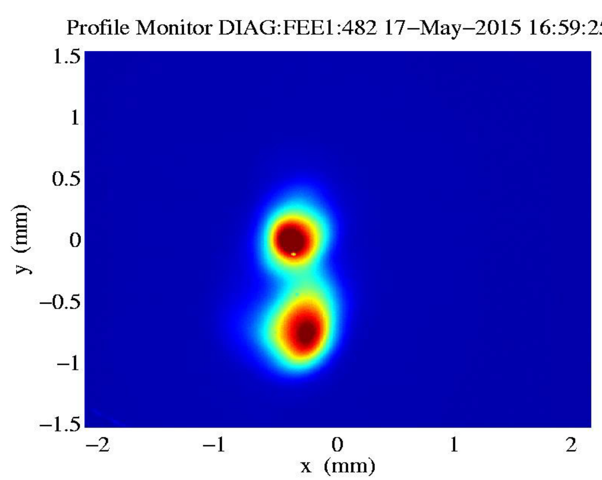

Figure 13: Two photon beams separated in y by a few spot sizes.

ISBN 978-3-95450-134-2

PHOTON DIAGNOSTIC

The photon beam is measured somewhat destructively by screens (Fig. 12 and 13) although at hard x-rays most of the photons go through. This gives a measurement of the transverse size, which is x and y and beam intensity. With a bend crystal also the energy distribution is measured (Fig. 12). A gas detector measures the beam intensity non-destructively and since it has a time response we can also measure the relative intensity of two bunches when they are enough separation like 25 ns. Figure 14 shows the gas detector raw waveform of 300 pulses with a 1:10 and a 2.5:5 intensity ratio. Since the two bunches are separated in y any vertical beam jitter changes the trajectory in the undulator and the intensity varies widely (Fig. 15).

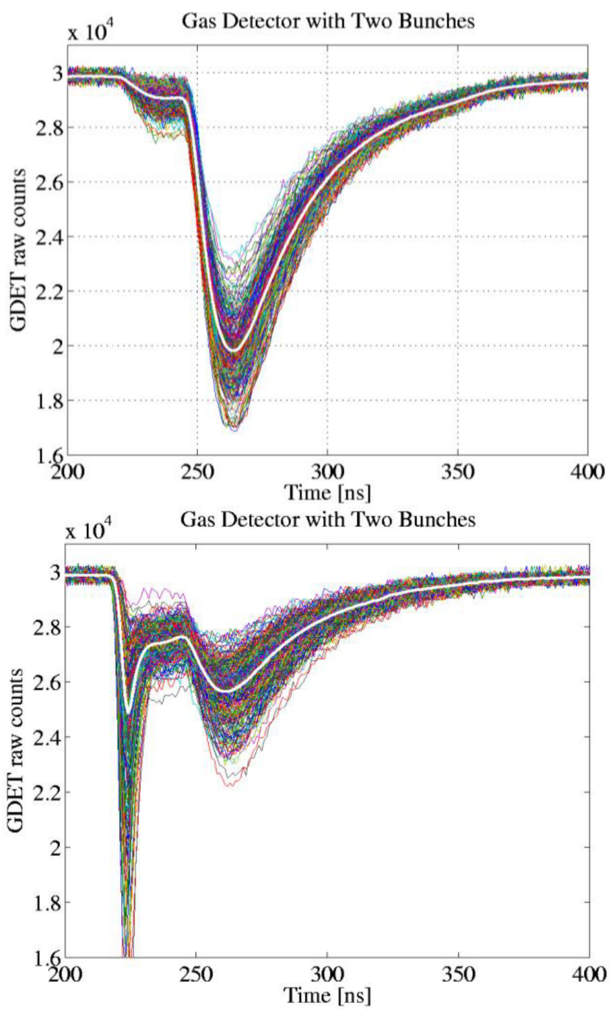

Figure 14: Gas detector raw waveforms and average (white) for different intensity ratios of the two bunches. The top shows an initial setup with 1:10 ratio for pump and probe, while the bottom shows a 2.5:5 ratio after the laser heater was timed for the first bunch. The spike in the front is an instrumental reaction to coherent synchrotron radiation. Therefore the integrated GDET signal typically uses the counts from 250 to 400 ns.

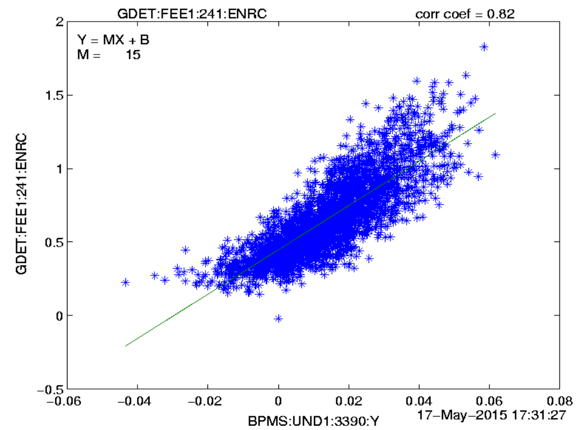

Figure 15: Integrated gas detector signal versus undulator position in y showing a strong correlation. Although the vertical jitter is not worse than typical running the different orbits of the two bunches away from the preferred center line makes it very jittery.

CONCLUSION

Two bunch operation with a few tens of ns time separation was studied and set up for an LCLS experiment which was successful in probing the effects of XFEL explosions in water droplets [4] (Fig 16). This setup with two bunches allows now time-resolved XFEL studies up to 40 ns, and soon beyond that. The micron-scale vertical separation of focused pulses at ns delays enables the study of propagating phenomena such as shock waves and other pressure-induced changes.

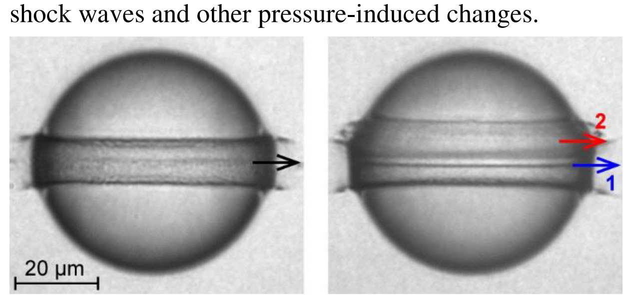

Figure 16: Visualizing the two-bunch mode at CXI (coherent x-ray imaging). Water droplets being hit by one (left) or two photon beams (right). The arrows indicate the XFEL beams.

REFERENCES

[1] A. Marinelli et al., “High-Intensity Double-Pulse X-Ray Free-Electron Laser”, Nature Communications 6, 6 Mar 2015, Article number: 6369.
[2] F.-J. Decker et al., “A Demonstration of Multi-Bunch Operation in the LCLS”, FEL 2010, Malmö, Sweden, WEPB33, p. 467.
[3] C.A. Stan, S. Boutet, et al., in preparation.
[4] C.A. Stan, private communication.

ISBN 978-3-95450-134-2

EFFECT OF MICROBUNCHING ON SEEDING SCHEMES FOR LCLS-II

G. Penn, J. Qiang, LBNL, Berkeley, CA 94720, USA
P. Emma, E. Hemsing, Z. Huang, G. Marcus,
T.O. Raubenheimer, L. Wang, SLAC, Menlo Park, CA 94025, USA

Abstract

External seeding and self-seeding schemes are particularly sensitive to distortions and fluctuations in the electron beam profile. Wakefields and the microbunching instability are important sources of such imperfections. Even at modest levels, their influence can degrade the spectrum and decrease the output brightness. These effects are evaluated for seeded FELs at the soft X-ray beam line of LCLS-II. FEL simulations are performed in GENESIS based on various realistic electron distributions obtained using the IMPACT tracking code. The sensitivity depends on both the seeding scheme and the output wavelength.

INTRODUCTION

At LCLS-II [1], the bandwidth is expected to be improved over SASE [2] through the use of self-seeding [3,4] schemes which filter out all but a narrow spectral bandwidth of the radiation somewhere in the middle of the undulators used for FEL amplification. Seeding using external lasers is another means by which a narrow spectrum can be produced, and includes other benefits such as more control over the x-ray pulse. Here we consider the self-seeding and echo-enabled harmonic generation (EEHG) schemes. Self-seeding is already being used at LCLS [5], while EEHG has been demonstrated at NLCTA [6] up to the 15th harmonic (160 nm).

Any attempt to generate coherent x-ray radiation from an electron beam is subject to phase variations caused by longitudinal variations in the electron bunch, through physical effects such as wake fields and the microbunching instability [7]. Laser heaters (LH) are currently used in LCLS to control the microbunching instability, and will be used in LCLS-II as well. In this paper, we consider two settings of the laser heater power, which produce microbunching at substantially different amplitude. The laser heater is set to that a slice energy spread of either 6 keV or 12 keV is produced at the end of the laser heater section, before bunch compression. We then characterize the sensitivity of each FEL scheme to microbunching by comparing the spectrum under these two settings.

The impact of wake fields is considered as well in these studies. When external lasers are used, they are modelled in an idealized fashion because the effect of laser errors is fairly well understood and broadly similar for different seeding schemes, except that EEHG has tighter tolerances on the laser power. It may be possible for carefully optimized lasers to improve performance even further, but because microbunching varies on a shot-by-shot basis there are limited possibilities to counteract this particular effect.

ELECTRON BEAM AND UNDULATOR PARAMETERS

The simulations shown below use particles obtained from start-to-end (S2E) simulations of the injector and linac accelerating the beam to 4 GeV, using the code IMPACT [8]. Previous studies [1,9] used beams derived from ASTRA [10] and ELEGANT [11] which included wake fields and coherent synchrotron radiation (CSR) but only included space charge forces at very low energies. The IMPACT simulations which generated the beams used here track a very large number of particles for higher fidelity, have a full 3D space charge model, and a better algorithm for CSR [12]. The nominal parameters for the electron beam and the main undulator sections for producing radiation are given in Table 1. The longitudinal phase space of the beams are shown in Fig. 1. Note the substantial decrease in levels of microbunching at the higher laser heater settings.

The final undulators have a period of 39 mm and cover a tuning range from 250 eV to 1.3 keV. We study x-ray radiation pulses at 540 eV and 1.2 keV. When external lasers are used, they operate at a wavelength of approximately 260 nm.

Table 1: Example Beam and Undulator Parameters for Soft X-ray Production at LCLS-II

Parameter	Symbol	Value
Electron Beam:		
Bunch charge	Q	300 pC
Electron energy	E	4 GeV
Peak current	I	1 kA
Emittance	ϵ_N	0.43 µm
Energy spread	σ_E	0.5 MeV
Beta function	β	15 m
Final undulators:		
Undulator period	λ_u	39 mm
Undulator segment length	L_{seg}	3.4 m
Break length	L_b	1.2 m
Min. magnetic gap	$g_{\min}$	7.2 mm
Max. undulator parameter	$K_{\max}$	5.48

LAYOUTS FOR DIFFERENT FEL SCHEMES

The layouts for the two main schemes are shown in Fig. 2. FEL simulations were performed using GENESIS [13]. These and other schemes have previously been considered in the LCLS-II Conceptual Design Report [14] for idealized

ISBN 978-3-95450-134-2

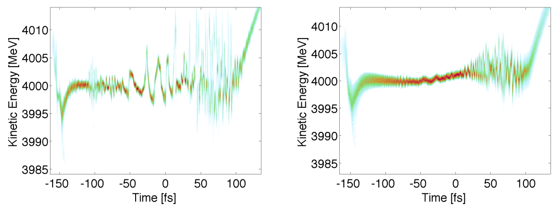

Figure 1: Longitudinal phase space for a 300 pC bunch with the laser heater inducing a 6 kev energy spread (left) and a 12 kev energy spread (right).

beams. Both beamlines should be capable of operating up to photon energies of 1.3 keV. For the self-seeding beamline it may be necessary to detune the first few undulator sections at lower photon energies, because the FEL gain rate is faster and it is undesirable to reach saturation upstream of the monochromator.

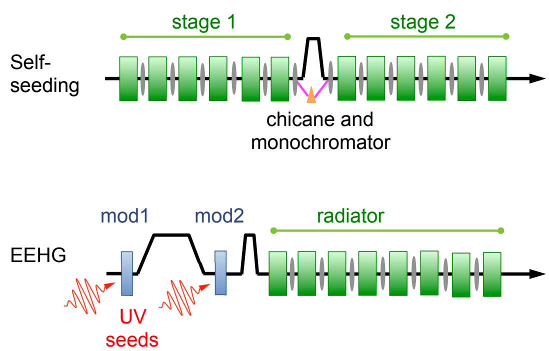

Figure 2: Beamline layouts using self-seeding (top) and EEHG (bottom).

Self-seeding Design and Layout

The self-seeding section is already part of the LCLS-II baseline, and involves only a small modification to the SASE beamline. One of the locations which would otherwise hold an undulator section will instead have a chicane and a monochromator. The chicane will fully debunch the electron beam (any value of $R_{56} \geq 10\,\mu\text{m}$ should suffice), and the monochromator will extract the SASE radiation field and allow only a narrow window in the spectrum to return to interact with the beam. The actual strength of the chicane will be adjusted so that the transit time of the electron beam will match that of the radiation field through the monochromator.

Here, we consider a monochromator resolving power of $R = 15000$, defined so that the bandwidth of the filtered radiation pulse will have a fwhm corresponding to $1/R$ of the target photon energy. The actual specifications and final design of the LCLS-II monochromator are still under development. Our current choice of a relatively large value for R is predominantly driven by a desire to highlight any effects which may cause even a small degradation in the bandwidth. We assume an efficiency of 2%; this means that in addition to eliminating out-of-bandwidth radiation, only 2% of the pulse energy originally within the bandwidth window makes it through the monochromator section due to losses. The monochromator used in LCLS as described in Ref. [5] has a resolving power in the range 2000 to 5000, and an efficiency between 7% and 15%.

EEHG Design and Layout

Echo-enabled harmonic generation (EEHG) [15] mixes modulations from two seed lasers, instead of using only one external laser as in HGHG. The first modulation is followed by a chicane which strongly overbunches the modulation. The chicane after the second modulation typically maximizes the bunching at the wavelength of the input laser. The overall bunching factor can be significant even at very high harmonics using fairly reasonable amplitudes of energy modulation.

Although the external lasers are not required to have the same wavelength, here both seed lasers have identical wavelengths close to 260 nm. The first undulator section is 3.2 m long, with a period of 0.1 m. The second undulator section is also 3.2 m long but with a period of 0.4 m, in order to reduce the amount of energy diffusion due to incoherent synchrotron radiation (ISR). Due to the combination of having fewer periods and sometimes requiring more energy modulation, the second laser needs a much higher peak power, up to 1 GW. To highlight the impact on the bandwidth, we take relatively long laser pulses with 400 fs fwhm. The output pulse is typically 75 fs fwhm.

Similarly, the first chicane has a much larger R_{56} of up to 15 mm, is longer and uses weaker magnets to reduce ISR. There is a tradeoff between reducing ISR and increasing the impact of intrabeam scattering (IBS) by adding to the chicane length.

After the bunching is generated, the electron beam goes directly into undulator sections with a 39 mm undulator period. Radiation is produced at the desired harmonic and amplified to saturation.

SIMULATION RESULTS

We show results for producing radiation at 1.2 keV, near the upper end of the tuning range for soft x-rays at LCLS-II, and at 540 eV. Wakefields are included in the simulation, with a nominal beam pipe diameter of 5 mm. However, because the initial stage of EEHG is especially sensitive to wake fields, and there is a relaxed undulator gap requirement for the modulating undulators, it was found advantageous to increase the beam pipe diameter in that section to 10 mm. Models for IBS were added within the same region, while ISR effects are already included in GENESIS.

The output spectrum profiles for a self-seeding beamline are shown in Fig. 3. The output pulse energy is 125 µJ at 1.2 keV with a 150 fs fwhm duration, and 331 µJ at 540 eV with a 110 fs fwhm duration. It is notable that the radiation at 540 eV is much more severely degraded when there is more microbunching than the radiation at 1.2 keV. For the chosen resolving power of $R = 15000$, the monochromator

ISBN 978-3-95450-134-2

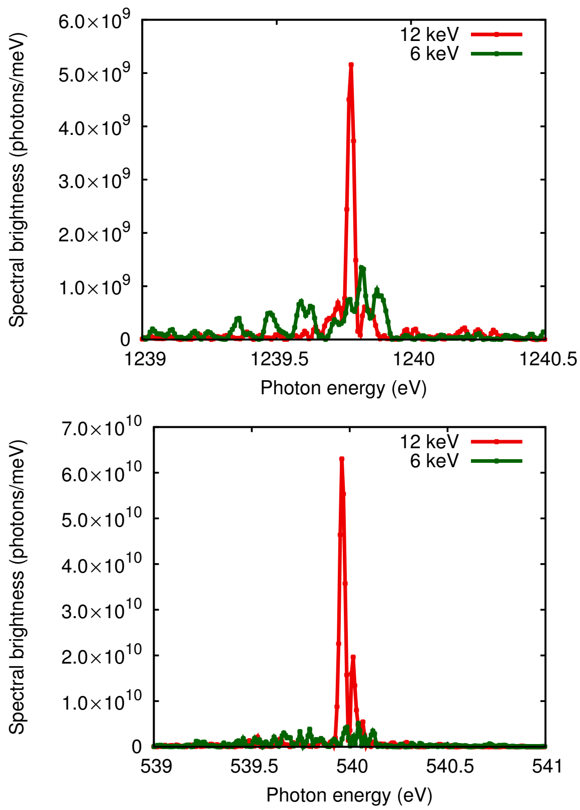

Figure 3: Spectral profiles of the final x-ray pulses for self-seeding, at different wavelengths and for different laser heater (LH) settings.

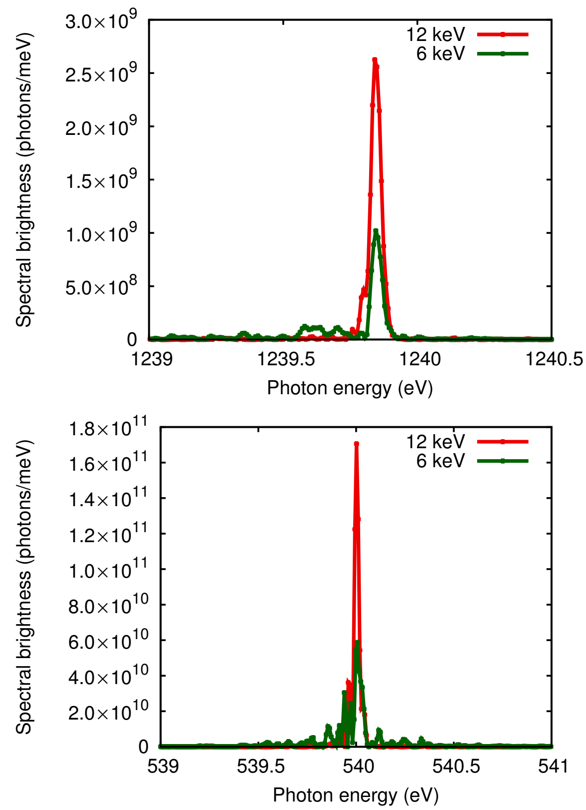

Figure 4: Spectral profiles of the final x-ray pulses for EEHG, at different wavelengths and for different laser heater (LH) settings.

does yield a longer coherence length at the lower photon energy. However, simulations with $R = 7000$ show a similar degradation at 540 eV when comparing the two laser heater settings. There appears to be a fundamental effect which is more of a concern at longer wavelengths than shorter wavelengths.

For EEHG starting from a pair of external lasers at 260 nm, the final x-ray properties are shown in Fig. 4. The output pulse energy is 32 µJ at 1.2 keV with a fwhm duration of 75 fs, and 638 µJ at 540 eV with a fwhm duration of 140 fs. The fwhm bandwidth is less than a factor of 2 from the transform limit when the high laser heater setting is used.

The above spectra are summarized in Fig. 5, in terms of the functional dependence of the fraction of pulse energy contained within a given bandwidth window, as that window is varied. It is particularly notable that for self-seeding, the spectrum at 540 eV with the high laser heater (LH) setting better than both spectra at 1.2 keV, while the spectrum at 540 eV with the low LH setting is worse than both of these spectra. For EEHG, on the other hand, the cumulative fractional energy curves fall into groups depending primarily on the strength of the LH.

CONCLUSION

As expected, seeding schemes perform better at lower harmonic jumps. However, self-seeding simulations show increased sensitivity to microbunching when radiating at longer wavelengths. While there is no harmonic jump in self-seeding, it is still somewhat surprising to see tighter tolerances being required at longer wavelengths. One possible explanation is that the resonance condition requires increased dispersion in the undulators at longer wavelengths. Energy modulations introduce phase modulations during the amplification process, and at low levels phase shifts are proportional to the dispersion and inversely proportional to the wavelength. Thus, the increased dispersion in the undulators should at least balance out the longer wavelength.

Another difference at longer wavelengths is that the FEL parameter is larger, which decreases the importance of the beam energy spreads on the growth rate. It is thus easier for regions of high current and high energy spread to produce significant amounts of unseeded radiation. Microbunching increases the number and amplitude of high current spikes in the beam, and only at shorter wavelengths will damping from the energy spread compensate for the excitation coming from the higher peak current.

The EEHG seeding scheme should produce long pulses with good coherence, assuming that the second seed laser can be tightly controlled. The parameter settings, especially the chicane strengths, must be very carefully set but are fairly robust to variations in electron bunch properties.

ISBN 978-3-95450-134-2

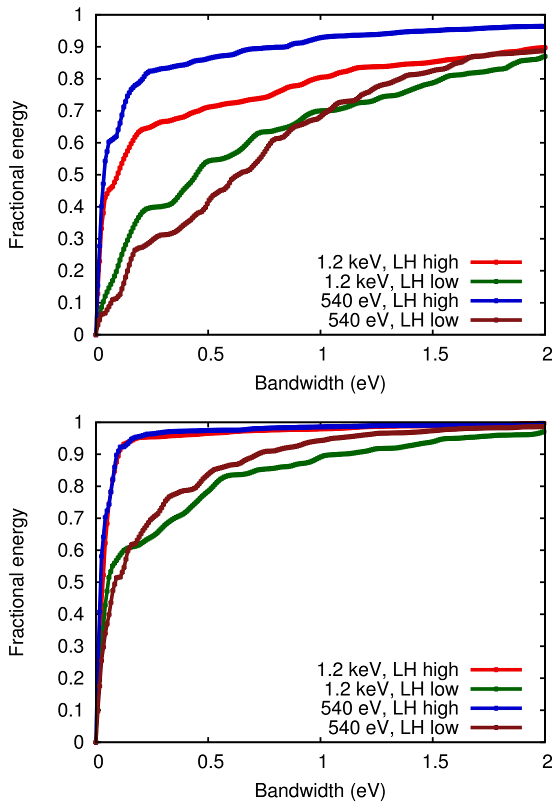

Figure 5: Spectral properties for self-seeding (top) and EEHG (bottom) for various wavelengths and laser heater settings, summarized in terms of the fraction of energy contained with a given bandwidth window.

In some cases, the spectrum and peak brigthness will be optimized by using fewer undulators than required to reach full saturation. Including more undulators can result in high-current portions of the electron bunch radiating in the SASE regime and spoiling the quality of the seeded output signal.

In all of the examples shown, it is clear that suppressing the microbunching instability as much as possible is crucial to optimizing performance when using either self-seeding or external seeding, whereas for SASE the broad spectrum tends to cover up the impact of microbunching at moderate levels. For the EEHG scheme, it was found to be important to reduce wake field forces within the initial bunching section of the beamline by doubling the beam pipe diameter.

ACKNOWLEDGMENT

This work was supported by the Director, Office of Science, Office of Basic Energy Sciences, of the U.S. Department of Energy under Contract Nos. DE-AC02-05CH11231 and DE-AC02-76SF00515.

REFERENCES

[1] G. Marcus, Y. Ding, P. Emma, Z. Huang, T. Raubenheimer, L. Wang, and J. Wu. FEL simulation and performance studies for LCLS-II. In *Proc. 36th Int. Free Electron Laser Conf.*, pages 456–460, Basel, Switzerland, 2014. JACoW. TUP032.

[2] R. Bonifacio, L. De Salvo, P. Pierini, N. Piovella, and C. Pellegrini. Spectrum, temporal structure, and fluctuations in a high-gain free-electron laser starting from noise. *Phys. Rev. Lett.*, 73:70–73, 1994.

[3] J. Feldhaus, E.L. Saldin, J.R. Schneider, E.A. Schmeidmiller, and M.V. Yurkov. Possible application of x-ray optical elements for reducing the spectral bandwidth of an x-ray SASE FEL. *Optics Commun.*, 140:341–352, 1997.

[4] G. Geloni, V. Kocharyan, and E. Saldin. A novel self-seeding scheme for hard x-ray FELs. *Journal of Modern Optics*, 58:1391–1403, 2011.

[5] D. Ratner, R. Abela, J. Amman, C. Behrens, D. Bohler, G. Bouchard, C. Bostedt, M. Boyes, K. Chow, D. Cocco, et al. Experimental demonstration of a soft x-ray self-seeded free-electron laser. *Phys. Rev. Lett.*, 114:054801, 2015.

[6] E. Hemsing, M. Dunning, C. Hast, T.O. Raubenheimer, S. Weathersby, and D. Xiang. Highly coherent vacuum ultraviolet radiation at the 15th harmonic with echo-enabled harmonic generation technique. *Phys. Rev. ST Accel. Beams*, 17:070702, 2014.

[7] Z. Zhang, Y. Ding, W.M. Fawley, Z. Huang, J. Krzywinski, A.A. Lutman, G. Marcus, A. Marinelli, and D. Ratner. Microbunching-induced sidebands in a seeded free-electron laser. In *These Proceedings: Proc. 37th Int. Free Electron Laser Conf.*, Daejeon, Korea, 2015. JACoW. WEP084.

[8] J. Qiang, R.D. Ryne, M. Venturini, A.A. Zholents, and I.V. Pogorelov. High resolution simulation of beam dynamics in electron linacs for x-ray free electron lasers. *Phys. Rev. ST Accel. Beams*, 12:100702, 2009.

[9] G. Penn et al. FEL simulation and performance studies for LCLS-II. In *Proc. 36th Int. Free Electron Laser Conf.*, pages 223–226, Basel, Switzerland, 2014. JACoW. TUP032.

[10] K. Flöttmann. Astra: A space charge tracking algorithm. Technical report, DESY, Hamburg, 2000. User's manual available at http://www.desy.de/ mpyflo/.

[11] M. Borland. Elegant. Report LS-287, Advanced Photon Source, 2000.

[12] G. Marcus, Y. Ding, P.J. Emma, Z. Huang, H.-D. Nuhn, T. Raubenheimer, L. Wang, J. Qiang, and M. Venturini. High fidelity start-to-end numerical particle simulations and performance studies for LCLS-II. In *These Proceedings: Proc. 37th Int. Free Electron Laser Conf.*, Daejeon, Korea, 2015. JACoW. TUP007.

[13] S. Reiche. GENESIS 1.3: a fully 3D time-dependent FEL simulation code. *Nucl. Instr. Meth. A*, 429:243–248, 1999.

[14] LCLS-II Design Study Group. LCLS-II conceptual design report. Report LCLSII-1.1-DR-0001-R0, SLAC, January 2014.

[15] G. Stupakov. Using the beam-echo effect for generation of short-wavelength radiation. *Phys. Rev. Lett.*, 102:074801, 2009.

ISBN 978-3-95450-134-2

INFLUENCE OF SEED LASER WAVEFRONT IMPERFECTIONS ON HGHG SEEDING PERFORMANCE

T. Plath*, C. Lechner, Universität Hamburg, Germany
S. Ackermann, J. Bödewadt, DESY, Hamburg, Germany

Abstract

To enhance the spectral and temporal properties of a free-electron laser, the FEL process can be seeded by an external light field. The quality of this light field strongly influences the final characteristics of the seeded FEL pulse. To push the limits of a seeding scheme and reach the smallest possible wavelengths it is therefore crucial to have a thorough understanding of relations between laser parameters and seeding performance. In this contribution, we numerically study the influence of laser wavefront imperfections on high-gain harmonic generation seeding at the seeding experiment at FLASH.

INTRODUCTION

To overcome statistical fluctuations of the radiation generated by a free-electron laser (FEL) that starts up from noise, the FEL process can be seeded by an external coherent source. In case of seeding schemes like high-gain harmonic generation (HGHG), a laser is used to imprint a sinusoidal energy modulation on the electron bunch. The quality of this modulation and the resulting bunching is strongly determined by the imperfections of the seed laser.

Since it is not practical to place a wavefront sensor at the region of interaction within the modulator undulator in order to measure laser wavefronts directly, often only the transverse intensity profile on screens can be used to diagnose the light field. From these measurements one can measure the transverse laser spot size as well as calculate the beam quality factor M^2.

Typically, simulations of seeding schemes are conducted with a perfect wavefront of the seed light field. Such a laser beam has a beam quality factor of $M^2 = 1$. As the beam quality factor degrades, additional modes arise in the transverse profile and the intensity distribution as well as the phase of the laser degrades in quality. Figure 1 shows exemplary the intensity profile of a laser beam with $M^2 = 1.0$, $M^2 = 2.0$ and $M^2 = 3.0$.

Using numerical methods we have investigated the influence of wavefront imperfections with a beam quality factor of up to $M^2 = 5.8$.

NUMERICAL METHODS

All FEL simulations presented in this contribution have been conducted with GENESIS 1.3 [1]. The simulations have been conducted for the experimental seeding setup at FLASH1 [2]. The relevant parameters are given in Table 1.

The transfer matrix option of GENESIS 1.3 has been used in order to both match the beam into the radiator and introduce the right amount of dispersive strength to bunch the electron beam. Thus, this simulation does not include any collective effects.

Table 1: Simulation Parameters for FEL Simulations at the Seeding Experiment at FLASH

Lattice modulator		
Undulator period	λ_u	20 cm
Periods per undulator	N_u	6
Undulator parameter	K_{rms}	1.9
Lattice radiator		
Number of undulators		4
Undulator period	λ_u	31.4 mm
Periods per undulator	N_u	60 (4th one: 120)
Undulator parameter	K_{rms}	1.8
Laser pulse		
Wavelength	λ_L	267 nm
Peak power	P_L	300 MW
FWHM duration	$\Delta\tau$	50 fs
Electron beam		
Peak current	I_{max}	1500 A
Energy	E	675 MeV
Energy spread	σ_E	200 keV
Normalized emittance	$\epsilon_{n\,x}, \epsilon_{n\,y}$	1.5 mm mrad

To properly model the seed laser imperfections, a field file that gives the complex electric field on each point of a three-dimensional grid has been used. This field was generated with the numeric algorithm described in [3]. It is based on the description of partially coherent beams using Hermite-Gaussian modes and allows the Monte Carlo driven generation of a modal composition for a given value of M^2.

In order to keep the axial symmetry of the seed field, only TEM_{mn} modes with even m, n have been considered. Since there are many possible combinations generating the same beam quality factors, the one with the minimum number of modes has been chosen. The total beam size has been kept constant along all profiles of a simulation run leading to the TEM_{00} mode getting smaller and less intense with higher M^2 as can be seen in Figure 2.

SIMULATION RESULTS

For a sufficient modulation to be built up even for the higher values of M^2, we chose a seed laser peak power of 300 MW, a full-width half maximum seed duration of $\Delta\tau = 50$ fs and a FWHM spot size of the laser beam of 800 µm.

ISBN 978-3-95450-134-2

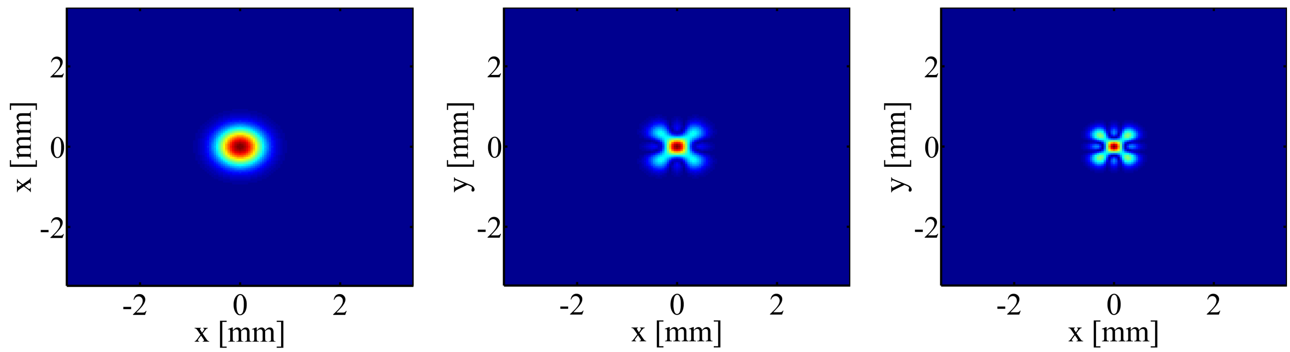

Figure 1: Transverse intensity profile of a laser beam with M^2 = 1.0 (left), M^2 = 2.0 (center) and M^2 = 3.0 (right). The color code shows the relative intensity on a linear scale, where dark red is the are with most intensity and blue is no intensity.

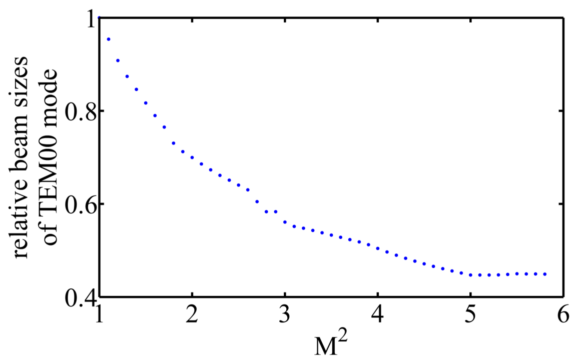

Figure 2: Relative transverse size of the TEM_{00} mode as a function of its beam quality factor M^2.

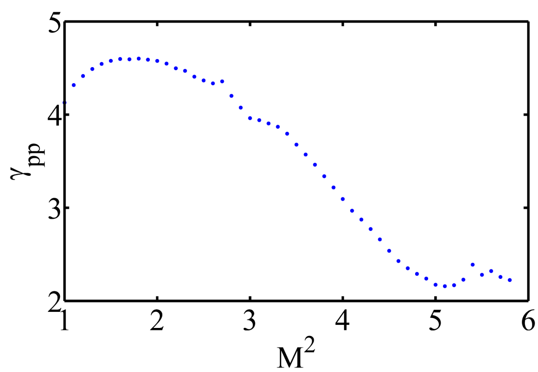

Figure 3: The modulation amplitude γ_{pp} induced by the seed laser as a function of its beam quality factor M^2.

Figure 3 shows the total modulation amplitude as a function of the M^2 of the seed light field. As seen before, the transverse size TEM_{00} carrying most of the beams intensity decreases with higher M^2. As new modes arise in the transverse profile also the power in the fundamental mode decreases.

The amplitude of the energy modulation decreases with higher M^2, since the TEM_{00} mode's intensity deacreses. Within the first few datapoints between M^2 = 1.0 and M^2 = 1.7 the modulation amplitude, however, rises. In this regime the transverse size of the TEM_{00} decreases faster than the square root of its power and thus the intensity rises.

For each particle distribution, the optimum R_{56} for bunching on the 7th harmonic of the laser wavelength has been calculated, and the transfermatrix of the corresponding chicane has been applied.

The resulting FEL power after the sFLASH undulator is shown in Figure 4. It decreases rapidly between M^2 = 4.0 and M^2 = 5.0 indicating a higher saturation length for the following runs.

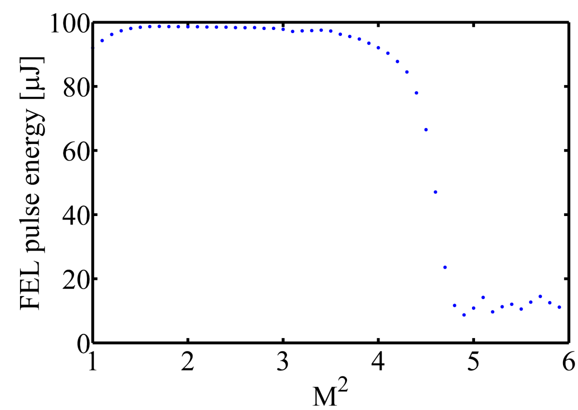

Figure 4: FEL pulse energy after the 4th radiator as a function of its beam quality factor M^2. The saturation energy increases rapidly between M^2 = 4.0 and M^2 = 5.0 and with this the power after the sFLASH undulators decreases.

Figure 5 shows a transverse map of the bunching phase of the bunched beam for M^2 = 5.0. The particle distribution has been binned transversely and the positions of the peaks with respect to the slice definition of GENESIS 1.3 have been analysed. For the outer layers, this analysis suffers from a small number of particles, further analysis will therefore focus on the central part of the bunch.

To further characterize the roughness of the wavefront, we have investigated the rms of all phases within a radius of $2\sigma_e$ in the electron bunch, where σ_e is its transverse rms width. Figure 6 shows these results as a function of M^2 of the input light field. It can be seen that the roughness increases at the same M^2 as the resulting FEL power decreases.

ISBN 978-3-95450-134-2

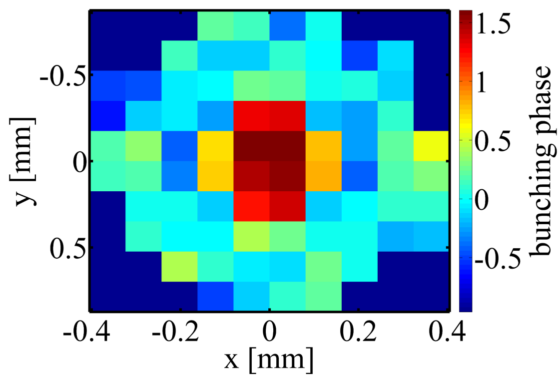

Figure 5: Transversely binned phase of the bunching in the electron bunch. The bunching is given in rad with respect to the center of one slice in GENESIS 1.3 for $M^2 = 5.0$.

The increasing roughness leads to a smaller bunching factor of the projected current distribution as already derived in [4].

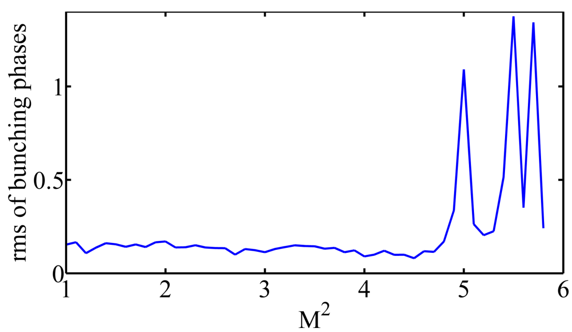

Figure 6: Roughness of bunching phases as a function of its beam quality factor M^2.

CONCLUSION AND OUTLOOK

The influence of the beam quality factor M^2 of a seed laser in an HGHG seeding setup has been studied considering the seeding hardware installed at FLASH1. With a seeding input power of 300 MW, the FEL signal at the end of the sFLASH undulator significantly decreases between $M^2 = 4.0$ and $M^2 = 5.0$. This is caused by the transverse inhomogeneous phase that results in a degraded bunchhing factor of the current profile and with this in an increased saturation length.

Future studies will analyse the characteristics of the resulting FEL pulse as well as the influence of different modal compositions for the same M^2. That will also determine the uncertainty of the study presented in this paper.

ACKNOWLEDGMENT

Supported by Federal Ministry of Education and Research of Germany under contract No. 05K1GU4 and 05K10PE1 and the German Research Foundation program graduate school 1355.

REFERENCES

[1] S. Reiche, "GENESIS 1.3: a fully 3D time-dependent FEL simulation code", Nuclear Instruments and Methods A 429, 1999, pp. 243-248.

[2] K. Hacker et al., "HGHG seeding at FLASH - First Lasing at 38 nm", FEL2015, Daejeon, WEP030, 2015.

[3] S. Ackermann et al., "Modal analysis of a seeded free-electron laser" Phys. Rev. ST Accel. Beams 16, 100702 (2013) `http://link.aps.org/doi/10.1103/PhysRevSTAB.16.100702`

[4] K. Hacker, "Tolerances for Echo-Seeding in the FLASH ORS Ssection", TESLA-FEL 2011-05, Hamburg, 2011.

ISBN 978-3-95450-134-2

FIRST LASING OF AN HGHG SEEDED FEL AT FLASH

Kirsten Hacker, Shaukat Khan, Robert Molo
DELTA, TU Dortmund, Germany
Sven Ackermann, Ralph Wolfgang Assmann, Jörn Bödewadt, Nagitha Ekanayake,
Bart Faatz, Ingmar Hartl, Rosen Ivanov, Tim Laarmann, Jost Müller, Holger Schlarb
DESY, Hamburg, Germany
Philipp Amstutz, Armin Azima, Markus Drescher, Leslie Lamberto Lazzarino,
Christoph Lechner, Theophilos Maltezopoulos, Tim Plath, Jörg Rossbach
University of Hamburg, Germany

Abstract

The free-electron laser facility FLASH at DESY operates in SASE mode with MHz bunch trains of high-intensity extreme ultraviolet and soft X-ray FEL pulses. A seeded beamline which is designed to be operated parasitically to the main SASE beamline has been used to test different external FEL seeding methods. First lasing at the 7th harmonic of a 266 nm seed laser using high-gain harmonic generation has been demonstrated.

INTRODUCTION

The seeding section at the Free-electron Laser in Hamburg (FLASH) facility was named sFLASH and designed to be operated in parallel with the FLASH1 and FLASH2 SASE sections [1] (Fig. 1). These three beamlines have been operated simultaneously in SASE mode with a peak current of 1.3 kA and wavelengths of 13.7 nm in FLASH1, 20 nm in FLASH2, and 38.1 nm in sFLASH. Operation of the sFLASH section in seeded-mode can potentially be done parasitically with <kA peak currents and improved quadrupole alignment.

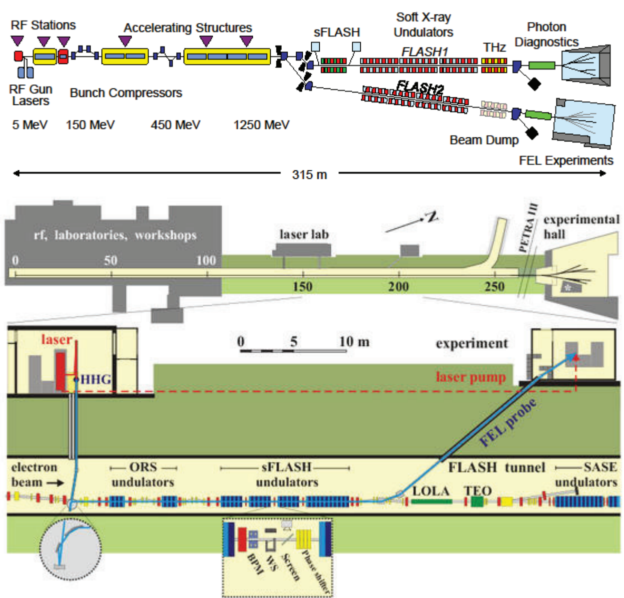

Figure 1: Layout of the FLASH facility and the sFLASH seeding section. The sFLASH section is designed to be operated in parallel with SASE generation in FLASH1 and FLASH2. It is followed by the RF deflector LOLA which makes longitudinal phase space distribution measurements. The seed laser is split so that part can be sent to the FEL user station for pump-probe experiments.

Seeding takes place when the electron bunch interacts with a laser pulse within an undulator magnet known as a modulator. The resulting sinusoidal energy modulation is transformed into a density modulation via longitudinal dispersion (Fig. 2). For a seeded FEL using the High-Gain Harmonic Generation (HGHG) scheme, microbunch trains with the periodicity of the seed laser wavelength will radiate at a harmonic of the microbunch repetition rate when they are sent through an FEL radiator tuned to that harmonic; shorter microbunches will have higher harmonic content [2,3].

For the first time at FLASH, lasing at the 7th harmonic of a 266 nm seed using high-gain harmonic generation has been demonstrated. The 266 nm seed pulses were generated from 800-nm Ti:sapphire light by using a frequency tripler made up of BBO crystals and crystalline quartz waveplates [4]. The mean pulse energy was (12±12) μJ, the maximum pulse energy was 75 μJ, and the estimated gain length was ~0.9 m. The bandwidth was 0.2 nm (FWHM) with $\Delta\lambda/\lambda = 5.2\times10^{-3}$. Future efforts will be concentrated on improving the stability of the seeded beam, parasitic operation, and progress towards Echo-Enabled Harmonic Generation (EEHG) [5,6] seeding.

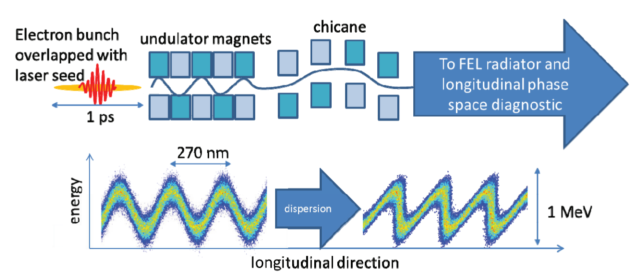

Figure 2: The HGHG experiment uses electron bunches with a peak current between 0.5 and 1 kA together with a 266 nm seed pulse, a 5 period undulator, and a chicane with ~100 μm of longitudinal dispersion.

MILESTONES

The HGHG seeding experiment was conceptualized in 2011 [5,7] and a dedicated seed injection setup was partially commissioned in 2012 [8], but filamentation of

ISBN 978-3-95450-134-2

the 266 nm seed stopped the project's progress. It was found that the filamentation problem was removed through the use of a thinner waveplate and timeplate in the frequency tripler. In 2013, a new effort [9] aimed to increase the flexibility of the experiment from single wavelength (266 nm) to multiwavelength (266, 400, and 800 nm) operation, but in commissioning attempts in 2014, problems with the new filters and multiwavelength dielectric mirrors installed in the injection line forced their replacement with the original hardware before seeding could be achieved in 2015.

The filters in the injection line steered the beam so that the seed position in the electron beamline was significantly different with the filters in or out, preventing spatial overlap with the electrons. The effect was not easily detectable with the diagnostics 6 meters upstream in the injection line.

The use of the multi-wavelength dielectric mirrors caused all three wavelengths emerging from the tripler: 800 nm, 400 nm, and 266 nm to be sent into the modulator and it appeared that when the modulator was tuned to be resonant at 266 nm, only 800 nm and 400 nm modulation was observed in measurements of the longitudinal phase space distribution of the seeded beam, making it impossible to identify any modulation at 266 nm, despite the adequate temporal separation of the 3 pulses.

An explanation for this observation of sub-harmonic modulation which is consistent with simulations is that an intensity gradient of the seed in the modulator could have been produced if the electron beam trajectory was at an angle with respect to the laser trajectory. Systematic scans of the sensitivity of the relative magnitude of the modulations to transverse overlap in the modulator were not, however, possible. An alternative possibility is that one of the electromagnetic modulator's 5 periods + 2 half periods was damaged, although this was not detected through in-tunnel measurements with a Hall probe or current meter.

The multi-wavelength dielectric mirrors also likely caused the polarization-dependent longitudinal splitting of the seed pulse which was observed with the longitudinal phase space distribution measurements of the 800 nm seeded electron bunch (Fig. 3). When the polarization of the 800 nm seed was in a mixed state as it propagated through the dielectric coatings on the mirrors, the *s* polarized light and *p* polarized light would travel different distances, leading to longitudinal splitting of the 50 fs (FWHM) pulses. After this splitting, the polarization was rotated again at a crystalline quartz window which would make a double pulse with the correct polarization for the modulator. With these mirrors, this effect would also likely be present at 400 nm and 266 nm.

In the original setup from 2011 [10], the waveplate locations and single-wavelength, 266 nm dielectric coatings were thinner and selected to avoid this problem. In 2014, the injection optics were returned to the 2011 design and a clear 266 nm modulation was observed with the longitudinal phase space diagnostic, however evidence of bunching in the radiator was not observed. The final barrier to FEL saturation was quadrupole alignment.

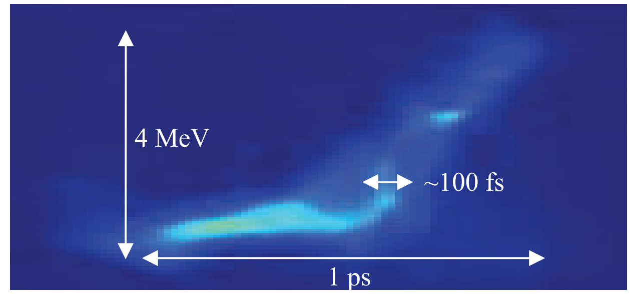

Figure 3: An RF deflecting cavity and a magnetic spectrometer are used to perform a measurement of the longitudinal phase space distribution of the 700 MeV, 0.3 kA seeded electron beam after the FEL radiator. The 800 nm, 50 fs (FWHM) seed imprinted on the electron bunch is split longitudinally, possibly via different path lengths traveled by *s* and *p* polarized light in multi-wavelength dielectric mirrors in the injection line. The 50 fs (FWHM) seed pulse length is measured prior to the entrance to the injection line.

As described in [7], the experiment would benefit from the addition of movers to the quadrupoles in the modulator section. Centering the quads with respect to the seed laser defined trajectory would ensure that the microbunches are not longitudinally smeared out in the radiator. In practice, turning off the most misaligned quadrupoles made the trajectory straight enough that FEL saturation was achieved in 2015 without the installation of movers on the quads. The seed laser and screens around the modulator and radiator segments were useful in establishing this trajectory.

FIRST LASING

As observed at Fermi in Trieste [3], the linearity of the electron bunch energy spread over the seeded region is important in establishing a narrow, stable FEL spectrum. The microbunching instability can also increase the slice energy spread of the electrons and degrade the FEL performance. Direct studies of these issues have not yet been conducted, however, it was observed in longitudinal phase space distribution measurements conducted with an RF deflector and a spectrometer that the linear energy chirp shown in Fig. 4 produced the narrowest FEL spectrum (Fig. 5), while a distribution showing a nonlinear chirp with significant microbunching instability produced a wider, more distorted spectrum [11].

The mean FEL pulse energy was (12±12) μJ, the maximum pulse energy was 75 µJ, and the estimated gain length was ~0.9 m. The background SASE signal was (2.6 ± 0.2) nJ. The bandwidth was 0.2 nm (FWHM) with $\Delta\lambda/\lambda = 5.2\cdot10^{-3}$. The jitter in the signal strength was dominated by pointing jitter of the seed.

ISBN 978-3-95450-134-2

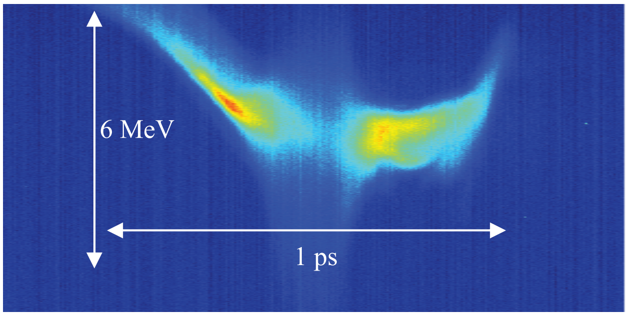

Figure 4: An RF deflecting cavity and a magnetic spectrometer are used to perform a measurement of the longitudinal phase space distribution of the 700 MeV, 0.5 kA, 266 nm seeded electron beam after the FEL radiator. The measurement is affected by the FEL process and the transverse beam size, as well as collective effects on the microbunches (see [12,13]).

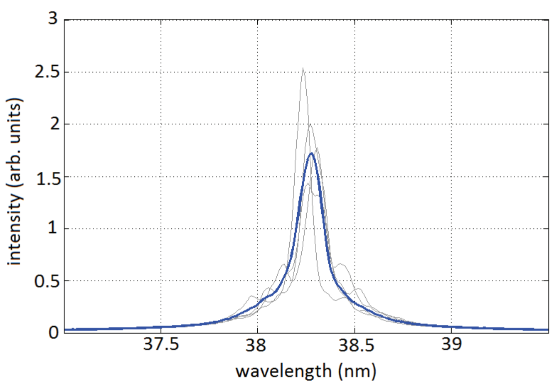

Figure 5: The FEL light is extracted from the beamline and reflected into a spectrometer. The blue curve is the average and the grey curves are individual shots.

The pointing jitter of the seed laser was initially the primary driver of variations in the intensity of the seeded FEL light, leading to 100% fluctuations as the transverse overlap changed by up to the full beam-diameter from shot to shot. After turning off un-necessary vacuum pumps and putting the IR light on the laser table into pipes in order to shield it from air currents, the pointing jitter improved by more than a factor of two.

FUTURE GOALS

After studying the performance of HGHG, the next step is to use the existing hardware to attempt an EEHG experiment (Fig. 6). Small changes to the hardware can provide adequate laser conditions for seeding at a wavelength of 266 nm in the first modulator and at 800 nm in the second modulator.

It was initially planned to use 266 nm in both modulators by splitting the 10 GW output of a single tripler [9], but tripler performance under those conditions has proven to be unstable. By reducing the bandwidth and lengthening the pulse sent into the tripler from 30 fs to 50 fs, better stability has been achieved, but at a cost to the desired peak power.

The goal is to attempt EEHG at the shortest wavelengths yet demonstrated and to determine the limitations of our ability to transport the fine EEHG microstructures into the radiator. With the 266/800 nm combination, we anticipate a minimum wavelength of 30 nm. By splitting the 800 nm pulses, to make the experiment with a combination of 266 nm and 400 nm, a minimum wavelength of 20 nm is expected (Fig. 7). A final upgrade with 266 nm in both modulators is expected to produce a minimum wavelength of 10 nm in the seeded radiators and to have the capability to be used to directly seed the downstream SASE undulators at a wavelength of 4-5 nm in a sort of directly seeded cascade [7].

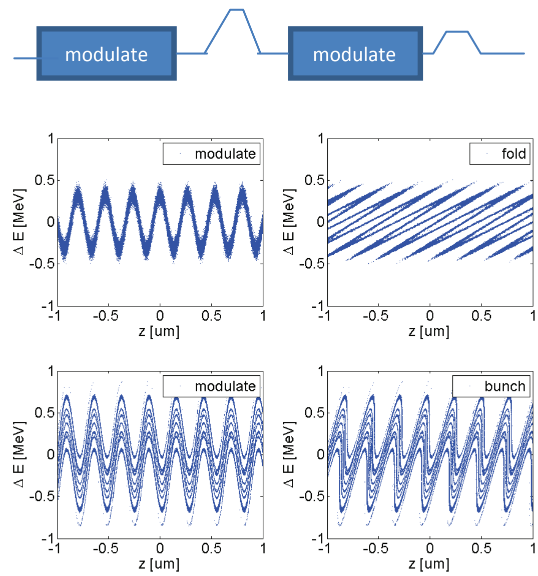

Figure 6: Echo-enabled harmonic generation (EEHG) uses two modulation stages in order to seed shorter wavelengths. It has not yet been demonstrated below 100 nm. A scheme using 266 nm in both stages is plotted.

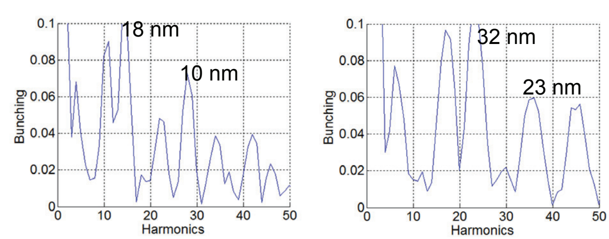

Figure 7: Harmonic content of 266/266 nm EEHG (left) and 266/800 nm EEHG (right). The sensitivity to electron beam energy jitter was taken into account in the selection of the operation points.

A key challenge of commissioning the seeding experiment at FLASH is related to the difficulty of working parasitically at an active user facility. Since demands for user beam time are high, access to the machine is limited. However, the potential to expand the user capabilities of the facility with an additional seeded beamline has kept the effort alive.

ISBN 978-3-95450-134-2

CONCLUSION

Commissioning of the HGHG seeding experiment at FLASH was started in 2012 and achieved success in 2015. The maximum pulse energy was 75 µJ and bandwidth was 0.2 nm (FWHM). Future goals include improving the stability of the HGHG seeded beam, testing the performance limitations, and working towards EEHG.

ACKNOWLEDGEMENTS

The authors would like to thank FLASH and the M-Division staff at DESY for their support. This work was funded by the Helmholtz Association Accelerator Reaseach and Development program, the Federal Ministry of Education and Research of Germany under contract No. 05K10PE1, 05K10PE3, 05K13GU4, and 05K13PE3, and the German Research Foundation program graduate school 1355.

REFERENCES

[1] M. Scholz, in *Proc. FEL Conf. 2015*, TUA04, Daejeon, Korea 2015.
[2] L.H. Yu, Phys. Rev. A 44, 5178 (1991).
[3] E. Allaria et al., Nature Photonics 6, 699 (2012).
[4] N. Ekanayake et al., in *Proc. FEL Conf. 2014*, MOP094, Basel, Switzerland (2014).
[5] G. Stupakov, Phys. Rev. Lett. 102, 074801 (2009).
[6] H. Deng, et al., Nat. Photonics 6, 360 (2012).
[7] K. Hacker, et al., DESY FEL Report No., TESLA-FEL 2011-04, (2011).
[8] K. Hacker, et al., in *Proc. FEL Conf. 2012*, TUPD13, Nara, Japan (2012).
[9] J. Boedewadt et al., in Proc. FEL Conf. 2013, WEPSO02, New York, USA (2013).
[10] K. Hacker, et al., DESY FEL Report No., TESLA-FEL 2011-06 (2011).
[11] J. Boedewadt et al., in *Proc IPAC Conf. 2015*, TUBC3, Richmond, USA (2015).
[12] K. Hacker, et al., in *Proc. FEL Conf. 2015*, WEP031, Daejeon, Korea (2015).
[13] C. Lechner, et al., in *Proc. FEL Conf. 2015*, TUA02, Daejeon, Korea (2015).

ISBN 978-3-95450-134-2

MEASUREMENTS AND SIMULATIONS OF SEEDED MICROBUNCHES WITH COLLECTIVE EFFECTS

K. Hacker*, R. Molo, S. Khan, DELTA, TU Dortmund, Germany
S. Ackermann, J. Boedewadt, M. Dohlus, N. Ekanayake, T. Laarmann, H. Schlarb, DESY, Hamburg, Germany
L. L. Lazzarino, C. Lechner, Th. Maltezopoulos, T. Plath, J. Rossbach, Universitaet Hamburg, Germany

Abstract

Measurements of the longitudinal phase-space distribution of electron bunches seeded with an external laser were done in order to study the impact of collective effects on seeded microbunches in free-electron lasers. When the collective effects of Coulomb forces in a drift space and coherent synchrotron radiation in a chicane are considered, velocity bunching of a seeded microbunch appears to be a viable alternative to compression with a magnetic chicane under high-gain harmonic generation seeding conditions. Measurements of these effects on seeded electron microbunches were performed with an RF deflecting structure and a dipole magnet which streak out the electron bunch for single-shot images of the longitudinal phase-space distribution. Particle tracking simulations in 3D predicted the compression dynamics of the seeded microbunches with collective effects.

INTRODUCTION

Seeding takes place when the electron bunch interacts with a laser pulse within an undulator magnet known as a modulator. The resulting sinusoidal energy modulation is transformed into a density modulation via longitudinal dispersion. For a seeded FEL using the High-Gain Harmonic Generation (HGHG) scheme, microbunch trains with the periodicity of the seed laser wavelength will radiate at a harmonic of the microbunch repetition rate when they are sent through an FEL radiator tuned to that harmonic; shorter microbunches will have higher harmonic content [1,2].

The longitudinal dispersion used to compress microbunches is typically provided through the energy-dependent path in a series of bending magnets which compose a magnetic chicane, but this will result in coherent synchrotron radiation (CSR) emitted by the tail of the bunch early in a bend catching up with the head of the bunch, producing an inhomogeneous energy loss along the bunch which is proportional to the peak current, bend radius, and bend length [3,4]. While typically of concern on the macrobunch scale due to nonlinear chirps which broaden the FEL spectrum, CSR is also of concern when it changes the energy, energy spread, or bunch length on the microbunch scale. Since the harmonic content of a seeded beam is given by the Fourier transform of the longitudinal current distribution, a change in the microbunch length has a direct impact on the high harmonic content. Here, we present simulations and measurements of the effect of CSR on the longitudinal phase-space distributions of seeded electron microbunches compressed in a chicane and we contrast it with the effect of Coulomb forces on seeded electron microbunches which are primarily compressed through velocity bunching in a drift space with quadrupole focusing optics.

In [5], the concept that Coulomb forces and velocity bunching could be used to reduce the energy spread for soft X-ray HGHG applications was investigated due to the requirement that the HGHG seeded beam in a proposed seeding design would need to drift for 20 meters before entering the radiator. Here, a condensed presentation is given of measurements and 3D simulations [6] performed with conditions at the Free-electron Laser in Hamburg (FLASH). The investigation of these microbunch collective effects was done with an RF deflector and dipole spectrometer which streak out a 700 MeV electron bunch for single-shot measurements of the particle distribution in longitudinal phase-space (Fig. 1). Quantitative agreement with simulations was observed within the error bars of the measurements and original physical interpretations are used to explain new effects discovered in the measurement method.

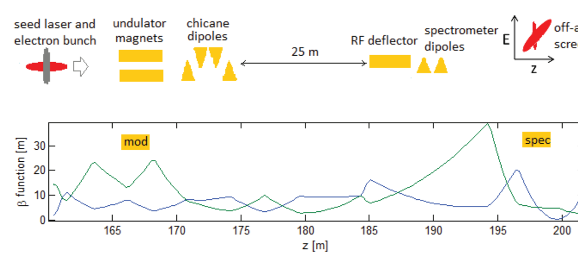

Figure 1: Layout of experimental setup. A seed laser is used to modulate the energy of the electron beam. The energy modulation is converted into density modulation through dispersion in a chicane, a drift, or in the dipoles of the spectrometer. The longitudinal phase space distribution is measured on an off-axis screen after the RF deflector and spectrometer.

MEASUREMENTS

Longitudinal phase space distribution measurements done at the Free-electron Laser in Hamburg (FLASH) are compared to particle tracking simulations for different compression settings of the chicane at the entrance to a 25-m long stretch of beamline with a beta-function which varies from 3 to 23 m and an average beam radius of

*kirsten.hacker@desy.de

ISBN 978-3-95450-134-2

135 µm (rms). The measurements were conducted with an RF deflector [7-9] which streaks out the longitudinal dimension of the electron bunch in the vertical direction. A dipole magnet horizontally deflects the electrons depending on their energies. The screen is rotated by 90 degrees, so that the vertical direction is the energy axis and the horizontal direction is the longitudinal axis.

In Fig. 2, we show a measurement of an uncompressed electron bunch with a region which has been seeded with a 60 fs (FWHM) pulse of 266 nm light. The chicane at the entrance to the drift was off. Due to CSR from in the first few centimeters of the spectrometer dipole, the average energy of the seeded region has been reduced relative to that of the surrounding particles.

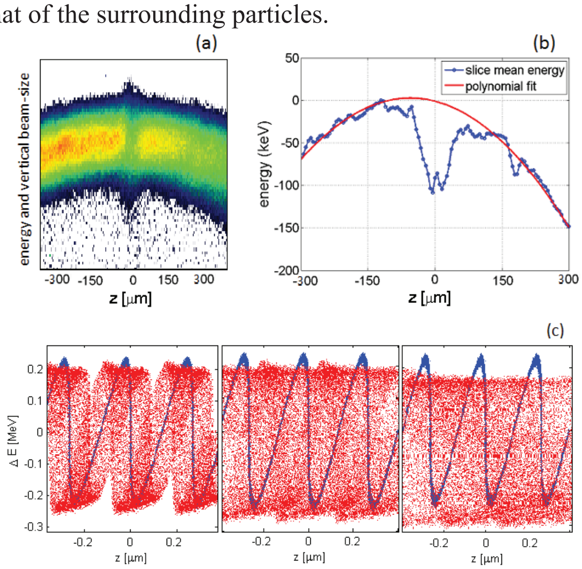

Figure 2: Measurement of seeded electron beam streaked out horizontally in time and vertically in energy (a) and measured average energy of longitudinal slices of the electron beam (b). In (b), the average energy of the seeded slices is lowered by 90 keV for a 56 A initial peak current and (700− 300) keV of energy modulation with a 266 nm seed duration of (100− 50) fs (FWHM). A CSRtrack simulation of a microbunched beam with a 7 keV slice energy spread prior to 400 keV (peak-to-peak) energy modulation is shown in (c) as it travels through the first 3 centimeters of the spectrometer. Prior to bunching, the peak current is 56 A and afterwards, it is 300 A. The blue, sinusoidal pattern is the particle distribution at the entrance to the bend. The red pattern shows that after 10 mm, the mean energy of the seeded portion has dropped by 15 keV, after 20 mm it has dropped by 25 keV, and above 30 mm, it has dropped by 50 keV.

In a measurement of the effect of the LSC wake on a beam seeded with 800 nm (Fig. 3), the longitudinal dispersion of the chicane directly after the modulator was scanned from zero up past η = 250 µm in order to measure the macroscopic effect of uncompressed (a), under-compressed (b), fully-compressed (c), and overcompressed (d)-(e) microbunches. Simulations of microbunches with an initial energy modulation of 1.3 MeV (rms) (f)-(j) are shown below each measurement (a)-(e). They correspond to conditions at the center of the seeded region of the measurements and were done in 3D with periodic boundary conditions [10]. Simulations of microbunches at a distance of σ from the center of the seeded region used an initial energy modulation of 0.65 MeV (rms) and they are plotted in (k)-(o).

The explanation of each macrobunch measurement (Fig. 3 top row) relies on controlled LSC impedances on the microbunch scale (bottom rows). For η = 20 µm, shown in column (a), the initial energy modulation profile was weakly affected by the LSC impedance because of the low peak current of the microbunches at the entrance to the drift space. In (b), where η = 50 µm, the micro-bunches are slightly undercompressed at the entrance to the drift space and the energy modulation for the majority of the particles is strongly reduced via the LSC impedance, despite the fact that a small fraction of extremely off-energy particles cause the rms energy spread to increase (g).

When the longitudinal dispersion is increased to 100 µm in (c), regions of increased and decreased energy spread are observed along the seeded portion, correlating with the peak current of the individual microbunches at the entrance to the drift. The central electrons of the seeded portion of (c) have an energy spread increase, as in (h), and the directly adjacent electrons have an energy spread reduction, as in (g). The behavior of the tails will be described later. As the central microbunches are folded over with 200 and 250 µm of dispersion, the wings of the seeded portion show an energy spread increase as they become fully (d) and overcompressed (e). The behavior of the tails is likely due to a distortion of the tails of the seed laser pulse, however, a peak current dependent transverse effect of CSR has not been fully ruled out.

Simulations of the RF deflector measurements were done using particle distributions transported with transfer matrices [11,12] in order to generate the color code which was used to interpret the slice energy spreads of the seeded regions of Fig. 3(a)-(e). The warmer colors correspond to decreased phase space density, a parameter which is inversely correlated with slice energy spread. The vertical dimensions of beam slices shown in the measurements roughly correspond to the slice energy spread of the beam at a given longitudinal position, however an absolute measurement of the slice energy spread from this data is affected by many factors, and for that reason, we employ a self-consistency analysis of relative changes dependent upon microbunch compression and peak current at the entrance to the drift.

The energy modulation is not purely in the vertical direction, due to a combination of longitudinal and vertical dispersion in the horizontally deflecting spectrometer. When temporal smearing of sharp structures is present, the color code has a systematic error in a direction which is opposite to that of the surrounding structures. This error is indicated by the dashed lines in Fig. 3.

In order to produce the pattern observed in Fig. 3(a)-(e), the slice energy spread of the central region must evolve

ISBN 978-3-95450-134-2

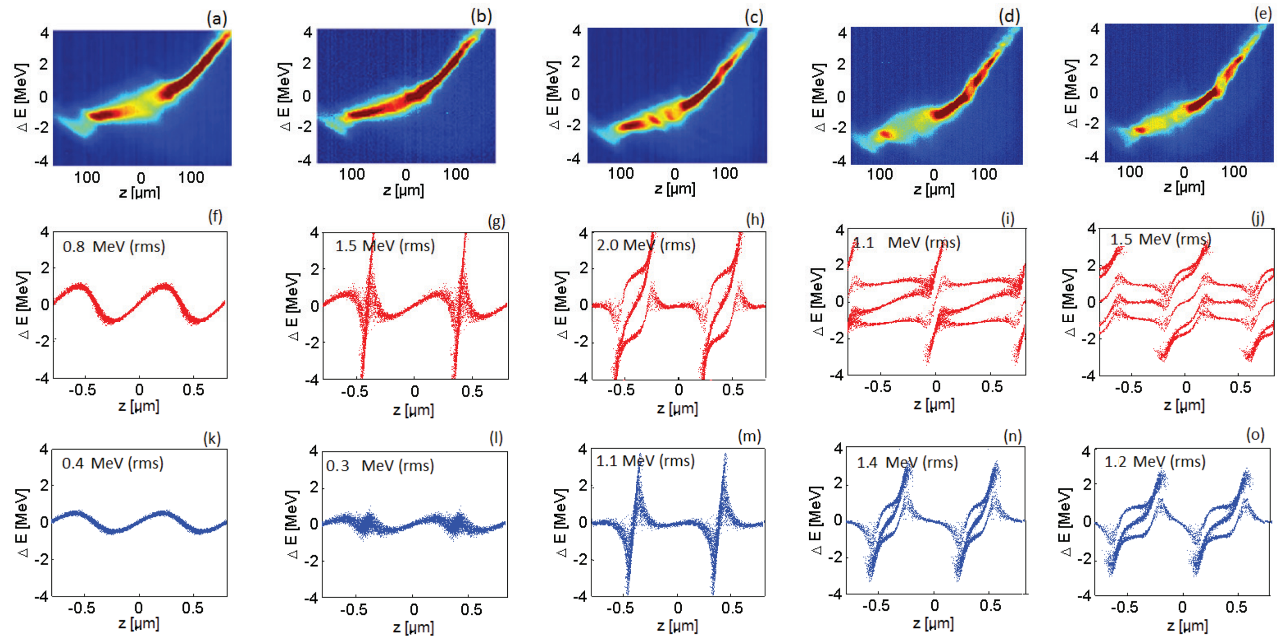

Figure 3: Measured longitudinal phase-space distribution of a seeded electron beam under the influence of LSC for uncompressed η = 20 μm (a), undercompressed, η = 50 μm (b), fully-compressed, η = 100 μm (c) and overcompressed η = 200-250 μm (d-e) microbunches. The color code corresponds to the number of electrons hitting the camera's pixels and is described in the text. Simulated longitudinal phase space distribution of microbunches after the 25 meter drift for the conditions described in (a)-(e) are below each measurement. Row (f)-(j) corresponds to the conditions at the center of the seeded region with an initial energy modulation of 1.3 MeV (rms) and an inital peak current of 300 A. Row (k)-(o) corresponds to the conditions at a distance of σ from the center of the seed with an inital energy modulation of 0.65 MeV (rms). The beam energy was 700 MeV with an average radius of 135 μm in the drift space. The head of the bunch is to the left and the peak current drops from 300 A to 250 A along the seeded portion. The emittance in the simulations is 1 mm mrad and the slice energy spread was 70 keV (rms).

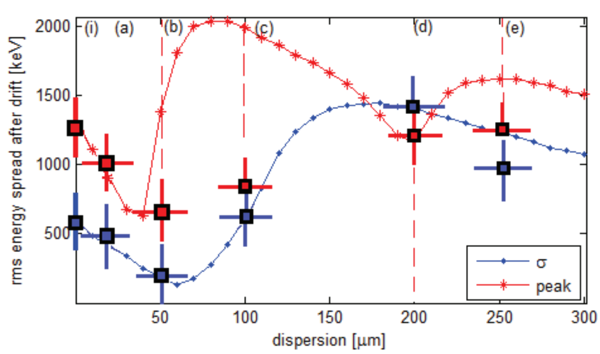

Figure 4: Simulation of the final rms energy spreads of seeded microbunches with initial energy modulations of 0.65 and 1.3 MeV (rms) corresponding to particles at σ and the peak of the seeded region in Fig. 3(a)-(e). Energy spread values derived from Fig. 3(a)-(e) are plotted as red and blue squares. The point labeled (i) corresponds to the expected energy modulation for measured laser and undulator parameters. Horizontal bars reflect the uncertainty in magnet hysteresis. The dashed lines extending upwards and downwards indicate measurement points which had a possible systematic error due to temporal smearing of sharp structures.

according to the upper curve of Fig. 4 while the surrounding regions at σ follow the lower curve. All data points at the peak of the seed and at a distance of σ from the peak follow the general pattern of the simulation and within the error bars of the laser and RF deflector measurements, the macroscopic changes in slice energy spread shown in Fig. 3(a)-(e) are in agreement with the simulated dynamics of the fine structures in Fig. 3(f)-(o).

The deviation of measurement point (e) from the model in Fig. 4 can be explained through laser heater concepts [13] which make use of the interaction of adjacent cycles which have unequal amplitudes. The explanation of the behavior of the tails for case (c) requires a non-Gaussian seed pulse with higher than expected energy modulation in the tails. Seeding experiments with drift spaces are required to further understand the implications for the preservation of fine structures as required for the HGHG microbunch compression in a drift or for LSC-EEHG concepts [14].

ISBN 978-3-95450-134-2

CONCLUSION

Simulations and measurements suggest that for beams with loose focusing and limited peak current, velocity bunching can produce a seeded microbunch with a smaller energy spread compared to the method of compression with a magnetic chicane. In support of this concept, RF deflector measurements showed the expected reduction of the slice energy spread of seeded microbunches after velocity bunching and the expected reduction of the average energy of seeded microbunches under the influence of CSR. The dependence of these reductions on longitudinal dispersion and peak current were in agreement with simulation. Concerns over the impact of microbunching instability coming from upstream of the seeding section did not manifest in the data but are not ruled out.

ACKNOWLEDGEMENTS

The authors would like to thank FLASH and the M-Division staff at DESY for their support. This work was funded by the Helmholtz Association Accelerator Research and Development program, the Federal Ministry of Education and Research of Germany under contract No. 05K10PE1, 05K10PE3, 05K13GU4, and 05K13PE3, and the German Research Foundation program graduate school 1355.

REFERENCES

[1] L.H. Yu, Phys. Rev. A 44,5178 (1991).
[2] E. Allaria *et al.*, Nature Photonics, 6, 699-704 (2012).
[3] Ya.S. Derbenev, J. Rossbach, E.L. Saldin, V.D. Shiltsev, DESY FEL Report No. TESLA-FEL 95-05, 1995.
[4] E.L. Saldin, E.A. Schneidmiller, M.V. Yurkov, DESY FEL Report No. TESLA-FEL 97-08, 1997.
[5] K. Hacker *et al.*, DESY FEL Report No. TELSA-FEL 2013-01.
[6] K. Hacker et al., submitted for publication Oct. 2014.
[7] O. Altenmueller, R. Larsen, G. Loew, Rev. Sci. Instrum. 35, 438 (1964).
[8] P. Emma, J. Frisch, P. Krejcik, SLAC Report No. LCLS-TN-00-12, (2000).
[9] C. Behrens, Ch. Gerth, and I. Zagorodnov, Proc. FEL Conf., WEPC45, Liverpool, United Kingdom, 2009.
[10] M. Dohlus, Ch. Henning, Periodic Poisson Solver for Particle Tracking, DESY 15-071.
[11] K.L. Brown, SLAC Report-75, (1982).
[12] K. Bongardt, CERN report No: LA-8668-MS, (1981).
[13] Z. Huang, M. Borland, P. Emma, J. Wu, C. Limborg, G. Stupakov, J. Welch, Phys. Rev. ST Accel. Beams 7, 074401 (2004).
[14] K. Hacker, Phys. Rev. ST Accel. Beams (2013).

ISBN 978-3-95450-134-2

DEVELOPMENT ACTIVITIES RELATED TO RF CABLES FOR GOOD PHASE STABILITY

Jinyul Hu#, Heung-Soo Lee, Heung-Sik Kang, PAL, POSTECH, Pohang, South Korea

Abstract

XFEL systems require extreme RF stabilities in amplitude and phase. RF cables as parts of the systems also require very high stabilities. RF cable measurements are performed to choose good cables. A simple measurement method and test results are presented. To enhance the phase stability of RF cables a prototype jacket surrounding a RF cable is constructed and the test result is described. Finally, a modification for phase measurement of RF cables is presented.

INTRODUCTION

XFEL(X-ray Free Electron Laser) systems can generate X-rays much brighter than those from current storage rings constructed around the world. In this strength, several XFEL construction projects are in progress. Among them are PAL-XFEL at PAL, South Korea, European XFEL at DESY, Germany[1], SwissFEL at PSI, Switzerland[2], and LCLS2 at SLAC, USA[3]. There are already two XFEL systems in operation, which are LCLS at SLAC[3] and SACLA in Japan[4]. But to achieve the X-rays planned, FEL machines must be very stable in several aspects including RF stabilities.

The required pulse-to-pulse RF stabilities for PAL-XFEL are 0.02% in rms amplitude and 0.03° in rms phase. Additionally, the drift of RF fields caused by the environmental temperature change must also be minimized to obtain stable X-rays. To consider the drift of RF illustratively, let us use Fig. 1.

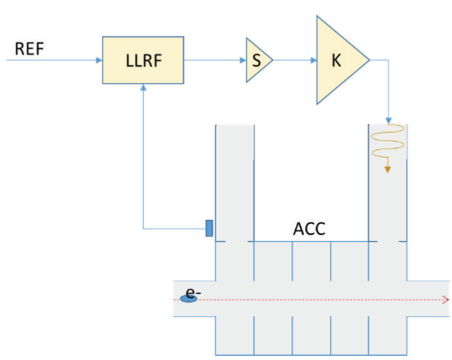

Figure 1 : RF station sketch.

Figure 1 shows a simplified RF station of a XFEL or a linac. The LLRF receives the reference CW(REF) through a coaxial cable, and it emits RF pulses into the SSA(S) through a coaxial cable. The SSA(S) amplifies the small RF pulses in mW level into kW level, which are sent through a coaxial cable to drive the klystron(K). The klystron(K) amplifies the RF pulses into about 80MW level and sends them to the accelerating column(ACC) through waveguides. Then the electron beams going through the column are accelerated synchronously with RF fields.

If all the components of Fig. 1 are not sensitive to the temperature variation and other causes, there will be no drift in RF fields, and there will be no needs to optimize the components and control by feedback. But in real situation, all the components are sensitive to temperature change more or less. So, each component should be optimized in temperature, or put in temperature controlled rack to minimize the drift. Though local feedback and global feedback corrects the drifts by temperature change, it should be preceded optimizing components to minimize the drifts by temperature change. The cables and waveguides applied must also be optimized with temperature change.

In this article, we present our activities to minimize the RF drifts within RF cables by temperature change for XFEL.

CABLE SELECTION ACTIVITES

Cable manufacturers do not always provide RF drift data by temperature variation. Some papers treating this topic[5] do not consider S-band used for PAL-XFEL. So, the drift measurement for our PAL-XFEL machine was carried out to select adequate RF cables.

Setup for RF Drift Measurement

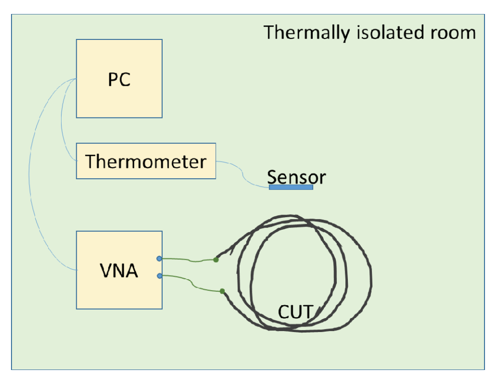

Figure 2 : RF drift measurement setup.

Figure 2 shows the simple setup invented for the drift measurement of cables. Within the thermally isolated room(usual room which is enclosed by ordinary wall), RF Vector Network Analyser(VNA) in connection with the cable under test(CUT), and the precision thermometer are used. PC for data acquisition is adopted. The above devices act as small heaters. With this setup, RF drift data along temperature are collected by the PC.

The drift data gathered include VNA drift also. The VNA drift must be removed from the data. To do the

#hjy@postech.ac.kr

ISBN 978-3-95450-134-2

removal, VNA drift data are gathered as shown in Fig. 3. The only difference is that two ports of VNA are connected directly.

The RF drift of the cable along temperature is finally obtained from the drift result of Fig. 2 eliminated by the drift result of Fig. 3. This method can be applied to measure amplitude and phase drift along temperature simultaneously for several RF cables.

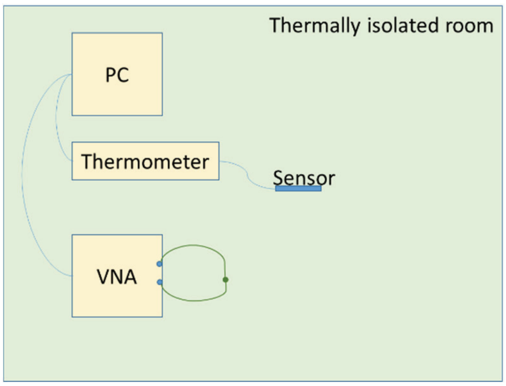

Figure 3 : The setup for VNA drift measurement.

Measurement Results

Several cables are measured to choose best one. Because the main frequency of PAL-XFEL is 2.856GHz, cables are measured mainly at this frequency. Though measurements are done for both amplitude and phase, phase change along temperature is mainly investigated because it is more critical for XFEL.

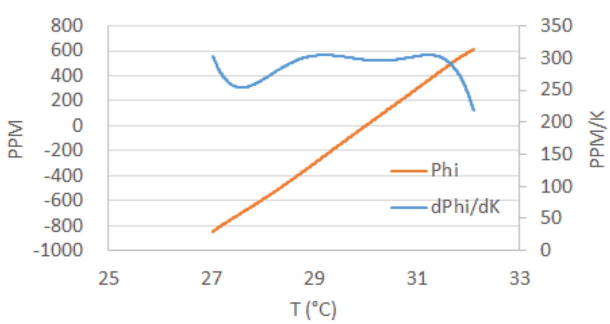

Figure 4 : Result of phase stability(drift) of RG-214. "Phi" means phase, and dPhi/dK means the rate of change of phase.

RG-214 is widely used because this cable is very flexible and can support high power. The measurement of RG-214 cable showed poor phase stability(drift) along temperature(Fig. 4). The slope of phase change along temperature is around 300PPM/K.

LMR cables are measured because this cable is often used instead of RG-214. LMR cables showed good phase stability. Among LMR cables tested, LMR400 showed best phase stability of 4~5PPM/K, LMR500 5~6PPM/K, and LMR600 about 9PPM/K.

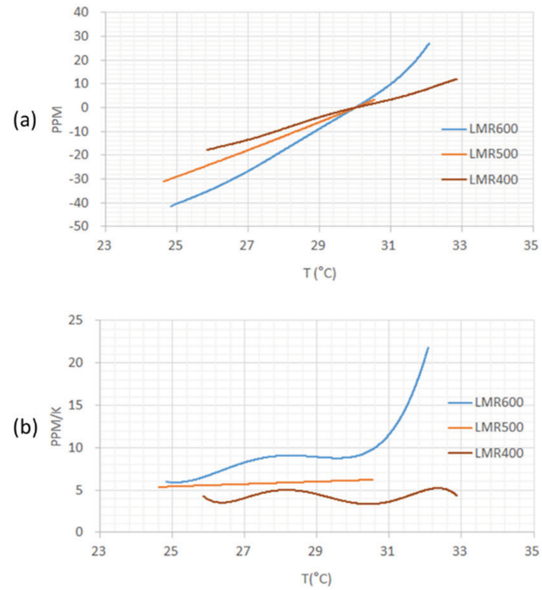

Figure 5 : Results of phase drifts of LMR400, 500, and 600. (a) means phase vs. temperature, and (b) means the slope of phase change.

Andrew cables are tested because these are widely used for current accelerators including PLS(Pohang Light Source) and LCLS. The measurement results showed that LDF2-50A(LDF2) has very good phase stability of <3PPM/K, but LDF4-50A(LDF4) did not have quite good phase stability compared with LDF2 and LMR 400 (Fig. 6). Figure 6 also shows an interesting point that the phase stabilities are different for two frequencies 1.3GHz and 2.856 GHz. That justifies our measurement for PAL-XFEL application.

RFS cables are widely used at DESY[5]. The measurement results showed very good phase stabilities of 2PPM for LCF38-50J(LCF38), and <3PPM for LCF12-50J(LCF12) for >25.5°C. Interestingly, LCF78-50J (LCF78) cable which is widely used for main drive line, showed good phase stability, but not excellency as the usage of main drive line for S-band.

From the test results, LMR400, RFS LCF38 and LCF12, and Andrew LDF2 cables are selected for PAL-XFEL application. Each of them is applied for different purposes; monitoring, feedback, and driving application.

ISBN 978-3-95450-134-2

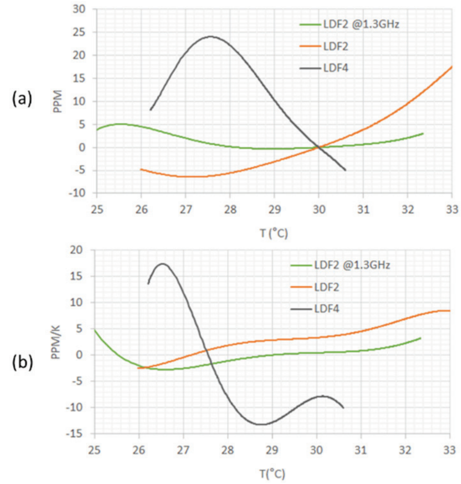

Figure 6 : Results of phase drifts of Andrew cables. (a) means phase vs. temperature, and (b) means the slope of phase change.

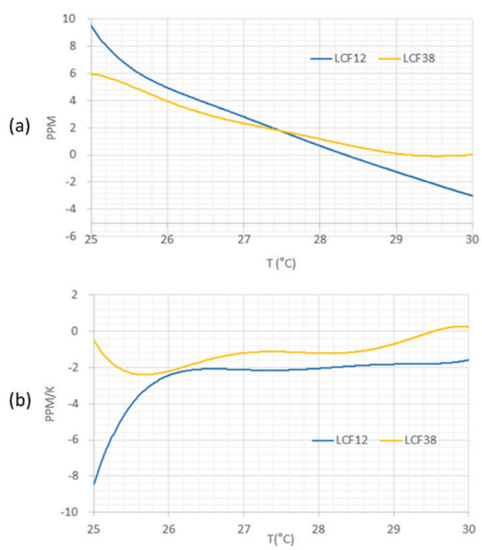

Figure 7: Results of phase drifts of Andrew cables. (a) means phase vs. temperature, and (b) means the slope of phase change.

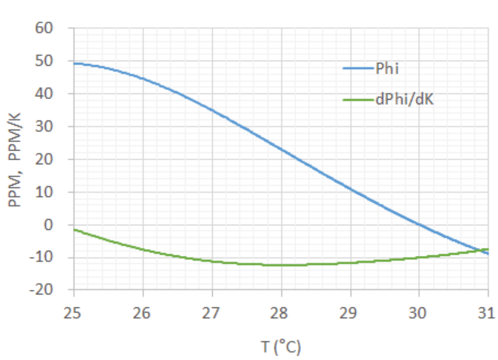

Figure 8 : Result of phase stability(drift) of LCF78-50J. "Phi" means phase, and dPhi/dK means the rate of change of phase.

JACKET FOR DRIFT REDUCTION

It is impossible to choose RF cable with no temperature drift. To reduce the RF drift of cable along temperature, a prototype jacket enclosing a RF cable is tested. The cross-section view(Fig. 4) is similar to the cable duct applied to SACLA[6].

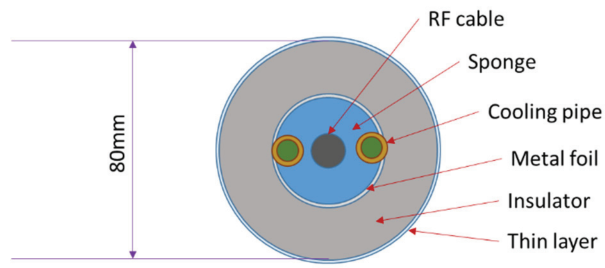

Figure 9 : The cross section of the jacket.

The temperature change at the surface of the RF cable within the jacket is measured at the setup of Fig. 5. By the chiller, the temperature of cooling water is controlled within ±0.05°C. The room temperature and the inner temperature of the jacket(DUT) are measured with the air conditioner turned on and off. The following result shows for the case of air conditioner turned on.

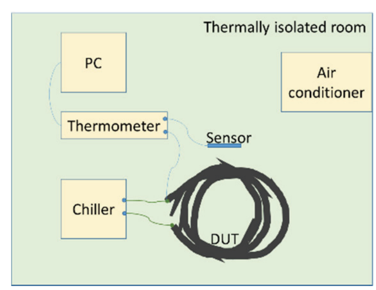

Figure 10 : The setup for Jacket measurement.

Figure 11 shows the result of measurement of the prototype jacket. The test range of environmental temperature is 27±2.5°C, which is very close to the temperature condition of PAL-XFEL gallery 26±2°C. For this environmental change, the inner temperature of the jacket is varied within ±0.25°C, which corresponds to about ±0.2°C for the condition of PAL-XFEL gallery.

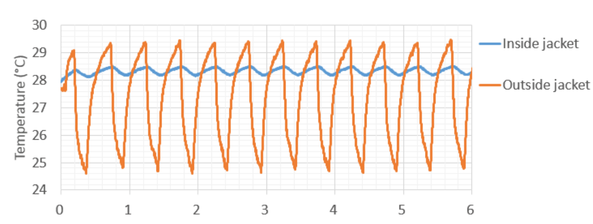

Figure 11 : The measured data for the prototype jacket.

To raise the performance of jacket, the thickness of the surrounding insulator will be increased from 80mm to

ISBN 978-3-95450-134-2

100mm in outer diameter. The upgraded jacket will be installed for PAL-XFEL this year.

MODIFICATION OF THE METHOD OF MEASUREMENT OF PHASE STABILITY

The measurement method of phase stability described in the previous section, have the weakness that the result of measurement includes the phase variation of the cable and the connectors assembled at both ends of the cable. To see the phase variation of the cable only, we propose a modified method slightly changed from the method. In the following the modified method is described.

We prepare two test cables of the same kind, but having different lengths. Next, we measure the phase variations of the two cables according to the method shown in Fig. 2. From the two results, we get the phase variation of the cable only, by eliminating the measured variation of the shorter cable from that of the longer cable.

CONCLUSION

XFEL machines require extremely stable RF fields. To achieve the requirements, the pulse-to-pulse stability and the drift stability of RF fields along temperature, must be optimized.

To optimize the drift stability of cables, a drift measurement method is invented. By the usage of the method, the cables having good phase stabilities are selected for PAL-XFEL.

To enhance the drift stabilities of cables, a prototype jacket is made and tested. The jacket showed the optimistic result. The improved jackets will be installed for PAL-XFEL this year.

The modified method of the RF drift measurement of cables along temperature is described to increase the measurement accuracy.

ACKNOWLEDGMENT

The authors deeply thank to Dr. Hiroshi Matsumoto, and Dr. Chang-Ki Min for their advices and valuable information.

REFERENCES

[1] http://www.xfel.eu
[2] http://www.psi.ch/swissfel
[3] https://portal.slac.stanford.edu/sites/lcls_public/lcls_ii
[4] http://xfel.riken.jp/eng
[5] K. Czuba, D. Sikora “Temperature Stability of Coaxial Cables”, ACTA PHYSICA POLONICA A, Vol. 119 No. 4(2001).
[6] N. Hosoda et al., “Construction of a Timing and Low-Level RF System for XFEL/SPRING-8”, TUPE024, Proceedings of IPAC’10, Kyoto, Japan(2010).

ISBN 978-3-95450-134-2

PRODUCTION STATUS OF ACCELERATOR COMPONENTS

N. Shigeoka#, M. Kimura, S. Miura, K. Okihira
Mitsubishi Heavy Industries, Ltd., Mihara, Hiroshima, Japan

Abstract

Mitsubishi Heavy Industries, LTD. (MHI) has been delivered various kinds of accelerator components to multiple FEL facilities. Recently we completed production of S-band accelerating structures for PAL-XFEL. Currently we are manufacturing C-band waveguide network for SwissFEL. Production status and results of above-mentioned products are reported in this paper.

INTRODUCTION

MHI has started manufacturing of accelerator components such as accelerating structures in 1960s. For example, in a field of normal conducting accelerator, in recent years, MHI had handled mass production of C-band choke-mode accelerating structures and SLED for Riken SACLA, production of DTL, SDTL (Separated DTL), ACS (Annular Coupled Structure) for JAEA/KEK J-PARC [1]. In latest years, MHI manufactured over 120 S-band accelerating structures for PAL-XFEL project [2-4] and shipment has completed in March 2015. In addition, MHI has accepted order of C-band waveguide network prototype (CWNP) for SwissFEL project [5] in June 2014 and has been already delivered to PSI in December 2014 [6]. MHI also has been accepted order of 26 C-band waveguide network series (CWNS) and the production of them is in progress now.

S-BAND ACCELERATING STRUCTURES FOR PAL-XFEL

Mass-production of the S-band 3 m long accelerating structure [7-8] started in June 2012 and finished at March 2015. Totally 120 structures has been delivered to PAL. Appearance of the structure is shown in Fig. 1 and main parameters are shown in Table 1.

Results of LLRF measurement after tuning are shown in Fig. 2. It shows excellent performance of production.

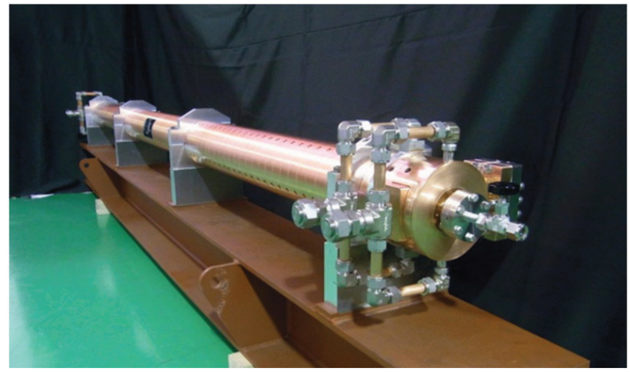

Figure 1: Appearance of the S-band accelerating structure for PAL-XFEL.

Table 1: Main Parameters of the S-band Accelerating Structure for PAL-XFEL

Item	Value
Operating frequency	2856 MHz
Accelerating type	C. G.
Phase shift per cavity	$2\pi/3$
Unloaded Q	13,000
Attenuation constant	0.56
Input / Output VSWR	< 1.05
Phase error	< +/- 2.5 degree
Number of cells	82 + 2 coupler cells
Filling time	0.84 μs
Length	3 m
Coupler type	Quasi-symmetrical

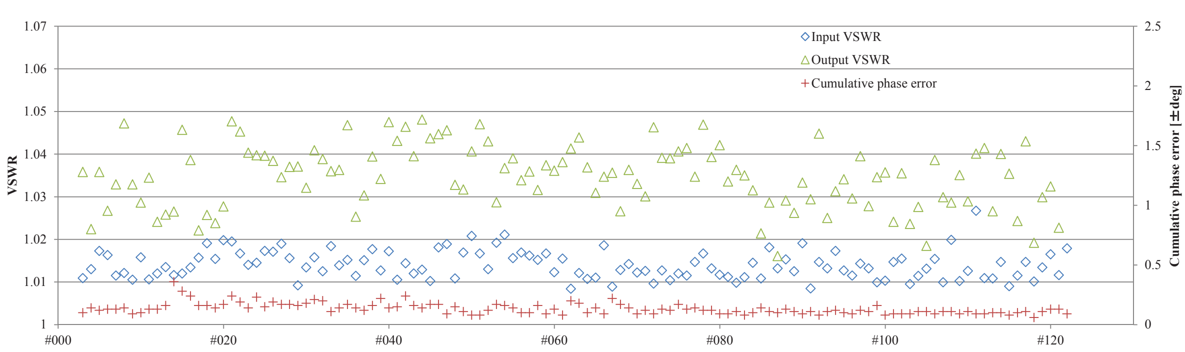

Figure 2: Input / Output VSWR and cumulative phase error of 120 S-band structure for PAL-XFEL after tuning.

#nobuyuki_shigeoka@mhi.co.jp

ISBN 978-3-95450-134-2

C-BAND WAVEGUIDE NETWORK FOR SwissFEL

The prototype waveguide (CWNP) has already installed by PSI in the test facility and high power test by PSI is planned. Additional 26 units (494 waveguides) will be delivered as a plan of series production (CWNS). 4 units of the CWNS have been already delivered to PSI in August 2015. Factory acceptance test results of the CWNP and first 4 units of the CWNS are shown below.

Overview of the waveguide network for LINAC 1 of SwissFEL is shown in Fig. 3. One waveguide network provides RF power from one klystron to four accelerating structure. Waveguide network for LINAC 1, 2 and 3 slightly differ from each other but basic configuration is common. Six directional couplers for RF monitor, three RF splitters and nine vacuum ports are included in one waveguide network. Specification of the waveguide network is shown in Table 2.

Table 2: Specification of the C-band Waveguide Network for SwissFEL

Item	Value
Bandwidth	5712 MHz +/- 20 MHz
Peak power	320 MW*
Average power	15 kW
Pulse repetition rate	1 – 100 Hz
VSWR	< 1.04
Operating pressure	< 1×10^{-6} Pa
Waveguide size	WR187
Flange type	C-band A-DESY
Coupling of the RF monitor	-60 +/- 2 dB (5712 +/- 3 MHz)
Directivity of the RF monitor	>25 dB (5712 +/- 20 MHz)
RF symmetry error of splitters	< 0.1 dB in amplitude < 3 degree in phase
RF leak to vacuum manifold	< -85 dB
Residual gas analysis (RGA)	The RGA spectrum must show no evidence of hydro carbons and the peaks > 40 Amu (excluding peak 44) should be < 0.1%
Outgassing rate	< 1.0×10^{-7} Pa・$m^3/(s\cdot m^2)$

*Maximum power in between the pulse compressor and the 1st splitter

Main part of the waveguide body is made from extruded ASTM class 2 oxygen-free copper (OFC). Waveguide flange is C-band A-DESY type. FUAR48 flanges are used for monitor ports. CF40 (ICF70) flanges are used for vacuum ports. Material of the each flange is SUS316L. RF flanges are copper plated.

Waveguide bodies, flanges and cooling pipes are assembled using vacuum brazing method.

In order to precisely fit to input flange of each accelerator structure, dimension accuracy between four interface flanges are +/- 0.2 mm.

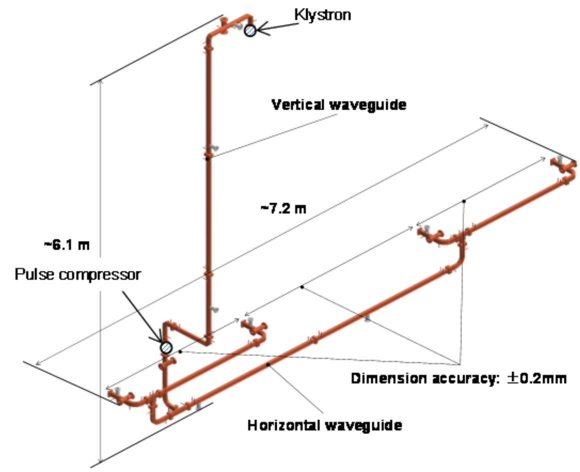

Figure 3: Overview of the C-band waveguide network for SwissFEL LINAC 1.

Directional Coupler for RF Monitor

Schematic of the directional coupler is shown in Fig. 4. Type of the monitor is a side-wall bidirectional coupler. Result of the LLRF measurement of coupling and directivity is shown in Fig. 5. All manufactured RF monitor complied with LLRF specification described in Table 2. Definitions of the values are as follows.

Coupling: S31 (-60 +/- 2 dB)
Directivity: S31 – S32 (> 25 dB)

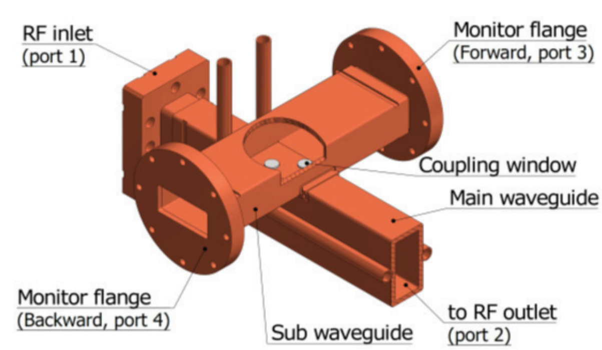

Figure 4: Schematic of the RF monitor.

ISBN 978-3-95450-134-2

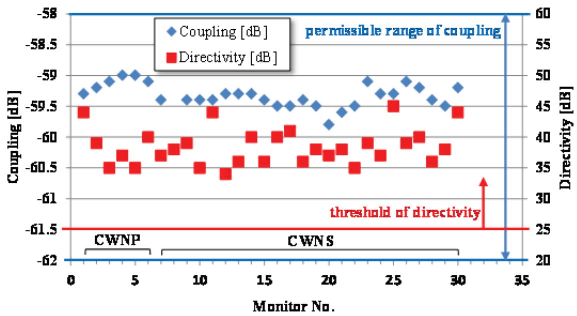

Figure 5: Coupling and directivity of RF monitors.

RF Splitter

RF Splitter divides RF power from inlet flange into 2 outlet flanges. Schematic of the H splitter is shown in Fig. 6. Two H splitters and one E splitter are included in one waveguide network unit.

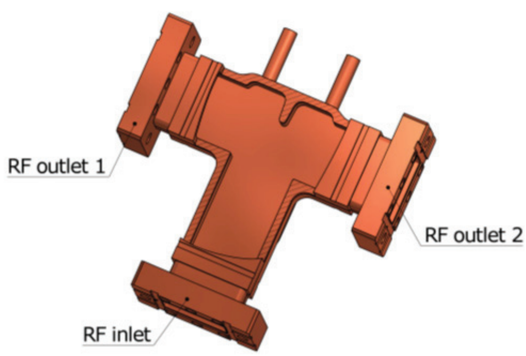

Figure 6: Schematic of the H splitter.

Result of the LLRF measurement of symmetry error is shown in Fig. 7. All splitters complied with LLRF specification described in Table 2.

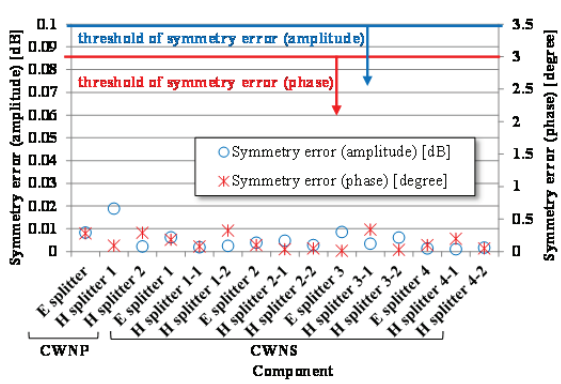

Figure 7: Symmetry error of splitters.

Residual Gas Analysis (RGA) and Outgassing Rate Measurement

RGA and outgassing rate measurement were carried out for the waveguide network. Regarding the CWNP, whole waveguide unit was divided into one vertical part and two horizontal parts then measured. Regarding the CWNS, one waveguide piece from each unit is picked up and assembled into one waveguide unit using 4 waveguide pieces then measured. Result of the RGA is shown in Fig. 8. There is no evidence of the hydrocarbons in mass spectrum.

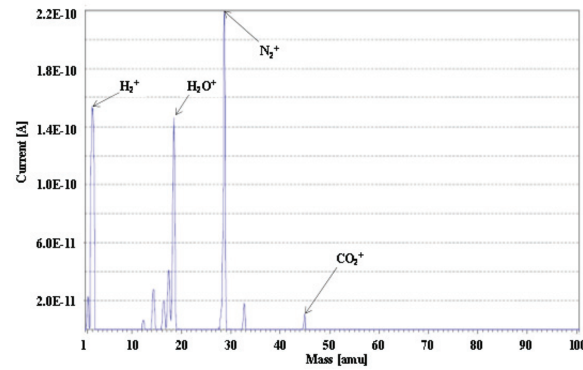

Figure 8: Residual gas analysis of the waveguide unit of CWNS (1st shipment).

Result of the outgassing rate is shown in Fig. 9. All results of the outgassing rate complied with the specification described in Table 2.

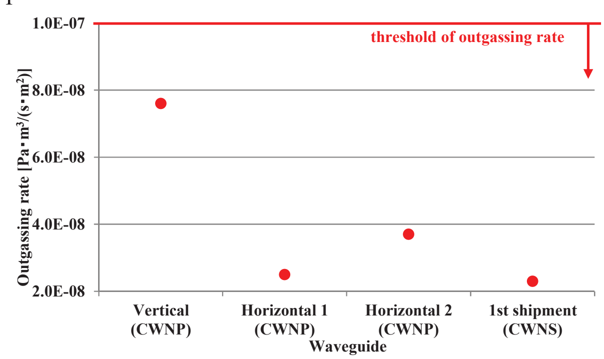

Figure 9: Outgassing rate of the CWNP and the CWNS.

CONCLUSION

Production status and result of two types of accelerator components are described in this paper. MHI keep contributing to the advance of the accelerator technology.

REFERENCES

[1] MHI Graph website: https://www.mhi-global.com/discover/graph/feature/no169.html
[2] J.-H. Han et al., "Status of the PAL-XFEL project," in Proceedings of 3rd Int. Particle Accelerator Conf., New Orleans, 2012, p. 1735.
[3] H.-S. Kang et al., "Current status of PAL-XFEL project," in Proceedings of 4th Int. Particle Accelerator Conf., Shanghai, 2013, p. 2074.
[4] I. S. Ko and J.-H. Han, "Current status of PAL-XFEL project", in Proceedings of 27th Linear Accelerator Conf., Geneva, 2014, MOIOB03.
[5] F. Loehl et al., "Status of the SwissFEL C-band Linac", in Proceedings of 36th International Free Electron Conf., Basel, 2014, 322.

ISBN 978-3-95450-134-2

[6] N. Shigeoka et al., “MHI’s Production Activities of Accelerator Components”, in Proceedings of 6th Int. Particle Accelerator Conf., Richmond, 2015, p. 2873.
[7] H.-S. Lee et al., “PAL-XFEL Accelerating Structures”, in Proceedings of 4th Int. Particle Accelerator Conf., Shanghai, 2013, p. 2806.
[8] S. Miura et al., “Development of S-band accelerating structure”, in Proceedings of 34th Int. Free-Electron Laser Conf., Nara, 2012, p. 153.

ISBN 978-3-95450-134-2

COMMISSIONING AND FIRST PERFORMANCE OF THE LINAC-BASED INJECTOR APPLIED IN THE HUST THz-FEL

T.N. Hu, Q.S. Chen,Y.Q. Xiong, B. Qin, P. Tan, L. Cao, J. Li, W. Chen
State Key Laboratory of Advanced Electromagnetic Engineering and Technology, HUST, Wuhan 430074, China
Y.J. Pei*, Z.X.Tang, Z.Y.Zhao, J.Liu
National Synchrotron Radiation Laboratory, USTC, Hefei 230029, China

Abstract

The construction of a compact high-power THz source based on the free electron laser(FEL), which is constructed in HUST, is undergoing. Before the end of 2014, we have installed most of the key components, completed conditioning of the LINAC-based FEL injector, and performed first beam experiment. During last 5 months, we have established a high efficient beam diagnostic system with a reliable online monitor platform and precise data processing methods. At present, longitudinal properties such as the micro-pulse width and the energy spread are kept to a reasonable level, while transverse emittance compensation by adjusting focusing parameters is still undergoing. In this paper, we will give the summary on the commissioning schedule, detailed commissioning plan, the development of the commissioning and first performance of the LINAC, etc.

INTRODUCTION

Brief Descriptions of the FEL-based LINAC

The THz-FEL facility is mainly composed of a novel EC-ITC RF gun (which consists of a DC electron gun and two independent standing-wave cavities), constant gradient travelling wave structure with a collinear absorbing load and an input coupler which makes the electric field be symmetry, and its focusing coil, beam diagnostics system, microwave power system, vacuum system, control system and so on [1]. The layout and main parameters of the LINAC are given by Fig. 1 and Table 1 respectively, and beam diagnostic equipments are sketched by Fig. 1 either.

By applying the EC-ITC RF gun as the pre-LINAC, and adopting the elements already exist these methods, the length of the whole beam line can be compressed into 2 m, which contributed to a more compact layout for the whole facility.

Beam Diagnostic System

For the sake of compactness, the beam diagnostic system should use the elements which already exist in the facility as far as possible [2]. As Fig. 1 shows, the online beam testing system contains two Toroids, one Flag with a fluorescent screen and a OTR screen, energy analysis system, two fluorescent targets, and three CCD(Charge-Coupled Device) cameras.

Table 1: Main Specifications

Parameter	Unit	Value
Energy	MeV	4-15
Current	A	0.571(Macro pulse)
Width	us ps	1-5(Macro pulse) 1-10(Micro pulse)
Energy spread	%	0.2-0.5
Nor. emittance	mm mrad	<15
RF frequency	MHz	2856
Input power	MW	20

In order to measure the beam length, we will adopt a method which is by means of a relation of electron energy and its phase in the Linac. When beam located at the "0" phase, the energy spread will change less. If the beam phase located in φ which is different from the "0", their energy spread will change and larger than initial energy spread. This change depend on beam length, so measuring these energy, energy spread and their phase, we can get pulse width [3].

Obviously, we will use quadrupole scanning technique perform normalized emittance measurement [4]. Since the beam matrix at Target2 can be written as Σ_1. And the beam matrix at the entrance of the Quadrupole chosen to be scanned is Σ_0. So that the two beam matrixes can be connected by the transmission matrix of the Quadrupole M, $\Sigma_1 = M\Sigma_0 M'$, If we change the current of the Quadrupole three times, three different beam spot sizes $\sigma_{11}(1)$, $\sigma_{11}(2)$, $\sigma_{11}(3)$ will be obtained on Target2 by CCD3, then we can obtain the following equation set,

$$\begin{pmatrix} \sigma_{11}(1) \\ \sigma_{11}(2) \\ \sigma_{11}(3) \end{pmatrix} = \begin{pmatrix} m^2_{11}(1) & 2m_{11}(1)m_{12}(1) & m^2_{12}(1) \\ m^2_{11}(2) & 2m_{11}(2)m_{12}(2) & m^2_{12}(2) \\ m^2_{11}(3) & 2m_{11}(3)m_{12}(3) & m^2_{12}(3) \end{pmatrix} \begin{pmatrix} \sigma_{11}(0) \\ \sigma_{12}(0) \\ \sigma_{22}(0) \end{pmatrix} \quad (1)$$

By solving above equation set, parameters used to calculate the normalized emittance can be determined, and the following formula should be used,

Authors to whom correspondence should be addressed.
Electronic addresses: yjpei@ustc.edu.cn

ISBN 978-3-95450-134-2

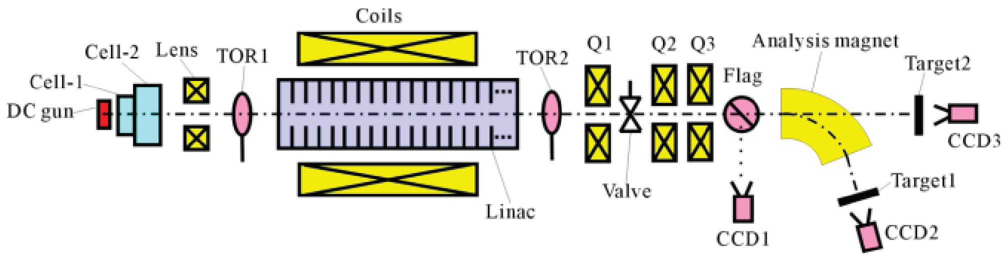

Figure 1: Layout of the HUST THz-FEL LINAC.

$$\varepsilon_x = \beta\gamma\sqrt{\sigma_{11}\sigma_{22} - \sigma^2_{12}} \tag{2}$$

where, β and γ are the relative velocity and relativity factor, respectively. Observed from Fig. 1, we apply an analysis magnet for the energy spread measurement. The whole energy analysis system can be expressed by Equation 3,

$$\begin{pmatrix} x_1 \\ x_1' \\ (\frac{\Delta p}{p})_1 \end{pmatrix} = \begin{pmatrix} m_{11} & m_{12} & m_{13} \\ m_{21} & m_{22} & m_{23} \\ m_{31} & m_{32} & m_{33} \end{pmatrix} \begin{pmatrix} x_0 \\ x_0' \\ (\frac{\Delta p}{p})_0 \end{pmatrix} \tag{3}$$

Under designing, by choosing suitable parameters, m_{12} is set to 0, and m_{11} should be designed close to 0 as far as possible. Then, by observe the beam spot on Flag and Target1, beam radii at these two position can be obtained, so that the energy spread can be calculated by Equation 4.

$$\frac{\Delta p}{p} = \sqrt{\sigma_1^2 - (m_{11} \cdot \sigma_0)^2} \;/\; m_{13} \tag{4}$$

BEAM COMMISSIONING

Commissioning of the Electron Gun

Before performing the beam commissioning for the LINAC, the vacuum of the whole system must have a stable level which is better than 5×10^{-6}Pa, and the conditioning work for the pre-injector and the travelling-wave accelerator must be completed. In addition, we must activate the DC electron gun. Table 2 shows the technical parameters of the gun.

Apparently, the calculate value of the perveance 2.10uP by using experiment results, is very close to the designed value 2.17uP.

The cathode activation can be conducted by following four steps,

- ***Cathode Disintegration:*** Under the vacuum condition of 1×10^{-5}Pa~1×10^{-4}Pa, add the filament current from 0 to 6.5A gradually.
- ***Thermal activation and low-voltage activation:*** make the filament current a little higher than the rated value (6.3A) and stay for a while; under the rated filament current, add the anode voltage from 0 to 10kV gradually.
- ***HV conditioning:*** reduce the filament current to 0, and add the anode voltage to 20kV gradually.
- ***Electron activation:*** under the rated filament current, add the anode voltage gradually, then test the emitting current and calculate the perveance, shown in Fig. 2. The electron gun activation is completed if the perveance matches with the designed value.

Table 2: Technical Parameters

Parameter	Rated value	Maximum value
Anode voltage	15kV	20kV
Emitting current	4.0A	
Perveance	2.17uP	
Waist radius	1.0mm	
Beam range	8.5mm	
Pulse width	4us	
Duty ratio	0.04%	
Filament voltage	6.0V	6.3V
Filament current	6.3A	6.5A

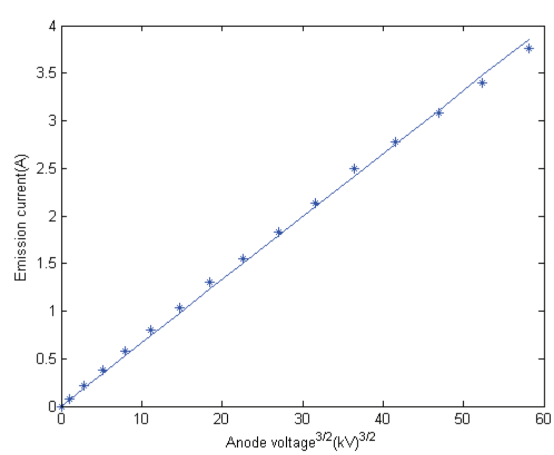

Figure 2: Measurement results for the perveance.

ISBN 978-3-95450-134-2

Commissioning of the LINAC

For the sake of compactness and cost-effectiveness, we only reserved sufficient space for key components and inevitable measurement tools on the beamline during the designing process, so that a more compact layout were obtained as described in Fig. 1. However, unavoidable difficulties and complications were induced in the beam commissioning process for the HUST THz-FEL LINAC. In order to fix these problems and pursue high-effectively commissioning methods, a simplified technology road-map is summarized based on many experiments and dynamic simulations, which is shown in Fig. 3.

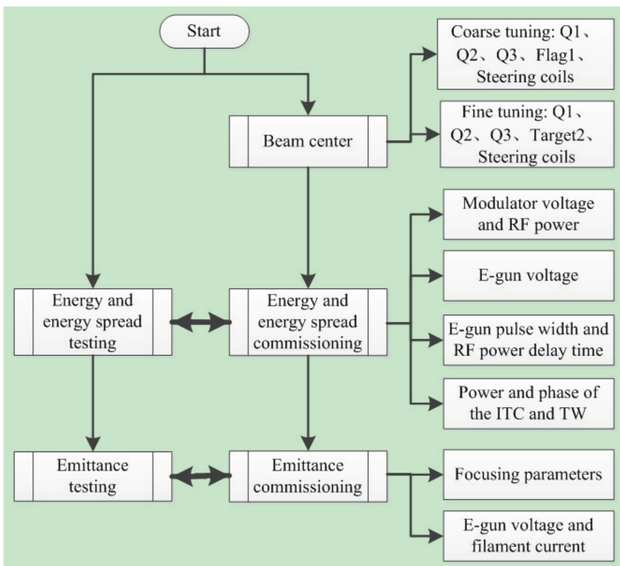

Figure 3: Technology Roadmap for beam commissioning.

FIRST BEAM EXPERIMENT

As mentioned above, we have established a high efficient beam commissioning scheme and beam diagnostic system. At present, several beam parameters such as energy spread, beam current, beam energy, etc. are tuned to a reasonable level, corresponding measurement results are listed in Table 3. Additionally, beam spot information of the energy analysis system is acquired by online monitor system, which is given in Fig. 4.

Table 3: Measurement Results

Parameter	Unit	Value
Energy	MeV	13
Current	A	0.744(Macro pulse)
Width	us	4(Macro pulse)
Energy spread	%	0.5
RF frequency	MHz	2856
Input power	MW	20

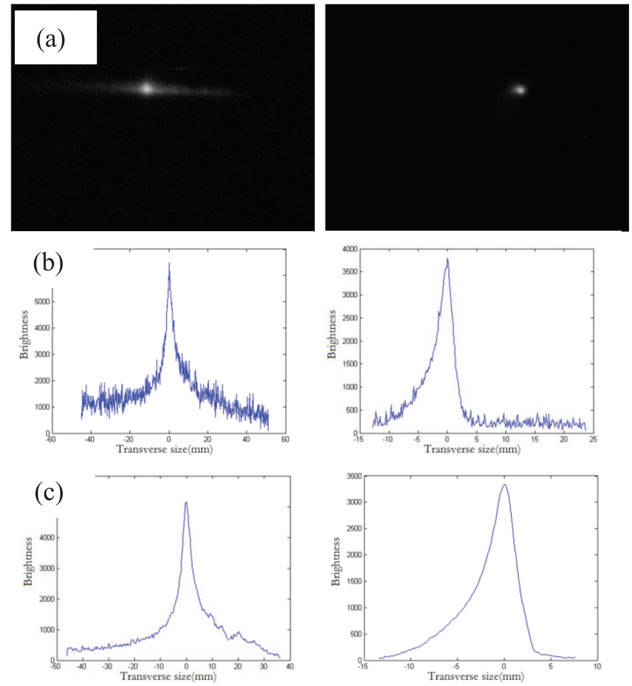

Figure 4: Beam spot information of the energy analysis system. (a) Beam spots on Target1 and Target2, (b) Brightness distributions of the Beam spots on Target1 and Target2, (c) Brightness distributions after picture processing.

CONCLUSIONS

Though some key parameters of the extracted beam from the HUST THz-FEL LINAC are tuned into a acceptable range by adopting a high efficient commissioning method, transverse emittance compensation by adjusting focusing parameters is still undergoing. And the stability of the whole system must be considered in the future commissioning .

ACKNOWLEDGMENT

The authors would like to thank Professor Kuanjun Fan and Lei Shang for consultations.

REFERENCES

[1] Y.J. Pei, et al., "Design of 14MeV Linac for THz source based FEL", Proceedings of IPAC2013, Shanghai, China. 2181-2183 (2013).
[2] T.N. Hu, et al., "Beam diagnostic of the Linac for the compact high-performance THz-FEL", Proceedings of the IPAC2015, VA, USA, 987-989 (2015).
[3] Y.J. Pei, et al., "R & D on a compact EC-ITC RF gun for FEL", Proceedings of IPAC'10, Kyoto, Japan. 1737-1739 (2010).
[4] H. Wiedemann, Particle Accelerator Physics: Basic Principles and Linear Beam Dynamics (Springer-Verlag, New York, 1993).

ISBN 978-3-95450-134-2

STUDY ON BEAM MODULATION TECHNIQUE USING A MASKED CHICANE AT FAST (FERMILAB ACCELERATOR SCIENCE AND TECHNOLOGY) FACILITY*

Y. M. Shin, Department of Physics, Northern Illinois University, Dekalb, IL 60115, USA, and FNAL, Batavia, IL 60510, USA
A. Green, Department of Physics, Northern Illinois University, Dekalb, IL 60115, USA
D. R. Broemmelsiek, D. J Crawford, A. Lumpkin, FNAL, Batavia, IL 60510, USA

Abstract

Longitudinal density modulations on electron beams can improve machine performance of beam-driven accelerators and FELs with resonance beam-wave coupling. The sub-ps beam modulation has been studied with a masked chicane by the analytic model and simulations with the beam parameters of the Fermilab Accelerator Science and Technology (FAST) facility. With the chicane design parameters (bending angle of 18°, bending radius of 0.95 m and R_{56} ~ - 0.19 m) and a nominal beam of 3-ps bunch length, the analytic model showed that a slit-mask with slit period 900 µm and aperture width 300 µm generates about 100-µm modulation periodicity with 2.4% correlated energy spread. With the designed slit mask and a 3- ps bunch, particle-in-cell simulations (CST-PS), including nonlinear energy distributions, space charge force, and coherent synchrotron radiation (CSR) effect, also result in ~ 100 µm of longitudinal modulation. The beam modulation has been extensively examined with three different beam conditions, 2.25 ps (0.25 nC), 3.25 ps (1 nC), and 4.75 ps (3.2 nC), by extended 3D tracking simulations (Elegant). The modulated bunch generation is tested by a slit-mask installed at the chicane of the ASTA 20-MeV injector beamline and the preliminary test result is presented in the paper.

INTRODUCTION

The masked chicane technique [1–3] has been investigated with the 50 MeV linac in the Fermilab Accelerator Science and Technology (FAST) facility, which is currently being constructed and commissioned in Fermilab [4]. A tungsten slit-mask is currently installed in a magnetic chicane, consisting of four bending dipole magnets, downstream of the 50 MeV photoinjector and the bunch performance and sub-ps micro-bunch generation capability are examined with analytic calculations and PIC simulations.

For the theoretical evaluation on bunching performance, the linear bunching theory is derived to check bunch-to-bunch distance and microbunch length with FAST nominal beam parameters (RMS bunch length $\sigma_{z,i}$ is 3 ps and energy ratio τ is around 0.1) are analyzed by the linear bunching theory, which was tested by beamline simulations using Elegant code and CST-PS. Space charge forces and CSRs are included in the simulations with nonlinear charge distribution over macro-particles. For Elegant simulations, bunch charge distribution and the beam spectra are mainly investigated with three different bunch charges, 0.25 nC, 1 nC, and 3.2 nC, under two RF-chirp conditions of minimum and maximum energy spreads. The corresponding bunch length for the maximally chirped beam is 2.25, 3.25, and 4.75 ps and the correlated energy spread is 3.1, 4.5, and 6.2 % respectively for bunch charge of 0.25 nC, 1 nC, and 3.2 nC.

*Work supported by the DOE contract No.DEAC02-07CH11359 to the Fermi Research Alliance LLC.

ANALYTIC DESIGN

The magnetic chicane is designed with four dipoles and a slit mask with slit spacing, *W*, and aperture width, *a*, is inserted in the middle of the bunch compressor (dispersion region). A positive linear energy-phase correlation is imposed by accelerating the beam off the crest of the RF wave in the linear accelerator before the beam is injected into the masked chicane. In this way, the chicane disperses and re-aligns the particles with respect to their energies in phase space. The input beam is then compressed and the phase space ellipse is effectively rotated toward the vertical. In the middle of the chicane, the beam is partially blocked by the transmission mask and holes are introduced in the energy-phase ellipse. The beam is deliberately over-bunched in the second half of the chicane and the beam ellipse is slightly rotated past the vertical. Accompanied with a steeper phase-space slope, the linear energy-phase correlation is preserved by over-bunching. The projection of the beam ellipse on the time axis therefore generates density modulations at a period smaller than the grid spacing.

The microscopic structure of a bunch can be controlled with a masked chicane under compression by adjusting the grid period and/or by varying the chicane magnetic field. In principle, if a grid period (or slit-spacing) is smaller than a hundred microns, a modulation wavelength of the bunched beam is possibly cut down to a few tens of microns. The beamline for the mask is originally designed with the four dipoles having bending angle of 18°, bending radius R = 0.95 m, and dipole separation D = 0.68 m. The 125 µm thick tungsten mask with a slit-array is designed with period of W = 900 µm and aperture width of a = 300 µm (~ 33 % transparency).

ISBN 978-3-95450-134-2

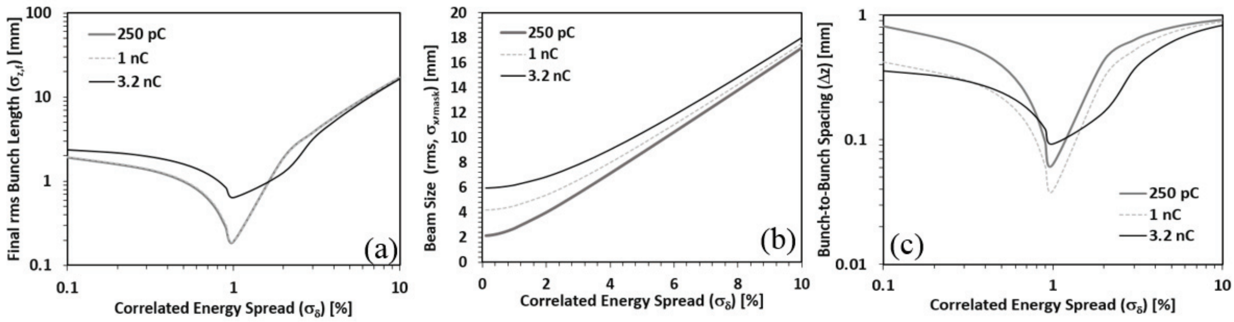

Figure 1: (a) Final bunch length (after BC1), (b) transverse beam size at X115, and (c) bunch-to-bunch distance (Δz) versus correlated energy spread (σ_δ) graphs with bunch charges of 250 pC, 1 nC, and 3.2 nC, calculated by the linear bunch compression theory.

For the 50 MeV chicane, R_{56} (longitudinal dispersion) = - 0.192 m and η_x (maximum transverse dispersion) = - 0.34 m. The bunch-to-bunch spacing (or modulation wavelength), Δz, is defined by the final bunch length divided by the number of micro-bunches in a compressed beam [2]. The final bunch length is

$$\sigma_{z,f} = \sqrt{(1+h_1R_{56})^2\sigma_{z,i}^2 + \tau^2 R_{56}^2 \sigma_{\delta i}^2}, \quad (1)$$

where h_1 is the first order chirp, $\sigma_{z,i}$ is the initial bunch length, $\sigma_{\delta i}$ is the initial un-correlated RMS energy spread, and τ is the energy ratio. The energy ratio is normally ~ 0.1 at FAST photoinjector beamline. Concerning correlated energy spread σ_δ, we have

$$\sigma_\delta^2 = \tau^2\sigma_{\delta i}^2 + h_1^2.\sigma_{z,i}^2. \quad (2)$$

The correlated energy spread, σ_δ, and transverse emittance, ε_x, normally determine a transverse beam size at the mask by

$$\sigma_{x,mask} = \sqrt{\varepsilon_x\beta_{x,mask} + (\eta_{x,mask}\sigma_\delta)^2}, \quad (3)$$

where $\beta_{x,mask}$ is the beta function and $\eta_{x,mask}$ is the transverse dispersion at the mask [5,6]. After passing through a slit-masked chicane, the number of micro-bunches of the compressed beam is determined by the transverse beam size at the mask, $\sigma_{x,mask}$, and the slit period, W, by

$$N_b = \frac{\sigma_{x,mask}}{W}. \quad (4)$$

The correlated energy spread,σ_δ, and transverse emittance, ε_x, normally determine a transverse beam size at the mask by

$$\sigma_{x,mask} = \sqrt{\varepsilon_x\beta_{x,mask} + (\eta_{x,mask}\sigma_\delta)^2}. \quad (5)$$

The bunch-to-bunch spacing of modulated beam, Δz, can thus be derived to be

$$\Delta z = W\frac{\sqrt{(1+h_1R_{56})^2\sigma_{z,i}^2 + \tau^2R_{56}^2\sigma_{\delta i}^2}}{\eta_{x,mask}h_1.\sigma_{z,i}} = W\frac{\sqrt{(\sigma_{z,i}+R_{56}\sigma_\delta)^2 + \tau^2R_{56}^2\sigma_{\delta i}^2}}{\eta_{x,mask}\sigma_\delta}. \quad (6)$$

The bunch length of microbunches is defined by $\sigma_{z,m}$ = T·Δz, where T (= a/W) is the mask transparency (~ 33 % here), with the calculated bunch-to-bunch spacing, assuming the time pattern of the beam is similar to the mask pattern [6].

The bunch lengths, compression ratios, and bunch-to-bunch distances with respect to correlated energy spreads,σ_δ, are examined for the beam with FAST nominal parameters [4]. The beam is maximally compressed and the final rms bunch length tends to be minimal, when σ_δ reaches 0.468% corresponding to σ_δ = -$\sigma_{z,i}/R_{56}$ and h_1 = - $1/R_{56}$. Continuously increasing σ_δ renders the beam less compressed and would make the beam rather stretched instead of being compressed. An amount of beam energy-spread determined by a beam injection condition with respect to RF-phase thus dictates the bunch length via the magnetic chicane. As shown in Fig. 1(b), the compress ratio is apparently in inverse proportion as a final bunch length (rms). Therefore, the compression ratio becomes infinite when the beam is maximally compressed. Figure 1(c) shows bunch-to-bunch distance (bunch modulation length) with correlated energy spread, σ_δ. The analytic calculation points out that the distance becomes ~ 100 µm with correlated energy spread of ~ 2.4%. With a 33.3% mask transparency, it is predicted that the ~ 100 µm spaced bunch produces a microbunch length of ~ 33 µm, corresponding to 100 fs in time.

SIMULATION ANALYSIS

In order to verify the analytic model, the masked chicane is simulated by Elegant with macro-particle data imported. For Elegant simulations, macro-particles are imported from a space-charge tracking code, ASTRA [7], which is combined with an extended analysis program called "Shower [8]" to include particle transition effect through a mask material. In order to analyse characteristics of the bunched beam, bunch profiles (charge distributions) at x-/y-planes and time axis are monitored at the image station positions, X110, 118, 121, and

ISBN 978-3-95450-134-2

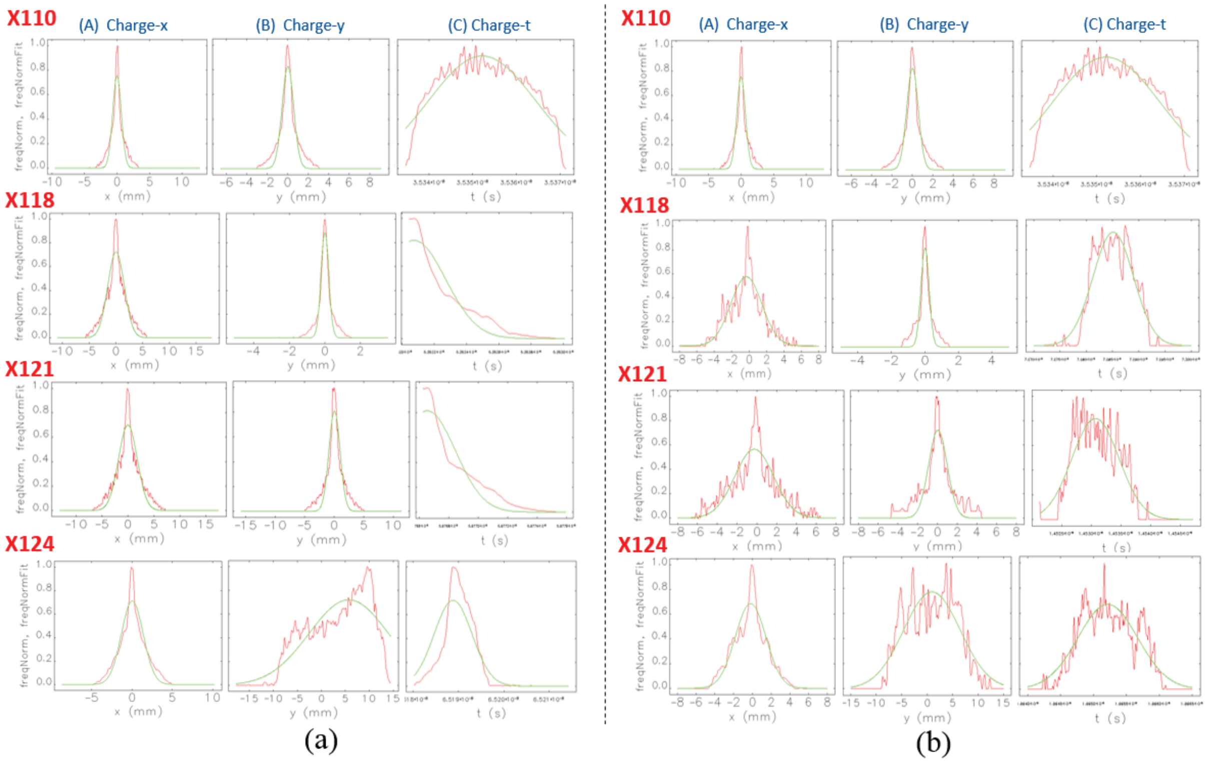

Figure 2: Simulation results with Elegant combined with Shower (Q = 3.2 nC and 50 MeV). Bunch profiles (a) without and (b) with a slit-mask at X115.

124, along the injector beamline, as shown in Fig. 2. The designed slit-mask with W = 900 µm and a = 300 µm is modelled with bunch charges of 250 pC, 1.0 nC and 3.2 nC. As theoretically analysed, the beam is strongly modulated with W = 900 µm and ~ 100 µm of modulation length (Δz), which is consistent with the peak (~ 3 THz) appearing in the beam spectrum. Two different bunching conditions with minimum and maximum energy spreads (on-crest and off-crest with maximum chirp) are examined with Elegant. Also, the simulation analysis includes three different bunch charges (0.25 nC, 1.0 nC and 3.2 nC). For the chirped beam with bunch charge of 0.25 nC, 1.0 nC and 3.2 nC, the rms bunch length is 2.25 ps, 3.25 ps, 4.75 ps and correlated energy spread 3.1%, 4.5% and 6.2% respectively. The normalized charge distributions of the injected beam with charge 3.2 nC are plotted in Fig. 2. Apparently, the beam charge profile follows approximately Gaussian distribution and the minimum energy chirp leads to about 1 % spread, which is far less than that of the chirped beam with linear energy distribution and 6.2% correlated energy.

While passing through the masked chicane, the initial linear energy-time distribution is reversed from positive to negative. This conforms to the principle of slit-masked chicane in micro bunch train generation. The beam with minimum energy chirp (red) appears not to carry a modulation pattern in the particle distribution. In such a condition, the presence of the slit-mask negligibly influences on the beam profile and the chicane behaves as a normal bunch compressor without modulating the beam. On the contrary, the beam modulation under the condition with maximum energy chirp (green) appears much stronger than that with minimum energy spread. It is found that modulation wavelengths of 0.25 nC, 1.0 nC and 3.2 nC are about 187 µm, 270 µm and 325 µm, corresponding to bunch lengths of 16 µm, 23 µm and 27 µm, respectively. Note that the linear model predicts 36 µm of bunch length under the same condition. Although there are some differences due to approximation in analytic model and some perspectives disregarded in Elegant simulations, those results show the feasibility of ~ 100 fs microbunch generation from the designed chicane. We also notice that the corresponding frequency of the bunch-to-bunch spacing is around 1.6 THz, 1.4 THz, and 1.2 THz, respectively. Taking into account all the theoretical and numerical analyses, a properly designed masked chicane can produce a micro-modulated bunch with RMS-bunch length around 100 fs under the optimum beam bunching condition.

PRELIMINARY TEST RESULT

A tungsten mask with W = 900 µm and a = 300 µm is placed in the X115 of BC1, as shown in Fig. 3. The bunch modulation is measured by using D122-X124 spectrometer and a skew-quad installed in BC1 with 20 MeV electron beam. Our simulation results indicate that a bunch modulation prominently appears with maximum energy chirp, so the X124 screen will most likely have a sliced beam image in y-axis (energy axis) in the case the bunch is modulated since the beam will be deflected with about 5–6 % correlated energy spread by

ISBN 978-3-95450-134-2

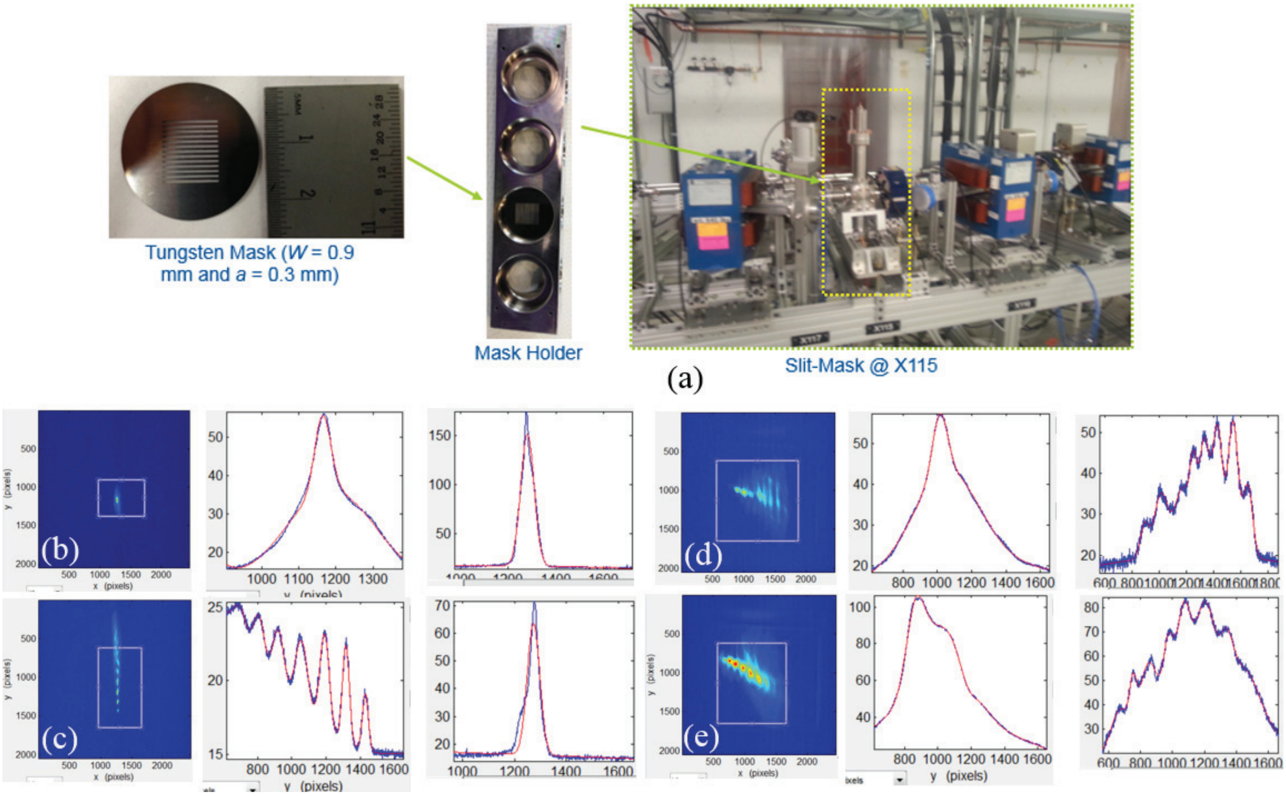

Figure 3: (a) Slit-mask installed in the X115 (BC1). (b) X120-focus with Q115 skew quad (b) OFF and (c) ON at 140 pC per micro-pulse. X124-focus with Q115 skew quad on, (d) 60 pC and (e) optimized.

D122 spectrometer magnet. Secondly, at the skew quadrupole, the particle gets a y-kick proportional to its x-position. This kick is converted to a y-position change at the screen (X121) downstream of the bunch compressor. As shown in Fig. 3, a strong modulation appears on the bunch at X121 and X124 without the skew-quad on (Figs . 3(c–d), while it is not shown with the skew-quad off (Fig. 3(b)). The slit-mask will be re-tested for full characterization measurements of the bunch modulation parameters after the FAST beamline is re-commissioned with 50 MeV.

CONCLUSION

Since bunch modulation of high brightness beams can significantly improve performance of accelerator-based coherent light sources and high energy linacs, we have investigated a simple way for micro-bunch train generation with a masked chicane, in particular with the bunch compressor at the 50 MeV. The linear model is derived to estimate performance of the designed masked chicane, indicating that the designed slit-mask produces σ_{ms} = 33µm long micro-bunches spaced with ~ 100 µm out of σ_t = 3 ps bunch with about 2.4 % correlated energy spread

ACKNOWLEDGMENT

We thank Jayakar C. Thangarj and Jinhao Ruan of Fermi National Accelerator Laboratory for the helpful discussion and technical supports.

REFERENCES

[1] D. C. Nguyen, B. E. Carlsten, NIMA 375, 597 (1996).
[2] P. Muggli, V.Yakimeno, M. Babzien, et al., PRL 101, 054801 (2008).
[3] J. C. Thangaraj, et al. PRST-AB 15, 110702 (2012).
[4] C. R. Prokop, et. al. NIMA 719, 17 (2013).
[5] Yipeng Sun, Tor Raubenheimer, Juhao Wu, SLAC-PUB-14327.
[6] Yipend Sun, Zhirong Huang, Yuantao Ding, Juhao Wu, SLAC-PUB-14335.
[7] http://tesla.desy.de/~meykopff/
[8] M. Borland, "User's Manual for Elegant", available online.

FEMTOSECOND TIMING DISTRIBUTION AT THE EUROPEAN XFEL

C. Sydlo, F. Zummack, J. Mueller, M. Felber, M.K. Czwalinna, C. Gerth, H. Schlarb,
DESY, Hamburg, Germany
S. Jablonski, Warsaw University of Technology, Warsaw, Poland

Abstract

Accurate timing synchronization on the femtosecond timescale is an essential installation for time-resolved experiments at free-electron lasers (FELs) such as FLASH and the upcoming European XFEL. To date the required precision levels can only be achieved by a laser-based synchronization system. Such a system has been successfully deployed at FLASH and is based on the distribution of femtosecond laser pulses over actively stabilized optical fibers. For time-resolved experiments and for special diagnostics it is crucial to synchronize various laser systems to the electron beam with a long-term stability of better than 10 fs.

The upcoming European XFEL has raised the demands due to its large number of stabilized optical fibers and a length of 3400 m. Specifically, the increased lengths for the stabilized fibers had necessitated major advancement in precision to achieve the requirement of less than 10 fs precision. This extensive rework of the active fiber stabilization has led to a system exceeding the current existing requirements and is even prepared for increasing demands in the future. This paper reports on the laser-based synchronization system focusing on the active fiber stabilization for the European XFEL, discusses major complications, their solutions and the most recent performance results.

INTRODUCTION

For the European XFEL a very strong emphasis is put on accurate timing and on the optical timing distribution. Already in the very first expansion stage 27 stations will receive optical synchronization with the option to extend this number to 44 stations. Additionally, the length of the accelerator increases by an order of magnitude compared to FLASH, which has a length of 300 m. This has necessitated a thorough planning and redesign of the existing optical synchronizationn system at FLASH. In the following an overview is given.

The master-oscillator (MO) distributes a stabilized 1.3 GHz reference to which the master laser-oscillator (MLO), with a repetition rate of 216.7 MHz (a sixth of the MO frequency), is locked. The stabilized pulse train from the MLO is split into multiple channels and guided to the individual link stabilization units (LSUs) through the free-space distribution (FSD). Each LSU actively stabilizes the effective length of its assigned optical link fiber, which can conveniently be guided through the entire FEL to stations obliged to femtosecond timing stability. One notable feature in this optical synchronization system is the slave laser-oscillator (SLO) at the end of the FEL. A sub-synchronization will be located in the experimental hall at the end of the beamlines to facilitate all the synchronization needs for the pump-probe lasers on-site. Additionally, it will stabilize all stations between 2.1 km and the end of the experimental hall. Hence, two more links with a length of 3.6 km are provided for SLO to MLO locking. On the one hand, this serves as a redundancy improving reliability and robustness. On the other hand, these two long links can be cross-correlated in-situ for diagnostics providing numbers for the actual synchronization accuracy.

CONCEPT

The optical synchronization system for the European XFEL will adopt to the greatest possible extent the proven and reliable system from FLASH. The long term experience with the optical synchronization system at FLASH has led to numerous enhancements and deeper understanding of the issues involved in such a complex and sensitive precision arrangement. Consequently, for the European XFEL an inimitable possibility arises to incorporate all the gathered knowledge from the bottom up into a new benchmark setting synchronization system.

The distribution of a highly stable optical pulse train to different stations along the complete European XFEL is divided into multiple steps which need individual attention.

The key system of the optical reference distribution is the master laser oscillator (MLO) which is stabilized by a phase-locked loop against the master oscillator (MO), which again is frequency stabilized by a Global Positioning System receiver to ensure best possible long term performance. The locking of the optical pulse train of the MLO against the RF signal of the MO requires a photodiode to convert the optical signal to an electrical for phase comparison. The phase difference is fed back by a feedback loop into the MLO. However, a conventional photodiode set-up is subjected to the AM-to-PM effect [1–3], where amplitude variations convert into phase variations. Despite the very high optical power stability of the deployed MLO minimising the degradation of phase variation due to the aforementioned effect, a more sophisticated method will be introduced for MLO locking. This method is inherently free of the AM-to-PM effect and has already proven high performance [4].

The stabilized optical pulse train is split free space by polarizing beam splitters into multiple channels to feed all link stabilization units (LSU). To accommodate the large number of LSUs - up to 24 LSUs are used on one optical table - they need to be placed efficiently. The optical free space path for each individual channel reaches a certain length. The lengths are kept identical to maintain identical beam parameters for each LSU. However, a distance of about 2 m has to be covered in free space on the optical table.

ISBN 978-3-95450-134-2

Conventional optical tables are composed of 4.8 mm thick steel plates as top and bottom sheet. Steel has a thermal expansion coefficient of about 10 ppm/K or about 33 fs/K/m [5]. For a climatization environment a thermal stability of 0.1 K is ambitious, but realistic. That would result in more than 6 fs drift for the optical table alone. Clearly, this is outside the acceptable range. Therefore, the optical table supporting the MLO and the LSUs - more specifically the top and bottom sheet - are made from Superinvar, which has a very low thermal expansion coefficient resulting in less than 1 fs/K/m [5]. Both sheets have been manufactured from Superinvar to avoid a bimetallic effect among other details. The most dominant contribution for drift is now the change of refractive index of air which is about 3 fs/K/m [6]. This issue can easily be overcome by placing the aforementioned laser locking scheme at the same distance from the MLO as the LSUs and exploiting common mode drift. While the temperature distribution on an optical table is usually not uniformly distributed due to the finite thermal conductivity, the temperature distribution of air is governed by movement. Consequently, this optical table incorporates dedicated holes for this purpose and a ventilation system is integrated into the climatization system.

The choice of Superinvar as top and bottom sheet demands to take great care with mounting optics and systems on it. The superior thermal performance of this material must not be degraded. Consequently, the classical clamping forks are banned as they apply mechanical stress and occupy a lot of valuable space. All the optics are mounted directly onto the optical table by cylindrical optical post which have been specifically designed to match the mechanical requirements. The small footprint of these post with a diameter of 24 mm is sufficiently small not to degrade the mechanical properties of the table. As a side effect the optical paths are kept in the 25 mm grid of the metric optical table simplifying optical alignment and diagnostics.

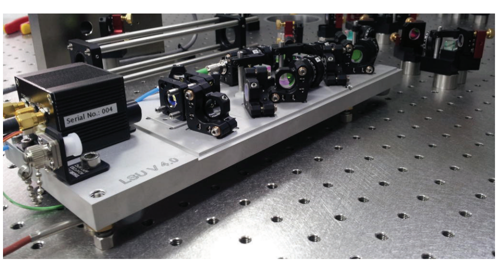

Figure 1: First link stabilization unit on optical table in the European XFEL.

Larger components required on this table - like the LSUs and MLO - received special feet for accurate placing. They are derived from the classical 3-point support which is commonly found on kinematic optical mounts. This is also a beneficial factor for the LSUs. While it sounds logical to also make the LSUs out of Superinvar to avoid thermal expansion and therefore resulting drift, we have chosen another approach. Superinvar is an expensive material and has a high lead time. However, a careful placing of the 3-point supports in the LSUs results in zero drift if a uniformly distributed temperature can be assumed. As the maximum dimension of the LSUs is 31 cm with a thickness of 15 mm, a material with reasonable thermal conductance is sufficient. In our case, we have chosen aluminum to avoid the aforementioned disadvantages, which provides a decent thermal conduction. Figure 1 presents an opened LSU made from aluminum on the Superinvar optical table in the European XFEL. One of the three 3-point supports is visible between the top sheet of the table and the LSU plate in the lower left corner of the photography. Additional rubber bumps are mounted for convenient assembly and storage; they do not touch the optical table when placed. Also, some of the custom mounts for optics are shown in the top right corner.

To complete the design concept logically consistent, all the optical delay stages and the supplementary fibers are also banned from this optical table. The optical delay lines are placed on a second optical table which is made from conventional steel. The frequent movement of this coarse delay correction introduces vibrations which must be kept away from the MLO. All the supplementary fibers - for amplification and dispersion compensation etc. - are placed in a compact 19 inch rack under the second optical table. This allows parallel working, commissioning and simplified maintenance.

EXPERIMENTAL RESULTS

The finalized design of the LSU has been manufactured in a small quantity for final tests before a large number has been sent to production. This test environment is kept identical to the previous experiments [7] and only the LSU itself has been replaced by the finalized production version. It should be noted that the used laboratory does neither feature a Superinvar table nor the new control electronics which is based on MTCA.4 [8]. The identical environment allows a concentrated test on the LSU alone.

Figure 2 presents the results of these test and confirms that the performance is identical to the previous test with a demonstrator set-up [7]. This result has released the large volume manufacturing for the European XFEL.

The following tests will concentrate on the fusion with the enhanced electronic performance of the MTCA.4 based system. While the most evident improvements are increased ADC and DAC sampling rates and resolutions for detection and regulation, here, another uniqueness will be introduced. The balanced detector - which is also an in-house development - will read out both photodiodes individually as this technique has a couple of advantages. First, the EMI situation is improved, as both photodiode signals are guided by two closely spaced low-crosstalk cables to two ADCs. The difference signal for locking is generated inside the regulation algorithm. This way any potential EMI will affect both cables highly identical which can be considered like a common mode distortion. The two single-ended ADC inputs can be regarded as a differential input. Any imbalance or offset error can be canceled out by the algorithms running on the

ISBN 978-3-95450-134-2

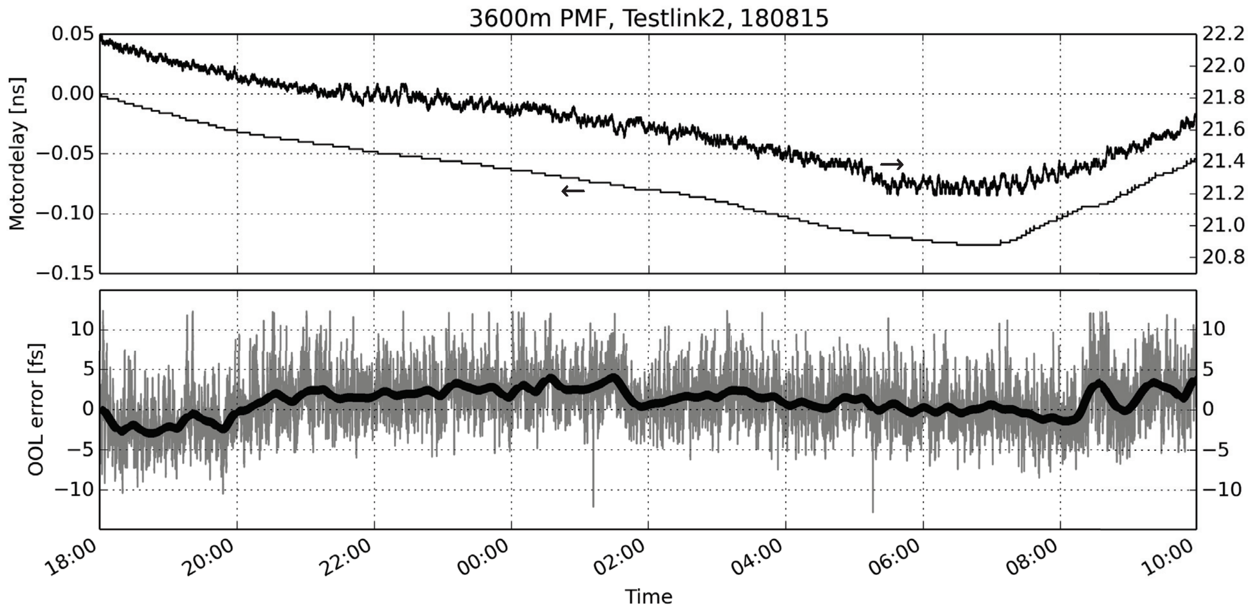

Figure 2: In the top graph the compensated length change of the fiber and the corresponding temperature is shown. The delay is given for one-way and therefore represents the drift of 3.6 km polarization maintaining fiber. The lower graph presents the measured residual out-of-loop timing error at the end of the stabilized fiber. Gray color shows the raw data, while the black line is a convolution with a Hanning-window of 1 h full length to distinguish between jitter and drift.

MTCA.4 system. Also, this technique features an inherent lock detection as both photodiodes carry some DC part in a locked state. This DC value provides additional relevant information of the link situation.

CURRENT STATUS

The main synchronization room in the European XFEL is ready for installations and the first optical set-ups are already built up. By the time of writing, the first MTCA.4 systems for the optical reference distribution are finalized and placed into their designated places. About 5 km of polarization maintaining fibers are already inserted which is about 25 %. These fibers serve the injector area, the photoinjector laser and the first LLRF station of the 2 km long LINAC. These fibers received a special custom jacket suitable for underground installations and complying with fire safety rules. To the best of our knowledge this is a unique feature in the accelerator community.

REFERENCES

[1] J. Taylor et al., "Characterization of power-to-phase conversion in high-speed P-I-N photodiodes", IEEE Photon. J. 3 140-51, 2011.

[2] W. Zang et al., "Amplitude to phase conversion of InGaAs pin photo-diodes for femtosecond lasers microwave signal generation", Appl. Phys. B 6 301-8, 2011.

[3] D.H. Phung et al., "Phase measurement of a microwave optical modulation: characterization and reduction of amplitude-to-phase conversion in 1.5μm high bandwidth photodiodes", J. Lightwave Technol. 32 3759-67, 2014.

[4] T. Lamb et al., "Femtosecond Stable Laser-to-RF Phase Detection for Optical Synchronization Systems", IBIC 2013, Oxford, Sept. 2013, TUPC33, http://www.JACoW.org

[5] Newport Corporation, http://www.newport.com

[6] P. E. Ciddor., "Refractive index of air: new equations for the visible and near infrared", Appl. Optics 35, 1566-1573, 1996.

[7] C. Sydlo et al., "Femtosecond timing distribution for the European XFEL", Proceedings of the 36th International Free Electron Laser Conference FEL 2014, August 25-29, 2014, Basel, Switzerland.

[8] M. Felber et al., "New MTCA.4-based hardware developments for the control of the optical synchronization systems at DESY", Proceedings of the 3rd International Beam Instrumentation Conference, IBIC 2014, September 14-18, 2014, Monterey, California, USA.

ISBN 978-3-95450-134-2

ELECTRON BEAM DIAGNOSTICS FOR FEL STUDIES AT CLARA

S. Spampinati#, University of Liverpool & The Cockcroft Institute, Cheshire, UK
D. Newton, University of Liverpool, Liverpool, UK

Abstract

CLARA (Compact Linear Accelerator for Research and Applications) is a proposed 250 MeV, 100-400 nm FEL test facility at Daresbury Laboratory [1]. The purpose of CLARA is to test and validate new FEL schemes in areas such as ultra-short pulse generation, temporal coherence and pulse-tailoring. Some of the schemes that can be tested at CLARA depend on a manipulation of the electron beam properties with characteristic scales shorter than the electron beam. In this article we describe the electron beam diagnostics required to carry on these experiments and simulations of FEL pulse and electron beam measurements.

INTRUDUCTION

Some of the most advanced schemes proposed to improve FEL performance depend on a manipulation of the electron beam properties with characteristic scales of several coherence lengths and shorter than the electron beam [2-4]. We are interested to test, among other schemes, mode locking FEL and femto-slicing for the production of trains of short pulses [4-7]. The implementation of these schemes at CLARA requires a 30 - 50 µm modulation of the beam energy acquired via the interaction with an infrared laser beam in a short undulator (modulator). The performance of these FEL schemes depends on this energy modulation. So monitoring the longitudinal phase space of the electron beam is important to perform and to realize these experiments. A deflecting cavity [8] installed in the last part of the FEL line will allow the longitudinal beam distribution to be observed on a screen placed after the dipole leading to the beam dump. The FEL line of CLARA, as shown in Fig. 1a, is composed of two modulators separated by a dispersive section, seventeen radiators and an afterburner section. The afterburner is composed by a series of short undulators and delay chicanes. A possible layout of the diagnostic system placed at the end of the CLARA undulator from the afterburner is shown in Fig. 1b.

In this design, the electron beam is deflected vertically by the deflecting cavity. This deflection maps the electron beam longitudinal coordinate to the vertical coordinate on an intercepting screen after the spectrometer dipole magnet; the dipole converts the particle's energy to the screen horizontal coordinate. Consequently, the electron beam longitudinal phase space is imaged on the screen, and the energy modulation taking place in the modulator can be studied and optimized. Another interesting application of this diagnostic beam line could be the study of the FEL process taking place in the different operation modes of CLARA.

#simone.spampinati@cockcroft.ac.uk

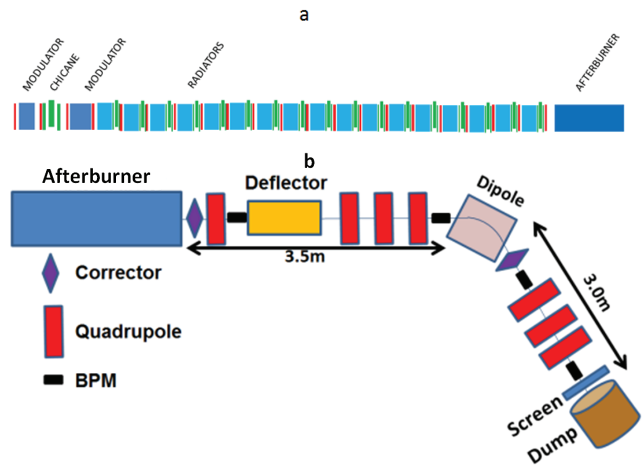

Figure 1: Top: FEl line of CLARA. Bottom: Layout of the phase space diagnostics composed by of a transverse deflector and an energy spectrometer.

OPTICS OPTIMIZATION AND RESOLUTIONS

The vertical beam size at the screen, after deflection, is [9]:

$$\sigma_y = \sqrt{\sigma_{y,0}{}^2 + (S\sigma_Z)^2} \tag{1}$$

where $\sigma_{y,0}$ the vertical beam size at the screen location without deflection is, σ_z is the longitudinal beam size and S is the calibration factor representing the strength of the beam deflection [9]:

$$S = \frac{e_0 V k}{pc}\sqrt{\beta_{yS}\beta_{yD}}\left|\sin\Delta\Psi\right| \tag{2}$$

here $k = \frac{2\pi}{\lambda}$ with λ = 10.01cm for an S-band cavity (frequency of 2.998 GHz). V_0 is the deflecting voltage, $\beta_{y,D}$ and $\beta_{y,S}$ are vertical betatron functions at the deflector and the screen, respectively. ΔΨ is the vertical betatron phase advance between the deflector and the screen. The size of the image of the beam detected on the screen will be increased by the system resolution (screen and CCD pixel size) and:

$$\sigma_y = \sqrt{\sigma_{y,0}{}^2 + \sigma_{screen}{}^2 + (S\sigma_Z)^2} \tag{3}$$

where σ_{Screen} is the screen and CCD resolution.

The longitudinal resolution of the screen image, $\sigma_{L,r}$ can be defined as the ratio of the non-deflected beam size on the screen to the calibration factor S [10]:

$$\sigma_{L,r} = \frac{pc}{e_0 V k \left|\sin\Delta\Psi\right|}\sqrt{\frac{\varepsilon_n}{\gamma\beta_{yD}} + \frac{(\sigma_{screen})^2}{\beta_{yS}\beta_{yD}}} \qquad (4)$$

The third term in Eq. 3 is equal to the quadratic sum of first two terms for $\sigma_z = \sigma_{L,r}$. The energy resolution of the spectrometer can be written as [10]:

$$\sigma_E = \sqrt{\frac{E^2}{\eta^2}\frac{\varepsilon_n\beta_x}{\gamma} + \frac{E^2}{\eta^2}(\sigma_{screen})^2 + (e_0 V k)^2\frac{\beta_y\varepsilon_n}{\gamma}} \qquad (5)$$

Here η is the horizontal dispersion at the screen. The first two terms represent the resolution of an energy spectrometer line, the third term is the energy spread induced by the deflector [11].

Equations 4 and 5 guide the optimization of the optics functions in the diagnostic beam line. The optimum phase advance between the deflector and the screen is $\Delta\psi = 90^\circ$. Large values of V and $\beta_{y,D}$ lead to a good longitudinal resolution but increase the energy resolution of the system via the induced energy spread. A large value of $\beta_{y,S}$ improves the total longitudinal resolution for a poor resolution screen but has to be narrowed to limit the total beam dimension on the screen given by Eq. 1. A small value of $\beta_{x,S}$ and a large value of η are required to have a good energy resolution.

STUDY OF BEAM ENERGY MODULATION

Figure 2 shows a possible optical solution, used to study the energy modulation (with a spatial period in the range 30-50 μm), from the entrance of the modulator to the screen. The radiators are at maximum gap and the intra-undulator quadrupoles are used along with the seven quadrupoles shown in Fig. 1 to give the required resolution. The optics shown is for beam energy of 150 MeV. The vertical betatron functions at the deflector and at the screen are 25 m and 0.95 m respectively. The calibration factor S, for a deflecting peak voltage of 5 MV and a RF frequency of 2.998 GHz, is ~10.2. The vertical rms beam size on the screen is 2.7 mm. The horizontal betatron function and dispersion at the screen are 1 m and 0.6 m. A longitudinal resolution of 4.7 μm and an energy resolution of 75 Kev are therefore achieved. A screen resolution of 20 μm is assumed. Similar optics and performances can be reached for beam energy of 250 MeV with a deflecting voltage of 7.5 MeV.

The reconstruction of the phase space requires short portions of the bunch to be resolved at the screen. An estimate of the length of these portions of the bunch, that

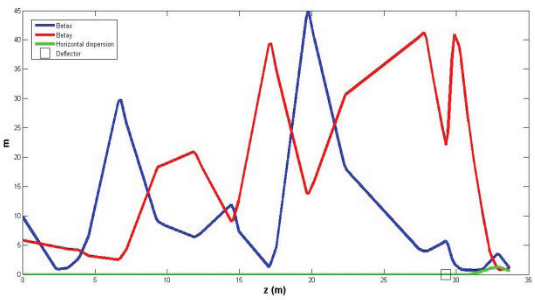

Figure 2: Possible optics from the exit of the modulator to the screen.

can be resolved, can be obtained by using the following simple approach [1, 12]: A portion of the longitudinal density distribution is modelled by two identical Gaussians with different centres in the bunch at a distance Δz. The sigma of the two Gaussians is σ_{screen} /s. This longitudinal test density distribution is reproduced in Fig. 3a. At the screen the separation between the two Gaussian is S·Δz while the sigma is $\sqrt{(\sigma_{y,0})^2 + (\sigma_{screen})^2}$. The vertical profile of the image on the screen is reproduced in Fig. 3b.

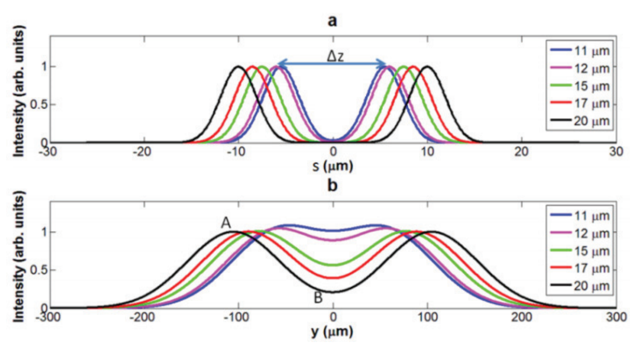

Figure 3: Top: Test longitudinal distributions represented by two Gaussians with a sigma of σ_{Screen} /S separated by a distance Δz. Bottom: Vertical profile on the screen for the distribution depicted above. A and B indicate respectively the values of the intensity of the peaks (the crests) and of the central local minimum (the valley) for any profile.

Simulations including the beam energy modulation in the modulator, the vertical deflection in the RF deflector and the beam transport up to the screen have been performed with the code ELEGANT [13] to test the performance of the diagnostic system introduced above. The parameters used in the simulations are listed in Table 1 and are taken from the CLARA CDR [1]. One-dimensional longitudinal space charge (LSC) and coherent synchrotron radiation (CSR) impedances are included in the simulations.

ISBN 978-3-95450-134-2

Table 1: Simulation Parameters

Parameter	Value	Unit
Macro-particles	2 10^6	
Beam energy	150	MeV
Current	150	A
Energy spread	50 (RMS)	Kev
Emittance	0.6 (RMS)	mm-mrad
Laser wavelength	40	µm
Laser pulse duration	500 (FWM)	fs
Laser pulse energy	10	µJ
Laser waist	2.5	mm
Deflecting frequency	2.998	GHz
Deflecting voltage	5	MV
Screen resolution	20 (RMS)	µm

Results of simulation are shown in Fig. 4. Figure 4a shows the phase space after the interaction in the modulator (see Fig. 1) with the 40 µm laser. Figure 4b shows the beam density distribution projected on the x-y plane at the end of the diagnostic beam line and it representing the screen image. The energy modulation is well evident as predicted above.

We can now compere the beam energy modulation after the laser-electron interaction with the measurements on the screen. We can derive the beam energy modulation on the screen image by using the theoretical value of the calibration factor S (Eq. 2) and of the horizontal dispersion at the screen location. Linear correlated energy spread induced by the deflector, LSC and CSR can be removed. The result is shown in Fig. 5 where the mean slice energy is plotted versus the slice longitudinal coordinate in the bunch. The red curve is the beam energy modulation derived by screen analysis (Fig. 4b) and the blue is the energy modulation present on the beam after the laser-electron interaction in the modulator (Fig. 4a). The agreement between the two curves is good.

STUDY OF THE FEL INTERACTION AND FEL PULSE

Recently a method to study FEL pulse length and fel intensity using a defector and an electron beam spectrometer has been proposed and applied to LCLS experiments [14, 15]. The beam phase space is measured with the FEL on and the FEL off. The application of the energy conservation principle permits to measure the temporal profile of the FEL pulse (E. vs t.) from the changes in the slice mean energy and energy spread induced by the lasing.

The diagnostics described above can be used to study the electron beam phase space with the FEL process on and off to apply this method. In this case the radiators are

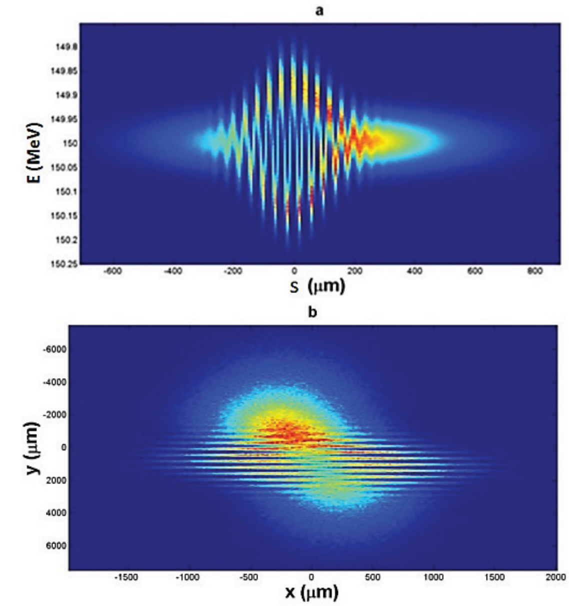

Figure 4: Top: Beam phase space after the interaction in the modulator (see Fig. 1) with the laser. Bottom: beam density distribution projected on the x-y plane at the end of the diagnostic beam line.

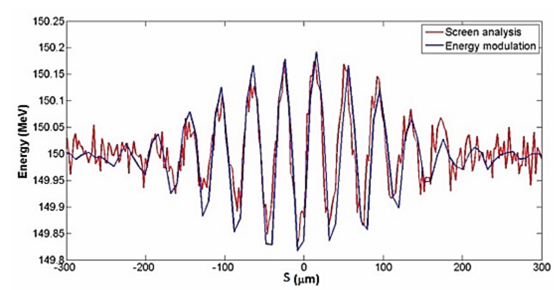

Figure 5: Beam energy modulation derived by the measurement analysis (red) compared with the one gained in the modulator (blue).

closed and the intra-radiator qudrupoles are set to ensure beta values required by FEL. We can use the quadrupoles placed after the last radiator to optimize the diagnostics resolutions according to Eq. 4 and Eq. 5. A quadrpupole in the middle of the afterburner has been considered in this case. A possible solution for the optics between the last radiator and the spectrometer screen is shown in Fig. 6. The vertical betatron functions at the deflector and at the screen are 19 m and 0.95 m respectively. The calibration factor S, for a defecting voltage of 5 MV and a RF frequency of 2.998 GHz, is ~9.2. The horizontal beta and dispersion at the screen are 1m and 0.6 m.

ISBN 978-3-95450-134-2

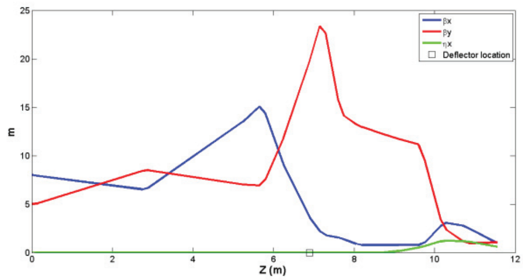

Figure 6: Possible optics from the exit of last radiator to the screen.

For this solution a longitudinal resolution of 5.2 µm and an energy resolution of 63 Kev are predicted by Equations 4 and 5.

As example we consider now the application of the technique described in [9, 14] and demonstrated in [15] to a single stage HGHG. The FEL process is simulated with GENESIS [16] and then the diagnostic line is simulated in ELEGANT as in example described above. In this case the first modulator is tuned at 800 nm to be resonant to a Ti:Sa laser and the radiator is tuned on the fourth harmonic of the seed laser (200 nm). In this case the electron beam has a peak current of 400 A, all the other parameters have the same values as in the previous case. The phase space after the modulator (reconstructed by the image on the diagnostic screen) is reproduced in Fig. 7a. The net energy exchange in this part of the HGHG scheme is negligible. The energy spread is increased on the part of the beam interacting with the laser while the central energy is not modified by the seed. Figure 7b reproduces the phase space after the radiator (5 modules). Radiation production in this stage implies that the beam energy is reduced while the FEL energy is increased. From the two measurements we can determine the slice energy loss induced from the FEL interaction:

$$\Delta E_{FEL}(t) = E_{FEL_{on}}(t) - E_{FEL_{off}}(t)$$

With the obtained time-sliced energy loss and current, laser profile is determined:

$$P_{FEL}(t) = \Delta E_{FEL}(t) \times I(t)$$

The FEL profile reconstructed from the energy loss is shown in Fig. 8 (blue curve) with the profile obtained by the simulation with GENESIS (red curve). The agreement between the two curves is good and in line with the predicted temporal and energy resolution of 15 fs and 10 MW respectively. The pulse duration (rms) of the reconstructed pulse is 55 fs while the simulated pulse has time duration of 66 fs (rms).

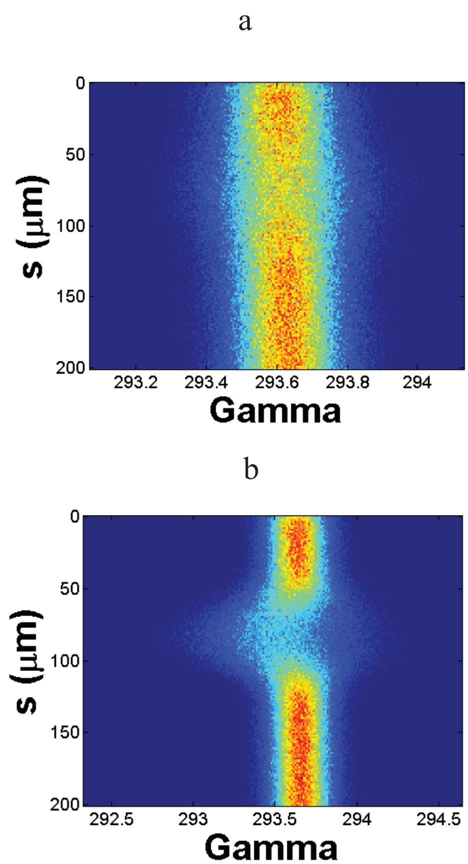

Figure 7: Electron beam phase space after the modulator (a) and after the first five modules of the radiator (b).

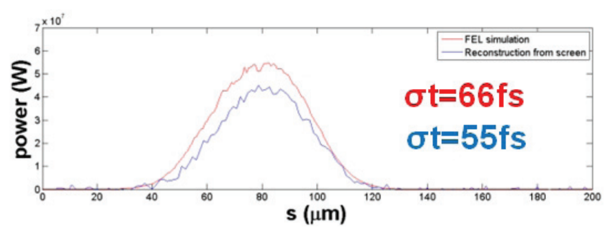

Figure 8: FEL profile as obtained by the simulation with GENESIS and by the screen image.

CONCLUSIONS

We have presented results on the viability of post-FEL diagnostics on CLARA to study the phase space of the beam after the beam energy modulation required by mode locking and sliced FEL schemes. Their expected performance and simulations of their utilization have been presented.

ACKNOWLEDGMENT

This work is funded by STFC (Science and Technology Facilities Council, UK).

ISBN 978-3-95450-134-2

REFERENCES

[1] J. A. Clarke et al., JINST 9, 05 (2014).
[2] A.A. Zholents, W.M. Fawley, Phys. Rev, Lett. 92, 224801 (2004).
[3] E. Kur, D.J. Dunning, B.W.J. McNeil, J. Wurtele & A.A. Zholents, New J. Phys. 13 063012 (2011).
[4] D.J. Dunning, B.W.J. McNeil and N.R. Thompson, Phys. Rev. Lett. 110, 104801 (2013).
[5] E.L. Saldin, E.A. Schneidmiller and M.V. Yurkov, Phys. Rev. ST Accel. Beams 9, 050702 (2006).
[6] N. R. Thompson and B.W.J. McNeil, Phys. Rev. Lett. 100,203901 (2008).
[7] L. Giannessi et al., Phys. Rev. Lett. 106 ,144801 (2011).
[8] G. A. Loew, O.H. Altenmueller, SLAC, PUB-135. Aug. 1965.
[9] Y. Ding et al., “Ultra-short electron bunch and X-ray temporal diagnostics with an x-band transverse deflecting cavity”, in: Proc. 1st Int. Beam Instrumentation Conf., Tsukuba, Japan, 2012, TUPA41.
[10] Y. Ding et al., “Commissioning of the X-band Transverse Deflector for Femtosecond Electron / X-Ray Pulse Length Measurements at LCLS”, in: Proc. 4th Int. Particle Accelerator Conf., Shanghai, 2013, WEOBB201.
[11] M. Cornacchia and P. Emma, Phys. Rev. ST Accel. Beams 5, 084001 (2002).
[12] P. Craievich et al., “A transverse RF deflecting cavity for FERMI@elettra project”, in: Proc. 8th European Workshop on Beam Diagnostics and Int. for Particle Accelerator Conf., Venice, 2007, TUPC10.
[13] M. Borland, ANL/APS Report No. LS-287 (2000).
[14] Y. Ding et al., Phys. Rev. ST Accel. Beams 14, 120701 (2011).
[15] C. Behrens at al. Nature communications 5, 3762 (2014).
[16] S. Reiche et al., Nucl. Instrum. Methods Phys. Res., Sect. A 429, 243 (1999).

ISBN 978-3-95450-134-2

THE PROTOTYPE OF NEW VARIABLE PERIOD UNDULATOR FOR NOVOSIBIRSK FREE ELECTRON LASER

I.V. Davidyuk , O.A. Shevchenko, V.G. Tcheskidov, N.A. Vinokurov, BINP, Novosibirsk, Russia

Abstract

To improve the parameters of the second stage Novosibirsk free electron laser one plans to replace the existing electromagnetic undulator by permanent-magnet variable-period undulator (VPU). The VPUs have several advantages compared to conventional undulators, which include wider radiation wavelength tuning range and an option to increase the number of poles for shorter periods with constant undulator length. Both these advantages will be realized in the new undulator under development in Budker INP.

The idea of the permanent-magnet VPU was proposed just several years ago and it has not been properly tested yet. There are some technical problems, which have to be solved before this idea can be implemented in practice. To check the solution of these problems we designed and manufactured a small undulator prototype, which has just several periods. In this paper, the results of mechanical and magnetic measurements of this undulator prototype are presented and compared with simulations.

INTRODUCTION

The VPU for the NovoFEL under development at Budker INP has a remarkable feature which is the possibility to change the number of periods. The new undulator will replace the electromagnetic one used in the second stage FEL. The old undulator has the period λ_u 120 mm and the field amplitude B_0 varying from zero to 0.13 T .It is installed on the bypass of the second horizontal track [1]. The tuning range of the existing FEL is 35 to 80 microns. Application of the VPU will allow shifting the short wavelength boundary to 15 microns [2].

The available free length for the undulator is four meters. Electron energy at the second stage FEL is 22 MeV. One can find most important parameters of the VPU in Table 1.

Table 1: Basic Undulator Parameters

Parameter	Limits
Undulator period λ_u (mm)	48 - 96
Radiation wavelength (μm)	15 - 70
Number of periods	40 - 80
Filed amplitude on the undulator axis (kGs)	0.94 – 1.9
Deflection parameter	0.42 – 1.79

UNDULATOR GEOMETRY

To ensure low diffraction losses at maximum radiation wavelength, the diameter of the circle inscribed into the aperture of undulator was chosen to be 50 mm. As field amplitude B exponentially decreases with growth of g/λ_u, where g is the undulator gap, one can obtain the limitation that λ_u should not be too small compared to g, so we chose minimum λ_u to be 48 mm. [2]

Each undulator block consists of one permanent magnet and two iron plates. The permanent magnets are made of NdFeB. In simulations we used a permanent magnet with a remanence of 1.3T. We optimized the dimensions of the magnets and iron plates to obtain a maximum field amplitude with a minimum period.

The transverse cross-sections of the iron plate and permanent magnet with final dimensions are presented in Fig. 1. The longitudinal sizes (thicknesses) are 20 mm for the magnets and 2 mm for the iron plates.

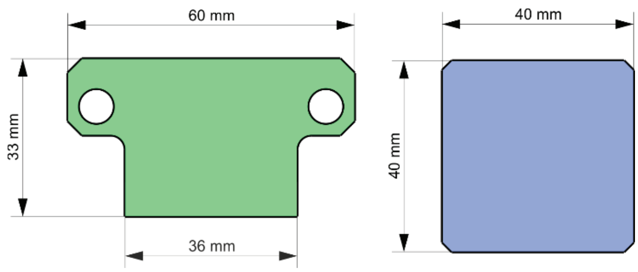

Figure 1: Transverse cross-sections of the iron plate and permanent magnet.

The opposite plates of two blocks adjacent in the longitudinal direction form one pole. Each couple of the right and left blocks at the top is combined in one unit, which can move as a whole, as can be seen from the Fig. 2. Each couple of the right and left blocks at the bottom also forms a similar movable unit.

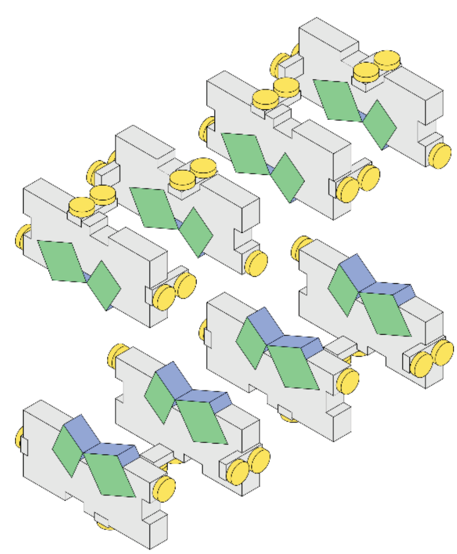

Figure 2: Undulator units disposition.

The top and bottom units are not connected. Blocks in one unit are tilted relative to each other, therefore the free aperture is a rhomb. This configuration provides field

ISBN 978-3-95450-134-2

amplitude growth with distance from the central axis in all directions. As a result, this undulator will focus the electron beam both horizontally and vertically. This feature is important because of the low (22 MeV) electron energy and, consequently, strong focusing by the undulator field.

Each unit has set of bearings that provide sufficient coefficient of friction to avoid significant undulator period tapering [2].

PROTOTYPE MECHANICAL DESIGN

Two prototypes of the VPU were manufactured in order to examine magnetic and mechanical undulator properties. Carcasses of undulators are made of aluminum and allow installing up to 8 units in row. One prototype has both upper and lower arrays of units and another one has just upper array and a metal plate in the horizontal symmetry plane that provides proper boundary conditions. One can see sketches of prototypes in Fig. 3. The first one is suitable for magnetic measurements and the second one is convenient to conduct mechanical measurements. Both prototypes have pusher screws in one side and stoppers in the middle, which allows changing the number of units and undulator period. There are deeperings in the inner side of frames for bearings.

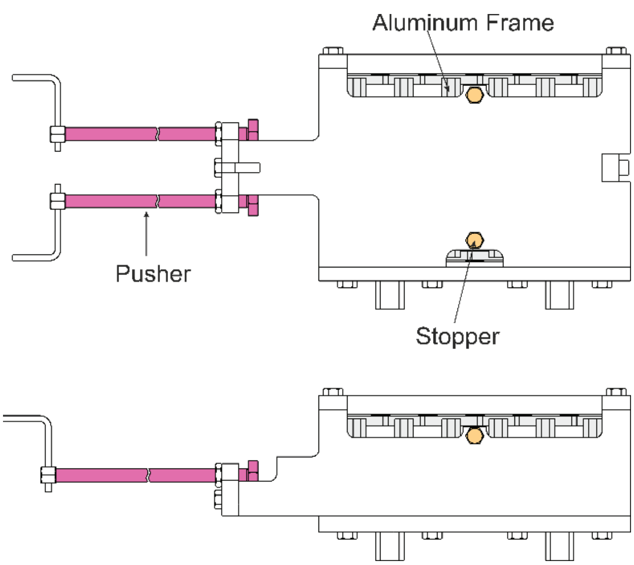

Figure 3: Sketches of VPU prototypes.

As it was said before undulator units consist of two magnets, four metal plates aluminum frame and set of bearings, as it is shown on Fig. 4. Bearings positions are optimized to avoid tilts of the unit.

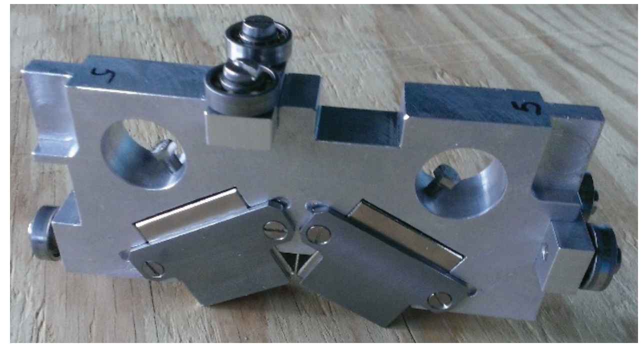

Figure.4: Undulator unit.

MAGNETIC MEASUREMENTS

To check results of three dimensional computer simulations of the field distribution in the undulator several mechanical and magnetic measurements were made.

One can measure the value of magnetic field produced by a single undulator unit at a given point with help of Hall sensor, as it is shown in Fig. 5. So one can compare magnetization of different units with value used in simulations.

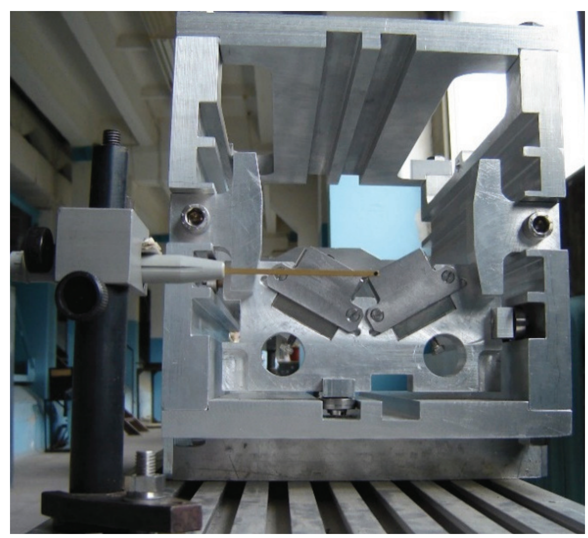

Figure 5: One point magnetic field measurement.

The mean value of longitudinal magnetic field measured by Hall detector at the 90 mm distance from unit is 97.8 Gs, while the magnetic field calculated in CST Studio software [3] in the same scheme is 97.3 Gs. It means that magnetizations of manufactured magnets are very close to project value 1.3 T. One can see deviation from the mean value of magnetization for all units in Fig. 6.

ISBN 978-3-95450-134-2

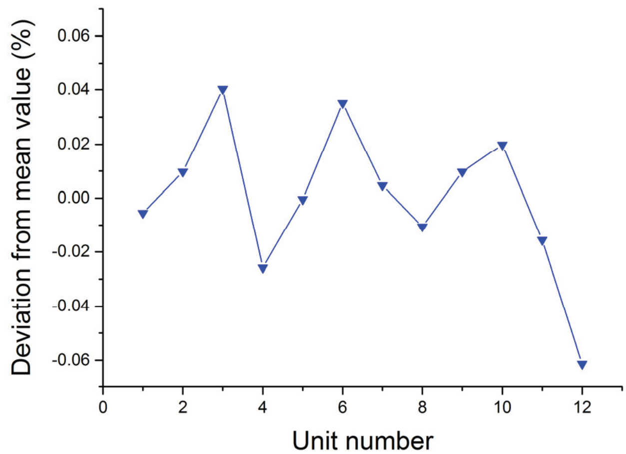

Figure 6: Variation of units field measured at given point.

MECHANICAL MEASUREMENTS AND COMPARISON WITH SIMULATIONS

Attraction force between upper and lower units placed in the magnetic field H can be described by Maxwell's stress tensor [4]. The vertical force can be found as integral of stress tensor over horizontal symmetry plane between two units. Using magnetic field distribution from simulations one can find the vertical attraction force and compare it to the measured one.

Figure 7: Measurement of the vertical attraction force.

One can see scheme of the experiment in Fig. 7. Lower unit was fixed and upper unit could be moved only vertically. The measured force was 60.42 N and the weight of the unit was 9.92 N, thus, attraction force is 50.5 N.

The force obtained from numerical calculation of simulated field is 50.85 N. Claimed error of the dynamometer is 0.1 N, measuring distance between units could also add error.

The prototype construction allows to fix outside units. In order to avoid errors related with displacement of inner units it was decided to measure longitudinal repulsive force using just three units: two fixed in the ends and one that we can shift in the middle, Fig. 8.

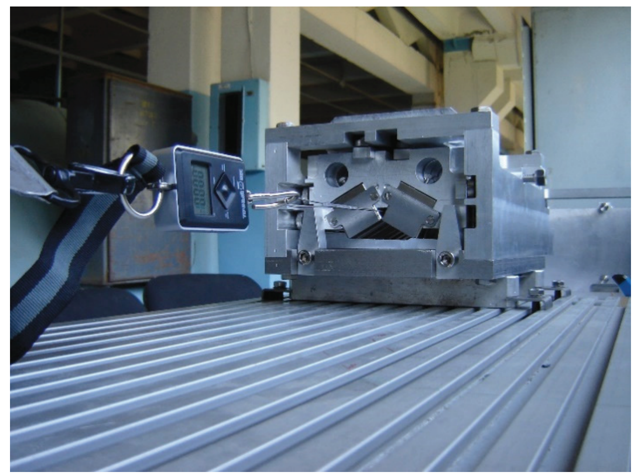

Figure 8: Measurement of longitudinal repulsive force.

One can see the dependence of repulsive force on the displacement of the middle unit in Fig. 9. In such a scheme, behavior of the force is almost linear due to absence of next unit with same magnetization.

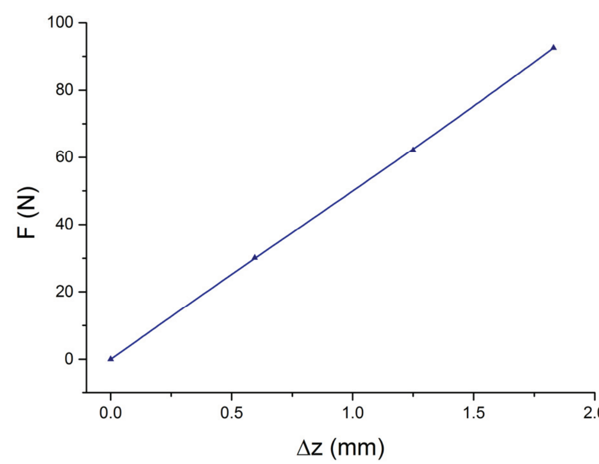

Figure 9: Dependence of repulsive force on the displacement.

As the period of undulator changes, the repulsive longitudinal force on shifted unit changes too. Fig. 10 shows the dependence of three-unit system rigidity (repulsive force normalized on shift) on the period of undulator. The results of simulations differ from measured values on short periods, where the error of measuring force is higher.

ISBN 978-3-95450-134-2

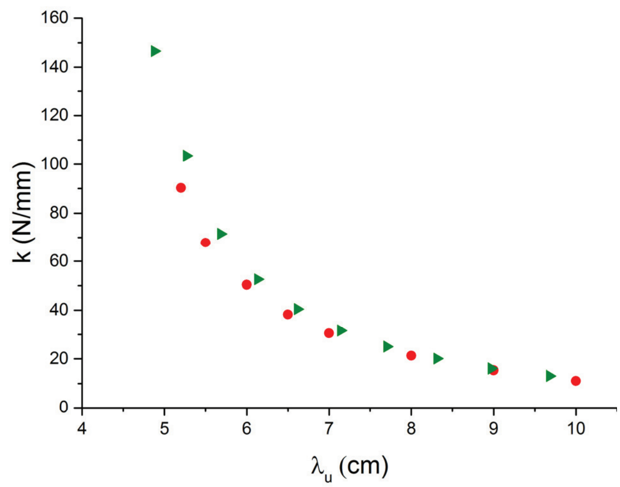

Figure.10: Dependence of three-unit system rigidity on the undulator period (green triangles – data from simulations, red dots – measured data).

In addition, prototype allow us to check the repeatability of the units distribution. Distances between units were measured in different periods several times.

Distribution of the units in different periods are shown in Fig. 11. Displacements of the units after the period change are shown in Fig. 12.

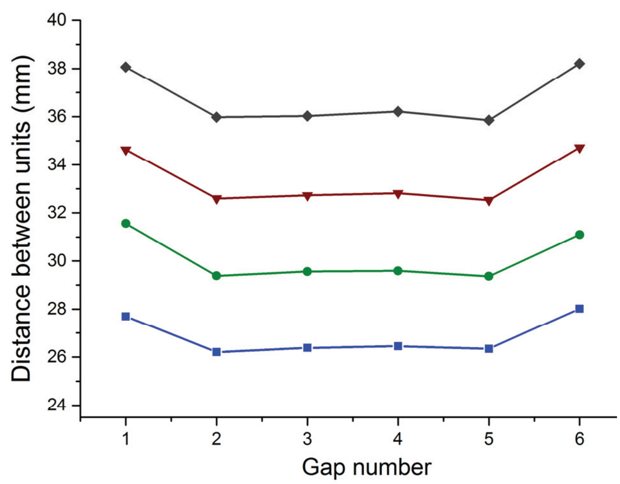

Figure 11: Distribution of the units in different periods.

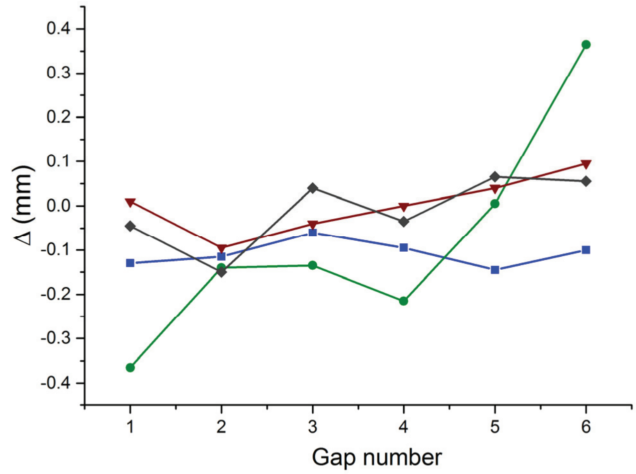

Figure 12: Displacements of the units after the period change.

CONCLUSION

Results of measurements obtained at VPU prototypes are in a good agreement with simulations. It confirms the feasibility of the variable period undulator concept. Valuable experience, which was obtained during prototype assembly, will be used for the full-scale undulator that is being designed and manufactured at BINP now.

REFERENCES

[1] O.A. Shevchenko, V. Arbuzov, K. Chernov, E. Dementyev. Proc. of FEL 2012, p. 361, Nara, Japan (2012)
[2] I.V. Davidyuk, O.A. Shevchenko, V.G. Tcheskidov, N.A. Vinokurov. Proc. of FEL 2014, p. 66, Basel, Switzerland (2014)
[3] CST Studio website: https://www.cst.com/Products/CSTEMS
[4] L. D. Landau and E. M. Lifshitz, The Classical Theory of Fields (Elsevier Science, Amsterdam, 1980)

ISBN 978-3-95450-134-2

STUDIES OF LCLS FEL DIVERGENCE*

J.L. Turner, P. Baxevanis, F.-J. Decker, Y. Ding, Z. Huang, J. Krzywinski, H. Loos, G. Marcus, N. Norvell, SLAC, Menlo Park, CA 94025, U.S.A.

Abstract

Simulations show various impacts on x-ray divergence. With the motivation to maximize intensity at the focus, these LCLS beam studies were designed to study parameter space and beam qualities impacting divergence, and therefore aperture related clipping and diffraction. With multiple simultaneous users, beam constraints increase, requiring an improving knowledge of the mechanism of impact of changing parameters. These studies have that goal in order to improve beam control.

MOTIVATION

Intensity lost at the focus is a strong function of capture by the mirror systems given the impact of diffraction, see Figure 1.

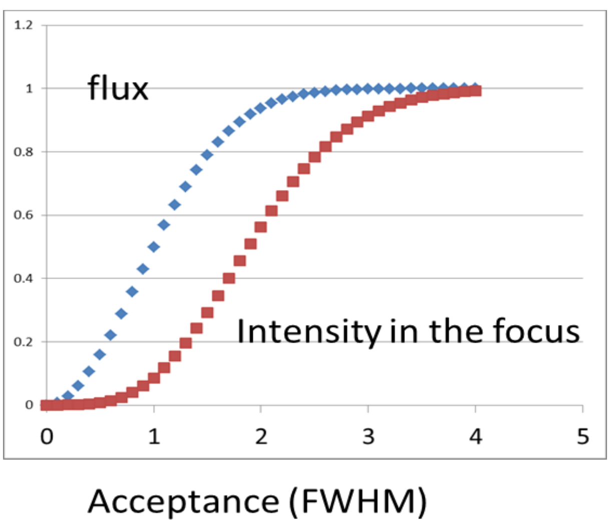

Figure 1: Vertical axis is relative intensity, horizontal axis acceptance of mirror systems cutting in both planes. Blue line is the intensity cut off by mirrors. Red line is the intensity at a downstream focus. Diffraction effects are taken into account.

STUDY APPROACH

We have made many measurements in the Front End Enclosure (FEE) where the distance is relatively close, 87 meters from the end of the undulator. Since increasing the FEL intensity via longitudinal collimation [1] (see Y. Ding's WEP024), we run into the dilemma of either saturating our diagnostic (YAGs) or attenuating the fundamental to the point where third harmonic will begin to impact the measurement. So we extend our measurements to a diagnostic near the Far Hall (FEH) 335 meters from the end of the undulator (Figure 2).

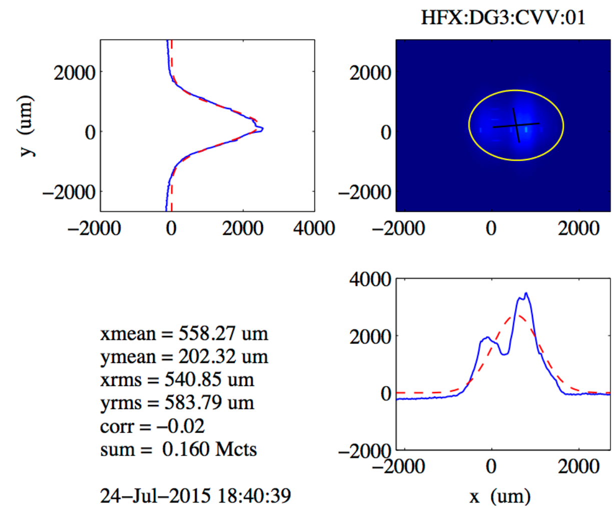

Figure 2: Beam size measured at the Far Hall 335 meters from the end of the undulator. Energy is 8.2 keV. Note the horizontal distortion is due to mirror figure error and diffraction effects [2].

Divergence Model

We applied Z. Huang and K. J. Kim approximation [3], derived in the linear regime, to calculate the photon source size (eq. 2) and the divergence (eq. 3). 1D gain length L_{1D}, in the equation 1, was generated using the Ming Xie parameterization [4]

$$\sigma_D = \sqrt{\lambda L_{1D} / 4\pi} \tag{1}$$

$$\sigma_{ph} \approx \sqrt{\sigma_D \sigma_{el}} \tag{2}$$

$$\sigma_\vartheta = \lambda / 4\pi\sigma_{ph} \tag{3}$$

Figure 3 shows confidence in the Z. Huang and K.J. Kim model (HK model) by corroboration with start to end simulation, which were performed using the GENESIS code [5]. The simulation produces a curved wave front at the end of the undulator, which is then back propagated to the source point, and forward propagated to imager points (see Figure 5).

Figure 4 shows that simulation at 300eV indicates the HK model, derived in the linear regime, should also be good in the non-linear regime.

*Work supported by U.S. Department of Energy, Office of Basic Energy Sciences, under Contract DE-AC02-76SF00515.

ISBN 978-3-95450-134-2

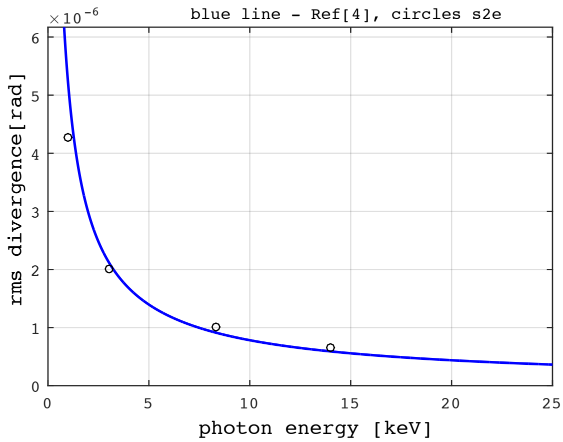

Figure 3: HK Divergence Model (blue line) compared to start-to-end simulations and forward propagation (circles).

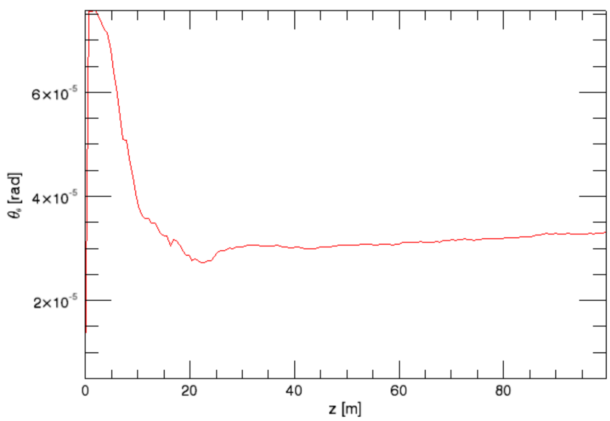

Figure 4: Simulation indicates that at 300 eV there is very small divergence change in the non-linear growth regime. This indicates the HK model should also predict divergence in the non-linear regime.

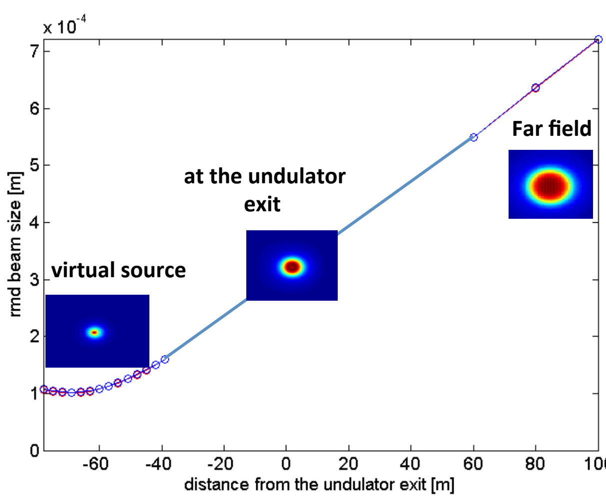

Figure 5: Simulation gives wave front at the exit of the undulator, then it is propagated backward and forward giving the waist (source) and the far field.

Measurements

X-ray beam profile and from that divergence measurements were made both at the 87 meter point and the 335 meter point at various energies near 9 keV. Profiles are fit with a Gaussian and rms values are recorded. Figure 6 shows simulation and model from Figure 3 with measurement results of various operating conditions landing within the rectangle drawn on the plot. This discrepancy of 1.5-2 μrad instead of near 1.0 μrad is the object of study.

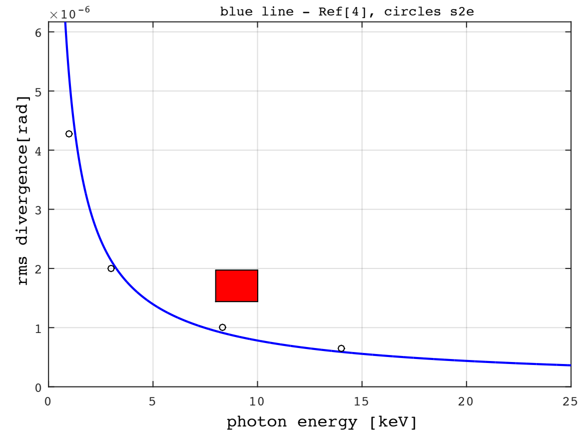

Figure 6: Recent hard x-ray divergence measurements over the past year are represented by the red rectangle.

At 8.2 keV studies were done to understand the difference between measurement and model. Electron beam beta-match in the undulator and undulator alignment were studied.

Beta match in the undulator required expert measurements of electron beam beta-match in the undulator using “beam finder wires” which were originally installed for alignment purposes. Measurement and matching using wire scanners upstream of the undulator leads to very good match in the undulator implying a good model of optics from the wires through the undulator. See Figure 7.

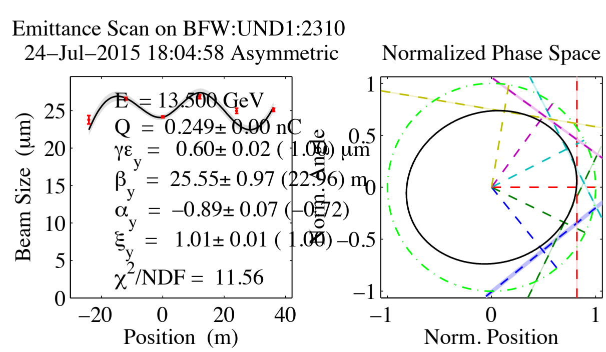

Figure 7: Vertical beta measurement in the undulator using 6 “beam finder wires”. Beta match parameter is 1.01 +/- 0.01 with perfect being 1.0.

ISBN 978-3-95450-134-2

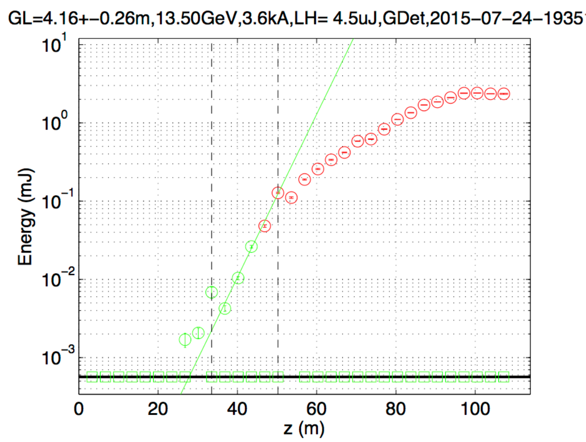

Figure 8: The gain length is measured by a system of gas detector PMTs (photomultiplier tubes) at different high voltage settings to achieve a large dynamic range.

Gain length was measured to insure input to our model was accurate see Figure 8 above.

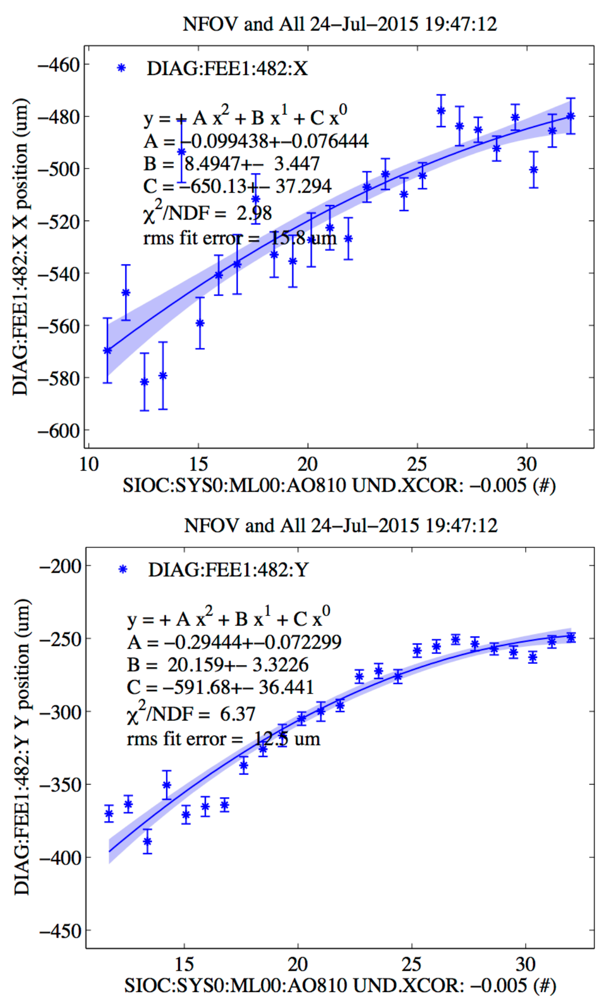

Figure 9: Electron beam is kicked at different points to suppress lasing beyond each point. X-ray position is measured at the imager 87 meters after the undulator.

Curvature of the electron orbit in the undulator was measured in the matched, 4 meter gainlength, 8.2 keV condition shown in Figure 9. Horizontal motion is the top plot, and vertical the bottom.

The electron beta match was varied using a single defocussing quadrupole. The out of plane match change was measured to be very small.

BMAG shown in the bottom plot of Figure 10 is an effective size magnification factor indicating how well the electron beta function is matched [6]. The matched condition was with the quadrupole at -91.4 kG.

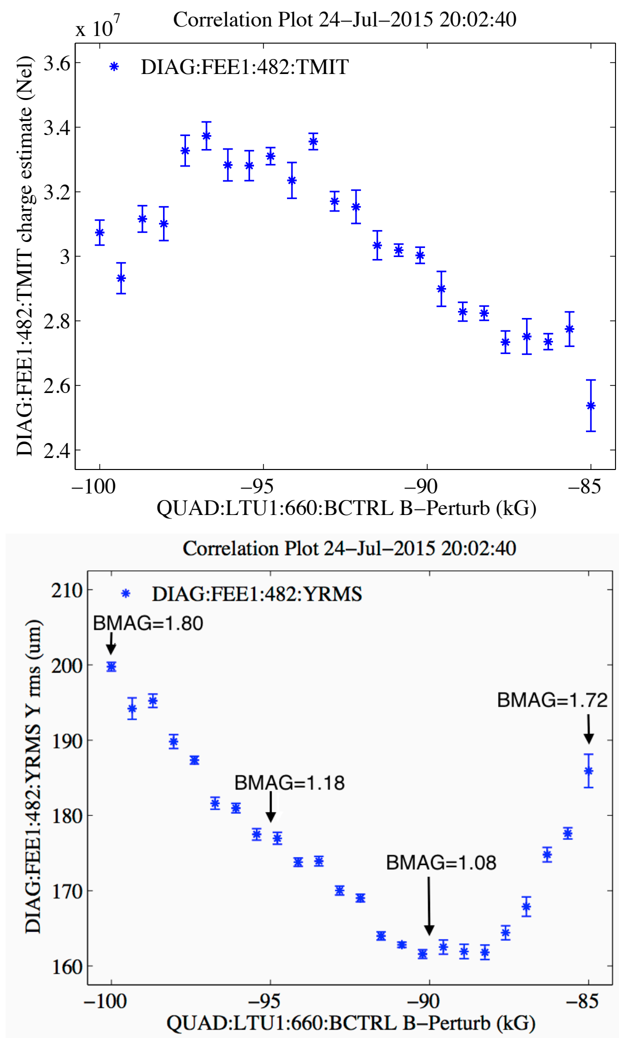

Figure 10: Top plot: x-ray intensity varies with quadrupole scan. Bottom plot: beam divergence changes with match change in the undulator.

SUMMARY

The hard x-ray divergence in LCLS still has an unknown factor of about 1.5 to 2.0 with respect to theory. Studies and improvements in theory and measurement toward understanding are on-going.

Orbit curvature doesn't appear large enough to cause this divergence discrepancy.

Study of matching vertical beta function into the undulator shows minimum divergence in the matched

ISBN 978-3-95450-134-2

condition as simulated by S. Reiche [7]. The intensity upstream of any x-ray focussing is not greatest at that matched condition however.

For normal operation, measurements of electron beam beta-match and x-ray divergence become very important when experiments are working in the focus.

REFERENCES

[1] Y. Ding et al., FEL15, Daejeon, Korea, WEP24, (2015); www.JACoW.org.

[2] J.L. Turner et al., “Transverse Size and Distribution of FEL X-ray Radiation of the LCLS” http://accelconf.web.cern.ch/AccelConf/FEL2011/papers/thoc4.pdf; www.JACoW.org.

[3] Z. Huang, K.J. Kim (2007). "Review of x-ray free-electron laser theory". Physical Review Special Topics - Accelerators and Beams 10 (3)

[4] M. Xie, Nucl. Instrum. and Methods A 445 (2000)59

[5] S. Reiche, Nucl. Instr. Meth. Phys. Res. Sec. A 429, 243 (1999).

[6] M. Sands, “A Beta Mismatch Parameter”, https://accelconf.web.cern.ch/accelconf/p07/PAPERS/TUPMS039.PDF , (1991)

[7] S. Reiche, “Coherence Properties of the LCLS X-ray Beam”, PAC07, https://accelconf.web.cern.ch/accelconf/p07/PAPERS/TUPMS039.PDF

ISBN 978-3-95450-134-2

CONTROL OF GAP DEPENDENT PHASE ERRORS ON THE UNDULATOR SEGMENTS FOR THE EUROPEAN XFEL

Yuhui Li, Joachim Pflueger
European XFEL, Notkestr 85, 22607 Hamburg, Germany

Abstract

Strong magnetic forces in long undulators always result in some girder deformation. This problem gets more serious in long gap tuneable undulators. In addition the deformation varies with changing forces at different gaps resulting in gap dependent phase errors. For the undulators for the European XFEL this problem has been studied thoroughly and quantitatively. A compensation method is presented which uses a combination of suitable shims and pole height tuning. It is exemplified by tuning one of the undulator segments for the European XFEL back to specs.

INTRODUCTION

The European X-ray free electron laser (EXFEL) facility is currently under construction [1]. It uses a superconducting accelerator with a maximum energy of up to 17.5 GeV and the concept of Self-Amplified-Spontaneous-Emission (SASE) [2,3]. Three gap tuneable undulator systems called SASE1, SASE2 and SASE3 are used. SASE1 and SASE2 are hard X-ray FELs using 35 undulator segments each with a period length of 40mm, called U40s. Their total length is 205m. By a suitable choice of beam energy and undulator gap the wavelength can be tuned from 0.05 to 0.4nm. SASE3 is a soft X-ray FEL using 21 undulator segments with a period length of 68mm, called U68s and a total length of 121m. Its wavelength can be tuned from 0.4 to 5.2nm. All undulator segments of the EXFEL are 5m long and use identical mechanical drive and support systems, which are designed to comply with worst case requirements. Table 1 gives a summary of specifications for the Undulator Systems for the EXFEL.

Table 1: Specifications of the Undulator Segments for the EXFEL

	SASE1/2	SASE3
Undulator Type	U40	U68
Period Length [mm]	40	68
Segment Length [m]	5	5
Operational Gap Range [mm]	10-20	10-25
K-Parameter Range	1.65 - 3.9	4 - 9
Max. Phase Error [Degree]	≤ 8	≤ 8
Radiation Wavelength [nm]	0.05-0.4	0.4 – 5.2

A strong magnetic force is acting between the girders of an undulator, which is proportional to the square of magnetic field and therefore strongly gap dependent as well. For example in an U68 operated at lowest gap of 10mm the maximum magnetic force amounts to about 17 tons. This leads to unavoidable mechanic deformation of the girders, resulting in a modulation of the parallel gap profile. Although it can be minimized by a suitable mechanic design, it cannot be avoided completely. Moreover, for given girder cross section, deformation increases with the 3rd power of its length. Therefore the mechanical design of the girders for the 5m long undulator segments for the EXFEL needed to be a compromise between acceptable girder deformation and technical effort i.e. amount of material and cross section.

In this paper the effects of girder deformation on EXFEL U40 undulator segments are studied and their gap dependence and impact on magnetic and optical properties are investigated. A method using a combination of shims and pole height tuning is described, which can be used to effectively reduce optical phase errors resulting from girder deformation. It is exemplified on an U40 undulator segment for the EXFEL.

PHASE ERRORS INDUCED BY GAP DEFORMATION

On all EXFEL undulators gap dependent parabolic deformation is observed to some extent. Pole Height Tuning (PHT) is used as the standard tool for field error correction, which allows to shift each pole verticall by about $\pm 300\mu m$ [4]. It is a perfect tool for static corrections of any deformation at one gap. In order to limit overall deformation and its effect on phase jitter a “Tuning Gap” was selected, which is about halfways inside the operational gap range. 14mm and 16mm were selected for U40s and U68s, respectively. At the tuning gap any deformation of the poles is completely eliminated using PHT. The resulting deformation profile of the poles is sketched in Fig.1 a-c): At lowest gap, Fig. 1a), there is only moderate concave gap deformation. At the tuning gap, Fig. 1b), there is none. Above the tuning gaps the gap deformation gets convex. Two points should be emphasized: 1.) Girder deformation is small and the typical pole height adjustments to compensate deformation are in the range ±50-60µm or less. 2.) The focus is on pole deformation. The deformation of the aluminum support girders cannot be changed. They are perfectly flat only under force free conditions at large gaps and gradually deform from flat to concave towards small gaps. This situation is sketched in Fig. 1a-c) as well.

The result of girder deformation is that the K-parameter slightly varies parabolically along the undulator axis by typically a few tenth of a percent as shown in Fig.1. As a result the phase error varies [5]:

ISBN 978-3-95450-134-2

$$\delta\varphi(z) = -\frac{4\pi}{1+2K^{-2}}\frac{\Delta g}{{\lambda_u}^2}\left(b+\frac{2cg}{\lambda_u}\right)\left(\frac{4}{3L_U^2}z^3-\frac{1}{5}z\right). \quad (1)$$

L_U is the undulator length. Δg is the local gap at undulator ends minus the local gap in the middle as defined in Fig.1), z is the longitudinal position in undulator, λ_u is the undulator period: The constants b and c are the fitting parameters for undulator field:

$$B_0 = a \cdot \exp\left[b\left(\frac{g}{\lambda_u}\right)+c\left(\frac{g}{\lambda_u}\right)^2\right] \quad (2)$$

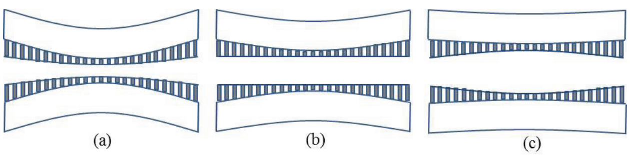

Figure 1: Girder and pole deformation on the EXFEL undulators with applied pole height tuning. (a) At small gaps Δg>0, concave case; (b) At the tuning gap Δg=0, flat case; (c) At large gaps Δg<0, convex case. The aluminium support girders gradually deform from convex at small gaps to flat at very large gaps.

For a purely parabolically shaped deformation like the one shown in Fig. 1 the resulting phase error has odd-symmetry with respect to the undulator center. The RMS phase jitter σ_φ obtained from $\delta\varphi(z)$ can be calculated from Eq. (1):

$$\sigma_\varphi = \sqrt{\frac{16}{1575}}\,\pi\,\frac{\left|\frac{b}{\lambda_u}+\frac{2c\,g}{{\lambda_u}^2}\right|}{1+2K^{-2}}N_U|\Delta g| \quad (3)$$

σ_φ is proportional to the product of the undulator period number N_U and the gap deformation Δg.

Using Eq. (3) the maximum gap deformation Δg is a function of the gap. The tolerance for the phase jitter, 8°, taken from table1 is a conservative choice and originated from Genesis1.3 studies reported in Ref. [5]. It depends on the absolute value for Δg in Eq.(3) meaning it is symmetric for positive and negative Δg corresponding to concave or convex deformation. Thereby a specification window for Δg is defined, as seen by the dashed lines in Fig. 2(a). It is seen that the tolerance for gap deformation increases with increasing gap.

Gap dependent deformation and phase jitter are shown in Fig. 2 for 10 representative U40s of the EXFEL. Considerable variation between individual devices is observed, which can be grouped in the classes: Hollow symbols, (X002, X045 X092, X044) indicate small, half-filled symbols (X043, X055) moderate and full symbols (X005, X006, X007) large gap dependence. All except the one marked with "+", X014, are inside the specification window.

The gap dependence of the phase jitter is shown in Fig. 2 b) for the same devices. Again, all except X014 are below the tolerance limit of 8°. The low deformation devices show low variation of phase jitter as well. On all devices the phase jitter shows a minimum of about 2 degrees near 14mm, which corresponds to the tuning gap.

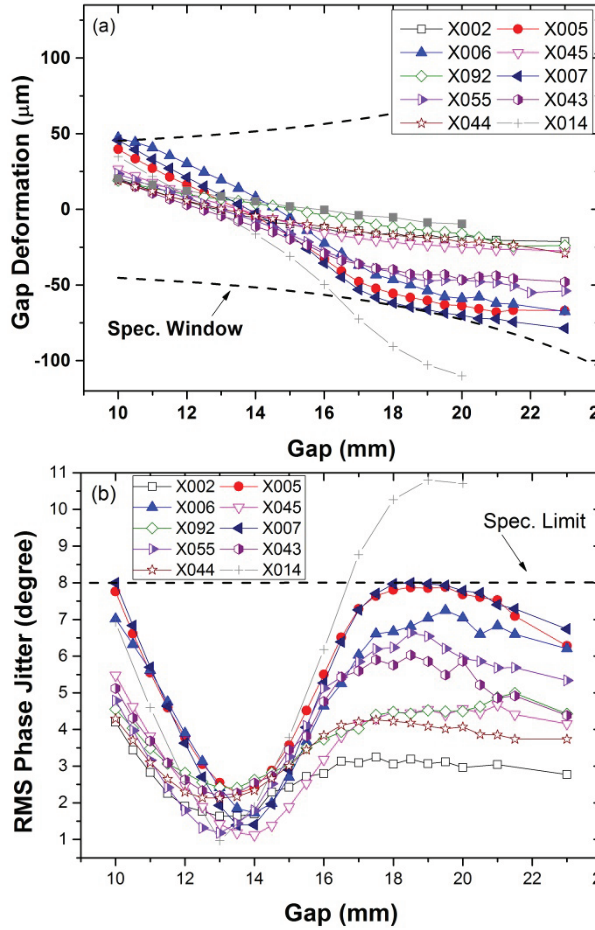

Figure 2: The status of 10 representative U40 undulator segments. a): Gap dependence of deformation. b): Gap dependence of RMS Phase Jitter. Specification limits are indicated.

COMPENSATION OF GAP DEPENDENCE

The reason of the observed variance in girder deformation is not fully understood and still under investigation. Fortunately for all devices except the X014 the Phase Errors are within specs. For this device a time consuming analysis of the mechanical support system and refurbishment was avoided in favour of a timely completion. Instead a compensation method based on using shims was developed, which is described below. It is closely related to the shimming method used at the EXFEL to tune the gap dependence of 1st field integrals of the phase shifters to very low tolerances [6-8].

Description of the Method

As demonstrated in Fig. 1 one can tune pole deformation to a symmetric balance between concave at small and convex at large gaps. However, total deformation cannot be reduced in this way. If it is too large the phase jitter gets out of the specification window as shown in Fig. 2 b). Using suitable shims, however, is an effective method to induce targeted gap dependent modifications of the magnetic field distribution [9-12].

Shims made of 0.1-0.4mm soft iron foil are used, which have the same dimensions like the magnet surface

ISBN 978-3-95450-134-2

[9, 10]. If placed on a magnet in between two poles the field of these two poles is weakened as sketched in Fig. 3. For symmetry reasons there is no net steering. This leads to a K parameter change of ΔK resulting in a phase jump of:

$$\Delta\varphi = 2\pi \frac{K \cdot \Delta K}{1+0.5K^2} \quad (4)$$

For shims ΔK is always negative and $\Delta\varphi$ is negative as well.

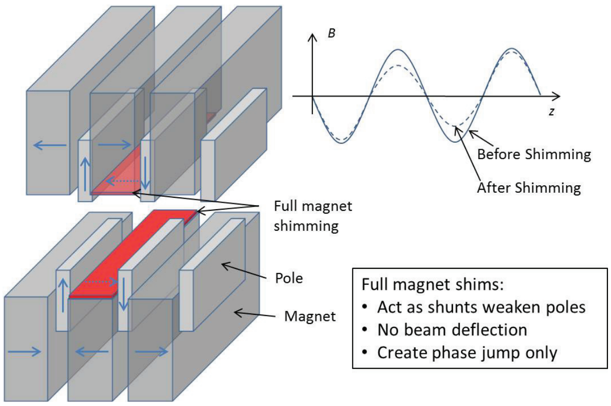

Figure 3: Principle of full magnet shims.

Alternatively a phase "jump" $\Delta\varphi$ can also be generated by pole tuning: By symmetrically changing the local gap of a pair of neighboring poles the sign of ΔK can be chosen and the strength can be varied continuously by increasing or decreasing the local gap. This is a marked difference to shimming.

The gap dependencies of shims and pole tuning were investigated experimentally. The results are presented in Fig. 4. Measurements were done using the U40-X014 again. On one period the pole height of two poles was adjusted symmetrically by -0.05, +0.025, +0.05 and +0.1mm. On another period sufficiently distant away full magnet shims of 0.1, 0.2, 0.3 and 0.4mm thickness were applied. The phase jump was measured for the operational gap range from 10 to 20mm in 2mm steps. The results are shown in Fig. 4a). The abscissa shows the amount of pole height tuning or the shim thickness, respectively. The amount of phase jump is given by the ordinate. For pole height tuning shown in the left upper part of Fig. 4a) it is observed that the phase jumps are proportional to the amount of tuning but for all gaps the jumps are identical. There is no gap dependence. Positive and negative jumps are possible. For shims the situation is different: There is significant gap dependence and all jumps are negative.

In addition Fig. 4a) gives a good impression of the linear dependence of the phase jumps on small pole adjustments or small shim thicknesses, which is an important assumption for both methods [6, 9, 10].

Phase jumps normalized to pole shifts or shim thicknesses are called signatures and are shown in Fig. 4b). Note for the sake of a direct comparison the sign of the signature for pole height tuning was reversed. These signatures are the basis for gap dependent phase tuning. It is obvious that shims and pole height tuning have different gap dependencies. This effect is used for compensation.

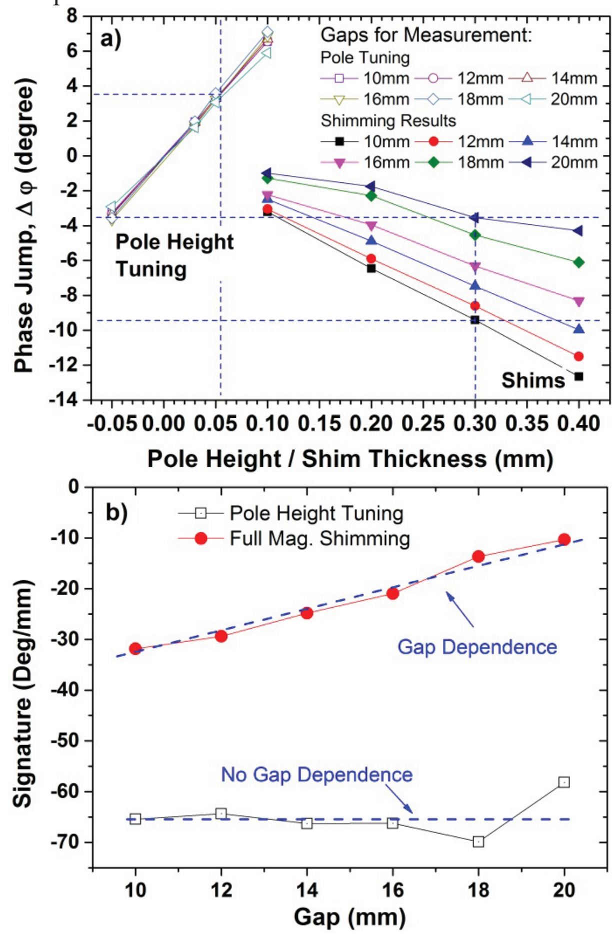

Figure 4: a) Gap dependence of phase jumps Δφ induced by tuning the height of a pair of poles and by shims of different thicknesses. The abscissa shows the amount of pole tuning or shim thickness. The dashed lines should guide the eye for the determination the shimming strengths, see text. b) Resulting signatures. For pole height tuning there is no gap dependence. Note, for direct quantitative comparison the sign of the signature of pole height tuning was reversed. The undulator X014 was used for the measurements.

Phase Tuning Example

The X014 is used as the example to demonstrate the tuning strategy. The original gap deformation and phase jitter after the standard EXFEL tuning procedure using a tuning gap of 14mm was already illustrated in Fig. 2: The gap deformation and phase jitter at small gaps is within and at large gaps is outside specs.

In a first step poles where retuned so that at 20mm gap the phase jitter is well within specs. This is done by shifting the tuning gap to 16mm where now the phase jitter is 1.19° only, see Fig. 5. This is the main work, since it requires to slightly retune all 248 poles of the undulator. Now at 10mm and 20mm 12.85° and 5.36° are obtained, respectively. Since pole tuning cannot reduce total deformation only the gap range of the phase error was shifted. Now the low gap region is out of specs as seen in Fig. 5.

ISBN 978-3-95450-134-2

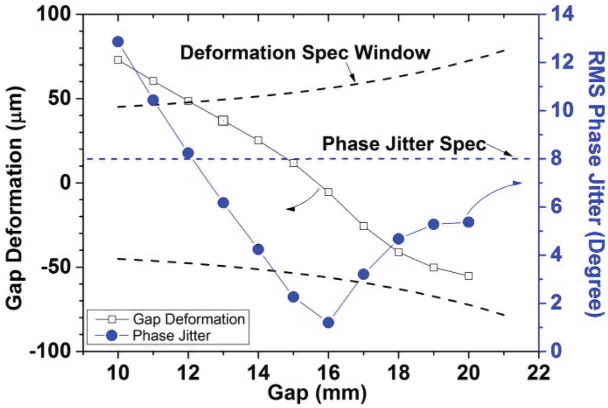

Figure 5: Effect of shifting the "Tuning Gap" to 16mm. Now at 20mm specifications on gap deformation (open squares) and the RMS phase jitter (full circles) are fulfilled, but exceeded at small gaps.

Next, the K-parameter for phase error calculation is slightly reduced resulting in an additional error, see Fig. 6 black and red curve. The K-Parameter is chosen such that the phase error at begin and end is about the same. For this purpose the K-parameter was reduced slightly by 0.0035 or 0.089% from 3.9009 to 3.8974. This initially increases the total phase error. But now there is a long section from z≈ -1300 to 1300mm where the phase error increases almost linearly with positive slope and the end sections with negative slope are shorter.

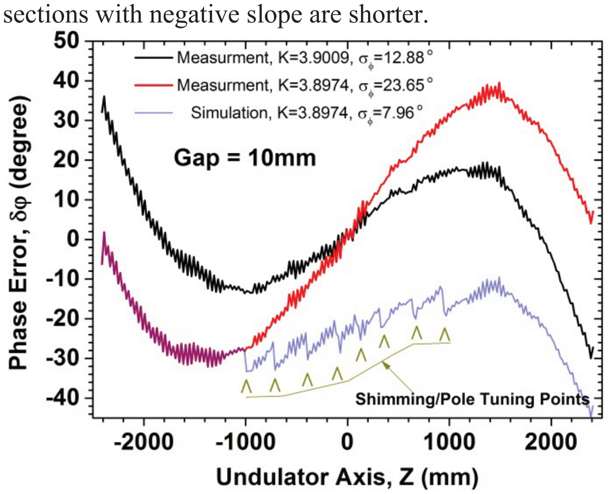

Figure 6: Phase error $\delta\varphi$ at 10mm gap. Black: K=3.9009, resulting in minimum RMS phase jitter of 12.88°. Red curve: K=3.8974 Phase error at start and end are approximately same. Blue: Expected phase error with K=3.8974 after shimming. The expected RMS error is 7.95°

In the linear section phase shims are placed, each reducing the phase error by a step amount. Parameters were selected by the following consideration using Figs. 6 and 4a): *(a)* In Fig. 6 the positive increase of phase errors in the center region extends from -30 to +40°. Only about 50° should be compensated by shims in order to limit the impact of the outer end sections with negative slope on the RMS phase jitter. However the properties at 20mm must stay unaffected. *(b)* In order to do so at that gap the effect of phase shims and pole height tuning must cancel mutually. Using the dashed lines as guides for the eye in Fig. 4a) it is seen that a 0.3mm shim at 20mm creates a negative phase jump of -3.5° which needs to be compensated by a pole shift of +0.055mm, which creates +3.5°. At 10mm this shim creates a phase jump of -9.5° while the pole contribution is constant at 3.5°. The net effect is -6° per shim/pole pair and consequently eight corrections are needed to compensate +48° and approximately fulfill the requirement. The effect of applying these corrections was simulated and is shown by the blue curve in Fig. 6. The RMS simulated phase jitter is 7.95° and inside EXFEL specs.

The final results for the optical phase are shown in Fig. 7a). The black line shows the measured phase error $\delta\varphi$ at the gap of 10mm. The blue circles show the simulated results shown in Fig. 6 shifted up by 24 degrees to match the same absolute scale. There is very good agreement. Finally Fig. 7b) shows the measured phase jitter as a function of the gap. It demonstrates that the RMS phase jitter at the gap of 10mm is reduced to 7.65 degrees, as expected. It is within specs at all gaps.

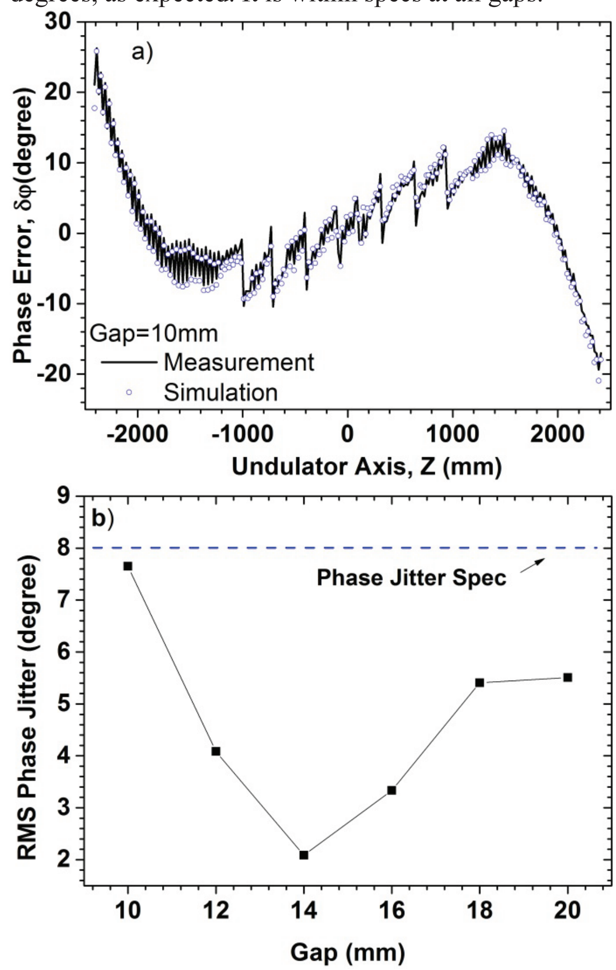

Figure 7. (a) Black curve: Measured phase error $\delta\varphi$ after tuning. Blue open circles: Simulation of Fig. 6 shifted by 24° to match scales. (b) Final gap dependence of the RMS phase jitter as a function of the undulator gap.

ISBN 978-3-95450-134-2

SUMMARY AND OUTLOOK

Gap dependent parabolic girder deformation is commonly observed on the Undulators for the EXFEL and is found to be the dominant source for the RMS Phase Jitter. Analytical formulae are developed which allow a quantitative evaluation and the definition of specifications. Results can be universally applied.

Considerable variation of girder deformation has been observed throughout the undulators built for the EXFEL so. While most are well within specs some come close, but only one out of 91 was found to be out of specs and girder deformation could not be tolerated.

For mitigation a systematic method using shims was developed and is presented in detail. It makes use of the different gap dependencies of full magnet shims and pole height tuning as used for tuning of the EXFEL devices. Measured gap signatures for both cases are used. With this method the RMS Phase Jitter observed initially on one device, which did not comply with specs, could be reduced by about 5° with very moderate effort and brought back to specifications.

Using the method described in this report an EXFEL U40 was treated: The negative effects resulting from gap dependent girder deformation of 110µm were compensated without negative side effects.

A potential application of the method, which would be straight forward to realize could be to significantly reduce the gap dependence of the phase jitter well below the specs given in the paper. This was not needed for EXFEL but might be of great use for long undulators in storage ring operated on high harmonics. For the EXFEL devices a phase jitter of 2° or less over the whole operational gap range seems feasible. Alternatively, the girder stiffness could be reduced by tolerating more mechanical gap deformation. Thus a trade-off between mechanical effort and moderate increase of magnetic measurements and tuning can be obtained.

REFERENCES

[1] M. Altarelli et al., "The European X-ray Free-electron Laser", Technical Design Report, ISBN 3-935702-17-5,2006; http://www.xfel.eu/dokumente/technical_documents

[2] A. M. Kondratenko and E. L. Saldin, Part. Accel. 10, 207 (1980).

[3] R. Bonifacio, C. Pellegrini, and L. M. Narducci, Opt. Commum. 50, 373 (1984).

[4] J. Pflüger, H. Lu, T. Teichmann, Nucl. Instr. and Meth. A429 (1999) 386

[5] Y. Li, B. Faatz, J. Pflueger, Phys. Rev ST-AB 11, 100701 (2008).

[6] Y. Li, J. Pflueger, "Tuning method for phase shifters with very low first field integral errors for the European X-ray Free Electron Laser" , Phys. Rev. ST-AB 8, 030703 (2015).

[7] Y. Li, J. Pflueger, "Compensation of gap dependent kicks by applying shims", Internal EXFEL report WP71/2012/15, unpublished.

[8] Y. Yang, Y. Li, H. Lu, F. Wolff-Fabris J. Pflueger, "Shimming Strategy for the Phase Shifters used in the European XFEL", Proceedings of the FEL2013, Aug 25-30, 2013, New York City, USA, Paper TUPSO42.

[9] J.M. Slater, S.C. Gottschalk, F.E. James, D.C. Quimby, K.E. Robinson, A.S. Valla, Rev. Sci. Instr. 60, (1989) 1881.

[10] D.C. Quimby, S.C. Gottschalk, F.E. James, K.E. Robinson, J.M. Slater, A.S. Valla, Nucl. Instr. and Meth. A285, (1989) 281.

[11] J. Chavanne, E. Chinchio, M. Diot, P. Elleaume, D. Frachon, X. Marechal, C. Mariaggi, F.Revol, Rev. Sci. Instr, 63, (1992) 317.

[12] J. Chavanne, P. Elleaume in "Undulators and Wigglers and their Applications", Taylor & Francis, London, Chapter 5.

ISBN 978-3-95450-134-2

EMITTANCE MEASUREMENTS AT THE PAL-XFEL INJECTOR TEST FACILITY

J. H. Lee, J. H. Han, J. H. Hong, H. Yang, C. H. Kim, S. J. Park, S. J. Lee, I. S. Ko
Pohang Accelerator Laboratory, Pohang, 37673, Korea

Abstract

The PAL-XFEL Injector Test Facility (ITF) at PAL has been operating for experimental optimization of electron beam parameters and for beam test of various accelerator components. It consists of a photocathode RF gun, two S-band accelerating structures, a laser heater system, and beam diagnostics such as ICTs, BPMs, screens, beam energy spectrometers and an RF deflector. Projected and slice emittance measurements were carried out by using single quadrupole scan. In this paper, we present the emittance measurements.

INTRODUCTION

PAL-XFEL is under construction. The building is ready and the accelerator components are being installed. PAL-XFEL will generate 0.1 nm FEL radiation using 10 GeV electron beam at the hard X-ray beamline and 1 nm FEL using 3 GeV beam at the soft X-ray beamline. The design parameter of the injector is 0.4 mm mrad slice emittance at 200 pC [1]. Injector Test Facility (ITF) have been operated to study the injector beam dynamics and to test the accelerator components.

EXPERIMENTAL SETUP

The ITF accelerator consists of an S-band 1.6 cell photocathode RF gun, two S-band accelerating columns, solenoids and beam diagnostics including quadrupoles, ICTs, BPMs, YAG/OTR screens, beam energy spectrometers and an RF deflector. A schematic layout is shown in Fig. 1. A quadrupole and a YAG screen for single quad scan are located at 13.22 m and 15.86 m from the cathode, respectively. We measure the electron beam energy using the beam energy spectrometers and the YAG screens. An RF deflector is located before at the quadrupole for studying longitudinal properties of a bunch. In the RF deflector, the transverse kick varies sinusoidally in time so each part of the electron bunch receives a time-dependent kick[2, 3].

Single Quad Scan

Single quadrupole scan was used for emittance measurements in this paper. The transformation matrix in beam dynamics is described as

$$\begin{pmatrix} x \\ x' \end{pmatrix} = M \begin{pmatrix} x_0 \\ x'_0 \end{pmatrix} = \begin{pmatrix} C & S \\ C' & S' \end{pmatrix} \begin{pmatrix} x_0 \\ x'_0 \end{pmatrix} \quad (1)$$

and

$$\begin{pmatrix} \beta \\ \alpha \\ \gamma \end{pmatrix} = \begin{pmatrix} C^2 & -2CS & S^2 \\ -CC' & CS' + C'S & -SS' \\ C'^2 & -2C'S' & S'^2 \end{pmatrix} \begin{pmatrix} \beta_0 \\ \alpha_0 \\ \gamma_0 \end{pmatrix} \quad (2)$$

Where, M is the beam transport matrix, α, β, γ is the twiss parameters. The transport matrix composed of drift space and quadrupole is represented as

$$M = M_d M_F, \qquad M_d = \begin{pmatrix} 1 & L \\ 0 & 1 \end{pmatrix},$$
$$M_F = \begin{pmatrix} 1 & 0 \\ -kl & 1 \end{pmatrix} = \begin{pmatrix} C & S \\ C' & S' \end{pmatrix}$$

M_d and M_F are drift space and quadrupole transformation matrices, respectively with thin lens approximation ($|k|l \ll 1$) [4]. k is the quadrupole strength, l is the effective length of the quadrupole, and L is distance between the quadrupole and screen. The beam emittance is related with the area of ellipse in phase space. Utilizing the definition of the ellipse equation in phase space and beam matrix,

$$\sigma_{11} = C^2 \sigma_{0,11} + 2SC\sigma_{0,12} + S^2 \sigma_{0,22} \quad (3)$$
$$\sigma_{11}\sigma_{22} - \sigma_{12}^2 = \epsilon^2 \quad (4)$$

Where,

$$\sigma = \begin{pmatrix} \sigma_{11} & \sigma_{12} \\ \sigma_{21} & \sigma_{22} \end{pmatrix} = \epsilon^2 \begin{pmatrix} \beta & -\alpha \\ -\alpha & \gamma \end{pmatrix}, \qquad \sigma_{12} = \sigma_{21}.$$

Using the above equations, we can get a relation as a function of quadrupole strength k [5]. Therefore, the beam emittance is calculated by measuring the beam size at different quadrupole strengths on YAG screen. The specifications of the quadrupole used for single quad scan is described in Table 1.

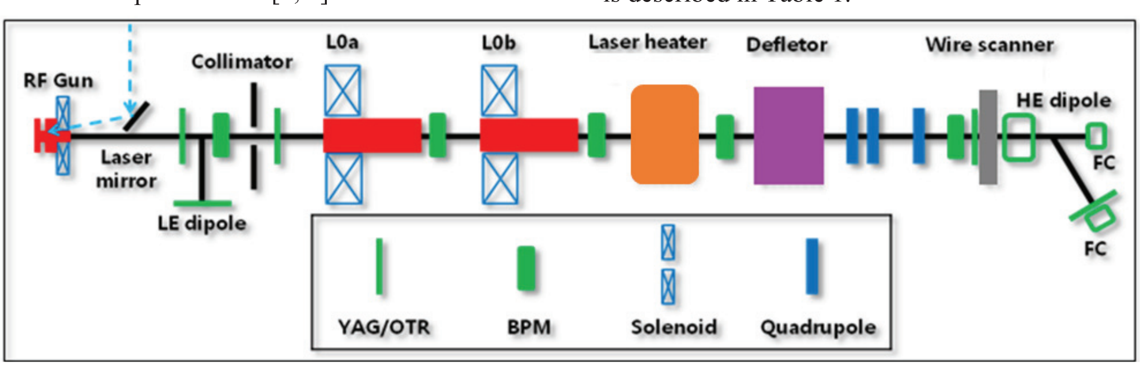

Figure 1: Schematic layout of Injector Test Facility at Pohang Accelerator Laboratory.

Table 1: Specifications of the Quadrupole for Single Quad Scan

Quadrupole parameter	Value	Unit
Effective length	14.7	cm
Max. quadrupole strength	27.97	$/m^2$

Beam Profile Measurement

Longitudinal and transverse shapes of a UV laser pulse dominate the electron beam formation right after beam emission from the cathode. Laser pulse lengths of 3 ps and 5 ps are used to measure projected and slice beam emittance. The measured longitudinal UV laser profile is shown in Fig. 2. A Gaussian fit was used for the pulse length measurements.

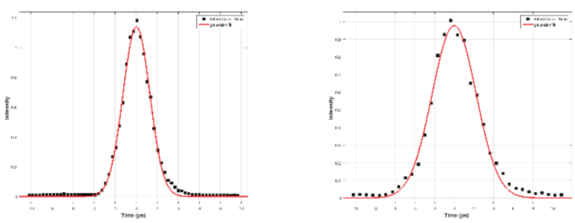

Figure 2: Longitudinal profiles of UV laser pulses. σ and FWHM of 3ps pulse are 1.27 and 3.00 ps, respectively (left). σ and FWHM of 5ps pulse are 2.22 and 5.23 ps, respectively (right).

For the emittance measurements, the phase of the gun was set to 34° from zero-crossing. The phase of the accelerating column was set to on-crest. Bunch charges of 20, 50, 100 and 200 pC were used for the projected emittance measurements. Bunch charge was monitored using the Bergoz Turbo-ICT during the measurements. A beam was accelerated to 68 MeV using the 1st accelerating column. The beam energy was measured using the spectrometer at 15.86 m.

Emittance measurements were done using the quadrupole and YAG screen at 13.22 and 15.86 m downstream of the cathode, respectively.

Slice emittance measurements were carried out using the same way as projected emittance measurements except for using the deflecting cavity for longitudinal streaking. The beam streaking was checked by measuring the beam

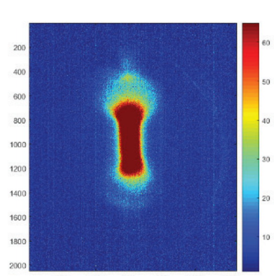

Figure 3: Streaked beam image by the RF deflector on the YAG screen. The head of a bunch is streaked to the top.

image on the YAG screen as the RF power in the deflecting cavity was changed (see Fig. 3). For the slice emittance measurements, a bunch was divided longitudinally to twenty slices. For each measurement, five beam images were taken and averaged.

RESULTS

Projected Emittance

The measurements were repeated using various machine conditions. Two laser pulse lengths, 3 and 5 ps FWHM, and four laser beam size, 0.5, 0.6, 0.8 and 1.0 mm full width, were used at 200 pC. Solenoid current of the RF gun was optimized in order to obtain best emittance value for each measurement.

The result of measurements is shown in Fig. 4. The solid lines represent 3 ps UV laser pulse length and the dashed lines represents 5 ps one. It shows a tendency that the projected emittance using a 3 ps laser is smaller than the one using a 5 ps. The smaller transverse laser size, the lower projected beam emittance.

Unfortunately, the projected emittance is generally higher than 0.8 mm mmrad and it is higher than the expected values from numerical simulations assuming ideal cases. The emittances at lowest beam charges converges towards some range. It may explain the thermal emittance of the photocathode, but its values are bigger than expected ones.

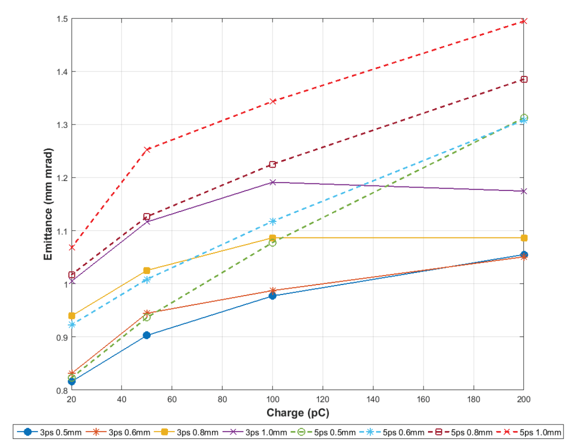

Figure 4: Measured projected emittances at different beam charges, UV laser sizes and pulse lengths. Solid lines describe the UV laser 3ps pulse length and dashed lines describe 5 ps.

Slice Emittance

An electron beam was accelerated up to 102 MeV after the second accelerating column. The phase of 2nd accelerating column was set to on crest. The beam was streaked using the RF deflector. As mentioned before, the slice emittance measurements were carried out using similar conditions as the projected emittance measurements. But, various phases of the 1st accelerating columns were used for the slice emittance measurements.

In case of a 5 ps UV laser, a central slice emittance has a

ISBN 978-3-95450-134-2

lowest value at conditions that are +34 degree RF gun phase, on crest 1st accelerating column phase and 0.8 mm transverse UV laser size. The top and middle figure in Fig. 5 were measured at 0.8 mm of laser size.

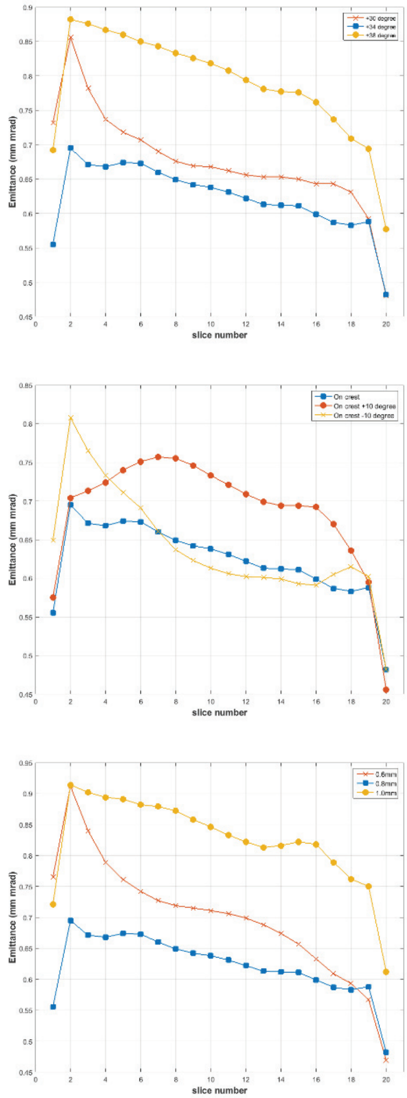

Figure 5: Measured slice emittance using laser 5 ps pulse length at different phase of RF gun (top), 1st accelerating column (middle) and UV laser size (bottom). The measurements of top and middle figure are performed at 0.8 mm laser size.

Measurements using 3 ps laser pulses are almost performed at 1.0 mm transverse laser size. A lowest central slice emittance was obtained under the conditions that are +30 degree of RF gun, -10 degree of 1st accelerating column phase from on crest. But the difference of slice emittance at the central slices through phase variation of the 1st accelerating column is unclear (see middle of Fig. 6). The central slice emittance at 0.8 mm transverse laser size represents a lowest value by comparison with 1.0 mm transverse laser size at +30 degree of RF gun phase and at on crest of 1st accelerating column phase (Fig. 7).

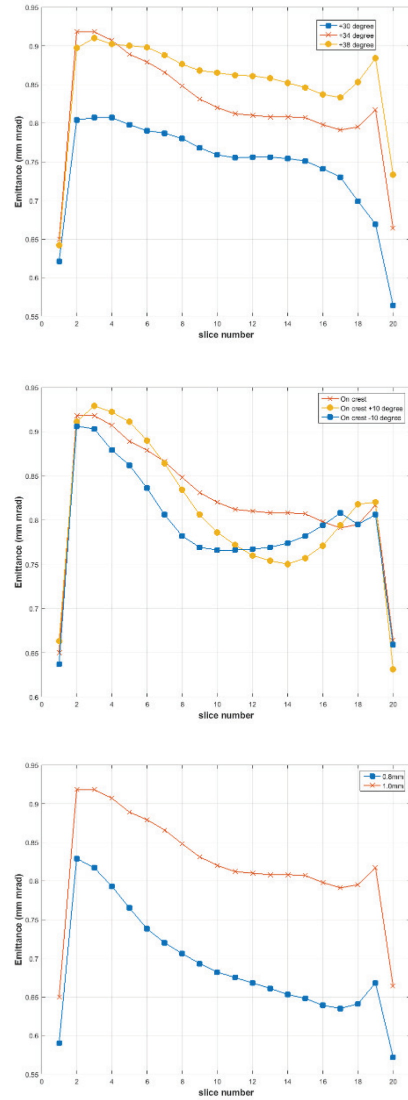

Figure 6: Measured slice emittance using laser 3 ps pulse length at different phase of RF gun (top), 1st accelerating column (middle) and UV laser size (bottom). The measurements shown in the top and middle figures were performed at 1.0 mm laser size.

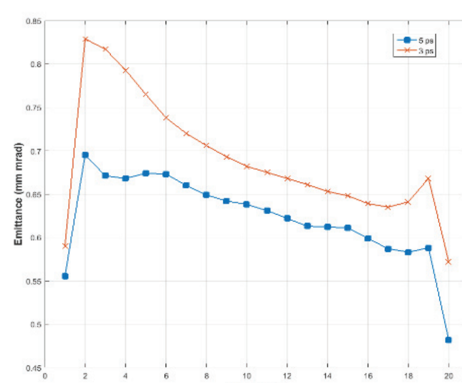

Figure 7: Comparison of optimized slice emittances with laser pulse 3 and 5 ps.

ISBN 978-3-95450-134-2

CONCLUSIONS

Projected and central slice emittances were over 1.0 mm mrad, 0.6 mm mrad at optimized conditions at 200 pC. It seems that the thermal emittance is higher than usually considered value, 1 mm mrad per 1 mm laser size. Additional effects from the non-perfect RF field and magnetic field might be the reason of the higher emittance as well.

REFERENCE

[1] J. Hong et al., "Development of Photocathode RF-Gun at PAL", in *Proceedings of 35th Int. Free Electron Laser Conf.*, New York, 2013, pp. 280-281.

[2] M. Huening et al., "Observation of Femtosecond Bunch Length Using a Transverse Deflecting Structure", in *proceedings of 27th Int. Free Electron Laser Conf.*, California, 2005, pp. 538-540.

[3] J. Shi et al., "A 3-cell Deflecting RF Cavity for Emittance Exchange Experiment at ANL", NIMA, 2008.

[4] H. Wiedermann, Particle Accelerator Physics 3rd edition, (Springer, 2007).

[5] U. Raich, "Accelerator Beam Diagnostics", U.S Particle Accelerator School, Albuquerque, 2009.

ISBN 978-3-95450-134-2

LONGITUDINAL ELECTRON BUNCH SHAPING EXPERIMENTS AT THE PAL-ITF *

Seong-Yeol Kim, Ji-Min Seok, Kook-Jine Moon, Moses Chung†, UNIST, Ulsan, 689-798, Korea
Heung-Sik Kang, Chul Hoon Kim, Juho Hong, Jang-Hui Han, PAL, Pohang, 790-834, Korea
J. Thangaraj, Fermilab, Batavia, IL 60510, USA

Abstract

Longitudinal shaping of electron beam has received much attention recently, due to its potential applications to THz generation, dielectric wakefield acceleration, improvement of FEL performance, and controlled space-charge modulation. Using a set of alpha-BBO crystals, shaping of laser pulse and electron bunch on the order of ps is tested at the Injector Test Facility (ITF) of Pohang Accelerator Laboratory (PAL). Initial experimental results will be presented with analytical theory and numerical simulations

INTRODUCTION

Bunch- and current-shaping of low energy electron beams are essential beam manipulation techniques for compact light sources, narrowband radiation generation, two-color FEL's, seeding techniques, advanced accelerators, mitigation of collective effects, and diagnostics [1]. To have a precise control of the longitudinal profile of the electron beam, a method to shape the photocathode drive laser is often used.

Several techniques to shape the longitudinal laser pulses of picosecond durations were introduced in recent years, such as line-delay technique, echelon lenses, acousto-optic programmable dispersive filter, or DAZZLER, to mention a few examples. In particular, the direct UV pulse shaping using alpha-BBO crystals is known to be a relatively cheap, compact, and power-efficient technique [2, 3].

In this work, we present initial experimental results on the shaping of laser pulses and electron bunches on the order of ps obtained at the Injector Test Facility (ITF) of Pohang Accelerator Laboratory (PAL) using a set of alpha-BBO crystals. We note that, for the PAL-XFEL, a flat-top longitudinal profile is considered in addition to the nominal Gaussian profile, for the improvement of projected emittances [4]. Using three sets of alpha-BBO crystals, for example, we indeed expect to have a flat-top beam distribution to a good approximation.

BASIC THEORY

The temporal separation between two polarizations, i.e., the ordinary wave (perpendicular to the optical axis) and the extraordinary wave (parallel to the optical axis) is given by [2]

$$\Delta t = L\left|\frac{1}{v_{ge}} - \frac{1}{v_{go}}\right| = \frac{L}{c}\left|n_{ge} - n_{go}\right| = \frac{L}{c}\Delta n_g, \quad (1)$$

where L is the length of the crystal, $v_{go} = c/n_{go}$ and $v_{ge} = c/n_{ge}$ are the group velocities of the o-wave and e-wave respectively. Here, c is the speed of light in vacuum, and n_{go} and n_{ge} are *group* indices of refraction of the o-wave and e-wave respectively.

We use commercially available alpha-BBO's for this experiment. The high temperature phase Barium Borate (alpha-BBO, α-BBO) is a negative uniaxial crystal with a strong birefringence (large Δn_g) over the broad transparent range from 189 nm to 3500 nm. Two alpha-BBO crystals of lengths 7.5 mm and 15 mm are used. Since the spot size of the UV laser (253 nm) used for this experiment is rather big, the clear aperture (diameter) of the alpha-BBO crystals are chosen to be 15 mm. An anti-reflection coating is applied on the surfaces of the alpha-BBO crystals, which also protects the surfaces from ambient moisture. The alpha-BBO crystals are kept inside the clean room to avoid moisture absorption, and they are mounted on the precision rotation stages.

The indices of refraction are given by the Sellmeier equations (λ in μm) as (see also Fig. 1)

$$n_o^2 = 2.7471 + 0.01878/(\lambda^2 - 0.01822) - 0.01354\lambda^2, \quad (2)$$

$$n_e^2 = 2.37153 + 0.01224/(\lambda^2 - 0.01667) - 0.01516\lambda^2. \quad (3)$$

The group index of refraction (n_g) is calculated from the index of refraction (n) as (see also Fig. 2)

$$n_g(\lambda) = n(\lambda) - \left(\frac{dn(\lambda)}{d\lambda}\right)\lambda. \quad (4)$$

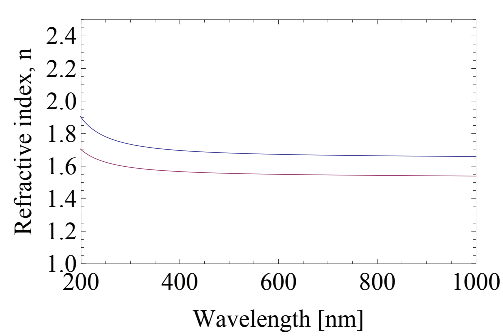

Figure 1: Indices of refraction for o-wave (blue) and e-wave (red) calculated by Sellmeier's formula.

For $L = 7.5$ mm, we expect $\Delta t = 6.55$ ps, and for $L = 15$ mm, $\Delta t = 13.1$ ps. The laser intensity of multiple Gaussian beams can be approximate as

$$I(t) = \sum_{i=1}^{n} \frac{1}{n} \exp\left(-\frac{(t-t_i)^2}{2\sigma_t^2}\right). \quad (5)$$

* This work was supported by the 2015 Research Fund (1.150124.01) of UNIST(Ulsan National Institute of Science and Technology)
† mchung@unist.ac.kr

ISBN 978-3-95450-134-2

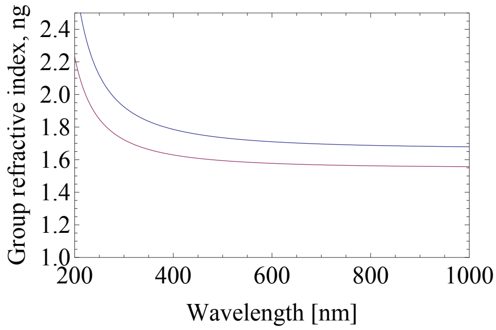

Figure 2: Group indices of refraction for o-wave (blue) and e-wave (red) calculated by Eq. (4).

where σ_t is the rms pulse length of the laser beam. We assumed that the peak intensity of the initial single Gaussian beam is normalized to be 1. Examples of multiply stacked Gaussian beams with FWHM = $2\sigma_t\sqrt{2\ln 2}$ = 3 ps are illustrated in Fig. 3.

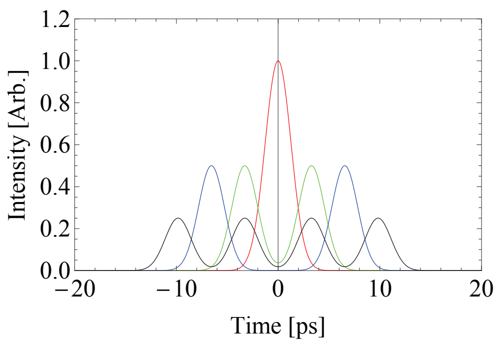

Figure 3: Examples of longitudinal profiles of the multiple Gaussian laser pulses. Each Gaussian has a FWHM of 3 ps. Red curve: single Gaussian, green curve: inserting alpha-BBO crystal of L = 7.5 mm, blue curve: inserting alpha-BBO crystal of L = 15 mm, black curve: inserting both the alpha-BBO crystals.

INJECTOR TEST FACILITY

To demonstrate performances of the sub-systems of the PAL-XFEL, and to develop high-brightness photo-cathode RF gun and various diagnostic techniques, the injector test facility (ITF) was constructed at PAL [4]. The ITF consists of a photo-cathode RF gun, a 30-mJ Ti:Sa laser system, two S-band (2.856 GHz) accelerating structures, two sets of klystron-modulator systems, and various instrumentations (screens, spectrometer magnets, Turbo Integrated Current Transformer etc.) [5]. A transverse deflecting cavity (S-band, 10-fs resolution) is installed at the end of the beamline, which allows longitudinal beam profile measurements [6]. In this experiment, beam profiles are measured using two YAG scintillator screen (indicated by screen 3 and screen 4 in Fig. 4) imaged with CCD cameras. The typical parameters for the ITF and electron beams are summarized in Table 1.

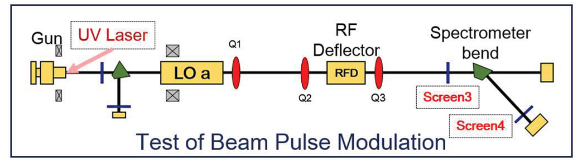

Figure 4: Beam elements and diagnostics setup at the Injector Test Facility (ITF).

Table 1: Summary of the ITF System and Typical Beam Parameters Used for this Experiment

Component	Parameter	Value	Unit
RF-gun	Operating frequency	2.856	GHz
	RF-pulse width	2	μs
	Repetition rate	10	Hz
Laser (UV)	FWHM	1.5 ~ 5.5	ps
	Wavelength	253	nm
Deflecting cavity	Operating frequency	2.856	GHz
	Structure length	1061.4	mm
	Operating mode	TM_{110}	-
	Temporal resolution	~ 10	fs
	Kick/$\sqrt{}$Power	2.7	MV/$\sqrt{}$MW
Electron beam	Energy	~ 81	MeV
	Charge	~ 200	pC
	Energy spread (rms)	0.1	%

LASER SYSTEM

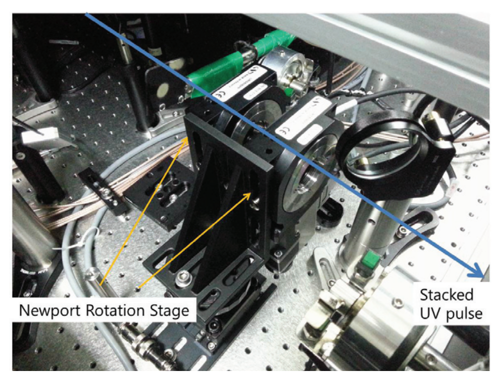

Figure 5: Optics setup for UV laser pulse stacking. The alpha-BBO crystals are mounted on the high-precision rotation stages. Minimum incremental motion of the stages is 0.0005°.

The ITF laser system provides both UV laser beam for the photocathode e-beam gun (see Fig. 5 for the setup used in this experiment) and IR laser beam for the laser heater. The main Ti:sapphire laser system generates >20 mJ picosecond pulses at 760 nm. The spectral bandwidth is limited to 1.5 nm, which is a compromise between good spatial mode in UV conversion and fast rise time in time domain. Time-domain measurement of ps laser pulses is based on the optical cross correlation method using nonlinear mixing in BBO crystal.

ISBN 978-3-95450-134-2

To obtain higher time resolution, fs pulses from the oscillator is mixed with the unknown ps pulses. A high speed data acquisition board is used to remove background noise and to measure each pulse of the cross correlation signal [4]. Measurement results with laser pulses of 3 ps FWHM are given in Fig. 6. The 45° orientation angle with respect to the optical axis of the crystal creates equal intensities for e-wave and o-wave [2, 3]. The relative intensity between the two waves could be controlled by a simple rotation of the optics axis. This ramped pulse generation would be investigated in the next experiment run.

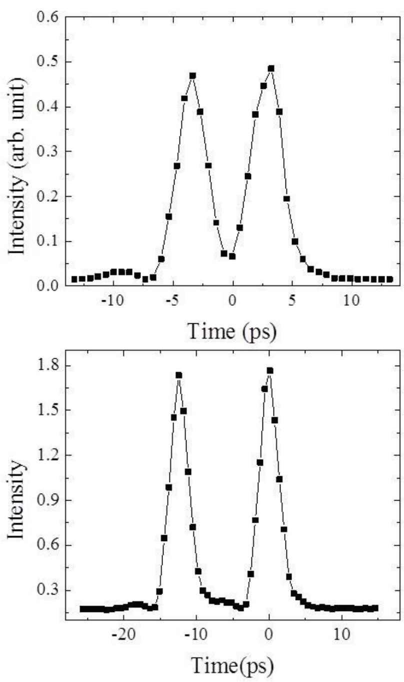

Figure 6: Results of the time-domain measurement of the multi-peak laser pulses: $L = 7.5$ mm (top) and $L = 15$ mm (bottom). Time differences between two peaks are measured to be 6.273 ps and 12.3665 ps, respectively, which are slightly smaller than the theoretical estimations.

RESULTS

To convert the pixel numbers in the screen images into the time difference, we first performed the calibration of the RF deflecting cavity. We measured the pixel numbers of the center of the beam images in screens 3 and 4 by scanning RF phase (1 degree step) of the deflecting cavity. For the operating frequency of 2.856 GHz, we note 1 degrees correspond to 0.973 ps. Based on the calibration data presented in Figs. 7 and 8, we obtain the calibration factors of 7.0735 fs/pixel for screen 3, and 9.5447 fs/pixel for screen 4.

Figure 9 shows the reference beam images generated by the 3 ps FWHM laser pulse. For both images, the measured FWHM's of the electron beam profiles are enlarged. In Figs. 10 and 11, screen images are taken after inserting alpha-BBO crystals of $L = 7.5$ mm and of $L = 15$ mm,

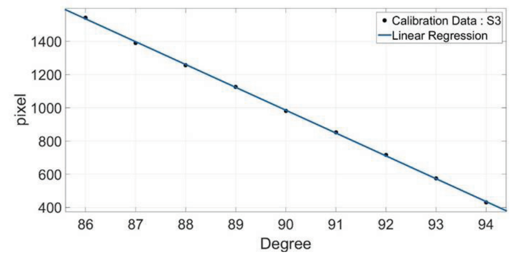

Figure 7: Calibration data for the longitudinal beam profile measurement using deflecting cavity and screen 3.

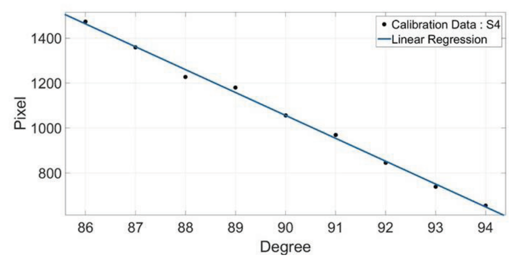

Figure 8: Calibration data for the longitudinal beam profile measurement using deflecting cavity and screen 4.

respectively. For both cases, the time differences between two peaks measured based on screen 3 (4.32 ps and 6.32 ps) are shorter than the analytical estimations (6.55 ps and 13.1 ps) and time-domain measurement of the lase pulses (6.273 ps and 12.3665 ps). Also the general trends are that the profiles estimated from the screen 4 are more widely spread. Particularly for the experiment with the longer crystal ($L = 15$ mm), the total bunch length increases too much that the transverse focusing is applied unevenly between head and tail (see blurred spots in the upper-left image in Fig. 11). We note that if the transverse beam size is too big, than the projected image generated by the deflecting cavity loses its resolution.

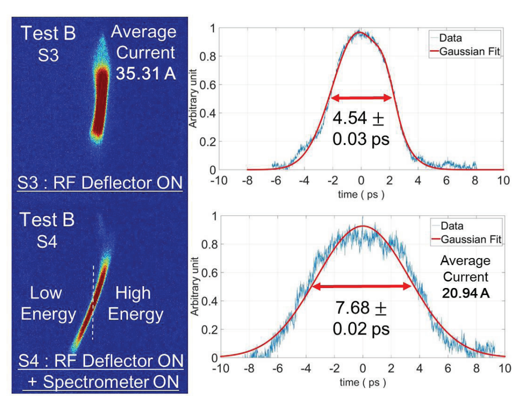

Figure 9: Beam images measured on screen 3 (top row) and screen 4 (bottom row) without inserting BBO crystals. The intensity profiles projected onto the vertical axis indicate time structure of the beam. A 3 ps FWHM laser pulse is used.

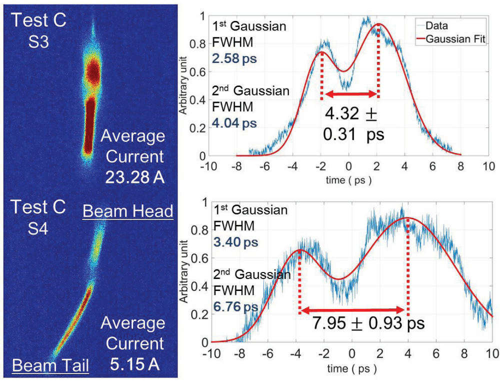

Figure 10: Beam images measured on screen 3 (top row) and screen 4 (bottom row) after inserting BBO crystal of L = 7.5 mm. A 3 ps FWHM laser pulse is used.

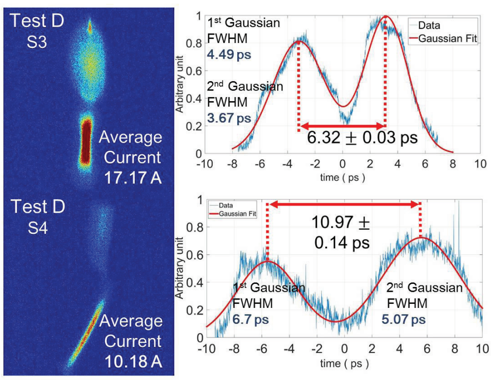

Figure 11: Beam images measured on screen 3 (top row) and screen 4 (bottom row) after inserting BBO crystal of L = 15 mm. A 3 ps FWHM laser pulse is used.

To test the possibility of flat beam profile generation, we apply 5 ps FWHM laser pulse after inserting alpha-BBO crystals of L = 7.5 mm. As illustrated in Fig. 12, it is clear that the two peaks are nearly overlapped and the beam center shows rather flat profile.

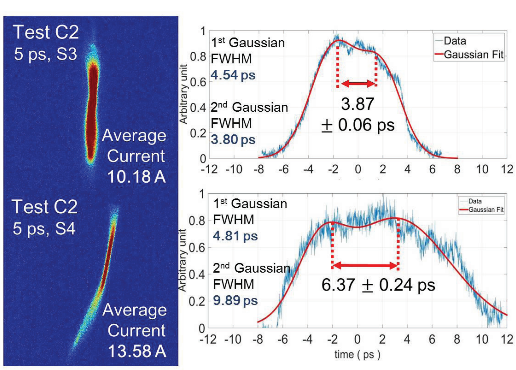

Figure 12: Beam images measured on screen 3 (top row) and screen 4 (bottom row) after inserting BBO crystal of L = 7.5 mm. A 5 ps FWHM laser pulse is used.

To examine the experimental results, we performed numerical simulations using ASTRA and ELEGANT codes. Since space-charge effects are strong at low beam energies, we used ASTRA code from the photocathode surface to the end of the accelerating cavity (L0a in Fig. 4). For the rest of the beamline, the ELEGANT code has been used to track particles. Reasonable agreements have been obtained as shown in Fig. 13. We plan to run more detailed simulations to fully understand our experimental results.

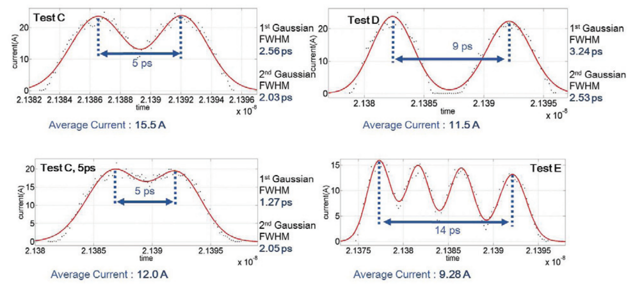

Figure 13: Simulation results obtained from ASTRA and ELEGANT codes.

CONCLUSIONS AND FUTURE WORK

As future work, we will further investigate methods to generate flat-top beam distributions for the PAL-XFEL. In addition, we plan to study the response of the longitudinally-modulated beam to a dechirper [7]. Understanding the interactions between electron beams of various longitudinal shapes with the wakefields generated by the dechirper will be important to assess the feasibility of the dechirper for use as a deflector.

REFERENCES

[1] P. Piot et al., "Overview of Alternative Bunch and Current-Shaping Techiniques for Low-Energy Electron Beams", MOD02, *These proceedings*, FEL2015, Daejeon, Korea (2015).

[2] J.G. Power et al., "High Frequency Bunch Train Generation from an RF Photoinjector at the AWA", MO6RFP047, *Proceedings of PAC09*, PAC'09, Vancouver, BC, Canada (2009).

[3] J. Thangaraj et al., "Z-SHAPER: A Picosecond UV Laser Pulse Shaping Channel at the Advanced Superconducting Test Accelerator", THPP059, *Proceedings of LINAC2014*, LINAC'14, Geneva, Switzerland (2014).

[4] *PAL-XFEL Technical Design Report* (Pohang Accelerator Laboratory, 2013).

[5] J. Hong et al., "Beam Measurement of Photocathode RF-Gun for PAL-XFEL", THP011, *Proceedings of FEL2014*, FEL'14, Basel, Switzerland (2014).

[6] J.-H. Lee et al., "Slice Emittance Measurement Using RF Deflecting Cavity at PAL-XFEL ITF", TUP013, *Proceedings of FEL2014*, FEL'14, Basel, Switzerland (2014).

[7] H.-S. Kang et al., "A Beam TEst of Corrugated Structure for Passive Linearizer', TUP093, *Proceedings of FEL2014*, FEL'14, Basel, Switzerland (2014).

ISBN 978-3-95450-134-2

NUMERICAL AND EXPERIMENTAL STUDIES ON ELECTRON BEAM PROPERTIES FROM ASYMMETRIC RF-GUN*

S. Rimjaem#, N. Chaisueb, N. Kangrang, E. Kongmon, K. Kosaentor, J. Saisut, C. Thongbai, W. Thongpakdi, P. Wichaisirimongkol
Plasma and Beam Physics Research Facility, Department of Physics and Materials Science, Faculty of Science, Chiang Mai University, Chiang Mai 50200, Thailand

Abstract

The electron linear accelerator at the Plasma and Beam Physics (PBP) Research Facility, Chiang Mai University (CMU), Thailand, is used to produce femtosecond electron bunches for generation of THz radiation. The main components of the PBP-CMU linac are a thermionic RF electron gun, an alpha magnet, an S-band travelling-wave linac structure, quadrupole lens, steering magnets, and various diagnostic components. The RF-gun consists of a 1.6 cell S-band standing-wave structure and a side-coupling cavity. The 2856 MHz RF wave is transmitted from the klystron to the gun through a rectangular waveguide input-port. Both the RF input-port and the side-coupling cavity cause an asymmetric electromagnetic field distributions inside the gun. This leads to asymmetric transverse shape with larger emittance value. Beam dynamic simulations were performed to investigate the effect of the asymmetric fields on the electron properties by using the code PARMELA. Simulation results suggest that the beam with a maximum kinetic energy of 2.51 MeV, a bunch charge of 0.21 nC and horizontal and vertical emittance values of 20.43 and 19.55 mm-mrad can be achieved. The experiments to investigate the performance of the RF-gun were performed. The results show that at optimal condition the gun can produce the beam of about 2 μs (FWHM) pulse width with a maximum kinetic energy of ~2.8 MeV and a macropulse charge of 850.1±34.7 nC.

INTRODUCTION

A linac-based THz radiation source at the Plasma and Beam Physics (PBP), Chiang Mai University, consists of an S-band thermionic RF electron gun, an alpha magnet, a travelling-wave linac structure, quadrupole focusing magnets, beam steering magnets, transition radiation stations and several diagnostic components. An electron source is a 1.6-cell S-band standing-wave RF-gun. A thermionic cathode is installed at the center of the rear wall of the first half-cell. A WR-284 rectangular RF waveguide is connected to the RF-gun at the radial wall of the full-cell. The RF wave from the full-cell is coupled to the half-cell through a side-coupling cavity. Opening holes between the main cavities and the RF input-port as well as the side-coupling cavity cause asymmetric electromagnetic field distributions inside the gun. In order to study the effect of this feature on the electron beam properties, 3D RF and beam dynamics simulations of the first PBP-CMU RF-gun were performed. The study results show that electron beams produced from asymmetric RF-gun have asymmetric transverse shape and larger transverse emittance than the beams produced from the symmetric one [1]. This RF-gun was dismounted from the PBP-CMU linac system. Then, the new RF-gun was installed in July 2011. It has both common and different features with the previous one. Numerical and experimental studies were conducted to investigate the characteristics and the performance of the new RF-gun.

PRESENT PBP-CMU RF-GUN

The current RF electron gun in the PBP-CMU linac system was constructed at the High-energy Optics and Electronics (HOPE) Laboratory, National Tsing Hau University and the National Synchrotron Radiation Research Center (NSRRC), Taiwan, R.O.C [2]. The design of this gun is similar to the first PBP-CMU RF-gun with some different features, which are a nose-cone thermionic cathode, an adjustable tuning plug, a smaller opening hole of the RF input-port on the full-cell radial wall. Moreover, cooling channels are located inside the wall of the gun cavities for better gun temperature control. The 3D drawing and the inner cut-view of the present PBP-CMU RF-gun are shown in Fig. 1.

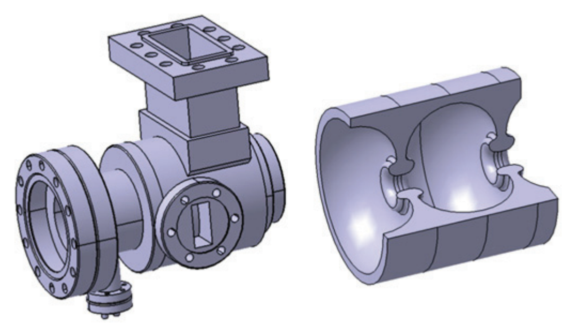

Figure 1: 3D drawing and inner cut-view of the present RF-gun at the PBP-CMU linac facility.

This RF-gun was transported from NSSRC to Chiang Mai University and has been installed as the electron source of the PBP-CMU linac after the cavity re-tuning process. According to the study results in [3], the flat-cathode is used instead of the nose-cone one to decrease the transverse emittance of electron beams at the RF-gun exit. The gun was operated with the forward RF peak power of 3.65 MW and 3 μs (FWHM) pulse width. The

*Work supported by the CMU Junior Research Fellowship Program.
#Corresponding author: sakhorn.rimjaem@cmu.ac.th

ISBN 978-3-95450-134-2

beam with a central kinetic energy of around 1.5 MeV and a beam macropulse current of 400 mA was obtained [4]. However, due to the incomplete copper plating at the area around the cathode heat-dam, the leak of the RF wave occurred. This led to the breakdown of the gun operation. Therefore, the repair of copper plating on the heat-dam surface was performed.

The cavity-tuning and low-level RF measurements in ambient air at the room temperature of 26.2°C were conducted to investigate the RF parameters of the gun. In addition, the bead-pull measurements were performed during the cavity-tuning process. Amplitudes of the electric field in the half and full cells was adjusted by moving the tuning plug inside the side-coupling cavity. The final ratio of the peak electric field at the center of the full-cell to that at the cathode position is 2.20. Results of RF measurements are listed in Table 1. The tuning plunger of this RF-gun has special design for allowing the re-adjustment of the field ratio even after the final fabrication and brazing process [2]. Therefore, the dependence of electron beam properties on the field ratio can be studied.

Table 1: Measured RF-Gun Parameters for π/2 –Mode

Parameters	Value
Resonant frequency	2855.68 MHz
Quality factor	12264
RF-coupling coefficient (β_{rf})	3.06
Field ratio (E_{p2}/E_{p1})	2.20

NUMERICAL SIMULATIONS

Simulations of Electromagnetic Fields

A computer code CST Microwave Studio (MWS) 2012[@] [5] was used to create a 3D model of the RF-gun (Fig. 2) for studying RF properties and electromagnetic field distributions inside the gun. The tuning-rod position was varied to obtain the field ratio as close as possible to the simulated value. This tuning process was difficult because it required the mesh adjustment for each tuning step. The best simulated peak field ratio (E_{p2}/E_{p1}) is 2.13 at the resonant frequency of 2855.73 MHz for π/2 operation mode. Simulated on-axis electric field profile along the beam propagating path was extracted and the result is agreed well to the measurement data (as shown in Fig. 3). Some RF parameters obtained from the MWS simulations for each mode are summarized in Table 2.

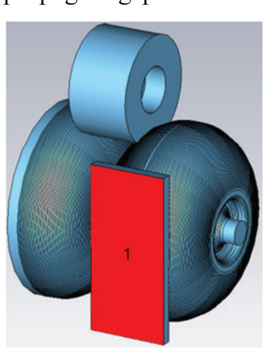

Figure 2: Simulated 3D MWS model of the RF-gun.

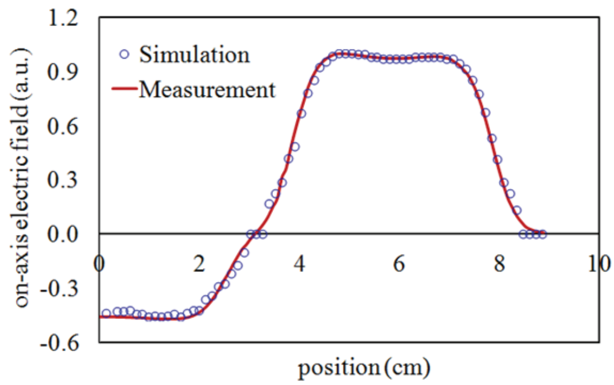

Figure 3: Simulated and measured on-axis electric field distributions inside the RF-gun.

Table 2: Summary of Simulated RF-Gun Parameters

Parameters		Value
Resonant frequency (MHz)	0-mode	2541.80
	π/2 –mode	2855.73
	π –mode	2868.74
Quality factor	0-mode	6647
	π/2 –mode	16943
	π –mode	13796
Field ratio (E_{p2}/E_{p1})	π/2 –mode	2.13

Beam Dynamics Simulations

A particle tracking code PARMELA [6] was used to study longitudinal particle distributions as well as transverse profiles and phase spaces of the electron bunch. In simulations, an electron bunch with a total charge of 0.91 nC per RF period are tracked through the electromagnetic fields, which were obtained from the RF simulation output from the program CST MWS. Radial and longitudinal mesh sizes used in simulations are 0.42 mm and 0.89 mm, respectively. The initial electron kinetic energy of 0.165 eV was used, which corresponds to the cathode temperature of 950°C.

Simulation results in Fig. 4 show that the longitudinal phase space distribution of the beam has linear energy-time correlation with a large fraction of particles accumulated at the head of the bunch. This particle distribution is suitable for the bunch compression using the alpha magnet. Unfortunately, the transverse phase spaces have asymmetric distributions (Fig. 5), which leads to a larger emittance value than the beam produced from the symmetric gun. Simulated parameters of the electron bunch at the RF-gun exit are listed in Table 3.

To study the beam transportation from the RF-gun to downstream components, the simple simulations including further drift length of 180 cm were conducted and the results are shown in Fig. 6. It is clearly seen that

ISBN 978-3-95450-134-2

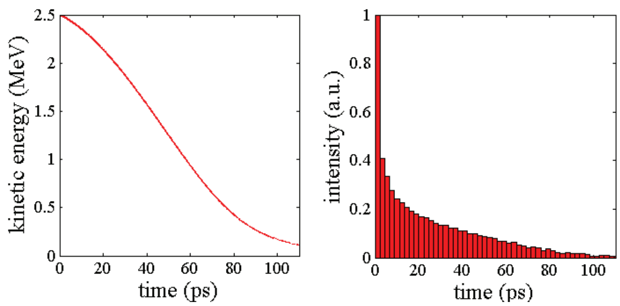

Figure 4: Simulated longitudinal phase space distribution and histogram at the RF-gun exit.

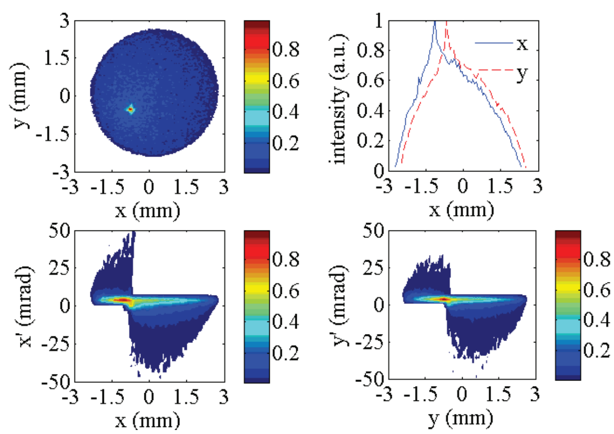

Figure 5: Simulated transverse phase space distributions at the RF-gun exit.

the beam width increases and it is bigger than the diameter of the beam tube (~2.5 cm) at about 70 cm downstream the gun exit. This distance corresponds to the vertex position of the alpha magnet. Energy slits inside the alpha magnet vacuum chamber are used to filter the electrons with low kinetic energies for sufficient post acceleration in the linac and for good beam transportation to the experimental stations. The fraction of useful electrons can be investigated experimentally, which is discussed in the experimental results section. In Fig. 6, the transverse beam emittance decreases when the beam travelling downstream the RF-gun. This is due to the particle lost along the propagating path.

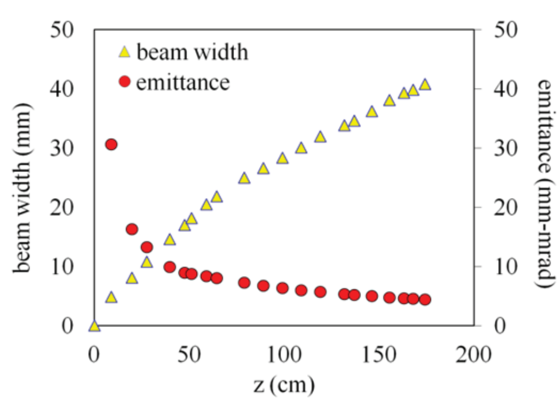

Figure 6: Beam width and beam transverse emittance evaluation from the gun exit through a 180 cm drift tube.

Table 3: Simulated Beam Parameters at the RF-Gun Exit

Parameter	Value
Electric field at cathode	30.62 MV/m
Electric field at full-cell center	64.86 MV/m
Maximum kinetic energy	2.51 MeV
Bunch charge	0.21 nC
Horizontal centroid position	-1.3 mm
Vertical centroid position	-0.7 mm
Horizontal rms beam size	1.150 mm
Vertical rms beam size	1.152 mm
Horizontal rms emittance	20.43 mm-mrad
Vertical rms emittance	19.55 mm-mrad

EXPERIMENTAL RESULTS

During the RF-gun commissioning and the beam characterizations in this study, we used the high power RF pulses with the repetition rate (*ppt*) of 10 Hz and the pulse width of about 3 μs (FWHM). The operating temperature of the RF-gun was controlled by using the cooling system with the precision of the measured temperature around 0.2°C. The high power RF measurements were done to clarify the optimal condition for the RF-gun operation. The RF-coupling coefficient (β_{rf}) was estimated from the amplitudes of forward and reflected RF waves as

$$\beta_{rf} = \frac{1 \pm \sqrt{P_r / P_f}}{1 \mp \sqrt{P_r / P_f}}, \quad (1)$$

where P_f and P_r are the peak powers of the forward and the reflected RF waves, respectively. The PBP-CMU RF-gun is over-coupled to an external RF source, the upper sign in Eq. (1) is used.

Results of high-power RF studies for three gun temperatures are reported in Table 4. It is noted that the forward and reflected RF peak powers (P_f and P_r) in Table 4 were considered at the optimal position, where the most RF absorption occurred.

Table 4: Results of High-Power RF Measurements

Parameters	32°C	34°C	36°C
P_f	3.44 MW	3.86 MW	3.47 MW
P_r	0.96 MW	1.23 MW	1.32 MW
β_{rf}	4.10	4.57	5.24

Current transformers CT1 and CT2 are used to measure electron charge per macropulse at the positions upstream

ISBN 978-3-95450-134-2

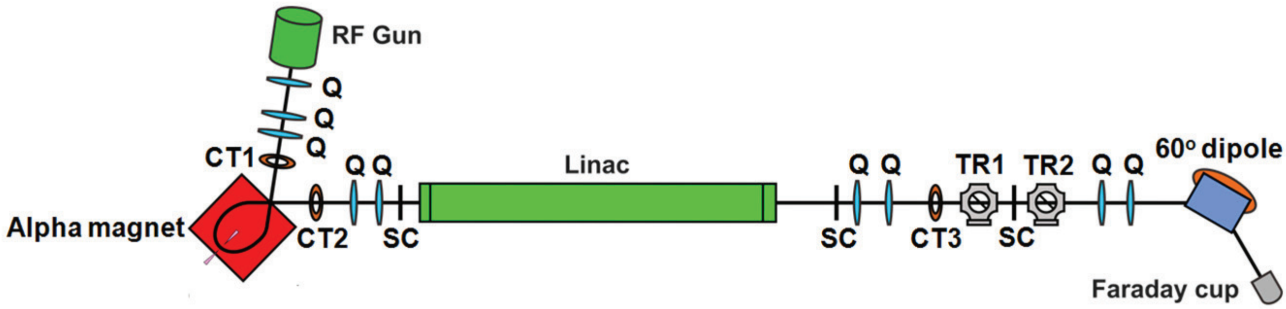

Figure 7: Schematic layout of the PBP-CMU linac system.

and downstream the alpha magnet (as shown in Fig. 7). The CT1 measurement results in Fig. 8 reveal that the RF-gun produced electron beams with the charge almost the same amount for all three considered gun temperatures. The overall results for 22 sets of measurements, which each set has 6 measurement points, show that the beam with the charge of 783.9±63.0 nC, 850.1±34.7 nC and 889.7±79.7 nC were achieved at the gun temperatures of 32, 34 and 36^{o}C, respectively. Although the beam charge values are similar for all three cases, but the gun can produce electron beams with small standard deviation at the gun temperature of 34^{o}C.

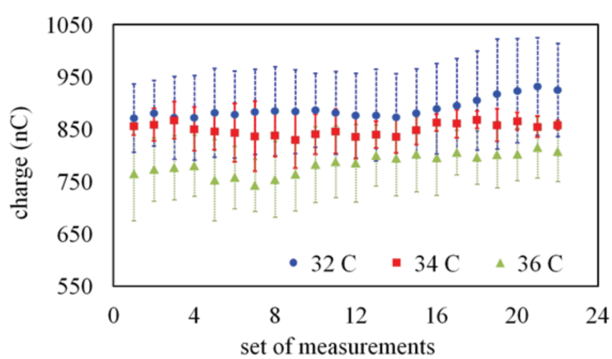

Figure 8: Results of charge measurements.

Electron beam energy was measured using energy slits inside the alpha magnet vacuum chamber. The electron charge values for each energy interval (0.2 MeV bin) for the gun temperature of 34^{o}C are shown in Fig. 9. About 50% beams with the kinetic energy lower than 1 MeV

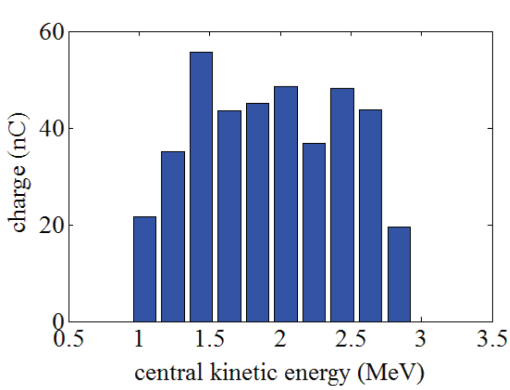

Figure 9: Energy spectrum for the cathode power of 27 W and the RF-gun temperature of 34^{o}C.

was filtered out using the low energy slit. The results in Fig. 9 show that electrons in the main part of the beam have energies in the range of 1.5-2.5 MeV. This beam will be transported further to be accelerated by the linac and will be used as the source of THz radiation.

CONCLUSION

The new RF-gun was installed as the electron source for the PBP-CMU linac system in 2011. Characteristics of this RF-gun are under the investigation. Numerical and experimental studies were performed to study the properties and the performance of the RF-gun. At optimal condition, the beams with maximum kinetic energy of around 2.8 MeV and the macropulse charge of 850.1±34.7 nC were measured at the gun temperature of 34^{o}C. The transverse projected emittance will be measured after the installation of the new diagnostics.

ACKNOWLEDGMENTS

This work has been supported by the CMU Junior Research Fellowship Program and the Department of Physics and Materials Science, Faculty of Science, Chiang Mai University. The authors grateful to the generous support for the RF-gun from the High-energy Optics and Electronics (HOPE) Laboratory, National Tsing Hau University and the National Synchrotron Radiation Research Center (NSRRC), Taiwan, R.O.C.

REFERENCES

[1] S. Rimjaem, K. Kusoljariyakul, C. Thongbai., Nucl. Instrum. Methods Phys. Res. A 736, 10 (2014).

[2] W.K. Lau et al., "*Characterization and Tuning of a Microwave Gun Cavity*", PAC'05, Knoxville, Tennessee, USA, May 2005, p. 1748 (2005); http://www.JACoW.org

[3] S. Rimjaem et al., Nucl. Instrum. Methods Phys. Res. A 533, 258 (2004).

[4] P. Boonpornprasert et al., "*RF Gun Commissioning for PBP-CMU Linac System*", AGRC'12, Chiang Mai, Thailand, p. ST-564 (2012).

[5] Microwave Studio, Computer Simulation Technology, Darmstadt, Germany; http://www.cst.com

[6] L.M. Young, J.H. Billen, *PARMELA*, Technical Note LA-UR-96-1835, Los Alamos National Laboratory (2002).

ISBN 978-3-95450-134-2

STUDY ON UNDULATOR RADIATION FROM FEMTOSECOND ELECTRON BUNCHES

N. Chaisueb†, S. Rimjaem, Plasma and Beam Physics (PBP) Research Facility, Department of Physics and Materials Science, Faculty of Science, Chiang Mai University, Chiang Mai 50200, Thailand

Abstract

Linac-based terahertz (THz) source at the Plasma and Beam Physics (PBP) Research Facility, Chiang Mai University (CMU), Thailand, consists of a thermionic RF electron gun, an alpha magnet for magnetic bunch compressor, a travelling wave S-band accelerating structure for post acceleration, and various beam diagnostic instruments. The PBP-CMU linac system can produce relativistic femtosecond electron bunches, which are used to generate coherent THz radiation via transition radiation technique. To increase the radiation intensity, an electromagnetic undulator will be added in the beam transport line. The designed electromagnetic undulator has 35 periods with a period length of 64 mm and a pole gap of 15 mm. This study investigates the dependence of the electron beam energy and longitudinal bunch length on the coherent undulator radiation. The numerical simulation and procedure to generate the undulator radiation in the THz regime by using femtosecond electron bunches produced at the PBP research facility is reported and discussed in this contribution. Numerical calculation result shows that the energy of the undulator radiation, which is produced from electron bunches with an energy of 5 - 20 MeV, a peak current of 33 - 55 A, and an effective bunch length of 180 - 300 fs can reach 14 μJ.

INTRODUCTION

In the last decade, electromagnetic radiation in the THz regime has become interesting spectrum in many applications. The THz radiation can pass through non-metallic materials, but it is reflected by metal and is absorbed by liquid. Due to this unique characteristic, the THz radiation is used in several researches involved THz spectroscopy and non-destructive distinguish analysis of different density materials, e.g. THz imaging, which can be used in many applications. For examples, it is used to detect metallic and non-metallic weapons, explosive materials, and drugs through concealing obstacles such as clothing or packaging. Therefore, it is useful for airport security, homeland security and defense [1]. Moreover, it is possibly used to observe the correctness of the integrated circuits, such as semiconductor devices and electronic cards, which are enclosed in non-metallic package [2]. A tooth cavity in enamel and the cancerous region compared to the healthy region of human tissue can also be detected by THz imaging [3]. This leads to widely studies in development of THz light sources, detectors, and several experimental techniques.

At Chiang Mai University, relativistic electron bunches produced from the PBP-CMU linac system was firstly used to generate THz radiation by transition radiation technique in March 2006 [4]. The electron beam is produced from the RF-gun with the maximum kinetic energy of about 2 - 2.5 MeV and a bunch length of around 100 - 200 ps [5]. The beam with long bunch length was then compressed and accelerated by using the alpha magnet and the travelling wave s-band linac structure, respectively. Then, it arrives at the experimental station with the bunch length of 180 - 300 fs and the total energy of 10 - 15 MeV. Transition radiation is emitted when electrons passing through a boundary between two different dielectric media. At the PBP facility, a thin Al-foil was placed in the electron's path at the experimental station. Then, the radiation is emitted from the interface between vacuum and the Al-foil resulting from an electric field discontinuity at the transition area of the materials with different dielectric constants. The radiation was, then, measured by using a Michelson interferometer and a pyroelectric detector. The spectrum of the THz transition radiation generated from electron beam with an electron energy of 10 MeV and a bunch length of 200 fs overs the wave number of about 80 cm^{-1} with the radiation energy of around 9 - 22 μJ per macropulse [4]. The produced THz radiation was used to create THz images via a transmission mode of imaging technique for several materials, such as cut-pattern in Al-foils, raw and cooked rice grains, water drop, and a fresh leaf [4].

The power of the THz radiation generated from the present setup of the PBP-CMU linac via transition radiation is merely in milliwatt scale resulting in low-resolution THz images. Therefore, a plan to increase the power or the intensity of the THz radiation by using a coherent undulator radiation method is conducted. This is in order to be able to apply the THz radiation in various researches for distinguishing material components with high resolution.

UNDULATOR MAGNET

In the future setup of the accelerator system, an electromagnetic undulator will be inserted as the new experimental station in the beam line as shown in Fig. 1. Typical undulator magnets compose of a periodic structure of dipole magnets. A static magnetic field is alternating along the length of the undulator with a certain period length. Electrons in a short bunch moving through the undulator magnetic field are oscillating in the transverse direction and emitting the radiation coherently. Therefore, the undulator radiation of femtosecond

†natthawut_chai@cmu.ac.th

ISBN 978-3-95450-134-2

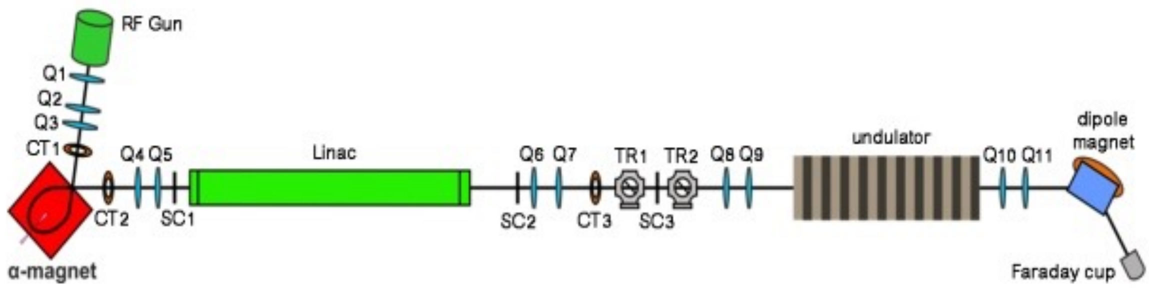

Figure 1: Future setup of the PBP CMU-linac with undulator magnet. The letters Q, CT, SC and TR represent quadrupole magnets, current transformers, screen stations, and transition radiation stations.

electron bunches is very intense, coherence, and is concentrated in the narrow band of spectrum.

An undulator radiation wavelength (λ_r) depends on undulator period length (λ_u), undulator parameter (K), and electron beam energy (E) as [6]

$$\lambda_r = \frac{\lambda_u}{2n\gamma^2}\left(1+\frac{K^2}{2}+\theta^2\gamma^2\right), \quad (1)$$

where $\gamma = E/m_e c^2$ is the Lorentz factor, m_e is the rest mass of electron and c is the speed of light. The harmonic number (n) is integer numbers 1,2,3,… and θ is the angle of observation related to the average beam direction. The undulator parameter can be calculated by using the following equation [6]

$$K = \frac{eB_0\lambda_u}{2\pi m_e c} = 0.934 B_0\lambda_u, \quad (2)$$

where B_0 is the peak magnetic field of the undulator. For $K \ll 1$, the fundamental harmonic $(n=1)$ is only considered. For $K \geq 1$, the radiation power is maximum at the fundamental harmonic and it is more intense for the first few harmonics.

The undulator magnet is designed and simulated for both 2D and 3D models with the computer codes SUPERFISH [7] and RADIA [8], correspondingly. Preliminary, this electromagnetic undulator consists of 71 magnet poles, return yokes and conducting coils. The pole number was correctly defined to be an odd number in order to have enough number of poles to guide the electron trajectory back to the mid-plane of the magnet. The number of period (N_p) is 35 periods with a period length of 64 mm and the pole gap of 15 mm. The maximum period number is limited by the length of available space for installation of the undulator magnet, which will be located downstream the linac and the transition radiation stations (TR1 and TR2) as shown in Fig. 1. This available space is around 2 - 2.5 m.

The undulator parameter or the magnetic field strength of the undulator can be adjusted by varying the coils' current or the width of the pole gap. Due to limitation of a vacuum chamber height located in the gap of the undulator, the desired undulator parameter will be reached by adjusting the coils' current. The magnetic field of the undulator is alternating in the vertical direction throughout the magnet length. Consequently, the field on the undulator axis of each pair of magnet poles (upper and lower poles) is similar to that of a dipole magnet, which is given by [9]

$$B_0 = \frac{\mu_0 NI}{h}, \quad (3)$$

where NI is the total coils current in terms of number of turns in a conducting coil and the current, h is the magnet pole gap, and μ_0 is the permeability in the vacuum. The relation between the undulator parameter and the total current considered from equation (2) and (3) is shown in Fig. 2. It shows that the undulator parameter obviously has a linear relation with the total current.

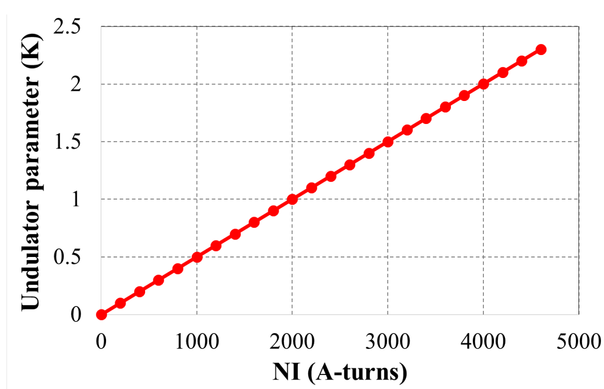

Figure 2: The undulator parameter as a function of the total current of the conducting coils.

Currently, the PBP-CMU linac system can produce femtosecond electron bunches with a typical electron energy up to 15 MeV. Higher beam energies (~20 - 25 MeV) can be achieved with higher feeding RF power. To study the dependence of the undulator specifications on the electron beam energy, we consider 5 cases of 5, 7, 10, 15, and 20 MeV electron beams. Then, the undulator wavelength and the undulator parameter are determined by using equations (1) and (2) for the first harmonic $(n=1)$ and only for on-axis radiation $(\theta = 0)$. The calculated

ISBN 978-3-95450-134-2

wavelength as a function of the undulator parameter for various electron beam energies is shown in Fig. 3.

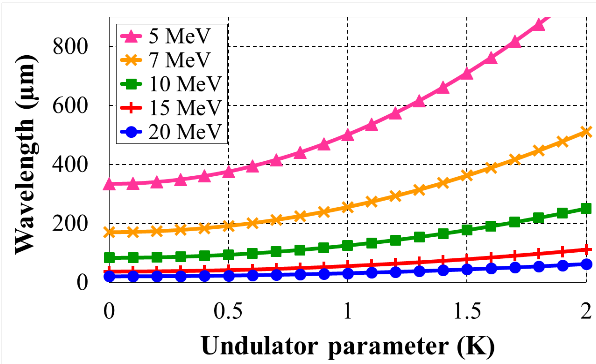

Figure 3: The undulator radiation wavelength as a function of the undulator parameter for the electron energies of 5, 7, 10, 15 and 20 MeV.

The undulator parameter is considered to be around 1, which is not required too high magnetic field. Figure 3 indicates that the wavelength range of the output radiation gets broader as the electron energy decreases for the undulator parameter up to 1. The wavelength of around 30 - 500 μm can be obtained at the undulator parameter of 1 with the total current of 2000 A-turns for electron beam energies of 10 MeV.

UNDULATOR RADIATION

The undulator radiation emitted from relativistic electrons subjected into periodic fields will be considered as the coherent synchrotron radiation (CSR) when the electron bunch length is equal or shorter than the radiation wavelength. This leads to properly add up of the emitted radiation from individual undulator poles in the forward direction and results in the enhancement of the radiation brightness as the brightness of the coherent radiation is proportional to the electron number squared. The defecting angle of the electron beam traveled in the undulator is no larger than the natural opening angle of the emission pattern in the laboratory frame. Consequently, the emitted radiation is collimated in forward direction and has narrow spectral range at a well-specified wavelength [10]. Nevertheless, the required spectral regime of the undulator radiation can be shifted by changing the undulator parameter that can be varied via adjusting the current of the conducting coils of the undulator magnet.

The total CSR energy (W_{coh}) depends on the radiation energy of a single electron (W_{1e}), the number of electron (N_e) squared, and the form factor (f_k) squared given by [11]

$$W_{coh} = W_{1e} N_e^2 f_k^2 , \tag{4}$$

where

$$W_{1e} = \frac{\pi q_e^2 N_p}{3\varepsilon_0 \lambda_u} K^2 \gamma^2 . \tag{5}$$

Here, q_e is the electron charge and ε_0 is the permittivity of free space. Typically, the form factor of the electron beam with the bunch length (σ) can be estimated to be the Gaussian distribution with a standard deviation (σ), where k is the wave vector expressed by [11]

$$f_k = e^{-\sigma^2 k^2} . \tag{6}$$

The emanated radiation features depend on the specific properties of the electron beam and the undulator magnet. The electron bunch charge (Q) at the experimental station is considered to be 25 pC which is equal to electrons [4]. This value was regarded throughout the calculation in this section. The peak current $(\hat{I})$ is defined by the bunch charge and the bunch length to be about 33 - 55 A, which can be calculated by the well-known formula

$$\hat{I} = \frac{Q}{\tau_{eff}} = \frac{Q}{\sqrt{2\pi}\sigma} , \tag{7}$$

where τ_{eff} is the effective bunch length. Specifications of the electron beam produced from the PBP-CMU linac and the designed undulator magnet are shown in Table 1.

Table 1: Summary of Electron Beam Properties of PBP-CMU Linac and The Designed Undulator Magnet

Parameters	Value
● Electron beam at the undulator entrance	
Electron energy	5 - 20 MeV
Bunch charge	25 pC
Bunch length	180 - 300 fs
Peak current	33 - 55 A
● Designed undulator magnet	
Undulator parameter	≈1
Period length	64 mm
Number of periods	35 periods
Pole gap	15 mm

The CSR wavelength as a function of the form factor for the electron bunch length of 180, 240, and 300 fs are presented in Fig. 4. The form factor is smaller when the electron bunch length increases or the electron bunch expands longitudinally. The calculation results in Fig. 4 show the proportional relation between the CSR wavelength and the form factor of electron beam. The radiation wavelength range generated from the short electron bunch is broader than that of the long electron bunch when considering in the form factor of 0.001 - 1.

ISBN 978-3-95450-134-2

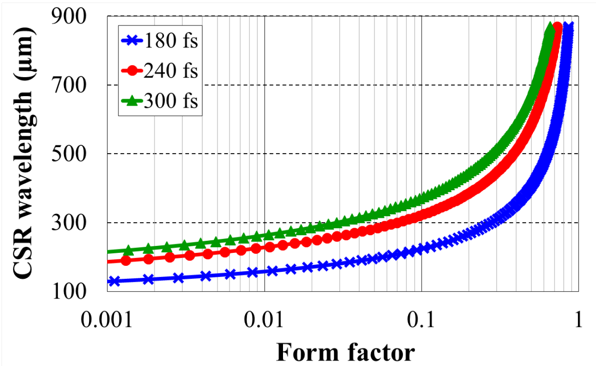

Figure 4: The CSR wavelength versus the electron form factor for the electron bunch length of 180, 240, and 300 fs.

Furthermore, Fig. 5 also shows the relation between the total CSR energy and the CSR wavelength considered for the chosen electron energy of 10 MeV and the bunch length of 180, 240, and 300 fs.

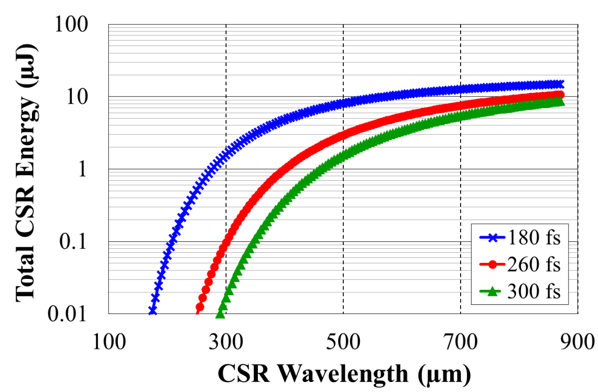

Figure 5: The total CSR energy as a function of the CSR wavelength for the electron bunch length of 180, 240 and 300 fs.

The graphs in Fig. 5 indicates that the total CSR energy is logarithmically increases and then saturates up to about 10 µJ at the CSR wavelength of 800 µm for all three bunch lengths. The radiation energy is higher when the electron bunch length is shorter at certain wavelength. When the 10 MeV electron beam with a bunch length of 180 fs and a bunch charge of 25 pC travels in the magnetic field of the undulator magnet with the undulator parameter of 1 and the undulator gap of 15 mm, the CSR energy of up to 14 µJ per microbunch can be obtained.

In general, the spectral brightness is determined to be the number of photons per second per unit solid angle per unit solid area in a constant fractional bandwidth [10]. While the width of the peak is a function of the number of undulator periods, the transverse size, and the divergence of the electron beam [12]. Preliminary study of the spectrum is considered by using the radiation simulation program called B2E with the ideal sinusoidal magnetic field. The ideal angular flux density, which is often used instead to present the radiation brightness, is calculated from the 10 MeV electron beam and the peak undulator field of 0.1674 T ($K \approx 1$) for the bunch lengths of 180, 240, and 300 fs. The results are shown in Fig. 6.

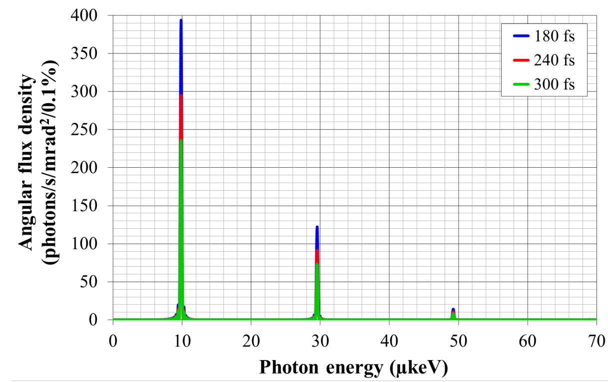

Figure 6: Angular flux density as a function of photon energy with the electron energy of 10 MeV for the bunch lengths of 180, 240, and 300 fs.

The result shows that the angular flux density at the fundamental harmonic for all electron bunch lengths is accomplished at the photon energy of 9.85 µkeV with a quasi-monochromatic peak of spectrum. Moreover, the angular flux density increases when the bunch length is shorter.

CONCLUSION

Preliminary study on coherent undulator radiation from femtosecond electron bunches was conducted. The undulator radiation wavelength and energy are tunable by adjusting the current of the conducting coils of the undulator magnet. The calculation results show that the radiation wavelength of around 30 - 500 µm can be obtained for the electron beam energies of 5 - 20 MeV. When the shorter electron bunch length is achieved, the short radiation wavelength is generated with the high radiation energy and high brightness. Further study with actual undulator magnetic field will be continue to study the performance of the setup.

ACKNOWLEDGEMENTS

The authors would like to express our essential gratitude to K. Thaijai-un for his initial design of the undulator. We would like to acknowledge the support by the Department of Physics and Materials Science, Faculty of Science, Chiang Mai University and the Science Achievement Scholarship of Thailand.

REFERENCES

[1] Wai Lam Chan et al., Rep. Prog. Phys. 70, 1325 (2007).
[2] G. P. Gallerano et al., J. Infrared. Milli. Terhz Waves 30, 1351 (2009).
[3] P. C. Ashworth et al., Opt. Express 17, 12444 (2009).

ISBN 978-3-95450-134-2

[4] J. Saisut, Ph.D Thesis, Chiang Mai University, (2011).

[5] S. Rimjaem et.al., Nucl. Instr. Meth. Phys. Res., Sect. A 10, 736 (2014).

[6] J. A. Clarke, *The Science and Technology of Undulators and Wigglers*, (New York: OUP, 2004), 231.

[7] L. M. Young, J. H. Billen, POISSON/SUPERFISH, Technical Note No. LA-UR-96-1834, Los Alamos National Laboratory (2006).

[8] RADIA, http://www.esrf.eu/Accelerators/Groups/InsertionDevices/Software/Radia

[9] K. Wille, *The Physics of Particle Accelerators*, (New York: OUP, 2000), 315.

[10] G. Brown et.al., Nucl. Instr. Meth. Phys. Res. 65, 208 (1983).

[11] D. Bocek, Ph.D Thesis, Stanford University, (2006).

[12] H. Winick et.al., Phys. Today 50, 34 (1981).

ISBN 978-3-95450-134-2

SIMULATION OF CASCADED LONGITUDINAL-SPACE-CHARGE AMPLIFIER AT THE FERMILAB ACCELERATOR SCIENCE & TECHNOLOGY (FAST) FACILITY*

A. Halavanau[1], and P. Piot[1,2]
[1] Department of Physics and Northern Illinois Center for Accelerator & Detector Development, Northern Illinois University, DeKalb, IL 60115, USA
[2] Accelerator Physics Center, Fermi National Accelerator Laboratory, Batavia, IL 60510, USA

Abstract

Cascaded longitudinal space-charge amplifier (LSCA) have been proposed as a mechanism to generate density modulation over a board spectral range. The scheme was recently demonstrated in the optical regime and confirmed the production of broadband optical radiation. In this paper we investigate, via numerical simulations, the performances of a cascaded LSCA beamline at the Fermilab Accelerator Science & Technology (FAST) facility to produce broadband ultraviolet radiation. Our studies are carried using a three-dimensional space charge algorithm coupled with ELEGANT and including a tree-based grid-less space-charge algorithm.

INTRODUCTION

It has been long recognized that collective effects such as coherent synchrotron radiation, wakefield and longitudinal space charge can lead to a microbunching instabilities when combined with bunch compressors (BC) commonly employed in electron linacs. Over the recent years, longitudinal space charge (LSC) has gained considerable interest as a simple mechanism to form attosecond structures on the bunch current distribution for the subsequent generation of intense broadband radiation pulses [1, 2].

The corresponding beamline configuration is relatively simple: it consists of focusing sections (e.g. FODO cells) which ensure the beam size is kept small and where energy modulations due to the space charge impedance accumulate, interspaced with BC sections. The BCs convert the incoming energy modulation into a density modulation. Several of these (FODO+BC) modules are cascaded so to result in a large final density modulation.

Motivated by the recent experimental demonstration of LSCA in the optical regime [2] along with the possible use of high-peak current beams produced in laser-plasma wakefield accelerators [3], we investigate the possible combination of a cascaded LSCA scheme to produce broadband ultraviolet radiation at the Fermilab Accelerator Science & Technology (FAST) facility which couples a high- brightness photoinjector with a superconducting accelerator [4].

* This work was supported by the US Department of Energy under contract DE-SC0011831 with Northern Illinois University. Fermilab is operated by Fermi Research Alliance, LLC under Contract No. DE-AC02-07CH11359 with the US DOE.

SIMULATION METHODS & SETUP

The simulation method employed for our numerical studies has been described elsewhere [5, 6]. In brief we simulate the beam dynamics simulation, including space charge effect, is modeled with the Barnes-Hut algorithm [7] within ELEGANT [8]. The space-charge kicks are applied at discrete user-defined locations using the ELEGANT's `script` command. In its current implementation, the calculations are rather slow (due to files being written out and read in at each space-charge kick location) but the algorithm is being implemented within the ELEGANT main distribution and will eventually be part of future ELEGANT releases.

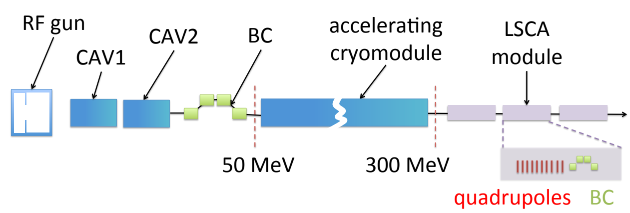

Figure 1: Overview of FAST Facility and the Proposed LSCA. The legend is as follows: "CAVx": accelerating cavities, "BC": magnetic chicane bunch compressor, the red and green rectangles are respectively quadrupole and dipole magnets.

The simulation setup is based on the configuration available at the FAST facility (formerly known as ASTA) [4]; see Fig. 1. In short, the beam is produced from a photocathode located in a $1+\frac{1}{2}$ radiofrequency (RF) gun and accelerated to $\sim$ 50 MeV by two superconducting TESLA cavities. Downstream of the cavities the beam can be manipulated (e.g. longitudinally compressed) and diagnosed before its injection in a ILC-type accelerating cryomodule composed of eight TESLA cavities. Downstream of the cryomodule, the beam, with energy up to $\sim$ 300 MeV, can be injected into the IOTA ring or transported to experiments arranged along a $\sim$ 70 m transport line. Conversely the 70-m beamline, with proper optics, could support the investigation of cascaded LSCAs to produce broadband ultraviolet radiation as discussed in this paper; see also Fig. 1.

Numerical optimization of the electron-beam formation and acceleration to $\sim$ 50 MeV was carried out with ASTRA [9] for various charges. The results combined with a mild bunch compression in the 50-MeV bunch compressor chicane, could produce bunches with peak current of

ISBN 978-3-95450-134-2

~ 500 A and slice parameters gathered in Table 1 [10]. For simplicity we take all the LSCA modules to be identical: they consist of 4 FODO-cell sections each followed by small-bending-angle chicanes. The introduced dispersion is minimal and does not affect the periodicity of the FODO.

Table 1: Beam Parameters Considered for the LSCA Simulations

Parameter	Value	Units
Lorentz factor, γ	600	–
slice charge, Q	20.0	pC
slice duration, τ	120	fs
peak current I	500	A
slice norm. emittance, $\varepsilon_{x,y}$	5×10^{-8}	m
slice momentum spread, σ_δ	10^{-4}	–
number of macroparticles, N	$[1-10] \times 10^6$	–

The slice was taken to have a Gaussian distributions in the transverse and longitudinal directions. The initial longitudinal phase space was taken to be uncorrelated and the initial Courant-Snyder parameters were matched to the FODO channel.

RESULTS

Optimization of First-stage LSCA

We start with the optimization of one module consisting of several FODO sections and one BC. We varied two parameters at this point - the length of the FODO sections and the bending angle in the chicane which affects its longitudinal dispersion R_{56}. As he goal of this study is to reach the shortest wavelength possible at FAST, we selected the range of very small chicane R_{56} where bunching factor with significant values at high frequency could be attained; see Fig. 2.

The estimated gain per one chicane in LSCA is proportional to the LSC impedance $Z(k, r)$ [3] following $G = Ck|R_{56}|\frac{I}{\gamma I_A}\frac{4\pi L_d|Z(k,r)|}{Z_0}e^{-\frac{1}{2}C^2k^2R_{56}^2\sigma_\delta^2}$, where R_{56} is the BC longitudinal dispersion, $I_A = 17$ kA is the Alfvèn current, L_d is the drift length, σ_δ is the rms fractional energy spread, $C \equiv \langle z\delta\rangle/\sigma_z$ is the chirp, and $Z_0 \equiv 120\pi$ is the free-space impedance. The exponential term in the equation induces a high-frequency cut-off of the modulation $R_{56} \approx -c/(\omega\sigma_\delta)$.

Throughout this paper the bunching factor is computed from the N-macro-particle distribution as $b(\omega) = |\sum_{m=1}^{N} e^{-i\omega t_m}|$ where t_m is the temporal coordinate of the m^{th} macro-particle within the bunch (here $\omega \equiv 2\pi f$ where f is the frequency of observation). We point out that our simulations are performed with $N = 10 \times 10^6$ (while the slice actually contains $N_e = 120 \times 10^6$ electrons). Therefore the noise floor [11] of the bunching factor is $\simeq 1/\sqrt{N_e} \simeq 9 \times 10^{-5}$ while our simulations are limited to noise floor of $\simeq 1/\sqrt{N} \simeq 3 \times 10^{-4}$. Nevertheless we have verified that the gain factor does not depends on the number of macro-particles used in the simulations [12].

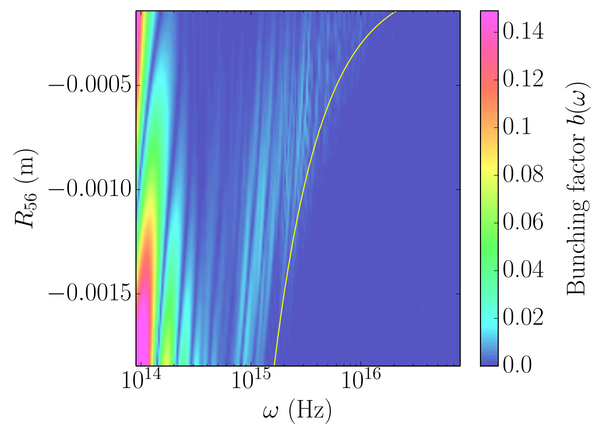

Figure 2: Bunching factor as a function of the longitudinal dispersion R_{56} and observation frequency ω. The yellow line $R_{56} \approx -c/(\omega\sigma_\delta)$ indicates the limit where the microbunching is suppressed due to momentum spread.

The resulting density modulation spectrum is wide and it narrows with the increase of chicane's bending angle. Although the optimal wavelength in this study is around $\lambda_{opt} \approx 650$ nm, the broadband feature of the amplification mechanism actually results in bunching factor enhancement at wavelengths reach the ultraviolet region of the spectrum as illustrated in Fig. 3. The latter figure reports the gain computed as the ratio between the final and initial bunching factors $|b_f(\omega)/b_i(\omega)|$. To smooth out the short-to-shot nature of the gain, the presented gain is average over 20 random realizations of the initial macro-particle distribution.

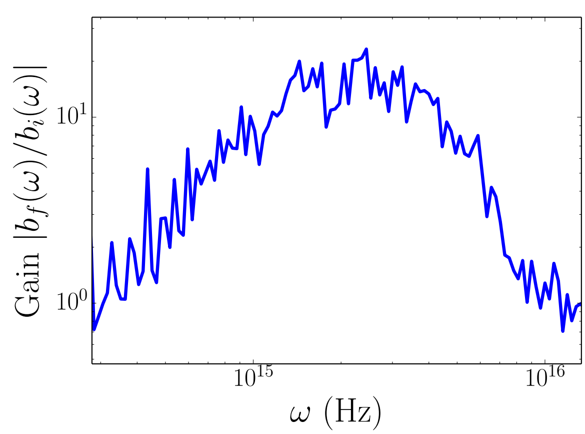

Figure 3: Gain curve as a function of frequency in the interval where significant gain is obtained. The curve is computed for a single (the first) LSCA module.

Simulation of a 3-stage LCSA

To simulate a 3-stage LCSA module, we iterated the process described in the previous section for each stage so to ensure the R_{56} is properly optimized. The simulations were

ISBN 978-3-95450-134-2

carried out in a piecewise fashion: the FODO channel of stage n was simulated with space charge, the output were passed to the subsequent BC. The R_{56} was optimized to provided the largest bunching factor. The optimized values for the R_{56} for first, second and third stage were respectively -3.64×10^{-4}, -2.79×10^{-4}, and -1.42×10^{-4} m.

The resulting distribution was rematched and passed to the $n + 1$ FODO channel where the process was repeated. As aforementioned the chicane have small R_{56} and single-particle dynamics do not affect the matching. However, in the presence of space charge and for a 300-MeV beam, we find that the matching is significantly deteriorated therefore requiring rematching of the beam parameters after each module.

The final phase space and resulting density modulation are presented on Fig. 4. One limitation found in the present study is the cumulated energy spread which leads to transverse emittance growth via chromatic aberration. This emittance dilution eventually leads suppression of the modulation (via an angular smearing effect). Note that at each stage the beam will acquire additional momentum spread which leads to additional emittance Overall this effect result in saturation of the gain in the final stages. For our three stage LSCA we obtained a gain (a the optimum wavelength) $G \approx 500$ for the given beam parameters. The final bunching factor downstream of the third stage appears in Fig. 5 (blue line).

Compressed Case

In addition introducing a longitudinal-phase-space chirp can significantly shift the wavelength region with significant gain to lower wavelength. Thus operating the cryomodule off-crest can compress the modulation wavelength to the ultraviolet regime at FAST: in our studies introducing a chirp $C \equiv \frac{d\delta}{dz}|_0 = 1667\ \mathrm{m}^{-1}$ results in a significant bunching factor (approximately 1%) at $\lambda \approx 140$ nm; see Fig. 5 (green trace). Here we note that for simplicity the chirp was "numerically applied" just before the last bunch compressor (thus its large value). In practice the chirp would be applied before the first LSCA module and therefore would be much smaller.

RADIATION PRODUCTION

Several radiation-production mechanisms can be considered. For simplicity we consider the case of a planar undulator. Given the beam energy of 300 MeV, and taking a undulator parameter of $K = 0.1$ yields a resonant wavelength $\lambda \simeq 1.4 \times 10^{-6}\lambda_u$, for an undulator period λ_u (corresponding to $\omega = 1.35 \times 10^{15}/\lambda_u$). A 10-cm undulator period will results in a frequency $\omega \simeq 1.2 \times 10^{16}\ \mathrm{s}^{-1}$ where the bunching factor scaled for 120M macroparticle is $5 \sim 10^{-2}$; see Fig. 5 (red trace). Simulations performed with GENESIS [13] (in steady state mode) indicate that a radiation energy of $\mathcal{E} \simeq 3$ ţJ could be reached.

SUMMARY

Using a grid-less code adapted from Astrophysics we have investigated the effect of three-dimensional LSC impedance and found that the possible use of a cascaded LSCA scheme at FAST can produce femtosecond microstructures in the longitudinal phase space with a period ranging from 140 to 700 nm. Our study involves beam parameters comparable to the ones achievable at FAST.

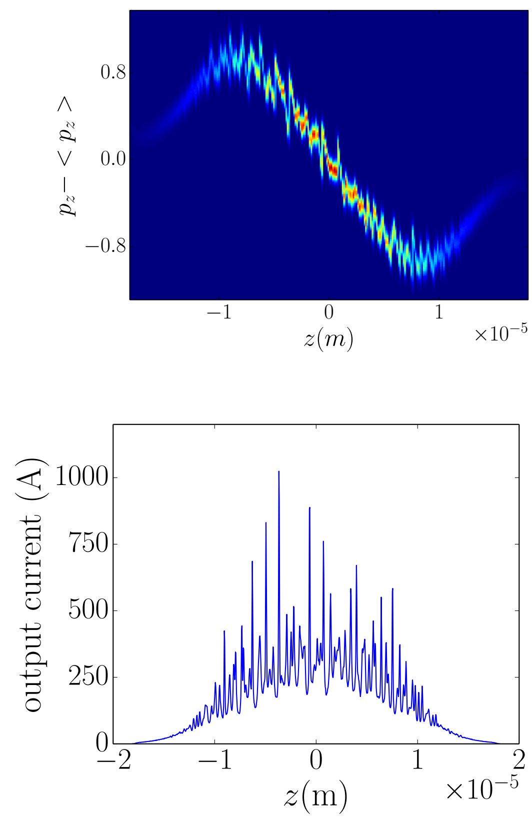

Figure 4: Longitudinal phase space (top density plot) and resulting density modulation (bottom plot) downstream of the third LSCA stage for $N = 10 \times 10^6$ macro-particles.

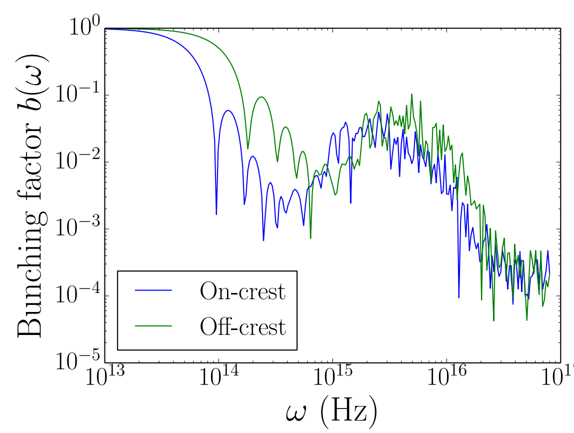

Figure 5: Simulated bunching factor downstream of the third LSCA stage for the case of an uncompressed (blue) and compressed (green) incoming beam.

ISBN 978-3-95450-134-2

REFERENCES

[1] E. A. Schneidmiller and M. V. Yurkov, Phys. Rev. ST Accel. Beams **13**, 110701 (2010).

[2] A. Marinelli, E. Hemsing, M. Dunning, D. Xiang, S. Weathersby, F. O'Shea, I. Gadjev, C. Hast, J. B. Rosenzweig, Phys. Rev. Lett. **110** 064804 (2013).

[3] M. Dohlus, E. Schneidmiller, M. V. Yurkov, C. Henning, F. J. Grüner, Proc. SPIE **8779**, 87791T (2013).

[4] E. Harms, J. Leibfritz, S. Nagaitsev, P. Piot, J. Ruan, V. Shiltsev, G. Stancari, A. Valishev, ICFA Beam Dyn.Newslett. **64** 133 (2014).

[5] A. Halavanau, P. Piot, in Proc. of the 2015 International Accelerator Conference (IPAC15), Richmond, VA, USA, 1853 (2015)

[6] A. Halavanau, P. Piot, ibid [5], p. 1850 (2015).

[7] J. Barnes and P. Hut, Nature, **324**, 446 (1986).

[8] M. Borland, Advanced Photon Source, Note LS-287, available from Argonne (unpublished 2000).

[9] P. Piot, Y.-E Sun, M. Church, in Proc. of the 2010 International Accelerator Conference (IPAC10), Kyoto, Japan, 4316 (2010).

[10] C. R. Prokop, P. Piot, B. E. Carlsten, M. Church, Nucl. Instrum. Meth. Sec. A **716**, 17 (2013).

[11] C. J. Hirschmugl, M. Sagurton, G. P. Williams, Phys. Rev. A **44**, 1316-1320 (1991).

[12] A. Halavanau, P. Piot, manuscript in preparation (2015).

[13] S. Reiche, Nucl. Instrum. Meth. Sec. A **429**, 243 (1999).

ISBN 978-3-95450-134-2

MINMIZATION OF THE EMITTANCE GROWTH INDUCED BY COHERENT SYNCHROTRON RADIATION IN ARC COMPRESSOR*

Xiyang Huang#, Xiaohao Cui, Yi Jiao, Gang Xu
Key Laboratory of Particle Acceleration Physics and Technology,
Institute of High Energy Physics, Chinese Academy of Sciences, Beijing, China

Abstract

Coherent synchrotron radiation (CSR) is a critical issue when electron bunches with short bunch length and high peak current transporting through a bending system in high-brightness light sources and linear colliders. For example, a high peak current of electron beam can be achieved by using magnetic bunch compressor, however, CSR induced transverse emittance growth will limit the performance of bunch compressor. In this paper, based on our 'two-dimensional point-kick analysis', an arc compressor with high compression factor is studied. Through analytical and numerical research, an easy optics design technique is introduced that could minimize the emittance dilution within this compressor. It is demonstrated that the strong compression of bunch length and the transverse emittance preservation can be achieved at the same time.

INTRODUCTION

In ERL designs, recirculation arcs are often used to compress the bunch length. In order to achieve compression, an ultra-relativistic electron beam with energy chirp passes through the bending system. Since the trajectory is curved, electrons emit coherent synchrotron radiation (CSR) and may induce energy modulation along the bunch and dilutes transverse emittance, leading to degradation of the beam quality [1-3]. To suppress the undesirable emittance growth, several design strategies have been proposed [4-8]. However, most of these designs reach a high compression factor by adopting a low bunch charge. In this paper, the point-kick analysis [8] is reviewed and be applied to an arc compressor consists of double bend achromats (DBAs) to achieve emittance preservation with high bunch charge.

POINT-KICK ANALYSIS OF CSR EFFECT

In the "steady-state" approximation for a Gaussian line-charge distribution beam, the CSR-induced rms relative energy spread depends linearly on both L_b and $\rho^{2/3}$ [9-11].

$$\Delta E_{rms} = 0.2459 \frac{eQ\mu_0 c_0^2 L_b}{4\pi\rho^{2/3}\sigma_z^{4/3}}, \qquad (1)$$

where e, Q, ρ, σ_z, L_b, μ_0, c_0 represent the charge of a single particle, the bunch charge, the bending radius of the orbit, the rms bunch length, the bending path, the permeability of vacuum, and the speed of light, respectively.

Therefore the CSR effect in a dipole was linearized by assuming $\delta(csr) = kL_b/\rho^{2/3}$, where k depends only on the bunch charge Q and the bunch length σ_z, and is in unit of $m^{1/3}$. In addition, it was shown that the CSR-induced coordinate deviations after a passage through a dipole can be equivalently formulated with a point-kick at the centre of the dipole (see Fig. 1), which is of the form [8]

$$X_k = \begin{pmatrix} \rho^{4/3}k[\theta\cos(\theta/2) - 2\sin(\theta/2)] \\ \sin(\theta/2)(2\delta + \rho^{1/3}k\theta) \end{pmatrix}, \qquad (2)$$

where $\delta = \delta_0 + \delta_{csr}$, is the particle energy deviation at the entrance of the dipole, with δ_0 being the initial particle energy deviation and δ_{csr} being that caused by CSR in the upstream path.

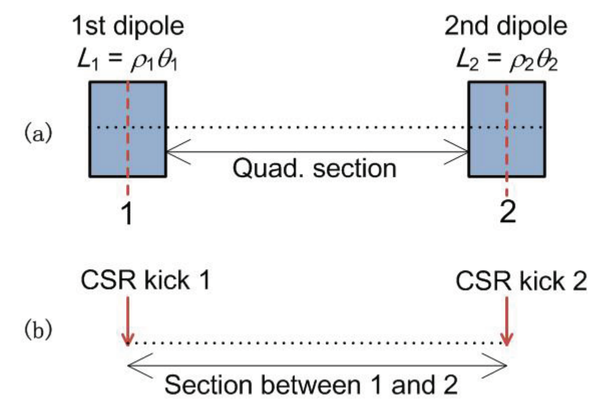

Figure 1: Schematic layout of a two-dipole achromat and physical model for the analysis of the CSR effect with two point kicks. The point 1 and 2 indicate the centres of the first and the second dipole, respectively.

EMITTANCE PRESERVATION OF A CHIRPED BEAM AFTER A DBA

In this section, we will present the derivation of the CSR-minimization condition for a DBA with symmetric layout. As sketched in Fig. 1, the bending angles of the first and the second dipole are denoted by θ, the bending radii of these dipoles are the same, denoted by ρ. According to the point-kick analysis, CSR kicks occur at the centres of the two dipoles (denoted by 1, 2, in Fig. 1), and between the adjacent kicks only one 2-by-2 transfer matrix of the horizontal betatron motion is considered. For simplicity, it is assumed that the initial particle coordinates relative to the reference trajectory are X_0 =

*work supported by National Natural Science Foundation of China (11475202, 11405187).
#huangxy@ihep.ac.cn

ISBN 978-3-95450-134-2

$(x_0, x_0')^\dagger = (0, 0)^\dagger$ and the energy deviation is $\delta = 0$. According to Eq. 2, the coordinates remain zero until the particle experiences the CSR-kick at point 1, where the particle coordinates are given by

$$X_1 = \begin{pmatrix} -\rho^{4/3} k_1 r \\ S\rho^{1/3} k_1 \theta \end{pmatrix}. \tag{3}$$

where $r = 2\sin(\theta/2) - \theta\cos(\theta/2)$, and $S = \sin(\theta/2)$. Since the symmetric DBA satisfied the achromat condition, the transport matrix can be expressed as (we assume that the Courant-Snyder (C-S) parameters are symmetric)

$$M_{12} = \begin{pmatrix} -1 & 0 \\ -\dfrac{2\alpha_1}{\beta_1} & -1 \end{pmatrix}. \tag{4}$$

After passing through the section between point 1 and 2, the particle experiences the second kick. Note that due to energy chirp, the bunch length of the beam is compressed and the coefficient $k_2 = m^{4/3} k_1$, where m is the compression factor of one DBA. Thus the CSR-induced particle coordinate deviations at point 2 are (the energy spread δ grows to $k\rho^{1/3}\theta$ at point 2)

$$X_2 = \begin{pmatrix} -rk_1\rho^{4/3}(-1+m^{4/3}) \\ k_1\rho^{1/3}[\dfrac{2r\alpha_1\rho}{\beta_1} + (1+m^{4/3})\theta S] \end{pmatrix}. \tag{5}$$

The final geometric emittance (the geometric emittance at the end of the DBA) in presence of the CSR effect can be estimated by

$$\begin{gathered} \varepsilon^2 = \varepsilon_0{}^2 + \varepsilon_0 \cdot d\varepsilon, \\ d\varepsilon = \frac{\theta^2}{144}(m^{4/3}+1)(\frac{q^2\rho^2 r^2}{\beta_1 S^2} + (\frac{-\rho\alpha_1 r}{\sqrt{\beta_1}S} + \sqrt{\beta_1}\theta)^2). \end{gathered} \tag{6}$$

where ε_0 is the unperturbed geometric emittance and $\alpha_2, \beta_2, \gamma_2$ are the C-S parameters at the centre of the second dipole of the DBA. In most cases $d\varepsilon \ll \varepsilon_0$, therefore the growth in unnormalized and normalized emittance due to CSR can be estimated by

$$\begin{gathered} \Delta\varepsilon = \varepsilon - \varepsilon_0 \approx \frac{1}{2} d\varepsilon, \\ \Delta\varepsilon_n = \varepsilon_n - \varepsilon_{n0} = \gamma\beta(\varepsilon - \varepsilon_0) \approx \frac{1}{2}\gamma\beta d\varepsilon, \end{gathered} \tag{7}$$

where β is the particle velocity relative to the speed of light, γ is the relativistic Lorentz factor, and the subscript n represents the normalized emittance. To achieve the emittance preservation, it is required to minimize Eq. 6, from which the linear CSR-suppression condition can be obtained,

$$\beta_1 / \alpha_1 = \rho(\theta\cot\frac{\theta}{2} - 2)/\theta. \tag{8}$$

In the particular case with $\theta \ll 1$, Eq. 8 can be simplify as

$$\beta_1 / \alpha_1 = -L_b / 6. \tag{9}$$

By expressing β_1 and α_1 in terms of β_0 and α_0, the above equation can be written as

$$\beta_0 = \frac{5\alpha_0 L_b}{12} \pm \frac{L_b}{12}\sqrt{\alpha_0^2 - 24}. \tag{10}$$

where in Eqs. 9 and 10 only the first significant terms with respect to θ are kept. It should also mentioning that in Eq. 10 the negative sign results better CSR-suppression effect, which is illustrated in Fig. 2.

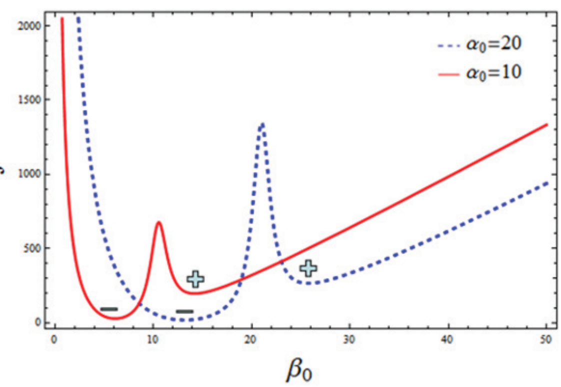

Figure 2: (color online) The lower β_0 solution has a lower particle invariant.

ARC COMPRESSOR

The compression arc can be consists of several identical DBAs, and the total compression factor is defined as $C = 1/(1+hR_{56})$ in first order, where h and R_{56} is the bunch energy chirp and the z-δ correlation term of transport matrix, respectively. To minimize the CSR-induced emittance growth after the arc, one should choose the proper initial C-S parameters, which satisfying Eq. 10. Since the energy chirp h increases along the arc, we concern about the emittance growth in the last DBA which has the largest compression factor. To contrast, the dependency of the emittance growth $\Delta\varepsilon_n$ on the initial C-S parameters is investigated with ELEGANT simulations, the initial beam distribution in phase space is generated accordingly to match the optics. The bunch charge in the simulations are 500 pC and the compression factor of the DBA is 4.5. The dipole bending radius and bending angle is 10m and 10 degrees, respectively. It can be seen from Fig. 3 that the emittance growth reaches a minimum as C-S parameters are close to the optimal value, which agrees reasonably well with the analytical prediction. Note that,

ISBN 978-3-95450-134-2

the minimum $\Delta\varepsilon_n$ is not exactly on the optimal value, this is because the bunch length is not invariant in the dipole.

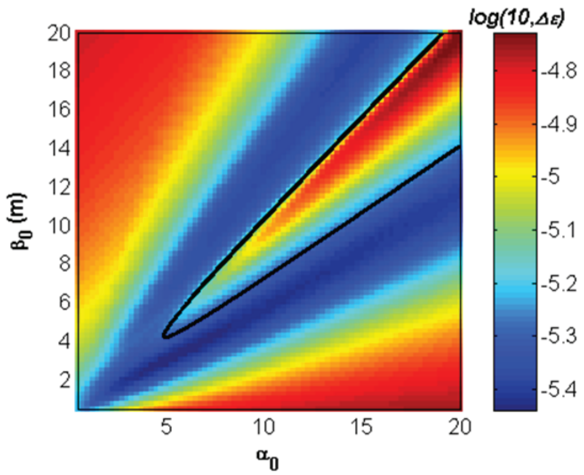

Figure 3: (color online) Numerical simulations of final emittance growth by scanning initial C-S parameters in a symmetric DBA with large compression factor 4.5. The initial transverse emittance is 1µm.rad. Black Line satisfying the CSR-suppression condition Eq. 10.

Now consider a periodical 192° arc compressor made of 8 DBA which satisfying the condition deduced above, some parameters of the lattice and the beam are listed in Table. 1 and R_{56} of the arc is 0.128m. To achieve a total compression factor $C = 45$, one need the energy chirp h = -7.6m^{-1} at the entrance of the arc. The initial C-S parameters can be chosen as $\beta_0 = 3$m, $\alpha_0 = 9$, which close to the suppression condition. It can be seen from Fig. 4 that at the end of the arc, the normalized emittance growth is at 0.1µm.rad level, which has a good agreement with Eq. 6 with scaling of the CSR effect with the beam parameters.

Table 1: Summary of the Simulation Parameters

Parameter	Value	Units
Bunch charge	500	pC
Normalized emittance	0.5	µm.rad
Beam energy	1	GeV
Energy spread	0.05	%
Initial bunch length	0.9	mm
Dipole bending radius	5.24	m
Dipole bending angle	12	degree
Final bunch length	2	µm
Final Normalized emittance	0.74	µm.rad

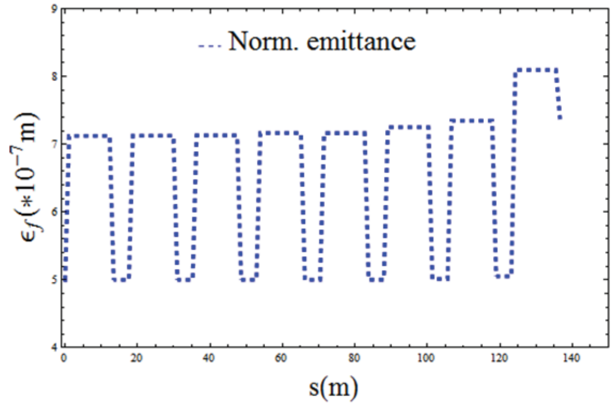

Figure 4: The normalized emittance along the arc. The emittance growth at the end is 0.24µm.rad.

DISCUSSIONS

By adopting a few modifications on the point-kick analysis, we have derived the generic condition for minimizing the CSR kicks in a linear regime. This condition provide a new way to suppress the CSR-induced growth emittance in an arc compressor made of identical symmetric DBAs with the beam of high bunch charge. It is worth mentioning that this analysis is based on the assumption that the bunch length does not change in the dipole, thus the compression factor in the last DBA should not be too large. On the other hand, from Eq. 6 the final emittance growth depends on β_1, the beta function at the centre of dipole should be cautiously tuned for both emittance preservation and optics symmetry.

REFERENCES

[1] R. Talman, Phys. Rev. Lett. **56**, 1429 (1986).
[2] P. Emma et al., Stanford Linear Accelerator Centre Report No. SLAC-PUB-7554, 1997.
[3] H. Braun et al., Phys. Rev. Lett., **84**, 658 (2000).
[4] S. V. Benson et al., J. Mod. Opt., **58**, 1438 (2011).
[5] J. H. Wu et al, "Coherent Synchrotron Radiation Analysis for the Photoinjected Energy Recovery Linac and UVFEL Projects at the NSLS", RPAH012, PAC'01, Chicago, USA.
[6] M. Shimada et al., Nucl. Instrum. Methods Phys. Res., Sect. A **575**, 315 (2007).
[7] S. Di Mitri et al., Euro. Phys. Lett, **109**, 62002 (2015).
[8] Y. Jiao, X. Cui, X. Huang and G. Xu, Phys. Rev. ST Accel. Beams, **17**,060701 (2014).
[9] Y. S. Derbenev et al., Stanford Linear Accelerator Centre Report No. SLAC-PUB-7181, 1996.
[10] E. L. Saldin et al., Nucl. Instrum. Methods Phys. Res., Sect. A **398**, 373 (1997).
[11] R. Hajima, Nucl. Instrum. Methods Phys. Res., Sect. A **528**, 335 (2004).

ISBN 978-3-95450-134-2

START-TO-END SIMULATION OF THE LCLS-II BEAM DELIVERY SYSTEM WITH REAL NUMBER OF ELECTRONS*

J. Qiang#, M. Venturini, C. Mitchell, C. Papadopoulos, LBNL, Berkeley, CA94720, USA
Y. Ding, P. Emma, Z. Huang, G. Marcus, Y. Nosochkov, T. O. Raubenheimer, L. Wang, M. Woodley, SLAC, Menlo Park, CA 94025, USA

Abstract

The LCLS-II as a next generation high repetition rate FEL based X-ray light source will enable significant scientific discoveries. In this paper, we report on progress in the design of the accelerator beam delivery system through start-to-end simulations. We will present simulation results for three charges, 20 pC, 100 pC and 300 pC that are transported through both the hard X-ray beam line and the soft X-ray beam line for FEL radiation.

INTRODUCTION

Next generation high brightness FEL X-ray light sources provide great opportunity for scientific discovery in many fields. The LCLS-II as an upgrade to the current LCLS FEL at SLAC will deliver photons of energy between 200 eV and 5 keV at a repetition rate as high as 1 MHz and is being actively designed under a multi-laboratory collaboration [1]. Figure 1 shows a schematic layout of the LCLS-II beam delivery system [2]. It consists of a high repetition rate photo-injector to generate and accelerate the electron beam to 100 MeV, a laser heater (LH) to suppress microbunching instability, a section of superconducting linac L1 to accelerate the beam to 250 MeV, a bunch compressor BC1, a second section of superconducting linac L2 to accelerate the beam to 1.6 GeV, a bunch compressor BC2, and a third section of superconducting linac L3 to accelerate the beam to 4 GeV, a long bypass transport line, and a magnetic kicker to spread the electron beam to a soft X-ray transport beam line and to a hard X-ray transport beam line. The superconduting linacs in all three sections are made of 1.3 GHz 9 cell superconducting cavities except the two cryomodules of 3.9 GHz third harmonic cavities right before the BC1 to linearize longitudinal phase space.

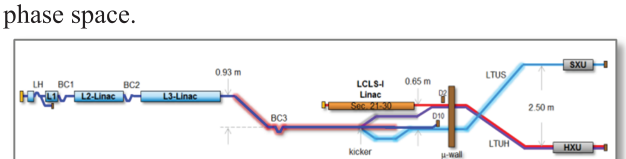

Figure 1: A schematic layout of the LCLS-II.

COMPUTATIONAL SETUP

All simulations presented in this study were done using a 3D parallel beam dynamics simulation framework IMPACT [3-5]. It includes a time-dependent 3D space-charge code module IMPACT-T to simulate photo-electron beam generation and acceleration through the photo RF gun, buncher and boosting cavities, and a position-dependent 3D space-charge code module to simulate electron beam transport through the superconducting linac system. Besides the 3D space-charge effects, the simulation also includes coherent synchrotron radiation (CSR) effects through a bending magnet, incoherent synchrotron radiation inside the bending magnet, RF cavity structure wakefield, and resistive wall wakefield. All simulations were done using the real number of electrons for three bunch charges, 20 pC, 100 pC, and 300 pC, to capture the initial shot noise of the beam, which can have important impact on the final beam quality and FEL performance due to the microbunching instability [6-8]. The total computational time takes from a few hours to about 14 hours on thousands of processors at the NERSC supercomputer center [9].

SIMULATION RESULTS

The simulation starts with an initial particle distribution behind the cathode. The choice of the initial electron beam parameters and the RF gun, the solenoid, the buncher cavity, and the boosting cavities parameters was based on a multi-variable multi-objective optimization [10]. Figure 2 shows the longitudinal phase space distribution and the current profile at the exit of the

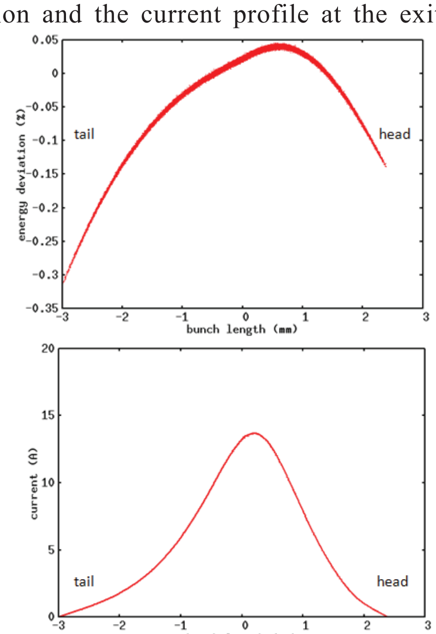

Figure 2: Longitudinal phase space (top) and current profile (bottom) at the exit of the injector.

*Work supported by the Director of the Office of Science of the US Department of Energy under Contract no. DEAC02-05CH11231 and Contract no. DE-AC02-76SF00515.
#jqiang@lbl.gov

ISBN 978-3-95450-134-2

injector for the nominal 100 pC charge case. The relative energy deviation in the longitudinal phase space is small but with noticeable nonlinear component that might affect the final beam compression. The peak current of the beam at this location is about 14 Ampere.

The electron beam coming out of the injector is sent through a laser heater chicane to increase its uncorrelated energy spread to suppress the microbunching instability. A detailed discussion of the microbunching instability in the LCLS-II is presented in the reference [6] of these proceedings. For the nominal 100 pC charge, we assumed a 7 keV increase of uncorrelated energy spread from the laser heater. After the laser heater, the electron beam is transported through the first section of the superconducting linac, the third harmonic linearizer, and the bunch compressor chicane BC1 to boost the beam energy and to increase the peak current. The RF accelerating gradient and the phase used in this section of linac are 12.72 MV/m and -12.7 degree respectively. The accelerating gradient and the phase used in the third harmonic cavity are 11.69 MV/m and -150 degree respectively. The bunch compressor BC1 has a compression factor of 6. The bending angle in this chicane is 0.1028 radian and the R56 of the chicane is 0.055 meters. Figure 3 shows the longitudinal phase space and the current profile after the BC1. The longitudinal phase space looks quite linear. The peak current is about 85 A with noticeable modulation due to the microbunching instability. After the BC1, the beam is further accelerated through the second section of the superconducting linac to 1.6 GeV before entering the second bunch compressor BC2. The accelerating gradient and the phase in this section of linac are 14.51 MV/m and -21 degree respectively. The bending angle in BC2 is 0.043 radian and the R56 of the chicane is 0.0379 m. This provides another compression factor of 8 to the beam.

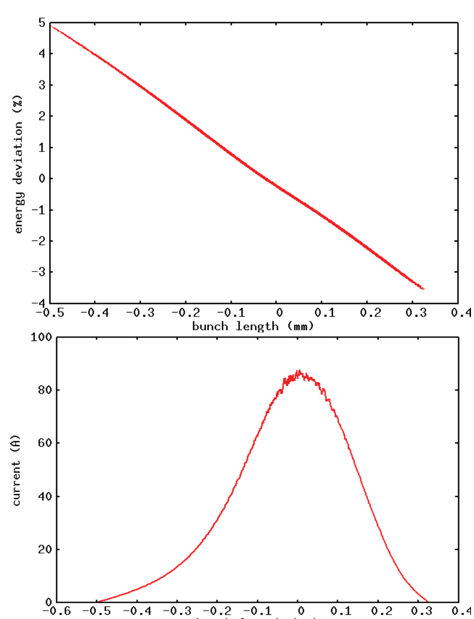

Figure 3: Longitudinal phase space (top) and current profile (bottom) at the exit of the BC1.

Figure 4 shows the longitudinal phase space distribution and the current profile after the BC2. Nonlinear tail forms around both ends of the beam and contributes to two large spikes in the current profile.

After the BC2, the electron beam is further accelerated through the third section of the superconducting linac to reach 4 GeV energy before entering the long transport beam line to the undulator hall. The RF gradient and the phase used in this section of linac are 14.71 MV/m and 0 degree respectively. The long transport beam line consists of a dogleg 1, a long bypass, and a spreader to a soft X-ray transport line and to a hard X-ray transport line. The final longitudinal phase spaces and the current profiles at the entrance to the soft X-ray FEL and the hard X-ray FEL are given in Figs. 5 and 6. Compared with the Fig. 4, the final longitudinal phase distribution becomes flatter and is dechirped by the resistive wakefield through the long transport line. The flat core of the beam is about 13 um with relatively small energy and current modulation due to the microbunching instability. Such a modulation might not present significant impact to the SASE FEL performance but can degrade the performance of the seeded FEL. The current and the energy modulation in the beam at the entrance to the soft X-ray FEL are worse than that at the entrance to the hard X-ray FEL. Study is ongoing to further improve both the soft X-ray and the hard X-ray transport beam lines to minimize the microbunching effects at the entrance to the undulator.

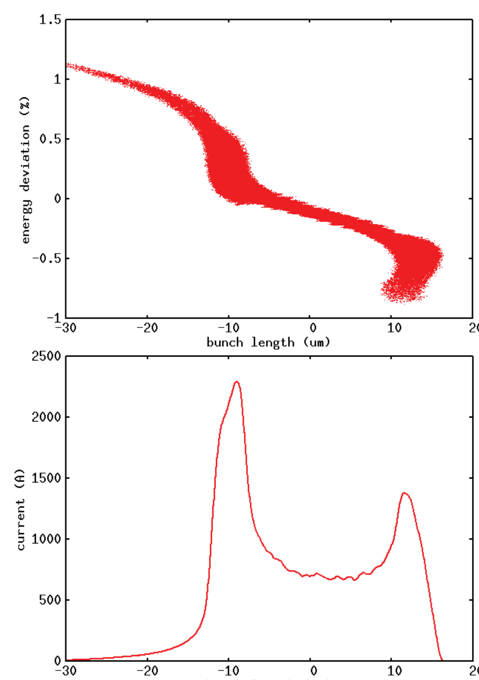

Figure 4: Longitudinal phase space (top) and current profile (bottom) at the exit of the BC2.

Figure 7 shows the transverse projected rms emittance evolution and the transverse center slice emittance (averaged over 5 slices) evolution through the linac and the hard X-ray transport beam line for the nominal 100 pC charge case. Some large spikes in the emittance are due to

ISBN 978-3-95450-134-2

the dispersion inside a chicane or a dogleg. The large projected rms emittance growth after the BC2 and the final dogleg is due to the CSR effects caused by these large current spikes in the beam. Some slice emittance growth is also noticed after the BC1 due to the nonlinear space-charge effects associated with the lattice mismatch and the strong focusing of the beam around this region. The final slice emittances in both horizontal (X) and veritical (X) planes are below 0.5 um. The projected X

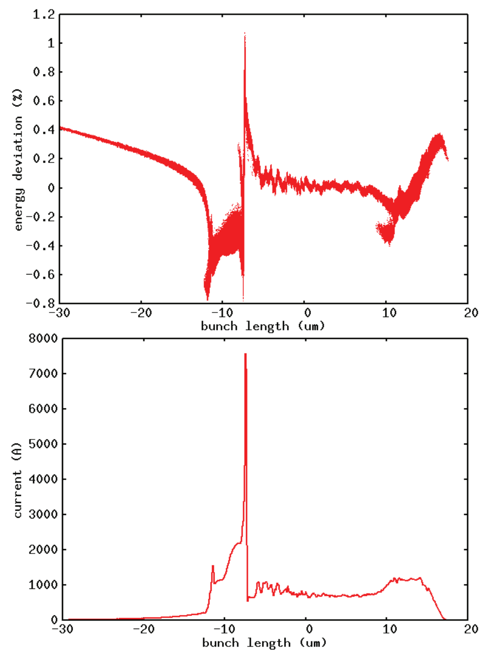

Figure 5: Longitudinal phase space (top) and current profile (bottom) at the entrance to the hard X-ray FEL.

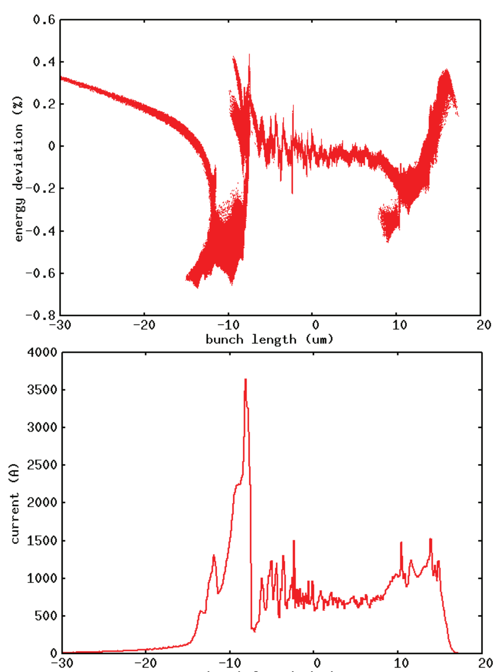

Figure 6: Longitudinal phase space (top) and current profile (bottom) at the entrance to the soft X-ray FEL.

emittance is about 1um and the projected Y emittance is about 0.5 um.

Besides the nominal 100 pC charge case, we also carried out start-to-end simulation using the real number of electrons for the 300 pC charge and the 20 pC charge. Figure 8 shows the final longitudinal phase space and current profile at the entrance to the hard X-ray FEL for the 300 pC charge. The core of the beam has about 60 um relatively flat distribution with a current beyond 800 A. The final projected transverse emittance is about 1.3 um

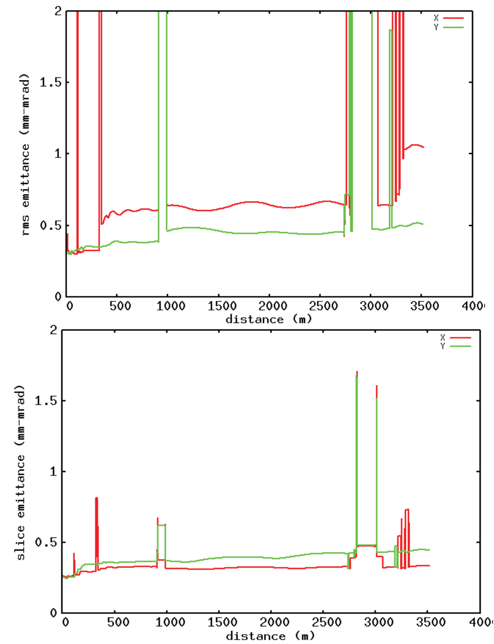

Figure 7: Transverse projected RMS emittance evolution (top) and slice emittance evolution (bottom) through the hard X-ray beam delivery system.

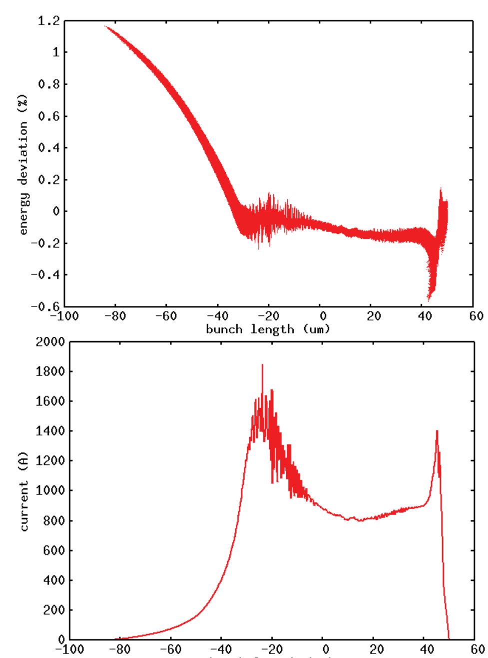

Figure 8: Final longitudinal phase space (top) and current profile (bottom) for the hard X-ray FEL with 300 pC.

ISBN 978-3-95450-134-2

in X and 0.94 um in Y. The center slice emittance is about 0.63 um in X and 0.59 um in Y. Similar phase space distribution and current profile are also obtained for the beam through the soft X-ray transport line.

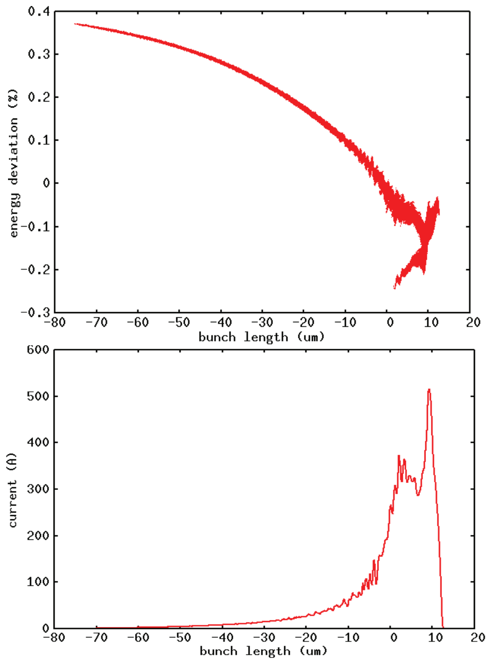

Figure 9: Final longitudinal phase space (top) and current profile (bottom) for the hard X-ray FEL with 20 pC.

Figure 9 shows the final longitudinal phase space and the current profile at the entrance to the hard X-ray FEL for the 20 pC charge case. The peak current in the core of the distribution is about 300 A with a length of about 9 um. The final projected rms emittances are 0.21 um in X and 0.13 in X. The center slice emittances are 0.13 um and 0.12 um in X and Y planes respectively.

SUMMARY AND DISCUSSIONS

As a summary, Table 1 gives some final beam parameters at the entrance to both the hard X-ray FEL (blue) and the soft X-ray FEL (brown) from the start-to-end simulations using real number of electrons. Those parameters that are important to the FEL performance include peak current inside the core, uncorrelated energy spread inside the core, total projected transverse RMS emittances, and core slice emittances. The 300 pC charge gives the largest ~900 A peak current inside the core of the beam. The nominal 100 pC charge leads to a final ~750 A peak current, and the 20 pC charge produces ~300 A peak current inside the core of the beam. The final transverse core slice emittances are below 1 um for all three charges. The total projected RMS emttiances are around 1 um for 100 pC and 300 pC charges except the one with 100 pC charge after the soft X-ray beam line. This large total projected emittance is due to the large fish tail shape distribution in the longitudinal-horizontal plane around the tail of the beam where a large energy tail is also observed in the top plot of the Fig. 6. This part of the beam might not contribute to the desired FEL radiation from the core of the beam in the downstream undulator. The final uncorrelated rms energy spread is below 600 keV for all three bunch charges.

Table 1: Final Beam Parameters at the Entrance to the Hard X-ray FEL (blue) and the Soft X-ray FEL (brown)

IMPACT Studies	I_peak (A)	σ_E (keV)	Proj. $\varepsilon_x / \varepsilon_y$ (mm-mrad)	Slice $\varepsilon_x / \varepsilon_y$ (mm-mrad)
20 pC	299	446	0.21/ 0.13	0.16 / 0.10
	294	444	0.23 / 0.12	0.15 / 0.10
100 pC	760	480	1.05 / 0.51	0.34 / 0.43
	755	592	3.5 / 0.44	0.34 / 0.42
300 pC	892	468	1.28 / 0.94	0.64/ 0.52
	921	529	1.21 / 0.90	0.56 / 0.53

The electron beam quality parameters listed in the Table 1 result in a reasonable FEL performance in the downstream undulators[7]. Further improvement to the quality of the beam is still undergoing. For example, recently, we have optimized the settings of the compensation chicane to further reduce the microbunching instability effects through the long transport line. We are also working on improving the beam current profile and reducing the microbunching effects by using a third bunch compressor right before the spreader. This bunch compressor helps to lower the compression factor needed in the first two stages and the peak current through the long bypass, which in principle will reduce the growth of the microbunching instability. This bunch compressor was used in the 20 pC charge case presented here. The challenge with this delayed compression is to remove the longitudinal energy chirp in the final beam distribution since the distance to the undulator entrance is short and the resistive wall wakefield might not be large enough to remove the energy chirp. Besides improving the longitudinal energy/density profile, we are also working on understanding the transverse emittance growth in the linac.

REFERENCES

[1] T. O. Raubenheimer, “Technical challenges of the LCLS-II CW X-ray FEL,” in proceedings of IPAC2015, Richmod, VA, USA.
[2] P. Emma et al., in proceedings of FEL’14, THP025.
[3] J. Qiang et al., PRST-AB 9, 044204 (2006).
[4] J. Qiang et al., J. of Comp. Phys., 163, 434 (2000).
[5] J. Qiang et al., PRST-AB 12, 100702 (2009).
[6] J. Qiang et al., PRST-AB 17, 030701 (2014).
[7] M. Venturini et al., “The microbunching instability and LCLS-II lattice design: lessons learned,” in these proceedings.
[8] G. Marcus et al., “High fidelity start-to-end numerical particle simulations and performance studies for LCLS-II,” in these proceedings.
[9] http://www.nersc.gov
[10] C. Papadopoulos et al, “RF injector beam dynamics optimization for LCLS-II,” SLAC-PUB-16210 (2014).

ISBN 978-3-95450-134-2

DISPERSION OF CORRELATED ENERGY SPREAD ELECTRON BEAMS IN THE FREE ELECTRON LASER

L.T. Campbell[1,2] and A.R. Maier[3]
[1]SUPA, Department of Physics, University of Strathclyde, Glasgow, UK
[2]ASTeC, STFC Daresbury Laboratory and Cockcroft Institute, Warrington, UK
[3]Center for Free-Electron Laser Science and Department of Physics,
University of Hamburg, Luruper Chaussee 149, 22761 Hamburg, Germany

Abstract

The effect of a correlated linear energy chirp in the electron beam in the FEL, and how to compensate for its effects by using an appropriate linear taper of the undulator magnetic field have previously been investigated considering relatively small chirps. In the following, it is shown that larger linear energy chirps, such as those found in beams produced by laser-plasma accelerators, exhibit dispersive effects in the undulator, and require a non-linear taper on the undulator field to properly optimise.

INTRODUCTION

In the FEL, it is well known that an energy spread correlated with the temporal bunch coordinate, or an energy chirp, in the electron beam can be compensated for by using an appropriate taper of the undulator magnetic field [1]. For the case of a linear energy chirp, it was previously derived that a linear taper is necessary, with gradient proportional to the gradient of the chirp, and this result was derived considering small variations in energy due to the chirp.

However, with the increased interest in novel accelerator concepts as FEL drivers, *e.g.* use of plasma accelerators [2–4] or the synthesis of broadband beams from linacs as in [5], the case of larger chirps has become more relevant. In this regime, dispersive effects can no longer be ignored, and the beam current and energy spread are a function of propagation distance through the undulator. Consequently, the gain length of the FEL is then itself a function of distance. In addition, dispersion due to the chirp will cause the gradient of the chirp to vary upon propagation, meaning that the taper necessary to compensate the chirp is also a function of undulator propagation length, and will not be linear.

FEL codes which employ 'slices' with periodic boundaries to model the electron beam [6–9] cannot model this dispersion properly, as the electrons cannot travel between slices, and so cannot model any current redistribution through the undulator. In addition, the Slowly Varying Envelope Approximation (SVEA) [10] means that they cannot model a broadband range of frequencies produced by large energy differences due to the chirp and/or a large taper. So-called 'unaveraged' FEL codes [11–15] are free of these limitations.

In the following, a general case of a large chirp which can be fully compensated with a taper is identified, which reduces to the previous, well known case only when dispersive effects are neglected. This simple case allows an analytic prediction for the variation in the gain length at a fixed frequency, which is compared to results from the unaveraged FEL code Puffin [11].

REVISITING THEORY IN SCALED NOTATION

Using the scaled notation of [11], the propagation distance through the undulator is scaled to the 1D gain length, and the temporal coordinate in the stationary radiation frame is scaled to the 1D cooperation length, so that, respectively,

$$\bar{z} = \frac{z}{L_g} \tag{1}$$

$$\bar{z}_2 = \frac{ct - z}{L_c}. \tag{2}$$

The scaled axial velocity of the jth electron is defined as

$$p_{2j} = \frac{d\bar{z}_{2j}}{d\bar{z}} = \frac{\beta_{zr}}{1 - \beta_{zr}} \frac{1 - \beta_{zj}}{\beta_{zj}}, \tag{3}$$

where $\beta_{zj} = v_{zj}/c$ is the z velocity in the undulator normalised to the speed of light. The subscript r denotes some reference velocity, which is usually sensible to take as the mean velocity of the beam, but which in general may be any velocity, as the model presented in [11] allows a broadband description of both the radiation field and the electron energies. The 'r' denotes the resonant condition for this reference velocity, so that the reference resonant frequency is denoted by

$$k_r = \frac{\beta_{zr}}{1 - \beta_{zr}} k_w, \tag{4}$$

and the electrons with $p_{2j} = 1$ are resonant with the reference frequency.

Tapering is achieved by varying $\alpha(\bar{z}) = \bar{a}_w(\bar{z})/\bar{a}_{w0}$, which is the relative change in the magnetic undulator field from its initial value, as defined in [16].

The gradient of an electron beam chirp may then be defined as

$$\frac{dp_2}{d\bar{z}_2} \approx -\frac{2}{\gamma_r} \frac{d\gamma}{d\bar{z}_2}, \tag{5}$$

assuming small deviations in energy, a small chirp so that

$$\frac{dp_2}{d\bar{z}_2} \ll 1, \tag{6}$$

ISBN 978-3-95450-134-2

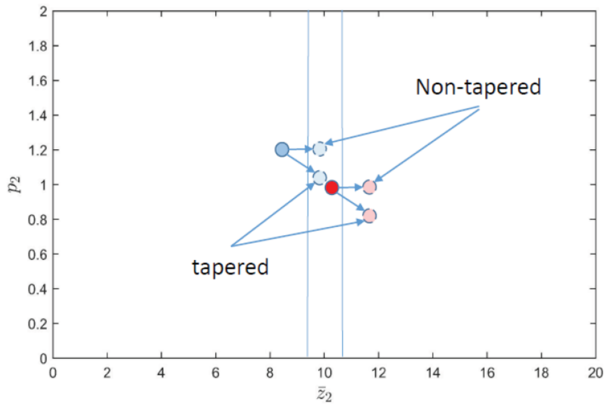

Figure 1: Showing the manipulation of p_2 by variation of the undulator magnetic field α. By altering the magnetic field, one may guide the blue electron to the correct value of p_2 to be resonant with the radiation in the blue slice indicated.

and small deviations in the undulator magnetic field, $\alpha \approx 1$.

Rewriting the formula for the taper required to compensate the detuning effect [1] from a chirp in the above notation, we obtain

$$\frac{d\alpha}{d\bar{z}} = -\frac{1+\bar{a}_{w0}^2}{\bar{a}_{w0}^2}\frac{1}{\gamma_r}\frac{d\gamma}{d\bar{z}_2}. \tag{7}$$

DISPERSIVE AND BROADBAND EFFECTS

To take into account dispersive effects, it is convenient to describe the system using the p_2 phase space. p_{2j} is the scaled velocity of the jth electron, and so describes, linearly, how the beam will disperse. It also linearly measures the resonant frequency of the electron; from Eq. (3)

$$p_{2j} = \frac{k_r}{k_j}, \tag{8}$$

so it is the inverse of the frequency scaled to the reference frequency.

Relaxing the constraint on the energies - once again allowing large energy changes - then Eq. (7) is no longer correct. In the 1D limit, and using a helical wiggler, from Eq. (3), p_{2j} may be defined as a function of α and γ as

$$p_{2j}(\bar{z}) = \frac{\gamma_r^2}{\gamma_j^2}\Big(\frac{1+\alpha(\bar{z})^2\bar{a}_{w0}^2}{1+\bar{a}_{w0}^2}\Big), \tag{9}$$

under the approximation that $\gamma_j, \gamma_r \gg 1$, ignoring any transverse velocity spread (1D limit), and ignoring any interaction with the radiation field (in the planar wiggler, one obtains the equivalent expression for p_{2j} averaged over the wiggle motion).

Using this definition, Figure 1 shows the effect of tapering in the $(\bar{z}_2, p_2)$ phase space, and shows what occurs when

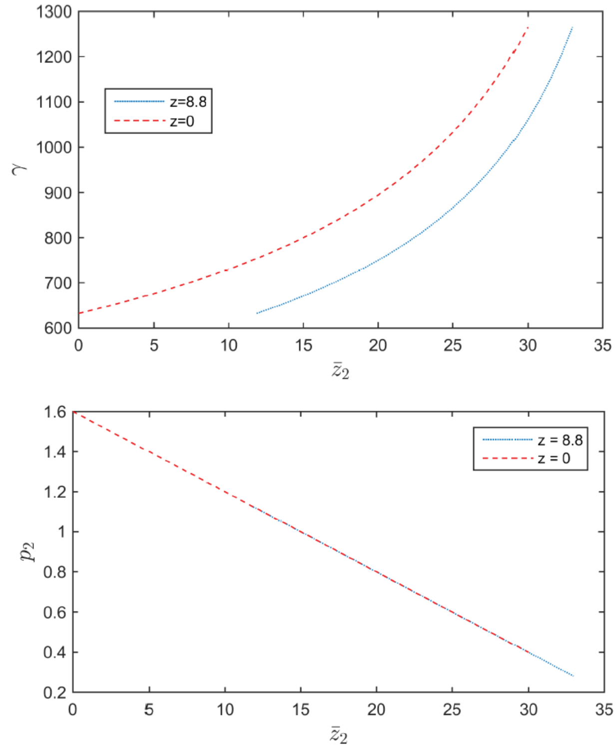

Figure 2: Top: The electron beam mean energy γ as a function of scaled temporal coordinate $\bar{z}_2$ at the start (red) and end (blue) of the undulator. Bottom: Same beam, now plotting the mean p_2 of the beam. The conversion from p_2 to γ can be obtained from Eq. (9). This is the stationary radiation frame, and the head of the beam is to the left, so the beam slips backwards through the field from left to right.

compensating for energy changes correlated in $\bar{z}_2$. The red electron, initially in the slice indicated, emits radiation at frequency k_r before slipping back to the right. Recall this is the stationary radiation frame, and the head of the pulse is to the left. The blue electron, slipping back into the thin slice, finds itself interacting with radiation it is not resonant with. By varying, or tapering, the magnetic field α, the value of p_2 of the blue electron can be manipulated, and reduced to the red electron's original value of p_2; therefore it is now resonant with the radiation in the slice originally emitted by the red electron.

Consequently, if an electron beam has an initial linear chirp in p_2, so that

$$\frac{dp_2}{d\bar{z}_2}\Big|_{\bar{z}=0} = m, \tag{10}$$

then the correct magnetic field taper to ensure the beam stays resonant should cause each electron to follow the line of the chirp defined by m. Figure 2 shows this. It plots the mean energy of a beam, and the corresponding mean p_2, as a function of $\bar{z}_2$, at the start ($\bar{z} = 0$) and end of an undulator tapered to compensate for the chirp. The taper may be derived from Eqs. (9) and (3), forcing $dp_{2j}/d\bar{z} = m$

ISBN 978-3-95450-134-2

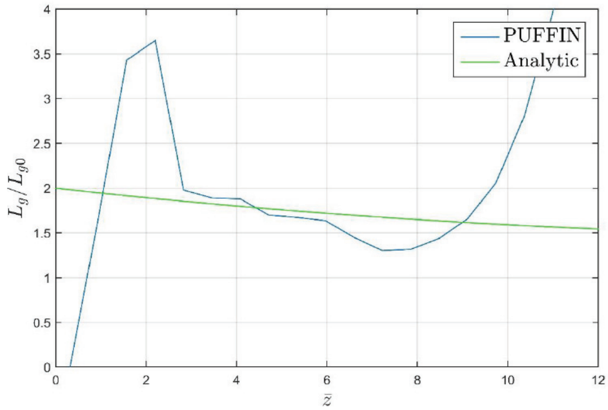

Figure 3: Variation in gain length as a function of distance through the undulator due to dispersive effects. Analytic from Eq. (19) (green) compared to numerical result from Puffin (blue).

and $d\gamma_j/d\bar{z} = 0$, and solving for α. The solution is found to be:

$$\alpha = \frac{1}{\bar{a}_{w0}}\sqrt{\exp(m\bar{z})(1+\bar{a}_{w0}^2) - 1}, \tag{11}$$

which reduces to the solution of Eq. (7) only when

$$|m\bar{z}| \ll 1 \tag{12}$$

and

$$\frac{\bar{a}_{w0}^2}{1+\bar{a}_{w0}^2} \sim 1. \tag{13}$$

For magnetic undulators, where $\bar{a}_{w0}^2 \gtrsim 1$, condition (13) is satisfied.

To measure the beam compression or decompression from this linear p_2 chirp, remembering that p_2 is the velocity of the electron in $\bar{z}_2$, then the change in the pulse width σ_{z2} is

$$\frac{d\sigma_{z2}}{d\bar{z}} = m\sigma_{z2}(\bar{z}). \tag{14}$$

From this, a stretch factor S is defined as

$$S(\bar{z}) = \frac{\sigma_{z2}(\bar{z})}{\sigma_{z20}} = \exp(m\bar{z}). \tag{15}$$

From this, it is seen that condition (12) is the limit of negligible dispersion in the undulator. This is different from the limit of a small chirp as previously identified in Eq. (7), which is simply

$$|m| \ll 1. \tag{16}$$

For a typical SASE FEL, $\bar{z} \approx 10 - 15$, so the dispersive condition is more restrictive by around an order of magnitude.

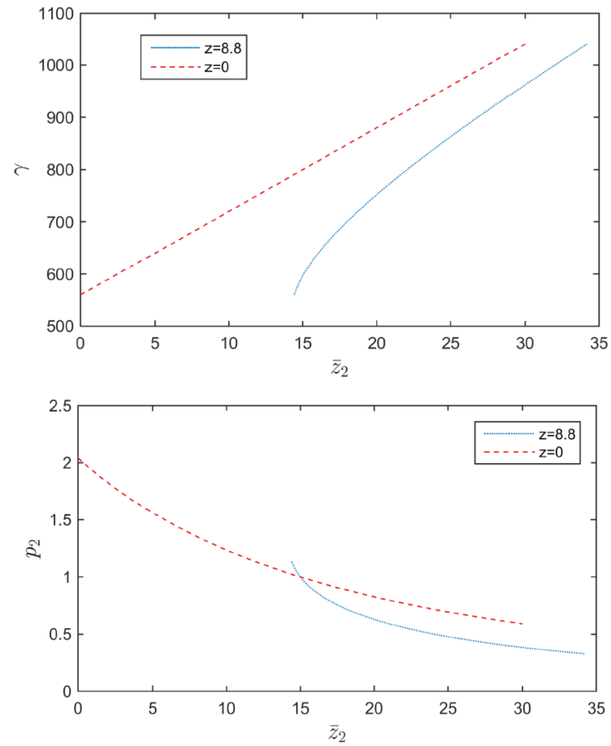

Figure 4: Same as Figure 2, now using an initially linear chirp in energy γ. The undulator is now tapered to try to keep the mean electron beam p_2 constant at $\bar{z}_2 = 15$. In this case, so that it is resonant with the reference frequency k_r, $p_2 = 1$ at $\bar{z}_2 = 15$. The undulator taper is calculated numerically and is not linear.

MEASURING THE EFFECT ON THE GAIN LENGTH

The dispersion has an effect on the '3D' gain length [17], as the compression/decompression will cause a change in the peak current and energy spread of the beam. The change in peak current can be analytically estimated very simply by

$$I(\bar{z}) = \frac{I_0(\bar{z}=0)}{S(\bar{z})}. \tag{17}$$

The dispersion will also alter the localised, or 'slice' energy spread of the beam. However, in this case, when using a linear chirp in p_2 with the taper in Eq. (11), every electron follows the line with gradient m in the $(\bar{z}_2, p_2)$ phase space (see Figure 2), so the slice p_2 spread does not change despite the compression/decompression. This will cause a corresponding variation in the transverse velocity spread, which will affect the gain length. Here, only the 1D case is considered, so the increased transverse spread has no effect.

The other consideration is that the gain length is different for each frequency; here, the frequency is linearly correlated with $\bar{z}_2$, and, because the taper is compensating perfectly, this correlation is fixed across the full undulator. Again refering to Figure 2, the mean p_2 at an instantaneous point in $\bar{z}_2$ remains constant, but the corresponding mean energy (from the top plot) is very different. Picking a coordinate initially in the center of the beam, $\bar{z}_{2c}$, with corresponding beam energy γ_c, which is a function of $\bar{z}$, then the normalized energy of the electron resonant with the fixed frequency is given by

$$\Gamma = \frac{\gamma_c}{\gamma_{c0}} = \left(\frac{1 + \alpha^2 \bar{a}_{w0}^2}{1 + \bar{a}_{w0}^2}\right)^{1/2}, \quad (18)$$

where $\gamma_{c0} = \gamma_c(\bar{z} = 0)$.

From the definition of the FEL parameter, the gain length then varies as

$$L_g(\bar{z}) = \frac{S(\bar{z})^{1/3}\Gamma(\bar{z})}{\alpha(\bar{z})^{2/3}} L_{g0}, \quad (19)$$

where L_{g0} is the gain length at $\bar{z} = 0$, and the gain length as referred to here is the M. Xie gain length, with only the energy spread parameter included.

A comparison of this analytic expression with the unaveraged FEL code Puffin is shown in Figure 3. Relevant parameters used are $\rho = 0.01$, $\bar{a}_{w0} = 2$, $\gamma_r = 800$ and $m = -0.04$, and slice spread of $\sigma_\gamma/\gamma_r = 1\%$. The gain length from Puffin is measured numerically from the radiated energy narrowly filtered around the frequency at $\bar{z}_{2c}$, and compares well with the analytic result. Note that the exponential gain region is $\bar{z} \approx 3$ to ≈ 8; before this is the startup regime where there is no gain, and after this the system is in saturation. There is good agreement in the exponential gain regime.

By using a linear chirp in *energy*, the beam compresses asymmetrically, and it is not possible the compensate for the detuning effect for all frequencies. Figure 4 plots the same quantities as Figure 2, but with a linear energy chirp, and the taper is calculated numerically to keep the reference frequency at $\bar{z}_2 = 15$ interacting with electrons resonant with it (so, in this case, keeping $p_2 = 1$). The same can be done for any frequency emitted, so it is possible to preferentially compensate for certain frequencies, but it is not possible to properly compensate for all frequencies.

However, this does not necessarily result in a higher power at that frequency. Other factors, such as the energy and slice spread, change differently for each frequency. Only the detuning effect is being compensated for; the other quantities (*e.g.* current), varying asymmetrically across the bunch, may result in less or more gain at other frequencies when all effects are accounted for.

Consequently, there is a large range of tapers which can be considered ‘optimum’. But the detuning effect can only be completely removed across the whole bunch when the beam has a linear chirp in p_2, and using the taper described in Eq. (11). In that case, the effect on the gain length can be easily predicted.

Note that, in the above, only 1D effects have been taken into account. There is no examination of the change in diffraction parameter, beam divergence parameter *etc.* (from [17]) occuring as a result of the dispersion. Preliminary work suggests that when these effects are included the impact on the gain can be more severe.

CONCLUSION

We have shown that the beam dispersion in the undulator is an important effect, and the constraint on when it appears is actually an order of magintude tighter than the condition of a ‘small’ chirp. A simple model was presented to take into account the dispersion, which allows an analytic solution for a matched taper to eliminate the detuning effect, and allows one to isolate the effects of the dispersion and measure them. It is shown that the unaveraged code Puffin agrees with this result.

ACKNOWLEDGEMENTS

We gratefully acknowledge the support of Science and Technology Facilities Council Agreement Number 4163192 Release #3; ARCHIE-WeSt High Performance Computer, EPSRC Grant EP/K000586/1; EPSRC Grant EP/M011607/1; and John von Neumann Institute for Computing (NIC) on JUROPA at Jülich Supercomputing Centre (JSC), under project HHH20.

REFERENCES

[1] E.L. Saldin *et al*, Phys. Rev. ST Accel. Beams **9**, 050702 (2006)

[2] A.R. Maier *et al*, Phys. Rev. X **2** (2012) 031019

[3] A. Aschikhin *et al*, The FLASHForward Facility at DESY, arXiv:1508.03192, (2015)

[4] B.Hidding *et al*, Tunable Electron Multibunch Production in Plasma Wakefield Accelerators, arXiv:1403.1109 (2014)

[5] E. Hemsing, G. Stupakov and D. Xiang, Rev. Mod. Phys. **86**, 897 (2014)

[6] H.P. Freund, Phys. Rev. E, **52**, 5401 (1995)

[7] S. Reiche, Nucl. Instr. and Meth. in Phys. Res. A **429**, 243-248 (1999)

[8] E.L. Saldin *et al*, Nucl. Instr. and Meth. in Phys. Res. A **429**, 233-237 (1999)

[9] W.M. Fawley, Proceedings of FEL 2006, BESSY, Berlin, Germany, 218-221 (2006)

[10] F.T. Arecchi and R. Bonifacio, IEEE J. Quantum Electron. **QE-1**, 169 (1965)

[11] L.T. Campbell and B.W.J. McNeil, Physics of Plasmas **19**, 093119 (2012)

[12] N. Piovella, Phys. Plasmas **6**, 3358 (1999)

[13] B.W.J. McNeil , G.R.M. Robb and D.A. Jaroszynski, Optics Comm. **165**, 65 (1999)

[14] S.I. Bajlekov, S.M. Hooker and R. Bartolini, Proc. FEL 2009 Liverpool, MOPC42 (2009)

[15] C. Maroli, V. Petrillo and M. Ferrario, Phys. Rev. ST Accel. Beams **14**, 070703 (2011)

[16] L.T. Campbell, B.W.J. McNeil and S. Reiche, New J. Phys.**16**, 103019 (2014)

[17] M. Xie, Nucl. Inst. Meth. Phys. Res. A 445, 59 (2000)

ISBN 978-3-95450-134-2

FEMTOSECOND X-RAY PULSE GENERATION WITH AN ENERGY CHIRPED ELECTRON BEAM

C. Emma, C. Pellegrini, UCLA, Los Angeles, CA 90095 USA
Y. Ding, G. Marcus, A. Lutman, Z. Huang, A. Marinelli, SLAC, Menlo Park, CA 94025, USA

Abstract

We study the generation of short (sub 10 fs) pulses in the X-ray spectral region using an energy chirped electron beam in a Self Amplified Spontaneous Emission Free Electron Laser (SASE FEL) and a self-seeding monochromator [1-4]. The monochromator filters a small bandwidth, short duration pulse from the frequency chirped SASE spectrum. This pulse is used to seed a small fraction of the long chirped beam, hence a short pulse with narrow bandwidth is amplified in the following undulators. We present start-to-end simulation results for LCLS operating in the soft X-ray self-seeded mode with an energy chirp of 1% over 30 fs and a bunch charge of 150 pC. We show the possibility to generate 5 fs pulses with a bandwidth 0.3 eV. We also assess the possibility of further shortening the pulse by utilizing one more chicane after the self-seeding stage and shifting the radiation pulse to a "fresh" part of the electron beam. Experimental study on this short pulse seeding mode has been planned at the LCLS.

INTRODUCTION

Ultrashort x-ray pulses of femtosecond to sub-femtosecond duration are important for time-resolved ultrafast studies in chemistry, biology, and material science. Operating in the self-amplied spontaneous radiation (SASE) mode [1], different schemes have been proposed in the past years to shorten the x-ray pulses. One such method, using a configuration similar to the selfseeding setup, was first proposed by Schroeder et al. [2]. In this mode, the electron beam has a time-energy correlation and a monochromator selects a narrow-bandwidth seed to interact wiith a small fraction of the chirped bunch. The central wavelength is determined by the monochromator hence the output central wavelength would be stable against beam energy jitter. In this paper we study the generation of femtosecond level pulses in start-to-end simulations for the LCLS beam.

A time-energy chirped beam can be generated in an overcompression mode in the second chicane compressor at LCLS. In this mode, the bunch head has higher beam energy than the tail. This chirped beam generates wide-bandwidth SASE radiation before the Soft X-ray Self Seeding (SXRSS) chicane. We choose the appropriate number of undulator sections to reach a radiation power on the 10MW level before the SXRSS monochromator. After the monochromator grating, we achieve a narrow-bandwidth seed determined by the monochromator resolving power. For a resolving power R the rms bandwidth is σ_m=1/(2.355*R). After the monochromator the pulse duration is given by [4]:

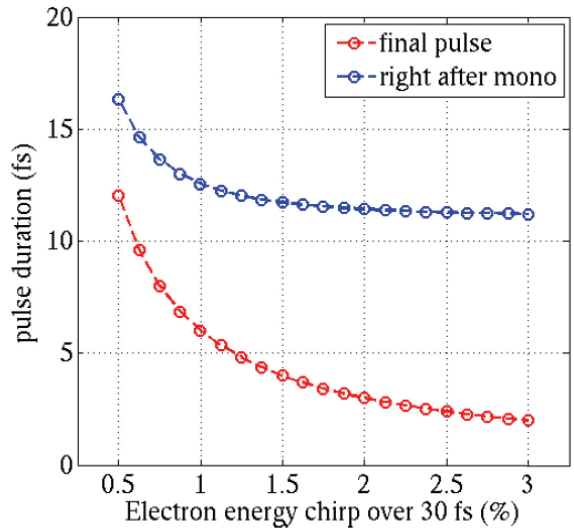

Figure 1: Theoretical expected pulse duration given by Eq. 1 right after the mono and at the end of the undulator. Prediction is in excellent agreement with simulation results for a beam with a 1 % chirp over 30 fs.

$$\sigma_{t,m}^2 = \frac{\sigma_\omega^2 + \sigma_m^2}{u^2} + \frac{1}{4\sigma_m^2} \tag{1}$$

where σ_ω is the SASE bandwidth, σ_m is the monochromator bandwidth and $u = \Delta\omega/\Delta t$ is the energy chirp on the beam. After the amplification process the pulse duration shortens and is dominated by the SASE bandwidth and the energy chirp $\sigma_{t,f} \approx \sigma_\omega/u$. The pulse length expected as a function of the electron beam chirp is shown in Fig. 1. Slippage of the radiation spike along the chirped beam requires reverse tapering of the undulator field in order to preserve the resonance condition and amplify a short pulse [5, 6]. In the amplifying section after the SXR monochromator only a small fraction of the chirped bunch is on resonance with the seed and will undergo microbunching at the radiation wavelength. To increase the gain and further shorten the pulse duration we consider using a second chicane as an additional delay to shift the radiation pulse to a "fresh" part of the beam downstream of the SXR monochromator. This ensures that the radiation will be continually amplified by a fresh bunch. The delay can be optimized to achieve shorter pulses and superradiant effects may also further shorten the pulse duration.

ISBN 978-3-95450-134-2

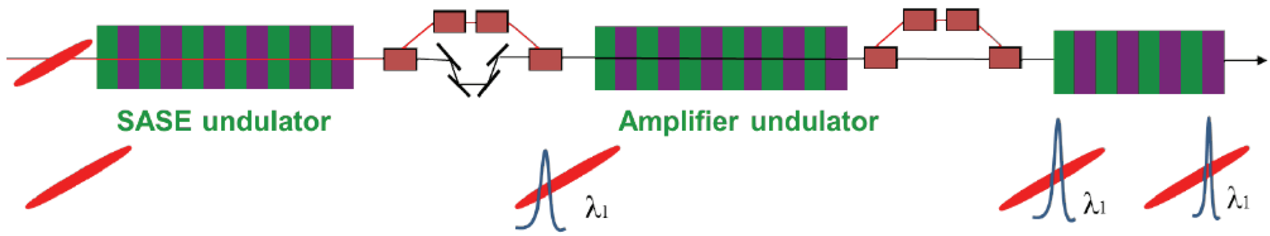

Figure 2: Schematic of the operation mode for soft x-ray self seeding with a chirped electron beam. The second chicane is used as an additional delay to shift the radiation to a “fresh" part of the electron bunch and shorten the pulse duration.

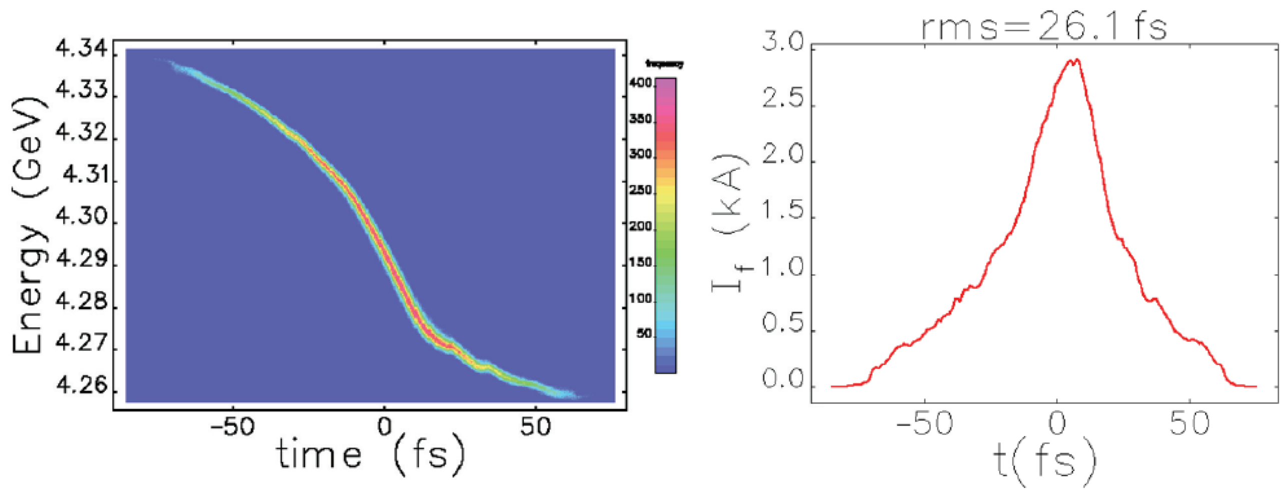

Figure 3: Longitudinal phase space and current profile for the LCLS beam with 150 pC charge and a chirp of 1 % over 30 fs in the core.

Table 1: GENESIS Simulation Parameters

Parameter Name	**Parameter Value**
Undulator:	
Undulator Period λ_w	30 mm
Undulator Parameter aw_0	2.4749
Electron Beam:	
Beam Energy E_0	4.3 GeV
Beam Peak Current I_{pk}	2.8 kA
Normalized Emittances $\epsilon_{x,n}/\epsilon_{y,n}$	0.4/0.4 μ m
Radiation:	
Radiation Wavelength λ_r	1.523 nm
(Before/after SXRSS chicane)	
Peak radiation power P_{in}	1.2GW/ 0.2MW
Pulse Duration FWHM σ_τ	17 fs→ 7 fs

START TO END SIMULATION STUDY FOR LCLS

Soft X-ray Self Seeding

We study the chirped seeding method in start to end simulations of the LCLS electron beam with a bunch charge of 150 pC and an energy chirp of 1% over 30 fs in the core part. The electron beam longitudinal phase space and current profile are shown in Fig. 3, the GENESIS simulation parameters are given in Table 1 [3] and a schematic of the undulator configuration is shown in Fig. 2. The first SASE section is 5 undulators long (20 m) and the SASE bandwidth generated is larger than 1% for this chirped beam. After the SXRSS monochromator with a resolving power of 5000 the bandwidth of the seed spike is 0.14 eV FWHM and the pulse length is approximately 13 fs consistent with the expected vaules from Eq. 1. We align the seed to the core part of the bunch and allow the bunch to amplify the radiation for 5 undulators between the SXRSS chicane and the second chicane. We find empirically that peak power is maximized for the shortest pulse duration with no tapering of the undulator K in the section between the two chicanes. This is due to the combined effects of radiation slippage towards the high energy part of the beam and electron beam energy loss due to the FEL process. The time domain and spectral evolution of the radiation between the SXRSS monochromator and the second chicane delay are shown in Fig. 4. At the second chicane after 20 m of amplification a peak power of 20 GW is achieved with a narrow bandwith of 0.3 eV and a pulse duration of 7 fs, also in excellent agreement with the theoretical prediction shown in Fig. 1.

ISBN 978-3-95450-134-2

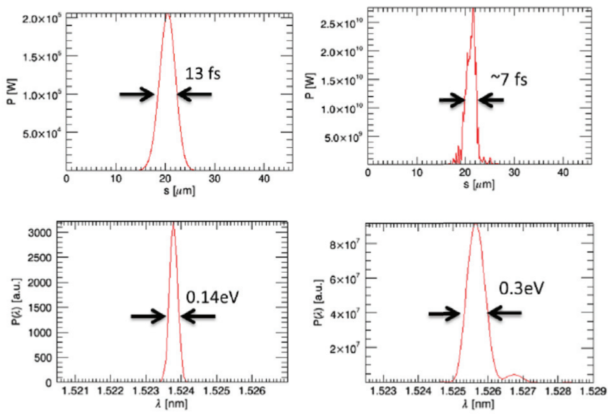

Figure 4: Evolution of the FEL pulse in the time and frequency domain for a chirped beam in the self-seeded operation mode. The left column is after the SXRSS monochromator and the right column is after 20 m of amplification before the second chicane.

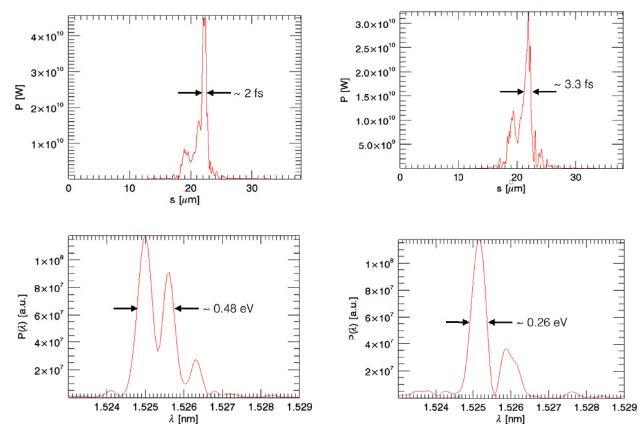

Figure 5: Time and frequency domain for a chirped beam in the self-seeded operation mode 4m downstream of the second chicane delay. The left column is for a 1 μm chicane delay and the right column is for 0.5 μm delay.

Fresh Bunch Technique

We then optimize the delay in the second chicane to further shorten the pulse and amplify using a fresh part of the electron beam. The time domain and spectrum 4 m downstream of the second chicane for two separate delays of 0.5 and 1 μm are shown in Fig. 5. Examining the spectral and time-domain evolution of the pulse we find that the shortest pulse ~ 2 fs, a FWHM bandwidth of 0.48 eV and a peak power of 45 GW is generated with a chicane delay of 1 μm. This delay corresponds to roughly half the pulse overlapped with fresh electrons. In this case the gain for the head of the radiation pulse is larger than for the tail and as a result the radiation pulse compresses in the time domain. For a larger delay of 2 μm the peak power of the radiation pulse increases but the pulse is longer in time ~ 6 fs. A smaller delay of 0.5 μm produces ~ 3.3 fs pulse with a cleaner spectrum and a peak power of 30 GW. The spectrum will ultimately become polluted if we amplify for more than two undulators after the second chicane due to the growth of the SASE from the chirped beam.

Experimental study of the chirp seeded mode are in progress at LCLS. Preliminary results show that pulses of ~ 10 fs time duration can be produced without using the second chicane delay. Data analysis for these experiments is ongoing.

CONCLUSION

We performed start to end simulations of femtosecond X-ray pulse generation using an energy chirped electron beam and a self-seeding monochromator at the LCLS. We consider a shceme originally proposed in Ref [2] in which a time-energy chirped electron beam is used to produce frequency chirped SASE, the frequency chirped SASE is filtered by a monochromator and recombined with the electron beam. A downstream undulator section is then used to amplify a narrow spike of radiation in both the time and frequency domain.

Using the LCLS start to end electron beam with 150 pC of charge and an energy chirp of 1 % over 30 fs in the core part we produce 12 GW of SASE power with >1 % bandwidth using 5 undulators before the SXRSS chicane. The large bandwidth improves wavelength stability after the monochromator against electron beam energy jitter coming from the linac. The monochromator selects a narrow bandwidth signal which is amplified in the following undulators by preserving the resonance condition over a short section of the chirped electron beam. The pulse duration after the monochromator is 17 fs and following 20 m of amplification, the pulse narrows to a FHWM duration of 7 fs and 20 GW peak power before the second chicane delay.

We then make use of the second chicane to introduce an additional delay and shift the radiation pulse to a “fresh" part of the electron beam. This increases the gain and with a 1 μ m delay reduces the pulse duration to ~ 2 fs, 4m downstream of the second delay. The peak power reaches 45 GW at this location. Smaller and larger delays are investigated, with larger delays producing higher peak powers but longer pulses. A shorter delay of 0.5 μ m reduces the peak power but produces a cleaner spectrum with a pulse duration ~ 3.3 fs. The main factor limiting further amplification is the growth of SASE from the chirped electron beam. Increasing the signal to noise ratio after the SXRSS monochromator will act to suppress this effect. Experimental investigations are ongoing at LCLS with initial results suggesting that ~ 10 fs pulses can be generated using the chirp-seeded configuration.

ISBN 978-3-95450-134-2

REFERENCES

[1] R. Bonifacio, C. Pellegrini, L. Narducci, Optics Communications, vol. 50, no. 6, p. 373, 1984.

[2] C. B. Schroeder, C. Pellegrini, S. Reiche, J. Arther and P. Emma, J. Opt. Soc. Am. B 19, 1782 (2002).

[3] S. Reiche, Nucl. Instr. Meth. Phys. Res. Sec. A 429, 243 (1999).

[4] S. Krinsky, Z. Huang, PRSTAB 6, 050702 (2003).

[5] Saldin, E. L. and Schneidmiller, E. A. and Yurkov, M. V., PRSTAB 9, 050702.

[6] L. Giannessi et al., Phys. Rev. Lett., 106(14):144801.

ISBN 978-3-95450-134-2

TAPERING STUDIES FOR TW LEVEL X-RAY FELS WITH A SUPERCONDUCTING UNDULATOR AND BUILT-IN FOCUSING*

C. Emma, C. Pellegrini, UCLA, Los Angeles, CA 90095 USA
K. Fang, J. Wu, SLAC, Menlo Park, CA 94025, USA

Abstract

Tapering optimization schemes for TeraWatt (TW) level X-ray Free Electron Lasers (FELs) are critically sensitive to the length of individual undulator and break sections. Break sections can be considerably shortened if the focusing quadrupole field is superimposed on the undulator field, increasing the filling factor and the overall extraction efficiency of the tapered FEL. Furthermore, distributed focusing reduces the FODO length and allows one to use smaller beta functions, reducing particle de-trapping due to betatron motion from the radial tails of the electron beam. We present numerical calculations of the tapering optimization for such an undulator using the three dimensional time dependent code GENESIS. Time dependent simulations show that 8 keV photons can be produced with over 3 TW peak power in a 100m long undulator. We also analyze in detail the time dependent effects leading to power saturation in the taper region. The impact of the synchrotron sideband growth on particle detrapping and taper saturation is discussed. We show that the optimal taper profile obtained from time independent simulation does not yield the maximum extraction efficiency when multi-frequency effects are included. A discussion of how to incorporate these effects in a revised model is presented.

INTRODUCTION

In this work we analyze the tapering optimization of a high efficiency [1] TW-level X-ray FEL using time independent and time dependent GENESIS simulations. We show that the solution obtained for the optimal taper profile in time independent simulations does not yield the maximum extraction efficiency when fully time dependent physics is included in the dynamics of the the electron beam and radiation field system. We study the optimization for a superconducting, 2 cm period, helical undulator with built in focusing. This undulator design is optimized for maximum efficiency, reduction of intra module undulator length, strong transverse focusing, short gain length and minimum total undulator length.

UNDULATOR DESIGN

We apply the tapering optimization method [2] to an undulator designed specifically to achiveve TW power X-ray pulses in the shortest possible undulator length. Our ideal undulator is superconducting, with a short 2 cm period and a peak on axis field B_0 of 1.6 T. For a double helix bifilar magnet with equal and opposite currents this field is given

Table 1: GENESIS Simulation Parameters

Parameter Name	Parameter Value
Beam Energy	12.975 GeV
Peak Current	4000 A
Normalized Emittances	0.3/0.3 μm rad
Average beta function	5 m
RMS Energy Spread	10^{-4}
Bunch Length	6 fs
Seed radiation power	5-25 MW
Radiation Wavelength	1.5 Å
Rayleigh Length	10 m
Undulator Period	2 cm
Undulator Parameter	3
Quadrupole Focusing Strength	26.4 T/m
Undulator Section Length	1 m
Undulator Break Length	20 cm
FEL parameter	1.66×10^{-3}
3-D Gain Length	65 cm

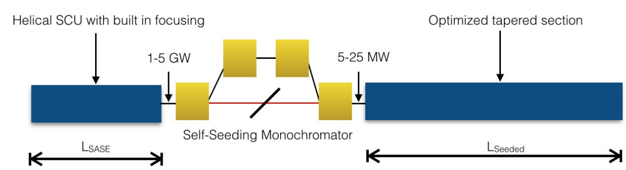

Figure 1: Schematic of the undulator for hard X-ray multi TW peak power output, designed to achieve high extraction efficiency in the shortest possible distance.

by [3]:

$$B_0 = \frac{4k_u I}{10^5}\left[k_u a K_0(k_u a) + K_1(k_u a)\right], \tag{1}$$

where I is the current in the coils, $k_u = 2\pi/\lambda_u$ is the undulator wavenumber, a is the helix radius and K_0 and K_1 are modified Bessel functions. For a helical bore radius $a = 7.5$ mm the total current required through the coils is $I = 484$ A which, considering coils of $\sim$ mm^2 surface area, gives a current density below the critical value for superconducting NbTi or Nb3Sn wires. From the point of view of operation a superconducting undulator has advantages such as resistance to radiation damage and reduced sensitivity to wakefields, for a more detailed description see Ref. [4]. The undulator is helically polarized as this increases the effect of refractive guiding in the post-saturation regime and improves the FEL performance [5].

* Work supported by: DOE Grant Number DE-SC0009983

ISBN 978-3-95450-134-2

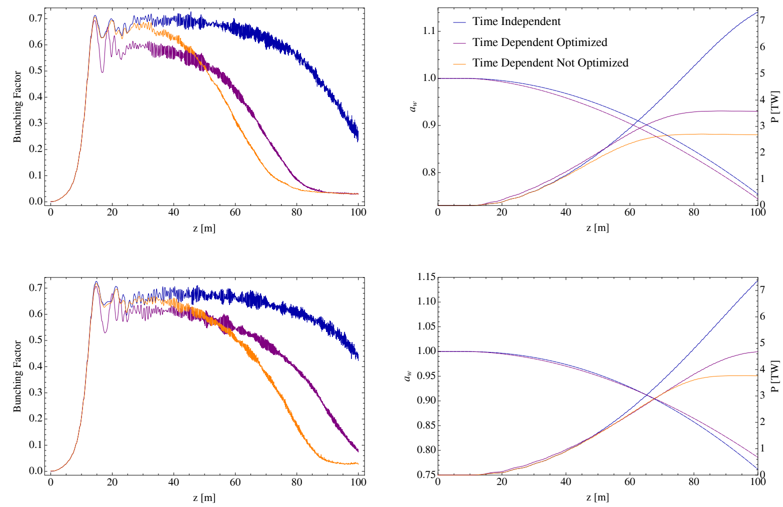

Figure 2: Bunching factor (left), taper profiles and FEL radiation power evolution (right) obtained from time independent and time dependent optimization. The top plots correspond to an iNput energy spread $\sigma_{E,0}$=3.1 MeV consistent with the SASE result from Fig. 1. The bottom plots are an alternate case with $\sigma_{E,0}$=1.5 MeV. In both cases z=0 is after the self-seeding monochromator and the input seed power is 5 MW.

In order to accomodate diagnostics a realistic undulator design must include periodic break sections, with longer breaks adversely affecting performance. This is due essentially to three effects. Firstly, diffraction effects are critical to the performance of a tapered FEL particularly for long, multiple Rayleigh length undulators. While these effects are mitigated by refractive guiding inside the undulator, there is no guiding during the break sections and the radiation size increases exponentially, reducing the field amplitude, causing particle detrapping and limiting the extraction efficiency. Secondly, a break of length L_b introduces a phase error $\Delta\Psi \sim L_b\delta/\gamma^2 = 2n\lambda_r\eta$ for a particle with relative energy offset $\eta = \delta\gamma/\gamma_r$ with respect to the resonant particle. Thus longer break sections increase electron phase mixing and reduce the bunching factor. Finally as a practical consideration, for a given total undulator length, longer break sections reduce the length of magnetic elements limiting the electron deceleration and over-all extraction efficiency. To minimize the break length we superimpose the focusing quadrupole field on the helical undulator field, similar to the design successfully tested in Ref. [6]. One advantage of distributed quadrupole focusing is the possibility to operate at small betatron beta function, due to the reduced FODO lattice length L_f. This minimizes the transverse beam envelope oscillation $\Delta\beta^2/\beta_{av}^2 = \beta_{av}L_f/(\beta_{av}^2 - L_f^2)$ which also degrades the FEL performance [7]. In our study the undulator magnetic field is tapered continuously and the section length is chosen to be 1 m, close to the 3-D gain length with 20 cm breaks in between.

Although this kind of undulator has never been constructed in the past, the parameters presented in this design are similar to what is currently being considered for an LCLS-II-like planar superconducting undulator with the addition of built in quadrupole focusing [4]. A full engineering and tolerance study of this undulator is needed before we can be confident that it is a feasible option for future high efficiency X-ray FEL facilities.

TAPERING OPTIMIZATION

Time Independent

We first obtain the optimal taper profile, maximizing the output power for a fixed 100 m undulator length in time independent simulations using the three dimensional FEL particle code GENESIS. The tapering law is written as:

$$a_w(z) = a_{w0} \times \left(1 - c \times (z - z_0)^d\right), \qquad (2)$$

where the parameters z_0, c, d are obtained by mutlidimensional scans which maximise the output power. The quadrupole focusing can also be tapered to further increase the extraction efficiency as shown in Ref. [2] but that will not be considered in this study. The optimal taper profile obtained from time independent optimization is shown in Fig. 3. The tapering order is approximately quadratic, which follows qualitatively from the fact that in time independent simulations the bunching factor and trapping fraction remain nearly constant in the tapered section and the dominant radiative process is coherent emission. The peak output power is 7.3 TW with an extraction efficiency of 14 %. It is important to note that there is no sign of the taper power saturating in the time independent case, which is not the case when time dependent effects are included.

Time Dependent Optimization

Using the optimal taper starting point obtained from time independent simulations, we perform time dependent scans over the taper order d and the taper strength $\Delta a_w/a_w$ =

ISBN 978-3-95450-134-2

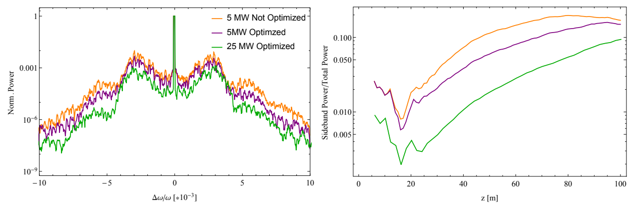

Figure 3: (left) Spectrum at half the undulator length and fractional sideband power (right) for the time independent optimized case and fully time dependent optimized for 5 MW and 25 MW input seed power and 1.5 MeV energy spread. Sideband power grows faster in the time independent optimized case, leading to particle detrapping and early saturation of the tapered FEL.

$c \times (L_w - z_0)^d$. As shown in Fig. 3, the values of the taper order and taper strength yielding the maximum power in time independent simulations are not the optimal choice of parameters once time dependent effects are included. The variation in peak power is more sensitive to variations in the taper profile in the time dependent cases. The optimal taper order is weaker than quadratic, and is reduced compared to the time independent case. This is due to the FEL increased sensitivity to particle detrapping when electron beam shot noise and multiple frequency effects are included.

Since the coherent emission power is proportional to the product of the number of trapped particles and the change in resonant energy (taper strength), a slower taper preserves the trapping for longer, maximising the product and the overall extraction efficiency. In the large energy spread case it is important to note that the time dependent optimized taper profile has a slower taper order but a larger over-all deceleration rate. This results in a worse particle capture in the early stages of the tapered section (z=10–50 m) but a reduction in detrapping in the remainder of the undulator. This can be understood by examining the functional form for the resonant phase:

$$\sin \Psi_R(z) = \chi \frac{|a'_w(z)|}{E(z)} \tag{3}$$

where $\chi = (2*me*c^2/e)(\lambda_w/2\lambda_s)(1/\sqrt{2}[JJ])$ is a constant independent of z and $E(z)$ is the electric field amplitude. The time dependent optimized taper reduces $|a'_w(z)|$ in the second half of the undulator z=50–100m, maintaining a larger bucket area in the region where the amplitude of the sidebands is more appreciable and the system is more sensitive to detrapping. From this it is clear that a fully optimized form of the taper profile should have an improved capture rate in the early stages with a profile similar to what one obtains from time independent optimization, and a slower decrease in the undulator field in the later stages when time dependent effects are more appreciable. This requires a more elaborate functional form for $a_w(z)$ and will be investigated in future work.

SIDEBAND INSTABILITY

The mechanism of sideband generation and amplification in free electron lasers can be summarized as follows [8]. Firstly, sidebands are generated due to amplitude and phase modulations of the electric field, due to the trapped particles undergoing synchrotron oscillations as they pass through the undulator. Using Maxwell's equations in the 1-D slowly varying envelope approximation we can write the evolution of the electric field amplitude and phase [8]:

$$a'_s = \frac{\omega_p^2}{2\omega_s c} a_w \left\langle \frac{\sin \Psi}{\gamma} \right\rangle \tag{4}$$

$$\delta k_s = \frac{\omega_p^2}{2\omega_s c} \frac{a_w}{a_s} \left\langle \frac{\cos \Psi}{\gamma} \right\rangle \tag{5}$$

where a_s is the dimensionless vector potential for the electric field, ω_p is the electron beam plasma frequency and Ψ is the ponderomotive phase. It is clear from these that as the electrons oscillate in the longitudinal phase space (Ψ, γ) the gain and the phase shift of the radiation field will be different at different locations in the undulator and, due to shot noise in the electron beam, at different locations along the bunch. This results in a temporal modulation of the radiation field giving rise to sidebands displaced from the central wavelength by a quantity proportional to the synchrotron period:

$$\lambda_{s'} \approx \lambda_s \left[1 \pm \frac{\lambda_w}{L_{sy}} \right] = \lambda_s \left[1 \pm \left(\frac{a_w a_s}{1 + a_w^2} \right)^{1/2} \right] \tag{6}$$

where L_{sy} is the synchrotron period. Once the sidebands are generated, the electron oscillations are driven by a multiple frequency ponderomotive potential, therefore the equations of motion and Maxwell's equations for the electric field, must be modified accordingly. An analysis of the simplest two frequency model shows that the coupled beam-radiation system is unstable and that the sideband amplitude will grow from noise for any realistic electron distribution [8]. When the strength of the sidebands exceeds a critical level, electron motion becomes chaotic leading to severe particle detrapping and a loss of amplification of the FEL signal [9]. Thus, as has been discussed by previous authors, suppressing the sideband instability is the key issue for tapered FEL designs [1], particularly those which are multiple synchrotron periods in length.

As is shown in Fig. 4 the time dependent optimized taper profile reduces sideband amplitude growth. This results in a reduction in particle loss and a delayed taper saturation, both evidenced in the increased bunching factor and output power in Fig. 2. In the simple case of constant sideband and carrier amplitude the diffusion coefficient caused by sideband excitations is proportional to the ratio of the power in the sidebands to the power in the FEL signal $D \propto C P_{s'}/P_s$ with the coefficient C depending on the type of sideband spectrum [9]. As is also shown in Fig. 4 this is reduced in the time dependent optimized case. The peak power improves

ISBN 978-3-95450-134-2

by 1 TW between the time dependent optimized and unoptimized cases, an overall improvement of 2 %. Despite the dedicated time dependent optimization we do not recover the single bucket extraction efficiency unlike results previously reported in Ref. [10].

CONCLUSION

In this paper we perform the first comparison of time independent and time dependent tapering optimization for a high efficiency seeded hard X-ray FEL. The comparison is done for an undulator design optimized to achieve TW peak powers in the shortest possible distance: helical, superconducting and with built-in focusing. We demonstrate that the taper profile yielding the maximum power in time independent optimizations does not correspond to the optimal solution when time dependent effects are included in the simulation. By performing time dependent scans of the taper order and the taper strength we show that the maximum output power in time dependent mode is achieved with a lower taper order compared to the time independent case. The difference is due to the increased sensitivity to particle detrapping in the time dependent case, mitigated by a slower taper profile in the later stages of the undulator where time dependent effects are more important. For an input energy spread of 3.1 MeV the final output power increases from 2.7 TW with the time independent taper profile to 3.7 TW with the profile obtained from dedicated time dependent scans.

We have also discussed the importance of the trade-off between energy spread and seed power at the entrance of the tapered undulator section. We show that using a “fresh bunch" with input energy spread of 1.5 MeV determined only by the linac we can decrease particle detrapping, maintain a larger bunching factor and improve the over-all performance. For the same seed power of 5 MW the maximum output power is 4.7 TW after the dedicated time dependent optimization. In a double-bunch system the input seed power can be larger without affecting the input energy spread. We have studied an optimal case with a 25 MW seed and 1.5 MeV energy spread and found that the output power reaches 6.3 TW at the end of the undulator, a 12 % efficiency which approaches the time independent result of 7.7 TW.

We identify the sideband instability as the fundamental time dependent effect which is not taken into account in time independent optimizations and limits the extraction efficiency by causing particle detrapping. Analyzing the fraction of energy in the sidebands in the σ_E =1.5 MeV case with a 5 MW seed, we show that the fraction of energy deposited in the sidebands is below 10 % for 70 m in the time dependent optimized taper profile while it exceeds 10 % after 40 m in the the time independent case reaching 14 % towards the end of the undulator.

While extending the simulation method of Ref. [2] to include time dependent effects significantly improves the performance of tapered X-FELs the current procedure is both time consuming and simulation intensive. The form of the taper profile $a_w(z)$ needs a more complicated functional dependence to optimize trapping in the early stages and reduce sideband growth in the later stages where time dependent effects play a more important role. With the enhanced understanding gained of the critical parameters limiting performance, such as the growth of the sideband instability, an improved algorithm can be developed which acts to directly suppress these effects. Such a scheme will be developed in future work.

REFERENCES

[1] N.M. Kroll, P.L. Morton, M. Rosenbluth, IEEE Journal of Quantum Electronics , vol. 17, p. 1436, 1981

[2] Y. Jiao et al., Phys. Rev. ST. AB., vol. 15, p. 050704, 2012

[3] W.R. Smythe, 1950, Static and Dynamic Electricity (McGraw-Hill, New York), p. 277.

[4] P. Emma et al., in FEL 2014 Conference proceedings, Basel, Switzerland, p. THA03, 2014.

[5] D. Prosnitz, A. Szoke, V.K. Neil, Phys. Rev. A, vol. 24, p. 1436, 1981

[6] A. Murokh et al., Nuclear Instruments and Methods in Physics Research Section A: Accelerators, Spectrometers, Detectors and Associated Equipment, vol. 507, no. 12, pp. 417-421, 2003.

[7] S. Reiche and E. Prat, in FEL 2012 Conference proceedings, Nara, Japan, p. MOOC02, 2012.

[8] N.R.M. Kroll, in Free Electron Generators of Coherent Radiation, pp. 147-174, Springer Berlin Heidelberg, 1979.

[9] S. Riyopoulos and C. M. Tang, Physics of Fluids, vol. 31, no. 11, pp. 3387-3402, 1988.

[10] B. Hafizi, A. Ting, P. Sprangle, and C. M. Tang, Physical Review A, vol. 38, no. 1, 1988.

ISBN 978-3-95450-134-2

ADVANCES ON THE LUNEX5 AND COXINEL PROJECTS

M. E. Couprie, C. Benabderrahmane, P. Berteaud, C. Bourassin-Bouchet, F. Bouvet, J. Bozek, F. Briquez, L. Cassinari, L. Chapuis, J. Daillant, J. Da Silva, D. Dennetière, Y. Dietrich, M. Diop, J. P. Duval, M. El Ajjouri, T. El Ajjouri, C. Herbeaux, N. Hubert, M. Khojoyan, M. Labat, N. Leclercq, A. Lestrade, A. Loulergue, P. Marchand, O. Marcouillé, J. L. Marlats, F. Marteau, C. Miron, P. Morin, A. Nadji, R. Nagaoka, F. Polack, F. Ribeiro, J. P. Ricaud, G. Sharma, P. Rommeluère, P. Roy, K. Tavakoli, M. Thomasset, M. Tilmont, M. A. Tordeux, M. Valléau, J. Vétéran, W. Yang, D. Zerbib, Synchrotron SOLEIL, France
S. Bielawski, C. Evain, M. Le Parquier, C. Szwaj, PhLAM/ CERLA, Lille, France
E. Roussel, FERMI@ELETTRA, Sincrotrone Trieste, Basovizza, Italy
G. Lambert, V. Malka, A. Rousse, C. Thaury, Lab. d'Optique Appliquée, Palaiseau, France
G. Devanz, C. Madec, A. Mosnier, CEA/DSM/IRFU/SACM, Saclay, France
D. Garzella, CEA/DSM/IRAMIS/ LIDyL, Saclay, France
N. Delerue, M. El Khaldi, W. Kaabi, F. Wicek, Laboratoire de l'Accélérateur Linéaire, Orsay, France
X. Davoine, CEA/DAM/DIF, Bruyère-Le-Châtel, France
A. Dubois, J. Lüning, LCPMR, Paris-VI, France

Abstract

LUNEX5 (free electron Laser Using a New accelerator for the Exploitation of X-ray radiation of 5th generation) aims at investigating compact and advanced Free Electron Laser (FEL). It comprises one one hand a 400 MeV superconducting linac for studies of advanced FEL schemes, high repetition rate operation (10 kHz), multi-FEL lines, and one the other hand a Laser Wake Field Accelerator (LWFA) for its qualification by a FEL application, an undulator line enabling advanced seeding and pilot user applications in the 40-4 nm spectral range. Following the CDR completion, different R&D programs were launched, as for instance on FEL pulse duration measurement, high repetition rate electro-optical sampling. The COXINEL ERC Advanced Grant aims at demonstrating LWFA based FEL amplification, thanks to a proper electron beam manipulation, with a test experiment under preparation. As a specific hardware is also under development such as a cryo-ready 3 m long undulator of 15 mm period is under development.

INTRODUCTION

Since the laser discovery [1] and the first FEL [2] in the infra-red in Stanford on MARK III, followed by the ACO FEL in Orsay [3] in the visible and UV, and then in the VUV using harmonic generation [4] in the VUV, free electron lasers count nowadays as unique light sources in terms of their properties. Since the early FEL times, performance characterisation and quest for improvement was one of the major concerns. For example, in the case of the Super-ACO storage ring based FEL in France [5,6], the FEL dynamics was actively studied [7-10] and led to the first use of a UV FEL, even in combination with synchrotron radiation for pump-probe two-color experiments [11-16]. Oscillators and coherent harmonic generation also enable adjustable polarisation thanks to the use of elliptically polarised undulators [17-18]. So far, FEL oscillators have been limited to the VUV [19] because of the issues related to the mirror performance and degradation at short wavelengths [20-21]. Short-wavelength FELs then evolved towards high-gain single-pass-based systems [22] in the SASE [23] and seeded [24] configurations. Presently, VUV-X tuneable coherent sub-ps pulses FEL light sources around the word provide record peak powers (typically GW), peak and average brilliance at short wavelengths. FEL user facilities (FLASH1, FLASH2 [25-26], FERMI@ELETTRA in the seeded configuration [27], LCLS [28] and SACLA [29] in the hard X-ray) enable to explore unknown phenomena in various scientific domains. Different directions are now explored for performance improvement.

In France, activity has been performed in the frame of international collaborations on seeding, enabling to reduce the intensity fluctuations, jitter, the saturation length, in particular with a seed being generated from high-order harmonics generated in gas [30-32]. There is also interest for two-color operation, with first studies on CLIO [33] and in the pulse splitting configuration [34]. Characterisation of FEL properties is also of concern, both transversally [35] and longitudinally [36].

LUNEX5 PROJECT

The LUNEX5 [37-41] demonstrator project (shown in Fig. 1) aims at exploring several directions for the production of short, intense, and coherent pulses between 40 and 4 nm on the first, third and fifth harmonics. It relies first on a 400-MeV superconducting linac (SC) with two to three modified XFEL-type cryomodules at 1.3 GHz for high repetition rate CW and thus multiple user operation. The electron bunch is compressed due to a dogleg with sextupoles, enabling phase space linearization and cancellation of the second order dispersion [41].

ISBN 978-3-95450-134-2

The FEL line is made of two modulators (period 30 mm) and four cryo-ready radiators (15-mm period) for the comparison of Echo Enabled Harmonic Generation (echo) [42] and HHG seeding in terms of FEL spectral and temporal properties. Two pilot user experiments in gas phase and condensed matter will qualify the FEL performance in the different cases.

In addition, another direction will explore the qualification of a laser plasma acceleration process [43] by a FEL application, using the same FEL line components and a specific transport line for handling the plasma electron beam properties (divergence (1 mrad) and energy spread (1%)) to enable FEL amplification [44-45].

The LUNEX5 R&D and complementary studies to the Conceptual Design Report are carried out on specific programs with their own funding. The progresses on the different R&D programs are described below.

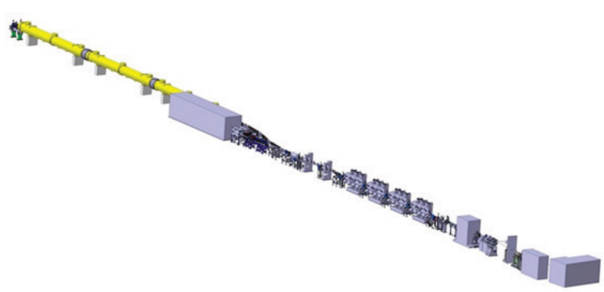

Figure 1: LUNEX5 sketch: cryomodules (yellow), LWFA laser hutch (grey), undulators (4 radiators and 2 echo modulators), pilot user experimental sections.

PARTIAL COHERENCE FEL PULSE MESUREMENT

Measuring and controlling the temporal properties of the radiation emitted by LUNEX5 is essential. A new method called MIX-FROG enabling to characterize these properties even in the presence of partial longitudinal coherence has been proposed and developed [36]. It is an extension of the FROG (Frequency Resolved Optical Gating) technique [46]. The measurement scheme relies on laser-dressed XUV photoionization: the evolution of the shot-averaged photoelectron spectrum with the laser/XUV delay provides a two-dimensional spectrogram (see Fig. 2a). The statistical properties of the XUV pulses accumulated during the measurement are then extracted from this spectrogram considering a superposition of coherent states [47] using a phase-retrieval algorithm, inspired from ptychography [48]. The ability of the technique to measure the pulses produced by LUNEX5 has been validated numerically. Fig. 2a shows the spectrogram expected in the EEHG configuration of LUNEX5 [49]. In this regime, partial longitudinal coherence will arise from the unavoidable arrival time jitter that exists between the laser and FEL pulses. The simulations show an impact of jitter on the spectrogram. The proposed technique however properly retrieves the LUNEX5 pulse, (see Fig. 2b), as well as the laser pulse and the envelope of the arrival time jitter (see Fig. 2c).

This technique provides a diagnostic for shot-to-shot pulse fluctuations, but it also enables the characterization of other phenomena that can reduce the pulse coherence, including the spatio-temporal pulse distortions or the limited resolution of the detection device.

The next step is to apply the technique on FEL experimental data. It can also be used for the characterisation of attosecond high-order harmonics or for infrared lasers.

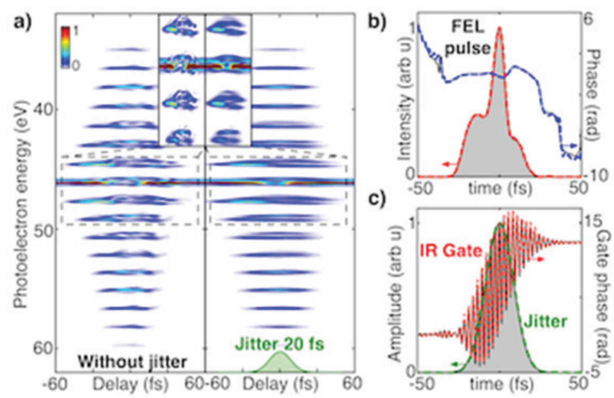

Figure 2: a) Photoelectrons spectra vs laser/FEL delay with and without arrival time jitter. In the presence of jitter, the new technique allows for the retrieval of b) the LUNEX5 pulse and of c) the laser pulse and the jitter envelop.

HIGH REPETITION RATE ELECTRO-OPTICAL SAMPLING

Operation of the LUNEX5 [37-41] demonstrator at high repetition rate (shown in Fig. 1) will also present challenges from the diagnostics point of view. This is particularly true for shot-by-shot electron bunch shape characterization.

Classical single-shot electro-optical sampling (EOS) schemes consist in encoding the electron bunch shape in the spectrum of a laser pulse. Then an optical spectrum analyzer (i.e., a grating and camera system) is used for the final detection. Though very efficient in the low-repetition case, this method cannot be directly applied to high repetition rates, because of the limited speed of current cameras (typically in the hundreds of kHz range).

We have tested an alternate method enabling to perform EOS at high repetition rates (88 MHz for the moment), using the so-called *time-stretch* strategy illustrated in Fig. 3 [50]. The principle is to slow down the EOS signal (with ps/sub-ps duration) down the nanosecond range, using dispersion in optical fibers. Eventually, the output of the system is a replica of the EOS signal (i.e., the bunch shape), magnified down to the nanosecond scale, and which can be recorded by an oscilloscope.

We performed a feasibility demonstration of this method, using Coherent Synchrotron Radiation (CSR) THz pulses (instead of bunch shapes). The EOS was performed in a GaP crystal, and the CSR pulses were

ISBN 978-3-95450-134-2

produced at the AILES beamline of the SOLEIL storage ring. Our EOS setup [51] was able to characterize individual THz CSR pulses emitted by the electron bunch at MHz rates. This strategy will thus be foreseen for the high repetition rate operation of LUNEX5.

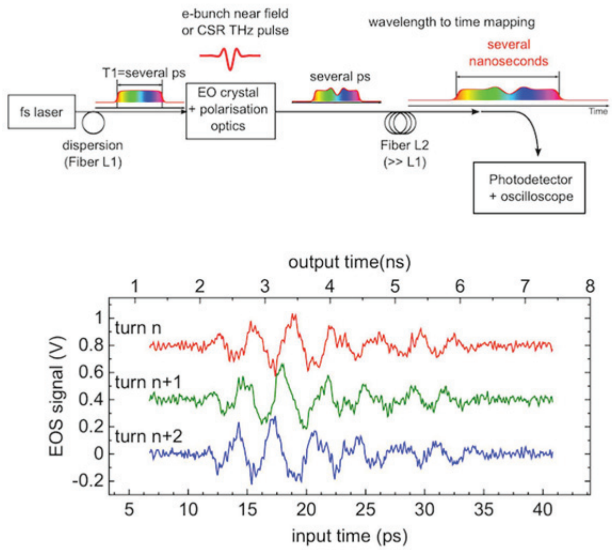

Figure 3: Time-stretched electro-optical sampling. Upper part: general principle (see Ref. 51 for the detailed setup). Lower part: typical series of single-shot EOS pulses. Note that the repetition rate of the pulses is ~1 MHz, but the EOS system is actually acquiring at 88 MHz acquisition rate.

SHORT PERIOD COMPACT UNDULATOR

SOLEIL has been pioneering in the development of $Pr_2Fe_{14}B$ based cryogenic undulators [52-55]. Cooling down the permanent magnet increases both the remanence and the coercivity. Because of the absence of Spin Reorientation Transition at 77 K, such a magnetic grade can also be directly used at the liquid nitrogen temperature. A first 2-meter long U18 undulator (18-mm period) is installed since 4 years on SOLEIL storage ring and operates successfully for the Nanoscopium long beamline with a gap of 5.5 mm. Performance are pushed further on LUNEX5 with a cryo-ready U15 (15-mm period) undulator of 3-m long and 3-mm gap for the FEL application.

The selected $Pr_2Fe_{14}B$ magnets with a coercivity of 1900 kA/m at 300 K and a remanence of 1.31 T enables operation at room temperature with a peak magnetic field of 1.59 T, and a cold regime at 77 K with a field of 1.74 T at 3-mm gap thanks to the increase of the remanence up to 1.55 T. The undulator construction is under progress.

TOWARDS CW OPERATION

There is a clear need for high repetition rate operation from the LUNEX5 user side, e.g. for coincidence experiment, photoemission and imaging.

In its last phase, the 400 MeV superconducting linac of LUNEX5 shall allow for a high repetition rate (10 kHz) multi-user operation by multiplexing the electron beam towards different FEL lines. That requires designing the RF system for continuous (CW) operation and the R&D programme LUCRECE was launched for this purpose. Within this framework, a 1.3-GHz superconducting accelerating structure and its related components (tuner, fundamental and HOM couplers, Helium manifold), based on the TESLA technology will be upgraded for CW operation. In parallel, a 1.3-GHz 20-kW CW solid state amplifier (SSA) will be developed, on the base of the SOLEIL technology already in use at lower frequencies (350 MHz and 500 MHz). The 20-kW CW operation of the complete RF unit including the cavity, the power source, as well as the associated LLRF and control systems, will then be validated in the CEA CryHoLab test station from high rate pulsed to CW operation. Performance will be compared at 1.8 K and at 2 K. LUCRECE will gather the three key laboratories of the Ile-de-France area, Synchrotron SOLEIL, CEA-IRFU and LAL with three industrial partners, Sigmaphi Electronics (SPE), ALSYOM and THALES. The joint work from CEA-IRFU & ALSYOM for the assembly of 103 cryomodules and from LAL & THALES for the supply of 800 couplers, as in-kind contribution to the European XFEL, will be extended to upgrade the equipment for use in CW regime. SOLEIL and SPE, which are already linked by an agreement of transfer of know-how in the domain of SSAs, will explore together the possibility of applying new emerging technologies. Finally, LUCRECE project aims at closely linking laboratories and companies in a process of technical valorisation with the aim to LUNEX5.

TOWARDS A DEMONSTRATION OF FEL AMPLIFICATION WITH ELECTRONS GENERATED WITH LASER PLASMA ACCELERATION

Laser Plasma Accelerator (LPA) presently provides an electron beam with a typical current of a few kA, a bunch length of a few fs, an energy in the few hundreds of MeV to several GeV range, a divergence of typically 1 mrad, an energy spread on the order of 1%, and a normalized emittance on the order of 1 π·mm·mrad. It is considered to use them to drive a FEL but a particular beam handling is necessary.

In a laser plasma wakefield accelerator [56-58], an intense laser pulse is focused in a light gas or in a mixture of heavy and light gases [59]. The rising edge of the laser ionizes the gas and creates a plasma. As the laser pulse propagates in the plasma, the ponderomotive force expels electrons from the optical axis, thus forming a cavity free of electrons in the laser wake, with large fields enabling electrons to be accelerated. The best electron beam performance has been achieved with colliding injection [60] and density transition injection [61].

ISBN 978-3-95450-134-2

One considers here in the LUNEX5 case (and in the COXINEL R&D program) electrons of several hundreds of MeV, dozens of pC charge, with 1-µm transverse size, 1-mrad divergence, and 1-µm longitudinal size (normalized emittance of ~1 π·mm·mrad), few-femtosecond duration and 1% energy spread. These values are close to what has been achieved but they require a specific handling to preserve the emittance and the bunch length in the transport. The proposed beam manipulation for COXINEL is the following: The beam is first strongly focused with adapted quadrupoles of high gradient close to the electron source and/or with a plasma lens [62]. The energy spread is handled in passing the electron beam through a decompression chicane, which sorts them in energy and can reduce typically the slice energy spread by one order of magnitude [63]. In addition, because of the energy-position correlation, the slices can be focused in synchronization with the optical wave advance, in the so-called chromatic matching scheme [64]. An example of FEL simulation in the seeded configuration is shown in Fig. 4. Further start-to-end simulations, starting from CALDER-PIC simulations, are also under way.

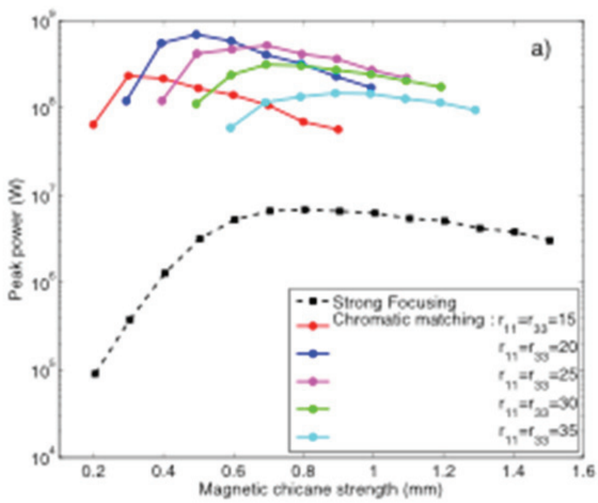

Figure 4: FEL peak power comparison versus chicane strength. Case of a 5-m undulator of 15-mm period and 1.5-T maximum field seeded with 10 kW at 40-nm wavelength and 400-MeV beam energy.

A test demonstration experiment is under preparation under the COXINEL and X-Five programs [65-67].

Electrons will be generated with the 2x60 TW laser at Lab. d'Optique Appliquée and equipment is under preparation at SOLEIL. The majority of the magnetic elements (see Fig. 5) of the transport line and their power supplies are under measurements. The cavity Beam Position Monitors (SwissFEL) and Turbo-Integrated Current Transformer (Bergoz) are under test on the SOLEIL linac. The profile meters are under design. The experiment of FEL amplification will be started at 200 nm with a 2-m long U20 undulator (which is ready) and a spectrometer (IHR320 Horiba), presently under test. The pumping system has been designed and is under procurement. Control will be performed with TANGO. This activity sets a first step within a larger prospect offer by the EuPRAXIA program on laser-plasma acceleration applications.

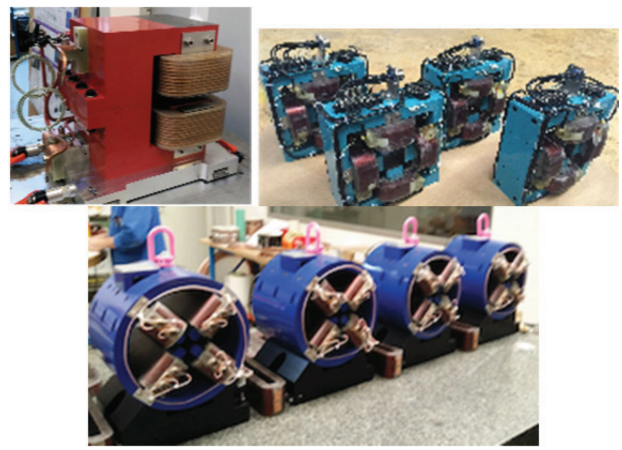

Figure 5: Picture of the COXINEL chicane dipoles, steerers and quadrupoles of the second refocusing set (manufactured by SEF).

CONCLUSION

The LUNEX5 R&D is under progress under various specific programs.

ACKNOWLEDGMENT

The work is supported by the European Commission (European Research Council Advanced Grants (COXINEL (340015), X-Five (339128), and Design studies EuPRAXIA), the Agence Nationale de la Recherche (Laboratoire d'Excellence Physique Atomes Lumière Matière- ANR-10-LABEX-0039 (FEL shaping, Ultrafast-X), IDEX Paris-Saclay (OPT2X), ANR (SP, DYNACO)), Labex CEMPI, the "Triangle de la Physique" (QUAPEVA) with collaborators from Sigmaphi (J.L. Lancelot, O. Cosson, F. Forest), the French Ministère chargé de la Recherche, Région Nord-Pas de Calais and FEDER, and the "region Ile-de-France" for the LUCRECE contract (partners Pascal Dupire (Sigmaphi Electronics), Thales Serge Sierra (THALES), Eric Giguet (Alsyom)), and the SOLEIL-VR collaboration (SP3-ID).

REFERENCES

[1] C.H. Townes, in L. Garwin *et al.*, Univ. of Chicago Press, 107-112 (2003).
[2] D.A.G. Deacon *et al.*, Phys. Rev. Lett. 38, 892-894 (1977).
[3] M. Billardon *et al.*, Phys. Rev. Lett. 51, 1652, (1983).
[4] B. Girard *et al.*, Phys. Rev. Lett. 53 (25) 2405-2408 (1984).
[5] M.E. Couprie *et al.*, Nucl.Inst. Meth. A 296, 13-19 (1990).
[6] M.E. Couprie *et al.*, Europhysics Letters 21(9), 909-914 (1993).

ISBN 978-3-95450-134-2

[7] M. Billardon, D. Garzella, M.E. Couprie, Phys. Rev. Lett. vol 69 (16), 2368-2371 (1992).
[8] T. Hara *et al*., Nucl.Inst. Meth. A 341, 21-23 (1994).
[9] M.E. Couprie *et al*., Phys. Rev E 53 (2), 1871-1889 (1996).
[10] M.E. Couprie *et al*., Nucl. Instr. Meth. A 407, 215-220 (1998).
[11] M.E. Couprie *et al*., Rev. of Scient. Inst. 65, 1495-1495, (1994).
[12] M. Marsi *et al*., Appl. Phys. Lett. 70, 895-897, (1997).
[13] M. Marsi *et al*., Journal of Electron Spectroscopy and Related Phenomena 94, 149-157 (1998).
[14] M.Marsi *et al*., Phys. Rev. B 61, R5070-R5073 (2000).
[15] L. Nahon *et al*., Nuclear Instr. Meth. A 429, 489-496 (1999).
[16] E. Renault *et al*., Nucl. Inst. Meth. A 475 (1-3), 617-624 (2001).
[17] M. Labat *et al*., Phys. Rev. Lett. 101, 164803 (2008).
[18] E. Allaria *et al*., Phys. Rev. Lett. 100, 174801 (2008).
[19] M. Trovo *et al*., A 483, 1-2, 157-161 (2002).
[20] M. Velghe *et al*., Nucl.Inst. Meth. A 296, 666-671 (1990).
[21] M.E. Couprie *et al*., Nucl. Instr. Meth. A 272 (1-2), 166-173 (1988).
[22] M.E. Couprie, J. M. Filhol, 2008 C. R. Physique 9, 487-506.
[23] A.M. Kondratenko, E.L. Saldin, Part. Acc. 10, 207 (1980).
[24] L.H. Yu *et al*., Science 289(5481), 932 (2000).
[25] W. Ackermann *et al*., Nature Photonics 1, 336-342 (2007).
[26] K. Honkavaara *et al*., Proceeding FEL Conf, Basel, Switzerland, Aug. 2014.
[27] E. Allaria *et al*., Nature Photon. 6 699–704 (2012).
[28] P. Emma *et al*., Nature Photonics 4, 641 (2010).
[29] T. Ishikawa *et al*., Nature Photonics 6, 540–544 (2012).
[30] G. Lambert *et al*. Nature Physics 4, (2008), 296-300.
[31] T. Togashi *et al*., Optics Express, 1, 317-324 (2011).
[32] M. Labat *et al*., Phys. Rev. Lett. 107, 224801 (2011).
[33] R. Prazeres *et al*., Eur. Phys. J. D3, 87 (1998).
[34] M. Labat *et al*, Phys. Rev. Lett. 103, 264801 (2009).
[35] R. Bachelard *et al*., Phys. Rev. Lett. 106, 234801 (2011).
[36] C. Bourassin-Bouchet and M. E. Couprie, Nature Communications 6, 6465 doi:10.1038 /ncomms7465 (2015).
[37] M.E. Couprie *et al*., J. of Phys. Conf. Series 425, 072001 (2013).
[38] M.E. Couprie *et al*., accepted in Review of Modern Optics.
[39] http://www.lunex5.com/spip.php?article34.
[40] M.E. Couprie *et al*. Proceeding FEL conf, Basel (2014).
[41] M.E. Couprie *et al*. Proceed. IPAC conf, Dresden, (2014).
[42] G. Stupakov, Phys. Rev. Lett., 102, 074801 (2009).
[43] T. Tajima *et al*., Phys. Rev. Lett. 43, 267 (1979).
[44] A. Loulergue *et al*. New J. Phys. 17 (2015) 023028 (2015).
[45] M.E. Couprie *et al*. J. Physics B: At., Mol., Opt. Phys. 47 234001 (2014).
[46] R. Trebino *et al*, Rev. of Scient. Inst., 68 3277-3295, (1997).
[47] D.T. Smithley *et al*., Phys. Rev. Lett. 70, 1244-1247 (1993).
[48] P. Thibault *et al*., Science 321, 379-382 (2008).
[49] C. Evain *et al*., Proceeding IPAC 2012, New Orleans, USA, 1611-1613 (2012).
[50] F. Coppinger *et al*., IEEE Transactions on Microwave Theory and Techniques 47, 1309 (1999).
[51] E. Roussel *et al*., Scientific Reports 5, 10330 (2015).
[52] C. Benabderrahmane *et al*. Nucl. Instr. Meth. Phys. Res. 669, 1-6 (2012).
[53] C. Benabderrahmane *et al*., Journal of Physics: Conference Series 425, 032019 (2013).
[54] M.E. Couprie *et al*. Proceeding of the SPIE conf, Praha, April 2015, to appear in IEEE.
[55] M. Valléau *et al*., Proceeding SRI 2015, New York.
[56] S. Mangles *et al*., Nature 431, 535 (2004).
[57] J. Faure *et al*., Nature 431, 541 (2004).
[58] C.G.R. Geddes *et al*., Nature, 431, 7008, 538-541(2004).
[59] M. Chen, *et al*., Journal of Applied Physics 99, 056109 (2006).
[60] J. Faure *et al*., Nature 444, 737 (2006).
[61] K. Schmid *et al*., Phys. Rev. ST Accel. Beams 13, 091301 (2010).
[62] C. Thaury *et al*., Demonstration of relativistic electron beam focusing by a laser-plasma lens, Nature Comm. 6, 6860 (2015).
[63] M.E. Couprie *et al*., Towards Free Electron Laser with Laser Plasma Accelerators, J. Physics B : At., Mol. Opt. Phys. 47 (2014) 234001 (12 pp) Special issues on compact x-ray sources (2014).
[64] A. Loulergue *et al*., Beam manipulation for compact laser wakefield accelerator based free-electron lasers, New J. Phys. 17 (2015) 023028 (2015).
[65] M.E. Couprie *et al*., Proceedings FEL'14, Basel, Switzerland 574-579 (2014).
[66] M.E. Couprie *et al*., Proceedings FEL'14, Basel, Switzerland 569-573 (2014).
[67] A. Loulergue *et al*. Proceeding SPIE, Prague, April 2015.

ISBN 978-3-95450-134-2

INCLUSION OF ADVANCED FIELDS AND BOUNDARY CONDITIONS IN THE ANALYTIC THEORY FOR HIGH GAIN FELs

P. Niknejadi and J.M.J. Madey
University of Hawai'i at Manoa, Honolulu, HI 96822, USA

Abstract

The efforts in realizing x-ray free electron lasers (FELs) and enhancing their performance has stimulated remarkable theoretical developments and experimental advances in the field. Yet, the successful operation of x-ray FELs based on the self-amplified spontaneous emission (SASE) principle which has made them a powerful new tool, has beckoned our attention for better understanding a comprehensive physical basis of the theory that has the potential to improve the temporal structure and spectral optimization of these sources. We have previously explained the advantages of including the coherent radiation reaction force as a part of the solution to the boundary value problem for FELs that radiate into "free space" (SASE FELs) and discussed how the advanced field of the absorber can interact with the radiating particles at the time of emission. Here we present the outline of our theoretical approach which follows from eigenmode analysis of optical guiding in FELs. We will also discuss in some detail the experimental setup that could verify and/or further our understanding of the the underlying physics of these devices.

INTRODUCTION

When formulated in the language of covariant action-at-a-distance, the solution to the boundary value problem corresponding to an oscillating particle within a spherical absorbing shell of arbitrary density is dominated by the interference of the retarded and advanced forces originating in the accelerated and absorbing particles [1]. This leads to a force on the accelerated particle exactly equal to that needed to match the power carried by radiation to the particles in the absorbing shell. Therefore a time-symmetric definition of electrodynamics provides non-diverging solution and origin for the radiation reaction field and satisfies Maxwell's energy integral [2]. In fact, it has also been shown that the action-at-a-distance formulation is not essential and the assumption of time-symmetry suffices for the conservation of energy [3]. The reliance of theory of SASE FELs on classical electrodynamics and their operational dependency on coherent radiation at femtosecond scale provides an excellent opportunity for the test and further study of the time-symmetric approach to electrodynamics.

DISCUSSION OF THE THEORY AND CONCEPT

Description of FEL interactions by Kimel and Elias [4] includes a viable model of the coherent radiation reaction in covariant form valid for radiation into free-space. In time-symmetric electrodynamics this can be introduced by taking in to account both the advanced and retarded field of the source and absorbing (non-emitting) particles. Applying that principle to the beam traveling in a SASE FEL, we start by considering both the advanced and retarded field/potential of both the absorber and the electrons (the emitter). It is important to note that in the absence of reflector/refractor/target in front of the electron beam traveling in z, the absorbers are the cosmological particles; and when including the effect of an absorber that far, the field and forces being considered approach the retarded field of experience). Now we must include half the retarded (outgoing) field of the emitters and the half the advanced (incoming) field of the target. The interaction of the advanced field of the target with the radiating electrons ensures energy conservation on the one hand, and on the other hand imposes the fields and forces initiated from the target on the source.

Non-reflecting Boundary Condition

The target mentioned above introduces a non-reflecting boundary condition to the system of the equations that must be solved. Here we refrain from calling the target an absorber to avoid confusion, since the role of the target is not absorbing the emitted photons but to be the origin of the advanced fields acting on the beam. For such signals carried on electromagnetic waves (advanced or retarded) the invariant interval $(cdt)^2 - dr^2$ between the emission of a wave and it's absorption at the non-reflecting boundary is always identically zero. So by that measure, which is the covariant statement of the distance in space-time separating transmitter and receivers, the emission and absorption of the retarded and advanced waves are all simultaneous. This has been illustrated in Figure 1. Note that the advanced wave of the non-reflecting boundary (mirror) co-propagates with the fields of the undulator acting on the electrons. (The characteristics of the mirror (partially reflecting) and why it was chosen for our experiment will be explained in the next section.)

Advanced Field and Evolution of Coherent Bunching in SASE

The SASE FEL starts from a randomly phased electron beam. After a few undulator periods the randomly phased electron beam gets bunched. The coherent radiation emitted by tightly bunched electron beams plays a critical role in the analysis and operation of free electron lasers. For conducting or reflecting (resonator mirror) FELs, a normal mode analysis of operation already includes the relevant boundary conditions. However, in order to arrive at a comprehensive first-principles field-based analysis of the intense radiation emitted into free-space by devices that work based on the

ISBN 978-3-95450-134-2

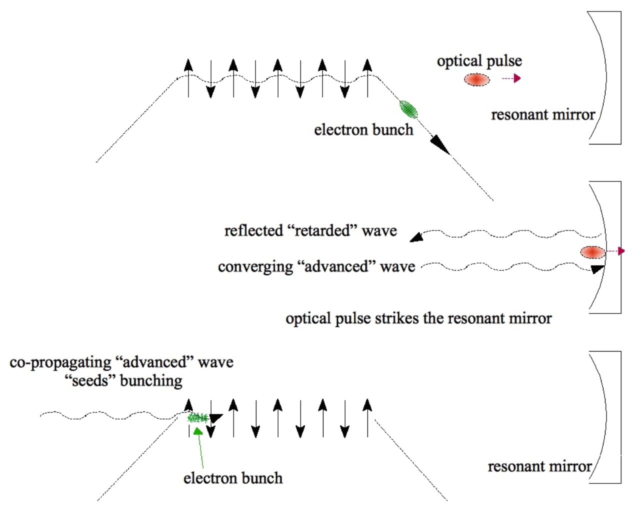

Figure 1: By the covariant statement of the distance in space-time separating transmitter and receivers, the emission and absorption of the retarded and advanced waves are all simultaneous. Presence of the mirror in front electron beam will introduce a co-propagation seed that can carry information that will improve the temporal coherence and the quality of the beam passing through the undulator.

SASE principle, including all target interactions, we also need to include the effect of boundary condition of the target.

EXPERIMENTAL TEST AND APPLICATION

The discussion of time-symmetric electrodynamics goes back to conversations between Wheeler, Feynman and Einstein. Since coherent emission is central to the operation of SASE FELs, not only could SASE FELs be instrumental in the study of this fundamental aspect of electrodynamics, their technology could potentially benefit from this previously un-utilized aspect of fundamental physics. The proposed setup provides just such opportunity.

Experimental Goal

Since SASE FELs operate based on the bunching induced by the co-propagating electrodynamic wave in these devices' undulator, they present the perfect set up for an experimental test of the model presented here. The goal of this experiment would be to evaluate the role of time-symmetric electrodynamics in operation of SASE FELs. We propose use of a multilayer bent-quartz crystal mirror at the end of the undulator to create the advanced field needed to alter the electron's bunching. This mirror will be curved (for the purpose of focusing) and be located in front of the bea and on it's transverse path right after the undulator. We ask the question: will the mirror's spontaneous response to the presence of the radiating beam (predicted by the time-symmetric electrodynamics) be able to carry phase information that will improve the temporal coherence and the quality of the beam passing through the undulator? The understanding gained from this experiment will be very important for both our current theoretical understanding and expanding the future applications of SASE FELS.

Set up and Required Parameters

Since the advanced co-propagating wave of the mirror will be acting as a seed laser the same condition that applies to the seeded FEL applies here: the seed power only has to exceed the spontaneous noise emitted into the coherent bandwidth and angle [5]. The wavelength of the radiation must match the spacing of the quartz lattice in one direction. Also the mirror must be located right after the undulator or beam dump to have access to a natural (unfiltered) SASE bandwidth. An optimal set of parameters for the experiment is presented in Table 1.

Table 1: Optimal Parametes for the Experimental Test

Radiation Beam	
Beam Wavelength	1 Angstrom
Bandwidth	Natural SASE BW
Pulse energy	1 mJ or less
Pulse Duration	70 fs
Spot size	micron range
Rep. Rate	1 Hz or Less

Bent Quartz Crystal Mirror

The bent quartz crystal mirror has two purposes. One is that only wavelengths that satisfy the Bragg condition pass through the mirror [6]. Second, the mirror will satisfy the non-reflecting boundary condition. Therefore if the radiation wavelength is tuned to the spacing of the lattice of the quartz we can expect that wavelength radiation to transfer phase information to the beam. Of course once the wavelength is shifted it will no longer be attenuated by the mirror and pass through. Significant improvement in the spectral coherence of the beam can be expected since the focusing (bent) multilayer quartz crystal (partially reflecting mirror) will simultaneously serve as a retroreflector and a filter. It is important to note that similar experiments have been conducted in the infrared regime with a dramatic improvement in the temporal coherence and spectral brightness of the emitted FEL radiation [7, 8]. Although the geometry of those experiments differ from what is proposed here, the physics is the same.

ANALYTICAL SOLUTION

An important question here is whether any of the currently used FEL theory or simulations can predict the effect of the advanced field on the FEL performance. In our study of simulations, we found that since we are looking for a previously un-utilized aspect of physics the result of the simulations could be unreliable. Therefore we looked for a method that gave us better physical insight.

ISBN 978-3-95450-134-2

Review of Xie's Theory of Optical Guiding

In this section Equations 1-6 are from Reference [9] and demonstrate how the interaction of the field of the electron and FEL is studied by eigenmode analysis of optical guiding in FELs. We take the same approach and solve for the coefficient of expansion when the initial condition includes the advanced field. In Xie's method the paraxial equation for FEL is reduced to a compact form: a Schödinger equation with a non-Hermitian Hamiltonian,

$$H = \begin{bmatrix} 0 & 1 & 0 \\ 0 & -L_1 & 1 \\ L_2 & 0 & 0 \end{bmatrix}, \tag{1}$$

where L_1 corresponds to the transverse Laplacian and detuning term and L_2 corresponds to the transverse density modulation of the paraxial wave equation for the FEL. The vector solution of this non-Hermitian Hamiltonian is

$$\psi = \begin{bmatrix} -i\frac{\partial \tilde{I}}{\partial \tau} \\ \tilde{a} \\ -L_2 \tilde{I} \end{bmatrix}. \tag{2}$$

Then the following initial condition is assumed

$$\psi(0) = \begin{bmatrix} 0 \\ \tilde{a}(0) \\ 0 \end{bmatrix}, \tag{3}$$

and the eigenmodes and eigenvectors are determined as:

$$\psi_n = V_n \exp(-i\lambda_n \tau)\, , V_n = \begin{bmatrix} \frac{1}{\lambda_n} \\ 1 \\ \frac{P_u(r_\perp)}{\lambda_n^2} \end{bmatrix}. \tag{4}$$

Then using the initial condition Equation 3 the expansion coefficient for the general solution and components of the field is solved.

$$\tilde{a} = \Sigma C_n V_n \exp(-i\lambda_n \tau) + \int C_\lambda g_\lambda \exp(-i\lambda_n \tau) d\lambda\, , \tag{5}$$

where the expansion coefficients for a discrete mode is

$$C_n = \frac{1}{N_n} < \tilde{a}(0) g_n >, \tag{6}$$

and the power coupling coefficient is

$$G_0 = \frac{|C_n|^2 < |g_n|^2 >}{< |\tilde{a}(0)|^2 >}. \tag{7}$$

Solution for an Initial Condition that Takes the Advanced Field into Account

As Xie states in [9] the three components of Equation 3 are, in order, the energy modulation of the electron beam, the amplitude of the radiation field and the density modulation of the electron beam. This complete picture allows for the direct inclusion of advance field. Due to the instantaneous propagation of the advanced field, initially the electrons in the beam would not have had the chance to see a density modulation. However, the advanced field could require energy modulation in the electron bunch. Therefore Equation 3 can be re-written for the case of including advanced field as:

$$\psi(0)_{adv} = \begin{bmatrix} \alpha(\nu,\tau)\tilde{a}(\tau_f) \\ \tilde{a}(0) + \tilde{a}(\tau_f) \\ 0 \end{bmatrix}. \tag{8}$$

Here τ_f is the focal distance of the quartz mirror and $\alpha(\nu,\tau)$ is a function relating the first two component of ψ_{adv}. For the simplest case, when the energy modulation is still small, expansion coefficients for the discrete mode now include a term that was contributed by the advanced field as shown here:

$$C_{n(adv)} = \frac{1}{N_n} < (\tilde{a}(0) + \tilde{a}(\tau_f)) g_n >, \tag{9}$$

therefore the power coupling coefficient will be stronger in this case. From this development we would expect that the initial condition would excite the lowest order optical mode which would couple with the electrons' field. Furthermore properties of the electron beam attributed to the higher mode will not appear in the advance field (due to the properties of the mirror) so they will not be amplified. A more detailed version of this calculation is presented elsewhere [10]. Initial result of a numerical study is shown in Figure 2 and Figure 3.

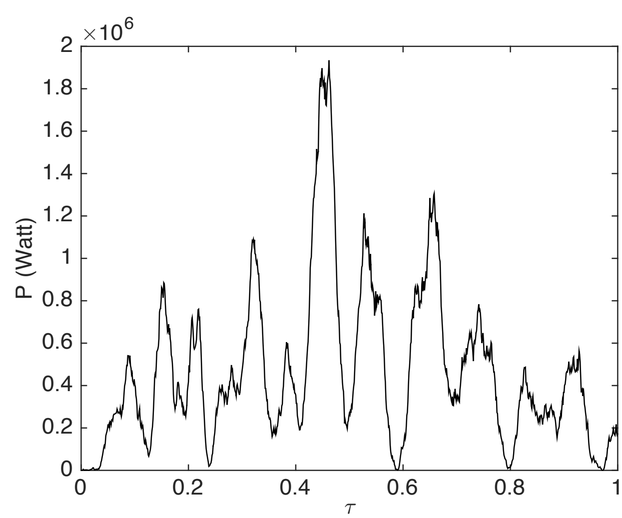

Figure 2: Typical SASE temporal profile with LCLS like parameters at 5 gain length without a non-reflecting boundary.

CONCLUSION

Here we discussed the importance and advantages of a comprehensive approach to electrodynamics for advance light sources like SASE FELs which is based on time-symmetric electrodynamics. A detailed picture of an experiment that would further our understanding in this area

ISBN 978-3-95450-134-2

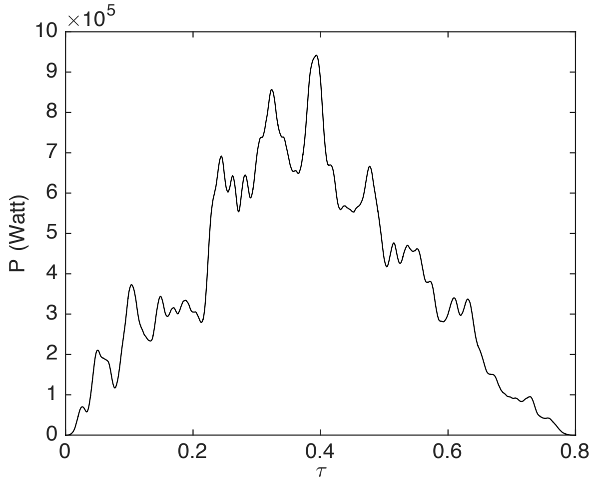

Figure 3: Typical SASE temporal profile with LCLS like parameters at 5 gain length with a non-reflecting boundary and including the advanced field.

was presented. Finally we took an analytic approach in order to determine exactly how inclusion of the advanced field in the analytic theory for high gain will change the solutions. We were able to demonstrate that an initial condition which takes the advanced field into account changes the expansion coefficients of a discrete mode. A numerical code in Matlab is being prepared which will be used for a more detailed study.

ACKNOWLEDGMENT

We wish to thanks Dr. Zhirong Huang for making his 1D FEL code available for our study and Jeremy Kowalczyk, Ian Howe, Erik Hemsing, Nicholas Wisniewski for many useful discussion. We are also grateful to the FEL Conference for their grant.

REFERENCES

[1] J. A. Wheeler, R. P. Feynman, Rev. Mod. Phys. 17, 157 (1945).

[2] P. Niknejadi et al., Phys. Rev. D 91 096006 (2015).

[3] S. Smith et al. (to be published).

[4] I. Kimel, L. Elias, Nuclear Instruments and Methods in Physics Research Section A: Accelerators, Spectrometers, Detectors and Associated Equipment 375, 565 (1996).

[5] Z. Huang, K.J. Kim, Phys. Rev. ST-AB, 10, 034801 (2007).

[6] E. P. Bertin, Crystals and Multilayer Langmuir-Blodgett Films Used as Analyzers in Wavelength-Dispersive X-Ray Spectrometers, in J. W. Robinson, Ed., Handbook of Spectroscopy, vol. 1, p. 157-166 (CRC Press, Cleveland, 1974).

[7] E.B. Szarmes and J.M.J. Madey, IEEE J. Quantum Electron., vol. 29, pp. 452-464, (1993).

[8] E.B. Szarmes and J.M.J. Madey, IEEE J. Quantum Electron., vol. 29, pp. 465-478, (1993).

[9] M. Xie et al. Phys. Rev. A 41 1662 (1990).

[10] P. Niknejadi et al. (to be published).

HIGH-POWER ULTRASHORT TERAHERTZ PULSES GENERATED BY A MULTI-FOIL RADIATOR WITH LASER-ACCELERATED ELECTRON PULSES

Jeongsang Jo[1], Young Uk Jeong[1], Seong Hee Park[1], Kitae Lee[1], Kyu-Ha Jang[1], Wooje Ryu[1], Hana Kim[1], Kyung Nam Kim[1], Boris Gudkov[1,2], Sergey Miginsky[1,2], Nikolay A. Vinokurov[1,2]

[1] Korea Atomic Energy Research Institute, 1045 Daedeok-Daero, Yuseong-gu, Daejeon, 305-353, Republic of Korea

[2] Budker Institute of Nuclear Physics, Siberian Branch of Russian Academy of sciences, 11 Lavrentyev Prospect, Novosibirsk 630090, Russia

Abstract

Terahertz (THz) wave is an attractive source for a variety of research including imaging, spectroscopy, security, etc. We proposed a new scheme of high-power and ultrashort THz generation by using the coherent transition radiation from a cone-shaped multi-foil radiator [1] and a rectangle-shaped multi-foil radiator. To perform the proof-of-principle of the multi-foil THz radiator, we used 80~100 MeV electron bunches from laser-plasma acceleration. While a cone-shaped multi-foil radiator has a circular polarization with a conic wave, we made a rectangle-shaped multi-foil radiator that has a linear polarization in a plane-like wave, which can be used more widely for various applications. We can easily control the power of multi-foil radiator by adjusting the number of foils. We compare the THz power ratio between 2 sheet and multi sheets using cooled bolometer. We will measure the pulse duration and bandwidth of the THz wave from the multi-foil radiators in a single-shot by using electro-optic sampling and cross-correlation method [2].

INTRODUCTION AND BACKGROUND

Since THz wave has different property to existing the electromagnetic wave, it is expected to be critical source in medical industry, security and various researches. But, the THz power from photo conductive antenna, Electro-optics and transition radiation is not sufficient to comercialize the item using the THz wave so far. It is dilemma in the THz industrial region. The new multifoil radiator may achieve gigawatt-level peak power using short electron bunch (70~100MeV, 25fs) [1].

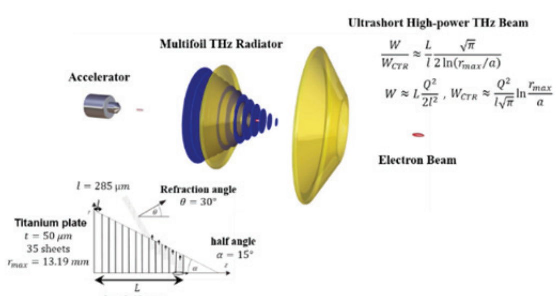

Figure 1: Radial polarization type multifoil radiator.

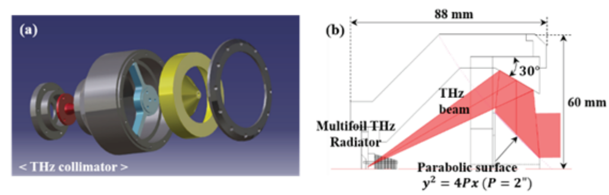

Figure 2. (a) 3D scheme of THz collimator with radiator, (b) The cross-sectional view of THz collimator.

Figure 1 is a THz generation process scheme of the radial polarization type multifoil radiator. 50 µm thickness Circular flat 35 sheets Ti plates with successively decreasing radii are stacked as a truncated cone. The gaps between Ti plates are filled with air and are equal. When short electron bunch propagate through Ti plates along z-axis, transition radiation is generated and is transferred to the edge of radiator along gap of Ti plate as waveguide. At edge of plate, all the transition radiation form one of the wavefront in phase. Then, the coherence wave pulse propagate outward with donut beam shape and it's collimated by special type collimator mirror in Fig. 2.

Figure 3 is linear polarization type radiator, it's consist of a half of the radial polarization type radiator with 5 µm thickness, 70 sheets Ti plates and collimation mirror. In the case that transition radiation by short electron bunch propagate upwards, it is radiated outward without collimation. Other case that transition radiation propagate downwards, it is collimated by parabolic reflector. This reflected and collimated beam is propagated along Ti plate. Finally, it is radiated outward with linear polarization as same process radial type radiator.

Figure 4 shows real image of the radial polarization type multifoil radiator and the linear polarization type multifoil radiator.

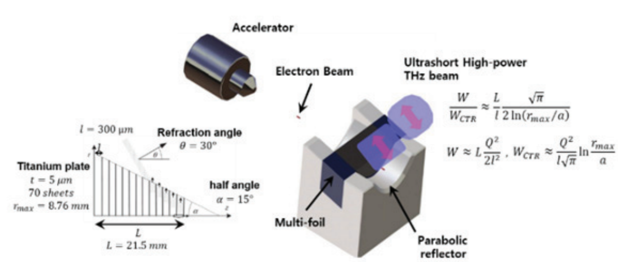

Figure 3: Linear polarization type multifoil radiator.

ISBN 978-3-95450-134-2

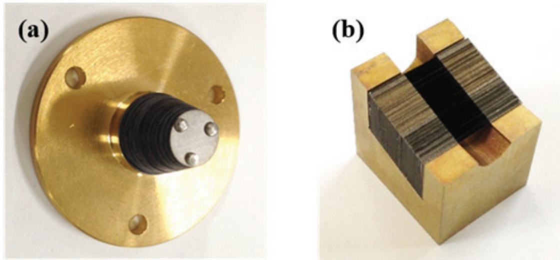

Figure 4: Real image of (a) Radial polarization type multifoil radiator, (b) Linear polarization type multifoil radiator.

Figure 5 is THz single pulse measurement scheme. We use 800 nm, 250 ps, 2.8 mJ and 10Hz chirped pulse amplification (CPA) laser. It is divided into two parts. One of ray is for probe beam. It has phase modulation by Electro-optics (EO) effect when THz beam and probe beam co-propagate through EO crystal temporally and spatially. We can distinguish modulation using two crossed polarizers system (near zero optical transmission). Other beam is for cross-correlation beam such as gating beam. Firstly, its 250ps pulse duration is converted to 50fs narrow pulse beam by two grating compressing system for high resolution in cross-correlation system. When gating beam and modulated probe beam are crossed at Beta Barium Borate (BBO) crystal temporally and spatially, some part of energy is converted to 400nm second harmonic beam (SHB) along bisectional angle of two beam line.

$$I_{SHG}(x) \propto \int_{-\infty}^{+\infty} I_{EO}(t+\tau) I_{gate}(t-\tau)dt \quad (1)$$

Finally, we can get the signal by subtracting probe beam from modulated probe beam and calibrate it by delay line for time difference between probe and gating beam. [2].

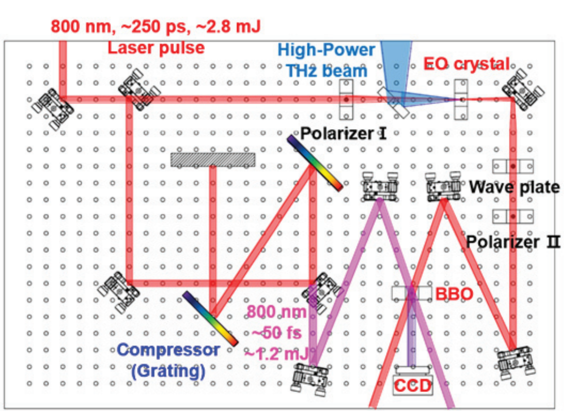

Figure 5: Single pulse measurement system.

RESULT

Figure 6 is the comparison of the power of 2 sheets and 70 sheets Ti plates with 5 µm thickness and 300 µm gap of linear polarization type multifoil radiator. The ratio of multi foil and single foil radiator is

$$\frac{W}{W_{CTR}} \approx \frac{L}{l} \frac{\sqrt{\pi}}{2\ln(r_{max}/a)}, \quad (2)$$

where L is the radiator total height along z-axis, l is the gap size between Ti plates, r_{max} is the radius of the Ti plate and a is the cross-sectional diameter along x-axis. The theory ratio is 27.23 and experiment ratio is 11.8. The reason of the difference is the diffraction of the edge of 2 sheet Ti plates radiator. Therefore, it is not properly collimated to cooled bolometer. In order to reduce this experiment error, we will use common 1 sheet Ti plate radiator.

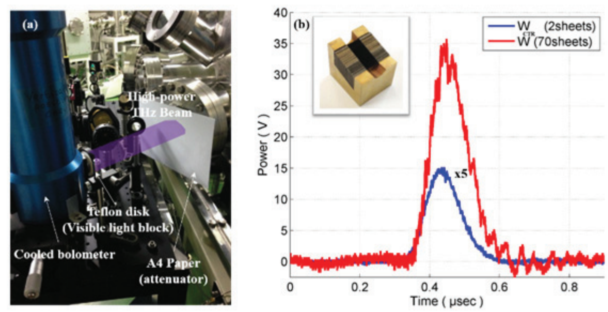

Figure 6: (a) THz power measurement system with cooled bolometer, visible light block and attenuator, (b) Comparison of the power for 2 sheets Ti plate and 70sheets Ti plates of linear polarization type multifoil radiator.

We use cross-correlation method for studying THz pulse from multifoil radiator and to match pulses timing between THz generation beam (30 fs), gate beam (50 fs) and probe beam (300 ps). Figure 7 are second harmonic beam between beams. Figire 7(a) is for matching pulse timing between THz pulse and probe pulse at EO crystal. Figure 7(b) is for matching pulse timing between modulated beam and gate pulse at BBO crystal. In the case that probe beam is modulated by electric field at EO crystal, we can find different part from SHB without unmodulated probe beam.

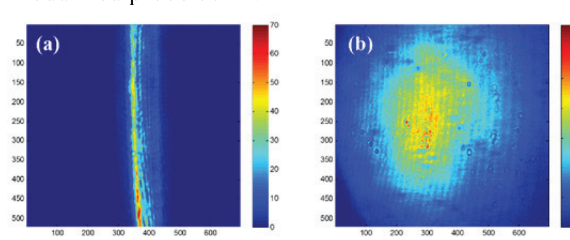

Figure 7: SHB Images of (a) THz generation beam (30 fs) and gate beam (50 fs), (b) Probe beam (300 ps) and gate beam (50 fs).

REFERENCES

[1] N. A. Vinokurov, Y. U. Jeong, "Generating High-Power Short Terahertz Electromagnetic Pulse with a Multifoil Radiator", Physical Review Letters 110, 064805 (2013).

[2] B. R. S. Marburg, "Electro-optic methods for Longitudinal Bunch Diagnostics at FLASH," Dissertation, des Departments Physik, der Universitat Hamburg, (2007).

ISBN 978-3-95450-134-2

MICROBUNCHING-INSTABILITY-INDUCED SIDEBANDS IN A SEEDED FREE-ELECTRON LASER

Z. Zhang[1,2], Y. Ding[1], W. M. Fawley[1], Z. Huang[1*], J. Krzywinski[1], A. Lutman[1], G. Marcus[1], A. Marinelli[1], and D. Ratner[1]
[1] SLAC, Menlo Park, CA 94025, USA
[2] Tsinghua University, Beijing 100084, China

Abstract

The measured spectrum of the soft X-ray self-seeding at the LCLS has a pedestal-like distribution around the seeded frequency, which limits the spectral purity and seeding applications without a post-undulator monochromator. In this paper, we study the origins of the pedestals and focus on the contributions of microbunching instability prior to the FEL undulator. We show that both energy and density modulations can induce sidebands in a seeded FEL. Theory and simulations are used to analyze the sideband content relative to the seeding signal. The results place a tight constraint on the longitudinal phase space uniformity for a seeded FEL.

INTRODUCTION

Many efforts have been devoted to improve the longitudinal coherence and spectral purity of the X-ray free-electron lasers (FELs) since the unequivocal success of existing facilities which are based on the self-amplified spontaneous emission (SASE) [1, 2]. While the relative bandwidth of SASE FELs are limited to at least 10^{-3} or larger, one can decrease the output bandwidth and increase the longitudinal coherence by initiating the FEL process with a coherent seed [3–6], or by imprinting the electron beam with a coherent density modulation (bunching) at the wavelength of interest [7–10]. Under ideal circumstances (high-quality seed of sufficient power and uniform electron beam, etc.), one can obtain completely coherent, high-power X-ray pulses that approach Fourier limit.

However, imperfections of the electron beam or of the seed will reduce the quality of the seeded FEL output [11–14]. In the measurement of self-seeded soft X-ray radiation spectrum at the Linac Coherent Light Source (LCLS) [6], there is often a pedestal-like distribution around the seeded frequency. In the absence of a post-undulator monochromator, this contamination limits the spectral purity and may degrade certain user applications. Further studies have ruled out the possibility that the pedestal-like distributions in the spectra come from the spectrometer noise or the monochromator optics. Microbunching instability growth of the electron beam prior to the undulator, mostly induced by the longitudinal space charge during the long-distance acceleration and drift sections [15, 16] and directly observed at the LCLS recently [17], is identified as the main source for these spectral pedestals. In this paper, we show that both energy and density modulations can induce sidebands in a seeded FEL. Theory and simulations are used to analyze the sideband content relative to the seeding signal. The results place a tight constraint on the longitudinal phase space uniformity for a seeded FEL.

* zrh@slac.stanford.edu

THEORETICAL ANALYSIS

To understand the basic physics of the pedestals, we consider a two-frequency system: the seed and the sideband. The FEL is seeded by a monochromatic radiation whose frequency is at or near the natural FEL resonant frequency ω_1 and the electron beam initially has a longitudinal long-wavelength modulation at frequency ω_s. We describe the longitudinal phase space of the electron beam with the electron ponderomotive phase $\theta \equiv (k_1 + k_u)z - \omega_1 t$ and normalized energy deviation from resonance $\eta \equiv (\gamma - \gamma_0)/\gamma_0$, where $k_1 (= \omega_1/c)$ and k_u are the wave numbers of the radiation and undulator. We will find the following dimensionless variables to be useful in the analysis:

$$\hat{z} \equiv 2k_u \rho z, \tag{1}$$

$$\hat{\eta} \equiv \frac{\eta}{\rho}, \tag{2}$$

$$a_\nu \equiv \frac{eK[JJ]}{8\gamma_0^2 mc^2 k_u \rho^2} E_\nu, \tag{3}$$

where the normalized frequency $\nu = 1 + \Delta\nu \equiv \omega/\omega_1$ and $\nu = 1$ is the resonant frequency. K is the normalized field of the undulator and $[JJ]$ is the Bessel function factor. With these dimensionless variables, the pendulum equations of the two-frequency system can be written as

$$\frac{d\theta}{d\hat{z}} = \hat{\eta}, \tag{4}$$

$$\frac{d\hat{\eta}}{d\hat{z}} = a_1 e^{i\theta} + a_s e^{i\nu\theta} + c.c., \tag{5}$$

$$\frac{da_1}{d\hat{z}} = -b_1, \tag{6}$$

$$\frac{da_s}{d\hat{z}} + i\Delta\nu a_s = -b_s, \tag{7}$$

with the bunching parameters at the seed and the sideband frequency

$$b_1 \equiv \langle e^{-i\theta} \rangle, \tag{8}$$

$$b_s \equiv \langle e^{-i\nu\theta} \rangle. \tag{9}$$

The subscript "1" denotes the variables of the seed and "s" the sideband, respectively. We also introduce the collective

ISBN 978-3-95450-134-2

momentum as

$$p_1 \equiv \langle \hat{\eta} e^{-i\theta} \rangle, \tag{10}$$
$$p_s \equiv \langle \hat{\eta} e^{-i\nu\theta} \rangle. \tag{11}$$

Initial Energy Modulation

Let us first consider an initial beam energy modulation: $A(s) = A_0 \cos(k_s s) = \frac{\Delta\gamma}{\gamma}\cos(k_s s)$. Using the scaled energy variable, we have

$$\hat{\eta}_0 = \frac{\hat{A}}{2} e^{i\Delta\nu\theta} + \text{complex conjugate}, \tag{12}$$

where the normalized modulation amplitude $\hat{A} = A_0/\rho$ and $k_s = \omega_s/c$ is the wave number of the modulation.

With the assumptions that $|a_s| \ll |a_1|$,$|b_s| \ll |b_1|$ and $|p_s| \ll |p_1|$, we can obtain the equations of the field amplitudes as

$$\frac{d^3 a_1}{d\hat{z}^3} \approx i a_1, \tag{13}$$
$$\frac{d^3 a_s}{d\hat{z}^3} + i\Delta\nu \frac{d^2 a_s}{d\hat{z}^2} \approx i\nu a_s + \nu^2 \hat{A} p_1. \tag{14}$$

Eq. (13) is the FEL cubic equation with the solution as

$$a_1(\hat{z}) = \sum_{l=1}^{3} D_l e^{-i\mu_l \hat{z}}, \tag{15}$$

where $D_{1,2,3}$ are the coefficients determined by the initial conditions and $\mu_{1,2,3}$ are the roots of the cubic equation

$$\mu_1 = 1, \quad \mu_2 = \frac{-1-\sqrt{3}i}{2}, \quad \mu_3 = \frac{-1+\sqrt{3}i}{2}. \tag{16}$$

If we consider the high-gain regime ($\hat{z} \gg 1$), $a_1(\hat{z})$ takes the simple form of

$$a_1(\hat{z}) = D_3 e^{-i\mu_3\hat{z}}. \tag{17}$$

Equation (14) is an inhomogeneous ordinary differential equation of a_s. If we assume $|\Delta\nu| < \rho$ (i.e., the sideband frequency shift is small compared to the FEL gain bandwidth), the sideband equation is simplified to

$$\frac{d^3 a_s}{d\hat{z}^3} \approx i a_s + i\hat{A} D_3 \mu_3^2 e^{-i\mu_3\hat{z}}. \tag{18}$$

The solution for the inhomogeneous equation in the high-gain regime with $a_s(0) = 0$ is

$$a_s(\hat{z}) = -\frac{i\hat{A}D_3}{3}\hat{z}e^{-i\mu_3\hat{z}} = -\frac{i\hat{A}}{3}\hat{z}a_1. \tag{19}$$

Thus the power ratio between the sideband and the seed radiation along the undulator is

$$\frac{P_s(\hat{z})}{P_1(\hat{z})} = \frac{\hat{A}^2}{9}\hat{z}^2 = \frac{(2k_u\rho z)^2}{9}\frac{A_0^2}{\rho^2}. \tag{20}$$

Eq. (20) applies to either lower or upper sideband with a frequency shift much less than the FEL gain bandwidth. The full treatment of this problem, valid for an arbitrary sideband frequency and also at FEL start-up, has been worked out by Lindberg [18].

We note that the ratio of the sideband power vs. the seed power grows quadratically with z and A_0. This can be understood qualitatively as follows. The energy modulation generates periodic local energy chirp along the electron beam $h(s) = h_0 \cos(k_s s)$. Together with the undulator R_{56}, the seed frequency or phase ϕ will be modulated according to

$$\frac{d\phi(s)}{ds} \sim h(s)R_{56}k_1 = h(s)2k_u z. \tag{21}$$

This phase modulation generates two lowest sidebands that have field amplitude proportional to h_0 (A_0) and z. If we take the seeding saturation at $2k_u\rho z = 9$, Eq. (20) stated that $A_0 < \frac{1}{3}\rho$ in order for the sideband to not exceed the seed power at saturation. Using the LCLS soft x-ray self-seeding parameters given in Table 1, this leads to $A_0 < 1$ MeV and is a very stringent requirement on the residual energy modulation at the undulator entrance.

Finally the single-frequency sideband analysis can be generalized to broadband sidebands driven by microbunching instability as

$$\frac{P_s(\hat{z})}{P_1(\hat{z})} = \frac{\hat{A}^2}{9}\hat{z}^2 = \frac{(2k_u\rho z)^2}{9}\int_0^{\Delta s}\frac{A(s)^2}{\rho^2}\frac{ds}{\Delta s}. \tag{22}$$

Here $A(s)$ is the energy centroid along the bunch coordinate s, and Δs is the bunch length of a flattop current profile.

Initial Density Modulation

The above analysis can be applied in a straightforward manner to modulations in current. Let us introduce an initial bunching parameter at the sideband frequency $\omega_s = \Delta\nu\omega_1$:

$$b_0 = \langle e^{-i\Delta\nu\theta} \rangle. \tag{23}$$

The sideband field equation for $\Delta\nu = \omega_s/\omega_1 < \rho$ becomes

$$\frac{d^3 a_s}{d\hat{z}^3} \approx i\nu a_s + i\nu a_1 b_0. \tag{24}$$

Similar to Eq. (20), the power ratio between the sideband and the seeding signal is

$$\frac{P_s(\hat{z})}{P_1(\hat{z})} = \frac{b_0^2}{9}\hat{z}^2 = \frac{(2k_u\rho z)^2}{9}b_0^2, \tag{25}$$

which also grows quadratically with the initial density modulation amplitude and the undulator length.

Combining Eqs. (14) and (24), we obtain the sideband driven by both energy and density modulations (the terms with $\hat{A}$ and b_0, respectively). Nevertheless, the typical residual density modulation is much smaller than the residual energy modulation (in units of ρ). For the microbunching instability, density and energy modulations are 90° out of

ISBN 978-3-95450-134-2

phase. In this case, the existence of the density modulation increases the lower sideband at the expense of upper sideband power and keeps the total sideband content approximately constant. Thus, the density modulation modifies the spectral pedestal shape without increasing the total spectral energy in the pedestals.

1-D SIMULATION

To verify the previous analytical considerations, we have numerically solved the time-dependent 1-D FEL equations for a number of initial modulation conditions to study the growth of the sideband power. Here we use the parameters of the soft X-ray self-seeding FEL experiment settings at the LCLS in Table 1. In the simulation, the electron beam is ideal with uniform current distribution and vanishing slice energy spread. The seed power distribution is also uniform. The energy modulations are added to the electron beam with cosine form with various periods and amplitudes. The modulation wavelength is 2 ~10 µm, which is the range of the microbunching instability observed in the experiment [17]. The modulation amplitude ranges from 0.1 MeV to 0.6 MeV, and the corresponding $\hat{A}$ is within 0.03 to 0.2.

Table 1: Simulation Parameters in 1-D FEL Code

Parameter	**Value**	**Unit**
Beam energy E	3.48	GeV
Slice energy spread	0	MeV
Normalized emittance ϵ_N	0.9	µm
Current I	1.4	kA
Average β	30	m
Undulator period λ_u	3	cm
FEL parameter ρ	8.6×10^{-4}	
Gain length L_G	1.6	m
Seeding wavelength λ_r	2.29	nm
Seeding power	20	kW
Energy modulation wavelength	2-10	µm
Energy modulation amplitude	0.1-0.6	MeV

The total field amplitude a and the bunching factor at the seed frequency b_1 for different energy modulation amplitudes are given in Fig. 1. The FEL reaches saturation around $\hat{z} = 9$. The total power of the FELs, which is proportional to a^2, is maintained while we increase the energy modulation amplitude. However, the bunching factor b_1 is reduced near the saturation at large modulation amplitude.

The FEL spectra along the undulator are shown in Fig. 2 to illustrate the growth of the sideband power. The spectra are normalized by the power of the seed (main peak), and the spectral unit is photon energy ($\Delta E = \hbar\omega_s$). There are two sideband peaks near the seed and their power ratios increase along the undulator. The difference between the lower and upper sideband peaks is due to the shape of the gain curve in FELs. The lower sideband has larger gain. It is also noted that when the first-order sideband becomes large enough, the second-order one will appear with larger energy offset. Here

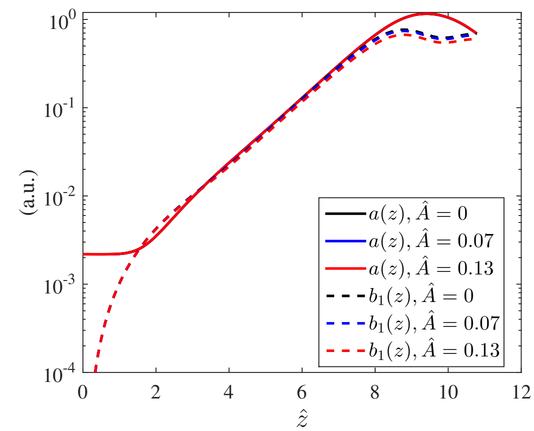

Figure 1: The total field amplitude a and bunching factor b_1 along the undulator with various energy modulation amplitude $\hat{A}$.

we only consider the first-order sideband as the second-order are always very small in our cases of interest.

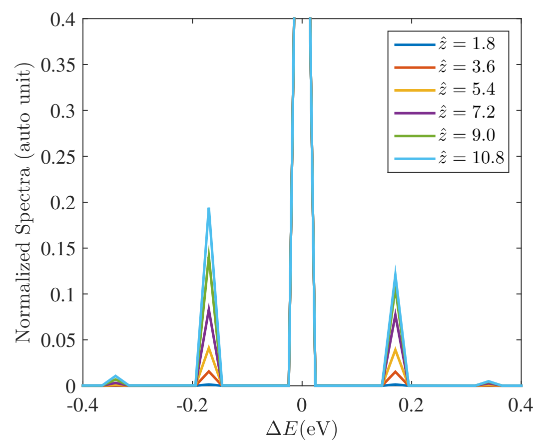

Figure 2: The spectra along the undulator length to illustrate the growth of the sideband power. The spectra are normalized by the power of the seed. The modulation wavelength is 8 µm and amplitude is $\hat{A} = 0.13$.

First we study the energy offset of the sideband peaks to the seed, as shown in Fig. 3. The energy offset of the two sideband peaks are the same and proportional to the inverse of the modulation wavelength. Simulation results show that the energy offset is independent of the modulation amplitude and undulator length.

To get the growth rate of the sideband power, we plot the power ratios of the lower sideband to the seed along the undulator for different modulation amplitudes in Fig. 4. The theoretical analysis predicts that the sideband power ratio grows quadratically with $\hat{z}$ and $\hat{A}$ (see Eq. 20) in the high-gain regime. We fit the simulation results at $\hat{z} > 1$ in Fig. 4 with second-order expressions of $\hat{A}$ and $\hat{z}$. The fitting coefficients of the curves are all around $\frac{1}{9}$ as predicted in the theory, which verifies the previous analysis.

ISBN 978-3-95450-134-2

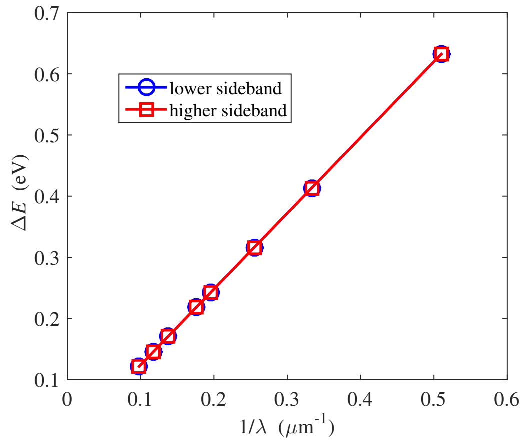

Figure 3: The energy offset of the sideband peaks to the seed versus the inverse of the modulation wavelength.

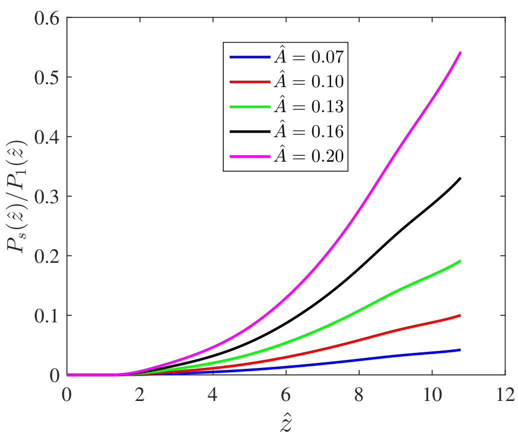

Figure 4: The ratio of the lower sideband to the seed along the undulator for different modulation amplitude.

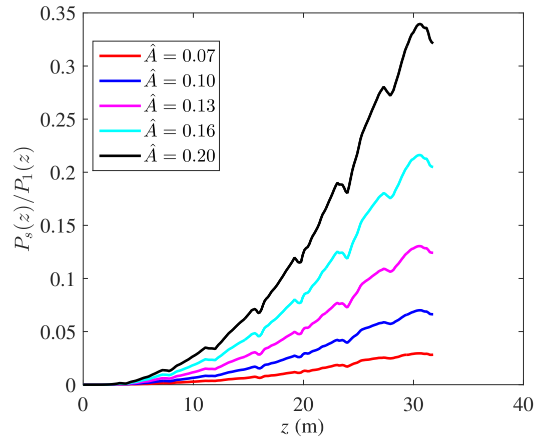

Figure 5: The ratio of the lower sideband to the seed along the undulator for different modulation amplitude in Genesis simulations.

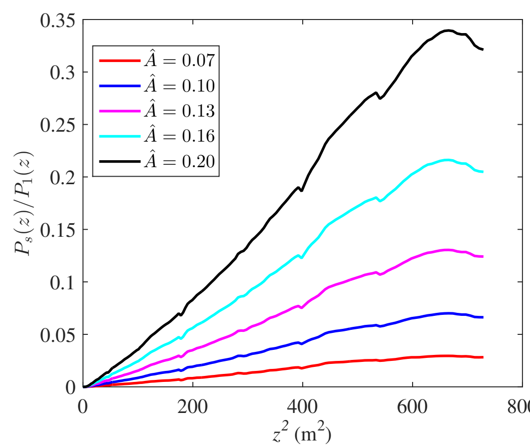

Figure 6: The ratio of the lower sideband to the seed versus the square of the undulator length (after removing the drifts) for different modulation amplitude in Genesis simulations.

3D GENESIS SIMULATIONS

3D Genesis [19] simulations were also performed to validate the theory and 1D simulations. We adopt similar parameters with the 1D simulations, but include the drifts between undulator sections. The energy offset of the sidebands are the same as found previously in the 1D simulations in Fig. 3. The power ratio along the undulator are shown in Fig. 5.

It can be seen that the power ratio of the sideband to the seed has a small drop at the beginning of new undulator sections in the Genesis simulations. This is because the upstream drift length matches the seed frequency and produces additional phase shifts (mismatches) for the sidebands. If we remove the drifts in the plot and use the square of the undulator length in Fig. 6 as the scale, the power ratio grows quadratically with the undulator length and modulation amplitude, which is consistent with the theory and 1D simulations.

SUMMARY

In this paper, we have investigated the effects of residual energy and density modulations on the output of a seeded FEL. A simple 1D theory is developed to estimate the sideband content and agrees well with simulations. The power ratio of the sidebands to the seeded signal grows quadratically with the modulation amplitude and undulator length before FEL saturation. Further work includes detailed comparison with the experimental observations and developing methods to produce a more uniform electron beam in the longitudinal phase space.

ACKNOWLEDGMENT

We thank C.-X. Tang and E. Allaria for useful discussions. This work was supported by U.S. Department of Energy Contract No. DE-AC02-76SF00515.

ISBN 978-3-95450-134-2

REFERENCES

[1] P. Emma *et al.*, Nat. Photonics 4, 641 (2010).

[2] T. Ishikawa *et al.*, Nat. Photonics 6, 540 (2012).

[3] J. Feldhaus, E. Saldin, J. Schneider, E. Schneidmiller, and M. Yurkov, Opt. Commun. 140, 341 (1997).

[4] G. Geloni, V. Kocharyan, E. Saldin, Journal of Modern Optics 58, 1391 (2011).

[5] J. Amann *et al.*, Nat. Photonics 6, 693 (2012).

[6] D. Ratner *et al.*, Phys. Rev. Lett. 114, 054801 (2015).

[7] L. H. Yu, Phys. Rev. A 44, 5178 (1991).

[8] G. Stupakov, Phys. Rev. Lett. 102, 074801 (2009).

[9] E. Allaria *et al.*, Nat. Photonics 6, 699 (2012).

[10] E. Allaria *et al.*, Nat. Photonics 7, 913 (2013).

[11] W. Fawley and G. Penn, Sincrontrone Trieste tech. note ST/F-TN-06/07 (2006).

[12] A. Lutman *et al.*, J. Phys. A: Math. Theor. 42, 085405 (2009).

[13] B. Ji *et al.*, Phys. Rev. ST Accel. Beams 13, 060701 (2010).

[14] A. Marinelli *et al.*, Phys. Rev. ST Accel. Beams 13, 070701 (2010).

[15] E. L. Saldin *et al.*, Nucl. Instrum. Methods Phys. Res. Sect. A 490, 1 (2002).

[16] Z. Huang *et al.*, Phys. Rev. ST Accel. Beams 7, 074401 (2004).

[17] D. Ratner *et al.*, Phys. Rev. ST Accel. Beams 18,030704 (2015).

[18] R. Lindberg, ANL tech. note AOP-TN-2015-028 (2015).

[19] S. Reiche, Nucl. Instrum. Methods A 429, 243 (1999).

ISBN 978-3-95450-134-2

CONCEPTUAL THEORY OF SPONTANEOUS AND TAPER-ENHANCED SUPERRADIANCE AND STIMULATED SUPERRADIANCE*

A. Gover, University of Tel-Aviv, Tel-Aviv, Israel
R. Ianconescu, University of Tel-Aviv, Tel-Aviv and Shenkar College, Ramat Gan, Israel
A. Friedman, Ariel University, Ariel, Israel
C. Emma, P. Musumeci, UCLA, Los Angeles, USA

Abstract

In the current work we outline the fundamental physical concepts of Spontaneous Superradiance (SR), Stimulated Superradiance (ST-SR), Taper-Enhanced Superradiance (TES) and Taper-Enhanced Stimulated Superradiance Amplification (TESSA), and compare their Fourier and Phasor formulations in a model of radiation mode expansion. Detailed further analysis can provide better design concepts of high power FELs and improved tapering strategy for enhancing the power of seeded short wavelength FELs. We further discuss the extensions of the model required for full description of these radiation processes, including diffraction and spectral widening effects.

INTRODUCTION

In the context of radiation emission from an electron beam Dicke's superradiance (SR) [1] is the enhanced radiation emission from a pre-bunched beam. Stimulated Superradiance (ST-SR) is the further enhanced emission of the bunched beam in the presence of a phase-matched radiation wave. These processes were analyzed for Undulator radiation in the framework of radiation field mode-excitation theory [2]. In the nonlinear saturation regime the synchronism of the bunched beam and an injected radiation wave may be sustained by wiggler tapering [3]. Same processes are instrumental also in enhancing the radiative emission in the tapered wiggler section of seeded FEL [4]. Here we outline the fundamental physical concepts of Spontaneous Superradiance (SR), Stimulated Superradiance (ST-SR), Taper-Enhanced Superradiance (TES) and Taper-Enhanced Stimulated Superradiance Amplification (TESSA), and compare their Fourier and Phasor formulations in a model of radiation mode expansion. Detailed further analysis can provide better design concepts of high power FELs and improved tapering strategy for enhancing the power of seeded short wavelength FELs. We further discuss the extensions of the model required for full description of these radiation processes, including diffraction [5] and spectral widening effects.

SUPERRADIANT AND STIMULATED SUPERRADIANCE OF SPONTANEOUS EMISSION

As a starting point we review the theory of superradiant (SR) and stimulated superradiant (ST_SR) emission from free electrons in a general radiative emission process. In this section we use a spectral formulation, namely, all fields are given in the frequency domain as Fourier transforms of the real time dependent fields:

$$\breve{A}(r,\omega) = \int_{-\infty}^{\infty} A(r,t)e^{i\omega t}\,dt \tag{1}$$

We use the radiation modes expansion formulation of [2], where the radiation field is expanded in terms of an orthogonal set of eigenmodes in a waveguide structure or in free space (eg. Hermite-Gaussian modes):

$$\{\tilde{E}_q(\underline{r}), \tilde{H}_q(\underline{r})\} = \{\tilde{E}_q(\underline{r}_\perp), \tilde{H}_q(\underline{r}_\perp)\}e^{ik_{qz}z} \tag{2}$$

$$\breve{E}(\underline{r},\omega) = \sum_{\pm q} C_q(z,\omega)\tilde{E}_q(\underline{r}) \tag{3}$$

$$\breve{H}(\underline{r},\omega) = \sum_{\pm q} C_q(z,\omega)\tilde{H}_q(\underline{r}) \tag{4}$$

The excitation equations of the mode amplitudes is:

$$\frac{d\tilde{C}_q(z,\omega)}{dz} = \frac{-1}{4P_q}\int d^2\underline{r}_\perp \underline{\tilde{J}}_\perp(\underline{r},\omega)\cdot\tilde{E}_q^*(\underline{r}), \tag{5}$$

which is formally integrated and given in terms of the initial mode excitation amplitude and the currents

$$\tilde{C}_q(z,\omega) - \tilde{C}_q(0,\omega) = -\frac{1}{4P_q}\int dV\,\underline{\tilde{J}}_\perp(\underline{r},\omega)\cdot\tilde{E}_q^*(\underline{r}), \tag{6}$$

where

$$P_q = \frac{1}{2}Re\iint \underline{\tilde{E}}_q \times \underline{\tilde{H}}_q d^2\underline{r}_\perp = \frac{|\tilde{E}_q(\underline{r}_\perp = 0)|^2}{2Z_q}A_{em}, \tag{7}$$

That defines the mode effective area A_{em} in terms of the field of the mode on axis $\tilde{E}_q(\underline{r}_\perp) = 0$.

For a particulate current (an electron beam):

$$J(\underline{r},t) = \sum_{j=1}^{N} -ev_j(t)\delta(\underline{r} - \underline{r}_j(t)) \tag{8}$$

The field amplitude increment appears as a coherent sum of contributions (energy wavepackets) from all the electrons in the beam: The contributions can be split into a spontaneous part (independent of the presence of radiation field) and stimulated (field dependent) parts:

$$\breve{C}_q^{out}(\omega) - \breve{C}_q^{in}(\omega) = -\frac{1}{4P_q}\sum_{j=1}^{N}\Delta\breve{W}_{qj} \tag{9}$$

* This research was supported in part by a grant from the United States-Israel Binational Science Foundation(BSF), Jerusalem, ISRAEL

$$\Delta\check{W}_{qj} = -e\int_{-\infty}^{\infty} v_j(t)\cdot\tilde{E}_q^*(r_j(t))e^{i\omega t}dt \quad (10)$$

$$\Delta\check{W}_{qj} = \Delta\check{W}_{qj}^0 + \Delta\check{W}_{qj}^{st} \quad (11)$$

Assuming a narrow cold beam where all particles follow the same trajectories, the spontaneous emission wavepacket contributions are identical except for a phase factor corresponding to their injection time t_{0j}.

$$\Delta\check{W}_{qj}^0 = \Delta\check{W}_{qe}^0 e^{i\omega t_{0j}} \quad (12)$$

where

$$\Delta\check{W}_{qe}^0 = -e\int_{-\infty}^{\infty} v_e^0(t)\cdot\tilde{E}_q^*(r_e^0(t))e^{i\omega t}dt. \quad (13)$$

The radiation mode amplitude at the output is composed of a sum of wavepacket contributions including the input field contribution (if any):

$$\check{C}_q^{out}(\omega) = \check{C}_q^{in}(\omega) + \Delta\check{C}_{qe}^0(\omega)\sum_{j=1}^{N} e^{i\omega t_{0j}} + \sum_{j=1}^{N}\Delta\check{C}_{qj}^{st} =$$
$$\check{C}_q^{in}(\omega) - \frac{1}{4P_q}\Delta\check{W}_{qe}^0\sum_{j=1}^{N} e^{i\omega t_{0j}} - \frac{1}{4P_q}\Delta\check{W}_{qe}^0\sum_{j=1}^{N}\Delta\check{W}_{qj}^{st} \quad (14)$$

so that the total spectral radiative energy from the electron pulse is

$$\frac{dW_q}{d\omega} = \frac{2}{\pi}P_q\left|C_q^{in}(\omega)\right|^2 =$$
$$\frac{2}{\pi}P_q\left\{\left|C_q^{in}(\omega)\right|^2 + \left|\Delta C_{qe}^{(0)}(\omega)\sum_{j=1}^{N} e^{i\omega t_{oj}}\right|^2 + \right.$$
$$\left[C_q^{in\,*}(\omega)\Delta C_{qe}^{(0)}(\omega)\sum_{j=1}^{N} e^{i\omega t_{oj}} + c.c.\right] +$$
$$\left.\left[C_q^{in\,*}(\omega)\sum_{j=1}^{N}\Delta C_{qj}^{st}(\omega) + c.c.\right]\right\} \equiv$$
$$\left(\frac{dW_q}{d\omega}\right)_{in} + \left(\frac{dW_q}{d\omega}\right)_{sp/SR} + \left(\frac{dW_q}{d\omega}\right)_{ST-SR} + \left(\frac{dW_q}{d\omega}\right)_{st} \quad (15)$$

Figures 1(a) and (b) represent the conventional spontaneous emission and superradiance emission that correspond to the second term in Eq. (15) where in 1(a) the wavepackets interfere randomly and in 1(b), in phase. Figure 1(d) represents the third term in Eq. (15) where the coherent constructive interference of a prebunched beam interferes with the input field with some phase offset. Figure 1(c) represents regular stimulated emission from a randomly injected electron beam (regular FEL). When the electrons in the beam are injected at random in a long pulse the second term in Eq. (15) contributes only to conventional shot-noise driven spontaneous emission [2, 6].

$$\left(\frac{dW_q}{d\omega}\right)_{sp} = \frac{1}{16}\left|\Delta\check{W}_{qe}^{(0)}\right|^2 N \quad (16)$$

Only when the electrons are bunched into a pulse shorter than an optical period $\omega(t_{0i}-t_0)\ll\pi$ or are periodically bunched, one gets enhanced superradiant spontaneous emission. Here we focus on periodic bunching, and following the formulation of [2] we write

$$\sum_{j=1}^{N} e^{i\omega t_{0j}} = \sum_{k=1}^{N_M}\sum_{j=1}^{N_N} e^{i\omega t_{0j}} = NM_b(\omega)M_M(\omega)e^{i\omega t_0}, \quad (17)$$

where

$$M_b(\omega) = \frac{1}{N_b}\left\langle\sum_{j=1}^{N_b} e^{i\omega t_{0j}}\right\rangle, \quad (18)$$

$$M_M(\omega) = \frac{1}{N_M}\left\langle\sum_{k=1}^{N_M} e^{i\omega t_{0k}}\right\rangle, \quad (19)$$

and

$$t_{0k} = t_0 + [k-(N_M/2)]2\pi/\omega_b \quad (20)$$

where now, neglecting beam noise, we assume identical microbunches of equal number of particles N_b and a uniform train of N_M microbunches (macropulse), such that the total number of particles is $N = N_bN_M$. For normalized Gaussian shaped microbunches

$$f(t) = \frac{1}{\sqrt{\pi}t_b}e^{-t^2/t_b^2} \quad (21)$$

and

$$M_b(\omega) = e^{-\omega^2 t_b^2/2}. \quad (22)$$

$M_M(\omega)$ comes out

$$M_M(\omega) = \frac{\sin(N_M\pi\omega/\omega_b)}{N_M\sin(\pi\omega/\omega_b)} \quad (23)$$

and consequently the superradiant spectral energy of the pulse is

$$\left(\frac{dW_q}{d\omega}\right)_{SR} = \frac{N^2}{8\pi P_q}\left|\Delta\check{W}_{qe}^{(0)}\right|^2|M_b(\omega)|^2|M_M(\omega)|^2, \quad (24)$$

and the stimulated superradiant at zero order approximation (the third term in Eq. (15) is

$$\left(\frac{dW_q}{d\omega}\right)_{ST-SR} = \frac{N}{2\pi}|\check{C}_q^{in}(\omega)|\left|\Delta\check{W}_{qe}^{(0)}\right|^2|M_b(\omega)||M_M(\omega)|cos\varphi, \quad (25)$$

where φ is the phase between the radiation field and the periodically bunched beam. For Undulator Radiation [2]:

$$\Delta\check{W}_{qj}^0 = -e\frac{v_{\perp 0}\cdot\tilde{E}_q^*}{2v_z}L\,\mathrm{sinc}(\theta L/2)e^{i\theta L/2}e^{i\omega t_{0j}}, \quad (26)$$

and the detuning parameter $\theta(\omega)$ is

$$\theta(\omega) = \frac{\omega}{v_z} - k_{zq}(\omega) - k_w. \quad (27)$$

ISBN 978-3-95450-134-2

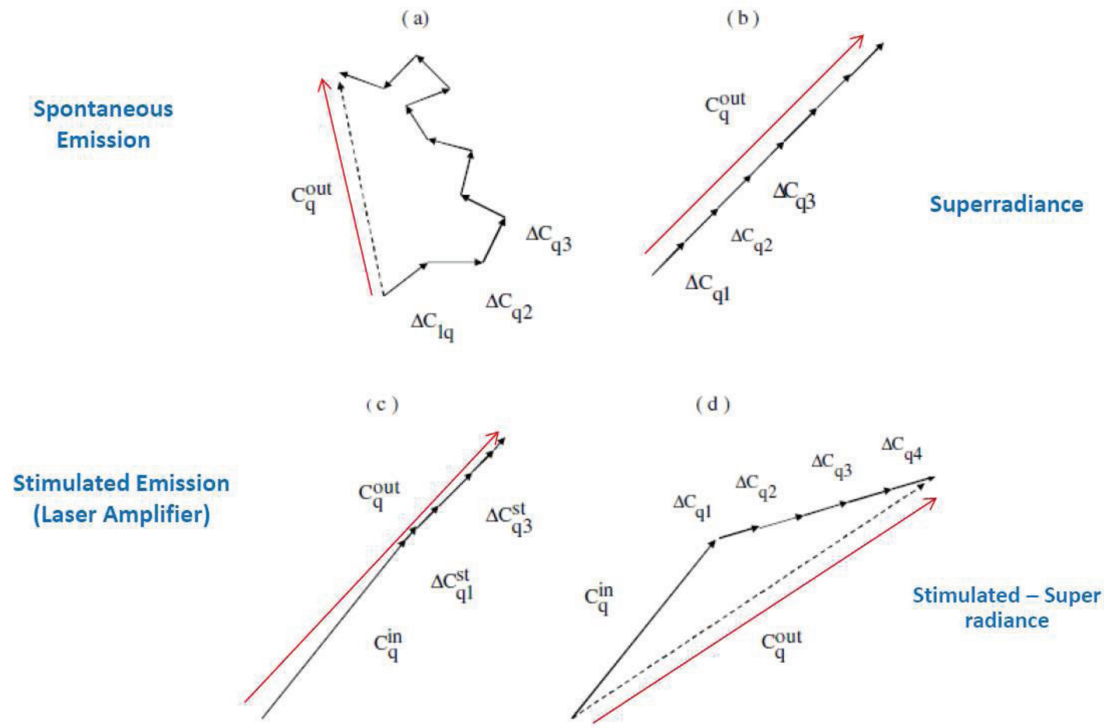

Figure 1: Different cases of radiation: (a) spontaneous emission, (b) superradiance, (c) stimulated emission and (d) stimulated superradiance.

The superradiant term is

$$\left(\frac{d\mathcal{W}_q}{d\omega}\right)_{SR} = \frac{N_b^2 e^2 Z_q}{16\pi}\left(\frac{a_w}{\beta_z\gamma}\right)^2 \frac{L^2}{A_m}|M_b(\omega)|^2 \operatorname{sinc}^2(\theta L/2) \tag{28}$$

and the stimulated superradiant term is

$$\left(\frac{d\mathcal{W}_q}{d\omega}\right)_{ST-SR} = |\breve{C}_q^{in}(\omega)| \frac{N_b^2 e^2 Z_q P_q}{4\pi N}\left(\frac{a_w}{\beta_z\gamma}\right)\frac{L}{A_m} |M_b(\omega)| \operatorname{sinc}(\theta L/2)\cos(\varphi - \theta L/2) \tag{29}$$

SINGLE FREQUENCY (PHASOR) FORMULATION

In the limit of a continuous train of microbunches or a long macropulse $N_M \gg 1$, the grid function $M_M(\omega)$ behaves like a comb of delta functions and narrows the spectrum of the prebunched beam SR and ST-SR Undulator Radiation to harmonics of the bunching frequencies $\omega = n\omega_b$. Instead of spectral energy one can then evaluate the average radiation power output by setting $M_M(\omega) = 1$ and dividing the spectral energy by the pulse duration: $T_M = N_M 2\pi/\omega_b$. Alternatively, one may have analyzed the continuous bunched beam problem from the start in a single frequency model using phasor formulation:

$$A(\underline{r}, t) = Re[\tilde{A}(\underline{r}, \omega)e^{-i\omega t}] \tag{30}$$

As in [5, 7, 8], we take a model of a periodically modulated e-beam current of a single frequency ω:

$$I(z, t) = I_0\{1 + Re[\tilde{M}_b e^{-i\omega(t - z/v_z)}\} \tag{31}$$

Assuming the beam has a normalized transverse profile distribution $f(\underline{r}_\perp)$. The transverse current density in the wiggler is:

$$\underline{J}_\perp(\underline{r}, \omega) = \frac{I_{m\perp}\hat{\mathbf{e}}_\perp}{2} f(\underline{r}_\perp)e^{i(\omega/v_z - k_w)z} \tag{32}$$

Where:

$$I_{m\perp}\hat{\mathbf{e}}_\perp = I_0\tilde{M}_b\frac{\tilde{\boldsymbol{\beta}}_w}{\beta_z} \tag{33}$$

Writing now the excitation equation in phasor formulation:

$$\tilde{C}_q(z) = \tilde{C}_q(0) - \frac{1}{4P_q}\int dV \underline{\tilde{J}}_\perp(\underline{r}, \omega)\cdot\tilde{E}_q^*(\underline{r}_\perp)e^{-ik_{zq}z}, \tag{34}$$

One obtains:

$$\tilde{C}_q(z) = \tilde{C}_q(0) - \frac{I_m}{8P_q}|\tilde{E}_q(0)|Fze^{i\theta z/2}\operatorname{sinc}(\theta z/2) \tag{35}$$

where

$$F = \frac{1}{|\tilde{E}_q(0)|}\int_{-\infty}^{\infty}\hat{e}_\perp\cdot\tilde{E}_q^*(\underline{r}_\perp)d^2r_\perp. \tag{36}$$

We remark that $F \simeq 1$ for a narrow beam. The time averaged radiation power will then be given by:

$$P_q(z) = P_q|C_q(z)|^2 = P_q(0) + P_{SR}(z) + P_{ST-SR}(z) \tag{37}$$

Where the superradiant and stimulated superradiant powers are:

$$P_{SR}(z) = \frac{1}{32}Z_q|I_m|^2F^2\frac{z^2}{A_{em}}\operatorname{sinc}^2(\theta z/2) \tag{38}$$

and

$$P_{ST-SR}(z) = \frac{1}{4}|I_m||E_\perp(0)|Fz\cos(\varphi_0^r - \varphi_0^b - \theta z/2) \\ \mathrm{sinc}(\theta z/2) \tag{39}$$

TAPER ENHANCED SUPERRADIANCE (TES) AND TAPER ENHANCED STIMULATED SUPERRADIANCE AMPLIFICATION (TESSA)

The underlying assumption in the calculation of spontaneous emission, superradiant spontaneous emission and (zero order) stimulated superradiant emission is that the beam energy loss as a result of radiation emission is negligible. When this is not the case the problem is a much harder nonlinear evolution problem. We now extend our model to the case of a continuously bunched electron beam interacting with a strong radiation field in an undulator, so that the electron beam loses an appreciable portion of its energy in favor of the radiation field. However in the case the injected radiation field power $P(0)$ is high enough to trap the bunched electrons in the buckets of the ponderomotive potential, one can conceive a concept of tapering the period or amplitude of the wiggler in such a way, that the phase velocity of the ponderomotive potential buckets will slow down in accordance with the energy loss of the bunched beam and the synchronism condition ($\theta \simeq 0$) continues to be kept [9]. In such a configuration Taper Enhanced Superradiance (TES) can continue to be produced [4, 5], but also as suggested in [3] there may be significant emission of Taper Enhanced Stimulated Superradiant Amplification (TESSA). This observation is particularly relevant to the case of seed injected tapered wiggler FEL. In this case (see Fig. 2) the tapered wiggler section would emit both TES and TESSA radiation, but the input field for the TESSA process is not arbitrary, but determined by the saturation power emitted by the constant wiggler parameters FEL section preceding the tapered wiggler section.

Start to end analysis and simulation of the tapered wiggler FEL were presented by numerous authors in attempt to maximize the radiation extraction efficiency and output power of the FEL [4, 5, 10–18]. A single frequency phasor analytical model has been recently presented by Schneidmiller and Yurkov [5] drawing attention to the radiation diffraction effect that must be taken into account in the tapered wiggler section. Emma et al have shown that a spectral analysis approach is necessary for including non negligible effects of shot noise and synchrotron oscillation side band radiation [18]. In this section we consider the tapering enhancement effect in the framework of the simple analytical model of radiation mode expansion and particularly drawing attention to the role of TESSA radiation emission process. Clearly a full 3D spectral numerical analysis is necessary for considering all the above mentioned effects and getting to reliable quantitative estimates of the radiation emission. But following [5] we suggest here an extended analytical analysis that can be used as a guideline for wiggler tapering strategy including TESSA contribution.

Applying for now our simplistic phasor analysis we assume that the bunched beam loses its average energy uniformly as a function of z in a way that depends on the radiation field evolution on axis $E(z)$:

$$\gamma(z) = \gamma(0) + \delta\gamma(z, E(z)) \tag{40}$$

The average axial velocity of the beam changes as a function of z both because because of wiggler amplitude tapering β_Z^0 and because of the energy loss $\delta\beta_z(z, E(z))$

$$\beta_z(z) = \beta_Z^0 + \delta\beta_z(z, E(z)) \tag{41}$$

The phase of the bunched beam relative to the ponderomotive wave is then:

$$\varphi(z) = \int_0^z \left[\theta^0(z') - k\frac{\delta\beta_z(z')}{[\beta_z^0(z')]^2}\right]dz' = \int_0^z \theta^E(z')dz', \tag{42}$$

where $\theta^E(z')$ is the resultant field dependent detuning parameter, and

$$\theta^0(z') = \frac{\omega}{v_Z^0(z')} - k_w(z') - k_{zq}(z') \tag{43}$$

is the would-be detuning parameter in the tapered wiggler in the absence of energy loss, consequently, from Eq. (34)

$$\check{C}_q(z) = \check{C}_q(0) - \frac{1}{8}I_0F\frac{|\check{E}_q(0)|}{P_q}e^{i\varphi_b} \\ \int_0^z \frac{a_w(z')}{\gamma(z')\beta_z(z')}|M_b(z')|e^{i\int_0^{z'}\theta^E(z'')dz''}dz' \tag{44}$$

Of course, in order to know $\delta\gamma(z, E(z))$ and consequently $\theta^E(z)$ one must solve the force equation for the bunched electron beam dynamics in the buckets of the slowing down ponderomotive potential. This part of the analysis is not attempted in the present work. We only assume the tapering strategy is optimal, such that we may assume with the consideration of the beam energy loss that the net taper and field depending detuning is constant: $\theta^E(z) = \theta^E(0)$. If we also assume as in [5] that the bunching amplitude and amplitude coefficient in the integrand are approximately constant, then the equation is integrable, resulting in:

$$\tilde{C}_q(z) = \tilde{C}_q(0) - \frac{I_m}{8P_q}|\tilde{E}_q(0)|Fze^{i\theta_0^E z/2}\,\mathrm{sinc}(\theta_0^E z/2) \tag{45}$$

Similarly to Eqs. (37), (38) and (39) for SR/ST-SR we get then for a tapered wiggler with tapering matched t_D the beam energy loss

$$P(z) = P(0) + P_{TES}(z) + P_{TESSA}(z) \tag{46}$$

where

$$P_{TES}(z) = \frac{1}{32}Z_q|I_m|^2F^2\frac{z^2}{A_{em}}\,\mathrm{sinc}^2(\theta_0^E z/2) \tag{47}$$

ISBN 978-3-95450-134-2

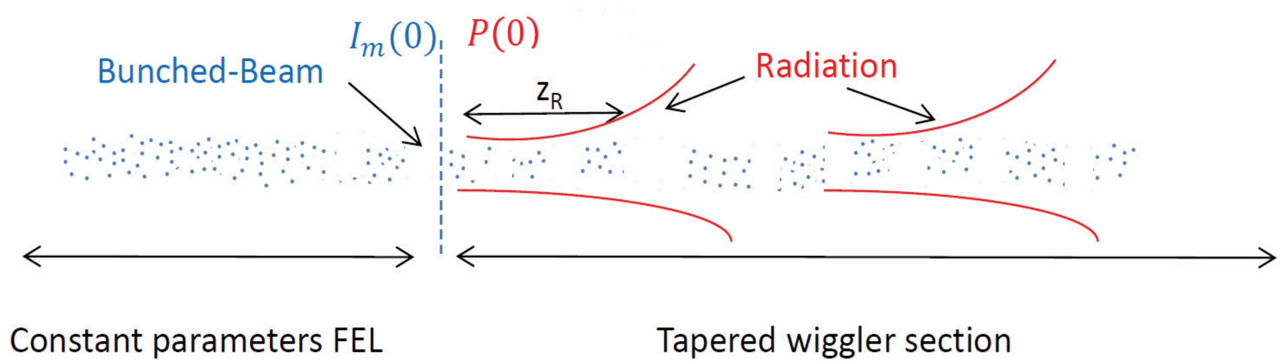

Figure 2: Constant wiggler vs taped wiggler.

and

$$P_{TESSA}(z) = \frac{1}{4}|I_m||E_\perp(0)|Fz\cos(\varphi_0^r - \varphi_0^b - \theta_0^E z/2) \operatorname{sinc}^2(\theta_0^E z/2). \tag{48}$$

For $\theta_0^E = 0$ and phase matched bunched current and radiation field $\varphi_0^r = \varphi_0^b$

$$P_{TES}(z) = \frac{1}{32} Z_q |I_m|^2 F^2 \frac{z^2}{A_{em}} \tag{49}$$

and

$$P_{TESSA}(z) = \frac{1}{4}|I_m|\sqrt{\frac{2Z_q}{A_{em}}}\sqrt{P_{in}}Fz \tag{50}$$

The ratio between the two contributions to the radiation power is

$$\frac{P_{TESSA}}{P_{TES}} = 8\frac{A_{em}}{Z_q I_m F z}\sqrt{\frac{2Z_q}{A_{em}}}\sqrt{P_{in}} = 8\frac{A_{em}}{Z_q I_m F z}E_{in}(0) \tag{51}$$

In Fig. 3 we show the Ratio of 0-order TESSA to TES for different initial power at $z = z_0$. Initially the TESSA

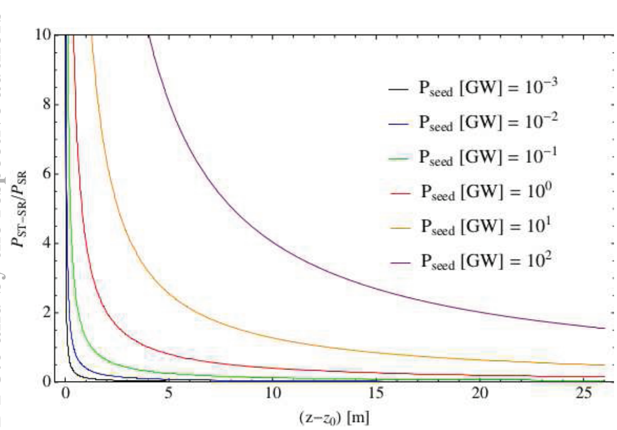

Figure 3: Ratio of 0-order TESSA to TES for different initial power at $z = z_0$.

power dominates the TES power, but evidently, for long interaction length the TES power that grows like z^2 exceeds the TESSA power that grows like z. At the beginning stages of interaction in the tapered wiggler the TESSA power may be significantly higher than the TES power if the initial radiation power P_{in} injected into the tapered section is large enough. This balance is demonstrated in Fig. 3 for the parameters of LCLS [15].

ELABORATION OF THE CONCEPTUAL MODEL

The classification of the spontaneous and stimulated emission processes of electron beams (shot noise spontaneous emission, SR and ST-SR emission) and the counterpart processes of TES and TESSA in a tapered wiggler is helpful as a guideline and general framework for more detailed and accurate analysis of realizable ratiative emission devices. Some progress has been made recently by various authors, but substantial analytical and simulation analyses are still required in order to optimize the radiation emission from practical sources.

Diffraction Effects

The radiation mode expansion formulation would be valid for a free diffraction case only for a wiggler length smaller than one Rayleigh length $L_w < z_R = \pi W_0^2/\lambda$. For longer lengths one should use a full multimode expansion analysis of the radiation field or rather a Fresnel diffraction analysis as was done by Schneidmiller et al for TES only [5].

Single vs Multi Frequency Analysis

The single frequency beam current steady state modulation model is too crude for obtaining reliable quantitative results in the case of the taper enhanced SR and ST-SR. A multifrequency spectral analysis (as in Eqs. (1,15) is required for taking full account of the trapped particle beam dynamics in the ponderomotive bucket in the tapered wiggler. This includes simulation of the synchrotron oscillations trajectories of the electron of the bunch trapped in the buckets, that differs from each other due to incomplete bunching, finite energy spread and emittance. This means that the beam modulation current evolves and diminishes (due to detrapping) along the interaction length. Further spectral

ISBN 978-3-95450-134-2

broadening effects that require more detailed spectral (time dependent) numerical simulations are evolvement of synchrotron oscillation side-band frequencies and shot noise effect [18].

TESSA

The TESSA contribution given in the present model calculation should be regarded only as "zero-order TESSA", because Eq. (48) does not take into consideration the enhanced stimulated SR emission that takes place when the radiation power grows along the interaction length, providing deepening of the trapping buckets and allowing more aggressive tapering strategy. This kind of non-linear dynamics "high gain TESSA" was analyzed numerically in [3].

REFERENCES

[1] R.H. Dicke, “Coherence in Spontaneous Radiation Processes”, Physical Review 93 (1): 99–110, (1954).

[2] A. Gover, “Superradiant and stimulated-superradiant emission in prebunched electron-beam radiators. I. Formulation”, Phys. Rev. ST-AB 8, 030701 (2005).

[3] J. Duris, A. Murokh, and P. Musumeci, “Tapering enhanced stimulated superradiant amplification”, New J.Phys. 17 063036, 2015.

[4] Y. Jiao et al, “Modeling and multidimensional optimization of a tapered free electron laser”, PRST-AB 15, (050704) (2012).

[5] E. A. Schneidmiller, M. V. Yurkov, “Optimization of a high efficiency free electron laser amplifier”, PRST-AB 18, 03070 (2015).

[6] R. Ianconescu, E. Hemsing, A. Marinelli, A. Nause and A. Gover, “Sub-Radiance and Enhanced-Radiance of undulator radiation from a correlated electron beam”, FEL 2015 Conference, August 23-28, Daejeon, Korea, 2015.

[7] M. Arbel et al, “Linear model formulation for superradiant and stimulated superradiant prebunched e-beam free-electron lasers”, PR-ST AB 17, 020705 (2014).

[8] I. Schnitzer and A. Gover, “The Prebunched Free Electron Laser in Various Operating Gain Regimes”, NIM-PR, A237 124-140, (1985).

[9] N.M. Kroll, P.L. Morton, M.N. Rosenbluth, “Free-Electron Lasers with Variable Parameter Wigglers”, IEEE J. Quant. Electron., VOL. QE-17, NO. 8, AUGUST 1981.

[10] J.M.Slater, “Tapered-Wiggler Free-Electron Laser Optimization”, IEEE J. Quant. Electron., VOL. QE-17, NO. 8, AUGUST 1981.

[11] D.C. Nguyen, H.P. Freund, “STAIR-STEP TAPERED WIGGLER FOR HIGH-EFFICIENCY FEL”, Proceedings of FEL 2006, BESSY, Berlin, Germany.

[12] D.C. Quimby and J.M. Slater, “Electron-Beam Quality Requirements for Tapered- Wiggler Free-Electron Lasers”, IEEE J. Quant. Electron., VOL. QE-21, NO. 7. JULY 1985.

[13] A. Bhowmik, R.A. COVER, and W. A. McMullin, “Comparison of dc Electric Field and Tapered Wiggler Free Electron Laser Efficiency Enhancement Schemes”, IEEE J. Quant. Electron., VOL. QE-21, NO. 7. JULY 1985.

[14] S.R. Chang, J. Joe, J.E. Scharer, “Nonlinear Analysis of Wiggler Taper, Mode Competition, and Space-Charge Effects For a 280-GHz Free Electron Laser”, IEEE TRANSACTIONS ON PLASMA SCIENCE. VOL. 18. NO. 3. JUNE 199O.

[15] C. Emma, K. Fang, J. Wu, C. Pellegrini, “High Efficiency, Multi-Terawatt X-ray free electron lasers”, Phys. Rev. ST-AB, 17, 110701 (2014).

[16] W. M. Fawley, Z. Huang, K.-J. Kim, and N. A. Vinokurov, “Tapered undulators for sase fels”, Nuclear Instruments and Methods in Physics Research Section A, vol. 483, no. 12, pp. 537-541, 2002, Proceedings of the 23rd International Free Electron Laser Conference and 8th FEL Users Workshop.

[17] A. Mak, F. Curbis, and S. Werin, “Model-based optimization of tapered free-electron lasers”, Phys. Rev. ST Accel. Beams, vol. 18, p. 040702, Apr 2015.

[18] C. Emma, K. Fang, J. Wu, and C. Pellegrini, “High Efficiency, Multi-Terawatt X-ray free electron lasers”, FEL 2015 Conference, August 23-28, Daejeon, Korea, 2015.

ISBN 978-3-95450-134-2

SMITH-PURCELL RADIATION FROM MICROBUNCHED BEAMS MODULATED AFTER PASSING THE UNDULATORS IN FELS*

D.Yu. Sergeeva[1,#], A.P. Potylitsyn[1,2], A.A. Tishchenko[1], M.N. Strikhanov[1],
[1] National Research Nuclear University MEPhI, Moscow, Russia
[2] National Research Tomsk Polytechnic University, Tomsk, Russia

Abstract

We suggest using the Smith-Purcell effect from microbunched beams modulated after passing the undulators in FELs as an extra source of monochromatic radiation. We investigate theoretically characteristics of Smith-Purcell radiation in THz and X-ray frequency regions for two types of distribution of the particles in the beam. The expression for spectral-angular distribution of such radiation is obtained and analyzed, both for fully and partially modulated beams. The intensity of Smith-Purcell radiation is shown to be able to increase both due to the periodicity of the beam and the periodicity of the target. The numerical results prove that such radiation source can be an effective instrument for different FEL users, supplementary for the main FEL source.

INTRODUCTION

Smith-Purcell radiation (SPR) is a promising scheme for creating the intense source of radiation. SPR is convenient for beam diagnostics because of large emission angles. The intensity of SPR is proportional to the squared number of strips in the periodic target (grating). Besides the intensity of radiation can be increased if it is generated by the beam having periodic inner structure. Such microbunched beams can be obtained in FEL, in the process of the beam modulation in undulator. Therefore, the beam after passing the undulator in FEL can generate intensive radiation from the grating before passing to a dump (see scheme in Fig. 1). Changing an emission angle it is possible to produce quasimonochromatic radiation with different wavelengths in a broad range in comparison with the modulation period.

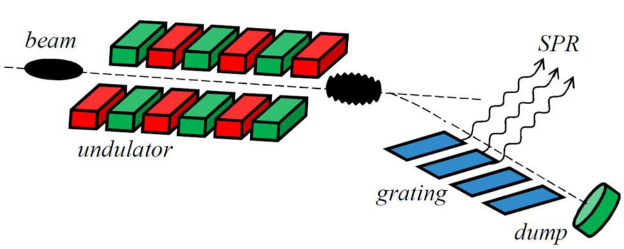

Figure 1: Scheme of using the microbunched beam modulated after passing the undulator for generating intensive Smith-Purcell radiation.

*Work supported by the Leverhulme Trust International Network, grant IN-2015-012 and by the Ministry of Science and Education of the Russian Federation, grant № 3.1110.2014/K.
#dysergeyeva@mephi.ru

We theoretically investigate SPR generated by the microbunched beam of relativistic electrons. The beam is assumed to have periodic internal structure with the period λ_0. The number of the particles with the charge e is N, the number of microbunches is N_b. The beam moves at a constant distance h above the grating surface with the constant velocity $\mathbf{v} = (v,0,0)$. The period of the grating is d, the single strip width is a, N_{st} is the number of the strips in the grating. The qualitative scheme is shown in Fig. 2.

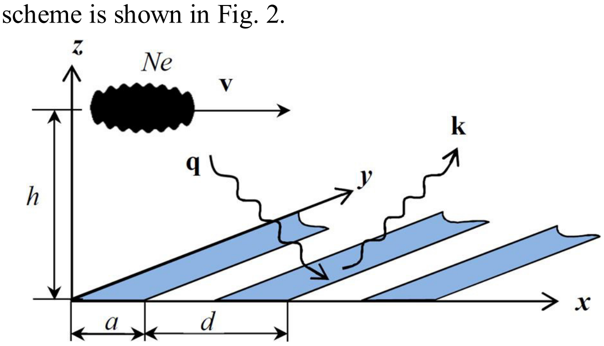

Figure 2: Qualitative scheme of generating the Smith-Purcell radiation.

MODULATED BEAM

The distribution of the particles in the modulated beam can be described by two ways. We will mark the values obtained for these distributions by f and g as the superscripts.

The first one is convenient to describe the beam which has a lot of microbunches with rather short delay between them. In this case the inner structure of each microbunch is negligible. Such kind of beams is produced, for example, in FELs like FLASH, Germany. The longitudinal profile of beam modulated in the undulator in this case can be described by the function

$$f_{long}(x) = \frac{2}{\sqrt{\pi}\sigma_x} \frac{\exp\left[-x^2/\sigma_x^2\right]\left(\mu + \sin^2\left(\pi x/\lambda_0\right)\right)}{1 + 2\mu - \exp\left[-\pi^2\sigma_x^2/\lambda_0^2\right]}, \quad (1)$$

with σ_x being the character size of the bunch in x direction; μ defining the “depth” of the modulation: if $\mu = 0$ then the beam is fully modulated, if $\mu \to \infty$ then the beam has the Gaussian form; λ_0 being the period of the modulation. The function in Eq. (1) is shown in Fig.3.

ISBN 978-3-95450-134-2

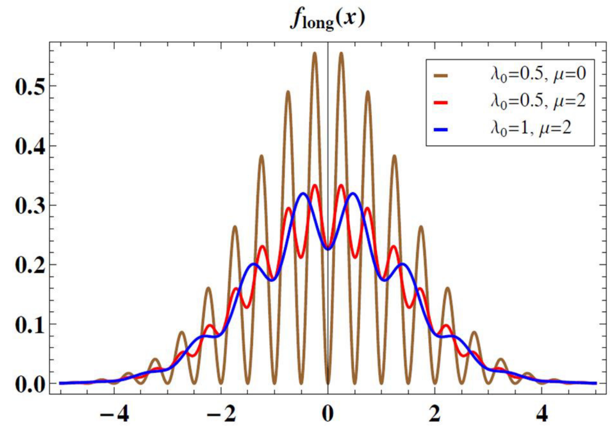

Figure 3: The longitudinal profile of the beam described by Eq. (1) for different parameters λ_0 and μ. For all curves $\sigma_x = 2$. The values x, λ_0, σ_x have the dimension of length and are measured in identical units.

The second distribution is convenient to describe the beam with not small delay between microbunches, or large size of microbunch. In this case the inner structure of each microbunch is taken into account. Such kind of the beam is produced, for example, in LUCX, Japan. There are about ten microbunches in the "train"[1]. The longitudinal distribution can be written as:

$$g_{long}(x) = \frac{1}{N_b\sqrt{\pi}\sigma'_x}\sum_{s=0}^{N_b-1}\exp\left[-(x-s\lambda_0)^2/\sigma'^2_x\right]. \tag{2}$$

Here σ'_x is the dispersion of a single microbunch, unlike σ_x in Eq. (1).

Function in Eq. (2) also can describe the partially modulated beam at $\lambda_0 < 4\sigma'_x$. This function is plotted in Fig. 4.

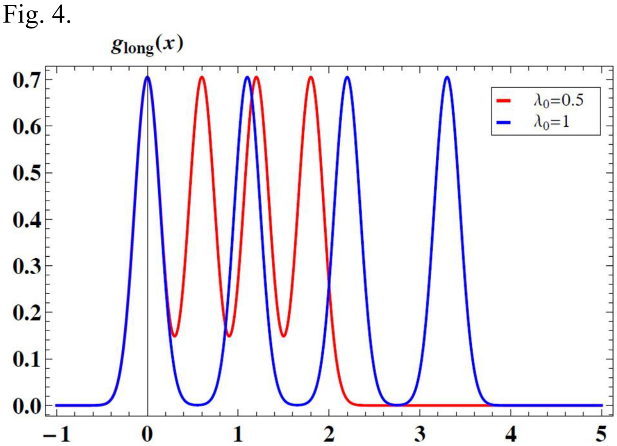

Figure 4: The longitudinal profile of the beam described by Eq. (2) for different parameters λ_0. For all curves $\sigma'_x = 0.2$, $N_b = 4$. The values x, λ_0, σ_x have the dimension of length and are measured in identical units.

The transversal distribution is assumed to be the same both for the $f_{tr}(x)$ and $g_{tr}(x)$:

$$f_{tr}(y,z) = g_{tr}(y,z) = \begin{cases} \dfrac{e^{-y^2/\sigma_y^2}}{\sqrt{\pi}\sigma_y\sigma_z}, & h-\dfrac{\sigma_z}{2} \le z \le h+\dfrac{\sigma_z}{2}, \\ 0, & z < h-\sigma_z/2,\ z > h+\sigma_z/2. \end{cases} \tag{3}$$

FORM-FACTOR FOR POLARIZATION RADIATION

In general the expression for the spectral-angular distribution of SPR has the following form [2]:

$$\frac{d^2W(\mathbf{n},\omega)}{d\omega d\Omega} = \frac{d^2W_1(\mathbf{n},\omega)}{d\omega d\Omega}GF, \tag{4}$$

where $d^2W_1(\mathbf{n},\omega)/d\omega d\Omega$ is the spectral-angular distribution of the radiation from a single electron (the center of the bunch) moving above a single strip, G is the factor defining the radiation from the grating, F is the so-called "form-factor" of the bunch, which can be written in the form [2-7]:

$$F = NF_{inc} + N(N-1)F_{coh}. \tag{5}$$

In Eq. (5) F_{inc} and F_{coh} are incoherent and coherent parts of the form-factor, correspondingly. We have to notice that $F_{inc} \ne 1$ in general case.

The expression for F can be found from qualitative approach in form similar to the form-factor for synchrotron radiation:

$$\begin{aligned} F_{inc} &= \int_V d^3r\left|e^{-i\mathbf{r}_m\mathbf{q}}\right|^2 f(\mathbf{r}), \\ F_{coh} &= \left|\int_V d^3re^{-i\mathbf{r}_m\mathbf{q}}f(\mathbf{r})\right|^2, \end{aligned} \tag{6}$$

where $f(\mathbf{r})$ is the function of distribution of the particles in the bunch, V is the volume of the bunch, $\mathbf{r}_m = \mathbf{r}-\mathbf{r}_0$, $\mathbf{r}_0$ is the radius-vector of the bunch center. It is important that for considered type of radiation the phase $\mathbf{r}_m\mathbf{q}$ is a complex value. All the values in Eq. (6) have to be written in a laboratory system of coordinates. That is why as opposed to the synchrotron radiation in the problems of diffraction or Smith-Purcell radiation there is a side of the target. The phase $\mathbf{r}_m\mathbf{q}$ for the case of polarization radiation was found in detail in the paper [8] from the conversation laws. For the coordinate system and geometry showing in the Fig. 2 the laws have the form

$$\begin{aligned} q_y &= k_y, \\ q &= k, \end{aligned} \tag{7}$$

and the dispersion relation for the virtual photons:

ISBN 978-3-95450-134-2

$$\omega = \mathbf{qv}, \tag{8}$$

where $\mathbf{k} = (k_x, k_y, k_z) = \mathbf{n}\,\omega/c$ is the wave-vector of the radiation in vacuum, $\mathbf{v}$ is the speed of the electron.

Solving the system of Eqs. (7) and (8) with help of equation

$$q = \sqrt{q_x^2 + q_y^2 + q_z^2}, \tag{9}$$

one can find the value $\mathbf{q}$ in Eq. (6) for the case of polarization radiation from the particle moving parallel to the target surface in form:

$$\mathbf{q} = \left(\frac{\omega}{v}, k_y, -i\sqrt{\frac{\omega^2}{v^2} + k_y^2 - \frac{\omega^2}{c^2}} \right). \tag{10}$$

Due to the qualitative difference between the natures of polarization types of radiation (diffraction radiation, transition radiation from a target of limited size, Smith-Purcell radiation) and synchrotron radiation, the differences in $\mathbf{q}$ and in the form-factor of the bunch arise.

RADIATION FROM MODULATED BEAM

Let us give the explicit form of expression for the spectral-angular distribution of the radiation for considered geometry.

Integrating in Eq. (6) with use of Eq. (10) for the beam with the function of distribution described in Eqs. (1)-(3), one can easily find the expression of the incoherent form-factor:

$$F_{inc} = F_{inc}^f = F_{inc}^g = \frac{sh(\rho\sigma_z)}{\rho\sigma_z}, \tag{11}$$

and coherent form-factors for different distributions $f_{long}(x) f_{tr}(y,z)$ and $g_{long}(x) g_{tr}(y,z)$:

$$F_{coh}^f = \frac{sh^2(\rho\sigma_z/2)}{(\rho\sigma_z/2)^2} \exp\left[-\frac{\sigma_y^2 k_y^2}{2} - \frac{\sigma_x^2 \xi^2}{2} \right] \times \left(\frac{1 + 2\mu - \exp\left[-\pi^2\sigma_x^2/\lambda_0^2 \right] ch\left(\pi\xi\sigma_x^2/\lambda_0 \right)}{1 + 2\mu - \exp\left[-\pi^2\sigma_x^2/\lambda_0^2 \right]} \right)^2, \tag{12}$$

and

$$F_{coh}^g = \frac{sh^2(\rho\sigma_z/2)}{(\rho\sigma_z/2)^2} \exp\left[-\frac{\sigma_y^2 k_y^2}{2} - \frac{\sigma_x'^2 \xi^2}{2} \right] \times \frac{1}{N_b^2} \frac{\sin^2(N_b\lambda_0\xi/2)}{\sin^2(\lambda_0\xi/2)}, \tag{13}$$

where we denoted

$$\xi = \omega/v, \ \rho = \sqrt{\xi^2 + k_y^2 - \omega^2/c^2}. \tag{14}$$

As a spectral-angular distribution of the radiation from a single electron at the optical and lower frequencies we chose the expression for the radiation from ideal conducting infinitely thin target. The expression was derived in the paper [9] and based on the theory of A.P. Kazantsev and G.I. Surdutovich [10] and adapted to the concerned coordinate system and geometry in[8]:

$$\frac{d^2W_1(\mathbf{n},\omega)}{d\hbar\omega d\Omega} = \frac{1}{137} \frac{\exp[-2\rho h]}{\pi^2\beta^3\rho^2\varphi^2} \left(\frac{\omega}{c} \right)^4 \sin^2\left(\frac{a\varphi}{2} \right) \times \left[\frac{\gamma^{-2}(1-n_y^2) + 2n_y^2}{\sqrt{1-n_y^2}} (1 - \beta n_x) + \gamma^{-2}\left(\beta(1-n_y^2) - n_x \right) \right]. \tag{15}$$

For X-ray frequency range we use the theory developed in [8, 11]:

$$\frac{d^2W_1(\mathbf{n},\omega)}{d\hbar\omega d\Omega} = \frac{1}{137} e^{-2\rho h} \left(\frac{\varepsilon(\omega)-1}{2\pi\beta\varphi\rho} \right)^2 \frac{\omega^4}{c^4} \sin^2\left(\frac{a\varphi}{2} \right) \times \frac{\left| \left[\mathbf{n}' \times \mathbf{n}' \times \left(\frac{\omega}{\beta c \gamma^2} \mathbf{e}_x + k_y \mathbf{e}_y - i\rho \mathbf{e}_z \right) \right] \right|^2}{\left| \rho - i(\omega/c)\sqrt{\varepsilon(\omega) - 1 + n_z^2} \right|^2}, \tag{16}$$

where $\varepsilon(\omega)$ is the dielectric permittivity of the target material described by the plasma frequency ω_p as

$$\varepsilon(\omega) = 1 - \omega_p^2/\omega^2, \ \omega >> \omega_p. \tag{17}$$

The factor G was also derived in the paper [8]:

$$G = \frac{\sin^2(N_{st} d\varphi/2)}{\sin^2(d\varphi/2)}, \tag{18}$$

where $\varphi = (\beta^{-1} - n_x)\omega/c$, d is a period of the grating, N_{st} is the number of the strips in the grating. This factor gives the well-known dispersion relation of SPR for $N_{st} >> 1$:

$$\lambda m = d(\beta^{-1} - n_x), \ m = 1, 2... \tag{19}$$

As a result, the spectral-angular distribution of the radiation at optical and lower frequencies has the form of Eqs. (4)-(5) with Eqs. (12)-(18).

RADIATION CHARACTERISTICS

For beam parameters of LUCX and FLASH the incoherent radiation is suppressed in comparison with the coherent one. That is why below we shall concentrate only on coherent radiation. As an example, the

ISBN 978-3-95450-134-2

comparison between F_{inc} and F_{coh}^{g} for terahertz frequencies is shown in Fig. 5. It can be seen that $F_{inc} \approx 1$ for wide range of wavelength. If F_{inc} and F_{coh}^{g} are multiplied by $N \sim 10^{10}$ and N^2 correspondingly, then coherent part will be more intensive (in more detail see [4]). In Fig. 5 we denote:

$$\mathbf{n} = \left(\cos\theta\cos\phi, \cos\theta\sin\phi, \sin\theta\right). \tag{20}$$

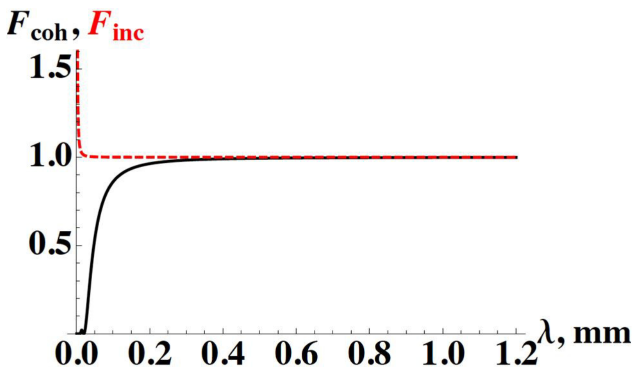

Figure 5: The comparison between F_{inc} (red dashed curve) and F_{coh}^{g} (black solid curve) for the beam of the size $\sigma_x = 3\mu m$, $\sigma_{y,z} = 14\mu m$, $\lambda_0 = 2\mu m$, $\phi = 0$, $\theta = 30^0$, $N_b = 10$, $\gamma = 16$ (energy of LUCX $E_e = 8MeV$).

From Eq. (13) the condition of strong enhancement of radiation intensity follows:

$$\lambda_0 = \beta\lambda s, \; s = 1, 2..., \tag{21}$$

that for ultrarelativistic particles, i.e. for $\gamma >> 1$, $\beta = \sqrt{1-\gamma^{-2}} \approx 1$ is $\lambda_0 \approx \lambda s, s = 1, 2...$. The similar condition can be found from Eq. (12):

$$\lambda_0 = \beta\lambda. \tag{22}$$

The spectral angular distribution of SPR at THz frequencies is shown in Fig. 6, at X-ray ones in Fig. 7.

For observation the most strong enhancement the wavelength of radiation λ should be very close to λ_0. For example, in Fig. 6 black curve is plotted for $\lambda_0 = \beta\lambda \approx 299\mu m$ and the radiation is most intensive; red curve is plotted for $\lambda_0 = 300\mu m$ and the radiation is less intensive. In Fig. 7 for $\lambda_0 = 10.001 nm$ the distributions of the radiation from the modulated beam and from Gaussian distributed beam in Fig. 7 are indistinguishable. If $\lambda_0 = 10.006 nm$, then all curves in Fig. 7 coincide with the blue curve. If $\lambda_0 = \lambda\beta$, then the radiation from modulated beam will be even much more intensive than in Fig. 7.

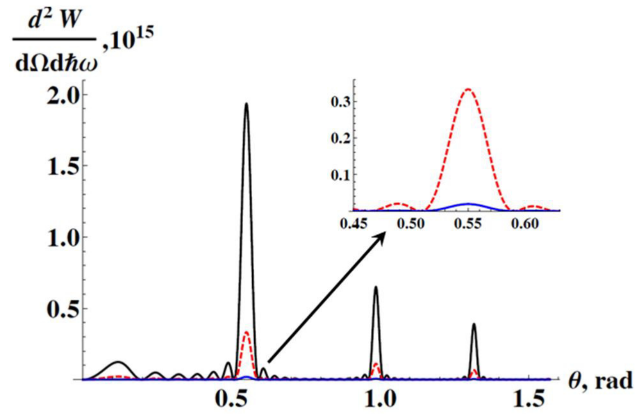

Figure 6: Spectral-angular distribution of SPR at THz frequencies plotted using Eqs. (4), (5), (13), (15), (18). Black solid curve: radiation from fully modulated beam with $\lambda_0 = \beta\lambda \approx 299\mu m$ (see Eq. (21) for $s = 1$), $N = 10^{10}$; red dashed curve: fully modulated beam with $\lambda_0 = 280\mu m$, $N = 10^{10}$; blue curve for the single microbunch ($N = 10^9$). For all curves $\sigma_x = 150\mu m$, $\sigma_{y,z} = 14\mu m$, $\lambda = 300\mu m$, $\phi = 0$, $N_b = 10$, $N_{st} = 7$, $\gamma = 16$ (energy of LUCX $E_e = 8MeV$), $h = 2mm$, $d = 2mm$, $a = 1mm$.

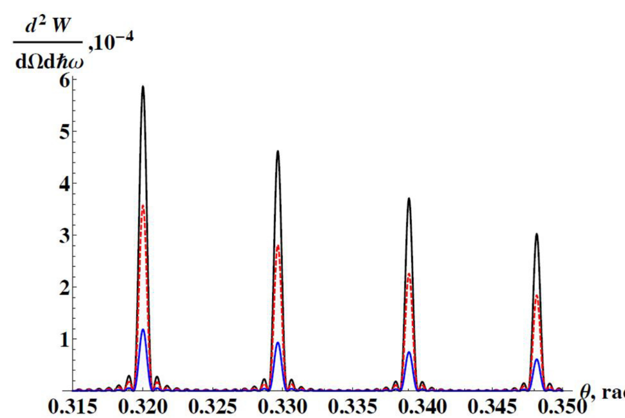

Figure 7: Spectral-angular distribution of SPR at X-ray frequencies plotted using Eqs. (4), (5), (12),(16), (18). Black solid curve: radiation from fully modulated beam $m = 0$; red dashed curve: partially modulated beam $m = 0.2$; blue dotted curve for the single not modulated bunch. For all curves $\sigma_x = 20\mu m$, $\sigma_{y,z} = 10\mu m$, $\lambda = 10nm$, $\phi = 0$, $N_b \approx 2000$, $N_{st} = 7$, $\gamma = 2000$ (energy of FLASH $E_e = 1GeV$), $h = 0.05mm$, $d = 6.5\mu m$, $a = d/2$, $\lambda_0 = 10.005nm$ (see Eq. (22)), $N = 10^{10}$, $\hbar\omega_p = 26.1eV$ (beryllium).

SUMMARY

In this paper we considered Smith-Purcell radiation generated by a microbunched beam modulated after passing the undulator in FELs, both for a conventional FEL, like FLASH, and also for the pre-bunched FEL, like LUCX (KEK).

ISBN 978-3-95450-134-2

We calculated the general analytical expression for the form-factor of the beam for polarization types of radiation that are defined by the edge of the target (diffraction radiation, Smith-Purcell radiation), and this expression differs from the form-factor for synchrotron radiation.

We show that the intensity of such radiation can be increased due to both the periodicity of the target and the periodicity of the beam, and strongly depends on the depth of modulation. So, the beam after undulator in FEL can be used as an effective supplementary source of radiation, in a wide range from THz to X-rays.

REFERENCES

[1] A. Aryshev, S. Araki, M. Fukuda et.al, Development of advanced THz generation schemes at KEK LUCX facility, in Proc. PASJ, SUP020 (2013).

[2] D.Yu. Sergeeva, A.A. Tishchenko, X-Ray Smith-Purcell Radiation from a Beam Skimming a Grating Surface, Proc. FEL2014, Switzerland , Basel, p. 378, (2015), http://jacow.org/

[3] D.Yu. Sergeeva, A.A. Tishchenko, M.N. Strikhanov, UV and X-ray diffraction and transition radiation from charged particles bunches, Nucl. Instrum. and Methods B **309**, 189 (2013).

[4] D.Yu. Sergeeva, A.A. Tishchenko M.N. Strikhanov, UV and X-ray diffraction radiation for submicron noninvasive diagnostics, in Proc. of IPAC 2013, China, Shanghai, pp. 616-619 (2013), http://jacow.org/

[5] H.L. Andrews, F.B. Taheri, J.Barros et.al, Longitudinal profile monitors using Coherent Smith-Purcell radiation, Nucl. Instr. and Methods A **740**, 212 (2014).

[6] G. Doucas, M.F. Kimmitt, A. Doria, G.P. Gallerano et al., Determination of longitudinal bunch shape by means of coherent Smith-Purcell radiation, Phys. Rev. ST Accel. Beams **5**, 072802 (2002).

[7] J.H. Brownell, J. Walsh, G. Doucas, Spontaneous Smith-Purcell radiation described through induced surface currents, Phys. Rev. E **57**, 1075 (1998).

[8] D.Yu. Sergeeva, A.A. Tishchenko, M.N. Strikhanov, Conical diffraction effect in optical and x-ray Smith-Purcell radiation, Phys. Rev. ST Accel. Beams **18**, 052801 (2015).

[9] N. Potylitsina-Kube, X. Artru, Diffraction radiation from ultrarelativictic particles passing through a slit. Determination of the electron beam divergence, Nucl. Instrum. Methods Phys. Res., Sect. B **201**, 172 (2003).

[10] A.P. Kazantsev, G.I. Surdutovich, Radiation of a charged particle passing close to a metal screen, Sov. Phys. Dokl. **7**, 990 (1963).

[11] A.P. Potylitsyn, M.I. Ryazanov, M.N. Strikhanov, A.A. Tishchenko, *Diffraction Radiation from Relativistic Particles*, ISBN 978-3-642-12512-6, Springer, Berlin Heidelberg, Germany (2011).

ISBN 978-3-95450-134-2

COMMISSIONING OF THE DELTA POLARIZING UNDULATOR AT LCLS*

H.-D. Nuhn#, S.D. Anderson, R.N. Coffee, Y. Ding, Z. Huang, M. Ilchen, Y. Levashov, A.A. Lutman, J. MacArthur, A. Marinelli, S.P. Moeller, F. Peters, Z. Wolf, SLAC National Accelerator Laboratory (SLAC), USA
A.B. Temnykh, Cornell University (CLASSE), USA
G. Hartmann, J. Viefhaus, Deutsches Elektronen-Synchrotron (DESY), Germany
J. Buck, European XFEL GmbH (XFEL.EU), Germany
A.O. Lindahl, University of Gothenburg Department of Physics, Sweden

Abstract

The Linac Coherent Light Source (LCLS) generates linearly polarized, intense, high brightness x-ray pulses from planar fixed-gap undulators. While the fixed-gap design supports a very successful and tightly controlled alignment concept, it provides only limited taper capability (up to 1% through canted pole and horizontal position adjustability) and lacks polarization control. The latter is of great importance for soft x-ray experiments. A new 3.2-m-long compact undulator (based on the Cornell University Delta design [1]) has been developed and installed in place of the last LCLS undulator segment (U33) in October 2014. This undulator provides full control of the polarization degree and *K* value. Used on its own, it produces fully polarized radiation in the selected state (linear, circular or elliptical) but at low intensity. To increase the output power by orders of magnitude, the electron beam is micro-bunched by several (~10) of the upstream LCLS undulator segments operated in the linear FEL regime. As unavoidable by-product, this micro-bunching process produces moderate amounts of horizontally linear polarized radiation which mixes with the radiation produced by the Delta undulator. This unwanted radiation component has been greatly reduced by the reverse taper configuration, as suggested by E. Schneidmiller and M. Yurkov [2]. Full elimination of the linear polarized component was achieved through spatial separation combined with transverse collimation. The paper describes these and other methods tested during commissioning, It also presents results of polarization measurements showing high degrees of circular polarization in the soft x-ray wavelength range (500 eV-1500 eV).

INTRODUCTION

The design and measurement plans for the first 3.2-m-long Delta undulator for the LCLS were described in an FEL2013 paper [3]. Since then, these plans have been implemented close to the original schedule; the parameters listed in Table 1 of the FEL2013 paper all apply. Installation occurred in October 2014. (Figure 1) Beam based commissioning took place from October 2014 to May 2015. During this period operational techniques were developed that allowed to operate the Delta undulator at performance levels significantly exceeding expectations. Beam based commissioning was followed by the first user experiments in June 2015. The following will discuss quadrant tuning, magnet field mapping, and beam based commissioning. Tuning and magnetic field mapping made use of experience obtained in the course of construction and testing of the 0.3-m model at Cornell and the 1-m long prototype at SLAC.

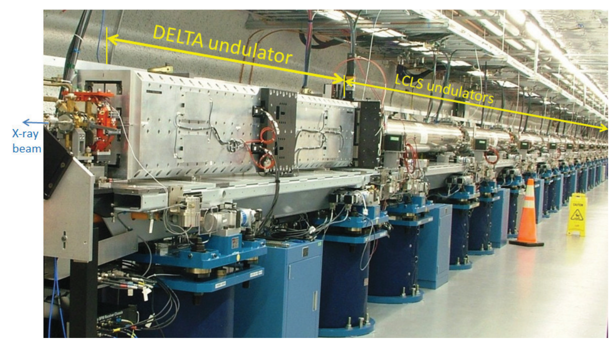

Figure 1: 3.2-m long LCLS Delta undulator installed at the end of the LCLS undulator line.

MAGNET BLOCKS

Each of the four rows of the Delta undulator contains 391 magnet blocks, four per period, arranged as Halbach array [4]. The first and last three blocks in each row are mounted at larger distances to the beam axis to accomplish end-field matching. Each magnet block is glued to an Al holder (Figure 2), which has been designed to also secure the magnet, mechanically, in case of glue

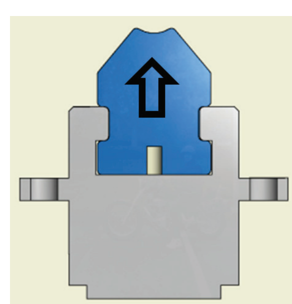

Figure 2: Ni coated PM blocks epoxied to Al holders. (Design by T. Montagne, SLAC)

* Work was supported by U.S. Department of Energy, Office of Basic Energy Sciences, under Contract DE-AC02-76SF00515. A.B. Temnykh is supported U.S. National Science Foundation awards DMR-0807731 and DMR-DMR-0936384
# nuhn@slac.stanford.edu

ISBN 978-3-95450-134-2

failure. 2000 regular mounted magnet block units and 60 individual blocks were purchased from AA International, Inc.

Block Sorting

After all blocks had been labelled, the amplitude and direction of their individual magnetic moments were measured with a Helmholtz coil at SLAC. The magnetic moment information was used to sort the blocks [5] before mounting them onto the carriers. The mounting fixture was designed to allow adjusting the position (distance to beam axis (y) and perpendicular direction (x)) of individual magnet blocks to enable virtual tuning (change of transverse magnet positions). Tuning was done separately for each quadrant.

Quadrant Tuning

For quadrant tuning, one of the two strongbacks was used as a support structure. For each quadrant the three carriers where mounted to the same location of the support strongback. The assembly was rotated such that the virtual beamline was positioned above the magnets (Figure 3).

Figure 3: Delta quadrant on the tuning bench.

A 2-sensor Sentron Hall probe was used to measure the magnetic field at the virtual beam axis as a function of the longitudinal (z) location. The mechanical positions of the magnets were measured and were used as constraints during virtual tuning to leave enough clearance for insertion of the vacuum chamber after the undulator was assembled (Figure 4).

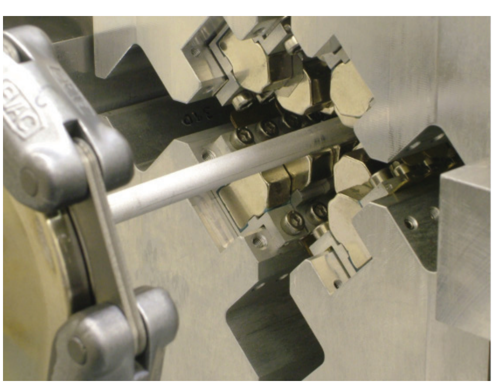

Figure 4: Delta undulator with vacuum chamber.

The measured fields of the four quadrants after tuning were combined numerically to a complete undulator and evaluated. The field integrals and phase shake values came out close to the tolerances in Table 2 of [3]. Errors due to mechanical tolerances and deformations of the strongbacks were introduced during final assembly because quadrants were mounted at strong back locations different from the ones used during tuning. These errors caused a significant increase in phase shake.

BENCH CHARACTERIZATION

After the Delta undulator was fully assembled (Figure 5), a number of measurements, both mechanical and magnetic, were performed to characterize the device and produce magnetic field maps vs. row positions.

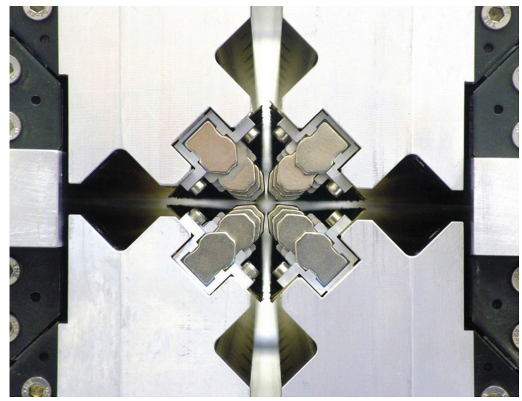

Figure 5: Front view of the fully assembled Delta undulator. Visible are the Al magnet block carriers and part of the precision rail system [6].

Mechanical Deformation Measurements

Dimensional changes of the strongback as function of row positions (different force directions) were measured with a coordinate measuring machine with relative position errors of less than 1 μm. As a result, the width and height of the Delta undulator change by about ±1.5 μm when changing the transverse forces (vertical or horizontal) between their extreme negative and positive amplitudes by adjusting row positions. This agrees well with the results of finite element modelling shown in Figure 6.

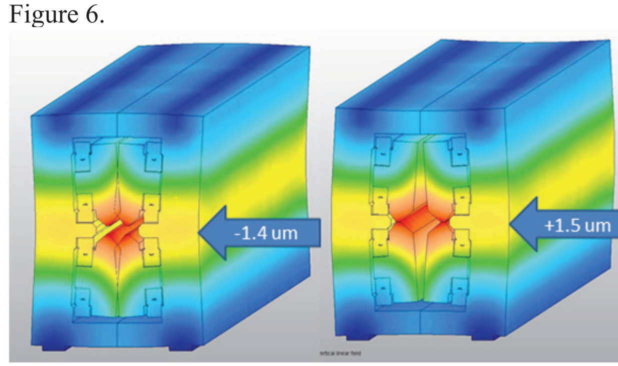

Figure 6: Shape deforming of Delta due to the transverse magnetic forces of ±15,000 N, according to finite element modeling.

ISBN 978-3-95450-134-2

Quadrant Moving and Position Control

The four magnet arrays shown in Figure 5 generate longitudinal forces of up to ±18,000 N between the quadrants depending on the relative longitudinal positions of all quadrants. Each quadrant can be moved independently in the longitudinal direction via so called drive units. Each of the four drive units consists of one spindle, roller nut, reduction gear and DC servo motor. The longitudinal position of the quadrants is measured relative to the common strongback using four inductive position sensors which feature a resolution of ±0.1 µm. The changing longitudinal force on the quadrants generates elastic deformations of the drive unit components, such as spindle, roller nut and bearings of up to ±75 µm for each quadrant. This effect is compensated by the position control system, which iterates the quadrant position setting by moving the four quadrants simultaneously until the four quadrant position readouts are matched with the demanded values. Operation experience has shown that quadrant position setting and control works reproducible within ±0.75 µm over the entire moving range of ±16 mm per quadrant and for all operated Delta configurations. The longitudinal elongation or contraction of the 3.2-meter-long magnet arrays due to the changing coupling forces was measured as ≤3.0 µm. One of the reasons that this small value is achievable comes from the fact that the drive units are positioned in the middle of Delta, which means one half of the magnet arrays is compressed while the other half is elongated at the same time. The drive unit position can be seen as the black part in the middle of Delta in Figure 7.

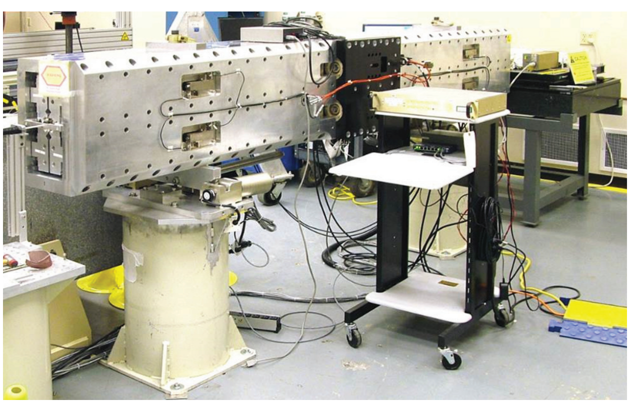

Figure 7: Delta undulator on the field mapping stand.

Magnetic Field Measurements

Magnetic field measurements were performed with a specially designed configuration of 6 Hall sensors packed as two 3-axis probes [3, 7, 8, 9]. Probe 1 was mounted close to the beam axis while probe 2 was transversely displaced by 200 µm, to allow estimates of the magnetic axis. The Hall probes were mounted at the end of a long carbon fiber tube which was guided through the device in an Al tube similar to the vacuum pipe used during operations. Figure 8 and Figure 9 show examples of B_x and B_y field measurements by probe 1 for the four main configurations (linear horizontal (LH), linear vertical (LV), circular left (CL) and circular right (CR)) at full strength.

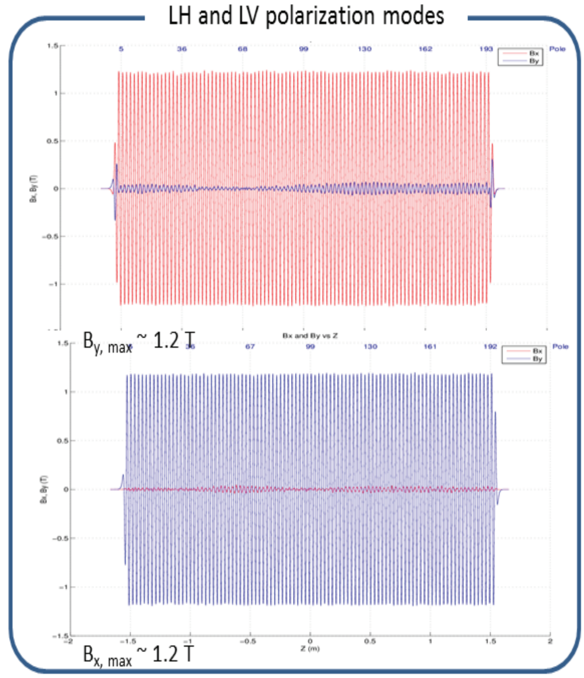

Figure 8: Undulator magnetic fields (red: $\boldsymbol{B_x}$, blue: $\boldsymbol{B_y}$) for the linear horizontal (LH) and linear vertical (LV) polarization modes at maximum *K* value.

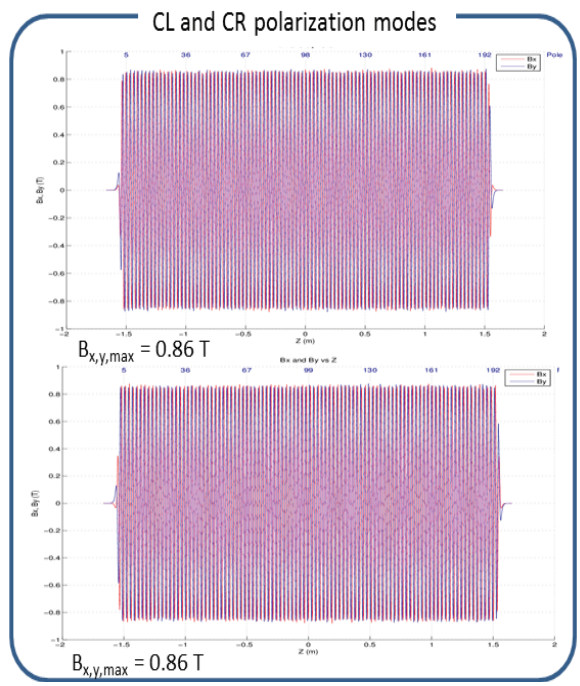

Figure 9: Undulator magnetic fields (red: $\boldsymbol{B_x}$, blue: $\boldsymbol{B_y}$) for the circular left (CL) and circular right (CR) polarization modes at maximum *K* value.

Field Integral Measurements

Field integral measurements were performed with a moving wire. The measurements were done for a number of row configurations. The information is used to

ISBN 978-3-95450-134-2

determine the change in beam steering. The dominant component comes from the environmental field (Earth field), which has not been corrected in this first version. Future versions will incorporate a correction coil or mu-metal shielding along the device to compensate these effects.

Magnetic Multipoles

In addition to field integrals, the moving wire was used to measure the quadrupole and skew quadrupole components in the Delta undulator.

While the quadrupole component came out close to expected, an unexpectedly large, first order skew quadrupole component was measured (0.55 T integrated gradient). Both components show only small dependence on *K* and polarization modes.

AFTERBURNER OPERATION

The spontaneous radiation that the Delta undulator produces from a regular electron bunch is quite small. It can be enhanced by several orders of magnitude by first micro-bunching the electrons at the optical wavelength in a SASE FEL process by regular LCLS undulator segments. This configuration of an undulator (micro-bunching undulator) operating in the linear regime followed by another undulator (in this case the Delta undulator) producing radiation with different characteristic is called afterburner configuration.

In this configuration, the Delta undulator produces significantly enhanced radiation amplitudes from the micro-bunched electron beam compared to the spontaneous radiation from the unmodified bunch.

Examples of different radiation characteristics used in afterburners are harmonics, i.e., the second undulator is tuned to a harmonic of the SASE undulator [10], and polarization, i.e., the second undulator produces a different polarization state than the SASE undulator segments. Different characteristics can be mixed.

In the afterburner configuration, the radiation produced by the micro-bunching undulator is often considered undesirable background when only the micro-bunching is needed to enhance the performance of the second undulator.

For the Delta undulator running to produce circular polarized radiation, schemes have been developed to minimize this background component. Those schemes include crossed polarized undulators, reverse taper, and beam splitting. They are explained in some detail, below.

Regular Afterburner

The Regular Afterburner scheme was the first scheme proposed for the Delta undulator. In all afterburner schemes, it is necessary to adjust the number of micro-bunching undulators, in order to balance the micro-bunching output and energy spread generated during the SASE process. (Figure 10 shows ten LCLS undulator segments being used in this example). A fine adjustment can be achieved by slightly detuning the first of those micro-bunching undulators. A minimum taper is applied (Figure 10) just enough to compensate for energy loss from spontaneous radiation and wakefields.

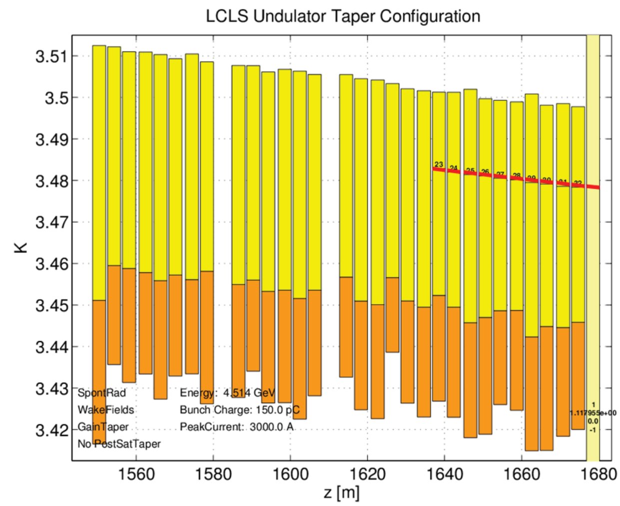

Figure 10: *K* values of the LCLS micro-bunching undulators segments for Delta operation in regular afterburner mode.

The efficiency of an afterburner configuration can be tested using a *K* resonance scan in which the *K* value of the Delta undulator is changed while the polarization mode is kept constant (Figure 11).

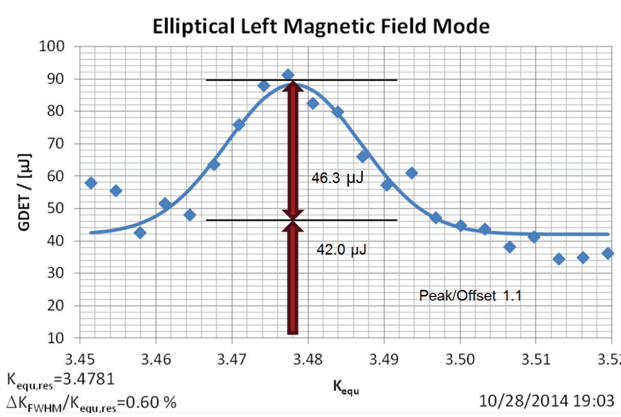

Figure 11: Delta resonance scan in elliptical left magnetic field mode (elliptical right polarization) in regular afterburner configuration.

In the scan, the x-ray intensity, measured by the gas detector or Direct Imager, is plotted against the *K* value, as derived through row positions using field mapping data. The scan results can be fitted by a Gaussian sitting on top of a slowly varying background. The ratio of the amplitude of the fitted Gaussian to the average amplitude of the background is called the contrast ratio.

Contrast ratios between 1 and 2.5 were achieved in this mode, depending on photon energy. The resonance scans also help determining the *K* values at which the Delta undulator is resonant to the micro-bunching undulators.

The degree of polarization can also be improved, following a proposal by Geloni et al. [11], by introducing a large (~20 m) spacing between the SASE and the Delta undulators and inserting slits in front of the Delta to

ISBN 978-3-95450-134-2

remove some of the diverging SASE radiation. This has not yet been tested on the Delta due to resource limitations and damage concerns.

Crossed Polarized Undulators

The crossed polarized undulator scheme produces circular polarized radiation by superposing the horizontally linear polarized radiation of the micro-bunching undulators with the radiation produced by the Delta undulator running in vertically linear polarization mode [12]. In this scheme, the radiation produced in the micro-bunching process is not considered undesirable background but is utilized. It is important to adjust the number of micro-bunching undulators to equalize the strength of their radiation and that produced by the micro-bunched electron beam in the Delta undulator.

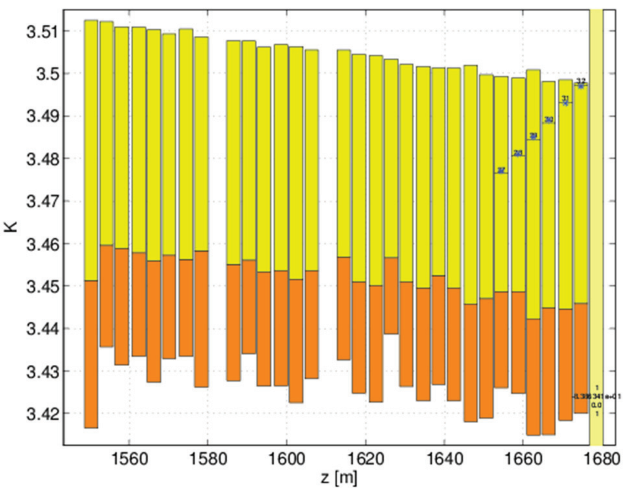

Figure 12: *K* values of the LCLS micro-bunching undulators segments for Delta operation in reverse taper mode.

A phase shifter in front of the Delta undulator is needed to adjust the phase between the two radiation components and thus the polarization mode (right circular, left circular, elliptical). A permanent magnet phase shifter was developed as part of the Delta project and installed just in front of the Delta undulator. It has been used to control the phase between the two radiation components (i.e., radiation of the micro-bunching undulator vs. radiation from the Delta undulator).

In the crossed polarized undulator scheme, the vertical polarized light produced from the spiky micro-bunching structure of the electron beam in the Delta undulator needs to be combined with the light produced during the micro-bunching process. Even though the total intensity of the horizontal and vertical components are about the same in the experiment, the time-dependent x-ray profiles can be quite different from horizontal to vertical since some parts of the bunch reach saturation much faster than other parts. As the experiment is conducted in the SASE mode, different time slices of the x-ray pulse will have different degrees of circular polarization. Due to the lack of any phase relationship among SASE spikes. The varying degrees of polarization along the SASE pulses will cause unpolarised radiation. Preliminary studies show that only relatively low intensity levels and low polarization degrees have been obtained with the cross undulator scheme with the Delta undulator. The degree of polarization in this scheme can be improved with a more-uniform electron bunch and increased temporal coherence [13].

Reverse Taper

The reverse taper scheme suggested by E. Schneidmiller and M. Yurkov [2] is an improvement of the afterburner scheme. By reversing the sign of the taper, i.e. by increasing the *K* values of the undulator segments instead of decreasing them along the undulator line (Figure 12), micro-bunching can built up with significantly reduced radiation amplitude. This method, which is described in more detail by MacArthur et al. [14] is more dependent on beam energy spread than the regular afterburner mode. Figure 13 shows the image of the 710 eV x-ray pulse produced with the reverse taper method. The image was taken with the Direct Imager, which is located about 88 m downstream of Delta undulator. It shows the combination of circular polarized Delta radiation (480 uJ) and linearly polarized radiation from the micro-bunching undulator segments (30 uJ).

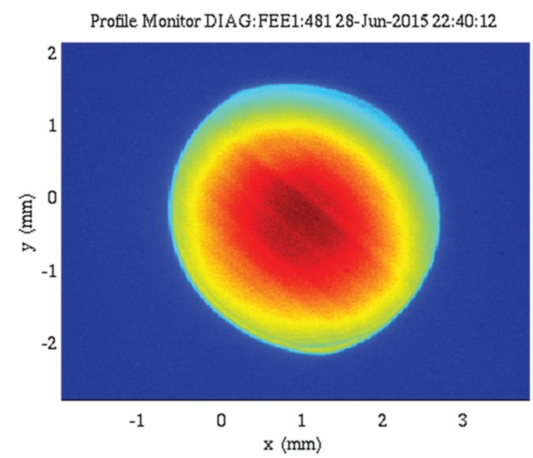

Figure 13: X-ray pulse image at 710 eV on Direct Imager in reverse taper contribution.

Beam Splitting

Beam splitting is a way of supressing the background component from the micro-bunching process. It is done by kicking the electron beam before entering the Delta undulator causing the electron beam and the background radiation beam to enter the Delta undulator under different angles. This beam kicking is controlled by the regular vertical corrector that is integrated in the quadrupole located at the end of the previous girder. The Delta undulator is detuned to be resonant to the off-axis component of the background radiation that still overlaps with it (Figure 14). Since there are about two gain lengths in the Delta undulator in the soft x-ray regime, simulations show that the micro-bunching orientation is readjusted to produce coherent radiation in the kicked direction. Detailed discussions of this method will be published elsewhere.

ISBN 978-3-95450-134-2

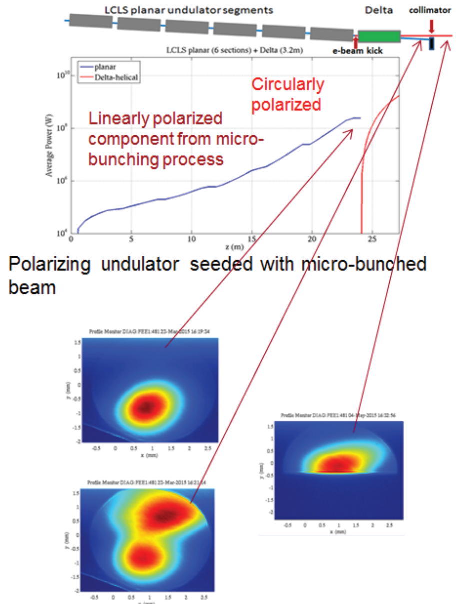

Figure 14: Beam splitting and collimation pushes degree of circular polarization close to 100 %.

POLARIMETER

The first measurements of the polarization degree of the radiation produced by the Delta undulator were done with a polarimeter developed at DESY [15], which is based on an array of 16 independently working time-of-flight spectrometers (TOF) aligned perpendicular to the plane of light propagation. The device measures the degree of linear polarization

$$P_{lin} \propto \sqrt{\frac{s_1^2 + s_2^2}{s_0^2}} \tag{1}$$

on a shot-by-shot basis. The equation is written in terms of the Stokes parameters, which are defined as

$$\begin{aligned} s_0 &= I_x + I_y \\ s_1 &= I_x - I_y \\ s_2 &= I_{45°} - I_{-45°} \\ s_3 &= I_{RCP} - I_{LCP} \end{aligned} \tag{2}$$

with

$$s_0^2 \geq s_1^2 + s_2^2 + s_3^2. \tag{3}$$

The equal sign applies if the light is fully polarized. Only in this case can the degree of circular polarization be deduced from P_{lin}

$$P_{circ} = \frac{|s_3|}{s_0} = \sqrt{1 - \frac{s_1^2 + s_2^2}{s_0^2}} = \sqrt{1 - P_{lin}{}^2}. \tag{4}$$

The assumption that that the pulse is fully polarized is expected to be quite accurate in the beam splitting scheme. In the crossed polarized scheme, the unpolarized component can be quite significant, as has been measured in this experiment, and the degree of circular polarization cannot be deduced from the measured degree of linear polarization according to equation (3).

The TOF polarimeter was used to measure the circular dichroism of sidebands in molecular oxygen in a two color scheme, allowing the direct measurement of a high degree of circular polarization for the regular and reverse taper schemes [16].

Table 1: Performance Overview over Afterburner Schemes

Scheme	E_{circ}/E_{lin}	P_{lin}	P_{circ}	E_{xray} (μJ)
Crossed Polarization			low	50
Regular Afterburner		0.5	0.87	50
Reverse Taper		0.3	0.96	480
Split Beams	≳100		~1	220

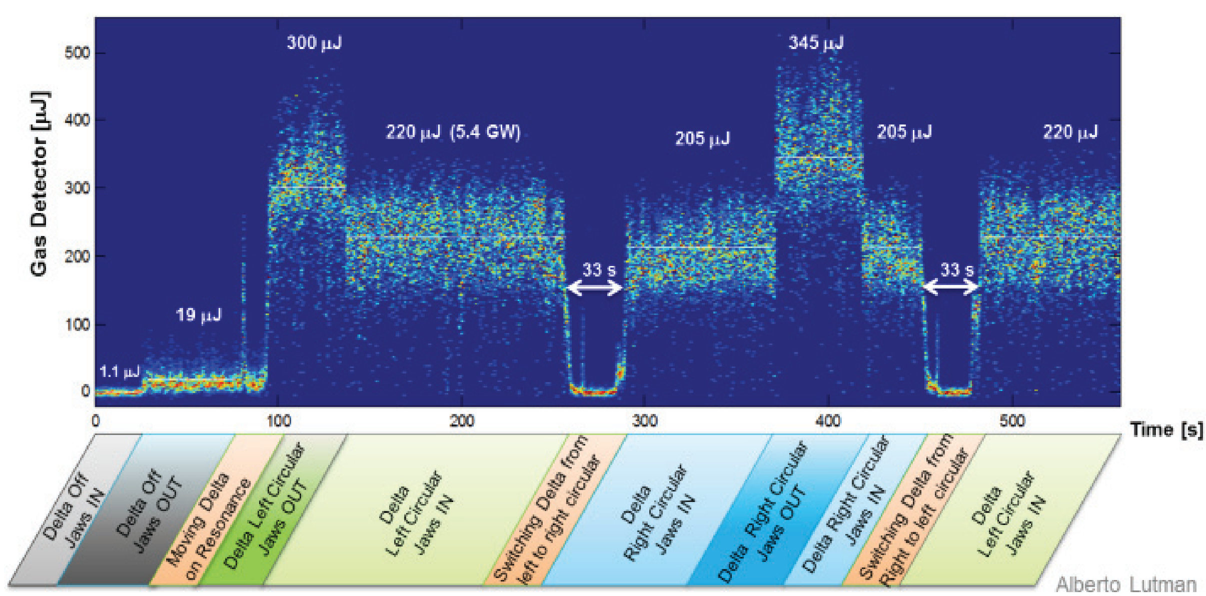

Figure 15: Delta polarization switching during operation.

ISBN 978-3-95450-134-2

USER EXPERIMENTS

The first user experiments were carried out in June 2015 in split beams mode [17, 18]. The effects of the difference between right and left circular polarized radiation produced by the Delta undulator using the beam splitting scheme was measured by x-ray magnetic circular dichroism (XMCD). It was confirmed that the degree of circular polarization is very close to 100%. Figure 15 shows the intensity during polarization switching as a function of time. The first part shows the background at 1.1 uJ with the collimators (Jaws) inserted. The next part shows the linear polarized radiation produced by the micro-bunching undulators at 19 uJ with the reverse taper scheme. When the Delta undulator is turned to resonance in left circular mode it adds 281 uJ to a total of 300 uJ. When the collimator jaws are inserted to remove the linear polarized component some of the circular polarized Delta light is cut in the process as well. The intensity drops to 220 uJ. Switching the Delta undulator from left to right circular polarization mode takes 33 s and generates a quite similar intensity (205 uJ). Later, switching back to left circular polarization mode takes the same time and reproduces the intensity quite well.

LESSONS LEARNED

Quadrants should not be moved to different support structures after tuning. Earth field compensation coils or mu-metal shielding along the Delta undulator should be included into the design. A small correctional skew quadrupole should be added in line with the Delta undulator.

FUTURE PLANS

Different beam modes have been tested when operating the Delta undulator. For example, two pulses with different color and polarization (for instance linear and circular) arriving with adjustable time delay have been created and will be reported in a separate publication. SLAC is developing a stronger version of the Delta undulator to be operated in the LCLS-II SXR beamline. The present plan is to produce up to three Delta undulators to be installed at the end of the SXR line.

ACKNOWLEDGEMENTS

We like to thank Leif Glaser, Frank Scholz, Jörn Seltmann, Ivan Shevchuk (DESY, Hamburg, Germany) and Jan Grünert (European XFEL) for providing the polarimeter and excellent support with running the device during Delta machine development shifts.

REFERENCES

[1] A. B. Temnykh. “Delta undulator for Cornell energy recovery linac.” In: Phys. Rev. ST Accel. Beams 11 (12 Dec. 2008), p. 120702.

[2] E.A. Schneidmiller, M.V. Yurkov, “Obtaining high degree of circular polarization at X-ray FELs via a reverse undulator taper”, arXiv:1308.3342 [physics.acc-ph].

[3] H.-D. Nuhn, S. Anderson, G. Bowden, Y. Ding, G. Gassner, Z. Huang, E.M. Kraft, Y. Levashov, F. Peters, F.E. Reese, J.J. Welch, Z. Wolf, J. Wu, A.B. Temnykh, “R&D Towards a Delta-Type Undulator for the LCLS,” *FEL2013*. SLAC-PUB-15743.

[4] K. Halbach, “Permanent Magnet Undulators,” Journal de Physique Colloques, 1983, 44 (C1), pp.C1-211-C1-216 <10.1051/jphyscol:1983120> <jpa-00222549>.

[5] Z. Wolf, "Magnet Block Sorting for the Delta Undulator" LCLS-TN-13-1.

[6] J.SCHNEEBERGER Maschinen AG, Switzerland.

[7] Z. Wolf, "Hall Element Angle Calibrations for the Delta Undulator" LCLS-TN-13-10.

[8] Z. Wolf, "Calculations of Fields on the Beam Axis of the Delta Undulator" LCLS-TN-13-11.

[9] Z. Wolf, "A Magnetic Measurement Plan for the Delta Undulator" LCLS-TN-13-4.

[10] H. D. Nuhn et al., “Characterization of Second Harmonic Afterburner Radiation at the LCLS”, in Proceedings of the 32nd International Free Electron Laser Conference (FEL2010), Malmo, Sweden (2010).

[11] G. Geloni, V. Kocharyan, E. Saldin, "Improvement of the crossed undulator design for effective circular polarization control in X-ray FELs", arXiv:1101.4085 [physics.acc-ph].

[12] K.-J. Kim, “A Synchrotron Radiation Source with Arbitrarily Adjustable Elliptical Polarization,” Nucl. Instr. Meth. 219 (1984) 425.

[13] E. Ferrari, “Single shot polarization characterization of XUV FEL pulses from crossed polarized undulators,” to be published in Nature Scientific Report, 2015.

[14] J. MacArthur, A. Marinelli, A.A. Lutman, H.-D. Nuhn, Z. Huang, “Energy spread constraints on field suppression in a reverse tapered undulator”, to be published in this conference.

[15] M. Ilchen, L. Glaser, F. Scholz, P. Walter, S. Deinert, A. Rothkirch, J. Seltmann, J. Viefhaus, P. Decleva, B. Langer, A. Knie and A. Ehresmann, M. Braune, G. Hartmann, A. Meissner, L. Tribedi, M. AlKhaldi, O. Al-Dossary, and U. Becker, “Angular Momentum Sensitive Two-Center Interference,” Phys. Rev. Lett. 112 023001 (2014).

[16] G. Hartmann et al. to be published.

[17] W. Schlotter et al. to be published.

[18] H. Dürr et al. to be published.

ISBN 978-3-95450-134-2

PHOTON DIAGNOSTICS AND PHOTON BEAMLINES INSTALLATIONS AT THE EUROPEAN XFEL

Jan Grünert, Andreas Koch, Naresh Kujala, Wolfgang Freund, Marc Planas, Florian Dietrich, Jens Buck, Jia Liu, Harald Sinn, Martin Dommach, Serguei Molodtsov, European XFEL GmbH, Albert-Einstein-Ring 19, 22761 Hamburg, Germany

Abstract

The European X-ray Free-Electron-Laser (XFEL.EU) is a new a 4th generation light facility which will deliver radiation with femtosecond and sub-Ångström resolution at MHz repetition rates, and is currently under construction in the Hamburg metropolitan area in Germany. Special diagnostics [1,2] for spontaneous radiation analysis is required to tune towards the lasing condition. Once lasing is achieved, diagnostic imagers [3], online monitors [4], and the photon beam transport system [5] need to cope with extreme radiation intensities. In 2015 the installation of machine equipment in the photon area of the facility is in full swing. This contribution presents the progress on final assemblies of photon diagnostics, the installation status of these devices as well as of the beam transport system, and recent design developments for diagnostic spectrometers and temporal diagnostics.

CONTENTS

This paper starts with a brief overview of the photon part of the European XFEL facility, outlines the photon diagnostics devices, details on the current status of the assembly of final devices. It continues with the status of the installations of photon diagnostics and beam transport system in the tunnels. Some recent design developments for advanced diagnostics are presented and finally, a schedule outlook is given.

INTRODUCTION

General Facility Layout

The general layout of the photon part of the European XFEL facility is shown in Fig.1 and is described in more detail elsewhere, e.g. in [5]. There are three undulators, of which the two called SASE1 and SASE2 provide hard X-ray FEL radiation up to 24keV in the fundamental, while SASE3 caters the soft X-ray domain below 3keV (SASE means self-amplified spontaneous emission). The photon diagnostics and beam transport system is located in all photon tunnels indicated in orange, called XTD1 through XTD10. The tunnels lead to the experimental hall XHEXP1, where in the startup phase there will be six experimental endstations. As an example for the beam transport and diagnostics layout, Fig. 2 shows the elements in the SASE1 beamline inside the tunnels XTD2 and XTD9 as well as shaft building XS3.

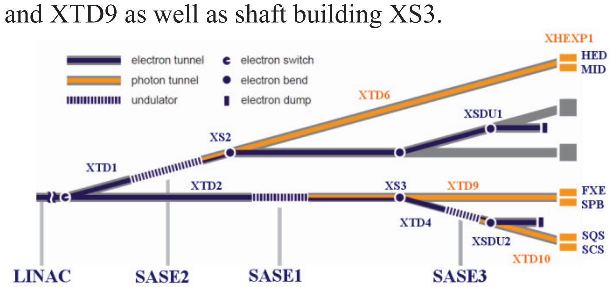

Figure 1: General facility layout, photon part

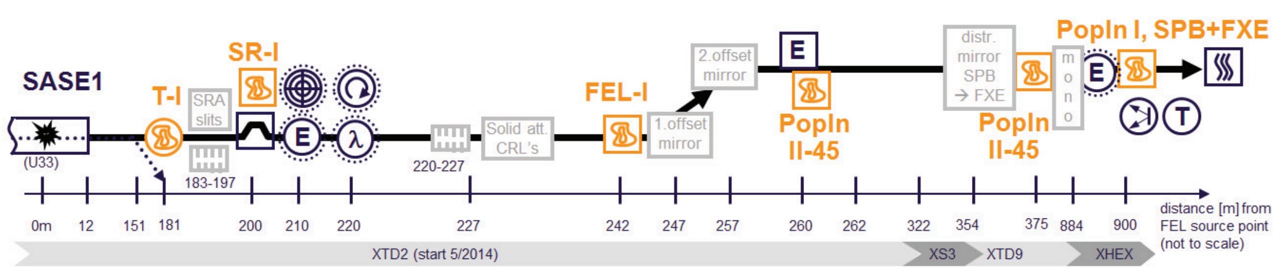

Figure 2: SASE1 beamline as an example for beam transport and diagnostics layout. Elements in the SASE1 beamline inside the tunnels XTD2 and XTD9 as well as shaft building XS3 are shown. Beam transport and optics elements are in grey, diagnostic imagers in orange, other diagnostics in black. From source to experimental hall, there are the transmissive imager (T-I), the synchrotron radiation absorber (SRA), the K-Monochromator with its spontaneous radiation imager (SR-I), the gas based online systems X-ray Gas Monitor (XGM) and PhotoElectron Spectrometer (PES) surrounded by differential pumping systems, the solid attenuators and Compound Refractive Lenses (CRLs), the FEL imager (FEL-I), the two offset mirrors, the MCP-based detector (denoted "E" here), a pop-in monitor type II-45°, the distribution mirror to switch between SPB and FXE endstation, another pop-in monitor type II-45°, a crystal monochromator, another XGM with its differential pumping, plus advanced diagnostics for timing and wavefront in the experimental endstation. Not shown is the HiREX spectrometer which was now added to the layout just upstream of the distribution mirror.

ISBN 978-3-95450-134-2

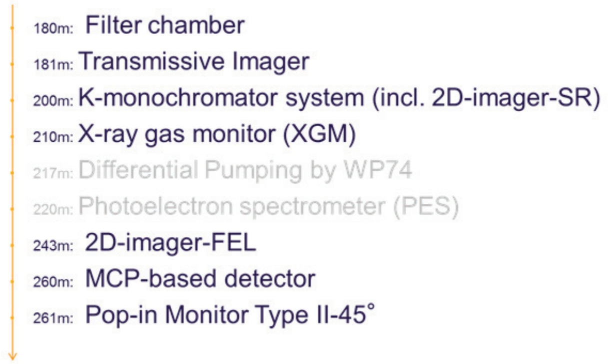

Figure 3: Sequence of diagnostics devices in the first equipped tunnel XTD2.

The sequence of diagnostics devices in the first equipped tunnel XTD2 (SASE1) is illustrated in more detail in Fig. 3. The device positions are given as a distance to the (theoretical) radiation source point in the third last undulator segment.

Timeline of Photon Diagnostics

2014

- Final assembly of first UHV-chambers: Imagers, K-mono, XGM (SASE1), PES (SASE3)
- Tunnel installation of first support structures (XTD2): Concrete pedestals and grouted steel pillars

2015

- Final assembly and tunnel installation of systems for SASE1 and SASE3
- Detailed design and production of the HiReX spectrometer, the modified PES for hard X-rays, and the Exit Slit and SR-imager-2D
- DAQ&Control System preparation, cabling, technical commissioning

2016

- Installation of remaining systems in SASE3
- Production/assembly/installation of SASE2 systems.

Status of Photon Diagnostics (WP74) in 2015

Several devices are built in-house at WP74: the 2D-imager-FELs, the K-Monochromators, the photo electron spectrometer PES, and the differential pumping stations. Pop-in monitors were and HiREX spectrometer as well as the 2D-imager-SR is in commercial production (after design by European XFEL), XGM and transmissive imager are produced and provided by DESY groups, the MCP-based detectors are provided by JINR at Dubna, Russia. The following devices are currently in the design and prototyping stage: Exit Slit Imager and Timing Diagnostics.

Diagnostics installations started in 2014 with the construction of concrete bases and installation of steel support pillars in tunnel XTD2. In 2015, the installation of the vacuum systems started with imagers and the K-monochromator for SASE1.

Perspectives until Fall 2015

The remaining diagnostics vacuum chambers destined for XTD2 will be installed, and also in XTD9 as soon as the tunnel conditions allow it in terms of humidity, cleanliness and infrastructure. Continuously pumped systems like the XGM require at least electrical power and pressurized air to be available, ideally also network for online device protection and monitoring.

Most SASE3 / XTD10 devices will be produced, the detailed designs for the HiREX and Exit Slit Imager will be finalized, the first 2D-imager-SR will be produced, and more diagnostics activities occur in the domain of temporal diagnostics.

Of all mentioned diagnostics devices, most are already required or used during the initial beam commissioning with spontaneous radiation before First Lasing, except systems that are only sensitive to XFEL radiation like the gas based systems which are crucial as soon as First Lasing is achieved.

PHOTON DIAGNOSTICS DEVICES

A detailed description of all photon diagnostics devices is given in [1] and in the Conceptual and Technical Design Documents, e.g. [2-4]. Here, we'll focus on the achieved status for the SASE1 devices and give some details about their implementation.

For all devices, before installation in the tunnel, particular emphasis was put on vacuum tests (RGA spectra) for conformity to the stringent beam transport UHV requirements and on checking all control items like motors and encoders for their correct performance. Also, all device-local patch panels were installed, wired and checked.

Transmissive Imager

This most upstream diagnostics device serves as a first monitor during initial commissioning. We use a slightly modified imager from the electron beam system, there called a standard „OTR-C" imager, and modified only the target arm to record photons instead of electrons. This modified scintillator holder was designed, produced and delivered to the DESY group that provides this imager.

K-Monochromator System

This system consists logically of a filter chamber, the actual K-monochromator (a two crystal, 2-bounce or 4-bounce monochromator for spontaneous radiation), and one imager for spontaneous radiation.

The filter chamber can be used for energy calibration of the K-mono by insertion of thin metal foils such as aluminum, chromium, copper, nickel, or molybdenium. The filter chamber holds up to 5 filter foils. Its alignment base plates were now designed and produced, all assembled and tests completed, RFI.

The K-mono device for SASE1 was designed, produced, assembled, tested and installed in XTD2, more details about this device see [2] (Fig. 4). Now the next two devices are under clean room assembly.

ISBN 978-3-95450-134-2

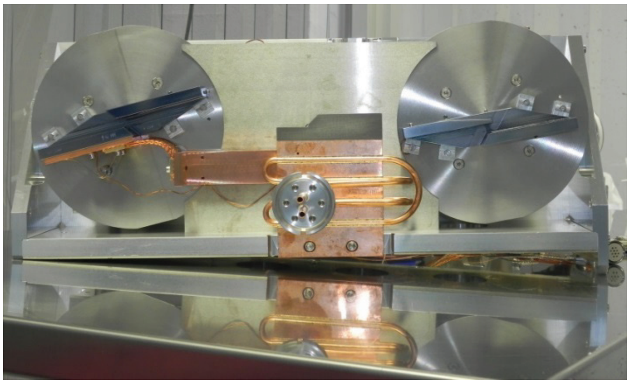

Figure 4: In-vacuum parts of the K-mono. Two Huber goniometers carry each a channel-cut silicon crystal, and the upstream crystal is water cooled.

The 2D-Imager-SR was fully designed down to workshop drawings in-house including its particular optical setup for optimum light collection of the faint spontaneous radiation of single undulator segments at large distances (Fig. 5). Its design contains YAG:Ce and Gd_2O_2S:Pr scintillators and a mirror on a manipulator in a UHV chamber, out-of-vacuum tandem lens optics (Leica Summilux 1.4/50 and Schneider Cinelux Ultra 2/110, f/0.95), a motorized iris, and a low noise camera (Photonic Science sCMOS, 16 bit, noise 0.92 e^- rms). This imager is in production at a commercial workshop and will be assembled at European XFEL in fall 2015.

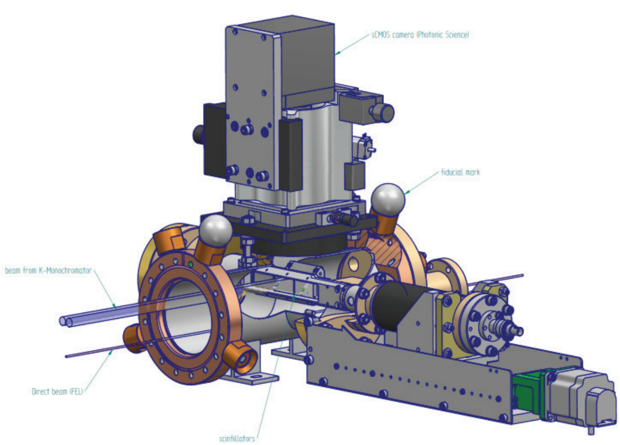

Figure 5: 2D-Imager-SR design sketch. The device can image the beam from the K-mono (indicated by the upper two larger diameter spontaneous radiation beams), or the direct beam when the K-Mono is not inserted (lower thin beam, typically FEL radiation), depending on its vertical positioning. The scintillators are inserted horizontally.

Pop-in Monitors

There are four types of these alignment monitors, details in [3]. The vacuum and motion parts of these monitors were designed in detail, produced and assembled by the company JJ X-ray, Denmark. Final assembly of the scintillators and mirrors is done at European XFEL as well as final vacuum and motor checks, see Fig. 6. The first such monitor was installed in XTD2 in April 2015, and more devices are continuously prepared for installation. In total, the facility will have 14 pop-in monitors.

Figure 6: Pop-in monitor type II-45° during final assembly.

MCP-based Detector

Each SASE beamline includes one monitor for SASE search and optimization, based on multi-channel plates (MCPs). This is a contribution by JINR, Dubna, Russia. All three systems were produced and vacuum tested. They each contain several integrating MCPs and one imaging MCP which is observed from outside the vacuum by an optical setup, in which a camera/lens combination sits on a motorized rail for focusing adjustment. The MCPs were checked without beam: signals were recorded during illumination with a UV light source and secondly by observing rare signal events caused by ions from the ion pump, see Fig. 7.

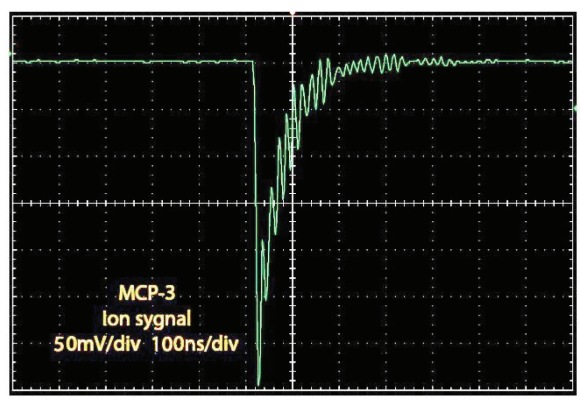

Figure 7: MCP-based detector signals

X-Ray Gas Monitor (XGM)

There are six XGMs in the facility to monitor online the beam position and intensity of the FEL radiation during beam delivery to the experiments. Each XGM consists of four vacuum chambers on a common girder, see Fig. 8, and can record fast shot-to-shot beam position and intensity as well as absolutely calibrated intensity. The latter is recorded slower but the shot-to-shot intensity is internally cross-referenced. Distribution of the XGMs: there is one XGM per beamline in the direct beam from

ISBN 978-3-95450-134-2

the undulator, upstream of offset mirrors. Additionally there is an XGM near the end of the photon tunnels in the SPB and HED branch and a last XGM in the SCS hutch. This system is contributed by the Tiedtke group (DESY), who have so far produced four devices and calibrated them with synchrotron radiation at the PTB, Berlin. Two more XGMs will be ready for installation beginning 2016.

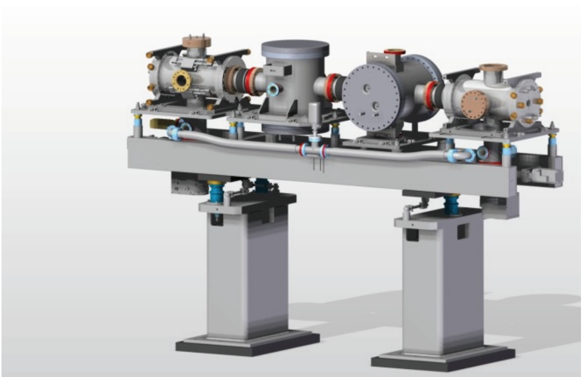

Figure 8: XGM model as built.

Photoelectron Spectrometer (PES)

This device [4] is for shot-to-shot spectrum and polarization monitoring. The detailed design for the SASE3 device was completed as well as for the fully motorized support. The SASE3 device was fully assembled and very successfully tested with X-ray FEL beam at AMO/LCLS which will be reported elsewhere.

This device was used in a scientific beamtime (PI Helml), a scientific in-house beamtime (PI Coffee), and for the commissioning of the DELTA undulator, see the presentation by J.Viefhaus in this conference. The SASE1 device requires development of modifications for hard X-ray application and will be therefor installed in a later installation phase. Hard X-ray High Resolution Single Shot Spectrometer (HiREX)

Hard X-ray High Resolution Single Shot Spectrometer (HiREX)

The HiREX, see Fig.9, will deliver high-resolution spectra during online beam operation, enabled by a transmissive grating of which the first order diffracted beam is sent on a bent crystal that disperses the spectrum on a flat linear detector. Various fixed bending radii and crystal reflections are planned to cover the hard X-ray range between 3 and 25keV, see Fig.10. The design documents explaining the physics and simulation results were completed [6] as well as the Technical Specifications Document for public tendering of the production, awarded in June. The detailed technical design is due in fall 2015 and one device will be installed in XTD9 in July 2016 for use in the SASE1 beamline.

Advanced Diagnostics

Prototype chambers are under construction for temporal diagnostics, mainly for two methods: spectral encoding for arrival time monitoring, and THz-streaking of rare gases for pulse duration monitoring.

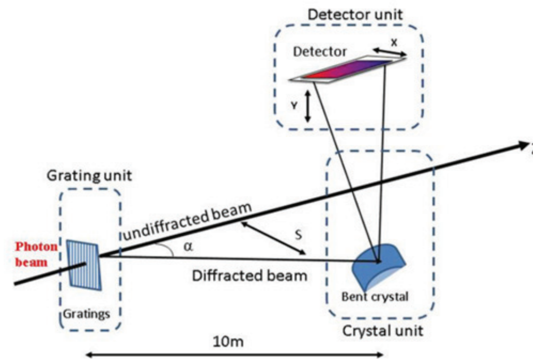

Figure 9: Schematic view of the HiREX setup.

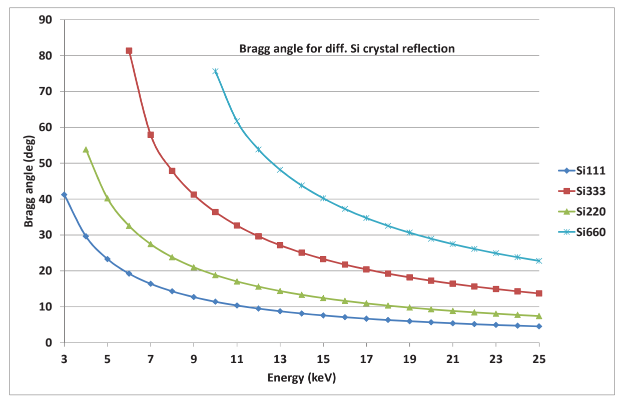

Figure 10: Bragg angles for the planned crystal reflections of the HiREX spectrometer in the hard X-ray range.

BEAM TRANSPORT INSTALLATIONS

The installation of the photon beam transport system started in 2014 when 140m of beamline in XTD2 became accessible for installation. The installations continued in 2015 with tunnel XTD9 where a huge length of 1050m had to be equipped, the larger part of this separated into two branch vacuum lines, leading to the SPB/SFX and the FXE instruments. Sections of 18m long vacuum pipes were mounted by joining three 6m pieces by orbital welding in the tunnel under clean room conditions. The remaining 20m of SASE1 beam transport in the connecting shaft building XS3 will be mounted last.

Large and heavy objects were mounted in the beamline, such as the supporting granites for the offset mirror chamber, see Fig. 11. Also, beam shaping devices like the compound refractive lenses (CRL) and the SRA were installed in XTD2. Not part of beam transport but inherently required for the operation, electronic racks were placed throughout the SASE1 tunnel area and started to get filled with control crates for the four Beckhoff loops controlling vacuum systems, motion control and encoders, equipment protection system (EPS) and backup loop.

ISBN 978-3-95450-134-2

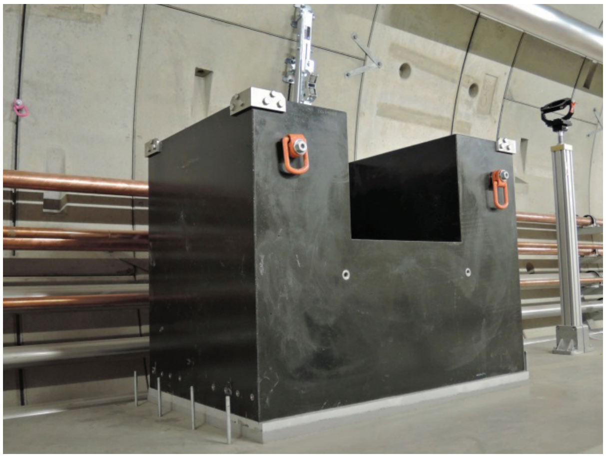

Figure 11: Support granite for the mirror chamber, installed on top of a concrete base.

The beam transport system now covers the entire SASE1 tunnel area, see Fig. 12 for a view of the many XTD9 support holders before installation of the vacuum pipes.

Figure 12: View into SASE1 tunnel XTD9.

SCHEDULE OUTLOOK

In 2015, the SASE1 vacuum and electrical installations will be finished, and the SASE3 installation starts including the mirror chamber and soft X-ray monochromator. The SASE3 detailed beam transport design was completed. The control system in SASE1 will be commissioned.

In 2016, more SASE1 installations are scheduled, including the hard X-ray monochromators, and the HiReX and PES spectrometers. SASE2 devices will be installed and SASE1 beam commissioning will start.

Finally, in 2017 the facility is ready for First Lasing and First Users!

CONLUSION

The final assembly and installation of the photon diagnostics and beam transport system for the European XFEL facility is on track for receiving beam end of 2016.

ACKNOWLEDGMENT

We would like to acknowledge all institutes and groups contributing to the presented work: E.Syresin and team at JINR, Dubna, Russia for the MCP-based detector work and measurements; K.Tiedtke group at FLASH/DESY for the XGM; the DESY team of J.Viefhaus at beamline P04 of PETRA3 for work on and experiments with the PES; C.David group at PSI, Switzerland for gratings of the HiREX spectrometer; A.Erko and J.Rehanek of HZB, Berlin contributed to the design of the K-monochromator and HiREX.

Also, we are grateful for the support to diagnostics implementation by other workpackages and groups in European XFEL such as WP73, the science groups, and the electronics groups CAS, AE, and ITDM.

REFERENCES

[1] J. Grünert, "Conceptual Design Report: Framework for X-Ray Photon Diagnostics at the European XFEL", XFEL.EU technical report TR-2012-003, April 2012.

[2] W. Freund, "The Undulator Commissioning Spectrometer for the European XFEL", DESY-2014-03060, XFEL.EU TN-2014-001-01.

[3] A. Koch et al., "Design and initial characterization of x-ray beam diagnostic imagers for the European XFEL", Proc. SPIE 9512, Advances in X-ray Free-Electron Lasers Instrumentation III, 95121R (May 12, 2015); doi:10.1117/12.2182463.

[4] J. Buck et al., "Time-of-flight photoemission spectroscopy from rare gases for non-invasive, pulse-to-pulse X-ray photon diagnostics at the European XFEL", Proc. SPIE 8504, X-Ray Free-Electron Lasers: Beam Diagnostics, Beamline Instrumentation, and Applications, 85040U (October 15, 2012); doi:10.1117/12.929805.

[5] H.Sinn et al., "Technical Design Report: X-Ray Optics and Beam Transport", December 2012, XFEL.EU TR-2012-006, doi:10.3204/XFEL.EU/TR-2012-006.

[6] J.Rehanek, N. Kujala, and J. Grünert, "Design Report Hard X-ray High-Resolution Single-Shot Spectro-meter (HX-HR-SSS)", December 2014, internal XFEL.EU report Alfresco Doc-ID: 13779761, available by request.

ISBN 978-3-95450-134-2

STATUS REPORT OF PAL-XFEL UNDULATOR PROGRAM

D.E. Kim*, Y.G. Jung, W.W. Lee, H.S. Kang, I.S. Ko, M.H. Cho,
H.G. Lee, S.B. Lee, B.G. Oh, H.S Suh, K.H. Park, PAL, POSTECH, Pohang, Korea
Suren Karabekyan, Joachim Pflueger, EU-XFEL, Hamburg, Germany

Abstract

PAL-XFEL is a SASE based FEL using S-band linear accelerator, photo cathode RF Gun, and hybrid undulator system for final lazing. The undulator system is based on EU-XFEL undulator design with necessary modifications. The changes include new magnetic geometry reflecting changed magnetic requirements, and EPICs based control system. The undulator system is in measurement and tuning stage targeting to finish installation within 2015. In this report, the development, tuning, measurement efforts for PAL-XFEL undulator system will be reported.

INTRODUCTION

The Pohang Accelerator Laboratory (PAL) has been developing SASE based light sources since 2011. The target wavelength is 0.1 nm for hard X-ray SASE radiation, with 10 GeV class S-band linear accelerator. For soft X-ray SASE, 3.0 nm FEL radiation using 3.15 GeV electron beam is assumed. To achieve this target, a few key components like low emittance (0.5 μm) photo cathode RF gun, and EU-XFEL style out vacuum undulator system are being developed [1]. For undulator system, there will be 18 undulators for hard X-ray line and 6 planar undulators with additional two EPUs (Elliptically Polarized Undulator) are expected for soft X-ray line. The EPUs will be used for polarization control at the last stages of lasing. The major parameters of the X-ray FEL and undulator line is slightly changed recently and the updated parameters are shown in Table 1. A minor changes were the magnetic gap and period. The gap was changed from old 7.2mm to 8.3 mm resulting period change from 24.4 mm to 26.0 mm maintaining 0.1 nm SASE lasing at 10 GeV electron beam energy. The number of required units for soft X-ray SASE line is estimated to be 6 units of 5 m long planar undulators with 2 additional EPUs. The major parameters of the undulator system is summarized in Table 1. And schematic layout of hard X-ray, and soft X-ray undulator lines are shown in Fig .1.

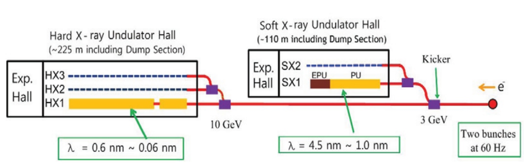

Figure 1: FEL undulator line plan of PAL-XFEL.

Table 1: Major Parameters of the PAL-XFEL Undulator System

Parameter	Unit	Value	Value
Undulator Line		HXU	SXU
Beam energy	GeV	10.0	3.15
Min gap	mm	8.30	8.30
Period	mm	26.0	35.0
Length	m	≃5.0	≃5.0
B_{eff}	T	0.812	1.016
K		1.973	3.321
Phase jitter	deg	< 7.0	< 7.0
Number		18+α	6+α

UNDULATOR SYSTEM

For the PAL-XFEL undulators, the EU-XFEL design and technology [2-4] was adopted and further developed. The EU-XFEL design is a well proven using standardization and optimization for mass serial production [3,4] and was successfully used for the production of 91 undulators for the EU-XFEL. The schematics and major subsystems are shown in Figure 2.

Following EU-XFEL, pole height tuning is used. The poles can be shifted by about ±150 μm in vertical direction and tilted by ±2 mrad using tuning studs and locking screws. This is a big advancement as compared to using conventional magnetic and/or non-magnetic shims. In contrast to shims, Pole Height Tuning is bi-polar and continuous. Magnetic shims are unipolar and only weaken poles. In addition they are only available in discrete steps. By using Pole Height Tuning an undulator can be readily assembled at a supplier. Provided that suitable a magnetic measurement facility is available the tuning is readily done in house.

At PAL a full scale prototype undulator was built. It is based on the EU-XFEL concept with some modification reflecting different magnetic periods and pole gaps. In addition, precision tilt meters were attached to the girders to monitor parallel motion. Unfortunately this prototype is based on the old magnetic periods of 24.4 mm and old magnetic gap of 7.2 mm. But it is, however, a good test bed to check the mechanical integrity and to develop the entire pole tuning schemes. The completed undulator was mechanically tested by installing precision external gap sensor by comparing the rotary encoder values and the actual gaps

POLE HEIGHT TUNING

For deeper analysis field measurements need to be analyzed. First, for each pole a local-K is defined for each pole using the following definition [5]. This is a half period field

* dekim@postech.ac.kr

ISBN 978-3-95450-134-2

integral around j-th pole of the field profile. Fluctuations of local K from the average describe the error. The difference of local K to the ideal K indicate error in the undulator field and by correcting local K to ideal K for each pole allows us to tune the undulator systematically.

The pole height corrections are calculated as described in ref. [6]. A linear system of equations is set up connecting the pole shift on a pole with index j to the local K change on a pole with index i. For HXU which has 191 periods, there are 382 poles resulting in a 382 by 382 system matrix. Since only three next nearest neighbors are used the matrix is diagonally dominant and there are only six side diagonals. This facilitates the solution and allows an iterative solution.

In Fig. 2, the calculated corrections from the measurement of as assembled undulator is shown in red circles. The blue circle represents that calculated pole height tuning from the measurement after 1st pole height tuning campaign. As shown in the figure, as assembled undulator requires maximum 40 μm corrections for each upper/lower magnet structures. After the 1st correction, the residual corrections are usually less than 5 μm which shows the impact and efficiency of the pole height tuning. The phase jitter of as assembled undulator is about 12-15 degrees. After the 1st implementation of the pole height tuning, the phase jitter reduces to 1-2 degrees.

The expected operating gap of the PAL-XFEL hard X-ray undulator (HXU) is between 8.3 mm to 12.5 mm producing 0.1 nm to 0.06 nm SASE radiation at 10 GeV e-beam energy. The undulator tuning gap is decided to be 9.5 mm balancing the errors for both extreme of the operating undulator gaps. Therefore, the HXU undulator is very optimal at the tuning gap, and deviates from the best condition as we move away from the tuning gap. In Fig. 3, the gap dependence of the phase jitter is shown. As can be seen in the Fig. 3, the phase jitter is lowest at the tuning gap and increases as we deviates from the tuning gap. But the phase jitters are within the requirements for all operating gaps. Note that in Fig. 3, phase jitter is shown up to 20 mm which is very large gap compared to the maximum operating gap.

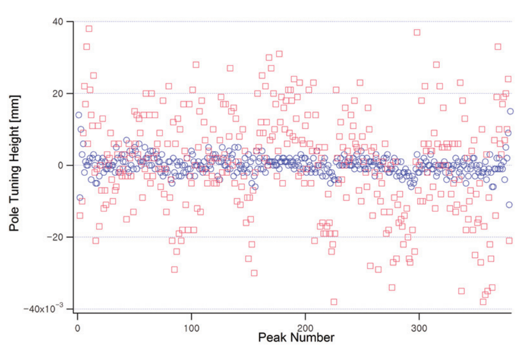

Figure 2: Calculated undulator pole height corrections. Red circles are correction data from as assembled. Blue circles are the calculated correction data based on the magnetic measurement after 1st pole height correction.

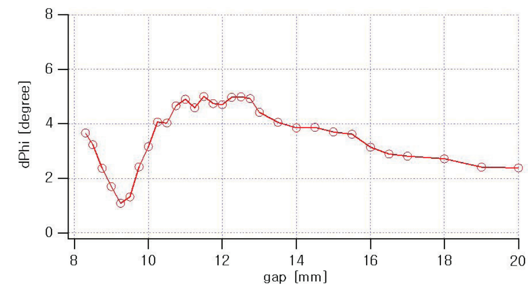

Figure 3: RMS phase jitter as a function of undulator gap. It's minimum at the tuning gap of 9.5 mm and increases as gap deviates from the tuning gap. The expected operating gap is from 8.3 mm to 12.5 mm.

In Fig. 4, the phase jitter distribution for several gaps are displayed. At tuning gap, the phase jitters are relatively flat and small. As gap deviates from the tuning gap, the phase jitter distribution shows typical S-structure which implies that the phase jitter error comes from the parabolic bending of the magnet structure. It's also evident that the polarity of the S-shape are opposite for minimum 8.3 mm gap and maximum operating gap of 12.5 mm. This means that the bending of the magnet structure is in opposite sign for minimum gap and maximum operating gap which is obvious from inspection. Also in Fig. 5, the orbits for several key gap within the operating gap range is shown.

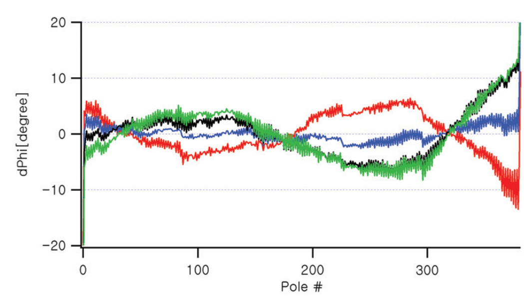

Figure 4: Phase jitters calculated at the several key gaps within the working gap ranges. The measured gaps are 8.3, 9.5, 11.0, 12.5 mm.

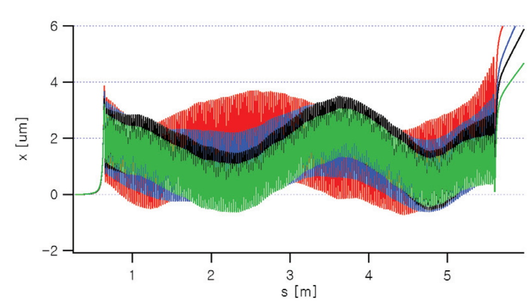

Figure 5: Selected x-orbits at undulator gaps g = 8.3 mm, 9.5 mm, 11.0 mm, and 12.5 mm.

ISBN 978-3-95450-134-2

Figure 6: Two undulators installed at the hard X-ray undulator hall. They are 1st undulator line and facing the wall.

CONCLUSIONS

PAL-XFEL is developing undulator system for its hard Xray undulator line, and soft undulator lines based on EU-XFEL undulator structure. Our modifications are redesign of the magnetic structure reflecting different magnetic gap, and periods including end sequences. Another modification includes the adaptation of the control system to EPICs.

An undulator prototype based on EU-XFEL design and modified for PAL-XFEL was built and tested. The local-K pole tuning procedure was developed and tested. For the field corrections the three next nearest neighbors were included into the correction signatures. Tuning was very effective, and a single iteration of pole height tuning could reduce the local-K fluctuations by one order of magnitude. The optical phase error at the tuning gap after pole height tuning is between 1 and 2 degrees. At the tuning gap, the undulator structure is well optimized. However, as we deviate from the tuning gap, the girder deforms in parabolic shape and the phase jitter shows typical S structure which is signature of the parabolic bending. For all operating gap range which is 8.3 mm to 12.5 mm for HXU undulators, the phase jitter meets the specification of 7 degrees. All other undulator properties, like entrance/exit kicks are also calculated from the magnetic measurements. All operation related data are tabulated, and fitted within the tuning gap range.

Currently, the measurement and correction procedures are setup and production measurements are going on for all undulators. And two undulators are installed in the undulator hall as shown in Fig. 6. Upto the end of Aug 2015, 8 undulators are expected to be ready for the HXU installation. With optimistic estimation, all 18 HXU undulators are expected to be installed in the undulator hall within 2015.

REFERENCES

[1] SwissFEL Conceptual Design Report, PSI Bericht Nr. 10-04 April 2012.

[2] Heung-Sik Kang, Jang Hui Han, Changbum Kim, Dong Eon Kim, Seung Hwan Kim, Heung Soo Lee, Ki-Hyeon Park, Sung-Ju Park, Tai-Hee Kang, In Soo Ko, "Current Status of PAL-XFEL Project", IPAC'13, May 2013, 2074-2076 (2013).

[3] M. Altarelli et al., "The European X-ray Free-electron Laser", Technical Design Report, ISBN 3-935702-17-5, 2006. http://www.xfel.eu/dokumente/technical_documents

[4] U. Englisch, Y. Li, J. Pflueger, "Tuning and Testing of the Prototype Undulator for European FEL", Proceedings of 34th Int. Free-Electron Laser Conf., Nara, 579-582 (2012).

[5] J. Pflueger, et. al. "Stats of the Undulator Systems for the European X-ray Free Electron Laser", Proceedings of the FEL2013, August 25-30, New York City, USA, p. 367-371 (2013).

[6] Y. Li, J. Pflueger, to be published in Journal of synchrotron Radiation.

ISBN 978-3-95450-134-2

List of Authors

Bold papercodes indicate primary authors

ISBN 978-3-95450-134-2

ISBN 978-3-95450-134-2

— L —

ISBN 978-3-95450-134-2

ISBN 978-3-95450-134-2

ISBN 978-3-95450-134-2

ISBN 978-3-95450-134-2

ISBN 978-3-95450-134-2

ISBN 978-3-95450-134-2

Institutes List

AIST
Tsukuba, Ibaraki, Japan
- Kuroda, R.
- Ogawa, H.
- Sei, N.
- Taira, Y.

Ankara University, Accelerator Technologies Institute
Golbasi / Ankara, Turkey
- Aksoy, A.A.
- Yavaş, Ö.

ANL
Argonne, Ilinois, USA
- Kim, K.-J.
- Kolodziej, T.
- Lindberg, R.R.
- Shu, D.
- Shvyd'ko, Yu.
- Stoupin, S.

Ariel University Center of Samaria, Faculty of Engineering
Ariel, Israel
- Einat, M.
- Kanter, M.
- Lasser, Y.
- Lurie, Yu.
- Yahalom, A.

Ariel University
Ariel, Israel
- Balal, N.
- Borodin, D.
- Bratman, V.L.
- Damti, A.
- Friedman, A.
- Magori, E.
- Vashdi, Y.

Assiut University
Assiut, Egypt
- Bakr, M. A.

AUT
Tehran, Iran
- Maraghechi, B.
- Salehi, E.

BERGOZ Instrumentation
Saint Genis Pouilly, France
- Bergoz, J.F.
- Stulle, F.

BINP SB RAS
Novosibirsk, Russia
- Arbuzov, V.S.
- Chernov, K.N.
- Davidyuk, I.V.
- Dementyev, E.N.
- Dovzhenko, B.A.
- Getmanov, Ya.V.
- Gudkov, B.A.
- Knyazev, B.A.
- Kolobanov, E.I.
- Kondakov, A.A.
- Kozak, V.R.
- Kozyrev, E.V.
- Kubarev, V.V.
- Kulipanov, G.N.
- Kuper, E.A.
- Kuptsov, I.V.
- Kurkin, G.Y.
- Medvedev, L.E.
- Miginsky, S.V.
- Motygin, S.V.
- Osipov, V.N.
- Ovchar, V.K.
- Petrov, V.M.
- Pilan, A.M.
- Popik, V.M.
- Repkov, V.V.
- Salikova, T.V.
- Scheglov, M.A.
- Sedlyarov, I.K.
- Serdobintsev, G.V.
- Serednyakov, S.S.
- Shevchenko, O.A.
- Skrinsky, A.N.
- Tararyshkin, S.V.
- Tcheskidov, V.G.
- Tribendis, A.G.
- Vinokurov, N.
- Vobly, P.

BNL
Upton, Long Island, New York, USA
- Altinbas, Z.
- Babzien, M.
- Belomestnykh, S.A.
- Brown, K.A.
- Brutus, J.C.
- Chubar, O.V.
- Curcio, A.J.
- Di Lieto, A.
- Fedurin, M.G.
- Folz, C.
- Gassner, D.M.
- Harvey, M.
- Jamilkowski, J.P.
- Jing, Y.C.
- Kayran, D.

ISBN 978-3-95450-134-2

- Kellermann, R.
- Kusche, K.
- Lambiase, R.F.
- Litvinenko, V.
- Mahler, G.J.
- Mapes, M.
- Meng, W.
- Miller, T.A.
- Minty, M.G.
- Narayan, G.
- Orfin, P.
- Pinayev, I.
- Pogorelsky, I.
- Polyanskiy, M.N.
- Rao, T.
- Reich, J.
- Sheehy, B.
- Skaritka, J.
- Smart, L.
- Smith, K.S.
- Snydstrup, L.
- Soria, V.
- Swinson, C.
- Than, R.
- Theisen, C.
- Tuozzolo, J.E.
- Wang, E.
- Wang, G.
- Xiao, B. P.
- Xin, T.
- Xu, W.
- Zaltsman, A.

CCPMR
Paris, France
- Dubois, A.

CEA/DAM/DIF
Arpajon, France
- Davoine, X.

CEA/DSM/DRECAM/SPAM
Gif-sur-Yvette, France
- Garzella, D.

CEA/DSM/IRFU
France
- Mosnier, A.

CEA/IRFU
Gif-sur-Yvette, France
- Devanz, G.
- Madec, C.

CERLA
Villeneuve d'Ascq, France
- Le Parquier, M.

CERN
Geneva, Switzerland
- Catalán Lasheras, N.
- Grudiev, A.
- Latina, A.
- Schulte, D.
- Stapnes, S.
- Syratchev, I.
- Wuensch, W.

CFEL
Hamburg, Germany
- Maier, A.R.

Chiang Mai University
Chiang Mai, Thailand
- Chaisueb, N.
- Damminsek, K.
- Rimjaem, S.
- Saisa-ard, C.
- Saisut, J.
- Suphakul, S.
- Thongbai, C.
- Thongpakdi, W.

Cockcroft Institute
Warrington, Cheshire, United Kingdom
- Dunning, D.J.
- Muratori, B.D.
- Siggel-King, M.R.F.
- Spampinati, S.
- Thompson, N.
- Williams, P.H.

Cornell University (CLASSE), Cornell Laboratory for Accelerator-Based Sciences and Education
Ithaca, New York, USA
- Finkelstein, K.
- Temnykh, A.B.

CSU
Fort Collins, Colorado, USA
- Freund, H.
- van der Slot, P.J.M.

Dawonsys
Siheung-City, Republic of Korea
- Kim, D.S.
- Lee, S.Y.
- Seo, M.

DELTA
Dortmund, Germany
- Bahnsen, F.H.
- Bolsinger, M.
- Hacker, K.E.

ISBN 978-3-95450-134-2

- Hilbrich, S.
- Jebramcik, M.A.
- Khan, S.
- Mai, C.
- Meyer auf der Heide, A.
- Molo, R.
- Rast, H.
- Shayeganrad, G.
- Ungelenk, P.

DESY Zeuthen
Zeuthen, Germany

- Bakr, M. A.
- Boonpornprasert, P.
- Donat, A.
- Good, J.D.
- Groß, M.
- Huck, H.
- Isaev, I.I.
- Jachmann, L.
- Kalantaryan, D.K.
- Khojoyan, M.
- Köhler, W.
- Kourkafas, G.
- Krasilnikov, M.
- Malyutin, D.
- Melkumyan, D.
- Oppelt, A.
- Otevřel, M.
- Pohl, M.
- Renier, Y.
- Rublack, T.
- Schultze, J.
- Stephan, F.
- Trowitzsch, G.
- Vashchenko, G.
- Wenndorff, R.W.
- Zhao, Q.T.

DESY
Hamburg, Germany

- Ackermann, S.
- Aßmann, R.W.
- Beutner, B.
- Bödewadt, J.
- Brenner, G.
- Butkowski, Ł.
- Czwalinna, M.K.
- Decking, W.
- Dinter, H.
- Dohlus, M.
- Ekanayake, N.
- Faatz, B.
- Felber, M.
- Feldhaus, J.
- Feng, G.
- Fenner, M.
- Gerth, C.
- Golz, T.
- Grün, C.
- Hartl, I.
- Hartmann, G.
- Heuer, M.
- Hoffmann, M.
- Honkavaara, K.
- Hüning, M.
- Ivanov, R.
- Janas, E.
- Kaernter, F.X.
- Killenberg, M.
- Klose, K.
- Kocharyan, V.
- Laarmann, T.
- Lamb, T.
- Lederer, S.
- Limberg, T.
- Maag, C.P.
- Marchetti, B.
- Mavrič, U.
- Müller, J.M.
- Peier, P.
- Przygoda, K.P.
- Rönsch-Schulenburg, J.
- Ruzin, S.
- Rybaniec, R.
- Safak, K.
- Saldin, E.
- Schlarb, H.
- Schneidmiller, E.
- Scholz, M.
- Schreiber, S.
- Serkez, S.
- Steffen, B.
- Stojanovic, N.
- Sydlo, C.
- Titberidze, M.
- Treusch, R.
- Viefhaus, J.
- Vogt, M.
- Xin, M.
- Yurkov, M.V.
- Zagorodnov, I.
- Zemella, J.
- Zummack, F.

Devi Ahilya University
Indore, India

- Mishra, G.

DICP
Dalian, People’s Republic of China

- Dai, D.X.
- Wang, G.L.
- Wu, G.R.
- Yang, X.M.
- Zhang, W.Q.

DLS
Oxfordshire, United Kingdom

ISBN 978-3-95450-134-2

- Bartolini, R.
- Martin, I.P.S.
- Sutter, J.

Elettra-Sincrotrone Trieste S.C.p.A.
Basovizza, Italy

- Abrami, A.
- Allaria, E.
- Badano, L.
- Bencivenga, F.
- Callegari, C.
- Capotondi, F.
- Castronovo, D.
- Cinquegrana, P.
- Coreno, M.
- Cornacchia, M.
- Cucini, R.
- Cudin, I.
- D'Auria, G.
- Danailov, M.B.
- De Monte, R.
- De Ninno, G.
- Delgiusto, P.
- Demidovich, A.A.
- Di Mitri, S.
- Diviacco, B.
- Fabris, A.
- Fabris, R.
- Fawley, W.M.
- Ferianis, M.
- Ferrari, E.
- Finetti, P.
- Furlan Radivo, P.
- Gaio, G.
- Gauthier, D.
- Gelmetti, F.
- Giannessi, L.
- Grulja, S.
- Iazzourene, F.
- Kiskinova, M.
- Krecic, S.
- Lonza, M.
- Mahne, N.
- Manfredda, M.
- Masciovecchio, C.
- Milloch, M.
- Parmigiani, F.
- Pedersoli, E.
- Penco, G.
- Pivetta, L.
- Plekan, O.
- Predonzani, M.
- Prince, K.C.
- Principi, E.
- Raimondi, L.
- Rebernik Ribič, P.
- Rossi, F.
- Roussel, E.
- Rumiz, L.
- Sauro, R.
- Scafuri, C.
- Serpico, C.
- Sigalotti, P.
- Spampinati, S.
- Sturari, L.
- Svandrlik, M.
- Svetina, C.
- Trovò, M.
- Vascotto, A.
- Veronese, M.
- Visintini, R.
- Zangrando, D.
- Zangrando, M.

ENEA C.R. Frascati
Frascati (Roma), Italy

- Giannessi, L.

FEL/Duke University
Durham, North Carolina, USA

- Hao, H.
- Mikhailov, S.F.
- Popov, V.
- Wu, Y.K.
- Yan, J.

Fermilab
Batavia, Illinois, USA

- Broemmelsiek, D.R.
- Crawford, D.J.
- Lumpkin, A.H.
- Piot, P.
- Shin, Y.-M.
- Thangaraj, J.C.T.
- Vivoli, A.

FNRF
Chiang Mai, Thailand

- Kangrang, N.

Huazhong University of Science and Technology, State Key Laboratory of Advanced Electromagnetic Engineering and Technology,
Hubei, People's Republic of China

- Cao, L.
- Chen, W.

HUST
Wuhan, People's Republic of China

- Chen, Q.S.
- Hu, T.
- Li, J.
- Qin, B.
- Tan, P.
- Xiong, Y.Q.

HZB
Berlin, Germany
- Malyutin, D.
- Wernet, Ph.

I-Tech
Solkan, Slovenia
- Cargnelutti, M.
- Žnidarčič, M.
- Zorzut, S.

IAP/RAS
Nizhny Novgorod, Russia
- Andrianov, A.V.
- Bandurkin, I.V.
- Bratman, V.L.
- Gacheva, E.
- Khazanov, E.
- Mironov, S.
- Poteomkin, A.
- Savilov, A.V.
- Zelenogorsky, V.

IBS
Daejeon, Republic of Korea
- Kim, K.H.

IHEP
Beijing, People's Republic of China
- Cui, X.
- Huang, X.Y.
- Jiao, Y.
- Xu, G.

IMP/CAS
Lanzhou, People's Republic of China
- Zhao, Q.T.

INRNE
Sofia, Bulgaria
- Asova, G.

ISIR
Osaka, Japan
- Fujimoto, M.
- Funakoshi, S.
- Furukawa, K.
- Irizawa, A.
- Isoyama, G.
- Kato, R.
- Kawase, K.
- Kubo, K.
- Tokuchi, A.
- Tsutsumi, R.
- Yaguchi, M.

IST
Chiang Mai, Thailand
- Kongmon, E.
- Kosaentor, K.
- Wichaisirimongkol, P.

JAEA
Ibaraki-ken, Japan
- Nishimori, N.

JAI
Oxford, United Kingdom
- Bartolini, R.
- Lyapin, A.

JASRI/RIKEN
Hyogo, Japan
- Ago, H.
- Hirata, K.
- Murakami, H.
- Ueno, G.
- Yamamoto, M.
- Yamashita, K.

JASRI/SPring-8
Hyogo-ken, Japan
- Fukami, K.

JINR
Dubna, Moscow Region, Russia
- Syresin, E.

JLab
Newport News, Virginia, USA
- Douglas, D.
- Hernandez-Garcia, C.
- Li, R.
- Tennant, C.

KAERI
Daejon, Republic of Korea
- Bae, S.
- Baek, I.H.
- Chae, M.S.
- Gudkov, B.A.
- Han, B.
- Jang, K.H.
- Jeong, Y.U.
- Jo, J.S.
- Kim, H.N.
- Kim, H.W.
- Kim, K.N.
- Kim, Y.
- Lee, K.
- Miginsky, S.V.
- Mun, J.
- Nam, J.H.

ISBN 978-3-95450-134-2

- Park, S. H.
- Park, S.
- Ryu, W.J.
- Setiniyaz, S.
- Shim, G.I.
- Vinokurov, N.

KAIST
Daejeon, Republic of Korea
- Ihee, H.
- Jeon, C.
- Jung, K.
- Kim, J.G.
- Kim, J.
- Yang, H.

KEK
Ibaraki, Japan
- Aryshev, A.
- Chen, S.
- Honda, Y.
- Konomi, T.
- Ohmi, K.
- Shevelev, M.
- Shimada, M.
- Yamamoto, N.
- Zhou, D.

KERI
Changwon, Republic of Korea
- Hwangbo, Y.H.
- Jeon, S.G.
- Kim, J.

Korea University Sejong Campus
Sejong, Republic of Korea
- Chung, H.

Kumamoto University, Department of Applied Chemistry and Biochemistry
Kumamoto, Japan
- Yoshida, K.

Kyoto Univeristy
Kyoto, Japan
- Nogi, T.

Kyoto University Graduate School of Energy Science
Kyoto, Japan
- Hachiya, K.

Kyoto University
Kyoto, Japan
- Katsurayama, T.
- Kii, T.
- Konstantin, T.
- Masuda, K.
- Morita, K.
- Murata, T.
- Nagasaki, K.
- Nogi, T.
- Ohgaki, H.
- Suphakul, S.
- Torgasin, K.
- Yamashita, H.
- Zen, H.

Kyungpook National University
Daegu, Republic of Korea
- Kim, E.-S.
- Park, S.

LAL
Orsay, France
- Delerue, N.
- El Khaldi, M.
- Kaabi, W.
- Wicek, F.

Lancaster University
Lancaster, United Kingdom
- Burt, G.
- Kolosov, O.V.
- Ratoff, P.N.
- Tovee, P.D.

LANL
Los Alamos, New Mexico, USA
- Anisimov, P.M.
- Bishofberger, K.
- Buechler, C.E.
- Carlsten, B.E.
- Duffy, L.D.
- Krawczyk, F.L.
- Lewellen, J.W.
- Marksteiner, Q.R.
- Nguyen, D.C.
- Russell, S.J.
- Sheffield, R.L.
- Yampolsky, N.A.

LBNL
Berkeley, California, USA
- Baptiste, K.M.
- Cork, C.W.
- De Santis, S.
- Dickinson, M.R.
- Doolittle, L.R.
- Doyle, J.A.
- Feng, J.
- Filippetto, D.
- Harris, G.L.

- Huang, G.
- Huang, R.
- Johnson, M.J.
- Jones, M.S.
- Kramasz, T.D.
- Kwiatkowski, S.
- Leitner, D.
- Lellinger, R.E.
- Mitchell, C.E.
- Moroz, V.
- Nasiatka, J.R.
- Norum, W.E.
- Padmore, H.A.
- Papadopoulos, C. F.
- Penn, G.
- Portmann, G.J.
- Qian, H.J.
- Qiang, J.
- Sannibale, F.
- Staples, J.W.
- Syversrud, D. L.
- Venturini, M.
- Vinco, M.
- Virostek, S.P.
- Wells, R.P.
- Zolotorev, M.S.

LEBRA
Funabashi, Japan
- Hayakawa, K.
- Hayakawa, Y.
- Inagaki, M.
- Nakao, K.
- Nogami, K.
- Sakai, T.
- Shishikura, F.
- Tanaka, T.

LOA
Palaiseau, France
- Lambert, G.
- Mahieu, B.
- Malka, V.
- Rousse, A.
- Thaury, C.

MAX-lab
Lund, Sweden
- Andersson, J.
- Curbis, F.
- Eriksson, M.
- Isaksson, L.
- Isinger, M.
- Karlberg, O.
- Kumbaro, D.
- Lindau, F.
- Mak, A.
- Mansten, E.
- Olsson, D.F.
- Thorin, S.
- Werin, S.

MEPhI
Moscow, Russia
- Lalayan, M.V.
- Sergeeva, D.Yu.
- Smirnov, A.Yu.
- Sobenin, N.P.
- Strikhanov, M.N.
- Tishchenko, A.A.

Mesa+
Enschede, The Netherlands
- Boller, K.-J.
- Strooisma, A.
- van der Slot, P.J.M.

MHI
Hiroshima, Japan
- Kimura, M.
- Miura, S.
- Okihira, K.
- Shigeoka, N.

MIT
Cambridge, Massachusetts, USA
- Callahan, P.T.
- Peng, M.Y.

MTA-PTE High-Field Terahertz Research Group
Péece, Hungary
- Fülöp, J.A.
- Tóth, Gy.

Nagoya University
Nagoya, Japan
- Hosaka, M.
- Takashima, Y.

National Technical University of Athens
Athens, Greece
- Gazis, E.N.

Nigde University
Nigde, Turkey
- Nergiz, Z.

Nihon University
Tokyo, Japan
- Komatsuzaki, Y.

NITTTR
Bhopal, India
- Jeevakhan, H.
- Purohit, P.K.

ISBN 978-3-95450-134-2

Northern Illinois Univerity
Dekalb, Illinois, USA
- Green, A.T.

Northern Illinois University
DeKalb, Illinois, USA
- Halavanau, A.
- Piot, P.

NPS
Monterey, California, USA
- Blau, J.
- Cohn, K. R.
- Colson, W.B.
- Ng, J.W.
- Price, M.J.

NSU
Novosibirsk, Russia
- Davidyuk, I.V.

NTHU
Hsinchu, Taiwan
- Chen, C.H.
- Chiu, Y.C.
- Huang, Y.-C.

NTUA
Athens, Greece
- Charitonidis, A.

Okayama University
Okayama, Japan
- Akita, F.
- Nakajima, Y.
- Shen, J.R.
- Shimizu, T.
- Suga, M.

PAL
Pohang, Kyungbuk, Republic of Korea
- Cho, M.-H.
- Choi, H. J.
- Gil, K.H.
- Han, J.H.
- Hong, J.H.
- Hu, J.
- Jeong, S.-H.
- Jung, Y.-G.
- Kang, H.-S.
- Kim, C.H.
- Kim, C.
- Kim, D.E.
- Kim, G.H.
- Kim, K.W.
- Kim, S.H.
- Ko, I.S.
- Kwon, S.J.
- Lee, H.-G.
- Lee, H.-S.
- Lee, S.B.
- Lee, S.J.
- Lee, W.W.
- Na, D.H.
- Oh, B.G.
- Parc, Y.W.
- Park, K.-H.
- Park, S.J.
- Park, S.S.
- Park, Y.J.
- Seo, K.W.
- Shin, D.C.
- Suh, H.S.
- Suh, Y.J.
- Yang, H.

PhLAM/CERCLA
Villeneuve d'Ascq Cedex, France
- Bielawski, S.
- Le Parquier, M.

PhLAM/CERLA
Villeneuve d'Ascq, France
- Evain, C.
- Szwaj, C.

PKU
Beijing, People's Republic of China
- Chen, J.E.
- Huang, S.
- Liu, K.X.
- Lu, X.Y.
- Qin, W.
- Tan, W.W.
- Yan, X.Q.
- Yang, D.Y.
- Yang, Y.
- Yang, Z.Q.
- Zeng, L.
- Zhao, G.
- Zhao, J.

POSCO ICT
Gyeonggi-do, Republic of Korea
- Jang, K.Y.
- Shin, H.S.

POSTECH
Pohang, Kyungbuk, Republic of Korea
- Cho, M.-H.
- Choi, W.S.
- Ko, I.S.
- Lee, J.

ISBN 978-3-95450-134-2

- Oh, B.H.
- Shim, C.H.
- Yoon, M.

PSI
Villigen PSI, Switzerland
- Aiba, M.
- Bettoni, S.
- Ganter, R.
- Hunziker, S.
- Orlandi, G.L.
- Ozkan Loch, C.
- Pedrini, B.
- Pedrozzi, M.
- Prat, E.
- Reiche, S.
- Rodriguez-Fernandez, A.
- Schietinger, T.

RAS/INR
Moscow, Russia
- Churanov, D.
- Kravchuk, L.V.
- Paramonov, V.V.
- Rybakov, I.V.
- Skasyrskaya, A.K.
- Zavadtsev, A.A.
- Zavadtsev, D.A.

RIKEN SPring-8 Center
Sayo-cho, Sayo-gun, Hyogo, Japan
- Hara, T.
- Inagaki, T.
- Kinjo, R.
- Kondo, C.
- Otake, Y.
- Takebe, H.
- Tanaka, H.
- Togawa, K.
- Yabashi, M.

Royal Holloway, University of London
Surrey, United Kingdom
- Boogert, S.T.
- Yamakawa, E.

Shanghai Jiao Tong University
Shanghai, People's Republic of China
- Xiang, D.

Shenkar College of Engineering and Design
Ramat Gan, Israel
- Ianconescu, R.

SINAP
Shanghai, People's Republic of China
- Chen, J.H.
- Chen, J.
- Chen, Z.H.
- Deng, H.X.
- Ding, J.G.
- Fang, G.P.
- Fang, W.
- Feng, C.
- Gu, M.
- Gu, Q.
- Hu, X.
- Huang, D.
- Huang, M.M.
- Leng, Y.B.
- Li, B.
- Lin, G.Q.
- Liu, B.
- Liu, Y.
- Sun, S.
- Wang, D.
- Wang, G.
- Wang, L.
- Yin, L.
- Yu, L.Y.
- Zhang, M.
- Zhang, W.
- Zhao, Z.T.
- Zhong, S.P.
- Zhou, Q.G.

SLAC
Menlo Park, California, USA
- Anderson, S.D.
- Arthur, J.
- Baxevanis, P.
- Benwell, A.L.
- Bohler, D.K.
- Brachmann, A.
- Campell, M.L.
- Coffee, R.N.
- Colocho, W.S.
- Decker, F.-J.
- Delor, J.T.
- Ding, Y.
- Dowell, D.
- Dunning, M.P.
- Emma, P.
- Fang, K.
- Fawley, W.M.
- Feng, Y.
- Field, R.C.
- Fisher, A.S.
- Frisch, J.C.
- Fry, A.R.
- Garcia, B.W.
- Gilevich, S.
- Hast, C.
- Hastings, J.B.
- Hemsing, E.
- Hogan, M.J.
- Huang, Z.

ISBN 978-3-95450-134-2

- Ilchen, M.
- Iverson, R.H.
- Krzywinski, J.
- Levashov, Yu.I.
- Lewandowski, J.R.
- Li, R.K.
- Li, Z.
- Loos, H.
- Lutman, A.A.
- MacArthur, J.P.
- Marcus, G.
- Marinelli, A.
- Maxwell, T.J.
- Moeller, S.P.
- Montanez, P.A.
- Norvell, N.P.
- Nosochkov, Y.
- Novokhatski, A.
- Nuhn, H.-D.
- Ortiz, E.
- Pellegrini, C.
- Peters, F.
- Ratner, D.F.
- Raubenheimer, T.O.
- Robinson, J.
- Rowen, M.
- Schafer, D.W.
- Schmerge, J.F.
- Sheppard, J.
- Smith, H.
- Stan, C.A.
- Stupakov, G.
- Sullivan, M.K.
- Tao, T.
- Turner, J.L.
- Van Hoover, Z.
- Vecchione, T.
- Vetter, S.
- Wang, L.
- Welch, J.J.
- Wolf, Z.R.
- Woodley, M.
- Wu, J.
- Zhou, F.

SLSA
Clayton, Australia

- Boland, M.J.
- Charles, T.K.
- Dowd, R.T.
- LeBlanc, G.
- Tan, Y.E.
- Wootton, K.P.
- Zhu, D.

Solaris
Kraków, Poland

- Bocchetta, C.J.
- Wawrzyniak, A.I.

SOLEIL
Gif-sur-Yvette, France

- Benabderrahmane, C.
- Berteaud, P.
- Bourassin-Bouchet, C.
- Bouvet, F.
- Bozek, J.D.
- Briquez, F.
- Brubach, J.B.
- Cassinari, L.
- Chapuis, L.
- Couprie, M.-E.
- Da Silva, J.
- Daillant, J.
- Dennetière, D.
- Dietrich, Y.
- Diop, M.
- Duval, J.P.
- El Ajjouri, M.E.
- El Ajjouri, T.K.
- Herbeaux, C.
- Hubert, N.
- Khojoyan, M.
- Labat, M.
- Leclercq, N.
- Lestrade, A.
- Loulergue, A.
- Lüning, J.
- Manceron, L.
- Marchand, P.
- Marcouillé, O.
- Marlats, J.L.
- Marteau, F.
- Miron, C.
- Morin, P.
- Nadji, A.
- Nagaoka, R.
- Polack, F.
- Ribeiro, F.
- Ricaud, J.P.
- Rommeluère, P.
- Roy, P.
- Sharma, G.
- Tavakoli, K.T.
- Thomasset, M.
- Tilmont, M.
- Tordeux, M.-A.
- Valléau, M.
- Vétéran, J.
- Yang, W.
- Zerbib, D.

Stanford University
Stanford, California, USA

- Li, S.

STFC/DL/ASTeC
Daresbury, Warrington, Cheshire, United Kingdom

- Angal-Kalinin, D.
- Brynes, A.D.
- Buckley, R.K.

- Buckley, S.R.
- Clarke, J.A.
- Cowie, L.S.
- Dunning, D.J.
- Fell, B.D.
- Goudket, P.
- Goulden, A.R.
- Hornickel, P.C.
- Jackson, F.
- Jamison, S.P.
- Jones, J.K.
- Marinov, K.B.
- McIntosh, P.A.
- McKenzie, J.W.
- Middleman, K.J.
- Militsyn, B.L.
- Moss, A.J.
- Muratori, B.D.
- Roper, M.D.
- Rudge, L.K.
- Saveliev, Y.M.
- Shepherd, B.J.A.
- Smith, R.J.
- Smith, S.L.
- Snedden, E.W.
- Surman, M.
- Thakker, T.T.
- Thompson, N.
- Valizadeh, R.
- Wheelhouse, A.E.
- Williams, P.H.

STFC/DL
Daresbury, Warrington, Cheshire, United Kingdom
- Atkinson, P.
- Bliss, N.
- Cash, R.J.
- Collomb, N.A.
- Cox, G.
- Diakun, G.P.
- Dobson, S.
- Gallagher, A.
- Griffiths, S.A.
- Hill, C.
- Hodgkinson, C.
- Holland, D.M.P.
- Jones, T.J.
- Martlew, B.G.
- Williams, J.

Tech-X
Boulder, Colorado, USA
- Smith, J.D.A.

The Hartree Centre, Science and Technology Facilities Council (STFC/DL)
Warrington, United Kingdom
- Allan, R.J.

The University of Liverpool
Liverpool, United Kingdom
- Craig, T.
- Newton, D.
- Siggel-King, M.R.F.
- Wei, Y.
- Weightman, P.
- Welsch, C.P.
- Wolski, A.

TPU
Tomsk, Russia
- Potylitsyn, A.

TUB
Beijing, People's Republic of China
- Du, Y.-C.
- Huang, W.-H.
- Zhang, Z.

TUL-DMCS
Łódź, Poland
- Kozak, T.
- Prędki, P.

TXUK
Warrington, United Kingdom
- Smith, J.D.A.

UCLA
Los Angeles, California, USA
- Curry, E.J.
- Duris, J.P.
- Emma, C.
- Fabbri, S.
- Gadjev, I.I.
- Musumeci, P.
- Nause, A.
- Pellegrini, C.
- Rosenzweig, J.B.
- Sudar, N.S.

UMAN
Manchester, United Kingdom
- Appleby, R.B.
- Hanahoe, K.
- Mete Apsimon, O.
- Owen, H.L.
- Xia, G.X.

Uni HH
Hamburg, Germany
- Ackermann, S.
- Amstutz, Ph.
- Azima, A.
- Drescher, M.
- Lazzarino, L.L.

ISBN 978-3-95450-134-2

- Lechner, C.
- Lishilin, O.
- Maltezopoulos, Th.
- Miltchev, V.
- Pathak, G.
- Plath, T.
- Rönsch-Schulenburg, J.
- Roßbach, J.

UNIST
Ulsan, Republic of Korea
- Chung, M.
- Seok, J.M.

University of California, San Diego (UCSD)
La Jolla, California, USA
- Hsu, S.

University of Gothenburg
Gothenburg, Sweden
- Lindahl, A.O.

University of Hawaii
Honolulu,, USA
- Madey, J.
- Niknejadi, P.

University of Huddersfield
Huddersfield, United Kingdom
- Kolano, A.M.

University of Nova Gorica
Nova Gorica, Slovenia
- De Ninno, G.
- Gauthier, D.

University of Oslo
Oslo, Norway
- Adli, E.
- Pfingstner, J.

University of Péece
Pécs, Hungary
- Almási, G.
- Csiha-Nagy, Zs.
- Fülöp, J.A.
- Hebling, J.
- Tibai, Z.

University of Science and Technology of Korea (UST)
Daejeon, Republic of Korea
- Jang, K.H.
- Jeong, Y.U.
- Kim, H.W.
- Lee, K.
- Miginsky, S.V.
- Park, S. H.
- Vinokurov, N.

University of Tel-Aviv, Faculty of Engineering
Tel-Aviv, Israel
- Gover, A.
- Ianconescu, R.
- Kleinman, H.
- Marks, H. S.

Università degli Studi di Trieste
Trieste, Italy
- Ferrari, E.

Uppsala University
Uppsala, Sweden
- Ekelöf, T.J.C.
- Hamberg, M.
- Jacewicz, M.
- Ruber, R.J.M.Y.
- Ziemann, V.G.

USTC/NSRL
Hefei, Anhui, People's Republic of China
- He, Z.G.
- Huang, R.
- Jia, Q.K.
- Li, H.T.
- Li, J.Y.
- Pei, Y.J.
- Tang, Zh. X.
- Wang, L.
- Xu, W.
- Zhang, S.C.

USTRAT/SUPA
Glasgow, United Kingdom
- Campbell, L.T.
- Colin, A.J.T.
- Henderson, J.
- Hidding, B.
- M^{C}Neil, B.W.J.
- Traczykowski, P.

UVSOR
Okazaki, Japan
- Hayashi, K.
- Katoh, M.
- Mirian, N.S.
- Yamazaki, J.

VDL ETG
Eindhoven, The Netherlands
- Janssen, X.J.A.

ISBN 978-3-95450-134-2

Virginia Polytechnic Institute and State University
Blacksburg, Virginia, USA
- Tsai, C.-Y.

Warsaw University of Technology, Institute of Electronic Systems
Warsaw, Poland
- Czuba, K.
- Jabłoński, S.

XFEL. EU
Hamburg, Germany
- Baranasic, B.
- Buck, J.
- Dietrich, F.
- Dommach, M.
- Freund, W.
- Geloni, G.
- Grünert, J.
- Karabekyan, S.
- Koch, A.
- Kujala, N.G.
- Li, Y.
- Liu, J.
- Madsen, A.
- Molodtsov, S.
- Pflüger, J.
- Planas, M.
- Sinn, H.

ISBN 978-3-95450-134-2

Participants List

— A —

Åkersten, Peter
ScandiNova Systems AB
Sweden

Andersson, Joel
Lund University
Sweden

Anisimov, Petr M
LANL
USA

Anno, Toshiro
Toshiba Electron Tubes and Devices Co.
Japan

— B —

Bach, Hong
LANL
USA

Bae, Sangyoon
KAERI
Korea

Baek, In Hyung
KAERI
Korea

Bahnsen, Fin Hendrik
Center for Synchrotron Radiation / DELTA
Germany

Baik, Sung-Hoon
KAERI
Korea

Bakr, Mahmoud
DESY
Germany

Balal, Nezah
Faculty of Engineering Ariel University
Israel

Bartolini, Riccardo
Diamond Light Source Ltd
UK

Bettoni, Simona
PSI
Switzerland

Bishofberger, Kip
LANL
USA

Blau, Joseph
Naval Postgraduate School
USA

Blokesch, Guido
Amgegon PPT GmbH
Germany

Boonpornprasert, Prach
DESY
Germany

Brachmann, Axel
SLAC
USA

— C —

Campbell, Lawrence
University of Strathclyde
UK

Cargnelutti, Manuel
Instrumentation Technologies
Slovenia

Carlsten, Bruce
LANL
USA

Chae, Moonsik
KAERI
Korea

Chaisueb, Natthawut
Chiang Mai University
Thailand

Chen, Si
KEK
Japan

Chin, Yong Ho
KEK
Japan

Choi, Hyojin
PAL-XFEL
Korea

Chrin, Jan
PSI
Switzerland

Christensen, Henning Bach
Danfysik
Denmark

Chung, Moses
Ulsan National Institute of Science
and Technology
Korea

Chung, Sang-Tai
MILIM
Korea

Clarke, Jim
STFC Daresbury Laboratory
UK

Cohn, Keith
Naval Postgraduate School
USA

Couprie, Marie-Emmanuelle
SOLEIL
France

Curbis, Francesca
Lund University
Sweden

Curry, Emma
UCLA
USA

— D —

Dahl-Petersen, Svend
Danfysik
Danmark

Damminsek, Kantaphon
Chiang Mai University
Thailand

Davidyuk, Igor
Budker INP
Russia

Debus, Alexander
Helmholtz-Zentrum Dresden-Rossendorf
Germany

Decker, Franz-Josef
SLAC
USA

Decking, Winfried
DESY
Germany

Deng, Haixiao
Shanghai Institute of Applied Physics
China

Di Mitri, Simone
Elettra-Sincrotrone Trieste
Italy

Ding, Yuantao
SLAC
USA

Dinter, Hannes
DESY
Germany

ISBN 978-3-95450-134-2

Doyle, Ross
Rayonix
USA

Duris, Joseph
UCLA
USA

— E —

Eaton, Douglas
ScandiNova
USA

Emma, Claudio
University of California
USA

— F —

Fawley, William
Sincrotrone Trieste + SLAC
USA

Fazio, Michael
SLAC National Accelerator Laboratory
USA

Fazio, Linda
SLAC National Accelerator Laboratory
USA

Felber, Matthias
DESY
Germany

Feng, Chao
Shanghai Institute of Applied Physics
China

Feng, Yiping
SLAC National Accelerator Laboratory
USA

Ferrari, Eugenio
Elettra-Sincrotrone Trieste
Italy

— G —

Gadjev, Ivan
UCLA
USA

Ganter, Romain
SwissFEL
Switzerland

Garcia, Bryant
SLAC National Accelerator Laboratory
USA

Gauthier, David
Elettra-Sincrotrone Trieste
Italy

Geloni, Gianluca
European XFEL
Germany

Gewinner, Sandy
FHI
Germany

Giannessi, Luca
Elettra-Sincrotrone Trieste
Italy

Good, James
DESY
Germany

Goryashko, Vitaliy
Uppsala University
Sweden

Green, Bertram
HZDR
Germany

Gruenert, Jan
European XFEL
Germany

Gudkov, Boris
BINP
Russia

— H —

Hama, Hyroyuki
Tohoku University
Japan

Hamberg, Mathias
Uppsala University
Sweden

Han, Jang-Hui
Pohang Accelerator Laboratory
Korea

Han, Byung Heon
KAERI
Korea

Hara, Toru
RIKEN
Japan

He, Zhigang
NSRL
China

Hemsing, Erik
SLAC National Accelerator Laboratory
USA

Hilbrich, Svenja
Center for Synchrotron Radiation / DELTA
Germany

Hogan, Mark
SLAC National Accelerator Laboratory
USA

Homma, Akira
Mitsubishi Heavy Industries
Japan

Honda, Yosuke
KEK
Japan

Hong, Juho
Pohang Accelerator Laboratory
Korea

Honkavaara, Katja
DESY
Germany

Hrovatin, Rok
Cosylab d.d.
Slovenia

Hu, Tongning
Huazhong University of Science
and Technology
China

Hu, Jinyul
Pohang Accelerator Laboratory
Korea

Huang, Xiyang
Institute of High Energy Physics
China

Huang, Senlin
Peking University
China

Huang, Zhirong
SLAC
USA

Huck, Holger
DESY Zeuthen
Germany

— I —

Ianconescu, Reuven
Shenkar College of Engineering
and Design
Israel

Ikeda, Naoaki
Mitsubishi Heavy Industries
Japan

ISBN 978-3-95450-134-2

Inagaki, Manabu
Nihon University
Japan

Ischebeck, Rasmus
PSI
Switzerland

Isoyama, Goro
Osaka University
Japan

— J —

Janas, Ewa
DESY
Germany

Jang, Kyu-Ha
KAERI
Korea

Jeevakhan, Hussain
National Institute of
Technical Teachers' Training
India

Jeong, Young Uk
KAERI
Korea

Jin, Xiuguang
High Energy Accelerator Research
Organization
Japan

Jo, Jeongsang
KAERI
Korea

Joseph, Weisheng
Naval Postgraduate School
USA

Jung, Kwangyun
KAIST
Korea

— K —

Kanasaki, hiroshi
Toshiba Electron Tubes and Devices Co.
Japan

Kang, Heung-Sik
Pohang Accelerator Laboratory
Korea

Kawase, Keigo
ISIR
Japan

Keens, simon
Ampegon AG
Switzerland

Khan, Shaukat
Center for Synchrotron Radiation / DELTA
Germany

Kim, Kwang Je
ANL
USA

Kim, Ha-Na
Chungnam National University
Korea

Kim, Hyun Woo
UST (KAERI)
Korea

Kim, Jinju
Gwangju Institute of Science
and Technology
Korea

Kim, Young-chan
Chungbuk National University
Korea

Kim, Kyung Hwan
IBS
Korea

Kim, KwangHoon
Pahang Accelerator Laboratory
Korea

Kim, Sang Hee
Pohang Acceleartor Laboratory
Korea

Kim, Byungnam
KAERI
Korea

Kim, Ilyou
Pohang Acceleartor Laboratory
Korea

Kim, Jinju
Gwangju Institute of Science
and Technology
Korea

Kim, Seongyeol
Ulsan National Institute of Science
and Technology
Korea

Kim, Changbum
Pohang Accelerator Laboratory
Korea

Kim, Gyehee
Wiener
Korea

Kim, Yongsam
Pohang Acceleartor Laboratory
Korea

Kim, Jaehoon
KERI
Korea

Kim, Jungwan
KAIST
Korea

Kim, Dong-eun
Pohang Acceleartor Laboratory
Korea

Kim, Cheol-Hoon
Pohang Acceleartor Laboratory
Korea

Kim, Yujong
KAERI
Korea

Kinjo, Ryota
RIKEN SPring-8 Center
Japan

Klein, Hans-Udo
Advanced Accelerator Technologies
Switzerland

Ko, In Soo
Pohang Acceleartor Laboratory
Korea

Kocharyan, Vitali
DESY
Germany

Koh, JoonHo
Postech
Korea

Kulipanov, Gennady
BINP
Russia

Kumar, Manoj
KAERI
Korea

Kuntzsch, Michael
Helmholtz-Zentrum Dresden-Rossendorf
Germany

Kurokawa, Shin-ichi
Cosylab/KEK
Japan

— L —

Labat, Marie
SOLEIL
France

Larsson, Mats
Stockholm University
Sweden

Lechner, Christoph
Uni Hamburg
Germany

Lee, Sojeong
Pohang Accelerator Laboratory
Korea

Lee, Shin-yeong
KAERI
Korea

Lee, Kitae
KAERI
Korea

Lee, Jaeyu
POSTECH
Korea

Lee, Hong Gi
Pohang Acceleartor Laboratory
Korea

Lee, Heung-Soo
Pohang Accelerator Laboratory
Korea

Lee, Sangbong
Pohang Accelerator Laboratory
Korea

Lee, JaeHyun
Pohang Accelerator Laboratory
Korea

Lee, Byeongno
KAERI
Korea

Lehnert, Ulf
Helmholtz-Center Dresden-Rossendorf
Germany

Lewandowski, James
SLAC National Accelerator Laboratory
USA

Lewellen, John
LANL
USA

Li, Heting
University of Science and
Technology of China
China

Li, Yuhui
European XFEL GmbH
Germany

Li, Renkai
SLAC National Accelerator Laboratory
USA

Lindholm, Mikael
ScandiNova Systems AB
Sweden

Liu, Xiao Qing
Shanghai Institute of Applied Physics
China

Liu, Bo
Shanghai Institute of Applied Physics
China

Loehl, Florian
Paul Scherrer Institute
Switzerland

Loos, Henrik
SLAC
USA

Loos, Jennifer
SLAC National Accelerator Laboratory
USA

Lundberg, Daniel
ScandiNova Systems AB
Sweden

— M —

Maag, Christoph
DESY
Germany

MacArthur, James
SLAC
USA

Mak, Alan
MAX IV Laboratory
Sweden

Marinelli, Agostino
SLAC National Accelerator Laboratory
USA

Marks, Harry
Tel Aviv University
Israel

Martin, Ian
Diamond Light Source Ltd
UK

McKenzie, Julian
STFC Daresbury Laboratory
UK

Miginsky, Sergey
BINP
Russia

Min, Chang-Ki
Pohang Acceleartor Laboratory
Korea

Minehara, Eisuke
The Wakasa Wan Energy Research Center
Japan

Mirian, Najmeh Sadat
IPL
Iran

Moon, Kookjin
Ulsan National Institute of Science
and Technology
Korea

Mun, Jungho
KAERI
Korea

Murata, Tomoya
Kyoto University Institute
of Advanced Energy
Japan

Murokh, Alex
RadiaBeam Technbologies
USA

— N —

Nakao, Keisuke
LEBRA
Japan

Nam, JinHee
KAERI
Korea

Nguyen, Dinh
LANL
USA

Niknejadi, Pardis
Student
USA

Nishimori, Nobuyuki
JAEA
Japan

Nogami, Kyoko
Nihon University
Japan

Nogi, Takeshi
Graduate School of Energy Science
Japan

Novokhatski, Alexander
SLAC National Accelerator Laboratory
USA

Nuhn, Heinz-Dieter
SLAC National Accelerator Laboratory
USA

— O —

Oh, Nak-kyun
VITZROTECH. CO.
Korea

OH, Bong Gi
Pohang Acceleartor Laboratory
Korea

Ohgaki, Hideaki
Kyoto University
Japan

— P —

Parc, Yong Woon
Pohang Accelerator Laboratory
Korea

Park, Seong Hee
Korea Atomic Energy Reserach Institute
Korea

Park, Sunjeong
Kyungpook National University
Korea

Park, Ki-Hyeon
Pohang Acceleartor Laboratory
Korea

Park, Jaeku
Pohang Accelerator Laboratory
Korea

Park, Soung Soo
Pohang Accelerator Laboratory
Korea

Park, Chinkun
Techvalley
Korea

Petit-Jean-Genaz, Christine
CERN
Switzerland

Pfingstner, Juergen
University of Oslo
Norway

Pflueger, Joachim
European XFEL
Germany

Pinayev, Igor
BNL
USA

Prat, Eduard
Paul Scherrer Institute
Switzerland

pretelli, miguel
OCEM Power Electronics
Italy

price, Michael
Naval Postgraduate School
USA

Prince, Kevin
Elettra-Sincrotrone Trieste
Italy

— Q —

Qian, Houjun
Lawrence Berkeley Lab
USA

Qin, Weilun
Peking University
China

— R —

Ratner, Daniel
SLAC
USA

Raubenheimer, Tor
SLAC
USA

Reiche, Sven
Paul Scherrer Institute
Switzerland

Rodriguez Fernandez, Angel
Paul Scherrer Institute
Switzerland

Roh, Sung-joo
VITZROTECH. CO.
Korea

Rossbach, Joerg
DESY & Hamburg University
Germany

Ryu, Woo-Je
KAERI
Korea

— S —

Saisaard, Chaipattana
Department of Physics and
Materials Science
Thailand

Saitiniyazi, Shadike
KAERI
Korea

Saldin, Evgeny
DESY
Germany

Sano, Yuji
Japan Science and Technology Agency
Japan

Schaa, Volker RW
GSI
Switzerland

Schietinger, Thomas
Paul Scherrer Institute
Switzerland

Schmidt, Bernhard
DESY
Germany

Schoellkopf, Wieland
Fritz-Haber-Institut
Germany

Scholz, Matthias
DESY
Germany

ISBN 978-3-95450-134-2

Schreiber, Siegfried
DESY
Germany

Seidel, Wolfgang
Helmholtz-Zentrum Dresden-Rossendorf
Germany

SEOK, JIMIN
UNIST
Korea

Sergeeva, Daria
National Research Nuclear
University MEPhI
Russia

Serkez, Svitozar
DESY
Germany

Shevchenko, Oleg
BINP
Russia

Shigeoka, Nobuyuki
Mitsubishi Heavy Industries
Japan

Shim, Chi Hyun
POSTECH
Korea

Shim, Gyu Il
KAERI
Korea

Shishikura, Fumio
LEBRA
Japan

Shvyd'ko, Yuri
Argonne National Laboratory
USA

Sohn, Younguk
Pohang Accelerator Laboratory
Korea

Spampinati, Simone
University of Liverpool
UK

Stefanic, Rok
Cosylab
Slovenia

Stephan, Frank
DESY
Germany

Stulle, Frank
Bergoz Instrumentation
France

Stupakov, Gennady
SLAC
USA

Sudar, Nicholas
UCLA Particle Beam Physics Laboratory
USA

Suh, Hyung Suck
Pohang Acceleartor Laboratory
Korea

Sydlo, Cezary
DESY
Germany

— T —

Taira, Yoshitaka
National Institute of Advanced Industrial
Science

Thompson, Neil
STFC Daresbury Laboratory
UK

Thorin, Sara
MAX-lab
Sweden

Tibai, Zoltan
University of Pecs
Hungary

Tishchenko, Alexey
National Research Nuclear
University MEPhI
Russia

Tsai, Cheng-Ying
Virginia Tech/Jefferson Lab
USA

Turner, James
SLAC National Accelerator Laboratory
USA

— V —

van der Slot, Peter
University of Twente
Netherlands

Vashchenko, Grygorii
DESY
Germany

Vecchione, Theodore
SLAC
USA

Venturini, Marco
LBNL
USA

Viefhaus, Jens
DESY
Germany

Vinokurov, Nikolay
BINP
Russia

— W —

Walker, Richard
Diamond Light Source Ltd
UK

Walker, Christine Walker
Diamond Light Source Ltd
UK

Wang, Dong
Shanghai Institute of Applied Physics
China

Wang, Lanfa
SLAC
USA

Wernet, Philippe
Helmholtz-Zentrum Berlin
Germany

— X —

Xiang, Dao
Shanghai Jiao Tong University
China

Xin, Ming
DESY
Germany

— Y —

Yabashi, Makina
RIKEN Spring-8 Center
Japan

Yamada, Michiaki
Mitsubishi Heavy Industries
Japan

Yan, Jun
Duke University
USA

Yang, Haeryong
Pohang Acceleartor Laboratory
Korea

ISBN 978-3-95450-134-2

Yang, Heewon
KAIST
Korea

Yeckel, Christopher
Stangenes
USA

Yurkov, Mikhail
DESY
Germany

— Z —

Zen, Heishun
Institute of Advanced Energy
Japan

Zeng, Ling
Peking University
China

Zhang, Zhen
Tsinghua University
China

Zhang, Wenyan
Shanghai Institute of Applied Physics
China

Zhang, Shukui
Jefferson Lab
USA

Zhao, Gang
Peking University (PKU)
Institute of Heavy Ion Physics
China

ZHAO, JIFEI
Institute of Heavy Ion Physics
China

Zhao, Zhentang
Shanghai Institute of Applied Physics
China

Zhou, Feng
SLAC
USA

Znidarcic, Matjaz
Instrumentation Technologies
Slovenia

ISBN 978-3-95450-134-2